

1

Standard Potentials

György Inzelt
Department of Physical Chemistry, Eötvös Loránd University, Budapest, Hungary

1.1	Introduction	3
1.2	Thermodynamic Basis of the Standard, Formal, and Equilibrium Potentials	5
1.2.1	The Problem of the Initial and Final States	6
1.2.2	Standard States and Activities	7
1.2.3	Electrolytes, Mean Activity	7
1.2.4	Electrochemical Potential, Galvani Potential Difference	8
1.2.5	Calculation of E_{cell}^{\oplus} from Calorimetric Data and ΔG^{\oplus} , ΔH^{\oplus} , ΔS^{\oplus} from Electrochemical Measurements	9
1.2.6	The Dependence of the Potential of Cell Reaction on the Composition	9
1.2.7	Determination of the Standard Electrode Potential (E^{\oplus}) from Electrochemical Measurements	11
1.2.8	Determination of E^{\oplus} from Thermodynamic Data	11
1.2.9	The Formal Potential (E_c°)	12
1.2.10	The Determination of E_c° by Cyclic Voltammetry	13
	References	15

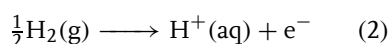
1.1 Introduction

Practically in every general chemistry textbook, one can find a table presenting the Standard (Reduction) Potentials in aqueous solution at 25 °C, sometimes in two parts, indicating the reaction condition: acidic solution and basic solution. In most cases, there is another table titled Standard Chemical Thermodynamic Properties (or Selected Thermodynamic Values). The former table is referred to in a chapter devoted to Electrochemistry (or Oxidation – Reduction Reactions), while a reference to the latter one can be found in a chapter dealing with Chemical Thermodynamics (or Chemical Equilibria). It is seldom indicated that the two types of tables contain redundant information since the standard potential values of a cell reaction ($E_{\text{cell}}^{\ominus}$) can be calculated from the standard molar free (Gibbs) energy change (ΔG^{\ominus}) for the same reaction with a simple relationship

$$E_{\text{cell}}^{\ominus} = \frac{-\Delta G^{\ominus}}{nF} = \left(\frac{RT}{nF} \right) \ln K \quad (1)$$

where n is the charge number of the cell reaction, which is the stoichiometric number equal to the number of electrons transferred in the cell reaction as formulated,

F is the Faraday constant, K is the equilibrium constant of the reaction, R is the gas constant, and T is the thermodynamic temperature. However, $E_{\text{cell}}^{\ominus}$ is not the standard potential of the electrode reaction (or sometimes called *half-cell reaction*), which is tabulated in the tables mentioned. It is the standard potential of the reaction in a chemical cell which is equal to the standard potential of an electrode reaction (abbreviated as standard electrode potential), E^{\ominus} , when the reaction involves the oxidation of molecular hydrogen to solvated protons



The notation $\text{H}^+(\text{aq})$ represents the hydrated proton in aqueous solution without specifying the hydration sphere. It means that the species being oxidized is always the H_2 molecule and E^{\ominus} is always related to a reduction. This is the reason why we speak of reduction potentials. In the opposite case, the numerical value of E^{\ominus} would be the same but the sign would differ. It should be mentioned that in old books, for example, in Latimer's book [1], the other sign convention was used; however, the International Union of Pure and Applied Chemistry (IUPAC) has introduced the unambiguous and authoritative usage in 1974 [2, 3].

Although the standard potentials, at least in aqueous solutions, are always related to reaction (2), that is, the standard hydrogen electrode (SHE) (see Ch. 18.3), it does not mean that other reference systems cannot be used or ΔG^\ominus of any electrochemically accessible reaction cannot be determined by measuring cell potential, E_{cell} , when both electrodes are at equilibrium. The cell as a whole is not at equilibrium (for if the cell reaction reaches its equilibrium then $E_{\text{cell}} = \Delta G_{\text{cell}} = 0$); however, no current flows through the external circuit, with all local charge-transfer equilibria across phase boundaries (except at electrolyte–electrolyte junctions) and local chemical equilibria within phases being established.

One may think that ΔG^\ominus and E^\ominus values in the tables cited are determined by calorimetry and electrochemical measurements, respectively. It is not so; the way of tabulations mentioned serves practical purposes only. Several “thermodynamic” quantities (ΔG^\ominus , ΔH^\ominus , ΔS^\ominus etc.) have been determined electrochemically, especially when these measurements were easier or were more reliable. On the other hand, E^\ominus values displayed in the tables mentioned have been determined mostly by calorimetric measurements since in many cases – owing to kinetic reasons, too slow or too violent reactions – it has been impossible to collect these data by using the measurement of the electric potential difference of a cell at suitable conditions. Quotation marks have been used in writing “thermodynamic”, as E^\ominus is *per se* also a thermodynamic quantity.

In some nonaqueous solvents, it is necessary to use a standard reaction other than the oxidation of molecular hydrogen. At present, there is no general choice of a standard reaction (reference electrode). Although in some cases

the traditional reference electrodes (e.g. saturated calomel, SCE, or silver/silver chloride) can also be used in organic solvents, much effort has been taken to find reliable reference reactions. The system has to meet the following criteria:

1. The reaction should be a one-electron transfer.
2. The reduced form should be a neutral molecule, and the oxidized form a cation.
3. The two components should have large sizes and spherical structures, that is, the $\Delta G_{\text{solvation}}$ should be low and practically independent from the nature of the solvent (the free energy of ion transfer from one solution to the other is small).
4. Equilibrium at the electrode must be established rapidly.
5. The standard potential must not be too high so that solvents are not oxidized.
6. The system must not change structure upon electron transfer.

The ferrocene/ferrocenium reference redox system at platinum fulfills these requirements fairly well [4–6]. Another system which has been recommended is bis(biphenyl)chromium (0)/bis(biphenyl)chromium (+1) (BCr^+/BCr) [5, 7]. Several other systems have been suggested, and used sporadically, such as cobaltocene/cobaltocenium, tris(2,2'-bipyridine) iron (I)/tris(2,2'-bipyridine) iron (0), $\text{Rb}^+/\text{Rb}(\text{Hg})$, and so on.

Ag/AgClO_4 or AgNO_3 dissolved in the nonaqueous solvent is also frequently used. It yields stable potentials in many solvents (e.g. in CH_3CN); however, in some cases its application is limited by a chemical reaction with the solvent.

The tables compiled usually contain E^\ominus values for simple inorganic reactions in

aqueous solutions mostly involving metals and their ions, oxides and salts, as well as some other important elements (H, N, O, S, and halogens). In special books (series), one can find E^\ominus values for more complicated reactions, for example, with the participation of metal complexes, and organic compounds [8–13]. The last authoritative reference work (on the standard potential in aqueous solutions) [13] – which has replaced the classic book of Latimer in this role – appeared in 1985.

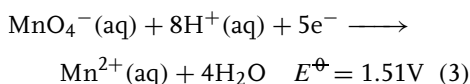
Many values of ΔG^\ominus , ΔH^\ominus , ΔS^\ominus , and E^\ominus found in these sources are based on rather old reports. The thermodynamic data have been continuously renewed by the US National Institute for Standards and Technology (NIST, earlier NBS = National Bureau of Standards and Technology) and its reports supply reliable data, which are widely used by the scientific community [14]. The numerical values of the quantities have also been changed because of the variation of the standard states and constants. Therefore, it is not surprising that E^\ominus values are somewhat different depending on the year of publication of the books. Despite the – usually slight – difference in the data and their uncertainty, E^\ominus values are very useful for predicting the course of any redox reactions including electrode processes. In the next subchapter, a short survey of the thermodynamic basis of the standard, formal, and equilibrium potentials, as well as the experimental access of these data, is given.

1.2

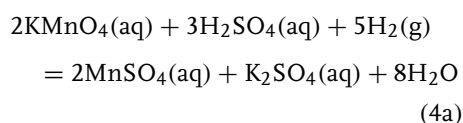
Thermodynamic Basis of the Standard, Formal, and Equilibrium Potentials

In the tables of standard potentials, usually the equation of electrode (half-cell)

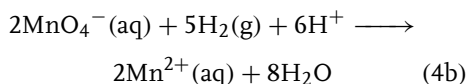
reactions are displayed, for example,



or just an abbreviated form is used: $E^\ominus (\text{MnO}_4^-/\text{Mn}^{2+}) = 1.51\text{V}$. The total chemical (cell) reaction formulated by neutral chemical species is



or considering charged reacting and product species is



The peculiarity of the cell reaction is that the oxidation and the reduction processes are separated in space and occur as heterogeneous reactions involving a charge-transfer step at the anode and the cathode, respectively, while electrons move through the external circuit, that is, electric current flows until the reaction reaches its equilibrium. In galvanic cells, the electric current (I) is used for energy production. Technically it is possible to measure the electric potential difference (E) between the electrodes or more exactly between the same metallic terminals attached to the electrodes even at the $I = 0$ condition (or by using a voltmeter of high resistance at $I \sim 0$). If the exchange current density (j_0) of both charge-transfer reactions is high, each electrode is at equilibrium, despite the fact that a small current flows. There is no equilibrium at electrolyte–electrolyte junctions; however, in many cases this junction potential can be diminished to a small value ($<1\text{mV}$). From this condition, it follows that the accuracy of the

determination of E^\ominus values is limited to ca 0.1–1 mV, depending on the system studied. However, the experimental error of the calorimetric determination of ΔG^\ominus , ΔH^\ominus , and ΔS^\ominus in many cases is not much smaller. Especially, the relative error in ΔS^\ominus is high and the calculation of low temperature values is sometimes problematic. The thermodynamic quantities are usually given with an accuracy of 0.1–0.001%. For instance, $\Delta G^\ominus = -477.2 \text{ kJ mol}^{-1}$ can be found for the formation of MnO_4^- ions [12]. It should be taken into consideration that 0.1 kJ mol^{-1} is equivalent to 1 mV. In fact, the problem is not the possible accuracy of the measurement of heat (temperature) or voltage since μV or μJ can be measured accurately.

There are several theoretical and practical difficulties regarding the determination of the exact values of the standard potential, which will be pointed out below.

1.2.1

The Problem of the Initial and Final States

The free energy functions are defined by explicit equations in which the variables are functions of the state of the system. The change of a state function depends only on the initial and final states. It follows that the change of the Gibbs free energy (ΔG) at fixed temperature and pressure gives the limiting value of the electrical work that could be obtained from chemical transformations. ΔG is the same for either the reversible or the explosively spontaneous path (e.g. $\text{H}_2 + \text{Cl}_2$ reaction); however, the amount of (electrical) work is different. Under reversible conditions

$$\Delta G = -nFE_{\text{cell}} \quad (5)$$

Equation (5) shows the fundamental relationship between Gibbs free energy change of the chemical reaction and the cell potential under reversible conditions (potential of the electrochemical cell reaction).

The calculation of ΔG from the caloric data is straightforward, independent of the path, that is, whether the reaction takes place in a single step or through a series of steps by using Hess's law and Nernst heat theorem [15–17]. Furthermore, we can calculate ΔG for the reaction of interest from the combination of other reactions involved for which the thermodynamic data are known. However, both the initial and final states in many cases are hypothetical. Even in the case of measurements executed very carefully and accurately, there might be problems in defining the states of the compounds, or even metals (!) that take part in the reaction.

This is the situation not only for reactions in which many components are involved and the product distribution strongly depends on the ratio of the participants (e.g. in reaction (3), at lower acidity the product is not Mn^{2+} (MnSO_4) but MnO_2 ; at higher acidity and KMnO_4 concentration the oxidation of H_2O to O_2 also occurs) but also for reactions which seem to be relatively simple. For instance, Ru^{3+} in aqueous solutions exists in the form $\text{Ru}(\text{H}_2\text{O})_6^{3+}$; however, in the presence of HCl , the whole series of complex ions, $[\text{Ru}^{\text{III}}\text{Cl}_n(\text{H}_2\text{O})_{6-n}]^{3-n}$ has been identified in aqueous solutions, and polymerization, hydrolysis, as well as formation of mixed valence compounds occur during reduction to Ru^{2+} [18–21].

Another example is the widely used $\text{PbO}_2(\text{s}, \text{cr})|\text{PbSO}_4(\text{s}, \text{cr})$ reversible electrode, where s is for solid and cr is

for crystalline. Cells containing this electrode can be used for the measurements of electromotive force ($E_{MF} \approx E_{cell}$) of high accuracy; however, the usual preparation methods yield a two-phase mixture of tetragonal and orthorhombic $PbO_2(cr)$, with the tetragonal form predominating [22]. This causes a variation in the E^\oplus values determined in different laboratories with 1 mV or more. An interesting problem has been addressed recently. In the last 20 years, new scanning probe techniques have been developed. With the help of the electrochemical scanning tunneling microscopy (ESTM), it is possible to handle metal clusters. It was found that for clusters containing $n < 20$ Ag atoms, the E^\oplus value determined was less by almost 2 V than that obtained for the bulk metal. In fact, this is not surprising since thermodynamic laws are valid only for high numbers of atoms, and the small clusters do not show the properties of a bulk metal, for example, there is no delocalization, and the band formation needs a large number of atoms. The effect was explained by the greater surface energy of small clusters compared to that of the bulk metal [23, 24].

1.2.2

Standard States and Activities

For ideal multicomponent systems, a simple linear relationship exists between the chemical potential (μ_i) and the logarithm of the mole fraction of solvent and solute, respectively.

$$\mu_i = \left(\frac{\partial G}{\partial n_i} \right)_{T, p, n_j \neq n_i} = \mu_i^\oplus + RT \ln x_i \quad (6)$$

where n_i and n_j are the mole numbers of the components, x_i is the mole fraction of component i , and μ_i^\oplus is the hypothetical standard state of unit mole fraction of

species i . Equation (6) is strictly valid only in the limit of infinite dilution in the case of solutions. In order to describe the behavior over the entire range of composition as a dimensionless quantity, the activity function (a_i) has been introduced. The activity can be expressed on different scales depending on the choice of the composition variable (mole fraction, molality, etc.) Mostly, the molality (moles of solute/1 kg solvent, $m_i = n_i/r_{\text{solvent}}$ in mol kg^{-1}) and the amount of concentration or, shortly, concentration (moles of solute/volume of solution, $c_i = n_i/V$ in mol m^{-3} or mol dm^{-3}) are used by electrochemists. The usage of molality is more correct because in this case, the possible volume change causes no problem; however, in the majority of the experiments in liquid phase there is no volume change, and c_i is certainly more popular than m_i .

The deviation from the ideal behavior is described conveniently by a function called *activity coefficient* (γ_i)

$$a_i = \gamma_{i,m} m_i / m_i^\oplus \quad \text{or} \quad a_i = \gamma_{i,c} c_i / c_i^\oplus \quad (7)$$

For the gases (it is of importance for gas electrodes)

$$a_i = f_i / f_i^\oplus \quad \text{or} \quad a_i = p_i / p^\oplus \quad (8)$$

where f is for the fugacity and p is for the pressure. Depending on the state of reference, the numerical value of a_i will vary; however, its standard state should be chosen in such a way that $\mu_i = \mu_i^\oplus$.

1.2.3

Electrolytes, Mean Activity

Electrolytes contain ions in more or less solvated (hydrated) forms and solvent molecules; however, undissociated molecules or ion associations, and so on may also be present. The composition of

a solution containing one or more electrolytes can be described defining the mole ratio or any other concentration of each ionic species. Most of the formulae have a close resemblance to those of the nonelectrolytes. There is, however, one important difference, namely, the concentrations of all the ionic species are not independent because the solution as a whole is electrically neutral. The electrical neutrality of the solution can be written as

$$\sum_i z_i m_i = 0 \quad \text{or} \quad \sum_i z_i c_i = 0 \quad (9)$$

where z_i is the charge number of ionic species i , which is a positive integer for cations and negative for anions. In fact, z_i is the ratio of the charge carried by ion i to the charge carried by the proton. No solution of a strong (fully dissociated) electrolyte is even approximately ideal even at highest dilution at which accurate measurements can be made; the infinitely dilute solution constitutes an idealized limiting case. The activity of the ionic species i can be given as

$$a_{i,c} = \gamma_{i,c} c_i / c^\ominus \quad \text{or} \quad a_{i,m} = \gamma_{i,m} m_i / m^\ominus \quad (10)$$

However, only the mean activity (a_\pm) or mean activity coefficient (γ_\pm) of an electrolyte can be determined by measurements, since in all processes, the electroneutral condition prevails. Note that

the indefiniteness of the individual activity coefficient is in connection with the impossibility of the determination of the single electrode potential.

Mean activity coefficient of electrolyte B in solution is given by

$$a_\pm = \exp \left[\frac{(\mu_B - \mu_B^\ominus)}{\nu RT} \right] \quad (11)$$

where μ_B is the chemical potential of the solute B in a solution containing B and other species, and μ_B^\ominus is the chemical potential of B in its standard state (see Table 1). A mole of the solute is defined in a way that it contains a group of ions of two kinds carrying an equal number of positive and negative charges – $B = K_{\nu+}^{z+} A_{\nu-}^{z-}$, and $\nu = \nu_+ + \nu_-$, $\sum z_i \nu_i = 0$. It follows that

$$a_\pm = a_B^{1/\nu} = (a_+^{\nu_+} a_-^{\nu_-})^{1/\nu} \quad (12)$$

and

$$\gamma_\pm = (\gamma_+^{\nu_+} \gamma_-^{\nu_-})^{1/\nu} \quad (13)$$

1.2.4

Electrochemical Potential, Galvani Potential Difference

The chemical potential of an ionic species depends on the electrical state of the phase (β), that is,

$$\mu_i^\beta = \tilde{\mu}_i^\beta - z_i F \varphi^\beta \quad (14)$$

Tab. 1 Standard states of mixtures

Solvent in solution	The reference state is the pure solvent at the same temperature ($a_{\text{solvent}} = 1$) At infinite dilution $\gamma_{\text{solvent}} \rightarrow 1$
Solute i in solution	The reference state is a hypothetical state at $x_i = 1$ or $m = 1 \text{ mol kg}^{-1}$ or $c = 1 \text{ mol dm}^{-3}$ solution, that is, a state that has the activity that such a solution would have if it obeyed the limiting law. It is set by extrapolation of Henry's law on the given basis. The temperature and pressure are the same as those of the solution under consideration.

where $\tilde{\mu}_i^\beta$ is the electrochemical potential of ion i in phase β , and φ^β is the inner potential of phase β .

It should be emphasized that the decomposition of $\tilde{\mu}_i$ into a chemical (μ_i) and an electrical ($z_i F \varphi$) component is arbitrary from strict thermodynamic point of view.

The general condition of equilibrium of a species i between phases α and β is

$$\tilde{\mu}_i^\alpha = \tilde{\mu}_i^\beta \quad (15)$$

The electrical potential difference (Galvani potential difference)

$$\varphi^\beta - \varphi^\alpha = \frac{\tilde{\mu}_i^\beta - \tilde{\mu}_i^\alpha}{z_i F} \quad (16)$$

can be measured only when the two phases have identical composition, for example, between two terminal copper wires (Cu, Cu') attached to the electrodes.

$$\begin{aligned} \varphi^{\text{Cu}} - \varphi^{\text{Cu}'} &= \frac{\tilde{\mu}_e^{\text{Cu}'} - \tilde{\mu}_e^{\text{Cu}}}{F} \\ &= E_{\text{cell}} \cong E_{\text{MF}} \end{aligned} \quad (17)$$

where e is for the electron.

1.2.5

Calculation of E_{cell}^\ominus from Calorimetric Data and ΔG^\ominus , ΔH^\ominus , ΔS^\ominus from Electrochemical Measurements

By combining Eq. (1) with the Gibbs-Helmholtz relation we obtain

$$\Delta H^\ominus = -nF \left(E_{\text{cell}}^\ominus + \frac{T \partial E_{\text{cell}}^\ominus}{\partial T} \right) \quad (18)$$

$$\Delta S^\ominus = nF \left(\frac{\partial E_{\text{cell}}^\ominus}{\partial T} \right) = - \left(\frac{\partial \Delta G^\ominus}{\partial T} \right)_p \quad (19)$$

ΔH can be determined calorimetrically, so as to obtain the value of ΔS from

the temperature function of the heat capacities ($C_p = (\partial H / \partial T)_p = T(\partial S / \partial T)_p$). However, the magnitude of $T \Delta S$ is often small, compared to that of ΔG and ΔH , and the relative error in ΔS determined in this way can be large. On the other hand, if accurate measurements of E_{MF} are made over a range of temperatures, the temperature coefficient of E_{cell} provides a more accurate value of ΔS . ($\partial E_{\text{cell}} / \partial T$) values are determined under conditions when the temperature of the whole cell is varied, that is, both electrodes are at the same temperature (isothermal cell). It is possible to keep the reference electrode at room temperature; however, in this case, the Seebeck effect (electromotive force in a thermocouple) appears. It is another example that thermodynamically – without further assumptions, simplifications, and conventions – only the whole cell (cell reaction) can be treated and interpreted.

1.2.6

The Dependence of the Potential of Cell Reaction on the Composition

If the stoichiometric equation of the cell reaction is

$$\sum_{\alpha} \sum_i v_i^\alpha A_i^\alpha = 0 \quad (20)$$

where A_i is for the components and α for the phases

$$\Delta G = \sum_{\alpha} \sum_i v_i^\alpha \tilde{\mu}_i^\alpha \quad (21)$$

At equilibrium between each contacting phases for the common constituents

$$\sum_{\alpha} \sum_i v_i^\alpha \tilde{\mu}_i^\alpha = 0 \quad (22)$$

If we consider a cell without liquid junction – which in fact is nonexistent,

through the effect of the liquid junction potential can be made negligible –

$$\Delta G = \sum_{\alpha} \sum_i v_i^{\alpha} \mu_i^{\alpha} = -nF E_{\text{cell}} \quad (23)$$

It follows that (for the sake of simplicity, the indication of phases further on is neglected)

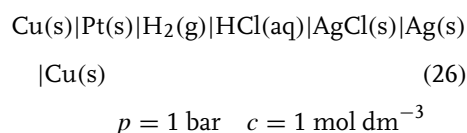
$$\begin{aligned} E_{\text{cell}} &= -\frac{1}{nF} \sum v_i \mu_i^{\oplus} - \frac{RT}{nF} \sum v_i \ln a_i \\ &= E_{\text{cell}}^{\oplus} - \frac{RT}{nF} \sum v_i \ln a_i \end{aligned} \quad (24)$$

If the reference electrode is the SHE

$$E_{\text{cell}}^{\oplus} = -\frac{1}{F} \left(\mu_{\text{H}^+}^{\oplus} - 0.5 \mu_{\text{H}_2}^{\oplus} \right) - \frac{1}{nF} \sum v_i \mu_i^{\oplus} \quad (25)$$

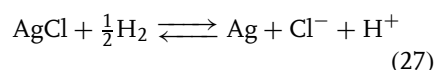
It has been mentioned that $E_{\text{cell}}^{\oplus} = E^{\oplus}$ when the reference system is the oxidation of molecular hydrogen to solvated (hydrated) protons. The standard electrode potential of the hydrogen electrode is chosen as 0 V. Thermodynamically it means that not only the standard free energy of formation of hydrogen ($\mu_{\text{H}_2}^{\oplus}$) is zero – which is a rule in thermodynamics (see Table 2) – but also that of the solvated hydrogen ion $\mu_{\text{H}^+}^{\oplus} = 0$!. (The old standard values of E^{\oplus} were calculated using $p^{\oplus} = 1 \text{ atm} = 101325 \text{ Pa}$. The new ones are related to 10^5 Pa (1 bar). It causes a difference in the potential of the SHE of + 0.169 mV, that

is, this value has to be subtracted from the E^{\oplus} values given previously in different tables. Since the large majority of the E^{\oplus} values have an uncertainty of at least 1 mV, this correction can be neglected.) When all components are in their standard states ($a_i = 1$ and $p^{\oplus} = 1 \text{ bar}$) $E_{\text{cell}} = E_{\text{cell}}^{\oplus} = E^{\oplus}$. However, a_i is not accessible by any electrochemical measurements, and only the mean activity can be determined. The cell represented by the cell diagram



is usually considered a cell without liquid junction. It is not entirely true, since the electrolyte is saturated with hydrogen and AgCl near the Pt and Ag|AgCl electrodes, respectively. In order to avoid the direct reaction between AgCl and H_2 , a long path is applied between the electrodes, or the HCl solution is divided into two parts separated by a diaphragm.

In this case, the cell reaction is as follows



From Eq. (24)

$$E_{\text{cell}} = E_{\text{Ag/AgCl}}^{\oplus} - \frac{RT}{F} \ln a_{\text{H}^+} a_{\text{Cl}^-} \quad (28)$$

Tab. 2 Standard states of pure substances

Solid	Pure solid in most stable form at $p^{\oplus} = 1 \text{ bar}$ (100 kPa) and the specified temperature (T) (usually $T = 298.15 \text{ K}$) the standard free energy of formation for any element is zero.
Liquid	Pure liquid in most stable form at $p^{\oplus} = 1 \text{ bar}$ and T .
Gas	Pure gas at unit fugacity; for ideal gas, fugacity is unity at $p^{\oplus} = 1 \text{ bar}$ and T ($f = p$ for ideal gas).

The activity of a pure solid or pure liquid at $p^{\oplus} = 1 \text{ bar}$ is equal to 1 at any temperature.

where $a_{\text{H}^+}a_{\text{Cl}^-} = a_{\pm}^2 = (\gamma_{\pm}c_{\text{HCl}}/c^{\ominus})^2 = (\gamma_{\pm}m_{\text{HCl}}/m^{\ominus})^2$

1.2.7

Determination of the Standard Electrode Potential (E^{\ominus}) from Electrochemical Measurements

Considering Eq. (28) we may write

$$E_{\text{cell}} + 2\frac{RT}{F} \ln m_{\text{HCl}}/m^{\ominus} = E_{\text{Ag}/\text{AgCl}}^{\ominus} - 2\frac{RT}{F} \ln \gamma_{\pm} \quad (29)$$

The value of the standard potential can be determined by measuring E_{cell} at various HCl concentrations and then by extrapolation to $m_{\text{HCl}} \rightarrow 0$, where $\gamma_{\pm} \rightarrow 1$, E^{\ominus} can be obtained.

In dilute electrolytes, where the Debye-Hückel limiting law prevails,

$$\lg \gamma_{\pm} = -A\sqrt{m_{\text{HCl}}} \quad (30)$$

where A is a constant.

Taking into account Eq. (30), we may rewrite Eq. (29) in the form

$$E_{\text{cell}} + 2\frac{RT}{F} \ln m_{\text{HCl}}/m^{\ominus} = E_{\text{Ag}/\text{AgCl}}^{\ominus} + 2\frac{RT}{F} A\sqrt{m_{\text{HCl}}} \quad (31)$$

In this way, a more accurate extrapolation to $m_{\text{HCl}} \rightarrow 0$ can be made from the $E_{\text{cell}} + 2\frac{RT}{F} \ln m_{\text{HCl}}/m^{\ominus}$ versus $A\sqrt{m_{\text{HCl}}}$ plot.

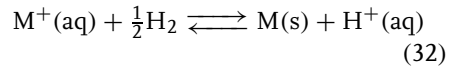
1.2.8

Determination of E^{\ominus} from Thermodynamic Data

With the help of the calorimetric method, ΔG^{\ominus} , ΔH^{\ominus} , and ΔS^{\ominus} can be determined for a given reaction, which is formulated in such a way that the participating species

are electrically neutral compounds and not ions in solution. From other techniques (e.g. mass spectrometry), the formation of an ion in gaseous state can be obtained. However, in the latter case the solvation (hydration) energy of the individual ions present in the solution is inaccessible, since only the heat of hydration of an electrolyte can be measured.

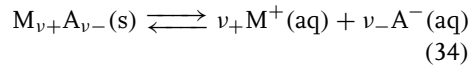
For a simple metal, dissolution/deposition



In accordance with Eq. (25), the formation of the chemical potential of the hydrated ion, $\text{M}^+(\text{aq})$, can be determined as

$$E_{\text{cell}}^{\ominus} = E^{\ominus} - \frac{1}{nF} \mu_{\text{M}^+}^{\ominus} \quad (33)$$

since $\mu_{\text{M}}^{\ominus} = 0$. However, $\mu_{\text{M}^+}^{\ominus}$ cannot be considered as the standard chemical potential of M^+ ion. It may be called the standard chemical potential of formation of this ion, since $\mu_{\text{M}^+}^{\ominus}$ is related to the formation of the hydrated hydrogen ion, and $\mu_{\text{H}^+}^{\ominus}$ was taken as zero, arbitrarily. When we want to calculate E^{\ominus} from thermodynamic data, it is necessary to set up equilibrium between the ions and the substance whose standard values are known. This is most often the solubility equilibrium.



For the equilibrium of a solid electrolyte and its saturated solution, one can write

$$\mu_{\text{MA}}(\text{s}) = \nu\mu_{\pm} = \mu_{\text{MA}}(\text{aq}) \quad (35)$$

$$K_s = \exp \left[\frac{\mu_{\text{MA}}^{\ominus}(\text{s}) - \nu_{+}\mu_{\text{M}}^{\ominus} - \nu_{-}\mu_{\text{A}}^{\ominus}}{RT} \right] = \frac{a_{\text{M}}^{\nu_{+}} a_{\text{A}}^{\nu_{-}}}{(a^{\ominus})^{\nu}} \quad (36)$$

The solubility product is

$$K_{\text{sp}} = c_{\text{M}}^{\nu_{+}} c_{\text{A}}^{\nu_{-}} \quad (37)$$

and therefore,

$$K_s = \frac{K_{\text{sp}}}{(c^{\oplus})^{\nu}} \gamma_{\pm}^{\nu} \quad (38)$$

The standard Gibbs energy of reaction (34) is

$$\Delta G^{\oplus} = -RT \ln K_s \quad (39)$$

and the entropy change can be obtained by the temperature dependence of K_s .

1.2.9

The Formal Potential ($E_c^{\circ'}$)

Beside E_{cell}^{\oplus} and E^{\oplus} , the so-called formal potentials, $E_{\text{cell},c}^{\circ'}$ and $E_c^{\circ'}$, are frequently used. The purpose of defining formal potentials is to have a “conditional constant” that takes into account the activity coefficients and side reaction coefficients (chemical equilibria of the redox species), since in many cases, it is impossible to calculate the resulting deviations because neither are the thermodynamic equilibrium constants known, nor is it possible to calculate the activity coefficients. Therefore, the potential of the cell reaction and the potential of the electrode reaction are expressed in terms of concentrations

$$E_{\text{cell}} = E_{\text{cell},c}^{\circ'} - \frac{RT}{nF} \sum \nu_i \ln \frac{c_i}{c^{\oplus}} \quad (40)$$

$$E = E_c^{\circ'} - \frac{RT}{nF} \sum \nu_i \ln \frac{c_i}{c^{\oplus}} \quad (41)$$

where

$$E_{\text{cell},c}^{\circ'} = E_{\text{cell}}^{\oplus} - \frac{RT}{nF} \sum \nu_i \ln \gamma_i \quad (42)$$

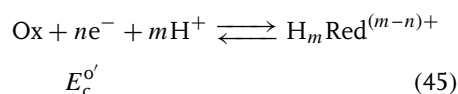
and

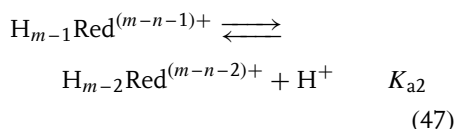
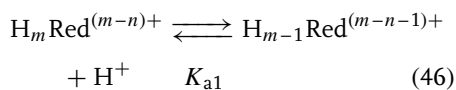
$$E_c^{\circ'} = E^{\oplus} - \frac{RT}{nF} \sum \nu_i \ln \gamma_i \quad (43)$$

when SHE is the reference electrode ($a_{\text{H}^+} = (p_{\text{H}_2}/p^{\oplus}) = 1$). Equation (41) is the well-known Nernst equation

$$E = E_c^{\circ'} + \frac{RT}{nF} \ln \frac{\pi c_{\text{ox}}^{\nu_{\text{ox}}}}{\pi c_{\text{red}}^{\nu_{\text{red}}}} \quad (44)$$

where π is for the multiplication of the concentrations of the oxidized (ox) and reduced (red) forms, respectively. The Nernst equation provides the relationship between the equilibrium electrode potential and the composition of the electrochemically active species. Note that the Nernst equation can be used only at equilibrium conditions. The formal potential is sometimes called as conditional potential indicating that it relates to specific conditions (e.g. solution composition), which usually deviate from the standard conditions. In this way, the complex or acid–base equilibria are also considered, since the total concentrations of oxidized and reduced species considered can be determined, for example, by potentiometric titration; however, without a knowledge of the actual compositions of the complexes (see our example in Sect 1.2.1.). In the case of potentiometric titration, the effect of the change of activity coefficients of the electrochemically active components can be diminished by applying inert electrolyte in high concentration (almost constant ionic strength). If the solution equilibria are known from other sources, it is relatively easy to include their parameters into the respective equations related to $E_c^{\circ'}$. The most common equilibria are the acid–base and the complex equilibria. In acid media, a general equation for the proton transfer accompanying the electron transfer is



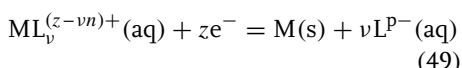


and so on. For $m = n = 2$

$$E = E_c^{\circ'} + \frac{RT}{nF} \ln \left(\frac{c_{\text{ox}}}{c_{\text{red}}} \frac{1 + K_{a1}a_{\text{H}^+} + a_{\text{H}^+}^2}{K_{a1}K_{a2}} \right) \quad (48)$$

The complex equilibria can be treated in a similar manner; however, one should not forget that each stability constant (K_i) of a metal complex depends on the pH and ionic strength.

The simplest and most frequent case is when metal ions (M^{z+}) can be reduced to the metal, which means that all the ligands ($\text{L}^{\text{p-}}$) will be liberated, that is,



In this case, the equilibrium potential is as follows:

$$E = E_{\text{c,ML/M}}^{\circ'} + \frac{RT}{zF} \ln \frac{c_{\text{ML}}}{c_{\text{L}}^\nu} \quad (50)$$

where c_{ML} and c_{L} are the concentrations of the complex and the ligand, respectively, and $E_{\text{c,ML/M}}^{\circ'}$ is the formal potential of reaction (49). Under certain conditions ($c_{\text{M}^{z+}} \ll c_{\text{L}}$), the stability constant (K) of the complex and ν can be estimated from the equilibrium potential E versus $\ln c_{\text{L}}$ plot by using the following equation:

$$E = E_c^{\circ'} - \frac{RT}{zF} \ln K - \frac{RT}{zF} \ln c_{\text{L}}^\nu \quad (51)$$

Amalgam formation shifts the equilibrium potential of a metal (polarographic

half-wave potential, $E_{1/2}$) into the direction of higher potentials owing to the free energy of the amalgam formation (ΔG_{amal}).

$$E = E_c^{\circ'} - \left(\frac{\Delta G_{\text{amal}}}{nF} \right) + \left(\frac{RT}{nF} \right) \ln (c_{\text{M}} + c_{\text{M}}) \quad (52)$$

$$E_{1/2} = E_c^{\circ'} - \left(\frac{\Delta G_{\text{amal}}}{nF} \right) + \left(\frac{RT}{nF} \right) \ln c_{\text{M}}(\text{sat}) \quad (53)$$

where $c_{\text{M}}(\text{sat})$ is the saturation concentration of the metal in the mercury. It is assumed that a_{Hg} is not altered, and $D_{\text{red}} = D_{\text{ox}}$, where D_{red} and D_{ox} are the respective diffusion coefficients.

In principle, $E_c^{\circ'}$ can be determined by the widely used electroanalytical techniques (e.g. polarography, cyclic voltammetry [25]). The combination of the techniques is also useful. It has been demonstrated recently where potentiometry, coulometry, and spectrophotometry have been applied [26]. The case of the cyclic voltammetry is examined below.

1.2.10

The Determination of $E_c^{\circ'}$ by Cyclic Voltammetry

Cyclic voltammetry has perhaps become the most popular electroanalytical, electrochemical technique [23, 27], and many reports have appeared in which $E_c^{\circ'}$ values were determined in this way. However, reliable formal potentials can be determined only for electrochemically reversible systems [28]. For any reversible redox system – provided that the electrode applied is perfectly inert, that is, there are

no chemical side reactions, no oxide formation etc. – the diagnostic criteria are as follows:

1. the peak currents are equal,

$$I_{pa} = I_{pc} \quad (54)$$

I_p is proportional to the square root of the scan rate.

2. the difference of the peak potential,

$$E_{pa} - E_{pc} = 2.218 \frac{RT}{nF} = \frac{57}{n} \text{ mV at 298 K} \quad (55)$$

and the peak potentials are independent of the scan rate ν ,

$$|E_p - E_{p/2}| = 2.218 \frac{RT}{nF} \quad (56)$$

where $E_{p/2}$ is measured at half of the peak current, $I_p/2$.

Since

$$E_{pc} = E_c^{o'} - 1.1 \frac{RT}{nF} - \frac{RT}{2nF} \ln \left(\frac{D_{ox}}{D_{red}} \right)^{1/2} \quad (57)$$

$$E_{pa} = E_c^{o'} + 1.1 \frac{RT}{nF} + \frac{RT}{2nF} \ln \left(\frac{D_{ox}}{D_{red}} \right)^{1/2} \quad (58)$$

where D_{ox} and D_{red} are the diffusion coefficient of the respective species, it follows

$$E_c^{o'} = 0.5(E_{pa} + E_{pc}) \quad (59)$$

It must be emphasized again that the mid-peak potential is equal to $E_c^{o'}$ for a simple, reversible redox reaction when neither any experimental artifact nor kinetic effect (ohmic drop effect, capacitive current, adsorption side reactions, etc.) occurs, and macroscopic inlaid disc electrodes are used, that is, the thickness of the diffusion layer is much higher than that of the diameter of the electrode.

A special case is when the electrochemically active components are attached to the metal or carbon (electrode) surface in the form of mono- or multilayers, for example, oxides, hydroxides, insoluble salts, metalloorganic compounds, transition-metal hexacyanides, clays, zeolites containing polyoxianions or cations, intercalative systems. The submonolayers of adatoms formed by underpotential deposition are neglected, since in this case, the peak potentials are determined by the substrate–adatom interactions (compound formation). From the ideal surface cyclic voltammetric responses, $E_c^{o'}$ can also be calculated as

$$E_c^{o'} = E_{pa} = E_{pc} \quad (60)$$

Other diagnostic criteria for the ideal surface responses are as follows:

$$I_{pa} = I_{pc} \quad (61)$$

$$I_p = \frac{n^2 F^2}{4RT} A \Gamma \nu \quad (62)$$

and

$$\Delta E_{p,1/2} = 3.53 \frac{RT}{nF} \quad (63)$$

where $\Delta E_{p,1/2}$ is the total width at half-height of either the cathodic or anodic wave, Γ is the apparent surface coverage of the electroactive species, A is the surface area, ν is the scan rate, and I_p is the respective peak current.

$$\text{If } L \gg (2Dt)^{1/2} \quad (64)$$

where L is the layer (film) thickness, D is the charge transport diffusion coefficient, and t is the timescale of the experiment; instead of a surface response, a regular diffusional behavior develops, and therefore Eqs (57–59) can be applied.

The interactions within the surface layer can also affect the surface response;

however, even so, $E_c^{\circ'}$ can be derived in many cases, since only $\Delta E_{p,1/2}$ will change.

Nevertheless, the mid-peak potentials determined by cyclic voltammetry and other characteristic potentials obtained by different electroanalytical techniques (such as pulse, alternating current, or square wave voltammetries) supply valuable information on the behavior of the redox systems. In fact, for the majority of redox reactions, especially for the novel systems, we have only these values. (The cyclic voltammetry almost entirely replaced the polarography which has been used for six decades from 1920. However, the abundant data, especially the half-wave potentials, $E_{1/2}$, are still very useful sources for providing information on the redox properties of different systems.)

References

1. W. M. Latimer, *Oxidation Potentials*, 2nd ed., Prentice-Hall, Englewood Cliffs, N.J., 1952.
2. R. Parsons, *Pure Appl. Chem.* **1974**, *37*, 503.
3. I. Mills, T. Cvitas, *Quantities, Units and Symbols in Physical Chemistry*, IUPAC, Blackwell Scientific Publications, London, Edinburgh, Boston, Melbourne, Paris, Berlin, Vienna, 1993.
4. Z. M. Koepp, H. Wendt, H. Strehlow, *Z. Elektrochem.* **1960**, *64*, 483.
5. G. Gritzner, J. Kuta, *Pure Appl. Chem.* **1984**, *56*, 461.
6. M. M. Baizer, H. Lund, (Eds.), *Organic Electrochemistry*, Marcel Dekker, New York, 1983.
7. G. Gritzner, *Pure Appl. Chem.* **1990**, *62*, 1839.
8. A. J. Bard, H. Lund, (Eds.), *The Encyclopedia of Electrochemistry of Elements*, Marcel Dekker, New York, 1973–1986.
9. G. Milazzo, S. Caroli, *Tables of Standard Electrode Potentials*, Wiley-Interscience, New York, 1977.
10. G. Charlot, A. Collumeau, M. J. C. Marchot, *Selected Constants. Oxidation-Reduction Potentials of Inorganic Substances in Aqueous Solution*, IUPAC, Butterworths, London, 1971.
11. M. Pourbaix, N. de Zoubov, J. van Muylder, *Atlas d' Equilibres Electrochimiques a 25°C*, Gauthier- Villars, Paris, 1963.
12. M. Pourbaix, (Ed.), *Atlas of Electrochemical Equilibria in Aqueous Solutions*, Pergamon-CEBELCOR, Brussels, 1966.
13. A. J. Bard, R. Parsons, J. Jordan, *Standard Potential in Aqueous Solution*, (Eds.), Marcel Dekker, New York, 1985.
14. M. W. Case, Jr., *Thermodynamical Tables Nat. Inst. Stand. Tech. J. Phys. Chem. Ref. Data, Monograph G*, **1998**, pp. 1–1951.
15. E. A. Guggenheim, *Thermodynamics*, North Holland Publications, Amsterdam, 1967.
16. R. A. Robinson, R. H. Stokes, *Electrolyte Solutions*, Butterworths Scientific Publications, London, 1959.
17. I. M. Klotz, R. M. Rosenberg, *Chemical Thermodynamics*, John Wiley, New York, Chichester, Brisbane, Toronto, Singapore, 1994.
18. F. A. Cotton, G. Wilkinson, C. A. Murillo et al., *Advanced Inorganic Chemistry*, Wiley, New York, 1999, pp. 1010–1039.
19. S. E. Livingstone, in *Comprehensive Inorganic Chemistry* (Eds.: J. C. Bailar, M. J. Emeléus, R. Nyholm et al.), Pergamon Press, Oxford, 1973, pp. 1163–1370, Vol. 3.
20. B. Chandret, S. Sabo-Etienne, in *Encyclopedia of Inorganic Chemistry* (Ed.: R. B. King), John Wiley, Chichester, 1994. Vol. 7.
21. M. M. Taqui Khan, G. Ramachandraiah, A. Prakash Rao, *Inorg. Chem.* **1986**, *25*, 665.
22. J. G. Albright, J. A. Rard, S. Serna et al., *J. Chem. Thermodyn.* **2000**, *32*, 1447.
23. A. J. Bard, L. R. Faulkner, *Electrochemical Methods*, John Wiley, New York, Chichester, Weinheim, Brisbane, Singapore, Toronto, 2001.
24. A. Henglein, *Ber. Bunsen-Ges. Phys. Chem.* **1990**, *94*, 600.
25. F. Scholz, in *Electrochemical Methods* (Ed.: F. Scholz), Springer, Berlin, Heidelberg, New York, 2002, 2005, pp. 9–28, Chapter I. 2.
26. M. T. Ramírez, A. Rojas-Hernández, I. González, *Talanta* **1997**, *44*, 31.

27. F. Marken, A. Neudeck, A. M. Bond, in *Electrochemical Methods* (Ed.: F. Scholz), Springer, Berlin, Heidelberg, New York, 2002, 2005, pp. 51–97, Chapter II. 1.
28. G. Inzelt, in *Electrochemical Methods* (Ed.: F. Scholz), Springer, Berlin, Heidelberg, New York, 2002, 2005, pp. 29–48, Chapter I. 3.

2 Standard, Formal, and Other Characteristic Potentials of Selected Electrode Reactions

György Inzelt
Eötvös Loránd University, Budapest, Hungary

2.1	Group 1 Elements	20
2.2	Group 2 Elements	22
2.3	Group 3 Elements	24
2.4	Group 4 Elements	30
2.5	Group 5 Elements	31
2.6	Group 6 Elements	32
2.7	Group 7 Elements	34
2.8	Group 8 Elements	36
2.9	Group 9 Elements	39
2.10	Group 10 Elements	41
2.11	Group 11 Elements	43
2.12	Group 12 Elements	47
2.13	Group 13 Elements	50
2.14	Group 14 Elements	53
2.15	Group 15 Elements	57

18 | 2 *Standard, Formal, and Other Characteristic Potentials of Selected Electrode Reactions*

2.16	Group 16 Elements	63
2.17	Group 17 Elements	68
2.18	Group 18 Elements	73
	Acknowledgment	73
	References	74

Over the last 20–30 years not too much effort has been made concerning the determination of standard potentials. It is mostly due to the funding policy all over the world, which directs the sources to new and fashionable research and practically neglects support for the quest for accurate fundamental data. A notable recent exception is the work described in Ref. 1, in which the standard potential of the cell Zn(Hg)_x (two phase)| $\text{ZnSO}_4(\text{aq})$ | $\text{PbSO}_4(\text{s})$ | Pb(Hg)_x (two phase) has been determined. Besides the measurements of electromotive force, determinations of the solubility, solubility products, osmotic coefficients, water activities, and mean activity coefficients have been carried out and compared with the previous data. The detailed analysis reveals that the uncertainties in some fundamental data such as the mean activity coefficient of ZnSO_4 , the solubility product of Hg_2SO_4 , or even the dissociation constant of HSO_4^- can cause uncertainties in the E^\ominus values as high as 3–4 mV. The author recommends this comprehensive treatise to anybody who wants to go deeply into the correct determination of E^\ominus values.

There are only a few groups that deal with the study of the thermodynamics of the electrochemical cell. Besides Ref. 1, it is appropriate to mention

Refs 2, 3, where the medium effects on $\text{M}_x\text{Hg}_{1-x}$ |MCl or MCl_2 |AgCl|Ag cells ($\text{M} = \text{Rb}, \text{Cs}, \text{Sr}, \text{Ba}$) were investigated, and Ref. 4, in which the influence of the activity of the supporting electrolyte on the formal potentials of ferricenium/ferrocene and decamethylferricenium/decamethylferrocene systems were studied with the help of the following cell:

$\text{Ag}|\text{AgClO}_4$ or $\text{TBAClO}_4(\text{CH}_3\text{CN})$ or $(\text{H}_2\text{O})|\text{poly}[\text{Ru}(\text{vbpy})_3(\text{ClO}_4)_n]|\text{Pt}$, where vbpy is 4-methyl-4'-vinyl-2,2'-bipyridine and TBA is tetra-*n*-butylammonium ion.

This chapter gives a selected compilation of the standard and other characteristic (formal, half-wave) potentials, as well as a compilation of the constant of solubility and/or complex equilibria. Mostly, data obtained by electrochemical measurements are given. In the cases when reliable equilibrium potential values cannot be determined, the calculated values (calcd) for the most important reactions are presented. The data have been taken extensively from previous compilations [5–13] where the original reports can be found, as well as from handbooks [13–16], but only new research papers are cited. The constant of solubility and complex equilibria were taken from Refs 6–11, 13, 17–21. The oxidation states (OSs), ionization energies (IEs) (first, second, etc.), and electron affinities (EAs) of the elements and the

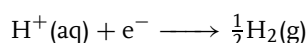
hydration enthalpy of some ions (ΔH_{hydr}) calculated on the basis of $\Delta H_{\text{hydr}}(\text{Cs}^+) = \Delta H_{\text{hydr}}(\text{I}^-)$ are also given. With the symbol of elements, the atomic number (lower index) and the mean relative atomic mass (upper index), the values that correspond either to the current best knowledge (IUPAC 2005) of the elements in natural terrestrial sources or to the mass number of the nuclide with the longest half-life, are also indicated. The electrode reactions and equilibria are organized according to the positions of the elements in the periodic table, starting from hydrogen and group 1 to group 18, including lanthanides and actinides [22, 23].

2.1

Group 1 Elements

Hydrogen ($^{1.0079}_1\text{H}$, ^2_1H), OS: +1, 0, -1; IE: 1312 kJ mol⁻¹; EA: -72.77 kJ mol⁻¹. $\Delta H_{\text{hydr}} = -1090$ kJ mol⁻¹.

$\text{H}^+ / \frac{1}{2}\text{H}_2$ couple



$$E^\ominus = 0.000 \text{ V}$$

The standard potential of the hydrogen electrode is taken as zero at all temperatures by convention [24, 25]. H does not refer to isotopically pure hydrogen ^1_1H but to a mixture of ^1_1H , and ^2_1H (deuterium, $^{2.014}\text{D}$) at the levels of natural abundance (99.985% of ^1_1H and 0.015% of ^2_1H). H_2 molecules possess nuclear spin isomers (ortho and para forms) that have significantly different physical and chemical properties. At ambient temperature, the equilibrium mixture is 3:1 for $^1_1\text{H}_2$ (ortho to para) and 2:1 for $^2_1\text{H}_2$. The para form becomes predominant below 200 K.

Taking into account the ionization constant of water ($K_w = a_{\text{H}^+}a_{\text{OH}^-}$) at 298.15 K, the equilibrium potentials can be calculated with the help of the Nernst equation at different pH values. Since $K_w = 1.008 \times 10^{-14}$ at $p_{\text{H}_2} = 1$ bar.

$$E_{\text{H}^+/\text{H}_2} = -0.414 \text{ V}(\text{pH } 7) \quad (1)$$

$$E_{\text{H}^+/\text{H}_2} = -0.828 \text{ V}(\text{pH } 14) \quad (2)$$

At $\text{pH} > 0$, the Hammett acidity function (H_0) [26, 27] can be used to estimate $E_{\text{H}^+/\text{H}_2}$:

$$E = \frac{RT}{F} \ln a_{\text{H}^+} \cong \frac{RT}{F} \ln \gamma_{\pm} c_{\text{H}^+} \cong -\frac{RT}{F} H_0 \quad (3)$$

The other strategy to determine the dependence of the equilibrium potential of any redox reaction on the hydrogen ion activity is the use of relative hydrogen electrode (RHE); that is, a hydrogen electrode immersed in the same solution. If the peak potential does not shift as a function of pH, it means that the hydrogen ion activity is involved in the same way as that characteristic of the hydrogen electrode (simple e^- , H^+ reaction). From the magnitude of the shift of E_p values, a conclusion can be drawn for the number of hydrogen ions accompanying the redox transformations of the species (e.g. 2e^- , H^+ ; e^- , 2H^+).

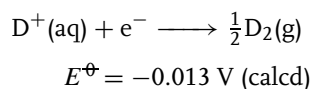
The equilibrium potential can be measured by using inert metals ($E_{\text{M}^+/\text{M}} > E_{\text{H}^+/\text{H}_2}$) and the exchange current density (j_0) for reaction $\text{H}^+ + \text{e}^- \rightleftharpoons \frac{1}{2}\text{H}_2$, which is higher than 10^{-4} A cm⁻². Besides Pt, Ir, Os, Pd, Rh, and Ru may be used. Because of the dissociative adsorption of H_2 molecules at these metals, no overpotential is needed to cover the rather high (431 kJ mol⁻¹) H-H bond energy.

On the other hand, the metal–hydrogen atom bond energy is not too high; therefore, it does not hinder the desorption process.

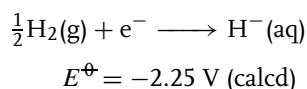
In aqueous solution, the potential window of stability of water is 1.23 V when $p_{\text{H}_2} = p_{\text{O}_2}$. However, at many electrodes, the hydrogen and oxygen evolution are kinetically hindered; therefore, it is possible to achieve a higher cell potential. Typical examples are Hg and Pb, in which $\log(j_0/\text{A cm}^{-2}) = -11.9$ and -12.6 , respectively.

$\text{D}^+/\frac{1}{2}\text{D}_2$ couple

Since the properties (e.g. dissociation energy, solvation enthalpy) of $\frac{2}{1}\text{H}(\text{D})$ substantially differ from those of $\frac{1}{1}\text{H}$, it is expected that the equilibrium potential under the same conditions will be different. The estimated value for the reaction is given as follows:

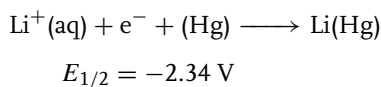
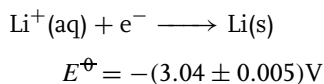


$\frac{1}{2}\text{H}_2/\text{H}^-$ couple



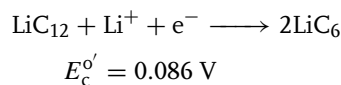
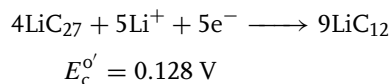
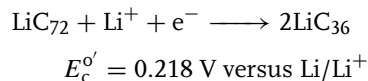
Solubility of H_2 in 100 g water at 1 bar and 20°C is 1.75×10^{-4} g.

Lithium (${}^{6.941}_{3}\text{Li}$), OS: +1, 0; IE: $520.2 \text{ kJ mol}^{-1}$. $\Delta H_{\text{hydr}} = -515 \text{ kJ mol}^{-1}$.

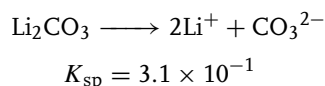


Lithium intercalation in graphite (1 mol dm^{-3} LiAsF_6 , ethylenecarbonate:

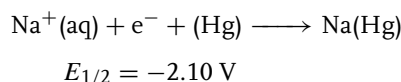
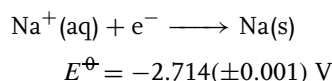
dimethylcarbonate 1 : 3) [28]



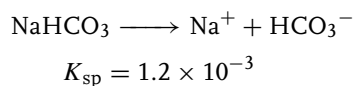
Solubility equilibrium:



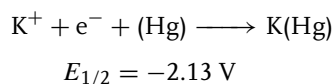
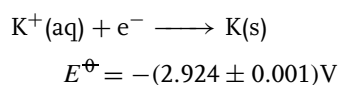
Sodium (${}^{22.989}_{11}\text{Na}$), OS: +1, 0; IE: $495.8 \text{ kJ mol}^{-1}$. $\Delta H_{\text{hydr}} = -405 \text{ kJ mol}^{-1}$.



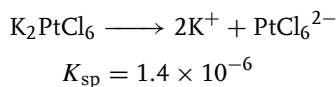
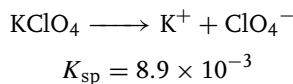
Solubility equilibrium:



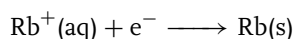
Potassium (${}^{39.098}_{19}\text{K}$), OS: +1, 0; IE: $418.8 \text{ kJ mol}^{-1}$. $\Delta H_{\text{hydr}} = -321 \text{ kJ mol}^{-1}$.



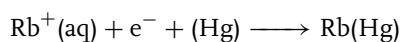
Solubility equilibria:



Rubidium ($^{85.467}_{37}\text{Rb}$), OS: +1, 0; IE: 403 kJ mol⁻¹. $\Delta H_{\text{hydr}} = -296$ kJ mol⁻¹.

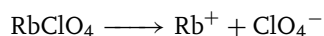


$$E^\ominus = -(2.924 \pm 0.001)\text{V}$$



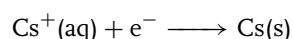
$$E_{1/2} = -2.12 \text{ V}$$

Solubility equilibrium:

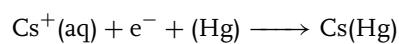


$$K_{\text{sp}} = 3.8 \times 10^{-3}$$

Cesium ($^{132.905}_{55}\text{Cs}$), OS: +1, 0; IE: 375.7 kJ mol⁻¹. $\Delta H_{\text{hydr}} = -263$ kJ mol⁻¹.

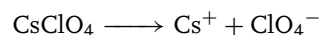


$$E^\ominus = -(2.923 \pm 0.001)\text{V}$$



$$E_{1/2} = -2.09 \text{ V}$$

Solubility equilibrium:



$$K_{\text{sp}} = 3.2 \times 10^{-3}$$

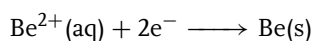
Francium ($^{223.02}_{87}\text{Fr}$)

No data are available

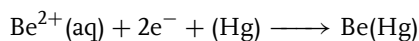
2.2

Group 2 Elements

Beryllium ($^{9.0121}_4\text{Be}$), OS: +2, (+1), 0; IE: 899, 1757.1 kJ mol⁻¹. $\Delta H_{\text{hydr}} = -4038$ kJ mol⁻¹.

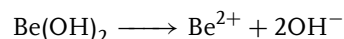


$$E^\ominus = -1.97 \text{ V (calcd)}$$



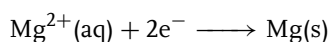
$$E_{1/2} \sim -1.8 \text{ V}$$

Solubility equilibrium:

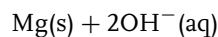
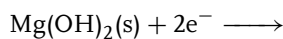


$$K_{\text{sp}} = 2.7 \times 10^{-10}$$

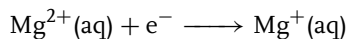
Magnesium ($^{24.305}_{12}\text{Mg}$), OS: +2, (+1), 0; IE: 737.7, 1450.7 kJ mol⁻¹. $\Delta H_{\text{hydr}} = -1922$ kJ mol⁻¹.



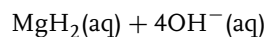
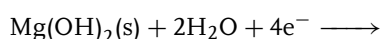
$$E^\ominus = -2.356 \text{ V (calcd)}$$



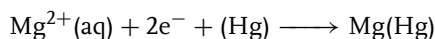
$$E^\ominus = -2.687 \text{ V (calcd)}$$



$$E^\ominus = -2.657 \text{ V (calcd)}$$

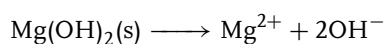


$$E^\ominus = -1.663 \text{ V (calcd)}$$

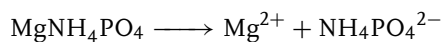


$$E_{1/2} \sim -2.53 \text{ V}$$

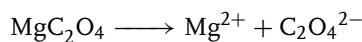
Solubility equilibria:



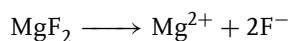
$$K_{\text{sp}} = 1.5 \times 10^{-11}$$



$$K_{\text{sp}} = 2.5 \times 10^{-12}$$



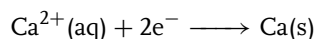
$$K_{\text{sp}} = 8.6 \times 10^{-5}$$



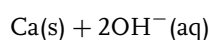
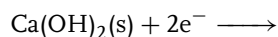
$$K_{\text{sp}} = 6.4 \times 10^{-9}$$

Calcium ($^{40.078}_{20}\text{Ca}$), OS: (+4), +2, (+1), 0, -2; IE: 589.8, 1145.4 kJ mol⁻¹.

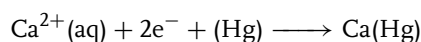
$$\Delta H_{\text{hydr}} = -1616 \text{ kJ mol}^{-1}.$$



$$E^{\ominus} = -(2.84 \pm 0.01)\text{V}$$



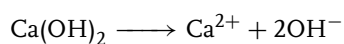
$$E^{\ominus} = -3.026 \text{ V}$$



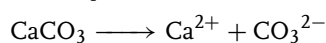
$$E^{\circ} = -(2.000 \pm 0.003) \text{ V}$$

$$(E_{1/2} = -1.974 \text{ V})$$

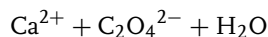
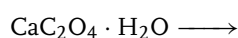
Solubility equilibria:



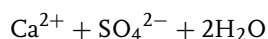
$$K_{\text{sp}} = 7.9 \times 10^{-6}$$



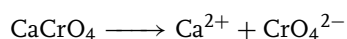
$$K_{\text{sp}} = 3.8 \times 10^{-9}$$



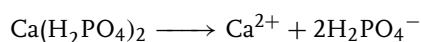
$$K_{\text{sp}} = 2.3 \times 10^{-9}$$



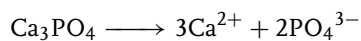
$$K_{\text{sp}} = 2.4 \times 10^{-5}$$



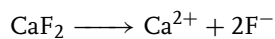
$$K_{\text{sp}} = 7.1 \times 10^{-4}$$



$$K_{\text{sp}} = 1.0 \times 10^{-3}$$

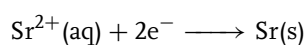


$$K_{\text{sp}} = 1.0 \times 10^{-25}$$

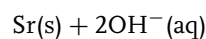
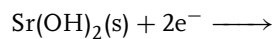


$$K_{\text{sp}} = 3.9 \times 10^{-11}$$

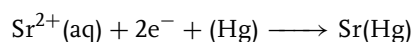
Strontium ($^{87.62}_{38}\text{Sr}$), OS: +2, 0; IE: 549.5, 1064.2 kJ mol⁻¹.



$$E^{\ominus} = -(2.89 \pm 0.01)\text{V}$$

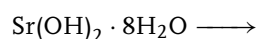


$$E^{\ominus} = -2.99 \text{ V}$$

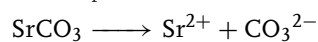


$$E^{\circ} = -1.901 \text{ V}$$

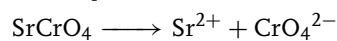
Solubility equilibria:



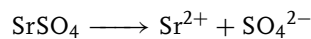
$$K_{\text{sp}} = 3.2 \times 10^{-4}$$



$$K_{\text{sp}} = 9.4 \times 10^{-10}$$

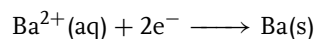


$$K_{\text{sp}} = 3.6 \times 10^{-5}$$

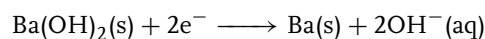


$$K_{\text{sp}} = 2.8 \times 10^{-7}$$

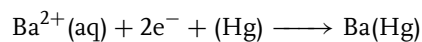
Barium ($^{137.327}_{56}\text{Ba}$), OS: +2, 0; IE: 503, 965.2 kJ mol⁻¹. $\Delta H_{\text{hydr}} = -1339 \text{ kJ mol}^{-1}$.



$$E^{\ominus} = -(2.92 \pm 0.01)\text{V}$$



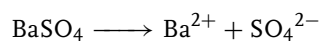
$$E^{\ominus} = -2.99 \text{ V}$$



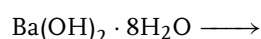
$$E^{\circ} = -1.717 \text{ V}$$

$$(E_{1/2} = -1.694 \text{ V})$$

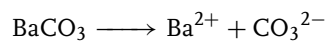
Solubility equilibria:



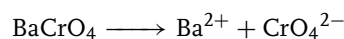
$$K_{\text{sp}} = 1.1 \times 10^{-10}$$



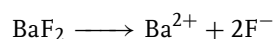
$$K_{\text{sp}} = 5 \times 10^{-3}$$



$$K_{\text{sp}} = 8.1 \times 10^{-9}$$

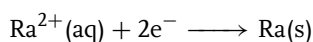


$$K_{\text{sp}} = 2.0 \times 10^{-10}$$

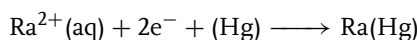


$$K_{\text{sp}} = 1.7 \times 10^{-6}$$

Radium ($^{226.0254}_{88}\text{Ra}$), OS: +2, 0; IE: 509.3, 979 kJ mol⁻¹.

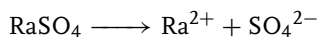


$$E^\ominus = -2.916 \text{ V (calcd)}$$



$$E_{1/2} \sim -1.85 \text{ V}$$

Solubility equilibrium:

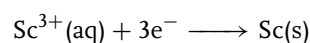


$$K_{\text{sp}} = 4.2 \times 10^{-15}$$

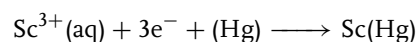
2.3

Group 3 Elements

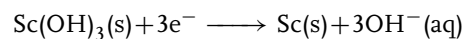
Scandium ($^{44.955}_{21}\text{Sc}$), OS: +3, 0; IE: 631, 4258 (I + II + III) kJ mol⁻¹.



$$E^\ominus = -2.03 \text{ V}$$

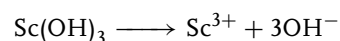


$$E_{1/2} = -1.51 \text{ V}$$

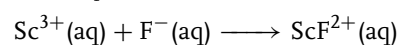


$$E^\ominus = -2.60 \text{ V}$$

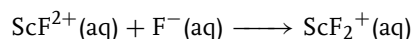
Solubility and complex equilibria:



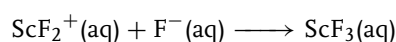
$$K_{\text{sp}} = 4 \times 10^{-31}$$



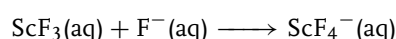
$$K = 1.2 \times 10^7$$



$$K = 6.5 \times 10^5$$

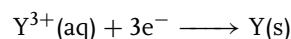


$$K = 3.0 \times 10^4$$

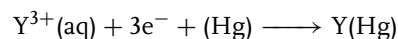


$$K = 7 \times 10^2$$

Yttrium ($^{88.9058}_{39}\text{Y}$), OS: +3, 0; IE: 617, 3760 (I + II + III) kJ mol⁻¹.

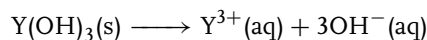


$$E^\ominus = -2.37 \text{ V (calcd)}$$



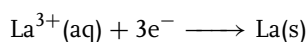
$$E_{1/2} \sim -1.6 \text{ V}$$

Solubility equilibrium:

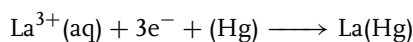


$$K_{\text{sp}} = 3.2 \times 10^{-25}$$

Lanthanum ($^{138.905}_{57}\text{La}$), OS: +3, 0; IE: 538, 3457 (I + II + III) kJ mol⁻¹. $\Delta H_{\text{hydr}}(\text{La}^{3+}) = -3235 \text{ kJ mol}^{-1}$.

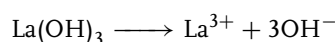


$$E^\ominus = -2.38 \text{ V}$$



$$E_{1/2} = -1.76 \text{ V}$$

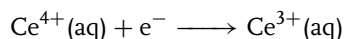
Solubility equilibrium:



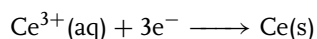
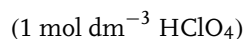
$$K_{\text{sp}} = 2 \times 10^{-22}$$

Cerium ($^{140.116}_{58}\text{Ce}$), OS: +4, +3, 0; IE: 534, 1047, 1940 kJ mol⁻¹. $\Delta H_{\text{hydr}}(\text{Ce}^{3+}) = -3370 \text{ kJ mol}^{-1}$.

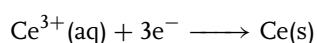
Acidic solutions



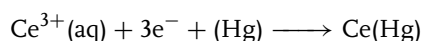
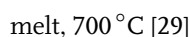
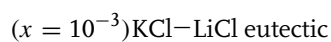
$$E^{\ominus} = 1.72 \text{ V}$$



$$E^{\ominus} = -2.34 \text{ V}$$

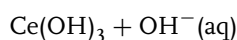
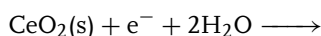


$$E_c^{\circ} = -3.065 \text{ V versus Ag|AgCl}$$

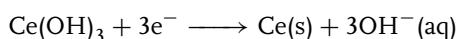


$$E_{1/2} = -1.73 \text{ V}$$

Basic solutions

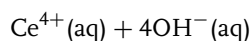
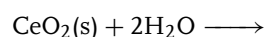


$$E^{\ominus} = -0.7 \text{ V}$$

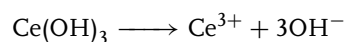


$$E^{\ominus} = -2.78 \text{ V}$$

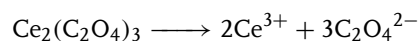
Solubility equilibria:



$$K_{\text{sp}} = 1 \times 10^{-63}$$

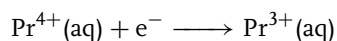


$$K_{\text{sp}} = 7.9 \times 10^{-23}$$

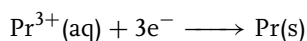


$$K_{\text{sp}} = 2.5 \times 10^{-29}$$

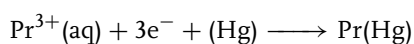
Praseodymium ($^{140.907}_{59}\text{Pr}$), OS: +4, +3, 0; IE: 522, 1018, 2090 kJ mol⁻¹.
 $\Delta H_{\text{hydr}}(\text{Pr}^{3+}) = -3413 \text{ kJ mol}^{-1}$.



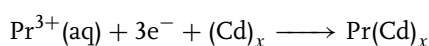
$$E^{\ominus} = 3.2 \text{ V (calcd)}$$



$$E^{\ominus} = -2.35 \text{ V}$$



$$E_{1/2} = -1.71 \text{ V}$$

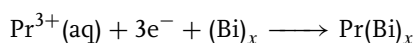


$$E_c^{\circ} = 0.561 \text{ V versus}$$

Pr (III)/Pr coexisting two

phases: Pr Cd₁₁ and Cd, LiCl-KCl

melt 673 °C [30]

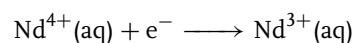


$$E_c^{\circ} = 0.741 \text{ V versus}$$

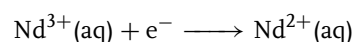
Pr (III)/Pr coexisting two phases:

PrBi and PrBi₂, 673 °C [30]

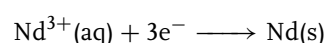
Neodymium ($^{144.24}_{60}\text{Nd}$), OS: +4, +3, +2, 0; IE: 530, 1034, 2128 kJ mol⁻¹.
 $\Delta H_{\text{hydr}}(\text{Nd}^{3+}) = -3442 \text{ kJ mol}^{-1}$.



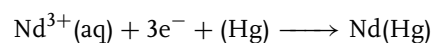
$$E^{\ominus} = 4.9 \text{ V (calcd)}$$



$$E^{\ominus} = -2.6 \text{ V (calcd)}$$

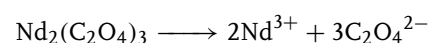


$$E^{\ominus} = -2.32 \text{ V}$$



$$E_{1/2} = -1.68 \text{ V}$$

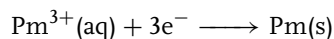
Solubility equilibrium:



$$K_{\text{sp}} = 5.9 \times 10^{-29}$$

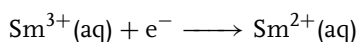
Promethium ($^{144.912}_{61}\text{Pm}$), OS: +3, 0; IE: 536, 1052, 2140 kJ mol⁻¹.

$$\Delta H_{\text{hydr}}(\text{Pm}^{3+}) = -3478 \text{ kJ mol}^{-1}.$$



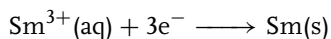
$$E^{\ominus} = -2.29 \text{ V}$$

Samarium ($^{150.36}_{62}\text{Sm}$), OS: +3, +2, 0; IE: 542, 1068, 2285 kJ mol⁻¹. $\Delta H_{\text{hydr}}(\text{Sm}^{3+}) = -3515 \text{ kJ mol}^{-1}$.

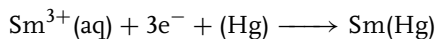


$$E^{\ominus} = -1.55 \text{ V}$$

$$(E_{1/2} = -1.44 \text{ V})$$

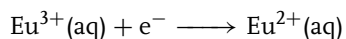


$$E^{\ominus} = -2.30 \text{ V}$$



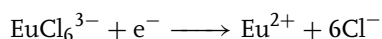
$$E_{1/2} = -1.73 \text{ V}$$

Europium ($^{151.964}_{63}\text{Eu}$), OS: +3, +2, 0; IE: 547, 1085, 2425 kJ mol⁻¹. $\Delta H_{\text{hydr}}(\text{Eu}^{3+}) = -3547 \text{ kJ mol}^{-1}$.



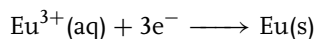
$$E^{\ominus} = -0.35 \text{ V}$$

$$(E_{1/2} = -0.39 \text{ V})$$

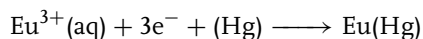


$$E^{\ominus'} = -0.971 \text{ V versus Ag|AgCl}$$

$$(x = 9.4 \times 10^{-3})\text{NaCl-KCl melt [31]}$$

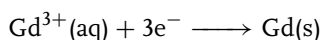


$$E^{\ominus} = -2.99 \text{ V}$$

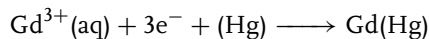


$$E_{1/2} = -2.23 \text{ V}$$

Gadolinium ($^{157.25}_{64}\text{Gd}$), OS: +3, 0; IE: 595, 1172, 1999 kJ mol⁻¹. $\Delta H_{\text{hydr}}(\text{Gd}^{3+}) = -3571 \text{ kJ mol}^{-1}$.

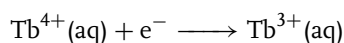


$$E^{\ominus} = -2.28 \text{ V}$$

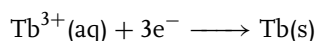


$$E_{1/2} = -1.68 \text{ V}$$

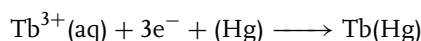
Terbium ($^{158.925}_{65}\text{Tb}$), OS: +4, +3, 0; IE: 569, 1112, 2122 kJ mol⁻¹. $\Delta H_{\text{hydr}}(\text{Tb}^{3+}) = -3605 \text{ kJ mol}^{-1}$.



$$E^{\ominus} = 3.1 \text{ V (calcd)}$$

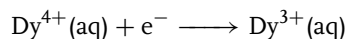


$$E^{\ominus} = -2.31 \text{ V}$$

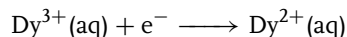


$$E_{1/2} = -1.65 \text{ V}$$

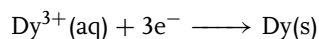
Dysprosium ($^{162.500}_{66}\text{Dy}$), OS: +4, +3, +2, 0; IE: 567, 1126, 2230 kJ mol⁻¹. $\Delta H_{\text{hydr}}(\text{Dy}^{3+}) = -3637 \text{ kJ mol}^{-1}$.



$$E^{\ominus} = 5.4 \text{ V (calcd)}$$

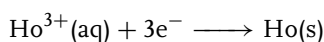


$$E^{\ominus} = -2.5 \text{ V}$$

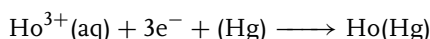


$$E^{\ominus} = -2.29 \text{ V}$$

Holmium ($^{164.930}_{67}\text{Ho}$), OS: +3, 0; IE: 574, 1139, 2221 kJ mol⁻¹. $\Delta H_{\text{hydr}}(\text{Ho}^{3+}) = -3667 \text{ kJ mol}^{-1}$.

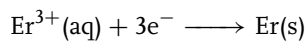


$$E^{\ominus} = -2.33 \text{ V}$$

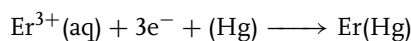


$$E_{1/2} = -1.61 \text{ V}$$

Erbium ($^{167.259}_{68}\text{Er}$), OS: +3, 0; IE: 581, 1151, 2207 kJ mol⁻¹. $\Delta H_{\text{hydr}}(\text{Er}^{3+}) = -3691 \text{ kJ mol}^{-1}$.

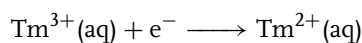


$$E^{\ominus} = -2.32 \text{ V}$$

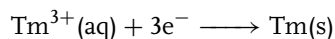


$$E_{1/2} = -1.60 \text{ V}$$

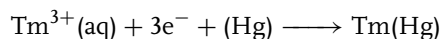
Thulium ($^{168.934}_{69}\text{Tm}$), OS: +3, +2, 0; IE: 589, 1163, 2305 kJ mol⁻¹. $\Delta H_{\text{hydr}}(\text{Tm}^{3+}) = -3717 \text{ kJ mol}^{-1}$.



$$E^{\ominus} = -2.3 \text{ V}$$

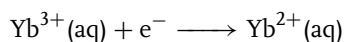


$$E^{\ominus} = -2.32 \text{ V}$$



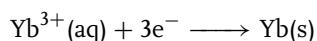
$$E_{1/2} = -1.57 \text{ V}$$

Ytterbium ($^{173.04}_{70}\text{Yb}$), OS: +3, +2, 0; IE: 603, 1175, 2408 kJ mol⁻¹. $\Delta H_{\text{hydr}}(\text{Yb}^{3+}) = -3739 \text{ kJ mol}^{-1}$.

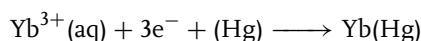


$$E^{\ominus} = -1.05 \text{ V}$$

$$(E_{1/2} = -1.13 \text{ V})$$

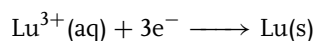


$$E^{\ominus} = -2.22 \text{ V}$$

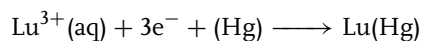


$$E_{1/2} = -1.73 \text{ V}$$

Lutetium ($^{174.967}_{71}\text{Lu}$), OS: +3, 0; IE: 513, 1341, 2054 kJ mol⁻¹. $\Delta H_{\text{hydr}}(\text{Lu}^{3+}) = -3760 \text{ kJ mol}^{-1}$.



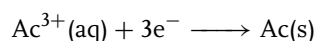
$$E^{\ominus} = -2.30 \text{ V}$$



$$E_{1/2} = -1.54 \text{ V}$$

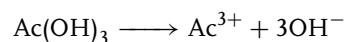
Actinium ($^{227.027}_{89}\text{Ac}$), OS: +3, 0; IE: 4284 (I + II + III) kJ mol⁻¹ [32].

The IE of all the actinides are estimated values based on the dependence of E^{\ominus} on IE [32].



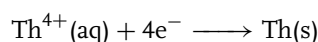
$$E^{\ominus} = -2.15 \text{ V}$$

Solubility equilibrium:

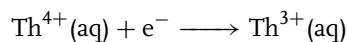


$$K_{\text{sp}} = 1.26 \times 10^{-21}$$

Thorium ($^{232.0381}_{90}\text{Th}$), OS: +4, (+3), 0; IE: 3628 (I + II + III) kJ mol⁻¹.

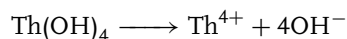


$$E^{\ominus} = -2.56 \text{ V}$$



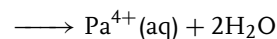
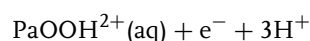
$$E^{\ominus} = -3.8 \text{ V}$$

Solubility equilibrium:

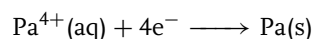


$$K_{\text{sp}} = 2.5 \times 10^{-49}$$

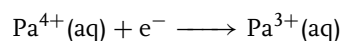
Protactinium ($^{231.0358}_{91}\text{Pa}$), OS: +5, +4, +3, 0; IE: 568 kJ mol⁻¹



$$E^{\ominus} = -0.1 \text{ V}$$

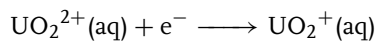


$$E^{\ominus} = -1.46 \text{ V}$$

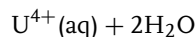
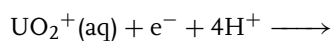


$$E^{\ominus} = -1.4 \text{ V}$$

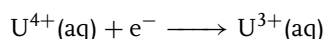
Uranium ($^{238.0289}_{92}\text{U}$), OS: +6, +5, +4, +3, 0; IE: 5023 (I + II + III) kJ mol⁻¹.



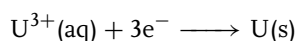
$$E^\ominus = 0.16 \text{ V}$$



$$E^\ominus = 0.38 \text{ V}$$



$$E^\ominus = -0.52 \text{ V}$$

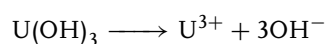


$$E^\ominus = -1.66 \text{ V}$$

$$E_c^{\circ'} = -1.283 \text{ V versus Ag|AgCl}$$

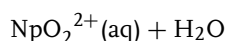
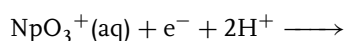
(1 wt % – AgCl) (LiCl–KCl
eutectic salt, 450 °C) [33]

Solubility equilibrium:

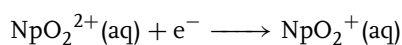


$$K_{\text{sp}} = 6.31 \times 10^{-23}$$

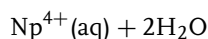
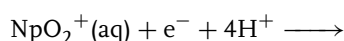
Neptunium ($^{237.0482}_{93}\text{Np}$), OS: +7, +6, +5, +4, +3, 0; IE: 4853 (I + II + III) kJ mol⁻¹.



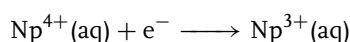
$$E^\ominus = 2.04 \text{ V}$$



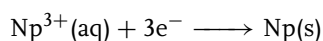
$$E^\ominus = 1.24 \text{ V}$$



$$E^\ominus = 0.66 \text{ V}$$



$$E^\ominus = 0.18 \text{ V}$$

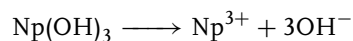


$$E^\ominus = -1.79 \text{ V}$$

$$E_c^{\circ'} = -1.484 \text{ V versus Ag|AgCl}$$

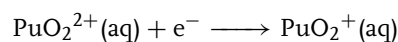
(LiCl–KCl eutectic salt, 450 °C) [33]

Solubility equilibrium:

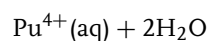
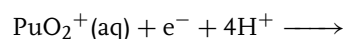


$$K_{\text{sp}} = 3.99 \times 10^{-23}$$

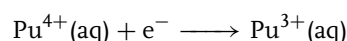
Plutonium ($^{244.0642}_{94}\text{Pu}$), OS: +7, +6, +5, +4, +3, 0; IE: 4531 (I + II + III) kJ mol⁻¹.



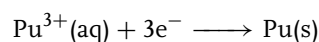
$$E^\ominus = 1.02 \text{ V}$$



$$E^\ominus = 1.04 \text{ V}$$



$$E^\ominus = 1.01 \text{ V}$$

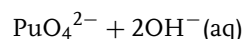
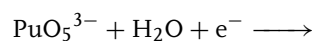


$$E^\ominus = -2.0 \text{ V}$$

$$E_c^{\circ'} = -1.593 \text{ V versus Ag|AgCl}$$

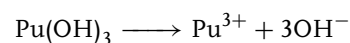
(LiCl–KCl eutectic salt, 450 °C) [33]

$$\text{or } E_c^{\circ'} = -1.571 \text{ V [34]}$$



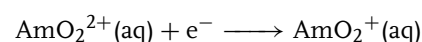
$$E_c^{\circ'} = 0.95 \text{ V (1 mol dm}^{-3} \text{ NaOH)}$$

Solubility equilibrium:

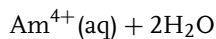
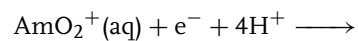


$$K_{\text{sp}} = 2.5 \times 10^{-23}$$

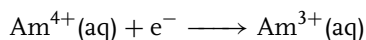
Americium ($^{243.061}_{95}\text{Am}$), OS: +6, +5, +4, +3, +2, 0; IE: 4405 (I + II + III) kJ mol⁻¹.



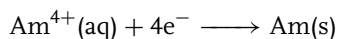
$$E^\ominus = 1.6 \text{ V}$$



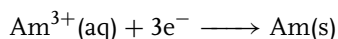
$$E^\ominus = 0.82 \text{ V}$$



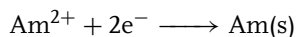
$$E^\ominus = 2.62 \text{ V (calcd)}$$



$$E^\ominus = -0.9 \text{ V}$$



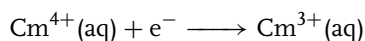
$$E^\ominus = -2.07 \text{ V}$$



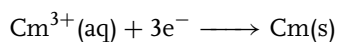
$$E_c^\ominus = -1.642 \text{ V versus Ag|AgCl}$$

(LiCl–KCl eutectic salt, 450 °C) [33]

Curium ($^{[247.07]}_{96}\text{Cm}$), OS: (+4), +3, 0; IE: 4424 (I + II + III) kJ mol⁻¹.

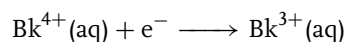


$$E^\ominus = 3.1 \text{ V (calcd)}$$



$$E^\ominus = -2.06 \text{ V (calcd)}$$

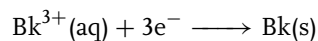
Berkelium ($^{[247.07]}_{97}\text{Bk}$), OS: (+4), +3, 0; IE: 4513 (I + II + III) kJ mol⁻¹.



$$E^\ominus = 1.67 \text{ V}$$

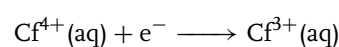
$$E_c^\ominus = 1.54 \text{ V (1 M HClO}_4\text{),}$$

$$1.37 \text{ V (1 M H}_2\text{SO}_4\text{)}$$

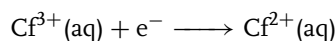


$$E^\ominus = -2.0 \text{ V (calcd)}$$

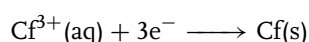
Californium ($^{[251.079]}_{98}\text{Cf}$), OS: (+4), +3, +2, 0; IE: 4646 (I + II + III) kJ mol⁻¹.



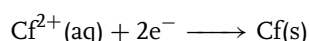
$$E^\ominus = 3.2 \text{ V (calcd)}$$



$$E^\ominus = -1.6 \text{ V}$$

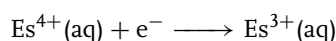


$$E^\ominus = -1.91 \text{ V}$$

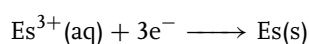


$$E^\ominus = -2.1 \text{ V}$$

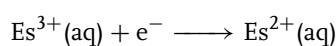
Einsteinium ($^{[252.083]}_{99}\text{Es}$), OS: (+4), +3, +2, 0; IE: 4531 (I + II + III) kJ mol⁻¹.



$$E^\ominus = 4.5 \text{ V (calcd)}$$

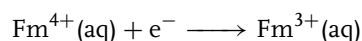


$$E^\ominus = -1.98 \text{ V}$$

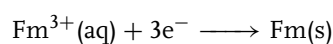


$$E^\ominus = -1.5 \text{ V}$$

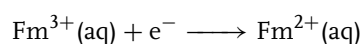
Fermium ($^{[257.095]}_{100}\text{Fm}$), OS: (+4), +3, 0; IE: 4598 (I + II + III) kJ mol⁻¹.



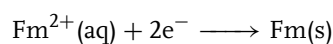
$$E^\ominus = 5.2 \text{ V (calcd)}$$



$$E^\ominus = -2.07 \text{ V}$$

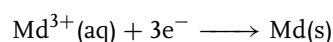


$$E^\ominus = -1.15 \text{ V}$$

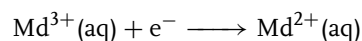


$$E^\ominus = -2.37 \text{ V}$$

Mendelevium ($^{[258.098]}_{101}\text{Md}$), OS: +3, +2, 0; IE: 4973 (I + II + III) kJ mol⁻¹.

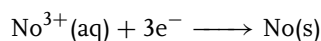


$$E^\ominus = -1.74 \text{ V}$$

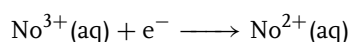


$$E^{\ominus} = -0.15 \text{ V}$$

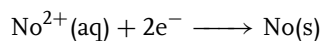
Nobelium ($^{258.098}_{102}\text{No}$), OS: +3, +2, 0; IE: 5526 (I + II + III) kJ mol⁻¹.



$$E^{\ominus} = -1.26 \text{ V}$$

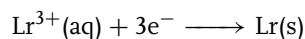


$$E^{\ominus} = 1.4 \text{ V}$$



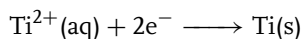
$$E^{\ominus} = -2.5 \text{ V}$$

Lawrencium ($^{262.109}_{103}\text{Lr}$), OS: +3, 0; IE: 4479 (I + II + III) kJ mol⁻¹.

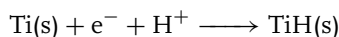


$$E^{\ominus} = -2.1 \text{ V (calcd)}$$

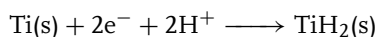
$$E^{\ominus} = -1.209 \text{ V (calcd)}$$



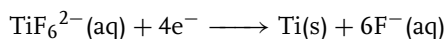
$$E^{\ominus} = -1.628 \text{ V (calcd)}$$



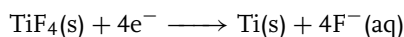
$$E^{\ominus} = -0.65 \text{ V (calcd)}$$



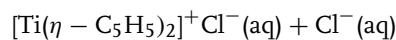
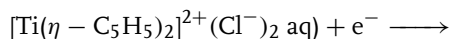
$$E^{\ominus} = -0.45 \text{ V (calcd)}$$



$$E^{\ominus} = -1.19 \text{ V (calcd)}$$



$$E^{\ominus} = -0.89 \text{ V (calcd)}$$



$$E_c^{\circ'} = -0.44 \text{ V } E_c^{\circ'} = -0.63 \text{ V}$$

versus Ag⁺/Ag (DMF,

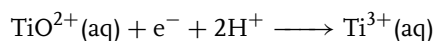
0.1 M TEAP)

2.4

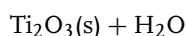
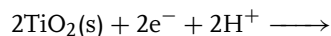
Group 4 Elements

Titanium ($^{47.867}_{22}\text{Ti}$), OS: +4, +3, +2, (+1), 0; IE: 658 kJ mol⁻¹.

Acidic solutions

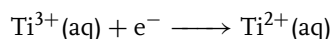


$$E^{\ominus} = 0.1 \text{ V (calcd)}$$



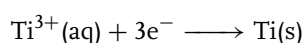
(both oxides are unhydrated)

$$E^{\ominus} = -0.556 \text{ V (calcd)}$$

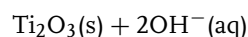
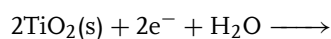


$$E^{\ominus} = -2.3 \text{ V (calcd) or}$$

$$E^{\ominus} = -0.37 \text{ V (calcd)}$$



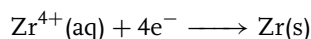
Basic solution



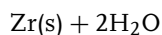
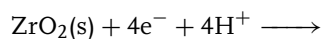
$$E^{\ominus} = -1.38 \text{ V (calcd)}$$

Standard potentials are calculated values. The electrochemical measurements have supplied contradictory values. This is mainly due to the formation of oxides and hydride films on the Ti surface, which causes it to behave as a noble metal. Titanium dissolves rapidly only in HF.

Zirconium ($^{91.224}_{40}\text{Zr}$), OS: +4, +3, +2, +1, 0; IE: 661 kJ mol⁻¹.

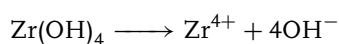


$$E^{\ominus} = -1.55 \text{ V (calcd)}$$



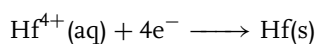
$$E^\ominus = -1.45 \text{ V (calcd)}$$

Solubility equilibrium:

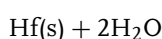
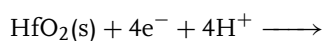


$$K_{\text{sp}} \sim 1 \times 10^{-56}$$

Hafnium ($^{178.49}_{72}\text{Hf}$), OS: +4, +3, +2, +1, 0; IE: 681 kJ mol⁻¹.



$$E^\ominus = -1.7 \text{ V (calcd)}$$



$$E^\ominus = -1.57 \text{ V (calcd)}$$

The experimental determination of E^\ominus values is hindered by the formation of surface oxides and polymeric species with oxo and hydroxo bridges in the solution. Hydrolysis practically always takes place even in strongly acidic media.

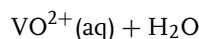
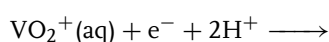
Rutherfordium ($^{261.108}_{104}\text{Rf}$)

No data are available.

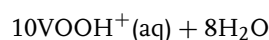
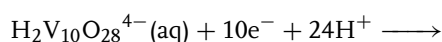
2.5

Group 5 Elements

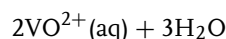
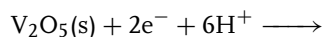
Vanadium ($^{50.941}_{23}\text{V}$), OS: +5, +4, +3, +2, 0; IE: 650 kJ mol⁻¹.



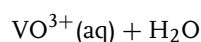
$$E^\ominus = 1.0 \text{ V}$$



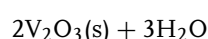
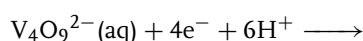
$$E^\ominus = 0.723 \text{ V}$$



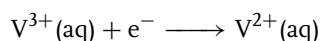
$$E^\ominus = 0.958 \text{ V}$$



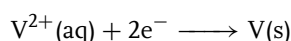
$$E^\ominus = 0.337 \text{ V}$$



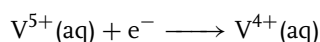
$$E^\ominus = 0.536 \text{ V}$$



$$E^\ominus = -0.255 \text{ V}$$



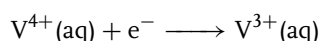
$$E^\ominus = -1.13 \text{ V}$$



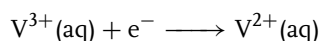
$$E_c^{\circ'} = 1.02 \text{ V (1 M HCl)}$$

$$E_c^{\circ'} = 1.02 \text{ V (1 M HClO}_4\text{)}$$

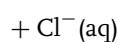
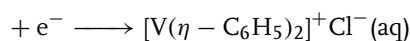
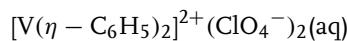
$$E_c^{\circ'} = 1.0 \text{ V (1 M H}_2\text{SO}_4\text{)}$$



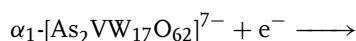
$$E_c^{\circ'} = 0.36 \text{ V (1 M H}_2\text{SO}_4\text{)}$$



$$E_c^{\circ'} = -0.267 \text{ V (1 M HCl)}$$



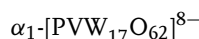
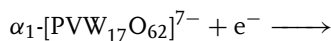
$$E_c^{\circ'} = -0.32 \text{ V (0.1 M HClO}_4\text{)}$$



$$E_c^{\circ'} = 0.575 \text{ V versus}$$

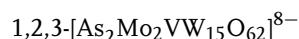
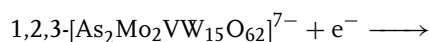
SCE (saturated calomel electrode)

SCE (pH 7) [35]



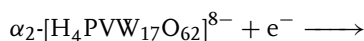
$$E_c^{o'} = 0.506 \text{ V versus}$$

SCE (pH 7) [35]



$$E_c^{o'} = 0.489 \text{ V versus}$$

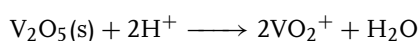
SCE (pH 7) [35]



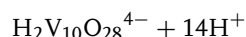
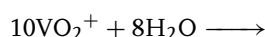
$$E_c^{o'} = -0.291 \text{ V versus}$$

SCE (pH 7) [35]

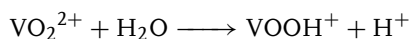
$E_c^{o'}$ values of several other Dawson-type V-substituted polyoxometalates can be found in Ref. 35 and the citations therein. Selected equilibria:



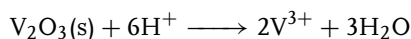
$$K = 3.42 \times 10^{-2}$$



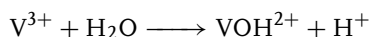
$$K = 1.8 \times 10^{-7}$$



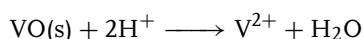
$$K = 4.4 \times 10^{-6}$$



$$K = 1.56 \times 10^{13}$$



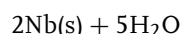
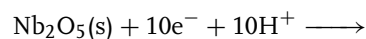
$$K = 1.17 \times 10^{-3}$$



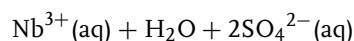
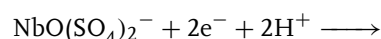
$$K = 3 \times 10^{10}$$

Uncertainties concerning the nature of the hydrolyzed and associated species call forth uncertainties in E^\oplus values.

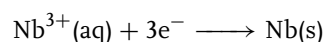
Niobium ($^{92.906}_{41}\text{Nb}$), OS: (+7), +5, +4, +3, +2, (+1), 0, (−1); IE: 664 kJ mol^{−1}.



$$E^\oplus = -0.65 \text{ V (calcd)}$$



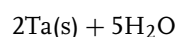
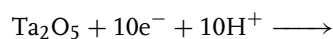
$$E^\oplus \sim -0.1 \text{ V}$$



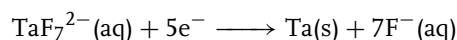
$$E^\oplus = -1.1 \text{ V (calcd)}$$

Niobium is always covered with an oxide layer. In aqueous solutions only some niobium compounds are soluble, mostly in the form niobate anions, for example, $[\text{H}_x\text{Nb}_6\text{O}_{19}]^{(8-x)-}$.

Tantalum ($^{180.948}_{73}\text{Ta}$), OS: +5, +4, +3, 0; IE: 761 kJ mol^{−1}.



$$E_c^{o'} = -0.81 \text{ V (pH 1)}$$



$$E_c^{o'} = -0.45 \text{ V}$$

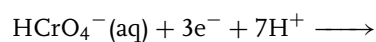
Dubnium ($^{262.114}_{105}\text{Db}$)

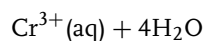
No data are available.

2.6

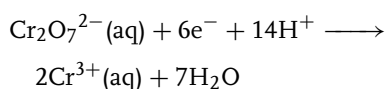
Group 6 Elements

Chromium ($^{51.996}_{24}\text{Cr}$), OS: +6, +3, +2, 0; IE: 652 kJ mol^{−1}.

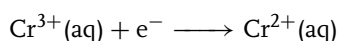




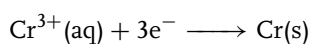
$$E^\ominus = 1.38 \text{ V (calcd)}$$



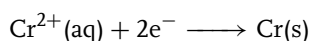
$$E^\ominus = 1.36 \text{ V}$$



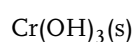
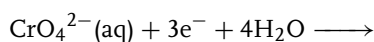
$$E^\ominus = -0.424 \text{ V}$$



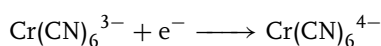
$$E^\ominus = -0.74 \text{ V}$$



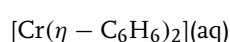
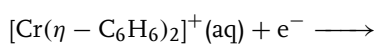
$$E^\ominus = -0.9 \text{ V}$$



$$E^\ominus = -0.11 \text{ V}$$



$$E_c^{\circ'} = -1.143 \text{ V (1 M KCN)}$$



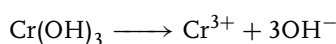
$$E_c^{\circ'} = -0.97 \text{ V (pH 2-12)}$$

$$E_c^{\circ'} = -0.93 \text{ V}$$

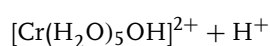
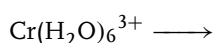
$$(0.1 \text{ M TEAP, CH}_3\text{CN})$$

Data for chromium amino carboxylate complexes can be found in Ref. 36.

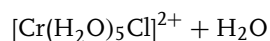
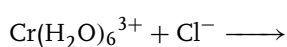
Solubility and complex equilibria:



$$K_{\text{sp}} = 1 \times 10^{-30}$$



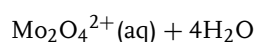
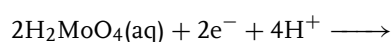
$$K = 1.6 \times 10^{-4}$$



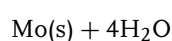
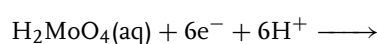
$$K = 0.1$$

Molybdenum ($^{95,94}_{42}\text{Mo}$), OS: +6, +5, +4, +3, +2, 0; IE: 685 kJ mol⁻¹.

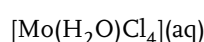
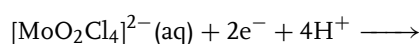
Acidic solutions



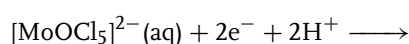
$$E^\ominus = 0.50 \text{ V (calcd)}$$



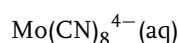
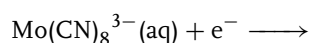
$$E^\ominus = 0.114 \text{ V (calcd)}$$



$$E_c^{\circ'} = 0.15 \text{ V (1 M HCl)}$$

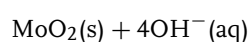
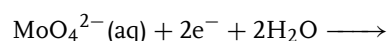


$$E_c^{\circ'} = -0.38 \text{ V (1 M HCl)}$$

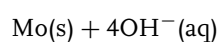
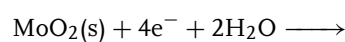


$$E_c^{\circ'} = 0.725 \text{ V (pH 7)}$$

Basic solutions



$$E^\ominus = -0.78 \text{ V (calcd)}$$



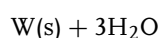
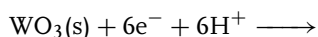
$$E^\ominus = -0.98 \text{ V (calcd)}$$

In solution Mo(VI) exists in the form of colorless MoO_4^{2-} anion at pH > 6. Acid hydrolysis results in the formation of polyanions, for example, $[\text{Mo}_8\text{O}_{26}]^{4-}$ (pH

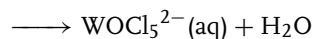
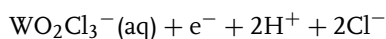
> 1) or $[\text{Mo}_{36}\text{O}_{112}]^{8-}$, $[\text{H}_2\text{Mo}_2\text{O}_6]^{2+}$ (pH > 1). In the presence of other oxanions heteropolyanions are formed, for example, $[\text{SiMo}_{12}\text{O}_{40}]^{4-}$, $\text{H}_3[\text{PMo}_{12}\text{O}_{40}]$.

Tungsten ($^{183.84}_{74}\text{W}$), OS: +6, +5, +4, +3, +2, +1, 0; IE: 770 kJ mol⁻¹.

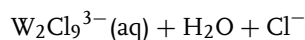
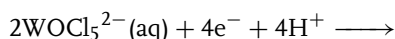
Acidic solutions



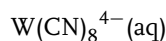
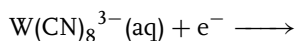
$$E^\ominus = -0.09 \text{ V}$$



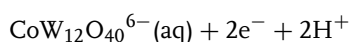
$$E_c^\ominus = 0.36 \text{ V (12 M HCl)}$$



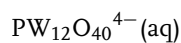
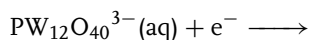
$$E_c^\ominus = -0.05 \text{ V (12 M HCl)}$$



$$E_c^\ominus = 0.457 \text{ V}$$

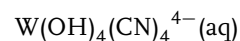
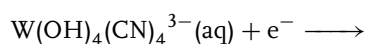


$$E_c^\ominus = -0.046 \text{ V (1 M H}_2\text{SO}_4)$$

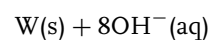
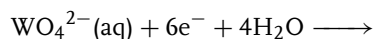


$$E_c^\ominus = -0.218 \text{ V (1 M H}_2\text{SO}_4)$$

Basic solutions



$$E_c^\ominus = -0.74 \text{ V (pH 13.7)}$$



$$E^\ominus = -1.074 \text{ V (calcd)}$$

Seaborgium ($^{266.122}_{106}\text{Sg}$)

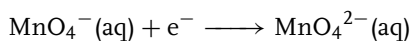
No data are available.

2.7

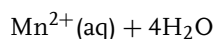
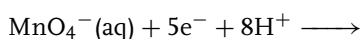
Group 7 Elements

Manganese ($^{54.938}_{25}\text{Mn}$), OS: +7, +6, +5, +4, +3, +2, +1, 0, -1; IE: 717 kJ mol⁻¹.

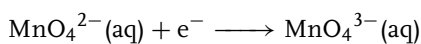
Acidic solutions



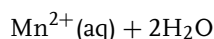
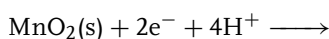
$$E^\ominus = 0.56 \text{ V}$$



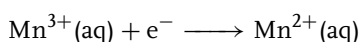
$$E^\ominus = 1.51 \text{ V (calcd)}$$



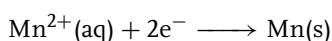
$$E^\ominus \sim 0.27 \text{ V}$$



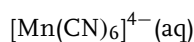
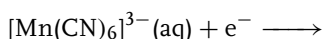
$$E^\ominus = 1.23 \text{ V (calcd)}$$



$$E^\ominus \sim 1.5 \text{ V (calcd)}$$

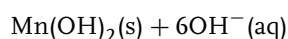
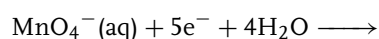


$$E^\ominus = -1.18 \text{ V (calcd)}$$

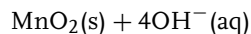
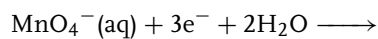


$$E^\ominus = -0.24 \text{ V}$$

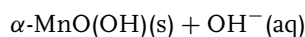
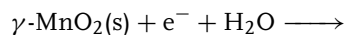
Basic solutions



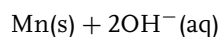
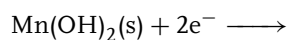
$$E^\ominus = 1.34 \text{ V (calcd)}$$



$$E^\ominus = 0.06 \text{ V (calcd)}$$



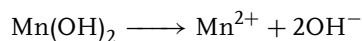
$$E^\ominus = 0.3 \text{ V (calcd)}$$



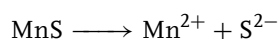
$$E^\ominus = -1.56 \text{ V (calcd)}$$

The determination of equilibrium (standard) potentials is rather problematic for several reasons; for instance, hydrolysis and disproportionation reactions, the existence of a large number of structural forms (e.g. α -, β -, γ -, δ - MnO_2), strong dependence on pH and ionic exchange processes, and the instability of the species in contact with water (e.g. Mn-metal–hydrogen evolution, MnO_4^- oxygen evolution; however, these processes are rather slow).

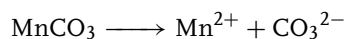
Solubility equilibria:



$$K_{\text{sp}} = 4 \times 10^{-14}$$



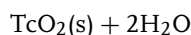
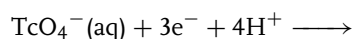
$$K_{\text{sp}} = 5.6 \times 10^{-16}$$



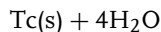
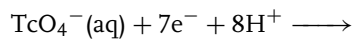
$$K_{\text{sp}} = 5.1 \times 10^{-10}$$

Technetium ($^{97.907}_{43}\text{Tc}$), OS: +7, +6, +5, +4, +2, +1, 0, (−1); IE: 702 kJ mol^{−1}.

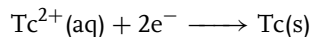
Acidic solutions



$$E^\ominus = 0.738 \text{ V}$$

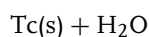
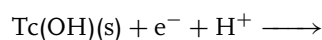


$$E^\ominus = 0.472 \text{ V (calcd)}$$

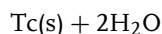
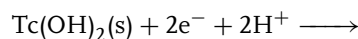


$$E^\ominus = 0.40 \text{ V (calcd)}$$

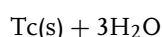
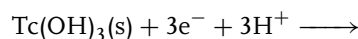
Basic solutions



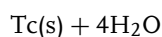
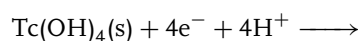
$$E^\ominus = 0.031 \text{ V}$$



$$E^\ominus = 0.072 \text{ V}$$



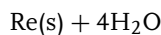
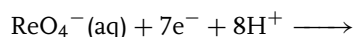
$$E^\ominus = 0.185 \text{ V}$$



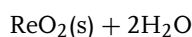
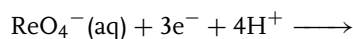
$$E^\ominus = 0.294 \text{ V}$$

Rhenium ($^{186.207}_{75}\text{Re}$), OS: +7, +6, +5, +4, +3, +2, +1, 0, −1; IE: 760 kJ mol^{−1}.

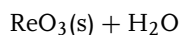
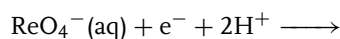
Acidic solutions



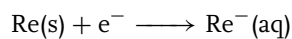
$$E^\ominus = 0.34 \text{ V}$$



$$E^\ominus = 0.51 \text{ V}$$

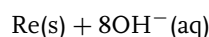
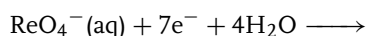


$$E^\ominus = 0.768 \text{ V}$$

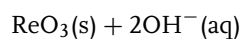
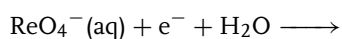


$$E^\ominus = -0.1 \text{ V (calcd)}$$

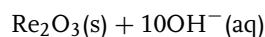
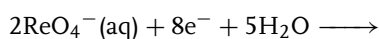
Basic solutions



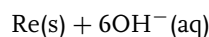
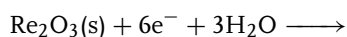
$$E^\ominus = -0.604 \text{ V}$$



$$E^\ominus = -0.89 \text{ V}$$



$$E^\ominus = -0.808 \text{ V (calcd)}$$



$$E^\ominus = -0.333 \text{ V (calcd)}$$

Bohrium ($^{264}_{107}\text{Bh}$)

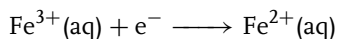
No data are available.

2.8

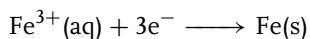
Group 8 Elements

Iron ($^{55.845}_{26}\text{Fe}$), OS: (+6), +3, +2, 0; IE: 759 kJ mol⁻¹.

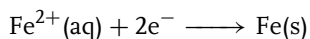
Acidic solutions



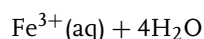
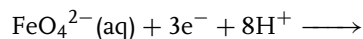
$$E^\ominus = 0.771 \text{ V}$$



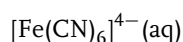
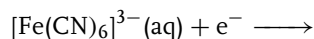
$$E^\ominus = -0.037 \text{ V (calcd)}$$



$$E^\ominus = -0.44 \pm 0.04 \text{ V}$$

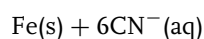
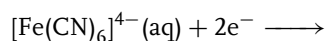


$$E^\ominus_c = 2.25 \text{ V [37]}$$

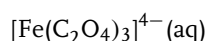
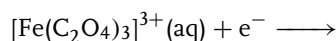


$$E^\ominus = 0.3610 (\pm 0.0005) \text{ V}$$

$$E^\ominus_c = 0.69 \text{ V (1 M H}_2\text{SO}_4)$$

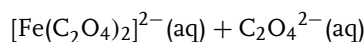
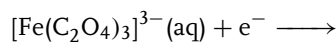


$$E^\ominus = -1.16 \text{ V}$$



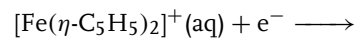
$$E^\ominus_c = 0.005 \text{ V}$$

$$(\text{Na}_2\text{C}_2\text{O}_4, c < 0.2\text{M})$$

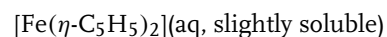


$$E^\ominus_c = 0.035 \text{ V}$$

$$(\text{Na}_2\text{C}_2\text{O}_4, c > 0.1\text{M})$$

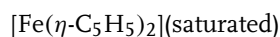
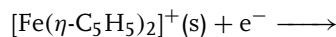


ferricenium



ferrocene

$$E^\ominus = (0.400 \pm 0.007) \text{ V}$$



$$E^\ominus_c = 0.637 \text{ V (1 M KCl,$$

$$0.01 \text{ M NH}_4\text{Cl})$$

$$E^\ominus_c = 0.618 \text{ V (1 M NaClO}_4,$$

$$0.01 \text{ M HClO}_4)$$

$$E^\ominus_c = 0.605 \text{ V (1.01 M HCl)}$$

$$E_c^{\circ'} = 0.539 \text{ V versus}$$

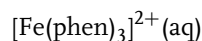
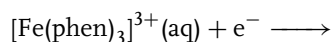
SHE (HCONH₂)

$$E_c^{\circ'} = 0.19 \text{ V versus SHE (CH}_3\text{CN)}$$

$$E_c^{\circ'} = 0.348 \text{ V versus}$$

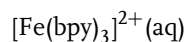
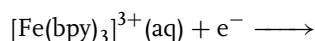
SHE(aq) (CH₃CN)

The formal potential of the substituted ferrocenes can be found in Ref. 38.



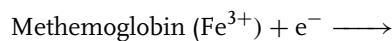
(phen = 1,10 phenanthroline)

$$E_c^{\circ'} = 1.13 \text{ V}$$



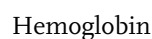
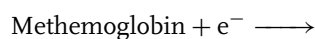
(bpy = 2, 2'-bipyridyl)

$$E_c^{\circ'} = 1.11 \text{ V}$$



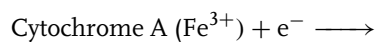
$$E_c^{\circ'} = 0.152 \text{ V (pH 7),}$$

$$0.282 \text{ V [39]}$$

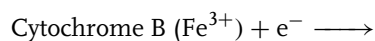


$$E_c^{\circ'} = 0.281 \text{ V (Lumbrians}$$

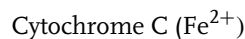
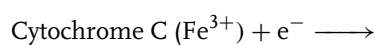
terrestis) [39]



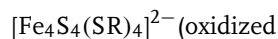
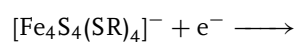
$$E_c^{\circ'} = 0.29 \text{ V (pH 7)}$$



$$E_c^{\circ'} = 0.04 \text{ V (pH 7)}$$



$$E_c^{\circ'} = 0.26 \text{ V (pH 7)}$$



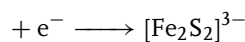
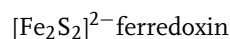
ferredoxin (Fe³⁺))(reduced

ferredoxin (Fe²⁺))

$$E_c^{\circ'} = -0.45 \text{ V [40] (depending}$$

on the source of the

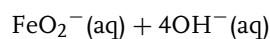
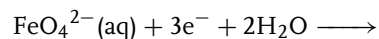
ferredoxins and the pH)



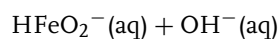
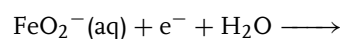
$$E_c^{\circ'} = -0.81 \text{ V [41]}$$

(Formal potentials of metal hexacyano-ferrates can be found in Ch. 11)

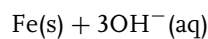
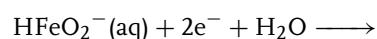
Basic solutions



$$E^{\oplus} \sim -0.55 \text{ V}$$



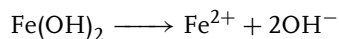
$$E^{\oplus} \sim -0.69 \text{ V}$$



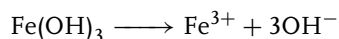
$$E^{\oplus} \sim -0.8 \text{ V}$$

The aqua complexes of Fe²⁺ and Fe³⁺, which are present in acid solutions, can hydrolyze to FeOH⁺, Fe(OH)²⁺, Fe(OH)₂⁺, and other ions at higher pH values, and the respective hydroxides precipitate. Weak anion complexes such as FeSO₄⁺, FeSO₄²⁺, or FeCl₂⁺ can also be formed.

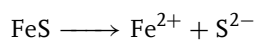
Solubility and complex equilibria:



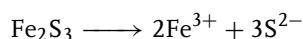
$$K_{\text{sp}} = 4.8 \times 10^{-16}$$



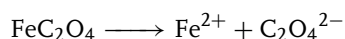
$$K_{\text{sp}} = 3.8 \times 10^{-38}$$



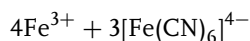
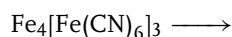
$$K_{\text{sp}} = 3.7 \times 10^{-19}$$



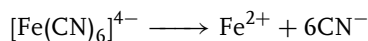
$$K_{\text{sp}} \sim 1 \times 10^{-88}$$



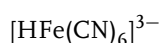
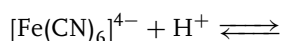
$$K_{\text{sp}} = 2.1 \times 10^{-7}$$



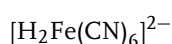
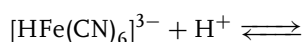
$$K_{\text{sp}} = 3 \times 10^{-41}$$



$$K = 1.3 \times 10^{-37}$$



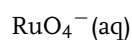
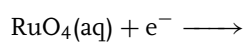
$$K = 1.2 \times 10^{-4}$$



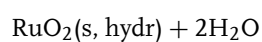
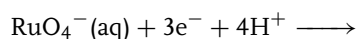
$$K = 2.2 \times 10^{-2}$$

Ruthenium ($^{101.07}_{44}\text{Ru}$), OS: +8, +7, +6, +4, +3, +2, 0; IE: 711 kJ mol⁻¹.

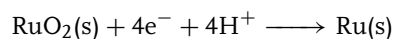
Acidic solutions



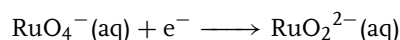
$$E^\ominus = 0.99 \text{ V (calcd)}$$



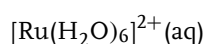
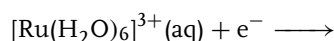
$$E^\ominus = 1.533 \text{ V (calcd)}$$



$$E^\ominus = 0.68 \text{ V (calcd)}$$

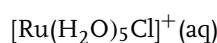
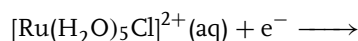


$$E^\ominus = 0.593 \text{ V (calcd)}$$

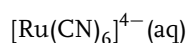
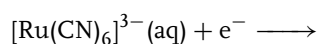


$$E_c^{\circ'} = 0.249 \text{ V}$$

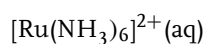
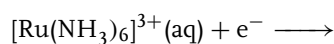
(*p*-toluenesulfonic acid)



$$E_c^{\circ'} = 0.086 \text{ V}$$

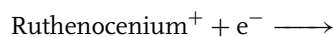


$$E_c^{\circ'} = (0.86 \pm 0.05) \text{ V (KCl)}$$



$$E_c^{\circ'} = (0.1 \pm 0.01) \text{ V (HClO}_4\text{)}$$

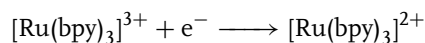
The formation of polymeric and mixed-valence complexes also occurs in aqueous solutions.



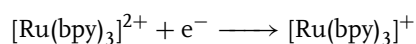
Ruthenocene

$$E_c^{\circ'} = 0.59 \text{ V versus Fc}^+/\text{Fc}$$

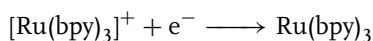
Formal potentials of ruthenium metallocenes can be found in Refs 42–44.



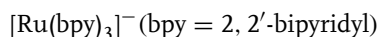
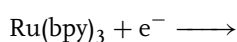
$$E_c^{\circ'} = 1.32 \text{ V}$$



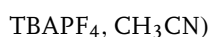
$$E_c^{\circ'} = -1.30 \text{ V}$$



$$E_c^{\circ'} = -1.49 \text{ V versus SCE}$$

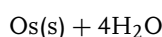
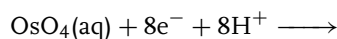


$$E_c^{\circ'} = -1.73 \text{ V (0.1 M}$$

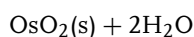
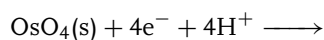


Formal potentials of dinuclear and hexanuclear Ru(II) bipyridine complexes (40 redox processes!) are given in Ref. 45.

Osmium ($^{190.23}_{76}\text{Os}$), OS: +8, +7, +6, +5, +4, +3, +2, +1, 0; IE: 840 kJ mol⁻¹.



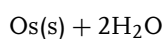
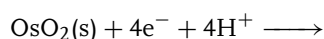
$$E^\Phi = 0.84 \text{ V (calcd)}$$



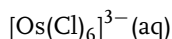
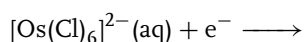
$$E^\Phi = 1.005 \text{ V (calcd)}$$

$$E_c^{\circ'} = 0.964 \text{ V}$$

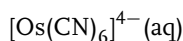
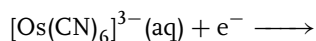
$$\text{pH} = 3.5 - 6.5$$



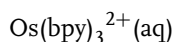
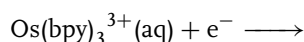
$$E^\Phi = 0.687 \text{ V (calcd)}$$



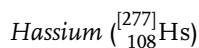
$$E^\Phi = 0.85 \text{ V (calcd)}$$



$$E^\Phi = 0.634 \text{ V}$$



$$E^\Phi = 0.885 \text{ V (calcd)}$$



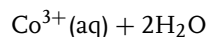
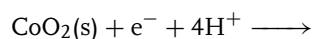
No data are available.

2.9

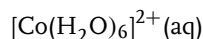
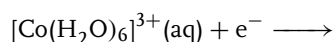
Group 9 Elements

Cobalt ($^{58.933}_{27}\text{Co}$), OS: (+4), +3, +2, (+1), 0; IE: 758 kJ mol⁻¹.

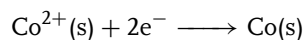
Acidic and nonaqueous solutions



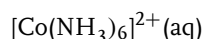
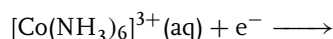
$$E^\Phi = 1.416 \text{ V}$$



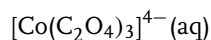
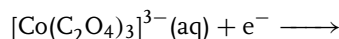
$$E_c^{\circ'} = 1.95 \text{ V (4 M HClO}_4\text{)}$$



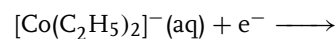
$$E^\Phi = -0.277 \text{ V (calcd)}$$



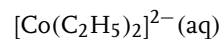
$$E_c^{\circ'} = 0.058 \text{ V (7 M NH}_3\text{,}$$



$$E_c^{\circ'} = 0.57 \text{ V (1 M KCl)}$$



(cobaltocenium)

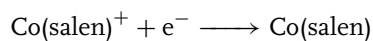


(cobaltocene)

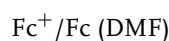
$$E_c^{\circ'} = -0.918 \text{ V}$$

$$E_c^{\circ'} = -1.146 \text{ V (CH}_3\text{CN)}$$

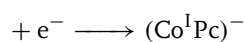
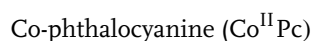
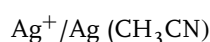
$$E_c^{\circ'} = -0.79 \text{ V (HCONH}_2\text{)}$$



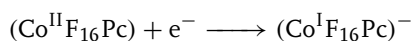
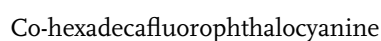
$$E_c^{o'} \sim -0.45 \text{ V versus}$$



$$E_c^{o'} \sim -0.37 \text{ V versus}$$



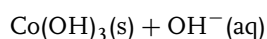
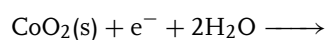
$$E_c^{o'} = -0.602 \text{ V (pH 13) [46]}$$



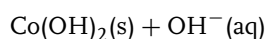
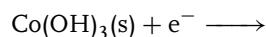
$$E_c^{o'} = -0.381 \text{ V [46]}$$

(Formal potential of other substituted Pc's can also be found in Ref. 46.)

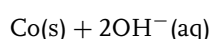
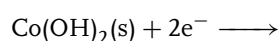
Basic solutions



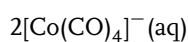
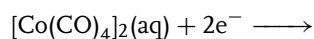
$$E^\ominus = 0.7 \text{ V}$$



$$E^\ominus = 0.17 \text{ V}$$

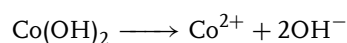


$$E^\ominus = -0.733 \text{ V}$$

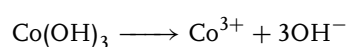


$$E^\ominus = -0.4 \text{ V}$$

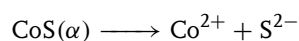
Solubility and complex equilibria:



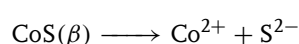
$$K_{\text{sp}} = 1.6 \times 10^{-18}$$



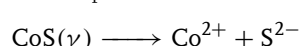
$$K_{\text{sp}} = 2.5 \times 10^{-43}$$



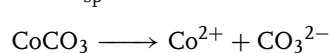
$$K_{\text{sp}} = 3.1 \times 10^{-23}$$



$$K_{\text{sp}} = 1.9 \times 10^{-27}$$

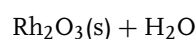
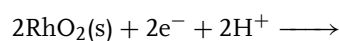


$$K_{\text{sp}} = 3 \times 10^{-26}$$

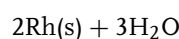
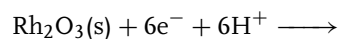


$$K_{\text{sp}} = 1 \times 10^{-17}$$

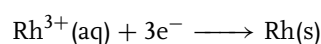
Rhodium ($^{102.905}_{45}\text{Rh}$), OS: (+6), (+5), (+4), +3, +2, (+1), 0, (−1); IE: 720 kJ mol^{−1}.



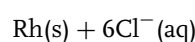
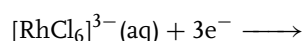
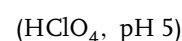
$$E^\ominus = 1.73 \text{ V (calcd)}$$



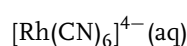
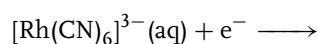
$$E^\ominus = 0.88 \text{ V (calcd)}$$



$$E^\ominus = 0.758 \text{ V (calcd)}$$

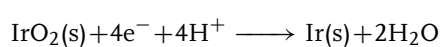


$$E^\ominus = 0.5 \text{ V (HCl)}$$

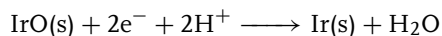


$$E^\ominus = 0.9 \text{ V}$$

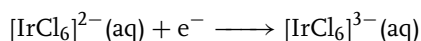
Iridium ($^{192.217}_{77}\text{Ir}$), OS: (+6), (+5), +4, +3, (+2), +1, 0; IE: 880 kJ mol^{−1}.



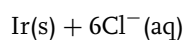
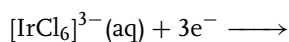
$$E_c^{\circ'} = (0.935 \pm 0.005) \text{ V}$$



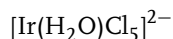
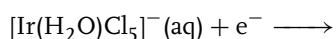
$$E_c^{\circ'} = (0.87 \pm 0.02) \text{ V (1 M H}_2\text{SO}_4\text{)}$$



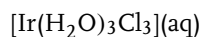
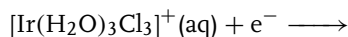
$$E_c^{\circ'} = 0.867 \text{ V (0.3 M HCl)}$$



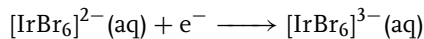
$$E^\oplus = 0.83 \text{ V (calcd)}$$



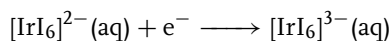
$$E_c^{\circ'} = 1.0 \text{ V (0.2 M HNO}_3\text{)}$$



$$E_c^{\circ'} = 1.30 \text{ V (0.4 M HClO}_4\text{)}$$



$$E_c^{\circ'} = 0.883 \text{ V (1 M HClO}_4\text{)}$$



$$E_c^{\circ'} = 0.49 \text{ V (1 M KI)}$$

Formal potentials of Ir–phosphine complexes in nonaqueous solutions can be found in Refs 47–49.

Meitnerium ($^{268.139}_{109}\text{Mt}$)

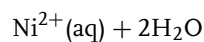
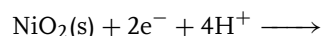
No data are available.

2.10

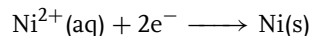
Group 10 Elements

Nickel ($^{58.6934}_{28}\text{Ni}$), OS: (+6), +4, +3, +2, 0; IE: 757 kJ mol⁻¹.

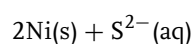
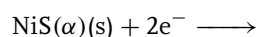
Acidic solutions



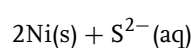
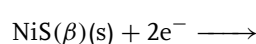
$$E^\oplus = 1.59 \text{ V (calcd)}$$



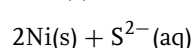
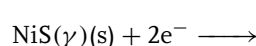
$$E^\oplus = -0.257 \text{ V}$$



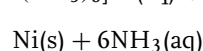
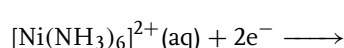
$$E^\oplus = -0.814 \text{ V}$$



$$E^\oplus = -0.96 \text{ V}$$

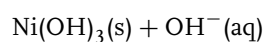
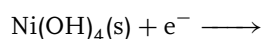


$$E^\oplus = -1.07 \text{ V}$$

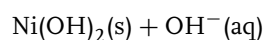
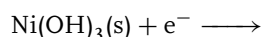


$$E^\oplus = -0.476 \text{ V}$$

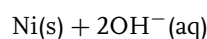
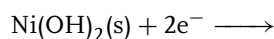
Basic solutions



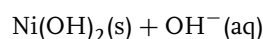
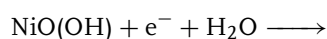
$$E^\oplus = 0.6 \text{ V (calcd)}$$



$$E^\oplus = 0.48 \text{ V (calcd)}$$

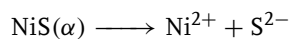


$$E^\oplus = -0.72 \text{ V}$$

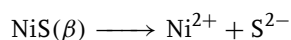


$$E_c^{\circ'} = 1.39 \text{ V (1 M NaOH)}$$

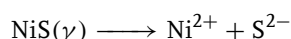
Solubility and other equilibria:



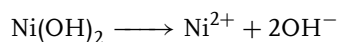
$$K_{\text{sp}} = 3 \times 10^{-21}$$



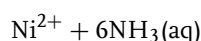
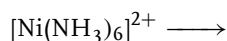
$$K_{\text{sp}} = 1 \times 10^{-26}$$



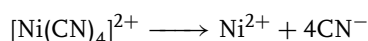
$$K_{\text{sp}} = 2 \times 10^{-28}$$



$$K_{\text{b}} = 1.6 \times 10^{-16}$$

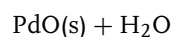
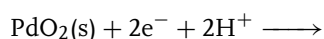


$$K = 1.8 \times 10^{-9}$$



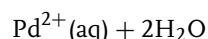
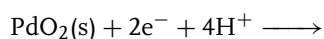
$$K = 1 \times 10^{-22}$$

Palladium ($^{106.42}_{46}\text{Pd}$), OS: (+6), +4, (+3), +2, (+1), 0; IE: 804 kJ mol⁻¹.

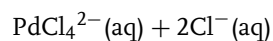
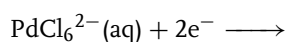


$$E^\ominus = 1.263 \text{ V (calcd)}$$

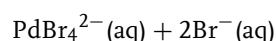
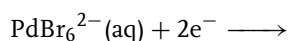
$$E^\ominus = 1.47 \text{ V (measured)}$$



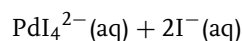
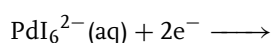
$$E^\ominus = 1.194 \text{ V}$$



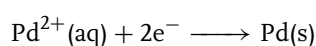
$$E^\ominus = 1.47 \text{ V (1 M HCl)}$$



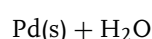
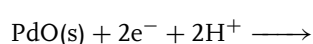
$$E^\ominus = 0.99 \text{ V (1 M KBr)}$$



$$E^\ominus = 0.48 \text{ V (1 M KI)}$$

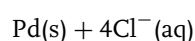
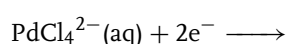


$$E^\ominus = (0.915 \pm 0.005)\text{V}(\text{HClO}_4)$$

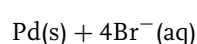
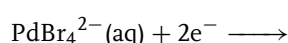


$$E^\ominus = 0.917 \text{ V (calcd)}$$

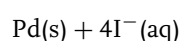
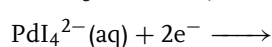
$$E^\ominus = 0.79 \text{ V (measured)}$$



$$E^\ominus = 0.62 \text{ V (1 M HCl)}$$



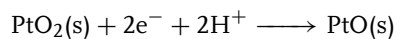
$$E^\ominus = 0.49 \text{ V (1 M KBr)}$$



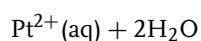
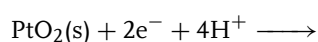
$$E^\ominus = 0.18 \text{ V (1 M KI)}$$

Palladium shows a great capacity for hydrogen absorption. This takes place with changes in the crystalline structure of the metal with the formation of Pd₂H or Pd₄H₂ hydrides.

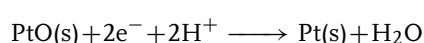
Platinum ($^{195.078}_{78}\text{Pt}$), OS: (+6), +4, (+3), +2, (+1), 0; IE: 870 kJ mol⁻¹.



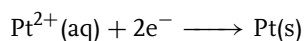
$$E^\ominus = 1.045 \text{ V (calcd)}$$



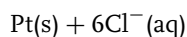
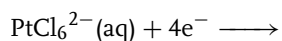
$$E^\ominus = 0.837 \text{ V (calcd)}$$



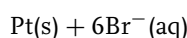
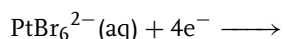
$$E^\ominus = 0.98 \text{ V (calcd)}$$



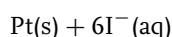
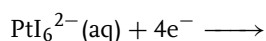
$$E^{\ominus} = 1.188 \text{ V}$$



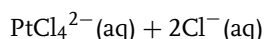
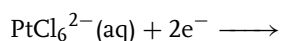
$$E^{\ominus} = 0.744 \text{ V}$$



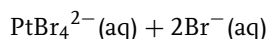
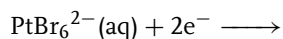
$$E^{\ominus} = 0.657 \text{ V}$$



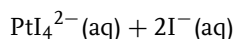
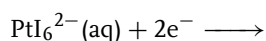
$$E_c^{\circ'} = 0.4 \text{ V (1 M NaI)}$$



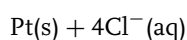
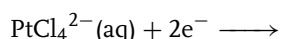
$$E^{\ominus} = 0.726 \text{ V}$$



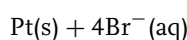
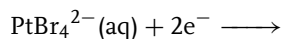
$$E^{\ominus} = 0.613 \text{ V}$$



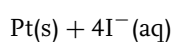
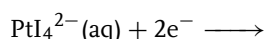
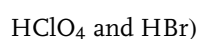
$$E^{\ominus} = 0.329 \text{ V}$$



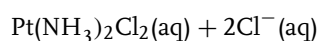
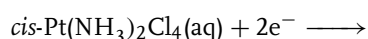
$$E_c^{\circ'} = 0.758 \text{ V}$$



$$E_c^{\circ'} = 0.698 \text{ V (3 M}$$



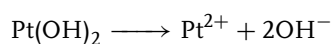
$$E_c^{\circ'} = 0.4 \text{ V (0.5 M NaI)}$$



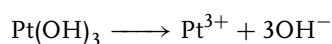
$$E_c^{\circ'} = 0.669 \text{ V (1 M NaCl)}$$

(cisplatin, cancer chemotherapy agent)

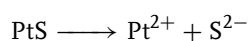
Solubility and complex equilibria:



$$K_{\text{sp}} \sim 10^{-24}$$



$$K_{\text{sp}} \sim 10^{-25}$$



$$K_{\text{sp}} \sim 10^{-68}$$

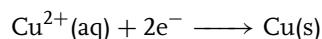
Darmstadtium ($^{[271]}_{110}\text{Ds}$)

No data are available.

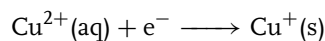
2.11 Group 11 Elements

Copper ($^{63.546}_{29}\text{Cu}$), OS: +2, +1, 0; IE: 745.3, 1957.3, 3577.6 kJ mol⁻¹.

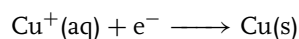
Acidic solutions



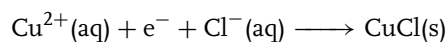
$$E^{\ominus} = 0.340 \text{ V}$$



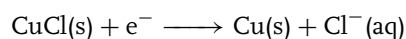
$$E^{\ominus} = 0.159 \text{ V}$$



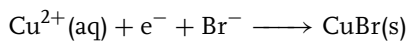
$$E^{\ominus} = 0.520 \text{ V}$$



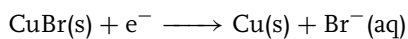
$$E^{\ominus} = 0.559 \text{ V}$$



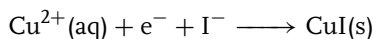
$$E^{\ominus} = 0.121 \text{ V}$$



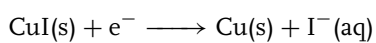
$$E^{\ominus} = 0.654 \text{ V}$$



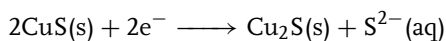
$$E^{\ominus} = 0.033 \text{ V}$$



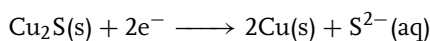
$$E^{\ominus} = 0.861 \text{ V}$$



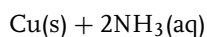
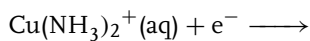
$$E^{\ominus} = -0.182 \text{ V}$$



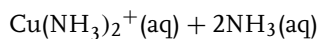
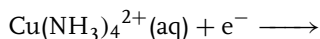
$$E^{\ominus} = -0.542 \text{ V}$$



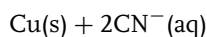
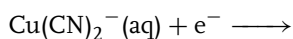
$$E^{\ominus} = -0.898 \text{ V}$$



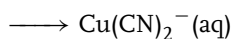
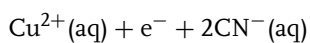
$$E^{\ominus} = -0.100 \text{ V}$$



$$E^{\ominus} = 0.10 \text{ V}$$

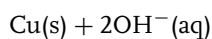
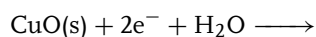


$$E^{\ominus} = -0.44 \text{ V}$$

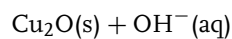
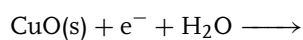


$$E^{\ominus} = 1.12 \text{ V}$$

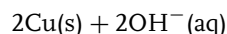
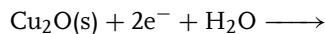
Basic solutions



$$E^{\ominus} = -0.29 \text{ V}$$

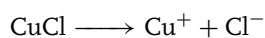


$$E^{\ominus} = -0.22 \text{ V}$$

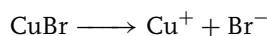


$$E^{\ominus} = -0.365 \text{ V}$$

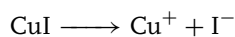
Solubility equilibria:



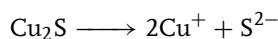
$$K_{\text{sp}} = 1.9 \times 10^{-7}$$



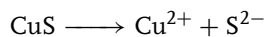
$$K_{\text{sp}} = 5.9 \times 10^{-9}$$



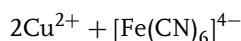
$$K_{\text{sp}} = 5.1 \times 10^{-12}$$



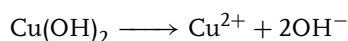
$$K_{\text{sp}} = 1.6 \times 10^{-48}$$



$$K_{\text{sp}} = 7.9 \times 10^{-37}$$



$$K_{\text{sp}} = 1.3 \times 10^{-16}$$



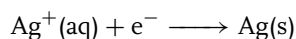
$$K_{\text{sp}} = 1.6 \times 10^{-19}$$

Complex equilibria

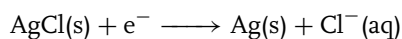
The information about the composition and stability of several Cu^{2+} complexes with nitrogen-containing and polyhydroxylic ligands can be found in Refs 50–65.

Silver ($^{107.862}_{47}\text{Ag}$), OS: (+3), (+2), +1, 0; IE: 731, 2072.6, 3359.4 kJ mol⁻¹.

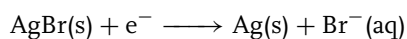
Acidic solutions



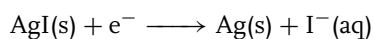
$$E^{\ominus} = 0.7991 \text{ V}$$



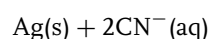
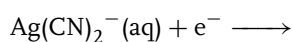
$$E^\ominus = 0.2223 \text{ V}$$



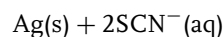
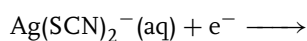
$$E^\ominus = 0.0711 \text{ V}$$



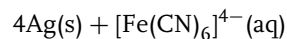
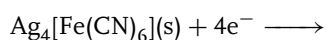
$$E^\ominus = -0.1522 \text{ V}$$



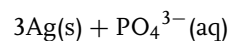
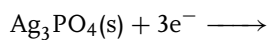
$$E^\ominus = -0.31 \text{ V}$$



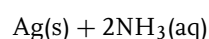
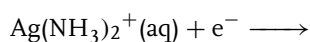
$$E^\ominus = 0.304 \text{ V}$$



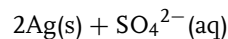
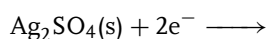
$$E^\ominus = 0.1478 \text{ V}$$



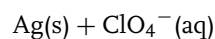
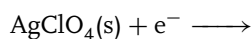
$$E^\ominus = 0.4525 \text{ V}$$



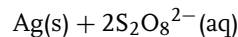
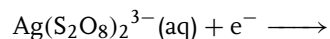
$$E^\ominus = 0.373 \text{ V}$$



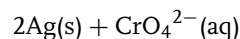
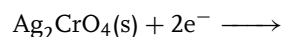
$$E^\ominus = 0.654 \text{ V}$$



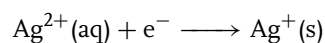
$$E^\ominus = 0.787 \text{ V}$$



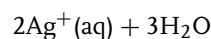
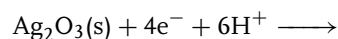
$$E^\ominus = -0.01 \text{ V}$$



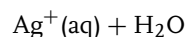
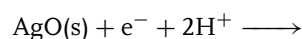
$$E^\ominus = 0.4491 \text{ V}$$



$$E^\ominus = 1.98 \text{ V}$$

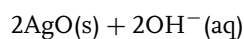
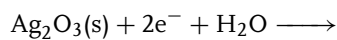


$$E^\ominus = 1.36 \text{ V}$$

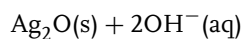
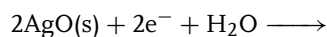


$$E^\ominus = 1.772 \text{ V}$$

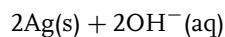
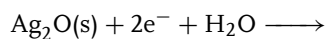
Basic solutions



$$E^\ominus = 0.739 \text{ V}$$

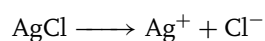


$$E^\ominus = 0.604 \text{ V}$$

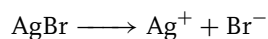


$$E^\ominus = 0.342 \text{ V}$$

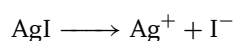
Solubility equilibria:



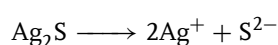
$$K_{\text{sp}} = 1.77 \times 10^{-10}$$



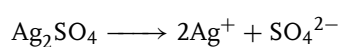
$$K_{\text{sp}} = 5.0 \times 10^{-13}$$



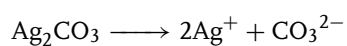
$$K_{\text{sp}} = 8.7 \times 10^{-17}$$



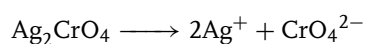
$$K_{\text{sp}} = 1 \times 10^{-50}$$



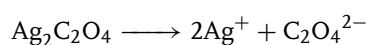
$$K_{\text{sp}} = 1.2 \times 10^{-5}$$



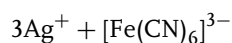
$$K_{\text{sp}} = 8 \times 10^{-12}$$



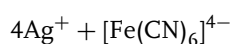
$$K_{\text{sp}} = 2.7 \times 10^{-12}$$



$$K_{\text{sp}} = 1.1 \times 10^{-11}$$

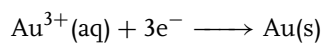


$$K_{\text{sp}} = 1 \times 10^{-20}$$



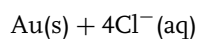
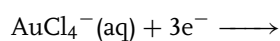
$$K_{\text{sp}} = 8.6 \times 10^{-45}$$

Gold ($^{196.966}_{79}\text{Au}$), OS: +3, (+2), +1, 0; IE: 890, 1973.3, (2895) kJ mol⁻¹.

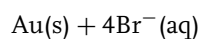
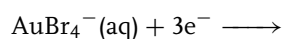


$$E^\ominus = 1.52 \text{ V}$$

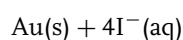
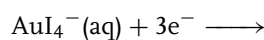
$$E_c' = 1.362 \text{ V (1 mol kg}^{-1} \text{ H}_2\text{SO}_4)$$



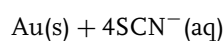
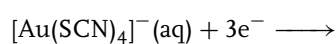
$$E^\ominus = 1.002 \text{ V}$$



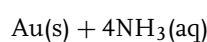
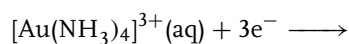
$$E^\ominus = 0.854 \text{ V}$$



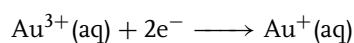
$$E^\ominus = 0.56 \text{ V}$$



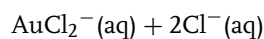
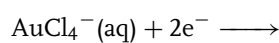
$$E^\ominus = 0.636 \text{ V}$$



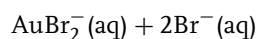
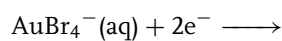
$$E^\ominus = 0.325 \text{ V}$$



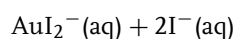
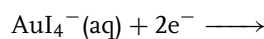
$$E^\ominus = 1.36 \text{ V}$$



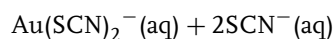
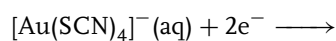
$$E^\ominus = 0.926 \text{ V}$$



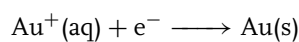
$$E^\ominus = 0.802 \text{ V}$$



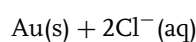
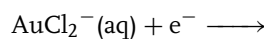
$$E^\ominus = 0.55 \text{ V}$$



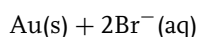
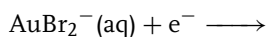
$$E^\ominus = -0.623 \text{ V}$$



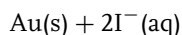
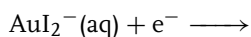
$$E^\ominus = 1.83 \text{ V}$$



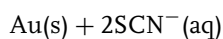
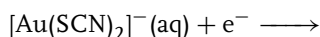
$$E^{\ominus} = 1.154 \text{ V}$$



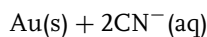
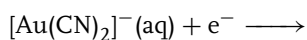
$$E^{\ominus} = 0.96 \text{ V}$$



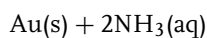
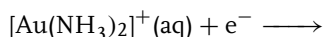
$$E^{\ominus} = 0.578 \text{ V}$$



$$E^{\ominus} = 0.662 \text{ V}$$

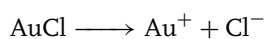


$$E_c^{\circ'} = -0.595 \text{ V (0.5 M KCN)}$$

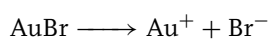


$$E_c^{\circ'} = 0.563 \text{ V (10 M NH}_4\text{NO}_3\text{)}$$

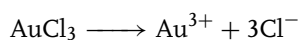
Solubility equilibria:



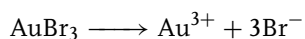
$$K_{\text{sp}} = 2 \times 10^{-3}$$



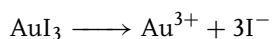
$$K_{\text{sp}} = 5 \times 10^{-17}$$



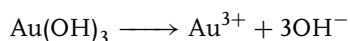
$$K_{\text{sp}} = 3.2 \times 10^{-25}$$



$$K_{\text{sp}} = 1.6 \times 10^{-23}$$



$$K_{\text{sp}} = 1 \times 10^{-46}$$



$$K_{\text{sp}} = 1 \times 10^{-53}$$

Röntgenium ($^{272}_{111}\text{Rg}$)

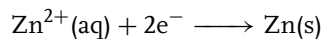
No data are available.

2.12

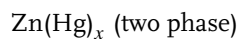
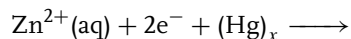
Group 12 Elements

Zinc ($^{65.409}_{30}\text{Zn}$), OS: +2, (+1), 0; IE: 906.1, 1733, 3831 kJ mol⁻¹.

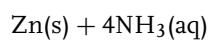
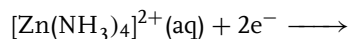
Acidic solutions



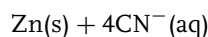
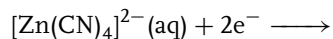
$$E^{\ominus} = -0.7626 \text{ V}$$



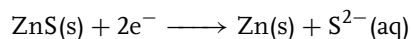
$$E^{\ominus} = -0.76175 \text{ V [1]}$$



$$E^{\ominus} = -1.04 \text{ V}$$

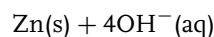
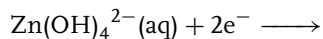


$$E^{\ominus} = -1.34 \text{ V}$$

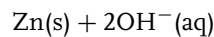
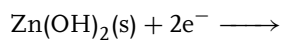


$$E^{\ominus} = -1.44 \text{ V}$$

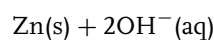
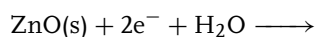
Basic solutions



$$E^{\ominus} = -1.285 \text{ V (calcd)}$$

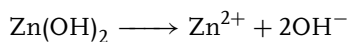


$$E^{\ominus} = -1.246 \text{ V}$$

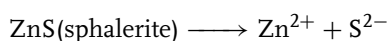


$$E^{\ominus} = -1.248 \text{ V}$$

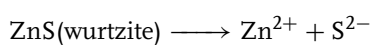
Solubility and complex equilibria:



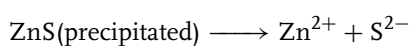
$$K_{\text{sp}} = 4.5 \times 10^{-17}$$



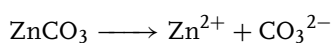
$$K_{\text{sp}} = 2.2 \times 10^{-27}$$



$$K_{\text{sp}} = 1.6 \times 10^{-23}$$



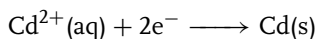
$$K_{\text{sp}} = 8.7 \times 10^{-23}$$



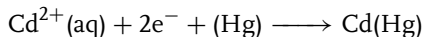
$$K_{\text{sp}} = 2 \times 10^{-10}$$

Cadmium ($^{112.411}_{48}\text{Cd}$), OS: +2, 0; IE: 876.5, 1631, 3644 kJ mol⁻¹.

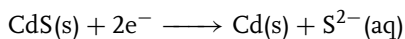
Acidic solutions



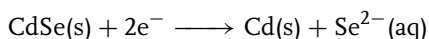
$$E^{\ominus} = -0.4025 \text{ V}$$



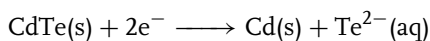
$$E^{\ominus} = -0.3515 \text{ V}$$



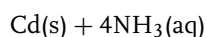
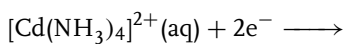
$$E^{\ominus} = -1.255 \text{ V}$$



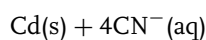
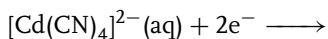
$$E^{\ominus} = -1.38 \text{ V}$$



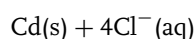
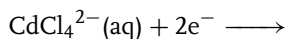
$$E^{\ominus} = -1.62 \text{ V}$$



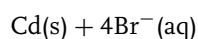
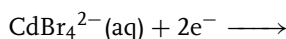
$$E^{\ominus} = -0.622 \text{ V}$$



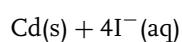
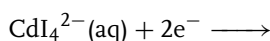
$$E^{\ominus} = -0.943 \text{ V}$$



$$E^{\ominus} = -0.453 \text{ V}$$

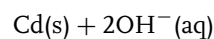
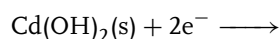


$$E^{\ominus} = -0.488 \text{ V}$$

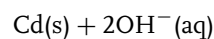
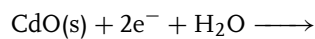


$$E^{\ominus} = -0.58 \text{ V}$$

Basic solutions

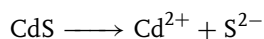


$$E^{\ominus} = -0.824 \text{ V}$$

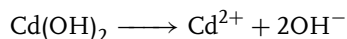


$$E^{\ominus} = -0.783 \text{ V}$$

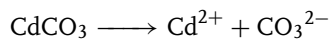
Solubility and complex equilibria:



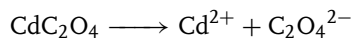
$$K_{\text{sp}} = 7 \times 10^{-28}$$



$$K_{\text{sp}} = 2.4 \times 10^{-13}$$



$$K_{\text{sp}} = 2.5 \times 10^{-14}$$

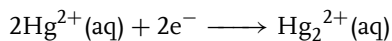


$$K_{\text{sp}} = 1.53 \times 10^{-8}$$

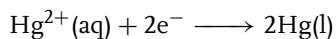
Data for several Cd²⁺ complexes can be found in Refs 65, 66.

Mercury ($^{200.59}_{80}\text{Hg}$), OS: +2, +1, 0; IE: 1007, 1809, 3300 kJ mol⁻¹.

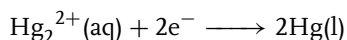
Acidic solutions



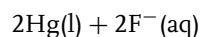
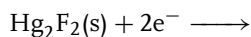
$$E^\ominus = 0.911 \text{ V}$$



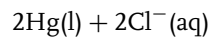
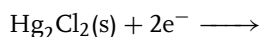
$$E^\ominus = 0.8535 \text{ V}$$



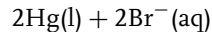
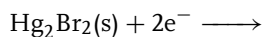
$$E^\ominus = 0.7960 \text{ V}$$



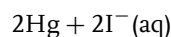
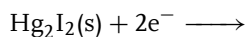
$$E^\ominus = 0.6562 \text{ V}$$



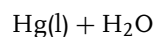
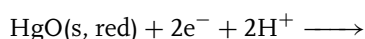
$$E^\ominus = 0.26816 \text{ V}$$



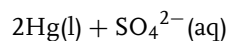
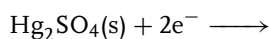
$$E^\ominus = 0.1392 \text{ V}$$



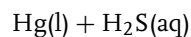
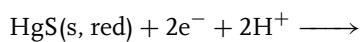
$$E^\ominus = -0.0405 \text{ V}$$



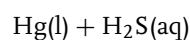
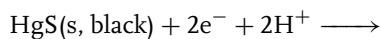
$$E^\ominus = 0.9256 \text{ V}$$



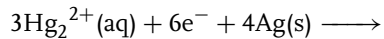
$$E^\ominus = 0.6136 \text{ V [1]}$$



$$E^\ominus = -0.096 \text{ V}$$

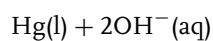
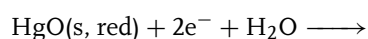


$$E^\ominus = -0.085 \text{ V}$$

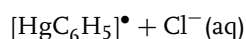
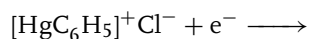


$$E_c^{\ominus'} = -0.85 \text{ V}$$

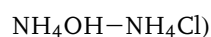
Basic and nonaqueous solutions



$$E^\ominus = 0.0977 \text{ V}$$



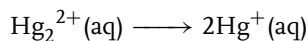
$$E_{1/2} = -0.123 \text{ V (0.2 M}$$



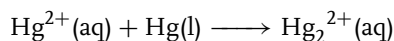
$$E_{1/2} = -0.544 \text{ V (0.1 M}$$



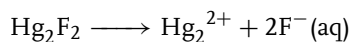
Solubility and other equilibria:



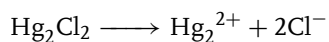
$$K_{\text{diss}} < 10^{-7}$$



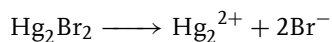
$$K = 87.9$$



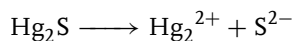
$$K_{\text{sp}} = 1.89 \times 10^{-5}$$



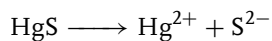
$$K_{\text{sp}} = 1.49 \times 10^{-18}$$



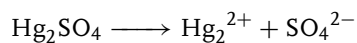
$$K_{\text{sp}} = 6.41 \times 10^{-23}$$



$$K_{\text{sp}} = 1 \times 10^{-47}$$



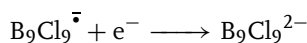
$$K_{\text{sp}} = 4 \times 10^{-53}$$



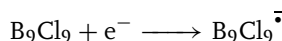
$$K_{\text{sp}} = 4.7 \times 10^{-7} - 8.1 \times 10^{-7}$$

$$E^\ominus = -1.241 \text{ V}$$

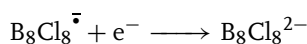
Nonaqueous solutions



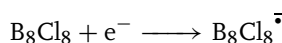
$$E_c^{\circ'} = -0.064 \text{ V [68]}$$



$$E_c^{\circ'} = 0.599 \text{ V}$$



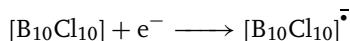
$$E_c^{\circ'} = 0.114 \text{ V}$$



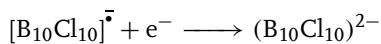
(0.1 M TBAPF₆|CH₂Cl₂,

$$c = 6.3 \times 10^{-4} \text{ mol dm}^{-3})$$

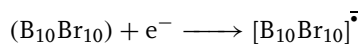
$$E_c^{\circ'} = 0.959 \text{ V}$$



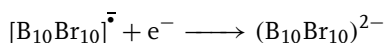
$$E_c^{\circ'} = 1.73 \text{ V [69]}$$



$$E_c^{\circ'} = 1.01 \text{ V}$$



$$E_c^{\circ'} = 1.77 \text{ V}$$



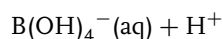
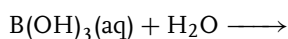
(0.1 mol dm⁻³ TBAPF₆-acetonitrile,

$$c = (2-4) \times 10^{-3} \text{ mol dm}^{-3})$$

$$E_c^{\circ'} = 1.14 \text{ V}$$

$E_c^{\circ'}$ values for other complexes (e.g. B₆X₆²⁻ (X = Cl, Br, I)) can be found in Ref. 70.

Dissociation equilibria:



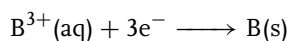
$$K = 1 \times 10^{-9}$$

2.13

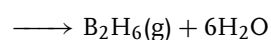
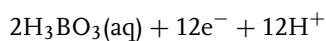
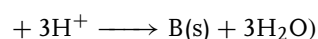
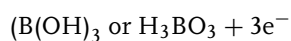
Group 13 Elements

Boron (^{10.811}₅B), OS: (+5), (+4), +3, (+2), (+1), 0; IE: 800.6, 2427.1, 3659.7 kJ mol⁻¹.

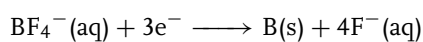
Acidic solutions



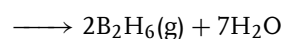
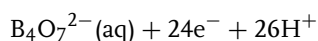
$$E^\ominus = -0.89 \text{ V (calcd)}$$



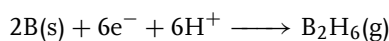
$$E^\ominus = -0.519 \text{ V (calcd)}$$



$$E^\ominus = -1.284 \text{ V}$$

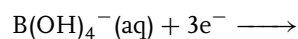


$$E^\ominus = -0.483 \text{ V (calcd)}$$

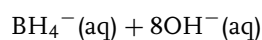
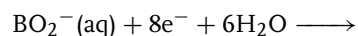


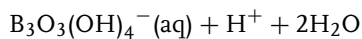
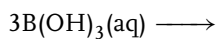
$$E^\ominus = -0.15 \text{ V (calcd)}$$

Basic solutions



$$E^\ominus = -1.811 \text{ V (calcd)}$$





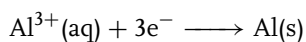
$$K = 1.4 \times 10^{-7}$$

(at higher concentrations \longrightarrow

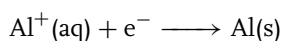
polymerization \longrightarrow increasing acidity)

Aluminum ($^{26.9815}_{13}\text{Al}$), OS: +3, (+1), 0;
IE: 557.5, 1816.7, 2744.8 kJ mol⁻¹.

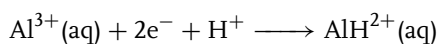
Acidic solutions



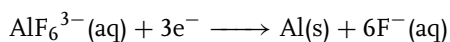
$$E^\ominus = -1.676 \text{ V (calcd)}$$



$$E^\ominus = 0.55 \text{ V}$$

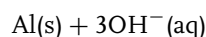
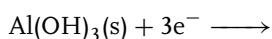


$$E^\ominus = -0.62 \text{ V (calcd)}$$

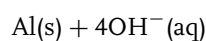
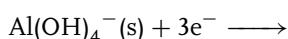


$$E^\ominus = -2.067 \text{ V (calcd)}$$

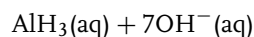
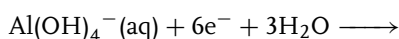
Basic solutions



$$E^\ominus = -2.3 \text{ V}$$

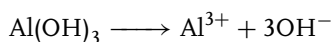


$$E^\ominus = -2.31 \text{ V}$$

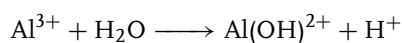


$$E^\ominus = -1.748 \text{ V}$$

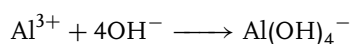
Solubility and other equilibria:



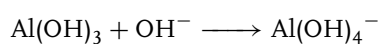
$$K_{\text{sp}} = 2.2 \times 10^{-32}$$



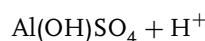
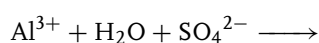
$$K = 1.4 \times 10^{-5}$$



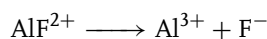
$$K = 6.8 \times 10^{-33}$$



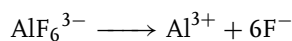
$$K = 3.1 \times 10^{-1}$$



$$K = 1.25 \times 10^{-2}$$



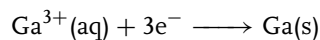
$$K = 7.4 \times 10^{-7}$$



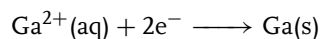
$$K = 1.44 \times 10^{-20}$$

Gallium ($^{69.723}_{31}\text{Ga}$), OS: +3, +2, (+1), 0;
IE: 578.8, 1979.3, 2963 kJ mol⁻¹.

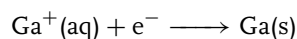
Acidic solutions



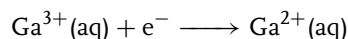
$$E^\ominus = -0.529 \text{ V (at 301 K)}$$



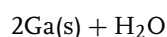
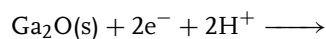
$$E^\ominus \sim -0.45 \text{ V (calcd)}$$



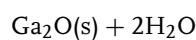
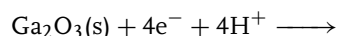
$$E^\ominus = -0.79 \text{ V (calcd)}$$



$$E^\ominus \sim -0.67 \text{ V (calcd)}$$

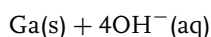
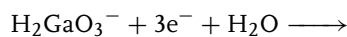


$$E^\ominus = -0.4 \text{ V (calcd)}$$



$$E^{\ominus} = -0.5 \text{ V (calcd)}$$

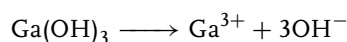
Basic solution



$$E^{\ominus} = -1.22 \text{ V (calcd)}$$

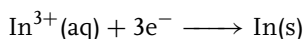
(Depending on the pH value, Ga^{3+} may also exist in the form of the following ions: $\text{Ga}(\text{OH})_2^+$, GaO^+ , GaO_2^- , H_2GaO_3^- , $\text{Ga}(\text{OH})_4^-$, HGaO_3^{2-} , GaO_3^{3-} , $[\text{Ga}_{2x}(\text{OH})_{5x}]^{5+}$.)

Solubility equilibrium:

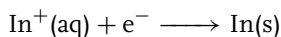


$$K_{\text{sp}} = 5 \times 10^{-37}$$

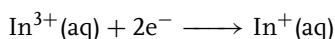
Indium ($^{114.818}_{48}\text{In}$), OS: +3, (+2), +1, 0;
IE: 558.3, 1820.6, 2704 kJ mol⁻¹.



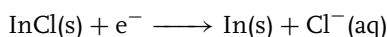
$$E^{\ominus} = -0.338 \text{ V}$$



$$E^{\ominus} = -0.126 \text{ V}$$



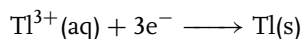
$$E^{\ominus} = -0.444 \text{ V}$$



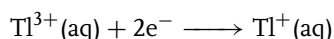
$$E^{\ominus} = -0.34 \text{ V (calcd)}$$

Thallium ($^{204.383}_{81}\text{Tl}$), OS: +3, (+2), +1;
IE: 589.4, 1971, 2878 kJ mol⁻¹.

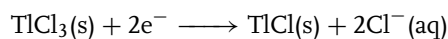
Acidic solutions



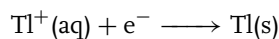
$$E^{\ominus} = 0.73 \text{ V}$$



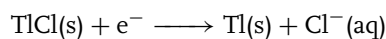
$$E^{\ominus} = 1.26 \text{ V}$$



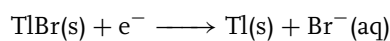
$$E^{\ominus} = 0.89 \text{ V}$$



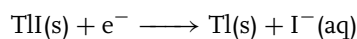
$$E^{\ominus} = -0.336 \text{ V}$$



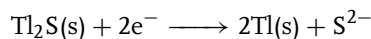
$$E^{\ominus} = -0.56 \text{ V}$$



$$E^{\ominus} = -0.413 \text{ V}$$

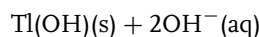
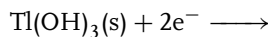


$$E^{\ominus} = -0.15 \text{ V}$$

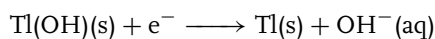


$$E^{\ominus} = -0.94 \text{ V}$$

Basic solutions

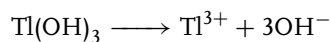


$$E^{\ominus} = -0.05 \text{ V}$$

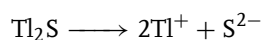


$$E^{\ominus} = -0.868 \text{ V}$$

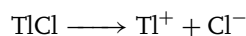
Solubility equilibria:



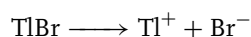
$$K_{\text{sp}} \sim 1.5 \times 10^{-44}$$



$$K_{\text{sp}} = 1 \times 10^{-24}$$



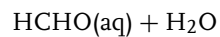
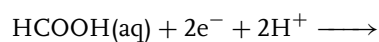
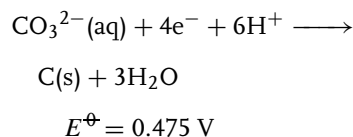
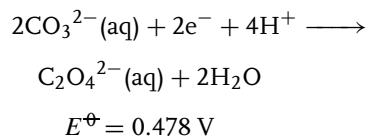
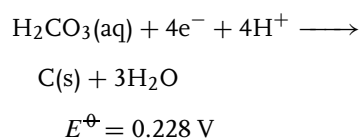
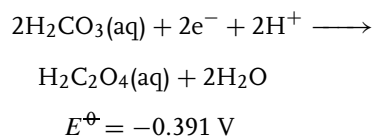
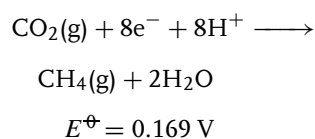
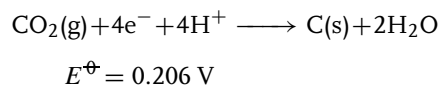
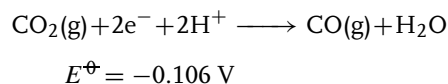
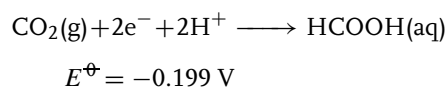
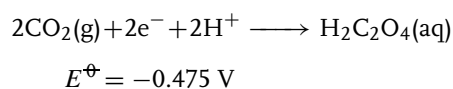
$$K_{\text{sp}} = 1.9 \times 10^{-4}$$



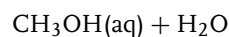
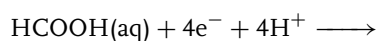
$$K_{\text{sp}} = 3.9 \times 10^{-6}$$

2.14 Group 14 Elements

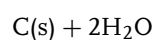
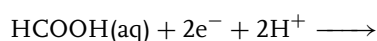
Carbon ($^{12.0107}_6\text{C}$), OS: +4, +2, 0, -2, (-4); IE: 1086.5, 2352.6, 4620.5, 6222.7 kJ mol⁻¹.



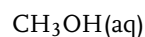
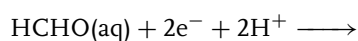
$$E^\ominus = 0.034 \text{ V}$$



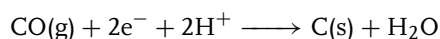
$$E^\ominus = 0.010 \text{ V}$$



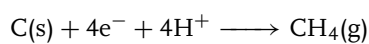
$$E^\ominus = 0.523 \text{ V}$$



$$E^\ominus = 0.232 \text{ V}$$



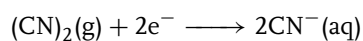
$$E^\ominus = 0.517 \text{ V}$$



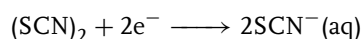
$$E^\ominus = 0.132 \text{ V}$$



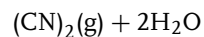
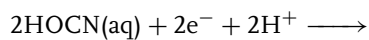
$$E^\ominus = 0.375 \text{ V}$$



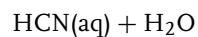
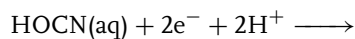
$$E^\ominus = -0.176 \text{ V}$$



$$E^\ominus = 0.77 \text{ V}$$



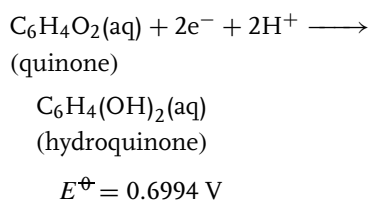
$$E^\ominus = -0.33 \text{ V}$$



$$E^\ominus = 0.02 \text{ V}$$

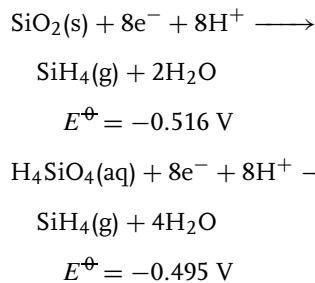
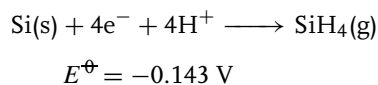
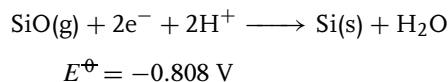
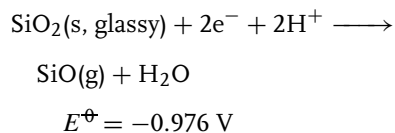
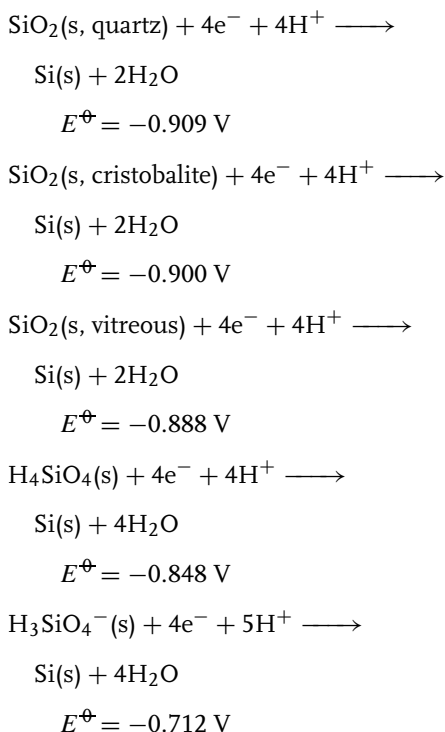
(The electrode reactions of these compounds are highly irreversible, therefore,

practically all E^\ominus values are calculated from caloric data. There is an irreversible adsorption (dissociative chemisorption) of CO_2 , CO , HCOOH , HCHO , and CH_3OH on platinum electrodes.)



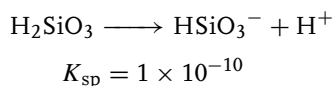
(There are several carbon compounds that exhibit reversible behavior. We refer to the quinone–hydroquinone system, which is used in pH-sensitive electrodes.) The solubility of CO_2 in 100 g water at 1 bar and 20°C is 0.172 g.

Silicon ($^{28.0855}_{14}\text{Si}$), OS: +4, (+2), 0, –4; IE: 786.3, 1576.5, 3228.3, 4354.4 kJ mol $^{-1}$.

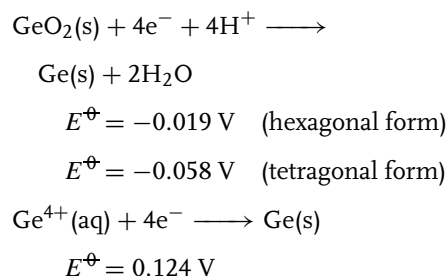


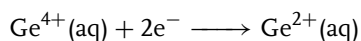
The E^\ominus values were calculated from thermodynamic data. There are a large number of different acids, especially of the polyacid type. The complex forms exist in equilibrium, which depends on the pH. There are several compounds with hydrogen, the general formula of which can be given as $\text{Si}_n\text{H}_{2n+2}$.

Solubility equilibrium:

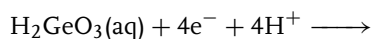


Germanium ($^{76.64}_{32}\text{Ge}$), OS: +4, +2, 0; IE: 761.2, 1537, 3301.2, 4409.4 kJ mol $^{-1}$.

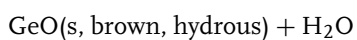
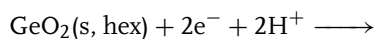




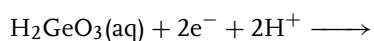
$$E^{\ominus} = 0.0 \text{ V}$$



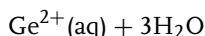
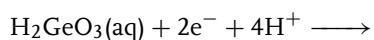
$$E^{\ominus} = 0.012 \text{ V}$$



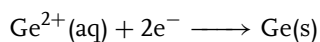
$$E^{\ominus} = -0.132 \text{ V}$$



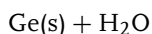
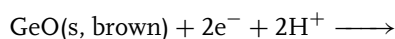
$$E^{\ominus} = -0.72 \text{ V}$$



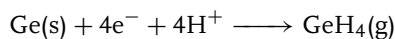
$$E^{\ominus} = -0.223 \text{ V}$$



$$E^{\ominus} = 0.247 \text{ V}$$



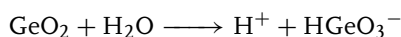
$$E^{\ominus} = 0.095 \text{ V}$$



$$E^{\ominus} = -0.42 \text{ V}$$

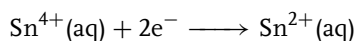
The E^{\ominus} values were calculated from thermodynamic data. In aqueous solutions, Ge^{4+} exist in different forms, such as $[\text{GeO}(\text{OH})_3]^{-}$ and $[\text{GeO}_2(\text{OH})_2]^{2-}$. Hydrides are of the type $\text{Ge}_n\text{H}_{2n+2}$ ($1 < n < 9$).

Solubility equilibrium:



$$K_{\text{sp}} = 1.1 \times 10^{-10}$$

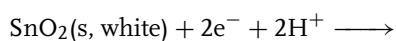
Tin ($^{118.71}_{50}\text{Sn}$), OS: +4, +2, (+1), 0; IE: 708.4, 1411.4, 2942.2, 3929.3 kJ mol⁻¹.



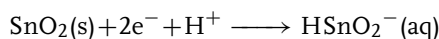
$$E^{\ominus} = 0.15 \text{ V (estimated)}$$

$$E^{\ominus}_{\text{c}} = 0.07 \text{ V (0.097 M HCl)}$$

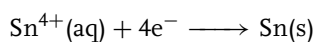
$$E^{\ominus}_{\text{c}} = 0.1325 \text{ V (2.023 M HCl)}$$



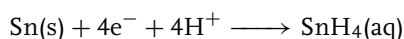
$$E^{\ominus} = 0.088 \text{ V (calcd)}$$



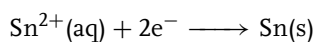
$$E^{\ominus} = -0.35 \text{ V (calcd)}$$



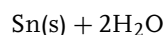
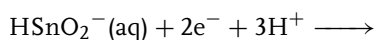
$$E^{\ominus} = -0.2 \text{ V (calcd)}$$



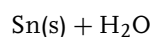
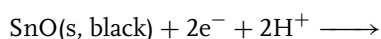
$$E^{\ominus} = -1.074 \text{ V (calcd)}$$



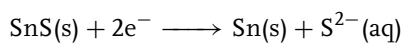
$$E^{\ominus} = -0.136 \text{ V (HCl)}$$



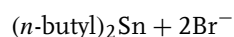
$$E^{\ominus} = 0.333 \text{ V (calcd)}$$



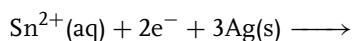
$$E^{\ominus} = -0.104 \text{ V (calcd)}$$



$$E^{\ominus} = -0.94 \text{ V (calcd)}$$

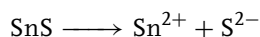


$$E^{\ominus} = 0.24 \text{ V (methanol) [71]}$$

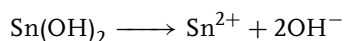


$$E_c^{\circ'} = -0.05 \text{ V}$$

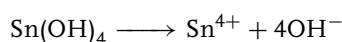
Solubility equilibria:



$$K_{\text{sp}} = 1 \times 10^{-20}$$



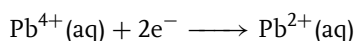
$$K_{\text{sp}} = 5 \times 10^{-26}$$



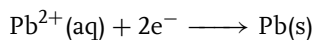
$$K_{\text{sp}} = 1 \times 10^{-56}$$

Lead ($^{207.2}_{82}\text{Pb}$), OS: +4, +2, 0; IE: 715.4, 1450, 3080.7, 4082.3 kJ mol⁻¹.

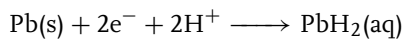
Acidic solutions



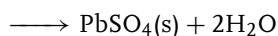
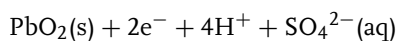
$$E^\ominus = 1.69 \text{ V}$$



$$E^\ominus = -0.125 \text{ V}$$

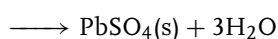
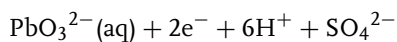


$$E^\ominus = -1.507 \text{ V}$$

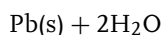
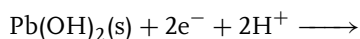


$$E^\ominus = 1.698 \text{ V } (\alpha\text{-PbO}_2)$$

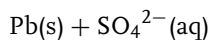
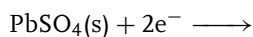
$$E^\ominus = 1.69 \text{ V } (\beta\text{-PbO}_2)$$



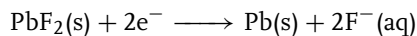
$$E^\ominus = 2.34 \text{ V (calcd)}$$



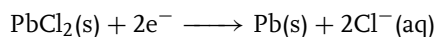
$$E^\ominus = 0.277 \text{ V (calcd)}$$



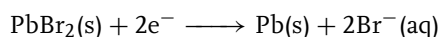
$$E^\ominus = -0.35277 \text{ V [1]}$$



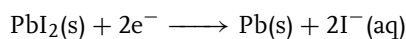
$$E^\ominus = -0.344 \text{ V}$$



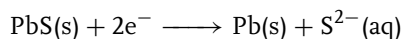
$$E^\ominus = -0.268 \text{ V}$$



$$E^\ominus = -0.28 \text{ V}$$

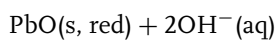
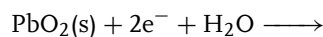


$$E^\ominus = -0.365 \text{ V}$$

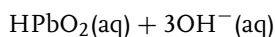
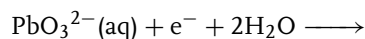


$$E^\ominus = -0.93 \text{ V (calcd)}$$

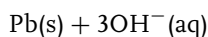
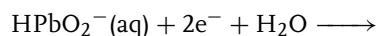
Basic solutions



$$E^\ominus = 0.247 \text{ V (calcd)}$$

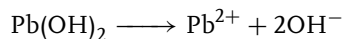


$$E^\ominus = 0.33 \text{ V (calcd)}$$

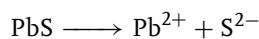


$$E^\ominus = -0.502 \text{ V (calcd)}$$

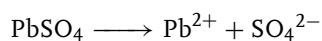
Solubility equilibria:



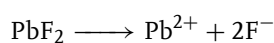
$$K_{\text{sp}} = 2.8 \times 10^{-16}$$



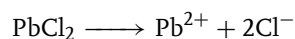
$$K_{\text{sp}} = 7 \times 10^{-29}$$



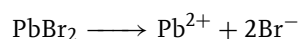
$$K_{\text{sp}} = 1.8 \times 10^{-8}$$



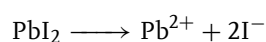
$$K_{\text{sp}} = 3.7 \times 10^{-8}$$



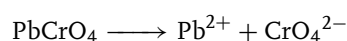
$$K_{\text{sp}} = 1.7 \times 10^{-5}$$



$$K_{\text{sp}} = 5 \times 10^{-5}$$



$$K_{\text{sp}} = 8.7 \times 10^{-9}$$



$$K_{\text{sp}} = 1.77 \times 10^{-14}$$

Complex equilibria

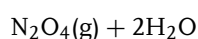
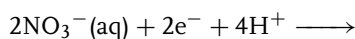
Recent data on several Pb^{2+} complexes can be found in Refs 59, 64.

2.15

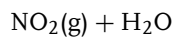
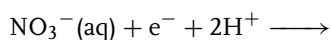
Group 15 Elements

Nitrogen ($^{14.0067}_{7}\text{N}$), OS: +5, +4, +3, +2, +1, 0, -1/3, -1, -2, -3; IE: 1402, 2856, 4577 kJ mol⁻¹, 16 920 (IV + V) kJ mol⁻¹.

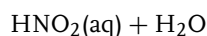
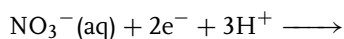
Acidic solutions



$$E^\ominus = 0.803 \text{ V (calcd)}$$

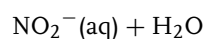
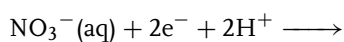


$$E^\ominus = 0.775 \text{ V (calcd)}$$

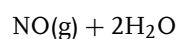
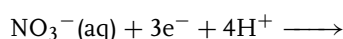


$$E^\ominus = 0.94 \text{ V (calcd)}$$

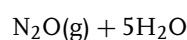
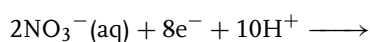
$$E^\ominus_{\text{c}} = 0.98 \text{ V (2–12 M HNO}_3\text{)}$$



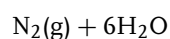
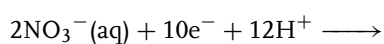
$$E^\ominus = 0.835 \text{ V (calcd)}$$



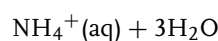
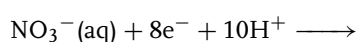
$$E^\ominus = 0.96 \text{ V}$$



$$E^\ominus = 1.116 \text{ V (calcd)}$$



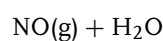
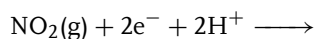
$$E^\ominus = 1.246 \text{ V (calcd)}$$



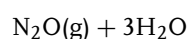
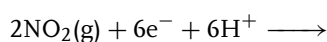
$$E^\ominus = 0.875 \text{ V (calcd)}$$



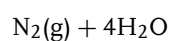
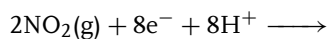
$$E^\ominus = 1.093 \text{ V (calcd)}$$



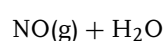
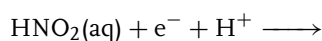
$$E^\ominus = 1.045 \text{ V (calcd)}$$



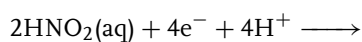
$$E^\ominus = 1.229 \text{ V (calcd)}$$

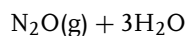


$$E^\ominus = 1.363 \text{ V (calcd)}$$

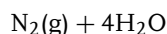
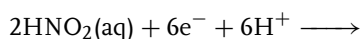


$$E^\ominus = 0.996 \text{ V}$$

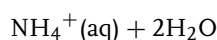
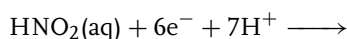




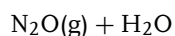
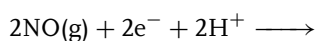
$$E^\ominus = 1.297 \text{ V (calcd)}$$



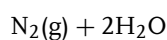
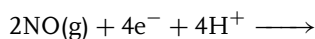
$$E^\ominus = 1.454 \text{ V (calcd)}$$



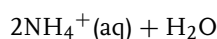
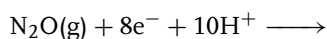
$$E^\ominus = 0.864 \text{ V (calcd)}$$



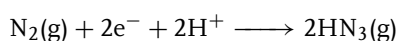
$$E^\ominus = 1.59 \text{ V (calcd)}$$



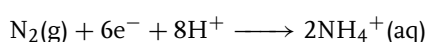
$$E^\ominus = 1.678 \text{ V (calcd)}$$



$$E^\ominus = 0.647 \text{ V (calcd)}$$

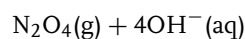
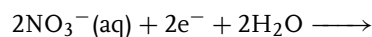


$$E^\ominus = -3.1 \text{ V (calcd)}$$

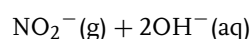
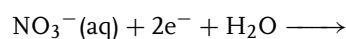


$$E^\ominus = 0.275 \text{ V (calcd)}$$

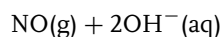
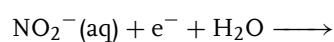
Basic solutions



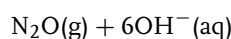
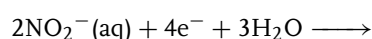
$$E^\ominus = -0.86 \text{ V (calcd)}$$



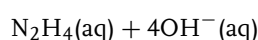
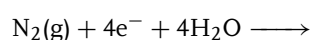
$$E^\ominus = 0.01 \text{ V (calcd)}$$



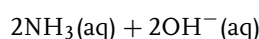
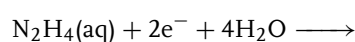
$$E^\ominus = 0.46 \text{ V (calcd)}$$



$$E^\ominus = 0.15 \text{ V (calcd)}$$



$$E^\ominus = -1.16 \text{ V (calcd)}$$



$$E^\ominus = 0.1 \text{ V}$$

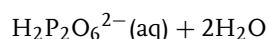
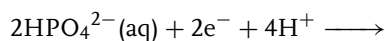
(Nitrogen fixation, that is, the conversion of N_2 to the nonzero OS, is thermodynamically possible; however, both the oxidation and the reduction of N_2 are kinetically hindered. Practically all of the electrode reactions of nitrogen compounds are irreversible; therefore, mostly, calculated E^\ominus values are given.)

Solubility of nitrogen in 100 g water at 1 bar and 20°C is 1.324×10^{-3} g.

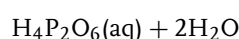
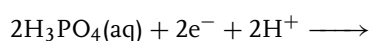
Solubility of ammonia in 100 g water at 1 bar and 20°C is 54 g.

Phosphorus ($^{30.9739}_{15}\text{P}$), OS: +5, +4, +3, +2, +1, 0, $-1/3$, -1 , -2 , -3 ; IE: 1402, 2856, 4577 kJ mol^{-1} , 16920 (IV + V) kJ mol^{-1} .

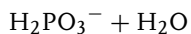
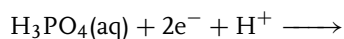
Acidic solutions



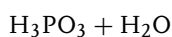
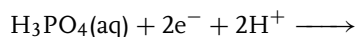
$$E^\ominus = -0.551 \text{ V}$$



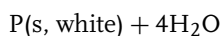
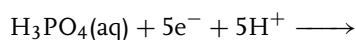
$$E^\ominus = -0.993 \text{ V}$$



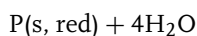
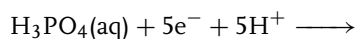
$$E^\ominus = -0.329 \text{ V}$$



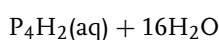
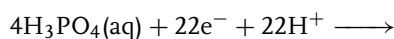
$$E^\ominus = -0.276 \text{ V}$$



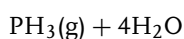
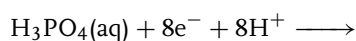
$$E^\ominus = -0.411 \text{ V}$$



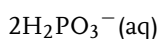
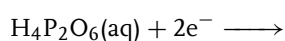
$$E^\ominus = -0.358 \text{ V}$$



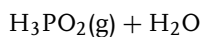
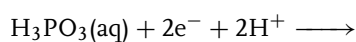
$$E^\ominus = -0.406 \text{ V}$$



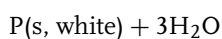
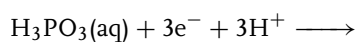
$$E^\ominus = -0.265 \text{ V}$$



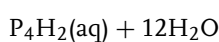
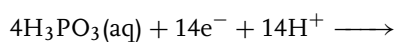
$$E^\ominus = 0.34 \text{ V}$$



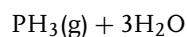
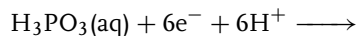
$$E^\ominus = -0.499 \text{ V}$$



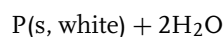
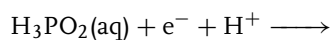
$$E^\ominus = -0.502 \text{ V}$$



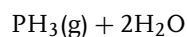
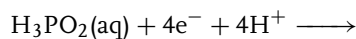
$$E^\ominus = -0.48 \text{ V}$$



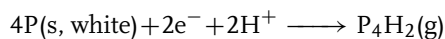
$$E^\ominus = -0.282 \text{ V}$$



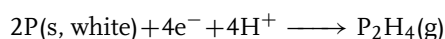
$$E^\ominus = -0.508 \text{ V}$$



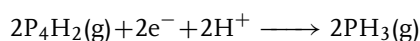
$$E^\ominus = -0.174 \text{ V}$$



$$E^\ominus = -0.347 \text{ V}$$

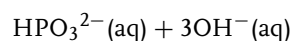
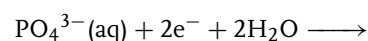


$$E^\ominus = -0.1 \text{ V}$$

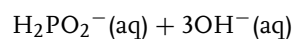
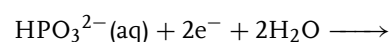


$$E^\ominus = 0.006 \text{ V}$$

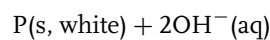
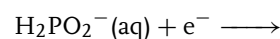
Basic solutions



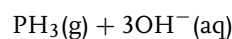
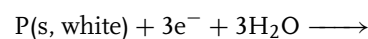
$$E^\ominus = -0.12 \text{ V}$$



$$E^\ominus = -1.57 \text{ V}$$



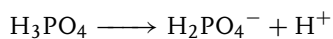
$$E^\ominus = -2.05 \text{ V}$$



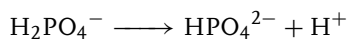
$$E^\ominus = -0.89 \text{ V}$$

The majority of the E^\ominus values are calculated from thermodynamic values.

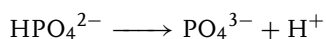
Dissociation and solubility equilibria:



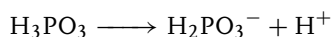
$$K = 7.5 \times 10^{-3}$$



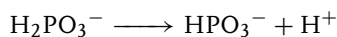
$$K = 6.2 \times 10^{-8}$$



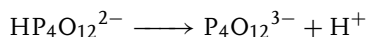
$$K = 1 \times 10^{-12}$$



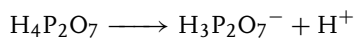
$$K = 1.6 \times 10^{-2}$$



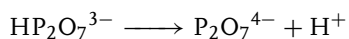
$$K = 2 \times 10^{-7}$$



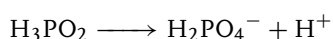
$$K = 1.8 \times 10^{-3}$$



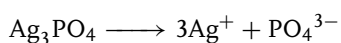
$$K = 10^{-1}$$



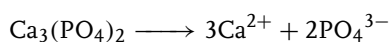
$$K = 2.4 \times 10^{-10}$$



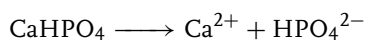
$$K = 8.5 \times 10^{-2}$$



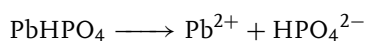
$$K_{\text{sp}} = 1.8 \times 10^{-18}$$



$$K_{\text{sp}} = 1 \times 10^{-25}$$



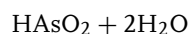
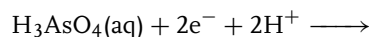
$$K_{\text{sp}} = 5 \times 10^{-6}$$



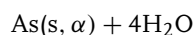
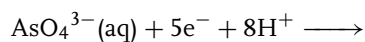
$$K_{\text{sp}} = 4 \times 10^{-12}$$

Arsenic ($^{74.921}_{33}\text{As}$), OS: +7, +5, +3, (+2), (+1), 0, (-1), -3; IE: 947, 1798, 2736 kJ mol⁻¹, 10 880 (IV + V) kJ mol⁻¹.

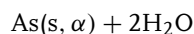
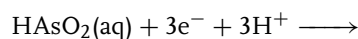
Acidic solutions



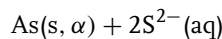
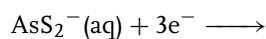
$$E^\ominus = 0.56 \text{ V}$$



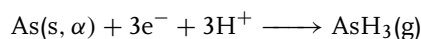
$$E^\ominus = 0.648 \text{ V}$$



$$E^\ominus = 0.24 \text{ V}$$

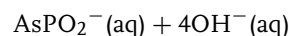
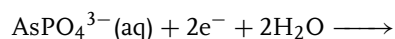


$$E^\ominus = -0.75 \text{ V}$$

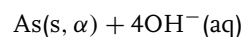
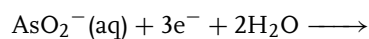


$$E^\ominus = -0.225 \text{ V}$$

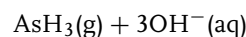
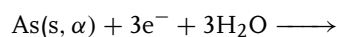
Basic solutions



$$\Delta E^\ominus = -0.67 \text{ V}$$



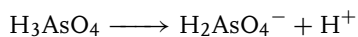
$$E^\ominus = -0.68 \text{ V}$$



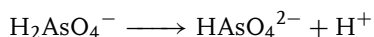
$$E^\ominus = -1.37 \text{ V}$$

Most of the E^\ominus values are calculated from thermodynamic data.

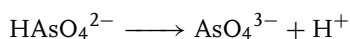
Dissociation and solubility equilibria:



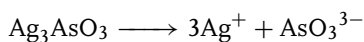
$$K = 4.8 \times 10^{-3}$$



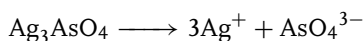
$$K = 1.7 \times 10^{-7}$$



$$K = 3 \times 10^{-12}$$



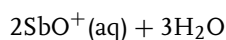
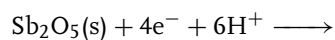
$$K_{\text{sp}} = 4.5 \times 10^{-19}$$



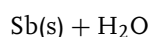
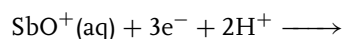
$$K_{\text{sp}} = 1 \times 10^{-19}$$

Antimony ($^{121.760}_{51}\text{Sb}$), OS: +5, +3, 0, -3; IE: 834, 1595, 2443 kJ mol⁻¹, 9636 (IV + V) kJ mol⁻¹.

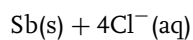
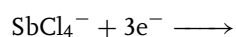
Strong acid solutions



$$E^\ominus = 0.605 \text{ V}$$

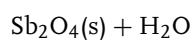
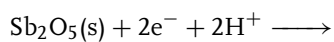


$$E^\ominus = 0.204 \text{ V}$$

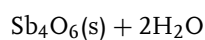
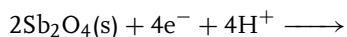


$$E_c' = 0.17 \text{ V (3.5–7 M HCl)}$$

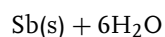
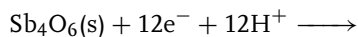
Acid and neutral solutions



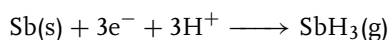
$$E^\ominus = 1.055 \text{ V (calcd)}$$



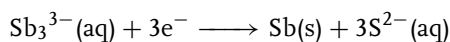
$$E^\ominus = 0.342 \text{ V (calcd)}$$



$$E^\ominus = 0.15 \text{ V}$$

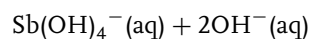
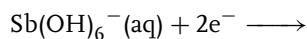


$$E^\ominus = -0.51 \text{ V}$$

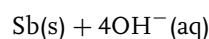
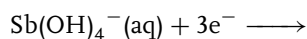


$$E^\ominus = -1.45 \text{ V}$$

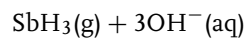
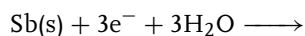
Basic solutions



$$E^\ominus = -0.465 \text{ V}$$

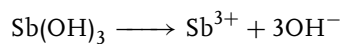


$$E^\ominus = -0.639 \text{ V}$$

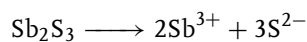


$$E^\ominus = -1.338 \text{ V}$$

Solubility equilibria:



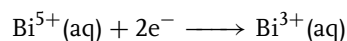
$$K_{\text{sp}} = 4 \times 10^{-42}$$



$$K_{\text{sp}} = 1 \times 10^{-30}$$

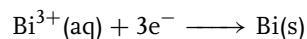
Bismuth ($^{208.98}_{83}\text{Bi}$), OS: +5, +3, 0, -3; IE: 703, 1610, 2466 kJ mol⁻¹, 9776 (IV + V) kJ mol⁻¹.

Acidic solutions

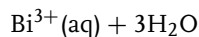
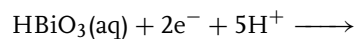


$$E_c' = 2.0 \text{ V (0.5 M H}^+,$$

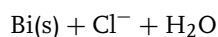
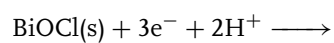
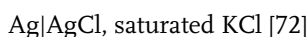
ionic strength, I = 2 M)



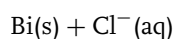
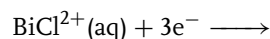
$$E^{\ominus} = 0.3172 \text{ V}$$



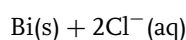
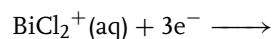
$$E_{\text{c}}^{\circ'} = 2.2 \text{ V versus}$$



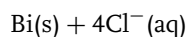
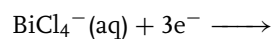
$$E^{\ominus} = 0.1697 \text{ V}$$



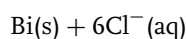
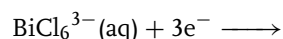
$$E^{\ominus} = 0.271 \text{ V}$$



$$E^{\ominus} = 0.249 \text{ V}$$

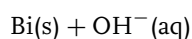
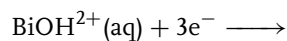


$$E^{\ominus} = 0.199 \text{ V}$$

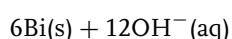
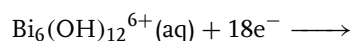


$$E^{\ominus} = 0.190 \text{ V}$$

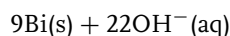
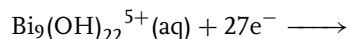
Basic solutions



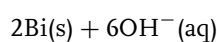
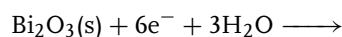
$$E^{\ominus} = 0.072 \text{ V (calcd)}$$



$$E^{\ominus} = -0.234 \text{ V (calcd)}$$

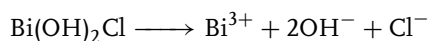


$$E^{\ominus} = -0.33 \text{ V (calcd)}$$

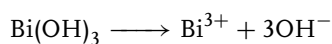


$$E^{\ominus} = -0.452 \text{ V (calcd)}$$

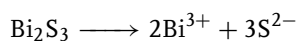
Solubility equilibria:



$$K_{\text{sp}} = 1.2 \times 10^{-35}$$



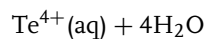
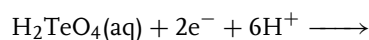
$$K_{\text{sp}} = 4.3 \times 10^{-31}$$



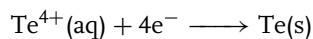
$$K_{\text{sp}} = 1.6 \times 10^{-72} \text{ (calcd)}$$

Tellurium ($^{127.6}_{52}\text{Te}$), OS: +6, +4, 0, (-1),
-2; IE: 869 kJ mol⁻¹,

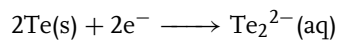
Acidic solutions



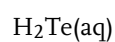
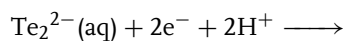
$$E^{\ominus} = 0.93 \text{ V (calcd)}$$



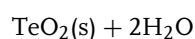
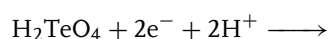
$$E^{\ominus} = 0.57 \text{ V}$$



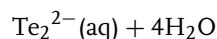
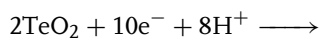
$$E^{\ominus} = -0.84 \text{ V}$$



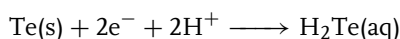
$$E^{\ominus} = -0.64 \text{ V}$$



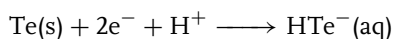
$$E^{\ominus} = 1.0 \text{ V}$$



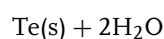
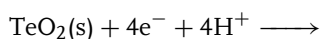
$$E^\ominus = 0.53 \text{ V}$$



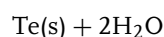
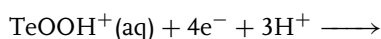
$$E^\ominus = -0.74 \text{ V}$$



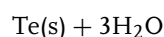
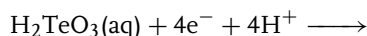
$$E^\ominus = -0.817 \text{ V}$$



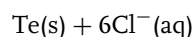
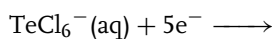
$$E^\ominus = 0.5213 \text{ V}$$



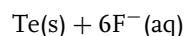
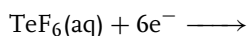
$$E^\ominus = 0.559 \text{ V}$$



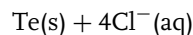
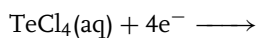
$$E^\ominus = 0.589 \text{ V}$$



$$E_c^{\circ'} = 0.63 \text{ V (3 M HCl)}$$

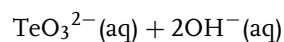
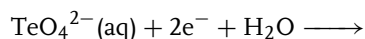


$$E^\ominus = 0.755 \text{ V}$$

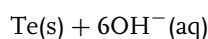
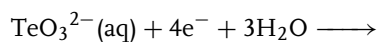


$$E^\ominus = 0.745 \text{ V}$$

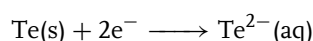
Basic solutions



$$E^\ominus = 0.07 \text{ V}$$

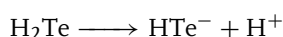


$$E^\ominus = -0.42 \text{ V}$$

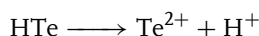


$$E^\ominus = -1.14 \text{ V}$$

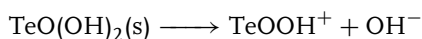
Dissociation equilibria:



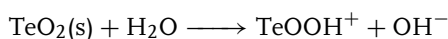
$$K = 2.3 \times 10^{-3}$$



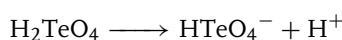
$$K = 1 \times 10^{-11}$$



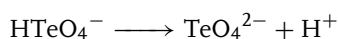
$$K_b = 1 \times 10^{-12}$$



$$K_b = 8.9 \times 10^{-17}$$

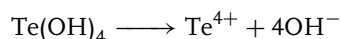


$$K = 2.1 \times 10^{-8}$$



$$K = 6.5 \times 10^{-12}$$

Solubility equilibrium:



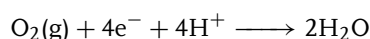
$$K = 1 \times 10^{-11}$$

2.16

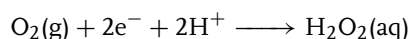
Group 16 Elements

Oxygen ($^{15.9994}_8\text{O}$), OS: (+2), 0, -2; IE: 1313.5 kJ mol⁻¹.

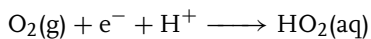
Acidic solutions



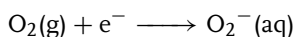
$$E^\ominus = 1.229 \text{ V}$$



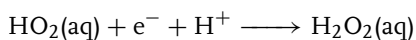
$$E^\ominus = 0.695 \text{ V}$$



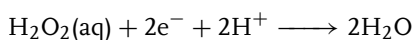
$$E^\ominus = -0.125 \text{ V}$$



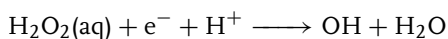
$$E^\ominus = -0.284 \text{ V}$$



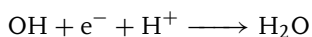
$$E^\ominus = 1.495 \text{ V}$$



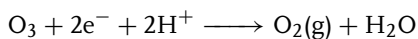
$$E^\ominus = 1.776 \text{ V}$$



$$E^\ominus = 0.71 \text{ V}$$

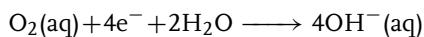


$$E^\ominus = 2.85 \text{ V (calcd)}$$

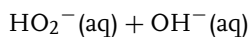
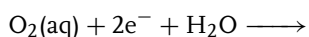


$$E^\ominus = 2.075 \text{ V (calcd)}$$

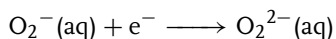
Basic solutions



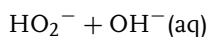
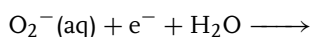
$$E^\ominus = 0.401 \text{ V}$$



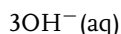
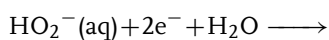
$$E^\ominus = -0.076 \text{ V}$$



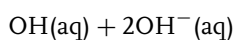
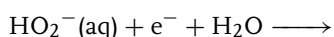
$$E^\ominus = -0.563 \text{ V}$$



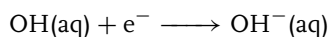
$$E^\ominus = 0.413 \text{ V}$$



$$E^\ominus = 0.878 \text{ V}$$

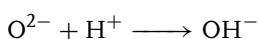


$$E^\ominus = -0.245 \text{ V}$$

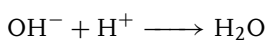


$$E^\ominus = 2.02 \text{ V}$$

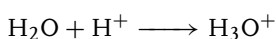
Proton affinities in gas phase:



$$A_{\text{H}^+} = -2860 \text{ kJ mol}^{-1}$$

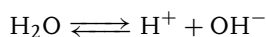


$$A_{\text{H}^+} = -1650 \text{ kJ mol}^{-1}$$

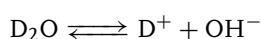


$$A_{\text{H}^+} = -695 \text{ kJ mol}^{-1}$$

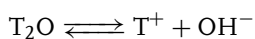
Dissociation equilibria:



$$K_{\text{W}} = 1.008 \times 10^{-14}$$

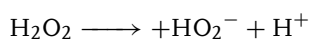


$$K_{\text{W}} = 1.95 \times 10^{-15}$$



(T for Tritium, ^3_1H)

$$K_{\text{W}} = 6 \times 10^{-6}$$

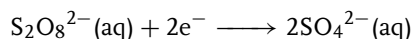


$$K = 2.4 \times 10^{-12}$$

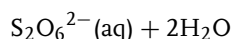
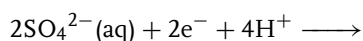
The solubility of oxygen in 100 g water at 1 bar and 20 °C is 4.42×10^{-3} g.

Sulfur ($^{32,065}_{16}\text{S}$), OS: +6, (+5), +4, +2, (+1), 0, -2; IE: 999.3 kJ mol⁻¹, EA: 200 and -414 kJ mol⁻¹.

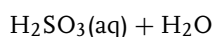
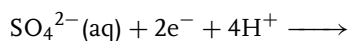
Acidic solutions



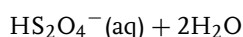
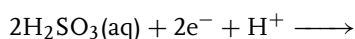
$$E^\ominus = 1.96 \text{ V}$$



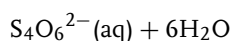
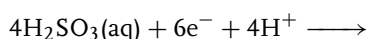
$$E^\ominus = -0.25 \text{ V}$$



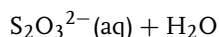
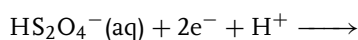
$$E^\ominus = 0.16 \text{ V}$$



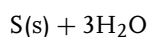
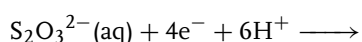
$$E^\ominus = -0.07 \text{ V}$$



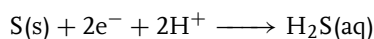
$$E^\ominus = 0.507 \text{ V}$$



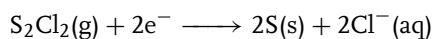
$$E^\ominus = 0.87 \text{ V}$$



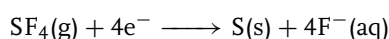
$$E^\ominus = 0.6 \text{ V}$$



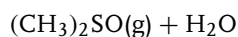
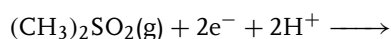
$$E^\ominus = 0.144 \text{ V}$$



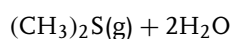
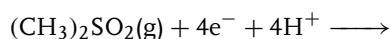
$$E^\ominus = 1.19 \text{ V}$$



$$E^\ominus = 0.97 \text{ V}$$

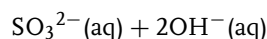
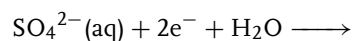


$$E^\ominus = 0.238 \text{ V (calcd)}$$

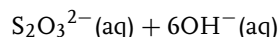
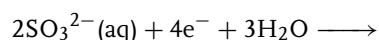


$$E^\ominus = 0.769 \text{ V (calcd)}$$

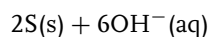
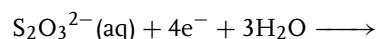
Basic solutions



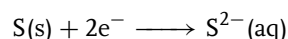
$$E^\ominus = -0.94 \text{ V}$$



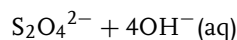
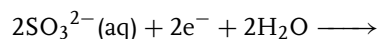
$$E^\ominus = -0.58 \text{ V}$$



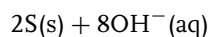
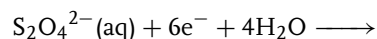
$$E^\ominus = -0.74 \text{ V}$$



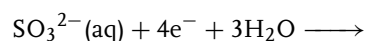
$$E^\ominus = -0.45 \text{ V}$$



$$E^\ominus = -1.13 \text{ V}$$



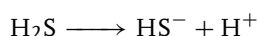
$$E^\ominus = -0.5 \text{ V}$$



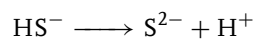
$$E^\ominus = -0.66 \text{ V}$$

The standard potentials of sulfur compounds are mostly calculated thermodynamically because the redox systems – except that of sulfite–dithionite – are irreversible. In excess sulfide, sulfur dissolves in the form of polysulfides.

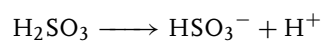
Dissociation equilibria:



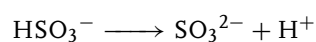
$$K = 9.1 \times 10^{-8}$$



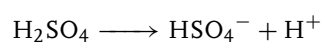
$$K = 1.2 \times 10^{-12}$$



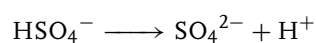
$$K = 1.7 \times 10^{-2}$$



$$K = 5 \times 10^{-6}$$



$$K > 10^3$$

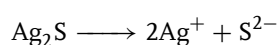


$$K = 1.26 \times 10^{-2} [7]$$

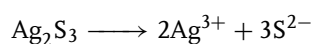
$$K = 1.02 \times 10^{-2}$$

$$- 1.08 \times 10^{-2} [1]$$

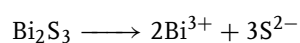
Solubility equilibria:



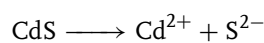
$$K_{\text{sp}} = 6 \times 10^{-51} \text{ (calcd)}$$



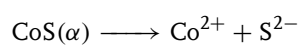
$$K_{\text{sp}} = 4 \times 10^{-29}$$



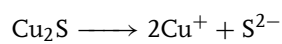
$$K_{\text{sp}} = 1.6 \times 10^{-72} \text{ (calcd)}$$



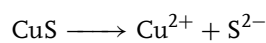
$$K_{\text{sp}} = 7 \times 10^{-28}$$



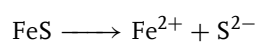
$$K_{\text{sp}} = 3.1 \times 10^{-23}$$



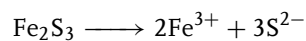
$$K_{\text{sp}} = 2 \times 10^{-47}$$



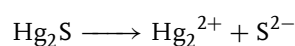
$$K_{\text{sp}} = 3.5 \times 10^{-38}$$



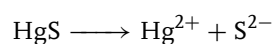
$$K_{\text{sp}} = 3.7 \times 10^{-19}$$



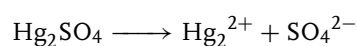
$$K_{\text{sp}} \sim 1 \times 10^{-88} \text{ (calcd)}$$



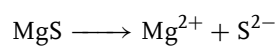
$$K_{\text{sp}} = 1 \times 10^{-47} \text{ (calcd)}$$



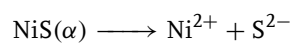
$$K_{\text{sp}} = 4 \times 10^{-53} \text{ (calcd)}$$



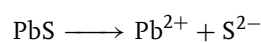
$$4.7 \times 10^{-7} < K_{\text{sp}} < 8.1 \times 10^{-7} [1]$$



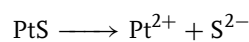
$$K_{\text{sp}} = 2 \times 10^{-15}$$



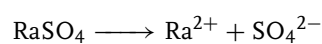
$$K_{\text{sp}} = 3 \times 10^{-21}$$



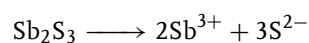
$$K_{\text{sp}} = 1.1 \times 10^{-29}$$



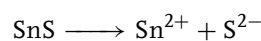
$$K_{\text{sp}} \sim 1 \times 10^{-68}$$



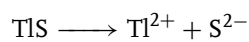
$$K_{\text{sp}} = 4.25 \times 10^{-11}$$



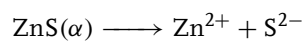
$$K_{\text{sp}} = 1 \times 10^{-30}$$



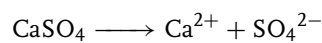
$$K_{\text{sp}} = 1 \times 10^{-28}$$



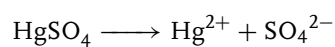
$$K_{\text{sp}} = 1 \times 10^{-24}$$



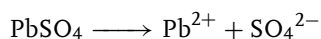
$$K_{\text{sp}} = 6.9 \times 10^{-20}$$



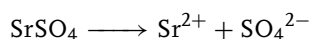
$$K_{\text{sp}} = 6.1 \times 10^{-5}$$



$$K_{\text{sp}} = 6.1 \times 10^{-7}$$



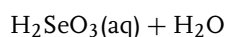
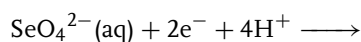
$$K_{\text{sp}} = 1.8 \times 10^{-8}$$



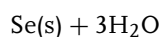
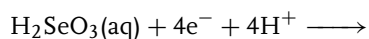
$$K_{\text{sp}} = 2.8 \times 10^{-7}$$

Selenium ($^{78.96}_{34}\text{Se}$), OS: +6, +5, +4, +3, +2, 0, -2; IE: 940.7 kJ mol⁻¹.

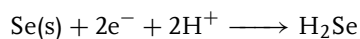
Acidic solutions



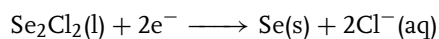
$$E^\ominus = 1.1 \text{ V (calcd)}$$



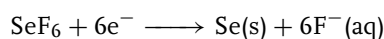
$$E^\ominus = 0.74 \text{ V}$$



$$E^\ominus = -0.11 \text{ V}$$

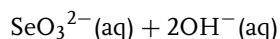
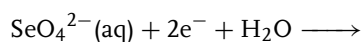


$$E^\ominus = 1.108 \text{ V}$$

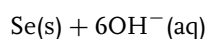
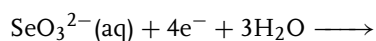


$$E^\ominus = 1.109 \text{ V}$$

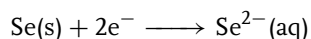
Basic solutions



$$E^\ominus = 0.03 \text{ V (calcd)}$$

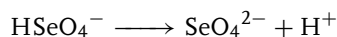


$$E^\ominus = -0.36 \text{ V}$$

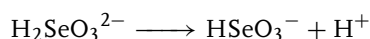


$$E^\ominus = 0.67 \text{ V}$$

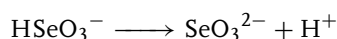
Dissociation equilibria:



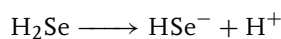
$$K = 8.9 \times 10^{-3}$$



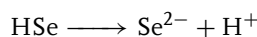
$$K = 2.7 \times 10^{-3}$$



$$K = 2.63 \times 10^{-7}$$



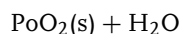
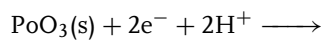
$$K = 1.88 \times 10^{-4}$$



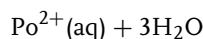
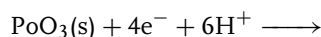
$$K = 1 \times 10^{-14}$$

Polonium ($^{208,982}_{84}\text{Po}$), OS: +6, +4, +2, 0, -2; IE: 813 kJ mol⁻¹.

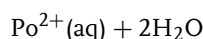
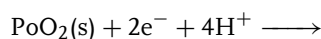
Acidic solutions



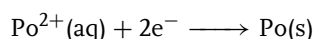
$$E^\ominus = 1.51 \text{ V}$$



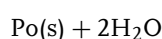
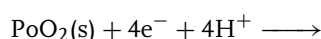
$$E^\ominus = 1.3 \text{ V}$$



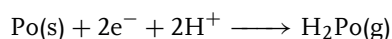
$$E^\ominus = 1.1 \text{ V}$$



$$E^\ominus = 0.37 \text{ V}$$

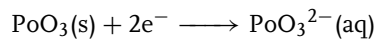


$$E^\ominus = 0.73 \text{ V}$$

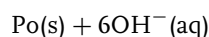
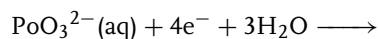


$$E^\ominus \sim 1 \text{ V}$$

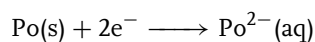
Basic solutions



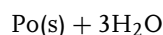
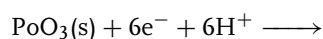
$$E^\ominus = 1.48 \text{ V}$$



$$E^\ominus = -0.5 \text{ V}$$



$$E^\ominus \sim 1.4 \text{ V}$$



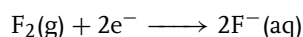
$$E^\ominus = 0.16 \text{ V}$$

Approximate E^\ominus values are obtained from the potentials of the deposition of Po and PoO_2 . Because of the emanation of high-energy α -particles, ozone, oxygen radicals, and peroxides are formed from water, which can oxidize Po^{2+} ions.

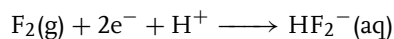
2.17

Group 17 Elements

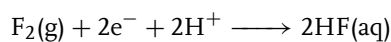
Fluorine ($^{18.998}_{9}\text{F}$), OS: 0, -1; IE: 1680 kJ mol⁻¹, EA: -332.6 kJ mol⁻¹.



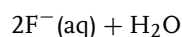
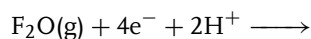
$$E^\ominus = 2.866 \text{ V (calcd)}$$



$$E^\ominus = 2.979 \text{ V (calcd)}$$

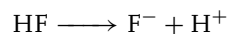


$$E^\ominus = 3.053 \text{ V (calcd)}$$



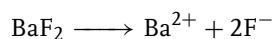
$$E^\ominus = 2.153 \text{ V (calcd)}$$

Dissociation equilibrium:

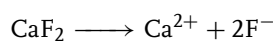


$$K = 3.53 \times 10^{-4}$$

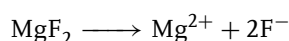
Solubility equilibria:



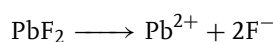
$$K_{\text{sp}} = 1.7 \times 10^{-6}$$



$$K_{\text{sp}} = 3.9 \times 10^{-11}$$



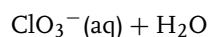
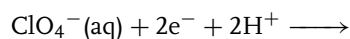
$$K_{\text{sp}} = 1.7 \times 10^{-9}$$



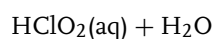
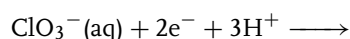
$$K_{\text{sp}} = 3.2 \times 10^{-8}$$

Chlorine ($^{35.453}_{17}\text{Cl}$), OS: +7, +5, +3, +1, 0, -1; IE: 1255.7 kJ mol⁻¹, EA: -348.7 kJ mol⁻¹.

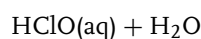
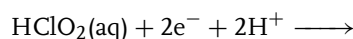
Acidic solutions



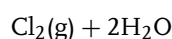
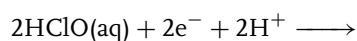
$$E^\ominus = 1.201 \text{ V}$$



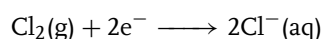
$$E^\ominus = 1.181 \text{ V}$$



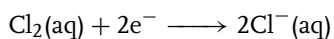
$$E^\ominus = 1.701 \text{ V}$$



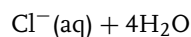
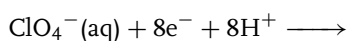
$$E^\ominus = 1.63 \text{ V}$$



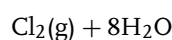
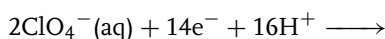
$$E^\ominus = 1.358 \text{ V}$$



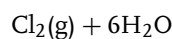
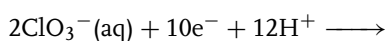
$$E^\ominus = 1.396 \text{ V}$$



$$E^\ominus = 1.387 \text{ V}$$



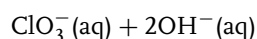
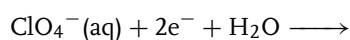
$$E^\ominus = 1.392 \text{ V}$$



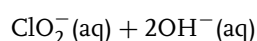
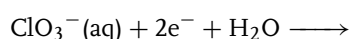
$$E^\ominus = 1.468 \text{ V}$$

The E^\ominus values for reactions including chlorine species with oxidation number of +1 or higher are calculated from thermodynamic data.

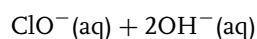
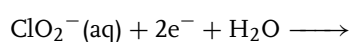
Basic solutions



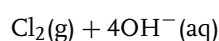
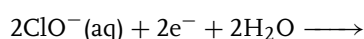
$$E^\ominus = 0.374 \text{ V}$$



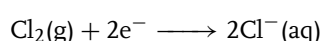
$$E^\ominus = 0.295 \text{ V}$$



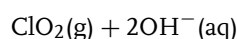
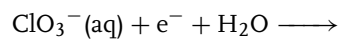
$$E^\ominus = 0.681 \text{ V}$$



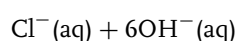
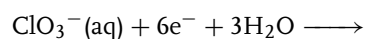
$$E^\ominus = 0.421 \text{ V}$$



$$E^\ominus = 1.358 \text{ V}$$

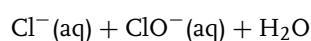


$$E^\ominus = -0.481 \text{ V}$$



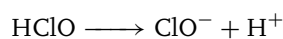
$$E^\ominus = 0.622 \text{ V}$$

Disproportionation equilibrium:



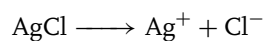
$$K = 9.64 \times 10^{-1}$$

Dissociation equilibrium:

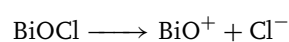


$$K = 5.6 \times 10^{-8}$$

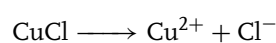
Solubility equilibria:



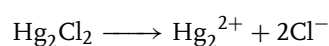
$$K_{\text{sp}} = 1.8 \times 10^{-10}$$



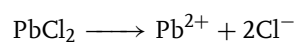
$$K_{\text{sp}} = 7 \times 10^{-9}$$



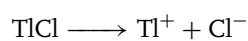
$$K_{\text{sp}} = 1.8 \times 10^{-7}$$



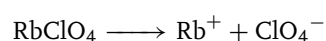
$$K_{\text{sp}} = 1.1 \times 10^{-18}$$



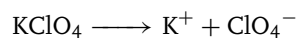
$$K_{\text{sp}} = 1.7 \times 10^{-5}$$



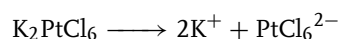
$$K_{\text{sp}} = 1.9 \times 10^{-4}$$



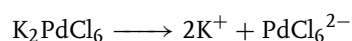
$$K_{\text{sp}} = 2.5 \times 10^{-3}$$



$$K_{\text{sp}} = 1.07 \times 10^{-2}$$



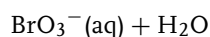
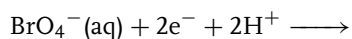
$$K_{\text{sp}} = 1.1 \times 10^{-5}$$



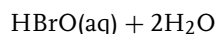
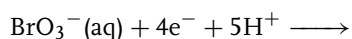
$$K_{\text{sp}} = 5.9 \times 10^{-6}$$

Bromine ($^{79.904}_{35}\text{Br}$), OS: +7, +5, +1, 0, -1; IE: $-324.5 \text{ kJ mol}^{-1}$.

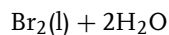
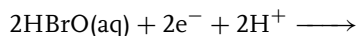
Acidic solutions



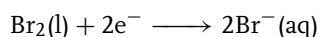
$$E^\ominus = 1.853 \text{ V}$$



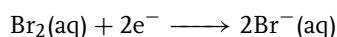
$$E^\ominus = 1.447 \text{ V}$$



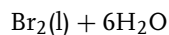
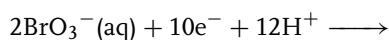
$$E^\ominus = 1.604 \text{ V}$$



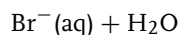
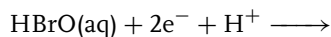
$$E^\ominus = 1.0652 \text{ V}$$



$$E^\ominus = 1.0874 \text{ V}$$

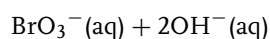
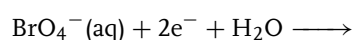


$$E^\ominus = 1.478 \text{ V}$$

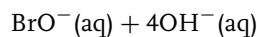
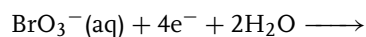


$$E^\ominus = 1.341 \text{ V}$$

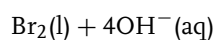
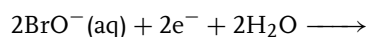
Basic solutions



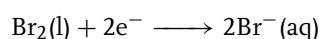
$$E^\ominus = 1.025 \text{ V}$$



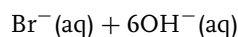
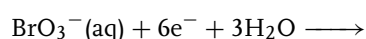
$$E^\ominus = 0.492 \text{ V}$$



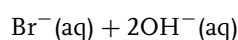
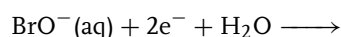
$$E^\ominus = 0.455 \text{ V}$$



$$E^\ominus = 1.0652 \text{ V}$$



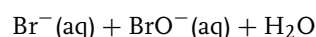
$$E^\ominus = 0.584 \text{ V}$$



$$E^\ominus = 0.766 \text{ V}$$

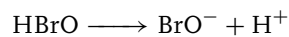
The standard potentials of the reactions involving bromine species with oxidation number of +1 or higher are calculated from thermodynamic data.

Disproportionation equilibrium:



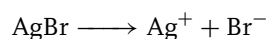
$$K = 9.7 \times 10^{-1}$$

Dissociation equilibrium:

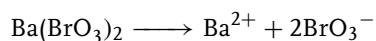


$$K = 2.06 \times 10^{-9}$$

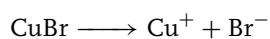
Solubility equilibria:



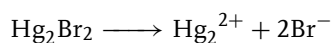
$$K_{\text{sp}} = 6.3 \times 10^{-3}$$



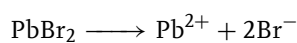
$$K_{\text{sp}} = 3.3 \times 10^{-5}$$



$$K_{\text{sp}} = 5.3 \times 10^{-9}$$



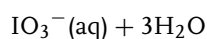
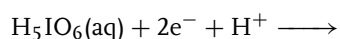
$$K_{\text{sp}} = 4.6 \times 10^{-23}$$



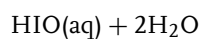
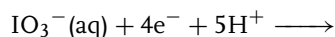
$$K_{\text{sp}} = 5 \times 10^{-5}$$

Iodine ($^{126.904}_{53}\text{I}$), OS: +7, +5, +3, +1, 0, -1; IE: $1008.7 \text{ kJ mol}^{-1}$, EA: $-295.3 \text{ kJ mol}^{-1}$.

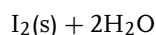
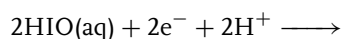
Acidic solutions



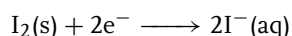
$$E^\ominus = 1.6 \text{ V (calcd)}$$



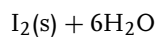
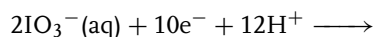
$$E^\ominus = 1.13 \text{ V}$$



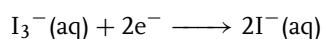
$$E^\ominus = 1.44 \text{ V}$$



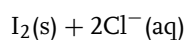
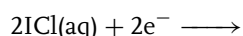
$$E^\ominus = 0.535 \text{ V}$$



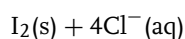
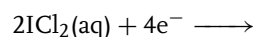
$$E^\ominus = 1.2 \text{ V}$$



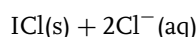
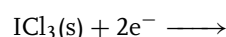
$$E^\ominus = 0.536 \text{ V}$$



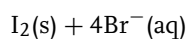
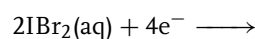
$$E^\ominus = 1.2 \text{ V}$$



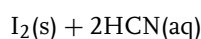
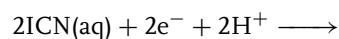
$$E^\ominus = 1.07 \text{ V}$$



$$E^\ominus = 1.312 \text{ V (calcd)}$$

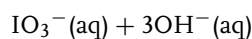
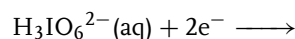


$$E^\ominus = 0.874 \text{ V (calcd)}$$

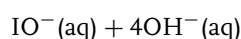
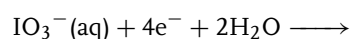


$$E^\ominus = 0.711 \text{ V}$$

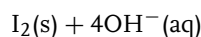
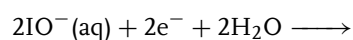
Basic solutions



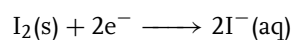
$$E^\ominus = 0.65 \text{ V (calcd)}$$



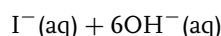
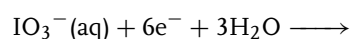
$$E^\ominus = 0.15 \text{ V}$$



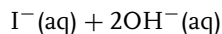
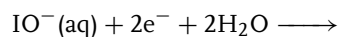
$$E^\ominus = 0.42 \text{ V}$$



$$E^\ominus = 0.535 \text{ V}$$

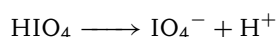


$$E^\ominus = 0.26 \text{ V}$$

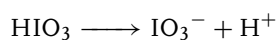


$$E^\ominus = 0.48 \text{ V}$$

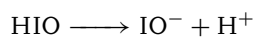
Dissociation equilibria:



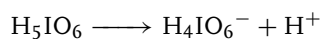
$$K = 2.3 \times 10^{-2}$$



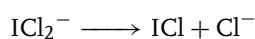
$$K = 1.7 \times 10^{-1}$$



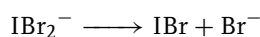
$$K = 2.29 \times 10^{-11}$$



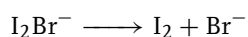
$$K = 5.1 \times 10^{-4}$$



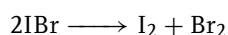
$$K = 6 \times 10^{-3}$$



$$K = 2.7 \times 10^{-13}$$

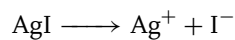


$$K = 8.19 \times 10^{-2}$$

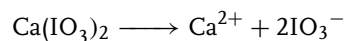


$$K = 1.8 \times 10^{-5}$$

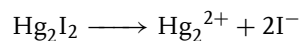
Solubility equilibria:



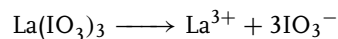
$$K_{\text{sp}} = 2.3 \times 10^{-16}$$



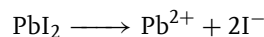
$$K_{\text{sp}} = 1.93 \times 10^{-6}$$



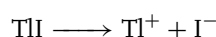
$$K_{\text{sp}} = 3.7 \times 10^{-29}$$



$$K_{\text{sp}} = 5.97 \times 10^{-10}$$



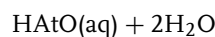
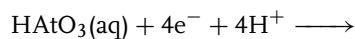
$$K_{\text{sp}} = 8.7 \times 10^{-9}$$



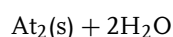
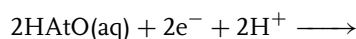
$$K_{\text{sp}} = 5.8 \times 10^{-8}$$

Astatine ($^{209.987}_{85}\text{At}$), OS: +5, +3, +1, 0, -1; IE: ca 926 kJ mol⁻¹, EA: ca -270 kJ mol⁻¹.

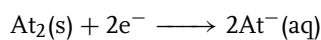
Acidic solutions



$$E^\ominus \sim 1.4 \text{ V}$$

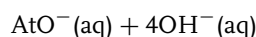
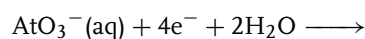


$$E^\ominus \sim 0.7 \text{ V}$$

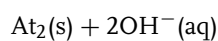
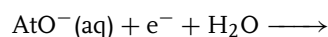


$$E^\ominus \sim 0.2 \text{ V}$$

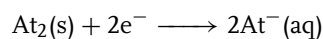
Basic solutions



$$E^\ominus \sim 0.5 \text{ V}$$



$$E^\ominus \sim 0 \text{ V}$$



$$E^\ominus \sim 0.2 \text{ V}$$

All the E^\ominus values are measured, but these are rather approximate values since At is an unstable element and rather dilute solutions ($c \sim 10^{-11} \text{ mol dm}^{-3}$) are used to test the redox properties.

2.18 Group 18 Elements

Helium (${}^{4.0026}_{2}\text{He}$), OS: 0; IE: 2372 kJ mol⁻¹.

No data are available.

Neon (${}^{20.1797}_{10}\text{Ne}$), OS: 0; IE: 2080 kJ mol⁻¹.

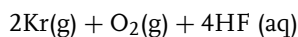
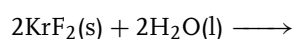
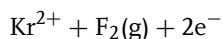
No data are available.

Argon (${}^{39.948}_{18}\text{Ar}$), OS: 0; IE: 1520 kJ mol⁻¹.

No data are available.

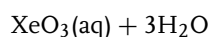
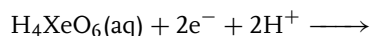
Solubility of argon in 100 g water at 1 bar and 20 °C is 5.99×10^{-3} g.

Krypton (${}^{83.798}_{36}\text{Kr}$), OS: +2, 0; IE: 1351 kJ mol⁻¹.

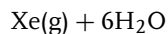
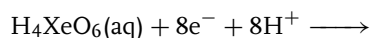


(fast decomposition)

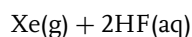
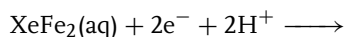
Xenon (${}^{131.293}_{54}\text{Xe}$), OS: +6, +4, +2, 0; IE: 1170 kJ mol⁻¹.



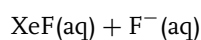
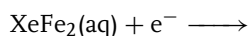
$$E^\ominus = 2.42 \text{ V}$$



$$E^\ominus = 2.18 \text{ V}$$

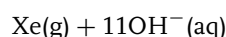
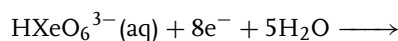


$$E^\ominus = 2.64 \text{ V}$$

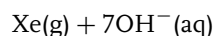
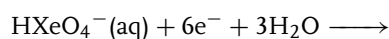


$$E^\ominus = 0.9 \text{ V}$$

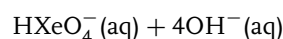
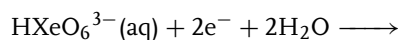
Basic solutions



$$E^\ominus = 1.18 \text{ V}$$



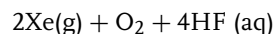
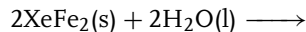
$$E^\ominus = 1.24 \text{ V}$$



$$E^\ominus = 0.99 \text{ V}$$

E^\ominus values are calculated

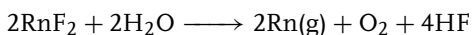
thermodynamically.



(decomposition, $t_{1/2} = 7 \text{ h}$)

Radon (${}^{222.017}_{86}\text{Rn}$), OS: +2, 0 IE: 1037 kJ mol⁻¹.

RnF_2 can be dissolved in anhydrous HF (Rn^{2+} , RnF^+ , RnF_3^-). In aqueous solutions, it reacts with water.



No electrochemical data are available.

Acknowledgment

Financial support from the Hungarian Scientific Research Fund, OTKA – TO46987, is acknowledged. The author expresses his thanks to Prof. G. Horányi for the careful reading of the manuscript and for his valuable comments.

References

1. J. G. Albright, J. A. Bard, S. Serna et al., *J. Chem. Thermodyn.* **2000**, 32, 1447.
2. L. Falciola, P. R. Mussini, T. Mussini et al., *J. Chem. Thermodyn.* **2004**, 36, 465.
3. L. Falciola, P. R. Mussini, T. Mussini et al., *J. Chem. Thermodyn.* **2005**, 37, 363.
4. J. Redepenning, E. Castro-Narro, G. Venkataraman et al., *J. Electroanal. Chem.* **2001**, 498, 192.
5. M. M. Baizer, H. Lund, (Eds.), *Organic Electrochemistry*, Marcel Dekker, New York, 1983
6. A. J. Bard, H. Lund, (Eds.), *The Encyclopedia of Electrochemistry of Elements*, Marcel Dekker, New York, 1973–1986
7. G. Milazzo, S. Caroli, *Tables of Standard Electrode Potentials*, Wiley-Interscience, New York, 1977
8. G. Charlot, A. Collumbeau, M. J. C. Marchot, *Selected Constants. Oxidation-Reduction Potentials of Inorganic Substances in Aqueous Solution*, IUPAC, Butterworths, London, 1971
9. M. Pourbaix, N. de Zoubov, J. van Muylder, *Atlas d'Equilibres Electrochimiques a 25°C*, Gauthier-Villars, Paris, 1963
10. M. Pourbaix, (Ed.), *Atlas of Electrochemical Equilibria in Aqueous Solutions*, Pergamon-CEBELCOR, Brussels, 1966
11. A. J. Bard, R. Parsons, J. Jordan, (Eds.), *Standard Potential in Aqueous Solution*, Marcel Dekker, New York, 1985
12. L. Meites, P. Zuman, A. Narayanan, *Handbook Series in Inorganic Chemistry*, CRC Press, Boca Raton, Florida, 1980–1988, Vols. 1–8.
13. B. P. Nikolskij, (Ed.), *Spravochnik Khimika*, Izd. Khimiya, Moscow, Leningrad, 1964, Vol. 3.
14. R. C. Weast, (Ed.), *CRC Handbook Chemistry and Physics*, CRC Press, Boca Raton, Florida, USA, 1989–1990.
15. H. Hotop, W. C. Lineberg, *J. Phys. Chem., Ref. Data* **1985**, 14, 731.
16. D. Dobos, *Electrochemical Data*, Akadémiai Kiadó, Budapest, 1975
17. W. F. Linke, *Solubilities: Inorganic and Metal-Organic Compounds*, American Chemical Society, Washington, DC, 1965, Vol. II.
18. D. D. Perrin, (Ed.), *Ionisation Constant of Inorganic Acids and Bases in Aqueous Solution*, Pergamon, Oxford, New York, Toronto, 1984
19. *Solubility Data Series*, Pergamon Press, 1979–1992, 1994–1996, Vols. 1–53, Vol. 54–65; *IUPAC-NIST Solubility Series*, Oxford University Press, 1998; *J. Phys. Chem. Reference Data* (Published quarterly), NIST, Gaithersburg, MD.
20. L. G. Sillén, A. E. Martell, *Stability Constants of Metal-ion Complexes, Special Publ. 17*, The Chemical Society, London, 1964
21. J. D. Cox, D. D. Wagman, V. A. Medvedev, *CODATA Key Values for Thermodynamics*, Hemisphere Publication Co., New York, 1989
22. N. N. Greenwood, A. Earnshaw, *Chemistry of the Elements*, Butterworth-Heinemann, 1997
23. IUPAC Periodic Table of the Elements, 14 January 2005, <http://www.iupac.org/reports/periodic-tables/>
24. R. Parsons, *Pure Appl. Chem.* **1974**, 37, 503.
25. I. Mills, T. Cvitas, *Quantities, Units and Symbols in Physical Chemistry*, IUPAC, Blackwell Science Publication, London, Edinburgh, Boston, Melbourne, Paris, Berlin, Vienna, 1993
26. M. A. Paul, F. A. Long, *Chem. Rev.* **1957**, 57, 1.
27. J. F. Coetze, C. D. Ritchie, (Eds.), *Solute-solvent Interactions*, Marcel Dekker, New York, 1969
28. M. D. Levi, D. Aurbach, *J. Electroanal. Chem.* **1997**, 421, 79.
29. H. N. Jena, T. Matthews, T. Subramanian, *J. Chem. Thermodyn.* **1996**, 28, 215.
30. Y. Castrillejo, M. R. Bermejo, P. Diaz Arocas et al., *J. Electroanal. Chem.* **2005**, 579, 343.
31. A. Kuznetsov, M. Gaune-Escard, *Electrochim. Acta* **2001**, 46, 1101.
32. R. Heyrovská, *J. Alloys Compd.* **2001**, 323–324, 614.
33. Y. Sakamura, T. Hijikata, K. Kinoshita et al., *J. Alloys Compd.* **1998**, 271–273, 592.
34. J. Serp, R. J. M. Konings, R. Malmbeck et al., *J. Electroanal. Chem.* **2004**, 561, 143.
35. B. Keita, I.-M. Mbomekalle, L. Nadjo et al., *Electrochem. Commun.* **2004**, 6, 978.
36. M. Hecht, F. A. Schultz, B. Speiser, *Inorg. Chem.* **1996**, 35, 5555.
37. J. Lee, D. A. Tryk, A. Fujishima et al., *Chem. Commun.* **2002**, 486.
38. M. D. Morris, G. L. Kok in *Encyclopedia of Electrochemistry of Elements* Eds.: A. J. Bard, H. Lund, (Eds.), Marcel Dekker, New York, 1979, Vol. 13. Chapter 1.
39. S. C. Dorman, J. P. Harrington, M. S. Martin et al., *J. Inorg. Biochem.* **2004**, 98, 185.

40. F. A. Armstrong in *Electroanalytical Methods for Biological Materials* Eds.: A. Brajter-Toth, J. Q. Chambers, (Eds.), Marcel Dekker, New York, 2002, Chapter 5.
41. A. E. F. Nassar, J. F. Rusling, M. Tominaga et al., *J. Electroanal. Chem.* **1996**, 416, 183.
42. E. Lindner, I. Krebs, R. Fawzi et al., *Organometallics* **1999**, 18, 480.
43. B. Gollas, B. Speiser, J. Sieglén et al., *Organometallics* **1996**, 15, 260.
44. B. Gollas, B. Speiser, I. Zagors et al., *J. Organomet. Chem.* **2000**, 602, 75.
45. M. Carrano, P. Ceroni, C. Fontanesi et al., *Electrochim. Acta* **2001**, 46, 3199.
46. D. Geraldo, C. Linares, Y.-Y. Chen et al., *Electrochem. Commun.* **2002**, 4, 182.
47. S. Buchmann, H. A. Mayer, B. Speiser et al., *Electrochim. Acta* **2003**, 48, 2725.
48. F. Novak, B. Speiser, H. A. Y. Mohammad et al., *Electrochim. Acta* **2004**, 49, 3841.
49. S. Buchmann, H. A. Mayer, B. Speiser et al., *Electrochim. Acta* **2001**, 46, 3207.
50. E. Norkus, A. Vaškelis, *Polyhedron* **1994**, 13, 3041.
51. E. Norkus, A. Vaškelis, J. Reklaitis, *Zh. Neorg. Khim.* **1986**, 31, 2318.
52. E. Norkus, A. Vaškelis, R. Vaitkus et al., *J. Inorg. Biochem.* **1995**, 60, 299.
53. E. Norkus, J. Vaičiūnienė, T. Vuorinen et al., *Carbohydr. Res.* **2003**, 339, 599.
54. E. Norkus, J. Vaičiūnienė, J. Reklaitis et al., *Chemija (Vilnius)* **2002**, 13, 119.
55. E. Norkus, J. Vaičiūnienė, J. Reklaitis et al., *Chemija (Vilnius)* **2002**, 13, 129.
56. E. Norkus, A. Vaškelis, J. Reklaitis et al., *Koord. Khim.* **1988**, 14, 325.
57. E. Norkus, G. Grincienė, T. Vuorinen et al., *Supramol. Chem.* **2003**, 15, 425.
58. E. Norkus, G. Grincienė, T. Vuorinen et al., *J. Incl. Phenom.* **2004**, 48, 147.
59. E. Norkus, G. Grincienė, R. Vaitkus, *Carbohydr. Res.* **2002**, 337, 1657.
60. E. Norkus, A. Vaškelis, I. Zakaitė, *Talanta* **1996**, 43, 465.
61. E. Norkus, A. Vaškelis, *Chemija (Vilnius)* **1995**, N4, 19.
62. E. Norkus, A. Vaškelis, I. Zakaitė et al., *Talanta* **1995**, 42, 1701.
63. E. Norkus, R. Pauliukaitė, *Pol. J. Chem.* **2000**, 74, 1231.
64. E. Norkus, I. Stalnionienė, D. C. Crans, *Heteroat. Chem.* **2003**, 14, 625.
65. E. Norkus, I. Stalnionienė, D. C. Crans, *Chemine Technologija (Kaunas)* **2002**, N4, 9.
66. E. Norkus, G. Grincienė, T. Vuorinen et al., *Int. J. Biol. Macromol.* **2003**, 33, 251.
67. H. L. Clever, S. A. Johnson, M. E. Derrick, *J. Phys. Chem. Ref. Data* **1985**, 14, 631.
68. B. Speiser, C. Tittel, W. Einholz et al., *J. Chem. Soc., Dalton Trans.* **1999**, 1741.
69. W. Einholz, K. Vaas, C. Wieloch et al., *Z. Anorg. Allg. Chem.* **2002**, 628, 258.
70. B. Speiser, T. Wizeman, M. Würde, *Inorg. Chem.* **2003**, 42, 4018.
71. J. F. Nemeth, L. R. Sherman, *Microchem. J.* **1997**, 56, 22.
72. J. Lee, Y. Einaga, A. Fujishima et al., *J. Electrochem. Soc.* **2004**, 151, E 265.

3

Redox Potential-structure Relationships in Coordination Compounds

Armando J.L. Pombeiro
Instituto Superior Técnico, Lisboa, Portugal

3.1	Introduction	79
3.2	Redox Potential Parameterization	80
3.2.1	Pickett's and Derived Models	80
3.2.1.1	The Ligand Parameter P_L and Metal Center Parameters E_s and β . .	80
3.2.1.2	Extensions of the Model	91
3.2.1.2.1	Dependence of the Ligand Parameter P_L on the Binding Metal Center	91
3.2.1.2.2	18-electron Complexes of the Types $[M_sLL']$ and $[M_sL_n]$	92
3.2.1.2.3	17- and 16-electron Compounds	93
3.2.1.3	Other Relationships	94
3.2.1.3.1	Effects of Isomerism	94
3.2.1.3.2	Relationships with Other Properties and Reactivity	95
3.2.2	Lever's Model	95
3.2.2.1	The Ligand Parameter E_L and the Metal Center Parameters S_M and I_M	95
3.2.2.2	Extensions of the Model	101
3.2.2.3	Other Relationships	103
3.2.3	Bursten's Model	104
3.3	Final Comments	104
	References	106

3.1 Introduction

Since long, redox potentials of coordination compounds have been correlated to many other features of these compounds, such as the highest occupied molecular orbital (HOMO) energy, the gas-phase ionization potential, the ligand field stabilization energy, the Hammett's σ and related constants, the energy of charge-transfer bands, infrared stretching frequencies, X-ray photoelectron spectroscopy binding energies, and ligand structural parameters in macrocyclic ligand complexes [1–7]. These properties are often markedly dependent on the electronic/structural features of the ligands and their binding metal centers, which suggests that it should be possible to define electrochemical parameters determined by the redox potential that could provide a measure of such ligand and metal site features.

For the sake of simplicity, the search for additive effects has oriented most of the research, and ligand additivity has been clearly recognized in some cases for many years. Hence, for the series of closely related 18-electron octahedral complexes $[\text{Mn}(\text{CO})_{6-x}(\text{CNR})_x]^+$ ($x = 1-6$) that undergo a single-electron reversible oxidation, the oxidation potential was shown to correlate linearly with the HOMO energy, a

greater stability of the latter corresponding to a higher value of the former [8]. In the same year, for the first-row transition metal complexes of the type $[\text{M}(\text{CO})_{6-x}\text{L}_x]^{y+}$, the linear relationship (1) between the oxidation potential and the degree of carbonyl substitution (x) was proposed by Pickett and Pletcher [9].

$$E^\theta = A + x \left(\frac{dE^\theta}{dx} \right)_L + 1.48 y \quad (1)$$

In this expression, y is the charge of the complex, A is a constant that depends upon the metal, the solvent, and the reference electrode, and $(dE^\theta/dx)_L$ can be considered as a measure of the L ligand effect, that is, the variation of the oxidation potential per each CO replacement by L. A separation between the ligand and the metal center effects is also evident.

These observations, in spite of expected limitations in terms of generality, have revealed a fundamental role for the development, at a latter stage, of systematic approaches.

The main ones are described in the following, that is, those based on the Pickett's, Lever's, and Bursten's models. In the first one, the potentials have typically been quoted relative to the saturated calomel electrode (SCE), whereas in the second one they have been referred to the normal hydrogen electrode (SHE). The

conversion of the former potentials (vs. SCE) into the latter (vs. SHE) is simply achieved by adding 0.245 V. Moreover, the use of the ferricinium/ferrocene redox couple has also been frequently encountered in the literature, and the potentials can be easily interconverted in the other scales by considering that for this redox couple, $E^\theta = 0.53, 0.55$, or 0.42 V vs. SCE (in 0.2 M $[\text{NBu}_4][\text{BF}_4]/\text{CH}_2\text{Cl}_2$, THF, or NCMe, respectively).

3.2

Redox Potential Parameterization

3.2.1

Pickett's and Derived Models

3.2.1.1 The Ligand Parameter P_L and Metal Center Parameters E_s and β

Pickett et al. [10] observed experimentally a linear relationship between the oxidation potentials of the members of a series of closed-shell octahedral-type complexes $[\text{M}_s\text{L}]$ (with a variable L ligand binding the 16-electron M_s metal site) and the oxidation potentials of the homologous complexes with the $[\text{Cr}(\text{CO})_5]$ site, that is, $[\text{Cr}(\text{CO})_5\text{L}]$. Such a relationship can be expressed by Eq. 2 (considering the carbonyl ligand and a general ligand L) in which the slope β , named the *polarizability of the metal site*, is a measure of the sensitivity of the redox orbital energy to a change in the ligand L.

$$\begin{aligned} E_{1/2}^{\text{ox}}[\text{M}_s\text{L}] - E_{1/2}^{\text{ox}}[\text{M}_s(\text{CO})] \\ = \beta \{ E_{1/2}^{\text{ox}}[\text{Cr}(\text{CO})_5\text{L}] \\ - E_{1/2}^{\text{ox}}[\text{Cr}(\text{CO})_6] \} \end{aligned} \quad (2)$$

The convenience of the definition of two other electrochemical parameters is evident from the analysis of this equation:

(1) The oxidation potential of the carbonyl complex with the $\{\text{M}_s\}$ center, that is, $E_{1/2}^{\text{ox}}[\text{M}_s(\text{CO})]$, which has been considered [10] a measure of the *electron richness (E_s) of the metal site* (the higher this richness, the lower the oxidation potential of the complex should be) (Eq. 3) and (2) the shift of the oxidation potential resulting from the replacement of one carbonyl ligand in $[\text{Cr}(\text{CO})_6]$ by one L ligand, that is, the difference $E_{1/2}^{\text{ox}}[\text{Cr}(\text{CO})_5\text{L}] - E_{1/2}^{\text{ox}}[\text{Cr}(\text{CO})_6]$ defined [10] as the *electrochemical ligand P_L parameter* (Eq. 4). This parameter is identical to $(dE^\theta/dx)_L$ in Eq. (1), for $\text{M}=\text{Cr}$ [9], and since it is a difference of redox potentials, it is not dependent on the reference electrode, in contrast to E_s . Equation (2) can then assume the form shown by Eq. (5) [10].

$$E_s\{\text{M}_s\} = E_{1/2}^{\text{ox}}[\text{M}_s(\text{CO})] \quad (3)$$

$$\begin{aligned} P_L(\text{L}) &= E_{1/2}^{\text{ox}}[\text{Cr}(\text{CO})_5\text{L}] \\ &\quad - E_{1/2}^{\text{ox}}[\text{Cr}(\text{CO})_6] \end{aligned} \quad (4)$$

$$E_{1/2}^{\text{ox}}[\text{M}_s\text{L}] = E_s + \beta P_L \quad (5)$$

The P_L parameter has been proposed [10] as a measure of the *net* electron-donor minus electron-acceptor ability of the ligand L: the higher this ability, the less stabilized will be the HOMO at $[\text{Cr}(\text{CO})_5\text{L}]$ and thus, the lower its oxidation potential and the lower the P_L value.

General behaviors are summarized in Table 1. For ligands such as carbon monoxide, isocyanides (CNR), carbynes, nitrosyl NO^+ and, although to a smaller extent, nitriles (NCR), which are not only σ donors but also good π acceptors, the *net* electron-donor ability is modest or poor and the P_L parameter has a high value. However, ligands that are not involved in π -bonding, such as ammonia (NH_3) and pyridine, exhibit lower P_L values that, nevertheless, are usually not

Tab. 1 General relationship between the electrochemical P_L ligand parameter and the electronic properties of the ligand (L) and its coordination M–L bond

L (example)	M–L bond	P_L
σ -donor and π -acceptor ($\equiv\text{CR}$, CO, CNR, NO^+ , NCR)	$\text{M} \begin{array}{c} \xrightarrow{\pi} \\ \xleftarrow{\sigma} \end{array} \text{L}$	High
σ -donor (NH_3 , pyridine)	$\text{M} \xleftarrow{\sigma} \text{L}$	Intermediate
Very strong σ -donor and eventually also π -donor (halide, $\text{C}\equiv\text{CR}^-$, H^- , N_3^- , NCNH^- , OH^-)	$\text{M} \begin{array}{c} \xleftarrow{\pi} \\ \xleftarrow{\sigma} \end{array} \text{L}$	Low

as low as those of ligands, typically halides, which are both σ - and π -electron donors. The hydride, alkynyls ($\text{C}\equiv\text{CR}^-$), hydrogen cyanamide (NCNH^-), and OH^- , also have rather low P_L values mainly as a result of their strong σ -electron donor character.

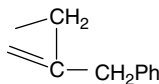
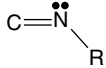
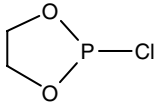
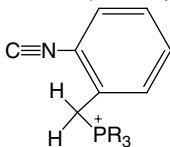
Hence, the P_L ligand parameter reflects, in an overall way, the combined σ - and π -electronic properties of the coordination M–L bond. It is noteworthy to mention that it relates to the variation of the free-energy difference of the redox processes (consider the known expression $\Delta G^\theta = -nFE^\theta$, in which n is the number of electrons transferred and F is the Faraday constant). It has analogies with the Hammett σ_p constant [11, 12] defined as $\log(K_X/K_H)$, that is, $\log K_X - \log K_H$, in which K_X and K_H are the acidic constants of the p -substituted benzoic acid $\text{HOOC}_6\text{H}_4\text{X}$ and of benzoic acid itself, respectively [13] (consider also the known relationship $\Delta G^\theta = -RT \ln K$).

The P_L parameter can be obtained in less direct (but often more convenient) ways than that corresponding to the immediate use of Eq. (4) (its definition expression) that requires the synthesis of the corresponding $[\text{Cr}(\text{CO})_5\text{L}]$ complex (which in many cases may even be unknown) and the measuring of its oxidation potential. In fact, if one knows

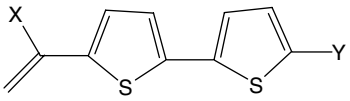
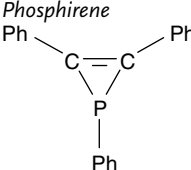
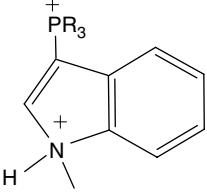
the oxidation potential of an 18-electron complex with ligand L coordinated to a metal center $\{\text{M}_s\}$ with known E_s and β parameters, the simple application of the general expression (5) allows the estimate of P_L for that ligand. If E_s and β are unknown for $\{\text{M}_s\}$, they can be obtained by applying the same Eq. (5) to at least two known members of the series (with known oxidation potentials), that is, $[\text{M}_s\text{L}']$ and $[\text{M}_s\text{L}'']$, provided L' and L'' are ligands with known P_L values. Other indirect modes of getting P_L are discussed in the following, and by using one or another approach, P_L values have already been proposed for a considerable variety of ligands. The currently known values of ligand P_L and metal center E_s and β parameters are depicted in Tables 2–8 [10, 14–48], since extensive and updated lists had not yet been provided. However, an extensive list of P_L values for carbyne, carbene, vinylidene, allenylidene and alkynyl ligands has been presented recently by Pombeiro [38].

Predictions of the P_L parameter for some (hypothetical) unsaturated diatomic ligands (e.g. SO^{2+} , NS^+ , PO^+ , CS , or CP^-) were also proposed [49] on the basis of linear correlations between experimentally determined P_L values and quantum-chemical MO indices for uncoordinated

Tab. 2 Values of the P_L ligand parameter for ligand L ^a

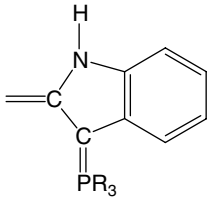
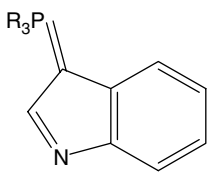
L	P_L/V	References
NO^+	+1.40	10
Carbynes ($\equiv\text{CR}$) ^b	+0.24 to +0.21	14
$\text{C}\equiv\text{NC}(\text{O})\text{Ph}^c$	+0.20	15
η^2 -Vinyl		
	+0.22	17
PF_3	+0.14	16
Aminocarbyne ($=\text{CNH}_2^+$)	+0.09	17
CO	0	10
$\text{P}\equiv\text{C-Bu}^{\text{td}}$	-0.04	18
N_2	-0.07	10
Isocyanides (bent) ^e		
	-0.07 to -0.18	19–22
Vinylidenes ($=\text{C}=\text{CHR}$) ^b	0 to -0.6	14, 38
PF_2NMe_2	-0.16	16
	-0.16	10
$\text{P}(\text{OPh})_3$	-0.18	10
η^2 -Allene ($\eta^2\text{-CH}_2=\text{C}=\text{CHPh}$) ^b	-0.21	17
Metallo-dinitriles ($\text{N}\equiv\text{C-X-C}\equiv\text{N-ML}_{n-1}$) ^f	-0.18 to -0.40	23
Nitriles ($\text{N}\equiv\text{CR}$) ^g	-0.23 to -0.58	10, 24
Ferricinium isocyanides ^h		
$\text{C}\equiv\text{N-Fc}^+$	-0.22	25, 26
$\text{C}\equiv\text{N-CH}_2\text{Fc}^+$	-0.28	25, 26
$\text{C}\equiv\text{N-CH}(\text{Men})\text{Fc}^+$	-0.28	25, 26
$\text{C}\equiv\text{N-BF}_3^-$	-0.24	15
Metallo-cyanides ($\text{C}\equiv\text{N-ML}_{n-1}$) ⁱ	-0.25 to -0.61	15, 27
	-0.28 to -0.36	28
$\text{PR}_3 = \text{PPh}_3$	-0.28	28
$\text{PPh}_2(\text{CH}_2\text{Ph})$	-0.30	28
PMe_3	-0.36	28
Allenylidenes ($=\text{C}=\text{C}=\text{CR}_2$) ^k	0 to -0.8	29, 38
Isocyanides (linear) ^l	-0.33 to -0.44	19–21, 30
$\text{C}\equiv\text{N-R}$		
PPh_3	-0.35	10
Bithiophene-carbenes	-0.38 to -0.62	31

Tab. 2 (continued)

<i>L</i>	<i>P_L/V</i>	<i>References</i>
 $X = \text{OEt}, Y = \text{C(OEt)} = \text{Cr(CO)}_5$ $X = \text{pyrrolidin-1-yl}, Y = \text{H}$ $X = \text{OEt}, Y = \text{H}$	 −0.38 −0.56 −0.62	 31 31 31
<i>Phosphirene</i>  PMePh_2	−0.43	32
<i>Protonated indole derivatives</i>	−0.44 to −0.62	28
 $\text{PR}_3 = \text{PPh}_3$ $\text{PPh}_2(\text{CH}_2\text{Ph})$ PMe_3	 −0.59 −0.62 −0.44	 28 28 28
PEt_3	−0.47	16
$\text{C}\equiv\text{N}-\text{BPh}_3^{-m}$	−0.51	33
<i>Cyanamides</i> ($\text{N}\equiv\text{C}-\text{NR}_2$) ⁿ	−0.57 to −0.85	34–37
<i>Oxocarbenes</i> ^o $=\text{C(OR)Y}$ $\text{R} = \text{alkyl, Ph}$ $\text{Y} = 2\text{-thienyl, 2-furyl, aryl}$	−0.51 to −0.64	38
<i>Pyridine</i>	−0.59	10
<i>Thiocarbenes</i> ^o $=\text{C(SR)Y}$ $\text{R} = \text{alkyl, Ph}$ $\text{Y} = 2\text{-furyl}$	−0.66 to −0.68	38
<i>Aminocarbenes</i> ^o $=\text{C(NRR')Y}$ $\text{NRR}' = \text{NH}_2, \text{NHCy}, \text{NMe}_2, \text{NEt}_2,$ $\text{aziridin-1-yl, azetidin-1-yl, pyrrolidin-1-yl, piperidin-1-yl}$ $\text{Y} = \text{alkyl, Ph, 2-furyl, 2-thienyl}$	−0.69 to −0.80	2, 38

(continued overleaf)

Tab. 2 (continued)

<i>L</i>	<i>P_L/V</i>	<i>References</i>
<i>Ferrocenyl-oxocarbenes</i> ^o		
$=C(OR)Y$ R = alkyl; Y = ferrocenyl	−0.70 to −0.9	38
NH ₃	−0.77	10
CF ₃ COO [−]	−0.78	10
	−0.79 to −0.87	28
PR ₃ = PPh ₃	−0.79	28
PPh ₂ (CH ₂ Ph)	−0.82	28
PMe ₃	−0.87	28
N≡C – NC(NH ₂) ₂ ^q	−0.86	39
N≡CNHCN ^r	−0.88	39
NCS [−]	−0.88	10
<i>Ferrocenyl-aminocarbenes</i> ^o	−0.99 to −1.1	38
$=C(\text{pyrrolidin-1-yl})Y$		
<i>Indole derivatives</i>		
	−0.92 to −1.0	28
PR ₃ = PPh ₃	−1.0	28
PPh ₂ (CH ₂ Ph)	−0.92	28
PMe ₃	−0.99	28
C≡N ^{−s}	−1.00	10
	−0.74	15
NCNCN ^{−t}	−1.14	39
NCO [−]	−1.16	10
I [−]	−1.15	10
Br [−]	−1.17	10
Cl [−]	−1.19	10
NCNC(O)Ph ^{−u}	−1.19	40
NCNC(O)Et ^{−v}	−1.19	40
NCNC(NH)NH ₂ ^{−x}	−1.22	39
<i>Alkynyls</i> (−C≡CR [−])	−0.9 to −1.7	2, 29, 38, 41, 42
H [−]	−1.22	10
N ₃ [−]	−1.26	10
NCNH ^{−y}	−1.34	37
S ₂ P(OEt) ₂ [−]	−1.34	43

Tab. 2 (continued)

<i>L</i>	<i>P_L</i> /V	References
Oxycarbenes (anionic) ^o {=C(O [−])Y}NMe ₄ ⁺ Y = 2-furyl, CH ₂ SiMe ₃ , 4-methylthiazol 2-yl, ferrocenyl	−1.1 to −1.7	38
OH [−]	−1.55	10

^aOrdered generally from higher to lower values; for some particular groups, see Tables 3–8.

^bAt the *trans*-{ReCl(dppe)₂} center.

^cBenzoylisocyanide at *trans*-{FeH(dppe)₂}⁺.

^dPhosphaalkyne (η^1 binding mode).

^eValues for bent isocyanides at electron-rich centers such as *trans*-{ReCl(dppe)₂} or *trans*-{TcH(dppe)₂}.

^fFor particular values see Table 5.

^gFor particular values see Tables 4 and 5.

^hOxidized ferrocenyl isocyanide ligands, with Fc⁺ = Fe(η^5 -C₅H₅) (η^5 -C₅H₄)⁺, Men = (1*R*,2*S*,5*R*)-2-isopropyl-5-methylcyclohexyl.

ⁱFor particular values see Table 3.

^jPhosphonium functionalized isocyanides.

^kAt the *trans*-{FeBr(depe)₂}⁺ center.

^lFor linear isocyanides at an electron-poor metal center such as {Cr(CO)₅}.

^mIsocyanotriphenylborate.

ⁿFor particular values see Table 6.

^o*P_L* values estimated from the data quoted in M.K. Lloyd, J.A. McCleverty, D.G. Orchard, et al., *J. Chem. Soc. Dalton Trans.*, 1973, 1743.

^pPhosphoylide-aminocarbenes; their protonated forms (possibly at the β -carbon of the carbene ring) have the following *P_L* values: −0.51 (PR₃ = PPh₃, PPh₂(CH₂Ph)), −0.60 (PR₃ = PMe₃) V.

^qCyanoguanidine, at *trans*-{Re(CNMe)(dppe)₂}⁺.

^rHydrogen dicyanamide, at *trans*-{Re(CNMe)(dppe)₂}⁺.

^sThe values −1.0 and −0.74 V have been estimated at the {Cr(CO)₅} and *trans*-{FeH(dppe)₂}⁺ centers, respectively.

^tDicyanamide.

^uAroylcyanamide, at *trans*-{Mo(NCN)(dppe)₂}²⁺.

^vAcylcyanamide, at *trans*-{Mo(NCN)(dppe)₂}²⁺.

^xMonodeprotonated form of cyanoguanidine, at *trans*-{Re(CNMe)(dppe)₂}⁺.

^yHydrogen-cyanamide, at *trans*-{Re(CNR)(dppe)₂}⁺ (R = alkyl).

diatomic molecules; the *P_L* parameter was then expressed as a linear function of the energies of the lowest unoccupied molecular orbital (LUMO) and HOMO of the free molecules, the former orbital behaving as the π -electron-acceptor orbital in the coordination, and the latter being the electron-donor orbital to the metal.

Nitrosyl (NO⁺), the ligands (carbynes, η^2 -vinyl and aminocarbynes) derived

from the protonation of alkyne-derived species or isocyanides, respectively, and benzoylisocyanide are stronger net electron acceptors than carbonyl, exhibiting positive *P_L* values in the following order: NO⁺ (+1.40 V) [10] > carbynes (CR) (+0.24 to +0.21 V) [14] \geq η^2 -vinyl (η^2 -CH₂CCH₂Ph) (+0.22 V) [17] > C \equiv NC(O)Ph (+0.20 V) [15] > aminocarbynes (CNH₂⁺) (+0.09 V) [17]

Tab. 3 Values of the P_L ligand parameter for metallo-cyanide $C\equiv N-ML_{n-1}^-$ and other cyano-adduct ligands^a

	P_L/V	References
$C\equiv N-BF_3^-$	-0.24	15
$C\equiv N-NiCl_2(PCy_3)^-$	-0.25	27
$C\equiv N-VCl_3(thf)_2^-$	-0.42	15
$C\equiv N-BPh_3^-$	-0.51	33
$C\equiv N-ReOCl_3(\mu-CN)FeH(dppe)_2^-$	-0.55	27
$C\equiv N-PdCl_2(PPh_3)^-$	-0.61	27

^aAt the *trans*-{FeH(dppe)₂}⁺ center for which $P_L(CN^-) = -0.74$ V [15].

(Table 2). For these C-ligated ligands, their coordination bonds have a multiple-bond order.

At the other extreme (Table 2) are the strongest net electron donors, such as the anionic ligands OH^- ($P_L = -1.55$ V) [10], anionic oxycarbenes $C(CO^-)Y$ ($P_L = -1.1$ to -1.7 V) [38], $S_2P(OEt)_2^-$ ($P_L = -1.34$ V) [43],

$NCNH^-$ (hydrogen-cyanamide) ($P_L = -1.34$ V) [37], N_3^- ($P_L = -1.26$ V) [10], H^- ($P_L = -1.22$ V) [10], $C\equiv CR^-$ (alkynyls) ($P_L = -0.9$ to -1.7 V) [2, 29, 38, 41, 42], $NCNC(NH)NH_2^-$ (monodeprotonated cyanoguanidine) ($P_L = -1.22$ V) [39], and $NCNC(O)R^-$ (acyl- or aroyl-cyanamide) ($P_L = -1.19$ V [40]), all of them with P_L values that commonly are

Tab. 4 Values of the P_L ligand parameter for organonitriles ($N\equiv CR$) at metal centers $\{M_5\}$ with a different electron-richness (E_S) [24]

	P_L/V	
	At <i>cis</i> -{ReCl(dppe) ₂ } ($E_S = 0.41$ V)	At <i>trans</i> -{FeBr(depe) ₂ } ⁺ ^a ($E_S = 1.32$ V)
NCC ₆ H ₄ NO ₂ -4	-0.23	-0.44
NCC ₆ H ₄ F-4	-0.27	-0.46
NCC ₆ H ₄ Cl-4	-0.27	-
NCPh	-0.29	-0.50
NCC ₆ H ₄ Me-4	-0.29	-0.52
NCCH ₂ C ₆ H ₄ Cl-4	-0.29	-
NCCH ₂ C ₆ H ₄ OMe-4	-	-0.55
NCBu ^t	-0.29	-
NCC ₆ H ₄ OMe-4	-0.30	-0.54
NCC ₆ H ₄ NEt ₂ -4	-0.33	-
NCMe	-	-0.55
NCtEt	-	-0.55
General expression	$P_L(NCR)\{cis-ReCl(dppe)_2\} = P_L(NCR)\{trans-FeBr(depe)_2\}^+ + 0.22$ V	

^aAt this center, the P_L values are expected to be comparable with those at {Cr(CO)₅} ($E_S = 1.50$ V), for example, at the latter: NCMe ($P_L = -0.58$ V [10]), NCPh ($P_L = -0.40$ V [10]).

Tab. 5 Values of the P_L ligand parameter for organodinitriles and metallo-dinitriles [23]

	P_L/V^a
$N\equiv C-X-C\equiv N$	
$N\equiv C-CH=CH-C\equiv N$	-0.32
$N\equiv C-C_6H_4-C\equiv N$	-0.34
$N\equiv C-CH_2CH_2-C\equiv N$	-0.41
$N\equiv C-X-C\equiv N-ML_{n-1}$	
$N\equiv C-CH=CH-C\equiv N-\{Fe^{II}H(dppe)_2\}^+$	-0.36
$N\equiv C-CH=CH-C\equiv N-\{Fe^{III}H(dppe)_2\}^{2+}$	-0.18
$N\equiv C-C_6H_4-C\equiv N-\{Fe^{II}H(dppe)_2\}^+$	-0.35
$N\equiv C-C_6H_4-C\equiv N-\{Fe^{III}H(dppe)_2\}^{2+}$	-0.35
$N\equiv C-CH_2CH_2-C\equiv N-\{Fe^{II}H(dppe)_2\}^+$	-0.40
$N\equiv C-CH_2CH_2-C\equiv N-\{Fe^{III}H(dppe)_2\}^{2+}$	-0.40

^aEstimated for dinitriles at the *trans*- $\{FeH(dppe)_2\}^+$ center [23].**Tab. 6** Values of the P_L ligand parameter for cyanamides at different metal centers

	P_L/V			
	At <i>trans</i> - $\{Fe(NCR)(depe)_2\}^+$ ($E_S = 2.0-1.7$ V)	At <i>trans</i> - $\{FeBr(depe)_2\}^+$ ($E_S = 1.32$ V)	At <i>trans</i> - $\{Re(CNR)(dppe)_2\}^+$ ($E_S = 1.15$ V)	At <i>trans</i> - $\{Mo(N_2)(dppe)_2\}$ ($E_S = -0.13$ V)
$N\equiv C-NH_2$	-0.82	-0.57	-0.85	—
$N\equiv C-NMe_2$	-0.79	-0.60	—	-0.72
$N\equiv C-NEt_2$	-0.78	-0.59	—	-0.70
References	35	36	37	34

even lower than those of the halides (P_L ca. -1.17 V). The other ligands lie between these two extremes.

The net electron acceptance of carbenes (Table 2) and related ligands [38] is weaker than that of CO and is very sensitive to the nature of the groups attached to the carbene carbon. Their P_L values spread over a remarkably wide range [14, 28, 31, 38], from vinylidenes $C=CHR$ (P_L from -0 to -0.6 V) [14, 38] to anionic oxycarbenes $C(O^-)Y$ (P_L from -1.1 to -1.7 V) [38], in the following the order: vinylidenes $C=CHR >$ allenylidenes $C=C=CR_2 >$ bithiophene-carbenes \geq

oxocarbenes $C(OR)Y >$ thiocarbenes $C(SR)Y >$ aminocarbenes $C(NRR')Y$, ferrocenyl-oxocarbenes \geq phos-phoylide-aminocarbenes $>$ ferrocenyl-aminocarbenes \gg anionic oxycarbenes $C(O^-)Y$.

Isocyanides also display over a wide range of P_L values (Table 2), from benzoyl isocyanide ($P_L = +0.20$ V) [15] with a net electron-acceptance similar to that of the carbyne ligands, down to the metallo-cyanide adduct $C\equiv N-PdCl_2(PPh_3)^-$ ($P_L = -0.61$ V) [27]. Between these limiting cases, one finds the following types ordered according to their net electron-acceptance (Tables 2

and 3): bent organoisocyanides [19–22] > ferricinium isocyanides (oxidized ferrocenyl isocyanides) such as $\text{C}\equiv\text{N}-\text{Fc}^+$ and related ones [25, 26], $\text{C}\equiv\text{N}-\text{BF}_3^-$ [15] > phosphonium isocyanides [28] \geq linear organoisocyanides [19–21, 30] > $\text{C}\equiv\text{N}-\text{BPh}_3^-$ [33]. The electronic properties of metallo-cyanide adducts $\text{C}\equiv\text{N}-\text{ML}_{n-1}^-$ (Table 3) [15, 27] are very much dependent on the nature of the metal Lewis acid $\{\text{ML}_{n-1}\}$.

Aryl phosphines, for example, PPh_3 and PMePh_2 , display a net electron-acceptor character comparable to those of linear organoisocyanides, and the latter phosphine has the same P_L value as phosphirene $\text{P}(\text{Ph})\text{C}(\text{Ph})=\text{C}(\text{Ph})$ (-0.43 V) [32]. However, PF_3 is a much stronger π -electron acceptor and weaker σ -donor ($P_L = +0.14$ V [16], slightly above that of the aminocarbyne CNH_2^+ , $+0.09$ V [17]).

The phosphalkyne $\text{P}\equiv\text{CBu}^t$, bonded in the η^1 mode, has a P_L value (-0.04 V) [18] that is very close to that of CO ($P_L = 0$ V). Since the former is not expected to be a good σ -donor, this similarity is accounted for by considering that it is also not an efficient π -acceptor [18]. A similar case is that of the N_2 ligand ($P_L = -0.07$ V [10]). Since P_L reflects the *net* π -electron acceptor minus σ -donor character, similar values can be found for both a strong π -acceptor/strong σ -donor ligand and a weak π -acceptor/weak σ -donor ligand.

Organonitriles are weaker net π -electron acceptors than comparable organoisocyanides, their P_L values (-0.23 to -0.58 V) [10, 24] (Tables 2 and 4) being lower than the corresponding ones for isocyanides. In the case of dinitriles, $\text{N}\equiv\text{C}-\text{X}-\text{C}\equiv\text{N}$, the effect of coordination of one of the cyano groups to any of the $\{\text{FeH}(\text{dppe})_2\}^{n+}$ ($n = 1$ or 2) centers was investigated (Table 5) [23] and the

significant increase of P_L for the fumaronitrile adduct upon Fe^{II} to Fe^{III} oxidation in $\text{N}\equiv\text{CCH}=\text{CHC}\equiv\text{N}\{\text{FeH}(\text{dppe})_2\}^{n+}$ (P_L increase from -0.36 to -0.18 V) was accounted for by the electronic communication through the unsaturated dinitrile.

Cyanamide $\text{N}\equiv\text{CNH}_2$, its dimeric form cyanoguanidine $\text{N}\equiv\text{CNC}(\text{NH}_2)_2$ and hydrogen dicyanamide $\text{N}\equiv\text{CNHCN}$ (Tables 2 and 6) are quite strong net electron-donor neutral ligands, with P_L values in the -0.85 to -0.88 V range [37, 39], when binding a *trans*- $\{\text{Re}(\text{NCR})(\text{dppe})_2\}^+$ ($\text{R} = \text{alkyl}$) center. They are even stronger than NH_3 and CF_3COO^- , and very close to NCS^- . Moreover, their derived anionic ligands are remarkably stronger electron-donors, dicyanamide NCNCN^- ($P_L = -1.14$ V) [39] being identical to NCO^- , the monodeprotonated form of cyanoguanidine ($P_L = -1.22$ V) [39] approaching N_3^- and hydrogen cyanamide NCNH^- ($P_L = -1.34$ V) [37] being one of the most effective electron donors.

Acyl and aroylcyanamides $\text{NCNC}(\text{O})\text{R}^-$ are also quite strong donors ($P_L = -1.19$ V) [40], similar to Cl^- , whereas organocyanamides NCNR_2 are much weaker electron-donors [35, 36], being comparable to cyanamide itself.

Indoles (functionalized with a phosphoylide group) (Table 2) are other N-coordinated ligands and behave as the most effective neutral electron-releasers with reported P_L values (-0.92 to -1.0 V) [28].

Protonation of a ligand normally leads to a significant increase in its net electron-withdrawing ability (or decrease of its net electron-donor character), as observed for the following pairs (P_L increase of 0.3 – 0.5 V) (Table 2): carbynes CCH_2R^+ versus vinylidenes $\text{C}=\text{CHR}$ [14], aminocarbyne CNH_2^+ versus isocyanide CNR [17],

protonated versus unprotonated aminocarbenes with a phosphoylide group [28], protonated versus unprotonated indole derivatives [28].

Oxidation of a moiety of a ligand can also result in a similar effect, as observed for the cationic Fe^{III} ferricinium-isocyanide $\text{C}\equiv\text{N}-\text{Fc}^+$ [25, 26] and fumaronitrile-iron $\text{N}\equiv\text{CCH}=\text{CHC}\equiv\text{N}\{\text{Fe}^{\text{III}}\text{H}(\text{dppe})_2\}^{2+}$ [23] ligands for which the P_L values have increased by 0.2 V relatively to related unoxidized ligands. However, if the redox center of the ligand does not communicate electronically with the coordinating atom or group, no effect is expected, as observed [23] in the case of the non-conjugated succinonitrile bridged ligand $\text{N}\equiv\text{CCH}_2\text{CH}_2\text{C}\equiv\text{N}\{\text{Fe}^{\text{III}}\text{H}(\text{dppe})_2\}^{2+}$.

Although the P_L parameter normally provides a reliable basis for the evaluation of the net electron donor/acceptor properties of ligands, as shown earlier, the comparison of their P_L values when ligating different metal centers has to be done with caution, in some cases, in view of the possible dependence of P_L on the type of the binding metal center (see in the following).

Concerning the estimate of the *electron-richness* (E_s) and *polarizability* (β) of a metal center $\{\text{M}_s\}$, one can apply the general Eq. (5) to as many as possible members (the minimum of two can lead to a high uncertainty) of series $[\text{M}_s\text{L}]$ with known oxidation potentials and known P_L for the corresponding L ligands. More directly, E_s is given (Eq. 3) as the oxidation potential for the carbonyl complex, that is, $[\text{M}_s(\text{CO})]$, when this is available. Indirect methods can also be used, namely by comparing the homologs of the series $[\text{M}_s\text{L}]$ and $[\text{M}'_s\text{L}]$, provided E_s and β are known for $\{\text{M}'_s\}$: those parameters are then given for $\{\text{M}_s\}$ from the intercept and the slope of Eq. (6) derived from the application of the general

Eq. (5) to both series.

$$\begin{aligned} E^{\text{ox}}[\text{M}_s\text{L}] - E^{\text{ox}}[\text{M}'_s\text{L}] &= (E_s\{\text{M}_s\} \\ &\quad - E_s\{\text{M}'_s\}) + (\beta\{\text{M}_s\} - \beta\{\text{M}'_s\})P_L(\text{L}) \end{aligned} \quad (6)$$

Other indirect methods are mentioned in the following.

The E_s and β values so far reported are listed in Table 7, the former in V versus SCE. A decrease of the electron-richness (increase of E_s) of a metal center is favored by an increase of charge and the presence of strong net electron-acceptor ligands such as CO and a carbyne. Hence, the least electron-rich centers are the dicationic carbonyl *trans*- $\{\text{Fe}(\text{CO})(\text{depe})_2\}^{2+}$ ($E_s = 2.3$ V vs. SCE) [35] or nitrile *trans*- $\{\text{Fe}(\text{NCR})(\text{depe})_2\}^{2+}$ ($E_s = 1.96$ to 1.65 V vs. SCE) [35] sites, the cationic carbyne dicarbonyl $\{\text{W}(\equiv\text{CR})(\text{CO})_2(\text{dppe})\}^+$ centers ($E_s = 1.69$ – 1.63 V) [30], the polycarbonyls $\{\text{M}(\text{CO})_5\}$ ($\text{M} = \text{Cr}, \text{Mo}, \text{W}$) ($E_s = 1.50$ V) [10, 28], and the cationic carbonyl *trans*- $\{\text{Re}(\text{CO})(\text{dppe})_2\}^+$ ($E_s = 1.42$ V) [20]. In contrast, the most electron-rich centers are the anionic or neutral ones, with a low metal oxidation state, *trans*- $\{\text{Mo}(\text{L})(\text{dppe})_2\}$ ($\text{L} = \text{N}_3^-, \text{NCPh}, \text{N}_2, \text{CO}$) with $E_s = -1.00, -0.40, -0.13$, or -0.11 V, respectively [10].

Within a series of related centers with a variable L ligand, the electron-richness increases, as expected, with the net electron-donor character of L and, interestingly, the polarizability also tends to increase in the same order. Hence, for instance, these parameters vary as follows in the *trans*- $\{\text{Re}(\text{L})(\text{dppe})_2\}^+$ series: $\text{L} = \text{CO}$ ($E_s = 1.42$ V, $\beta = 0.62$ [20]), aryl CNR ($E_s = 1.19$ – 1.17 V, $\beta = 0.75$ – 0.79) [19, 20], alkyl CNR ($E_s = 1.15$ V, $\beta = 0.90$ – 0.92) [19, 20], CN^- ($E_s = 0.78$ V, $\beta = 3.7$) [45], Cl^- ($E_s = 0.68$ V, $\beta = 3.4$) [21].

Tab. 7 Values of the electron-richness (E_S) and polarizability (β) parameters for 16-electron metal sites $\{M_S\}$

$\{M_S\}^a$	E_S/V vs. SCE	β	References
$\{Fe(CO)(depe)_2\}^{2+}$	2.3	–	35
$\{Fe(NCR)(depe)_2\}^{2+}$ R = aryl, alkyl	1.96–1.65	0.75–1.10	35
$W(\equiv C - CH=C(CH_2)_nCH_2)(dppe)^+$ n = 3	1.69	0.73	30
n = 6	1.63	0.61	30
$\{Cr(CO)_5\}$	1.50	1	10
$\{Mo(CO)_5\}$	1.50	0.86	28
$\{W(CO)_5\}$	1.50	0.90	28
$\{Re(CO)(dppe)_2\}^+$	1.42	0.62	20
$\{Re(N_2)(dppe)_2\}^+$	1.38	0.92	2
	1.20	0.74	10
$\{FeBr(depe)_2\}^+$	1.32	1.10	24
$\{Re(CNR)(dppe)_2\}^+$ R = C ₆ H ₄ Cl-4	1.19	0.75	19, 20
Ph	1.18	0.76	19, 20
C ₆ H ₄ Me-4	1.18	0.79	19, 20
C ₆ H ₄ OMe-4	1.17	0.82	19, 20
Me	1.15	0.90	19, 20
Bu [†]	1.15	0.92	19, 20
$\{FeH(dppe)_2\}^+$	1.04	1.0	10
$\{Mo(NO)(dppe)_2\}^+$	0.91	0.51	10
$\{Mn(CO)(dppm)_2\}^+$	0.86	0.75	44
$\{Re(CN)(dppe)_2\}$	0.78	3.7	45
$\{Re(NCS)(dppe)_2\}$	0.73	–	46
$\{Re(Cl)(dppe)_2\}$	0.68	3.4	21
$\{Re(NCO)(dppe)_2\}$	0.63	–	46
$\{Re(N_3)(dppe)_2\}$	0.55	–	46
<i>cis</i> - $\{Re(Cl)(dppe)_2\}$	0.41	1.88	24
$\{TcH(dppe)_2\}$	0.34	4.0	22
$\{Mo(CO)(dppe)_2\}$	–0.11	0.72	10
$\{Mo(N_2)(dppe)_2\}$	–0.13	0.84	10
$\{Mo(NCPh)(dppe)_2\}$	–0.40	0.82	10
$\{Mo(N_3)(dppe)_2\}^-$	–1.00	1.0	10
<i>mer</i> - $\{ReCl(N_2)[P(OMe)_3]_3\}$	–	1.0	47

^aWith *trans* geometry, except when stated otherwise.

In fact, effective electron-donors, such as hydride, Cl[–] or CN[–], present a low capacity to “buffer” changes in the electron density at the metal induced by a change in the *trans* L ligand (high β), whereas strong π -electron acceptors (such as NO⁺, carbyne, CO, or N₂) behave

in the opposite way (low β). Compare, for example, the centers with the highest β , *trans*- $\{TcH(dppe)_2\}$ (β = 4.0) [22], *trans*- $\{ReL(dppe)_2\}$ [L = Cl[–] (β = 3.4) [21], CN[–] (β = 3.7) [45], and *cis*- $\{Re(Cl)(dppe)_2\}$ (β = 1.88) [24], with those with the lowest β , *trans*- $\{Mo(NO)(dppe)_2\}^+$ (β =

0.51 [10]) and $\{W(\equiv CR)(CO)_2(dppe)\}^+$ ($\beta = 0.61\text{--}0.73$) [30]. In these carbyne complexes, the stabilization of the HOMO (high E_s) and its delocalization toward the strong π -electron acceptor carbyne (or CO) ligand, as indicated by MO calculations, result in an attenuating effect on changes of the HOMO energy (low β) upon variation of another ligand [30].

3.2.1.2 Extensions of the Model

3.2.1.2.1 Dependence of the Ligand Parameter P_L on the Binding Metal Center

In Pickett et al. initial general Eqs. (4) and (5), P_L was considered to be independent of the binding metal center. However, one should be aware that the net π -electron acceptance/ σ -donation of a ligand (measured by P_L) is not an intrinsic property of the ligand alone, but can also be determined by the π -electron releasing and the σ -acceptance ability of the particular binding metal center. For instance, if an unsaturated ligand has, in principle, a considerable π -electron acceptor character, this can be fulfilled only if the metal site is an effective π -electron donor.

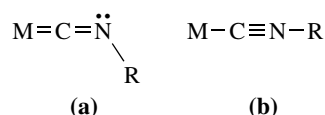
Such situations have been typically recognized by Pombeiro et al. for isocyanides [19–22] (Table 2), nitriles [24] (Table 4), cyanamides [34–37] (Table 6), and cyanide [15] (Table 2).

In fact, when ligating the electron-rich metal center $trans\text{-}\{ReCl(dppe)_2\}$ ($E_s = 0.68$ V) [21], with a high π -electron-releasing ability, the isocyanides behave as much stronger net electron acceptors than when ligating a much less electron-rich center such as $\{Cr(CO)_5\}$ ($E_s = 1.50$ V, in which the five CO ligands strongly compete for the available metal d -electron density), and present a bent geometry **a** (unless stereochemical effects prevent such bending). This was confirmed by the

single-crystal X-ray diffraction analysis of $trans\text{-}[ReCl(CNMe)(dppe)_2]$ (CNC bending angle of $139.4(10)^\circ$) [50]. Consistent with these observations, the strong π -electron acceptors, bent isocyanides, have higher P_L values (by ca. 0.26 V) than the linear ones (Eq. 7) [19–21].

$$P_L(\text{CNR bent}) = P_L(\text{CNR linear}) + 0.26 \quad (7)$$

The value of the P_L parameter for an isocyanide ligand (without a bulky R group) can then be used to predict whether the coordination mode is bent or linear, that is, with a dominant representation by form **a** or **b**, respectively.



An even higher correction of +0.34 V for the linear P_L value has been proposed [22] for isocyanides at $trans\text{-}\{TcH(dppe)_2\}$ with an electron-richness ($E_s = 0.34$ V) higher than that of the above Re(I) center.

Nitriles also exhibit P_L dependence on the type of metal center [24] (Table 4), and, for example, at the electron-richer $cis\text{-}\{ReCl(dppe)_2\}$ center ($E_s = 0.41$ V), their P_L values are ca. 0.22 V higher than at the much electron-poorer $trans\text{-}\{FeBr(depe)_2\}^+$ site ($E_s = 1.32$ V).

Besides the electron richness, other electronic properties of the metal center can also affect P_L , as demonstrated for cyanamides $N\equiv CNR_2$, which tend to behave as considerable net electron-donors (σ and π). In fact (Table 6), at the $trans\text{-}\{FeBr(depe)_2\}^+$ center ($E_s = 1.32$ V), with the Br^- ligand [36], they act as weaker electron-donors than at $trans\text{-}\{Mo(N_2)(dppe)_2\}$ (much electron-richer, $E_s = -0.13$ V) [34], $trans\text{-}\{Re(CNR)(dppe)_2\}^+$ (electron-richer, $E_s =$

1.15 V) [37], *trans*-{Fe(NCR)(depe)₂}²⁺ (electron-poorer, $E_s = 1.7\text{--}2.0$ V) [35], with a N₂, CNR, or NCR ligand. The strong electron-release from the *trans* bromo ligand in the first center, in contrast with the appreciable π -electron acceptance by the *trans*-N₂, CNR, or NCR ligands in the other centers, hampers the electron-donation from the cyanamides, whereas the opposite effect occurs for the other metal sites.

A similar effect conceivably accounts for the higher P_L value (-0.74 V) (weaker net electron-donation) of the cyanide ligand and estimated [15] at *trans*-{FeH(dppe)₂}⁺ with the strong donor *trans*-hydride, in comparison with that (-1.0 V) [10] obtained at {Cr(CO)₅} and also proposed at *trans*-{MoL(dppe)₂} (L = CO, N₂) with the strong net electron-acceptor L ligand, in spite of the lower electron-richness of the former Fe^{II} site ($E_s = 1.04$ V) relatively to the latter ($E_s = -0.11$ or -0.13 V) molybdenum centers.

The dependence of the P_L ligand parameter on the type of binding metal center is a limitation of the Pickett's model, but a similar difficulty is encountered for the E_L Lever parameter (see in the following) for which the need for corrections has been recognized for ligands such as CO and CNR. Such a type of limitation is inherent to any additive model that tries to separate the effects of ligands and metal centers on the redox potential, and add them as independent components, in contrast with the situation of the real molecule in which those effects are mutually dependent.

Nevertheless, such a difficulty should not be exaggerated since one should take into account that even the conventional Hammett's σ_p constant, of a widely recognized significance for the comparison of the electron donor/acceptor character of substituents, has required corrections in

a number of cases, namely for those with enhanced direct resonance with the reaction center, for which σ_p^+ values should instead be used [13].

3.2.1.2.2 18-electron Complexes of the Types [M_sLL'] and [M_sL_n] The oxidation potentials of particular types of complexes can be predicted from the knowledge of the oxidation potentials of related ones by using expressions derived from the application to particular situations of the fundamental Eqs. (3)–(5), as shown by Pombeiro in the following cases.

A simple situation concerns the 18-electron mixed-ligand complexes [M_sLL'] whose oxidation potential was shown [19] to be the average of those of the corresponding complexes with two identical (L or L') ligands, [M_sL₂] and [M_sL'₂] (Eq. 8), provided that the metal sites {M_sL} and {M_sL'} present analogous polarizabilities.

$$E_{1/2}^{\text{ox}}[\text{M}_s\text{LL}'] = \frac{1}{2}\{E_{1/2}^{\text{ox}}[\text{M}_s\text{L}_2] + E_{1/2}^{\text{ox}}[\text{M}_s\text{L}'_2]\} \quad (8)$$

Through the application of the general Eqs. (3)–(5) to complexes of the type [M_sL₂] and the related [M_sL'L] ones presenting a suitable auxiliary {M_sL'} metal site with the basic {M_s} core, it has been possible to establish [20] relationships from which E_s and β of the {M_sL} center (Eqs. 9 and 10, respectively), as well as the oxidation potential of the complexes [M_sL₂] (Eq. 11), can be predicted, provided that one knows the oxidation potential of the dicarbonyl [M_s(CO)₂], the E_s and β of the auxiliary {M_sL'} site, and the P_L values of L and the auxiliary L' ligand.

$$E_s\{\text{M}_s\text{L}\} = \left[1 - \frac{P_L(\text{L})}{P_L(\text{L}')} \right] E_{1/2}^{\text{ox}}[\text{M}_s(\text{CO})_2] + \frac{P_L(\text{L})}{P_L(\text{L}')} E_s\{\text{M}_s\text{L}'\} \quad (9)$$

$$\beta\{M_s L\} = \frac{\left[1 - \frac{P_L(L)}{P_L(L')}\right] E_s\{M_s L'\} - \left[1 - \frac{P_L(L)}{P_L(L')}\right] E_{1/2}^{\text{ox}}[M_s(\text{CO})_2] + \beta\{M_s L'\} P_L(L)}{P_L(L')} \quad (10)$$

$$\begin{aligned} E_{1/2}^{\text{ox}}[M_s L_2] &= \left[1 - \frac{P_L(L)}{P_L(L')}\right]^2 E_{1/2}^{\text{ox}}[M_s(\text{CO})_2] \\ &+ \left[\frac{2P_L(L)}{P_L(L')} - \frac{P_L^2(L)}{P_L^2(L')}\right] E_s\{M_s L'\} \\ &+ \frac{P_L^2(L)}{P_L(L')} \beta\{M_s L'\} \end{aligned} \quad (11)$$

These expressions have been applied to the series isocyanide and carbonyl complexes of rhenium(I) *trans*-[ReL₂(dppe)₂]⁺ (L = CNR, CO) [19, 20] and of nitrile and carbonyl compounds of iron(II) *trans*-[FeL₂(depe)₂]²⁺ (L = NCR, CO) [35], and the E_s and β values of the corresponding *trans*-{ReL(dppe)₂}⁺ and *trans*-{FeL(depe)₂}²⁺ centers, which are given in Table 9, have been discussed earlier.

The basic Eqs. (3)–(5) have also been extended [2, 51] to complexes of the type [M_sL_n] ($n = 2$ or 3 ; $n = 1$ was the initial case) in which {M_s} denotes a 14- or 12-electron metal binding site, respectively (see Eqs. 12–14).

$$E_{1/2}^{\text{ox}}[M_s L_n] = E_s + \beta P_{nL} \quad (12)$$

$$E_s = E_{1/2}^{\text{ox}}[M_s(\text{CO})_n] \quad (13)$$

$$\begin{aligned} P_{nL} &= E_{1/2}^{\text{ox}}[\text{Cr}(\text{CO})_{6-n} L_n] \\ &- E_{1/2}^{\text{ox}}[\text{Cr}(\text{CO})_6] \end{aligned} \quad (14)$$

The P_{nL} ligand parameter is then the shift in the oxidation potential resulting from the replacement of n CO ligands in [Cr(CO)₆] by n L ligands, and should reflect the overall effect of these ligands, that

is, their combined net electron-acceptor minus donor ability.

The P_{nL} value is the sum of the n individual P_L values (Eq. 15) when the n ligands exhibit independent electronic effects, usually being in mutually *cis* positions and behaving as electron acceptors or donors that are neither very strong nor very weak [2, 51].

$$P_{nL} = n P_L \quad (15)$$

3.2.1.2.3 17- and 16-electron Compounds

The model can, in principle, be extended to open-shell complexes as suggested by Pombeiro et al. [24] for 17-electron complexes of the types *cis*-[ReCl(L)(dppe)₂]⁺ and *trans*-[FeBr(L)(depe)₂]²⁺, with a 15-electron Re^{II} or Fe^{III} center, respectively.

The general forms of Eqs. (3)–(5) can still be preserved, but now the metal center {M_s} is a 15-electron site whose E_s and β parameters have been estimated from the linear plots of the second oxidation potential ^{II} $E_{1/2}^{\text{ox}}$ (Re^{II/III} or Fe^{III/IV}) of the starting 18-electron complexes *cis*-[ReCl(L)(dppe)₂] or *trans*-[FeBr(L)(depe)₂]⁺ versus P_L : *cis*-{ReCl(dppe)₂}⁺ ($E_s = 1.42$ V, $\beta = 1.30$), *trans*-{FeBr(depe)₂}²⁺ ($E_s = 1.98$ V, $\beta = 1.30$) [24] (Table 8).

Extensions to series of complexes with lower numbers of valence electrons can also be anticipated, provided their redox potentials become available. This possibility has also been demonstrated by Pombeiro et al. [48] for the particularly significant case of square planar 16-electron complexes with T-shaped 14-electron metal centers, namely the Rh^I series [Rh(O[⊖]O)(CO)L] (O[⊖]O = acac, bac) (Table 8). The forms of the general expressions (3)–(5) can still be preserved, but [M_sL] now represents a square planar 16-electron complex and {M_s} a T-shaped 14-electron metal site,

Tab. 8 Values of the electron-richness (E_s) and polarizability (β) parameters for 15-electron and 14-electron metal sites $\{M_S\}$

	E_s/V vs. SCE	β	References
15-electron $\{M_S\}$			
<i>trans</i> - $\{Fe^{III}Br(depe)_2\}^{2+}$	1.98	1.30	24
<i>cis</i> - $\{Re^{II}(Cl)(dppe)_2\}^+$	1.42	1.30	24
14-electron $\{M_S\}^a$			
$\{Rh(acac)(CO)\}^b$	1.64	1.96	48
$\{Rh(bac)(CO)\}^c$	ca. 2.2	ca. 3.3	48

^aSquare planar.^bacac = MeC(O)CHC(O)Me[−].^cRather preliminary data based on only two members of the series.bac = PhC(O)CHC(O)Me[−].

whereas P_L , in view of the shortage of data for such a type of complexes, can maintain its meaning (Eq. 4) as the shift of redox potential of $[Cr(CO)_6]$ upon replacement of one CO ligand by L.

The advantages of using the same definition of P_L as for the 18-electron complexes is evident, benefiting from the knowledge of its values for a good number of L ligands and allowing the direct estimate of others without the need of further relationships for conversion between the two types of structures. However, one can expect some limitations to such a proposal resulting from the consideration, for comparison of ligand effects on redox potentials, of nonisoelectronic series of complexes [48].

3.2.1.3 Other Relationships

3.2.1.3.1 Effects of Isomerism Geometrical isomers of coordination compounds can exhibit different values of redox potential, as accounted for, in various cases, by simple d_π orbital level splitting diagrams or by MO calculations. The dependence of the relative stability and redox behavior of the geometrical isomers on the electronic configuration of the metal is also

well known [52, 53], and the possibility to estimate the redox potentials of these isomers is a matter of high significance toward the establishment of the type of mechanism of electron-transfer induced isomerizations, a subject that has been recently reviewed [52].

The Pickett's model and extensions thereof have the potential to deal with such situations, namely involving *cis/trans* or *mer/fac* octahedral complexes, provided the E_s and β parameters are known for the corresponding isomeric metal centers. Although this application still remains virtually unexplored, the following case is illustrative. The *trans*- and *cis*- $\{ReCl(dppe)_2\}$ centers display quite different values of those parameters: $E_s = 0.68$ V, $\beta = 3.4$ [21] for the former, and $E_s = 0.41$ V, $\beta = 1.88$ [24] for the latter. Hence, for example, for the carbonyl ($P_L = 0$) complexes $[ReCl(CO)(dppe)_2]$, the *cis* isomer is oxidized at a lower potential than the *trans* (0.41 vs. 0.68 V), whereas for the nitrile $[ReCl(NCR)(dppe)_2]$ complexes, with P_L (NCR) in the range from -0.23 to -0.33 V [24] (Table 4), the reverse occurs.

These *cis* isomers undergo anodically induced isomerizations to the corresponding

oxidized trans isomers, via an electron-transfer-catalyzed (ETC) process in the case of the carbonyl complexes [54], or via a double square ECEC-type mechanism for the nitrile complexes [55, 56], as determined by the relative isomeric oxidation potentials.

3.2.1.3.2 Relationships with Other Properties and Reactivity

The earlier mentioned electrochemical parameters, in particular, P_L of a ligand L (or, in an equivalent way, see Eq. (5), the redox potential of a complex with that ligand), can be correlated [1, 2] with other properties of the complexes that are also determined by electronic features of ligands and metal sites, namely of their coordination bonds. Examples include infrared stretching frequencies of unsaturated ligands such as CO, N₂, CNR, NCR, or NO [37, 46–48, 57–60], ligand substituent effects as measured by Hammett and related constants [21, 60, 61] and photoelectron binding energies or gas-phase vertical ionization potentials [16].

On the basis of the above mentioned electrochemical parameters, it is also possible to propose *criteria* for *ligand coordination* to a metal center and for *chemical reactivity*.

Examples of the former criteria are as follows: metal centers with a low electron-richness (high E_s) bind preferably ligands that are strong electron donors (low P_L values); coordination of N₂ is favored by a high electron-richness (low E_s) and a high polarizability (β) of the metal center [10, 11]. *Trans*-[ReCl(N₂)(dppe)₂] is an example of a rather stable N₂ complex with such features (the E_s and β values of the binding metal center are 0.68 V and 3.4, respectively [21]).

Correlations with the chemical reactivity include (1) the stronger coordination ability of isocyanides and higher

activation to protonation, in comparison with dinitrogen, a weaker π -acceptor with a lower versatility to accommodate to an electronic change in the metal center [62], (2) the activation of N₂ toward electrophilic or nucleophilic attack, upon coordination to an electron-rich or to an electron-poorer metal center (as measured by E_s), respectively [10, 58], (3) the influence of a co-ligand (its P_L value) on the stability of the coordination bond of N₂ and on the reactivity of this ligand toward protonation or alkylation [57], and (4) the electroactivation of metal-hydride bonds (increase of the rate of H⁺ loss, upon anodically induced heterolytic metal-H bond cleavage, with the P_L of an isocyanide co-ligand) [23, 63]. The metal–metal interaction in some dinuclear complexes was also shown to increase with the P_L value (reflecting the π -electron acceptance) of the dinitrile bridging ligand [23].

3.2.2

Lever's Model

3.2.2.1 The Ligand Parameter E_L and the Metal Center Parameters S_M and I_M

This model, proposed by Lever in 1990 [64, 65], one decade after the Pickett's model was introduced [10], has become the most popular one mainly due to its wider scope of application and wider availability of data. It has been the object of extensive reviews [66, 67] including a very recent one [67] and therefore will not be treated herein in such a great detail.

It is based on the proposed additive contribution of all the ligands to the redox potential of a complex with the $[M^{n+1/n}]$ redox couple, expressed by Eq. (16) in volts versus SHE, where S_M (slope) and I_M (intercept) depend upon the metal and redox couple, the spin state and the stereochemistry, and E_L is an additive

electrochemical ligand parameter.

$$E_{1/2}[M^{n+1/n}] = S_M(\Sigma E_L) + I_M/V \text{ vs. SHE} \quad (16)$$

The E_L parameter for each ligand L was obtained through a statistical analysis of the reported redox potentials of the large number of complexes with the $Ru^{III/II}$ redox couple and the possible ligands, as given by Eq. 17 (alternatively in some cases using Hammett relationships [68–71]).

$$E_{1/2}[Ru^{III/II}] = \Sigma E_L(L) \quad (17)$$

Hence, ideally, for the $Ru^{III/II}$ complexes, S_M should be unity and I_M null. In contrast to the P_L parameter, E_L is dependent on the reference electrode and commonly is referred to the SHE.

Values of those parameters have already been proposed for many ligands (E_L) and a considerable number of metal centers (S_M and I_M), mainly by Lever [64–67, 72] and occasionally by others [14, 15, 24, 27, 29, 35, 38, 41, 48, 71, 73–77]. Examples concerning the former parameter are listed in Table 9 and an extensive list for many carbyne, carbene, vinylidene, allenylidene and alkynyl ligands has been proposed recently by Pombeiro [38]. Tables 10–12 list the proposed S_M and I_M values for the binding metal centers so far studied.

Since the linear relationship (18) has been experimentally observed [64] (for a considerable number of ligands) between E_L and P_L , both reflecting the net electron-donor/acceptor character of the ligand, the two sets of values are expected to follow parallel trends and one can derive any of them from the knowledge of the other one. Hence, the earlier mentioned ligand comparisons based on P_L should, in general, be also valid for the E_L scale, and one could complete the corresponding Tables (2 and 9, respectively) by estimating

the missing data using Eq. (18).

$$P_L = 1.17E_L - 0.86 \quad (18)$$

However, this expression should be used with caution. In fact, it appears to be invalid for ligands (like CO [22, 46, 64], carbynes [14] and isocyanides [22, 28, 64]) that are strong π -acceptors (with an extensive π -stabilizing influence on the HOMO energy), when the need to introduce positive corrections to E_L has been recognized (compare with the above P_L corrections for isocyanides, nitriles, and cyanide). Corrective terms can also be added to the general expression (16), which then assumes, for carbonyl complexes, the form (19) [67] in which x is the number of CO π^* -orbitals that interact with the HOMO and c is an empirical correction. Further corrections ($c'x'$, etc.) can be added if the complex has also other strong π -acceptor ligands, for example, isocyanides. Each of these corrections can reach values up to 0.3 V [28, 64, 67].

$$E_{1/2}[M^{n+1/n}] = S_M(\Sigma E_L) + I_M + cx \quad (19)$$

Hence, for such ligands, the estimate of E_L or P_L by using Eq. (18) should be avoided, whenever possible, and separate methods based on the corresponding models are preferable. Moreover, Eq. (16) also requires corrective terms and its use thus becomes less convenient.

Examples of ligands whose E_L values have been recently estimated by using directly the Lever model, with disagreeing values obtained from expression (18), include the benzoylisocyanide $C\equiv NC(O)Ph$ ($E_L = 0.60$ V vs. SHE [15]), a number of metallo-cyanide and other cyano-adducts such as $C\equiv N-ML_{n-1}^-$ ($M = V^{III}, Re^V, Ni^{II}, Pd^{II}$) ($E_L = +0.19$ to -0.14 V vs. SHE [15, 27]), $C\equiv N-BF_3^-$ ($E_L = 0.20$ V vs. SHE [15]) and $C\equiv N-BPh_3^-$ ($E_L = -0.05$ V vs. SHE [15]) (Table 9).

Tab. 9 Values of the Lever E_L parameter of selected ligands^a

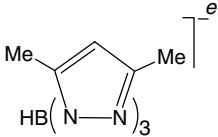
<i>L</i>	E_L/V vs. SHE	References
NO ⁺	>1.5	64, 67
Carbynes ($\equiv\text{CR}$)	ca.1.2	14
CO	0.99	64
<i>N</i> -Methylpyrazinium	0.79	64
CH ₂ =CH ₂	0.76	64
2,2'-Bipyrazinium	0.75	64
Alkyl nitrites (RONO)	0.72 to 0.70	64
P(C ₆ H ₄ OMe-4) ₃	0.69	73
P(NC ₄ H ₄) ₃ ^b	0.69	48
=C=CHCO ₂ R	0.62	14
C \equiv NC(O)Ph	0.60	15
PPh(NC ₄ H ₄) ₂ ^b	0.60	48
C \equiv N-CH ₂ Ph	0.56	64
=C=CH ₂	0.56	14
P(OC ₆ H ₄ Me-3) ₃	0.54	48
PPh ₂ (NC ₄ H ₄) ^b	0.53	48
=C=CHPh	0.52	14
=C=CHC ₆ H ₄ Me-4	0.51	14
=C=CHBu ^t	0.50	14
P(OC ₆ H ₄ Me-4) ₃	0.50	48
N \equiv C-C ₆ H ₄ -C \equiv N-4	0.49(aq.)	64
Ph ₂ PCH=CHPPh ₂	0.49	64
Me ₂ S=O	0.57	74
Ph ₂ PC \equiv CPPh ₂	0.46	64
=C=C=CPh ₂	0.46 ^c	29, 38
Norbornadiene	0.46	64
C \equiv N-Bu ⁿ	0.45	64
Pcy ₃	0.45	48
Ph ₂ AsCH ₂ CH ₂ AsPh ₂	0.44	64
Ph ₂ PCH ₂ PPh ₂ (dppm)	0.43	64
Pyrimidinium	0.43	64
=C=C=C(Me)Ph	0.42	29, 38
P(OMe) ₃	0.42	64
=C=C=CEt ₂	0.41	29, 38
C \equiv N-Ph	0.41	64
N \equiv C-C ₆ H ₄ Cl-4	0.40(aq.)	64
PPh ₂ (C ₆ H ₄ OMe-4)	0.40	48
PPh ₃	0.39	64
AsPh ₃	0.38	64
SbPh ₃	0.38	64
N \equiv C-C ₆ H ₄ OMe-4	0.38	64
N \equiv C-CH=CH ₂	0.38	64
N \equiv C-C ₆ H ₄ Me-4	0.37	64
Ph ₂ PCH ₂ CH ₂ PPh ₂ (dppe)	0.36	64
2,2'-Bipyrazine	0.36	64
N \equiv CMe	0.34	64
PMe ₂ Ph	0.34	64

(continued overleaf)

Tab. 9 (continued)

L	E_L/V vs. SHE	References
PMe ₃	0.33	64
S(Me)Ph	0.33	64
Pyrazine	0.33	64
Pyridine, 3,5-dichloro	0.33	64
Bipyrimidine	0.31	64
SMe ₂	0.31	64
Pyridine, 4-acetyl	0.30	64
Quinoline	0.29	64
Pyrimidine	0.29	64
Et ₂ PCH ₂ CH ₂ PEt ₂ (depe)	0.28	24
4,4'-Bipyridine	0.27	64
Pyridine, 4-chloro	0.26(aq.)	64
Indazole	0.26	76
1,10-Fenanthroline	0.26	64
Isonicotinamide	0.26(aq.)	64
2,2'-Bipyridine	0.259	64
Pyridine	0.25	64
Pyridine, 4-phenyl	0.23	64
4,4'-Bithiazole	0.20	64
Pyrazole	0.20	64
C≡N-BF ₃ ⁻	0.20	15
C≡N-NiCl ₂ (PCy ₃) ⁻	0.19	27
1,2,4-Triazole	0.18	64
Trifluorosulfonate	0.13	64
NH ₂ Bu	0.13	64
Imidazole	0.12	64
NH ₃	0.07	64
ClO ₄ ⁻	0.06	64
NH ₂ Pr ⁱ	0.05	64
H ₂ O	ca. 0.04	64
C≡N-VCl ₃ (thf) ₂ ⁻	0.03	15
NO ₂ ⁻	0.02	64
C≡N ⁻	0.02	64
	-0.26 ^d	15
Dimethylglyoximate	0.01	64
C≡N-BPh ₃ ⁻	-0.05	15
PhC(O)CHC(O)CH ₃ ⁻ (bac)	-0.06	64
SCN ⁻	-0.06	64
CH ₃ C(O)CHC(O)CH ₃ ⁻ (acac)	-0.08	64
8-Hydroxyquinolate	-0.09	64
C≡N-ReOCl ₃ (μ-CN)FeH(dppe) ₂ ⁻	-0.09	27
NO ₃ ⁻	-0.11	64
Dimethyldithiocarbamate	-0.12	64
4-CH ₃ C ₆ H ₄ SO ₃ ⁻	-0.13	64
S=C(NH ₂) ₂ (thiourea)	-0.13	64
C≡N-PdCl ₂ (PPh ₃) ⁻	-0.14	27
CF ₃ COO ⁻	-0.15	64
Oxalate	-0.17	64
1,2,4-Triazolate	-0.17	64

Tab. 9 (continued)

<i>L</i>	E_L/V vs. SHE	References
Br [−]	−0.22	64
	−0.23	73
Pyrazolate	−0.24	64
Cl [−]	−0.24	64
I [−]	−0.24	64
H [−]	−0.30	64
N ₃ [−]	−0.30	64
HCOO [−]	−0.30	64
Alkynyls (−C≡C−R [−])	−0.1 to −0.7	29, 38, 41
F [−]	−0.42	64
SC ₆ H ₄ Me-4 [−]	−0.48	64
Benzohydroxamate(2 [−])	−0.52	64
SPh [−]	−0.53	64
SEt [−]	−0.56	64
Alkyls, aryls, NO [−]	−0.70 to −0.90	67

^aFor di- or poly-dentate ligands, E_L refers to each ligating arm.

^b*N*-Pyrrolylphosphine.

^cThe value of 0.71 V has been proposed [75] at a 4-coordinate metal center with S_M and I_M values obtained from a restricted number of data points (see Table 10).

^dAt *trans*-[FeH(dppe)₂]⁺.

^eHydrotris(3,5-dimethylpyrazolyl)borate.

However, Eq. (18) appears to be valid for both allenylidenes =C=C=CR₂ and alkynyls −C≡CR[−], giving E_L values comparable to those obtained from the general expression (16) [29, 38, 41, 48].

Other recently proposed E_L values on the basis of the general Eq. (16) include (1) indazole ($E_L = 0.26$ V vs. SHE [76]), which thus is shown to be a weaker net electron-donor than the previously studied triazole and imidazole (Table 9), (2) the *N*-pyrrolylphosphines PPh_{*n*}(NC₄H₄)_{3−*n*} (*n* = 0–2) ($E_L = 0.69$ – 0.53 V vs. SHE) [48] that behave as weaker net electron-donors than organophosphines, the electron-releasing ability decreasing with the increase

of the number of *N*-pyrrolyl groups, and (3) the hydro-tris(3,5-dimethylpyrazolyl)borate [HB{NNC(Me)CHC(Me)}₃][−] ligand (i.e. each of its N-ligating arms) ($E_L = -0.23$ V vs. SHE [73]) that acts as a net electron-donor identical to pyrazolate ($E_L = -0.24$ V vs. SHE [64]).

The pyrrolylphosphines and the tris-(pyrazolyl)borate derivative were investigated [48, 73] at square-planar tetra-coordinate Rh^I complexes for which the Lever model was then extended (see in the following).

In organic media, the particular net charge of the complex usually appears

Tab. 10 Values of the S_M and I_M parameters for six-coordinate complexes in organic medium^a

Redox couple	S_M	I_M/V vs. SHE	References
Nb ^{V/IV}	0.76	1.24	64
Nb ^{IV/III}	0.75	−0.12	64
Ta ^{V/IV}	0.79	0.66	64
	1.17	−0.86	64
Cr ^{III/II} (LS)	1.18	−1.72	64
Cr ^{III/II} (HS)	0.84	−1.18	64
Cr ^{I/0}	0.52	−1.75	64
Mo ^{I/0}	0.74	−2.25	64
Mo ^{II/I}	0.81	−1.76	64
Tc ^{IV/III}	1.00	0.65	65
Tc ^{III/II}	1.28	−0.89	65
Tc ^{II/I}	1.42	−2.09	65
Re ^{IV/III}	0.86	0.51	65
Re ^{III/II}	1.17	−0.88	65
Re ^{II/I} (upper)	0.76	−0.95	65
Re ^{II/I} (lower)	0.27	−1.43	65
Fe ^{IV/III} (particular) ^b	1.49	−0.18	24
Fe ^{III/II} (LS)	1.10	−0.43	64
Fe ^{III/II} (LS)	1.07	−0.3	35
(particular) ^c			
Fe ^{III/II} (LS)	1.32	−0.57	24
(particular) ^d			
Fe ^{III/II} (HS)	0.89	−0.25	64
Ru ^{IV/III}	1.03	1.68	76
Ru ^{III/II}	0.97	0.04	64
Os ^{III/II}	1.01	−0.40	64

^aLS = low spin; HS = high spin.^bEstablished for the series *trans*-[FeBrL(depe)₂]^{2+/3+} (L = CO, aryl and alkyl N≡CR).^cEstablished for the series *trans*-[FeL₂(depe)₂]^{2+/3+} (L = CO, aryl and alkyl N≡CR, N≡C−NR₂).^dEstablished for the series *trans*-[FeBrL(depe)₂]^{+ / 2+} (L = CO, aryl and alkyl N≡CR, Br[−]).

not to have a relevant effect on the redox potential, since complexes with the common $M^{n+1/n}$ redox couple but with different net charges (determined by the ligands) exhibit the same S_M and I_M values (these are dependent on the difference in free energy of solvation for the pair of ions involved) [67]. However, in water, solvation effects can play an important role and different sets of values are

expected for different charges (Table 11). The Ru^{III/II} couple has been the most studied one: in water, the 2+/1+ charged couple has $S_M = 1.14$, $I_M = -0.35$ V vs. SHE [64], whereas the 1−/2− charged one in aqueous phosphate buffer (pH 7) exhibits $S_M = 0.88$, $I_M = 0.46$ V vs. SHE [76], and these values are also distinct from those quoted ($S_M = 0.97$, $I_M = 0.04$ vs. SHE [64]) for organic media.

Tab. 11 Values of the S_M and I_M parameters for six-coordinate complexes in aqueous medium^a

Redox couple	S_M	I_M/V vs. SHE	References
Cr ^{III/II}	0.58	−1.12	64
Fe ^{III/II} (LS)	0.68	0.24	64
Ru ^{III/II} (2+/1+) ^b	1.14	−0.35	64
Ru ^{III/II} (1−/2−) ^{b,c}	0.88	0.46	76
Os ^{III/II}	1.61	−1.30	64

^aLS = low spin.^bCharges of the complexes in the oxidized and reduced forms given in brackets.^cIn aqueous phosphate buffer (pH 7).

The high generality of Lever Eq. (16) also brings some drawbacks. In order to be applicable to all the six-coordinate complexes with a certain $M^{n+1/n}$ redox couple, it cannot distinguish among either particular series of complexes or isomeric forms with different redox potentials, and linearity may fail for all the wide range of the available ΣE_L values. These limitations are usually not serious, or at least can be overcome much easier, with the Pickett Eq. (5) that concerns a series of closely related $[M_S L]$ complexes with a specific metal center $\{M_S\}$ and with a single variable ligand L. Hence, for each particular series, the more restricted Pickett equation is expected to be more accurate than the more general Lever expression that is not able to reflect subtle variations in the electronic and structural properties of the ligands and metal sites.

Therefore, different S_M , I_M sets of values have already been proposed by Pombeiro et al. for particular series of Fe^{III/II} complexes, such as *trans*-[FeL₂(depe)₂]^{2+/3+} (L = CO, aryl and alkyl NCR, NCNH₂) ($S_M = 1.07$, $I_M = -0.3$ V vs. SHE [35]) and *trans*-[FeBr(L)(depe)₂]⁺²⁺ (L = CO, NCR, Br[−]) ($S_M = 1.32$, $I_M = -0.57$ V vs. SHE [24]), that fit better the experimental data than

the Lever general one ($S_M = 1.10$, $I_M = -0.43$ V vs. SHE [64]) (Table 10).

Incidentally, the *trans*-[FeBr(L)(depe)₂]^{+2+/3+} series has also allowed to propose [24] parameter values for a Fe^{IV/III} redox couple: $S_M = 1.49$, $I_M = -0.18$ V vs. SHE.

In order to overcome the isomeric limitations, correction terms have to be introduced (see Eq. 19) [64] to account for the different isomeric redox potentials, whereas the loss of linearity in the relationship between the redox potential and ΣE_L , for a wide range of the latter, requires the consideration [65] of different expressions along the ΣE_L scale or of curved relationships, as observed for the Re^{I/II} redox systems. More recent studies of series of Re^I-nitrile [24] and Re^I-vinylidene [14] complexes have provided some supporting testimony for a curved overall relationship.

3.2.2.2 Extensions of the Model

Lever's model has been typically applied only to six-coordinate complexes, but recently it has been extended by Pombeiro et al. to square planar *four-coordinate* Rh^{I/II} complexes ($S_M = 1.68$, $I_M = -0.87$ V vs. SHE [47, 73]) and, although still restricted

Tab. 12 Values of the S_M and I_M parameters for four- and five-coordinate complexes in organic medium

Redox couple		S_M	I_M/V vs. SHE	References
4-coordinate	Rh ^{I/II} (square planar) ^a	1.68	−0.87	48, 73
5-coordinate	Rh ^{I/IIb}	0.80	−0.95	48
	Fe ^{III/IIc}	1.60	–	64
	Mn ^{III/IIc}	0.38	–	64

^aThe values of $S_M = 1.83$ and $I_M = -1.22$ V vs. SHE have been proposed [75] on the basis of a smaller number of data points.

^bOn the basis of a rather limited number of monohydride complexes.

^cOn the basis of a rather limited number of porphyrin complexes and with an uncertain E_L value for the porphyrin core.

to a rather small number of available monohydride complexes, to *five-coordinate* Rh^{I/II} compounds [48] (Table 12). Other S_M and I_M values for the four-coordinate Rh^{I/II} complexes had been proposed by Werner et al. [75] on the basis of a smaller number of data points.

Applications of the model to Ru *clusters* have been reported namely by Toma et al. [78] and Keister et al. [79, 80], and, for example, for the single-electron oxidation of the 48-electron complexes of the type [Ru₃(μ-H)₃(μ₃-CX) (CO)_{9-n}L_n], expression (20) is followed [79, 80], being derived from the general Lever's equation with inclusion of a Hammett term concerning the methylidyne X substituent. The observed value of S_{M3} (0.37) (vs. the unity expected for a monometallic Ru center) is indicative of an effective delocalization of the ligand effects over the three Ru atoms [79].

For the μ-oxo centered [Ru₃(μ₃-O)(μ₂-CH₃COO)₆L₃]ⁿ⁺ (L = *N*-heterocyclic ligand e.g. pyridine, pyrazine, and derivatives) clusters, the general form of Lever Eq. (16) was shown to be valid for

successive oxidation processes, with the slope (S_M) tending to decrease with the increase of the average metal oxidation state, that is, from unity for the Ru₃^{III,III,II/III,II,II} redox couple to 0.48 to the Ru₃^{IV,IV,III/IV,III,III} pair [78].

$$E_{1/2}[M^{n+1/n}] = S_{M3} \Sigma E_L + 2.303 \left(\frac{RT}{F} \right) \rho \sigma_p^+(X) + I_{M3} \quad (20)$$

The Lever's model has also been extended to *sandwich* and *half-sandwich complexes* with π-cyclopentadienyl or π-arene ligands [66, 67, 69]. The E_L parameter for the π-ligands has been defined [69] on the basis of the low spin Fe^{III/II} redox couple, by Eqs. (21) or (22), for homoleptic sandwich [Fe(π-L)₂] or mixed sandwich [Fe(π-L₁)(π-L₂)] complexes, respectively.

$$E_L(\pi-L) = \frac{1}{2} E_{1/2}[\text{Fe}^{\text{III/II}}] \quad (21)$$

$$E_{1/2}[\text{Fe}^{\text{III/II}}] = E_L(\pi-L_1) + E_L(\pi-L_2) \quad (22)$$

E_L values have thus been proposed [66, 67, 69] for a great number of π-ligands, also by using the observed correlation

between E_L of the substituted π -ligand and the Hammett's substituent constant. The study was performed with π -complexes of various first row transition metal centers whose S_M and I_M values were also obtained.

Lever's approach has also been extended to reduction processes *centered at ligands* [66, 67]. Thus, for a complex $[M(LL)WXYZ]$ with a reducible ligand LL and other co-ligands W, X, Y, and Z, the reduction potential of LL to LL^- , bound to M^{n+} , is given by Eq. (23) in which S_L is a measure of the influence of the W, X, Y, Z ligands on the reducible LL ligand via the metal center, and I_L , for $S_L = 0$, is the reduction potential of the free ligand [66, 67].

$$E_{1/2}[LL^{o/-}(M^n)] = S_L \Sigma E_L(WXYZ) + I_L \quad (23)$$

Combination and rearrangement of Eqs. (16) and (23) lead to expression (24) that correlates linearly the ligand-centered reduction potential with the metal centered oxidation potential (d is the denticity of the reducible LL ligand). The slope of this line is S_L/S_M , and the intercept is a constant for the particular reducible ligand [66].

$$E_{1/2}[LL^{o/-}(M^n)] = \left(\frac{S_L}{S_M} \right) E_{1/2}[M^{n+1/n}(LL)] + \left[I_L - \left(\frac{S_L}{S_M} \right) I_M - S_L d \Sigma E_L(LL) \right] \quad (24)$$

Effects on the redox potential of substituents at the reducible ligand have also been investigated and linear correlations recognized with the Hammett's σ constant [66, 67].

3.2.2.3 Other Relationships

Linear correlations between $E_L(L)$ and Hammett substituent constants for substituted π -cyclopentadienyl and π -arene ligands [69], for other substituted ligands,

such as pyridines, bipyridines, and diketones [68], as well as for a number of unsubstituted ligands [71], have been well established and allowed the estimate of previously unknown E_L values (see also the earlier text).

The E_L Lever parameter was also shown [71] to correlate linearly with other parameters that measure the net electron-donor character of a ligand (L), namely the Tolman's electronic parameter (TEP) [81] for phosphines and a computed electronic parameter (CEP) [71] based (as TEP) on the infrared $A_{1g}(\text{CO})$ frequency in complexes $[\text{NiL}(\text{CO})_3]$, which is determined by the electronic effect of L.

Relationships between redox potentials and the energy ($h\nu$) of a *metal-to-ligand charge transfer* (MLCT) band have been well documented and expressed, for complexes $[M(LL)WXYZ]$, in a simplified way, by Eq. (25) in which C is a constant and $\Delta E(\text{Redox})$ is given by Eq. (26), that is, the difference between the metal centered oxidation potential and the ligand centered reduction potential [67].

$$h\nu(\text{MLCT}) = \Delta E(\text{Redox}) + C \quad (25)$$

$$\Delta E(\text{Redox}) = E_{1/2}[M^{n+1/n}(LL)] - E_{1/2}[LL^{o/-}(M^n)] \quad (26)$$

Since these redox potentials can be expressed as function of the E_L parameter (Eqs. 5 and 23), the MLCT energy can be given by Eq. (27) or (28) (C' and C'' are constants) as a function of E_L .

$$h\nu(\text{MLCT}) = (S_M - S_L) E_{1/2}[M^{n+1/n}] + C' \quad (27)$$

$$h\nu(\text{MLCT}) = (S_M - S_L) \Sigma E_L(WXYZ) + C'' \quad (28)$$

However, correlations with the emission energy of emission spectra are still rare.

The applications of these and related expressions to various types of complexes have been reviewed by Lever [66, 67].

3.2.3

Bursten's Model

This model was proposed by Bursten [82] in 1982. It assumes a linear correlation (with a negative slope) between the HOMO energy and the oxidation potential of octahedral d^6 metal complexes of the type $[ML_nL'_{6-n}]$ (L = stronger π -acceptor than L'), this potential (viz. HOMO energy) being determined in an additive way by the effects (B) of all the nL and $(6-n)L'$ ligands and by the effects (C) of the ligands, xL and $(4-x)L'$, that π -interact with the metal d_π orbital comprised in the HOMO of the complex (Eq. 29 in which A° depends on the metal atom, in particular its oxidation state, and trivially on the solvent and reference electrode).

$$E_{1/2} = A^\circ + nB^L + (6-n)B^{L'} + xC^L + (4-x)C^{L'} \quad (29)$$

This equation assumes the simplified form (30) in which the constants A , B , and C are given by Eqs. (31)–(33).

$$E_{1/2} = A + nB + xC \quad (30)$$

$$A = A^\circ + 6B^{L'} + 4C^{L'} \quad (31)$$

$$B = B^L - B^{L'} \quad (32)$$

$$C = C^L - C^{L'} \quad (33)$$

Parameter B (electrostatic term) reflects the difference between the abilities of L and L' to electrostatically stabilize the metal d orbitals (difference between the net electron-acceptor characters of these ligands), whereas parameter C (bonding term) is determined by the difference between the abilities of L

(typically CO) and L' to stabilize (by π -acceptance) the metal d_π orbital involved in the HOMO. The latter term is isomer dependent and allows to differentiate isomeric potentials. Hence, for example, although $n = 2$ for both *trans*- and *cis*- $[ML_2L'_4]$, these isomers have different x values (0 and 1, respectively) and therefore should exhibit different oxidation potentials (Eq. 30), that is, $E_{1/2} = A + 2B$ for *trans* and $A + 2B + C$ for *cis*.

Although the model has been extended to other types of coordination compounds [83, 84], namely d^1 metal octahedral complexes such as $[MCl_{6-n}(NCMe)_n]^{-2+n}$ ($M = Nb^{IV}, Ta^{IV}; n = 0-2$) [84], its application still remains little explored [82–84].

The Bursten's model can be correlated to the Pickett's model by considering the relationship between the corresponding ligand parameters, as shown by Datta [85]. In fact, by applying the former model (Eq. 30) to $[Cr(CO)_5L]$ ($n = 5, x = 3$) and $[Cr(CO)_6]$ ($n = 6, x = 4$) and taking into account the definition of P_L (Eq. 4), one obtains Eq. (34), which substantiates the importance, in the ligand P_L parameter, of both the overall electrostatic ligand effects and π -effects at the HOMO, expressed by the corresponding terms of the Bursten equation.

$$P_L = -(B + C) \quad (34)$$

Ligand additivity implications to the Pickett's model for complexes of the type $[ML_4L'L'']$ have also been recognized [85].

3.3

Final Comments

The redox potential of a complex contains a rich information on its electronic/structural properties, that is, of

its ligands and binding metal center. However, in order to extract that information, it is necessary to find out how the value of the redox potential reflects all the ligand and metal effects. This can be attempted, in indirect ways, by searching for relationships between the redox potential and other properties of the complexes, or, in a more direct and quantitative way, by ligand and metal parametrization of the redox potential which thus is directly related to the electronic/structural features of the ligands and binding metal sites. For this purpose, the ligand and metal effects are separated, considered to be independent and their contributions are added to give the redox potential. This additivity assumption, necessary for the simplification of the complex dependence of the redox potential on those factors, naturally has considerable limitations since it does not take into account, for example, synergisms between the ligands and the metal, interactions among the ligands and the possible dependencies of the ligand effects on the particular metal centers and of the metal centers on the particular ligands.

Therefore, the limitations of the parametrization models should reflect the relative extents of additivity on which they are based, which are also related to their generality.

The Lever's model appears as the most general and attractive one. Since it assumes a complete additivity, with all the ligand effects treated separately and being independent from the metal, its application is rather general and simple. For instance, to estimate the redox potential of a particular complex, one simply has to add the contributions of all the ligands, ΣE_L , and affect the total ligand effect by the effects associated to the $M^{n+1/n}$ redox couple (S_M , I_M), which are assumed to be fully independent of the

ligands. The risk of failure in particular cases parallels the high generality and a good answer to subtle changes in structure or composition of the complexes should not be expected.

In contrast, the Pickett's model, in its original form, is based on a minimum additivity, since only one ligand (L) is treated separately, the others being associated to the metal in the common $\{M_s\}$ center that is considered as a whole. The set of ligand and metal center parameters is applicable only to the complexes with that $\{M_s\}$ center and therefore the model has a much lower generality than the Lever's one. However, it is expected to be more accurate for the particular series of complexes it concerns and to respond in a better way to structure/composition changes, including geometrical isomeric differences, a type of situation that is also accounted for by the Bursten's model (although in a different way and so far applied only to limited series of complexes), but not by the Lever's model which then requires the inclusion of less convenient correction terms. Corrections have also to be applied when dealing with very strong π -acceptor ligands.

Hence, these models are somehow of complementary characters and efforts should be directed toward their developments and wider applications, including those situations in which the additivity fails. Extensions of the Pickett's and Lever's models have already been proposed to overcome their limitations, as discussed above, and in some cases the dependency of the ligand parameters on the metal centers and generalizations to types (with different electron-counts, structures, compositions, etc.) of complexes, metal centers and ligands not included in the original proposals, have already been successfully treated.

Further developments will undoubtedly follow, but one should not expect to reach a single and simple overall redox potential-structure relationship with a universal use in Coordination Chemistry, in preference to a number of relationships with a lower generality that conceivably will deal more appropriately with correspondingly more restricted areas of application.

References

1. A. J. L. Pombeiro, *Portugaliae Electrochim. Acta* **1983**, 1, 19.
2. A. J. L. Pombeiro, *New J. Chem.* **1997**, 21, 649.
3. A. J. L. Pombeiro, C. Amatore, (Eds.), *Trends in Molecular Electrochemistry* Marcel Dekker/FontisMedia, New York/Lausanne, 2004.
4. A. J. L. Pombeiro, J. McCleverty, (Eds.), *Molecular Electrochemistry of Inorganic, Bioinorganic and Organometallic Compounds* NATO ASI Series, Kluwer, Dordrecht, The Netherlands, 1993.
5. P. Zanello, *Inorganic Electrochemistry. Theory, Practice and Application*, Royal Society of Chemistry, Cambridge, 2003.
6. D. Astruc, *Electron Transfer and Radical Processes in Transition-Metal Chemistry*, VCH, New York, 1995.
7. A. Vlcěk, *Chemtracts – Inorg. Chem.* **1993**, 5, 1.
8. A. C. Sarapu, R. F. Fenske, *Inorg. Chem.* **1975**, 14, 247.
9. C. J. Pickett, D. Pletcher, *J. Organometal. Chem.* **1975**, 102, 327.
10. J. Chatt, C. T. Kan, G. J. Leigh et al., *J. Chem. Soc. Dalton Trans.* **1980**, 2032.
11. J. Chatt, *Coord. Chem. Rev.* **1982**, 43, 337.
12. C. J. Pickett, in *Comprehensive Coordination Chemistry* (Eds.: G. Wilkinson, R. D. Gillard, J. A. McCleverty et al.), Pergamon Press, Oxford, 1987, p. 493, Vol. 1, ch. 8.3.
13. C. Laurence, B. Wojtkowiak, *Ann. Chim.* **1970**, 5, 163.
14. S. S. P. R. Almeida, A. J. L. Pombeiro, *Organometallics* **1997**, 16, 4469.
15. S. S. P. R. Almeida, M. F. C. Guedes da Silva, J. J. R. Fraústo da Silva et al., *Portugaliae Electrochim. Acta* **2001**, 19, 371.
16. C. J. Pickett, in *Electrochemistry* (Ed.: D. Pletcher), Royal Society of Chemistry, Cambridge, 1983, 81, Vol. 8.
17. M. A. N. D. A. Lemos, A. J. L. Pombeiro, *J. Organomet. Chem.* **1988**, 356, C79.
18. M. F. Meidine, M. A. N. D. A. Lemos, A. J. L. Pombeiro et al., *J. Chem. Soc. Dalton Trans.* **1998**, 3319.
19. M. F. N. N. Carvalho, A. J. L. Pombeiro, *J. Chem. Soc. Dalton Trans.* **1989**, 1209.
20. A. J. L. Pombeiro, *Inorg. Chim. Acta* **1985**, 103, 95.
21. A. J. L. Pombeiro, C. J. Pickett, R. L. Richards, *J. Organomet. Chem.* **1982**, 224, 285.
22. Y. Wang, A. J. L. Pombeiro, L. Kaden, et al., in *Molecular Electrochemistry of Inorganic, Bioinorganic and Organometallic Compounds* (Eds.: A. J. L. Pombeiro, J. McCleverty), NATO ASI Series, Kluwer, Dordrecht, The Netherlands, 1993, p. 63.
23. A. I. F. Venâncio, M. L. Kuznetsov, M. F. C. Guedes da Silva et al., *Inorg. Chem.* **2002**, 41, 6456.
24. M. F. C. Guedes da Silva, L. M. D. R. S. Martins, J. J. R. Fraústo da Silva et al., *Collect. Czech. Chem. Commun.* **2001**, 66, 139.
25. T. El-Shihi, F. Siglmüller, R. Herrmann et al., *J. Organomet. Chem.* **1987**, 335, 239.
26. T. El-Shihi, F. Siglmüller, R. Herrmann et al., *Portugaliae Electrochim. Acta* **1987**, 5, 179.
27. S. S. P. R. Almeida, M. F. C. Guedes da Silva, A. J. L. Pombeiro, *Collect. Czech. Chem. Commun.* **2003**, 68, 1663.
28. G. Facchin, M. Mozzon, R. A. Michelin et al., *J. Chem. Soc. Dalton Trans.* **1992**, 2827.
29. A. I. Venâncio, M. F. Guedes da Silva, L. M. D. R. S. Martins, J. J. R. Fraústo da Silva, A. J. L. Pombeiro *Organometallics* **2005**, 24, 4654.
30. L. Zhang, M. F. C. Guedes da Silva, M. L. Kuznetsov et al., *Organometallics* **2001**, 20, 2782.
31. A. Limberg, M. A. N. D. A. Lemos, A. J. L. Pombeiro et al., *Portugaliae Electrochim. Acta* **1995**, 13, 319.
32. A. J. L. Pombeiro, M. T. A. R. S. Costa, Y. Wang et al., *J. Chem. Soc. Dalton Trans.* **1999**, 3755.
33. S. S. P. R. Almeida, M. F. C. Guedes da Silva, J. J. R. Fraústo da Silva et al., *J. Chem. Soc. Dalton Trans.* **1999**, 467.

34. S. M. P. R. M. Cunha, M. F. C. Guedes da Silva, A. J. L. Pombeiro, *Portugaliae Electrochim. Acta* **1999**, 17, 221.
35. L. M. D. R. S. Martins, A. J. L. Pombeiro, *Portugaliae Electrochim. Acta* **1996**, 14, 151.
36. L. M. D. Ribeiro, A. J. L. Pombeiro, *Portugaliae Electrochim. Acta* **1995**, 13, 329.
37. M. F. N. N. Carvalho, A. J. L. Pombeiro, *J. Organomet. Chem.* **1991**, 410, 347.
38. A. J. L. Pombeiro, *J. Organometal. Chem.* **2005**, in press (special issue on Carbene Chemistry).
39. M. F. N. N. Carvalho, A. J. L. Pombeiro, A. Hills et al., *J. Organometal. Chem.* **1993**, 469, 179.
40. E. C. B. A. Alegria, S. M. P. R. M. Cunha, L. M. D. R. S. Martins et al., *Portugaliae Electrochim. Acta* **2004**, 22, 19.
41. A. I. F. Venâncio, L. M. D. R. S. Martins, A. J. L. Pombeiro, *Portugaliae Electrochim. Acta* **2003**, 21, 85.
42. A. Hills, D. L. Hughes, N. Kashef et al., *J. Chem. Soc. Dalton Trans.* **1992**, 1775.
43. L. Zhang, M. P. Gamasa, J. Gimeno et al., *Eur. J. Inorg. Chem.* **2000**, 1707.
44. G. A. Carriedo, V. Riera, N. G. Connelly et al., *J. Chem. Soc. Dalton Trans.* **1987**, 1769.
45. M. F. C. Guedes da Silva, J. J. R. Fraústo da Silva, A. J. L. Pombeiro et al., *J. Chem. Soc. Dalton Trans.* **1996**, 2763.
46. Y. Wang, A. J. L. Pombeiro, *Portugaliae Electrochim. Acta* **1993**, 11, 111.
47. M. F. N. N. Carvalho, A. J. L. Pombeiro, *Portugaliae Electrochim. Acta* **1989**, 7, 101.
48. M. F. C. Guedes da Silva, A. M. Trzeciak, J. J. Ziolkowski et al., *J. Organometal. Chem.* **2001**, 620, 174.
49. G. A. Katsoulos, M. P. Sigalas, C. A. Tsipis, *Inorg. Chim. Acta* **1989**, 158, 225.
50. M. F. N. N. Carvalho, M. T. Duarte, A. M. Galvão et al., *J. Organometal. Chem.* **1994**, 469, 79.
51. A. J. L. Pombeiro, *Portugaliae Electrochim. Acta* **1985**, 3, 41.
52. A. J. L. Pombeiro, M. F. C. Guedes da Silva, M. A. N. D. A. Lemos, *Coord. Chem. Rev.* **2001**, 219–221, 53.
53. A. M. Bond, R. Colton, *Coord. Chem. Rev.* **1997**, 166, 161.
54. M. F. C. Guedes da Silva, C. M. P. Ferreira, J. J. R. Fraústo da Silva et al., *J. Chem. Soc. Dalton Trans.* **1998**, 4139.
55. M. F. C. Guedes da Silva, J. J. R. Fraústo da Silva, A. J. L. Pombeiro et al., *Organometallics* **1994**, 13, 3943.
56. M. F. C. Guedes da Silva, J. J. R. Fraústo da Silva, A. J. L. Pombeiro et al., *Inorg. Chem.* **1998**, 37, 2344.
57. J. Chatt, G. J. Leigh, H. Neukomm et al., *J. Chem. Soc. Dalton Trans.* **1980**, 121.
58. G. J. Leigh, R. H. Morris, C. J. Pickett et al., *J. Chem. Soc. Dalton Trans.* **1981**, 300.
59. J. Chatt, W. Hussain, G. J. Leigh et al., *J. Chem. Soc. Dalton Trans.* **1985**, 1131.
60. M. F. C. Guedes da Silva, J. J. R. Fraústo da Silva, A. J. Pombeiro, *J. Chem. Soc. Dalton Trans.* **1994**, 3299.
61. G. Butler, J. Chatt, G. J. Leigh et al., *J. Chem. Soc. Dalton Trans.* **1979**, 113.
62. A. J. L. Pombeiro, *Rev. Port. Quím.* **1981**, 23, 179.
63. M. A. N. D. A. Lemos, A. J. L. Pombeiro, *J. Organometal. Chem.* **1992**, 438, 159.
64. A. B. P. Lever, *Inorg. Chem.* **1990**, 29, 1271.
65. A. B. P. Lever, *Inorg. Chem.* **1991**, 30, 1980.
66. A. B. P. Lever, E. S. Dodsworth, *Inorganic Electronic Structure and Spectroscopy*, John Wiley & Sons, New York, 1999, p. 227.
67. A. B. P. Lever, in *Comprehensive Coordination Chemistry II* (Ed.: A. B. P. Lever), 2004, p. 251, Vol. 2. ch. 2.19.
68. M. Masui, A. B. P. Lever, *Inorg. Chem.* **1993**, 32, 2199.
69. S. Lu, V. V. Strelets, M. F. Ryan et al., *Inorg. Chem.* **1996**, 35, 1013.
70. S. I. Gorelsky, A. B. P. Lever, *Can. J. Appl. Spectr.* **2003**, 48, 93.
71. L. Perrin, E. Clot, O. Eisenstein et al., *Inorg. Chem.* **2001**, 40, 5806.
72. For an updated list, see Lever's website <http://www.chem.yorku.ca/profs/lever>.
73. A. M. Trzeciak, B. Borak, Z. Ciunik et al., *Eur. J. Inorg. Chem.* **2004**, 1411.
74. M. F. C. Guedes da Silva, A. J. L. Pombeiro, S. Geremia et al., *J. Chem. Soc. Dalton Trans.* **2000**, 1363.
75. I. Kovacic, O. Gevert, H. Werner et al., *Inorg. Chim. Acta* **1998**, 275–276, 435.
76. E. Reisner, V. B. Arion, M. F. C. Guedes da Silva et al., *Inorg. Chem.* **2004**, 43, 7083.
77. R. C. Rocha, F. N. Rein, H. E. Toma, *Inorg. Chem. Commun.* **2002**, 5, 891.
78. H. E. Toma, K. Araki, A. D. P. Alexiou et al., *Coord. Chem. Rev.* **2001**, 219, 187.

79. D. J. Bierdeman, J. B. Keister, D. A. Jelski, J. *Organometal. Chem.* **2001**, 633, 51.
80. W. G. Feighery, H. Yao, A. F. Hollenkamp et al., *Organometallics* **1998**, 17, 872.
81. C. A. Tolman, *Chem. Rev.* **1977**, 77, 313.
82. B. E. Bursten, *J. Am. Chem. Soc.* **1982**, 104, 1299.
83. B. E. Bursten, M. R. Green, *Prog. Inorg. Chem.* **1988**, 36, 393.
84. B. E. Bursten, M. R. Green, V. Katovic et al., *Jr. Inorg. Chem.* **1986**, 25, 831.
85. D. Datta, *J. Chem. Soc. Dalton Trans.* **1986**, 1907.

4

Molecular Hydrogen, Hydride, and Dihydrogen Complexes

Christopher J. Pickett
John Innes Centre, Norwich, UK

4.1	Molecular Hydrogen	111
4.2	Hydride and Dihydrogen Complexes	112
	References	113

4.1 Molecular Hydrogen

The electrochemical reduction of protons to dihydrogen at an electrode and the reverse of this reaction, oxidation of molecular hydrogen to protons have been intimately bound up with the development of the theory of electrochemical kinetics over the last century. The interconversion is of considerable technological importance, impacting on areas such as: corrosion; embrittlement [1–5]; fuel cells [6–12]; electrolytic production of hydrogen [13–18]; hydrogen/hydride storage materials [19–24]; water splitting and photoelectrochemical devices [25–29]; and proton conducting/exchange materials [30–35]. The literature is necessarily vast [36–38].

Low activation energy barrier for the adsorption/cleavage of dihydrogen to give adsorbed H atoms (H_{ad}) and its converse recombination of H_{ad} to give dihydrogen, is critical to the performance of electrocatalytic materials with large standard heterogeneous rate constants for the $H_2/2H^+$ couple [36, 39]. The first spectroscopic detection of adsorbed H atoms (H_{ad}) on platinum was made in the late 1980s and there have been several related spectroscopic studies of potential-dependent forms of H_{ad} on platinum and other metals [40–42]. Detailed mechanisms of the

hydrogen evolution reaction at bulk metals [2, 4, 43–51], at single crystals or epitaxial films [41, 52–55], at metals with surface adatoms [56–59], at various alloys and intermetallic phases [60–66], at conducting oxides [67], and at semiconductor electrodes have been proposed [27, 28, 68]. Absorption of dihydrogen into bulk materials to form hydride phases, hydrogen evolution/uptake by metals and H-atom mobility/recombination mechanisms within metallic phases and the electrochemical behavior of solid metal hydrides have received considerable attention, particularly in the context of hydrogen storage materials, application in batteries such as rechargeable Ni–MH alkaline cells, and hydrogen embrittlement [69–75].

Correlations between electrochemical reduction rates, electronic structure and heats of adsorption of dihydrogen [47, 76], the relationship between the work function and the electrochemical behavior of metals [77], and the possible role of proton tunneling [78, 79] have been developed. Quantum chemical approaches to hydrogen evolution/oxidation [80–82] have included the application of DFT methods for the recognition of transition metal sulfide materials [16] with electrocatalytic properties similar to those of platinum [83]. Figure 1 shows a comparison of the calculated free energy diagrams for hydrogen evolution

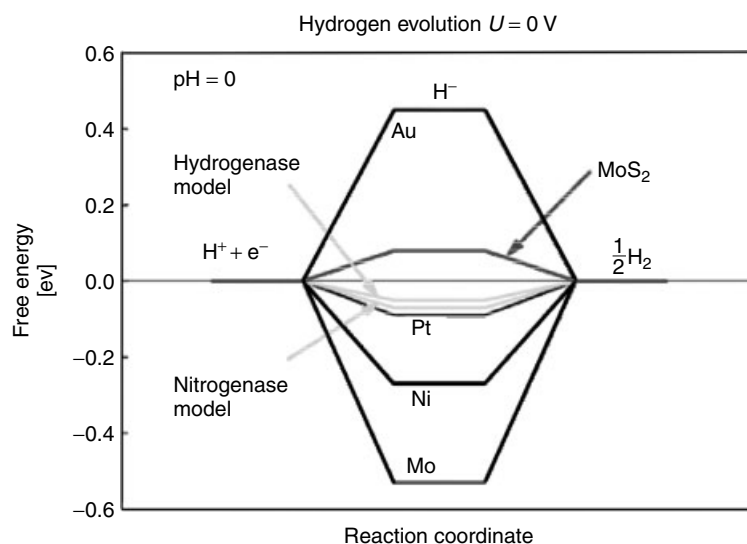


Fig. 1 Calculated free energy diagram for hydrogen evolution at a potential $U = 0$ V relative to the standard hydrogen electrode at $\text{pH} = 0$. The free energy of $\text{H}^+ + \text{e}^-$ is by definition the same as that of $\frac{1}{2}\text{H}_2$ at standard conditions. The free energy of H atoms bound to different catalysts is then found by calculating the free energy with respect to molecular hydrogen including zero-point energies and entropy terms (reprinted from Ref. 83 with permission).

on various materials together with that for two enzyme models. Incorporation of platinum or palladium nanoparticles into polymers to give hybrid electrocatalytic materials has received some attention [84, 85].

4.2 Hydride and Dihydrogen Complexes

Direct electrochemical studies of the hydride ion in a LiCl-KCl eutectic at 425°C at an iron electrode have shown that the anion is oxidized near 0.65 V versus Li^+/Li in a one-electron process which leads to the formation of dihydrogen with high current efficiency via surface combination of H_{ad} .

The hydride *ligand* is found bound in a terminal fashion to a vast range of metal centers or as a bridging ligand

between two or more metal centers. Dihydrogen can oxidatively add to a coordinatively unsaturated metal center to give either *cis*-dihydrides or η^2 -dihydrogen (sideways-bound H_2) complexes. The relative stability and the interconversion of *cis*-dihydride/ η^2 -dihydrogen systems is sensitive to the nature of the metal, its oxidation state and the coligands around it, particularly the ligand “trans” to the dihydrogen/dihydride group. These same factors also strongly influence M-H bonding in terms of whether or not the hydrogen ligand is hydridic (H^-), acidic (H^+), or radical (H^\bullet) in character. There has been considerable interest in correlations between redox potential as a measure of the electron-richness of a metal complex containing hydride or dihydrogen ligands and the $\text{p}K_{\text{a}}$ of these ligands [86–89] or the stability of dihydrogen

complexes [88]. This has covered a wide range of transition metal complexes and has addressed periodic trends. The consequence of electrochemical oxidation or reduction on the character the hydride ligand together with mechanistic aspects related to the changes in the hydride ligands following their oxidation has been widely described [90–94]. Interconversion of *cis*-dihydride/ η^2 -dihydrogen systems via electrode reactions [95, 96] is mechanistically of great interest but a clear-cut example of one-electron oxidation of a dihydride leading to a stable dihydrogen complex remains elusive. A key series of papers has dealt with the heterolytic and homolytic cleavage of the metal–hydride (M–H) bond in which redox potential measurements for 17-electron/18-electron couples have been used in thermochemical cycles to calculate M–H bond dissociation energies [97–100].

The electrosynthesis of hydride complexes directly from molecular hydrogen at atmospheric pressure by reduction of Mo(II) and W(II) tertiary phosphine precursors in moderate yield has been described as also the electrosynthesis of trihydride complexes of these metals by reduction of M(IV) dihydride precursors [101, 102]. Hydrogen evolution at the active site of molybdenum nitrogenases [103] is intimately linked with biological nitrogen fixation and the electrochemistry of certain well-defined mononuclear molybdenum and tungsten hydrido species has been discussed in this context [104, 105].

Electrocatalysis of proton reduction by metal complexes in solution has been widely studied [106–111] and confinement of molecular electrocatalysts for this process in polymeric films has also received some attention [111, 112]. This area has received much impetus from biochemical and structural studies of the iron-only

and nickel hydrogenases [113]. For example, it is evident that a di-iron dithiolate assembly provides the active site of the iron-only hydrogenase and electrochemical studies of synthetic compounds related to this site have provided some insight into both how the enzyme might work and the possibility of generating new types of electrocatalysts for hydrogen evolution or uptake [107, 114–123]. Whereas a wide range of model di-iron complexes catalyze hydrogen evolution, they do so at overpotentials far removed from equilibrium for the $2\text{H}^+/\text{H}_2$ couple and none have so far demonstrated electrocatalysis of hydrogen oxidation.

References

1. G. Jerkiewicz, *Prog. Surf. Sci.* **1998**, *57*, 137–186.
2. J. O. Bockris, J. McBreen, L. Nanis, *J. Electrochem. Soc.* **1965**, *112*, 1025.
3. E. J. Kelly, *J. Electrochem. Soc.* **1965**, *112*, 124–131.
4. M. A. V. Devanathan, Z. Stachurski, *J. Electrochem. Soc.* **1964**, *111*, 619–623.
5. R. N. Iyer, H. W. Pickering, M. Zamanzadeh, *J. Electrochem. Soc.* **1989**, *136*, 2463–2470.
6. G. J. K. Acres, J. C. Frost, G. A. Hards et al., *Catal. Today* **1997**, *38*, 393–400.
7. N. Toshima, T. Yonezawa, *New J. Chem.* **1998**, *22*, 1179–1201.
8. R. Doshi, V. L. Richards, J. D. Carter et al., *J. Electrochem. Soc.* **1999**, *146*, 1273–1278.
9. L. Carrette, K. A. Friedrich, U. Stimming, *Chem. Phys. Chem.* **2000**, *1*, 162–193.
10. N. M. Markovic, P. N. Ross, *Surf. Sci. Rep.* **2002**, *45*, 121–229.
11. C. S. Song, *Catal. Today* **2002**, *77*, 17–49.
12. T. Matsumoto, T. Komatsu, K. Arai et al., *Chem. Commun.* **2004**, 840–841.
13. M. Elbatouny, M. Strongin, G. P. Williams et al., *Phys. Rev. Lett.* **1981**, *46*, 269–272.
14. H. Vandenborre, P. Vermeiren, R. Leysen, *Electrochim. Acta* **1984**, *29*, 297–301.
15. B. Keita, L. Nadjo, *J. Electroanal. Chem.* **1985**, *191*, 441–448.

16. A. Sobczynski, A. Yildiz, A. J. Bard et al., *J. Phys. Chem.* **1988**, 92, 2311–2315.
17. A. Lasia, A. Rami, *J. Electroanal. Chem.* **1990**, 294, 123–141.
18. M. Sadakane, E. Steckhan, *Chem. Rev.* **1998**, 98, 219–237.
19. P. H. L. Notten, P. Hokkeling, *J. Electrochem. Soc.* **1991**, 138, 1877–1885.
20. C. Liu, Y. Y. Fan, M. Liu et al., *Science* **1999**, 286, 1127–1129.
21. P. Chen, X. Wu, J. Lin et al., *Science* **1999**, 285, 91–93.
22. Q. Y. Wang, J. K. Johnson, *J. Phys. Chem. B* **1999**, 103, 4809–4813.
23. H. M. Cheng, Q. H. Yang, C. Liu, *Carbon* **2001**, 39, 1447–1454.
24. M. Hirscher, M. Becher, M. Haluska, *Appl. Phys. A: Mater. Sci. Process.* **2001**, 72, 129–132.
25. N. Toshima, M. Kuriyama, Y. Yamada et al., *Chem. Lett.* **1981**, 793–796.
26. P. A. Brugger, P. Cuendet, M. Gratzel, *J. Am. Chem. Soc.* **1981**, 103, 2923–2927.
27. D. E. Aspnes, A. Heller, *J. Phys. Chem.* **1983**, 87, 4919–4929.
28. Y. I. Kim, S. J. Atherton, E. S. Brigham et al., *J. Phys. Chem.* **1993**, 97, 11802–11810.
29. A. Kudo, M. Sekizawa, *Chem. Commun.* **2000**, 1371–1372.
30. W. T. Grubb, L. W. Niedrach, *J. Electrochem. Soc.* **1960**, 107, 131–135.
31. K. D. Kreuer, *Chem. Mater.* **1996**, 8, 610–641.
32. T. Norby, *Solid State Ionics* **1999**, 125, 1–11.
33. S. M. Haile, D. A. Boysen, C. R. I. Chisholm et al., *Nature* **2001**, 410, 910–913.
34. K. D. Kreuer, *J. Membr. Sci.* **2001**, 185, 29–39.
35. Q. F. Li, R. H. He, J. O. Jensen et al., *Chem. Mater.* **2003**, 15, 4896–4915.
36. J. O. M. Bockris, A. K. N. Reddy, *Modern Electrochemistry*, Plenum Press, New York, 1998, Vol. 1.
37. J. O. M. Bockris, A. K. N. Reddy, M. Gamboa-Aldeco, *Modern Electrochemistry*, Kluwer Academic, Dordrecht, 2000, Vol. 2A.
38. J. O. M. Bockris, A. K. N. Reddy, *Modern Electrochemistry*, Kluwer Academic, Dordrecht, 2000, Vol. 2B.
39. B. E. Conway, B. V. Tilak, *Electrochim. Acta* **2002**, 47, 3571–3594.
40. R. J. Nichols, A. Bewick, *J. Electroanal. Chem.* **1988**, 243, 445–453.
41. A. Peremans, A. Tadjeddine, *J. Chem. Phys.* **1995**, 103, 7197–7203.
42. Z. Q. Tian, B. Ren, Y. X. Chen et al., *J. Chem. Soc., Faraday Trans.* **1996**, 92, 3829–3838.
43. B. Post, C. F. Hiskey, *J. Am. Chem. Soc.* **1950**, 72, 4203–4208.
44. J. O. Bockris, A. M. Azzam, *Trans. Faraday Soc.* **1952**, 48, 145–160.
45. J. O. Bockris, E. C. Potter, *J. Chem. Phys.* **1952**, 20, 614–628.
46. J. O. M. Bockris, E. C. Potter, *J. Electrochem. Soc.* **1952**, 99, 169–186.
47. B. E. Conway, J. O. Bockris, *J. Chem. Phys.* **1957**, 26, 532–541.
48. N. Pentland, J. O. Bockris, E. Sheldon, *J. Electrochem. Soc.* **1957**, 104, 182–194.
49. J. L. Weininger, M. W. Breiter, *J. Electrochem. Soc.* **1964**, 111, 707–712.
50. P. K. Wrona, A. Lasia, M. Lessard et al., *Electrochim. Acta* **1992**, 37, 1283–1294.
51. T. H. Yang, S. I. Pyun, *J. Electroanal. Chem.* **1996**, 414, 127–133.
52. N. M. Markovic, S. T. Sarraf, H. A. Gasteiger et al., *J. Chem. Soc., Faraday Trans.* **1996**, 92, 3719–3725.
53. N. M. Markovic, B. N. Grgur, P. N. Ross, *J. Phys. Chem. B* **1997**, 101, 5405–5413.
54. J. Barber, S. Morin, B. E. Conway, *J. Electroanal. Chem.* **1998**, 446, 125–138.
55. N. M. Markovic, C. A. Lucas, V. Climent et al., *Surf. Sci.* **2000**, 465, 103–114.
56. N. Furuya, S. Motoo, *J. Electroanal. Chem.* **1976**, 72, 165–175.
57. N. Furuya, S. Motoo, *J. Electroanal. Chem.* **1977**, 78, 243–256.
58. N. Furuya, S. Motoo, *J. Electroanal. Chem.* **1978**, 88, 151–160.
59. N. Furuya, S. Motoo, *J. Electroanal. Chem.* **1979**, 98, 195–202.
60. M. M. Jaksic, *Electrochim. Acta* **1984**, 29, 1539–1550.
61. M. M. Jaksic, *J. Mol. Catal.* **1986**, 38, 161–202.
62. L. L. Chen, A. Lasia, *J. Electrochem. Soc.* **1991**, 138, 3321–3328.
63. C. L. Fan, D. L. Piron, A. Slebo et al., *J. Electrochem. Soc.* **1994**, 141, 382–387.
64. B. N. Grgur, N. M. Markovic, P. N. Ross, *J. Phys. Chem. B* **1998**, 102, 2494–2501.
65. M. Ciureanu, D. H. Ryan, J. O. Stromolsen et al., *J. Electrochem. Soc.* **1993**, 140, 579–584.

66. H. Ezaki, M. Morinaga, S. Watanabe, *Electrochim. Acta* **1993**, 38, 557–564.
67. T. C. Wen, C. C. Hu, *J. Electrochem. Soc.* **1992**, 139, 2158–2163.
68. H. Gerischer, N. Muller, O. Haas, *J. Electroanal. Chem.* **1981**, 119, 41–48.
69. B. E. Conway, G. Jerkiewicz, *J. Electroanal. Chem.* **1993**, 357, 47–66.
70. P. H. L. Notten, R. E. F. Einerhand, J. L. C. Daams, *J. Alloys Compd.* **1994**, 210, 221–232.
71. C. Lim, S. I. Pyun, *Electrochim. Acta* **1994**, 39, 363–373.
72. A. Rose, S. Maniguet, R. J. Mathew et al., *Phys. Chem. Chem. Phys.* **2003**, 5, 3220–3225.
73. T. H. Yang, S. Pyun, Y. Yoon, *Electrochim. Acta* **1997**, 42, 1701–1708.
74. T. H. Yang, S. I. Pyun, *Electrochim. Acta* **1996**, 41, 843–848.
75. J. Kleperis, G. Wojcik, A. Czerwinski et al., *J. Solid State Electrochem.* **2001**, 5, 229–249.
76. R. Parsons, *Trans. Faraday Soc.* **1958**, 54, 1053–1063.
77. S. Trasatti, *J. Electroanal. Chem.* **1972**, 39, 163–166.
78. B. E. Conway, M. Salomon, *J. Chem. Phys.* **1964**, 41, 3169–3169.
79. J. O. M. Bockris, D. B. Matthews, *J. Chem. Phys.* **1966**, 44, 298–299.
80. A. B. Anderson, D. B. Kang, *J. Phys. Chem. A* **1998**, 102, 5993–5996.
81. C. G. Van de Walle, J. Neugebauer, *Nature* **2003**, 423, 626–628.
82. J. K. Norskov, T. Bligaard, A. Logadottir et al., *J. Electrochem. Soc.* **2005**, 152, J23–J26.
83. B. Hinnemann, P. G. Moses, J. Bonde et al., *J. Am. Chem. Soc.* **2005**, 127, 5308–5309.
84. A. Leone, W. Marino, B. R. Scharifker, *J. Electrochem. Soc.* **1992**, 139, 438–443.
85. H. Bonnemann, R. M. Richards, *Eur. J. Inorg. Chem.* **2001**, 2455–2480.
86. M. T. Bautista, E. P. Cappellani, S. D. Drouin et al., *J. Am. Chem. Soc.* **1991**, 113, 4876–4887.
87. G. Jia, R. H. Morris, *J. Am. Chem. Soc.* **1991**, 113, 875–883.
88. R. H. Morris, *Inorg. Chem.* **1992**, 31, 1471–1478.
89. E. P. Cappellani, S. D. Drouin, G. C. Jia et al., *J. Am. Chem. Soc.* **1994**, 116, 3375–3388.
90. M. Martelli, G. Schiavon, S. Zecchin et al., *Inorg. Chim. Acta* **1975**, 15, 217–220.
91. O. B. Ryan, M. Tilset, *J. Am. Chem. Soc.* **1991**, 113, 9554–9561.
92. K. T. Smith, C. Romming, M. Tilset, *J. Am. Chem. Soc.* **1993**, 115, 8681–8689.
93. K. T. Smith, M. Tilset, R. Kuhlman et al., *J. Am. Chem. Soc.* **1995**, 117, 9473–9480.
94. A. J. L. Pombeiro, *New J. Chem.* **1997**, 21, 649–660.
95. K. A. Earl, G. C. Jia, P. A. Maltby et al., *J. Am. Chem. Soc.* **1991**, 113, 3027–3039.
96. A. A. Zlota, M. Tilset, K. G. Caulton, *Inorg. Chem.* **1993**, 32, 3816–3821.
97. M. Tilset, V. D. Parker, *J. Am. Chem. Soc.* **1989**, 111, 6711–6717.
98. V. Skagestad, M. Tilset, *J. Am. Chem. Soc.* **1993**, 115, 5077–5083.
99. M. Tilset, *J. Am. Chem. Soc.* **1992**, 114, 2740–2741.
100. M. Tilset, J. R. Hamon, P. Hamon, *Chem. Commun.* **1998**, 765–766.
101. T. I. Alsalihi, C. J. Pickett, *J. Chem. Soc., Dalton Trans.* **1985**, 1255–1264.
102. S. A. Fairhurst, R. A. Henderson, D. L. Hughes et al., *J. Chem. Soc., Chem. Commun.* **1995**, 1569–1570.
103. T. Le Gall, S. K. Ibrahim, C. A. Gormal et al., *Chem. Commun.* **1999**, 773–774.
104. D. L. Hughes, S. K. Ibrahim, C. J. Pickett et al., *Polyhedron* **1994**, 13, 3341–3348.
105. C. J. Pickett, *J. Biol. Inorg. Chem.* **1996**, 1, 601–606.
106. T. H. Chao, J. H. Espenson, *J. Am. Chem. Soc.* **1978**, 100, 129–133.
107. M. Razavet, V. Artero, M. Fontecave, *Inorg. Chem.* **2005**, 44, 4786–4795.
108. I. Okura, S. Nakamura, K. Nakamura, *J. Mol. Catal.* **1979**, 6, 71–73.
109. I. Bhugun, D. Lexa, J. M. Saveant, *J. Am. Chem. Soc.* **1996**, 118, 3982–3983.
110. V. Grass, D. Lexa, J. M. Saveant, *J. Am. Chem. Soc.* **1997**, 119, 7526–7532.
111. T. Abe, F. Taguchi, H. Imai et al., *Polym. Adv. Technol.* **1998**, 9, 559–562.
112. S. Cosnier, A. Deronzier, N. Vlachopoulos, *J. Chem. Soc., Chem. Commun.* **1989**, 1259–1261.
113. D. J. Evans, C. J. Pickett, *Chem. Soc. Rev.* **2003**, 32, 268–275.
114. F. Gloaguen, J. D. Lawrence, T. B. Rauchfuss, *J. Am. Chem. Soc.* **2001**, 123, 9476–9477.

115. S. J. Borg, T. Behrsing, S. P. Best et al., *J. Am. Chem. Soc.* **2004**, 126, 16988–16999.
116. C. Tard, X. M. Liu, D. L. Hughes et al., *Chem. Commun.* **2005**, 133–135.
117. C. Tard, X. M. Liu, S. K. Ibrahim et al., *Nature* **2005**, 433, 610–613.
118. D. S. Chong, I. P. Georgakaki, R. Mejia-Rodriguez et al., *Dalton Trans.* **2003**, 4158–4163.
119. M. Y. Darensbourg, E. J. Lyon, X. Zhao et al., *Proc. Natl. Acad. Sci. U.S.A.* **2003**, 100, 3683–3688.
120. C. M. Alvarez, M. E. Garcia, M. T. Rueda et al., *Organometallics* **2005**, 24, 650–658.
121. V. Artero, M. Fontecave, *Coord. Chem. Rev.* **2005**, 249, 1518–1535.
122. J. F. Capon, F. Gloaguen, P. Schollhammer et al., *Coord. Chem. Rev.* **2005**, 249, 1664–1676.
123. V. Vijaikanth, J. F. Capon, F. Gloaguen et al., *Electrochem. Commun.* **2005**, 7, 427–430.

5

Redox Properties, Electrochemistry of Oxygen

Maurice L'Her

Université de Bretagne Occidentale, Brest Cedex, France

5.1	Introduction	119
5.2	Atomic and Physical Properties	120
5.3	Thermodynamics of the Redox Processes	122
5.4	Electrochemistry at Metal and Carbon Electrodes	128
5.4.1	Electrochemistry in Aqueous Solutions	128
5.4.1.1	Electrochemistry on Platinum	129
5.4.1.2	Electrochemistry on Other Metals and Electrode Materials	135
5.4.2	Electrochemistry in Nonaqueous Media	136
5.5	Electrochemistry at Electrodes Modified with Metal Complexes	137
5.5.1	Studies in Solution	138
5.5.2	ORR at Modified Electrodes	138
	References	140

5.1

Introduction

Capable of deleterious effects and of destruction of the organisms on earth, oxygen also sustains life, through the respiration of plants and animals; this element is known mainly for this beneficial property. Most of the constituents of the living species should spontaneously burn in air, some of the reduced species of oxygen, the nasty radicals, are noxious when others, like water, are essential to life. These compounds are the products, or intermediates, of the natural reduction reaction of oxygen, respiration, for example. The balance between these two opposing influences reflects the control of most oxygen redox reactions by kinetics; if they were governed by thermodynamics, the reactions would be less numerous and less oxygen intermediates would be known. In the living organisms, where appropriate catalysts have been selected by evolution, various reduction pathways are known. For the chemist too, this offers the opportunity to govern the reactions provided, of course, that he has found the appropriate catalyst, which is not always the case, as illustrated by the problem of the oxygen electrode for fuel cells.

Even if it was known since centuries that air was constituted by more than one

constituent, one of which was essential for combustion (in the fifteenth century, Leonardo da Vinci knew that), the gas was isolated, prepared and studied by Scheele and Priestley, who worked independently, around 1773–1774; the Swedish chemist was quite certainly the first to work on it, but Priestley published his observations before Scheele. The gas received various names, for example, “pure air,” “fire air,” “dephlogisticated air,” as at that time the *phlogiston* theory had vigorous supporters, Priestley being one of these. After a meeting with him in Paris, Lavoisier repeated experiments and rapidly came to the conclusion that this gas was an element; this sealed the fate of the *phlogiston* theory and the beginning of a new era for chemistry. Lavoisier built up the theories of combustion, respiration, and of the oxidation reactions. He named the new element *Oxygen* from two greek roots meaning “acid generator” ($\alpha\acute{\kappa}\upsilon\upsilon$ –: sharp, acid and $\gamma\epsilon\nu$ –: generate).

The triatomic molecule allotrope of oxygen was discovered in 1839 by Schönbein who detected it from its smell and thus named it *ozone* ($\omicron\zeta\epsilon\iota\nu$ ozein: emitting a smell). The nature of the molecule was established in 1865 by Soret. Thénard discovered hydrogen peroxide in 1818. Water was known as an *Element*, from Thales of Milet (~600 B. C.) to the time of Cavendish

and Priestley who, by combination of dephlogisticated (oxygen) and phlogisticated (hydrogen) airs, established that water was a combination.

5.2

Atomic and Physical Properties

Oxygen is present as three stable isotopes, abundance of which varies slightly with its natural source, so that the precision of its atomic weight is limited to 15.9994 ± 0.0003 . ^{16}O is the most abundant (99.760%; A_r : 15.994915), the two others being ^{17}O (0.037%; A_r : 16.999) and ^{18}O (0.200%; A_r : 17.999). Oxygen gas can be enriched above 95% in these isotopes, which are very useful as tracers for the study of reaction mechanisms and kinetics, ^{18}O being particularly helpful for that. ^{17}O would have been used more extensively for nuclear magnetic resonance (NMR) studies (nuclear spin $I = 5/2$) if the sensitivity had not been so low, due to its reduced abundance, and to the signal broadening from its quadrupolar nature. Some radioactive isotopes exist, but are not of great help for studies because of their short lifetimes, the most stable being ^{15}O , the half-life of which is only 122 s. In its ground state, dioxygen is a triplet because the molecule has two electrons, in π orbitals, with parallel spins: $^3\Sigma^-_g$ (Fig. 1). A singlet excited state, $^1\Delta_g$, the energy of which is $94.72 \text{ kJ mol}^{-1}$ higher, can be reached by light irradiation in the presence of a sensitizer, as well as a second excited singlet state, $^1\Sigma^+_g$, $157.85 \text{ kJ mol}^{-1}$ above the ground state. Of importance for some of the points discussed in the following, is the fact that the bond dissociation energy of the oxygen molecule is rather high, $493.4 \text{ kJ mol}^{-1}$.

Another allotropic form of oxygen is ozone, the triatomic molecule O_3 ; present

as traces in the upper atmosphere, it is produced in a dioxygen atmosphere at room temperature and pressure, by UV irradiation and by the silent electric discharge, or by electrolysis of acidic aqueous solutions. Ozone is unstable as a gas, as well as in its liquid and solid phases, which are explosive.

Atomic oxygen, O, is a very elusive species, which is too reactive to exist in appreciable concentration under ordinary conditions and cannot be isolated. In its $^3\text{P}_2$ ground state, it has two unpaired electrons. This species is produced in some photochemical processes and in the formation of O_3 in the discharge ozonizer; however, its reaction on ozone to give two molecules of O_2 is highly favored ($\Delta H_{298}^\ominus = -394 \text{ kJ mol}^{-1}$). O is an important intermediate, a strong oxidizing agent, involved in many reactions in the chemistry of the upper atmosphere.

Apart from the allotropic forms of the element, O_2 and O_3 , which are reactive species, oxidizing agents, oxygen is found on earth mostly as compounds of its O^{2-} reduced state; that is, the case of water and of the many oxides such as those of silicon and of many metals in the earth crust. Another form in which it can be found is hydrogen peroxide and the peroxides; this redox state is unstable so that the corresponding compound, and particularly hydrogen peroxide, cannot accumulate under the conditions of life on earth. Hydrogen peroxide was discovered in 1818 by Thénard, when the chemistry of oxygen became the object of intense studies. Hydrogen peroxide is now produced in very large quantities through the reduction of oxygen from air by hydrogen gas, a reaction that requires a mediator, 2-ethylanthraquinone, and a catalyst for the reduction of the mediator.

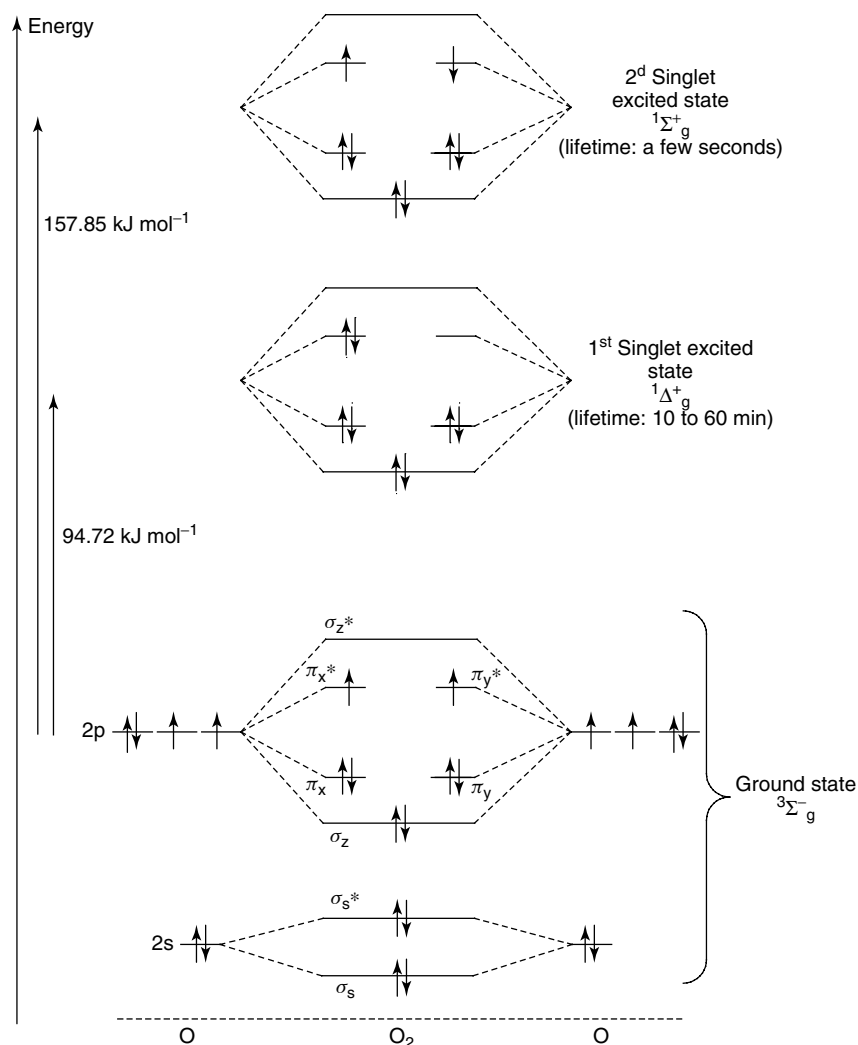


Fig. 1 Molecular orbital diagram for oxygen.

The electronic configuration of atomic oxygen is $1s^2, 2s^2, 2p_x^2, 2p_y^1, 2p_z^1$ in its ground state (3P_2), so that two unpaired electrons occupy the upper levels. In molecular O_2 , which is more stable because of the bond formation energy, which is $-493.4 \text{ kJ mol}^{-1}$, the molecular orbital of the $^3\Sigma_g^-$ ground state is:

$$KK(\sigma_s)^2(\sigma_s^*)^2(\sigma_p)^2(\pi_x)^2(\pi_y)^2(\pi_x^*)^1(\pi_y^*)^1$$

as illustrated in Fig. 1. The bond order is 2 because 8 electrons are in bonding levels and 4 of them in antibonding orbitals; of these latter, 2 (in π_x^* and π_y^*) are unpaired, which explains why molecular oxygen is paramagnetic. In O_2 , O_2^- , and O_2^{2-} the bond lengths are respectively 1.21, 1.28, and 1.49 Å, corresponding to decreasing bond energies; this is consistent with the bond orders of 2, 1.5,

and 1 [1]. From the orbital diagram it is easily understood why O_2 accepts 1 and 2 electrons, which leads to the superoxide and the peroxide ions.

At ordinary temperatures, H_2O_2 is a liquid denser ($d = 1.4425 \text{ g cm}^{-3}$ at 20°C) and more viscous (1.249 cP at 20°C), and also more highly associated, than water. As expected from the bond order, O–O in hydrogen peroxide is a single bond with a low rotational barrier due to repulsive interactions between the O–H bond and the lone-pair of electrons on the O atom. As a consequence, the O–O–H angle, as well as the dihedral angle H–O–O–H (Fig. 2), vary greatly with the very different environments of the molecule in the gas phase and various solids (H_2O_2 crystals, crystalline hydrates, crystals of metal salts etc.) [2–4].

In ozone, each of the three O atoms is bound to its neighbor through a σ -bond (1.278 Å), the angle being 116.5° to 117° the two terminal atoms are 2.18 Å apart, a distance shorter than the van der Waals distance (2.8 Å). Owing to the delocalization of the π electrons, the O–O bond in ozone has a multiple bond character, which is reflected in the bond distance.

Of importance for redox chemistry and electrochemistry, as well as for its metabolism and applications, is the solubility of oxygen in various media (Table 1). Owing to its importance, the solubility of oxygen in water has been extensively studied and is well-documented [4–17]. This nonpolar molecule is less soluble in water than in organic solvents, that is why fluorocarbons where O_2 is highly soluble have been envisaged for oxygen transfer. In aqueous solutions, salts influence oxygen solubility as does temperature also (Table 1), gases being more soluble in cold solvents; the solubility of oxygen, as well as its diffusivity, decreases when the concentration of KOH or acids increases.

5.3

Thermodynamics of the Redox Processes

The thermodynamics of the redox systems related to O_2 and its allotropic forms, to hydrogen peroxide and to water have been examined in various books and reviews [18–23], the most recent and complete being the compilation by Hoare,

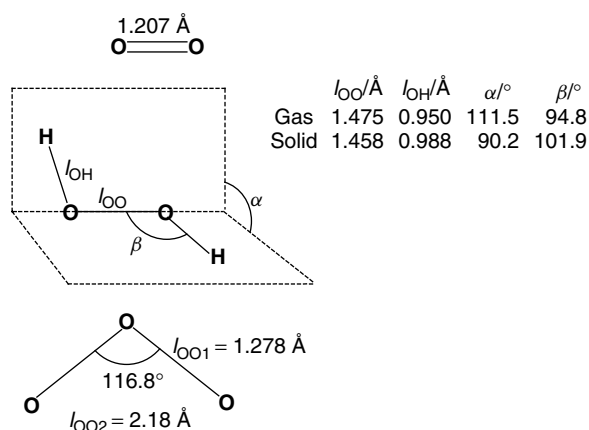


Fig. 2 Bond lengths and angles for O_2 , H_2O_2 , and O_3 .

Tab. 1 Solubility of oxygen in liquid media

	θ [°C]	Solubility	References
Aqueous solution			
		(mmol kg ⁻¹)	
H ₂ O	20	1.35 ± 0.01	14
H ₂ O	35	1.07 ± 0.02	14
H ₂ O	50	0.91 ± 0.02	14
0.015 NaOH	22	1.320 (calculated)	14
0.075 NaOH	22	1.287 (calculated)	14
0.25 NaOH	22	1.197 (calculated)	14
Sea water			
		(mmol l ⁻¹)	
Salinity: 34‰	0	1.70	6–8
Salinity: 34‰	10	1.34	6–8
Salinity: 34‰	20	1.11	6–8
Salinity: 34‰	35	0.85	6–8
Salinity: 34‰	20	1.21	6–8
Solvent			
		(mmol l ⁻¹)	
DMSO		2.1	10, 12
DMF		4.7	10, 12
Py		4.8	10, 12
AN		8.0	10, 12
Hydrocarbons		~10	12
Fluorocarbons		~25	12
Et ₂ O	25	20.1	4
CCl ₄	25	13.3	4
Me ₂ CO	25	12.3	4
C ₆ H ₆	25	9.8	4

Note: Solutions in equilibrium with O₂ at a pressure of 10⁵ Pa.

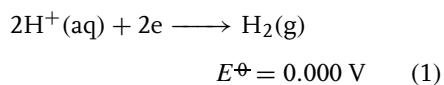
AN: acetonitrile; DMF: dimethylformamide; DMSO: dimethylsulfoxide;

Py: pyridine

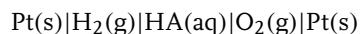
which refers to the critically selected thermodynamic values, published under the auspices of IUPAC [24].

Owing to the allotropic forms of oxygen, to its various redox states, and related chemical species that are thermodynamically stable or exist for kinetic reasons, a lot of redox reactions are usually described. However, many of them are not really important for the common works, particularly for those in solutions; consequently, only some of them have been described here. The publications cited earlier can be searched for data useful for the calculation of Gibbs energy or potentials of particular reactions.

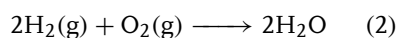
The standard electrode potentials are referred to the standard potential of the hydrogen electrode:



which is zero at all temperatures. An electrode potential is measured through the study of an electrochemical cell, for example:



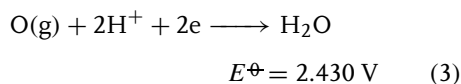
to which corresponds the reversible chemical reaction:



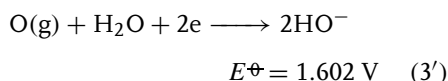
The Gibbs energy of such a reaction varies with temperature, and thus the standard potential of the other redox couple than H^+/H_2 . When not specified, the temperature is 25 °C (298.15 K) so that the standard potentials cited in the text or in (1, 2, 3) are in E^\ominus/V , at 25 °C. The potential/pH diagram for some redox systems related to oxygen is presented in Fig. 3.

As evidenced by the high values of the redox potentials (Scheme 1), atomic oxygen is a powerful oxidant but, of course, these values cannot be measured. The standard potentials of the following half-cell

reactions have been calculated [24]:



in acidic media and, in basic solutions:



Oxygen has an oxidation number of +2 in some fluorides [25,] which also stabilize the dioxygenyl cation O_2^+ [26], redox states which are not stable, of course, in solutions. The common redox reactions

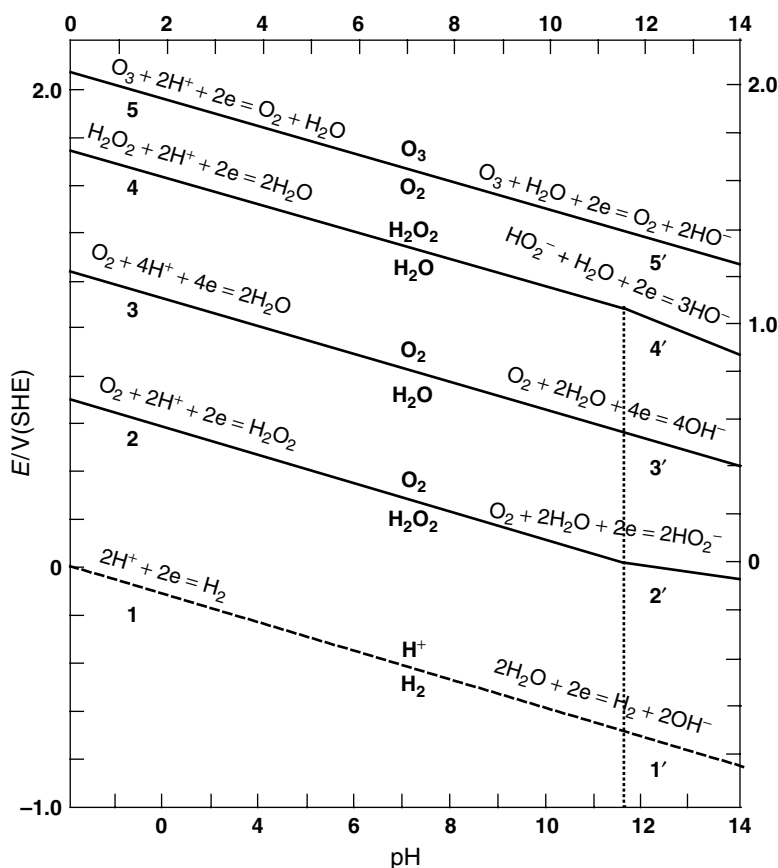
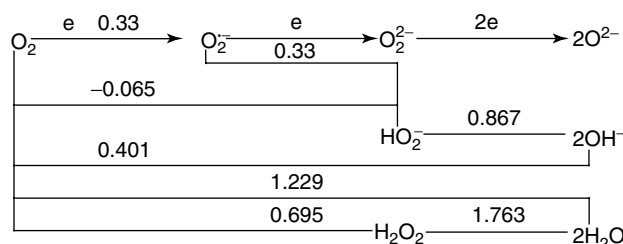
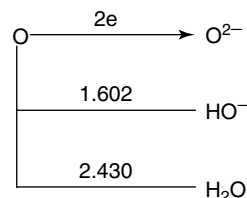


Fig. 3 Potential/pH diagram for oxygen.

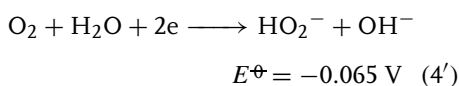
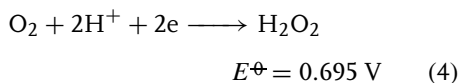
Scheme 1 Redox systems of atomic oxygen (V vs. SHE).**Scheme 2** Redox systems of molecular oxygen (V vs. SHE).

of molecular oxygen are illustrated in Scheme 2, where the electron exchanges occur on lines when the species modified by protonation appear in columns, as in the well-known *square schemes*; the second line illustrates the redox reactions in alkaline aqueous solutions, and the third line in acidic media.

The product of the one-electron reduction of O_2 , the superoxide ion, $O_2^{\cdot -}$, is highly unstable in acidic-aqueous solutions where its protonated form, the peroxy radical HO_2 ($pK = 4.8$), decomposes to ozone, oxygen, and hydrogen peroxide; experiments have shown that the two latter compounds are produced almost quantitatively, when only traces of ozone are found. In alkaline solutions, the superoxide ion is more stable; even if it decomposes spontaneously to O_2 and $HO_2^{\cdot -}$ ($\Delta G^\ominus = -51.13 \text{ kJ mol}^{-1}$), it has been studied by polarography in NaOH solutions, in the presence of compounds that adsorb at the surface of the electrode and slow down the protonation of $O_2^{\cdot -}$. From these electrochemical experiments

and from radiolysis, it appears that E^\ominus for the $O_2/O_2^{\cdot -}$ couple is close to 0.33 V [24, 27].

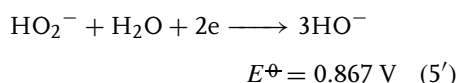
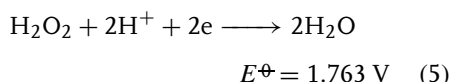
The two-electron reduction of O_2 leads to the peroxide ion, O_2^{2-} , which is stable in basic aqueous solutions as $HO_2^{\cdot -}$ and as hydrogen peroxide, H_2O_2 , in acidic media. Hydrogen peroxide is a very weak acid ($pK_1 = 11.6$), which does not lose its second proton in aqueous alkaline solutions ($16 < pK_2 < 18$) [19, 24, 28]. The potential of the two-electron reduction reaction, in acidic and basic aqueous media, has been calculated from thermodynamic data (Scheme 2):



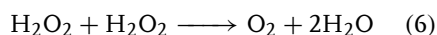
These theoretical values have been supported by experimental measurements, at least in acidic media; it is apparently more

difficult to study the O_2/HO_2^- couple in solutions of bases [24].

The following two-electron reduction of the peroxide produces water under acidic conditions and the hydroxyl ion at higher pH:



It thus appears that hydrogen peroxide is a very powerful oxidizer, which should oxidize water. The comparison of (4,4') and (5,5') shows that H_2O_2 should oxidize itself (Fig. 3); in other words, hydrogen peroxide solutions should decompose by disproportionation:

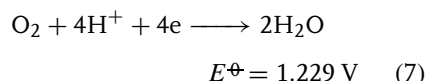


However, the solutions are fairly stable when stored in clean vessels and protected from light, because reaction (6) is slow, as well as the oxidation of water; but, dust, metal ions, and organic traces can catalyze the reactions; the effervescence of H_2O_2 in contact with traces of hemoglobin is a well-known illustration of the catalytic disproportionation of the peroxide. The decomposition of concentrated solutions induced by impurities can be explosive.

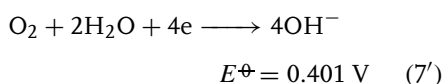
The direct reduction of O_2 to H_2O is of paramount importance, in many respects; considering the large number of reactions in which oxygen and its derivatives are involved, this process is highly energetic, delivering 4 electrons and issuing a harmless product. In vivo, it uses a freely available substrate and does not produce very deleterious radical species; for industry, it is a very good way to produce energy, that is, electricity,

without pollution and at low cost. Reality is yet somewhat different because of kinetic impediments, the O–O bond being difficult to break.

The potential of reaction (7) has not really been determined by measurement:

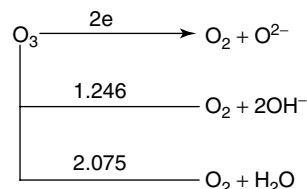


$E^\ominus = 1.229 \text{ V}$ has been calculated from the Gibbs energy of formation of liquid water, which is $\Delta G^\ominus = -237.178 \text{ kJ mol}^{-1}$ at 25°C [13, 29]. In basic aqueous media, the reaction is (7'):



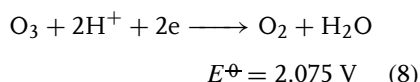
the standard potential of which is calculated from $E^\ominus(7)$ and from the ionization constant of water at 25°C ($K_W = 1.008 \cdot 10^{-14}$ [30]) (Scheme 2).

The $\text{O}_2/\text{H}_2\text{O}$ system is very slow so that the exchange current at equilibrium is extremely low ($10^{-10}/10^{-9} \text{ A cm}^{-2}$); as a consequence, any other reaction at the electrode will hamper its study and that could be the reaction of impurities or other redox reactions involving the electrode itself. The so-called *noble metals* are not really inert and do interact with oxygen; a platinum surface in contact with an O_2 saturated solution adsorbs oxygen as an electronically conducting monolayer but can be further oxidized to PtO, PtO_2 . A detailed analysis of these phenomena, which falls outside the scope of the present review, can be found elsewhere [31]. A platinum electrode, when a complete electronically conducting monolayer of Pt–O is formed at the surface of the metal, behaves as an ideally inert electrode; in such conditions, rest potentials dependent on pO_2 and pH can be measured during a few hours, close to

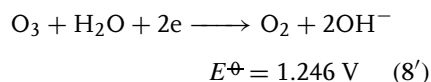
Scheme 3 Redox systems of ozone (V vs. SHE).

1.23 V. This had been observed for the first time by Bockris and Huq [32], then by a few other groups. The same has also been observed on Rh electrodes, but Au, Pd, and Ir are unsuitable for such measurements, the rest potentials being mixed potentials [31].

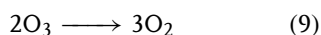
Ozone is, of course, a more powerful oxidant, which is reduced to O_2 in acidic media, following the half-cell reaction (Scheme 3):



and in basic solutions through:



From the standard potentials of (8) and (7) it is evident that O_3 will oxidize water to O_2 , the result being the following reaction; in other words, O_3 is thermodynamically unstable in water:



In pure, anhydrous, nonaqueous solvents, O_2 is reduced by a one-electron step because the superoxide ion, $\text{O}_2^{\cdot-}$, is stable in the absence of proton. For a long time, superoxide has been considered as quite an unreactive and uninteresting species, until 1960, when its electrochemical generation and implication in enzymatic reactions were discovered [33]. This is why the first reduction wave of oxygen in solvents like

CH_3CN , dimethylsulfoxide, dimethylformamide (DMF) and pyridine, of course, is reversible at the timescale of cyclic voltammetry; the first unambiguous studies appeared in 1965, the radical being identified by electron spin resonance (ESR) [34, 35]. The reversibility has been demonstrated by cyclic voltammetry in pyridine; even in a basic medium, the second reduction step occurring at a much more negative potential is irreversible [36]. In the presence of proton donors, and, of course, in protic solvents, it is known that $\text{O}_2^{\cdot-}$ is unstable and that the reduction of O_2 proceeds via a two-electron step [10, 27, 37]. The superoxide ion is moderately basic ($\text{p}K_A = 4.4$, in water), less than O_2^{2-} , so that the potential of $\text{O}_2^{\cdot-}/\text{HO}_2^-$ becomes higher than that of $\text{O}_2/\text{O}_2^{\cdot-}$. As a consequence, the superoxide disproportionates into O_2 and HO_2^- , in the presence of proton sources. An evaluation of the solvent effect on the redox potential of the $\text{O}_2/\text{O}_2^{\cdot-}$ system is not easy because of the difficulty in comparing the potential scales in various media but, obviously, assuming that the junction potential between the aqueous SCE and every solvent does not exist is far from correct [12]; adopting any extrathermodynamic hypothesis would be better. The important shift in the one-electron reduction of O_2 to $\text{O}_2^{\cdot-}$, almost 0.5 V, has been attributed to the solvation of $\text{O}_2^{\cdot-}$, which is much more strongly solvated by water than by the aprotic media; hexamethylphosphorotriamide (HMPT) is the solvent where the $\text{O}_2/\text{O}_2^{\cdot-}$ potential is

Tab. 2 Redox potentials of $O_2/O_2^{\cdot-}$ in solvents [37]

Solvent	E^\ominus/V , vs. Fc^+/Fc
DMSO	−1.15
AN	−1.21
DMF	−1.26; −1.33
PY	−1.13
DCM	−1.26
NMA	−0.87
HMPT	−1.52
PC	−1.14
Q	−1.30

Note: AN: acetonitrile; DCM: dichloromethane; DMF: dimethylformamide; DMSO: dimethylsulfoxide; HMPT: hexamethylphosphorotriamide; NMA: *N*-methylacetamide; PC: propylene carbonate; PY: pyridine; Q: quinoline

the most negative (Table 2) [37, 38]. The superoxide ion can be prepared in liquid NH_3 and in some melts like alkali halides or hydroxides; however, in most of the other melts the chemistry of oxygen is complicated by the intrinsic properties of the media that can exchange O^{2-} ions or because of their redox behavior [37].

5.4

Electrochemistry at Metal and Carbon Electrodes

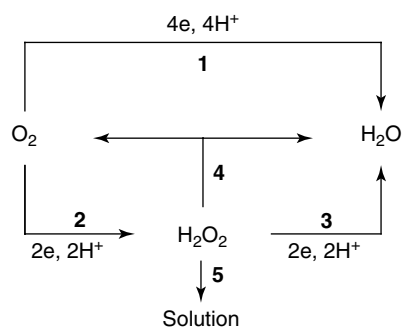
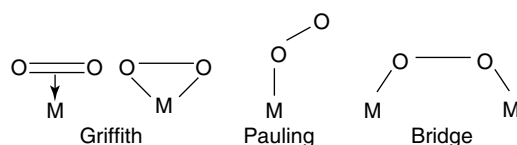
Of great interest in lots of domains, oxygen has been studied by voltammetry under very different experimental conditions. As its reaction is under kinetic control, the electrode reaction is influenced by various factors, in particular by the nature of the electrode and of the solution. The metal, through its chemical properties and surface states, which influence the adsorption–desorption of electroactive species or

intermediates, drives the reaction along different pathways, depending on many factors. As a consequence, the oxygen reduction reaction (ORR) not only is highly dependent on the experimental conditions but is also a subject of controversy, particularly about the exact nature of the pathways of catalysis and rate determining steps. Of paramount importance for the reduction reactions, like (4) and (7), is the availability of proton, so that ORR follows different routes in protic and aprotic environments.

5.4.1

Electrochemistry in Aqueous Solutions

Oxygen can be reduced to water through the $4e$ and $4H^+$ reaction, pathway 1 in Scheme 4, energetically favorable, or to hydrogen peroxide ($HO_2^{\cdot-}$ in alkaline media) following pathway 2. These two reactions can occur simultaneously and independently on the same electrode, as two parallel processes. When the disproportionation reaction of H_2O_2 is very fast and occurs at the surface of the electrode, the overall process is apparently the reduction to water, the peroxide being, however, an intermediate. A genuine $4e$ reduction implies that the $O-O$ bond is broken at a very early stage of the reaction, during adsorption, so that no peroxidic species can be detected at the electrode surface. Hydrogen peroxide is not a stable compound and decomposes more or less rapidly (Path. 4, Scheme 4); it can only be detected when it is rather stable and escapes to the solution (Path. 5, Scheme 4) or when appropriate experimental techniques are used (e.g. rotating ring-disk electrode). The main question is whether hydrogen peroxide is produced as an intermediate or in a parallel reaction and this opens the way to controversy as the time window of

Scheme 4 Reduction of molecular oxygen.**Scheme 5** Binding of oxygen to metal.

the experiment is essential and because there is no consensus about what is an intermediate.

This is not the only subject of debate; the nature of the adsorbed forms of oxygen and reaction products on the electrode surface has been widely discussed, as well as the various steps of ORR. Very often, for conditions apparently similar, for example, the same electrode and solution, observations made by two research groups are different and so are, of course, the deductions and the pathways for the electrode reaction. There are so many possible steps, reactions and species that various combinations can be envisaged; moreover, as other methods for observing the species or intermediates involved in the electrode reaction are rare, electrochemistry is often the only source of experimental facts. As for other multiparametric problems, when a plausible explanation is found, there is no certainty that this is the only possibility and the correct solution. Moreover, experimental conditions that look identical are not really exactly similar; the problem

of contamination of electrode surfaces by impurities is a good example of that.

Oxygen binding to a metal can be represented by models sketched on Scheme 5, and it is understandable that the two atoms of the oxygen molecule linked to two metal atoms of the surface (bridge) is the most favorable position for weakening the O—O bond, leading to its dissociation. Recent *ab initio* calculations (DFT) have shown that the (111), (100), and (110) surfaces of Pt have different properties for the adsorption of O₂, O, OH, OOH, and H₂O₂, which should influence differently the mechanism of ORR [39].

5.4.1.1 Electrochemistry on Platinum

Platinum, an incomparable metal for most electrochemists, is also the best electrode material for oxygen reduction, unsurpassed despite its cost, so that most of the studies about ORR have been performed on electrodes made of this metal. One of the targets of the earlier studies on oxygen has been to scrutinize the reversibility of the redox

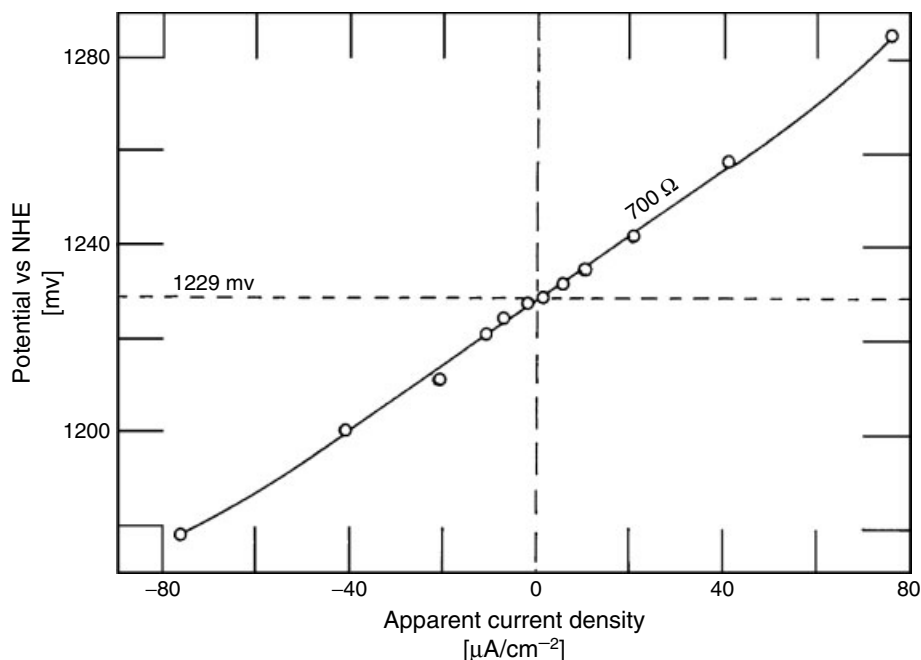


Fig. 4 Potential versus current for the reversible $\text{O}_2/\text{H}_2\text{O}$ system on a bright platinum surface (Reproduced with permission from Ref. 44).

system. Hoar, in 1933, was the first to show that extrapolated Tafel lines crossed at 1.23 V (vs. SHE), the theoretical E^\ominus value calculated from thermodynamic data [40]. This has been extensively studied later by Bockris [32, 41] and Hoare [24, 31, 42, 43] who concluded that the $\text{O}_2/\text{H}_2\text{O}$ reaction was observed on the $\text{Pt}(\text{O})/\text{O}_2$ reversible electrode [31, 44]. The reversibility is illustrated in Fig. 4, where there is continuity from the cathodic to the anodic regions, with the zero current potential at 1.229 V. As the current evolution is very similar on the cathodic and the anodic branches, which is the sign of a reversible reaction, it must be concluded that the cathodic process is the reverse of the anodic reaction. This latter generates O_2 from H_2O oxidation, the first step of which is a 1e exchange; as a consequence,

for the reverse process, the O–O bond rupture must happen before the first electron addition. However, observing that behavior is not easy because the exchange current at 1.23 V is very low ($\sim 10^{-10} \text{ A cm}^{-2}$) [45]. Any chemical or electrochemical treatment of the surface, or modification of the solution will change the surface state of the electrode, for example, by reduction of the oxide layer and by adsorption of ions or molecules. When higher reduction currents flow, at lower potentials, $\delta\eta/\delta \log i$ the slope of Tafel plots ($\eta = f(\log i)$; η being the overvoltage) changes because the electrode surface, and thus the reduction mechanism, is modified. Damjanovic has attributed this evolution to a change in O_2 adsorption, following a Langmuir isotherm (constant heat of adsorption) on bare platinum and a Temkin isotherm

(heat of adsorption decreasing linearly with coverage) on an oxide covered surface [46, 47]. The presence of some electroactive species in solution will generate, at 1.23 V, more current than ORR itself, even at very low concentration; the impurity concentration must be maintained lower than $10^{-10} \text{ mol l}^{-1}$ to allow the study of the 4e ORR near its equilibrium [48]. Measurements were possible only after careful pretreatments of the electrodes and extensive, lengthy, purification of the solutions by electrolysis.

The voltage more currently measured at $i = 0$ is close to 1.0 V, different from the potential corresponding to the reversible reaction of oxygen (7). Various hypothesis have been presented about the origin of this potential [31, 45], which, most people agree about, is a mixed potential. For Damjanovic, this could be a mixed potential for which the cathodic half-reaction would be oxygen reduction, the anodic component being oxidation of impurities [45]. This is far from being unanimously approved, but none of the other hypothesis is largely accepted [43]. In acidic aqueous solutions (HClO_4 , H_2SO_4), the surface is progressively oxidized above 0.8 V and it is accepted that it becomes a platinum-oxide electrode above 1.0 V, the oxide existing as multilayers in some conditions. Below 1 V, down to ~ 0.8 V, oxygen is present on the platinum surface as adsorbed species (e.g. OH^- , O^{2-}), this chemisorbed oxygen constituting a film not thicker than a monolayer [31, 45, 49]. Below 0.6 V no species is detectable on the free platinum surface, until ~ 0.2 V, when adsorbed hydrogen appears from proton reduction. Adsorbed species cannot be detected by ellipsometry, but the formation of oxide at about 1 V is observed by this technique [50].

Voltammetry and the kinetic studies are highly dependent on these surface states of the metal and on the experimental conditions that influence them. From the very large number of studies in acidic, neutral, and basic media, emerged a rather general agreement about the influence of the platinum surface, of the purity of the solution, and about the global reaction. However, and not surprisingly as the main criterion for drawing conclusions is the slope of the Tafel plots, very large number of mechanistic schemes have been presented and extensively discussed along the years, but with no definite conclusion [45, 51–53].

In acidic media, the reduction current at a rotating electrode rises below 0.9 V, reaches a plateau at about 0.5 V, and decreases sharply below 0.1 V (Fig. 5). The rotating ring-disk electrode (RRDE) has been used since earlier studies by Frumkin and Nekrasov [54–56], in order to detect the production of H_2O_2 during the cathodic process; peroxide is detected by oxidation on the platinum ring electrode, away from the reduction site of oxygen, on the central Pt disk. From Fig. 5, it is obvious that no peroxide is formed above 0.1 V, so that oxygen is reduced to water. This has been reported by many authors [22, 45, 46, 48, 53, 57, 58]. It has also been reported that in unpurified acidic solutions some hydrogen peroxide is produced, since the beginning of the reduction [58]. These observations led to the conclusion that H_2O and H_2O_2 are simultaneously produced, in parallel reactions, the peroxide on catalytic sites deactivated by adsorption of impurities.

Considering the reversibility of the $\text{O}_2/\text{H}_2\text{O}$ system at potentials close to 1.23 V, as illustrated in Fig. 4, it must be concluded that breaking the O–O bond is not the rate determining step

as the electron transfer is reversible. Moreover, peroxide has not been identified as an intermediate in water oxidation to oxygen, the reaction corresponding to the anodic current in Fig. 4. This reversible behavior occurs only close to the standard potential, at low current densities, when the platinum surface is covered by a film of oxide; on this Pt(O)/O₂ electrode, the addition of electron occurs after the O–O bond breaking [31]. However, for most experiments where O₂ reduction is the objective and higher currents requested, the electrode potential is much lower than 1.2 V. Under such conditions, the electrode surface is not Pt(O) anymore and it is well known that on the bare metal surface the reaction is a faster, but irreversible, 4e reduction to water [58]. From the Tafel slopes and from pH and pO₂ dependence, many research groups have proposed very different interpretations of the important steps of the overall reaction, none being really satisfactory. The mechanistic studies are mainly based on the interpretation of the slopes of Tafel, which are dependent on surface states of platinum and adsorption.

It must be mentioned that when precautions have been taken to get a clean Pt surface, no peroxide is produced above 0.1 V (Fig. 5). However, the production of H₂O₂ is observed when care in the preparation of the electrode or purification of the solution has been insufficient [59]. At electrode potentials lower than 0.2 V, when species in relation with hydrogen evolution are adsorbed, peroxide is produced in a parallel way to the 4e reaction. The catalytic site density diminishes, so that it is tempting to hold this responsible for the decrease in bond breaking because bridging an O₂ molecule between two adjacent metal atoms (Scheme 5) becomes more difficult when other species

are bound too and deactivate the surface for oxygen adsorption.

On platinum single crystals in contact with 1 N H₂SO₄ or HClO₄ solutions, in the 0.9–1.0 V domain where the platinum surface is oxygenated, no difference was observed between Pt(111) and Pt(100) or the stepped surfaces, the oxygenated metal surface being uniformly active [60]. Yet, it has been shown that Pt(111) is less active than Pt(100) and Pt(110) in sulfuric acid and this has been attributed to the inhibiting effect of strongly adsorbed HSO₄[−] [61]. By carefully controlling the state of the surface to prevent its evolution and reconstruction when its potential is cycled, differences have been observed between the three single-crystal electrodes in H₂SO₄ or HClO₄ solutions, Pt(110) being the most active, probably because of a stronger adsorption of O₂; absolutely no H₂O₂ is produced even at 0.1 V [62]. Hydrogen is more strongly bound to Pt(111), which could explain why the reduction to peroxide occurs on this platinum surface below 0.2 V. DFT calculation have shown that adsorbed oxygen is so stable on Pt(111) that it cannot be appreciably reduced at high potentials and reduction is allowed when the potential is lowered, which decreases oxygen stability [63].

In alkaline solutions, electrochemistry of oxygen is not as greatly affected by purification of the solutions as in acidic media [45]. Since the earlier RRDE experiments, it has been shown that H₂O₂ is the main product of the reduction in the activation domain but is not detected anymore at lower potentials, when the electrode reaction is limited by mass transport [59, 64, 65]. The existence of two potential regions for ORR in alkaline media is also illustrated by the Tafel plots, as those reported in Fig. 6 [66]. The existence of two

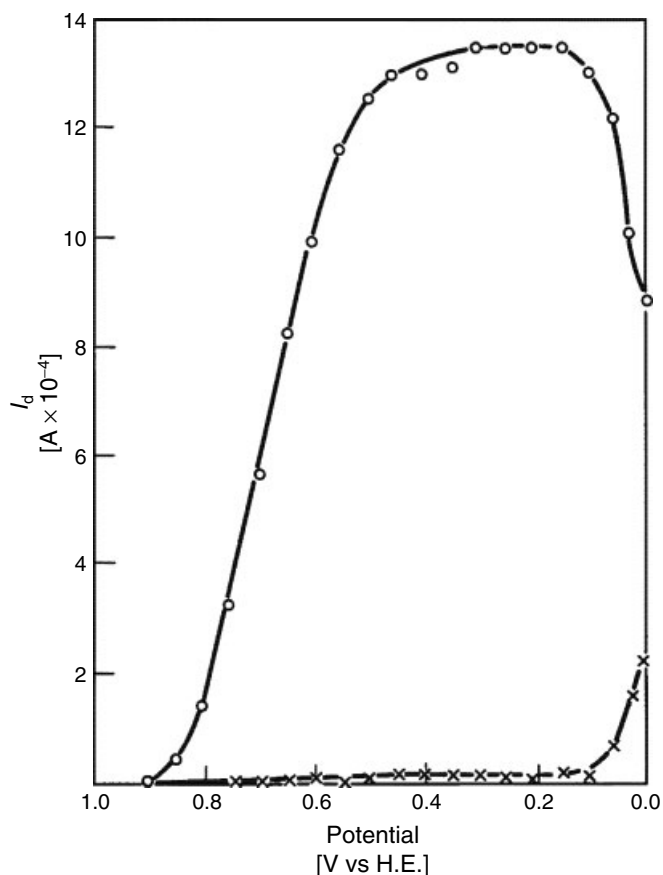


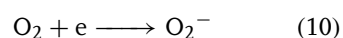
Fig. 5 Oxygen reduction at a rotating ring(Pt)-disk(Pt) electrode in 0.1 N H_2SO_4 . $p\text{O}_2 = 1 \text{ atm}$; $\omega = 120\pi \text{ s}^{-1}$; \circ : disk current, \times : ring current; the 0.1 N H_2SO_4 solution has been purified by electrolysis (5 to 10 h) at 0.3 V/SHE, on a Pt gauze (Reproduced with permission from Ref. 57).

different slopes has been reported many times, with an agreement about the first one at higher potentials (60 mV/log); the values reported for higher current densities, where the slope is much steeper, differ more [40, 46, 67]. Recent studies about polycrystalline platinum surfaces have shown that the reduction of O_2 is dependent on the behavior of the peroxide, an intermediate in the reduction process in basic media, which is influenced by the pretreatment of the electrode [68, 69].

Single-crystal surfaces behave quite differently, almost no peroxide being produced on Pt(111) in contact with 0.1 M KOH, the authors attributing this to the fact that OH^- is adsorbed reversibly on this surface, but irreversibly adsorbed on Pt(100) and Pt(110) [61, 70]. Experiments conducted with platinum microdisc electrodes (2.5 to 12.5 μm) have unambiguously shown how the apparent number of electron for O_2 reduction is dependent on mass transfer [71].

From these various observations it can be concluded that H_2O_2 in neutral media and HO_2^- in basic solutions are the major products of the reduction of O_2 , the further $2e$ reduction to water being limited by a slow step. The disproportionation or reduction of the peroxide is then time dependent. It can thus be understood why the apparent number of electrons for the reduction of O_2 in these media will differ with the surface state of the Pt electrode, the timescale of the experiment or the rotation rate of the electrode. There is a general agreement about the fact that H_2O_2 is an intermediate in O_2 reduction on platinum, in a basic environment; however, various reduction schemes have been proposed, with very different adsorbed intermediates and mechanisms

[52]. Owing to the influence of the surface state, to the evolution of the electrode along one experiment as well as from an experiment to another, it is understandable that conflicting interpretations exist. Nevertheless, there is some agreement about the fact that the rate determining step is the first electron addition, at low current density [59, 66, 70–72]:



It is also agreed that the slope becomes much steeper because of a change in the regime, when the oxygen adsorption becomes the rate determining reaction instead of the electrochemical step (Fig. 6) [70, 73–76]. This has also been suggested from experiments by scanning electrochemical microscopy [77]. This

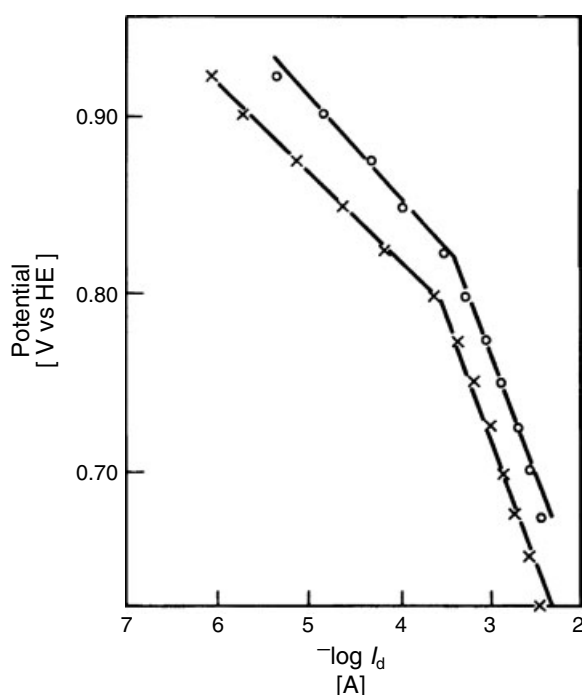


Fig. 6 Current/potential for O_2 reduction at platinum disk electrodes (0.18 cm^2), in 0.1 M KOH . \circ : prereduced Pt, \times : not prereduced Pt (Reproduced with permission from Ref. 66).

technique, also adapted by the authors to works in acidic media [78], could be useful for looking more closely at the activity of catalytic surfaces.

For obvious reasons related to the necessary reduction of the amount of catalyst used in fuel cells, ORR has been studied on thin films of platinum deposited onto glassy carbon or titanium [73, 79] and on small metal particles on carbon [80–82]. The reduction of the Pt film thickness (<1 nm), as well as of the size of the particles (diam. < 3 nm), induces a moderate loss of activity attributed to differences in the adsorption of O_2 on the metal surface.

5.4.1.2 Electrochemistry on Other Metals and Electrode Materials

From the comparison of calculated oxygen and OH adsorption energies to M(111) versus activity of the metals toward O_2 reduction, a peak shaped curve is obtained, Pt being situated almost on top of the volcano plot [63]; palladium and platinum activities should be quite close. The relation between the amount of adsorbed oxygen and the number of unpaired d electrons of the metal had been mentioned earlier [48].

The reversible O_2 potential has not been observed on palladium, due to the existence of a local cell, but O_2 evolves from water oxidation on a PdO_2 covered surface and the reduction mechanism is supposed to be the same as on Pt, the rate determining step being the first electron addition [31]. In basic media, the reduction on Pd proceeds mainly through the 4e mechanism, which has been attributed to a high catalytic activity for the peroxide reduction, or disproportionation [83, 84].

Silver is also an efficient metal for the catalysis of O_2 reduction to water by the 4e reaction, in alkaline media; the overvoltage

is, however, higher than that on platinum. H_2O_2 is produced during the reduction on Ag, but at very low concentration as silver is a good catalyst for the peroxide decomposition [31]. RRDE experiments have shown that H_2O_2 production is lower than 2% (0.1 M KOH) but considerably higher when the electrode surface has been contaminated [59].

On rhodium, the reversible potential for O_2/H_2O has been observed, after treatment of the electrode with concentrated nitric acid. On an Ir surface, this treatment does not produce the oxygen layer, which would induce the reduction by a similar mechanism [31]. The oxidation scheme of water on Rh and Ir is not clear as conflicting opinions exist [31, 45]. Oxygen is reduced to water on a Rh electrode in pure acidic media, H_2O_2 being produced in the presence of impurities; the peroxide is, however, an intermediate of the reduction in basic conditions [85, 86]. The reduction of O_2 on Ir electrodes in acid solutions is the same as on Pt, with a higher overvoltage however, probably because Ir does not promote efficiently the disproportionation of H_2O_2 [31].

On gold, the electrochemistry is dominated by the Au_2O_3/Au system ($E^\ominus = 1.36$ V); the reversible behavior of O_2/H_2O has never been observed on that electrode. Oxygen does not evolve from H_2O oxidation until the electrode surface is completely covered with oxide. The oxidation wave of OH^- to water is well defined on a gold electrode and appears at higher potential than on Pt [77]. In acid as well as in basic solutions, the overvoltage for O_2 reduction is higher than on platinum [31]. In acidic media, when the reaction occurs on oxide, this reduction is reported to go to water at high potentials and to H_2O_2 simultaneously (0.35–0.55 V); at lower potentials, H_2O_2 is further reduced

to water. In alkaline solutions, peroxide is an intermediate in the reduction path, further reduced to water [45, 87, 88]. It has been shown that peroxide is produced since the very beginning of the ORR [89, 90]. From MO calculation, it has been concluded that the 4e reduction is impossible on Au, because no dissociative chemisorption of oxygen occurs [59].

Nickel presents no interest for the reduction of O_2 , but this metal is used as electrode material for the oxidation of OH^- to O_2 , which proceeds over surface oxides of different composition, depending on the potential [31, 45].

The two well-separated waves for the reduction of oxygen on mercury were reported by Heyrovsky [91]. The first wave corresponds to the 2e reduction of O_2 to H_2O_2 in acidic or neutral solutions and to HO_2^- in basic media, species that are reduced to water or OH^- at lower potentials. Jacq and Bloch have developed the “square-scheme” concept for the discussion of the mechanism of O_2 reduction on Hg and on carbon [28].

Alloys of noble metals have been tested for O_2 reduction [31] and some should even be more efficient than Pt [63]. These metals are expensive so that other materials have been tested, like bronze, some being even slightly better electrocatalysts than platinum [45]; however, they do not seem to be stable enough. The factors governing oxygen reduction on oxides used as cathodes in fuel cells have been reviewed recently [92].

Another material has some importance for oxygen reduction, not as an electrocatalyst but because other properties make it a good supporting material for catalysts; that is, carbon, graphite, used with dispersed platinum particles or adsorbed coordination compounds. The main reduction product on carbon itself

is peroxide; the nature of carbon, for example, the orientation of the electrode surface versus the graphite planes, is essential. “Edge plane” graphite (graphitic planes perpendicular to the electrode surface) is a much better electrocatalyst than “basal plane” graphite [93, 94]. Different mechanisms and limiting steps have been proposed for O_2 reduction on carbon [75, 93], the only unquestionable statement being that ORR is a 2e process.

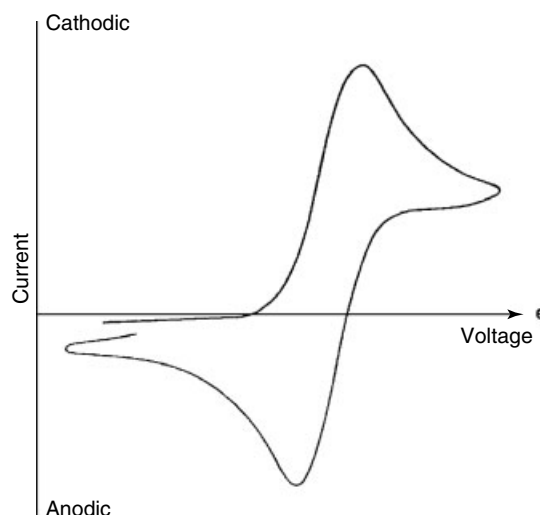
5.4.2

Electrochemistry in Nonaqueous Media

No wonder the electrochemical behavior of O_2 is totally different in aprotic media as proton, driving ORR with electron, is lacking in nonprotic solvents when potential sources, like water, are carefully eliminated.

The reversibility of the O_2/O_2^- system (reaction 10) in dimethylsulfoxide (DMSO), DMF, acetonitrile, pyridine, acetone, and methylene chloride has been demonstrated by cyclic voltammetry [35] (Fig. 7); the UV-visible and ESR spectra of superoxide being recorded after preparation of O_2^- solutions in pyridine by electrolysis [95]. Analysis of the first reduction wave on the dropping mercury electrode, in DMSO, proved that 1e is exchanged at -0.7 V versus SCE, a quite low potential for O_2 reduction; a second reduction step is observed at -2.4 V. In butyronitrile, the formal potential for O_2/O_2^- is more negative than in DMSO [96]. Upon addition of proton donor (phenol, strong acids), the wave at -0.7 V becomes a 2e irreversible wave, peroxide being the product of the reduction [12, 34]. The effect of solvents on the redox potential of O_2/O_2^- has been reported and examined [10, 12], but these results must be compared with precaution as the uncertainty due to the

Fig. 7 Cyclic voltammetry of O_2 in pyridine, at a stationary mercury drop electrode. Reference electrode: aqueous SCE; scan rate: 45 mV s^{-1} ; potential scale: from -0.6 to -1.05 V (Reproduced with permission from Ref. 35).



junction potential between the aqueous calomel electrode and the nonaqueous media is unknown and could vary significantly. This potential has been measured for a larger number of solvents, versus the ferrocenium/ferrocene couple: in most of them $E^\ominus(O_2/O_2^-)$ is close to -0.7 V , -0.8 V , a drift toward more negative potentials being observed for DMF, sulfolane, quinoline, and HMPT ($\sim -1.0 \text{ V}$) [37, 38].

The redox properties of oxygen in inorganic solvents has also been reviewed [37]. In liquid ammonia, O_2^- is obtained by reduction of O_2 by alkaline metals; the first of the two electroreduction steps of oxygen to O_2^- is reversible. In anhydrous alkaline hydroxides melts, O_2 is reduced to a mixture of peroxide and superoxide, the two redox systems O_2^-/O_2^{2-} and O_2^{2-}/O^{2-} being reversible; in molten nitrates, O_2/O_2^- and O_2^-/O_2^{2-} are reversible. CO_2 and SO_3 being acceptors of O_2^- , the electrochemical behavior of oxygen is highly dependent on the partial pressure of the corresponding anhydride over molten carbonates and sulfates and on the concentration of O^{2-} ; H_2O , a strong

acid in such media, has a great influence on electrochemistry. Owing to the high temperatures, most redox systems are reversible, for example, O_2/CO_3^{2-} on Pt in carbonates.

5.5 Electrochemistry at Electrodes Modified with Metal Complexes

Since Fenton's work in the late nineteenth century, the role of transition metals in oxygen chemistry is known, but the formation of oxygen adducts with coordination metal complexes and their importance for O_2 activation have been studied much later [1, 97]. The lively interest in ORR catalysis comes from its utmost importance to the development of fuel cells and this justifies that only a few studies have been done with metal complexes in solution; most have been devoted to carbon electrodes modified by immobilization of a catalyst. The research for good catalysts that could be efficient substitutes for the expensive platinum naturally moved toward porphyrins,

key constituents of many redox enzymes involved in the fixation and activation of oxygen, *in vivo* [98, 99]; closely related, but more robust macrocyclic compounds, the phthalocyanines have even been more extensively studied.

5.5.1

Studies in Solution

Solution studies have been performed as providing greater possibilities for mechanistic investigations; however, they are not really numerous. In aqueous solutions, adequate media for experiments aimed at energy production, they are limited by the very poor solubility of macrocyclic complexes. The electrocatalytic activity of soluble iron and cobalt porphyrins, and phthalocyanines, (bearing carboxylic or tetraalkylammonium functions) have been compared [100]. It was concluded that dissolved iron catalysts promote the reduction to water, H_2O_2 being often an intermediate, when in the presence of cobalt complexes ORR goes to water; functional groups at the periphery of the macrocycles affect the catalysis through their influence on the redox potentials of the complexes. Cobalt complexes of porphyrins and cofacial diporphyrins are slightly soluble in concentrated acid solutions, the biscobalt compounds promoting the 4e reduction of O_2 [101].

In solvents, the complexes of metal ions with organic ligands are more soluble, which makes studies easier; moreover, in anhydrous and aprotic media, it is possible to reduce the catalysts and their oxygen complexes out of reach of protons and thus to study the first steps of the catalytic cycle. It has been possible to show by studies in benzonitrile that the mixed-valence $\text{Co}^{\text{III}}\text{Co}^{\text{II}}$ redox state of the

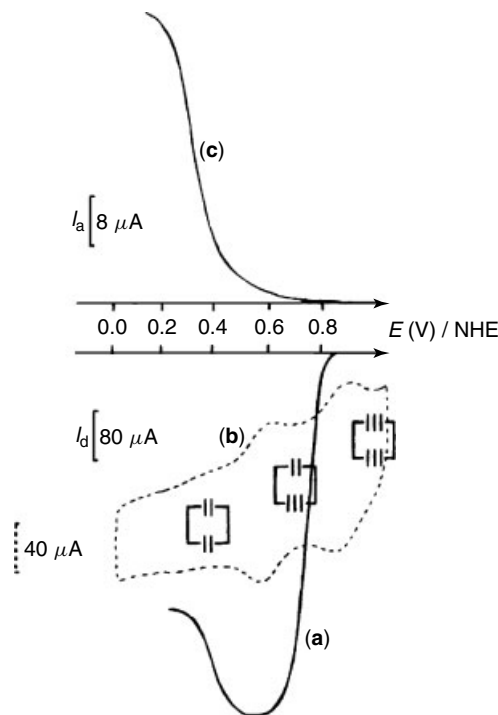
biscobalt cofacial diporphyrin binds O_2 strongly [102].

5.5.2

ORR at Modified Electrodes

Surface functionalization, by chemical reaction or adsorption, is a good way to attach catalytic groups to solid electrodes and modify their properties [103, 104]. For the electroreduction of oxygen, carbon electrodes modified by adsorption or coatings of metal complexes are convenient and have been extensively used. Adsorbed cobalt porphyrins, phthalocyanines, and tetraazaannulene complexes catalyze O_2 reduction to H_2O_2 [100, 105–108]. Iron derivatives promote the 4e reduction all over the pH range, even if H_2O_2 production is sometimes detected at low pH [100, 108–110]. Cobalt complexes catalyze O_2 reduction with a lower overvoltage than do iron compounds, because the $\text{M}^{\text{III}}/\text{M}^{\text{II}}$ redox potential is much higher for cobalt [100, 108]. In many cases, however, it has been shown that oxygen is reduced to water on electrodes modified with cobalt phthalocyanines [111]. This always occurs when aggregates or dense polymeric phases are present at the surface of the electrode and suggests that the molecule of oxygen can bind to two cobalt centers, by analogy with what has been observed with cofacial porphyrins. Electrodes modified by these diporphyrins promote the 4e ORR when the distance between the two metal centers is adequate for the binding of O_2 to both centers [106, 112, 113]. The mixed-valence complex, $\text{Co}^{\text{III}}\text{Co}^{\text{II}}$, which was shown to strongly bind O_2 in solution, is also generated when the diporphyrin is adsorbed on the graphite electrode surface [114, 115]. From the voltammograms depicted in Fig. 8, there is no doubt left about the role of this mixed-valence compound in

Fig. 8 Catalysis of O_2 reduction at a ring-disk electrode in contact with an aqueous 0.5 M H_2SO_4 solution, the graphite disk (EPGE) being modified by adsorption of a biscobalt diporphyrin, Co_2FTF_4 . (a) Disk current, solution saturated with oxygen, $pO_2 = 1$ atm; rotation rate: 100 r min^{-1} ; scan rate: 5 mV s^{-1} . (b) Detection of H_2O_2 on the Pt ring, $E_{ring} = 1.33\text{ V}$. (c) Cyclic voltammetry at the EPGE disk, under nitrogen; scan rate = 100 mV s^{-1} (Reproduced with permission from Ref. 116).



the catalytic reduction of oxygen to water, as the 4e reduction is active only in the potential domain where the $Co^{III}Co^{II}$ redox state exists; the reduction to peroxide occurs when both cobalt centers are reduced to Co^{II} . It has been unambiguously proved that Co^{III} in the mixed-valence biscobalt porphyrin acts as a Lewis acid center for O_2 binding and can be replaced by Lu^{III} or Sc^{III} [116].

These electrodes modified with metal complexes could have been substitutes for expensive platinum if they had been usable under conditions compatible with requirements for efficient fuel cells. However, they are not stable, particularly in contact with acidic media, which results from demetallation. This is known since the early works with N_4 macrocycles and heat treatment has been proposed to enhance the durability of the carbon

modified electrodes [117]. Since, very different hypothesis have been proposed to explain the improvement observed after pyrolysis of the modified electrodes, which depend on many factors and of course on the temperature of treatment ($300^\circ C$ to $1000^\circ C$). It seems quite clear that the macrocyclic compounds exist after treatments at moderate temperatures (up to $600^\circ C$), but obvious that they are destroyed by pyrolysis at about $800^\circ C$, which, however, gives the best results for oxygen reduction. Nevertheless, the exact nature of the catalytic site is still under discussion: for example, metal, metal and nitrogen, oxides [118–120]. However, such electrodes do not seem to be efficient substitutes for platinum/carbon electrodes.

Quite recently, with the aim to develop implantable miniaturized biofuel cells to power devices like sensors, the reduction

of oxygen has been studied at surfaces modified by various enzymes, proteins, wired to the electrodes [121, 122]. For the development of viable devices of this kind, which use enzymes and must function in vivo for reasonable periods of time, many problems must be solved.

References

1. R. D. Jones, D. A. Summerville, F. Basolo, *Chem. Rev.* **1979**, 79, 139.
2. R. L. Redington, N. B. Olson, P. C. Cross, *J. Chem. Phys.* **1962**, 36, 1311.
3. J.-M. Savariault, M. S. Lehman, *J. Am. Chem. Soc.* **1980**, 102, 1298.
4. N. N. Greenwood, A. Earnshaw, *Chemistry of the Elements*, Pergamon Press, Oxford, 1984.
5. K. E. Gubbins, R. D. J. Walker, *J. Electrochem. Soc.* **1965**, 112, 469.
6. C. N. Murray, J. P. Riley, *Deep-Sea Res.* **1969**, 16, 311.
7. R. F. Weiss, *Deep-Sea Res.* **1970**, 17, 721.
8. E. Wilhelm, R. Battino, R. J. Wilcock, *Chem. Rev.* **1977**, 77, 219.
9. R. Battino, *Oxygen and Ozone*, Pergamon Press, Oxford, 1981, Vol. 7.
10. D. T. Sawyer, G. Chiericato, C. T. Angelis et al., *Anal. Chem.* **1982**, 54, 1720.
11. L. H. Gevantman, in *CRC Handbook of Chemistry and Physics* (Ed.: D. R. Lide), 72nd ed., CRC Press, Boca Raton, 1991–1992.
12. D. T. Sawyer, A. Sobkowiak, J. L. Roberts, *Electrochemistry for Chemists*, John Wiley & Sons, New York, 1995.
13. R. Perry, D. W. Green, J. O. Maloney, *Perry's Chemical Engineer's Handbook*, 7th ed., McGraw-Hill, New York, 1997.
14. J. Salminen, P. Koukarri, *Calculation of Solubility of Oxygen and pH in Aqueous H_2O_2 –NaOH– O_2 System Using Pitzer-Setschenow Model*, 2002, <http://www.vtt.fi/pro/pro5/pro56/chemsheetmaterialaali/porto/index.htm>
15. T. Rettich, R. Battino, E. Wilhelm, *J. Chem. Thermodyn.* **2000**, 32, 1145.
16. D. Tromans, *Ind. Eng. Chem. Res.* **2000**, 39, 805.
17. F. Millero, F. Huang, L. Laferiere, *Mar. Chem.* **2002**, 78, 217.
18. W. M. Latimer, *The Oxidation States of the Elements and their Potentials in Aqueous Solutions*, 2nd ed., Prentice Hall, Englewood Cliffs, 1952.
19. M. Pourbaix, *Atlas d'équilibres électrochimiques*, Gauthier-Villars, Paris, 1963.
20. A. J. de Béthune, N. A. Swendeman Loud, *Standard Aqueous Potentials and Temperature Coefficients at 25°C.*, Hampel, Skokie, 1964.
21. M. Pourbaix, *Atlas of Electrochemical Equilibria in Aqueous Solutions*, NACE, Houston, 1974.
22. D. T. Sawyer, A. Sobkowiak, J. L. Roberts, *Electrochemistry for Chemists*, 2nd ed., John Wiley & Sons, Inc., New York, 1995.
23. D. T. Sawyer, *Oxygen Chemistry*, Oxford University Press, New York, 1991.
24. J. P. Hoare, in *Standard Potentials in Nonaqueous Solutions* (Eds.: A. J. Bard, R. Parsons, J. Jordan), Marcel Dekker, New York, 1985.
25. A. G. Streng, *Chem. Rev.* **1963**, 63, 607.
26. R. J. Gillespie, J. Passmore, *Acc. Chem. Res.* **1971**, 4, 413.
27. Y. A. Ilan, G. Czapski, D. Meisel, *Biochim. Biophys. Acta* **1976**, 430, 209.
28. J. Jacq, O. Bloch, *Electrochim. Acta* **1970**, 15, 1945.
29. *CRC Handbook of Chemistry and Physics*, (Ed.: D. R. Lide), 83rd ed., CRC Press, Boca Raton, 2002.
30. P. N. Ross, *Hydrogen*, Marcel Dekker, New York, 1985.
31. J. P. Hoare, *The Electrochemistry of Oxygen*, Interscience, John Wiley & Sons, New York, 1968.
32. J. O. M. Bockris, A. K. M. S. Huq, *Proc. R. Soc. London* **1956**, A237, 277.
33. D. T. Sawyer, S. J. Valentine, *Acc. Chem. Res.* **1981**, 14, 393.
34. D. L. Maricle, W. G. Hodgson, *Anal. Chem.* **1965**, 37, 1562.
35. M. E. Peover, B. S. White, *J. Chem. Soc., Chem. Commun.* **1965**, 183.
36. J. Wilshire, D. T. Sawyer, *Acc. Chem. Res.* **1979**, 12, 105.
37. D. Bauer, J.-P. Beck, *J. Electroanal. Chem.* **1972**, 40, 233.
38. D. Bauer, M. Bréant, in *Electroanalytical Chemistry* (Ed.: A. J. Bard), Marcel Dekker, New York, 1975, Vol. 8.
39. A. Panchenko, M. T. M. Koper, T. E. Shubina, *J. Electrochem. Soc.* **2004**, 151, A2016.

40. T. P. Hoar, *Proc. R. Soc. London* **1933**, A142, 628.
41. A. Damjanovic, J. O. M. Bockris, *Electrochim. Acta* **1966**, 11, 376.
42. J. P. Hoare, *J. Electrochem. Soc.* **1965**, 112, 602.
43. J. P. Hoare, (Ed.), *Oxygen*, Marcel Dekker, New York, 1974, Vol. 2.
44. J. P. Hoare, *J. Electrochem. Soc.* **1965**, 112, 849.
45. A. Damjanovic, in *Modern Aspects of Electrochemistry* (Eds.: J. O. M. Bockris, B. E. Conway), Plenum Publishing Corporation, New York, 1969, Vol. 5.
46. A. Damjanovic, V. Brusic, *Electrochim. Acta* **1967**, 12, 615.
47. A. Damjanovic, M. Genshaw, *Electrochim. Acta* **1970**, 15, 1281.
48. J. O. M. Bockris, A. K. N. Reddy, *Modern Electrochemistry*, Plenum Publishing Corporation, New York, 1970, Vol. 2.
49. S. Gilman, in *Electroanalytical Chemistry* (Ed.: A. J. Bard), Marcel Dekker, New York, 1967, Vol. 2.
50. A. K. N. Reddy, M. Genshaw, J. O. M. Bockris, *J. Electroanal. Chem.* **1964**, 8, 406.
51. A. Damjanovic, A. Dey, J. O. M. Bockris, *Electrochim. Acta* **1966**, 11, 791.
52. D. S. Gnanamuthu, J. V. Petrocelli, *J. Electrochem. Soc.* **1967**, 114, 1036.
53. A. J. Appleby, *J. Electroanal. Chem.* **1993**, 357, 117.
54. A. N. Frumkin, L. N. Nekrasov, *Dokl. Akad. Nauk SSSR* **1959**, 126, 115.
55. L. Müller, L. N. Nekrasov, *Dokl. Akad. Nauk SSSR* **1964**, 154, 437.
56. L. Müller, L. N. Nekrasov, *Electrochim. Acta* **1964**, 9, 1015.
57. A. Damjanovic, M. Genshaw, J. O. M. Bockris, *J. Electrochem. Soc.* **1967**, 114, 466.
58. J. O. M. Bockris, S. Srinivasan, *J. Electroanal. Chem.* **1966**, 11, 350.
59. P. Fischer, J. Heitbaum, *J. Electroanal. Chem.* **1980**, 112, 231.
60. P. N. Ross, *J. Electrochem. Soc.* **1979**, 126, 78.
61. N. M. Markovic, H. A. Gasteiger, P. N. J. Ross, *J. Phys. Chem.* **1995**, 99, 3411.
62. J. Perez, H. M. Villulas, E. R. Gonzalez, *J. Electroanal. Chem.* **1997**, 435, 179.
63. J. K. Nørskov, J. Rossmeisl, A. Logadotti et al., *J. Phys. Chem. B* **2004**, 108, 17886.
64. L. N. Nekrasov, L. Müller, *Dokl. Akad. Nauk SSSR* **1963**, 149, 1107.
65. W. J. Albery, M. L. Hitchman, *Ring-Disc Electrodes*, Clarendon Press, Oxford, 1971.
66. A. Damjanovic, M. Genshaw, J. O. M. Bockris, *J. Electrochem. Soc.* **1967**, 114, 1107.
67. D. T. Sawyer, R. J. Day, *Electrochim. Acta* **1963**, 8, 589.
68. C. Paliteiro, E. Correia, *J. Electrochem. Soc.* **2000**, 147, 3445.
69. C. Paliteiro, L. Batista, *J. Electrochem. Soc.* **2000**, 147, 3436.
70. N. M. Markovic, H. A. Gasteiger, P. N. Ross, *J. Phys. Chem.* **1996**, 100, 6715.
71. D. Pletcher, S. Sotiropoulos, *J. Electroanal. Chem.* **1993**, 356, 109.
72. G. Bianci, T. Mussini, *Electrochim. Acta* **1965**, 10, 445.
73. K. Tammeveski, M. Arulepp, T. Tenno et al., *Electrochim. Acta* **1997**, 42, 2961.
74. M. Tarasevitch, *Elektrokhimiya* **1973**, 9, 578.
75. K. Kinoshita, *Electrochemical Oxygen Technology*, John Wiley & Sons, New York, 1992.
76. M. R. Tarasevitch, A. Sadkowsky, E. B. Yeager, *Comprehensive Treatise of Electrochemistry*, Plenum Publishing Corporation, New York, 1983, Vol. 7.
77. B. Liu, A. J. Bard, *J. Phys. Chem. B* **2002**, 106, 12801.
78. J. L. Fernandez, A. J. Bard, *Anal. Chem.* **2003**, 75, 2967.
79. K. Tammeveski, T. Tenno, J. Claret et al., *Electrochim. Acta* **1997**, 42, 893.
80. L. Genies, R. Faure, R. Durand, *Electrochim. Acta* **1998**, 44, 1317.
81. A. Gamez, D. Richard, P. Gallezot et al., *Electrochim. Acta* **1996**, 41, 307.
82. K. Kinoshita, *J. Electrochem. Soc.* **1990**, 137, 845.
83. C.-C. Chang, T.-C. Wen, H.-J. Tien, *Electrochim. Acta* **1997**, 42, 557.
84. Y.-F. Yang, Y.-H. Zhou, C.-S. Cha, *Electrochim. Acta* **1995**, 40, 2579.
85. M. Genshaw, A. Damjanovic, J. O. M. Bockris, *J. Phys. Chem.* **1967**, 71, 3722.
86. L. N. Nekrasov, E. I. Khrushcheva, N. A. Shumilova, *Elektrokhimiya* **1966**, 2, 363.
87. A. Damjanovic, M. Genshaw, J. O. M. Bockris, *J. Electroanal. Chem.* **1967**, 15, 173.
88. M. Genshaw, A. Damjanovic, J. O. M. Bockris, *J. Electroanal. Chem.* **1967**, 15, 163.
89. S. Strbac, R. R. Adzic, *Electrochim. Acta* **1996**, 41, 2903.
90. R. W. Zurilla, R. K. Sen, E. B. Yeager, *J. Electrochem. Soc.* **1978**, 125, 1103.

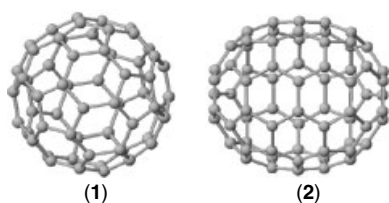
91. J. Heyrovsky, *Trans. Faraday Soc.* **1924**, 19, 785.
92. S. B. Adler, *Chem. Rev.* **2004**, 104, 4791.
93. I. Morcos, E. B. Yeager, *Electrochim. Acta* **1970**, 15, 953.
94. E. B. Yeager, *Electrochim. Acta* **1984**, 29, 1527.
95. W. Slough, *J. Chem. Soc., Chem. Commun.* **1965**, 184.
96. R. N. Bagchi, A. M. Bond, F. Scholz et al., *J. Am. Chem. Soc.* **1989**, 111, 8270.
97. A. E. Martell, D. T. Sawyer, (Eds), *Oxygen Complexes and Oxygen Activation by Transition Metals*, Plenum Publishing Corporation, New York, 1987.
98. J. P. Collman, *Acc. Chem. Res.* **1977**, 10, 265.
99. M. Momenteau, C. Reed, *Chem. Rev.* **1994**, 94, 659.
100. N. Kobayashi, W. A. Nevin, *Appl. Organometal. Chem.* **1996**, 10, 579.
101. R. R. Durand, J. P. Collman, F. C. Anson, *J. Electroanal. Chem.* **1983**, 151, 289.
102. Y. Le Mest, M. L'Her, J. P. Collman et al., *J. Am. Chem. Soc.* **1986**, 108, 533.
103. M. S. Wrighton, *Science* **1986**, 231, 32.
104. R. W. Murray, *Acc. Chem. Res.* **1980**, 13, 135.
105. H. Behret, G. Sandstede, *Z. Phys. Chem.* **1978**, 113, 97.
106. J. P. Collman, M. Marrocco, P. Denisevich et al., *J. Electroanal. Chem.* **1979**, 101, 117.
107. A. Van Der Putten, A. Elzing, W. Visscher et al., *J. Electroanal. Chem.* **1987**, 221, 95.
108. J. H. Zagal, M. Gulppi, M. Isaacs et al., *Electrochim. Acta* **1998**, 44, 1349.
109. K. Shigehara, F. C. Anson, *J. Phys. Chem.* **1982**, 86, 2776.
110. D. Ricard, A. Didier, M. L'Her et al., *C. R. Chim.* **2002**, 5, 33.
111. M. L'Her, A. Pondaven, in *The Porphyrin Handbook*, Vol. 16, *Phthalocyanines* (Eds.: K. M. Kadish, K. M. Smith, R. Guilard), Academic Press, Amsterdam, 2003.
112. C. K. Chang, H. Y. Liu, I. Abdalmuhdi, *J. Am. Chem. Soc.* **1984**, 106, 2725.
113. J. P. Collman, P. Wagenknecht, J. E. Hutchison, *Angew. Chem., Int. Ed. Engl.* **1994**, 33.
114. E. Ngameni, Y. Le Mest, M. L'Her et al., *J. Electroanal. Chem.* **1987**, 220.
115. J. P. Collman, N. H. Hendricks, C. R. Leidner et al., *Inorg. Chem.* **1988**, 27, 387.
116. R. Guilard, S. Brandès, C. Tardieux et al., *J. Am. Chem. Soc.* **1995**, 117, 11721.
117. H. Jahnke, M. Schoenborn, G. Zimmermann, *Top. Curr. Chem.* **1976**, 61, 133.
118. I. T. Bae, D. A. Tryk, D. A. Scherson, *J. Phys. Chem. B* **1998**, 102, 4114.
119. A. L. Bouwkamp-Wijnoltz, W. Visscher, J. A. R. van Veen et al., *J. Phys. Chem. B* **2002**, 106, 12993.
120. F. Jaouen, S. Marcotte, J.-P. Dodelet et al., *J. Phys. Chem. B* **2003**, 107, 1376.
121. A. Heller, *Phys. Chem. Chem. Phys.* **2004**, 6, 209.
122. S. Calabrese Barton, J. Gallaway, P. Atanasov, *Chem. Rev.* **2004**, 104, 4867.

6.1 Fullerenes

*Lourdes E. Echegoyen, M. Ángeles Herranz,
and Luis Echegoyen
Clemson University, Clemson, South Carolina, USA*

6.1.1 Introduction

Following the fascinating discovery of C_{60} and C_{70} (**1** and **2**) in 1985 [1] and their isolation in multigram quantities in 1990 [2], several larger carbon-based spheroids, the higher fullerenes, were also isolated and characterized [3–7]. These included some stable isomers of C_{76} , C_{78} , and C_{84} among others. Together C_{60} , C_{70} , and the higher fullerenes represent a unique family of three-dimensional building blocks that possess distinctive electronic properties with an enormous potential for materials science applications [8].



The high electron affinity (EA) of C_{60} was initially predicted using Hückel Molecular

Orbital (HMO) Theory [9, 10]. The only possible isomer of the proposed (and later confirmed) icosahedral C_{60} , (**1**), was theoretically described as having a closed-shell configuration consisting of 30 bonding molecular orbitals (MO) with 60 π electrons (see Fig. 1). The completely occupied HOMO (highest occupied molecular orbital) was calculated to be 1.5–2.0 eV lower than the antibonding LUMO (lowest unoccupied molecular orbital). The LUMO was predicted to be triply degenerate and energetically low lying, suggesting an exceptionally high affinity for up to six electrons in solution. Soon after, the electron affinity of C_{60} was measured as 2.65 eV [10], confirming theoretical predictions.

Similar calculations were made for the only possible isomer of C_{70} [11–13] that obeys the “isolated pentagon rule” [4, 6] and for some of the most stable isomers of the higher fullerenes [11, 14–16]. On the basis of their easily accessible LUMOs and high electron affinities, all stable members of the fullerene family were expected to display very rich cathodic electrochemistry.

Calculated and experimentally determined values of EAs and ionization energies (IE) of selected members of the fullerene family are shown in Table 1. The magnitude of these values clearly indicates that fullerenes easily accept electrons

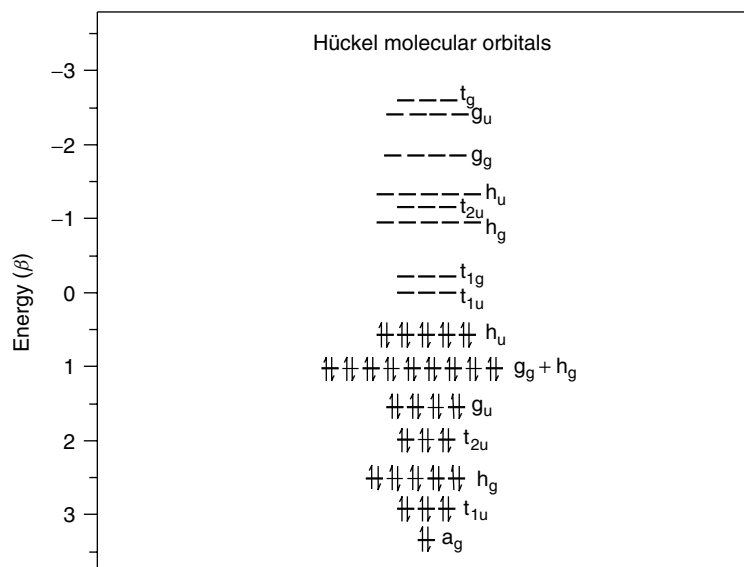


Fig. 1 Hückel energy levels of C_{60} together with one component of the triply degenerate t_{1u} set of molecular orbitals that become populated upon alkali metal doping or electrochemical reduction.

Tab. 1 Calculated and experimental electron affinities (EA_c and EA_1) and ionization energies (IE_c and IE_1) of selected fullerenes

	EA_c [eV] ^a	EA_1 [eV] ^b	IE_c [eV] ^a	IE_1 [eV] ^c
C_{60}	2.7	2.66	7.8	7.57
C_{70}	2.8	2.67	7.3	7.36
C_{76} (D_2 isomer)	3.2	2.90 ^d	6.7	7.34 ^d
C_{78} (C_{2v} isomer)	3.4	3.12 ^d	6.8	7.26 ^d
C_{82} (C_2 isomer)	3.5	3.14 ^d	6.6	7.25 ^d
C_{84} (D_2 isomer)	3.5	3.14 ^d	7.0	7.17 ^d
C_{84} (D_{2d} isomer)	3.3	7.0		

^aValues reported are averages from two levels of Hartree–Fock (HF) modified neglect of diatomic overlap (MNDO) theory in Ref. 15.

^bFrom Ref. 17.

^cFrom Ref. 18.

^dValues reported for a mixture of stable isomers formed during the synthetic procedure.

[9, 15, 17, 18], but their oxidation is somewhat difficult. Furthermore, electron affinity increases and ionization energy decreases with the number of carbons in the cage, indicating that the higher

fullerenes should be easier to reduce and oxidize than C_{60} or C_{70} (see the following).

Before embarking on a detailed discussion on the electrochemistry of fullerenes, it is important to emphasize that the

fascination with the electronic properties of these compounds has gone beyond studies of the pristine molecules. For example, alkali metal-doped anion radical salts of C_{60} are superconducting at low temperatures [19], and reaction of C_{60} with the organic donor TDAE (tetrakis(dimethylamino)ethylene) results in an organic ferromagnet [20]. A detailed discussion of these topics is, however, beyond the scope of this chapter and will not be addressed here. Encapsulation of one or more metal atoms or a small molecule inside fullerene cages, endohedral metallofullerenes, has also attracted special attention due to the possibility of unusual physicochemical properties not found in the pristine fullerenes [21]. Furthermore, the reactivity of fullerenes is enhanced by pyramidalization of the sp^2 carbon, and it differs significantly from the reactivity of planar aromatics, providing fullerenes with the extraordinary ability to easily undergo addition reactions [8, 22–26]. As a consequence, numerous transformations have been developed and an enormous number of fullerene derivatives have been prepared with the aim of exploring and exploiting its electron-donor/acceptor capabilities.

This chapter presents an up-to-date account of the redox properties of the pristine fullerenes and a large number of their derivatives as revealed by electrochemical studies in solution. The description here is as exhaustive as possible, although not completely comprehensive due to the large number of reports on the subject that have appeared over the years. A section on electrosynthesis of fullerene derivatives is included, with special emphasis on the retro-cyclopropanation reaction, a reaction that has led to the formation of novel derivatives as well as

isomers not easily attainable by synthetic methods.

6.1.2

Electrochemistry of C_{60} and C_{70}

6.1.2.1 Reduction of C_{60}

The triple degeneracy of the LUMO of C_{60} was confirmed experimentally in several steps between 1990 and 1992 with the detection of C_{60}^- and C_{60}^{2-} [27], C_{60}^{3-} [28], C_{60}^{4-} [29], C_{60}^{5-} [30], and finally C_{60}^{6-} [31]. Owing to limitations in the solvent potential window, the elusive hexaanion species was only detected when the experiment was carried out under vacuum, at low temperature (-10°C), and using a 0.1 M tetra-*n*-butylammonium hexafluorophosphate (TBAPF₆) electrolyte solution in a solvent mixture consisting of toluene/acetonitrile (PhMe/MeCN) in a 4 to 1 ratio. Under these conditions, using cyclic voltammetry (CV) (Fig. 2a) and differential-pulse voltammetry (DPV) (Fig. 2b), six successive, fully reversible, one-electron reductions are easily observed [31]. The potentials measured are shown on Table 2. As expected, on the basis of the triply degenerate LUMO, the potential separation between any two successive reductions is relatively constant, 450 ± 50 mV. On the voltammetric timescale, C_{60}^- through C_{60}^{6-} appear to be chemically stable. However, only C_{60}^- through C_{60}^{4-} are stable when generated by controlled potential coulometry (CPC) under vacuum, using toluene/acetonitrile as solvent.

Also included in Table 2 are the reduction potentials of C_{60} using different combinations of solvent, supporting electrolyte, and temperature. It is evident from these results that the above factors have a notable effect on the cathodic electrochemistry of C_{60} [30–37].

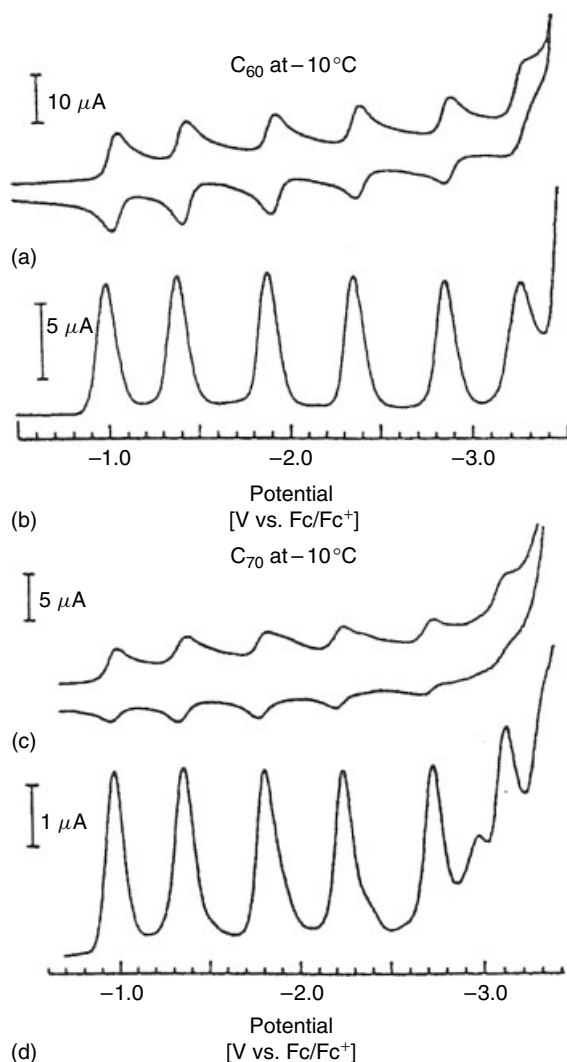


Fig. 2 Reduction of C₆₀ and C₇₀ in MeCN/PhMe at -10 °C using (a and c) cyclic voltammetry at a 100 mV s⁻¹ scan rate and (b and d) differential-pulse voltammetry at a 25 mV s⁻¹ scan rate. Reprinted with permission from Ref. 31. Copyright © 1992 American Chemical Society.

This same solvent and supporting electrolyte dependence effect is observed for C₇₀ and for the higher fullerenes (see the following).

The solubility of the electrogenerated species also depends upon the choice of solvent and supporting electrolyte [38]. For example, C₆₀⁰ is insoluble in DMF and THF, but all of its anions readily dissolve in these solvents. In acetonitrile, C₆₀⁰ is

also insoluble, but a soluble dianion can be generated from a suspension in the presence of K⁺, Cs⁺, or Ca²⁺ cations. A soluble trianion can also be prepared in acetonitrile if TBA⁺, K⁺, Na⁺, or Ca²⁺ cations are present. These acetonitrile solutions have been used to study the conductivities of electrodeposited films of C₆₀ [38] and for the synthesis of singly bonded C₆₀ dimers [39].

Tab. 2 Half-wave reduction potentials (in V vs. Fc/Fc^+) of C_{60} using various solvents, supporting electrolytes, and temperatures

Solvent ^a	Supporting electrolyte	Temperature [°C]	E_1	E_2	E_3	E_4	E_5	E_6	References
PhMe/MeCN	TBAPF ₆	−10	−0.98	−1.37	−1.87	−2.35	−2.85	−3.26	31
PhMe/DMF	TBAPF ₆	−60	−0.82	−1.26	−1.82	−2.33	−2.89	−3.34 ^b	33
Liq. NH ₃ ^c	KI	−70	−1.04	−1.56	−2.00	−2.37	−2.43	−3.03	34
Benzene	THAClO ₄	+45	−0.83	−1.29	−1.89	−2.48	−3.07		30
MeCN ^d	TBAClO ₄	+22	−1.24	−1.73	−2.19	−2.78			32
Pyridine	TBAClO ₄	+22	−0.86	−1.38	−1.80	−2.33			32
DMF	TBAClO ₄	+22	−0.77	−1.23	−1.82	−2.36			32
PhCN	TBAClO ₄	+22	−0.92	−1.34	−1.82				32
THF	TBABF ₄	−60	−0.96	−1.53	−2.11	−2.60	−3.13	−3.59	35
	TBABF ₄	+25	−0.93	−1.52	−2.08	−2.57	−3.08		35
	TBAClO ₄	+22	−0.90	−1.49	−2.06	−2.56			32
DCM	TBAPF ₆	+22	−1.02	−1.41	−1.87				32
	TBAClO ₄	+22	−1.00	−1.39	−1.84 ^e				32
	TBABF ₄	+25	−1.01	−1.40					27
TCE	TBAPF ₆	+25	−1.06						36
ODCB	TBAPF ₆	+25	−1.13	−1.50	−1.94	−2.41			37

PhMe = toluene; MeCN = acetonitrile; DMF = dimethylformamide; PhCN = benzonitrile; THF = tetrahydrofuran; DCM = dichloromethane; TCE = 1, 1, 2, 2-tetrachloroethane; DMA = dimethylamine; ODCB = *o*-dichlorobenzene; TBA = tetra-*n*-butylammonium; THA = tetra-*n*-hexylammonium; $\text{PPN}^+ = [(\text{C}_6\text{H}_5)_3\text{P}]_2\text{N}^+$.

^aGlassy carbon electrode. All others use Pt.

^bAnodic peak potential.

^cOwing to the presence of surface waves upon reoxidation, anodic peak potentials are reported.

^dControlled potential electrolysis used to generate C_{60}^- due to insolubility of C_{60} in MeCN.

^eScan rate $> 5 \text{ V s}^{-1}$.

6.1.2.2 Reduction of C_{70}

Hückel MO calculations of C_{70} , (2), indicated that the structure of C_{70} had D_{5h} symmetry. It consisted of an elongated C_{60} obtained by cutting C_{60} 's truncated icosahedron at the equator and inserting a belt of five hexagons [10, 11, 40]. Although, the LUMO of C_{70} is not threefold degenerate like that of C_{60} , calculations indicated the existence of three levels, one single and two degenerate (LUMO and LUMO + 1), with a very small energy separation. The energy of these orbitals was found to be practically identical to that of C_{60} [11, 12]. Consequently, C_{70} was expected to behave electrochemically very much

like C_{60} . Indeed, in toluene/acetonitrile, six reduction waves are observed, but unlike C_{60} , all six waves can be detected at room temperature (see Fig. 2c,d) [31]. Reduction potentials for C_{70} obtained under various conditions of solvent and temperature are presented in Table 3. Note that the first and second reduction potentials of C_{60} and C_{70} in toluene/acetonitrile are nearly identical. However, from the trianion up to and including the hexaanion, C_{70} becomes increasingly easier to reduce than C_{60} . The phenomenon has been explained in terms of a simple charge-separation delocalization model. Since C_{70} is larger than C_{60} , adding the third electron would be

Tab. 3 Half-wave reduction potentials (in V vs. Fc/Fc^+) of C_{70} using various solvents, supporting electrolytes, and temperatures

Solvent ^a	Supporting electrolyte	Temperature [°C]	E_1	E_2	E_3	E_4	E_5	E_6	References
PhMe/ MeCN ^b	TBAPF ₆	−10	−0.97	−1.34	−1.78	−2.21	−2.70	−3.70	31
DMA ^{c,d}	TBABr	−65	−0.45	−0.90	−1.34	−1.77	−2.33	−2.80	41
ODCB ^e	TBAPF ₆	+25	−1.10	−1.46	−1.86	−2.27			37
THF	n/r ^f	+25	−0.85	−1.41	−1.95				28
PhCN	n/r ^f	+25	−0.91	−1.32					28
PhMe/DCM	TBAPF ₆	n/r ^f	−0.91	−1.28	−1.70				40, 42
DCM	n/r ^f	+25	−0.97	−1.35	−1.76				28
	TBAPF ₆	+25	−0.93	−1.31	−1.73	−2.09			43
TCE	TBAPF ₆	+25	1.02						36

^aSee Table 2 for solvent abbreviations.^bGlassy carbon electrode. All others use Pt.^cCathodic peak potential.^dVs. Ag/AgCl.^eScan rate = 20 mV s^{−1}.^fNot reported.

easier if the charges are separated by larger distances or if they can be delocalized over a larger number of carbon atoms [41].

6.1.2.3 Oxidation of C_{60} and C_{70}

Initial calculations had indicated that C_{60} and C_{70} had closed-shell configurations and that the HOMOs of both molecules were energetically low lying. The HOMO of C_{60} was predicted to be fivefold degenerate [9, 10], while C_{70} appeared as having 10 occupied orbital states around the HOMO energy. In addition, the corresponding IEs were estimated to have high values, 7.8 and 7.3 eV, respectively (see Table 1). These results suggested that C_{60} and C_{70} should not be readily oxidizable. In fact, most studies on the anodic electrochemistry of C_{60} indicate irreversible behavior (see Table 4) [30, 31, 42–45]. The first study, performed on a film of C_{60} in acetonitrile, showed a chemically irreversible wave at +1.6 V vs. Fc/Fc^+ [45]. In another report, chemically irreversible waves were observed at

+1.30 V vs. Fc/Fc^+ for both C_{60} and C_{70} in benzonitrile/TBAPF₆ [30]. No change was observed by lowering the temperature to −15 °C or by increasing the scan rate up to 50 V s^{−1}. Four electrons were transferred during oxidation as indicated by peak current intensities, which was confirmed by CPC at 1.44 V vs. Fc/Fc^+ . Other studies with C_{60} in dichloromethane (DCM) and dichloroethene (DCE) also showed an irreversible wave at +1.32 and 1.28 V, respectively vs. Fc/Fc^+ [32]. For a mixture of C_{60} and C_{70} , the observation of two oxidation peaks in close proximity at 1.65 and 1.75 V vs. Ag/AgCl was reported [42]. In this study, it was observed that oxidation currents were approximately double those of the single-electron reduction waves. On the basis of these observations, the existence of two two-electron transfers was suggested.

To date, the only truly reversible oxidation of C_{60} and C_{70} has been observed in 1,1,2,2-tetrachloroethane (TCE) [36, 46].

Tab. 4 Half-wave oxidation potentials and HOMO–LUMO gaps in solution (in V vs. Fc/Fc^+) of C_{60} and C_{70} using various solvents, supporting electrolytes, and temperatures

	<i>Solvent</i> ^a	<i>Supporting electrolyte</i>	<i>Temperature</i> [°C]	E_1^{ox}	E_2^{ox}	$\langle E_1^{\text{ox}} - E_1^{\text{red}} \rangle$	<i>References</i>
C_{60}	MeCN ^b	TBAPF ₄	n/r ^c	+1.60 ^d			45
	PhCN	TBAPF ₆	RT	+1.30 ^d			30
	DCE	TBAClO ₄	22	+1.28 ^d			32
	DCM	TBAClO ₄	22	+1.32 ^d			32
	TCE	TBAPF ₆	RT	+1.26		2.32	36
	ODCB	TBAPF ₆	n/r ^c	+1.32		2.45	37
$\text{C}_{60} + \text{C}_{70}$	DCM	TBAPF ₆	n/r ^c	+1.65 ^{e,f}	+1.75 ^{e,f}		41
C_{70}	PhCN	TBAPF ₆	RT	+1.30 ^b			30
	TCE	TBAPF ₆	RT	+1.20	+1.75	2.22	36
	ODCB	TBAPF ₆	n/r ^c	+1.21		2.31	37

^aSee Table 2 for solvent abbreviations.^bFilm of C_{60} in MeCN.^cNot reported.^dChemically irreversible.^eIt was not reported which of these potentials corresponds to C_{60} and which one to C_{70} .^fAdsorption observed.

In this solvent, using CV and Osteryoung square-wave voltammetry (OSWV) under high vacuum conditions at room temperature, C_{60} displays a one-electron, chemically reversible oxidation wave at +1.26 V vs. Fc/Fc^+ . TBAPF₆ was used as the supporting electrolyte. Under the same conditions, the first one-electron oxidation of C_{70} occurs at +1.20 V, 60 mV more negative (easier to oxidize) than that of C_{60} . Both oxidations are electrochemically quasireversible with $\Delta E_{\text{pp}} \cong 80$ mV. In addition, a second oxidation wave is observed for C_{70} close to the limit of the solvent potential window at +1.75 V. However, this wave appears to be chemically irreversible (see Fig. 3) [36].

TCE containing 1–10% trifluoromethanesulfonic acid ($\text{CF}_3\text{SO}_3\text{H}$) and TBAPF₆ as supporting electrolyte has been used as a medium for the bulk electrolytic generation of long-lived, stable solutions

of the cation radical of C_{60} , $\text{C}_{60}^{\bullet+}$, for electron paramagnetic resonance (EPR) and UV–VIS–NIR studies [46]. The same medium, however, results in unstable $\text{C}_{70}^{\bullet+}$, whose UV–VIS–NIR and EPR spectroscopic data indicate the presence of oxidized species other than $\text{C}_{70}^{\bullet+}$. Table 4 summarizes relevant oxidation potential results for C_{60} and C_{70} .

The potential difference between the first reduction and the first oxidation is a good measure of the HOMO–LUMO energy difference (the HOMO–LUMO gap) in solution. For C_{60} and C_{70} , these gaps are 2.32 and 2.22 V, respectively, at room temperature in TCE [36].

Recently, it has been shown that there are two distinct classes of fullerenes. The first class, which includes C_{60} , C_{70} , and several stable isomers of the higher fullerenes, have large HOMO–LUMO gaps and are soluble in many organic

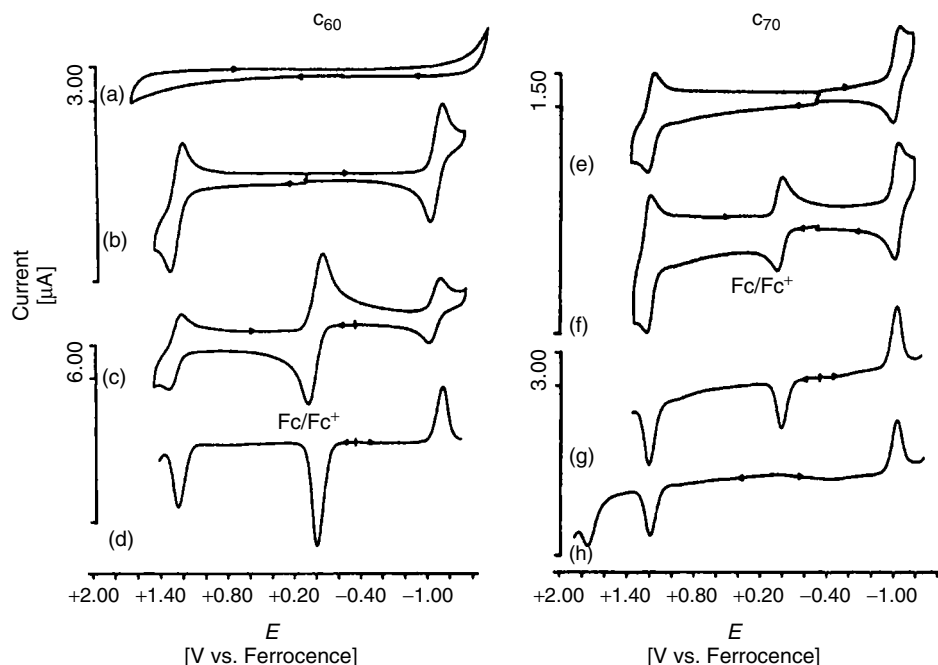


Fig. 3 CV and OSWV scans for C_{60} and C_{70} in 0.1 M TBAPF₆/TCE at room temperature. CVs were run at a scan rate of 100 mV s⁻¹, while OSWVs were run at 60 mV s⁻¹. (a) CV of background solvent–electrolyte system. (b) CV with C_{60} , no ferrocene added. The cathodic and anodic cyclic scans were performed separately. (c) Same as (b) after addition of ferrocene. (d) OSWV of the solution in (c). Cathodic and anodic scans were performed separately. (e) CV

of C_{70} without added ferrocene. Cathodic and anodic cyclic scans were performed separately. (f) Same as (e) after addition of ferrocene. (g) OSWV of the solution in (f). Cathodic and anodic cyclic scans were performed separately. (h) OSWV of the solution as in (e), without ferrocene added, scanned to more positive potential to show the second oxidation wave for C_{70} . Reprinted with permission from Ref. 36. Copyright © 1993 American Chemical Society.

solvents. The second class, which includes C_{74} , C_{80} (I_h), and other selected isomers of the higher fullerenes are either free radicals or have small HOMO–LUMO gaps [47]. These small-band gap fullerenes are kinetically unstable and tend to react readily to form insoluble polymerized solids.

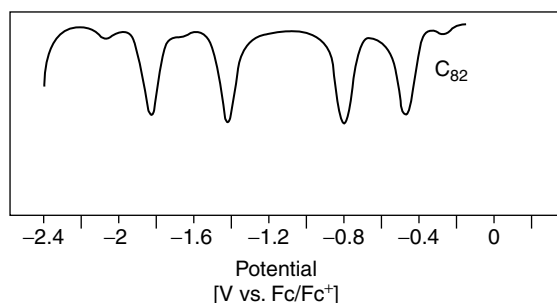
6.1.3

Electrochemistry of the Higher Fullerenes, C_{76} , C_{78} , C_{82} , and C_{84}

The chemistry of the higher fullerenes has developed at a slower pace than that

of the smaller cages mainly because the former are present in very small quantities in fullerene soot [3]. To complicate matters, more than one stable constitutional isomer exists for each of the higher fullerenes [7, 15], a fact that has created difficulties with their isolation and purification. Consequently, reports on their redox properties did not begin to appear until 1991, soon after pure samples in milligram quantities became available [6, 7, 48, 49]. In some of the initial studies, isomers of different symmetries were not separated, and multiple redox waves

Fig. 4 Square-wave voltammograms for C_{82} with a 610-mV potential gap between the second and third reductions. Reprinted with permission from Ref. 58. Copyright © 2000 Elsevier.



were observed [50, 51]. Under these conditions, assigning a particular wave to a given isomer was difficult or impossible. In recent years, advances in separation methods have allowed the isolation of individual isomers for electrochemical studies and for derivatization [44, 50–57]. Thus, a compilation of reduction potentials of the pristine higher fullerenes and some of the most notable endohedral metallofullerenes studied thus far is presented in Tables 5–8. Oxidation potentials, along with the corresponding values of the HOMO–LUMO gaps in solution,

are presented in Table 9. Individual cases are discussed in the following, according to cage size and isomer symmetry. On the basis of some of these electrochemical measurements, it has been recently suggested that among all stable fullerenes there exist two distinct types with different electronic structures: those with evenly spaced reductions like C_{60} and C_{70} , and those whose reductions are not evenly spaced like C_{78} and C_{82} (see Fig. 4). A correlation between electronic differences and endohedral metallofullerene formation has been proposed [58].

Tab. 5 Half-wave reduction potentials (in V vs. Fc/Fc⁺) of C_{76} using various solvents, supporting electrolytes, and temperatures

	<i>Solvent</i> ^a	<i>Supporting electrolyte</i>	<i>Temperature [°C]</i>	<i>E</i> ₁	<i>E</i> ₂	<i>E</i> ₃	<i>E</i> ₄	<i>E</i> ₅	<i>E</i> ₆	<i>References</i>
C_{76}	PhCN	TBAPF ₄	RT	−0.76 ^b	−1.19 ^a	−1.72 ^a	−2.06 ^b			59
		PPN ⁺ Cl [−]	n/r ^c	−0.78	−1.16	−1.70				61
	DCM	TBAPF ₄	RT	−0.79	−1.12	−1.57				59
		TBAPF ₆	RT	−0.83	−1.15	−1.64	−2.01			44
	ODCB	TBAPF ₆	n/r ^c	−1.00	−1.30	−1.76	−2.15			37
	TCE	TBAPF ₆	RT	−0.83	−1.12					60
		PPN ⁺ Cl [−]	n/r ^c	−0.91						61
	PhMe /MeCN	TBAPF ₆	−15	−0.83	−1.17 ^d	−1.68 ^d	−2.10 ^d	−2.61 ^d	−3.04 ^{d,e}	50

^aSee Table 2 for solvent abbreviations.

^bScan rate = 1 V s^{−1}.

^cNot reported.

^dScan rate = 2 V s^{−1}.

^eMay be irreversible.

Tab. 6 Half-wave reduction potentials (in V vs. Fc/Fc^+) of C_{78} using various solvents, supporting electrolytes, and temperatures

	<i>Solvent^a</i>	<i>Supporting electrolyte</i>	<i>Temperature [°C]</i>	<i>E₁</i>	<i>E₂</i>	<i>E₃</i>	<i>E₄</i>	<i>E₅</i>	<i>E₆</i>	<i>References</i>
C_{78}	TCE	TBAPF ₆	RT	−0.77	−1.08					60
	TCE	PPN ⁺ Cl [−]	n/r ^b	−0.79	−1.13					61
	PhCN	PPN ⁺ Cl [−]	n/r ^b	−0.64	−1.06					61
$\text{C}_{2v}\text{--}\text{C}_{78}$	DCM	TBAPF ₆	RT	−0.70	−1.04	−1.72	−2.07			44
	PhMe	TBAPF ₆	−15	−0.72 ^c	−1.08 ^c	−1.79 ^c	−2.18 ^c	−2.45 ^c	−2.73 ^c	50
	/MeCN									
$\text{D}_3\text{--}\text{C}_{78}$	DCM	TBAPF ₆	RT	−0.64	−0.94	−1.70	−2.05			44

^aSee Table 2 for solvent abbreviations.^bNot reported.^cScan rate = 2 V s^{−1}.**Tab. 7** Half-wave reduction potentials (in V vs. Fc/Fc^+) of C_{82} and its endohedral metalloderivatives using various solvents and supporting electrolytes

	<i>Solvent^a</i>	<i>Supporting electrolyte</i>	<i>E₁</i>	<i>E₂</i>	<i>E₃</i>	<i>E₄</i>	<i>E₅</i>	<i>E₆</i>	<i>References</i>
$\text{C}_{82}^{\text{b,c}}$	ODCB	TBAPF ₆	−0.69	−1.04	−1.58	−1.94			58, 73
	Pyridine	TBAClO ₄	−0.47	−0.80	−1.42	−1.84			70
$\text{La@C}_{82}\text{--A}$	ODCB	TBAPF ₆	−0.42	−1.37	−1.53	−2.26	−2.46		73, 74
$\text{La@C}_{82}\text{--B}$	ODCB	TBAPF ₆	−0.47	−1.40 ^d		−2.01	−2.40		74
$\text{Pr@C}_{82}\text{--A}$	ODCB	TBAPF ₆	−0.39	−1.35	−1.46	−2.21			67, 69
$\text{Pr@C}_{82}\text{--B}$	ODCB	TBAPF ₆	−0.48	−1.39 ^d		−1.99			67, 69
$\text{Y@C}_{82}\text{--A}$	ODCB	TBAPF ₆	−0.34	−1.34 ^d		−2.22	−2.47		74
Ce@C_{82}	ODCB	TBAPF ₆	−0.41	−1.41	−1.53	−1.79	−2.25	−2.50	73
Ga@C_{82}	ODCB	TBAPF ₆	−0.39	−1.38 ^d		−2.22 ^{d,e}	−2.47		73
	PhMe/MeCN ^f	TBAPF ₆	−0.25	−1.25 ^d	−2.05	−2.17	−2.35	−2.58	72
Sm@C_{82}	PhMe/MeCN ^f	TBAPF ₆	−0.28	−0.63	−1.52	−1.88	−2.03	−2.32 ^g	72
$\text{Sc}_2\text{@C}_{82}$ (III)	Pyridine	TBAClO ₄	−0.87 ^d	−1.29 ^d	−1.85 ^e				58
$\text{Sc}_2\text{@C}_{82}$ (I) ^h	Pyridine	TBAClO ₄		−1.26 ^d	−1.88				58
$\text{Eu}_2\text{@C}_{82}$ (III)	Pyridine	TBAClO ₄	−0.87	−1.26					58

^aSee Table 2 for solvent abbreviations.^bMajor isomer of C_2 (a) symmetry.^cScan rate = 20 mV s^{−1}.^dTwo-electron process.^eIrreversible.^fConducted at −10 °C.^gUnexplained unusual peak height.^hImpure sample.

Tab. 8 Half-wave reduction potentials (in V vs. Fc/Fc^+) of C_{84} using various solvents, supporting electrolytes, and temperatures

	<i>Solvent</i> ^a	<i>Supporting electrolyte</i>	E_1	E_2	E_3	E_4	E_5	E_6	<i>References</i>
C_{84} ^b	PhCN	TEAPF ₆	−0.63	−0.95	−1.28	−1.58	−1.87		50
	TCE	TBAPF ₆	−0.67	−0.96	−1.27				60
	PhMe/MeCN	TBAPF ₆	−0.67	−1.00	−1.34	−1.72	−1.99		51
$\text{D}_2\text{--C}_{84}$ (IV)	Pyridine	TBAClO ₄	−0.65	−0.98	−1.34	−1.75			53
		TBAPF ₆	−0.56	−0.88	−1.24	−1.67			54
	PhCN	PPN ⁺ Cl [−]	−0.60	−0.96	−1.37	−1.60	−1.77		78
$\text{D}_{2d}\text{--C}_{84}$ (II)	TCE	TBAPF ₆	−0.78	−1.06					78
	ODCB	TBAPF ₆	−0.74	−1.03	−1.36	−1.71			37
	Pyridine	TBAPF ₆	−0.55	−0.86	−1.20	−1.59	−2.40		54
	PhCN	PPN ⁺ Cl [−]	−0.61	−0.96	−1.33	−1.63			78
	TCE	TBAPF ₆	−0.79	−1.10					78
$\text{C}_2\text{--C}_{84}$ (IV)	Pyridine ^c	TBAPPF ₆	−0.42	−0.73	−1.46	−1.90			54
	Pyridine ^d	TBAClO ₄	−0.46	−0.77	−1.58	−1.98	−2.27		53
	PhCN	PPN ⁺ Cl [−]	−0.28	−0.63	−1.46				78
	TCE	TBAPF ₆	−0.59	−0.90					78
$\text{D}_{2d}\text{--C}_{84}$ (I)	PhCN	PPN ⁺ Cl [−]	−0.64	−0.98	−1.37				78
	TCE	TBAPF ₆	−0.94						78
$\text{C}_5\text{--C}_{84}$ (b)	PhCN	PPN ⁺ Cl [−]	−0.43	−0.79					78
	TCE	TBAPF ₆	−0.77						78
$\text{D}_2\text{--C}_{84}$ (II)	PhCN	PPN ⁺ Cl [−]	−0.46	−0.80	−1.15	−1.51			78
	TCE	TBAPF ₆	−0.79	−1.10					78

^aSee Table 2 for solvent abbreviations.^bMixture of two major isomers, $\text{D}_2\text{--C}_{84}$ (IV) and $\text{D}_{2d}\text{--C}_{84}$ (II).^cThe “new isomer” in Ref. 54 is now presumed to be the C_2 (IV) isomer, see Ref. 78.^dRedox potentials for the D_{2d} isomer in Ref. 53 have been reassigned to the C_2 -b isomer. See Ref. 54 for details.

6.1.3.1 Reduction and Oxidation of C_{76}

Only one structure of C_{76} has a closed-shell configuration. It possesses D_2 symmetry and is therefore chiral [48]. Its two enantiomers, C_{76} and *ent*- C_{76} are normally isolated as a 1:1 racemic mixture. Four reversible reduction couples corresponding to 0/−1, −1/−2, −2/−3, and −3/−4 can be observed by CV in PhCN, DCM, and ODCB (see Table 5) [37, 59]. Six evenly spaced waves have been detected in a 4:1 (v/v) PhMe/MeCN mixture at −15 °C, but the sixth reduction is observed at the limit of the solvent potential window and appears to be irreversible

[50]. In TCE, only the first two reduction waves are detected by OSWV. However, this solvent allows the calculation of the HOMO–LUMO gap in solution because a reversible first oxidation wave, 0/+1, is observed when using TCE (see the following) [60]. Note that the first reduction potentials for C_{76} in all four solvents are 100–200 mV more positive than the corresponding ones for C_{60} (see Table 2). Considering the higher electron affinity of C_{76} (see Table 1), this is not an unexpected result. One reversible oxidation wave is observed in DCM [44], while in TCE, two oxidation waves are observed [60, 61]. The

Tab. 9 Half-wave oxidation potentials (in V vs. Fc/Fc⁺) and HOMO–LUMO gap in solution of the higher fullerenes

	<i>Solvent</i> ^a	<i>Supporting electrolyte</i>	<i>E</i> ₁ ^{ox}	<i>E</i> ₂ ^{ox}	(<i>E</i> ₁ ^{ox} – <i>E</i> ₁ ^{red})	<i>References</i>
C ₇₆	TCE	TBAPF ₆	+0.81	+1.30 ^b	1.64	60
	DCM	TBAPF ₆	+0.84		1.67	44
	ODCB	TBAPF ₆	+0.73		1.73	37
C _{2v} –C ₇₈	TCE	TBAPF ₆	+0.95	+1.43	1.72	60
	PhMe/MeCN	TBAPF ₆	+0.90 ^b		1.62 ^c	50
D ₃ –C ₇₈	TCE	TBAPF ₆	+0.70	+1.17	+1.47	60
	DCM	TBAPF ₆	+0.74		+1.38	44
C ₈₂ ^{d,e}	ODCB	TBAPF ₆	+0.72		1.41	58, 73
La@C ₈₂ -A	ODCB	TBAPF ₆	+0.07	+1.07 ^b	0.49	73, 74
La@C ₈₂ -B	ODCB	TBAPF ₆	–0.07	+1.08 ^b	0.40	74
Pr@C ₈₂ -A	ODCB	TBAPF ₆	+0.07	+1.08 ^b	0.46	67
Pr@C ₈₂ -B	ODCB	TBAPF ₆	–0.07	+1.05 ^b	0.41	67
Y@C ₈₂ -A	ODCB	TBAPF ₆	+0.10	+1.07 ^b	0.44	74
Ce@C ₈₂	ODCB	TBAPF ₆	+0.08	+1.08 ^b	0.49	73
Ga@C ₈₂	ODCB	TBAPF ₆	+0.09	+1.08 ^b	0.48	73
	PhMe/MeCN ^f	TBAPF ₆	+0.20		0.45	72
C ₈₄ ^g	TCE	TBAPF ₆	+0.93		1.60	60
D ₂ –C ₈₄ (IV)	ODCB	TBAPF ₆	+0.88		1.62	37
C ₂ –C ₈₄ (IV)	TCE	TBAPF ₆	+0.88		1.47	78
D _{2d} –C ₈₄ (I)	TCE	TBAPF ₆	+0.91		1.85	78
C ₅ –C ₈₄ (b)	TCE	TBAPF ₆	+0.86		1.63	78
D ₂ –C ₈₄ (II)	TCE	TBAPF ₆	+0.89		1.68	78

^aSee Table 2 for solvent abbreviations.^bIrreversible.^cCalculated from data in Ref. 50.^dMajor isomer of C₂ (a) symmetry.^eScan rate = 20 mV s^{–1}.^fConducted at –10 °C.^gMixture of two major isomer, D₂–C₈₄ (IV) and D_{2d}–C₈₄ (II).

first one is chemically reversible and electrochemically quasireversible. It occurs at +0.81 V, making C₇₆ about 450 mV easier to oxidize than C₆₀. The second oxidation in TCE occurs at +1.30 V, but it is chemically irreversible (see Table 9). Others have reported chemically irreversible first and second oxidations in various solvents such as PhMe/MeCN mixtures, DCM, and THF under different conditions of temperature and/or supporting electrolyte [50, 59].

6.1.3.2 Reduction and Oxidation of C₇₈

There are five possible constitutional isomers of C₇₈ whose structures possess closed-shell electronic configurations [15, 62]. The two most abundant of these, C_{2v}–C₇₈ and D₃–C₇₈ have been studied extensively by CV and OSWV. In the first study carried out at –15 °C in PhMe/MeCN, the C_{2v} isomer displays six one-electron reductions, with the sixth one being irreversible. All waves are

evenly spaced with an average potential separation of 325 ± 59 mV, except for a larger separation of 710 mV observed between the second and third redox couples (see Table 6). One irreversible oxidation step is also observed under the above conditions (see Table 9) [50].

An isomeric mixture of the C_{2v} and D_3 isomers in TCE displays only two one-electron reduction waves by OSWV. The waves correspond to the 0/−1 and −1/−2 redox processes and overlap at −0.77 and −1.08 V vs. Fc/Fc^+ [60]. The anodic scan, however, shows four oxidation waves, consisting of two pairs of consecutive small and large waves. Each pair has been assigned, on the basis of their current: intensity ratio, to the two isomers in the mixture, which exist in a 1:5 ratio of $C_{2v}:D_3$ – C_{78} (see Table 9) [62]. The assignment of D_3 – C_{78} as the easier to oxidize isomer is in agreement with the previously calculated HOMO energies for the two isomers [63].

In another study involving C_{78} , a pure sample of the C_{2v} isomer was prepared using the cyclopropanation-retrocyclopropanation reaction sequence [44, 64]. This reaction scheme consists of a controlled potential electrolytic (CPE) reduction of a previously synthesized cyclopropane derivative of the isomer, leading to removal of the cyclopropane moiety(s), (see Sect. 6.1.5). A pure sample of the D_3 isomer was obtained by high performance liquid chromatography (HPLC) as previously described [49, 65]. The redox behavior of both isomers, in DCM at room temperature, reveals that their cathodic electrochemistry is indeed very similar (although not identical) in this solvent [44]. The first two reductions are easier for the D_3 isomer by 60 and 100 mV, respectively, while the third and fourth reductions are nearly identical for the two

isomers. Partial confirmation of the anodic results in TCE was also obtained. A reversible one-electron oxidation is observed at +0.74 V for the D_3 isomer in DCM (see Table 9). However, neither the second oxidation for the D_3 isomer nor the two oxidations for the C_{2v} isomer were observed because of limitations in the solvent potential window.

6.1.3.3 Reduction and Oxidation of C_{82}

The C_{82} fullerene is considered the prototypical cage to form endohedral metallofullerenes. In fact, a molecule consisting of a Lanthanum atom inside an 82-carbon cage, denoted $La@C_{82}$, was detected and produced in macroscopic quantities before the pristine cage was isolated [5, 66]. Other metals (M) such as Ca, Sc, Y, Ga, and several lanthanides have been trapped inside C_{82} as well, and in some cases more than one isomeric structure of the particular $M@C_{82}$ has been identified [21, 58, 67–69]. Furthermore, a few bi- and trimetallic endohedrals, $M_2@C_{82}$ and $M_3@C_{82}$, have also been prepared [58, 70]. Some of these compounds, along with the pristine C_{82} cage have been studied electrochemically [21, 58, 67–74]. Incorporation of a metal atom inside C_{82} increases the EA of the carbon cage [17], and consequently, reduction potentials are much more positive for endohedral C_{82} compounds than for the empty fullerene by an average of 275 mV (see Table 7). In addition, the first reversible oxidation of $M@C_{82}$ occurs at potentials very close to that of the oxidation of ferrocene, making these compounds moderate electron donors (see Table 9) [70].

Of notable importance here is the fact that although there are nine possible stable isomers of C_{82} , ^{13}C NMR measurements combined with theoretical calculations have shown that only one isomer with

C_2 symmetry, the $C_{2(a)}$ isomer, is the most stable and the one produced as the empty cage [75, 76]. However, it has been shown that formation of endohedral metallofullerenes involves electron transfer from the HOMO of the incorporated metal to the LUMO of the cage [70]. For example, in $La@C_{82}$, the La atom is in the +3 state, while the cage is in the -3 state, which gives a formal charge state of $La^{+3}@C_{82}^{-3}$ [70]. This transfer of electrons changes the electronic structure and consequently the relative stability of the carbon cage [77]. Thus, the most favorable cage for endohedral formation is not the $C_{2(a)}$ isomer of C_{82} because negative charges on the C_{82} spheroid change dramatically the order of relative stability of the different isomers [77]. Recently, two isomers of $La@C_{82}$ have been extracted and isolated, $La@C_{82}\text{-A}$ and $La@C_{82}\text{-B}$, and their symmetry has been determined by ^{13}C NMR as C_{2v} and C_s , respectively [68]. These results confirm prior calculations of relative energies of the C_{82}^{3-} and C_{82}^{2-} , which clearly demonstrate that the $C_{2(a)}$ isomer is significantly destabilized upon reduction, while the C_{2v} and C_s isomers become much more stable upon reduction to the di- and trianion [77]. Similar conclusions have been reached for isomers of $Pr@C_{82}$, $Sc@C_{82}$, and $Y@C_{82}$

[67, 74, 77]. Thus, a direct comparison of redox potentials between empty C_{82} (C_2 symmetry) and endohedral C_{82} (C_{2v} and C_s symmetries) is unfair considering cage symmetry differences. At the present time, and probably due to their instability as empty cages, the C_{2v} and C_s isomers of C_{82} have not been isolated; thus, their redox behavior is unknown.

6.1.3.4 Reduction and Oxidation of C_{84}

C_{84} can be any of 24 stable isomers that satisfy the “isolated pentagon rule” [4, 6] and possess closed-shell electronic configurations [15]. Before successful HPLC separation and characterization of major and some minor isomers was achieved [53, 55, 56], electrochemical studies of C_{84} involved a mixture of its two major isomers, $D_2(IV)$ and $D_{2d}(II)$, which at the time could only be isolated as a 2:1 mixture [50, 51, 60]. In solvents such as pyridine, PhCN, and DMF/PhMe, the mixture displayed multiple redox waves, making assignment difficult. In the first OSWV study of the separated isomers, $D_2\text{-}C_{84}(IV)$ displayed four one-electron evenly spaced reductions in pyridine (see Table 8 and Fig. 5) [53]. However, the reduction potentials of the isomer reported as $D_{2d}(II)$ in that same study are now believed to correspond to one of the minor isomers of C_{84} , the $C_2(IV)$

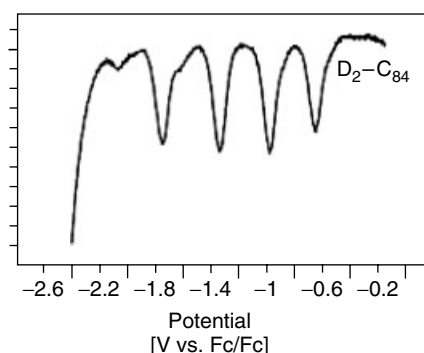


Fig. 5 Square-wave voltammograms for $D_2\text{-}C_{84}$ with sequential, approximately evenly spaced reductions. Reprinted with permission from Ref. 58. Copyright © 2000 Elsevier.

isomer [54, 78], and it is reported as such in Table 8.

In a later study, the cyclopropanation-retro-cyclopropanation reaction sequence (Bingel-retro-Bingel) mentioned earlier was used to isolate the two major constitutional isomers plus a minor isomer of C_{84} [54]. The redox properties of these isomers were investigated in pyridine by OSWV. Four reduction peaks were observed for the $D_2(IV)$ isomer during the cathodic scan and five for the $D_{2d}(II)$. Interestingly, values for the peak reduction potentials of these major isomers were similar, and successive reductions were evenly separated by about 360 mV. The fourth and fifth waves of the $D_{2d}(IV)$ isomer were, however, separated by 810 mV, and no fifth wave was observed for the $D_2(II)$ isomer within the solvent potential window. These results indicate that the LUMOs of both isomers are nearly doubly degenerate, but the LUMO + 1 is much higher in energy in both cases. Two important features are noteworthy for the third (minor) isomer obtained in that study, which is now presumed to be the $C_2-C_{84}(IV)$ based on recent results [78]. First, a large gap of 730 mV is observed between the second and third reduction waves indicating that the LUMO is nondegenerate. In other solvents, this gap is as large as 810 mV (see Table 8). Second, at potentials ranging from -0.28 to -0.50 V depending on the solvent, this isomer is the easiest to reduce of all members of the fullerene family, making it an excellent candidate for the preparation of charge-transfer complexes [79].

Other minor isomers of C_{84} have also been successfully isolated, and their redox behavior studied in different solvent [78]. These results are also presented in Tables 8 and 9.

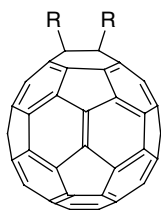
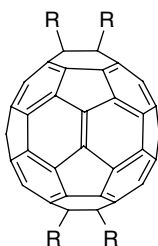
The best solvent to obtain reversible oxidation waves of fullerenes has been, undoubtedly, TCE [60, 78]. One reversible oxidation has been observed for all isomers of C_{84} studied so far. Oxidations are irreversible in pyridine and in PhCN [53, 54, 78]. Oxidation potentials along with HOMO–LUMO gaps in solution for all the higher fullerenes are presented in Table 9. Note that the higher fullerenes have a smaller experimental HOMO–LUMO gap than C_{60} and C_{70} , and these experimental values correlate well with theoretical predictions [60, 78].

6.1.4

Electrochemistry of C_{60} Derivatives

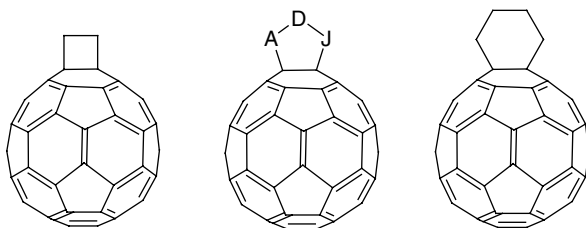
The covalent chemistry of fullerenes has developed very rapidly in the past decade in an effort to modify fullerene properties for a number of applications such as photovoltaic cells, infrared detectors, optical limiting devices, chemical gas sensors, three-dimensional electroactive polymers, and molecular wires [8, 25, 26, 80–82]. Systematic studies of the redox properties of C_{60} derivatives have played a crucial role in the characterization of their unique electronic properties, which lie at the center of these potential applications. Furthermore, electrochemical techniques have been used to synthesize and separate new fullerene derivatives and their isomers as well as to prepare fullerene containing thin films and polymers. In this section, to facilitate discussion of their redox properties, C_{60} derivatives have been classified in three groups on the basis of the type of attachment of the addend to the fullerene. In group one, the addends are attached via single bonds to the C_{60} surface as shown in Fig. 6(a) and are referred to as *singly bonded functionalized derivatives*. The group includes

Singly bonded functionalized derivatives

R = H, Alkyl group^a, F^bR = alkyl group^{a,c}^aAlkyl groups may be at 1,2- or a 1,4-position^bFluorofullerenes are actually multifluorinated^cThe second set may be at other positions within the fullerene

(a)

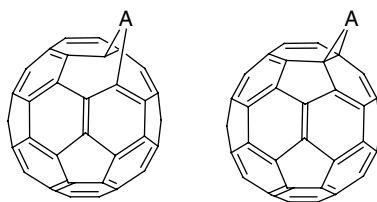
Cycloaddition products



A, D, J = C, N, O, Si, or R R = any functional group

(b)

Cyclopropanated derivatives

A = C-R₂, N-R, O, transition metal-R₂
R = H or any functional group

(c)

Fig. 6 Classification of C₆₀ derivatives. Reprinted with permission from Ref. 83. Copyright © 2000 John Wiley & Sons, Inc.

the hydrofullerenes, the alkylfullerenes, and the fluorofullerenes among others. Group two, referred to as *cycloaddition products*, includes derivatives for which

a cycloaddition reaction results in the formation of four-, five-, or six-membered rings. The ring may be heterocyclic (see Fig. 6b). The third group contains

derivatives in which a cyclopropane ring serves as the point of attachment to the fullerene surface. These are referred to as *cyclopropanated derivatives*, and the group includes methanofullerenes, fulleroids, iminofullerenes, fullerene epoxides, and transition metal derivatives (see Fig. 6c).

6.1.4.1 Singly bonded Functionalized Derivatives of C₆₀

6.1.4.1.1 Hydrofullerenes Only two hydrogenated derivatives of C₆₀ have been characterized electrochemically: the dihydrofullerene, C₆₀H₂, and a multihydrogenated derivative, C₆₀H₃₆. Reduction of dihydrofullerene (C₆₀H₂) is generally characterized by potentials that are 70–140 mV more negative than the corresponding ones for C₆₀ [84–86]. At room temperature and fast scan rates (2 V s^{−1}), up to four reversible one-electron reductions are

observed in PhMe/MeCN (see Table 10). However, at slower scan rates, decomposition results in the formation of the parent C₆₀ and the release of H₂. When reduction is carried out at −50 °C, two one-electron, reversible reductions are observed in PhMe/DMF, which correspond to C₆₀H₂[−] and C₆₀H₂^{2−}. Further reduction to the tri- and tetra-anions results once again in decomposition with formation of C₆₀^{3−} and C₆₀^{4−}.

Two chemically irreversible, multielectron oxidation steps are observed in PhCN at (peak potential) +1.13 and +1.35 V vs. Fc/Fc⁺ for C₆₀H₂. Irreversibility persists even at scan rates up to 8 V s^{−1}. The first oxidation is consistent with the loss of two protons and two electrons from C₆₀H₂ to form C₆₀. The second oxidation has been attributed to the formation of C₆₀⁺, since the peak potential for that step is in good agreement with other reported

Tab. 10 Half-wave redox potentials (in V vs. Fc/Fc⁺) of hydrofullerene derivatives using various solvents supporting electrolytes and temperatures

	Solvent ^a	Supporting electrolyte	Temperature [°C]	E ₁ ^{ox}	E ₁ ^{red}	E ₂ ^{red}	E ₃ ^{red}	E ₄ ^{red}	References
C ₆₀	PhMe/DMF	TBAClO ₄	−50		−0.89	−1.34	−1.90	−2.40	85
C ₆₀ H ₂	PhMe/DMF	TBAClO ₄	−50		−1.02	−1.46	−2.07 ^b	−2.59 ^b	85
	PhCN/MeCN ^{c,d}	TBAPF ₆	RT		−1.05	−1.44	−1.99	−2.36	84
	PhCN ^{c,d}	TBAPF ₆	RT	+1.13 ^{e,f}	−1.04	−1.43	−2.01		84
	DCM ^{c,d}	TBAPF ₆	RT		−1.11	−1.57	−2.18		84
C ₆₀	PhMe/DMSO	TBAPF ₆	+2		−1.00	−1.46	−2.01		86
C ₆₀ H ₂	PhMe/DMSO	TBAPF ₆	+2		−1.14	−1.57	−2.18		86
C ₆₀ H ₃₆	THF	TBAPF ₆	+14		−3.24				87
			−38		−3.18				87
	DCM	TBAPF ₆	−47	+1.22 ^{e,f}					87
	MeCN	TBAPF ₆	−28	+1.25 ^{e,f}					87

^aSee Table 2 for solvent abbreviations. DMSO = dimethylsulfoxide.

^bProduct decomposes to the corresponding C₆₀ anion.

^cScan rate > 1.0 V s^{−1}.

^dCompare potentials to those of C₆₀ in this solvent reported in Table 2, Ref. 32.

^eIrreversible.

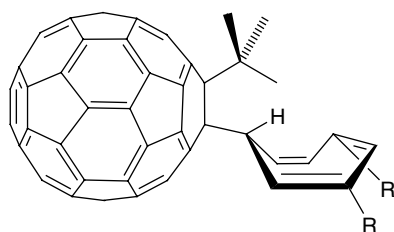
^fPeak potential.

values under similar conditions (see also Table 4) [84].

The highly hydrogenated derivative, $C_{60}H_{36}$ displays only one reversible reduction in THF, which appears to involve two electrons [87]. Reductions are observed at -3.24 and -3.18 V vs. Fc/Fc^+ when the voltammetry is conducted at $+14$ and -38 °C respectively. These highly negative potentials approach the value for the reduction of benzene (see Table 10), and support the notion that as fullerene double bonds become saturated, reduction becomes more difficult. No oxidation was obtained in THF, but the compound oxidizes irreversibly in DCM and MeCN at $+1.22$ and $+1.25$ V vs. Fc/Fc^+ at -47 and -28 °C respectively.

6.1.4.1.2 Alkylfullerenes The original alkylfullerenes prepared by Kadish and coworkers have the general formula $C_{60}R_2$ (dialkylfullerenes) (see Fig. 7) and $C_{60}R_4$ (tetraalkylfullerenes) and were studied by CV or DPV. $C_{60}R_2$ exist as either 1,2 or 1,4 isomers, while many more isomers exist for $C_{60}R_4$. In most cases, dialkylfullerenes exhibit three reversible reduction waves that are 90–150 mV more negative than the corresponding ones for pure C_{60} , and no significant effect in the reduction potential is observed by changing the alkyl group (see Table 11) [88–93]. The first

reduction potentials of 1,2 and 1,4 isomers are the same within experimental error, but the second and third reductions differ by 50 mV, with the 1,2 isomer being easier to reduce [90]. The tetraalkylfullerenes are ca. 140 mV more difficult to reduce than the dialkyl derivatives and ca. 260 mV more difficult to reduce than the parent C_{60} . A pentaphenylfullerene has also been studied by CV, and its first reduction occurs at a potential that is ca. 500 mV more negative than that of C_{60} in the same solvent, supporting electrolyte and temperature [94]. Apparently, as the fullerene cage becomes increasingly functionalized, reductions become more difficult, since each sequential loss of a double bond induces a cathodic shift [91]. Evidence for the latter has been obtained in studies involving mono- through hexakis-methano adducts of C_{60} [95]. Interestingly, decomposition of alkylfullerenes to the parent C_{60} upon electrochemical reduction has not been reported, indicating that their anions are more stable than those of hydrofullerenes. In fact, a pK_a of 5.7 has been determined for $t\text{-Bu}C_{60}H$, a value that makes this alkylfullerene one of the strongest acids made up of only carbon and hydrogen, and consequently its conjugate anion, $t\text{-Bu}C_{60}^-$, one of the most stable hydrocarbon anions [92, 93].



(3a): R = H
(3b): R = *tert*-Bu
(3c): R = cyclopropyl

Fig. 7 Selected alkylfullerenes (3a–c).

Tab. 11 Half-wave redox potentials (in V vs. Fc/Fc⁺) of alkylfullerene derivatives using various solvents supporting electrolytes and temperatures

	Solvent ^a	Supporting electrolyte	Temperature [°C]	E ₁ ^{ox}	E ₁ ^{red}	E ₂ ^{red}	E ₃ ^{red}	E ₄ ^{red}	References
C ₆₀ (CH ₃) ₂	PhCN ^b	TBAClO ₄	25		−1.03 ^c	−1.45 ^c	−2.00 ^c		88
1,2-C ₆₀ (PhCH ₂) ₂	PhCN ^b	TBAClO ₄	RT		−0.96 ^c	−1.37 ^c	−1.89 ^c		89, 90
1,4-C ₆₀ (PhCH ₂) ₂	PhCN ^b	TBAClO ₄	RT		−0.97 ^c	−1.42 ^c	−1.94 ^c		89, 90
C ₆₀ (C ₂ H ₅) ₂	PhCN ^b	TBAClO ₄	RT		−1.00 ^c	−1.43 ^c			91
C ₆₀ (C ₄ H ₉) ₂	PhCN ^b	TBAClO ₄	RT		−0.99 ^c	−1.39 ^c			91
C ₆₀ (CH ₃) ₄	PhCN ^b	TBAClO ₄	n/r ^d		−1.17 ^c	−1.57 ^c			91
C ₆₀ (n-C ₄ H ₉) ₄	PhCN ^b	TBAClO ₄	n/r ^d		−1.14 ^c	−1.55 ^c			91
<i>t</i> -BuC ₆₀ H	THF ^b	n/r ^d	n/r ^d		−1.01	−1.57	−2.18		92
C ₆₀	ODCB	TBAPF ₆	n/r ^d	+1.37 ^e	−1.09	−1.48	−1.93	−2.42	93
<i>t</i> -BuC ₆₀ H	ODCB	TBAPF ₆	n/r ^d	+1.43 ^e	−1.22	−1.59	−2.13		93
(3a) ^f	ODCB	TBAPF ₆	n/r ^d	+1.36	−1.18	−1.56	−2.06		93
(3b) ^f	ODCB	TBAPF ₆	n/r ^d	+1.41	−1.19	−1.59	−2.09		93
(3c) ^f	ODCB	TBAPF ₆	n/r ^d	+1.38	−1.20	−1.58	−2.10		93
C ₆₀ Ph ₅ H	THF ^b	TBAClO ₄	−78		−1.45	−2.10			94

^aSee Table 2 for solvent abbreviations.^bCompare potentials to those of C₆₀ in this solvent reported on Table 2, Ref. 32.^cE_{1/2} recalculated from the original data using the reported value for Fc/Fc⁺ in 0.1 M TBAClO₄/PhCN solution of −0.45 V vs. SCE, which appears in Ref. 37.^dNot reported.^eIrreversible.^fSee Fig. 7.

6.1.4.1.3 Fluorofullerenes Electron affinities of polyfluorinated C₆₀ derivatives such as C₆₀F₄₈ and C₆₀F₄₆ are almost 1.5 eV higher than those of the parent fullerene [96]. As expected, these compounds undergo their first reduction at potentials considerably more positive than those of pure C₆₀ under similar conditions (see Table 12) [97–99]. For example, C₆₀F₄₈ undergoes a first, reversible, one-electron reduction at +0.79 V (vs. SCE). Its second reduction is irreversible, and formation of C₆₀F₄₈^{2−} is followed by a chemical process involving the loss of F[−] and formation of C₆₀F₄₇[−]. The latter species undergoes a reversible reduction to form C₆₀F₄₇^{2−} at +0.37 V (vs. SCE). Other polyfluorinated derivatives such as C₆₀F₁₈ and C₆₀H₃₆ undergo similar

irreversible reduction processes under the same conditions, suggesting that the fluorine atoms are involved in the mechanism of the chemical reactions coupled to the electron transfer process [97, 100]. Some of these polyfluorinated compounds have been used as cathode materials on solid-state lithium cells [101].

6.1.4.1.4 Other Singly bonded Derivatives

A few other derivatives of C₆₀ bearing functional groups attached to the sphere via single bonds deserve mention here.

One of these is C₆₀Ph₅Cl, which was reported as the first derivative of C₆₀ to undergo two reversible one-electron oxidations, labeled O₁ and O₂ in Fig. 8(a) (see Table 12) [102]. Another striking feature of this compound involves its

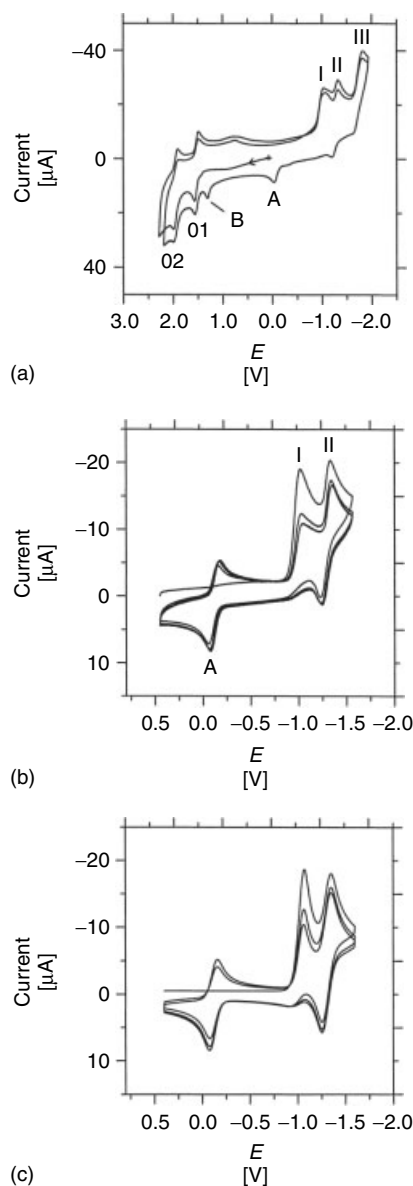


Fig. 8 (a) Multiple-scan CV curve of a 0.5 mM $\text{C}_{60}\text{Ph}_5\text{Cl}$, 0.05 M $\text{Bu}_4\text{NPF}_6 \cdot \text{CH}_2\text{Cl}_2$ solution. Scan rate = 0.5 V s^{-1} ; $T = -50^\circ\text{C}$; the working electrode is platinum. The initial scan starts anodically and the successive scans are performed without the renewal of the diffusion layer. (b) A limited region of scan (a) that excludes the B, O₁, O₂, and III processes. (c) Digitally simulated CV curve of scan (b) according to the mechanism outlined in the text. Reprinted with permission from Ref. 102. Copyright © 2000 American Chemical Society.

run, two additional irreversible oxidation peaks, labeled A and B in Fig. 8(a), are detected. However, reversing the scan immediately after A to exclude B, O₁, and O₂, makes A reversible (see Fig. 8b). Backed by digital simulations (Fig. 8c) and by analogy with the behavior of $\text{C}_{60}\text{Ph}_5\text{H}$ [94], the authors suggest that the compound breaks into a Cl^- and a $\text{C}_{60}\text{Ph}_5^-$ anion upon reduction at this potential. The individual fragments then undergo separate irreversible reoxidation processes and appear to reassemble into the original molecule as shown in Sch. 1.

Komatsu and coworkers prepared 1-octynyl- C_{60} , (4), reduced it chemically using *t*-BuOK, and observed the redox properties of the resulting anion, (4⁻), by CV (see Table 12) [103]. A one-electron irreversible oxidation is observed at -0.39 V (vs. Fc/Fc^+), and the corresponding reduction is shifted to -1.20 V . The authors have proposed that this large negative shift of the cathodic peak ($\Delta_{\text{pp}} = 0.81 \text{ V}$) is due to a chemical process involving the formation of a dimer of the corresponding radical as shown in Sch. 2.

The ferrocene–fullerene dyad, (5) (see Fig. 9), represents the first example of a fullerene-based dyad where the donor

behavior upon reductive/oxidative cycling. In the cathodic scan, three reductions are observed, labeled I, II, and III, but notably the first one is an irreversible, two-electron reduction, observed at -1.05 (vs. SCE). If a successive anodic scan is

Tab. 12 Half-wave redox potentials (in V vs. F_c/F_c^{+}) of fluorofullerene and other special singly bonded derivatives of C_{60} using various solvents, supporting electrolytes and temperatures

	Solvent ^a	Supporting electrolyte	Temperature [°C]	E_1^{ox}	E_2^{ox}	E_1^{red}	E_2^{red}	E_3^{red}	References
C_{60}	DCM	TBAPF ₆	25			−0.88 ^b	−1.32 ^b		97
$C_{60}F_{48}$	DCM	TBAPF ₆	25			+0.53 ^b	+0.18 ^{b,c}		97, 98
$C_{60}F_{47}$	DCM	TBAPF ₆	25				+0.37 ^{c,d}	−0.12 ^{d,e}	98
$C_{60}F_{46}$	DCM	TBAPF ₆	25			+0.51 ^b	+0.01 ^{b,c}		97, 99
$C_{60}F_{36}$	DCM	TBAPF ₆	25			−0.05 ^b	−0.48 ^b		97
$C_{60}Ph_5Cl$	DCM	TBAPF ₆	−50	+1.52 ^d	+1.93 ^d	−1.05 ^{c,d}	−1.30 ^d	−1.80 ^d	102
Hex−C≡C− $C_{60}^{−}$ K ⁺	THF	TBAPF ₄	n/r ^f	−0.39(−1.20) ^g		−1.55	−2.08	−2.75	103
Hex−C≡C− $C_{60}^{−}$ Li ⁺	DMSO	TBAPF ₄	n/r ^f	−0.32(−0.94) ^g		−1.21	−1.72	−2.33	103
(5)	ODCB	TBAPF ₆	RT	+0.73 ^h	+1.46 ⁱ	−0.63	−1.00	−1.48	104
(6)	ODCB	TBAPF ₆	RT	+0.54					104
(7)	ODCB	TBAPF ₆	RT		+1.41	−0.58	−0.95	−1.43	104

^a See Table 2 for solvent abbreviations.

^b Vs. Ag/AgCl.

^c Irreversible.

^d Vs. SCE.

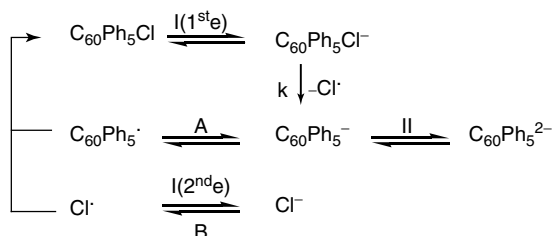
^e $C_{60}F_{48}^{2-}$ loses F^{-} to form $C_{60}F_{47}^{-}$, which can be reduced to $C_{60}F_{47}^{2-}$.

^f Not reported.

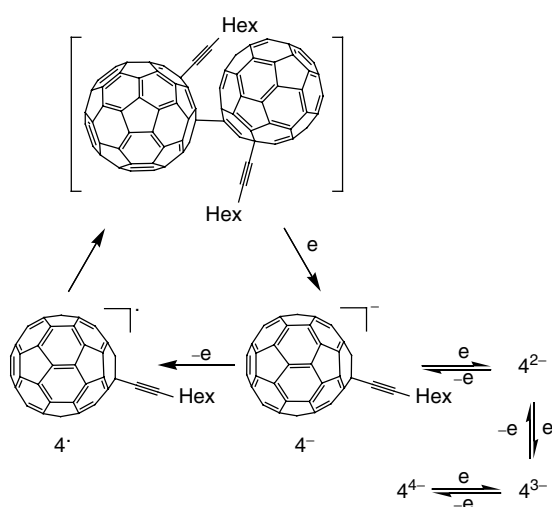
^g Peak potentials, E_{pa} (E_{pc}). Potential in parenthesis is the corresponding reduction peak.

^h Ferrocene-centered oxidation.

ⁱ N-centered oxidation.



Scheme 1 Mechanistic details for the CV behavior of $C_{60}Ph_5Cl$. Reprinted with permission from Ref. 102. Copyright © 2000 American Chemical Society.



Scheme 2 Electrochemistry of 1-octynyl- C_{60} carbanion (**4**), including the formation of a dimer upon a one-electron oxidation. Reprinted with permission from Ref. 103. Copyright © 1996 American Chemical Society.

(ferrocene) and acceptor (fullerene) groups are connected via a single bond [104]. The main goal behind the concept of fullerene-based donor-acceptor dyads is to develop systems with unique electronic and photophysical properties. To this end, effective coupling between two electroactive groups must be established in order to promote intramolecular energy transfer or electron transfer, and/or to generate long-lived charge separated states. The CV of dyad (**5**) reveals two oxidation processes. The first one, occurring at +0.73 V (vs. Fc/Fc^+), is a reversible, ferrocene-based, one-electron process, while the second one, occurring at +1.47 V is irreversible and centered on the azafullerenyl nitrogen. The first oxidation is significantly positively shifted

by 183 mV with respect to that of the parent ferrocene, (**6**). This indicates the existence of intramolecular charge transfer, ICT, from the ferrocene donor to the azafullerenyl acceptor. In addition, four successive, reversible, one-electron reductions are observed (see Table 12) with relatively constant potential separation. The four reductions are fullerene-based and are shifted negatively by ca. 50 to 57 mV with respect to those of the parent analog (**7**), again indicating the presence of intramolecular electronic interactions [104].

6.1.4.2 Cycloaddition Products

A wide variety of fullerene adducts have been synthesized by covalent addition

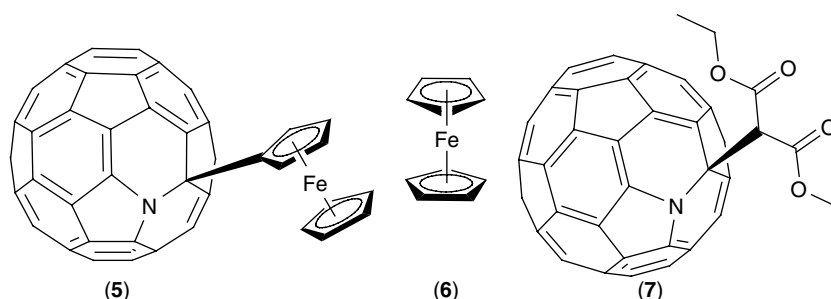


Fig. 9 Ferrocenyl hydroazafullerene (5), a singly bonded ferrocene–fullerene dyad, and reference compounds (6) and (7).

across fullerene double bonds [25]. Cycloadditions and specially, Diels–Alder [8] and 1,3-dipolar [82] cycloadditions are the most commonly employed methods for the preparation of [60] fullerene derivatives bearing a five-, or a six-membered ring connection to the C_{60} surface.

In general, the redox properties of these derivatives also depend upon the number of addends linked to the C_{60} cage, and with few exceptions they reduce at potentials within the range observed for all other derivatives of C_{60} [105].

One of the first studies of the electrochemical properties of cycloaddition

products reported the electron-withdrawing effect of silicon and oxygen on the reduction potential of several fullerene derivatives (see Fig. 10 and Table 13) [106]. Although in all cases the presence of substituents shifts the first reduction to more negative potentials, the effect follows the order $Si > C > O$, indicating that, as expected, oxygen has the strongest electron-withdrawing effect. This study inspired many researchers to pursue the preparation of C_{60} derivatives whose reduction potential could be tuned by the use of different electron-withdrawing substituents (see the following) [107–111].

Tab. 13 Half-wave reduction potentials at room temperature (in V vs. Fc/Fc^+) of representative examples of cycloaddition derivatives of C_{60} with oxygen-, carbon- and silicon-containing groups

	<i>Solvent</i> ^{a,b}	<i>Supporting electrolyte</i>	E_1	E_2	E_3	<i>References</i>
C_{60}	ODCB	TBAPF ₆	−1.13	−1.50	−1.95	106
(8)	ODCB	TBAPF ₆	−1.23	−1.58	−2.11	106
(9)	ODCB	TBAPF ₆	−1.23	−1.60	−2.14	106
(10)	ODCB	TBAPF ₆	−1.21	−1.57	−2.11	106
(11)	ODCB	TBAPF ₆	−1.14	−1.52	−2.02	106
(12)	ODCB	TBAPF ₆	−1.13	−1.50	−1.99	106
(13)	ODCB	TBAPF ₆	−1.28	−1.66	−2.16	106
(14)	ODCB	TBAPF ₆	−1.29	−1.67	−2.18	106

^aSee Table 2 for solvents abbreviations.

^bScan rate = 200 mV s^{−1}.

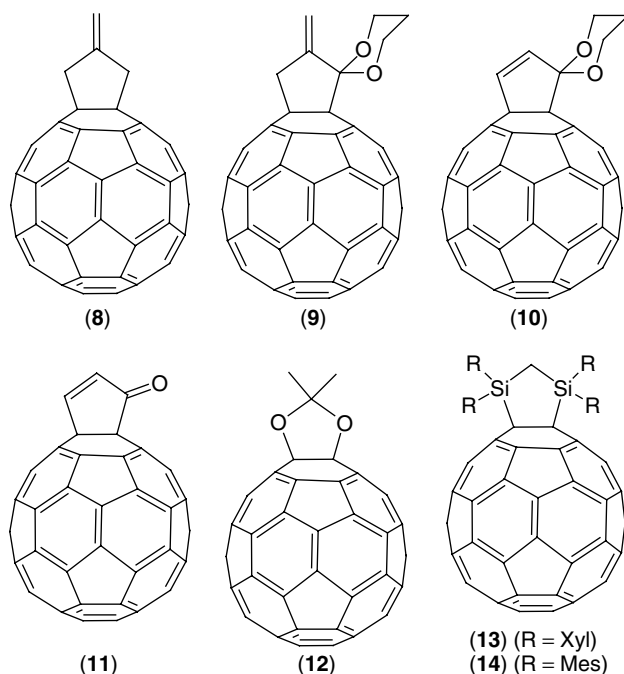


Fig. 10 Some representative examples of cycloaddition derivatives of C₆₀ bearing oxygen-, carbon-, and silicon-containing groups.

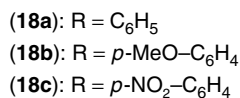
One other remarkable property of fullerenes and their derivatives is that they are very easily excited from the ground state to the singlet excited state by low energy light in the UV and visible regions. This singlet state is short lived (a few nanoseconds) as it rapidly converts to the much longer-lived triplet state (tens to hundreds of microseconds). The combination of this property with the high electron affinity of fullerenes results in materials capable of photoinduced electron transfer [110]. In fact, upon irradiation, some fullerene derivatives efficiently give rise to a rapid charge separation followed by a slow charge recombination in the dark [79]. Consequently, the search for systems with a more efficient and long-lived charge separation, and thus suitable for use in photovoltaic

devices, has stimulated the investigation of the redox behavior of cycloaddition products of C₆₀ containing either electron-donor or electron-withdrawing units. In the following sections, the electrochemical characteristics of these two types of cycloadducts will be described in detail.

6.1.4.2.1 C₆₀ Electron-acceptor Cyclo-

adducts A few examples of recently prepared cycloaddition products containing electron-withdrawing groups are shown in Fig. 11. Their corresponding redox potentials are listed in Table 14.

In compounds (15), (16), and (17), attachment of cyano groups to the C₆₀ substituent has been carried out in an attempt to increase the electron affinity of the fullerene sphere. Indeed, the first



potential of (15) is positively by 170 mV with respect to that of C₆₀ [112]. (16) and (17) in the electroactive tetracyano-*p*-methane (TCNQ) and dicyano-*p*-methane (DCNQI) substituents, respectively. Consequently, the CVs of

these derivatives in PhMe/MeCN show four reduction waves, two of which are addend-based and the other two are fullerene-based. The first reduction of **(16)** appears as a two-electron, reversible wave at -0.38 V, and the first and third reductions of **(17)** appear as one-electron,

Tab. 14 Half-wave reduction potentials (in V vs. SCE, T = 25 °C) of some cycloaddition derivatives of C₆₀

	<i>Solvent</i> ^a	<i>Supporting electrolyte</i>	<i>E</i> ₁	<i>E</i> ₂	<i>E</i> ₃	<i>E</i> ₄	<i>E</i> ₅	<i>E</i> ₆	<i>References</i>
(15)	CH ₂ Cl ₂	TBAPF ₆	−0.40	−0.97	−1.42	–	–	–	112
(16)	PhMe/MeCN	TBAClO ₄	−0.38 ^b	−0.65	−1.06	−1.67	–	–	113
(17)	PhMe/MeCN	TBAClO ₄	−0.32 ^b	−0.64	−0.98 ^b	−1.07	–	–	113
C ₆₀	ODCB/MeCN	TBAClO ₄	−0.59	−0.99	−1.48	−2.05	–	–	115
(18a)	ODCB/MeCN	TBAClO ₄	−0.55	−0.97	−1.46	−2.22	–	–	115
(18b)	ODCB/MeCN	TBAClO ₄	−0.57	−0.99	−1.44	−2.23	–	–	115
(18c)	ODCB/MeCN	TBAClO ₄	−0.51	−0.91	−1.19	−2.21	–	–	115
(19)	ODCB/MeCN	TBAClO ₄	−0.68	−1.09	−1.64	−2.22	–	–	115
C ₆₀	THF	TBAPF ₆	−0.35	−0.94	−1.50	−1.99	−2.50	–	116
(20)	THF	TBAPF ₆	−0.29	−0.79	−1.34	−1.84	−2.66 ^c	−3.15 ^c	116
(21)-trans-1	THF	TBAPF ₆	−0.26	−0.67	−1.36	−1.75	−2.42 ^c	–	116
(21)-trans-2	THF	TBAPF ₆	−0.27	−0.74	−1.53	−1.93	−2.60 ^c	–	116
(21)-cis-2	THF	TBAPF ₆	−0.33	−0.84	−1.52	−1.99	−2.67 ^c	–	116
C ₆₀	PhMe/MeCN	TBAClO ₄	−0.60	−1.00	−1.52	−2.04	–	–	113, 117
(22a)	PhMe/MeCN	TBAClO ₄	−0.51 ^b	−0.68	−1.17	−1.74	–	–	117
(22b)	PhMe/MeCN	TBAClO ₄	−0.63	−0.77 ^b	−1.11	−1.32 ^b	–	–	117
(22c)	PhMe/MeCN	TBAClO ₄	−0.21 ^b	−0.64	−1.07	−1.68	–	–	117

^aSee Table 2 for solvents abbreviations.^bAddend-based reductions.^cData obtained at −60 °C.

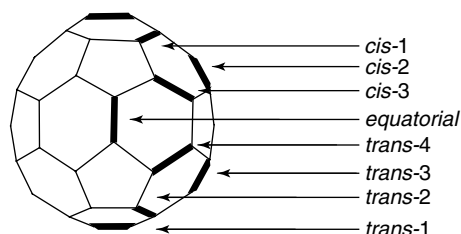
reversible waves, at −0.32 and −0.98 V respectively. These reductions are all addend-based [113]. However, the first C₆₀-based reductions of (16) and (17) occur at potentials ca. 50 mV more positive than those of pure C₆₀ (shown under E₂ in Table 14), suggesting that the cyano groups are too far removed from the sphere to induce any substantial effect on its reduction potential. Similar observations of clearly separated addend-based and C₆₀-based electrochemistry have been obtained previously for other related dyads [83, 114].

The electrochemical properties of cycloaddition derivatives of C₆₀ bearing pyrazolines such as (18a–c) (see Fig. 11) have been reported recently [115]. Their first reduction potential occurs 40–80 mV

more positive than the corresponding one for pure C₆₀, demonstrating an increase in the electron affinity of the C₆₀ chromophore (see Table 14). Interestingly, the analog compound, (19), bearing a pyrrolidino rather than a pyrazolino substituent, is 90 and 130 mV more difficult to reduce than C₆₀ and (18a), respectively, suggesting that the presence of two heteroatoms as opposed to one in the attached ring may be responsible for the observed shift in potential.

The observation of six fullerene-based reductions for a series of *N*-methylfulleropyrrolidinium iodide salts, including (20) in Fig. 11, has been described. In general, these derivatives exhibit reduction potentials that are positively shifted by up to 200 mV with

Fig. 12 Nomenclature used to describe bis-adducts.



respect to those of C_{60} (see Table 14) [109]. In a more recent study [116], the same authors reported the electrochemical properties of the corresponding bis-fulleropyrrolidinium ions (**21**), which are, in general, slightly easier to reduce than the monoadduct (**20**). The nomenclature used to describe bis-adducts of C_{60} is shown in Fig. 12. More interesting, however, is the comparison of the redox potentials of (**21**) with those of the parent C_{60} . The presence of the two positive charges in (**21**) produce a stabilizing effect of the reduced bis-adducts, particularly for the *trans*-1 and *trans*-2 isomers, where the positive charges are located on opposite hemispheres. The first and second reductions are 90 and 270 mV, respectively, more positive for the *trans*-1 isomer than for C_{60} . The optimal electrochemical behavior of these derivatives has prompted the investigation of their photoinduced ICT properties, which are currently under way [110].

Finally, cycloadducts (**22a–c**) exhibit an addend-based first reduction wave, which is very close to the first reduction potential of pristine C_{60} . Remarkably, as shown in Table 14, the choice of substituent on the *p*-benzoquinone moiety affects the redox behavior of these derivatives. By controlling the relative energy of the LUMO of the organic addend with respect to the LUMO of C_{60} , the first reduction process may be forced to occur at either the C_{60} cage or the organic addend, allowing for tunability of these electron-acceptor

systems and making them very attractive for further applications [117].

6.1.4.2.2 C_{60} -Electron Donor Cycloadducts

A strong driving force behind the synthesis of novel C_{60} -based donor–acceptor (D–A) molecules is the fact that photovoltaic devices using a composite blend of C_{60} or C_{60} derivatives as the acceptor and a donor conducting polymer derived from polyphenylene vinylene (PPV) or polythiophene demonstrated a highly efficient charge separation [118]. The performance of this type of device is sensitive to the morphology of the blend, which ideally should form a bicontinuous microphase separated network to allow bipolar charge transport. In this type of bulk heterojunction device, however, if the donor and acceptor molecules in the two phases are incompatible, uncontrolled phase separation is observed, producing a bad contact at the junction. To avoid this, an alternative approach is based on covalently connecting donor (hole conducting) and acceptor (electron conducting) moieties [119, 120].

Evidently, the existence of electronic interactions between the D and A units in the ground state can be unequivocally established on the basis of electrochemical studies. A recent report has reviewed the electrochemical properties of donor-linked fullerenes as a function of the attached chromophores including transition metal structures,

porphyrins, phthalocyanines, tetrathiafulvalenes (TTF), ferrocene, oligomers, dendrimers, supramolecular arrays, dimethylaniline (DMA), and other heterocyclic donors [121]. The results described here correspond to recent selected examples of cycloaddition C_{60} -based D–A systems (see Figs. 13 and 14), which exhibit remarkable electrochemical properties. Their redox properties are summarized in Table 15.

Several fullerene-oligophenylenevinylene (OPV) hybrids such as (23) have been prepared. Comparison of the reduction potentials of (23) with those of C_{60} shows a shift to more negative values by 100 mV. In contrast, a slightly positive shift was observed for the OPV-based oxidation of (23) by about 40 mV with respect to the corresponding model compound, (24). The shifts appear to be a consequence of a small electronic interaction between the

donating OPV moiety and the accepting C_{60} sphere. This was confirmed by photophysical investigations [122].

The use of functionalized polypyridyl-ruthenium(II) complexes with an electron-accepting fullerene core as building blocks in devices that perform light and/or redox-induced functions is an area under intense study. The presence of more than one ruthenium center provides greater flexibility in terms of redox potentials, excited state energies, and ground state absorption than a single metal center [127]. Polypyridylruthenium(II) complexes are known for their multiple reduction processes (see Fig. 15a), and dyad (27) is no exception. In fact, dyad (27) consists of a bimetallic ruthenium complex bridged to a fulleropyrrolidine moiety via a rigid androstane spacer. Consequently, the CV of (27) displays additional reduction processes associated

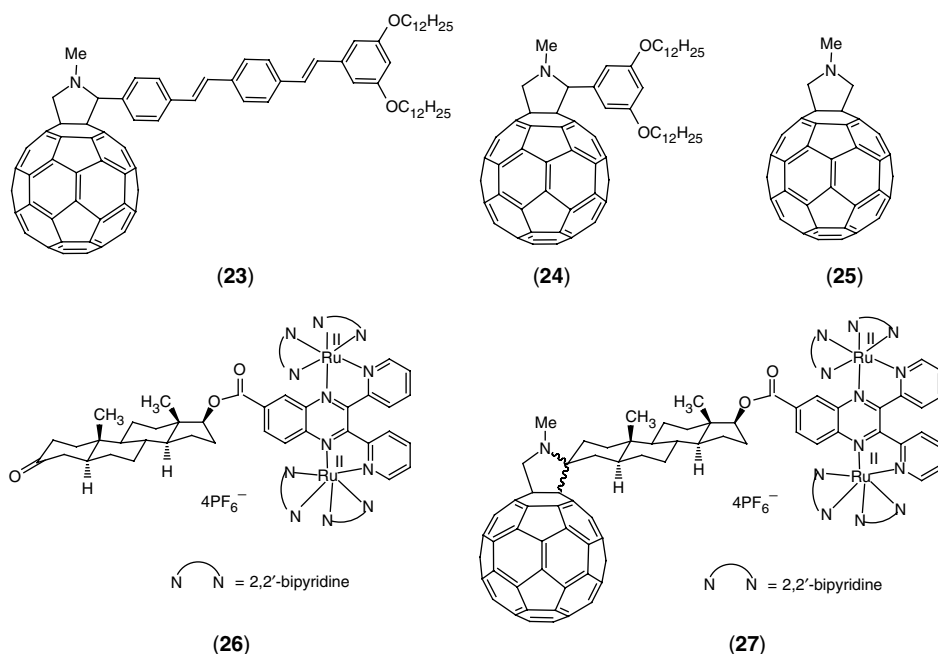


Fig. 13 Representative examples of cycloaddition derivatives of C_{60} bearing electron-donor moieties.

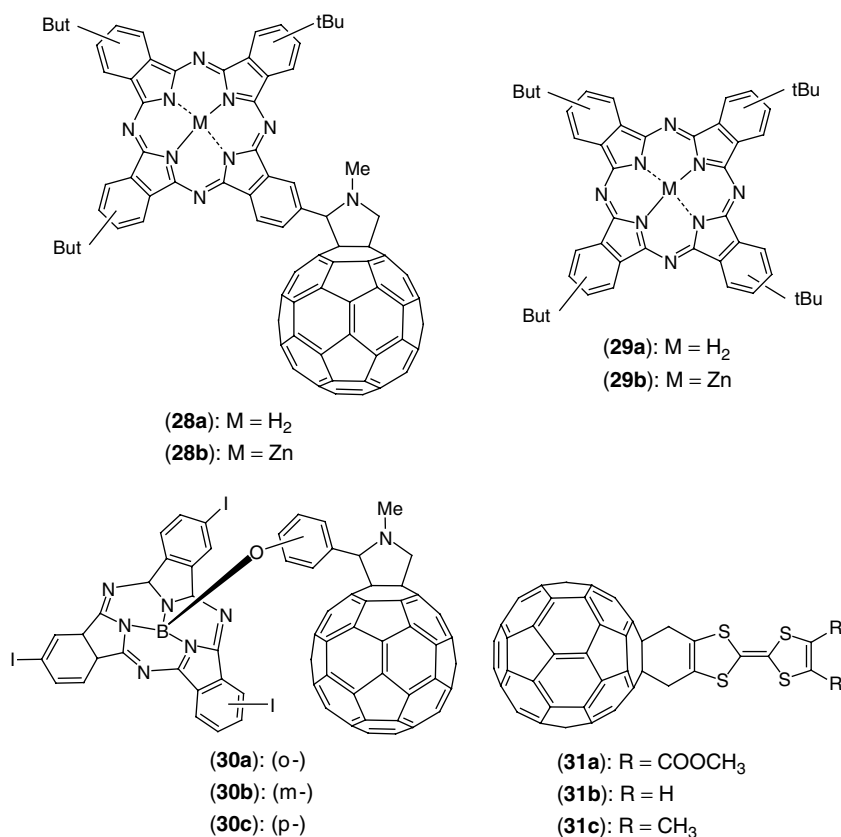


Fig. 14 More representative examples of cycloaddition derivatives of C_{60} bearing electron-donor moieties.

with the C_{60} chromophore (see Fig. 15b). To properly assign reduction potentials, model compounds (**25**) and (**26**) were prepared and electrochemically analyzed as well. It can be clearly established from the reduction potentials in Table 15 that the first, third, and fifth reduction processes are ligand centered, while the second, fourth, and sixth are fullerene-based. The absence of potential shifts with respect to the model compounds indicate that there is essentially no electronic interaction between the fullerene and the bimetallic ruthenium complex [123].

Phtalocyanine dyads (**28a,b**) and sub-phtalocyanine dyads (**30a–c**) (Fig. 14) are porphyrin analogs with unique electrochemical properties. Comparison of the redox potentials of (**28a**) and (**28b**) with those of model compounds (**25**) and (**29a**) and (**29b**) (see Table 15) indicate that the dyads retain the electronic properties of the individual units. However, all the phtalocyanine-centered processes in both dyads are positively shifted with respect to those of the model phtalocyanines, (**29a,b**). Additionally, the observed C_{60} -centered reduction potentials of both dyads are shifted to more negative values

Tab. 15 Half-wave redox potentials in V (vs. Fc/Fc⁺, SCE, or Ag/Ag⁺) of representative examples of C₆₀-based donor–acceptor systems

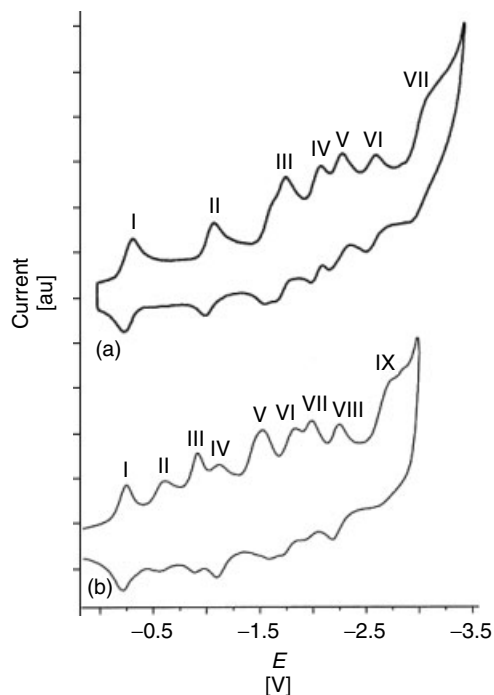
	<i>Solvent</i> ^a	<i>Supporting electrolyte</i>	<i>E</i> ₁ ^{ox}	<i>E</i> ₂ ^{ox}	<i>E</i> ₁ ^{red}	<i>E</i> ₂ ^{red}	<i>E</i> ₃ ^{red}	<i>E</i> ₄ ^{red}	<i>E</i> ₅ ^{red}	<i>References</i>
C ₆₀ ^b	ODCB	TBAPF ₆	–	–	–0.55	–0.93	–1.36	–1.82	–	122
(23) ^b	ODCB	TBAPF ₆	+1.35 ^c	–	–0.65	–1.02	–1.53	–1.95	–	122
(24)	ODCB	TBAPF ₆	+1.35	+1.55 ^c	–0.64	–1.01	–1.52	–1.97	–	122
(25) ^{d,e}	THF	TBAH	–	–	–0.47	–1.05	–1.70	–2.16	–2.93	123
(26) ^e	THF	TBAH	+1.54 ^f	+1.71 ^f	–0.23	–0.91	–1.41 ^g	–1.81	–1.97	123
									–2.26	
(27) ^e	THF	TBAH	+1.52 ^f	+1.70 ^f	–0.23 ^h	–0.49	–0.89 ^h	–1.07	–1.41 ^{g,h}	123
									–1.71 ^{g,h}	
(25) ^{b,d}	ODCB	TBAPF ₆	–	–	–0.66	–1.02	–1.53	–1.97	–	124
(28a) ^b	ODCB	TBAPF ₆	+0.85	+0.96	–0.66	–0.79 ^h	–1.02	–1.18 ^h	–1.57	124
(28b) ^b	ODCB	TBAPF ₆	+0.67	+1.32	–0.70	–1.07 ^{h,i}	–1.07	–1.22 ^h	–1.63	124
(29a) ^b	ODCB	TBAPF ₆	+0.74	+0.94	–0.86	–1.18				124
(29b) ^b	ODCB	TBAPF ₆	+0.61	+1.26	–1.08	–1.38	–1.62			124
(25) ^{d,j}	THF	TBAPF ₆	–	–	–0.91	–1.43	–2.02	–	–	125
(30a) ^j	THF	TBAPF ₆	0.82	–	–1.02	–1.39 ^h	–1.56	–	–	125
(30b) ^j	THF	TBAPF ₆	0.78	0.99	–1.00	–1.35 ^h	–1.51	–	–	125
(30c) ^j	THF	TBAPF ₆	0.85	1.04	–1.04	–1.38 ^h	–1.57	–	–	125
C ₆₀ ^j	ODCB	TBAPF ₆	–	–	–1.11	–1.52	–1.99	–2.48	–	126
(31a) ^{j,k}	ODCB	TBAPF ₆	0.13	0.65	–1.21	–1.63	–1.99	–2.57	–	126
(31b) ^j	ODCB	TBAPF ₆	–0.08	0.43	–1.17	–1.53	–2.05	–2.49	–	126
(31c) ^j	ODCB	TBAPF ₆	–0.15	0.41	–1.18	–1.55	–2.06	–2.52	–	126

^aSee Table 2 for solvents abbreviations.^bAg/AgCl as reference electrode.^cIrreversible process, peak potentials.^d*N*-methylfulleropyrrolidine.^eSCE as reference electrode.^fAcetonitrile solution.^gObtained from digital simulations.^hAddend-based reduction processes.ⁱThe first Pc-based reduction wave was overlapped with the second C₆₀-based one.^jHalf-wave redox potentials vs. Fc/Fc⁺.^kAn additional quasireversible wave is observed at –2.24 V.

when compared to those of the model fulleropyrrolidine (25). Specifically, in the case of the Zn-complexed dyad (28b), all C₆₀-based reductions are shifted to more negative values by about 50–100 mV. These results clearly indicate some degree of charge transfer in the ground state from the donating phthalocyanine to the

fullerene acceptor. In order to establish whether the effects observed were due to inter- or intramolecular interactions, CVs and OSWVs were obtained for 1 : 1 molar mixtures of the corresponding model compounds. Analysis of those results indicate that although small shifts are also observed for the mixtures indicating a small degree

Fig. 15 Cyclic voltammograms at 25 °C in THF of: (a) **(26)** and (b) **(27)**. Scan rate = 0.5 V s⁻¹, working electrode: Pt. Reprinted with permission from Ref. 123. Copyright © 2001 Wiley-VCH Verlag.



of intermolecular interactions (through space), the shifts observed for the covalently linked dyads are larger, and consequently intramolecular interactions must also be present [124].

For subphthalocyanine dyads (**30a–c**), electrochemical studies suggest that in the ground state the electronic effects that dominate are through-bond and not through-space, since they follow the expected behavior for the ortho and para, and the weakest electronic effect for the meta isomer [125].

The last group of dyads considered here are those that incorporate TTFs in their structure. TTFs are powerful organic donors, which, when linked to the fullerene core and engaged in charge-separation processes, gain rather than lose aromaticity [128]. The modification of the donor strength on the TTF moiety in dyads (**31a–c**) allows the tuning of the

HOMO–LUMO gap of these structures, which have important consequences on their electrochemical and photophysical properties [126].

6.1.4.3 Cyclopropanated Derivatives of C₆₀

In this group of derivatives, we have included all compounds in which attachment of the substituent results in the formation of a cyclopropane ring on the surface of C₆₀. The bridging atom may be carbon, nitrogen, a transition metal, or oxygen (epoxyfullerene). Basic structures for these compounds are shown in Fig. 16. The electrochemistry of representative examples of all of these derivatives has been reviewed previously [83], and only general observations are presented below, along with some specific examples of new derivatives with novel electrochemical behavior.

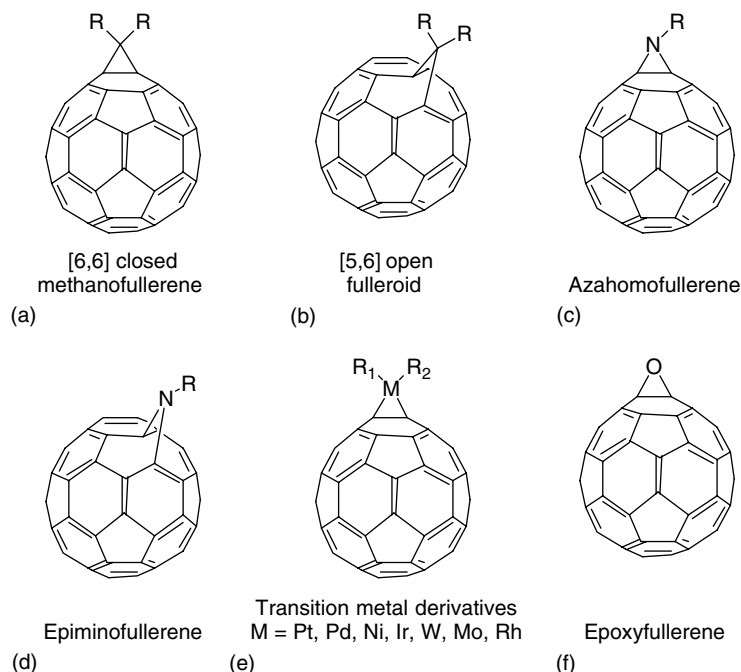


Fig. 16 Basic structures of cyclopropanated derivatives of C_{60} .

6.1.4.3.1 C-bridged Cyclopropanated Derivatives: Methanofullerenes and Fulleroids

The so-called methanofullerenes [129] and fulleroids [130] have the general formula $C_{61}R_1R_2$. Their difference results from the location of the cyclopropane ring on the C_{60} surface. In methanofullerenes, the bridge is located across the junction of two six-membered rings forming a [6,6]closed structure, while in fulleroids the bridge occurs at the junction between a five- and a six-membered ring forming a [5,6]open structure on the C_{60} surface (see Fig. 16a,b). Two other isomers, [6,6]open and [5,6]closed are possible, but have not been identified. They do not preserve the [5]radialene structure of C_{60} , and are, therefore, unstable [131, 132]. The [5,6]open or fulleroid isomer is the kinetic product during synthesis [130, 133], and it may be

induced to isomerize to the [6,6]closed or methanofullerene product either thermally, photochemically, or electrochemically [83]. As with their cycloaddition product analogs, methanofullerenes reduce at potentials 100–150 mV more negative than pure C_{60} , but this may vary depending on the electron-donating/withdrawing ability of the addend and on its orientation [83]. In addition, it has been demonstrated that as the number of addends increase, reductions occur at increasingly more negative potentials and become irreversible. The latter effect is attributed to the stepwise loss of conjugation, which results in higher energy LUMOs. For the same reason, oxidations occur at increasingly more positive potentials as more addends are attached to the fullerene core [83].

An important difference between methanofullerenes and fulleroids is that

while fulleroids retain the 60π -electron configuration of the parent C_{60} , formation of methanofullerenes results in partial loss of conjugation. The two bridgehead carbon atoms in methanofullerenes are sp^3 hybridized, and consequently only 58π -electrons remain on the surface.

However, this loss of conjugation does not seem to affect the electron affinity of methanofullerenes. Numerous studies have shown that the redox potentials of methanofullerenes do not differ significantly from those of their fulleroid analogs [83], and until the year 2000,

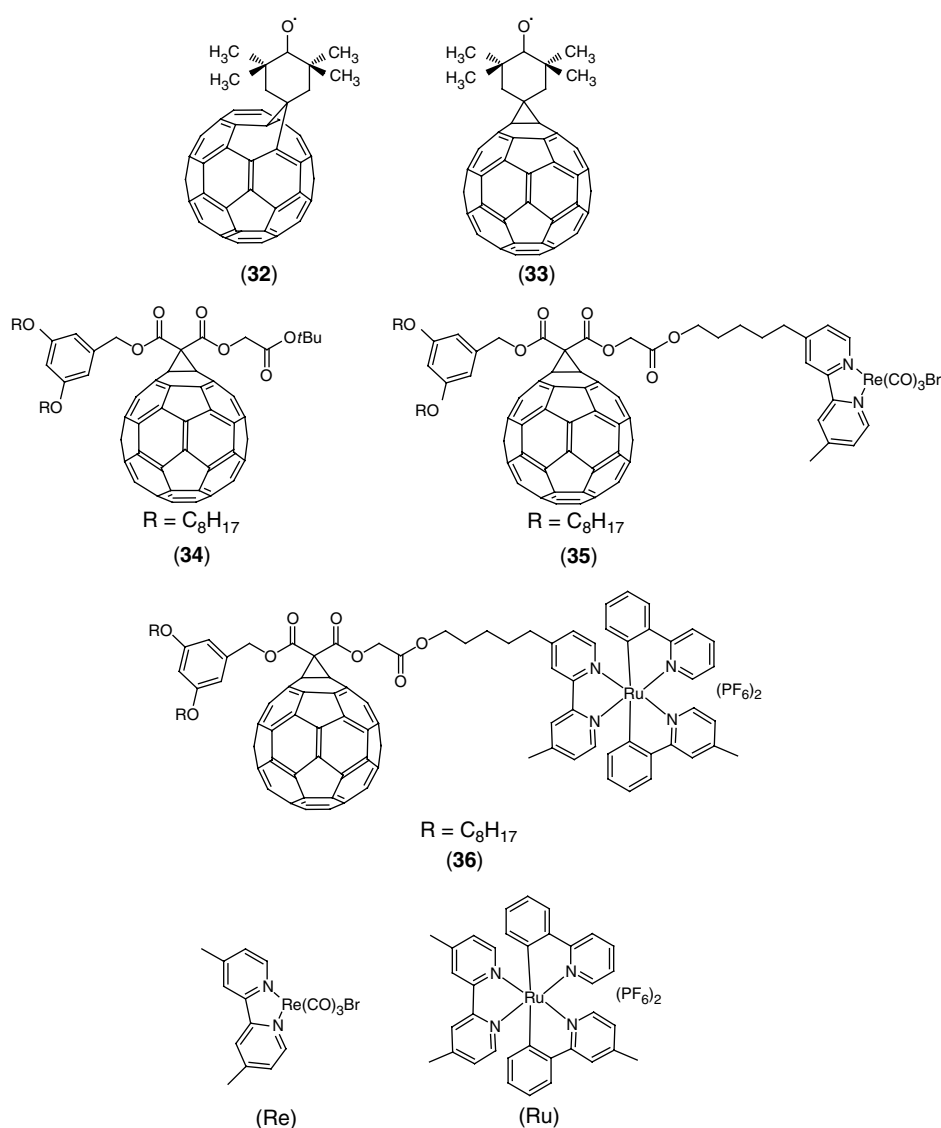


Fig. 17 Some selected cyclopropanated derivatives of C_{60} .

differences had been observed only after the third [35, 134], fourth [35], or fifth [135, 136] electron reduction depending on the temperature, solvent, and substituent. However, a study on TEMPO-C₆₁ in THF (see (32) and (33) in Fig. 17) presented quite interesting results [137]. Oxidations and reductions occur essentially at the same potentials for both isomers on the CV timescale (see Table 16), and reductions are, as expected, cathodically shifted by ca. 100 mV with respect to pristine C₆₀. However, the first reduction wave of fulleroid (32) appears irreversible at room temperature, while the corresponding wave for methanofullerene (33) is reversible. Bulk electrolysis of fulleroid (32) at a potential corresponding

to the first reduction results in its isomerization to methanofullerene (33) after injection of a single electron, contrary to other reported cases of fulleroid to methanofullerene conversions.

A few other interesting molecular architectures exhibiting uncharacteristic electrochemical behavior have been constructed on the basis of the methanofullerene building block. These include two methanofullerene-substituted bipyridine ligands complexed to rhenium and ruthenium ((35) and (36) in Fig. 17), which were prepared as possible candidates for photoinduced electron transfer processes [138]. In addition, three fullerene crown ether conjugates ((38), (39), and (40) in Fig. 18) have

Tab. 16 Half-wave redox potentials (in V vs. Fc/Fc⁺) of selected cyclopropane derivatives of C₆₀ at 25 °C

	<i>Solvent</i> ^a	<i>Supporting electrolyte</i>	<i>E</i> ₁ ^{ox}	<i>E</i> ₁ ^{red}	<i>E</i> ₂ ^{red}	<i>E</i> ₃ ^{red}	<i>E</i> ₄ ^{red}	<i>E</i> ₅ ^{red}	<i>References</i>
(32) ^b	THF	TBAH	+0.94	−0.42	−1.01	−1.57 ^c	−1.65	−2.12	137
(33) ^b	THF	TBAH	+0.95	−0.44	−1.03	−1.50 ^c	−1.64	−2.11	137
TEMPO ^b	THF	TBAH	+0.85	−1.47					137
(34)	DCM	TBAPF ₆		−1.03	−1.41	−1.83			138
Re	DCM	TBAPF ₆	+0.92 ^c	−1.88					138
(35)	DCM	TBAPF ₆	+0.96 ^d	−0.99	−1.37	−1.83 ^d			138
Ru	DCM	TBAPF ₆	+0.92	−1.76					138
(36)	DCM	TBAPF ₆	+0.91	−1.02	−1.40	−1.81 ^d			138
(37)	DCM/MeCN	TBAPF ₆ ^e		−0.94	−1.36				139
(37)	DCM/MeCN	TBAPF ₆ /KPF ₆ ^f		−0.95	−1.36				139
(38)	DCM/MeCN	TBAPF ₆ ^e		−1.04	−1.51				139
(38)	DCM/MeCN	TBAPF ₆ /KPF ₆ ^f		−0.95	−1.36				139
(39)	DCM/MeCN	TBAPF ₆ ^e		−1.02	−1.48				139
(39)	DCM/MeCN	TBAPF ₆ /KPF ₆ ^f		−0.97	−1.43				139
(40)	DCM/MeCN	TBAPF ₆ ^e		−1.05	−1.47				139
(40)	DCM/MeCN	TBAPF ₆ /KPF ₆ ^f		−1.01	−1.46				139

^aSee Table 2 for solvent abbreviations.

^bVs. SCE.

^cIrreversible.

^dDielectronic process.

^eIn the presence of one equivalent of [2.2.2]cryptand.

^fIn the presence of one equivalent of [2.2.2]cryptand and a 10-fold excess of KPF₆.

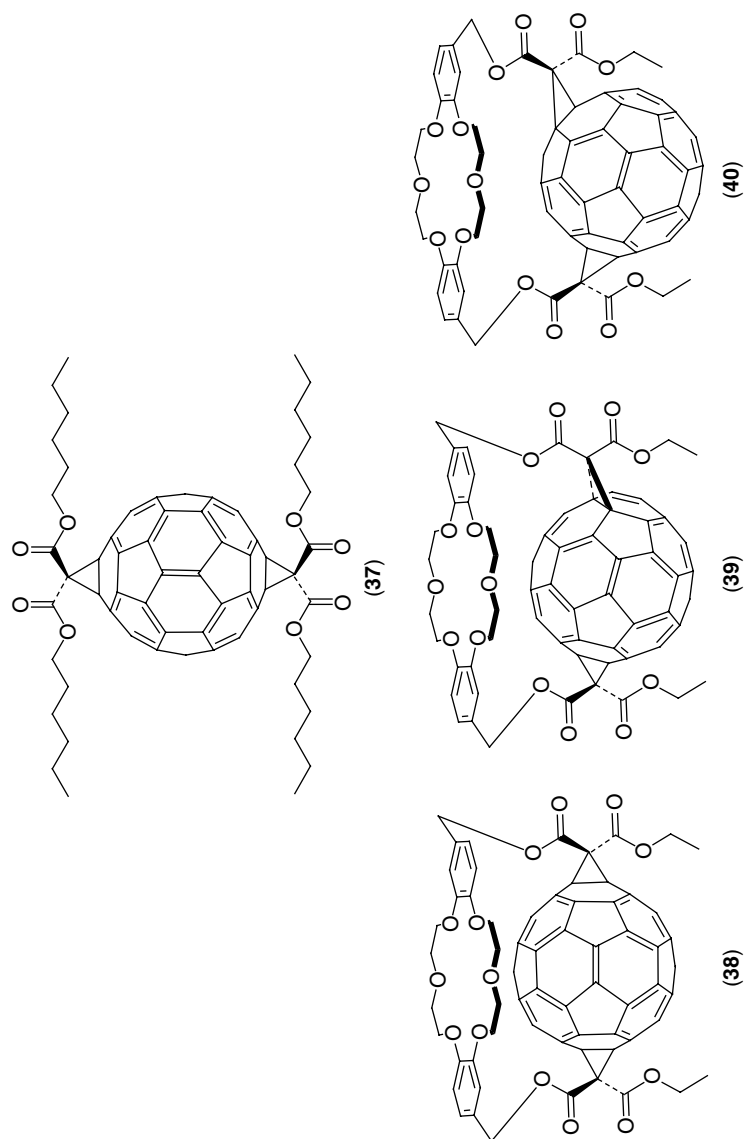


Fig. 18 Other cyclopropanated derivatives of C_{60} .

been synthesized with the goal of forming fullerene-based amphiphilic, supramolecular complexes, which may be tunable by metal ion recognition and capable of monolayer formation [139]. The redox potentials of all these compounds are presented in Table 16 along with those of model analogs (34), **Re,Ru**, and (37), respectively, for comparison.

In the cathodic region, the voltammograms of (35) and (36) display two reversible one-electron reduction waves and a third two-electron reduction process. The first two waves correspond to C_{60} -centered reductions, while the third corresponds to the overlap of simultaneous one-electron processes taking place at the metal center as well as the fullerene. In addition, a metal-centered oxidation is observed in both dyads. In the case of the ruthenium dyad, (36), oxidation and reduction potentials remain essentially unchanged when compared to the corresponding ones in model compounds **Ru** and (34), respectively, indicating that there is no electronic interaction between the ruthenium complex and the fullerene. The two moieties must be far from each other in an extended conformation that prevents through-space interaction. On the other hand, the C_{60} -centered reduction potentials of the rhenium dyad, (35), are ca. 40 mV more positive than those of model compound (34). The metal-centered oxidation of the dyad is also shifted to a more positive potential. These results suggest that the dyad adopts a conformation in which the two moieties are in close proximity, so that a small electronic interaction between the two takes place [138].

Electrochemical studies of fullerene crown ether conjugates (38), (39), and (40) yielded fascinating results. The three compounds differ only in the points of attachment of the tangential crown

moiety to the fullerene, causing the crown to be at three different distances from the surface of the sphere. The distance increases in the order (38) < (39) < (40). A significant degree of perturbation of the electronic properties of the fullerene moiety was observed in all three cases in the presence and absence of crown ether bound potassium. In the absence of bound cation, which was imposed by the addition of one equivalent of [2.2.2]cryptand, the proximity of the ether oxygens to the surface of the sphere induces a negative shift of ca. 80–110 mV in the first reduction potentials of all three compounds with respect to those of the model compound (37). This negative shift is attributed to a through-space electron-donating effect of the crown ether oxygens. Remarkably, however, addition of a 10-fold excess of KPF_6 causes a shift toward more positive potentials of 90, 50, and 40 mV respectively for (38), (39), and (40). These positive shifts correlate directly with the distance of the bound potassium to the C_{60} surface in all three compounds. At these distances, potassium withdraws electron density away from the fullerene surface, causing the observed positive shift [135, 139].

At this point, it is important to indicate that a very large number of C-bridged cyclopropanated fullerene derivatives undergo irreversible reduction processes leading to the removal of the addend and recovery of the pristine parent fullerene. The process has been advantageously used in electrosynthetic procedures, and thus a separate section covering the electrochemically induced retro-cyclopropanation reaction is presented later in this chapter (see Sect. 6.1.5.2). A number of other C-bridged cyclopropanated derivatives will be discussed there.

6.1.4.3.2 Other Cyclopropanated Derivatives of C_{60}

Like their C-bridged relatives, N-bridged cyclopropanated derivatives of C_{60} also exist in two isomeric forms: [6,6]closed or epimino- and [5,6]open or azahomofullerenes (see Fig. 16). The redox properties of significant representatives of this family of derivatives have been reviewed before [83, 140], and their one significant characteristic is that as expected, the electron-withdrawing ability of bridging nitrogen increases the electron affinity of the sphere. As a result, these compounds generally reduce at potentials close to the reduction potentials of pure C_{60} .

A large number of cyclopropanated derivatives of C_{60} in which the bridging atom is an electron rich transition metal (see Fig. 16) such as Pt, Pd, Ni, Ir, W, Mo, and Rh has been reported. Their electrochemical properties have been reviewed [83, 141, 142] and, in general, reductions are C_{60} centered and negatively shifted with respect to those of pure C_{60} , while oxidations are metal centered. In most cases, however, the first reduction is accompanied by breakage of the carbon-metal bonds and recovery of the pristine [60] fullerene. In multiadduct derivatives, the breakage occurs in a stepwise manner.

Reduction of epoxyfullerene $C_{60}O$ results in the formation of a polymer film on the surface of the electrode [143, 144]. Three one-electron voltammetric waves are observed, the first one of which corresponds to the formation of $C_{60}O^-$, which decomposes to C_{60} . The second wave corresponds to the formation of C_{60}^{2-} , which is the polymer initiator, and the third wave corresponds to C_{60}^{3-} .

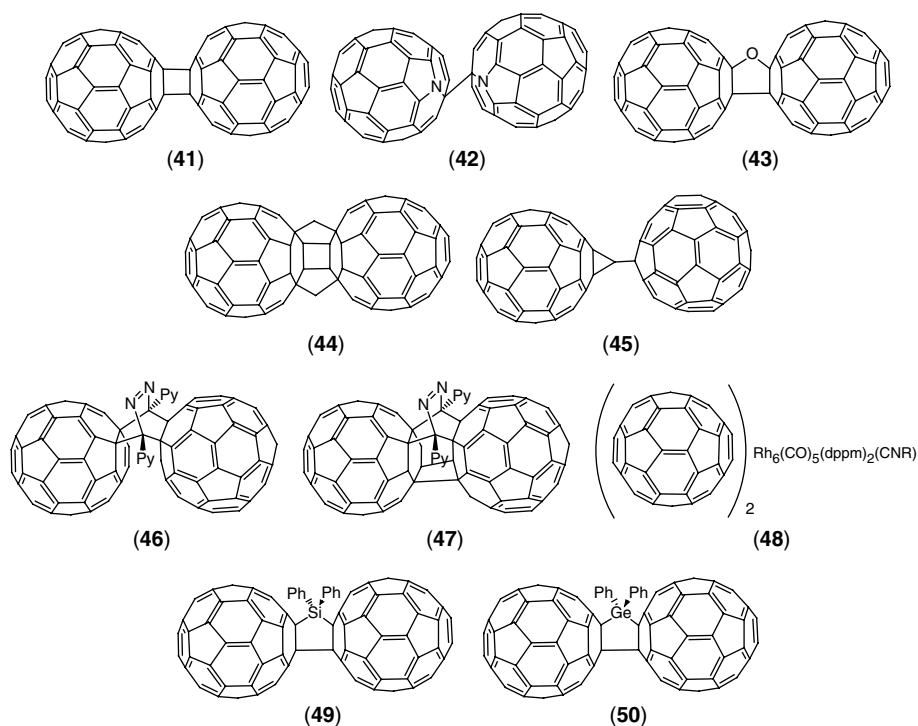
6.1.4.4 C_{60} -dimers

The proximity of two C_{60} units introduces yet another novel method of influencing the electronic behavior of each of the

spheres, since the presence of one may affect the electrochemistry of the other. With this in mind, several fullerene dimers have been prepared to date, using different connecting bridges. Some of these structures, (41–50), are shown in Fig. 19 [145–156], and their corresponding redox potentials are listed in Table 17. Initial studies were not very encouraging. For example, compound (42) and others bearing an acetylene or a phenylene spacer displayed superimposable two-electron redox waves corresponding to the simultaneous reduction of the individual spheres, indicating an absence of electronic coupling between the two spheres [145, 146, 149]. C_{120} , (41), underwent a homolytic cleavage upon one-electron reduction, resulting in the recovery of two C_{60} molecules [147]. Cleavage has also been inferred from voltammetric results of a C_{60} – C_{70} cross-dimer [148]. The first breakthrough was achieved with dimer (43), $C_{120}O$, whose voltammetry, after deconvolution, displayed three sets of closely spaced but separate and independent one-electron reduction waves (see Table 17). Similar results have been obtained recently for dimers (44–50) (see Fig. 20). One notable feature in the voltammetry of these dimers, which is also evident from the redox potentials listed in Table 17, is the increased separation between waves in each consecutive pair. This property has been attributed to an increase in Coulombic repulsion between the negatively charged fullerene cages as each individual cage is reduced.

6.1.4.5 Electrochemistry of C_{70} Derivatives

The redox behavior of C_{70} derivatives is very similar to that of derivatives of C_{60} . Fewer examples have been characterized electrochemically, but the redox potentials of some representative ones, including $C_{70}H_2$, the methano [70]

Fig. 19 C₆₀-dimers.Tab. 17 Half-wave redox potentials (in V vs. Fc/Fc⁺) of C₆₀ dimers at room temperature

	Solvent ^a	Supporting electrolyte	E_{1a}^{red}	$E_{1b}^{red,b}$	E_{2a}^{red}	$E_{2b}^{red,c}$	E_{3a}^{red}	$E_{3b}^{red,d}$	References
(43)	ODCB	TBAP	−0.84	−0.88	−1.24	−1.30	−1.82	−1.96	149
(44)	ODCB	TBAP	−1.20 ^e		−1.60 ^e		−1.82 ^e		150
(45)	ODCB	TBAP	−1.04	−1.12	−1.44	−1.53	−1.99	−2.16	151
(46)	ODCB	TBAP	−1.09	−1.15	−1.52	−1.58	−2.11	−2.19	152
(47)	ODCB	TBAP	−1.11	−1.20	−1.56	−1.63	−2.03	−2.32	152
(48)	ODCB	TBAP	−1.19	−1.38	−1.62	−1.86	−2.12	−2.41	153
(49)	ODCB	TBAPF ₄	−1.04	−1.13	−1.46	−1.54	−1.94	−2.08	154
(50)	ODCB	TBAPF ₄	−1.06	−1.15	−1.50	−1.58	−1.98	−2.12	155

^aSee Table 2 for solvent abbreviations.^bPotential corresponds to first reduction of the second fullerene cage.^cPotential corresponds to second reduction of the second fullerene cage.^dPotential corresponds to third reduction of the second fullerene cage.^eWaves are split in two.

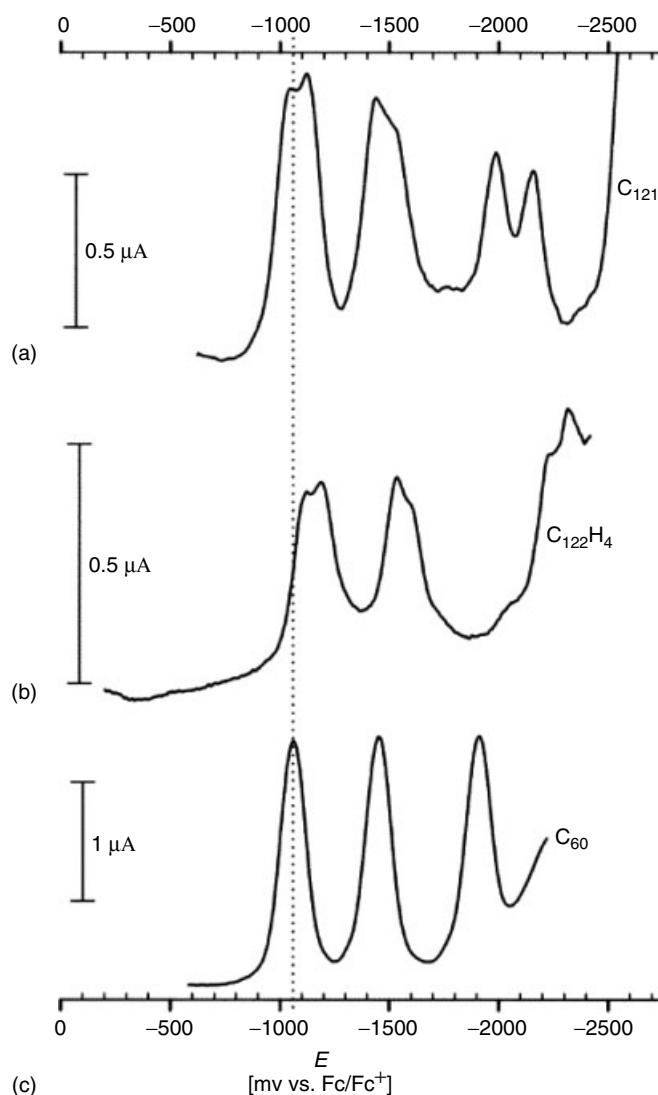


Fig. 20 Differential-pulse voltammogram of C_{121} , (45) (a), square-wave voltammogram of $C_{122}H_4$, (44) (b), and C_{60} (c) in *o*-dichlorobenzene with 0.1 M TBAP as supporting electrolyte. The first reduction potential of C_{60} is shown by the dotted line. Reprinted with permission from Ref. 152. Copyright © 2001 American Chemical Society.

fullerene derivatives $C_{70}R_2$ with $R = CO(C_2H_5O)_2H$ or $CO_2CH_2CO_2Et$, and (51–53) (see Fig. 21), are shown in Table 18 [44, 85, 157–160].

Notably, methano [70] monoadducts and the dihydro derivatives reduce at potentials ca. 90–130 mV more negative than pure C_{70} . Also, as with their C_{60} analogs, the

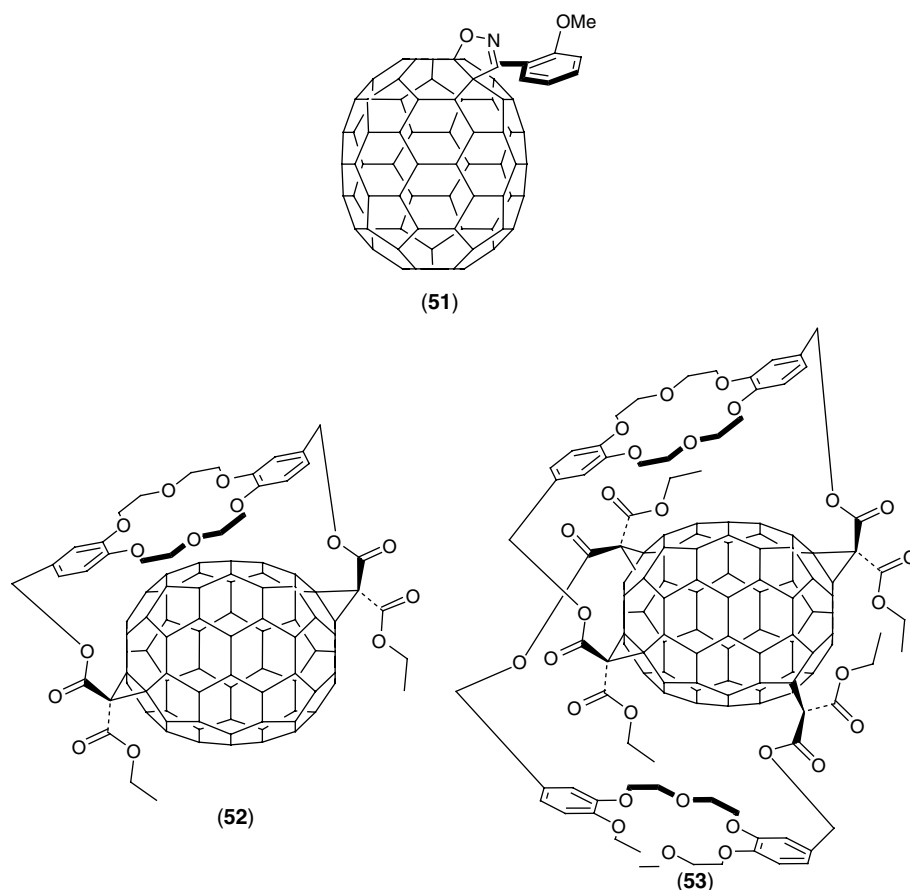


Fig. 21 Selected derivatives of C_{70} .

first reduction of C_{70} methanoadducts becomes increasingly more difficult as the number of addends increases, as shown by the mono to tetrakis series $C_{71}R_2$ – $C_{74}R_8$ in Table 18 [44].

The isoxazoline derivative, (51), displays essentially no shift in reduction potentials with respect to those of C_{70} , indicating a strong electron-withdrawing effect from the isoxazoline moiety [157].

Even more remarkable results were observed, however, for the $C_{70}Ph_2$ through $C_{70}Ph_{10}$ series [159]. In this series, addends are located around the “waist” of

the C_{70} spheroid, and each singly bonded phenyl addend saturates a carbon atom in the cage, decreasing the π -electron conjugation. Interestingly, however, the di- and tetraphenyl adducts appear to be electrochemically and chemically stable, both displaying reversible reductions at potentials that are more positive than those of the corresponding parent C_{70} . This phenomenon is attributed to the inductive effect of the phenyl groups that renders the cage a better electron acceptor. As the cage is sequentially saturated in $C_{70}Ph_{6-10}$, reduction potentials become increasingly

Tab. 18 Half-wave reduction potentials (in V vs. Fc/Fc^+) of selected C_{70} derivatives

	Solvent ^a	Supporting electrolyte	Temperature [°C]	E_1	E_2	E_3	E_4	E_5	E_6	References
C_{70}	PhMe/DMF	TBAP	-50	-0.91	-1.34	-1.83				85
7,8- C_{70}H_2	PhMe/DMF	TBAP	-50	-1.04	-1.48	-1.96				85
1,9- C_{70}H_2	PhMe/DMF	TBAP	-50	-1.03	-1.52	-1.93				85
(51) ^b	PhMe/MeCN	n/r ^c	n/r ^c	-0.98	-1.37	-1.79	-2.24			156
C_{70}	DCM	TBAPF ₆	+25	-0.93	-1.31	-1.73	-2.09			157
C_{71}R_2	DCM	TBAPF ₆	+25	-1.02	-1.39					157
$\text{R}=\text{CO}_2(\text{C}_2\text{H}_4\text{O})_2\text{H}$										
C_{71}R_2	DCM	TBAPF ₆	+25	-1.05	-1.44 ^d	-1.84	-2.02			44
C_{72}R_4	DCM	TBAPF ₆	+25	-1.11	-1.47 ^d	-1.88	-2.06			44
C_{73}R_6	DCM	TBAPF ₆	+25	-1.13	-1.52	-2.15				44
C_{74}R_8	DCM	TBAPF ₆	+25	-1.23	-1.45	-1.65				44
$\text{R}=\text{CO}_2\text{CH}_2\text{CO}_2\text{Et}$										
C_{70}^e	THF	TBAH	+25	-0.35	-0.91	-1.44	-1.88	-2.40	-2.86	158
$\text{C}_{70}\text{Ph}_2^e$	THF	TBAH	+25	-0.25	-0.79	-1.43	-1.93	-2.13	-2.50 ^d	158
$\text{C}_{70}\text{Ph}_4^e$	THF	TBAH	+25	-0.25 ^f	-0.83 ^f	-1.35 ^f	-1.82	-2.30		158
$\text{C}_{70}\text{Ph}_6^e$	THF	TBAH	+25	-0.47	-1.00	-1.60 ^d	-2.10	-2.30 ^d		158
$\text{C}_{70}\text{Ph}_8^e$	THF	TBAH	+25	-0.91	-1.37	-2.13	-2.44			158
$\text{C}_{70}\text{Ph}_{10}^e$	THF	TBAH	+25	-1.34 ^d	-2.00	-2.58 ^d				158

(continued overleaf)

Tab. 18 (continued)

	Solvent ^a	Supporting electrolyte	Temperature [°C]	E ₁	E ₂	E ₃	E ₄	E ₅	E ₆	References
(52)	PhMe/MeCN	TBAPF ₆	+25	-1.13	-1.57					159
(52) + KPF ₆ ^g	PhMe/MeCN	TBAPF ₆	+25	-1.05						159
(53)	PhMe/MeCN	TBAPF ₆	+25	-1.44	-1.74 ^h					159
(53) + KPF ₆	PhMe/MeCN	TBAPF ₆	+25	-1.27 ⁱ						159

^aSee Table 2 for solvent abbreviations.
^bCompare potentials to those of C₇₀ in this solvent reported on Table 3.
^cNot reported.
^dIrreversible.
^eVs. SCE.
^fValue corresponds to the first wave in a pair of waves.
^gOne equivalent of KPF₆.
^hCathodic peak potential. Reversibility is difficult to ascertain due to the presence of another small redox couple from an impurity.
ⁱTwo equivalents of KPF₆.

more negative. For $C_{70}Ph_{10}$ and $C_{70}Ph_6$, irreversibility is observed after the first and third waves, respectively, and waves corresponding to the redox potentials of pristine C_{70} are observed. This suggests the presence of an electrochemical, chemical, electrochemical (ECE) mechanism, which results in addend removal. Interestingly, this irreversibility is not observed in $C_{70}Ph_8$ until the fourth wave.

Electrochemical studies of [70] fullerene crown ether derivatives (52) and (53) also yielded fascinating results [160]. The reduction potentials of both compounds were obtained in the presence and absence of KPF_6 to determine the effect of cation complexation by the crown ether on the electron affinity of the cage. In the case of (52), the cathodic scan shows two reversible redox couples in the absence of added cation. Addition of one equivalent of KPF_6 results in an anodic shift of 80 mV with respect to the noncomplexed compound, suggesting an electrostatic effect between the positively charged ion and the reduced cage. Interestingly, (53), which bears two crown ether addends tangential to the cage, also displays two reversible reduction waves in the absence of added cation, but addition of only one equivalent results in the appearance of two new redox couples that must correspond to the 1:1 and 1:2 host–guest complexes. Addition of two equivalents of KPF_6 results in only one redox couple that is anodically shifted by 170 mV with respect to the corresponding couple in uncomplexed (53). Note that the magnitude of the cation-induced anodic shift in (53) is about twice that observed for (52), indicating that there is no cooperative effect between the two binding sites.

A mixture of hydrofullerenes $C_{70}H_{36-46}$ composed of 50% $C_{70}H_{36}$, 20% $C_{70}H_{38}$,

14% $C_{70}H_{44}$, and 15% $C_{70}H_{46}$ was studied by CV in THF and DCM at various temperatures. At +13 °C, reduction of the mixture in THF is characterized by one reversible and one irreversible wave at -3.18 and -3.37 V vs. Fc/Fc^+ , respectively. At temperatures below -34 °C, only a single reversible reduction is observed at -3.16 V. Oxidation of the mixture in DCM at -31 °C is characterized by a broad, irreversible peak at +1.22 V vs. Fc/Fc^+ [161].

6.1.4.6 Electrochemistry of C_{76} , C_{78} , and C_{84} Derivatives

Very few studies have been carried out on derivatives of the higher fullerenes. The reason for this may be attributed to the lower abundance of the parent compounds in fullerene soot, which has prevented their ample use in synthetic investigations. To complicate matters, C_{76} , C_{78} , and C_{84} exist as 2, 5, and 24 possible constitutional isomers, respectively; a fact that makes separation and purification procedures more difficult. As a result, only a couple of studies have been published on the electrochemistry of derivatives of the higher fullerenes [44, 54].

The redox properties of three pairs of diastereomeric mono-methanoadducts of C_{76} bearing a bis(phenylbutyl)malonate addend (see 54 in Fig. 22) have been studied by steady-state voltammetry (SSV) [44]. Two of the three pairs of diastereomers reduce at potentials more positive than those of the parent [76] fullerene, while the other pair is actually more difficult to reduce. Interestingly, in contrast with similar C_{60} and C_{70} derivatives, the di- and trianions of these C_{76} monoadducts are much more chemically stable. In fact, the retro-cyclopropanation reaction (see Sect. 6.1.5.2 below), which removes the malonate addend, occurs in very low yields

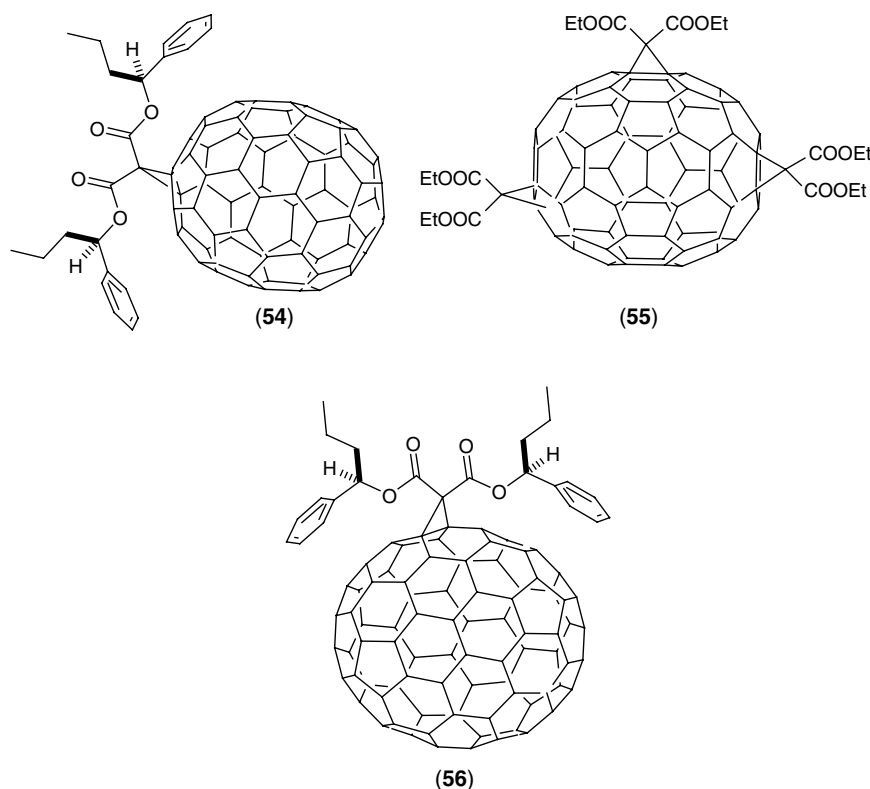


Fig. 22 C₂-symmetrical C₇₆ diastereoisomer (*S*, *S^f* A)-**54**, C_{2v}-C₇₈ tris-adduct (±)-**55** and, C₂-symmetrical monoadduct (**56**) of achiral D_{2d}-C₈₄.

for these compounds, supporting their higher stability.

The redox properties of two bis-adduct and four tris-adduct derivatives of C₇₈ (see (55) in Fig. 22) have also been reported [44]. In all cases, at least four one-electron reduction steps and one oxidation are observed. All reductions occur at more negative potentials than those of the pristine cage, while the oxidation is facilitated. The first one-electron reduction is reversible, but the second one is irreversible for half of the derivatives. In fact, the second reduction results in a chemical transformation leading to the observation of the parent cage redox

couples. Indeed, CPE of these derivatives of C₇₈ results in an electrochemically induced retro-cyclopropanation reaction in which the pristine cage is recovered (see Sect. 6.1.5.2 below).

The only electrochemical study on derivatives of C₈₄ describes the use of the Bingel-retro-Bingel protocol, now known as the *retro-cyclopropanation reaction* (see Sect. 6.1.5.2), to isolate the two major isomers of pure C₈₄ by removing bis(phenylbutyl)malonate addends from mono and bis-adducts of C₈₄ (see (56) in Fig. 22) [54]. CV profiles in DCM (+0.12 M TBAPF₆) of two different monoadducts and four different

bis-adducts were obtained before CPE was performed. The voltammetries revealed that in all cases only the first reduction out of four that was observed at 25 °C was reversible. Lowering the temperature improved reversibility.

A very clear pattern was observed for a large number of bismalonate derivatives of C₆₀, C₇₀, C₇₆, C₇₈, and C₈₄. The second or in some cases the third reduction appears irreversible, and CPE leads to the recovery of the parent fullerene. A detailed account of a systematic investigation of this phenomenon is presented in the next section.

6.1.5 Electrosynthesis

The use of controlled potential electrolysis of fullerenes has thus far been used as a synthetic tool in two general ways. One method has involved the preparation of fullerene derivatives from the reaction of electrochemically generated anions of the pristine cages with electrophiles. The second method has involved an electrochemically induced retro-synthetic reaction of fullerene derivatives, which results in a number of different products, some of which have not been achieved by chemical synthesis. Both methods are described in the following, but special

emphasis is placed on the second method due to its novel results.

6.1.5.1 Electrosynthesis of C₆₀ and C₇₀ Derivatives

C₆₀ is considered an electrophile or electron acceptor because of its high electron affinity. Once reduced, C₆₀ behaves as a nucleophile or electron donor. The high stability of its anions has been used advantageously in reactions with electrophiles such as alkyl halides and gem-dihalo compounds. Reaction of the C₆₀ dianion with alkyl halides results in the formation of C₆₀R₂ (R = CH₃, C₂H₅, *n*-C₄H₉, or C₆H₅CH₂) and C₆₀R₄ (R = CH₃, *n*-C₄H₉, or C₆H₅CH₂) [88, 91, 162, 163]. Addition of a gem-dihalo compound yields methanofullerenes of the type C₆₁RR' (R = H or CO₂Et and R' = H, CO₂Et, *t*-butyl, or CN) [164]. The experimental method to produce these derivatives electrosynthetically has been described in detail elsewhere [[83] and references therein], and the same procedure has been used more recently to prepare the C₇₀ derivative C₇₀(C₆H₅CH₂)₂ [165]. In addition, several (inorganic) fulleride salts have also been obtained using electrosynthetic and electrocrystallization methods. These methods are also described in a recent review [166].

A mechanistic study on the formation of C₆₀R₂ and C₆₀RR' from the C₆₀ dianion

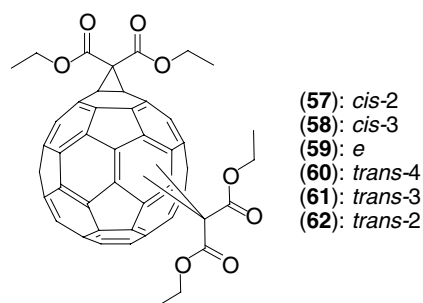


Fig. 23 C₆₀ bis-adducts (57–62).

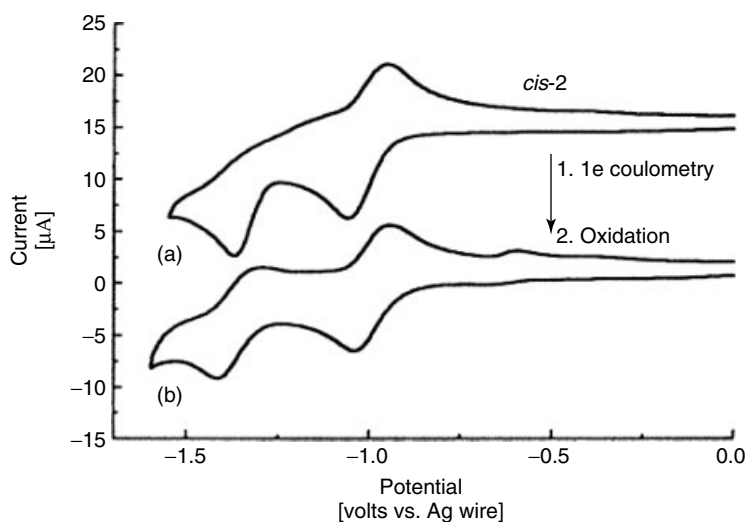
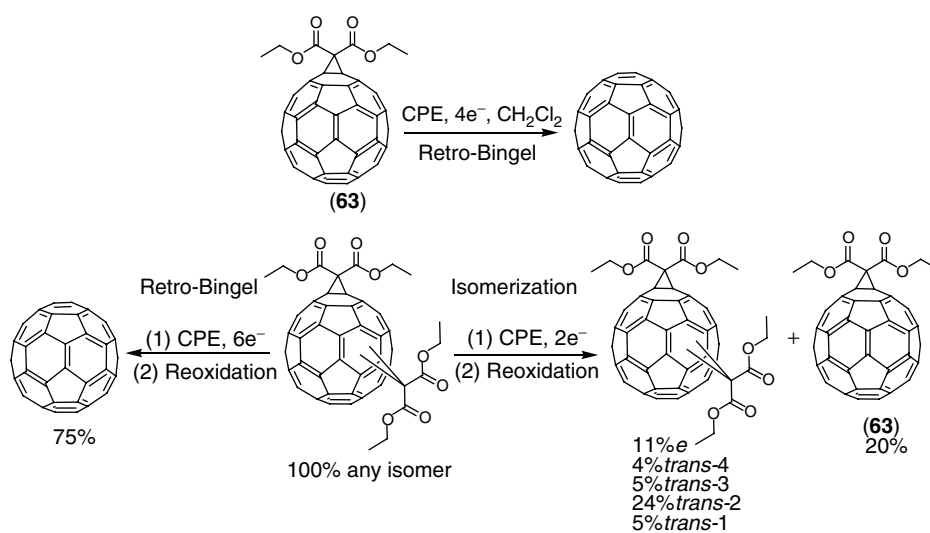


Fig. 24 (a) CV of *cis*-2 bis-adduct (**57**) in CH_2Cl_2 (+0.1 M Bu_4NPF_6) using a scan rate of 100 mV s^{-1} . (b) Voltammogram recorded after coulometrically controlled one electron per molecule electrolysis, followed by reoxidation, clearly showing that the second reduction has become more chemically reversible. The working electrode was a glassy carbon minielectrode. Reprinted with permission from Ref. 168. Copyright © 1998 American Chemical Society.



Scheme 3 Retro-Bingel and isomerization reactions.

and the alkyl halides RX and $R'X$ reports that the reaction occurs in two distinct steps. In the first step, an electron transfer occurs from C_{60}^{2-} to RX resulting in the formation of $C_{60}R^-$. This is followed by an S_N2 reaction of $C_{60}R^-$ with $R'X$ where $C_{60}RR'$ is produced [167].

6.1.5.2 Electrochemically Induced Retro-cyclopropanation Reactions

The removal of methano addends from fullerenes using CPE is an efficient and versatile procedure, which has been successfully employed in the separation of enantiomers and constitutional isomers of the higher fullerenes, for the isomerization of bis- and tris-adducts of C_{60} , and more recently, for the selective removal of one addend in the presence of another.

These studies were initiated upon observing that the *cis*-2-bis-methano-fullerene, (57), was the only one of six bis isomers available synthetically (see Fig. 23) that exhibited an irreversible second reduction wave by CV and SSV [105]. A one-electron CPE of (57) in DCM at the first reduction potential followed by reoxidation

resulted in the complete disappearance of (57) and the appearance of a mixture of other bis isomers. The CV of (57) before electrolysis and that of the resulting mixture after electrolysis is shown in Fig. 24. Interestingly, CPE of all other synthetic isomers, (58–62), at their first reduction potential did not result in any isomerization and only the corresponding starting materials were recovered [168]. Isomerization of (58–62) occurred, however, after addition of two electrons per molecule by CPE followed by reoxidation. Interestingly, column chromatography of the products yielded two fractions. The first fraction contained a mixture of bis-adducts whose product distribution was essentially the same regardless of which isomer was electrolyzed: 23% *e*, 44–53% *trans*-2, and ca. 10% each of *trans*-1, *trans*-3, and *trans*-4. No *cis* isomers were recovered. These results indicated that the methano adducts were migrating on the surface of C_{60} to form certain isomers preferentially, which according to theoretical calculations were indeed the isomers with higher stability [169]. The second fraction contained only

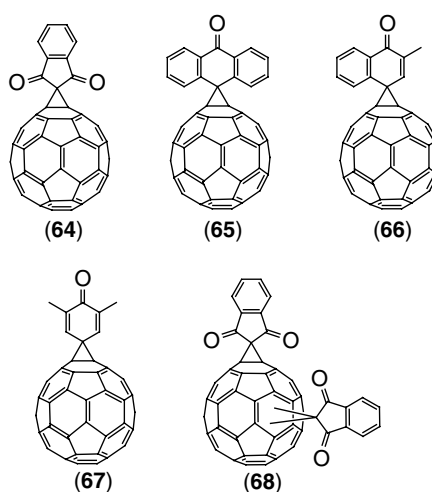


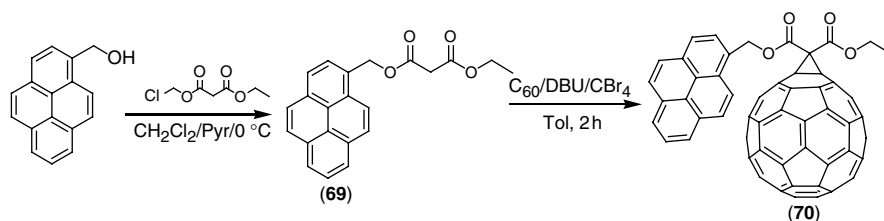
Fig. 25
Spiromethanofullerenes that exhibit retro-cyclopropanation reactions under reductive electrochemistry.

monoadduct, (63) (see Sch. 3), which resulted from the loss of one of the Bingel addends.

After addition of two-electron equivalents, the current for the CPE performed earlier on (58–62) did not reach background levels. In fact, a substantial amount of current remained. If electrolysis was allowed to continue until the current decreased to background level, a total of six electrons per molecule were added, and analysis of the products after reoxidation indicated that both addends had been completely removed, producing C_{60} in about 75% yield. These results are summarized in Sch. 3.

Clearly, depending on the number of electrons per molecule added during CPE, either removal of the addends [170] or an isomerization reaction was attained. The former reaction was initially called the *retro-Bingel reaction* [64], since it was the reverse of the Bingel addition of methano addends to C_{60} [171]. The generality of the retro-Bingel and isomerization reactions has since been tested using other multiple-malonate adducts of C_{60} [172, 173]. In fact, the reaction has made it possible to isolate the C_{2v} isomer of C_{78} , a new C_{78} bis-adduct, and new isomers of C_{84} [44, 54].

Further investigation has proved that addend removal is not limited to Bingel-type



Scheme 4 Synthesis of the Bingel derivative (70).

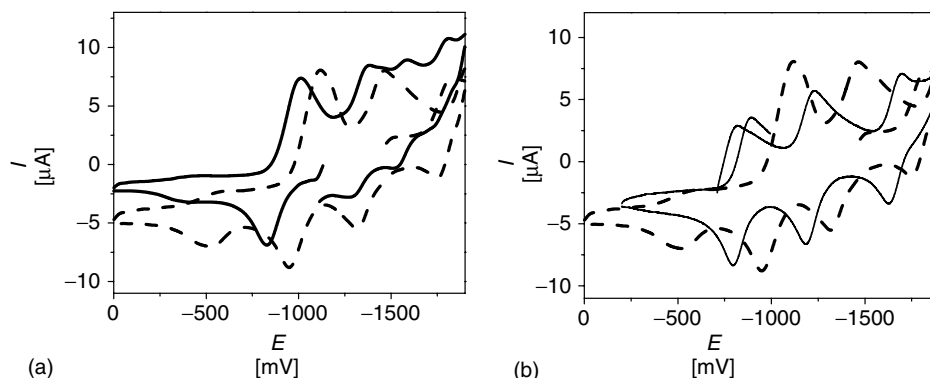


Fig. 26 Reductive electrochemistry data for (70). (a) Solid line: cyclic voltammogram after one-electron reduction; dashed line: cyclic voltammogram after 2.2 electron reduction. (b) Dashed line: cyclic voltammogram after 2.2

electron reduction; solid line: cyclic voltammogram after reoxidation. Reprinted with permission from Ref. 177. Copyright © 2003 American Chemical Society.

adducts. Other cyclopropanated derivatives of C_{60} such as (64–66) and (68) (see Fig. 25) also undergo efficient addend removal to form C_{60} upon CPE in DCM, a fact that has led to renaming the reaction “the electrochemically induced retro-cyclopropanation reaction of fullerenes” [174, 175]. A particularly interesting observation provided more insight into the possible mechanism of the reaction. CPE of compound (67) did

not result in the formation of C_{60} , and the starting material was not recovered either. This observation along with the fact that reduction of C_{84} to the dianion in DCM led to formation of $C_{84} > (CH_2)_n$ [54] pointed in the direction of anion reactivity with the solvent. Thus, CPE of several cyclopropanated derivatives including (64) was conducted in THF instead. After addition of 1.8 electrons per molecule, reoxidation, and purification, product analysis

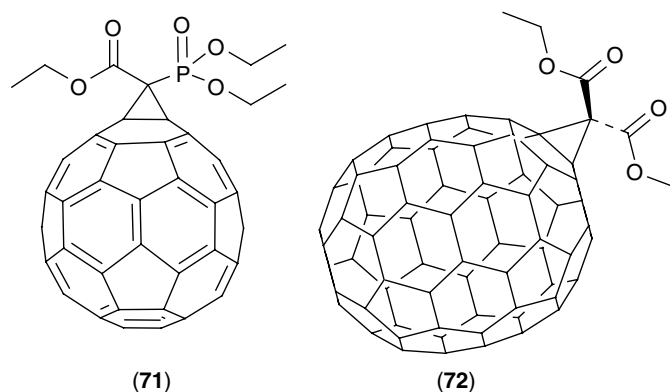


Fig. 27 Cyclopropanated derivatives (71) and (72).

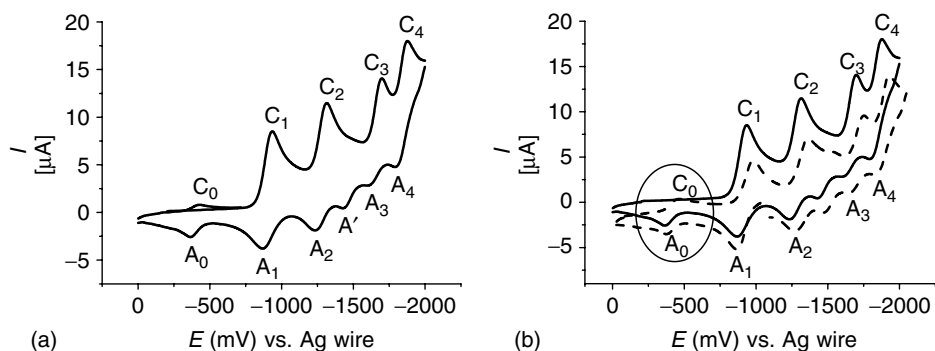
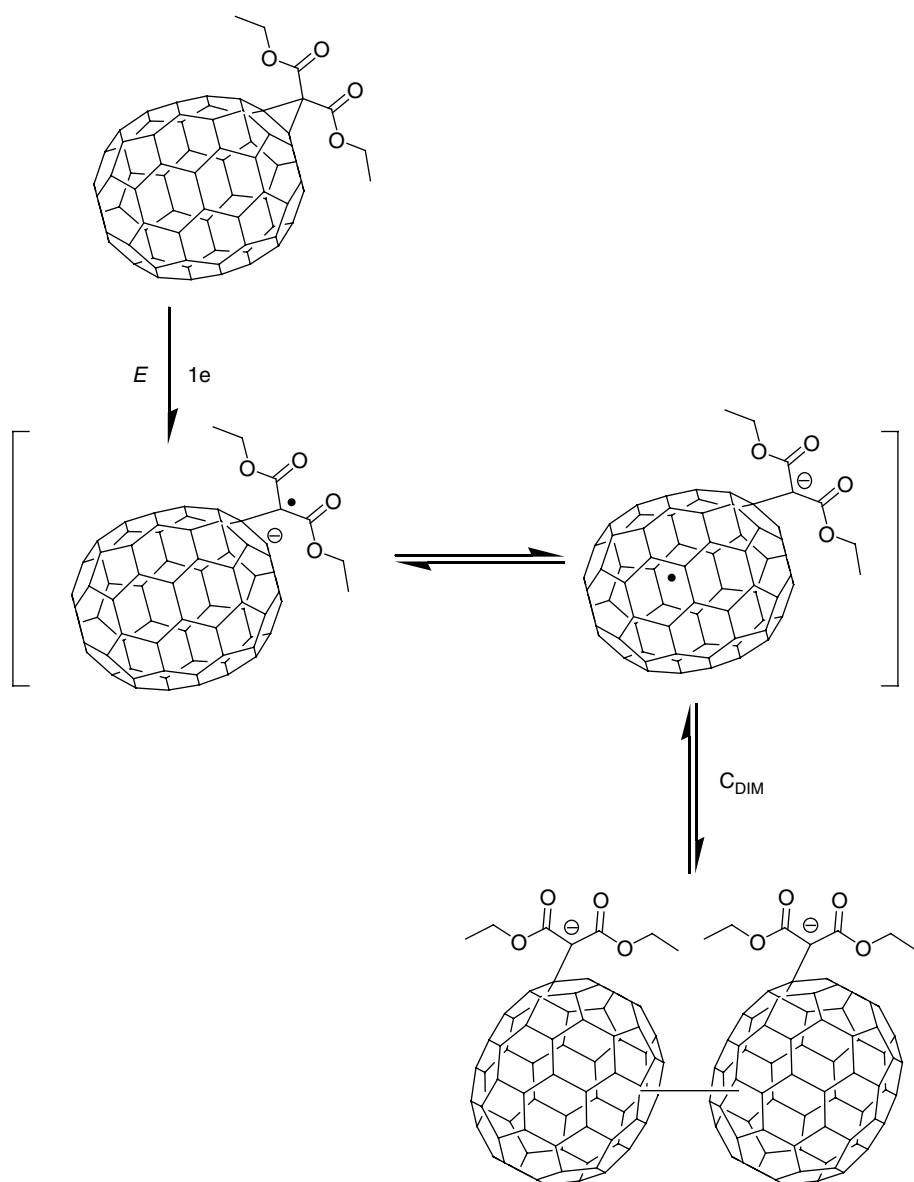


Fig. 28 Reductive electrochemistry data for (72). Cyclic voltammetric curves for a 0.1-mM CH_2Cl_2 solution of (72) at 100 mV s^{-1} , glassy carbon as a working electrode, Pt-mesh as a counter electrode, and a Ag wire as a quasi-reference electrode, $T = 25^\circ\text{C}$, $TBAPF_6$ (0.1 M) was used as supporting electrolyte.

(a) Cyclic voltammogram of (72). (b) Solid line: starting CV under high vacuum conditions; dashed line: cyclic voltammogram obtained after one-electron reduction of (72). Reprinted with permission from Ref. 178. Copyright © 2003 Wiley-VCH Verlag.



Scheme 5 Proposed mechanism for the formation of dimeric C₇₀ derivatives from electroreduced (**72**) (radical position and connecting bond between the C₇₀ units are chosen arbitrarily with respect to possible regioisomers). Reprinted with permission from Ref. 178. Copyright © 2003 Wiley-VCH Verlag.

indicated the presence of 27% recovered (64), 40% C₆₀, and more interestingly, 14% bis-adducts, (68) [175, 176]. Similar results were obtained for other adducts, and a possible mechanism involving the formation of a dimer intermediate in which two fullerene cages share one or two addends was proposed to explain these results [175].

Throughout these investigations attempts to isolate reaction intermediates

had been fruitless, and the fate of removed cyclopropane groups was unknown. To this end, methanofullerene (70) bearing a fluorescent bis-pyrene malonate was prepared according to Sch. 4 and submitted to CPE [177]. After transferring, approximately 2.2 electrons per molecule followed by reoxidation, product analysis yielded 48% C₆₀, 50% of the highly fluorescent bis-pyrene malonate (69), and

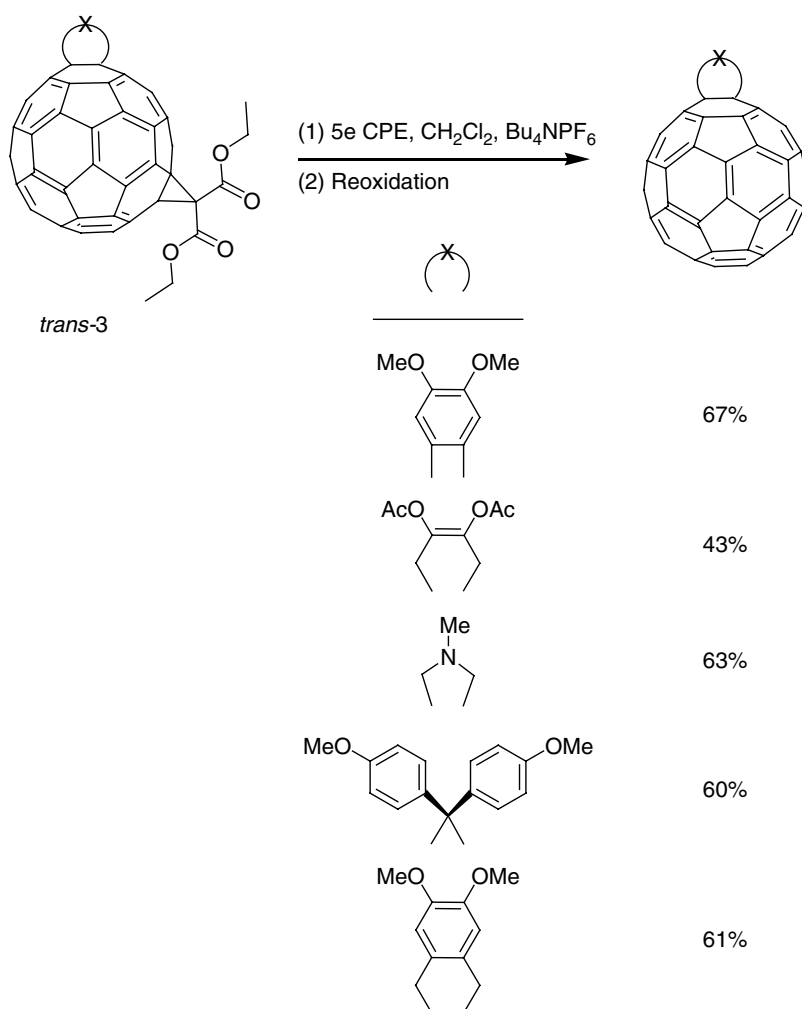


Fig. 29 Selective removal of bis(ethoxycarbonyl)methano addends in mixed C₆₀ bis-adducts.

traces of another fluorescent compound with polarity close to that of C₆₀. Thus, the elusive addend appeared to be intact after electrolytic removal. More significant, however, was the observation that the CV obtained before reoxidation showed the presence of a new redox couple at 500 mV more positive than the first fullerene-based reduction (see Fig. 26). This redox couple was attributed to a stable intermediate since its CV trace remained intact until reoxidation, at which point it disappeared.

Similar observations were made in a separate study carried out with compound (71) (see Fig. 27) [178]. In this case, the appearance of the new redox couple occurred after transferring 2.3 electrons per molecule, and most remarkably and once again, at a potential 500 mV more positive than the first fullerene-based reduction. At about the same time, two relevant articles reporting the formation of singly bonded C₆₀ and C₇₀ dimers [179, 180] appeared. Furthermore, since a redox couple similar to the ones mentioned earlier had been previously observed during CPE of a C₇₀-Bingel monoadduct (72 in Fig. 27) [64], the electrolytic behavior of (72) was restudied, paying particular attention to the formation of dimeric species. The CVs before and after a one-electron CPE of (72) are shown in Fig. 28, where the expected new redox couple can be clearly observed at a potential approximately 500 mV more positive than the first reduction. To obtain additional information about this intermediate, the EPR spectrum of the electrolysis mixture was recorded. The two signals observed were in reasonable agreement with those reported for an ionic complex of the C₇₀ dimer mentioned earlier [180]. Attempts to trap this intermediate resulted

in decomposition, which is probably the result of weakness of the intercage bond. However, CPE of (72) followed by quenching with CH₃I yielded a product displaying a $m/z = 2081$ peak by matrix assisted laser desorption ionization (MALDI) mass spectrometry, a value that is consistent with dimer formation (plus two methyl groups, molecular oxygen, and sodium) as shown in the postulated mechanism in Sch. 5. Support for the ring-opening step of the mechanism has been obtained by digital simulation [181].

The usefulness of the retrocyclopropanation reaction is even more remarkable than previously anticipated. It was questioned whether this reaction allowed the selective removal of a Bingel-type addend while leaving addends of a different type unaffected. A variety of mixed bis-adducts such as those shown in Fig. 29, were prepared, all of which contained a bis(ethoxycarbonyl)methano group [182]. In all cases, CPE led to the selective removal of the Bingel addend in over 60% yield, while the other one was retained, confirming that the reaction may be used in a synthetic protection-deprotection protocol to prepare novel fullerene derivatives.

References

1. H. W. Kroto, J. R. Heath, S. C. O'Brien et al., *Nature* **1985**, 318, 162–163.
2. W. Krätschmer, L. D. Lamb, K. Fostiropoulos et al., *Nature* **1990**, 347, 354–358.
3. F. Diederich, R. Ettl, Y. Rubin et al., *Science* **1991**, 252, 548–551.
4. R. Ettl, I. Chao, F. Diederich et al., *Nature* **1991**, 353, 149–153.
5. K. Kikuchi, N. Nakahara, T. Wakabayashi et al., *Chem. Phys. Lett.* **1992**, 188, 177–180.

6. F. Diederich, R. L. Whetten, *Acc. Chem. Res.* **1992**, 25, 119–126.
7. C. Thilgen, A. Herrmann, F. Diederich, *Angew. Chem., Int. Ed. Engl.* **1997**, 36, 2269–2280.
8. D. M. Guldi, N. Martin, (Eds.), *Fullerenes: From Synthesis to Optoelectronic Properties*, Kluwer, Norwell, 2002.
9. R. C. Haddon, L. E. Brus, K. Raghavachari, *Chem. Phys. Lett.* **1986**, 125, 459–464.
10. L. S. Wang, J. Conceicao, C. Jin et al., *Chem. Phys. Lett.* **1991**, 182, 5–11.
11. P. W. Fowler, J. Woolrich, *Chem. Phys. Lett.* **1986**, 125, 459–464.
12. S. Saito, A. Oshiyama, *Phys. Rev. B* **1991**, 44, 11532–11535.
13. J. Baker, P. W. Fowler, P. Lazzeretti et al., *Chem. Phys. Lett.* **1991**, 184, 182–186.
14. J. R. Colt, G. E. Scuseria, *J. Phys. Chem.* **1992**, 96, 10265–10268.
15. J. Cioslowski, *Electronic Structure Calculations on Fullerenes and Their Derivatives*, Oxford University Press, New York, 1995, Chapters 3, 4, and 5, and references therein.
16. P. W. Fowler, P. W. Ceulemans, *J. Phys. Chem.* **1995**, 99, 508–511.
17. O. V. Boltalina, D. B. Ponomarev, L. N. Sidorov, *Mass Spectrom. Rev.* **1997**, 16, 333–351.
18. O. V. Boltalina, I. N. Ioffe, L. N. Sidorov et al., *J. Am. Chem. Soc.* **2000**, 122, 9745–9749.
19. R. C. Haddon, *Acc. Chem. Res.* **1992**, 25, 127–133.
20. P.-M. Allemand, K. C. Khemani, A. Koch et al., *Science* **1991**, 253, 301–303.
21. S. Nagase, K. Kobayashi, T. Akasaka, in *Fullerenes: Chemistry, Physics, and Technology* (Eds.: K. M. Kadish, R. S. Ruoff), Wiley, New York, 2000, pp. 395–436.
22. A. Hirsch, *Angew. Chem., Int. Ed. Engl.* **1993**, 32, 1138–1141.
23. R. Taylor, R. M. Walton, *Nature* **1993**, 363, 685–693.
24. F. Diederich, *Nature* **1994**, 369, 199–207.
25. A. Hirsch, *Chemistry of the Fullerenes*, Thieme, Stuttgart, 1994.
26. A. Hirsch, (Ed.), *Fullerenes and Related Structures*, Springer, Berlin, 1999.
27. R. E. Haufler, J. Conceicao, L. P. F. Chibante et al., *J. Phys. Chem.* **1990**, 94, 8634–8636.
28. P.-M. Allemand, A. Koch, F. Wudl et al., *J. Am. Chem. Soc.* **1991**, 113, 1050–1051.
29. D. Dubois, K. M. Kadish, S. Flanagan et al., *J. Am. Chem. Soc.* **1991**, 113, 4364–4366.
30. D. Dubois, K. M. Kadish, S. Flanagan et al., *J. Am. Chem. Soc.* **1991**, 113, 7773–7774.
31. Q. Xie, E. Perez-Cordero, L. Echegoyen, *J. Am. Chem. Soc.* **1992**, 114, 3978–3980.
32. D. Dubois, G. Moninot, W. Kutner et al., *J. Phys. Chem.* **1992**, 96, 7137–7145.
33. Y. Ohsawa, T. Saji, *J. Chem. Soc., Chem. Commun.* **1992**, 781–782.
34. F. Zhou, C. Jeboulet, A. J. Bard, *J. Am. Chem. Soc.* **1992**, 114, 11004–11006.
35. F. Paolucci, M. Marcaccio, S. Roffia et al., *J. Am. Chem. Soc.* **1995**, 117, 6572–6580.
36. Q. Xie, F. Arias, L. Echegoyen, *J. Am. Chem. Soc.* **1993**, 115, 9818–9981.
37. T. Wakahara, A. Han, Y. Niino et al., *J. Mater. Chem.* **2002**, 12, 2061–2064.
38. W. Koh, D. Dubois, W. Kutner et al., *J. Phys. Chem.* **1993**, 97, 6871–6879.
39. F. Cheng, Y. Murata, K. Komatsu, *Org. Lett.* **2002**, 4, 2541–2544.
40. G. E. Scuseria, *Chem. Phys. Lett.* **1991**, 180, 451–456.
41. D. M. Cox, S. Bethal, M. Disko et al., *J. Am. Chem. Soc.* **1991**, 113, 2940–2944.
42. K. Meerholz, P. Tschuncky, J. Heinze, *J. Electroanal. Chem.* **1993**, 347, 425–433.
43. S. M. Gorum, M. A. Greaney, D. M. Cox et al., *Mater. Res. Soc. Symp. Proc.* **1991**, 206, 651–658.
44. C. Boudon, J.-P. Gisselbrecht, M. Gross et al., *J. Am. Chem. Soc.* **1998**, 120, 7860–7868.
45. C. Jeboulet, A. Bard, F. Wudl, *J. Am. Chem. Soc.* **1991**, 113, 5456–5457.
46. R. Webster, G. A. Heath, *Phys. Chem. Chem. Phys.* **2001**, 3, 2588–2594.
47. M. D. Diener, J. M. Alford, *Nature* **1998**, 393, 668–671.
48. R. Ettl, I. Chao, F. Diederich et al., *Nature* **1991**, 353, 149–153.
49. F. Diederich, R. L. Whetten, C. Thilgen et al., *Science* **1991**, 254, 1768–1770.
50. J. P. Selegue, J. P. Shaw, T. F. Guarr, in *Recent Advances in the Chemistry and Physics of Fullerenes and Related Materials* (Eds.: K. M. Kadish, R. S. Ruoff), The Electrochemical Society, Pennington, 1994, pp. 1274–1291, Vol. 94–24.

51. P. L. Boulas, M. T. Jones, R. S. Ruoff et al., *J. Phys. Chem.* **1996**, *100*, 7573–7579.
52. T. J. S. Dennis, T. Kai, T. Tomiyama et al., *Chem. Commun.* **1998**, 619–620.
53. M. R. Anderson, H. C. Dorn, S. A. Stevenson et al., *J. Electroanal. Chem.* **1998**, *444*, 151–154.
54. J. Crassous, J. Rivera, N. S. Fender et al., *Angew. Chem., Int. Ed. Engl.* **1999**, *38*, 1613–1617.
55. N. Tagmatarchis, A. G. Avent, K. Prassides et al., *Chem. Commun.* **1999**, 1023–1024.
56. T. J. S. Dennis, T. Kai, K. Asato et al., *J. Phys. Chem. A* **1999**, *103*, 8747–8752.
57. G.-W. Wang, M. Saunders, A. Khong et al., *J. Am. Chem. Soc.* **2000**, *122*, 3216–3217.
58. M. R. Anderson, H. C. Dorn, S. A. Stevenson, *Carbon* **2000**, *38*, 1663–1670.
59. Q. Li, F. Wudl, C. Thilgen et al., *J. Am. Chem. Soc.* **1992**, *114*, 3994–3996.
60. Y. Yang, F. Arias, L. Echegoyen et al., *J. Am. Chem. Soc.* **1995**, *117*, 7801–7804.
61. J. A. Azamar-Barrios, P. E. Muñoz, A. Pénicaud, *J. Chem. Soc., Faraday Trans.* **1997**, *93*, 3119–3123.
62. F. Diederich, R. L. Whetten, C. Thilgen et al., *Science* **1991**, *254*, 1768–1770.
63. J. R. Colt, G. E. Scuseria, *Chem. Phys. Lett.* **1992**, *199*, 505–512.
64. R. Kessinger, J. Crassous, A. Herrmann et al., *Angew. Chem., Int. Ed. Engl.* **1998**, *37*, 1919–1922.
65. A. Herrmann, F. Diederich, *J. Chem. Soc., Perkin Trans. 2* **1997**, 1679–1684.
66. Y. Chai, T. Guo, C. Jin et al., *J. Phys. Chem.* **1991**, *95*, 7564–7568.
67. T. Akasaka, S. Okubo, M. Kondo et al., *Chem. Phys. Lett.* **2000**, *319*, 153–156.
68. T. Akasaka, T. Wakahara, S. Nagase et al., *J. Phys. Chem.* **2001**, *105*, 2971–2974.
69. T. Wakahara, S. Okubo, M. Kondo et al., *Chem. Phys. Lett.* **2002**, *360*, 235–239.
70. H. Shinohara, in *Fullerenes: Chemistry, Physics, and Technology* (Eds.: K. M. Kadish, R. S. Ruoff), Wiley, New York, 2000, pp. 357–393.
71. P. B. Burbank, J. R. Gibson, H. C. Dorn et al., *J. Electroanal. Chem.* **1996**, *417*, 1–4.
72. B. Sun, M. Li, H. Luo et al., *Electrochim. Acta* **2002**, 3545–3549.
73. T. Suzuki, K. Kikuchi, F. Oguri et al., *Tetrahedron* **1996**, *52*, 4973–4982.
74. K. Kikuchi, Y. Nakao, S. Suzuki et al., *J. Am. Chem. Soc.* **1994**, *116*, 9367–9368.
75. Y. Achiba, K. Kikuchi, Y. Aihara et al., *Mater. Res. Soc. Symp. Proc.* **1995**, *359*, 3–9.
76. Z. Slanina, S.-L. Lee, K. Kobayashi et al., *J. Mol. Struct. (Theochem)* **1995**, *339*, 89–93.
77. K. Kobayashi, S. Nagase, *Chem. Phys. Lett.* **1998**, *282*, 325–329.
78. J. A. Azamar-Barrios, T. J. S. Dennis, S. Sadhukan et al., *J. Phys. Chem. A* **2001**, *105*, 4627–4632.
79. N. Martín, L. Sánchez, B. Illescas et al., *Chem. Rev.* **1998**, *98*, 2527–2547.
80. F. Diederich, C. Thilgen, *Science* **1996**, *271*, 317–323.
81. F. Diederich, R. Kessinger, *Acc. Chem. Res.* **1999**, *32*, 537–545.
82. M. Prato, *J. Mater. Chem.* **1997**, *7*, 1097–1109.
83. L. Echegoyen, F. Diederich, L. E. Echegoyen, in *Fullerenes: Chemistry Physics and Technology* (Eds.: R. Ruoff, K. M. Kadish), Wiley, New York, 2000, pp. 1–51.
84. T. F. Guarr, M. S. Meier, V. K. Vance et al., *J. Am. Chem. Soc.* **1993**, *115*, 9862–9863.
85. P. Boulas, F. D'Souza, C. C. Henderson et al., *J. Phys. Chem.* **1993**, *97*, 13435–13437.
86. M. E. Niyazimbetov, D. H. Evans, S. A. Lerke et al., *J. Phys. Chem.* **1994**, *98*, 13093–13098.
87. A. S. Lobach, V. V. Strelets, in *Recent Advances in the Chemistry and Physics of Fullerenes and Related Materials*, (Eds.: P. V. Kamat, D. M. Guldi, K. M. Kadish), The Electrochemical Society, Pennington, 1999, pp. 38–46, Vol. 99–12.
88. C. Caron, R. Subramanian, F. D'Souza et al., *J. Am. Chem. Soc.* **1993**, *115*, 8505–8506.
89. R. Subramanian, K. M. Kadish, M. N. Vijayashree et al., *J. Phys. Chem.* **1996**, *100*, 16327–16335.
90. K. M. Kadish, X. Gao, E. V. Caemelbecke et al., *J. Phys. Chem.* **2000**, *104*, 3878–3883.
91. F. D'Souza, C. Caron, R. Subramanian, in *Recent Advances in the Chemistry and Physics of Fullerenes and Related Materials* (Eds.: K. M. Kadish, R. S. Ruoff), The Electro-

- chemical Society, Pennington, 1994, pp. 768–778, Vol. 94–24.
92. P. J. Fagan, P. J. Krusic, D. H. Evans et al., *J. Am. Chem. Soc.* **1992**, *114*, 9697–9699.
 93. T. Kitagawa, T. Tanaka, Y. Takata et al., *Tetrahedron* **1997**, *53*, 9965–9976.
 94. H. Ikura, S. Mori, M. Sawamura et al., *J. Org. Chem.* **1997**, *62*, 7912–7913.
 95. C. Boudon, J.-P. Gisselbrecht, M. Gross et al., *Helv. Chim. Acta* **1995**, *78*, 1334–1344.
 96. R. Hettich, C. Jin, R. N. Compton, *Int. J. Mass. Spectrom. Ion Processes* **1984**, *138*, 263–274.
 97. N. Liu, Y. Morio, F. Okino et al., *Synth. Met.* **1997**, *86*, 2289–2290.
 98. F. Zhou, G. J. Van Berkel, B. T. Donovan, *J. Am. Chem. Soc.* **1994**, *116*, 5485–5486.
 99. N. Liu, H. Touhara, F. Okino et al., *J. Electrochem. Soc.* **1996**, *143*, 2267–2272.
 100. G. A. Burley, A. G. Avent, O. V. Boltalina et al., *Org. Biomol. Chem.* **2003**, *1*, 2015–2023.
 101. T. Suzuki, Y. Maruyama, T. Akasaka et al., *J. Am. Chem. Soc.* **1994**, *116*, 1359–1363.
 102. P. R. Birkett, R. Taylor, N. K. Wachter et al., *J. Am. Chem. Soc.* **2000**, *122*, 4209–4212.
 103. Y. Murata, K. Motoyama, K. Komatsu, *Tetrahedron* **1996**, *52*, 5077–5090.
 104. F. Hauke, A. Hirsch, S.-G. Liu et al., *Chem. Phys. Chem.* **2002**, *3*, 195–205.
 105. F. Cardullo, P. Seiler, L. Isaac et al., *Helv. Chim. Acta* **1997**, *80*, 343–371.
 106. T. Suzuki, Y. Maruyama, T. Akasaka et al., *J. Am. Chem. Soc.* **1994**, *116*, 1359–1363.
 107. J. C. Hummelen, B. Knight, J. Pavlovich et al., *Science* **1995**, *269*, 1554–1556.
 108. B. Knight, N. Martín, T. Ohno et al., *J. Am. Chem. Soc.* **1997**, *119*, 9871–9882 and references cited therein.
 109. T. da Ros, M. Prato, M. Carano et al., *J. Am. Chem. Soc.* **1998**, *120*, 11645–11648.
 110. D. M. Guldi, M. Prato, *Acc. Chem. Res.* **2000**, *33*, 695–703.
 111. X.-W. Wei, A. D. Darwish, O. V. Boltalina et al., *Angew. Chem., Int. Ed. Engl.* **2001**, *40*, 2989–2992.
 112. L. Fan, F. Li, Y. Li et al., *Chem. Phys. Lett.* **1998**, *294*, 443–446.
 113. B. Illescas, N. Martín, C. Seoane, *Tetrahedron Lett.* **1997**, *38*, 2015–2018.
 114. M. Diekers, A. Hirsch, S. Pyo et al., *Eur. J. Org. Chem.* **1998**, 1111–1121.
 115. F. Langa, P. de la Cruz, E. Espíldora et al., *J. Org. Chem.* **2001**, *66*, 5033–5041.
 116. M. Carano, T. da Ros, M. Fonti et al., *J. Am. Chem. Soc.* **2003**, *125*, 7139–7144.
 117. B. M. Illescas, N. Martín, C. Seoane et al., *J. Org. Chem.* **1997**, *62*, 7585–7591.
 118. G. Yu, J. Gao, J. C. Hummelen et al., *Science* **1995**, *270*, 1789–1791.
 119. J.-F. Nierengarten, J.-F. Eckert, D. Felder et al., *Carbon* **2000**, *38*, 1587–1598.
 120. M. M. Wienz, J. M. Kroon, W. J. H. Verhees et al., *Angew. Chem., Int. Ed. Engl.* **2003**, *42*, 3371–3375.
 121. L. Echegoyen, M. A. Herranz, in *Developments in Fullerene Science* (Fullerenes: From synthesis to Optoelectronic Properties), (Eds.: D. M. Guldi, N. Martin), Kluwer Academic Publishers, The Netherlands, 2002, pp. 267–293, Vol. 4 and references cited therein.
 122. J.-F. Eckert, J.-F. Nicoud, J.-F. Nierengarten et al., *J. Am. Chem. Soc.* **2000**, *122*, 7467–7479.
 123. D. M. Guldi, M. Maggini, E. Menna et al., *Chem. Eur. J.* **2001**, *7*, 1597–1605.
 124. A. Gouloumis, S.-G. Liu, A. Sastre et al., *Chem. Eur. J.* **2000**, *6*, 3600–3607.
 125. D. González-Rodríguez, T. Torres, D. M. Guldi et al., *Org. Lett.* **2002**, *4*, 335–338.
 126. J. Llacay, J. Veciana, J. Vidal-Gancedo et al., *J. Org. Chem.* **1998**, *63*, 5201–5210.
 127. V. Balzani, A. Juris, M. Venturi et al., *Chem. Rev.* **1996**, *96*, 759–833.
 128. N. Martín, J. L. Segura, *Angew. Chem., Int. Ed. Engl.* **2001**, *40*, 1372–1409.
 129. A. B. Smith III, R. M. Strongin, L. Brard et al., *J. Am. Chem. Soc.* **1993**, *115*, 5829–5830.
 130. T. Suzuki, Q. Li, K. C. Khemani et al., *J. Am. Chem. Soc.* **1992**, *114*, 7301–7302.
 131. L. Isaacs, F. Diederich, *Helv. Chim. Acta* **1993**, *76*, 2454–2464.
 132. R. J. Taylor, *J. Chem. Soc., Perkin Trans.* **1992**, 3–6.
 133. L. Isaacs, A. Wehrsig, F. Diederich, *Helv. Chim. Acta* **1993**, *76*, 1231–1250.
 134. M. Eiermann, F. Wudl, M. Prato et al., *J. Am. Chem. Soc.* **1994**, *116*, 8364–8365.

135. F. Arias, L. Echegoyen, S. R. Wilson et al., *J. Am. Chem. Soc.* **1995**, *117*, 1422–1427.
136. F. Arias, Q. Xie, Y. Wu et al., *J. Am. Chem. Soc.* **1994**, *116*, 6388–6394.
137. P. Ceroni, F. Conti, C. Corvaja et al., *J. Phys. Chem. A* **2000**, *104*, 156–163.
138. N. Armaroli, G. Accorsi, D. Felder et al., *Chem. Eur. J.* **2002**, *78*, 2314–2323.
139. J.-P. Bourgeois, P. Seiler, M. Fibbioli et al., *Helv. Chim. Acta* **1999**, *82*, 1572–1595.
140. L. Echegoyen, L. E. Echegoyen, *Acc. Chem. Res.* **1998**, *31*, 593–601.
141. A. L. Balch, M. M. Olmstead, *Chem. Rev.* **1998**, *98*, 2123–2165.
142. P. Zanello, in *Chemistry at the Beginning of the Third Millenium* (Eds.: L. Fabrizzi, A. Poggi), Springer, Berlin, 2000, pp. 247–278.
143. M. Ferduco, D. A. Costa, A. L. Balch et al., *Angew. Chem., Int. Ed. Eng.* **1995**, *34*, 194–196.
144. K. Winkler, D. A. Costa, A. L. Balch et al., *J. Phys. Chem.* **1995**, *99*, 17431–17436.
145. P. Timmerman, L. E. Witschel, F. Diederich et al., *Helv. Chim. Acta* **1996**, *79*, 6–20.
146. T. Suzuki, Q. Li, K. C. Khemani et al., *J. Am. Chem. Soc.* **1992**, *114*, 7300–7301.
147. G.-W. Wang, K. Komatsu, Y. Murata et al., *Nature* **1997**, *387*, 583–586.
148. K. Komatsu, K. Fujiwara, Y. Murata, *Chem. Commun.* **2000**, 1583–1584.
149. J. C. Hummelen, B. Knight, J. Pavlovich et al., *Science* **1995**, *269*, 1554–1556.
150. A. L. Balch, D. A. Costa, W. R. Fawcett et al., *J. Phys. Chem.* **1996**, *100*, 4823–4827.
151. N. Drago, H. Shimotani, M. Hayashi et al., *J. Org. Chem.* **2000**, *65*, 3269–3273.
152. N. Drago, H. Shimotani, J. Wang et al., *J. Am. Chem. Soc.* **2001**, *123*, 1294–1301.
153. Y. Murata, M. Suzuki, K. Komatsu, *Chem. Commun.* **2001**, 2338–2339.
154. K. Lee, H. Song, B. Kim et al., *J. Am. Chem. Soc.* **2002**, *124*, 2872–2873.
155. K. Fujiwara, K. Komatsu, *Org. Lett.* **2002**, *4*, 1039–1041.
156. Y. Murata, A. Han, K. Komatsu, *Tetrahedron Lett.* **2003**, *44*, 8199–8201.
157. M. S. Meier, M. Poplawska, A. L. Compton et al., *J. Am. Chem. Soc.* **1994**, *116*, 7044–7048.
158. J.-F. Nierengarten, A. Herrmann, R. R. Tykwinski et al., *Helv. Chim. Acta* **1997**, *80*, 293–316.
159. A. Avent, P. R. Birkett, M. Carano et al., *J. Chem. Soc., Perkin Trans. 2* **2002**, 140–145.
160. M. J. van Eis, I. Pérez-Núñez, L. A. Muslinkina et al., *J. Chem. Soc., Perkin Trans. 2* **2001**, 1890–1892.
161. A. S. Lobach, V. V. Strelets, *Russ. Chem. Bull., Int. Ed.* **2001**, *50*, 996–999.
162. K.-M. Mangold, W. Kutner, L. Dunsch et al., *Synth. Methods* **1996**, *77*, 73–76.
163. K. M. Kadish, X. Gao, E. Van Caemelbecke et al., *J. Phys. Chem. A* **1998**, *102*, 3898–3906.
164. P. L. Boulas, Y. Zuo, L. Echegoyen, *Chem. Commun.* **1996**, 1547–1548.
165. K. M. Kadish, X. Gao, O. Gorelik et al., *J. Phys. Chem. A* **2000**, *104*, 2902–2907.
166. C. Reed, R. D. Bolskar, *Chem. Rev.* **2000**, *100*, 1075–1120.
167. S. Fukuzumi, T. Suenobu, T. Hirasaka et al., *J. Am. Chem. Soc.* **1998**, *120*, 9220–9227.
168. R. Kessinger, M. Gómez-López, C. Boudon et al., *J. Am. Chem. Soc.* **1998**, *120*, 8545–8546.
169. A. Hirsch, I. Lamparth, H. R. Karfunkel, *Angew. Chem., Int. Ed. Engl.* **1994**, *33*, 437–438.
170. F. Arias, Y. Yang, L. Echegoyen, in *Recent Advances in the Chemistry and Physics of Fullerenes and Related Materials* (Eds.: R. D. Ruoff, K. M. Kadish), The Electrochemical Society, Pennington, 1995, pp. 200–212, Vol. 95-10.
171. C. Bingel, *Chem. Ber.* **1993**, *126*, 1957–1959.
172. L. E. Echegoyen, F. D. Djojo, A. Hirsch et al., *J. Org. Chem.* **2000**, *65*, 4994–5000.
173. N. S. Fender, B. Nuber, D. I. Schuster et al., *J. Chem. Soc., Perkin Trans. 2* **2000**, 1924–1928.
174. M. W. J. Beulen, L. Echegoyen, J. A. Rivera et al., *Chem. Commun.* **2000**, 917–918.
175. M. W. J. Beulen, J. A. Rivera, M. A. Herranz et al., *Chem. Commun.* **2001**, 407–408.
176. M. W. J. Beulen, J. A. Rivera, M. A. Herranz, et al., *J. Org. Chem.* **2001**, *66*, 4393–4398.

177. M. A. Herranz, C. T. Cox, L. Echegoyen, *J. Org. Chem.* **2003**, 68, 5009–5012.
178. M. Ocafrain, M. A. Herranz, L. Marx et al., *Chem. Eur. J.* **2003**, 9, 4811–4819.
179. F. Cheng, Y. Murata, K. Komatsu, *Org. Lett.* **2002**, 4, 2541–2544.
180. D. V. Konarev, S. S. Khasanov, I. I. Vorontsov et al., *Chem. Commun.* **2002**, 2548–2549.
181. M. Carano, L. Echegoyen, *Chem. Eur. J.* **2003**, 9, 1974–1981.
182. R. Kessinger, N. S. Fender, L. E. Echegoyen et al., *Chem. Eur. J.* **2002**, 6, 2184–2192.

6.2 Electrochemical Reactions of Carbon Dioxide

Daniel L. DuBois
National Renewable Energy Laboratory,
Golden, Colorado, USA

6.2.1 Introduction

Carbon dioxide is the ultimate source of the various carbon-based materials used in our daily lives. These include food, fossil fuels, natural and synthetic fibers, wood for construction materials, and so on. The process that fixes the carbon in these materials is photosynthesis, the biological conversion of sunlight, water, and carbon dioxide into a variety of reduced organic materials. During photosynthesis, sunlight is transformed into electrical energy in the form of separated charges, then via electron transfer and chemical steps this energy is changed into chemical energy stored in the form of C–H and C–C bonds by reduction of carbon dioxide. Photosynthesis occurs on a very large scale fixing some 200 gigatons of carbon dioxide annually [1]. Because of its importance, it is natural that scientists would want to mimic the fixation of carbon dioxide.

The abundance and nontoxic nature of carbon dioxide also make it an attractive carbon feedstock. Potential sources of carbon dioxide include the atmosphere (where it is present in concentrations of approximately 370 ppm), natural reservoirs including natural gas wells and pure CO₂ wells, waste streams of fermentation reactions, and flue stacks from power plants, cement production, and so on. Because CO₂ is not toxic, development of chemical processes in which CO₂ can be used to

replace toxic substrates such as phosgene and volatile organic solvents are being sought. The nontoxic nature of CO₂ makes it an ideal substrate and solvent for drug synthesis and food processing.

Use of CO₂ is also attractive from the perspective of reducing the amount of CO₂ that human activities contribute to the atmosphere (approximately 20–30 gigatons of CO₂ per year) [2]. However, two conditions must be met to achieve CO₂ mitigation if CO₂ is used as a feedstock: (1) the energy source required for these processes should not come from the combustion of fossil fuels, and (2) the source of CO₂ should not be a natural reservoir that already sequesters CO₂. If the combustion of fossil fuels is the source of the energy for a process that uses CO₂, it is likely that more CO₂ will be produced by combustion than is consumed in the chemical process. However, if the source of energy is one that does not produce CO₂ (such as wind turbines, solar cells, or nuclear reactors), production of carbon-based products from CO₂ reduction using these energy sources would result in a net fixation of CO₂. Even after these materials are degraded or combusted, there would be no net contribution to atmospheric carbon dioxide. If the source of CO₂ is a natural reservoir, CO₂ that is already sequestered will be released into the atmosphere when the carbon-based material produced by reduction is burned or degraded via natural processes. The overall result would be the transformation of sequestered CO₂ into atmospheric CO₂, which has the same net effect as the combustion of fossil fuels. Finally, the amount of CO₂ consumed must be very large to have a significant impact on the 20–30 gigatons of CO₂ produced by mankind. Only fuels and construction materials are consumed on a

sufficiently large scale to have a significant impact on the overall carbon budget.

It is the objective of this review to provide an overview of electrochemical processes involving CO₂. It is not intended to be an exhaustive review, but rather to provide a brief but reasonably comprehensive introduction to the area. Most of this research is in its early stages, and the processes discussed represent what may be possible in the future in terms of the electrochemical production of chemicals directly from CO₂. This review will be organized in terms of the degree of reduction of CO₂. It will begin with a brief discussion of bonding of CO₂ to different metal complexes to illustrate some of the various bonding modes that have been observed. The next subject will be electrochemical processes, in which CO₂ is bound and released during an electrochemical cycle, but no irreversible bond formation or cleavage occurs. Then one-electron reductions of CO₂ in which C–C bonds are formed will be discussed followed by two-, four-, six-, and eight-electron reductions of CO₂. Reductions by two or more electrons require the cleavage of C–O and/or the formation of C–H or C–C bonds. In a few cases, information on the mechanism is known, but in most cases, mechanistic information is lacking. More time is devoted to those processes in which the mechanisms are reasonably well understood, because they provide the basis for rational approaches to improving catalytic processes and designing new ones.

6.2.2

CO₂ Binding

6.2.2.1 Modes of CO₂ Binding

CO₂ is a weak acid, and its reactions and bonding characteristics reflect this acidity.

The lowest unoccupied molecular orbital of CO₂ resides predominantly on the carbon atom, and hence carbon is the site at which bases bind. Water reacts with CO₂ to form carbonic acid, and in the process a new C–O bond is formed and the O–C–O bond angle decreases from 180° to approximately 120°. Similarly, amines, alkoxides, carbanions, and a variety of other nucleophiles react with CO₂ by forming a new bond between the nucleophile and carbon. In all of these cases, the resulting CO₂ fragment is strongly bent. When metal surfaces and transition metal complexes interact with CO₂, it is typically via a similar M–C bond. A wide variety of bonding modes between transition metal complexes and CO₂ have been determined by X-ray structural studies. This subject is reviewed in detail by Gibson [3]. Four of the more common bonding modes observed for transition metal CO₂ complexes are shown schematically by structures (1–4). The formation of an M–C bond is the one common feature. In these structures, μ indicates that the CO₂ molecule bridges two or more metals with the subscript indicating the number of metal ions bridged. The number of bonds or significant interactions (n) between CO₂ and the metal or metals to which it is bound is indicated by η^n . The simplest bonding mode is η^1 and has been observed for Rh(diars)₂Cl(CO₂), (1) [4]. This structural motif can be viewed as the result of a nucleophilic attack of the rhodium center on CO₂ to transfer a pair of electrons to CO₂ with formation of a Rh(III) complex. It is analogous to the attack of a strong carbon nucleophile, such as a Grignard reagent, on CO₂ to form a carboxylic acid. The strength of this interaction is dependent on the ligand trans to the C atom of CO₂. If this trans ligand is lost, to form a five-coordinate complex, less electron density is transferred to CO₂ [5].

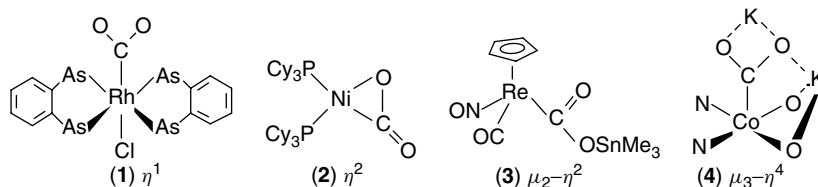
A second common structural arrangement for CO₂ binding to a single metal center is the η^2 bonding mode observed for a variety of metal complexes. Examples include both late and early transition metals, such as Ni(PCy₃)₂(CO₂), (2), [6] and Cp₂Nb(CH₂SiMe₃)(CO₂) [7]. This type of bonding can be rationalized in terms of electron transfer to the carbon atom of CO₂ to produce CO₂ bending, and electron transfer back to the metal atom via a negatively charged oxygen atom. Complexes of this type typically have O–C–O bond angles between 130 and 136°, which is somewhat larger than those observed for other modes of bonding. A variety of examples are known in which a nucleophilic metal center (M₁) interacts with the carbon atom of CO₂ and one or more electrophilic metal centers interact with the oxygen atoms of CO₂ as shown in structures (3) and (4) [8–10]. These electrophilic interactions are important because they stabilize the M–C bond. The number of additional bonds to CO₂ occurring through the oxygen atoms ranges from 1 to 4. Coordination through a single oxygen with no M–C bond is also possible. One structurally characterized example of this mode of bonding has been reported, and the U–O–C (171.1°) and O–C–O (178.0°) bond angles are nearly linear [11].

The structures observed for these discrete metal–CO₂ complexes illustrate that the binding of CO₂ can be quite variable. The situation is even more complex on electrode surfaces. Most metal electrodes

will be polycrystalline and present multiple surfaces with many different binding sites on each surface. In addition, it is likely that the surface will change as a function of the applied potential. This may be the result of structural changes; adsorption or desorption of solvents, hydrogen atoms, and so on; and/or because surface atoms with increasingly negative charge interact more strongly with the carbon atom of CO₂. In addition, chemisorption, in which the C–O bond is cleaved is much more common on metal surfaces than for discrete complexes [12]. However, the properties that influence the mode of binding on surfaces should be the same as those observed for the structurally characterized complexes discussed earlier.

6.2.2.2 Thermodynamics and Kinetics of CO₂ Binding to Substrates

Table 1 lists some of the binding constants and rate constants measured for the reaction of CO₂ with redox-active molecules. Various techniques have been used to measure these constants including cyclic voltammetry, pulsed radiolysis, and bulk electrolysis followed by UV–visible spectral measurements. The binding constants span an enormous range from less than 1 to 10¹⁵ M^{−1} [13–17]. Co(I) and Ni(I) macrocyclic complexes have been studied in some detail [13–16]. For the cobalt complexes, the CO₂ binding constants (*K*) and second-order rate constants for CO₂ binding (*k_f*) are largely determined by the Co(II/I) reduction potentials

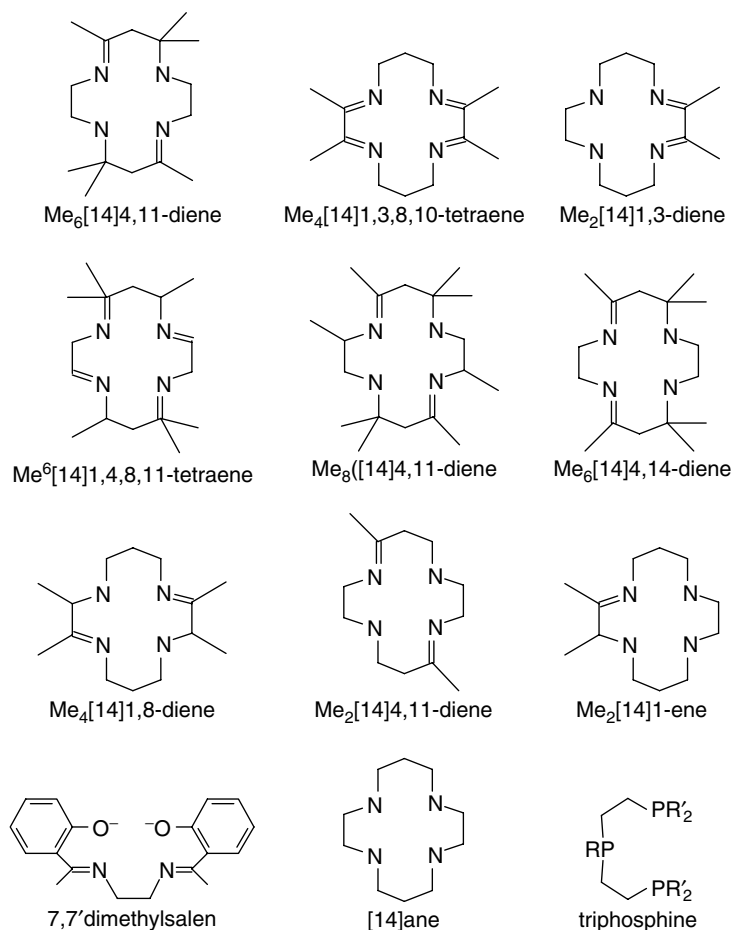


Tab. 1 CO₂ binding constants and rates for selected redox-active compounds

Compound	$E_{1/2}[V]^a$	$K [M^{-1}]^b$	$k_f [M^{-1} s^{-1}]^c$	$k_r [s^{-1}]^d$	Solvent ^e	References
Co(Me ₄ [14]1,3,8,10-tetraene) ⁺	−0.76	<0.5			CH ₃ CN	14
Co(Me ₂ [14]1,3-diene) ⁺	−1.31	<4 <0.5			DMSO CH ₃ CN	15 14
Co(Me ₆ [14]1,4,8,11-tetraene) ⁺	−1.42	<4			DMSO	15
Co(Me ₈ [14]4,11-diene) ⁺	−1.70	4.0			CH ₃ CN	14
Co(Me ₆ [14]4,14-diene)	−1.74	7 26			DMSO CH ₃ CN	15 14
Co(<i>meso</i> -Me ₆ [14]4,11-diene) ⁺	−1.74	1.7×10^2			CH ₃ CN	14
Co(<i>rac</i> -Me ₆ [14]4,11-diene) ⁺	−1.74	6.0×10^6 2.6×10^2 1.2×10^4			H ₂ O DMSO CH ₃ CN	 15 14
Co(Me ₄ [14]1,8-diene) ⁺	−1.80	3.0×10^4 1.8×10^4 4.0×10^4 3.0×10^3 4.5×10^8 9×10^4 1×10^5	1.7×10^8	0.38	DMSO DMF PC THF H ₂ O CH ₃ CN	15 15 15 15 14 14
Co(Me ₂ [14]4,11-diene) ⁺	−1.91	7×10^5	3.7×10^8		DMSO CH ₃ CN	15 14
Co(Me ₂ [14]1-ene) ⁺	−2.05	Irreversible			DMSO	15
Ni([14]ane) ⁺	−1.89	3×10^6 Irreversible			CH ₃ CN DMSO	14 15
Co(7,7'-dimethylsalen) ^{−f}	−1.73 −1.65 −1.84	16 500 120 2	3.2×10^7	2.0×10^6	H ₂ O THF, NaTf THF, LiTf THF, Bu ₄ Tf	16 15 15 15
2,6-Di- ^t Bu-benzoquinone (−2)	−1.86	1.1×10^{15}			CH ₃ CN	17
Phenanthrenequinone (−2)	−1.59	6.7×10^{11}			CH ₃ CN	17
2,3-Dicyanobenzoquinone (−2)	−0.77	5.6×10^3			CH ₃ CN	17
2,3-Dichloro-5,6-dicyanobenzoquinone (−2)	−0.65	3.6			CH ₃ CN	17

^aV vs. SCE for the (II/I) redox couples of the cobalt and nickel complexes and the quinone (−1/−2) couples. ^bEquilibrium constant for the reaction of a metal complex or a quinone dianion with CO₂. ^cSecond-order rate constant for CO₂ binding. ^dFirst-order rate constant for loss of CO₂ from a M–CO₂ complex. ^eSolvent used in the study. ^fDifferent binding constants for this compound reflect the effects of using different salts of the triflate anion (Tf) as indicated in the solvent column.

List of Ligands



with minor roles being played by specific steric interactions. It can be seen that no measurable binding is observed for reduction potentials more positive than -1.65 V vs. the ferrocene/ferrocenium couple. For redox potentials more negative than -1.9 V, the binding was classified as irreversible [15]. Studies of solvent effects for $[\text{Co}(\text{rac-Me}_6[14]4,11\text{-diene})]^+$ indicate that changing from one organic solvent to another does not significantly change the binding constants of CO_2 to these

metal complexes [14, 15]. However, the equilibrium constants for the *rac* and *meso* isomers of $[\text{Co}(\text{Me}_6[14]4,11\text{-diene})]^+$ are approximately 10^4 larger in water than in acetonitrile (CH_3CN), dimethylsulfoxide (DMSO), and other organic solvents. This may be due to enhanced hydrogen bonding in water, and intramolecular hydrogen bonding to ligand NH protons has been demonstrated for these complexes as well [13]. Comparison of the binding constants for $\text{Ni}([14]\text{ane})^+$ reveals that CO_2

binding in water [16] is much weaker, $K = 16$, than in dimethyl sulfoxide in which the binding has been characterized as irreversible [15]. The reason for this difference is not clear. The nature of the cation in the supporting electrolyte can have a significant influence on the CO_2 binding constants, especially in solvents such as tetrahydrofuran (THF), where ion pairing is more likely to occur than in solvents with higher dielectric constants. For example, the binding constant of $[\text{Co}(7,7'\text{-dimethylsalen})]^{-1}$ for CO_2 in THF is over 100 times larger when the NaCF_3SO_3 is the supporting electrolyte compared to $\text{Bu}_4\text{NCF}_3\text{SO}_3$ (see Table 1) [15].

The CO_2 binding constants of a series of quinone dianions (see Table 1) are much larger than those of the Co(I) macrocycles for the same redox potential. This is probably a reflection of much stronger C–O bonds compared to M–C bonds. The binding constants of the quinone dianions also exhibit a linear dependence on potential of the $(-1/-2)$ couple of the quinones [17]. Because the binding constants of the quinones vary over a large range as a function of the oxidation state, they have been studied for their ability to bind and release CO_2 when carried through an electrochemical cycle [17]. Pumping experiments in which CO_2 concentrations have been increased from 0.5% CO_2 in a CO_2/N_2 feed gas to 100% CO_2 in an exit gas have been described using 2,6-di-*t*-Bu-benzoquinone as the CO_2 carrier in propylene carbonate [18]. Such cycles might be useful for recovery of CO_2 from dilute gas streams or from the atmosphere. Electrochemical cycles based on molten carbonate fuel cells have also been proposed for CO_2 separation and recovery [19, 20].

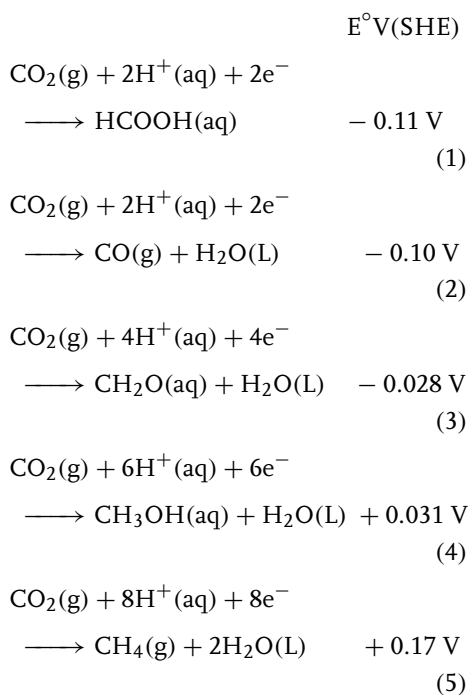
From the data in Table 1, it can be seen that CO_2 binding constants for electrochemically active molecules span

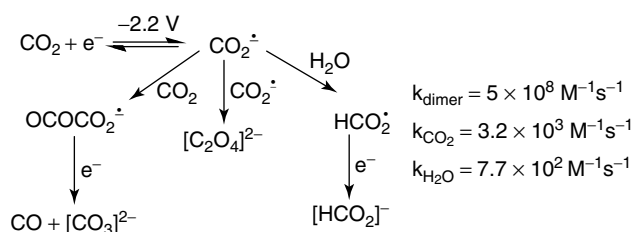
an enormous range. Understanding the features that control this binding will be critical for developing catalysts or carriers that are ideal for specific applications.

6.2.3

Electrochemical CO_2 Reduction

Because CO_2 is the final product of combustion, reactions of CO_2 generally require a significant input of energy and result in the reduction of CO_2 . This energy requirement can be chemical energy stored in highly reactive bonds and intermediates, but of more relevance to this review are the reduction potentials required for electrochemical reactions. The electrochemical potentials required for the reduction of CO_2 to a variety of one-carbon products are shown in reactions (1–5) [12]. These potentials are all within a couple of tenths of a volt of the potential required for the reduction of protons to hydrogen.





Scheme 1

In general, reactions (1–5) require catalysts, and so the chemistry discussed in the following sections will deal predominantly with the role of catalysts in different chemical transformations. Catalysts are of two basic types, homogeneous and heterogeneous. Homogeneous catalysts are molecules that are evenly distributed throughout a solution, and as a result, the catalytic reactions occur in solution. A heterogeneous catalyst is a solid, and the catalytic reaction occurs at the interface between the solid and a liquid or a gas phase. It is generally easier to determine mechanisms for reactions that occur in solution, than it is for reactions that occur on electrode surfaces. The concentrations of catalysts and reagents are more easily controlled in solution, and a wider range of spectroscopic studies are routinely available, especially nuclear magnetic resonance techniques. It is also easier to control structural features of homogeneous catalysts. This makes it possible to probe detailed structure–activity relationships. For these reasons, most of the mechanistic studies discussed in the following sections are of homogeneous or molecular catalysts.

Heterogeneous catalysts on the other hand, offer significant practical advantages. Perhaps the most important of these is that heterogeneous catalysts are generally more easily recovered from the reaction mixture. If the catalyst is the

electrode itself, or if it is attached to the electrode surface, removing the electrode from the solution also results in the separation and recovery of the catalyst. For homogeneous catalysts, solvent removal and separation of the catalyst from the supporting electrolyte are required. A second attractive feature of heterogeneous catalysts is that they are frequently more robust than homogeneous catalysts. In general, this review will emphasize mechanistic studies, and as a result, homogeneous catalysis is strongly emphasized. However, there are a number of very interesting reactions catalyzed by heterogeneous catalysts that have no homogeneous analogs, and these reactions will also be described.

6.2.3.1 One-electron Reduction to Oxalate

The outer-sphere one-electron reduction of CO_2 leads to the formation of the $\cdot\text{CO}_2^-$ radical anion. In dry dimethylformamide, the $\text{CO}_2/\cdot\text{CO}_2^-$ couple has been experimentally determined to be -2.21 V vs. standard calomel electrode (SCE) or approximately -2.6 V vs. the ferrocene/ferrocenium couple [21, 22]. From pulse radiolysis experiments, the reduction potential of CO_2 is -1.90 V vs. the SHE in water (-2.14 V vs. SCE) [23]. Theoretical calculations have been used to calculate the contributions of various factors to the reduction potential of CO_2 . These include the electron affinity of CO_2 ,

stretching and bending contributions that are required to change the geometry of CO_2 from linear to bent, solvation energies, and so on [12]. The interaction between the electrode surface and CO_2 must be negligible, for an outer-sphere electron transfer to occur. Once the CO_2 radical ion is formed, different reaction pathways are available depending on the medium. Saveant and coworkers have suggested that the $\bullet\text{CO}_2^-$ radical anion formed at the electrode surface can undergo three different homogeneous reactions depending on the reaction conditions (Sch. 1) [21, 22]. In the middle reaction of Sch. 1, two $\bullet\text{CO}_2^-$ radical anions react to form oxalate. This reaction is fast in both water ($1.3 \times 10^9 \text{ M}^{-1} \text{ s}^{-1}$) [24] and organic solvents such as dimethylformamide ($5 \times 10^8 \text{ M}^{-1} \text{ s}^{-1}$) [25]. This reduction involves only one electron per carbon atom and results in the formation of a C–C bond. This C–C bond formation is significant as a potential starting point for the synthesis of multicarbon organic products.

It can be seen from the relative rate constants shown in Sch. 1 that the products formed will depend on the reaction conditions [26]. The production of formate, as shown by the right-hand reaction in Sch. 1, will be enhanced in protic solvents or in more acidic solutions. In water, formic acid is the main product. The production of CO, as shown by the left-hand reaction in Sch. 1, will be enhanced in rapidly stirred solutions in which locally high concentrations of the $\bullet\text{CO}_2^-$ radical anion cannot buildup. This will decrease the probability of a bimolecular reaction between $\bullet\text{CO}_2^-$ radical anions. In quiet solutions and high current densities, the $\bullet\text{CO}_2^-$ radical anion concentration should be high in the diffusion layer, favoring formation of oxalate.

The reduction of carbon dioxide on graphite electrodes modified with cobalt phthalocyanine has been reported to yield oxalic acid and glycolic acid [27]. Reduction of CO_2 at unmodified glassy carbon electrodes and graphite electrodes in basic aqueous solutions containing tetramethylammonium ions has also been reported to produce oxalate and glycolic acid [28, 29]. The relatively positive reduction potential (-0.74 V vs. SCE at pH 10) was attributed to the specific adsorption of the triethylammonium cation. The strongly adsorbed cations are thought to stabilize the $\bullet\text{CO}_2^-$ radical anion formed by CO_2 reduction. This interaction of the negative charge of the radical anion with the adsorbed cations results in significantly more positive potentials for CO_2 reduction. In this case, oxalate production is also thought to occur by dimerization of adsorbed radical anions rather than dimerization of $\bullet\text{CO}_2^-$ radical anions in solution. Similar studies at lead electrodes have also been reported [30].

Silver and palladium porphyrins [31], nickel macrocycles [32], and organic molecules such as benzoate esters and benzonitrile have been reported to act as homogeneous catalysts for the reduction of CO_2 to oxalate. It appears from mechanistic studies of the aromatic organic catalysts that the oxalate formation again proceeds through the formation of the $\bullet\text{CO}_2^-$ radical anion, but in this case, the electron transfer is proposed to occur via a nucleophilic attack of the aromatic radical anion ($\text{ArO}^-\bullet$) on CO_2 . In the case of a benzoate ester, this nucleophilic attack involves the formation of a bond between the carbon atom of CO_2 and the oxygen atom of the radical anion of the ester. This C–O bond undergoes a homolytic cleavage reaction to regenerate the

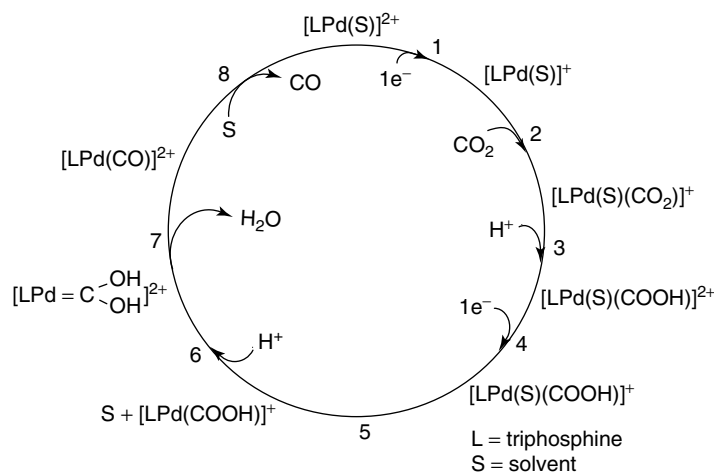
benzoate ester catalyst and the $\bullet\text{CO}_2^-$ radical anion. This inner-sphere mechanism is favored over an outer-sphere mechanism because all of the data could not be fit with a single Marcus correlation line as expected for an outer-sphere mechanism. $\text{Ni}^{(\text{I})}$ complexes are also thought to react with CO_2 to form the $\bullet\text{CO}_2^-$ radical anion in a similar manner, except that formation and cleavage of a Ni–C bond is proposed instead of a C–O bond [32]. The $\bullet\text{CO}_2^-$ radical anion that is formed in this inner-sphere process undergoes dimerization to form oxalate in dry dimethylformamide solutions as discussed earlier. The important point is that the CO_2 radical anion can form by either inner-sphere or outer-sphere electron transfer mechanisms. Once the radical anions are formed, rapid dimerization to oxalate occurs.

6.2.3.2 Two-electron Reduction to Carbon Monoxide

In Sch. 1, if the $\bullet\text{CO}_2^-$ radical anion reacts with CO_2 in solution, CO is formed via a dimeric intermediate in which a C–O bond is formed. A second electron transfer to this intermediate from either the electrode or $\bullet\text{CO}_2^-$ leads to the formation of carbon monoxide. The ultimate result of this pathway is the formation of the two-electron reduction product, carbon monoxide, and carbonate. In this reaction, a second CO_2 molecule acts as the acceptor of the oxide ion formed in the two-electron reduction of CO_2 to CO. Many of the features of these reactions are common to the catalyzed reactions discussed in the following. Because free $\bullet\text{CO}_2^-$ is not present in the catalyzed two-electron reductions of CO_2 to CO, the reduction potentials can be considerably less negative than that required to form $\bullet\text{CO}_2^-$.

A number of homogeneous catalysts are known for the electrochemical reduction of CO_2 to CO. These include macrocyclic complexes of iron, cobalt, and nickel; bipyridine complexes of Re, Ru, Os, Rh, and Ir; and triphosphine complexes of palladium. Although this list is not exhaustive, it does include the systems that have been most extensively studied. In 1980, several of the discrete macrocyclic complexes of cobalt shown in Table 1 were reported to produce a mixture of CO and hydrogen when electrolyzed under CO_2 in water or aqueous acetonitrile solutions [33]. This led to a number of studies directed at understanding this catalytic process in more detail and the development of new classes of catalysts. From these studies, a rather general picture of the mechanism for the transition metal catalyzed reduction of CO_2 to CO has emerged. One such mechanism for $[\text{Pd}(\text{triphosphine})(\text{solvent})]^{2+}$ complexes is shown in Sch. 2 [34, 35]. This catalytic mechanism has been studied in some detail, and it illustrates important steps that are common to all catalysts known to reduce CO_2 to CO. It is also clear from Sch. 2 that even a simple two-electron reduction of CO_2 to CO involves a number of discrete steps that must occur in a coordinated fashion for catalysis to occur. To simplify this catalytic cycle, four general processes will be considered. These steps are (1) electron transfer to form a reduced metal complex, (2) CO_2 binding to the metal complex, (3) CO bond cleavage with a formal loss of O^{2-} , and (4) loss of CO.

In the process of reducing CO_2 to CO, two electrons must be transferred, but these electron transfer steps have intervening chemical steps between them. For example, in Sch. 2, one-electron transfer occurs immediately before CO_2 binding, and the second electron transfer occurs two steps later, after protonation of



Scheme 2

the bound CO_2 . Clearly, the two-electron transfer steps are not concerted. This is a fairly general observation for catalyzed reductions of CO_2 .

In Sch. 2, the reduction of $\text{Pd}(\text{II})$ to $\text{Pd}(\text{I})$ is immediately followed by CO_2 binding (step 2) to form a metal carboxylate complex. For the $[\text{Pd}(\text{triphosphine})(\text{solvent})]^{2+}$ catalysts shown in Sch. 2, this is the rate-determining step at high acid concentrations ($>0.01 \text{ M}$) with second-order rate constants ranging from 5 to $300 \text{ M}^{-1} \text{ s}^{-1}$ [35]. As observed for the binding constants illustrated in Table 1, the rate constants for the reaction of these palladium catalysts with CO_2 are dependent on the potential of the $\text{Pd}(\text{II}/\text{I})$ couple. In this case, a linear dependence is observed between $\ln(k)$ and $E_{1/2}$ [36]. The use of bimetallic palladium complexes can lead to even faster catalysts without increasing the overpotentials required, but these bimetallic complexes are also significantly less stable [36]. These enhanced rates presumably arise from the second palladium atom forming a $\text{Pd}-\text{O}$ bond in addition to a $\text{Pd}-\text{C}$ bond to the first Pd atom.

These first two steps, electron transfer and CO_2 binding, are also common to Fe, Co, and Ni macrocyclic complexes. For these catalysts, one-electron reductions corresponding to $\text{Fe}(\text{I}/0)$ [37–40], $\text{Fe}(\text{II}/\text{I})$ [41], $\text{Co}(\text{II}/\text{I})$ [42–44], and $\text{Ni}(\text{II}/\text{I})$ [45] couples are followed by reaction with CO_2 . However, for these catalytic systems, which operate at much more negative potentials than the Pd complexes, the rate-determining step is not the reaction of CO_2 with the reduced metal species. This reaction is very rapid. As shown in Table 1, the rate of reaction of $\text{Co}(\text{I})$ (*rac*- $\text{Me}_6[14]4,11$ -diene) with CO_2 is $1.7 \times 10^8 \text{ M}^{-1} \text{ s}^{-1}$ [14]. In addition, $E_{1/2}$ for the $\text{M}(\text{II}/\text{I})$ couple of cobalt and nickel macrocycles under CO_2 in aprotic media are typically shifted toward cathodic potentials, but remain fully reversible [15]. These results indicate that CO_2 binding is fast and reversible for this class of complexes. Similarly, the $\text{Fe}(0)$ species formed on reduction of derivatives of $\text{Fe}(\text{II})$ tetraphenylporphyrins react very rapidly with CO_2 [37, 38].

An interesting case arises in the electrochemical reduction of CO_2 to CO

by $\text{Re}(\text{bipy})(\text{CO})_3\text{Cl}$ (where bipy is 2,2'-bipyridine). For this compound, reduction occurs on the bipy ligand [46]. The resulting radical anion is not reactive with CO_2 [47–50]. In order for reaction to occur, the chloride ligand must be lost accompanied by electron transfer to Re [47]. The 17-electron rhenium species formed by this electron transfer reacts with CO_2 , and this mechanism results in the so-called one-electron pathway observed for this catalyst. A second two-electron pathway appears to involve reduction to form $\text{Re}(\text{bipy})(\text{CO})_3^-$ followed by reaction with CO_2 [51]. For this rhenium complex and its derivatives, multiple pathways following formation of the carboxylate complexes have been proposed [47, 52].

As discussed in the preceding two paragraphs, electrocatalytic reduction of CO_2 to CO by homogeneous catalysts always involves the binding of CO_2 to a reduced form of the catalyst. Although this can be the rate-determining step, normally it is not. The rate-determining step appears to be controlled by the potential at which the catalytic reaction occurs. For those catalysts that are reduced at very negative potentials, CO_2 binding is not the rate-determining step. For those catalysts operating at more positive potentials, CO_2 binding is more likely to be rate limiting.

For reduced catalysts in solution, protonation competes with the reaction with CO_2 (step 2 of Sch. 2). Protonation of the reduced metal results in the formation of a transition metal hydride, which may ultimately lead to the formation of hydrogen or formate. Protonation can be quite fast and favorable. For example, $[\text{Co}^{\text{I}}(\text{rac-Me}_6[14]4,11\text{-diene})]^+$ has binding constants of $2.5 \times 10^8 \text{ M}^{-1}$ and $2.5 \times 10^{11} \text{ M}^{-1}$ ($\text{p}K_{\text{a}} = 11.4$) for the reaction with CO_2 and protons, respectively [53]. Similarly, the rate constants for binding protons

($3.0 \times 10^9 \text{ M}^{-1} \text{ s}^{-1}$) are larger than that for binding CO_2 ($1.7 \times 10^8 \text{ M}^{-1} \text{ s}^{-1}$). If the species should come to equilibrium in aqueous solutions at pH 5 and saturated with CO_2 (approximately 0.06 M), both the $[\text{Co}^{\text{I}}\text{L}(\text{CO}_2)]^+$ complex and the hydride should be present at significant concentrations. It is not surprising that hydrogen is also formed during the reduction of CO_2 to CO by this catalyst in water [33]. In order to favor the production of CO, it is necessary to limit the availability of protons. $[\text{Ni}(\text{cyclam})]^+$ has binding constants of 63 M and 16 M for H^+ and CO_2 , respectively, in water, and rate constants of $3 \times 10^7 \text{ M}^{-1} \text{ s}^{-1}$ and $3.2 \times 10^7 \text{ M}^{-1} \text{ s}^{-1}$ for reaction with H^+ and CO_2 , respectively [16]. In this case, for CO_2 saturated aqueous solutions at pH 5, the production of the CO_2 complex should be favored. As a result, the selective production of CO using this catalyst is expected. The $[\text{Pd}(\text{triposphine})(\text{solvent})]^{2+}$ catalysts shown in Sch. 2 produce CO with current efficiencies of nearly 90% in strongly acidic solutions (0.1 M H^+ and 0.18 M CO_2 in dimethylformamide) [36]. This means that there is a preference for the Pd^{I} intermediate to react with CO_2 and not with protons.

Once CO_2 has added to the reduced metal complex, C–O bond cleavage must occur to form CO. This process normally begins by the reaction of an acid with the oxygen atom of the bound CO_2 molecule. In Sch. 2, step 3 is the protonation of the metal carboxylate to form a metallocarboxylic acid. $\text{p}K_{\text{a}}$ values for metallocarboxylic acids have been reported that range from 14 to 2.5 [14]. It is thus reasonable that the Pd^{I} carboxylate formed in step 2 is protonated in strong acid. Instead of interacting with protons, metal carboxylates can also interact with a second CO_2 molecule or a Lewis acid such as

Na^+ or Mg^{2+} . In catalytic reactions involving $\text{Fe}^{(0)}$ porphyrins, protons, a second CO_2 molecule, or Mg^{2+} and CO_2 play the role of oxide acceptor to form water, carbonate, and MgCO_3 , respectively [38]. The reactions of the iron carboxylate with these Lewis acids are thought to be fast and not rate determining. For the cobalt and nickel macrocyclic catalysts, CO_2 is the ultimate oxide acceptor with formation of bicarbonate salts in addition to CO, but it is not clear what the precise pathway is for decomposition of the carboxylate to CO [33]. The influence of alkali metal ions on CO_2 binding for these complexes was discussed earlier [15]. It appears the interactions between bound CO_2 and these ions are fast and reversible, and one would presume that reactions between protons and bound CO_2 are rapid as well.

For the $[\text{Pd}(\text{triposphine})(\text{solvent})]^{2+}$ complexes, the metalcarboxylic acid formed in step 3 of Sch. 2 is not ready to undergo C–O bond cleavage. In order for this reaction to occur, an additional electron transfer, solvent loss, and a second protonation have to occur. Of particular interest in this sequence is the loss of a weakly coordinated solvent molecule (step 5), to produce a vacant site on the metal for water to occupy as the C–O bond of CO_2 is broken to form coordinated CO and coordinated water [34, 35]. This C–O bond cleavage reaction is the slow step in the catalytic cycle for these catalysts at low acid concentrations, and a vacant coordination site is required for this reaction to occur. C–O bond cleavage is also the slow step for $\text{Fe}(\text{porphyrin})$ catalysts at low acid concentrations (H^+ , Mg^{2+} , or CO_2) [37–39]. In this case, a vacant coordination site is not required. However, the potentials at which catalysis occurs in this case (approximately -2.0 V vs. ferrocene/ferrocenium) is much more negative than those

of the $[\text{Pd}(\text{triposphine})(\text{solvent})]^{2+}$ complexes (-1.1 to -1.4 V). This more negative potential should facilitate loss of water (or carbonate) to cleave the C–O bond. As a result, a vacant coordination site may not be required to achieve high catalytic rates, but a large overpotential is observed.

Breaking the C–O bond, step 7 of Sch. 2, results in the formation of a metal carbonyl complex in which CO is bound to the metal. Completion of the catalytic cycle requires CO dissociation. Cleavage of the M–C bond of the metal carbonyl complex that results from C–O bond cleavage is rapid for both the $[\text{Pd}(\text{triposphine})(\text{solvent})]^{2+}$ and $\text{Fe}(\text{porphyrin})$ complexes. For the palladium triphosphine system, the $\text{Pd}^{(\text{II})}$ and $\text{Pd}^{(\text{I})}$ species formed during the catalytic cycle have little affinity for CO [34, 35]. For the iron porphyrin system, an $\text{Fe}^{(\text{II})}(\text{CO})$ intermediate is formed with a strong Fe–CO bond, but upon reduction to $\text{Fe}(0)$ the CO is rapidly expelled [39–42]. Studies of $\text{Co}(\text{salophen})$ catalysts suggest that the loss of CO is a possible rate-determining step [54]. It was shown that a $[\text{Co}^{(\text{I})}(\text{salophen})(\text{CO})]^-$ complex is formed during the catalytic cycle, and that the release of CO from these complexes is slow. For $[\text{Co}^{(\text{I})}(\text{rac-Me}_6[14]4,11\text{-diene})(\text{CO})]^+$, the rate of CO loss has been reported to be 3 s^{-1} [53]. For the latter two cobalt complexes, either the cleavage of the Co–C bond or the cleavage of the C–O bond may be the rate-determining step, but the slow loss of CO provides an upper limit to the rate at which these catalysts can operate. As a result, efforts to improve the catalytic rates of these cobalt macrocyclic complexes should focus on increasing the rates of C–O and M–C bond cleavage reactions.

The multiple steps shown in Sch. 2 and discussed earlier for various catalysts for reduction of CO_2 to CO, indicates that

even a relatively simple two-electron process can be quite complex. However, these complex systems have the following common features. (1) The metal is reduced in two discrete one-electron steps. (2) The reaction of the reduced metal complex with CO_2 forms a $\text{M}-\text{C}$ bond. (3) The oxygen atoms of the resulting metal carboxylate interact with Lewis or protic acids to produce $\text{C}-\text{O}$ bond cleavage. (4) Finally, the $\text{M}-\text{CO}$ bond must be broken to produce free CO . Any of these steps can be the rate-determining step. Catalysts that operate by this general mechanism significantly reduce the overpotentials associated with direct electrochemical reduction of CO_2 , and the current efficiencies and rates can be quite high.

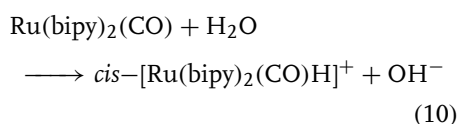
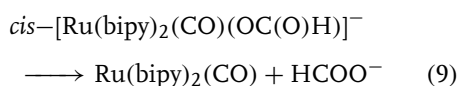
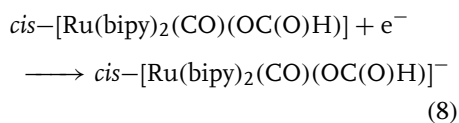
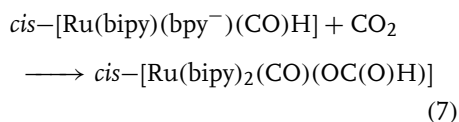
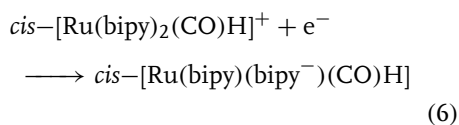
Inorganic and organometallic complexes adsorbed on electrode surfaces provide a transition between homogeneous and heterogeneous catalysts. A very interesting case is the reduction of CO_2 to CO by $[\text{Ni}(\text{cyclam})]^+$ complexes adsorbed on Hg [45]. These complexes appear to exhibit higher activities, higher selectivities, and higher turnover numbers as adsorbed species than they do as homogeneous species. The adsorbed species is $[\text{Ni}^{(\text{I})}(\text{cyclam})]^+$, and a structural rearrangement is required for adsorption [55, 56]. The precise nature of this structural rearrangement is not known. Similarly, carbon electrodes modified with cobalt phthalocyanines have been reported to produce CO [57–59]. Polymeric thin films of $\text{Ru}(\text{bipy})(\text{CO})_2$ on carbon and platinum have been formed by the electrochemical reduction of a variety of precursors in solution [60, 61]. These films are active catalysts for the reduction of CO_2 to CO in both organic solvents and in water. Similarly, polymeric films derived from the electrochemical polymerization of vinylbipyridine and vinylterpyridine complexes

of Re and Co , and polypyrrole/Schiff-base complexes of nickel that catalyze the electrochemical reduction of CO_2 to CO and formate [62–64] have been described.

Electrochemical reductions of CO_2 at a number of metal electrodes have been reported [12, 65, 66]. CO has been identified as the principal product for Ag and Au electrodes in aqueous bicarbonate solutions at current densities of 5.5 mA cm^{-2} [67]. Different mechanisms for the formation of CO on metal electrodes have been proposed. It has been demonstrated for Au electrodes that the rate of CO production is proportional to the partial pressure of CO_2 . This is similar to the results observed for the formation of CO_2 adducts of homogeneous catalysts discussed earlier. There are also a number of spectroscopic studies of CO_2 bound to metal surfaces [68–70], and the formation of strongly bound CO from CO_2 on Pt electrodes [71]. These results are consistent with the mechanism proposed for the reduction of CO_2 to CO by homogeneous complexes described earlier and shown in Sch. 2. Alternative mechanistic pathways for the formation of CO on metal electrodes have proposed the formation of $\text{M}-\text{COOH}$ species by (1) insertion of CO_2 into $\text{M}-\text{H}$ bonds on the surface or (2) by outer-sphere electron transfer to CO_2 followed by protonation to form a COOH radical and then adsorption of the neutral radical [12]. Certainly, protonation of adsorbed CO_2 by a proton on the surface or in solution would be reasonable. However, insertion of CO_2 into a surface hydride would seem unlikely based on precedents in homogeneous catalysis. CO_2 insertion into transition metal hydrides complexes invariably leads to formation of formate complexes in which $\text{C}-\text{H}$ bonds rather than $\text{O}-\text{H}$ bonds have been formed, as discussed in the next section.

6.2.3.2.1 Two-electron Reduction of CO₂ to Formate/formic Acid

As shown on the right-hand side of Sch. 1, protonation of the radical anion of CO₂ followed by a second electron transfer leads to formation of the formate ion. A number of catalysts also mediate the reduction of CO₂ to formate, but at much less negative potentials. In contrast to the electrochemical reduction of CO₂ to CO, no C–O bond is broken. A C–H bond is formed instead. An example of a proposed catalytic cycle for formate formation is shown by reactions (6–10) for *cis*-[Ru(bipy)₂(CO)H]⁺ [72]. In reaction (6), a one-electron reduction occurs on a bipyridine ring, which enhances the electron density on the hydride ligand. This increased electron density promotes insertion of CO₂ into the M–H bond to form a formate ligand (reaction 7). CO₂ insertion is followed by a second one-electron reduction of the resulting formate complex (reaction 8). Loss of the formate ion (reaction 9) and protonation of the resulting Ru(0) complex by water (reaction 10) completes the cycle. The key features of this catalytic cycle are the formation of a nucleophilic hydride that can attack CO₂ to form a C–H bond and the cleavage of the Ru–O bond to eliminate formate.



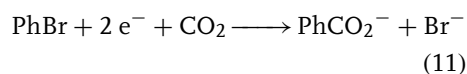
In the mechanism shown in reactions (6–10), a transition metal hydride acts as a hydride donor. The direct reaction of metal hydrides and carbon dioxide has been studied in some detail [73–76], and these studies demonstrate the feasibility of hydride transfer to form formate complexes. Other studies have suggested formyl (MC(O)H) complexes as hydride donors in the reduction of CO₂ to formate [77], and some formyl complexes are sufficiently good hydride donors to transfer a hydride to CO₂ [76, 78]. So, hydride transfer reactions from both transition metal hydrides and formyl complexes are reasonable from an energetic perspective. In reactions (6–10), the formation of the proposed ruthenium hydride takes place via protonation of a reduced metal complex, a well-known reaction. The formation of a formyl complex presumably takes place via protonation of a reduced carbonyl complex. This could take place through a bent carbonyl complex. There is some evidence for the formation of bent carbonyl complexes for Rh(II)porphyrin complexes [79], and their reactivity with hydrogen has been studied. Formation of a hydride carbonyl complex followed by hydride migration to the carbonyl ligand is also possible. Generally, this migration reaction is not favored. To provide the necessary driving force for migration, formyl formation may be accompanied by ring closure of a dangling pyridyl ligand [80]. Reactions 6–10 presents a fairly simplified mechanism for the formation of formate, but it may not be as general

as the mechanism shown in Sch. 2 for CO formation. Certainly, there is more debate regarding the details of proposed steps.

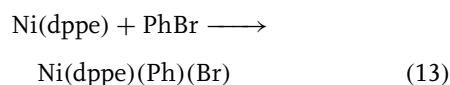
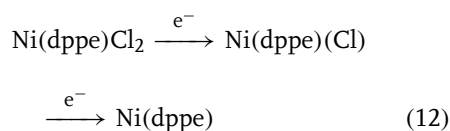
Formate production has also been reported for electropolymerized films of $[\text{Co}(\text{4-vinylterpyridine})_2]^{2+}$ on glassy carbon electrodes in dimethylformamide solutions [63]. Interestingly, the product of this same catalytic system in aqueous solutions is formaldehyde [81]. Other heterogeneous systems that produce formate include Cd, Sn, Pb, In, and Zn electrodes in aqueous media [12] (see also Vol VII 5.2.3). It is likely that the pathway to formate formation on metal electrodes follows the sequence of M–H bond formation followed by CO_2 insertion to form a M–OC(O)H species followed by desorption from the electrode surface.

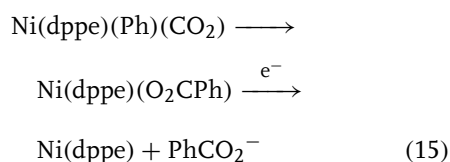
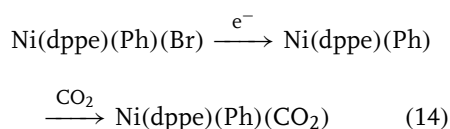
6.2.3.2.2 Two-electron Reductions of CO_2 Involving Formation of a C–C Bond Instead of forming a C–H bond, two-electron reduction of CO_2 may also result in the formation of C–C bonds. Reaction of Grignard reagents with CO_2 has been used for many years to prepare carboxylic acids. In general, the uncatalyzed electrochemical carboxylation of organic halides results in the formation of esters. These esters are formed by the reaction of the carboxylate anion that forms at the cathode with unreacted organic halide in solution. As a result, carboxylation of no more than 50% of the original halide is possible. However, benzyl chlorides can be reduced in the presence of CO_2 at graphite electrodes in single compartment cells with aluminum anodes to form the corresponding carboxylic acid in good yields (80–90%) [82]. Using an Fe–Mo cluster, $[(\text{C}_2\text{H}_5)_4\text{N}]_3[\text{Fe}_6\text{Mo}_2\text{S}_8(\text{SC}_2\text{H}_5)_9]$, electrochemical reduction of CO_2 in the presence of thioesters results in the formation of α -keto acids [83].

From a mechanistic perspective, the best understood system for C– CO_2 bond formation is the catalytic electrocarboxylation of bromoarenes in the presence of a transition metal catalyst, reaction (11) [84–87]. This reaction is selective and occurs at room temperature and 1 atm of CO_2 .

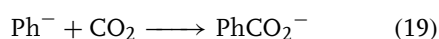
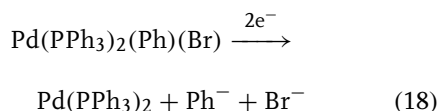
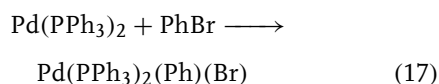
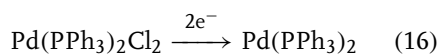


The carboxylation reaction shown in reaction (11) is catalyzed by both nickel and palladium phosphine complexes. For example, $\text{Ni}(\text{dppe})\text{Cl}_2$ (where dppe is 1,2-bis(diphenylphosphino)ethane) and $\text{Pd}(\text{PPh}_3)_2\text{Cl}_2$ both catalyze reaction (11) [84–86]. Mechanistic studies have been carried out on these two systems, and the results indicate that two different mechanisms are involved. In the case of the Ni complex, the first step is the reduction of $\text{Ni}(\text{dppe})\text{Cl}_2$ to a transient $\text{Ni}(\text{dppe})$ species [85]. This process occurs in two one-electron steps (reaction 12). Bromobenzene then oxidatively adds to $\text{Ni}(\text{dppe})$ to form $\text{Ni}(\text{dppe})(\text{Br})(\text{Ph})$, reaction (13). The resulting $\text{Ni}(\text{II})$ aryl species is reduced in a one-electron process to form $\text{Ni}(\text{dppe})(\text{Ph})$, which reacts rapidly with CO_2 to form a Ni– CO_2 intermediate as shown in reaction (14). The rate-determining step for the overall catalytic reaction is the insertion of CO_2 into the Ni–aryl bond, reaction (15) step 1. This reaction is followed by a final one-electron reduction to regenerate $\text{Ni}(\text{dppe})$, the true catalyst in the cycle (reaction 15, step 2).



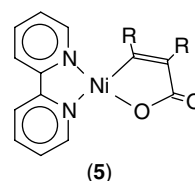


For the $\text{Pd(Ph}_3\text{)}_2\text{Cl}_2$ catalyzed carboxylation of bromobenzene, $\text{Pd(Ph}_3\text{)}_2\text{Cl}_2$ is reduced in a single two-electron step to form $\text{Pd(PPh}_3\text{)}_2$ (reaction 16) followed by oxidative addition of bromobenzene (reaction 17) [84]. In contrast to the Ni(dppe)(Ph)(Br) complex, $\text{Pd(PPh}_3\text{)}_2\text{(Ph)(Br)}$ undergoes a single two-electron reduction followed by expulsion of the aryl anion (reaction 18). The anion then reacts with CO_2 to form PhCO_2^- (reaction 19). In this case, the role of the Pd complex is simply to reduce the overpotential associated with the reduction of bromobenzene to form the phenyl anion. These two different mechanisms for these closely related complexes indicate that it is difficult to predict precise reaction pathways. However, both complexes effectively carboxylate PhBr.



The formation of C–C bonds between CO_2 and alkenes and alkynes can also be

catalyzed. For example, benzonitrile catalyzes the reductive coupling of CO_2 and styrene to form mono- and dicarboxylic acid products [88]. This transformation requires very negative potentials (-2.15 V vs. SCE), and is not very selective. Carbon dioxide can also be incorporated into alkynes in a catalytic reaction using nickel 2,2'-bipyridine complexes as catalysts [89]. The catalytic process requires a single compartment cell and the use of magnesium as the counter electrode. For this catalytic system, Mg^{2+} ions are required for cleavage of a metallocycle, structure (5), to form the ultimate product. Depending on the nature of the substituents, selectivities in this case can be reasonably high. An extension of this chemistry is the sequential reductive coupling of two molecules of CO_2 to butadiene to form 4-hexene-1,6-dioic acid, the unhydrogenated precursor to adipic acid [90]. Adipic acid is used in the synthesis of Nylon. Although these C–C bond forming reactions are not commercially developed, they do indicate that in the future, electrochemical coupling of various organic substrates to CO_2 may provide attractive routes to various carboxylic acids and their derivatives.



6.2.3.3 Four-electron Reductions of CO_2

Four-electron reductions of CO_2 are rather unusual. As discussed above, the reduction of CO_2 to formate is observed at films of $[\text{Co(4-vinylterpyridine)}_2]^{2+}$ on glassy carbon electrodes in dimethylformamide solutions [63]. These same films are reported to produce formaldehyde in

aqueous solutions at potentials of approximately -1.3 V vs. ferrocene [81]. Films of $[\text{Cr}(\text{4-vinylterpyridine})_2]^{2+}$ and $[\text{Fe}(\text{4-vinylterpyridine})_2]^{2+}$ on glassy carbon electrodes also catalyzed the reduction of CO_2 to formaldehyde with current efficiencies of 87 and 28%, respectively. Kinetic studies indicated that the reaction is first order in catalyst and first order in CO_2 . The reaction rates were observed to be much lower for formaldehyde production than they were for the formation of formate. This was attributed to a four-electron reduction being more difficult than a two-electron reduction.

Another very interesting reaction, is the four-electron reduction of CO_2 to acetone [91, 92]. $[\text{Ru}(\text{bipy})_2(\text{qu})(\text{CO})]^{2+}$ (where qu is quinoline) catalyzes the reduction of CO_2 to CO in acetonitrile using LiBF_4 as the supporting electrolyte. When the solvent is changed to a 1:1 mixture of acetonitrile and DMSO and Me_4NBF_4 is used as the supporting electrolyte, CO is the main product (42%) but a significant amount of acetone (16%) is also formed. In the production of acetone, CO_2 is the source of carbonyl moiety, and the Me_4N^+ functions as the methylating agent. In this reaction, it has been proposed that $[\text{Ru}(\text{bipy})_2(\text{qu})(\text{CO})]$ reacts with NMe_4^+ to form $[\text{Ru}(\text{bipy})_2(\text{qu})(\text{C}(\text{O})\text{CH}_3)]^+$ in which the carbonyl moiety acts as a nucleophile and the methyl group on nitrogen acts as an electrophile. Further study and development of this very interesting reaction is clearly warranted, because it would provide useful insights into pathways resulting in the four-electron reduction of CO_2 and the formation of C–C bonds.

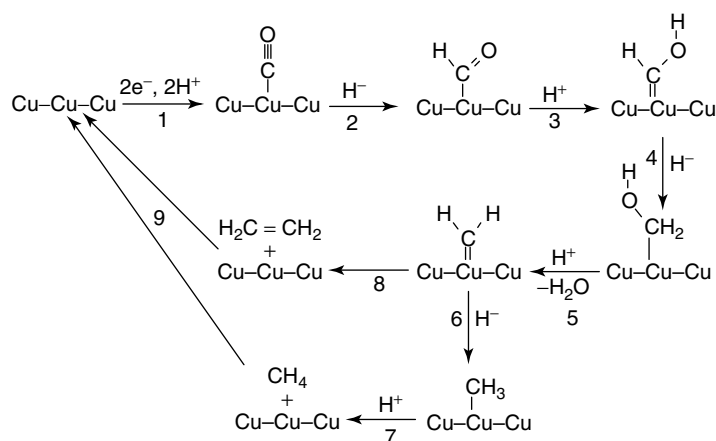
6.2.3.4 Six-electron Reduction to Methanol

Although traces of methanol have been observed in the reduction of CO_2 using homogeneous catalysts [93], heterogeneous

catalysts appear to be superior for this reaction to date. Reduction of CO_2 at molybdenum electrodes to produce methanol (Faradaic efficiencies of 50–100%) proceeds at room temperature at -0.8 V vs. SCE [94]. The chief drawback to the use of molybdenum electrodes for producing methanol is that the current densities are very low. Other metals showing interesting activity for the production of methanol included Ag, W, and Os [12]. Unfortunately, the mechanisms for methanol formation are not known for any of these catalysts.

6.2.3.5 Eight- and Twelve-electron Reductions of CO_2 to Methane and Ethylene

The electrochemical reduction of CO_2 to form hydrocarbons has been studied on several electrodes. The production of methane at both ruthenium and Cu electrodes has been reported. For ruthenium, electrolysis of CO_2 in aqueous solutions containing 0.1 M H_2SO_4 resulted in current efficiencies as high as 20% for methane production at 65°C [12, 95]. The potentials were modest (-0.39 V vs. SCE), but current densities were low (0.3 mA cm^{-2}). In contrast, constant current electrolysis of CO_2 saturated solutions (0.5 M KHCO_3 in water) at copper electrodes produced a mixture of products including methane, ethylene, hydrogen, CO, and formate [98]. At 0°C , the Faradaic efficiency for CH_4 production was 65%. At higher temperatures, the efficiency for methane production decreased while that for ethylene production increased to 20% at 40°C . Further studies resulted in Faradaic efficiencies of up to nearly 50% for ethylene formation when KCl, KClO_4 , or K_2SO_4 were used as supporting electrolytes. In some cases, significant quantities of ethanol (20% Faradaic efficiency)



Scheme 3

were also formed [98]. The production of hydrocarbons is favored for potentials negative of -1.3 V versus the NHE, and CO formation is favored for potentials positive of -1.2 V. More recent studies of single crystal electrodes of copper and platinum have shown that the products formed are dependent on the crystal plane and the presence or absence of steps [99–101]. For homogeneous catalysts, such features correspond to vacant or weakly solvated coordination sites.

Scheme 3 accounts for the various products formed, and it is consistent with known transformations in organometallic chemistry. In the first step, CO_2 is reduced in a proton-coupled two-electron process to form adsorbed CO. That CO is an intermediate in the reduction of CO_2 to hydrocarbons is supported by the following observations. (1) Reduction of CO at copper electrodes under the same conditions gives a similar distribution of hydrocarbon products. Reduction of formate, on the other hand, gave no hydrocarbon products [98, 102]. (2) CO on the electrode surface could be detected by cyclic voltammetry measurements. Fourier transform

infrared measurements showed a band at 2087 cm^{-1} , consistent with a terminal CO ligand bound to Cu [103]. (3) Factor analysis suggests that CO, methane, and ethylene production are strongly correlated [104]. All of the data together leave little doubt that hydrocarbon formation proceeds through adsorbed or bound CO. The steps for the formation of this bound CO are probably similar to those shown in Sch. 2.

CO formation on copper electrodes appears to be accompanied by hydride formation as well [103]. In Sch. 3, the surface bound CO is reduced by a hydride transfer reaction to form a formyl species as shown in step 2. There are precedents in organometallic chemistry for late transition metal hydrides reducing bound CO [105–109]. Protonation of the adsorbed formyl in step 3 results in the formation of a hydroxycarbene species [110, 111]. This hydroxycarbene species could be considered to be an adsorbed and rearranged form of formaldehyde, and the reduction of formaldehyde at a copper electrode has been reported to form hydrocarbons [102]. However, reduction of

formaldehyde at copper electrodes has also been reported to form primarily methanol and hydrogen [98]. Hydride transfer to the hydroxycarbene species, step 4, is expected to form an adsorbed hydroxymethyl species [106, 112]. Reactions of MCH_2OH complexes with protons or Lewis acids followed by loss of water (step 5) result in the formation of an adsorbed methylene species [113–115]. A hydride transfer, step 6, then normally leads to the formation of a methyl complex, $\text{M}-\text{CH}_3$ [106, 116]. Protonation of the $\text{M}-\text{CH}_3$ species (step 7) leads to methane [106, 116]. If instead of a hydride transfer step, two methylene units couple as shown in step 8, then ethylene will be produced. The coupling of two methylene units would be anticipated to require more energy than methylene insertion into a $\text{Cu}-\text{H}$ bond. This would explain the preference at low temperatures for methane formation while higher temperatures favor ethylene formation. Similarly, the formation of methane from a $\text{Cu}-\text{CH}_3$ group requires a proton. This would account for the electrolyte dependence for methane versus ethylene production. Hori has suggested that different pH values of the solutions at the interface with the electrode are responsible for the observed electrolyte dependence, even though bulk solution pH values may be the same [98]. Those supporting electrolytes that favor higher proton concentrations near the electrode surface favor methane formation, while lower proton concentrations favor ethylene formation. The coupling of methylene groups may also be involved in the formation of carbon deposits that deactivate the electrode surface [102]. Experiments in which the electrode potential is periodically cycled to positive potentials have shown that carbon formation and electrode deactivation can be reduced or eliminated [117, 118].

The eight- and twelve-electron reductions of CO_2 to methane and ethylene, are very exciting results for two reasons. First, these results demonstrate that complex multielectron reductions are possible. Second, they illustrate the close relationship that exists between reactions observed for discrete molecular complexes and reactions observed on metal surfaces.

6.2.4

Sequential Two-electron Reductions of CO_2 Catalyzed by Enzymes

In the preceding sections, we have discussed the reduction of CO_2 by one, two, four, six, eight, and twelve electrons. A single homogeneous or heterogeneous catalyst catalyzes all of these reactions. Another possible route to multielectron reduction of CO_2 is to carry out sequential two-electron reductions, with each step using a different catalyst. In fact, this is the process that is used in nature. In photosynthetic reactions using the Calvin cycle, CO_2 reacts with a 5-carbon sugar, ribulose biphosphate, to form two molecules of phosphoglyceric acid. This reaction is catalyzed by the enzyme ribulose biphosphate carboxylase (RuBisCO) and involves both the formation and cleavage of $\text{C}-\text{C}$ bonds [119]. In this respect, it is similar to the carboxylation reactions described earlier. The phosphoglyceric acid is phosphorylated and then reduced in a second two-electron step involving nicotinamide adenine dinucleotide phosphate (NADPH). Overall, a four-electron reduction of CO_2 to the level of a sugar (or formaldehyde) is achieved in photosynthesis.

Using biological catalysts, or enzymes, is therefore an attractive approach for trying to reduce CO_2 to a variety of specific products. However, the direct reduction of

enzymes at electrode surfaces is not generally feasible. The active sites frequently lie within the interior of the enzyme, and therefore they are not readily accessible to the electrode surface. This requires the use of mediators such as methyl viologen. These mediators are reversibly reduced at the electrode surface and are small enough to diffuse into the interior of the enzyme to effect reduction of the active site. In one of the first studies using this approach, a semiconductor electrode was illuminated in the presence of methylviologen, CO_2 , and formate dehydrogenase [120]. In this case, illumination of the semiconductor results in charge separation with the electrons going to the semiconductor solution interface where reduction of methylviologen occurs. The reduced methylviologen carrier in turn reduces the active site of formate dehydrogenase, which reduces CO_2 to formate. This example illustrates not only the use of an electron mediator, but also the coupling of photon absorption and charge separation with CO_2 reduction. Numerous examples of photoelectrochemical reduction of CO_2 at semiconductor electrodes have been reported, but the mechanistic details are generally not known [121–123]. Reduction of CO_2 to CO using carbon monoxide dehydrogenase has also been reported [124].

More complex reductions of CO_2 by enzyme cascades have also been achieved. A combination of an electron mediator and two enzymes, formate dehydrogenase and methanol dehydrogenase, was used to reduce CO_2 to methanol. This system operates with current efficiencies as high as 90% and low overpotentials (approximately -0.8 V vs. SCE at pH 7) [125]. The high selectivity and energy efficiency of this system indicate the potential of enzyme cascades. There are also drawbacks to these systems. In general, enzymes are

not very stable and are frequently sensitive to light, oxygen, pH, and so on. Like homogeneous catalysts, they are difficult to separate from the reaction mixture. However, studies such as these indicate that in the future cascades of enzymes, homogeneous catalysts, or heterogeneous catalysts or combinations of all of these different catalyst types may be able to efficiently reduce CO_2 to a variety of products selectively and efficiently.

6.2.5 Summary

Electrochemical reactions involving CO_2 are an important class of reactions. They provide the basis for developing new methods for CO_2 recovery and the production of future feedstocks and fuels. Fundamental studies that increase our understanding of the ways in which CO_2 interacts with electrochemically active molecules and surfaces are critical to the rational development of catalysts that can reduce CO_2 along specific pathways to desired products. Preliminary studies of CO_2 binding to molecular compounds have established that electron density plays an important role in the strength and rates of these interactions. However, the use of secondary interactions to control binding of CO_2 is in its infancy. A thorough understanding of these secondary interactions is of fundamental importance for designing electrochemical CO_2 pumps and highly selective catalysts. One- and two-electron reductions can lead to the formation of oxalate and carboxylates in which C–C bonds are formed. This is an essential step in the formation of more complex molecules from CO_2 . The direct production of ethylene at copper electrodes is a striking example of a very complex multielectron reduction

that uses only CO₂ to produce a chemical feedstock that is used in a large range of reactions. Two-electron electrocarboxylation reactions suggest the possibility of selectively building up complex molecules in a predetermined manner. A better understanding of the factors controlling low energy pathways for the formation of C–C bonds is critical for future development of feedstocks from CO₂. The multielectron reduction of CO₂ to methanol and methane represent important initial studies that indicate that production of high energy-density fuels by electrochemical reduction of CO₂ should be considered an attractive future approach for storing solar and wind energy and other intermittent forms of energy.

Acknowledgment

The support of the Director's Discretionary Research and Development Program of the National Renewable Energy Laboratory during the writing of this manuscript is gratefully acknowledged.

References

1. D. O. Hall, K. K. Rao, *Photosynthesis*, 5th ed., Cambridge University Press, Cambridge, 1994, Chapter 1.
2. C. M. White, B. R. Strazisar, E. J. Granite et al., *J. Air Waste Manage. Assoc.* **2003**, 53, 645–715.
3. D. H. Gibson, *Chem. Rev.* **1996**, 96, 2063–2095.
4. J. C. Calabrese, T. Herskovitz, J. B. Kinney, *J. Am. Chem. Soc.* **1983**, 105, 5914.
5. E. Fujita, L. R. Furenliid, M. W. Renner, *J. Am. Chem. Soc.* **1997**, 119, 4549–4550.
6. M. Aresta, C. F. Nobile, *J. Chem. Soc., Chem. Commun.* **1975**, 636.
7. G. S. Bristow, P. B. Hitchcock, M. F. Lapert, *J. Chem. Soc., Chem. Commun.* **1981**, 1145.
8. D. H. Gibson, M. Ye, B. A. Sleadd et al., *Organometallics* **1995**, 14, 1242.
9. G. Fachinetti, C. Floriani, P. F. Zanazzi, *J. Am. Chem. Soc.* **1978**, 100, 7405.
10. S. Gambarotta, F. Arena, C. Floriani et al., *J. Am. Chem. Soc.* **1982**, 104, 5082–5092.
11. I. Castro-Rodriguez, H. Nakai, L. N. Zakharov et al., *Science* **2004**, 305, 1757–1759.
12. K. W. Frese Jr. in *Electrochemical and Electrocatalytic Reactions of Carbon Dioxide* (Eds.: B. P. Sullivan, K. Krist, H. E. Guard), Elsevier, New York, 1993, Chapter 6.
13. E. Fujita, C. Creutz, N. S. Sutin et al., *J. Am. Chem. Soc.* **1991**, 113, 343–353.
14. C. Creutz in *Electrochemical and Electrocatalytic Reactions of Carbon Dioxide* (Eds.: B. P. Sullivan, K. Krist, H. E. Guard), Elsevier, New York, 1993, Chapter 2.
15. M. H. Schmidt, G. M. Miskelly, N. S. Lewis, *J. Am. Chem. Soc.* **1990**, 112, 3420–3426.
16. C. A. Kelly, Q. G. Mulazzani, M. Venturi et al., *J. Am. Chem. Soc.* **1995**, 117, 4911–4919.
17. D. L. DuBois, A. Miedaner, W. Bell in *Electrochemical and Electrocatalytic Reactions of Carbon Dioxide* (Eds.: B. P. Sullivan, K. Krist, H. E. Guard), Elsevier, New York, 1993, Chapter 4.
18. P. Scovazzo, J. Poshusta, D. L. DuBois et al., *J. Electrochem. Soc.* **2003**, 150, D91–D98.
19. J. L. Weaver, J. Winnick, *J. Electrochem. Soc.* **1983**, 130, 20–28.
20. J. Winnick, *Chem. Eng. Prog.* **1990**, 41–46.
21. C. Amatore, J. M. Savéant, *J. Am. Chem. Soc.* **1981**, 103, 5021–5023.
22. C. Amatore, L. Nadjó, J. M. Savéant, *Nouv. J. Chim.* **1984**, 8, 565–566.
23. H. A. Schwarz, R. W. Dodson, *J. Phys. Chem.* **1989**, 93, 409–414.
24. P. Neta, R. E. Huie, A. B. Ross, *J. Phys. Chem. Ref. Data* **1988**, 17, 1027.
25. A. Gennaro, A. A. Isse, J. M. Savéant et al., *J. Am. Chem. Soc.* **1996**, 118, 7190–7196.
26. C. Amatore, J. M. Saveant, *J. Electroanal. Chem.* **1981**, 125, 23–39.
27. S. Meshitsuka, M. Ichikawa, K. Tamaru, *J. Chem. Soc., Chem. Commun.* **1974**, 158–159.
28. B. R. Eggins, E. M. Bennett, E. A. McMullan, *J. Electroanal. Chem.* **1996**, 408, 165–171.
29. B. R. Eggins, E. M. Brown, E. A. McNeill et al., *Tetrahedron Lett.* **1988**, 29, 945–948.

30. B. R. Eggins, C. Ennis, R. McConnell et al., *J. Appl. Electrochem.* **1997**, 27, 706–712.
31. J. Y. Becker, B. Vainas, R. Eger et al., *J. Chem. Soc., Chem. Commun.* **1985**, 1471–1472.
32. M. Rudolph, S. Dautz, E. G. Jäger, *J. Am. Chem. Soc.* **2000**, 122, 10821–10830.
33. B. Fisher, R. Eisenberg, *J. Am. Chem. Soc.* **1980**, 102, 7363–7365.
34. D. L. DuBois, *Comments Inorg. Chem.* **1997**, 19, 307.
35. D. L. DuBois, R. C. Haltiwanger, A. Miedaner, *J. Am. Chem. Soc.* **1991**, 114, 8753–8764.
36. P. R. Bernatis, A. Miedaner, R. C. Haltiwanger et al., *Organometallics* **1994**, 13, 4835–4843; B. D. Steffey, C. J. Curtis, D. L. DuBois, *Organometallics* **1995**, 14, 4937–4943.
37. I. Bhugun, D. Lexa, J. M. Savéant, *J. Am. Chem. Soc.* **1994**, 116, 5015–5016.
38. M. Hammouche, D. Lexa, M. Momenteau et al., *J. Am. Chem. Soc.* **1991**, 112, 8455–8466.
39. I. D. Bhugun, D. Lexa, J. M. Savéant, *J. Am. Chem. Soc.* **1996**, 118, 1769–1776.
40. T. Dhanasekaran, J. Grodkowski, P. Neta et al., *J. Phys. Chem. A* **1999**, 103, 7742–7748.
41. J. Grodkowski, P. Neta, E. Fujita et al., *J. Phys. Chem. A* **2002**, 106, 4772–4778.
42. T. Ogata, S. Yanagida, B. S. Brunschwig et al., *J. Am. Chem. Soc.* **1995**, 117, 6708–6716.
43. A. A. Isse, A. Gennaro, E. Vianello, *J. Mol. Catal.* **1991**, 70, 197–208.
44. D. J. Pearce, D. Pletcher, *J. Electroanal. Chem.* **1986**, 197, 317–330.
45. M. Beley, J. P. Collin, R. Ruppert et al., *J. Am. Chem. Soc.* **1986**, 108, 7461–7467.
46. J. Hawecker, J. M. Lehn, R. Ziessel, *Helv. Chim. Acta* **1986**, 69, 1990–2012.
47. Y. Hayashi, S. Kita, B. S. Brunschwig et al., *J. Am. Chem. Soc.* **2003**, 125, 11976–11987.
48. G. J. Stor, J. W. M. van Outersterp, D. J. Stufke, *Organometallics* **1995**, 14, 1115–1131.
49. P. Christensen, A. Hamnett, A. V. G. Muir et al., *J. Chem. Soc., Dalton Trans.* **1992**, 1455–1463.
50. F. P. A. Johnson, M. W. George, F. Hartl et al., *Organometallics* **1996**, 15, 3374–3387.
51. B. P. Sullivan, C. M. Bolinger, D. Conrad et al., *J. Chem. Soc., Chem. Commun.* **1985**, 1414–1416.
52. D. H. Gibson, X. Yin, H. Y. He et al., *Organometallics* **2003**, 22, 337–346.
53. C. Creutz, H. A. Schwarz, J. F. Wishart et al., *J. Am. Chem. Soc.* **1991**, 113, 3361–3371.
54. A. A. Isse, A. Gennaro, E. Vianello et al., *J. Mol. Catal.* **1991**, 70, 197–208.
55. G. B. Balazs, F. C. Anson, *J. Electroanal. Chem.* **1992**, 322, 325–345.
56. M. Fujihira, Y. Hirata, K. Suga, *J. Electroanal. Chem.* **1990**, 292, 199–215.
57. C. M. Lieber, N. S. Lewis, *J. Am. Chem. Soc.* **1984**, 106, 5033–5034.
58. T. Atoguchi, A. Aramata, A. Kazusaka et al., *J. Electroanal. Chem.* **1991**, 318, 309–320.
59. N. Furuya, K. Matsui, *J. Electroanal. Chem.* **1989**, 271, 181–191.
60. M. N. Collomb-Dunand-Sauthier, A. Deronzier, R. Ziessel, *Inorg. Chem.* **1994**, 33, 2961–2967.
61. S. Chardon-Noblat, A. Deronzier, R. Ziessel et al., *Inorg. Chem.* **1997**, 36, 5384–5389.
62. P. Christensen, A. Hamnett, A. V. G. Muir et al., *J. Chem. Soc., Dalton Trans.* **1994**, 90, 459–469.
63. H. C. Hurrell, A. L. Mogstad, D. A. Usifer et al., *Inorg. Chem.* **1989**, 28, 1080–1084.
64. C. Arana, S. Yan, M. Keshavarz-K et al., *Inorg. Chem.* **1992**, 31, 3680–3682.
65. B. R. Eggins, J. McNeill, *J. Electroanal. Chem.* **1983**, 148, 17–24.
66. Y. B. Vassiliev, V. S. Bagotzky, N. V. Osetrova et al., *J. Electroanal. Chem.* **1985**, 189, 271–294.
67. Y. Hori, K. Kikuchi, S. Suzuki, *Chem. Lett.* **1985**, 1695–1698.
68. A. J. McQuillan, P. J. Hendra, M. Fleischman, *J. Electroanal. Chem.* **1975**, 65, 933–944.
69. B. Aurian-Blajeni, M. H. Habib, I. Taniguchi et al., *J. Electroanal. Chem.* **1983**, 157, 399–404.
70. K. Chandrasekaran, J. O. M. Bockris, *Surf. Sci.* **1987**, 185, 495–514.
71. B. Beden, A. Bewick, M. Razaq et al., *J. Electroanal. Chem.* **1982**, 139, 203–206.
72. J. R. Pugh, M. R. M. Bruce, B. P. Sullivan et al., *Inorg. Chem.* **1991**, 30, 86–91.
73. D. J. Darensbourg, H. P. Wiegreffe, P. W. Wiegreffe, *J. Am. Chem. Soc.* **1990**, 112, 9252–9257.

74. D. J. Darensbourg, P. Wiegreffe, C. G. Rioridan, *J. Am. Chem. Soc.* **1990**, 112, 5759.
75. B. P. Sullivan, T. J. Meyer, *Organometallics* **1986**, 5, 1500–1502.
76. D. L. DuBois, D. E. Berning, *Appl. Organomet. Chem.* **2000**, 14, 860–862.
77. K. Toyohara, H. Nagao, T. Mizukawa et al., *Inorg. Chem.* **1995**, 34, 5399–5400.
78. W. W. Ellis, A. Miedaner, D. H. Gibson et al., *J. Am. Chem. Soc.* **2002**, 124, 1926–1932.
79. B. B. Wayland, A. E. Sherry, G. Poszmik et al., *J. Am. Chem. Soc.* **1992**, 114, 1673–1681.
80. D. H. Gibson, J. G. Andino, S. Bhamidi et al., *Organometallics* **2001**, 20, 4956–4964.
81. J. A. R. Sende, C. R. Arana, L. Hernández et al., *Inorg. Chem.* **1995**, 34, 3339–3348.
82. G. Silvestri, S. Gambino, G. Filardo et al., *Angew. Chem., Int. Ed. Engl.* **1984**, 23, 979–980.
83. N. Komeda, H. Nagao, T. Matsui et al., *J. Am. Chem. Soc.* **1992**, 114, 3625–3630.
84. C. Amatore, A. Jutand, F. Khalil et al., *J. Am. Chem. Soc.* **1992**, 114, 7076–7085.
85. C. Amatore, A. Jutand, *J. Am. Chem. Soc.* **1991**, 113, 2819–2825.
86. J. F. Fauvarque, C. Chevrot, A. Jutand et al., *J. Organomet. Chem.* **1984**, 264, 273–281.
87. G. Zheng, M. Stradiotto, L. Li, *J. Electroanal. Chem.* **1998**, 453, 79–88.
88. G. Filardo, S. Gambino, G. Silvestri, *J. Electroanal. Chem.* **1984**, 177, 303–309.
89. S. Dérien, E. Duñach, J. Périchon, *J. Am. Chem. Soc.* **1991**, 113, 8447–8454.
90. J. Bringmann, E. Dinjus, *Appl. Organomet. Chem.* **2001**, 15, 135–140.
91. T. Mizukawa, K. Tsuge, H. Nakajima et al., *Angew. Chem., Int. Ed. Engl.* **1999**, 38, 362–363.
92. H. Nakajima, Y. Kushi, H. Nagao et al., *Organometallics* **1995**, 14, 5093–5098.
93. H. Nagao, T. Mizukawa, Tanaka, *Chem. Lett.* **1993**, 955–958.
94. D. P. Summers, K. W. Frese Jr., *J. Electroanal. Chem.* **1986**, 205, 219–232.
95. K. W. Frese Jr., S. Leach, *J. Electrochem. Soc.* **1985**, 132, 259–260.
96. Y. Hori, K. Kikuchi, A. Murata et al., *Chem. Lett.* **1986**, 897–898.
97. Y. Hori, A. Murata, R. Takahashi et al., *J. Chem. Soc., Chem. Commun.* **1988**, 17–19.
98. Y. Hori, A. Murata, R. Takahashi, *J. Chem. Soc., Faraday Trans. 1* **1989**, 85, 2309–2326.
99. Y. Hori, I. Takahashi, O. Koga et al., *J. Mol. Catal. A: Chem.* **2003**, 199, 39–47.
100. N. Hoshi, Y. Hori, *Electrochim. Acta* **2000**, 45, 4263–4270.
101. N. Hoshi, E. Sato, Y. Hori, *J. Electroanal. Chem.* **2003**, 540, 105–110.
102. D. W. DeWulf, T. Jiu, A. J. Bard, *J. Electrochem. Soc.* **1989**, 136, 1686–1691.
103. Y. Hori, A. Murata, T. Tsukamoto et al., *Electrochim. Acta* **1994**, 2495–2500.
104. A. Sammells, R. L. Cook in *Electrochemical and Electrocatalytic Reactions of Carbon Dioxide* (Eds.: B. P. Sullivan, K. Krist, H. E. Guard), Elsevier, New York, 1993, Chapter 7.
105. A. Miedaner, D. L. DuBois, C. J. Curtis et al., *Organometallics* **1993**, 12, 299–303.
106. C. Lapinte, D. Catheline, D. Astruc, *Organometallics* **1988**, 7, 1683–1691.
107. G. O. Nelson, C. E. Sumner, *Organometallics* **1986**, 5, 1983–1990.
108. M. D. Farnos, B. A. Woods, B. B. Wayland, *J. Am. Chem. Soc.* **1986**, 108, 3659–3663.
109. B. D. Dombek, *Organometallics* **1985**, 4, 1707–1712.
110. D. H. Gibson, S. K. Mandal, K. Owens et al., *Organometallics* **1990**, 9, 1936–1942.
111. A. Asdar, C. Lapinte, L. Toupet, *Organometallics* **1989**, 8, 2708–2717.
112. C. P. Casey, M. A. Andrews, D. R. McAlister et al., *J. Am. Chem. Soc.* **1980**, 102, 1927–1933.
113. W. Tam, G.-Y. Lin, W.-K. Wong et al., *J. Am. Chem. Soc.* **1982**, 104, 141–152.
114. A. T. Patton, C. E. Strouse, C. B. Knobler et al., *J. Am. Chem. Soc.* **1983**, 105, 5804–5811.
115. J. R. Sweet, W. A. G. Graham, *J. Am. Chem. Soc.* **1982**, 104, 2811–2815.
116. J. H. Merrifield, J. M. Fernandez, W. E. Buhro et al., *Inorg. Chem.* **1984**, 23, 4022–4029.
117. R. Shiratsuchi, Y. Aikoh, G. Nogami, *J. Electrochem. Soc.* **1993**, 140, 3479–3482.
118. B. Jermann, J. Augustynski, *Electrochim. Acta* **1994**, 39, 1891–1896.
119. D. O. Hall, K. K. Rao, *Photosynthesis*, 5th ed., Cambridge University Press, Cambridge, 1994, Chapter 6.
120. B. Parkinson, P. Weaver, *Nature* **1984**, 309, 148–149.

121. N. S. Lewis, G. A. Shreve in *Electrochemical and Electrocatalytic Reactions of Carbon Dioxide* (Eds.: B. P. Sullivan, K. Krist, H. E. Guard), Elsevier, New York, 1993, Chapter 6.
122. A. Fujishima, D. A. Tryk, T. N. Rao in *Advances in Chemical Conversions for Mitigating Carbon Dioxide, Studies in Surface Science and Catalysis Vol. 114* (Eds.: T. Inui, M. Anpo, K. Izui et al.), Elsevier, Tokyo, 1998, pp. 31–42.
123. S. Yanagida, Y. Wada, K. Murakoshi in *Advances in Chemical Conversions for Mitigating Carbon Dioxide, Studies in Surface Science and Catalysis* (Eds.: T. Inui, M. Anpo, K. Izui et al.), Elsevier, Tokyo, 1998, pp. 183–194, Vol. 114.
124. W. Shin, S. H. Lee, J. W. Shin et al., *J. Am. Chem. Soc.* **2003**, *125*, 14688–14689.
125. S. Kuwabata, R. Tsuda, H. Yoneyama, *J. Am. Chem. Soc.* **1994**, *116*, 5437–5443.

6.3 Carbon Monoxide and Binary Metal Carbonyls

*Christopher J. Pickett
John Innes Centre, Norwich, UK*

6.3.1 Electrochemical Reduction and Oxidation of Carbon Monoxide

Electrochemical reduction of carbon monoxide in dry nonaqueous media at moderate to low pressures leads to the formation of the 1,3-cyclobutanedione dianion (squarate) at current efficiencies, up to about 45% depending on the cathode material [1, 2]. In aqueous solution, electroreduction can lead to the formation of methane and other hydrocarbon products. The role of the metal/adatom in determining the extent of CO and hence hydrocarbon formation during the reduction of carbon dioxide is related to the ability of the electrode material to favor CO formation (Cu, Au, Ag, Zn, Pd, Ga, Ni, and Pt) and stabilize HCCO^- [3, 4].

Electrooxidation of carbon monoxide to carbon dioxide at platinum has been extensively studied mainly not least because of the technological importance of its role in methanol oxidation in fuel cells [5] and in poisoning hydrogen fuel cells [6]. Enhancing anodic oxidation of CO is critical, and platinum surfaces modified with ruthenium or tin, which favor oxygen atom adsorption and transfer to bound CO, can achieve this [7, 8].

Fundamental studies of CO binding to platinum surfaces have shown that the vibrational stark effect and binding energetics are related to the nature of surface coordination of CO as terminally bound or bridging [9, 10]. The spectroelectrochemical behavior of polynuclear platinum

carbonyls have been studied as models for surface-bound CO [11]; see Sect. 6.3.2 below.

6.3.2 Binary Metal Carbonyls

In the mid-1960s, Dessy and coworkers [12, 13] provided an extensive survey of the anodic and cathodic reactions of transition metal organometallic species, including binary (homoleptic) carbonyls, and this provided a stimulus for many later detailed studies. Whereas the electrochemistry of heteroleptic transition metal carbonyls is covered elsewhere in this volume, that of the binary carbonyls, which is covered here, provides paradigms for the electrochemistry of their substituted counterparts. A key aspect is the generation of reactive 17-electron or 19-electron intermediates that can play key roles in the electrocatalytic processes and electron-transfer catalysis of CO substitution by other ligands.

6.3.2.1 Mononuclear Carbonyls

Specific reviews of the electrochemistry of mononuclear carbonyls have not appeared. The primary oxidation of the mononuclear carbonyls leads to the formation of 17-electron radical cations with half-lives in the order of seconds or less in MeCN electrolytes [14, 15]. Decay may take place by disproportionation, CO loss, and/or nucleophilic attack. Electrogeneration in solvents of low nucleophilicity such as trifluoroacetic acid can enhance the stability of the cations and indicates that nucleophilic attack is a major pathway for decay. This is concordant with the stability order $[\text{Cr}(\text{CO})_6]^+ > [\text{Fe}(\text{CO})_5]^+ \gg [\text{Ni}(\text{CO})_4]^+$, where the lower coordination numbers favor nucleophilic attack and

further oxidation [16]. This is also consistent with the observation that $[\text{Mo}(\text{CO})_6]^+$ and $[\text{W}(\text{CO})_6]^+$, which have larger metal centers and a tendency for seven coordination in M(II) oxidation states, so far remain undetected in electrochemical systems. In general, the substitution of CO in mononuclear 18-electron systems by donor ligands such as amines, phosphines, or halides allows oxidation to occur at less positive potentials because the 17-electron metalloradicals are stabilized and less reactive. For example, the 17-electron neutral complexes $[\text{Cr}(\text{CO})_5\text{X}]$, where X = halide or pseudohalide, are stable, isolable species [17]. The importance of a cationic charge in promoting nucleophilic attack is emphasized by the comparative stability of the paramagnetic 17-electron species $[\text{V}(\text{CO})_6]$, which are indefinitely stable in nonpolar solvents, and $[\text{Cr}(\text{CO})_6]^+$, which is not so [14, 18, 19]. In the 17-electron carbonyl complexes, the M–CO bonds are weakened by diminished backbonding to CO; this favors an intimate associative mechanism involving nucleophilic attack and concerted CO loss from a 19-electron intermediate or transition state. It accounts for the relative stability of the 18-electron cation $[\text{Mn}(\text{CO})_6]^+$ vis-a-vis $[\text{Cr}(\text{CO})_6]^+$ and of the lower reactivity of the 17-electron carbonyl cations with donor coligands such as phosphines or amines [20].

Electrochemical reduction of mononuclear binary carbonyls on the preparative timescale generally leads to CO loss and the formation of dinuclear dianionic products. For example, $\text{M}(\text{CO})_6$ (M = Cr, Mo, or W) undergoes irreversible electrochemical reduction near -2.7 V versus SCE in tetrahydrofuran (THF) containing $[\text{NBu}_4][\text{BF}_4]$. The product of the reductions are the dinuclear dianions $[\text{M}_2(\text{CO})_{10}]^{2-}$ [14, 21], although under some conditions

polynuclear products can also be obtained [22]. It was initially proposed that the primary step involved a single-electron transfer with fast CO loss and subsequent dimerization of the 17-electron radical anion $[\text{M}(\text{CO})_5]^-$ [21]. A subsequent study showed that a common intermediate detected on the voltammetric timescale was the 18-electron species $[\text{M}(\text{CO})_5]^{2-}$ formed by a two-electron ECE process and that the overall one-electron reduction observed in preparative electrolysis arises by the attack of this dianion on the parent material in the bulk solution – the same mechanism operates for the reduction of $\text{Fe}(\text{CO})_5$ to $[\text{Fe}_2(\text{CO})_8]^{2-}$, but electrolysis in a flow cell allows the synthesis of the primary mononuclear product $[\text{Fe}(\text{CO})_4]^{2-}$ [23, 24].

6.3.2.2 Dinuclear and Polynuclear Binary Carbonyls

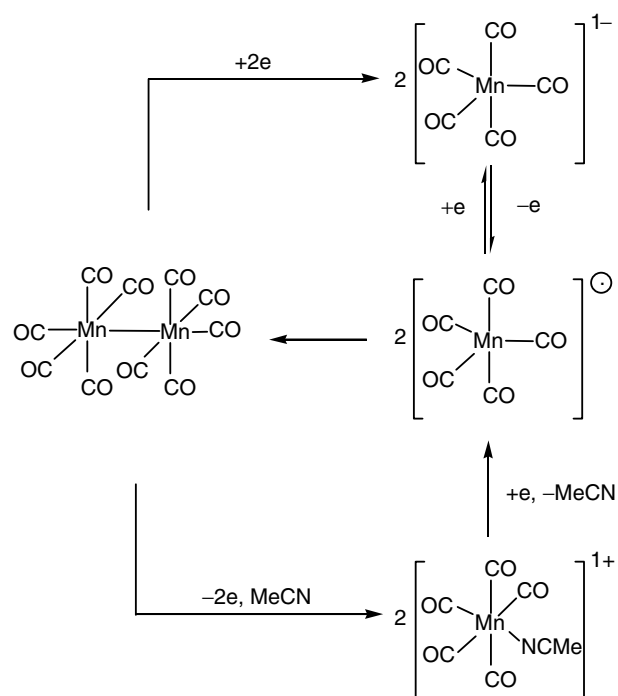
The electrochemical oxidation and reduction of $\text{Mn}_2(\text{CO})_{10}$ provides an exemplar for organometallic metal–metal-bonded systems. Electrochemical oxidation in a coordinating solvent (S) or in the presence of a ligand (L) leads to a two-electron cleavage of the metal–metal bond and the formation of the 18-electron cation $[\text{Mn}(\text{CO})_5(\text{S} \text{ or } \text{L})]^+$ – electrochemical reduction of this type of product generally leads to the regeneration of the metal–metal-bonded product; for example, when S = MeCN, the parent molecule $\text{Mn}_2(\text{CO})_{10}$ is regenerated essentially in a quantitative manner. Electrochemical reduction of $\text{Mn}_2(\text{CO})_{10}$ also leads to the cleavage of the metal–metal bond in a two-electron process, which generates the monoanion $[\text{Mn}(\text{CO})_5]^-$.

Reoxidation of this anion leads to the regeneration of the parent material at inert anodes via the formation of the 17-electron radical [12–14, 25]. These reactions are

summarized in Sch. 1. The thermodynamics of these and related systems have been studied. For the two-electron couples, such as $2[\text{Mn}(\text{CO})_5(\text{MeCN})]^+/\text{Mn}_2(\text{CO})_{10}$, $E_c^{\oplus'}$ was estimated to be +0.30 versus SSCE (saturated sodium chloride calomel electrode), and for $\text{Mn}_2(\text{CO})_{10}/2[\text{Mn}(\text{CO})_5]^-$ it was estimated to be -0.69 V versus SSCE. These values were obtained by an equilibration technique. For one-electron couples such as $\text{Mn}(\text{CO})_5/[\text{Mn}(\text{CO})_5]$, $E_c^{\oplus'}$ was found to be -0.08 V versus SSCE, as measured by fast-scan microelectrode cyclic voltammetry [26]. Cross-coupling reactions of electrogenerated radicals [27] and electrochemical substitution processes have been studied *in situ* by FTIR spectroelectrochemistry [28].

The electrochemistry of polynuclear carbonyl complexes has been reviewed

[29–31]. Electron-transfer catalysis of substitution of CO by a donor ligand in a trinuclear iron carbonyl system provided early examples of how the generation of reactive metalloradical species can give rise to intermediates that *oxidize* at the potential of the primary *reduction* process, with consequently low charge consumption; that is, the electron acts as a catalyst [32–34]. Major structural changes can result from the electrochemical reduction of trinuclear binary carbonyls [35, 36]. This is exemplified by the electrochemical reduction of $\text{Ru}_3(\text{CO})_{12}$; this irreversible two-electron process proceeds via an EE mechanism, with the opening of the triruthenium ring being concerted with the first electron-transfer step. The reduction product, presumed to be open-chain $[\text{Ru}_3(\text{CO})_{12}]^{2-}$, is very



Scheme 1 Electrochemical transformations of $\text{Mn}_2(\text{CO})_{10}$.

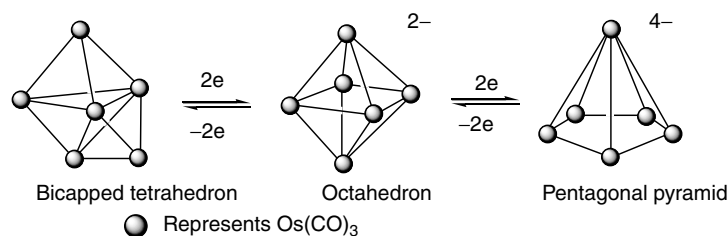
rapidly consumed by a second-order process to give $[\text{Ru}_3(\text{CO})_{11}]^{2-}$ and by a competing first-order process to give a species, possibly an acetone adduct, which then slowly decays to $[\text{Ru}_3(\text{CO})_{11}]^{2-}$ [35].

Structural reorganization associated with successive reversible two-electron reductions of $[\text{Os}_6(\text{CO})_{18}]$, as illustrated by Sch. 2, can have low energy barriers. The primary reduction proceeds without the detection of an intervening monoanion and with a small activation energy barrier for the conversion of the bicapped tetrahedron to the octahedral dianion of 8 kcal mol^{-1} , as shown in Sch. 2; the structure of the tetraanion in Sch. 2 is deduced from theoretical calculations [36].

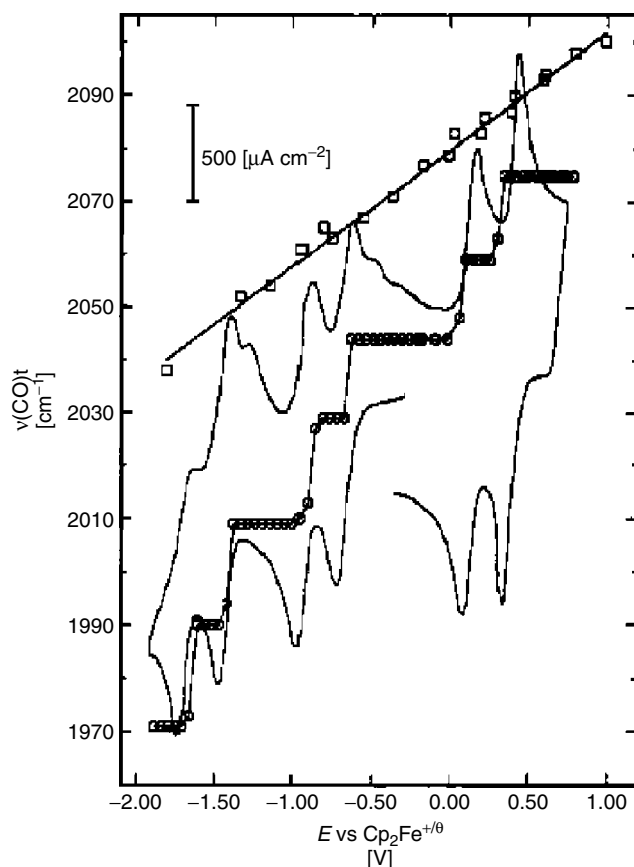
An intriguing link between the electronic and bonding properties of large, ionizable metal polynuclear carbonyl clusters and that of chargeable metal surfaces on which CO is adsorbed has been found. Thus, infrared spectroelectrochemistry has been used to explore the vibrational properties of the high-nuclearity platinum carbonyl clusters $[\text{Pt}_{24}(\text{CO})_{30}]^{n-}$, $[\text{Pt}_{26}(\text{CO})_{32}]^{n-}$, and $[\text{Pt}_{38}(\text{CO})_{44}]^{n-}$ as a function of the charge n in a range of solvents. The clusters exhibit reversible voltammetric and spectroelectrochemical behavior, with a sequence of redox steps spanning $n = 0$ to -10 , with $E_c^{\oplus'}$ between ca 0.5 and -2.5 V versus ferrocene–ferrocenium. Largely, two-electron

steps are observed for $[\text{Pt}_{26}(\text{CO})_{32}]^{n-}$, involving even-charge states ($n = -2, -4, -6, -8$, and -10). Sequential one-electron steps are found for $[\text{Pt}_{24}(\text{CO})_{30}]^{n-}$ and $[\text{Pt}_{38}(\text{CO})_{44}]^{n-}$, although the regions of electrode potential over which odd-charge states ($n = -1, -3, -5, -7$) are stable (i.e. the spacings between $E_c^{\oplus'}$ values) are markedly smaller than those for the even-charge states. The CO stretching frequencies for the bridging ($\nu(\text{CO})_b$) and especially the terminal ($\nu(\text{CO})_t$) coordinated CO ligands decrease systematically as n becomes more negative; for example, $\nu(\text{CO})_t$ for $[\text{Pt}_{24}(\text{CO})_{30}]^{n-}$ diminishes by $15\text{--}20 \text{ cm}^{-1}$ per added electron. Comparisons with the potential (and consequent) charge-dependent properties of CO adlayers at corresponding platinum electrode–solution interfaces can be made because these systems also display decreases in $\nu(\text{CO})_t$ and $\nu(\text{CO})_b$ as the electrode potential, E , and hence the surface charge, is made more negative, as usually ascribed either to increased $d\pi(\text{Pt})$ to $\pi^*(\text{CO})$ backbonding or to a Stark effect (Sch. 3).

The $\nu(\text{CO})_t$ – E slopes for saturated CO adlayers at both single-crystal and polycrystalline Pt–nonaqueous interfaces are noticeably smaller than those for the corresponding solvated Pt carbonyl clusters. These differences are explained as being chiefly due to larger “effective



Scheme 2 Structural reorganization accompanying the electron-transfer reactions of $\text{Os}_6(\text{CO})_{18}$.



Scheme 3 Terminal $\nu(\text{CO})$ frequencies (squares) versus redox potential for $[\text{Pt}_{24}(\text{CO})_{30}]^{n-}$; the circles show the corresponding response of $\nu(\text{CO})$ on poly crystalline platinum (from Ref. 37 with permission).

surface" capacitances (i.e. charge- $E_c^{\oplus'}$ dependencies) for the clusters than those measured for the electrode–solution interfaces and have been rationalized by a simple geometric electrostatic model [37]. The electrochemical behavior of the bimetallic $[\text{H}_{6-n}\text{Ni}_{38}\text{Pt}_6(\text{CO})_{48}]^{n-}$ ($n = 4-6$) clusters show that up to six different oxidation states are accessible. The difference in the formal electrode potentials of consecutive redox couples of both series is almost constant and is around 0.3 V. It is argued that this is because there is no

well-defined HOMO–LUMO gap, and the clusters display semiconductor-like behavior; moreover, the transition from semiconductor to metallic behavior might occur upon a ca 50% increase in the nuclearity of clusters currently available [38].

References

1. G. Silvestri, S. Gambino, G. Filardo et al., *Electrochim. Acta* **1978**, 23, 413.
2. M. Shibata, D. Omori, N. Furuya et al., *Electrochemistry* **1999**, 67, 355.

3. Y. Hori, A. Murata, R. Takahashi, *Chem. Lett.* **1987**, 1665.
4. Y. Hori, H. Wakabe, T. Tsukamoto et al., *Electrochim. Acta* **1994**, 39, 1833.
5. S. Gilman, *J. Phys. Chem.* **1964**, 68, 707.
6. A. L. Dicks, *J. Power Sources* **1996**, 61, 113–124.
7. H. A. Gasteiger, N. M. Markovic, P. N. Ross, *J. Phys. Chem.* **1995**, 99, 8945–8949.
8. M. Watanabe, S. Motoo, *J. Electroanal. Chem.* **1975**, 60, 275–283.
9. S. A. Wasileski, M. T. M. Koper, M. J. Weaver, *J. Am. Chem. Soc.* **2002**, 124, 2796.
10. S. Z. Zou, M. J. Weaver, *J. Phys. Chem.* **1996**, 100, 4237.
11. J. D. Roth, G. J. Lewis, L. K. Safford et al., *J. Am. Chem. Soc.* **1992**, 114, 6159.
12. R. E. Dessy, F. E. Stary, R. B. King et al., *J. Am. Chem. Soc.* **1966**, 88, 471.
13. R. E. Dessy, L. A. Bares, *Acc. Chem. Res.* **1972**, 5, 415.
14. C. J. Pickett, D. Pletcher, *J. Chem. Soc., Chem. Commun.* **1975**, 879.
15. C. J. Pickett, D. Pletcher, *J. Chem. Soc., Chem. Commun.* **1974**, 660.
16. C. J. Pickett, D. Pletcher, *J. Chem. Soc., Dalton Trans.* **1976**, 636.
17. A. M. Bond, J. A. Bowden, R. Colton, *Inorg. Chem.* **1974**, 13, 602.
18. R. N. Bagchi, A. M. Bond, R. Colton et al., *J. Am. Chem. Soc.* **1986**, 108, 3352.
19. A. M. Bond, R. Colton, *Inorg. Chem.* **1976**, 15, 2036.
20. A. M. Bond, P. A. Dawson, B. M. Peake et al., *Inorg. Chem.* **1977**, 16, 2199.
21. C. J. Pickett, D. Pletcher, *J. Chem. Soc., Dalton Trans.* **1976**, 749.
22. A. Seurat, P. Lemoine, M. Gross, *Electrochim. Acta* **1978**, 23, 1219.
23. C. Amatore, P. J. Krusic, J. N. Verpeaux, *Organometallics* **1988**, 11, 2426.
24. C. Amatore, P. J. Krusic, S. U. Pedersen et al., *Organometallics* **1995**, 14, 640.
25. P. Lemoine, A. Giraudeau, M. Gross, *Electrochim. Acta* **1976**, 21, 1.
26. J. R. Pugh, T. J. Meyer, *J. Am. Chem. Soc.* **1992**, 114, 3784.
27. D. J. Kuchynka, J. K. Kochi, *Inorg. Chem.* **1989**, 28, 855.
28. R. E. Wittig, C. P. Kubiak, *J. Electroanal. Chem.* **1995**, 393, 75.
29. P. Lemoine, *Coord. Chem. Rev.* **1988**, 83, 169.
30. W. E. Geiger, N. G. Connely, *Adv. Organomet. Chem.* **1985**, 24, 87.
31. S. R. Drake, *Polyhedron* **1990**, 9, 455.
32. A. Darchen, C. Mahe, H. Patin, *J. Chem. Soc., Chem. Commun.* **1982**, 243.
33. A. J. Downard, B. H. Robinson, J. Simpson, *J. Organomet. Chem.* **1987**, 320, 363.
34. D. Astruc, *Angew. Chem., Int. Ed. Engl.* **1988**, 27, 643.
35. B. Tulyathan, W. E. Geiger, *J. Am. Chem. Soc.* **1985**, 107, 5960.
36. J. E. Cyr, P. H. Rieger, *Organometallics* **1991**, 10, 2153.
37. J. D. Roth, G. J. Lewis, L. K. Safford et al., *J. Am. Chem. Soc.* **1992**, 114, 6159.
38. F. F. De Biani, C. Femoni, M. C. Iapalucci et al., *Inorg. Chem.* **1999**, 38, 3721.

7.1 Molecular Nitrogen and Dinitrogen Complexes

Christopher J. Pickett
John Innes Centre, Norwich, UK

7.1.1 Molecular Nitrogen

A single study reports the electrochemical oxidation of molecular nitrogen (dinitrogen) at platinum microelectrode, together with the oxidation of inert gases [1]. There have been several reports of the heterogeneous electroreduction of dinitrogen to ammonia. These include studies of gas-diffusion electrodes coated with metallophthalocyanines [2, 3], industrial iron catalysts at high pressure [4], and ruthenium electrodes [5]. Ammonia has been synthesized from its elements at atmospheric pressure in a solid-state proton (H^+)-conducting cell reactor. Hydrogen flowing over the anode was converted into protons that were transported through the solid electrolyte and reached the cathode (palladium) over which nitrogen was passing. At $570^\circ C$ and atmospheric pressure, about 78% of the electrochemically supplied hydrogen was converted into ammonia [6].

Electroreduction titanium(IV) isopropoxide under molecular nitrogen at 1 atm in diglyme led to the generation of titanium nitride species that could be hydrolyzed to yield ammonia [7]. The electrochemical reduction of dinitrogen to ammonia in aqueous electrolytes using vanadium(IV) catecholate mediators and other transition metal systems has been reported, including the titanocene species [8–10].

7.1.2 Nitrogen Hydrides: Ammonia and Hydrazine

The kinetics of the electrochemical oxidation of ammonia on platinum to dinitrogen in basic electrolytes has been extensively studied. In the widely supported mechanism originally suggested by Gerischer and Mauerer [11], the active intermediate in the selective oxidation to N_2 is a partly dehydrogenated ammonia adsorbate, $NH_{2,ads}$ or NH_{ads} . The atomic nitrogen adsorbate N_{ads} , which is apparently formed at more positive potentials, is inactive toward N_2 production at room temperature. Generally, only platinum and iridium electrodes exhibit steady-state N_2 production at potentials at which no sur-

face oxides are formed in contrast to metals with a high propensity for atomic nitrogen formation, such as ruthenium, rhodium, and palladium which show at the most only a transient activity toward N_2 production [12]. Surface-enhanced Raman spectroscopy (SERS) has recently revealed a band near 460 cm^{-1} on palladium exposed to ammonia which has been attributed to inactivating chemisorbed atomic N [13]. Both ammonia and hydrazine also have potential utility in fuel cells.

The selective electrosynthesis of hydrazine either by oxidation of ammonia or by reduction of dinitrogen has not been achieved because both thermodynamically and kinetically hydrazine is easier to oxidize than ammonia, and easier to reduce than dinitrogen. Indirect methods for its electrosynthesis have been reported [14, 15]. For example, NCl_3 was electrosynthesized in CCl_4 by diaphragmless electrolysis of NH_4Cl in H_2O-CCl_4 . Treating this solution with an aqueous solution of NH_3 yielded NH_2Cl . The latter transforms to 3,3-diaziridines under the action of a methylethylketone-containing aqueous solution of NH_3 , which on hydrolysis with sulfuric acid gave the hydrazinium sulfate in 75% to 77% yield based on NH_2Cl [15]. Both hydrazine and ammonia have potential utility as anode reactants in fuel cells. Thus, there have been a wide range of studies of hydrazine oxidation at carbon and noble metals and these anode materials are modified by ad-atoms, inorganic complexes such as Prussian blue, or by electropolymers [16–25].

7.1.3

Dinitrogen Complexes of the Transition Metals

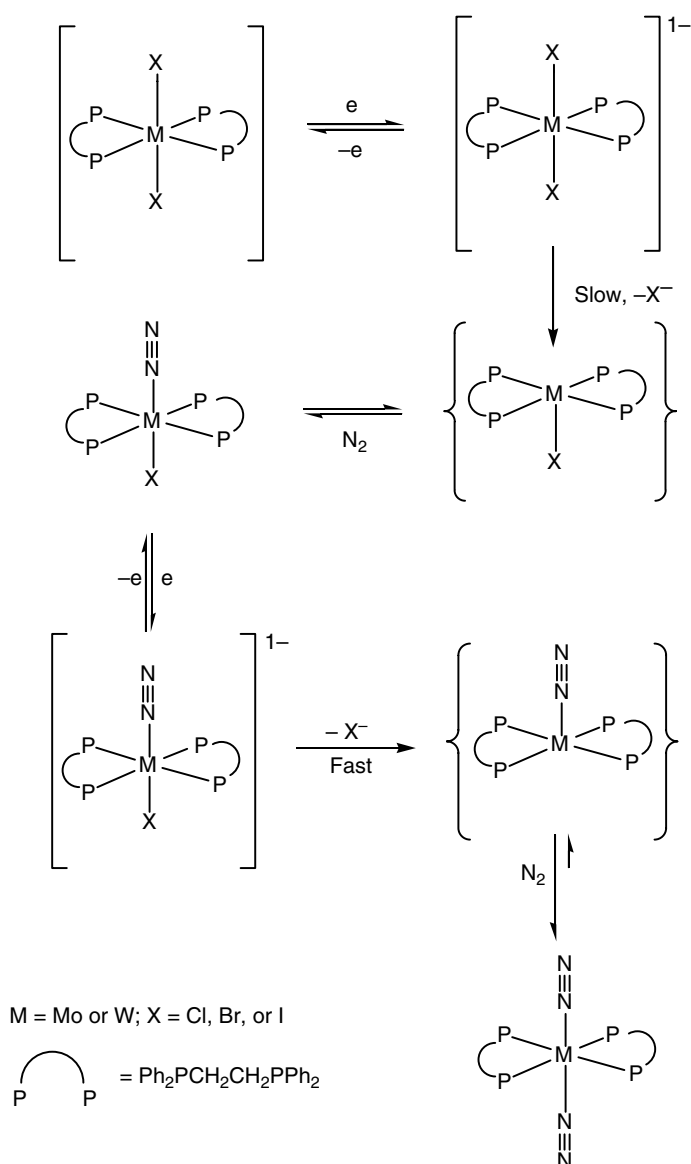
The chemistry and electrochemistry of well-defined dinitrogen complexes have

been studied in the context of understanding how the iron–molybdenum or related metallocenters in the Mo, V, and Fe – nitrogenases might function; how stoichiometric or electrocatalytic systems might be developed for nitrogen fixation at low temperatures and pressures; and how new routes from molecular nitrogen to organonitrogen products might be uncovered. Molecular nitrogen forms more or less stable complexes with transition metals in low or intermediate oxidation states. Two major types of coordination are observed: end-on terminally bound and bridging between two transition metal centers. In the terminally bound mode, it behaves as a σ -donor/ π^* -acceptor ligand in a fashion similar to that of carbon monoxide. In the bridging mode, dinitrogen is a σ -donor and a π^* -acceptor ligand or π -donor ligand, depending on the $d\pi$ -donor/acceptor capacity of the metals. For both modes of bonding, the stable species have an 18-electron, closed-shell configuration around the metal center [26].

Mononuclear 18-electron dinitrogen complexes generally undergo successive reversible one-electron oxidations to moderately stable 17-electron and unstable 16-electron species, which parallels the behavior of their carbonyl analogs. Measurements of formal oxidation potentials have been widely used to probe the influence of coligands on dinitrogen complexes, and correlations of $E_{1/2}$ measured by cyclic voltammetry with infrared $\nu(N_2)$ frequencies have been noted [27, 28]. A further analogy with the electrochemistry of transition metal carbonyl systems is the observation of certain octahedral Mo and W bis-dinitrogen systems of a redox linked cis–trans isomerism associated with the 17-electron/18-electron couple [29, 30].

17-electron dinitrogen intermediates are involved in electrochemical pathways to dinitrogen complexes and also in the formation of N–C bonds through radical attack on bound N_2 (see Sect. 3.4)

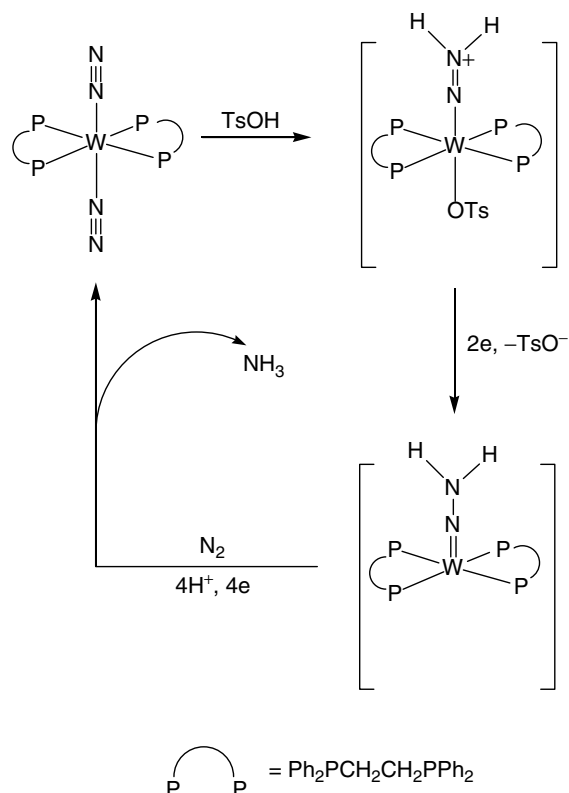
Dinitrogen complexes of molybdenum and tungsten have been electrochemically synthesized from molecular nitrogen at 1 atm and higher oxidation state (II, IV, or V) Mo or W precursors. For example, in



Scheme 1 Electrochemical synthesis of dinitrogen complexes of Mo and W from M(II) precursors.

a tetrahydrofuran electrolyte at mercury or platinum $\text{trans-[Mo}^{\text{II}}\text{Cl}_2(\text{Ph}_2\text{PCH}_2\text{CH}_2\text{PPh}_2)_2]$ was reduced to $\text{trans-[Mo}(\text{N}_2)_2(\text{Ph}_2\text{PCH}_2\text{CH}_2\text{PPh}_2)_2]$, which could be isolated in good yield – the proposed mechanism of this reduction is given in Sch. 1 [31, 32]. The electrosyntheses of this dinitrogen complex and its tungsten analog is possible from molecular nitrogen and Mo or W (IV) oxo, imide, or hydrazide precursors [33–35]. Hydrazide derivatives can be directly synthesized by protonation of $\text{trans-[M}(\text{N}_2)_2(\text{Ph}_2\text{PCH}_2\text{CH}_2\text{PPh}_2)_2]$ (where M = Mo or W). The electrochemical reduction of the tungsten hydrazide $\text{trans-[W(NNH}_2)(\text{TsO})(\text{Ph}_2\text{PCH}_2\text{CH}_2\text{PPh}_2)_2]^+$ ($\text{TsO} = p\text{-C}_6\text{H}_5\text{SO}_3$) under dinitrogen

yields ammonia and regenerates the parent dinitrogen complex in good yield thus establishing the basis for an electrochemical nitrogen fixing cycle [36, 37] Sch. 2. A catalytic reduction of molecular nitrogen through a molybdenum triamidoamine dinitrogen complex has been developed by Schrock and Yandulov. This system probably involves similar hydrazide and imide intermediates [38–41]. The relevance of electron-transfer chemistry of molybdenum and tungsten model compounds to the mechanism of biological nitrogen fixation at the functional group level has been discussed [42]. The formation of nitrogen–carbon bonds by reactions of $\text{trans-[M}(\text{N}_2)_2(\text{Ph}_2\text{PCH}_2\text{CH}_2\text{PPh}_2)_2]$



Scheme 2 Electrosynthesis of ammonia via tungsten bis(ditertiaryphosphine) species.

(M = Mo or W) with alkyl halides has opened the way for the electrosynthesis of organoamines, organohydrazines, cyanides, aminocarbynes organonitriles, and amino acids. These are discussed in Sect. 3.4 [35, 43, 44].

The electrochemistry of dinitrogen bridging two porphyrin ligated ruthenium centers has been studied as a possible route to fixed nitrogen [45–47]. Diazene stabilized by bonding to two iron centers in a FeS system has been advanced as a structural model of a plausible intermediate in biological nitrogen fixation [48–50].

References

1. T. Dibble, S. Bandyopadhyay, J. Ghoroghchian et al., *J. Phys. Chem.* **1986**, 90, 5275.
2. N. Furuya, H. Yoshida, *J. Electroanal. Chem.* **1989**, 272, 263.
3. N. Furuya, H. Yoshida, *J. Electroanal. Chem.* **1989**, 263, 171.
4. C. G. Yiokari, G. E. Pitselis, D. G. Polydoros et al., *J. Phys. Chem. A* **2000**, 104, 10600.
5. S. Y. Zhang, X. Y. Zhang, Z. S. Zhang et al., *Chem. Lett.* **2003**, 32, 440.
6. G. Marnellos, S. Zisekas, M. Stoukides, *J. Catal.* **2000**, 193, 80.
7. E. E. van Tamel, R. B. Fechter, S. W. Schnelle et al., *J. Am. Chem. Soc.* **1969**, 91, 1551.
8. A. F. Zueva, A. E. Shilov, A. D. Styrkas et al., *Russ. J. Phys. Chem. USSR* **1972**, 46, 435.
9. V. V. Strelets, O. N. Efimov, L. A. Nikonova et al., *Zh. Fiz. Khim.* **1976**, 50, 1019.
10. J. Y. Becker, S. Avraham, B. Posin, *J. Electroanal. Chem.* **1987**, 230, 143.
11. H. Gerische, A. Maurer, *J. Electroanal. Chem.* **1970**, 25, 421.
12. A. C. A. de Voors, M. T. M. Koper, R. A. van Santen et al., *J. Electroanal. Chem.* **2001**, 506, 127.
13. A. C. A. de Voors, M. F. Mrozek, M. T. M. Koper et al., *Electrochem. Commun.* **2001**, 3, 293.
14. Z. Ali, R. Bauer, W. Schon et al., *J. Appl. Electrochem.* **1980**, 10, 97.
15. B. V. Lyalin, V. A. Petrosyan, *Russ. J. Electrochem.* **1999**, 35, 523.
16. B. C. Wang, X. Q. Cao, *J. Electroanal. Chem.* **1991**, 309, 147.
17. G. Schulzek, D. Baresel, *J. Electroanal. Chem.* **1972**, 35, 73.
18. U. Scharf, E. W. Grabner, *Electrochim. Acta* **1996**, 41, 233.
19. D. W. Pang, B. H. Deng, Z. L. Wang, *Electrochim. Acta* **1994**, 39, 847.
20. G. Kokkinidis, P. D. Jannakoudakis, *J. Electroanal. Chem.* **1981**, 130, 153.
21. S. M. Golabi, H. R. Zare, *J. Electroanal. Chem.* **1999**, 465, 168.
22. S. M. I. Golabi, F. Noor-Mohammadi, *J. Solid State Electrochem.* **1998**, 2, 30.
23. U. Eisner, E. Gileadi, *J. Electroanal. Chem.* **1970**, 28, 81.
24. L. Doubova, M. Fabrizio, G. Mengoli et al., *Electrochim. Acta* **1990**, 35, 1425.
25. S. Antoniadou, A. D. Jannakoudakis, E. Theodoridou, *Synth. Met.* **1989**, 30, 295.
26. R. A. Henderson, G. J. Leigh, C. J. Pickett, *Adv. Inorg. Chem.* **1983**, 27, 197.
27. W. Hussain, G. J. Leigh, H. M. Ali et al., *J. Chem. Soc., Dalton Trans.* **1984**, 1703.
28. J. Chatt, W. Hussain, G. J. Leigh et al., *J. Chem. Soc., Dalton Trans.* **1985**, 1131.
29. T. A. George, J. R. D. Debor, B. B. Kaul et al., *Inorg. Chem.* **1992**, 31, 1295.
30. T. A. George, R. K. Hayes, M. Y. Mohammed et al., *Inorg. Chem.* **1989**, 28, 3269.
31. T. I. Alsali, C. J. Pickett, *J. Chem. Soc., Dalton Trans.* **1985**, 1255.
32. J. Talarmin, T. I. Alsali, C. J. Pickett et al., *J. Chem. Soc., Dalton Trans.* **1992**, 2263.
33. D. L. Hughes, M. Y. Mohammed, C. J. Pickett, *J. Chem. Soc., Chem. Commun.* **1988**, 1481.
34. M. Y. Mohammed, C. J. Pickett, *J. Chem. Soc., Chem. Commun.* **1988**, 1119.
35. W. Hussain, G. J. Leigh, C. J. Pickett, *J. Chem. Soc., Chem. Commun.* **1982**, 747.
36. C. J. Pickett, J. Talarmin, *Nature* **1985**, 317, 652.
37. C. J. Pickett, K. S. Ryder, J. Talarmin, *J. Chem. Soc., Dalton Trans.* **1986**, 1453.
38. D. V. Yandulov, R. R. Schrock, *Science* **2003**, 301, 76.
39. D. V. Yandulov, R. R. Schrock, *Can. J. Chem.* **2005**, 83, 341.
40. D. V. Yandulov, R. R. Schrock, *Inorg. Chem.* **2005**, 44, 1103.
41. D. V. Yandulov, R. R. Schrock, *J. Am. Chem. Soc.* **2002**, 124, 6252.
42. C. J. Pickett, *J. Biol. Inorg. Chem.* **1996**, 1, 601.

43. A. Hills, D. L. Hughes, C. J. Macdonald et al., *J. Chem. Soc., Dalton Trans.* **1991**, 121.
44. D. L. Hughes, S. K. Ibrahim, C. J. Macdonald et al., *J. Chem. Soc., Chem. Commun.* **1992**, 1762.
45. J. P. Collman, J. E. Hutchison, M. A. Lopez et al., *J. Am. Chem. Soc.* **1991**, 113, 2794.
46. J. P. Collman, J. E. Hutchison, M. A. Lopez et al., *J. Am. Chem. Soc.* **1992**, 114, 8066.
47. J. P. Collman, J. E. Hutchison, M. S. Ennis et al., *J. Am. Chem. Soc.* **1992**, 114, 8074.
48. D. Sellmann, W. Soglowek, F. Knoch et al., *Angew. Chem., Int. Ed. Engl.* **1989**, 28, 1271.
49. D. Sellmann, J. Kappler, M. Moll et al., *Inorg. Chem.* **1993**, 32, 960.
50. D. Sellmann, J. Sutter, *J. Biol. Inorg. Chem.* **1996**, 1, 587.

7.2

Nitrogen Oxides and Oxyanions

György Inzelt

Eötvös Loránd University, Budapest, Hungary

György Horányi

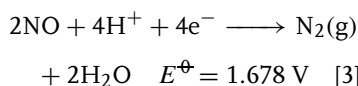
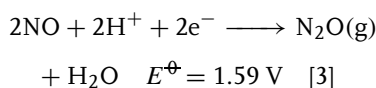
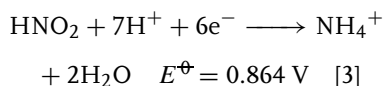
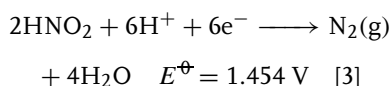
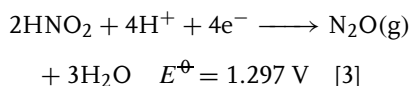
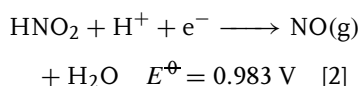
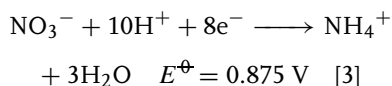
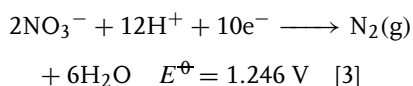
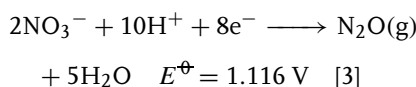
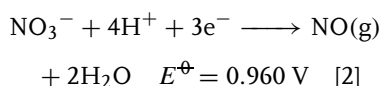
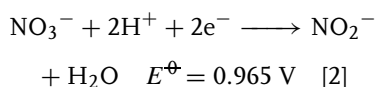
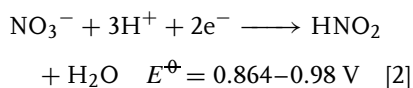
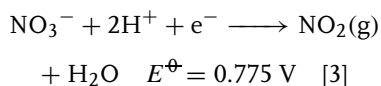
Institute of Materials and Environmental Chemistry, Budapest, Hungary

7.2.1

Fundamentals

The redox transformations of nitrogen oxides and nitrogen containing oxyanions have been thoroughly studied in connection with nitrogen fixation, with environmental problems, and recently with the physiological effect of NO. Although E^\ominus values calculated from thermodynamic data have been published [1–3], reliable electrochemically determined ones are available only for some redox reactions. This is the result of the rather complex nature of the electrode processes, for example, follow-up reactions and pH dependences. The E^\ominus values of several transformations involving different oxidation states are rather close to each other and, which makes the thing more complicated, to the decomposition of H_2O . It means that at a given potential rather complex reaction schemes may be operative, and the pH changes occurring during the reaction may also alter the composition of the reaction products.

The electrochemical transformations of the oxygen containing compounds involve all the 10 oxidation states. The most important reactions are as follows:



The standard potential values presented above are mostly derived from thermodynamic data [3]; however, where it was possible, the electrochemically measured values [2] are given.

7.2.2

Practical and Theoretical Importance of the Field

Electrocatalytic processes have been used for the production of useful chemicals, for instance, N_2O and NH_2OH from nitrates.

During the last decade, groundwater, the main source of drinking water, has been contaminated worldwide with nitrate owing to the extensive use of artificial fertilizers. High nitrate concentration in drinking water is fatal for infants, leading to the “blue baby syndrome,” and through a transformation into nitrosamine can cause cancer and hypertension.

Owing to these problems, the elaboration of denitrification technologies is a central task of environmental chemistry. Electrochemical denitrification is considered as a possible version because of its advantageous environmental compatibility, versatility, safety, and cost-effectiveness in comparison with biological, ion exchange, chemical, and catalytic methods.

The physiological importance of nitric oxide should also be mentioned. It plays an important role in smooth muscle relaxation, platelet inhibition, neurotransmission, immune regulation, and penile erection (Nobel Prize in 1998 for the discovery of its role in the cardiovascular system). The importance of NO in biological systems stimulated the development of electrochemical sensors and the investigation of the electrochemical behavior of that compound.

From theoretical aspects, the simple inorganic compounds of nitrogen may serve as model species for the clarification of elementary steps involved in electrocatalytic transformations at polycrystalline and single-crystal electrodes.

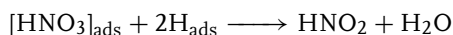
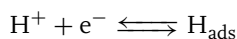
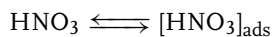
7.2.3

Electrochemical Transformations of NO_2^- , NO_3^- (HNO_2 , HNO_3)

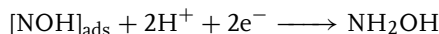
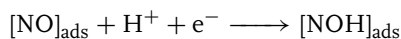
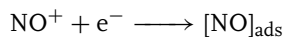
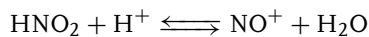
The problem of the kinetics and mechanism of electroreduction of NO_2^- and NO_3^- has been the subject of several studies since the 1960s [4–16].

The mechanism of the reduction is very complex; a series of homogenous and heterogeneous chemical reactions may occur, beside the pure electrochemical processes.

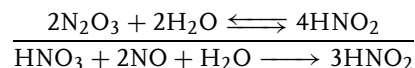
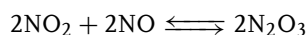
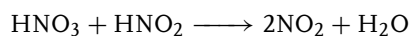
For instance, the first steps of the reduction of HNO_3 were described [12] by the relatively simple reactions:



However, these steps are followed by further charge transfer steps:



and also by autocatalytic processes in the solution phase:



It was established that for the interpretation of phenomena occurring at a platinum electrode, the competitive adsorption of hydrogen and the anions (involving the reacting ones) should be taken into consideration [13–15].

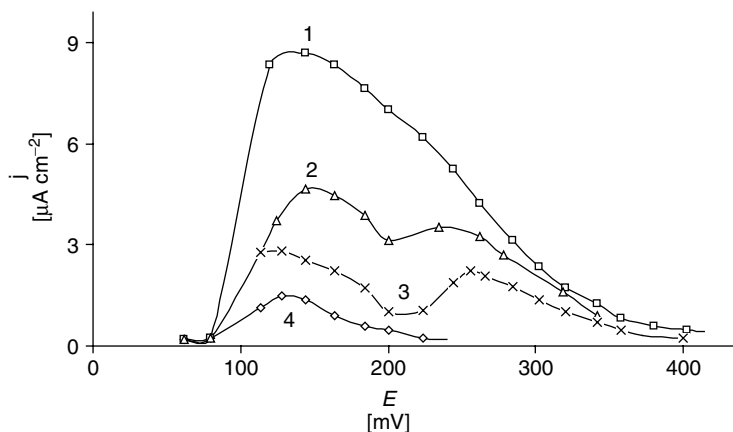


Fig. 1 Polarization curves of HNO_3 ($c = 5 \times 10^{-2} \text{ mol dm}^{-3}$) obtained in the presence of various supporting electrolytes. (1) $1 \text{ mol dm}^{-3} \text{ HClO}_4$; (2) $1 \text{ mol dm}^{-3} \text{ HClO}_4 + 1 \times 10^{-1} \text{ mol dm}^{-3} \text{ H}_3\text{PO}_4$; (3) $1 \text{ mol dm}^{-3} \text{ H}_2\text{SO}_4$; (4) $1 \text{ mol dm}^{-3} \text{ HClO}_4 + 1 \times 10^{-4} \text{ mol dm}^{-3} \text{ HCl}$.

Thus, the anion dependent shape of the polarization curves presented in Fig. 1 can be explained

1. in terms of displacement of the reacting anion by the hydrogen adsorption occurring at low potentials;
2. by the adsorption competition of the anion of the supporting electrolyte with the reacting species.

An electrocatalytic effect of Pb adatoms on Ag, Pt, and Au electrodes in NO_3^- reduction has been described [17–19].

The role of complexes and modifiers in the reduction has been discussed in [20–24]. The investigation of the liquid phase catalytic hydrogenation of NO_3^- , NO_2^- , and NH_2OH at tungsten carbide catalyst furnished interesting information concerning the electrocatalytic properties of the latter [25].

In the course of electrooxidation and/or reduction of NH_3 , NH_2OH , NO_3^- , and NO_2^- at Pt-black electrodes, adsorbates of very similar properties have been found [26].

These adsorbates can be reduced to ammonia and oxidized to nitrogen. In contrast to the adsorbates of the other compounds, adsorbed nitrite can also be reduced to nitrogen oxides (in addition to ammonia). The combination of cyclic voltammetry (CV) and on-line mass spectrometry (MS) has proved that the adsorbates do not consist solely of triple bonded nitrogen.

The adsorption and oxidation of hydrazine on electrodispersed and electrofaceted Pt electrodes [27] furnish another interesting example for the influence of crystalline surface composition on the electrocatalytic properties of the electrode.

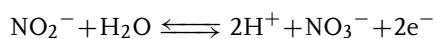
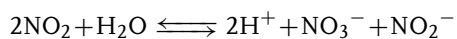
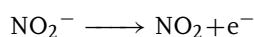
Reduction of NO (and NO_2^-) was studied at polycrystalline [28] and single crystal [29] Pt electrodes and a structure-sensitive behavior has been observed.

A comparative study of NO_3^- and NO_2^- reduction at platinum metals has been reported in [30].

The oxidation of NO_2^- was reinvestigated by Piela et al. [31, 32] at gold, platinum, glassy carbon, and oxide layer

covered gold and platinum electrodes recently.

It was observed that the oxide layer formed on gold and platinum surfaces hinders the oxidation process. According to the authors, the electrooxidation on pure electrode surfaces can be described by the following reaction sequence:



This reaction scheme involves the second-order homogeneous disproportionation of NO_2 . It was stated that the rate of the latter process is independent of the electrode material, the supporting electrolyte, the presence of oxygen, and the pH of the solution.

Various modified electrodes have been used for the investigation of the oxidation process [33–37].

An aluminum electrode modified by a chemically deposited palladium pentacyanonitrosylferrate film was reported in [33]. Vitreous carbon electrode modified with cobalt phthalocyanine was used in [34]. Electrocatalytic activity of nanostructured polymeric tetra-ruthenated porphyrin film was studied in [35]. Codeposition of Pt nanoparticles and Fe(III) species on glassy-carbon electrode resulted in significant catalytic activity in nitrite oxidation [36]. It was shown that the photocatalytic oxidation at a TiO_2/Ti film electrode can be electrochemically promoted [37].

The oxidation and reduction behavior of nitrite at carbon nanotube microelectrodes was studied with the aim of preparation of a sensor [38].

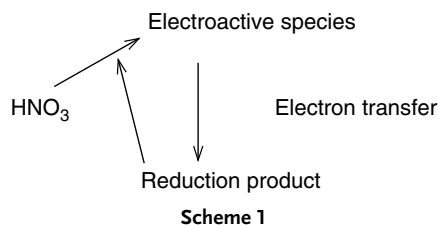
The investigation of electrochemical, electrocatalytic, and catalytic reduction of nitrite and nitrate have attracted much

attention during the last decades owing to their role in pollution of surface water and groundwater systems. The motivation of these studies was, on the one hand, to elaborate methods for the reductive elimination of these contaminating species and to create sensors for their detection and quantitative determination, on the other hand [39–49].

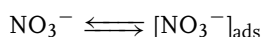
A series of publications was devoted to the electrocatalytic reduction of nitrate by the Eindhoven group [50–54]. On the basis of these works, a comparative study was performed to determine the reactivity of nitrate ions in 0.1 mol dm^{-3} concentration on eight different polycrystalline electrodes (platinum, palladium, rhodium, ruthenium, iridium, copper, silver, and gold) in acidic solution using cyclic voltammetry, chronoamperometry, and differential electrochemical mass spectroscopy (DEMS) [50].

It was found that the electrocatalytic activity strongly depends on the nature of the electrode; it decreases in the order $\text{Rh} > \text{Ru} > \text{Ir} > \text{Pd}$ and Pt for the transition-metal electrodes and in the order $\text{Cu} > \text{Ag} > \text{Au}$ for the coinage metals. It was concluded that the rate-determining step on Ru, Rh, Ir, Pt, Cu, and Ag is the reduction of nitrate to nitrite. It was assumed that chemisorbed nitric oxide is the key surface intermediate in the nitrate reduction. It was suggested that ammonia and hydroxylamine are the main products on transition-metal electrodes. This is in agreement with the known mechanism for NO reduction, which forms N_2O or N_2 only if NO is present in the solution. On Cu the production of gaseous NO was found, which was explained by the weaker binding of NO to Cu as compared to the transition metals.

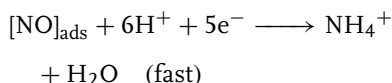
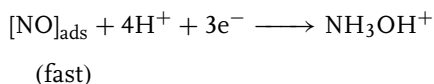
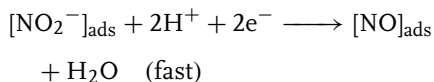
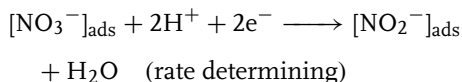
In a recent study [51], the influence of nitrate concentration and acidity on



the reduction of nitrate at platinum was investigated. In this work, two different reduction mechanisms were distinguished: direct and indirect mechanism. According to the authors, the reduction occurs via direct mechanism at low nitrate concentrations involving the following steps:



(in equilibrium)



The indirect mechanism is considered only at high nitrate concentrations (>2 M) in highly acidic environment (>2 M) in the presence of nitrite.

It is assumed that under the conditions mentioned, nitrate itself is not the electroactive species. Another species is involved in the electron transfer reaction and the product of this reaction reacts with HNO_3 to reproduce the electroactive species. The following schematic overview (Sch. 1) of the indirect reaction was given in [51]:

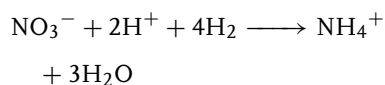
The adsorption and reduction of NO_3^- ions at Au and Pt electrodes was studied by in situ fourier transform infrared (FTIR) spectroscopy [55]. Possible adsorption geometries were suggested for adsorbed nitrate ions and for nitrite ions formed by reduction.

The effect of inorganic cations on the electroreduction of nitrate ions at platinized platinum electrodes has been studied in [56, 57].

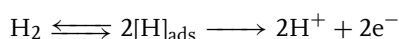
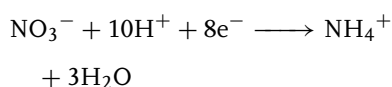
It was shown that modification of the electrode surface by Ni^{2+} , Co^{2+} , Cd^{2+} , Ge^{4+} , and Sn^{2+} cations (adatoms) enhances the catalytic activity and there are changes in the selectivity with respect to ammonium ions and hydroxylamine.

Electrochemical quartz crystal microbalance studies at Sn-modified Pt and Au electrodes allowed a further insight into the kinetics and mechanism of the reduction process [58, 59]. The problems connected with the chemisorption of NO_3^- ions were discussed in [30, 60].

Electrochemical aspects of liquid phase heterogeneous transformations [61–69] have also to be mentioned. In these cases, either the solid phase is a catalyst or the solid phase is a reaction partner. At least two coupled redox partners are present. The catalytic reduction of nitrate with molecular hydrogen in acidic aqueous phase at a solid catalyst



is composed of two coupled electrochemical processes [61].



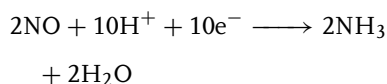
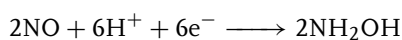
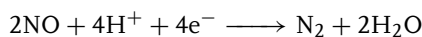
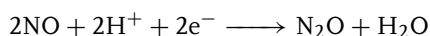
Instead of H_2 , another reducing agent can be used, for example, HCOOH . Thus, the study of electrochemical properties of the catalyst could contribute to a better understanding of the catalytic process (for detailed information see [62, 63], some other papers relevant to the field are [64, 65]).

Reduction of nitrate (and nitrite) occurs by interaction with the metal, for example, by metallic iron that has been widely studied for elaborating a technology to remove nitrate from water [66–70]. The very principle of this procedure that the anodic transformation (dissolution) corrosion of metallic iron $\text{Fe}(0)$ leading to the formation of $\text{Fe}(\text{II})$ and $\text{Fe}(\text{III})$ species is coupled with the reduction process. The effect of pH and the iron-to-nitrate ratio, temperature, and mass transport were studied under various conditions in order to elaborate a suitable technology.

7.2.4

Electrochemistry and Electrochemical Detection of NO

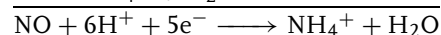
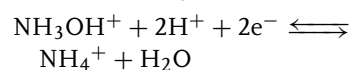
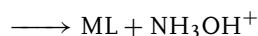
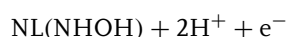
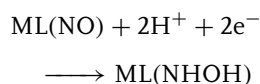
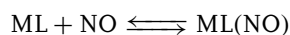
Mostly noble metal electrodes [71–75] and modified glassy-carbon electrodes [76–81] have been used. In the case of platinum electrodes, the formation of four products characterized by the following equations was observed [74, 75].



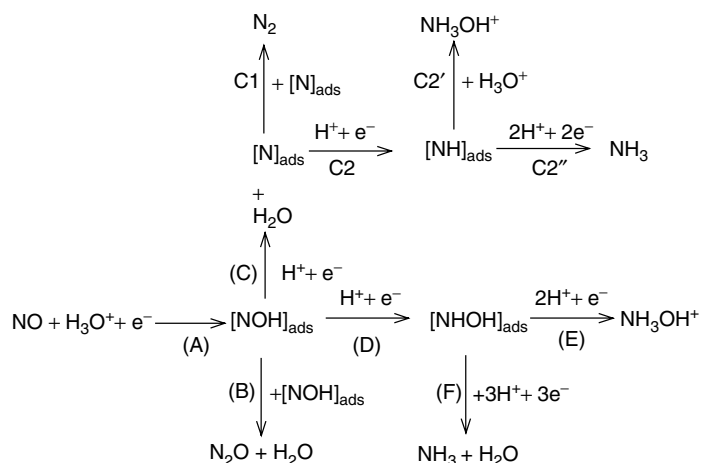
At high potentials, N_2O was the unique product while the other products appeared at lower potentials. In [74], the catalytic activities of Pt, Pd, Rh, and Ru electrodes were compared in the presence of perchloric acid supporting electrolyte and the following reaction scheme (Sch. 2) was given by the authors.

In works by Ogura and coworkers [76–81], the optimal conditions for the transformation of NO into NH_3 were studied using modified glassy-carbon electrodes and platinum electrodes in the presence of various iron complexes.

They arrived at the conclusion that in the electrode processes, NO linked to the complex (ML) is involved according to the following reaction scheme:



Detailed and fundamental studies of the mechanistic aspects of the electrochemical reduction and oxidation of nitric oxide were carried out by the Eindhoven group [82, 83] on a series of metals (Pt, Pd, Rh, Ru, Ir, and Au) both in the case of polycrystalline and well-defined single-crystal surfaces. It was found that the reduction process at all metals studied shows a high selectivity with respect to N_2O production at high potentials while at low potentials the formation of NH_3 is the dominant

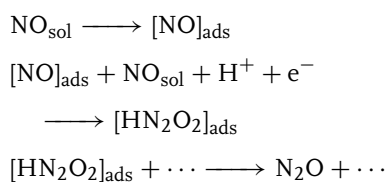


Scheme 2

process. N_2 is formed at intermediate potentials.

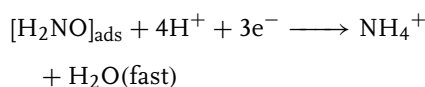
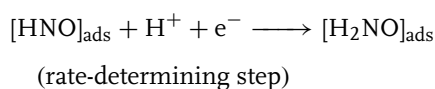
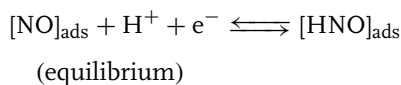
A marked difference was found in the behavior of adsorbed NO and NO in solution phase. Adsorbed NO can be reduced only to hydroxylamine and/or ammonia, while the reduction of NO in solution leads to the formation of N_2O and N_2 as well.

The following mechanism for the reduction of bulk NO was suggested in the case of polycrystalline platinum:



where the second step is rate determining. The protonated NO dimer is only formed when NO is present in the solution.

In the case of single-crystal platinum, the formation of NH_3 was formulated as follows:



In a series of publications by the Alicante group (see [84] and [85] and references cited therein), the voltammetric (cyclic voltammetry) and spectroscopic (*in situ* FTIR) characterization of NO adlayers on $\text{Pt}(h,k,l)$ and $\text{Rh}(h,k,l)$ was performed.

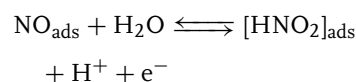
It was found that the N–O stretching frequency is potential dependent. For $\text{Rh}(111)$, it was observed that with increasing potential the bridge-bonded NO changes into linearly bonded species.

Adsorption and oxidation of NO adlayers on $\text{Pt}(111)$ was studied by using *in situ* surface X-ray diffraction and *ex situ* X-ray photoemission spectroscopy [86]. Molecular adsorption of NO was observed independently of the preparation of the adlayer.

A surface mediated oxidation process of NO toward NO_2 was observed at higher potential.

The oxidation mechanism of nitric oxide at single and polycrystalline platinum and other metals was surveyed in [82].

In the case of polycrystalline platinum, the existence of an electrochemical equilibrium



is assumed as the first step in the oxidation. The question of the further steps is a subject of intense speculation as the oxidation reaction is very sensitive to the oxidation state of the Pt surface causing poor reproducibility of the experiments. Studies on Au, Pd, Ru, and Ir lead to the conclusion that NO oxidation is not very metal dependent.

As mentioned earlier, monitoring of NO in biological samples *in vivo* and in real time is desirable in many fields of NO research. Although several techniques are available for measurement of NO in biological samples, the electrochemical method is most advantageous because of its speed and sensitivity. Since the first commercially available electrochemical NO detection system, many NO electrodes have been developed with dimensions from micrometer to centimeter, and with detection limits in the low nanomolar range. Depending on the working principle, three main types of electrodes can be distinguished [87]:

1. Electrodes based on the principle of Clark's electrode with gas permeable membranes. These sensors are used in many different fields.
2. Electrodes obtained by coating Nafion and cellulose acetate on electrode surface or the combination of Nafion/NO selective membranes and nonconducting polymer-modified electrode.

3. Sensors based on the electrocatalytic oxidation of NO by a modified layer (IrO₂, palladium metalloporphyrin modified electrodes).

More details are given in [88–94].

The electrochemical reduction of nitric oxide in solid-state electrochemical cell is an interesting field surveyed in [95]. The working principle of the cells is the cathodic reduction of NO to nitrogen and oxygen anions. In [95], the properties of various types of solid-state electrochemical cells used for NO reduction are presented and discussed. It is shown that the cathode materials with a high redox capacity and oxygen vacancies are most active for the electrochemical reduction of nitric oxide, whereas noble metal-based electrodes show a much lower selectivity. As an alternative route, the promotion of the reduction with a reductive agent is also considered.

According to [96], electrochemical methods, especially the application of cyclic voltammetry, could be a powerful tool to find suitable catalysts for NO_x removal from combustion products. Investigation of electrocatalytic properties of vitamin B₁₂ toward oxidation and reduction of nitric oxide was reported in [97]. The catalytic activity of *meso*-tetraphenyl-porphyrin cobalt for nitric oxide oxidation in methanolic solution and in Nafion film was reported in [98].

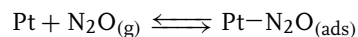
7.2.5

Reactions of N₂O

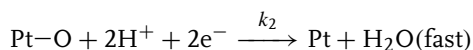
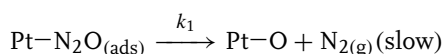
Indirect evidences for N₂O adsorption are reported in a study [99] of the effect of Pb, Cd, and Tl adatoms on the reduction process of N₂O at polycrystalline Pt electrodes. N₂O reduction was studied in detail owing to its use as a probe

of hydrogen adsorption and/or anion adsorption [100].

In a series of publications by Attard and coworkers (see [101] and literature cited therein), the adsorption and reduction of N_2O at single crystal and polycrystalline noble metal electrodes were studied. It was demonstrated that N_2O adsorption can be a useful tool to probe the anion adsorption. According to the authors, the reduction of N_2O can be described by the preequilibrium characterized by K equilibrium constant,



followed by



It was assumed that the equilibrium follows a Langmuir isotherm with competitive adsorption of ions (the coverages of which are potential dependent), then the rate of reduction was formulated as

$$\text{Rate} = k_1 K P_{N_2O}$$

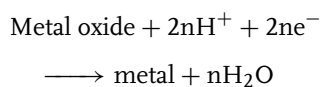
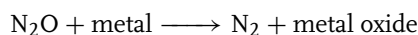
$$(1 - \theta_{N_2O} - \underbrace{\theta_{anion} - \theta_{hydrogen} - \theta_{oxide}}_{\text{potential dependent}})$$

It was demonstrated that there is a direct correspondence between the potential of zero total charge and the maximum rate of N_2O reduction.

Reduction of N_2O was used as model electrocatalytic reaction on well-defined surfaces [102, 103]. Pt(111) and Pt(100) electrodes covered with Rh adlayers were prepared for these studies. It was shown that the adsorptive and catalytic activity of the adlayers differs from those of the bulk single-crystal electrodes.

In [104], the electrochemical reduction of N_2O involving protons transported through a polyelectrolyte-coated porous glass wall was reported using zinc, lead, iron, and copper cathode.

In [105], a reduction procedure involving the permeation of hydrogen through palladized Pd sheet electrodes is described. The electrocatalytic activity of various metal (Ti, Zr, Nb, Mo, Fe, Ni, Pd, Pt, Cu, As, Au, Zn, Al, In, Sn, Pb) and metal oxide (ZnO , In_2O_3 , SnO_2 , doped Fe_2O_3 , NiO) electrodes in N_2O reduction was compared in [106, 107]. It was shown that the Faradaic efficiency for N_2 formation strongly depends on the electrode materials. The general scheme



was suggested for the interpretation of the phenomena observed.

A significant part of these studies was carried out with noble metal electrodes mainly with Pt and Pd, thus information relevant to the subject of the present section can also be found in Chapter 17 dealing with the electrochemistry of Pt and Pd.

Acknowledgment

Financial support from the Hungarian Scientific Research Fund is acknowledged. (Grants OTKA T046987 G.I., T045888 G.H.)

References

1. J. T. Maloy, in *Standard Potentials in Aqueous Solution* (Eds.: A. J. Bard, R. Parsons,

- J. Jordan), Marcel Dekker, New York, 1985, pp. 127–139, Chap. 7.
2. W. J. Plieth, in *Encyclopedia of the Electrochemistry of the Elements* (Ed.: A. J. Bard), Marcel Dekker, New York, 1973–1980.
3. M. Pourbaix, N. Zoubov, in *Atlas D'équilibres Électrochimiques at 25°C* (Ed.: M. Pourbaix), Gauthier-Villars, Paris, 1963.
4. G. Schmid, M. A. Lobeck, *Ber. Bunsen-Ges. Phys. Chem.* **1969**, 73, 189.
5. G. Schmid, M. A. Lobeck, H. Keiser, *Ber. Bunsen-Ges. Phys. Chem.* **1970**, 74, 1036.
6. G. Schmid, M. A. Lobeck, H. Keiser, *Ber. Bunsen-Ges. Phys. Chem.* **1972**, 76, 151.
7. R. R. Gadde, S. Bruckenstein, *J. Electroanal. Chem.* **1974**, 50, 163.
8. J. F. van der Plas, E. Barendrecht, *J. R. Netherlands Chem. Soc.* **1977**, 96, 133.
9. H. N. Heckner, G. Schmid, *Electrochim. Acta* **1971**, 16, 131.
10. H. N. Heckner, *J. Electroanal. Chem.* **1973**, 44, 9.
11. H. N. Heckner, *J. Electroanal. Chem.* **1977**, 83, 51.
12. J. F. van der Plas, E. Barendrecht, *Electrochim. Acta* **1980**, 25, 1463.
13. G. Horányi, E. M. Rizmayer, *J. Electroanal. Chem.* **1982**, 140, 347.
14. G. Horányi, E. M. Rizmayer, *J. Electroanal. Chem.* **1983**, 143, 323.
15. G. Horányi, E. M. Rizmayer, *J. Electroanal. Chem.* **1985**, 188, 265.
16. H. L. Li, J. Q. Chambers, D. T. Hobbs, *J. Appl. Electrochem.* **1988**, 18, 454.
17. J. Garcia-Domenech, M. A. Climent, A. Aldaz et al., *J. Electroanal. Chem.* **1983**, 159, 223.
18. F. El Omar, R. Durand, *J. Electroanal. Chem.* **1984**, 178, 343.
19. J. Garcia-Domenech, J. L. Vazquez, A. Aldaz, *An. Quim.* **1986**, 82, 433.
20. I. Taniguchi, N. Nakashima, K. Yasukouchi, *J. Chem. Soc., Chem. Commun.* **1986**, 1813.
21. I. Taniguchi, N. Nakashima, K. Matsushita et al., *J. Electroanal. Chem.* **1987**, 224, 199.
22. S. Kuwabata, S. Uezumu, K. Tanaka et al., *J. Chem. Soc., Chem. Commun.* **1986**, 135.
23. M. Belay, J. P. Collin, R. Ruppert et al., *J. Chem. Soc., Chem. Commun.* **1984**, 1315.
24. M. H. Barley, K. Takenchi, W. R. Murphy et al., *J. Chem. Soc., Chem. Commun.* **1985**, 507.
25. G. Horányi, E. M. Rizmayer, *J. Electroanal. Chem.* **1982**, 132, 119.
26. S. Wasmus, E. J. Vasini, M. Krausa et al., *Electrochim. Acta* **1994**, 39, 23.
27. M. D. Garcia Azorero, M. L. Marcos, J. González Velasco, *Electrochim. Acta* **1994**, 39, 1909.
28. M. J. Foral, S. H. Langer, *Electrochim. Acta* **1991**, 36, 299.
29. S. Ye, H. Kita, *J. Electroanal. Chem.* **1993**, 346, 489.
30. O. A. Petrii, T. Ya. Safonova, *J. Electroanal. Chem.* **1992**, 331, 897.
31. B. Piela, P. K. Wrona, *J. Electrochem. Soc.* **2002**, 149, E55.
32. B. Piela, P. Piela, P. K. Wrona, *J. Electrochem. Soc.* **2002**, 149, E357.
33. M. H. Pournaghi-Azar, H. Dastango, *J. Electroanal. Chem.* **2004**, 567, 211.
34. C. A. Caro, F. Bedioui, J. H. Zagal, *Electrochim. Acta* **2002**, 47, 1489.
35. H. Winnischofer, S. de Souza Lima, K. Araki et al., *Anal. Chim. Acta* **2003**, 480, 97.
36. S. Wang, Y. Yin, X. Lin, *Electrochem. Commun.* **2004**, 6, 259.
37. C.-C. Sun, T.-C. Chou, *J. Mol. Catal., A* **2000**, 151, 133.
38. Y.-Di. Zhao, W.-De. Zang, Q.-M. Luo et al., *Microchem. J.* **2003**, 75, 189.
39. M. Guo, J. Chen, J. Li et al., *Anal. Chim. Acta* **2005**, 532, 71.
40. W. Gao, J. Chen, X. Gan et al., *Catal. Today* **2004**, 93, 95, 333.
41. H.-Y. Hu, N. Goto, I. K. Fujie, *Water Res.* **2001**, 35, 2789.
42. S. Kerkeni, E. Lamy-Pitara, J. Barbier, *Catal. Today* **2002**, 75, 35.
43. K. T. Ranjit, B. Viswanathan, *J. Photochem. Photobiol., A* **2003**, 154, 299.
44. B. Keita, F. Girard, L. Nadjo et al., *J. Electroanal. Chem.* **2001**, 508, 70.
45. T. McCormac, B. Fabre, G. Bidan, *J. Electroanal. Chem.* **1997**, 427, 155.
46. K. T. Ranjit, B. Viswanathan, *J. Photochem. Photobiol., A* **1997**, 108, 73.
47. C. Reuben, E. Galun, H. Cohen et al., *J. Electroanal. Chem.* **1995**, 396, 233.
48. W. Sun, S. Zhang, H. Liu et al., *Anal. Chim. Acta* **1999**, 388, 103.
49. W. Sun, S. Zhang, X. Lin et al., *J. Electroanal. Chem.* **1999**, 469, 63.
50. G. E. Dima, A. C. A. de Vooy, M. T. M. Koper, *J. Electroanal. Chem.* **2003**, 554, 15.

51. M. T. de Groot, M. T. M. Koper, *J. Electroanal. Chem.* **2004**, 562, 81.
52. J. F. E. Gootzen, L. Lefferts, J. A. R. van Veen, *Appl. Catal., A* **1999**, 188, 127.
53. J. F. E. Gootzen, P. G. J. M. Peeters, J. M. B. Dukers et al., *J. Electroanal. Chem.* **1997**, 434, 171.
54. A. C. A. de Vooys, R. A. van Santen, J. A. R. van Veen, *J. Mol. Catal., A* **2000**, 154, 203.
55. M. C. P. M. da Cunha, M. Weber, F. C. Nart, *J. Electroanal. Chem.* **1996**, 414, 163.
56. T. Y. Safonova, O. A. Petrii, *J. Electroanal. Chem.* **1998**, 448, 211.
57. T. Y. Safonova, O. A. Petrii, *Russ. J. Electrochem.* **1998**, 34, 1137.
58. K. Tada, K. Shimazu, *J. Electroanal. Chem.* **2005**, 577, 303.
59. K. Tada, T. Kawaguchi, K. Shimazu, *J. Electroanal. Chem.* **2004**, 572, 93.
60. Y. Safonova, O. A. Petrii, *Russ. J. Electrochem.* **1995**, 31, 1269.
61. G. Horányi, *Catal. Today* **1994**, 19, 285.
62. U. Prüsse, M. Hähnlein, J. Daum et al., *Catal. Today* **2000**, 55, 79.
63. S. Kerkeni, E. Lamy-Pitara, J. Barbier, *Catal. Today* **2002**, 75, 35.
64. W. Gao, N. Guan, J. Chen et al., *Appl. Catal., B* **2003**, 46, 341.
65. F. Gauthard, F. Epron, J. Barbier, *J. Catal.* **2003**, 220, 182.
66. Y. H. Huang, T. C. Zhang, *Water Res.* **2004**, 38, 2631.
67. S. Choe, H. M. Liljestrang, J. Khim, *Appl. Geochem.* **2004**, 19, 225.
68. Y.-M. Chen, C.-W. Li, S.-S. Chen, *Chemosphere* **2005**, 59, 753.
69. C.-P. Huang, H.-W. Wang, P.-C. Chiu, *Water Res.* **1998**, 32, 2257.
70. J. L. Ginner, P. J. J. Alvarez, S. L. Smith et al., *Environ. Eng. Sci.* **2004**, 21, 219.
71. L. Paseka, J. Vonkova, *Electrochim. Acta* **1980**, 25, 1251.
72. L. Paseka, A. Hodiner, *Electrochim. Acta* **1982**, 27, 1461.
73. J. A. Colucci, M. J. Foral, S. H. Langer, *Electrochim. Acta* **1985**, 30, 521.
74. J. A. Colucci, M. J. Foral, S. H. Langer, *Electrochim. Acta* **1985**, 30, 1675.
75. M. J. Foral, S. H. Langer, *Electrochim. Acta* **1988**, 33, 257.
76. K. Ogura, T. Ozeki, *Electrochim. Acta* **1981**, 26, 877.
77. K. Ogura, M. Watanabe, *Electrochim. Acta* **1982**, 27, 111.
78. K. Ogura, H. Ishikawa, *Electrochim. Acta* **1983**, 28, 167.
79. K. Ogura, Y. Tanaka, *J. Electroanal. Chem.* **1984**, 161, 121.
80. K. Ogura, H. Ishikawa, *J. Chem. Soc., Faraday Trans. 1* **1984**, 80, 2243.
81. K. Ogura, S. Yamasaki, *J. Appl. Electrochem.* **1985**, 15, 279.
82. A. C. A. de Vooys, G. L. Beltramo, B. van Riet et al., *Electrochim. Acta* **2004**, 49, 1307.
83. A. C. A. de Vooys, M. T. M. Koper, R. A. van Santen et al., *J. Catal.* **2001**, 202, 387.
84. A. Rodes, V. Climent, J. M. Orts et al., *Electrochim. Acta* **1998**, 44, 1077.
85. A. Rodes, R. Gómez, J. M. Pérez et al., *Electrochim. Acta* **1996**, 41, 729.
86. E. Casero, C. Alonso, J. A. Martín-Gago et al., *Surf. Sci.* **2002**, 507, 688.
87. X. Zhang, J. Lin, L. Cardoso et al., *Electroanalysis* **2002**, 14, 697.
88. N. Pereira-Rodrigues, V. Albin, M. Koude-lka-Hep et al., *Electrochem. Commun.* **2002**, 4, 922.
89. B. W. Allen, C. A. Piantadosi, L. A. Coury Jr., *Nitric Oxide* **2000**, 4, 75.
90. K.-C. Ho, Y.-H. Tsou, *Sens. Actuators, B* **2001**, 77, 253.
91. B. W. Allen, C. A. Piantadosi, *Nitric Oxide* **2003**, 8, 243.
92. M. S. Joshi, J. R. Lancaster Jr., X. Liu et al., *Nitric Oxide* **2001**, 5, 561.
93. X. Zhang, L. Cardosa, M. Broderick et al., *Electroanalysis* **2000**, 12, 1113.
94. M. Pontie, H. Lecture, F. Bedioui, *Sens. Actuators, B* **1999**, 56, 1.
95. K. Kammer, *Appl. Catal., B* **2005**, 58, 33.
96. J. Zhu, Z. Zhao, D. Xiao et al., *Electrochem. Commun.* **2005**, 7, 58.
97. S. L. Vilakazi, T. Nyokong, *Electrochim. Acta* **2000**, 46, 453.
98. A. V. Kashevskii, J. Lei, A. Y. Safronov et al., *J. Electroanal. Chem.* **2002**, 531, 71.
99. G. Ritzoulis, *J. Electroanal. Chem.* **1992**, 327, 209.
100. H. Eber, R. Parsons, G. Ritzoulis et al., *J. Electroanal. Chem.* **1989**, 262, 181.
101. G. A. Attard, A. Ahmadi, *J. Electroanal. Chem.* **1995**, 389, 175.
102. F. J. G. de Dios, R. Gómez, J. M. Feliu, *Electrochem. Commun.* **2001**, 3, 659.
103. R. Gómez, F. J. G. de Dios, J. M. Feliu, *Electrochim. Acta* **2004**, 49, 1195.

104. K. Kanazawa, H. Yamamura, M. Nakayama et al., *J. Electroanal. Chem.* **2002**, 521, 127.
105. Y. Yoshida, S. Ogata, S. Nakamatsu et al., *Electrochim. Acta* **1999**, 44, 3585.
106. A. Kudo, A. Mine, *J. Electroanal. Chem.* **1996**, 408, 267.
107. A. Kudo, A. Mine, *Appl. Surf. Sci.* **1997**, 122, 538.

8 Sulfur

E. Levillain
ANGERS Cedex, France

A. Demortier and J.-P. Lelieur
LILLE Cedex, France

8.1	Introduction	255
8.2	Sulfur and Polysulfide Ions in Solution	256
8.2.1	Nonaqueous Solvents	256
8.2.2	Aqueous Solutions	259
8.3	Electroreduction of Sulfur and Redox Properties of Polysulfides	260
8.3.1	“Classical” Nonaqueous Solvents	260
8.3.2	Liquid Ammonia	263
8.3.3	Aqueous Solutions	264
8.4	Electrooxidation of Sulfur	265
8.5	Applied Electrochemistry	266
8.5.1	Electrosynthesis	266
8.5.2	Batteries, Solar Cells, and Sulfurization	266
8.5.3	Environmental Chemistry	267
8.6	Conclusion	268
	References	268

8.1 Introduction

Sulfur is a rather exceptional element for several aspects. It can assume various oxidation states [1] and in these oxidation states it exists in a great number of different chemical forms. Sulfur is a constituent of a large number of industrial products (H_2SO_4 , rubber vulcanization, for instance) and is also at the origin of a major pollutant (SO_2) [2]. Sulfur can exist in more than ten allotropic forms at room temperature, that is, in a variety not found with any other element [3–5]. Orthorhombic sulfur is the most stable form at room temperature. It contains crown-shaped S_8 molecules, which are stacked in a complex array. It can also be mentioned that the liquid and gaseous phases of sulfur are very complex [6, 7]. Undoubtedly, the existence of catenated species is a general feature of sulfur chemistry and is the basic reason for its complexity.

Sulfur has been intensively studied for at least 30 years because it is very attractive as a cathode-active material for high-energy density electrochemical cells [8]. This is easily understood because sulfur can be reduced to sulfide and has a high theoretical specific capacity.

In this review, we shall mainly consider the electrochemical behavior of sulfur and polysulfide ions (i.e. the reduced forms of sulfur) in solution. Recent works (see Sect. 8.3.1) gave a better understanding of the elementary steps leading from sulfur S_8 to polysulfide ions S_n^{2-} (or S_n^-) in non-aqueous solvents. This has been achieved by using spectroscopic techniques for the identification of chemical species, the direct coupling of spectroscopic and electrochemical techniques, and by using digital simulation calculations for the validation of the proposed models.

Only the inorganic polysulfides (and more specifically the alkali polysulfides) will be considered. Furthermore, we shall not review the electrochemical properties of S_xO_y ions or molecules. It must be noted that a comprehensive review, devoted to the oxidation of sulfur(IV) oxides, oriented toward the atmospherically relevant processes and mechanisms, appeared in 1995 [9]. However, the solutions of SO_2 have been the matter of recent works, which clarify the understanding of the electrochemical reduction of SO_2 in solution [10], but these works will not be reviewed here.

In the first section, the main characteristics of solutions of sulfur and polysulfides in nonaqueous solvents and water are summarized. Then, the electroreduction of

sulfur and redox properties of polysulfides will be analyzed. The electrooxidation of sulfur will also be examined. Finally, some electrochemical applications of sulfur and polysulfides are presented.

8.2

Sulfur and Polysulfide Ions in Solution

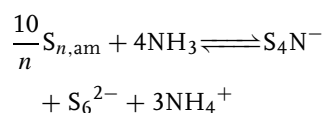
8.2.1

Nonaqueous Solvents

When sulfur S_8 is solubilized, two cases are experimentally observed:

1. The cyclic molecule S_8 is maintained. This is the more usual case and it is observed in various solvents: DMSO (dimethyl sulfoxide), DMF (dimethyl formamide), CS_2 , methanol, and so on, [2, 11, 12]. In this review, we shall denote them as *classical solvents*. The solutions of sulfur in these solvents are almost uncolored, slightly yellow, and absorbing in the UV range. A strong coloration of these solutions would indicate the presence of impurities (e.g. amines) in the solvent. The best evidence that the S_8 molecule is kept intact in these solutions is provided by Raman spectroscopy [13, 14]. It must be noted that the rate of dissolution is rather slow; the equilibrium is reached, at room temperature, after about one day.
2. Sulfur S_8 is dissolved through a disproportionation process, which can be reversible or not reversible. The only solvent, which dissolves sulfur by a reversible disproportionation process, is liquid ammonia NH_3 . In this solvent, the dissolution of sulfur gives the reduced form S_6^{2-} in equilibrium with S_3^- , and oxidized forms of sulfur,

mainly S_4N^- . Along with the formation of this species, NH_4^+ , the corresponding acid to NH_3 , is formed. In a solution of sulfur in liquid ammonia, there is no more sulfur in the form of S_8 , but a large fraction of sulfur is still in the zero oxidation state in a form that is not yet identified [15], and denoted as $S_{n,am}$, assuming that this species involves n sulfur atoms interacting with ammonia. This notation allows writing the disproportionation process of dissolution of sulfur in ammonia [16] as:

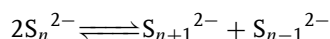


The dissolution of sulfur in ammonia has been known for more than 100 years [17]. The identification of the chemical species in these solutions was a matter of confusion until the identification of S_4N^- and S_3^- , by Chivers and Lau [18] and Bernard et al. [19], using Raman spectroscopy. When considering the species formed in the dissolution process, it is quite remarkable that this dissolution is reversible: sulfur is recovered after evaporation of ammonia. These solutions are strongly colored (blue), mainly due to the electronic absorption band of S_4N^- at 580 nm. It must be mentioned that this dissolution is moderately fast at room temperature (but much slower than the dissolution of alkali metals) and that the rate is much slower when temperature decreases. It should also be mentioned that concentrated solutions of sulfur in liquid ammonia can be used as the solution at the positive electrode of a secondary battery. The solution at the negative electrode can be a solution of alkali metal in liquid ammonia [20], the electrodes being

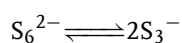
separated by a membrane. Both electrode solutions of this battery are liquid down to about 200 K. The emf of the cell in open circuit is close to 2.35 V. However, it is not possible to get satisfactory density currents from this cell.

The dissolution of sulfur in primary and secondary amines also gives highly colored solutions [21, 22], but this “dissolution” is not reversible. The color of these solutions is caused by polysulfides. The presence of reduced forms of sulfur in these solutions suggests the existence of a disproportionation process, but the oxidized form(s) of sulfur have not yet been identified. Therefore, the process of “dissolution” of sulfur in amines is not clarified.

The understanding of the reduction process of sulfur requires the identification of the reduced forms of sulfur, that is, polysulfides S_n^{2-} or S_n^- . The phase diagrams of M_2S-S_8 systems (where M is an alkali-metal cation) have been reviewed [23], as also the properties of polysulfide melts [24]. Many polysulfides have been characterized in the solid state by x-ray diffraction, infrared and Raman spectroscopy [25]. The identification of polysulfides in solution is often rather difficult. The reason is that the dissolution of a M_2S_n polysulfide leads, for most of them, to a disproportionation process of the type:



Consequently, the dissolution of a well-defined solid polysulfide can lead to the coexistence of several polysulfides. Furthermore, the dissolution of S_6^{2-} occurs with its dissociation into S_3^- :



The identification of the radical anion S_3^- has been unambiguously clarified less than 35 years ago, after some years of confusion between S_3^- and S_2^- . This species is characterized by a visible absorption band (~ 610 nm) and by a Raman vibration band (~ 540 cm^{-1}). It has been recognized by Chivers [26, 27] that the occurrence of this radical is “ubiquitous.” This species is partly responsible for the strong coloration (deep blue) of alkali polysulfides in electron pair donor solvents.

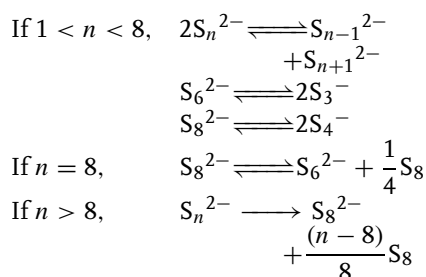
Obviously, in solution, S_3^- is not stable against oxidation. It is stable in the mineral *lapis lazuli*, and the industrial ultramarine blue pigment [28]. In these materials, the radical S_3^- is encapsulated in the β -cages of the sodalite structure, which protects it against oxidation. In ultramarine pigments, another radical anion polysulfide, S_2^- , has been observed. It is the yellow chromophore of these pigments [28, 29]. To our knowledge, it has never been observed in solution. It is supposed to originate from the dissociation of S_4^{2-} . This dissociation is perhaps significant at high temperatures, like those of the synthesis of ultramarine pigments or those of doping of alkali halide crystals. S_3^- and S_2^- radicals have also been observed in the alkali halides doped with sulfur [30, 31]. Another radical anion polysulfide, S_4^- , has been identified, by EPR experiments, in solution in DMF, originating from the dissociation of S_8^{2-} , which is the least reduced polysulfide in this solvent [32].

Undoubtedly, the unambiguous identification of S_3^- played a key role in understanding the electrochemistry of sulfur and polysulfides in nonaqueous solutions. Presently, some general model that would be able to describe the distribution of polysulfides in “classical” nonaqueous

solvents is emerging[33]. This model is based on the following hypothesis. Obviously, the constants of the equilibria would depend on the solvent.

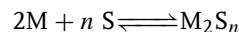
1. S^{2-} ion is the most completely reduced polysulfide.
2. S_8^{2-} ion is the least reduced polysulfide.
3. The radical anions are only S_3^- and S_4^- ; they result from the dissociation of S_6^{2-} and S_8^{2-} . These equilibria are temperature dependent.
4. S_n^{2-} dianions are, at least, partly disproportionated. These disproportionation equilibria are almost temperature independent.
5. Sulfur is not disproportionated.

With these considerations, the following reactions can be written:



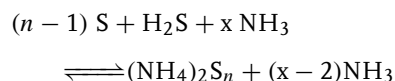
This last equation should be used if a solid of the overall composition M_2S_n with $n > 8$ is in solution. It should be noted that solids with the overall composition M_2S_n

can be synthesized in liquid ammonia:



After evaporation of ammonia, and after drying under high vacuum, the M_2S_n solid is obtained. The dissolution of the solid M_2S_n in a given solvent can also be obtained directly in the solvent by the reaction of sulfide M_2S with $(n-1) S$.

The reduction of sulfur by hydrogen sulfide in liquid ammonia leads to $(NH_4)_2S_n$, ammonium polysulfide solutions, following:



In these solutions, the S_n^{2-} polysulfides are in a more acidic solution than in $Li_2S_n-NH_3$. The comparison of the spectroscopic characteristics between $(NH_4)_2S_n-NH_3$ and $Li_2S_n-NH_3$ allows observing the influence of acidity of the solution on the disproportionation equilibria. It was observed that S_n^{2-} is more disproportionated in ammonium solutions than in lithium solutions [15, 16].

Interestingly, S_7^{2-} ion has never been observed in solution. Thermodynamic data are summarized in Table 1.

Significant progress has been achieved in the identification of polysulfides in non-aqueous solvents, mainly by application of Raman spectroscopy. However, there are

Tab. 1 Values of the dissociation constants of S_6^{2-} ($K_3 = [S_3^-]^2/[S_6^{2-}]$) and S_8^{2-} ($K_4 = [S_4^-]^2/[S_8^{2-}]$) and of the disproportionation constants of S_8^{2-} ($K_8 = [S_6^{2-}][S_8]^{1/4}/[S_8^{2-}]$) in nonaqueous solvents with supporting electrolyte at room temperature [32]

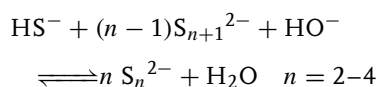
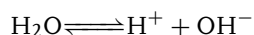
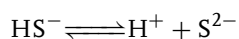
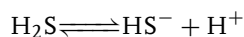
Nonaqueous solvent	DMF	DMSO	DMA	CH ₃ CN	NH ₃
K_3 (M)	0.04	0.0077	0.043	0.012	0.005
K_4 (M)	10^{-9}	?	$2 \cdot 10^{-3}$?	/
K_8 (M ^{1/4})	$2 \cdot 10^{-3}$	$2 \cdot 10^{-3}$	$8.6 \cdot 10^{-4}$	$1.6 \cdot 10^{-2}$	/

presently too little data to determine the mechanism of the effect of the solvent. Nevertheless, the identification has been very useful for the interpretation of the electrochemical processes.

8.2.2

Aqueous Solutions

Sulfur is weakly soluble in H_2O (10^{-8} M at 298 K) [33, 34], but Na_2S is very soluble [35]. In deaerated aqueous solutions, the alkali-metal polysulfide system contains, in addition to H_2O and alkali-metal cations, OH^- , H^+ , H_2S , HS^- , S^{2-} , S_2^{2-} , S_3^{2-} , S_4^{2-} , and S_5^{2-} . It is usually considered that S_5^{2-} is the least reduced polysulfide in water. However, it has been reported, in several papers [26, 36], that in basic aqueous solutions, at high temperatures, a blue color is observed, suggesting the stability of S_3^- . The polysulfide equilibrium constants, interrelating polysulfide speciation, K_A , K_B , and K_C , have been well established [36, 37]. The species in solution are related by the equilibria:



which provide the following equilibrium constants:

$$K_1 = [\text{H}^+][\text{HS}^-]/[\text{H}_2\text{S}]$$

$$K_2 = [\text{H}^+][\text{S}^{2-}]/[\text{HS}^-]$$

$$K_W = [\text{H}^+][\text{OH}^-]/[\text{H}_2\text{O}]$$

$$K_A = [\text{S}_2^{2-}]^2/([\text{HS}^-][\text{OH}^-][\text{S}_3^{2-}])$$

$$K_B = [\text{S}_3^{2-}]^3/([\text{HS}^-][\text{OH}^-][\text{S}_4^{2-}]^2)$$

$$K_C = [\text{S}_4^{2-}]^4/([\text{HS}^-][\text{OH}^-][\text{S}_5^{2-}]^3)$$

The water dissociation equilibrium constant, K_W , and the first acid dissociation constant of H_2S , K_1 , are both well documented. Several studies have confirmed that K_2 , the second acid dissociation constant of H_2S , has a value of 10^{-17} [38–43], and not as previously assumed 10^{-12} [38]. This results in a substantial revision of known metal sulfide solubilities [44]. Noticeably, the concentrations of S^{2-} , S_2^{2-} , S_3^{2-} , S_4^{2-} , and S_5^{2-} polysulfides depend on pH and their stabilities increase with pH. A distribution of polysulfides in aqueous solutions, as a potential–pH diagram, has been proposed [45] (Fig. 1).

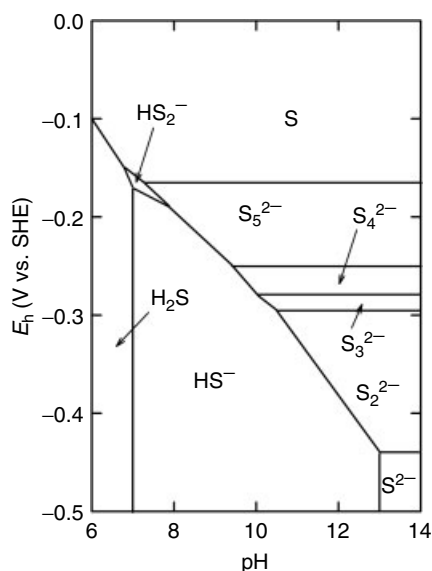
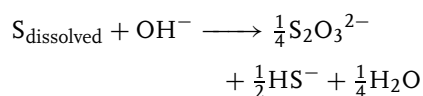


Fig. 1 E_h –pH diagram for the sulfur–water system at 298 K with concentrations of 0.2 mM for $\text{S}(-\text{II})$ species and 1 μM for polysulfide species [45].

Some works [36, 37, 46] have shown that aqueous polysulfide solutions are unstable, and sulfur, dissolved as polysulfide, decomposes to thiosulfate, $\text{S}_2\text{O}_3^{2-}$ in agreement with the observed net consumption of dissolved sulfur



Each polysulfide S_n^{2-} can be considered to contain $(n - 1)$ zerovalent sulfur and contributes to $\text{S}_{\text{dissolved}}$. The distribution of species and measured and modeled rate of polysulfide decomposition are investigated for a wide range of polysulfide solution compositions from 298 K to 358 K. At temperatures up to 358 K, polysulfide solutions are extremely stable under conditions of high polysulfide concentration and low KOH concentrations. Under these conditions, zerovalent sulfur dissolved in these solutions should be stable on the order of years.

8.3

Electroreduction of Sulfur and Redox Properties of Polysulfides

8.3.1

“Classical” Nonaqueous Solvents

The electroreduction of sulfur in nonaqueous solvents (DMF, DMSO etc.) has been studied by several authors for the past 35 years [47–60]. Experimentally, a solution of sulfur is yellow (pale) and the reduced solutions are intensely colored. Electrochemically, the response of the electroreduction of sulfur in classical organic solvent (DMF, DMA, DMSO, CH_3CN etc.) is similar. The reduced forms, that is, polysulfides S_n^{2-} or S_n^- , have characteristic absorption bands in the visible range. Structurally, sulfur is a ring and polysulfides are expected to be linear chains. To understand the electrochemical behavior of sulfur, it was necessary to take into account these structural aspects. This was done only in 1997 [60].

The electroreduction of sulfur was first studied in DMSO by Merrit and Sawyer

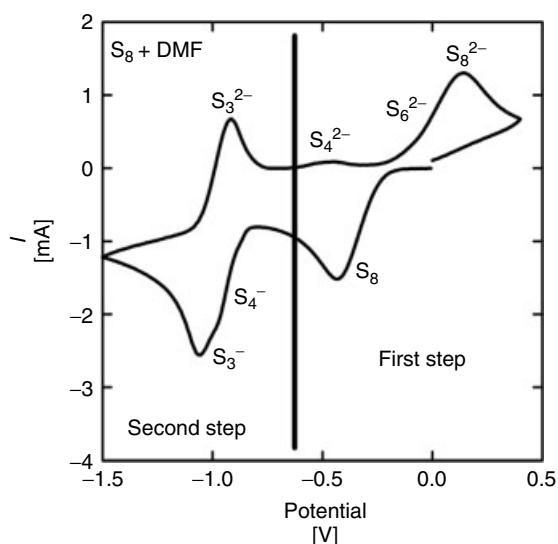


Fig. 2 Cyclic voltammogram of a S_8 + DMF solution (2.5 mM, 293 K; 1 V s^{-1} ; working electrode Pt-electrode; pseudoreference electrode Pt-wire).

in 1970 [47]. In the first interpretation of their experiments, they claimed that S_8 is reducible to give S_8^{2-} . In 1972, Bonnaterre [49] showed that S_8 is reduced through a two-electron process. This last interpretation was confirmed later, in particular, in 1985 by Baranski [53] using microelectrodes, and also by the numerical simulation of Xie [54]. Seel [51] showed

that, in “classical” solvents, the S_8^{2-} polysulfide ion is the least reduced polysulfide. The proof of structural changes (ring shape into linear chains) is recent [59].

Cyclic voltammetry (Fig. 2) and spectroelectrochemical studies (Fig. 3) in DMF have shown that the first step of the reduction of sulfur proceeds via an ECE process with a reversible chemical reaction (C) that

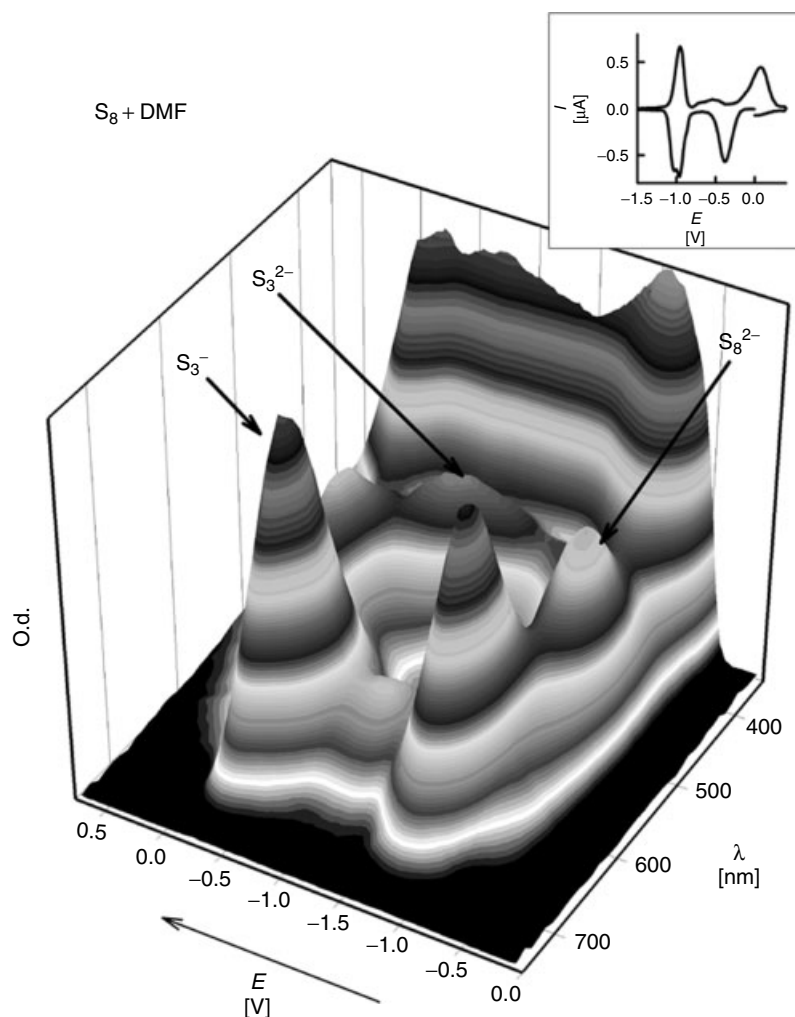
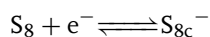
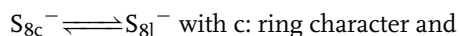


Fig. 3 Spectroelectrochemical experiment of a S_8 + DMF solution (2.5 mM, 293 K; 0.005 V s^{-1} ; $200 \text{ } \mu\text{m}$; working electrode Pt-electrode; pseudoreference electrode Pt-wire). O.d.: optical density.

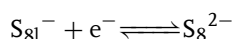
takes into account the ring-opening step of S_8 :



– 1.05 V (vs. Fc^+/Fc) at 293 K



l: linear character

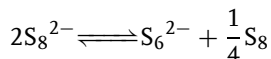


– 0.70 V (vs. Fc^+/Fc) at 293 K

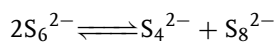
In addition, spectroelectrochemical studies [55–57, 59] have undoubtedly shown that S_6^{2-}/S_3^- polysulfides were produced during the reduction step. These polysulfides originate from the disproportionation of S_8^{2-} into S_6^{2-} and S_8 . Noticeably, S_8^{2-} is weakly dissociated into S_4^- . Park et al. [55, 56] would have identified this radical anion at 700 nm by spectroelectrochemistry but this assignment remains to be confirmed. It should be noted that recent works tried to keep the previous interpretations of the electrochemical reduction of sulfur but without success [61–64].

A further step in the reduction of sulfur is also observed (Fig. 2). This step displays a reversible reduction wave close to –1.8 V (vs. Fc^+/Fc at 293 K in DMF) and

a “prewave” at a potential slightly higher. The prewave is clearly observed at low scan rates, at high temperatures, and under thin layer conditions. It is noteworthy that the second step is not detected at low temperatures (233 K). The assignment of these two reductions has been controversial. In 1973, Sawyer [48] assigned them to the reduction of HS_8^- and S_8^{2-} . In 1974, Badoz-Lambling [50] assigned them to the reduction of S_6^{2-} and, in 1981, Paris [52] assigned them to the reduction of S_8^{2-} and S_6^{2-} . In fact, it has been necessary to study the electrochemical behavior of polysulfide solutions to reach the basic fact: only the radical anions S_3^- and S_4^- are reducible. The study of Li_2S_n + DMF solutions, investigated by cyclic voltammetry (Fig. 4) and time-resolved spectroelectrochemical experiments, allowed to propose the following mechanism [60]:



Disproportionation of S_8^{2-}



Disproportionation of S_6^{2-}

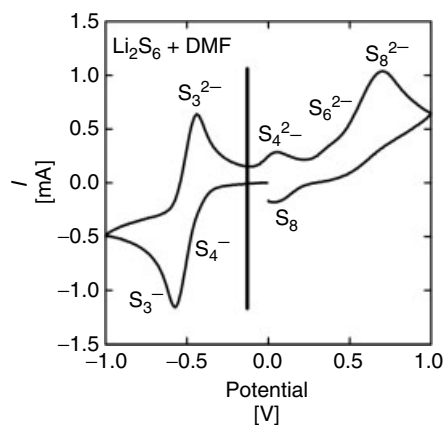
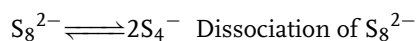
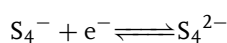


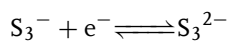
Fig. 4 Cyclic voltammogram of a Li_2S_6 + DMF solution (2.5 mM, 293 K; 1 V s^{-1} ; working electrode Pt-electrode; pseudoreference electrode Pt-wire).

Tab. 2 Redox potentials and charge-transfer coefficients in DMF at 293 K [60]

Redox couple	S_3^-/S_3^{2-}	S_4^-/S_4^{2-}	S_8/S_{8c}^-	S_6^-/S_6^{2-}	S_{8l}^-/S_{n8}^-
Redox potential (V vs. Fc^+/Fc)	−1.80	−1.30	−1.05	−0.85	−0.70
Charge-transfer coefficient	0.5	0.5	0.35	0.6	0.7



$$-1.30 \text{ V (vs. } Fc^+/Fc) \text{ at } 293 \text{ K}$$



$$-1.80 \text{ V (vs. } Fc^+/Fc) \text{ at } 293 \text{ K}$$

The study of Li_2S_n + DMF solutions [60] also allowed to characterize the electrochemical properties of polysulfides: only redox couples of the type S_n^-/S_n^{2-} are involved. The chemical reactions coupled to charge transfers are classical dissociation and disproportionation equilibria: no complex rearrangement reaction or transient species has been necessary. Redox potentials and charge-transfer coefficients of the redox couples involved in sulfur and polysulfide solutions are summarized in Table 2.

Therefore, a complete description of the redox properties of sulfur and polysulfides in classical organic solvents has been obtained on the following basis: only S_8 and the radical anions S_n^- are reducible and only the dianions S_n^{2-} and S_8 are oxidable. The electrochemical process has been validated in DMF by comparing simulations and the experimental data in a wide range of temperatures (233 to 313 K) and scan rates (0.005 to 2.0 Vs^{-1}). It can be reasonably extended to other organic solvents. Thermodynamic and kinetic parameters have been discussed in Ref. 60. It must be noted that Paris et al. [58] describe the reduction of sulfur

and the generation of polysulfides in a completely different way, involving the dissociation of S_8 into S_2 . A spectroscopic evidence of such dissociation has not been given.

The spectroelectrochemical experiments in a wide range of temperature and scan rate have been a powerful tool for understanding the complex redox properties of sulfur and polysulfides in DMF and numerical simulations have been essential to validate the proposed electrochemical mechanisms.

It is expected that this model should be valid in other “classical” nonaqueous solvents. However, such a check would be useful, but it requires the dissolution of M_2S_n solids of well-controlled stoichiometry n .

8.3.2

Liquid Ammonia

Liquid ammonia is not a classical solvent for sulfur because it dissolves sulfur in the course of a reversible and slow disproportionation process as has been described earlier. Ammonia is a very useful solvent for the investigation of polysulfides because it allows their synthesis with an easy control of their stoichiometry. After evaporation of ammonia and drying under high vacuum, a solid with the overall composition M_2S_n is obtained. The solid is either a polysulfide or a mixture of polysulfide(s) with sulfur, depending

on n and on the metal cation M . The spectroscopic studies of $Li_2S_n-NH_3$ solutions suggest that S_6^{2-} is the less reduced polysulfide in ammonia [65], but electrochemical experiments show that it is slightly disproportionated [66]. The electrochemical study of solutions of lithium polysulfides ($Li_2S_n + NH_3$) and ammonium polysulfides ($(NH_4)_2S_n + NH_3$) allowed the specific study of the reduction of S_3^- [67] and the oxidation of S_4^{2-} and S_6^{2-} ions [66]. This study has shown the key role of S_3^- in the redox properties of these solutions. In all lithium polysulfide solutions with $n > 3$, S_3^- and S_3^{2-} species are present at equilibrium, as the consequence of the disproportionation processes of S_n^{2-} . S_3^- and S_3^{2-} are the conjugated species of the same redox couple; consequently, the equilibrium potential of these solutions is well defined. By using the theory of cyclic voltammetry for this situation [68], it was possible to interpret the experimental voltammograms and the electrochemical impedance diagrams for Li_2S_4 and $(NH_4)_2S_4$ solutions in liquid ammonia [69]. It has been shown that for $(NH_4)_2S_4$ solutions, the electron transfer reaction between S_3^- and S_3^{2-} is coupled with a reversible homogeneous reaction between S_3^{2-} and NH_4^+ (the acidic form of NH_3). These experimental data display the influence of the acidity of the solution, not only on the disproportionation equilibria but also, as a consequence, on the electrochemical processes. The electrochemical properties of the polysulfide ions are similar to those observed in “classical” nonaqueous solvents. But, the spectroelectrochemical experiments have shown the formation of a solid species during the oxidation of S_8^{2-} ion. This solid species has been assigned to sulfur because dissolution of sulfur via a redox

disproportionation process is very slow in liquid ammonia. Noticeably, the oxidized form of sulfur, S_4N^- , has been observed during this process and the sulfur, in the zero oxidation number state (but different from S_8), is not reducible in liquid ammonia.

Ammonia is a very special solvent of sulfur, but it gives the possibility of preparing very well-defined $Li_2S_n-NH_3$ (or $M_2S_n-NH_3$) and $(NH_4)_2S_n-NH_3$ solutions. The electrochemical studies of these solutions have been very useful for understanding the electrochemical properties of polysulfide solutions.

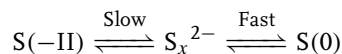
8.3.3

Aqueous Solutions

The electrochemical behavior of sulfur, sulfide (HS^- , S^{2-}) and polysulfide ions in water is much less documented than for nonaqueous solvents. Experimental studies are less numerous and do not include a systematic study versus the stoichiometry n of polysulfides M_2S_n . The conclusions of these investigations are often speculative, since the experimental curves do not display strong evidence for chemical species involved in the proposed mechanisms. Moreover, the very low solubility of sulfur in water does not allow the study of its electrochemical reduction in water.

The system $S(-II)/S(0)$ (Fig. 1) has been studied by cyclic voltammetry on gold [70, 71] and platinum electrodes [72]. For a solution of $S(-II)$ at $pH = 9.3$ (major species HS^-) and at $pH = 13$ (major species S^{2-}) and for a gold electrode [70, 71], underpotential deposition of sulfide ion to form a monolayer of chemisorbed sulfur occurs in the potential range of -0.65 to -0.45 V/SHE. An anodic peak is observed

between -0.1 and 0.3 V/SHE, corresponding to sulfur deposition resulting from the oxidation of S(–II). During this process, the formation of soluble polysulfide ions, through the reaction between sulfur and soluble S(–II) ions cannot be excluded. The characterization, by XPS, of the film deposited on the electrode gives evidence of elemental sulfur S_8 [70]. The spectrum also indicates the presence of sulfur in a form different from S_8 . The binding energy shows a substantial interaction between the monolayer (that can be seen as gold sulfide) and the sulfur in the deposit. In negative direction, one or two reduction peaks are observed in the voltammograms, assigned to the formation of soluble polysulfide ions by reduction of sulfur on the electrode (cathodic stripping). These experimental results have been interpreted by the following mechanism [70]:



On Pt-electrode [72], there is no evidence for the underpotential deposition of a monolayer. The voltammograms that have the same shape as for Au electrode were interpreted by the same mechanism. These studies have been completed by electrochemical impedance spectroscopy (EIS) as a function of the electrode potential. For Au and Pt electrodes [73, 74], the increase in the charge-transfer resistance in the potential range of sulfur deposition shows that the sulfur layer either partially blocks the electrode, or that the layer is poorly conducting. In their work, Anani et al. [75] gave cyclic voltammograms, recorded with a graphite electrode, for solutions of Na_2S_4 in water and for Na_2S_4 in 0.25 M NaOH. According to the experimental results given in the paper, these solutions seem

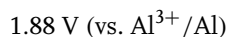
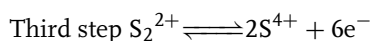
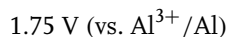
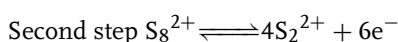
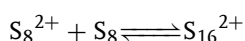
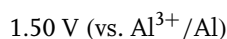
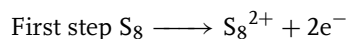
to be characterized by a well-defined equilibrium potential, as for solutions in nonaqueous solvents. The broad anodic peak current observed at a sweep rate of 100 mV s^{-1} may result from at least two successive electrode reactions, as is shown by the two peaks resolved at lower scan rate. No mechanism has been proposed for these observations, but it would be interesting to examine the interpretation of these experiments on the basis of the interpretation given for the polysulfide solutions in nonaqueous solvents.

8.4 Electrooxidation of Sulfur

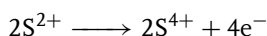
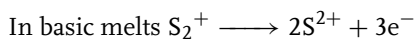
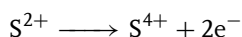
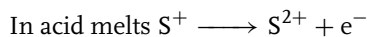
As early as 1804, it was reported that sulfur dissolves in oleum to give brown, green or blue solutions [76]. As for solutions of sulfur in liquid ammonia, the nature of the colored species has been controversial. It was shown 30 years ago that sulfur can be oxidized with $S_2O_6F_2$, AsF_5 , or SbF_5 in various solvents (H_2SO_4 , $HFSO_3$, HF, oleum) to polyatomic cations: S_{16}^{2+} , S_8^{2+} , S_4^{2+} [77–80]. The observation of EPR signal for these solutions led the authors to believe that the species are S_8^+ and S_4^+ radicals presumably in equilibrium with their dimers S_{16}^{2+} and S_8^{2+} , respectively. By using the EPR spectrum of 92% ^{33}S enriched sulfur, Low and Beaudet [81] concluded that the sulfur radical in 65% oleum is S_5^+ .

Surprisingly, electrooxidation of sulfur is only known in molten salts and in fluorosulfuric acid. In accordance with Fehrmann [82], the species S_{16}^{2+} , S_8^{2+} , S_4^{2+} , S_2^{2+} , S^{2+} , and S^{4+} are formed by oxidation of sulfur in molten $AlCl_3-NaCl$ at 150°C .

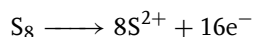
The following mechanism has been proposed by Marassi [83] in this medium at 150–250 °C:



The electrochemistry of sulfur in fluoro-sulfuric acid has been studied by Herlem [84, 85]. Sulfur dissolves only in boiling HFSO_3 to give colored solutions. The proposed mechanism assumes S^+ and S^{2+} as the starting ions:



In acetonitrile, a high irreversible wave is observed at 2.42 V (vs. SCE) by cyclic voltammetry. A 16-electron process has been proposed by Le Guillanton [86, 87]:



The consumption of 16 Faradays per mole has been confirmed by coulometry. The presence of intermediate species (S_8^{2+} , S_4^{2+} , and S_2^{2+}) is not totally dismissed.

In the presence of Lewis acids (AlCl_3 , SnCl_4), a second irreversible 16-electron process is observed at 2.90 V, leading to S^{4+} [87].

8.5

Applied Electrochemistry

8.5.1

Electrosynthesis

A complete review details new methods of preparation for thio-organic compounds derived from the electrogenerated species S_n^{2-} and S_n^{2+} with a sacrificial carbon-sulfur electrode [88]. Through reactions with various substrates, it is possible to prepare thiophenes, sulfur-containing heterocycles, sulfides, trisulfides, and so on. High selectivity and regioselectivity have been observed in reaction with S_n^{2+} . Recent works allowed testing the reactivity of electrogenerated polysulfide ions toward nucleophilic substitution of alkyl halides [89], acyl thioanhydrides and anhydrides [90], S-phenyl thiol [91], acyl chlorides [92] and allene derivatives [93].

It can also be noted that an electrochemical process for the decomposition of hydrogen sulfide into its constituents in an aqueous alkaline solution has been presented [75, 94].

8.5.2

Batteries, Solar Cells, and Sulfurization

Rechargeable cells with a sulfur cathode, a sodium anode, and a solid electrolyte such as β -alumina have been much investigated [8]. They are operated at about 618 K, temperature at which sodium and sulfur are both liquid.

Another approach is to use a lithium/sulfur cell with nonaqueous electrolyte systems. Rechargeable lithium batteries are being developed for portable power applications such as electric vehicles, partly because of their specific energy ranges 100–150 Wh kg^{-1} (and

theoretical specific energies in the range 425–890 Wh kg⁻¹). Further increases in battery specific energy are limited by the extent of lithium intercalation into transition metal oxides, resulting in capacities in the range of 100–150 mAh g⁻¹ of active material. A battery based on the lithium/(elemental) sulfur redox couple has, in contrast, a theoretical specific capacity of 1672 mAh g⁻¹ of active material and a theoretical specific energy of 2600 Wh kg⁻¹, assuming complete reaction to the product Li₂S. Therefore, there is a strong incentive to develop Li/S batteries.

A Li/S battery with a 100% sulfur positive electrode is impossible to discharge at low temperatures because sulfur is both ionically and electronically resistive. A practical Li/S cell must therefore incorporate well-distributed electronically conducting and lithium ion-conducting phases in the positive electrode. Prior studies of Li/S cells with liquid electrolytes faced the serious problems of low active material utilization and poor rechargeability, due to the insulating nature of sulfur and Li₂S, and due to the loss of active material in the form of soluble polysulfide reaction to lower-order sulfides (e.g. Li₂S₂, Li₂S). In addition, degradation of the Li electrode in liquid organic electrolytes limited the performance of such cells [95–99].

Aqueous polysulfide electrolytes are regularly the matter of fundamental photoelectrochemical studies (see Sect. 5.2 in Volume 6) and of the development of high-energy efficiency and highly stable photoelectrochemical solar cells [100, 101]. Aqueous polysulfide solution chemistry is also of importance to the pulp and paper industry [102], and provides an opportunity for a battery cathode based on the

high storage capacity of zerovalent sulfur in concentrated aqueous polysulfide electrolytes [103].

The sulfurization of semiconducting surfaces by dipping the material in aqueous sulfide solutions is generally used for the following applications:

- To allow the growth of another semiconducting material having the sulfide ion as the anion component, for example, CdS. The SILAR process has been proposed. For InP (*n*), the mechanism of sulfurization (the first step of CdS deposition) has been described [104]: reversible adsorption of HS⁻ ions, followed by the irreversible expulsion of P³⁻ anions (as PH₃) and the formation of an indium sulfide. A concomitant deoxidation takes place.
- To protect the lasing face of diode lasers against the growth of oxides. Generally, these oxides absorb the emitted light, leading to the destruction of the device.

Sulfurization can be performed by simple dipping or under applied (anodic) bias. For GaAs, the anodization of this material in the presence of (NH₄)₂S [105–108] leads to the formation of Ga(II+)S(–II), GaS, which implies redox reactions between Ga³⁺ ions issued from the material and sulfide ions.

8.5.3

Environmental Chemistry

Characterization of inorganic sulfur speciation in marine and freshwater porewaters is critical to our understanding of metal and sulfur cycling in sediments. Since coprecipitation and/or adsorption on FeS_(s) and formation of discrete authigenic sulfide minerals can effectively remove trace metals, many metal cycling studies are

based on measurements of sulfide and iron concentrations in porewaters, as well as acid volatile sulfides and pyrite in sediments [109–114]. However, a lack of exact data on sulfur speciation, that is, concentrations of polysulfides and elemental sulfur, in sediment porewaters, limits the interpretation of these results [115].

Various polarographic techniques have been successfully used to measure elemental sulfur, S^0 , and sulfide (H_2S and HS^-) concentrations in laboratory solutions [116], salt water [117], saline lake [118], freshwater [119], lake porewaters [120], salt marsh sediments [109, 120], and marine porewaters [121]. Using stripping square wave voltammetry, researchers have been able to measure sulfide species at nanomolar concentrations [118–120, 122, 123]. Recently, cyclic and linear sweep voltammeteries have been used to quantify elemental sulfur S^0 , hydrogenosulfide (HS^-) and polysulfides (S_n^{2-}) with fast scan rates ($1V\ s^{-1}$) [124]: for example, in estuarine sediments (from Rehoboth Bay, an inland bay located in Delaware), the sulfur speciation was found to change throughout a core profile, with S^0 dominant in the top layers (0–6 cm), S_n^{2-} dominant in the transition zone (6–7 cm), and HS^- dominant in the deeper sediment (>7 cm).

8.6

Conclusion

This review has shown the complexity of the chemistry and the electrochemistry of sulfur, polysulfide ions, and sulfur cations. This complexity originates from the ability of sulfur to form catenated species, which leads to disproportionation and dissociation equilibria.

Significant progress has been achieved in the interpretation of the reduction of

sulfur in DMF. This has been possible because of the progress made in understanding the electrochemical properties of polysulfide solutions in liquid ammonia and in DMF. This has been greatly supported by the association of spectroscopic, electrochemical, and numerical digital simulation techniques. It would certainly be useful to check the proposed models in various solvents.

It seems useful to understand the mechanisms involved in the chemistry and in the electrochemistry of sulfur and polysulfides. During the last 10 years, more than 90 papers dealing with solvothermal synthesis of chalcogenides M_xE or binary chalcogenides $M_xM'_yE_z$ ($E = S, Se, \text{ or } Te$) have been published. In a typical process, a metal and/or a metallic salt is heated in a solvent (benzene, toluene, pyridine, ethylenediamine, water, etc.) at 100–200 °C in the presence of an excess of chalcogen (see for instance Ref. 125). These empirical syntheses would benefit from a sound understanding of the involved mechanisms.

Finally, it must be emphasized that the mechanism of the influence of the solvent (even among the “classical” solvents) has not been examined.

References

1. S. I. Zhdanov, in *Encyclopedia of Electrochemistry of the Elements* (Ed.: A. J. Bard), Marcel Dekker, New York, 1982, pp. 273, Vol. 6.
2. B. Meyer, *Sulfur, Energy and Environment*, Elsevier, New York, 1977.
3. B. Meyer, (Ed.), *Elemental Sulfur, Chemistry and Physics*, Interscience, New York, 1965.
4. B. Meyer, *Chem. Rev.* **1976**, 76, 367.
5. M. Schmidt in *Homoatomic Rings and Chains* (Ed.: A. L. Rheingold), Elsevier, New York, 1977, p. 463.
6. M. Andercut, *Mod. Phys. Lett. B* **1996**, 25, 1267.

7. P. Lenain, E. Picquenard, J. Corset et al., *Ber. Bunsen-Ges. Phys. Chem.* **1988**, 92, 859.
8. R. P. Tisher, (Ed.), *The Sulfur Electrode*, Academic Press, New York, 1983.
9. C. Brandt, R. Van Eldik, *Chem. Rev.* **1995**, 95, 119.
10. E. Potteau, E. Levillain, J. P. Lelieur, *J. Electroanal. Chem.* **1999**, 476, 15.
11. F. N. Tebbe, E. Wasserman, W. G. Peet et al., *J. Am. Chem. Soc.* **1982**, 104, 4971.
12. J. B. Richard, M. Aparicio-Razo, D. K. Roe, *J. Electrochem. Soc.* **1990**, 137, 2143.
13. D. W. Scott, J. P. Mac Cullough, *J. Mol. Spectrosc.* **1964**, 13, 313.
14. M. Smidt, *Angew. Chem., Int. Ed. Engl.* **1973**, 12, 445.
15. P. Dubois, J. P. Lelieur, G. Lepoutre, *Inorg. Chem.* **1988**, 27, 3032.
16. P. Dubois, J. P. Lelieur, G. Lepoutre, *Inorg. Chem.* **1989**, 28, 195.
17. G. Gore, *Proc. R. Soc. London* **1873**, 21, 140.
18. T. Chivers, C. Lau, *Inorg. Chem.* **1982**, 21, 453.
19. L. Bernard, J. P. Lelieur, G. Lepoutre, *New J. Chem.* **1985**, 9, 199.
20. L. Bernard, A. Demortier, J. P. Lelieur et al., *J. Phys. Chem.* **1984**, 88, 3833.
21. W. G. Hodgson, S. A. Buckler, G. Peters, *J. Am. Chem. Soc.* **1963**, 85, 543.
22. F. P. Daly, C. W. Brown, *J. Phys. Chem.* **1973**, 77, 1859; **1976**, 80, 480.
23. J. Sanster, A. D. Pelton, *J. Phase Equilib.* **1997**, 18, 78; **1997**, 18, 82; **1997**, 18, 89; **1997**, 18, 97.
24. B. Cleaver in *The Sulfur Electrode* (Ed.: R. P. Tisher), Academic Press, New York, 1983.
25. O. El Jaroudi, E. Picquenard, A. Demortier et al., *Inorg. Chem.* **1999**, 38, 2394; **2000**, 39, 2593.
26. T. Chivers, *Nature* **1974**, 252, 32.
27. T. Chivers in *Homoatomic Rings and Chains* (Ed.: A. L. Rheingold), Elsevier, New York, 1977, p. 499.
28. F. Seel, *Stud. Inorg. Chem.* **1984**, 5, 67.
29. N. Gobeltz, A. Demortier, J. P. Lelieur et al., *New J. Chem.* **1996**, 20, 19.
30. J. Schneider, B. Dischler, A. Rauber, *Phys. Status Solidi* **1966**, 13, 141.
31. W. Holzer, W. F. Murphy, H. J. Bernstein, *J. Mol. Spectrosc.* **1969**, 32, 13.
32. E. Levillain, P. Leghié, N. Gobeltz et al., *New J. Chem.* **1997**, 21, 335.
33. C. Courty, *C. R. Acad. Sci. Paris* **1971**, 273, 193.
34. J. Boulegue, *Phosphorus Sulfur* **1978**, 5, 127.
35. W. F. Giggenbach, *Inorg. Chem.* **1971**, 10, 1036.
36. W. F. Giggenbach, *Inorg. Chem.* **1974**, 13, 1724.
37. S. Licht, G. Hodes, J. Manassen, *Inorg. Chem.* **1986**, 25, 2486.
38. S. R. Rao, L. G. Hepler, *Hydrometallurgy* **1977**, 2, 293.
39. B. Meyer, K. Ward, K. Koshlap et al., *Inorg. Chem.* **1983**, 22, 2345.
40. S. Licht, J. Manassen, *J. Electrochem. Soc.* **1987**, 134, 918.
41. F. Forouzan, K. Longo, S. Licht, *Anal. Chem.* **1990**, 62, 1356.
42. S. Licht, K. Longo, D. Peramunage et al., *J. Electroanal. Chem.* **1991**, 318, 111.
43. D. Peramunage, F. Forouzan, S. Licht, *Anal. Chem.* **1994**, 66, 378.
44. S. Licht, *J. Electrochem. Soc.* **1988**, 135, 2971.
45. I. C. Hamilton, R. Woods, *J. Appl. Electrochem.* **1983**, 13, 783.
46. S. Licht, J. Davis, *J. Phys. Chem.* **1997**, 101, 2540.
47. M. V. Merritt, D. T. Sawyer, *Inorg. Chem.* **1970**, 9, 211.
48. R. P. Martin, W. H. Doub, J. L. Roberts et al., *Inorg. Chem.* **1973**, 12, 1921.
49. R. P. Bonnaterre, G. Cauquis, *J. Chem. Soc., Chem. Commun.* **1972**, 5, 293.
50. J. Badoz-Lambling, R. Bonnaterre, G. Cauquis et al., *Electrochim. Acta* **1976**, 21, 119.
51. F. Seel, H. J. Guttler, G. Simon et al., *Pure Appl. Chem.* **1977**, 49, 46.
52. J. Paris, V. Plichon, *Electrochim. Acta* **1981**, 26, 1823.
53. A. S. Baranski, W. R. Fawcett, C. M. Gilberts, *Anal. Chem.* **1985**, 57, 166.
54. N. X. Xie, T. X. Huang, *Acta Chim. Sinica* **1988**, 46, 631; **1989**, 47, 227.
55. B. S. Kim, S. M. Park, *J. Electrochem. Soc.* **1993**, 140, 115.
56. D.-H. Han, B.-S. Kim, S.-J. Choi et al., *J. Electrochem. Soc.* **2004**, 151, E283.
57. F. Gaillard, E. Levillain, *J. Electroanal. Chem.* **1995**, 398, 77.
58. G. Bossier, J. Paris, *New J. Chem.* **1995**, 104, 391.
59. F. Gaillard, E. Levillain, M. C. Dhamelin-court et al., *J. Raman Spectrosc.* **1997**, 28, 511.

60. E. Levillain, F. Gaillard, P. Leghié et al., *J. Electroanal. Chem.* **1997**, 420, 167; **1997**, 432, 129; **1997**, 440, 243.
61. A. Evans, M. I. Montenegro, D. Pletcher, *Electrochem. Commun.* **2001**, 3, 514.
62. P. Leghié, J.-P. Lelieur, E. Levillain, *Electrochem. Commun.* **2002**, 4, 406.
63. A. Evans, M. I. Montenegro, D. Pletcher, *Electrochem. Commun.* **2002**, 4, 626.
64. P. Leghié, J.-P. Lelieur, E. Levillain, *Electrochem. Commun.* **2002**, 4, 628.
65. P. Dubois, J. P. Lelieur, G. Lepoutre, *Inorg. Chem.* **1988**, 27, 73.
66. E. Levillain, F. Gaillard, A. Demortier et al., *J. Electroanal. Chem.* **1996**, 405, 85.
67. E. Levillain, A. Demortier, J. P. Lelieur, *J. Electroanal. Chem.* **1995**, 394, 103; **1995**, 394, 205.
68. A. Demortier, C. Jehoulet, *J. Electroanal. Chem.* **1990**, 283, 15.
69. C. Jehoulet, A. Demortier, J. P. Lelieur, *J. Electroanal. Chem.* **1990**, 292, 153; **1990**, 296, 77.
70. A. N. Buckley, I. C. Hamilton, R. Woods, *J. Electroanal. Chem.* **1987**, 216, 213.
71. A. Briceno, S. Chander, *J. Appl. Electrochem.* **1990**, 20, 506.
72. J. Szynekarczuk, P. G. Komorowski, J. C. Donini, *Electrochim. Acta* **1994**, 39, 2285.
73. A. Briceno, S. Chander, *J. Appl. Electrochem.* **1990**, 20, 512.
74. J. Szynekarczuk, P. G. Komorowski, J. C. Donini, *Electrochim. Acta* **1995**, 40, 487.
75. A. A. Anani, Z. Mao, R. E. White et al., *J. Electrochem. Soc.* **1990**, 137, 2703.
76. C. F. Bucholz, *Gehlen's Neues J. Chem.* **1804**, 3, 7.
77. R. J. Gillespie, J. Passmore, P. K. Ummat et al., *Inorg. Chem.* **1971**, 10, 1327.
78. G. C. Davies, R. J. Gillespie, J. J. Park et al., *Inorg. Chem.* **1971**, 10, 2781.
79. R. J. Gillespie, P. K. Ummat, *Inorg. Chem.* **1972**, 11, 1674.
80. J. Passmore in *Homoatomic Rings and Chains* (Ed.: A. L. Rheingold), Elsevier, New York, 1977, p. 539.
81. H. S. Low, R. A. Beaudet, *J. Am. Chem. Soc.* **1976**, 98, 3849.
82. R. Fehrmann, N. J. Bjerrum, F. W. Poulsen, *Inorg. Chem.* **1978**, 17, 1195.
83. R. Marassi, G. Mamantov, S. E. Springer et al., *J. Electrochem. Soc.* **1979**, 126, 231.
84. S. Adhami, M. Herlem, *J. Electroanal. Chem.* **1970**, 26, 363.
85. M. Herlem, A. Thiebault, S. Adhami, *Anal. Lett.* **1972**, 5, 309.
86. G. Le Guillanton, D. Elothmani, Q. T. Do et al., *J. Electrochem. Soc.* **1994**, 141, 316.
87. G. Le Guillanton, D. Elothmani, C. Lopez et al., *New J. Chem.* **1994**, 18, 239.
88. G. Le Guillanton, *Sulfur Rep.* **1992**, 12, 405.
89. A. Ahrika, J. Robert, M. Anouti et al., *Acta Chem. Scand.* **1999**, 53, 513.
90. J. Robert, M. Anouti, J. Paris, *New J. Chem.* **1998**, 22, 53.
91. A. Ahrika, M. Anouti, J. Robert et al., *J. Chem. Soc., Perkin Trans. 2* **1997**, 3, 473.
92. J. Robert, M. Anouti, M. Abarbi et al., *J. Chem. Soc., Perkin Trans. 2* **1997**, 9, 1759.
93. A. Kunugi, K. Kuwamura, M. Inoue et al., *Electrochim. Acta* **1996**, 41, 1987.
94. Z. Mao, A. Anani, R. E. White et al., *J. Electrochem. Soc.* **1991**, 138, 1299.
95. R. D. Rauh, K. M. Abraham, G. F. Pearson et al., *J. Electrochem. Soc.* **1979**, 126, 523.
96. H. Yamin, E. Peled, *J. Power Sources* **1983**, 9, 281.
97. H. Yamin, A. Gorenshtein, J. Penciner et al., *J. Electrochem. Soc.* **1988**, 135, 1045.
98. G. G. Bikbaeva, A. A. Gavrilova, V. S. Kolosnitsyn, *Russ. J. Electrochem.* **1993**, 29, 715.
99. D. Marmorstein, T. H. Yu, K. A. Striebel et al., *J. Power Sources* **2000**, 89, 219.
100. S. Licht, *Nature* **1987**, 330, 148.
101. S. Licht, G. Hodes, R. Tenne et al., *Nature* **1987**, 326, 893.
102. M. Behm, D. Simonsson, *J. Appl. Electrochem.* **1997**, 27, 507.
103. D. Peramunage, S. Licht, *Science* **1993**, 261, 1029.
104. T. Moreau, A. Etcheberry, M. Herlem et al., *C. R. Acad. Sci. Paris* **1989**, 308 sér. II, 275.
105. S. Delalande, R. Majorel, J. Olivier et al., *Ecasia 95 Proceedings* (Eds.: H. J. Mathieu, B. Reihl, D. Briggs), Wiley & Sons, Chichester and New-York, 1996, p. 327.
106. C. Debiemme-Chouvy, S. Delalande, M. Herlem et al., *SOTAPOCS XXVII, Electrochem. Soc. Proc.* **1997**, 97–21, 223.
107. S. Delalande, C. Debiemme-Chouvy, M. Herlem et al., *SOTAPOCS XXVII, Electrochem. Soc. Proc.* **1997**, 97–21, 209.
108. C. Debiemme-Chouvy, C. Wartelle, F.-X. Sauvage, *J. Phys. Chem. B* **2004**, 108, 18291.
109. G. W. Luther III, A. E. Giblin, R. Varsolona, *Limnol. Oceanogr.* **1985**, 30, 727.

110. M. A. Huerta-Diaz, A. Tessier, R. Carigana, *Appl. Geochem.* **1993**, 13, 213.
111. G. Gianmarco, R. Azzoni, M. Bartoli et al., *Water, Air, Soil Pollut.* **1997**, 99, 363.
112. J. W. Morse, *Mar. Chem.* **1994**, 46.
113. D. A. Cooper, J. W. Morse, *Environ. Sci. Technol.* **1998**, 32, 327.
114. C. Gagnon, A. Mucci, E. Pelletier, *Mar. Chem.* **1996**, 42, 195.
115. F. Wang, A. Tessier, J. Buffe, *Limnol. Oceanogr.* **1998**, 43, 1353.
116. N. Batina, I. Ciglenecki, B. Cosovic, *Anal. Chim. Acta* **1992**, 267, 157.
117. S. M. Theberge, G. W. Luther, A. W. Farrenkopf, *Deep Sea Res.* **1997**, 44, 1381.
118. I. Ciglenecki, Z. Kodba, B. Cosovic, *Mar. Chem.* **1996**, 53, 101.
119. T. F. Rozan, G. Benoit, G. W. Luther III, *Environ. Sci. Technol.* **1999**, 33, 3021.
120. G. W. Luther III, T. M. Church, A. E. Giblin et al., *Org. Mar. Geochem.* **1986**, 305, 340.
121. G. W. Luther III, P. J. Brendel, B. L. Lewis et al., *Limnol. Oceanogr.* **1998**, 43, 325.
122. G. W. Luther III, E. Tsamakis, *Mar. Chem.* **1989**, 27, 165.
123. I. Ciglenecki, B. Cosovic, *Electroanalysis* **1997**, 9, 775.
124. T. F. Rozan, S. M. Theberge, G. W. Luther III, *Anal. Chim. Acta* **2000**, 415, 175.
125. Q. Lu, J. Hu, K. Tang et al., *Inorg. Chem.* **2000**, 39, 1606.

9 The Electrochemistry of Halogens

Frank Marken
University of Bath, Bath, UK

9.1	Introduction	275
9.2	The Electrochemistry of Fluorine	277
9.2.1	Introduction	277
9.2.2	Electrochemical Generation of Fluorine	277
9.2.3	Electrofluorination in Synthesis	278
9.2.4	Gas and Ion Sensors for Fluorine and Fluoride	281
9.3	The Electrochemistry of Chlorine	281
9.3.1	Introduction	281
9.3.2	Electrogeneration of Chlorine Gas	281
9.3.3	In Situ Electrogeneration of Chlorine	283
9.3.4	Miscellaneous Methods and Applications Involving Electrogenerated Chlorine	284
9.3.5	Sensors for Chlorine and Chloride	285
9.4	The Electrochemistry of Bromine	285
9.4.1	Introduction	285
9.4.2	Electrochemical Generation of Bromine	285
9.4.3	Electrobromination in Synthesis	287
9.4.4	Electrogenerated Bromine as Redox Mediator	288
9.4.5	Electrobromination Processes in Room Temperature Ionic Liquids	289
9.4.6	Miscellaneous Methods and Applications Involving Electrogenerated Bromine	289
9.4.7	Sensors for Bromine and Bromide	290
9.5	The Electrochemistry of Iodine	291
9.5.1	Introduction	291
9.5.2	Electrochemical Studies of Iodine Generation	291

9.5.3	Electroiodination and Electrogenerated Iodine as a Redox Mediator in Electrosynthesis	293
9.5.4	Miscellaneous Methods and Applications Involving Iodine Redox Systems	294
9.5.5	Application of Iodine as a Redox Mediator in Electroanalysis	295
9.5.6	Sensors for Iodine and Iodide	296
9.6	The Electrochemistry of Astatine	297
9.6.1	Introduction	297
9.6.2	Electrochemical Studies	298
	References	298

9.1

Introduction

The halogens (from the Greek “hals + gennan” for “salt formers”) play a special and important role in fundamental and technical electrochemistry. The electrochemical (anodic) formation of the free halogens or their more highly oxidized forms has been widely employed in synthetic and analytical processes. The bulk generation of chlorine from chloride (in the chlor-alkali electrolysis process [1]), the bulk or in situ generation of fluorine (in electrofluorination processes [2]), as well as the in situ generation of aggressive reagents employed in waste decontamination [3] or in mediated electrosynthetic processes (e.g. in the electroepoxidation of olefins [4]) are processes that have been developed to provide alternatives to reactions involving the addition of bulk reagents. In particular, the in situ formation of reactive intermediates such as fluorine or bromine offer relatively clean and nonhazardous alternatives to bulk chemical use and will be of considerable future importance. The halogenides are ubiquitous and versatile as inert electrolytes as well as precursors for highly reactive redox intermediates of electrochemical processes.

Owing to their considerable oxidizing power, the fully reduced $-I$ redox state is

the naturally most abundant redox state for all halogens (only iodine and astatine can occur naturally in higher oxidation states; chlorine oxides and perchlorate are present in traces). The availability of higher redox states can be of technical importance (e.g. for periodate mediated oxidation reactions) and is generally dependent on the chemical environment (solvent, pH, T, etc.). As one might expect, the heavier halogens exhibit more inert higher oxidation states. However, there are exceptions such as the highly unstable perbromate, BrO_4^- . The reversible standard potentials for the formation of the halogens from aqueous halide solutions decrease when going to the heavier halogens and follow approximately the trend of the hydration energies. Some further key chemical properties and important physical constants for the halogens are summarized in Table 1.

The availability of the halogens in the earth's crust are 0.027 w% (F), 0.19 w% (Cl), 6×10^{-4} w% (Br), and 6×10^{-6} w% (I). The radioactive astatine (from the Greek “astatos” for “unstable”), with 3×10^{-24} w% occurs naturally only as a radioactive fission product of uranium (with a half-life of 8.3 h or less) and can be synthesized by fusion of bismuth with α -particles [11].

The electrochemistry of the halogens strongly depends on the solvent,

Tab. 1 Some physical properties of halogens [5, 6]

	<i>Fluorine</i>	<i>Chlorine</i>	<i>Bromine</i>	<i>Iodine</i>	<i>Astatine</i>
Relative atomic weight/[au]	18.9984	35.453	79.904	126.9045	210 ^a
Color of gas	Very weak yellow	Yellow–green	Red–brown	Violet	–
Melting point / °C	–219.61	–101.00	–7.25	113.60	ca. 300
Critical point/ °C	–129	143.5	311	–	–
Atomic radius/10 ^{–10} m	0.64	0.99	1.14	1.33	1.4
Ionic radius/10 ^{–10} m	1.33	1.81	1.96	2.20	2.27
Gibbs energy of hydration/kJ mol ^{–1} ^b	–472	–347	–321	–283	–247
E ⁰ (X [–] /X ₂) in aqueous acid/V vs. NHE	2.866	1.358	1.065	0.621	0.2
Atomic electron affinity/eV	3.401	3.613	3.363	3.059	ca. 2.8
Atomic ionization energy/eV	17.423	12.968	11.813	10.451	9.5
X–X bond distance/10 ^{–10} m	1.42	1.9881	2.2809	2.666	ca. 2.8
X–X bond dissociation energy/kJ mol ^{–1}	158.1	243.52	192.99	151.34	95.0
HX pK _A (298 K) ^c	3.17	–6.1	–8.9	–9.3	–
Azeotrope with H ₂ O (1 bar)/w%	35.37	20.24	47.63	56.7	–

^a Astatine is highly radioactive and only produced and isolated in very small quantities; isotope with the longest half-life (8.3 h) considered.

^b Taken from Ref. 7.

^c Acidity constants in water [8, 9]. Note that H₃O⁺F[–] ion pair formation is responsible for the strong deviation seen in the value for HF [10].

conditions, and environment and, for example, species such as Br⁺, I⁺, or At⁺ have been reported as useful reactive intermediates. These “hypervalent” species are highly reactive and are readily generated electrochemically in donor solvents such as pyridine [12]. These highly reactive intermediates form adducts with olefins and aromatic π -systems and play an important role in electrosynthetic processes (vide infra) in spite of being only poorly characterized.

Fundamental and practical information about the electrochemistry of the halogens is available in considerable depth from the Pourbaix diagrams [13], from the collection

of standard potentials in aqueous solution [14], and from standard textbooks [6] and resources [15]. In the following chapters, an overview is provided highlighting recent developments in the fundamental understanding and the application of halogens in electrochemical processes. In particular, advances in electrode materials and process designs leading to more efficient or novel electrochemical processes are considered. Areas such as the development of boron-doped diamond electrode materials and novel room temperature ionic liquid reaction media are included. Further, more fundamental and critical information is available in earlier reviews [16, 17].

9.2

The Electrochemistry of Fluorine

9.2.1

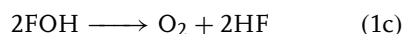
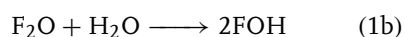
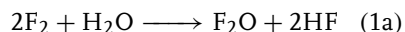
Introduction

Fluorine was discovered in electrochemical experiments conducted by Henri Moissan [18, 19] in 1886. He discovered that solutions of KF in HF remain liquid and electrically conducting even at ambient temperatures and during electrolysis, he was able to isolate fluorine as a pale yellow gas for the first time. Fluorine as well as hydrofluoric acid are highly toxic and should be handled only with extreme care [20].

Owing to its chemically highly aggressive nature, fluorine is difficult and hazardous to handle and it can be manufactured only via the electrolytic oxidation of fluoride. Fluorine gas has been produced commercially since 1946 and has found applications in many areas of fluorine chemistry (polymers, surfactants, lubricants, thermally stable liquids, blood replacement and pharmaceuticals, propellants, etc.). Inorganic fluorides such as SF₆ and UF₆ [21] have technical applications. Fluorous solvent systems [22] provide novel reaction environments fundamentally different from both aqueous and hydrocarbon media [23] and fluorine has been employed as a marker or spin label [24].

A critical and comprehensive review of fluorine redox chemistry has been given by Kuhn [17] and much fundamental information is also available from Bard [14] and from Pourbaix [13]. The most important redox states for fluorine are – I (fluoride, fluormonoxide) and 0 (fluorine) and the hypothetical reversible standard potentials for these systems are given below. The highly unstable oxide F₂O is

obtained by reacting fluorine with traces of water and further reaction leads to the formation of thermally unstable HOF, oxygen, and HF (Eq. 1).

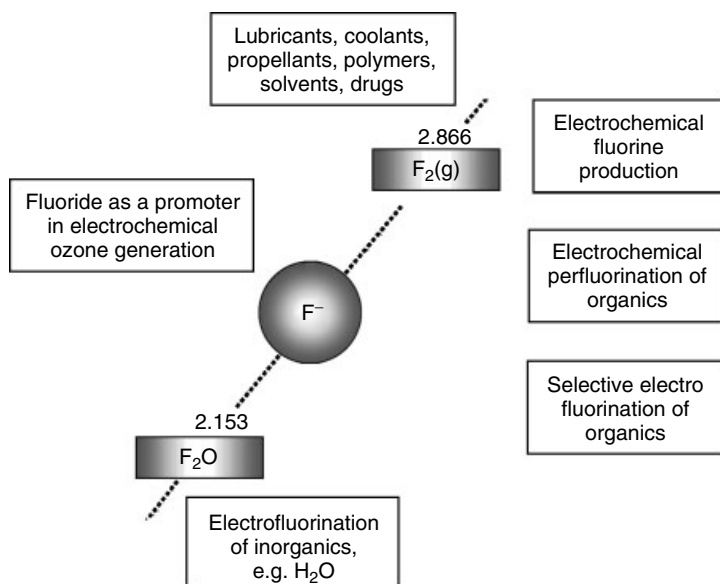


Hydrofluoric acid in contact with water behaves anomalous when compared to the heavier halogens. The hydrogen–fluoride bond is relatively strong and ion pairs of the type H₃O⁺F[–] exist rather than free hydronium ions [10]. Anhydrous HF is an electrically conducting liquid (3HF = H₂F⁺ + HF₂[–] occurs) with a normal boiling point of 19.5 °C. Scheme (1) summarizes the most important forms, the standard potentials in acidic aqueous media, and typical applications of fluorine.

9.2.2

Electrochemical Generation of Fluorine

Owing to the extremely high standard potential of fluorine, only electrochemical methods are available for the oxidation of fluoride to fluorine. In order to generate fluorine gas commercially, a process based on electrolysis in a eutectic mixture of KF and HF with a melting point of 82 °C has been developed [25, 26]. Problems due to the high cell voltages and rapid carbon anode degradation are encountered. During the electrolysis process, a film of fluorinated carbon forms at the anode surface and leads to poor wetting. Additional problems arise from fluorine gas bubbles adhering to the electrode and substantially increasing the overpotential [27]. A theoretical model for this process based on a “fluidized” layer has been proposed recently [28] and processes at C electrodes in



Scheme 1 Redox states, reversible standard potentials (in V vs. NHE, in acidic aqueous environments [13, 14]), and some applications of fluorine.

KF–(HF)₂ electrolyte media have been further dissected [29]. Detailed information about the industrial process is available [17, 30].

9.2.3

Electrofluorination in Synthesis

Avoiding handling, storage, and transport of toxic and highly reactive reaction intermediates is one of the benefits of the electrochemical in situ generation of reagents. For fluorine chemistry, this approach is of particular value. The direct electrofluorination of organics [31] is a process carried out in a scale of ca. 100–1000 ton year^{−1} and there are mainly two technical processes, the Simons process and the Phillips process [32]. The Simons process is employed for the perfluorination of organic substrates and involves electrolysis of a dispersion of substrate in anhydrous HF at a nickel anode. In the Phillips process,

the substrate is supplied through a porous carbon anode into the molten KF–2HF electrolyte. Products are formed via statistical replacement of hydrogen in an apparent radical reaction scheme. Much of the progress made over recent years has been reviewed by Misra et al. [33]

Electrochemical fluorination (ECF) has been applied to the formation of both inorganic and organic target molecules. In spite of the formation of side products and the inevitable destruction of the initial substrate, mild electrofluorination conditions allow most of the functional groups or heteroatoms (N, O, S) in the starting material to be conserved. Among numerous perfluorinated substances produced by ECF there are perfluorinated tertiary amines, perfluoroethers, and perfluorocarbons. Those substances are of considerable interest for industry being inert, environmental comparatively friendly, nonflammable, and fire-safe liquids with

applications as coolants or as liquid dielectrics in various technical applications and over a wide temperature range. The derivatives of fluoroanhydrides of carbonic and sulfonic acids are efficient surfactants needed in transportation and metallurgy. The derivatives of perfluoromethyl- or perfluoroethyl- sulfonic acids are very promising raw materials for electrolytes in a new generation of electrochemical power sources. On the other hand, ECF has some disadvantages that may limit its usage. One important disadvantage is destructive fluorination of the initial substrate that occurs simultaneously with the synthesis of a perfluorinated target molecule. Often, a product mixture is isolated and the yield of the target substance may happen to be rather small. Fluorination of molecules containing 9 or more side chain carbons often results in gums that tend to accumulate in the electrolyte and to stick to the electrode surface thus complicating the use of continuous electrolysis process.

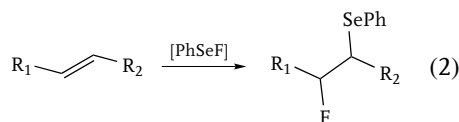
In a recent review, Tao et al. [34] describe the partial fluorination and the perfluorination of organics with particular emphasis on medically important compounds and pharmaceuticals. The selective electrofluorination (SEF) of olefins and active methylene groups is reviewed by Noel et al. [35] In the case of heterocycles, nuclear fluorination is known to be the predominant process. However, in aromatic compounds, nuclear substitution as well as addition proceeds simultaneously, leading to the formation of a mixture of products. The influence of solvents, supporting electrolytes, and adsorption on product yield and selectivity is summarized and evaluated. Dimethoxyethane is found to be a superior solvent for SEF processes. Redox mediators have been employed to minimize anode passivation and to achieve better current efficiencies.

Nitrogen bases containing perfluoroalkyl substituents have been synthesized using redox catalysts as mediators. Important biologically active molecules containing fluoro-substituents have been prepared by SEF methods. The fluorination of dimethylcarbonates has been described by Takehara et al. [36] A very selective and mild electrofluorination method has been reported by Fang et al. [37] Acetonitrile is employed as an inert solvent with $\text{Et}_3\text{N}\cdot\text{HF}$ as supporting electrolyte and as a fluorine source. The fluorination of pyridine yielded 4-fluoropyridine in good yield.

The electrofluorination of acetophenone and benzophenone takes place in anhydrous HF and in the presence of solvents such as chloroform and acetonitrile [38]. The fluorination of the aromatic rings occurred to various extent. Further uses of anhydrous hydrogen fluoride as a liquid environment for electrofluorination processes have been reported, for example, by Matalin et al. [39]. In particular, systems with low conductivity in liquid hydrogen fluoride and nonselective processes have been studied and optimized. The fluorination of benzene and halobenzenes in the presence of $\text{Et}_4\text{NF}-(\text{HF})_n$ in an undivided cell has been studied by Horio et al. [40] Cathodic dehalogenation is observed to accompany the anodic fluorination process.

Mild electrofluorination is possible with much higher selectivity when fluorine is replaced by adducts such as in situ generated PhSeF , Br_2F^- , $\text{Ar}-\text{IF}_2$ [41], or interhalogen compounds [42] such as IF_5 [43]. A very mild approach to introducing fluorine into organic molecules can be based on a redox mediator containing fluoride bound to a reactive electrophile. Uneyama et al. pioneered the use of electrogenerated fluoroselenols [44] (see Eq. 2). The reagent is generated anodically in situ from a selenophenol in the presence

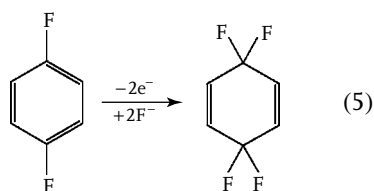
of fluoride.



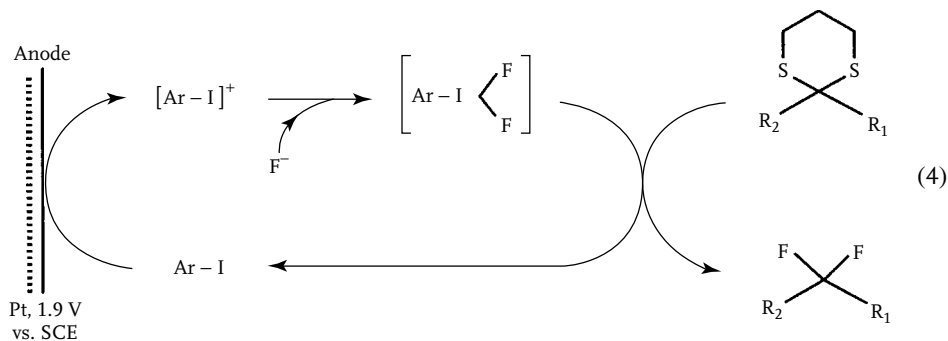
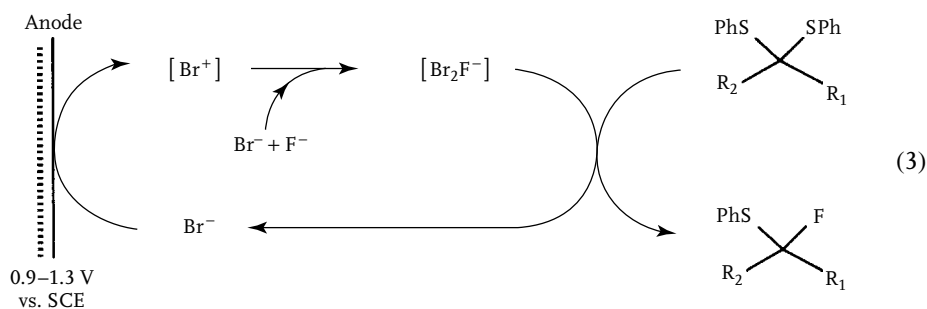
This type of reagent allows a very selective and mild introduction of fluorine. Fuchigami et al. pioneered a similar approach for the desulfurisation fluorination employing hypervalent bromine (Eq. 3) and iodine (Eq. 4) reagents [45].

The electrode material for electrofluorination processes is important, and new materials with high conductivity but chemically inert surface characteristics are desirable. Materials such as Ni, Monel, or Hastalloy are commonly employed [46] and the use of Pt has been pioneered by Schmidt [47]. Boron-doped diamond is a novel electrode material with a chemically highly inert surface suitable for

application in harsh environments such as the electrofluorination in anhydrous HF [48]. Okino et al. [49] demonstrated the fluorination of 1,4-difluorobenzene in $Et_4NF-(HF)_4$ containing electrolyte solutions (see Eq. 5). A comparison with graphite and platinum demonstrated the benefits of boron-doped diamond.



An interesting aspect of fluoride applications in electrochemistry is the beneficial effect that fluoride-containing electrolyte media have on the anodic formation of ozone. Oxidized forms of fluoride are known to result in the formation of persulfate and peroxide, but for the



electrochemical ozone generation, no direct participation in the reaction has been reported. It has been proposed that for anodes made of PbO_2 the coverage of the electrode with intermediates is affected by the presence of fluoride [50]. The ozone formation process has also been observed at other electrode materials such as boron-doped diamond [51].

9.2.4

Gas and Ion Sensors for Fluorine and Fluoride

The rapid detection and determination of fluorine as a highly toxic gas is of importance in industry and both solid-state semiconductor and polymer electrolyte solutions have been suggested. Moritz et al. [52] developed a semiconductor field-effect structure $\text{Si}/\text{SiO}_2/\text{Si}_3\text{N}_4/\text{LaF}_3/\text{Pt}$, which, as an all solid-state device, allowed the determination of 0.01 to 1000 ppm fluorine. In a related report, a three-phase boundary charge transfer reaction at an $\text{AlF}_3/\text{Pt}/\text{gas}$ interface has been proposed as a key step in the overall fluorine detection mechanism [53]. At elevated temperatures of up to 530°C also the electrochemical determination of fluorocarbons ($\text{CF}_3\text{CH}_2\text{F}$, CF_3CCl_3 , $\text{CF}_3\text{CH}_2\text{Cl}$, CHClF_2 , CCl_2F_2 , CCl_3F) at semiconductor structures has been reported [54].

Room temperature sensors based on a V_2O_5 -graphite cathode and a polyethylene oxide-based electrolyte were reported by Sathiyamoorthi et al. [55]. The gas is sampled through the porous cathode and for both chlorine and fluorine good sensitivity and rapid response times were observed.

Ion-selective electrodes for fluoride trace analysis are commercially available and effective down to a level of mg dm^{-3} [56]. A recent textbook by Cattrall [57] gives background information to the theory

and design of ion-selective electrodes and, in particular, to the mechanism of the fluoride-selective electrode. The potentiometric detection mechanism is usually based on the interaction of fluoride anions with a LaF_3 membrane, which in turn is in contact with a reference solution [58]. Doping of the LaF_3 membrane with EuF_2 introduces vacancies and allows ion conductivity and selectivity to be improved [59].

9.3

The Electrochemistry of Chlorine

9.3.1

Introduction

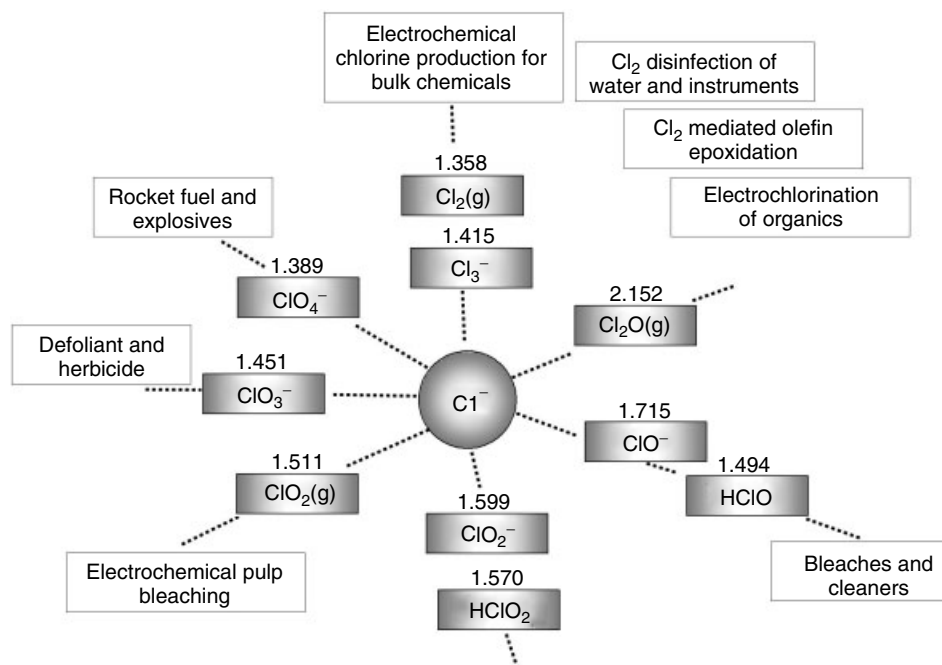
Chlorine (from the Greek “chloros” for “yellow-green”) is the most abundant halogen (0.19 w% of the earth’s crust) and plays a key role in chemical processes. The chlor-alkali industry has been in operation since the 1890s and improvements in the technology are still important and noticeable, for example, the transition from the mercury-based technology to membrane cells [60]. Most chlorine produced today is used for the manufacture of polyvinyl chloride, chloroprene, chlorinated hydrocarbons, propylene oxide, in the pulp and paper industry, in water treatment, and in disinfection processes [61]. A summary of typical redox states of chlorine, standard potentials for acidic aqueous media, and applications is given in Scheme 2.

Information about the history and technical importance of the electrochemistry of chlorine is available from earlier reviews [62] and data collections [14].

9.3.2

Electrogeneration of Chlorine Gas

Chlorine is a widely used bulk chemical with numerous applications on a megaton



Scheme 2 Redox states, reversible standard potentials (in acidic aqueous environment), and applications of chlorine [13, 14].

scale [63, 64]. The electrochemical generation of chlorine from chloride has become a standard process often carried out on site in order to avoid transport of compressed chlorine. Only recently in 2004 just outside Texas (US) an accident caused by a train derailment resulted in the release of a toxic cloud of chlorine and demonstrated the inherent dangers of transporting large amounts liquid chlorine [65].

The bulk generation of chlorine from brine has been carried out at graphite electrodes (anodes) until the 1960s [66]. In the process, the graphite was slowly consumed causing exposure of the environment with chlorohydrocarbons and a need for regularly replacing electrodes. A further problem was the substantial overpotential for chlorine evolution of about 500 mV on carbon anodes. This high overpotential

caused the competing oxygen evolution process to introduce impurities and losses in efficiency. Electrocatalysts such as platinum undergo considerable dissolution (1 g per 5 ton chlorine) in the 25% brine solution typically employed in chlorine electrogeneration and therefore cannot be used. However, new ceramic electrodes, dimensionally stable anodes or DSAs [67] based on anodized titanium modified with catalytic oxides, then revolutionized this process. For the chlorine production, ruthenium oxide coatings on titanium anodes reduced the overpotential for the chlorine evolution to 50 mV while increasing the overpotential for the competing oxygen evolution. Reliable anodes for the harsh conditions employed during anodic formation of chlorine and lifetimes of up to 10 years are now available. However,

novel electrode systems are still under development and a recent review summarizes some advances in ceramic film design and analysis [68]. The effect of the thickness of the porous ceramic layer has been investigated [69]. The failure of DSAs during chlorine evolution usually is linked to the leaching of metals, such as ruthenium, from the anode surface [70]. A kinetic study on the chlorine formation process at Ti/RuO₂ electrodes has been reported [71] and the sol-gel formation of TiO₂/RuO₂ films for DSA applications has been studied [72]. The effects of particle size and aging on electrode kinetics and leaching have been evaluated.

A new development during the last decade was the introduction of boron-doped diamond as an electrode material and work is continuing on analyzing the properties and the possible benefits of this material in electrochemical processes [73]. The chemical inertness of diamond carbon reduces the problems with losses of anode material and the boron doping introduces electrical conductivity. Thin films of boron-doped diamond have been grown, for example, onto titanium substrates and tested. A high overvoltage for the chlorine evolution process on boron-doped diamond has been reported by Beck et al. [74] However, Ferro et al. [75] showed that a comparison of various carbon anodes with boron-doped diamond suggest similar performance and that the application of boron-doped diamond, for example, in seawater electrolysis (for hypochlorite formation [76]) is realistic. It is likely that the type (doping level, roughness) and history of boron-doped diamond is in part responsible for differences in the characteristics of boron-doped diamond surfaces. Attempts have been made to embed electrocatalysts into the surface of boron-doped diamond electrodes [77].

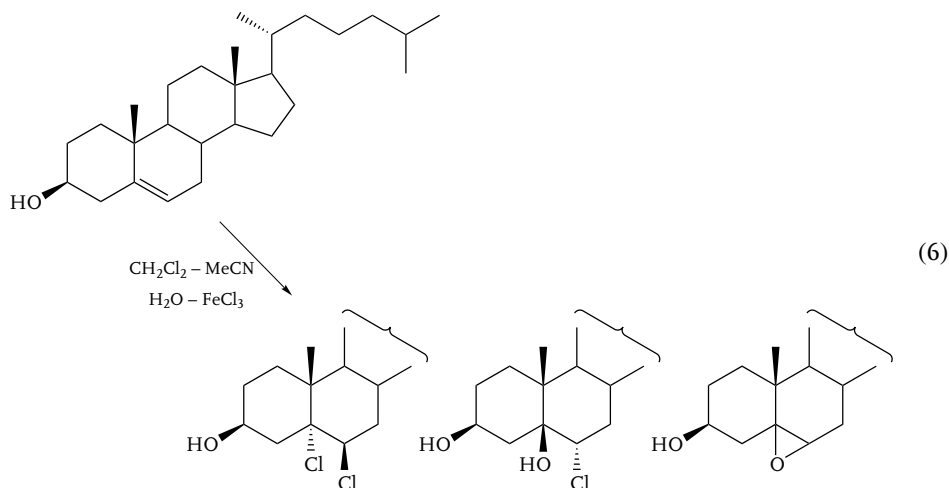
A further important application of chlorine is in the disinfection of drinking water. In a recent review by Bergmann et al. [78], processes in simple undivided cells are discussed and the high efficiency of titanium-based DSAs when compared to platinum and diamond is pointed out.

9.3.3

In Situ Electrogeneration of Chlorine

Chlorine may be regarded as a reactive intermediate in electrochemical processes and chlorination of many substrates can be achieved simply by in situ anodic generation of chlorine. Indeed, often electrolysis in the presence of chloride leads to mechanistic ambiguities and/or the formation of chlorinated side products [79].

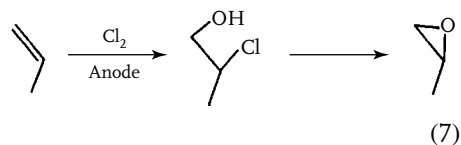
Over recent years, the electrochlorination of a wide range of substrates has been reported. The direct halogenation of benzene has been studied at Pt and Rh electrodes and the in situ spectroelectrochemical monitoring of the process with confocal microprobe Raman methods allowed optimization of the reaction conditions [80]. Toluene has been chlorinated at DSAs and the kinetics of this process have been explored in detail [81]. The electrochlorination of 1,4-dimethoxy-2-*tert*-butylbenzene has been reported in CCl₄ and in acetonitrile environments [82]. A difference in mechanism has been proposed to explain the observation of 1,4-dimethoxy-2-*tert*-butyl-5-chlorobenzene and 1,4-dimethoxy-2-*tert*-butyl-6-chlorobenzene, respectively, as the main products. Succinimide is electrochlorinated to give *N*-chlorosuccinimide at platinum electrodes, but the process has been reported to be relatively inefficient due to side reactions (when compared



to electrobromination under the same conditions) [83]. The chlorination of unsaturated steroids [84] and the stereoselective electrochlorination of a steroidal 5,6-olefin has been reported by Maki et al. [85]. The dichloro product as well as the chlorohydrin have been obtained (Eq. 6).

In similar electrochlorination experiments, propionaldehyde [86], ethylene [87], tetramethylpiperidine derivatives [88], amines [89], acetone [90], and polymers [91] have been converted into chloro derivatives. Mechanistic studies have aimed at elucidating the role of chloronium intermediates [92], water [93], and of redox mediators such as Ce^{4+} [94] in the electrochlorination process.

The formation of epoxides is synthetically a very important transformation. The indirect epoxidation of olefins (see Eq. 7) in the presence of electrogenerated chlorine (or bromine) [95] is a commercial process in which chlorine is recycled and not part of the product. The products such as propylene oxide are key intermediates in many further chemical processes.



9.3.4

Miscellaneous Methods and Applications Involving Electrogenerated Chlorine

The photoelectrochemical production of chlorine at nanocrystalline titanium dioxide thin film electrodes exposed to UV light has been reported [96]. In this process, the energy from photons substantially reduces the overpotential required for the chlorine evolution process and therefore less harsh conditions are required. Metal doping of the TiO_2 photoelectrocatalyst was explored but found to be not beneficial for this process. In future, this kind of process could be of practical value, in particular, for water treatment and disinfection applications requiring low levels of chlorine.

Electrochemical processes in plasmas have recently attracted renewed attention [97]. Plasmas contain ionic species in a

gaslike state and electrodes placed into the plasma zone allow electrochemical measurements. Janek and coworkers explored the reactivity of silver electrodes in a chlorine rf plasma environment [98]. Both potentiostatic and galvanostatic experiments have been conducted and the growth of AgCl at the electrode surface was monitored. The morphology of the film was dependent on the applied potential and the experimental conditions and the transport of charges across the AgCl film was found to be rate limiting [99].

The use of chlorine in a fuel cell system for space power applications has been suggested [100]. The Cl_2/H_2 system is based on a proton-exchange membrane fuel cell design and is shown to give superior power and energy density when compared to conventional systems.

9.3.5

Sensors for Chlorine and Chloride

Sensing of chlorine is possible with a phthalocyanine-based optode that is electrochemically reset [101]. Also a direct electrochemical Clark-type sensor employing carbon electrodes has been investigated [102]. For this type of sensor, the various types of carbon gave different responses and the edge-plane sites of graphitic electrodes were identified as electrochemically active. Both chlorine reduction and chlorine evolution were studied and the effects of the trichloride anion, Cl_3^- , were highlighted.

Ion-selective sensors for chloride are commercially available [103]. Both fundamental and practical information concerning the theory, design, and operation of chloride-selective electrodes is available from a recent textbook [57]. Sensor membranes for potentiometric chloride detection have been formed from Ag_2S (as ion

conductor) and AgCl. Heterogeneous sensor membranes have been formed from silver chloride and silicone rubber [104] and other types of membrane materials [105]. Chloride ion-selective electrodes suffer from interference, in particular, from bromide and iodide anions.

9.4

The Electrochemistry of Bromine

9.4.1

Introduction

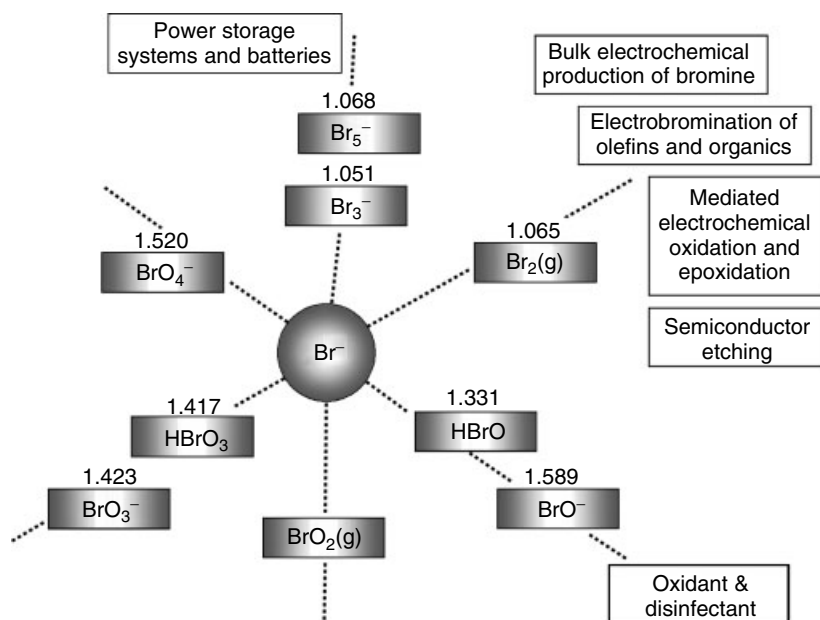
Bromine (from the Greek “bromos” for “stench”) has found applications in flue gas desulfurization [106], in the design for a large-scale electrical power storage facility [107], in many flame retardants, for fire extinguishers, and in pharmaceuticals. Electrobromination processes have been employed directly and indirectly, and bromates are produced [108] and detected [109] electrochemically. Perbromates when compared to perchlorates and periodates are chemically very unstable. A summary of redox states, standard potentials in acidic aqueous media, and typical applications is shown in Scheme 3.

Much fundamental information and data about the electrochemistry of bromine and the applications of bromine are available in earlier reviews [110] and data collections [13, 14].

9.4.2

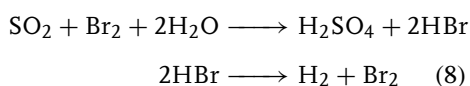
Electrochemical Generation of Bromine

Bromine can be generated from bromide at many types of electrodes and in many solvent environments. Industrial scale bromine formation has been employed recently in a flue gas desulfurization reaction [111]. The process involves anodic



Scheme 3 Redox states, reversible standard potentials (in acidic aqueous environment), and applications of bromine [13, 14].

formation of Br_2 at ruthenium oxide coated titanium electrodes (DSAs) and reaction of bromine with SO_2 in the solution phase (see Eq. 8). Hydrobromic acid is reformed and SO_2 is removed in the form of sulfuric acid.



The type and reactivity of the products formed in the bromide oxidation process may differ. Vojinovic et al. [112] have investigated the formation of bromine in propylene carbonate. The tribromide anion, Br_3^- , was identified as the main product and an unwanted reaction of the solvent with the active bromine was observed.

In aqueous media, kinetic studies at various types of platinum surfaces have been

reported [113] and a strong effect of the surface on the rate of bromine formation was observed. A careful study of the process taking into account platinum oxide formation and adsorbed intermediates has been reported by Conway et al. [114]. Similarities in the mechanism when compared to the chlorine evolution reaction are pointed out. Further studies in aqueous media and at platinum electrodes appeared for the case of neutral [115] and for alkaline media [116]. The effect of a poly(*para*-phenylene) film on the surface of a platinum electrode on the bromine evolution process was studied. The study uses stationary and rotating electrodes and concludes that in sulfuric acid solution a catalytic process is observed [117].

Graphite and carbon electrodes are most commonly employed in industrial applications. Recent work on a large-scale redox battery systems based on

the $\text{Br}^-/\text{Br}_3^-$ redox system [107] employed carbon composites. The work was aimed at providing a buffer system for the output of power stations in order to provide power at peak time and to recharge during periods of low power demand. Prototype plants were built in the United Kingdom and in the United States [118]. Depending on the reaction conditions during bromine electrogeneration, some types of carbon can be prone to deterioration. The electrochemical intercalation of bromine into graphite, which occurs under more extreme conditions, has been studied by Izumi et al. [119]. Loss of conductivity and widening of the carbon lattice spacing have been observed.

The suitability of boron-doped diamond as anode material for the generation of aggressive reagents, such as bromine, has been investigated. Vinokur et al. reported that the electron transfer at boron-doped diamond electrodes is strongly affected by the nature of the electrode process. Inner-sphere processes such as the bromine evolution from bromide seem to be kinetically slow, [73, 120] in particular, when occurring positive of a potential of approximately -0.05 V vs. SCE. This is currently limiting possible wider applications of boron-doped diamond electrode materials.

9.4.3

Electrobromination in Synthesis

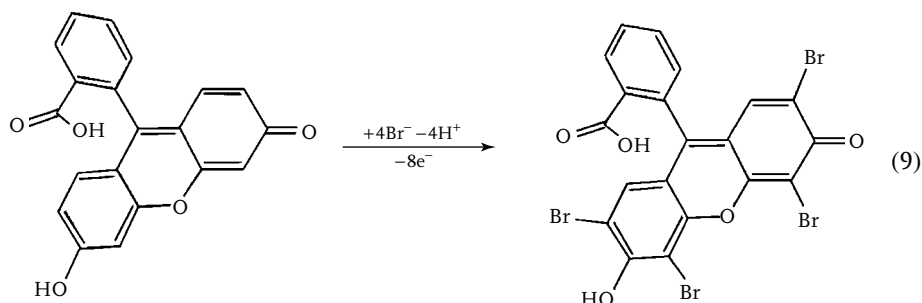
The electrobromination of organics with in situ generated bromine offers a clean and relatively nonhazardous way of producing bromo-substituted products. The bromination of hexane, cyclohexene, and styrene has been studied in a mixed aqueous/DMF electrolyte system [121]. The mechanism for this process yielding

geminal dibromides was investigated by computer simulation methods.

A comparison of the chemical bromination and the electrochemical bromination of germacrene D and geraniol has been reported [122]. In these multiolefinic systems, region selectivity is important and a better selectivity in the electrochemical bromination process is observed. Dimedon halogen derivatives have been obtained with in situ generated bromine [123]. Both 2-bromo- and 2,2-dibromodimedone are obtained in good yield and purity in a process conducted in an undivided cell. The regioselective electrobromination of benzofuran was reported by Tanaka et al. [124]. The products 5-bromobenzofuran, 5,7-dibromobenzofuran (obtained in acetic acid, H_2O , NH_4Br), and 2,3-dibromo-2,3-dihydrobenzofuran (obtained in CH_2Cl_2 , H_2O , NaBr) were obtained depending on the choice of conditions, solvent, and electrolyte.

The in situ formation of *N*-bromosuccinimide (NBS) has been reported and optimized by Krishnamoorthy et al. [83]. The process is operated at a platinum electrode and a reduced efficiency due to side reactions is observed. A maximum yield of 55% is reported. The use of in situ generated NBS and bromine for the synthesis of nucleosides from silylated pyrimidines has been studied. Nokami et al. [125] suggest the use of only catalytic amounts of NBS or bromine and regeneration of the catalyst by anodic electrolysis in an undivided cell system.

Eosin is a dye that is obtained by reaction of fluorescein with bromine (Eq. 9). This reaction has been carried out in batch and flow reactors, and both eosin and erythrosine (the tetraiodine derivative) have been obtained. The mechanism and



benefits of the method are discussed [126]. In a related study, the effect of different reaction media, such as carbonate, acetate, or ammonia containing aqueous solutions, has been addressed [127]. Optimized conditions for the formation of eosin have been determined and a dimensionally stable ceramic electrode $\text{Ti}/\text{TiO}_2/\text{RuO}_2$ was employed.

The reaction of unsaturated hydrocarbons with bromine is synthetically important. Unsaturated fatty acids have been electrobrominated in an acetic acid/acetonitrile medium and at platinum electrodes [128]. The mechanism and rate constant for the process with oleic, erucic, and linoleic acid were elucidated. The α -bromination of α,β -unsaturated ketones has been reported [129] on the basis of the electrolysis of a substrate/ $\text{CF}_3\text{COOH}/\text{CuBr}/\text{Et}_4\text{NOTs}/\text{MeCN}$ reaction system. CuBr is present as a catalyst.

The use of electrogenerated bromine for the analytical determination of pharmaceuticals has been reported by Abdullin

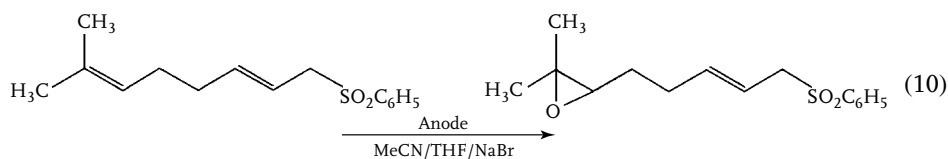
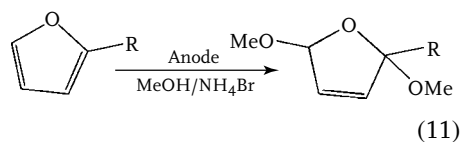
et al. [130]. In this process, bromine generated at the electrode surface is employed for the coulometric detection of aromatic amines such as anesthesine, novocaine, paracetamol, sulgin, or sulfadimezine. The mechanism and stoichiometry of the process is discussed.

9.4.4

Electrogenerated Bromine as Redox Mediator

Electrogenerated bromine can also be used as a mediator in catalytic electrolysis processes. The regioselective formation of epoxides is of high synthetic value and has been reported [131] (Eq. 10)

In a similar manner, bromine has been employed as an oxidant for glucose to calcium gluconate [132] and for the methoxylation of furan [133] (Eq. 11).



9.4.5

Electrobromination Processes in Room Temperature Ionic Liquids

Ionic liquids attract considerable attention as a novel reaction environment for electrochemical reactions and electrobromination processes in ionic liquids and are an interesting new area of research activity. Ionic liquids are nonvolatile and electrically conducting, thereby allowing products to be removed simply by pervaporation. There is no need for added electrolytes and new types of electrolysis cell coupled to high vacuum systems can be developed. The oxidation of bromide at platinum electrodes immersed in room temperature ionic liquid 1-butyl-3-methylimidazolium bis(trifluoromethylsulfonyl)imide has been studied by Compton and coworkers [134]. A two-step process has been detected with at lower potential formation of Br_3^- , which is followed by the direct formation of Br_2 at higher potentials. The association of the cation 1-butyl-3-methylimidazolium, BMIM^+ , with bromide is observed, which reduces the stability of Br_3^- in ionic liquid media compared to acetonitrile. The electrobromination of cyclohexene in ionic liquid media has been shown to give 1,2-dibromocyclohexane in good yields [135]. A novel and nonhazardous ionic liquid reagent, pentylpyridinium tribromide, with the properties of bromine but very low vapor pressure has recently been proposed by Salazar and Dorta as a new chemical reagent for bromination reactions [136]. The benefits and mechanistic details for the addition of trihalides, for example, Br_3^- , to unsaturated compounds in ionic liquid solvent systems have been reported [137].

9.4.6

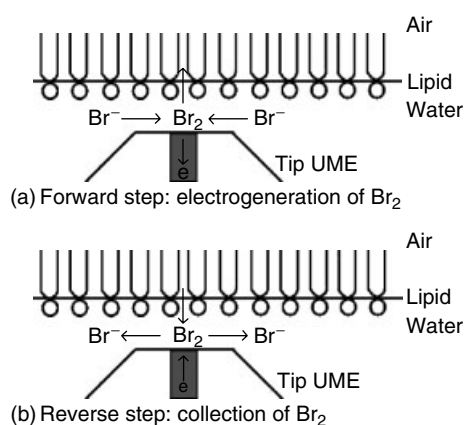
Miscellaneous Methods and Applications Involving Electrogenerated Bromine

The transfer of bromine across liquid–liquid and gas–liquid interfaces is of considerable interest, for example, for sensor systems or for fundamental insights in the effects of bromine in the environment. A new methodology for kinetic studies at a lipid layer has been reported by Zhang et al. [138]. A microelectrode immersed in the aqueous phase is placed in close distance to a lipid surface layer in contact with a gas phase. The oxidation of bromide at the electrode causes the formation of bromine, which in part escapes through the lipid layer into the gas phase (see Scheme 4).

As the distance between electrode and interface is reduced, kinetic effects due to the lipid layer reducing the flux of bromine becomes measurable. Several types of lipids have been investigated and a barrier effect due to L- α -phosphatidylethanolamine distearoyl is reported.

Bromine has been employed as a powerful etchant for semiconductors and for metals. Silicon etching in a fluoride/bromine environment occurs with a diffusion controlled rate both at (100) and at (111) surfaces and affects the photoluminescence of the semiconductor [139]. Chemical etching was also observed for *p*-type GaP immersed in methanolic bromine solution [140]. The dissolution of gold by reaction with bromine is affected by minerals present in contact with the gold. Depending on the type of mineral and the solution composition, significant changes in gold dissolution/leaching rate are reported [141].

Finally, bromine has found application in power storage and battery systems. A



Scheme 4 Schematic of scanning electrochemical microscopy – double potential step chronoamperometry (SECM-DPSC) measurements. (a) In the forward step, Br_2 is produced via the oxidation of Br^- . (b) At t_{switch} , the potential is reversed to collect Br_2 by reduction to Br^- .

regenerative fuel cell system based on polysulfide/bromine half-cells has been developed [107] and studied [107, 142]. Much of this work is patent protected and not in the open literature. However, some studies have emerged, for example, on the effect of graphite electrode materials [143]. Another type of power storage system has been developed and studied on the basis of the zinc/bromine half-cells [144].

9.4.7

Sensors for Bromine and Bromide

The detection and monitoring of bromine is important in various fields of application. In industrial processes, bromine is employed, for example, for the desulfurization of flue gas and an on-line detector enables the process to be optimized. The presence of bromine in the atmosphere has been implicated in processes such as ozone depletion, [145] and devices for monitoring the release of bromine and bromine derivatives are desirable. Bromide monitoring is of interest in industrial contexts, photographic developers, environmental, and in medical samples.

Potentiometric devices for the detection of bromine can be based, for example,

on liquid membranes or solid operating at room temperature. Niizeki et al. [146] demonstrated a sandwich device with a RuO_2 sensor electrode, a PbBr_2 – KBr solid electrolyte and a Pb reference electrode. The open circuit EMF (electro motive force) of the cell measured at room temperature was reproducible and agreed closely with the value calculated from the Nernst equation in the concentration range of 0.00075 to 25.7 vol% bromine in air. The 90% response time of the sensor was less than 1 min at concentrations higher than 0.1 vol% bromine. A sensor device for bromine based on a conducting polymer was proposed by Przyluski et al. [147]

The potentiometric determination of bromide anions with ion-selective electrodes is possible with commercial electrodes that are commonly based on solid Ag_2S – AgBr ion conductor membranes [148–150]. Recently, a novel liquid film sensor has been proposed by Ganjali et al. [151] Determination of bromide was reliable without significant interference from common ions such as chloride and iodide, and was reported down to a micromolar level. The electroactive species in the liquid membrane

was a bis(4-hydroxyphenyl) 1,4-diaza-1,3-butadiene-Hg(II) complex. A similar sensitivity was observed with a PVC-based membrane with 14-phenyldibenzo-xanthenium bromide as the membrane carrier [152]. A solid contact bromide sensitive device was investigated by Stefanova et al. [153]

A spectroelectrochemical sensor has been developed for the bromide monitoring in industrial brine samples [154]. The bromide is oxidized to bromine and a sensitive colorimetric reaction with chloramine-T is employed for detection with a fiber-optic device.

Bromine has also been suggested for an indirect detection process for the determination of tetracyclines in pharmaceutical formulations [155]. A bromine/hydrogen peroxide-based electrogenerated chemiluminescence reaction is shown to be enhanced by tetracycline derivatives and detection levels down to the $\mu\text{g dm}^{-3}$ level are reported on the basis of this enhancement effect.

The determination of ammonium, arsenic, thiosulfate, allyl alcohol, and iodide has been achieved with a bromine redox mediator. Tomcik et al. [156] employ interdigitated microelectrodes at which bromine is generated at one set of electrodes and collected at a second set of electrodes. The reaction of the bromine with the analytes allows quantitative determination down to a micromolar level.

9.5

The Electrochemistry of Iodine

9.5.1

Introduction

Iodine (from the Greek “ioeides” for “colored violet”) has the ability to exist

in many redox states and forms. Iodine is a solid with a melting point of 113.6°C and perhaps surprisingly the resulting brown liquid shows electrical conductivity due to the formation of $\text{I}_3^+ \text{I}_3^-$ ion pairs [157]. Then, in the gas phase, violet iodine readily forms charge transfer complexes and therefore often exhibits a brown color in donor solvents such as water, pyridine, or ethanol.

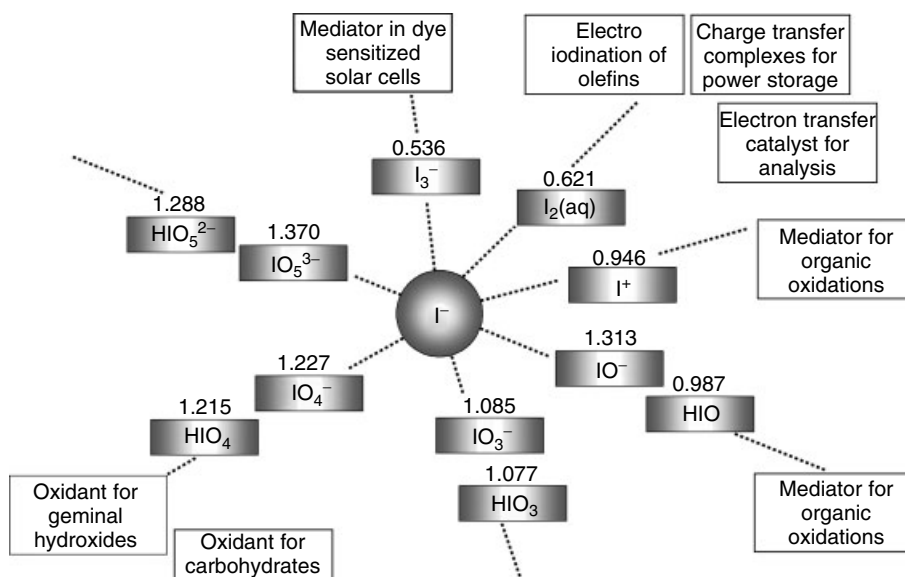
Collections of fundamental and thermodynamic data can be found in an earlier review [158] and in standard resources [13, 14]. However, due to the reactivity of iodine there are many less common or more reactive forms of iodine that have been less well characterized. For example, a blue I_2^+ cation, a brown I_3^+ , or a green I_5^+ cation are formed in concentrated sulfuric acid and I^+ is stabilized in donor environments such as pyridine [159]. So-called “hypervalent” iodine reagents have been developed as a versatile oxidation tool in organic synthesis and often iodine derivatives are employed as electron transfer catalysts. Some fundamental thermodynamic data and typical applications of iodine are summarized in Scheme 5.

9.5.2

Electrochemical Studies of Iodine Generation

Iodine is formed anodically from iodide and at a relatively mild potential that is accessible at common electrode materials. Most studies of iodine electrogeneration are aimed at analytical or electrosynthetic applications of iodine, but there are also some specific uses such as the I_3^-/I^- redox system in dye sensitized solar cells.

At ambient temperature, the electrochemical formation of iodine from iodide causes the formation of a solid product at the electrode surface. The formation of

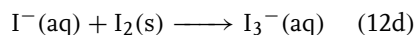
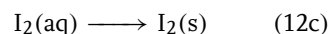
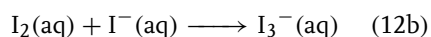
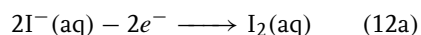


Scheme 5 Redox states, reversible standard potentials (in acidic aqueous environment), and typical applications of iodine [13, 14].

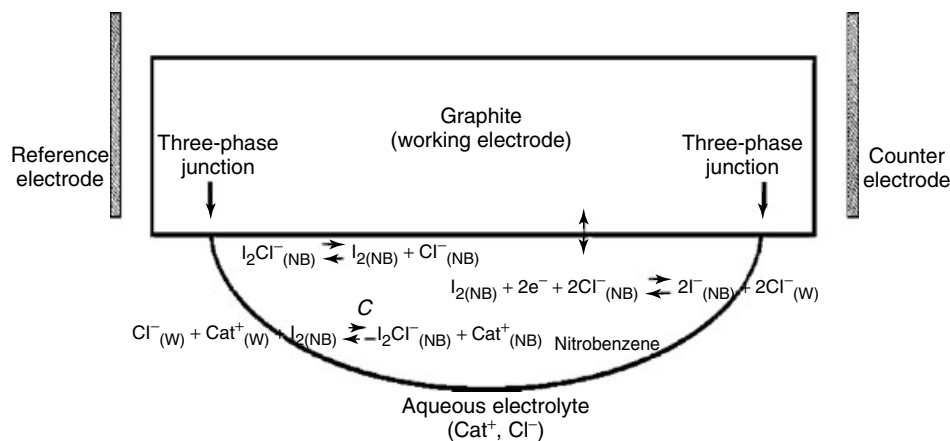
iodine at gold macro- and microelectrodes was studied by Zhang et al. [160]. Quartz crystal microbalance measurements are reported and the process at the microelectrode was optimized for analytical detection purposes down to micromolar iodide concentrations.

The mechanism of the iodide formation at platinum immersed in aqueous electrode was recently studied by laser-activated voltammetry in a channel flow cell system [161]. In this technique, solid deposits of iodine are removed from the electrode continuously by short nanosecond high-power laser pulses. By removing deposits on electrode surfaces within a channel flow cell, the voltammetric measurements becomes time independent and data can be analyzed and modeled quantitatively. Laser activation using a 10-Hz pulsed Nd:YAG 532-nm laser was shown to remove bulk iodine from the electrode surface so that under sustained pulsed

irradiation a steady state surface evolved. The iodide oxidation was reproducibly studied. When the concentration and flow rate dependence of the voltammetric wave shape were modeled, the mechanism was shown to be the following (Eq. 12).



For these processes, the formal redox potential for reaction in Eq. 12(a) was 0.358 V vs. SCE in 0.1 M H_2SO_4 , the equilibrium constant for reaction in Eq. 12(b) has been reported as 580 M^{-1} . The forward rate constant for the reaction in Eq. 12(b) was $1 \times 10^5 \text{ mol}^{-1} \text{ cm}^3 \text{ s}^{-1}$, the solubility of I_2 (Eq. 12(c)) was $1.85 \times 10^{-3} \text{ M}$, and the heterogeneous rate constant for the reaction in Eq. 12(d) was $1.6 \times 10^{-3} \text{ cm s}^{-1}$. Images for the iodine deposit on platinum



Scheme 6 Electrode assembly with a droplet of nitrobenzene containing dissolved iodine attached to a graphite electrode. The electrode is immersed in an aqueous electrolyte solution containing chloride ions [162].

were obtained by in situ atomic force microscopy.

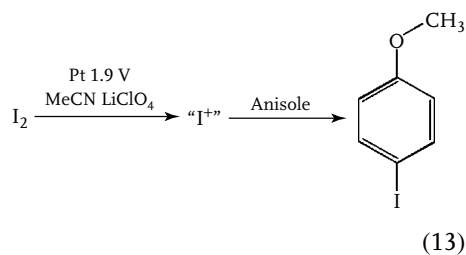
The reactivity of iodine has been investigated at liquid–liquid–electrode triple-phase boundary systems. Scholz et al. [162] demonstrated that the reduction of iodine dissolved in a nitrobenzene microdroplet triggered the transfer of cations from the aqueous into the organic solution phase (Scheme 6). In addition, the formation of I_2Cl^- interhalogen anions in the organic phase was discovered and shown to be the key to the overall process.

The redox process within the organic solution droplet was reported to be coupled to the transfer of cations between organic and aqueous phase, and the reversible potential for the transfer has been correlated with the known Gibbs energies for transfer. The iodine-based measurement at the triple-phase boundary can be employed as a method to determine the Gibbs energy for transfer of cations. A similar scheme employing iodine and bromine-interhalogen anions was developed also for the transfer of anions [163].

9.5.3

Electroiodination and Electrogenerated Iodine as a Redox Mediator in Electrosynthesis

Iodine is reactive toward unsaturated aliphatic hydrocarbons and the “iodine number” is a well-known measure for the degree of unsaturation of fatty acids [164]. The electroiodination of unsaturated and aromatic hydrocarbons also is well known and can be achieved, for example, by electrogeneration of “ I^+ ” in acetonitrile [165] (Eq. 13). The reaction has been proposed to be consistent with a conventional homogeneous electrophilic aromatic substitution.



The efficient formation of diaryliodonium salts during the electrolysis of aryliodides has been reported by Peacock and Pletcher [166]. The electroiodination of a 3D-aromatic molecule, dodecahydro-7,8-dicarba-*nido*-undecaborate has also been reported [167]. The iodination (and bromination) of dimedone has been reported to yield 2-iododimedone, which formally is an electrophilic substitution reaction [123]. In a similar process, the indirect electrochemical oxidation of aliphatic ketones in an alkaline NaI/NaOH solution environment has been shown to yield α,α -diiodoketones, which rapidly rearrange to give unsaturated conjugated esters [168]. Dibenzoylmethane has been converted into dibenzoyliodomethane [169]. Terminal acetylenes have been iodinated in the presence of NaI. However, this process was proposed to proceed via oxidation of the acetylene [170].

Iodine may be employed as a mediator to achieve α -hydroxylation of carbonyl compounds. In basic methanolic solution containing iodide, oxidation was reported to lead to α -iodo ketones, which further reacted to give α -hydroxy ketals [171]. The electrolysis of alkylidenemalonates in the presence of iodide as a mediator has been shown to yield cyclopropane derivatives [172].

The electrochemical transformation of 2-methoxy- and 2-methylphenols to give orthoquinoid cyclohexadienone synthons with the aid of iodanes has been reported [173]. Iodanes (or “hypervalent” iodine [174, 175]) are a large family of reagents [176, 177] and often beneficial as clean and recyclable reagents [178]. The two most often utilized reagents are 2-Iodoxybenzoic (IBX) acid and 1,1,1-triacetoxy-1,1-dihydro-1,2-benziodoxol-3(1H)-one (Dess–Martin periodinane, DMP) (see Scheme 7). These

reagents are mild and selective and are useful for a wide range of processes.

Finally, the electroiododofluorination of alkynes and alkenes has been reported [179]. The process occurs with high regioselectivity and is based on the anodic formation of an iodonium ion in the presence of iodide and fluoride.

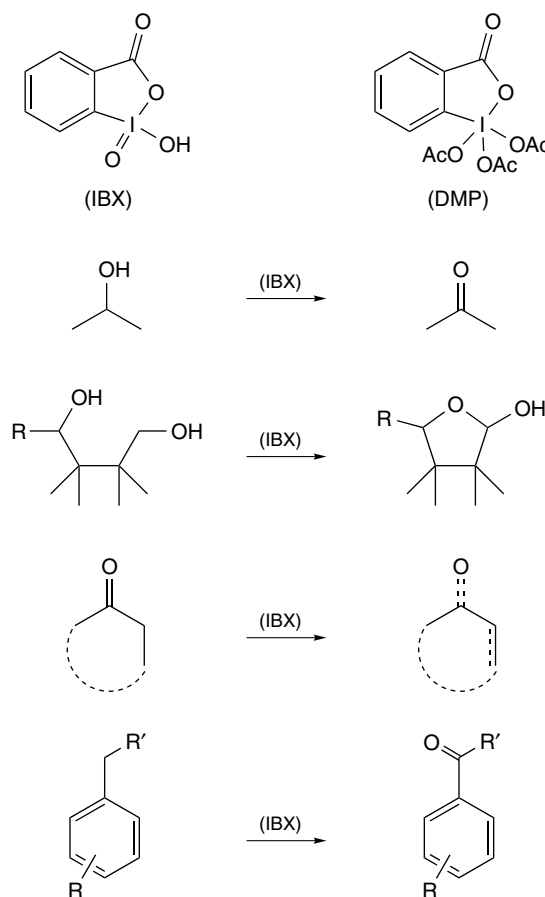
9.5.4

Miscellaneous Methods and Applications Involving Iodine Redox Systems

In dye sensitized solar cells (or “Grätzel cells” [180, 181]), a redox mediator is required to allow charges to be transported from the mesoporous and light sensitive TiO_2 film to the cathode. Although other systems have been studied, the equilibrium potential, mobility, and stability of the I_3^-/I^- system are most suitable for this application and most cells developed to date employ the iodine redox system in an organic solvent environment.

Iodine-based power storage devices have been developed by exploiting the ability of iodine to form charge transfer complexes [182]. Benzidine–iodine charge transfer complexes in polymer membranes are investigated and the electrode reaction is established. Much more fundamental studies of the formation and electrochemical reactivity of phenazine–iodine charge transfer complexes have been reported by Galus and coworkers [183]. Different types of electrochemical experiments and the Gibbs free energy of the phenazine–iodine complex are reported. In pellets formed with graphite powder, surprisingly fast mass transport was observed under applied potential conditions. Experiments as a function of thickness of the graphite/phenazine–iodine layer indicate that the electrochemical process occurs throughout the film. Charge transfer

Scheme 7 Iodanes and their application in oxidation processes.



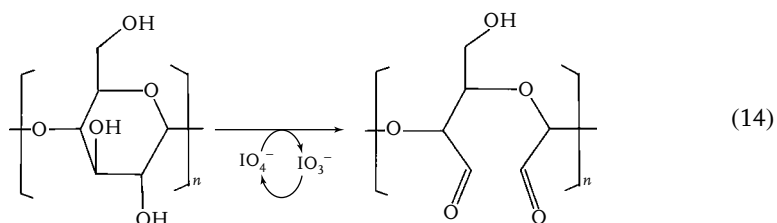
complexes formed from phenothiazines and iodine have been studied by cyclic voltammetry [184].

Similar to chlorine and bromine, iodine may be employed as a reagent for etching semiconductor surfaces. The kinetic study of the etching of InP in iodine solutions has been reported by Vermeir et al. [185]. Single crystal surfaces in contact with iodine solution were studied and a particularly slow rate of etching at (111) surfaces was observed. An interaction of electrochemical and iodine etching processes was suggested.

9.5.5

Application of Iodine as a Redox Mediator in Electroanalysis

Iodine has the ability to catalyze many redox processes that are otherwise kinetically extremely slow. The detection and determination of As(III) in the form of arsenite is an important problem in the context of drinking water supply. The direct electrochemical As(III)/As(V) oxidation at various types of electrodes is not possible. However, in the presence of electrogenerated iodine, the As(III)/As(V) oxidation



can be observed [186]. The mechanism and kinetics of this process have been studied and the resulting process allows the sensitive determination of As(III) in aqueous samples.

The oxidation of sulfite and thiosulfate becomes facile in the presence of iodide and novel disposable microband sensor electrodes have been developed by Williams and coworkers [187] to allow fast amperometric determination. A similar approach was proposed for the determination of sulfite in wine [188]. In this method, a coulometric titration is carried out in which S(IV) is indirectly oxidized to S(VI). Speciation of SO_2 and sulfite was achieved down to micromolar levels. Sulfide and hydrogen sulfide can be determined electrochemically in the presence of an iodide mediator [189]. This process may be further enhanced at elevated temperatures.

Drugs such as 2-thiobarbituric acid are oxidized in the presence of iodide mediators. In aqueous media, an electroiodination process occurs and the resulting voltammetric signal allows quantitative determination [190]. A similar methodology with a limit of detection at ca. $40 \mu\text{M}$ level has been developed for barbiturates [191]. Also, catechin as a model system for polyphenols was studied in the presence of an iodide redox mediator [192].

Similar to iodide, periodates IO_4^- are also very useful redox mediator systems in the presence of aliphatic alcohols and carbohydrates. For example, the C–C bond

fission process resulting from the oxidation of vicinal dihydroxy compounds is of considerable interest in both electrosynthesis [193] and in electroanalysis (Eq. 14).

Torimura et al. [194] developed an analytical approach capable of determining subnanomolar amounts of carbohydrates based on the indirect detection of iodate, IO_3^- , at a glassy carbon electrode. The method was applied as a postcolumn detection system for HPLC separation.

9.5.6

Sensors for Iodine and Iodide

The gas phase detection of iodine vapor with an electrochemical probe has been investigated [195]. The $\text{Ag}|\text{AgI}|\text{Au}$ electrochemical cell was observed to be sensitive to interference from both oxygen and humidity. A sensor based on a $\text{Ag}|\text{Ag}(\text{Cs})\text{I}|$ graphite electrode system has been reported by Sola et al. [196]. Temperature effects were studied and the effect of CsI doping of the AgI explored to widen the working temperature range.

Iodine and iodine derivatives are ubiquitous in nature and a report describing the determination of iodine in environmental and biological samples has been published [197]. Electrochemical techniques are important, in particular, for inorganic iodine species in aqueous media. The direct detection of iodine by differential pulse and stripping voltammetry has been reported

by Tian et al. [198]. Submicromolar detection limits for determinations in aqueous media and at platinum electrodes were observed. The biamperometric determination of iodide and iodate has been described by Bozina et al. [199] and the working potential range and pH were optimized. The flow-injection analysis of iodate in table salt by electrochemical detection at glassy carbon electrodes was developed by Jakmunee et al. [200]. Finally, the effect of a layer of lecithin on the electrochemical behavior of iodine at a glassy carbon electrode was studied by Karabaliev et al. [201]. In this work, a thin monolayer-type film of the lipid was formed at the electrode|solution interface and the behavior of the lipid membrane as a function of potential and type of redo system was explored. Strong time-dependent relaxation effects due to membrane reorganization processes were observed.

The determination of iodide with ion-selective electrodes is possible with commercial sensors often based on ion conducting $\text{Ag}_2\text{S}-\text{AgI}$ solid membranes [57]. A PVC membrane-based sensor employing a silver complex with thiourea derivatives has been reported by El Aamrani et al. [202]. Interference from thiocyanate and bromide was investigated and a limit of detection in the nanomolar range was determined. A study assessing the performance

of different types of solid ion conducting membranes in flow-injection analysis has been published [203]. A new ion-selective electrode for triiodide, I_3^- , has been investigated by Suzuki et al. [204] A PVC-based membrane with a Mn(II) tetraphenylporphyrin complex incorporated was employed. The electrode was observed to be highly specific and sensitive, down into a micromolar concentration range. Finally, a review of the surface study of ion-selective electrodes for iodide determination by Cattrall and Demarco has appeared [205] with detailed information about the surface structure, sensitivity, and morphology – response time correlation for a range of ion-selective electrode systems.

9.6

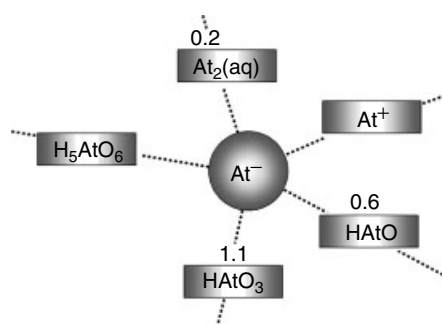
The Electrochemistry of Astatine

9.6.1

Introduction

Astatine (from the Greek “astatos” unstable) is highly unstable and radioactive. It was synthesized in 1940 by D. R. Corson, K. R. MacKenzie, and E. Segre at the University of California by bombarding bismuth with α -particles. The resulting $^{209-211}\text{At}$ isotopes are relatively long-lived

Scheme 8 Redox states, reversible standard potentials (in acidic aqueous environment), and applications of astatine [14].



and can be distilled from the target by heating in air. Astatine occurs naturally as a fission product in uranium decay. The total amount of astatine present in the earth's crust is less than 50 g.

Astatine has properties very similar to those of iodine, but has a more metallic character. The oxidation of astatide to astatine occurs at a potential ca. 0.4 V less positive compared to that for the oxidation of iodine. Fundamental information about the redox chemistry of astatine is available in an earlier review [158] and standard data collections [14]. A summary of the approximate standard potentials and known redox states is given in Scheme 8.

9.6.2

Electrochemical Studies

Only limited information about the electrochemical properties of astatine is available. The formation of a singly positively charged cation, At^+ , in aqueous and other solvent environments has been observed. A study in a nitric acid environment investigated the adsorption into ion exchange materials of this cation [206]. In a similar study in aqueous perchloric acid, the mobility of At^+ was found to change with pH and the presence of a strongly water bound species, $\text{At}(\text{H}_2\text{O})_2^+$, with a $\text{p}K_{\text{A}}$ of ca. 1.5 was proposed [207].

References

1. D. Pletcher, F. C. Walsh, *Industrial Electrochemistry*, Chapman & Hall, London, 1982 and references cited therein.
2. N. L. Weinberg, in *Technique of Electroorganic Synthesis, Part II* (Ed.: N. L. Weinberg), Wiley, New York, 1975, pp. 1–82.
3. O. J. Murphy, S. Srinivasan, B. E. Conway, (Eds.), *Electrochemistry in Transition*, Plenum Press, New York, 1992.
4. H. Fees, H. Wendt, in *Technique of Electrochemistry, Part III* (Ed.: N. L. Weinberg), Wiley, New York, 1982, pp. 81–178.
5. D. R. Lide, (Ed.), *CRC Handbook of Chemistry and Physics*, 74th ed., CRC Press, London, 1993.
6. A. F. Hollemann, E. Wiberg, *Inorganic Chemistry*, Academic Press, New York, 2001.
7. Y. Marcus, *Ion Properties*, Marcel Dekker, New York, 1997.
8. G. T. Hefter, *J. Solution Chem.* **1984**, *13*, 457–470.
9. R. T. Myers, *J. Chem. Educ.* **1976**, *53*, 17–19.
10. A. F. Hollemann, E. Wiberg, *Inorganic Chemistry*, Academic Press, New York, 2001, p. 425.
11. A. F. Hollemann, E. Wiberg, *Inorganic Chemistry*, Academic Press, New York, 2001, p. 423.
12. A. F. Hollemann, E. Wiberg, *Inorganic Chemistry*, Academic Press, New York, 2001, p. 424.
13. M. Pourbaix, *Atlas of Electrochemical Equilibria in Aqueous Solutions*, Cebalcor, Brussels, 1974.
14. A. J. Bard, R. Parsons, J. Jordan, (Eds.), *Standard Potentials in Aqueous Solution*, Marcel Dekker, New York, 1985.
15. V. Gutmann, (Ed.), *Halogen Chemistry*, Academic Press, New York, 1967.
16. A. J. Bard, (Ed.), *Encyclopedia of Electrochemistry of the Elements*, Marcel Dekker, New York, 1973, Vol. I.
17. A. J. Bard, (Ed.), *Encyclopedia of Electrochemistry of the Elements*, Marcel Dekker, New York, 1975, Vol. IV.
18. H. Moissan, *C. R. Acad. Sci.* **1886**, *102*, 1534.
19. J. W. Mellor, *Comprehensive Treatise on Inorganic Chemistry*, Longmans, London, 1922, p. 5, Vol. 2.
20. W. Wirth, C. Gloxhuber, *Toxikologie*, Thieme Verlag, Stuttgart, 1985.
21. D. Pletcher, F. C. Walsh, *Industrial Electrochemistry*, Chapman & Hall, London, 1982, p. 249.
22. D. J. Adams, P. J. Dyson, S. J. Tavener, *Chemistry in Alternative Reaction Media*, Wiley, New York, 2004.
23. C. Reichardt, *Solvents and Solvent Effects in Organic Chemistry*, Wiley-VCH, Weinheim, 2003.
24. M. A. Danielson, J. J. Falke, *Ann. Rev. Biophys. Biomol. Struct.* **1996**, *25*, 163–195.

25. H. Wendt, G. Kreysa, *Electrochemical Engineering*, Springer, Berlin, 1999, p. 315.
26. D. Pletcher, F. C. Walsh, *Industrial Electrochemistry*, Blackie Academic, London, 1993, p. 249 and references cited therein.
27. F. Lantelme, H. Groult, *J. Electrochem. Soc.* **2004**, *151*, D121–D126.
28. H. Groult, D. Devilliers, F. Lantelme et al., *J. Electrochem. Soc.* **2002**, *149*, E485–E492.
29. H. Groult, *J. Fluorine Chem.* **2003**, *119*, 173–189.
30. D. Pletcher, F. C. Walsh, *Industrial Electrochemistry*, Blackie Academic, London, 1993, p. 249f.
31. W. V. Childs, L. Christensen, F. W. Klink, in *Organic Electrochemistry* (Eds.: H. Lund, M. M. Baizer), Marcel Dekker, New York, 1991, p. 1103f.
32. D. Pletcher, F. C. Walsh, *Industrial Electrochemistry*, Blackie Academic, London, 1993, p. 319.
33. S. N. Misra, A. D. Jethva, M. S. Gohil et al., *Rev. Chem. Eng.* **2003**, *19*, 357–385.
34. H. S. Tao, M. G. Li, L. F. Wu et al., *Prog. Chem.* **2004**, *16*, 213–219.
35. M. Noel, V. Suryanarayanan, *J. Appl. Electrochem.* **2004**, *34*, 357–369.
36. M. Takehara, S. Watanabe, N. Nanbu et al., *Synth. Commun.* **2004**, *34*, 1367–1375.
37. B. Fang, H. Tao, X. Kan et al., *Heterocyclic Commun.* **2004**, *10*, 305–306.
38. B. A. Shainyan, Y. S. Danilevich, A. A. Grigor'eva et al., *Russ. J. Org. Chem.* **2003**, *39*, 1581–1586.
39. V. A. Matalin, G. I. Kaurova, D. D. Moldavskiy et al., *Fluorine Notes* **2003**, *6*, 31.
40. H. Horio, K. Momota, K. Kato et al., *Electrochim. Acta* **1996**, *41*, 1611–1618.
41. K. Uneyama, in *New Challenges in Organic Electrochemistry* (Ed.: T. Osa), Gordon & Breach, Amsterdam, 1998, pp. 221–235.
42. N. N. Greenwood, *Revs. Pure Appl. Chem. (Australia)* **1951**, *1*, 84–120 and references cited therein.
43. N. Yoneda, *J. Fluorine Chem.* **2004**, *125*, 7–17.
44. K. Uneyama, in *New Challenges in Organic Electrochemistry* (Ed.: T. Osa), Gordon & Beach Science Publications, Amsterdam, 1998, p. 226f.
45. T. Fuchigami, T. Fujita, *J. Org. Chem.* **1994**, *51*, 7190.
46. A. T. Kuhn, in *Encyclopedia of Electrochemistry of the Elements* (Ed.: A. J. Bard), Marcel Dekker, New York, 1975, p. 43f, Vol. IV.
47. H. Schmidt, H. D. Schmidt, *J. Prakt. Chem.* **1955**, *274*, 105.
48. F. Okino, Y. Kawaguchi, H. Touhara et al., *J. Fluorine Chem.* **2004**, *125*, 1715–1722.
49. F. Okino, H. Shibata, S. Kawasaki et al., *Electrochem. Solid State Lett.* **1999**, *2*, 382–384.
50. L. M. Da Silva, L. A. De Faria, J. F. C. Boodts, *Electrochim. Acta* **2003**, *48*, 699–709.
51. L. M. Da Silva, M. H. P. Santana, J. F. C. Boodts, *Quim. Nova* **2003**, *26*, 880–888.
52. W. Moritz, L. Bartholomäus, *Electrochim. Acta* **2000**, *46*, 271–277.
53. L. Bartholomäus, W. Moritz, *Solid State Ionics* **2000**, *132*, 31–37.
54. W. Moritz, L. Bartholomäus, U. Roth et al., *Anal. Chim. Acta* **1999**, *393*, 49–57.
55. R. Sathiyamoorthi, R. Chandrasekaran, T. Mathanmohan et al., *Sens. Actuators, B* **2004**, *B99*, 336–339.
56. S. X. Shi, Z. G. Zhu, R. Suo et al., *Anal. Sci.* **2003**, *19*, 671–673.
57. R. W. Cattrall, *Chemical Sensors*, Oxford University Press, Oxford, 1997.
58. M. Bralic, N. Radic, S. Brinic et al., *Talanta* **2001**, *55*, 581–586.
59. J. Wang, *Analytical Electrochemistry*, Wiley, New York, 2000, p. 157.
60. D. Pletcher, F. C. Walsh, *Industrial Electrochemistry*, Chapman & Hall, London, 1982, p. 177f.
61. D. E. Danly, C. J. H. King, in *Organic Electrochemistry* (Ed.: H. Lund, M. M. Baizer), Marcel Dekker, New York, 1991, p. 1285f.
62. T. Mussini, G. Faita, in *Encyclopedia of Electrochemistry of the Elements*, (Ed.: A. J. Bard), Marcel Dekker, New York, 1973, pp. 1–56, Vol. I.
63. D. Pletcher, F. C. Walsh, *Industrial Electrochemistry*, Chapman & Hall, London, 1982, p. 173f.
64. H. Wendt, G. Kreysa, *Electrochemical Engineering*, Springer, Berlin, 1999, p. 291f.
65. Marc. Reisch, *Chem. Eng. News* **2004**, 82(27), 5.
66. D. Pletcher, F. C. Walsh, *Industrial Electrochemistry*, Chapman & Hall, London, 1982.
67. S. Trasatti, *Electrochim. Acta* **2000**, *45*, 2377–2385.
68. V. V. Tilak, C. P. Chem, *Proc. Electrochem. Soc.* **1995**, 95–11, 32–50.

69. Y. G. Chirkov, V. I. Rostokin, *Russ. J. Electrochem.* **2002**, 38, 280–284.
70. C. E. Vallet, B. V. Tilak, R. A. Zuhr et al., *Proc. Electrochem. Soc.* **1995**, 95–11, 338–360.
71. J. L. Fernandez, M. R. Gennero de Chialvo, A. C. Chialvo, *Electrochim. Acta* **2002**, 47, 1129–1136.
72. V. Panic, A. Dekanski, S. Milonjic et al., *Electrochim. Acta* **2000**, 46, 415–421.
73. N. Vinokur, B. Miller, Y. Avyigal et al., *J. Electrochem. Soc.* **1996**, 143, L238–L240.
74. F. Beck, W. Kaiser, H. Krohn, *Electrochim. Acta* **2000**, 45, 4691–4695.
75. S. Ferro, A. De Battisti, I. Duo et al., *J. Electrochem. Soc.* **2000**, 147, 2614–2619.
76. R. Ferrigno, C. Comninellis, V. Reid et al., *Electrochim. Acta* **1999**, 44, 2871–2878.
77. F. Montilla, E. Morallon, I. Duo et al., *Electrochim. Acta* **2003**, 48, 3891–3897.
78. H. Bergmann, T. Iourtchouk, K. Schoeps, *GDCh-Monographien* **2001**, 23, 155–162.
79. H. Lund, M. M. Baizer, *Organic Electrochemistry*, Marcel Dekker, New York, 1991, p. 1094.
80. G. K. Liu, B. Ren, R. A. Gu et al., *Chem. Phys. Lett.* **2002**, 364, 593–598.
81. T. Raju, C. A. Basha, V. Krishnan et al., *Bull. Electrochem.* **1997**, 13, 206–208.
82. L. Appelbaum, D. Danovich, G. Lazanes et al., *J. Electroanal. Chem.* **2001**, 499, 39–47.
83. S. Krishnamoorthy, R. K. Srinivasan, M. Noel, *Bull. Electrochem.* **2000**, 16, 544–550.
84. S. Milisavljevic, R. D. Vukicevic, *J. Serb. Chem. Soc.* **2004**, 69, 941–947.
85. S. Maki, K. Konno, S. Ohba et al., *Tetrahedron Lett.* **1998**, 39, 3541–3542.
86. K. A. Maksimov, K. M. Balaeva, Y. A. Yuzbekov et al., *Russ. J. Appl. Chem.* **1995**, 68, 524–526.
87. Y. V. Saltykov, T. A. Kenova, V. L. Kornienko, *Russ. J. Electrochem.* **1996**, 32, 99–100.
88. I. Y. Zhukova, S. A. Pozhidaeva, E. S. Kagan et al., *Zhur. Organ. Khim.* **1993**, 29, 751–757.
89. V. A. Petrosyan, B. V. Lyalin, A. V. Smetanin, *Bull. Acad. Sci. USSR Div. Chem. Sci.* **1990**, 39, 542–546.
90. V. G. Malaev, V. A. Ilyushin, *Bull. Acad. Sci. USSR Div. Chem. Sci.* **1989**, 38, 406–407.
91. D. A. Ashurov, A. D. Duniyamiliev, A. V. Dzhabbarov, *J. Appl. Chem. USSR* **1991**, 64, 407–408.
92. M. Novak, C. Visy, *Electrochim. Acta* **1983**, 28, 507–510.
93. C. Visy, M. Novak, *J. Electroanal. Chem.* **1990**, 296, 571–581.
94. Y. Takasu, M. Masaki, Y. Matsuda et al., *J. Appl. Electrochem.* **1986**, 16, 304–306.
95. K. Scott, C. Odouza, W. Hui, *Chem. Eng. Sci.* **1992**, 47, 2957–2962.
96. M. V. B. Zanoni, J. J. Sene, H. Selcuk et al., *Environ. Sci. Technol.* **2004**, 38, 3203–3208.
97. D. J. Caruana, S. P. McCormack, *Electrochem. Commun.* **2002**, 4, 780–786.
98. M. Vennekamp, J. Janek, *Z. Anorg. Allg. Chem.* **2003**, 629, 1851–1862.
99. M. Vennekamp, J. Janek, *J. Electrochem. Soc.* **2003**, 150, C723–C729.
100. E. B. Anderson, E. J. Taylor, G. G. A. Wilemski, *J. Power Sources* **1994**, 47, 321–328.
101. P. Gründler, *Chemische Sensoren*, Springer, Berlin, 2004, p. 222.
102. E. R. Lowe et al., *Anal. Bioanal. Chem.* **2005**, 382, 1169–1174.
103. E. Sucman, J. Bednar, *Electroanalysis* **2003**, 15, 866–871.
104. J. Wang, *Analytical Electrochemistry*, Wiley, New York, 2000, p. 159.
105. M. M. G. Antonisse, D. N. Reinhoudt, *Electroanalysis* **1999**, 11, 1035–1048.
106. K. A. Halhouli, A. I. Aly, B. M. Abu-Ashour, *Chemosphere* **1999**, 38, 3181–3192.
107. F. C. Walsh, *Pure Appl. Chem.* **2001**, 73, 1819–1837.
108. K. Scott, W. Taama, B. R. Williams, *J. Appl. Electrochem.* **1998**, 28, 259–268.
109. A. Salimi, V. Alizadeh, H. Hadadzadeh, *Electroanalysis* **2004**, 16, 1984–1991.
110. T. Mussini, G. Faita, in *Encyclopedia of Electrochemistry of the Elements* (Ed.: A. J. Bard), Marcel Dekker, New York, 1973, pp. 57–90, Vol. I.
111. D. Pletcher, F. C. Walsh, *Industrial Electrochemistry*, Chapman & Hall, London, 1982, p. 379.
112. V. Vojinovic, S. Mentus, V. Komnenic, *J. Electroanal. Chem.* **2003**, 547, 109–113.
113. D. Halasz, C. Visy, A. Szucs et al., *React. Kinet. Catal. Lett.* **1992**, 48, 177–188.
114. B. E. Conway, Y. Phillips, S. Y. Qian, *J. Chem. Soc., Faraday Trans.* **1995**, 91, 283–293.

115. A. Wu, Y. Sun, *Huaxue Chuanganqi* **1998**, 18, 70–73.
116. A. Wu, Y. Sun, *Huaxue Gongye Yu Gongcheng (Tianjin)* **1999**, 16, 270–274.
117. M. D. Levi, E. Y. Pisarevskaya, *Elektrokhi-miya* **1991**, 27, 1267–1274.
118. D. Pletcher, F. C. Walsh, *Chem. Ind.* **2001**, 18, 564.
119. I. Izumi, J. Sato, N. Iwashita et al., *Synth. Met.* **1995**, 75, 75–77.
120. N. Vinokur, B. Miller, Y. Avyigal et al., *Proc. Electrochem. Soc.* **1996**, 96–9, 149–158.
121. J. Malyszko, T. Niewiadomski, *Pol. J. Chem.* **1993**, 67, 1637–1645.
122. T. Ogamino, K. Mori, S. Yamamura et al., *Electrochim. Acta* **2004**, 49, 4865–4869.
123. D. Nematollahi, N. Akaberi, *Bull. Electrochem.* **2001**, 17, 61–64.
124. H. Tanaka, Y. Kawakami, M. Kuroboshi et al., *Heterocycles* **2001**, 54, 825–831.
125. J. Nokami, M. Osafune, Y. Ito et al., *Chem. Lett.* **1999**, 28, 1053–1054.
126. D. Vasudevan, C. A. Basha, *Bull. Electrochem.* **2000**, 16, 341–344.
127. D. Vasudevan, P. N. Anantharaman, *J. Appl. Electrochem.* **1993**, 23, 808–812.
128. J. Malyszko, E. Malyszko, E. Rutkowska-Ferchichi et al., *Anal. Chim. Acta* **1998**, 376, 357–364.
129. M. Mitani, T. Kobayashi, K. Koyama, *Chem. Commun.* **1991**, 1418–1419.
130. I. F. Abdullin, N. N. Chernysheva, G. K. Budnikov, *J. Anal. Chem.* **2002**, 57, 629–631.
131. J. Volke, F. Liska, *Electro-Chemistry in Organic Synthesis*, Springer, Berlin, 1994, p. 132.
132. M. M. Baizer, in *Organic Electrochemistry* (Ed.: H. Lund, M. M. Baizer), Marcel Dekker, New York, 1991, p. 1428.
133. J. Simonet, in *Organic Electrochemistry* (Ed.: H. Lund, M. M. Baizer), Marcel Dekker, New York, 1991, p. 1243.
134. G. D. Allen, M. C. Buzzeo, C. Villagran et al., *J. Electroanal. Chem.* **2005**, 575, 311–320.
135. G. D. Allen, M. C. Buzzeo, L. G. Davies et al., *J. Phys. Chem. B* **2004**, 108, 16322–16327.
136. J. Salazar, R. Dorta, *Synlett* **2004**, 1318–1320.
137. C. Chiappe, D. Pieraccini, *J. Org. Chem.* **2004**, 69, 6059–6064.
138. J. Zhang, P. R. Unwin, *Phys. Chem. Chem. Phys.* **2003**, 5, 3979–3983.
139. P. M. M. C. Bressers, M. Plakman, J. J. Kelly, *J. Electroanal. Chem.* **1996**, 406, 131–137.
140. K. Strubbe, W. P. Gomes, *J. Electrochem. Soc.* **1993**, 140, 3301–3305.
141. M. T. van Meersbergen, L. Lorenzen, J. S. J. van Deventer, *Miner. Eng.* **1993**, 6, 1067–1079.
142. S. H. Ge, B. L. Yi, H. M. Zhang, *J. Appl. Electrochem.* **2004**, 34, 181–185.
143. S. H. Ge, B. L. Yi, Y. Fu et al., *Dianyuan Jishu* **2002**, 26, 355–358.
144. I. Vogel, A. Moebius, *Electrochim. Acta* **1991**, 36, 1403–1408.
145. J. S. Daniel, S. Solomon, R. W. Portmann et al., *J. Geophys. Res. Atmos.* **1999**, 104, 23871–23880.
146. Y. Niizeki, S. Shibata, *Solid State Ionics* **1997**, 104, 159–162.
147. J. Przyluski, C. Budrowski, *Synth. Met.* **1991**, 41, 1163.
148. D. Pletcher, F. C. Walsh, *Industrial Electrochemistry*, Chapman & Hall, London, 1982, p. 607f.
149. I. M. P. L. V. O. Ferreira, J. L. F. C. Lima, L. S. M. Rocha, *Fresenius' J. Anal. Chem.* **1993**, 347, 314–319.
150. T. Masadome, Y. Asano, T. Nakamura, *Talanta* **1999**, 50, 595–600.
151. M. R. Ganjali, M. Tahami, T. Poursaberi et al., *Anal. Lett.* **2003**, 36, 347–360.
152. M. Shamsipur, S. Rouhani, A. Mohajeri et al., *Anal. Chim. Acta* **2000**, 418, 197–203.
153. O. K. Stefanova, Z. S. Alagova, G. A. Khripun, *Russ. J. Appl. Chem.* **1995**, 68, 1212–1213.
154. C. Zhu, G. M. Hieftje, *Anal. Chim. Acta* **1992**, 256, 97–103.
155. X. W. Zheng, Y. Mei, Z. J. Zhang, *Anal. Chim. Acta* **2001**, 440, 143–149.
156. P. Tomcik, D. Bustin, I. Novotny, *Chem. Listy* **2001**, 95, 18–21.
157. A. F. Holleman, E. Wiberg, N. Wiberg, *Inorganic Chemistry*, Academic Press, New York, 2001, p. 416.
158. P. G. Desideri, L. Lepri, D. Heimler, in *Encyclopedia of Electrochemistry of the Elements* (Ed.: A. J. Bard), Marcel Dekker, New York, 1973, pp. 91–155, Vol. I.
159. A. F. Holleman, E. Wiberg, N. Wiberg, *Inorganic Chemistry*, Academic Press, New York, 2001, p. 420.
160. W. Zhang, H. Zha, B. Yao et al., *Talanta* **1998**, 46, 711–716.

161. R. P. Akkermans, F. L. Qiu, S. L. Roberts et al., *J. Phys. Chem. B* **1999**, *103*, 8319–8327.
162. V. Mirceski, R. Gulaboski, F. Scholz, *Electrochem. Commun.* **2002**, *4*, 814–819.
163. V. Mirceski, F. Scholz, *J. Electroanal. Chem.* **2002**, *522*, 189–198.
164. F. Schynowski, W. Schwack, *Chemosphere* **1996**, *33*, 2255–2262.
165. L. Ebersson, J. H. P. Utley, O. Hamerich, in *Organic Electrochemistry* (Ed.: H. Lund, M. M. Baizer), Marcel Dekker, New York, 1991, p. 1094f.
166. M. J. Peacock, D. Pletcher, *Tetrahedron Lett.* **2000**, *41*, 8995–8998.
167. V. L. Shirokii, D. A. Rudakov, A. V. Bazhanov et al., *Russ. J. Electrochem.* **2004**, *40*, 212–214.
168. F. Barba, M. N. Elinson, J. Escudero et al., *Electrochim. Acta* **1998**, *43*, 973–976.
169. D. Nematollahi, A. Afkhami, M. A. Zolfigol et al., *Bull. Electrochem.* **2000**, *16*, 89–91.
170. I. Nishiguchi, O. Kanbe, K. Itoh et al., *Synlett* **2000**, 89–91.
171. M. J. Zacuto, D. W. Cai, *Tetrahedron Lett.* **2005**, *46*, 447–450.
172. M. N. Elinson, S. K. Feducovich, A. A. Zakharenkov et al., *Mendeleev Commun.* **1999**, 20–22.
173. S. Quideau, L. Pouysegu, D. Deffieux et al., *Arkivoc* **2003**, 106–119.
174. V. V. Zhdankin, *Curr. Org. Synth.* **2005**, *2*, 121–145.
175. G. F. Koser, *Adv. Heterocycl. Chem.* **2004**, *86*, 225–292.
176. T. Wirth, *Angew. Chem., Int. Ed. Engl.* **2001**, *40*, 2812–2814.
177. V. V. Zhdankin, D. N. Litvinov, A. Y. Kopyosov et al., *Chem. Commun.* **2004**, 106–107 and references cited therein.
178. H. Tohma, A. Maruyama, A. Maeda et al., *Angew. Chem., Int. Ed. Engl.* **2004**, *43*, 3595–3598.
179. S. Kobayashi, M. Sawaguchi, S. Ayuba et al., *Synlett* **2001**, 1938–1940.
180. N. Papageorgiou, W. F. Maier, M. Gratzel, *J. Electrochem. Soc.* **1997**, *144*, 876–884.
181. P. J. Cameron, L. M. Peter, S. Hore, *J. Phys. Chem. B* **2005**, *109*, 930–936 and references cited therein.
182. O. N. Srivastava, R. A. Singh, *Bull. Electrochem.* **1999**, *15*, 372–375.
183. A. Szadkowska, P. K. Wrona, Z. Galus, *J. Phys. Org. Chem.* **2003**, *16*, 661–668.
184. R. Singh, R. A. Singh, *Mol. Cryst. Liq. Cryst. Sci. Technol., Sect. C* **1998**, *9*, 343–362.
185. I. E. Vermeir, W. P. Gomes, *J. Electrochem. Soc.* **1996**, *143*, 1319–1325.
186. G. Hignett, J. D. Wadhawan, N. S. Lawrence et al., *Electroanalysis* **2004**, *16*, 897–903.
187. H. Rajantie, D. E. Williams, *Analyst* **2001**, *126*, 1882–1887.
188. D. Lowinsohn, M. Bertotti, *Food Add. Contam.* **2001**, *18*, 773–777.
189. A. K. Rzaeva, M. M. Asadov, A. L. Shabanov, *Azerbaijdzhanskii Khim. Z.* **2002**, 17–20.
190. D. Nematollahi, J. Rahimi, M. Hesari et al., *Iran. J. Chem. Chem. Eng. Int. Ed.* **2001**, *20*, 90–95.
191. D. Nematollahi, M. Hesari, *J. Anal. Chem.* **2001**, *56*, 1109–1112.
192. V. Castaignede, H. Durliat, M. Comtat, *Anal. Lett.* **2003**, *36*, 1707–1720.
193. J. Volke, F. Liska, *Electrochemistry in Organic Synthesis*, Springer, Berlin, 1994.
194. M. Torimura, K. Kano, T. Ikeda et al., *J. Chromatogr., A* **1997**, *790*, 1–8.
195. V. G. Goffman, B. U. Shaimerodinov, I. M. Kotelkin et al., *Russ. J. Electrochem.* **1993**, *29*, 1324–1326.
196. M. E. Sola, H. G. Rotstein, J. C. Bazan, *J. Solid State Electrochem.* **2002**, *6*, 279–283.
197. J. S. Edmonds, M. Morita, *Pure Appl. Chem.* **1998**, *70*, 1567–1584.
198. Y. Tian, W. B. Song, Y. X. Jiang et al., *Chem. J. Chin. Univ.* **1999**, *20*, 28–31.
199. T. V. Bozina, O. E. Ruvinskii, *J. Anal. Chem.* **2003**, *58*, 1069–1072.
200. J. Jakmunee, K. Grudpan, *Anal. Chim. Acta* **2001**, *438*, 299–304.
201. M. Karabaliev, V. Kochev, *Electrochem. Commun.* **2001**, *3*, 367–371.
202. F. Z. El Aamrani, J. Garcia-Raurich, A. Sastre et al., *Anal. Chim. Acta* **1999**, *402*, 129–135.
203. D. E. Davey, D. E. Mulcahy, G. R. O'Connell, *Electroanalysis* **1996**, *8*, 274–279.
204. H. Suzuki, H. Nakagawa, M. Mifune et al., *Anal. Sci.* **1993**, *9*, 351–354.
205. R. W. Cattrall, R. Demarco, *Select. Electrode Rev.* **1992**, *14*, 169–193.
206. F. C. Wang, Y. V. Norseev, V. A. Khalkin et al., *Radiokhimiya* **1963**, *5*, 351–355.
207. M. Milanov, V. Doberenz, V. A. Khalkin et al., *J. Radioanal. Nucl. Chem.* **1984**, *83*, 291–299.

10 Silicon

*Marius Chemla**

Université Pierre et Marie Curie, Paris, Cedex 05, France

*Died in summer 2005; contact: Pr. Didier Devilliers, Université Pierre et Marie Curie, Paris Cedex, France.

10.1	Introduction	305
10.1.1	Thermodynamics of Silicon Compounds	306
10.1.2	Electrochemical Reactions of Si Compounds Dissolved in the Electrolyte	307
10.2	The Silicon Electrodes	308
10.2.1	Prominent Role of the Space Charge Layer	309
10.2.2	The Flat Band Potential of Silicon	310
10.2.3	Electrochemical Impedance Spectroscopy (EIS) of the Space Charge Layer	312
10.2.4	Linear Sweep Voltammetry of Si Electrode in HF Solutions	314
10.2.5	Formation of Porous Silicon	318
10.2.6	Growth of Anodic Oxide Layers	320
10.3	Chemical/Electrochemical Reactions at Open-circuit Potential	322
10.3.1	Oxide Growth by the RCA Cleaning Process	322
10.3.2	Etching of Monocrystalline Silicon	324
10.3.3	Electroless Nucleation of Metal Contaminants on Si Surface	327
10.3.4	Electrochemical Photovoltaic Cells	329
	References	331

10.1 Introduction

In the periodic table of the elements, the position of silicon is in the fourth column, which, for the light elements, is the frontier between metals and nonmetals. While the characteristics of a metal are well defined by their electronic structure, atoms of this group possess four valence electrons and form an infinitely spreading network of the diamond type with covalent tetrahedral bonding. In this group, silicon (like germanium) is a typical semiconductor. In this material, the energy levels of electrons are divided into a lower almost filled valence band and an upper unfilled conductance band separated by a not too large energy gap. For silicon at 300 K, the width of the band gap $E_C - E_V$ is 1.12 eV. The average energy level of electrons corresponding to the equilibrium distribution is called the *Fermi level*, which, in contrast with metals, is situated within the band gap.

The applications of silicon in the electronics industry are so important that the major part of this report will be devoted to the electrochemistry of the elemental silicon crystals used as semiconductors. In fact, the extremely efficient surface treatment of Si wafers needed for the construction of ultra large-scale

integration (ULSI) circuits is based on the “wet process” originally developed by Kern and Puotinen at RCA company. This most widespread technology employs oxidizing reactants in alkaline as well as acidic aqueous solutions, the mechanism of the reactions being strictly electrochemical. Moreover, electrochemical corrosion and etching occur in HF solutions, which are often used in processing. In addition, anodic oxide growth was proposed to build up insulating layers on silicon. The formation of porous silicon layers was also investigated for its luminescence properties. Finally, electrochemical reactions are often involved for the solar energy conversion in the semiconductor liquid-junction solar cells (SLJSC). In the fundamental studies undertaken for the interpretation of all these processes, it is important to recall that the electrochemical charge transfer at the interface must account for the space charge distribution within the semiconductor, and its dependence on the applied potential. Moreover, when the purpose is to identify the specific properties of n- or p-type semiconductors, it is necessary to carry the experiments in a light sheltered device.

The electrical conductance of semiconductors is derived from the mobility of charge carriers, holes h^+ in the valence band and free electrons e^- in the

conductance band. According to the Fermi energy distribution function, the number of negative n and positive p charge carriers at thermal equilibrium is given by the relation analogous to the mass action law:

$$n p = N_C N_V \exp -\frac{E_C - E_V}{kT}, \quad (1)$$

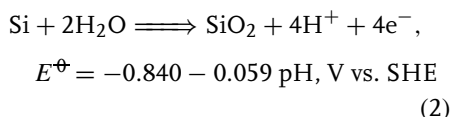
Thus, for high purity silicon at room temperature, the intrinsic carrier density, for h^+ and e^- , is equal to $1.45 \cdot 10^{10} \text{ cm}^{-3}$. But, in all practical uses, the electronic properties of the silicon substrate are changed by doping agents. Doping by electron donors such as phosphorus (5 external electrons) results in the substitution of P atoms in place of Si and generates excess electrons in the conduction band. Alternatively, doping by boron (only 3 external electrons) generates free positive holes in the valence band. These transformations lead easily to higher charge carrier density, generally 10^{15} to 10^{18} cm^{-3} , and thus form n -type or p -type semiconductors in which the concentration of the opposite sign carriers is negligible. When the doping level is more than 10^{18} cm^{-3} , a qualitative change of the semiconductor properties occurs leading to a degeneracy effect, which induces a metallic character. The material is called *degenerated semiconductor*, and the electronic properties are similar to those of a metal.

10.1.1

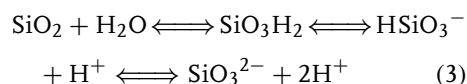
Thermodynamics of Silicon Compounds

Usually, the thermodynamic properties involved in the electrochemical reactions of Si element are presented in the Pourbaix diagram showing the lines where one species is transformed into another as a function of the potential and pH values. In the case of Si, this presentation is not necessary. In fact, the standard

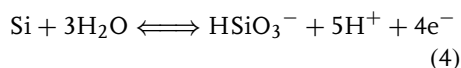
potential of Si in aqueous solutions is extremely negative, so that a bare sample of Si cannot be in equilibrium with any aqueous solution. Theoretical calculations mention the transient formation of SiH_4 , but this hydride is not stable in the presence of water and leads to the generation of SiO_2 . Thus, in the absence of complexing reactants, the electrochemical process gives rise to a silicon oxide layer following the overall reaction written as:



The value of this standard potential is slightly modified depending on the solid oxide structure and reaches -0.857 V for the quartz structure. In most acidic or neutral solutions, this silicon oxide forms a protecting layer. However, when the solution pH is increased, the oxide will give rise to various sparingly soluble compounds due to the following dissociation reactions:

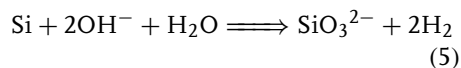


The acidity constants K_1 and K_2 of the silicic acid are equal to 10^{-10} and 10^{-12} respectively. As a result, in the pH range near 10, the reaction (2) could be written as:

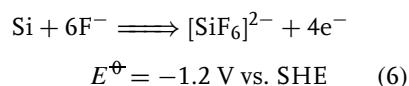


Nevertheless, the calculated standard potential given in Eq. (2) remains valid with a good precision. When pH value is higher than 12, the solubility of silicate ion grows rapidly and then corrosion process

occurs with hydrogen gas evolution:



When the solution contains HF or fluoride species, the oxide layer is rapidly dissolved, and the electrochemical reaction yields soluble complex ions, so that the surface is no longer protected against the corrosion process.



Again, the standard potential is negative enough to induce the mechanism of electrochemical corrosion. We just have to point out that the kinetics of corrosion is very sensitive to the surface structure of the material and the presence of defects or impurities.

Finally, it is worth recalling that the Si element reacts with molecular O_2 to form SiO_2 following an exoenergetic reaction ($\Delta G = -798 \text{ kJ mol}^{-1}$). The main conclusion of these thermodynamic properties is that, in most applications, the Si substrate is always covered with a native oxide protecting layer.

10.1.2

Electrochemical Reactions of Si Compounds Dissolved in the Electrolyte

All the stable Si species in solutions are under the tetravalent oxidation state. No studies of electron transfer between soluble Si compounds can be found in the literature. Several investigations were devoted to the electrochemical deposition of elemental silicon from solute species.

By analogy with the Hall–Heroult process for electrowinning of aluminum, first attempts used molten salt electrolytes at high temperature [1]. Silicon oxide

dissolved in cryolite has been extensively investigated, and the method was able to yield 99.9 to 99.99% pure silicon. A graphite anode was used, and the gases generated by the electrochemical reaction were mixtures of CO and CO_2 . A pilot plant working at 1000°C was built in 1960 and was operated until 1966 with deposition currents up to 3000 A. The major inconvenience with this process is that the silicon is produced as small solid crystals that include particles of electrolyte. In trials to produce silicon above its melting point, the eutectic BaO/ SiO_2 system was used at 1450°C with the addition of BaF_2 to lower the melt viscosity. The purity of Si produced from the barium silicate melts was about 99.98%, close to the quality required to produce 10% efficiency solar cells. Other techniques using silicon fluoride in molten alkali fluorides were proposed for electrowinning or electrorefining, and showed that the production of 99.99% pure silicon could be achieved by pulsed electrolysis.

Finally, the deposition of amorphous silicon (a-Si), interesting both for solar cells and hard protective coatings, can be achieved at temperatures close to ambient using anhydrous aprotic organic solvents. Several electrolyte compositions were used; for example, silicon chlorides or fluorides in tetrahydrofuran/toluene, (alternatively formamide/ethylene glycol); mixed solvents were efficient for the formation of thick chemically stable coatings on metals, and also dendrites, sponge, and powder to produce 99.99% pure silicon ingots after melting.

A large number of studies were undertaken mainly in the period 1960–1990 aiming at the production of solar grade silicon (SGSi) with a purity substantially higher than that of the metallurgical grade silicon (MGSi). Until now, all these experiments

have been done on a small laboratory scale. It is worth recalling that, for the extreme purity required in microelectronics, the starting source of silicon is first transformed into a volatile component such as a chlorosilane, SiCl_4 , SiHCl_3 , or SiH_2Cl_2 , which can be purified by fractional distillation until the level of most impurities is below 1 ppba (part per billion atoms). The elemental granulated Si, generated by chemical vapor decomposition, is used to grow single crystals, which are necessary for highly integrated devices. Usually, the single crystal is obtained by the Czochralski (CZ) method, which consists of slowly pulling a small initial crystal of the proper orientation from a melt contained in a crucible rotating at a suitable rate [2].

10.2

The Silicon Electrodes

Electrochemical properties of silicon single crystals, usually cuts of semiconductor wafers, have to be considered under two distinct respects: (1) As an electrode, silicon is a source of charge carriers, electrons or positive holes, involved in electrochemical reactions, and whose surface concentration is a determining parameter for the rate of charge transfer. (2) As a chemical element, silicon material is also involved in redox transformations such as electroless deposition, oxide generation, and anodic etching, or corrosion processes.

The experimental practice for the study of current/potential characteristics requires the formation of an ohmic contact on the back of the electrode. The simplest technique consists in the application of a very thin layer of Ga–In eutectic liquid alloy, which wets the surface easily. But in the most rigorous method used in production lines, a highly doped 750-nm

layer is generated by implantation, and then an Al–Cu film 1.5 μm thick, deposited by evaporation, is alloyed to the substrate by annealing at 450°C in a $\text{N}_2\text{--H}_2$ reducing atmosphere. Currently, the electrodes are pieces cut in Si wafers, CZ grown, and oriented (100) or (111), moderately doped 10^{15} to 10^{17} cm^{-3} having a resistivity from 15 to 0.1 $\Omega\text{ cm}$. The samples, mirror polished by the producer with a profile RMS (root mean square) value near 0.15–0.20 nm, are preferably cleaned following the RCA technique, which consists of two important steps. First, the surface is treated by a mixture of hydrogen peroxide with aqueous ammonia solution called SC1 (standard clean #1), which is an efficient oxidizing reagent. It transforms most of the organic impurities into soluble compounds, and induces an etching of a few surface atomic layers giving rise to a uniform oxide film completely free of particles. In the second step, a dilute HF solution (DHF) is used to dissolve this oxide layer and leads to a rather stable surface structure made of terminal Si–H bonds.

The behavior of silicon electrodes has been investigated using a wide range of electrochemical techniques, such as the following specific examples:

1. Steady state or dynamic potential and current relationship
2. Current or potential versus time to provide information on transient species
3. Capacitance–potential relationship to reveal the position of semiconductor bands
4. Impedance-frequency spectroscopy to yield the electronic components equivalent circuits
5. Same measurements under illumination to emphasize the effect of the generated minority carriers.

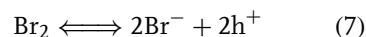
In addition to the electrochemical techniques, many surface analytical techniques are constantly in use, such as ellipsometry for the surface thin oxide thickness, multiple reflection infrared spectroscopy (MIR), and X-ray photoelectron spectroscopy (XPS) for surface layer composition, total reflection X-ray fluorescence spectroscopy (TXRFS) for the metal surface contaminants, and naturally atomic force microscopy (AFM) for the surface roughness profile.

10.2.1

Prominent Role of the Space Charge Layer

The main difference between metals and semiconductors is that the density of carriers at the electrode/solution interface is a prevailing factor in the kinetics of electrochemical processes. When the electrode is in contact with a redox couple in the solution, the equilibrium condition requires the Fermi levels of the semiconductor and solution to be equal [3]. Fermi energy levels in semiconductors are defined relative to the energy of an electron in vacuum, while the potentials in solution are referred to the standard hydrogen electrode. The two scales are related by the theoretical value for the Fermi level of the platinum in the SHE, which is -4.5 eV vs. vacuum. Then superimposing both scales leads to predicting whether electrons or holes are involved in the exchange current. In this scale, the binding energy of electrons in oxidizing species is very strong so that their potential energy level is deep near the valence band of silicon. Then the exchange of charge between the electrode and the solution proceeds through holes. For example, following Gerischer [4], various oxidizing species such as IrCl_6^{2-} or Br_2 will inject h^+ holes in the valence band as the

consequence of the reaction:



Respectively, electrons in reducing reactants are weakly bound; thus, redox couples with a negative standard potential vs. SHE are positioned in the upper part of the diagram, that is, in the vicinity of the conduction band level in the semiconductor electrode.

Doping a p-type semiconductor generates fixed acceptor sites with a density N_A , and an equal number of mobile carriers with an opposite charge h^+ , whose distribution is controlled by the local value of the potential $\Phi(x)$, following the Boltzmann function so that the mobile charge distribution is given by:

$$\rho(\text{h}^+) = eN_A \exp - \left(\frac{e\Phi}{kT} \right) \quad (8)$$

In turn this distribution contributes to the local potential, so that the potential profile is controlled by the Poisson equation:

$$\Delta\Phi = \left(\frac{eN_A}{\varepsilon\varepsilon_0} \right) \left(1 - \exp - \left(\frac{e\Phi}{kT} \right) \right) \quad (9)$$

where ε and ε_0 are the permittivity of the substrate and of the vacuum respectively.

The basic theory of the kinetics of charge-transfer reactions is that the electron transfer is most probable when the energy levels of the initial and final states of the system coincide [5] following the Franck–Condon principle. Thus, the efficiency of the redox reaction processes is primarily controlled by the energy overlap between the quantum states in the energy bands of the semiconductor and the donor and acceptor levels of the reactants in the electrolyte (Fig. 1). In the ideal case, the anodic current density is given by the

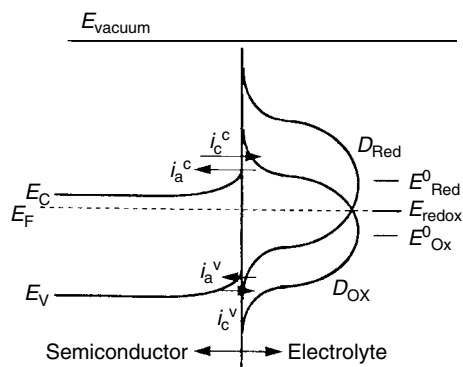


Fig. 1 Illustration of the electron transfer as anodic and cathodic current via the conduction and valence band (after Zhang [6]).

formal equation:

$$i = zF \int k(E)N_V(E)D_{\text{Red}}(E)dE - zF \int k(E)N_O(E)D_{\text{Ox}}(E)dE \quad (10)$$

where N_V and N_O are the densities of vacant and occupied states in the semiconductor, D_{Red} and D_{Ox} are the densities of donor and acceptor sites in the electrolyte, and $k(E)$ is the transition coefficient, which strongly depends on the interaction of reacting molecules with the surface.

Often, the overlap between the electronic states of the semiconductor and the levels in the electrolyte is unfavorable. However, the electrochemical reaction can proceed via additional surface states, always existing at surface defects on the electrode.

An externally applied potential controls the Fermi level of the semiconductor with respect to the reference electrode in the solution. Changes of the potential affect the potential drop across the semiconductor/electrolyte interface. In most situations of electrochemical reactions, the potential drop in the solution Helmholtz layer can be neglected, and thus a gradient of potential is generated in the “space charge

layers” within the Si substrate. This condition results in the bending of energy levels of both the conduction and valence bands, and a change of the charge distribution following Eq. (8). An important consequence is that, in the case of n-Si substrate polarized at positive potentials, bending the energy levels upwards generates a depletion layer of electrons, which are the mobile charge carriers. A symmetrical situation creates a hole depletion layer in p-Si samples. A reverse bias potential condition contributes to building up a charge accumulation layer. These properties can be used to predict the path of the charge-transfer reactions.

10.2.2

The Flat Band Potential of Silicon

The frontier between the depletion and the accumulation situations of the space charge layer is defined by the flat band potential. In fact, when the potential is constant all along the thickness of the electrode, the mobile charge (and naturally the fixed charge) distribution is uniform. In the case of the interface of Si electrode with an electrolyte, the corresponding bias potential has to be determined with respect to the reference electrode. The value of the flat band potential V_{fb} is expected

to depend on several factors such as, n- or p-type Si, doping agent concentration, nature of the solvent, and components of solute species.

The general method for the determination of the flat band potential is based on the Mott–Schottky linear plot based on capacitance/voltage relation. Starting from Eq. (9) the space charge distribution was calculated, and its potential dependence lead to the derivation of a model equivalent to a capacitance, given by:

$$C_{SC} = \left[\frac{e\epsilon\epsilon_0 N_A}{2 \left(V_{fb} - V_S - \frac{kT}{e} \right)} \right]^{1/2} \quad (11)$$

Where V_S is the potential value at the surface of the electrode. Then plotting the value of $1/C_{SC}^2$ versus the applied potential E should yield a straight line whose intercept with the E axis represents the flat band potential, and the slope is used for the calculation of N , the charge carrier density in the semiconductor. A typical example of Mott–Schottky plot is given in Fig. 2 [7]; in this graph, the extrapolated values of the fb potential are +0.8 V and −0.6 V vs. SCE for p-Si and n-Si respectively.

On the other hand, a considerable amount of experimental flat band potential

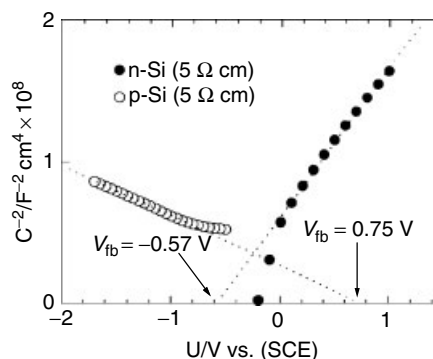
Tab. 1 Flat band potentials of silicon materials determined in the dark in various solutions

Sample	Electrolyte	V_{fb} vs. SCE
p-type		
(100) 10 Ω cm	0.1% HF	+0.16
(100) 8 Ω cm	1% HF	+1.76
(100) 0.5 Ω cm	5% HF	+1.3
n-type		
(100) 3 Ω cm	1% HF	−0.46
(100) 0.1 Ω cm	1% HF	−0.57
(100) 0.01 Ω cm	5% HF	−0.42

data are reported by Zhang [6]; a few of them are reported in Table 1.

Although results concerning n-type Si are not too much scattered, it is difficult to recognize any convergence in p-type Si. We underline the difficulty in obtaining such results, because, due to the standard potential of the element, Si material tends to be covered with a chemical oxide layer in most aqueous solutions, and is subject to anodic etching in HF containing solutions. We could expect a better coherence in nonaqueous solvents. However, according to Lewis and Bocarsly [2], Mott–Schottky plots in those solvents exhibit substantial frequency dispersion. Additionally, the measured intercepts seem to be critically dependent upon the utilized solvent/electrolyte combination. The

Fig. 2 Mott–Schottky plots of n-type and p-type Si (5 Ω cm) in NH_4Cl 0.5 M + HF 0.5 M aqueous solution (after Ottow et al. [7]).



wide range of reported values of V_{fb} for n-type Si in nonaqueous solvents indicates the disparity in experimental results. Corrosion and passivation in nonaqueous solvents are not well understood for silicon photoelectrodes. Morrison [3] claimed that oxide growth is beneficial, and perhaps necessary, for Si anode stability.

10.2.3

Electrochemical Impedance Spectroscopy (EIS) of the Space Charge Layer

A more reliable method for the determination of the fb potential can be drawn from a thorough investigation of the complete impedance diagram equivalent to the space charge layer. In fact, the main difficulty encountered in the Mott–Schottky plot is the rather wide range potential for the C^{-2} extrapolation, which necessarily lead to values where electrochemical reactions contribute to changing the surface properties of the substrate. Moreover, the expected linear relationship shows a significant deviation, which is explained

by the partitioning of the total voltage applied to the electrode between a potential drop in the space charge layer and another potential drop in the Helmholtz layer.

Most often, the electrochemical impedance spectroscopy (EIS) measurements are undertaken with a potentiostat, which maintains the electrode at a precisely constant bias potential. A sinusoidal perturbation of ± 10 mV in a frequency range from 10^5 to 10^{-2} Hz is superimposed on the electrode, and the response is acquired by an impedance analyzer. In the case of semiconductor/electrolyte interfaces, the equivalent circuit fitting the experimental data is modeled as one and sometimes two loops involving a capacitance imaginary term in parallel with a purely ohmic resistance R .

Generally, depending on the bias potential, the EIS leads to RC equivalent circuit loops representing both the space charge and the interface impedance components. The complete set of imaginary versus real impedance data leads to the construction of a semicircle that can be

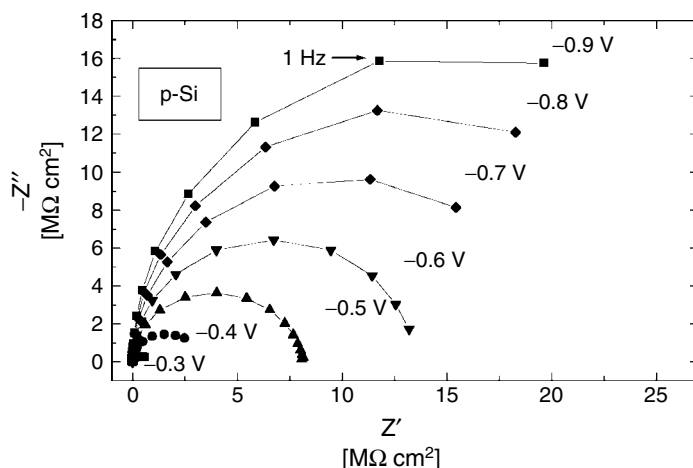


Fig. 3 Successive impedance diagrams in the dark of p-Si substrates in 5% HF solution at different bias potential in the depletion regime.

modeled by numerical software to derive the R and C components. In the range of bias potentials where a depletion layer is formed within the semiconductor, the Nyquist diagram is an almost perfect semicircle, which is easily attributed to the space charge. Instead of paying attention to the capacitance value, it is more efficient to study the resistance R term of the observed loop. This R term is simply represented by the diameter of the semicircle. Figure 3 shows a series of semicircles, which are the Nyquist diagrams obtained in the dark at various negative bias potentials. The sample was p-Si doped at the level of ca. 10^{16} at cm^{-3} , and the capacitance values in this interval of potential were in the range of a few 10^{-8} F cm^{-2} in agreement with the expected values for a depletion layer. The resistance R term in this interval increases from 2 to 35 $\text{M}\Omega \text{ cm}^2$. The diagrams obtained with p-Si are more reliable because, owing to the surface properties of the electrode at cathodic bias potential, the measurements are obtained under almost zero current density.

A similar procedure can be used to determine the space charge distribution in n-type Si in the dark with a positive bias polarization so as to generate a depletion layer within the semiconductor substrate. In this case, the situation is somewhat different because the positive polarization in HF results in an anodic etching of the sample with a nonnegligible current density near $7 \mu\text{A cm}^{-2}$. Nevertheless, similar results were obtained, the components of the equivalent circuit were a capacitance of a few 10^{-8} F cm^{-2} , and a resistance term ranging from 1 to 10 $\text{M}\Omega \text{ cm}^2$ for a bias potential varying from -0.1 to $+0.9$ V vs. SCE.

In a fundamental treatment of the carrier density [8] in the space charge layer,

the calculation started from the complete Poisson Eq. (9), which was developed in the low potential approximation to permit the linearization of the exponential term and to derive the potential distribution $\Phi(x)$ at a bias polarization close to the flat band potential. Then, using Eq. (8) the density $\rho(h^+)$ of mobile carriers was calculated and was used to express the resistance R_{SC} of the space charge layer as a function of the surface potential V_{S} referred to the fb value:

$$R_{\text{SC}} - R_0 = R_0 \left(\frac{\varepsilon \varepsilon_0}{k T N_{\text{D}}} \right)^{1/2} (V_{\text{fb}} - V_{\text{S}}) \quad (12)$$

where R_0 is the intrinsic resistivity of the wafer material. Eq. (12) shows that $(R_{\text{SC}} - R_0)$ cancels out for the flat band situation.

As shown in Fig. 3, the measured resistance R_{SC} in the depletion regime can reach several $\text{M}\Omega \text{ cm}^2$, but Eq. (12) indicates that it becomes equal to the effective resistance of the substrate which is less than $1 \Omega \text{ cm}^2$ at the fb potential. Then the term $1/R_{\text{SC}}$ is almost equal to zero under the depletion regime, and suddenly rises very sharply to almost infinity when the potential approaches the fb value (Fig. 4). This effect is extremely useful for a simple determination of the fb potential, which is found near 0 V vs. SCE, for p-type Si in a 5% HF aqueous solution. The procedure seems more rigorous, because it does not deal with an extrapolation method, and, owing to the sharp variation of the conductance, it needs just a few impedance measurements in the immediate vicinity of the fb potential. This method of investigation of the space charge layer, which reveals the formation of a depletion layer that is several $\text{M}\Omega$ resistant, leads

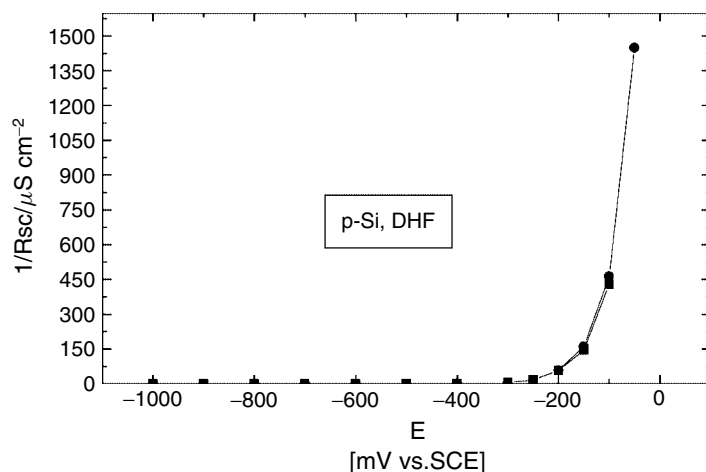


Fig. 4 Reciprocal of the depletion layer resistance of p-type Si in the dark as a function of the bias potential applied to the Si substrate.

to a simple comprehensive interpretation of the electrochemical response of silicon electrodes.

10.2.4

Linear Sweep Voltammetry of Si Electrode in HF Solutions

A “bare” surface of silicon can only exist in fluoride containing solutions. In reality, in these media, the electrode is considered to be “passive” due to the coverage by Si–H_x terminal bonds. Nevertheless, the interface Si/HF electrolyte constitutes a basic example for the study of electrochemical processes at the Si electrode. In this system, the silicon must be considered both as a charge carrier reservoir in cathodic reactions, and as an electrochemical reactant under anodic polarization. Moreover, one must keep in mind that, according to the standard potential of the element, both anodic and cathodic charge transfers are involved simultaneously (corrosion process) in a wide range of potentials.

An interesting feature of Eq. (10) formalism is its similarity with the usual

Butler–Volmer equation for the current–voltage relationship:

$$i = zF k_0 \left[C_{\text{red}} \exp \left(\alpha n F \left(\frac{E - E_0}{RT} \right) \right) - C_{\text{ox}} \exp - \left(\beta n F \left(\frac{E - E_0}{RT} \right) \right) \right] \quad (13)$$

This Eq. (13) is derived from the fundamental electrochemical kinetics at metal electrodes and mainly accounts for the mechanism of the transformation, but the Gerischer Eq. (10) introduces an additional term accounting for the density of available mobile carriers at the electrode surface.

However, silicon material in an aqueous solution is not a system in equilibrium. It is considered as a mixed system containing two redox couples with standard electrode potentials E_1 and E_2 separated by a wide interval. Then Eq. (13) must be modified to account for both components:

$$i = i_{01} \exp \left(\alpha F \left(\frac{E - E_1}{RT} \right) \right) - i_{02} \exp - \left(\beta F \left(\frac{E - E_2}{RT} \right) \right) \quad (14)$$

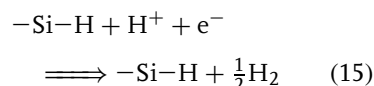
where i_{01} and E_1 hold for the exchange current and the equilibrium potential of the silicon material, and i_{02} and E_2 are the exchange current and the equilibrium potential of the oxidizing species, that is, the proton/hydrogen couple.

Several results concerning the electrochemical reactions at the Si/HF interface have been published. Some were focused on the cathodic processes, others on the anodic etching reaction, and the influence of various parameters, such as doping level, influence of light, surface structure or presence of redox reactants, was investigated. A synthetic picture of anodic and cathodic behavior of both p- and n-type Si substrate, in the simplest condition of a pure 5% HF aqueous solution, in the dark is presented (see Fig. 5).

A: Cathodic behavior

The only cathodic process in HF solutions is the hydrogen evolution reaction (HER), which is important in that it is involved in almost all reactions at both anodic and cathodic potentials. The silicon electrode can be passivated by hydrogen termination

of the surface Si dangling bonds. Even though the cathodic current density could be high, the Si–H layered surface is not expected to undergo any drastic change of structure following the electrochemical reaction:



The charge transfer for H_2 evolution proceeds almost entirely over the conduction band, a conclusion that is mainly supported by the graphs obtained with n-type Si in comparison with p-type electrodes.

With an n-type Si electrode, the reduction current density increases exponentially with decreasing potential, the apparent Tafel slope was found equal to 140–160 mV/decade. This is much higher than the 60 mV/decade required for the processes that are limited by the supply of electrons from the semiconductor whose space charge is under the accumulation regime. In other words, the HER at the Si surface is a slow electron transfer, that is, a relatively large overpotential is required to

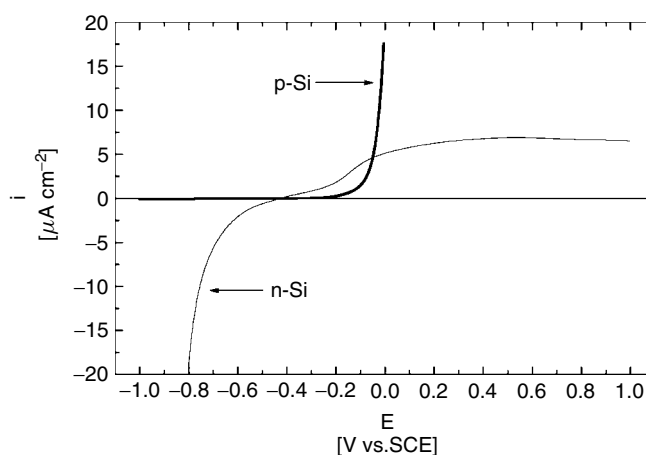


Fig. 5 Current/voltage characteristics of p- and n-type Si substrates in the dark in a 5% HF aqueous solution.

obtain an appreciable reaction rate. For example, the potential for the onset of HER on “bare” Si is 300 mV more negative than on platinized Si.

As shown in Fig. 5, the current density for HER on p-Si, in the dark, at cathodic bias voltage is almost equal to zero, in fact it hardly reaches a limiting value near $\approx 50 \text{ nA cm}^{-2}$ even at -1.0 V vs. SCE . It is interesting to recall that such a small value for p-Si will provide the favorable conditions for the measurement of electrochemical impedance diagrams. Naturally, this limiting current is classically attributed to the limiting diffusion flux of the mobile electron minority carriers in the space charge layer [6].

$$i_n^{\text{lim}} = \frac{e D_n n_0}{L_n} \quad (16)$$

where D_n , n_0 , and L_n , are the diffusion constant, the equilibrium concentration, and the diffusion length of the negative charge carriers in p-type Si. This Eq. (16) is linked to the assumption that bulk thermal generation is the only source of minority carriers.

Data from electrochemical impedance diagrams yield a simplified quantitative analysis for an appropriate interpretation of the linear sweep voltammetry (LSV) experiments. In fact, the Si electrode potential measured with respect to the reference electrode represents the value within the bulk of the material. The direct current flow for the electrochemical reaction has to overcome the resistance of the space charge layer, which can reach extremely high values when a depletion layer is formed. For p-type Si in the potential range for the HER onset, this excess surface resistance is over $10^7 \Omega \text{ cm}^2$. Thus, even with a bias of -1 V , the DC cannot exceed 100 nA cm^{-2} , and even

less according to the necessary overvoltage associated with the slow reaction rate.

The specific behavior of semiconductors is exemplified by the influence of several factors such as:

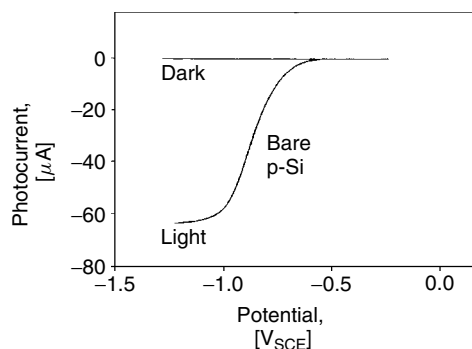
1. The effect of the depletion layer in p-type Si is easily circumvented by light irradiation of the electrode. In fact, the current/voltage graph is drastically affected by the partitioning of the total applied potential $\Delta\Phi_T$ between the space charge drop $\Delta\Phi_{SC}$ and the contribution of the interfacial charge transfer $\Delta\Phi_{CT}$.

$$\Delta\Phi_T = \Delta\Phi_{SC} + \Delta\Phi_{CT} \quad (17)$$

For potentials at which the silicon is in a depletion situation, the major part of the applied bias voltage will concern the semiconductor space charge and generate a high electric field within this surface layer. In this case, light illumination will generate electron-hole pairs, which are steadily separated by the driving force of the local electric field. Holes are attracted toward the bulk of the substrate, while the minority carriers (e^-) are pushed to the Si/electrolyte interface and produce an inversion layer that is available for the HER process. At low current density, the depletion layer is now filled with electrons and its resistance term is almost zero. Naturally, at negative bias potential, the current density reaches a limiting plateau proportional to the photon flux (Fig. 6).

2. The doping level of the silicon substrate is a determining parameter for the density of mobile carriers at the interface, even when the electrode is in the accumulation regime. Zhang [6] determined the cathodic current/voltage graphs for an n-type sample doped 10^{17} and 10^{19}

Fig. 6 Current/voltage curves for naked p-type Si in the dark, and under illumination at 632.8 nm, 2.5 mW cm^{-2} (after Zhang [6]).



at cm^{-3} respectively. Naturally, the current of the latter at a constant potential was higher than the former. But the current density ratio for these samples was only a factor between 2 and 3, instead of the factor 100 of the carrier concentration. This result points out the interference of the separate contributions of both the surface electron density and the slow rate kinetics for HER charge transfer.

B: Anodic behavior

In the positive branch of the i/V graph, anodic dissolution process will remove material from silicon crystals. The conditions for optimal etching of silicon have been extensively explored for micromachining or surface polishing in the fabrication of electronic devices. Most generally, the etch rate of silicon in HF solutions is isotropic among the various crystalline orientations. The etch rate of silicon at room temperature at the open-circuit potential (OCP) is very low, on the order of $10^{-4} \text{ nm s}^{-1}$, which is equivalent to 100 nA cm^{-2} , in aqueous HF solutions.

Under anodic bias potential, the behavior of n-type Si in the HF solution must be discussed because of the onset of a depletion layer with a resistance of several megaohms per square centimeter, which should limit the DC density to less than

$1 \mu\text{A cm}^{-2}$. But the experiments show a plateau value at $5\text{--}6 \mu\text{A cm}^{-2}$. This result could be easily interpreted according to the extremely high reactivity of transient bare Si^0 surface states. In Gerischer's treatment, the minority carrier density and the current value are modified by a term g_s , the surface generation rate of mobile charge carriers. In many systems, there may be several sources of minority carrier generation, for example, through the surface states. Surface states are always present on silicon electrodes in fluoride containing solutions and are associated with the dissolution of the silicon. This process is the result of the dual redox character of the Si/HF interface at which holes h^+ carriers are consumed during the oxidation of Si material. The kinetics of this reaction is equivalent to a flux of electrons generated at the level of the conduction band near the interface.

The interpretation of the anodic branch of LSV for p-Si is apparently more simple because the current increases following an exponential variation with a Tafel slope of $\approx 60\text{--}80 \text{ mV/decade}$. In this case, an accumulation layer is generated, and then the current is only controlled by the kinetics of the electrochemical reaction, which involves several successive steps. It is not necessary to account for the various reaction paths proposed by many authors.

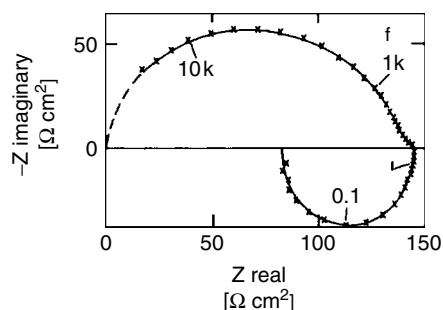
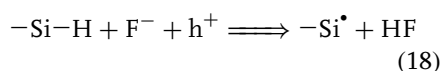
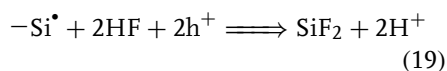


Fig. 7 Complex plane impedance plot for p-type Si in 1% HF solution, in the dark, at bias potential 0 V vs. SCE (after Vanmaekelberg et al. [9]).

The complete electrochemical behavior of the system can be described assuming the following steps [9]:



The transient surface species $-\text{Si}^\bullet$, which is extremely reactive, immediately undergoes successive steps of oxidation, which are written as:



The soluble divalent SiF_2 compound is in turn transformed by disproportionation into SiF_6^{2-} and elemental amorphous silicon. This mechanism is responsible for the effective dissolution valence of Si, which was found to be equal to 2 in the range of potential between 0 and +0.4 V/SCE.

The electrochemical reaction rate for the anodic etching of Si in HF was very rapid. This is confirmed by the electrochemical impedance diagram of Fig. 7 that shows a real component equal to $\approx 150 \Omega \text{ cm}^2$, and is the result of the high reactivity of the transient bare $-\text{Si}^\bullet$ sites that appear under anodic current. The detailed mechanism of the transformation was investigated by EIS, which revealed quite an unusual inductive loop, which is shown in Fig. 7. Such a diagram was obtained by modeling the reaction kinetics based

on the existence of rather stable $-\text{Si}-\text{H}$ surface sites giving rise to an extremely reactive intermediate $-\text{Si}^\bullet$ site, which, after dissolution, regenerates the original stable $-\text{Si}-\text{H}$ terminal dangling bond. The transition from a passive behavior to a very active surface is responsible for the inductive component of the complex impedance.

10.2.5

Formation of Porous Silicon

The $i-V$ characteristics, in HF solutions, in Fig. 5 was intentionally limited to low values of current density. When the p-Si electrode is polarized to more positive potentials, the anodic current rises exponentially reaching a first maximum near 30 mA cm^{-2} at +0.5 V vs. SCE. Beyond this point, electropolishing of the Si surface is observed. However, in the exponential range of potential, where the anodic current density is ca. $1-4 \text{ mA cm}^{-2}$, the Si surface is altered by the formation of a new structure made of porous silicon (PS). Simultaneously, hydrogen evolution occurs indicating an electrochemical/chemical mechanism resulting from the effective dissolution valence that can vary from 2 to 4 depending on the HF concentration and the electrode potential. In a first approximation, the hydrogen evolution could be assigned to a chemical

oxidation of Si^{II} (Eq. 19) by protons leading to Si^{IV} and H_2 . But the mechanism is more elaborate in the case of PS formation; a dissolution valence as low as 0.5 was measured for thick PS layers. This property is the consequence of the direct chemical dissolution of highly reactive silicon nanocrystals by HF.

Also, from Fig. 5 it appears that the anodic current density with n-type Si is extremely low due to the buildup of the depletion layer with a more than $1 \text{ M}\Omega$ resistance. In fact, obtaining a few mA cm^{-2} with n-type Si in the dark needs a very high polarization potential, up to 6–10 V so as to induce breakdown within the highly resistant depletion layer. Nevertheless, PS structure can be obtained on n-type Si, either using heavily doped samples, alternatively under light activated silicon surfaces.

After the discovery, in 1990, of luminescence displayed by porous silicon, the published literature is enormous since this material has extremely rich morphological features, with properties that are very different from those of silicon. The growth rate can vary over a wide range depending on formation conditions. For example, using heavily doped n-type Si in 3% HF the rate is almost constant at 10 nm s^{-1} , the PS thickness being a linear function of time up to $10 \mu\text{m}$. The morphology of pores is not well characterized, although most of the pores are straight in the direction perpendicular to the (100) plane, and clearly separated. The mechanism for the propagation of pore needlelike cavities is explained by the random existence of very reactive sites such as $-\text{Si}^\bullet$ on a passive $-\text{Si}-\text{H}$ surface. During PS formation at an anodic potential, the tip of pores dissolves preferentially by electrochemical process. But the pore wall areas dissolve only chemically at a very low rate.

The chemical dissolution does not depend on potential but on the time of immersion and the total surface area. Many other parameters are determined on the general morphology of the pores and their distribution. We can cite the type and the level of doping, the HF concentration, and the applied potential or the excitation by light. Owing to the formation of hydrogen bubbles, the space within the pores may not be filled by electrolyte. Ethanol is often added to facilitate evacuation of H_2 . It is clear that, depending on the specific electrochemical conditions, quite different morphologies are obtained, depth and inner diameter of the pores, interconnected channels, random distribution in size and position.

A lot of potentialities are expected for applications in many wide fields. The most important one is the efficient luminescence in the near infrared and the whole visible range. In addition, PS is an active host for rare earth emitters, for example, Nd or Er, as well as dye solutions.

Moreover, the high surface area of this structure makes it very effective in the production of on-chip capacitors, and in the adsorption of various contaminants in the gaseous atmosphere, or the adsorption of biological molecules in solutions. For a better specificity of these applications, well-defined structures are preferred. For example, the inefficient luminescence observed from inhomogeneous material of low porosity originates from microscopic areas of high porosity. Using micropatterning for pore initiation, regularly spaced pore arrays can be produced. The position of pore nucleation can be determined by etch pits, the technique being limited to macroporous PS, since present lithographic resolution is in the range of hundreds of nanometers. For example formation of pore arrays $2 \mu\text{m}$ in diameter

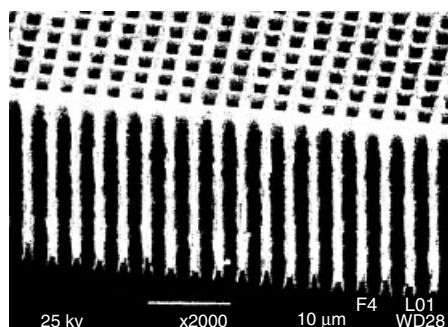


Fig. 8 Scanning electron microscope images of a photonic crystal formed by macroporous silicon obtained on n-type Si (after Pavese et al. [10]).

and up to 400 μm deep on a silicon wafer in the direction (100) has been reported [10] (Fig. 8).

Presently, the studies on porous silicon are considered to be a very promising field for advanced research oriented in the photonic materials to make light emitting diodes (LED), and mostly as sensors and biosensors of various components in solutions as well as in gaseous phases.

10.2.6

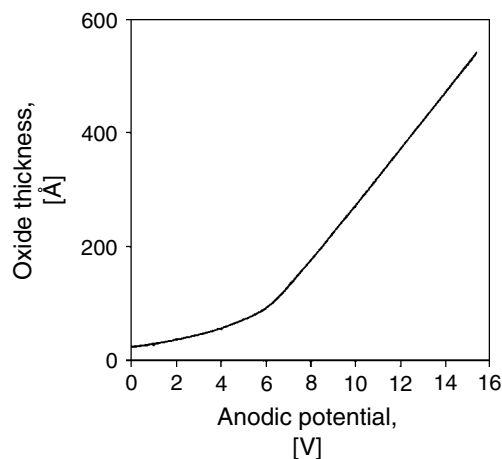
Growth of Anodic Oxide Layers

In nonalkaline and nonfluoride aqueous solutions, silicon substrates behave as essentially inert electrodes due to the presence of a thin oxide film. Even in alkaline solutions, silicon is passivated by an oxide film at anodic potentials beyond the passivation peak. Very small current can pass through the passivated silicon surface of n- or p-type materials in the dark or under illumination. Depending on the pH of the electrolyte, oxidized surface sites $\text{Si}-\text{OH}$ are more or less ionized into anionic species $\text{Si}-\text{O}^-$ owing to the acido-basic properties of such radicals; so that the passivation current can vary in a wide range from a few $\mu\text{A cm}^{-2}$ in KOH to less than 1 nA cm^{-2} in acidic solutions, HCl, H_2SO_4 . The passivating layers on silicon are composed

of amorphous and nonstoichiometric oxides containing varying amounts of water and hydroxyl ions, the composition is not the same near the Si/SiO_x as near the $\text{SiO}_x/\text{electrolyte}$ interface. The nonstoichiometric composition of the anodically formed oxide film can be expressed as SiO_x with a higher value close to $x = 2$ near the electrolyte, and a lower value in the deep layers near the surface. The structures of these oxides on n- or p-type materials are similar, but are not stable and tend to change with time. The layer acts as a barrier to the interaction between the electrode and the electrolyte resulting in a drastic reduction of electrochemical reactions.

Anodization can be carried out in inorganic or organic solutions at constant potential or constant current. Under galvanostatic mode, the voltage increases with time, along with an increase of the oxide thickness. But the electrode surface always reaches a limiting structure and the system starts oscillating. Then the oxide film is physically broken, with the appearance of pits and nodules. In nitrate, phosphate, or borate aqueous solutions it was observed that the maximum allowed voltage could not exceed 200 V. But organic solvents such as glycols or alcohols allowed the formation of thicker oxides at higher voltages in excess of 500 V. Naturally, some

Fig. 9 Thickness of anodized oxide film measured by ellipsometry as a function of voltage above the passivation peak (after Zhang [6]).

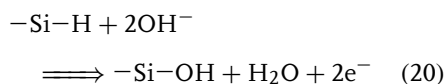


water is necessary for the growth and the electrical properties of the anodic oxide. The amount of water closely correlates the breakdown potential.

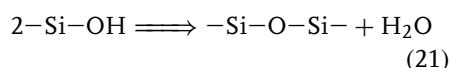
The thickening of the oxide layer is controlled by the local electric field on the order of 10^6 – 10^7 V cm $^{-1}$, and the conductivity of the growing oxide. In alkaline solutions, due to the nonnegligible conductance induced by the ionization of hydroxyl groups, rather thick oxide layers can be obtained. For a given applied potential, the thickness reaches a limiting value that can be as high as 60 nm. Figure 9 shows the experimental limiting thickness obtained in a KOH solution as a function of the bias potential, the average slope being ≈ 0.8 nm V $^{-1}$. But it is also clear that the forming voltage in KOH cannot exceed 20 V, mainly due to the conductance of Si–O $^-$ ionized sites. A similar growth pattern is observed in NH $_4$ OH solutions. But in acidic non-HF solutions, much more insulating layers are grown yielding a limiting thickness that can hardly exceed 1 nm.

Several mechanisms were described in the literature, accounting for both the surface oxidation of the electrode

and the subsequent formation of solubilized species. Concerning the growth of the surface oxide in alkaline solutions, the main path can be summarized in the following steps. The primary reaction is the transformation of the –Si–H terminal bond into the silanol group:



Because of the polarization by the –Si–OH bond, the –Si–Si–back bonds are weakened and attacked by H $_2$ O molecules to generate new –Si–H and –Si–OH terminations. Again, the Si–H are oxidized into silanol, and simultaneously these silanol groups are condensed into siloxane bridges:



Thus, a new layer of oxide is generated as schematically shown in Fig. 10. Water molecules are present in the oxide structure incorporated during the oxidation process. This water combines with

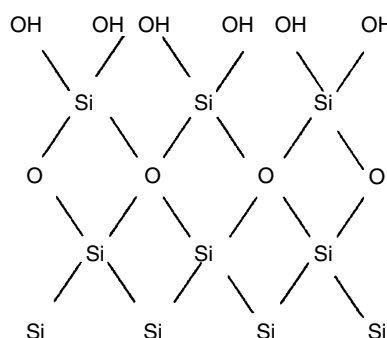


Fig. 10 Schematic illustration of the formation of Si—O—Si bonds in KOH solution at potentials more positive than the passivation potential (after Zhang [6]).

bridges —Si—O—Si— to form pairs of non-bridging —Si—OH groups.

Surface layers of silicon oxide are important in semiconductor device fabrication as interlayer dielectrics for capacitors, isolation of conducting layers, or as masking materials. However, anodic oxides, due to their relatively poor electrical properties, breakdown voltage, and leakage current, have not yet found much use in device technology, and cannot compete with thermal oxides obtained at high temperatures of 700 to 900 °C.

10.3

Chemical/Electrochemical Reactions at Open-circuit Potential

10.3.1

Oxide Growth by the RCA Cleaning Process

A clean silicon surface is critical in the production of smaller and faster logic and memory devices. A typical process flow for advanced integrated circuits consists of 300 to 500 steps, 30% of them being wafer cleaning operations. Trace amounts of impurities such as Na^+ ions, metals, and particles are especially detrimental in the reliability of finished devices. This is the main reason why nonvolatile reactants (alkali, alkaline earth as well as any metal

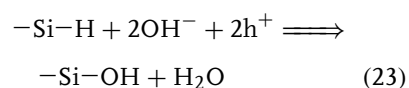
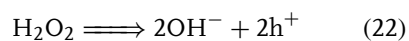
salts, even at the ppb level) must absolutely be absent in all the solutions used in the various steps of the wet treatment. For example, diffusion of such impurities in the insulating oxide layers is responsible for a large amount of yield losses.

Presently, the most widespread cleaning technology is the RCA wet processing that was originally initiated by Kern and Puotinen [11] in 1970. But since several years, the formulation of the solutions have continually been optimized in order to meet the requirements for the miniaturization of the circuits at the submicron level, and also for the economic and environmental factors. In this process, a first step is the removal of the native oxide protecting film by DHF solution, which leads to a bare hydrophobic H-terminated surface. The next step is a treatment called SC1 (Standard Clean #1) using an ammonia/hydrogen peroxide mixture (APM), which is very efficient to grow a new protecting silicon oxide layer and to release the surface from particle contamination. In fact, the oxides grown in SC1 are hydrophilic as a consequence of their surface silanol, Si—OH groups, which are more or less ionized in the alkaline solution. This is an important effect because it results in the generation of the Zeta potential, which is in the same polarity for the substrate surface

and particles so as to cause a repulsive electric force. In the following steps, this oxide layer is removed by DHF, and the remaining metal contaminants are removed by a hot aqueous solution called SC2, made of a HCl/hydrogen peroxide mixture (HPM). This acidic treatment will also generate a new protective extremely thin oxide layer.

In these processes, the oxide growth takes place at the expense of the Si substrate, and is considered as a special case of etching. In a simplified approximation, the reaction could be considered as purely chemical. However, owing to the wide variations of the OCP by the reactants, to treat the etching of silicon as a purely chemical reaction with no involved electrochemical mechanism is inappropriate. The existence of an exchange current is consistent with the setup of a definite OCP, including a charge transfer, e^- or h^+ , between surface sites and the reactants in solution. Finally, the oxide growth can be classified as anodic oxidation at OCP. The reaction of hydrogen peroxide with a bare

hydrophobic silicon surface can be written as:



This equation being equivalent to Eq. (20), leads to a fast removal of $Si-H_x$ terminal bonds; the subsequent thickening of the oxide is again explained by the break of the Si backbonds induced by the polarization of $Si-OH$, and the formation of siloxane groups as in Eq. (21).

The experimental results mainly obtained by EIS supported the mechanism of the build up of an oxide passive layer. They lead to the determination of quantitative parameters related to the change of surface reactivity. The measurements constituted a series of impedance diagrams obtained at successive time intervals. Examples given in Fig. 11 represent [12] the time variation of the Nyquist diagram resulting from the build up of an insulating layer, after reaction of SC1 on an initially bare hydrophobic

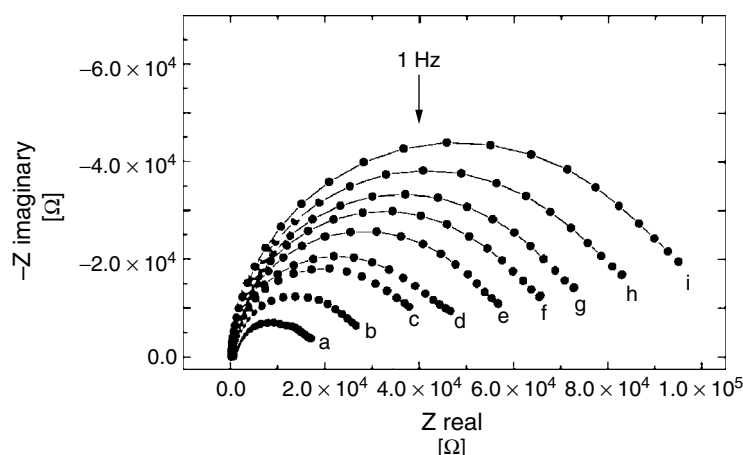


Fig. 11 Successive impedance diagrams of initially hydrophobic p-Si, in the dark, in an $NH_3 + H_2O_2$ solution; a, b, c, d, e, f, g, h, i, the diagrams are recorded at time intervals of 8 min (after Bertagna et al. [12]).

p-type Si surface. These impedance plots, obtained at the OCP, that is, at zero current potential, are well shaped semicircles, the center being very close to the real axis, each corresponding to a simple RC circuit. In fact, the system is quite equivalent to a semiconductor/oxide/electrolyte (SOE) capacitor, showing some similarities with a metal/oxide semiconductor (MOS) structure.

The resistance term is characteristic of the leakage current of the oxide layer dielectric. The series of diagrams show a steep increase of the polarization resistance from 5×10^3 to more than $3 \times 10^5 \Omega \text{ cm}^2$. It is interesting to note that voltammetric records in a narrow range of potential ± 50 mV near the OCP lead to the same value of the polarization resistance. One could expect that the capacitance should accordingly decrease. But infrared ATR spectroscopy (attenuated total reflection) demonstrated that the increase of resistance was partly due to the gradual change to a more compact and well-defined structure of the oxide. This figure reveals the buildup of an insulating oxide layer, leading to a hydrophilic final bright surface, showing no defect with a scanning electron microscope.

Nevertheless, we recall that, in alkaline solutions, the silanol groups are partly dissociated into $-\text{Si}-\text{O}^-$ anionic sites owing to their acido-basic character. As a result, this oxide structure is loose and is permeable to water molecules and chemical reactants, so that the reaction can proceed by diffusion through the layer and lead to a uniform protecting layer. The acido-basic character is well demonstrated by the transformation operated by dipping the oxidized sample in an acidic HCl solution. The polarization resistance, which was equal to a few $10^5 \Omega \text{ cm}^2$, suddenly is

raised to more than $10^7 \Omega \text{ cm}^2$. This result reveals the neutralization of $-\text{Si}-\text{O}^-$ sites to $-\text{Si}-\text{OH}$ groups, followed by the condensation into highly insulating siloxane $-\text{Si}-\text{O}-\text{Si}-$ bridges.

10.3.2

Etching of Monocrystalline Silicon

The term etching refers to the dissolution processes at OCP of silicon samples immersed in an electrolyte solution. The technique has been extensively explored for its useful applications in the fabrication of electronic devices, surface polishing, and micromachining. For example, it is widely used for the production of cantilevers for the AFM technology.

Again it seems not necessary to discuss the considerations of the chemical versus electrochemical reaction mechanism. It is clear from the extremely negative standard potential of silicon, from Eqs. (2) and (6), that the Si electrode is in all aqueous solutions a dual redox system, characterized by its OCP, which is the resultant of an anodic Si dissolution current and a simultaneous reduction of oxidizing species in solution. The oxidation of silicon gives four electrons that are consumed in the reduction reaction. Experimental results show clearly that the steady value of the OCP is narrowly dependent on the redox potential of the solution components. In solutions containing only HF, alternatively alkaline species, the oxidizing component is simply the proton H^+ or the H_2O molecule respectively.

In this respect, etching is considered as an electrochemical process, taking place under the OCP conditions. The charge-transfer mechanism is the same as the electrochemical corrosion, and the reaction rate is derived from

Eq. (14):

$$i_{\text{corr}} = \sqrt{i_{01}i_{02}} \exp \left[\alpha F \left(\frac{E_2 - E_1}{2RT} \right) \right] \quad (24)$$

where i_{01} and i_{02} are the exchange currents, and E_1 and E_2 the equilibrium potentials of the reducing and oxidizing species of the dual redox system.

Owing to the requirement of Si compounds solubilization, the main etching solutions can be either fluoride-based, alternatively high pH alkaline solutions. A large number of experimental data of etch rate and selectivity are given in the review by Zhang [6]. It is indicated that, for a given silicon material and solution composition, the etch rate may vary significantly when it is measured by different investigators. In fact, we can add that the reaction is extremely sensitive to surface defects so that the etch rate of the same sample measured in the clean room of an integrated circuits production line is often much lower than in a common laboratory.

In acidic fluoride solutions, the etch rate is low in the low-pH region, due to the large coverage of passivating Si–H surface bonds. A maximum rate was observed near a pH value of 6, and is attributed to the competing reactions of Si with HF, HF_2^- , and OH^- species. In fact, the Si–H bond is practically nonpolarized and thus has a high degree of chemical stability. In contrast, the ionic character of Si–OH or Si–F bonds results in a strong polarization and weakening of the back bonds of the surface Si atoms, thus enhancing the chemical attack of the material. Since this process is more likely to occur at surface defects resulting in their removal, a prolonged immersion in HF solution should lead to a more atomically smooth surface. In general, the specificity of HF etching is to generate a uniform surface.

In HF solutions, the etch rate can be increased by addition of effective oxidizing agents. For example, addition of CrO_3 increases the etch rate following the increase of hole concentration resulting from the reduction of Cr^{VI} . Other oxidants such as Br_2 or H_2O_2 are interesting candidates for the treatment of silicon leading to a clean and flat surface at the level of a few tenths of a nanometer. The mixture HF– HNO_3 is one of the most widely used isotropic etchants of (100) oriented Si surfaces. The dissolution rate is maximum for the composition at 33% HF and 23% HNO_3 , and can reach a value as high as $28 \mu\text{m s}^{-1}$, which is equivalent to a current density of 90 A cm^{-2} . This mixture can be diluted with water so as to offer a wide range of etch rates.

A different group of etchants based on alkaline solutions is also widely used for silicon micromachining. The simplest reactant is KOH, but the nonvolatile K element is undesirable because it is often adsorbed at the sample surface. Other alkaline solutions such as hydrazine, ethanolamine, or a mixture of ethylene diamine and pyrocatechol were proposed. The most useful alkaline solutions are NH_4OH , or tetramethyl ammonium hydroxide (TMAH). The latter has the advantage of being a strong base like KOH and producing only volatile compounds after cleaning.

The most characteristic feature of alkaline solution etching is its anisotropic nature [13]. For example, in 20% KOH at room temperature, the etch rate at the OCP of the (100) plane is a hundredfold higher than the (111) plane. In general, because of the anisotropic etching process, the morphology of the surface shows smooth ideal (111) sidewalls thus forming micropylamids on (100) wafers, as shown in Fig. 12.

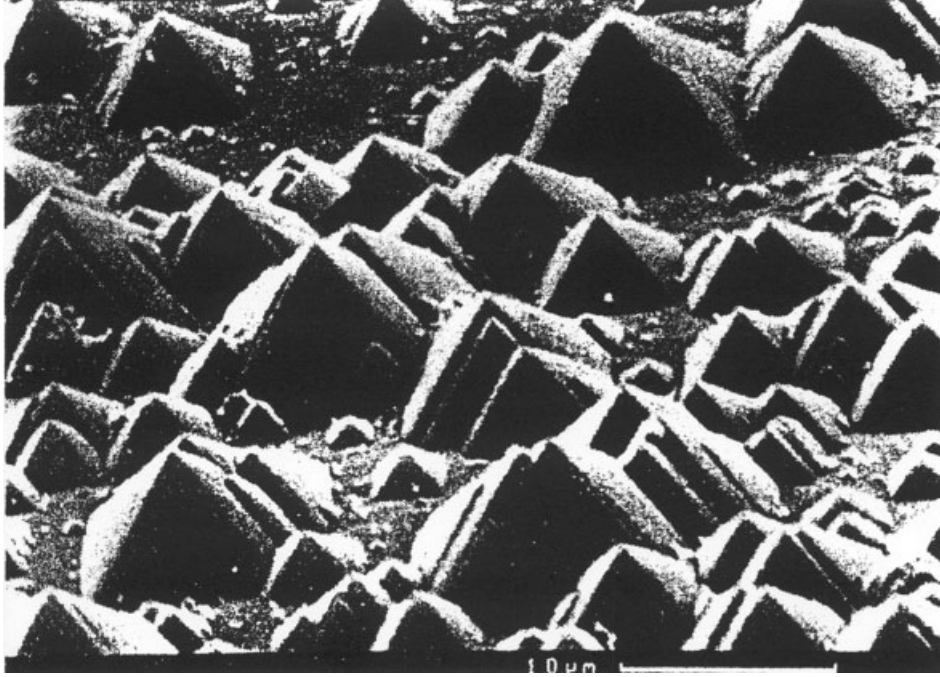
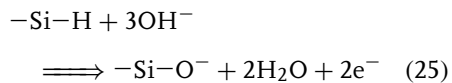


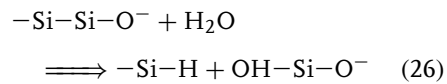
Fig. 12 SEM micrographs of a p-type (100) sample etched 30 min at V_{OCp} in 4 M KOH at 70 °C (after Bressers et al. [13]).

The mechanism of silicon etching in alkaline solutions is a process of material dissolution with a simultaneous hydrogen evolution. The main soluble product is a silicic anion $\text{SiO}_2(\text{OH})_2^{2-}$ that can further be condensed to form polysilicic anions. In fact, due to the acido-basic ionization of OH radicals in a highly alkaline solution, Eq. (19) should be modified as follows:



Again, because of the polarization by the $\text{Si}-\text{O}^-$ group, the $-\text{Si}-\text{Si}-$ back bonds are weakened and attacked by H_2O molecules to generate new $-\text{Si}-\text{H}$ and $-\text{Si}-\text{OH}$ terminations, and induce the detachment of low molecular weight

soluble species, ending at $\text{SiO}_2(\text{OH})_2^{2-}$. A simplified presentation of the reaction can be [6]:



The etch rate of silicon in KOH may vary from as low as 0.1 nm s^{-1} in dilute solution at room temperature to as high as 200 nm s^{-1} in 40% KOH near 90 °C. The etch rate of silicon single crystals always depends on the surface plane orientation in all dissolving solutions, but the effect is maximum for alkaline solutions. The (111) surface is the slowest etching plane in all reported investigations. This result can be convincingly correlated by the back bond theory, that is, the surface atoms on the (111) plane have 3 bonds connected to

the substrate lattice, while those of (100) have only 2, recalling that the action of OH^- ions reduces the strength of the back bonds.

The formation of hillocks correspond to crystallographic structures defined by 4 (111) planes resulting from the anisotropic etching. The process depends strongly on operating conditions, and readily proceeds on poorly cleaned surfaces, and in etchants containing some impurities. For example, hillocks may result from local masking by contaminants or deposits of reaction products such as hydrogen gas microbubbles. The pyramidal hillocks have been found to be associated with a microheterogeneity, a few nanometers in size, at the apex of the micropyramid. Initially, the pyramids at the surface are tiny, but new pyramids are generated while the existing ones grow. When the surface is fully covered with hillocks, the overall etch rate is slowed down so as to result in the structure represented in Fig. 12.

10.3.3

Electroless Nucleation of Metal Contaminants on Si Surface

Ultraclean and defect-free silicon surfaces constitute a major requirement for the advanced processing of SLSI (super large-scale integration) in the last test technology device manufacturing. Dielectric breakdown, which occurs during the final electrical tests, is often generated by metallic contamination at the level of 10^{10} at cm^{-2} . In some circumstances, spontaneous metallic contamination occurs during the cleaning steps, especially in HF solutions, when traces of copper or iron contaminants undergo a reduction reaction at the naked silicon surface, thus generating unwanted metallic nanoparticles. These precipitates, even at a

nanoscopic level, concentrate at the Si/gate oxide interface and are responsible for the defective final SLSI devices. For this reason, chemicals used in the wet treatment processes must reach a high degree of purity at the ppb and even ppt level. Such a purity can be controlled by high performance induction coupled plasma mass spectrometry (ICPMS). In addition, silicon surface metallic impurities can now be quantified, with a detection limit less than 10^9 at cm^{-2} using extremely sensitive techniques such as TXRFS. This spectroscopy is an important tool both to identify and to measure the surface distribution of the contaminants. Additionally, AFM surface scanning is also a powerful method to detect the presence of particles at the nanoscopic scale.

Fundamental studies were undertaken for establishing a technology that prevents metallic contamination and eventually for obtaining characterization criteria for the surface state evaluation. These studies were limited to systems constituted by electronic grade silicon in contact with high purity deaerated HF solutions in the dark. Much work was dedicated to the surface contamination by copper ions impurities present in HF solutions at the ppb level. In fact, trace amounts of copper are often encountered in the solutions used in the production lines, for example, in the chemical/mechanical polishing techniques. Owing to the negative electrode potential of Si element, the spontaneous metallic nucleation process is a consequence of an electroless deposition mechanism [14]. As an electrochemical process, OCP recordings proved to be extremely useful for providing a response associated with the nucleation process. In fact, this parameter takes advantage of the electrocatalytic properties of the nanosized Cu particles. The OCP is the resultant of

the electrochemical reactivity of the anodic and cathodic surface sites on the Si electrode. Starting with Eq. (14), the OCP is defined from the condition $i = 0$:

$$E_{(\text{OCP})} = \frac{1}{2}(E_{\text{Si}} + E_{\text{H}}) + \frac{RT}{F} \ln \left(\frac{i_{02}}{i_{01}} \right) \quad (27)$$

This equation reveals that the direct measurement of the OCP gives information related to the electrochemical reactivity of the anodic and cathodic sites.

Interesting results were obtained by this method as shown in Fig. 13, which depicts the drastic effect of Cu nucleation on the OCP value. These curves first show the initial OCP recorded during 3 min in the dark, in oxygen free pure DHF, on 6 separate n-type silicon samples. This value is quite reproducible for the whole set of samples.

A trace amount of Cu^{2+} ions was then introduced in the cell so as to reach the concentration indicated on the curves of Fig. 13. It immediately resulted in a steep rise of the OCP toward more positive values.

Owing to the very small copper surface concentration, such a high change of potential could not be assigned to a contribution of the deposited copper. This feature was analyzed, through Eq. (27) in terms of the catalytic properties for proton reduction kinetics of the very small, nanometer sized, copper nuclei generated on the silicon surface. To understand the effect of the catalytic sites, it is worth noting that the exchange current of the anodic reaction of Si, Eq. (6), is a constant but the compensating cathodic reaction of hydrogen should be separated into two contributions accounting for two possible

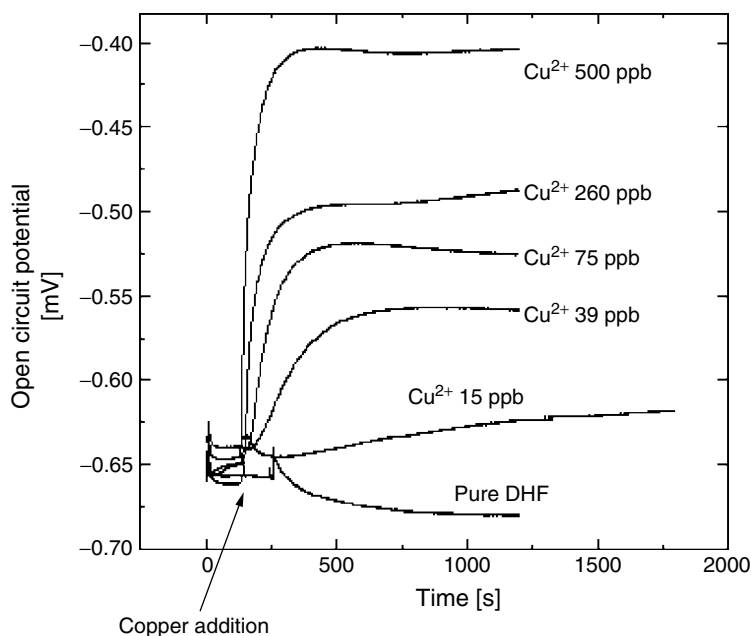


Fig. 13 Time dependence of the OCP at n-type silicon, in the dark, in a thoroughly deaerated 5% HF solution, upon addition of trace amounts of copper ions (after Chemla et al. [14]).

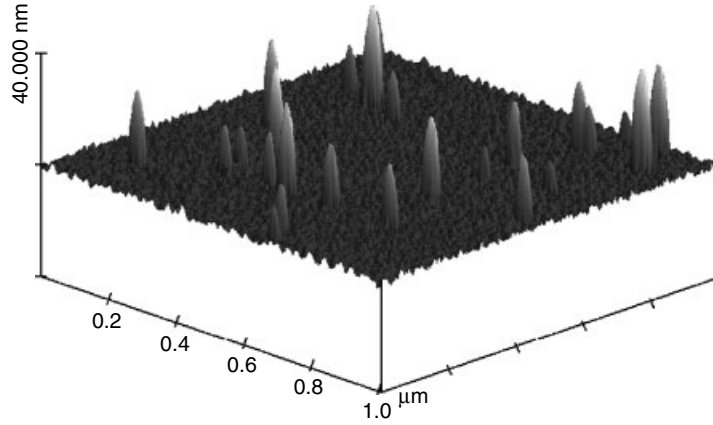
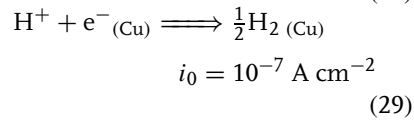
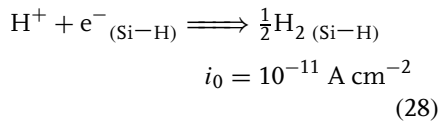


Fig. 14 TMAFM observation of copper nuclei generated in the dark on a p-type Si surface after dipping for 1 min. in a 5% DHF solution containing 1 ppm Cu^{2+} ions (after Chemla et al. [14]).

reactions sites, (1) on the Si surface, and (2) on the Cu nuclei.



It is well known that the exchange current density on the Si surface passivated by Si-H terminal bonds is extremely low, ca. 10^{-10} to $10^{-11} \text{ A cm}^{-2}$. On the other hand, the same exchange current on metallic copper is near $10^{-7} \text{ A cm}^{-2}$, and certainly much higher on nanoscopic particles. At this first stage, the copper nuclei are generated on the clean Si surface, as presented in Fig. 14, which shows the first Cu particles observed by atomic force microscopy working in tapping mode (TMAFM). The amount of Si material consumed for the electroless deposition is quite negligible. The needlelike shape of the nuclei on the AFM scan is not real. The appearance is only due to the scale

difference, $1 \mu\text{m}$ along the $x \times y$ axes and 40 nm for the z -axis.

It was demonstrated that the growth of Cu nuclei goes on with time, while the OCP values of Fig. 13 reach a plateau after a long time. This effect was attributed to a weaker catalytic effect of the large copper clusters that balance the continuing increase in the size of the clusters.

On the other hand, the condition of zero current leads necessarily to the conclusion that the corrosion current of the Si substrate in DHF is strongly enhanced, correlated with the increase in the HER at catalytic sites. After a longer time, this fact mainly results in generating corrosion pits in the immediate neighborhood of the metallic nuclei due to the formation of short-circuited nanoscale electrochemical cells.

10.3.4

Electrochemical Photovoltaic Cells

The most direct solar energy conversion for the production of electricity [15] is

based on solid-state–photovoltaic cells. There are two types of purely solid-state devices, one based on p–n junction photocells, and the second consisting of a Schottky type metal–semiconductor junction. The light excitation leads to the formation of electron-hole pairs, which are separated by the electric field across the space charge in the vicinity of the junction. The corresponding photocurrent in the reverse direction is proportional to the light intensity. The photopotential U_{ph} is measured under open-circuit conditions, that is, when the external current is zero. Presently, solar energy conversion efficiencies of up to 20% have been obtained with single crystal devices, and around 9% with polycrystalline or amorphous layers.

Similar photovoltaic cells can be made of semiconductor/liquid junctions. For example, the system could consist of an n-type semiconductor and an inert metal counterelectrode, in contact with an electrolyte solution containing a suitable reversible redox couple. At equilibrium, the electrochemical potential of the redox system in solution is aligned with the Fermi level of the semiconductor. Upon light excitation, the generated holes move toward the Si surface and are consumed for the oxidation of the red species. The charge transfer at the Si/electrolyte interface should account for the width of occupied states in the semiconductor and the range of the energy states in the redox system as represented in Fig. 1.

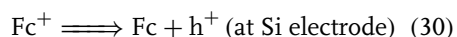
The stability of silicon electrodes contacting an aqueous electrolyte is a severe problem in regenerative solar systems. As mentioned previously, the standard electrode potential of a silicon element is negative enough to induce an electrochemical reaction mechanism, giving rise to an insulating surface silicon oxide in the absence of complexing reactants. On the

other hand, in highly alkaline, or alternatively in fluoride containing solutions, a corrosion process, even extremely slow, will gradually alter the effectiveness of the system.

For this reason, an interesting photoelectrochemical cell based on an n-type Si electrode in an aqueous solution containing the Br_2/Br^- redox couple cannot be operated at a steady regime for a long time, because the charge carriers have to overcome a high energy barrier due to the formation of a thin oxide layer. In this context, it should be mentioned that the height of the barrier can be reduced by a procedure of metal nanoparticles deposition. For example, Pt metal clusters 10 nm in diameter can be deposited on n-type Si surfaces. If the barrier height at the metal/semiconductor junction is not too large, the photoholes generated by light excitation can enter the metal via a quantum mechanical penetration process. Then the maximum photovoltage is determined by the standard potential of the redox couple, and the photocurrent is only carried by electrons transferred via the metal nanoparticles. This was actually found with n-type Si electrodes working with the Br_2/Br^- couple, and with very high photovoltages up to 0.68 V at a current density of 20 mA cm^{-2} were obtained in a corresponding electrochemical photovoltaic cell.

A stable configuration can only be achieved when nonaqueous solvents are involved. For example, a photoelectrochemical cell can be operated using the ferrocene/ferrocinium couple at an n-type Si electrode in a pure methanol solvent. This system is of special interest because the rate-determining steps can be analyzed in detail. Using Si as an electrode in CH_3OH or CH_3CN requires that the solvent is completely water free in order

to avoid any growth of an insulating oxide layer that would block a charge transfer across the interface. It was found that the photovoltage rises linearly with an increase in the redox potential of the solution. In fact, the redox potential value can be varied by using different derivatives of ferrocene. The highest photovoltage, 0.67 V at 20 mA cm^{-2} , was obtained with the use of dimethyl ferrocene ($E^\ominus = +0.15 \text{ V}$ vs. SCE). In addition, it was shown that the forward current involves positive holes following a valence band process:



Interestingly, this forward current is not controlled by the interface charge-transfer kinetics but entirely by the diffusion and recombination of holes injected into the valence band. This was demonstrated by using differently doped Si electrodes having different diffusion lengths for holes.

It has then to be concluded that the charge transfer in the ferrocene/ferrocenium couple in this specific solvent is a fast process at the timescale of the hole diffusion in the semiconductor space charge layer. However, at the present time, it seems that the constraints arising from the construction of a perfectly tight device will hinder the development of these electrochemical photovoltaic cells.

References

1. D. Elwell, G. M. Rao, *J. Appl. Electrochem.* **1988**, 18, 15.
2. N. S. Lewis, A. B. Bocarsly in *Semiconductor Electrodes* (Ed.: H. O. Finklea), Elsevier, New York, 1988.
3. S. R. Morrison, *Electrochemistry of Semiconductor and Oxidized Metal Electrodes*, Plenum Press, New York, 1981.
4. H. Gerischer, M. Lübke, *J. Electrochem. Soc.* **1988**, 135, 2782.
5. H. Gerischer, *Electrochim. Acta* **1990**, 35, 1677.
6. X. G. Zhang, *Electrochemistry of Silicon and its Oxide*, Kluwer Academic/Plenum Publishers, New York, 2001, p. 75.
7. S. Ottow, G. S. Popkurov, H. Föll, *J. Electroanal. Chem.* **1998**, 455, 29.
8. M. Chemla, V. Bertagna, R. Erre et al., *Electrochem. Solid State Lett.* **2003**, 6, G7.
9. D. Vanmaekelberg, P. C. Searson, *J. Electrochem. Soc.* **1994**, 141, 697.
10. L. Pavesi, Z. Gaburro, L. Dal Negro et al., *Opt. Lasers Eng.* **2003**, 39, 345.
11. W. Kern, D. A. Puotinen, *RCA Rev.* **1970**, 31, 186.
12. V. Bertagna, R. Erre, F. Rouelle et al., *J. Solid State Electrochem.* **2001**, 5, 306.
13. P. M. M. C. Bressers, J. J. Kelly, J. G. E. Gardeniers et al., *J. Electrochem. Soc.* **1996**, 143, 1744.
14. M. Chemla, T. Homma, V. Bertagna et al., *J. Electroanal. Chem.* **2003**, 559, 111.
15. R. Memming in *Topics in Current Chemistry, Electrochemistry II* (Ed.: E. Steckhan), Springer Verlag, Berlin Heidelberg, 1988, p. 79.

11 Alkali Metals

Jody Redepenning
University of Nebraska, Lincoln, Nebraska, USA

11.1	Introduction	335
11.2	Secondary Lithium-ion Batteries	335
11.3	Standard Potentials in Aqueous Solutions	336
11.4	Temperature Dependence of Standard Potentials	340
11.5	Alkali Metal Hydrides	340
11.6	Pourbaix Diagrams	341
11.7	Amalgams	343
11.8	Formation of Binary Compounds	343
11.9	Nonaqueous Solvents	345
	References	348

11.1 Introduction

In the final decades of the twentieth century, some of the most technologically significant advances in electrochemistry were located within the seemingly narrow confines of group 1 in the periodic table. More specifically, in the 1980s and 1990s the development and mass production of rechargeable lithium-ion batteries helped usher in a technological renaissance in communication and computation. In large part, this renaissance was one of mobility. The advent of inexpensive and lightweight secondary batteries with high-energy densities helped facilitate the proliferation of lightweight “cellular” telephones and portable laptop computers. These batteries also facilitated the development and popularity of portable music players, and have become an integral part of industry transforming technologies such as digital photography and videography.

The market for rechargeable lithium batteries has risen steadily since they were introduced in the early 1990s. Between 1995 and 2002, the worldwide production of lithium-ion cells grew at an annual rate of approximately 100 000 cells per year, and at the time of this publication, annual worldwide production is nearly one billion cells valued at four billion

US dollars [1]. It has been estimated that in 2004 the US lithium battery market was valued at \$2.1 billion [2]. Despite the magnitude of the US market, nearly all of the manufacturing capability for these cells is found in Japan, Korea, and China.

It should also be noted that the demand for primary lithium batteries remains strong, particularly in military applications where there is high demand for lightweight and disposable power supplies for portable electronic devices. In fact, the US General Accounting Office (GAO) has indicated that primary lithium batteries were one of seven items for which “supply shortages reduced operational capability and increased risk to [US] troops” [3].

11.2 Secondary Lithium-ion Batteries

The focus of this chapter is on the electrochemistry of alkali metals, not on the specific technological developments that have led to the successful production of rechargeable lithium batteries, but given the impact of this technology, a brief overview is warranted. The evolving story of commercially successful rechargeable lithium batteries describes the balance of safety with economic concerns, and the balance of fundamental science with

empiricism. In the last 15 years, many hurdles have been overcome to achieve the high-energy and power capacities anticipated for lithium-ion batteries in comparison to Ni–Cd batteries. Because of the large cell potential, which is often greater than 3.6 V, a significant effort has been devoted to finding a stable and economical solvent/electrolyte system with high ionic conductivity. Although there are now many variations, the use of LiPF₆ electrolyte in propylene carbonate (PC) has proven to be quite successful. Both can be obtained at modest cost in highly pure forms. Both are highly stable in the desired potential range, and although LiPF₆ is susceptible to the formation of hydrolysis products that can compromise cell performance, the device can be packaged such that water contamination is minimized. The breakthrough that enabled the reproducible recharging of lithium batteries was the implementation of graphitic anodes and cobalt oxide cathodes, which can reproducibly intercalate lithium ions. This “rocking chair technology” facilitates the migration (rocking) of lithium ions between the intercalating electrodes to provide excellent mechanical and chemical stability on scales ranging from the macroscopic to the atomic. These technologies were integrated by Sony, which marketed the first commercially successful lithium-ion battery in 1991.

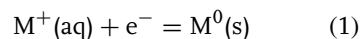
Since 1991, a significant research effort, in academia and in industry, has focused on fundamental science and on incremental improvements of the technologies that have made Li-ion batteries a success. These incremental improvements have dispersed the ownership of the intellectual property over a large number of entities. In regard to the fundamental science of these cells, it is clear that both the structure of the electrodes and the mechanisms that allow

them to function are highly complex. For example, the intercalating anodes exhibit an intricate morphology, which includes a passivation layer that is sensitive to solvent, electrolyte, and any impurities that may be present [4]. Solution additives can be introduced to attenuate deleterious side reactions or to stabilize the passivating surface layer [5]. Additionally, although their exact function is still unclear, the addition of chelates such as crown ethers may facilitate the intercalation process and prevent unwanted side reactions by making the lithium ion a weaker electrophile [6]. Readers interested in a more thorough review of the design criteria for electrolyte solutions for lithium-ion batteries are directed to a review by Aurbach et al. [7]. Comprehensive treatments of the research and development of primary and secondary lithium batteries can be found in a number of recent books [8–10].

11.3

Standard Potentials in Aqueous Solutions

In making a transition to a quantitative discussion of the electrochemistry of the alkali metals, we begin with a discussion of standard potentials. Table 1 provides a list of standard potentials for half-reactions that take the generic form found in Eq. (1)



where $M^+(aq)$ is an alkali metal cation, and $M^0(s)$ is a pure alkali metal.

For the most part, the standard potentials shown in Table 1 have converged on values for which there is little uncertainty. With the exception of the francium couple, the first column of standard potentials is calculated from standard free energies of formation provided by the National Institute of Science and Technology

Tab. 1 Standard potentials (in V versus standard hydrogen electrode (SHE)) for alkali metals and their monovalent cations in water at 298.15 K

Half-reaction	E° (from ΔG°) [11]	E° (Lewis) [12]	E° (measure)
$\text{Li}^+ + \text{e}^- = \text{Li}^0$	−3.040	−3.027	−3.040 [13]
$\text{Na}^+ + \text{e}^- = \text{Na}^0$	−2.714	−2.715	−2.713 [14]
$\text{K}^+ + \text{e}^- = \text{K}^0$	−2.936	−2.925	−2.924 [15]
$\text{Rb}^+ + \text{e}^- = \text{Rb}^0$	−2.943	−2.924	—
$\text{Cs}^+ + \text{e}^- = \text{Cs}^0$	−3.027	—	−2.923 [16]
$\text{Fr}^+ + \text{e}^- = \text{Fr}^0$	−2.9 [17]	—	—

(NIST) [1, 2]. These values are in close agreement with those reported in the classic work of Latimer [18]. The second column of standard potentials shows values measured by Lewis et al. [12]. These measurements, which were performed using dilute alkali metal amalgams that were stable enough to be used in aqueous solutions, have long served as the benchmarks for subsequent refined measurements. The final column shows more refined measurements of standard potentials for alkali metal couples in water [5–8].

At first glance, the standard potentials listed in Table 1 are largely nondescript. All are quite similar, with the possible exception of the sodium couple, which might appear to be anomalously positive. These values are qualitatively consistent with the simple picture that develops upon consideration of the electronic structures of the metals and their oxidized monovalent cations. Each of the metals exhibits an electronic structure that can be symbolized by (noble gas) ns^1 , where the principal quantum number (n) ranges from $2 \leq n \leq 7$. For example, the electronic structure for potassium is $[\text{Ar}]4s^1$, that is, $1s^2 2s^2 2p^6 3s^2 3p^6 4s^1$. Each of the alkali metals can easily lose one electron to give a stable monovalent metal cation that is isoelectronic with the noble gas

immediately preceding it in the periodic table. To summarize, simple arguments based on chemical periodicity lead to the conclusion that the alkali metals are easily oxidized to monovalent cations, and that highly negative electrode potentials are required to reduce these stable cations to their elemental forms.

While the above description has qualitative merit at an introductory level, it is important to recognize that the ground state electronic configurations apply to unassociated *atoms*. Ionization (oxidation) of a metal *phase* in a solvent produces solvated ions, and the stability of these ions is an important influence on the value of the standard potential. Descriptions of alkali metal electrochemistry that are more informative than descriptions based on ground state electronic configurations and periodicity can be obtained by inspection of simple thermodynamic balance sheets. One scheme for assigning the contributions to the oxidation process in solutions is shown in Fig. 1.

The standard free energy of formation of a gaseous metal ion, $\Delta G_f^\circ(\text{M}^+, \text{g})$, can be viewed as the sum of the standard free energy of sublimation, $\Delta G_f^\circ(\text{M}^0, \text{g})$, and the free energy of ionization, $\Delta G_{\text{ioniz}}^\circ$. The standard entropy of a monatomic gas is very nearly equal to the standard entropy of its corresponding monatomic gaseous

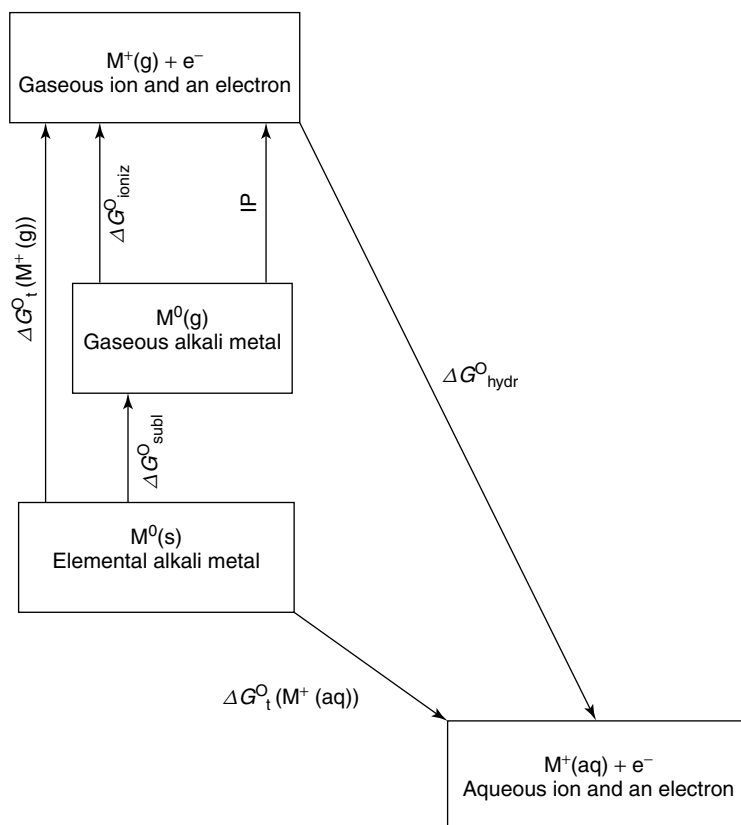


Fig. 1 Formation of aqueous cation from element in its standard state.

ion. Both are largely translational. Consequently the entropies of ionization of a monatomic gas are near zero, making $\Delta G_{\text{ioniz}}^{\circ}$ nearly equal to IP (ionization potential), which is the measurable quantity described by Eq. 2.

$$\text{IP} = \Delta H_{\text{f}}^{\circ}(\text{M}^{+}, \text{g}) - \Delta H_{\text{f}}^{\circ}(\text{M}^0, \text{g}) \quad (2)$$

For those who are interested in a more detailed explanation of Fig. 1, including a thorough review of the entropic contributions, chapters in the two books by Marcus are highly recommended [19, 20].

The standard free energy of formation of the aqueous metal ion, $\Delta G_{\text{f}}^{\circ}(\text{M}^{+}(\text{aq}))$,

can be calculated using Eq. (3).

$$\Delta G_{\text{f}}^{\circ}(\text{M}^{+}(\text{aq})) = \Delta G_{\text{f}}^{\circ}(\text{M}^{+}(\text{g})) + \Delta G_{\text{hydr}}^{\circ} \quad (3)$$

Thermodynamic data relevant to the schematic diagram shown in Figure 1 are found in Table 2. Values relevant to the hydrogen electrode are also included for comparison.

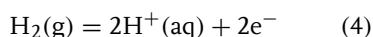
The information tabulated in Table 2 is provided on both the absolute and relative scales. Note that if $\Delta G_{\text{f}}^{\circ}(\text{H}^{+}(\text{g}))$ and $\Delta G^{\circ}(\text{H}^{+}, (\text{hydr}))$ from Table 2 (1523.2 and $-1056 \text{ kJ mol}^{-1}$, respectively on the absolute scale) are used in Eq. (3) to determine

Tab. 2 Contributions to standard free energy of formation of aqueous ions (kJ mol⁻¹) [9, 10]

Couple	ΔG_f° (M ⁺ (g))	ΔG_f° (M ⁰ (g))	Ionization potential	$\Delta G_{\text{hydr}}^\circ$ (absolute)	$\Delta G_{\text{hydr}}^\circ$ (relative)	ΔG_f° (M ⁺ (aq)) (absolute)	ΔG_f° (M ⁺ (aq)) (relative)
H/H ⁺	1523.2	203.25 ^a	1318	-1056	0	467.2	0
Li/Li ⁺	654.8	126.66	526	-481	575.2	173.8	-293.4
Na/Na ⁺	580.5	76.76	502	-375	680.7	205.5	-261.7
K/K ⁺	487.3	60.59	425	-304	752.5	183.3	-283.9
Rb/Rb ⁺	464.0	—	409	-281	775.1	183.0	-284.2
Cs/Cs ⁺	432.7	49.12	382	-258	798.4	174.7	-292.5

^aThis is the bond dissociation energy for H₂(g).

$\Delta G_f^\circ(\text{H}^+(\text{aq}))$, a value of 467.2 kJ mol⁻¹ is obtained for the formation of H⁺(aq) from H₂(g).



If we adopt the usual convention that the half-cell potential for the cell in Eq. (4) is taken to be zero, then we also need to adopt a relative convention in which $\Delta G_f^\circ(\text{H}^+(\text{aq}))$ is zero. Consequently, values of $\Delta G_{\text{hydr}}^\circ$ on the relative scale are taken to be +1056 kJ mol⁻¹ of $\Delta G_{\text{hydr}}^\circ$ on the absolute scale. The resulting values of $\Delta G_f^\circ(\text{M}^+(\text{aq}))$ on the relative scale are in good agreement with the standard potentials listed in Table 1.

If we examine Table 2 in a stepwise fashion, proceeding from cesium to potassium, there is no information that stands out as being anomalous. The atoms with smaller atomic numbers have smaller atomic radii, and as the radii gradually decrease, the respective $\Delta G_f^\circ(\text{M}^0, \text{g})$ increase. As the atomic radii decrease, the increase in $\Delta G_f^\circ(\text{M}^+, \text{g})$ is offset to some extent by increasingly negative $\Delta G_{\text{hydr}}^\circ$; thus $\Delta G_f^\circ(\text{M}^+(\text{aq}))$ (and E°) remain essentially constant. It appears that the only exception to this trend might be $\Delta G_f^\circ(\text{Na}^+(\text{aq}))$, but the unusually small

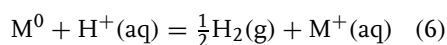
value for the free energy of formation of Na⁺(aq) and the unusually positive standard potential for the Na⁰/Na⁺ couple are red herrings in recognizing the periodic trends. A more detailed consideration that includes H₂/H⁺ shows that Li⁰/Li⁺ is the anomaly, not Na⁰/Na⁺. The IPs of Li⁰(g) and Na⁰(g) are quite similar, despite the fact that the atomic radius (r) of lithium (1.34 Å) is much smaller than that of sodium (1.54 Å). $\Delta G_f^\circ(\text{Li}^+(\text{g}))$ is much smaller than might be expected on the basis of a trend that includes $\Delta G_f^\circ(\text{H}^+(\text{g}))$. Note that $\Delta G_f^\circ(\text{Li}^+(\text{g})) - \Delta G_f^\circ(\text{Na}^+(\text{g}))$ is only 74.3 kJ mol⁻¹, and of this amount, 49.9 kJ mol⁻¹ is due to the larger $\Delta G_{\text{subl}}^\circ$ of lithium compared to sodium. The small $\Delta G_f^\circ(\text{Li}^+(\text{g}))$ can be attributed to the fact that shielding of the valence electron from the nuclear charge is much more efficient in lithium than in sodium. Indeed, the effective nuclear charge (often symbolized by Z_{eff}) is only 1.3 for lithium, but is 2.5 for sodium; thus, Z_{eff}/r for lithium and sodium are more similar than might otherwise be expected, as are the IPs. The result is a standard potential for the Li⁰/Li⁺ couple that is more negative than might be expected on the basis of qualitative periodic trends from Cs⁰/Cs⁺ to H₂/H⁺.

11.4 Temperature Dependence of Standard Potentials

The standard potentials listed in Table 1 are all at 298.15 K. Given that not all electrochemistry is done at 298.15 K, it is useful to consider the temperature dependence of the standard potentials for the alkali metals. The temperature dependence can be obtained from the change in entropy, which is given by Eq. (5).

$$\Delta S^\circ = nF \left(\frac{\partial E}{\partial T} \right)_P \quad (5)$$

So, for the reaction of a generic alkali metal (M^0) with hydrogen ions as shown in Eq. (6),



the temperature dependence of the standard potential is given by Eq. (7).

$$\left(\frac{\partial E}{\partial T} \right)_P = [S^\circ(H^+, aq) + S^\circ(M^0)] - \left[\frac{S^\circ(H_2, g)}{2} + S^\circ(M^+, aq) \right] \quad (7)$$

$$M^+(aq) + H^+(aq) + 2e^- = MH(cr) \quad (8)$$

Table 3 provides entropies for those species that are needed to determine the temperature dependence of standard potentials for alkali metal redox couples. All of these entropies were obtained from values published by NIST [11]. The resulting temperature dependences agree well with values tabulated by Bratsch [17].

11.5 Alkali Metal Hydrides

Lithium hydride and sodium hydride are the only alkali metal hydrides of much practical importance. They are useful when it is desirable for proton (or hydrogen atom) transfers to accompany electron-transfer events. Because these hydrides react quickly with water to form alkali metal hydroxides and hydrogen gas, they are frequently used as drying agents, particularly for hydrocarbons and ethers. Care should be exercised in using them to dry solvents that are not predried, and they should not be used to dry alcohols or halogenated solvents.

Standard potentials for half-cells that take the following generic form,

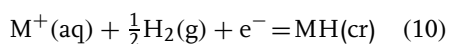
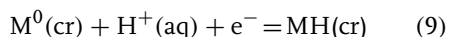
Tab. 3 Standard entropies for alkali metals and aqueous metal ions, and temperature dependences of their standard potentials

Half-reaction	$S^\circ(M^0)$ [J mol ⁻¹ K ⁻¹]	$S^\circ(M^+, aq)$ [J mol ⁻¹ K ⁻¹]	$\left(\frac{\partial E}{\partial T} \right)_P$ [μV K ⁻¹]
H ⁺ (aq) + e ⁻ = 1/2H ₂ (g)	130.684	0	0
Li ⁺ (aq) + e ⁻ = Li ⁰	29.12	13.4	-0.514
Na ⁺ (aq) + e ⁻ = Na ⁰	51.21	59.0	-0.758
K ⁺ (aq) + e ⁻ = K ⁰	64.18	102.5	-1.074
Rb ⁺ (aq) + e ⁻ = Rb ⁰	76.78	121.50	-1.141
Cs ⁺ (aq) + e ⁻ = Cs ⁰	85.23	133.05	-1.173

are found in Table 4. Half-cell potentials for specific examples can be determined from the standard free energies of formation of the relevant alkali metal hydrides and aqueous ions. The NIST tables are again useful for these determinations; however, the standard free energies of formation of KH, RbH, and CsH have not been measured reliably [11]. Consequently, estimates of standard potentials provided by Bratsch are listed for KH, RbH, and CsH [17]. The free energies of formation listed for KH, RbH, and CsH in Table 4 have been calculated on the basis of known free energies of formation of the aqueous metal ions and Bratsch's estimates of standard potentials.

The information contained in Table 4 can also be used to determine standard

potentials for other half-cells that contain alkali metal hydrides. Two alternative expressions take the following general forms



Standard potentials for specific examples of these half-reactions are found in Table 5.

11.6 Pourbaix Diagrams

The information in the preceding equations can be summarized in a highly informative graphical form popularized

Tab. 4 Standard free energies of formation and standard potentials for alkali metal hydrides in water

Half-reaction	$\Delta G_f^\circ (MH, \text{cr})$ [kJ mol ⁻¹]	$\Delta G_f^\circ (M^+, \text{aq})^b$ [kJ mol ⁻¹]	E° (V versus SHE)
$\text{Li}^+ + \text{H}^+ + 2e^- = \text{LiH}$	-68.35	-293.31	-1.166
$\text{Na}^+ + \text{H}^+ + 2e^- = \text{NaH}$	-33.46	-261.905	-1.184
$\text{K}^+ + \text{H}^+ + 2e^- = \text{KH}$	-34.3 ^a	-283.27	-1.29 [17]
$\text{Rb}^+ + \text{H}^+ + 2e^- = \text{RbH}$	-27.3 ^a	-283.98	-1.33 [17]
$\text{Cs}^+ + \text{H}^+ + 2e^- = \text{CsH}$	-29.6 ^a	-292.02	-1.36 [17]

^aCalculated on the basis of estimates of the standard potential found in the last column of this table.

^bThese same standard free energies of formation were used to calculate the standard potentials listed in Table 1.

Tab. 5 Standard potential for hydridic half-cells containing alkali metals

Half-reaction	E° [V]	Half-reaction	E° [V]
$\text{Li}^0 + \text{H}^+ + e^- = \text{LiH}$	0.708	$\text{Li}^+ + 1/2H_2 + e^- = \text{LiH}$	-2.331
$\text{Na}^0 + \text{H}^+ + e^- = \text{NaH}$	0.347	$\text{Na}^+ + 1/2H_2 + e^- = \text{NaH}$	-2.368
$\text{K}^0 + \text{H}^+ + e^- = \text{KH}$	0.355	$\text{K}^+ + 1/2H_2 + e^- = \text{KH}$	-2.58 [17]
$\text{Rb}^0 + \text{H}^+ + e^- = \text{RbH}$	0.283	$\text{Rb}^+ + 1/2H_2 + e^- = \text{RbH}$	-2.66 [17]
$\text{Cs}^0 + \text{H}^+ + e^- = \text{CsH}$	0.307	$\text{Cs}^+ + 1/2H_2 + e^- = \text{CsH}$	-2.72 [17]

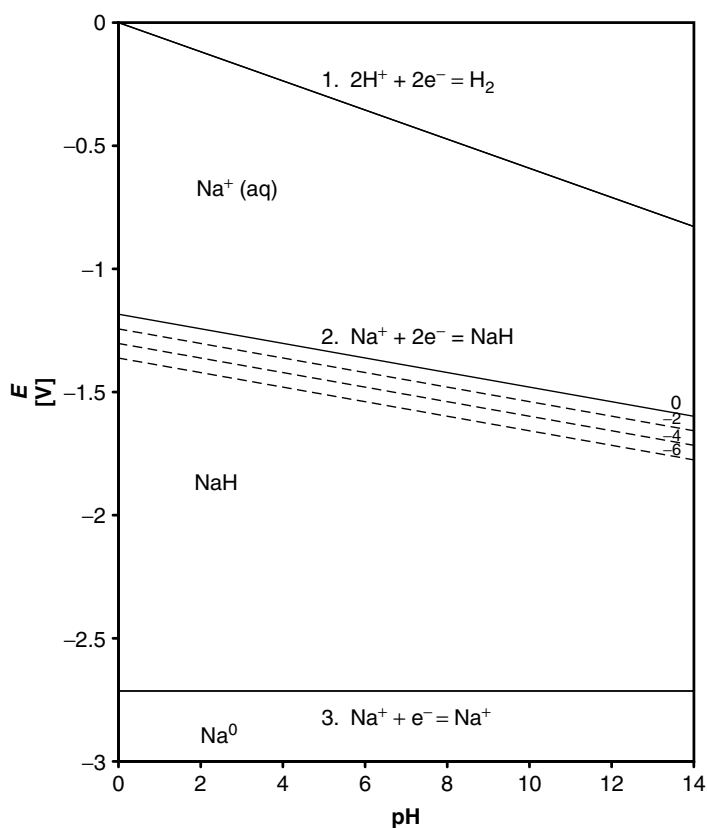


Fig. 2 Potential-pH diagram for sodium.

by Pourbaix [21]. In such displays, sometimes called *predominance-region plots*, half-cell potentials are plotted versus pH to describe the redox behavior of the element of interest. The predominant species are usually clearly indicated in each region, the borders of which are formed by relevant half-cell reactions or precipitation reactions. Such a diagram for sodium is shown in Fig. 2.

Lines 1–3 in Fig. 2 were calculated on the following basis:

$$\begin{aligned} \text{Line 1. } E_1 &= E_1^\circ - 0.0592 \log a(\text{H}_2) \\ &\quad - 0.0592 \text{ pH} \end{aligned} \quad (11)$$

where $E_1^\circ = 0 \text{ V}$ and $a(\text{H}_2) = 1$.

$$\begin{aligned} \text{Line 2. } E_2 &= E_2^\circ + 0.0592 \log a(\text{Na}^+, \text{aq}) \\ &\quad - 0.0296 \text{ pH} \end{aligned} \quad (12)$$

where $E_2^\circ = -1.184$ (from Table 4) and $a(\text{Na}^+, \text{aq}) = 1$. Cases where $\log a(\text{Na}^+, \text{aq}) = -2, -4, -6$ are shown as dotted lines.

$$\begin{aligned} \text{Line 3. } E_3 &= E_3^\circ - 0.0592 \log a(\text{Na}^+, \text{aq}) \end{aligned} \quad (13)$$

where $E_3^\circ = -2.714 \text{ V}$ (from Table 1) and $a(\text{Na}^+, \text{aq}) = 1$.

On the scale at which these plots are usually made, potential-pH plots for the

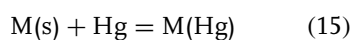
other alkali metals are quite similar to that shown for sodium. Detailed plots can be prepared using information found in Tables 1 and 4, and equations analogous to Eqs (11–13). Pourbaix has compiled similar plots, which are slightly different in detail because they contain thermodynamic information that has now been refined [21].

11.7 Amalgams

The potentials of half-cells that are constructed using amalgams are important whenever one is interested in performing reactions in a media in which hydrogen evolution at the metal–solution interface might interfere with the reaction of interest. Consequently, half-cell potentials for alkali metal amalgams are important to synthetic chemists and electrochemists alike. The standard potential for a metal amalgam in contact with a solution of its monovalent cation ($E^\circ(\text{M}^+/\text{M}(\text{Hg}))$) can be related to that of the pure metal in contact with its monovalent cation (E°_{M}) as shown in Eq. (14)

$$E^\circ(\text{M}^+/\text{M}(\text{Hg})) = E^\circ_{\text{M}} + \frac{RT}{nF} \log a(\text{M}^+)_{\text{s}} - \frac{RT}{nF} \ln a(\text{M}(\text{Hg})) \quad (14)$$

where $a(\text{M}(\text{Hg}))$ is the activity of the metal in the mercury amalgam and $a(\text{M}^+)_{\text{s}}$ is the metal ion activity in solution. The difference in these standard potentials can be used directly to calculate standard free energy of amalgamation for the reaction shown in Eq. (15).



A number of detailed thermodynamic comparisons of half-cells containing alkali metal and alkali metal amalgams are available. For example, Cogley and Butler examined cell potentials as a function of amalgam concentration for the cell shown below [22].



The cell design represented by Eq. (16) is noteworthy. For this cell, the activity of lithium ions in solution is irrelevant to the overall cell potential because both the anode and the cathode exhibit the same dependence on lithium-ion activity. Consequently, the cell potential can be written using the relatively simple expression shown in Eq. (17),

$$E = E^\circ_{\text{Li}(\text{Hg})} - E^\circ_{\text{Li}} - \frac{RT}{F} \ln(X_{\text{Li}}\gamma_{\text{Li}}) \quad (17)$$

where $E^\circ_{\text{Li}(\text{Hg})}$ is the standard potential for the lithium amalgam, E°_{Li} is the standard potential for solid lithium (see Table 1), X_{Li} is the mole fraction of lithium in the amalgam, and γ_{Li} is the activity coefficient of lithium in the amalgam. Other alkali metal amalgams can be treated in a similar fashion. Standard potentials and free energies of amalgamation for alkali metal amalgams are found in Table 6. For more detailed discussions of amalgam properties and thermodynamics, the reader is directed to peruse the works by Guminski et al. [23–25].

11.8 Formation of Binary Compounds

Up to this point, most of the discussions in this chapter have focused on descriptions of electrochemical half-cells of the

Tab. 6 Standard potentials (in V versus SHE) and free energies of amalgamation (in kJ mol⁻¹) for alkali metal amalgams and their monovalent cations in water

<i>Element</i>	$E_{\text{M(Hg)}}^{\circ}$ [24]	$E_{\text{M(Hg)}}^{\circ} - E_{\text{M}}^{\circ}$	$\Delta G_{\text{amalgam}}^{\circ}$
Li	-2.195	0.845	-81.5
Na	-1.958	0.755	-72.8
K	-1.975	0.949	-91.6
Rb	-1.970	0.973	-93.9
Cs	-1.950	0.974	-94.0

alkali metals. Of course, any redox event that includes such a half-cell must include at least one other half-cell, and the driving force for the overall reaction depends on the potentials of both half-cells. Furthermore, the thermodynamics of coupled chemical reactions such as precipitations or complexations may have a profound influence on redox reactions. Such reactions can even drive electron-transfer events that might otherwise be unfavorable. A thorough review of this subject matter is far beyond the scope of this chapter, but a brief overview of a small subset is viable. The subset considered here is the formation of binary alkali metal compounds. Many of the compounds described can be prepared by direct reaction of an alkali metal with another species in its elemental form, but such procedures are frequently not the preferred synthetic routes.

One informative means of organizing a discussion of binary alkali metal compounds is by group in the periodic table. The overview provided below begins with binary alloys formed with other alkali metals and ends with binary compounds formed with halogens. The focus is primarily on second row elements. More detailed discussions can be found in the books concerning inorganic chemistry [26, 27].

Binary compounds do not form between any given alkali metal and another alkali metal, nor do binary compounds form with alkaline earth metals. However, a number of binary alloys do form, and the phase diagrams for these alloys exhibit a high degree of diversity. Phase diagrams for binary alloys of alkali metals with other alkali metals and with alkaline earth metals can be found in a compilation edited by Massalski [28]; many other binary alloys of the alkali metals are also included. Binary compounds containing alkali metals and boron are quite rare. There have been apparently no reports of alkali metal borides until 1963 when the synthesis of NaB₆ was first described [29]. Alkali metal borides are presently of little practical utility, but they provide valuable information in helping to discern periodic trends in chemical reactivity. For a more detailed review of this interesting class of compounds, the reader is directed to the works by Hagenmuller [30]. Alkali metals do not react with carbon to give saltlike structures with what are nominally C⁴⁻ anions in the lattice. Instead, they form solids that are better described as acetylides containing C₂²⁻ anions. Alkali metal nitrides can be produced by a variety of methods, but only lithium reacts directly with N₂ to produce Li₃N. Sanderson has pointed out that the interaction between the nitrogen and the

lithiums in Li_3N has significant covalent character; hence, it is unlikely that the nitrogen in this compound should be treated as a “true” nitride (N^{3-}) ion [27]. Among the binary compounds formed by the alkali metals, the compounds formed with oxygen are certainly the most diverse. The multiple formal oxidation states of oxygen in conjunction with size diversity of the alkali metal cations produces an interesting array of materials. The elements from sodium through cesium can form stable solid superoxides, which take the form MO_2 . All are very strong oxidizing agents. Lithium superoxide is not formed, possibly because of a strong interaction between oxygen and lithium, which weakens the oxygen–oxygen bond. All of the alkali metals burn in air to give peroxides, but little Li_2O_2 is formed because of the unusually high stability of Li_2O . All of the alkali metal oxides are basic oxides, in other words, they react with water to give hydroxides. All of the hydroxides are highly soluble in water. Consequently, metal hydroxide phases do not appear in Pourbaix diagrams such as the one shown in Fig. 2. Binary compounds with lithium ions and small or highly charged anions are often more stable than analogs with the other alkali metals. In large part, this is due to the very high charge density of the lithium ion, which results in very large lattice energies for the resulting solids. LiH , like Li_3N mentioned above, serves as an example. LiH is much more stable and generally much less reactive than NaH . Finally, the well-known alkali metal halides exist largely as one to one compounds, all of which exhibit large lattice energies. The most notable exceptions are the triiodides, MI_3 , which increase in stability as one proceeds down the periodic table.

Much of the phenomenology described above can be found in more quantitative

forms in Fig. 3 and in tables provided by NIST [11]. Figure 3 is designed to provide graphical representations of the periodic trends present for binary compounds of the alkali metals. The information is sorted by anion so that periodic trends can be identified more readily. All of the raw data used to construct the plots shown in Fig. 3 were previously tabulated by Reed [31]. The NIST tables provide additional thermodynamic data for those interested in detailed information or in performing their own thermodynamic calculations [11].

11.9 Nonaqueous Solvents

The electrochemical behavior described above has been limited to solid-state or aqueous systems. Such systems are certainly important because of their widespread applicability, but a significant amount of electrochemical research has been performed in nonaqueous solvents. The justifications for performing nonaqueous experiments are frequently straightforward. Many nonpolar or neutral compounds exhibit low solubilities in nonaqueous solutions, and one or more oxidation states of many redox couples are not stable in water. This reactivity can occur because of the acidic nature of water, or because of its intrinsic basicity. Alternatively, the reactivity can be caused by the strong solvating properties of water or to the fact that one or more oxidation states of a redox couple might be oxidized or reduced by water. Use of a nonaqueous solvent is frequently a convenient means of circumventing these problems. The practical utility of nonaqueous electrochemical cells is particularly noteworthy in electroorganic synthesis and in the development of

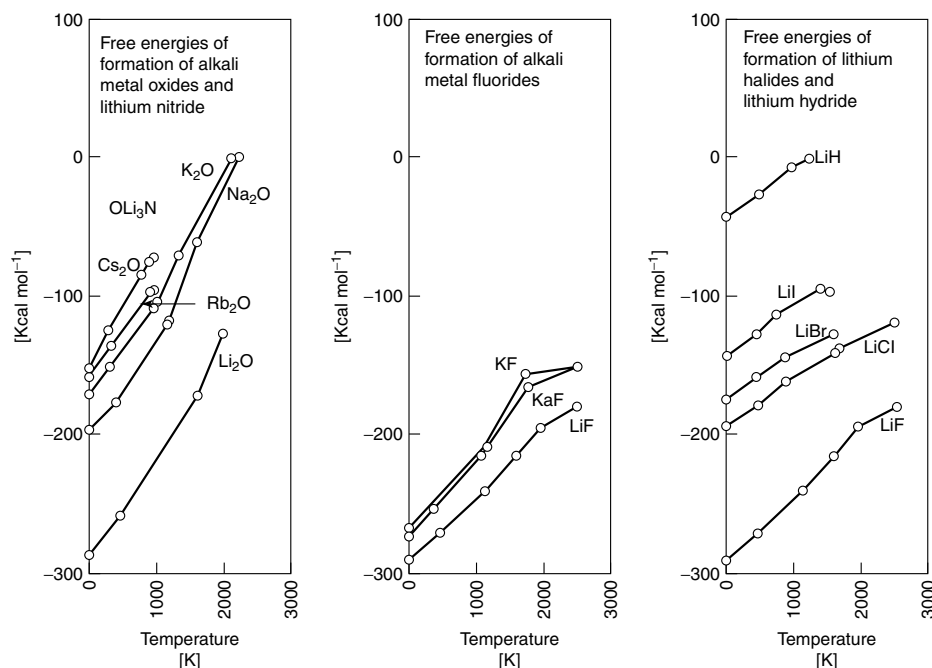


Fig. 3 Temperature dependence of standard free energies of formation for binary compounds with alkali metals.

high-energy batteries. Readers interested in more details are directed to a review, and the more than nine hundred references therein [32].

Unfortunately, in many nonaqueous solvents there is no completely unambiguous way of determining half-cell potentials. This ambiguity stems from the fact that the free energies of transfer (ΔG_t°) of individual ions from one solvent to another are not knowable. (It should be noted that no ambiguity necessarily exists if one is content with comparing “whole-cell” potentials in different solvents. This is true because the free energies of transfer of dissolved salts are knowable.) Some type of extrathermodynamic assumption is usually necessary to compare half-cell potentials measured in one solvent to those measured in some other solvent. Popovich has provided excellent

discussions of these extrathermodynamic assumptions [33], which appear to have converged such that reasonable estimates of ΔG_t° for single ions can now be made.

Marcus has tabulated ΔG_t° for a variety of ions, from water to a variety of solvents [34]. Values for the alkali metal ions ($\Delta G_t^\circ(\text{M}^+, \text{w} \rightarrow \text{s})$) are included in Table 7. $\Delta G_t^\circ(\text{Ag}^+, \text{w} \rightarrow \text{CH}_3\text{CN})$ are included for comparative purposes because the Ag/Ag^+ couple is a reliable reference half-cell in a number of different solvents. $\Delta G_t^\circ(\text{H}^+, \text{w} \rightarrow \text{s})$ are included because they are needed to determine the influence that pH might have on half-cells containing alkali metals. These numbers are also useful in revealing important periodic trends. To provide a frame of reference in comparing the various ions, entries in Table 7 are sorted by $\Delta G_t^\circ(\text{Na}^+, \text{w} \rightarrow \text{s})$.

Tab. 7 Free energies of transfer, $\Delta G_t^\circ(M^+, w \rightarrow s)$ (in kJ mol⁻¹) [34]

<i>Solvent</i>	<i>H</i> ⁺	<i>Li</i> ⁺	<i>Na</i> ⁺	<i>K</i> ⁺	<i>Rb</i> ⁺	<i>Cs</i> ⁺	<i>Ag</i> ⁺
NH ₃	-97	-35	-17	-12	-13	-15	-100
DMSO	-19	-15	-13	-13	-10	-13	-35
DMF	-18	-10	-10	-10	-10	-11	-21
FA	-10	-10	-8	-4	-5	-6	-15
EG	-5	0	-2	-2	-	-	-
THF	-	8	0	6	5	-7	-3
MeOH	10	4	8	10	10	9	7
Acetone	-	10	10	4	4	4	-13
PC	50	24	15	5	-1	-7	19
CH ₃ CN	46	25	15	8	6	6	-31
Pyridine	-28	18	16	14	13	11	-57
PhCN	-	36	21	19	15	13	-18
MeNO ₂	95	48	32	15	11	6	21
PhNO ₂	33	38	36	21	19	18	30
CH ₂ Cl ₂	-	-	58	32	24	22	-

DMSO: dimethyl sulfoxide; DMF: *N, N*-dimethylformamide; FA: formamide; EG: ethylene glycol; THF: tetrahydrofuran; MeOH: methanol; PC: propylene carbonate; PhCN: benzonitrile; MeNO₂: nitromethane; PhNO₂: nitrobenzene.

The $\Delta G_t^\circ(M^+, w \rightarrow s)$ for all of the alkali metal ions follow similar trends. Generally speaking, $\Delta G_t^\circ(M^+, w \rightarrow s)$ are thermodynamically favorable for transfers from water to solvents that exhibit large dielectric constants and large donor numbers. (See Ref. 35 for a discussion of donor numbers.) The transfers are generally unfavorable when made to solvents with small dielectric constants and small donor numbers. Furthermore, because of its high charge density, lithium ion exhibits the largest range of $\Delta G_t^\circ(M^+, w \rightarrow s)$. The properties of lithium ions that either stabilize or destabilize its presence in various solvents are exaggerated by its small size and large effective charge. The influence of solvent basicity is clearly evident, particularly for $\Delta G_t^\circ(H^+, w \rightarrow s)$ when the solvents are ammonia or pyridine; the Lewis acidity of the ions can also play an important role, as is evident for solvents that readily form

coordinate covalent bonds with silver ions. Consequently, cell potentials (comprised of alkali metal half-cells measured versus a Ag/Ag⁺ reference) in solvents such as pyridine, ammonia, and the nitriles, are significantly smaller than those measured in many other solvents, including water. Readers interested in a more detailed discussion of ion solvation in various solvents, including multiparameter fits to various ion and solvent properties, are directed to peruse the work by Marcus [36].

Finally, although the free energies of transfers found in Table 7 are quite useful in comparing cell potentials measured in various solvents, these values are insufficient to adequately interpret potentials measured under many non-aqueous conditions. The primary reason for this difficulty stems from the manner in which $\Delta G_t^\circ(M^+, w \rightarrow s)$ is defined. For example, $\Delta G_t^\circ(Na^+, w \rightarrow CH_3CN)$ is associated with the transfer of sodium ions

in their standard state (i.e. at infinite dilution in water) to acetonitrile where they are also in their standard state (i.e. at infinite dilution in acetonitrile). Since most electrochemical measurements are made under conditions where the ions are far from their standard states, and since methods by which the actual conditions can be related to the standard state are infrequently available in nonaqueous solvents (in other words, the activity coefficients for the ions in nonaqueous solvents are frequently not known), the contributions of individual half-cell potentials to the overall cell potential are frequently ambiguous. Sadly, if fundamental research concerning the thermodynamic behavior of nonaqueous electrochemical cells continues at its present rate, these ambiguities may remain for decades.

References

1. R. J. Brodd, *Factors Affecting U. S. Production Decisions: Why are There No Volume Lithium-Ion Battery Manufacturers in the United States?* ATP Working Paper Series, Working Paper 05-01, National Institute of Standards and Technology, Gaithersburg, June 2005.
2. M. Rajan, Press release, Lithium battery sales to reach \$2.7 Billion by 2009, in reference to RGB-210N *Lithium Batteries: Materials and Markets*, Business Communications Company, Norwalk, August 19, 2004.
3. *Defense Logistics: Actions Needed to Improve the Availability of Critical Items during Current and Future Operations*, Report GAO-05-0275, United States Government Accountability Office, April 2005, p. 19 ff.
4. D. Aurbach, The electrochemical behavior of active metal electrodes in nonaqueous solutions in *Nonaqueous Electrochemistry* (Ed.: D. Aurbach), Marcel Dekker, New York, 1999.
5. D. Aurbach, The role of surface films on electrodes in Li-ion batteries in *Advances in Lithium Batteries* (Eds.: W. A. van Schalkwijk, B. Scrosati), Kluwer Academic Publishers, New York, 2002.
6. A. M. Belostotskii, E. Markevich, D. Aurbach, *J. Coord. Chem.* **2004**, 57, 1047.
7. D. Aurbach, Y. Talyosef, B. Markovsky et al., *Electrochim. Acta* **2004**, 50, 247.
8. G. Pistoia, (Ed.), *Lithium Batteries: New Materials, Development and Perspectives*, Elsevier Science, Amsterdam, 1994.
9. W. A. van Schalkwijk, B. Scrosati, (Eds.), *Advances in Lithium Batteries*, Kluwer Academic Publishers, New York, 2002.
10. G.-M. Nazri, G. Pistoia, (Eds.), *Lithium Batteries: Science and Technology*, Kluwer Academic Publishers, Norwell, 2003.
11. D. D. Wagman, B. H. Evans, V. B. Parker et al., *The NBS Tables of Chemical and Thermodynamic Properties: Selected Values for Inorganic and C₁ and C₂ Organic Substances in SI Units*, American Chemical Society, New York, 1982.
12. (a) G. N. Lewis, C. A. Kraus, *J. Am. Chem. Soc.* **1910**, 32, 1459. (b) G. N. Lewis, F. G. Keyes, *J. Am. Chem. Soc.* **1913**, 35, 340. (c) G. N. Lewis, W. L. Argo, *J. Am. Chem. Soc.* **1915**, 37, 1983.
13. R. Huston, J. N. Butler, *J. Phys. Chem.* **1968**, 72, 4263.
14. E. R. Smith, J. K. Taylor, *J. Res. Natl. Bur. Stand* **1940**, 25, 731.
15. A. J. Dill, L. M. Itzkowitz, O. Popovych, *J. Phys. Chem.* **1968**, 72, 4580.
16. H. E. Bent, G. S. Forbes, A. F. Fortziatti, *J. Am. Chem. Soc.* **1939**, 61, 709.
17. S. G. Bratsch, *J. Phys. Chem. Ref. Data* **1989**, 18, 1.
18. W. M. Latimer, *Oxidation Potentials*, 2nd ed., Prentice Hall, Englewood Cliffs, 1952.
19. Y. Marcus, Chapter 5. Ion hydration *Ion Solvation*, Wiley-Interscience, New York, 1985.
20. Y. Marcus, Chapter 8. Thermodynamic data for hydrated ions, *Ion Properties*, Marcel Dekker, New York, 1997.
21. M. Pourbaix, *Atlas of Electrochemical Equilibria in Aqueous Solutions*, National Association of Corrosion Engineers, Houston, 1974.
22. D. Cogley, J. N. Butler, *J. Phys. Chem.* **1968**, 72, 1017.
23. C. Guminski, *J. Mater. Sci.* **1989**, 24, 2661.
24. T. Mussini, P. Longhi, S. Rondinini, *Ann. Chim.* **1983**, 73, 357.
25. C. Guminski, Z. Galus, in *Solubility Data Series, Metals in Mercury* (Eds.: C. Hirayama), Pergamon Press, Oxford, 1986.

26. R. T. Sanderson, *Chemical Periodicity*, Reinhold Publishing, New York, 1960.
27. F. A. Cotton, G. Wilkinson, C. A. Murillo et al., *Advanced Inorganic Chemistry*, 6th ed., John Wiley & Sons, New York, 1999.
28. T. B. Massalski, (Ed.), *Binary Alloy Phase Diagrams*, ASM International, Materials Park, 1990.
29. P. Hagenmuller, *C. R. Biol.* **1963**, 257, 1294.
30. R. Naslain, J. Etourneau, P. Hagenmuller, V. Alkali metal borides in *Boron and Refractory Borides* (Ed.: V. I. Matkovich), Springer-Verlag, New York, 1977.
31. T. B. Reed, *Free Energy of Formation of Binary Compounds: An Atlas of Charts for High-Temperature Chemical Calculations*, MIT Press, Cambridge, 1971.
32. J. Barthel, Nonaqueous electrolyte solutions in chemistry and modern technology in *Topics in Current Chemistry* (Ed.: F. L. Boschke), Springer-Verlag, New York, 1983, Vol. 111.
33. (a) O. Popovich, Estimation of medium effects for single ions in non-aqueous solvents in *Treatise on Analytical Chemistry, Part 1* (Eds.: I. M. Kolthoff, P. J. Elving), John Wiley & Sons, New York, 1970, p. 73 ff, Vol. 1. See also (b) O. Popovich, Transfer activity coefficients (medium effects) in *Treatise on Analytical Chemistry, Part 1*, 2nd ed., (Eds.: I. M. Kolthoff, P. J. Elving), John Wiley & Sons, New York, 1979, p. 711, Vol. 1.
34. Y. Marcus, Chapter 15. Ion-solvent preferences, *Ion Properties*, Marcel Dekker, New York, 1997.
35. V. Gutmann, *The Donor-Acceptor Approach to Molecular Interactions*, Plenum Publishing, New York, 1978.
36. Y. Marcus, M. J. Kamlet, R. W. Taft, *J. Phys. Chem.* **1988**, 92, 3613.

12

Titanium, Zirconium, and Hafnium

Christopher J. Pickett
John Innes Centre, Norwich, UK

12.1	Syntheses of Coordination Complexes by Anodic Dissolution of the Metal	353
12.2	Electrochemistry in Molten Salts	353
12.3	Metallocene Systems	353
12.4	Porphyrin, Phthalocyanine, and Other Systems	355
	References	355

12.1

Syntheses of Coordination Complexes by Anodic Dissolution of the Metal

Anodic dissolution of metals in the presence of ligands allows the syntheses of various coordination complexes, and these have included examples of the preparation of a limited number of titanium complexes. For example, anodic dissolution of Ti in the presence of CO and cyclopentadienyl monomer is reported to yield $[\text{Ti}(\eta^5\text{-C}_5\text{H}_5)_2(\text{CO})_2]$ [1]. This field has been reviewed but has not been extensively developed since the early work of Tuck and coworkers [2, 3].

12.2

Electrochemistry in Molten Salts

The electrochemical reduction of TiCl_4 and ZrCl_4 , in chloroaluminate melts and other molten salt systems, to lower valent halides has been fairly widely studied [4–7]. This has also been extended to studies of centered hexanuclear Zr halide clusters. Thus, ambient temperature AlCl_3 -1-ethyl-3-methylimidazolium chloride (ImCl) molten salts, both basic (40/60 mol% AlCl_3 /ImCl) and acidic (60/40 mol% AlCl_3 /ImCl), were used in an electrochemical investigation of clusters

$[(\text{Zr}_6\text{ZCl}_{12})\text{Cl}_6]^{n-}$ ($\text{Z}=\text{Be, B, C, Mn, Fe}$); in basic melts, the clusters generally show two reversible reduction steps at potentials that are strongly dependent on the net charge on the cluster ($n-$) [8]. The electrochemistry of $[\text{Ti}(\eta^5\text{-C}_5\text{H}_5)_2\text{Cl}_2]$ has also been examined in acidic and basic melts [9].

12.3

Metallocene Systems

Electrochemical studies of the Ti group of metals have been far and away, dominated by studies of metallocene complexes. The primary reduction of the dihalides $[\text{M}(\eta^5\text{-C}_5\text{H}_5)_2\text{X}_2]$ ($\text{M}=\text{Ti, Zr, or Hf}$) in nonaqueous solvents is a reversible single electron-transfer step to give the labile M(III) monoanions [10–12] from which a halide ligand can be reversibly displaced by a solvent or by a free ligand. For example, electrochemical reduction of $[\text{Ti}(\eta^5\text{-C}_5\text{H}_5)_2\text{Cl}_2]$ in the presence of PMe_3 gives the Ti(III) species $[\text{Ti}(\eta^5\text{-C}_5\text{H}_5)_2\text{Cl}(\text{PMe}_3)]$ which can undergo a further reversible one-electron reduction with chloride loss and the formation of $[\text{Ti}(\eta^5\text{-C}_5\text{H}_5)_2(\text{PMe}_3)_2]$ [13].

Various studies have examined the effect of substituents of the cyclopentadienyl ring on electrochemical behavior [14–16].

For example, in $\text{Zr}(\eta^5\text{-C}_5\text{H}_{5-n}\text{Me}_n)_2\text{Cl}_2$ complexes, E° for the one-electron reduction shifts to more negative values by 0.071 V per methyl group for $n = 1\text{--}4$. A deviation from this linear dependence is observed for $\text{Zr}(\eta^5\text{-C}_5\text{Me}_5)_2\text{Cl}_2$, which is attributed to the steric hindrance between rotating C_5Me_5 ligands, which tend to decrease the angle between the cyclopentadienyl rings, and consequently the energy difference between the frontier orbitals [15].

Systematic studies of complexes with ansa bridges in which two rings are linked by a bridging group have been reported. For example, the electronic influence of unbridged and ansa-bridged ring substituents on a zirconocene center has been studied by means of IR spectroscopic, electrochemical, and computational methods. The reduction potentials of the dichloride complexes $[\text{Zr}(\eta^5\text{-C}_5\text{H}_4\text{R})_2\text{Cl}_2]$ (R = substituent) do not correlate well with Hammett $\sigma(\text{meta})$ parameters, thereby suggesting that factors other than the substituent inductive effect also influence E° . Ansa bridges with single-atom linkers, for example $[\text{Me}_2\text{C}]$ and $[\text{Me}_2\text{Si}]$, exert a net electron-withdrawing effect, but the effect is diminished upon increasing the length of the bridge – with a linker comprising a three-carbon chain, the $[\text{CH}_2\text{CH}_2\text{CH}_2]$ ansa bridge becomes electron donating. In contrast to the electron-withdrawing effect observed for a single $[\text{Me}_2\text{Si}]$ ansa bridge, a pair of vicinal $[\text{Me}_2\text{Si}]$ ansa bridges exert an electron-donating effect relative to that of the single bridge. DFT calculations demonstrated that the electron-withdrawing effect of the $[\text{Me}_2\text{C}]$ and $[\text{Me}_2\text{Si}]$ ansa bridges is due to stabilization of the cyclopentadienyl ligand acceptor orbital, which subsequently enhances backdonation from the metal. The calculations also indicate that the electron-donating effect of two vicinal

$[\text{Me}_2\text{Si}]$ ansa bridges, relative to that of a single bridge, is a result of it enforcing a ligand conformation that reduces backdonation from the metal [16].

Mono and dialkyl complexes such as $[\text{Ti}(\eta^5\text{-C}_5\text{H}_5)_2\text{Me}_2]$ also display reversible single electron reduction to the $\text{M}(\text{III})$ anions which can decay by the loss of the cyclopentadienyl anion [17]. An instructive review on molecular electrochemistry of metallocene dichloride and dimethyl complexes of group four metals emphasizes redox, photophysical, and photochemical properties of homologous bent metallocenes, and a comparative analysis of a variety of electron-transfer induced transformations and ligand-to-metal charge-transfer excited states is given for bent metallocene complexes upon systematic variation of the identity of the metal ion (Ti , Zr , or Hf), ancillary π , and monodentate σ – (Cl , Me : linear correlations exist between energies of optical and redox HOMO-to-LUMO electron transitions) [18].

Titanocene units have been exploited in the formation of heterobimetallic complexes [19] and in the construction of organometallic macrocycles [20]. For example, bis(alkynyl) titanocene derivatives of the type $\{[\text{Ti}](\text{C}\equiv\text{CSiMe}_3)_2\}$, where $[\text{Ti}] = \text{Ti}(\eta^5\text{-C}_5\text{H}_4\text{SiMe}_3)_2$, can act as “ π tweezers” for Cu (I) or Ag (I) complexes and electrochemical studies indicate a strong intramolecular interaction with the group 11 metal held in place by the organometallic π tweezers [19]. Brief electrochemical studies of related bimetallic or polymetallic systems with ligating thiolate or phosphine appendages on the titanocene unit have also been reported [21, 22].

There have been some electrochemical studies of monocyclopentadienyl Ti and Zr systems including $[\text{Ti}$ or $\text{Zr}(\eta^5\text{-C}_5\text{H}_5)_2\text{R}_2]$,

where R is a chelating phosphine ligand such as CH₂PPh₂ [23, 24].

12.4

Porphyrin, Phthalocyanine, and Other Systems

The electrochemical reductions of oxo-, peroxy-, η^2 -azobenzene, and phenylimido Ti(IV) porphyrin complexes have been described, and the mechanism of the two-electron reduction of the peroxy-species to the oxo (compound) established [25, 26].

A range of neutral, singly and doubly oxidized heteroleptic double-decker complexes of the type [M(IV)(P)(Pc)](*n*), where *n* = 0, +1, or +2, M = Zr or Hf, P = the dianion of octaethylporphyrin (OEP) or tetraphenylporphyrin (TPP), and Pc = the dianion of phthalocyanine, has been reported. Each oxidized or reduced compound was characterized by UV–visible and/or EPR spectroscopy. The neutral compounds all undergo two reversible ring-centered oxidations and two reversible ring-centered reductions. The redox potentials were found to depend upon the type of macrocycle. They also vary with the size of metal ion in the case of oxidation but not in reduction, where *E*^o values are relatively unaffected and shift by only 20–40 mV upon going from Hf(P)(Pc) to Th(P)(Pc), as compared to a much larger 220–280 mV shift between *E*^o for the first oxidation of the same compounds [27].

References

1. J. Grobe, B. H. Schneider, H. Zimmermann, *Z. Anorg. Allg. Chem.* **1981**, 481, 107.
2. D. G. Tuck, *Pure Appl. Chem.* **1979**, 51, 2005.
3. M. C. Chakravorti, G. V. B. Subrahmanyam, *Coord. Chem. Rev.* **1994**, 135, 65.
4. K. W. Fung, G. Mamantov, *J. Electroanal. Chem.* **1972**, 35, 27.
5. B. Gilbert, K. W. Fung, G. Mamantov, *Inorg. Chem.* **1975**, 14, 1802.
6. H. Linga, Z. Stojek, R. A. Osteryoung, *J. Am. Chem. Soc.* **1981**, 103, 3754.
7. R. T. Carlin, R. A. Osteryoung, J. S. Wilkes, *Inorg. Chem.* **1990**, 29, 3003.
8. D. Sun, T. Hughbanks, *Inorg. Chem.* **1999**, 38, 992.
9. R. J. Gale, R. Job, *Inorg. Chem.* **1981**, 20, 42.
10. A. Fakhr, Y. Mugnier, B. Gautheron et al., *J. Organomet. Chem.* **1986**, 302, C7–C9.
11. E. Samuel, D. Guery, J. Vedel et al., *Organometallics* **1985**, 4, 1073.
12. A. Fakhr, Y. Mugnier, B. Gautheron et al., *Nouv. J. Chim.* **1986**, 601.
13. I. M. M. Füssing, D. Pletcher, R. J. Whitby, *J. Organomet. Chem.* **1994**, 470, 109.
14. J. Langmaier, Z. Samec, V. Varga et al., *J. Organomet. Chem.* **1999**, 579, 323.
15. J. Langmaier, Z. Samec, V. J. Varga et al., *J. Organomet. Chem.* **1999**, 584, 348.
16. C. E. Zachmanoglou, A. Docrat, B. M. Bridgewater et al., *J. Am. Chem. Soc.* **2002**, 125, 9525.
17. A. Chaloyard, A. Dormond, J. Tirouflet et al., *J. Chem. Soc., Chem. Commun.* **1980**, 214.
18. G. V. Loukova, V. V. Strelets, *Collect. Czech. Chem. Commun.* **2001**, 66, 185.
19. T. Stein, H. Lang, R. Holze, *J. Electroanal. Chem.* **2002**, 520, 163.
20. E. Delgado, M. A. Garcia, E. Gutierrez-Puebla et al., *Inorg. Chem.* **1998**, 37, 6684.
21. I. Ara, E. Delgado, J. Formies et al., *J. Chem. Soc., Dalton Trans.* **1996**, 3201.
22. G. S. White, D. W. Stephan, *Inorg. Chem.* **1985**, 24, 1499.
23. M. Etienne, R. Choukroun, D. Gervais, *J. Chem. Soc., Dalton Trans.* **1984**, 915.
24. T. Malinski, D. Chang, J. M. Latour et al., *Inorg. Chem.* **1984**, 23, 3947.
25. I. M. M. Füssing, D. Pletcher, R. S. Whitby, *J. organomet. Chem.* **1994**, 470, 109.
26. S. D. Gray, J. L. Thorman, V. A. Adamian et al., *Inorg. Chem.* **1998**, 37, 1.
27. R. Guillard, J. M. Barbe, A. Iblnlfassi et al., *Inorg. Chem.* **1995**, 34, 72.

13 Vanadium Electrochemistry

Michael J. Shaw

Southern Illinois University Edwardsville, Edwardsville, Illinois, USA

13.1	Introduction	359
13.2	Vanadium(I) and Lower	359
13.3	Vanadium(II)	361
13.4	Vanadium(III)	362
13.5	Vanadium(IV)	367
13.6	Vanadium(V)	371
13.7	Oxovanadium(III)	372
13.8	Oxovanadium(IV)	372
13.9	Oxovanadium(V)	376
	References	379

13.1 Introduction

This chapter primarily covers studies of the electrochemistry of vanadium, which have appeared in the literature during the period 1985–2005. The material is organized on the basis of the oxidation state of the starting complex and is not meant to be an exhaustive review. Cyclic voltammetry (CV) studies outnumber other methods of electrochemistry for the study of vanadium complexes, and redox potentials will be reported as referenced to the $\text{Cp}_2\text{Fe}^{0/+}$ couple in the appropriate solvent except as noted [1].

The known electrochemistry of coordination complexes of vanadium covers a range of eight oxidation states, from $\text{V}(-\text{II})$ to $\text{V}(\text{V})$. “Soft” ligands such as arene, tropylium, and cyclopentadienyl groups are often found in low-valent V complexes, that is, $\text{V}(0)$, $\text{V}(\text{I})$, and $\text{V}(\text{II})$. To obtain negative oxidation states, strong π -acidic ligands such as RNC , CO , and CN^- are necessary. Many organometallic species have reversible reduction chemistry, which results in oxidation states as low as $\text{V}(-\text{II})$ being formed reversibly at an electrode surface on the cyclic voltammetry timescale.

Higher oxidation states are stabilized by “hard” ligands, which often have N- or O-atoms as donor atoms. Examples

include the triazanonane ligands, and biochemically relevant groups such as carboxylates and pyrazole rings. A large section of high-oxidation state vanadium chemistry deals with oxovanadium species for which $\text{VO}(\text{IV})$ - and $\text{VO}(\text{V})$ -containing species are the most common. Some imidovanadium complexes have also been examined.

The standard aqueous redox chemistry of vanadium and the other group 5 elements is summarized in the Latimer diagrams shown in Fig. 1 [2]. Under standard acidic aqueous conditions, the stability of the +5 oxidation state increases for the heavier group 5 elements at the expense of the +4 and +3 states.

13.2 Vanadium(I) and Lower

Fewer electrochemical studies have been performed on low-oxidation-state complexes of vanadium, compared to higher oxidation states. Complexes in oxidation states lower than $\text{V}(\text{I})$ are limited to those which contain ligands such as strong π acids (CO and RNC), arenes, or tropylium. For example, the $[\text{Cp}_2\text{Co}][\text{V}(\text{CO})_6]$ salt contains $\text{V}(-\text{I})$ which undergoes a reversible oxidation at -0.54 V in CH_2Cl_2 to form the 17-electron $\text{V}(0)$ species [3].

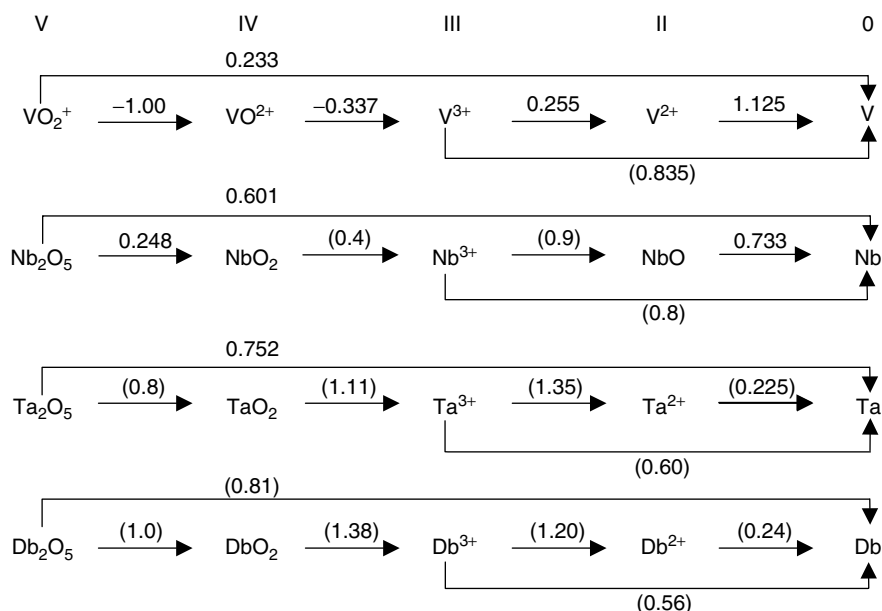


Fig. 1 Latimer diagram for the aqueous chemistry of the group 5 elements.

Congeneric Nb species are known [4]. A (trimp₂)V(NO)(CO)₂ complex (trimp₂ = ^tBuSi(CH₂PMe₂)₃) has been reported [5] which undergoes a reversible oxidation to the cationic V(O) complex at -0.74 V versus Cp₂Fe/CH₂Cl₂ and a second, irreversible oxidation at 0.61 V. More highly reduced complexes of vanadium have been prepared, but their electrochemistry has evidently not been explored. The electrochemical synthesis of CpV(CO)₄ from a vanadium anode, cyclopentadiene, and 115 bar of CO at 100 °C in DMF has been reported [6].


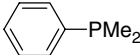
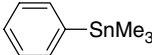

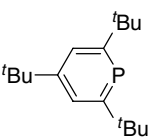
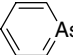
Some work has been performed with bis(arene)vanadium and bis(heteroarene) vanadium complexes [7–10]. As indicated for the selected complexes shown in Table 1, replacement of benzene by phosphabenzene and arsabenzene lowers the reduction potential. This counterintuitive result has been explained in terms of a greater positive charge on the metal

arising from loss of π -orbital degeneracies, higher dipole moments, and the increased electron affinity of the ligand relative to benzene. Alkyl substituents on these rings appear to have the expected effect on redox potentials, and substituents with heavier (yet electron-rich) atoms have little effect on oxidation potentials but facilitate reduction.

The (η^6 -C₆H₅PMe₂)V complex is coordinated to the CpMn(CO) fragment as a bidentate diphosphine ligand and its reduction becomes irreversible with $E_{pc} = -2.68$ V. On the other hand, the V-based oxidation is hardly affected, shifting 30 mV to values more negative.

A growing body of work deals with CpV(cycloheptatrienyl) complexes and derivatives, which are formally V(0), if the cycloheptatrienyl (tropylium) ligand is considered to have a +1 charge [11–13]. The parent complex has a facile reversible oxidation (-0.17 V) in THF but it cannot

Tab. 1 Redox potentials of some bis(arene)vanadium complexes in DME versus SCE

Arene						
–/0	–2.71	–2.52	–2.58	–1.99	–2.25	–2.02
0/+	–0.35	–0.27	–0.33	0.18	–0.10	0.10
+ /2+	0.24 ^a	na	0.58 ^a	1.02 ^a	0.86 ^a	0.87 ^a

^aIrreversible: E_{pa} only.

be reduced within this solvent's potential window. The Nb and Ta congeners have even more facile oxidations (–1.18 and –1.54 V, respectively) because they form THF adducts. The Nb complex can be reduced, but the Ta complex cannot. The question of tropylium bonding to the group 5 metals and the difference in electrochemistry were explored with photoelectron spectroscopy [14], and it was concluded that although the bonding in these complexes is hard to describe via an oxidation state formalism because of extensive delocalization of d electrons onto the ligand, it is not inappropriate to call tropylium a trivalent ligand attached to a d^1 complex.

13.3 Vanadium(II)

Electrochemical studies on V(II) complexes have been relatively few compared to the quantity of work on higher oxidation states. The recent discovery of a general synthesis has improved the availability of data on derivatives of vanadocene [15, 16]. For example, E_c^\oplus values of L_2V decrease in the order $L = \text{indenyl}$ (–2.38 V versus $\text{Cp}_2\text{Fe/THF}$) > Cp (–2.72 V versus

$\text{Cp}_2\text{Fe/THF}$) > Cp^* (< –3.0 V versus $\text{Cp}_2\text{Fe/THF}$), the latter being outside the observable solvent window [17]. Coordination of the π -acid CO to these vanadocenes moves their reduction potentials to more positive values by ca 0.4 V, consistent with the CO ligand's π -acidic properties. For indenyl derivatives, ring-slippage plays a role in the electrochemical consequences of electron transfer. On the CV timescale, $(\text{Ind})_2\text{V}(\text{CO})_2$ displays two apparently Nernstian reductions at $E_c^{\oplus'} = -1.06$ and -1.58 V versus $\text{Cp}_2\text{Fe/THF}$, but chemical reduction with sodium naphthalenide results in the formation of $(\text{Ind})\text{V}(\text{CO})_4$ and $\text{V}(\text{CO})_6^-$ as the only characterized products [17].

A bimetallic vanadocene analog (Fig. 2) where a cyclooctatetraendiyl ligand is coordinated η^5- to each V atom was studied at –38 °C and shown to have a reversible reduction at very negative potentials [18]. If the Cp ligands are bound together by a short bridging group as shown in Fig. 2, then there is a reversible oxidation at mild potentials, otherwise the oxidation is irreversible. There is also a second, irreversible oxidation. The electrons involved in the oxidation reactions come from the V–V bond which explains the destabilization of these structures upon oxidation.

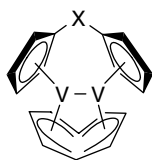


Fig. 2 syn-Cyclooctatetraendiyl complex. X = SiMe₂, GeMe₂, SnMe₂, 2H.

Air and moisture stable tricarbade-caboranyl (CH₃C₃B₇H₉) analogs of vanadocene, which possess only one unpaired electron have recently been reported [19]. The five forms obtained differ in the enantiomeric form of the tricarbade-caboranyl ligand, the relative orientation of the two ligands, or the position of methyl groups on the ligands. These complexes have redox features which are much more positive (e.g. the reduction is 2.9 V more positive) than the corresponding features of Cp₂V, a feature attributed to the ability of the ligand to stabilize metals in low oxidation states.

The six-coordinate octahedral polypyridyl [V(bipy)(terpy)L]ⁿ⁺ complexes (bipy = 1, 8-bipyridine, terpy = terpyridine; L = Cl⁻: *n* = +1; L = H₂O, MeCN: *n* = +2) were found to undergo major structural changes upon 1e⁻ oxidation to form species which are susceptible to further oxidation to V(IV) [20, 21].

A study of an extensive set of pyridine complexes was conducted using voltammetry [22]. The complexes [V(py)₄L₂], V(Et-py)₄L₂, [V(py)₆]²⁺, [V(py)₅]²⁺, [V(py)₄]²⁺ were prepared or studied *in situ* in pyridine (py = pyridine, Et-py = X-ethylpyridine). These compounds undergo either reversible or irreversible one-electron oxidations as did the [V(CH₃CN)_{6-n}L_n]⁺²⁻ⁿ (*n* = 0, 2, 4) and a set of V(dmpe) complexes. It was found that the affinity of the ligand L for the V(II) oxidation state could be determined from the *E*_c⁰ values which varied in the order L = CF₃SO₃⁻ < I⁻ < SCN⁻ < Br⁻ <

AlH₄⁻ < BH₄⁻ < Cl⁻ < Ph⁻ < N₃⁻ < H⁻. This order corresponds to increasing affinity for V(II).

13.4

Vanadium(III)

Electrochemically characterized V(III) species are plentiful relative to the paucity of complexes which have been examined in lower oxidation states. Such species have been characterized in aqueous, nonaqueous, and ionic solvents.

In contrast to the facile reduction of aqueous V(III) (-0.26 V versus NHE) [23, 24], coordination of anionic polydentate ligands decreases the reduction potential dramatically. The reduction of the seven-coordinate capped-octahedral [23] [V(EDTA)(H₂O)]⁻ complex (*E*_c⁰ = -1.440 V versus Cp₂Fe/H₂O) has been studied extensively [25, 26]. The redox reaction shows moderately slow electron-transfer kinetics, but is independent of pH in the range from 5.0 to 9.0, with no follow-up reactions, a feature that reflects the substitutional inertness of both oxidation states. In the presence of nitrate ion, reduction of [V(EDTA)(H₂O)]⁻ results in electrocatalytic regeneration of this V(III) complex. The mechanism was found to consist of two second-order pathways – a major pathway due to oxidation of V(II) by nitrate, and a minor pathway which is second order in nitrate. This mechanism is different from the comproportionation observed during

the stepwise two-electron reduction of the V(IV)-EDTA complex in the presence of nitrate [27]. The redox potentials of a series of V(III) complexes of EDTA analogs have also been measured [23] and they occur at comparable potentials. The values of ΔH° and ΔS° for the reduction of $[\text{V}(\text{EDTA})(\text{H}_2\text{O})]^-$ have been measured by voltammetric methods to be 72 kJ mol^{-1} and $-85 \text{ J mol}^{-1} \text{ K}^{-1}$ respectively [23].

Vanadium complexes with polydentate ligands, which have all-nitrogen or mixed nitrogen/oxygen-donor ligand sets, have been especially popular. V(III) complexes with amine/phenolato or catecholato ligand sets have biochemical relevance [28, 29]. For amine-phenolato complexes, as the number of O-atoms in the coordination sphere of the V atom increases, the V(III/IV) couple shifts to more negative values [28]. These hard-donor atoms bind well to V(III), which is a hard Lewis acid [30]. Many of these complexes adopt octahedral coordination geometry, but a fair number of trigonal prismatic complexes have also been observed.

One interesting octahedral complex is based on the N,N',N,N' -bis[(2-hydroxybenzyl)(2-methylpyridyl)]ethylenediamine ligand (BBPEN), a derivative of the common Schiff base called *salen* [31]. The $[\text{V}(\text{BBPEN})]\text{PF}_6$ complex has the four

nitrogen donor atoms in the same plane and the phenolate O-atoms are located axially. This complex is unusual (but not unique) among V(III) species in that it displays three apparently Nernstian electron-transfer processes. The data suggests that the V(II) to V(V) oxidation states are accessible apparently without major structural changes. The dianionic ligand shifts the V(II/III) couple to -1.79 V versus $\text{Cp}_2\text{Fe}/\text{MeCN}$, but the V(III/IV) couple is much more facile (0.27 V versus $\text{Cp}_2\text{Fe}/\text{MeCN}$), and even the V(IV/V) couple can be observed (1.11 V versus $\text{Cp}_2\text{Fe}/\text{MeCN}$).

Another popular ligand motif has been the 2.2.2-triazanonane ligand (TAN) and its derivatives. This ligand coordinates in a fac-octahedral fashion to V(III) centers. In such complexes, these ligands leave three coordination sites vacant. The N,N',N'' -tris(*t*-butyl)-2.2.2-triazanonane ligand coordinates to VCl_3 to form a labile octahedral complex, which has a Nernstian oxidation at 0.78 V versus $\text{Cp}_2\text{Fe}/\text{MeCN}$ and irreversible reductions at -0.64 and -1.46 V versus $\text{Cp}_2\text{Fe}/\text{MeCN}$. Chelation stabilizes a wider range of oxidation states of the TAN-derived compounds. An example of one of a series [32, 33] of hexadentate ligands is shown in Fig. 3. The octahedral V complex made with this ligand has three apparently Nernstian redox

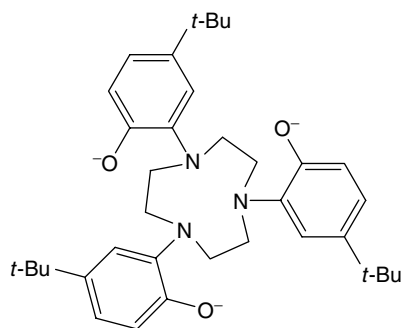


Fig. 3 A hexadentate triazacyclononane ligand.

processes at 0.38, -0.50 , and -2.41 V versus $\text{Cp}_2\text{Fe}/\text{MeCN}$ due to the V(IV/V), V(III/IV), and V(III/II) couples respectively. This trianionic ligand shifts the now-reversible V(III/II) couple to considerably more negative potentials, but also stabilizes the V(IV) and V(V) oxidation states. Bimetallic examples are also known. An example is the dimetallic $[(\text{TAN})\text{Cr}(\mu\text{-O})(\mu\text{-CH}_3\text{CO}_2)\text{V}(\text{TAN})]$ complex which has an oxidation at -0.63 V versus $\text{Cp}_2\text{Fe}/\text{MeCN}$ [34] and which displays strong ferromagnetic coupling between the two vanadium centers. Protonation of the complex at the oxo-ligand makes the reduction more facile ($E_c^{\oplus'} = -1.29$ V versus $\text{Cp}_2\text{Fe}/\text{MeCN}$). The vanadium-based redox processes on the analogous V_2 ($E_c^{\oplus'}(\text{ox}) = -0.26$ V, $E_c^{\oplus'}(\text{red}) = -2.11$ V), Cr_2 , and RuV ($E_c^{\oplus'}(\text{ox}) = -0.18$ V, $E_c^{\oplus'}(\text{ox}) = -2.08$ V versus Cp_2Fe) complexes [35] have also been studied. Cyclic ligands which contain four N-donor sites have also been studied [36].

The redox potentials of trigonal prismatic complexes span a similar range as that observed for octahedral V(III) complexes. The complexes $\text{V}(\text{bpy})(\text{Cl}_4\text{Cat})_2$ ($\text{bpy} = 2, 2'$ -bipyridine, $\text{Cl}_4\text{Cat} = \text{tetrachlorocatecholato}$) and $\text{V}(\text{bpy})(\text{acac})(\text{Cl}_4\text{Cat})$ have V(III/II) couples at -1.74 and -1.75 V versus $\text{Cp}_2\text{Fe}/\text{MeCN}$ respectively. The V(III/IV) couples are -0.35 and -0.50 V, respectively, values which are comparable to the octahedral TAN complexes above. However, the V(IV/V) couples are at 0.92 and 0.06 V versus $\text{Cp}_2\text{Fe}/\text{MeCN}$ respectively, a significant difference when compared to the other two couples [28].

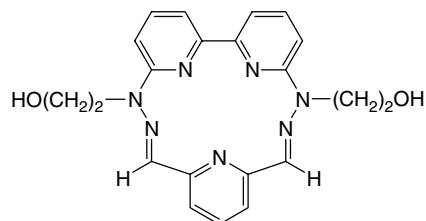
Octahedral “scorpionate” complexes of the $[\text{HB}(\text{pz})_3]^-$ (Tp) and $[\text{HB}(3,5\text{-Me}_2\text{pz})_3]^-$ (Tp*) ligands ($\text{pz} = \text{pyrazole}$, $3, 5\text{-Me}_2\text{pz} = 3, 5\text{-dimethylpyrazole}$) have

been prepared and studied using voltammetry [37]. The $[\text{Tp}'_2\text{V}]\text{BPh}_4$ ($\text{Tp}' = \text{Tp}, \text{Tp}^*$) complexes show reversible features in their voltammograms ($E_c^{\oplus'} = -0.42$ (Tp) and -0.68 (Tp*) V versus $\text{Cp}_2\text{Fe}/\text{CH}_2\text{Cl}_2$) and can be reduced to the neutral V(II) complexes, which appear stable on the bulk electrolysis timescale. The values of $E_c^{\oplus'}$ were found to be solvent dependent. On the other hand, while the $\text{Tp}'\text{VCl}_2(\text{DMF})$ complexes show reversible oxidation behavior by voltammetry ($E_c^{\oplus'} = 1.28$ (Tp) and 1.22 V (Tp*) versus $\text{Cp}_2\text{Fe}/\text{CH}_2\text{Cl}_2$), bulk electrolysis revealed the V(IV) species to be unstable over longer time periods. However, the presence of an oxo-ligand, as in $\text{Tp}'\text{V}(\text{O})\text{Cl}(\text{DMF})$ and $\text{Tp}'\text{V}(\text{O})(\text{acac})(\text{DMF})$ ($\text{acac} = 2, 4\text{-pentanedionate}$) stabilizes the V(IV) and V(V) oxidation state considerably ($1.07 > E_c^{\oplus'} > 1.21$ V). It appears that TpV complexes with anionic $(\text{PhO})_2\text{PO}_2^-$ ligands which bridge to other metal complexes have reversible V(III/II) reduction features [38].

The highly distorted octahedral complex $[\text{mer-V}(\text{pic})_3]$ ($\text{pic} = \text{picolinic acid}$, a tryptophan metabolite) oxidizes over time to the $[\text{VO}(\text{pic})_2]$ complex in aqueous solution [39]. Conductivity measurements revealed that the species is a nonelectrolyte, and voltammetry indicated a reversible oxidation at 0.635 V and reduction at -1.01 V versus Ag/AgCl , values which are more positive than usually observed for comparable complexes. This feature was attributed to delocalization of d electrons [39].

It is possible for an appropriately designed ligand to force a seven-coordinate pentagonal bipyramidal structure upon a V(III) complex. An example is the Schiff-base ligand shown in Fig. 4 [40]. In the $[\text{VCl}_2]\text{Cl}$ complex the five nitrogen donor atoms are in a single plane and

Fig. 4 A planar pentadentate ligand.



there are two axial Cl^- ligands. This cationic complex has a single reduction at -0.97 V versus Ag/AgCl/DMSO, which is comparable to that of the anionic EDTA complex described above.

Stereoisomerism in a ligand set can have a profound influence on the observed electrochemical behavior of pentagonal bipyramidal structures. For example, a set of dinuclear V(III) complexes with bridging oxo ligands, benzoate ligands, and specially designed bridging heptadentate ligands (Fig. 5a) was examined [41]. Two isomers of a distorted pentagonal bipyramidal species were examined electrochemically. The first was characterized by single crystal X-ray diffraction to have the structure depicted in Fig. 5b [41], and the second appeared to be an isomer where coordinated carboxylate and pyridyl groups

had exchanged places. Interestingly, this small structural change results in significant changes in the redox chemistry. The isomer shown in Fig. 5b has two reversible oxidation features evident in CV studies ($E_c^{\oplus'} = 0.65, 1.02$ V versus Ag/AgCl in MeOH); however, its stereoisomer has two irreversible features under the same conditions ($E_c^{\oplus'} = 0.81, 1.22$ V versus Ag/AgCl in MeOH). No reductions were reported in this system; however, another bimetallic pentagonal bipyramidal complex based on the ligand shown in Fig. 6 with axial H_2O ligands displayed two closely spaced reduction features at mildly negative potentials (-1.19 V versus $\text{Cp}_2\text{Fe}/\text{MeCN}$) [42].

Organometallic derivatives of V(III) are somewhat rare. The Cp_2VBr and Cp^*VBr complexes undergo irreversible oxidation processes at 0.40 and 0.31 V versus Cp_2Fe

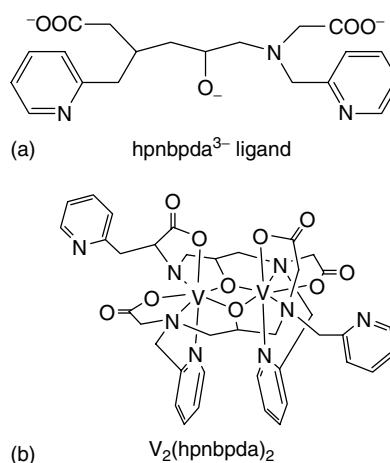


Fig. 5 Pentagonal bipyramidal complexes.

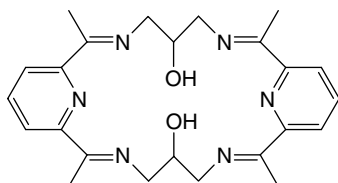


Fig. 6 A planar pentadentate Schiff-base that forms bimetallic complexes.

respectively. The Cp_2VCl species was investigated previously [43]. Coordination of tetracyanoethylene to these complexes results in oxidation to the V(IV) species, as indicated by EPR measurements [44], but the resulting $\text{Cp}_2\text{VBr}(\text{TCNE})$ and $\text{Cp}_2^*\text{VBr}(\text{TCNE})$ complexes are then more difficult to reduce ($E_{\text{pc}} = -0.75$ and -0.93 V versus Cp_2Fe respectively). Three $[\text{L}_2\text{V}(\text{VO})_2]\text{PF}_6$ derivatives (L = indenyl, Cp, Cp^*) have been investigated [45,] and while their reduction potentials decrease in the order L = indenyl > Cp > Cp^* , only the indenyl derivative ($E_c^{\ominus'} = -1.06$ V versus $\text{Cp}_2\text{Fe}/\text{THF}$) showed chemically reversible electrode kinetics. The $[\text{Cp}^*\text{V}(\mu\text{-Cl})_2]_3$ cluster has a reversible oxidation at 0.5 V versus $\text{Cp}_2\text{Fe}/\text{THF}$, but the electrode kinetics appear very slow with $\Delta E_p = 400$ mV [46].

The $\text{V}(\text{mes})_3(\text{THF})$ (mes = mesityl) complex displays a reversible oxidation at -0.25 V versus $\text{Cp}_2\text{Fe}/\text{THF}$, and a reversible reduction at -2.50 V versus $\text{Cp}_2\text{Fe}/\text{THF}$ although the latter appears to have slow electrode kinetics [47]. If the atmosphere is switched from Ar to N_2 , new electrochemical features appear. CV and bulk electrolysis studies showed that the new electrode product was $[(\text{mes})_3\text{V} - \text{N} \equiv \text{N} - \text{V}(\text{mes})_3]^{2-}$. This species can be oxidized to a monoanion at -2.25 V versus $\text{Cp}_2\text{Fe}/\text{THF}$ and reduced to a trianion at -2.81 V versus $\text{Cp}_2\text{Fe}/\text{THF}$. Attempts to generate the trianion by bulk electrolysis result in decomposition, but both the anion and dianion yield ammonia and hydrazine upon protonolysis. The anion's

irreversible oxidation at $E_{\text{pa}} = -1.35$ V versus $\text{Cp}_2\text{Fe}/\text{THF}$ results in regeneration of $\text{V}(\text{mes})_3(\text{THF})$ [47].

V(III) complexes with sulfur-containing ligands are somewhat rare. An example is the $(\text{NEt}_4)_2[\text{V}_2(\text{dte})_4]$ salt (dte = 1,2-dithiolatoethane) [48], which can be oxidized by the strongly coupled ($\Delta E > 450$ mV) mixed-valence V(III)/V(IV) species at $E_c^{\ominus'} = -0.48$ V versus $\text{Ag}/\text{AgCl}/\text{MeCN}$.

A series of $[\text{V}_3(\mu^3\text{-O})(\kappa^2\text{-O}_2\text{CR})_6\text{L}_3]\text{ClO}_4$ complexes (R = Me, Et, 4-anisole; L = pyridine, 4-picoline, lutidine) has been prepared as models for V-containing impurities in crude oils [49]. These complexes feature octahedral geometry around each V atom, which are bridged symmetrically by the carboxylate groups. At the center of the cluster is a trigonal-planar O atom. These compounds undergo Nernstian reductions in the range -1.32 to -1.61 V versus $\text{Cp}_2\text{Fe}/\text{CH}_2\text{Cl}_2$, values that appear to be more facile than monomeric complexes with similar ligand sets. At high scan rates, reversibility was observed for the oxidations ($0.46 - 0.77$ V versus $\text{Cp}_2\text{Fe}/\text{CH}_2\text{Cl}_2$) in the CV scans. A second, irreversible reduction was also observed at -1.7 to -1.9 V versus $\text{Cp}_2\text{Fe}/\text{CH}_2\text{Cl}_2$.

No redox features are observed for VCl_3 dissolved in 1-ethyl-3-methyl-1*H*-imidazolium chloride (EMIC)/ AlCl_3 until excess Cl^- is added. The main species formed appears to be $[\text{VCl}_6]^{3-}$, although $[\text{VCl}_5]^{2-}$ and $[\text{VCl}_4]^-$ are also present, and these species may be oxidized reversibly

at 1.00, 1.23, and 1.33 V versus Al wire in 0.4 EMIC/0.6 AlCl₃ melt. Oxidation of V(III) under these conditions appears to yield V(IV) complexes as indicated by spectrophotometry [50].

13.5 Vanadium(IV)

Analytical techniques such as adsorptive stripping voltammetry rely on complex formation to improve detection limits of metals such as V(IV) and V(V) [51]. An example is in the use of cupferron and KBrO₃ as additives to acidic aqueous solutions, which result in the adsorption of the V(V)-cupferron complex to the electrode surface that catalyzes the reduction of the BrO₃[−] ion in solution. This technique has good selectivity over Cu, Pb, Cd, Fe, and Ti, but the response is dependent on pH.

A series of enterobactin analogs has been prepared as structural analogs to Fe(III) complexes. These species have facile oxidation processes ($E_c^{\oplus} = -0.53$ to -1.00 V versus Cp₂Fe/DMF) and are based on three catecholato ligands joined to a central aromatic ring (Fig. 7) or nitrogen atom by amide bridges [52]. The parent [V(cat)₃]^{2−} (cat = 1,2-catecholato)

species has reversible oxidation and reduction processes at -0.42 and -1.24 V versus Cp₂Fe/MeCN, respectively [53], and so the electron withdrawing effect of the carbonyl substituents on the catecholato ligands moves the V(IV/V) couple to more positive potentials. Similarly, a comparison of compounds with catecholato- and 3,5-di-*t*-butylcatecholato ligands found that substitution by the more electron-releasing *t*-butyl groups moved the redox potentials to more negative values by 0.35 V [53]. In contrast, substitution of the methyl groups on the acac ligand (acac = 2,4-pentanedionato) results in little change from the redox potential observed for the [V(acac)₃]⁺⁰ couple at -1.30 V versus Cp₂Fe/MeCN. Mixed dionato/catecholato complexes displayed the same trend.

Interestingly, a homoleptic 2-mercapto phenolate complex *fac*-[V(mcp)₃]^{2−} can be prepared from VO(acac)₂ (as can the catecholato analog) by displacement of the acac and oxo ligands [54]. Similar to the catecholato complex, the structure is described as octahedral distorted toward trigonal prismatic. The redox features of this compound appear at values more negative than its catecholato analog. The Nernstian V(IV/V)

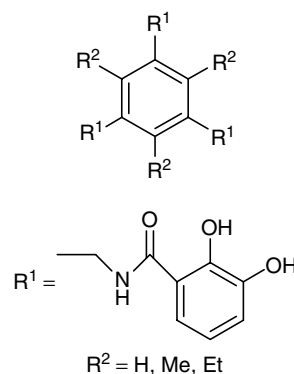


Fig. 7 An enterobactin analog.

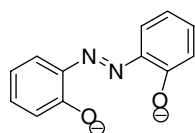


Fig. 8 Tridentate azo(2-phenolate) ligand.

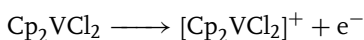
oxidation occurs at $E_c^{\oplus'} = -0.27$ V versus Ag/AgCl/MeCN, but this complex has an irreversible reduction at -1.08 V versus Ag/AgCl/MeCN. The irreversibility of this reduction is unexpected, given the reversibility of the catecholato and maleonitriledithiolate (vide infra) analogs.

V(IV) complexes that are coordinated by six sulfur donor atoms are also known. For example, $[\text{AsPh}_4][\text{V}(\text{mnt})_3]$ (mnt = maleonitriledithiolate) displays three redox features on cyclic voltammetry, which correspond to the reversible V(V/IV), V(IV/III), and quasireversible V(III/II) couples at 0.17, -0.87 , and -2.12 V versus $\text{Cp}_2\text{Fe}/\text{CH}_2\text{Cl}_2$ [55]. The surface normalized incident Fourier transform infrared spectroscopy (SNIFTIRS) spectroelectrochemical technique was used to determine that the extent of π bonding of the mnt ligand increases as the metal's oxidation state is lowered through examination of the $\nu(\text{CN})$ frequencies in the various oxidation states. This technique was particularly effective in the determination of the spectral features of the short-lived V(II) species.

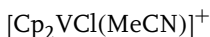
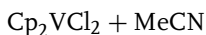
As for V(III), trigonal prismatic complexes, and trigonally distorted octahedral complexes are not uncommon for V(IV) [56]. The ligand set exerts a stronger influence on the redox potentials, whether the coordination geometry is octahedral or trigonal prismatic, at least to a first approximation. A series of compounds made with tridentate and tetradentate ligands with N- and O-donor atoms such as the azophenol derivative shown in Fig. 8 has both reversible oxidations and reductions.

The former $E_c^{\oplus'}$ values range from 0.51 to 0.92 V versus $\text{Cp}_2\text{Fe}/\text{CH}_2\text{Cl}_2$ and the latter from 1.09 to 1.32 V.

A variety of vanadocene-derived organometallic species has been studied by electrochemical means. Cp_2VCl_2 has been studied under a variety of conditions [57]. In MeCN, the oxidation appears well behaved by CV, but rotating-disk and channel-electrode voltammetry studies show that the oxidized complex undergoes follow-up chemistry shown in Eqs (1–3):



$$E_{1/2} = 1.00\text{V versus SCE/MeCN} \quad (1)$$



However, these studies also noted photocurrent at -0.10 and 0.75 V versus $\text{Cp}_2\text{Fe}/\text{MeCN}$, which reached a maximum at 325 nm, a wavelength coincident with no spectral feature in Cp_2VCl_2 . This photocurrent appears to be due to the formation of Cp_2VCl by homolytic photocleavage of a V–Cl bond.

In THF, Cp_2VCl_2 has two irreversible reductions that each lead to chloride loss ($E_c^{\oplus'} = -1.15$ and -2.20 V versus $\text{Cp}_2\text{Fe}/\text{THF}$), which ultimately lead to the observation of the reversible couple for vanadocene at -3.27 V versus $\text{Cp}_2\text{Fe}/\text{THF}$ [58]. In acetonitrile, a series of substituted vanadocene dichlorides ($(\text{C}_5\text{H}_4\text{R})_2\text{VCl}_2$, R = Me, ^iPr , ^tBu) [59] is

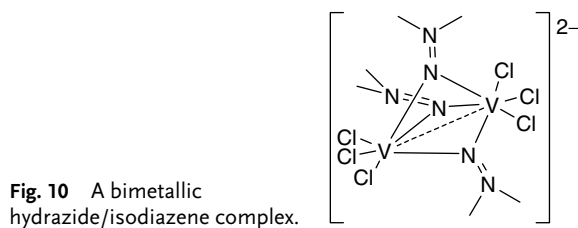
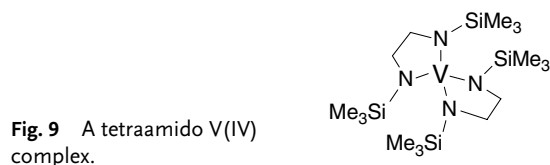
reported to have reversible oxidations at ca 0.52 V versus $\text{Cp}_2\text{Fe}/\text{MeCN}$ and irreversible reductions at ca -0.36 and -1.38 V versus $\text{Cp}_2\text{Fe}/\text{MeCN}$. The disparity in values is most likely due to electrode kinetics rather than extreme differences in E° values. The analogous 1,1,2,2-tetramethylethylene-bridged *ansa*-metallocene also shows irreversible reductions at $E_c^{\Phi'} = -1.50$ and -2.40 V versus $\text{Cp}_2\text{Fe}/\text{THF}$, but the corresponding vanadocene species reduction is much less reversible because the *ansa*-bridge prevents the rings from attaining coplanarity.

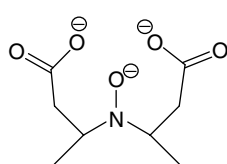
Vanadocene(IV) complexes can act as potent spermicides, which function as modulators of cellular redox potential and exert pleiotropic effects that result in the cessation of sperm motility through depolarization of mitochondrial membranes [60, 61]. An example of a spermicidal complex is $[\text{Cp}_2\text{V}(\kappa^2\text{-S}_2\text{CNEt})]^+$ which has a reversible reduction at $E_c^{\Phi'} = -0.92$ V versus $\text{Cp}_2\text{Fe}/\text{MeCN}$ and an irreversible oxidation at 0.56 V versus $\text{Cp}_2\text{Fe}/\text{MeCN}$, potentials that are within the usual range of the biochemically accessible redox values. Nitrogen donors appear to result in less negative reduction

potentials, that is, $[\text{Cp}_2\text{V}(\text{bipy})]^+$ and $[\text{Cp}_2\text{V}(\text{phen})]^+$ (phen = phenanthroline) at -0.63 and -0.62 V versus $\text{Cp}_2\text{Fe}/\text{MeCN}$ respectively [61].

Other electrochemically characterized organometallic V(IV) complexes are rare. The thiolate bridged $[\text{Cp}(\text{CO})_2\text{V}(\mu\text{-SR})_2\text{V}(\text{CO})_2\text{Cp}]$ (R = Me, Et, Ph) have reversible reduction processes that range from -1.89 to -2.01 V versus $\text{Cp}_2\text{Fe}/\text{THF}$ in addition to two other irreversible reduction processes at more negative potentials. For R = Me, an oxidation at -0.20 V versus $\text{Cp}_2\text{Fe}/\text{THF}$ is reported. Reductive bulk electrolysis results in the decomposition of $[\text{Cp}(\text{CO})_2\text{V}(\mu\text{-SMe})_2\text{V}(\text{CO})_2\text{Cp}]$ by loss of SMe^- [62].

An example of a tetrahedral tetraamido V(IV) complex, bis(*N,N'*-bistrimethylsilylethylenediamine)vandium(IV) was reported (Fig. 9) [63,] which had reversible oxidation and “quasireversible” reduction features in its CV at 0.41 and -1.51 V versus $\text{Ag}/\text{AgCl}/\text{THF}$ respectively. A second, irreversible ligand-based oxidation was observed at 1.34 V. A related bimetallic complex forms when $\text{VCl}_3(\text{THF})_3$ is treated with dimethylhydrazine (Fig. 10) where three N_2Me_2 units bridge the two V atoms which are joined by



Fig. 11 HIDPA³⁻ ligand.

a single bond [64]. The structures indicate that two of the N₂Me₂ units are dianionic hydrazido ligands, but the third is a neutral isodiazeno ligand which preserves the V(IV) oxidation state. Consistently, this complex has a reversible oxidation at 0.30 V versus Cp₂Fe/CH₂Cl₂ and a further irreversible oxidation at 1.30 V versus Cp₂Fe/CH₂Cl₂ which correspond to the loss of the electrons in the V–V bond.

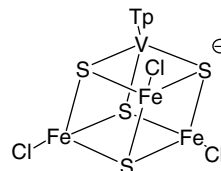
V(IV) is a biologically active oxidation state, acting as an electron-transfer mediator in enzymes such as amavadin, which catalyzes the formation of disulfides [65]. Amavadin is a V(IV) complex found in mushrooms of the genus *Amanita* in which two (*S,S*)-2,2'-(hydroxyimino)dipropionic acid (HIDPA³⁻) ligands (Fig. 11) and two water molecules coordinate to the metal atom [66]. This [V(HIDPA)₂(H₂O)₂]²⁻ complex has been shown to undergo Michaelis-Menton electrocatalysis in the presence of thiols such as HS(CH₂)₂COOH. Addition of the thiol yields enhanced anodic peak current, but at very high thiol concentrations, the catalytic activity is suppressed, consistent with the inner-sphere oxidation of the thiol. The carboxylic acid group was shown to be important for the reaction in a position 2 or 3 bonds away from the SH group.

Porphyrin complexes of V(IV) have rich electrochemistry, but few such complexes have been explored in detail by electrochemical methods. An example of a complex whose electrochemistry has been elaborated is (TTP)VCl₂ (TTP =

tetra-*p*-tolylporphyrinate) [67]. At –30 °C, this complex has two-one electron reductions to the V(III) and V(II) states respectively at –0.16 and –1.81 V versus Cp₂Fe/THF on the CV timescale. These reductions initiate a fast solvent-for-chloride substitution process which results in electroactive (TTP)VCl(THF) complexes that can react with the starting material to form electroactive halo-bridged dimers. The V(II) [(TTP)VCl(THF)]⁻ complex forms at $E_c^{\theta'} = -1.46$ V versus Cp₂Fe/THF and then loses the second Cl⁻ ligand to form the electroactive [(TTP)V(THF)₂] complex.

Bacteria in Mo-deficient environments produce a vanadium(IV) – containing an alternative to the usual FeMo nitrogenase. This alternative is less active than the usual form of the enzyme. A series of complexes made by ligand substitution on the [(DMF)₃VFe₃S₄X₃]⁻ (X = Cl⁻, Br⁻, I⁻) cubane structure where the V atom is located in an octahedral coordination environment have quasireversible reduction features at 0.17 > $E_c^{\theta'}$ > 0.12 V versus Ag/AgCl/MeCN and irreversible reductions at –1.12 > E_{pc} > –1.20 V versus Ag/AgCl/MeCN. The similarities in the potentials indicate that the LUMOs lack significant contribution from ligand-based orbitals; however, the Tp derivative [TpVFe₃S₄Cl₃]⁻ (Fig. 12) has a much more facile reduction (–0.68 V), which is attributed to π back-donation while its oxidation is relatively close to those of the DMF complexes at 0.00 V [68, 69]. Similar cubane structures with chelating dithiocarbamate ligands have also been studied [70].

Fig. 12 A cubane-based tripyrazolylborate-V complex.



A number of other cubane complexes of V(IV) have been reported. $[\text{Cp}^*\text{V}(\text{N})]_4$ can be reduced reversibly at $E_c^{\ominus'} = 0.16$ V versus $\text{Cp}_2\text{Fe}/\text{THF}$ [71]. A similar cubane complex $[\text{TpV}(\text{O}_3\text{POPh})]_4$ where phosphate groups bridge three TpV units displays four oxidation features, of which two are reversible (0.68, 1.13 V versus $\text{Ag}/\text{AgCl}/\text{CH}_2\text{Cl}_2$) and two are irreversible. Although bulk electrolysis at a potential suitable to remove one electron from the complex resulted in decomposition [72].

13.6 Vanadium(V)

Electrochemically characterized V(V) complexes which lack oxo ligands are somewhat rare. Many of those which are known are the result of preparative studies guided by CV results on V(IV) systems. For example, a series of imidovanadium(IV) complexes containing the tetradentate dianionic 5,7,12,14-tetramethyldibenzo[*b, i*] [1, 4, 8, 11] tetraazacyclotetradecinato moiety (TMTAA^{2-}) was reported [73], and diamagnetic vanadium(V) cations $[(\text{TMTAA})\text{V} = \text{NR}]^+$ (**4**) were prepared by oxidation of

their neutral V(IV) precursors with 1 equivalent of $[\text{Cp}_2\text{Fe}]\text{SbF}_6$. The V(IV) complexes have a reversible oxidation in the range -0.12 to -0.16 V versus $\text{Cp}_2\text{Fe}/\text{CH}_2\text{Cl}_2$, and similar values have been found for the corresponding oxo complexes [74, 75].

For nonoxo and nonimido complexes, ligands which bear high charge and can stabilize high-oxidation states are necessary. An example is the $[\text{N}_3\text{S}_2]^{3-}$ ion, which forms six-membered chelate rings through the terminal nitrogen atoms (N and S atoms alternate), reminiscent of the acac ligand [76, 77]. An example is the octahedral $\text{V}(\text{phen})(\text{dtbc})(\text{N}_3\text{S}_2)$ complex (dtbc = 4, 6-*t*-Bu₂-catecholato) which undergoes reversible reductions at $E_c^{\ominus'} = -0.33$ and -1.47 V versus $\text{Cp}_2\text{Fe}/\text{CH}_2\text{Cl}_2$.

The tridentate biquinone ligand shown in Fig. 13 (HDBQI^{3-}) can adopt five different charges, of which the most negative (-3) is shown. Calculations have been performed and they indicate that the octahedral $\text{V}(\text{HDBQI})_2$ complex has two different forms of the ligand, one in the -2 state and one in the -3 state. This complex has a reversible ligand-based oxidation and a reversible metal-based reduction at mildly negative potentials [78].

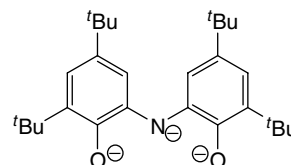


Fig. 13 Reduced biquinone derivative.

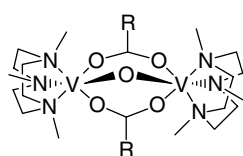


Fig. 14 Dimetallic μ -carboxylato complex.

13.7 Oxovanadium(III)

Electrochemically characterized V(III) complexes with oxo ligands are exceedingly rare. A study which probed the nature of spin exchange coupling in dimetallic μ -oxo- μ -bis-carboxylato complexes of 1,4,7-trimethyl-1,4,7-triazacyclononane, Fig. 14 [79] emerged. As the electron withdrawing ability of the R group on the RCO_2^- carboxylato ligand increases, the compounds become harder to oxidize ($0.58 > E_c^{\Theta'} > -0.02$ V versus $\text{Cp}_2\text{Fe}/\text{MeCN}$) but easier to reduce ($-1.43 > E_c^{\Theta'} > -1.87$ V versus $\text{Cp}_2\text{Fe}/\text{MeCN}$). Protonation of the oxo-ligand dramatically changes the spin coupling of the complexes from $S = 2$ ferromagnetic to $S = 0$ antiferromagnetic but how this change affects redox potentials is not known [79].

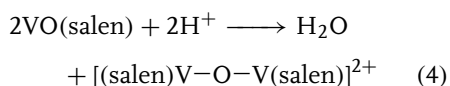
13.8 Oxovanadium(IV)

In octahedral vanadyl complexes, the weakest ligand is usually found *trans*- to the oxo group. The $\nu(\text{V}=\text{O})$ stretching frequency is indicative of the ligand *trans*- to the $\text{V}=\text{O}$ bond. As σ -donor ability increases, $\nu(\text{V}=\text{O})$ decreases [80]. This trend was examined in a series of compounds $[\text{VO}(\text{DCP})\text{L}_2]$ ($\text{DCP} = 2,6\text{-dicarboxylatopyridine}$, $\text{L}_2 = (\text{H}_2\text{O})_2$, *o*-phenanthroline, bipyridine) which displayed reversible reduction chemistry

($-1.63 < E_c^{\Theta'} < -1.68$ V versus $\text{Cp}_2\text{Fe}/\text{DMF}$), but irreversible oxidation chemistry ($0.40 > E_{\text{pa}} > 0.25$ V versus $\text{Cp}_2\text{Fe}/\text{DMF}$) [80]. This observation is contrary to the expected trend because the $\text{V}=\text{O}$ group usually stabilizes the lifetime of the VO(V) state and destabilizes the lifetime of the VO(III) state.

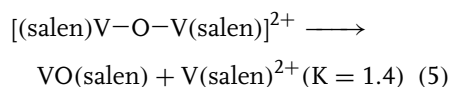
The weakening of the ligand bonded *trans*- to the oxo group results in a large number of square-pyramidal VO(IV) complexes where the oxo-ligand occupies the apical site. Such complexes can serve as useful oxidation catalysts. For example, $\text{VO}(\text{acac})_2$ is a good catalyst for the oxidative (by O_2) polymerization of diphenylsulfide [81] and is used for the epoxidation of allylic alcohols with Me_3COOH [82]. Its electrochemistry has been examined in detail elsewhere [83].

Planar tetradentate Schiff-base ligands are extremely common for VO(IV) complexes. The prototypal example, $\text{VO}(\text{salen})$, has been studied under a variety of conditions. Under nonaqueous acidic conditions the chemistry is complicated by dimerization driven by the release of water (Eq. 4) [84].



$\text{VO}(\text{salen})$ is oxidized reversibly at 0.08 V versus $\text{Cp}_2\text{Fe}/\text{MeCN}$, but in the presence of H^+ or the Lewis acid $[\text{Ph}_3\text{C}]^+$, a reversible wave at more positive potentials ($E_c^{\Theta'} = 0.25$ V versus $\text{Cp}_2\text{Fe}/\text{MeCN}$) is observed in addition to the expected wave at

0.54 V versus $\text{Cp}_2\text{Fe}/\text{MeCN}$ for the oxidation of $[(\text{salen})\text{V}-\text{O}-\text{V}(\text{salen})]^{2+}$ [84]. The wave at 0.25 V was assigned to the $\text{V}(\text{salen})^{3+/2+}$ couple, a complex which is probably solvated by MeCN and which forms by disproportionation of the $[(\text{salen})\text{V}-\text{O}-\text{V}(\text{salen})]^{2+}$ complex (Eq. 5):



Six-coordinate $\text{V}(\text{IV}/\text{III})$ couples (e.g. $[\text{V}(\text{salen})(\text{MeCN})_2]^{2+/+} E_c^{\oplus} = \text{at } 0.53 \text{ V}$ versus $\text{Ag}/\text{AgCl}/\text{MeCN}$) are usually more accessible than $\text{VO}(\text{IV}/\text{III})$ couples (e.g. $[\text{VO}(\text{salen})]^{0/-}$ at -1.6 V versus $\text{Ag}/\text{AgCl}/\text{MeCN}$ [84]). The oxidation of the square-pyramidal $\text{VO}(\text{salen})$ complex in $\text{CH}_2\text{Cl}_2/\text{NBu}_4\text{BF}_4$ at 0.18 V versus $\text{SCE}/\text{CH}_2\text{Cl}_2$ results in coordination of BF_4^- and formation of the structurally characterized neutral octahedral complex $(\text{VO}(\text{salen})\text{BF}_4)$ [85]. The formation constant of the $\text{V}(\text{V})$ complex was evaluated and found to be 1.1×10^2 . In more donating solvents, the reversible couple appears at -0.24 V to -0.35 V versus SCE . These results highlight the preference of $\text{VO}(\text{V})$ to be octahedrally coordinated.

Optically active Schiff-base oxovanadium(IV) complexes catalyze the asymmetric oxidation of sulfides to sulfoxides by peroxides [86]. The catalytically active species is $\text{VO}(\text{V})$ rather than $\text{VO}(\text{IV})$ and is formed in situ under the reaction conditions. A series of related complexes based on the optically active ligand shown in Fig. 15 shows linear dependence of their oxidation E_c^{\oplus} values on the Hammett parameters of functional group X. These values ranged from 0.18 V versus $\text{Cp}_2\text{Fe}/\text{DMSO}$ for $\text{X} = \text{NO}_2$ to -0.18 V for $\text{X} = \text{OCH}_3$ [87]. A few complexes of planar tetradentate non-Schiff base ligands have also been investigated [88].

In the solid state, there appear to be two common types of five-coordinate $\text{VO}(\text{IV})$ complexes of tetradentate dianionic Schiff bases. Green derivatives have $\nu(\text{V}=\text{O})$ close to 980 cm^{-1} and yellow-brown derivatives have $\nu(\text{V}=\text{O})$ around 880 cm^{-1} [89]. In solution, the N,N' -2,2-dimethyltrimethylenebis[salicylideneimine] (salnptn) ligand forms the complexes shown in Fig. 16 as expected, but it is orange in the solid state with very close axial $\text{V}-\text{O}=\text{V}$ contacts and $\nu(\text{V}=\text{O})$ at 871 cm^{-1} [89]. This complex

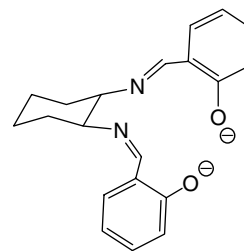


Fig. 15 Optically active Schiff-base ligand.

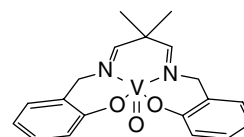


Fig. 16 Square-pyramidal $\text{VO}(\text{IV})$ complex.

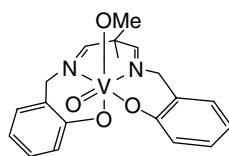


Fig. 17 Octahedral VO(V) product.

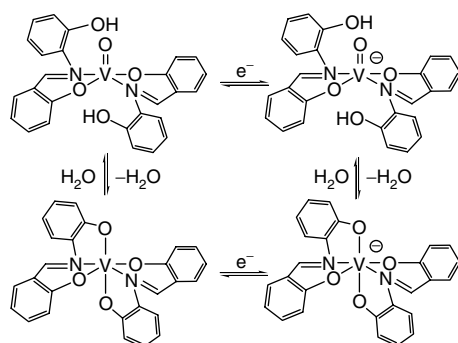


Fig. 18 Square scheme reduction mechanism for loss of the V=O group.

can be reversibly oxidized at 0.152 V versus $\text{Cp}_2\text{Fe}/\text{MeCN}$ and the corresponding VO(V) complex can be isolated as its BF_4^- salt by chemical oxidation. In the presence of methanol, the oxidized product reacts to form the complex shown in Fig 17, where the presence of the π -basic oxo and methoxide ligand force the Schiff-base ligand to adopt a rare, nonplanar conformation.

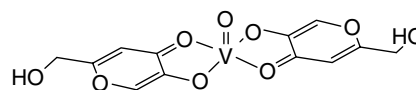
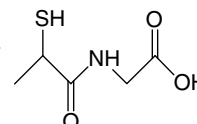
A key characteristic of square-pyramidal VO(IV) complexes is their preference to lose oxo ligands and become six-coordinate V(III) species upon reduction [37, 90]. This structural change is often a fast following reduction and can require only trace amounts of H^+ from protic species for oxo-ligand loss as H_2O to occur. A well-defined example of such a transformation is shown in Fig. 18 [91]. The starting VO(HSalamp) $_2$ complex (Fig. 18, top left) is in equilibrium with the octahedral nonoxo complex V(Salamp) $_2$, but the rate of interconversion is relatively slow. Following one-electron reduction of

VO(HSalamp) $_2$, H_2O is quickly lost to form the $\text{V}(\text{Salamp})_2^-$ anion. Spectroelectrochemical measurements reveal the reversibility of the overall conversion. In contrast, the oxidation process is completely reversible ($E_c^{\oplus'} = 0.57$ V versus $\text{Ag}/\text{Ag}^+/\text{CH}_2\text{Cl}_2$) as confirmed by controlled potential electrolysis.

The octahedrally coordinated Tp^*VO (3,5-dimethylpyrazole)($\eta^1\text{-O}_2\text{CR}$) complex ($\text{R} = (\eta^5\text{-C}_5\text{H}_4)\text{CpFe}$) displays a reversible oxidation due to the ferrocenyl moiety in the carboxylate ligand at $E_c^{\oplus'} = 0.15$ V versus $\text{Cp}_2\text{Fe}/\text{CH}_2\text{Cl}_2$ and an irreversible oxidation due to the V atom at $E_{\text{pa}} = 0.86$ V similar to other carboxylate complexes [92, 93]. Bulk oxidation at 0.45 V versus $\text{Cp}_2\text{Fe}/\text{CH}_2\text{Cl}_2$ resulted in the formation of a cationic species which could be reduced back to the starting material; however, the oxidized V(IV)-Fe(III) complex is EPR silent.

There has been considerable interest in the coordination chemistry of biologically relevant complexes of VO(IV) [94]. The

Fig. 19 Kojic acid complex.

Fig. 20
N-(2-Mercaptopropionyl)glycine.

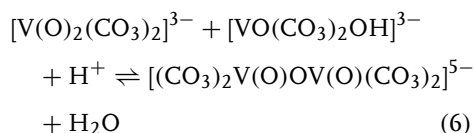
redox properties of complexes with deprotonated amide ligands [95], penicillamine-ester ligands [95], glycinate [96], and phenylalaninate [96] ligands have been reported. The glucose-lowering VO(ma)₂ and VO(ka)₂ (ka = kojic acid) (Fig 19) complexes (ma = maltol) were studied in aqueous solution over a range of pH values, and were found to undergo an oxidation characterized by slow electron transfer that appears to be less chemically reversible at high values of pH (>8) [97]. Ligand dissociation complicated the electrochemistry at pH values less than 5.

Glutathione is a tripeptide, which is a principle intracellular defense against oxidative stress. Models of its interaction with VO(IV) were prepared using sulfhydryl-containing pseudopeptides such *N*-(2-mercaptothiopropionyl)glycine (H₃mpg) shown in Fig. 20 [98]. The [NH₄Et₃][VO(mpg)(phen)][−] salt was characterized spectroscopically and by X-ray diffraction techniques and displays severely distorted octahedral coordination. This complex has a reversible reduction whose $E_c^{\oplus'}$ is solvent-dependent by CV ($E_c^{\oplus'} = -2.06$ V versus Cp₂Fe/MeCN and -2.44 V versus Cp₂Fe/CH₂Cl₂) but which appears more uniform by polarography (-1.92 V versus Cp₂Fe/MeCN versus -2.03 V versus Cp₂Fe/CH₂Cl₂). The irreversible oxidation appears to be much

less solvent-dependent (-0.83 V versus Cp₂Fe/MeCN).

A pair of triazocyclononane derivatives [99] [LVO(SCN)] were found to undergo a reversible oxidation process at $E_c^{\oplus'} = 0.26$ V versus Ag/AgCl/MeCN, but form oxo-bridged mixed-valence dimers [LV(O)OV(O)L]⁺ on reaction with water. Compounds with the [(O)VOV(O)]³⁺ core form a large class of mixed-valent compounds [100]. This example has two reversible electron transfers at $E_c^{\oplus'} = 0.59$ and -0.75 V versus Ag/AgCl/MeCN, corresponding to a Robin and Day Class I delocalized system. The delocalization of these species does not strongly depend on the V–O–V angle [99], but does depend on the presence of π -donor ligands in the $x-y$ plane. Such donors stabilize the V(V) state, but destabilize the V(IV) state in which the occupied d_{xy} orbital has an antibonding character, leading to localization. In this example, the [L¹V(O)OV(O)L¹]⁺ is delocalized because all ligands are predominantly σ donors, but the [L²V(O)OV(O)L²]⁺ is localized because of the phenylato group.

In a related example, the mixed-valence V₂O₃ core forms when vanadyl sulfate is oxidized in a pH = 7.5 HCO₃[−]/CO₃^{2−} buffer. This complex has a reversible oxidation whose potential is pH dependent since the mixed-valence dimer forms by the following equilibrium (Eq. 6):



The $[\text{VO}(\text{CO}_3)_2\text{OH}]^{3-}$ species is apparently the form of vanadyl sulfate present under these conditions and the $[\text{V}(\text{O})_2(\text{CO}_3)_2]^{3-}$ species is formed from the monomeric V(IV) species by oxidation. Similar processes result in the formation of the V_2O_3 core when a V(V) source is reduced in the same buffer [101].

Research related to the use of vanadium phosphates or V_2O_5 as oxidants of gases such as CO and SO_2 in commercial processes shows that solid vanadyl sulfate can serve as a gas-permeable solid-phase electrolyte [102]. Two reversible redox features are observable at slow scan rates ($20\text{--}150\text{ mV s}^{-1}$) by CV in a gas-tight two-electrode cell packed with powdered $\text{VOSO}_4 \cdot 3\text{H}_2\text{O}$ between a 10-mm carbon disk and a 3-mm glassy carbon electrode. The V(IV/V) couple was observed at 0.55 V versus C, and the V(IV/III) couple was observed at -0.97 V . Unlike in aqueous solution where vanadyl sulfate is reduced to $[\text{V}(\text{H}_2\text{O})_6]^{3+}$, the $\text{V}=\text{O}$ bond in the solid remains intact. The oxidation of CO(g) can be observed when it is introduced into this cell.

13.9

Oxovanadium(V)

Stabilization of the V(V) oxidation state by the $\text{V}=\text{O}$ group is well established in vanadyl coordination chemistry, but there are fewer electrochemically characterized examples of VO(V) complexes than for VO(IV) [32].

Schiff-base complexes are popular motifs for VO(V) chemistry. It is often observed that the reduction potentials of

such complexes become more negative as the energy of the ligand to metal charge transfer band in the UV-vis spectrum moves to a higher energy [103]. A variety of ligands have been recently reported which range from bidentate to pentadentate [104]. The effect of decreasing the number of N-donor atoms and increasing O-donor atoms in the coordination sphere of the metal seems to move the reduction potential to more negative values. Five-coordinate square-pyramidal structures and six-coordinate octahedral structures (with varying amounts of distortion) are known. As expected, the six-coordinate species is more difficult to reduce by ca 0.1 V in the case where the sixth ligand is an alcohol [105]. These reductions to VO(IV) are often reversible. The effect of the alkoxo group is to move the reduction potential to more negative values, at least compared to carboxylato groups [106]. Octahedral VO complexes of methylated α -D-mannopyranoside and β -D-ribofuranoside with *N*-salicylidene-glycinate as an ancillary ligand have facile reductions at -0.70 V versus $\text{Cp}_2\text{Fe}/\text{MeCN}$.

A series of 12-mixed-ligand complexes of substituted catecholates and tridentate Schiff bases (made from 8-aminoquinoline and salicylaldehyde derivatives) was prepared, and each showed a reversible reduction to the corresponding VO(IV) species in the range -0.70 to -0.85 V versus $\text{Cp}_2\text{Fe}/\text{CH}_2\text{Cl}_2$. A second, irreversible reduction was also observed corresponding to the loss of the oxo-ligand, as previously described. In DMSO, the CV response of these complexes diminished as they converted to the corresponding VO_2^+ complexes, with loss of the catecholato ligand [107].

VO(V) complexes with flexible polydentate ligands can adopt isomeric structures in solution, even though they favor

Fig. 21 A flexible polydentate ligand.

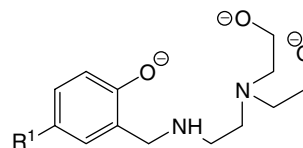
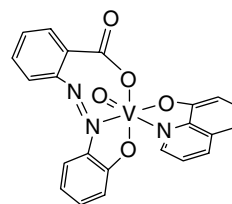


Fig. 22 Azobenzene complex.



one structure in the solid state [108]. An example is the ligand shown in Fig. 21 ($R^1 = \text{H, OMe, Br, NO}_2, \text{H}$). The corresponding salicylaldimine Schiff-base complex displays only one structure in solution [108]. For the ligand in Fig. 21, two VO(V) complexes exist in solution which differ by fac- and mer- arrangement of the alkoxide ligands. Both types display irreversible reductions complicated by solubility problems, and their reduction peak potentials vary over a 200-mV range depending on the identity of R^1 . This variation does not correlate with the Hammett constants σ_p for the substituents R^1 , but other series of Schiff-base ligands do show Hammett correlations [87].

Structural motifs related to Schiff-base ligands have been explored. Three tridentate ligands have been coordinated to the VO(quin) fragment (quin = 8-quinolinato). The octahedral azobenzene complex VO(quin)(2-hydroxy-2'-carboxy-5-methylazobenzene) shown in Fig. 22 has a reversible reduction (by CV and controlled potential electrolysis) at ca -0.31 V versus $\text{Cp}_2\text{Fe}/\text{CH}_2\text{Cl}_2$. This potential is 0.58 V more positive than the potential found in the analogous Schiff-base VO(quin) (*N*-(1-hydroxyethyl)salicylaldimine) complex. The latter complex reduction is also

reversible on the electrolysis timescale, although the reduced product is air-sensitive [106]. However, when the ancillary ligand is replaced by the related acetylacetone benzoylhydrazone ligand, the reduction loses much of its reversibility ($E_{\text{pc}} = -0.33$ V versus $\text{Ag}/\text{AgCl}/\text{CH}_2\text{Cl}_2$) [109].

cis-VO₂ complexes with tridentate Schiff-base ligands also appear, and they sometimes have five-coordinate square-pyramidal structures with one oxo-ligand at the apex. Many of these species have reversible features in their CVs at $E_c^{\oplus'} = \text{ca } -0.07$ V versus $\text{Ag}/\text{AgCl}/\text{MeOH}$ and can undergo a photoreduction in the solid state which can be reversed by dissolution [110].

Oxidation of d^0 V(V) complexes must occur at the ligands. Although many oxidations are irreversible, some reversible processes are known. For example, the square-pyramidal bimetallic complex shown in Fig. 23 has two reversible oxidations ($E_c^{\oplus'} = -0.05$ and 0.37 V versus $\text{Cp}_2\text{Fe}/\text{MeCN}$), the first of which results in a cationic ligand radical species, on the basis of its $E_c^{\oplus'}$ value, its EPR spectrum, and UV-vis data [111]. The complex also shows two closely spaced reductions ($E_c^{\oplus'} = -1.26$ and -1.36 V

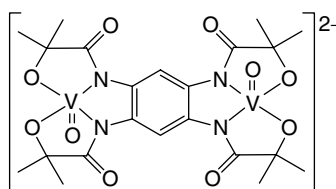


Fig. 23 Square-pyramidal bimetallic complex.

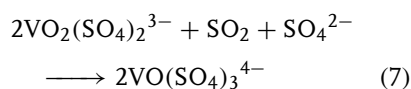
versus $\text{Cp}_2\text{Fe}/\text{MeCN}$) which are at more negative potentials because of the anionic nature of the complexes [111].

While many complexes feature $\text{VO(IV)}-\text{O}-\text{VO(IV)}$ moieties, and $\text{VO(IV)}-\text{O}-\text{VO(V)}$ represent the largest class of mixed-valence compounds known [100], electrochemically characterized $\text{VO(V)}-\text{O}-\text{VO(V)}$ are rare [112]. A series of three such complexes has been prepared, including $[(\text{abd})\text{OV}-\text{O}-\text{VO}(\text{abd})]$ which features tridentate abd ligands and square-pyramidal coordination geometry around each V atom. These complexes are reduced in the range $-0.25 < E_c^{\oplus'} < -0.16$ V versus $\text{Cp}_2\text{Fe}/\text{CH}_2\text{Cl}_2$ and the mixed-valence products are stable on the bulk electrolysis timescale and they display temperature-dependent delocalization of the unpaired electron.

The extent of delocalization in $\text{VO(IV)}-\text{O}-\text{VO(V)}$ is sensitive to the ligands present in the molecule. A series of complexes based on tetradentate TAN ligands showed Robin and Day Class 1 delocalization when the pendant donor site was a carboxyl ligand, but showed Class 3 delocalization when the donor site was a phenoxide ligand [99].

Highly oxygenated VO(V) complexes can be electrosynthesized. $\text{K}_2[\text{VO}(\text{O}_2)_2\text{F}]$, $\text{K}[\text{VO}(\text{O}_2)_2(\text{X})]$ ($\text{X} = \text{H}_2\text{O}$, O_2 , bipyridine, 1,10-phenanthroline), and similar species have been generated by the dissolution of vanadium anodes in the presence of H_2O_2 , HF and various ligands [113, 114]. Such complexes effect unusual oxidations of substrates such as cresols. Vanadium

peroxide complexes have been recognized as two-electron oxidants for the oxidation of organic substrates in chemical and biological systems [115, 116]. A molten V_2O_5 /alkali pyrosulfite catalyst for the oxidation of gaseous SO_2 used in H_2SO_4 manufacture and more recently in the desulfurization of power plant flue gas has been investigated. The formation of V(IV) and V(V) species in sulfate-saturated melts was documented [117] and their redox reaction with SO_2 was found to follow Eq. (7).



The overall mechanism remains controversial since the species formed appear to be very dependent on conditions such as the presence of water, whether the pyrosulfate melt is acidic or basic, and the alkali metal present [118]. V_2O_5 appears to be reduced in molten $\text{K}_2\text{S}_2\text{O}_7$ at 400°C under Ar in two steps; a reduction to V(IV) which is reversible at low concentrations and a second step to V(III) [118]. The presence of Li^+ accelerates the reduction.

There is very little information on organometallic V(V) species, but the related octahedral $\text{Tp}^*\text{VO}(\text{OMe})_2$ was found to be representative of a series of Tp and Tp^* alkoxide complexes. The Tp^* complexes are more difficult to reduce than the Tp derivatives, but the identity of the alkoxide ligand had little effect on the observed electrochemical features. The complex can be reduced at $E_c^{\oplus'} = -0.96$ V

versus SCE/CH₂Cl₂, but there is little reversibility in the CV at 0.3 V s⁻¹. The reduction appears to involve the loss of the alkoxide ligand. In methanol, or in the presence of a base, the reversibility is enhanced and $E_c^{\oplus'} = -0.26$ V versus SCE/MeOH [119, 120].

References

- W. E. Geiger, N. G. Connelly, *Chem. Rev.* **1996**, 96, 877–910.
- G. V. Ionova, V. Pershina, E. Johnson et al., *J. Phys. Chem.* **1992**, 96, 11096–11101.
- G. Pampaloni, U. Koelle, *J. Organomet. Chem.* **1994**, 481, 1–6.
- M. C. Barybin, J. E. Ellis, M. K. Pomije et al., *Inorg. Chem.* **1998**, 37, 6518–6527.
- T. W. Hayton, P. J. Daff, P. Legzdins et al., *Inorg. Chem.* **2002**, 41, 4114–4126.
- J. Grobe, B. H. Schneider, H. Zimmermann, *Z. Anorg. Allg. Chem.* **1981**, 481, 107–116.
- C. Elschenbroich, J. Kroker, M. Nowotny et al., *Organometallics* **1999**, 18, 1495–1503.
- J. Chakravarty, S. Dutta, A. Chakravorty, *Organometallics* **1993**, 12, 3373–3378.
- C. Elschenbroich, E. Schmidt, B. Metz et al., *Z. Anorg. Allg. Chem.* **1999**, 625, 875–886.
- C. Elschenbroich, T. Isenburg, B. Metz et al., *J. Organomet. Chem.* **1994**, 481, 153–165.
- C. Elschenbroich, P. Kuehlkamp, J. Koch et al., *Chem. Ber.* **1996**, 129, 871–878.
- C. Elschenbroich, O. Schiemann, O. Burghaus et al., *Organometallics* **1999**, 18, 3273–3277.
- C. Elschenbroich, J. Plackmeyer, J. Pebler et al., *Inorg. Chem.* **2005**, 44, 955–963.
- J. C. Green, M. L. H. Green, N. Kaltsoannis et al., *Organometallics* **1992**, 11, 3353–3361.
- J. A. Belot, R. D. McCullough, A. L. Rhein gold et al., *Organometallics* **1996**, 15, 5062–5065.
- Y. Mugnier, C. Moise, E. Laviron, *Nouv. J. Chim.* **1982**, 6, 197–200.
- G. A. Miller, M. J. Therien, W. C. Troglor et al., *J. Organomet. Chem.* **1990**, 383, 271–278.
- B. Bachmann, F. Hahn, J. Heck et al., *Organometallics* **1989**, 8, 2523–2543.
- M. D. Wasczak, Y. Wang, A. Gard et al., *J. Am. Chem. Soc.* **2001**, 123, 2783–2790.
- L. E. Bennett, H. Taube, *Inorg. Chem.* **1968**, 7, 254–261.
- J. C. Dobson, H. Taube, *Inorg. Chem.* **1989**, 28, 1310–1315.
- P. Ghosh, H. Taube, T. Hasegawa et al., *Inorg. Chem.* **1995**, 34, 5761–5775.
- H. Ogino, T. Nagata, K. Ogino, *Inorg. Chem.* **1989**, 28, 3656–3659.
- N. Kato, *Polyhedron* **1989**, 8, 1949–1951.
- M. Hecht, F. Mathias, W. Ronald, *J. Phys. Chem.* **1996**, 100, 14248–14255.
- M. Hecht, F. Mathias, W. Ronald, *J. Phys. Chem.* **1996**, 100, 14240–14247.
- N. Kato, K. Aoki, *J. Electroanal. Chem. Interfacial Electrochem.* **1989**, 261, 309–314.
- C. L. Simpson, C. G. Pierpont, *Inorg. Chem.* **1992**, 31, 4308–4313.
- K. Ramesh, R. Mukherjee, *J. Chem. Soc., Dalton Trans.* **1991**, 3259–3262.
- M. Chatterjee, S. Ghosh, N. Saktiprosad et al., *Polyhedron* **1997**, 16, 2917–2923.
- A. Neves, A. S. Ceccato, S. M. D. Erthal et al., *Inorg. Chim. Acta* **1991**, 187, 119–121.
- A. Sokolowski, B. Adam, T. Weyhermueller et al., *Inorg. Chem.* **1997**, 36, 3702–3710.
- U. Auerbach, V. Della, S. P. C. Beatric et al., *J. Chem. Soc., Chem. Commun.* **1990**, 1004–1006.
- R. Hotzelmann, K. Wieghardt, *Inorg. Chem.* **1993**, 32, 114–116.
- R. Hotzelmann, K. Wieghardt, J. Ensling et al., *J. Am. Chem. Soc.* **1992**, 114, 9470–9483.
- H. Kelm, H.-J. Krueger, *Inorg. Chem.* **1996**, 35, 3533–3540.
- M. Mohan, S. M. Holmes, R. J. Butcher et al., *Inorg. Chem.* **1992**, 31, 2029–2034.
- N. S. Dean, L. M. Mokry, M. R. Bond et al., *Inorg. Chem.* **1996**, 35, 3541–3547.
- M. Chatterjee, S. Ghosh, A. K. Nandi, *Polyhedron* **1997**, 16, 2917–2923.
- L. Y. Chung, E. C. Constable, M. S. Khan et al., *Inorg. Chim. Acta* **1991**, 185, 93–96.
- K. Kanamori, K. Yamamoto, T. Okayasu et al., *Bull. Chem. Soc. Jpn.* **1997**, 70, 3031–3040.
- P. E. Kruger, B. Moubaraki, K. S. Murray, *J. Chem. Soc., Dalton Trans.* **1996**, 1223–1228.
- Y. Mugnier, C. Moise, E. Laviron, *Nouv. J. Chim.* **1982**, 6, 197–200.

44. F. Baumann, M. Heilmann, W. Matheis et al., *Inorg. Chim. Acta* **1996**, 251, 239–248.
45. G. A. Miller, M. J. Therien, W. C. Troglor, *J. Organomet. Chem.* **1990**, 383, 271–278.
46. C. D. Abernethy, F. Bottomley, A. Decken et al., *Organometallics* **1997**, 16, 1865–1869.
47. R. Ferguson, E. Solari, C. Floriani et al., *J. Am. Chem. Soc.* **1997**, 119, 10104–10115.
48. J. R. Rambo, S. L. Castro, K. Folting et al., *Inorg. Chem.* **1996**, 35, 6844–6852.
49. S. L. Castro, W. E. Streib, J.-S. Sun et al., *Inorg. Chem.* **1996**, 35, 4462–4468.
50. K. R. Hanz, T. L. Riechel, *Inorg. Chem.* **1997**, 36, 4024–4028.
51. G. M. Greenway, G. Wolfbauer, *Anal. Chim. Acta* **1995**, 312, 15–25.
52. Z. Hou, T. D. P. Stack, C. J. Sunderland et al., *Inorg. Chim. Acta* **1997**, 263, 341–355.
53. C. J. Hawkins, T. A. Kabanos, *Inorg. Chem.* **1989**, 28, 1084–1087.
54. P. R. Klich, A. T. Daniher, P. R. Challen et al., *Inorg. Chem.* **1996**, 35, 347–356.
55. S. P. Best, S. A. Ciniawsky, D. G. Humphrey, *J. Chem. Soc., Dalton Trans.* **1996**, 2945–2949.
56. E. Ludwig, H. Hefele, E. Uhlemann et al., *Z. Anorg. Allg. Chem.* **1995**, 621, 23–28.
57. R. G. Compton, J. Booth, J. J. Eklund, *J. Chem. Soc., Dalton Trans.* **1994**, 1711–1715.
58. S. T. Hamdi, S. M. Aliwi, *Z. Phys. Chem. (Munich)* **1991**, 174, 199–209.
59. J. A. Belot, R. D. McCullough, A. L. Rhein gold et al., *Organometallics* **1996**, 15, 5062–5065.
60. P. Ghosh, S. Ghosh, O. J. D'Cruz et al., *J. Inorg. Biochem.* **1998**, 72, 89–98.
61. P. Ghosh, A. T. Kotchevar, D. D. DuMez et al., *Inorg. Chem.* **1999**, 38, 3730–3737.
62. F. Y. Petillon, P. Schollhammer, J. Talarmin, *J. Organomet. Chem.* **1991**, 411, 159–170.
63. W. A. Herrmann, M. Denk, R. W. Albach et al., *Chem. Ber.* **1991**, 124, 683–689.
64. C. Le Floch, R. A. Henderson, D. L. Hughes et al., *J. Chem. Soc., Chem. Commun* **1993**, 175–176.
65. M. F. C. Guedes da Silva, J. A. L. da Silva, J. J. R. Frausto da Silva et al., *J. Am. Chem. Soc.* **1996**, 118, 7568–7573.
66. E. M. Armstrong, R. L. Beddoes, L. J. Calviou et al., *J. Am. Chem. Soc.* **1993**, 115, 807–808.
67. P. Reeb, Y. Mugnier, *J. Organomet. Chem.* **1988**, 339, 89–96.
68. S. M. Malinak, K. D. Demadis, D. Coucouvanis, *J. Am. Chem. Soc.* **1995**, 117, 3126–3133.
69. D. V. Fomitchev, C. C. McLauchlan, R. H. Holm, *Inorg. Chem.* **2002**, 41, 958–966.
70. Y. Zhang, Q. Liu, Y. Deng et al., *Polyhedron* **1999**, 18, 3153–3163.
71. C. D. Abernethy, F. Bottomley, A. Decken et al., *Organometallics* **1996**, 15, 1758–1759.
72. T. Otieno, L. M. Mokry, M. R. Bond et al., *Inorg. Chem.* **1996**, 35, 850–856.
73. H. Schumann, *Inorg. Chem.* **1996**, 35, 1808–1813.
74. H. Schumann, *Z. Naturforsch., B* **1995**, 50, 1494–1504.
75. D. L. Davies, A. J. Grist, *Inorg. Chim. Acta* **1994**, 216, 217–221.
76. T. A. Kabanos, A. M. Z. Slawin, D. J. Williams et al., *J. Chem. Soc., Chem. Commun.* **1990**, 193–194.
77. T. A. Kabanos, J. D. Woollins, *J. Chem. Soc., Dalton Trans.* **1991**, 1347–1350.
78. T. Ren, *Inorg. Chim. Acta* **1995**, 229, 195–202.
79. P. Knopp, K. Wiegardt, *Inorg. Chem.* **1991**, 30, 4061–4066.
80. M. Chatterjee, S. Ghosh, B.-M. Wu et al., *Polyhedron* **1998**, 17, 1369–1374.
81. E. Tsuchida, K. Yamamoto, O. Oyaizu et al., *Inorg. Chem.* **1994**, 33, 1056–1063.
82. C. K. Sams, K. A. Joergensen, *Acta Chem. Scand.* **1995**, 49, 839–847.
83. M. A. Nawi, T. L. Riechel, *Inorg. Chem.* **1981**, 20, 1974–1978.
84. E. Tsuchida, K. Oyaizu, E. L. Dewi et al., *Inorg. Chem.* **1999**, 38, 3704–3708.
85. K. Oyaizu, E. L. Dewi, E. Tsuchida, *Inorg. Chem.* **2003**, 42, 1070–1075.
86. H. Schmidt, M. Bashirpoor, D. Rehder, *J. Chem. Soc., Dalton Trans.* **1996**, 3865–3870.
87. K. Nakajima, K. Kojima, M. Kojima et al., *Bull. Chem. Soc. Jpn.* **1990**, 63, 2620–2630.
88. K. K. Nanda, S. Mohanta, S. Ghosh et al., *Inorg. Chem.* **1995**, 34, 2861–2869.
89. S. A. Fairhurst, D. L. Hughes, U. Kleinkes et al., *J. Chem. Soc., Dalton Trans.* **1995**, 321–326.
90. Y. Zhang, R. H. Holm, *Inorg. Chem.* **1990**, 29, 911–917.
91. J. Dai, H. Wang, M. Mikuriya, *Polyhedron* **1996**, 15, 1801–1806.

92. D. Collison, F. E. Mabbs, S. S. Turner et al., *J. Chem. Soc., Dalton Trans.* **1997**, 1201–1204.
93. D. Collison, D. R. Eardley, F. E. Mabbs et al., *Inorg. Chem.* **1993**, 32, 664–671.
94. G. E. M. Winter, A. Butler, *Biochemistry* **1996**, 35, 11805–11811.
95. T. A. Kabanos, A. D. Keramidas, A. B. Papaioannou et al., *J. Chem. Soc., Chem. Commun* **1993**, 643–645.
96. S. Mondal, S. Dutta, A. Chakravorty, *J. Chem. Soc., Dalton Trans.* **1995**, 1115–1120.
97. V. G. Yuen, P. Caravan, L. Gelmini et al., *J. Inorg. Biochem.* **1997**, 68, 109–116.
98. A. J. Tasiopoulos, A. N. Troganis, A. Evangelou et al., *Chem. – Eur. J.* **1999**, 5, 910–921.
99. D. Schulz, T. Weyhermueller, K. Wieghardt et al., *Inorg. Chim. Acta* **1995**, 240, 217–229.
100. C. G. Young, *Coord. Chem. Rev.* **1989**, 96, 89–251.
101. R. Meier, G. Werner, R. Kirmse et al., *Z. Anorg. Allg. Chem.* **1990**, 583, 209–222.
102. W. Gorski, J. A. Cox, *Langmuir* **1995**, 11, 3603–3604.
103. G. Asgedom, A. Sreedhara, C. P. Rao, *Polyhedron* **1995**, 14, 1873–1879.
104. C. P. Rao, A. Sreedhara, P. V. Rao et al., *J. Chem. Soc., Dalton Trans.* **1998**, 2383–2394.
105. S. P. Rath, S. Mondal, A. Chakravorty, *Inorg. Chim. Acta* **1997**, 263, 247–253.
106. S. P. Rath, T. Ghosh, S. Mondal, *Polyhedron* **1997**, 16, 4179–4186.
107. G. Asgedom, A. Sreedhara, C. P. Rao et al., *Polyhedron* **1996**, 15, 3731–3739.
108. W. Plass, *Z. Anorg. Allg. Chem.* **1997**, 623, 461–477.
109. S.-X. Liu, S. Gao, *Polyhedron* **1997**, 17, 81–84.
110. G. Asgedom, A. Sreedhara, J. Kivikoski et al., *J. Chem. Soc., Dalton Trans.* **1995**, 2459–2466.
111. S. W. Gordon-Wylie, B. L. Claus, C. P. Horwitz et al., *Chem. – Eur. J.* **1998**, 4, 2173–2181.
112. J. Chakravarty, S. Dutta, A. Chakravorty, *J. Chem. Soc., Dalton Trans.* **1993**, 2857–2858.
113. M. C. Chakravorti, S. Ganguly, G. V. B. Subrahmanyam et al., *Polyhedron* **1993**, 12, 683–687.
114. M. C. Chakravorti, S. Ganguly, M. Bhattacharjee, *Polyhedron* **1994**, 13, 695–699.
115. A. Butler, M. J. Clague, G. E. Meister, *Chem. Rev.* **1994**, 94, 625–638.
116. Z. Liu, F. C. Anson, *Inorg. Chem.* **2001**, 40, 1329–1333.
117. S. B. Rasmussen, K. M. Eriksen, R. Fehrmann, *J. Phys. Chem. B* **1999**, 103, 11282–11289.
118. T. Horita, N. Sakai, T. Kawada et al., *J. Electrochem. Soc.* **1995**, 142, 2621–2624.
119. S. Holmes, C. J. Carrano, *Inorg. Chem.* **1991**, 30, 1231–1235.
120. C. J. Carrano, M. Mohan, S. M. Holmes et al., *Inorg. Chem.* **1994**, 33, 646–655.

15 Chromium, Molybdenum and Tungsten

Christopher J. Pickett
John Innes Centre, Norwich, UK

15.1	Introduction	389
15.2	Electrochemical Oxidation	389
15.2.1	Mononuclear Carbonyls	389
15.2.2	Tertiary Phosphine Complexes: Redox Linked cis–trans Isomerism	390
15.2.3	Tertiary Phosphine Complexes: Intermediate Oxidation States and Ligand-centered Oxidative Transformations	391
15.2.4	Arene and Cyclopentadienyl Derivatives	391
15.2.4.1	Zero Oxidation State Complexes	391
15.2.4.2	Intermediate and Higher Oxidation State Cyclopentadienyl Complexes	392
15.2.5	Pyrazolylborate Derivatives	393
15.3	Electrochemical Reduction	393
15.3.1	The Hexacarbonyls	393
15.3.2	Substituted Hexacarbonyls: Ligand-centered Reduction	394
15.3.3	Haptotropic Rearrangements – Ring Slippage	394
15.3.4	Intermediate and Higher Oxidation State Complexes	395
15.3.5	Electrochemical Transformation of Ligands at {M(Ph ₂ PCH ₂ CH ₂ PPh ₂) ₂ } Centers	395
	References	396

15.1 Introduction

This chapter deals with aspects of the electrochemistry of coordination and the organometallic compounds of Cr, Mo, and W. Emphasis is placed on the electrochemistry of the lower and intermediate oxidation states species in which the metal center is generally stabilized with carbonyl, cyclopentadienyl, or tertiary phosphine ligands, as this area has progressed rapidly over the last 20 years or so. Molybdenum complexes with bis-bidentate tertiary phosphine coligands provide a redox platform at which ligands can be transformed in stoichiometric or catalytic reactions, and some emphasis is placed on the electrochemical aspects of this chemistry. The electron-transfer reactions of molybdenum sulfur complexes have received enormous attention in the last three decades, not least because of their relevance to molybdo enzymes such as the nitrate reductases, xanthine oxidases, and the iron molybdenum protein of nitrogenase. For this reason, a separate section is devoted to molybdenum sulfur ligand systems. In general, rather than an exhaustive survey, those systems that illustrate generic aspects of the electrochemistry of both the groups and of the wider aspects of transition metal coordination

or organometallic chemistry are given the most attention. Polyoxometallate electrochemistry of Cr, Mo or W is covered in Chapter 3.

15.2 Electrochemical Oxidation

15.2.1 Mononuclear Carbonyls

The prototypically zero oxidation state complexes of the group are the binary hexacarbonyls $M(CO)_6$. Early studies of the electrochemistry of these 18-electron closed-shell systems in nonaqueous electrolytes has perhaps been seminal in understanding the electron-transfer reactions of more substituted systems and of metal carbonyls in general.

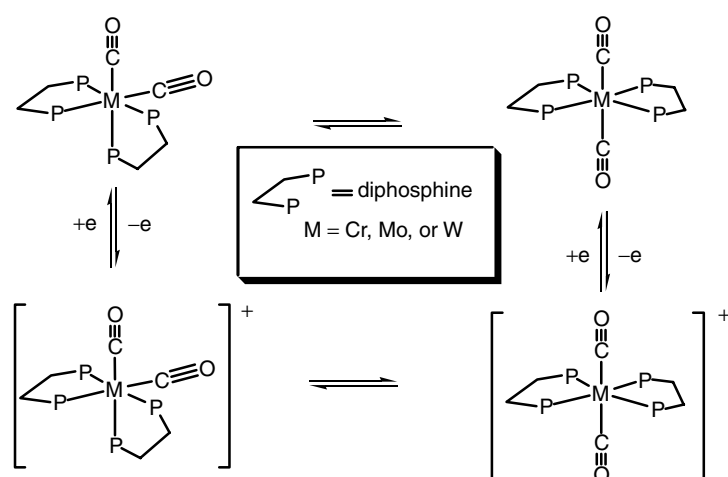
$Cr(CO)_6$ undergoes a primary diffusion-controlled one-electron oxidation near +1.5 V versus SCE in MeCN or CF_3COOH containing $[NBu_4][BF_4]$ to give the unstable paramagnetic $Cr^{I}17$ -electron radical cation, [1, 2] whereas $Mo(CO)_6$ and $W(CO)_6$ both undergo irreversible multi-electron oxidation at a similar potential under the same conditions [2]. This can be attributed to the ease of attack by nucleophiles on the larger Mo and W cation centers – the tendency of these metals

to form seven-coordinate complexes in their intermediate oxidation states is well established [3]. Replacing one or more CO ligands on the metal center can lead to stabilization of the 17-electron cation because all substitutions of a π^* CO by a ligand L or anion X^- must lead to enhanced electron density at the metal, with the exception of PF_3 . This has two consequences: (1) lower electrophilicity of the 17-electron cation, and (2) stabilizing the metal carbonyl bond. Thus, in the latter case, a decomposition pathway via loss of CO from the 17-electron species as a consequence of weaker backdonation from metal to CO in the oxidized state, can be compensated for by the presence of one or more donor ligands. For example, the anions $[Cr(CO)_5X]^-$ ($X = \text{halide or CN}$) undergo fully reversible one-electron oxidation to give stable, isolable 17-electron products [3]. Comparison of the effect of substituents L or X^- on the $E_{1/2}^{\text{ox}}$ of $[Cr(CO)_5L]$ or $[Cr(CO)_5X]^-$ has provided a scale of the net electron-donating influence of a substituent, the P_L scale, as discussed in Chapter 1 [4].

15.2.2

Tertiary Phosphine Complexes: Redox Linked cis–trans Isomerism

Formally replacing four CO ligands in $M(CO)_6$ ($M = \text{Mo or W}$) by two bidentate tertiary phosphine ligands both enhances the electron density on the metal center and sterically inhibits nucleophilic attack on the 17-electron cation. For example, *trans*- $[Mo(CO)_2(Ph_2PCH_2CH_2PPh_2)_2]$ undergoes reversible electrochemical oxidation to the Mo(I) cation, Sch. 1. The electrochemistry of this type of P4 tertiary phosphine complexes is particularly interesting in that they can exhibit redox linked cis–trans isomerism, Sch. 1. Detailed electrochemical studies of such Cr, Mo, and W systems by Bond and coworkers provided the paradigm analysis of the thermodynamics and kinetics of this type of isomerism [3, 5–10], which has now been recognized in a wide range of systems [11], including complexes in which CO is replaced by other π -acceptor ligands such as isocyanides or by N_2 [12, 13].



Scheme 1 Scheme of squares for cis–trans redox isomerism.

15.2.3

**Tertiary Phosphine Complexes:
Intermediate Oxidation States and
Ligand-centered Oxidative Transformations**

The 16-electron *tertiary* phosphine complexes $\text{trans}[\text{MX}_2\{\text{R}_2\text{P}(\text{CH}_2)_n\text{PR}_2\}_2]$ ($\text{M} = \text{Cr}, \text{Mo}$ or W ; $\text{X} = \text{halide}, \text{CN}, \text{SCN}$, or thiolate; $\text{R} = \text{alkyl}$ or aryl ; $n = 1, 2$, or 3) show two successive reversible one-electron oxidation processes in non-aqueous solvents, corresponding to the M(III)/M(II) and M(IV)/M(III) couples. The M(III) species are stable on the preparative timescale whereas the M(IV) 14-electron dicationic species are generally less stable. Comparison of crystallographic data for the 15-electron cation $\text{trans}[\text{MoCl}_2\{\text{Ph}_2\text{P}(\text{CH}_2)_2\text{PPh}_2\}_2]^+$ and its 16-electron parent shows that the average $\text{M}-\text{P}$ bond lengthens by about 0.1 \AA upon one-electron oxidation, and this is attributed to diminished backdonation from the metal to the phosphine ligands [14].

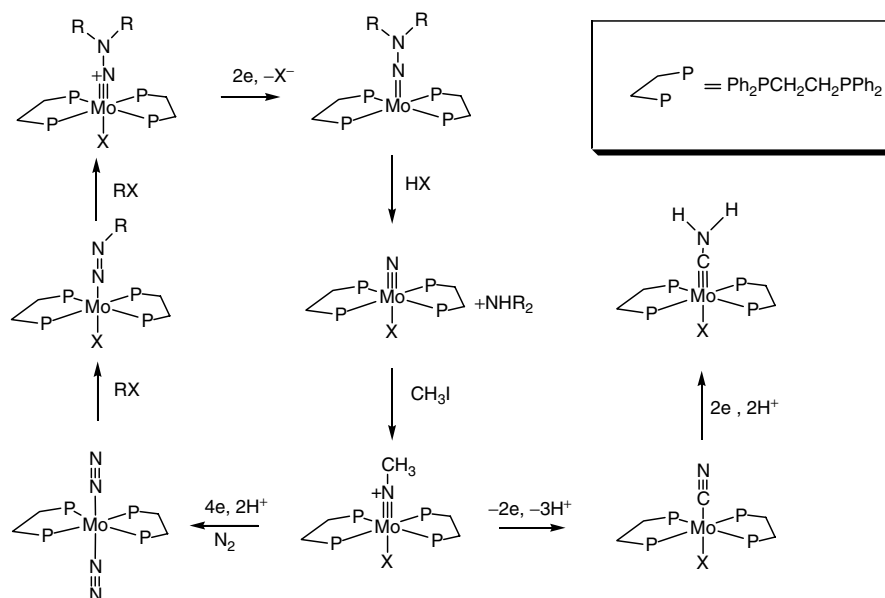
A range of multiply bonding ligands such as $=\text{O}$, $\equiv\text{N}$, $\equiv\text{NMe}^+$, and $\equiv\text{NNH}_2^+$ are supported at M^{IV} sites, for example, as in $\text{trans}[\text{MoCl}(\text{NMe})(\text{Ph}_2\text{PCH}_2\text{CH}_2\text{PPh}_2)_2]^+$. Such diamagnetic complexes undergo one-electron reversible oxidation to the paramagnetic M^{V} dications, which are moderately stable when generated in solvents of low nucleophilicity. The electrogenerated dication $[\text{MoCl}(\text{NMe})(\text{Ph}_2\text{PCH}_2\text{CH}_2\text{PPh}_2)_2]^{2+}$ has been studied by EPR and ENDOR which has shown that the MoNMe moiety remains linear [15]. The methyl group in $\text{trans}[\text{MoCl}(\text{NMe})(\text{Ph}_2\text{PCH}_2\text{CH}_2\text{PPh}_2)_2]^+$ can be deprotonated with a strong base to yield a Mo^{IV} methyleneamide complex $\text{trans}[\text{MoCl}(\text{NCH}_2)(\text{Ph}_2\text{PCH}_2\text{CH}_2\text{PPh}_2)_2]$. Remarkably, electrochemical oxidation of this species leads to rearrangement of the

MoNC framework to MoCN with *formal* reduction of the metal center (from 18-electron) Mo^{IV} to (16-electron) Mo^{II} [16], Sch. 2. The utility of the square-planar $\{\text{M}(\text{Ph}_2\text{PCH}_2\text{CH}_2\text{PPh}_2)_2\}$ assembly as a platform for electrochemical transformation of ligands in the axial position is further exemplified in the section on reduction.

15.2.4

Arene and Cyclopentadienyl Derivatives15.2.4.1 **Zero Oxidation State Complexes**

There has been much early work on the oxidative electrochemistry of π -arene complexes of the chromium group. Three CO or six ligands on $\text{M}(\text{CO})_6$ can formally be replaced by arenes to give respectively $[\text{M}(\eta^6\text{-arene})(\text{CO})_3]$ or $[\text{M}(\eta^6\text{-arene})_2]$ complexes ($\text{M} = \text{Cr}, \text{Mo}$, or W). These undergo reversible one-electron oxidation at potentials dependent upon the arene substituents. There have been various experimental and theoretical analyses of such effects, including free-energy correlations between free and coordinated ligand redox potentials [17]. The stabilization of the metal-centered 17-electron radical cation $[\text{Cr}(\eta^6\text{-C}_6\text{H}_6)(\text{CO})_3]^+$ has recently been achieved using an electrolyte of low nucleophilicity, $[\text{NBu}_4][\text{B}(\text{C}_6\text{F}_5)_4]-\text{CH}_2\text{Cl}_2$, a system which has wide application for stabilizing electrophilic metallo complexes [18]. The electronic interplay between arene tricarbonyl chromium units linked by spacer groups has been systematically examined [19]. The ferrocenyl (Fc) group attached to the benzene ring in $[\text{Cr}(\eta^6\text{-FcC}_6\text{H}_5)(\text{CO})_3]$ functions as a reversible redox switch by providing a mechanism for the chromium center to be oxidatively activated to ligand substitution and addition reactions [20]. The initial oxidation occurs at the ferrocenyl



Scheme 2 Electrochemical and chemical transformations of nitrogen ligands.

group promoting CO substitution by, for example, $\text{P}(\text{OEt})_3$. Internal electron transfer from Cr to Fe accompanies this CO substitution, with the result that the ferrocenium group in reverts to ferrocenyl, thus closing the redox switch. Cyclopentadienyl complexes such as anionic $[\text{Cr}(\eta^5\text{-C}_5\text{H}_5)(\text{CO})_3]^-$ (isoelectronic with the neutral arene tricarbonyl analog) and certain CO substituted derivatives also undergo reversible one-electron oxidation to 17-electron, neutral metal-centered radicals [21]. The isolable mixed-sandwich 17-electron metallocene $[\text{Mo}(\eta^5\text{-C}_5\text{H}_5)(\eta^6\text{-C}_6\text{Ph}_6)]$ has been shown to undergo reversible one-electron oxidation and reduction reactions to the 16-electron and 18-electron species by voltammetry and coulometry; notably the 16-electron cation can form an adduct with $[\text{PF}_6]^-$ in dichloromethane [22].

Chromium tricarbonyl complexes with arenes bonded to rigid polynorbornyl-type

spacers have been studied by cyclic voltammetry and controlled-potential coulometry. The binuclear complexes undergo two reversible oxidations. In one system in which the metal centers are at a distance of 6.48 Å, the two-redox steps are separated by 140 mV. This magnitude of interaction between the two-redox sites is ascribed to efficient through-bond coupling through the bicyclic spacer. Some characterization of the cation radicals was accomplished by low-temperature IR and ESR studies [19].

15.2.4.2 Intermediate and Higher Oxidation State Cyclopentadienyl Complexes

Electrochemical oxidation of the M(IV) bis-cyclopentadienyl complexes such as $[\text{Mo}(\eta^5\text{-C}_5\text{H}_5)_2\text{X}_2]$, where X is an anionic ligand, have been widely studied. Invariably, such complexes undergo reversible oxidation to the M(V) species

in nonaqueous electrolytes [23]. A recent sonoelectrochemical study of $[\text{Mo}(\eta^5\text{-C}_5\text{H}_5)_2\text{Cl}_2]$ suggests, surprisingly, that ultrasound promotes the displacement of Cl^\bullet from the 17-electron cation by MeCN and subsequent disproportionation [24]. One or both $\text{X} = \text{halide}$ groups in $[\text{Mo}(\eta^5\text{-C}_5\text{H}_5)_2\text{X}_2]$ can be replaced by alkyl ligands, and cyclic voltammetry studies show that they undergo one-electron oxidation. Not unexpectedly, the ease of oxidation of these complexes decreases in the order $\text{Me;Me} > \text{Me;Bu} > \text{Bu;Bu} > \text{Et;Et} > \text{Cl;Me} > \text{Br;Me}$ [25]. The amide thiolate complex $[\text{Mo}(\eta^5\text{-C}_5\text{H}_5)_2(\text{NHCH}(\text{COO Me})(\text{CH}_2\text{S}))]$, which is formed by the reaction of $[\text{Mo}(\eta^5\text{-C}_5\text{H}_5)_2\text{Cl}_2]$ with cysteine methyl ester, displays a remarkable electrochemistry insofar as a redox linked rotamerism is observed in which the $\text{C}=\text{O}$ group of the amide is orientated toward the metal in the 17-electron cationic form and is predominately rotated away from the metal in the parent neutral 18-electron complex [26].

Anodic oxidations of the Mo(II) bis-cyclopentadienyl alkyne compound $\text{Mo}(\eta^5\text{-C}_5\text{H}_5)_2(\eta^2\text{-C}_2\text{Ph}_2)$, and of metal-alkene analogs such as $\text{Mo}(\eta^5\text{-C}_5\text{H}_5)_2(\eta^2\text{-C}_2\text{H}_4)$ involve a reversible one-electron oxidation at very facile potentials. The $\nu(\text{CC})$ alkyne stretch in the IR spectrum of 17-electron Mo -alkyne cation (1824 cm^{-1}) was shifted by 50 cm^{-1} to a higher wave number to that of its parent, consistent with a decrease in the metal-alkyne interaction in the Mo(III) cation.

15.2.5

Pyrazolylborate Derivatives

Pyrazolylborate anions such as $[\text{HB}(3,5\text{-Me}_2\text{C}_3\text{HN}_2)_3]^-$ (Tp^*) are isoelectronic with

the cyclopentadienide anion and serve in a similar capacity as ligands which “occupy” three facial sites. McCleverty and coworkers have very extensively studied the chemistry and electrochemistry of Mo and W systems containing these type of ligands [27] and have particularly developed the syntheses to probe systematically the electronic and magnetic interactions between bimetallic systems linked by bridging units such as $4,4'\text{-NC}_5\text{H}_4(\text{CH}=\text{CH})_n\text{C}_5\text{H}_4\text{N}$ and have notably explored such materials for second-harmonic generation [27–33].

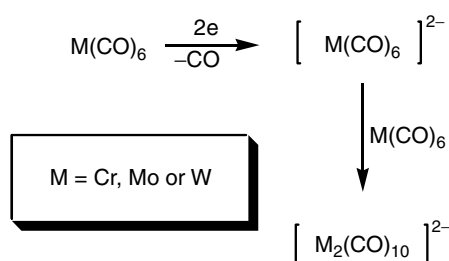
15.3

Electrochemical Reduction

15.3.1

The Hexacarbonyls

$\text{M}(\text{CO})_6$ complexes all undergo irreversible electrochemical reduction in nonaqueous electrolytes at peak potentials close to -2.7 V versus SCE in tetrahydrofuran (THF) containing $[\text{NBu}_4][\text{BF}_4]$. The product of the reductions are the dinuclear dianions $[\text{M}_2(\text{CO})_{10}]^{2-}$ although under some conditions polynuclear products can also be obtained, Sch. 3 [2]. It was initially proposed that the primary step involved a single-electron transfer with fast CO loss and subsequent dimerization of the 17-electron radical anion $[\text{M}(\text{CO})_5]^-$ [34]. A subsequent study showed that a common intermediate detected on the voltammetric timescale was the 18-electron species $[\text{M}(\text{CO})_5]^{2-}$ and that the overall one-electron process observed in preparative electrolysis arises by attack of the dianion on the parent material in the bulk solution, Sch. 2 [35].



Scheme 3 Pathway for reduction of group VI hexacarbonyls.

15.3.2

Substituted Hexacarbonyls: Ligand-centered Reduction

By the same notion that replacing one or more CO ligands in M(CO)_6 by a ligand, generally L, raises the energy of the HOMO and makes oxidation more accessible, the enhanced charge on the metal as a consequence of substitution raises the energy of the LUMO and shifts the reduction of $\text{M(CO)}_5\text{L}$ beyond -2.7V versus SCE – generally outside of the reduction range of the electrolyte system. However, with certain N ligands such as TCNE, 2,2'-bipyridyl, and phenanthroline, low-lying π^* orbitals allow *ligand-centered* reduction and the electrochemistry of such systems has received attention, most notably by the group of Kaim, in the context of hyperfine interactions, photophysics, solvatochromic properties, and redox induced substitution chemistry, as have binuclear systems in which a group bridging two metal centers undergoes ligand-centered reduction [36–41].

15.3.3

Haptotropic Rearrangements – Ring Slippage

In the sections above, we have seen that addition of an electron to an 18-electron octahedral complex can lead to the fast expulsion of a ligand as in the case of

$[\text{Cr(CO)}_6]$ or if the metal center bears a ligand with low-lying π^* system the “extra” electron can reside on the ligand. There is an additional way in which extra electrons can be accommodated in the reduction of closed-shell 18-electron systems and that is by a change in hapticity of an unsaturated π -hydrocarbon ligand. Examples are well documented for a wide range of metal centers, and the work of Geiger’s group has been at the forefront of delineating redox induced changes in hapticity [42, 43]. Examples for chromium group systems are limited but include an early example in which an η^6 -naphthalene complex $[\text{Cr}(\eta^6\text{-C}_{10}\text{H}_8)(\text{CO})_3]$ rearranges to $[\text{Cr}(\eta^4\text{-C}_{10}\text{H}_8)(\text{CO})_3]^{2-}$ upon two-electron reduction [44] and stepwise hapticity changes in an indenyl ligand (Ind) [45]. Thus, the chemically reversible two-electron reduction of the dication $[\text{Mo}(\eta^5\text{-Ind})(\eta^5\text{-C}_5\text{H}_5)\{\text{P(OMe)}_3\}_2]^{2+}$ to $[\text{Mo}(\eta^3\text{-Ind})(\eta^5\text{-C}_5\text{H}_5)\{\text{P(OMe)}_3\}_2]^{2+}$ proceeds through a one-electron intermediate. The structures of the parent η^5 complex and the η^3 product were determined by X-ray diffraction studies and these have shown that the slip-fold distortion angle of the indenyl ring increases from 4.1 to 21.7° . Cyclic voltammetry and bulk electrolysis were employed to define the thermodynamics and heterogeneous charge-transfer kinetics of reactions. Molecular orbital calculations

(density functional theory and extended Huckel) predicted that metal–indenyl bonding in the monocationic intermediate is approximately midway between that of the η^5 and η^3 hapticities (slip angle = 11.4°). The measured electron-transfer rate constants $k(s)$ are consistent with only minor inner-sphere reorganizational energies being necessary for the electron-transfer reactions, showing that a full η^5/η^3 hapticity change may require only small inner-sphere reorganization energies when this is concomitant with stepwise one electron–transfer processes. The indenyl ligand in the monocation was best described as donating approximately four π electrons to Mo by combining a traditional η^3 linkage with two “half-strength” Mo–C bonds.

15.3.4

Intermediate and Higher Oxidation State Complexes

The electrochemical reduction of Mo(II) and W(II) halido complexes such as *trans*-[MoCl₂{Ph₂P(CH₂)₂PPh₂}₂] has been examined in the presence of a range of substrates by cyclic voltammetry, coulometry, and preparative electrolysis. The initial reversible one-electron step is followed by loss of a halide ligand and binding of a solvent or small molecules such as H₂, N₂, CO, or isocyanide; further electron transfer leads to the loss of the remaining halide group and binding of the substrate to give isolable M(0) complexes such as *trans*-[M(N₂)₂{Ph₂P(CH₂)₂PPh₂}₂] in moderate yields [46]. The electrochemical reduction of the 15-electron molybdenum(III) complex [MoCl₃(dpepp)], dpepp = Ph₂PCH₂CH₂P(Ph)CH₂CH₂PPh₂, has been studied in the presence of PPh₃ under argon and under molecular nitrogen. The primary reduction of the trichloride involves

a reversible single-electron transfer to give the unstable 16-electron molybdenum(II) anion [MoCl₃(dpepp)][−]. Loss of chloride from this anion, prior to or following further electron transfer, provides two principal pathways to molybdenum(0) products, [Mo(η^6 -C₆H₅PPh₂)(dpepp)] under Ar or *cis*-[Mo(N₂)₂(dpepp)(PPh₃)] under molecular nitrogen, a relatively high potential pathway via molybdenum(I) solvated intermediates and a low potential pathway via *trans*-[MoCl₂(dpepp)(PPh₃)]. The *cis*-dinitrogen complex is unstable on the preparative timescale, small amounts of *trans*-[Mo(N₂)₂(dpepp)(PPh₃)] are formed, presumably by isomerization, but the major product is the η^6 -arene complex [47]. Preparative electrochemical reduction of Mo(0) or W(0) compounds from MoCl₅ or from WCl₆ has been shown. For example, reduction of MoCl₅ at a mercury pool in a THF electrolyte under molecular nitrogen at one atmosphere and in the presence of the free phosphine ligand affords *trans*-[Mo(N₂)₂{Ph₂P(CH₂)₂PPh₂}₂] [46].

15.3.5

Electrochemical Transformation of Ligands at {M(Ph₂PCH₂CH₂PPh₂)₂} Centers

The square-planar {M(Ph₂PCH₂CH₂PPh₂)₂} assembly provides a robust platform for reductive transformation of a multiply bonded ligand occupying an axial position and, in certain cases, released as a product molecule. Such transformations include reduction of coordinated cyanide to an aminocarbene ligand; conversion of organoimide ligands to amines or amino acids; reductive coupling of diazomethane ligands; and the conversion of hydrazides to hydrazines [16, 48–56]. Illustrative reactions are shown in Sch. 2.

References

1. C. J. Pickett, D. Pletcher, *J. Chem. Soc., Chem. Commun.* **1974**, 660.
2. C. J. Pickett, D. Pletcher, *J. Chem. Soc., Dalton Trans.* **1975**, 879.
3. A. M. Bond, R. Colton, *Coord. Chem. Rev.* **1997**, 166, 161.
4. J. Chatt, C. T. Kan, G. J. Leigh et al., *J. Chem. Soc., Dalton Trans.* **1980**, 2032.
5. A. M. Bond, R. Colton, F. Daniels et al., *J. Am. Chem. Soc.* **1993**, 115, 9556.
6. A. M. Bond, R. Colton, S. W. Feldberg et al., *Organometallics* **1991**, 10, 3320.
7. A. M. Bond, R. Colton, J. J. Jackowski, *Inorg. Chem.* **1975**, 14, 2526.
8. A. M. Bond, R. Colton, K. McGregor, *Inorg. Chem.* **1986**, 25, 2378.
9. A. M. Bond, D. J. Darensbourg, E. Mocellin et al., *J. Am. Chem. Soc.* **1981**, 103, 6827.
10. A. M. Bond, B. S. Grabaric, J. J. Jackowski, *Inorg. Chem.* **1978**, 17, 2153.
11. A. J. L. Pombeiro, M. da Silva, M. Lemos, *Coord. Chem. Rev.* **2001**, 219, 53.
12. T. A. George, J. R. D. Debord, B. B. Kaul et al., *Inorg. Chem.* **1992**, 31, 1295.
13. T. A. George, R. K. Hayes, M. Y. Mohammed et al., *Inorg. Chem.* **1989**, 28, 3269.
14. T. Al Salih, M. T. Duarte, J. Da Silva et al., *J. Chem. Soc., Dalton Trans.* **1993**, 3015.
15. D. L. Hughes, D. J. Lowe, M. Y. Mohammed et al., *J. Chem. Soc., Dalton Trans.* **1990**, 2021.
16. A. Hills, D. L. Hughes, C. J. Macdonald et al., *J. Chem. Soc., Dalton Trans.* **1991**, 121–129.
17. L. P. Yureva, L. N. Nekrasov, S. M. Peregu-dova, *Usp. Khim.* **1993**, 62, 135.
18. N. Camire, A. Nafady, W. E. Geiger, *J. Am. Chem. Soc.* **2002**, 124, 7260.
19. J. W. Merkert, W. E. Geiger, M. N. Paddon-row et al., *Organometallics* **1992**, 11, 4109.
20. L. K. Yeung, J. E. Kim, Y. K. Chung et al., *Organometallics* **1996**, 15, 3891.
21. K. A. E. O'Callaghan, S. J. Brown, J. A. Page et al., *Organometallics* **1991**, 10, 3119.
22. I. C. Quarmby, R. C. Hemond, F. J. Feher et al., *J. Organomet. Chem.* **1999**, 577, 189.
23. J. C. Kotz, W. Vining, W. Coco et al., *Organometallics* **1983**, 2, 68.
24. R. G. Compton, J. C. Eklund, S. D. Page et al., *J. Chem. Soc., Dalton Trans.* **1995**, 389.
25. M. J. Calhorda, M. A. D. F. Carrondo, A. R. Dias et al., *Organometallics* **1991**, 10, 483.
26. M. C. Durrant, S. A. Fairhurst, D. L. Hughes et al., *J. Chem. Commun.* **1997**, 2379.
27. J. A. McCleverty, *Chem. Soc. Rev.* **1983**, 12, 331.
28. J. A. McCleverty, M. D. Ward, *Acc. Chem. Res.* **1998**, 31, 842.
29. S. L. W. McWhinnie, J. A. Thomas, T. A. Hamor et al., *Inorg. Chem.* **1996**, 35, 760.
30. B. J. Coe, C. J. Jones, J. A. McCleverty et al., *J. Chem. Soc., Chem. Commun.* **1989**, 1485.
31. A. Das, J. C. Jeffery, J. P. Maher et al., *Inorg. Chem.* **1993**, 32, 2145.
32. A. M. W. C. Thompson, D. Gatteschi, J. A. McCleverty et al., *Inorg. Chem.* **1996**, 35, 2701.
33. V. A. Ung, D. A. Bardwell, J. C. Jeffery et al., *Inorg. Chem.* **1996**, 35, 5290.
34. C. J. Pickett, D. Pletcher, *J. Chem. Soc., Dalton Trans.* **1976**, (8), 749–752.
35. C. Amatore, P. J. Krusic, S. U. Pedersen et al., *Organometallics* **1995**, 14, 640.
36. W. Kaim, *Chem. Ber.-Rec.* **1982**, 115, 910.
37. W. Kaim, *Inorg. Chem.* **1984**, 23, 3365.
38. W. Kaim, *J. Organomet. Chem.* **1984**, 264, 317.
39. W. Kaim, *J. Organomet. Chem.* **1984**, 262, 171.
40. W. Kaim, *Inorg. Chem.* **1984**, 23, 504.
41. W. Kaim, W. Bruns, S. Kohlmann et al., *Inorg. Chim. Acta* **1995**, 229, 143.
42. W. J. Bowyer, W. E. Geiger, *J. Am. Chem. Soc.* **1985**, 107, 5657.
43. W. J. Bowyer, J. W. Merkert, W. E. Geiger et al., *Organometallics* **1989**, 8, 191.
44. R. D. Rieke, W. P. Henry, J. S. Arney, *Inorg. Chem.* **1987**, 26, 420.
45. M. E. Stoll, P. Belanzoni, M. J. Calhorda et al., *J. Am. Chem. Soc.* **2001**, 123(43), 10595–10606.
46. T. I. Al Salih, C. J. Pickett, *J. Chem. Soc., Dalton Trans.* **1985**, (6), 1255–1264.
47. J. Talarmin, T. I. Al Salih, C. J. Pickett et al., *J. Chem. Soc., Dalton Trans.* **1992**, 2263.
48. T. Adachi, D. L. Hughes, S. K. Ibrahim et al., *J. Chem. Soc., Chem. Commun.* **1995**, 1081.
49. Y. Alias, M. L. Abasq, F. Barriere et al., *Chem. Commun.* **1998**, 675.
50. Y. Alias, S. K. Ibrahim, M. A. Queiros et al., *J. Chem. Soc., Dalton Trans.* **1997**, 4807.
51. S. A. Fairhurst, D. L. Hughes, S. K. Ibrahim et al., *J. Chem. Soc., Dalton Trans.* **1995**, 1973.
52. D. L. Hughes, S. K. Ibrahim, C. J. Pickett et al., *J. Chem. Soc., Chem. Commun.* **1994**, 425.

53. D. L. Hughes, D. J. Lowe, M. Y. Mohammed et al., *Polyhedron* **1989**, 8, 1653.
54. D. L. Hughes, M. Y. Mohammed, C. J. Pickett, *J. Chem. Soc., Dalton Trans.* **1989**, 1399.
55. C. J. Pickett, G. J. Leigh, *J. Chem. Soc., Chem. Commun.* **1981**, 20, 1033–1035.
56. C. J. Pickett, J. E. Tolhurst, A. Copenhaver et al., *J. Chem. Soc., Chem. Commun.* **1982**, 1071.

16

Electrochemistry of the Group 7 Elements: Manganese, Technetium, and Rhenium

*Franklin A. Schultz, Cole T. Duncan, and Matthew A. Rigby
Indiana University- Purdue University Indianapolis, Indianapolis, Indiana, USA*

16.1	Manganese	401
16.1.1	Introduction	401
16.1.2	Mononuclear Complexes with Acyclic and Other Common Ligands	401
16.1.2.1	Redox Potentials	401
16.1.2.2	Coupled Chemical and Electrochemical Reactions	406
16.1.2.3	Electron-transfer Kinetics	406
16.1.3	Mononuclear Complexes with Porphyrins, Schiff Bases, Phthalocyanine, and Related Macrocyclic Ligands	409
16.1.3.1	Introduction	409
16.1.3.2	Studies in Nonaqueous Media	409
16.1.3.3	Studies in Aqueous Media	411
16.1.3.4	Electrocatalytic Studies	412
16.1.4	Binuclear and Polynuclear Complexes	415
16.1.4.1	Introduction	415
16.1.4.2	Studies in Nonaqueous Media	415
16.1.4.3	Studies in Aqueous Media	421
16.1.5	Biological Systems	423
16.1.5.1	Introduction	423
16.1.5.2	Manganese Catalase	423
16.1.5.3	Manganese Peroxidase	423
16.1.5.4	Manganese Superoxide Dismutase	425
16.1.5.5	Oxygen-evolving Center in Photosystem II	426
	References	431
16.2	Technetium	435
16.2.1	Introduction	435
16.2.2	Mononuclear Complexes	435
16.2.2.1	Oxo Complexes	435
16.2.2.2	Homoleptic and Mixed-ligand Complexes	436
16.2.3	Binuclear Complexes	440

16.2.3.1	Oxo-bridged Complexes	440
16.2.3.2	Metal–metal-bonded Complexes	440
	References	442
16.3	Rhenium	444
16.3.1	Introduction	444
16.3.2	Mononuclear Complexes	444
16.3.2.1	Oxo Complexes	444
16.3.2.2	Homoleptic and Mixed-ligand Complexes	449
16.3.3	Polynuclear Complexes	451
16.3.3.1	Oxo-bridged Complexes	451
16.3.3.2	Metal–metal-bonded Complexes	452
16.3.3.3	Supramolecular Arrays	453
16.3.3.4	Carbon Dioxide Fixation	454
	References	455
	Ligand Abbreviations	456

16.1 Manganese

16.1.1 Introduction

Manganese is the third most abundant transition element [1]. It is present in a number of industrial, biological, and environmental systems, representative examples of which include manganese oxide batteries [2]; the oxygen-evolving center of photosystem II (PSII) [3]; manganese catalase, peroxidase, superoxide dismutase (SOD), and other enzymes [4, 5]; chiral epoxidation catalysts [6]; and deep ocean nodules [7]. Oxidation–reduction chemistry plays a central role in the function of most, if not all, of these examples.

The coordination chemistry [8] and electrochemical properties [9–11] of manganese-containing compounds have been reviewed on a number of occasions. These collections contain primarily thermodynamic and (to a lesser extent) kinetic information on compounds of relatively simple composition. The objective in this chapter is to provide a descriptive summary of the electrochemical properties of a wide range of manganese compounds. There is generous coverage of coordination complexes, which seeks to illustrate relationships between structure and

reactivity by emphasizing the influence of coordination environment on oxidation state preference, reactivity, and mechanism. This approach provides a convenient framework for the discussion of electron-transfer reactivity that is important in many applications. The topics covered include mononuclear manganese complexes; Schiff base, porphyrin, and phthalocyanine complexes; bi- and polynuclear complexes; and Mn in biological systems.

16.1.2 Mononuclear Complexes with Acyclic and Other Common Ligands

16.1.2.1 Redox Potentials

Manganese forms a large number of mononuclear complexes in oxidation states II, III, and IV with acyclic and other common ligands. The complexes primarily are six-coordinate species with octahedral or pseudo-octahedral geometries. Some exceptions to this categorization are the tetraoxo anions in oxidation states V, VI, and VII and the manganocenes. Table 1 contains electrochemical data for representative redox couples in which the Mn coordination environment remains invariant with oxidation state. Many entries are for homoleptic complexes, but some species with mixed

Tab. 1 Electrochemical properties of mononuclear manganese complexes with acyclic and other common ligands

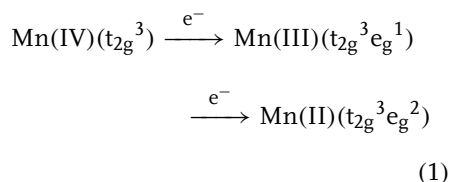
Oxidation state change	Mn coordinate shell	Electrode reaction	Solvent/supporting electrolyte	E^0 , V versus NHE	k_s , cm s^{-1}	References
VII/VI	O ₄	$\text{MnO}_4^- + e^- \rightleftharpoons \text{MnO}_4^{2-}$	H ₂ O/1.0 M NaOH	+0.59	2.4×10^{-2}	12
VI/V	O ₄	$\text{H}_2\text{O} + \text{MnO}_4^{2-} + e^- \rightleftharpoons \text{MnO}_3(\text{OH})^{2-} + \text{OH}^-$	H ₂ O/1.0 M NaOH	+0.31	2.5×10^{-3}	12, 13
IV/III	C ₆	$\text{Mn}(\text{CN})_6^{2-} + e^- \rightleftharpoons \text{Mn}(\text{CN})_6^{3-}$	Formamide/0.1 M TEAClO ₄	+1.06		14
IV/III	C ₆	$\text{Mn}(\text{CN})_6^{2-} + e^- \rightleftharpoons \text{Mn}(\text{CN})_6^{3-}$	CH ₃ CN/0.1 M TEAClO ₄	+0.41		14
IV/III	N ₆	$\text{Mn}(\text{Tp})_2^{2+} + e^- \rightleftharpoons \text{Mn}(\text{Tp})_2^+$	C ₂ H ₄ Cl ₂ /0.1 M TBAPF ₆	+2.01	4.9×10^{-2}	15
IV/III	N ₄ O ₂	$\text{Mn}(\text{bbpen})^{2+} + e^- \rightleftharpoons \text{Mn}(\text{bbpen})^+$	CH ₃ CN/0.1 M TBAPF ₆	+1.13		16
IV/III	N ₃ O ₃	$\text{Mn}(\text{8-Q})_3^+ + e^- \rightleftharpoons \text{Mn}(\text{8-Q})_3$	CH ₃ CN/0.1 M TEAClO ₄	+1.18		17
IV/III	N ₃ O ₃	$\text{Mn}(\text{phox})_3^+ + e^- \rightleftharpoons \text{Mn}(\text{phox})_3$	CH ₃ CN/0.05 M TEAPF ₆	+0.68		18
IV/III	N ₂ O ₄	$\text{Mn}(\text{als})_2^+ + e^- \rightleftharpoons \text{Mn}(\text{als})_2$	CH ₃ OH/0.1 M TEAClO ₄	+0.74		19
IV/III	O ₆	$\text{Mn}(\text{bpyO}_2)_3^{4+} + e^- \rightleftharpoons \text{Mn}(\text{bpyO}_2)_3^{3+}$	CH ₃ CN/0.1 M TPAClO ₄	+1.86		20
IV/III	O ₆	$\text{Mn}(\text{tripod})_2^{2+} + e^- \rightleftharpoons \text{Mn}(\text{tripod})_2^+$	CH ₃ CN/unspecified	+1.77		21
IV/III	O ₆	$\text{Mn}(\text{acac})_3^+ + e^- \rightleftharpoons \text{Mn}(\text{acac})_3$	CH ₃ CN/0.1 M TBAClO ₄	+1.21		22
IV/III	O ₃ S ₃	$\text{Mn}(\text{hpt})_3^+ + e^- \rightleftharpoons \text{Mn}(\text{hpt})_3$	2CH ₃ CN:1CH ₂ Cl ₂ /0.1 M TEAClO ₄	+0.61		23
IV/III	S ₆	$\text{Mn}(\text{Et}_2\text{dto})_3^+ + e^- \rightleftharpoons \text{Mn}(\text{Et}_2\text{dto})_3$	CH ₃ CN/0.15 M TEAClO ₄	+0.57	4×10^{-1}	24
III/II	C ₆	$\text{Mn}(\text{CNCH}_3)_6^{3+} + e^- \rightleftharpoons \text{Mn}(\text{CNCH}_3)_6^{2+}$	CH ₃ CN/0.1 M TEAClO ₄	+1.78		25
III/II	C ₆	$\text{Mn}(\text{CN})_6^{3-} + e^- \rightleftharpoons \text{Mn}(\text{CN})_6^{4-}$	Formamide/0.1 M TEAClO ₄	-0.43 ^a		14

III/II	C ₆	$\text{Mn}(\text{CN})_6^{3-} + \text{e}^- \rightleftharpoons \text{Mn}(\text{CN})_6^{4-}$	CH ₃ CN/0.1 M TEAClO ₄	-1.33		14
III/II	C ₁₀	$\text{Mn}(\text{Cp}^*)_2^+ + \text{e}^- \rightleftharpoons \text{Mn}(\text{Cp}^*)_2$	CH ₃ CN/0.1 M TBABF ₄	-0.32	$\geq 4 \times 10^0$	26, 27
III/II	N ₆	$\text{Mn}(\text{bpy})_3^{3+} + \text{e}^- \rightleftharpoons \text{Mn}(\text{bpy})_3^{2+}$	CH ₃ CN/0.1 M TPAClO ₄	+1.60		28
III/II	N ₆	$\text{Mn}(\text{NH}_3)_6^{3+} + \text{e}^- \rightleftharpoons \text{Mn}(\text{NH}_3)_6^{2+}$	NH ₃ /1 M NH ₄ NO ₃	+0.81	6.5×10^{-5}	29
III/II	N ₆	$\text{Mn}(\text{Tp})_2^+ + \text{e}^- \rightleftharpoons \text{Mn}(\text{Tp})_2$	C ₂ H ₄ Cl ₂ /0.1 M TBAPF ₆	+0.76	5.3×10^{-5}	15
III/II	N ₆	$\text{Mn}(\text{tacn})_3^{3+} + \text{e}^- \rightleftharpoons \text{Mn}(\text{tacn})_2^{2+}$	H ₂ O/0.1 M KCl (276 K)	+0.68		30
III/II	N ₆	$\text{Mn}(\text{sar})_3^{3+} + \text{e}^- \rightleftharpoons \text{Mn}(\text{sar})_2^{2+}$	H ₂ O/0.1 M CF ₃ SO ₃ H	+0.53		31
III/II	N ₄ O ₂	$\text{Mn}(\text{bbpen})^+ + \text{e}^- \rightleftharpoons \text{Mn}(\text{bbpen})$	CH ₃ CN/0.1 M TBAPF ₆	+0.27		16
III/II	N ₃ O ₃	$\text{Mn}(\text{8-Q})_3 + \text{e}^- \rightleftharpoons \text{Mn}(\text{8-Q})_3^-$	CH ₃ CN/0.1 M TEAClO ₄	+0.16		17
III/II	N ₃ O ₃	$\text{Mn}(\text{phox})_3 + \text{e}^- \rightleftharpoons \text{Mn}(\text{phox})_3^-$	CH ₃ CN/0.05 M TEAPF ₆	-0.22		18
III/II	N ₂ O ₄	$\text{Mn}(\text{als})_2^- + \text{e}^- \rightleftharpoons \text{Mn}(\text{als})_2^{2-}$	CH ₃ OH/0.1 M TEAClO ₄	+0.02		19
III/II	O ₆	$\text{Mn}(\text{H}_2\text{O})_6^{3+} + \text{e}^- \rightleftharpoons \text{Mn}(\text{H}_2\text{O})_6^{2+}$	6.15 M H ₂ SO ₄ , 7.5 M H ₂ SO ₄	+1.49	2.5×10^{-6} , 3.4×10^{-5}	32, 33
III/II	O ₆	$\text{Mn}(\text{bpyO}_2)_3^{3+} + \text{e}^- \rightleftharpoons \text{Mn}(\text{bpyO}_2)_3^{2+}$	CH ₃ CN/0.1 M TPAClO ₄	+1.11		20
III/II	O ₆	$\text{Mn}(\text{tripod})_2^+ + \text{e}^- \rightleftharpoons \text{Mn}(\text{tripod})_2$	CH ₂ Cl ₂ /unspecified	+0.36	7×10^{-7}	21
III/II	O ₆	$\text{Mn}(\text{acac})_3 + \text{e}^- \rightleftharpoons \text{Mn}(\text{acac})_3^-$	CH ₃ CN/0.1 M TBAClO ₄	+0.15	4.5×10^{-1}	22, 34
III/II	O ₃ S ₃	$\text{Mn}(\text{hpt})_3 + \text{e}^- \rightleftharpoons \text{Mn}(\text{hpt})_3^-$	2CH ₃ CN:1CH ₂ Cl ₂ /0.1 M TEAClO ₄	-0.11		23
III/II	S ₆	$\text{Mn}(\text{Et}_2\text{dto})_3 + \text{e}^- \rightleftharpoons \text{Mn}(\text{Et}_2\text{dto})_3^-$	CH ₃ CN/0.15 M TEAClO ₄	+0.03	6×10^{-1}	24
II/I	C ₆	$\text{Mn}(\text{CNCH}_3)_6^{2+} + \text{e}^- \rightleftharpoons \text{Mn}(\text{CNCH}_3)_6^+$	CH ₃ CN/0.1 M TEAClO ₄	+0.62		25
II/I	C ₆	$\text{Mn}(\text{CN})_6^{4-} + \text{e}^- \rightleftharpoons \text{Mn}(\text{CN})_6^{5-}$	H ₂ O/1 M NaCN	-1.11 ^a	2.6×10^{-1}	35
II/I	C ₁₀	$\text{Mn}(\text{Cp}^*)_2 + \text{e}^- \rightleftharpoons \text{Mn}(\text{Cp}^*)_2^-$	CH ₃ CN/0.1 M TBABF ₄	-1.93		26
II/O	O ₆	$\text{Mn}(\text{H}_2\text{O})_6^{2+} + 2\text{e}^- \rightleftharpoons \text{Mn}^0(\text{Hg})$	H ₂ O/1 M LiClO ₄	-1.20	4×10^{-4}	36

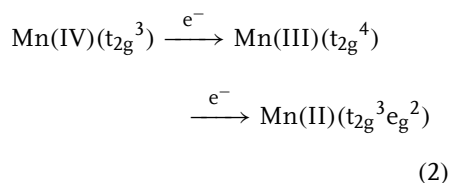
^a Values of -0.24 and -1.06 V versus NHE have been obtained for the $\text{Mn}(\text{CN})_6^{3-}/4-$ and $\text{Mn}(\text{CN})_6^{4-}/5-$ couples, respectively, by redox titrimetry in 2 M NaCN/H₂O [37].

donor atom sets are included. Potentials extend from +0.41 to +2.01 V versus NHE for $\text{Mn}^{\text{IV/III}}$ couples [12–24], from –1.33 to +1.78 V for $\text{Mn}^{\text{III/II}}$ couples [14–19, 25–34], and from –1.93 to +0.62 V for $\text{Mn}^{\text{II/I}}$ couples [25, 26, 35]. The large ranges reflect the significant influences of the charge and donor/acceptor properties of the ligand(s). Thus, oxidized forms are stabilized and negative potentials result with negatively charged, strong σ -donor ligands (e.g. CN^-), whereas reduced forms are stabilized and positive potentials result with neutral π -acceptor ligands (e.g. isocyanides, diimines). Consequently, one-electron oxidants or reductants exhibiting a very large range of potentials can be produced at mononuclear Mn centers.

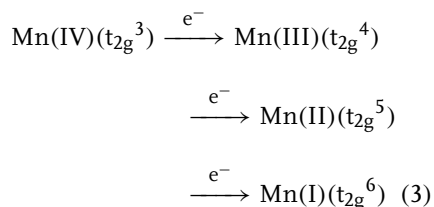
The d-electron configurations most commonly observed for Mn (IV) through Mn (II) electron-transfer reactions involve Mn (III) in the high-spin state ($t_{2g}^3 e_g^1$):



However, low-spin $\text{Mn(III)}(t_{2g}^4)$ is found in some instances (e.g. for Tp^- and its substituted derivatives [15]), resulting in the observation of:

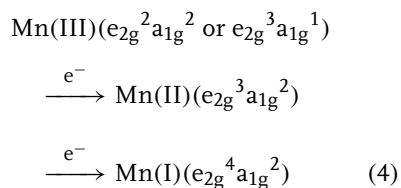


Strong field CN^- stabilizes low-spin Mn in oxidation states I through IV and is unique in stabilizing a four-member redox series:



Isocyanides stabilize low-spin Mn(I), (II), and (III) and form a redox sequence encompassing the last three members of Eq. (3). The potentials in Eq. (3) are very solvent-dependent for the negatively charged cyanide complexes. The reduced forms are stabilized relative to the oxidized forms by strong hydrogen bond interactions, which produce positive E° shifts of 0.6–0.9 V in proton-donating solvents. The magnitude of the effect is such that the potential of the $\text{Mn(CN)}_6^{4-/5-}$ couple in H_2O is more positive than that of the $\text{Mn(CN)}_6^{3-/4-}$ couple in CH_3CN (Table 1).

Decamethylmanganocene (D_{5d}) undergoes chemically reversible and kinetically facile electron-transfer reactions encompassing the Mn(III), (II), and (I) oxidation states:



$[\text{Mn(Cp}^*)_2]^{+/0/-}$ is low spin in all oxidation states. However, unsubstituted high-spin Mn(Cp)_2 is extremely reactive and has not been characterized electrochemically [26, 38].

Simple one-electron reduction of manganese tetraoxo anions in aqueous solution is observed only under very alkaline conditions. Hydroxide ion concentrations greater than 0.4 and 10 M are required

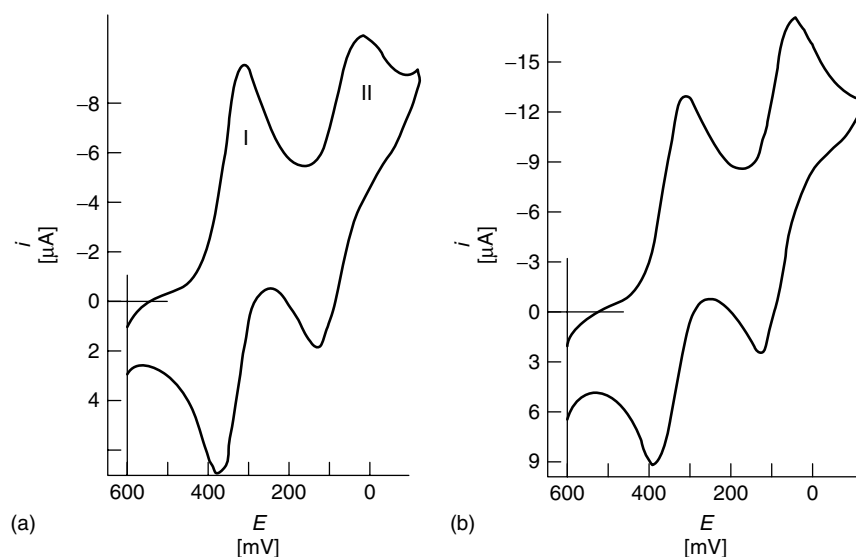
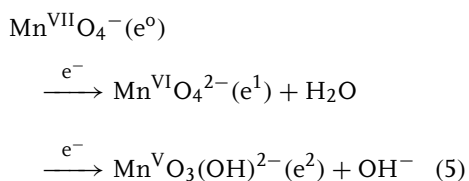


Fig. 1 Cyclic voltammograms of electrode reactions of the $\text{MnO}_4^{2-}/3-$ (I) and $\text{MnO}_4^{2-}/3-$ (II) couples in 1 M NaOH; 0.001 M KMnO_4 , $\nu = 1.5 \text{ V min}^{-1}$; (a) carbon paste electrode and (b) glassy carbon electrode (reprinted from Ref. 12, Copyright 1979 with permission from Elsevier).

to stabilize MnO_4^{2-} and MnO_4^{3-} , respectively, and to produce the following electron-transfer sequence:



Here, the electrochemical reduction of MnO_4^{2-} is accompanied by protonation under certain conditions. As shown in Fig. 1 [12], the close proximity of the $\text{Mn}^{\text{VII}}/\text{VI}$ and $\text{Mn}^{\text{VI}}/\text{V}$ electrode reactions reflects the positive shift in the $\text{Mn}^{\text{VI}}/\text{V}$ potential because of proton addition in the second step of Eq. (5). Under more acidic conditions, MnO_4^{2-} reduction proceeds to $\text{Mn}^{\text{IV}}\text{O}_2$ or to $\text{Mn}^{\text{II}}(\text{H}_2\text{O})_6^{2+}$.

For heteroleptic complexes not included in Table 1, redox potentials can be estimated by ligand additivity principles

[39–41]. Lever has successfully predicted $\text{Mn}^{\text{II/I}}$ potentials of 24 Mn-carbonyl complexes containing halide, pseudohalide, isonitrile, and phosphine co-ligands, with additivity parameters derived from the potentials of $\text{Ru}^{\text{III/II}}$ couples [39]. An important consideration for heteroleptic complexes is the influence of isomerism on redox thermodynamics. For $\text{Mn}(\text{CO})_n(\text{CNR})_{6-n}$ complexes, with $n = 2$ or 3, the $\text{Mn}^{\text{II/I}}$ potentials for cis/trans and fac/mer pairs differ by as much as 0.2 V [40]. The effect arises from the different σ -donor and π -acceptor abilities of carbonyl (CO) and isocyanide and their influence on the energy of the highest energy occupied molecular orbital (HOMO).

The electron-transfer reactions in Table 1 primarily are metal-centered processes. As a result, the separation between the potentials of successive electrode reactions generally is large. Values of $\Delta E^\circ = E_{\text{IV/III}}^\circ - E_{\text{III/II}}^\circ$ in Table 1 range from

0.5 to 1.7 V, and the corresponding comproportionation constants, $K_{\text{com}} = \exp(F\Delta E^{\circ'}/RT)$, range from 3×10^8 to 5×10^{28} . The larger values of $\Delta E^{\circ'}$ (e.g. CN^-) are consistent with highly metal-localized electron transfers, whereas as smaller values (e.g. Et_2dtc^-) indicate more effective distribution of charge upon a change in oxidation state.

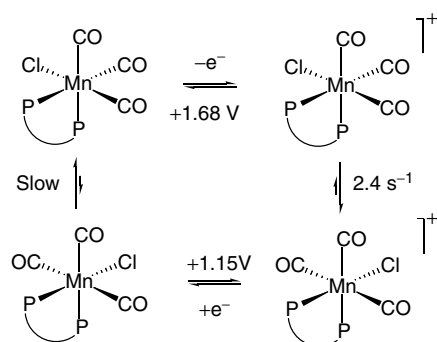
16.1.2.2 Coupled Chemical and Electrochemical Reactions

The influence of isomerism is revealed in the mechanistic electrochemistry of Mn carbonyls. One-electron oxidation of *fac*- $\text{Mn}(\text{CO})_3(\text{dpm})\text{Cl}$ ($\text{dpm} = \text{bis}-(\text{diphenylphosphino})\text{methane}$) is followed by rapid rearrangement of *fac*- $[\text{Mn}(\text{CO})_3(\text{dpm})\text{Cl}]^+$ to *mer*- $[\text{Mn}(\text{CO})_3(\text{dpm})\text{Cl}]^+$ [42]. However, reduction of the *mer*-Mn(II) species (protected against photolytic or solvolytic decomposition) to *mer*- $\text{Mn}(\text{CO})_3(\text{dpm})\text{Cl}$ is not followed by the facile rearrangement to the thermodynamically favored *fac*- $\text{Mn}(\text{CO})_3(\text{dpm})\text{Cl}$. The mechanism is summarized in Sch. 1, from which it is evident that (1) the *fac* isomer is thermodynamically favored in the Mn(I) state and the *mer* isomer in the Mn(II) state, (2) the *fac* isomer is 0.5 V more oxidizing than the *mer* isomer, and (3) the 17-e^- Mn^{II} species is kinetically more reactive than the 18-e^- Mn^{I} species.

Further structure-dependent reactivity is illustrated by the electrochemistry of 18-electron *trans*- $[\text{Mn}(\text{CO})_2(\eta^2\text{-dppe})_2]^+$ [I^+ , $\text{dppe} = 1, 2\text{-bis}(\text{diphenylphosphino})\text{ethane}$] (Fig. 2) [43]. As summarized in Sch. 2, the initial one-electron reduction of I^+ produces the metastable 19-electron species, I^* , which rapidly ($k_2 \approx 4 \times 10^6 \text{ s}^{-1}$) extrudes one end of a coordinated dppe ligand and forms the 17-electron *trans*- $[\text{Mn}(\text{CO})_2(\eta^2\text{-dppe})(\eta^1\text{-dppe})]$, II^* . This five-coordinate complex is reduced at the potential of initial reduction, affording two-electron transfer by an electrochemical-chemical-electrochemical (ECE) mechanism: $\text{I}^+ + 2\text{e}^- \rightarrow \text{II}^-$. Reversible one-electron electrochemistry of the II^*/II^- couple is observed on a subsequent cyclic scan at positive potentials (peaks B and C, Fig. 2). An interesting aspect of this voltammogram is the curve-crossing at -1.6 V . This phenomenon results from the contribution of the homogeneous chemical reaction, $\text{I}^+ + \text{II}^- \rightleftharpoons 2\text{II}^*$, to the electrochemical response, producing an ECE-disproportionation (DISP) mechanism.

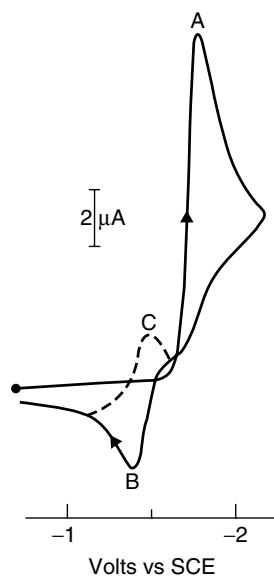
16.1.2.3 Electron-transfer Kinetics

Electrochemical electron-transfer rate constants have been measured less frequently



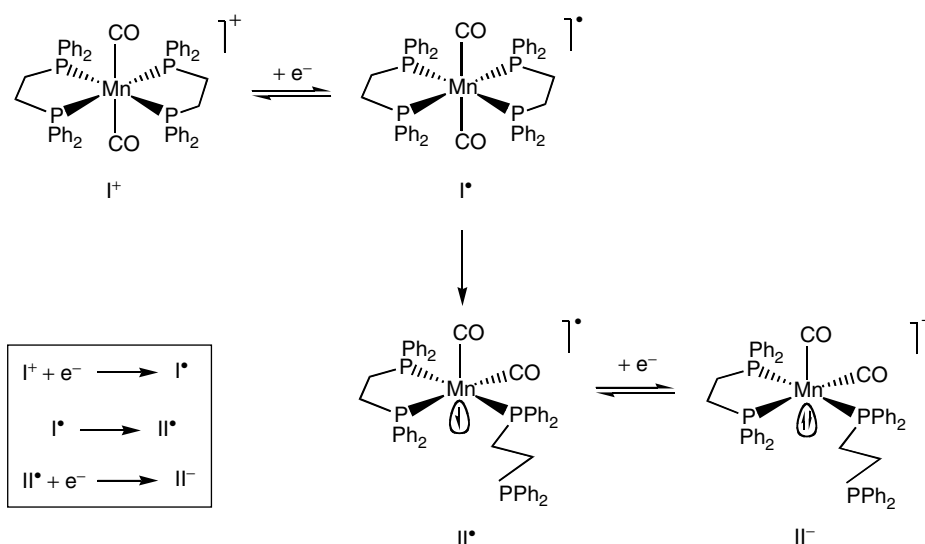
Scheme 1 Mechanism of electrochemically induced *fac*/*mer* isomerization of $\text{Mn}(\text{CO})_3(\text{dpm})\text{Cl}$ in $\text{CH}_3\text{CN}/0.1 \text{ M TEAClO}_4$ [42].

Fig. 2 Negative-scan cyclic voltammogram of 5×10^{-3} M $[\text{Mn}(\text{CO})_2(\text{dppe})_2] \text{PF}_6$ ($\text{I}^+ \text{PF}_6^-$) in THF, containing 0.3 M TBAClO₄ at $\nu = 0.5 \text{ V s}^{-1}$ (reprinted with permission from Ref. 43, Copyright 1988 American Chemical Society).



than redox potentials for these mononuclear manganese complexes. Even so, the values of $k_{s,h}$ in Table 1 encompass a range of 7 orders of magnitude. In circumstances in which little inner-shell reorganization accompanies electron transfer, as in the reduction of low-spin $\text{Mn}(\text{CN})_6^{4-}$ (t_{2g}^5) to low-spin $\text{Mn}(\text{CN})_6^{5-}$ (t_{2g}^6) (Eq. 3), $k_{s,h}$ is large (0.26 cm s^{-1}) [35]. However, in cases in which there is a change in the number of antibonding e_g^* electrons, structural change ensues and the rate constant can be much smaller. This is illustrated by the oxidation of $[\text{Mn}^{\text{II}}(\text{tripod})_2]$ ($t_{2g}^3 e_g^2$) to $[\text{Mn}^{\text{III}}(\text{tripod})_2]^+$ ($t_{2g}^3 e_g^1$), where $k_{s,h} = 7 \times 10^{-7} \text{ cm s}^{-1}$ (Fig. 3) [21]. Figure 4, which

depicts the sequential one-electron oxidations of $[\text{Mn}^{\text{II}}(\text{Me}_2\text{pzb})_2]$ ($\text{Me}_2\text{pzb}^- = \text{Tp}^{*-} = \text{hydrotris}(3,5\text{-dimethylpyrazol-1-yl})\text{borate}$) species [15], further illustrates the



Scheme 2 Mechanism of the two-electron reduction of $[\text{Mn}(\text{CO})_2(\eta^2\text{-dppe})_2]^+$ (I^+) to $[\text{Mn}(\text{CO})_2(\eta^2\text{-dppe})(\eta^1\text{-dppe})]$ (II^-) [43].

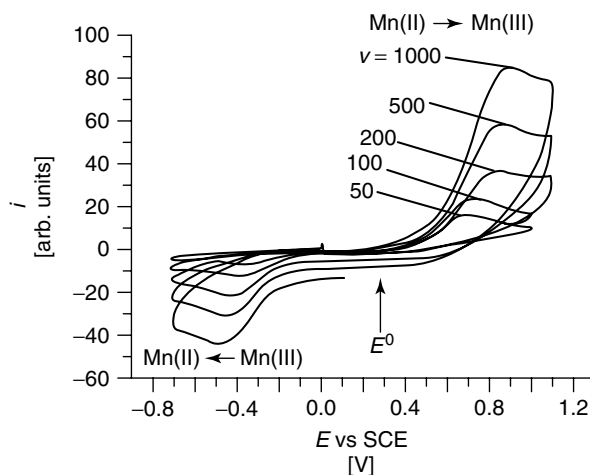


Fig. 3 Cyclic voltammograms for the oxidation of $[\text{Mn}^{\text{II}}(\text{tripod})_2]$ in CH_2Cl_2 at sweep rates of 50–1000 mV s^{-1} (reprinted from Ref. 21, Copyright 2002 with permission from Wiley-VCH).

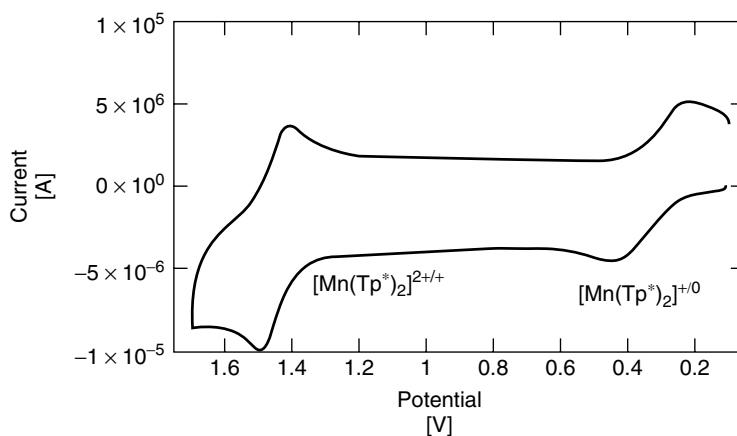


Fig. 4 Oxidative cyclic voltammogram of $2.4 \times 10^{-4} \text{ M Mn}^{\text{II}}(\text{Me}_2\text{pzb})_2$ in 1,2-dichloroethane containing 0.1 M TBAPF₆ at $\nu = 0.1 \text{ V s}^{-1}$ (reprinted with permission from Ref. 15, Copyright 2003 American Chemical Society).

influence of inner-shell reorganizations on electron-transfer rate. Here, $k_{\text{s,h}} = 5.9 \times 10^{-4} \text{ cm s}^{-1}$ for the oxidation of high-spin $[\text{Mn}^{\text{II}}(\text{Me}_2\text{pzb})_2]$ ($t_{2g}^3 e_g^2$) to low-spin $[\text{Mn}^{\text{III}}(\text{Me}_2\text{pzb})_2]^+$ (t_{2g}^4), which is accompanied by a large change in the average

Mn–N bond distance ($\Delta\text{Mn–N} = 0.26 \text{ \AA}$) [44], and $k_{\text{s,h}} = 1.1 \times 10^{-2} \text{ cm s}^{-1}$ for the oxidation of low-spin $[\text{Mn}^{\text{III}}(\text{Me}_2\text{pzb})_2]^+$ (t_{2g}^4) to low-spin $[\text{Mn}^{\text{IV}}(\text{Me}_2\text{pzb})_2]^{2+}$ (t_{2g}^3), for which the structural change is much less ($\Delta\text{Mn–N} = 0.025 \text{ \AA}$) [44].

16.1.3

Mononuclear Complexes with Porphyrins, Schiff Bases, Phthalocyanine, and Related Macrocyclic Ligands

16.1.3.1 Introduction

Manganese complexes with porphyrins, Schiff bases (SBs), and related ligands are of interest as catalysts for the epoxidation of olefins [6]; as models for the behavior of catalases, SODs, cytochrome P450, and other metalloenzymes [4, 5, 45]; and as the active component of membrane electrodes with unusual anion selectivities [46]. Because they are catalytic scavengers of reactive oxygen- and nitrogen-containing species, they have also been tested for their efficacy in the treatment of oxidative stress [47]. In addition, Mn–phthalocyanines are of interest as dyes and in display devices because of their intense coloration and resistance to degradation [48].

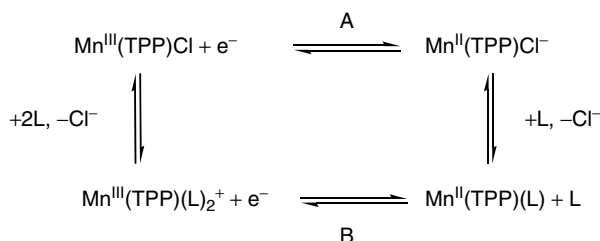
The utility of these complexes derives from the robustness provided by the equatorial coordination of the macrocyclic or polydentate ligand plus the ability to modulate chemical and physical properties and reactivity patterns by changing axial ligation and/or ligand substituent groups. Replacement of H with electron-donating or -withdrawing groups on the porphyrin skeleton or appended aromatic substituents can shift the potential of metal- or ligand-centered electron transfer by more than 0.5 V [49–51]. In addition, ligand substituents impart favorable solubility properties, steric constraints, or structural features not found in the unsubstituted porphyrin complex. Ligand structures and abbreviations are found in the Appendix.

The most common oxidation states in these complexes are Mn(III) and Mn(II). The more highly oxidized forms can be stabilized by strongly electron-donating

ligands or by appropriate control of experimental conditions. For Mn–porphyrins and phthalocyanines, the ligand-centered reductions producing metal-bound π anion and dianion species occur at potentials that are about 1.4 V more negative than that for $\text{Mn(III)} \rightarrow \text{Mn(II)}$ reduction. The ligand-centered reactions are separated by ~ 0.4 V. Depending on conditions, ligand-centered oxidations producing metal-bound π cation and dication species also may occur at potentials that are about 1 V more positive than the $\text{Mn}^{\text{III/II}}$ value and may precede, follow, or coincide with Mn(III) oxidation.

16.1.3.2 Studies in Nonaqueous Media

Because of its high reactivity and unsuitable solubility characteristics, complexes of the unsubstituted porphine (H_2P) are rarely investigated. The most widely studied manganoporphyrins are the tetraphenylporphyrin species, Mn(TPP)X , where X^- is a monodentate axial ligand. In noncoordinating, aprotic solvents, Mn(TPP)X is a five-coordinate, high-spin (d^4) complex in which the Mn(III) atom is displaced ~ 0.23 Å ($\text{X}^- = \text{Cl}^-$) above the porphyrin plane [52]. Reduction of Mn(TPP)Cl in a noncoordinating solvent occurs without a change in ligation but the Mn atom further extends to ~ 0.69 Å above the plane [53]. This large inner-shell reorganization causes the rate of heterogeneous $\text{Mn}^{\text{III/II}}$ electron transfer to be slow – $k_{\text{s,h}} = 2 \times 10^{-3} \text{ cm s}^{-1}$ [54, 55]. Electrochemical behavior is influenced dramatically by the presence of a coordinating solvent or a strong axial ligand (e.g. CH_3OH , py), which converts the Mn(III) form to a six-coordinate species with axial bis-ligation, while the Mn(II) form retains the five-coordinate geometry with the new axial ligand. Scheme 3 summarizes this reactivity, which produces demonstrable



Scheme 3 Electrode half-reaction scheme for five- and six-coordinate Mn(III) porphyrins [56–58].

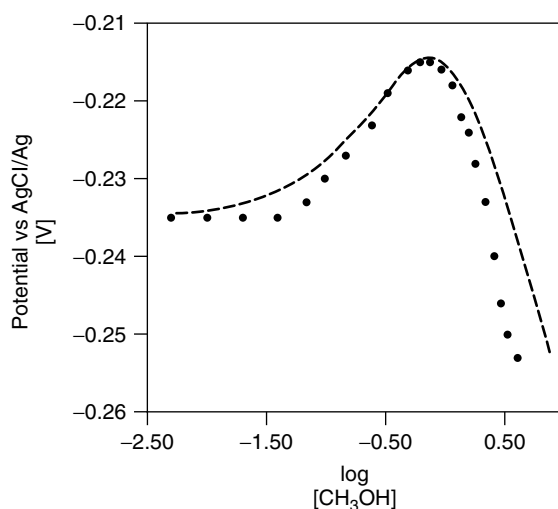


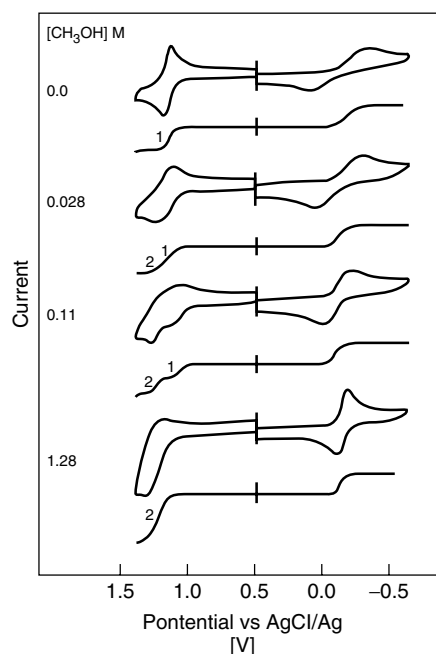
Fig. 5 Dependence of the potential of $\text{Mn}^{\text{III}}(\text{TPP})\text{Cl}$ reduction on CH_3OH concentration in 1,2-dichloroethane containing 0.1 M Et_4NCl at 296 K; (●) experimental data, (–) calculated data (reprinted with permission from Ref. 58, Copyright 1992 American Chemical Society).

effects on the thermodynamics of electron transfer. The $\text{Mn}^{\text{III/II}}$ potential is no longer dependent on the counterion present in the initial complex but rather depends on the nature and concentration of the new axial ligand [56–58]. Under appropriate conditions, the electrode potential can exhibit a biphasic dependence on the concentration of the added ligand, as illustrated in Fig. 5. The kinetics of $\text{Mn}^{\text{III/II}}$ electron transfer also is influenced by this change in composition. As shown in Fig. 6, the voltammetric peak potential separation decreases and the electron-transfer rate increases upon conversion to the six-coordinate species, which has its Mn atom in the porphyrin plane. Enhancement of

the $\text{Mn}^{\text{III/II}}$ electron-transfer rate by this axial bis-ligation is observed in both electrochemical [58] and homogeneous [59] experiments. The spectroscopic signatures of Mn^{III} and Mn^{II} porphyrins also are sensitive to the state of axial ligation, and these features have been used to characterize Mn–porphyrin species [60, 61].

Table 2 contains redox potentials for representative porphyrin, SB, and related complexes in nonaqueous solvents. These data primarily illustrate the influence of axial ligation and porphyrin substituents on the $\text{Mn}^{\text{III/II}}$ potential. Planar macrocyclic ligands such as phthalocyanine and corrole provide an equatorial coordination environment similar to that of porphyrins.

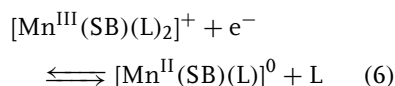
Fig. 6 Cyclic voltammograms at a 1.6-mm diameter Pt electrode (200 mV s^{-1}) and steady state voltammograms at a $25\text{-}\mu\text{m}$ diameter Pt electrode (20 mV s^{-1}) for oxidation and reduction of $8.5 \times 10^{-4} \text{ M Mn}^{\text{III}}(\text{TPP})\text{Cl}$ at 241 K in 1,2-dichloroethane containing 0.1 M TBABF_4 in the presence of $0\text{--}1.28 \text{ M CH}_3\text{OH}$. The peak potential separation at 200 mV s^{-1} for cyclic voltammetric reduction of $\text{Mn}^{\text{III}}(\text{TPP})\text{Cl}$ at 296 K in 1,2-dichloroethane decreases from ca 220 mV in $0 \text{ M CH}_3\text{OH}$ to ca 70 mV in $\geq 1 \text{ M CH}_3\text{OH}$ (reprinted with permission from Ref. 58, Copyright 1992 American Chemical Society).



In the case of dinegative Pc^{2-} , the $\text{Mn}^{\text{III/II}}$ potential is similar to that of the porphyrins [62]. However, the trinegative tpc^{3-} ligand [63] shifts potentials to negative values and enables observation of $\text{Mn}^{\text{IV/III}}$ and $\text{Mn}^{\text{V/IV}}$ redox processes (Table 2).

The electrochemistry of Mn–Schiff base complexes closely parallels that of the Mn-porphyrins. A $\text{Mn}^{\text{III/II}}$ redox process is observed near 0 V versus NHE. In addition to changes in substituent groups and axial ligation, the variation of the donor atom set and denticity is possible with SBs. Redox potentials can be tuned over a range of $\sim 0.5 \text{ V}$ by using one or more of these modifications [65, 66]. The state of axial ligation often is not fully characterized for Mn–Schiff base complexes. However, it appears that many $\text{Mn}(\text{III})$ forms are high-spin, six-coordinate d^4 species and that the $\text{Mn}(\text{II})$ forms presumably are high-spin, five-coordinate d^5 species. Thus, for a

tetradentate SB ligand, the generic $\text{Mn}^{\text{III/II}}$ half-reaction is represented as:



Manganese (IV) and (V) complexes with a multiply bonded oxo ligand are potentially important intermediates in catalytic and biological processes. Although observed transiently, these species have not been generated in a stable form by electrochemical methods in aprotic media. However, strongly donating ligands such as the deprotonated tetraamide macrocycle (mac^{4-}) [68] enable access to high-valent oxo systems, as exemplified by the $[\text{Mn}^{\text{V/IV}}\text{O}(\text{mac})]^{-/2-}$ system in Table 2.

16.1.3.3 Studies in Aqueous Media

Manganese porphyrins can be solubilized in aqueous solution by the attachment of charged functional groups to the porphyrin

Tab. 2 Electrochemical data for manganese complexes with porphyrins, Schiff bases, and related macrocyclic ligands in nonaqueous media

Complex	Electrode Reaction ^a	Conditions	$E^{\circ/b}$, V versus NHE	References
<i>Five-coordinate porphyrins</i>				
Mn ^{III} (TPP)ClO ₄	A	CH ₃ CN/0.1 M TBAClO ₄	−0.43	57
Mn ^{III} (TPP)Cl	A	CH ₃ CN/0.1 M TBAClO ₄	−0.47	57
Mn ^{III} (TPP)N ₃	A	CH ₃ CN/0.1 M TBAClO ₄	−0.53	57
Mn ^{III} (tdcmp)Cl	A	C ₆ H ₅ CN/0.1 M TBAClO ₄	+0.05	50
Mn ^{III} (DPPF ₂₀)Cl	A	C ₆ H ₅ CN/0.1 M TBAClO ₄	−0.20	51
Mn ^{III} (DMHP)Cl	A	CH ₃ CN/0.1 M TPAClO ₄	−0.61	64
Mn ^{III} (EtioP)Cl	A	CH ₃ CN/0.1 M TPAClO ₄	−0.69	64
Mn ^{III} (tdmpp)Cl	A	C ₆ H ₅ CN/0.1 M TBAClO ₄	−0.81	50
<i>Six-coordinate porphyrins</i>				
Mn ^{III} (TPP)(CH ₃ OH) ₂ ⁺	B	CH ₂ Cl ₂ /0.1 M TEACl/1 M CH ₃ OH	−0.42	58
Mn ^{III} (TPP)(dmsO) ₂ ⁺	B	CH ₂ Cl ₂ /0.1 M TEAClO ₄ /1 M DMSO	−0.49	57
Mn ^{III} (TPP)(py) ₂ ⁺	B	CH ₂ Cl ₂ /0.1 M TEAClO ₄ /1 M py	−0.54	57
<i>Schiff bases</i>				
Mn ^{III} (salophen) ⁺	6	DMSO/0.1 M TEAClO ₄	−0.36	65
Mn ^{III} (saldpt) ⁺	6	DMSO/0.1 M TEAClO ₄	−0.44	66
Mn ^{III} (salen) ⁺	6	CH ₃ CN/0.1 M TBAClO ₄	−0.52	67
<i>Others</i>				
Mn ^{III} (Pc) ⁺		DMSO/TEAClO ₄	−0.32	62
Mn ^{IV} (tpc)Cl		CH ₂ Cl ₂ /0.1 M TBAClO ₄	+0.79 ^c −0.31 ^d	63
Mn ^V O(mac) [−]		DMSO/0.1 M TBAPF ₆	−0.27 ^c	68

^a From Sch. 3 or text.^b Mn^{III/II} potential, except as indicated.^c Mn^{V/IV} potential.^d Mn^{IV/III} potential.

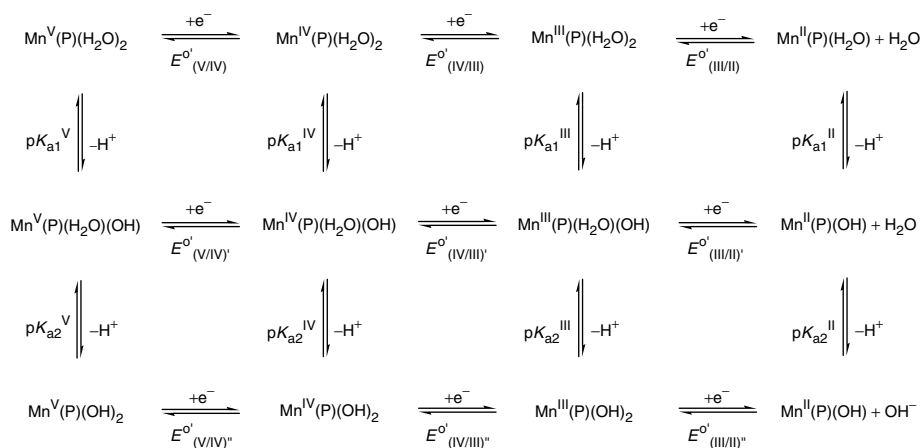
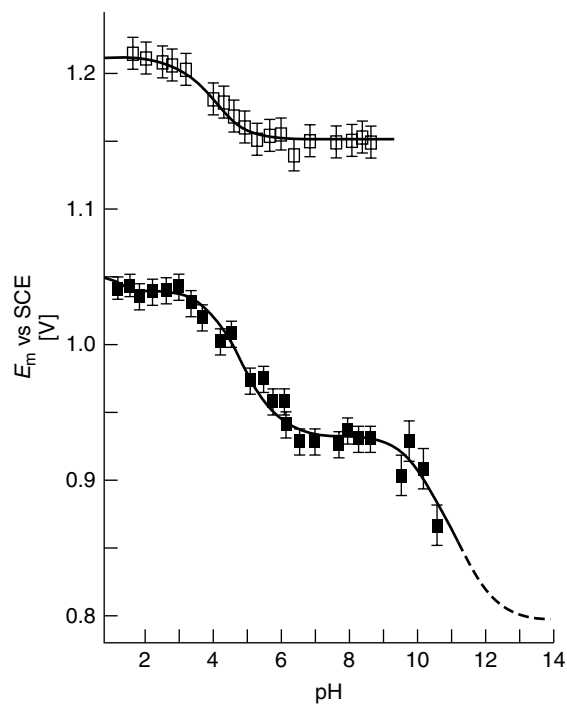
skeleton or its appended phenyl rings. The behavior of the tetrasulfonated TDM-SPP system is represented in Fig. 7 [69]. Sequential Mn^{V/IV} and Mn^{IV/III} electron-transfer reactions are observed from pH 1 to 10. At the highest acidities both axial ligands of Mn are H₂O, and E° values are independent of pH. The axial H₂O ligands become deprotonated as pH is increased. Thus, under some conditions, half-reactions involve both H⁺ and e[−] transfer, and E° values become pH dependent. Overall behavior is described by the sequence of reactions in Sch. 4. Data for selected aqueous Mn–porphyrin

systems are collected in Table 3. Accessible oxidation states, electrode potentials, and p*K*_a values are dependent on porphyrin substituents and experimental conditions. For this reason, the entire range of oxidation and protonation states has not been observed for a single system. Moreover, manganese porphyrins with a fully deprotonated oxo ligand (i.e. Mn^V = O) have not been observed under these conditions.

16.1.3.4 Electrocatalytic Studies

High-valent oxomanganese species are important intermediates in industrially significant catalytic reactions and are model

Fig. 7 Aqueous solution electrode potentials as a function of pH for Mn(TDMSP)(X)₂ porphyrins, with X = H₂O or OH[−] axial ligands. Top curve (□): Mn^{IV} → Mn^V oxidation; bottom curve (■): Mn^{III} → Mn^{IV} oxidation (reprinted with permission from Ref. 69, Copyright 1991 American Chemical Society).



Scheme 4 Electron- and proton-transfer reactions of manganese porphyrins in aqueous media.

reactants of similar catalytic processes in biological systems (e.g. cytochrome P450) [45, 75]. The mechanism of olefin epoxidation has been studied electrochemically

using Mn(TPP)Cl [76] or Mn(salen)Cl [66] as the source of manganese. As shown in Fig. 8, the oxidative process is initiated by the reduction of Mn(TPP)Cl (believed

Tab. 3 Electrochemical data for manganese porphyrins in aqueous media^a

Porphyrin	Axial ligation	<i>E</i> ^o , V versus NHE			Proton ionization			References
		V/IV	IV/III	III/II	oxidation state	p <i>K</i> _{a1}	p <i>K</i> _{a2}	
H ₂ TDMSPP	(H ₂ O) ₂	+1.45	+1.28		V	3.7		69
	(H ₂ O)(OH)	+1.39	+1.17		IV	4.1–4.7	9.9	
	(OH) ₂		+0.9		III	5.8	12.2	
H ₂ TDCSPP	(H ₂ O) ₂		+1.44		V			70
	(H ₂ O)(OH)		+1.29		IV	1.8		
	(OH) ₂				III	4.4		
H ₂ TMPyP	(H ₂ O) ₂			+0.02	III	8.0	10.6	71,72
H ₂ TMAP	(H ₂ O) ₂			−0.13	III	11.4		73
H ₂ DMHP	(H ₂ O)(OH)			−0.33 ^b				74

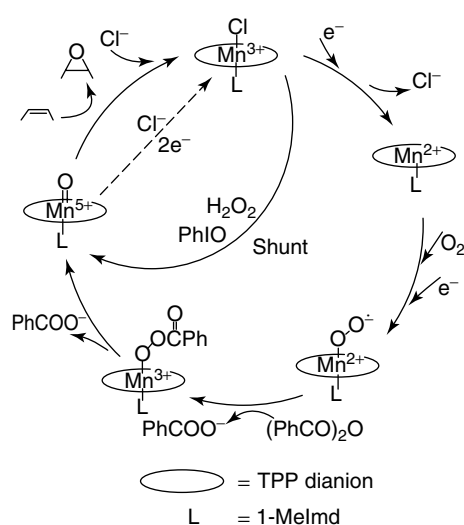
^a Defined on the basis of the half-reactions in Sch. 4.^b 47.5% ethanol in H₂O.

Fig. 8 Proposed mechanism of electrocatalytic epoxidation of olefins by manganese-porphyrin catalysts (reprinted with permission from Ref. 76, Copyright 1986 American Chemical Society).

to exist as Mn(TPP)(1-MeIm)Cl in the presence of excess 1-methylimidazole) in an O₂-saturated solution, which produces five-coordinate [Mn(TPP)(Im)]. This complex binds O₂ in an axial position and is reduced by a second electron to the Mn(II)-peroxo species, [Mn^{III}(TPP)(O₂)(1-MeIm)]⁻. Benzoic anhydride, which is added to the solution as an electrophilic

activator, reacts with the bound peroxo and forms a Mn^V=O center upon displacement of two moles of benzoate ion. This highly reactive Mn^V=O species then epoxidizes the olefin. Although direct electrochemical reduction of Mn^V=O presumably contributes to a loss of faradaic efficiency, product yields of 48–56% have been achieved.

16.1.4 Binuclear and Polynuclear Complexes

16.1.4.1 Introduction

Manganese forms a number of bi- and polynuclear complexes. In many cases, the metal centers are bridged by oxo- or O-donor ligands (consistent with the affinity of Mn for this element) and are capped by N-donor or other ligands at the remaining coordination sites. The most common structural forms discussed in this section are depicted in Chart 1. Interest in these compounds is predicated on the presence of multiple Mn atoms in close proximity to one another at several enzyme active sites [4, 5] and at the oxygen-evolving center of PSII [3]. In addition, manganese centers of high nuclearity

are being investigated actively as single-molecule magnets [77–79].

16.1.4.2 Studies in Nonaqueous Media

Among the earliest compounds investigated are those containing the binuclear di- μ -oxo core represented by (1). The complexes are isolated as mixed-valent Mn(IV,III) species, with four N-donor atoms from two bipyridyl or two phenanthroline ligands bound to each metal. The cyclic voltammetric response [80–82] of the more stable phen system, $[\text{Mn}_2\text{O}_2(\text{phen})_2]^{3+}$ is reproduced in Fig. 9. It consists of a one-electron oxidation to the Mn(IV,IV) species, $[\text{Mn}_2\text{O}_2(\text{phen})_2]^{4+}$, and a one-electron reduction to the Mn(III,III) species, $[\text{Mn}_2\text{O}_2(\text{phen})_2]^{2+}$:

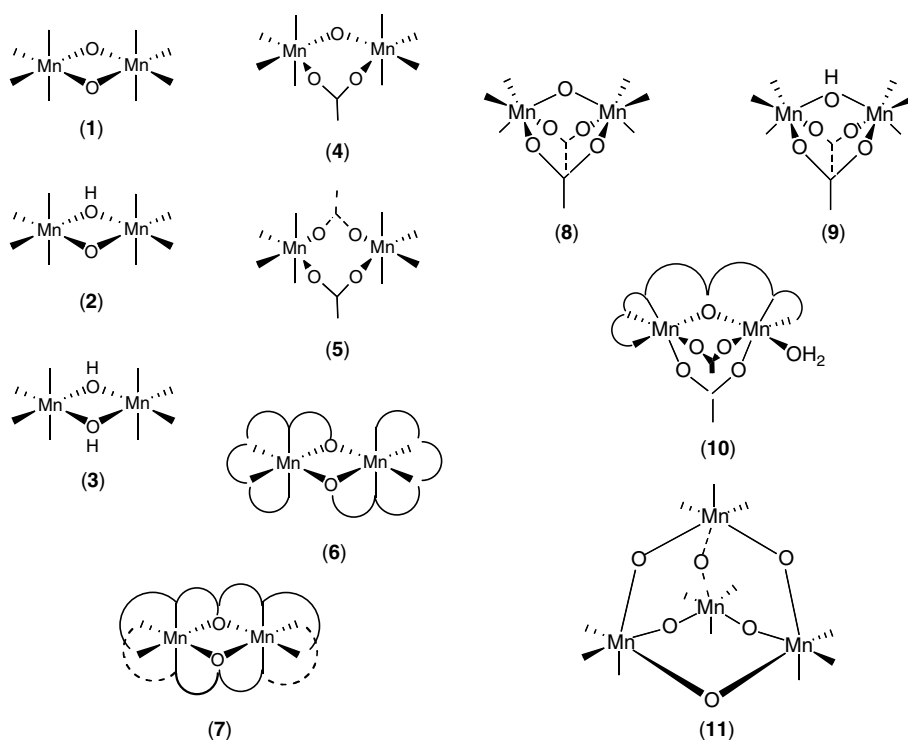


Chart 1 Polynuclear metal structures in Chapter 16.

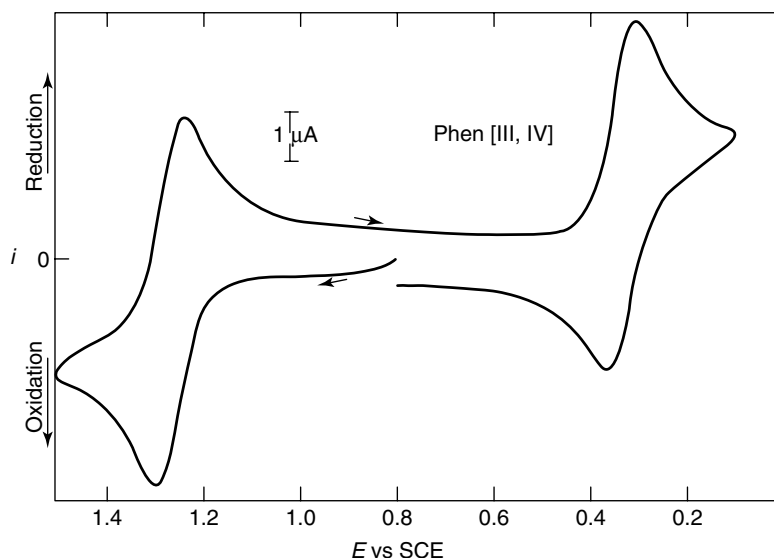
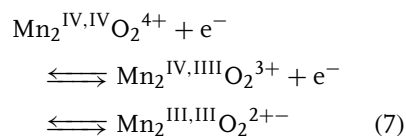


Fig. 9 Cyclic voltammogram for the oxidation and reduction of the $[\text{Mn}_2\text{O}_2(\text{phen})_4]^{3+}$ dimer at $\nu = 0.1 \text{ V s}^{-1}$ in $\text{CH}_3\text{CN}/0.3 \text{ M TEAClO}_4$ (reprinted with permission from Ref. 81, Copyright 1977 American Chemical Society).



The half-reaction potentials for these and the related redox couples are represented in Table 4. The large separation between potentials implies a large electrostatic interaction between Mn centers, which strongly stabilizes the intermediate mixed-valent state with respect to disproportionation. However, it is interesting to note from magnetic properties that the two Mn atoms in $[\text{Mn}_2\text{O}_2(\text{phen})_2]^{3+}$ are only weakly antiferromagnetically coupled ($J = -147 \text{ cm}^{-1}$) [83], indicating that there is little direct metal–metal interaction in the complex.

The potentials represented by Eq. (7) can be tuned in several ways. One approach is to replace one or more of the heterocyclic nitrogen donors with

a saturated amine, as reflected by the potentials of the (bispicen) versus (phen)₂ or (bpy)₂ complexes in Table 4 [84]. This change produces a negative shift of 300–400 mV in both the (IV,IV)/(IV,III) and (IV,III)/(III,III) potentials. A second strategy is to place sterically demanding substituents at key positions on the ligands. As illustrated by the comparison of the E° values for the bispicMe₂en versus bispicen [84] and pebMe₂pma versus pebpma [85, 86] complexes, the placement of a methyl group at the 6-position of the coordinating pyridyl groups produces positive shifts of 400–500 mV in the (IV,IV)/(IV,III) and (IV,III)/(III,III) potentials. Weaker metal–ligand bonding is caused by steric hindrance from these methyl substituents and is reflected in the changes in Mn–N bond distances and N–Mn–N bond angles at these sites [86].

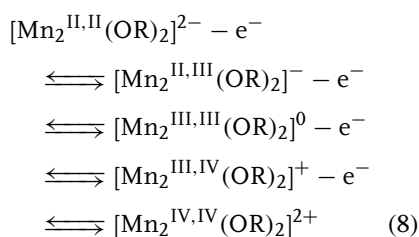
Tab. 4 Nonaqueous electrochemical data for binuclear manganese complexes

Structure	Capping ligands	Solvent/supporting electrolyte	E° , V versus NHE				References
			(IV,IV)/(IV,III)	(IV,III)/(III,III)	(III,III)/(II,II)	(III,II)/(II,II)	
1	(phen) ₂	(phen) ₂	CH ₃ CN/0.1 M TPAClO ₄	+1.57	+0.65		80
1	(phen) ₂	(phen) ₂	CH ₃ CN/0.3 M TEAClO ₄	+1.50	+0.57		81
1	(phen) ₂	(phen) ₂	CH ₃ CN/0.1 M TBAPF ₆	+1.54	+0.63		82
1	(bpy) ₂	(bpy) ₂	CH ₃ CN/0.1 M TPAClO ₄	+1.56	+0.60		80
1	(bpy) ₂	(bpy) ₂	CH ₃ CN/0.3 M TEAClO ₄	+1.49	irrev		81
1	bispicen	bispicen	CH ₃ CN/0.1 M TEAClO ₄	+1.16	+0.32		84
1	bispicMe ₂ en	bispicMe ₂ en	CH ₃ CN/0.1 M TEAClO ₄	+1.54	+0.77		84
1	pebpma	pebpma	CH ₃ CN/0.1 M TEAClO ₄	+1.24	+0.43		85
1	pebMe ₂ pma	pebMe ₂ pma	CH ₃ CN/0.1 M TBAClO ₄	+1.78	+0.98		86
2	(phen) ₂	(phen) ₂	CH ₃ CN/0.1 M TBAPF ₆		+0.61		82
3	(phen) ₂	(phen) ₂	CH ₃ CN/0.1 M TBAPF ₆			−0.10	82
1	bpia	bpia	CH ₃ CN/0.1 M TBAPF ₆	+1.24	+0.47		87
4	bpia	bpia	CH ₃ CN/0.1 M TBAPF ₆	+1.44	+1.22	+0.37	87
5	bpia	bpia	DMF/0.1 M TBAPF ₆			+0.89	87
6	hbpmc	hbpmc	CH ₃ CN/0.1 M TBAClO ₄			+0.95	87
7	(salmp) ₂	(salmp) ₂	CH ₃ CN/0.1 M TBAClO ₄	+1.34	+0.99	+0.20	88
8	HB(pz) ₃ [−]	HB(pz) ₃ [−]	CH ₃ CN/0.1 M TBAClO ₄	+1.86	+1.14 (qr)	−0.56 (irr)	89
8	Me ₃ tacn	Me ₃ tacn	CH ₃ CN/0.1 M TBAPF ₆	+1.85	+1.22	+0.11	90
9	Me ₃ tacn	Me ₃ tacn	CH ₃ CN/0.1 M TBAPF ₆			+1.14	90
8	bpy, Cl [−]	bpy, Cl [−]	DMF		+1.08	+0.69	91

Another strategy for modifying potentials is to alter the composition of the bridge between the metal centers. This can be done by protonation, which produces (2) and (3) in nonaqueous media. Larsen et al. [82] measured the energetics of electron-, proton-, and H-atom-transfer reactions for $[\text{Mn}_2\text{O}_2(\text{phen})_4]^{n+}$ complexes in CH_3CN and found that protonation greatly increases the ease of reduction. For example the E° for $\text{Mn(III,III)} \rightarrow \text{Mn(III,II)}$ reduction of the $[\text{Mn}_2(\text{O})(\text{OH})]^{3+}$ form (2) nearly equals that for $\text{Mn(IV,III)} \rightarrow \text{Mn(III,III)}$ reduction of the $[\text{Mn}_2\text{O}_2]^{3+}$ form (1) (Table 4). Thus, protonation can facilitate multi-electron transfer at oxo-bridged manganese centers. In addition, the donor strength of bridging ligands and redox potentials can be modified by replacing μ -oxo units with carboxylate (e.g. CH_3CO_2^-) (4,5) [87] or phenolate (6) [92] groups.

A particularly interesting example of binuclear Mn electrochemistry is that reported by Holm et al. for the $[\text{Mn}_2(\text{salmp})_2]^n$ ($n = 2+, 1+, 0, 1-, 2-$) complex [88]. H_3salmp is a pentadentate SB ligand that bridges both Mn centers by means of a centrally positioned phenolate group (7). $[\text{Mn}_2(\text{salmp})_2]^n$ undergoes four chemically reversible one-electron transfers,

encompassing five oxidation levels over a potential range of 1.5 V.



As shown by the cyclic voltammetric response in Fig. 10, the peak potential separation of the initial $\text{Mn(II,II)} \rightarrow \text{Mn(II,III)}$ electrode reaction is much larger than that of the other steps. This suggests significant inner-shell reorganization and a small rate of heterogenous electron transfer for oxidation of the fully reduced Mn(II,II) state. Similar kinetic sluggishness is observed for Mn(III)/Mn(II) electron-transfer reactions of some mononuclear complexes (see Sects 16.1.2 and 16.1.3).

A second structural motif in binuclear manganese chemistry is the triply bridged structure in which one μ -oxo unit has been replaced by two bridging carboxylates (8 in Sect. 16.1.4). The remaining coordination sites on each metal are commonly occupied by a tridentate tripod or a macrocyclic ligand such as HB(pz)_3^-

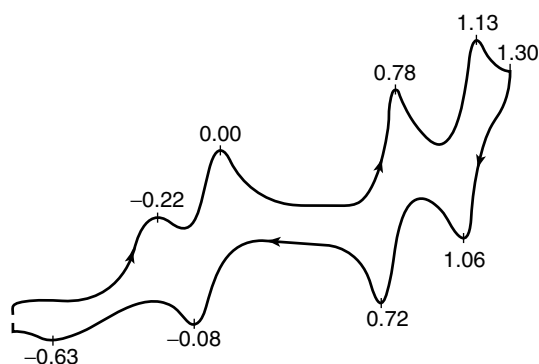
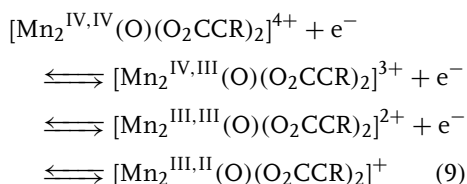


Fig. 10 Cyclic voltammogram for the oxidation of $[\text{Mn}_2(\text{salmp})_2]^{2-}$ in CH_3CN at $\nu = 0.05 \text{ V s}^{-1}$. Peak potentials in V versus SCE [+0.24 V versus NHE] are shown on the voltammetric trace (reprinted with permission from Ref. 88, Copyright 1991 American Chemical Society).

(Tp[−]) [89] or Me₃tacn [90]. Other combinations such as bidentate bipyridyl plus monodentate chloride ligands are possible [91]. These complexes have been prepared and studied as models for catalase, ribonucleotide reductase, and related manganese-containing enzymes [93]. [(Tp)₂Mn₂(O)(O₂CCR)₂]^{2+/+/0/−} [90] and [(Me₃tacn)₂Mn₂(O)(O₂CCR)₂]^{4+/3+/2+/+} [91] participate in four-membered redox series, which cover a potential range of ca 1.7 V.

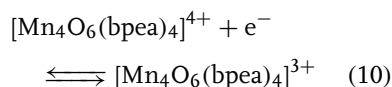


It is interesting to note that the (IV,IV)/(IV,III) and (IV,III)/(III,III) potentials of the [Mn₂(O)(O₂CCR)₂]ⁿ⁺ complexes (**8** in Sect. 16.1.4) with Tp[−] and Me₃tacn capping ligands are similar to one another and also to those of the [Mn₂O₂]ⁿ⁺ complexes (**1**) with terminal bpy and phen ligands (Table 4). The latter observation presumably is a result of the charge compensation that occurs when two mononegative bridging carboxylates replace a single, dinegative bridging oxo ligand. The comparative influence of Tp[−], tacn, and aromatic diimine ligands on metal-centered redox potentials has been discussed in Ref. 15.

[Mn₂(O)(O₂CCR)₂]ⁿ⁺ redox potentials also can be modified by protonation of the single μ -oxo bridge. The μ -hydroxo [(Me₃tacn)₂Mn₂^{II,II}(OH)(O₂CCR)₂]⁺ complex (**9** in Sect. 16.1.4) has been prepared and found to undergo sequential one-electron oxidations to [(Me₃tacn)₂Mn₂^{III,II}(OH)(O₂CCR)₂]²⁺ and [(Me₃tacn)₂Mn₂^{III,III}(OH)(O₂CCR)₂]³⁺ (Table 4) [90]. The change in potential upon protonation

is similar to that observed for di- μ -oxo species and increases the potential of Mn(III,III) → Mn(III,II) reduction to a value near that for Mn(IV,III) → Mn(III,III) reduction in the unprotonated complex.

Manganese exhibits a tendency to form structures of higher nuclearity, especially ones that are supported by bridging oxo ligands. An example that has been well-characterized structurally and electrochemically is the tetranuclear adamantane-like cluster, [Mn₄O₆(bpea)₄]⁴⁺ [94, 95], which is of interest for its relevance to the oxygen-evolving center (OEC) of PSII. Bpea is the tridentate *N,N*-bis(2-pyridylmethyl)ethylamine ligand, which binds to the vacant coordination sites in (**11** in Sect. 16.1.4). [Mn₄O₆(bpea)₄]⁴⁺ undergoes a chemically reversible one-electron reduction (Eq. 10) at +0.50 V in CH₃CN:



and exhibits coupled electron–proton-transfer chemistry in aqueous media [94]. It is of interest to note that the fully oxidized Mn(IV)₄ center in [Mn₄O₆(bpea)₄]⁴⁺ is achieved at a very accessible potential.

Manganese complexes of higher nuclearity are being investigated as single-molecule magnets (SMMs). An example is the Mn₁₂ cluster, [Mn₁₂O₁₂(O₂CCHCl₂)₁₆(H₂O)₄]⁰, whose structure in its two-electron reduced form ([Mn₁₂]^{2−}) is shown in Fig. 11 [96]. The [Mn₁₂]⁰, [Mn₁₂][−], and [Mn₁₂]^{2−} states of this structure have ground-state spin values of *S* = 10, 19/2, and 10, respectively. The oxidized forms have a larger barrier to magnetization relaxation and therefore exhibit SMM behavior at higher temperatures. The influence of oxidation level

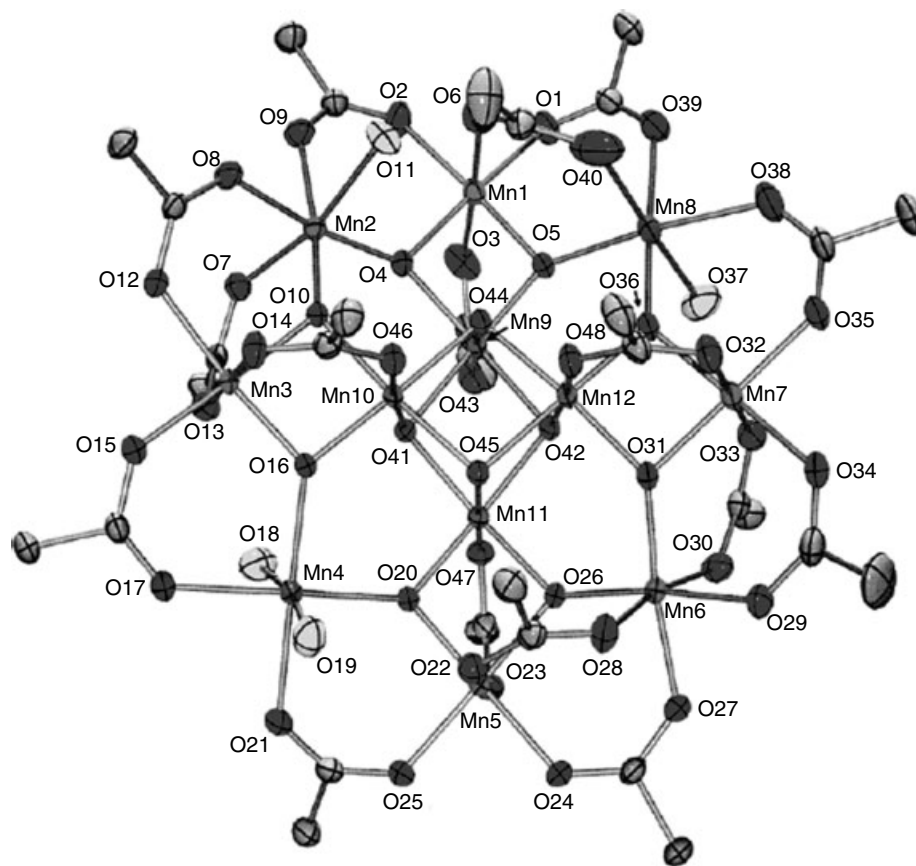
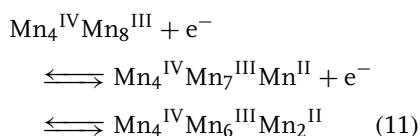


Fig. 11 Structure of the $(\text{PPh}_4)_2[\text{Mn}_{12}\text{O}_{12}(\text{O}_2\text{CCHCl}_2)_{16}(\text{H}_2\text{O})_4] \cdot 4\text{CH}_2\text{Cl}_2 \cdot \text{H}_2\text{O}$ dianion. Atoms Mn4 and Mn8 are reduced from Mn(III) to Mn(II) upon reduction of $[\text{Mn}_{12}]^0$ to $[\text{Mn}_{12}]^{2-}$.

Atoms Mn9 through Mn12 form the $\text{Mn}_4^{\text{IV}}\text{O}_4$ core at the center of the molecule (reprinted with permission from Ref. 96, Copyright 2003 American Chemical Society).

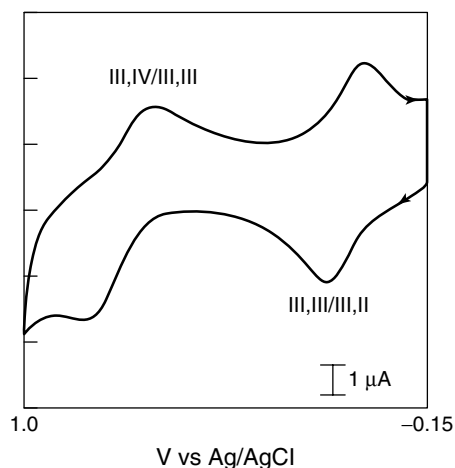
on magnetic properties is of fundamental importance in these compounds. The $[\text{Mn}_{12}\text{O}_{12}(\text{O}_2\text{CCHCl}_2)_{16}(\text{H}_2\text{O})_4]^0$ cluster exhibits reductions at +1.55 and +1.25 V in CH_3CN :



It is of interest to note that Mn(III) rather than Mn(IV) sites are reduced in

Eq. (11) and that the $\text{Mn}_4^{\text{IV}}\text{Mn}_7^{\text{III}}\text{Mn}^{\text{II}}$ and $\text{Mn}_4^{\text{IV}}\text{Mn}_6^{\text{III}}\text{Mn}_2^{\text{II}}$ reduction products are trapped valence species. Figure 11 shows that the dodecamangano cluster consists of a central Mn_4O_4 cubane unit surrounded by a nonplanar ring of eight Mn atoms that are bridged by and connected to the core by eight $\mu_3\text{-O}^{2-}$ ions. Sixteen bridging dichloroacetate ions and four H_2O groups are ligated to the eight Mn atoms in the ring. In the neutral $[\text{Mn}_{12}]$ form, the four central Mn atoms

Fig. 12 Cyclic voltammogram of $[\text{Mn}_2\text{O}_2(\text{phen})_4]^{3+}$ in pH 4.5 phosphate buffer at an activated glassy carbon electrode; $\nu = 0.1 \text{ V s}^{-1}$ (reprinted with permission from Ref. 97, Copyright 1992 American Chemical Society).



are Mn(IV) and the eight Mn atoms in the ring are Mn(III). On the basis of bond valence sum analyses of the structurally characterized products [96], Mn atoms at positions 4 and 8 are reduced in Eq. (11). The relative ease of reduction of these sites presumably results from their partial coordination by H_2O , which is less strongly donating than oxo or dichloroacetato ligands.

16.1.4.3 Studies in Aqueous Media

The electrochemistry of oxo-bridged manganese complexes in aqueous solution is characterized by coupled electron and proton-transfer reactions. The cyclic voltammetric behavior of $[\text{Mn}_2^{\text{IV,III}}\text{O}_2(\text{phen})_4]^{3+}$ in aqueous pH 4.5 phosphate buffer is illustrated in Fig. 12 [97]. It is of interest to compare this result with that obtained for the same complex dissolved in CH_3CN (Fig. 9). Two one-electron reactions are observed in each case. However, these correspond to $\text{Mn}(\text{IV,IV}) \rightarrow \text{Mn}(\text{IV,III})$ and $\text{Mn}(\text{IV,III}) \rightarrow \text{Mn}(\text{III,III})$ reductions in the nonaqueous solvent and to $\text{Mn}(\text{IV,III}) \rightarrow \text{Mn}(\text{III,III})$ and $\text{Mn}(\text{III,III}) \rightarrow \text{Mn}(\text{III,II})$ reductions in

H_2O . Moreover, the half-reactions in aqueous solution exhibit a pH dependence corresponding to the addition of one proton in conjunction with each electron. Thus, under the conditions of Fig. 12, the $[\text{Mn}_2^{\text{IV,III}}\text{O}_2]^{3+}$ center (1) is converted to an $[\text{Mn}_2^{\text{III,III}}\text{O}(\text{OH})]^{3+}$ center (2) in the first reduction and to an $[\text{Mn}_2^{\text{III,II}}(\text{OH})_2]^{3+}$ center (3) in the second. Electrode half-reactions, Nernst equations, and $\text{p}K_{\text{a}}$ values for the phen complex and for several related systems are summarized in Table 5. Precise data are somewhat difficult to obtain for these systems owing to the slow electron-transfer kinetics ($k_{\text{s,h}} \approx 10^{-3} \text{ cm}^2 \text{ s}^{-1}$ or less), the need to activate the working electrode surface to achieve a useful response, and the limited stability of some species in the presence of coordinating buffers. Nonetheless, $\text{p}K_{\text{a}}$ values for the bpy complex obtained from the Pourbaix diagram in Ref. 93 lead to pH-independent potentials of +1.1 and +0.5 V, respectively, for $[\text{Mn}_2^{\text{IV,III}}\text{O}(\text{OH})]^{3+}$ and $[\text{Mn}_2^{\text{IV,III}}\text{O}_2]^{3+}$ reduction, values that compare reasonably well to the results in Table 4, given the difference in solvent environments.

Tab. 5 Aqueous electrochemical data for binuclear manganese complexes

Half-reaction	Nernst equation (V versus NHE)	$pK_{a1}^{IV,III}$	$pK_{a1}^{III,II,III}$	$pK_{a1}^{III,II}$	References
$[Mn_2^{IV,III}O_2(phen)_4]^{3+} + H^+ + e^- \rightleftharpoons [Mn_2^{III,III}O(OH)(phen)_4]^{3+}$	$E^o = +1.30 - 0.079 \text{ pH}$		9.15		97
$[Mn_2^{IV,III}O_2(bpy)_4]^{3+} + H^+ + e^- \rightleftharpoons [Mn_2^{III,III}O(OH)(bpy)_4]^{3+}$	$E^o = +1.21 - 0.064 \text{ pH}$	2.3	11.0 (14.6) ^a		98
$[Mn_2^{IV,III}O_2(bispicen)_2]^{3+} + H^+ + e^- \rightleftharpoons [Mn_2^{III,III}O(OH)(bispicen)_2]^{3+}$	Na		8.35		99, 100
$[Mn_2^{IV,III}O_2(edda)_2]^- + H^+ + e^- \rightleftharpoons [Mn_2^{III,III}O(OH)(edda)_2]^-$	$E^o = +1.22 - 0.07 \text{ pH}$				100
$[Mn_2^{III,III}O(OH)(phen)_4]^{3+} + H^+ + e^- \rightleftharpoons [Mn_2^{III,II}(OH)_2(phen)_4]^{3+}$	$E^o = +0.62 - 0.066 \text{ pH}$			(11.5) ^a	97

^a Data in parentheses determined in CH₃CN [82].

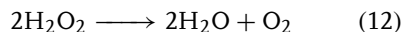
16.1.5

Biological Systems16.1.5.1 **Introduction**

Manganese is an element that is essential for life. It is present at the active site of many enzymes [4, 5]. Those enzymes in which the metal center is involved in a redox process are manganese catalase [101], peroxidase [102], and SOD [103]. In addition, a cluster containing four Mn and one Ca atoms in the water-oxidizing center (WOC) of PSII is the site at which dioxygen is produced photosynthetically on Earth [3, 104].

16.1.5.2 **Manganese Catalase**

Hydrogen peroxide, which is a by-product of the process of O_2 utilization by aerobic organisms, is a toxic substance. Its toxicity is ameliorated by the disproportionation of H_2O_2 into H_2O and O_2



This process is catalyzed by a variety of catalase enzymes, the most common being the heme catalases, which accomplish the two-electron chemistry of Eq. (12) at a mononuclear heme center. Here, both the iron and its surrounding porphyrin ligand participate to the extent of one electron each in the redox process. Manganese catalases contain a binuclear Mn center and cycle between $Mn_2(II,II)$ and $Mn_2(III,III)$ oxidation states while carrying out the disproportionation of H_2O_2 . The enzyme can

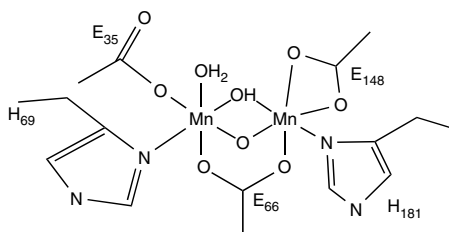
also exist in a superoxidized $Mn_2(III,IV)$ state, which does not destroy its catalytic activity.

The active site structure of the $Mn_2(III,III)$ form of *Lactobacillus plantarum* is depicted in Fig. 13 [105, 106]. The Mn centers are bridged by oxo, hydroxo, and carboxylato ligands in a manner similar to the binuclear structures (8–10) in Sect. 16.1.4. A proposed mechanism for hydrogen peroxide dismutation by Mn catalase is presented in Fig. 14. A number of model studies of H_2O_2 disproportionation employing bridged binuclear Mn complexes have been conducted [107].

16.1.5.3 **Manganese Peroxidase**

Peroxidases catalyze the oxidation of a wide variety of substrates through utilization of hydrogen peroxide. Manganese peroxidase is a heme protein that also contains a mononuclear Mn center linked to the iron-protoporphyrin IX prosthetic group through a propionate residue on the porphyrin [102, 105]. Manganese peroxidases are found in white rot fungi, where they serve to degrade lignin, a polyphenolic substance in woody plants that is otherwise resistant to degradation. As shown in the catalytic cycle in Fig. 15, Mn^{III} is produced by an electron-transfer reaction with the H_2O_2 -oxidized ferric porphyrin, at which point it diffuses into the lignin matrix and initiates the degradation of the polymer via phenol radical formation. Direct electron transfer between electrodes

Fig. 13 A schematic drawing of the active site of manganese catalase from *Lactobacillus plantarum* (reprinted from Ref. 105, Copyright 2003 with permission from Elsevier).



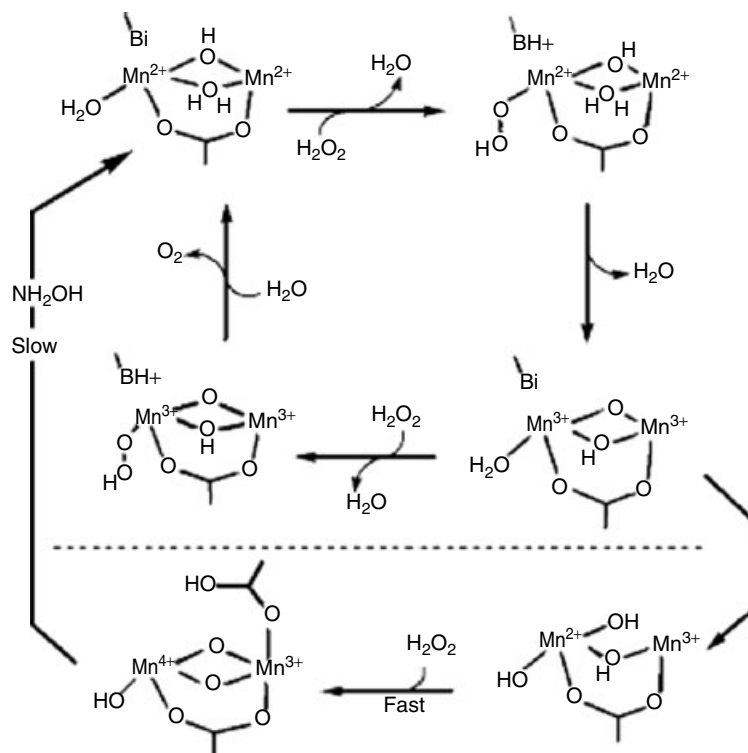


Fig. 14 Proposed mechanism for disproportionation of H_2O_2 by manganese catalase (reprinted with permission from Ref. 107, Copyright 2004 American Chemical Society).

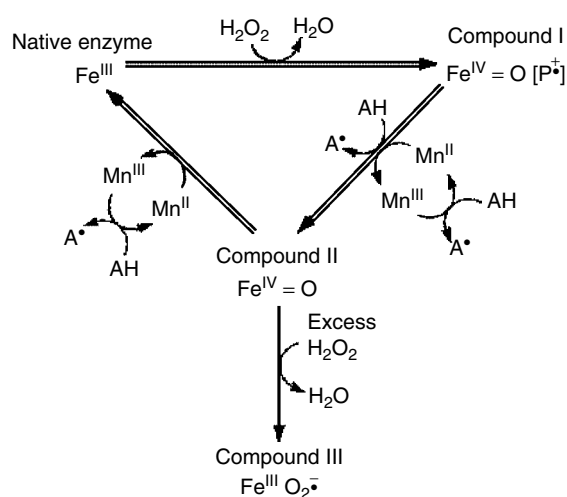
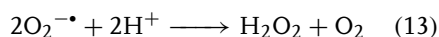


Fig. 15 Catalytic cycle of manganese peroxidase (Reprinted with permission from Ref. 102, Copyright 2000, Marcel Dekker).

and ligninolytic redox enzymes has been achieved, and the $\text{Fe}^{\text{III/II}}$ -heme potential has been measured [108]. However, the potential of the $\text{Mn}^{\text{III/II}}$ couple in Mn peroxidase has not been determined.

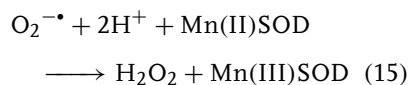
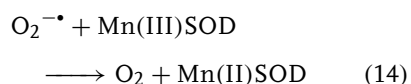
16.1.5.4 Manganese Superoxide Dismutase

Superoxide ion, $\text{O}_2^{\bullet-}$, is a highly toxic substance that is also a by-product of oxygen utilization in aerobic organisms. Its decomposition into H_2O_2 and O_2 ,



is catalyzed by SOD enzymes [103], of which there are Mn-, Fe-, Ni-, and Cu/Zn-containing forms. Absence of or defects in MnSOD are thought to be linked to disease states in humans.

The active site of manganese SOD contains a single five-coordinate Mn bound to three histidine imidazoles, a monodentate aspartate carboxylate, and a solvent molecule (H_2O or OH^- , depending on the oxidation state) [103]. The catalytic cycle of the enzyme, which is illustrated in Fig. 16, incorporates the following oxidative and reductive steps:



Electron transfer is coupled with proton transfer involving the metal-bound solvent molecule. For Eqs (14) and (15) to be thermodynamically favorable, the potential of the $\text{Mn}^{\text{III/II}}$ -SOD couple must lie between the values for superoxide oxidation and reduction ($\text{O}_2^{\bullet-} \rightarrow \text{O}_2 + \text{e}^-$, $E^\circ = -0.16$ V; $\text{O}_2^{\bullet-} + 2\text{H}^+ \rightarrow \text{H}_2\text{O}_2 + \text{e}^-$, $E^\circ = +0.89$ V at pH 7) [109]. The potential has been measured for MnSOD from several organisms. From the results summarized in Table 6, the $\text{Mn}^{\text{III/II}}$ potential is intermediate to the values of the $\text{O}_2/\text{O}_2^{\bullet-}$ and $\text{O}_2^{\bullet-}/\text{H}_2\text{O}_2$ couples in all cases and hence is capable of accomplishing the Eqs (14) and (15). Values of E° have been measured for wild-type and two mutated forms of human MnSOD. There are only small differences in E° , from which it is suggested that the role of the mutated His30 and Tyr34 residues is to support proton transport rather than redox potential tuning [110]. The E° value from *Escherichia coli* is constant from pH 7.0 to 8.5 but decreases dramatically at higher pH ($\Delta E^\circ/\Delta \text{pH} \approx -140$ mV) [111, 112]. The pH dependence of the Mn(III/II) potential has not been studied for other organisms. It is interesting to note that the Fe-substituted form of MnSOD has $E^\circ = -0.24$ V and that the Mn-substituted form of FeSOD has $E^\circ > 0.96$ V [105]. These altered enzyme forms are ineffective in superoxide dismutation.

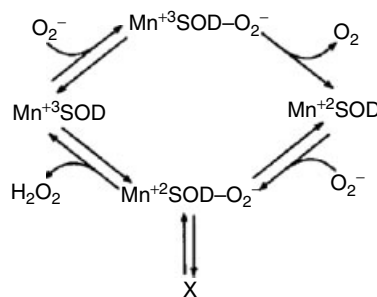


Fig. 16 Catalytic cycle of manganese superoxide dismutase; X is a dead-end peroxide complex (Reprinted with permission from Ref. 103, Copyright 2000, Marcel Dekker).

Tab. 6 Redox potentials of manganese superoxide dismutase

Organism	Method ^a	pH	$E^{\circ'}$, V versus NHE	References
WT Human	A	7.8	$+0.40 \pm 0.03$	110
H30N Human	A	7.8	$+0.37 \pm 0.03$	110
Y34F Human	A	7.8	$+0.44 \pm 0.03$	110
<i>Escherichia coli</i>	B	7.0	$+0.42$	111
<i>Escherichia coli</i>	C	7.0	$+0.31$	112
<i>Bacillus stearothermophilus</i>	C	7.0	$+0.26$	112

^a A: Chemically mediated spectroelectrochemical titration; B: Cyclic voltammetry at a 3-mercaptopropionic acid–modified Au electrode; C: Chemically mediated coulometric titration.

16.1.5.5 Oxygen-evolving Center in Photosystem II

The photosynthetic oxidation of water to O_2 is responsible for the generation of virtually all the dioxygen in the planet. This reaction is accomplished at a tetra-manganese cluster – now known to also contain Ca^{2+} and require Cl^- and possibly bicarbonate ion as cofactors – that lies at the oxidizing terminus of PSII in higher plants, green algae, and cyanobacteria (Fig. 17) [3, 104, 113]. The understanding

of the structure and function of this OEC or WOC, although still incomplete, has advanced considerably in concert with the knowledge of the structural and redox properties of mono-, bi-, and polynuclear manganese complexes described in the earlier parts of this chapter.

Photosynthesis is initiated by the absorption of a photon, which produces a charge-separated $P680^+Pheo^-$ state between P680, a special arrangement of four chlorophyll *a* molecules, and pheophytin

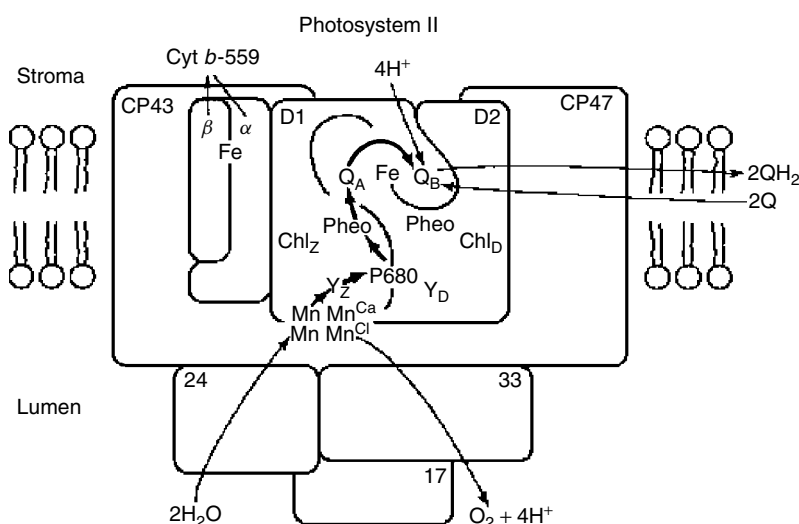
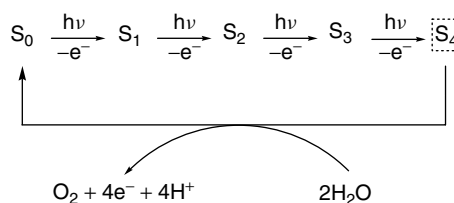
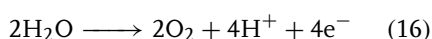


Fig. 17 A schematic drawing of photosystem II (Reprinted with permission from Ref. 113, Copyright 2000, Marcel Dekker).

Scheme 5 The S-state cycle of the oxygen-evolving center in photosystem II [114].



(Pheo). The negative charge is passed from Pheo[−] to the reducing terminus of PSII, where carbohydrate biomass is produced by the fixation of CO₂ and H₂O. The positive charge is passed from P680⁺ to a redox-active tyrosine residue (Y_Z−OH), which in its deprotonated radical form (Y_Z−O[•]) serves as the immediate oxidant of the OEC. This transfer of charge drives the OEC through a sequence of four one-electron steps known as the *S-state cycle* [114] (Sch. 5). Absorption of three photons promotes the OEC from its S₀ to the S₃ state. Absorption of a fourth photon and promotion to the S₄ state is accompanied by the almost simultaneous release of O₂ and return to the S₀ level. The OEC, therefore, is able to store charge and release it in a concerted manner to accomplish the four-electron oxidation of water to O₂:



The potential of Eq. (16) at pH 7 is +0.81 V [115]. As shown in Table 7, P680⁺

and Y_Z−O[•] are sufficiently potent oxidants to drive the individual steps in the S-state cycle and to convert water to dioxygen. The need for a catalyst and a mechanism for multielectron reaction is evident from the very positive potentials of the one-electron steps in H₂O to O₂ conversion [109]. It is of interest to note that the *E*^{o'} values of the individual S_{*i*} → S_{*i*+1} conversions are approximately equal. This indicates that proton transfer or a compositional or structural change must accompany each electron transfer to maintain the OEC potential at an accessible level. Although coupled electron–proton (or hydrogen atom) transfer maintains the requisite overall charge neutrality with each step, a proton-addition sequence of 1:0:1:2 also is likely. There is general agreement that the average oxidation state of Mn in the tetramanganese cluster advances from +3.25 to +4.25 upon S₀ → S₄ conversion, but there is no consensus on the formal oxidation state assignments at each stage in the cycle. The possibilities considered

Tab. 7 Redox potentials and oxidation state assignments of photosystem II components

Half-reaction	Potential, V versus NHE ^a	OEC state	Oxidation state assignments
P680 ⁺ + e [−] → P680	+1.12	S ₀	Mn ₄ (II,III,IV,IV) or Mn ₄ (III,III,III,IV)
Y _Z −O [•] + H ⁺ + e [−] → Y _Z −OH	+0.97	S ₁	Mn ₄ (III,III,IV,IV)
S ₁ + e [−] → S ₀	< +0.70	S ₂	Mn ₄ (III,IV,IV,IV)
S ₂ + e [−] → S ₁	+0.925	S ₃	Mn ₄ (IV,IV,IV,IV) or Mn ₄ (III,IV,IV,IV)-O [•]
S ₃ + e [−] → S ₂	+0.925	S ₄	Mn ₄ (IV,IV,IV,V) or Mn ₄ (IV,IV,IV,IV)-O [•]

^a From Ref. 104.

most likely on the basis of current evidence from XAS, EPR, and other spectroscopic experiments are included in Table 7.

Included among these are the steps in which electron transfer is assumed to involve an oxo ligand rather than a metal.

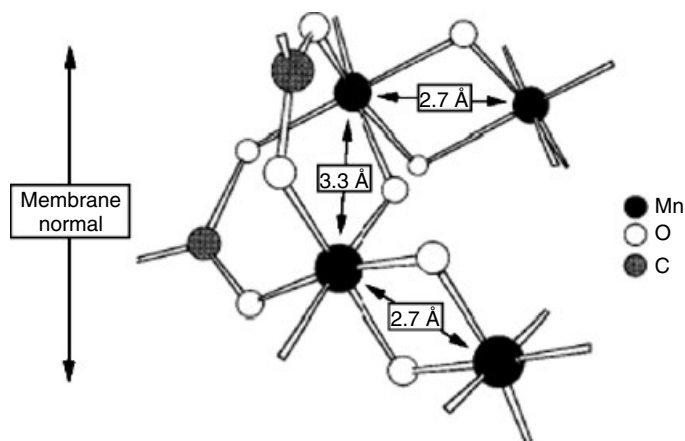


Fig. 18 A proposed model structure of the OEC of photosystem II (reprinted with permission from Ref. 3, Copyright 1996 American Chemical Society).

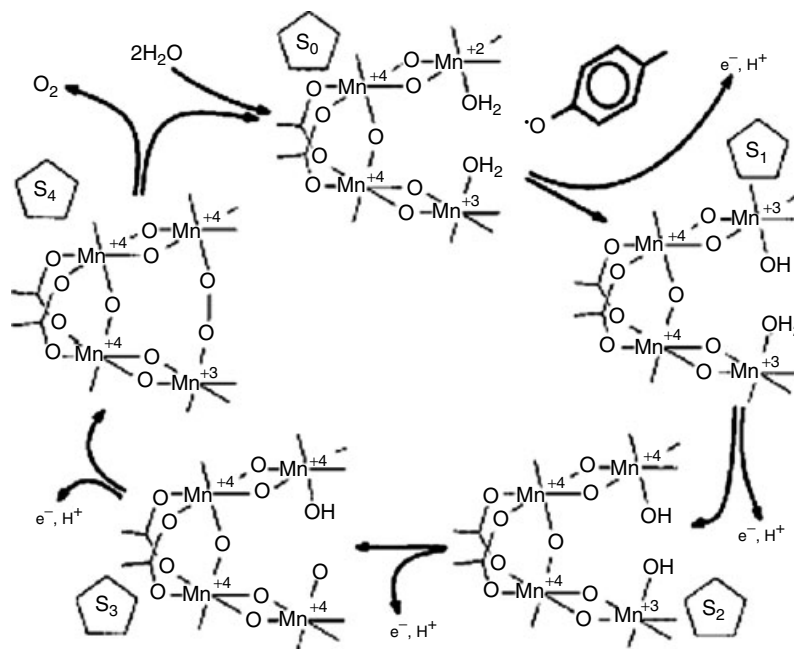


Fig. 19 A proposed mechanism for O_2 evolution from photosystem II based on the model structure in Fig. 18 (Reprinted with permission from Ref. 118, Copyright 1997, American Association for the Advancement of Science).

Many chemical model studies and proposed mechanisms have been presented for the OEC in PSII [3, 104, 116–128]. These draw heavily on the redox and coordination chemistry discussed in Sect. 16.1.4 and on the extensive work with isolated biological materials. Space does not permit full coverage; thus, only some of the more significant stages in the model and mechanism development are described in the following paragraphs.

An early model of the Mn complex in the OEC of PSII is shown in Fig. 18 [3]. This C-shaped structure consists of two di- μ -oxo-bridged Mn units connected by a single μ -oxo plus two di- μ -carboxylato bridges. These features are similar to (1) and (8), respectively, in Sect. 16.1.4. Important components of the model are the Mn-Mn distances of 2.7 Å in the di- μ -oxo unit and 3.3 Å in the mono- μ -oxo unit, which are consistent with the values obtained by EXAFS of the OEC in PSII. Although it was proposed initially that O₂ forms from the bridging oxo ligands, this possibility has been discounted.

An important stage in the OEC model development based on this C-shaped cluster is shown in Fig. 19 [118]. This description established the role of the neutral tyrosyl radical (Y_Z-O•) derived from the Tyr161 residue on the D1 polypeptide as the primary oxidant of the Mn₄ cluster. In addition, the Y_Z-OH/Y_Z-O• redox system provides a means of coupling proton transfer to electron transfer during the S-state cycle. It has been argued that these H⁺/e⁻ exchanges are accomplished exclusively by hydrogen atom transfer on

the basis of the approximate energetic equivalence of O-H bonds in Y_Z-OH and manganese-bound ligands. However, it is likely that H⁺ and e⁻ transfer is not so tightly concerted in all stages of O₂ evolution and that protons and electrons may move along separate paths in the higher S-state conversions [129]. The model in Fig. 19 also recognizes the possibility that dioxygen may be formed (via μ -peroxo species) at a terminal rather than at a bridging Mn site within the OEC. The development of O₂ evolution model chemistry has received considerable impetus from recent X-ray spectroscopic [128, 130, 131] and 3.2–3.5-Å resolution crystallographic [132, 133] studies, which reveal a prominent role for Ca²⁺. The structures shown in Fig. 20, which contain Ca²⁺ either as an integral component of a Mn₃Ca cluster or bridged across a multinuclear

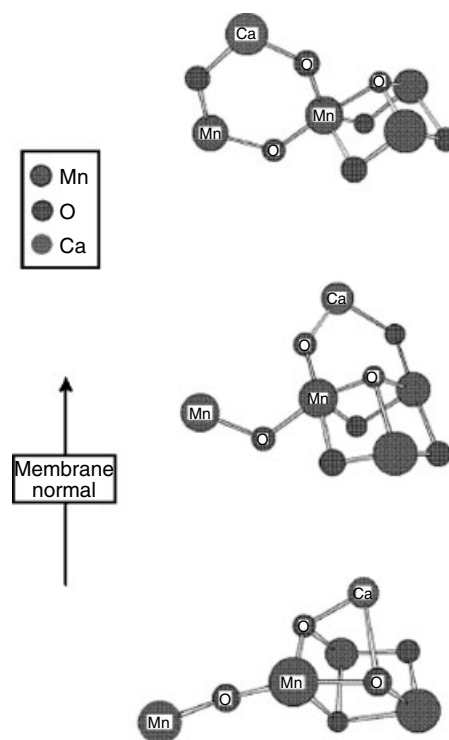


Fig. 20 Some proposed model structures of the OEC in photosystem II incorporating four Mn and one Ca atom (Reprinted with permission from Ref. 128, Copyright 2005, Springer-Verlag).

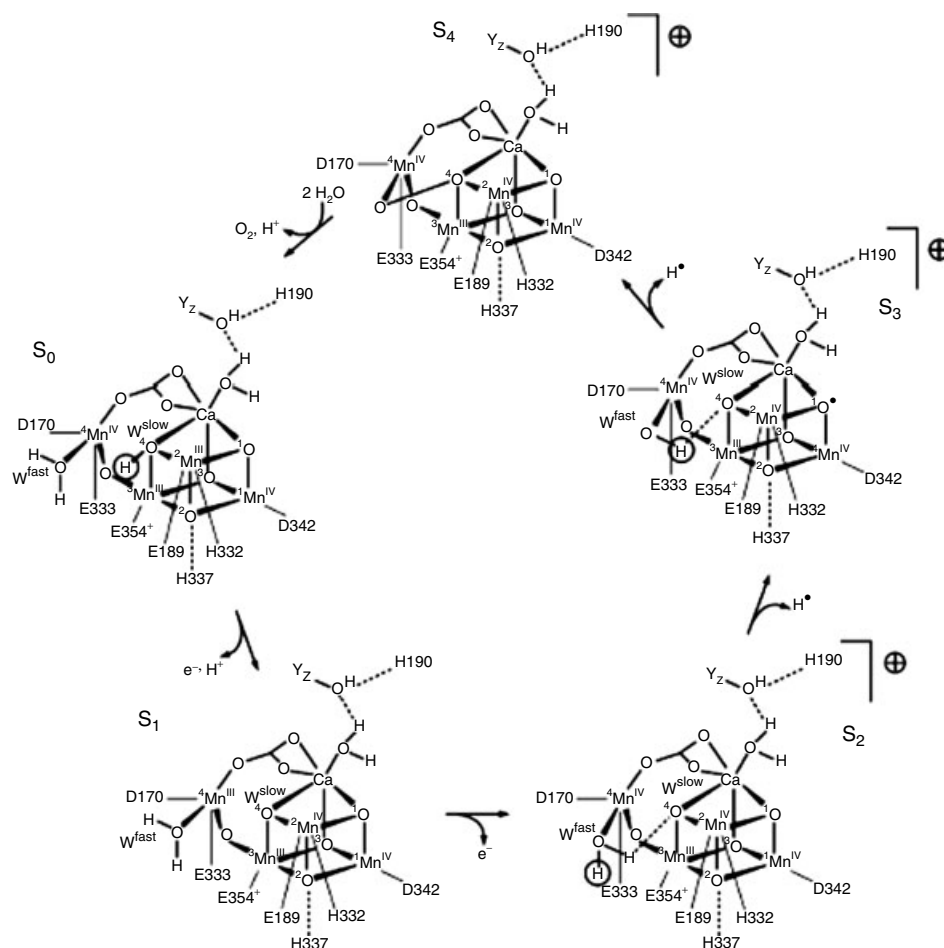


Fig. 21 A proposed mechanism for O_2 evolution from photosystem II based on a 4Mn-1Ca cluster (reprinted from Ref. 125, Copyright 2004 with permission from the Royal Society of Chemistry).

Mn array, are consistent with the experimentally established Mn-Ca distance of ~ 3.4 Å. Although seemingly implausible, intimate binding of Ca^{2+} is supported by the observation that Ca can be incorporated in MnO_2 minerals [134] and by the recent synthesis of an $\text{Mn}_{13}\text{Ca}_2$ cluster containing an Mn_4CaO_4 unit [135]. An important feature of these models is the presence of a “dangling” Mn atom connected the main cluster via a mono- μ -oxo or μ_4 -oxo bridge. One proposed mechanism based on recent

findings is shown in Fig. 21 [125]; other interpretations have been presented [122, 127, 129, 131]. Some important points to be resolved while achieving an understanding of the molecular basis of dioxygen evolution include the details of proton-transfer reactions; whether oxidations of the OEC involve solely metal-centered electron transfers or the formation of oxy radicals in some instances; the specific roles of Ca^{2+} and Cl^- ; and the details of the $\text{S}_2 \rightarrow \text{S}_3$ transition, which is thought

to involve a change in the Mn coordination number or structure within the Mn_4CaO_4 cluster [131].

References

1. J. J. Morgan, in *Metal Ions in Biological Systems*, (Eds.: A. Sigel, H. Sigel), Marcel Dekker, Basel, Switzerland, 2000 Vol. 37., Chapter 1.
2. M. M. Thackeray, *Prog. Solid State Chem.* **1997**, 1, 1–71.
3. V. K. Yachandra, K. Sauer, M. P. Klein, *Chem. Rev.* **1996**, 96, 2927–2950.
4. V. L. Pecoraro, (Ed.), *Manganese Redox Enzymes*, VCH Publishers, New York, 1992.
5. A. Sigel, H. Sigel, (Eds.), *Metal Ions in Biological Systems*, Marcel Dekker: Basel, Switzerland, 2000, Vol. 37.
6. T. Katsuki, *Coord. Chem. Rev.* **1995**, 140, 189–214.
7. G. P. Glasby, in *Marine Geochemistry*, (Eds.: H. Schulz, M. Zabel), Springer-Verlag, Berlin, 2000, pp. 335–372.
8. (a) F. A. Cotton, G. Wilkinson, C. A. Murillo et al., *Advanced Inorganic Chemistry*, 6th ed., John Wiley & Sons: New York, 1999, pp. 757–775. (b) D. C. Weatherburn, S. Mandel, S. Mukopadhyay et al., in *Comprehensive Coordination Chemistry II*, (Eds.: J. A. McCleverty, T. J. Meyer), 2nd ed., Elsevier, Amsterdam, 2004, Vol. 5, Chapter 5.1.
9. C. C. Liang, in *Encyclopedia of the Electrochemistry of the Elements*, (Ed.: A. J. Bard), Marcel Dekker, New York, 1973 Vol. 1, Chapter. I-6.
10. J. C. Hunter, A. Kozawa, in *Standard Potentials in Aqueous Solution*, (Eds.: A. J. Bard, R. Parsons, J. Jordan), Marcel Dekker, New York, 1985 Chapter. 15.
11. (a) T. A. Zordan, L. G. Hepler, *Chem. Rev.* **1968**, 68, 737–745. (b) S. G. Bratsch, *J. Phys. Chem. Ref. Data* **1989**, 18, 1–21.
12. K. Sekula-Brzezinska, P. K. Wrona, Z. Galus, *Electrochim. Acta* **1979**, 24, 555–563.
13. D. B. Freeman, G. Mamantov, *Electrochim. Acta* **1976**, 21, 257–261.
14. G. Gritzner, K. Danksagmüller, V. Gutmann, *J. Electroanal. Chem.* **1978**, 90, 203–210.
15. D. C. L. De Alwis, F. A. Schultz, *Inorg. Chem.* **2003**, 42, 3616–3622.
16. A. Neves, S. M. D. Erthal, I. Vencato et al., *Inorg. Chem.* **1992**, 31, 4749–4755.
17. K. Yamaguchi, D. T. Sawyer, *Inorg. Chem.* **1985**, 24, 971–976.
18. M. Hoogenraad, K. Ramkisoensing, S. Gorter et al., *Eur. J. Inorg. Chem.* **2002**, 377–387.
19. S. K. Chandra, P. Basu, D. Ray et al., *Inorg. Chem.* **1990**, 29, 2423–2428.
20. M. M. Morrison, D. T. Sawyer, *Inorg. Chem.* **1978**, 17, 338–339.
21. U. Kölle, U. Englert, *Eur. J. Inorg. Chem.* **2002**, 165–170.
22. G. Gritzner, H. Murauer, V. Gutmann, *J. Electroanal. Chem.* **1979**, 101, 185–200.
23. V. Manivannan, S. Dutta, P. Basu et al., *Inorg. Chem.* **1993**, 32, 769–771.
24. H. Yasuda, K. Suga, S. Aoyagui, *J. Electroanal. Chem.* **1978**, 86, 259–270.
25. P. M. Treichel, G. E. Dirreen, H. J. Mueh, *J. Organomet. Chem.* **1972**, 44, 339–352.
26. J. L. Robbins, N. M. Edelstein, S. R. Cooper et al., *J. Am. Chem. Soc.* **1979**, 101, 3853–3857.
27. T. Gennett, D. F. Milner, M. J. Weaver, *J. Phys. Chem.* **1985**, 89, 2787–2794.
28. M. M. Morrison, D. T. Sawyer, *Inorg. Chem.* **1978**, 17, 333–337.
29. O. R. Brown, S. Clarke, *J. Electroanal. Chem.* **1976**, 70, 87–93.
30. K. Wiegardt, W. Schmidt, W. Herrmann et al., *Inorg. Chem.* **1983**, 22, 2953–2956.
31. P. A. Anderson, I. I. Creaser, C. Dean et al., *Aust. J. Chem.* **1993**, 46, 449–463.
32. A. T. Kuhn, *J. Chem. Soc., Faraday Trans.* **1983**, 79, 417–430.
33. E. Bishop, P. Cofré, *Analyst* **1981**, 106, 429–432.
34. W. R. Fawcett, M. Opallo, *J. Electroanal. Chem.* **1992**, 331, 815–830.
35. M. Orlik, Z. Galus, *J. Electroanal. Chem.* **1994**, 366, 97–103.
36. J. Broda, Z. Galus, *Electrochim. Acta* **1983**, 28, 1523–1528.
37. W. D. Treadwell, W. E. Rath, *Helv. Chim. Acta* **1952**, 35, 2259–2275.
38. N. Hebenanz, F. H. Köhler, G. Müller et al., *J. Am. Chem. Soc.* **1986**, 108, 3281–3289.
39. A. B. P. Lever, *Inorg. Chem.* **1990**, 29, 1271–1285.
40. B. E. Bursten, *J. Am. Chem. Soc.* **1982**, 104, 1299–1304.

41. C. J. Pickett, D. Pletcher, *J. Organomet. Chem.* **1975**, 102, 327–333.
42. A. M. Bond, B. S. Grabaric, Z. Grabaric, *Inorg. Chem.* **1978**, 17, 1013–1018.
43. D. J. Kuchynka, J. K. Kochi, *Inorg. Chem.* **1988**, 27, 2574–2581.
44. Changes in Mn–N bond distances taken from, F. Hossain, *Synthesis, Structure and Characterization of Low-spin Mn(III)-Bis[poly(pyrazolyl)borate] Complexes*, M.S. Thesis; Indiana University-Purdue University Indianapolis, Indianapolis, IN; 2004
45. B. Meunier, S. P. de Visser, S. Shaik, *Chem. Rev.* **2004**, 104, 3947–3980.
46. N. A. Chaniotakis, A. M. Chasser, M. E. Meyerhoff et al., *Anal. Chem.* **1988**, 60, 185–188.
47. I. Batinic-Haberle, I. Spasojevic, R. D. Stevens et al., *J. Chem. Soc., Dalton Trans.* **2002**, 2689–2696.
48. A. B. P. Lever, *J. Porphyr. Phthalocya.* **2004**, 8, 1327–1342.
49. K. M. Kadish, *Prog. Inorg. Chem.* **1986**, 34, 435–605.
50. M. Autret, Z. Ou, A. Antonini et al., *J. Chem. Soc., Dalton Trans.* **1996**, 2793–2797.
51. R. Guillard, K. Perie, J.-M. Barbe et al., *Inorg. Chem.* **1998**, 37, 973–981.
52. A. Tulinsky, B. M. L. Chen, *J. Am. Chem. Soc.* **1977**, 99, 3647–3651.
53. R. B. Van Atta, C. E. Strouse, L. K. Hanson et al., *J. Am. Chem. Soc.* **1987**, 109, 1425–1434.
54. D. Feng, F. A. Schultz, *Inorg. Chem.* **1988**, 27, 2144–2149.
55. X. H. Mu, F. A. Schultz, *J. Electroanal. Chem.* **1993**, 353, 349–355.
56. K. M. Kadish, S. Kelly, *Inorg. Chem.* **1979**, 18, 2968–2971.
57. S. L. Kelly, K. M. Kadish, *Inorg. Chem.* **1982**, 21, 3631–3639.
58. X. H. Mu, F. A. Schultz, *Inorg. Chem.* **1992**, 31, 3351–3357.
59. I. Nakanishi, S. Fukuzumi, J.-M. Barbe et al., *Eur. J. Inorg. Chem.* **2000**, 1557–1562.
60. R. D. Arasasingham, T. C. Bruice, *Inorg. Chem.* **1990**, 29, 1422–1427.
61. X. H. Mu, F. A. Schultz, *Inorg. Chem.* **1995**, 34, 3835–3837.
62. A. B. P. Lever, P. C. Minor, J. P. Wilshire, *Inorg. Chem.* **1981**, 20, 2550–2553.
63. E. Steene, T. Wondimagegn, A. Ghosh, *J. Phys. Chem. B* **2001**, 105, 11406–11413.
64. L. J. Boucher, H. K. Garber, *Inorg. Chem.* **1970**, 9, 2644–2649.
65. R. K. Boggess, J. W. Hughes, W. M. Coleman et al., *Inorg. Chim. Acta* **1980**, 38, 183–189.
66. W. M. Coleman, R. R. Goehring, L. T. Taylor et al., *J. Am. Chem. Soc.* **1979**, 101, 2311–2315.
67. C. P. Horwitz, S. E. Creager, R. W. Murray, *Inorg. Chem.* **1990**, 29, 1006–1011.
68. J. M. Workman, R. D. Powell, A. D. Procyk et al., *Inorg. Chem.* **1992**, 31, 1550–1551.
69. T. W. Kaaret, G. H. Zhang, T. C. Bruice, *J. Am. Chem. Soc.* **1991**, 113, 4652–4656.
70. S. Jeon, T. C. Bruice, *Inorg. Chem.* **1992**, 31, 4843–4848.
71. M. Rodriguez, A. J. Bard, *Inorg. Chem.* **1992**, 31, 1129–1135.
72. A. Harriman, G. Porter, *J. Chem. Soc., Faraday Trans. II* **1979**, 75, 1532–1542.
73. A. Bettelheim, D. Ozer, R. Parash, *J. Chem. Soc., Faraday Trans. I* **1983**, 79, 1555–1564.
74. D. G. Davis, J. G. Montalvo Jr. *Anal. Chem.* **1969**, 41, 1195–1202.
75. M. K. Stern, J. T. Groves, in *Manganese Redox Enzymes*, (Ed.: V. L. Pecoraro), VCH Publishers, New York, 1992 Chapter. 11.
76. S. E. Creager, S. A. Raybuck, R. W. Murray, *J. Am. Chem. Soc.* **1986**, 108, 4225–4227.
77. O. Kahn, *Molecular Magnetism*, VCH Publishers, New York, 1993
78. K. Takeda, K. Awaga, *Springer Ser. Chem. Phys.* **2003**, 70, 41–57.
79. P. Thornton, *Ann. Rep. Prog. Chem., Sect. A: Inorg. Chem.* **2004**, 100, 217–227.
80. M. M. Morrison, D. T. Sawyer, *J. Am. Chem. Soc.* **1977**, 99, 257–258.
81. S. R. Cooper, M. Calvin, *J. Am. Chem. Soc.* **1977**, 99, 6623–6630.
82. A. S. Larsen, K. Wang, M. A. Lockwood et al., *J. Am. Chem. Soc.* **2002**, 124, 10112–10123.
83. P. M. Plaskin, R. C. Stouffer, M. Mathew et al., *J. Am. Chem. Soc.* **1972**, 94, 2121–2122.
84. P. A. Goodson, A. R. Oki, J. Glerup et al., *J. Am. Chem. Soc.* **1990**, 112, 6248–6254.
85. A. R. Oki, J. Glerup, D. J. Hodgson, *Inorg. Chem.* **1990**, 29, 2435–2441.
86. Y. Gultneh, T. B. Yisgedu, Y. T. Tesema et al., *Inorg. Chem.* **2003**, 42, 1857–1867.
87. M. U. Triller, W.-Y. Hsieh, V. L. Pecoraro et al., *Inorg. Chem.* **2002**, 41, 5544–5554.

88. S. B. Yu, C. P. Wang, E. P. Day et al., *Inorg. Chem.* **1991**, 30, 4067–4074.
89. J. E. Sheats, R. S. Czernuszewicz, G. C. Dismukes et al., *J. Am. Chem. Soc.* **1987**, 109, 1435–1444.
90. K. Wieghardt, U. Bossek, B. Nuber et al., *J. Am. Chem. Soc.* **1988**, 110, 7398–7411.
91. L. Dubois, D.-F. Xiang, X.-S. Tan et al., *Inorg. Chem.* **2003**, 42, 750–760.
92. C. Hureau, E. Anxolabéhère-Mallart, M. Nierlich et al., *Eur. J. Inorg. Chem.* **2002**, 2710–2719.
93. G. C. Dismukes, *Chem. Rev.* **1996**, 96, 2909–2926.
94. C. E. Dubé, D. W. Wright, S. Pal et al., *J. Am. Chem. Soc.* **1998**, 120, 3704–3716.
95. H. Visser, C. E. Dubé, W. H. Armstrong et al., *J. Am. Chem. Soc.* **2002**, 124, 11008–11017.
96. M. Soler, W. Wernsdorfer, K. A. Abboud et al., *J. Am. Chem. Soc.* **2003**, 125, 3576–3588.
97. R. Manchanda, H. H. Thorp, G. W. Brudvig et al., *Inorg. Chem.* **1992**, 31, 4040–4041.
98. H. H. Thorp, J. E. Sarneski, G. W. Brudvig et al., *J. Am. Chem. Soc.* **1989**, 111, 9249–9250.
99. P. A. Goodson, J. Glerup, D. J. Hodgson et al., *Inorg. Chem.* **1990**, 29, 503–508.
100. R. Manchanda, H. H. Thorp, G. W. Brudvig et al., *Inorg. Chem.* **1991**, 30, 494–497.
101. D. W. Yoder, J. Hwang, J. E. Penner-Hahn, in *Metal Ions in Biological Systems*, (Eds.: A. Sigel, H. Sigel), Marcel Dekker, Basel, Switzerland, 2000 Vol. 37, Chapter. 16.
102. M. H. Gold, H. L. Youngs, M. D. Sollewijn Gelpke, in *Metal Ions in Biological Systems*, (Eds.: A. Sigel, H. Sigel), Marcel Dekker, Basel, Switzerland, 2000 Vol. 37, Chapter. 17.
103. J. W. Whittaker, in *Metal Ions in Biological Systems*, (Eds.: A. Sigel, H. Sigel), Marcel Dekker, Basel, Switzerland, 2000 Vol. 37, Chapter. 18.
104. C. W. Hoganson, G. T. Babcock, in *Metal Ions in Biological Systems*, (Eds.: A. Sigel, H. Sigel), Marcel Dekker, Basel, Switzerland, 2000 Vol. 37, Chapter. 19.
105. D. C. Weatherburn, S. Mandel, S. Mukopadhyay et al., in *Comprehensive Coordination Chemistry II*, (Eds.: J. A. McCleverty, T. J. Meyer), 2nd ed., Elsevier, Amsterdam, 2004, pp. 100–101. Vol. 5, Chapter. 5.1.
106. V. V. Barynin, M. M. Whittaker, S. V. Antonyuk et al., *Structure* **2001**, 9, 725–738.
107. A. J. Wu, J. E. Penner-Hahn, V. L. Pecoraro, *Chem. Rev.* **2004**, 104, 903–938.
108. A. Christenson, N. Dimcheva, E. E. Fera-pontova et al., *Electroanalysis* **2004**, 16, 1074–1092.
109. D. T. Sawyer, A. Sobkowiak, J. L. Roberts Jr. *Electrochemistry for Chemists*, 2nd ed., Wiley-Intersciences, New York, 1995, Chapter. 9.
110. V. J.-P. Lévêque, C. K. Vance, H. S. Nick et al., *Biochemistry* **2001**, 40, 10586–10591.
111. Y. Tian, L. Mao, T. Okajima et al., *Anal. Chem.* **2004**, 76, 4162–4168.
112. G. D. Lawrence, D. T. Sawyer, *Biochemistry* **1979**, 18, 3045–3050.
113. R. J. Debus, in *Metal Ions in Biological Systems*, (Eds.: A. Sigel, H. Sigel), Marcel Dekker, Basel, Switzerland, 2000 Vol. 37, Chapter. 20.
114. B. Kok, B. Forbush, M. McGloin, *Photochem. Photobiol.* **1970**, 11, 457–476.
115. J. P. Hoare, in *Standard Potentials in Aqueous Solution*, (Eds.: A. J. Bard, R. Parsons, J. Jordan), Marcel Dekker, New York, 1985 Chapter. 4.
116. V. K. Yachandra, V. J. DeRose, M. J. Latimer et al., *Science* **1993**, 263, 675–679.
117. K. Wieghardt, *Angew. Chem., Int. Ed. Engl.* **1994**, 33, 725–728.
118. C. W. Hoganson, G. T. Babcock, *Science* **1997**, 277, 1953–1956.
119. C. Tommos, G. T. Babcock, *Acc. Chem. Res.* **1998**, 31, 18–25.
120. V. L. Pecoraro, M. J. Baldwin, M. T. Caudle et al., *Pure Appl. Chem.* **1998**, 70, 925–929.
121. J. Limburg, J. S. Vrettos, L. M. Liable-Sands et al., *Science* **1999**, 283, 1524–1527.
122. J. S. Vrettos, J. Limburg, G. W. Brudvig, *Biochim. Biophys. Acta* **2001**, 1503, 229–245.
123. S. Mukopadhyay, S. K. Mandal, S. Bhaduri et al., *Chem. Rev.* **2004**, 104, 3981–4026.
124. J. P. McEvoy, G. W. Brudvig, *Phys. Chem. Chem. Phys.* **2004**, 6, 4754–4763.
125. J. Messinger, *Phys. Chem. Chem. Phys.* **2004**, 6, 4764–4771.
126. P. E. M. Siegbahn, *Inorg. Chem.* **2000**, 39, 2923–2935.
127. M. Lundberg, P. E. M. Siegbahn, *Phys. Chem. Chem. Phys.* **2004**, 6, 4772–4780.
128. K. Sauer, J. Yano, V. K. Yachandra, *Photosynth. Res.* **2005**, 85, 73–86.
129. J. Barber, K. Ferreira, K. Maghlaoui et al., *Phys. Chem. Chem. Phys.* **2004**, 6, 4737–4742.

130. R. M. Cinco, J. J. Robblee, J. Messinger et al., *Biochemistry* **2004**, *43*, 13271–13282.
131. M. Haumann, C. Müller, P. Liebisch et al., *Biochemistry* **2005**, *44*, 1894–1908.
132. K. N. Ferreira, T. M. Iverson, K. Maghlaoui et al., *Science* **2004**, *303*, 1831–1838.
133. J. Biesiadka, B. Loll, J. Kern et al., *Phys. Chem. Chem. Phys.* **2004**, *6*, 4733–4736.
134. K. Sauer, V. K. Yachandra, *Proc. Natl. Acad. Sci. U.S.A.* **2002**, *99*, 8631–8636.
135. A. Mishra, W. Wernsdorfer, K. A. Abboud et al., *Chem. Commun.* **2005**, 54–56.

16.2 Technetium

16.2.1 Introduction

There are no stable isotopes of technetium. The element is obtained from fission reactions rather than from natural sources. The most commonly encountered isotopes are ^{99}Tc , a weak 292-keV β^- emitter with a half-life of 2.1×10^5 yr, and $^{99\text{m}}\text{Tc}$, a metastable form that decays to ^{99}Tc with the emission of a 140-keV γ photon with a half-life of ca 6 h. The coordination chemistry [1, 2] and electrochemistry [3] of technetium have been reviewed on several occasions.

Aside from interest in the properties of this relatively unexplored element, a primary reason for studying the electrochemistry of technetium is its utilization in nuclear medicine [4, 5]. Because of its relatively short half-life, the $^{99\text{m}}\text{Tc}$ isotope is well suited and widely applied to the radiopharmaceutical imaging of the bone and the heart, liver, kidney, and brain. The so-called first-generation imaging agents rely on the inherent biodistribution of technetium complexes (or their *in vivo* by-products) to reach an intended destination. Because this distribution varies with charge, size, lipophilicity, and other properties that depend on the oxidation state, extensive electrochemical investigations have been conducted on actual and model technetium radiopharmaceuticals [4]. More recently, second-generation imaging agents based on stable technetium complexes have emerged, which serve as a scaffold for the attachment of a biological molecule (e.g. a peptide, metallopeptide, monoclonal antibody) that can target a specific receptor site. The knowledge of

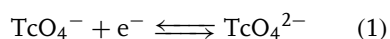
Tc redox properties, however, remains an essential component of second-generation applications.

This chapter covers the electrochemistry of technetium complexes in oxidation states I through VII and focuses on mononuclear Tc(II) through Tc(V) species that are actual or model components of radiopharmaceuticals. In addition, technetium forms mononuclear complexes with multiply bonded oxo groups, binuclear complexes with bridging oxygen atoms, and binuclear complexes with unsupported metal–metal bonds. These structural features are rare or unknown in manganese chemistry. Thus, the electrochemistry of technetium differs considerably from that of manganese but is comparable to that of its higher congener, rhenium.

16.2.2 Mononuclear Complexes

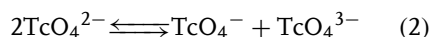
16.2.2.1 Oxo Complexes

The tetraoxo pertechnetate ion is a much less potent oxidant than its permanganate counterpart. A value of $E^{\circ'} = -1.50$ V versus NHE has been measured for the potential of the one-electron couple in Eq. (1) in CH_3CN [6].



A much more positive value of $E^{\circ'} = -0.88$ V is estimated in aqueous solution at $\text{pH} \geq 11$ by using short-time pulse techniques [7, 8]. The aqueous electrochemistry of TcO_4^- is complex. Under alkaline conditions, it is proposed that the protonation of TcO_4^{2-} and/or the expansion of its coordination shell follows Eq. (1) and produces a more easily reduced Tc(VI) species, resulting in a multielectron transfer [8]. The subsequent reduction can

be blocked by the addition of gelatin, which allows the chemical disproportionation reaction to occur:



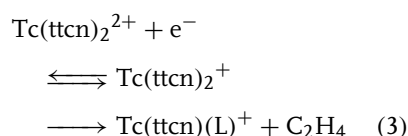
The estimated rate constant of Eq. (2) in 1 M NaOH is $k \approx 1.5 \times 10^5 \text{ M}^{-1} \text{ s}^{-1}$ [7]. In noncomplexing acid media, a three-electron reduction to Tc(IV) with the deposition of TcO_2 is observed [9].

Mononuclear oxo and nitrido complexes of Tc can be isolated with a variety of ancillary ligands. These compounds undergo reversible one-electron reactions encompassing oxidation states IV through VI [10–12] (Table 1).

16.2.2.2 Homoleptic and Mixed-ligand Complexes

A wide variety of mononuclear homoleptic and mixed-ligand technetium complexes without oxo ligands have been characterized in the oxidation states I through VI. The values of $E^{\circ'}$ for representative systems are represented in Table 1 [13–27]. The range of potentials accessible via ligand tuning for a given metal-centered redox event approaches 2 V. Soft sulfur, phosphorus, and arsenic donor ligands are notable for their ability to stabilize lower oxidation states and to produce stable complexes with biologically compatible redox potentials. The molar absorptivity of such compounds is frequently large, which enables the determination of $E^{\circ'}$ by using spectroelectrochemistry in addition to conventional voltammetric methods. The determination of $E^{\circ'}$ for the $\text{Tc}(\text{dmpe})_3^{2+/+}$ couple by using spectroelectrochemistry in an optically transparent thin-layer electrode (OTTLE) cell is illustrated in Fig. 1 [19]. As is

customary for second and third transition row elements, mononuclear Tc complexes are in the low-spin state. Hence, electron-transfer reactions proceed without large inner-shell reorganization, and electron-transfer rates are high. An exception to such a generally reversible response is the cathodic behavior of $\text{Tc}(\text{ttcn})_2^{2+}$. The reduction of this complex at +0.26 V is accompanied by the release of C_2H_4 and formation of a Tc(III) complex containing one trithiacyclononane (ttcn) and one tridentate acyclic $\text{L}^{2-} = ^-\text{SCH}_2\text{CH}_2\text{SCH}_2\text{CH}_2\text{S}^-$ ligand [17]:



The reliable prediction of redox potentials as a function of composition is useful in the synthetic design and application of technetium and other transition metal complexes. A parametric procedure for doing so on the basis of ligand additivity principles has been developed by Lever [28]. Lu et al. [29] used this scheme to correlate $\text{Tc}^{\text{IV/III}}$, $\text{Tc}^{\text{III/II}}$, and $\text{Tc}^{\text{II/I}}$ potentials with the composition of octahedral technetium complexes containing halide, nitrogen, and phosphorus donor ligands. The results are illustrated in Fig. 2 [29], where the observed potentials are plotted according to

$$E_{\text{obs}}^{\circ'} = S_{\text{M}}[\Sigma E_{\text{L}}(\text{L})] + I_{\text{M}} \quad (4)$$

where S_{M} and I_{M} are the slope and intercept of the correlation line and $\Sigma E_{\text{L}}(\text{L})$ is the sum of the ligand parameters. It is assumed that S_{M} and I_{M} are constant for a given metal and oxidation state, provided the coordination number, stereochemistry, and spin state do not

Tab. 1 Electrochemical data for mononuclear technetium complexes

Oxidation state change	Tc coordinate shell	Electrode reaction	Solvent/supporting electrolyte	$E^{\circ'}$, V versus NHE	References
<i>Oxo and nitrido complexes</i>					
VII/VI	O ₄	$\text{TcO}_4^- \rightleftharpoons \text{TcO}_4^{2-}$	CH ₃ CN/0.05 M TMAIO ₄	-1.50	6
VII/VI	O ₄	$\text{TcO}_4^- \rightleftharpoons \text{TcO}_4^{2-}$	H ₂ O/pH 12	-0.64	7, 8
VI/V	NCl ₄	$\text{TcNCl}_4^- + e^- \rightleftharpoons \text{TcNCl}_4^{2-}$	CH ₂ Cl ₂ /TBAPF ₆	+0.45	10
VI/V	OCl ₄	$\text{TcOCl}_4 + e^- \rightleftharpoons \text{TcOCl}_4^-$	CH ₂ Cl ₂ /TBAPF ₆	+2.08	10
V/V	OS ₄	$\text{TcO}(\text{mnt})_2^- + e^- \rightleftharpoons \text{TcO}(\text{mnt})_2^{2-}$	CH ₃ CN/0.1 M TBACIO ₄	-0.40	11
V/V	ON ₂ O ₃	$\text{TcO}(\delta\text{-Q})(\text{SB}) + e^- \rightleftharpoons \text{TcO}(\delta\text{-Q})(\text{SB})^-$	CH ₃ CN/0.1 M TEACIO ₄	-0.28	12
<i>Homoleptic complexes</i>					
VI/V	O ₆	$\text{Tc}(\text{DTBCat})_3 + e^- \rightleftharpoons \text{Tc}(\text{DTBCat})_3^-$	CH ₂ Cl ₂ /TBAPF ₆	+0.28	13
V/V	O ₆	$\text{Tc}(\text{mepp})_3^{2+} + e^- \rightleftharpoons \text{Tc}(\text{mepp})_3^+$	CH ₃ CN/0.1 M TEACIO ₄	+1.27	14
V/V	O ₆	$\text{Tc}(\text{DTBCat})_3^- + e^- \rightleftharpoons \text{Tc}(\text{DTBCat})_3^{2-}$	CH ₂ Cl ₂ /TBAPF ₆	-0.39	13
IV/III	N ₆	$\text{Tc}(\text{NCS})_6^{2-} + e^- \rightleftharpoons \text{Tc}(\text{NCS})_6^{3-}$	CH ₃ CN/0.1 M TBACIO ₄	+0.42	15
IV/III	O ₆	$\text{Tc}(\text{mepp})_3^+ + e^- \rightleftharpoons \text{Tc}(\text{mepp})_3$	CH ₃ CN/0.1 M TEACIO ₄	-0.54	13
III/II	S ₆	$\text{Tc}(\text{ttcn})_2^{3+} + e^- \rightleftharpoons \text{Tc}(\text{ttcn})_2^{2+}$	CH ₃ CN	+1.51	16, 17
II/I	C ₆	$\text{Tc}(\text{CNMe})_6^{2+} + e^- \rightleftharpoons \text{Tc}(\text{CNMe})_6^+$	CH ₃ CN/TEACIO ₄	+1.06	18
II/I	P ₆	$\text{Tc}(\text{dmpe})_3^{2+} + e^- \rightleftharpoons \text{Tc}(\text{dmpe})_3^+$	DMF/0.5 M TEACIO ₄	+0.62	19
II/I	S ₆	$\text{Tc}(\text{ttcn})_2^{2+} + e^- \rightleftharpoons \text{Tc}(\text{ttcn})_2^+$	CH ₃ CN	+0.26 (irr) ^a	17
<i>Mixed-ligand complexes</i>					
V/IV	P ₃ S ₃	$\text{Tc}(\text{2-Ph}_2\text{PC}_6\text{H}_4\text{S})_3^{2+} + e^- \rightleftharpoons \text{Tc}(\text{2-Ph}_2\text{PC}_6\text{H}_4\text{S})_3^+$	CH ₂ Cl ₂ /TBABF ₄	+1.91	20
IV/III	N ₄ Cl ₂	$\text{Tc}(\text{Me}_2\text{bpy})_2\text{Cl}_2^{2+} + e^- \rightleftharpoons \text{Tc}(\text{Me}_2\text{bpy})_2\text{Cl}_2^+$	DMA/0.5 M TBAPF ₆	+1.13	21
IV/III	N ₄ Cl ₂	$\text{Tc}(\text{py})_4\text{Cl}_2^{2+} + e^- \rightleftharpoons \text{Tc}(\text{py})_4\text{Cl}_2^+$	DMA/0.5 M TBAPF ₆	+1.34	21
IV/III	N ₃ Cl ₃	$\text{Tc}(\text{terpy})\text{Cl}_3^+ + e^- \rightleftharpoons \text{Tc}(\text{terpy})\text{Cl}_3$	DMA/0.5 M TBAPF ₆	+0.67	21
IV/III	N ₃ Cl ₃	$\text{Tc}(\text{py})_3\text{Cl}_3^+ + e^- \rightleftharpoons \text{Tc}(\text{py})_3\text{Cl}_3$	DMA/0.5 M TBAPF ₆	+0.79	21
IV/III	N ₂ P ₂ Cl ₂	$\text{Tc}(\text{bpy})(\text{PMe}_2\text{Ph})_2\text{Cl}_2^{2+} + e^- \rightleftharpoons \text{Tc}(\text{bpy})(\text{PMe}_2\text{Ph})_2\text{Cl}_2^+$	CH ₃ CN/0.1 M TEACIO ₄	+1.27	22
IV/III	N ₂ P ₂ O ₂	$\text{Tc}(\text{PPh}_3)_2(\text{acac})_2\text{en}^{2+} + e^- \rightleftharpoons \text{Tc}(\text{PPh}_3)_2(\text{acac})_2\text{en}^+$	PC/0.1 M TEACIO ₄	+0.92	23

(continued overleaf)

Tab. 1 (continued)

Oxidation state change	Tc coordinate shell	Electrode reaction	Solvent/supporting electrolyte	E° , V versus NHE	References
IV/III	P ₃ S ₃	$\text{Tc}(2\text{-Ph}_2\text{PC}_6\text{H}_4\text{S})_3^+ + \text{e}^- \rightleftharpoons \text{Tc}(2\text{-Ph}_2\text{PC}_6\text{H}_4\text{S})_3$	CH ₂ Cl ₂ /TBABF ₄	+1.16	20
IV/III	P ₄ S ₂	$\text{Tc}(\text{dmpe})_2(\text{tdt})^{2+} + \text{e}^- \rightleftharpoons \text{Tc}(\text{dmpe})_2(\text{tdt})^+$	DMF/0.5 M TEAClO ₄	+0.88	24
IV/III	As ₄ S ₂	$\text{Tc}(\text{diars})_2(\text{SPh})_2^{2+} + \text{e}^- \rightleftharpoons \text{Tc}(\text{diars})_2(\text{SPh})_2^+$	DMF/0.5 M TEAClO ₄	+1.14	25
III/II	N ₅ Cl	$\text{Tc}(\text{py})_5\text{Cl}^{2+} + \text{e}^- \rightleftharpoons \text{Tc}(\text{py})_5\text{Cl}^+$	DMA/0.5 M TBAPF ₆	+0.09	21
III/II	N ₄ Cl ₂	$\text{Tc}(\text{Me}_2\text{bpy})_2\text{Cl}_2^+ + \text{e}^- \rightleftharpoons \text{Tc}(\text{Me}_2\text{bpy})_2\text{Cl}_2$	DMA/0.5 M TBAPF ₆	-0.16	21
III/II	N ₄ Cl ₂	$\text{Tc}(\text{py})_4\text{Cl}_2^+ + \text{e}^- \rightleftharpoons \text{Tc}(\text{py})_4\text{Cl}_2$	DMA/0.5 M TBAPF ₆	-0.38	21
III/II	N ₃ Cl ₃	$\text{Tc}(\text{terpy})\text{Cl}_3 + \text{e}^- \rightleftharpoons \text{Tc}(\text{terpy})\text{Cl}_3^-$	DMA/0.5 M TBAPF ₆	-0.34	21
III/II	N ₃ Cl ₃	$\text{Tc}(\text{py})_3\text{Cl}_3 + \text{e}^- \rightleftharpoons \text{Tc}(\text{py})_3\text{Cl}_3^-$	DMA/0.5 M TBAPF ₆	-0.79	21
III/II	N ₂ P ₂ Cl ₂	$\text{Tc}(\text{bpy})(\text{PMe}_2\text{Ph})_2\text{Cl}_2^+ + \text{e}^- \rightleftharpoons \text{Tc}(\text{bpy})(\text{PMe}_2\text{Ph})_2\text{Cl}_2$	CH ₃ CN/0.1 M TEAClO ₄	+0.11	22
III/II	N ₂ P ₂ O ₂	$\text{Tc}(\text{PPh}_3)_2(\text{acac})_2\text{en}^+ + \text{e}^- \rightleftharpoons \text{Tc}(\text{PPh}_3)_2(\text{acac})_2\text{en}$	PC/0.1 M TEAClO ₄	-0.69	23
III/II	P ₃ S ₃	$\text{Tc}(2\text{-Ph}_2\text{PC}_6\text{H}_4\text{S})_3 + \text{e}^- \rightleftharpoons \text{Tc}(2\text{-Ph}_2\text{PC}_6\text{H}_4\text{S})_3^-$	CH ₂ Cl ₂ /TBABF ₄	+0.06	20
III/II	P ₄ S ₂	$\text{Tc}(\text{depe})_2(\text{Et}_2\text{dtc})^{2+} + \text{e}^- \rightleftharpoons \text{Tc}(\text{depe})_2(\text{Et}_2\text{dtc})^+$	DMF/0.5 M TEAClO ₄	+0.51	26
III/II	P ₄ S ₂	$\text{Tc}(\text{dmpe})_2(\text{tdt})^+ + \text{e}^- \rightleftharpoons \text{Tc}(\text{dmpe})_2(\text{tdt})$	DMF/0.5 M TEAClO ₄	-0.40	24
III/II	P ₄ Cl ₂	$\text{Tc}(\text{dmpe})_2\text{Cl}_2^+ + \text{e}^- \rightleftharpoons \text{Tc}(\text{dmpe})_2\text{Cl}_2$	DMF/0.5 M TEAClO ₄	-0.03	19
III/II	As ₄ S ₂	$\text{Tc}(\text{diars})_2(\text{SPh})_2^+ + \text{e}^- \rightleftharpoons \text{Tc}(\text{diars})_2(\text{SPh})_2$	DMF/0.5 M TEAClO ₄	-0.12	25
III/II	As ₄ Cl ₂	$\text{Tc}(\text{diars})_2\text{Cl}_2^+ + \text{e}^- \rightleftharpoons \text{Tc}(\text{diars})_2\text{Cl}_2$	DMF/0.5 M TEAClO ₄	+0.14	25, 27
II/I	N ₅ Cl	$\text{Tc}(\text{py})_5\text{Cl}^+ + \text{e}^- \rightleftharpoons \text{Tc}(\text{py})_5\text{Cl}$	DMA/0.5 M TBAPF ₆	-0.84	21
II/I	N ₄ Cl ₂	$\text{Tc}(\text{py})_4\text{Cl}_2 + \text{e}^- \rightleftharpoons \text{Tc}(\text{py})_4\text{Cl}_2^-$	DMA/0.5 M TBAPF ₆	-1.33	21
II/I	N ₃ Cl ₃	$\text{Tc}(\text{py})_3\text{Cl}_3^- + \text{e}^- \rightleftharpoons \text{Tc}(\text{py})_3\text{Cl}_3^{2-}$	DMA/0.5 M TBAPF ₆	-1.72	21
II/I	P ₄ S ₂	$\text{Tc}(\text{depe})_2(\text{Et}_2\text{dtc})^+ + \text{e}^- \rightleftharpoons \text{Tc}(\text{depe})_2(\text{Et}_2\text{dtc})$	DMF/0.5 M TEAClO ₄	-0.34	26
II/I	P ₄ S ₂	$\text{Tc}(\text{dmpe})_2(\text{tdt}) + \text{e}^- \rightleftharpoons \text{Tc}(\text{dmpe})_2(\text{tdt})^-$	DMF/0.5 M TEAClO ₄	-1.02	24
II/I	P ₄ Cl ₂	$\text{Tc}(\text{dmpe})_2\text{Cl}_2 + \text{e}^- \rightleftharpoons \text{Tc}(\text{dmpe})_2\text{Cl}_2^-$	DMF/0.5 M TEAClO ₄	-1.21	19
II/I	As ₄ S ₂	$\text{Tc}(\text{diars})_2(\text{SPh})_2 + \text{e}^- \rightleftharpoons \text{Tc}(\text{diars})_2(\text{SPh})_2^-$	DMF/0.5 M TEAClO ₄	-1.02	25
II/I	As ₄ Cl ₂	$\text{Tc}(\text{diars})_2\text{Cl}_2 + \text{e}^- \rightleftharpoons \text{Tc}(\text{diars})_2\text{Cl}_2^-$	DMF/0.5 M TEAClO ₄	-1.06	25, 27

^a Irreversible reduction (see text).

Fig. 1 Spectroelectrochemical characterization of the $\text{Tc}(\text{dmpe})_2^{2+/+}$ redox couple in 0.5 M TEAClO_4 /propylene carbonate. Applied potential in V versus NHE for traces (a)–(j) – +0.80, +0.60, +0.58, +0.56, +0.54, +0.52, +0.50, +0.48, +0.46, and +0.30. For $\text{Tc}(\text{dmpe})_2^{2+/+}$ in propylene carbonate, $E^\circ = +0.53$ V (reprinted with permission from Ref. 19, Copyright 1984 American Chemical Society).

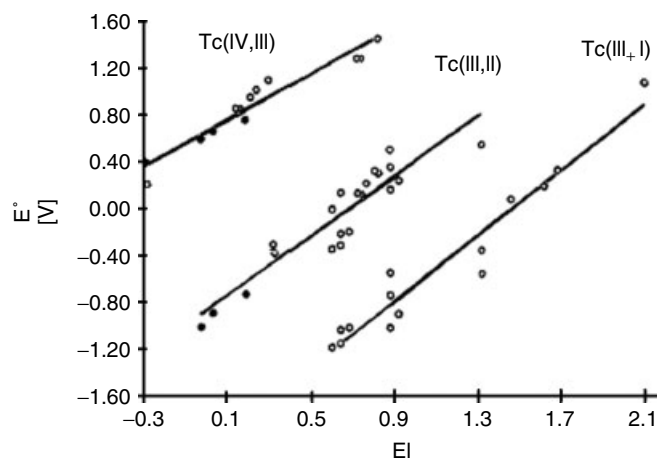
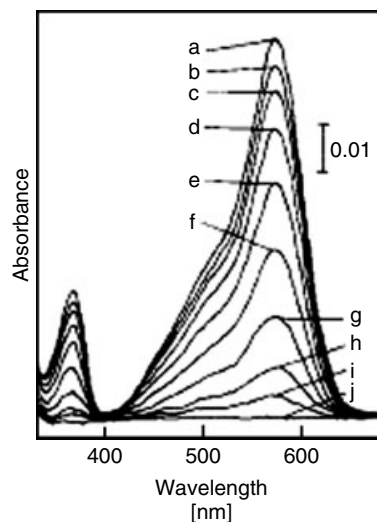


Fig. 2 Plots of E° for $\text{Tc}^{\text{IV/III}}$, $\text{Tc}^{\text{III/II}}$, and $\text{Tc}^{\text{II/I}}$ redox couples versus the sum of ligand parameters, according to Eq. (4) (reprinted with permission from Ref. 29, Copyright 1990 American Chemical Society).

change. Figure 2 shows an excellent correlation with the predictions. The plots for the $\text{Tc}^{\text{IV/III}}$, $\text{Tc}^{\text{III/II}}$, and $\text{Tc}^{\text{II/I}}$ couples are linear and nearly parallel. The slopes of $S_M = 1.00 \pm 0.10$, 1.29 ± 0.08 , and 1.39 ± 0.12 , respectively, are quite large relative to values of other transition elements and indicate an excellent means

of modulating technetium-based redox potentials through the adjustment of ligand composition.

In some cases, agreement with the predictions of the Lever parameterization scheme is not exact. For example, Table 1 shows that the $\text{Tc}^{\text{III/II}}$ potentials of $\text{Tc}(\text{Me}_2\text{bpy})_2\text{Cl}_2^{+/0}$ and $\text{Tc}(\text{terpy})\text{Cl}_3^{0/-}$

are 0.22 and 0.45 V more positive than the values for $\text{Tc}(\text{py})_4\text{Cl}_2^{+/0}$ and $\text{Tc}(\text{py})_3\text{Cl}_3^{0/-}$ [21]. Such differences are not observed for the corresponding $\text{Tc}^{\text{IV/III}}$ potentials. Because py, bpy, and terpy have nearly identical ligand parameters per diimine N donor [28], these results indicate that polypyridyl ligands are more effective than a comparable number of monopyridines in stabilizing $\text{Tc}(\text{II})$ versus $\text{Tc}(\text{III})$.

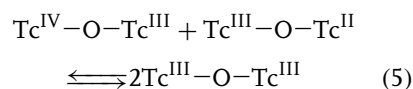
16.2.3

Binuclear Complexes

16.2.3.1 Oxo-bridged Complexes

Technetium forms a number of binuclear complexes in which the metal atoms are joined by a single oxygen bridge and do not contain any multiply bonded oxo groups (1, Chart 1). These complexes undergo reversible electron transfers encompassing the $\text{Tc}^{\text{IV}}-\text{O}-\text{Tc}^{\text{IV}}$, $\text{Tc}^{\text{IV}}-\text{O}-\text{Tc}^{\text{III}}$, $\text{Tc}^{\text{III}}-\text{O}-\text{Tc}^{\text{III}}$, and $\text{Tc}^{\text{III}}-\text{O}-\text{Tc}^{\text{II}}$ oxidation states. As shown by the examples in Table 2 [30, 31], experimentally observed redox potentials and oxidation states depend significantly on the ligands bound to the $\text{Tc}-\text{O}-\text{Tc}$ unit. The replacement of a diimine nitrogen donor with a monodentate, negatively charged ligand shifts the potential in the negative direction and stabilizes the higher oxidation state.

An interesting result in Table 2 is the large difference between $E^{\circ'}_{(\text{IV,III})/(\text{III,III})}$ and $E^{\circ'}_{(\text{III,III})/(\text{III,II})}$ for the oxo-bridged complexes in comparison to the adjacent values $E^{\circ'}_{(\text{IV,IV})/(\text{IV,III})} - E^{\circ'}_{(\text{IV,III})/(\text{III,III})}$ and $E^{\circ'}_{(\text{III,III})/(\text{III,II})} - E^{\circ'}_{(\text{III,II})/(\text{II,II})}$. The values of $\Delta E^{\circ'} = E^{\circ'}_{(\text{IV,III})/(\text{III,III})} - E^{\circ'}_{(\text{III,III})/(\text{III,II})}$ range from 1.27 to 1.39 V. These differences correspond to disproportionation constants, $K_{\text{com}} = \exp(F\Delta E^{\circ'}/RT)$, for the equilibrium reaction



on the order of 10^{21} to 10^{23} . Such values suggest a large thermodynamic stabilization of the $(d^4) \text{Tc}^{\text{III}}-\text{O}-\text{Tc}^{\text{III}}$ (d^4) oxidation state, which presumably is promoted by the single μ -oxo bridge.

16.2.3.2 Metal-metal-bonded Complexes

The octachloroditechnetate ion, $\text{Tc}_2\text{Cl}_8^{2-}$, was among the first compounds recognized as containing a metal-metal quadruple bond [32]. The electrochemical data for this and several other metal-metal-bonded Tc_2 complexes are represented in Table 2 [32–35]. Ligands bind at the equatorial positions around each metal in the

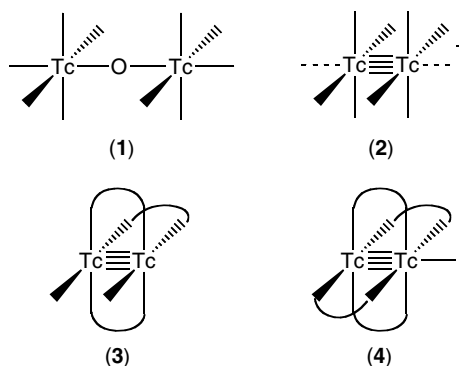


Chart 1 Structures of binuclear technetium centers.

Tab. 2 Electrochemical data for binuclear oxo-bridged and metal–metal-bonded technetium complexes

<i>Tc(III,III) complex</i>	<i>Solvent/supporting electrolyte</i>	<i>E°', V versus NHE</i>					<i>References</i>
		(IV,IV)/ (IV,III)	(IV,III)/ (III,III)	(III,III)/ (III,II)	(III,II)/ (II,II)	(II,II)/ (I,I)	
<i>Oxo-bridged complexes</i>							
$\text{Tc}_2\text{O}(\text{tpy})_2(\text{Me}_2\text{bpy})_2^{4+}$	DMA/TBAPF ₆		+1.24	−0.14	−0.39		30
$\text{Tc}_2\text{O}(\text{bpy})_4\text{Cl}_2^{2+}$	$\text{CH}_3\text{CN}/0.1 \text{ M TEAClO}_4$	+1.53	+0.86	−0.38 ^a			31
$\text{Tc}_2\text{O}(\text{bpy})_4\text{Br}_2^{2+}$	$\text{CH}_3\text{CN}/0.1 \text{ M TEAClO}_4$	+1.56	+0.90	−0.37 ^a			31
$\text{Tc}_2\text{O}(\text{phen})_4(\text{OH})_2^{2+}$	$\text{CH}_3\text{CN}/0.1 \text{ M TEAClO}_4$	+1.53	+0.86	−0.53			31
<i>Metal–metal-bonded complexes</i>							
$\text{Tc}_2\text{Cl}_8^{2-}$	EtOH/10 vol% 12 M HCl			+0.38			32
$\text{Tc}_2\text{Cl}_4(\text{PEt}_2)_4^{2+}$	$\text{CH}_2\text{Cl}_2/0.2 \text{ M TBAPF}_4$			+1.58	+0.22		33
$\text{Tc}_2(\text{CH}_3\text{CN})_{10}^{4+}$	$\text{CH}_3\text{CN}/0.1 \text{ M TBAPF}_6$				−0.18	−0.92(irr) ^b	34
$\text{Tc}_2(\text{DPhF})_3\text{Cl}_2$	$\text{CH}_2\text{Cl}_2/0.1 \text{ M TBAPF}_6$			+0.70	−0.80		35
$\text{Tc}_2(\text{DPhF})_4\text{Cl}$	$\text{CH}_2\text{Cl}_2/0.1 \text{ M TBAPF}_6$			+0.34	−1.03		35

^a $\text{H}_2\text{O}/0.1 \text{ M LiCl}$.^b Irreversible reduction (see text).

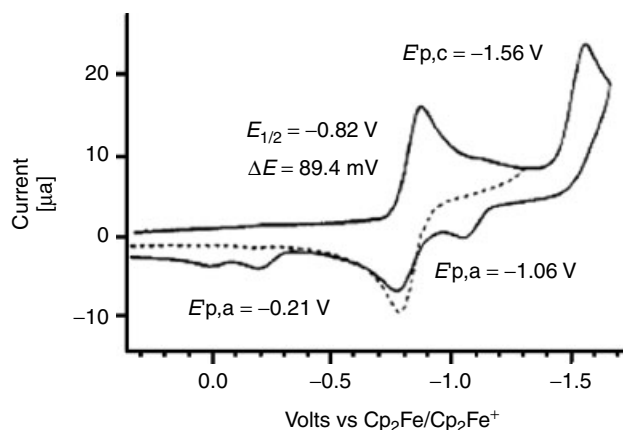


Fig. 3 Cyclic voltammetric reduction of $\text{Tc}_2(\text{CH}_3\text{CN})_{10}^{4+}$ at $\nu = 0.2 \text{ V s}^{-1}$ in $\text{CH}_3\text{CN}/0.1 \text{ M TBAPF}_6$ (reprinted with permission from Ref. 34, Copyright 1995 American Chemical Society).

Tc_2^{n+} unit (**2**) and in some instances at the axial positions as well. Axial binding is weak, as exemplified by $\text{Tc}_2(\text{CH}_3\text{CN})_{10}^{4+}$, where the CH_3CN ligands at these positions exchange rapidly with the solvent molecules [34]. Some bidentate ligands, such as diphenylformamidinate ($\text{DPhF}^- = \text{C}_6\text{H}_5\text{NHCHNHC}_6\text{H}_5^-$), can bridge the metal centers, resulting in structures with three paddlewheel units and one Cl^- bound to each metal ($\text{Tc}_2(\text{DPhF})_3\text{Cl}_2$, **3**) or four paddlewheel units and a single axial Cl^- ($\text{Tc}_2(\text{DPhF})_4\text{Cl}$, **4**) [35].

Quadruply bonded $\text{Tc}_2^{\text{III,III}}$ has the electron configuration $\sigma^2\pi^4\delta^2$. Reduction produces $\text{Tc}_2^{\text{III,II}}$, $\text{Tc}_2^{\text{II,II}}$, $\text{Tc}_2^{\text{II,I}}$, and $\text{Tc}_2^{\text{I,I}}$ centers, with configurations of $\sigma^2\pi^4\delta^2\delta^*$, $\sigma^2\pi^4\delta^2\delta^{*2}$, $\sigma^2\pi^4\delta^2\delta^{*2}\pi^*$, and $\sigma^2\pi^4\delta^2\delta^{*2}\pi^{*2}$ and metal–metal bond orders of 3.5, 3.0, 2.5, and 2.0, respectively. Exemplary data for several compounds of this type are presented in Table 2. Triply bonded $\text{Tc}_2^{\text{II,II}}(\text{CH}_3\text{CN})_{10}^{4+}$ undergoes reversible one-electron reduction to the uncommon $\sigma^2\pi^4\delta^2\delta^{*2}\pi^*$ state (Fig. 3) [34]. However, further reduction

weakens the metal–metal bond to the point that the complex is not chemically stable.

References

1. F. A. Cotton, G. Wilkinson, C. A. Murillo et al., *Advanced Inorganic Chemistry*, 6th ed., John Wiley & Sons, New York, 1999, pp. 974–1000.
2. R. Alberto, in *Comprehensive Coordination Chemistry II*, (Eds.: J. A. McCleverty, T. J. Meyer), 2nd ed., Elsevier, Amsterdam, 2004, Vol. 5, Chapter. 5.2.
3. R. J. Magee, T. J. Cardwell, in *Encyclopedia of Electrochemistry of the Elements*, (Ed.: A. J. Bard), Marcel Dekker, New York, 1973 Vol. 2, Chapter. II-4.
4. E. Deutsch, K. L. Libson, S. Jurisson et al., *Prog. Inorg. Chem.* **1983**, 30, 75–139.
5. M. J. Clarke, L. Podbielski, *Coord. Chem. Rev.* **1987**, 89, 253–331.
6. L. Astheimer, K. Schwochau, *J. Inorg. Nucl. Chem.* **1976**, 38, 1131–1134.
7. G. Kissel, S. W. Feldberg, *J. Phys. Chem.* **1969**, 73, 3082–3088.
8. A. Founta, D. A. Aikens, H. M. Clark, *J. Electroanal. Chem.* **1987**, 219, 221–246.
9. B. L. Lawson, S. M. Scheiffers, T. C. Pinkerton, *J. Electroanal. Chem.* **1984**, 177, 167–181.

10. J. Baldas, G. A. Heath, S. A. Macgregor et al., *J. Chem. Soc., Dalton Trans.* **1998**, 2303–2314.
11. A. Davison, C. Orvig, H. S. Trop et al., *Inorg. Chem.* **1980**, 19, 1988–1992.
12. F. Refosco, U. Mazzi, E. Deutsch et al., *Inorg. Chem.* **1988**, 27, 4121–4127.
13. L. A. de Learie, R. C. Haltiwanger, C. G. Pierpont, *J. Am. Chem. Soc.* **1989**, 111, 4324–4328.
14. D. S. Edwards, S. Liu, M. J. Poirier et al., *Inorg. Chem.* **1994**, 33, 5607–5609.
15. H. S. Trop, A. Davison, A. G. Jones et al., *Inorg. Chem.* **1980**, 19, 1105–1110.
16. D. J. White, H.-J. Küppers, A. J. Edwards et al., *Inorg. Chem.* **1992**, 31, 5351–5352.
17. G. E. D. Mullen, P. J. Blower, D. J. Price et al., *Inorg. Chem.* **2000**, 39, 4093–4098.
18. M. J. Abrams, A. Davison, A. G. Jones et al., *Inorg. Chem.* **1983**, 22, 2798–2800.
19. A. Ichimura, W. R. Heineman, J.-L. Vanderheyden et al., *Inorg. Chem.* **1984**, 23, 1272–1278.
20. J. R. Dilworth, A. J. Hutson, S. Morton et al., *Polyhedron* **1992**, 11, 2151–2155.
21. J. Barrera, A. K. Burrell, J. C. Bryan, *Inorg. Chem.* **1996**, 35, 335–341.
22. B. E. Wilcox, E. Deutsch, *Inorg. Chem.* **1991**, 30, 688–693.
23. A. Ichimura, W. R. Heineman, E. Deutsch, *Inorg. Chem.* **1985**, 25, 2134–2139.
24. T. Konno, J. R. Kirchoff, M. J. Heeg et al., *J. Chem. Soc., Dalton Trans.* **1992**, 3069–3075.
25. T. Konno, M. J. Heeg, J. A. Stuckey et al., *Inorg. Chem.* **1992**, 31, 1173–1181.
26. K.-I. Okamoto, B. Chen, J. R. Kirchoff et al., *Polyhedron* **1993**, 12, 1559–1568.
27. R. W. Hurst, W. R. Heineman, E. Deutsch, *Inorg. Chem.* **1981**, 20, 3298–3303.
28. A. B. P. Lever, *Inorg. Chem.* **1990**, 29, 1271–1285.
29. J. Lu, A. Yamano, M. J. Clarke, *Inorg. Chem.* **1990**, 29, 3483–3487.
30. J. Barrera, J. C. Bryant, *Inorg. Chem.* **1996**, 35, 1825–1830.
31. J. Lu, C. D. Hiller, M. J. Clarke, *Inorg. Chem.* **1993**, 32, 1417–1423.
32. F. A. Cotton, E. Pedersen, *Inorg. Chem.* **1975**, 14, 383–387.
33. C. J. Burns, A. K. Burrell, F. A. Cotton et al., *Inorg. Chem.* **1994**, 33, 2257–2264.
34. J. C. Bryan, F. A. Cotton, L. M. Daniels et al., *Inorg. Chem.* **1995**, 34, 1875–1883.
35. F. A. Cotton, S. C. Haefner, A. P. Sattelberger, *Inorg. Chem.* **1996**, 35, 7530–7537.

16.3 Rhenium

16.3.1 Introduction

Rhenium is a rare element, having eluded discovery until 1925. Its chemistry [1, 2] and electrochemistry [3, 4] have been reviewed on previous occasions. The properties of Re compounds closely parallel those of Tc, and, although many comparative studies have been conducted on the two elements, the rhenium literature is the more extensive. The properties of both elements are quite distinct from those of manganese.

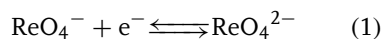
Interest in the electrochemistry of rhenium derives in part from its role in nuclear medicine [5], where compounds containing the high-energy, β^- -emitting ^{186}Re and ^{188}Re isotopes find use in the radiation therapy of cancer. As is the case for technetium, the electrochemical properties are helpful in projecting the distribution and stability of these radiopharmaceuticals in a biological environment. Also, the investigation of nonradioactive Re compounds provides a useful guide to the behavior of radioactive Tc congeners. Although similar in many respects – especially with regard to homoleptic and other mononuclear complexes – Re compounds generally are less oxidizing and kinetically more inert than their Tc analogs. Other distinguishing characteristics of rhenium include (1) the existence of high-valent mononuclear oxo complexes, whose aqueous electrochemical behavior provides useful insight to coupled electron-proton transfer reactions [6]; (2) the formation of hydride complexes exhibiting well-defined electrochemistry [7]; (3) the incorporation in supramolecular arrays, which have applications in

molecular sieving, sensing, and catalysis [8]; and (4) the utilization as a catalyst for photo- or electrochemically initiated carbon dioxide reduction [9].

16.3.2 Mononuclear Complexes

16.3.2.1 Oxo Complexes

A value of $E^{\circ'} = -2.06$ V versus NHE has been measured for one-electron reduction of the perrhenate ion, ReO_4^- , in CH_3CN (Eq. 1) [10], although the flow of additional current on the plateau of the wave indicates that the initial electrode product is not chemically stable.



The electrochemical behavior of ReO_4^- in aqueous solution is irreversible and not well-characterized. The estimated one-electron potential for the $\text{ReO}_4^-/^{2-}$ couple in aqueous alkaline solution [3] (Table 1) is slightly more negative than that for $\text{TcO}_4^-/^{2-}$ (Table 1 of Sect. 16.2). In aqueous acid media, reduction is thought to proceed by a two-electron transfer from Re(VII) to Re(V) [11], followed by disproportionation and formation of ReO_2 [12].

Rhenium forms a number of mono-oxo, *cis*-dioxo, and *trans*-dioxo complexes in oxidation states IV through VII. Reversible, proton-independent, one-electron potentials for several systems are represented in Table 1 [13–22, 35, 36]. As is the case for Tc, a large change in $E^{\circ'}$ for a given redox step can be produced by changing the ancillary ligands.

Of particular interest are the proton-coupled multielectron transfers of high-valent oxorhenium (poly)pyridyl complexes [6, 15–18, 35]. This behavior is

Tab. 1 Electrochemical data for mononuclear rhenium complexes

Oxidation state change	Re coordinate shell	Electrode reaction	Solvent/supporting electrolyte	E° , V versus NHE	References
<i>Oxo complexes</i>					
VII/VI	O ₄	$\text{ReO}_4^- + e^- \rightleftharpoons \text{ReO}_4^{2-}$	CH ₃ CN/0.05 M TEAClO ₄	-2.06	10
VII/VI	O ₄	$\text{ReO}_4^- + e^- \rightleftharpoons \text{ReO}_4^{2-}$	H ₂ O (alkaline)	-0.70	3
VII/VI	O ₂ N ₃ Cl	$\text{c-ReO}_2(\text{Tp})\text{Cl}^+ + e^- \rightleftharpoons \text{c-ReO}_2(\text{Tp})\text{Cl}$	CH ₃ CN/0.1 M TBAPF ₆	+1.57	13
VII/VI	O ₂ O ₄	$\text{c-ReO}_2(\text{DTBcat})_2^- + e^- \rightleftharpoons \text{c-ReO}_2(\text{DTBcat})_2^{2-}$	CH ₃ CN/0.2 M TBABF ₄	-0.77	14
VI/V	O ₂ N ₄	$\text{t-ReO}_2(\text{py})_4^{2+} + e^- \rightleftharpoons \text{t-ReO}_2(\text{py})_4^+$	CH ₃ CN/0.1 M TBAPF ₆	+1.61	15
VI/V	O ₂ N ₄	$\text{t-ReO}_2(\text{py})_4^{2+} + e^- \rightleftharpoons \text{t-ReO}_2(\text{py})_4^+$	H ₂ O/pH 2	+1.49	16, 17
VI/V	O ₂ N ₄	$\text{c-ReO}_2(\text{bpy})(\text{py})_2^{2+} + e^- \rightleftharpoons \text{c-ReO}_2(\text{bpy})(\text{py})_2^+$	CH ₃ CN/0.1 M TBAPF ₆	+1.01	15
VI/V	O ₂ N ₄	$\text{c-ReO}_2(\text{bpy})(\text{py})_2^{2+} + e^- \rightleftharpoons \text{c-ReO}_2(\text{bpy})(\text{py})_2^+$	H ₂ O/pH 2	+0.87	17
VI/V	O ₂ N ₄	$\text{c-ReO}_2(\text{bpy})(\text{py})_2^{2+} + e^- \rightleftharpoons \text{c-ReO}_2(\text{bpy})(\text{py})_2^+$	CH ₃ CN/0.1 M TBAPF ₆	+2.44	18
VI/V	ON ₄ O	$\text{t-ReO}(\text{OMe})(4\text{-Mepy})_4^{3+} + e^- \rightleftharpoons \text{t-ReO}(\text{OMe})(4\text{-Mepy})_4^{2+}$	CH ₃ CN/0.1 M TBAPF ₆	+1.22	19
VI/V	ON ₂ O ₂ Cl	$\text{ReO}(\text{hoz})_2\text{Cl}^+ + e^- \rightleftharpoons \text{ReO}(\text{hoz})_2\text{Cl}$	CH ₃ CN/0.1 M TBAPF ₆	-0.50	18
V/IV	ON ₄ O	$\text{t-ReO}(\text{OMe})(4\text{-Mepy})_4^{2+} + e^- \rightleftharpoons \text{t-ReO}(\text{OMe})(4\text{-Mepy})_4^+$	CH ₃ CN/0.1 M TEAClO ₄	-0.74	20
V/IV	ON ₂ O ₃	$\text{ReO}(\text{g-Q})(\text{SB}) + e^- \rightleftharpoons \text{ReO}(\text{g-Q})(\text{SB})^-$	CH ₃ CN/0.2 M TBABF ₄	-1.74	21
V/IV	ON ₃ O ₂	$\text{ReO}(\text{pzTp})(\text{OCH}_2\text{CH}_2\text{O}) + e^- \rightleftharpoons \text{ReO}(\text{pzTp})(\text{OCH}_2\text{CH}_2\text{O})^-$	CH ₃ CN/0.2 M TBABF ₄	-1.38	21
V/IV	ON ₃ OS	$\text{ReO}(\text{pzTp})(\text{OCH}_2\text{CH}_2\text{S}) + e^- \rightleftharpoons \text{ReO}(\text{pzTp})(\text{OCH}_2\text{CH}_2\text{S})^-$	CH ₃ CN/0.2 M TBABF ₄	-1.18	21
V/IV	ON ₃ S ₂	$\text{ReO}(\text{pzTp})(\text{SCH}_2\text{CH}_2\text{S}) + e^- \rightleftharpoons \text{ReO}(\text{pzTp})(\text{SCH}_2\text{CH}_2\text{S})^-$	CH ₃ CN/0.1 M TBAClO ₄	-0.81	22
V/IV	OS ₄	$\text{ReO}(\text{mnt})_2^- + e^- \rightleftharpoons \text{ReO}(\text{mnt})_2^{2-}$	CH ₃ CN/0.1 M TBAPF ₆	-1.36	18
IV/III	ON ₄ O	$\text{t-ReO}(\text{OMe})(4\text{-Mepy})_4^+ + e^- \rightleftharpoons \text{t-ReO}(\text{OMe})(4\text{-Mepy})_4$	H ₂ O/pH 2	-0.28	17
V/III	O ₂ N ₄	$\text{c-ReO}_2(\text{py})_4^{2+} + 3\text{H}^+ + 2e^- \rightleftharpoons \text{t-Re}(\text{OH})(\text{OH}_2)(\text{py})_4^{2+}$	H ₂ O/pH 2	-0.07	17
V/III	O ₂ N ₄	$\text{c-Re}(\text{OH})(\text{OH}_2)(\text{bpy})(\text{py})_2^{2+} + 2e^- \rightleftharpoons \text{c-Re}(\text{OH})(\text{OH}_2)(\text{bpy})(\text{py})_2$			
III/II	O ₂ N ₄	$\text{t-Re}(\text{OH})(\text{OH}_2)(\text{py})_4^{2+} + \text{H}^+ + e^- \rightleftharpoons \text{t-Re}(\text{OH}_2)_2(\text{py})_4^{2+}$			
III/II	O ₂ N ₄	$\text{c-Re}(\text{OH})(\text{OH}_2)(\text{bpy})(\text{py})_2^{2+} + \text{H}^+ + e^- \rightleftharpoons \text{c-Re}(\text{OH}_2)_2(\text{bpy})(\text{py})_2$			

(continued overleaf)

Tab. 1 (continued)

Oxidation state change	Re coordinate shell	Electrode reaction	Solvent/supporting electrolyte	E° , V versus NHE	References
<i>Homoleptic complexes</i>					
VI/IV	C ₈	$\text{Re}(\text{CN})_8^{2-} + \text{e}^- \rightleftharpoons \text{Re}(\text{CN})_8^{3-}$	CH ₃ CN	+1.64	23
VI/IV	O ₆	$\text{Re}(\text{Cl}_4\text{Cat})_3 + \text{e}^- \rightleftharpoons \text{Re}(\text{Cl}_4\text{Cat})_3^-$	CH ₂ Cl ₂ /TBAPF ₆	+1.06	24
VI/IV	O ₆	$\text{Re}(\text{DTBCat})_3 + \text{e}^- \rightleftharpoons \text{Re}(\text{DTBCat})_3^-$	CH ₂ Cl ₂ /TBAPF ₆	-0.13	24
V/IV	N ₆	$\text{Re}(\text{NCS})_6^- + \text{e}^- \rightleftharpoons \text{Re}(\text{NCS})_6^{2-}$	CH ₂ Cl ₂ /0.2 M TBAPF ₆	+1.27	25
V/IV	O ₆	$\text{Re}(\text{Cl}_4\text{Cat})_3^- + \text{e}^- \rightleftharpoons \text{Re}(\text{Cl}_4\text{Cat})_3^{2-}$	CH ₂ Cl ₂ /TBAPF ₆	-0.11	24
V/IV	O ₆	$\text{Re}(\text{DTBCat})_3^- + \text{e}^- \rightleftharpoons \text{Re}(\text{DTBCat})_3^{2-}$	CH ₂ Cl ₂ /TBAPF ₆	-0.99	24
V/IV	P ₃ S ₃	$\text{Re}(\text{2-Ph}_2\text{PC}_6\text{H}_4\text{S})_3^{2+} + \text{e}^- \rightleftharpoons \text{Re}(\text{2-Ph}_2\text{PC}_6\text{H}_4\text{S})_3^+$	CH ₂ Cl ₂ /0.2 M TBAPF ₆	+1.68	26
IV/III	C ₇	$\text{Re}(\text{CN})_7^{3-} + \text{e}^- \rightleftharpoons \text{Re}(\text{CN})_7^{4-}$	CH ₃ CN	-0.64	23
IV/III	N ₆	$\text{Re}(\text{NCS})_6^{2-} + \text{e}^- \rightleftharpoons \text{Re}(\text{NCS})_6^{3-}$	CH ₂ Cl ₂ /0.2 M TBAPF ₆	-0.04	25
IV/III	P ₃ S ₃	$\text{Re}(\text{2-Ph}_2\text{PC}_6\text{H}_4\text{S})_3^+ + \text{e}^- \rightleftharpoons \text{Re}(\text{2-Ph}_2\text{PC}_6\text{H}_4\text{S})_3$	CH ₂ Cl ₂ /0.2 M TBAPF ₆	+0.90	26
IV/III	Cl ₆	$\text{ReCl}_6^{2-} + \text{e}^- \rightleftharpoons \text{ReCl}_6^{3-}$	CH ₂ Cl ₂	-0.88	27
III/II	N ₆	$\text{Re}(\text{NCS})_6^{3-} + \text{e}^- \rightleftharpoons \text{Re}(\text{NCS})_6^{4-}$	CH ₂ Cl ₂ /0.2 M TBAPF ₆	-1.39	25
III/II	N ₄ S ₂	$\text{Re}(\text{tsc})_2^+ + \text{e}^- \rightleftharpoons \text{Re}(\text{tsc})_2$	DMF/0.1 M TBAPF ₆	-0.27	28
III/II	P ₃ S ₃	$\text{Re}(\text{2-Ph}_2\text{PC}_6\text{H}_4\text{S})_3 + \text{e}^- \rightleftharpoons \text{Re}(\text{2-Ph}_2\text{PC}_6\text{H}_4\text{S})_3^-$	CH ₂ Cl ₂ /0.2 M TBAPF ₆	-0.32	26
III/II	S ₆	$\text{Re}(\text{ttcn})_2^{3+} + \text{e}^- \rightleftharpoons \text{Re}(\text{ttcn})_2^{2+}$	CH ₃ CN/0.1 M TBAPF ₆	+1.11	29
III/II	C ₆	$\text{Re}(\text{CNTol})_6^{2+} + \text{e}^- \rightleftharpoons \text{Re}(\text{CNTol})_6^+$	CH ₂ Cl ₂ /0.1 M TBAPF ₆	+1.44	30
II/I	N ₆	$\text{Re}(\text{terpy})_2^{2+} + \text{e}^- \rightleftharpoons \text{Re}(\text{terpy})_2^+$	DMA/0.5 M TBAPF ₆	+0.12	31
II/I	N ₆	$\text{Re}(\text{bpy})_2^{2+} + \text{e}^- \rightleftharpoons \text{Re}(\text{bpy})_2^+$	DMA/0.5 M TBAPF ₆	-0.33	31
II/I	N ₄ S ₂	$\text{Re}(\text{tsc})_2 + \text{e}^- \rightleftharpoons \text{Re}(\text{tsc})_2^-$	DMF/0.1 M TBAPF ₆	-0.83	28
II/I	P ₆	$\text{Re}(\text{dmpe})_3^{2+} + \text{e}^- \rightleftharpoons \text{Re}(\text{dmpe})_3^+$	DMF/0.5 M TEAClO ₄	+0.52	32

Mixed-ligand complexes					
V/IV	HO ₄ P ₂	$\text{ReH}(\text{acac})_2(\text{PPh}_3)_2^{2+} + \text{e}^- \rightleftharpoons \text{ReH}(\text{acac})_2(\text{PPh}_3)_2^+$	CH ₂ Cl ₂ /0.1 M TBAPF ₆	+1.05	7
IV/III	HO ₄ P ₂	$\text{ReH}(\text{acac})_2(\text{PPh}_3)_2^+ + \text{e}^- \rightleftharpoons \text{ReH}(\text{acac})_2(\text{PPh}_3)_2$	CH ₂ Cl ₂ /0.1 M TBAPF ₆	-0.24	7
IV/III	N ₄ Cl ₂	$\text{Re}(\text{bpy})_2\text{Cl}_2^{2+} + \text{e}^- \rightleftharpoons \text{Re}(\text{bpy})_2\text{Cl}_2^+$	DMA/0.5 M TBAPF ₆	+1.06	31
IV/III	N ₃ Cl ₃	$\text{Re}(\text{terpy})\text{Cl}_3^+ + \text{e}^- \rightleftharpoons \text{Re}(\text{terpy})\text{Cl}_3$	DMA/0.5 M TBAPF ₆	+0.52	31
IV/III	N ₃ Cl ₃	$\text{Re}(\text{py})_3\text{Cl}_3^+ + \text{e}^- \rightleftharpoons \text{Re}(\text{py})_3\text{Cl}_3$	DMA/0.5 M TBAPF ₆	+0.45	31
IV/III	N ₂ P ₂ Cl ₂	$\text{Re}(\text{bpy})(\text{PMe}_2\text{Ph})_2\text{Cl}_2^{2+} + \text{e}^- \rightleftharpoons \text{Re}(\text{bpy})(\text{PMe}_2\text{Ph})_2\text{Cl}_2^+$	CH ₃ CN/0.1 M TEAClO ₄	+1.12	33
IV/III	O ₄ P ₂	$\text{Re}(\text{acac})_2(\text{PPh}_3)_2^{2+} + \text{e}^- \rightleftharpoons \text{Re}(\text{acac})_2(\text{PPh}_3)_2^+$	CH ₂ Cl ₂ /0.1 M TBAPF ₆	+1.17	7
III/II	N ₄ Cl ₂	$\text{Re}(\text{bpy})_2\text{Cl}_2^+ + \text{e}^- \rightleftharpoons \text{Re}(\text{bpy})_2\text{Cl}_2$	DMA/0.5 M TBAPF ₆	-0.17	31
III/II	N ₃ Cl ₃	$\text{Re}(\text{terpy})\text{Cl}_3 + \text{e}^- \rightleftharpoons \text{Re}(\text{terpy})\text{Cl}_3^-$	DMA/0.5 M TBAPF ₆	-0.49	31
III/II	N ₃ Cl ₃	$\text{Re}(\text{py})_3\text{Cl}_3 + \text{e}^- \rightleftharpoons \text{Re}(\text{py})_3\text{Cl}_3^-$	DMA/0.5 M TBAPF ₆	-1.11	31
III/II	N ₂ P ₂ Cl ₂	$\text{Re}(\text{bpy})(\text{PMe}_2\text{Ph})_2\text{Cl}_2^+ + \text{e}^- \rightleftharpoons \text{Re}(\text{bpy})(\text{PMe}_2\text{Ph})_2\text{Cl}_2$	CH ₃ CN/0.1 M TEAClO ₄	-0.15	33
III/II	P ₄ Cl ₂	$\text{Re}(\text{dmpe})\text{Cl}_2^+ + \text{e}^- \rightleftharpoons \text{Re}(\text{dmpe})\text{Cl}_2$	DMF/0.5 M TEAClO ₄	-0.22	34
III/II	As ₄ Cl ₂	$\text{Re}(\text{diars})\text{Cl}_2^+ + \text{e}^- \rightleftharpoons \text{Re}(\text{diars})\text{Cl}_2$	DMF/0.5 M TEAClO ₄	-0.12	34
III/II	O ₄ P ₂	$\text{Re}(\text{acac})_2(\text{PPh}_3)_2^+ + \text{e}^- \rightleftharpoons \text{Re}(\text{acac})_2(\text{PPh}_3)_2$	CH ₂ Cl ₂ /0.1 M TBAPF ₆	-0.52	7
II/I	N ₄ Cl ₂	$\text{Re}(\text{bpy})_2\text{Cl}_2 + \text{e}^- \rightleftharpoons \text{Re}(\text{bpy})_2\text{Cl}_2^-$	DMA/0.5 M TBAPF ₆	-1.01	31
II/I	N ₃ Cl ₃	$\text{Re}(\text{py})_3\text{Cl}_3^- + \text{e}^- \rightleftharpoons \text{Re}(\text{py})_3\text{Cl}_3^{2-}$	DMA/0.5 M TBAPF ₆	-1.81	31
II/I	P ₄ Cl ₂	$\text{Re}(\text{dmpe})\text{Cl}_2 + \text{e}^- \rightleftharpoons \text{Re}(\text{dmpe})\text{Cl}_2^-$	DMF/0.5 M TEAClO ₄	-1.36	34
II/I	As ₄ Cl ₂	$\text{Re}(\text{diars})\text{Cl}_2 + \text{e}^- \rightleftharpoons \text{Re}(\text{diars})\text{Cl}_2^-$	DMF/0.5 M TEAClO ₄	-1.25	34

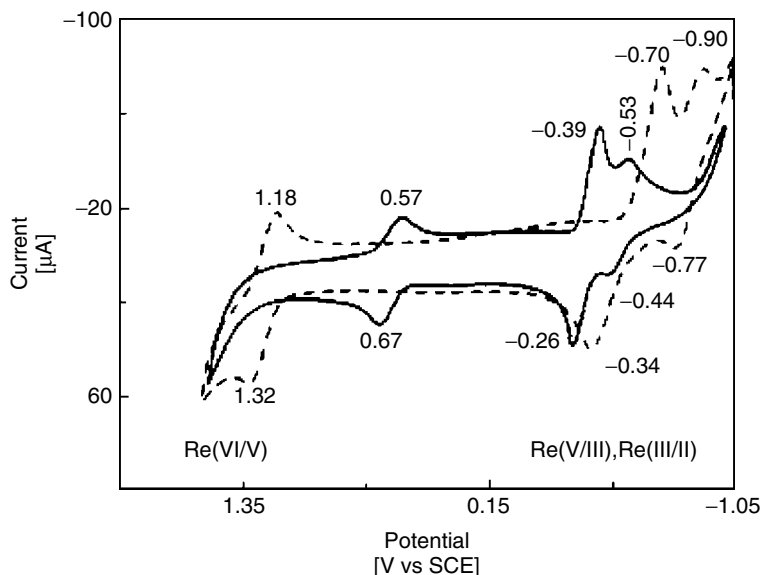
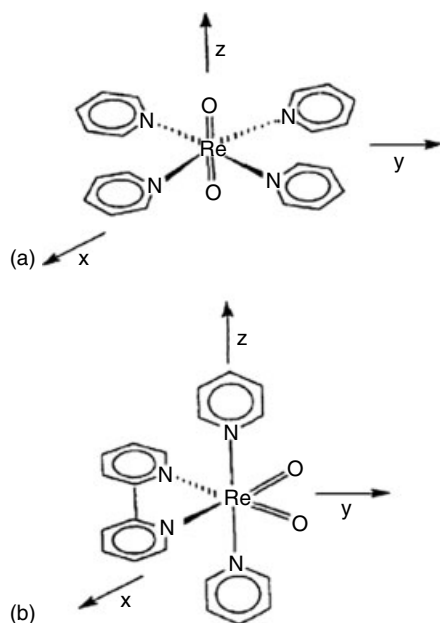


Fig. 1 Cyclic voltammograms of $\text{ReO}_2(\text{bpy})(\text{py})_2^+$ (solid line) and $\text{ReO}_2(\text{py})_4^+$ (dashed line) at pH 2 on a glassy carbon working electrode (reprinted with permission from Ref. 17, Copyright 1990 American Chemical Society).

illustrated by the aqueous, pH 2, cyclic voltammograms of $\text{cis-ReO}_2(\text{bpy})(\text{py})_2^+$



and $\text{trans-ReO}_2(\text{py})_4^+$ (Fig. 1) [17]. The one-electron $\text{Re(V)} \rightarrow \text{Re(VI)}$ potentials are proton independent from pH 1 to 11 and are close to the values observed in CH_3CN . However, the potential for oxidation of trans-ReO_2^+ complex is 0.6 V more positive than that for the oxidation of the cis-ReO_2^+ . Conversely, the proton-coupled $\text{Re(V)} \rightarrow \text{Re(III)}$ and $\text{Re(III)} \rightarrow \text{Re(II)}$ reductions of the cis and trans isomers occur at more nearly equal potentials, and the cis form exhibits the more positive $E^{\circ'}$ (Fig. 1). The difference in $\text{Re}^{\text{VI/V}}$ potentials is attributed to the oxo group geometry [35]. The redox orbital of the trans complex is d_{xy} , which lies in the equatorial plane and experiences little interaction with the oxo groups (Fig. 2) [35]. However, the redox orbital of the

Fig. 2 Structures of (a) $\text{trans-ReO}_2(\text{py})_4^+$ and (b) $\text{cis-ReO}_2(\text{bpy})(\text{py})_2^+$ (reprinted from Ref. 35, Copyright 1995 with permission from Elsevier).

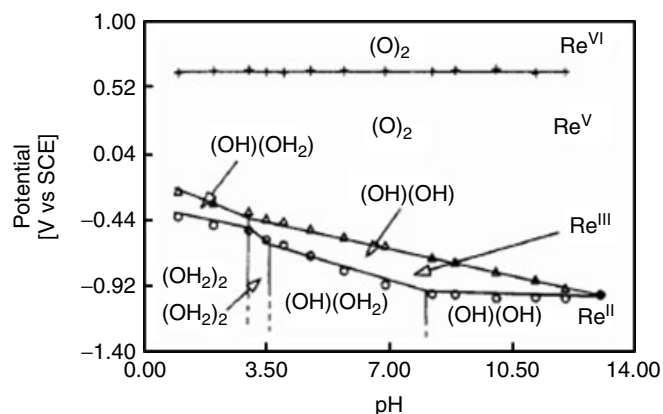
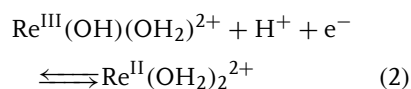
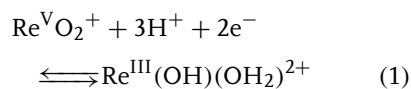


Fig. 3 Pourbaix diagram for $\text{ReO}_2(\text{bpy})(\text{py})_2^+$ (reprinted with permission from Ref. 17, Copyright 1990 American Chemical Society).

cis complex is a composite of the d_{xz} and d_{yz} orbitals, which interact unfavorably with one or more oxo $p-\pi^*$ orbitals and favor $d^2 \rightarrow d^1$ electron removal. The electron-transfer kinetics of *cis*- $\text{ReO}_2(\text{bpy})(\text{py})_2^+$ and *trans*- $\text{ReO}_2(\text{py})_4^+$ also differ; $(k_{s,h})_{\text{trans}}/(k_{s,h})_{\text{cis}} \approx 3$ at highly ordered pyrolytic graphite electrodes. The smaller rate constant for *cis*- $\text{ReO}_2(\text{bpy})(\text{py})_2^+$ corresponds to an approximate 4-kJ mol^{-1} difference in barrier height, which is assigned to a $\text{Re}-\text{N}(\text{bpy})$ stretching mode that is observed only for the *cis* complex [35].

Reduction of the ReO_2^+ species at pH 2 (Fig. 1) is accompanied by the addition of three protons and two electrons in the first step followed by the addition of one proton and one electron in the second step. The corresponding half-reactions (Table 1) are



Proton stoichiometries change as pH is altered and are influenced by oxo group

geometry and pyridyl ligand identity. The Pourbaix diagram of *cis*- $\text{ReO}_2(\text{bpy})(\text{py})_2^+$ (Fig. 3) [17] is representative of the observed behavior.

The apparent kinetics of proton-coupled $\text{Re}^{\text{V/III}}$ electron transfer also are dependent on oxo group geometry; here $(k_{s,h})_{\text{cis}}/(k_{s,h})_{\text{trans}} \approx 100$ [36]. It is proposed that the apparent kinetics is controlled by the thermodynamic accessibility of the intermediate $\text{Re}(\text{IV})$ state, whose effective potential is modulated by protonation, oxo group geometry, and pyridyl ligand substituents.

16.3.2.2 Homoleptic and Mixed-ligand Complexes

Rhenium forms a large number of mononuclear nonoxo complexes in oxidation states I through VI. The redox potentials of selected examples are included in Table 1. The majority of compounds are octahedral. However, notable exceptions include the pentagonal bipyramidal $\text{Re}(\text{CN})_7^{3-/4-}$ ($E^\circ = -0.64\text{ V}$) and the square antiprismatic $\text{Re}(\text{CN})_8^{2-/3-}$ ($E^\circ = +1.64\text{ V}$) couples [23]. The latter complexes are similar in behavior to the isoelectronic Mo species.

The electrochemistry of Re and Tc complexes is frequently compared. Rhenium compounds are more difficult to reduce in a given oxidation state. Comparison of values from Table 1 of Sect. 16.2 and Table 1 of Sect. 16.3 at identical ligand composition indicates that Re potentials are 0.2–0.6 V more negative than those of Tc, with the smaller differences occurring more frequently in the lower oxidation states. Lever constructed an electrochemical parameterization scheme on the basis of the ligand additivity principles for 119 Re redox couples [37]. The results are shown in Fig. 4. The lines for the $\text{Re}^{\text{IV/III}}$, $\text{Re}^{\text{III/II}}$, and $\text{Re}^{\text{II/I}}$ couples are not as cleanly parallel as they are for $\text{Tc}^{\text{IV/III}}$, $\text{Tc}^{\text{III/II}}$, and $\text{Tc}^{\text{II/I}}$ (Fig. 2 of Sect. 16.2). Moreover, two lines are apparent for

$\text{Re}^{\text{II/I}}$ couples. The upper line is dominated by complexes containing electron-withdrawing CO and isocyanide ligands. However, the structural or bonding significance of the two $\text{Re}^{\text{II/I}}$ correlation lines is not clear.

A change in the coordination number accompanies oxidation or reduction of some Re complexes. For example, oxidation of $\text{Re}^{\text{I}}(\text{terpy})_2^+$ in the presence of free chloride ion produces seven-coordinate $\text{Re}^{\text{III}}(\text{terpy})_2\text{Cl}^+$ via the following reaction sequence [31]:

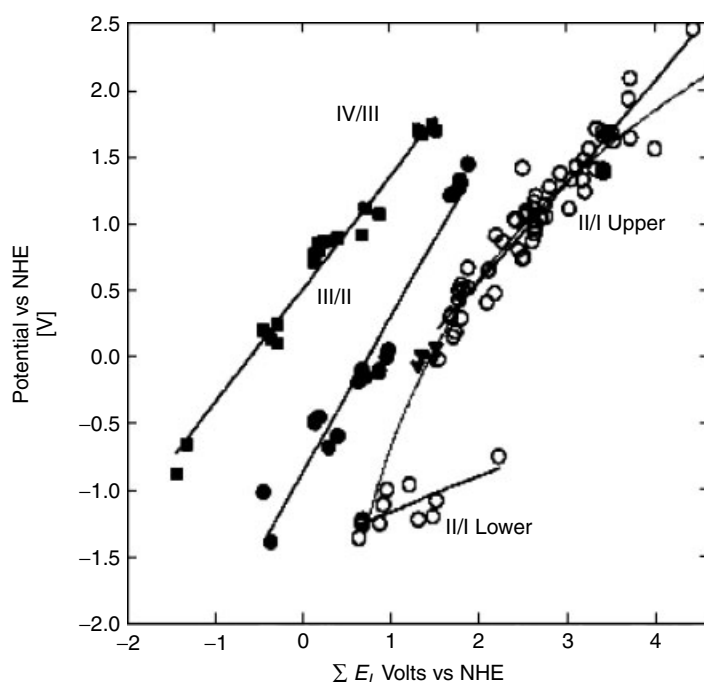
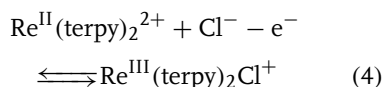
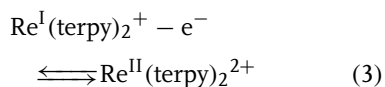


Fig. 4 Plot of $E^{\circ'}$ for $\text{Re}^{\text{IV/III}}$, $\text{Re}^{\text{III/II}}$, and $\text{Re}^{\text{II/I}}$ redox couples versus the sum of ligand parameters (reprinted with permission from Ref. 37, Copyright 1990 American Chemical Society).

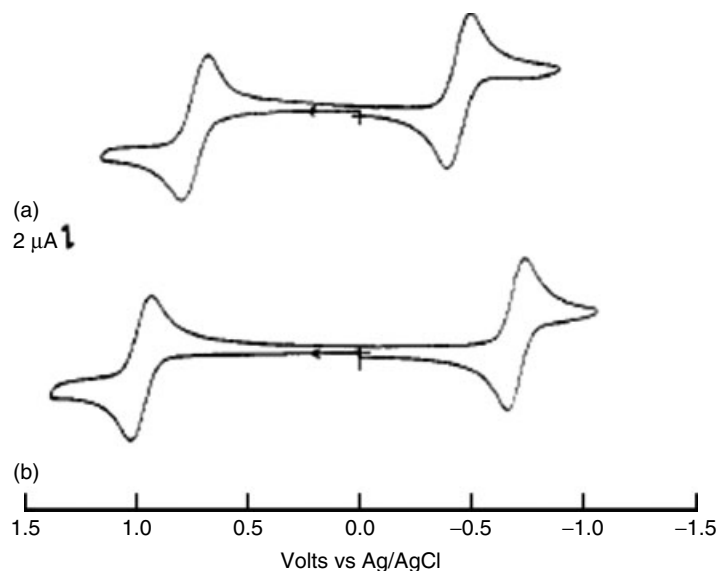


Fig. 5 Cyclic voltammograms of $\text{ReH}(\text{acac})_2(\text{PPh}_3)_3^+$ in $\text{CH}_2\text{Cl}_2/0.1 \text{ M TBAPF}_6$ (a) prior to and (b) following exhaustive electrolysis at $+1.1 \text{ V}$ versus NHE (reprinted with permission from Ref. 7, Copyright 1990 American Chemical Society).

Reduction of $\text{Re}^{\text{III}}(\text{terpy})_2\text{Cl}^+$ is irreversible and re-forms $\text{Re}^{\text{I}}(\text{terpy})_2^+$ in a two-electron reaction. Other seven-coordinate complexes [e.g. $\text{Re}^{\text{III}}(\text{bpy})_3(\text{CNBu}^t)^{3+}$] are generated in this manner and exhibit similar reactivity [31].

The seven-coordinate hydrido complex, $\text{Re}^{\text{IV}}\text{H}(\text{acac})_2(\text{PPh}_3)_2^+$, also undergoes a change in coordination number upon oxidation [7]. As shown in the upper trace (a) in Fig. 5, this compound exhibits a reversible one-electron oxidation at $E^{\circ'}_{\text{V/IV}} = +1.05 \text{ V}$ and a reversible one-electron reduction at $E^{\circ'}_{\text{IV/III}} = -0.24 \text{ V}$. Exhaustive electrolysis at $+1.1 \text{ V}$ produces the six-coordinate $\text{Re}(\text{III})$ complex, $\text{Re}^{\text{III}}(\text{acac})_2(\text{PPh}_3)_2^+$, which exhibits a reversible one-electron oxidation at $E^{\circ'}_{\text{IV/III}} = +1.17 \text{ V}$ and a reversible one-electron reduction at $E^{\circ'}_{\text{III/II}} = -0.52 \text{ V}$ (Fig. 5b). Although similar in appearance and potential, the two sets of electrode

reactions involve different pairs of oxidation states.

16.3.3

Polynuclear Complexes

16.3.3.1 Oxo-bridged Complexes

Although relatively few oxo-bridged rhenium complexes have been characterized electrochemically, several studies have been conducted on $\text{Re}(\text{V})$ complexes containing a linear $\text{O}=\text{Re}-\text{O}-\text{Re}=\text{O}$ unit (**1**, Chart 1). Dithiocarbamate complexes such as $\text{Re}_2\text{O}_3(\text{Et}_2\text{dtc})_4$ exhibit a reversible $\text{Re}^{\text{V,V}} \rightarrow \text{Re}^{\text{V,IV}}$ reduction at $E^{\circ'} = -1.13 \text{ V}$ in CH_3CN [38]. Complexes with SB ligands such as $\text{Re}_2\text{O}_3(\text{salen})_2$ exhibit one-electron $\text{Re}^{\text{V,V}} \rightarrow \text{Re}^{\text{VI,V}}$ and $\text{Re}^{\text{VI,V}} \rightarrow \text{Re}^{\text{VI,VI}}$ oxidations at $+0.76$ and $+1.29 \text{ V}$ and a one-electron $\text{Re}^{\text{V,V}} \rightarrow \text{Re}^{\text{V,IV}}$ reduction at -0.82 V in $\text{C}_2\text{H}_4\text{Cl}_2$ [39].

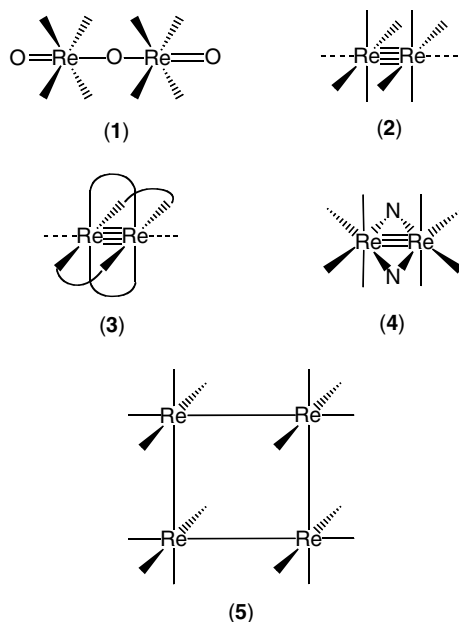


Chart 1 Structures of polynuclear rhenium centers.

Multiple metal–metal bonds have since been found in Re and many other transition metal complexes [41]. The structure of the unsupported Re_2^{6+} unit (2) is shown in Chart 1. Bonds to the ligands in the equator around each metal may be staggered or eclipsed depending on electronic structure, and solvent or unidentate ligands may bind weakly at the axial positions. In some cases, polydentate ligands may bridge the metal–metal-bonded unit (3).

Electrochemical data for a number of multiply bonded Re_2 complexes are represented in Table 2 [42–50]. The oxidation of quadruply bonded $\text{Re}_2^{\text{III,III}}$ ($\sigma^2\pi^4\delta^2$) produces $\text{Re}_2^{\text{III,IV}}$ and $\text{Re}_2^{\text{IV,IV}}$ centers with configurations of $\sigma^2\pi^4\delta^1$ and $\sigma^2\pi^4$ and formal metal–metal bond orders of 3.5 and 3.0, respectively. Reduction produces a $\sigma^2\pi^4\delta^2\delta^{*1}$ $\text{Re}_2^{\text{III,II}}$ center, also with a bond order of 3.5. The sequential one-electron potentials in Table 2 are widely

16.3.3.2 Metal–metal-bonded Complexes

The octachlorodirhenate ion, $\text{Re}_2\text{Cl}_8^{2-}$, was the first substance recognized to contain a metal–metal quadruple bond [40].

Tab. 2 Electrochemical data for metal–metal-bonded rhenium complexes

(Re III,III) complex	Solvent/supporting electrolyte	E° , V versus NHE				References
		(IV,IV)/ (IV,III)	(IV,III)/ (III,III)	(III,III)/ (III,II)	(III,II)/ (II,II)	
$\text{Re}_2\text{Cl}_8^{2-}$	$\text{CH}_3\text{CN}-\text{CH}_2\text{Cl}_2$ (1 : 1) / 0.5 M TBAPF ₆	+2.08 ^c	+1.64 ^c	−0.44		42, 43
$\text{Re}_2\text{Cl}_6(\text{PEt}_3)_2$	CH_2Cl_2 / 0.2 M TBAPF ₆			+0.14		44, 45
$\text{Re}_2\text{Cl}_5(\text{PEt}_3)_3^+$	CH_2Cl_2 / 0.2 M TBAPF ₆			+0.58	−0.64	44, 45
$\text{Re}_2\text{Cl}_4(\text{PEt}_3)_4^{2+}$	CH_2Cl_2 / 0.2 M TBAPF ₆			+1.04	−0.16	44, 45
$\text{Re}_2\text{Cl}_2(\text{OOCe}_2)_4^a$	CH_2Cl_2 / 0.2 M TBAPF ₆			−0.10		46, 47
$\text{Re}_2(\text{NCS})_8^{2-}$	n-PrCN / 0.4 M TBAPF ₆		+1.30	0.00	−0.70	48
$\text{Re}_2(\text{NCS})_{10}^{4-b}$	CH_2Cl_2 / 0.5 M TBAPF ₆	+0.66	+0.20	−1.11 ^d		49, 50

^a Axial Cl^- ligands.

^b $\text{Re}_2(\mu\text{-NCS})_2(\text{NCS})_8^{4-}$.

^c Evaluated at 220 K.

^d Irreversible two-electron reaction (see text).

spaced, indicating strong interaction between metals, and the $E^{\circ'}$ values for a particular redox step are influenced significantly by the charge and donor properties of the ligands.

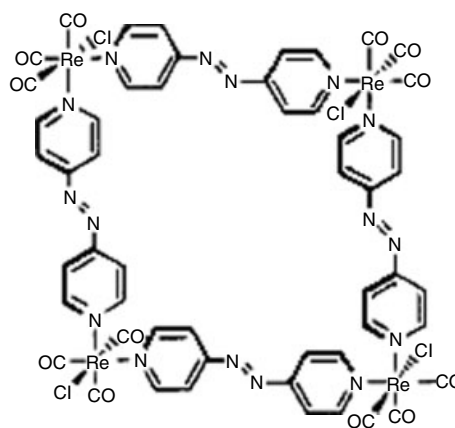
Electrochemical oxidation or reduction of Re_2^{n+} complexes is frequently followed by chemical reactions leading to products with altered structure or composition. For example, the exhaustive oxidation of $\text{Re}_2^{\text{II,II}}\text{Cl}_4(\text{PEt}_2)_4$ to $\text{Re}_2^{\text{III,II}}\text{Cl}_4(\text{PEt}_2)_4^+$ and $\text{Re}_2^{\text{III,III}}\text{Cl}_4(\text{PEt}_2)_4^{2+}$ is followed by chemical reactions that produce $\text{Re}_2^{\text{III,II}}\text{Cl}_5(\text{PEt}_2)_3$, $\text{Re}_2^{\text{III,III}}\text{Cl}_5(\text{PEt}_2)_3^+$, and $\text{Re}_2^{\text{III,III}}\text{Cl}_6(\text{PEt}_2)_2$ [44, 45]. The reactions involve scavenging of additional Cl^- ligands by complexes in the higher oxidation states. In the four-membered $\text{Re}_2(\text{NCS})_8^{-2/-3/-4-}$ redox chain [48], oxidation of $\text{Re}_2^{\text{III,III}}(\text{NCS})_8^{2-}$ is also followed by ligand scavenging and rearrangement to $\text{Re}_2^{\text{IV,IV}}(\text{NCS})_{10}^{2-}$ [49, 50]. This compound has been formulated as an edge-shared bioctahedral complex, $\text{Re}_2(\mu\text{-NCS})_2(\text{NCS})_8^{2-}$, containing two N-bonded bridging thiocyanate ligands (4). The electronic configuration is $\sigma^2\pi^2\delta^2$, which is consistent with a metal–metal bond order of 3.0. Reduction of $\text{Re}_2^{\text{IV,IV}}(\mu\text{-NCS})_2(\text{NCS})_8^{2-}$ proceeds by

two sequential, reversible one-electron transfers to $\text{Re}_2^{\text{III,III}}(\mu\text{-NCS})_2(\text{NCS})_8^{4-}$, which are then followed by an irreversible two-electron reduction that forms a product similar to $\text{Re}_2^{\text{II,II}}(\text{NCS})_8^{4-}$ [50].

16.3.3.3 Supramolecular Arrays

Rhenium complexes are used in the construction of robust supramolecular arrays having strong metal–ligand bonds. Assemblies in the form of triangles, squares, rectangles, and the like possess capabilities for host–guest interactions and molecular recognition and have promise in areas such as sensing, catalysis, molecular sieving, and energy storage and conversion [8, 51–53]. The *fac*- $\text{Re}(\text{CO})_3\text{Cl}$ unit is frequently employed as an element in such structures. An example is the molecular square $[\text{Re}(\text{CO})_3\text{Cl}(\mu\text{-azp})]_4$ (5 and Fig. 6) which is assembled from four $\text{Re}(\text{CO})_3\text{Cl}$ moieties and four bridging 4,4'-azopyridine (azp) ligands [51]. The compound exhibits four successive reductions at -0.01 , -0.45 , -0.74 , and -1.07 V and a single, reversible four-electron oxidation at $E^{\circ'} = +2.03$ V in DMF. The reductions are assigned to ligand-centered electron transfers; the oxidation is assigned to

Fig. 6 Structural representation of $[\text{Re}(\text{CO})_3\text{Cl}(\mu\text{-azp})]_4$, (5) (reprinted with permission from Ref. 51, Copyright 2000 American Chemical Society).



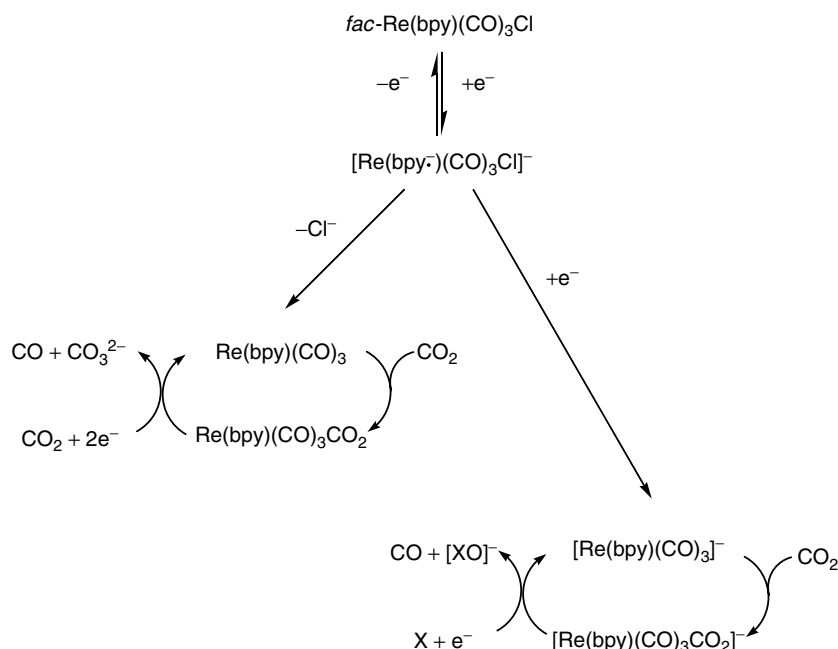


Fig. 7 Proposed one- and two-electron mechanisms for electrocatalytic reduction of CO_2 by $\text{fac-Re(bpy)(CO)}_3\text{Cl}$; X is an oxide ion acceptor (adapted from Ref. 55).

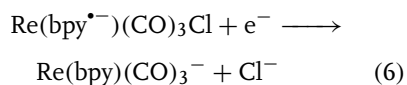
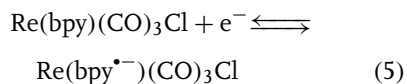
the removal of one electron each from the four noninteracting Re(I) atoms. The light-harvesting capacity of polynuclear rhenium centers and their capacity for reversible multielectron transfer is of interest with regard to applications in energy storage and conversion.

16.3.3.4 Carbon Dioxide Fixation

Low-valent rhenium complexes are effective in the catalytic reduction of carbon dioxide. The conversion can be accomplished photolytically or electrochemically and is of interest with regard to fuel production and greenhouse gas remediation [9]. Electrocatalytic reduction of CO_2 to CO is initiated by the reduction of $\text{fac-Re(bpy)(CO)}_3\text{Cl}$ or a related complex and can be accomplished in homogeneous solution [54, 55] or on a polymer-modified electrode surface [56]. Catalytic current

efficiency is high and generally is in excess of 90%.

The mechanism of electrocatalytic CO_2 reduction has been studied in some detail [57–60] but is not fully understood. A proposed mechanism from an early investigation [55] is shown in Fig. 7. The initial step in the reaction is the reversible reduction of $\text{fac-Re(bpy)(CO)}_3\text{Cl}$ ($E^{\circ'} = -1.1$ V in CH_3CN), which is assigned to the bipyridyl-centered electron transfer (Eq. 5). This is followed by a second step (Eq. 6) at ca -1.5 V, which is irreversible at room temperature and may be accompanied by loss of Cl^- :



Carbon dioxide reduction is thought to proceed via metallocarboxylate intermediate(s) formed by coordination of CO₂ to the electron-rich Re center, although discrete steps in the process cannot be unambiguously assigned. The timing of Cl[−] displacement from and CO₂ adduction to the Re(bpy)(CO)₃ unit are important mechanistic parameters. Most interpretations are based on a one-electron pathway, involving the interaction of CO₂ with the product of Eq. (5); a two-electron pathway, involving interaction of CO₂ with the product of Eq. (6); or a combination of these steps. Additional mechanistic considerations are the role dimeric rhenium intermediates and likely proton sources.

References

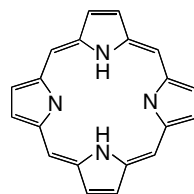
1. F. A. Cotton, G. Wilkinson, C. A. Murillo et al., *Advanced Inorganic Chemistry*, 6th ed., John Wiley & Sons, New York, 1999, pp. 974–1000.
2. U. Abram, in *Comprehensive Coordination Chemistry II*, (Eds.: J. A. McCleverty, T. J. Meyer), 2nd ed., Elsevier, Amsterdam, 2004, Vol. 5, Chapter 5.3.
3. R. J. Magee, T. J. Cardwell, in *Encyclopedia of Electrochemistry of the Elements*, (Ed.: A. J. Bard), Marcel Dekker, New York, 1973 Vol. 2, Chapter II-4.
4. R. J. Magee, H. Blumstein, in *Standard Potentials in Aqueous Solution*, (Eds.: A. J. Bard, R. Parsons, J. Jordan), Marcel Dekker, New York, 1985, pp. 444–451.
5. K. Hashimoto, K. Yoshihara, *Top. Curr. Chem.* **1996**, 176, 275–291.
6. M. S. Ram, L. M. Skeens-Jones, C. S. Johnson et al., *J. Am. Chem. Soc.* **1995**, 117, 1411–1421.
7. M. Leeaphon, P. E. Fanwick, R. A. Walton, *Inorg. Chem.* **1990**, 29, 4348–4351.
8. P. H. Dinolfo, J. T. Hupp, *Chem. Mater.* **2001**, 13, 3113–3125.
9. E. Fujita, B. S. Brunschwig, in *Electron Transfer in Chemistry. Catalysis of Electron Transfer, Heterogeneous and Gas-Phase Systems*, (Eds.: S. Fukuzumi, T. E. Mallouk, Y. Haas), Wiley-VCH, Weinheim, 2001 Vol. 4, pp. 88–126.
10. L. Astheimer, K. Schwochau, *J. Inorg. Nucl. Chem.* **1976**, 38, 1131–1134.
11. D. W. Letcher, T. J. Cardwell, R. J. Magee, *J. Electroanal. Chem.* **1970**, 25, 473–479.
12. M. Gross, P. Lemoine, J. Brenet, *Electrochim. Acta* **1971**, 16, 1787–1795.
13. D. D. DuMez, J. M. Mayer, *Inorg. Chem.* **1998**, 37, 445–453.
14. J. R. Dilworth, S. K. Ibrahim, S. R. Khan et al., *Polyhedron* **1990**, 9, 1323–1329.
15. M. S. Ram, L. M. Jones, H. J. Ward et al., *Inorg. Chem.* **1991**, 30, 2928–2938.
16. D. W. Pipes, T. J. Meyer, *J. Am. Chem. Soc.* **1985**, 107, 7201–7202.
17. M. S. Ram, C. S. Johnson, R. L. Blackburn et al., *Inorg. Chem.* **1990**, 29, 238–244.
18. M. S. Ram, L. M. Skeens-Jones, C. S. Johnson et al., *J. Am. Chem. Soc.* **1995**, 117, 1411–1421.
19. C. C. Van Kirk, V. Béreau, M. M. Abu-Ornar et al., *J. Electroanal. Chem.* **2003**, 541, 31–38.
20. R. Seeber, G. A. Mazzocchin, U. Mazzi et al., *Polyhedron* **1986**, 5, 1975–1986.
21. A. Paulo, Â. Domingos, A. P. de Matos et al., *Inorg. Chem.* **1994**, 33, 4729–4737.
22. A. Davison, C. Orvig, H. S. Trop et al., *Inorg. Chem.* **1980**, 19, 1988–1992.
23. M. V. Bennett, J. R. Long, *J. Am. Chem. Soc.* **2003**, 125, 2394–2395.
24. L. A. de Learie, R. C. Haltiwanger, C. G. Pierpont, *Inorg. Chem.* **1987**, 26, 817–821.
25. J. E. Hahn, T. Nimry, W. R. Robinson et al., *J. Chem. Soc., Dalton Trans.* **1978**, 1232–1236.
26. J. R. Dilworth, A. J. Hutson, S. Morton et al., *Polyhedron* **1992**, 11, 2151–2155.
27. G. A. Heath, K. A. Moock, D. W. A. Sharp et al., *J. Chem. Soc., Dalton Trans.* **1985**, 1503–1505.
28. A. R. Cowley, J. R. Dilworth, P. S. Donnelly et al., *J. Chem. Soc., Dalton Trans.* **2003**, 748–754.
29. G. E. D. Mullen, P. J. Blower, D. J. Price et al., *Inorg. Chem.* **2000**, 39, 4093–4098.
30. P. M. Treichel, J. P. Williams, *J. Organomet. Chem.* **1977**, 135, 39–51.
31. L. E. Helberg, S. D. Orth, M. Sabat et al., *Inorg. Chem.* **1996**, 35, 5584–5594.
32. J. R. Kirchoff, M. R. Allen, B. V. Cheesman et al., *Inorg. Chim. Acta* **1997**, 262, 195–202.
33. B. E. Wilcox, E. Deutsch, *Inorg. Chem.* **1991**, 30, 688–693.
34. J. R. Kirchoff, W. R. Heineman, E. Deutsch, *Inorg. Chem.* **1987**, 36, 3108–3113.

35. X. L. Zhang, J. T. Hupp, G. D. Danzer, *J. Electroanal. Chem.* **1995**, 380, 229–235.
36. L. M. Jones-Skeens, X. L. Zhang, J. T. Hupp, *Inorg. Chem.* **1992**, 32, 3879–3881.
37. A. B. P. Lever, *Inorg. Chem.* **1991**, 30, 1980–1985.
38. A. Ichimura, T. Kajino, T. Kitagawa, *Inorg. Chim. Acta* **1988**, 147, 27–31.
39. L. A. Bottomley, P. E. Wojciechowski, G. B. Holder, *Inorg. Chim. Acta* **1997**, 255, 149–155.
40. F. A. Cotton, *Inorg. Chem.* **1965**, 4, 334–336.
41. F. A. Cotton, R. A. Walton, *Multiple Bonds between Metal Atoms*, 2nd ed., Oxford University Press, New York, 1993.
42. F. A. Cotton, E. Pedersen, *Inorg. Chem.* **1975**, 14, 383–387.
43. G. A. Heath, R. G. Raptis, *Inorg. Chem.* **1991**, 30, 4106–4108.
44. D. J. Salmon, R. A. Walton, *J. Am. Chem. Soc.* **1978**, 100, 991–993.
45. P. Brant, D. J. Salmon, R. A. Walton, *J. Am. Chem. Soc.* **1978**, 100, 4424–4430.
46. F. A. Cotton, E. Pedersen, *J. Am. Chem. Soc.* **1975**, 97, 303–308.
47. V. Srinivasan, R. A. Walton, *Inorg. Chem.* **1980**, 19, 1635–1640.
48. G. A. Heath, R. G. Raptis, *J. Am. Chem. Soc.* **1993**, 115, 3768–3769.
49. S. P. Best, R. J. H. Clark, D. G. Humphrey, *Inorg. Chem.* **1995**, 34, 1013–1014.
50. R. J. H. Clark, D. G. Humphrey, *Inorg. Chem.* **1996**, 35, 2053–2061.
51. S.-S. Sun, A. J. Lees, *J. Am. Chem. Soc.* **2000**, 122, 8956–8967.
52. P. H. Dinolfo, M. E. Williams, C. L. Stern et al., *J. Am. Chem. Soc.* **2004**, 126, 12989–13001.
53. B. Gholamkhash, H. Mametuka, K. Koike et al., *Inorg. Chem.* **2005**, 44, 2326–2336.
54. J. Hawecker, J.-M. Lehn, R. Ziessel, *J. Chem. Soc., Chem. Commun.* **1984**, 328–330.
55. P. Sullivan, C. M. Bolinger, D. Conrad et al., *J. Chem. Soc., Chem. Commun.* **1985**, 1414–1416.
56. T. R. O'Toole, L. D. Margerum, T. D. Westmoreland et al., *J. Chem. Soc., Chem. Commun.* **1985**, 1416–1417.
57. A. I. Breikss, H. D. Abruña, *J. Electroanal. Chem.* **1986**, 201, 347–358.
58. P. Christensen, A. Hamnett, A. V. G. Muir et al., *J. Chem. Soc., Dalton Trans.* **1992**, 1455–1463.
59. F. Paolucci, M. Marcaccio, C. Paradisi et al., *J. Phys. Chem. B* **1998**, 102, 4759–4769.
60. Y. Hayashi, S. Kita, B. S. Brunshwig et al., *J. Am. Chem. Soc.* **2003**, 125, 11976–11987.

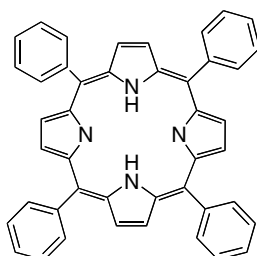
Ligand Abbreviations

Abbreviation	Name
8-HQ	8-Quinolinol
acac [−]	Acetylacetonate
bisimMe ₂ en	<i>N, N'</i> -Dimethyl- <i>N, N'</i> -bis(imidazol-4-ylmethyl)ethane-1,2-diamine
bispicen	<i>N, N'</i> -Bis(2-pyridylmethyl)-1,2-ethanediamine
bispicMe ₂ en	<i>N, N'</i> -Bis((6-methylpyrid-2-yl)methyl)ethane-1,2-diamine
bpea	<i>N, N'</i> -Bis(2-pyridylmethyl)ethylamine
bpia	Bis(picoly)(<i>N</i> -methylimidazol-2-yl)amine
bpy	2,2'-Bipyridine
bpyO ₂	2, 2'-Bipyridine-1,1'-dioxide
Cp ^{∗−}	Decamethylcyclopentadienide
Et ₂ dtc [−]	<i>N, N'</i> -Diethyldithiocarbamate
H ₂ als	<i>N</i> -(2-Carboxyethyl)salicylideneamine
H ₂ bbpen	<i>N, N'</i> -Bis(2-hydroxybenzyl)- <i>N, N'</i> -bis(2-pyridylmethyl)ethylenediamine

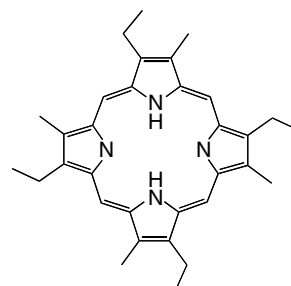
H ₂ DMHP	Hematoporphyrin IX dimethylester = 2, 7, 12, 18-tetramethyl-3,8-di(2-hydroxyethyl)-13,17-di(methylpropionato)porphyrin
H ₂ DPPF ₂₀	5,10,15,20-Tetrakis(pentafluorophenyl)-2,3,7,8,12,13,17,18-octaphenylporphyrin
H ₂ EtioP	2,7,12,17-Tetramethyl-3,8,13,18-tetraethylporphyrin
H ₂ Pc	Phthalocyanine
H ₂ saldpt	1,7-Diamino-4-azaheptanebis(salicylaldimine)
H ₂ salen	<i>N</i> , <i>N'</i> -Ethylenebis(salicylaldimine)
H ₂ salophen	<i>N</i> , <i>N'</i> - <i>o</i> -Phenylenebis(salicylaldimine)
H ₂ tdcmpp	2,3,7,8,12,13,17,18-Octachloro-5,10,15,20-tetrakis(3,5-dichloro-2,6-dimethoxyphenyl)porphyrin
H ₂ TDCSPP	5,10,15,20-Tetrakis(2,6-dichloro-3-sulfonatophenyl)porphyrin
H ₂ tdmpp	5,10,15,20-Tetrakis(2,6-dimethoxyphenyl)porphyrin
H ₂ TDMSP	5,10,15,20-Tetrakis(2,6-dimethyl-3-sulfonatophenyl)porphyrin
H ₂ TMAP	5,10,15,20-Tetrakis(4- <i>N</i> , <i>N'</i> , <i>N''</i> -trimethylanilinium)porphyrin
H ₂ TMPyP	5,10,15,20-Tetrakis(<i>N</i> -methyl-4-pyridyl)porphyrin
H ₂ TPP	5,10,15,20-Tetrakis(phenyl)porphyrin
H ₃ salmp	2-(Bis(salicylideneamino)methyl)phenol
H ₃ tpc	<i>meso</i> -Tris(phenyl)corrole
H ₄ mac	5,6-(4,5-Dichlorobenzo)-3,8,11,13-tetraoxo-2,3,9,9-tetramethyl-12,12-diethyl-1,4,7,10-tetraazacyclotridecane
HB(pz) ₃ [−]	Hydrotris(pyrazol-1-yl)borate
hbpme	<i>N</i> -(2-Hydroxybenzyl)- <i>N</i> , <i>N'</i> -bis(2-pyridylmethyl)ethane-1,2-diamine
Hhpt	1-Hydroxy-2-pyridinethione
Hphox	2-(2'-Hydroxyphenyl)oxazoline
Me ₃ tacn	<i>N</i> , <i>N'</i> , <i>N''</i> -Trimethyl-1,4,7-triazacyclononane
pebMe ₂ pma	2-(2-Pyridyl)ethylbis(6-methyl-2-pyridylmethyl)amine
pebpma	2-(2-Pyridyl)ethylbis(2-pyridylmethyl)amine
phen	1,10-Phenanthroline
sar	3,6,10,13,16,19-Hexaazabicyclo[6.6.6]eicosane
tacn	1,4,7-Triazacyclononane
Tp [−]	Hydrotris(pyrazol-1-yl)borate
tripod [−]	Cyclopentadienyltris(diethylphosphito-P)cobaltate(1-)



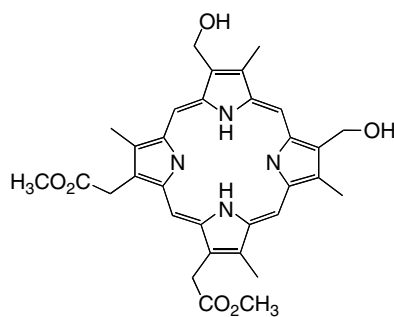
Porphine (H_2P)



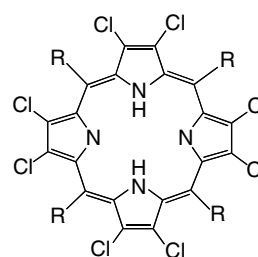
H_2TPP



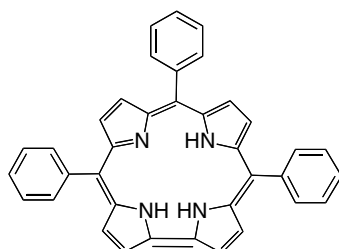
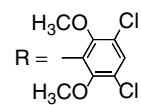
H_2EtioP



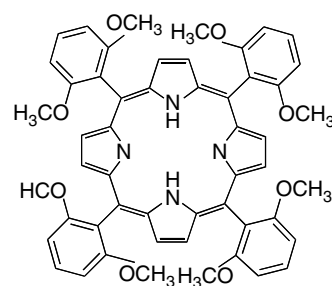
H_2DMHP



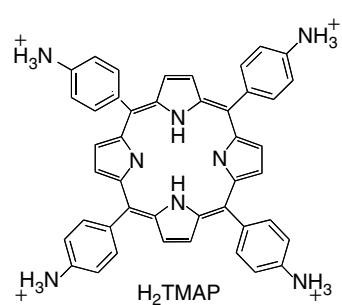
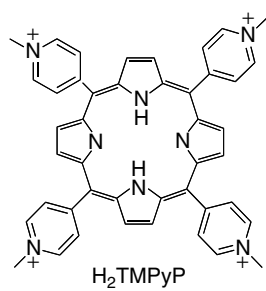
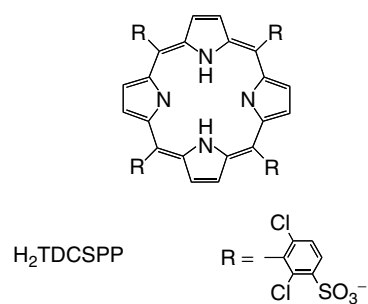
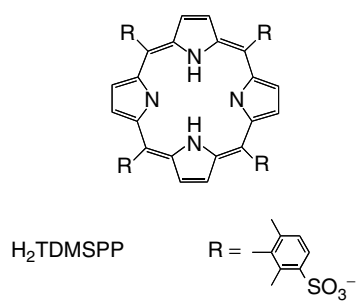
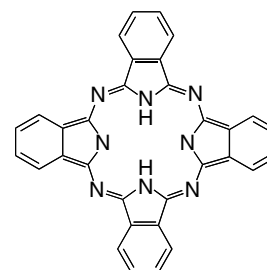
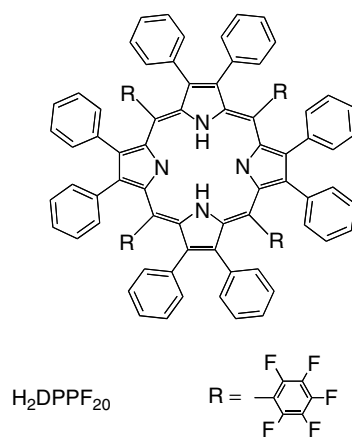
$H_2tdcmpp$

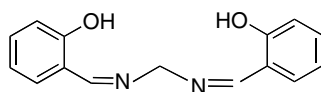


H_3tpc

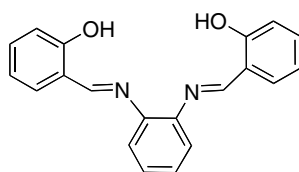


H_2tdmpp

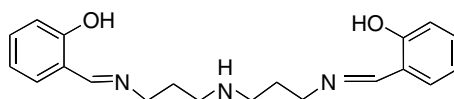




H₂salen



H₂salophen



H₂saldpt

16

Electrochemistry of the Group 7 Elements: Manganese, Technetium, and Rhenium

*Franklin A. Schultz, Cole T. Duncan, and Matthew A. Rigby
Indiana University- Purdue University Indianapolis, Indianapolis, Indiana, USA*

16.1	Manganese	401
16.1.1	Introduction	401
16.1.2	Mononuclear Complexes with Acyclic and Other Common Ligands	401
16.1.2.1	Redox Potentials	401
16.1.2.2	Coupled Chemical and Electrochemical Reactions	406
16.1.2.3	Electron-transfer Kinetics	406
16.1.3	Mononuclear Complexes with Porphyrins, Schiff Bases, Phthalocyanine, and Related Macrocyclic Ligands	409
16.1.3.1	Introduction	409
16.1.3.2	Studies in Nonaqueous Media	409
16.1.3.3	Studies in Aqueous Media	411
16.1.3.4	Electrocatalytic Studies	412
16.1.4	Binuclear and Polynuclear Complexes	415
16.1.4.1	Introduction	415
16.1.4.2	Studies in Nonaqueous Media	415
16.1.4.3	Studies in Aqueous Media	421
16.1.5	Biological Systems	423
16.1.5.1	Introduction	423
16.1.5.2	Manganese Catalase	423
16.1.5.3	Manganese Peroxidase	423
16.1.5.4	Manganese Superoxide Dismutase	425
16.1.5.5	Oxygen-evolving Center in Photosystem II	426
	References	431
16.2	Technetium	435
16.2.1	Introduction	435
16.2.2	Mononuclear Complexes	435
16.2.2.1	Oxo Complexes	435
16.2.2.2	Homoleptic and Mixed-ligand Complexes	436
16.2.3	Binuclear Complexes	440

16.2.3.1	Oxo-bridged Complexes	440
16.2.3.2	Metal–metal-bonded Complexes	440
	References	442
16.3	Rhenium	444
16.3.1	Introduction	444
16.3.2	Mononuclear Complexes	444
16.3.2.1	Oxo Complexes	444
16.3.2.2	Homoleptic and Mixed-ligand Complexes	449
16.3.3	Polynuclear Complexes	451
16.3.3.1	Oxo-bridged Complexes	451
16.3.3.2	Metal–metal-bonded Complexes	452
16.3.3.3	Supramolecular Arrays	453
16.3.3.4	Carbon Dioxide Fixation	454
	References	455
	Ligand Abbreviations	456

16.1 Manganese

16.1.1 Introduction

Manganese is the third most abundant transition element [1]. It is present in a number of industrial, biological, and environmental systems, representative examples of which include manganese oxide batteries [2]; the oxygen-evolving center of photosystem II (PSII) [3]; manganese catalase, peroxidase, superoxide dismutase (SOD), and other enzymes [4, 5]; chiral epoxidation catalysts [6]; and deep ocean nodules [7]. Oxidation–reduction chemistry plays a central role in the function of most, if not all, of these examples.

The coordination chemistry [8] and electrochemical properties [9–11] of manganese-containing compounds have been reviewed on a number of occasions. These collections contain primarily thermodynamic and (to a lesser extent) kinetic information on compounds of relatively simple composition. The objective in this chapter is to provide a descriptive summary of the electrochemical properties of a wide range of manganese compounds. There is generous coverage of coordination complexes, which seeks to illustrate relationships between structure and

reactivity by emphasizing the influence of coordination environment on oxidation state preference, reactivity, and mechanism. This approach provides a convenient framework for the discussion of electron-transfer reactivity that is important in many applications. The topics covered include mononuclear manganese complexes; Schiff base, porphyrin, and phthalocyanine complexes; bi- and polynuclear complexes; and Mn in biological systems.

16.1.2 Mononuclear Complexes with Acyclic and Other Common Ligands

16.1.2.1 Redox Potentials

Manganese forms a large number of mononuclear complexes in oxidation states II, III, and IV with acyclic and other common ligands. The complexes primarily are six-coordinate species with octahedral or pseudo-octahedral geometries. Some exceptions to this categorization are the tetraoxo anions in oxidation states V, VI, and VII and the manganocenes. Table 1 contains electrochemical data for representative redox couples in which the Mn coordination environment remains invariant with oxidation state. Many entries are for homoleptic complexes, but some species with mixed

Tab. 1 Electrochemical properties of mononuclear manganese complexes with acyclic and other common ligands

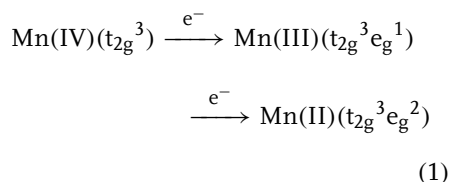
Oxidation state change	Mn coordinate shell	Electrode reaction	Solvent/supporting electrolyte	E^0 , V versus NHE	k_s , cm s^{-1}	References
VII/VI	O ₄	$\text{MnO}_4^- + e^- \rightleftharpoons \text{MnO}_4^{2-}$	H ₂ O/1.0 M NaOH	+0.59	2.4×10^{-2}	12
VI/V	O ₄	$\text{H}_2\text{O} + \text{MnO}_4^{2-} + e^- \rightleftharpoons \text{MnO}_3(\text{OH})^{2-} + \text{OH}^-$	H ₂ O/1.0 M NaOH	+0.31	2.5×10^{-3}	12, 13
IV/III	C ₆	$\text{Mn}(\text{CN})_6^{2-} + e^- \rightleftharpoons \text{Mn}(\text{CN})_6^{3-}$	Formamide/0.1 M TEAClO ₄	+1.06		14
IV/III	C ₆	$\text{Mn}(\text{CN})_6^{2-} + e^- \rightleftharpoons \text{Mn}(\text{CN})_6^{3-}$	CH ₃ CN/0.1 M TEAClO ₄	+0.41		14
IV/III	N ₆	$\text{Mn}(\text{Tp})_2^{2+} + e^- \rightleftharpoons \text{Mn}(\text{Tp})_2^+$	C ₂ H ₄ Cl ₂ /0.1 M TBAPF ₆	+2.01	4.9×10^{-2}	15
IV/III	N ₄ O ₂	$\text{Mn}(\text{bbpen})^{2+} + e^- \rightleftharpoons \text{Mn}(\text{bbpen})^+$	CH ₃ CN/0.1 M TBAPF ₆	+1.13		16
IV/III	N ₃ O ₃	$\text{Mn}(\text{8-Q})_3^+ + e^- \rightleftharpoons \text{Mn}(\text{8-Q})_3$	CH ₃ CN/0.1 M TEAClO ₄	+1.18		17
IV/III	N ₃ O ₃	$\text{Mn}(\text{phox})_3^+ + e^- \rightleftharpoons \text{Mn}(\text{phox})_3$	CH ₃ CN/0.05 M TEAPF ₆	+0.68		18
IV/III	N ₂ O ₄	$\text{Mn}(\text{als})_2^+ + e^- \rightleftharpoons \text{Mn}(\text{als})_2$	CH ₃ OH/0.1 M TEAClO ₄	+0.74		19
IV/III	O ₆	$\text{Mn}(\text{bpyO}_2)_3^{4+} + e^- \rightleftharpoons \text{Mn}(\text{bpyO}_2)_3^{3+}$	CH ₃ CN/0.1 M TPAClO ₄	+1.86		20
IV/III	O ₆	$\text{Mn}(\text{tripod})_2^{2+} + e^- \rightleftharpoons \text{Mn}(\text{tripod})_2^+$	CH ₃ CN/unspecified	+1.77		21
IV/III	O ₆	$\text{Mn}(\text{acac})_3^+ + e^- \rightleftharpoons \text{Mn}(\text{acac})_3$	CH ₃ CN/0.1 M TBAClO ₄	+1.21		22
IV/III	O ₃ S ₃	$\text{Mn}(\text{hpt})_3^+ + e^- \rightleftharpoons \text{Mn}(\text{hpt})_3$	2CH ₃ CN:1CH ₂ Cl ₂ /0.1 M TEAClO ₄	+0.61		23
IV/III	S ₆	$\text{Mn}(\text{Et}_2\text{dto})_3^+ + e^- \rightleftharpoons \text{Mn}(\text{Et}_2\text{dto})_3$	CH ₃ CN/0.15 M TEAClO ₄	+0.57	4×10^{-1}	24
III/II	C ₆	$\text{Mn}(\text{CNCH}_3)_6^{3+} + e^- \rightleftharpoons \text{Mn}(\text{CNCH}_3)_6^{2+}$	CH ₃ CN/0.1 M TEAClO ₄	+1.78		25
III/II	C ₆	$\text{Mn}(\text{CN})_6^{3-} + e^- \rightleftharpoons \text{Mn}(\text{CN})_6^{4-}$	Formamide/0.1 M TEAClO ₄	-0.43 ^a		14

III/II	C ₆	$\text{Mn}(\text{CN})_6^{3-} + \text{e}^- \rightleftharpoons \text{Mn}(\text{CN})_6^{4-}$	CH ₃ CN/0.1 M TEAClO ₄	-1.33		14
III/II	C ₁₀	$\text{Mn}(\text{Cp}^*)_2^+ + \text{e}^- \rightleftharpoons \text{Mn}(\text{Cp}^*)_2$	CH ₃ CN/0.1 M TBABF ₄	-0.32	$\geq 4 \times 10^0$	26, 27
III/II	N ₆	$\text{Mn}(\text{bpy})_3^{3+} + \text{e}^- \rightleftharpoons \text{Mn}(\text{bpy})_3^{2+}$	CH ₃ CN/0.1 M TPAClO ₄	+1.60		28
III/II	N ₆	$\text{Mn}(\text{NH}_3)_6^{3+} + \text{e}^- \rightleftharpoons \text{Mn}(\text{NH}_3)_6^{2+}$	NH ₃ /1 M NH ₄ NO ₃	+0.81	6.5×10^{-5}	29
III/II	N ₆	$\text{Mn}(\text{Tp})_2^+ + \text{e}^- \rightleftharpoons \text{Mn}(\text{Tp})_2$	C ₂ H ₄ Cl ₂ /0.1 M TBAPF ₆	+0.76	5.3×10^{-5}	15
III/II	N ₆	$\text{Mn}(\text{tacn})_3^{3+} + \text{e}^- \rightleftharpoons \text{Mn}(\text{tacn})_2^{2+}$	H ₂ O/0.1 M KCl (276 K)	+0.68		30
III/II	N ₆	$\text{Mn}(\text{sar})_3^{3+} + \text{e}^- \rightleftharpoons \text{Mn}(\text{sar})_2^{2+}$	H ₂ O/0.1 M CF ₃ SO ₃ H	+0.53		31
III/II	N ₄ O ₂	$\text{Mn}(\text{bbpen})^+ + \text{e}^- \rightleftharpoons \text{Mn}(\text{bbpen})$	CH ₃ CN/0.1 M TBAPF ₆	+0.27		16
III/II	N ₃ O ₃	$\text{Mn}(\text{8-Q})_3 + \text{e}^- \rightleftharpoons \text{Mn}(\text{8-Q})_3^-$	CH ₃ CN/0.1 M TEAClO ₄	+0.16		17
III/II	N ₃ O ₃	$\text{Mn}(\text{phox})_3 + \text{e}^- \rightleftharpoons \text{Mn}(\text{phox})_3^-$	CH ₃ CN/0.05 M TEAPF ₆	-0.22		18
III/II	N ₂ O ₄	$\text{Mn}(\text{als})_2^- + \text{e}^- \rightleftharpoons \text{Mn}(\text{als})_2^{2-}$	CH ₃ OH/0.1 M TEAClO ₄	+0.02		19
III/II	O ₆	$\text{Mn}(\text{H}_2\text{O})_6^{3+} + \text{e}^- \rightleftharpoons \text{Mn}(\text{H}_2\text{O})_6^{2+}$	6.15 M H ₂ SO ₄ , 7.5 M H ₂ SO ₄	+1.49	2.5×10^{-6} , 3.4×10^{-5}	32, 33
III/II	O ₆	$\text{Mn}(\text{bpyO}_2)_3^{3+} + \text{e}^- \rightleftharpoons \text{Mn}(\text{bpyO}_2)_3^{2+}$	CH ₃ CN/0.1 M TPAClO ₄	+1.11		20
III/II	O ₆	$\text{Mn}(\text{tripod})_2^+ + \text{e}^- \rightleftharpoons \text{Mn}(\text{tripod})_2$	CH ₂ Cl ₂ /unspecified	+0.36	7×10^{-7}	21
III/II	O ₆	$\text{Mn}(\text{acac})_3 + \text{e}^- \rightleftharpoons \text{Mn}(\text{acac})_3^-$	CH ₃ CN/0.1 M TBAClO ₄	+0.15	4.5×10^{-1}	22, 34
III/II	O ₃ S ₃	$\text{Mn}(\text{hpt})_3 + \text{e}^- \rightleftharpoons \text{Mn}(\text{hpt})_3^-$	2CH ₃ CN:1CH ₂ Cl ₂ /0.1 M TEAClO ₄	-0.11		23
III/II	S ₆	$\text{Mn}(\text{Et}_2\text{dto})_3 + \text{e}^- \rightleftharpoons \text{Mn}(\text{Et}_2\text{dto})_3^-$	CH ₃ CN/0.15 M TEAClO ₄	+0.03	6×10^{-1}	24
II/I	C ₆	$\text{Mn}(\text{CNCH}_3)_6^{2+} + \text{e}^- \rightleftharpoons \text{Mn}(\text{CNCH}_3)_6^+$	CH ₃ CN/0.1 M TEAClO ₄	+0.62		25
II/I	C ₆	$\text{Mn}(\text{CN})_6^{4-} + \text{e}^- \rightleftharpoons \text{Mn}(\text{CN})_6^{5-}$	H ₂ O/1 M NaCN	-1.11 ^a	2.6×10^{-1}	35
II/I	C ₁₀	$\text{Mn}(\text{Cp}^*)_2 + \text{e}^- \rightleftharpoons \text{Mn}(\text{Cp}^*)_2^-$	CH ₃ CN/0.1 M TBABF ₄	-1.93		26
II/O	O ₆	$\text{Mn}(\text{H}_2\text{O})_6^{2+} + 2\text{e}^- \rightleftharpoons \text{Mn}^0(\text{Hg})$	H ₂ O/1 M LiClO ₄	-1.20	4×10^{-4}	36

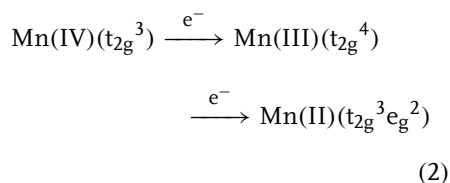
^a Values of -0.24 and -1.06 V versus NHE have been obtained for the $\text{Mn}(\text{CN})_6^{3-}/4-$ and $\text{Mn}(\text{CN})_6^{4-}/5-$ couples, respectively, by redox titrimetry in 2 M NaCN/H₂O [37].

donor atom sets are included. Potentials extend from +0.41 to +2.01 V versus NHE for $\text{Mn}^{\text{IV/III}}$ couples [12–24], from –1.33 to +1.78 V for $\text{Mn}^{\text{III/II}}$ couples [14–19, 25–34], and from –1.93 to +0.62 V for $\text{Mn}^{\text{II/I}}$ couples [25, 26, 35]. The large ranges reflect the significant influences of the charge and donor/acceptor properties of the ligand(s). Thus, oxidized forms are stabilized and negative potentials result with negatively charged, strong σ -donor ligands (e.g. CN^-), whereas reduced forms are stabilized and positive potentials result with neutral π -acceptor ligands (e.g. isocyanides, diimines). Consequently, one-electron oxidants or reductants exhibiting a very large range of potentials can be produced at mononuclear Mn centers.

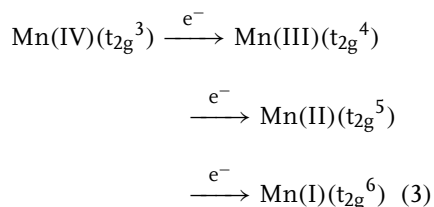
The d-electron configurations most commonly observed for Mn (IV) through Mn (II) electron-transfer reactions involve Mn (III) in the high-spin state ($t_{2g}^3 e_g^1$):



However, low-spin $\text{Mn(III)}(t_{2g}^4)$ is found in some instances (e.g. for Tp^- and its substituted derivatives [15]), resulting in the observation of:

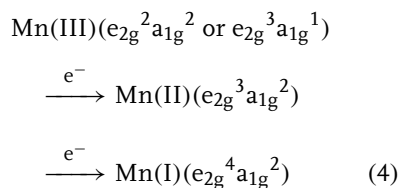


Strong field CN^- stabilizes low-spin Mn in oxidation states I through IV and is unique in stabilizing a four-member redox series:



Isocyanides stabilize low-spin Mn(I), (II), and (III) and form a redox sequence encompassing the last three members of Eq. (3). The potentials in Eq. (3) are very solvent-dependent for the negatively charged cyanide complexes. The reduced forms are stabilized relative to the oxidized forms by strong hydrogen bond interactions, which produce positive E° shifts of 0.6–0.9 V in proton-donating solvents. The magnitude of the effect is such that the potential of the $\text{Mn(CN)}_6^{4-/5-}$ couple in H_2O is more positive than that of the $\text{Mn(CN)}_6^{3-/4-}$ couple in CH_3CN (Table 1).

Decamethylmanganocene (D_{5d}) undergoes chemically reversible and kinetically facile electron-transfer reactions encompassing the Mn(III), (II), and (I) oxidation states:



$[\text{Mn(Cp}^*)_2]^{+/0/-}$ is low spin in all oxidation states. However, unsubstituted high-spin Mn(Cp)_2 is extremely reactive and has not been characterized electrochemically [26, 38].

Simple one-electron reduction of manganese tetraoxo anions in aqueous solution is observed only under very alkaline conditions. Hydroxide ion concentrations greater than 0.4 and 10 M are required

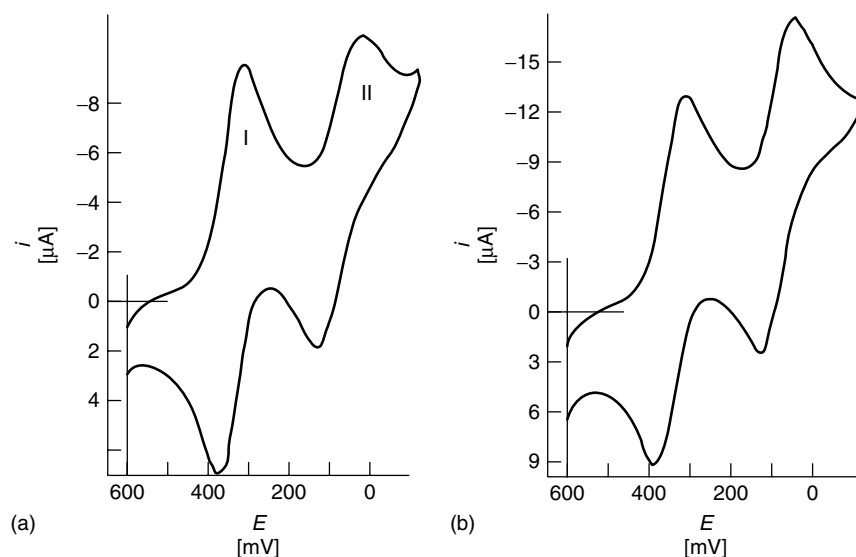
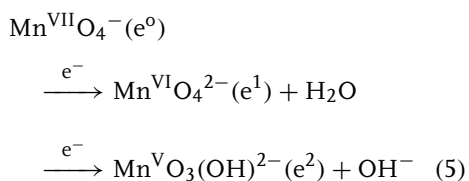


Fig. 1 Cyclic voltammograms of electrode reactions of the $\text{MnO}_4^{2-}/3-$ (I) and $\text{MnO}_4^{2-}/3-$ (II) couples in 1 M NaOH; 0.001 M KMnO_4 , $\nu = 1.5 \text{ V min}^{-1}$; (a) carbon paste electrode and (b) glassy carbon electrode (reprinted from Ref. 12, Copyright 1979 with permission from Elsevier).

to stabilize MnO_4^{2-} and MnO_4^{3-} , respectively, and to produce the following electron-transfer sequence:



Here, the electrochemical reduction of MnO_4^{2-} is accompanied by protonation under certain conditions. As shown in Fig. 1 [12], the close proximity of the $\text{Mn}^{\text{VII}}/\text{VI}$ and $\text{Mn}^{\text{VI}}/\text{V}$ electrode reactions reflects the positive shift in the $\text{Mn}^{\text{VI}}/\text{V}$ potential because of proton addition in the second step of Eq. (5). Under more acidic conditions, MnO_4^{2-} reduction proceeds to $\text{Mn}^{\text{IV}}\text{O}_2$ or to $\text{Mn}^{\text{II}}(\text{H}_2\text{O})_6^{2+}$.

For heteroleptic complexes not included in Table 1, redox potentials can be estimated by ligand additivity principles

[39–41]. Lever has successfully predicted $\text{Mn}^{\text{II/I}}$ potentials of 24 Mn-carbonyl complexes containing halide, pseudohalide, isonitrile, and phosphine co-ligands, with additivity parameters derived from the potentials of $\text{Ru}^{\text{III/II}}$ couples [39]. An important consideration for heteroleptic complexes is the influence of isomerism on redox thermodynamics. For $\text{Mn}(\text{CO})_n(\text{CNR})_{6-n}$ complexes, with $n = 2$ or 3, the $\text{Mn}^{\text{II/I}}$ potentials for cis/trans and fac/mer pairs differ by as much as 0.2 V [40]. The effect arises from the different σ -donor and π -acceptor abilities of carbonyl (CO) and isocyanide and their influence on the energy of the highest energy occupied molecular orbital (HOMO).

The electron-transfer reactions in Table 1 primarily are metal-centered processes. As a result, the separation between the potentials of successive electrode reactions generally is large. Values of $\Delta E^\circ = E_{\text{IV/III}}^\circ - E_{\text{III/II}}^\circ$ in Table 1 range from

0.5 to 1.7 V, and the corresponding comproportionation constants, $K_{\text{com}} = \exp(F\Delta E^{\circ'}/RT)$, range from 3×10^8 to 5×10^{28} . The larger values of $\Delta E^{\circ'}$ (e.g. CN^-) are consistent with highly metal-localized electron transfers, whereas as smaller values (e.g. Et_2dtc^-) indicate more effective distribution of charge upon a change in oxidation state.

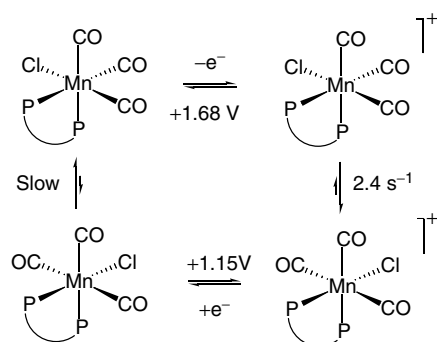
16.1.2.2 Coupled Chemical and Electrochemical Reactions

The influence of isomerism is revealed in the mechanistic electrochemistry of Mn carbonyls. One-electron oxidation of *fac*- $\text{Mn}(\text{CO})_3(\text{dpm})\text{Cl}$ ($\text{dpm} = \text{bis}-(\text{diphenylphosphino})\text{methane}$) is followed by rapid rearrangement of *fac*- $[\text{Mn}(\text{CO})_3(\text{dpm})\text{Cl}]^+$ to *mer*- $[\text{Mn}(\text{CO})_3(\text{dpm})\text{Cl}]^+$ [42]. However, reduction of the *mer*-Mn(II) species (protected against photolytic or solvolytic decomposition) to *mer*- $\text{Mn}(\text{CO})_3(\text{dpm})\text{Cl}$ is not followed by the facile rearrangement to the thermodynamically favored *fac*- $\text{Mn}(\text{CO})_3(\text{dpm})\text{Cl}$. The mechanism is summarized in Sch. 1, from which it is evident that (1) the *fac* isomer is thermodynamically favored in the Mn(I) state and the *mer* isomer in the Mn(II) state, (2) the *fac* isomer is 0.5 V more oxidizing than the *mer* isomer, and (3) the 17-e^- Mn^{II} species is kinetically more reactive than the 18-e^- Mn^{I} species.

Further structure-dependent reactivity is illustrated by the electrochemistry of 18-electron *trans*- $[\text{Mn}(\text{CO})_2(\eta^2\text{-dppe})_2]^+$ [I^+ , $\text{dppe} = 1, 2\text{-bis}(\text{diphenylphosphino})\text{ethane}$] (Fig. 2) [43]. As summarized in Sch. 2, the initial one-electron reduction of I^+ produces the metastable 19-electron species, I^\bullet , which rapidly ($k_2 \approx 4 \times 10^6 \text{ s}^{-1}$) extrudes one end of a coordinated dppe ligand and forms the 17-electron *trans*- $[\text{Mn}(\text{CO})_2(\eta^2\text{-dppe})(\eta^1\text{-dppe})]$, II^\bullet . This five-coordinate complex is reduced at the potential of initial reduction, affording two-electron transfer by an electrochemical-chemical-electrochemical (ECE) mechanism: $\text{I}^+ + 2\text{e}^- \rightarrow \text{II}^-$. Reversible one-electron electrochemistry of the $\text{II}^\bullet/\text{II}^-$ couple is observed on a subsequent cyclic scan at positive potentials (peaks B and C, Fig. 2). An interesting aspect of this voltammogram is the curve-crossing at -1.6 V . This phenomenon results from the contribution of the homogeneous chemical reaction, $\text{I}^+ + \text{II}^- \rightleftharpoons 2\text{II}^\bullet$, to the electrochemical response, producing an ECE-disproportionation (DISP) mechanism.

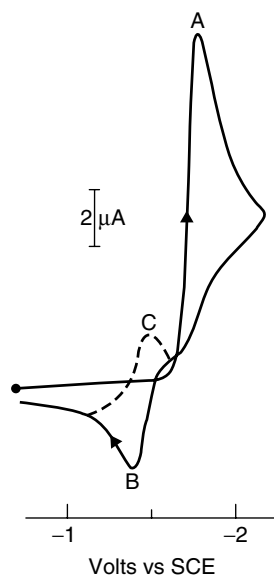
16.1.2.3 Electron-transfer Kinetics

Electrochemical electron-transfer rate constants have been measured less frequently



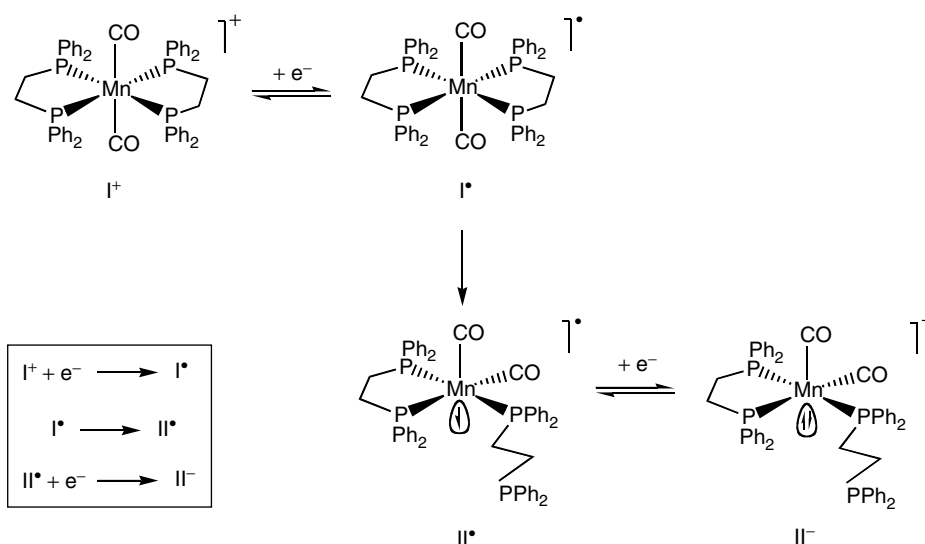
Scheme 1 Mechanism of electrochemically induced *fac*/*mer* isomerization of $\text{Mn}(\text{CO})_3(\text{dpm})\text{Cl}$ in $\text{CH}_3\text{CN}/0.1 \text{ M TEAClO}_4$ [42].

Fig. 2 Negative-scan cyclic voltammogram of 5×10^{-3} M $[\text{Mn}(\text{CO})_2(\text{dppe})_2] \text{PF}_6$ ($\text{I}^+ \text{PF}_6^-$) in THF, containing 0.3 M TBAClO₄ at $\nu = 0.5 \text{ V s}^{-1}$ (reprinted with permission from Ref. 43, Copyright 1988 American Chemical Society).



than redox potentials for these mononuclear manganese complexes. Even so, the values of $k_{s,h}$ in Table 1 encompass a range of 7 orders of magnitude. In circumstances in which little inner-shell reorganization accompanies electron transfer, as in the reduction of low-spin $\text{Mn}(\text{CN})_6^{4-}$ (t_{2g}^5) to low-spin $\text{Mn}(\text{CN})_6^{5-}$ (t_{2g}^6) (Eq. 3), $k_{s,h}$ is large (0.26 cm s^{-1}) [35]. However, in cases in which there is a change in the number of antibonding e_g^* electrons, structural change ensues and the rate constant can be much smaller. This is illustrated by the oxidation of $[\text{Mn}^{\text{II}}(\text{tripod})_2]$ ($t_{2g}^3 e_g^2$) to $[\text{Mn}^{\text{III}}(\text{tripod})_2]^+$ ($t_{2g}^3 e_g^1$), where $k_{s,h} = 7 \times 10^{-7} \text{ cm s}^{-1}$ (Fig. 3) [21]. Figure 4, which

depicts the sequential one-electron oxidations of $[\text{Mn}^{\text{II}}(\text{Me}_2\text{pzb})_2]$ ($\text{Me}_2\text{pzb}^- = \text{Tp}^{*-} = \text{hydrotris}(3,5\text{-dimethylpyrazol-1-yl})\text{borate}$) species [15], further illustrates the



Scheme 2 Mechanism of the two-electron reduction of $[\text{Mn}(\text{CO})_2(\eta^2\text{-dppe})_2]^+$ (I^+) to $[\text{Mn}(\text{CO})_2(\eta^2\text{-dppe})(\eta^1\text{-dppe})]$ (II^-) [43].

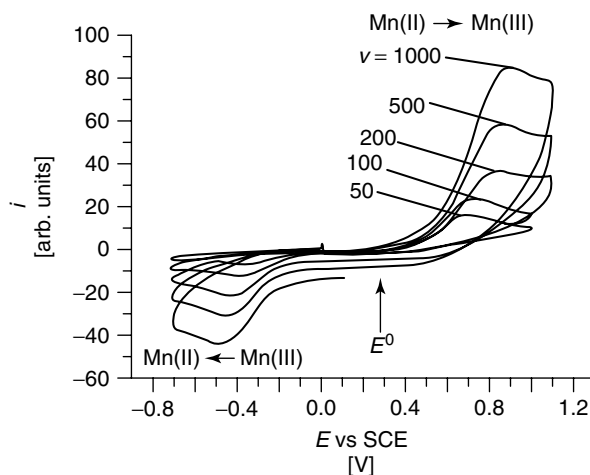


Fig. 3 Cyclic voltammograms for the oxidation of $[\text{Mn}^{\text{II}}(\text{tripod})_2]$ in CH_2Cl_2 at sweep rates of 50–1000 mV s^{-1} (reprinted from Ref. 21, Copyright 2002 with permission from Wiley-VCH).

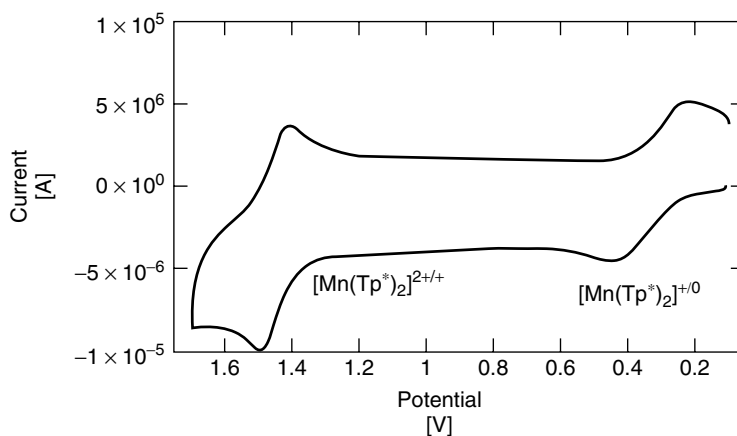


Fig. 4 Oxidative cyclic voltammogram of $2.4 \times 10^{-4} \text{ M Mn}^{\text{II}}(\text{Me}_2\text{pzb})_2$ in 1,2-dichloroethane containing 0.1 M TBAPF_6 at $\nu = 0.1 \text{ V s}^{-1}$ (reprinted with permission from Ref. 15, Copyright 2003 American Chemical Society).

influence of inner-shell reorganizations on electron-transfer rate. Here, $k_{\text{s,h}} = 5.9 \times 10^{-4} \text{ cm s}^{-1}$ for the oxidation of high-spin $[\text{Mn}^{\text{II}}(\text{Me}_2\text{pzb})_2]$ ($t_{2g}^3 e_g^2$) to low-spin $[\text{Mn}^{\text{III}}(\text{Me}_2\text{pzb})_2]^+$ (t_{2g}^4), which is accompanied by a large change in the average

Mn–N bond distance ($\Delta \text{Mn–N} = 0.26 \text{ \AA}$) [44], and $k_{\text{s,h}} = 1.1 \times 10^{-2} \text{ cm s}^{-1}$ for the oxidation of low-spin $[\text{Mn}^{\text{III}}(\text{Me}_2\text{pzb})_2]^+$ (t_{2g}^4) to low-spin $[\text{Mn}^{\text{IV}}(\text{Me}_2\text{pzb})_2]^{2+}$ (t_{2g}^3), for which the structural change is much less ($\Delta \text{Mn–N} = 0.025 \text{ \AA}$) [44].

16.1.3

Mononuclear Complexes with Porphyrins, Schiff Bases, Phthalocyanine, and Related Macrocyclic Ligands

16.1.3.1 Introduction

Manganese complexes with porphyrins, Schiff bases (SBs), and related ligands are of interest as catalysts for the epoxidation of olefins [6]; as models for the behavior of catalases, SODs, cytochrome P450, and other metalloenzymes [4, 5, 45]; and as the active component of membrane electrodes with unusual anion selectivities [46]. Because they are catalytic scavengers of reactive oxygen- and nitrogen-containing species, they have also been tested for their efficacy in the treatment of oxidative stress [47]. In addition, Mn–phthalocyanines are of interest as dyes and in display devices because of their intense coloration and resistance to degradation [48].

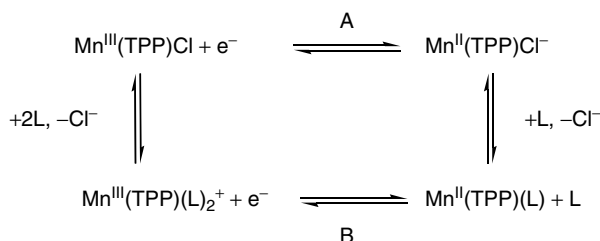
The utility of these complexes derives from the robustness provided by the equatorial coordination of the macrocyclic or polydentate ligand plus the ability to modulate chemical and physical properties and reactivity patterns by changing axial ligation and/or ligand substituent groups. Replacement of H with electron-donating or -withdrawing groups on the porphyrin skeleton or appended aromatic substituents can shift the potential of metal- or ligand-centered electron transfer by more than 0.5 V [49–51]. In addition, ligand substituents impart favorable solubility properties, steric constraints, or structural features not found in the unsubstituted porphyrin complex. Ligand structures and abbreviations are found in the Appendix.

The most common oxidation states in these complexes are Mn(III) and Mn(II). The more highly oxidized forms can be stabilized by strongly electron-donating

ligands or by appropriate control of experimental conditions. For Mn–porphyrins and phthalocyanines, the ligand-centered reductions producing metal-bound π anion and dianion species occur at potentials that are about 1.4 V more negative than that for $\text{Mn(III)} \rightarrow \text{Mn(II)}$ reduction. The ligand-centered reactions are separated by ~ 0.4 V. Depending on conditions, ligand-centered oxidations producing metal-bound π cation and dication species also may occur at potentials that are about 1 V more positive than the $\text{Mn}^{\text{III/II}}$ value and may precede, follow, or coincide with Mn(III) oxidation.

16.1.3.2 Studies in Nonaqueous Media

Because of its high reactivity and unsuitable solubility characteristics, complexes of the unsubstituted porphine (H_2P) are rarely investigated. The most widely studied manganoporphyrins are the tetraphenylporphyrin species, Mn(TPP)X , where X^- is a monodentate axial ligand. In noncoordinating, aprotic solvents, Mn(TPP)X is a five-coordinate, high-spin (d^4) complex in which the Mn(III) atom is displaced ~ 0.23 Å ($\text{X}^- = \text{Cl}^-$) above the porphyrin plane [52]. Reduction of Mn(TPP)Cl in a noncoordinating solvent occurs without a change in ligation but the Mn atom further extends to ~ 0.69 Å above the plane [53]. This large inner-shell reorganization causes the rate of heterogeneous $\text{Mn}^{\text{III/II}}$ electron transfer to be slow – $k_{\text{s,h}} = 2 \times 10^{-3} \text{ cm s}^{-1}$ [54, 55]. Electrochemical behavior is influenced dramatically by the presence of a coordinating solvent or a strong axial ligand (e.g. CH_3OH , py), which converts the Mn(III) form to a six-coordinate species with axial bis-ligation, while the Mn(II) form retains the five-coordinate geometry with the new axial ligand. Scheme 3 summarizes this reactivity, which produces demonstrable



Scheme 3 Electrode half-reaction scheme for five- and six-coordinate Mn(III) porphyrins [56–58].

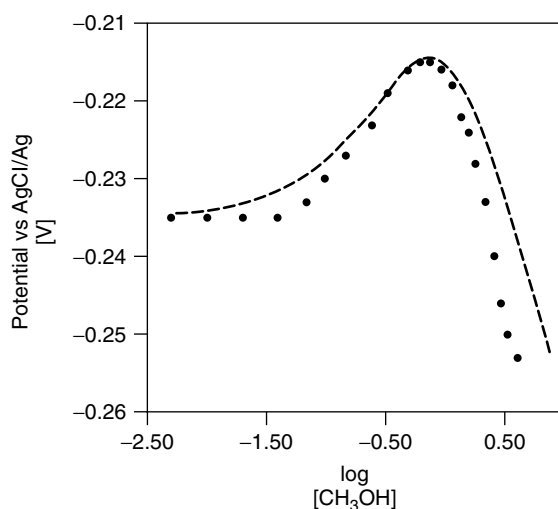


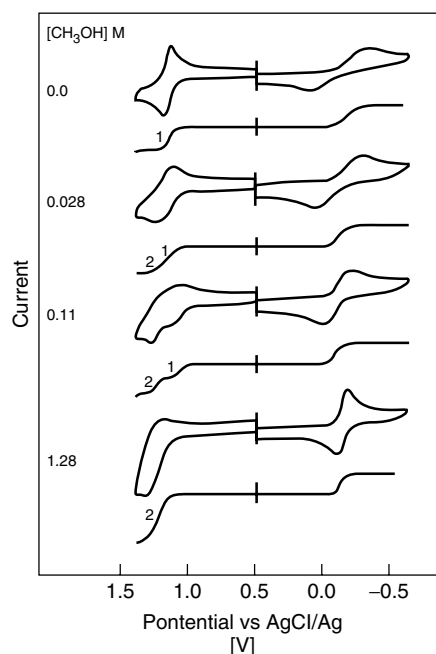
Fig. 5 Dependence of the potential of $\text{Mn}^{\text{III}}(\text{TPP})\text{Cl}$ reduction on CH_3OH concentration in 1,2-dichloroethane containing 0.1 M Et_4NCl at 296 K; (●) experimental data, (–) calculated data (reprinted with permission from Ref. 58, Copyright 1992 American Chemical Society).

effects on the thermodynamics of electron transfer. The $\text{Mn}^{\text{III/II}}$ potential is no longer dependent on the counterion present in the initial complex but rather depends on the nature and concentration of the new axial ligand [56–58]. Under appropriate conditions, the electrode potential can exhibit a biphasic dependence on the concentration of the added ligand, as illustrated in Fig. 5. The kinetics of $\text{Mn}^{\text{III/II}}$ electron transfer also is influenced by this change in composition. As shown in Fig. 6, the voltammetric peak potential separation decreases and the electron-transfer rate increases upon conversion to the six-coordinate species, which has its Mn atom in the porphyrin plane. Enhancement of

the $\text{Mn}^{\text{III/II}}$ electron-transfer rate by this axial bis-ligation is observed in both electrochemical [58] and homogeneous [59] experiments. The spectroscopic signatures of Mn^{III} and Mn^{II} porphyrins also are sensitive to the state of axial ligation, and these features have been used to characterize Mn–porphyrin species [60, 61].

Table 2 contains redox potentials for representative porphyrin, SB, and related complexes in nonaqueous solvents. These data primarily illustrate the influence of axial ligation and porphyrin substituents on the $\text{Mn}^{\text{III/II}}$ potential. Planar macrocyclic ligands such as phthalocyanine and corrole provide an equatorial coordination environment similar to that of porphyrins.

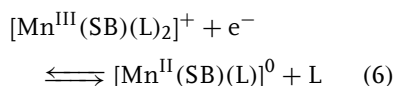
Fig. 6 Cyclic voltammograms at a 1.6-mm diameter Pt electrode (200 mV s^{-1}) and steady state voltammograms at a 25- μm diameter Pt electrode (20 mV s^{-1}) for oxidation and reduction of $8.5 \times 10^{-4} \text{ M Mn}^{\text{III}}(\text{TPP})\text{Cl}$ at 241 K in 1,2-dichloroethane containing 0.1 M TBABF₄ in the presence of 0–1.28 M CH₃OH. The peak potential separation at 200 mV s^{-1} for cyclic voltammetric reduction of $\text{Mn}^{\text{III}}(\text{TPP})\text{Cl}$ at 296 K in 1,2-dichloroethane decreases from ca 220 mV in 0 M CH₃OH to ca 70 mV in $\geq 1 \text{ M CH}_3\text{OH}$ (reprinted with permission from Ref. 58, Copyright 1992 American Chemical Society).



In the case of dinegative Pc^{2-} , the $\text{Mn}^{\text{III/II}}$ potential is similar to that of the porphyrins [62]. However, the trinegative tpc^{3-} ligand [63] shifts potentials to negative values and enables observation of $\text{Mn}^{\text{IV/III}}$ and $\text{Mn}^{\text{V/IV}}$ redox processes (Table 2).

The electrochemistry of Mn–Schiff base complexes closely parallels that of the Mn-porphyrins. A $\text{Mn}^{\text{III/II}}$ redox process is observed near 0 V versus NHE. In addition to changes in substituent groups and axial ligation, the variation of the donor atom set and denticity is possible with SBs. Redox potentials can be tuned over a range of $\sim 0.5 \text{ V}$ by using one or more of these modifications [65, 66]. The state of axial ligation often is not fully characterized for Mn–Schiff base complexes. However, it appears that many $\text{Mn}(\text{III})$ forms are high-spin, six-coordinate d^4 species and that the $\text{Mn}(\text{II})$ forms presumably are high-spin, five-coordinate d^5 species. Thus, for a

tetradentate SB ligand, the generic $\text{Mn}^{\text{III/II}}$ half-reaction is represented as:



Manganese (IV) and (V) complexes with a multiply bonded oxo ligand are potentially important intermediates in catalytic and biological processes. Although observed transiently, these species have not been generated in a stable form by electrochemical methods in aprotic media. However, strongly donating ligands such as the deprotonated tetraamide macrocycle (mac^{4-}) [68] enable access to high-valent oxo systems, as exemplified by the $[\text{Mn}^{\text{V/IV}}\text{O}(\text{mac})]^{-/2-}$ system in Table 2.

16.1.3.3 Studies in Aqueous Media

Manganese porphyrins can be solubilized in aqueous solution by the attachment of charged functional groups to the porphyrin

Tab. 2 Electrochemical data for manganese complexes with porphyrins, Schiff bases, and related macrocyclic ligands in nonaqueous media

Complex	Electrode Reaction ^a	Conditions	$E^{\circ/b}$, V versus NHE	References
<i>Five-coordinate porphyrins</i>				
Mn ^{III} (TPP)ClO ₄	A	CH ₃ CN/0.1 M TBAClO ₄	−0.43	57
Mn ^{III} (TPP)Cl	A	CH ₃ CN/0.1 M TBAClO ₄	−0.47	57
Mn ^{III} (TPP)N ₃	A	CH ₃ CN/0.1 M TBAClO ₄	−0.53	57
Mn ^{III} (tdcmp)Cl	A	C ₆ H ₅ CN/0.1 M TBAClO ₄	+0.05	50
Mn ^{III} (DPPF ₂₀)Cl	A	C ₆ H ₅ CN/0.1 M TBAClO ₄	−0.20	51
Mn ^{III} (DMHP)Cl	A	CH ₃ CN/0.1 M TPAClO ₄	−0.61	64
Mn ^{III} (EtioP)Cl	A	CH ₃ CN/0.1 M TPAClO ₄	−0.69	64
Mn ^{III} (tdmpp)Cl	A	C ₆ H ₅ CN/0.1 M TBAClO ₄	−0.81	50
<i>Six-coordinate porphyrins</i>				
Mn ^{III} (TPP)(CH ₃ OH) ₂ ⁺	B	CH ₂ Cl ₂ /0.1 M TEACl/1 M CH ₃ OH	−0.42	58
Mn ^{III} (TPP)(dmsO) ₂ ⁺	B	CH ₂ Cl ₂ /0.1 M TEAClO ₄ /1 M DMSO	−0.49	57
Mn ^{III} (TPP)(py) ₂ ⁺	B	CH ₂ Cl ₂ /0.1 M TEAClO ₄ /1 M py	−0.54	57
<i>Schiff bases</i>				
Mn ^{III} (salophen) ⁺	6	DMSO/0.1 M TEAClO ₄	−0.36	65
Mn ^{III} (saldpt) ⁺	6	DMSO/0.1 M TEAClO ₄	−0.44	66
Mn ^{III} (salen) ⁺	6	CH ₃ CN/0.1 M TBAClO ₄	−0.52	67
<i>Others</i>				
Mn ^{III} (Pc) ⁺		DMSO/TEAClO ₄	−0.32	62
Mn ^{IV} (tpc)Cl		CH ₂ Cl ₂ /0.1 M TBAClO ₄	+0.79 ^c −0.31 ^d	63
Mn ^V O(mac) [−]		DMSO/0.1 M TBAPF ₆	−0.27 ^c	68

^a From Sch. 3 or text.^b Mn^{III/II} potential, except as indicated.^c Mn^{V/IV} potential.^d Mn^{IV/III} potential.

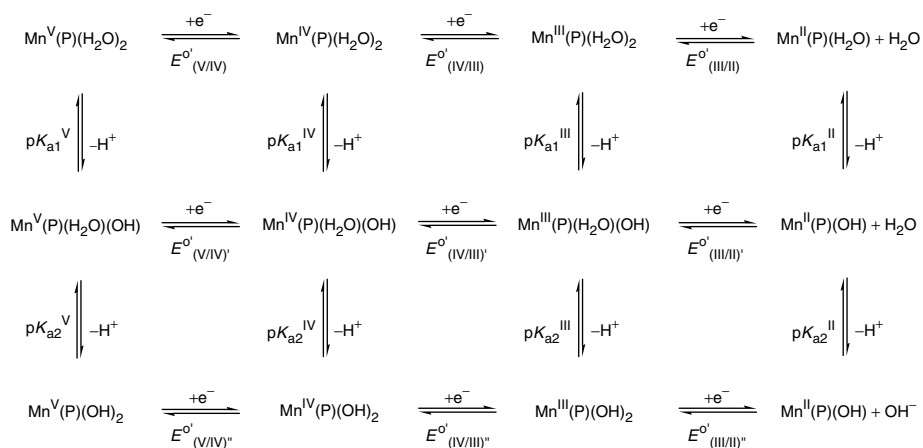
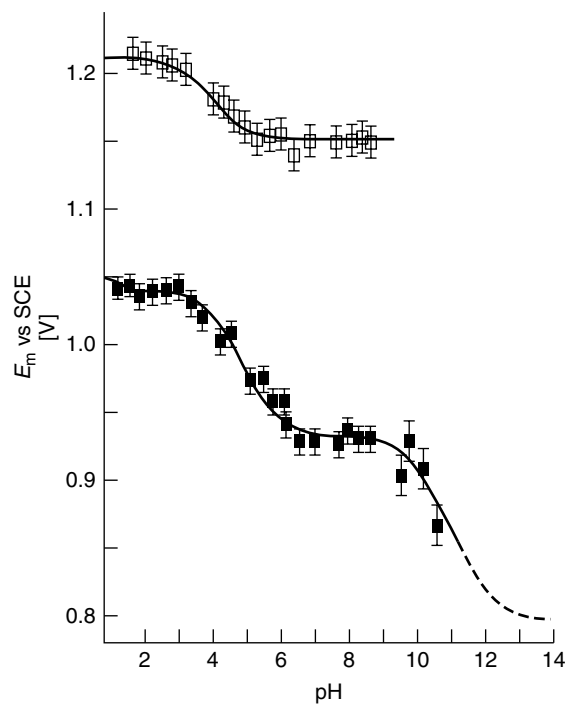
skeleton or its appended phenyl rings. The behavior of the tetrasulfonated TDM-SPP system is represented in Fig. 7 [69]. Sequential Mn^{V/IV} and Mn^{IV/III} electron-transfer reactions are observed from pH 1 to 10. At the highest acidities both axial ligands of Mn are H₂O, and E° values are independent of pH. The axial H₂O ligands become deprotonated as pH is increased. Thus, under some conditions, half-reactions involve both H⁺ and e[−] transfer, and E° values become pH dependent. Overall behavior is described by the sequence of reactions in Sch. 4. Data for selected aqueous Mn–porphyrin

systems are collected in Table 3. Accessible oxidation states, electrode potentials, and p*K*_a values are dependent on porphyrin substituents and experimental conditions. For this reason, the entire range of oxidation and protonation states has not been observed for a single system. Moreover, manganese porphyrins with a fully deprotonated oxo ligand (i.e. Mn^V = O) have not been observed under these conditions.

16.1.3.4 Electrocatalytic Studies

High-valent oxomanganese species are important intermediates in industrially significant catalytic reactions and are model

Fig. 7 Aqueous solution electrode potentials as a function of pH for Mn(TDMSP)(X)₂ porphyrins, with X = H₂O or OH[−] axial ligands. Top curve (□): Mn^{IV} → Mn^V oxidation; bottom curve (■): Mn^{III} → Mn^{IV} oxidation (reprinted with permission from Ref. 69, Copyright 1991 American Chemical Society).



Scheme 4 Electron- and proton-transfer reactions of manganese porphyrins in aqueous media.

reactants of similar catalytic processes in biological systems (e.g. cytochrome P450) [45, 75]. The mechanism of olefin epoxidation has been studied electrochemically

using Mn(TPP)Cl [76] or Mn(salen)Cl [66] as the source of manganese. As shown in Fig. 8, the oxidative process is initiated by the reduction of Mn(TPP)Cl (believed

Tab. 3 Electrochemical data for manganese porphyrins in aqueous media^a

Porphyrin	Axial ligation	<i>E</i> °, V versus NHE			Proton ionization			References
		V/IV	IV/III	III/II	oxidation state	p <i>K</i> _{a1}	p <i>K</i> _{a2}	
H ₂ TDMSPP	(H ₂ O) ₂	+1.45	+1.28		V	3.7		69
	(H ₂ O)(OH)	+1.39	+1.17		IV	4.1–4.7	9.9	
	(OH) ₂		+0.9		III	5.8	12.2	
H ₂ TDCSPP	(H ₂ O) ₂		+1.44		V			70
	(H ₂ O)(OH)		+1.29		IV	1.8		
	(OH) ₂				III	4.4		
H ₂ TMPyP	(H ₂ O) ₂			+0.02	III	8.0	10.6	71,72
H ₂ TMAP	(H ₂ O) ₂			−0.13	III	11.4		73
H ₂ DMHP	(H ₂ O)(OH)			−0.33 ^b				74

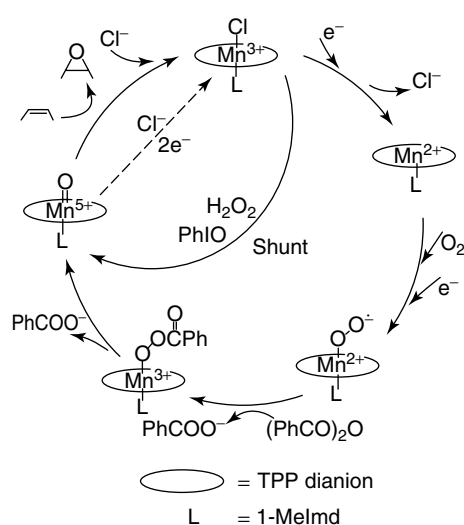
^a Defined on the basis of the half-reactions in Sch. 4.^b 47.5% ethanol in H₂O.

Fig. 8 Proposed mechanism of electrocatalytic epoxidation of olefins by manganese-porphyrin catalysts (reprinted with permission from Ref. 76, Copyright 1986 American Chemical Society).

to exist as $\text{Mn}(\text{TPP})(1\text{-MeIm})\text{Cl}$ in the presence of excess 1-methylimidazole) in an O_2 -saturated solution, which produces five-coordinate $[\text{Mn}(\text{TPP})(\text{Im})]$. This complex binds O_2 in an axial position and is reduced by a second electron to the $\text{Mn}(\text{II})$ -peroxo species, $[\text{Mn}^{\text{III}}(\text{TPP})(\text{O}_2)(1\text{-MeIm})]^-$. Benzoic anhydride, which is added to the solution as an electrophilic

activator, reacts with the bound peroxo and forms a $\text{Mn}^{\text{V}}=\text{O}$ center upon displacement of two moles of benzoate ion. This highly reactive $\text{Mn}^{\text{V}}=\text{O}$ species then epoxidizes the olefin. Although direct electrochemical reduction of $\text{Mn}^{\text{V}}=\text{O}$ presumably contributes to a loss of faradaic efficiency, product yields of 48–56% have been achieved.

16.1.4 Binuclear and Polynuclear Complexes

16.1.4.1 Introduction

Manganese forms a number of bi- and polynuclear complexes. In many cases, the metal centers are bridged by oxo- or O-donor ligands (consistent with the affinity of Mn for this element) and are capped by N-donor or other ligands at the remaining coordination sites. The most common structural forms discussed in this section are depicted in Chart 1. Interest in these compounds is predicated on the presence of multiple Mn atoms in close proximity to one another at several enzyme active sites [4, 5] and at the oxygen-evolving center of PSII [3]. In addition, manganese centers of high nuclearity

are being investigated actively as single-molecule magnets [77–79].

16.1.4.2 Studies in Nonaqueous Media

Among the earliest compounds investigated are those containing the binuclear di- μ -oxo core represented by (1). The complexes are isolated as mixed-valent Mn(IV,III) species, with four N-donor atoms from two bipyridyl or two phenanthroline ligands bound to each metal. The cyclic voltammetric response [80–82] of the more stable phen system, $[\text{Mn}_2\text{O}_2(\text{phen})_2]^{3+}$ is reproduced in Fig. 9. It consists of a one-electron oxidation to the Mn(IV,IV) species, $[\text{Mn}_2\text{O}_2(\text{phen})_2]^{4+}$, and a one-electron reduction to the Mn(III,III) species, $[\text{Mn}_2\text{O}_2(\text{phen})_2]^{2+}$:

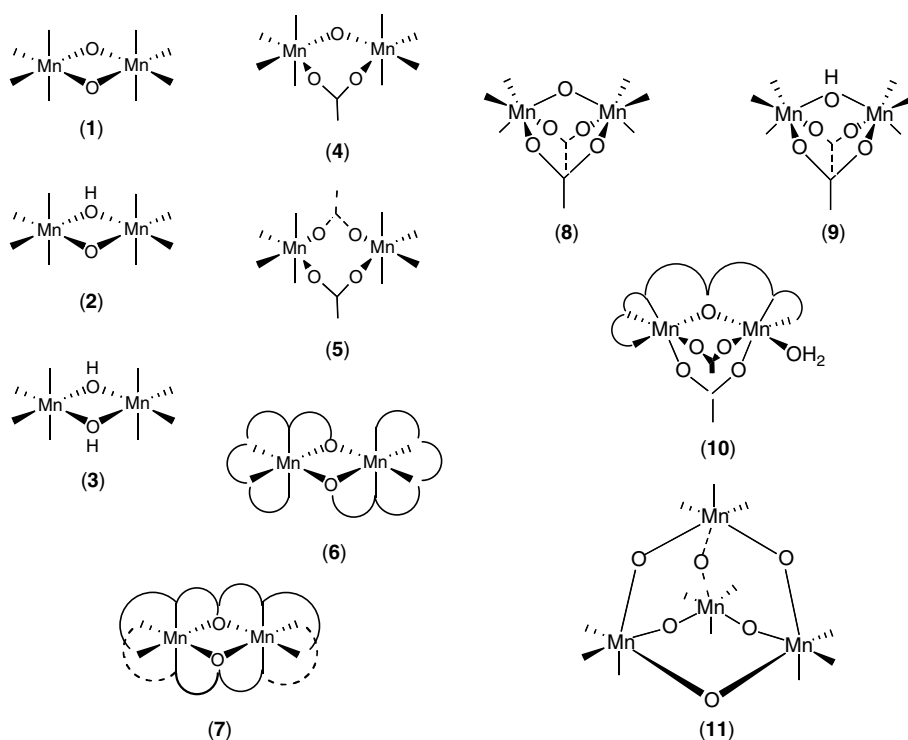


Chart 1 Polynuclear metal structures in Chapter 16.

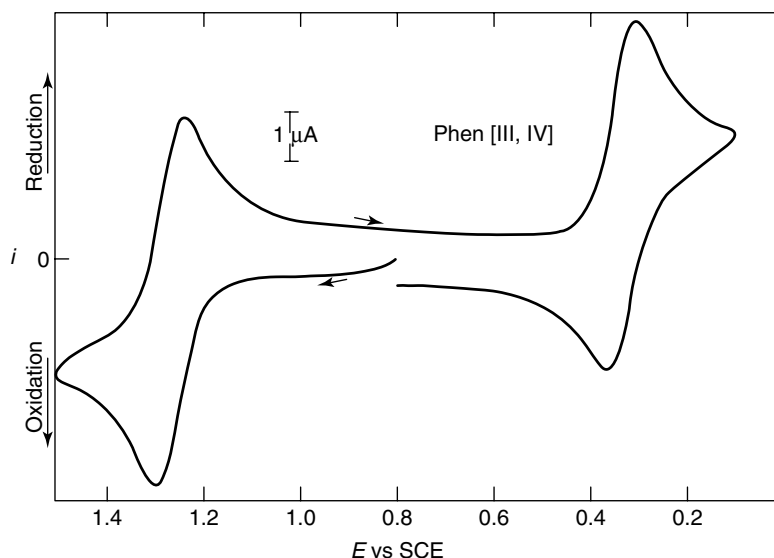
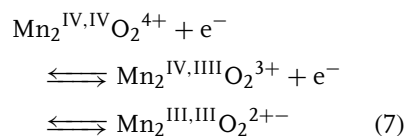


Fig. 9 Cyclic voltammogram for the oxidation and reduction of the $[\text{Mn}_2\text{O}_2(\text{phen})_4]^{3+}$ dimer at $\nu = 0.1 \text{ V s}^{-1}$ in $\text{CH}_3\text{CN}/0.3 \text{ M TEAClO}_4$ (reprinted with permission from Ref. 81, Copyright 1977 American Chemical Society).



The half-reaction potentials for these and the related redox couples are represented in Table 4. The large separation between potentials implies a large electrostatic interaction between Mn centers, which strongly stabilizes the intermediate mixed-valent state with respect to disproportionation. However, it is interesting to note from magnetic properties that the two Mn atoms in $[\text{Mn}_2\text{O}_2(\text{phen})_2]^{3+}$ are only weakly antiferromagnetically coupled ($J = -147 \text{ cm}^{-1}$) [83], indicating that there is little direct metal–metal interaction in the complex.

The potentials represented by Eq. (7) can be tuned in several ways. One approach is to replace one or more of the heterocyclic nitrogen donors with

a saturated amine, as reflected by the potentials of the (bispicen) versus (phen)₂ or (bpy)₂ complexes in Table 4 [84]. This change produces a negative shift of 300–400 mV in both the (IV,IV)/(IV,III) and (IV,III)/(III,III) potentials. A second strategy is to place sterically demanding substituents at key positions on the ligands. As illustrated by the comparison of the E° values for the bispicMe₂en versus bispicen [84] and pebMe₂pma versus pebpma [85, 86] complexes, the placement of a methyl group at the 6-position of the coordinating pyridyl groups produces positive shifts of 400–500 mV in the (IV,IV)/(IV,III) and (IV,III)/(III,III) potentials. Weaker metal–ligand bonding is caused by steric hindrance from these methyl substituents and is reflected in the changes in Mn–N bond distances and N–Mn–N bond angles at these sites [86].

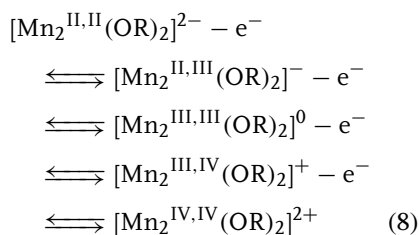
Tab. 4 Nonaqueous electrochemical data for binuclear manganese complexes

Structure	Capping ligands	Solvent/supporting electrolyte	E° , V versus NHE				References
			(IV,IV)/(IV,III)	(IV,III)/(III,III)	(III,III)/(II,II)	(III,II)/(II,II)	
1	(phen) ₂	(phen) ₂	CH ₃ CN/0.1 M TPAClO ₄	+1.57	+0.65		80
1	(phen) ₂	(phen) ₂	CH ₃ CN/0.3 M TEAClO ₄	+1.50	+0.57		81
1	(phen) ₂	(phen) ₂	CH ₃ CN/0.1 M TBAPF ₆	+1.54	+0.63		82
1	(bpy) ₂	(bpy) ₂	CH ₃ CN/0.1 M TPAClO ₄	+1.56	+0.60		80
1	(bpy) ₂	(bpy) ₂	CH ₃ CN/0.3 M TEAClO ₄	+1.49	irrev		81
1	bispicen	bispicen	CH ₃ CN/0.1 M TEAClO ₄	+1.16	+0.32		84
1	bispicMe ₂ en	bispicMe ₂ en	CH ₃ CN/0.1 M TEAClO ₄	+1.54	+0.77		84
1	pebpma	pebpma	CH ₃ CN/0.1 M TEAClO ₄	+1.24	+0.43		85
1	pebMe ₂ pma	pebMe ₂ pma	CH ₃ CN/0.1 M TBAClO ₄	+1.78	+0.98		86
2	(phen) ₂	(phen) ₂	CH ₃ CN/0.1 M TBAPF ₆		+0.61		82
3	(phen) ₂	(phen) ₂	CH ₃ CN/0.1 M TBAPF ₆			−0.10	82
1	bpia	bpia	CH ₃ CN/0.1 M TBAPF ₆	+1.24	+0.47		87
4	bpia	bpia	CH ₃ CN/0.1 M TBAPF ₆	+1.44	+1.22	+0.37	87
5	bpia	bpia	DMF/0.1 M TBAPF ₆			+0.89	87
6	hbpmc	hbpmc	CH ₃ CN/0.1 M TBAClO ₄			+0.95	87
7	(salmp) ₂	(salmp) ₂	CH ₃ CN/0.1 M TBAClO ₄	+1.34	+0.99	+0.20	88
8	HB(pz) ₃ [−]	HB(pz) ₃ [−]	CH ₃ CN/0.1 M TBAClO ₄	+1.86	+1.14 (qr)	−0.56 (irr)	89
8	Me ₃ tacn	Me ₃ tacn	CH ₃ CN/0.1 M TBAPF ₆	+1.85	+1.22	+0.11	90
9	Me ₃ tacn	Me ₃ tacn	CH ₃ CN/0.1 M TBAPF ₆			+1.14	90
8	bpy, Cl [−]	bpy, Cl [−]	DMF		+1.08	+0.69	91

Another strategy for modifying potentials is to alter the composition of the bridge between the metal centers. This can be done by protonation, which produces (2) and (3) in nonaqueous media. Larsen et al. [82] measured the energetics of electron-, proton-, and H-atom-transfer reactions for $[\text{Mn}_2\text{O}_2(\text{phen})_4]^{n+}$ complexes in CH_3CN and found that protonation greatly increases the ease of reduction. For example the E° for $\text{Mn(III,III)} \rightarrow \text{Mn(III,II)}$ reduction of the $[\text{Mn}_2(\text{O})(\text{OH})]^{3+}$ form (2) nearly equals that for $\text{Mn(IV,III)} \rightarrow \text{Mn(III,III)}$ reduction of the $[\text{Mn}_2\text{O}_2]^{3+}$ form (1) (Table 4). Thus, protonation can facilitate multi-electron transfer at oxo-bridged manganese centers. In addition, the donor strength of bridging ligands and redox potentials can be modified by replacing μ -oxo units with carboxylate (e.g. CH_3CO_2^-) (4,5) [87] or phenolate (6) [92] groups.

A particularly interesting example of binuclear Mn electrochemistry is that reported by Holm et al. for the $[\text{Mn}_2(\text{salmp})_2]^n$ ($n = 2+, 1+, 0, 1-, 2-$) complex [88]. H_3salmp is a pentadentate SB ligand that bridges both Mn centers by means of a centrally positioned phenolate group (7). $[\text{Mn}_2(\text{salmp})_2]^n$ undergoes four chemically reversible one-electron transfers,

encompassing five oxidation levels over a potential range of 1.5 V.



As shown by the cyclic voltammetric response in Fig. 10, the peak potential separation of the initial $\text{Mn(II,II)} \rightarrow \text{Mn(II,III)}$ electrode reaction is much larger than that of the other steps. This suggests significant inner-shell reorganization and a small rate of heterogenous electron transfer for oxidation of the fully reduced Mn(II,II) state. Similar kinetic sluggishness is observed for Mn(III)/Mn(II) electron-transfer reactions of some mononuclear complexes (see Sects 16.1.2 and 16.1.3).

A second structural motif in binuclear manganese chemistry is the triply bridged structure in which one μ -oxo unit has been replaced by two bridging carboxylates (8 in Sect. 16.1.4). The remaining coordination sites on each metal are commonly occupied by a tridentate tripod or a macrocyclic ligand such as HB(pz)_3^-

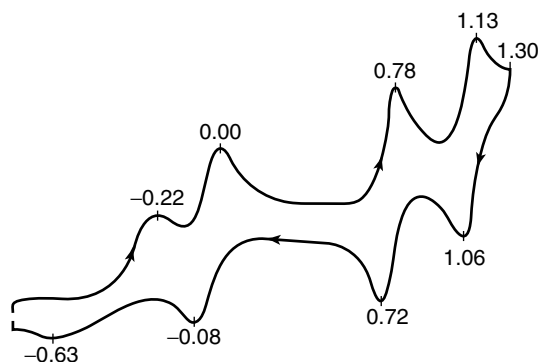
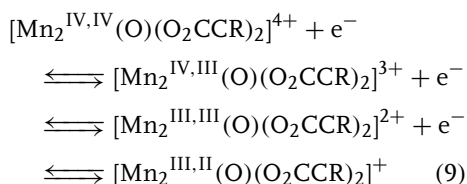


Fig. 10 Cyclic voltammogram for the oxidation of $[\text{Mn}_2(\text{salmp})_2]^{2-}$ in CH_3CN at $\nu = 0.05 \text{ V s}^{-1}$. Peak potentials in V versus SCE [+0.24 V versus NHE] are shown on the voltammetric trace (reprinted with permission from Ref. 88, Copyright 1991 American Chemical Society).

(Tp[−]) [89] or Me₃tacn [90]. Other combinations such as bidentate bipyridyl plus monodentate chloride ligands are possible [91]. These complexes have been prepared and studied as models for catalase, ribonucleotide reductase, and related manganese-containing enzymes [93]. [(Tp)₂Mn₂(O)(O₂CCR)₂]^{2+/+/0/−} [90] and [(Me₃tacn)₂Mn₂(O)(O₂CCR)₂]^{4+/3+/2+/+} [91] participate in four-membered redox series, which cover a potential range of ca 1.7 V.

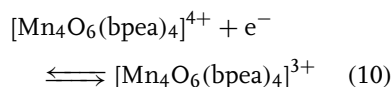


It is interesting to note that the (IV,IV)/(IV,III) and (IV,III)/(III,III) potentials of the [Mn₂(O)(O₂CCR)₂]ⁿ⁺ complexes (**8** in Sect. 16.1.4) with Tp[−] and Me₃tacn capping ligands are similar to one another and also to those of the [Mn₂O₂]ⁿ⁺ complexes (**1**) with terminal bpy and phen ligands (Table 4). The latter observation presumably is a result of the charge compensation that occurs when two mononegative bridging carboxylates replace a single, dinegative bridging oxo ligand. The comparative influence of Tp[−], tacn, and aromatic diimine ligands on metal-centered redox potentials has been discussed in Ref. 15.

[Mn₂(O)(O₂CCR)₂]ⁿ⁺ redox potentials also can be modified by protonation of the single μ -oxo bridge. The μ -hydroxo [(Me₃tacn)₂Mn₂^{II,II}(OH)(O₂CCR)₂]⁺ complex (**9** in Sect. 16.1.4) has been prepared and found to undergo sequential one-electron oxidations to [(Me₃tacn)₂Mn₂^{III,II}(OH)(O₂CCR)₂]²⁺ and [(Me₃tacn)₂Mn₂^{III,III}(OH)(O₂CCR)₂]³⁺ (Table 4) [90]. The change in potential upon protonation

is similar to that observed for di- μ -oxo species and increases the potential of Mn(III,III) → Mn(III,II) reduction to a value near that for Mn(IV,III) → Mn(III,III) reduction in the unprotonated complex.

Manganese exhibits a tendency to form structures of higher nuclearity, especially ones that are supported by bridging oxo ligands. An example that has been well-characterized structurally and electrochemically is the tetranuclear adamantane-like cluster, [Mn₄O₆(bpea)₄]⁴⁺ [94, 95], which is of interest for its relevance to the oxygen-evolving center (OEC) of PSII. Bpea is the tridentate *N,N*-bis(2-pyridylmethyl)ethylamine ligand, which binds to the vacant coordination sites in (**11** in Sect. 16.1.4). [Mn₄O₆(bpea)₄]⁴⁺ undergoes a chemically reversible one-electron reduction (Eq. 10) at +0.50 V in CH₃CN:



and exhibits coupled electron–proton-transfer chemistry in aqueous media [94]. It is of interest to note that the fully oxidized Mn(IV)₄ center in [Mn₄O₆(bpea)₄]⁴⁺ is achieved at a very accessible potential.

Manganese complexes of higher nuclearity are being investigated as single-molecule magnets (SMMs). An example is the Mn₁₂ cluster, [Mn₁₂O₁₂(O₂CCHCl₂)₁₆(H₂O)₄]⁰, whose structure in its two-electron reduced form ([Mn₁₂]^{2−}) is shown in Fig. 11 [96]. The [Mn₁₂]⁰, [Mn₁₂][−], and [Mn₁₂]^{2−} states of this structure have ground-state spin values of *S* = 10, 19/2, and 10, respectively. The oxidized forms have a larger barrier to magnetization relaxation and therefore exhibit SMM behavior at higher temperatures. The influence of oxidation level

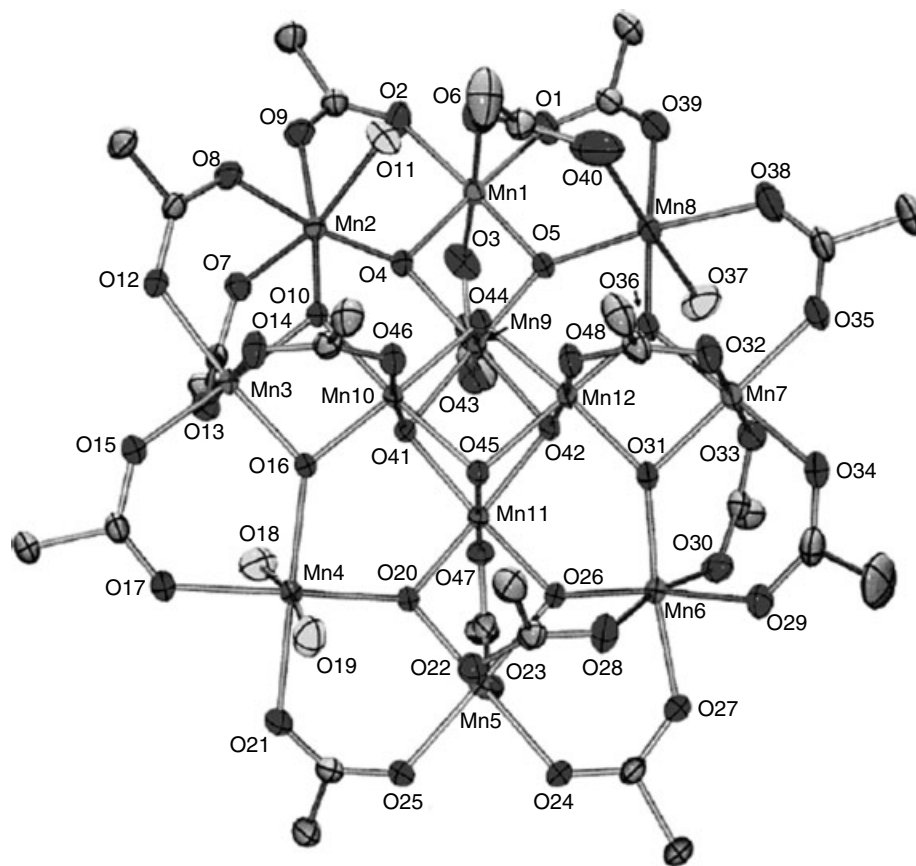
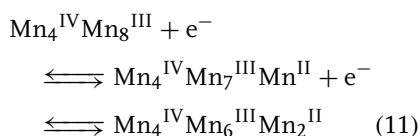


Fig. 11 Structure of the $(\text{PPh}_4)_2[\text{Mn}_{12}\text{O}_{12}(\text{O}_2\text{CCHCl}_2)_{16}(\text{H}_2\text{O})_4] \cdot 4\text{CH}_2\text{Cl}_2 \cdot \text{H}_2\text{O}$ dianion. Atoms Mn4 and Mn8 are reduced from Mn(III) to Mn(II) upon reduction of $[\text{Mn}_{12}]^0$ to $[\text{Mn}_{12}]^{2-}$.

Atoms Mn9 through Mn12 form the $\text{Mn}_4^{\text{IV}}\text{O}_4$ core at the center of the molecule (reprinted with permission from Ref. 96, Copyright 2003 American Chemical Society).

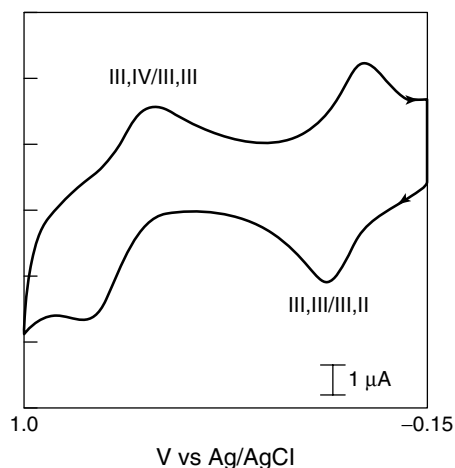
on magnetic properties is of fundamental importance in these compounds. The $[\text{Mn}_{12}\text{O}_{12}(\text{O}_2\text{CCHCl}_2)_{16}(\text{H}_2\text{O})_4]^0$ cluster exhibits reductions at +1.55 and +1.25 V in CH_3CN :



It is of interest to note that Mn(III) rather than Mn(IV) sites are reduced in

Eq. (11) and that the $\text{Mn}_4^{\text{IV}}\text{Mn}_7^{\text{III}}\text{Mn}^{\text{II}}$ and $\text{Mn}_4^{\text{IV}}\text{Mn}_6^{\text{III}}\text{Mn}_2^{\text{II}}$ reduction products are trapped valence species. Figure 11 shows that the dodecamangano cluster consists of a central Mn_4O_4 cubane unit surrounded by a nonplanar ring of eight Mn atoms that are bridged by and connected to the core by eight $\mu_3\text{-O}^{2-}$ ions. Sixteen bridging dichloroacetate ions and four H_2O groups are ligated to the eight Mn atoms in the ring. In the neutral $[\text{Mn}_{12}]$ form, the four central Mn atoms

Fig. 12 Cyclic voltammogram of $[\text{Mn}_2\text{O}_2(\text{phen})_4]^{3+}$ in pH 4.5 phosphate buffer at an activated glassy carbon electrode; $\nu = 0.1 \text{ V s}^{-1}$ (reprinted with permission from Ref. 97, Copyright 1992 American Chemical Society).



are Mn(IV) and the eight Mn atoms in the ring are Mn(III). On the basis of bond valence sum analyses of the structurally characterized products [96], Mn atoms at positions 4 and 8 are reduced in Eq. (11). The relative ease of reduction of these sites presumably results from their partial coordination by H_2O , which is less strongly donating than oxo or dichloroacetato ligands.

16.1.4.3 Studies in Aqueous Media

The electrochemistry of oxo-bridged manganese complexes in aqueous solution is characterized by coupled electron and proton-transfer reactions. The cyclic voltammetric behavior of $[\text{Mn}_2^{\text{IV,III}}\text{O}_2(\text{phen})_4]^{3+}$ in aqueous pH 4.5 phosphate buffer is illustrated in Fig. 12 [97]. It is of interest to compare this result with that obtained for the same complex dissolved in CH_3CN (Fig. 9). Two one-electron reactions are observed in each case. However, these correspond to $\text{Mn(IV,IV)} \rightarrow \text{Mn(IV,III)}$ and $\text{Mn(IV,III)} \rightarrow \text{Mn(III,III)}$ reductions in the nonaqueous solvent and to $\text{Mn(IV,III)} \rightarrow \text{Mn(III,III)}$ and $\text{Mn(III,III)} \rightarrow \text{Mn(III,II)}$ reductions in

H_2O . Moreover, the half-reactions in aqueous solution exhibit a pH dependence corresponding to the addition of one proton in conjunction with each electron. Thus, under the conditions of Fig. 12, the $[\text{Mn}_2^{\text{IV,III}}\text{O}_2]^{3+}$ center (1) is converted to an $[\text{Mn}_2^{\text{III,III}}\text{O}(\text{OH})]^{3+}$ center (2) in the first reduction and to an $[\text{Mn}_2^{\text{III,II}}(\text{OH})_2]^{3+}$ center (3) in the second. Electrode half-reactions, Nernst equations, and $\text{p}K_{\text{a}}$ values for the phen complex and for several related systems are summarized in Table 5. Precise data are somewhat difficult to obtain for these systems owing to the slow electron-transfer kinetics ($k_{\text{s,h}} \approx 10^{-3} \text{ cm}^2 \text{ s}^{-1}$ or less), the need to activate the working electrode surface to achieve a useful response, and the limited stability of some species in the presence of coordinating buffers. Nonetheless, $\text{p}K_{\text{a}}$ values for the bpy complex obtained from the Pourbaix diagram in Ref. 93 lead to pH-independent potentials of +1.1 and +0.5 V, respectively, for $[\text{Mn}_2^{\text{IV,III}}\text{O}(\text{OH})]^{3+}$ and $[\text{Mn}_2^{\text{IV,III}}\text{O}_2]^{3+}$ reduction, values that compare reasonably well to the results in Table 4, given the difference in solvent environments.

Tab. 5 Aqueous electrochemical data for binuclear manganese complexes

Half-reaction	Nernst equation (V versus NHE)	$pK_{a1}^{IV,III}$	$pK_{a1}^{III,II}$	$pK_{a1}^{II,I}$	References
$[Mn_2^{IV,III}O_2(phen)_4]^{3+} + H^+ + e^- \rightleftharpoons [Mn_2^{III,III}O(OH)(phen)_4]^{3+}$	$E^o = +1.30 - 0.079 \text{ pH}$		9.15		97
$[Mn_2^{IV,III}O_2(bpy)_4]^{3+} + H^+ + e^- \rightleftharpoons [Mn_2^{III,III}O(OH)(bpy)_4]^{3+}$	$E^o = +1.21 - 0.064 \text{ pH}$	2.3	11.0 (14.6) ^a		98
$[Mn_2^{IV,III}O_2(bispicen)_2]^{3+} + H^+ + e^- \rightleftharpoons [Mn_2^{III,III}O(OH)(bispicen)_2]^{3+}$	Na		8.35		99, 100
$[Mn_2^{IV,III}O_2(edda)_2]^- + H^+ + e^- \rightleftharpoons [Mn_2^{III,III}O(OH)(edda)_2]^-$	$E^o = +1.22 - 0.07 \text{ pH}$				100
$[Mn_2^{III,III}O(OH)(phen)_4]^{3+} + H^+ + e^- \rightleftharpoons [Mn_2^{III,II}(OH)_2(phen)_4]^{3+}$	$E^o = +0.62 - 0.066 \text{ pH}$			(11.5) ^a	97

^a Data in parentheses determined in CH₃CN [82].

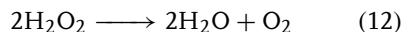
16.1.5

Biological Systems16.1.5.1 **Introduction**

Manganese is an element that is essential for life. It is present at the active site of many enzymes [4, 5]. Those enzymes in which the metal center is involved in a redox process are manganese catalase [101], peroxidase [102], and SOD [103]. In addition, a cluster containing four Mn and one Ca atoms in the water-oxidizing center (WOC) of PSII is the site at which dioxygen is produced photosynthetically on Earth [3, 104].

16.1.5.2 **Manganese Catalase**

Hydrogen peroxide, which is a by-product of the process of O_2 utilization by aerobic organisms, is a toxic substance. Its toxicity is ameliorated by the disproportionation of H_2O_2 into H_2O and O_2



This process is catalyzed by a variety of catalase enzymes, the most common being the heme catalases, which accomplish the two-electron chemistry of Eq. (12) at a mononuclear heme center. Here, both the iron and its surrounding porphyrin ligand participate to the extent of one electron each in the redox process. Manganese catalases contain a binuclear Mn center and cycle between $Mn_2(II,II)$ and $Mn_2(III,III)$ oxidation states while carrying out the disproportionation of H_2O_2 . The enzyme can

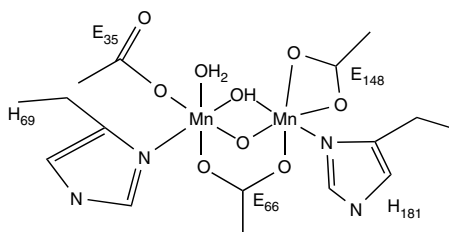
also exist in a superoxidized $Mn_2(III,IV)$ state, which does not destroy its catalytic activity.

The active site structure of the $Mn_2(III,III)$ form of *Lactobacillus plantarum* is depicted in Fig. 13 [105, 106]. The Mn centers are bridged by oxo, hydroxo, and carboxylato ligands in a manner similar to the binuclear structures (8–10) in Sect. 16.1.4. A proposed mechanism for hydrogen peroxide dismutation by Mn catalase is presented in Fig. 14. A number of model studies of H_2O_2 disproportionation employing bridged binuclear Mn complexes have been conducted [107].

16.1.5.3 **Manganese Peroxidase**

Peroxidases catalyze the oxidation of a wide variety of substrates through utilization of hydrogen peroxide. Manganese peroxidase is a heme protein that also contains a mononuclear Mn center linked to the iron-protoporphyrin IX prosthetic group through a propionate residue on the porphyrin [102, 105]. Manganese peroxidases are found in white rot fungi, where they serve to degrade lignin, a polyphenolic substance in woody plants that is otherwise resistant to degradation. As shown in the catalytic cycle in Fig. 15, Mn^{III} is produced by an electron-transfer reaction with the H_2O_2 -oxidized ferric porphyrin, at which point it diffuses into the lignin matrix and initiates the degradation of the polymer via phenol radical formation. Direct electron transfer between electrodes

Fig. 13 A schematic drawing of the active site of manganese catalase from *Lactobacillus plantarum* (reprinted from Ref. 105, Copyright 2003 with permission from Elsevier).



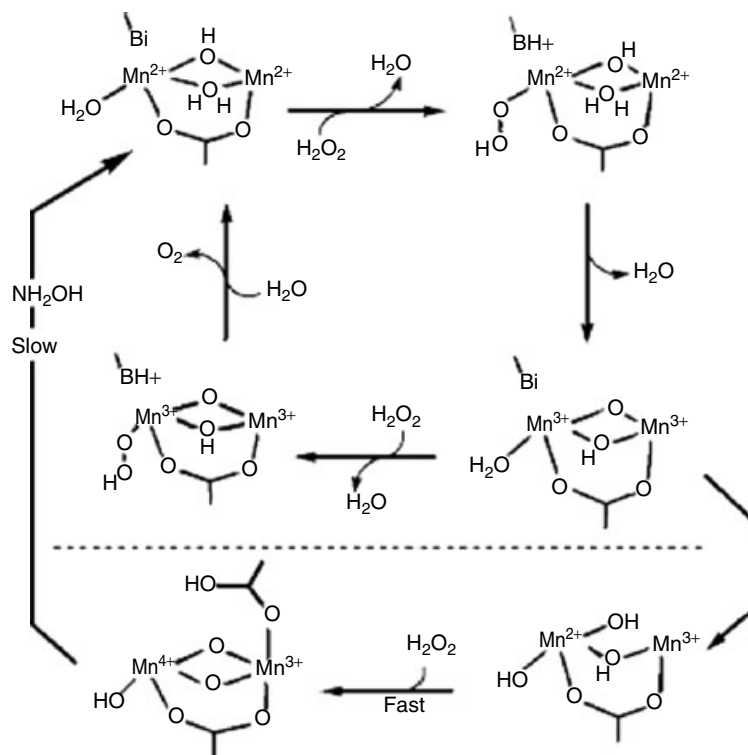


Fig. 14 Proposed mechanism for disproportionation of H_2O_2 by manganese catalase (reprinted with permission from Ref. 107, Copyright 2004 American Chemical Society).

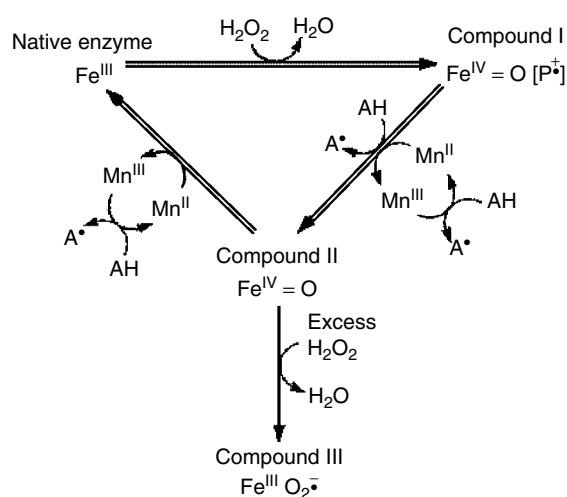
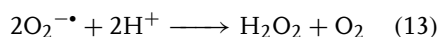


Fig. 15 Catalytic cycle of manganese peroxidase (Reprinted with permission from Ref. 102, Copyright 2000, Marcel Dekker).

and ligninolytic redox enzymes has been achieved, and the $\text{Fe}^{\text{III/II}}$ -heme potential has been measured [108]. However, the potential of the $\text{Mn}^{\text{III/II}}$ couple in Mn peroxidase has not been determined.

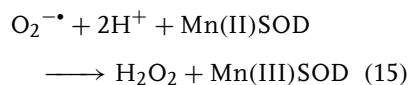
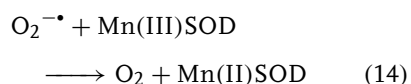
16.1.5.4 Manganese Superoxide Dismutase

Superoxide ion, $\text{O}_2^{\bullet-}$, is a highly toxic substance that is also a by-product of oxygen utilization in aerobic organisms. Its decomposition into H_2O_2 and O_2 ,



is catalyzed by SOD enzymes [103], of which there are Mn-, Fe-, Ni-, and Cu/Zn-containing forms. Absence of or defects in MnSOD are thought to be linked to disease states in humans.

The active site of manganese SOD contains a single five-coordinate Mn bound to three histidine imidazoles, a monodentate aspartate carboxylate, and a solvent molecule (H_2O or OH^- , depending on the oxidation state) [103]. The catalytic cycle of the enzyme, which is illustrated in Fig. 16, incorporates the following oxidative and reductive steps:



Electron transfer is coupled with proton transfer involving the metal-bound solvent molecule. For Eqs (14) and (15) to be thermodynamically favorable, the potential of the $\text{Mn}^{\text{III/II}}$ -SOD couple must lie between the values for superoxide oxidation and reduction ($\text{O}_2^{\bullet-} \rightarrow \text{O}_2 + \text{e}^-$, $E^{\circ'} = -0.16 \text{ V}$; $\text{O}_2^{\bullet-} + 2\text{H}^+ \rightarrow \text{H}_2\text{O}_2 + \text{e}^-$, $E^{\circ'} = +0.89 \text{ V}$ at pH 7) [109]. The potential has been measured for MnSOD from several organisms. From the results summarized in Table 6, the $\text{Mn}^{\text{III/II}}$ potential is intermediate to the values of the $\text{O}_2/\text{O}_2^{\bullet-}$ and $\text{O}_2^{\bullet-}/\text{H}_2\text{O}_2$ couples in all cases and hence is capable of accomplishing the Eqs (14) and (15). Values of $E^{\circ'}$ have been measured for wild-type and two mutated forms of human MnSOD. There are only small differences in $E^{\circ'}$, from which it is suggested that the role of the mutated His30 and Tyr34 residues is to support proton transport rather than redox potential tuning [110]. The $E^{\circ'}$ value from *Escherichia coli* is constant from pH 7.0 to 8.5 but decreases dramatically at higher pH ($\Delta E^{\circ'}/\Delta \text{pH} \approx -140 \text{ mV}$) [111, 112]. The pH dependence of the Mn(III/II) potential has not been studied for other organisms. It is interesting to note that the Fe-substituted form of MnSOD has $E^{\circ'} = -0.24 \text{ V}$ and that the Mn-substituted form of FeSOD has $E^{\circ'} > 0.96 \text{ V}$ [105]. These altered enzyme forms are ineffective in superoxide dismutation.

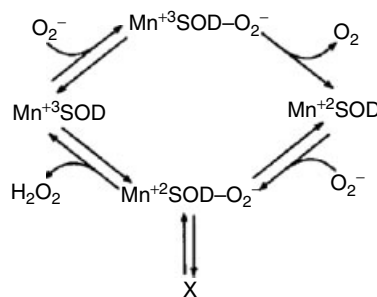


Fig. 16 Catalytic cycle of manganese superoxide dismutase; X is a dead-end peroxide complex (Reprinted with permission from Ref. 103, Copyright 2000, Marcel Dekker).

Tab. 6 Redox potentials of manganese superoxide dismutase

Organism	Method ^a	pH	$E^{\circ'}$, V versus NHE	References
WT Human	A	7.8	$+0.40 \pm 0.03$	110
H30N Human	A	7.8	$+0.37 \pm 0.03$	110
Y34F Human	A	7.8	$+0.44 \pm 0.03$	110
<i>Escherichia coli</i>	B	7.0	$+0.42$	111
<i>Escherichia coli</i>	C	7.0	$+0.31$	112
<i>Bacillus stearothermophilus</i>	C	7.0	$+0.26$	112

^a A: Chemically mediated spectroelectrochemical titration; B: Cyclic voltammetry at a 3-mercaptopropionic acid–modified Au electrode; C: Chemically mediated coulometric titration.

16.1.5.5 Oxygen-evolving Center in Photosystem II

The photosynthetic oxidation of water to O_2 is responsible for the generation of virtually all the dioxygen in the planet. This reaction is accomplished at a tetra-manganese cluster – now known to also contain Ca^{2+} and require Cl^- and possibly bicarbonate ion as cofactors – that lies at the oxidizing terminus of PSII in higher plants, green algae, and cyanobacteria (Fig. 17) [3, 104, 113]. The understanding

of the structure and function of this OEC or WOC, although still incomplete, has advanced considerably in concert with the knowledge of the structural and redox properties of mono-, bi-, and polynuclear manganese complexes described in the earlier parts of this chapter.

Photosynthesis is initiated by the absorption of a photon, which produces a charge-separated $P680^+Pheo^-$ state between P680, a special arrangement of four chlorophyll *a* molecules, and pheophytin

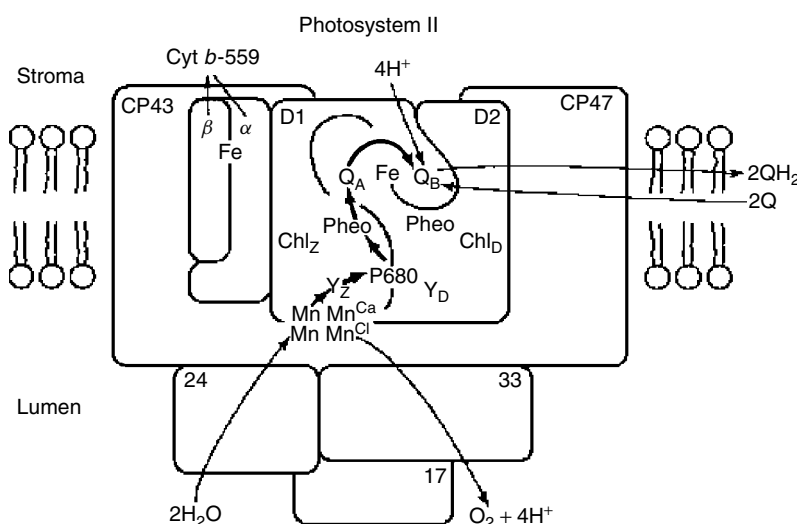
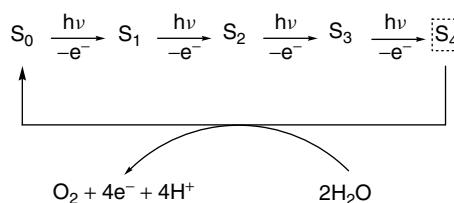
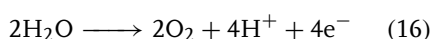


Fig. 17 A schematic drawing of photosystem II (Reprinted with permission from Ref. 113, Copyright 2000, Marcel Dekker).

Scheme 5 The S-state cycle of the oxygen-evolving center in photosystem II [114].



(Pheo). The negative charge is passed from Pheo[−] to the reducing terminus of PSII, where carbohydrate biomass is produced by the fixation of CO₂ and H₂O. The positive charge is passed from P680⁺ to a redox-active tyrosine residue (Y_Z−OH), which in its deprotonated radical form (Y_Z−O[•]) serves as the immediate oxidant of the OEC. This transfer of charge drives the OEC through a sequence of four one-electron steps known as the *S-state cycle* [114] (Sch. 5). Absorption of three photons promotes the OEC from its S₀ to the S₃ state. Absorption of a fourth photon and promotion to the S₄ state is accompanied by the almost simultaneous release of O₂ and return to the S₀ level. The OEC, therefore, is able to store charge and release it in a concerted manner to accomplish the four-electron oxidation of water to O₂:



The potential of Eq. (16) at pH 7 is +0.81 V [115]. As shown in Table 7, P680⁺

and Y_Z−O[•] are sufficiently potent oxidants to drive the individual steps in the S-state cycle and to convert water to dioxygen. The need for a catalyst and a mechanism for multielectron reaction is evident from the very positive potentials of the one-electron steps in H₂O to O₂ conversion [109]. It is of interest to note that the *E*^{o'} values of the individual S_{*i*} → S_{*i*+1} conversions are approximately equal. This indicates that proton transfer or a compositional or structural change must accompany each electron transfer to maintain the OEC potential at an accessible level. Although coupled electron–proton (or hydrogen atom) transfer maintains the requisite overall charge neutrality with each step, a proton-addition sequence of 1:0:1:2 also is likely. There is general agreement that the average oxidation state of Mn in the tetramanganese cluster advances from +3.25 to +4.25 upon S₀ → S₄ conversion, but there is no consensus on the formal oxidation state assignments at each stage in the cycle. The possibilities considered

Tab. 7 Redox potentials and oxidation state assignments of photosystem II components

Half-reaction	Potential, V versus NHE ^a	OEC state	Oxidation state assignments
P680 ⁺ + e [−] → P680	+1.12	S ₀	Mn ₄ (II,III,IV,IV) or Mn ₄ (III,III,III,IV)
Y _Z −O [•] + H ⁺ + e [−] → Y _Z −OH	+0.97	S ₁	Mn ₄ (III,III,IV,IV)
S ₁ + e [−] → S ₀	< +0.70	S ₂	Mn ₄ (III,IV,IV,IV)
S ₂ + e [−] → S ₁	+0.925	S ₃	Mn ₄ (IV,IV,IV,IV) or Mn ₄ (III,IV,IV,IV)-O [•]
S ₃ + e [−] → S ₂	+0.925	S ₄	Mn ₄ (IV,IV,IV,V) or Mn ₄ (IV,IV,IV,IV)-O [•]

^a From Ref. 104.

most likely on the basis of current evidence from XAS, EPR, and other spectroscopic experiments are included in Table 7.

Included among these are the steps in which electron transfer is assumed to involve an oxo ligand rather than a metal.

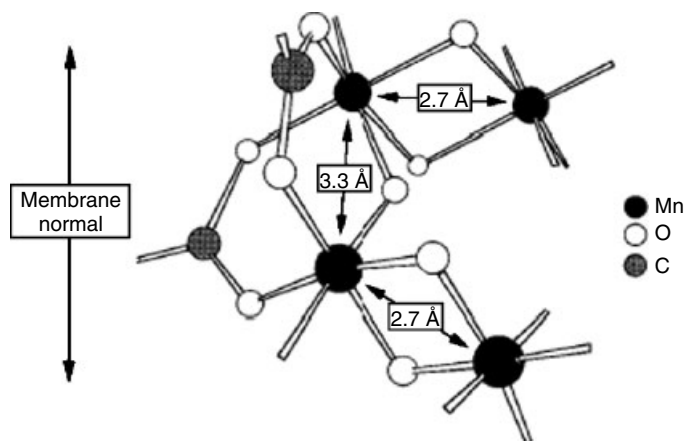


Fig. 18 A proposed model structure of the OEC of photosystem II (reprinted with permission from Ref. 3, Copyright 1996 American Chemical Society).

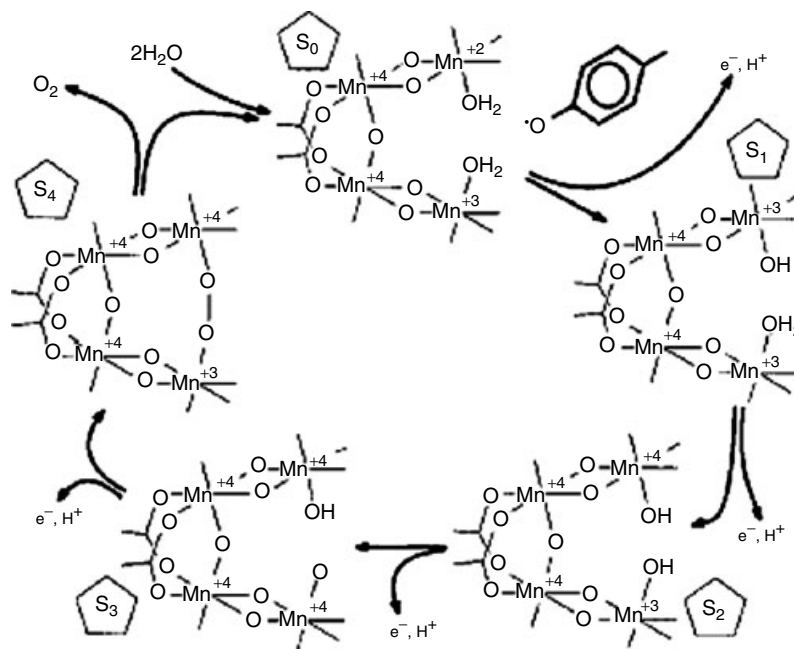


Fig. 19 A proposed mechanism for O_2 evolution from photosystem II based on the model structure in Fig. 18 (Reprinted with permission from Ref. 118, Copyright 1997, American Association for the Advancement of Science).

Many chemical model studies and proposed mechanisms have been presented for the OEC in PSII [3, 104, 116–128]. These draw heavily on the redox and coordination chemistry discussed in Sect. 16.1.4 and on the extensive work with isolated biological materials. Space does not permit full coverage; thus, only some of the more significant stages in the model and mechanism development are described in the following paragraphs.

An early model of the Mn complex in the OEC of PSII is shown in Fig. 18 [3]. This C-shaped structure consists of two di- μ -oxo-bridged Mn units connected by a single μ -oxo plus two di- μ -carboxylato bridges. These features are similar to (1) and (8), respectively, in Sect. 16.1.4. Important components of the model are the Mn-Mn distances of 2.7 Å in the di- μ -oxo unit and 3.3 Å in the mono- μ -oxo unit, which are consistent with the values obtained by EXAFS of the OEC in PSII. Although it was proposed initially that O₂ forms from the bridging oxo ligands, this possibility has been discounted.

An important stage in the OEC model development based on this C-shaped cluster is shown in Fig. 19 [118]. This description established the role of the neutral tyrosyl radical (Y_Z-O[•]) derived from the Tyr161 residue on the D1 polypeptide as the primary oxidant of the Mn₄ cluster. In addition, the Y_Z-OH/Y_Z-O[•] redox system provides a means of coupling proton transfer to electron transfer during the S-state cycle. It has been argued that these H⁺/e⁻ exchanges are accomplished exclusively by hydrogen atom transfer on

the basis of the approximate energetic equivalence of O-H bonds in Y_Z-OH and manganese-bound ligands. However, it is likely that H⁺ and e⁻ transfer is not so tightly concerted in all stages of O₂ evolution and that protons and electrons may move along separate paths in the higher S-state conversions [129]. The model in Fig. 19 also recognizes the possibility that dioxygen may be formed (via μ -peroxo species) at a terminal rather than at a bridging Mn site within the OEC. The development of O₂ evolution model chemistry has received considerable impetus from recent X-ray spectroscopic [128, 130, 131] and 3.2–3.5-Å resolution crystallographic [132, 133] studies, which reveal a prominent role for Ca²⁺. The structures shown in Fig. 20, which contain Ca²⁺ either as an integral component of a Mn₃Ca cluster or bridged across a multinuclear

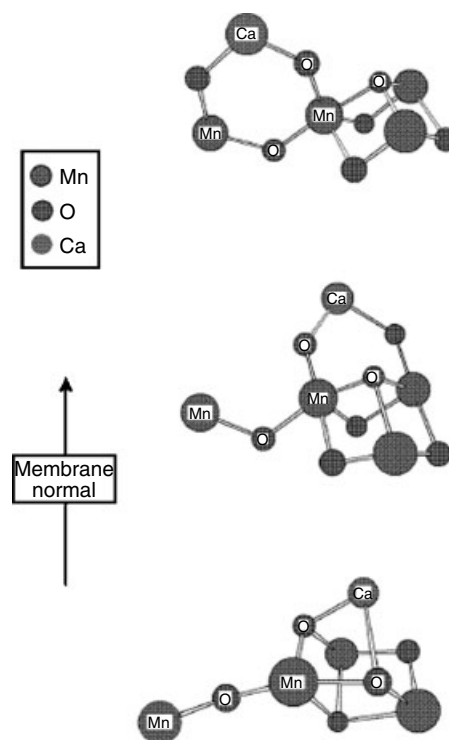


Fig. 20 Some proposed model structures of the OEC in photosystem II incorporating four Mn and one Ca atom (Reprinted with permission from Ref. 128, Copyright 2005, Springer-Verlag).

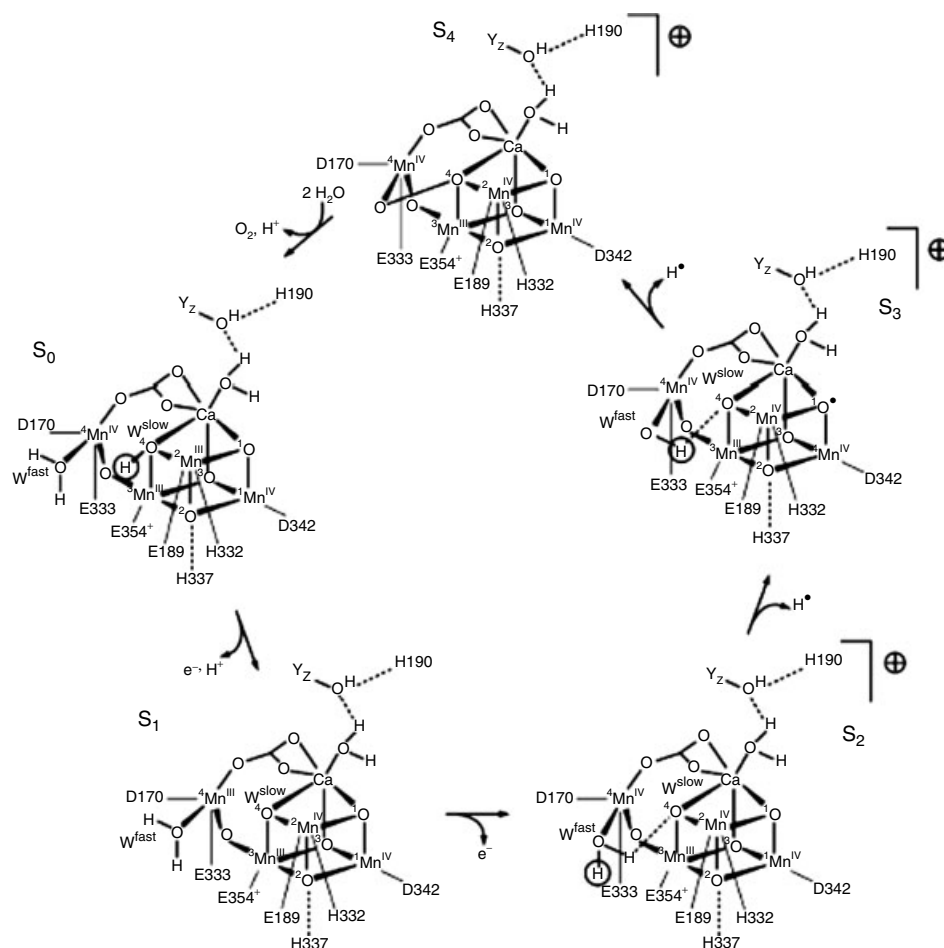


Fig. 21 A proposed mechanism for O_2 evolution from photosystem II based on a 4Mn-1Ca cluster (reprinted from Ref. 125, Copyright 2004 with permission from the Royal Society of Chemistry).

Mn array, are consistent with the experimentally established Mn-Ca distance of ~ 3.4 Å. Although seemingly implausible, intimate binding of Ca^{2+} is supported by the observation that Ca can be incorporated in MnO_2 minerals [134] and by the recent synthesis of an $\text{Mn}_{13}\text{Ca}_2$ cluster containing an Mn_4CaO_4 unit [135]. An important feature of these models is the presence of a “dangling” Mn atom connected the main cluster via a mono- μ -oxo or μ_4 -oxo bridge. One proposed mechanism based on recent

findings is shown in Fig. 21 [125]; other interpretations have been presented [122, 127, 129, 131]. Some important points to be resolved while achieving an understanding of the molecular basis of dioxygen evolution include the details of proton-transfer reactions; whether oxidations of the OEC involve solely metal-centered electron transfers or the formation of oxy radicals in some instances; the specific roles of Ca^{2+} and Cl^- ; and the details of the $\text{S}_2 \rightarrow \text{S}_3$ transition, which is thought

to involve a change in the Mn coordination number or structure within the Mn_4CaO_4 cluster [131].

References

1. J. J. Morgan, in *Metal Ions in Biological Systems*, (Eds.: A. Sigel, H. Sigel), Marcel Dekker, Basel, Switzerland, 2000 Vol. 37., Chapter 1.
2. M. M. Thackeray, *Prog. Solid State Chem.* **1997**, 1, 1–71.
3. V. K. Yachandra, K. Sauer, M. P. Klein, *Chem. Rev.* **1996**, 96, 2927–2950.
4. V. L. Pecoraro, (Ed.), *Manganese Redox Enzymes*, VCH Publishers, New York, 1992.
5. A. Sigel, H. Sigel, (Eds.), *Metal Ions in Biological Systems*, Marcel Dekker: Basel, Switzerland, 2000, Vol. 37.
6. T. Katsuki, *Coord. Chem. Rev.* **1995**, 140, 189–214.
7. G. P. Glasby, in *Marine Geochemistry*, (Eds.: H. Schulz, M. Zabel), Springer-Verlag, Berlin, 2000, pp. 335–372.
8. (a) F. A. Cotton, G. Wilkinson, C. A. Murillo et al., *Advanced Inorganic Chemistry*, 6th ed., John Wiley & Sons: New York, 1999, pp. 757–775. (b) D. C. Weatherburn, S. Mandel, S. Mukopadhyay et al., in *Comprehensive Coordination Chemistry II*, (Eds.: J. A. McCleverty, T. J. Meyer), 2nd ed., Elsevier, Amsterdam, 2004, Vol. 5, Chapter 5.1.
9. C. C. Liang, in *Encyclopedia of the Electrochemistry of the Elements*, (Ed.: A. J. Bard), Marcel Dekker, New York, 1973 Vol. 1, Chapter. I-6.
10. J. C. Hunter, A. Kozawa, in *Standard Potentials in Aqueous Solution*, (Eds.: A. J. Bard, R. Parsons, J. Jordan), Marcel Dekker, New York, 1985 Chapter. 15.
11. (a) T. A. Zordan, L. G. Hepler, *Chem. Rev.* **1968**, 68, 737–745. (b) S. G. Bratsch, *J. Phys. Chem. Ref. Data* **1989**, 18, 1–21.
12. K. Sekula-Brzezinska, P. K. Wrona, Z. Galus, *Electrochim. Acta* **1979**, 24, 555–563.
13. D. B. Freeman, G. Mamantov, *Electrochim. Acta* **1976**, 21, 257–261.
14. G. Gritzner, K. Danksagmüller, V. Gutmann, *J. Electroanal. Chem.* **1978**, 90, 203–210.
15. D. C. L. De Alwis, F. A. Schultz, *Inorg. Chem.* **2003**, 42, 3616–3622.
16. A. Neves, S. M. D. Erthal, I. Vencato et al., *Inorg. Chem.* **1992**, 31, 4749–4755.
17. K. Yamaguchi, D. T. Sawyer, *Inorg. Chem.* **1985**, 24, 971–976.
18. M. Hoogenraad, K. Ramkisoensing, S. Gorter et al., *Eur. J. Inorg. Chem.* **2002**, 377–387.
19. S. K. Chandra, P. Basu, D. Ray et al., *Inorg. Chem.* **1990**, 29, 2423–2428.
20. M. M. Morrison, D. T. Sawyer, *Inorg. Chem.* **1978**, 17, 338–339.
21. U. Kölle, U. Englert, *Eur. J. Inorg. Chem.* **2002**, 165–170.
22. G. Gritzner, H. Murauer, V. Gutmann, *J. Electroanal. Chem.* **1979**, 101, 185–200.
23. V. Manivannan, S. Dutta, P. Basu et al., *Inorg. Chem.* **1993**, 32, 769–771.
24. H. Yasuda, K. Suga, S. Aoyagui, *J. Electroanal. Chem.* **1978**, 86, 259–270.
25. P. M. Treichel, G. E. Dirreen, H. J. Mueh, *J. Organomet. Chem.* **1972**, 44, 339–352.
26. J. L. Robbins, N. M. Edelstein, S. R. Cooper et al., *J. Am. Chem. Soc.* **1979**, 101, 3853–3857.
27. T. Gennett, D. F. Milner, M. J. Weaver, *J. Phys. Chem.* **1985**, 89, 2787–2794.
28. M. M. Morrison, D. T. Sawyer, *Inorg. Chem.* **1978**, 17, 333–337.
29. O. R. Brown, S. Clarke, *J. Electroanal. Chem.* **1976**, 70, 87–93.
30. K. Wiegardt, W. Schmidt, W. Herrmann et al., *Inorg. Chem.* **1983**, 22, 2953–2956.
31. P. A. Anderson, I. I. Creaser, C. Dean et al., *Aust. J. Chem.* **1993**, 46, 449–463.
32. A. T. Kuhn, *J. Chem. Soc., Faraday Trans.* **1983**, 79, 417–430.
33. E. Bishop, P. Cofré, *Analyst* **1981**, 106, 429–432.
34. W. R. Fawcett, M. Opallo, *J. Electroanal. Chem.* **1992**, 331, 815–830.
35. M. Orlik, Z. Galus, *J. Electroanal. Chem.* **1994**, 366, 97–103.
36. J. Broda, Z. Galus, *Electrochim. Acta* **1983**, 28, 1523–1528.
37. W. D. Treadwell, W. E. Rath, *Helv. Chim. Acta* **1952**, 35, 2259–2275.
38. N. Hebenanz, F. H. Köhler, G. Müller et al., *J. Am. Chem. Soc.* **1986**, 108, 3281–3289.
39. A. B. P. Lever, *Inorg. Chem.* **1990**, 29, 1271–1285.
40. B. E. Bursten, *J. Am. Chem. Soc.* **1982**, 104, 1299–1304.

41. C. J. Pickett, D. Pletcher, *J. Organomet. Chem.* **1975**, 102, 327–333.
42. A. M. Bond, B. S. Grabaric, Z. Grabaric, *Inorg. Chem.* **1978**, 17, 1013–1018.
43. D. J. Kuchynka, J. K. Kochi, *Inorg. Chem.* **1988**, 27, 2574–2581.
44. Changes in Mn–N bond distances taken from, F. Hossain, *Synthesis, Structure and Characterization of Low-spin Mn(III)-Bis[poly(pyrazolyl)borate] Complexes*, M.S. Thesis; Indiana University-Purdue University Indianapolis, Indianapolis, IN; 2004
45. B. Meunier, S. P. de Visser, S. Shaik, *Chem. Rev.* **2004**, 104, 3947–3980.
46. N. A. Chaniotakis, A. M. Chasser, M. E. Meyerhoff et al., *Anal. Chem.* **1988**, 60, 185–188.
47. I. Batinic-Haberle, I. Spasojevic, R. D. Stevens et al., *J. Chem. Soc., Dalton Trans.* **2002**, 2689–2696.
48. A. B. P. Lever, *J. Porphyr. Phthalocya.* **2004**, 8, 1327–1342.
49. K. M. Kadish, *Prog. Inorg. Chem.* **1986**, 34, 435–605.
50. M. Autret, Z. Ou, A. Antonini et al., *J. Chem. Soc., Dalton Trans.* **1996**, 2793–2797.
51. R. Guillard, K. Perie, J.-M. Barbe et al., *Inorg. Chem.* **1998**, 37, 973–981.
52. A. Tulinsky, B. M. L. Chen, *J. Am. Chem. Soc.* **1977**, 99, 3647–3651.
53. R. B. Van Atta, C. E. Strouse, L. K. Hanson et al., *J. Am. Chem. Soc.* **1987**, 109, 1425–1434.
54. D. Feng, F. A. Schultz, *Inorg. Chem.* **1988**, 27, 2144–2149.
55. X. H. Mu, F. A. Schultz, *J. Electroanal. Chem.* **1993**, 353, 349–355.
56. K. M. Kadish, S. Kelly, *Inorg. Chem.* **1979**, 18, 2968–2971.
57. S. L. Kelly, K. M. Kadish, *Inorg. Chem.* **1982**, 21, 3631–3639.
58. X. H. Mu, F. A. Schultz, *Inorg. Chem.* **1992**, 31, 3351–3357.
59. I. Nakanishi, S. Fukuzumi, J.-M. Barbe et al., *Eur. J. Inorg. Chem.* **2000**, 1557–1562.
60. R. D. Arasasingham, T. C. Bruice, *Inorg. Chem.* **1990**, 29, 1422–1427.
61. X. H. Mu, F. A. Schultz, *Inorg. Chem.* **1995**, 34, 3835–3837.
62. A. B. P. Lever, P. C. Minor, J. P. Wilshire, *Inorg. Chem.* **1981**, 20, 2550–2553.
63. E. Steene, T. Wondimagegn, A. Ghosh, *J. Phys. Chem. B* **2001**, 105, 11406–11413.
64. L. J. Boucher, H. K. Garber, *Inorg. Chem.* **1970**, 9, 2644–2649.
65. R. K. Boggess, J. W. Hughes, W. M. Coleman et al., *Inorg. Chim. Acta* **1980**, 38, 183–189.
66. W. M. Coleman, R. R. Goehring, L. T. Taylor et al., *J. Am. Chem. Soc.* **1979**, 101, 2311–2315.
67. C. P. Horwitz, S. E. Creager, R. W. Murray, *Inorg. Chem.* **1990**, 29, 1006–1011.
68. J. M. Workman, R. D. Powell, A. D. Procyk et al., *Inorg. Chem.* **1992**, 31, 1550–1551.
69. T. W. Kaaret, G. H. Zhang, T. C. Bruice, *J. Am. Chem. Soc.* **1991**, 113, 4652–4656.
70. S. Jeon, T. C. Bruice, *Inorg. Chem.* **1992**, 31, 4843–4848.
71. M. Rodriguez, A. J. Bard, *Inorg. Chem.* **1992**, 31, 1129–1135.
72. A. Harriman, G. Porter, *J. Chem. Soc., Faraday Trans. II* **1979**, 75, 1532–1542.
73. A. Bettelheim, D. Ozer, R. Parash, *J. Chem. Soc., Faraday Trans. I* **1983**, 79, 1555–1564.
74. D. G. Davis, J. G. Montalvo Jr. *Anal. Chem.* **1969**, 41, 1195–1202.
75. M. K. Stern, J. T. Groves, in *Manganese Redox Enzymes*, (Ed.: V. L. Pecoraro), VCH Publishers, New York, 1992 Chapter. 11.
76. S. E. Creager, S. A. Raybuck, R. W. Murray, *J. Am. Chem. Soc.* **1986**, 108, 4225–4227.
77. O. Kahn, *Molecular Magnetism*, VCH Publishers, New York, 1993
78. K. Takeda, K. Awaga, *Springer Ser. Chem. Phys.* **2003**, 70, 41–57.
79. P. Thornton, *Ann. Rep. Prog. Chem., Sect. A: Inorg. Chem.* **2004**, 100, 217–227.
80. M. M. Morrison, D. T. Sawyer, *J. Am. Chem. Soc.* **1977**, 99, 257–258.
81. S. R. Cooper, M. Calvin, *J. Am. Chem. Soc.* **1977**, 99, 6623–6630.
82. A. S. Larsen, K. Wang, M. A. Lockwood et al., *J. Am. Chem. Soc.* **2002**, 124, 10112–10123.
83. P. M. Plaskin, R. C. Stouffer, M. Mathew et al., *J. Am. Chem. Soc.* **1972**, 94, 2121–2122.
84. P. A. Goodson, A. R. Oki, J. Glerup et al., *J. Am. Chem. Soc.* **1990**, 112, 6248–6254.
85. A. R. Oki, J. Glerup, D. J. Hodgson, *Inorg. Chem.* **1990**, 29, 2435–2441.
86. Y. Gultneh, T. B. Yisgedu, Y. T. Tesema et al., *Inorg. Chem.* **2003**, 42, 1857–1867.
87. M. U. Triller, W.-Y. Hsieh, V. L. Pecoraro et al., *Inorg. Chem.* **2002**, 41, 5544–5554.

88. S. B. Yu, C. P. Wang, E. P. Day et al., *Inorg. Chem.* **1991**, 30, 4067–4074.
89. J. E. Sheats, R. S. Czernuszewicz, G. C. Dismukes et al., *J. Am. Chem. Soc.* **1987**, 109, 1435–1444.
90. K. Wieghardt, U. Bossek, B. Nuber et al., *J. Am. Chem. Soc.* **1988**, 110, 7398–7411.
91. L. Dubois, D.-F. Xiang, X.-S. Tan et al., *Inorg. Chem.* **2003**, 42, 750–760.
92. C. Hureau, E. Anxolabéhère-Mallart, M. Nierlich et al., *Eur. J. Inorg. Chem.* **2002**, 2710–2719.
93. G. C. Dismukes, *Chem. Rev.* **1996**, 96, 2909–2926.
94. C. E. Dubé, D. W. Wright, S. Pal et al., *J. Am. Chem. Soc.* **1998**, 120, 3704–3716.
95. H. Visser, C. E. Dubé, W. H. Armstrong et al., *J. Am. Chem. Soc.* **2002**, 124, 11008–11017.
96. M. Soler, W. Wernsdorfer, K. A. Abboud et al., *J. Am. Chem. Soc.* **2003**, 125, 3576–3588.
97. R. Manchanda, H. H. Thorp, G. W. Brudvig et al., *Inorg. Chem.* **1992**, 31, 4040–4041.
98. H. H. Thorp, J. E. Sarneski, G. W. Brudvig et al., *J. Am. Chem. Soc.* **1989**, 111, 9249–9250.
99. P. A. Goodson, J. Glerup, D. J. Hodgson et al., *Inorg. Chem.* **1990**, 29, 503–508.
100. R. Manchanda, H. H. Thorp, G. W. Brudvig et al., *Inorg. Chem.* **1991**, 30, 494–497.
101. D. W. Yoder, J. Hwang, J. E. Penner-Hahn, in *Metal Ions in Biological Systems*, (Eds.: A. Sigel, H. Sigel), Marcel Dekker, Basel, Switzerland, 2000 Vol. 37, Chapter. 16.
102. M. H. Gold, H. L. Youngs, M. D. Sollewijn Gelpke, in *Metal Ions in Biological Systems*, (Eds.: A. Sigel, H. Sigel), Marcel Dekker, Basel, Switzerland, 2000 Vol. 37, Chapter. 17.
103. J. W. Whittaker, in *Metal Ions in Biological Systems*, (Eds.: A. Sigel, H. Sigel), Marcel Dekker, Basel, Switzerland, 2000 Vol. 37, Chapter. 18.
104. C. W. Hoganson, G. T. Babcock, in *Metal Ions in Biological Systems*, (Eds.: A. Sigel, H. Sigel), Marcel Dekker, Basel, Switzerland, 2000 Vol. 37, Chapter. 19.
105. D. C. Weatherburn, S. Mandel, S. Mukopadhyay et al., in *Comprehensive Coordination Chemistry II*, (Eds.: J. A. McCleverty, T. J. Meyer), 2nd ed., Elsevier, Amsterdam, 2004, pp. 100–101. Vol. 5, Chapter. 5.1.
106. V. V. Barynin, M. M. Whittaker, S. V. Antonyuk et al., *Structure* **2001**, 9, 725–738.
107. A. J. Wu, J. E. Penner-Hahn, V. L. Pecoraro, *Chem. Rev.* **2004**, 104, 903–938.
108. A. Christenson, N. Dimcheva, E. E. Fera-pontova et al., *Electroanalysis* **2004**, 16, 1074–1092.
109. D. T. Sawyer, A. Sobkowiak, J. L. Roberts Jr. *Electrochemistry for Chemists*, 2nd ed., Wiley-Intersciences, New York, 1995, Chapter. 9.
110. V. J.-P. Lévêque, C. K. Vance, H. S. Nick et al., *Biochemistry* **2001**, 40, 10586–10591.
111. Y. Tian, L. Mao, T. Okajima et al., *Anal. Chem.* **2004**, 76, 4162–4168.
112. G. D. Lawrence, D. T. Sawyer, *Biochemistry* **1979**, 18, 3045–3050.
113. R. J. Debus, in *Metal Ions in Biological Systems*, (Eds.: A. Sigel, H. Sigel), Marcel Dekker, Basel, Switzerland, 2000 Vol. 37, Chapter. 20.
114. B. Kok, B. Forbush, M. McGloin, *Photochem. Photobiol.* **1970**, 11, 457–476.
115. J. P. Hoare, in *Standard Potentials in Aqueous Solution*, (Eds.: A. J. Bard, R. Parsons, J. Jordan), Marcel Dekker, New York, 1985 Chapter. 4.
116. V. K. Yachandra, V. J. DeRose, M. J. Latimer et al., *Science* **1993**, 263, 675–679.
117. K. Wieghardt, *Angew. Chem., Int. Ed. Engl.* **1994**, 33, 725–728.
118. C. W. Hoganson, G. T. Babcock, *Science* **1997**, 277, 1953–1956.
119. C. Tommos, G. T. Babcock, *Acc. Chem. Res.* **1998**, 31, 18–25.
120. V. L. Pecoraro, M. J. Baldwin, M. T. Caudle et al., *Pure Appl. Chem.* **1998**, 70, 925–929.
121. J. Limburg, J. S. Vrettos, L. M. Liable-Sands et al., *Science* **1999**, 283, 1524–1527.
122. J. S. Vrettos, J. Limburg, G. W. Brudvig, *Biochim. Biophys. Acta* **2001**, 1503, 229–245.
123. S. Mukopadhyay, S. K. Mandal, S. Bhaduri et al., *Chem. Rev.* **2004**, 104, 3981–4026.
124. J. P. McEvoy, G. W. Brudvig, *Phys. Chem. Chem. Phys.* **2004**, 6, 4754–4763.
125. J. Messinger, *Phys. Chem. Chem. Phys.* **2004**, 6, 4764–4771.
126. P. E. M. Siegbahn, *Inorg. Chem.* **2000**, 39, 2923–2935.
127. M. Lundberg, P. E. M. Siegbahn, *Phys. Chem. Chem. Phys.* **2004**, 6, 4772–4780.
128. K. Sauer, J. Yano, V. K. Yachandra, *Photosynth. Res.* **2005**, 85, 73–86.
129. J. Barber, K. Ferreira, K. Maghlaoui et al., *Phys. Chem. Chem. Phys.* **2004**, 6, 4737–4742.

130. R. M. Cinco, J. J. Robblee, J. Messinger et al., *Biochemistry* **2004**, *43*, 13271–13282.
131. M. Haumann, C. Müller, P. Liebisch et al., *Biochemistry* **2005**, *44*, 1894–1908.
132. K. N. Ferreira, T. M. Iverson, K. Maghlaoui et al., *Science* **2004**, *303*, 1831–1838.
133. J. Biesiadka, B. Loll, J. Kern et al., *Phys. Chem. Chem. Phys.* **2004**, *6*, 4733–4736.
134. K. Sauer, V. K. Yachandra, *Proc. Natl. Acad. Sci. U.S.A.* **2002**, *99*, 8631–8636.
135. A. Mishra, W. Wernsdorfer, K. A. Abboud et al., *Chem. Commun.* **2005**, 54–56.

16.2 Technetium

16.2.1 Introduction

There are no stable isotopes of technetium. The element is obtained from fission reactions rather than from natural sources. The most commonly encountered isotopes are ^{99}Tc , a weak 292-keV β^- emitter with a half-life of 2.1×10^5 yr, and $^{99\text{m}}\text{Tc}$, a metastable form that decays to ^{99}Tc with the emission of a 140-keV γ photon with a half-life of ca 6 h. The coordination chemistry [1, 2] and electrochemistry [3] of technetium have been reviewed on several occasions.

Aside from interest in the properties of this relatively unexplored element, a primary reason for studying the electrochemistry of technetium is its utilization in nuclear medicine [4, 5]. Because of its relatively short half-life, the $^{99\text{m}}\text{Tc}$ isotope is well suited and widely applied to the radiopharmaceutical imaging of the bone and the heart, liver, kidney, and brain. The so-called first-generation imaging agents rely on the inherent biodistribution of technetium complexes (or their *in vivo* by-products) to reach an intended destination. Because this distribution varies with charge, size, lipophilicity, and other properties that depend on the oxidation state, extensive electrochemical investigations have been conducted on actual and model technetium radiopharmaceuticals [4]. More recently, second-generation imaging agents based on stable technetium complexes have emerged, which serve as a scaffold for the attachment of a biological molecule (e.g. a peptide, metalloprotein, monoclonal antibody) that can target a specific receptor site. The knowledge of

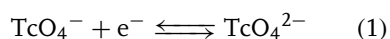
Tc redox properties, however, remains an essential component of second-generation applications.

This chapter covers the electrochemistry of technetium complexes in oxidation states I through VII and focuses on mononuclear Tc(II) through Tc(V) species that are actual or model components of radiopharmaceuticals. In addition, technetium forms mononuclear complexes with multiply bonded oxo groups, binuclear complexes with bridging oxygen atoms, and binuclear complexes with unsupported metal–metal bonds. These structural features are rare or unknown in manganese chemistry. Thus, the electrochemistry of technetium differs considerably from that of manganese but is comparable to that of its higher congener, rhenium.

16.2.2 Mononuclear Complexes

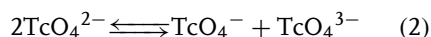
16.2.2.1 Oxo Complexes

The tetraoxo pertechnetate ion is a much less potent oxidant than its permanganate counterpart. A value of $E^{\circ'} = -1.50$ V versus NHE has been measured for the potential of the one-electron couple in Eq. (1) in CH_3CN [6].



A much more positive value of $E^{\circ'} = -0.88$ V is estimated in aqueous solution at $\text{pH} \geq 11$ by using short-time pulse techniques [7, 8]. The aqueous electrochemistry of TcO_4^- is complex. Under alkaline conditions, it is proposed that the protonation of TcO_4^{2-} and/or the expansion of its coordination shell follows Eq. (1) and produces a more easily reduced Tc(VI) species, resulting in a multielectron transfer [8]. The subsequent reduction can

be blocked by the addition of gelatin, which allows the chemical disproportionation reaction to occur:



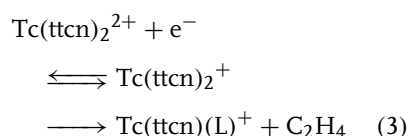
The estimated rate constant of Eq. (2) in 1 M NaOH is $k \approx 1.5 \times 10^5 \text{ M}^{-1} \text{ s}^{-1}$ [7]. In noncomplexing acid media, a three-electron reduction to Tc(IV) with the deposition of TcO_2 is observed [9].

Mononuclear oxo and nitrido complexes of Tc can be isolated with a variety of ancillary ligands. These compounds undergo reversible one-electron reactions encompassing oxidation states IV through VI [10–12] (Table 1).

16.2.2.2 Homoleptic and Mixed-ligand Complexes

A wide variety of mononuclear homoleptic and mixed-ligand technetium complexes without oxo ligands have been characterized in the oxidation states I through VI. The values of $E^{\circ'}$ for representative systems are represented in Table 1 [13–27]. The range of potentials accessible via ligand tuning for a given metal-centered redox event approaches 2 V. Soft sulfur, phosphorus, and arsenic donor ligands are notable for their ability to stabilize lower oxidation states and to produce stable complexes with biologically compatible redox potentials. The molar absorptivity of such compounds is frequently large, which enables the determination of $E^{\circ'}$ by using spectroelectrochemistry in addition to conventional voltammetric methods. The determination of $E^{\circ'}$ for the $\text{Tc}(\text{dmpe})_3^{2+/+}$ couple by using spectroelectrochemistry in an optically transparent thin-layer electrode (OTTLE) cell is illustrated in Fig. 1 [19]. As is

customary for second and third transition row elements, mononuclear Tc complexes are in the low-spin state. Hence, electron-transfer reactions proceed without large inner-shell reorganization, and electron-transfer rates are high. An exception to such a generally reversible response is the cathodic behavior of $\text{Tc}(\text{ttcn})_2^{2+}$. The reduction of this complex at +0.26 V is accompanied by the release of C_2H_4 and formation of a Tc(III) complex containing one trithiacyclononane (ttcn) and one tridentate acyclic $\text{L}^{2-} = ^-\text{SCH}_2\text{CH}_2\text{SCH}_2\text{CH}_2\text{S}^-$ ligand [17]:



The reliable prediction of redox potentials as a function of composition is useful in the synthetic design and application of technetium and other transition metal complexes. A parametric procedure for doing so on the basis of ligand additivity principles has been developed by Lever [28]. Lu et al. [29] used this scheme to correlate $\text{Tc}^{\text{IV/III}}$, $\text{Tc}^{\text{III/II}}$, and $\text{Tc}^{\text{II/I}}$ potentials with the composition of octahedral technetium complexes containing halide, nitrogen, and phosphorus donor ligands. The results are illustrated in Fig. 2 [29], where the observed potentials are plotted according to

$$E_{\text{obs}}^{\circ'} = S_{\text{M}}[\Sigma E_{\text{L}}(\text{L})] + I_{\text{M}} \quad (4)$$

where S_{M} and I_{M} are the slope and intercept of the correlation line and $\Sigma E_{\text{L}}(\text{L})$ is the sum of the ligand parameters. It is assumed that S_{M} and I_{M} are constant for a given metal and oxidation state, provided the coordination number, stereochemistry, and spin state do not

Tab. 1 Electrochemical data for mononuclear technetium complexes

Oxidation state change	Tc coordinate shell	Electrode reaction	Solvent/supporting electrolyte	$E^{\circ'}$, V versus NHE	References
<i>Oxo and nitrido complexes</i>					
VII/VI	O ₄	$\text{TcO}_4^- \rightleftharpoons \text{TcO}_4^{2-}$	CH ₃ CN/0.05 M TMAIO ₄	-1.50	6
VII/VI	O ₄	$\text{TcO}_4^- \rightleftharpoons \text{TcO}_4^{2-}$	H ₂ O/pH 12	-0.64	7, 8
VI/V	NCl ₄	$\text{TcNCl}_4^- + e^- \rightleftharpoons \text{TcNCl}_4^{2-}$	CH ₂ Cl ₂ /TBAPF ₆	+0.45	10
VI/V	OCl ₄	$\text{TcOCl}_4 + e^- \rightleftharpoons \text{TcOCl}_4^-$	CH ₂ Cl ₂ /TBAPF ₆	+2.08	10
V/V	OS ₄	$\text{TcO}(\text{mnt})_2^- + e^- \rightleftharpoons \text{TcO}(\text{mnt})_2^{2-}$	CH ₃ CN/0.1 M TBACIO ₄	-0.40	11
V/V	ON ₂ O ₃	$\text{TcO}(\delta\text{-Q})(\text{SB}) + e^- \rightleftharpoons \text{TcO}(\delta\text{-Q})(\text{SB})^-$	CH ₃ CN/0.1 M TEACIO ₄	-0.28	12
<i>Homoleptic complexes</i>					
VI/V	O ₆	$\text{Tc}(\text{DTBCat})_3 + e^- \rightleftharpoons \text{Tc}(\text{DTBCat})_3^-$	CH ₂ Cl ₂ /TBAPF ₆	+0.28	13
V/V	O ₆	$\text{Tc}(\text{mepp})_3^{2+} + e^- \rightleftharpoons \text{Tc}(\text{mepp})_3^+$	CH ₃ CN/0.1 M TEACIO ₄	+1.27	14
V/V	O ₆	$\text{Tc}(\text{DTBCat})_3^- + e^- \rightleftharpoons \text{Tc}(\text{DTBCat})_3^{2-}$	CH ₂ Cl ₂ /TBAPF ₆	-0.39	13
IV/III	N ₆	$\text{Tc}(\text{NCS})_6^{2-} + e^- \rightleftharpoons \text{Tc}(\text{NCS})_6^{3-}$	CH ₃ CN/0.1 M TBACIO ₄	+0.42	15
IV/III	O ₆	$\text{Tc}(\text{mepp})_3^+ + e^- \rightleftharpoons \text{Tc}(\text{mepp})_3$	CH ₃ CN/0.1 M TEACIO ₄	-0.54	13
III/II	S ₆	$\text{Tc}(\text{ttcn})_2^{3+} + e^- \rightleftharpoons \text{Tc}(\text{ttcn})_2^{2+}$	CH ₃ CN	+1.51	16, 17
II/I	C ₆	$\text{Tc}(\text{CNMe})_6^{2+} + e^- \rightleftharpoons \text{Tc}(\text{CNMe})_6^+$	CH ₃ CN/TEACIO ₄	+1.06	18
II/I	P ₆	$\text{Tc}(\text{dmpe})_3^{2+} + e^- \rightleftharpoons \text{Tc}(\text{dmpe})_3^+$	DMF/0.5 M TEACIO ₄	+0.62	19
II/I	S ₆	$\text{Tc}(\text{ttcn})_2^{2+} + e^- \rightleftharpoons \text{Tc}(\text{ttcn})_2^+$	CH ₃ CN	+0.26 (irr) ^a	17
<i>Mixed-ligand complexes</i>					
V/IV	P ₃ S ₃	$\text{Tc}(2\text{-Ph}_2\text{PC}_6\text{H}_4\text{S})_3^{2+} + e^- \rightleftharpoons \text{Tc}(2\text{-Ph}_2\text{PC}_6\text{H}_4\text{S})_3^+$	CH ₂ Cl ₂ /TBABF ₄	+1.91	20
IV/III	N ₄ Cl ₂	$\text{Tc}(\text{Me}_2\text{bpy})_2\text{Cl}_2^{2+} + e^- \rightleftharpoons \text{Tc}(\text{Me}_2\text{bpy})_2\text{Cl}_2^+$	DMA/0.5 M TBAPF ₆	+1.13	21
IV/III	N ₄ Cl ₂	$\text{Tc}(\text{py})_4\text{Cl}_2^{2+} + e^- \rightleftharpoons \text{Tc}(\text{py})_4\text{Cl}_2^+$	DMA/0.5 M TBAPF ₆	+1.34	21
IV/III	N ₃ Cl ₃	$\text{Tc}(\text{terpy})\text{Cl}_3^+ + e^- \rightleftharpoons \text{Tc}(\text{terpy})\text{Cl}_3$	DMA/0.5 M TBAPF ₆	+0.67	21
IV/III	N ₃ Cl ₃	$\text{Tc}(\text{py})_3\text{Cl}_3^+ + e^- \rightleftharpoons \text{Tc}(\text{py})_3\text{Cl}_3$	DMA/0.5 M TBAPF ₆	+0.79	21
IV/III	N ₂ P ₂ Cl ₂	$\text{Tc}(\text{bpy})(\text{PMe}_2\text{Ph})_2\text{Cl}_2^{2+} + e^- \rightleftharpoons \text{Tc}(\text{bpy})(\text{PMe}_2\text{Ph})_2\text{Cl}_2^+$	CH ₃ CN/0.1 M TEACIO ₄	+1.27	22
IV/III	N ₂ P ₂ O ₂	$\text{Tc}(\text{PPh}_3)_2(\text{acac})_2\text{en}^{2+} + e^- \rightleftharpoons \text{Tc}(\text{PPh}_3)_2(\text{acac})_2\text{en}^+$	PC/0.1 M TEACIO ₄	+0.92	23

(continued overleaf)

Tab. 1 (continued)

Oxidation state change	Tc coordinate shell	Electrode reaction	Solvent/supporting electrolyte	E° , V versus NHE	References
IV/III	P ₃ S ₃	$\text{Tc}(2\text{-Ph}_2\text{PC}_6\text{H}_4\text{S})_3^+ + \text{e}^- \rightleftharpoons \text{Tc}(2\text{-Ph}_2\text{PC}_6\text{H}_4\text{S})_3$	CH ₂ Cl ₂ /TBABF ₄	+1.16	20
IV/III	P ₄ S ₂	$\text{Tc}(\text{dmpe})_2(\text{tdt})^{2+} + \text{e}^- \rightleftharpoons \text{Tc}(\text{dmpe})_2(\text{tdt})^+$	DMF/0.5 M TEAClO ₄	+0.88	24
IV/III	As ₄ S ₂	$\text{Tc}(\text{diars})_2(\text{SPh})_2^{2+} + \text{e}^- \rightleftharpoons \text{Tc}(\text{diars})_2(\text{SPh})_2^+$	DMF/0.5 M TEAClO ₄	+1.14	25
III/II	N ₅ Cl	$\text{Tc}(\text{py})_5\text{Cl}^{2+} + \text{e}^- \rightleftharpoons \text{Tc}(\text{py})_5\text{Cl}^+$	DMA/0.5 M TBAPF ₆	+0.09	21
III/II	N ₄ Cl ₂	$\text{Tc}(\text{Me}_2\text{bpy})_2\text{Cl}_2^+ + \text{e}^- \rightleftharpoons \text{Tc}(\text{Me}_2\text{bpy})_2\text{Cl}_2$	DMA/0.5 M TBAPF ₆	-0.16	21
III/II	N ₄ Cl ₂	$\text{Tc}(\text{py})_4\text{Cl}_2^+ + \text{e}^- \rightleftharpoons \text{Tc}(\text{py})_4\text{Cl}_2$	DMA/0.5 M TBAPF ₆	-0.38	21
III/II	N ₃ Cl ₃	$\text{Tc}(\text{terpy})\text{Cl}_3 + \text{e}^- \rightleftharpoons \text{Tc}(\text{terpy})\text{Cl}_3^-$	DMA/0.5 M TBAPF ₆	-0.34	21
III/II	N ₃ Cl ₃	$\text{Tc}(\text{py})_3\text{Cl}_3 + \text{e}^- \rightleftharpoons \text{Tc}(\text{py})_3\text{Cl}_3^-$	DMA/0.5 M TBAPF ₆	-0.79	21
III/II	N ₂ P ₂ Cl ₂	$\text{Tc}(\text{bpy})(\text{PMe}_2\text{Ph})_2\text{Cl}_2^+ + \text{e}^- \rightleftharpoons \text{Tc}(\text{bpy})(\text{PMe}_2\text{Ph})_2\text{Cl}_2$	CH ₃ CN/0.1 M TEAClO ₄	+0.11	22
III/II	N ₂ P ₂ O ₂	$\text{Tc}(\text{PPh}_3)_2(\text{acac})_2\text{en}^+ + \text{e}^- \rightleftharpoons \text{Tc}(\text{PPh}_3)_2(\text{acac})_2\text{en}$	PC/0.1 M TEAClO ₄	-0.69	23
III/II	P ₃ S ₃	$\text{Tc}(2\text{-Ph}_2\text{PC}_6\text{H}_4\text{S})_3 + \text{e}^- \rightleftharpoons \text{Tc}(2\text{-Ph}_2\text{PC}_6\text{H}_4\text{S})_3^-$	CH ₂ Cl ₂ /TBABF ₄	+0.06	20
III/II	P ₄ S ₂	$\text{Tc}(\text{depe})_2(\text{Et}_2\text{dtc})^{2+} + \text{e}^- \rightleftharpoons \text{Tc}(\text{depe})_2(\text{Et}_2\text{dtc})^+$	DMF/0.5 M TEAClO ₄	+0.51	26
III/II	P ₄ S ₂	$\text{Tc}(\text{dmpe})_2(\text{tdt})^+ + \text{e}^- \rightleftharpoons \text{Tc}(\text{dmpe})_2(\text{tdt})$	DMF/0.5 M TEAClO ₄	-0.40	24
III/II	P ₄ Cl ₂	$\text{Tc}(\text{dmpe})_2\text{Cl}_2^+ + \text{e}^- \rightleftharpoons \text{Tc}(\text{dmpe})_2\text{Cl}_2$	DMF/0.5 M TEAClO ₄	-0.03	19
III/II	As ₄ S ₂	$\text{Tc}(\text{diars})_2(\text{SPh})_2^+ + \text{e}^- \rightleftharpoons \text{Tc}(\text{diars})_2(\text{SPh})_2$	DMF/0.5 M TEAClO ₄	-0.12	25
III/II	As ₄ Cl ₂	$\text{Tc}(\text{diars})_2\text{Cl}_2^+ + \text{e}^- \rightleftharpoons \text{Tc}(\text{diars})_2\text{Cl}_2$	DMF/0.5 M TEAClO ₄	+0.14	25, 27
II/I	N ₅ Cl	$\text{Tc}(\text{py})_5\text{Cl}^+ + \text{e}^- \rightleftharpoons \text{Tc}(\text{py})_5\text{Cl}$	DMA/0.5 M TBAPF ₆	-0.84	21
II/I	N ₄ Cl ₂	$\text{Tc}(\text{py})_4\text{Cl}_2 + \text{e}^- \rightleftharpoons \text{Tc}(\text{py})_4\text{Cl}_2^-$	DMA/0.5 M TBAPF ₆	-1.33	21
II/I	N ₃ Cl ₃	$\text{Tc}(\text{py})_3\text{Cl}_3^- + \text{e}^- \rightleftharpoons \text{Tc}(\text{py})_3\text{Cl}_3^{2-}$	DMA/0.5 M TBAPF ₆	-1.72	21
II/I	P ₄ S ₂	$\text{Tc}(\text{depe})_2(\text{Et}_2\text{dtc})^+ + \text{e}^- \rightleftharpoons \text{Tc}(\text{depe})_2(\text{Et}_2\text{dtc})$	DMF/0.5 M TEAClO ₄	-0.34	26
II/I	P ₄ S ₂	$\text{Tc}(\text{dmpe})_2(\text{tdt}) + \text{e}^- \rightleftharpoons \text{Tc}(\text{dmpe})_2(\text{tdt})^-$	DMF/0.5 M TEAClO ₄	-1.02	24
II/I	P ₄ Cl ₂	$\text{Tc}(\text{dmpe})_2\text{Cl}_2 + \text{e}^- \rightleftharpoons \text{Tc}(\text{dmpe})_2\text{Cl}_2^-$	DMF/0.5 M TEAClO ₄	-1.21	19
II/I	As ₄ S ₂	$\text{Tc}(\text{diars})_2(\text{SPh})_2 + \text{e}^- \rightleftharpoons \text{Tc}(\text{diars})_2(\text{SPh})_2^-$	DMF/0.5 M TEAClO ₄	-1.02	25
II/I	As ₄ Cl ₂	$\text{Tc}(\text{diars})_2\text{Cl}_2 + \text{e}^- \rightleftharpoons \text{Tc}(\text{diars})_2\text{Cl}_2^-$	DMF/0.5 M TEAClO ₄	-1.06	25, 27

^a Irreversible reduction (see text).

Fig. 1 Spectroelectrochemical characterization of the $\text{Tc}(\text{dmpe})_2^{2+/+}$ redox couple in 0.5 M TEAClO_4 /propylene carbonate. Applied potential in V versus NHE for traces (a)–(j) – +0.80, +0.60, +0.58, +0.56, +0.54, +0.52, +0.50, +0.48, +0.46, and +0.30. For $\text{Tc}(\text{dmpe})_2^{2+/+}$ in propylene carbonate, $E^\circ = +0.53$ V (reprinted with permission from Ref. 19, Copyright 1984 American Chemical Society).

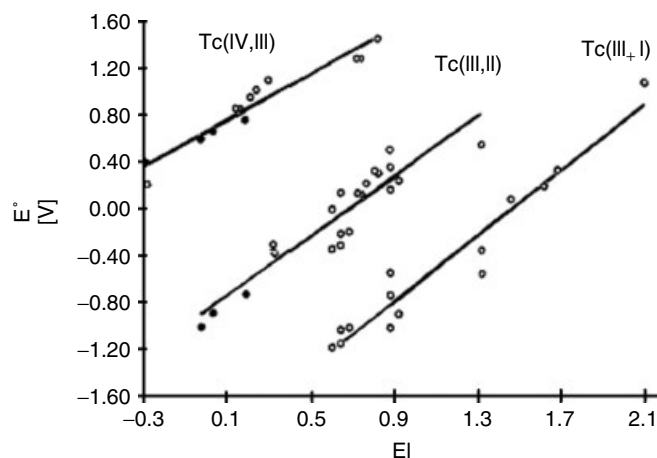
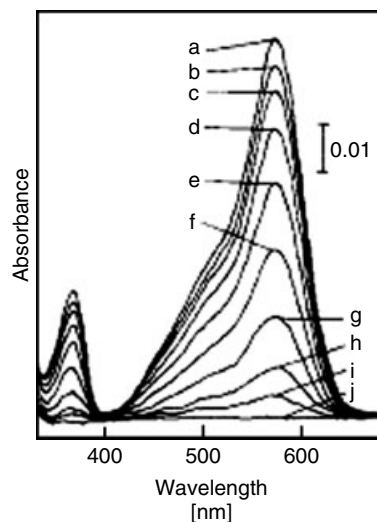


Fig. 2 Plots of E°' for $\text{Tc}^{\text{IV/III}}$, $\text{Tc}^{\text{III/II}}$, and $\text{Tc}^{\text{II/I}}$ redox couples versus the sum of ligand parameters, according to Eq. (4) (reprinted with permission from Ref. 29, Copyright 1990 American Chemical Society).

change. Figure 2 shows an excellent correlation with the predictions. The plots for the $\text{Tc}^{\text{IV/III}}$, $\text{Tc}^{\text{III/II}}$, and $\text{Tc}^{\text{II/I}}$ couples are linear and nearly parallel. The slopes of $S_M = 1.00 \pm 0.10$, 1.29 ± 0.08 , and 1.39 ± 0.12 , respectively, are quite large relative to values of other transition elements and indicate an excellent means

of modulating technetium-based redox potentials through the adjustment of ligand composition.

In some cases, agreement with the predictions of the Lever parameterization scheme is not exact. For example, Table 1 shows that the $\text{Tc}^{\text{III/II}}$ potentials of $\text{Tc}(\text{Me}_2\text{bpy})_2\text{Cl}_2^{+/0}$ and $\text{Tc}(\text{terpy})\text{Cl}_3^{0/-}$

are 0.22 and 0.45 V more positive than the values for $\text{Tc}(\text{py})_4\text{Cl}_2^{+/0}$ and $\text{Tc}(\text{py})_3\text{Cl}_3^{0/-}$ [21]. Such differences are not observed for the corresponding $\text{Tc}^{\text{IV/III}}$ potentials. Because py, bpy, and terpy have nearly identical ligand parameters per diimine N donor [28], these results indicate that polypyridyl ligands are more effective than a comparable number of monopyridines in stabilizing $\text{Tc}(\text{II})$ versus $\text{Tc}(\text{III})$.

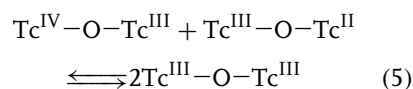
16.2.3

Binuclear Complexes

16.2.3.1 Oxo-bridged Complexes

Technetium forms a number of binuclear complexes in which the metal atoms are joined by a single oxygen bridge and do not contain any multiply bonded oxo groups (1, Chart 1). These complexes undergo reversible electron transfers encompassing the $\text{Tc}^{\text{IV}}-\text{O}-\text{Tc}^{\text{IV}}$, $\text{Tc}^{\text{IV}}-\text{O}-\text{Tc}^{\text{III}}$, $\text{Tc}^{\text{III}}-\text{O}-\text{Tc}^{\text{III}}$, and $\text{Tc}^{\text{III}}-\text{O}-\text{Tc}^{\text{II}}$ oxidation states. As shown by the examples in Table 2 [30, 31], experimentally observed redox potentials and oxidation states depend significantly on the ligands bound to the $\text{Tc}-\text{O}-\text{Tc}$ unit. The replacement of a diimine nitrogen donor with a monodentate, negatively charged ligand shifts the potential in the negative direction and stabilizes the higher oxidation state.

An interesting result in Table 2 is the large difference between $E^{\circ'}_{(\text{IV,III})/(\text{III,III})}$ and $E^{\circ'}_{(\text{III,III})/(\text{III,II})}$ for the oxo-bridged complexes in comparison to the adjacent values $E^{\circ'}_{(\text{IV,IV})/(\text{IV,III})} - E^{\circ'}_{(\text{IV,III})/(\text{III,III})}$ and $E^{\circ'}_{(\text{III,III})/(\text{III,II})} - E^{\circ'}_{(\text{III,II})/(\text{II,II})}$. The values of $\Delta E^{\circ'} = E^{\circ'}_{(\text{IV,III})/(\text{III,III})} - E^{\circ'}_{(\text{III,III})/(\text{III,II})}$ range from 1.27 to 1.39 V. These differences correspond to disproportionation constants, $K_{\text{com}} = \exp(F\Delta E^{\circ'}/RT)$, for the equilibrium reaction



on the order of 10^{21} to 10^{23} . Such values suggest a large thermodynamic stabilization of the $(d^4) \text{Tc}^{\text{III}}-\text{O}-\text{Tc}^{\text{III}}$ (d^4) oxidation state, which presumably is promoted by the single μ -oxo bridge.

16.2.3.2 Metal-metal-bonded Complexes

The octachloroditechnetate ion, $\text{Tc}_2\text{Cl}_8^{2-}$, was among the first compounds recognized as containing a metal-metal quadruple bond [32]. The electrochemical data for this and several other metal-metal-bonded Tc_2 complexes are represented in Table 2 [32–35]. Ligands bind at the equatorial positions around each metal in the

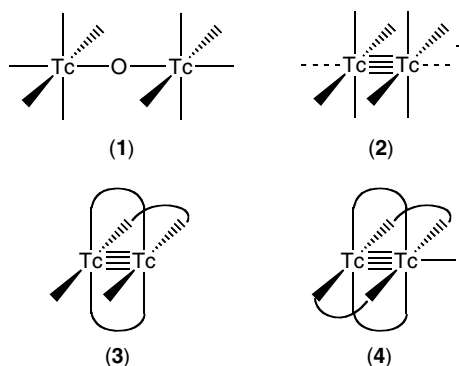


Chart 1 Structures of binuclear technetium centers.

Tab. 2 Electrochemical data for binuclear oxo-bridged and metal–metal-bonded technetium complexes

<i>Tc(III,III) complex</i>	<i>Solvent/supporting electrolyte</i>	<i>E°', V versus NHE</i>					<i>References</i>
		(IV,IV)/ (IV,III)	(IV,III)/ (III,III)	(III,III)/ (III,II)	(III,II)/ (II,II)	(II,II)/ (I,I)	
<i>Oxo-bridged complexes</i>							
$\text{Tc}_2\text{O}(\text{tpy})_2(\text{Me}_2\text{bpy})_2^{4+}$	DMA/TBAPF ₆		+1.24	−0.14	−0.39		30
$\text{Tc}_2\text{O}(\text{bpy})_4\text{Cl}_2^{2+}$	$\text{CH}_3\text{CN}/0.1 \text{ M TEAClO}_4$	+1.53	+0.86	−0.38 ^a			31
$\text{Tc}_2\text{O}(\text{bpy})_4\text{Br}_2^{2+}$	$\text{CH}_3\text{CN}/0.1 \text{ M TEAClO}_4$	+1.56	+0.90	−0.37 ^a			31
$\text{Tc}_2\text{O}(\text{phen})_4(\text{OH})_2^{2+}$	$\text{CH}_3\text{CN}/0.1 \text{ M TEAClO}_4$	+1.53	+0.86	−0.53			31
<i>Metal–metal-bonded complexes</i>							
$\text{Tc}_2\text{Cl}_8^{2-}$	EtOH/10 vol% 12 M HCl			+0.38			32
$\text{Tc}_2\text{Cl}_4(\text{PEt}_2)_4^{2+}$	$\text{CH}_2\text{Cl}_2/0.2 \text{ M TBAPF}_4$			+1.58	+0.22		33
$\text{Tc}_2(\text{CH}_3\text{CN})_{10}^{4+}$	$\text{CH}_3\text{CN}/0.1 \text{ M TBAPF}_6$				−0.18	−0.92(irr) ^b	34
$\text{Tc}_2(\text{DPhF})_3\text{Cl}_2$	$\text{CH}_2\text{Cl}_2/0.1 \text{ M TBAPF}_6$			+0.70	−0.80		35
$\text{Tc}_2(\text{DPhF})_4\text{Cl}$	$\text{CH}_2\text{Cl}_2/0.1 \text{ M TBAPF}_6$			+0.34	−1.03		35

^a $\text{H}_2\text{O}/0.1 \text{ M LiCl}$.^b Irreversible reduction (see text).

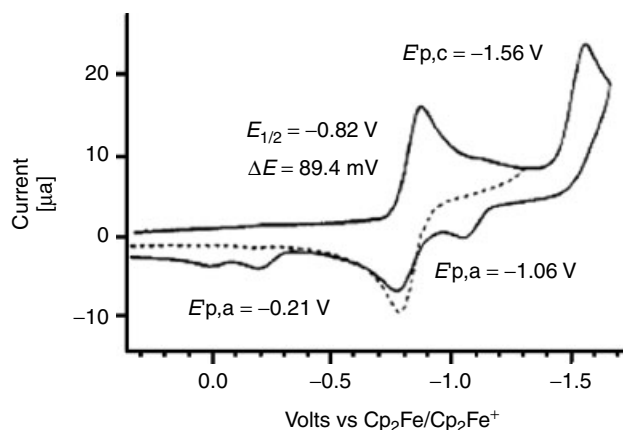


Fig. 3 Cyclic voltammetric reduction of $\text{Tc}_2(\text{CH}_3\text{CN})_{10}^{4+}$ at $\nu = 0.2 \text{ V s}^{-1}$ in $\text{CH}_3\text{CN}/0.1 \text{ M TBAPF}_6$ (reprinted with permission from Ref. 34, Copyright 1995 American Chemical Society).

Tc_2^{n+} unit (**2**) and in some instances at the axial positions as well. Axial binding is weak, as exemplified by $\text{Tc}_2(\text{CH}_3\text{CN})_{10}^{4+}$, where the CH_3CN ligands at these positions exchange rapidly with the solvent molecules [34]. Some bidentate ligands, such as diphenylformamidinate ($\text{DPhF}^- = \text{C}_6\text{H}_5\text{NHCHNHC}_6\text{H}_5^-$), can bridge the metal centers, resulting in structures with three paddlewheel units and one Cl^- bound to each metal ($\text{Tc}_2(\text{DPhF})_3\text{Cl}_2$, **3**) or four paddlewheel units and a single axial Cl^- ($\text{Tc}_2(\text{DPhF})_4\text{Cl}$, **4**) [35].

Quadruply bonded $\text{Tc}_2^{\text{III,III}}$ has the electron configuration $\sigma^2\pi^4\delta^2$. Reduction produces $\text{Tc}_2^{\text{III,II}}$, $\text{Tc}_2^{\text{II,II}}$, $\text{Tc}_2^{\text{II,I}}$, and $\text{Tc}_2^{\text{I,I}}$ centers, with configurations of $\sigma^2\pi^4\delta^2\delta^*$, $\sigma^2\pi^4\delta^2\delta^{*2}$, $\sigma^2\pi^4\delta^2\delta^{*2}\pi^*$, and $\sigma^2\pi^4\delta^2\delta^{*2}\pi^{*2}$ and metal–metal bond orders of 3.5, 3.0, 2.5, and 2.0, respectively. Exemplary data for several compounds of this type are presented in Table 2. Triply bonded $\text{Tc}_2^{\text{II,II}}(\text{CH}_3\text{CN})_{10}^{4+}$ undergoes reversible one-electron reduction to the uncommon $\sigma^2\pi^4\delta^2\delta^{*2}\pi^*$ state (Fig. 3) [34]. However, further reduction

weakens the metal–metal bond to the point that the complex is not chemically stable.

References

1. F. A. Cotton, G. Wilkinson, C. A. Murillo et al., *Advanced Inorganic Chemistry*, 6th ed., John Wiley & Sons, New York, 1999, pp. 974–1000.
2. R. Alberto, in *Comprehensive Coordination Chemistry II*, (Eds.: J. A. McCleverty, T. J. Meyer), 2nd ed., Elsevier, Amsterdam, 2004, Vol. 5, Chapter. 5.2.
3. R. J. Magee, T. J. Cardwell, in *Encyclopedia of Electrochemistry of the Elements*, (Ed.: A. J. Bard), Marcel Dekker, New York, 1973 Vol. 2, Chapter. II-4.
4. E. Deutsch, K. L. Libson, S. Jurisson et al., *Prog. Inorg. Chem.* **1983**, 30, 75–139.
5. M. J. Clarke, L. Podbielski, *Coord. Chem. Rev.* **1987**, 89, 253–331.
6. L. Astheimer, K. Schwochau, *J. Inorg. Nucl. Chem.* **1976**, 38, 1131–1134.
7. G. Kissel, S. W. Feldberg, *J. Phys. Chem.* **1969**, 73, 3082–3088.
8. A. Founta, D. A. Aikens, H. M. Clark, *J. Electroanal. Chem.* **1987**, 219, 221–246.
9. B. L. Lawson, S. M. Scheiffers, T. C. Pinkerton, *J. Electroanal. Chem.* **1984**, 177, 167–181.

10. J. Baldas, G. A. Heath, S. A. Macgregor et al., *J. Chem. Soc., Dalton Trans.* **1998**, 2303–2314.
11. A. Davison, C. Orvig, H. S. Trop et al., *Inorg. Chem.* **1980**, 19, 1988–1992.
12. F. Refosco, U. Mazzi, E. Deutsch et al., *Inorg. Chem.* **1988**, 27, 4121–4127.
13. L. A. de Learie, R. C. Haltiwanger, C. G. Pierpont, *J. Am. Chem. Soc.* **1989**, 111, 4324–4328.
14. D. S. Edwards, S. Liu, M. J. Poirier et al., *Inorg. Chem.* **1994**, 33, 5607–5609.
15. H. S. Trop, A. Davison, A. G. Jones et al., *Inorg. Chem.* **1980**, 19, 1105–1110.
16. D. J. White, H.-J. Küppers, A. J. Edwards et al., *Inorg. Chem.* **1992**, 31, 5351–5352.
17. G. E. D. Mullen, P. J. Blower, D. J. Price et al., *Inorg. Chem.* **2000**, 39, 4093–4098.
18. M. J. Abrams, A. Davison, A. G. Jones et al., *Inorg. Chem.* **1983**, 22, 2798–2800.
19. A. Ichimura, W. R. Heineman, J.-L. Vanderheyden et al., *Inorg. Chem.* **1984**, 23, 1272–1278.
20. J. R. Dilworth, A. J. Hutson, S. Morton et al., *Polyhedron* **1992**, 11, 2151–2155.
21. J. Barrera, A. K. Burrell, J. C. Bryan, *Inorg. Chem.* **1996**, 35, 335–341.
22. B. E. Wilcox, E. Deutsch, *Inorg. Chem.* **1991**, 30, 688–693.
23. A. Ichimura, W. R. Heineman, E. Deutsch, *Inorg. Chem.* **1985**, 25, 2134–2139.
24. T. Konno, J. R. Kirchoff, M. J. Heeg et al., *J. Chem. Soc., Dalton Trans.* **1992**, 3069–3075.
25. T. Konno, M. J. Heeg, J. A. Stuckey et al., *Inorg. Chem.* **1992**, 31, 1173–1181.
26. K.-I. Okamoto, B. Chen, J. R. Kirchoff et al., *Polyhedron* **1993**, 12, 1559–1568.
27. R. W. Hurst, W. R. Heineman, E. Deutsch, *Inorg. Chem.* **1981**, 20, 3298–3303.
28. A. B. P. Lever, *Inorg. Chem.* **1990**, 29, 1271–1285.
29. J. Lu, A. Yamano, M. J. Clarke, *Inorg. Chem.* **1990**, 29, 3483–3487.
30. J. Barrera, J. C. Bryant, *Inorg. Chem.* **1996**, 35, 1825–1830.
31. J. Lu, C. D. Hiller, M. J. Clarke, *Inorg. Chem.* **1993**, 32, 1417–1423.
32. F. A. Cotton, E. Pedersen, *Inorg. Chem.* **1975**, 14, 383–387.
33. C. J. Burns, A. K. Burrell, F. A. Cotton et al., *Inorg. Chem.* **1994**, 33, 2257–2264.
34. J. C. Bryan, F. A. Cotton, L. M. Daniels et al., *Inorg. Chem.* **1995**, 34, 1875–1883.
35. F. A. Cotton, S. C. Haefner, A. P. Sattelberger, *Inorg. Chem.* **1996**, 35, 7530–7537.

16.3 Rhenium

16.3.1 Introduction

Rhenium is a rare element, having eluded discovery until 1925. Its chemistry [1, 2] and electrochemistry [3, 4] have been reviewed on previous occasions. The properties of Re compounds closely parallel those of Tc, and, although many comparative studies have been conducted on the two elements, the rhenium literature is the more extensive. The properties of both elements are quite distinct from those of manganese.

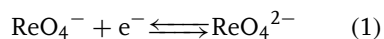
Interest in the electrochemistry of rhenium derives in part from its role in nuclear medicine [5], where compounds containing the high-energy, β^- -emitting ^{186}Re and ^{188}Re isotopes find use in the radiation therapy of cancer. As is the case for technetium, the electrochemical properties are helpful in projecting the distribution and stability of these radiopharmaceuticals in a biological environment. Also, the investigation of nonradioactive Re compounds provides a useful guide to the behavior of radioactive Tc congeners. Although similar in many respects – especially with regard to homoleptic and other mononuclear complexes – Re compounds generally are less oxidizing and kinetically more inert than their Tc analogs. Other distinguishing characteristics of rhenium include (1) the existence of high-valent mononuclear oxo complexes, whose aqueous electrochemical behavior provides useful insight to coupled electron-proton transfer reactions [6]; (2) the formation of hydride complexes exhibiting well-defined electrochemistry [7]; (3) the incorporation in supramolecular arrays, which have applications in

molecular sieving, sensing, and catalysis [8]; and (4) the utilization as a catalyst for photo- or electrochemically initiated carbon dioxide reduction [9].

16.3.2 Mononuclear Complexes

16.3.2.1 Oxo Complexes

A value of $E^{\circ'} = -2.06$ V versus NHE has been measured for one-electron reduction of the perrhenate ion, ReO_4^- , in CH_3CN (Eq. 1) [10], although the flow of additional current on the plateau of the wave indicates that the initial electrode product is not chemically stable.



The electrochemical behavior of ReO_4^- in aqueous solution is irreversible and not well-characterized. The estimated one-electron potential for the $\text{ReO}_4^-/^{2-}$ couple in aqueous alkaline solution [3] (Table 1) is slightly more negative than that for $\text{TcO}_4^-/^{2-}$ (Table 1 of Sect. 16.2). In aqueous acid media, reduction is thought to proceed by a two-electron transfer from Re(VII) to Re(V) [11], followed by disproportionation and formation of ReO_2 [12].

Rhenium forms a number of mono-oxo, *cis*-dioxo, and *trans*-dioxo complexes in oxidation states IV through VII. Reversible, proton-independent, one-electron potentials for several systems are represented in Table 1 [13–22, 35, 36]. As is the case for Tc, a large change in $E^{\circ'}$ for a given redox step can be produced by changing the ancillary ligands.

Of particular interest are the proton-coupled multielectron transfers of high-valent oxorhenium (poly)pyridyl complexes [6, 15–18, 35]. This behavior is

Tab. 1 Electrochemical data for mononuclear rhenium complexes

Oxidation state change	Re coordinate shell	Electrode reaction	Solvent/supporting electrolyte	E° , V versus NHE	References
<i>Oxo complexes</i>					
VII/VI	O ₄	$\text{ReO}_4^- + e^- \rightleftharpoons \text{ReO}_4^{2-}$	CH ₃ CN/0.05 M TEAClO ₄	-2.06	10
VII/VI	O ₄	$\text{ReO}_4^- + e^- \rightleftharpoons \text{ReO}_4^{2-}$	H ₂ O (alkaline)	-0.70	3
VII/VI	O ₂ N ₃ Cl	$\text{c-ReO}_2(\text{Tp})\text{Cl}^+ + e^- \rightleftharpoons \text{c-ReO}_2(\text{Tp})\text{Cl}$	CH ₃ CN/0.1 M TBAPF ₆	+1.57	13
VII/VI	O ₂ O ₄	$\text{c-ReO}_2(\text{DTBcat})_2^- + e^- \rightleftharpoons \text{c-ReO}_2(\text{DTBcat})_2^{2-}$	CH ₃ CN/0.2 M TBABF ₄	-0.77	14
VI/V	O ₂ N ₄	$\text{t-ReO}_2(\text{py})_4^{2+} + e^- \rightleftharpoons \text{t-ReO}_2(\text{py})_4^+$	CH ₃ CN/0.1 M TBAPF ₆	+1.61	15
VI/V	O ₂ N ₄	$\text{t-ReO}_2(\text{py})_4^{2+} + e^- \rightleftharpoons \text{t-ReO}_2(\text{py})_4^+$	H ₂ O/pH 2	+1.49	16, 17
VI/V	O ₂ N ₄	$\text{c-ReO}_2(\text{bpy})(\text{py})_2^{2+} + e^- \rightleftharpoons \text{c-ReO}_2(\text{bpy})(\text{py})_2^+$	CH ₃ CN/0.1 M TBAPF ₆	+1.01	15
VI/V	O ₂ N ₄	$\text{c-ReO}_2(\text{bpy})(\text{py})_2^{2+} + e^- \rightleftharpoons \text{c-ReO}_2(\text{bpy})(\text{py})_2^+$	H ₂ O/pH 2	+0.87	17
VI/V	O ₂ N ₄	$\text{c-ReO}_2(\text{bpy})(\text{py})_2^{2+} + e^- \rightleftharpoons \text{c-ReO}_2(\text{bpy})(\text{py})_2^+$	CH ₃ CN/0.1 M TBAPF ₆	+2.44	18
VI/V	ON ₄ O	$\text{t-ReO}(\text{OMe})(4\text{-Mepy})_4^{3+} + e^- \rightleftharpoons \text{t-ReO}(\text{OMe})(4\text{-Mepy})_4^{2+}$	CH ₃ CN/0.1 M TBAPF ₆	+1.22	19
VI/V	ON ₂ O ₂ Cl	$\text{ReO}(\text{hoz})_2\text{Cl}^+ + e^- \rightleftharpoons \text{ReO}(\text{hoz})_2\text{Cl}$	CH ₃ CN/0.1 M TBAPF ₆	-0.50	18
V/IV	ON ₄ O	$\text{t-ReO}(\text{OMe})(4\text{-Mepy})_4^{2+} + e^- \rightleftharpoons \text{t-ReO}(\text{OMe})(4\text{-Mepy})_4^+$	CH ₃ CN/0.1 M TEAClO ₄	-0.74	20
V/IV	ON ₂ O ₃	$\text{ReO}(\text{g-Q})(\text{SB}) + e^- \rightleftharpoons \text{ReO}(\text{g-Q})(\text{SB})^-$	CH ₃ CN/0.2 M TBABF ₄	-1.74	21
V/IV	ON ₃ O ₂	$\text{ReO}(\text{pzTp})(\text{OCH}_2\text{CH}_2\text{O}) + e^- \rightleftharpoons \text{ReO}(\text{pzTp})(\text{OCH}_2\text{CH}_2\text{O})^-$	CH ₃ CN/0.2 M TBABF ₄	-1.38	21
V/IV	ON ₃ OS	$\text{ReO}(\text{pzTp})(\text{OCH}_2\text{CH}_2\text{S}) + e^- \rightleftharpoons \text{ReO}(\text{pzTp})(\text{OCH}_2\text{CH}_2\text{S})^-$	CH ₃ CN/0.2 M TBABF ₄	-1.18	21
V/IV	ON ₃ S ₂	$\text{ReO}(\text{pzTp})(\text{SCH}_2\text{CH}_2\text{S}) + e^- \rightleftharpoons \text{ReO}(\text{pzTp})(\text{SCH}_2\text{CH}_2\text{S})^-$	CH ₃ CN/0.1 M TBAClO ₄	-0.81	22
V/IV	OS ₄	$\text{ReO}(\text{mnt})_2^- + e^- \rightleftharpoons \text{ReO}(\text{mnt})_2^{2-}$	CH ₃ CN/0.1 M TBAPF ₆	-1.36	18
IV/III	ON ₄ O	$\text{t-ReO}(\text{OMe})(4\text{-Mepy})_4^+ + e^- \rightleftharpoons \text{t-ReO}(\text{OMe})(4\text{-Mepy})_4$	H ₂ O/pH 2	-0.28	17
V/III	O ₂ N ₄	$\text{t-ReO}_2(\text{py})_4^+ + 3\text{H}^+ + 2e^- \rightleftharpoons \text{t-Re}(\text{OH})(\text{OH}_2)(\text{py})_4^{2+}$	H ₂ O/pH 2	-0.07	17
V/III	O ₂ N ₄	$\text{c-ReO}_2(\text{bpy})(\text{py})_2^+ + 3\text{H}^+ + 2e^- \rightleftharpoons \text{c-Re}(\text{OH})(\text{OH}_2)(\text{bpy})(\text{py})_2^{2+}$			
III/II	O ₂ N ₄	$\text{c-Re}(\text{OH})(\text{OH}_2)(\text{bpy})(\text{py})_2^{2+} + e^- \rightleftharpoons \text{c-Re}(\text{OH})(\text{OH}_2)(\text{bpy})(\text{py})_2^+$			
III/II	O ₂ N ₄	$\text{t-Re}(\text{OH})(\text{OH}_2)(\text{py})_4^{2+} + e^- \rightleftharpoons \text{t-Re}(\text{OH})(\text{OH}_2)(\text{py})_4^+$			
III/II	O ₂ N ₄	$\text{c-Re}(\text{OH})(\text{OH}_2)(\text{bpy})(\text{py})_2^{2+} + e^- \rightleftharpoons \text{c-Re}(\text{OH})(\text{OH}_2)(\text{bpy})(\text{py})_2^+$			

(continued overleaf)

Tab. 1 (continued)

Oxidation state change	Re coordinate shell	Electrode reaction	Solvent/supporting electrolyte	E° , V versus NHE	References
<i>Homoleptic complexes</i>					
VI/IV	C ₈	$\text{Re}(\text{CN})_8^{2-} + \text{e}^- \rightleftharpoons \text{Re}(\text{CN})_8^{3-}$	CH ₃ CN	+1.64	23
VI/IV	O ₆	$\text{Re}(\text{Cl}_4\text{Cat})_3 + \text{e}^- \rightleftharpoons \text{Re}(\text{Cl}_4\text{Cat})_3^-$	CH ₂ Cl ₂ /TBAPF ₆	+1.06	24
VI/IV	O ₆	$\text{Re}(\text{DTBCat})_3 + \text{e}^- \rightleftharpoons \text{Re}(\text{DTBCat})_3^-$	CH ₂ Cl ₂ /TBAPF ₆	-0.13	24
V/IV	N ₆	$\text{Re}(\text{NCS})_6^- + \text{e}^- \rightleftharpoons \text{Re}(\text{NCS})_6^{2-}$	CH ₂ Cl ₂ /0.2 M TBAPF ₆	+1.27	25
V/IV	O ₆	$\text{Re}(\text{Cl}_4\text{Cat})_3^- + \text{e}^- \rightleftharpoons \text{Re}(\text{Cl}_4\text{Cat})_3^{2-}$	CH ₂ Cl ₂ /TBAPF ₆	-0.11	24
V/IV	O ₆	$\text{Re}(\text{DTBCat})_3^- + \text{e}^- \rightleftharpoons \text{Re}(\text{DTBCat})_3^{2-}$	CH ₂ Cl ₂ /TBAPF ₆	-0.99	24
V/IV	P ₃ S ₃	$\text{Re}(\text{2-Ph}_2\text{PC}_6\text{H}_4\text{S})_3^{2+} + \text{e}^- \rightleftharpoons \text{Re}(\text{2-Ph}_2\text{PC}_6\text{H}_4\text{S})_3^+$	CH ₂ Cl ₂ /0.2 M TBAPF ₆	+1.68	26
IV/III	C ₇	$\text{Re}(\text{CN})_7^{3-} + \text{e}^- \rightleftharpoons \text{Re}(\text{CN})_7^{4-}$	CH ₃ CN	-0.64	23
IV/III	N ₆	$\text{Re}(\text{NCS})_6^{2-} + \text{e}^- \rightleftharpoons \text{Re}(\text{NCS})_6^{3-}$	CH ₂ Cl ₂ /0.2 M TBAPF ₆	-0.04	25
IV/III	P ₃ S ₃	$\text{Re}(\text{2-Ph}_2\text{PC}_6\text{H}_4\text{S})_3^+ + \text{e}^- \rightleftharpoons \text{Re}(\text{2-Ph}_2\text{PC}_6\text{H}_4\text{S})_3$	CH ₂ Cl ₂ /0.2 M TBAPF ₆	+0.90	26
IV/III	Cl ₆	$\text{ReCl}_6^{2-} + \text{e}^- \rightleftharpoons \text{ReCl}_6^{3-}$	CH ₂ Cl ₂	-0.88	27
III/II	N ₆	$\text{Re}(\text{NCS})_6^{3-} + \text{e}^- \rightleftharpoons \text{Re}(\text{NCS})_6^{4-}$	CH ₂ Cl ₂ /0.2 M TBAPF ₆	-1.39	25
III/II	N ₄ S ₂	$\text{Re}(\text{tsc})_2^+ + \text{e}^- \rightleftharpoons \text{Re}(\text{tsc})_2$	DMF/0.1 M TBAPF ₆	-0.27	28
III/II	P ₃ S ₃	$\text{Re}(\text{2-Ph}_2\text{PC}_6\text{H}_4\text{S})_3 + \text{e}^- \rightleftharpoons \text{Re}(\text{2-Ph}_2\text{PC}_6\text{H}_4\text{S})_3^-$	CH ₂ Cl ₂ /0.2 M TBAPF ₆	-0.32	26
III/II	S ₆	$\text{Re}(\text{ttcn})_2^{3+} + \text{e}^- \rightleftharpoons \text{Re}(\text{ttcn})_2^{2+}$	CH ₃ CN/0.1 M TBAPF ₆	+1.11	29
III/II	C ₆	$\text{Re}(\text{CNTol})_6^{2+} + \text{e}^- \rightleftharpoons \text{Re}(\text{CNTol})_6^+$	CH ₂ Cl ₂ /0.1 M TBAPF ₆	+1.44	30
II/I	N ₆	$\text{Re}(\text{terpy})_2^{2+} + \text{e}^- \rightleftharpoons \text{Re}(\text{terpy})_2^+$	DMA/0.5 M TBAPF ₆	+0.12	31
II/I	N ₆	$\text{Re}(\text{bpy})_2^{2+} + \text{e}^- \rightleftharpoons \text{Re}(\text{bpy})_2^+$	DMA/0.5 M TBAPF ₆	-0.33	31
II/I	N ₄ S ₂	$\text{Re}(\text{tsc})_2 + \text{e}^- \rightleftharpoons \text{Re}(\text{tsc})_2^-$	DMF/0.1 M TBAPF ₆	-0.83	28
II/I	P ₆	$\text{Re}(\text{dmpe})_3^{2+} + \text{e}^- \rightleftharpoons \text{Re}(\text{dmpe})_3^+$	DMF/0.5 M TEAClO ₄	+0.52	32

Mixed-ligand complexes					
V/IV	HO ₄ P ₂	$\text{ReH}(\text{acac})_2(\text{PPh}_3)_2^{2+} + \text{e}^- \rightleftharpoons \text{ReH}(\text{acac})_2(\text{PPh}_3)_2^+$	CH ₂ Cl ₂ /0.1 M TBAPF ₆	+1.05	7
IV/III	HO ₄ P ₂	$\text{ReH}(\text{acac})_2(\text{PPh}_3)_2^+ + \text{e}^- \rightleftharpoons \text{ReH}(\text{acac})_2(\text{PPh}_3)_2$	CH ₂ Cl ₂ /0.1 M TBAPF ₆	-0.24	7
IV/III	N ₄ Cl ₂	$\text{Re}(\text{bpy})_2\text{Cl}_2^{2+} + \text{e}^- \rightleftharpoons \text{Re}(\text{bpy})_2\text{Cl}_2^+$	DMA/0.5 M TBAPF ₆	+1.06	31
IV/III	N ₃ Cl ₃	$\text{Re}(\text{terpy})\text{Cl}_3^+ + \text{e}^- \rightleftharpoons \text{Re}(\text{terpy})\text{Cl}_3$	DMA/0.5 M TBAPF ₆	+0.52	31
IV/III	N ₃ Cl ₃	$\text{Re}(\text{py})_3\text{Cl}_3^+ + \text{e}^- \rightleftharpoons \text{Re}(\text{py})_3\text{Cl}_3$	DMA/0.5 M TBAPF ₆	+0.45	31
IV/III	N ₂ P ₂ Cl ₂	$\text{Re}(\text{bpy})(\text{PMe}_2\text{Ph})_2\text{Cl}_2^{2+} + \text{e}^- \rightleftharpoons \text{Re}(\text{bpy})(\text{PMe}_2\text{Ph})_2\text{Cl}_2^+$	CH ₃ CN/0.1 M TEAClO ₄	+1.12	33
IV/III	O ₄ P ₂	$\text{Re}(\text{acac})_2(\text{PPh}_3)_2^{2+} + \text{e}^- \rightleftharpoons \text{Re}(\text{acac})_2(\text{PPh}_3)_2^+$	CH ₂ Cl ₂ /0.1 M TBAPF ₆	+1.17	7
III/II	N ₄ Cl ₂	$\text{Re}(\text{bpy})_2\text{Cl}_2^+ + \text{e}^- \rightleftharpoons \text{Re}(\text{bpy})_2\text{Cl}_2$	DMA/0.5 M TBAPF ₆	-0.17	31
III/II	N ₃ Cl ₃	$\text{Re}(\text{terpy})\text{Cl}_3 + \text{e}^- \rightleftharpoons \text{Re}(\text{terpy})\text{Cl}_3^-$	DMA/0.5 M TBAPF ₆	-0.49	31
III/II	N ₃ Cl ₃	$\text{Re}(\text{py})_3\text{Cl}_3 + \text{e}^- \rightleftharpoons \text{Re}(\text{py})_3\text{Cl}_3^-$	DMA/0.5 M TBAPF ₆	-1.11	31
III/II	N ₂ P ₂ Cl ₂	$\text{Re}(\text{bpy})(\text{PMe}_2\text{Ph})_2\text{Cl}_2^+ + \text{e}^- \rightleftharpoons \text{Re}(\text{bpy})(\text{PMe}_2\text{Ph})_2\text{Cl}_2$	CH ₃ CN/0.1 M TEAClO ₄	-0.15	33
III/II	P ₄ Cl ₂	$\text{Re}(\text{dmpe})\text{Cl}_2^+ + \text{e}^- \rightleftharpoons \text{Re}(\text{dmpe})\text{Cl}_2$	DMF/0.5 M TEAClO ₄	-0.22	34
III/II	As ₄ Cl ₂	$\text{Re}(\text{diars})\text{Cl}_2^+ + \text{e}^- \rightleftharpoons \text{Re}(\text{diars})\text{Cl}_2$	DMF/0.5 M TEAClO ₄	-0.12	34
III/II	O ₄ P ₂	$\text{Re}(\text{acac})_2(\text{PPh}_3)_2^+ + \text{e}^- \rightleftharpoons \text{Re}(\text{acac})_2(\text{PPh}_3)_2$	CH ₂ Cl ₂ /0.1 M TBAPF ₆	-0.52	7
II/I	N ₄ Cl ₂	$\text{Re}(\text{bpy})_2\text{Cl}_2 + \text{e}^- \rightleftharpoons \text{Re}(\text{bpy})_2\text{Cl}_2^-$	DMA/0.5 M TBAPF ₆	-1.01	31
II/I	N ₃ Cl ₃	$\text{Re}(\text{py})_3\text{Cl}_3^- + \text{e}^- \rightleftharpoons \text{Re}(\text{py})_3\text{Cl}_3^{2-}$	DMA/0.5 M TBAPF ₆	-1.81	31
II/I	P ₄ Cl ₂	$\text{Re}(\text{dmpe})\text{Cl}_2 + \text{e}^- \rightleftharpoons \text{Re}(\text{dmpe})\text{Cl}_2^-$	DMF/0.5 M TEAClO ₄	-1.36	34
II/I	As ₄ Cl ₂	$\text{Re}(\text{diars})\text{Cl}_2 + \text{e}^- \rightleftharpoons \text{Re}(\text{diars})\text{Cl}_2^-$	DMF/0.5 M TEAClO ₄	-1.25	34

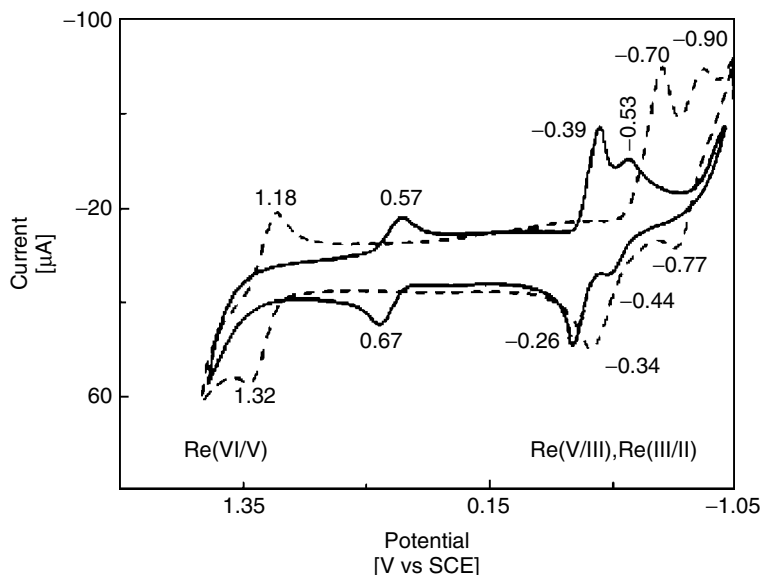
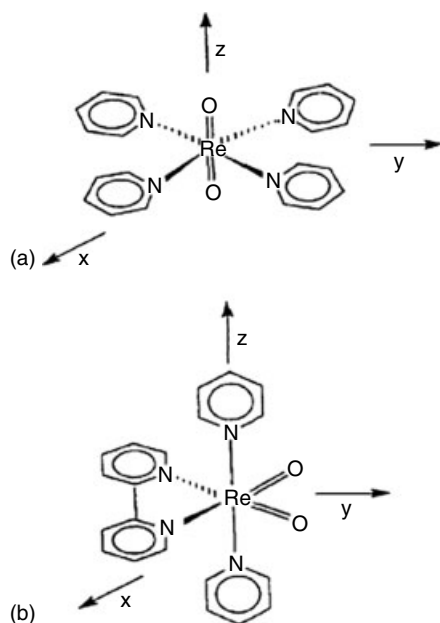


Fig. 1 Cyclic voltammograms of $\text{ReO}_2(\text{bpy})(\text{py})_2^+$ (solid line) and $\text{ReO}_2(\text{py})_4^+$ (dashed line) at pH 2 on a glassy carbon working electrode (reprinted with permission from Ref. 17, Copyright 1990 American Chemical Society).

illustrated by the aqueous, pH 2, cyclic voltammograms of $\text{cis-ReO}_2(\text{bpy})(\text{py})_2^+$



and $\text{trans-ReO}_2(\text{py})_4^+$ (Fig. 1) [17]. The one-electron $\text{Re(V)} \rightarrow \text{Re(VI)}$ potentials are proton independent from pH 1 to 11 and are close to the values observed in CH_3CN . However, the potential for oxidation of trans-ReO_2^+ complex is 0.6 V more positive than that for the oxidation of the cis-ReO_2^+ . Conversely, the proton-coupled $\text{Re(V)} \rightarrow \text{Re(III)}$ and $\text{Re(III)} \rightarrow \text{Re(II)}$ reductions of the cis and trans isomers occur at more nearly equal potentials, and the cis form exhibits the more positive $E^{\circ'}$ (Fig. 1). The difference in $\text{Re}^{\text{VI/V}}$ potentials is attributed to the oxo group geometry [35]. The redox orbital of the trans complex is d_{xy} , which lies in the equatorial plane and experiences little interaction with the oxo groups (Fig. 2) [35]. However, the redox orbital of the

Fig. 2 Structures of (a) $\text{trans-ReO}_2(\text{py})_4^+$ and (b) $\text{cis-ReO}_2(\text{bpy})(\text{py})_2^+$ (reprinted from Ref. 35, Copyright 1995 with permission from Elsevier).

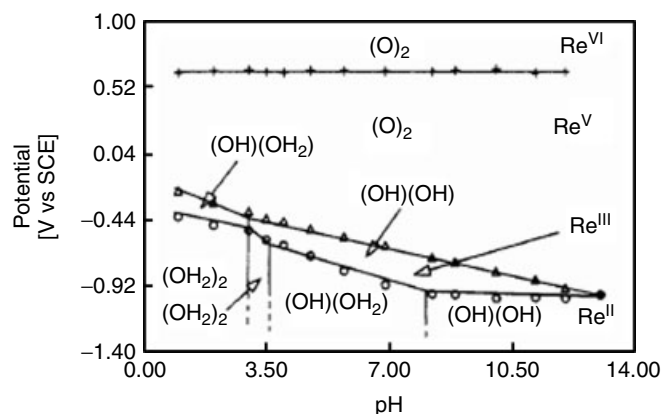
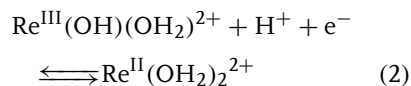
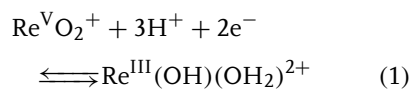


Fig. 3 Pourbaix diagram for $\text{ReO}_2(\text{bpy})(\text{py})_2^+$ (reprinted with permission from Ref. 17, Copyright 1990 American Chemical Society).

cis complex is a composite of the d_{xz} and d_{yz} orbitals, which interact unfavorably with one or more oxo $p-\pi^*$ orbitals and favor $d^2 \rightarrow d^1$ electron removal. The electron-transfer kinetics of *cis*- $\text{ReO}_2(\text{bpy})(\text{py})_2^+$ and *trans*- $\text{ReO}_2(\text{py})_4^+$ also differ; $(k_{s,h})_{\text{trans}}/(k_{s,h})_{\text{cis}} \approx 3$ at highly ordered pyrolytic graphite electrodes. The smaller rate constant for *cis*- $\text{ReO}_2(\text{bpy})(\text{py})_2^+$ corresponds to an approximate 4-kJ mol^{-1} difference in barrier height, which is assigned to a $\text{Re}-\text{N}(\text{bpy})$ stretching mode that is observed only for the *cis* complex [35].

Reduction of the ReO_2^+ species at pH 2 (Fig. 1) is accompanied by the addition of three protons and two electrons in the first step followed by the addition of one proton and one electron in the second step. The corresponding half-reactions (Table 1) are



Proton stoichiometries change as pH is altered and are influenced by oxo group

geometry and pyridyl ligand identity. The Pourbaix diagram of *cis*- $\text{ReO}_2(\text{bpy})(\text{py})_2^+$ (Fig. 3) [17] is representative of the observed behavior.

The apparent kinetics of proton-coupled $\text{Re}^{\text{V/III}}$ electron transfer also are dependent on oxo group geometry; here $(k_{s,h})_{\text{cis}}/(k_{s,h})_{\text{trans}} \approx 100$ [36]. It is proposed that the apparent kinetics is controlled by the thermodynamic accessibility of the intermediate $\text{Re}(\text{IV})$ state, whose effective potential is modulated by protonation, oxo group geometry, and pyridyl ligand substituents.

16.3.2.2 Homoleptic and Mixed-ligand Complexes

Rhenium forms a large number of mononuclear nonoxo complexes in oxidation states I through VI. The redox potentials of selected examples are included in Table 1. The majority of compounds are octahedral. However, notable exceptions include the pentagonal bipyramidal $\text{Re}(\text{CN})_7^{3-/4-}$ ($E^\circ = -0.64\text{ V}$) and the square antiprismatic $\text{Re}(\text{CN})_8^{2-/3-}$ ($E^\circ = +1.64\text{ V}$) couples [23]. The latter complexes are similar in behavior to the isoelectronic Mo species.

The electrochemistry of Re and Tc complexes is frequently compared. Rhenium compounds are more difficult to reduce in a given oxidation state. Comparison of values from Table 1 of Sect. 16.2 and Table 1 of Sect. 16.3 at identical ligand composition indicates that Re potentials are 0.2–0.6 V more negative than those of Tc, with the smaller differences occurring more frequently in the lower oxidation states. Lever constructed an electrochemical parameterization scheme on the basis of the ligand additivity principles for 119 Re redox couples [37]. The results are shown in Fig. 4. The lines for the $\text{Re}^{\text{IV/III}}$, $\text{Re}^{\text{III/II}}$, and $\text{Re}^{\text{II/I}}$ couples are not as cleanly parallel as they are for $\text{Tc}^{\text{IV/III}}$, $\text{Tc}^{\text{III/II}}$, and $\text{Tc}^{\text{II/I}}$ (Fig. 2 of Sect. 16.2). Moreover, two lines are apparent for

$\text{Re}^{\text{II/I}}$ couples. The upper line is dominated by complexes containing electron-withdrawing CO and isocyanide ligands. However, the structural or bonding significance of the two $\text{Re}^{\text{II/I}}$ correlation lines is not clear.

A change in the coordination number accompanies oxidation or reduction of some Re complexes. For example, oxidation of $\text{Re}^{\text{I}}(\text{terpy})_2^+$ in the presence of free chloride ion produces seven-coordinate $\text{Re}^{\text{III}}(\text{terpy})_2\text{Cl}^+$ via the following reaction sequence [31]:

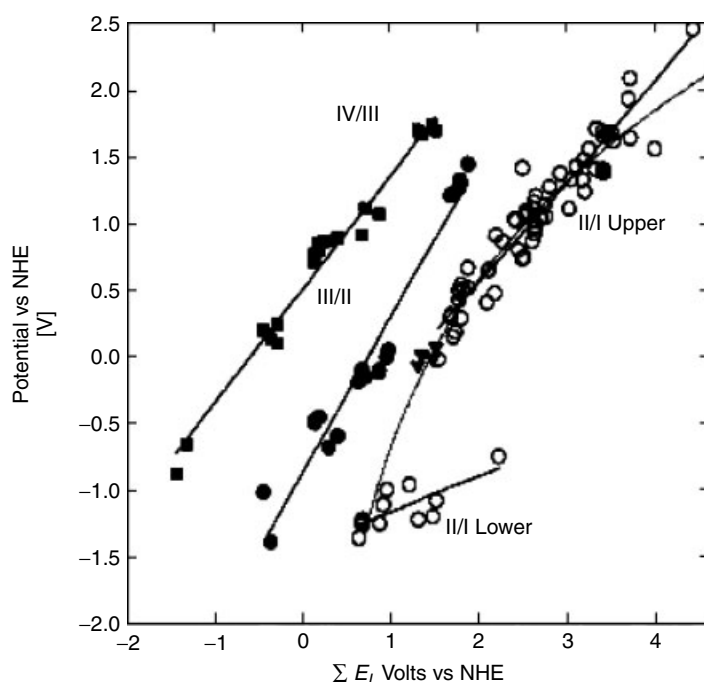
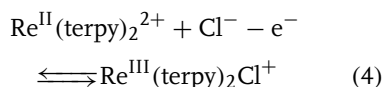
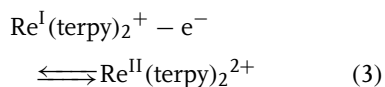


Fig. 4 Plot of $E^{\circ'}$ for $\text{Re}^{\text{IV/III}}$, $\text{Re}^{\text{III/II}}$, and $\text{Re}^{\text{II/I}}$ redox couples versus the sum of ligand parameters (reprinted with permission from Ref. 37, Copyright 1990 American Chemical Society).

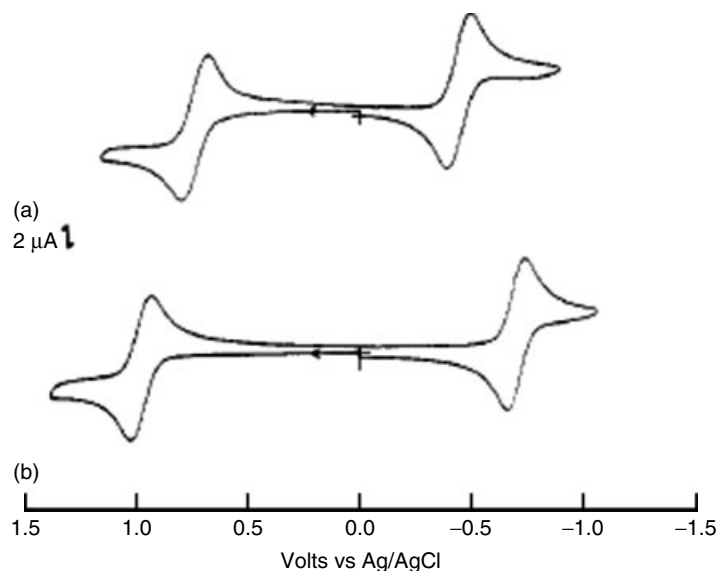


Fig. 5 Cyclic voltammograms of $\text{ReH}(\text{acac})_2(\text{PPh}_3)_3^+$ in $\text{CH}_2\text{Cl}_2/0.1 \text{ M TBAPF}_6$ (a) prior to and (b) following exhaustive electrolysis at $+1.1 \text{ V}$ versus NHE (reprinted with permission from Ref. 7, Copyright 1990 American Chemical Society).

Reduction of $\text{Re}^{\text{III}}(\text{terpy})_2\text{Cl}^+$ is irreversible and re-forms $\text{Re}^{\text{I}}(\text{terpy})_2^+$ in a two-electron reaction. Other seven-coordinate complexes [e.g. $\text{Re}^{\text{III}}(\text{bpy})_3(\text{CNBu}^t)^{3+}$] are generated in this manner and exhibit similar reactivity [31].

The seven-coordinate hydrido complex, $\text{Re}^{\text{IV}}\text{H}(\text{acac})_2(\text{PPh}_3)_2^+$, also undergoes a change in coordination number upon oxidation [7]. As shown in the upper trace (a) in Fig. 5, this compound exhibits a reversible one-electron oxidation at $E^{\circ'}_{\text{V/IV}} = +1.05 \text{ V}$ and a reversible one-electron reduction at $E^{\circ'}_{\text{IV/III}} = -0.24 \text{ V}$. Exhaustive electrolysis at $+1.1 \text{ V}$ produces the six-coordinate $\text{Re}(\text{III})$ complex, $\text{Re}^{\text{III}}(\text{acac})_2(\text{PPh}_3)_2^+$, which exhibits a reversible one-electron oxidation at $E^{\circ'}_{\text{IV/III}} = +1.17 \text{ V}$ and a reversible one-electron reduction at $E^{\circ'}_{\text{III/II}} = -0.52 \text{ V}$ (Fig. 5b). Although similar in appearance and potential, the two sets of electrode

reactions involve different pairs of oxidation states.

16.3.3

Polynuclear Complexes

16.3.3.1 Oxo-bridged Complexes

Although relatively few oxo-bridged rhenium complexes have been characterized electrochemically, several studies have been conducted on $\text{Re}(\text{V})$ complexes containing a linear $\text{O}=\text{Re}-\text{O}-\text{Re}=\text{O}$ unit (**1**, Chart 1). Dithiocarbamate complexes such as $\text{Re}_2\text{O}_3(\text{Et}_2\text{dtc})_4$ exhibit a reversible $\text{Re}^{\text{V,V}} \rightarrow \text{Re}^{\text{V,IV}}$ reduction at $E^{\circ'} = -1.13 \text{ V}$ in CH_3CN [38]. Complexes with SB ligands such as $\text{Re}_2\text{O}_3(\text{salen})_2$ exhibit one-electron $\text{Re}^{\text{V,V}} \rightarrow \text{Re}^{\text{VI,V}}$ and $\text{Re}^{\text{VI,V}} \rightarrow \text{Re}^{\text{VI,VI}}$ oxidations at $+0.76$ and $+1.29 \text{ V}$ and a one-electron $\text{Re}^{\text{V,V}} \rightarrow \text{Re}^{\text{V,IV}}$ reduction at -0.82 V in $\text{C}_2\text{H}_4\text{Cl}_2$ [39].

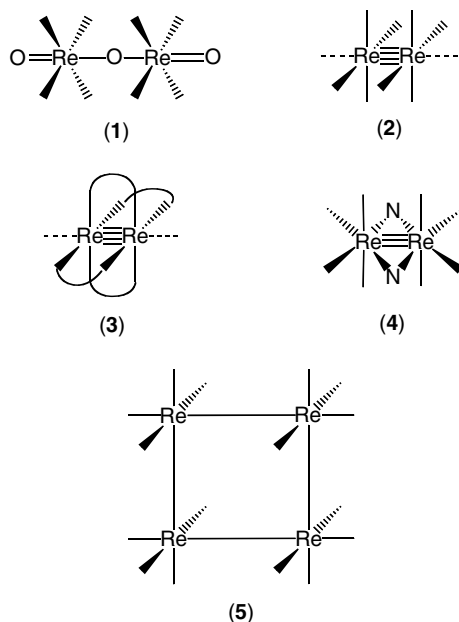


Chart 1 Structures of polynuclear rhenium centers.

Multiple metal–metal bonds have since been found in Re and many other transition metal complexes [41]. The structure of the unsupported Re_2^{6+} unit (2) is shown in Chart 1. Bonds to the ligands in the equator around each metal may be staggered or eclipsed depending on electronic structure, and solvent or unidentate ligands may bind weakly at the axial positions. In some cases, polydentate ligands may bridge the metal–metal-bonded unit (3).

Electrochemical data for a number of multiply bonded Re_2 complexes are represented in Table 2 [42–50]. The oxidation of quadruply bonded $\text{Re}_2^{\text{III,III}}$ ($\sigma^2\pi^4\delta^2$) produces $\text{Re}_2^{\text{III,IV}}$ and $\text{Re}_2^{\text{IV,IV}}$ centers with configurations of $\sigma^2\pi^4\delta^1$ and $\sigma^2\pi^4$ and formal metal–metal bond orders of 3.5 and 3.0, respectively. Reduction produces a $\sigma^2\pi^4\delta^2\delta^{*1}$ $\text{Re}_2^{\text{III,II}}$ center, also with a bond order of 3.5. The sequential one-electron potentials in Table 2 are widely

16.3.3.2 Metal–metal-bonded Complexes

The octachlorodirhenate ion, $\text{Re}_2\text{Cl}_8^{2-}$, was the first substance recognized to contain a metal–metal quadruple bond [40].

Tab. 2 Electrochemical data for metal–metal-bonded rhenium complexes

(Re III,III) complex	Solvent/supporting electrolyte	E° , V versus NHE				References
		(IV,IV)/ (IV,III)	(IV,III)/ (III,III)	(III,III)/ (III,II)	(III,II)/ (II,II)	
$\text{Re}_2\text{Cl}_8^{2-}$	$\text{CH}_3\text{CN}-\text{CH}_2\text{Cl}_2$ (1 : 1) / 0.5 M TBAPF ₆	+2.08 ^c	+1.64 ^c	−0.44		42, 43
$\text{Re}_2\text{Cl}_6(\text{PEt}_3)_2$	CH_2Cl_2 / 0.2 M TBAPF ₆			+0.14		44, 45
$\text{Re}_2\text{Cl}_5(\text{PEt}_3)_3^+$	CH_2Cl_2 / 0.2 M TBAPF ₆			+0.58	−0.64	44, 45
$\text{Re}_2\text{Cl}_4(\text{PEt}_3)_4^{2+}$	CH_2Cl_2 / 0.2 M TBAPF ₆			+1.04	−0.16	44, 45
$\text{Re}_2\text{Cl}_2(\text{OOCe}_2)_4^a$	CH_2Cl_2 / 0.2 M TBAPF ₆			−0.10		46, 47
$\text{Re}_2(\text{NCS})_8^{2-}$	n-PrCN / 0.4 M TBAPF ₆		+1.30	0.00	−0.70	48
$\text{Re}_2(\text{NCS})_{10}^{4-b}$	CH_2Cl_2 / 0.5 M TBAPF ₆	+0.66	+0.20	−1.11 ^d		49, 50

^a Axial Cl^- ligands.

^b $\text{Re}_2(\mu\text{-NCS})_2(\text{NCS})_8^{4-}$.

^c Evaluated at 220 K.

^d Irreversible two-electron reaction (see text).

spaced, indicating strong interaction between metals, and the $E^{\circ'}$ values for a particular redox step are influenced significantly by the charge and donor properties of the ligands.

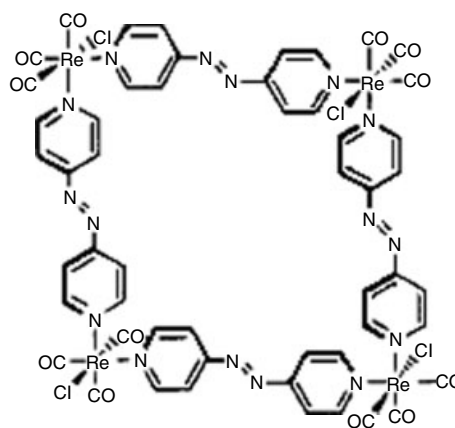
Electrochemical oxidation or reduction of Re_2^{n+} complexes is frequently followed by chemical reactions leading to products with altered structure or composition. For example, the exhaustive oxidation of $\text{Re}_2^{\text{II,II}}\text{Cl}_4(\text{PEt}_2)_4$ to $\text{Re}_2^{\text{III,II}}\text{Cl}_4(\text{PEt}_2)_4^+$ and $\text{Re}_2^{\text{III,III}}\text{Cl}_4(\text{PEt}_2)_4^{2+}$ is followed by chemical reactions that produce $\text{Re}_2^{\text{III,II}}\text{Cl}_5(\text{PEt}_2)_3$, $\text{Re}_2^{\text{III,III}}\text{Cl}_5(\text{PEt}_2)_3^+$, and $\text{Re}_2^{\text{III,III}}\text{Cl}_6(\text{PEt}_2)_2$ [44, 45]. The reactions involve scavenging of additional Cl^- ligands by complexes in the higher oxidation states. In the four-membered $\text{Re}_2(\text{NCS})_8^{-2/-3/-4-}$ redox chain [48], oxidation of $\text{Re}_2^{\text{III,III}}(\text{NCS})_8^{2-}$ is also followed by ligand scavenging and rearrangement to $\text{Re}_2^{\text{IV,IV}}(\text{NCS})_{10}^{2-}$ [49, 50]. This compound has been formulated as an edge-shared bioctahedral complex, $\text{Re}_2(\mu\text{-NCS})_2(\text{NCS})_8^{2-}$, containing two N-bonded bridging thiocyanate ligands (4). The electronic configuration is $\sigma^2\pi^2\delta^2$, which is consistent with a metal–metal bond order of 3.0. Reduction of $\text{Re}_2^{\text{IV,IV}}(\mu\text{-NCS})_2(\text{NCS})_8^{2-}$ proceeds by

two sequential, reversible one-electron transfers to $\text{Re}_2^{\text{III,III}}(\mu\text{-NCS})_2(\text{NCS})_8^{4-}$, which are then followed by an irreversible two-electron reduction that forms a product similar to $\text{Re}_2^{\text{II,II}}(\text{NCS})_8^{4-}$ [50].

16.3.3.3 Supramolecular Arrays

Rhenium complexes are used in the construction of robust supramolecular arrays having strong metal–ligand bonds. Assemblies in the form of triangles, squares, rectangles, and the like possess capabilities for host–guest interactions and molecular recognition and have promise in areas such as sensing, catalysis, molecular sieving, and energy storage and conversion [8, 51–53]. The *fac*- $\text{Re}(\text{CO})_3\text{Cl}$ unit is frequently employed as an element in such structures. An example is the molecular square $[\text{Re}(\text{CO})_3\text{Cl}(\mu\text{-azp})]_4$ (5 and Fig. 6) which is assembled from four $\text{Re}(\text{CO})_3\text{Cl}$ moieties and four bridging 4,4'-azopyridine (azp) ligands [51]. The compound exhibits four successive reductions at -0.01 , -0.45 , -0.74 , and -1.07 V and a single, reversible four-electron oxidation at $E^{\circ'} = +2.03$ V in DMF. The reductions are assigned to ligand-centered electron transfers; the oxidation is assigned to

Fig. 6 Structural representation of $[\text{Re}(\text{CO})_3\text{Cl}(\mu\text{-azp})]_4$, (5) (reprinted with permission from Ref. 51, Copyright 2000 American Chemical Society).



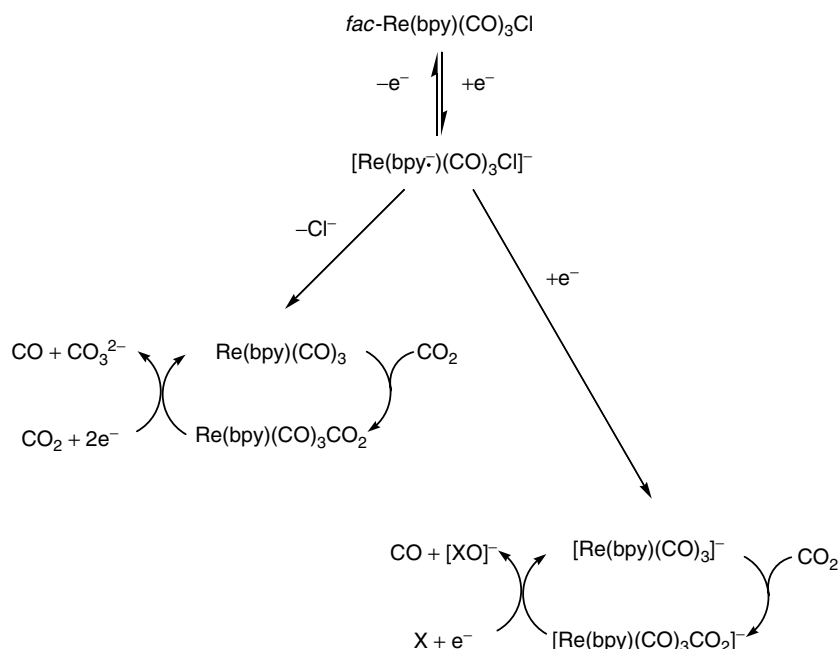


Fig. 7 Proposed one- and two-electron mechanisms for electrocatalytic reduction of CO_2 by $\text{fac-Re(bpy)(CO)}_3\text{Cl}$; X is an oxide ion acceptor (adapted from Ref. 55).

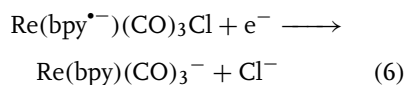
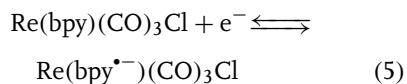
the removal of one electron each from the four noninteracting Re(I) atoms. The light-harvesting capacity of polynuclear rhenium centers and their capacity for reversible multielectron transfer is of interest with regard to applications in energy storage and conversion.

16.3.3.4 Carbon Dioxide Fixation

Low-valent rhenium complexes are effective in the catalytic reduction of carbon dioxide. The conversion can be accomplished photolytically or electrochemically and is of interest with regard to fuel production and greenhouse gas remediation [9]. Electrocatalytic reduction of CO_2 to CO is initiated by the reduction of $\text{fac-Re(bpy)(CO)}_3\text{Cl}$ or a related complex and can be accomplished in homogeneous solution [54, 55] or on a polymer-modified electrode surface [56]. Catalytic current

efficiency is high and generally is in excess of 90%.

The mechanism of electrocatalytic CO_2 reduction has been studied in some detail [57–60] but is not fully understood. A proposed mechanism from an early investigation [55] is shown in Fig. 7. The initial step in the reaction is the reversible reduction of $\text{fac-Re(bpy)(CO)}_3\text{Cl}$ ($E^{\circ'} = -1.1$ V in CH_3CN), which is assigned to the bipyridyl-centered electron transfer (Eq. 5). This is followed by a second step (Eq. 6) at ca -1.5 V, which is irreversible at room temperature and may be accompanied by loss of Cl^- :



Carbon dioxide reduction is thought to proceed via metallocarboxylate intermediate(s) formed by coordination of CO₂ to the electron-rich Re center, although discrete steps in the process cannot be unambiguously assigned. The timing of Cl[−] displacement from and CO₂ adduction to the Re(bpy)(CO)₃ unit are important mechanistic parameters. Most interpretations are based on a one-electron pathway, involving the interaction of CO₂ with the product of Eq. (5); a two-electron pathway, involving interaction of CO₂ with the product of Eq. (6); or a combination of these steps. Additional mechanistic considerations are the role dimeric rhenium intermediates and likely proton sources.

References

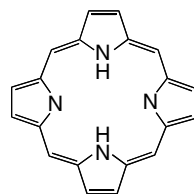
1. F. A. Cotton, G. Wilkinson, C. A. Murillo et al., *Advanced Inorganic Chemistry*, 6th ed., John Wiley & Sons, New York, 1999, pp. 974–1000.
2. U. Abram, in *Comprehensive Coordination Chemistry II*, (Eds.: J. A. McCleverty, T. J. Meyer), 2nd ed., Elsevier, Amsterdam, 2004, Vol. 5, Chapter 5.3.
3. R. J. Magee, T. J. Cardwell, in *Encyclopedia of Electrochemistry of the Elements*, (Ed.: A. J. Bard), Marcel Dekker, New York, 1973 Vol. 2, Chapter II-4.
4. R. J. Magee, H. Blumstein, in *Standard Potentials in Aqueous Solution*, (Eds.: A. J. Bard, R. Parsons, J. Jordan), Marcel Dekker, New York, 1985, pp. 444–451.
5. K. Hashimoto, K. Yoshihara, *Top. Curr. Chem.* **1996**, 176, 275–291.
6. M. S. Ram, L. M. Skeens-Jones, C. S. Johnson et al., *J. Am. Chem. Soc.* **1995**, 117, 1411–1421.
7. M. Leeaphon, P. E. Fanwick, R. A. Walton, *Inorg. Chem.* **1990**, 29, 4348–4351.
8. P. H. Dinolfo, J. T. Hupp, *Chem. Mater.* **2001**, 13, 3113–3125.
9. E. Fujita, B. S. Brunschwig, in *Electron Transfer in Chemistry. Catalysis of Electron Transfer, Heterogeneous and Gas-Phase Systems*, (Eds.: S. Fukuzumi, T. E. Mallouk, Y. Haas), Wiley-VCH, Weinheim, 2001 Vol. 4, pp. 88–126.
10. L. Astheimer, K. Schwochau, *J. Inorg. Nucl. Chem.* **1976**, 38, 1131–1134.
11. D. W. Letcher, T. J. Cardwell, R. J. Magee, *J. Electroanal. Chem.* **1970**, 25, 473–479.
12. M. Gross, P. Lemoine, J. Brenet, *Electrochim. Acta* **1971**, 16, 1787–1795.
13. D. D. DuMez, J. M. Mayer, *Inorg. Chem.* **1998**, 37, 445–453.
14. J. R. Dilworth, S. K. Ibrahim, S. R. Khan et al., *Polyhedron* **1990**, 9, 1323–1329.
15. M. S. Ram, L. M. Jones, H. J. Ward et al., *Inorg. Chem.* **1991**, 30, 2928–2938.
16. D. W. Pipes, T. J. Meyer, *J. Am. Chem. Soc.* **1985**, 107, 7201–7202.
17. M. S. Ram, C. S. Johnson, R. L. Blackburn et al., *Inorg. Chem.* **1990**, 29, 238–244.
18. M. S. Ram, L. M. Skeens-Jones, C. S. Johnson et al., *J. Am. Chem. Soc.* **1995**, 117, 1411–1421.
19. C. C. Van Kirk, V. Béreau, M. M. Abu-Ornar et al., *J. Electroanal. Chem.* **2003**, 541, 31–38.
20. R. Seeber, G. A. Mazzocchin, U. Mazzi et al., *Polyhedron* **1986**, 5, 1975–1986.
21. A. Paulo, Â. Domingos, A. P. de Matos et al., *Inorg. Chem.* **1994**, 33, 4729–4737.
22. A. Davison, C. Orvig, H. S. Trop et al., *Inorg. Chem.* **1980**, 19, 1988–1992.
23. M. V. Bennett, J. R. Long, *J. Am. Chem. Soc.* **2003**, 125, 2394–2395.
24. L. A. de Learie, R. C. Haltiwanger, C. G. Pierpont, *Inorg. Chem.* **1987**, 26, 817–821.
25. J. E. Hahn, T. Nimry, W. R. Robinson et al., *J. Chem. Soc., Dalton Trans.* **1978**, 1232–1236.
26. J. R. Dilworth, A. J. Hutson, S. Morton et al., *Polyhedron* **1992**, 11, 2151–2155.
27. G. A. Heath, K. A. Moock, D. W. A. Sharp et al., *J. Chem. Soc., Dalton Trans.* **1985**, 1503–1505.
28. A. R. Cowley, J. R. Dilworth, P. S. Donnelly et al., *J. Chem. Soc., Dalton Trans.* **2003**, 748–754.
29. G. E. D. Mullen, P. J. Blower, D. J. Price et al., *Inorg. Chem.* **2000**, 39, 4093–4098.
30. P. M. Treichel, J. P. Williams, *J. Organomet. Chem.* **1977**, 135, 39–51.
31. L. E. Helberg, S. D. Orth, M. Sabat et al., *Inorg. Chem.* **1996**, 35, 5584–5594.
32. J. R. Kirchoff, M. R. Allen, B. V. Cheesman et al., *Inorg. Chim. Acta* **1997**, 262, 195–202.
33. B. E. Wilcox, E. Deutsch, *Inorg. Chem.* **1991**, 30, 688–693.
34. J. R. Kirchoff, W. R. Heineman, E. Deutsch, *Inorg. Chem.* **1987**, 36, 3108–3113.

35. X. L. Zhang, J. T. Hupp, G. D. Danzer, *J. Electroanal. Chem.* **1995**, 380, 229–235.
36. L. M. Jones-Skeens, X. L. Zhang, J. T. Hupp, *Inorg. Chem.* **1992**, 32, 3879–3881.
37. A. B. P. Lever, *Inorg. Chem.* **1991**, 30, 1980–1985.
38. A. Ichimura, T. Kajino, T. Kitagawa, *Inorg. Chim. Acta* **1988**, 147, 27–31.
39. L. A. Bottomley, P. E. Wojciechowski, G. B. Holder, *Inorg. Chim. Acta* **1997**, 255, 149–155.
40. F. A. Cotton, *Inorg. Chem.* **1965**, 4, 334–336.
41. F. A. Cotton, R. A. Walton, *Multiple Bonds between Metal Atoms*, 2nd ed., Oxford University Press, New York, 1993.
42. F. A. Cotton, E. Pedersen, *Inorg. Chem.* **1975**, 14, 383–387.
43. G. A. Heath, R. G. Raptis, *Inorg. Chem.* **1991**, 30, 4106–4108.
44. D. J. Salmon, R. A. Walton, *J. Am. Chem. Soc.* **1978**, 100, 991–993.
45. P. Brant, D. J. Salmon, R. A. Walton, *J. Am. Chem. Soc.* **1978**, 100, 4424–4430.
46. F. A. Cotton, E. Pedersen, *J. Am. Chem. Soc.* **1975**, 97, 303–308.
47. V. Srinivasan, R. A. Walton, *Inorg. Chem.* **1980**, 19, 1635–1640.
48. G. A. Heath, R. G. Raptis, *J. Am. Chem. Soc.* **1993**, 115, 3768–3769.
49. S. P. Best, R. J. H. Clark, D. G. Humphrey, *Inorg. Chem.* **1995**, 34, 1013–1014.
50. R. J. H. Clark, D. G. Humphrey, *Inorg. Chem.* **1996**, 35, 2053–2061.
51. S.-S. Sun, A. J. Lees, *J. Am. Chem. Soc.* **2000**, 122, 8956–8967.
52. P. H. Dinolfo, M. E. Williams, C. L. Stern et al., *J. Am. Chem. Soc.* **2004**, 126, 12989–13001.
53. B. Gholamkhass, H. Mametuka, K. Koike et al., *Inorg. Chem.* **2005**, 44, 2326–2336.
54. J. Hawecker, J.-M. Lehn, R. Ziessel, *J. Chem. Soc., Chem. Commun.* **1984**, 328–330.
55. P. Sullivan, C. M. Bolinger, D. Conrad et al., *J. Chem. Soc., Chem. Commun.* **1985**, 1414–1416.
56. T. R. O'Toole, L. D. Margerum, T. D. Westmoreland et al., *J. Chem. Soc., Chem. Commun.* **1985**, 1416–1417.
57. A. I. Breikss, H. D. Abruña, *J. Electroanal. Chem.* **1986**, 201, 347–358.
58. P. Christensen, A. Hamnett, A. V. G. Muir et al., *J. Chem. Soc., Dalton Trans.* **1992**, 1455–1463.
59. F. Paolucci, M. Marcaccio, C. Paradisi et al., *J. Phys. Chem. B* **1998**, 102, 4759–4769.
60. Y. Hayashi, S. Kita, B. S. Brunshwig et al., *J. Am. Chem. Soc.* **2003**, 125, 11976–11987.

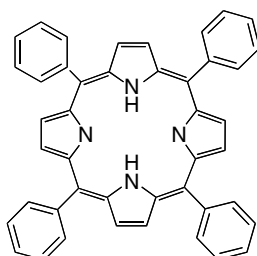
Ligand Abbreviations

Abbreviation	Name
8-HQ	8-Quinolinol
acac [−]	Acetylacetonate
bisimMe ₂ en	<i>N, N'</i> -Dimethyl- <i>N, N'</i> -bis(imidazol-4-ylmethyl)ethane-1,2-diamine
bispicen	<i>N, N'</i> -Bis(2-pyridylmethyl)-1,2-ethanediamine
bispicMe ₂ en	<i>N, N'</i> -Bis((6-methylpyrid-2-yl)methyl)ethane-1,2-diamine
bpea	<i>N, N'</i> -Bis(2-pyridylmethyl)ethylamine
bpia	Bis(picoly)(<i>N</i> -methylimidazol-2-yl)amine
bpy	2,2'-Bipyridine
bpyO ₂	2, 2'-Bipyridine-1,1'-dioxide
Cp ^{*−}	Decamethylcyclopentadienide
Et ₂ dtc [−]	<i>N, N</i> -Diethyldithiocarbamate
H ₂ als	<i>N</i> -(2-Carboxyethyl)salicylideneamine
H ₂ bbpen	<i>N, N'</i> -Bis(2-hydroxybenzyl)- <i>N, N'</i> -bis(2-pyridylmethyl)ethylenediamine

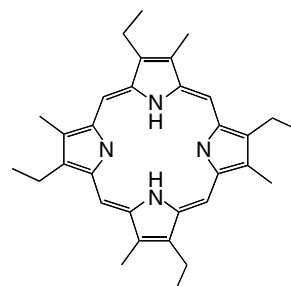
H ₂ DMHP	Hematoporphyrin IX dimethylester = 2, 7, 12, 18-tetramethyl-3,8-di(2-hydroxyethyl)-13,17-di(methylpropionato)porphyrin
H ₂ DPPF ₂₀	5,10,15,20-Tetrakis(pentafluorophenyl)-2,3,7,8,12,13,17,18-octaphenylporphyrin
H ₂ EtioP	2,7,12,17-Tetramethyl-3,8,13,18-tetraethylporphyrin
H ₂ Pc	Phthalocyanine
H ₂ saldpt	1,7-Diamino-4-azaheptanebis(salicylaldimine)
H ₂ salen	<i>N</i> , <i>N'</i> -Ethylenebis(salicylaldimine)
H ₂ salophen	<i>N</i> , <i>N'</i> - <i>o</i> -Phenylenebis(salicylaldimine)
H ₂ tdcmpp	2,3,7,8,12,13,17,18-Octachloro-5,10,15,20-tetrakis(3,5-dichloro-2,6-dimethoxyphenyl)porphyrin
H ₂ TDCSPP	5,10,15,20-Tetrakis(2,6-dichloro-3-sulfonatophenyl)porphyrin
H ₂ tdmpp	5,10,15,20-Tetrakis(2,6-dimethoxyphenyl)porphyrin
H ₂ TDMSP	5,10,15,20-Tetrakis(2,6-dimethyl-3-sulfonatophenyl)porphyrin
H ₂ TMAP	5,10,15,20-Tetrakis(4- <i>N</i> , <i>N'</i> , <i>N''</i> -trimethylanilinium)porphyrin
H ₂ TMPyP	5,10,15,20-Tetrakis(<i>N</i> -methyl-4-pyridyl)porphyrin
H ₂ TPP	5,10,15,20-Tetrakis(phenyl)porphyrin
H ₃ salmp	2-(Bis(salicylideneamino)methyl)phenol
H ₃ tpc	<i>meso</i> -Tris(phenyl)corrole
H ₄ mac	5,6-(4,5-Dichlorobenzo)-3,8,11,13-tetraoxo-2,3,9,9-tetramethyl-12,12-diethyl-1,4,7,10-tetraazacyclotridecane
HB(pz) ₃ [−]	Hydrotris(pyrazol-1-yl)borate
hbpme	<i>N</i> -(2-Hydroxybenzyl)- <i>N</i> , <i>N'</i> -bis(2-pyridylmethyl)ethane-1,2-diamine
Hhpt	1-Hydroxy-2-pyridinethione
Hphox	2-(2'-Hydroxyphenyl)oxazoline
Me ₃ tacn	<i>N</i> , <i>N'</i> , <i>N''</i> -Trimethyl-1,4,7-triazacyclononane
pebMe ₂ pma	2-(2-Pyridyl)ethylbis(6-methyl-2-pyridylmethyl)amine
pebpma	2-(2-Pyridyl)ethylbis(2-pyridylmethyl)amine
phen	1,10-Phenanthroline
sar	3,6,10,13,16,19-Hexaazabicyclo[6.6.6]eicosane
tacn	1,4,7-Triazacyclononane
Tp [−]	Hydrotris(pyrazol-1-yl)borate
tripod [−]	Cyclopentadienyltris(diethylphosphito-P)cobaltate(1-)



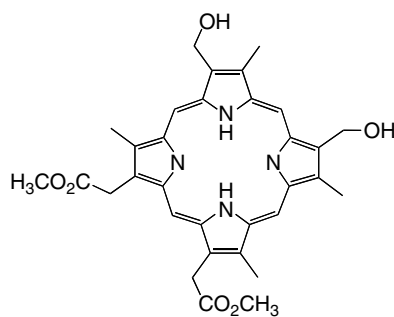
Porphine (H_2P)



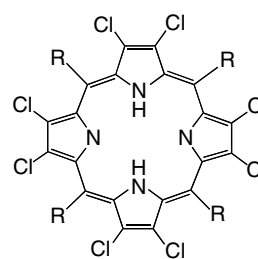
H_2TPP



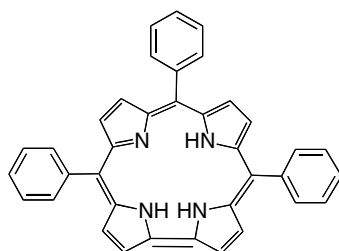
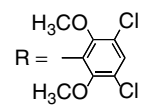
H_2EtioP



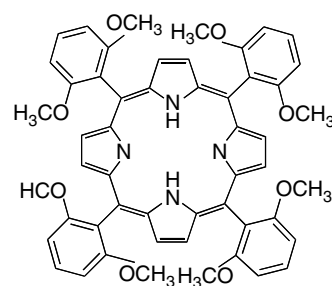
H_2DMHP



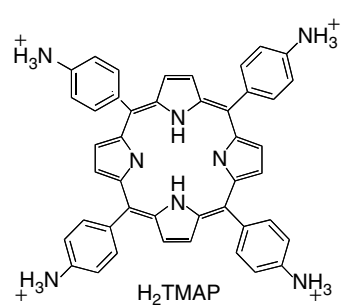
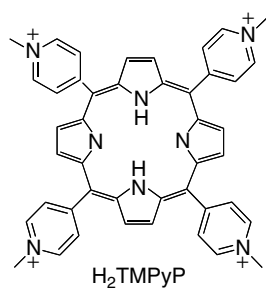
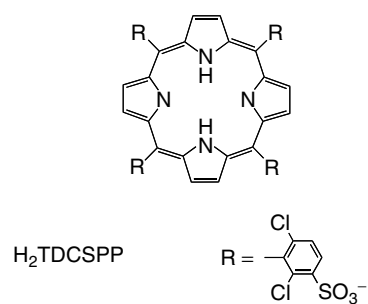
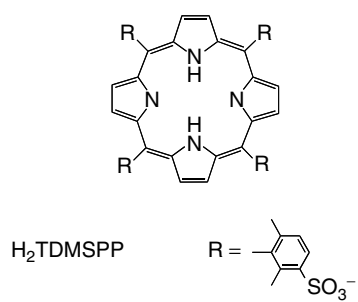
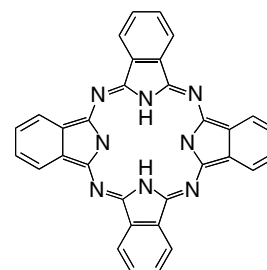
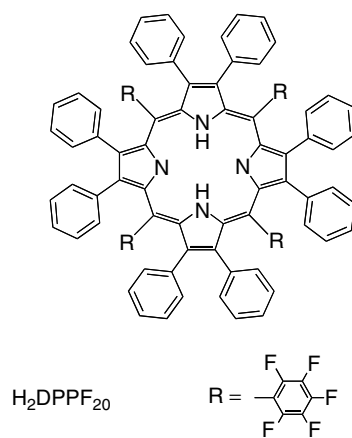
$H_2tdcmpp$

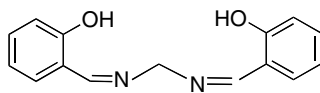


H_3tpc

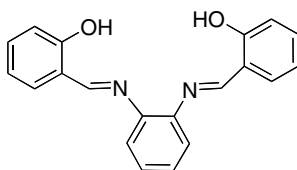


H_2tdmpp

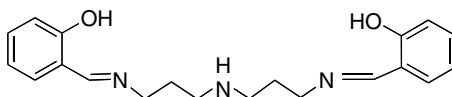




H₂salen



H₂salophen



H₂saldpt

18

The Nickel Group (Nickel, Palladium, and Platinum)

György Inzelt
Eötvös Loránd University, Budapest, Hungary

György Horányi
Institute of Materials and Environmental
Chemistry (IMEC), Budapest, Hungary

18.1	Nickel	499
18.1.1	Fundamentals	499
18.1.2	Surface Changes at Atomic Level as a Function of Potential	500
18.1.3	Adsorption Studies	503
18.1.4	Spontaneous Reduction of Anions at Ni Surface	505
18.1.5	Electrochemical Oscillation during Nickel Dissolution	506
18.1.6	New Findings on the Dissolution/Deposition Processes	507
18.1.7	Nickel–Hydrogen Systems	508
18.1.8	Nickel Oxide and Nickel Hydroxide	509
18.2	Palladium	510
18.2.1	Fundamentals	510
18.2.2	New Findings on the Dissolution and Deposition of Palladium	511
18.2.3	Hydrogen and Oxygen Sorption in/at Palladium Electrodes	513
18.2.4	Electrosorption and Electrocatalytic Processes	514
18.3	Platinum	515
18.3.1	Fundamentals	515
18.3.2	Effect of Adsorption and Surface Structure on the Voltammetric Behavior of Platinum Electrodes	516
18.3.2.1	Adsorption of Hydrogen, Oxygen, and Anions	516
18.3.2.2	Well-defined Platinum Surfaces	518
18.3.2.3	Faceted and Platinized Platinum Electrodes	519
18.3.2.4	Surface Structure and Reactivity	520
	Acknowledgment	523
	References	523

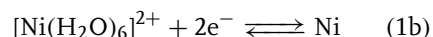
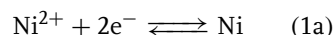
18.1 Nickel

18.1.1 Fundamentals

The oxidation number of nickel in its compounds ranges from 0 to +4; however, +2 state is the most important one. In fact, there is no other stable, higher oxidation state than +4, therefore, the redox chemistry of nickel is poorer as compared with the other two metals of this group. Ni^{2+} ions in a hydrated form can be found in aqueous solutions of NiCl_2 , NiSO_4 , $\text{Ni}(\text{NO}_3)_2$, and so on. $\text{Ni}(\text{II})$ is the typical oxidation state in several, stable water-soluble complexes such as $[\text{Ni}(\text{NH}_3)_4]^{2+}$, $[\text{Ni}(\text{CN})_4]^{2-}$, and $[\text{Ni}(\text{NH}_3)_6]^{2+}$, as well as in sparingly soluble simple compounds, for example, $\text{Ni}(\text{II})$ -dimethylglyoxime, $\text{KNi}[\text{Fe}(\text{CN})_6]$, $\text{K}_2\text{Ni}[\text{Fe}(\text{CN})_6]$.

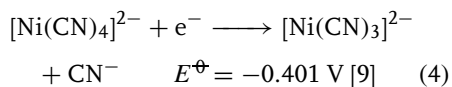
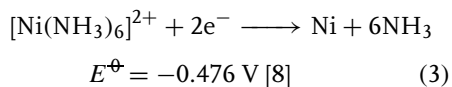
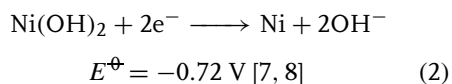
Although the nickel-containing systems have been extensively studied also by electrochemical methods [1] due to their practical importance, for example, in electrochemical power sources (Ni-Fe , Ni-Cd , Li-NiF_2 batteries), in corrosion-resistant alloys (tableware, coins, industrial instruments) as well as due to their interesting (magnetic, spectral, catalytic) properties most of the standard potentials of electrode

reactions involving nickel compounds have been calculated from nonelectrochemical (calorimetric and solubility) data [2]. Even for the simplest reaction

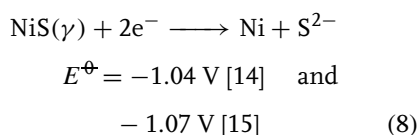
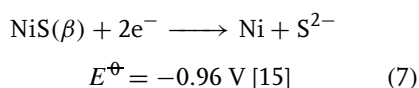
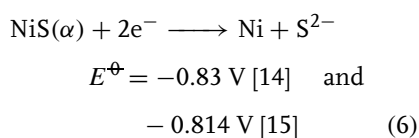
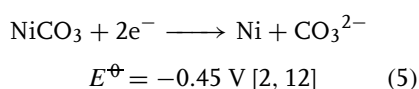


there is a rather large scattering of the published standard potential values determined by the measurements of the electromotive force (E_{MF}), for example, -0.248 V [3], -0.231 V [4], -0.227 V [5], and -0.246 V [6]. This scattering of data is presumably related to the difficulties in the attainment of a true equilibrium state. At present the most accepted value is $E^\ominus = -0.257$ V [2] that was calculated on the basis of the Gibbs energy change of the reaction (ΔG) [7]; however, different values for ΔG as well as for the reaction entropy (ΔS) can be found in the literature [2].

Further standard potentials measured electrochemically at 25°C are as follows:



These values differ from those calculated from ΔG values, for example, for reaction (3) $E^\ominus = 0.49$ V is given in Refs. 10, 11. E^\ominus values for several reactions estimated by using thermodynamical data can be found in the literature [1–13]. Perhaps the most accurate ones are those calculated from the solubility products, for example,



Nickel sulfide is a good example why – beside the uncertainty of the thermal values mentioned before – diverse E^\ominus values have been determined, inasmuch as the formation and ratios of different forms depend on the conditions, for example, on the acidity and temperature of the solution from which the precipitation is executed.

The system, which is of practical importance (Edison storage battery, electrocatalysis in organic synthesis), is the $\text{NiOOH}|\text{Ni}(\text{OH})_2$ couple (electrode). Somewhat surprisingly – since it is a widely studied and applied electrode – the mechanism and the true nature of the oxidized species are not fully understood yet [1, 2, 16]. The formal potential depends on the KOH concentration and is ca. 1.3 V. It follows that it is unstable in aqueous solutions and is also an oxidizing agent for various organic compounds.

There have been many polarographic measurements devoted to the reduction of Ni(II). Not only Ni(II) compounds in “noncomplexing” supporting electrolytes such as alkali chlorides, nitrates, perchlorates have been investigated, but a wide range of complexes have also been studied [1, 17]. The half-wave potential of the polarographic wave ($E_{1/2}$) depends on the experimental conditions (ionic strength, nature of anions); however, its value is typically -1.1 ± 0.1 V in aqueous solutions. $E_{1/2}$ values determined for complexes range between ca. -0.3 to -0.7 V, for example, $-0.7 \text{ V} < E_{1/2} < -0.91 \text{ V}$ for $[\text{Ni}(\text{SCN})_x]^{(2-x)+}$, $-1.36 \text{ V} < E_{1/2} < -1.47 \text{ V}$ for $[\text{Ni}(\text{CN})_4]^{2-}$, $-1.05 \text{ V} < E_{1/2} < -1.22 \text{ V}$ for $[\text{Ni}(\text{NH}_3)_6]^{2+}$, $-0.751 \text{ V} < E_{1/2} < -1.16 \text{ V}$ for $[\text{Ni}(\text{Py})_6]^{2+}$ have been reported. The voltammetric characteristics, the kinetic, the mechanistic, and double-layer properties of the nickel electrodes and compounds have been compiled in Ref. 1 including an extensive literature survey until 1971. Further on we review the new results obtained in the last 15 years.

18.1.2

Surface Changes at Atomic Level as a Function of Potential

A detailed electrochemical study of Ni(111) electrodes in H_2SO_4 solution in conjunction with in situ scanning tunneling microscopy (STM) and in situ surface X-ray scattering methods (SXS, x-ray diffraction and x-ray reflectivity) was carried out by Scherer et al. [18].

The main results of the study are as follows: Ni(111) samples, prepared via annealing in H_2 and exposure to air at room temperature, are covered by a smooth three-to-four-layers thick NiO(111) film with parallel $(\text{NiO}[1\bar{1}0])\parallel(\text{NiO}[1\bar{1}0])$

and antiparallel $(\text{NiO}[1\bar{1}0])\parallel(\text{NiO}[1\bar{1}0])$ in-plane orientation. Electrochemical reduction at potentials $\geq -0.40 \text{ V}_{\text{Ag}/\text{AgCl}}$ results in the formation of a well-defined, oxide-free surface with large terraces, a low surface mobility, and a (1×1) lattice on the atomic scale. X-ray reflectivity data indicate vertical lattice expansion for the topmost Ni layer and a strongly bound sulfate or oxygen species. Active Ni dissolution commences at potentials $\geq -0.25 \text{ V}_{\text{Ag}/\text{AgCl}}$ by a step-flow mechanism, followed by the rapid formation of large three-dimensional etch pits, leading to considerable surface roughening. In situ STM observations of the passive film formation show at potentials $\geq -0.10 \text{ V}_{\text{Ag}/\text{AgCl}}$ the nucleation and growth of an initial “grainy” phase, which is attributed to a Ni hydroxide, followed by a slower restructuring process. According to combined STM and SXS data, the resulting steady state passive film exhibits a duplex structure, with a crystalline, inner $\text{NiO}(111)$ layer, consisting of exclusively antiparallel oriented grains $(\text{NiO}[1\bar{1}0])\parallel(\text{NiO}[1\bar{1}0])$, which are slightly tilted relative to the substrate lattice, and a porous, probably amorphous hydroxide phase on top. The thickness of the crystalline NiO film increases with potential by $14\text{--}17 \text{ \AA V}^{-1}$. In addition, structural changes of the oxide film during immersion of Ni samples into the sulfuric acid solution at potentials in the passive range and after immersion from the electrolyte were observed, which indicate the slow conversion of the air formed into the passive oxide and the (partial) reformation of the air-formed oxide, respectively.

In a series of publications, the results of anodic dissolution and passivation of well-defined single-crystal surfaces of Ni (and other metals) and its alloys were presented by Marcus et al. [19–24]. Their approach aimed at a better understanding

of corrosion phenomena at the atomic and molecular level.

STM was used to study ex situ (in air) the thin oxide films (passive films) grown on $\text{Ni}(111)$ by anodic polarization in $0.05 \text{ mol dm}^{-3} \text{ H}_2\text{SO}_4$. Atomic resolution imaging demonstrated the crystalline character of the oxide film and the epitaxy with the substrate. Two levels of roughening with respect to the nonpolarized surfaces were observed: on a mesoscopic scale and on the atomic scale. The roughening on the mesoscopic scale increases with higher polarization potentials. The observed roughness was attributed to the result of the competition between metal dissolution and nucleation and growth of the oxide film. The roughening on the atomic scale is independent of the polarization potential. It is evidenced by the formation of a stepped crystalline lattice whose parameters fit those of a (111) -oriented NiO surface. The presence of steps indicated a tilt of (8 ± 5) degrees of the surface of the film with respect to the (111) orientation. The possible epitaxial relationships resulting from the surface tilt are discussed. Local variations of the film thickness at the step edges are likely to result from the surface tilt and may constitute preferential sites for the local breakdown of passivity.

In other papers by the same group, the effects of sulfur adsorbed or segregated on the Ni surface on corrosion or passivation were described, including the sulfur-induced enhancement of dissolution and the blocking of passivation. It was shown how the conditions of stability of adsorbed sulfur monolayers could be predicted on thermodynamical grounds and this was illustrated by a potential–pH diagram for adsorbed sulfur on nickel in water at 25°C . (See Refs. 22, 25–29 and papers cited therein.)

In [30] on cyclic voltammetry (CV), x-ray and UV photoelectron spectroscopy (XPS, UPS) were employed to study the electrochemical deposition and dissolution of nickel on a polycrystalline gold electrode, in a 0.1-mol dm^{-3} NiSO_4 electrolyte. The modification of the Ni/Au interface upon thermal treatment in ultrahigh vacuum was also investigated. Depending on the applied potential, two distinct Ni chemical states were observed. At -0.5 V vs. SCE an oxidized Ni phase, mainly Ni(OH)_2 , was formed, whereas at potentials lower than -0.8 V , nucleation of reduced Ni species surrounded by hydroxidized nickel occurred. The systematic investigation of the adsorbate species' binding energies as a function of the applied potential revealed that hydroxidized nickel precipitates on the gold electrode, while reduced nickel species directly deposit on the electrode surface via the reduction of Ni^{2+} ions. Heating the Ni/Au interface to 650 K decomposes the adsorbed nickel film forming a new compound containing a Au–Ni intermetallic component.

A study of the electrodeposition and electrochemical dissolution of ultrathin Ni films on Ag(111) electrodes in Watts electrolyte by in situ STM, electrochemical quartz crystal microbalance (EQCM), and cyclic voltammetry was reported in [31]. It was stated that Ni deposition starts at potentials negative of -0.72 V vs. SCE , where an incommensurate, (111)-oriented film with an in-plane lattice rotation of 0.5° relative to the Ag substrate lattice was formed. The lateral nearest neighbor spacing is as in bulk Ni (0.249 nm) for a film thickness greater than or equal to 3 ML and expanded for monolayer (0.254 nm) and bilayer (0.252 nm) films. Depending on the deposition potential, three growth regimes, resulting in different deposit morphologies, were observed:

At low overpotentials, a smooth Ni film was formed via a 2D step-flow growth process, commencing at steps of the Ag substrate. At medium overpotentials, a transformation from 2D step-flow to 3D growth took place resulting in the selective formation of Ni multilayer islands along the Ag steps. At even higher overpotentials, 3D islands were formed at the steps and on the substrate terraces. The size of the Ni multilayer islands was independent of the terrace widths, indicating that Ni growth proceeds via direct discharge at step sites ("direct deposition"). The transition from 2D to 3D growth as well as the change in island shape with overpotential could be rationalized by a different potential dependence of the various microscopic nucleation and growth processes. The multilayer growth at steps was attributed to next-layer nucleation at the structural defect induced by the Ag–Ni boundary and could be described quantitatively as a function of deposition time by a simple 2D model. A place exchange of Ni with Ag surface atoms and encapsulation of Ni islands by Ag is observed. It was found that the dissolution of the electrodeposited multilayer Ni films proceeds via step-flow etching, with a higher dissolution rate for the Ni monolayer as compared to higher Ni layers.

The application of STM to in situ studies of nickel electrodes under potential control was reported in [32].

Using atomic force microscopy (AFM), the kinetic surface roughening in electrochemical dissolution of nickel films at a low constant current density was studied in order to reveal the scaling laws [33]. The surface measurements of AFM exhibited the oscillatory variation of the interface width with time, which made it impossible to determine the growth exponent β . The oscillatory behavior of surface

roughening was explained by the presence of unstable passive films formed on the nickel film surface. The roughness exponent $\alpha = 0.94 \pm 0.04$ calculated from the AFM images of the anodic dissolved surface was almost equal to that predicted by the diffusion-driven growth model.

18.1.3

Adsorption Studies

The study of the adsorption phenomena of ions and organic species on nickel electrodes may contribute to a better understanding of the electrode processes occurring at the nickel/electrolyte interface.

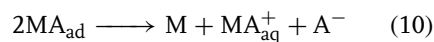
In the last few decades, the study of adsorption phenomena at nickel electrodes by a radiotracer method has been the subject of several studies (see [34–40] and literature cited therein). Most of these studies were carried out at smooth electrodes; however, in some cases, nickel powder and Raney-nickel catalysts were used.

Pioneering work was done in this field by Schwabe [34, 35]. Substantial and very informative radiotracer adsorption studies carried out by him and his coworkers using Pt, Ni, and Fe sheets and evaporated films, using labeled anions in order to interpret the role of anions in the corrosion and passivation processes [34, 35].

A radiotracer method was elaborated for the study of the adsorption phenomena on nickel electrodes formed by electrodeposition of nickel (“nickelized” nickel electrode). Adsorption studies were carried out with labeled HCl, H₂SO₄, H₃PO₄, thiourea, phenylacetic, and acetic acids in 0.1 mol dm^{−3} HClO₄ supporting electrolyte. The potential dependence of the adsorption of these species was determined in the potential range −200 to +200 mV vs. relative hydrogen electrode (RHE). It was found

that a significant potential-dependent adsorption occurs at low concentrations (10^{−3}–10^{−4} mol dm^{−3}) of the species studied in the course of the anodic dissolution of the electrode.

There is no doubt that specific adsorption of anions and organic species occurs in a wide potential range as the experiments were carried out in 0.1 mol dm^{−3} HClO₄ supporting electrolyte at low concentrations (10^{−3}–10^{−5} mol dm^{−3}) of the species studied. It was found that the adsorption of anions exerts some influence on the anodic dissolution rate; however, this effect is very far from that observed in the case of thiourea. In the latter case, the rate of anodic dissolution was significantly influenced by the presence of thiourea, even at its very low concentration. This behavior was ascribed to the strong interaction of thiourea with the metal ions and the formation of complexes both on the metal surface and in the solution phase. The phenomena presented were considered as a result of the adsorption competition of the species studied with ClO₄[−] ions. Three fundamental mechanisms were formulated for the active dissolution: (1) aquo–ligand, (2) hydroxo–ligand, and (3) anion–ligand mechanisms. The last of the mentioned mechanisms is formulated as follows:



It is assumed that these three mechanisms are operating simultaneously and depend on the experimental conditions if one of them becomes predominant in the overall process. The significant adsorption of anions found at low potentials where

the dissolution rate is small, the reversibility of the adsorption with respect to the potential, and the mobility of the adsorbed species all support the possibility of the anion–ligand mechanism.

The incorporation of chloride ions in passive films formed on nickel in Cl^- -containing acid solution and the entry of Cl^- into passive films formed in Cl^- -free solution and subsequently exposed to Cl^- were investigated by Marcus and Herbelin [41, 42] by electrochemical measurements, ESCA (Electron Spectroscopy for Chemical Analysis) and using in situ radiotracer (Cl-36) methods. It was found that at potentials in the active region, chloride ions are adsorbed on the nickel surface and form a thin hydroxy-chloride layer. They observed that the amount of Cl^- increases with potential (beyond the equivalent full monolayer coverage) up to the active/passive potential where a marked drop of the Cl^- surface concentration takes place. In the passive region, chloride ions are incorporated in the passive film. When the film is formed in Cl^- -containing solution at potentials below the pitting potential, Cl^- ions are found in the outer hydroxide layer and at the metal/oxide interface. When the film is formed without Cl^- in the solution, and then exposed to Cl^- , chloride ions are found in the outer hydroxide layer with the same concentration as the one found after passivation in Cl^- -containing solution, whereas no significant amount of Cl^- is found in the inner oxide. The concentration of Cl^- in the passive film has been measured. The Cl^- concentration in the hydroxide layer is approximately $10^{-2} \text{ mol dm}^{-3}$ (i.e. $\text{Cl}^-/(\text{Cl}^- + \text{OH}^-)$ approximately 10%) for $\text{Cl}^- = 5 \times 10^{-3} \text{ mol dm}^{-3}$ in the solution. At potentials above the pitting potential, measurements have been performed during the incubation period in order to investigate

the mechanisms of pit initiation, the hydroxide layer acts as a reservoir for Cl^- , which enters the passive film. A critical concentration of Cl^- in the oxide layer of approximately $10^{-2} \text{ mol cm}^{-3}$ has been measured in the stage immediately preceding pitting. A similar critical concentration in the film has been measured for different Cl^- concentrations in the solution.

The passive film was found to have a bilayer structure both in the absence and in the presence of Cl^- in the stage preceding pitting. The passive film does not become thinner in the presence of Cl^- ; on the contrary a growth of the film is observed when Cl^- is added to the electrolyte. Cl^- must be adsorbed in order to penetrate into the film but the surface coverage of adsorbed Cl^- always remains very low, as Cl^- starts to enter the passive film at low surface coverage. The view of pit initiation emerging from the above results is the following. Marked modifications of the passive film are caused by the presence of Cl^- . Cl^- is incorporated or enters the hydroxide layer by a chemical reaction probably involving place exchange of OH^- and Cl^- . Above a certain potential, Cl^- enters the inner oxide layer. A critical concentration of Cl^- in the film is reached, of the order of $10^{-2} \text{ mol cm}^{-3}$ for nickel.

The study of the effect of the adsorptions of various additives on the anodic dissolution has been the subject of several studies. For instance, the influence of the adsorption of N species on the anodic dissolution of Ni was studied in [43]. The dissolution and passivation of Ni in nitrite-containing acid solutions were investigated by Auger spectroscopy, AFM, and conventional electrochemical techniques. It was found that the dissolution/passivation of the Ni surface is consistent with a competition between adsorbed OH^- and nitrogen-containing

species with a potential-dependent surface coverage. Nitrogen-containing species hinder the passivation of the Ni surface, shifting the formation of the complex nickel-hydroxide/oxide film to more positive potential values. The dynamics of the dissolving interface, followed by AFM, reflect first the competition of adsorbed species, leading to the development of protrusions and cavities, and finally the formation of the passive film that promotes surface smoothening by a preferential dissolution of the protrusion tips under ohmic control.

An investigation of the adsorption of pyrazine and pyridine on nickel electrodes by in situ surface-enhanced Raman spectroscopy was reported in [44]. The result suggests that both pyrazine and pyridine were strongly adsorbed onto the substrates. It also implies that pyridine was adsorbed perpendicularly onto the substrate, while pyrazine adsorbed onto the substrate in a slightly tilted vertical configuration.

18.1.4

Spontaneous Reduction of Anions at Ni Surface

It is an almost general view that the nature of anions present in the electrolyte solutions affects the dissolution process of nickel.

This effect is explained by the role of the specific adsorption of anions. It is assumed that the specific adsorption of ClO_4^- ions is negligible [45, 46], and no chemical changes occur in the course of the electrochemical study of anodic dissolution and corrosion of nickel [47].

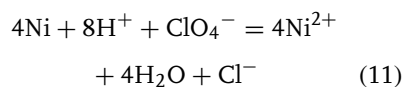
Detailed mechanistic conclusions are drawn from such studies without taking into account the possible reduction of ClO_4^- ions under the conditions of the experiments.

In a series of recent communications [48–50], it was demonstrated that the reduction of ClO_4^- ions takes place during the corrosion of Cu, Al, Zn, Ni, and Fe in deoxygenated HClO_4 solutions.

Both the dissolution rate of Ni and the reduction of ClO_4^- should depend on the acid concentration and temperature. The results obtained are summarized in Table 1. A given amount of Ni powder was dissolved in an excess of perchloric acid.

From the data presented in Table 1, the molar ratio of the Cl^- ions formed to nickel dissolved is independent of HClO_4 concentration. The influence of temperature is not strong as a temperature change of 25°C results in less than a doubling in the value of B/A .

Considering the equation



the formation of 1 mol Cl^- should be accompanied by the oxidation of 4 mol of nickel; thus, at 50°C , the efficiency of the reduction process referred to in the total amount of dissolved Ni is about 1.5% and at 20°C is around 1%.

Although the data obtained do not allow far reaching conclusions to be drawn, it can be stated that owing to the high adsorbability of Cl^- ions, the possible role of Cl^- ions formed at Ni electrodes in HClO_4 solutions cannot be neglected in the interpretation of phenomena observed in such systems. It was assumed that no significant amount of Cl-containing intermediates of reaction (11) accumulate in the solution phase. It was shown that the rate of interaction of ClO_3^- ions with Ni is significantly higher than that of ClO_4^- under comparable conditions.

Data presented in Table 2 provides an unambiguous proof of the occurrence of

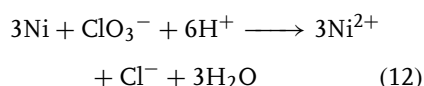
Tab. 1 Interaction of HClO₄ with nickel

Temperature [°C]	c_{HClO_4} [mol dm ⁻³]	A amount of dissolved Ni [10 ⁻² mol]	Bc_{Cl^-} formed [10 ⁻⁵ mol]	B/A [10 ⁻³]
25	3	3.57	7.5	2.1
40	3	3.9	12	3.07
50	3	3.9	13.5	3.46
25	1	1.26	2.6	2
40	1	1.27	4.3	3.38
50	1	1.27	4.9	3.85

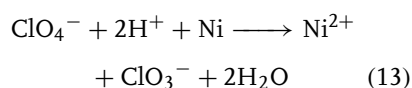
Tab. 2 Reduction of ClO₃⁻ ions by Ni. Amount of Ni 6 × 10⁻³ mol, temperature 25 °C, volume 50 cm³

Electrolyte [mol dm ⁻³]	c_{NaClO_3} [mol dm ⁻³]	Contact time [min]	c_{Cl^-} [mol dm ⁻³]
HClO ₄			
1	0	60	$c < 10^{-5}$
1	5×10^{-2}	60	1.5×10^{-2}
1	5×10^{-1}	15	3.9×10^{-2}
H ₂ SO ₄			
0.5	5×10^{-2}	60	1.24×10^{-2}
0.5	5×10^{-1}	15	3.9×10^{-2}

the following overall process:



This has a very high rate when compared with reaction (11). This means that we may assume that reaction (13) is the rate-determining process in the reduction of perchlorate ions:



18.1.5

Electrochemical Oscillation during Nickel Dissolution

The structure of complex behavior in anodic nickel dissolution was analyzed and

discussed in a series of papers by Lev and coworkers [51, 52].

In [53], oscillatory wave patterns observed during electrochemical dissolution of a nickel wire in acidic media was reported. It was shown that space-averaged potential or current oscillations are associated with the creation of an inhomogeneous current distribution, and that the selection of a specific spatial current pattern depends on the current control mode of the electrochemical cell. In the almost potentiostatic (fixed potential) mode of operation, a train of traveling pulses prevails, whereas antiphase oscillations occur in the galvanostatic (constant average current) mode.

In [52], a modeling of periodic and chaotic dynamics in anodic dissolution

was presented. The observed and modeled behavior include bistability, periodic oscillations bounded by Hopf and saddle loop bifurcations, the disappearance of these transitions in a double-zero singularity and the existence of chaotic solutions, which are bounded by a period-doubling transition. The modeling and parameter estimation were based on comparison of the experimental and simulated bifurcation maps, showing domains of different characteristic behaviors in the plane of applied constant current versus acid concentration. Qualitative agreement between the observed and predicted maps has been obtained. In [54], the delay and memory effects in bifurcations of nickel electrodis-solution were experimentally demonstrated.

18.1.6

New Findings on the Dissolution/Deposition Processes

During the last decades, a great number of papers dealing with anodic or spontaneous dissolution of polycrystalline nickel were published. Only some illustrative examples could be mentioned here. In [55], the anodic dissolution of nickel was studied galvanostatically in hydrochloric acid solutions of various concentrations. The reaction orders with respect to chloride ion and hydrogen ion concentrations were determined.

The corrosion behavior and dissolution mechanism of nickel in acid solutions with hydrogen sulfide (H_2S) was studied. It was found that the dissolution of nickel is influenced by both the nickel sulfide layer formed on the electrode surface and the acceleration effect of H_2S [56].

In [57], investigations of nickel dissolution in sulfuric acid solution have been performed by using an electrochemical microgravimetry (EQCM). On the basis of

reaction parameters obtained experimentally, the active dissolution mechanism of nickel has been explained by the Bockris mechanism.

Apparent activation energy of the anodic dissolution of nickel in sulfuric acid solutions in the presence of Cl^- and CNS^- ions was determined in [58].

Finally, it should be mentioned that according to some authors [59] anomalous – nonelectrochemical – dissolution has to be considered for the interpretation of the overall dissolution process of nickel in solutions containing oxygen. Although the idea is very interesting, the explanation presented seems to be questionable.

In [60], electrochemical deposition and stripping of nickel at a polycrystalline gold film electrode was studied by cyclic voltammetry and surface conductance.

In a series of publications by Gomez et al. [61–63], the electrodeposition of nickel on a vitreous carbon electrode has been investigated.

In [61], the influence of the nickel(II) concentration on the deposition process, in [62], the influence of potential on deposit morphology, while in [63], the morphology and structure of nickel nuclei as a function of the conditions of electrodeposition were studied. In the latter, the effects of growth rate (affected by the temperature and/or the nickel concentration), bath composition, and deposition time (particularly at low overpotentials) on the morphology of nickel nuclei were analyzed.

Pure nickel electrodeposits with macropores were prepared from electrolytic solutions of $0.2 \text{ mol dm}^{-3} \text{ NiCl}_2$ and NH_4Cl with concentrations varying between 0.25 and 4 mol dm^{-3} [64]. The effects of the electrodeposition current density and the NH_4Cl concentration on the surface morphology were determined. Surface area, faradaic efficiency, and fractal dimension

of the cross section of the electrodeposits were also evaluated. From these results, it was concluded that highly porous metallic matrices could be obtained, with very high roughness factors and excellent mechanical resistance, yet at very high apparent current densities of electrodeposition (5 A cm^{-2}). The use of this type of electrodeposition bath is suggested for the preparation of Raney-nickel electrodes, in order to improve the accessibility of reactants to the electrode surface.

18.1.7

Nickel–Hydrogen Systems

An analog of the platinized platinum electrode is the black or gray nickel electrode, which under certain experimental conditions can be used as the hydrogen electrode instead of the platinum electrode [65]. This electrode can be obtained by electrochemical deposition of nickel under the experimental conditions described in [65]. The real surface areas of these electrodes significantly surpass their geometric surface areas. In addition, potential-dependent adsorption of hydrogen occurs on the nickel surface and the measurement of the hydrogen capacity of the electrode in alkaline medium offers a tool for the determination of the real surface area [66].

However, because of overlapping of the adsorbed hydrogen oxidation region and that of adsorbed oxygen reduction the separation of these regions is difficult. Another difficulty is the slowness of the electrochemical processes leading to the formation of the layers of adsorbed hydrogen or oxygen.

In [67], an optoelectrochemical method (OEM) or a combination of electrochemical and ellipsometric methods, was developed for unambiguous evaluation of surface state and electrocatalytic properties of smooth standardized and modified

nickel electrodes in alkaline solutions. The method is based on the (1) insensitivity of ellipsometric method to hydrogen adsorption at least within the wavelengths interval 500–700 nm and (2) proportionality between changes in the amount of adsorbed oxygen and ellipsometric parameter, Δ . The simple method elaborated by the authors enabled them to obtain reliable roughness factor values.

The adsorption of hydrogen could be accompanied by its absorption as well.

Although it has been known for more than a century that large amounts of hydrogen can be loaded into nickel cathodes by electrolysis [68, 69], systematic work on the $\text{Ni}|\text{H}_2$ system was only initiated much later.

Almost fifty years ago, Baranowski et al. [70] and Baranowski and Smialowski [71] reported that, using sulfuric acid electrolyte and current densities $\leq 20 \text{ mA cm}^{-2}$, Ni cathodes could be converted into nonstoichiometric NiH_x ($x < 1$) hydride. A few years later, the nature of NiH_x was established by identifying two separate phases, β and α , as for the PdH_x analog [69, 72]. Both β - and α -hydrides formed by electrolysis of aqueous H_2SO_4 at Ni: the former, much more hydrogen-rich than the latter (H/Ni atom ratios of ≈ 0.8 for β and ≈ 0.03 for α), decomposes quickly with H_2 evolution [73, 74].

According to Baranowski and subsequent authors, the electrolytic formation of NiH_x is conditioned by factors such as the presence in the electrolyte of small amounts ($\approx 10^{-3} \text{ mol dm}^{-3}$) of a S, As, or Se compound [75], and the pH of the electrolyte. It has been stated in Ref. 73 that electrolytic hydriding of Ni failed in alkaline media. More recently, the validity of this statement was questioned by Bernardini et al. [76, 77]. According to [76, 77], considering of apparent similarity

between Ni and Pd hydrides, there is no reason why NiH_x should be obtained from acid electrolytes only. If there is a correlation between overvoltage and equivalent hydrogen pressure, the formation of unstable β NiH_x should be easier in alkaline media where larger overvoltages than in acid can generally be applied.

In [76], the feasibility of obtaining Ni hydride through electrolytic reduction of aqueous $0.6 \text{ mol dm}^{-3} \text{ K}_2\text{CO}_3$ at Ni electrodes of different types (solid Ni, Ni-fiber composite, and sintered Ni) was investigated. It was found that potentiostatic electrolyses at the beginning of the hydrogen evolution reaction (*her*) lead to the formation of several hydrogenated species of Ni, which generally become degraded when more negative potentials are applied. The species oxidized reversibly with the *her* was identified as the β -Ni hydride phase, whereas the nature of the Ni hydrides oxidized at more positive potentials could not be definitely established. The interaction of Ni samples on open circuit with H_2 dissolved in the electrolyte was found to form the same Ni hydride species as that achieved after electrolysis.

This approach was critically evaluated in a communication by Baranowski [78] pointing out that probably surface or subsurface hydrides are formed in alkaline solutions, instead of the bulk, three-dimensional hydride. It is stressed in [78] that the idea of the equivalence between overvoltage and thermodynamic activity, considered in [76, 77] is a misleading and unfounded concept.

Recently, by application of x-ray diffraction technique, evidences proving the

formation of β - NiH_x phase in the presence of promoters (S, As_2O_3 , Sb, and GeO_2) were reported in [79].

Dependencies of the β - NiH_x phase volume fraction on the nature and concentration of the promoter, changing current density and changing duration were presented and the phenomena observed were explained with the assumption that NiAs-type compounds take part in the formation of nickel hydride.

In contrast to the views asserting the reality of formation of NiH_x phase in alkaline media in the presence of promoters, Monev found [80] a very distinct pH effect in the formation of the hydride phase in the presence of H_2SeO_3 . According to [80], the nickel hydride formation terminates at pH value over 2.1.

18.1.8

Nickel Oxide and Nickel Hydroxide

Nickel oxides and hydroxides play an important role in the passivity of nickel in aqueous solutions, in oxidizing ionic

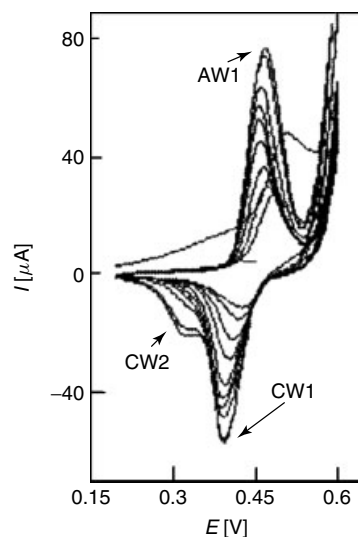


Fig. 1 A typical response of Ni to cyclic polarization in $0.1 \text{ mol dm}^{-3} \text{ NaOH}$. Potential measured against $\text{Hg}|\text{HgO}$ electrode. Scan rate: 60 mV s^{-1} . Explanation see in the text [91].

melts, and in the formation of electrodes related to batteries. Nickel hydroxide electrode is used for organic electrosynthesis, first of all for electrochemical oxidation.

Figure 1 shows a typical response of Ni to cyclic polarization in alkaline medium [81–91]. The redox wave pair AW1/CW1 is associated with the redox process $\text{Ni(OH)}_2 \leftrightarrow \text{NiOOH} + \text{H}^+ + \text{e}^-$. The current grows with the number of potential scans indicating the progressive enrichment of the electroactive species Ni^{2+} and Ni^{3+} in the surface. Prolonged polarization results in a stationary state. The anodic peak potential varies depending on the process of polarization of Ni oxides as a result of repeated polarization. The small cathodic wave CW2 developed during the later stages of polarization indicates the alteration of phase of Ni oxides [88]. The strong current increase following the anodic wave AW1 is the result of the oxygen evolution reaction. The intensity of this reaction also grows with advancing polarization, suggesting a correlation between the oxygen evolution and the concentration of Ni^{3+} sites. The first positive potential scan generates a monotonically elevated current flow giving a peak at a potential more positive than in the subsequent potential cycles. The peak shift is indicative of an overpotential required for the nucleation and growth of NiOOH. The enhanced baseline current, being most pronounced in the first scan, is associated with the oxidation of Ni to Ni^{2+} . α -NiOOH, β -NiOOH, and γ -NiOOH were structurally identified.

In a recent publication [89], processes taking place on a Ni electrode were investigated with the EQCM. At potentials negative of about -500 mV vs. SCE, a closed frequency loop was observed without irreversible changes in the mass of the electrode. It was found that the phase

transition $\alpha \rightarrow \beta$ -Ni(OH)₂, taking place at potentials positive to -500 mV vs. SCE, is accompanied by an irreversible increase in the mass of the electrode. When Ni(OH)₂ was further oxidized, the frequency increase is followed by a decrease indicating the transport of various species in both directions, that is, from and into the electrode. The authors arrived at the conclusion that during the Ni(OH)₂ oxidation reaction, the transport of species responsible for the mass increase is slower than the charge-transfer process.

The applicability of positron lifetime spectroscopy for the characterization of the partly charged nickel hydroxide was investigated [90]. The positron lifetime spectra of β -Ni(OH)₂/ β -NiOOH systems were presented. Three different parts of the annihilation curves were observed and identified.

In a recent communication [91], Ni surface alloyed with Cu, Ti, or Cu + Ti by ion implantation was examined for its redox and electrocatalytic activities by cyclic voltammetry. The surface was characterized by XPS, x-ray, and electron diffraction, as well as by electron and atomic force microscopies. This type of material exhibited a unique voltammetric response of Ni and was shown to stabilize the β -modification of the Ni oxide/hydroxide. It was demonstrated that the morphology and microstructure differ from those of bulk materials.

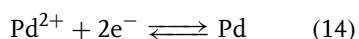
18.2 Palladium

18.2.1 Fundamentals

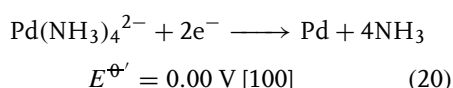
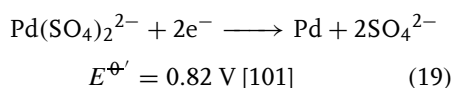
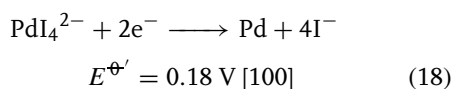
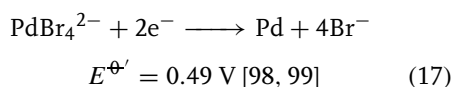
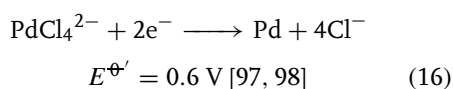
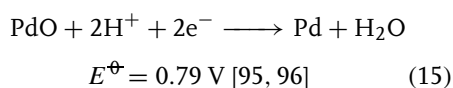
The oxidation number of palladium in compounds ranges from 0 to +6; however,

+2 and +4 states occur most frequently [92, 93].

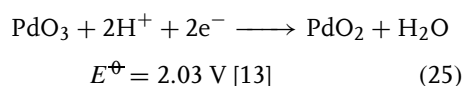
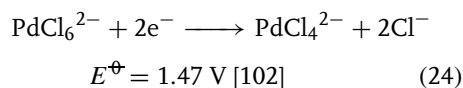
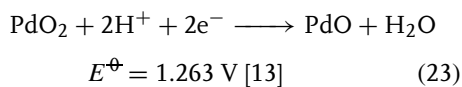
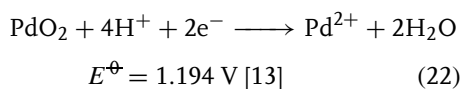
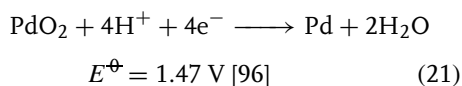
For the process



the most reliable standard potential value is $E^\ominus = 0.915 \pm 0.005 \text{ V}$ [94]; however, 0.945 V or 0.987 V formal potentials have also been reported [92, 93]. Similarly, diverse E^\ominus and formal potential ($E^{\ominus'}$) values can be found in the literature for other electrode reactions. For selected systems, the electrochemically measured values will be given.



The uncertainty in the E^\ominus and $E^{\ominus'}$ values are even higher in the case of Pd(IV) and Pd(VI) states.



The interfacial chemistry of palladium electrodes (polycrystalline and single crystal) was surveyed by Soriaga et al. recently [103]. According to the authors, the “remarkably rich interfacial chemistry of palladium” may have its origin in the anomalously weak intermetallic palladium–palladium bond, a circumstance that is expected not only to enhance lateral surface mobilities but also to facilitate the disruption of substrate–substrate bonds and/or the formation of substrate–adsorbate bonds.

In a survey dealing with palladium electrode, it is not possible to avoid mentioning the cold fusion controversy, started in 1989, where Pd electrode played and plays a central role. Hundreds of papers relating to palladium electrode are dealing exclusively with cold fusion and related subjects. The status of “cold fusion” was summarized in [104], recently.

18.2.2

New Findings on the Dissolution and Deposition of Palladium

Only a few illustrative examples taken from the literature of the last few years could be presented here.

The deposition of Pd on well-ordered single crystalline Au surfaces, Au(111), Au(110), and Au(100) has been studied by Kolb et al. especially with regard to the initial stages [105–107].

Pd was deposited onto Au from aqueous solutions of its chlorine compounds, for example, Pd_2Cl_2 or K_2PdCl_4 . It was stated that from such electrolytes, prior to

palladium deposition, $[\text{PdCl}_4]^{2-}$ adsorbs on the bare Au(111) and Au(100) surfaces and forms ordered adlayers, the structures of which were studied by in situ STM [105–108]. This complex anion has also been found to adsorb on the first Pd monolayer on Au(111) [105], whereas it is displaced by chloride in the case of Pd on Au(100) [106]. On these unreconstructed Au(111) and Au(100) surfaces, palladium nucleates first at surface defects like monoatomic high steps, and at higher overpotentials also on terraces [105, 106]. In the underpotential deposition (UPD) region, a pseudomorphic Pd monolayer is formed in Au(111) [105, 109]. No alloy formation was observed for this system [105], while a Pd/Au surface alloy is formed when Pd is deposited onto Au(100) [106]. Deviations in the electrochemical properties of thin Pd films on Au(100) from those of well-ordered Pd(100) surfaces [110] are most probably caused by this alloying process.

Soriaga and coworkers [111–113] discovered that the anodic dissolution Pd(111) and Pd(100) single-crystal electrodes in pure H_2SO_4 solutions was catalyzed by the presence of monolayers of iodine chemisorbed on these surfaces. Large anodic peaks were found for the dissolution even in noncorrosive electrolyte solutions only when the surfaces of Pd were modified by the iodine adlayer.

Further important results based mostly on in situ STM study were reported by Itaya and coworkers [114]. Iodine pretreatment was accomplished simply by immersion of the clean electrode, without potential control, in an aqueous 1-mM solution of iodide for 5 min. Unadsorbed iodide was removed by rinsing with pure water.

It was shown by Soriaga et al. [115] that this unique type of dissolution can be used for the selective and quantitative anodic

stripping of Pd films electrodeposited on Pt substrates. This method can also be used for Pd-coverage determinations, a major advantage if catalysis-induced coverage changes are to be monitored.

The dependence of adsorption properties and texture on electrolytic palladium deposits on the deposition potential was investigated by Tsirlina et al. [116]. It was found that, in sulfuric acid solutions, the palladium dissolution, which accompanies the oxygen adsorption, obscures the adsorption behavior of the deposits with respect to oxygen. Assumptions were made about the predominant crystallographic orientation (100) of the surface of some palladium deposits being dependent on the deposition potential and about the presence of regions whose adsorption properties are anomalous with respect to copper. The assumptions are based on a comparative analysis of the copper adsorption data and x-ray diffraction patterns. In addition to sites of crystalline palladium, the deposits were found to have disordered areas as well.

Regularities of formation of a palladium oxide layer and its cathodic reduction in $0.5 \text{ mol dm}^{-3} \text{ H}_2\text{SO}_4$ at 0.5–1.3 V (SHE) were studied by cyclic voltammetry, XPS, and EQCM [117]. It was shown that a Pd electrode dissolves electrochemically in $0.5 \text{ mol dm}^{-3} \text{ H}_2\text{SO}_4$ when its potential is cycled between 0.5 and 1.3 V. It was suggested that anodic process at 0.5–1.3 V (SHE) represents electrochemical oxidation of palladium, yielding a surface layer of poorly soluble $\text{Pd}(\text{OH})_2$ and/or PdO phases, as expressed by the equation $\text{Pd} + 2\text{H}_2\text{O} = \text{Pd}(\text{OH})_2/\text{PdO}_s + 2\text{H}^+ + 2\text{e}^-$. This surface layer, $\text{Pd}(\text{OH})_2/\text{PdO}_s$, undergoes reduction during the cathodic process. It was found that about 5% of the total amount of ionized palladium dissolves in electrolyte.

18.2.3

Hydrogen and Oxygen Sorption in/at Palladium Electrodes

A great number of papers devoted to the investigation of hydrogen absorption and adsorption can be found in the literature. Some new developments will be considered here.

It is a well-known and a widely recognized fact that the electrical resistance of palladium is a function of its hydrogen content. In [118], some problems on the resistance method regarding the in situ measurement of hydrogen content is discussed.

In [119], the hydrogen adsorption and desorption reactions in thin palladium electrodes were studied using the potential step method in order to analyze the mechanism of phase transformation. Transient current responses were recorded at the onset of the potential step for 47 μm thick Pd electrodes in 1 mol dm⁻³ H₂SO₄ at ambient temperature. A model based on a moving boundary mechanism was proposed to account for the experimental $i-t$ curves. It was found that the hydrogen adsorption reaction shows interfacial kinetic limitations and only numerical solutions can be obtained. Such kinetic limitations were not found for the desorption reaction and a semianalytical solution that satisfactorily fits the experimental data was proposed.

During the last two decades, hydrogen adsorption and absorption were shown to play a central role in a whole series of papers by Czerwinski and coworkers [120–133].

The EQCM method is used to evaluate the processes that occur in/on the palladium electrode in acid and basic solutions. It was concluded that hydrogen electrosorption in palladium is accompanied by an additional frequency shift of

the crystal that could be attributed to the stresses generated inside the Pd metal. A nonlinear dependence between the mass change and the charge consumed during hydrogen oxidation in the Pd electrode was found for hydrogen absorbed in the α - and β -phases.

This effect created significant problems with the objective estimation of the amount of sorbed hydrogen inside the palladium electrode using the EQCM method.

The study of hydrogen and deuterium electrosorption in palladium limited volume electrodes (LVE) was carried out by the same group in both acidic and basic solutions [124, 130, 134]. It was found that the hydrogen capacity, H(D)/Pd, measured electrochemically, depends significantly on sweep rate in cyclic voltammetric experiments and also on the thickness of the LVE. Two different mechanisms of hydrogen desorption, that is, the electrochemical oxidation and the nonelectrochemical recombination step, which take place in parallel within the Pd–LVE, have been postulated.

A decrease in hydrogen capacity (H/Pd ratio) with increasing temperature was observed. Hydrogen absorption was found to be dependent on the composition of the surrounding electrolyte solution.

The first systematic study on the oxide growth at Pd electrodes under well-defined potentiostatic conditions was reported in [135]. The impact of temperature variation on the development of Pd surface oxides was investigated in aqueous H₂SO₄. Various theoretical models were applied in order to elucidate the growth kinetics and mechanism in relation to the experimental conditions.

In a series of publications by Burke [136–140], the electrochemical and electrocatalytic behavior of palladium was

studied. The phenomena observed were explained similarly to other noble metals by the assumption of the role of premono-layer oxidation and formation of hydrous oxides.

18.2.4

Electrosorption and Electrocatalytic Processes

Some relatively simple examples will be presented.

The mechanism of the evolution of hydrogen on palladium in alkaline medium and associated internal damage phenomena were discussed in a recent paper by Bockris and Minevski [141]. The aim of the paper was to get support for their belief concerning the occurrence of nuclear reaction inside the metal. However, the authors arrived at the conclusion that the results obtained could be explained by an atomic-molecular (nonnuclear) model.

The electrocatalytic reduction of NO_3^- ions on noble metal electrodes has been the subject of several studies. (The reduction of nitrate has recently gained renewed attention in view of its relevance to pollution control.)

Comparative studies of catalytic activity of various metals, alloys, and adatom-modified metals were carried out.

For instance, the electrocatalytic reduction of nitrate ions on Pt, Pd, and Pt + Pd electrodes activated with Ge was studied in [142, 143].

It was found that underpotentially deposited germanium strongly enhances the reduction rate of nitrate. The reduction of nitrite is enhanced to a lesser extent, whereas germanium is inactive for NO and hydroxylamine reduction. It is of interest that the well-known inhibition of the nitrate reduction at low potentials was absent for germanium-modified electrodes.

A proportionality between the activity and the germanium coverage was reported. The authors arrived at the conclusion that germanium is involved in the rate-determining step, which is the reduction of nitrate to nitrite and its role is to bind the oxygen atom of nitrate. The higher activities found for Pt + Pd electrodes was explained in terms of changes in the electronic structure of the metals as a result of alloying.

Similar studies on palladium/copper electrodes was carried out using differential electrochemical mass spectroscopy (DEMS), rotating ring-disk electrodes and EQCM [144]. In acidic electrolytes, the activity increased linearly with Cu coverage; in alkaline electrolytes, a different dependence on coverage was observed.

Recently, the electrochemical behavior saturated alcohols, that is, propargyl alcohol ($\text{HC}\equiv\text{CCH}_2\text{OH}$, PA) [145], benzyl alcohol ($\text{C}_6\text{H}_5\text{CH}_2\text{OH}$, BA) [146] and allyl alcohol [147], has been studied at Pd electrodes in an acid medium by cyclic voltammetry, chronoamperometry, and on-line mass spectrometry. For BA, it was observed that the fragmentation of the molecules occurs at potentials in the hydrogen adsorption/absorption region of palladium, whereas for PA the adsorbates maintain the C_3 -chain. On the other hand, the yields of the electroreduction and electrooxidation products for both PA and BA differ from those obtained at Pt [146, 148, 149].

In the case of allyl alcohol, the on-line mass spectrometry (DEMS) allowed the detection of the volatile products generated during the electroreduction and electrooxidation processes. C_3 -hydrocarbons (propene and propane) and acrolein were detected as the bulk products, whereas C_2 -hydrocarbons and CO_2 are related to the adsorbed species. The dissociation of the alcohol produces ethine in

the 0.10–0.35 V potential range, which reduces to ethane. Adsorbed acrolein and C₂-hydrocarbonated residues seem to be formed in addition to CO-like species. The results were compared with those previously obtained at platinum and gold, as well as with other unsaturated alcohols, that is, benzyl and propargyl alcohol.

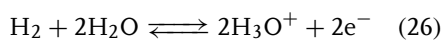
Similar studies were carried out with benzoic acid on porous palladium electrodes [150]. The objective of this work was to investigate the adsorption processes and the reactivity of benzoic acid on different noble metals, in order to compare these results with those obtained for related aromatic compounds. On-line mass spectroscopy analysis of volatile products revealed that the adsorption of benzoic acid is irreversible at platinum while it is mainly reversible on palladium. Accordingly, different catalytic activity of platinum and palladium was found in the electrooxidation.

18.3 Platinum

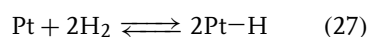
18.3.1 Fundamentals

Platinum electrodes are widely used as an inert electrode in redox reactions because the metal is most stable in aqueous and nonaqueous solutions in the absence of complexing agents, as well as because of its electrocatalytic activity. The inertness of the metal does not mean that no surface layers are formed. The true double-layer (ideal polarized electrode) behavior is limited to ca. 200–300 mV potential interval depending on the crystal structure and the actual state of the metal surface, while at low and high potentials, hydrogen and oxygen adsorption (oxide formation) respectively, occur.

First of all, the important role of platinum as the metal part of the standard hydrogen electrode (SHE), which is the primary standard in electrochemistry should be mentioned. The standard potential of an electrode reaction (standard electrode potential) is defined as the value of the standard potential of a cell reaction when that involves the oxidation of molecular hydrogen to solvated (hydrated) protons (hydrogen ions):



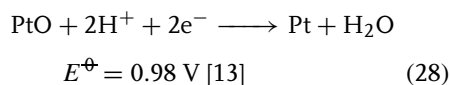
The standard state is the hypothetical ideal solution of molality 1 mol kg^{−1} (or the relative activity of H₃O⁺, $a_{\text{H}_3\text{O}^+} = 1$) at standard pressure. The standard pressure is 1 bar (earlier 1 atm = 1.01325 bar; however, the shift is only 0.00026 V at the potential scale). By definition, the potential of this electrode is zero. Although the standard potential should not depend on the material of the metal, the SHE exclusively contains a platinum wire or a platinum sheet covered with platinum black (platinized platinum). Owing to the spontaneous dissociation (dissociative chemisorption) of H₂ at Pt

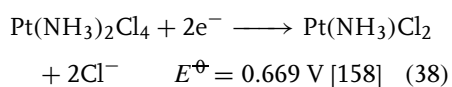
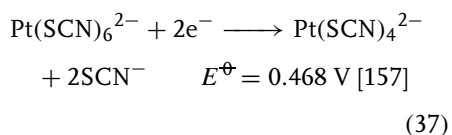
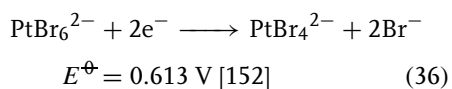
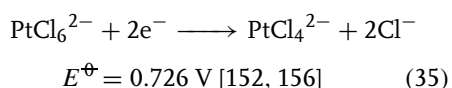
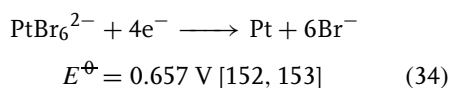
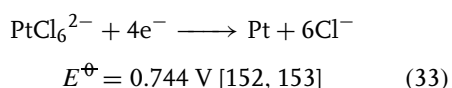
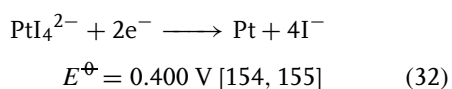
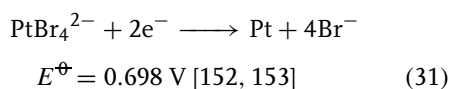
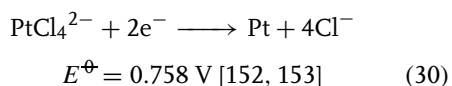
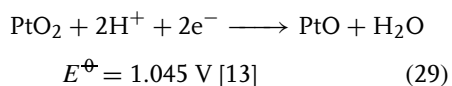


and the not-too-high Pt–H bond energy, the exchange current is high and the electrode process is electrochemically reversible [151].

In its compounds, Pt has oxidation states +2 and +4. The redox reactions – except the formation of surface oxides, hydroxides, and hydrides – take place with participation of its complexes.

Some important systems and the corresponding E^\ominus and $E^{\ominus'}$ values are as follows.





Data for several ammine-halo, ammine-ethylenediamine, halo-nitro-amine, halo-nitro-triammine, chloro-alkyl-ammine, alcohol-ammine, tetra-amino, pyridine-chloro, picoline-chloro, quinoline-chloro, phenanthroline-ammine-chloro, and so on, complexes have been compiled in [159, 160]. Some regularities have been found, for example, E^\ominus of Pt halo-complexes decreases with the increasing atomic number of the halogen atom; the successive substitution of NH_3 for chloro ligands causes the decrease of

E^\ominus ; the introduction of different ligands in the amine complexes increases E^\ominus according to the order $\text{I} < \text{CN} < \text{SCN} < \text{Br} < \text{Cl} < \text{NO}_2$ [159, 160]. Finally, we mention the famous cisplatin, *cis*- $\text{Pt}(\text{NH}_3)_2\text{Cl}_2$, which is a very powerful cancer chemotherapy drug [161]. Its effect was discovered by Rosenberg [162] accidentally when he investigated the influence of electric field on living cells. He used supposedly inert platinum electrodes to study the suspension of live *Escherichia coli* bacteria. It was found that, as a consequence of dissolution of Pt, cisplatin was formed which had a devastating effect on the bacteria.

18.3.2

Effect of Adsorption and Surface Structure on the Voltammetric Behavior of Platinum Electrodes

18.3.2.1 Adsorption of Hydrogen, Oxygen, and Anions

The “classical” voltammetric curve used generally for the presentation of hydrogen and oxygen adsorption on polycrystalline Pt is shown in Fig. 2.

It is well known that the shape of the curve depends on the nature of the anion(s) present in the system. In reality, there is an overall behavior reflecting simultaneous H/O and anion adsorption.

It was demonstrated that the radiotracer method, using labeled anions, is an adequate tool to follow anion adsorption in the course of voltammetric measurements and to gain simultaneous information on hydrogen and anion adsorption [163]. Coupling voltammetric and radiometric measurements in the study of platinized platinum electrodes gave insight in the anion-hydrogen atom coadsorption process.

Figure 3(a) shows the count rate originating from radiolabeled HSO_4^- adsorption vs. E (voltradiometric curve)

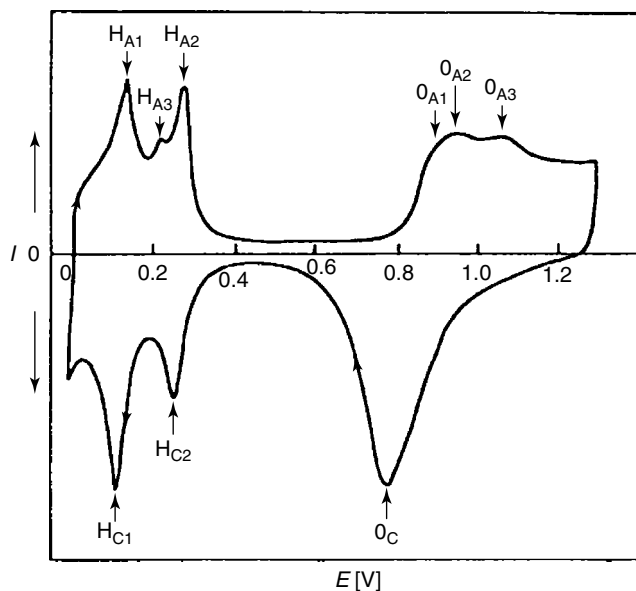


Fig. 2 Cyclic voltammogram of Pt in $0.5 \text{ mol dm}^{-3} \text{ H}_2\text{SO}_4$.

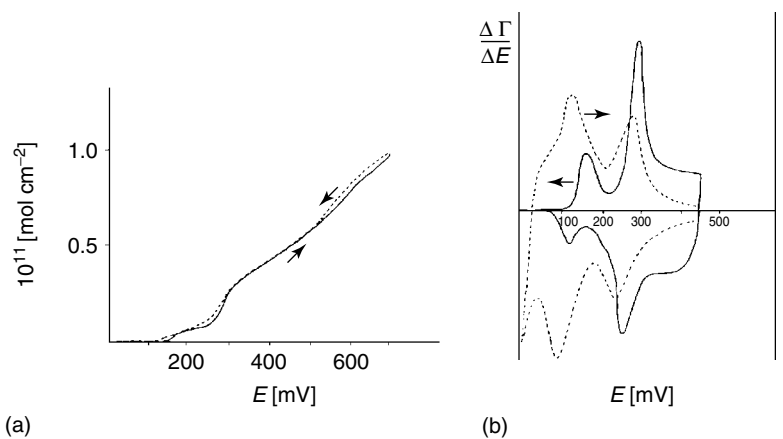


Fig. 3 (a) Voltradiometric Γ vs. E curve in the potential range 14–710 mV; sweep rate 0.25 mV s^{-1} ; $1.7 \times 10^{-3} \text{ mol dm}^{-3} \text{ H}_2\text{SO}_4$ in $1 \text{ mol dm}^{-3} \text{ HClO}_4$. (b) Shape of the $\Delta\Gamma/\Delta E$ vs. E (—) and voltammetric curves (---) in the potential range 10–450 mV; sweep rate 0.15 mV s^{-1} ($\Delta\Gamma/\Delta E$ and I arbitrary units) [163].

curve traced in the potential range from 15 to 710 mV with a sweep rate of 0.25 mV s^{-1} in the presence of labeled H_2SO_4 ($c = 1.7 \times 10^{-3} \text{ mol dm}^{-3}$)

in $1 \text{ mol dm}^{-3} \text{ HClO}_4$. From data presented in Fig. 3(a) the $d\Gamma/dE$ vs. E curve (differential voltradiometric curve) can be calculated, which may be considered as the

counterpart of the corresponding voltammetric curve. In Fig. 3(b), the $\Delta\Gamma/\Delta E$ vs. E and voltammetric curves are compared. From the comparison of these curves it can be stated that the position of the anion adsorption peaks in the hydrogen adsorption region are not far from those of the hydrogen adsorption. The most pronounced difference may be observed between the first hydrogen and anion peaks.

There are indications in the literature for the overlap of the oxide and hydrogen regions of platinum electrodes in aqueous acid solution [164]. The extent to which the hydrous oxide reduction process overlaps with the hydrogen adsorption region was investigated for platinum in acid solution. At least three distinct hydrous oxide reduction peaks (or regions) were observed and in some cases one of these peaks commenced at ca. 0.0 V, that is, it was almost totally within the hydrogen gas evolution region. Following repeated hydrous oxide growth and reduction, which disrupted and thus activated the metal surface, a sequence of four low-level premonolayer oxidation peaks (each of which has been noted earlier by other authors) appeared in the positive sweep. The transitions giving rise to such peaks were assumed to be mediator generation reactions, which strongly influence electrocatalytic processes occurring on platinum at low potentials.

18.3.2.2 Well-defined Platinum Surfaces

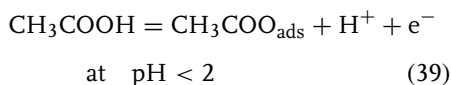
Fundamental questions connected with the characterization of the double layer at well-defined single-crystal faces of solid metals have been reviewed and surveyed several times by Hamelin [165–169].

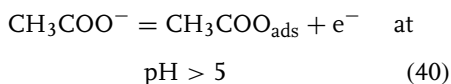
Since the early 1980s, cyclic voltammetry has been used to characterize single-crystal electrodes in terms of surface order, presence or absence of defects, contaminations, and so on. In some cases, the

voltammograms have also been used for identification of adsorbates, mostly based on electric charge calculation. However, since the double-layer charging and surface reactions such as underpotential deposition and anion adsorption may occur in parallel, it is difficult to break down the total voltammetric charge into all of its individual components. Therefore, interpretation from voltammetry alone, used as a tool for the adsorbed species identification, may be ambiguous. This has been, for instance, the case with the interpretation of the “unusual adsorption states” on the Pt(111) electrode [170–179].

Although at a very early stage of the studies the appearance of the unusual peak on the voltammograms of Pt(111) was explained by anion adsorption for a long period, the view that it should be ascribed to hydrogen adsorption (or incorporation of hydrogen) was widely accepted by many researchers. Recently, the hydrogen adsorption model has been rejected on the basis of reexamination of the problem by the most eminent proponents of the model studying the unusual desorption states on Pt(111) electrodes by CO and I displacement method. First they arrived at the conclusion that the results obtained confirm that the charge associated with the unusual states is at least formally compatible with the exchange of one electron per three surface platinum atoms.

In accordance with this view, the occurrence of the unusual peaks on the cyclic voltammograms observed in acetic acid/acetate system was ascribed to a one-electron transfer process of acetic acid/acetate ions according to the equations [180]:





There are, however, many evidences demonstrating that the existence of the unusual states cannot be easily explained with the charge transfer to, or from the anions (or other species). For instance, recent spectroscopic studies do not support the occurrence of electron transfer in the case of anion adsorption [174, 176, 181–185].

A very important and confusing observation is that the charge involved in the unusual states in various solutions is nearly independent of the nature of the anion, including organic anions. This aspect of the unusual states cannot be easily reconciled with the charge transfer to, or from the anion as a mechanistic origin of the pseudocapacitive current generated by the reversibly adsorbed anions on Pt(111).

Results obtained from careful examination of the pH effects on the potentiodynamic behavior of the Pt(111) electrode in acidified perchlorate solutions [180] advocate in favor of the assumption that water and not ClO_4^- anions are involved in the unusual adsorption states in the double-layer region of Pt(111). Presumably, H_2O dissociation and OH deprotonation are responsible for the two main electrode processes in the double-layer region of Pt(111) in NaClO_4 solutions.

For instance, in situ Fourier transform infrared (FTIR) spectroscopy has been used by Faguy et al. [176] to study the potential-dependent changes in anion structure and composition at the surface of Pt(111) electrodes in HSO_4^- -containing solutions. From the infrared differential normalized relative reflectance data, the maximum rate of intensity changes for three infrared bands can be obtained. Two modes associated with the adsorbed anion

and one mode assigned to species is not adequately described as either sulfate or bisulfate; the data are more consistent with an adsorbed $\text{H}_3\text{O}^+ - \text{SO}_4^{2-}$ ion pair, possibly with the three unprotonated sulfate oxygens interacting with Pt sites.

Since the number of papers dealing with the electrochemistry of Pt single crystals exceeds several hundreds, only some of them, published in the last few years could be referred to [179, 186–205].

18.3.2.3 Faceted and Platinized Platinum Electrodes

A series of papers by Arvia and coworkers [206–215] demonstrated that metal electrode surfaces with preferred crystallographic orientation and different roughnesses could be created through the application of periodic potential treatments.

It was found that changes in the voltammetric response of polycrystalline platinum electrodes in the direction expected for preferred oriented surface electrodes can be achieved using a fast repetitive potential perturbation.

Faceted platinized platinum surfaces with preferred crystallographic orientation were prepared by square-wave potential-modulated DC electrodeposition [216].

A fast repetitive triangular potential sweep (10^4 V s^{-1} between 0.05 and 1.5 V for 2 h) was applied to platinized platinum electrode [217]. This treatment resulted in a considerable decrease in the real surface area and in the formation of a (100)-type preferentially oriented surface structure.

A detailed comparison of the voltammetric behavior of platinum single-crystal and faceted electrodes was also given [218].

A different approach to the preparation of preferentially oriented surfaces on polycrystalline systems has been demonstrated by Sumino and Shibata [219]. It has been shown that a fast-cycling treatment

is not required for obtaining deposits with preferential orientation [176]. A platinum electrode with a single-crystal (100) surface was obtained by annealing a thin platinum film electrodeposited on a polycrystalline platinum foil.

Considering these results it was an important task to reconsider some questions connected with the technique of platinization, examining whether the method of platinization has some influence on the voltammetric behavior of the platinized surfaces. In [220], attempts were made to demonstrate that the voltammetric behavior of the platinized system could depend on the experimental conditions of the deposition carried out by a simple galvanostatic method.

On the basis of the results obtained, it could be stated without any doubt that the voltammetric behavior of the electrodes studied depends strongly on both the composition of the platinization solution and the current density of the deposition. The number of the peaks (pseudopeaks) and shoulders appearing on the voltammograms changes from two to four and the ratios of the heights of these peaks also change significantly. This behavior differed somewhat from that expected on the basis of classical views concerning the voltammetric behavior of a platinized system. On the other hand, this conclusion per se cannot be considered as a completely new statement. Various kinds of platinized and supported platinum catalyst electrodes were studied in the literature in order to reveal the relationship between their electrocatalytic (electrosorption) behavior and the structure of the deposited layer. (See, for instance, Refs. 221–225 and the literature cited therein.) It has been shown in these studies that the electrocatalytic activity and, occasionally, the character of the hydrogen adsorption at the deposited

platinum particles depends strongly on the preparation, and consequently on the structure of the deposited layer and on the dimension (size) of the deposited particles. For instance, in [225] in connection with the investigation of the electrocatalytic properties of ultrafine platinum particles it has been stated that the ratio of the amount of strongly adsorbed hydrogen to that of weakly adsorbed hydrogen decreased with decreasing platinum particle size. It was assumed that the adsorption strength of the hydrogen on the Pt(100) plane of the small platinum particles grew weaker with decreasing particle size.

The similarity of the shape of the voltammetric curves of platinized system to those reported for electrodes treated by the fast repetitive potential perturbation technique or obtained by annealing electrodeposited platinum and the appearance of signs characteristic for stepped surfaces allows us to assume that these phenomena should be ascribed to the similarities in the surface structure.

This probably means that it entails a common feature leading to the formation of electrodes with ordered domains of single-crystal or stepped surfaces. It is evident that further studies are required to elucidate the mechanism of the process resulting in such systems by simple platinization. For practical reasons, it will be of importance to study the electrocatalytic behavior of these systems.

18.3.2.4 Surface Structure and Reactivity

The study of the link between the surface structure of an electrode and its reactivity in electrode processes is considered as an important element of the investigations in modern electrochemistry.

In the frame of electrocatalysis and fuel cell-oriented research, a vast amount of data was collected during the last decades,

first of all concerning the reactivity of simple organic compounds at various Pt and Pd surfaces. These questions will not be discussed in this chapter. In the following, only the reduction of two anions, ClO_4^- and NO_3^- ions will be considered as model species for the demonstration of the complex problem of “structure and reactivity.”

The investigation of adsorption phenomena occurring on Pt and Pd electrodes is an important task for the clarification of their behavior in electrocatalytic processes. A characteristic feature for these systems is the hydrogen adsorption reflected by the shape of voltammetric curves taken under suitable conditions. This experimental approach constitutes the intersection point where the problem of perchlorate

reduction and the investigation of electrosorption behavior of prospective fuel cell electrodes touch each other.

It was (and perhaps is) a general belief in the literature that perfect voltammograms reflecting H adsorption on the “catalytic” electrodes can be obtained in HClO_4 solution.

The distortion of voltammetric curves in the presence of ClO_4^- ions is firm evidence for the occurrence of the reduction process. This effect is shown in Fig. 4 for the case of Pt with high real surface areas.

In Fig. 4, voltammograms of platinized electrodes prepared under various conditions are shown. For the sake of comparison, the corresponding voltammograms in HClO_4 and H_2SO_4 solutions are presented [226].

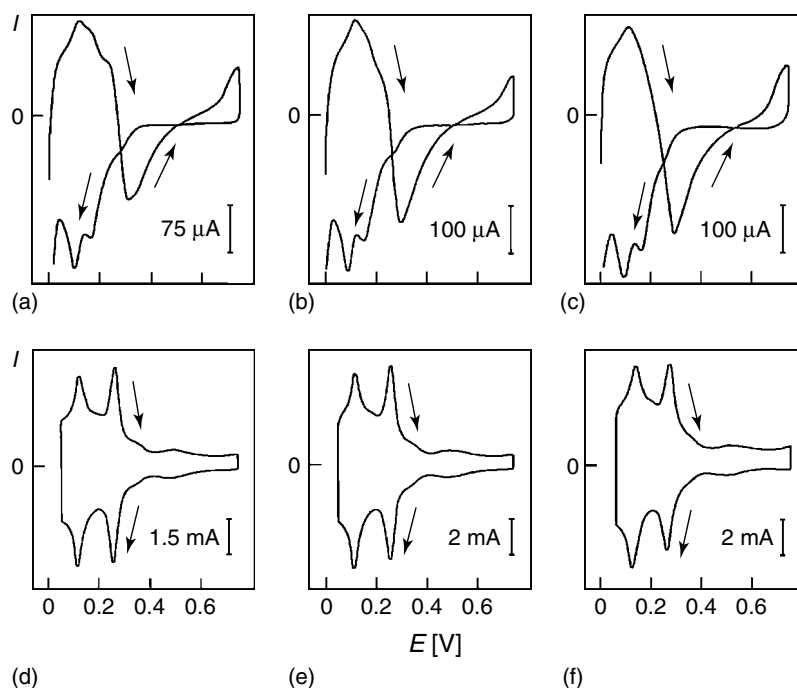


Fig. 4 Voltammogram of three different Pt/Pt electrodes: (a–c) in 3 mol dm^{-3} HClO_4 , sweep rate = 1 mV s^{-1} ; (d–f) in 0.5 mol dm^{-3} H_2SO_4 , sweep rate = 20 mV s^{-1} [226].

The features characteristic of these systems are as follows:

1. The reduction process occurs, almost exclusively, during the positive sweep.
2. Generally, no reaction can be observed on the negative sweeps, but the shape, height, and position of the corresponding hydrogen peak differ significantly from those expected.

3. The distortion of the anodic peak gradually disappears during subsequent cycles.

The reduction of NO_3^- ions at platinum electrodes has been studied by several authors during the last decade [227–230]. Thus, we have the relevant fundamental information about the behavior of the system. The most important information

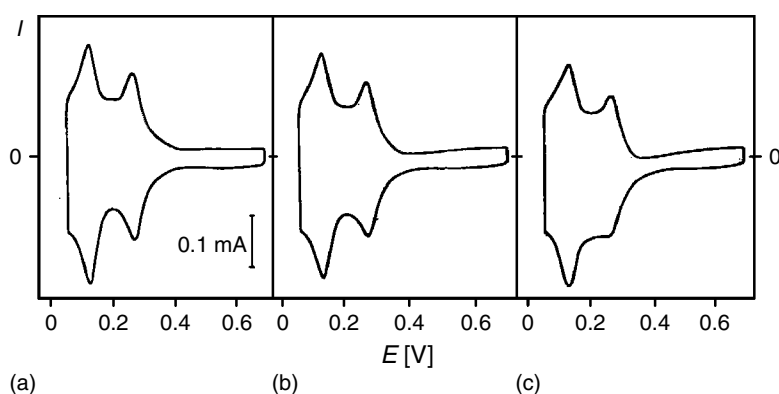


Fig. 5 Cyclic voltammograms of a platinized platinum electrode (type I) in (a) $0.25 \text{ mol dm}^{-3} \text{H}_2\text{SO}_4$, (b) $0.25 \text{ mol dm}^{-3} \text{H}_2\text{SO}_4 + 10^{-3} \text{ mol dm}^{-3} \text{HNO}_3$ and (c) $0.25 \text{ mol dm}^{-3} \text{H}_2\text{SO}_4 + 10^{-2} \text{ mol dm}^{-3} \text{HNO}_3$. Sweep rate, 20 mV s^{-1} [235].

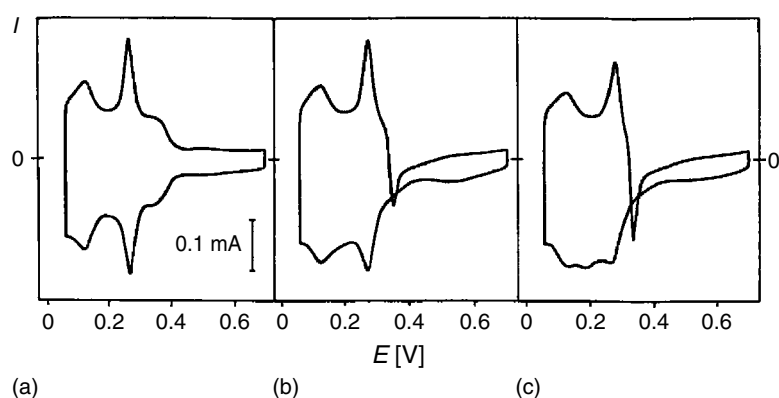


Fig. 6 Cyclic voltammograms of a platinized platinum electrode (type II) in (a) $0.25 \text{ mol dm}^{-3} \text{H}_2\text{SO}_4$, (b) $0.25 \text{ mol dm}^{-3} \text{H}_2\text{SO}_4 + 10^{-3} \text{ mol dm}^{-3} \text{HNO}_3$, and (c) $0.25 \text{ mol dm}^{-3} \text{H}_2\text{SO}_4 + 10^{-2} \text{ mol dm}^{-3} \text{HNO}_3$. Sweep rate, 20 mV s^{-1} [235].

is that hydrogen adsorption inhibits the reduction of NO_3^- ions. This means that in acid media the reduction rate is zero on surfaces covered by adsorbed hydrogen and a measurable reduction can only be observed at potentials above 50–100 mV. The current (absolute value) versus potential curve goes through a maximum.

The role of the various crystal faces in the reduction of nitrite, nitrate, and other oxygen-containing nitrogen compounds has been studied recently [231, 232].

It has also been shown [173, 233, 234] that the catalytic activity of various crystal faces of platinum for the reduction of NO_3^- ions is very different. This means that similar effects should be expected in the case of platinized systems with various preferred crystallographic orientations [235].

Figures 5 and 6 show the voltammograms of two types of platinized systems obtained in $0.25 \text{ mol dm}^{-3} \text{ H}_2\text{SO}_4$ supporting electrolyte in the absence and presence of NO_3^- ions. Figure 5(a) shows the voltammetric behavior of the classical polycrystalline electrode (type I) in H_2SO_4 solution, while Fig. 6(a) is for an electrode with preferred (100) orientation (type II).

It follows from a comparison of Fig. 5(b) and (c) with Fig. 6(b) and (c) that the electrocatalytic reduction of NO_3^- ions depends strongly on structural factors, reflected by the voltammetric behavior in pure H_2SO_4 solution. This observation is in accordance with earlier findings [173, 233, 234] that (100) crystal faces have an excellent catalytic activity toward the reduction of NO_3^- ions compared with the other low index planes.

The absence of a distinct catalytic activity in the case of the type I electrode at the HNO_3 concentrations studied can be considered to be normal behavior if we take into consideration the results of some

previous studies showing that HSO_4^- and SO_4^{2-} anions inhibit NO_3^- reduction to some extent via competitive adsorption [228]. In the light of this fact, we should consider the cathodic spikes on curves in Fig. 6(b) and (c) as dramatic evidence of the high catalytic activity of type II electrodes.

However, it is known from steady state reduction studies that the rate of the reduction process at all potential values is significantly higher in HClO_4 supporting electrolyte owing to the lower adsorbability of ClO_4^- ions on platinum.

Acknowledgment

Financial supports from the Hungarian Scientific Research Fund, OTKA – TO46987 (G. I.) and OTKA – TO49888 (G. H.) are acknowledged.

References

1. A. J. Arvia, D. Posadas in *Encyclopedia of Electrochemistry of Elements* (Ed.: A. J. Bard), Marcel Dekker, New York, 1975, pp. 212–421, Vol. III.
2. A. J. Arvia, D. Posadas in *Standard Potentials in Aqueous Solution* (Eds.: A. J. Bard, R. Parsons, J. Jordan), Marcel Dekker, New York, 1985, pp. 321–339, Chapter 12I.
3. F. Murate, *Bull. Chem. Soc. Jpn.* **1928**, 3, 57.
4. M. M. Haring, E. G. van de Bosche, *J. Phys. Chem.* **1929**, 33, 161.
5. I. Colombier, *C. R. Acad. Sci. Paris* **1934**, 199, 273.
6. M. A. López-López, *C. R. Acad. Sci. Paris* **1963**, 256, 2594; **1962**, 255, 3170.
7. G. Milazzo, S. Caroli, *Tables of Chemical Thermodynamic Properties*, National Bureau of Standards, US Government Printing Office, Washington, 1982.
8. A. J. de Béthune, N. A. Swendeman Loud, *Standard Aqueous Electrode Potentials and Temperature Coefficients*, Hampel, Skokie, 1964.
9. V. Gaglioti, G. Sartori, P. Silvestroni, *Ric. Sci.* **1947**, 17, 624.

10. B. P. Nikolskii, O. N. Grigorov, M. E. Pozin et al., (Eds.), *Spravochnik Khimika*, Izd. Khimiya, Moscow, Leningrad, 1964, Vol. 3.
11. J. Bjerrum, G. Schwarzenbach, L. G. Sillén, *Stability Constants, Inorganic Ligands*, The Chemical Society, London, 1958, Vol. 2.
12. W. M. Latimer, *Oxidation Potentials*, 2nd ed., Prentice Hall, Englewood Cliffs, 1952.
13. M. Pourbaix, (Ed.), *Atlas of Electrochemical Equilibria in Aqueous Solutions*, Pergamon-CEBELCOR, Brussels, 1966.
14. A. Thiel, H. Gessner, Z. *Anorg. Allg. Chem.* **1914**, 86, 49.
15. A. Ringbom, *Solubility of Sulfides*, Report to Anal. Sec., IUPAC, 1953.
16. I. A. Cotton, G. Wilkinson, C. A. Murillo et al., *Advanced Inorganic Chemistry*, 6th ed., Wiley, New York, Chichester, Weinheim, Brisbane, Singapore, Toronto, 1999, pp. 835–854, Part 3, 17 G.
17. L. Meites, P. Zuman, (Eds.), *CRC Handbook Series in Inorganic Chemistry*, CRC Press, Boca Raton, 1985, Vol. IV.
18. J. Scherer, B. M. Ocko, O. M. Magnussen, *Electrochim. Acta* **2003**, 48, 1169.
19. P. Marcus, J. M. Grimal, *Corros. Sci.* **1990**, 31, 377.
20. V. Maurice, H. Talah, P. Marcus, *Surf. Sci.* **1993**, 284, 1431.
21. V. Maurice, H. Talah, P. Marcus, *Surf. Sci.* **1994**, 304, 98.
22. P. Marcus, *Electrochim. Acta* **1998**, 43, 109.
23. V. Maurice, L. H. Klein, P. Marcus, *Surf. Interface Anal.* **2002**, 34, 139.
24. A. Machet, A. Galtayries, P. Marcus et al., *Surf. Interface Anal.* **2002**, 34, 197.
25. P. Marcus, E. Protopopoff, *Corros. Sci.* **1997**, 39, 1741.
26. J. Oudar, P. Marcus, *Appl. Surf. Sci.* **1979**, 3, 48.
27. A. Teissier, P. Marcus, J. Oudar, *C. R. Acad. Sci. Ser. II* **1981**, 292, 395.
28. P. Marcus, J. Oudar, I. Olefjord, *Mater. Sci. Eng.* **1980**, 42, 191.
29. S. Bouquet, G. Lorang, J. P. Langeron et al., *J. Microsc. Spectrosc. Electron.* **1982**, 7, 447.
30. S. Zafeiratos, F. E. Paloukis, S. G. Neophytides, *J. Phys. Chem. B* **2004**, 108, 1371.
31. A. Lachenwitzer, S. Morin, O. M. Magnussen et al., *Phys. Chem. Chem. Phys.* **2001**, 3, 3351.
32. O. Lev, F. R. Fan, A. J. Bard, *J. Electrochem. Soc.* **1988**, 135, 783.
33. M. Saitou, A. Makabe, T. Tomoyose, *J. Chem. Phys.* **2000**, 113, 2397.
34. K. Schwabe, *Electrochim. Acta* **1962**, 6, 223.
35. K. Schwabe, W. Schwenke, *Electrochim. Acta* **1964**, 9, 1003.
36. J. O. M. Bockris, D. A. J. Swinkels, *J. Electrochem. Soc.* **1964**, 111, 736.
37. N. A. Balashova, S. A. Lilin, *Elektrokhimiya* **1973**, 9, 637.
38. N. A. Balashova, N. T. Gorokhova, S. A. Lilin, *Elektrokhimiya* **1973**, 9, 666.
39. R. S. Vakhidov, M. N. Bakirov, *Elektrokhimiya* **1975**, 11, 282.
40. P. Fouilloux, M. Reppelin, P. Bussiere, *Int. J. Appl. Radiat. Isot.* **1972**, 23, 567.
41. J. M. Herbelin, N. Barbouth, P. Marcus, *J. Electrochem. Soc.* **1990**, 137, 3410.
42. P. Marcus, J. M. Herbelin, *Corros. Sci.* **1993**, 34, 1123.
43. A. G. Munoz, G. Benitez, M. E. Vela et al., *Langmuir* **2004**, 20, 2361.
44. Q. J. Huang, X. F. Lin, Z. L. Yang et al., *J. Electroanal. Chem.* **2004**, 563, 121.
45. S. Y. Zhao, S. H. Chen, H. Y. Ma et al., *J. Appl. Electrochem.* **2002**, 32, 231.
46. H. Y. Ma, G. Q. Li, S. C. Chen et al., *Corros. Sci.* **2002**, 44, 1177.
47. F. Zucchi, M. Fonsati, G. Trabanelli, *J. Appl. Electrochem.* **1998**, 28, 441.
48. M. Ujvári, G. Láng, G. Horányi, *J. Appl. Electrochem.* **2001**, 31, 1171.
49. M. Ujvári, G. Láng, G. Horányi, *J. Appl. Electrochem.* **2002**, 32, 581.
50. G. Láng, M. Ujvári, G. Horányi, *Corros. Sci.* **2003**, 45, 1.
51. O. Lev, A. Wolffberg, M. Sheintuch et al., *Chem. Eng. Sci.* **1988**, 43, 1339.
52. D. Haim, O. Lev, L. M. Pismen et al., *J. Phys. Chem.* **1992**, 96, 2676.
53. O. Lev, M. Sheintuch, L. M. Risemen et al., *Nature* **1988**, 336, 458.
54. M. T. M. Koper, B. D. Aguda, *Phys. Rev. E* **1996**, 54, 960.
55. E. E. Abd El Aal, W. Zakria, A. Diab et al., *J. Mater. Eng. Perform.* **2003**, 12, 172.
56. X. Cheng, H. Ma, S. Chen et al., *Corros. Sci.* **2000**, 42, 299.
57. M. Itagaki, H. Nakazawa, K. Watanabe et al., *Corros. Sci.* **1997**, 39, 901.
58. V. P. Grigor'ev, V. M. Kravchenko, I. M. Gershanova, *Prot. Met.* **2004**, 40, 214.
59. G. Beck-Nielsen, F. de Fontenay, H. Roulson, *Electrochim. Acta* **1997**, 42, 1847.

60. M. H. Fonticelli, D. Posadas, R. I. Tucceri, *J. Electroanal. Chem.* **2003**, 553, 157.
61. E. Gomez, C. Muller, R. Pollina et al., *J. Electroanal. Chem.* **1992**, 333, 47.
62. E. Gomez, C. Muller, W. G. Proud et al., *J. Appl. Electrochem.* **1992**, 22, 872.
63. E. Gomez, R. Pollina, E. Valles, *J. Electroanal. Chem.* **1995**, 397, 111.
64. C. A. Marozzi, A. C. Chialvo, *Electrochim. Acta* **2000**, 45, 2111.
65. S. I. Berezina, G. S. Vozdvizhenskii, G. P. Dezider'ev, *Dokl. Akad. Nauk SSSR* **1951**, 77, 53.
66. A. G. Pshenichnikov, *J. Res. Inst. Catal., Hokkaido Univ.* **1982**, 30, 137.
67. A. G. Pshenichnikov, L. A. Brkal'tseva, Z. I. Kudryavtseva, *Electrochim. Acta* **2000**, 45, 4143.
68. F. M. Raoult, *C. R. Biol.* **1869**, 69, 826.
69. R. A. Oriani, J. P. Hirth, M. Smialowski, (Eds.), *Hydrogen Degradation of Ferrous Alloys*, Noyes Publications, Norwich, N.Y. **1985**.
70. B. Baranowski, Z. Szklarska-Smialowska, M. Smialowski, *Bull. Acad. Pol. Sci., Ser. Sci. Chim. Geol.* **1958**, 6, 179.
71. B. Baranowski, M. Smialowski, *Int. J. Phys. Chem. Solids* **1959**, 12, 206.
72. M. L. Wayman, G. C. Weatherli, *Bull. Alloy Phase Diag.* **1989**, 10, 569.
73. B. Baranowski, Z. Szklarska-Smialowska, *Electrochim. Acta* **1964**, 9, 1497.
74. Z. Szklarska-Smialowska, M. Smialowski, *J. Electrochem. Soc.* **1963**, 110, 444.
75. H. Jarmolowicz, M. Smialowski, *J. Catal.* **1962**, 1, 165.
76. M. Bernardini, N. Comisso, G. Davolio et al., *J. Electroanal. Chem.* **1998**, 442, 125.
77. M. Bernardini, N. Comisso, G. Mengoli et al., *J. Electroanal. Chem.* **1998**, 457, 205.
78. B. Baranowski, *J. Electroanal. Chem.* **1999**, 472, 182.
79. R. Juskašnas, I. Valsiūnas, V. Jasulaitienė et al., *Electrochim. Acta* **2002**, 47, 4239.
80. M. Monev, *Electrochim. Acta* **2001**, 46, 2373.
81. M. Fleischmann, K. Korinek, D. Pletcher, *J. Chem. Soc., Perkin Trans.* **1972**, 2, 1396.
82. P. F. F. Luo, T. Kuwana, D. K. Paul et al., *Anal. Chem.* **1996**, 68, 3330.
83. H. Bode, K. Dehmelt, J. Witte, *Electrochim. Acta* **1966**, 11, 1079.
84. R. S. Schreiber Guzman, J. R. Vilche, A. J. Arvia, *J. Electrochem. Soc.* **1978**, 125, 1578.
85. F. Hahn, B. Bede, M. J. Croissant et al., *Electrochim. Acta* **1986**, 31, 1578.
86. J. L. Weininger, M. W. Breiter, *J. Electrochem. Soc.* **1963**, 110, 484.
87. D. A. Corrigan, R. M. Bendert, *J. Electrochem. Soc.* **1989**, 136, 723.
88. I. G. Casella, M. Gatta, *J. Electrochem. Soc.* **2002**, 149, B465.
89. M. Grden, K. Klimek, A. Czerwinski, *J. Solid State Electrochem.* **2004**, 8, 390.
90. K. Süvegh, T. S. Horányi, A. Vértess, *Electrochim. Acta* **1988**, 33, 1061.
91. M. T. Pham, M. F. Maitz, E. Richter et al., *J. Electroanal. Chem.* **2004**, 572, 185.
92. J. F. Llopis, I. Colom in *Encyclopedia of Electrochemistry of Elements* (Ed.: A. J. Bard), Marcel Dekker, New York, 1976, pp. 259–276, Vol. VI.
93. F. Colom in *Standard Potentials in Aqueous Solution* (Eds.: A. J. Bard, R. Parsons, J. Jordan), Marcel Dekker, New York, 1985, pp. 339–345, Chapter 12IIA.
94. R. M. Izatt, D. Eatough, J. J. Christensen, *J. Chem. Soc. A* **1967**, 1301.
95. H. Kleykamp, *Z. Phys. Chem. (Frankfurt)* **1970**, 71, 142.
96. J. P. Hoare, *J. Electrochem. Soc.* **1964**, 111, 611.
97. V. I. Kravtsov, M. I. Zelinski, *Elektrokhimiya* **1966**, 2, 1138.
98. N. M. Nikolaeva, L. D. Tsvedodub, A. M. Ehrenburg, *Izv. Sib. Otd. Nauk SSSR, Ser. Khim.* **1978**, 44.
99. A. B. Fasman, G. G. Kut'yukov, D. V. Sokolski, *Zh. Neorg. Khim.* **1965**, 10, 1338.
100. R. N. Goldberg, L. H. Hepler, *Chem. Rev.* **1968**, 68, 229.
101. E. Jackson, D. A. Pantony, *J. Appl. Electrochem.* **1971**, 1, 283.
102. A. A. Grinberg, A. S. Shamsiev, *Zh. Obshch. Khim.* **1942**, 12, 55.
103. M. P. Soriaga, Y.-G. Kim, J. E. Soto, *Interfacial chemistry of palladium electrodes in Interfacial Electrochemistry, Theory, Experiment, and Applications* (Ed.: A. Wieckowski), Marcel Dekker, New York, 1999.
104. D. J. Nagel, *Radiat. Phys. Chem.* **1998**, 51, 653.
105. L. A. Kibler, M. Kleinert, R. Randler et al., *Surf. Sci.* **1999**, 443, 19.
106. L. A. Kibler, M. Kleinert, D. M. Kolb, *Surf. Sci.* **2000**, 461, 155.
107. L. A. Kibler, M. Kleinert, V. Lazarescu et al., *Surf. Sci.* **2002**, 498, 175.

108. H. Naohara, S. Ye, K. Uosaki, *J. Electroanal. Chem.* **1999**, 473, 2.
109. M. Takahasi, Y. Hayashi, J. Mizuki et al., *Surf. Sci.* **2000**, 461, 213.
110. M. Baldauf, D. M. Kolb, *J. Phys. Chem.* **1996**, 100, 11375.
111. J. A. Schimpf, J. R. McBride, M. P. Soriaga, *J. Phys. Chem.* **1993**, 97, 10518.
112. J. A. Schimpf, J. B. Abreu, M. P. Soriaga, *Langmuir* **1993**, 9, 3331.
113. W. F. Temesghen, J. B. Abreu, R. J. Barriga et al., *Surf. Sci.* **1997**, 385, 336.
114. K. Itaya, Atomic-scale aspects of anodic dissolution of metals: studies by in situ scanning tunneling microscopy in *Interfacial Electrochemistry, Theory, Experiment, and Applications* (Ed.: A. Wieckowski), Marcel Dekker, New York, 1999.
115. E. A. Lafferty, Y.-G. Kim, M. P. Soriaga, *Electrochim. Acta* **1998**, 44, 1031.
116. G. A. Tsirlina, S. B. Baronov, F. M. Spiridonov et al., *Russ. J. Electrochem.* **2000**, 36, 1179.
117. K. Juodkazis, J. Juodkazyte, B. Sebek et al., *Russ. J. Electrochem.* **2003**, 39, 954.
118. W.-S. Zhang, Z.-F. Zhang, Z.-L. Zhang, *J. Electroanal. Chem.* **2002**, 528, 1.
119. P. Millet, M. Srour, R. Faure et al., *Electrochem. Commun.* **2001**, 3, 478.
120. A. Czerwinski, M. Grden, M. Lukaszewski, *J. Solid State Electrochem.* **2004**, 8, 411.
121. A. Czerwinski, M. Grden, M. Lukaszewski, *Anal. Lett.* **2004**, 37, 967.
122. M. Lukaszewski, M. Grden, A. Czerwinski, *J. Phys. Chem. Solids* **2004**, 65, 523.
123. M. Lukaszewski, A. Czerwinski, *Electrochim. Acta* **2003**, 48, 2435.
124. A. Czerwinski, I. Kiersztyn, M. Grden, *J. Solid State Electrochem.* **2003**, 7, 321.
125. M. Lukaszewski, K. Kusmierczyk, J. Kotoski et al., *J. Solid State Electrochem.* **2003**, 7, 69.
126. M. Grden, K. Kusmierczyk, A. Czerwinski, *J. Solid State Electrochem.* **2002**, 7, 43.
127. M. Grden, A. Piascik, Z. Koczorowski et al., *J. Electroanal. Chem.* **2002**, 532, 35.
128. J. Kleperis, G. Wojcik, A. Czerwinski et al., *J. Solid State Electrochem.* **2001**, 5, 229.
129. M. Y. Rusanova, M. Grden, A. Czerwinski et al., *J. Solid State Electrochem.* **2001**, 5, 212.
130. A. Czerwinski, I. Kiersztyn, M. Grden, *J. Electroanal. Chem.* **2000**, 492, 128.
131. M. Grden, J. Kotoski, A. Czerwinski, *J. Solid State Electrochem.* **2000**, 4, 273.
132. M. Grden, J. Kotoski, A. Czerwinski, *J. Solid State Electrochem.* **1999**, 3, 348.
133. M. Grden, A. Czerwinski, J. Golimowski et al., *J. Electroanal. Chem.* **1999**, 460, 30.
134. A. Czerwinski, I. Kiersztyn, M. Grden et al., *J. Electroanal. Chem.* **1999**, 471, 190.
135. L. H. Dall'Antonia, G. Tremiliosi-Filho, G. Jerkiewicz, *J. Electroanal. Chem.* **2001**, 502, 72.
136. L. D. Burke, J. K. Casey, *J. Electrochem. Soc.* **1993**, 140, 1292.
137. L. D. Burke, J. K. Casey, *J. Appl. Electrochem.* **1993**, 23, 573.
138. L. D. Burke, D. T. Buckley, *J. Electrochem. Soc.* **1996**, 143, 845.
139. L. D. Burke, L. C. Nagle, *J. Electroanal. Chem.* **1999**, 461, 52.
140. L. D. Burke, L. M. Hurley, *J. Solid State Electrochem.* **2003**, 7, 327.
141. J. O'M. Bockris, Z. Minevski, *Int. J. Hydrogen Energy* **2000**, 25, 747.
142. J. F. E. Gootzen, P. G. J. M. Peeters, J. M. B. Dukers et al., *J. Electroanal. Chem.* **1997**, 434, 171.
143. J. F. E. Gootzen, L. Lefferts, J. A. R. van Veen, *Appl. Catal., A-Gen.* **1999**, 188, 127.
144. A. C. A. de Vooy, R. A. van Santen, J. A. R. van Veen, *J. Mol. Catal. A Chem.* **2000**, 154, 203.
145. M. C. Arévalo, J. L. Rodríguez, E. Pastor, *J. Electroanal. Chem.* **1999**, 472, 71.
146. J. L. Rodríguez, R. M. Souto, S. González et al., *Electrochim. Acta* **1998**, 44, 1415.
147. M. C. Arévalo, J. L. Rodríguez, E. Pastor, *J. Electroanal. Chem.* **2001**, 505, 62.
148. R. M. Souto, J. L. Rodríguez, G. Pastor et al., *Electrochim. Acta* **2000**, 45, 1645.
149. E. Pastor, S. Wasmus, T. Iwasita et al., *J. Electroanal. Chem.* **1994**, 371, 167.
150. R. M. Souto, J. L. Rodríguez, L. Fernandez-Merida et al., *J. Electroanal. Chem.* **2000**, 494, 127.
151. G. Inzelt in *Electroanalytical Methods* (Ed.: F. Scholz), Springer, Berlin, Heidelberg, New York 2002, pp. 39–43.
152. D. Grinstrup, *Acta Chem. Scand.* **1972**, 26, 1527.
153. D. Grinstrup, I. Leden, *Acta Chem. Scand.* **1968**, 22, 1163.
154. A. A. Grinberg, V. B. Ptitsyn, V. N. Lavrentiev, *Zh. Fiz. Khim.* **1937**, 10, 661.

155. A. A. Grinberg, M. I. Gelfman, *Dokl. Akad. Nauk SSSR* **1960**, 133, 1081.
156. A. T. Hubbard, F. C. Anson, *Anal. Chem.* **1966**, 38, 58.
157. Y. N. Kukushkin, S. Ch. Dkhara, *Zh. Neorg. Khim.* **1970**, 15, 1585.
158. Y. N. Kukushkin, S. Ch. Dkhara, *Zh. Neorg. Khim.* **1969**, 14, 2816.
159. J. F. Llopis, I. Colom in *Encyclopedia of Electrochemistry of Elements* (Ed.: A. J. Bard), Marcel Dekker, New York, 1976, pp. 169–219, Vol. VI.
160. F. Colom in *Standard Potentials in Aqueous Solution* (Eds.: A. J. Bard, R. Parsons, J. Jordan), Marcel Dekker, New York, 1985, pp. 345–365, Chapter 12 IIB.
161. B. Lippert, (Ed.), *Cisplatin: Chemistry and Biochemistry of a Leading Anticancer Drug*, Wiley-VCH, Weinheim, 1999.
162. B. Rosenberg, L. Van Camp, J. E. Trosko et al., *Nature* **1969**, 222, 385.
163. G. Horányi, E. M. Rizmayer, *J. Electroanal. Chem.* **1987**, 218, 337.
164. L. D. Burke, A. J. Ahern, *J. Solid State Electrochem.* **2001**, 5, 553.
165. A. Hamelin in *Trends in Interfacial Electrochemistry* (Ed.: A. F. Silva), D. Reidel Publishing Company, Dordrecht, 1986, p. 83.
166. A. Hamelin in *Modern Aspects of Electrochemistry* (Eds.: B. E. Conway, R. E. White, J. O. M. Bockris), Plenum Press, New York, 1985, p. 1, Vol. 16.
167. A. Hamelin, *J. Electroanal. Chem.* **1996**, 407, 1.
168. A. Hamelin, A. M. Martins, *J. Electroanal. Chem.* **1996**, 407, 13.
169. A. Hamelin, *J. Electroanal. Chem.* **1995**, 386, 1.
170. J. Clavilier, R. Faure, G. Guinet et al., *J. Electroanal. Chem.* **1980**, 107, 205.
171. F. T. Wagner, R. N. Ross Jr., *J. Electroanal. Chem.* **1983**, 150, 141.
172. K. Al Jaaf-Golze, D. M. Kolb, D. Scherson, *J. Electroanal. Chem.* **1986**, 200, 353.
173. N. Markovic, M. Hanson, G. McDougall et al., *J. Electroanal. Chem.* **1986**, 214, 555.
174. P. W. Faguy, N. Markovic, R. R. Adzic et al., *J. Electroanal. Chem.* **1990**, 289, 245.
175. E. Herrero, J. M. Feliu, A. Wieckowski et al., *Surf. Sci.* **1995**, 325, 131.
176. P. W. Faguy, N. S. Marinkovic, R. R. Adzic, *J. Electroanal. Chem.* **1996**, 407, 209.
177. A. Zolfaghari, G. Jerkiewicz, *J. Electroanal. Chem.* **1997**, 422, 1.
178. T. Fukuda, A. Aramata, *J. Electroanal. Chem.* **1997**, 440, 153.
179. V. Lazarescu, J. Clavilier, *Electrochim. Acta* **1998**, 44, 931.
180. T. Fukuda, A. Aramata, *J. Electroanal. Chem.* **1999**, 467, 112.
181. F. C. Nart, T. Iwasita, M. Weber, *Electrochim. Acta* **1994**, 39, 961.
182. T. Iwasita, A. Rodes, E. Pastor, *J. Electroanal. Chem.* **1995**, 383, 181.
183. E. Pastor, A. Rodes, T. Iwasita, *J. Electroanal. Chem.* **1996**, 404, 61.
184. Y. Shingaya, K. Hirota, H. Ogasawara et al., *J. Electroanal. Chem.* **1996**, 409, 103.
185. Y. Shingaya, M. Ito, *J. Electroanal. Chem.* **1999**, 467, 299.
186. R. Gómez, J. M. Orts, B. Álvarez-Ruiz et al., *J. Phys. Chem. B* **2004**, 108, 228.
187. V. Climent, B. A. Coles, R. G. Compton et al., *J. Electroanal. Chem.* **2004**, 561, 157.
188. J. Mostany, E. Herrero, J. M. Feliu et al., *J. Electroanal. Chem.* **2004**, 558, 19.
189. M. D. Maciá, E. Herrero, J. M. Feliu, *J. Electroanal. Chem.* **2003**, 554–555, 25.
190. R. Gómez, J. M. Feliu, *J. Electroanal. Chem.* **2003**, 554–555, 145.
191. K. Domke, E. Herrero, A. Rodes et al., *J. Electroanal. Chem.* **2003**, 552, 115.
192. R. Albalat, J. Claret, A. Rodes et al., *J. Electroanal. Chem.* **2003**, 550–551, 53.
193. B. Álvarez, A. Rodes, J. M. Pérez et al., *J. Phys. Chem. B* **2003**, 107, 2018.
194. F. J. Vidal-Iglesias, N. García-Aráez, V. Montiel et al., *Electrochem. Commun.* **2003**, 5, 22.
195. R. Gómez, F. J. G. de Dios, J. M. Feliu, *Electrochim. Acta* **2004**, 49, 1195.
196. A. Berná, A. Rodes, J. M. Feliu, *Electrochim. Acta* **2004**, 49, 1257.
197. A. Berná, A. Rodes, J. M. Feliu, *J. Electroanal. Chem.* **2004**, 563, 49.
198. B. Álvarez, J. M. Feliu, J. Clavilier, *Electrochem. Commun.* **2002**, 4, 379.
199. J. M. Orts, E. Louis, L. M. Sander et al., *Electrochim. Acta* **1998**, 44, 1221.
200. J. M. Orts, E. Louis, L. M. Sander et al., *Surf. Sci.* **1998**, 416, 371.
201. R. Gómez, J. M. Orts, J. M. Feliu et al., *J. Electroanal. Chem.* **1997**, 432, 1.
202. J. M. Orts, R. Gómez, J. M. Feliu et al., *Langmuir* **1997**, 13, 3016.

203. G. A. Attard, O. Hazzazi, P. B. Wells et al., *J. Electroanal. Chem.* **2004**, 568, 329.
204. E. Herrero, B. Álvarez, J. M. Feliu et al., *J. Electroanal. Chem.* **2004**, 567, 139.
205. M. D. Baciá, J. M. Campiña, E. Herrero et al., *J. Electroanal. Chem.* **2004**, 564, 141.
206. A. C. Chialvo, W. E. Triaca, A. J. Arvia, *J. Electroanal. Chem.* **1983**, 146, 93.
207. J. C. Canullo, W. E. Triaca, A. J. Arvia, *J. Electroanal. Chem.* **1984**, 175, 337.
208. R. M. Cerviño, W. E. Triaca, A. J. Arvia, *J. Electrochem. Soc.* **1985**, 132, 266.
209. R. M. Cerviño, W. E. Triaca, A. J. Arvia, *J. Electroanal. Chem.* **1985**, 182, 51.
210. A. J. Arvia, J. C. Canullo, E. Custidiano et al., *Electrochim. Acta* **1986**, 31, 1359.
211. W. E. Triaca, T. Kessler, J. C. Canullo et al., *J. Electrochem. Soc.* **1987**, 134, 1165.
212. A. Visitin, J. C. Canullo, W. E. Triaca et al., *J. Electroanal. Chem.* **1988**, 239, 67.
213. A. E. Bolzan, A. M. Castro Luna, A. Visitin et al., *Electrochim. Acta* **1988**, 33, 1743.
214. A. J. Arvia, R. C. Salvarezza, W. E. Triaca, *Electrochim. Acta* **1989**, 34, 1057.
215. A. Visitin, W. E. Triaca, A. J. Arvia, *J. Electroanal. Chem.* **1990**, 284, 465.
216. B. Bittins-Cattaneo, E. Santos, W. Vielstich, *Electrochim. Acta* **1986**, 31, 1495.
217. E. Custidiano, A. C. Chialvo, A. J. Arvia, *J. Electroanal. Chem.* **1985**, 196, 423.
218. R. M. Cerviño, W. E. Triaca, A. J. Arvia, *Electrochim. Acta* **1985**, 30, 1323.
219. M. Sumino, S. Shibata, *Denki Kagaku* **1988**, 56, 286.
220. I. Bakos, G. Horányi, *J. Electroanal. Chem.* **1992**, 332, 147.
221. R. P. Petukhova, I. I. Astakhov, B. I. Podlovchenko, *Elektrokhimiya* **1971**, 7, 1548.
222. Yu. D. Gamburg, R. P. Petukhova, B. I. Podlovchenko et al., *Elektrokhimiya* **1974**, 10, 751.
223. T. D. Gladisheva, B. I. Podlovchenko, *Elektrokhimiya* **1978**, 14, 182.
224. V. S. Bagotzky, L. S. Kanevsky, V. Sh. Palanker, *Electrochim. Acta* **1973**, 18, 473.
225. Y. Takasu, Y. Fujii, K. Yasuda et al., *Electrochim. Acta* **1989**, 34, 453.
226. I. Bakos, G. Horányi, *J. Electroanal. Chem.* **1993**, 347, 383.
227. G. Horányi, E. M. Rizmayer, *J. Electroanal. Chem.* **1982**, 140, 347.
228. G. Horányi, E. M. Rizmayer, *J. Electroanal. Chem.* **1983**, 143, 323.
229. K. Nishimura, K. Machida, M. Enyo, *Electrochim. Acta* **1991**, 36, 877.
230. O. A. Petrii, T. Ya. Safonova, *J. Electroanal. Chem.* **1992**, 331, 897.
231. S. Ye, H. Hattori, H. Kita, *Ber. Bunsen-Ges. Phys. Chem.* **1992**, 96, 1884.
232. S. Ye, H. Kita, *J. Electroanal. Chem.* **1993**, 346, 489.
233. A. S. Homa, E. Yeager, B. D. Cahan, *J. Electroanal. Chem.* **1983**, 150, 181.
234. F. El Omar, R. Durand, *J. Electroanal. Chem.* **1984**, 178, 343.
235. I. Bakos, G. Horányi, *J. Electroanal. Chem.* **1994**, 370, 309.

18

The Nickel Group (Nickel, Palladium, and Platinum)

György Inzelt
Eötvös Loránd University, Budapest, Hungary

György Horányi
Institute of Materials and Environmental
Chemistry (IMEC), Budapest, Hungary

18.1	Nickel	499
18.1.1	Fundamentals	499
18.1.2	Surface Changes at Atomic Level as a Function of Potential	500
18.1.3	Adsorption Studies	503
18.1.4	Spontaneous Reduction of Anions at Ni Surface	505
18.1.5	Electrochemical Oscillation during Nickel Dissolution	506
18.1.6	New Findings on the Dissolution/Deposition Processes	507
18.1.7	Nickel–Hydrogen Systems	508
18.1.8	Nickel Oxide and Nickel Hydroxide	509
18.2	Palladium	510
18.2.1	Fundamentals	510
18.2.2	New Findings on the Dissolution and Deposition of Palladium	511
18.2.3	Hydrogen and Oxygen Sorption in/at Palladium Electrodes	513
18.2.4	Electrosorption and Electrocatalytic Processes	514
18.3	Platinum	515
18.3.1	Fundamentals	515
18.3.2	Effect of Adsorption and Surface Structure on the Voltammetric Behavior of Platinum Electrodes	516
18.3.2.1	Adsorption of Hydrogen, Oxygen, and Anions	516
18.3.2.2	Well-defined Platinum Surfaces	518
18.3.2.3	Faceted and Platinized Platinum Electrodes	519
18.3.2.4	Surface Structure and Reactivity	520
	Acknowledgment	523
	References	523

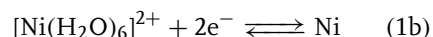
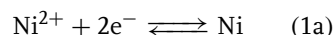
18.1 Nickel

18.1.1 Fundamentals

The oxidation number of nickel in its compounds ranges from 0 to +4; however, +2 state is the most important one. In fact, there is no other stable, higher oxidation state than +4, therefore, the redox chemistry of nickel is poorer as compared with the other two metals of this group. Ni^{2+} ions in a hydrated form can be found in aqueous solutions of NiCl_2 , NiSO_4 , $\text{Ni}(\text{NO}_3)_2$, and so on. $\text{Ni}(\text{II})$ is the typical oxidation state in several, stable water-soluble complexes such as $[\text{Ni}(\text{NH}_3)_4]^{2+}$, $[\text{Ni}(\text{CN})_4]^{2-}$, and $[\text{Ni}(\text{NH}_3)_6]^{2+}$, as well as in sparingly soluble simple compounds, for example, $\text{Ni}(\text{II})$ -dimethylglyoxime, $\text{KNi}[\text{Fe}(\text{CN})_6]$, $\text{K}_2\text{Ni}[\text{Fe}(\text{CN})_6]$.

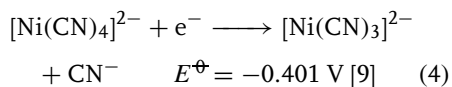
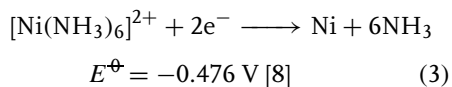
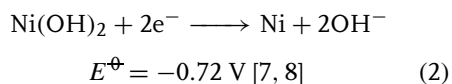
Although the nickel-containing systems have been extensively studied also by electrochemical methods [1] due to their practical importance, for example, in electrochemical power sources (Ni-Fe , Ni-Cd , Li-NiF_2 batteries), in corrosion-resistant alloys (tableware, coins, industrial instruments) as well as due to their interesting (magnetic, spectral, catalytic) properties most of the standard potentials of electrode

reactions involving nickel compounds have been calculated from nonelectrochemical (calorimetric and solubility) data [2]. Even for the simplest reaction

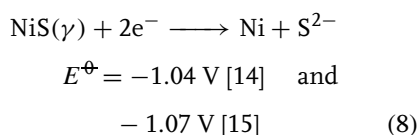
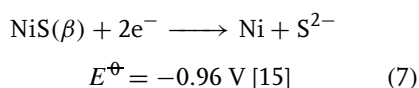
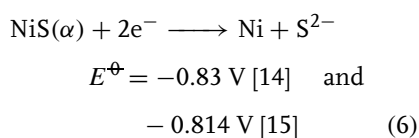
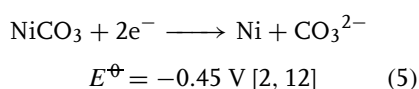


there is a rather large scattering of the published standard potential values determined by the measurements of the electromotive force (E_{MF}), for example, -0.248 V [3], -0.231 V [4], -0.227 V [5], and -0.246 V [6]. This scattering of data is presumably related to the difficulties in the attainment of a true equilibrium state. At present the most accepted value is $E^\ominus = -0.257$ V [2] that was calculated on the basis of the Gibbs energy change of the reaction (ΔG) [7]; however, different values for ΔG as well as for the reaction entropy (ΔS) can be found in the literature [2].

Further standard potentials measured electrochemically at 25°C are as follows:



These values differ from those calculated from ΔG values, for example, for reaction (3) $E^\ominus = 0.49$ V is given in Refs. 10, 11. E^\ominus values for several reactions estimated by using thermodynamical data can be found in the literature [1–13]. Perhaps the most accurate ones are those calculated from the solubility products, for example,



Nickel sulfide is a good example why – beside the uncertainty of the thermal values mentioned before – diverse E^\ominus values have been determined, inasmuch as the formation and ratios of different forms depend on the conditions, for example, on the acidity and temperature of the solution from which the precipitation is executed.

The system, which is of practical importance (Edison storage battery, electrocatalysis in organic synthesis), is the $\text{NiOOH}|\text{Ni}(\text{OH})_2$ couple (electrode). Somewhat surprisingly – since it is a widely studied and applied electrode – the mechanism and the true nature of the oxidized species are not fully understood yet [1, 2, 16]. The formal potential depends on the KOH concentration and is ca. 1.3 V. It follows that it is unstable in aqueous solutions and is also an oxidizing agent for various organic compounds.

There have been many polarographic measurements devoted to the reduction of Ni(II). Not only Ni(II) compounds in “noncomplexing” supporting electrolytes such as alkali chlorides, nitrates, perchlorates have been investigated, but a wide range of complexes have also been studied [1, 17]. The half-wave potential of the polarographic wave ($E_{1/2}$) depends on the experimental conditions (ionic strength, nature of anions); however, its value is typically -1.1 ± 0.1 V in aqueous solutions. $E_{1/2}$ values determined for complexes range between ca. -0.3 to -0.7 V, for example, $-0.7 \text{ V} < E_{1/2} < -0.91 \text{ V}$ for $[\text{Ni}(\text{SCN})_x]^{(2-x)+}$, $-1.36 \text{ V} < E_{1/2} < -1.47 \text{ V}$ for $[\text{Ni}(\text{CN})_4]^{2-}$, $-1.05 \text{ V} < E_{1/2} < -1.22 \text{ V}$ for $[\text{Ni}(\text{NH}_3)_6]^{2+}$, $-0.751 \text{ V} < E_{1/2} < -1.16 \text{ V}$ for $[\text{Ni}(\text{Py})_6]^{2+}$ have been reported. The voltammetric characteristics, the kinetic, the mechanistic, and double-layer properties of the nickel electrodes and compounds have been compiled in Ref. 1 including an extensive literature survey until 1971. Further on we review the new results obtained in the last 15 years.

18.1.2

Surface Changes at Atomic Level as a Function of Potential

A detailed electrochemical study of Ni(111) electrodes in H_2SO_4 solution in conjunction with in situ scanning tunneling microscopy (STM) and in situ surface X-ray scattering methods (SXS, x-ray diffraction and x-ray reflectivity) was carried out by Scherer et al. [18].

The main results of the study are as follows: Ni(111) samples, prepared via annealing in H_2 and exposure to air at room temperature, are covered by a smooth three-to-four-layers thick NiO(111) film with parallel $(\text{NiO}[1\bar{1}0])\parallel(\text{NiO}[1\bar{1}0])$

and antiparallel $(\text{NiO}[1\bar{1}0])\parallel(\text{NiO}[1\bar{1}0])$ in-plane orientation. Electrochemical reduction at potentials $\geq -0.40 \text{ V}_{\text{Ag}/\text{AgCl}}$ results in the formation of a well-defined, oxide-free surface with large terraces, a low surface mobility, and a (1×1) lattice on the atomic scale. X-ray reflectivity data indicate vertical lattice expansion for the topmost Ni layer and a strongly bound sulfate or oxygen species. Active Ni dissolution commences at potentials $\geq -0.25 \text{ V}_{\text{Ag}/\text{AgCl}}$ by a step-flow mechanism, followed by the rapid formation of large three-dimensional etch pits, leading to considerable surface roughening. In situ STM observations of the passive film formation show at potentials $\geq -0.10 \text{ V}_{\text{Ag}/\text{AgCl}}$ the nucleation and growth of an initial “grainy” phase, which is attributed to a Ni hydroxide, followed by a slower restructuring process. According to combined STM and SXS data, the resulting steady state passive film exhibits a duplex structure, with a crystalline, inner $\text{NiO}(111)$ layer, consisting of exclusively antiparallel oriented grains $(\text{NiO}[1\bar{1}0])\parallel(\text{NiO}[1\bar{1}0])$, which are slightly tilted relative to the substrate lattice, and a porous, probably amorphous hydroxide phase on top. The thickness of the crystalline NiO film increases with potential by $14\text{--}17 \text{ \AA V}^{-1}$. In addition, structural changes of the oxide film during immersion of Ni samples into the sulfuric acid solution at potentials in the passive range and after immersion from the electrolyte were observed, which indicate the slow conversion of the air formed into the passive oxide and the (partial) reformation of the air-formed oxide, respectively.

In a series of publications, the results of anodic dissolution and passivation of well-defined single-crystal surfaces of Ni (and other metals) and its alloys were presented by Marcus et al. [19–24]. Their approach aimed at a better understanding

of corrosion phenomena at the atomic and molecular level.

STM was used to study ex situ (in air) the thin oxide films (passive films) grown on $\text{Ni}(111)$ by anodic polarization in $0.05 \text{ mol dm}^{-3} \text{ H}_2\text{SO}_4$. Atomic resolution imaging demonstrated the crystalline character of the oxide film and the epitaxy with the substrate. Two levels of roughening with respect to the nonpolarized surfaces were observed: on a mesoscopic scale and on the atomic scale. The roughening on the mesoscopic scale increases with higher polarization potentials. The observed roughness was attributed to the result of the competition between metal dissolution and nucleation and growth of the oxide film. The roughening on the atomic scale is independent of the polarization potential. It is evidenced by the formation of a stepped crystalline lattice whose parameters fit those of a (111) -oriented NiO surface. The presence of steps indicated a tilt of (8 ± 5) degrees of the surface of the film with respect to the (111) orientation. The possible epitaxial relationships resulting from the surface tilt are discussed. Local variations of the film thickness at the step edges are likely to result from the surface tilt and may constitute preferential sites for the local breakdown of passivity.

In other papers by the same group, the effects of sulfur adsorbed or segregated on the Ni surface on corrosion or passivation were described, including the sulfur-induced enhancement of dissolution and the blocking of passivation. It was shown how the conditions of stability of adsorbed sulfur monolayers could be predicted on thermodynamical grounds and this was illustrated by a potential–pH diagram for adsorbed sulfur on nickel in water at 25°C . (See Refs. 22, 25–29 and papers cited therein.)

In [30] on cyclic voltammetry (CV), x-ray and UV photoelectron spectroscopy (XPS, UPS) were employed to study the electrochemical deposition and dissolution of nickel on a polycrystalline gold electrode, in a 0.1-mol dm^{-3} NiSO_4 electrolyte. The modification of the Ni/Au interface upon thermal treatment in ultrahigh vacuum was also investigated. Depending on the applied potential, two distinct Ni chemical states were observed. At -0.5 V vs. SCE an oxidized Ni phase, mainly Ni(OH)_2 , was formed, whereas at potentials lower than -0.8 V , nucleation of reduced Ni species surrounded by hydroxidized nickel occurred. The systematic investigation of the adsorbate species' binding energies as a function of the applied potential revealed that hydroxidized nickel precipitates on the gold electrode, while reduced nickel species directly deposit on the electrode surface via the reduction of Ni^{2+} ions. Heating the Ni/Au interface to 650 K decomposes the adsorbed nickel film forming a new compound containing a Au–Ni intermetallic component.

A study of the electrodeposition and electrochemical dissolution of ultrathin Ni films on Ag(111) electrodes in Watts electrolyte by in situ STM, electrochemical quartz crystal microbalance (EQCM), and cyclic voltammetry was reported in [31]. It was stated that Ni deposition starts at potentials negative of -0.72 V vs. SCE , where an incommensurate, (111)-oriented film with an in-plane lattice rotation of 0.5° relative to the Ag substrate lattice was formed. The lateral nearest neighbor spacing is as in bulk Ni (0.249 nm) for a film thickness greater than or equal to 3 ML and expanded for monolayer (0.254 nm) and bilayer (0.252 nm) films. Depending on the deposition potential, three growth regimes, resulting in different deposit morphologies, were observed:

At low overpotentials, a smooth Ni film was formed via a 2D step-flow growth process, commencing at steps of the Ag substrate. At medium overpotentials, a transformation from 2D step-flow to 3D growth took place resulting in the selective formation of Ni multilayer islands along the Ag steps. At even higher overpotentials, 3D islands were formed at the steps and on the substrate terraces. The size of the Ni multilayer islands was independent of the terrace widths, indicating that Ni growth proceeds via direct discharge at step sites ("direct deposition"). The transition from 2D to 3D growth as well as the change in island shape with overpotential could be rationalized by a different potential dependence of the various microscopic nucleation and growth processes. The multilayer growth at steps was attributed to next-layer nucleation at the structural defect induced by the Ag–Ni boundary and could be described quantitatively as a function of deposition time by a simple 2D model. A place exchange of Ni with Ag surface atoms and encapsulation of Ni islands by Ag is observed. It was found that the dissolution of the electrodeposited multilayer Ni films proceeds via step-flow etching, with a higher dissolution rate for the Ni monolayer as compared to higher Ni layers.

The application of STM to in situ studies of nickel electrodes under potential control was reported in [32].

Using atomic force microscopy (AFM), the kinetic surface roughening in electrochemical dissolution of nickel films at a low constant current density was studied in order to reveal the scaling laws [33]. The surface measurements of AFM exhibited the oscillatory variation of the interface width with time, which made it impossible to determine the growth exponent β . The oscillatory behavior of surface

roughening was explained by the presence of unstable passive films formed on the nickel film surface. The roughness exponent $\alpha = 0.94 \pm 0.04$ calculated from the AFM images of the anodic dissolved surface was almost equal to that predicted by the diffusion-driven growth model.

18.1.3

Adsorption Studies

The study of the adsorption phenomena of ions and organic species on nickel electrodes may contribute to a better understanding of the electrode processes occurring at the nickel/electrolyte interface.

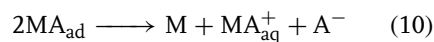
In the last few decades, the study of adsorption phenomena at nickel electrodes by a radiotracer method has been the subject of several studies (see [34–40] and literature cited therein). Most of these studies were carried out at smooth electrodes; however, in some cases, nickel powder and Raney-nickel catalysts were used.

Pioneering work was done in this field by Schwabe [34, 35]. Substantial and very informative radiotracer adsorption studies carried out by him and his coworkers using Pt, Ni, and Fe sheets and evaporated films, using labeled anions in order to interpret the role of anions in the corrosion and passivation processes [34, 35].

A radiotracer method was elaborated for the study of the adsorption phenomena on nickel electrodes formed by electrodeposition of nickel (“nickelized” nickel electrode). Adsorption studies were carried out with labeled HCl, H₂SO₄, H₃PO₄, thiourea, phenylacetic, and acetic acids in 0.1 mol dm^{−3} HClO₄ supporting electrolyte. The potential dependence of the adsorption of these species was determined in the potential range −200 to +200 mV vs. relative hydrogen electrode (RHE). It was found

that a significant potential-dependent adsorption occurs at low concentrations (10^{−3}–10^{−4} mol dm^{−3}) of the species studied in the course of the anodic dissolution of the electrode.

There is no doubt that specific adsorption of anions and organic species occurs in a wide potential range as the experiments were carried out in 0.1 mol dm^{−3} HClO₄ supporting electrolyte at low concentrations (10^{−3}–10^{−5} mol dm^{−3}) of the species studied. It was found that the adsorption of anions exerts some influence on the anodic dissolution rate; however, this effect is very far from that observed in the case of thiourea. In the latter case, the rate of anodic dissolution was significantly influenced by the presence of thiourea, even at its very low concentration. This behavior was ascribed to the strong interaction of thiourea with the metal ions and the formation of complexes both on the metal surface and in the solution phase. The phenomena presented were considered as a result of the adsorption competition of the species studied with ClO₄[−] ions. Three fundamental mechanisms were formulated for the active dissolution: (1) aquo–ligand, (2) hydroxo–ligand, and (3) anion–ligand mechanisms. The last of the mentioned mechanisms is formulated as follows:



It is assumed that these three mechanisms are operating simultaneously and depend on the experimental conditions if one of them becomes predominant in the overall process. The significant adsorption of anions found at low potentials where

the dissolution rate is small, the reversibility of the adsorption with respect to the potential, and the mobility of the adsorbed species all support the possibility of the anion–ligand mechanism.

The incorporation of chloride ions in passive films formed on nickel in Cl^- -containing acid solution and the entry of Cl^- into passive films formed in Cl^- -free solution and subsequently exposed to Cl^- were investigated by Marcus and Herbelin [41, 42] by electrochemical measurements, ESCA (Electron Spectroscopy for Chemical Analysis) and using in situ radiotracer (Cl-36) methods. It was found that at potentials in the active region, chloride ions are adsorbed on the nickel surface and form a thin hydroxy-chloride layer. They observed that the amount of Cl^- increases with potential (beyond the equivalent full monolayer coverage) up to the active/passive potential where a marked drop of the Cl^- surface concentration takes place. In the passive region, chloride ions are incorporated in the passive film. When the film is formed in Cl^- -containing solution at potentials below the pitting potential, Cl^- ions are found in the outer hydroxide layer and at the metal/oxide interface. When the film is formed without Cl^- in the solution, and then exposed to Cl^- , chloride ions are found in the outer hydroxide layer with the same concentration as the one found after passivation in Cl^- -containing solution, whereas no significant amount of Cl^- is found in the inner oxide. The concentration of Cl^- in the passive film has been measured. The Cl^- concentration in the hydroxide layer is approximately $10^{-2} \text{ mol dm}^{-3}$ (i.e. $\text{Cl}^-/(\text{Cl}^- + \text{OH}^-)$ approximately 10%) for $\text{Cl}^- = 5 \times 10^{-3} \text{ mol dm}^{-3}$ in the solution. At potentials above the pitting potential, measurements have been performed during the incubation period in order to investigate

the mechanisms of pit initiation, the hydroxide layer acts as a reservoir for Cl^- , which enters the passive film. A critical concentration of Cl^- in the oxide layer of approximately $10^{-2} \text{ mol cm}^{-3}$ has been measured in the stage immediately preceding pitting. A similar critical concentration in the film has been measured for different Cl^- concentrations in the solution.

The passive film was found to have a bilayer structure both in the absence and in the presence of Cl^- in the stage preceding pitting. The passive film does not become thinner in the presence of Cl^- ; on the contrary a growth of the film is observed when Cl^- is added to the electrolyte. Cl^- must be adsorbed in order to penetrate into the film but the surface coverage of adsorbed Cl^- always remains very low, as Cl^- starts to enter the passive film at low surface coverage. The view of pit initiation emerging from the above results is the following. Marked modifications of the passive film are caused by the presence of Cl^- . Cl^- is incorporated or enters the hydroxide layer by a chemical reaction probably involving place exchange of OH^- and Cl^- . Above a certain potential, Cl^- enters the inner oxide layer. A critical concentration of Cl^- in the film is reached, of the order of $10^{-2} \text{ mol cm}^{-3}$ for nickel.

The study of the effect of the adsorptions of various additives on the anodic dissolution has been the subject of several studies. For instance, the influence of the adsorption of N species on the anodic dissolution of Ni was studied in [43]. The dissolution and passivation of Ni in nitrite-containing acid solutions were investigated by Auger spectroscopy, AFM, and conventional electrochemical techniques. It was found that the dissolution/passivation of the Ni surface is consistent with a competition between adsorbed OH^- and nitrogen-containing

species with a potential-dependent surface coverage. Nitrogen-containing species hinder the passivation of the Ni surface, shifting the formation of the complex nickel-hydroxide/oxide film to more positive potential values. The dynamics of the dissolving interface, followed by AFM, reflect first the competition of adsorbed species, leading to the development of protrusions and cavities, and finally the formation of the passive film that promotes surface smoothening by a preferential dissolution of the protrusion tips under ohmic control.

An investigation of the adsorption of pyrazine and pyridine on nickel electrodes by in situ surface-enhanced Raman spectroscopy was reported in [44]. The result suggests that both pyrazine and pyridine were strongly adsorbed onto the substrates. It also implies that pyridine was adsorbed perpendicularly onto the substrate, while pyrazine adsorbed onto the substrate in a slightly tilted vertical configuration.

18.1.4

Spontaneous Reduction of Anions at Ni Surface

It is an almost general view that the nature of anions present in the electrolyte solutions affects the dissolution process of nickel.

This effect is explained by the role of the specific adsorption of anions. It is assumed that the specific adsorption of ClO_4^- ions is negligible [45, 46], and no chemical changes occur in the course of the electrochemical study of anodic dissolution and corrosion of nickel [47].

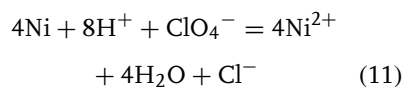
Detailed mechanistic conclusions are drawn from such studies without taking into account the possible reduction of ClO_4^- ions under the conditions of the experiments.

In a series of recent communications [48–50], it was demonstrated that the reduction of ClO_4^- ions takes place during the corrosion of Cu, Al, Zn, Ni, and Fe in deoxygenated HClO_4 solutions.

Both the dissolution rate of Ni and the reduction of ClO_4^- should depend on the acid concentration and temperature. The results obtained are summarized in Table 1. A given amount of Ni powder was dissolved in an excess of perchloric acid.

From the data presented in Table 1, the molar ratio of the Cl^- ions formed to nickel dissolved is independent of HClO_4 concentration. The influence of temperature is not strong as a temperature change of 25°C results in less than a doubling in the value of B/A .

Considering the equation



the formation of 1 mol Cl^- should be accompanied by the oxidation of 4 mol of nickel; thus, at 50°C , the efficiency of the reduction process referred to in the total amount of dissolved Ni is about 1.5% and at 20°C is around 1%.

Although the data obtained do not allow far reaching conclusions to be drawn, it can be stated that owing to the high adsorbability of Cl^- ions, the possible role of Cl^- ions formed at Ni electrodes in HClO_4 solutions cannot be neglected in the interpretation of phenomena observed in such systems. It was assumed that no significant amount of Cl-containing intermediates of reaction (11) accumulate in the solution phase. It was shown that the rate of interaction of ClO_3^- ions with Ni is significantly higher than that of ClO_4^- under comparable conditions.

Data presented in Table 2 provides an unambiguous proof of the occurrence of

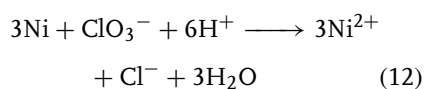
Tab. 1 Interaction of HClO₄ with nickel

Temperature [°C]	c_{HClO_4} [mol dm ⁻³]	A amount of dissolved Ni [10 ⁻² mol]	Bc_{Cl^-} formed [10 ⁻⁵ mol]	B/A [10 ⁻³]
25	3	3.57	7.5	2.1
40	3	3.9	12	3.07
50	3	3.9	13.5	3.46
25	1	1.26	2.6	2
40	1	1.27	4.3	3.38
50	1	1.27	4.9	3.85

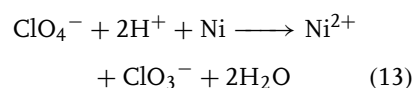
Tab. 2 Reduction of ClO₃⁻ ions by Ni. Amount of Ni 6 × 10⁻³ mol, temperature 25 °C, volume 50 cm³

Electrolyte [mol dm ⁻³]	c_{NaClO_3} [mol dm ⁻³]	Contact time [min]	c_{Cl^-} [mol dm ⁻³]
HClO ₄			
1	0	60	$c < 10^{-5}$
1	5×10^{-2}	60	1.5×10^{-2}
1	5×10^{-1}	15	3.9×10^{-2}
H ₂ SO ₄			
0.5	5×10^{-2}	60	1.24×10^{-2}
0.5	5×10^{-1}	15	3.9×10^{-2}

the following overall process:



This has a very high rate when compared with reaction (11). This means that we may assume that reaction (13) is the rate-determining process in the reduction of perchlorate ions:



18.1.5

Electrochemical Oscillation during Nickel Dissolution

The structure of complex behavior in anodic nickel dissolution was analyzed and

discussed in a series of papers by Lev and coworkers [51, 52].

In [53], oscillatory wave patterns observed during electrochemical dissolution of a nickel wire in acidic media was reported. It was shown that space-averaged potential or current oscillations are associated with the creation of an inhomogeneous current distribution, and that the selection of a specific spatial current pattern depends on the current control mode of the electrochemical cell. In the almost potentiostatic (fixed potential) mode of operation, a train of traveling pulses prevails, whereas antiphase oscillations occur in the galvanostatic (constant average current) mode.

In [52], a modeling of periodic and chaotic dynamics in anodic dissolution

was presented. The observed and modeled behavior include bistability, periodic oscillations bounded by Hopf and saddle loop bifurcations, the disappearance of these transitions in a double-zero singularity and the existence of chaotic solutions, which are bounded by a period-doubling transition. The modeling and parameter estimation were based on comparison of the experimental and simulated bifurcation maps, showing domains of different characteristic behaviors in the plane of applied constant current versus acid concentration. Qualitative agreement between the observed and predicted maps has been obtained. In [54], the delay and memory effects in bifurcations of nickel electrodis-solution were experimentally demonstrated.

18.1.6

New Findings on the Dissolution/Deposition Processes

During the last decades, a great number of papers dealing with anodic or spontaneous dissolution of polycrystalline nickel were published. Only some illustrative examples could be mentioned here. In [55], the anodic dissolution of nickel was studied galvanostatically in hydrochloric acid solutions of various concentrations. The reaction orders with respect to chloride ion and hydrogen ion concentrations were determined.

The corrosion behavior and dissolution mechanism of nickel in acid solutions with hydrogen sulfide (H_2S) was studied. It was found that the dissolution of nickel is influenced by both the nickel sulfide layer formed on the electrode surface and the acceleration effect of H_2S [56].

In [57], investigations of nickel dissolution in sulfuric acid solution have been performed by using an electrochemical microgravimetry (EQCM). On the basis of

reaction parameters obtained experimentally, the active dissolution mechanism of nickel has been explained by the Bockris mechanism.

Apparent activation energy of the anodic dissolution of nickel in sulfuric acid solutions in the presence of Cl^- and CNS^- ions was determined in [58].

Finally, it should be mentioned that according to some authors [59] anomalous – nonelectrochemical – dissolution has to be considered for the interpretation of the overall dissolution process of nickel in solutions containing oxygen. Although the idea is very interesting, the explanation presented seems to be questionable.

In [60], electrochemical deposition and stripping of nickel at a polycrystalline gold film electrode was studied by cyclic voltammetry and surface conductance.

In a series of publications by Gomez et al. [61–63], the electrodeposition of nickel on a vitreous carbon electrode has been investigated.

In [61], the influence of the nickel(II) concentration on the deposition process, in [62], the influence of potential on deposit morphology, while in [63], the morphology and structure of nickel nuclei as a function of the conditions of electrodeposition were studied. In the latter, the effects of growth rate (affected by the temperature and/or the nickel concentration), bath composition, and deposition time (particularly at low overpotentials) on the morphology of nickel nuclei were analyzed.

Pure nickel electrodeposits with macropores were prepared from electrolytic solutions of $0.2 \text{ mol dm}^{-3} \text{ NiCl}_2$ and NH_4Cl with concentrations varying between 0.25 and 4 mol dm^{-3} [64]. The effects of the electrodeposition current density and the NH_4Cl concentration on the surface morphology were determined. Surface area, faradaic efficiency, and fractal dimension

of the cross section of the electrodeposits were also evaluated. From these results, it was concluded that highly porous metallic matrices could be obtained, with very high roughness factors and excellent mechanical resistance, yet at very high apparent current densities of electrodeposition (5 A cm^{-2}). The use of this type of electrodeposition bath is suggested for the preparation of Raney-nickel electrodes, in order to improve the accessibility of reactants to the electrode surface.

18.1.7

Nickel–Hydrogen Systems

An analog of the platinized platinum electrode is the black or gray nickel electrode, which under certain experimental conditions can be used as the hydrogen electrode instead of the platinum electrode [65]. This electrode can be obtained by electrochemical deposition of nickel under the experimental conditions described in [65]. The real surface areas of these electrodes significantly surpass their geometric surface areas. In addition, potential-dependent adsorption of hydrogen occurs on the nickel surface and the measurement of the hydrogen capacity of the electrode in alkaline medium offers a tool for the determination of the real surface area [66].

However, because of overlapping of the adsorbed hydrogen oxidation region and that of adsorbed oxygen reduction the separation of these regions is difficult. Another difficulty is the slowness of the electrochemical processes leading to the formation of the layers of adsorbed hydrogen or oxygen.

In [67], an optoelectrochemical method (OEM) or a combination of electrochemical and ellipsometric methods, was developed for unambiguous evaluation of surface state and electrocatalytic properties of smooth standardized and modified

nickel electrodes in alkaline solutions. The method is based on the (1) insensitivity of ellipsometric method to hydrogen adsorption at least within the wavelengths interval 500–700 nm and (2) proportionality between changes in the amount of adsorbed oxygen and ellipsometric parameter, Δ . The simple method elaborated by the authors enabled them to obtain reliable roughness factor values.

The adsorption of hydrogen could be accompanied by its absorption as well.

Although it has been known for more than a century that large amounts of hydrogen can be loaded into nickel cathodes by electrolysis [68, 69], systematic work on the $\text{Ni}|\text{H}_2$ system was only initiated much later.

Almost fifty years ago, Baranowski et al. [70] and Baranowski and Smialowski [71] reported that, using sulfuric acid electrolyte and current densities $\leq 20 \text{ mA cm}^{-2}$, Ni cathodes could be converted into nonstoichiometric NiH_x ($x < 1$) hydride. A few years later, the nature of NiH_x was established by identifying two separate phases, β and α , as for the PdH_x analog [69, 72]. Both β - and α -hydrides formed by electrolysis of aqueous H_2SO_4 at Ni: the former, much more hydrogen-rich than the latter (H/Ni atom ratios of ≈ 0.8 for β and ≈ 0.03 for α), decomposes quickly with H_2 evolution [73, 74].

According to Baranowski and subsequent authors, the electrolytic formation of NiH_x is conditioned by factors such as the presence in the electrolyte of small amounts ($\approx 10^{-3} \text{ mol dm}^{-3}$) of a S, As, or Se compound [75], and the pH of the electrolyte. It has been stated in Ref. 73 that electrolytic hydriding of Ni failed in alkaline media. More recently, the validity of this statement was questioned by Bernardini et al. [76, 77]. According to [76, 77], considering of apparent similarity

between Ni and Pd hydrides, there is no reason why NiH_x should be obtained from acid electrolytes only. If there is a correlation between overvoltage and equivalent hydrogen pressure, the formation of unstable β NiH_x should be easier in alkaline media where larger overvoltages than in acid can generally be applied.

In [76], the feasibility of obtaining Ni hydride through electrolytic reduction of aqueous $0.6 \text{ mol dm}^{-3} \text{ K}_2\text{CO}_3$ at Ni electrodes of different types (solid Ni, Ni-fiber composite, and sintered Ni) was investigated. It was found that potentiostatic electrolyses at the beginning of the hydrogen evolution reaction (*her*) lead to the formation of several hydrogenated species of Ni, which generally become degraded when more negative potentials are applied. The species oxidized reversibly with the *her* was identified as the β -Ni hydride phase, whereas the nature of the Ni hydrides oxidized at more positive potentials could not be definitely established. The interaction of Ni samples on open circuit with H_2 dissolved in the electrolyte was found to form the same Ni hydride species as that achieved after electrolysis.

This approach was critically evaluated in a communication by Baranowski [78] pointing out that probably surface or subsurface hydrides are formed in alkaline solutions, instead of the bulk, three-dimensional hydride. It is stressed in [78] that the idea of the equivalence between overvoltage and thermodynamic activity, considered in [76, 77] is a misleading and unfounded concept.

Recently, by application of x-ray diffraction technique, evidences proving the

formation of β - NiH_x phase in the presence of promoters (S, As_2O_3 , Sb, and GeO_2) were reported in [79].

Dependencies of the β - NiH_x phase volume fraction on the nature and concentration of the promoter, changing current density and changing duration were presented and the phenomena observed were explained with the assumption that NiAs-type compounds take part in the formation of nickel hydride.

In contrast to the views asserting the reality of formation of NiH_x phase in alkaline media in the presence of promoters, Monev found [80] a very distinct pH effect in the formation of the hydride phase in the presence of H_2SeO_3 . According to [80], the nickel hydride formation terminates at pH value over 2.1.

18.1.8

Nickel Oxide and Nickel Hydroxide

Nickel oxides and hydroxides play an important role in the passivity of nickel in aqueous solutions, in oxidizing ionic

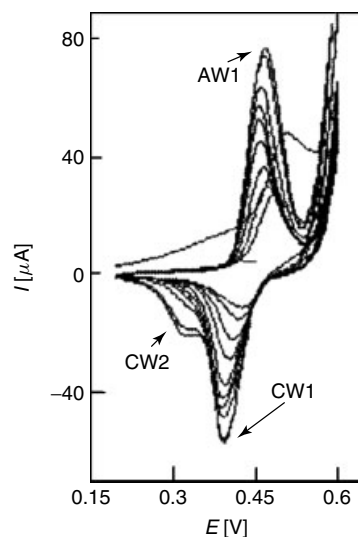


Fig. 1 A typical response of Ni to cyclic polarization in $0.1 \text{ mol dm}^{-3} \text{ NaOH}$. Potential measured against $\text{Hg}|\text{HgO}$ electrode. Scan rate: 60 mV s^{-1} . Explanation see in the text [91].

melts, and in the formation of electrodes related to batteries. Nickel hydroxide electrode is used for organic electrosynthesis, first of all for electrochemical oxidation.

Figure 1 shows a typical response of Ni to cyclic polarization in alkaline medium [81–91]. The redox wave pair AW1/CW1 is associated with the redox process $\text{Ni(OH)}_2 \leftrightarrow \text{NiOOH} + \text{H}^+ + \text{e}^-$. The current grows with the number of potential scans indicating the progressive enrichment of the electroactive species Ni^{2+} and Ni^{3+} in the surface. Prolonged polarization results in a stationary state. The anodic peak potential varies depending on the process of polarization of Ni oxides as a result of repeated polarization. The small cathodic wave CW2 developed during the later stages of polarization indicates the alteration of phase of Ni oxides [88]. The strong current increase following the anodic wave AW1 is the result of the oxygen evolution reaction. The intensity of this reaction also grows with advancing polarization, suggesting a correlation between the oxygen evolution and the concentration of Ni^{3+} sites. The first positive potential scan generates a monotonically elevated current flow giving a peak at a potential more positive than in the subsequent potential cycles. The peak shift is indicative of an overpotential required for the nucleation and growth of NiOOH. The enhanced baseline current, being most pronounced in the first scan, is associated with the oxidation of Ni to Ni^{2+} . α -NiOOH, β -NiOOH, and γ -NiOOH were structurally identified.

In a recent publication [89], processes taking place on a Ni electrode were investigated with the EQCM. At potentials negative of about -500 mV vs. SCE, a closed frequency loop was observed without irreversible changes in the mass of the electrode. It was found that the phase

transition $\alpha \rightarrow \beta$ -Ni(OH)₂, taking place at potentials positive to -500 mV vs. SCE, is accompanied by an irreversible increase in the mass of the electrode. When Ni(OH)₂ was further oxidized, the frequency increase is followed by a decrease indicating the transport of various species in both directions, that is, from and into the electrode. The authors arrived at the conclusion that during the Ni(OH)₂ oxidation reaction, the transport of species responsible for the mass increase is slower than the charge-transfer process.

The applicability of positron lifetime spectroscopy for the characterization of the partly charged nickel hydroxide was investigated [90]. The positron lifetime spectra of β -Ni(OH)₂/ β -NiOOH systems were presented. Three different parts of the annihilation curves were observed and identified.

In a recent communication [91], Ni surface alloyed with Cu, Ti, or Cu + Ti by ion implantation was examined for its redox and electrocatalytic activities by cyclic voltammetry. The surface was characterized by XPS, x-ray, and electron diffraction, as well as by electron and atomic force microscopies. This type of material exhibited a unique voltammetric response of Ni and was shown to stabilize the β -modification of the Ni oxide/hydroxide. It was demonstrated that the morphology and microstructure differ from those of bulk materials.

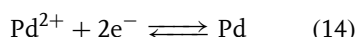
18.2 Palladium

18.2.1 Fundamentals

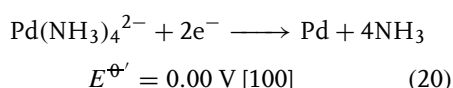
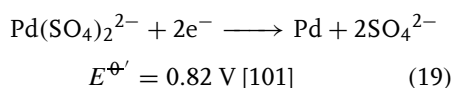
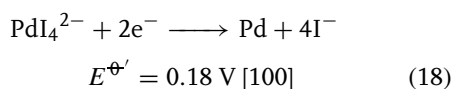
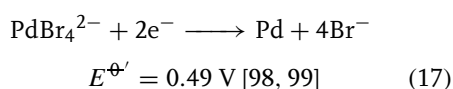
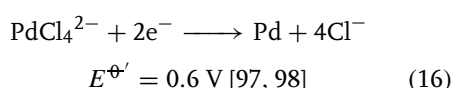
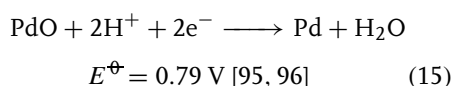
The oxidation number of palladium in compounds ranges from 0 to +6; however,

+2 and +4 states occur most frequently [92, 93].

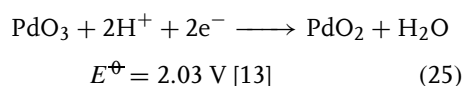
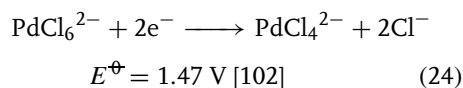
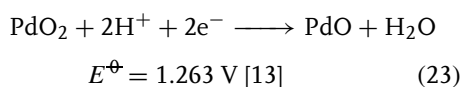
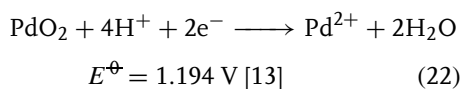
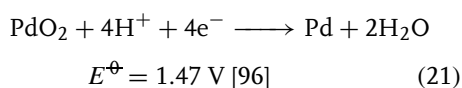
For the process



the most reliable standard potential value is $E^\ominus = 0.915 \pm 0.005 \text{ V}$ [94]; however, 0.945 V or 0.987 V formal potentials have also been reported [92, 93]. Similarly, diverse E^\ominus and formal potential ($E^{\ominus'}$) values can be found in the literature for other electrode reactions. For selected systems, the electrochemically measured values will be given.



The uncertainty in the E^\ominus and $E^{\ominus'}$ values are even higher in the case of Pd(IV) and Pd(VI) states.



The interfacial chemistry of palladium electrodes (polycrystalline and single crystal) was surveyed by Soriaga et al. recently [103]. According to the authors, the “remarkably rich interfacial chemistry of palladium” may have its origin in the anomalously weak intermetallic palladium–palladium bond, a circumstance that is expected not only to enhance lateral surface mobilities but also to facilitate the disruption of substrate–substrate bonds and/or the formation of substrate–adsorbate bonds.

In a survey dealing with palladium electrode, it is not possible to avoid mentioning the cold fusion controversy, started in 1989, where Pd electrode played and plays a central role. Hundreds of papers relating to palladium electrode are dealing exclusively with cold fusion and related subjects. The status of “cold fusion” was summarized in [104], recently.

18.2.2

New Findings on the Dissolution and Deposition of Palladium

Only a few illustrative examples taken from the literature of the last few years could be presented here.

The deposition of Pd on well-ordered single crystalline Au surfaces, Au(111), Au(110), and Au(100) has been studied by Kolb et al. especially with regard to the initial stages [105–107].

Pd was deposited onto Au from aqueous solutions of its chlorine compounds, for example, Pd_2Cl_2 or K_2PdCl_4 . It was stated that from such electrolytes, prior to

palladium deposition, $[\text{PdCl}_4]^{2-}$ adsorbs on the bare Au(111) and Au(100) surfaces and forms ordered adlayers, the structures of which were studied by in situ STM [105–108]. This complex anion has also been found to adsorb on the first Pd monolayer on Au(111) [105], whereas it is displaced by chloride in the case of Pd on Au(100) [106]. On these unreconstructed Au(111) and Au(100) surfaces, palladium nucleates first at surface defects like monoatomic high steps, and at higher overpotentials also on terraces [105, 106]. In the underpotential deposition (UPD) region, a pseudomorphic Pd monolayer is formed in Au(111) [105, 109]. No alloy formation was observed for this system [105], while a Pd/Au surface alloy is formed when Pd is deposited onto Au(100) [106]. Deviations in the electrochemical properties of thin Pd films on Au(100) from those of well-ordered Pd(100) surfaces [110] are most probably caused by this alloying process.

Soriaga and coworkers [111–113] discovered that the anodic dissolution Pd(111) and Pd(100) single-crystal electrodes in pure H_2SO_4 solutions was catalyzed by the presence of monolayers of iodine chemisorbed on these surfaces. Large anodic peaks were found for the dissolution even in noncorrosive electrolyte solutions only when the surfaces of Pd were modified by the iodine adlayer.

Further important results based mostly on in situ STM study were reported by Itaya and coworkers [114]. Iodine pretreatment was accomplished simply by immersion of the clean electrode, without potential control, in an aqueous 1-mM solution of iodide for 5 min. Unadsorbed iodide was removed by rinsing with pure water.

It was shown by Soriaga et al. [115] that this unique type of dissolution can be used for the selective and quantitative anodic

stripping of Pd films electrodeposited on Pt substrates. This method can also be used for Pd-coverage determinations, a major advantage if catalysis-induced coverage changes are to be monitored.

The dependence of adsorption properties and texture on electrolytic palladium deposits on the deposition potential was investigated by Tsirlina et al. [116]. It was found that, in sulfuric acid solutions, the palladium dissolution, which accompanies the oxygen adsorption, obscures the adsorption behavior of the deposits with respect to oxygen. Assumptions were made about the predominant crystallographic orientation (100) of the surface of some palladium deposits being dependent on the deposition potential and about the presence of regions whose adsorption properties are anomalous with respect to copper. The assumptions are based on a comparative analysis of the copper adsorption data and x-ray diffraction patterns. In addition to sites of crystalline palladium, the deposits were found to have disordered areas as well.

Regularities of formation of a palladium oxide layer and its cathodic reduction in $0.5 \text{ mol dm}^{-3} \text{ H}_2\text{SO}_4$ at 0.5–1.3 V (SHE) were studied by cyclic voltammetry, XPS, and EQCM [117]. It was shown that a Pd electrode dissolves electrochemically in $0.5 \text{ mol dm}^{-3} \text{ H}_2\text{SO}_4$ when its potential is cycled between 0.5 and 1.3 V. It was suggested that anodic process at 0.5–1.3 V (SHE) represents electrochemical oxidation of palladium, yielding a surface layer of poorly soluble $\text{Pd}(\text{OH})_2$ and/or PdO phases, as expressed by the equation $\text{Pd} + 2\text{H}_2\text{O} = \text{Pd}(\text{OH})_2/\text{PdO}_s + 2\text{H}^+ + 2\text{e}^-$. This surface layer, $\text{Pd}(\text{OH})_2/\text{PdO}_s$, undergoes reduction during the cathodic process. It was found that about 5% of the total amount of ionized palladium dissolves in electrolyte.

18.2.3

Hydrogen and Oxygen Sorption in/at Palladium Electrodes

A great number of papers devoted to the investigation of hydrogen absorption and adsorption can be found in the literature. Some new developments will be considered here.

It is a well-known and a widely recognized fact that the electrical resistance of palladium is a function of its hydrogen content. In [118], some problems on the resistance method regarding the in situ measurement of hydrogen content is discussed.

In [119], the hydrogen adsorption and desorption reactions in thin palladium electrodes were studied using the potential step method in order to analyze the mechanism of phase transformation. Transient current responses were recorded at the onset of the potential step for 47 μm thick Pd electrodes in 1 mol dm⁻³ H₂SO₄ at ambient temperature. A model based on a moving boundary mechanism was proposed to account for the experimental $i-t$ curves. It was found that the hydrogen adsorption reaction shows interfacial kinetic limitations and only numerical solutions can be obtained. Such kinetic limitations were not found for the desorption reaction and a semianalytical solution that satisfactorily fits the experimental data was proposed.

During the last two decades, hydrogen adsorption and absorption were shown to play a central role in a whole series of papers by Czerwinski and coworkers [120–133].

The EQCM method is used to evaluate the processes that occur in/on the palladium electrode in acid and basic solutions. It was concluded that hydrogen electrosorption in palladium is accompanied by an additional frequency shift of

the crystal that could be attributed to the stresses generated inside the Pd metal. A nonlinear dependence between the mass change and the charge consumed during hydrogen oxidation in the Pd electrode was found for hydrogen absorbed in the α - and β -phases.

This effect created significant problems with the objective estimation of the amount of sorbed hydrogen inside the palladium electrode using the EQCM method.

The study of hydrogen and deuterium electrosorption in palladium limited volume electrodes (LVE) was carried out by the same group in both acidic and basic solutions [124, 130, 134]. It was found that the hydrogen capacity, H(D)/Pd, measured electrochemically, depends significantly on sweep rate in cyclic voltammetric experiments and also on the thickness of the LVE. Two different mechanisms of hydrogen desorption, that is, the electrochemical oxidation and the nonelectrochemical recombination step, which take place in parallel within the Pd–LVE, have been postulated.

A decrease in hydrogen capacity (H/Pd ratio) with increasing temperature was observed. Hydrogen absorption was found to be dependent on the composition of the surrounding electrolyte solution.

The first systematic study on the oxide growth at Pd electrodes under well-defined potentiostatic conditions was reported in [135]. The impact of temperature variation on the development of Pd surface oxides was investigated in aqueous H₂SO₄. Various theoretical models were applied in order to elucidate the growth kinetics and mechanism in relation to the experimental conditions.

In a series of publications by Burke [136–140], the electrochemical and electrocatalytic behavior of palladium was

studied. The phenomena observed were explained similarly to other noble metals by the assumption of the role of premono-layer oxidation and formation of hydrous oxides.

18.2.4

Electrosorption and Electrocatalytic Processes

Some relatively simple examples will be presented.

The mechanism of the evolution of hydrogen on palladium in alkaline medium and associated internal damage phenomena were discussed in a recent paper by Bockris and Minevski [141]. The aim of the paper was to get support for their belief concerning the occurrence of nuclear reaction inside the metal. However, the authors arrived at the conclusion that the results obtained could be explained by an atomic-molecular (nonnuclear) model.

The electrocatalytic reduction of NO_3^- ions on noble metal electrodes has been the subject of several studies. (The reduction of nitrate has recently gained renewed attention in view of its relevance to pollution control.)

Comparative studies of catalytic activity of various metals, alloys, and adatom-modified metals were carried out.

For instance, the electrocatalytic reduction of nitrate ions on Pt, Pd, and Pt + Pd electrodes activated with Ge was studied in [142, 143].

It was found that underpotentially deposited germanium strongly enhances the reduction rate of nitrate. The reduction of nitrite is enhanced to a lesser extent, whereas germanium is inactive for NO and hydroxylamine reduction. It is of interest that the well-known inhibition of the nitrate reduction at low potentials was absent for germanium-modified electrodes.

A proportionality between the activity and the germanium coverage was reported. The authors arrived at the conclusion that germanium is involved in the rate-determining step, which is the reduction of nitrate to nitrite and its role is to bind the oxygen atom of nitrate. The higher activities found for Pt + Pd electrodes was explained in terms of changes in the electronic structure of the metals as a result of alloying.

Similar studies on palladium/copper electrodes was carried out using differential electrochemical mass spectroscopy (DEMS), rotating ring-disk electrodes and EQCM [144]. In acidic electrolytes, the activity increased linearly with Cu coverage; in alkaline electrolytes, a different dependence on coverage was observed.

Recently, the electrochemical behavior saturated alcohols, that is, propargyl alcohol ($\text{HC}\equiv\text{CCH}_2\text{OH}$, PA) [145], benzyl alcohol ($\text{C}_6\text{H}_5\text{CH}_2\text{OH}$, BA) [146] and allyl alcohol [147], has been studied at Pd electrodes in an acid medium by cyclic voltammetry, chronoamperometry, and on-line mass spectrometry. For BA, it was observed that the fragmentation of the molecules occurs at potentials in the hydrogen adsorption/absorption region of palladium, whereas for PA the adsorbates maintain the C_3 -chain. On the other hand, the yields of the electroreduction and electrooxidation products for both PA and BA differ from those obtained at Pt [146, 148, 149].

In the case of allyl alcohol, the on-line mass spectrometry (DEMS) allowed the detection of the volatile products generated during the electroreduction and electrooxidation processes. C_3 -hydrocarbons (propene and propane) and acrolein were detected as the bulk products, whereas C_2 -hydrocarbons and CO_2 are related to the adsorbed species. The dissociation of the alcohol produces ethine in

the 0.10–0.35 V potential range, which reduces to ethane. Adsorbed acrolein and C₂-hydrocarbonated residues seem to be formed in addition to CO-like species. The results were compared with those previously obtained at platinum and gold, as well as with other unsaturated alcohols, that is, benzyl and propargyl alcohol.

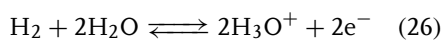
Similar studies were carried out with benzoic acid on porous palladium electrodes [150]. The objective of this work was to investigate the adsorption processes and the reactivity of benzoic acid on different noble metals, in order to compare these results with those obtained for related aromatic compounds. On-line mass spectroscopy analysis of volatile products revealed that the adsorption of benzoic acid is irreversible at platinum while it is mainly reversible on palladium. Accordingly, different catalytic activity of platinum and palladium was found in the electrooxidation.

18.3 Platinum

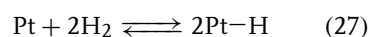
18.3.1 Fundamentals

Platinum electrodes are widely used as an inert electrode in redox reactions because the metal is most stable in aqueous and nonaqueous solutions in the absence of complexing agents, as well as because of its electrocatalytic activity. The inertness of the metal does not mean that no surface layers are formed. The true double-layer (ideal polarized electrode) behavior is limited to ca. 200–300 mV potential interval depending on the crystal structure and the actual state of the metal surface, while at low and high potentials, hydrogen and oxygen adsorption (oxide formation) respectively, occur.

First of all, the important role of platinum as the metal part of the standard hydrogen electrode (SHE), which is the primary standard in electrochemistry should be mentioned. The standard potential of an electrode reaction (standard electrode potential) is defined as the value of the standard potential of a cell reaction when that involves the oxidation of molecular hydrogen to solvated (hydrated) protons (hydrogen ions):



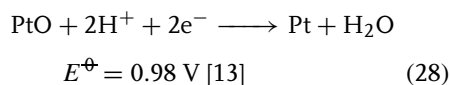
The standard state is the hypothetical ideal solution of molality 1 mol kg⁻¹ (or the relative activity of H₃O⁺, $a_{\text{H}_3\text{O}^+} = 1$) at standard pressure. The standard pressure is 1 bar (earlier 1 atm = 1.01325 bar; however, the shift is only 0.00026 V at the potential scale). By definition, the potential of this electrode is zero. Although the standard potential should not depend on the material of the metal, the SHE exclusively contains a platinum wire or a platinum sheet covered with platinum black (platinized platinum). Owing to the spontaneous dissociation (dissociative chemisorption) of H₂ at Pt

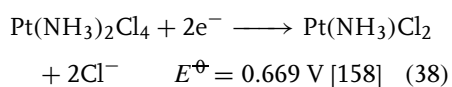
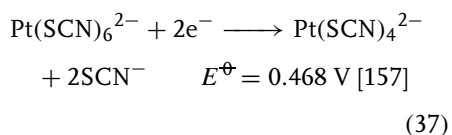
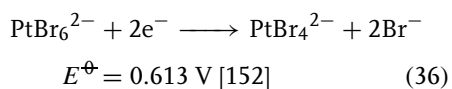
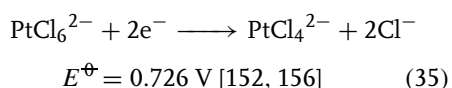
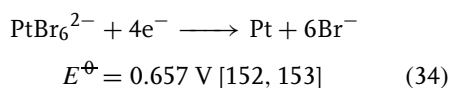
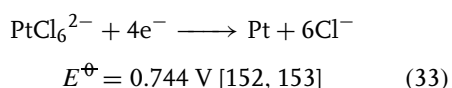
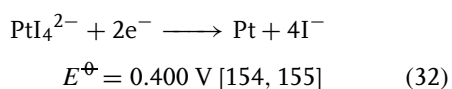
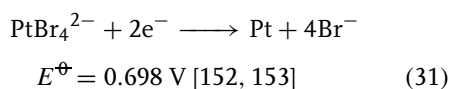
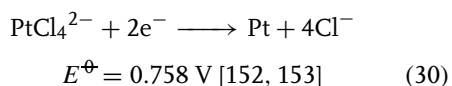
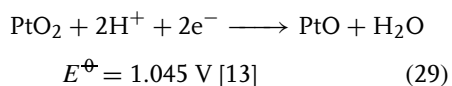


and the not-too-high Pt–H bond energy, the exchange current is high and the electrode process is electrochemically reversible [151].

In its compounds, Pt has oxidation states +2 and +4. The redox reactions – except the formation of surface oxides, hydroxides, and hydrides – take place with participation of its complexes.

Some important systems and the corresponding E^\ominus and $E^{\ominus'}$ values are as follows.





Data for several ammine-halo, ammine-ethylenediamine, halo-nitro-amine, halo-nitro-triammine, chloro-alkyl-ammine, alcohol-ammine, tetra-amino, pyridine-chloro, picoline-chloro, quinoline-chloro, phenanthroline-ammine-chloro, and so on, complexes have been compiled in [159, 160]. Some regularities have been found, for example, E^\ominus of Pt halo-complexes decreases with the increasing atomic number of the halogen atom; the successive substitution of NH_3 for chloro ligands causes the decrease of

E^\ominus ; the introduction of different ligands in the amine complexes increases E^\ominus according to the order $\text{I} < \text{CN} < \text{SCN} < \text{Br} < \text{Cl} < \text{NO}_2$ [159, 160]. Finally, we mention the famous cisplatin, *cis*- $\text{Pt}(\text{NH}_3)_2\text{Cl}_2$, which is a very powerful cancer chemotherapy drug [161]. Its effect was discovered by Rosenberg [162] accidentally when he investigated the influence of electric field on living cells. He used supposedly inert platinum electrodes to study the suspension of live *Escherichia coli* bacteria. It was found that, as a consequence of dissolution of Pt, cisplatin was formed which had a devastating effect on the bacteria.

18.3.2

Effect of Adsorption and Surface Structure on the Voltammetric Behavior of Platinum Electrodes

18.3.2.1 Adsorption of Hydrogen, Oxygen, and Anions

The “classical” voltammetric curve used generally for the presentation of hydrogen and oxygen adsorption on polycrystalline Pt is shown in Fig. 2.

It is well known that the shape of the curve depends on the nature of the anion(s) present in the system. In reality, there is an overall behavior reflecting simultaneous H/O and anion adsorption.

It was demonstrated that the radiotracer method, using labeled anions, is an adequate tool to follow anion adsorption in the course of voltammetric measurements and to gain simultaneous information on hydrogen and anion adsorption [163]. Coupling voltammetric and radiometric measurements in the study of platinized platinum electrodes gave insight in the anion-hydrogen atom coadsorption process.

Figure 3(a) shows the count rate originating from radiolabeled HSO_4^- adsorption vs. E (voltradiometric curve)

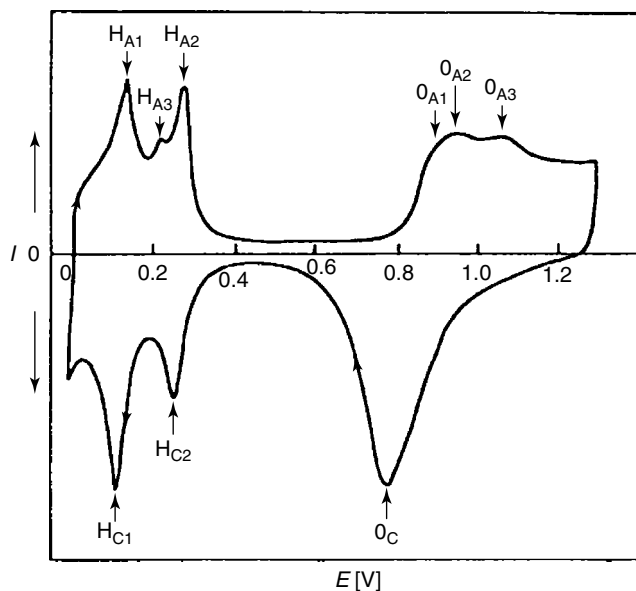


Fig. 2 Cyclic voltammogram of Pt in $0.5 \text{ mol dm}^{-3} \text{ H}_2\text{SO}_4$.

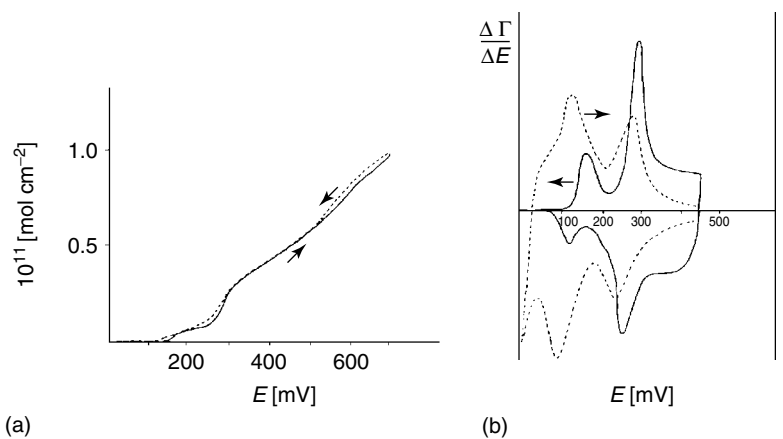


Fig. 3 (a) Voltradiometric Γ vs. E curve in the potential range 14–710 mV; sweep rate 0.25 mV s^{-1} ; $1.7 \times 10^{-3} \text{ mol dm}^{-3} \text{ H}_2\text{SO}_4$ in $1 \text{ mol dm}^{-3} \text{ HClO}_4$. (b) Shape of the $\Delta\Gamma/\Delta E$ vs. E (—) and voltammetric curves (---) in the potential range 10–450 mV; sweep rate 0.15 mV s^{-1} ($\Delta\Gamma/\Delta E$ and I arbitrary units) [163].

curve traced in the potential range from 15 to 710 mV with a sweep rate of 0.25 mV s^{-1} in the presence of labeled H_2SO_4 ($c = 1.7 \times 10^{-3} \text{ mol dm}^{-3}$)

in $1 \text{ mol dm}^{-3} \text{ HClO}_4$. From data presented in Fig. 3(a) the $d\Gamma/dE$ vs. E curve (differential voltradiometric curve) can be calculated, which may be considered as the

counterpart of the corresponding voltammetric curve. In Fig. 3(b), the $\Delta\Gamma/\Delta E$ vs. E and voltammetric curves are compared. From the comparison of these curves it can be stated that the position of the anion adsorption peaks in the hydrogen adsorption region are not far from those of the hydrogen adsorption. The most pronounced difference may be observed between the first hydrogen and anion peaks.

There are indications in the literature for the overlap of the oxide and hydrogen regions of platinum electrodes in aqueous acid solution [164]. The extent to which the hydrous oxide reduction process overlaps with the hydrogen adsorption region was investigated for platinum in acid solution. At least three distinct hydrous oxide reduction peaks (or regions) were observed and in some cases one of these peaks commenced at ca. 0.0 V, that is, it was almost totally within the hydrogen gas evolution region. Following repeated hydrous oxide growth and reduction, which disrupted and thus activated the metal surface, a sequence of four low-level premonolayer oxidation peaks (each of which has been noted earlier by other authors) appeared in the positive sweep. The transitions giving rise to such peaks were assumed to be mediator generation reactions, which strongly influence electrocatalytic processes occurring on platinum at low potentials.

18.3.2.2 Well-defined Platinum Surfaces

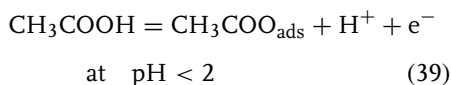
Fundamental questions connected with the characterization of the double layer at well-defined single-crystal faces of solid metals have been reviewed and surveyed several times by Hamelin [165–169].

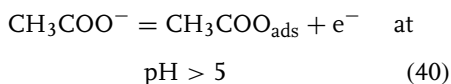
Since the early 1980s, cyclic voltammetry has been used to characterize single-crystal electrodes in terms of surface order, presence or absence of defects, contaminations, and so on. In some cases, the

voltammograms have also been used for identification of adsorbates, mostly based on electric charge calculation. However, since the double-layer charging and surface reactions such as underpotential deposition and anion adsorption may occur in parallel, it is difficult to break down the total voltammetric charge into all of its individual components. Therefore, interpretation from voltammetry alone, used as a tool for the adsorbed species identification, may be ambiguous. This has been, for instance, the case with the interpretation of the “unusual adsorption states” on the Pt(111) electrode [170–179].

Although at a very early stage of the studies the appearance of the unusual peak on the voltammograms of Pt(111) was explained by anion adsorption for a long period, the view that it should be ascribed to hydrogen adsorption (or incorporation of hydrogen) was widely accepted by many researchers. Recently, the hydrogen adsorption model has been rejected on the basis of reexamination of the problem by the most eminent proponents of the model studying the unusual desorption states on Pt(111) electrodes by CO and I displacement method. First they arrived at the conclusion that the results obtained confirm that the charge associated with the unusual states is at least formally compatible with the exchange of one electron per three surface platinum atoms.

In accordance with this view, the occurrence of the unusual peaks on the cyclic voltammograms observed in acetic acid/acetate system was ascribed to a one-electron transfer process of acetic acid/acetate ions according to the equations [180]:





There are, however, many evidences demonstrating that the existence of the unusual states cannot be easily explained with the charge transfer to, or from the anions (or other species). For instance, recent spectroscopic studies do not support the occurrence of electron transfer in the case of anion adsorption [174, 176, 181–185].

A very important and confusing observation is that the charge involved in the unusual states in various solutions is nearly independent of the nature of the anion, including organic anions. This aspect of the unusual states cannot be easily reconciled with the charge transfer to, or from the anion as a mechanistic origin of the pseudocapacitive current generated by the reversibly adsorbed anions on Pt(111).

Results obtained from careful examination of the pH effects on the potentiodynamic behavior of the Pt(111) electrode in acidified perchlorate solutions [180] advocate in favor of the assumption that water and not ClO_4^- anions are involved in the unusual adsorption states in the double-layer region of Pt(111). Presumably, H_2O dissociation and OH deprotonation are responsible for the two main electrode processes in the double-layer region of Pt(111) in NaClO_4 solutions.

For instance, in situ Fourier transform infrared (FTIR) spectroscopy has been used by Faguy et al. [176] to study the potential-dependent changes in anion structure and composition at the surface of Pt(111) electrodes in HSO_4^- -containing solutions. From the infrared differential normalized relative reflectance data, the maximum rate of intensity changes for three infrared bands can be obtained. Two modes associated with the adsorbed anion

and one mode assigned to species is not adequately described as either sulfate or bisulfate; the data are more consistent with an adsorbed $\text{H}_3\text{O}^+ - \text{SO}_4^{2-}$ ion pair, possibly with the three unprotonated sulfate oxygens interacting with Pt sites.

Since the number of papers dealing with the electrochemistry of Pt single crystals exceeds several hundreds, only some of them, published in the last few years could be referred to [179, 186–205].

18.3.2.3 Faceted and Platinized Platinum Electrodes

A series of papers by Arvia and coworkers [206–215] demonstrated that metal electrode surfaces with preferred crystallographic orientation and different roughnesses could be created through the application of periodic potential treatments.

It was found that changes in the voltammetric response of polycrystalline platinum electrodes in the direction expected for preferred oriented surface electrodes can be achieved using a fast repetitive potential perturbation.

Faceted platinized platinum surfaces with preferred crystallographic orientation were prepared by square-wave potential-modulated DC electrodeposition [216].

A fast repetitive triangular potential sweep (10^4 V s^{-1} between 0.05 and 1.5 V for 2 h) was applied to platinized platinum electrode [217]. This treatment resulted in a considerable decrease in the real surface area and in the formation of a (100)-type preferentially oriented surface structure.

A detailed comparison of the voltammetric behavior of platinum single-crystal and faceted electrodes was also given [218].

A different approach to the preparation of preferentially oriented surfaces on polycrystalline systems has been demonstrated by Sumino and Shibata [219]. It has been shown that a fast-cycling treatment

is not required for obtaining deposits with preferential orientation [176]. A platinum electrode with a single-crystal (100) surface was obtained by annealing a thin platinum film electrodeposited on a polycrystalline platinum foil.

Considering these results it was an important task to reconsider some questions connected with the technique of platinization, examining whether the method of platinization has some influence on the voltammetric behavior of the platinized surfaces. In [220], attempts were made to demonstrate that the voltammetric behavior of the platinized system could depend on the experimental conditions of the deposition carried out by a simple galvanostatic method.

On the basis of the results obtained, it could be stated without any doubt that the voltammetric behavior of the electrodes studied depends strongly on both the composition of the platinization solution and the current density of the deposition. The number of the peaks (pseudopeaks) and shoulders appearing on the voltammograms changes from two to four and the ratios of the heights of these peaks also change significantly. This behavior differed somewhat from that expected on the basis of classical views concerning the voltammetric behavior of a platinized system. On the other hand, this conclusion per se cannot be considered as a completely new statement. Various kinds of platinized and supported platinum catalyst electrodes were studied in the literature in order to reveal the relationship between their electrocatalytic (electrosorption) behavior and the structure of the deposited layer. (See, for instance, Refs. 221–225 and the literature cited therein.) It has been shown in these studies that the electrocatalytic activity and, occasionally, the character of the hydrogen adsorption at the deposited

platinum particles depends strongly on the preparation, and consequently on the structure of the deposited layer and on the dimension (size) of the deposited particles. For instance, in [225] in connection with the investigation of the electrocatalytic properties of ultrafine platinum particles it has been stated that the ratio of the amount of strongly adsorbed hydrogen to that of weakly adsorbed hydrogen decreased with decreasing platinum particle size. It was assumed that the adsorption strength of the hydrogen on the Pt(100) plane of the small platinum particles grew weaker with decreasing particle size.

The similarity of the shape of the voltammetric curves of platinized system to those reported for electrodes treated by the fast repetitive potential perturbation technique or obtained by annealing electrodeposited platinum and the appearance of signs characteristic for stepped surfaces allows us to assume that these phenomena should be ascribed to the similarities in the surface structure.

This probably means that it entails a common feature leading to the formation of electrodes with ordered domains of single-crystal or stepped surfaces. It is evident that further studies are required to elucidate the mechanism of the process resulting in such systems by simple platinization. For practical reasons, it will be of importance to study the electrocatalytic behavior of these systems.

18.3.2.4 Surface Structure and Reactivity

The study of the link between the surface structure of an electrode and its reactivity in electrode processes is considered as an important element of the investigations in modern electrochemistry.

In the frame of electrocatalysis and fuel cell-oriented research, a vast amount of data was collected during the last decades,

first of all concerning the reactivity of simple organic compounds at various Pt and Pd surfaces. These questions will not be discussed in this chapter. In the following, only the reduction of two anions, ClO_4^- and NO_3^- ions will be considered as model species for the demonstration of the complex problem of “structure and reactivity.”

The investigation of adsorption phenomena occurring on Pt and Pd electrodes is an important task for the clarification of their behavior in electrocatalytic processes. A characteristic feature for these systems is the hydrogen adsorption reflected by the shape of voltammetric curves taken under suitable conditions. This experimental approach constitutes the intersection point where the problem of perchlorate

reduction and the investigation of electrosorption behavior of prospective fuel cell electrodes touch each other.

It was (and perhaps is) a general belief in the literature that perfect voltammograms reflecting H adsorption on the “catalytic” electrodes can be obtained in HClO_4 solution.

The distortion of voltammetric curves in the presence of ClO_4^- ions is firm evidence for the occurrence of the reduction process. This effect is shown in Fig. 4 for the case of Pt with high real surface areas.

In Fig. 4, voltammograms of platinized electrodes prepared under various conditions are shown. For the sake of comparison, the corresponding voltammograms in HClO_4 and H_2SO_4 solutions are presented [226].

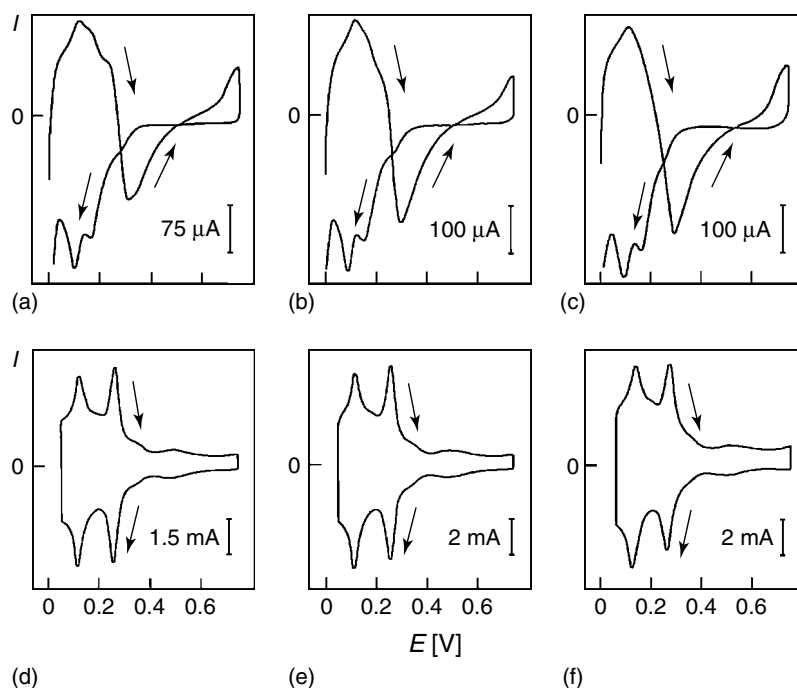


Fig. 4 Voltammogram of three different Pt/Pt electrodes: (a–c) in 3 mol dm^{-3} HClO_4 , sweep rate = 1 mV s^{-1} ; (d–f) in 0.5 mol dm^{-3} H_2SO_4 , sweep rate = 20 mV s^{-1} [226].

The features characteristic of these systems are as follows:

1. The reduction process occurs, almost exclusively, during the positive sweep.
2. Generally, no reaction can be observed on the negative sweeps, but the shape, height, and position of the corresponding hydrogen peak differ significantly from those expected.

3. The distortion of the anodic peak gradually disappears during subsequent cycles.

The reduction of NO_3^- ions at platinum electrodes has been studied by several authors during the last decade [227–230]. Thus, we have the relevant fundamental information about the behavior of the system. The most important information

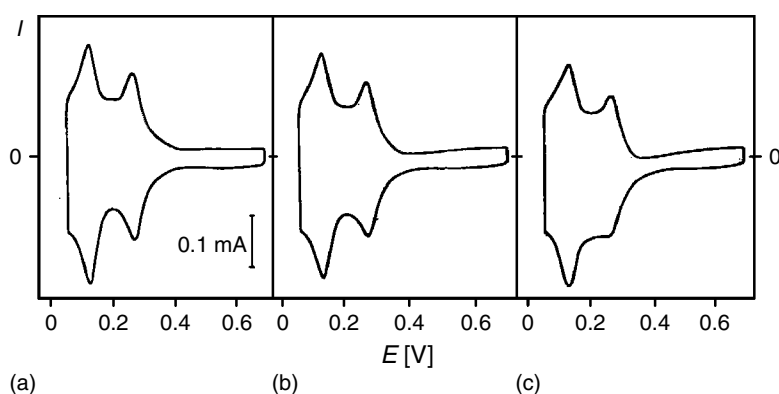


Fig. 5 Cyclic voltammograms of a platinized platinum electrode (type I) in (a) $0.25 \text{ mol dm}^{-3} \text{H}_2\text{SO}_4$, (b) $0.25 \text{ mol dm}^{-3} \text{H}_2\text{SO}_4 + 10^{-3} \text{ mol dm}^{-3} \text{HNO}_3$ and (c) $0.25 \text{ mol dm}^{-3} \text{H}_2\text{SO}_4 + 10^{-2} \text{ mol dm}^{-3} \text{HNO}_3$. Sweep rate, 20 mV s^{-1} [235].

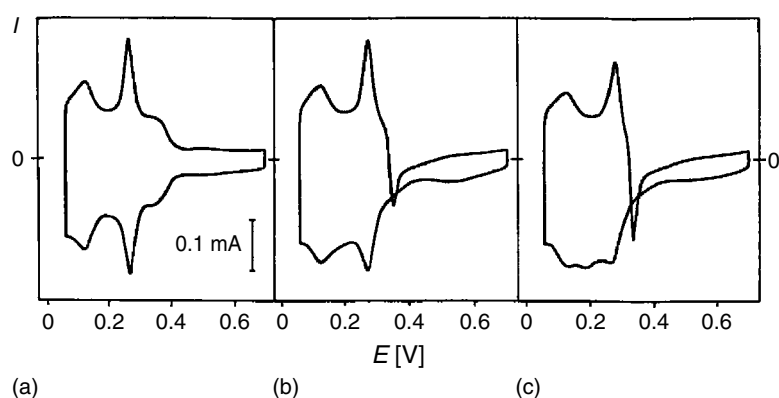


Fig. 6 Cyclic voltammograms of a platinized platinum electrode (type II) in (a) $0.25 \text{ mol dm}^{-3} \text{H}_2\text{SO}_4$, (b) $0.25 \text{ mol dm}^{-3} \text{H}_2\text{SO}_4 + 10^{-3} \text{ mol dm}^{-3} \text{HNO}_3$, and (c) $0.25 \text{ mol dm}^{-3} \text{H}_2\text{SO}_4 + 10^{-2} \text{ mol dm}^{-3} \text{HNO}_3$. Sweep rate, 20 mV s^{-1} [235].

is that hydrogen adsorption inhibits the reduction of NO_3^- ions. This means that in acid media the reduction rate is zero on surfaces covered by adsorbed hydrogen and a measurable reduction can only be observed at potentials above 50–100 mV. The current (absolute value) versus potential curve goes through a maximum.

The role of the various crystal faces in the reduction of nitrite, nitrate, and other oxygen-containing nitrogen compounds has been studied recently [231, 232].

It has also been shown [173, 233, 234] that the catalytic activity of various crystal faces of platinum for the reduction of NO_3^- ions is very different. This means that similar effects should be expected in the case of platinized systems with various preferred crystallographic orientations [235].

Figures 5 and 6 show the voltammograms of two types of platinized systems obtained in $0.25 \text{ mol dm}^{-3} \text{ H}_2\text{SO}_4$ supporting electrolyte in the absence and presence of NO_3^- ions. Figure 5(a) shows the voltammetric behavior of the classical polycrystalline electrode (type I) in H_2SO_4 solution, while Fig. 6(a) is for an electrode with preferred (100) orientation (type II).

It follows from a comparison of Fig. 5(b) and (c) with Fig. 6(b) and (c) that the electrocatalytic reduction of NO_3^- ions depends strongly on structural factors, reflected by the voltammetric behavior in pure H_2SO_4 solution. This observation is in accordance with earlier findings [173, 233, 234] that (100) crystal faces have an excellent catalytic activity toward the reduction of NO_3^- ions compared with the other low index planes.

The absence of a distinct catalytic activity in the case of the type I electrode at the HNO_3 concentrations studied can be considered to be normal behavior if we take into consideration the results of some

previous studies showing that HSO_4^- and SO_4^{2-} anions inhibit NO_3^- reduction to some extent via competitive adsorption [228]. In the light of this fact, we should consider the cathodic spikes on curves in Fig. 6(b) and (c) as dramatic evidence of the high catalytic activity of type II electrodes.

However, it is known from steady state reduction studies that the rate of the reduction process at all potential values is significantly higher in HClO_4 supporting electrolyte owing to the lower adsorbability of ClO_4^- ions on platinum.

Acknowledgment

Financial supports from the Hungarian Scientific Research Fund, OTKA – TO46987 (G. I.) and OTKA – TO49888 (G. H.) are acknowledged.

References

1. A. J. Arvia, D. Posadas in *Encyclopedia of Electrochemistry of Elements* (Ed.: A. J. Bard), Marcel Dekker, New York, 1975, pp. 212–421, Vol. III.
2. A. J. Arvia, D. Posadas in *Standard Potentials in Aqueous Solution* (Eds.: A. J. Bard, R. Parsons, J. Jordan), Marcel Dekker, New York, 1985, pp. 321–339, Chapter 12I.
3. F. Murate, *Bull. Chem. Soc. Jpn.* **1928**, 3, 57.
4. M. M. Haring, E. G. van de Bosche, *J. Phys. Chem.* **1929**, 33, 161.
5. I. Colombier, *C. R. Acad. Sci. Paris* **1934**, 199, 273.
6. M. A. López-López, *C. R. Acad. Sci. Paris* **1963**, 256, 2594; **1962**, 255, 3170.
7. G. Milazzo, S. Caroli, *Tables of Chemical Thermodynamic Properties*, National Bureau of Standards, US Government Printing Office, Washington, 1982.
8. A. J. de Béthune, N. A. Swendeman Loud, *Standard Aqueous Electrode Potentials and Temperature Coefficients*, Hampel, Skokie, 1964.
9. V. Gaglioti, G. Sartori, P. Silvestroni, *Ric. Sci.* **1947**, 17, 624.

10. B. P. Nikolskii, O. N. Grigorov, M. E. Pozin et al., (Eds.), *Spravochnik Khimika*, Izd. Khimiya, Moscow, Leningrad, 1964, Vol. 3.
11. J. Bjerrum, G. Schwarzenbach, L. G. Sillén, *Stability Constants, Inorganic Ligands*, The Chemical Society, London, 1958, Vol. 2.
12. W. M. Latimer, *Oxidation Potentials*, 2nd ed., Prentice Hall, Englewood Cliffs, 1952.
13. M. Pourbaix, (Ed.), *Atlas of Electrochemical Equilibria in Aqueous Solutions*, Pergamon-CEBELCOR, Brussels, 1966.
14. A. Thiel, H. Gessner, Z. Anorg. Allg. Chem. **1914**, 86, 49.
15. A. Ringbom, *Solubility of Sulfides*, Report to Anal. Sec., IUPAC, 1953.
16. I. A. Cotton, G. Wilkinson, C. A. Murillo et al., *Advanced Inorganic Chemistry*, 6th ed., Wiley, New York, Chichester, Weinheim, Brisbane, Singapore, Toronto, 1999, pp. 835–854, Part 3. 17 G.
17. L. Meites, P. Zuman, (Eds.), *CRC Handbook Series in Inorganic Chemistry*, CRC Press, Boca Raton, 1985, Vol. IV.
18. J. Scherer, B. M. Ocko, O. M. Magnussen, *Electrochim. Acta* **2003**, 48, 1169.
19. P. Marcus, J. M. Grimal, *Corros. Sci.* **1990**, 31, 377.
20. V. Maurice, H. Talah, P. Marcus, *Surf. Sci.* **1993**, 284, 1431.
21. V. Maurice, H. Talah, P. Marcus, *Surf. Sci.* **1994**, 304, 98.
22. P. Marcus, *Electrochim. Acta* **1998**, 43, 109.
23. V. Maurice, L. H. Klein, P. Marcus, *Surf. Interface Anal.* **2002**, 34, 139.
24. A. Machet, A. Galtayries, P. Marcus et al., *Surf. Interface Anal.* **2002**, 34, 197.
25. P. Marcus, E. Protopopoff, *Corros. Sci.* **1997**, 39, 1741.
26. J. Oudar, P. Marcus, *Appl. Surf. Sci.* **1979**, 3, 48.
27. A. Teissier, P. Marcus, J. Oudar, *C. R. Acad. Sci. Ser. II* **1981**, 292, 395.
28. P. Marcus, J. Oudar, I. Olefjord, *Mater. Sci. Eng.* **1980**, 42, 191.
29. S. Bouquet, G. Lorang, J. P. Langeron et al., *J. Microsc. Spectrosc. Electron.* **1982**, 7, 447.
30. S. Zafeiratos, F. E. Paloukis, S. G. Neophytides, *J. Phys. Chem. B* **2004**, 108, 1371.
31. A. Lachenwitzer, S. Morin, O. M. Magnussen et al., *Phys. Chem. Chem. Phys.* **2001**, 3, 3351.
32. O. Lev, F. R. Fan, A. J. Bard, *J. Electrochem. Soc.* **1988**, 135, 783.
33. M. Saitou, A. Makabe, T. Tomoyose, *J. Chem. Phys.* **2000**, 113, 2397.
34. K. Schwabe, *Electrochim. Acta* **1962**, 6, 223.
35. K. Schwabe, W. Schwenke, *Electrochim. Acta* **1964**, 9, 1003.
36. J. O. M. Bockris, D. A. J. Swinkels, *J. Electrochem. Soc.* **1964**, 111, 736.
37. N. A. Balashova, S. A. Lilin, *Elektrokhimiya* **1973**, 9, 637.
38. N. A. Balashova, N. T. Gorokhova, S. A. Lilin, *Elektrokhimiya* **1973**, 9, 666.
39. R. S. Vakhidov, M. N. Bakirov, *Elektrokhimiya* **1975**, 11, 282.
40. P. Fouilloux, M. Reppelin, P. Bussiere, *Int. J. Appl. Radiat. Isot.* **1972**, 23, 567.
41. J. M. Herbelin, N. Barbouth, P. Marcus, *J. Electrochem. Soc.* **1990**, 137, 3410.
42. P. Marcus, J. M. Herbelin, *Corros. Sci.* **1993**, 34, 1123.
43. A. G. Munoz, G. Benitez, M. E. Vela et al., *Langmuir* **2004**, 20, 2361.
44. Q. J. Huang, X. F. Lin, Z. L. Yang et al., *J. Electroanal. Chem.* **2004**, 563, 121.
45. S. Y. Zhao, S. H. Chen, H. Y. Ma et al., *J. Appl. Electrochem.* **2002**, 32, 231.
46. H. Y. Ma, G. Q. Li, S. C. Chen et al., *Corros. Sci.* **2002**, 44, 1177.
47. F. Zucchi, M. Fonsati, G. Trabanelli, *J. Appl. Electrochem.* **1998**, 28, 441.
48. M. Ujvári, G. Láng, G. Horányi, *J. Appl. Electrochem.* **2001**, 31, 1171.
49. M. Ujvári, G. Láng, G. Horányi, *J. Appl. Electrochem.* **2002**, 32, 581.
50. G. Láng, M. Ujvári, G. Horányi, *Corros. Sci.* **2003**, 45, 1.
51. O. Lev, A. Wolffberg, M. Sheintuch et al., *Chem. Eng. Sci.* **1988**, 43, 1339.
52. D. Haim, O. Lev, L. M. Pismen et al., *J. Phys. Chem.* **1992**, 96, 2676.
53. O. Lev, M. Sheintuch, L. M. Risemen et al., *Nature* **1988**, 336, 458.
54. M. T. M. Koper, B. D. Aguda, *Phys. Rev. E* **1996**, 54, 960.
55. E. E. Abd El Aal, W. Zakria, A. Diab et al., *J. Mater. Eng. Perform.* **2003**, 12, 172.
56. X. Cheng, H. Ma, S. Chen et al., *Corros. Sci.* **2000**, 42, 299.
57. M. Itagaki, H. Nakazawa, K. Watanabe et al., *Corros. Sci.* **1997**, 39, 901.
58. V. P. Grigor'ev, V. M. Kravchenko, I. M. Gershanova, *Prot. Met.* **2004**, 40, 214.
59. G. Beck-Nielsen, F. de Fontenay, H. Roulson, *Electrochim. Acta* **1997**, 42, 1847.

60. M. H. Fonticelli, D. Posadas, R. I. Tucceri, *J. Electroanal. Chem.* **2003**, 553, 157.
61. E. Gomez, C. Muller, R. Pollina et al., *J. Electroanal. Chem.* **1992**, 333, 47.
62. E. Gomez, C. Muller, W. G. Proud et al., *J. Appl. Electrochem.* **1992**, 22, 872.
63. E. Gomez, R. Pollina, E. Valles, *J. Electroanal. Chem.* **1995**, 397, 111.
64. C. A. Marozzi, A. C. Chialvo, *Electrochim. Acta* **2000**, 45, 2111.
65. S. I. Berezina, G. S. Vozdvizhenskii, G. P. Dezider'ev, *Dokl. Akad. Nauk SSSR* **1951**, 77, 53.
66. A. G. Pshenichnikov, *J. Res. Inst. Catal., Hokkaido Univ.* **1982**, 30, 137.
67. A. G. Pshenichnikov, L. A. Brkal'tseva, Z. I. Kudryavtseva, *Electrochim. Acta* **2000**, 45, 4143.
68. F. M. Raoult, *C. R. Biol.* **1869**, 69, 826.
69. R. A. Oriani, J. P. Hirth, M. Smialowski, (Eds.), *Hydrogen Degradation of Ferrous Alloys*, Noyes Publications, Norwich, N.Y. 1985.
70. B. Baranowski, Z. Szklarska-Smialowska, M. Smialowski, *Bull. Acad. Pol. Sci., Ser. Sci. Chim. Geol.* **1958**, 6, 179.
71. B. Baranowski, M. Smialowski, *Int. J. Phys. Chem. Solids* **1959**, 12, 206.
72. M. L. Wayman, G. C. Weatherli, *Bull. Alloy Phase Diag.* **1989**, 10, 569.
73. B. Baranowski, Z. Szklarska-Smialowska, *Electrochim. Acta* **1964**, 9, 1497.
74. Z. Szklarska-Smialowska, M. Smialowski, *J. Electrochem. Soc.* **1963**, 110, 444.
75. H. Jarmolowicz, M. Smialowski, *J. Catal.* **1962**, 1, 165.
76. M. Bernardini, N. Comisso, G. Davolio et al., *J. Electroanal. Chem.* **1998**, 442, 125.
77. M. Bernardini, N. Comisso, G. Mengoli et al., *J. Electroanal. Chem.* **1998**, 457, 205.
78. B. Baranowski, *J. Electroanal. Chem.* **1999**, 472, 182.
79. R. Juskašnas, I. Valsiūnas, V. Jasulaitienė et al., *Electrochim. Acta* **2002**, 47, 4239.
80. M. Monev, *Electrochim. Acta* **2001**, 46, 2373.
81. M. Fleischmann, K. Korinek, D. Pletcher, *J. Chem. Soc., Perkin Trans.* **1972**, 2, 1396.
82. P. F. F. Luo, T. Kuwana, D. K. Paul et al., *Anal. Chem.* **1996**, 68, 3330.
83. H. Bode, K. Dehmelt, J. Witte, *Electrochim. Acta* **1966**, 11, 1079.
84. R. S. Schreiber Guzman, J. R. Vilche, A. J. Arvia, *J. Electrochem. Soc.* **1978**, 125, 1578.
85. F. Hahn, B. Bede, M. J. Croissant et al., *Electrochim. Acta* **1986**, 31, 1578.
86. J. L. Weininger, M. W. Breiter, *J. Electrochem. Soc.* **1963**, 110, 484.
87. D. A. Corrigan, R. M. Bendert, *J. Electrochem. Soc.* **1989**, 136, 723.
88. I. G. Casella, M. Gatta, *J. Electrochem. Soc.* **2002**, 149, B465.
89. M. Grden, K. Klimek, A. Czerwinski, *J. Solid State Electrochem.* **2004**, 8, 390.
90. K. Süvegh, T. S. Horányi, A. Vértess, *Electrochim. Acta* **1988**, 33, 1061.
91. M. T. Pham, M. F. Maitz, E. Richter et al., *J. Electroanal. Chem.* **2004**, 572, 185.
92. J. F. Llopis, I. Colom in *Encyclopedia of Electrochemistry of Elements* (Ed.: A. J. Bard), Marcel Dekker, New York, 1976, pp. 259–276, Vol. VI.
93. F. Colom in *Standard Potentials in Aqueous Solution* (Eds.: A. J. Bard, R. Parsons, J. Jordan), Marcel Dekker, New York, 1985, pp. 339–345, Chapter 12IIA.
94. R. M. Izatt, D. Eatough, J. J. Christensen, *J. Chem. Soc. A* **1967**, 1301.
95. H. Kleykamp, *Z. Phys. Chem. (Frankfurt)* **1970**, 71, 142.
96. J. P. Hoare, *J. Electrochem. Soc.* **1964**, 111, 611.
97. V. I. Kravtsov, M. I. Zelinski, *Elektrokhimiya* **1966**, 2, 1138.
98. N. M. Nikolaeva, L. D. Tsvedodub, A. M. Ehrenburg, *Izv. Sib. Otd. Nauk SSSR, Ser. Khim.* **1978**, 44.
99. A. B. Fasman, G. G. Kut'yukov, D. V. Sokolski, *Zh. Neorg. Khim.* **1965**, 10, 1338.
100. R. N. Goldberg, L. H. Hepler, *Chem. Rev.* **1968**, 68, 229.
101. E. Jackson, D. A. Pantony, *J. Appl. Electrochem.* **1971**, 1, 283.
102. A. A. Grinberg, A. S. Shamsiev, *Zh. Obshch. Khim.* **1942**, 12, 55.
103. M. P. Soriaga, Y.-G. Kim, J. E. Soto, *Interfacial chemistry of palladium electrodes in Interfacial Electrochemistry, Theory, Experiment, and Applications* (Ed.: A. Wieckowski), Marcel Dekker, New York, 1999.
104. D. J. Nagel, *Radiat. Phys. Chem.* **1998**, 51, 653.
105. L. A. Kibler, M. Kleinert, R. Randler et al., *Surf. Sci.* **1999**, 443, 19.
106. L. A. Kibler, M. Kleinert, D. M. Kolb, *Surf. Sci.* **2000**, 461, 155.
107. L. A. Kibler, M. Kleinert, V. Lazarescu et al., *Surf. Sci.* **2002**, 498, 175.

108. H. Naohara, S. Ye, K. Uosaki, *J. Electroanal. Chem.* **1999**, 473, 2.
109. M. Takahasi, Y. Hayashi, J. Mizuki et al., *Surf. Sci.* **2000**, 461, 213.
110. M. Baldauf, D. M. Kolb, *J. Phys. Chem.* **1996**, 100, 11375.
111. J. A. Schimpf, J. R. McBride, M. P. Soriaga, *J. Phys. Chem.* **1993**, 97, 10518.
112. J. A. Schimpf, J. B. Abreu, M. P. Soriaga, *Langmuir* **1993**, 9, 3331.
113. W. F. Temesghen, J. B. Abreu, R. J. Barriga et al., *Surf. Sci.* **1997**, 385, 336.
114. K. Itaya, Atomic-scale aspects of anodic dissolution of metals: studies by in situ scanning tunneling microscopy in *Interfacial Electrochemistry, Theory, Experiment, and Applications* (Ed.: A. Wieckowski), Marcel Dekker, New York, 1999.
115. E. A. Lafferty, Y.-G. Kim, M. P. Soriaga, *Electrochim. Acta* **1998**, 44, 1031.
116. G. A. Tsirlina, S. B. Baronov, F. M. Spiridonov et al., *Russ. J. Electrochem.* **2000**, 36, 1179.
117. K. Juodkazis, J. Juodkazyte, B. Sebek et al., *Russ. J. Electrochem.* **2003**, 39, 954.
118. W.-S. Zhang, Z.-F. Zhang, Z.-L. Zhang, *J. Electroanal. Chem.* **2002**, 528, 1.
119. P. Millet, M. Srour, R. Faure et al., *Electrochem. Commun.* **2001**, 3, 478.
120. A. Czerwinski, M. Grden, M. Lukaszewski, *J. Solid State Electrochem.* **2004**, 8, 411.
121. A. Czerwinski, M. Grden, M. Lukaszewski, *Anal. Lett.* **2004**, 37, 967.
122. M. Lukaszewski, M. Grden, A. Czerwinski, *J. Phys. Chem. Solids* **2004**, 65, 523.
123. M. Lukaszewski, A. Czerwinski, *Electrochim. Acta* **2003**, 48, 2435.
124. A. Czerwinski, I. Kiersztyn, M. Grden, *J. Solid State Electrochem.* **2003**, 7, 321.
125. M. Lukaszewski, K. Kusmierczyk, J. Kotoski et al., *J. Solid State Electrochem.* **2003**, 7, 69.
126. M. Grden, K. Kusmierczyk, A. Czerwinski, *J. Solid State Electrochem.* **2002**, 7, 43.
127. M. Grden, A. Piascik, Z. Koczorowski et al., *J. Electroanal. Chem.* **2002**, 532, 35.
128. J. Kleperis, G. Wojcik, A. Czerwinski et al., *J. Solid State Electrochem.* **2001**, 5, 229.
129. M. Y. Rusanova, M. Grden, A. Czerwinski et al., *J. Solid State Electrochem.* **2001**, 5, 212.
130. A. Czerwinski, I. Kiersztyn, M. Grden, *J. Electroanal. Chem.* **2000**, 492, 128.
131. M. Grden, J. Kotoski, A. Czerwinski, *J. Solid State Electrochem.* **2000**, 4, 273.
132. M. Grden, J. Kotoski, A. Czerwinski, *J. Solid State Electrochem.* **1999**, 3, 348.
133. M. Grden, A. Czerwinski, J. Golimowski et al., *J. Electroanal. Chem.* **1999**, 460, 30.
134. A. Czerwinski, I. Kiersztyn, M. Grden et al., *J. Electroanal. Chem.* **1999**, 471, 190.
135. L. H. Dall'Antonia, G. Tremiliosi-Filho, G. Jerkiewicz, *J. Electroanal. Chem.* **2001**, 502, 72.
136. L. D. Burke, J. K. Casey, *J. Electrochem. Soc.* **1993**, 140, 1292.
137. L. D. Burke, J. K. Casey, *J. Appl. Electrochem.* **1993**, 23, 573.
138. L. D. Burke, D. T. Buckley, *J. Electrochem. Soc.* **1996**, 143, 845.
139. L. D. Burke, L. C. Nagle, *J. Electroanal. Chem.* **1999**, 461, 52.
140. L. D. Burke, L. M. Hurley, *J. Solid State Electrochem.* **2003**, 7, 327.
141. J. O'M. Bockris, Z. Minevski, *Int. J. Hydrogen Energy* **2000**, 25, 747.
142. J. F. E. Gootzen, P. G. J. M. Peeters, J. M. B. Dukers et al., *J. Electroanal. Chem.* **1997**, 434, 171.
143. J. F. E. Gootzen, L. Lefferts, J. A. R. van Veen, *Appl. Catal., A-Gen.* **1999**, 188, 127.
144. A. C. A. de Vooy, R. A. van Santen, J. A. R. van Veen, *J. Mol. Catal. A Chem.* **2000**, 154, 203.
145. M. C. Arévalo, J. L. Rodriguez, E. Pastor, *J. Electroanal. Chem.* **1999**, 472, 71.
146. J. L. Rodriguez, R. M. Souto, S. González et al., *Electrochim. Acta* **1998**, 44, 1415.
147. M. C. Arévalo, J. L. Rodriguez, E. Pastor, *J. Electroanal. Chem.* **2001**, 505, 62.
148. R. M. Souto, J. L. Rodriguez, G. Pastor et al., *Electrochim. Acta* **2000**, 45, 1645.
149. E. Pastor, S. Wasmus, T. Iwasita et al., *J. Electroanal. Chem.* **1994**, 371, 167.
150. R. M. Souto, J. L. Rodriguez, L. Fernandez-Merida et al., *J. Electroanal. Chem.* **2000**, 494, 127.
151. G. Inzelt in *Electroanalytical Methods* (Ed.: F. Scholz), Springer, Berlin, Heidelberg, New York 2002, pp. 39–43.
152. D. Grinstrup, *Acta Chem. Scand.* **1972**, 26, 1527.
153. D. Grinstrup, I. Leden, *Acta Chem. Scand.* **1968**, 22, 1163.
154. A. A. Grinberg, V. B. Ptitsyn, V. N. Lavrentiev, *Zh. Fiz. Khim.* **1937**, 10, 661.

155. A. A. Grinberg, M. I. Gelfman, *Dokl. Akad. Nauk SSSR* **1960**, 133, 1081.
156. A. T. Hubbard, F. C. Anson, *Anal. Chem.* **1966**, 38, 58.
157. Y. N. Kukushkin, S. Ch. Dkhara, *Zh. Neorg. Khim.* **1970**, 15, 1585.
158. Y. N. Kukushkin, S. Ch. Dkhara, *Zh. Neorg. Khim.* **1969**, 14, 2816.
159. J. F. Llopis, I. Colom in *Encyclopedia of Electrochemistry of Elements* (Ed.: A. J. Bard), Marcel Dekker, New York, 1976, pp. 169–219, Vol. VI.
160. F. Colom in *Standard Potentials in Aqueous Solution* (Eds.: A. J. Bard, R. Parsons, J. Jordan), Marcel Dekker, New York, 1985, pp. 345–365, Chapter 12 IIB.
161. B. Lippert, (Ed.), *Cisplatin: Chemistry and Biochemistry of a Leading Anticancer Drug*, Wiley-VCH, Weinheim, 1999.
162. B. Rosenberg, L. Van Camp, J. E. Trosko et al., *Nature* **1969**, 222, 385.
163. G. Horányi, E. M. Rizmayer, *J. Electroanal. Chem.* **1987**, 218, 337.
164. L. D. Burke, A. J. Ahern, *J. Solid State Electrochem.* **2001**, 5, 553.
165. A. Hamelin in *Trends in Interfacial Electrochemistry* (Ed.: A. F. Silva), D. Reidel Publishing Company, Dordrecht, 1986, p. 83.
166. A. Hamelin in *Modern Aspects of Electrochemistry* (Eds.: B. E. Conway, R. E. White, J. O. M. Bockris), Plenum Press, New York, 1985, p. 1, Vol. 16.
167. A. Hamelin, *J. Electroanal. Chem.* **1996**, 407, 1.
168. A. Hamelin, A. M. Martins, *J. Electroanal. Chem.* **1996**, 407, 13.
169. A. Hamelin, *J. Electroanal. Chem.* **1995**, 386, 1.
170. J. Clavilier, R. Faure, G. Guinet et al., *J. Electroanal. Chem.* **1980**, 107, 205.
171. F. T. Wagner, R. N. Ross Jr., *J. Electroanal. Chem.* **1983**, 150, 141.
172. K. Al Jaaf-Golze, D. M. Kolb, D. Scherson, *J. Electroanal. Chem.* **1986**, 200, 353.
173. N. Markovic, M. Hanson, G. McDougall et al., *J. Electroanal. Chem.* **1986**, 214, 555.
174. P. W. Faguy, N. Markovic, R. R. Adzic et al., *J. Electroanal. Chem.* **1990**, 289, 245.
175. E. Herrero, J. M. Feliu, A. Wieckowski et al., *Surf. Sci.* **1995**, 325, 131.
176. P. W. Faguy, N. S. Marinkovic, R. R. Adzic, *J. Electroanal. Chem.* **1996**, 407, 209.
177. A. Zolfaghari, G. Jerkiewicz, *J. Electroanal. Chem.* **1997**, 422, 1.
178. T. Fukuda, A. Aramata, *J. Electroanal. Chem.* **1997**, 440, 153.
179. V. Lazarescu, J. Clavilier, *Electrochim. Acta* **1998**, 44, 931.
180. T. Fukuda, A. Aramata, *J. Electroanal. Chem.* **1999**, 467, 112.
181. F. C. Nart, T. Iwasita, M. Weber, *Electrochim. Acta* **1994**, 39, 961.
182. T. Iwasita, A. Rodes, E. Pastor, *J. Electroanal. Chem.* **1995**, 383, 181.
183. E. Pastor, A. Rodes, T. Iwasita, *J. Electroanal. Chem.* **1996**, 404, 61.
184. Y. Shingaya, K. Hirota, H. Ogasawara et al., *J. Electroanal. Chem.* **1996**, 409, 103.
185. Y. Shingaya, M. Ito, *J. Electroanal. Chem.* **1999**, 467, 299.
186. R. Gómez, J. M. Orts, B. Álvarez-Ruiz et al., *J. Phys. Chem. B* **2004**, 108, 228.
187. V. Climent, B. A. Coles, R. G. Compton et al., *J. Electroanal. Chem.* **2004**, 561, 157.
188. J. Mostany, E. Herrero, J. M. Feliu et al., *J. Electroanal. Chem.* **2004**, 558, 19.
189. M. D. Maciá, E. Herrero, J. M. Feliu, *J. Electroanal. Chem.* **2003**, 554–555, 25.
190. R. Gómez, J. M. Feliu, *J. Electroanal. Chem.* **2003**, 554–555, 145.
191. K. Domke, E. Herrero, A. Rodes et al., *J. Electroanal. Chem.* **2003**, 552, 115.
192. R. Albalat, J. Claret, A. Rodes et al., *J. Electroanal. Chem.* **2003**, 550–551, 53.
193. B. Álvarez, A. Rodes, J. M. Pérez et al., *J. Phys. Chem. B* **2003**, 107, 2018.
194. F. J. Vidal-Iglesias, N. García-Aráez, V. Montiel et al., *Electrochem. Commun.* **2003**, 5, 22.
195. R. Gómez, F. J. G. de Dios, J. M. Feliu, *Electrochim. Acta* **2004**, 49, 1195.
196. A. Berná, A. Rodes, J. M. Feliu, *Electrochim. Acta* **2004**, 49, 1257.
197. A. Berná, A. Rodes, J. M. Feliu, *J. Electroanal. Chem.* **2004**, 563, 49.
198. B. Álvarez, J. M. Feliu, J. Clavilier, *Electrochem. Commun.* **2002**, 4, 379.
199. J. M. Orts, E. Louis, L. M. Sander et al., *Electrochim. Acta* **1998**, 44, 1221.
200. J. M. Orts, E. Louis, L. M. Sander et al., *Surf. Sci.* **1998**, 416, 371.
201. R. Gómez, J. M. Orts, J. M. Feliu et al., *J. Electroanal. Chem.* **1997**, 432, 1.
202. J. M. Orts, R. Gómez, J. M. Feliu et al., *Langmuir* **1997**, 13, 3016.

203. G. A. Attard, O. Hazzazi, P. B. Wells et al., *J. Electroanal. Chem.* **2004**, 568, 329.
204. E. Herrero, B. Álvarez, J. M. Feliu et al., *J. Electroanal. Chem.* **2004**, 567, 139.
205. M. D. Baciá, J. M. Campiña, E. Herrero et al., *J. Electroanal. Chem.* **2004**, 564, 141.
206. A. C. Chialvo, W. E. Triaca, A. J. Arvia, *J. Electroanal. Chem.* **1983**, 146, 93.
207. J. C. Canullo, W. E. Triaca, A. J. Arvia, *J. Electroanal. Chem.* **1984**, 175, 337.
208. R. M. Cerviño, W. E. Triaca, A. J. Arvia, *J. Electrochem. Soc.* **1985**, 132, 266.
209. R. M. Cerviño, W. E. Triaca, A. J. Arvia, *J. Electroanal. Chem.* **1985**, 182, 51.
210. A. J. Arvia, J. C. Canullo, E. Custidiano et al., *Electrochim. Acta* **1986**, 31, 1359.
211. W. E. Triaca, T. Kessler, J. C. Canullo et al., *J. Electrochem. Soc.* **1987**, 134, 1165.
212. A. Visitin, J. C. Canullo, W. E. Triaca et al., *J. Electroanal. Chem.* **1988**, 239, 67.
213. A. E. Bolzan, A. M. Castro Luna, A. Visitin et al., *Electrochim. Acta* **1988**, 33, 1743.
214. A. J. Arvia, R. C. Salvarezza, W. E. Triaca, *Electrochim. Acta* **1989**, 34, 1057.
215. A. Visitin, W. E. Triaca, A. J. Arvia, *J. Electroanal. Chem.* **1990**, 284, 465.
216. B. Bittins-Cattaneo, E. Santos, W. Vielstich, *Electrochim. Acta* **1986**, 31, 1495.
217. E. Custidiano, A. C. Chialvo, A. J. Arvia, *J. Electroanal. Chem.* **1985**, 196, 423.
218. R. M. Cerviño, W. E. Triaca, A. J. Arvia, *Electrochim. Acta* **1985**, 30, 1323.
219. M. Sumino, S. Shibata, *Denki Kagaku* **1988**, 56, 286.
220. I. Bakos, G. Horányi, *J. Electroanal. Chem.* **1992**, 332, 147.
221. R. P. Petukhova, I. I. Astakhov, B. I. Podlovchenko, *Elektrokhimiya* **1971**, 7, 1548.
222. Yu. D. Gamburg, R. P. Petukhova, B. I. Podlovchenko et al., *Elektrokhimiya* **1974**, 10, 751.
223. T. D. Gladisheva, B. I. Podlovchenko, *Elektrokhimiya* **1978**, 14, 182.
224. V. S. Bagotzky, L. S. Kanevsky, V. Sh. Palanker, *Electrochim. Acta* **1973**, 18, 473.
225. Y. Takasu, Y. Fujii, K. Yasuda et al., *Electrochim. Acta* **1989**, 34, 453.
226. I. Bakos, G. Horányi, *J. Electroanal. Chem.* **1993**, 347, 383.
227. G. Horányi, E. M. Rizmayer, *J. Electroanal. Chem.* **1982**, 140, 347.
228. G. Horányi, E. M. Rizmayer, *J. Electroanal. Chem.* **1983**, 143, 323.
229. K. Nishimura, K. Machida, M. Enyo, *Electrochim. Acta* **1991**, 36, 877.
230. O. A. Petrii, T. Ya. Safonova, *J. Electroanal. Chem.* **1992**, 331, 897.
231. S. Ye, H. Hattori, H. Kita, *Ber. Bunsen-Ges. Phys. Chem.* **1992**, 96, 1884.
232. S. Ye, H. Kita, *J. Electroanal. Chem.* **1993**, 346, 489.
233. A. S. Homa, E. Yeager, B. D. Cahan, *J. Electroanal. Chem.* **1983**, 150, 181.
234. F. El Omar, R. Durand, *J. Electroanal. Chem.* **1984**, 178, 343.
235. I. Bakos, G. Horányi, *J. Electroanal. Chem.* **1994**, 370, 309.

19

Electrochemistry of Cobalt-containing Species

Michael J. Johnson and Dennis G. Peters
Indiana University, Bloomington, Indiana

19.1	Introduction	531
19.2	Electrochemistry of Cobalt-containing Species with Inorganic Ligands	531
19.2.1	Half-reactions Involving Aquated Cobalt(II) and Cobalt(III)	532
19.2.2	Effect of Complexing Agents on Potentials for the Cobalt(II)–Cobalt(0) and Cobalt(III)–Cobalt(II) Couples	532
19.2.3	Potential of the Cobalt(II)–Cobalt(0) Couple in Molten Salts	533
19.2.4	Existence of Cobalt(I) in Aqueous Cyanide Solutions	533
19.2.5	Electrochemical Determination of Cobalt	534
19.2.6	Electrodeposition of Cobalt	534
19.3	Electrochemistry of Organocobalt Species	535
19.3.1	Direct Oxidations and Reductions	536
19.3.1.1	Dicobalt and Metal-cluster Complexes	536
19.3.1.2	Modified Electrodes	539
19.3.1.3	Schiff-base Complexes	540
19.3.1.4	Cobalt-containing Porphyrins, Corroles, and Porphycenes	540
19.3.1.5	Macrocyclic Tetraamines	541
19.3.2	Catalytic Processes	544
19.3.2.1	Oxygen	544
19.3.2.2	Carbon Dioxide	548
19.3.2.3	Catalytic Interactions of Cobalt-containing Species with Alkyl and Aryl Halides	549
19.3.2.4	Hydrazine	551
	References	552

19.1 Introduction

Two early references provide detailed information about the electrochemistry of cobalt species, particularly those involving inorganic ligands. First, there is a comprehensive review [1] that gives thermodynamic data principally for the cobalt(III)–cobalt(II) and cobalt(II)–cobalt(0) redox couples in a variety of aqueous, nonaqueous, and molten salt media, along with electron-transfer rate constants and mechanistic information for complexes possessing inorganic and organic ligands. Second, there are extensive data tables [2] listing electrochemical characteristics for many cobalt-containing complexes. These two sources cover most of the literature up to approximately 1980. Another briefer compilation of standard potentials and other thermodynamic data for cobalt species can be found in the IUPAC-commissioned volume that appeared in 1985 [3].

Much of the foundational work concerning organocobalt species can be found elsewhere. A comprehensive examination of the literature up to 1994 appears in a pair of reference series [4, 5], with the former covering research up to 1982 and the latter covering work between 1982 and 1994. Each series contains a chapter on

cobalt-containing complexes and clusters, including discussions about the synthesis, characterization, and reactions of several different classes of organometallic complexes, as well as further information in other chapters.

This chapter consists of two main parts: (1) an initial, shorter section that discusses briefly some of the more classic fundamentals of the electrochemical behavior of inorganic cobalt-containing species and (2) a second, longer section that surveys the electrochemistry of cobalt species with organic ligands, including some that mimic biologically important species, as well as the use of electrogenerated complexes of cobalt for catalytic purposes, with emphasis on the most recent findings. On the basis of the necessarily limited size of this chapter, the interested reader seeking more information is encouraged to consult other publications by authors identified in the list of references.

19.2 Electrochemistry of Cobalt-containing Species with Inorganic Ligands

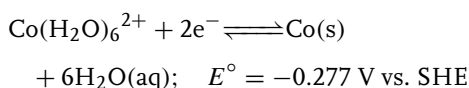
Most of the electrochemistry that deals with cobalt compounds bearing strictly inorganic ligands is of vintage character, so only a brief account of that body

of knowledge is presented here, with pertinent references. On the other hand, more attention is devoted to two topics, namely, (1) the electrochemical determination of cobalt and (2) the electrodeposition of cobalt, with emphasis on more recent publications.

19.2.1

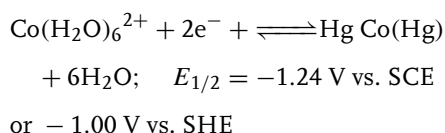
Half-reactions Involving Aquated Cobalt(II) and Cobalt(III)

In an aqueous medium, where water is the only significant ligand, the half-reaction and standard potential for the cobalt(II)–cobalt(0) couple can be written as



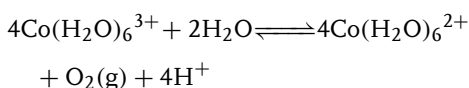
If one considers a strongly acidic solution ($\text{pH} = 0$), the preceding standard potential indicates that elemental cobalt should be thermodynamically capable of reducing hydrogen ion to form $\text{Co}(\text{H}_2\text{O})_6^{2+}$ and H_2 . However, this process is actually slow at room temperature, so cobalt metal is not an effective reducing agent.

Many polarographic studies of the reduction of cobalt(II) to form an amalgam at a dropping mercury electrode have been reported, but most of the work has focused on systems involving complexes with ligands other than water [1, 2]. In one of the few investigations of the behavior of $\text{Co}(\text{H}_2\text{O})_6^{2+}$ (in aqueous 0.1 M potassium nitrate) [3], the following information was deduced:

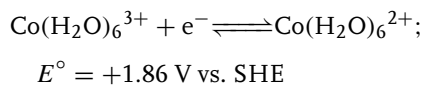


However, in the presence of 0.006% gelatin or 0.005% Triton X-100 as a maximum suppressor, the half-wave potential was -1.25 V vs. SCE (or -1.01 V vs. SHE) and -1.48 V vs. SCE (or -1.24 V vs. SHE), respectively [6]. Furthermore, this process does not exhibit the normal electrochemical characteristics of a reversible reaction.

Cobalt(III) is a potent oxidant in an aqueous solution and, in the absence of a complexing agent that can stabilize cobalt(III), it is rapidly reduced to cobalt(II) with the concomitant oxidation of water to dioxygen:



In the past, there has been controversy [1] regarding both the true identity of the cobalt(III) species present in an aqueous medium and the standard potential for its one-electron reduction to cobalt(II). However, according to Warnqvist [7], as well as Davies and Warnqvist [8], there is good reason to conclude that $\text{Co}(\text{H}_2\text{O})_6^{3+}$ is the predominant species in a 3 M perchloric acid solution and that the cobalt(III)–cobalt(II) couple in this medium can be represented as follows:

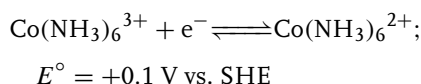


19.2.2

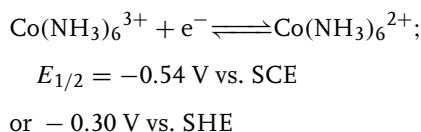
Effect of Complexing Agents on Potentials for the Cobalt(II)–Cobalt(0) and Cobalt(III)–Cobalt(II) Couples

When a ligand, other than water, which can form complexes with cobalt(III) and cobalt(II) is present, the standard potentials for the cobalt(II)–cobalt(0) and cobalt(III)–cobalt(II) couples differ from

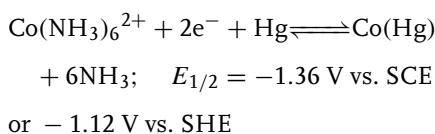
the values given earlier, depending on the relative stabilities of the particular complex ions. Rock [9] has offered some arguments, based on ligand-field theory, to account for the observed shifts in standard potentials for the cobalt(III)–cobalt(II) couple in the presence of several different ligands. In an aqueous ammonia solution, cobalt(III) and cobalt(II) are both complexed by NH_3 ligands, but the formation constant for $\text{Co}(\text{NH}_3)_6^{3+}$ ($\beta_6 = 1.45 \times 10^{35}$) is much larger than that for $\text{Co}(\text{NH}_3)_6^{2+}$ ($\beta_6 = 2.45 \times 10^4$), so the standard potential for the cobalt(III)–cobalt(II) couple is much less positive than the value quoted earlier for the system involving the hexaaqua cations:



Thus, the $\text{Co}(\text{NH}_3)_6^{3+}$ complex is quite stable in the presence of excess aqueous ammonia and, indeed, $\text{Co}(\text{NH}_3)_6^{2+}$ undergoes spontaneous and rapid air oxidation to $\text{Co}(\text{NH}_3)_6^{3+}$. A polarogram for the reduction of $\text{Co}(\text{NH}_3)_6^{3+}$ in an aqueous buffer consisting of 2.5 M ammonia and 0.1 M ammonium chloride exhibits two waves, the first corresponding to a one-electron reduction.



followed, at a more negative potential, by a two-electron process:



Notice that, owing to the higher stability of $\text{Co}(\text{NH}_3)_6^{2+}$ in comparison to

$\text{Co}(\text{H}_2\text{O})_6^{2+}$, the polarographic half-wave potential for reduction of $\text{Co}(\text{NH}_3)_6^{2+}$ (-1.36 V vs. SCE) is more negative than the half-wave potential for the reduction of $\text{Co}(\text{H}_2\text{O})_6^{2+}$ (-1.24 V vs. SCE).

19.2.3

Potential of the Cobalt(II)–Cobalt(0) Couple in Molten Salts

Several investigations have been made of the reduction of cobalt(II) to cobalt(0) in molten salt media. For a eutectic melt of LiCl – KCl at 450°C [10], a 1:1 NaCl – KCl melt at 450°C [11], and a MgCl_2 – NaCl – KCl (50:30:20 mol%) mixture at 475°C [12], the apparent standard potentials for the cobalt(II)–cobalt(0) couple have been deduced to be -1.207 V , -1.277 V , and -1.046 V , respectively, each with respect to a chlorine–chloride ion reference electrode.

19.2.4

Existence of Cobalt(I) in Aqueous Cyanide Solutions

In a classic study, Hume and Kolthoff [13] obtained polarographic evidence that, in a 1 M aqueous solution of potassium cyanide, $\text{Co}(\text{H}_2\text{O})(\text{CN})_5^{3-}$ is irreversibly reduced at a dropping mercury electrode to a cobalt(I) species, the composition of which was not elucidated. Furthermore, the cobalt(I) complex was reported to undergo neither oxidation nor reduction. In addition, the cobalt(III) complex, $\text{Co}(\text{H}_2\text{O})(\text{CN})_5^{2-}$, was seen to be reducible at the dropping mercury electrode, whereas $\text{Co}(\text{CN})_6^{3-}$ is not electroactive. In earlier work [14], cobalt(II) cyanide complexes were reduced electrolytically to cobalt(I) cyanide species.

19.2.5

Electrochemical Determination of Cobalt

Two polarographic methods have been developed for the determination of cobalt(II) at concentrations ranging from approximately 1 to 80 mM in an aqueous sample. For the first method [15], which is suitable for samples containing large amounts of nickel(II), the cobalt(II) is oxidized to $\text{Co}(\text{NH}_3)_6^{3+}$ in an ammoniacal medium with the aid of sodium perborate, after which the cobalt(III) species is determined. A second procedure [16] entails the use of lead dioxide in an acetic acid–acetate buffer containing oxalate to convert cobalt(II) to the $\text{Co}(\text{C}_2\text{O}_4)_3^{3-}$ ion, which can be subjected to polarographic reduction. This latter approach is well suited to the determination of cobalt in the presence of copper(II), iron(III), nickel(II), tin(IV), and zinc(II), whereas the chief interferences are cerium, chromium, manganese, and vanadium.

Clement and Paris [17] have devised a pair of methods for the determination of cobalt in steels, especially materials encountered in the nuclear industry. In the first technique, suitable for the analysis of solutions containing 8 to 160 mM cobalt(II), iron(III) is used to oxidize cobalt(II) in a picolinic acid medium, after which the resulting iron(II) is titrated potentiometrically with a standard solution of cerium(IV). An alternative procedure, for concentrations of cobalt(II) below 8 mM, involves a constant-current coulometric titration with electrogenerated cerium(IV) to measure the iron(II) that arises from the original reaction between cobalt(II) and iron(III).

Preliminary results have been published [18] that describe the voltammetric determination of cobalt(II) in molten

heavy-metal fluoride glass in a matrix consisting of a $\text{ZrF}_4\text{--BaF}_2\text{--LaF}_3\text{--AlF}_3\text{--NaF}$ melt at 500 °C. Sharma and coworkers have developed a method, based on the use of differential pulse polarography and conventional polarography, for the determination of cobalt(II) in natural waters containing nickel [19] and in industrial wastewater containing cadmium, chromium, and lead [20]. An adsorptive stripping voltammetric method for the determination of cobalt(II) at the 10^{-7} to 10^{-5} M level has been explored [21], although the full analytical merit of the method has not been evaluated; the procedure involves the use of a mercury cathode in a borate buffer (pH = 9.3) containing 10^{-4} M dimethylglyoxime as the accumulating reagent.

Although the preceding methods pertain mainly to aqueous solutions initially containing cobalt(II), the analysis of organocobalt compounds poses some additional problems. In particular, if one is interested in determining the cobalt content of an organometallic species, it might be necessary to carry out a preliminary wet- or dry-ashing procedure to prepare an aqueous sample for subsequent electrochemical analysis.

19.2.6

Electrodeposition of Cobalt

For the period from the beginning of 1975 to the middle of 2004, more than 750 citations pertaining either directly or peripherally to the electrodeposition of cobalt were retrieved from a literature search by means of SciFinder Scholar, but the overwhelming majority of those references were to works involving cobalt-containing alloys. Consequently, in this summary, mention is restricted to articles concerning just the deposition of

pure cobalt. Other topics such as the electrowinning, electrorefining, and electropolishing of cobalt have been treated in an earlier review [1].

A method for the constant-current deposition of cobalt onto a brass cathode in an acidic solution ($\text{pH} = 1$) containing cobalt(II) sulfate and vanadium pentoxide has been published [22]. Franklin and Aktan [23] discussed the effect of adsorbable tetra-*n*-butylammonium cations on the electrodeposition of cobalt onto a platinum cathode in a medium consisting of cobalt(II) nitrate and sodium chloride. Nucleation and crystal growth of cobalt electrodeposited from sulfate baths were investigated by means of potentiostatic and potentiodynamic techniques [24], and a comparable study of the deposition of cobalt onto polycrystalline gold was performed [25]. In addition, the effect of electrolysis conditions on the crystal orientation and morphology of cobalt deposited from sulfate media has been probed [26]. Magnetic properties of cobalt layers, ranging from 25 to 100 nm in thickness and electrodeposited onto polycrystalline copper, have been studied [27]. Using the technique of X-ray diffraction, Cohen-Hyams and coworkers [28] found that cobalt deposited onto copper films covering silicon wafers in borate-citrate media of pH 7 can achieve either a face-centered cubic or hexagonal close-packed structure, depending on the potential employed. Electrodeposition of cobalt onto glassy carbon in a borate buffer of pH 5 is enhanced when ultrasound is employed [29]. Other reports have dealt with the effects of added thiourea and saccharin on the surface roughness of cobalt coatings [30]; on the relationship between magnetic and morphological properties of electrodeposited cobalt on vitreous carbon and copper substrates [31]; and on the use

of gluconate baths for the deposition of cobalt on steel [32].

A series of papers by Tseung and coworkers [33–37] has focused on the deposition of cobalt onto nickel and titanium electrodes; the last of these references deals with the mechanism of reduction of cobalt(II) to elemental cobalt in a dimethylformamide medium. Electrodeposition of cobalt onto a copper cathode has been accomplished in a room-temperature chloroaluminate molten salt [38]. Another example of the deposition of cobalt from a molten salt is found in work by Chen and Sun [39], who reduced cobalt(II) onto nickel, tungsten, and copper cathodes from a mixture of zinc(II) chloride and 1-ethyl-3-methylimidazolium chloride at 80 °C. For the preparation of radioactive sources, cobalt-60 (without any inactive cobalt carrier) has been electrodeposited onto stainless-steel planchets [40]. Nanostructured cobalt films have been electrodeposited from lyotropic liquid crystalline media onto gold layers covering glass microscope slides [41], and the magnetic anisotropy and domain structure of electrodeposited cylindrical cobalt nanowires have been examined [42]. Using a phosphorous acid medium, Li [43] electrodeposited hexagonal cobalt particles into the pores of anodically formed films of aluminum oxide. Fabrication of two different cobalt nanostructures – one a hollow nanotube and the other a nanowire composed of nanowhiskers – has been accomplished via electrodeposition into a pore-wall modified alumina membrane [44].

19.3

Electrochemistry of Organocobalt Species

Organocobalt species are of great interest to researchers, the most obvious

reason being for their catalytic abilities, which will be covered in a later section. Further topics include the characterization of metal-cluster stability, metal-center to metal-center interactions in multinuclear metal-containing complexes, improved electrodes and sensors, advancements in conducting polymer films, and the development and characterization of mimics for naturally occurring biomolecules, especially vitamin B₁₂. Coverage presented in the following will be divided into two sections, one dealing with the direct electrochemical reactions of organocobalt species and another concerning the catalytic properties of cobalt-containing organometallic complexes.

19.3.1

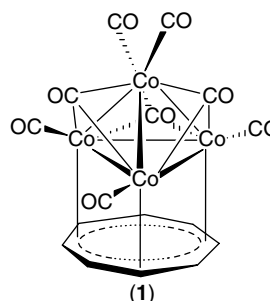
Direct Oxidations and Reductions

In this section, we present material dealing with the direct oxidation and reduction of a variety of organocobalt species, including complexes with more than one cobalt center, electrodes functionalized with cobalt complexes, cobalt-containing Schiff-base complexes, cobalt porphyrins and corroles, and macrocyclic tetraamines.

19.3.1.1 Dicobalt and Metal-cluster Complexes

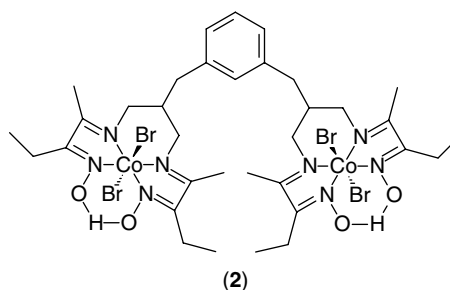
A great deal of emphasis has been placed on the study of transition-metal complexes containing two or more metal centers. These complexes are useful as model systems for the study of intermolecular interactions between metal centers as well as the examination of electron-transfer reactions between donor and acceptor species.

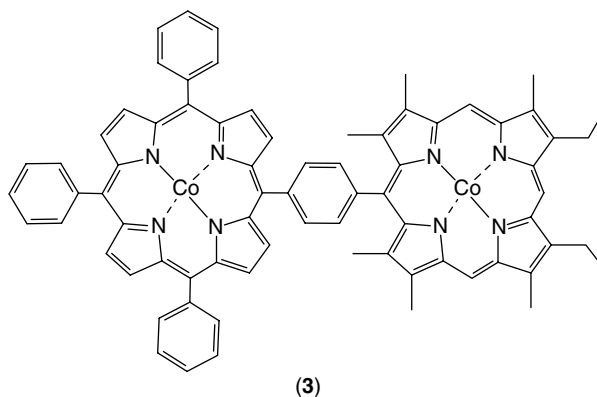
Fiedler and coworkers [45] undertook the examination of a family of tetracobalt carbonyl clusters, each with a facial cyclooctatetraene ligand (1).



Polarographic and cyclic voltammetric studies showed the formation of dianions, with one of the dianionic complexes exhibiting further chemical reactivity. Bulk electrolysis and infrared spectroelectrochemistry were used to confirm the decomposition of the dianionic tetranuclear clusters to stable tricobalt anions.

Experiments involving dicobalt species have focused mainly on the interaction or communication between the two metal centers. Variations in the connecting or bridging ligands can cause distinct differences in the overall oxidation and reduction potentials for the two metal centers. Metal centers separated by rigid alkyne moieties [46] differ in the degree of interaction between the cobalt centers, depending on the number of alkyne units used in the bridge, whereas Costa-type complexes with a *m*-xylene spacer [47], (2), and mixed ligand diporphyrins [48], (3), undergo completely discrete metal-center reactions. Complexes of the latter





types [47, 48] are useful as catalysts for selective dimerization where two radicals can be formed and held in close proximity.

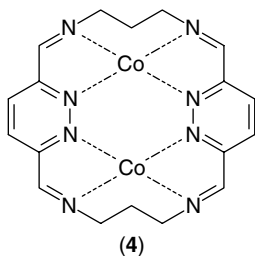
Dicobalt species have also been shown to result in cobalt's possessing characteristically unstable oxidation states. A binary cofacial dicobalt porphyrin species has been shown to undergo a pair of one-electron oxidation steps as well as a pair of one-electron reduction steps [49]; the two cobalt centers behave essentially independently of one another, so that mixed-valence complexes can be generated. Brooker and coworkers [50] investigated a pyridazine Schiff-base macrocycle with two cobalt centers (4), each of which could undergo a separate one-electron oxidation or reduction to produce a species capable of existing in five different combinations of redox states. Most interesting about this complex is the formation of cobalt

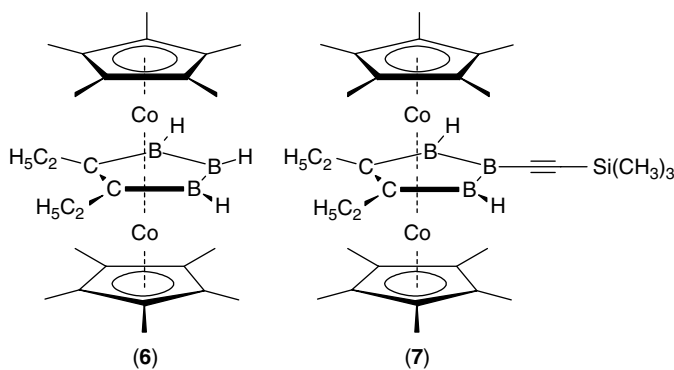
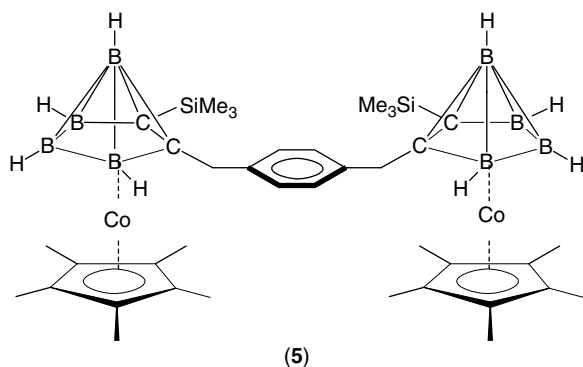
in the +1 oxidation state. In addition, Dimitrou et al. [51] synthesized tetracobalt complexes that are oxidizable to yield one of the metal centers in the +4 oxidation state.

Reduction of a dicobaltacarborane sandwich complex (5) is a two-electron process, and the metal centers are independent, noncommunicating sites [52]. In related work [53], it was observed that a cyclic voltammogram for the reduction of (6) at a platinum cathode in either dimethoxyethane or dimethylformamide containing tetra-*n*-butylammonium hexafluorophosphate consists of three well-resolved stages of reduction, each corresponding to a one-electron process at each cobalt center.

In a more recent investigation, Yao and coworkers [54] studied the electrochemical behavior of several alkynyl-substituted cobaltacarboranes, including (7).

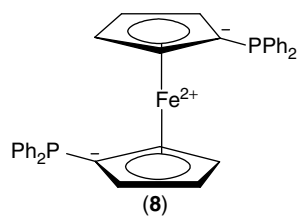
Ferrocenylphosphine ligands are receiving a great deal of attention due to their applications both in complexes for homogeneous catalysis and as redox-active moieties. Their usefulness stems from their ability to exhibit a variety of bonding modes, ranging from their chelating a single metal center to their bridging two or more metal



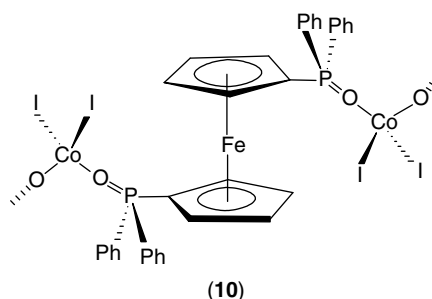
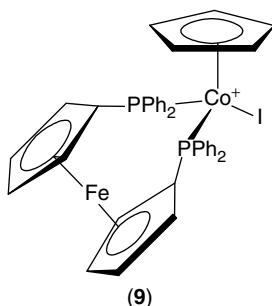


centers. Complexes incorporating the 1,1'-bis(diphenylphosphino)ferrocene ligand (abbreviated hereafter as dppf), (8), are expected to demonstrate redox chemistry characteristic of both the iron center of the ferrocene moiety and the other transition-metal center present in the molecule. Therefore, studies of the extent with which these two metal centers interact, and the dependence of this interaction on the associated ligands, can be used to tune the redox potentials of both the metal center and the ferrocene–ferricenium couple.

Aviles et al. [55] conducted a study of the $[\text{CpCoI}(\text{dppf})]\text{I}$ monomer (9) as well as the $[\text{CoI}_2(\text{dppfO}_2)]$ complex (10). Results for the former complex showed the distinct reduction of the iron center, followed



by rapid loss of an iodine atom and reduction of the cobalt center to the +1 oxidation state; no results were reported for the latter complex. Other investigations by Gerbase et al. [56] and by McAdam et al. [57–59] demonstrated similar metal-centered redox chemistry; however, the focus of these works was placed mainly on the iron center. In addition, electrochemical studies of monomeric and

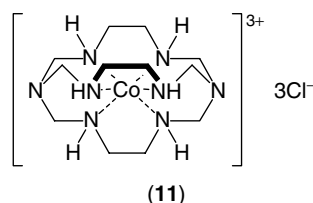


linked metal carbonyl clusters with a *closo*- Si_2Co_4 pseudo-octahedral core [60] as well as some cobalt-containing metal-cluster cations [61] have been reported.

19.3.1.2 Modified Electrodes

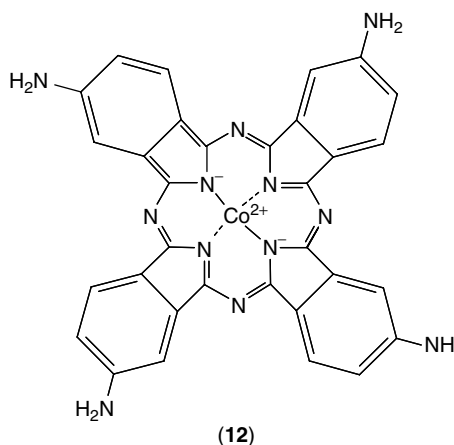
Modifying an electrode by adsorption or bonding of molecules onto its surface, or through the use of polymer coatings or other thick phases bearing redox sites, is used to catalyze otherwise slow electrochemical reactions. Depositing polymer films on electrodes has also led to improvements in electrode stability as well as to the development of chemical sensors and biosensors, to applications involving directing and controlling mediated charge-transfer processes, and to the design of potential-dependent polymer films for color displays. Much of the work in this field has appeared in the older literature and has focused on the incorporation of organocobalt catalysts into polymer films, or the development of catalytically active films, for the detection of oxygen. Recent studies have involved (1) the development of new polymer films for incorporating organocobalt species and (2) the effects of pH on the redox chemistry of the cobalt couples.

Dewald and Chen [62] studied the effects that pH has on the cobalt(III)–cobalt(II) couple of $\text{Co}(\text{sep})$ [sep = sepulchrate



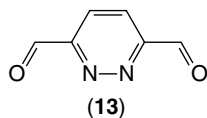
trichloride], (11), immobilized in a Nafion film on a graphite electrode; prior to this publication, only one other report had been made on the incorporation of a cage complex into a Nafion film.

Brown and coworkers [63] examined the behavior of a cobalt-containing tetraaminophthalocyanine-based polymer (12) and the effects of pH on the cobalt(III)–cobalt(II) redox couple.



19.3.1.3 Schiff-base Complexes

Although there has been a great deal of research concerning how platinum(II) complexes bind to biological molecules and the likely mechanism of antitumor activity of these platinum-containing species, far less attention has been paid to the properties of other metal complexes in this arena. Recent attention has fallen on cobalt(II)–Schiff base complexes, as several have been discovered to have promise as antiviral agents. A review of recent work has appeared elsewhere [64], so the topic will not be covered here; however, in addition to focusing on recent developments, emphasis is placed on the introduction of the new head unit, 3,6-diformylpyridazine (13), into Schiff-base macrocyclic electrochemistry.



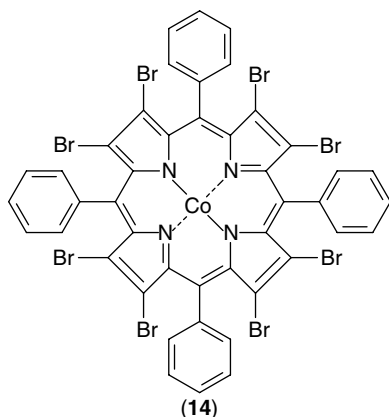
19.3.1.4 Cobalt-containing Porphyrins, Corroles, and Porphycenes

There is tremendous interest in the electrochemical reactivity of iron- and cobalt-containing porphyrins toward small molecules, because such knowledge provides a better understanding of the reactions of naturally occurring hemoproteins. Studies of the binding of NO by metalloporphyrins have aided our understanding of how NO interacts with heme-containing molecules, and the addition of electron-withdrawing substituents to the porphyrin ring structure has resulted in a class of highly efficient oxygen-transfer catalysts that show a strong resistance to chemical degradation. Although not studied as much as their iron-containing counterparts, cobalt

porphyrins have begun to receive more attention.

Research by Kadish, Han, and Endo [65] has helped to develop some preliminary aspects of the interactions of cobalt porphyrins with organic molecules. These workers reported that only ring-centered reductions can be observed in organic solvents for cobalt(II) porphyrins σ -bonded to organic moieties. Furthermore, organic molecules linked to the cobalt center can undergo migration to one of the nitrogen atoms of the porphyrin ring when the complex is oxidized. Also, reduction of the system leads to formation of an anion, either with or without the loss of an alkyl group, and the process depends on the identities of the solvent and the alkyl group, as well as on the timescale of the experiment.

In subsequent research, Kadish and coworkers [66] demonstrated that a tetraphenylphosphine (TPP) complex could be modified to tune the potential for the cobalt(III)–cobalt(II) and cobalt(II)–cobalt(I) redox couples by substitution of bromine atoms on the ring structure. As prior work had entailed the synthesis and characterization of TPP with mono-, di-, tri-, and tetrabromo substitutions, the reduction and oxidation of complexes bearing six to eight bromo moieties was investigated in the later research [66]. In addition, the possibility of electrogenerating $[(\text{TPPBr}_x)\text{Co}(\text{I})]^-$ with $x = 1-7$ from the octabrominated compound (14) through the use of controlled-potential electrolysis was examined. As halogenated porphyrins show an exceptionally high catalytic efficiency for oxidizing organic substances, this synthesis provides a simpler approach to tuning the potential at which the catalysis occurs.



Two publications by Kadish et al. considered the reactivity of NO with cobalt porphyrin [67] and with the tetrabromo derivative [68]. Both sets of experiments showed a relatively strong stabilization of cobalt(II) upon binding with a molecule of NO. Strong binding of pyridine by cobalt(III) was also demonstrated in the latter article. Additional papers from the research group of Kadish pertaining to the electrochemistry of cobalt-containing species involve ligands such as octachloroporphyrin [69], β -brominated-pyrrole tetraphenylporphyrin [70], symmetrical and unsymmetrical porphyrins [71], diaza-18-crown-6 porphyrin [72], and an anthracenyl-bridged porphyrin-corrole bismacrocycle [73].

L'Her and coworkers [74] investigated the electrochemical behavior of several face-to-face dicobaltaporphyrins linked together via anthracenyl, biphenylenyl, and other bridges. These authors concluded that the first and third oxidation steps are ligand-based, whereas the second stage of oxidation is the one-electron conversion of cobalt(II) to cobalt(III).

Recent work by Nagata et al. [75] has demonstrated the photoactivation of a cobalt porphyrin complex. Covalently

linked porphyrin–acceptor systems (15) are being actively studied as models for photoinduced electron transfer in photosynthesis. Photoinduced electron transfer in this system leads to a “reactive” cobalt(II) state, but a fast intermolecular back-electron transfer readily forms the cobalt(III) species again and makes the process nonproductive.

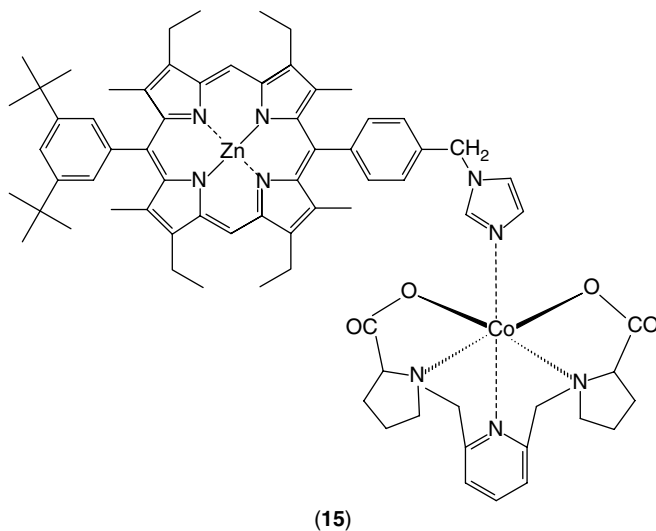
In 1992, Kadish and coworkers [76] reported results for the first comprehensive study of the electrochemical oxidation and reduction of some metallocorroles, including (OMC)Co(PPh₃) (16), where OMC denotes the trianion of 2,3,7,8,12,13,17,18-octamethylcorrole.

Subsequent investigations were undertaken of cobalt corroles with modified structures [77] and with cobalt in higher oxidation states [78]. In addition, cobalt-containing corrole dimers were studied [79], cobalt biscalcoroles were investigated [80, 81], the influence of various alkyl and aryl substituents on the electrochemical behavior of cobalt corroles was probed [82], and the effects of solvents on the electrochemistry of these compounds was examined [83].

Finally, some aspects of the electrochemistry of cobalt(II) porphycenes (17) have been discussed in two relatively recent articles [84, 85].

19.3.1.5 Macrocyclic Tetraamines

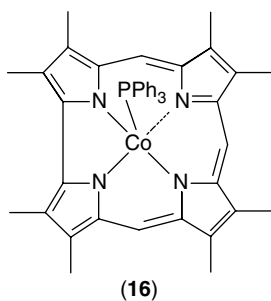
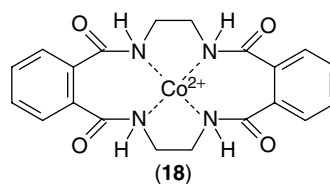
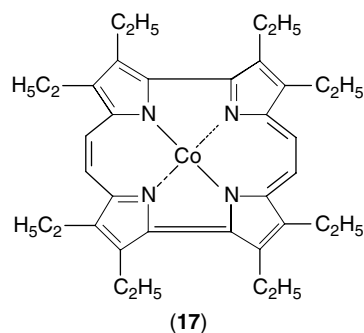
This class of compounds, which includes 1,4,8,11-tetraazacyclotetradecane (otherwise known as *cyclam*), consists of a cyclic macrostructure containing four central nitrogen atoms. These nitrogens form a complex with a transition metal, holding it in the center of a square-planar configuration. Often, the cavity size formed by the macrocycle will stabilize one oxidation state of the transition metal over others due to the size of the metal center



and the available room for interactions between the metal and the central nitrogen atoms. Such interactions have been known to stabilize metal ions in unusually high oxidation states.

Siddiqi and Mathew [86] successfully synthesized and characterized dibenzo[c,k][1,6,9,14]tetraazacyclohexadecane[2,5,10,13]tetraone with a cobalt(II) center (18).

Within the chosen range of potentials, two well-resolved one-electron reductions and a single two-electron oxidation were observed, each of which is irreversible. Formation of cobalt(I) was responsible for the first step of reduction, with the second



reduction affording cobalt(0); the oxidation led to the regeneration of cobalt(II). Simon et al. [87] synthesized cobalt(II) cyclam one nitrogen atom of which was linked to a pyrrole group via a pentamethylene group; electropolymerization of this species on glassy carbon afforded a film that proved

to be active for the electrocatalytic reduction of oxygen. In another study, Choi [88] demonstrated the stabilization of cobalt(I) in a di-*N*-carboxymethylated tetraaza macrocycle (19), with cobalt(I) being irreversibly produced via reduction of the cobalt(II) precursor.

Polar organic compounds containing sulfur and nitrogen atoms, as well as their complexes with transition metals, are known to be good corrosion inhibitors, among other possible applications. Jovanović et al. [89] recently studied the electrochemical behavior of eight cobalt(III) cyclams, each bearing an additional bidentate dithiocarbamate ligand, the species with morpholine dithiocarbamate being an example (20).

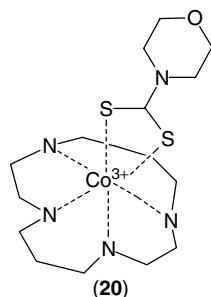
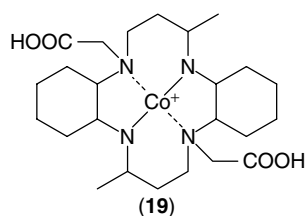
Preliminary results showed that these types of compounds are possible inhibitors of the corrosion of iron in acids. This anti-corrosion behavior is believed to arise from the fact that a dithiocarbamate-substituted cobalt cyclam can affect the hydrogen evolution reaction within the system. A

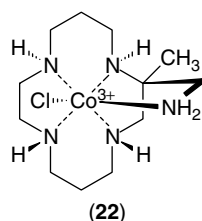
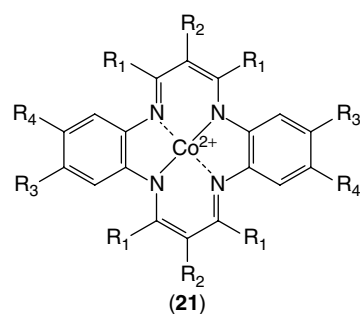
subsequent electrochemical investigation of cobalt-containing species involving aza-macrocycles and β -diketonato ligands was carried out by Babic–Samardzija and coworkers [90].

Studies of tetraaza[14]annulene complexes have also been conducted to improve the action of catalysts and for the development of new materials, such as conducting polymer films and electrochromic polymers. Intrinsic characteristics of these compounds can be altered if ring size, substituents, degree of unsaturation, conjugation of the rings, or the overall charge of the ligand is varied. Lelj et al. [91] and Lukes and coworkers [92] demonstrated the effects of substitution on the behavior of some tetraazaannulenes. In the former study [91], the peak potentials associated with two ligand-based oxidations were determined with respect to the substitution of methyl, ethyl, and phenyl moieties onto the ring structure. Despite the change in the anodic peak potentials for ligands with various substituents, the difference in the peak potentials for the two stages of oxidation was always approximately 0.43 V. In addition, a stabilization of cobalt(III) was observed, which was greatest for the phenyl-substituted compound and least for the ethyl-substituted complex. For the latter study [92], the redox potential for the cobalt(III)–cobalt(II) couple was tuned by variation of the extent of methyl substitution on a dibenzotetraaza[14]annule (21).

In a recent publication by Miry and coworkers [93], the cobalt(II) complex of dibenzotetraaza[14]annulene was anodically polymerized from a benzonitrile solution onto carbon and platinum electrodes.

Complexes of metals with tetraaza-macrocycles possessing pendant arms are currently being considered as models for biologically relevant systems. Such species generally possess a metal ion bound to





a centrally located quartet of nitrogen atoms in a square-planar arrangement with one or two associated monodentate ligands, making the biological system specific for a particular function. In an earlier study [94], and again in a more recent paper [95], the extent of stabilization of the cobalt center was observed for a variety of modified cobalt(III) tetraazamacrocyclic complexes possessing pendant-arm substituents; the pendant arm consisted of an alkyl chain with a terminal amine group occupying one of the axial coordination sites of cobalt (22). Quite possibly, the stability of these compounds results from the octahedral coordination about the central cobalt ion. Both investigations revealed the extra stability of the electrogenerated cobalt(II) center (in comparison with ordinary cobalt(II) cyclam), and pH was found to exert a strong influence on the redox processes due to protonation of the pendant-arm amines.

One final point of interest was reported by Simon and coworkers [96].

They presented the first synthesis of cobalt(III) cyclam in the absence of oxygen. Generally, for such a procedure, molecular oxygen is used to convert cobalt(II) to cobalt(III). However, because there are systems for which oxygen is undesirable, preparation of cobalt(III) cyclam from a refluxing mixture of tri(acetylacetonato)cobalt(III) and cyclam is a significant accomplishment.

19.3.2

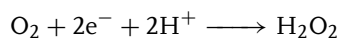
Catalytic Processes

In this section, we discuss processes in which cobalt-containing catalysts are employed for a variety of applications such as the reductions of molecular oxygen, carbon dioxide, and halogenated organic compounds as well as the oxidation of hydrazine.

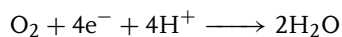
19.3.2.1 Oxygen

Without doubt, the area of greatest interest in the realm of cobalt chemistry is catalytic interactions of cobalt complexes with molecular oxygen. Much of this effort stems from the goal to improve the efficiency of fuel-cell electrodes, although the characterization of organocobalt species as models for biological molecules is also of significance. Platinum is the primary material used for the air electrode of fuel cells; however, the desire is to replace expensive platinum with highly potent materials that are less costly to synthesize and manufacture.

Main reactions involving the catalytic reduction of dioxygen fall into one of two categories. Molecular oxygen undergoes either a two-electron reduction (generally in the presence of individual catalyst molecules).



or a four-electron reduction (requiring two catalyst molecules to be in close proximity):

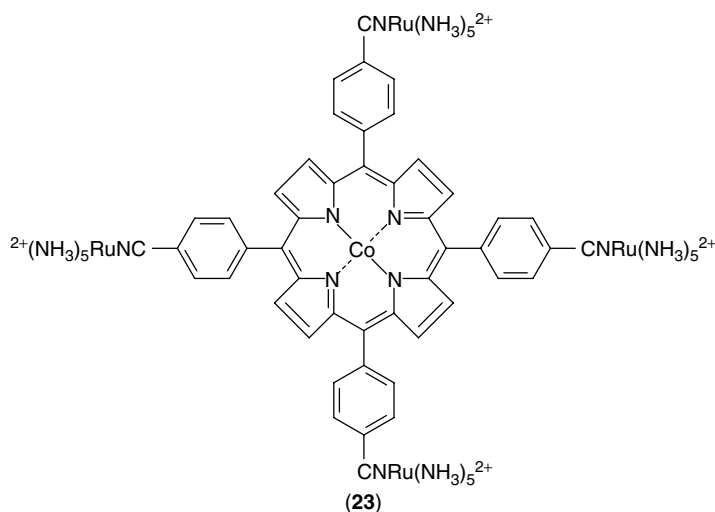


In the first reaction, the two-electron reduction of molecular oxygen is followed by protonation of the resulting anionic species to yield hydrogen peroxide. On the other hand, the second reaction requires cleavage of the dioxygen bond, followed ultimately by protonation of hydroxide ions to afford water; this process has not been observed unless each of the oxygen atoms is able to bind to a unique metal center.

Cobalt porphyrins have been some of the most studied catalysts for oxygen reduction, due in part to their strong interaction with molecular oxygen and the ease with which they catalyze the reduction at low potentials. Anson and coworkers [97] performed a study of the simplest of cobalt porphyrins, cobalt porphine, in the hope of gaining a baseline for the observed reactions of other porphyrins. Instead, they observed a very different process from most other monomeric cobalt porphyrins.

Cobalt porphine promotes the reduction of O_2 in two steps, both of which occur at unusually positive potentials; the first step results in the formation of water rather than hydrogen peroxide.

Further work by Anson's group sought to find the effects that would cause the four-electron reaction to occur as the primary process. Studies with ruthenated complexes [[98], and references therein], (23), demonstrated that π back-bonding interactions are more important than intramolecular electron transfer in causing cobalt porphyrins to promote the four-electron process over the two-electron reaction. Ruthenated complexes result in the formation of water as the product of the primary catalytic process. Attempts to simulate this behavior without the use of transition-metal substituents (e.g. ruthenated moieties) to enhance the transfer of electron density from the meso position to the porphyrin ring [99] met with limited success. Also, the use of *p*-hydroxy substituents produced small positive shifts in the potential at which catalysis occurs.



Only two of the substituted porphyrins caused the desired four-electron reduction, and the process took place in two distinct steps, first to produce hydrogen peroxide and then to form water. However, the use of ruthenated complexes led to the direct four-electron reduction of dioxygen.

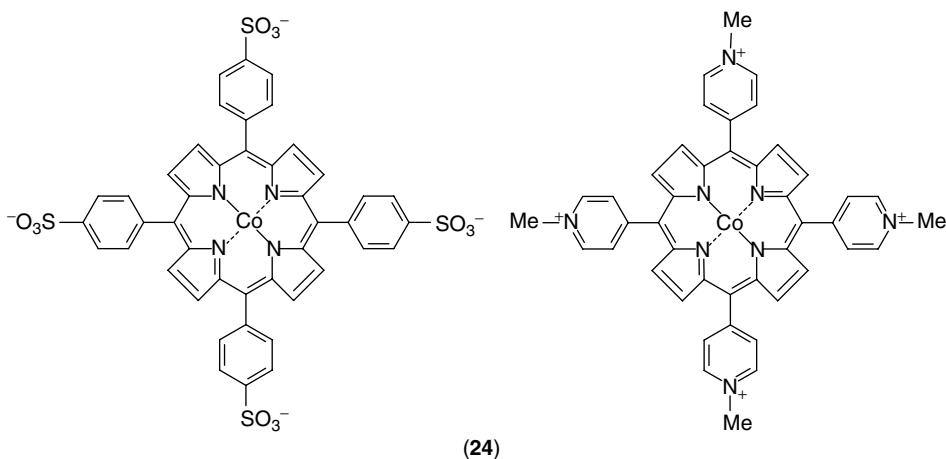
Recently, the Anson group sought to find the elusive $\text{Co}-\text{O}_2$ adduct that is supposedly formed as an intermediate for the electron-transfer reaction [100]. A 1-methylimidazole-substituted “picket fence” porphyrin was chosen due to its high affinity for molecular oxygen. Unfortunately, the desired adduct was not observed; instead, the four-molecule “picket” appended to one side of the porphyrin ring actually hindered the catalytic reduction of molecular oxygen.

Improvement in promoting the four-electron reduction of molecular oxygen has been achieved by the direct adsorption or film coating of the catalyst onto the surface of an electrode. Apparently, the rationale for this approach rests on the formation of an oxygen bridge between two adjacent cobalt centers. Thus, the close association of adsorbed porphyrin monomers or the formation of cobalt porphyrin dimers, either via direct polymerization or charge interaction of two monomeric units, is deemed to be critical for this process. These latter statements are easily observed in other work by Anson’s group [101]. When cobalt(II) tetramethylporphyrin is adsorbed onto the edge plane of a pyrolytic graphite electrode, the adsorbed species catalyzes the reduction of molecular oxygen via a process that is unusual in several different ways. First, the electroreduction occurs at a significantly more positive value than the formal potential either for the adsorbed porphyrin or for other monomeric porphyrins reported in the literature. Under typical cyclic voltammetric

conditions, the catalyst causes dioxygen to undergo a diffusion-controlled, four-electron reduction. Also, the contribution to the voltammetric response from the adsorbed monomer is still prominent and remains visible even as it acts to catalyze the reduction. Other cobalt porphyrins adsorbed onto a graphite electrode provided similar results [102]. Using two porphyrins without substituents in the meso ring positions affords both water and hydrogen peroxide, whereas those with meso substituents yield only hydrogen peroxide. It was argued that the presence of only hydrogen or small alkyl groups in the meso positions of the porphyrin ring results in the spontaneous formation of van der Waals dimers, and it is these dimers that lead to the formation of water via the four-electron reduction.

Ion-paired cobalt porphyrin dimers [103], (24), have also been shown to yield results that are similar to those for the van der Waals dimers discussed earlier. As individual units, the positively or negatively charged monomers are known to adsorb irreversibly onto the surface of glassy carbon electrodes. These surfaces then catalytically reduce molecular oxygen via a two-electron process. Individual monomers are also known to form stable dimers with monomers of the opposite charge when mixed together in solution. A study involving the use of a rotating disk electrode revealed that the ion-paired cobalt porphyrin dimer promotes the four-electron reduction of dioxygen with 98% efficiency.

Other studies [104–107] have shown varying degrees of success for the modification of electrode surfaces to achieve the desired four-electron reduction. Use of a monolayer film of cobalt tetraphenylporphyrin on a gold(111) surface [104] results in hydrogen peroxide as the predominant

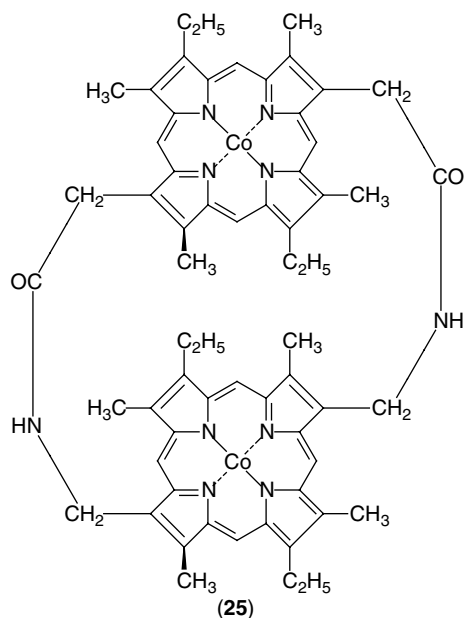


product, whereas the combination of the same cobalt-containing porphyrin with silica-metal oxide films [105, 106] afforded water as the main product. A set of flexible dimers [107], studied as possible models for cytochrome c oxidase, showed varying degrees of catalytic conversion of dioxygen to water.

One final novel approach for the preparation of catalytically active electrodes for chemical fuel cells has been heat-treating metal N_4 -chelates onto the surface of graphite [108–110]. By pyrolyzing cobalt porphyrins onto the graphite surface, one can observe a greatly enhanced catalytic ability for the reduction of molecular oxygen. One study [108] revealed that substituted pyrroles can be used to prepare modified electrodes having a much higher catalytic activity than an electrode modified with cobalt tetraphenylporphyrin. Another investigation [109] showed that a moderately active surface can be formed by application of the catalyst to the electrode via a Nafion film prior to the pyrolysis step. A third study [110] involving cobalt cyclam demonstrated a much lower catalytic effectiveness than any other catalyst examined

via this method. However, the one goal of all of these studies was the development of an efficient and inexpensive electrode that can be used to replace platinum.

For at least 20 years, the research group of L'Her has been engaged in a number of investigations of the use of cobalt-containing macrocycles for the catalytic reduction of molecular oxygen. Some early work [111] centered on the oxygen-binding properties of a mixed-valence cobalt(III)–cobalt(II) cofacial diporphyrin species (25), whereas a later study [112] was concerned with the binding of dioxygen by the product of the two-electron oxidation of (25) under strictly anhydrous conditions. When adsorbed onto a graphite electrode, (25) is a potent catalyst for the four-electron reduction of dioxygen [113]. In another report, the effect of the distance between the two cofacial porphyrin moieties was examined, and it was discovered that, for the largest separation, the two cobalt centers are oxidized or reduced simultaneously because they are noninteracting; however, for smaller distances of separation, the two cobalt centers are oxidized and reduced separately [114].



Multilayers of a species having a structure very similar to that of (25) were found to be adsorbed onto graphite and to promote the four-electron reduction of oxygen, but the process is potential-dependent and hydrogen peroxide can be formed at potentials negative with respect to that of the cobalt(III)–cobalt(II) couple [115]. Additional work along the lines of the already mentioned papers include studies of the effect of potential on the electroreflectance of a dicobalt bisporphyrin adsorbed onto graphite and gold surfaces [116], of the possible intermediacy of a μ -superoxo complex during the catalytic reduction of

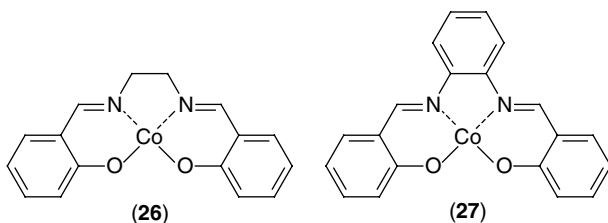
dioxygen by an oxidized form of a dicobalt cofacial bisporphyrin [117], of the catalytic activity of some heterodinuclear cofacial biphenylene- or anthracene-bridged bisporphyrins [118], and of some structural and mechanistic aspects of the catalytic reduction of dioxygen by dicobalt face-to-face diporphyrins [119].

As a last point, it should be mentioned that cobalt(II) salen (26) and cobalt(II) salophen (27) are known to interact with molecular oxygen in solution. Dioxygen forms a peroxo bridge between two cobalt centers, resulting in an often-undesired dicobalt(III) species that can attenuate the efficiency of electrogenerated cobalt(I) salen or cobalt(I) salophen for other reactions of interest, for example, the catalytic reduction of alkyl halides discussed in the following text.

On the other hand, the two-to-one adduct arising from the spontaneous reaction between dioxygen and a pair of either cobalt(II) salen or cobalt(II) salophen species provides an avenue for the catalytic reduction of dioxygen to the superoxide ion, $O_2^{\cdot -}$ [120].

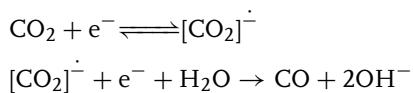
19.3.2.2 Carbon Dioxide

Experimentation with the catalytic reduction of carbon dioxide has stemmed from several important factors. Its presence as a “greenhouse” gas within the atmosphere has led to the need to find effective methods to lower its concentration. Also, as

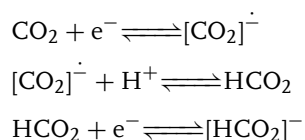


one of the most abundant sources of carbon, its possible use as a precursor for the synthesis of organic compounds makes it a much-sought alternative to crude oil. Finally, the fixation of carbon dioxide is an important step in the photosynthetic process. Research pertaining to electrocatalysts for the reduction of carbon dioxide may help to elucidate the biomolecules responsible for this process as well as the mechanisms involved.

Several organocobalt species have been observed to catalyze the two-electron reduction of carbon dioxide. Depending on the pathway for reduction that is followed, different products arise. If the reaction proceeds via rapid sequential uptake of two electrons, carbon monoxide is produced:



However, in the presence of a proton donor, a slow secondary electron transfer may be preceded by a chemical reaction:



Protonation of the last product affords formic acid.

Often intertwined with the catalytic reduction of carbon dioxide is the reduction of protons to form hydrogen gas. This competitive process takes place because of the relatively modest cathode potential required for hydrogen evolution. Moreover, some catalysts can shift the potential needed for the evolution of hydrogen into the region of the catalytic reduction of carbon dioxide, thereby decreasing the efficiency for the desired process involving carbon dioxide. This problem was

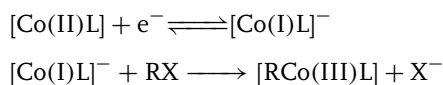
reported by Grodkowski et al. [121], who examined the behavior of an electrogenerated cobalt(I) corrole as a catalyst for CO₂ reduction, and in an earlier paper by Abe et al. [122], who investigated the catalytic reduction of CO₂ at a graphite electrode coated with cobalt octacyanophthalocyanine. In both accounts, the major products of the reduction were CO and H₂. In the former work, the slowness of the reaction with CO₂ at potentials corresponding to those of the cobalt(II)–cobalt(I) couple may have allowed concomitant hydrogen evolution to occur. In the latter research, the reduction of carbon dioxide occurred most selectively in an aqueous medium of pH 9.3; nevertheless, the CO-to-H₂ ratio was still approximately 10.

On the other hand, in two other papers, the formation of hydrogen gas was not mentioned, whereas carbon monoxide and formic acid were both observed as products. In studies carried out by Ogura and coworkers [123], electrogenerated [Co(PPh₃)₂L]⁰ (where L is a substituted quinoline, bipyridine, or phenanthroline moiety) was employed as a catalyst for the reduction of CO₂ in anhydrous organic solvents, conditions for which the current efficiency for production of CO (the main product) was 83%. Similarly, in an investigation done by Behar et al. [124], who used cobalt porphyrins as catalysts in an acetonitrile medium, the formation of both carbon monoxide and formic acid was noted; however, the catalytic species did not appear to contain cobalt(I), but rather a cobalt(0) species complexed with carbon dioxide.

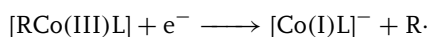
19.3.2.3 Catalytic Interactions of Cobalt-containing Species with Alkyl and Aryl Halides

Electrogenerated cobalt(I) salen (**26**) and its analogs are well known as *catalysts*

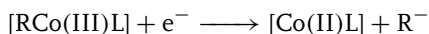
for the one-electron reduction of organic halides (RX). Fundamentally, the process (with (26) denoted by [Co(II)L]) involves the reversible reduction of cobalt(II) salen to cobalt(I) salen, followed by rapid oxidative addition of the cobalt(I) species to RX to form an organocobalt(III) salen:



Formation of the organocobalt(III) salen intermediate is the essential step in the process. Once formed, the organocobalt(III) salen species can undergo another one-electron reduction. If the organic moiety has little affinity for an electron, the reduction affords cobalt(I) salen and an organic radical:



An example of this behavior is seen for the catalytic reduction of iodoethane [125]. On the other hand, if the organic moiety is electron attracting, cobalt(II) salen and a carbanion are formed:



This latter behavior is encountered in the catalytic reduction of ethyl chloroacetate [126].

Although the bond between cobalt and the organic moiety of the organocobalt(III) salen can be readily photolyzed to give cobalt(II) salen and an organic radical, these species usually recombine if formed in a solvent cage.

Some of the earlier work pertaining to the cobalt(I) salen-catalyzed reduction of organic halides is mentioned in a recent review [127]. Fry and coworkers have examined in detail the catalytic reductions by electrogenerated cobalt(I) salen of both

benzal chloride [128] and benzotrichloride [129], and other investigations of the cobalt(I) salen-catalyzed reductions of alkyl halides and dihalides have been reported [130–132]. A number of studies of the use of electrogenerated cobalt(I) species (in particular, cobalt(I) salen, vitamin B₁₂s, and cobalt(I) phthalocyanine) as catalysts for the reductive cleavage of halogenated organic compounds in homogeneous phases and in bicontinuous microemulsions have been described by Rusling and his colleagues [133–135]. Catalytic degradation of Freon-113 (1,1,2-trichloro-1,2,2-trifluoroethane) by electrogenerated cobalt(I) salen has recently been reported [136].

It is possible to observe the reversible one-electron oxidation of cobalt(II) salen to cobalt(III) salen in a nonaqueous solvent such as acetonitrile [137]:

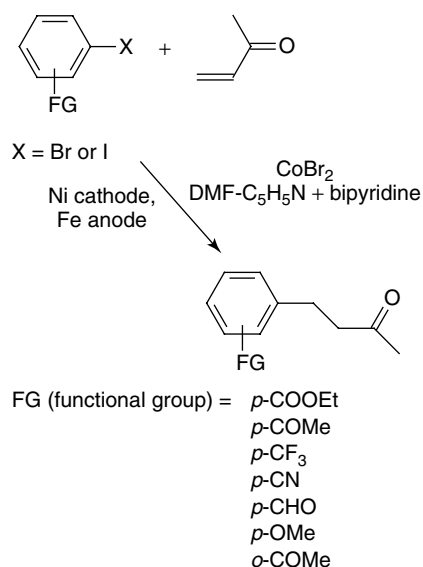


Parenthetically, it should be mentioned that, although electrogenerated cobalt(III) salen should be capable of serving as a catalyst for a variety of indirect oxidations, no report of an application has yet appeared in the literature.

Other publications dealing with the catalytic ability of electrogenerated cobalt(I) species have appeared. Cob(I)alamin reacts with 1,4-dibromobutane to yield a tetramethylene-1,4-di-Co_β-cobalamin complex [138]. Alkyl radicals (which arise from the oxidative addition of cobalt(I) tetraphenyl porphyrin to an alkyl halide) have been found to migrate from the cobalt center to a nitrogen of a pyrrole ring [139].

In a series of investigations [140–146], Gomes et al. utilized cobaltous bromide (although some work was done with cobaltous chloride) as a precursor for the catalytic reduction of aryl halides in the presence of activated olefins to afford

adducts in which carbon–carbon bonds are formed, as exemplified by the following process:



Electroreduction of the cobalt(II) salt in a mixture of either dimethylformamide–pyridine or acetonitrile–pyridine as solvent, often in the presence of bipyridine, produces a catalytically active cobalt(I) complex which is believed to be cobalt(I) bromide with attached bipyridine ligands (or pyridine moieties in the absence of bipyridine). As quickly as it is electrogenerated, the active catalyst reduces an aryl halide, after which the resulting aryl radical can undergo coupling with an acrylate ester [141], a different aryl halide (to form a biaryl compound) [142], an activated olefin [143], an allylic carbonate [144], an allylic acetate [144, 145], or a

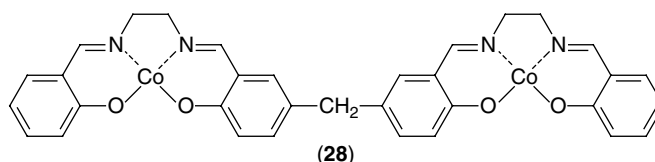
vinyl acetate [146]. It is notable that in all these studies a sacrificial iron anode was used and, in some of the work, it was found that the desired coupling product could not be formed in the absence of iron as the anode material. It is still unknown exactly what role iron plays in the catalytic process.

In recent research, Shimakoshi et al. [147] synthesized a novel complex consisting of two cobalt salen moieties joined by a methylene bridge (28).

In a fashion similar to that of cobalt salen, distinct redox chemistry can be observed for each of the two cobalt centers of (28). Coulometric studies showed that the complex can undergo a one-electron reduction as well as a one-electron oxidation of each cobalt center and that there is no interaction between those cobalt centers. Thus, the two metal centers can be used as separate catalytic sites for the reduction of halogenated organic compounds. In the same article [147] is a list of literature citations of work done over the past 20 years by the group of Hiseada on the catalytic behavior of electroreduced vitamin B₁₂ derivatives.

19.3.2.4 Hydrazine

Hydrazine compounds are widely used as fuels, corrosion inhibitors, catalysts, and dyes. However, such compounds are recognized as toxic agents; consequently, their detection and processing are of much concern. Only a few recent papers pertain to the catalytic oxidation of hydrazine [148–150], with special emphasis



on the use of chemically modified electrodes. Direct oxidation of hydrazine at unmodified electrodes is rendered difficult by the relatively high overpotential for the process, so catalysts are needed to allow work at more convenient potentials.

References

1. N. Maki, N. Tanaka, in *Encyclopedia of Electrochemistry of the Elements* (Ed.: A. J. Bard), Marcel Dekker, New York, 1975, pp. 43–210, Vol. III.
2. L. Meites, P. Zuman, A. Narayanan et al., *CRC Handbook Series in Inorganic Electrochemistry*, CRC Press, Boca Raton, 1980, Vol. I.
3. N. Maki, N. Tanaka, in *Standard Potentials in Aqueous Solution* (Eds.: A. J. Bard, R. Parsons, J. Jordan), Marcel Dekker, New York, 1985, pp. 367–382.
4. G. Wilkinson, F. G. A. Stone, E. W. Abel, *Comprehensive Organometallic Chemistry*, Pergamon Press, Oxford, 1982.
5. E. W. Abel, F. G. A. Stone, G. Wilkinson, *Comprehensive Organometallic Chemistry II*, Pergamon Press, Oxford, 1995.
6. E. T. Verdier, G. Baptiste, *J. Electroanal. Chem.* **1965**, 10, 42–50.
7. B. Warnqvist, *Inorg. Chem.* **1970**, 9, 682–684.
8. G. Davies, B. Warnqvist, *J. Chem. Soc., Dalton Trans.* **1973**, 900–902.
9. P. A. Rock, *Inorg. Chem.* **1968**, 7, 837–840.
10. H. A. Laitinen, C. H. Liu, *J. Am. Chem. Soc.* **1958**, 80, 1015–1020.
11. S. N. Flengas, T. R. Ingraham, *J. Electrochem. Soc.* **1959**, 106, 714–721.
12. H. C. Gaur, W. K. Behl, *J. Electroanal. Chem.* **1963**, 5, 261–269.
13. D. N. Hume, I. M. Kolthoff, *J. Am. Chem. Soc.* **1949**, 71, 867–869.
14. W. D. Treadwell, D. Huber, *Helv. Chim. Acta* **1943**, 26, 10–17.
15. J. I. Watters, I. M. Kolthoff, *Anal. Chem.* **1949**, 21, 1466–1469.
16. I. M. Kolthoff, J. I. Watters, *Anal. Chem.* **1950**, 22, 1422–1426.
17. G. Clement, M. R. Paris, *Anal. Chim. Acta* **1979**, 110, 227–232.
18. Z. Zhiping, D. R. MacFarlane, *J. Non-Cryst. Solids* **1992**, 140, 215–219.
19. P. Sharma, S. Kumbhat, C. Rawat, *Int. J. Environ. Anal. Chem.* **1992**, 48, 201–207.
20. P. Sharma, C. Rawat, *J. Indian Chem. Soc.* **1995**, 72, 283–284.
21. F. Cordon, S. A. Ramirez, G. J. Gordillo, *J. Electroanal. Chem.* **2002**, 534, 131–141.
22. G. R. Lakshminarayanan, E. S. Chen, J. C. Sadak et al., *J. Electrochem. Soc.* **1976**, 123, 1612–1616.
23. T. C. Franklin, A. Aktan, *J. Electrochem. Soc.* **1988**, 135, 1636–1638.
24. E. Guevas, J. Torrent-Burgues, *Port. Electrochim. Acta* **2001**, 19, 237–245.
25. L. H. Mendoza-Huizar, J. Robles, M. Palomar-Pardave, *J. Electroanal. Chem.* **2003**, 545, 39–45.
26. H. Nakano, K. Nakahara, S. Kawano et al., *J. Appl. Electrochem.* **2002**, 32, 43–48.
27. T. S. Eagleton, J. P. G. Farr, *Trans. Inst. Met. Finish.* **2002**, 80, 9–12.
28. T. Cohen-Hyams, W. D. Kaplan, J. Yahalom, *Electrochem. Solid State Lett.* **2002**, 5, C75–C78.
29. S. Floate, M. Hyde, R. G. Compton, *J. Electroanal. Chem.* **2002**, 523, 49–63.
30. R. F. Renner, K. C. Liddell, *J. Appl. Electrochem.* **2002**, 32, 621–627.
31. E. Gomez, E. Valles, *J. Appl. Electrochem.* **2002**, 32, 693–700.
32. S. S. Abd El Rehim, M. A. M. Ibrahim, M. M. Dankeria, *J. Appl. Electrochem.* **2002**, 32, 1019–1027.
33. S. P. Jiang, Y. Z. Chen, J. K. You et al., *J. Electrochem. Soc.* **1990**, 137, 3374–3380.
34. S. P. Jiang, A. C. C. Tseung, *J. Electrochem. Soc.* **1990**, 137, 3381–3386.
35. S. P. Jiang, A. C. C. Tseung, *J. Electrochem. Soc.* **1990**, 137, 3387–3393.
36. C. Q. Cui, S. P. Jiang, A. C. C. Tseung, *J. Electrochem. Soc.* **1990**, 137, 3418–3423.
37. C. Q. Cui, S. P. Jiang, A. C. C. Tseung, *J. Electrochem. Soc.* **1991**, 138, 94–100.
38. J. A. Mitchell, W. R. Pitner, C. L. Hussey et al., *J. Electrochem. Soc.* **1996**, 143, 3448–3455.
39. P.-Y. Chen, I.-W. Sun, *Electrochim. Acta* **2001**, 46, 1169–1177.
40. P. Sahoo, S. V. Narasimhan, *Bull. Electrochem.* **1998**, 14, 22–25.
41. P. N. Bartlett, P. N. Birkin, M. A. Ghanem et al., *J. Electrochem. Soc.* **2001**, 148, C119–C123.

42. J. Henry, K. Ounadjela, L. Piraux et al., *Eur. Phys. J. B* **2001**, 20, 35–54.
43. L. Li, *J. Mater. Sci. Lett.* **2001**, 20, 1459–1461.
44. J. Bao, Z. Xu, J. Hong et al., *Scr. Mater.* **2004**, 50, 19–23.
45. J. Fiedler, C. Nervi, D. Osella et al., *J. Chem. Soc., Dalton Trans.* **2002**, 3705–3711.
46. J. Classen, R. Gleiter, F. Rominger, *Eur. J. Inorg. Chem.* **2002**, 2040–2046.
47. H. Shimakoshi, M. Koga, Y. Hisaeda, *Bull. Chem. Soc. Jpn.* **2002**, 75, 1553–1558.
48. K. M. Kadish, N. Guo, E. Van Caemelbecke et al., *J. Porphyrins Phthalocyanines* **1998**, 2, 439–450.
49. Y. Le Mest, M. L'Her, J. Courtot-Coupez et al., *J. Electroanal. Chem.* **1985**, 184, 331–346.
50. S. Brooker, R. J. Kelly, P. G. Plieger, *Chem. Commun.* **1998**, 1079–1080.
51. K. Dimitrou, A. D. Brown, G. Christou et al., *Chem. Commun.* **2001**, 1284–1285.
52. M. Stephan, J. Hauss, U. Zenneck et al., *Inorg. Chem.* **1994**, 33, 4211–4215.
53. M. Stephan, P. Mueller, U. Zenneck et al., *Inorg. Chem.* **1995**, 34, 2058–2067.
54. H. Yao, M. Sabat, R. N. Grimes et al., *Organometallics* **2003**, 22, 2581–2593.
55. T. Aviles, A. Dinis, J. Orlando Goncalves et al., *J. Chem. Soc., Dalton Trans.* **2002**, 4595–4602.
56. A. E. Gerbase, E. J. S. Vichi, E. Stein et al., *Inorg. Chim. Acta* **1997**, 266, 19–27.
57. C. J. McAdam, N. W. Duffy, B. H. Robinson et al., *J. Organomet. Chem.* **1997**, 527, 179–190.
58. C. J. McAdam, J. J. Brunton, B. H. Robinson et al., *J. Chem. Soc., Dalton Trans.* **1999**, 2487–2496.
59. L.-A. Hore, C. J. McAdam, J. L. Kerr et al., *Organometallics* **2000**, 19, 5039–5048.
60. C. Evans, G. J. Harfoot, J. S. McIndoe et al., *J. Chem. Soc., Dalton Trans.* **2002**, 4678–4683.
61. A. R. Manning, C. J. McAdam, A. J. Palmer et al., *J. Chem. Soc., Dalton Trans.* **2003**, 4472–4481.
62. H. D. Dewald, J. Chen, *Microchem. J.* **1997**, 56, 197–206.
63. K. L. Brown, J. Shaw, M. Ambrose et al., *Microchem. J.* **2002**, 72, 285–298.
64. S. Brooker, *Eur. J. Inorg. Chem.* **2002**, 2535–2547.
65. K. M. Kadish, B. C. Han, A. Endo, *Inorg. Chem.* **1991**, 30, 4502–4506.
66. F. D'Souza, A. Villard, E. Van Caemelbecke et al., *Inorg. Chem.* **1993**, 32, 4042–4048.
67. G. B. Addo-Richter, S. J. Hodge, G.-B. Yi et al., *Inorg. Chem.* **1996**, 35, 6530–6538.
68. K. M. Kadish, Z. Ou, X. Tan et al., *J. Chem. Soc., Dalton Trans.* **1999**, 1595–1602.
69. M. Autret, Z. Ou, A. Antonini et al., *J. Chem. Soc., Dalton Trans.* **1996**, 2793–2797.
70. K. M. Kadish, J. Li, E. Van Caemelbecke et al., *Inorg. Chem.* **1997**, 36, 6292–6298.
71. K. M. Kadish, N. Guo, E. Van Caemelbecke et al., *J. Porphyrins Phthalocyanines* **1998**, 2, 439–450.
72. K. M. Kadish, J. Shao, Z. Ou et al., *J. Porphyrins Phthalocyanines* **2000**, 4, 639–648.
73. R. Guillard, F. Jerome, C. P. Gros et al., *C. R. Acad. Sci., Ser. IIC: Chim.* **2001**, 4, 245–254.
74. Y. Le Mest, M. L'Her, J.-Y. Saillard, *Inorg. Chim. Acta* **1996**, 248, 181–191.
75. T. Nagata, Y. Kikuzawa, A. Osuka, *Inorg. Chim. Acta* **2003**, 342, 139–144.
76. K. M. Kadish, W. Koh, P. Tagliatesta et al., *Inorg. Chem.* **1992**, 31, 2305–2313.
77. V. A. Adamian, F. D'Souza, S. Licoccia et al., *Inorg. Chem.* **1995**, 34, 532–540.
78. S. Will, J. Lex, E. Vogel et al., *Inorg. Chem.* **1996**, 35, 5577–5583.
79. K. M. Kadish, V. A. Adamian, E. Van Caemelbecke et al., *J. Am. Chem. Soc.* **1998**, 120, 11986–11993.
80. R. Guillard, F. Jerome, J.-M. Barbe et al., *Inorg. Chem.* **2001**, 40, 4856–4865.
81. K. M. Kadish, Z. Ou, J. Shao et al., *Inorg. Chem.* **2002**, 41, 3990–4005.
82. R. Guillard, C. P. Gros, F. Bolze et al., *Inorg. Chem.* **2001**, 40, 4845–4855.
83. K. M. Kadish, J. Shao, Z. Ou et al., *Inorg. Chem.* **2003**, 42, 4062–4070.
84. F. D'Souza, P. Boulas, A. M. Aukauloo et al., *J. Phys. Chem.* **1994**, 98, 11885–11891.
85. K. M. Kadish, P. L. Boulas, M. Kisters et al., *Inorg. Chem.* **1998**, 37, 2693–2700.
86. Z. A. Siddiqi, V. J. Mathew, *Polyhedron* **1994**, 13, 799–805.
87. E. Simon, E. Sable, H. Handel et al., *Electrochim. Acta* **1999**, 45, 855–863.
88. K.-Y. Choi, *Inorg. Chem. Commun.* **2002**, 5, 220–222.
89. V. M. Jovanović, K. Babic-Samardzija, S. P. Sovilj, *Electroanal.* **2001**, 13, 1129–1135.
90. K. Babic-Samardzija, S. P. Sovilj, V. M. Jovanović, *J. Serb. Chem. Soc.* **2003**, 68, 989–999.

91. F. Lelj, G. Morelli, G. Ricciardi et al., *Inorg. Chim. Acta* **1990**, 176, 189–194.
92. P. J. Lukes, A. C. McGregor, T. Clifford et al., *Inorg. Chem.* **1992**, 31, 4697–4699.
93. C. Miry, D. Le Brun, J.-M. Kerbaol et al., *J. Electroanal. Chem.* **2000**, 494, 53–59.
94. J. Taraszewska, G. Rosłonek, B. Korybut-Daszkiewicz, *J. Electroanal. Chem.* **1991**, 297, 245–255.
95. B. Korybut-Daszkiewicz, J. Taraszewska, K. Zieba et al., *Eur. J. Inorg. Chem.* **2003**, 1741–1747.
96. E. Simon, P. L'Haridon, R. Pichon et al., *Inorg. Chim. Acta* **1998**, 282, 173–179.
97. C. Shi, B. Steiger, M. Yuasa et al., *Inorg. Chem.* **1997**, 36, 4294–4295.
98. B. Steiger, F. C. Anson, *Inorg. Chem.* **1997**, 36, 4138–4140.
99. M. Yuasa, B. Steiger, F. C. Anson, *J. Porphyrins Phthalocyanines* **1997**, 1, 181–188.
100. B. Steiger, F. C. Anson, *Inorg. Chem.* **2000**, 39, 4579–4585.
101. C. Shi, F. C. Anson, *Inorg. Chem.* **1998**, 37, 1037–1043.
102. E. Song, C. Shi, F. C. Anson, *Langmuir* **1998**, 14, 4315–4321.
103. F. D'Souza, Y.-Y. Hsieh, G. R. Deviprasad, *Chem. Commun.* **1998**, 1027–1028.
104. S. Yoshimoto, A. Tada, K. Suto et al., *Langmuir* **2003**, 19, 672–677.
105. C. A. Pessoa, Y. Gushikem, *J. Porphyrins Phthalocyanines* **2001**, 5, 537–544.
106. A. M. Castellani, Y. Gushikem, *J. Colloid Interface Sci.* **2000**, 230, 195–199.
107. C. J. Chang, Y. Deng, D. G. Nocera et al., *Chem. Commun.* **2000**, 1355–1356.
108. A. L. Bouwkamp-Wijnoltz, W. Visscher, J. A. R. Van Veen et al., *Electrochim. Acta* **1999**, 45, 379–386.
109. T. Okada, M. Yoshida, T. Hirose et al., *Electrochim. Acta* **2000**, 45, 4419–4429.
110. H. Kalvelage, A. Mecklenburg, U. Kunz et al., *Chem. Eng. Technol.* **2000**, 23, 803–807.
111. Y. Le Mest, M. L'Her, J. P. Collman et al., *J. Am. Chem. Soc.* **1986**, 108, 533–535.
112. Y. Le Mest, M. L'Her, *J. Chem. Soc., Chem. Commun.* **1995**, 1441–1442.
113. E. Ngameni, Y. Le Mest, M. L'Her et al., *J. Electroanal. Chem.* **1987**, 220, 247–257.
114. Y. Le Mest, M. L'Her, J. P. Collman et al., *J. Electroanal. Chem.* **1987**, 234, 277–295.
115. J. P. Collman, N. H. Hendricks, C. R. Leidner et al., *Inorg. Chem.* **1988**, 27, 387–393.
116. E. Ngameni, A. Laouenan, M. L'Her et al., *J. Electroanal. Chem.* **1991**, 301, 207–226.
117. J. P. Collman, J. E. Hutchison, M. A. Lopez et al., *J. Am. Chem. Soc.* **1992**, 114, 9869–9877.
118. R. Guillard, S. Brandes, C. Tardieux et al., *J. Am. Chem. Soc.* **1995**, 117, 11721–11729.
119. Y. Le Mest, C. Inisan, A. Laouenan et al., *J. Am. Chem. Soc.* **1997**, 119, 6095–6106.
120. B. Ortiz, S.-M. Park, *Bull. Korean Chem. Soc.* **2000**, 21, 405–411.
121. J. Grodkowski, P. Neta, E. Fujita et al., *J. Phys. Chem. A* **2002**, 106, 4772–4778.
122. T. Abe, H. Imai, T. Yoshida et al., *J. Porphyrins Phthalocyanines* **1997**, 1, 315–321.
123. A. G. M. Mostafa Hossain, T. Nagaoka, K. Ogura, *Electrochim. Acta* **1997**, 42, 2577–2585.
124. D. Behar, T. Dhanasekaran, P. Neta et al., *J. Phys. Chem. A* **1998**, 102, 2870–2877.
125. K. S. Alleman, D. G. Peters, *J. Electroanal. Chem.* **1998**, 451, 121–128.
126. L. J. Klein, K. S. Alleman, D. G. Peters et al., *J. Electroanal. Chem.* **2000**, 481, 24–33.
127. D. G. Peters, in *Organic Electrochemistry*, 4th ed. (Eds.: H. Lund, O. Hammerich), Marcel Dekker, New York, 2000, p. 368.
128. A. J. Fry, A. H. Singh, *J. Org. Chem.* **1994**, 59, 8172–8177.
129. S. A. Kaufman, T. Phaniiphand, A. J. Fry, *Tetrahedron Lett.* **1996**, 37, 8105–8108.
130. A. A. Isse, A. Gennaro, E. Vianello, *J. Electroanal. Chem.* **1998**, 444, 241–245.
131. K. S. Alleman, D. G. Peters, *J. Electroanal. Chem.* **1999**, 460, 207–213.
132. D. Pletcher, H. Thompson, *J. Electroanal. Chem.* **1999**, 464, 168–175.
133. D.-L. Zhou, J. Gao, J. F. Rusling, *J. Am. Chem. Soc.* **1995**, 117, 1127–1134.
134. D.-L. Zhou, H. Carrero, J. F. Rusling, *Langmuir* **1996**, 12, 3067–3074.
135. J. F. Rusling, D.-L. Zhou, *J. Electroanal. Chem.* **1997**, 439, 89–96.
136. J. D. Persinger, J. L. Hayes, L. J. Klein et al., *J. Electroanal. Chem.* **2004**, 568, 157–165.
137. M. J. Samide, D. G. Peters, *J. Pharm. Biomed. Anal.* **1999**, 19, 193–203.
138. B. Kräutler, T. Dérier, P. Liu et al., *Angew. Chem., Int. Ed. Engl.* **1995**, 34, 84–86.
139. G. Zheng, M. Stradiotto, L. Li, *J. Electroanal. Chem.* **1998**, 453, 79–88.

140. P. Gomes, C. Gosmini, J.-Y. Nédélec et al., *Tetrahedron Lett.* **2000**, 41, 3385–3388.
141. P. Gomes, C. Gosmini, J.-Y. Nédélec et al., *Tetrahedron Lett.* **2002**, 43, 5901–5903.
142. P. Gomes, H. Fillon, C. Gosmini et al., *Tetrahedron* **2002**, 58, 8417–8424.
143. P. Gomes, C. Gosmini, J. Périchon, *Synlett* **2002**, 1673–1676.
144. P. Gomes, C. Gosmini, J. Périchon, *J. Org. Chem.* **2003**, 68, 1142–1145.
145. P. Gomes, C. Gosmini, J. Périchon, *Org. Lett.* **2003**, 5, 1043–1045.
146. P. Gomes, C. Gosmini, J. Périchon, *Tetrahedron* **2003**, 59, 2999–3002.
147. H. Shimakoshi, W. Ninomiya, Y. Hisaeda, *J. Chem. Soc., Dalton Trans.* **2001**, 1971–1974.
148. G. Cepria, J. R. Castillo, *J. Appl. Electrochem.* **1998**, 28, 65–70.
149. S.-M. Chen, *Electrochim. Acta* **1998**, 43, 3359–3369.
150. C. A. Pessoa, Y. Gushikem, S. Nakagaki, *Electroanal.* **2002**, 14, 1072–1076.

20

A Few Selected Aspects of Electrode-induced Reactions at Mono- and Dinuclear Molybdenum–sulfur Centers

Dedicated to the memory of Alain Talarmin

*Francois Y. Pétilion, Philippe Schollhammer, and Jean Talarmin
Université de Bretagne Occidentale, 29283 Brest Cedex 3, France*

20.1	Introduction	567
20.2	Mononuclear Mo–S Centers	567
20.2.1	Electron Transfer-induced Structure Change	567
20.2.2	Electrochemically Induced Metal–ligand Bonds Cleavage	568
20.2.3	Electrochemical Transformation of Ligands	571
20.3	Dinuclear Thiolate-bridged Molybdenum Complexes	573
20.3.1	Electron Transfer-induced Structure Changes	573
20.3.2	Electron Transfer-induced and Electron Transfer-catalyzed Ligand Substitution	576
20.3.3	Electrochemically Induced Metal–Ligand Bonds Cleavage	577
20.3.4	Electrochemical Deprotection of a Substrate-binding Site	581
20.3.5	Electrochemical Transformations of Bound Substrate	582
20.4	Conclusion	588
	Acknowledgments	589
	References	589

20.1

Introduction

A large number of studies devoted to metal–sulfur centers are motivated by the occurrence of such arrangements at the active site of various metalloenzymes [1–13]. Mononuclear complexes with Mo=O function(s) and possessing sulfur ligands in their coordination sphere have been extensively investigated since they can be seen as models of the active site of enzymes such as nitrate- and DMSO reductases or sulfite- and xanthine oxidases [1–4]. On the other hand, a large variety of mono-, di-, and polynuclear Mo–S centers have been synthesized in order to produce functional models of the Mo–nitrogenase since the exact nature (mono-, di- or polynuclear) of the metal center, where N₂ interacts within the iron–molybdenum cofactor (FeMo–co) of the enzyme is still unknown [4–8].

Although many studies of Mo–S complexes make use of electrochemical techniques, and particularly of cyclic voltammetry (CV), this is often restricted to measurements of redox potentials, and to discussions of their variation with structure or of their relationships with spectroscopic properties. Such examples can be found in the above-mentioned reviews. In this article, we will comment

on a few studies where chemical reactions such as structural changes, metal–ligand bond(s) cleavage, substitution, transformations of ligands, were induced or catalyzed by electron transfer step(s). This will be illustrated, in the case of mononuclear Mo–S centers, by complexes in which the sulfur ligands are supplied by a tetrathioether macrocycle, by dithiocarbamates, or by ligands providing a mixed thiolate/thioether donor set. In the case of binuclear complexes, we will focus on compounds where thiolate bridges link the metal centers, although examples of compounds containing sulfide or thioether groups will be briefly mentioned.

20.2

Mononuclear Mo–S Centers

20.2.1

Electron Transfer-induced Structure Change

The occurrence of structure changes as a result of electron transfer steps is well-documented [14–16]. Such a reaction has been observed for a molybdenum complex of the macrocyclic tetrathioether Me₈[16]aneS₄ (Me₈[16]aneS₄ = 3,3,7,7,11,11,15,15-octamethyl-1,5,9,13-tetrathiacyclohexadecane) [17–20], which is among the

rare [21] Mo–S site able to bind N_2 [18]. The electrochemical behavior of the Mo(II) precursor of the bis- N_2 complex, namely *trans*-[MoX₂(Me₈[16]aneS₄)] **1** (X = Cl, Br), has been investigated in order to compare with the phosphorus-ligated analog, *trans*-[MoX₂(dppe)₂] (X = Cl, Br) [22]. The oxidation of **1** (X = Br) [20] at room temperature appeared as an uncomplicated, reversible, diffusion-controlled one-electron step with $E_{1/2}^{ox} = -0.52$ V/Fc (Fc = ferrocene). However, the CV recorded at -55°C in dichloromethane showed two partially reversible oxidation processes, at -0.65 V and -0.47 V. The temperature-dependence of the oxidation of **1** was assigned to the occurrence of dynamic equilibria involving two different conformers of the neutral and cationic complexes, differing by the “all-up” (*syn*) or “up-up-down-down” (*anti*) conformation of the carbon ring atoms of the crown thioether (Sch. 1) [20].

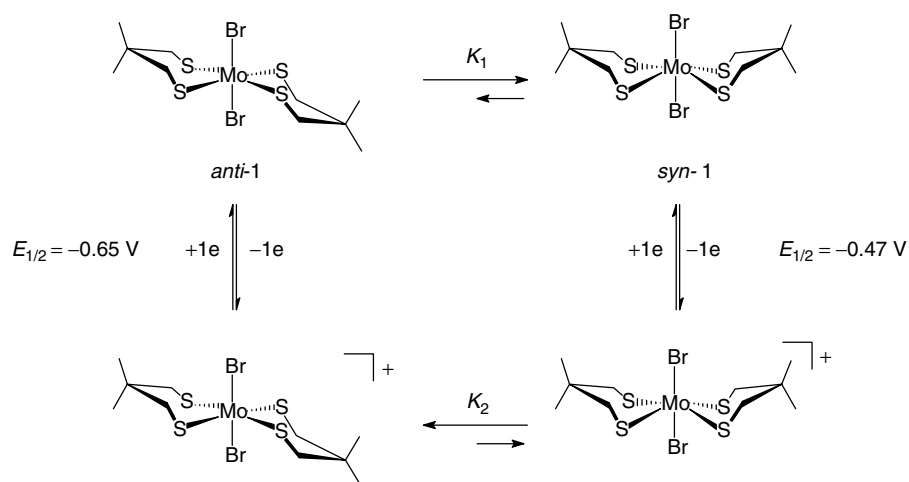
This assignment is supported by the X-ray crystal structures of **1** and **1**⁺ (X = Br), which show the different arrangements adopted by the macrocyclic ligand in the

neutral Mo(II) complex (*syn*) and in the Mo(III) cation (*anti*) [20]. The fluxional behavior of the complexes was rationalized in terms of electronic effects, since the *anti* conformation favored at the Mo(III) level would maximize net charge donation by the sulfur ligands and compensate for the decrease of the electron density at the metal center resulting from the one-electron oxidation. It is also interesting to note that the two axial sites are not equivalent for the *syn* conformation of the macrocycle [19]. Therefore, the one-electron oxidation of **1** might induce a different reactivity of the complex, not only because of the change in the metal oxidation state but also, possibly, because of different geometric/steric requirements.

20.2.2

Electrochemically Induced Metal–ligand Bonds Cleavage

The electrochemical behavior of the seven-coordinate complexes [MoOX₂(dte)₂] **2** (X = Cl, Br; dte = S₂CNEt₂), [MoO(cat)



Scheme 1 Carbon ring atoms at the front and at the back were omitted for clarity; potentials are relative to Fc^+/Fc .

(dtc)₂] **3**, and [MoO(dtc)₃]⁺ **4**⁺ has been investigated in order to evaluate the role of the metal environment on the electron transfer processes [23]. The reduction of **2–4**⁺ was shown to result in metal–ligand bonds cleavage, according to mechanisms that depend on the nature of the ligands present in the coordination sphere.

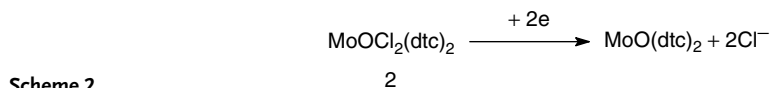
The CV of [MoOX₂(dtc)₂] **2** in MeCN showed that the complex reduces in an irreversible two-electron step, with the elimination of both halide ligands (Sch. 2). The metal product of the electrochemical reduction, [MoO(dtc)₂], detected by CV through its reduction and oxidation systems, was obtained by controlled-potential reduction of **2** (2 F mol^{−1} **2**).

The process in Sch. 2 is chemically reversible since controlled potential oxidation of [MoO(dtc)₂] in the presence of an excess chloride regenerated **2** after the transfer of ca. 2F mol^{−1} [MoO(dtc)₂]. The detailed mechanism represented in Sch. 3

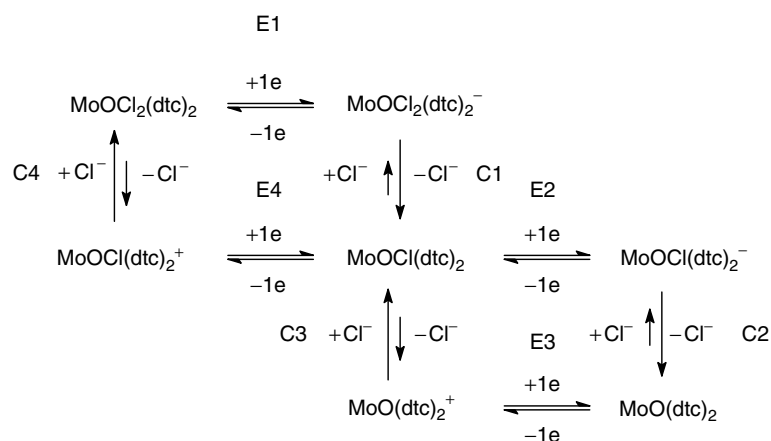
was confirmed by investigations of the individual steps.

The loss of a halide from **2** (step C4) was shown to be a reversible reaction, which was more shifted toward the monohalide cation for X = Br than for X = Cl. The electrochemical steps E2 and E4 were studied using the Mo(V) complex [MoOCl(dtc)₂]. The reduction of **2** follows the E1-C1-E2-C2 pathway and the oxidation of [MoO(dtc)₂] the E3-C3-E4-C4 pathway [23].

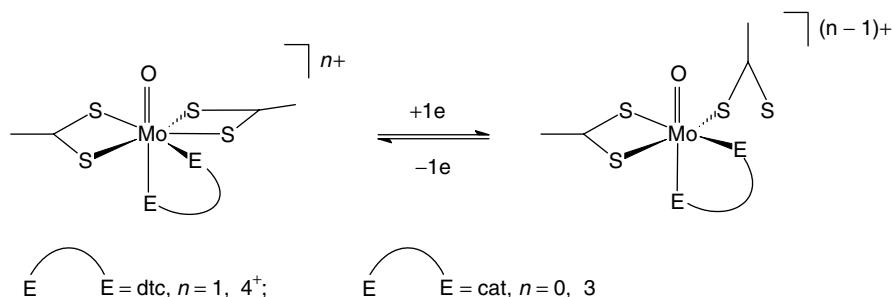
The two-electron reduction of both **3** and **4**⁺ resulted in the elimination of a dtc[−] ligand [23]. For these compounds, the two-electron reduction could be resolved in two separate one-electron steps. The first electron transfer for both **3** and **4**⁺ led to partial dissociation of a dtc ligand; nevertheless this step was quasi-reversible, as evidenced by the scan rate dependence of the peak-to-peak separation (ΔE_p) [24] (Sch. 4). This was assigned to the fact that the decoordinated sulfur atom



Scheme 2



Scheme 3



Scheme 4

remained at proximity of the metal center, thus allowing the reverse reaction to take place [24].

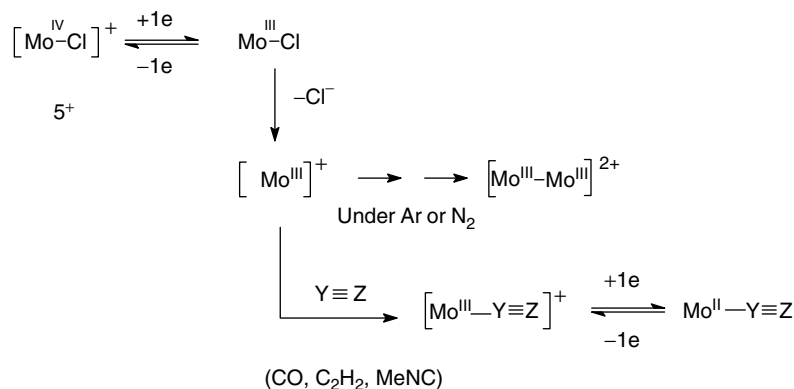
The apparent rate constant of the heterogeneous electron transfer (k_s^{app}) was about 100 times larger for 4^+ than for **3** [24]. Furthermore, k_s^{app} for **3** was dependent on the nature of the catecholate ligand (Cl_4cat , NO_2cat , cat , DTBcat) [24]. This indicated that the activation barrier contains a substantial contribution from the catecholate ligand and that the Gibbs free energy of activation for the process in Sch. 4 accounts for reorganization of the entire coordination sphere.

The cleavage of one equatorial Mo–X or Mo–S bond upon one-electron reduction of **2**, **3**, and 4^+ was assigned to unfavorable electrostatic interactions between the lobes of the half-filled Mo $4d_{xy}$ antibonding orbital and the five equatorial metal–ligand bonding electron pairs [23]. This interpretation was confirmed by the fact that the Mo(VI)/Mo(V) reduction of six-coordinate complexes (i.e. with four equatorial ligands) was found fully reversible, as expected [25].

In the following example, the electrochemical cleavage of the Mo–Cl bond of the seven-coordinate complex $[\text{MoCl}(\text{dtc})_2(\text{dppe})]^+$ ($\text{dtc} = \text{S}_2\text{CNR}_2$; $\text{R} = \text{Me}$ or Et ; $\text{dppe} = \text{Ph}_2\text{PCH}_2\text{CH}_2\text{PPh}_2$)

generated a vacant site that binds nitrogenase substrates (C_2H_2 , MeNC) or inhibitor (CO). The first reduction of $[\text{MoCl}(\text{dtc})_2(\text{dppe})]^+$ ($[\text{Mo–Cl}]^+$) 5^+ in MeCN under argon occurred according to an EC process [26]. The chemical reactions following the one-electron transfer step, which were responsible for complicated CV curves, could be suppressed at fast scan rates. Under these conditions, reduction of 5^+ appeared as a partially reversible couple. Controlled potential electrolysis under argon at the potential of the first reduction afforded a $[\text{Mo}^{\text{III}}-\text{Mo}^{\text{III}}]^{2+}$ dimer after transfer of $1 \text{ F mol}^{-1} 5^+$ (Sch. 5). Whereas the CV under N_2 was the same as under argon, the presence of other $\text{Y}\equiv\text{Z}$ substrates (CO , C_2H_2 , MeNC) resulted in a simplification of the cyclic voltammograms, since a single two-electron (ECE) reduction was observed. This clearly indicated binding of $\text{Y}\equiv\text{Z}$ to the Mo(III) intermediate generated by the EC process (Sch. 5). However, only the carbonyl derivative $[\text{Mo}(\text{CO})(\text{dtc})_2(\text{dppe})]$ could be obtained by controlled potential electrolysis ($2 \text{ F mol}^{-1} 5^+$). Electrolyses performed in the presence of acetylene afforded the dimer $[\text{Mo}^{\text{III}}-\text{Mo}^{\text{III}}]^{2+}$ after the transfer of $1 \text{ F mol}^{-1} 5^+$.

These experiments demonstrated that, although C_2H_2 and MeNC bind at the electrogenerated Mo(III) site (Sch. 5), these



Scheme 5

substrates, but not CO, were lost after one-electron reduction of the $\{\text{Mo}^{\text{III}}\text{-Y}\equiv\text{Z}\}$ complex [26].

Complexes with thiolate/thioether ligands such as dtdt [dtdt = 1,2-bis(2-mercaptophenylthio)ethane] have been extensively investigated [7] as they provide a coordination sphere similar to that found at the active site of various metalloenzymes [1–4]. $[\text{Mo}(\text{NO})\text{Cl}(\text{dtdt})]$ **6** showed a rich electrode-induced reactivity [27]. **6** undergoes two diffusion-controlled reduction steps, the first one ($E_{1/2}^{\text{red1}} = -0.70 \text{ V/Fc}$) was reversible at room temperature, while the second ($E_{1/2}^{\text{red2}} = -2.20 \text{ V/Fc}$) showed some reversibility only at low temperature. Whereas controlled potential reduction at the first step afforded the stable monoanion, electrolysis at the potential of the second process was found to generate the highly reduced species $[\text{Mo}(\text{NO})(1,2\text{-C}_6\text{H}_4\text{S}_2)_2]^{3-}$ **7**³⁻, in an overall 4e transfer (Sch. 6). Thus, the 4e-reduction of **6** caused the cleavage of the Mo—Cl bond, as well as the cleavage of two C—S bonds, the latter resulting in the extrusion of ethylene from the ligand backbone.

Gas chromatographic analyses during the electrolysis showed that C_2H_4 release

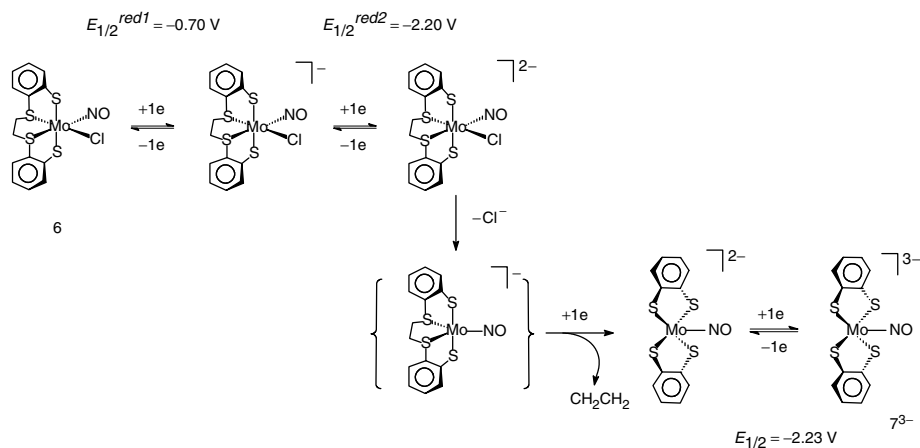
started after 2 F mol^{-1} **6** had passed, Sch. 6 [27].

20.2.3

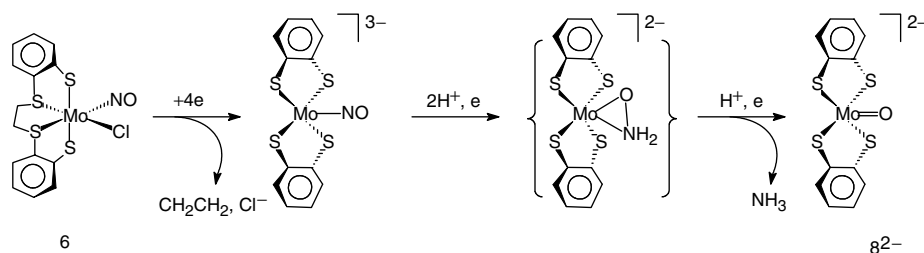
Electrochemical Transformation of Ligands

A particularly interesting aspect of electrochemistry is that it may allow transformations of bound substrates, by coupling proton(s) and electron(s) transfers. This makes possible to mimic certain steps of the reactions driven by metalloenzymes. For example, the nitrosyl ligand in **7**³⁻ (Sch. 6) is activated toward protic attack. Controlled potential reduction of **6** at the potential of the second process in the presence of PhOH (5–10 equiv) as a proton source consumed 6 F mol^{-1} **6** and afforded the molybdenum oxide $[\text{MoO}(1,2\text{-C}_6\text{H}_4\text{S}_2)_2]^{2-}$ **8**²⁻ and ammonia. The reductive cleavage of the N—O bond was proposed to involve a hydroxylamide intermediate, Sch. 7 [27]. Relevant to this is the fact that the chemical reduction of $[\text{Mo}(\text{NO})_2(\text{dtdt})]$ by sodium borohydride or hydrazine in methanol produced $[\text{Mo}(\text{NO})(\text{NH}_2\text{O})(\text{dtdt})]$ with a side-on hydroxylaminyl ligand [28].

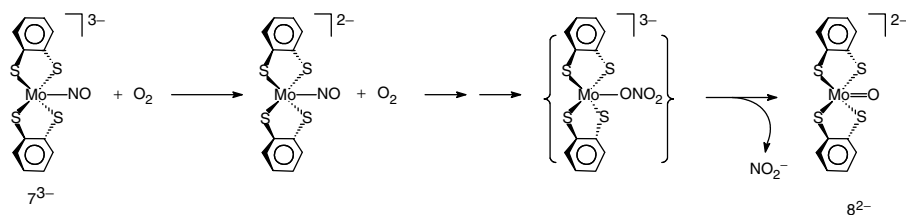
The nitrosyl ligand in **7**³⁻ is also activated toward attack by molecular oxygen.



Scheme 6 Species in braces is a postulated intermediate.



Scheme 7 Species in braces is a postulated intermediate.



Scheme 8 Species in braces is a postulated intermediate.

The first step of the mechanism leading to the formation of 8^{2-} and free nitrite from the reaction of 7^{3-} with O_2 probably involved a single electron transfer. Subsequent radical–radical coupling of the products, to afford a molybdenum-bound nitrate, followed by N–O bond cleavage would eventually lead to the observed products (Sch. 8) [27].

The electrochemical study of the seven-coordinate complex $[Mo(N_2RR')(dtc)_3]^+$ 9^+ ($R, R' = \text{alkyl or aryl}$, $dtc = S_2CNMe_2$) provided an example of electrode-induced activation of a hydrazido(2–) ligand. Complex 9^+ was shown to reduce in two separate diffusion-controlled one-electron steps, with the first one reversible on the CV timescale at room temperature and

moderate scan rate ($\nu > 0.3 \text{ V s}^{-1}$) [29]. On longer timescale at room temperature, the one-electron reduced complex **9** was not stable and was involved in chemical reactions so that the reduction of 9^+ at the potential of the first step occurred according to an ECE-type process. Controlled potential reduction at the first or at the second step afforded the same product **10**, after the transfer of $2 \text{ F mol}^{-1} 9^+$. Product **10** could not be characterized, but it was shown to retain an organodinitrogen moiety. The electronic strain resulting from the two-electron reduction of 9^+ was proposed to be relieved either by partial dissociation of one of the dtc ligands (see Sch. 4) or by bending of the hydrazido(2-) group followed by protonation at $N\alpha$ (Sch. 9). The latter possibility is entirely consistent with the observed release of the substituted hydrazine $\text{H}_2\text{NNRR}'$ upon treatment of **10** with HCl [29].

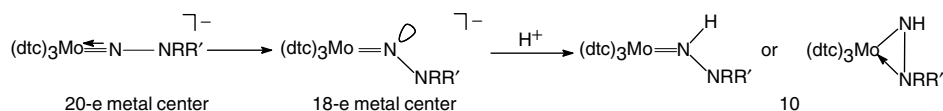
20.3 Dinuclear Thiolate-bridged Molybdenum Complexes

20.3.1 Electron Transfer-induced Structure Changes

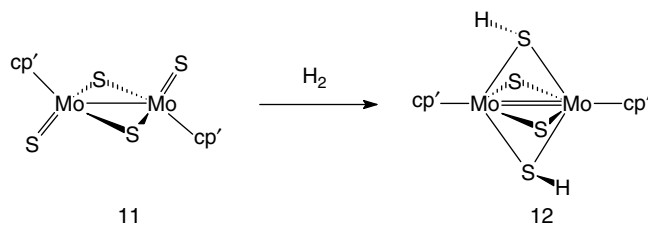
Electron transfers may lead to modifications of the metal-sulfur core of binuclear sulfur-bridged complexes. The CV of $[\text{M}_2\text{S}_2(\text{cp}')_2(\mu\text{-S})_2]$ **11** ($\text{M} = \text{Mo}$ or W , $\text{cp}' = \eta\text{-C}_5\text{H}_5\text{-}_n\text{Me}_n$) [30] showed that the first reduction was a one-electron process,

whose reversibility was dependent on the nature of the metal centers. Whereas the reduction of the tungsten complex was reversible on the CV timescale, that of the Mo analog ($\text{cp}' = \text{cp}^* = \eta\text{-C}_5\text{Me}_5$) was not. This was assigned to an isomerization of the core, from the bis-bridged $[\text{M}_2\text{S}_2(\mu\text{-S})_2]$ structure of **11** to the more compact $[\text{M}_2(\mu\text{-S})_4]$ core of **12**, which would be easier for the Mo complex than for the W one [30]. Although the product of the one-electron reduction of **11** was not isolated, the reductively induced structure change could be compared to that resulting from the reaction of **11** with dihydrogen (Sch. 10) [31]. The structure change is best illustrated by the shortening of the Mo-Mo distance from 2.905 \AA in **11** ($\text{cp}' = \text{cp}^*$) to 2.582 \AA in an analog of **12** ($\text{cp}' = \text{Me-cp}$, $\text{SR} = \text{SMe}$ instead of SH) [31].

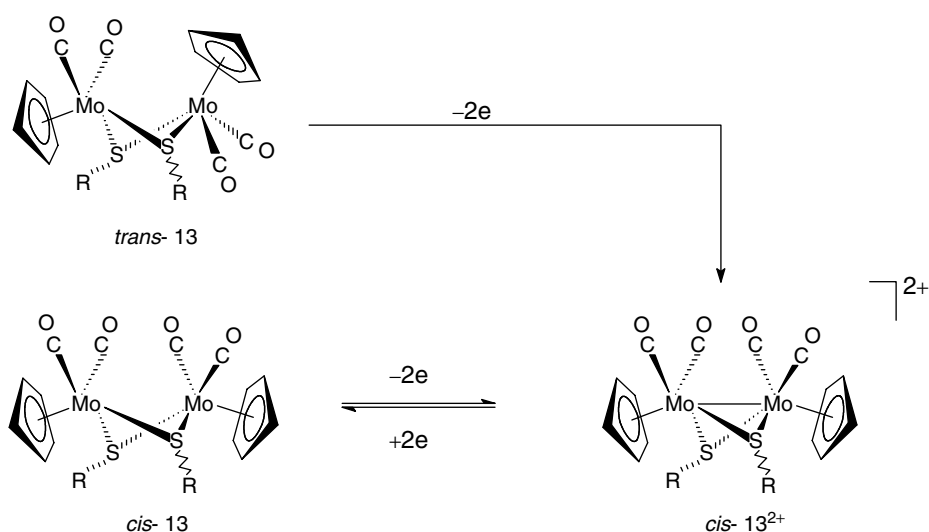
Other examples of electron transfer-induced modifications of metal-sulfur cores have been reported. In the case of *trans*- $[\text{M}_2(\text{cp})_2(\mu\text{-SR})_2(\text{CO})_4]$ (*trans*-**13**: $\text{M} = \text{Mo}$, $\text{R} = \text{Me}$, ^tBu , Ph ; *trans*-**14**: $\text{M} = \text{W}$, $\text{R} = \text{Me}$; $\text{cp} = \eta\text{-C}_5\text{H}_5$), the electrochemical oxidation is an irreversible two-electron process, which led to the dication with the *cis* arrangement of the CO ligands (Sch. 11). The presence of an M-M single bond in *cis*-**13**²⁺ was evidenced by the X-ray crystal structure of the dication ($\text{R} = ^t\text{Bu}$) [32]. The other isomer, *cis*- $[\text{M}_2(\text{cp})_2(\mu\text{-SR})_2(\text{CO})_4]$ (*cis*-**13**: $\text{M} = \text{Mo}$, $\text{R} = \text{Me}$, ^tBu , Ph ; *cis*-**14**: $\text{M} = \text{W}$, $\text{R} = \text{Me}$) was shown to oxidize in a reversible, “single step” two-electron transfer (Sch. 11).



Scheme 9



Scheme 10



Scheme 11

Although there are no crystal structures of corresponding couples of cis - $[M_2(cp)_2(\mu-SR)_2(CO)_4]^{0/2+}$ complexes, the metal–metal separations in cis - 13^{2+} [$R = tBu$, $d(Mo-Mo) = 3.008 \text{ \AA}$] [32] and in an analog of cis -14, namely cis - $[W_2(cp)_2(\mu-S^iPr)_2(CO)_4]$ [$d(W \dots W) = 3.835 \text{ \AA}$] [33], have been reported. It is thus likely that the reversible two-electron process leads to substantial changes in the M_2S_2 core dimensions ($M \dots M$ distance, $M-S-M$ and $S-M-S$ bond angles). The peak-to-peak separation of the reversible, “single step” two-electron transfer ($M = Mo$, $\Delta E_p = 40 \text{ mV}$ in thf; 35 mV in CH_3CN ; $M = W$, $\Delta E_p = 60 \text{ mV}$ in thf; 35 mV in

CH_3CN ; $\nu = 0.2 \text{ V s}^{-1}$) indicated that the electrode process was not a Nernstian two-electron transfer but involved two successive one-electron steps, with the second thermodynamically more favorable than the first one [32]. Therefore, the reversible, overall two-electron process in Sch. 11 is better represented by two successive, reversible, one-electron steps involving a thermodynamically unstable and undetected cation intermediate (see Sch. 13; EE process, or ECE process, where the chemical step C is a fast, reversible deformation of the M_2S_2 core). In agreement with this, it should be noted that the oxidation of cis - $[Mo_2(cp^*)_2(\mu-SMe)_2(CO)_4]$ cis -13* also

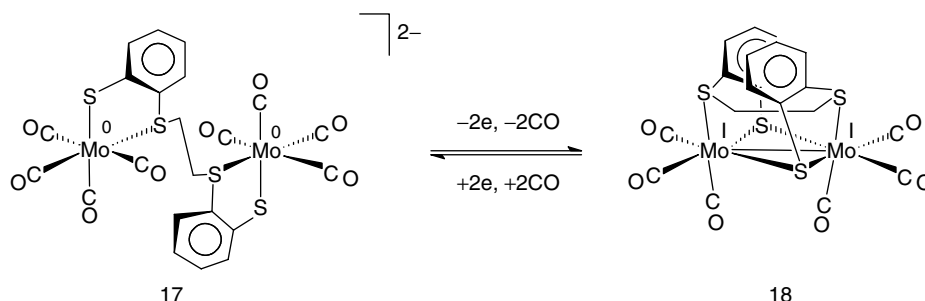
occurred in a single step, reversible two-electron transfer with $\Delta E_p = 40$ mV in thf ($\Delta E_p = 35$ mV in CH_3CN), whereas two separate ($\Delta E_{1/2} = 70$ mV), reversible one-electron couples (ΔE_p ca. 60 mV) were observed in CH_2Cl_2 [34]. This illustrates the effect of the solvent on the separation of successive electron transfer processes [35–37]; in the present case, it resulted from a better solvation of the dication by solvents such as MeCN and thf as compared to dichloromethane [34].

Similarly, the $[\text{M}_2(\mu\text{-SR})_2(\text{CO})_8]^{0/2-}$ complexes ($\text{M} = \text{Mo}$, **15/15**²⁻; $\text{M} = \text{W}$, **16/16**²⁻; $\text{R} = \text{Ph}$, ^tBu, Bz) are related by a reversible, overall two-electron process [38–41]. As for *cis*- $[\text{M}_2(\text{cp})_2(\mu\text{-SR})_2(\text{CO})_4]$, the 2e process causes important structural changes of the M_2S_2 core, with the formation of an M–M single bond resulting in the decrease of $d(\text{M} \dots \text{M})$ by ca. 1 Å upon oxidation [42–46]. Detailed investigations and simulations of the electrochemical process for $[\text{W}_2(\mu\text{-SBz})_2(\text{CO})_8]^{2-}$ led to the conclusion that the oxidation consisted of two successive reversible one-electron steps, with $\Delta E^{o'} \approx 0$ V [41].

The fact that the electrochemical oxidation of *cis*- $[\text{M}_2(\text{cp})_2(\mu\text{-SR})_2(\text{CO})_4]$ and of $[\text{M}_2(\mu\text{-SR})_2(\text{CO})_8]^{2-}$ is reversible despite the amount of structural reorganization involved suggests that these changes require low activation energy. Extended Hückel Molecular Orbital (EHMO) calculations on the model complex *cis*-**13**²⁺ ($\text{R} = \text{H}$) indicated that the Lowest Unoccupied Molecular Orbital (LUMO) was the $\sigma^*_{\text{Mo-Mo}}$ level [47]. Weakening of the Mo–Mo bond by adding one electron into this orbital might cause an increase in the metal–metal separation. This would result in the stabilization of the semi-occupied orbital, as shown by the Walsh diagram associated with the variations of the Mo_2S_2

core dimensions, which in turn would trigger the transfer of the second electron at the same potential as the first one [48]. Therefore, “the nuclear displacements that occur along the two-electron reaction coordinate serve to favor the thermodynamics of the second charge transfer” (quotation from Ref. 41).

However, the occurrence of major structural changes, including the formation of an M–M bond, upon reduction or oxidation of a complex with an M_2E_2 core does not necessarily result in an overall two-electron transfer. Indeed, although the first oxidation of the iron complex $[\text{Fe}_2(\text{cp})_2(\mu\text{-SMe})_2(\text{CO})_2]$ causes a shortening of the $\text{Fe} \dots \text{Fe}$ distance by ca. 0.5 Å, the formation of the dication occurs in two well-separated reversible one-electron steps [48, 49]. EHMO calculations indicated that the LUMO of the dication possesses metal–metal antibonding character and the Walsh diagram associated with the Fe_2S_2 core deformations showed similar stabilization of this orbital as in the case of *cis*-**13**²⁺, so that an overall two-electron transfer might have been expected [48]. Investigations of the electrochemical oxidation of $[\text{Fe}_2(\text{cp})_2(\mu\text{-SMe})_2(\text{CO})_2]$, $[\text{Fe}_2(\text{cp})_2(\mu\text{-PPh}_2)_2(\text{CO})_2]$, and $[\text{Mo}_2(\text{cp})_2(\mu\text{-SMe})_4]$ demonstrated [49] that the standard heterogeneous electron transfer rate constant, k_s , was about the same for the iron compounds (both of which undergo important structure change upon oxidation) as for the molybdenum complex whose structure is little affected by oxidation [50]. The reasons why the heterogeneous electron transfers are fast for complexes **13–16** and for the above iron compounds despite the structural changes involved, which is in apparent contradiction with the Marcus–Hush theory [51, 52], are still unclear [41, 48, 49]. Also, the reasons why



Scheme 12

$[\text{Fe}_2(\text{cp})_2(\mu\text{-SMe})_2(\text{CO})_2]$ and $[\text{Fe}_2(\text{cp})_2(\mu\text{-PPh}_2)_2(\text{CO})_2]$ undergo two discrete one-electron oxidation steps while complexes **13**, **14**, **15**^{2−}, and **16**^{2−} oxidize in an overall two-electron process are not well understood [41, 48, 49].

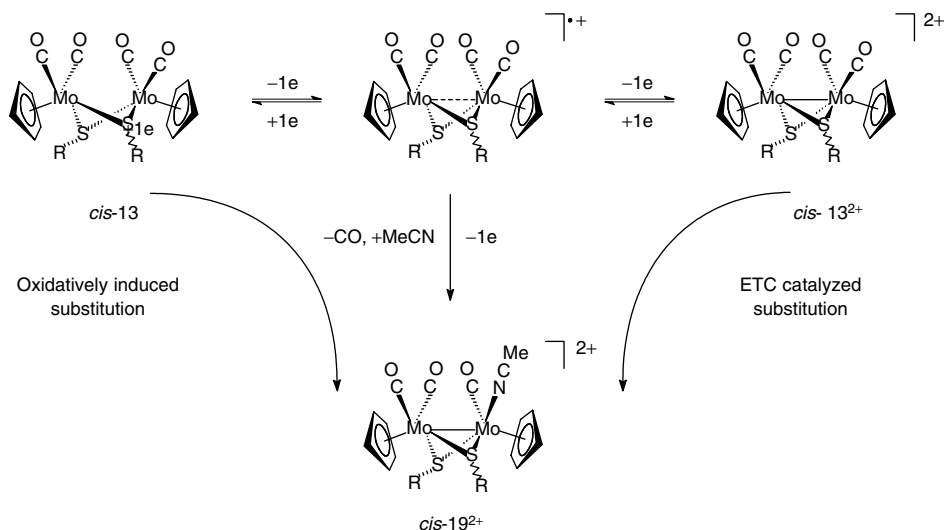
Although the redox reactions in Sch. 12 have not been achieved electrochemically, they illustrate another type of redox-induced structural change in a dimolybdenum compound with a sulfur-rich coordination sphere. In this case, $\text{Mo}_2(\mu\text{-S})_2$ ring opening in **18** (cleavage of Mo–Mo and Mo–S bonds) is associated with the exposure of vacant coordination sites, and the uptake of two carbonyl ligands in **17** [7, 53].

20.3.2

Electron Transfer-induced and Electron Transfer-catalyzed Ligand Substitution

Controlled potential oxidation of **13** (*cis* and *trans* isomers) in a MeCN electrolyte at room temperature produced variable amounts of the acetonitrile substituted derivative $\text{cis-}[\text{Mo}_2(\text{cp}')_2(\mu\text{-SR})_2(\text{CO})_3(\text{MeCN})]^{2+}$ *cis-19*²⁺ (R = Me, Ph; cp' = cp or cp*) along with *cis-13*²⁺ [34, 54]. However, *cis-19*²⁺ was the major product when the electrolysis was performed at 40–45 °C. Interestingly, the electrochemical reduction of *cis-13*²⁺ under similar

conditions also produced *cis-19*²⁺, with a low charge consumption, according to an Electron Transfer Chain (ETC) catalyzed reaction. The catalytic role of electrons was evidenced by initiating the substitution reaction by passage of a small amount of charge (typically 0.05–0.1 F mol^{−1} *cis-13*²⁺), and by monitoring the formation of *cis-19*²⁺ by CV after the electrolysis was stopped. Since neither **13** nor *cis-13*²⁺ reacted with MeCN on the electrolysis timescale, the formation of *cis-19*²⁺ from both the electrochemical oxidation of **13** and the electrochemical reduction of *cis-13*²⁺ involved a cation intermediate (Sch. 13) [34, 54]. The formation of the substituted complex with a *cis* geometry (as evidenced by the X-ray crystal structure of *cis-19*²⁺, R = Ph; cp' = cp) from both the *cis* and *trans* isomers of **13** (R = Me) suggested that the substitutionally labile intermediate cation might have a singly SR-bridged structure [54]. In the case where cp' = cp, controlled potential electrolyses (oxidation of **13** and reduction of *cis-13*²⁺) performed in the presence of ^tBuNC afforded the isocyanide singly substituted analog of *cis-19*²⁺ [54]. Doubly substituted ^tBuNC complexes could be obtained by electrochemical reduction of the singly substituted precursor in the presence of an excess ligand, according to an ETC process [54].



Scheme 13

Complexes 15^{2-} and 16^{2-} were also shown to undergo oxidatively induced substitution of MeCN for CO. In this case, however, doubly substituted derivatives were obtained via the singly substituted species, which could not be isolated, but was detected by CV [40].

20.3.3

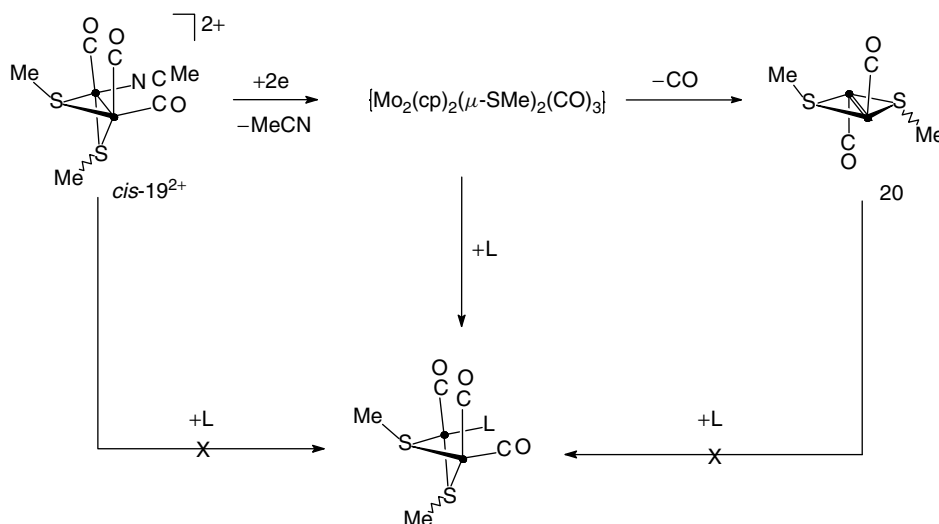
Electrochemically Induced Metal–Ligand Bonds Cleavage

Electrochemical cleavage of metal–ligand bond(s) is a convenient way of generating vacant coordination sites at a metal center (see Sch. 5). The eliminated ligand can be neutral (L) or anionic (X).

Cleavage of a Mo–L bond. The electrochemical reduction of the acetonitrile complex *cis*-19²⁺ is an overall two-electron process leading to the cleavage of the Mo–NCMe bond. The CV of *cis*-[Mo₂(cp')₂(μ-SR)₂(CO)₃(MeCN)]²⁺ appeared to be strongly dependent upon the nature of the sulfur substituents and of the

cp' ring [34, 55]. When R = Me and cp' = cp, the CV under N₂ or Ar showed an irreversible two-electron reduction, and the redox systems of the electrogenerated *trans*-[Mo₂(cp)₂(μ-SMe)₂(CO)₂], **20**, (Sch. 14), which was produced by controlled potential electrolysis. However, the phenyl analog was also obtained by controlled potential reduction of *cis*-19²⁺ (R = Ph), along with *trans*-[Mo₂(cp)₂(μ-SPh)₂(CO)₄]. This is consistent with the fact that the kinetic product of the electrochemical two-electron reduction of *cis*-19²⁺ (R = Ph), detected by CV, was not *trans*-[Mo₂(cp)₂(μ-SPh)₂(CO)₂]. The kinetic product was assigned as a tricarbonyl intermediate [55]. Although the methyl analog was not detected by CV ($v \leq 1 \text{ V s}^{-1}$), its transient formation was evidenced by trapping experiments. Indeed, the CV of *cis*-19²⁺ (R = Me) in the presence of a substrate L (L = CO or ^tBuNC) showed the formation of *cis*-[Mo₂(cp)₂(μ-SMe)₂(CO)₃(L)] (Sch. 14).

The electrochemistry of *cis*-[Mo₂(cp')₂(μ-SMe)₂(CO)₃(MeCN)]²⁺ was also affected

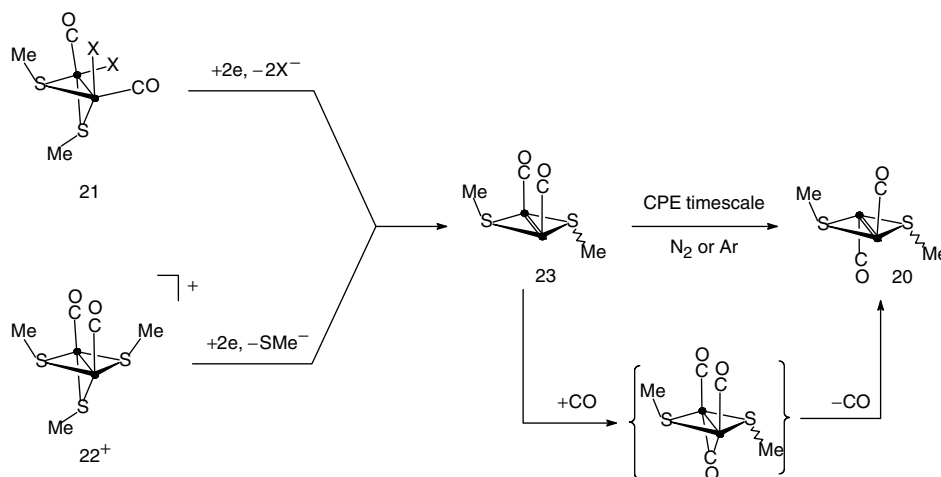


Scheme 14 • = Mo–cp'; the product in braces was not detected.

by the nature of the cp' rings. In addition to the effect on the redox potentials, the substitution of cp* for cp resulted in the stabilization of the Mo–NCMe bond. Instead of the irreversible two-electron reduction of the cp analog, that of the cp* complex $cis-19^{*2+}$ occurred in two successive one-electron steps, both reversible at low temperature (inert atmosphere, MeCN, thf or CH₂Cl₂ electrolyte) [34]. The reduction of $cis-19^{*2+}$ under CO in thf at 40 °C (or in CH₂Cl₂) was an irreversible two-electron (ECE) process affording $cis-13^*$. In contrast, two one-electron steps were still observed under CO in a MeCN electrolyte. Although the first reduction remained reversible at moderate scan rate ($\nu = 0.2 \text{ V s}^{-1}$) under these conditions, the occurrence of an ECE-type mechanism, where the chemical step consisted in the reversible decoordination of MeCN from the radical cation, could be evidenced [34]. The product formed at the first reduction was $cis-13^*$, whereas $trans-13^*$ was obtained after the second (irreversible) reduction had been traversed.

This suggested that two tricarbonyl species with *cis* and *trans* arrangements of the cp* ligands were formed transiently. These experiments illustrate the effects of “spectator” ligands on the mechanism and products of electrochemical processes. Therefore, the differences in the electrochemical behavior of $cis-[Mo_2(cp')_2(\mu-SMe)_2(CO)_3(MeCN)]^{2+}$ for cp' = cp or cp* were assigned to a stronger Mo–NCMe bond for cp' = cp*, and to the longer lifetimes of $cis-19^{*n+}$ ($n = 0, 1$) and of the cp* tricarbonyl intermediates as compared to their cp analogs [34].

Cleavage of Mo–X bonds. An example of the reductive cleavage of Mo–S(R) bonds is shown in Schs. 4 and 12. Similarly, the electrochemical two-electron reduction of $[Mo_2(cp)_2(\mu-SMe)_2(CO)_2(X)_2]^{2+}$ 21, (X = Cl, Br) and of $[Mo_2(cp')_2(\mu-SMe)_3(CO)_2]^{2+}$, 22⁺ (cp' = cp or cp*) afforded a reactive site, assigned as the transient $cis-[Mo_2(cp)_2(\mu-SMe)_2(CO)_2]$ 23, by cleavage of two M–X bonds [56]. Complex 23 rearranged to the stable *trans* isomer 20 on the electrolysis timescale (Sch. 15).



Scheme 15 • = Mo–cp; the nature of the product in braces was not demonstrated.

The *cis* dicarbonyl intermediate **23** could not be isolated, although it was longer lived when $\text{cp}' = \text{cp}^*$ [57] than when $\text{cp}' = \text{cp}$. The *cis* \rightarrow *trans* isomerization of the dicarbonyl complex is catalyzed by CO, presumably via an unstable CO-bridged intermediate, which would decay to the *trans* isomer and carbon monoxide (Sch. 15) [56].

EHMO calculations performed on the reactants, products, and possible intermediates of the reactions shown in Sch. 15 supported the proposed mechanism [58]. Thus, steric and electronic factors combine to make **23** a good substrate-binding site: it has an uncongested Mo_2S_2 face and a low-lying LUMO available to hold an incoming nucleophile. The proposed mechanism remains valid if the CO substrate is replaced by other two-electron donor ligands such as isocyanide [56] or cyanide [59].

$[\text{Mo}_2(\text{cp})_2(\mu\text{-SMe})_3(\text{CO})_2]^+$ derives from **13**²⁺ by substitution of two carbonyl ligands by a methylthiolate anion. Similarly, $[\text{Mo}_2(\mu\text{-SPh})_3(\text{CO})_6]^-$ is derived from **15** by replacement of two COs by a SPh bridge.

It should be noted that the reduction of $[\text{Mo}_2(\mu\text{-SPh})_3(\text{CO})_6]^-$, as that of **15**, occurred in a single, reversible two-electron step [46]. In contrast, the reduction of $[\text{Mo}_2(\text{cp})_2(\mu\text{-SMe})_3(\text{CO})_2]^+$ was an essentially irreversible (ECE) process leading to the cleavage of two Mo–S bonds (Sch. 15). The difference might be partly due to the fact that, in $[\text{Mo}_2(\mu\text{-SPh})_3(\text{CO})_6]^-$, the excess charge resulting from the reduction can be dissipated by the six CO ligands.

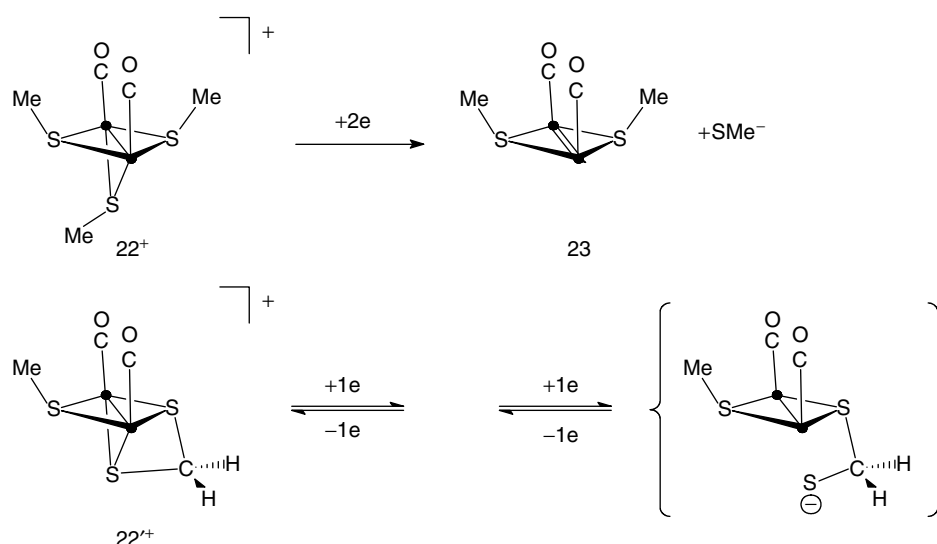
An analog of **22**⁺, $[\text{Mo}_2(\text{cp})_2(\mu\text{-S}_2\text{CH}_2)(\mu\text{-SMe})(\text{CO})_2]^+$ **22'**⁺ has been synthesized by Rakowski DuBois [60]. **22'**⁺ undergoes a reversible, “single step” two-electron reduction ($E_{1/2}^{\text{red}} = -1.41 \text{ V/Fc}$; $\Delta E_p = 35 \text{ mV}$ for $\nu = 0.04 \text{ V s}^{-1}$) in MeCN, whereas two overlapping reversible one-electron reductions were observed in thf ($E_{1/2}^{\text{red1}} = -1.43 \text{ V/Fc}$, $\Delta E_p^{\text{red1}} \approx 80 \text{ mV}$; $E_{1/2}^{\text{red2}} = -1.52 \text{ V/Fc}$, $\Delta E_p^{\text{red2}} \approx 100 \text{ mV}$ for $\nu = 0.2 \text{ V s}^{-1}$) [61]. Although the redox system(s) of **22'**⁺ (in MeCN and in thf) were not fully reversible ($i_p^a/i_p^c < 1$), the reduction of **22'**⁺ appears much more reversible than that of **22**⁺ on the basis of the

measured anodic-to-cathodic peak current ratios. Therefore, the substitution of two methylthiolate bridges by one 1,1-dithiolate bridge, which has a limited influence on the redox potentials of these complexes (22^+ : $E_{1/2}^{red} = -1.47$ V/Fc in MeCN [56]), has a pronounced effect on the reversibility of the electrode process. The nature of the chemical reaction coupled to the reduction of 22^+ was not determined. However, the fact that the reduction of 22^+ is more reversible than that of 22^+ could be due to the (initial) bidentate coordination of the S_2CH_2 fragment in 22^+ . If the reduction of 22^+ (like that of 22^+) resulted in the cleavage of the two Mo–S bonds trans to the carbonyl ligands, the de-coordinated S atom would remain in the metal's coordination sphere, making the reverse reactions possible (Sch. 16). Such an example has been reported in the case of mononuclear complexes (see Sch. 4).

Although *trans*-[Mo₂(cp)₂(μ-SMe)₂(CO)₂] **20** shows an interesting reactivity with substrates such as isocyanides

and cyanide [59], it can be seen as arising from the deactivation of electrogenerated sites, namely {[Mo₂(cp)₂(μ-SMe)₂(CO)₃]} (Sch. 14) and *cis*-[Mo₂(cp)₂(μ-SMe)₂(CO)₂] **23** (Sch. 15). It is clear that such a reaction could prevent the formation of the desired (site-substrate) complex, and the subsequent metal-assisted reduction of the substrate, if the substrate-binding step is slow or reversible, as it could be when dinitrogen is involved.

The problem raised by the deactivation of vacant site could be solved by the design of a protective device such as a *redox-switchable hemilabile ligand*, RHL [62]. Ideally, the protective device should (1) be activated by an electronic (redox) or chemical (pH) instruction, (2) open the binding site only in the presence of the substrate, (3) function reversibly so that the site is protected back when the bound substrate is lost (due to reversibility of the binding step or due to decoordination during subsequent steps). An example of an electrochemically



Scheme 16 • = Mo–cp; the nature of the product in braces was not demonstrated.

activated protecting group is provided in the following.

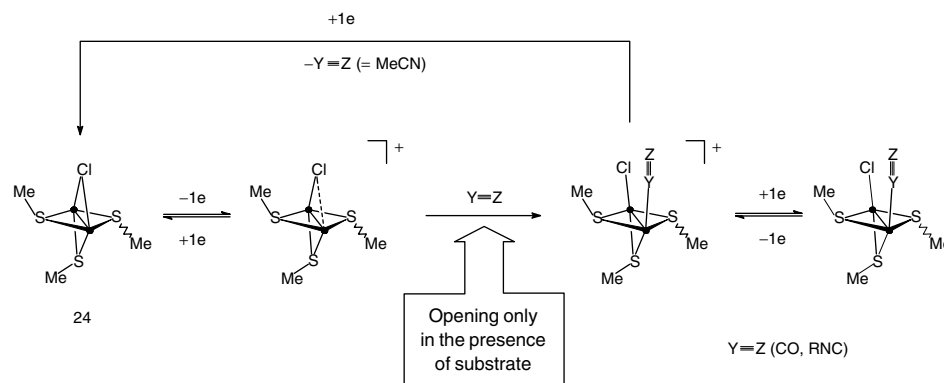
20.3.4

Electrochemical Deprotection of a Substrate-binding Site

The chloride-bridged complex $[\text{Mo}_2(\text{cp})_2(\mu\text{-SMe})_3(\mu\text{-Cl})]$ **24** [63] is unreactive toward $\text{Y}\equiv\text{Z}$ molecules such as CO, MeCN, or RNC; in contrast, **24**⁺ was shown to react with these substrates [64]. **24** undergoes two successive quasi-reversible one-electron oxidations in a thf- (or dichloromethane) $[\text{NBu}_4][\text{PF}_6]$ electrolyte. Controlled potential electrolysis at the potential of the first step in thf or CH_2Cl_2 afforded the paramagnetic cation after the passage of ca. 1F mol^{-1} **24**. That the oxidized complex retained the quadruply bridged structure of its neutral precursor was indicated by the EPR spectrum of **24**⁺ (-50°C , CH_2Cl_2), showing hyperfine coupling consistent with delocalization of the unpaired electron over two equivalent molybdenum nuclei (Class III complex [65]). In contrast, the first oxidation occurred according to an EC process in MeCN. In this solvent, the one-electron oxidation of **24** led

to the opening of the chloride bridge and to the binding of MeCN at the exposed metal site [64]. The EPR spectrum of $[\text{Mo}_2(\text{cp})_2(\mu\text{-SMe})_3(\text{Cl})(\text{NCMe})]^+$ was consistent with the localization of the unpaired electron on one Mo center (Class I complex [65]). Similar spectra were obtained for analogous substituted complexes where the bound substrate was CO or an isocyanide molecule [64]. These reactions are illustrated in Sch. 17.

Since **24** does not react with $\text{Y}\equiv\text{Z}$ (CO, MeCN, RNC), the one-electron oxidation can be seen as “unlocking” the access to a coordination site. However, in the absence of $\text{Y}\equiv\text{Z}$, the chloride ligand remains in a bridging position, thus preventing the premature opening of the site. Furthermore, when the bound substrate is lost, which is the case for the MeCN ligand upon one-electron reduction of $[\text{Mo}_2(\text{cp})_2(\mu\text{-SMe})_3(\text{Cl})(\text{NCMe})]^+$, the chloride ligand moves back in the bridging position, thus preventing decomposition of the complex (Sch. 17). Therefore, the $\mu\text{-Cl}$ atom in **24** appears as an effective protective device, which possesses the desired properties (1)–(4) mentioned earlier.



Scheme 17 • = Mo-cp.

Modifications at the Mo_2S_3 core affect the electron transfer-induced reactivity of the chloride bridge. A complex closely related to **24**, namely $[\text{Mo}_2(\text{cp})_2(\mu\text{-S}_2\text{CH}_2)(\mu\text{-SMe})(\mu\text{-Cl})]$ **24'**, has been reported [60]. Comparison of the redox potentials of both species indicates that the $\{\text{Mo}_2(\mu\text{-SMe})_3\}$ core is slightly more electron-rich than $\{\text{Mo}_2(\mu\text{-S}_2\text{CH}_2)(\mu\text{-SMe})\}$ and that substitution of two SMe bridges by a bridging 1,1-dithiolate has a more pronounced effect for **24/24'** (**24**: $E_{1/2}^{\text{ox1}} = -0.40 \text{ V/Fc}$; $E_{1/2}^{\text{ox2}} = 0.34 \text{ V/Fc}$, $\text{thf}-[\text{NBu}_4][\text{PF}_6]$ [64]; **24'**: $E_{1/2}^{\text{ox1}} = -0.29 \text{ V/Fc}$; $E_{1/2}^{\text{ox2}} = 0.37 \text{ V/Fc}$, $\text{MeCN}-[\text{NBu}_4][\text{BF}_4]$ [60]) than for $(22^+)/(22'^+)$ (as seen earlier). In addition to producing this electronic effect, the substitution affects the reactivity of the complexes. Indeed, the first oxidation of **24'** is reversible on the CV timescale in MeCN [60]. Therefore, **24'** is missing the oxidatively induced reactivity of **24** (cf. Sch. 17). Examination of the electrochemical behavior of an other analog of **24**, $[\text{Mo}_2(\text{cp})_2(\mu\text{-SMe})_2(\mu\text{-PPh}_2)(\mu\text{-Cl})]$ **24''**, confirms the influence of the Mo_2E_3 core on the reactivity at the chloride bridge. Although the first oxidation of **24''** looks quasi-reversible in $\text{MeCN}-[\text{NBu}_4][\text{BF}_4]$, the reactivity of **24''** can be described by a mechanism similar to that in Sch. 17, with the substrate-binding step being a dynamic equilibrium, however [66].

20.3.5

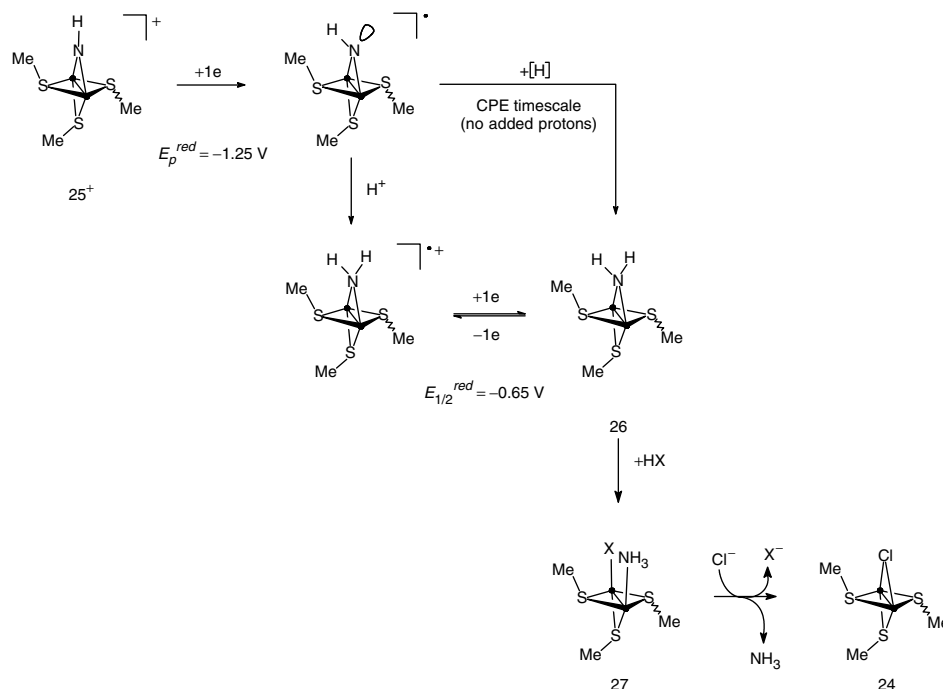
Electrochemical Transformations of Bound Substrate

A large part of the research involving metal–sulfur complexes (metal = molybdenum or iron) is aimed at designing functional models of the active site of nitrogenase, the iron–molybdenum cofactor, FeMo-co [4–8, 12, 13]. Only a very

limited number of dinitrogen complexes containing sulfur in the metal coordination sphere have been obtained [21]. However, a not so limited number of mono- or binuclear metal–sulfur sites react with nitrogenous molecules or ions to afford complexes containing $\{\text{N}\}$ or $\{\text{N}-\text{N}\}$ fragments bound to the metal center(s). Studies of the latter may give new insights in the mechanism of the enzyme-driven reactions.

In the family of compounds with the $\{\text{Mo}_2(\text{cp})_2(\mu\text{-SMe})_3\}$ core, complexes with ammine (NH_3) [67, 68], amido (NH_2^-) [67–69], imido (NH^{2-}) [68, 70], substituted diazene ($\text{R}-\text{N}=\text{N}-\text{H}$) or isodiazene/hydrazido(2–) [$\text{R}(\text{H})\text{N}=\text{N}/\text{R}(\text{H})\text{N}-\text{N}^{2-}$], and diazenido ($\text{R}-\text{N}=\text{N}^-$) [68, 71, 72] ligands have been isolated and characterized. Among them, the amido/imido complexes are related by a reduction step. Also, cleavage of the $\text{N}=\text{N}$ bond of diazene or isodiazene/hydrazido(2–) ligands, to produce imido or amido derivatives, requires several $\{\text{H}^+/\text{e}\}$ transfer steps.

The imido complex $[\text{Mo}_2(\text{cp})_2(\mu\text{-SMe})_3(\mu\text{-NH})]^+$ **25**⁺ undergoes an irreversible one-electron (EC) reduction [70]. Controlled potential electrolysis afforded the amido analog $[\text{Mo}_2(\text{cp})_2(\mu\text{-SMe})_3(\mu\text{-NH}_2)]$ **26** almost quantitatively after the transfer of 1F mol^{-1} **25**⁺. The amido complex was not the primary reduction product; the latter was assigned as a rearranged imide radical (Sch. 18), which is able to abstract a H-atom from the environment (supporting electrolyte, solvent, or adventitious water) on the electrolysis timescale. In the presence of protons, the reduction of **25**⁺ became a two-electron (ECE) process. This is consistent with the protonation at the nitrogen lone pair of the primary reduction product, followed by reduction of the resulting amido cation



Scheme 18 • = Mo–cp; X = TsO.

(Sch. 18). It must be noted that **25**⁺ can be protonated by HBF₄/Et₂O (or by HTsO) in MeCN. The protonation step producing [Mo₂(cp)₂(μ-SMe)₃(μ-NH₂)]²⁺ **26**²⁺ allowed the formation of the μ-amido to take place (CE process) at a potential about 600 mV less negative than the reduction of the imide cation **25**⁺ [70].

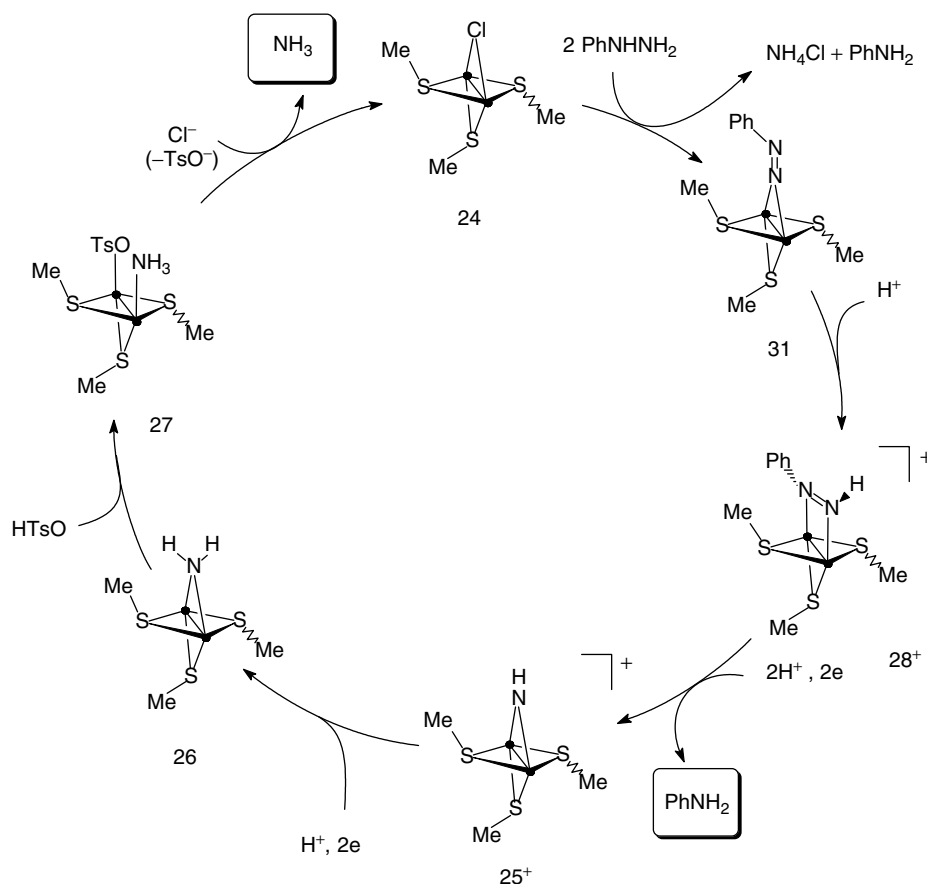
Controlled potential reduction of **25**⁺ in the presence of 3 equiv acid and 2–2.5 equiv [NEt₄][Cl] in a thf electrolyte produced [Mo₂(cp)₂(μ-SMe)₃(μ-Cl)] **24** (>95%) and [NH₄][Cl] (ca. 70% mol [NH₄]⁺ per mol of **25**⁺), after the transfer of 2 F mol⁻¹ **25**⁺. This demonstrated that an imide group bridging two molybdenum atoms in a sulfur environment can be reduced to ammonia via amide (**26**) and ammine (**27**) intermediates [70].

The electrochemical reductions of complexes with an organodiazene ligand [Mo₂(cp)₂(μ-SMe)₃(μ-η¹:η¹-H-N=N-R)]⁺ **28**⁺ (R = Me, Ph) and with a methylhydrazido(2-) (or isodiazene) ligand [Mo₂(cp)₂(μ-SMe)₃(μ-η¹-NN(H)Me)]⁺ **29**⁺ have been investigated [73]. Compounds **28**⁺ and **29**⁺ were obtained by protonation of the diazenido precursors [Mo₂(cp)₂(μ-SMe)₃(μ-μ-η¹:η¹-N=N-R)] **30**, or [Mo₂(cp)₂(μ-SMe)₃(μ-η¹-NNR)] **31** (R = Me or Ph). Complex **28**⁺ (R = Ph) undergoes a reversible one-electron reduction, which is followed by a chemical step (EC process). In the presence of acid, the reduction became irreversible with a substantial increase of the corresponding peak current (almost doubled at $v = 1$ V s⁻¹), indicative of the occurrence of a rapid ECE mechanism. At lower scan rates ($v \leq 0.4$ V s⁻¹),

the plot of the current function ($i_p^{red}/v^{1/2}$) versus scan rate deviates markedly from linearity thus showing that more electrons were transferred on a longer timescale. In agreement with this, controlled potential reduction of 28^+ ($R = Ph$) in the presence of an excess acid HX (4–6 equiv HX = HTsO or CF_3CO_2H ; thf-[NBu₄][PF₆] electrolyte) was completed after 4 to 6 F mol⁻¹ 28^+ (depending on the amount of acid) have been consumed. The electrolysis afforded either $[Mo_2(cp)_2(\mu-SMe)_3(\mu-NH_2)]$ **26** or $[Mo_2(cp)_2(\mu-SMe)_3(NH_3)(X)]$ **27** (depending on the amount of acid) and aniline. The dependence of the charge

passed on the amount of added acid suggested that H₂ might also be produced [73]. The formation of **26** (or **27**) and of PhNH₂ demonstrated that the N=N bond of the Ph–N=N–H ligand had been reductively cleaved. This allowed the construction of the cycle shown in Sch. 19 [68].

In contrast, no N=N bond rupture was observed in the case of the methyldiazene ligand (Sch. 20). However, electrochemical reduction of the hydrazido(2–)/isodiazene isomer $[Mo_2(cp)_2(\mu-SMe)_3(\mu-\eta^1-NN(H)Me)]^+$ **29**⁺ in the presence of acid also afforded **26** and methylamine, showing that the N–N bond had been cleaved



Scheme 19 • = Mo–cp.



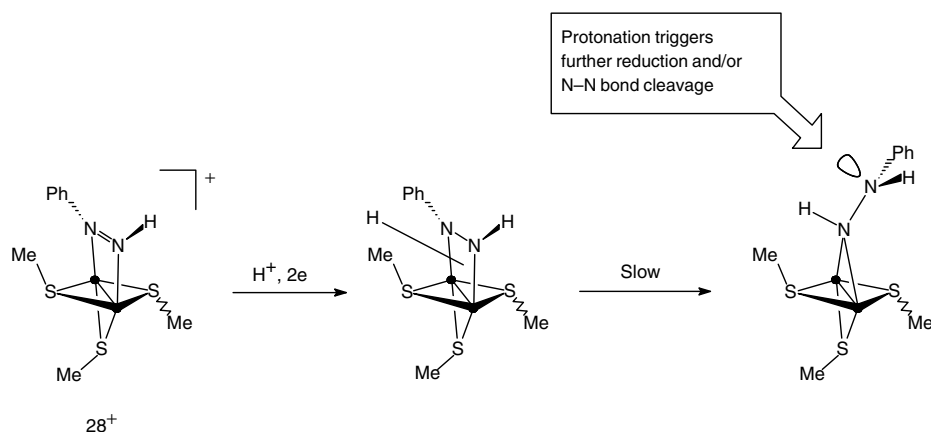
● = Mo-cp; X = TsO or CF₃CO₂.

(Sch. 20) [73]. In this case also, it is likely that dihydrogen was a coproduct of the electrolysis.

The behavior of 28^+ in terms of reductive cleavage of the N=N bond was thus different depending on whether R = Me or Ph. This was assigned to the electronic effect of the R substituent on the strength of the Mo–N(R) bond: whereas electron withdrawing R (R = Ph) would allow the release of the N(R) end of the ligand from the metal and a $\mu\text{-}\eta^1 : \eta^1 \rightarrow \mu\text{-}\eta^1$ rearrangement, probably at the hydrazido(1–) stage of the reduction process (Sch. 21), the electron-releasing Me substituent would not [73]. When R = Ph, protonation at the lone pair of the distant N atom would either cause the N–N bond cleavage in the resulting

cation, or allow further reduction of the latter and eventually N–N bond cleavage (Sch. 21). The fact that the metal product arising from the N–N bond rupture, respectively a bent imide cation or radical, was shown to reduce to **26** (or **27**) in the presence of acid, at a potential about 1 V less negative than the reduction of **28**⁺ (R = Ph), is consistent with the proposed mechanism [70, 73].

From the effect of the R substituent on the mechanism and products of the reduction of **28**⁺ (R = Me or Ph), it was concluded that reductive cleavage of the N=N bond of a $\mu\text{-}\eta^1\text{:}\eta^1$ coordinated organodiazene might occur only in particular cases. Therefore, this type of coordination might be a dead-end as far as the N=N bond cleavage is



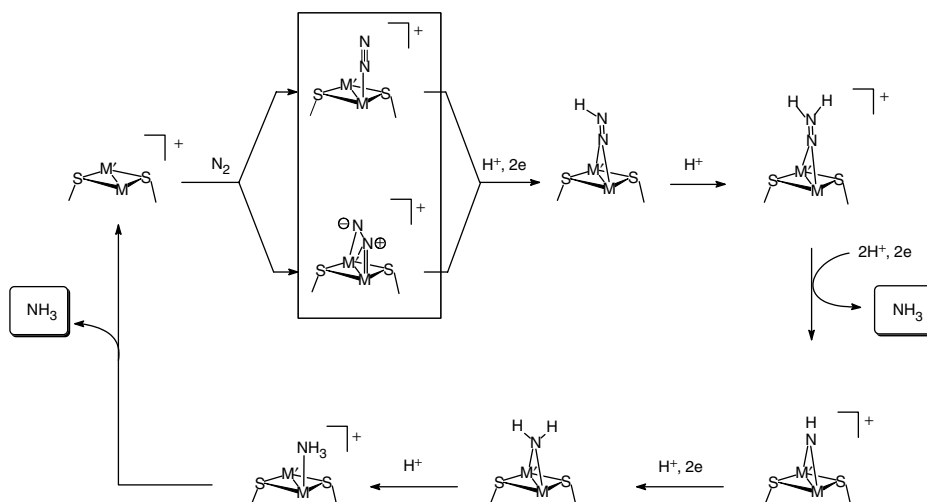
Scheme 21 • = Mo–cp.

concerned, at least at the $\{\text{Mo}_2(\text{cp})_2(\mu\text{-SMe})_3\}$ core [73].

In the earlier examples, the binuclear complexes with a $\{\text{Mo}_2\text{S}_3\}$ core clearly cannot be seen as modeling the metal sites in FeMo–co since it is known to contain a single molybdenum center [74]. However, what is suggested by these studies is that several steps (if not all) of the reduction of dinitrogen to ammonia by Mo–nitrogenase could take place at a

bimetallic-sulfur site. The different steps in Sch. 22 (M and M' could be similar or different) were proposed on the bases of the chemistry and electrochemistry involving the $\{\text{Mo}_2(\text{cp})_2(\mu\text{-SMe})_3\}$ core, except for the key N_2 -binding step (boxed in Sch. 22), which has not been observed yet [73].

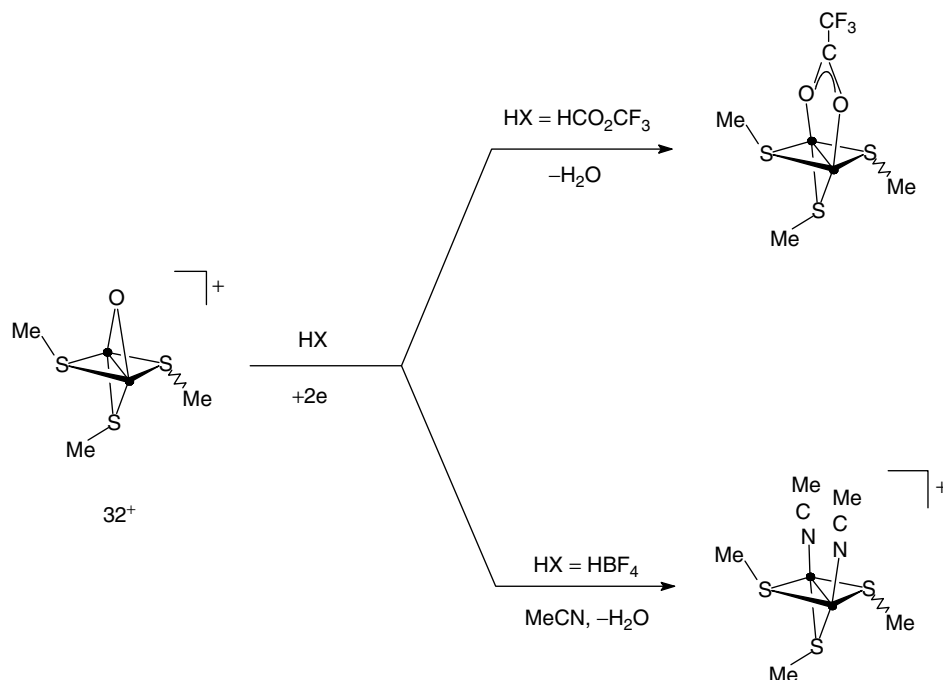
The electrochemical study of the μ -oxo complex $[\text{Mo}_2(\text{cp})_2(\mu\text{-SMe})_3(\mu\text{-O})]^+ 32^+$ [75], which is isoelectronic with the

Scheme 22 Proposed cycle for the reduction of N_2 at a bimetallic-sulfur site.

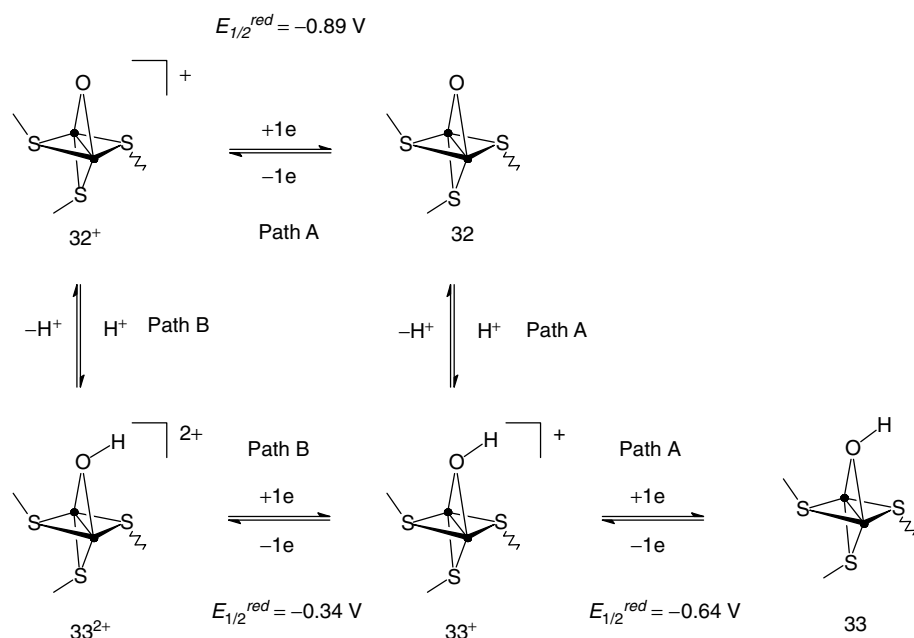
imido derivative 25^+ , is another example of electrochemically induced transformation of a ligand (the oxo bridge) and of the electrochemical generation of substrate-binding sites. In this study, it was shown that the controlled potential reduction of 32^+ in the presence of acid resulted in the protonation of the oxo bridge, which was eventually released as a water molecule, after transfer of ca. $2F \text{ mol}^{-1}$ 32^+ , when a coordinating anion or solvent was present (Sch. 23).

The detailed investigation of the reduction mechanism by CV in $\text{thf}-[\text{NBu}_4][\text{PF}_6]$ showed that the first steps of the reduction of 32^+ in the presence of acid occurred according to an $\text{EC}_{\text{rev}}\text{E}$ mechanism in which the intervening chemical reaction is a protonation equilibrium (Sch. 24, Path A). Therefore, in the presence of 1 equiv acid, the diffusion-controlled, one-electron

reduction of 32^+ ($E_{1/2}^{\text{red}} = -0.89 \text{ V/Fc}$) is replaced by a pseudo reversible two-electron system observed at $E_{1/2}^{\text{red}} \sim -0.7 \text{ V/Fc}$ ($\Delta E_p \sim 120 \text{ mV}$) that is at a potential intermediate between those of 32^+ and of the hydroxo-bridged complex 33^+ ($E_{1/2}^{\text{red}} = -0.64 \text{ V/Fc}$). As its imido analog 25^+ (as seen earlier), 32^+ could also be protonated by $\text{HBF}_4/\text{H}_2\text{O}$ in $\text{thf}-[\text{NBu}_4][\text{PF}_6]$. Therefore, reduction of 32^+ can take place according to a CE process (Sch. 24, Path B), at a potential by ca. 0.4 V less negative than in the absence of this protonation step ($E_{1/2}^{\text{red}} \sim -0.7 \text{ V/Fc}$), via the hydroxo dication 33^{2+} . This kind of mechanism where protonation of a ligand substantially facilitates the reduction of a metal center might be relevant to biological processes involving redox enzymes, due to the restricted potential range accessible to natural reductants.



Scheme 23 • = Mo-cp.



Scheme 24 • = Mo–cp.

The square scheme in Sch. 24 allowed estimating the effect of the reduction of the complexes on the basicity of the oxo bridge, in the $33^{2+}/32^+$ and $33^+/32$ couples. The ΔpK_a was found to be ca. 9 units in $\text{thf} - [\text{NBu}_4][\text{PF}_6]$ ($E_{1/2}^{red} (33^{2+}/33^+) = -0.34 \text{ V/Fc}$) and 11 units in $\text{MeCN} - [\text{NBu}_4][\text{PF}_6]$ ($E_{1/2}^{red} (33^{2+}/33^+) = -0.24 \text{ V/Fc}$). Although these values are only approximate due to the quasi-reversible character of the $33^{2+}/33^+$ couple, they illustrate the substantial effect of the reduction of 32^+ on the basicity of the oxo bridge.

20.4

Conclusion

Electrochemistry is a powerful analytical and synthetic tool. The few examples described earlier illustrate that control of the electron transfers by controlling

the electrode potential allows selective transformations of complexes or those of bound substrates, which would be difficult, or impossible, to accomplish chemically.

Beyond thermodynamic information, CV gives access to reaction mechanisms, which is one of the fundamental challenges of molecular electrochemistry, through the detection of intermediates, and to the kinetics of chemical steps coupled to the electron transfer events. In this way, useful chemical information is also provided. The use of electrochemical techniques can help understand mechanisms (or part of them) of biological processes, involving $\{\text{H}^+/\text{e}\}$ transfer steps, catalyzed by metalloenzymes, through the investigations of much less complicated model compounds. In the field of biomimetic chemistry, detailed investigations of the effect of a redox step on the acid/base properties of a ligand, and conversely,

examinations of the consequences of protonating an even weakly basic ligand on the reduction potential and mechanism of the metal center(s) of synthetic models are particularly needed.

Acknowledgments

Part of the studies described in this contribution comes from the authors' laboratory. We are thankful to our coworkers and students who took an active part in these studies, and whose names can be found in the references.

References

1. R. H. Holm, *Coord. Chem. Rev.* **1990**, *100*, 183–221; R. H. Holm, *Chem. Rev.* **1987**, *87*, 1401–1449, and references therein.
2. C. D. Garner, S. Bristow, in *Molybdenum Enzymes, Metal Ions in Biology*, Vol. 7 (Ed.: T. G. Spiro), Wiley, New York, 1985, pp. 343–410, Chapter 7, and references therein.
3. R. S. Pilato, E. I. Stiefel, in *Bioinorganic Catalysis*, 2nd ed. (Eds.: J. Reedijk, E. Bouwman), Marcel Dekker, New York, 1999, pp. 81–152, Chapter 6, and references therein.
4. R. H. Holm, P. Kennepohl, E. I. Solomon, *Chem. Rev.* **1996**, *96*, 2239–2314, and references therein.
5. R. H. Holm, E. D. Simhon, in *Molybdenum Enzymes, Metal Ions in Biology*, Vol. 7 (Ed.: T. G. Spiro), Wiley, New York, 1985, pp. 1–87, Chapter 1, and references therein.
6. D. Coucouvanis, in *Molybdenum Enzymes, Cofactors, and Model Systems*, ACS Symposium Series 535 (Eds.: E. I. Stiefel, D. Coucouvanis, W. E. Newton), American Chemical Society, Washington, DC, 1993, pp. 304–331, Chapter 20, and references therein.
7. D. Sellmann, in *Molybdenum Enzymes, Cofactors, and Model Systems*, ACS Symposium Series 535 (Eds.: E. I. Stiefel, D. Coucouvanis, W. E. Newton), American Chemical Society, Washington, DC, 1993, pp. 332–345, Chapter 20, and references therein.
8. M. Hidai, Y. Mizobe, *Chem. Rev.* **1995**, *95*, 1115–1133, and references therein.
9. M. Rakowski DuBois, *J. Clust. Sci.* **1996**, *7*, 293–315; M. Rakowski DuBois, *Chem. Rev.* **1989**, *89*, 1–9, and references therein.
10. P. Zanello, *Coord. Chem. Rev.* **1988**, *83*, 199–275, and references therein.
11. H.-B. Kraatz, P. M. Boorman, *Coord. Chem. Rev.* **1995**, *143*, 35–69, and references therein.
12. F. Y. Pétillon, P. Schollhammer, J. Talarmin et al., *Coord. Chem. Rev.* **1998**, *178–180*, 203–247, and references therein.
13. J. R. Dilworth, N. Weathley, *Coord. Chem. Rev.* **2000**, *199*, 89–158, and references therein.
14. W. E. Geiger, *Prog. Inorg. Chem.* **1985**, *33*, 275–352, and references therein.
15. D. H. Evans, K. M. O'Connell, in *Electroanalytical Chemistry* (Ed.: A. J. Bard), Marcel Dekker, New York, 1986, pp. 113–207, Vol. 14, and references therein.
16. A. J. L. Pombeiro, M. F. Guedes da Silva, M. A. N. D. A. Lemos, *Coord. Chem. Rev.* **2001**, *219–221*, 53–80, and references therein.
17. T. Yoshida, T. Adachi, T. Ueda et al., *Angew. Chem., Int. Ed. Engl.* **1987**, *26*, 1171–1172; T. Yoshida, T. Adachi, T. Ueda et al., *Angew. Chem., Int. Ed. Engl.* **1989**, *28*, 1040–1042; T. Adachi, N. Sasaki, T. Ueda et al., *J. Chem. Soc., Chem. Commun.* **1989**, 1320–1322.
18. T. Yoshida, T. Adachi, M. Kaminaka et al., *J. Am. Chem. Soc.* **1988**, *110*, 4872–4873.
19. T. Yoshida, T. Adachi, K. Kawazu et al., *Angew. Chem., Int. Ed. Engl.* **1991**, *30*, 982–984.
20. T. Adachi, M. D. Durrant, D. L. Hughes et al., *J. Chem. Soc., Chem. Commun.* **1992**, 1464–1467.
21. D. Sellmann, B. Hautsch, A. Rössler et al., *Angew. Chem., Int. Ed. Engl.* **2001**, *40*, 1505–1507.
22. T. I. Al Salih, C. J. Pickett, *J. Chem. Soc., Dalton Trans.* **1985**, 1255–1264.
23. J. R. Bradbury, F. A. Schultz, *Inorg. Chem.* **1986**, *25*, 4408–4416.
24. F. A. Schultz, *J. Electroanal. Chem.* **1986**, *273*, 169–174.
25. J. U. Mondal, F. A. Schultz, *Inorg. Chim. Acta* **1989**, *157*, 5–7.
26. J. R. Dilworth, B. D. Neaves, C. J. Pickett et al., *Inorg. Chem.* **1983**, *22*, 3524–3529.
27. S. K. Ibrahim, C. J. Pickett, *J. Chem. Soc., Chem. Commun.* **1991**, 246–249.

28. D. Sellmann, B. Seubert, F. Knoch et al., *Z. Naturforsch* **1991**, 46b, 1449–1458.
29. B. L. Crichton, J. R. Dilworth, C. J. Pickett et al., *J. Chem. Soc., Dalton Trans.* **1981**, 419–424.
30. O. A. Rajan, M. McKenna, J. Noordik et al., *Organometallics* **1984**, 3, 831–840.
31. M. Rakowski DuBois, D. L. DuBois, M. C. VanDerveer et al., *Inorg. Chem.* **1981**, 20, 3064–3071.
32. J. Courtot-Coupez, M. Guéguen, J. E. Guerschais et al., *J. Organomet. Chem.* **1986**, 312, 81–95.
33. A. Shaver, B. Soo Lum, P. Bird et al., *Inorg. Chem.* **1990**, 29, 1832–1835.
34. F. Y. Pétillon, S. Poder-Guillou, P. Schollhammer et al., *New J. Chem.* **1997**, 21, 477–494.
35. E. Ahlberg, O. Hammerich, V. D. Parker, *J. Am. Chem. Soc.* **1981**, 103, 844–849.
36. R. G. Finke, R. H. Voegeli, E. D. Laganis et al., *Organometallics* **1983**, 2, 347–350.
37. D. T. Pierce, W. E. Geiger, *J. Am. Chem. Soc.* **1992**, 114, 6063–6073.
38. B. Zhuang, J. W. McDonald, F. A. Schultz et al., *Organometallics* **1984**, 3, 943–945.
39. B. Zhuang, J. W. McDonald, F. A. Schultz et al., *Inorg. Chim. Acta* **1985**, 99, L29–L31.
40. D. A. Smith, B. Zhuang, W. E. Newton et al., *Inorg. Chem.* **1987**, 26, 2524–2531.
41. J. B. Fernandes, L. Qun Zhang, F. A. Schultz, *J. Electroanal. Chem.* **1991**, 297, 145–161.
42. D. J. Darensbourg, K. M. Sanchez, J. Reibenspies, *Inorg. Chem.* **1988**, 27, 3636–3643.
43. B. Zhuang, L. R. Huang, L. J. He et al., *Acta Chim. Sin.* **1986**, 4, 294–300.
44. B. Zhuang, L. Huang, Y. Yang et al., *J. Struct. Chem.* **1985**, 4, 103–106.
45. B. Zhuang, L. Huang, L. He et al., *Inorg. Chim. Acta* **1989**, 157, 85–90.
46. B. Zhuang, H. Sun, G. Pan et al., *J. Organomet. Chem.* **2001**, 640, 127–139.
47. M. El Khalifa, F. Y. Pétillon, J.-Y. Saillard et al., *Inorg. Chem.* **1989**, 28, 3849–3855.
48. P. Madec, K. W. Muir, F. Y. Pétillon et al., *J. Chem. Soc., Dalton Trans.* **1999**, 2371–2383.
49. T. E. Gennett, W. E. Geiger, B. Willett et al., *J. Electroanal. Chem.* **1987**, 222, 151–160.
50. N. G. Connelly, L. F. Dahl, *J. Am. Chem. Soc.* **1970**, 92, 7470–7472.
51. R. A. Marcus, *J. Chem. Phys.* **1965**, 43, 679.
52. N. S. Hush, *Electrochim. Acta* **1968**, 13, 1005.
53. D. Sellmann, G. Binker, J. Schwarz et al., *J. Organomet. Chem.* **1987**, 323, 323–338.
54. M. Guéguen, J. E. Guerschais, F. Y. Pétillon et al., *J. Chem. Soc., Chem. Commun.* **1987**, 557–559; M. El Khalifa, M. Guéguen, R. Mercier et al., *Organometallics* **1989**, 8, 140–148.
55. M. Guéguen, F. Y. Pétillon, J. Talarmin, *Organometallics* **1989**, 8, 148–154.
56. F. Gloaguen, C. Le Floch, F. Y. Pétillon et al., *Organometallics* **1991**, 10, 2004–2011.
57. F. Y. Pétillon, P. Schollhammer, J. Talarmin unpublished results.
58. M. El Khalifa, J.-Y. Saillard, F. Gloaguen et al., *New J. Chem.* **1992**, 16, 847–854.
59. M.-L. Abasq, D. L. Hughes, F. Y. Pétillon et al., *J. Chem. Soc., Dalton Trans.* **1997**, 2279–2291.
60. D. S. Tucker, S. Dietz, K. G. Parker et al., *Organometallics* **1995**, 14, 4325–4333.
61. M. Rakowski DuBois, J. Talarmin, unpublished results.
62. A. M. Allgeier, C. A. Mirkin, *Angew. Chem., Int. Ed. Engl.* **1998**, 37, 894–908, and references therein.
63. M. B. Gomes de Lima, J. E. Guerschais, R. Mercier et al., *Organometallics* **1986**, 5, 1952–1964.
64. F. Barrière, Y. Le Mest, F. Y. Pétillon et al., *J. Chem. Soc., Dalton Trans.* **1996**, 3967–3976.
65. M. B. Robin, P. Day, *Adv. Inorg. Chem. Radiochem.* **1967**, 10, 247.
66. C. Le Roy, F. Y. Pétillon, K. W. Muir et al., submitted for publication.
67. F. Y. Pétillon, P. Schollhammer, J. Talarmin, *J. Chem. Soc., Dalton Trans.* **1997**, 4019–4024.
68. F. Y. Pétillon, P. Schollhammer, J. Talarmin et al., *Inorg. Chem.* **1999**, 38, 1954–1955.
69. P. Schollhammer, F. Y. Pétillon, S. Poder-Guillou et al., *Chem. Commun.* **1996**, 2633–2634.
70. J.-Y. Cabon, C. Le Roy, K. W. Muir et al., *Chem. Eur. J.* **2000**, 6, 3033–3042.
71. P. Schollhammer, E. Guénin, F. Y. Pétillon et al., *Organometallics* **1998**, 17, 1922–1924.
72. P. Schollhammer, B. Didier, N. Le Grand et al., *Eur. J. Inorg. Chem.* **2002**, 658–663.
73. N. Le Grand, K. W. Muir, F. Y. Pétillon et al., *Chem. Eur. J.* **2002**, 8, 3115–3127.
74. J. S. Kim, D. C. Rees, *Science* **1992**, 257, 1677–1682; O. Einsle, F. A. Teczan, S. L. A. Andrade et al., *Science* **2002**, 297, 1696–1700.
75. M. Le Hénanf, C. Leroy, K. W. Muir et al., *Eur. J. Inorg. Chem.* **2004**, 1687–1700.

21

Aspects of Metallo-sulfur Clusters' Electrochemistry

Frédéric Barrière
Université de Rennes, Rennes, France

21.1	Introduction	593
21.2	Abiological Iron–Sulfur Clusters' Electrochemistry: The Black Roussinate as an Example	594
21.3	Models of Iron–Sulfur Centers in Protein	595
21.3.1	Models of $\text{Fe}(\text{SR})_4$ Sites	595
21.3.2	Models of $\text{Fe}_2\text{S}_2(\text{SR})_4$ Sites	596
21.3.3	Models of Linear $\text{Fe}_3\text{S}_4(\text{SR})_4$ or Cuboidal $\text{Fe}_3\text{S}_4(\text{SR})_3$ Sites	596
21.3.4	Models of $\text{Fe}_4\text{S}_4(\text{SR})_4$ Sites, The Iron-protein of Nitrogenase as an Example	597
21.4	Bridged Iron–Sulfur Molecular Assemblies	599
21.4.1	Nitrogenases	599
21.4.1.1	Introduction	599
21.4.1.2	Electrochemistry of the Fe_8S_7 P Cluster and Models	601
21.4.1.3	Electrochemistry of the MoFe_7S_9 FeMo Cofactor and Models	602
21.4.2	Hydrogenases	603
21.5	Conclusions	604
	References	605

21.1 Introduction

Iron–sulfur cluster synthesis in the laboratory and the subsequent study of their electrochemical properties has been driven and stimulated by the occurrence and characterization of such centers in many redox enzymes. The reason for the ubiquitous occurrence of these clusters in the biological world may rest on the abundance and wide availability of these two elements on earth. However, the chemical properties of iron and sulfur also seem well suited to meet the needs of some proteins in terms of electron transfer and catalysis. Indeed, iron electrochemical properties (discussed in Chapter 16) bring some latitude in spin and oxidation states for these centers. Here again, iron oxidation state two and three are overwhelmingly dominant, especially because of the moderate oxidizing and reducing potentials available in biology. Sulfur fills the coordination sphere of iron, yielding pseudotetrahedral centers. Two types of sulfur ligands are found: thiolate and sulfide. The thiolate itself is in fact cysteinate, from the natural cysteine amino acid, and provides an anchor between the active inorganic center and the protein within? it is buried. Cysteinate may coordinate in a terminal fashion or in a bridging fashion between two iron

centers. Sulfide ligands are found bridging two or three centers usually, but in some instances also up to six iron atoms as in one of the characterized structures of a nitrogenase metal–sulfur site (the P cluster, *vide infra*). Sulfur being in the third row of the periodical classification of the elements, its diffuse orbitals and low-lying empty d orbitals are likely to participate in strong hydrogen bonds or even in a reaction leading to protonation of the ligand to hydrosulfide. This combination of individual atomic properties, together with the assembly of biological iron–sulfur clusters ranging from one to as many as seven iron centers, which may also accommodate other metals, give these chemical assemblies a large modularity as elementary pieces of the complex living world [1]. Of course, in trying to mimic and understand these biological inorganic centers, chemists have produced an immense array of original, abiological clusters, interesting in their own right, and by nature electrochemically active, which also contribute to the understanding of the properties of this family of compounds, whether they are biological or not [2]. It is only fair and right to recall that iron–sulfur chemistry perhaps started with the synthesis of $[\text{Fe}_4\text{S}_3(\text{NO})_7]^-$ and related species by Roussin in 1858 [3]. This example shows that terminal coordination at iron is not

restricted to thiolate (NO here), especially in synthetic species, and many other terminal ligands may be found. Even in biology, some unexpected ligands may occur as we shall discuss later for hydrogenase (see also Sect. 16.2.2.4).

This section is organized as follows: we first start with a discussion of the electrochemical behavior of the Roussin-type synthetic iron–sulfur clusters for their historic importance and as an interesting introduction to poly iron–sulfur centers' redox chemistry. Then we review iron–sulfur centers in proteins and artificial models in the order of increasing iron content. Finally, biological iron–sulfur centers and artificial models directly linked to other inorganic centers, the so-called bridged molecular assemblies, are considered,

with a focus on nitrogenases and hydrogenases.

21.2

Abiological Iron–Sulfur Clusters'

Electrochemistry: The Black Roussinate as an Example

A recent review on abiological iron–sulfur clusters should be the primary entry reference to anyone wishing to gain information on this wide field [2]. Indeed, Ogino et al. provide a comprehensive source of data, of synthetic, structural, spectroscopic, and electrochemical nature, on many synthetic iron–sulfur clusters. The electrochemical properties of Roussin's black anion [3] have been investigated

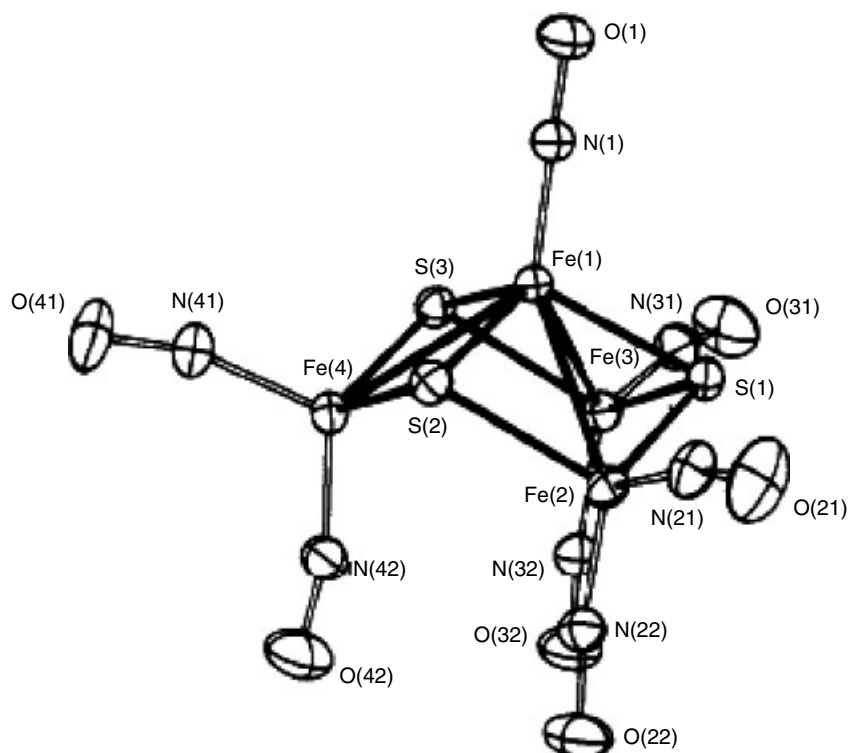


Fig. 1 Structure of $[(\text{NO})\text{Fe}(\mu_3\text{-S})_3\text{Fe}_3(\text{NO})_6]^-$ (from Ref. 4).

[4]. The $[(\text{NO})\text{Fe}(\mu_3\text{-S})_3\text{Fe}_3(\text{NO})_6]^-$ anion (cf Fig. 1) is best described as a trigonal pyramid of iron with each of its face being capped by a triply bridging sulfur atom. The apical iron atom capping the pyramid has one terminal nitrosyl ligand and shares metal–metal bonds with all three iron atoms of the pyramid base. These iron atoms do not themselves share metal–metal bonds and have two nitrosyl ligands each: one axial and one equatorial. The idealized point group symmetry of the cluster is C_{3v} . NO is a strong π -acceptor ligand, so that it is expected to stabilize electron-rich metal centers. The black Roussinate monoanion is indeed sequentially and reversibly reducible in three consecutive monoelectronic steps to three more reduced states, at the rather negative potentials of -0.68 , -1.26 , and -1.75 V versus saturated calomel electrode (SCE) in acetonitrile. The paramagnetic dianion has been generated in tetrahydrofuran by sodium naphthalenide reduction, and then crystallized. The structure of the dianion confirmed that there is no major structural change upon reduction, as was suggested by the chemical and electrochemical reversibility of the reduction. When the crystal structures of the mono- and dianion with the same countercation (Et_4N^+) are compared, the very good π -acceptor nature of the nitrosyl ligand is noticeable in a significantly shorter average N–O bond

length in the reduced state (1.646 versus 1.667 Å) and longer Fe–N distance (1.176 versus 1.161 Å). Because all three redox processes are reversible, it is anticipated that the cluster does not experience major structural change upon reduction. The trianion could only be studied and generated in solution by sodium reduction in hexamethylphosphortriamide.

21.3

Models of Iron–Sulfur Centers in Protein

The synthesis, structures, and properties of analogs of iron–sulfur protein active sites has been recently reviewed by Venkateswara Rao and Holm [5]. In the order of increasing iron content, these sites are of $\text{Fe}(\text{SR})_4$, $\text{Fe}_2\text{S}_2(\text{SR})_4$, $\text{Fe}_3\text{S}_4(\text{SR})_4$, or $\text{Fe}_3\text{S}_4(\text{SR})_3$, and $\text{Fe}_4\text{S}_4(\text{SR})_4$ stoichiometry (cf. Fig. 2) and are now briefly treated.

21.3.1

Models of $\text{Fe}(\text{SR})_4$ Sites

Although not a metallic cluster, the simplest iron–sulfur center of proteins and its synthetic analogs are discussed here. $[\text{Fe}(\text{SR})_4]^-$ synthetic species are generally reversibly reduced to $[\text{Fe}(\text{SR})_4]^{2-}$ in aprotic solvents at potentials controlled, or tuned, by the nature of R. For example, $E_{1/2} = -1.11$ V versus SCE for $[\text{Fe}(\text{SPr}^i)_4]^{1-/2-}$

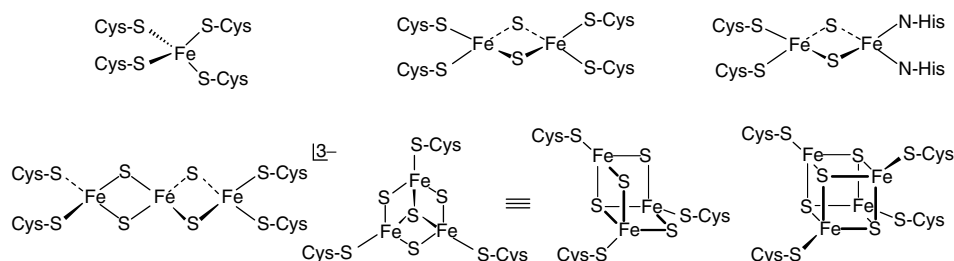


Fig. 2 Structures of simple iron–sulfur centers in proteins (from Ref. 5).

and -0.52 V for $[\text{Fe}(\text{SPh})_4]^{1-/2-}$. Functionalization of the phenyl ring allows for alteration of the Fe (III/II) redox potential via specific $\text{N}-\text{H}\cdots\text{S}$ hydrogen bonds, an effect that is of relevance to biological sites. For example, a positive shift of 250 mV is obtained with respect to $[\text{Fe}(\text{SPh})_4]^{1-/2-}$ when $\text{R} = 2-(\text{MeCONH})\text{C}_6\text{H}_4$ in acetonitrile. Water soluble derivatives like $[\text{Fe}(\text{SCH}_2\text{CH}_2\text{OH})_4]^{1-/2-}$ ($E_{1/2} = -0.35$ V) are more biologically relevant because of the solvent and associated hydrogen-bonding properties. However, specific interactions from the protein cannot be fully reproduced. Indeed, the redox potential of $[\text{Fe}(\text{SCH}_2\text{CH}_2\text{OH})_4]^{1-/2-}$ in water is close to the lower limit of FeS_4 sites in rubredoxin proteins (-0.1 to $+0.1$ V versus standard hydrogen electrode (SHE)).

21.3.2

Models of $\text{Fe}_2\text{S}_2(\text{SR})_4$ Sites

The synthetic $[\text{Fe}_2\text{S}_2(\text{SPh})_4]^{2-}$ complex has been shown to undergo two reductions in acetonitrile or dimethylformamide (DMF) at $E_{1/2} = -1.13$ and -1.41 V versus SCE. Again, $\text{N}-\text{H}\cdots\text{S}$ hydrogen bonds with functionalized phenyl groups shift this redox potential toward positive values. The first reduction product, $[\text{Fe}_2\text{S}_2(\text{SR})_4]^{3-}$, has some instability as it tends to dimerize to the more stable cubane-type cluster $[\text{Fe}_4\text{S}_4(\text{SR})_4]^{2-}$, with concomitant release of two equivalents of thiolate and one equivalent of disulfide. The biologically relevant cluster oxidation states involve the $[\text{Fe}_2\text{S}_2(\text{SR})_4]^{2-/3-}$ couple. Heteroligated biological site exists in Rieske protein where one of the iron centers is ligated to the polypeptide backbone via two histidine residues instead of cysteine. Accurate models for this site are not available although it is possible to get N_2S_2 terminal coordination by ligand

substitution reaction of $[\text{Fe}_2\text{S}_2\text{Cl}_4]^{2-}$ with bidentate chelating ligands. The very air-sensitive all-ferrous state ($[\text{Fe}_2\text{S}_2]^0$ core) of a Rieske protein has been generated and characterized, with E^0 for the $[\text{Fe}_2\text{S}_2]^{1+/0}$ couple being -0.73 V versus SHE at pH 7, that is, 1 V more negative than for $[\text{Fe}_2\text{S}_2]^{2+/1+}$ [6]. The $[\text{Fe}_2\text{S}_2]^0$ core is stabilized by protonation of one of the bridging sulfides at $\text{pH} > 9.8$. The basic nature of the bridging sulfide in iron-sulfur clusters is an important property that has been studied extensively [7].

21.3.3

Models of Linear $\text{Fe}_3\text{S}_4(\text{SR})_4$ or Cuboidal $\text{Fe}_3\text{S}_4(\text{SR})_3$ Sites

Linear $\text{Fe}_3\text{S}_4(\text{SR})_4$ clusters have been found in partially unfolded proteins, but are not known to exist as functional centers to date. Synthetic analogs comprise the all-ferric $[\text{Fe}_3\text{S}_4(\text{SPh})_4]^{3-}$ species (a $[\text{Fe}_3\text{S}_4]^{1+}$ core) that may be reduced to the corresponding $[\text{Fe}_3\text{S}_4]^0$ core at -1.35 V versus SCE in acetonitrile (-1.66 V for the ethylthiolate derivative).

The cuboidal $\text{Fe}_3\text{S}_4(\text{SR})_3$ sites have the Fe_4S_4 cubane-type structure of which one iron corner is missing. This open structure can accommodate a fourth metal ion, as in the aconitase enzyme that binds Fe^{2+} after one-electron reduction of the $[\text{Fe}_3\text{S}_4(\text{SCys})_3]^{2-}$ center. The enzyme then becomes active, and catalyzes the isomerization of citrate to isocitrate at the fourth iron site. The first synthetic analog of the "open-cube" $\text{Fe}_3\text{S}_4(\text{SR})_3$ sites has only been obtained recently [8]. It involves the uses of a tridentate thiolate ligand (LS_3) that acts as a cavitand for the Fe_3S_4 open-cube core. A whole new chemistry is being developed from this structure with binding of a fourth site-differentiated iron center or other metal fragments. The model

cluster exhibits two-electron-transfer processes involving the $[\text{Fe}_3\text{S}_4(\text{LS}_3)]^{2-/3-}$ and $[\text{Fe}_3\text{S}_4(\text{LS}_3)]^{3-/4-}$ of which only the first one is of biological relevance (redox potentials are -0.79 and -1.72 V respectively, versus SCE in acetonitrile).

21.3.4

Models of $\text{Fe}_4\text{S}_4(\text{SR})_4$ Sites, The Iron-protein of Nitrogenase as an Example

Fe_4S_4 clusters with cysteinate ligation at iron, in their $[\text{Fe}_4\text{S}_4]^{1+/2+/3+}$ redox states, are of pervasive occurrence in iron–sulfur proteins, functioning mostly as electron transfer relays as in ferredoxins ($1+/2+$, -0.3 to -0.8 V range versus normal hydrogen electrode (NHE)) and high potential iron-proteins ($2+/3+$, $+0.1$ to $+0.5$ V range versus NHE). Examples are also known where they are implied in catalysis [1, 5]. Mo-nitrogenase [9] is an enzyme responsible for the reduction of atmospheric nitrogen to ammonia. It comprises two proteins: the iron-protein and the molybdenum-protein. The Fe-protein specifically reduces the MoFe-protein with its Fe_4S_4 cluster cycling between the $[\text{Fe}_4\text{S}_4]^{1+}$ and $[\text{Fe}_4\text{S}_4]^{2+}$ redox states at a potential of -0.31 V versus NHE, that is lowered by about 0.1 V upon nucleotide binding. The Fe_4S_4 cluster is symmetrically bridged between the α -subunits of the iron-protein and is accessible to solvent molecules (H_2O). Vicinal amino-acid residues provide NH-S hydrogen bonds from amide groups to the iron–sulfur center. The $[\text{Fe}_4\text{S}_4]^0$ state can be artificially generated as a stable center within the iron-protein of nitrogenase (-0.79 V versus NHE); however, it is not known if this state is biologically relevant [10].

The iron–sulfur cluster of the iron-protein in its $[\text{Fe}_4\text{S}_4]^{1+}$ redox state exists in a mixture of spin states of similar energy

in frozen solution ($S = 3/2$ and $S = 1/2$). However, proton nuclear magnetic resonance (NMR) analysis suggests that in standard conditions, only one spin state is populated ($S = 1/2$). Proton NMR spectroscopy is useful for the analysis of paramagnetic iron–sulfur clusters (those with the $[\text{Fe}_4\text{S}_4]^{1+}$ and $[\text{Fe}_4\text{S}_4]^{3+}$ core). Indeed, significant low or high field hyperfine isotropic shifts for the resonance of the protons bound at the carbon β to an iron center greatly simplify the analysis of the chemical environment of each iron center of the protein even if the signal is usually broad. ^{57}Fe Mössbauer spectroscopy is a method of choice to assign the overall core oxidation state of a native or synthetic iron–sulfur cluster. There exists an empirical linear relationship between the ^{57}Fe Mössbauer spectroscopy isomer shift (i.s.) and the oxidation state (or mean oxidation state) of an iron center (or a cluster of iron centers) in a pseudotetrahedral sulfur environment [5].

Synthetic structural models for the Fe_4S_4 clusters have been known for three decades now [5]. They are readily prepared by self-assembly from ferric or ferrous chloride, a source of reduced sulfur and thiolates, acting as ligands to the iron sites (Fig. 2). Ligand substitution reactions at the iron centers allow the tuning over a large window of their redox potential that is linearly linked to the electron donor/acceptor properties of the ligands, usually an alkyl or phenyl thiolate, or a halide. Crystal structures of model Fe_4S_4 clusters with thiolate ligands are available for all $[\text{Fe}_4\text{S}_4]^{1+/2+/3+}$ redox states, the $[\text{Fe}_4\text{S}_4]^0$ state being only transiently generated in solution.

It has been shown that the Fe_4S_4 cluster of the Fe-protein can be further reduced with nonbiological reductants from the

$[\text{Fe}_4\text{S}_4]^{1+}$ to the $[\text{Fe}_4\text{S}_4]^0$ (all-ferrous) redox state, which suggests that the Fe-protein could transfer two electrons per reduction cycle to the MoFe-protein [10]. Although there is no precedence for a functional $[\text{Fe}_4\text{S}_4]^0$ state in biology, this is an attractive proposal considering (1) that substrates of nitrogenase can be reduced by multiple of two electrons, (2) that the dicubane structure of both the P cluster and the FeMo cofactor (vide infra) is perhaps tailored to accept two electrons at once, and (3) the homodimeric structure of the Fe-protein that may bind two donor molecules at a time [9, 10]. Moreover, the redox potential originally reported for the $[\text{Fe}_4\text{S}_4]^{1+/0}$ redox couple (-0.46 V versus NHE) was well within physiological range and only 150 mV negative to that of the $[\text{Fe}_4\text{S}_4]^{2+/1+}$ redox couple. The biological relevance of the $[\text{Fe}_4\text{S}_4]^0$ oxidation state, however, is contentious. In synthetic models with thiolate ligands, the all-ferrous redox state ($[\text{Fe}_4\text{S}_4]^0$) can be detected transiently in some instances at the cyclic voltammetry timescale, and has been first generated, but not isolated, as a persistent species in solution in the case of $\text{Fe}_4\text{S}_4(\text{PR}_3)_4$ bearing less biologically relevant phosphine ligands known to stabilize reduced oxidation states of metal complexes. Recently [11], the first Fe_4S_4 cluster in the zero oxidation state has been synthesized and characterized. Each iron atom has terminal cyanide ligands that allow the stabilization of such a reduced core. Indeed, compared to other clusters with terminal thiolate ligands, the redox potential of $[\text{Fe}_4\text{S}_4(\text{CN})_4]^{0/1+}$ is shifted positive by about 0.3 V. In acetonitrile, the $[\text{Fe}_4\text{S}_4(\text{CN})_4]^{0/1+}$ couple is detected at -1.42 V versus SCE and the $[\text{Fe}_4\text{S}_4(\text{CN})_4]^{1+/2+}$ at -0.44 V.

Such a narrow potential separation ($\Delta E = 0.15$ V) between the $2+/1+$ and

$1+/0$ redox couples of the iron-protein Fe_4S_4 cluster, was hard to reconcile with redox potentials of synthetic models. Indeed, a range of models with ligands differing by their charge, structure, and electron-withdrawing properties, has been studied electrochemically in dipolar aprotic organic solvent electrolytes (MeCN, DMF, dimethylsulfoxide (DMSO)) in order to assess the effect of the direct environment of the cluster core on its redox potentials [12]. The measured ΔE between the $2+/1+$ and $1+/0$ redox potentials of model clusters with thiolate ligands remains consistently in the range $\text{ca } 0.70 \pm 0.05$ V in organic solvent electrolytes, and $\text{ca } 0.40 \pm 0.02$ V in water. The reported absolute potential for the one-electron reduction of $[\text{Fe}_4\text{S}_4]^{1+}$ in nitrogenase was also too high compared to model system values generally reported to be in the range -1.50 to -1.85 V (SCE) in organic solvent electrolytes and $\text{ca } -1.2$ V (SCE) in water. Recently, the redox potential for the $[\text{Fe}_4\text{S}_4]^{1+/0}$ couple of the iron-protein has been measured at -0.79 V (NHE; i.e. $\text{ca } -1.03$ V SCE), corresponding to a ΔE of 0.48 V between the two redox couples, more in line with experimental and theoretical redox potential and associated ΔE in model clusters [12, 13].

The polypeptide environment of the iron-protein Fe_4S_4 cluster appreciably stabilizes the $[\text{Fe}_4\text{S}_4]^0$ state compared to corresponding model clusters. This can be assigned to the network of hydrogen bonds between the protein residues and the cluster sulfide groups, and, to some extent, to the accessibility of water molecules to the cluster. However, the iron-protein iron-sulfur cluster in its $[\text{Fe}_4\text{S}_4]^{1+}$ state does not appear to be reducible *in vivo* by known physiological electron donors, unless a currently unknown mechanism, such as a protein conformation change,

stabilizes the $[\text{Fe}_4\text{S}_4]^0$ state even more. Accurate synthetic models have helped to understand the structural, spectroscopic, and electronic properties of the Fe_4S_4 cluster, particularly that of the iron-protein of nitrogenase. Whether or not the $[\text{Fe}_4\text{S}_4]^0$ state is implied in the physiological electron-transfer chain in nitrogenase remains to be proven. However, the sole fact that this latter state can be generated as a stable center within the protein encourages the quest for stable synthetic models in the all-ferrous state and bearing terminal thiolate ligands. These future models might bear a ligand scaffold mimicking the immediate stabilizing protein environment of the native cluster. In particular, it would be interesting to study the effect in terms of structure and associated electronic properties (electron transfer) of specific hydrogen bonds to the bridging sulfides as a function of the oxidation state of the cluster core. The modeling of a dielectric medium similar to the polarity and Lewis acidity experienced by iron–sulfur centers within proteins might be imposed by ligands sharing both covalent and noncovalent bonds to the cluster core.

More complex iron–sulfur centers in the MoFe-protein of Mo-nitrogenase are discussed next.

21.4 Bridged Iron–Sulfur Molecular Assemblies

More complex assemblies of iron and sulfur, sometimes extended to other metals like nickel, molybdenum, vanadium, or other iron centers are found in some enzymes, that catalyze the transformation of small molecules [1, 14]. Among these centers, we will focus next on the P cluster and the FeMo cofactor of nitrogenase and on the H cluster of the iron-only hydrogenase.

21.4.1

Nitrogenases

21.4.1.1 Introduction

The most extensively studied nitrogenase enzyme contains two kinds of transition metals, namely, iron and molybdenum, and is called *molybdenum nitrogenase* [9]. In growth conditions where molybdenum concentration is low, a nitrogenase dependant on iron and vanadium is expressed [15]. When both molybdenum and vanadium are unavailable, a third type of nitrogenase is expressed that contains iron as the only transition metal [16]. The vanadium-nitrogenase and iron-only nitrogenases, also known as *alternative nitrogenases*, are related to the molybdenum nitrogenase but are all genetically distinct. A fourth and completely different “nonconventional” type of nitrogenase is known; it also contains iron and molybdenum, but couples dinitrogen reduction to the oxidation of superoxide and carbon monoxide [17].

Mo-nitrogenase is the only one for which both detailed structural and mechanistic data are available [9, 18]. The enzymatic complex comprises two proteins: the iron-protein and the molybdenum-iron-protein. The Fe-protein is an α_2 -homodimer with a Fe_4S_4 cluster (vide supra) bridging the two α -subunits via four iron-cysteinate ligations. Each α -monomer of the iron-protein possesses a nucleotide-binding site (ATP or ADP). The Fe-protein is a specific reductant of the MoFe-protein, an event that depends on, and is coupled to, the hydrolysis of MgATP. The MoFe-protein is an $\alpha_2\beta_2$ tetramer and contains two types of metal–sulfur centers: the so-called P cluster of Fe_8S_7 stoichiometry that is located at the interface of each homologous α – β subunit, and the FeMo cofactor (MoFe_7S_9) found in each α -subunit.

Two different structures are known for the P cluster (cf. Fig. 3) and are assigned to different cluster core oxidation states. In the reduced or P^N (native) state, the Fe_8S_7 cluster can be described as two Fe_4S_4 cubes sharing one common hexacoordinate sulfur atom, the iron atoms being linked to the protein by cysteinate ligands, two of them bridging the subcubes. In the P^{OX} state, oxidized by two electrons relative to P^N , the central sulfur atom loses two bonds with two iron atoms in one of the subcubes, thus becoming more open. The tetrahedral coordination of these two iron atoms is then completed by extra ligations from neighboring cysteine and serine residues.

The FeMo-cofactor structure can be viewed as the assembly of two incomplete

$Fe_4(\mu_3-S)_3$ and $MoFe_3(\mu_3-S)_3$ subcubes, linked together by three central μ_2-S bridging sulfide ligands (cf. Fig. 4). The six central iron atoms form an approximate trigonal prism centered on a light atom "Y" that has only been structurally recognized recently [18b]. The identity of the light atom has been proposed to be either nitrogen, carbon, or oxygen. Recently, the possibility of "Y" being a nitrogen atom seems to have been excluded [18d]. The pseudo-octahedral coordination of molybdenum is completed by the exogenous bidentate (*R*)-homocitrate ligand and by imidazole from a neighboring histidine residue. A cysteine residue, covalently bound to the tetrahedral apical iron atom, provides the cofactor with its other protein ligation.

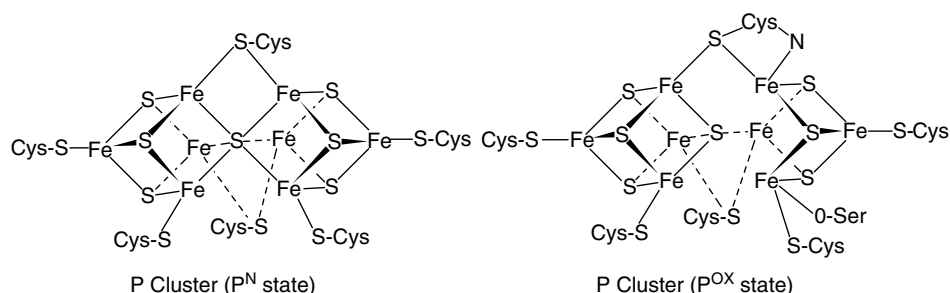


Fig. 3 Known structures of the P cluster of nitrogenase in two oxidation states.

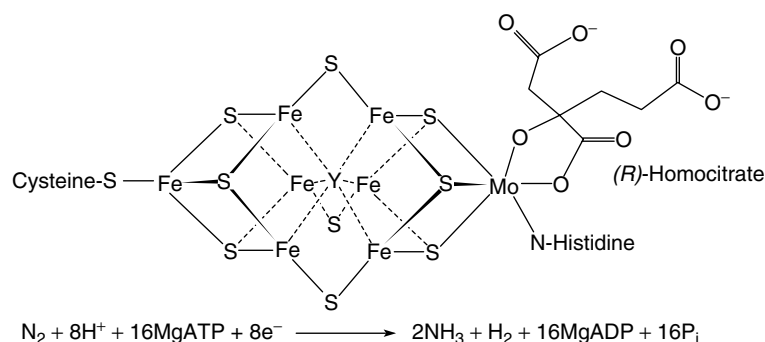


Fig. 4 Structures of the FeMo cofactor of nitrogenase (Y is C, N, or O) and limiting stoichiometry of the catalyzed reaction.

The electrons transferred from the Fe_4S_4 cluster of the iron-protein to the molybdenum-iron-protein are believed to shuttle through the P cluster before eventually reaching FeMo-co where N_2 binding, reduction, and protonation occurs.

The limiting stoichiometry for the reduction of one equivalent of dinitrogen by Mo-nitrogenase to two equivalents of ammonia involves the hydrolysis of 16 MgATP and the production of one molecule of dihydrogen, as outlined in Fig. 4. The three metal clusters found in Mo-nitrogenase belong to the diverse class of iron–sulfur prosthetic centers largely distributed in all living organisms. However, while the Fe_4S_4 center is a common cluster found in many other iron–sulfur proteins (*vide supra*), the P cluster and the FeMo cofactor represent unique structures in biology to date.

21.4.1.2 Electrochemistry of the Fe_8S_7 P Cluster and Models

The Fe_8S_7 inorganic core of the P cluster has been synthesized from tetramethylthiourea, 2,4,6-triisopropylbenzenethiol, elemental sulfur, and iron(II)bis(ditrimethylsilylamide) in toluene, in the respective 3/12/7/8 ratio [19]. The differences between the model and the native P cluster lie within the nature of the ligands to the iron–sulfur sites, the iron atoms' oxidation states and the shorter bond distances in the model around the central hexacoordinated sulfur. While the iron atoms are terminated or bridged by cysteinate ligands in the P cluster, different ligations are involved in the model. Indeed, the two opposite apical iron sites of the synthetic cluster have a terminal bis-amide ligation; thiourea completes the tetrahedral coordination of two opposite central iron atoms, and the two remaining pairs of opposite iron centers are linked by a bis-amide bridge. The tighter amide

bridge of the model compared to the cysteinate bridge found in the MoFe-protein explains the shorter $\mu_6\text{S}$ –Fe bonds and shorter distance between opposite central iron atoms in the model. ^{57}Fe Mössbauer spectroscopy of the model compound distinguishes two iron sites in a 3/1 ratio: each quadrupole doublet's isomer shift and quadrupole splitting are consistent respectively with six Fe(II) and two Fe(III), the former assigned to the six central iron atoms and the latter assigned to the two opposite apical iron centers. The oxidation state of the model (six ferrous/two ferric) is therefore directly related to that of the P cluster in the P^{OX} state. Nevertheless, the structure of the Fe_8S_7 core of the model resembles closely that of the P^{N} state, which is likely because the bridging amide prevents a more open structure similar to that of P^{OX} .

The model cluster has been reported to be very sensitive to oxygen and heat. This is consistent with the known instability of the P cluster toward extraction from the MoFe-protein. It is perhaps for this reason that no redox potentials were reported for the model.

In the as-isolated state [9], the diamagnetic P cluster can be oxidized to the P^{1+} and P^{2+} (P^{OX}) states at a midpoint potential of -0.309 V (NHE at pH 8). The identical midpoint potential for both the $\text{P}^{\text{N}}/\text{P}^{1+}$ and $\text{P}^{1+}/\text{P}^{2+}$ couples may be accounted for by a model in which both halves of the P cluster may be oxidized separately, and by the structural change observed between P^{N} and P^{OX} . The P^{2+} state (P^{OX}) may be further oxidized to P^{3+} ($\text{P}^{\text{SUPEROX}}$) at $E_{\text{m}} = 0.09$ V. With $E_{\text{m}} = -0.309$ V for $\text{P}^{\text{N}}/\text{P}^{\text{OX}}$, the P cluster seems well positioned for electron transfer from the MgATP bound iron–protein ($E_{\text{m}} = -0.600$ V). In a complex between

the iron–protein and the molybdenum–iron-protein, the P^N/P^{OX} E_m value is shifted negative to -0.390 V while that of the Fe_4S_4 cluster in the Fe-protein is -0.620 V. This may be required for the P cluster to be a better reductant of the FeMo cofactor. The additional cysteine and serine residues' ligation to the P cluster in the P^{OX} state have been proposed to serve as proton donor. Indeed, the E_m value for the P^{1+}/P^{2+} couple varies linearly with pH in the range pH 6.0 to 8.4 (-53 mV per pH unit). Despite these electrochemical data on the P-cluster redox potential and oxidation state, it is not yet clear as to which ones are relevant to the biological process, how this center reduces the FeMo cofactor, and whether it is the only specific iron–sulfur structure capable of sustaining nitrogenase reactivity [9c].

21.4.1.3 Electrochemistry of the MoFe₇S₉ FeMo Cofactor and Models

The FeMo cofactor (or M center) in the MoFe-protein is in the native paramagnetic M^N state. Reduction of the MoFe-protein by the Fe-protein results in the reduction of FeMo-co from the M^N state to the M^R state at a potential estimated to be less than -0.465 V (NHE). The electron paramagnetic resonance (EPR) silent M^R state is only transiently produced during catalysis, and relaxes to the M^N state when catalysis stops. The intimate consequences of the M^N state reduction are not precisely known. A more oxidized diamagnetic state may also be generated (M^{OX}) at -0.042 V but its biological relevance is unclear [9].

The electrochemistry of the extracted FeMo cofactor has also been studied in depth [20]. Extracted *N*-methyl formamide (NMF) solutions of FeMo-co contain the intact cluster, probably with retention of the exogenous homocitrate ligand. Protein ligation are replaced with NMF ligands at

Mo and apical Fe. The as-isolated FeMo-co in reducing conditions (dithionite) is in the EPR active ($S = 3/2$) so-called “semireduced” state. FeMo-co^{semired} may be oxidized to FeMo-co^{ox} at -0.32 V (NHE), a process that is complicated by a redox-linked isomerization of mono- to bidentate coordination mode of the $MeNHCHO^-$ anion at the apical iron atom. Addition of thiophenolate to the solution simplifies the redox process by ligand substitution at this iron site. A partially reversible one-electron reduction step, corresponding to FeMo-co^{semired/red} is observed at about -1 V, followed by an irreversible process at some 150 mV more negative. The ox/semireduced/reduced triad is proposed to be associated with the cluster core reduction while the last process would be more localized at the molybdenum center. Interaction of extracted FeMo-co with substrates or inhibitors like proton, carbon monoxide or cyanide is informative given that (1) no interaction between dinitrogen and FeMo-co has been shown, (2) nitrogenase is also a hydrogenase, (3) CO binds to FeMo-co in the MoFe-protein. Details of these interactions may be found in Ref. 20. In short, the semireduced state of extracted FeMo-co catalyzes H_2 evolution at high acidity (-0.28 V) in the presence of thiophenol (both an acid and ligand for the apical iron site). At low acidity, H_2 evolution occurs at the reduced FeMo-co state. CO binding to the iron–sulfur core involves a two-electron reduction of the semireduced FeMo-co. Upon CO release, the semireduced state is recovered via oxidation by protons. The third-electron-transfer process (reduced/super reduced) is associated with a second CO binding site, probably at Mo. Accurate models of the FeMo cofactor are not available but are being actively pursued [21].

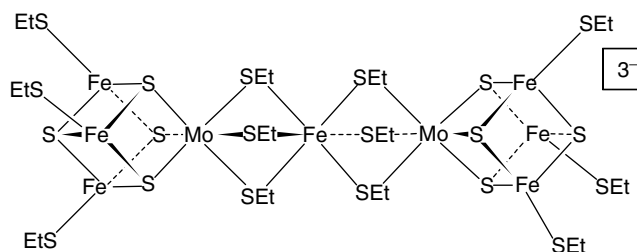


Fig. 5 The double cubane $[\text{Mo}_2\text{Fe}_7\text{S}_8(\text{SET})_{12}]^{3-}$ cluster.

The fragment of FeMo-co that has been most accurately modeled by synthetic clusters is its molybdenum cap. Indeed, cubane-like MoFe_3S_4 clusters reproduce very well the first and second coordination sphere of molybdenum in nitrogenase. MoFe_3S_4 clusters are usually synthesized from the double cubane $[\text{Mo}_2\text{Fe}_7\text{S}_8(\text{SET})_{12}]^{3-}$ (Fig. 5) whose central iron bridge can be cleaved to yield independent MoFe_3S_4 monocubes [22, 23]. The $[\text{Mo}_2\text{Fe}_7\text{S}_8(\text{SET})_{12}]^{3-}$ double cubane has an interesting electrochemistry. The first reduction is associated with the central low-spin iron(III) center. The monoelectronic reduction to iron(II) is associated with a spin state change, confirmed by Mössbauer spectroscopy, and by an increase of the Fe–S bond length by an average of 0.2 Å. Electrochemically, these structural and spin state changes translate into a quasi-reversible reduction (slow electron transfer) as shown by an increase of the ΔE_p at low temperature (ΔE_p increase from 80 to 270 mV between 293 and 243 K). The two other redox-active sites in this cluster are the equivalent MoFe_3S_4 cubes that undergo a monoelectronic reduction at very close potentials (about 90 mV apart). Only under low temperature conditions are the two redox processes fully reversible. At room temperature, the cubane reductions are associated with a reversible opening of some of the

thiolate bridges to the central iron center. The cubane reduction potentials are consistent with the $[\text{MoFe}_3\text{S}_4]^{2+/3+}$ core oxidation state. The inherent lability of the central iron bridge in $[\text{Mo}_2\text{Fe}_7\text{S}_8(\text{SET})_{12}]^{3-}$ allows synthesis of independent MoFe_3S_4 cubes that are good structural models of the molybdenum center of nitrogenase. In isolated monocubane, three redox processes may be observed electrochemically, involving the $[\text{MoFe}_3\text{S}_4]^{1+/2+}$, $[\text{MoFe}_3\text{S}_4]^{2+/3+}$, and $[\text{MoFe}_3\text{S}_4]^{3+/4+}$ couples. Direct synthesis of MoFe_3S_4 or VFe_3S_4 clusters is also possible from $\text{TpMoS}(\text{S}_4)$, FeCl_2 and $\text{NaSET}/\text{PPh}_3$ (Tp is hydro(trispyrazolyl)borate(1-)) [23c].

21.4.2

Hydrogenases

The iron-only hydrogenase is a nice example of an electron-transfer path paved with different iron–sulfur clusters within a protein. The [Fe]-hydrogenase from *Clostridium pasteurianum* and *Desulfovibrio desulfuricans* consists of one Fe_2S_2 and three Fe_4S_4 centers, ending at the H cluster that comprises a Fe_4S_4 center bridged via a cysteine residue to a dinuclear iron site [24a]. The structure of the H cluster and hydrogen evolution by dinuclear models of its di-iron subsite have already been discussed in Sect. 16.2.2.4. Recently, a synthetic model of the whole

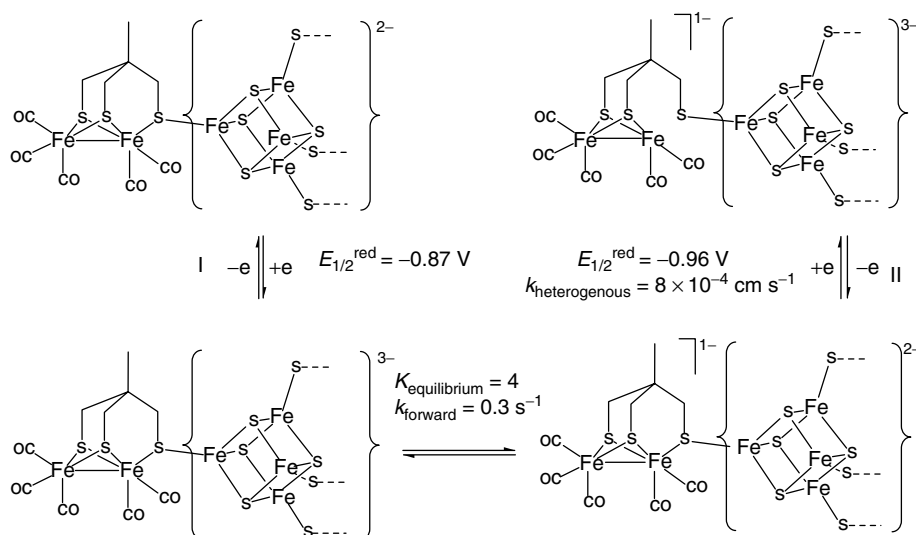


Fig. 6 Reduction of the H-cluster analog and interconversion of redox processes (from Ref. 24b).

structure of the H cluster has been published [24]. The key to the synthesis of the model cluster rests on the use of the tridentate thiolate cavitand ligand, already discussed in Sect. 21.3.3, that prevents expansion of the Fe_4S_4 cluster. The electrochemical reduction of the H-cluster model at -0.87 V versus Ag/AgCl (process I, Fig. 6) is associated with the reversible decoordination from the di-iron site of the bridging thiolate. The decoordination corresponds to a formal intramolecular electron transfer from the reduced cubane to the di-iron site (process II, Fig. 6). The reoxidized cubane then undergoes a reduction at -0.96 V . The interconverting redox processes I and II have been satisfactorily simulated. The accurate structural analog of the H cluster is also a good functional model as it catalyzes H_2 evolution in the presence of acid (4,6-dimethyl pyridinium in MeCN). The catalytic current potential is shifted some 200 mV positive in the presence of the catalyst ($E_p = -1.13 \text{ V}$) but the current

remains within some 5% of the current in the absence of the catalyst.

21.5

Conclusions

The association of sulfur and iron into simple to more complex molecular assemblies allows a great flexibility of electron transfer relays and catalysis in metalloproteins. Indeed, the array of different structures, the interactions with amino-acid residues and solvent and their effect on redox potential and spectroscopic signatures is both inspiring for chemists and electrochemists, and of paramount importance for the study of these centers in native conditions. Most of the simpler natural clusters have been synthesized and studied in the laboratory. Particularly, the multiple redox and spin states can be studied on pure synthetic samples with electrochemical and spectroscopic techniques such as EPR or ^{57}Fe Mössbauer spectroscopy. More complex assemblies still resist structural

and functional modeling by artificially synthesized complexes, with the notable exception of the H cluster of hydrogenase. The FeMo cofactor of nitrogenase combines both a difficult structure to be synthesized and an extremely difficult reaction to catalyze under ambient condition. This and other challenges are partly driving the development of more rational iron–sulfur chemistry and electrochemistry that extend well beyond the present restricted number of iron–sulfur sites of biological relevance.

References

- H. Beinert, R. H. Holm, E. Münck, *Science* **1997**, *277*, 653–659.
- H. Ogino, S. Inomata, H. Tobita, *Chem. Rev.* **1998**, *98*, 2093–2121.
- M. L. Roussin, *Ann. Chim. Phys.* **1858**, *52*, 285.
- S. D’Addario, F. Demartin, L. Grossi et al., *Inorg. Chim. Acta* **1993**, *207*, 1153–1160.
- P. Venkateswara Rao, R. H. Holm, *Chem. Rev.* **2004**, *104*, 527–559.
- E. J. Leggate, E. Bill, T. Essigke et al., *Proc. Natl. Acad. Sci. U.S.A.* **2004**, *101*, 10913–10918.
- R. A. Henderson, *Chem. Rev.* **2005**, *105*, 2365–2438.
- (a) J. Zhou, R. H. Holm, *J. Am. Chem. Soc.* **1995**, *117*, 11353. (b) J. Zhou, Z. Hu, E. Münck et al., *J. Am. Chem. Soc.* **1996**, *118*, 1966.
- (a) B. K. Burgess, D. J. Lowe, *Chem. Rev.* **1996**, *96*, 2983–3010. (b) R. Y. Igarashi, L. C. Seefeldt, The mechanism of Mo-dependent nitrogenase: thermodynamics and kinetics in *Nitrogenase and Chemical Models*. (Eds.: B. E. Smith, R. L. Richards, W. E. Newton), Kluwer, Amsterdam, 2004, pp. 97–140, chapter 5. (c) Y. Hu, M. C. Corbett, A. W. Fay et al., *Proc. Natl. Acad. Sci. U.S.A.* **2005**, *102*, 13825–13830.
- (a) G. D. Watt, K. R. N. Reddy, *J. Inorg. Biochem.* **1994**, *53*, 281–294. (b) M. Guao, F. Sulc, M. W. Ribbe et al., *J. Am. Chem. Soc.* **2002**, *124*, 12100–12101.
- (a) T. A. Scott, H.-C. Zhou, *Angew. Chem., Int. Ed. Engl.* **2004**, *43*, 5628–5631. (b) T. A. Scott, C. P. Berlinguette, R. H. Holm et al., *Proc. Natl. Acad. Sci. U.S.A.* **2005**, *102*, 9741–9744.
- C. Zhou, J. W. Raebiger, B. M. Segal et al., *Inorg. Chim. Acta* **2000**, *300–302*, 892–902.
- R. A. Torres, T. Lovell, L. Noodleman et al., *J. Am. Chem. Soc.* **2003**, *125*, 1923–1936.
- (a) R. H. Holm, *Pure Appl. Chem.* **1995**, *67*, 217–224. (b) C. L. Drennan, J. W. Peters, *Curr. Opin. Struct. Biol.* **2003**, *13*, 220–226.
- (a) R. R. Eady, *Coord. Chem. Rev.* **2003**, *237*, 23–30. (b) B. J. Hales, Vanadium nitrogenase in *Nitrogenase and Chemical Models*. (Eds.: B. E. Smith, R. L. Richards, W. E. Newton), Kluwer, Amsterdam, 2004, pp. 255–279, chapter 10.
- K. Schneider, A. Müller, Iron-only nitrogenase: exceptional catalytic, structural and spectroscopic features in *Nitrogenase and Chemical Models*. (Eds.: B. E. Smith, R. L. Richards, W. E. Newton), Kluwer, Amsterdam, 2004, pp. 281–307, chapter 11.
- (a) M. Ribbe, D. Gadkari, O. Meyer, *J. Biol. Chem.* **1997**, *272*, 26627–26633. (b) D. Gadkari, Superoxide dependant nitrogenase in *Nitrogenase and Chemical Models*. (Eds.: B. E. Smith, R. L. Richards, W. E. Newton), Kluwer, Amsterdam, 2004, pp. 309–332, chapter 12.
- (a) J. B. Howard, D. C. Rees, *Chem. Rev.* **1996**, *96*, 2965–2982. (b) O. Einsle, F. A. Tezcan, S. L. A. Andrade et al., *Science* **2002**, *297*, 1696–1700. (c) F. A. Tezcan, J. T. Kaiser, D. Mustaphi et al., *Science* **2005**, *309*, 1377–1380. (d) T.-C. Yang, N. K. Maeser, M. Laryukhin et al., *J. Am. Chem. Soc.* **2005**, *127*, 12804–12805.
- Y. Ohki, Y. Sunada, M. Honda et al., *J. Am. Chem. Soc.* **2003**, *125*, 4052–4053.
- (a) C. J. Pickett, K. A. Vincent, S. K. Ibrahim et al., *Chem. – Eur. J.* **2003**, *9*, 76–87. (b) F. Barrière, M. C. Durrant, C. J. Pickett, Chemical Models, Theoretical calculations, and the reactivity of isolated Iron-Molybdenum cofactor. in *Nitrogenase and Chemical Models*. (Eds.: B. E. Smith, R. L. Richards, W. E. Newton), Kluwer, Amsterdam, 2004, chapter 7, pp. 161–199.
- S. C. Lee, R. H. Holm, *Proc. Natl. Acad. Sci. U.S.A.* **2003**, *100*, 3595–3600.
- R. H. Holm, E. D. Simhon, Molybdenum-Tungsten-Iron-Sulfur chemistry: Current status and relevance to the Native Cluster

- of Nitrogenase in *Molybdenum Enzymes*. (Ed.: T. G. Spiro), Wiley, New York, 1985, pp. 1–87. (b) R. H. Holm, *Adv. Inorg. Chem.* **1992**, 38, 1–71. (c) D. Coucouvanis, S. M. Malinak, *Prog. Inorg. Chem.* **2001**, 49, 599–662.
23. R. E. Palermo, R. Singh, J. K. Bashkin et al., *J. Am. Chem. Soc.* **1984**, 106, 2600–2612. (b) F. Barrière, D. J. Evans, D. L. Hughes et al., *J. Chem. Soc., Dalton Trans.* **1999**, 957–964. (c) D. V. Fomitchev, C. C. McLauchlan, R. H. Holm, *Inorg. Chem.* **2002**, 41, 958–966.
24. (a) R. Cammack, *Nature* **1999**, 397, 214–215. (b) C. Tard, X. Liu, S. K. Ibrahim et al., *Nature* **2005**, 433, 610–613.

22

Electrochemistry of Isopoly and Heteropoly Oxometalates

Bineta Keita and Louis Nadjo
Laboratoire de Chimie Physique, Université Paris-Sud, Orsay Cedex,
France

22.1	Introduction	611
22.1.1	Definitions	611
22.1.2	General Properties, Literature, and Topics Covered	611
22.2	A simplified Overview of the Formation of POMs	614
22.3	Fundamental Redox Mechanisms of POMs at Electrodes	615
22.3.1	Electrochemical Reductions of Selected Plenary POMs: α - $[\text{SiW}_{12}\text{O}_{40}]^{4-}$, α - $[\text{PW}_{12}\text{O}_{40}]^{3-}$, α - $[\text{P}_2\text{W}_{18}\text{O}_{62}]^{6-}$, and α - $[\text{H}_2\text{W}_{12}\text{O}_{40}]^{6-}$	616
22.3.1.1	Aqueous Media	616
22.3.1.2	Nonaqueous and Mixed Solvents	619
22.3.2	Quinone/hydroquinone-like Behaviors in the First Several Reduction Waves of POMs	623
22.4	Selected Achievements that Illustrate the Basic Behaviors of Plenary POMs at Electrodes	625
22.4.1	Heterogeneous One-electron Exchange of α - $[\text{SiW}_{12}\text{O}_{40}]^{4-}$ in Dimethylformamide	625
22.4.2	The Reduction Potential of the One-electron Wave and the Role of the Central Heteroatom	626
22.4.3	Isomerization upon Reduction	626
22.4.4	POM-solvent Interactions as Probed by the Redox Potentials of Two POMs	627
22.4.5	Structure of Electrolyte Solutions As Probed by the Electrochemical Behaviors of POMs	629
22.4.6	Cation and Pressure Effects on the Electrochemistry of 12- Tungstocobaltate and 12-Tungstophosphate Ions in Acidic Aqueous Solution	630

22.5	Mixed Addenda and Other Substituted POMs	632
22.5.1	Comparison of Valence Trapping in Uniform and Mixed Addenda Plenary POMs	632
22.5.2	Lacunary and Transition Metal–substituted POMs	635
22.5.2.1	Lacunary POMs	635
22.5.2.2	Transition Metal–monosubstituted POMs	637
22.5.2.3	An Interesting Case of Mixing up of Substituent and Tungsten Waves: α_1 - and α_2 -[Fe ^{III} (OH ₂)P ₂ W ₁₇ O ₆₁] ⁷⁻	646
22.5.3	Sandwich-type POMs	649
22.5.3.1	Electron Transfer Behaviors of Multi-iron Sandwich-type POMs . . . Ion-pairing: pH Effects: Diferric and Triferric Sandwich-type Complexes: Mixed-Metal Sandwich-type Complexes:	649 653 654 655 656
22.5.3.2	Electrochemical Probing of Siderophoric Behavior in Sandwich-type Multi-iron Wells–Dawson Heteropolytungstates	658
22.6	Recent Developments	660
22.6.1	Electrochemistry of a New Family of Wells–Dawson Anions: Semivacant Tungstophosphates and Arsenates [H ₄ XW ₁₈ O ₆₂] ⁷⁻ (X = P or As)	660
22.6.1.1	Evidence for an Influence of the Dissymmetry on the Voltammetric Behavior of PW ₁₈ : Comparison with P ₂ W ₁₈	660
22.6.2	Recent Achievements in Apparently Direct Multiple Electron Transfers on the First Waves of POMs	662
22.6.2.1	Electrochemistry of the Multi-nickel Polyoxoanions [Ni ₆ As ₃ W ₂₄ O ₉₄ (H ₂ O) ₂] ¹⁷⁻ , [Ni ₃ Na(H ₂ O) ₂ (AsW ₉ O ₃₄) ₂] ¹¹⁻ , and [Ni ₄ Mn ₂ P ₃ W ₂₄ O ₉₄ (H ₂ O) ₂] ¹⁷⁻	664
22.6.2.2	Electrochemistry of the Iron(III)-substituted Keggin Dimer, [Fe ₆ (OH) ₃ (A- α -GeW ₉ O ₃₄ (OH) ₃) ₂] ¹¹⁻	667
22.6.3	Theoretical Approaches	667
22.6.3.1	Electronic Structures of POMs Explain their Redox Behaviors and the Relative Stability of Reduced Forms	667
22.6.3.2	An Extended Hückel Calculations Approach to a Qualitative Understanding of the Initial Electron Transfer Site in Dawson-type POMs	668
22.7	Electrocatalysis	672
22.7.1	Basic Concepts of Homogeneous Catalysis of Electrode Reactions . .	672
22.7.2	Selected Electrocatalysis in Homogeneous Solution	673
22.7.2.1	Electrocatalytic Reductions	674
22.7.2.1.1	Electrocatalytic reduction of nitrite and nitrate Studies with [{Cu ^{II} (H ₂ O)} ₂ Cu ^{II} ₂ (X ₂ W ₁₅ O ₅₆) ₂] ¹⁶⁻ (abbreviated in the following as Cu ₄ X ₄ W ₃₀ with X = P or As)	675 675

	Cooperative effect of Mn- and Fe-centers within $\text{Mn}_2\text{Fe}_2\text{P}_4\text{W}_{30}$ in the electrocatalytic reduction of nitrite	676
	Evaluation of the behaviors of $\text{Ni}_3\text{P}_2\text{W}_{18}$, $\text{Ni}_4\text{Mn}_2\text{P}_3\text{W}_{24}$, $\text{Ni}_6\text{As}_3\text{W}_{24}$, and $\text{Fe}_6\text{Ge}_2\text{W}_{18}$ in the electrocatalytic reduction of nitrate and nitrite	678
22.7.2.1.2	Electrocatalytic Reduction of Dioxygen and Hydrogen Peroxide	680
	Electrocatalytic reduction of dioxygen in the presence of α - $\text{P}_2\text{W}_{15}\text{Mo}_2\text{Cu}$	680
	Reduction of dioxygen and hydrogen peroxide by $\text{Cu}_4\text{X}_4\text{W}_{30}$ (X = P or As)	684
	Electrocatalytic reduction of dioxygen and hydrogen peroxide in the presence of $\text{Mn}_2\text{Fe}_2\text{X}_4$ (X = P or As)	685
22.7.2.2	Electrocatalytic Oxidations	687
22.7.2.2.1	$[\text{Ru}^{\text{III}}(\text{H}_2\text{O})\text{PW}_{11}\text{O}_{39}]^{4-}$ and $[\text{Ru}^{\text{III}}(\text{H}_2\text{O})\text{SiW}_{11}\text{O}_{39}]^{5-}$ as an Electrochemical Oxygen Transfer Catalysts	687
22.7.2.2.2	α - $[\text{Cr}^{\text{III}}(\text{H}_2\text{O})\text{PW}_{11}\text{O}_{39}]^{4-}$ and α_2 - $[\text{Cr}^{\text{III}}(\text{OH}_2)\text{P}_2\text{W}_{17}\text{O}_{61}]^{7-}$ as Oxygen Transfer Catalysts in Electrochemistry	687
22.7.2.2.3	A Detailed Study of $\text{K}_n[\text{Mn}^{\text{II}}(\text{OH}_2)\text{SiW}_{11}\text{O}_{39}]^{(6-n)-}$ as Oxidation Electrocatalyst	689
22.7.2.2.4	Catalytic Oxidation of NAD(P)H: A Continuously Improved Selection of Suitable POMs	690
22.8	Conclusion	695
	Acknowledgment	695
	References	695

22.1 Introduction

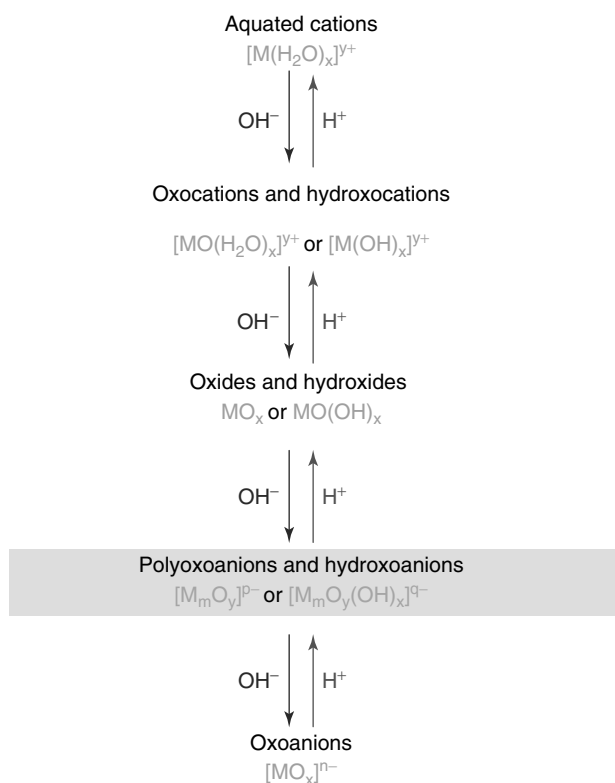
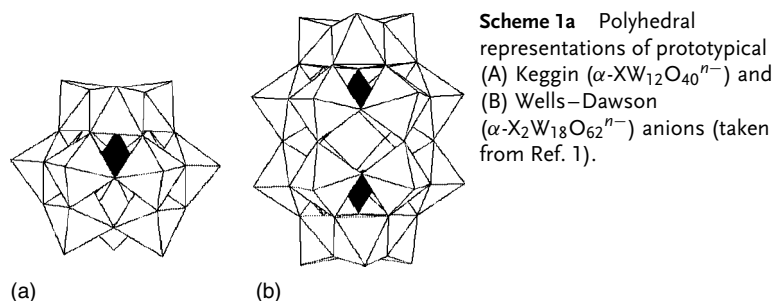
22.1.1 Definitions

Polyoxometalates (POMs for convenience) constitute a unique class of molecular metal-oxygen clusters, remarkable in several respects: the multitude of their properties based on their sizes, shapes, charge densities, and reversible redox potentials, and their enormous diversity of structures. Even though there are metal oxide clusters that are neutral or cationic, the present text will adopt the simplified view that most POMs are anionic structures constituted of early transition-metal elements in their highest oxidation state, hence their usual designation as early transition-metal-oxygen-anion clusters. These atoms in positive oxidation state constitute the so-called addenda atoms. Condensation of MO_6 octahedra, mostly with $\text{M}^{z+} = \text{W}^{6+}$, Mo^{6+} and V^{5+} , gives isopolyanions or isopoly compounds. Heteropolyanions are obtained when a large number of MO_6 octahedra are condensed with a much smaller proportion of another atom in positive oxidation state (the so-called heteroatom). In the following text, POM will be kept as the general term, but these other designations might also be used

occasionally. The structures of the vast majority of POMs studied in electrochemistry are primarily derived from the Keggin structure and the Dawson structure. These two basic precursor structures are sketched in Sch. 1. POMs of these groups are characterized by the M/X ratio, where M designates the addenda atom and X the heteroatom. The Keggin structure belongs to the 12/1 series and the Dawson structure to the 18/2 series.

22.1.2 General Properties, Literature, and Topics Covered

The interest in the redox, catalytic, and electrocatalytic properties of unsubstituted and substituted polyoxometalates arouses much attention [2–15] because they are a versatile family of molecular metal-oxide clusters with applications in catalysis as well as in medicine and material science. Such versatility must be traced to at least two main characteristics. First, the size and mass of these unique molecular oxides place their solution chemistry in an intermediate position between small molecule solution chemistry and infinite lattice solid-state chemistry. Second, their redox behaviors may be very flexible and finely tuned on purpose, by changing smoothly their composition, with a



Scheme 1b Formal sequence of hydrolysis reactions linking metal cations, oxyions, and polymeric oxides (adapted from Ref. 4).

tremendously diverse variety of structures [6].

Keeping first with unsubstituted POMs, their oxidized forms may only accept electrons; in contrast, their reduced forms,

owing to their electron and proton transfer and/or storage abilities, may behave as donors or acceptors of several electrons while maintaining their structure. In this series, most POMs may be considered

as close mimics of mixed-metal oxides and therefore, be studied as their soluble analogs, at least as regards their catalytic properties in photochemistry and electrochemistry. As a consequence, extensive attention was exercised to their acidity and redox capabilities as oxidation catalysts in heterogeneous vapor phase catalysis, and more recently, in homogeneous phase catalysis [7]. An enlightening example is the comparative study of POMs and semiconductor metal oxides as catalysts in the photochemical oxidative degradation of thioethers that demonstrates that POMs remain active even under anaerobic conditions [16].

Turning now to the ability of unsubstituted POMs to generate lacunary species and then metal cation-substituted derivatives, it appears that a virtually enormous family of compounds might result. The impetus for their study was triggered by the seminal remark of Baker [17] that monosubstituted POMs can be considered as the analogs of metalated porphyrins and used in catalytic processes with the advantage, relative to their organic counterparts, of thermal stability, robustness, and inertness toward oxidizing environments.

The foregoing remarks suggest strongly that electrochemistry should be an invaluable technique to study several aspects of POMs properties. Following the pioneering work of Souchay who demonstrated that polarography is suitable for the study of oxometalate solutions, electrochemical techniques are now extensively used in diverse directions: distinguish between isopoly and heteropoly anions and even between two isomers by establishing appropriate fingerprints; follow the kinetics of transformation of most of these compounds or establish potential-pH diagrams; establish reaction mechanisms; study electron transfer processes, catalytic

and electrocatalytic pathways, and so on. Among remarkable results, electrochemical reduction avoids secondary reactions like the exchange of some elements of the oxometalate with those of the reducing agent. For instance, in the reduction of molybdic species by SnCl_2 , substitution of Mo by Sn was observed [18]. Electrochemistry allows sequential additions of electrons and allows to demonstrate that the reduced species, most of which, but by no means all, are intensely blue (and henceforth named *heteropolyblues*, HBP), are stable in a larger pH domain than the oxidized forms and that this domain extends toward more alkaline pH values as the number of added electrons increases [19–23].

In short, most work on POMs address primarily their pH of formation, the stability of the various complexes with emphasis on their analytical properties, homogeneous catalysis, radiochemical, and photochemical behaviors. All these properties have been described in a series of excellent reviews, which usually include short developments on their electrochemistry and redox catalysis properties [2–9, 24–28]. The reader is referred to these reviews for general descriptions of POMs synthesis, structures, and reactivity. Among these reviews, particular attention is drawn to those few containing substantial developments on electron transfer behaviors and the electrochemistry of POMs [2, 4, 5, 7–9, 24–28].

In the present chapter devoted to the electrochemistry of POMs, our purpose is not to provide an exhaustive review of all the papers in which some electrochemical aspects of POMs intervene, but rather to emphasize the fundamental principles that govern the vast majority, if not all, of the electron transfer behaviors of these chemicals at electrodes and help to explain their electrocatalytic properties. As

a consequence, illustrative examples will be selected. Details not necessary to establish the mechanisms will be omitted or not commented and can be found in the original papers. The reader is referred to exhaustive reviews and to the current literature for these particular details. Therefore, in addition of seminal papers, particular attention is exercised toward the literature covering the period from 1996 to 2004 to provide a satisfactory overlap with the two following reviews: (1) a 1998 review [8] devoted to the properties of POMs as electrocatalysts; (2) a development in Volume 10 of the present series that considers the electrocatalysis with POMs attached to electrode surfaces [9]. Therefore, the examples selected in the following text will highlight the molecular aspects of the electrochemistry of POMs in solution.

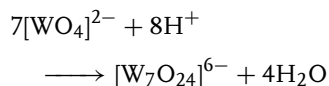
22.2

A simplified Overview of the Formation of POMs

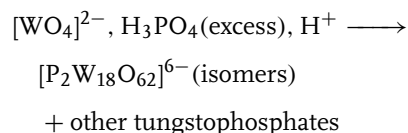
Although POMs have been known for about 200 years [6d,e,f] a large number of novel polyoxoanions with unexpected shapes and sizes are still being discovered. However, despite this diversity that precludes from complete rational and systematic design of synthesis for all POMs, a few guidelines can be retained. For specific details, the reader is referred to books, reviews, and original papers [3–7, 27]. Primarily, the evolution of aquated metal cations in aqueous solution depends on the pH of the medium, going from the hydrated cation $[M(H_2O)_x]^{n+}$, viable in very acidic medium, to the oxoanion $[MO_x]^{n-}$ obtained in very basic solution (see Sch. 1b). The route between these two extremes is populated by a series of more or less stable oxocations and hydroxocations,

oxides and hydroxides, and finally polyoxoanions and hydroxoanions, which are the focus of our study.

More specifically, acidification of $[MO_x]^{n-}$ oxoanion-containing solutions in appropriate experimental conditions (pH, concentration, temperature. . .) results in polycondensation of these oxoanions to build up large and eventually giant anionic species, the so-called Polyoxoanions or Polyanions (POMs). Such assemblies are known with transition metals in high oxidation states, among which the d^0 states of vanadium, molybdenum, and tungsten are the most common ones. Polycondensation of the same oxoanion gives an Isopolyoxoanion $[M_mO_y]^{p-}$. The structures can be viewed as the association of tetrahedral $[MO_4]$ (mainly vanadium) and/or octahedral $[MO_6]$ groups sharing corners, edges, and/or faces. As an example, paratungstate $[W_7O_{24}]^{6-}$ is synthesized by acidification of tungstate solutions according to the stoichiometry:



When polycondensation of these “addenda atoms” is carried out in the presence of another oxoanion containing an “heteroatom” X, an Heteropolyanion is obtained, formulated as $[X_xM_mO_y]^{q-}$. X belongs usually to the main group elements (B, Si, Ge, P, As, . . .) but can also be a metal.



The two foregoing examples illustrate the variability of experimental conditions and suggest the necessity of further

specific conditions for isolation of a pure sample of the desired POM.

Usually, addition of an appropriate counterion, commonly an alkali metal, ammonium, or tetraalkylammonium permits the isolation of the polyanion. Lithium and sodium salts are generally more water-soluble than those of the larger cations. In contrast, salts of alkylammonium and similar cations are insoluble in water but can be recrystallized from several nonaqueous solvents.

POMs can be viewed as assemblies of discrete fragments of oxides with definite sizes and shapes. These assemblies represent usually thermodynamically stable arrangements, even though their formation, especially in the case of polytungstates, is rather under kinetic control [3]. Most of them keep their identity in aqueous and nonaqueous solutions.

In short, the mechanism of formation of POMs is far from well understood and commonly proposed descriptions as self-assembly are rather elusive. Only syntheses in aqueous solutions are briefly outlined. Actually, successful POM formations in nonaqueous media were also described, without any deeper insight into the reaction pathways. Therefore, attempts at rationalization of the hitherto mysterious equilibria that generate polyoxometalates are necessary so that, eventually, straightforward syntheses of novel species might be designed. In contrast, a better knowledge exists as regards the transformation mechanisms of a POM into another one or the partial degradation pathways of a POM. As a matter of fact, rational stereospecific methods of synthesis of substituted POMs were developed starting from appropriate lacunary species [3, 4, 6a,b].

Finally, a survey of the literature confirms the evolution of such systems to be controlled by numerous, apparently

insignificant, parameters. For instance, the sequence of adding reagents might be important [4]. It was also shown that the concentration of a counterion like Na^+ plays an important role in the evolution of a system apparently as “simple” as the hydrolysis of molybdate in aqueous medium [5].

The above considerations show that the rational synthesis and structural characterization of new POMs remain a challenge. Nevertheless, the potentially attractive catalytic properties of such species are a strong motivation to undergo this kind of research.

22.3 Fundamental Redox Mechanisms of POMs at Electrodes

The possibilities of POMs compositions and structures are virtually enormous, and the number of these molecules actually prepared and characterized continues to grow unabated. However, examination of their short electrochemical studies, which are becoming a usual part of their characterization, shows that a limited selection of representative groups of POMs is sufficient for a description of the main electrochemical behaviors of this class of chemicals. Therefore, α -Keggin- and Dawson-type heteropolyanions of phosphotungstate, silicotungstate, phosphomolybdate, and silicomolybdate; mixed addenda heteropolyanions, and transition-metal substituted heteropolyanions including sandwich-type derivatives were selected for the present article.

Unless otherwise stated, most studies were performed by cyclic voltammetry with freshly polished glassy carbon working electrode (GC) and a saturated calomel reference electrode (SCE).

22.3.1

Electrochemical Reductions of Selected

Plenary POMs: α -[SiW₁₂O₄₀]⁴⁻,
 α -[PW₁₂O₄₀]³⁻, α -[P₂W₁₈O₆₂]⁶⁻, and
 α -[H₂W₁₂O₄₀]⁶⁻

When no confusion is possible, these POMs will be abbreviated as SiW₁₂, PW₁₂, P₂W₁₈, and H₂W₁₂ respectively

22.3.1.1 **Aqueous Media**

A first point of concern is the knowledge of the pH domain where the molecule under scrutiny is stable. For these classical POMs, such domains were determined and found to be shifted to more alkaline pH values as the number of added electrons increases [19–23]. H₄SiW₁₂O₄₀, H₃PW₁₂O₄₀, and H₆P₂W₁₈O₆₂ are known as *strong acids in aqueous solutions*, presumably with a uniform acidity [29]. In addition, each reduction step increases the negative charge density on the

POMs and hence, their basicity. Therefore, the electrochemical observations are anticipated to depend on the acidity functions of the various classical mineral acids, HClO₄, H₂SO₄, and HCl, used as supporting electrolytes.

In their usual pH domains of stability, starting from low to high pH values, the electrochemistry of the three heteropolyanions, SiW₁₂, PW₁₂, P₂W₁₈, shows at least two successive one-electron waves followed eventually by multielectron waves [4, 30]. This observation is consistent with the very strong acidity of these POMs [29], even in the solid state as demonstrated for H₄SiW₁₂O₄₀ and H₃PW₁₂O₄₀ [31]. Even though a two-electron reduction on the first wave of H₄SiW₁₂O in solutions more concentrated than 5 M HCl was occasionally mentioned [32], only recently was this possibility of apparently direct two-electron reductions on the first waves of these POMs generalized and

Tab. 1 Reduction peak potentials (E_{pc}) vs. SCE and anodic-to-cathodic peak separations (ΔE_p) for 10⁻³ M α -K₆P₂W₁₈O₆₂ with various hydrochloric acid concentrations in water^a (taken from Ref. 33c)

Medium	$n_{app.}^b$ ($n_{corr.}$)	$-E_{pC_1}^c$ [mV]	ΔE_{p_1} [mV]	$-E_{pC_2}$ [mV]	ΔE_{p_2} [mV]	$-E_{pC_3}$ [mV]	ΔE_{p_3} [mV]	$-E_{pC_4}$ [mV]	ΔE_{p_4} [mV]	$-E_{pC_5}$ [mV]
1 M HCl	1 (1.0)	-5	55	135	50	380	30	610	25	805
2 M HCl	1.06 (1.08)	-5	55	125	50	365	30	595	25	~800
3 M HCl		~ -5		115		345	30	565	20	~780
4 M HCl		~ -5		90		330	30	550	20	

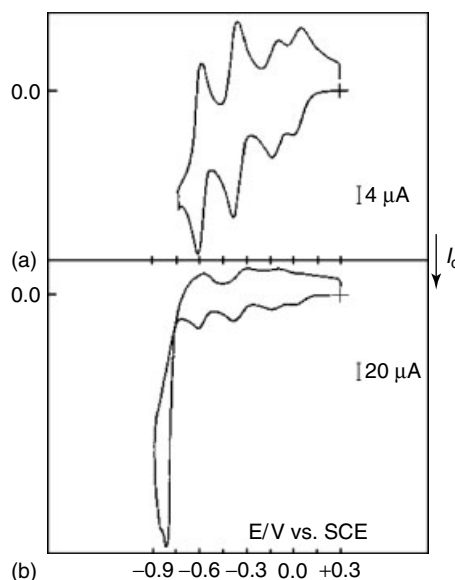
Medium	$n_{app.}^b$ ($n_{corr.}$)	$-E_{pC_1}^c$ [mV]	ΔE_{p_1} [mV]	$-E_{pC_2}$ [mV]	ΔE_{p_2} [mV]	$-E_{pC_3}$ [mV]	ΔE_{p_3} [mV]	$-E_{pC_4}$ [mV]
6 M HCl	1.40 (1.54)	65		100	290	25	515	20
8 M HCl	1.50 (1.73)	35		60	275	25	495	20
12.4 M HCl	1.54 (1.96)	-5		30	240	25	460	20

^aMissing values correspond to very ill-defined patterns. The potential sweep rate is 100 mV s⁻¹.

^b $n_{app.}$ is the apparent electron number for the first voltammetric wave, $n_{corr.}$ is the same value corrected for viscosity effects.

^cWhen the two first waves are merged, the new numbering of waves is obvious.

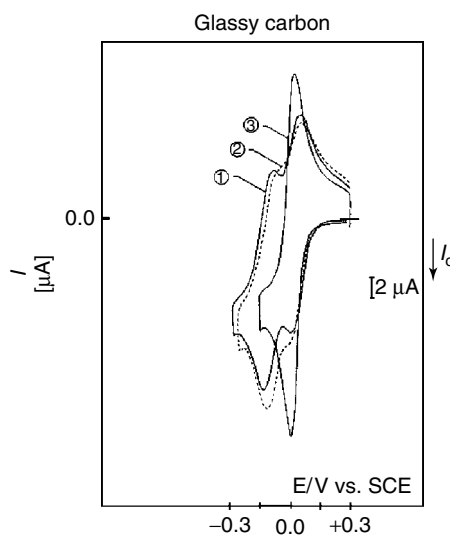
Fig. 1 Cyclic voltammetry pattern at a glassy carbon electrode (GC Tokai, Japan) with 10^{-3} M α - $\text{K}_6\text{P}_2\text{W}_{18}\text{O}_{62}$ in 1 M HCl supporting electrolyte. Sweep rate: 100 mV s^{-1} ; electrode surface area: 0.07 cm^2 ; (a) voltammetric pattern restricted to the four first waves of $[\text{P}_2\text{W}_{18}\text{O}_{62}]^{6-}$; (b) the whole voltammetric pattern showing ill-defined reoxidation peaks on potential reversal (taken from Ref. 33c).



studied systematically [33b,c]. The results for P_2W_{18} are the most complete because, among the three POMs, this molecule turned out to be the most soluble up to the highest acid concentrations. Table 1 summarizes the quantitative parameters associated with the cyclic voltammograms of 10^{-3} M P_2W_{18} dissolved in various HCl concentrations in water. Figures 1 through 3 illustrate the main evolutions of these CVs. Figure 1(a) shows the CV obtained in 1 M HCl. Four waves appear, with electrons numbers being 1 : 1 : 2 : 2. It was demonstrated previously that six electrons could be added to P_2W_{18} and reversibly removed [33, 34].

Figure 1(b) shows that scanning the potential up to the fifth wave complicates the voltammetric pattern. In the following, the pattern is restricted to a potential domain in which no undesirable derivatization of the electrode surface was observed [28]. For this acid concentration and

Fig. 2 Evolution of the cyclic voltammetry pattern with hydrochloric acid concentration in water with 10^{-3} M α - $\text{K}_6\text{P}_2\text{W}_{18}\text{O}_{62}$. The figure is restricted to the merging process of the first two waves. Curve 1: 1 M HCl; Curve 2: 3 M HCl; Curve 3: 12.4 M HCl. Sweep rate: 100 mV s^{-1} ; electrode surface area: 0.07 cm^2 (taken from Ref. 33c).



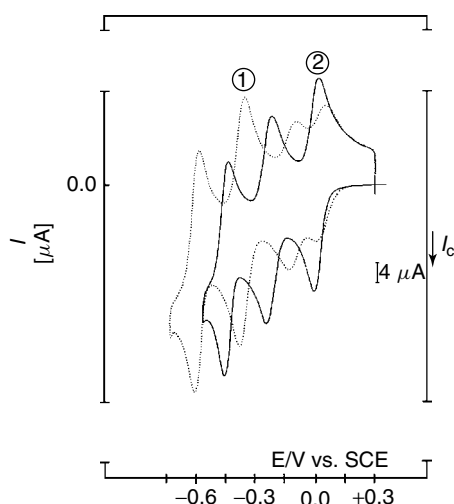


Fig. 3 Final voltammetric pattern obtained with 10^{-3} M α -K₆P₂W₁₈O₆₂ in 12.4 M HCl (Curve 2) from the set of four waves (Curve 1) observed in 1 M HCl. Sweep rate: 100 mV s^{-1} ; electrode surface area: 0.07 cm^2 (taken from Ref. 33c).

with a potential scan rate of 100 mV s^{-1} , the anodic-to-cathodic peak separations quoted in Table 1 fit the 1:1:2:2 electron numbers. The corresponding waves may feature diffusion-controlled processes. This conclusion was checked to be true for the first reduction process. The evolution of the voltammetric pattern when the hydrochloric acid concentration increases is described by Table 1 and sketched in Fig. 2. Already at 2 M HCl, all the waves move in the positive potential direction, except for the first one that remains at its initial potential location. This evolution continues with increasing concentrations of HCl until the first and the second waves are practically merged into a broad composite wave at 6 M HCl for potential scan rates between 20 mV s^{-1} and 500 mV s^{-1} . For the sake of simplicity and continuity, this combined wave is renumbered 1 as it is clear from Table 1. In more and more acidic solutions, the peak current intensity of this composite wave grows larger and larger, while its reduction peak potential becomes less negative and the anodic-to-cathodic peak potential

difference decreases down to 30 mV in 12.4 M HCl. The final voltammetric pattern appears also on Fig. 2. At such high concentration of hydrochloric acid, the change in viscosity of the solution [33a] must be taken into account to demonstrate consistently that the wave has now the characteristics of an overall, apparently direct, two-electron transfer process. Figure 3 shows the final pattern of three waves in 12.4 M HCl, from the set of four initial waves in 1 M HCl of Fig. 1. The chemical reversibility of these two-electron waves is reminiscent of the electrochemical behaviors of quinone/hydroquinone systems in molecular electrochemistry and suggests the use of this unifying analogy, which is developed in the following.

The same kind of experiments was carried out with HClO₄. The observations in the two media parallel each other. At the same concentration of 4 M, HClO₄ is much stronger an acid than HCl, as the first two waves of P₂W₁₈ are already merged in the former medium while they are not in the latter. Concentrations of HClO₄ higher than 7 M could not be used, due to the very poor solubility of P₂W₁₈ in these media.

SiW₁₂ behaves in much the same way as P₂W₁₈ in perchloric acid. The final unique two-electron wave obtained in strongly acid solution from the initial set of two one-electron waves in 1 M HClO₄ is built-up by the same mechanism as observed for P₂W₁₈, which is the gradual positive potential shift of the second wave. It is also noted that the merging of the first

two waves of P_2W_{18} is complete at 4 M $HClO_4$ while it only begins for SiW_{12} . This observation supports the idea that the two-electron reduction product of P_2W_{18} is more basic than that of SiW_{12} . Results for other acids can be found in the original papers [33b,c,d].

PW_{12} turns out to be sparingly soluble in concentrated acid solutions. The first three waves feature 1:1:2 electron processes. On varying the perchloric acid concentration from 1 M to 4 M, the first two waves move to more negative potentials while the third one moves in the positive direction. The first wave goes from a value corresponding to one electron to 0.95 electron. This last value was corrected to 1.0 electron when taking into account the change in viscosity of the various media. The anodic-to-cathodic peak potential separation remains constant throughout. Higher concentrations of $HClO_4$ are precluded by the poor solubility of PW_{12} in these media. A concentration as high as 6 M has been possible for HCl . Much the same phenomena are observed as in $HClO_4$. In particular, the height of the first wave, corrected for viscosity effects, corresponds to one electron whatever the medium.

It thus appeared that coalescence of the first waves of P_2W_{18} or SiW_{12} could be achieved only in very high acidity media. A complete simulation of all these processes over the entire acidity range would require the input of a large number of parameters [35]. The merging of the third and fourth waves of P_2W_{18} upon increasing the acidity of the supporting electrolyte could only be simulated [35].

In contrast with the examples of P_2W_{18} and SiW_{12} , much more ordinary pH media were sufficient to obtain the coalescence of the first two one-electron waves of H_2W_{12} [35]. As a matter of fact, at pH above 4.0, the initial reduction processes of H_2W_{12}

involve two successive one-electron waves with their potentials independent of pH. Figure 4 shows the voltammetric behavior of 10^{-3} M H_2W_{12} solutions in the pH range 2–7 in aqueous NaCl (0.5 M). When the pH decreases below 4.0, the second wave diminishes in intensity while the first one increases. The evolution of the voltammetric pattern appears in Fig. 4.

Typically, a single wave is observed at pH = 3.4. This gradually sharpens and below pH 3.2 begins to move to more positive potentials as the pH is decreased. At pH 1.1, the anodic-to-cathodic peak potential separation is 55 mV, consistent with a chemically reversible two-electron process comprising two unresolved one-electron events. The whole evolution could be simulated, on the basis of the following scheme and on an established program (DIGISIM V 2.0 and partly 2.1, Bioanalytical Systems, West Lafayette, IN) in which unknown parameters are adjusted. The relevant parameters are gathered in Table 2 and the corresponding voltammograms are represented by dots in Fig. 4. The hypotheses and adjustments necessary to achieve a satisfactory simulation of the case of H_2W_{12} indicate the difficulty of the task in more sophisticated media. Nonetheless, the achievement is important as a quantitative support of the more general classical nine-member box scheme that summarizes the possible intermediates for all two-electron two-proton reactions such as the quinone/hydroquinone systems. This general scheme that applies in a wide variety of experimental conditions will be discussed after examination of electron transfer behaviors of the same plenary POMs in other solvents and mixed solvents.

23.3.1.2 Nonaqueous and Mixed Solvents

Nonaqueous solvents and their mixtures with various amounts of water are

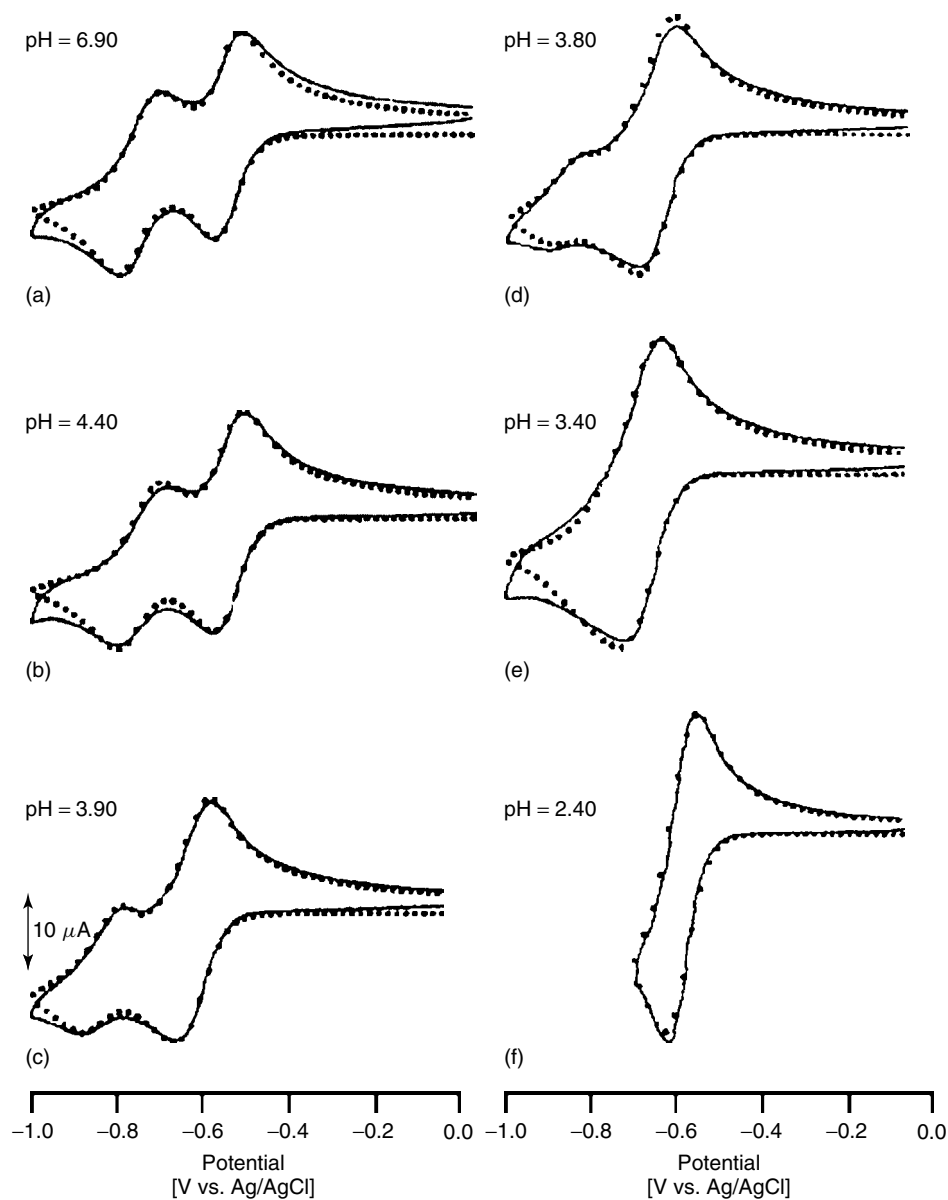


Fig. 4 Cyclic voltammograms of solutions of $(\text{NH}_4)_6[\text{H}_2\text{W}_{12}\text{O}_{40}]$ (1 mM) in aqueous NaCl (0.5 M); $\nu = 100 \text{ mV s}^{-1}$; full line: experiment; dotted line: simulation (taken from Ref. 35).

interesting because they may promote ion-pairing of oxidized and/or reduced forms of POMs with small cations such as H^+ , Li^+ , and Na^+ , and thus orient

the reduction pathways observed for these molecules. These behaviors must be traced both to the basicity of these solvents and also to their permittivity [33, 36–39].

Tab. 2 Parameters for simulation of cyclic voltammetry of 1 mM solution of $[\text{H}_2\text{W}_{12}\text{O}_{40}]^{6-}$ in aqueous NaCl (0.5M)

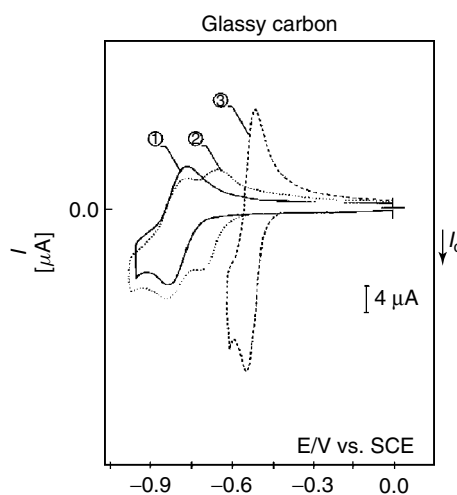
$[\text{H}_2\text{W}_{12}\text{O}_{40}]^{6-}$			
Couple	$0'/1'$	$1'/2'$	$1'h/2'h$
$E'_{1/2}$, mV	−555	−755	−585
ΔE_p , mV	72	101	
Protonic equil.	$K_{1'h}$	$K_{2'h}$	$K_{2'h2}$
	2.8×10^3	2.4×10^6	3.0×10^3
Disproprn equil.	$21' \rightleftharpoons 0' + 2'$	$1' + 1'h \rightleftharpoons 0' + 2'h$	$21'h \rightleftharpoons 0' + 2'h_2$
Equil. const	4×10^{-4}	0.35	
Diffusion coeff.	D_{anion}	D_{H^+}	
$10^6 \text{ cm}^2 \text{ s}^{-1}$	2.0	19	

The action of H^+ from perchloric acid on the reduction of SiW_{12} , P_2W_{18} , and PW_{12} in DMF in the presence of 0.1 M lithium perchlorate is studied as a representative example [33b,33c]. Perchloric acid is known to be strong in DMF [36]. The evolution of the voltammetric pattern of 10^{-3} M $\text{K}_4\text{SiW}_{12}\text{O}_{40}$ (abbreviated as $\text{K}_4\text{SiW}_{12}$) is shown in Fig. 5. For clarity, the pattern in this figure is restricted to the evolution of the first one-electron wave of this salt in DMF + 0.1 M LiClO_4 , upon stepwise addition of HClO_4 . With the acid, a new wave appears, more positive than the previous one and grows at its expense when the acid concentration is raised. The evolution ends up in the formation of a two-electron wave.

Table 3 gives in more detail the evolution of the whole voltammetric pattern. The

first waves in the absence of acid are in electron ratios 1:1:2. Their smooth evolution upon perchloric acid addition ends up in a set of three new waves in electron ratios 2:2:4, the last value varying with the acid concentrations. Completely similar trends are obtained with 10^{-3} M $\text{K}_6\text{P}_2\text{W}_{18}\text{O}_{62}$ in DMF. Here again, a new wave appears on addition of acid, albeit at a smaller acid to POM ratio, underscoring the higher basicity and/or ion-pairing ability of P_2W_{18} compared with SiW_{12} . Again, PW_{12} behaves differently and the experiments could be started directly with

Fig. 5 Voltammetric pattern obtained with 10^{-3} M $\alpha\text{-K}_4\text{SiW}_{12}\text{O}_{40}$ in DMF + 0.1 M LiClO_4 solution – Curve 1: in the absence of acid; Curve 2: with 2×10^{-3} M perchloric acid; curve 3: with 5×10^{-1} M HClO_4 . The pattern is restricted to the evolution of the first wave observed in the absence of acid. Sweep rate: 100 mV s^{-1} ; GC electrode surface area: 0.07 cm^2 (taken from Ref. 33c).



Tab. 3 Reduction peak potentials (E_{pc}) versus SCE and anodic-to-cathodic peak separations (ΔE_p) for 10^{-3} M α -K₄SiW₁₂O₄₀ in dimethylformamide with various perchloric acid concentrations^a (taken from Ref. 33c)

[HClO ₄] mM	$n_{app.}^b$	$-E_{pC1}^c$ [mV]	ΔE_{p1} [mV]	$-E_{pC2}$ [mV]	ΔE_{p2} [mV]	$-E_{pC3}$ [mV]
0	1	840	75	1060	115	1320

[HClO ₄] mM	$n_{app.}^b$	$-E_{pC1}^c$ [mV]	ΔE_{p1} [mV]	$-E_{pC2}$ [mV]	ΔE_{p2} [mV]	$-E_{pC3}$ [mV]	ΔE_{p3} [mV]	$-E_{pC4}$ [mV]
2	~0.90	720	60	845	70	~1030		1315
4	1.34	715	75	~850		~1030		~1250
5	1.56	705	75	~850		~1030		~1200
6	1.63	700	75	~855	~75	~1040		~1175
8	1.69	680	65	~855	~90	~1070		
10	1.74	670	60	~835	~80	~1070		
20	1.81	645	50	775	60	~1040		~1170
40	1.85	615	45	735	50	~1000		~1170
100	1.85	595	45	705	45	~1000		
500	1.79	545	35	655	40	~920		
1000	1.72	525	30	650	30	900	30	~1050

^aThe solvent contains 0.1 M LiClO₄ for all the solutions. The potential sweep rate is 100 mV s⁻¹; missing values correspond to very ill-defined patterns.

^b $n_{app.}$ is the apparent electron number for the first voltammetric wave.

^cWhen a new wave appears, the renumbering of waves is obvious.

its acidic form. Up to 4 M HClO₄, the first two one-electron waves of PW₁₂ remain monoelectronic throughout.

Such effect of small cations on the voltammetric behaviors of α -[SiMo₁₂O₄₀]⁴⁻ and α -[PMo₁₂O₄₀]³⁻ in acetone and acetonitrile was investigated recently [37]. For the α -[SiMo₁₂O₄₀]⁴⁻ complex, the presence of Li⁺ or Na⁺ caused the one-electron wave to be converted into a two-electron wave at ca. 0.3 V more positive than the first one-electron wave. In the presence of Li⁺ or Na⁺, the α -[PMo₁₂O₄₀]³⁻ complex underwent a two-electron reduction at the same potential as the original first one-electron wave in CH₃COCH₃, whereas it exhibited only successive

one-electron waves in CH₃CN. The addition of a trace amount of H⁺ produced new two-electron waves at more positive potentials. These observations were rationalized by considering both the greater basicity of CH₃COCH₃ compared to that of CH₃CN (Donor Number DN: CH₃CN, 14.1; CH₃COCH₃, 17.1) [38] on the one hand and the greater relative permittivity of CH₃CN ($\epsilon_r = 35.9$) than CH₃COCH₃ ($\epsilon_r = 20.7$) [39]. An even more striking solvent and small cations effect could be demonstrated for the 18-molybdodiphosphate complex [(P₂O₇)Mo₁₈O₅₄]⁴⁻ that contains [P₂O₇]⁴⁻ as heteroion [40]. Unlike the usual Dawson complexes that consist of two A-type XMo₉ units (X = S, P, As),

the $[(P_2O_7)Mo_{18}O_{54}]^{4-}$ complex has a structure based on two B-type PMo_9 fragments. For this molecule, the presence of small cations such as H^+ , Li^+ , and Na^+ caused one-electron wave to be converted into four- and two-electron waves in a complex manner. With the addition of a trace amount of H^+ , a four-electron reduction wave was obtained in solvents of weaker basicity like acetone, acetonitrile, or propylene carbonate; the relative permittivity does not affect the appearance of the four-electron wave. Two-electron waves were obtained in solvents of stronger basicity like *N,N*-dimethylformamide (DMF), *N,N*-dimethylacetamide (DMA), and *N*-methylpyrrolidinone (NMP). With the addition of Li^+ or Na^+ , the one-electron waves were converted into two-electron waves only in acetone, indicating that the conversion can occur in solvents of both weak basicity and low relative permittivity. The interaction of Li^+ toward the reduced forms of the Dawson $[S_2Mo_{18}O_{62}]^{4-}$ polyoxometalate anion was interpreted in the same framework by considering this cation as a moderately strong Lewis acid [41]. In the 95:5 $CH_3CN + H_2O$ solvent mixture (0.1 M NBu_4ClO_4), the voltammetric behavior obtained upon

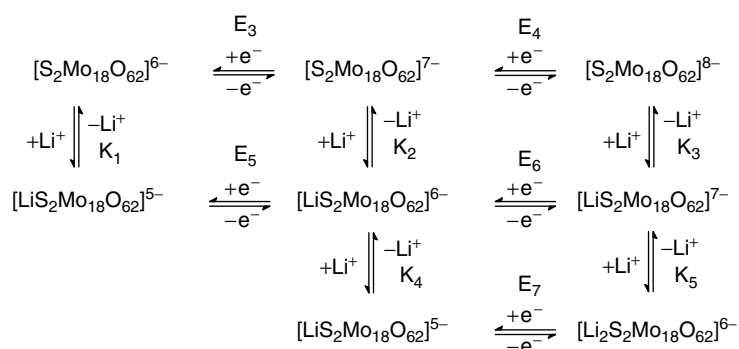
stepwise addition of Li^+ is analogous to that observed upon addition of $HClO_4$ [41b], except that Li^+ appears to act as a weaker acid than H^+ . Following experimental observations, it is assumed that $[S_2Mo_{18}O_{62}]^{4-}$ and its one-electron reduced species do not interact with Li^+ . Then, the various possibilities sketched in Sch. 2 involving an extensive series of reversible potentials and equilibrium constants could be simulated. Parameters used to simulate cyclic voltammograms are gathered in Table 4.

Phenomenologically, the reactions between reduced forms of $[S_2Mo_{18}O_{62}]^{4-}$ and Li^+ are analogous to those with H^+ , with acidity strength being in the order $HClO_4 > LiClO_4 > H_2O$. However, as this simulation involves a significant number of unknown parameters, the coherent set of data obtained cannot be assumed to be unique.

22.3.2

Quinone/hydroquinone-like Behaviors in the First Several Reduction Waves of POMs

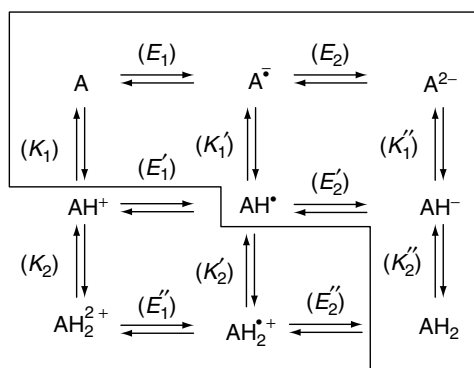
Whatever the solvent and the salt used as supporting electrolyte, it appears that the first several waves of POMs could be



Scheme 2 General scheme for the interaction of lithium cation with the reduced forms of $[S_2Mo_{18}O_{62}]^{6-}$ (Ref. 41a).

Tab. 4 (a) See Ref. 41a. (b) Diffusion coefficient used in the simulation was $1.4 \times 10^{-5} \text{ cm}^2 \text{ s}^{-1}$ for Li^+ and $6.4 \times 10^{-6} \text{ cm}^2 \text{ s}^{-1}$ for all polyoxo anions. (c) Reversible charge transfer process simulated by use of value of $10^{-4} \text{ cm s}^{-1}$ for the heterogeneous charge transfer rate constant (k_s) and 0.5 for the charge transfer (α). (d) Reversible conditions achieved by making the rate constant for both forward (k_f) and reverse (k_b) reaction of homogeneous chemical reactions extremely fast

Charge transfer reactions ^c	$E_{1/2} [\text{V}]$
$[\text{S}_2\text{Mo}_{18}\text{O}_{62}]^{4-} + \text{e}^- \rightleftharpoons [\text{S}_2\text{Mo}_{18}\text{O}_{62}]^{5-}$	-0.12
$[\text{S}_2\text{Mo}_{18}\text{O}_{62}]^{5-} + \text{e}^- \rightleftharpoons [\text{S}_2\text{Mo}_{18}\text{O}_{62}]^{6-}$	-0.11
$[\text{S}_2\text{Mo}_{18}\text{O}_{62}]^{6-} + \text{e}^- \rightleftharpoons [\text{S}_2\text{Mo}_{18}\text{O}_{62}]^{7-}$	-0.73
$[\text{S}_2\text{Mo}_{18}\text{O}_{62}]^{7-} + \text{e}^- \rightleftharpoons [\text{S}_2\text{Mo}_{18}\text{O}_{62}]^{8-}$	-0.91
$[\text{LiS}_2\text{Mo}_{18}\text{O}_{62}]^{5-} + \text{e}^- \rightleftharpoons [\text{LiS}_2\text{Mo}_{18}\text{O}_{62}]^{6-}$	-0.56
$[\text{LiS}_2\text{Mo}_{18}\text{O}_{62}]^{6-} + \text{e}^- \rightleftharpoons [\text{LiS}_2\text{Mo}_{18}\text{O}_{62}]^{7-}$	-0.67
$[\text{Li}_2\text{S}_2\text{Mo}_{18}\text{O}_{62}]^{5-} + \text{e}^- \rightleftharpoons [\text{Li}_2\text{S}_2\text{Mo}_{18}\text{O}_{62}]^{6-}$	-0.60
Chemical reactions ^d	K/M^{-1}
$[\text{S}_2\text{Mo}_{18}\text{O}_{62}]^{6-} + \text{Li}^+ \rightleftharpoons [\text{LiS}_2\text{Mo}_{18}\text{O}_{62}]^{5-}$	$10^1 (K_1)$
$[\text{S}_2\text{Mo}_{18}\text{O}_{62}]^{7-} + \text{Li}^+ \rightleftharpoons [\text{LiS}_2\text{Mo}_{18}\text{O}_{62}]^{6-}$	$5 \times 10^2 (K_2)$
$[\text{S}_2\text{Mo}_{18}\text{O}_{62}]^{8-} + \text{Li}^+ \rightleftharpoons [\text{LiS}_2\text{Mo}_{18}\text{O}_{62}]^{7-}$	$10^6 (K_3)$
$[\text{LiS}_2\text{Mo}_{18}\text{O}_{62}]^{6-} + \text{Li}^+ \rightleftharpoons [\text{Li}_2\text{S}_2\text{Mo}_{18}\text{O}_{62}]^{5-}$	$10^3 (K_4)$
$[\text{LiS}_2\text{Mo}_{18}\text{O}_{62}]^{7-} + \text{Li}^+ \rightleftharpoons [\text{Li}_2\text{S}_2\text{Mo}_{18}\text{O}_{62}]^{6-}$	$8 \times 10^3 (K_5)$



Scheme 3 Nine-member box scheme summarizing the possible intermediates for all two-electron, two-proton reactions (taken from Ref. 2).

considered to follow the same mechanistic scheme as quinones. As a representative example, H^+ will be selected as the active cation in the supporting electrolyte (Sch. 3).

$E_1, E_2, E'_1, E'_2, E''_1, E''_2$ are the normal potentials of the various redox couples

and $K_1, K_2, K'_1, K'_2, K''_1, K''_2$ are the acid dissociation constants.

It is assumed that $E_1 > E_2$. Then the actual reaction mechanism depends on the relative rates of proton and electron transfers [42–44]. The whole set of experimental results suggests clearly two main

reaction pathways, depending on the solvent. Taking SiW_{12} in water as an example, its second wave was found to shift to less negative potentials, the peak potential of its first wave remaining unchanged when the perchloric acid concentration was varied in the range 1–4 M. From 5–7 M perchloric acid concentration, this phenomenon continues, while the first wave now grows at the expense of the second one, conceivably due to the very close proximity of the redox potentials of the two couples [45–47]. Obviously, the behavior in water is consistent with a reaction mechanism in which the second electron transfer is followed by a protonation shifting in the positive potential direction of this step. This mechanism leads to the formation of an overall, apparently direct two-electron process. In the present case, an Electrochemical-Electrochemical-Chemical (EEC) pathway is followed. Nuances of this mechanism and/or thermodynamically equivalent pathways can be found and were described previously [42, 48].

In DMF, the appearance, upon addition of acid, of a new wave located at a more positive potential than the former first wave in the absence of acid suggests strongly that the preferred reaction pathway should feature a Chemical-Electrochemical-Electrochemical-Chemical pathway (CEEC) or Chemical-Electrochemical-Chemical-Electrochemical pathway (CECE). The foregoing considerations indicate, however, that determination of the kinetic parameters of the reaction, in water as well as in DMF, is a formidable task that, up to now, could be carried out only in selected experimental conditions.

All these considerations apply also to heteropolymolybdates, with the general remark that they are more easily reduced than heteropolytungstates and that the

media where they are stable must be carefully selected.

22.4

Selected Achievements that Illustrate the Basic Behaviors of Plenary POMs at Electrodes

22.4.1

Heterogeneous One-electron Exchange of $\alpha\text{-[SiW}_{12}\text{O}_{40}]^{4-}$ in Dimethylformamide

The one electron exchange of $\alpha\text{-[SiW}_{12}\text{O}_{40}]^{4-}$ in dimethylformamide was studied with the aim to obtain a deeper insight into the formal analogy between quinones and POMs as regards their respective electron transfer kinetics [49]. In particular, it was of interest to check whether the simpler treatments of Marcus [50], commonly applied to quinoidic compounds [51], can be also applied to POMs to evaluate quantitative parameters of electron transfer kinetics. Cyclic voltammetry was used for this purpose. Important experimental details can be found in the original paper. Great care was exercised to collect experimental data without ohmic drop and without adsorption effects. Table 5 gathers the values of diffusion coefficients, heterogeneous rate constants k_s , collision number Z_{het} , free enthalpy of activation $\Delta G_{\text{T}}^\ddagger$ and standard free enthalpy of activation ΔG_{298}^\ddagger for the reduction of 10^{-3} M $\text{K}_4\text{SiW}_{12}\text{O}_{40}$ in DMF containing 0.1 M LiClO_4 . Several approximations were discussed in detail and have permitted to evaluate a theoretical value of $\Delta G_{\text{th}}^\ddagger$ between 0.22 and 0.43 eV, in fairly acceptable agreement with the experimental value, considering the very crude approximations used in the estimation of $\Delta G_{\text{th}}^\ddagger$. It appears that the

Tab. 5 Diffusion coefficient, heterogeneous rate constant k_s , collision number Z_{het} , free enthalpy of activation DG_T^\ddagger and standard free enthalpy of activation DG_{298}^\ddagger for the reduction of 10^{-3} M α -K₄SiW₁₂O₄₀ in DMF containing 0.1 M LiClO₄ (taken from Ref. 49)

$T/^\circ\text{C}$	$10^6 D \text{ cm}^{-2} \text{ s}^{-1}$	$10^3 k_s \text{ cm}^{-2} \text{ s}^{-1}$	$Z_{\text{het}} \text{ cm}^{-1} \text{ s}^{-1}$	DG_T^\ddagger/eV	$DG_{298}^\ddagger/\text{eV}$
25	3.12	9.19	1171	0.302	0.302
10	2.39	5.16	1141	0.300	0.302
0	2.24	3.57	1120	0.298	0.301
-10	1.88	2.26	1100	0.297	0.301
-30	1.19	0.895	1057	0.293	0.299

bulkiness and structure of this POM, resulting on a very small surface charge, are the main parameters favoring its straightforward comparison with organic compounds like quinones.

22.4.2

The Reduction Potential of the One-electron Wave and the Role of the Central Heteroatom

Detailed studies of this problem were performed for Keggin-type heteropolytungstates and heteropolymolybdates. It came out that the reducibility increases in the sequence α -, β - and γ -isomers according to the number of M₃O₁₃ rotated groups [4, 52, 53]. A related question of interest concerns the influence or fate of the central heteroatom during the reduction of heteropolyanions. It was shown that the reductions of α -[PW₁₂O₄₀]³⁻, α -[SiW₁₂O₄₀]⁴⁻, α -[Fe^{III}W₁₂O₄₀]⁵⁻, α -[Co^{II}W₁₂O₄₀]⁶⁻, and α -[H₂W₁₂O₄₀]⁶⁻ in 1 M H₂SO₄, electrons can be added without protonation until the charge of the reduced species is -6 [30a]. Further reduction is always accompanied by protonation keeping the overall ionic charge at -6. In the case of α -[Fe^{III}W₁₂O₄₀]⁵⁻ and α -[Co^{II}W₁₂O₄₀]⁶⁻ where the central heteroatom might be reduced, the reduction takes place only

on the tungsten atoms and no Fe(II) and Co(I) species were observed. In the absence of protonation in aqueous solutions, the reduction of α -[XW₁₂O₄₀]^{*n*-} (X = P(V), Si(IV), Ge(IV), Fe(III), B(III), Co(II), H₂, Cu(I)) is featured by two one-electron processes. Their potentials are linearly dependent on the ionic charge by -0.18 V per unit charge [Chapter 6 in Ref. 4, 54a,b,c as sketched in Fig. 6]. The same trend is also reported in organic solvents [54d].

In short, the central heteroatom was admitted to intervene in the reduction of these POMs essentially by the overall ionic charge it imposes to the molecule. Recently, however, the Si center was shown, by XPS, FTIR, and ESR, to be partly reduced in the one-electron reduction species of α -[SiMo₁₂O₄₀]⁴⁻ [55].

22.4.3

Isomerization upon Reduction

Possibilities of isomerization of POMs, during their reduction processes, were reported [56]. For example, the one-electron reduction of the γ^* -isomer of [S₂W₁₈O₆₂]⁴⁻ leads to isolation of the α -isomer and this transformation is associated with the [S₂W₁₈O₆₂]⁴⁻/[S₂W₁₈O₆₂]⁵⁻ [56]. However, the transformation could not be detected on the timescale of

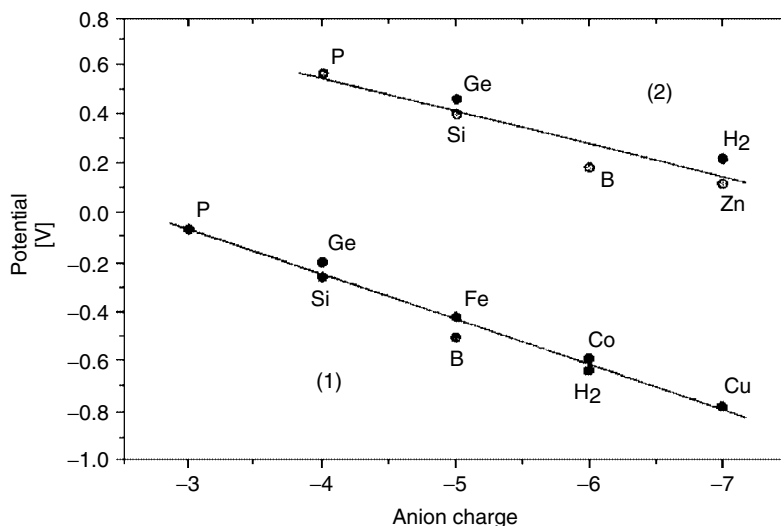


Fig. 6 Dependence of the first one-electron reduction potentials (in V vs. SCE) on the negative charge: (1) $XW_{12}O_{40}^{n-}$, $X = P, Si, Ge, Fe, B, Co, H_2, Cu$; and (2) $XW_{11}VO_{40}^{n-}$, $X = P, Si, Ge, B, H_2, Zn$ (taken from Ref. 8).

cyclic voltammetry up to a scan rate of 10 V s^{-1} and was solved by X-ray crystallography. The available data suggest that either (1) the γ^* - α equilibrium favors one of the isomers in solution for both redox states or (2) the isomerization is slow on the cyclic voltammetry timescale but the difference in $E_{1/2}$ for the α - $[S_2W_{18}O_{62}]^{4-}/\alpha$ - $[S_2W_{18}O_{62}]^{5-}$ and γ - $[S_2W_{18}O_{62}]^{4-}/\gamma$ - $[S_2W_{18}O_{62}]^{5-}$ couples cannot be resolved by cyclic voltammetry.

22.4.4

POM-solvent Interactions as Probed by the Redox Potentials of Two POMs

α - $K_4SiW_{12}O_{40}$ (SiW_{12}) and α - $K_6P_2W_{18}O_{62}$ (P_2W_{18}) were selected as representative examples to enlarge the current knowledge of ion-solvent interactions [34]. In related studies, cations have received considerable attention [57], but anions suitable for work in nonaqueous media are scarce [57a, 58]. The best representative examples are

hexacyanoferrate(III)/hexacyanoferrate(II) and hexacyanomanganate(III)/hexacyanomanganate(II) redox couples that contain cyano groups. Therefore, the high nominal negative charge of SiW_{12} and P_2W_{18} as well as the lack of cyano groups were anticipated to be of interest.

The following discussion is based on the study of the first voltammetric waves of SiW_{12} and P_2W_{18} respectively, in the various media, with 0.1 M $LiClO_4$ as supporting electrolyte except in water where $HClO_4$ was used [34]. The reference system was ferrocene-ferricinium. These waves were checked to be one-electron chemically reversible processes in all the solvents used in the following. The main results are gathered in Table 6.

They show that the electron transfer is reversible or quasi-reversible, the deviation from reversibility remaining quite modest for scan rates from 10 mV s^{-1} to 100 mV s^{-1} . Although the reversibility of the ferrocene-ferricinium in all the

Tab. 6 Cyclic voltammetry data for the reduction of 10^{-3} M solution of α -K₄SiW₁₂O₄₀ or α -K₆P₂W₁₈O₆₂ in various solvents. T = 25 °C; working electrode: glassy carbon disk. Sweep rate: 100 mV s⁻¹ (taken from Ref. 34)

Solvent	SiW ₁₂ O ₄₀ K ₄		P ₂ W ₁₈ O ₆₂ K ₆	
	-E _{pc} [mV]	ΔE _p [mV]	-E _{pc} [mV]	ΔE _p [mV]
N, N-dimethylformamide (DMF)	1297	75	1087	75
Dimethylsulfoxide (DMSO)	1130	60–65	910	63
N-methylformamide (NMF)	756	57	485	63
Formamide (FA)	574	60	295	55
Water (H ₂ O) + 1 M HClO ₄	340	55	95	55

E_{pc}: reduction peak potential measured versus the reduction peak potential of ferricinium in the same medium.

ΔE_p: anodic-to-cathodic peak potential difference. The supporting electrolyte is 0.1M LiClO₄.

solvents was verified, only the reduction peak potentials are quoted in Table 6, instead of standard potentials, taking the reduction peak potential of ferricinium in the relevant medium as a reference. This procedure was shown to be useful in an attempt to extend the correlation to water in the series of solvents [34]. The reduction peak potentials of SiW₁₂ and P₂W₁₈ depend strongly on the nature

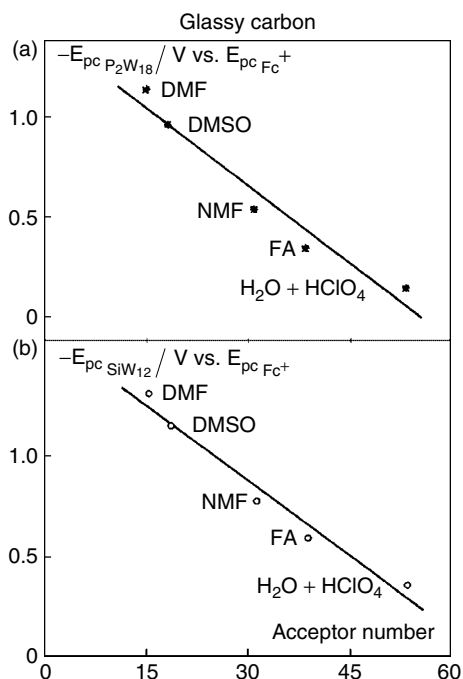
of the solvent. On the assumption that preferential solvation of the molecules by residual water was not prevalent, the following conclusions emerge from the discussion based on the bulk properties of the solvents, gathered in Table 7; (1) the dielectric continuum model of Born is not successful in correlating solvent effects with redox potentials of POMs [34, 57b, 57c, 58], a conclusion also reached for

Tab. 7 Solvent parameters [dielectric constant (ε), dipole moment (μ), acceptor number (AN) and free enthalpy of transfer (DG^o_{tr}) of the chloride ion from N, N-dimethylformamide as reference solvent (taken from Ref. 34)

Solvent	ε	μ ^a Debye	AN	-ΔG _{tr} (Cl ⁻) kJ mol ⁻¹
N, N-dimethylformamide (DMF)	36.7	3.82	16.0	0
Dimethylsulfoxide (DMSO)	46.7	3.96	19.3	+6
N-methylformamide (NMF)	182.4	3.83	32.1	+25
Formamide (FA)	109.5	3.73	39.8	+33
Water (H ₂ O)	78.5	1.87	54.8	+46

^a1 Debye = 3.3356 × 10⁻³⁰ C.m.

Fig. 7 Relationship between the reduction peak potential, E_{pc} , of α -K₆P₂W₁₈O₆₂ or α -K₄SiW₁₂O₄₀ versus the reduction peak potential, E_{pcFc+} , of ferricinium and the acceptor number of studied solvents. Abbreviations are the same as in Tables 6 and 7. The solid line is the best linear regression fit to all the experimental points, including water as a solvent. (a) α -K₆P₂W₁₈O₆₂: correlation coefficient for the solid line: 0.974. The correlation coefficient for the best fit to “nonaqueous solvents” only is 0.994. (b) α -K₄SiW₁₂O₄₀: correlation coefficient for the solid line: 0.983. The correlation coefficient for the best fit to “nonaqueous solvents” only is 0.995 (taken from Ref. 34).



cyano complexes of iron and manganese; (2) in contrast, the Lewis-type concept that proved satisfactory for ion-solvent interactions [57, 58] was successful here also.

The Gutmann acceptor number is one quantitative expression of this solvent parameter. Figure 7 shows that the reduction peak potentials of SiW₁₂ and P₂W₁₈ respectively correlate satisfactorily with the acceptor numbers of the corresponding solvents. The correlation coefficient is above 0.99 for the line including only “nonaqueous” solvents, and is still larger than 0.97 when the H₂O/HClO₄ was included as a solvent. Alternatively, the free enthalpies (ΔG_{tr}^0) of transfer of the chloride ion express also quantitatively the electron-pair acceptor properties of solvents. Figure 8 shows good correlations for SiW₁₂ and P₂W₁₈ reduction peak potentials with this parameter, with correlation coefficients as high as 0.999. As such

strikingly good correlation coefficients were obtained also for hexacyano complexes [58], it can be concluded that any specific interaction between the solvents and anions in this work are small, absent or smoothly parallel each other. Furthermore, a plot of the reduction peak potentials data for SiW₁₂ versus those for P₂W₁₈ gives a straight line with a slope close to unity, thus indicating that solvent effects must be very similar for both systems.

22.4.5

Structure of Electrolyte Solutions As Probed by the Electrochemical Behaviors of POMs

Sizes, shapes, diffusion coefficients, redox behaviors, and spectroscopic properties of oxidized and reduced forms of POMs make these species eminently suitable for a variety of physicochemical studies [4, 18, 19, 22, 23, 30a–d]. Owing to the minimal

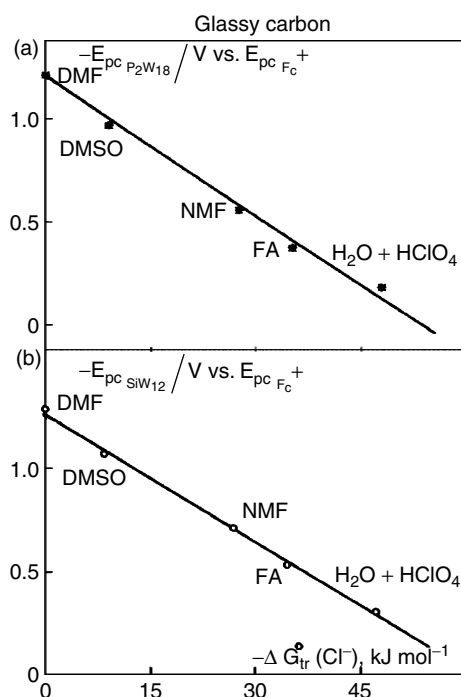


Fig. 8 Relationship between the reduction peak potential, E_{pc} , of $\alpha\text{-K}_6\text{P}_2\text{W}_{18}\text{O}_{62}$ or $\alpha\text{-K}_4\text{SiW}_{12}\text{O}_{40}$ versus the reduction peak potential, E_{pcFc}^+ , of ferricinium and the free enthalpy of transfer of the chloride ion, $\Delta G_{tr}(Cl^-)$, taking DMF as the reference solvent. Abbreviations are the same as in Tables 6 and 7. The solid line is the best linear regression fit to all the experimental points, including water as a solvent. (a) $\alpha\text{-K}_6\text{P}_2\text{W}_{18}\text{O}_{62}$: correlation coefficient for the solid line: 0.996. The correlation coefficient for the best fit to “nonaqueous solvents” only is 0.999. (b) $\alpha\text{-K}_4\text{SiW}_{12}\text{O}_{40}$: correlation coefficient for the solid line: 0.999. The correlation coefficient for the best fit to “nonaqueous solvents” only is also 0.999 (taken from Ref. 34).

solvation and ion-pairing of SiW_{12} and PW_{12} in concentrated aqueous solutions of alkali-metal salts, these species were used to probe the structure of electrolyte solutions [33a,b]. Ion-water interactions in highly concentrated solutions are currently a matter of interest that has benefited from the modern developments of various spectroscopies, including NMR, X-ray scattering, and IR studies. A classification of commonly used ions has resulted, among which Li^+ , Na^+ , H_3O^+ ... are net-structure making ions, while K^+ , Cl^- , ClO_4^- are net-structure breaking ions [59]. In contrast, other IR results would suggest that Li^+ , Na^+ , and K^+ are net-structure breaking species at high concentrations. It was anticipated that the electrochemical behaviors of SiW_{12} might allow a cross-check of this classification. Electrochemical measurements were supplemented

by UV-visible spectroscopy and viscosity measurements. In the absence of any salt added to acid, it was easy to obtain the following order of structure breaking ability for anions: $\text{ClO}_4^- > \text{Cl}^- > \text{SO}_4^{2-}$, HSO_4^- [33a]. For cations, the structure-making abilities were in the order $\text{Li}^+ > \text{Na}^+ \gg \text{K}^+$. With special attention paid to the case of K^+ , electrochemical data suggest unambiguously a small net-structure making ability for K_2SO_4 .

22.4.6

Cation and Pressure Effects on the Electrochemistry of 12-Tungstocobaltate and 12-Tungstophosphate Ions in Acidic Aqueous Solution

Also, cation and pressure effects were studied on two selected POMs, $\text{CoW}_{12}\text{O}_{40}^{5-/6-}$ (CoW_{12}) and $\text{PW}_{12}\text{O}_{40}^{3-/4-}$

($\text{PW}_{12}^{3-/4-}$) and $\text{PW}_{12}\text{O}_{40}^{4-/5-}$ ($\text{PW}_{12}^{4-/5-}$), with the aim to extend investigations on electron transfer chemistry of anions at electrodes to couples other than cyanometalates that could arguably represent special cases because of the “softness” conferred by the π -acceptor action of the cyano ligands [60]. Indeed, marked cation effects have been reported on the reduction potentials of heteropolyoxometalates in aqueous [33a,d, 61a], organic [37, 40], and aqueous organic media [61b,c,d] and also on the rates of self-exchange [62] and of net redox reactions [25], [61a, 63] although it has not always been clear whether the effects observed are cation specific or arise in a general way from ionic strength. The study as a function of pressure has permitted to clarify the role of various cations in the reduction process. The half-wave potentials for the CoW_{12} couple become moderately more positive with increasing electrolyte concentration and cationic charge and also in the sequences $\text{Li}^+ \approx \text{Na}^+ < \text{NH}_4^+ \leq \text{H}^+ < \text{K}^+ < \text{Rb}^+ < \text{Cs}^+$ and $\text{Na}^+ < \text{Mg}^{2+} < \text{Ca}^{2+} < \text{Eu}^{3+}$. The mean diffusion coefficients for CoW_{12}

with the 1:1 electrolytes are independent of electrolyte concentration and rise only slightly from Li^+ to Cs^+ , averaging $(2.4 \pm 0.3) \times 10^{-6} \text{ cm}^2 \text{ s}^{-1}$. It was found [60] that $E_{1/2}$, $\ln D$ and $\ln k_{\text{el}}$ are linear functions of the pressure, the slopes of which therefore gave, respectively, mean values of the reaction volume relative to $\text{Ag}/\text{AgCl}/\text{NaCl}(\text{satd})$ $\Delta V_{\text{Ag}/\text{AgCl}} (= -F(\delta E_{1/2}/\delta P)_{\text{T}})$, the volume of activation for diffusion $\Delta V_{\text{diff}}^{\ddagger} (= -RT(\delta \ln D/\delta P)_{\text{T}})$ and the volume of activation $\Delta V_{\text{el}}^{\ddagger} (= -RT(\delta \ln k_{\text{el}}/\delta P)_{\text{T}})$ of the electrode reaction for the aqueous $\text{CoW}_{12}\text{O}_{40}^{5-/6-}$ couple, over the pressure range 0–204 MPa.

Figure 9 illustrates the results for k_{el} . Neither the volume of activation for diffusion $\Delta V_{\text{diff}}^{\ddagger}$ (average $-0.9 \pm 1.1 \text{ cm}^3 \text{ mol}^{-1}$) nor the electrochemical cell reaction volumes $\Delta V_{\text{Ag}/\text{AgCl}}$ average $(-22 \pm 2 \text{ cm}^3 \text{ mol}^{-1})$ for the CoW_{12} couple show significant dependence on electrolyte identity or concentration. For the $\text{PW}_{12}^{3-/4-}$ and $\text{PW}_{12}^{4-/5-}$ couples $\Delta V_{\text{Ag}/\text{AgCl}} = -14$ and $-26 \text{ cm}^3 \text{ mol}^{-1}$, respectively, suggesting a dependence on $\Delta(z^2)$ (z = ionic

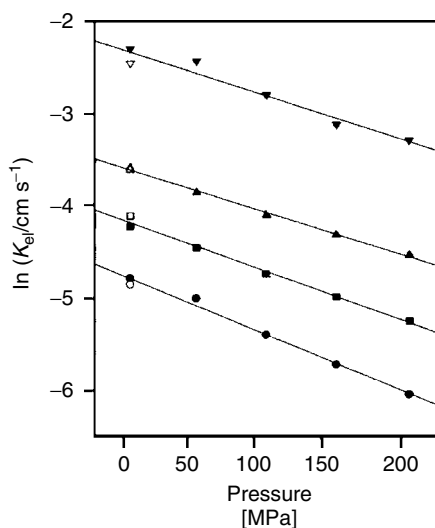


Fig. 9 Pressure and supporting electrolyte concentration dependences of rate constants k_{el} for the $\text{CoW}_{12}\text{O}_{40}^{5-/6-}$ electrode reaction in aqueous KCl at 25.0 C, $[\text{KCl}] = 0.10$ (●), 0.20 (■), 0.50 (▲), and 1.00 (▼) mol L^{-1} ; hollow symbols represent return to low pressure after the pressure cycle. $[\text{K}_6\text{CoW}_{12}\text{O}_{40}] = 1.0 \text{ mmol L}^{-1}$ (taken from Ref. 60).

charge number), which would fit the Born-Drude-Nernst theory of electrostriction of solvent in the form $\Delta V_{\text{Ag/AgCl}} = \Delta V_{\text{ref}} + B\Delta(z^2/r)$ in the one-electron reduction of an electroactive species with an effective radius r , and B being a positive constant at a given pressure. Actually, comparison of these $\Delta V_{\text{Ag/AgCl}}$ with those for CoW_{12} and other anion–anion couples shows that the Born-Drude-Nernst approach fails in this context. For aqueous electrode reactions of CoW_{12} as for other anionic couples such as cyanometalates, the standard rate constants k_{el} show specific cation catalysis ($\text{Na}^+ < \text{K}^+ < \text{Rb}^+ < \text{Cs}^+$), and $\Delta V_{\text{el}}^\ddagger$ is invariably positive, in the presence of supporting electrolytes. For the heavier group 1 cations, $\Delta V_{\text{el}}^\ddagger$ is particularly large ($10\text{--}15\text{ cm}^3\text{ mol}^{-1}$), consistent with a partial dehydration of the cation to facilitate catalysis if the electron transfer process. The positive values of $\Delta V_{\text{el}}^\ddagger$ for the CoW_{12} couple cannot be attributed to rate control by solvent dynamics, which would lead to $\Delta V_{\text{el}}^\ddagger \leq \Delta V_{\text{diff}}^\ddagger$, that is, to negative or zero $\Delta V_{\text{el}}^\ddagger$ values. These results stand in sharp contrast to those for aqueous cationic couples, for which k_{el} shows relatively little influence of the nature of the counterion and $\Delta V_{\text{el}}^\ddagger$ is always negative.

22.5

Mixed Addenda and Other Substituted POMs

22.5.1

Comparison of Valence Trapping in Uniform and Mixed Addenda Plenary POMs

As far as the first electron fixation site on plenary POMs is concerned, a distinction must be made between those containing a single addenda ion like W(VI) , Mo(VI) , or V(V) and those in which at least two

different addenda ions are present. As a consequence of such substitution, the electrochemical character of these POMs can be widely modulated [54c].

Symmetries in the structures of the POMs result in the equivalence of several metal centers detectable, for example, by NMR on fully oxidized species, and by EPR and/or NMR on their reduced analogs [30f, 64–69]. In agreement with the complete structural equivalence of the twelve tungsten atoms of the α -Keggin anions, EPR experiments show that the “blue” electron is delocalized over all the tungsten centers in the one-electron reduced species, for instance in $\alpha\text{-[PW}_{12}\text{O}_{40}]^{4-}$ [30f]. Ample confirmation by EPR and also NMR of this pioneering work exists in the literature for this compound and several others and even on two-electron reduced Keggin derivatives [65]. In contrast, the electron is localized on the more reducible atom at room temperature in the one-electron-reduced mixed addenda POMs. In short, substitution of one or several W atom(s) by Mo or V atom(s), reveals that the added electrons can be trapped according to various timescales, over certain atoms in the case of monosubstitution and/or regions for multisubstituted derivatives [30f, 66, 67, 69–71]. The following order of decreasing oxidizing ability is found: $\text{V(V)} > \text{Mo(VI)} > \text{W(VI)}$.

Such equivalence raises the following question in the molecular electrochemistry of these compounds: in the absence of other possible mechanistic complications, related usually to pH or ion-pairing of the counteranions, can it be expected that symmetry equivalent metal centers will be reduced simultaneously or will the interactions between adjacent metal centers induce a stepwise reduction. (The problem of pure electron transfer reactions to and from molecules containing at least

two identical redox centers has received appropriate attention in several studies. Two main classes are described: The first class of compounds gathers those cases in which noninteracting redox centers are present and for which successive electron transfers are expected to follow simple statistics, in the absence of coupled chemical steps. For example, see [71a–c]. The second group includes molecules in which various phenomena (including conjugation, ion-pairing, solvation changes, and structural variations) induce or reveal interactions between the sites, and comparatively, differences between their half reaction potentials. These constitute the majority of published examples. For example, see [71d–h]) [72].

Despite the structural equivalence of the twelve metal centers in the α -PW₁₂O₄₀^{3–} Keggin anion, a stepwise reduction of the tungsten centers is observed [30f]. EPR experiments on this species show that the added electron is delocalized (type II in the scheme proposed by Robin and Day) [4]. Over all 12 tungsten centers suggesting that there is communication

between the metal centers. (The delocalized electron undergoes localization at low temperatures, otherwise the mixed valence compound is classified as type III under the scheme of Robin and Day.) In general, complete delocalization of the added electrons over all 12 metal centers appears to be the rule for all unsubstituted, highly symmetrical α -Keggin anions. Introduction of lower symmetry results in a variation in the degree of valence trapping [66, 67, 69].

Unlike the spherical α -Keggin anion, the Wells–Dawson structure is shaped like a prolate ellipsoid [73], consisting of six “cap” tungsten centers and twelve “belt” tungsten centers. The nonequivalence of the “cap” and “belt” tungsten sites raises the issue of the initial site of the electron transfer. Various lines of experimental evidence all converge to support that the added electrons are first introduced into the “belt” tungsten sites [54a, 65–70, 74–77]. As will be elaborated in the following, extended Hückel calculations provide a qualitative understanding of the initial electron transfer site in these compounds [78]. Tables 8 through 11

Tab. 8 Half-wave potential for the various complexes at pH = 4.7. The values in this table are essentially those from Ref. 79, but the same measurements were also carried out in Refs. 14,83, with small numerical variations that have no consequence on the interpretations. The numbering of the substituent(s) follows the IUPAC recommendations

Compound	$E_{1/2}$ (V vs. SCE) (number of electrons)	References
P ₂ W ₁₈	+0.04 (1)	14, 79, 83
(4)-P ₂ MoW ₁₇ (α_1)	+0.39 (1)	14, 79, 83
(1)-P ₂ MoW ₁₇ (α_2)	+0.23 (1)	14, 79, 83
(1,2,3)-P ₂ Mo ₃ W ₁₅	+0.26 (1)	14, 79, 83
(4, 9, 10, 15)-P ₂ Mo ₄ W ₁₄	+0.48 (2)	79
(1,4, 9, 10, 16)-P ₂ W ₁₃ Mo ₅	+0.46 (1)	79
(1, 4, 9, 10, 15)-P ₂ W ₁₃ Mo ₅	+0.47 (2)	79
(1, 4, 9, 10, 15, 16)-P ₂ W ₁₂ Mo ₆	+0.45 (2)	79
P ₂ Mo ₁₈	+0.32 (2)	79, 83

Tab. 9 Half-wave potential for the various complexes. The values in this table are taken from Ref. 80. The numbering of the substituent(s) follows the IUPAC recommendations

Compound	pH	$E_{1/2}$ (V vs. SCE) (number of electrons)
α -As ₂ W ₁₈	1	+0.08 (1)
(4)-As ₂ W ₁₇ (α_1)	4,6	−0.47 (2)
(1)-As ₂ W ₁₇ (α_2)	4,6	−0.44 (2)
(1, 2)-As ₂ W ₁₅ Mo ₂	4,6	−0.42 (2)
(1)-As ₂ W ₁₇ Mo (α_2)	1	+0.28 (1)
(4)-As ₂ W ₁₇ Mo (α_1)	1	+0.45 (1)
(1,2) – As ₂ W ₁₆ Mo ₂	1	+0.29 (1)
(1,2,3)-As ₂ W ₁₅ Mo ₃	1	+0.31 (1)
(1)-As ₂ W ₁₇ V (α_2)	1	+0.46 (1)
(1,2)-As ₂ W ₁₆ V ₂	1	+0.42 (2)
(1,2,3)-As ₂ W ₁₅ V ₃	1	+0.32 (3)

Tab. 10 Half-wave potential for various V-substituted complexes. The numbering of the substituent(s) follows the IUPAC recommendations

Compound	pH	$E_{1/2}$ (V vs. SCE) (number of electrons)	References
(4)-P ₂ W ₁₇ V (α_1)	5.5 (Li+)	+0.48 (1)	81
(1)-P ₂ W ₁₇ V (α_2)	5.5 (Li+)	+0.39 (1)	81
(1,2)-P ₂ W ₁₆ V ₂	5.5 (Li+)	+0.27 (1)	81
(1,2,3)-P ₂ W ₁₅ V ₃	5.5 (Li+)	+0.23 (1)	81
(1,2,3)-P ₂ W ₁₅ V ₃	7.0 (Li+)	+0.11 (1)	81
(4)-P ₂ W ₁₇ V (α_1)	4.7(Na+)	+0.51 (1)	74, 81
(1)-P ₂ W ₁₇ V (α_2)	4.7(Na+)	+0.41 (1)	74, 81
(4)-P ₂ W ₁₇ V (α_1)	7	+0.48 (1)	82
(1)-P ₂ W ₁₇ V (α_2)	7	+0.39 (1)	82
(1,2)-P ₂ W ₁₆ V ₂	7	+0.28 (2)	82

gather the reduction half-wave potentials or peak potentials of selected Dawson-type POMs [14, 15, 74–82].

In the formulae of these anions, oxygen atoms and charges were omitted. Experimental evidence proved that the first waves observed for Mo(VI)- and V(V)-substituted derivatives are restricted to the reduction of these cations. The interpretations are based on the comparisons of the reduction potentials of the same element within

α_1 and α_2 -substituted Dawson anions and also with those of the corresponding unsubstituted derivatives. Specifically, it appears that α_1 -P₂MoW₁₇, which contains the Mo atom in an equatorial position, is more easily reduced than P₂Mo₁₈ [79]. In contrast, α_2 -P₂MoW₁₇ in which the Mo atom is in one cap is less reducible than P₂Mo₁₈. This observation is in agreement with the proposal that P₂W₁₈ is initially reduced at one of the twelve equatorial

Tab. 11 Half-wave potential for variously substituted complexes at pH = 1. The values are culled from Ref. 83. The numbering of the substituent(s) follows the IUPAC recommendations

Compound	$E_{1/2}$ (V vs. SCE) (number of electrons)
P ₂ W ₁₈	+0.04 (1)
(1,2)-P ₂ W ₁₆ Mo ₂	+0.27 (1)
(1,2,3)-P ₂ W ₁₅ Mo ₂ V	+0.46 (1) (V ^V /V ^{IV})
(1,2,3)-P ₂ W ₁₅ MoV ₂	+0.37 (2) (V ^V /V ^{IV})
(1,2,3)-P ₂ W ₁₅ V ₃	+0.42 (1) (V ^V /V ^{IV})
(1,2)-P ₂ W ₁₆ V ₂	+0.36 (2)
(4)-P ₂ W ₁₇ V (α_1)	+0.49 (1)
(1)-P ₂ W ₁₇ V (α_2)	+0.41 (1)

tungsten atoms. This conclusion can be extended to P₂Mo₁₈ itself, as suggested by the results in Tables 8–11. In short and in complete analogy with the Keggin model, a stepwise reduction of the equivalent metal centers is also seen in the Wells–Dawson POMs, with various degrees of valence trapping observed upon the introduction of other addenda atom substituents.

22.5.2

Lacunary and Transition Metal–substituted POMs

This section is separated from the former one, even though mixed addenda POMs are mostly, if not exclusively, synthesized from the appropriate lacunary precursors and can be viewed normally as substituted POMs. At least two reasons can be invoked to justify such dichotomy: first, a substitutionally labile position is available on the transition metal substituted into the POMs framework, which is not the case with mixed addenda compounds; second, these transition metal centers are usually the active sites for catalytic and electrocatalytic reactions and might deserve special attention.

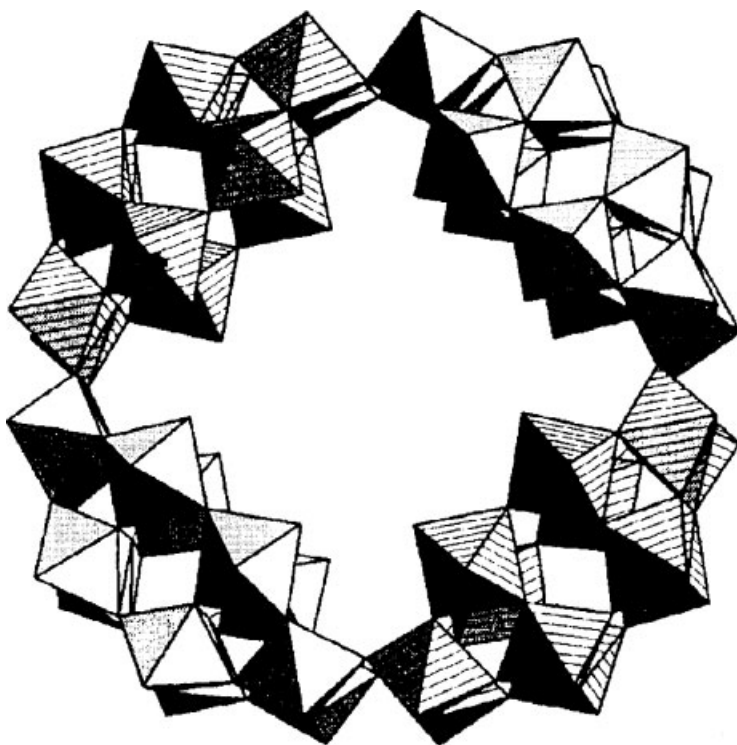
The so-called mono “lacunary” POMs are derived from plenary Keggin, (XM₁₂O₄₀), or Dawson, (P₂W₁₈O₆₂), anions by the removal of one MO unit to yield (XM₁₁O₃₉) or (P₂W₁₇O₆₁) respectively. (Note that charges are omitted for convenience.) Trivalent species, XW₉O₃₄ and X₂W₁₅O₅₆ and even hexavacant species like X₂W₁₂O₄₈ are the precursors of new families of POMs, some of which will also be studied briefly in the following text. In most, but not all cases, the free lacunary polyanions are independently stable. Metal ion binding occurs at the octahedral vacant site(s). In addition of being interesting in its own right, the electrochemistry of lacunary POMs is useful for comparison with the redox processes of the framework in the corresponding plenary compounds and in the transition metal–substituted derivatives.

22.5.2.1 **Lacunary POMs**

Various lines of experimental evidence confirm the very low surface charge density, at least for symmetrical plenary Keggin- and Dawson-type POMs [33a,d, 84]. For example, a simple linear variation

of the first reduction potentials of α -[XW₁₂O₄₀]ⁿ⁻ with the anion charge is observed under conditions without protonation [4, 54]. Extension of these remarks to the corresponding lacunary species and to their first transition metal ion-substituted derivatives do not seem straightforward, possibly owing to the change of symmetry in the charge distribution in the molecules, in conjunction with the increase of the overall negative charge. As a matter of fact, the lacunary POMs are known to exhibit “a donor set of hard oxide ions while the adjacent d⁰ (Mo^{VI}, W^{VI}) atoms provide acceptor orbitals” [85]. As a consequence, the first framework reduction wave in the cyclic voltammogram of these lacunary derivatives appears usually

as a reversible two-electron process, in pH media where the corresponding plenary complexes still undergo a reversible one-electron reduction. In this context, the cyclic voltammetric behavior of selected Keggin- and Dawson-type POMs was studied as a function of electrolyte composition [86a]. The buffer capacity of the electrolyte appeared as an important parameter that can be used to reveal the symmetry or dissymmetry in charge distribution within each oxometalate. A fully symmetrical POM like [P₂W₁₈O₆₂]⁶⁻ exhibits a uniform protonability, while its α_1 and α_2 lacunary derivatives present stepwise acid–base equilibria, owing to their charge dissymmetry. The behavior of these sites is revealed readily in unbuffered or



Scheme 4 Structure of the anion [P₈W₄₈O₁₈₄]⁴⁰⁻. The four building blocks are easily identified (taken from Ref. 86b).

poorly buffered media at $\text{pH} = 3$. In short, it is shown [86a] that cations other than the proton, even in very high excess, fail to give rise to the classical voltammograms of lacunary POMs. The same behavior was observed also for $\alpha_2[\text{P}_2\text{Mo}_2\text{W}_{15}\text{O}_{61}]^{10-}$, $\alpha[\text{PW}_{11}\text{O}_{39}]^{7-}$, $\alpha[\text{SiW}_{11}\text{O}_{39}]^{8-}$, but to a lesser extent in $\alpha_2[\text{Ni}(\text{OH}_2)\text{P}_2\text{W}_{17}\text{O}_{61}]^{8-}$ and $\alpha_2[\text{Zn}(\text{OH}_2)\text{P}_2\text{W}_{17}\text{O}_{61}]^{8-}$ [86a]. The phenomenon was very severe with $[\text{H}_2\text{P}_2\text{W}_{12}\text{O}_{48}]^{12-}$ [86a] and was also studied in some detail on its remarkably stable and inert cyclic tetramer $\text{K}_{28}\text{Li}_5\text{H}_7\text{P}_8\text{W}_{48}\text{O}_{184} \cdot 92\text{H}_2\text{O}$ (P_8W_{48} for convenience) [86b]. The structure of this crown POM is sketched in Sch. 4.

A constant $\text{pH} = 3$ value, was selected to start the experiments. It was made up with H_2SO_4 without or with potassium hydrogenophthalate (PHP) and the appropriate concentration of Li_2SO_4 or LiCl to maintain the total concentration of Li^+ constant. First pH measurements illustrated by Fig. 10 give some insight into the acid–base equilibria of the oxidized form of the crown complex. Proton consumption occurs even with the smallest concentration of POM used in that work. The results are easily explained by taking into account the buffer capacity of the various media. A fast increase of the pH is observed in chloride medium as a consequence of the absence of any buffer capacity. In pure sulfate solution, the hydrogen sulfate anion $[\text{HSO}_4]^-$ confers some

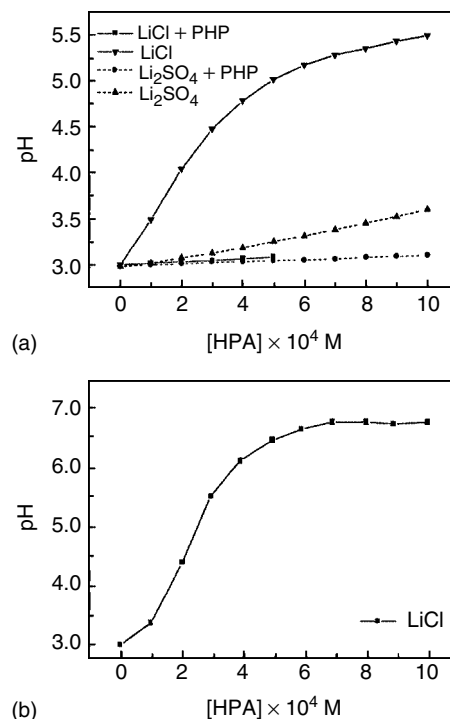
buffer capacity to the medium. Finally, the mixture $\text{Li}_2\text{SO}_4 + \text{PHP}$ is slightly more efficient than $\text{LiCl} + \text{PHP}$, as the former contains two-proton donors. The cyclic voltammograms in Fig. 11 shows the behaviors observed during the redox processes of P_8W_{48} . The voltammetric patterns speak by themselves. In particular, the increase in Li^+ concentration does not compensate for the lack of buffer capacity of the supporting electrolyte, an observation that underscores again the essential role of proton sources in the electrochemistry of lacunary POMs.

22.5.2.2 Transition

Metal–monosubstituted POMs

In addition to structural studies, one of the main incentives to synthesize and characterize these transition metal–substituted complexes is the remark that they might

Fig. 10 Evolution of the pH of an initially pH 3 solution as a function of the concentration of the relevant heteropolyanion. The compositions of the four starting pH 3 electrolytes were respectively: ($\text{H}_2\text{SO}_4 + 1\text{M LiCl}$); ($\text{H}_2\text{SO}_4 + 0.5\text{M Li}_2\text{SO}_4$); ($\text{H}_2\text{SO}_4 + 1\text{M LiCl} + 0.069\text{M PHP}$); ($\text{H}_2\text{SO}_4 + 0.5\text{M Li}_2\text{SO}_4 + 0.069\text{M PHP}$). (a) P_8W_{48} ; (b) P_2W_{12} . For further details, see text (taken from Ref. 86b).



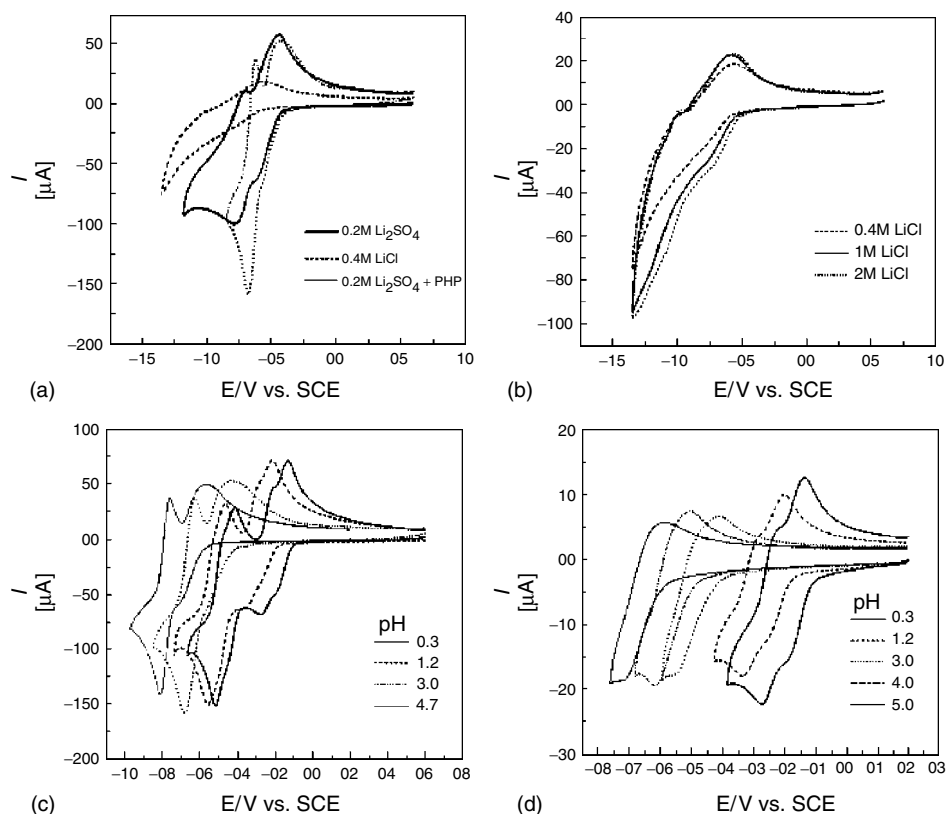
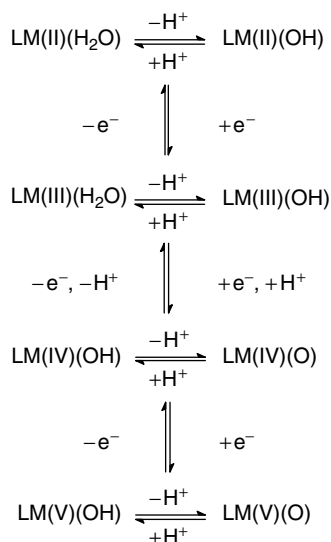


Fig. 11 Evolution of the cyclic voltammograms of P_8W_{48} as a function of the composition of the supporting electrolyte. Scan rate: 10 mV s^{-1} . (a) $5 \times 10^{-4} \text{ M } P_8W_{48}$ in several pH 3 solutions: ($H_2SO_4 + 0.4 \text{ M LiCl}$); ($H_2SO_4 + 0.2 \text{ M Li}_2SO_4$); ($H_2SO_4 + 0.2 \text{ M Li}_2SO_4 + 0.069 \text{ M PHP}$). (b) $5 \times 10^{-4} \text{ M } P_8W_{48}$ in several pH 3 solutions: ($H_2SO_4 + 0.4 \text{ M LiCl}$); ($H_2SO_4 + 1 \text{ M LiCl}$); ($H_2SO_4 + 2 \text{ M LiCl}$). (c) $5 \times 10^{-4} \text{ M } P_8W_{48}$ in various pH solutions: pH = 4.7: ($0.1 \text{ M CH}_3\text{COOLi/CH}_3\text{COOH} + 1 \text{ M LiCl}$); pH = 3:

($H_2SO_4 + 0.069 \text{ M PHP} + 0.5 \text{ M Li}_2SO_4$); pH = 1.2: ($H_2SO_4 + 0.5 \text{ M Li}_2SO_4$); pH = 0.3: (0.5 M H_2SO_4). (d) $10^{-4} \text{ M } P_8W_{48}$ in various pH solutions; the study is restricted to the first wave obtained at pH 5 and to its evolution for lower pH values; pH = 4 and pH = 5: ($0.1 \text{ M CH}_3\text{COOLi/CH}_3\text{COOH} + 1 \text{ M LiCl}$); pH = 3: ($H_2SO_4 + 0.069 \text{ M PHP} + 0.5 \text{ M Li}_2SO_4$); pH = 1.2: ($H_2SO_4 + 0.5 \text{ M Li}_2SO_4$); pH = 0.3: (0.5 M H_2SO_4). For further details, see text (taken from Ref. 86b).

serve as catalysts and electrocatalysts [17]. With the lacunary POM functioning as a ligand, two global stoichiometries were observed: 1 : 1 metal-ligand and 1 : 2 metal-ligand complexes. In the 1 : 1 complexes formed predominantly with “octahedral” metal ions, the POM is a pentadentate ligand, whereas the metal can be viewed

as 8-coordinate in 1 : 2 complexes. The number of such complexes is virtually enormous and very numerous examples were reported. The sixth coordination site on the substituent metal in the 1 : 1 complexes may be occupied by a variety of ligands, usually a water molecule as most syntheses are carried out in that medium.



Scheme 5 General electrochemical behavior of transition metal–substituted POMs (taken from Ref. 8).

The POM ligands in these complexes undergo, at least one, but generally two reversible two-electron reductions, with the addition of between two and three protons in acidic solutions. Eventually, the two-electron reductions split into two one-electron reductions when the pH of the electrolyte is raised. These behaviors are the same as observed with the plain precursor lacunary complexes, albeit at a different potential location as will be shown in the following. We consider the metal centers in their role of active oxidation sites. A behavior that can be viewed as general is sketched in Sch. 5 [8].

Usually, the aquametal(III) is reducible to aquametal(II) and oxidizable to the corresponding oxometal(IV), hydroxometal(IV) and oxometal(V) derivatives depending on the character of the incorporated metals. Further oxidations to oxometal(VI) and –(VII) are possible in the cases of metals like rhenium [87]. The interest of hydroxometal and oxometal species as oxidation catalysts in synthetic applications must be stressed.

The formal potentials of substituent metals are modulated by numerous influences among which those of the central heteroion and the addenda ions must be highlighted, in addition of the effects of pH, counterions, additives, solvents, and so on. For example, the redox potential of the Mn(III/II) couple was found to increase with $X = \text{B} < \text{Zn} < \text{Si} < \text{Ge} < \text{P}$ [88]. In aqueous solutions, the pH of the supporting electrolyte might induce deprotonation of the aquametal or hydroxymetal, thus changing its redox potential. The labile water molecule on the sixth site of the substituent metal can be substituted by a large variety of other ligands, including other solvents, with an expected consequence on the redox potential. In addition to these general trends, more specific insights can be obtained by detailed descriptions of selected experiments. Among complementary issues of interest in electrochemical studies, particular attention should be drawn to questions including, but not exhaustively: the redox activity of the transition metal centers within the POMs, when that is visible; the influence on their location on the framework of the molecule and eventually, the number and mutual influences of these centers in the molecules; the redox activity of the POM framework and the appropriate comparison with a precursor, and so on. These points are studied in the literature [13, 15, 30f, 74, 79, 81, 85, 88, 89]. The electrochemistry of metal ion complexes derived from α_1 - and α_2 -[P₂W₁₇O₆₁]^{10–} illustrates most of the features of interest [15]. The complexes substituted by Ca(II), V(V), Mn(II), Fe(III), Co(II), Ni(II), Cu(II), and Zn(II) were synthesized in the α_1 and in the α_2 series. Complexes with V(V)

and Mo(VI) were also added for the sake of comparison. As a matter of fact, an interesting issue concerns the choice of

the more appropriate precursor to which to compare the cyclic voltammograms of metal ion-substituted POMs. For this

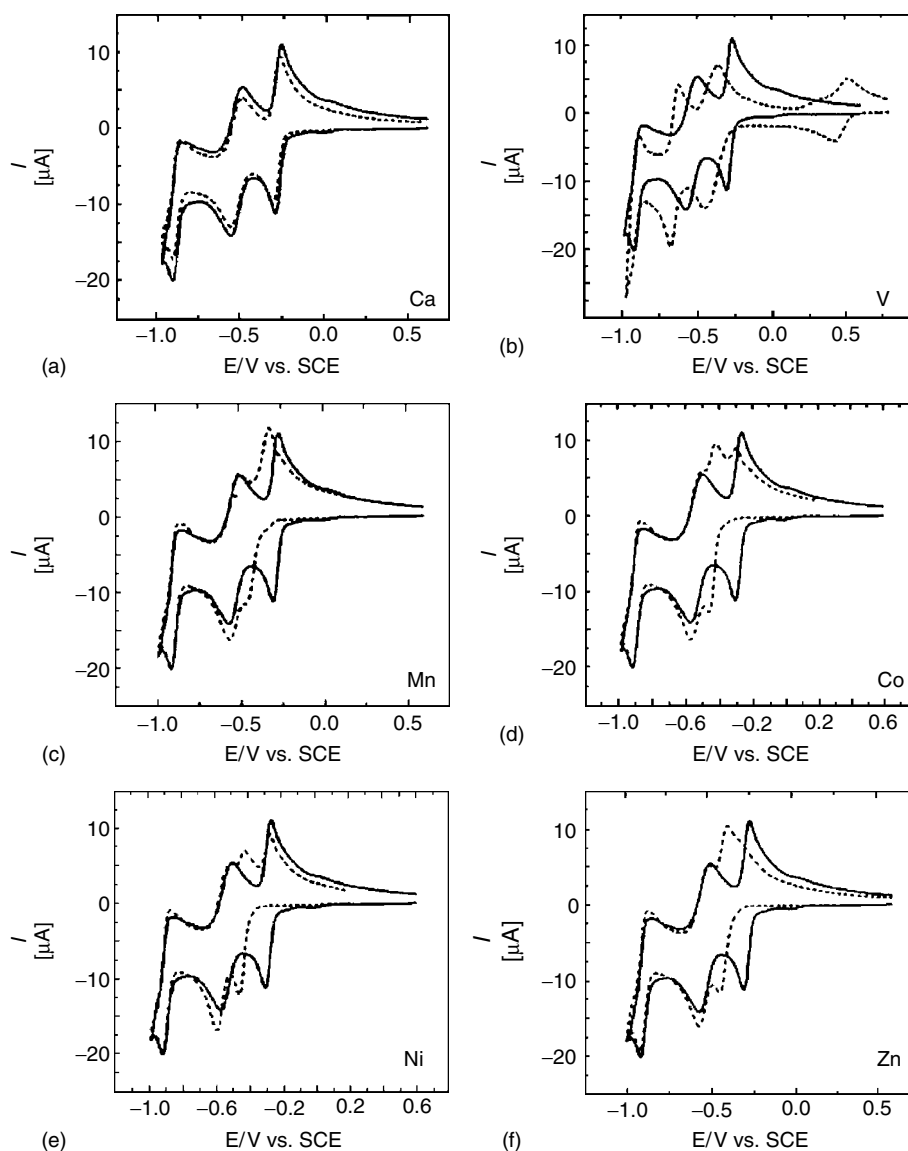


Fig. 12 Comparison of the cyclic voltammograms of $\alpha_1\text{-P}_2\text{W}_{17}$ with those of its substituted complexes in 0.2 M $\text{Na}_2\text{SO}_4 + \text{H}_2\text{SO}_4$ (pH 3) medium. Scan rate: 10 mV s^{-1} . Concentration $c_0 = 2.5 \cdot 10^{-4} \text{ M}$ for

each complex. The substituent cation is indicated on each curve. The full line corresponds to the lacunary species. For further details, see text (taken from Ref. 15).

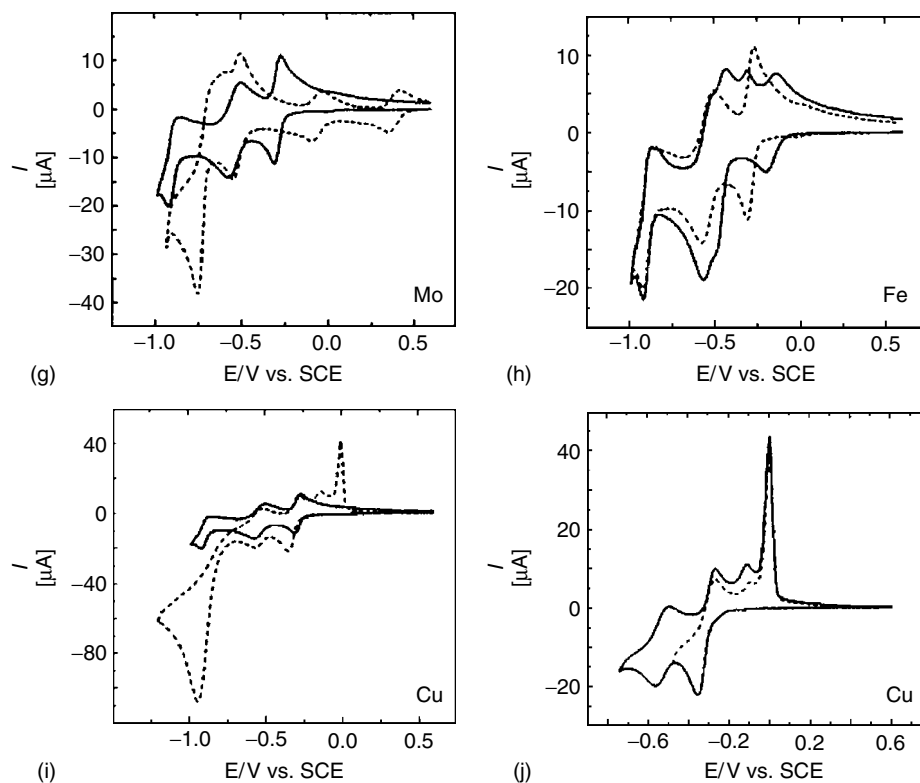


Fig. 12 (Continued).

purpose, the substituted compounds are symbolized by $(P_2W_{17})(ZL)$, where Z is the substituent metal cation and L the terminal ligand [4, 14, 89]. This formula permits to take also into account mixed addenda complexes, and two groups of POMs can be distinguished: the first group is constituted by those complexes in which $Z = W^{6+}$, Mo^{6+} , V^{5+} or V^{4+} and $L = O^{2-}$ and the second group gathers complexes with $Z = M^{n+}$ and $L = H_2O$ where M^{n+} is the metal cation. The complexes of the first group, which encompasses plenary and mixed addenda POMs, can be considered as really “saturated” compounds while the others are not. As a matter of fact, these two groups behave differently in electrochemistry [14, 15, 89], and the

voltammetry of the second group is better considered as deriving from that of the precursor lacunary species.

For convenience, two groups are distinguished among these substituted compounds, depending on whether the potential location of the redox activity of the substituent heterometal cation, in cases when it is visible on cyclic voltammograms is far or close to that of the tungsten framework. A pH = 3 medium (0.2 M $Na_2SO_4 + H_2SO_4$) was selected for this study.

In the α_1 series, Fig. 12(a–f) gather the cyclic voltammograms of those complexes in which the redox activity of the transition metal cation, when visible, occurs far from the potential locations of the waves

associated with the tungsten framework. In each case, the cyclic voltammogram of the α_1 lacunary complex was superimposed for direct comparison. Among these figures, the voltammogram of the Ca(II)-substituted complex is remarkable because it is close to that of the lacunary species. In the pH = 3 medium, $\alpha\text{P}_2\text{W}_{18}$ was observed to grow during the decomposition of the calcium-substituted derivative. Also traces of $[\text{H}_2\text{P}_2\text{W}_{12}\text{O}_{48}]^{12-}$ were detected on the voltammograms. This compound is known to be formed concurrently with $\alpha_1\text{-}[\text{P}_2\text{W}_{17}\text{O}_{61}]^{10-}$ upon degradation of $\alpha\text{P}_2\text{W}_{18}$. Here its presence can be attributed to the formation of $\alpha_1\text{-}[\text{P}_2\text{W}_{17}\text{O}_{61}]^{10-}$ as an intermediate in the Ca(II)-substituted complex transformation at pH 3. Further details on this transformation can be found in the original paper [15]. For the whole series of complexes, it could have been expected, on a purely electrostatic basis, that the addition of a substituent metal cation should just lower the negative charge on the precursor lacunary species and thus facilitate the electron transfer. Such a reasoning would not take into account any specific modification like acid–base properties brought about by each substituent cation. Parameters like the size of each ion, its electronic configuration, its favorite geometry in complexes, the possibility and extent of Jahn-Teller effect, should contribute to the specificity. Throughout the series of compounds, the interplay of these characteristics results in the fact that the first tungsten wave in the substituted complexes appears at a more negative potential location than in the precursor species. Furthermore, in the cases of V(V) and Mn(II), Fig. 12(b) and (c), respectively, this wave tends to split up, which can be attributed to a lowering in basicity of the intermediate reduction species. Another general trend

is the tendency to the appearance of a small second wave associated with the first reduction step, in-line with the composite nature of this first reduction step.

Redox behaviors of the incorporated metal cations are diverse. In the potential domains explored, no electrochemical activity was detected for Ni(II) or Zn(II). The Co(II) center can be oxidized to Co(III). A well-behaved, reversible one-electron wave is observed for the oxidation of V(IV) to V(V) and the subsequent reduction of V(V) to V(IV). The case of Mn(II) is more striking, as at least two fairly stable states are obtained, featuring the Mn(II)/Mn(III) and Mn(III)/Mn(IV) steps.

Figure 12(g–j) illustrates the cases in which the substituent metal cations are reduced in the potential vicinity of the tungsten framework. This situation is encountered with Mo(VI), Fe(III), and Cu(II) cations. The cyclic voltammogram of $\alpha_1\text{P}_2\text{MoW}_{17}$ begins with two well-behaved, largely separated one-electron waves, followed by a two-electron wave. The first one features the reduction of the molybdenum center, the other two are associated with the redox activity of the tungsten framework. The observation of two successive one-electron waves is unique in the series under examination and is rationalized as already explained previously. The molybdenum-substituted compound must be considered as a really “saturated or plenary” species. Therefore, the appropriate comparison must be made with another “plenary” POM like $\alpha\text{P}_2\text{W}_{18}$ or $[\text{P}_2\text{Mo}_{18}\text{O}_{62}]^{6-}$. The better reducibility of the molybdenum over the tungsten atom must also be taken into account. The observed order of potentials in cyclic voltammetry ensues. A relatively detailed account of the study of the Fe(III)-substituted POM will be given in the following as an interesting

example of mixing up of iron and tungsten waves in appropriate pH conditions. It is just worth stressing here the obvious

difference between the cyclic voltammogram of the Fe(III)-complex and the precursor lacunary species in Fig. 12(h–j)

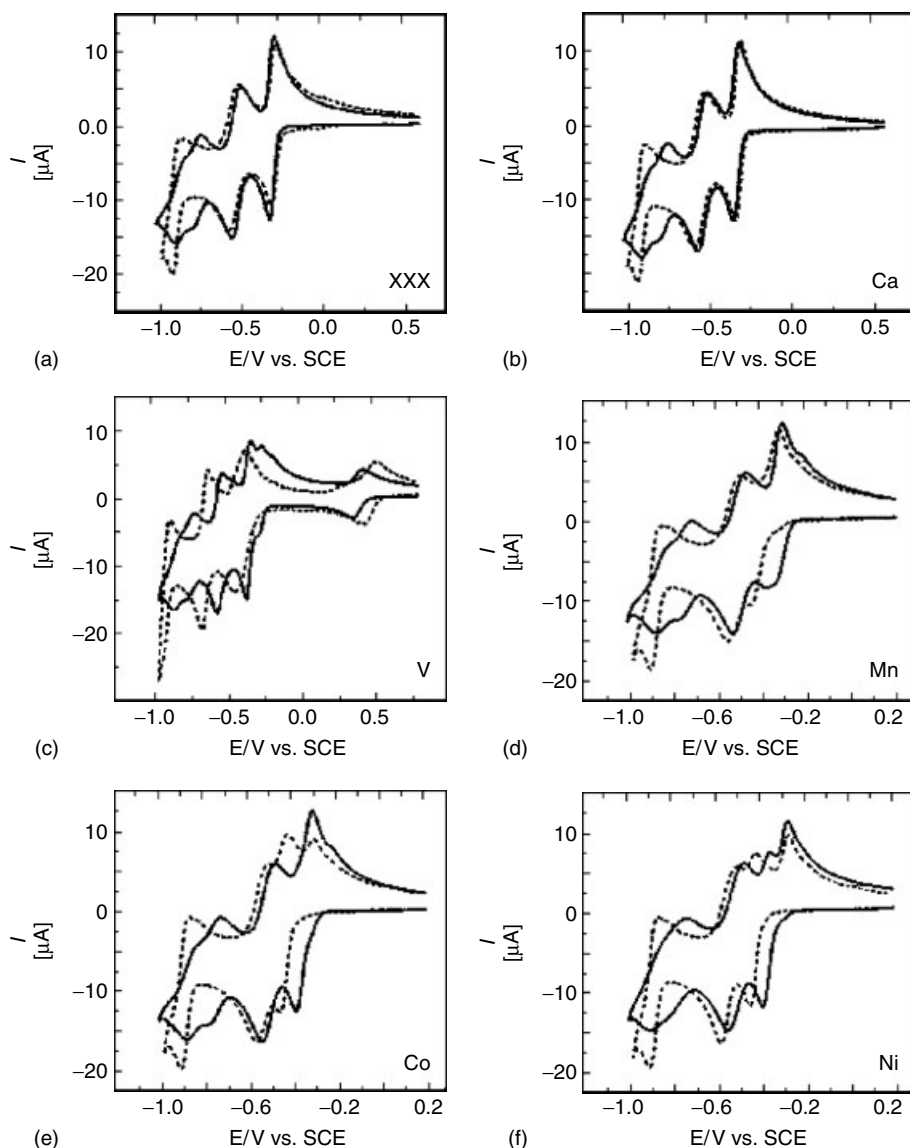


Fig. 13 Comparison of the cyclic voltammograms of α_1 and α_2 -P₂W₁₇ and comparison of their metal cation-substituted derivatives in 0.2 M Na₂SO₄ + H₂SO₄ (pH 3) medium. Scan rate: 10 mV s⁻¹. Concentration

$c_0 = 2.5 \cdot 10^{-4}$ M for each complex. The substituent cation is indicated on each curve. The full line corresponds to the α_2 species. For further details, see text (taken from Ref. 15).

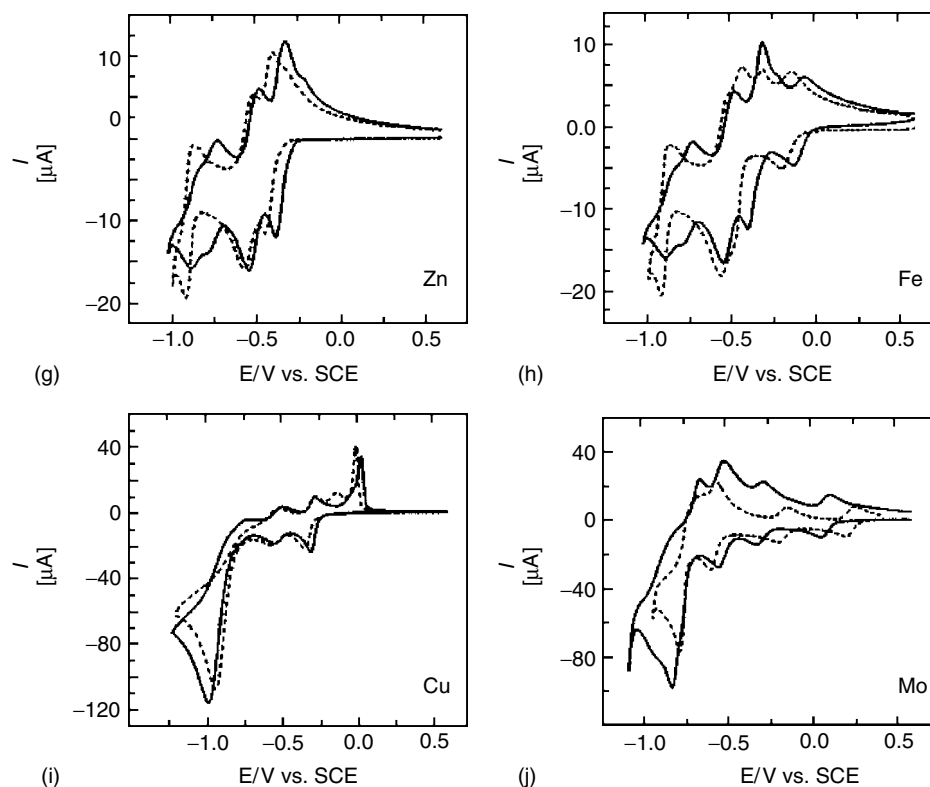


Fig. 13 (Continued).

illustrates the voltammetric behavior of the Cu(II)-substituted POM. The current intensity of the first slightly composite wave is obviously larger than that of the precursor lacunary species at the same concentration, thus signaling at least a partial merging of the copper and tungsten waves in this pH medium. Coulometry on this wave gives four electrons per molecule [90]. The two less negative oxidation waves are attributed to the oxidation of copper (Fig. 12j). One of them is clearly a desorptive oxidation process and its shape indicates that the deposition of copper has occurred during the negative potential directed scan. The large current intensity and chemically irreversible wave in the cyclic voltammogram of the copper

complex reflects the interference of the hydrogen evolution reaction.

Coming to the comparison of the α_1 and α_2 series, the possibilities of isomerization and/or decomposition of the precursor lacunary complexes and, presumably, of their metal ion-substituted derivatives, make it necessary to insure first that no fast conversion occurs, in particular from the α_1 structure to the α_2 one. Figure 13(a) compares the cyclic voltammograms of the two lacunary complexes in the pH 3 medium. The main difference appears on the “third” redox system: a single two-electron, reversible wave is obtained for the α_1 complex; in contrast, the corresponding system for the α_2 isomer is clearly constituted by two,

closely spaced, presumably one-electron waves. This observation is taken as a good distinctive fingerprint of the α_2 complex. In Fig. 13(b–j), the distinction between most compounds of the two groups is obtained readily, owing to the particular fingerprint of the α_2 series. In addition to the special fingerprint in Fig. 13(a–g), at least two other general trends appear: they concern the first redox system associated with the tungsten framework. First, it is split into two unequal steps, the preponderance of one step over the next being a function of the particular substituent metal cation. Second, on average, the cathodic peak potential is more negative in the α_1 than

in the α_2 series. These observations are quantified in Table 12.

This behavior can be understood on the following basis. It was inferred from the comparison of the stability constants of the complexes that they reflect steric effects and that the vacancy in the α_2 position is more prone to deformation than that in the α_1 position [91, 92]. Then the abilities of these two kinds of sites to accommodate various metal cations being different and in favor of the α_2 position, it is obvious that the reduction potentials should become less negative as the negative charge on the anion decreases. Furthermore, it has been proposed [30f, 74] and experimental evidence [79] and

Tab. 12 Reduction peak potentials versus SCE for the first tungsten wave in the various complexes and comparison with the first peak potential of the appropriate lacunary species; electrolyte: 0.2 M $\text{Na}_2\text{SO}_4 + \text{H}_2\text{SO}_4$ (pH = 3) medium (taken from Ref. 15)

Substituent in the complex	α_1 series		α_2 series	
	$-E_p[\text{mV}]$ for the 1 st W-wave	ΔE_p [mV]	$-E_p[\text{mV}]$ for the 1 st W-wave	ΔE_p [mV]
□	306	0	320	0
Ca	318	12	334	14
V	446	140	(280)	
			372	52
Mn	(330)		(358)	
	468	162	394	74
Fe	500	194	(340)	
			402	82
Co	462	156	(330)	
			392	72
Ni	460	154	(325)	
			406	86
Cu	(254)		306	−14
	350	44		
Zn	450	144	(300)	
			386	66
Mo	88	−218	236	−84

^aScan rate: 10 mV s^{−1}. The numbers in brackets correspond to the first part of composite waves and are not considered for the calculation of ΔE_p values. For further details, see text.

$\Delta E_p = (E_{p,\text{lacunary}} - E_{p,\text{substituted}})$ 1st W-wave.

theoretical approach support [78] that $\alpha\text{P}_2\text{W}_{18}$ is initially reduced at one of the twelve equivalent tungsten atoms. Then introduction of electrons in any α_1 position should markedly influence the reduction processes of the tungsten atoms, and, in particular, drive their potentials in the negative direction in comparison of the α_2 derivatives. This situation is indeed observed throughout.

22.5.2.3 An Interesting Case of Mixing up of Substituent and Tungsten Waves: α_1 - and α_2 -[Fe^{III}(OH₂)P₂W₁₇O₆₁]⁷⁻

It is usual that the first reduction wave of commonly studied POMs be monoelectronic or, at the utmost, bielectronic [89]. As a consequence, energetically favorable catalytic processes that require larger numbers of electrons can only be accomplished at fairly negative potentials where the necessary number of charges is accumulated and delivered by the POM framework; hence the search for strategic parameters that could favor apparently multiple electron uptake on the first wave of POMs. The present case deserves emphasis as a simple illustrative example that proved to be very beneficial in the electrocatalytic reduction of nitrite.

In the preceding section, the electrochemistry of copper-substituted derivatives shows an example of mixing up of the substituent metal cation and tungsten waves, but this process was accompanied by the deposition of Cu⁰. Analogous merging was studied in detail in the case of α_1 - and α_2 -[Fe^{III}(OH₂)P₂W₁₇O₆₁]⁷⁻, where this complicating feature was absent [89].

In a pH = 2 medium, the main differences in the cyclic voltammograms of α_1 - and α_2 -[Fe^{III}(OH₂)P₂W₁₇O₆₁]⁷⁻ appear in Fig. 14 and can be summarized as follows: (1) a Fe³⁺ cation filling the vacancy in the

α_2 position introduces nearly no influence in the cyclic voltammogram in which, except for the one-electron “Fe” wave, all the others correspond strictly to those of α_2 -[P₂W₁₇O₆₁]¹⁰⁻; (2) the presence of the iron substituent in the α_1 position modifies substantially the electron transfer pattern associated with the first two waves of α_1 -[P₂W₁₇O₆₁]¹⁰⁻. The “Fe” wave peak intensity is larger and its potential location more negative than the corresponding parameters of α_2 -[Fe^{III}(OH₂)P₂W₁₇O₆₁]⁷⁻. A rationale for this observation was proposed by considering the symmetry of the PO₄ tetrahedron in each of the compounds of the series [89, 93]: its symmetry is C_{3v} in $\alpha\text{P}_2\text{W}_{18}$; it turns to T_d, very close to C_{3v}, in the PO₄ tetrahedron belonging to the half lacunary moiety of α_2 -[P₂W₁₇O₆₁]¹⁰⁻. In this case, little perturbation is to be expected from the addition of a heteroatom in the α_2 position, which is actually observed. In contrast, the corresponding PO₄ tetrahedron in α_1 -[P₂W₁₇O₆₁]¹⁰⁻ assumes a C_s symmetry, which would favor a stronger coupling of the heterometal with the tungsten atoms in the “belt” of the Dawson POM.

Gradual lowering of the solution pH down to pH = 0.16 shows the steady increase of the “iron” wave intensity, which reaches finally a current corresponding to the consumption of 3.0 electrons per molecule, a value confirmed by coulometry. Following literature result that whatever the pH dependence of the “iron” wave in classical POMs [94] it involves only one electron, the reasonable assumption is that the observed three-electron wave should feature the merging of the one-electron process of Fe³⁺ with a two-electron process of tungsten. Noteworthy is the reversibility of the pH effect. Upon gradual addition of NaOH in the pH = 0.16 solution up to the pH = 2, the cyclic

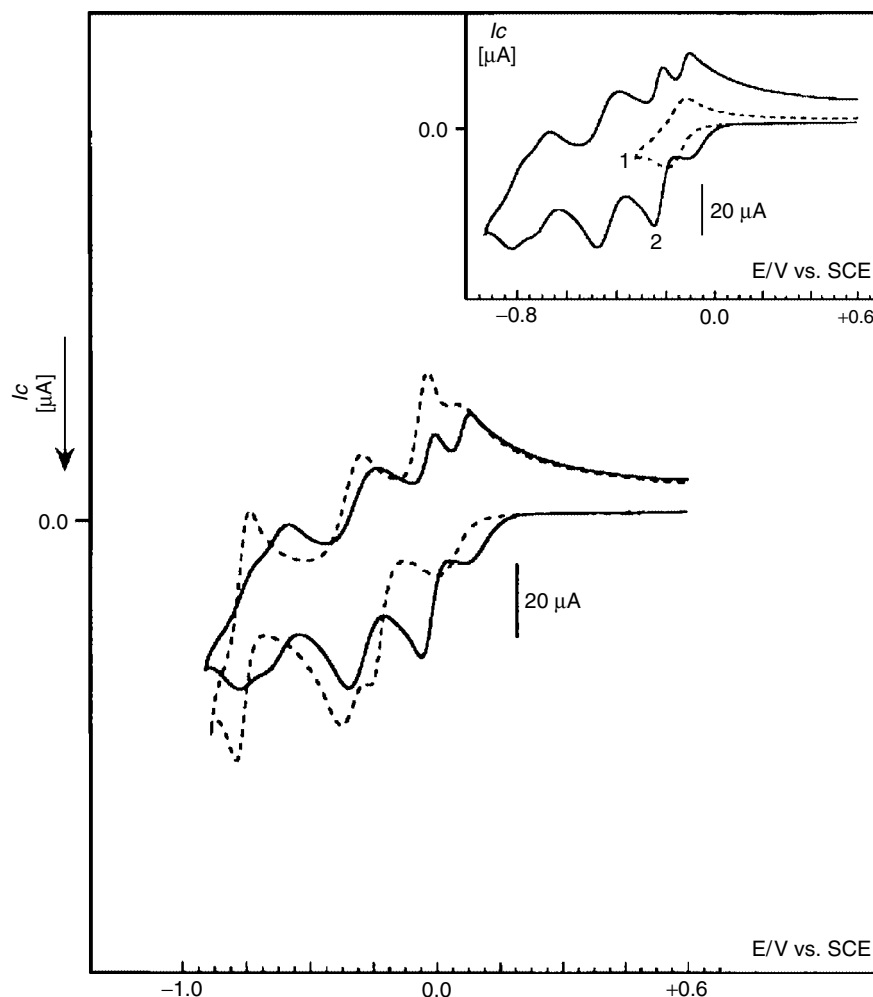


Fig. 14 Comparison of the cyclic voltammograms observed in a pH = 2 medium (0.2 M Na₂SO₄ + H₂SO₄) for 5 × 10⁻⁴ M solution of the substituted POM α₁FeP₂W₁₇ (Curve 1) and α₂FeP₂W₁₇ (Curve 2). Inset: comparison of the first wave of α₁FeP₂W₁₇ (Curve 1) with that of α₂FeP₂W₁₇ (Curve 2). Scan rate: 100 mV s⁻¹ (taken from Ref. 89).

voltammogram goes back exactly through the same situations obtained when the pH was made to decrease by addition of H₂SO₄. Coulometry and spectroelectrochemistry experiments were carried out with the aim to confirm the preceding observations. Figure 15 gathers spectroelectrochemistry results obtained, essentially at pH = 2. For clarity and simplicity,

shown here are the spectra corresponding to exhaustive reduction of the relevant POM. For each POM, the electrolysis potential was fixed at the reversal potential of the first wave on the cyclic voltammogram. Fig. 15(a) pertains to the reduced form of α₁-[P₂W₁₇O₆₁]¹⁰⁻ which was checked previously to be stable in the pH = 2 medium. The spectra of α₁-[Fe^{III}(OH₂)P₂W₁₇O₆₁]⁷⁻

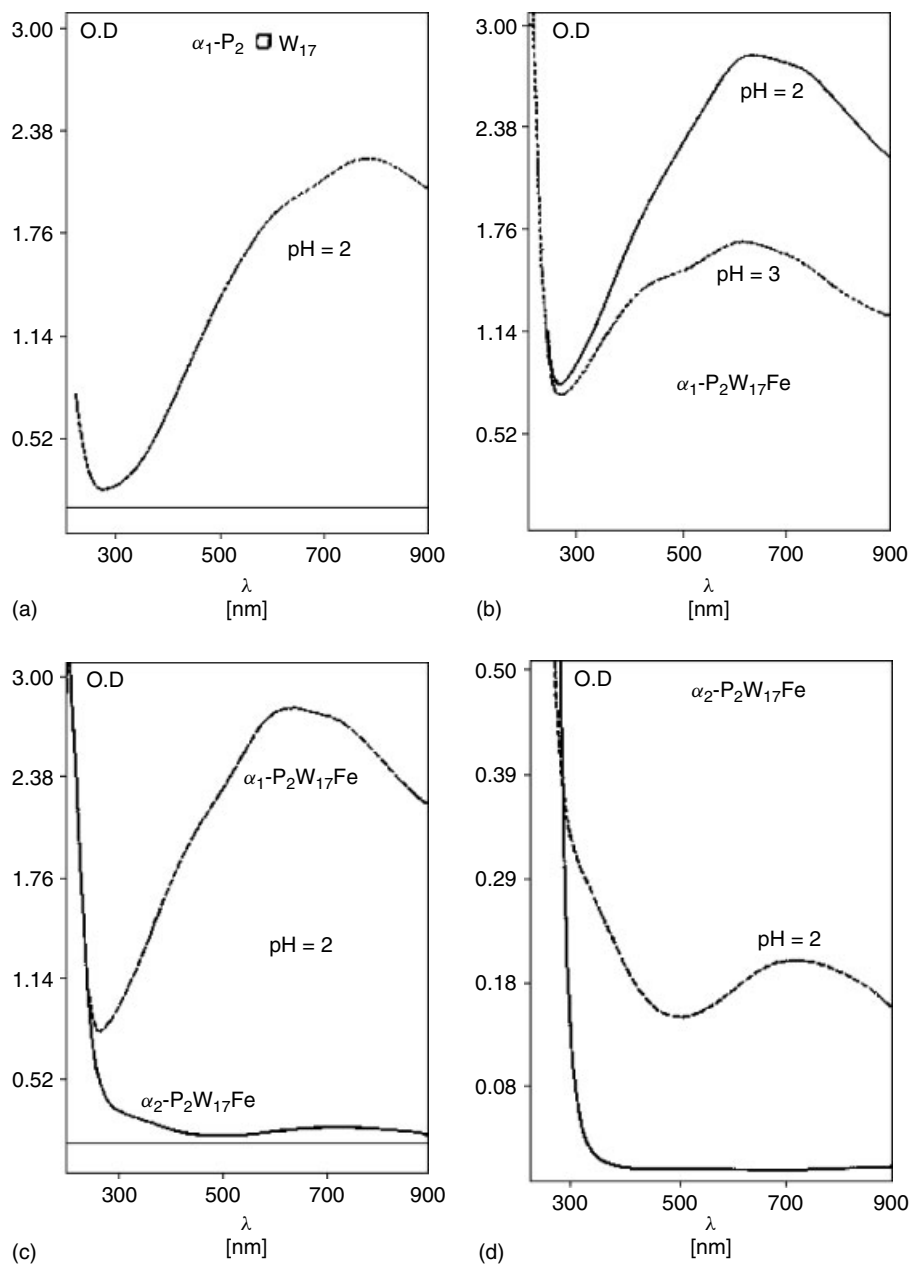


Fig. 15 Final UV-visible spectra run at the end of spectroelectrochemistry experiments. The concentration of POM is 10^{-3} M throughout, except for the spectrum A for which the concentration is $2.8 \cdot 10^{-4}$ M (taken from Ref. 89).

at pH = 2 and pH = 3 are shown in Fig. 15(b). Exactly the same concentration of the POM was used. Following analogous assignments [22, 85, 95–97], the d–d band for Fe(II) appears around 525 nm and the broad band extending into the near-infrared region is assigned to “metal” to “ligand” charge transfers, specifically Fe(II) → W(VI) charge transfer up to the coexistence of Fe(II) and W(V) [96]. In this case, the chromophore W(V) can be expected to contribute the most to the absorption, owing to the more delocalized character of a “tungstic” electron in this environment. The intensities of absorption bands in Fig. 15(b) are in agreement with this line of reasoning and also with the number of electrons consumed in coulometry at each pH (1.08 at pH = 3 and 1.80 at pH = 2). Finally, it was observed that the blue color observed for reduced α_1 -[Fe^{III}(OH₂)P₂W₁₇O₆₁]⁷⁻ became deeper and deeper as the pH of the medium was made more and more acidic. It was checked that the increase in optical density observed in Fig. 15(b) cannot be attributed mainly to a variation in extinction coefficient of the reduced species as described for other POMs [22, 97]. The observations for α_1 - and α_2 -[Fe^{III}(OH₂)P₂W₁₇O₆₁]⁷⁻ are contrasted in Fig. 15(c). They underscore and confirm the differences obtained in cyclic voltammetry and coulometry. Fig. 15(d) shows the spectrum of α_2 -[Fe^{III}(OH₂)P₂W₁₇O₆₁]⁷⁻ (solid line) and that of its reduced form on a magnified scale. The d–d band of Fe(II) appears now around 440 nm and the Fe(II) → W(VI) charge transfer band is small, in agreement with electrochemistry conclusions. The smaller extinction coefficient of reduced α_2 -[Fe^{III}(OH₂)P₂W₁₇O₆₁]⁷⁻ compared to that of reduced α_1 -[Fe^{III}(OH₂)P₂W₁₇O₆₁]⁷⁻ may be attributed to a stronger trapping

of the electron on the Fe center when it occupies an α_2 position.

Thus, in this example, combination of pH effects and spectroelectrochemistry proves very beneficial in the detailed study of merging of POM waves.

22.5.3

Sandwich-type POMs

Transition metal–substituted POMs (TM-SPs) can be considered as the largest subclass of polyanions [6]. Within the class of TMSPs, the sandwich-type compounds represent the largest family. In short, sandwich-type POMs are formed by the fusion of two trivacant α -XW₉O₃₄ⁿ⁻ (X = P(V), As (V), Si(IV), Fe(III), Co(II), Cu(II), or Zn(II)), α -XW₉O₃₃ⁿ⁻ (X = As(III), Sb(III), Bi(III), Se(IV), or Te(IV)), or α -X₂W₁₅O₅₆ⁿ⁻ (X = P(V) or As(V)) units via two or more d-electron centers and now constitute one of the largest classes of transition metal–substituted heteropolytungstates. To date, the Hervé-[98], Weakley-[99], Krebs-[100], and Knoth-[101] type sandwich polyanions can be distinguished. The synthesis of fundamentally novel, discrete polyanions is among the most interesting, but also the most difficult challenges in POM chemistry. Transition metal–substituted, sandwich-type polyanions are of particular interest, because of their highly tunable nature, coupled with their chemical robustness. This unique combination of properties is of interest for applications in several areas, including catalysis, electrocatalysis, medicine, and material science [102].

22.5.3.1 Electron Transfer Behaviors of Multi-iron Sandwich-type POMs

In parallel with the explosion of sandwich-type POMs synthesis and characterization, their electrochemistry is studied, both on

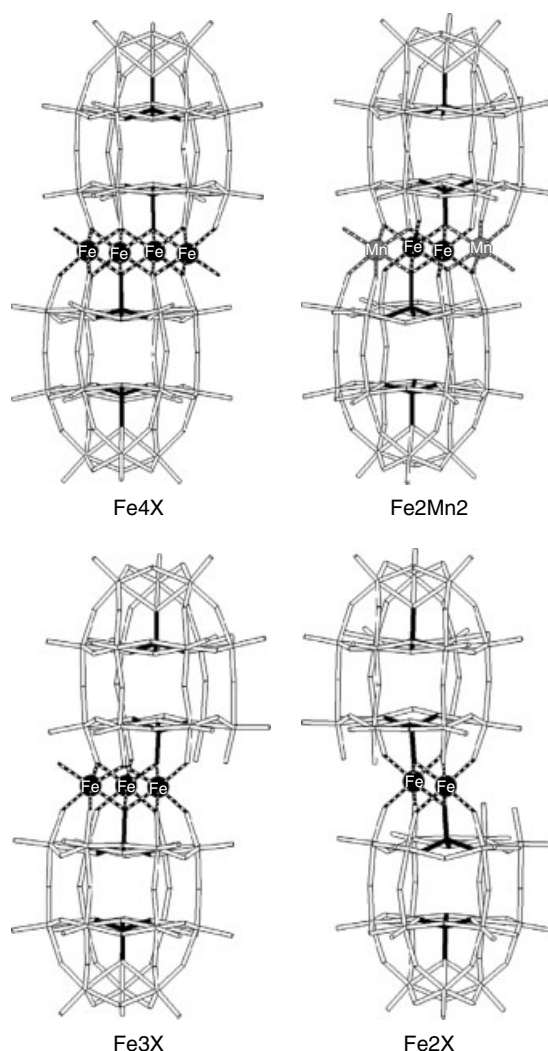
their own interest and also to find out the effects of accumulation of transition metal centers on catalytic and electrocatalytic properties. The same general trends encountered in the preceding section with POMs monosubstituted with a transition metal cation are also observed with sandwich-type species. Electrochemical studies [1, 103–121] indicate the existence of two groups of substituents: (1) the metal cations showing a redox activity within these complexes, with an expected pH dependence of the electrochemistry of the centers bearing a water molecule; (2) the metal cations electrochemically silent in the sandwich complexes; in that case, only a slight modification of the peak potential locations of the ligand waves is observed in comparison with those of the precursor lacunary species. Ni(II)- and Zn(II)-substituted derivatives belong to this group [103, 104, 113, 114].

Some specific behaviors are encountered. As expected, Cu(II)-containing complexes [103, 115, 121] show a deposition of copper upon reduction, and the redox behaviors of Mn(II) within Mn(II)-sandwich complexes were also studied [109, 110, 112, 119]. Electron transfer behaviors of multi-iron sandwich-type oxometalates reveal several illustrative features and these POMs are selected for a detailed electrochemical description [1]. Eight several recently reported multi-iron Wells–Dawson sandwich-type POMs (including **Fe4As4**, **Fe4P4**, $\alpha\alpha\alpha\alpha$ -Na₁₆(NaOH₂)₂(Fe^{III})₂(X₂W₁₅O₅₆)₂ (X = As(V) (**Fe2As4**) or P(V) (**Fe2P4**)), $\alpha\alpha\beta\alpha$ -Na₁₄(NaOH₂)(Fe^{III}OH₂)(Fe^{III})₂(X₂W₁₅O₅₆)₂ (X = As(V) (**Fe3As4**) or P(V) (**Fe3P4**)) and the mixed-metal complexes, $\alpha\beta\beta\alpha$ -Na₁₄(Mn^{II}OH₂)₂(Fe^{III})₂(X₂W₁₅O₅₆)₂ (X = As(V) (**Fe2Mn2As4**) or As(V) (**Fe2Mn2P4**)), (see Sch. 6 for structures)

are used to identify and quantify the interactions between adjacent Fe(III) (or Mn(II)) centers, and electrochemical measurements illustrate how ion-pairing, pH, and electrolyte compositions affect the redox properties of the complexes.

In addition, these results show also how the redox properties of the sandwich-type POMs are affected by the metal population of the central unit. All of these compounds are stable, at least in the timescale of these voltammetric studies, in the pH = 5 buffer (1 M CH₃COOLi and CH₃COOH) medium selected for their studies. The electrochemistry of the lacunary species (α -P₂W₁₅O₅₆¹²⁻ and α -As₂W₁₅O₅₆¹²⁻) were previously described [80, 103, 117]. In contrast with the voltammograms of α -As₂W₁₅O₅₆¹²⁻ and α -P₂W₁₅O₅₆¹²⁻, those of **Fe4As4** and **Fe4P4** show four new waves in the potential domain +0.2 through –0.5 V. Figure 16(a) compares the CVs of α -P₂W₁₅O₅₆¹²⁻ and **Fe4P4**. The four new waves are attributed to the reduction of the four Fe(III) centers within the sandwich complex. At pH 3 (2 M NaCl + HCl), the formal potentials for the Fe(III)/Fe(II) redox couples are: 0.227, 0.124, –0.016, and –0.093 V (vs. SCE), respectively. These locations are distinctly positive of the first W-wave of α -P₂W₁₅O₅₆¹²⁻ and **Fe4P4** (Fig. 16a). This is consistent with the fact that Fe(III) is known to be more easily reduced than W(VI) centers within substituted heteropolytungstates [89]. Corresponding data for the other complexes can be found in the original paper [1]. The reduction of W(VI) centers is also influenced by the presence of the Fe(III) centers in the sandwich molecule. The first wave of α -P₂W₁₅O₅₆¹²⁻, which is slightly composite, is now split into two waves in **Fe4P4**. This behavior is related to differences in the acid–base properties of the two POMs. In analogy with the CVs of α -As₂W₁₅O₅₆¹²⁻

Scheme 6 Combination wireframe/ball-and-stick representations of the eight multi-iron Wells–Dawson sandwich-type complexes studied in this section (taken from Ref. 1).



and $\alpha\text{-P}_2\text{W}_{15}\text{O}_{56}^{12-}$, those of **Fe4As4** and **Fe4P4** are also very similar to each other. The presence of the arsenic heteroatom facilitates the reduction of both the Fe(III) and W(VI) centers (Fig. 16b). The number of W(VI)-waves observed for **Fe4As4** or **Fe4P4**, and hence, the electron number for each wave, depends on the pH of the electrolyte. Rather classical electrochemical behaviors were observed for the W(VI) centers in these complexes. Therefore,

the focus of these studies remains exclusively with the Fe(III) centers. Fig. 16(c) shows the stepwise reduction of the Fe(III) centers in **Fe4P4**, with the domain restricted to the Fe(III) redox processes. The X-ray crystal structures of **Fe4As4** and **Fe4P4** suggest that there are two types of symmetry-equivalent Fe(III) centers [99d, 111a]. There are two “external” Fe(III) sites which share two oxygen atoms with one $\alpha\text{-X}_2\text{W}_{15}\text{O}_{56}^{12-}$ unit and three oxygen

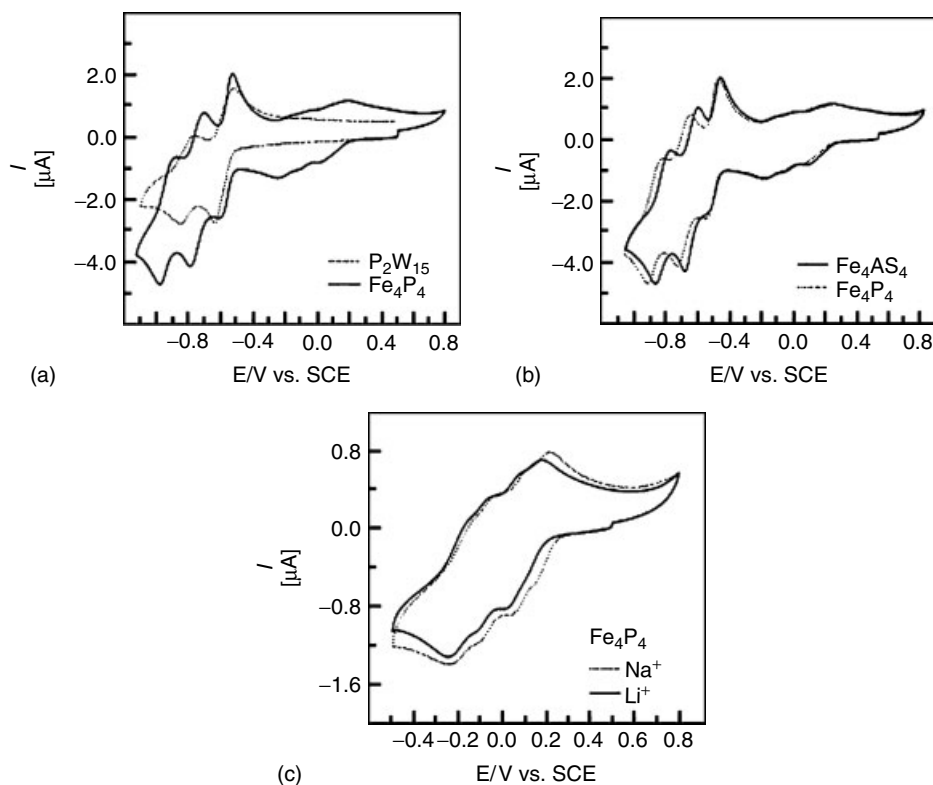


Fig. 16 Cyclic voltammograms of **Fe₄As₄** and **Fe₄P₄** ($2 \cdot 10^{-4} M$). The scan rate was 10 mV s^{-1} , the working electrode was glassy carbon, and the reference electrode was SCE. All measurements were performed in a $1 M CH_3COOLi + 1 M$

CH_3COOH (pH = 5) buffer solution except in (c), where the dotted line represents a measurement taken in a $0.5 M Na_2SO_4 + NaOH$ (pH = 5) buffer solution (taken from Ref. 1).

atoms with the other $\alpha\text{-X}_2W_{15}O_{56}^{12-}$ unit. The sixth vertex of the octahedra is composed of a water molecule. The sixth vertex of the two “internal” Fe(III) sites is composed of an additional oxygen atom from one of the two $\alpha\text{-X}_2W_{15}O_{56}^{12-}$ units (rather than a water ligand). The structural data alone would suggest that there would be two groups of redox processes rather than four. The complete splitting into four distinct one-electron reduction processes suggests that there is some type of electronic communication involving the Fe(III) centers. This possibility deserves

careful consideration because it might compete with others (Although coupling between the Fe-centers is invoked as an explanation for the separation (or lack thereof) of the various reduction waves, the behavior for reduction of these centers (whether clearly sequential or not) may also depend simply on the effect of the extra negative charge the POM takes on each time a Fe(III) center is reduced to Fe(II). Literature has solved the case of the first reduction potentials of several Keggin species under conditions of no protonation. The correlation line has a

slope of -0.18 V/unit charge (see Refs. 4 and 54a). The same correlation was also suggested for select examples of second reduction potentials (see Ref. 30a). In the latter case, only highly symmetrical POMs with little or no ion-pairing were addressed and the reduced centers were all W-based. In the multi-iron compounds we address here, electrons are localized essentially in the Fe_4 central unit where ion-pairing is extensively operative and in competition with protonation. In addition, we have to consider the Wells–Dawson trivacant species as the precursors in the synthesis of the present sandwich complexes. Therefore, only a semiquantitative evaluation of this phenomenon can be made at best. However, the observation of a broad, single large cathodic current featuring the combined series of one-electron reduction processes of the four Fe-centers made on $[\text{Fe}_4(\text{OH}_2)_{10}(\beta\text{-XW}_9\text{O}_{33})_2]^{n-}$ ($n = 6$, $\text{X} = \text{As}^{\text{III}}$, Sb^{III} ; $n = 4$, $\text{X} = \text{Se}^{\text{IV}}$, Te^{IV}) in which Fe centers are not directly connected (Ref. 107a) supports the idea of electronic communication between Fe centers. It can therefore be concluded that the stepwise addition of electrons required in molecular electrochemistry and the subsequent stepwise increase in the overall negative charge of the POM are not sufficient to split the waves measurably in a case where direct influence between structurally equivalent centers does not exist.). This interaction must generate and/or reinforce inequivalence among the sites, especially in the reduced state, and it is also consistent with the magnetic measurements. Finally, it is worth noting that all of the voltammetric patterns of **Fe4As4** and **Fe4P4** are perfectly well defined and well behaved at $\text{pH} = 5$. This observation is in contrast with the report that **Fe4P4** shows ill-defined waves with very small intensity in media of $\text{pH} > 4$ [118]. These differences

may be due to differences in the media used to collect these measurements. This point was checked by running the CV in the same electrolyte (0.5 M Na_2SO_4 and NaOH , $\text{pH} = 5$) as that used in Ref. 118. The results in Fig. 4(c) show that the waves remain perfectly well-defined (dotted line curve) with no current decrease observed compared to the curve recorded in acetate medium (solid line curve). The lesson from these comparisons is that the most severe attention must be paid to the challenging problem of the synthesis and characterization of sandwich-type POMs.

Ion-pairing: Although ion-pairing, pH effects, and ionic strength effects all exist simultaneously and act in competition, the data presented in Fig. 16(c) allows the opportunity to discuss the first of these phenomena. In this system, an overall positive shift is observed for the Fe(III) centers when a Na_2SO_4 -based medium is used instead of CH_3COOLi . Since the two systems have the same ionic strength and pH (even though the buffer capacity is greater for CH_3COOLi), this positive shift must be due in part to the nature of the cation. It was previously shown that Na^+ engages in more intimate ion-pairing with POMs than Li^+ since the hydrodynamic radius of Li^+ is greater than Na^+ [61c,d] (Ref. 94a) have also shown that reduced forms of Fe(III)-monosubstituted Keggin anions engage in ion-pairing with alkali-metal cations.). The positive shift of the Fe(III) centers increases with increased ion-pairing (i.e. $\text{K}^+ > \text{Na}^+ > \text{Li}^+$). For example, with both the pH and ionic strength kept constant, the formal potential measured for the Fe(III)/Fe(II) couple in $\text{Ge}(\text{FeOH}_2)\text{W}_{11}\text{O}_{39}^{5-}$ is more positive with a Na^+ counteranion than Li^+ . Complexes **Fe4As4** and **Fe4P4**, however,

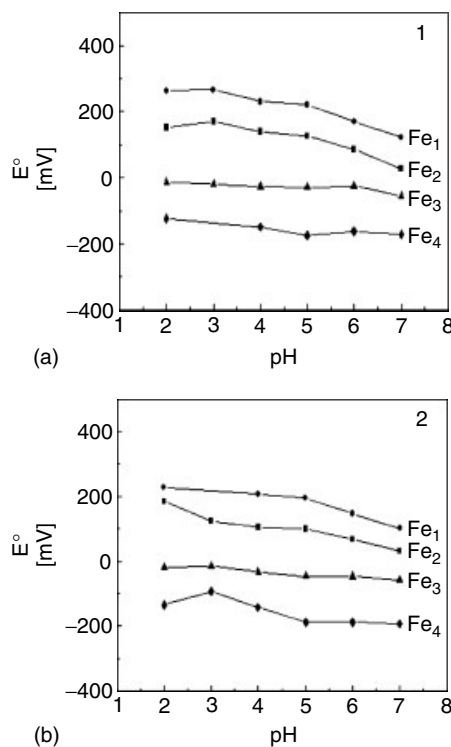
contain four Fe(III) centers and could display more complex ion-pairing behavior. In addition, the two Fe(III) sites with ionizable terminal water ligands add further complexity since ion-pairing and protonation can compete [94]. Figure 16(c) illustrates this complexity by showing that cation influences differ from one wave to the next. For example, the second and fourth redox couples (which are better behaved) experience a 35 mV shift and a negligibly small shift, respectively, with the change of Na^+ to Li^+ medium. The shift due to cation effects is larger for the first two redox couples. To further illustrate the competition between ion-pairing and protonation of the terminal water ligands, the pH of the system was lowered from five to three, prepared with 0.5 M Li_2SO_4 and H_2SO_4 or 0.5 M Na_2SO_4 and H_2SO_4 . The results suggest that protonation supersedes ion-pairing with decreasing pH. These general trends are in good agreement with the apparent $\text{p}K_a$ values measured previously. Complex **Fe4As4** gave results similar to **Fe4P4** under the same experimental conditions. The nature of the cation of the supporting electrolyte has a similar effect on W(VI) waves as described previously for monosubstituted Keggin derivatives [94]. For the remaining electrochemical studies, Na^+ is the countercation used since most of the POMs studied here were originally synthesized as Na^+ salts.

pH Effects: The behaviors of the W(VI) waves within POMs as a function of pH were the subject of several previous investigations [3, 4, 28, 89, 94, 103, 107, 122]. The same types of variations were roughly observed within the present multi-iron sandwich-type derivatives, but these were not the focus of this particular study. For the present purpose, pH effects (from $\text{pH} = 2$ to $\text{pH} = 7$) were studied by adding

an appropriate amount of concentrated mineral acid or base to a 2 M solution of NaCl. The high concentration of NaCl is intended to minimize any effect induced by small ionic strength variations. The observation of interest is to determine how changes in pH affect the formal potentials of the Fe(III) waves. Provisionally, it is worth noting that changes in pH might induce the merging of two or more of these waves, although that phenomenon was not observed in these studies.

Figure 17 represents the formal potential variations between pH 2 and pH 7 for each of the Fe(III) centers in **Fe4As4** and **Fe4P4**. The four Fe(III) centers are numbered according to their formal potentials from the least negative (Fe_1) to the most negative (Fe_4). The formal potentials of the Fe(III)/Fe(II) redox couples do not vary smoothly with pH. Analogous intricate pH dependence was previously described in the case of a single Fe(III) center within monosubstituted Keggin derivatives [94]. Electronic communication between Fe(III) centers in the sandwich-type derivatives might render their formal potential variations pH interdependent, and possibly, might also render them more complex. Nevertheless, some new trends do appear in Fig. 17. Focusing first on **Fe4As4**, Fe_1 and Fe_2 centers show almost parallel formal potential variations, with a small domain of quasi-independence from pH 2 to 3 and then again from pH 4 to 5. The variation is roughly linear above pH 5, with a slope of 55 mV/pH. In contrast, the formal potential for Fe_3 is nearly independent for pH values up to 6, and then it begins to vary slightly above this value. For Fe_4 , a linear variation is obtained from pH 3 to 5 with a slope of 26 mV/pH. Then it is fairly pH independent for higher pH values. Even though the present observations specifically concern the Fe(III)/Fe(II)

Fig. 17 Plot of the formal potentials of **Fe4As4** (a) and **Fe4P4** (b) as function of pH for the four one-electron Fe(III)-centered redox processes. The Fe(III) centers are labeled FeX (with $X = 1, 2, 3$, or 4) from the most positive to the least positive reduction potential. The pH 2–3 solutions are composed of 2 M NaCl + HCl, the pH 4–5 solutions are composed of 2 M NaCl + 0.1 M CH_3COONa + 0.1 M CH_3COOH , and the pH 6–7 solutions are composed of 2 M NaCl + 0.05 M NaH_2PO_4 + 0.05 M NaOH (taken from Ref. 1).



redox couples and not solely the Fe(III) redox states, the formal potential variations follow the trends expected from the knowledge of apparent pK_a values. In particular, the zones of pH independence are consistent with the possibility that ion-pairing supersedes protonation. Furthermore, the formal potentials of the two internal Fe(III) centers are not expected to depend directly on pH. The observed dependence must therefore be traced back to the electronic communication between all of the Fe(III) centers. The same trends were observed for **Fe4P4** as well, albeit with only small differences, presumably linked to differences induced by the different heteroatoms (As vs. P) within these complexes. Finally, ion-pairing and pH effects converge during the reduction processes to suggest that external Fe(III) centers are reduced first.

This is consistent with Pope's report on $(\text{MnOH}_2)_2(\text{Mn})_2(\text{PW}_9\text{O}_{34})_2^{10-}$, in which it was discovered that oxidation first occurs at the aquated Mn centers [112]. However, due to the low intensity of the observed effects and to the fact that oxidation and reduction might involve different molecular orbitals, support or invalidation for the present hypothesis should be sought through complementary theoretical calculations.

Diferric and Triferric Sandwich-type Complexes: Figure 18 shows, in superposition, the voltammograms of **Fe4As4**, **Fe3As4**, and **Fe2As4**, restricted to the waves attributed to the reductions of the Fe(III) centers only. Several conclusions emerge from these patterns. For each CV, the number of waves corresponds to the

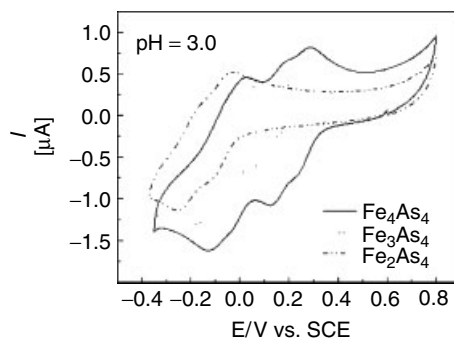


Fig. 18 Cyclic voltammograms of **Fe₄As₄**, **Fe₃As₄**, and **Fe₂As₄** in 2×10^{-4} M, pH = 3 (2M NaCl + HCl) buffer solution. The scan rate was 10 mV s^{-1} , the working electrode was glassy carbon, and the reference electrode was SCE (taken from Ref. 1).

number of Fe(III) atoms in each complex. These observations suggest there are sufficiently strong interactions between the Fe(III) centers in each of the complexes to induce complete splitting of their redox processes into separate steps. Magnetization measurements were used to identify and quantify the antiferromagnetic interactions between the edge-sharing Fe^{III} units, in complete agreement with electrochemical conclusions [1]. Qualitatively, the overall current intensities are also consistent with the number of Fe(III) atoms in each complex. The number of Fe(III) centers was also checked by controlled potential coulometry measurements, which give three electrons per molecule for **Fe₃As₄** and **Fe₃P₄** and two electrons per molecule for **Fe₂As₄** and **Fe₂P₄** for the exhaustive reduction of these centers. At pH 3, the following values were determined: 3.95 ± 0.05 electrons per molecule for **Fe₄As₄** and **Fe₄P₄** at -0.250 V (vs. SCE); 2.95 ± 0.06 electrons per molecule for **Fe₃As₄** and **Fe₃P₄** with the potential set at -0.300 V (vs. SCE); 1.95 ± 0.07 electrons per molecule for **Fe₂As₄** and **Fe₂P₄** at -0.360 V (vs. SCE). The CV patterns shift in the negative potential direction with a decrease in the number of Fe(III) atoms. This is most likely related to the overall increase in the negative charge of the POM due to the decrease in the

number of Fe(III) atoms. It is probably also related to $\text{p}K_{\text{a}}$ differences in the reduced forms. The formal potentials measured from the CVs of the Fe(III)-only complexes can be found in the original paper.

The relative potential shifts of the waves also seem to support the distinction between the external $\text{Fe}^{\text{III}}\text{O}_5(\text{OH}_2)$ centers and the internal $\text{Fe}^{\text{III}}\text{O}_6$ centers within the present complexes. Previously, we concluded that the external $\text{Fe}^{\text{III}}\text{O}_5(\text{OH}_2)$ centers are likely reduced before the internal $\text{Fe}^{\text{III}}\text{O}_6$ ones. Indeed, the CVs of **Fe₃As₄** and **Fe₃P₄** show the disappearance of a wave attributable to an external $\text{Fe}^{\text{III}}\text{O}_5(\text{OH}_2)$ center in **Fe₄As₄** and **Fe₄P₄**. The CVs of **Fe₂As₄** and **Fe₂P₄**, which have no external $\text{Fe}^{\text{III}}\text{O}_5(\text{OH}_2)$ centers, also agree with this hypothesis since only two waves attributable to internal $\text{Fe}^{\text{III}}\text{O}_6$ centers are observed. These conclusions are also supported by the apparent $\text{p}K_{\text{a}}$ values.

Mixed-Metal Sandwich-type Complexes: Characterization of the mixed-metal multi-iron sandwich complexes indicated that they are stable from pH 0 to 7. This thoroughly-checked observation is in contrast with the instability of several mixed-metal sandwich-type complexes claimed in Ref. 120. In **Fe₂Mn₂P₄**,

the presence of Mn(II) modifies the characteristics of the Fe(III) and W(VI) waves that are observed at slightly more positive potentials than in compound **Fe2P4**. Figure 19 compares the Fe(III)-based redox processes of complexes **Fe2P4** and **Fe2Mn2P4**. Controlled potential coulometry confirms that exhaustive reduction of these centers consumes 2.00 ± 0.05 electrons per molecule. Examination of Fig. 19(a) shows that the

first wave of **Fe2P4** is larger than that of **Fe2Mn2P4** and it has a tendency to merge with the second wave. Thus, an ECE- or EEC-type process seems to be favored in the former complex. This observation leads to the conclusion that the reduced form of **Fe2Mn2P4** is less basic than the corresponding form of **Fe2P4**. Support for the important influence of basicity is illustrated in Fig. 19(b). At pH 5, the two Fe(III)-based

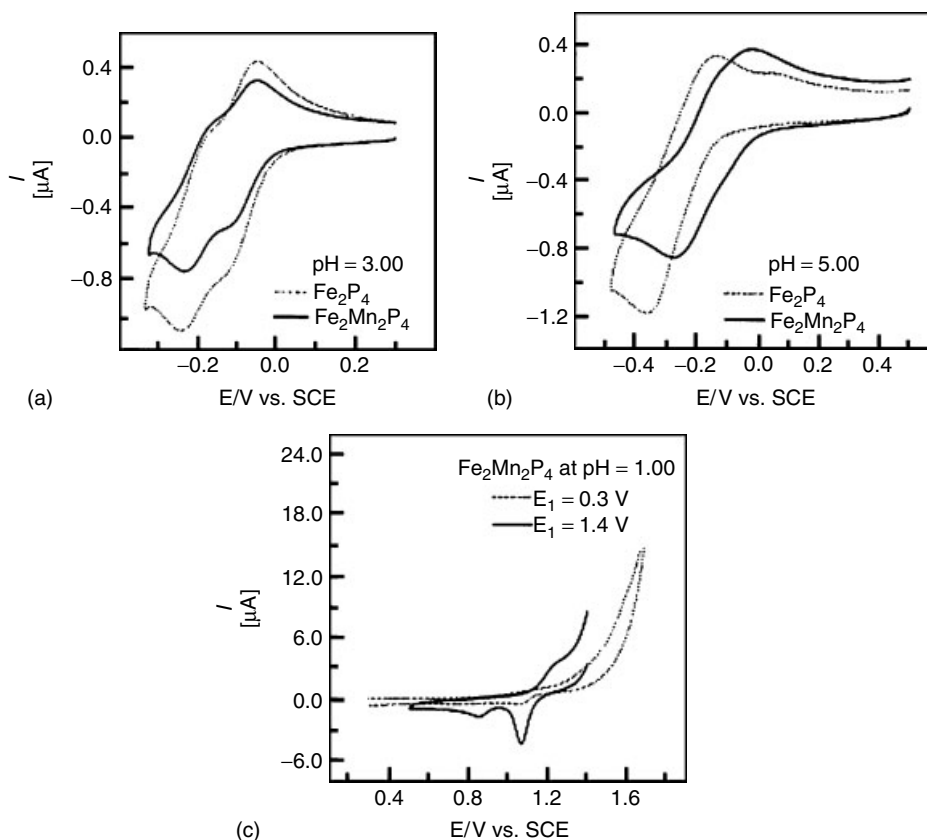


Fig. 19 Cyclic voltammograms of **Fe2P4** and **Fe2Mn2P4** in different buffer solutions. The concentration of the POM was 2×10^{-4} M in all the solutions. The scan rate was 10 mV s^{-1} , the working electrode was glassy carbon, and the reference electrode was SCE. (a) Comparison of **Fe2P4** and **Fe2Mn2P4** in a pH = 3 buffer (0.5 M

$\text{Na}_2\text{SO}_4 + \text{H}_2\text{SO}_4$); (b) Comparison of **Fe2P4** and **Fe2Mn2P4** in a pH = 5 medium (1 M $\text{CH}_3\text{COOLi} + 1 \text{ M CH}_3\text{COOH}$); (c) Study of the Mn(II) centers in **Fe2Mn2P4** in a pH = 1 medium (0.5 M $\text{Na}_2\text{SO}_4 + \text{H}_2\text{SO}_4$). E_i = initial potential. See the text for more details (taken from Ref. 1).

waves merge in both complexes with coalescence being somewhat incomplete for **Fe₂Mn₂P₄**, which shows a slightly composite wave. Such differences in the pK_a values of the two complexes might be explained by considering that **Fe₂Mn₂P₄** should behave much like a saturated complex while **Fe₂P₄** is more lacunary in nature. The differences in behavior of the arsenic analogs (complexes **Fe₂As₄** and **Fe₂Mn₂As₄**) are less clear than those of the corresponding phosphorus analogs. The results suggest a clear influence of the central heteroatom, P or As, that consists (at pH 3) of an overall positive shift of the Fe(III) waves without a current increase when P is replaced by As. A tentative explanation for this lack of current variation is that the relevant pK_a values in the reduced forms of the As derivatives are very close from one complex to another.

A detailed study of the Mn(II) wave in complex **Fe₂Mn₂P₄** reveals, as expected, that the oxidation process becomes more difficult (i.e. moves toward more positive potentials) when the pH of the supporting electrolyte decreases. This point is illustrated for pH = 1 in Fig. 19(c) where this process is kinetically sluggish. However, pretreating the electrode surface by pausing its potential at +1.4 V for a short time (120 s) prior to scanning the potential in the negative direction clearly reveals the presence of Mn(II). Under these conditions, two reduction waves were observed, accompanied on potential reversal by a fairly well-behaved oxidation wave for the Mn(II) centers. This result is also shown in Fig. 19(c). Separation of the reduction into two steps is less pronounced in a pH 3 medium, where only a shoulder is observed. Examination of all these results together suggests that, for the two pH values

we have explored (pH 3 and 5), the oxidation of Mn(II) to Mn(IV) is followed on potential reversal by the stepwise reduction of Mn(IV). In addition, holding the potential at a selected positive value activates the electrode surface faster than continuous potential cycling. Continuous potential cycling of the electrode through the domain in which the oxidation of interest is expected constitutes another nuance of the activation of the glassy carbon surface electrode in the study of POM-based Mn(II) centers. Steckhan and Sadakane found that this procedure gradually revealed the presence of the two waves of $\alpha\text{-Si}(\text{MnOH}_2)\text{W}_{11}\text{O}_{39}^{6-}$ in a pH 6 phosphate buffer [123]. In contrast, it was shown previously that the merging of the two redox systems of Mn(II) in $\alpha_2\text{-P}_2(\text{MnOH}_2)\text{Mo}_2\text{W}_{15}\text{O}_{61}^{8-}$ results in a composite broad wave while cycling in a pH 6 phosphate medium (with concomitant deposition of an electroactive film on the electrode surface) [14].

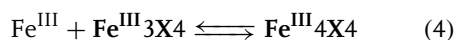
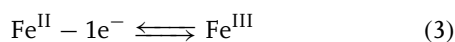
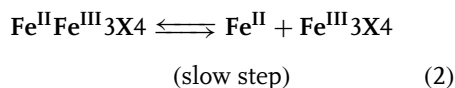
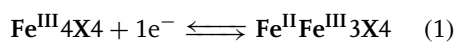
22.5.3.2 Electrochemical Probing of Siderophoric Behavior in Sandwich-type Multi-iron Wells–Dawson Heteropolytungstates

The formation of sandwich-type POMs from solutions of metal cations and trivalent heteropolytungstate species may alternatively be viewed as means to sequester cations from solution [116]. The question then arises if reversible dissociation of the metal cations from the multidentate ligands is possible as well. The sequestration and subsequent release of metal cations under appropriate conditions is of considerable interest in waste decontamination technology as well as in medicine [124]. Following these ideas, the demetallation process of ten multi-iron Wells–Dawson polyoxometalates is studied by cyclic

voltammetry and controlled potential coulometry. Eight sandwich-type complexes $(\alpha\alpha\alpha\alpha\text{-Na}_{16}(\text{NaOH}_2)_2(\text{Fe}^{\text{III}})_2(\text{X}_2\text{W}_{15}\text{O}_{56})_2$, $\alpha\alpha\beta\alpha\text{-Na}_{14}(\text{NaOH}_2)_2(\text{Fe}^{\text{III}}\text{OH}_2)(\text{Fe}^{\text{III}})_2(\text{X}_2\text{W}_{15}\text{O}_{56})_2$, $\alpha\beta\beta\alpha\text{-Na}_{12}(\text{Fe}^{\text{III}}\text{OH}_2)_2(\text{Fe}^{\text{III}})_2(\text{X}_2\text{W}_{15}\text{O}_{56})_2$, and $\alpha\beta\beta\alpha\text{-Na}_{14}(\text{Mn}^{\text{II}}\text{OH}_2)_2(\text{Fe}^{\text{III}})_2(\text{X}_2\text{W}_{15}\text{O}_{56})_2$ (where $\text{X} = \text{P(V)}$ or As(V)) and two monomeric complexes $(\alpha\text{-Na}_{11}(\text{P}_2(\text{Fe}^{\text{III}}\text{Cl})_2(\text{Fe}^{\text{III}}\text{OH}_2)\text{W}_{15}\text{O}_{59})$ and $\alpha\text{-Na}_{11}(\text{As}_2(\text{Fe}^{\text{III}}\text{Cl})_2(\text{Fe}^{\text{III}}\text{OH}_2)\text{W}_{15}\text{O}_{59}))$ were selected for this study.

Specifically, Fig. 20 shows representative slow potential scan rate cyclic voltammograms of Fe_4P_4 and Fe_4As_4 in a $\text{pH} = 3$ solution and also as a function of ionic strength for this last complex. A demetallation process of the reduced POMs was detected as appears on this figure. Detailed study of the whole process

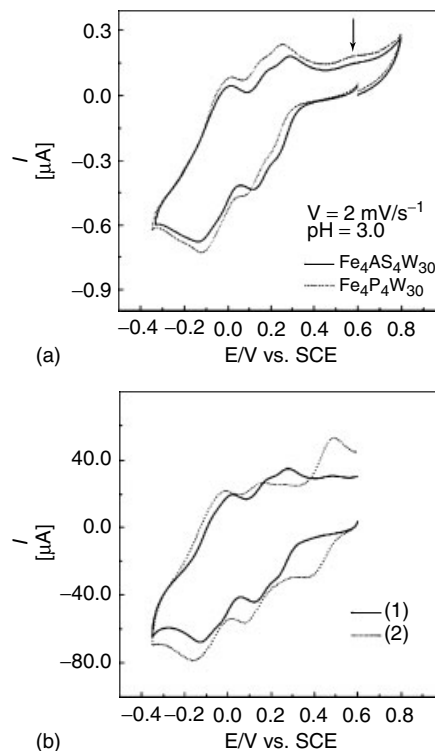
was performed as a function of several parameters including the pH , the ionic strength, and the composition of the electrolyte. The observations lead to the conclusion that the following reaction pattern applies, in which Eq. (4) may be only partially operable on the timescale of cyclic voltammetry:



In short, all ten complexes considered here show Fe(III) waves that are well separated from the redox activity of the

Fig. 20 Cyclic voltammograms of complexes **Fe₄P₄** and **Fe₄As₄** (2×10^{-4} M). The scan rate was 2 mV s^{-1} and the reference electrode was SCE. All measurements were performed in a $2 \text{ M NaCl} + \text{HCl}$ ($\text{pH} 3$) buffer solution.

(a) The working electrode was glassy carbon (3 mm diameter). The arrow indicates the oxidation of free Fe(II) ; (b) The working electrode was a glassy carbon plate (4 cm^2) that was used for the exhaustive controlled potential reduction of the Fe(III) centers within **Fe₄As₄**, followed by an attempt at their regeneration. The cyclic voltammogram before electrolysis is marked “1” while the cyclic voltammogram after the forward and backward electrolyses is indicated by a “2.” See the text for more details (taken from Ref. 116).



W(VI) centers. At room temperature and under mild conditions, iron release from the complexes is observed upon reduction of the Fe(III) centers. This release is controlled by the ionic strength of the medium, the nature and concentration of the anions present in the supporting electrolyte, and by the pH of the solution. This behavior parallels those described for most siderophores that depend on the same parameters.

It is noteworthy that the analogous ejection of Fe(II) was observed previously upon reduction of the single Fe(III) center within α_2 -[Fe(OH₂) P₂W₁₇O₆₁]⁷⁻ [89] and α -[Fe(OH₂) ZnW₁₁O₃₉]⁷⁻ [122].

22.6

Recent Developments

22.6.1

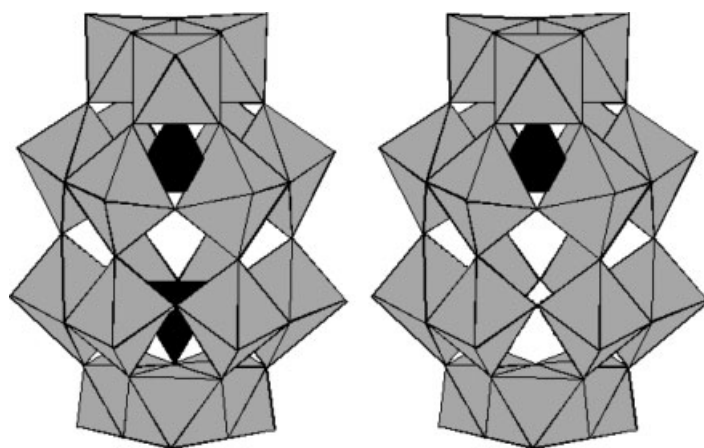
Electrochemistry of a New Family of Wells–Dawson Anions: Semivacant Tungstophosphates and Arsenates [H₄XW₁₈O₆₂]⁷⁻ (X = P or As)

Following the pioneering synthesis of [H₄PW₁₈O₆₂]⁷⁻ (PW₁₈ for convenience)

[187], the general possibility of establishing a novel Dawson-type family structures with two different central heteroatoms was demonstrated with the syntheses of [H₄XW₁₈O₆₂]⁷⁻ (X = P or As), their monolacunary species and their first transition metal ion derivatives [103, 125, 126]. The new structure is sketched in Sch. 7 and was confirmed very recently by direct X-ray crystallography determination [127, 128].

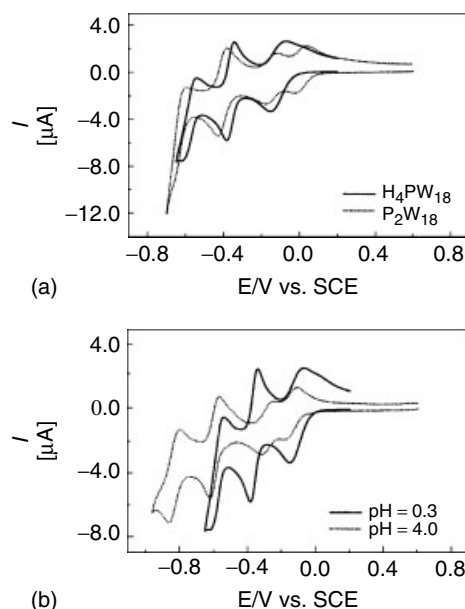
22.6.1.1 Evidence for an Influence of the Dissymmetry on the Voltammetric Behavior of PW₁₈: Comparison with P₂W₁₈

The comparison of the voltammetric characteristics of PW₁₈ and P₂W₁₈ is useful to highlight the peculiarities of the former complex. Figure 21 shows in superimposition the cyclic voltammograms (CVs) of the two complexes in a pH 0.3 sulfate medium. The potential domain was selected to avoid any deleterious derivatization of the electrode surface [28]. Furthermore, such domain is the most useful for elucidation of electrocatalytic processes. Here, the voltammetric pattern is restricted to the first three waves observed for PW₁₈ in this medium. In



Scheme 7 Schematic representations of the Dawson-type tungstodiphosphate and tungstomonophosphate (taken from Ref. 125).

Fig. 21 Cyclic voltammograms (CVs) run on 5×10^{-4} M solutions of the relevant polyoxometalates; scan rate: 10 mV s^{-1} ; working electrode: glassy carbon; reference electrode: SCE. (a) comparison of the CVs observed in a pH 3 medium (0.2 M $\text{Na}_2\text{SO}_4 + \text{H}_2\text{SO}_4$) for the two unsubstituted tungstophosphates: PW_{18} and P_2W_{18} ; (b) pH effect on the CV of PW_{18} . For further details, see text (taken from Ref. 125).



the same conditions, the voltammetry of P_2W_{18} is known [29] and is constituted by two one-electron waves followed by two two-electron waves. These waves feature reversible diffusion-controlled processes. The comparison of the CVs of the two POMs is shown in Fig. 21(a) and is enlightening. The first wave of PW_{18} represents unambiguously a two-electron chemically reversible process. This point was checked by controlled potential coulometry. The two subsequent waves also feature two-electron processes. In short, the pattern for PW_{18} is constituted by a set of three reversible diffusion-controlled waves. This observation was expanded by a brief study of the pattern as a function of pH. Figure 21(b) illustrates this point and shows, in superimposition, the CVs of PW_{18} at pH 0.3 and 4. With the increase in pH, the formerly two-electron wave splits into two supposedly one-electron processes. No attempt was made to ascertain quantitatively that the

splitting was complete at pH 4. Turning more specifically to the comparison of the voltammetric behaviors of the two POMs, all the observations point to the higher basicity of the reduced forms of PW_{18} compared to those of P_2W_{18} . The results fit in the following scheme that could have been forecast from the structures. Formally, PW_{18} is constituted by two A-type half-anions that can be formulated H_4W_9 and PW_9 respectively. A loose analogy might induce one to point out the similarity between the hydrogenated fragment of PW_{18} and $[\text{H}_2\text{W}_{12}\text{O}_{40}]^{6-}$ (H_2W_{12}). This analogy should be expressed in terms of compared basicity between PW_{18} and P_2W_{18} , with reference to the known basicity influence in the reduction of H_2W_{12} compared to those of the corresponding species of classical Keggin-type POMs [33c, 129, 130]. As a matter of fact, polarograms (and voltammograms) of H_2W_{12} at pH < 3.5, show three waves of 2, 2, and ca. 10 electrons each [35, 129, 130], in conditions in which

the first two reductions of its analogs $[\text{PW}_{12}\text{O}_{40}]^{3-}$ and $[\text{SiW}_{12}\text{O}_{40}]^{4-}$ and even the Dawson-type P_2W_{18} , are one-electron pH-independent processes. Therefore, the pH-dependent voltammetric behavior observed for PW_{18} in comparison with that of P_2W_{18} can be paralleled with that of H_2W_{12} vis à vis $[\text{PW}_{12}\text{O}_{40}]^{3-}$ and $[\text{SiW}_{12}\text{O}_{40}]^{4-}$. It must be concluded that PW_{18} and its first several reduced species show larger basicity compared to the corresponding species of P_2W_{18} . Provisionally, it is worth mentioning, in contrast, that roughly 6 M HCl solution was necessary to make the first two waves of P_2W_{18} merge [33c]; the concentration of acid reaches 7–8 M HCl in the case of $[\text{SiW}_{12}\text{O}_{40}]^{4-}$. Such merging could not be achieved for $[\text{PW}_{12}\text{O}_{40}]^{3-}$ in solution [33c] and was only realized inside polymer matrices [130]. This observation is rewarding and constitutes a good step in the continuous search for means to accumulate electrons on the first or the first several waves of POMs in mild conditions. To our knowledge, this series of compounds represent the first example in which a two-electron W-wave in a saturated species is found to appear at relatively less negative potential and mild acidity than generally obtained in classical Dawson HPAs in aqueous media. This constitutes one of the favorable conditions for eventual electrocatalytic processes.

Following the synthesis of pure $[\text{H}_4\text{PW}_{18}\text{O}_{62}]^{7-}$ (PW_{18}), its derivatives monosubstituted by M ($\text{M} \equiv \text{Mo}^{\text{VI}}, \text{V}^{\text{IV}}, \text{V}^{\text{V}}, \text{Mn}^{\text{II}}, \text{Fe}^{\text{III}}, \text{Co}^{\text{II}}, \text{Ni}^{\text{II}}, \text{Cu}^{\text{II}}, \text{and Zn}^{\text{II}}$) were obtained. Their cyclic voltammetry behaviors were studied as a function of pH and systematically compared with those of their analogs derived from the symmetrical $[\text{P}_2\text{W}_{18}\text{O}_{62}]^{6-}$ (P_2W_{18}). The fingerprint observed for $\alpha_2\text{-P}_2\text{W}_{17}\text{M}$ derivatives in pH 3 media consisted in the splitting of the

third W-redox system into two one-electron closely spaced waves, in contrast with the same system in $\alpha_1\text{-P}_2\text{W}_{17}\text{M}$. This peculiarity was also obtained for several of the present $\alpha_2\text{-PW}_{17}\text{M}$ in pH 3 medium and confirmed that α_2 -substituted derivatives were indeed prepared. The disappearance of this peculiar behavior in some other derivatives is consistent with smooth variations of acid–base properties from one derivative to the next.

Comparison with the electrochemistry of $[\text{H}_4\text{AsW}_{18}\text{O}_{62}]^{7-}$ with that of the P analog reveals only small differences between the two plenary species. In contrast, a remarkable difference in stability was observed for the lacunary derivatives. Unlike its phosphorus analog, the defect species of $[\text{H}_4\text{AsW}_{18}\text{O}_{62}]^{7-}$ was sufficiently stable for a few voltammetric runs. For the two series, several lines of experimental evidence converge to indicate that the substitution occurs in the α_2 position. As a consequence, in the case of $[\text{H}_4\text{AsW}_{18}\text{O}_{62}]^{7-}$ substituted derivatives, the cyclic voltammetry properties of substituted compounds could be studied as a function of pH and systematically compared with those of the lacunary precursor rather than with those of their analogs derived from the symmetrical species $[\text{As}_2\text{W}_{18}\text{O}_{62}]^{6-}$.

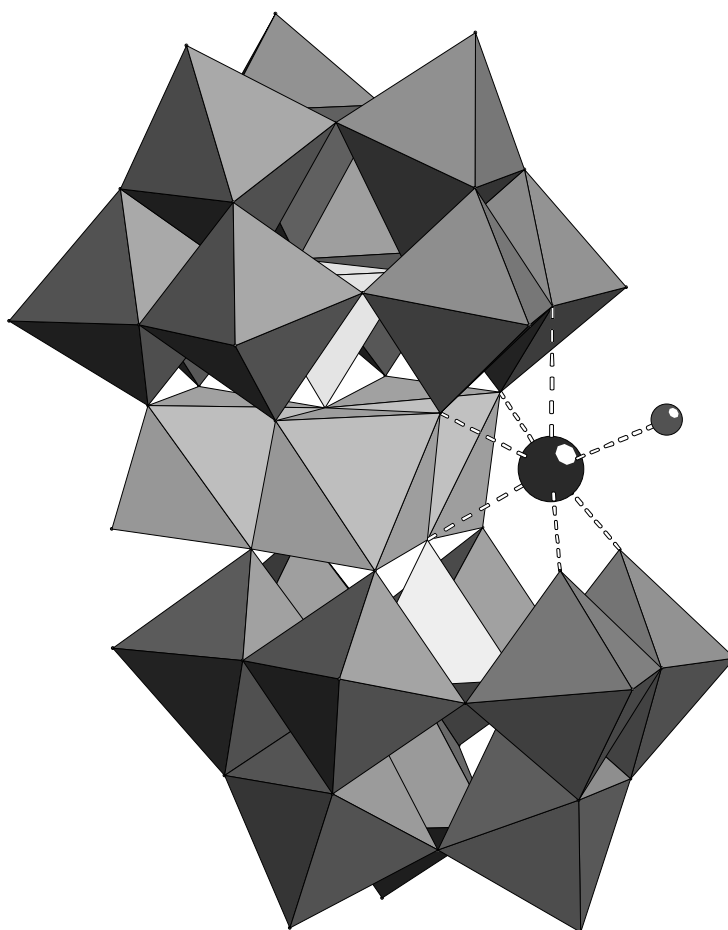
22.6.2

Recent Achievements in Apparently Direct Multiple Electron Transfers on the First Waves of POMs

An issue that is being considered with attention concerns the possibility to achieve multiple electron transfers on the first wave of POMs. The aim is twofold: (1) save energy by favoring those electrocatalytic processes that necessitate several electron to be performed; (2) avoid the

derivatization of the electrode surface. In this context and with particular regard to the electrochemistry and correlatively the use of these POMs in electrocatalysis, three factors were identified recently that promote their multielectron transfer reactions: first, the pH [2] of the solution that also determines the stability domain of the POM; second, a “substituent effect” was identified in which one or more of the skeletal d^0 (usually W^{VI} or Mo^{VI}) centers

of the POM structure are replaced by other d^0 centers and/or by d-electron containing transition metal cations [11, 13–15, 103, 111, 113, 125]; of particular interest for the present purpose, it was found that accumulation of such substituted centers is more favorable for electrocatalytic processes compared to the results observed with the corresponding monosubstituted derivatives [103, 111]; third, the nature of the central heteroatom was



Scheme 8 Combined polyhedral/ball-and-stick representation of $[Ni_3Na(H_2O)_2(AsW_9O_{34})_2]^{11-}$. The AsO_4 , WO_6 , and NiO_6 polyhedra are shown in yellow, red, and green, respectively. The sodium atom is shown as a blue ball and its terminal water molecule as a red ball (taken from Ref. 106).

found to influence the potential locations of the first several waves [111b]. A comparison of a series of monosubstituted Wells–Dawson tungstodiphosphates and tungstodiarсенates revealed that the presence of the As heteroatom drives the first several voltammetric waves in the positive potential direction [111b]. As illustration of these lines, several POMs which engage in multiple electron transfer in the potential domain of their first redox wave were synthesized and studied. However, before going into descriptions of the results, it is worth emphasizing both the difficulty of the syntheses and the necessity for these POMs to be stable in the

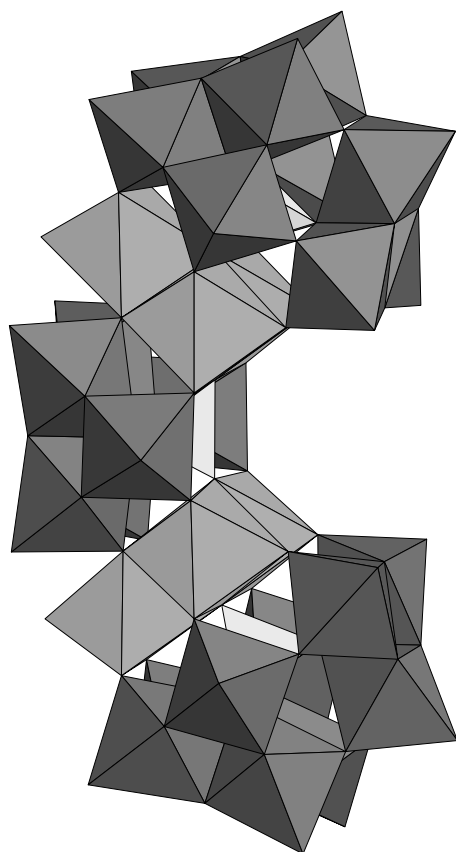
media in which they are studied. In the following, the selection is restricted to stable POMs, even though several others were synthesized with larger numbers of metallic centers.

22.6.2.1 Electrochemistry of the Multi-nickel Polyoxoanions

$[\text{Ni}_6\text{As}_3\text{W}_{24}\text{O}_{94}(\text{H}_2\text{O})_2]^{17-}$,
 $[\text{Ni}_3\text{Na}(\text{H}_2\text{O})_2(\text{AsW}_9\text{O}_{34})_2]^{11-}$, and
 $[\text{Ni}_4\text{Mn}_2\text{P}_3\text{W}_{24}\text{O}_{94}(\text{H}_2\text{O})_2]^{17-}$

The structures of these new POMs are sketched in Schs. 8 and 9 [108].

$[\text{Ni}_4\text{Mn}_2\text{P}_3\text{W}_{24}\text{O}_{94}(\text{H}_2\text{O})_2]^{17-}$ ($\text{Ni}_4\text{Mn}_2\text{P}_3\text{W}_{24}$). Figure 22(a) compares, in a pH 3 medium, the cyclic voltammograms of $\text{Ni}_4\text{Mn}_2\text{P}_3\text{W}_{24}$ and of the original precursor used for its synthesis, $\text{Ni}_3\text{P}_2\text{W}_{18}$ [106]. In the negative potential domain, only the first two redox couples located just before proton reduction are represented. The CVs of the two complexes are very similar in shape, with the pattern for $\text{Ni}_4\text{Mn}_2\text{P}_3\text{W}_{24}$ located slightly more negatively in potential. This observation might be traced to the difference in the overall negative charges of the complexes. As a matter of fact, with the assumption that all other factors act practically in the same way, it is expected that $\text{Ni}_4\text{Mn}_2\text{P}_3\text{W}_{24}$ with 17 negative charges should be more difficult to reduce than $\text{Ni}_3\text{P}_2\text{W}_{18}$ with only 12 negative charges [4, 54a,b,c]. It must be noted, however, that the magnitude of this difference might be modulated by acido-basic properties of the reduced forms of the complexes. As observed previously for $\text{Ni}_3\text{P}_2\text{W}_{18}$, these two waves are attributed to redox processes of W^{VI} centers. In the positive potential domain, only $\text{Ni}_4\text{Mn}_2\text{P}_3\text{W}_{24}$ shows a wave



Scheme 9 Polyhedral representation of $[\text{Ni}_6\text{As}_3\text{W}_{24}\text{O}_{94}(\text{H}_2\text{O})_2]^{17-}$. The AsO_4 , WO_6 , and NiO_6 polyhedra are shown in yellow, red, and green, respectively (taken from Ref. 108).

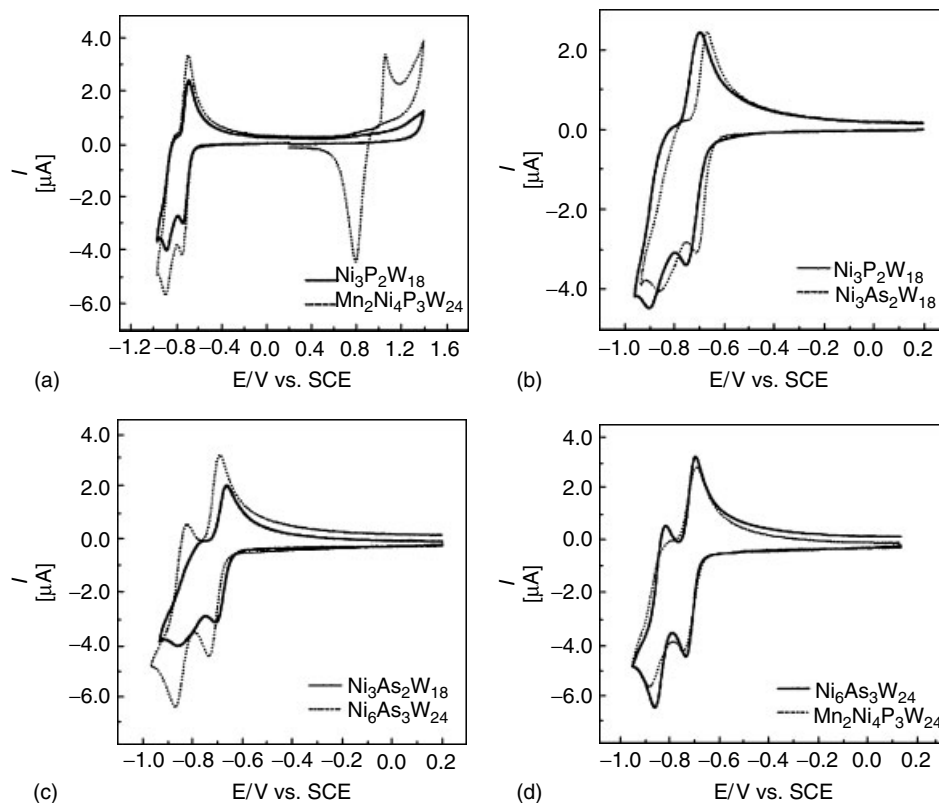


Fig. 22 (a) Comparison of the cyclic voltammograms of 2×10^{-4} M $\text{Ni}_3\text{P}_2\text{W}_{18}$ and $\text{Mn}_2\text{Ni}_4\text{P}_3\text{W}_{24}$, respectively, at pH 3 (0.2 M $\text{Na}_2\text{SO}_4 + \text{H}_2\text{SO}_4$). Scan rate: 10 mV s^{-1} ; working electrode: polished glassy carbon; reference electrode: SCE. For further details, see text. (b) Comparison of the cyclic voltammograms of 2×10^{-4} M $\text{Ni}_3\text{P}_2\text{W}_{18}$ and $\text{Ni}_3\text{As}_2\text{W}_{18}$, respectively, at pH 3 (0.2 M $\text{Na}_2\text{SO}_4 + \text{H}_2\text{SO}_4$). Scan rate: 10 mV s^{-1} ; working electrode: polished glassy carbon; reference electrode: SCE. For further details, see text. (c) Comparison of the cyclic

voltammograms of 2×10^{-4} M $\text{Mn}_2\text{Ni}_4\text{P}_3\text{W}_{24}$ and $\text{Ni}_6\text{As}_3\text{W}_{24}$, respectively, at pH 3 (0.2 M $\text{Na}_2\text{SO}_4 + \text{H}_2\text{SO}_4$). Scan rate: 10 mV s^{-1} ; working electrode: polished glassy carbon; reference electrode: SCE. For further details, see text. (d) Comparison of the cyclic voltammograms of 2×10^{-4} M $\text{Ni}_6\text{As}_3\text{W}_{24}$ and $\text{Mn}_2\text{Ni}_4\text{P}_3\text{W}_{24}$, respectively, at pH 3 (0.2 M $\text{Na}_2\text{SO}_4 + \text{H}_2\text{SO}_4$). Scan rate: 10 mV s^{-1} ; working electrode: polished glassy carbon; reference electrode: SCE. For further details, see text (taken from Ref. 108).

with a peak located at +1.058 V, featuring the oxidation of Mn^{II} centers.

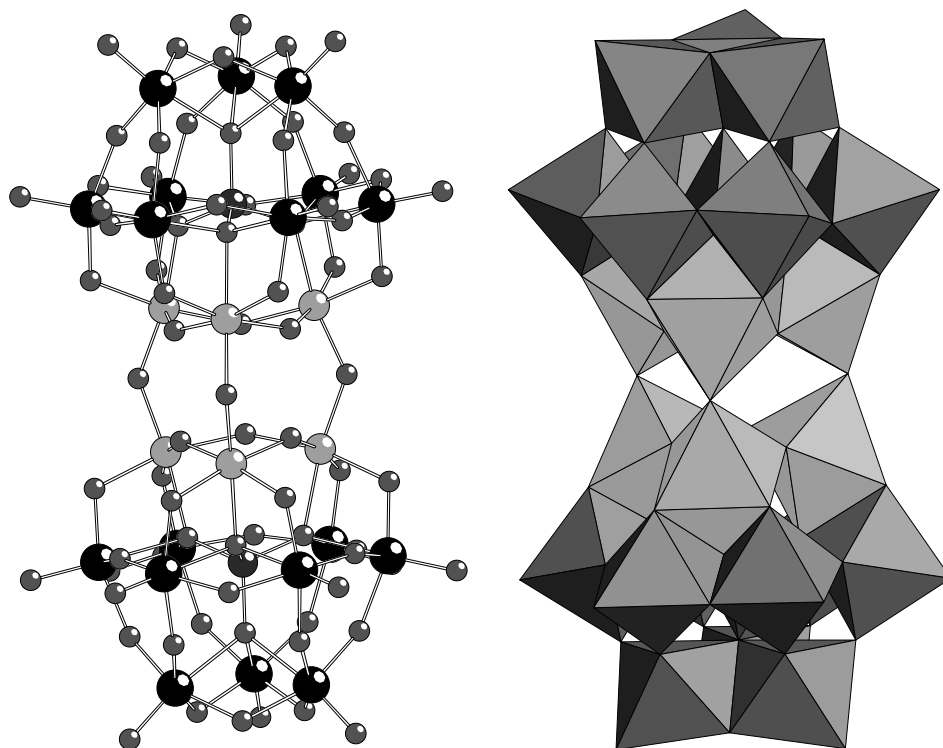
$[\text{Ni}_6\text{As}_3\text{W}_{24}\text{O}_{94}(\text{H}_2\text{O})_2]^{17-}$ ($\text{Ni}_6\text{As}_3\text{W}_{24}$) and $[\text{Ni}_3\text{Na}(\text{H}_2\text{O})_2(\text{AsW}_9\text{O}_{34})_2]^{11-}$ ($\text{Ni}_3\text{As}_2\text{W}_{18}$). The CV of $\text{Ni}_3\text{As}_2\text{W}_{18}$ is also constituted by two reversible waves, which are located in a more positive potential

domain than that of its P analog $\text{Ni}_3\text{P}_2\text{W}_{18}$ as shown in Fig. 22(b). This observation is in agreement with results on other heteropolyanions for which the presence of As instead of P as the central heteroatom facilitates the reduction process [111b]. In analogy to the case of $\text{Ni}_3\text{P}_2\text{W}_{18}$, the

second wave is followed by the reduction of protons. Furthermore, controlled potential coulometric determination at -0.730 V in a pH 3 medium confirms that four electrons are consumed per molecule in the first wave, as already observed previously for the P analog [106]. In short, the electrochemical and IR characterizations as well as elemental analysis converge to confirm that $\text{Ni}_3\text{As}_2\text{W}_{18}$ and $\text{Ni}_3\text{P}_2\text{W}_{18}$ have the same structure.

On the basis of CV it is possible to clearly distinguish $\text{Ni}_6\text{As}_3\text{W}_{24}$ and $\text{Ni}_3\text{As}_2\text{W}_{18}$ as shown in Fig. 22(c). In agreement with the difference in charges of the two polyanions, the more heavily negative one, $\text{Ni}_6\text{As}_3\text{W}_{24}$, is slightly more

difficult to reduce than $\text{Ni}_3\text{As}_2\text{W}_{18}$. As the two molecules are not expected to have the same diffusion coefficient, the simple comparison of the peak current intensities of the respective CVs of $\text{Ni}_6\text{As}_3\text{W}_{24}$ and $\text{Ni}_3\text{As}_2\text{W}_{18}$ cannot be used for an accurate determination of the number of electrons on the latter species. Nevertheless, it can be easily concluded that this number of electrons is larger for $\text{Ni}_6\text{As}_3\text{W}_{24}$. Figure 22(d) compares the CVs of $\text{Ni}_6\text{As}_3\text{W}_{24}$ and $\text{Ni}_4\text{Mn}_2\text{P}_3\text{W}_{24}$ and as expected the compound with P as the heteroatom is more difficult to reduce than its As-analog [111b]. These two polyanions are likely to have fairly similar diffusion coefficients;



Scheme 10 Ball and stick (left) and polyhedral (right) representations of $[\text{Fe}_6(\text{OH})_3(\text{A-}\alpha\text{-GeW}_9\text{O}_{34}(\text{OH})_3)_2]^{11-}$ (**1**). The color code is as follows: iron (green), tungsten (black), germanium (blue) and oxygen (red) (taken from Ref. 107b).

therefore, their CVs can be compared straightforwardly and correspond to the same number of electrons, albeit for the potential locations. Controlled potential coulometry performed at pH 3 on the first W-wave of these two compounds indicates that these waves correspond to six-electron processes for each polyanion.

22.6.2.2 Electrochemistry of the Iron(III)-substituted Keggin Dimer, $[\text{Fe}_6(\text{OH})_3(\text{A-}\alpha\text{-GeW}_9\text{O}_{34}(\text{OH})_3)_2]^{11-}$

The complex $\text{Fe}_6\text{Ge}_2\text{W}_{18}$ (Sch. 10) was found to be stable between pH = 3 and pH = 7 [107].

Figure 23 shows the cyclic voltammogram of $\text{Fe}_6\text{Ge}_2\text{W}_{18}$ obtained at a scan rate of 10 mV s^{-1} , in a pH 3 sulfate medium ($0.2 \text{ M Na}_2\text{SO}_4 + \text{H}_2\text{SO}_4$). The pattern is restricted to the two waves that feature respectively the reduction of Fe^{3+} centers and the first W-wave. In the following text, attention is focused on the reduction of Fe^{3+} centers. Its reduction peak potential is observed at $E_{\text{pc}} = -0.248 \text{ V vs. SCE}$. A loose comparison with the corresponding E_{pc} values for free Fe^{3+} ($E_{\text{pc}} = 0.074 \text{ V vs. SCE}$) and $[\text{Fe}_4(\text{H}_2\text{O})_{10}(\beta\text{-AsW}_9\text{O}_{33})_2]^{6-}$ ($E_{\text{pc}} = -0.126 \text{ V vs. SCE}$) in the same electrolyte [107a], supports the usual expectation that the order of peak potentials should follow the overall negative charges of the complexes, under the

complementary assumption of otherwise identical influences. Whatever the scan rate from 1000 mV s^{-1} down to 2 mV s^{-1} , no splitting of the single Fe-wave of $\text{Fe}_6\text{Ge}_2\text{W}_{18}$ was observed. Controlled potential coulometry with the potential set at -0.400 V vs. SCE indicates the consumption of 6.08 ± 0.05 electrons per molecule, thus confirming the simultaneous one-electron reduction of each of the six Fe-centers. As a good piece of evidence that the tungsten-oxo framework was not reduced, the electrolysis did not give the characteristic blue color. Exchange of a relatively high number of electrons in polyoxometalate electrochemistry was described previously. In cases when such exchanges are associated with proton consumption, the buffer capacity of the supporting electrolyte might influence the shape and potential location of the voltammetric waves [86a,b]. This point was also studied in the paper.

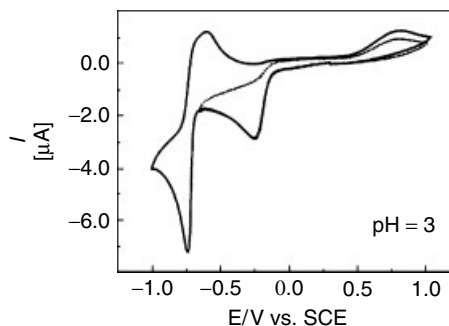
22.6.3

Theoretical Approaches

22.6.3.1 Electronic Structures of POMs Explain their Redox Behaviors and the Relative Stability of Reduced Forms

As a consequence of the high number of heavy atoms in POMs in addition to the complexity of the problems

Fig. 23 Cyclic voltammograms in a $2 \cdot 10^{-4} \text{ M}$ solution of $\text{Fe}_6\text{Ge}_2\text{W}_{18}$ complex in pH = 3 media; working electrode: glassy carbon; reference electrode: SCE. pH = 3 sulfate medium ($0.2 \text{ M Na}_2\text{SO}_4 + \text{H}_2\text{SO}_4$); superposition of the CVs restricted to the Fe-wave and to the Fe-wave and the first W-redox processes; scan rate: 10 mV s^{-1} (taken from Ref. 107b).



of interest, attempts at direct theoretical rationalization of observations and/or prediction of behaviors are rather limited. A remarkable characteristic, however, is that different issues were tackled as directly as possible, whatever the available theoretical tools at hand at the moment. Even the earliest theoretical works on polyoxometalates using the simple semiempirical extended Hückel approach are devoted to problems as complicated as the comparison of the catalytic and structural properties of heteropolycompounds [131], or the behaviors of polyoxometalates as models of oxide catalysts [132]. Other achievements include the Molecular Orbital Theory treatment of the photodimerization of cyclohexene and methane by decatungstate anions [133] or the oxidative dehydrogenation of methanol by metal oxide surfaces [134]. Progressively, more sophisticated *ab initio* or DFT methods are being introduced [135–150]. Their ability to tackle problems as diverse as the acidity and basicity of polyoxometalates [142, 143], the localization or delocalization of metal electrons in reduced species [140, 141, 144, 147, 150] is receiving increasing attention. Among several very interesting examples, a recent DFT study [150] focuses on the relative stability, upon reduction, of the five isomers of $[\text{PW}_{12}\text{O}_{40}]^{3-}$. In the oxidized form, the energy grows as follows $\alpha < \beta < \gamma < \delta < \epsilon$ and fits the experimental findings. The reduced clusters behave differently as long as the β form becomes the most stable isomer after the second reduction. The γ isomer also gains stability upon reduction, but not enough to be competitive with β . For the fourfold reduced $[\text{PW}_{12}\text{O}_{40}]^{3-}$ cluster, the energy difference computed between β and γ in solution is 11 kcal mol^{-1} . This large difference proves that the $\beta \rightarrow \gamma$ isomerization is not favored upon simple reduction. The other isomers, δ and ϵ , are

much more unstable than α or β in any reduction state.

22.6.3.2 An Extended Hückel Calculations Approach to a Qualitative Understanding of the Initial Electron Transfer Site in Dawson-type POMs

The nonequivalence of the “cap” and “equatorial” atoms in Well–Dawson anions raises the problem of the initial site of electron transfer in such structures. In a pioneering work [30f], a striking similarity of magnetic and ESR properties in $[\text{WOX}_5]^{2-}$ complexes and Keggin and Dawson one-electron blues was pointed out. Comparisons of the widths of the spectra and, especially, observation of the distinctly longer relaxation times in reduced 2:18 anions than in the other anions guide Pope et al. to the following statement: “This may mean that it is the ‘equatorial’ (non-Keggin-like) tungsten atoms which are reduced first in 2:18 anions” [30f]. Since then, various lines of experimental evidence, culled from the results of different techniques, converge to support the fact that the added electrons should first be introduced into the equatorial atoms [54a, 65–71, 74–77]. Yet, a direct theoretical proof was lacking and was sought through extended Hückel calculations [78].

The nonequivalence of the “cap” (α_2 positions) and the “belt” (α_1 positions) metal atoms in $\text{P}_2\text{W}_{18}\text{O}_{62}^{6-}$ is reflected by the composition of metal-centered vacant orbitals (Fig. 24). It is worth noting that the lowest unoccupied molecular orbital (LUMO) (a_1'') is almost entirely developed on the α_1 positions (96%), with equal weights on each of the twelve metal atoms. With the reasonable assumption that the initial electron transfer involves the LUMO of the starting species, the shape of

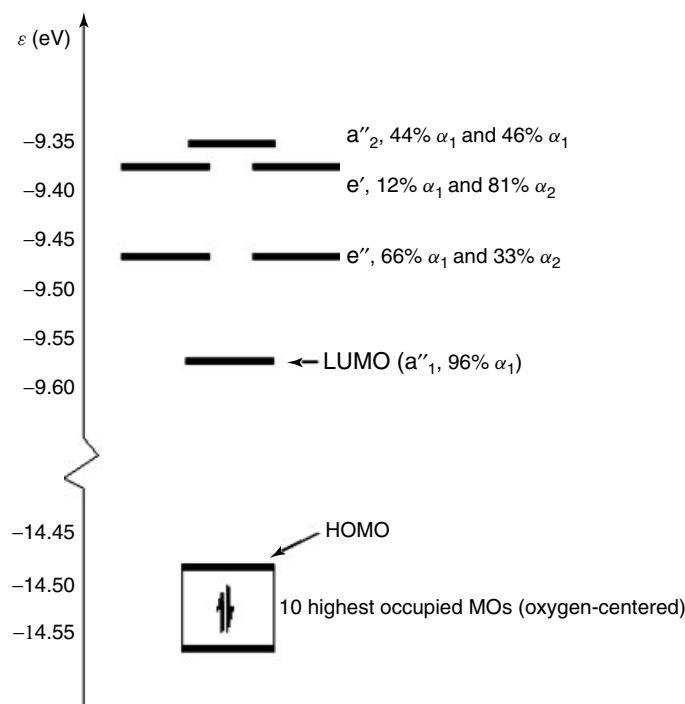


Fig. 24 Selected frontier orbitals of the $\text{P}_2\text{W}_{18}\text{O}_{62}^{6-}$ heteropolyanion (EH calculations). The symmetry and the contributions of the α_1 and α_2 positions to the six lowest vacant MOs are given (taken from Ref. 78).

this molecular orbital nicely rationalizes the experimental evidence that the added electrons should first be introduced into the equatorial atoms. Interestingly, the composition of the vacant orbitals located above the LUMO is very different. For instance, in the first set of degenerate MOs, of e'' symmetry, the orbitals are spread out over both the α_1 (61%) and the α_2 (33%) positions in such a way that almost equal weights are found for the eighteen metal centers (12 and 6 in the α_1 and the α_2 positions, respectively). In the second set of degenerate MOs (e'), the orbitals are mainly located on the α_2 positions (81% instead of only 12% for the twelve α_1 positions). Finally, the sixth low-lying vacant orbital (a''_1) is developed on both the α_1 (44%) and the α_2 (46%) positions.

The shape and the energies of the metal-centered vacant molecular orbitals are sensitive to the substitution of W atom(s) by more electronegative metal atom(s) (Mo for instance). Assuming the geometry of the substituted $\text{P}_2\text{W}_{18-x}\text{Mo}_x\text{O}_{62}^{6-}$ heteropolyanions is identical to that of the unsubstituted species, the electronegativity perturbation can be accounted for, in the first approximation, by the lowering of the atomic orbital energies on the substituted metal center(s) [151]. Any substitution in the α_1 ("belt") position(s) leads to a LUMO of lower energy, still developed on the α_1 positions, but mainly centered on the α_1 -Mo center(s). For instance, with a single α_1 -Mo atom, the LUMO is lowered by 0.08 eV and remains located on the "belt" (93%). However, instead of an

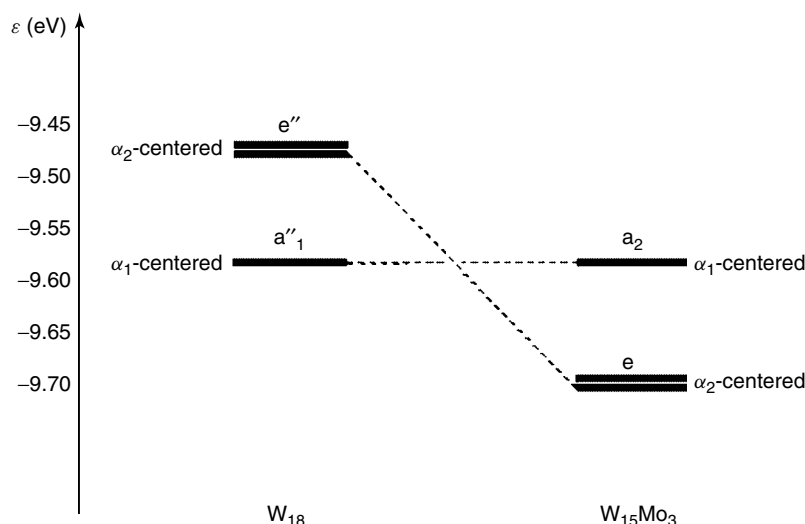


Fig. 25 Energy crossing between the lowest unoccupied MOs of the $\text{P}_2\text{W}_{18}\text{O}_{62}^{6-}$ heteropolyanion upon substitution by three molybdenum centers in a “cap” (α_2 positions) (EH calculations) (taken from Ref. 78).

equal weight of about 8% on each metal atom, 45% of the LUMO is now concentrated on the single α_1 -Mo center. Note that such a localization of the LUMO upon substitution was also reported by Poblet and colleagues for α -Keggin anions (DFT orbitals) [148]. The same conclusions apply for compounds with several α_1 substituted centers. On the contrary, substitution at the α_2 position(s) lets this α_1 -centered vacant orbital unchanged but stabilizes the MOs developed on the α_2 sites. Therefore, a dramatic change in the localization of the LUMO can occur with respect to the unsubstituted compound, as it is illustrated in Fig. 25 for the (1, 2, 3)- $\text{P}_2\text{Mo}_3\text{W}_{15}\text{O}_{62}^{6-}$ complex with three Mo centers in one cap. In this compound, a set of two degenerate LUMOs of the symmetry (C_{3v}), centered on the three α_2 -Mo positions (86%), are now located 0.10 eV below the α_1 -centered (94%) vacant orbital that has been left unchanged by the

substitution. Even for a single substitution, the LUMO is located at 80% on the α_2 -Mo center and its energy is 0.06 eV below that of the belt-centered vacant orbital. In the “mixed” face-substituted complex, with four α_1 -Mo and two α_2 -Mo centers, the LUMO remains located on the four substituted α_1 positions (82%) while the vacant MO just above is mainly developed on the two substituted α_2 positions (77%). Finally, in the fully substituted Mo_{18} compound, the situation is identical to that found in the starting W_{18} species, with a LUMO entirely developed on the twelve α_1 centers. A nice correlation is thus found between the localization of the LUMO (either α_1 - or α_2 -centered) and the nature of the first reduction site in the substituted $\text{P}_2\text{W}_{18-x}\text{Mo}_x\text{O}_{62}^{6-}$ heteropolyanions deduced from the experimental evidences recalled earlier.

Finally, the HOMO–LUMO energy gap depends on the substitution pattern

since the HOMO level (oxygen-centered) remains unchanged while the LUMO level (metal-centered) is lowered when more electronegative metal centers are introduced. It is illustrated in Fig. 26 for the $P_2W_{18}O_{62}^{6-}$ heteropolyanion and

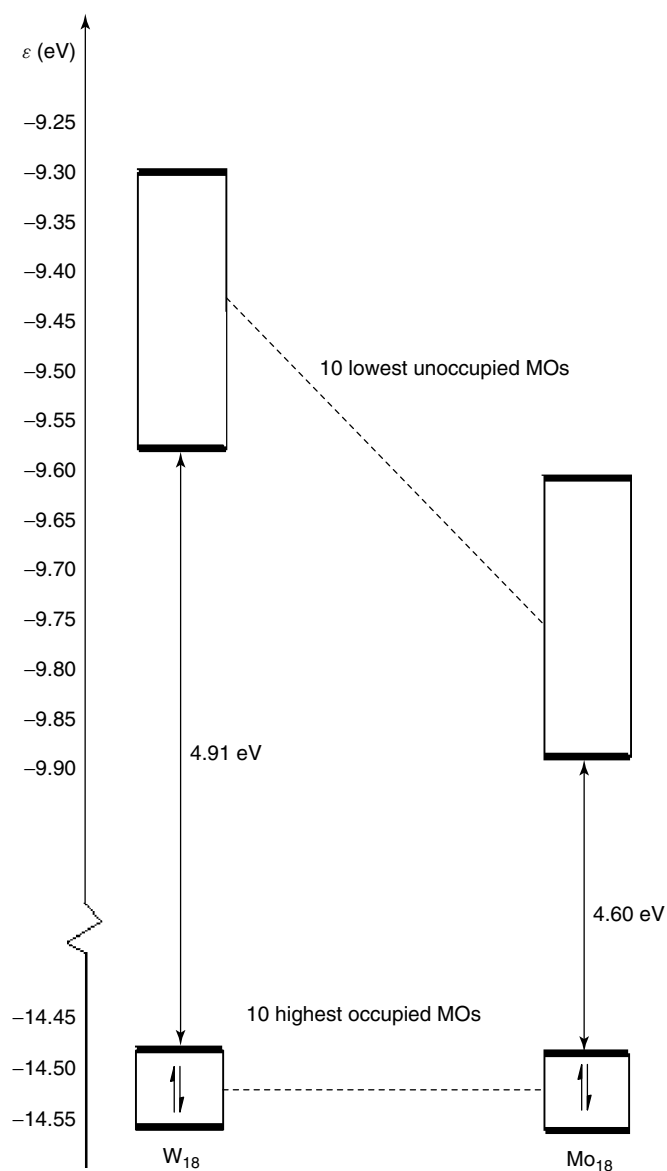


Fig. 26 Energy change of the ten highest occupied (oxygen-centered) and the ten lowest unoccupied (metal-centered) MOs in going from the $P_2W_{18}O_{62}^{6-}$ heteropolyanion to its molybdenum analog $P_2Mo_{18}O_{62}^{6-}$ (EH calculations) (taken from Ref. 78).

its fully substituted analog $P_2Mo_{18}O_{62}^{6-}$. The HOMO energy level is -14.48 eV in both complexes but the LUMO energy level is lower by 0.31 eV in the Mo_{18} species (-9.88 instead of -9.57 eV in the tungsten analog). Such a lowering of the LUMO level upon substitution can be correlated with the easier reduction of the Mo substituted species (Table 8).

In conclusion, it was shown that the experimental evidence for an initial electron transfer site in an equatorial position (α_1) of the unsubstituted Dawson-type $P_2W_{18}O_{62}^{6-}$ heteropolyanion can be rationalized by the “belt”-centered character of the LUMO. The change of the reduction site ($\alpha_1 \rightarrow \alpha_2$) upon substitution in the “cap” region (α_2 site) by a more electronegative metal center (Mo for instance) is also consistent with the localization of the LUMO on the substituted center(s).

22.7 Electrocatalysis

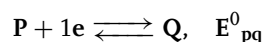
Possibilities of electrocatalysis of reactions at electrodes are among the powerful incentives for the electrochemical study of POMs. Interesting results were obtained both in electrocatalytic reductions and oxidations, provided the appropriate form of the POM is used. Two recent reviews devoted to the electrochemical properties of polyoxometalates as electrocatalysts are available [8, 9]. The second one focuses more specifically on electrocatalysis on modified electrodes. In the present text, attention will be drawn specially to the basic principles that could be considered to govern most of solution processes. The principles will be illustrated by several recent experimental results, even though earlier achievements will also be described briefly.

Strictly speaking, electrocatalysis applies to the “dependence of the electrode reaction rate on the nature of the electrode material” [152]. In the following, this term will be used in a broader sense and will be admitted to include the possibility that the catalyst be homogeneously dissolved in the electrolyte solution as well as the case where the catalyst is attached to the electrode surface. A short chapter on the electrocatalysis of inorganic chemicals by chemically modified electrodes can also be found in Vol. 10 of this Encyclopedia [9].

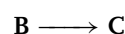
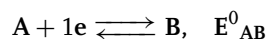
22.7.1 Basic Concepts of Homogeneous Catalysis of Electrode Reactions

The first observations of catalytic phenomena in electrochemistry in the early 1930s were followed by attempts at modelization on the example of hydrogen peroxide reduction in the 1940s. A general framework was expressed, in which electron exchange occurred in solution between the reduced catalyst and the substrate, thus regenerating the catalyst and explaining the observed catalytic effect. In short, electron transfers to or from a molecule must be viewed as a succession of elementary electrochemical and chemical reaction steps. Such simplified reaction schemes served as the basis for theoretical analysis of catalytic phenomena. In molecular electrochemistry, electrochemical reductions can therefore be sketched by the following reaction schemes:

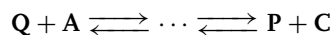
For the catalyst (P) :



For the substrate (A) :



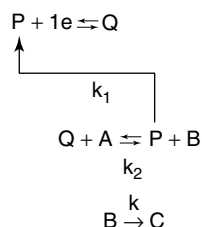
The catalytic effect is reflected in the interaction of Q with A, resulting in the regeneration of P.



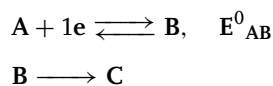
The only thermodynamic condition then required for this reaction to be driven from left to right is that the standard molar free enthalpy of the reaction be negative, that is, the following inequality must hold: $E^0_{PQ} < E^0_{AC}$, where E^0_{AC} represents the standard redox potential of the A/C couple.

However, this overall scheme might feature two types of successive reaction steps. The first one considers the possibility of solution electron transfers; the second one goes through the formation of an adduct.

The first scheme is simple and reads as follows:

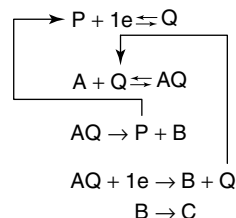


It is worth reminding that the direct reduction of the substrate is realized according to the following pathways:



The catalyst constitutes an electron shuttle between the electrode and the solution, where it is engaged in a direct redox electron transfer with the substrate. This type of catalysis is termed *redox catalysis*.

The second reaction scheme reads:



In this case, the reduced form of the catalyst builds up with the substrate a relatively unstable adduct AQ, which then decomposes, eventually after further reduction at the electrode surface or in solution. Finally, either the oxidized form P of the catalyst or its reduced form Q is regenerated. As regards the substrate, its reduction follows the aforementioned E.C. (Electrochemical Chemical) mechanism. This type of catalysis is termed *chemical catalysis*. Finally, it must be pointed out that the clear-cut distinction between redox catalysis and chemical catalysis might be difficult, but amounts ultimately to a detailed study of the nature of the redox reaction.

22.7.2

Selected Electrocatalysis in Homogeneous Solution

In principle, the choice of a specific electrochemical technique is not crucial in the study of electrocatalytic processes. However, from a practical and qualitative point of view, cyclic voltammetry is, in most cases, suited for a rapid assessment of an electrocatalytic process triggered by POMs. The interest stems from the following general behavior: most POMs undergo a series of reversible one- and two-electron reductions and these reduced forms act usually as the active species, inducing an increase of the corresponding

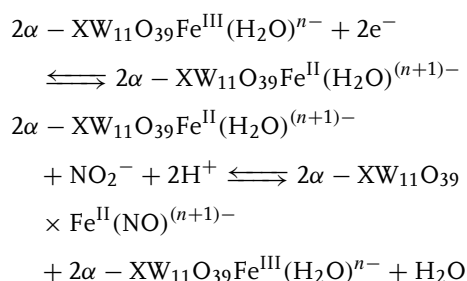
cathodic current and a concomitant loss of its reversibility.

22.7.2.1 Electrocatalytic Reductions

Table 13 gathers the main electrocatalytic processes triggered by POMs dissolved in solution. The electrocatalytic reductions of dioxygen, hydrogen peroxide and of several NO_x including nitrite, nitric oxide, and nitrate are selected for a more detailed description.

Electrocatalysis of the reduction of HNO₂ and NO was demonstrated in the late 1980s independently by Anson et al. [153d] and by Keita et al. [157, 158]. Since then, this reaction has been selected and is being used worldwide as a classical test of the electrocatalytic properties of the POMs. Consideration of [Fe(H₂O)SiW₁₁O₃₉]^{6−} (**SiW₁₁Fe** for

short), one of the electrocatalysts proposed by Anson [153d], is particularly enlightening: a Fe-nitrosyl complex is formed upon reduction of the Fe center and the actual catalytic process to obtain ammoniac occurs at more negative potentials where the necessary number of charges is accumulated and delivered by the W-framework. The overall mechanism up to the Fe-nitrosyl formation involves the following steps [153d]:



Tab. 13 Electrocatalytic reductions by homogeneously dissolved heteropolyanions

Catalyst	Reduction	condition	References
SiW ₁₂ O ₄₀ ^{4−}	h.e.r.	Acidic solution	33b,c
	Nitrite reduction	Buffer	153a
	O ₂ reduction	Triflate buffer (pH 2)	154
SiMo ₁₂ O ₄₀ ^{4−}	Chlorate reduction	50%(v/v) dioxane-water (0.5 M H ₂ SO ₄)	153b
	Nitrite reduction		155
PMo ₁₂ O ₄₀ ^{3−}	Chlorate reduction	50%(v/v) dioxane-water (0.5 M H ₂ SO ₄)	153b
P ₂ W ₁₈ O ₆₂ ^{6−}	Nitrite reduction	Buffer	153c
XW ₁₁ O ₃₉ Fe ^{III} (H ₂ O) ^{n−} (X = P, As, Si, Ge)	Nitrite reduction	Buffer	156
SiW ₁₁ O ₃₉ Fe ^{III} (H ₂ O) ^{5−}	H ₂ O ₂ reduction	Buffer	94b
P ₂ W ₁₇ O ₆₁ Fe ^{III} (H ₂ O) ^{8−}	H ₂ O ₂ reduction	Sulfate buffer (pH 3)	94b
	Nitrite reduction	Acetate buffer (pH 5)	
PW ₁₁ O ₃₉ Ru ^{III} (H ₂ O) ^{4−}	DMSO reduction	Sulfate buffer (pH 2)	85
	h.e.r.		
K ₁₇ [Ln(As ₂ W ₁₇ O ₆₁) ₂] (Ln = La, Pr, Sm, Eu, Gd, Dy, Tm)	Nitrite reduction	Acetate buffer (pH 5.5)	153e
Nd(SiMo ₇ W ₄ O ₃₉) ₂ ^{13−}	Bromate reduction	Buffer	153f

X = Si, Ge, n = 5; X = P, As, n = 4

Nitrous acid was shown to be the reactive intermediate depending on the pH domain explored. As a matter of fact, the following sequence is known: $\text{HNO}_2 \rightleftharpoons \text{H}^+ + \text{NO}_2^-$ $pK_a = 3.3$ at 18°C and HNO_2 disproportionates in fairly acidic solution: $3\text{HNO}_2 \rightleftharpoons \text{HNO}_3 + 2\text{NO} + \text{H}_2\text{O}$. The rate of this reaction is known to be low.

However, a loss in selectivity and a low yield ensue [153d] from electrode derivatization [28]. Recently, to avoid the shortcomings encountered with SiW_{11}Fe , several alternative POMs were proposed [8, 10, 157–159]. Among all of these potentially acceptable candidates, N_2O was obtained with a quantitative yield of 100% with molybdc and molybdo-tungstic POMs [10]. A supramolecular compound like $[\text{P}_8\text{W}_{48}\text{O}_{184}]^{40-}$, with only W-centers, can also be used to reduce NO efficiently without derivatization of the electrode surface [86b]. Finally, mixed addenda POMs and also sandwich-type complexes have the advantage of accumulating metal centers known for their catalytic behaviors in the reduction of NO_x , or alternatively in the reductions of dioxygen and hydrogen peroxide; in cases they are electroactive within the POM, they permit generally a substantial positive shift of the potential because these metal centers are easier to reduce than the W-centers of the polytungstic framework [1, 103, 115]. Specifically, Cu, Ni, and Fe-centers were the most efficient among metal ion substituents. In addition, their efficiency was enhanced by the presence of Mo atoms [159, 160]. A cooperative effect was also noted between Mn- and Fe-centers as will be shown in the following text.

The electrocatalytic reduction of nitrate by reduced POMs was demonstrated for the first time [160a]. Following general

conclusions emerge from recent achievements in NO_x reductions. In $\text{pH} < 4$ media, most POMs are active for the reduction of nitrite (which is actually a mixture of HNO_2 and NO). In contrast, for $\text{pH} > 4$ media where nitrite itself is the main species in solution, few examples of electrocatalysis exist and Cu-substituted POMs are the most efficient. For the reduction of nitrate, Cu- and Ni-containing POMs show a good efficiency. In addition, $\text{Ni}_4\text{Mn}_2\text{P}_3\text{W}_{24}$, $\text{Ni}_6\text{As}_3\text{W}_{24}$, and $\text{Fe}_6\text{Ge}_2\text{W}_{18}$ With their six-electron first waves proved remarkably efficient in the electrocatalytic reduction of nitrate. These observations are taken into account for the selection of following examples.

22.7.2.1.1 Electrocatalytic reduction of nitrite and nitrate

Studies with $[(\text{Cu}^{\text{II}}(\text{H}_2\text{O}))_2\text{Cu}^{\text{II}}_2(\text{X}_2\text{W}_{15}\text{O}_{56})_2]^{16-}$ (abbreviated in the following as $\text{Cu}_4\text{X}_4\text{W}_{30}$ with X = P or As) This example is selected to compare nitrate reduction with the more classical nitrite reduction [115]. Correlatively, the study of the possible intermediate or final product in this reaction, namely nitrite, was also to be considered. All the experiments were carried out at $\text{pH} = 5$.

The oxidized forms of these two sandwich-type POMs are stable from $\text{pH} 3$ to at least $\text{pH} 7$. Their characterization by cyclic voltammetry revealed the stepwise reduction of the Cu^{2+} centers within the POMs, before Cu° deposition on the glassy carbon electrode surface [115]. Phenomena are described mainly for the P-derivative and are the same for the As-analog.

The cyclic voltammograms in Fig. 27 sketch the main observations with $\text{Cu}_4\text{P}_4\text{W}_{30}$ as a catalyst; they were run at the same scan rate as a function of the excess parameter γ ($\gamma = C^\circ_{\text{NO}_3^-}/C^\circ_{\text{POM}}$). Starting from $\gamma = 0$, it is seen that addition of even

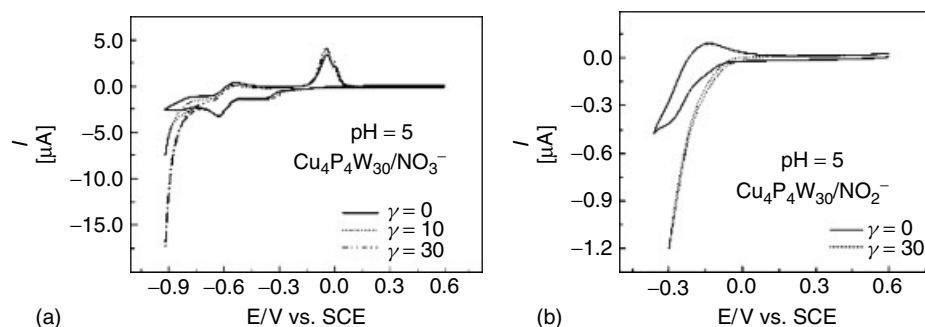


Fig. 27 Electrocatalysis of NO_x reduction in the presence of 2×10^{-4} M Cu₄P₄W₃₀ in a pH 5 medium. The scan rate was 2 mV s^{-1} , the working electrode was glassy carbon and the reference electrode was SCE. (a) Nitrate (b) nitrite. For more detailed information, see text (taken from Ref. 115).

a small amount of nitrate to the solution induces a large cathodic current increase just negative of the peak potential location of the first W-wave. Concomitantly, the reversibility of the second W-wave is suppressed even for small γ values. These observations indicate an efficient reduction of nitrate anions by reduced species of Cu₄P₄W₃₀. The catalytic efficiencies CAT (defined as $\text{CAT} = 100 \times [I_{(\text{POM}+\text{NO}_3^-)} - I_{(\text{POM})}^d]/I_{(\text{POM})}^d$ where $I_{(\text{POM}+\text{NO}_3^-)}$ represents the reduction peak current observed for the POM in the presence of nitrate and $I_{(\text{POM})}^d$ is the corresponding reduction peak current for the POM alone) varies from 194 to 580% when γ increases from $\gamma = 10$ to $\gamma = 30$. The corresponding CAT values for Cu₄As₄W₃₀ are 203 and 607% for $\gamma = 10$ and $\gamma = 30$ respectively. It is likely from these values that the nature of the central heteroatom (P or As) does not influence significantly the catalytic process. It is worth pointing out that no direct reduction of nitrate anions on glassy carbon electrode is observed in the potential domain explored here in the absence of heteropolyanion [160a].

In addition to these experiments, we have checked that the probable

intermediates in the reduction of nitrate, namely NO and NO₂⁻, are also efficiently reduced by the reduced Cu₄X₄W₃₀ at a less negative potential than necessary for nitrate itself. As an example, Fig. 27(b) shows the reduction of NO₂⁻ by Cu₄P₄W₃₀. It comes out that Cu²⁺ retain its catalytic properties upon complexation with an heteropolyanion, accompanied by supplementary advantages; these advantages include the possibility to accumulate Cu²⁺ active centers and also the possibility to fabricate highly reduced species with the electrons accumulated in the reduced W-framework of the heteropolyanion.

As a whole, it was found that the electrocatalytic reduction of nitrate, nitrite, and nitric oxide proceeds efficiently from pH 3 to 7.

Cooperative effect of Mn- and Fe-centers within Mn₂Fe₂P₄W₃₀ in the electrocatalytic reduction of nitrite In the preceding sections, it was well established that Fe(III)-substituted POMs catalyze the reduction of NO and/or NO₂⁻ [1]. The first step in this process is the formation of a complex with the Fe(II) form of the POM and nitrogen oxide.

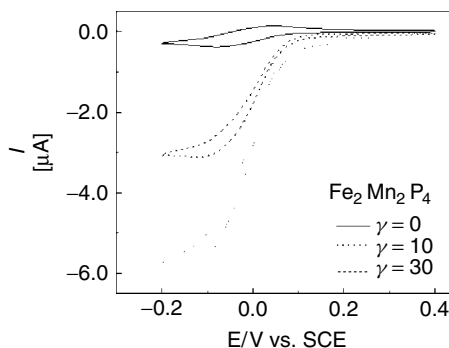
The actual catalytic step takes place with remarkable enhancement of the current intensity, and it occurs at more negative potentials in the reduction domain, where the W(VI) centers accumulate a suitable number of electrons within the complex framework for subsequent delivery. With the goal of saving energy by moving the electron reservoir closer to the Fe(III)-reduction potential, several Wells–Dawson-type monosubstituted derivatives were previously synthesized, including α_1 -(FeOH₂) P₂W₁₇O₆₁⁷⁻ and α_2 -(FeOH₂)P₂Mo₂W₁₅O₆₁⁷⁻ in which the Fe- and W-waves or Fe- and Mo-waves merge in appropriate pH media [14, 159]. This strategy turns out to be favorable, and the entire catalytic process shows up at the reduction potential of the Fe(III) center, which is now observed concomitantly with the Mo(VI) or W(VI) reduction waves. The same phenomenon is observed here.

These results are illustrated briefly with **Fe2Mn2P4** in Fig. 28, with NaNO₂ as the starting substrate. An important current intensity increase is observed with increasing γ values (γ is the excess parameter defined as $\gamma = C^\circ(\text{NO}_x)/C^\circ(\text{POM})$) at the reduction potential of the Fe(III) centers in a pH 1 solution in which a mixture of HNO₂ and NO must be considered. In this potential

domain, no reduction is observed for NO or HNO₂ present in the solution. Figure 28 shows unambiguously that the catalytic process begins simultaneously with the reduction of the Fe(III) centers. Furthermore, it is worth noting the high efficiency of the electrocatalysis, even though modest γ values were used. Finally, in the timescale of cyclic voltammetry, **Fe2P4** shows the same phenomenon as **Fe2Mn2P4** concerning the electrocatalytic reduction of NO and NO₂⁻. However, the latter complex might be a better choice for this catalytic process due to the improved stability of its Fe(II) forms [109]. Under the same experimental conditions, **Fe2Mn2As4** also shows good catalytic efficiency for the reduction of nitrite. In addition, its activity at 0 V is 25% higher than that of **Fe2Mn2P4** due to the slight positive potential shift of the Fe(III) waves in the former complex compared with the latter due to the different heteroatoms (i.e. As vs. P).

However, in a pH = 5 medium, the catalytic process (obtained with NaNO₂ as the starting substrate) is no longer observed in the iron reduction–potential domain, but is relegated to the reduction potential of the first W-wave. This observation is in full agreement with the expected absence of NO and HNO₂ in this medium.

Fig. 28 Cyclic voltammetry study of the electrocatalytic reduction of nitrite with a 2×10^{-4} M solution of **Fe2Mn2P4** in a pH = 1 medium (0.5 M Na₂SO₄ + H₂SO₄). The scan rate was 2 mV s^{-1} , the working electrode was glassy carbon, and the reference electrode was SCE (taken from Ref. 1).



In contrast, experiments with pure NO [10, 155] at pH = 5 show that the catalytic process starts directly in the iron reduction–potential domain. We have also checked the catalytic reduction of NO at pH = 1. All these results converge to designate NO as the species electrocatalytically reduced by the present complexes throughout the pH domain evaluated.

Evaluation of the behaviors of $\text{Ni}_3\text{P}_2\text{W}_{18}$, $\text{Ni}_4\text{Mn}_2\text{P}_3\text{W}_{24}$, $\text{Ni}_6\text{As}_3\text{W}_{24}$, and $\text{Fe}_6\text{Ge}_2\text{W}_{18}$ in the electrocatalytic reduction of nitrate and nitrite A few general conclusions can be drawn from literature results before going into specific details [107b, 113]. These POMs, specifically those exhibiting six-electron first waves, constitute unique examples of multielectron catalysts active in the electrocatalytic reduction of nitrate without derivatization of the electrode surface. In addition, highly reduced products were obtained, because nitrite is reduced at a less negative potential than nitrate whatever the pH from acidic to neutral media. With the examples of $\text{Ni}_4\text{Mn}_2\text{P}_3\text{W}_{24}$ and $\text{Ni}_6\text{As}_3\text{W}_{24}$, it was demonstrated that the availability of large number of electrons is not a sufficient condition for an efficient catalysis of nitrate reduction. As a matter of fact, the crown POM P_8W_{48} does not perform such a catalysis, despite the eight electrons available in its first reduction step. Finally, Fe-centers within POMs are usually poor catalysts for the reduction of nitrate. Therefore, it is remarkable that they turned out to be efficient in the particular structure of $\text{Fe}_6\text{Ge}_2\text{W}_{18}$.

Coming to details, cyclic voltammetry was used to evaluate the activity of $\text{Ni}_3\text{P}_2\text{W}_{18}$ and $\text{Mn}_2\text{Ni}_4\text{P}_3\text{W}_{24}$ in the electrocatalytic reduction of nitrate. The choice of the substrate is tricky, as nitrate is difficult to reduce. Other few examples

where POMs have proven to be useful in this system have been described recently [13, 103, 160]. For this purpose, the excess parameter is an operational parameter defined as $\gamma = C^{\circ}_{\text{NO}_3^-}/C^{\circ}_{\text{POM}}$. The electrocatalysis is characterized by the catalytic efficiency CAT, defined as follows: $\text{CAT} = 100 \times [I_{(\text{POM}+\text{NO}_3^-)} - I^d_{(\text{POM})}]/I^d_{(\text{POM})}$ where $I_{(\text{POM}+\text{NO}_3^-)}$ is the peak current for reduction of the heteropolyanion (POM) in the presence of NO_3^- and $I^d_{(\text{HPA})}$ is the corresponding diffusion peak current for the HPA alone. CAT values are sufficient to compare the efficiencies for a given electrocatalytic process either for one compound as a function of pH or for two compounds at the same experimental conditions. However, it must be recognized that a more detailed comparison would necessitate determination of the nature and yields of the final products, which was considered beyond the scope of this work. As a first example, CAT values were measured in the presence of $\text{Ni}_3\text{P}_2\text{W}_{18}$ for the electrocatalytic reduction of nitrate in a pH 2 sulfate medium. CAT was measured at -0.840 V and varies from 2098 to 2733 for $\gamma = 500$ and $\gamma = 1000$ respectively. These values indicate an efficient electrocatalysis of the reduction of nitrate by $\text{Ni}_3\text{P}_2\text{W}_{18}$ at pH 2. Furthermore, several tests with NO_2^- and/or with NO under the aforementioned conditions confirm that these species are easily reduced electrocatalytically at substantially less negative potentials than nitrate [10]. Insofar as nitrite and NO are known to appear as intermediates in the reduction of nitrate on various metals, the present results would suggest that highly reduced species should be obtained in the electrocatalytic reduction of nitrate in the presence of $\text{Ni}_3\text{P}_2\text{W}_{18}$. Also, the number of accumulated electrons in the polyoxoanion framework at the potential where the transformation of

nitrate takes place is large enough for a complete reduction, which constitutes a complementary circumstance supporting the preceding assumption.

The media of pH 3 and 5, respectively, were selected to compare the efficiencies of $\text{Ni}_3\text{P}_2\text{W}_{18}$ and $\text{Mn}_2\text{Ni}_4\text{P}_3\text{W}_{24}$ in the electrocatalytic reduction of nitrate, because the latter complex is not very stable at pH 2. Whatever the pH, $\text{Mn}_2\text{Ni}_4\text{P}_3\text{W}_{24}$ was found to be the more efficient of the two complexes: its CAT values were four and seven times larger, at pH 3 and 5 respectively, than those measured for $\text{Ni}_3\text{P}_2\text{W}_{18}$ under the same conditions.

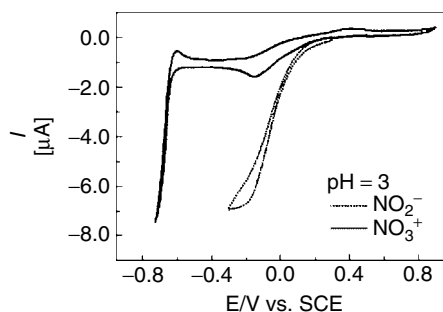
The results for these two complexes were compared with the efficiencies obtained with $\text{Ni}_4\text{P}_2\text{W}_{18}$ and $\text{NiPW}_{11}(\text{Ni}(\text{OH}_2)\text{PW}_{11}\text{O}_{39})^{5-}$ in the pH 5 medium where all these complexes are stable. The efficiencies for $\text{Ni}_3\text{P}_2\text{W}_{18}$ and $\text{Ni}_4\text{P}_2\text{W}_{18}$ turned out to be comparable. In contrast, NiPW_{11} shows a negligibly small activity toward the electrocatalytic reduction of nitrate in this medium.

Finally, comparisons of the efficiencies of several Ni-substituted tungstophosphates vis-à-vis the catalytic electroreduction of nitrate suggest that an increase of the Ni centers incorporated in stable sandwich-type polyoxoanions has a very beneficial effect.

The electrocatalytic behavior of **Fe6Ge2W18** toward the reduction of nitrite

and nitrate was tested at pH = 3. In the absence of either of the two NO_x , the voltammetric pattern is that of Fig. 29. Upon addition of even modest amounts of nitrite, a large cathodic current enhancement was observed, starting in a potential domain positive to the Fe-wave. This observation must be linked with the beneficial accumulation of electrons in the POM framework. It was checked that NO is also electrocatalytically reduced in the same potential domain. Concerning nitrate, it is worth reminding that a comparative study of several metal ion-substituted heteropolyanions including α_1 - and α_2 - $\text{P}_2\text{W}_{17}\text{M}$ and α_2 - $\text{P}_2\text{W}_{15}\text{Mo}_2\text{M}$ where $\text{M} \equiv \text{V}^{\text{IV}}, \text{Mn}^{\text{II}}, \text{Fe}^{\text{III}}, \text{Co}^{\text{II}}, \text{Ni}^{\text{II}}, \text{Cu}^{\text{II}}, \text{Zn}^{\text{II}}$ and \Rightarrow (where \Rightarrow indicates the absence of M) most heteropolyanions, except those substituted by Cu or Ni do not show any important electrocatalytic ability toward its reduction [160a]. Specifically, Fe^{III} -substituted heteropolyanions are not efficient in the electrocatalytic reduction of nitrate [160a]. Such observation complies with literature where Epstein et al. had shown that efficient oxidation of Fe^{II} by nitrate necessitates a catalyst [160b]. In contrast, the electrocatalytic reduction of nitrate was observed here when the first W-reduction processes were reached. Furthermore, the potential domain where this electrocatalysis was obtained is comparable with those of the best

Fig. 29 Cyclic voltammograms in a $2 \cdot 10^{-4}$ M solution of $\text{Fe}_6\text{Ge}_2\text{W}_{18}$ complex in pH = 3 acetate medium ($0.4\text{M CH}_3\text{COONa} + \text{ClCH}_2\text{COOH}$); superposition of the CVs run in the presence of $6 \cdot 10^{-3}$ M of nitrite and of $2 \cdot 10^{-1}$ M of nitrate; scan rate: 2 mV s^{-1} (taken from Ref. 107b).



HPA-based electrocatalysts [113]. Owing to the slightly positive location of the W-wave of $\text{Fe}_6\text{Ge}_2\text{W}_{18}$ relative, for example, to that of $[\text{Ni}_4\text{Mn}_2\text{P}_3\text{W}_{24}\text{O}_{94}]^{17-}$ [113] the electrocatalytic reduction of nitrate at pH 3 begins roughly 100 mV positive in the case of the former complex. Comparison of the nitrite and nitrate electrocatalysis patterns is enlightening: insofar as nitrite and NO are known to appear as intermediates in the reduction of nitrate on various metals, the potential locations of the corresponding waves would suggest that highly reduced species should be obtained in the electrocatalytic reduction of nitrate in the presence of $\text{Fe}_6\text{Ge}_2\text{W}_{18}$. Provisionally, the remarkable activity of $\text{Fe}_6\text{Ge}_2\text{W}_{18}$ in the electrocatalytic reduction of nitrate is worth emphasizing as it constitutes the first example, to our knowledge, in which such an efficiency is demonstrated for a Fe-containing POM. Finally and in agreement with expectations, it was noted that $\text{Fe}_6\text{Ge}_2\text{W}_{18}$ catalyses also the electroreductions of dioxygen and hydrogen peroxide.

22.7.2.1.2 Electrocatalytic Reduction of Dioxygen and Hydrogen Peroxide These two processes must be emphasized because reduction of dioxygen, and eventually hydrogen peroxide, features the usually claimed pathway for reoxidation of reduced POMs after the participation of the latter in oxidation processes. As a consequence, electrocatalysis of dioxygen and hydrogen peroxide reduction is a valuable catalytic test with most new POMs [154, 156, 161].

In aqueous solution, the catalytic reduction of hydrogen peroxide was observed on the wave corresponding to the reduction of Fe(III) to Fe(II) within $\alpha\text{-}[\text{Fe}(\text{OH}_2)\text{SiW}_{11}\text{O}_{39}]^{5-}$ and $\alpha\text{-}[\text{Fe}(\text{OH}_2)\text{P}_2\text{W}_{17}\text{O}_{61}]^{8-}$ [156]. The rate constants for the process triggered by the

Fe(II) forms were evaluated at 9×10^2 and $1.16 \times 10^4 \text{ M}^{-1} \text{ s}^{-1}$ for the two complexes respectively. The mechanism involves complicated competing reactions including Fe(II), Fe(III), Fe(IV), and Fe(V) complexes, species that are usually invoked in metalloporphyrin chemistry.

Two examples are selected to describe and discuss the electrocatalytic reduction of dioxygen, the first one with a TMSP [161] and the second one with a sandwich-type complex [162]. The discussion reflects the questions encountered also with usual plenary POMs.

Electrocatalytic reduction of dioxygen in the presence of $\alpha_2\text{-P}_2\text{W}_{15}\text{Mo}_2\text{Cu}$

The main features of the dioxygen electrocatalytic reduction in the presence of $\alpha_2\text{-P}_2\text{W}_{15}\text{Mo}_2\text{Cu}$, in a pH = 3 medium, are illustrated in Fig. 30(b) by a selection of cyclic voltammograms. The direct reduction of dioxygen on the glassy carbon surface is observed at a fairly negative potential. In contrast, its electrocatalysis occurs readily in the potential domain that was demonstrated previously to correspond mainly to the reduction of Mo centers. It is worth emphasizing that the voltammetric pattern indicates no obvious deposition of copper in this domain. Qualitatively, the efficiency of the catalysis is already revealed even for an excess parameter ($\gamma = C^\circ_{\text{O}_2}/C^\circ_{\text{POM}}$) as low as $\gamma = 2$. The catalytic efficiency CAT is a useful parameter and is defined as follows: $\text{CAT} = 100 \times [I_{(\text{POM}+\text{O}_2)} - I^d_{(\text{POM})}]/I^d_{(\text{POM})}$ where $I_{(\text{POM}+\text{O}_2)}$ is the peak current for reduction of the heteropolyanion (POM) in the presence of O_2 and $I^d_{(\text{POM})}$ is the corresponding diffusion peak current for the HPA alone. For $\gamma = 10$, CAT calculated at -0.060V is 2.5 times larger than for $\gamma = 2$. Whatever

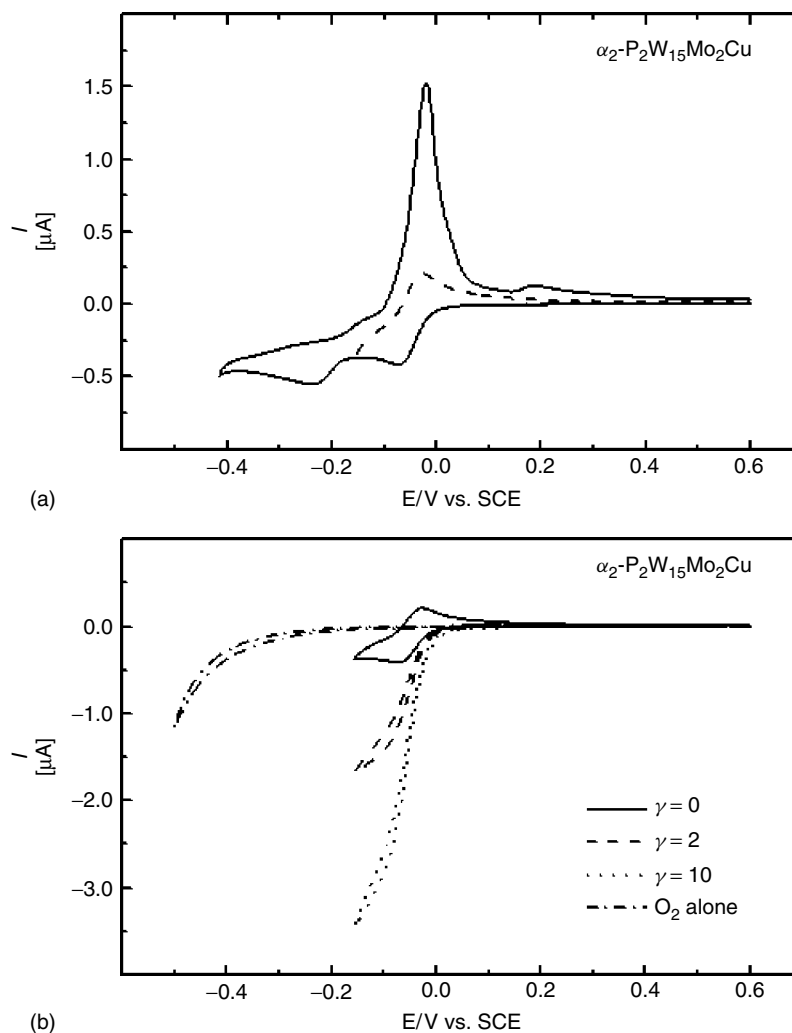


Fig. 30 Cyclic voltammograms (scan rate: 2 mV s^{-1}) observed in $0.2 \text{ M Na}_2\text{SO}_4 + \text{H}_2\text{SO}_4$ (pH 3); the working electrode was glassy carbon and the reference electrode was SCE. (a) $10^{-4} \text{ M } \alpha_2\text{-P}_2\text{W}_{15}\text{Mo}_2\text{Cu}$. The choice of the reversal potentials help to distinguish the various steps. (b) dioxygen alone and $10^{-4} \text{ M } \alpha_2\text{-P}_2\text{W}_{15}\text{Mo}_2\text{Cu}$ in the presence of different concentrations of dioxygen. For further details, see text (taken from Ref. 161).

the value of γ , the polarogram shape of the cyclic voltammogram at low scan rates must be noted. Also worthy of notice is the observation that the plateau current for these polarograms at fixed γ value does not depend on the scan

rate. These details facilitate the evaluation of the overall rate constant of the catalytic process [163] which is found to be: $k = 2.110^3 \text{ M}^{-1} \text{ s}^{-1}$. After completion of the dioxygen reduction experiments, the initial voltammogram under argon was

routinely restored by bubbling the inert gas through the solution. This result is an indication that no irreversible complex was formed between dioxygen and the oxidized POM. At slow scan rate, the electrocatalytic activity is also observed on the other waves beyond the first one. A correct comparison with the activity of a solution of pure copper sulfate is plagued or, at least, made difficult by several parameters: the difference in diffusion coefficient between the POM and Cu^{2+} ; some deposition of copper modifying the electrode surface area; the potential at which the catalysis begins, and so on. Nonetheless, even ignoring these shortcomings, the catalytic efficiency of the POM was found to remain better than that of Cu^{2+} alone. A remarkable example of additivity and/or cooperativity of the influences of Mo and Cu centers was found in this study.

The closeness of the reduction potentials of Mo and Cu centers within the molecule of $\alpha_2\text{-P}_2\text{W}_{15}\text{Mo}_2\text{Cu}$ at most pH values, where the catalysis occurs, raises the question of the actual role of each particular atom in the electrocatalytic reduction of dioxygen. Various parameters of the system were studied to clarify the situation. The lacunary heteropolyanion $\alpha_2\text{-P}_2\text{W}_{15}\text{Mo}_2$ develops no dioxygen reduction catalysis in the potential domain of reduction of Mo moieties, even though the Mo centers are reduced at the same potential in both the lacunary and the Cu-substituted complexes. Indeed, a catalytic effect is seen to start at the substantially more negative potential corresponding to the first reduction wave of W-centers. Provisionally, it is worth noting that such catalysis of the dioxygen reduction on the W waves is encountered in most of the heteropolyanions studied to-date. Keeping specifically with the Mo atom, it was found also that the first wave of $\alpha_2\text{-P}_2\text{W}_{15}\text{Mo}_3$

does not show any catalytic activity toward dioxygen, even though sufficiently energetic electrons are available. It must be concluded, at the very least, that the Mo centers alone within $\alpha_2\text{-P}_2\text{W}_{15}\text{Mo}_2\text{Cu}$ are not the loci of the observed catalysis process.

$\alpha_2\text{-P}_2\text{W}_{17}\text{Cu}$ was selected to test and compare the catalytic ability of another closely related Cu-containing heteropolyanion in the dioxygen electrocatalytic reduction. Its electrochemistry at pH 3 was studied previously [90]. Its first wave was observed at a more negative potential than the Mo wave of $\alpha_2\text{-P}_2\text{W}_{15}\text{Mo}_2\text{Cu}$. Copper deposition during the first reduction wave of $\alpha_2\text{-P}_2\text{W}_{17}\text{Cu}$ was revealed by the characteristic stripping oxidation wave on potential reversal [90]. In this compound, the first W-wave was shown to overlap partly with the copper wave. Spectroelectrochemistry studies indicated, however, that the two-electron reduction of Cu^{2+} is complete before any significant reduction of W moieties.

In this work, the electrocatalytic dioxygen reduction by reduced $\alpha_2\text{-P}_2\text{W}_{17}\text{Cu}$ is indeed observed. In contrast with the case of $\alpha_2\text{-P}_2\text{W}_{15}\text{Mo}_2\text{Cu}$, the catalytic wave current intensity depends on the scan rate. The characteristic stripping oxidation wave of the copper deposited during the cathodic processes diminishes drastically upon increase of the γ values. All these observations together point to a prominent role of the copper center within $\alpha_2\text{-P}_2\text{W}_{17}\text{Cu}$ in the catalytic reduction of dioxygen, albeit at a substantially more negative potential than observed with $\alpha_2\text{-P}_2\text{W}_{15}\text{Mo}_2\text{Cu}$.

Figure 31 compares the currents of the catalytic waves obtained in identical experimental conditions with $\alpha_2\text{-P}_2\text{W}_{15}\text{Mo}_2\text{Cu}$ and $\alpha_2\text{-P}_2\text{W}_{17}\text{Cu}$ respectively. The electrocatalytic process is less favorable with the latter complex,

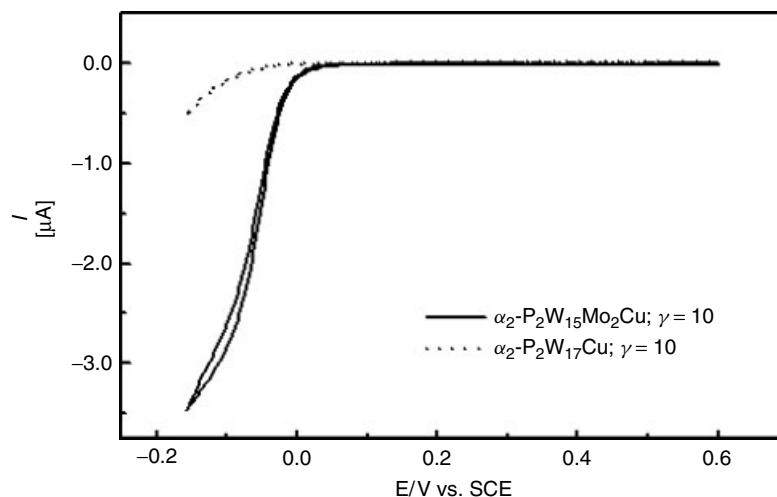


Fig. 31 Cyclic voltammograms (scan rate: 2 mV s^{-1}) observed in $0.2 \text{ M Na}_2\text{SO}_4 + \text{H}_2\text{SO}_4$ (pH 3); the working electrode was glassy carbon and the reference electrode was SCE. Comparison of the behaviors of $10^{-4} \text{ M } \alpha_2\text{-P}_2\text{W}_{17}\text{Cu}$ and $10^{-4} \text{ M } \alpha_2\text{-P}_2\text{W}_{15}\text{Mo}_2\text{Cu}$ in the presence of dioxygen. For further details, see text (taken from Ref. 161).

in which the catalysis can be admitted to be triggered essentially by the Cu center. In other words, no synergism could be observed between the W and Cu influences in the explored potential domain. In contrast, this result, associated with the lack of “intrinsic” activity of Mo centers, highlights the cooperativity between Mo and Cu centers within $\alpha_2\text{-P}_2\text{W}_{15}\text{Mo}_2\text{Cu}$ in the electrocatalytic dioxygen reduction.

The question arises as to the actual sequence of events that end up in the reduction of dioxygen into water. Even though complementary investigation is needed before a complete answer could be proposed, several observations are worth mentioning provisionally. The reoxidation of reduced heteropolyanions by dioxygen after the catalytic processes in which they participate is a popular practice. Its mechanism was generally and indistinctly explained to go through an intermediate adduct formation accompanied by inner sphere electron transfers [164].

Recently a clarification by Duncan and Hill [165] established clearly that simple outer sphere electron transfer might be the actual pathway in the case of unsubstituted POMs; in the case of vanadium-substituted derivatives, the conclusion was less clear-cut. The present results should be considered in the framework of metal ion-substituted complexes. In other words, the reasoning parallels those used in the dioxygen electroreduction by copper-containing organometallic complexes. In these examples, “Cu(I)–O₂” constitutes the favorite intermediate [166]. Here, the proximity of the reduction potentials of Mo and Cu²⁺ centers within $\alpha_2\text{-P}_2\text{W}_{15}\text{Mo}_2\text{Cu}$ at appropriately selected pH values suggests strongly that such a mechanism could be operative. Furthermore, the efficiency of the catalysis would indicate that the reduction potential of the adduct is very close to or even more positive than that of Mo centers. Tentatively, mixed acceptor orbitals containing both Mo and

Cu contributions can be suggested to exist.

Finally, the possibility that a specificity of the Mo/Cu association exists to favor the observed cooperativity should be considered. Even though the present work is performed in homogeneous conditions, a parallel was, tentatively, made with the case of catalytic solid electrodes prepared for the reduction of dioxygen into water: specifically, $(\text{Ru}_{1-x}\text{Mo}_x)_y\text{SeO}_z$ layers containing very small amounts of Mo realize the four-electron reduction of dioxygen in acidic media [167]. The presence of Mo was demonstrated to be required to favor the catalytic process. The mechanistic assumption that guided to the synthesis and study of such layers is that oxygen is adsorbed by Mo due to its higher interaction energy among the surface atoms, but the electrocatalysis must occur at the ruthenium. Such cooperativity can be considered as a successful operational hypothesis.

Reduction of dioxygen and hydrogen peroxide by $\text{Cu}_4\text{X}_4\text{W}_{30}$ (X = P or As) Direct

dioxygen reduction occurs at fairly negative potential on glassy carbon electrode [115]. In the presence of the sandwich-type complexes of this work, this reduction is observed readily on the first Cu^{2+} reduction wave as shown in Fig. 32. For $\gamma = 10$, the catalytic efficiency, CAT, reaches values as high as 615 and 722% for $\text{Cu}_4\text{P}_4\text{W}_{30}$ and $\text{Cu}_4\text{As}_4\text{W}_{30}$ respectively. The small difference between the two CAT values result from the fact that Cu^{2+} is slightly more easily reduced in the As-containing complex. Analogous results were obtained recently with Mn-sandwich complexes [110].

The possible final products are hydrogen peroxide and water. Electrolyses were performed at the peak potential location E_{pc1} of the first Cu^{2+} reduction wave to try and determine the identity of the final product. In each experiment, enough charge was passed through the solution to generate 13 mM to 27 mM H_2O_2 if this substance were the final product. At the end of each electrolysis, the amount of generated H_2O_2 was tested by the spectrophotometry, using

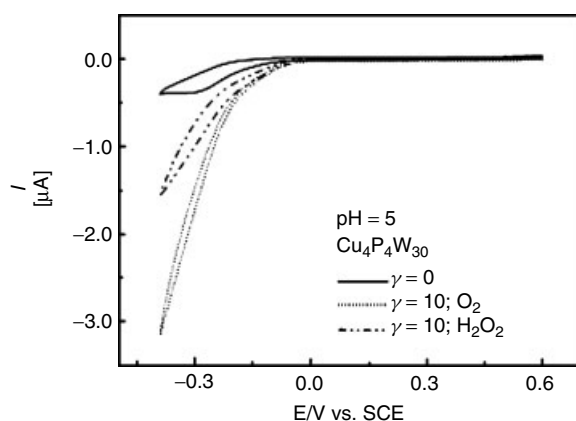


Fig. 32 Electrocatalysis of O_2 and H_2O_2 reductions in the presence of 10^{-4} M $\text{Cu}_4\text{P}_4\text{W}_{30}$ in a pH 5 medium. The scan rate was 2 mV s^{-1} , the working electrode was glassy carbon and the reference electrode was SCE. For more detailed information see text (taken from Ref. 115).

the sensitive $\text{Ti}(\text{SO}_4)_2$ as reagent [168]. In all batches, only traces of H_2O_2 were detected. This observation indicates that the final product of the reduction of dioxygen by the present sandwich complexes is essentially water. The intermediacy of H_2O_2 can be suspected, as traces of this substance are detected. However, Fig. 32 confirms that H_2O_2 is also efficiently reduced in the presence of $\text{Cu}_4\text{P}_4\text{W}_{30}$, for example. Finally, it must be concluded that the electrocatalytic reduction of dioxygen features an overall four-electron process.

Finally, it is worth noting that much the same results as obtained here in the reduction of nitrate, nitrite, dioxygen, and hydrogen peroxide with $\text{Cu}_4\text{As}_4\text{W}_{30}$ are observed also with the semivacant analog $\text{H}_8\text{Cu}_4\text{As}_2\text{W}_{30}$ ($[\alpha\beta\beta\alpha\text{-(Cu}^{\text{II}}\text{OH}_2)_2(\text{Cu}^{\text{II}})_2(\text{AsW}_{15}(\text{OH}_2)_3(\text{OH})\text{O}_5)_2]^{12-}$).

Electrocatalytic reduction of dioxygen and hydrogen peroxide in the presence of $\text{Mn}_2\text{Fe}_2\text{X}_4$ (X = P or As) In this example selected from recent work [162], the studies of the electrocatalytic reductions of O_2 and H_2O_2 were performed in a pH = 5 medium. The efficiency of the catalysis is again evaluated by an excess parameter γ , which is defined as $C^\circ(\text{O}_2)/C^\circ(\text{POM})$ for dioxygen and $C^\circ(\text{H}_2\text{O}_2)/C^\circ(\text{POM})$ for hydrogen peroxide (C° = concentration of the relevant species indicated in parentheses). The catalytic efficiency (CAT) is defined as follows: $\text{CAT} = 100 \times [\text{I}(\text{POM} + \text{O}_2 \text{ or } \text{H}_2\text{O}_2) - \text{I}^{\text{d}}(\text{POM})]/\text{I}^{\text{d}}(\text{POM})$, where $\text{I}(\text{POM} + \text{O}_2 \text{ or } \text{H}_2\text{O}_2)$ is the current for the reduction of the POM in the presence of O_2 or H_2O_2 and $\text{I}^{\text{d}}(\text{POM})$ is the corresponding diffusion current for the POM alone. Selected values of cat-

Tab. 14 Selected values of catalytic efficiencies measured at $E = -420$ mV vs. SCE in a pH 5 medium (1 M $\text{CH}_3\text{COOLi} + \text{CH}_3\text{COOH}$) for O_2 and H_2O_2 reductions with various electrocatalysts^a

Complex	CAT	
	O_2	H_2O_2
$\text{Zn}_2\text{Fe}_2\text{As}_4$	680	334
$\text{Zn}_2\text{Fe}_2\text{P}_4$	817	222
$\text{Mn}_2\text{Fe}_2\text{As}_4$	944	464
$\text{Mn}_2\text{Fe}_2\text{P}_4$	1055	380

^aThe scan rate was 2 mV s^{-1} . The catalytic efficiency (CAT) is defined as follows:

$\text{CAT} = 100 \times [\text{I}(\text{POM} + \text{O}_2 \text{ or } \text{H}_2\text{O}_2) - \text{I}^{\text{d}}(\text{POM})]/\text{I}^{\text{d}}(\text{POM})$, where $\text{I}(\text{POM} + \text{O}_2 \text{ or } \text{H}_2\text{O}_2)$ is the current for the reduction of the POM in the presence of O_2 or H_2O_2 and $\text{I}^{\text{d}}(\text{POM})$ is the corresponding diffusion current for the POM alone.

alytic efficiencies (CAT) for the reduction of dioxygen and hydrogen peroxide are included in Table 14. CAT values were measured at -420 mV vs. SCE, in the potential domain of the Fe(III)-reduction waves.

Corresponding CAT values for $\text{Mn}_2\text{Fe}_2\text{X}_4$ (X = P or As) were also measured and included for comparison. Under the same experimental conditions, the phosphorus-containing complexes, $\text{M}_2\text{Fe}_2\text{P}_4$ (M = Zn(II) or Mn(II)), are more efficient than their arsenic analogs, $\text{M}_2\text{Fe}_2\text{As}_4$ (M = Zn(II) or Mn(II)), for dioxygen reduction, while the opposite is true for hydrogen peroxide reduction. This observation underscores the difficulty for anticipating which electrocatalyst would be more efficient when an inner sphere pathway is operative. The electrocatalytic

processes observed here remain efficient in other media, and they establish the utility of the Fe(III) centers within these mixed-metal sandwich complexes even in media of low proton availability. There is still ample room for optimization of the selected media for efficient electrocatalytic processes within these compounds.

Examination of the dioxygen and hydrogen peroxide electrocatalytic processes discussed here may also shed some light on possible reaction pathways. Dioxygen does not coordinate to Fe(III) but it does coordinate to Fe(II). Then, the presence of another reduced Fe center could drive the catalytic process to completion by carrying out immediate further reduction of the Fe–O₂ adduct. In-line with these observations, the

measured catalytic efficiencies decrease when the number of F''-centers decrease [111a, 1]. Also noteworthy is that the synthesis of $M_2Fe_2X_4$ ($M = Zn(II)$ or $Mn(II)$; $X = P$ or As) from Fe_2X_4 ($X = P$ or As) diminishes the overall negative charge of the POM, rendering its reduction more facile, and ultimately, saving energy during the electrocatalytic process.

Indeed, other electrocatalytic processes were studied, including the pioneering work on chlorate reduction by the six-electron reduction product of 12-molybdophosphate in water-dioxane solutions [169]. This process, extended to bromate, has become a classical test of the electrocatalytic abilities of several POMs [see Table 13].

Tab. 15 Electrochemical oxidations catalyzed by heteropolyanions

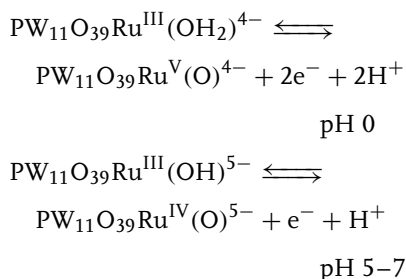
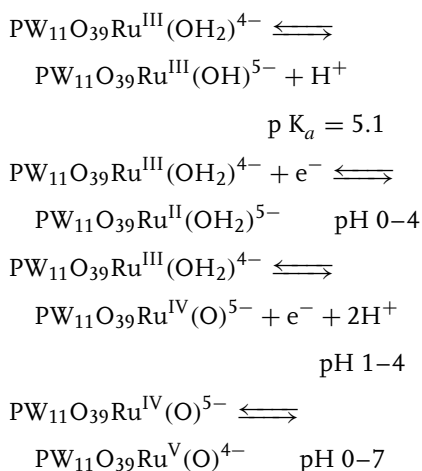
Catalyst	Substrate	Products	Conditions	References
α -PW ₁₁ O ₃₉ Ru(H ₂ O) ⁴⁻	Me ₂ SO	Me ₂ SO ₂	Electrolysis, sulfate buffer (pH 1) 1.1 V vs. SCE, divided cell, room temperature	85
	Alcohols	carbonyl compounds	acetate buffer, room temperature	169
α -Q ₅ SiW ₁₁ O ₃₉ Ru ^a	Olefins	aldehydes	double-mediator electrolysis CH ₂ Cl ₂ -H ₂ O, NaIO ₃ , undivided cell, 50° C, PbO ₂ anode, Pt cathode	170
α -PW ₁₁ O ₃₉ Cr(H ₂ O) ⁴⁻	Alcohols	carbonyl compounds	Sulfate buffer (pH 1), room temperature	171
P ₂ W ₁₇ O ₆₁ Cr(H ₂ O) ⁷⁻ α -SiW ₁₁ O ₃₉ Mn(H ₂ O) ⁶⁻	Alcohols	carbonyl compounds	Electrolysis, phosphate buffer (pH 6) 1.25 V vs. Ag/AgCl, divided cell, room temperature, C anode, Pt cathode	153g + h
α_2 -P ₂ W ₁₇ O ₆₂ V ⁸⁻	NADH	NAD ⁺	Phosphate buffer (pH 7), room temperature	82, 172–174
α_1 -P ₂ W ₁₇ O ₆₂ V ⁸⁻ α_1 -P ₂ W ₁₇ MoO ₆₂ ⁶⁻				

^aQ = tetrabutylammonium.

22.7.2.2 Electrocatalytic Oxidations

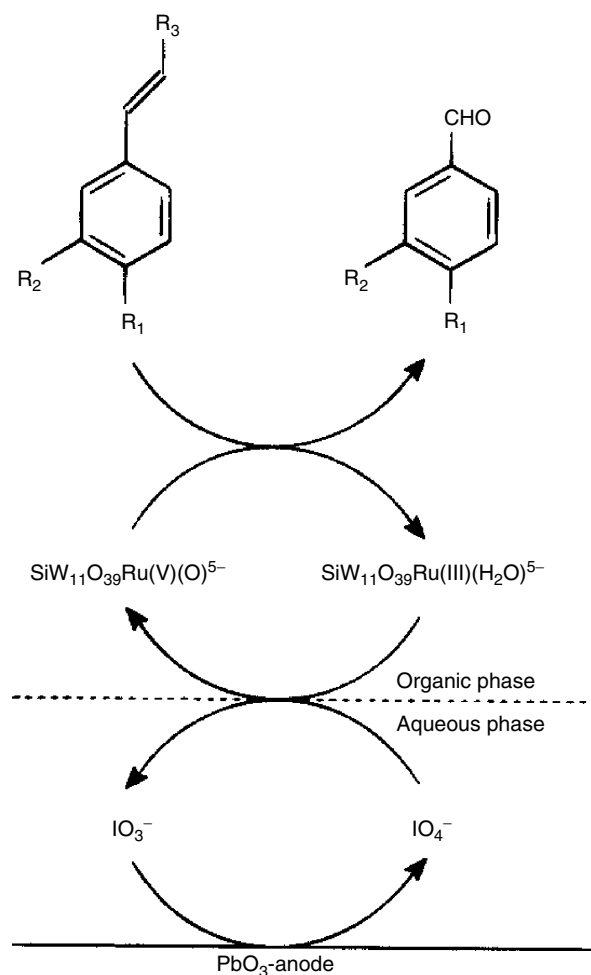
Table 15 gathers the main electrocatalytic processes triggered by POMs dissolved in solution. Most of these examples highlight the prominent role of the metal substituted into the POM framework. The catalyst can be considered as soluble POM-supported catalytic centers, with the advantage, relative to their organic counterparts, of thermal stability, robustness, and inertness toward oxidizing environments of the ligand. With this view, most electrochemically-assisted catalytic oxidation reactions described in the literature were designed to parallel analogous known effective processes in organometallic chemistry.

22.7.2.2.1 $[\text{Ru}^{\text{III}}(\text{H}_2\text{O})\text{PW}_{11}\text{O}_{39}]^{4-}$ and $[\text{Ru}^{\text{III}}(\text{H}_2\text{O})\text{SiW}_{11}\text{O}_{39}]^{5-}$ as an Electrochemical Oxygen Transfer Catalysts Depending on the pH domain studied in acidic solution, $[\text{Ru}^{\text{III}}(\text{H}_2\text{O})\text{PW}_{11}\text{O}_{39}]^{4-}$ ($\text{PW}_{11}\text{O}_{39}\text{Ru}^{\text{III}}(\text{H}_2\text{O})$ for short) was demonstrated to exhibit three reversible redox couples corresponding to the Ru center processes [85]. These redox couples can be assigned to the aquaruthenium (II), oxoruthenium (IV), and oxoruthenium (V) as sketched in the following equations:

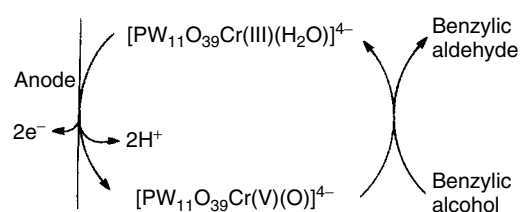


The two-electron oxidation to generate the oxoruthenium(V) constitutes the basis of an electrocatalytic oxidation of Dimethylsulfoxide to dimethylsulfone with >90% current efficiency and a modest total turnover of 40 for the catalyst. Substitution of π -acids to the water molecule stabilizes the Ru(II) form and shifts all the redox potentials in the positive direction, so that the Ru(IV/III) and Ru(V/III) couples are no longer seen on the voltammograms, owing to the absence of an aqua ligand [175]. The oxoruthenium (V) species were also shown to oxidize alcohols. The quaternary ammonium salt of the tungstosilicate analog, $\text{SiW}_{11}\text{O}_{39}\text{Ru}^{\text{III}}(\text{OH}_2)^{5-}$ was used to catalyze the periodate-mediated oxidative cleavage of olefins [170, 176]. However, electrochemical investigation and direct electrochemical oxidation of this compound failed, as also the electrochemical regeneration of the active oxoruthenium(V) species. Yet, Steckhan and Kandzia [177] found an elegant two-phase double-mediator system based on this complex. In this system sketched in Sch. 11, the IO_4^- was regenerated at the PbO_2 anode in the aqueous phase and various olefins were converted to the corresponding aldehydes in the organic phase.

22.7.2.2.2 $\alpha\text{-}[\text{Cr}^{\text{III}}(\text{H}_2\text{O})\text{PW}_{11}\text{O}_{39}]^{4-}$ and $\alpha_2\text{-}[\text{Cr}^{\text{III}}(\text{OH}_2)\text{P}_2\text{W}_{17}\text{O}_{61}]^{7-}$ as Oxygen Transfer Catalysts in Electrochemistry Following the intensive study of the oxygen

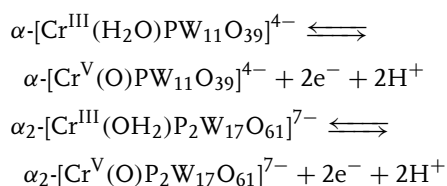


Scheme 11 Indirect electrochemical oxidation cleavage of alkenes using a double-mediator system consisting of IO_4^- and ruthenium tungstosilicate (taken from Ref. 8).



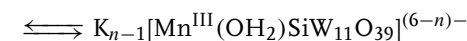
Scheme 12 Electrocatalytic oxidation of benzylic alcohol to benzylic aldehyde using $[\text{Cr}^{\text{III}}(\text{OH}_2)\text{PW}_{11}\text{O}_{39}]^{4-}$ as redox catalyst taken from Ref. 8).

transfer abilities of these POMs by the groups of Pope [171] and Hill [178], Rong and Anson evaluated the possibility to use them as electrocatalysts in water [179]. The reduction of Cr(III) to Cr(II) could not be observed by cyclic voltammetry at pH = 1. The following steps were demonstrated:

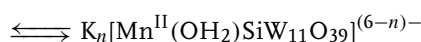
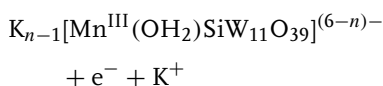


The electrochemically generated $\text{Cr}^{\text{V}}=\text{O}$ complexes are able to oxidize alcohols to carbonyl compounds according to the following catalytic cycle, sketched in Sch. 12.

22.7.2.2.3 A Detailed Study of $\text{K}_n[\text{Mn}^{\text{II}}(\text{OH}_2)\text{SiW}_{11}\text{O}_{39}]^{(6-n)-}$ as Oxidation Electrocatalyst Pope and coworkers [112] were the first to identify that the chemical or electrochemical oxidation of Mn(II) center within $\text{K}_n[\text{Mn}^{\text{II}}(\text{OH}_2)\text{SiW}_{11}\text{O}_{39}]^{(6-n)-}$ yields a $\text{Mn}^{\text{IV}}(\text{OH})$ complex rather than a $\text{Mn}^{\text{V}}(\text{O})$ complex. An electrochemical confirmation of the formation of the complex $\text{K}_{n-1}[\text{Mn}^{\text{IV}}(\text{OH})\text{SiW}_{11}\text{O}_{39}]^{(6-n)-}$ was obtained in cyclic voltammetry by observing the average redox potential when pH and potassium concentration were changed in the electrolyte [153g,h]. Reproducible cyclic voltammograms could be run only either after pretreatment of the electrode by continuous cycling between 1.3 and 0 V vs. Ag/AgCl or by starting the CV from 1.3 V where the manganese was oxidized to Mn(IV). The following overall steps are in agreement with observations.

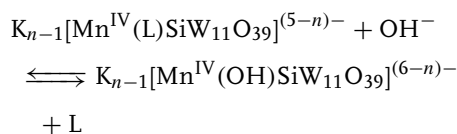
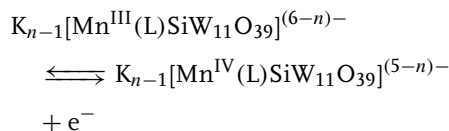
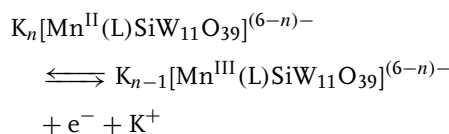
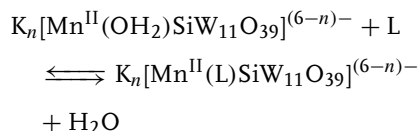


($E_{1/2} = 0.99\text{V}$ vs. Ag/AgCl at pH = 6.0)

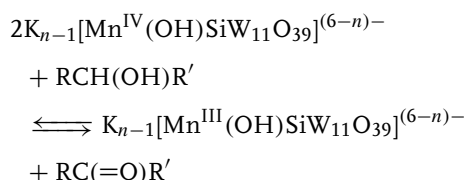


($E_{1/2} = 0.53\text{V}$ vs. Ag/AgCl at pH = 6.0)

These steps were explained in more detail by the following sequence of events, by taking into account the competition between a water molecule and a counterion L in the electrolyte ($\text{L} = \text{H}_2\text{PO}_4^-$ or HPO_4^{2-} in phosphate buffer) to occupy the sixth site on the Mn atom.



The complex $\text{K}_{n-1}[\text{Mn}^{\text{IV}}(\text{L})\text{SiW}_{11}\text{O}_{39}]^{(6-n)-}$ was shown to be efficient in the oxidation of different alcohols via hydride ion transfer.



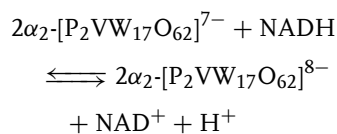
22.7.2.2.4 Catalytic Oxidation of NAD(P)H: A Continuously Improved Selection of Suitable POMs

This research is triggered by at least two reasons: (1) the importance of NAD(P)H/NAD(P)⁺ redox couples in biological systems is known, as is known the dependence of oxidation mechanisms on the oxidants [14, 82, 172–174]; (2) the possibility of developing amperometric biosensors for NAD(P)⁺-dependent dehydrogenases. As a consequence, much attention is devoted to the regeneration of these coenzymes in their reduced or oxidized forms for their application in biosensors or in enzymatic synthesis [180]. Here, we are concerned with electrochemical regeneration [181].

However, the oxidation of NAD(P)H to NAD(P)⁺ at practical rates on most electrode materials proceeds only at high overpotentials [182] and often fouling of the electrode surface has been observed. This situation induces the search for suitable mediators or electrode modification processes to accelerate the highly irreversible oxidation of NAD(P)H. The stability of the reaction products in the presence of each other is also a necessary condition for usefulness.

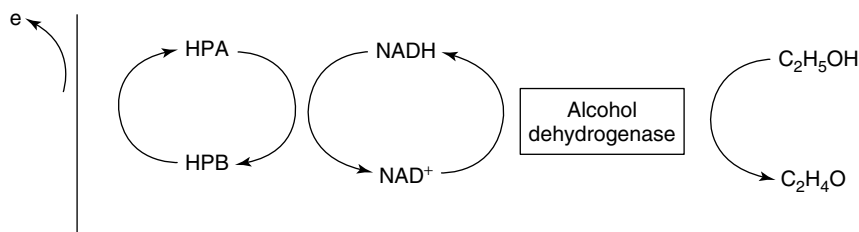
The first studies were devoted to NADH. The challenge was to select POMs likely to meet all these criteria and be stable in neutral alkaline media. As a matter of fact, quantitative studies in fairly acidic

solutions are precluded by the known rapid hydration of NADH below pH = 6. Nadjö and Keita demonstrated an efficient oxidation of NADH by several vanado-tungstophosphoric heteropolyanions, stable at pH = 7 [14, 82, 172–174]. The correct stoichiometry of NADH to POM was found, by spectrophotometry and coulometry, to be 1 : 2, thus indicating that the POM acts as a one-electron oxidant. The stability of the mixtures was established. In addition, complete regeneration of NADH was obtained from NAD⁺ in the mixtures with the heteropolyblue (HPB) in the presence of alcohol dehydrogenase (ADH) and ethanol. Thus, the catalytic process sketched in Sch. 13 is fully established.



The kinetics of NADH oxidation by three vanado-tungstodiphosphoric species were studied at pH = 7 by the stopped flow technique [82], giving values in complete agreement with electrochemistry results to be discussed in the following.

Figure 33 shows a representative example of the oxidation of NADH by POMs using cyclic voltammetry at a scan rate of 5 mV s⁻¹. Other examples can be found in the original papers. Typically, the system $\alpha_1\text{-[P}_2\text{VW}_{17}\text{O}_{62}]^{7-}$ /NADH is shown. The



Scheme 13 General catalytic redox process of NADH triggered by POMs (taken from Ref. 174).

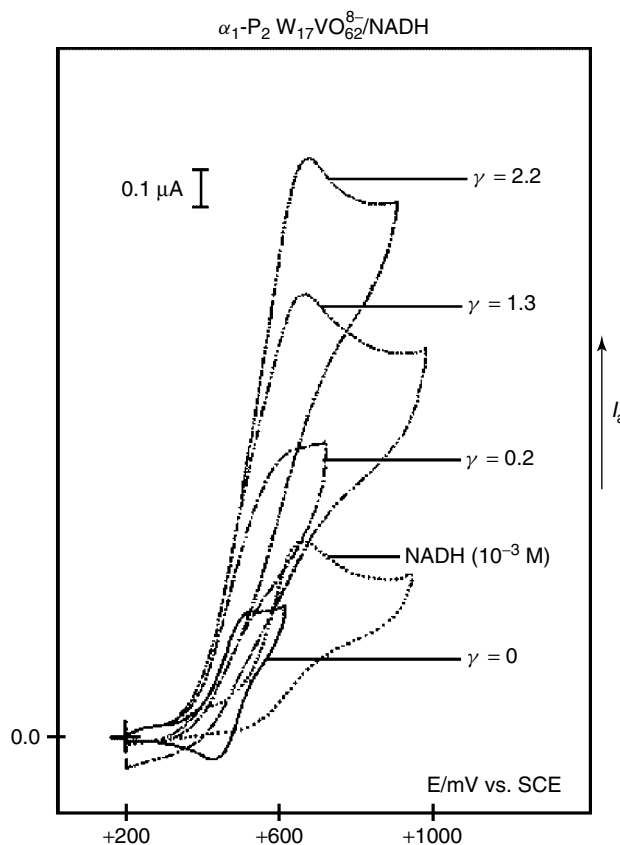


Fig. 33 Cyclic voltammograms obtained for the system $\alpha_1\text{P}_2\text{W}_{17}\text{VO}_{62}^{8-}/\text{NADH}$. Electrolyte pH 7 phosphate buffer. Reference electrode SCE; working electrode: 1 mm diameter Pt disk. The solutions contain 10^{-3} M $\alpha_1\text{P}_2\text{W}_{17}\text{VO}_{62}^{8-} + 10^{-3}\gamma$ M NADH, except for the one containing 10^{-3} M NADH alone. Scan rate $v = 5 \text{ mV s}^{-1}$ (taken from Ref. 174).

excess parameter ($\gamma = C_{\text{NADH}}^{\circ}/C_{\text{POM}}^{\circ}$) values appear on each curve. It is worth noting, in Fig. 33, the cyclic voltammogram associated with the first redox system of the POM and corresponding to a one-electron diffusion-controlled process ($\gamma = 0$). Also, the cyclic voltammogram featuring the direct oxidation of NADH on the electrode surface in the same medium is shown. The other curves in this figure show the evolution of the CV of the POM upon addition of various amounts

of NADH. For $\gamma \neq 0$, it is observed that the anodic current component of the one-electron system of the HPB increases substantially and the corresponding reduction process is suppressed at the scan rate used for these CVs. The evolution of the CVs is easily understood on the basis of a fast oxidation of NADH by the oxidized form of the POM.

Determinations of rate constants for the catalytic process were carried out by double potential step chronocoulometry

Tab. 16 Standard potential for the first redox system of each POM and second-order rate constant k derived from DPSC experiments on HPB/NADH systems at pH = 7. Each value of k is the average of at least five experiments. The values of γ are not necessary, but have been added to give a better idea of the experimental conditions (taken from Ref. 174)

HPB	$\alpha_1\text{-P}_2\text{W}_{17}\text{VO}_{62}^{8-}$	$\alpha_1\text{-P}_2\text{W}_{17}\text{MoO}_{62}^{7-}$	$\alpha_2\text{-P}_2\text{W}_{17}\text{VO}_{62}^{8-}$	$\text{P}_2\text{W}_{16}\text{V}_2\text{O}_{62}^{9-}$	$\alpha_2\text{-P}_2\text{W}_{17}\text{MoO}_{62}^{7-}$
E° (mV vs. SCE)	477.5	395.5	392.5	277.5	225
γ	10	10	10	10	20
K ($\text{M}^{-1} \times \text{s}^{-1}$)	1.5×10^4	6.9×10^2	6.4×10^2	7.1	1.2

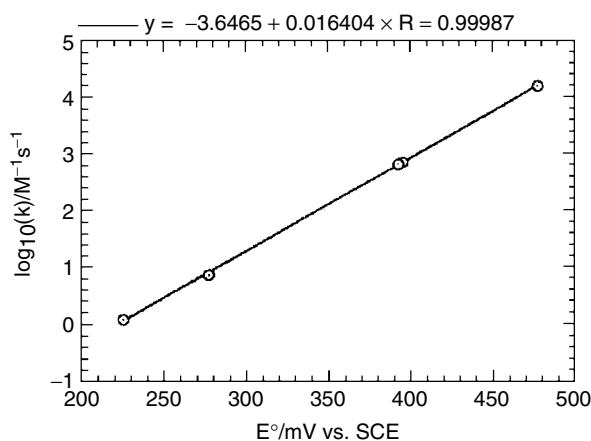


Fig. 34 Plot of $\log k$ versus the one-electron redox potentials E of the POMs (taken from Ref. 174).

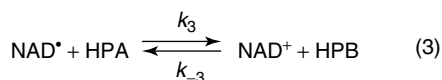
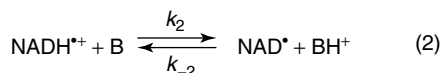
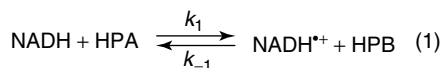
[183]. The experiments were performed under pseudo first order rate conditions. The results are gathered in Table 16, which also gives the standard potential for the first redox system of each POM. Figure 34 shows the plot of $\log_{10}k$ as a function of the one-electron redox potentials of the POMs. A straight line is obtained with a slope of 16.4 V^{-1} .

A detailed mechanistic pathway could be written (Sch. 14) and discussed.

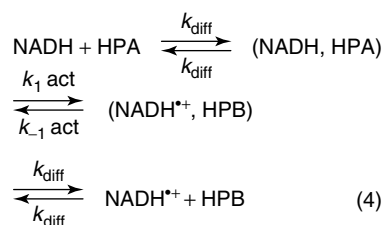
It is shown first that hydride transfer is not a likely reaction pathway. The rate-limiting step is established to be the initial one-electron transfer by using rate constants obtained by independent

measurements. Then to go deeper into the mechanism, the initial one-electron rate-limiting step was developed into three successive steps in Sch. 15 in which (NADH, HPA) and (NADH⁺, HPB) represent the reactants in their reaction sites, whereas NADH + HPA and NADH⁺ + HPB represent the reactants and products beyond the average distance of diffusion; k_{diff} is the diffusion-limited rate constant, k_{1act} and $k_{\text{-1act}}$ are the activation-controlled rate constants. Each of these steps could be, in principle, rate-limiting [184]. However, the experimental results in Fig. 34 indicate that the diffusional separation of the HPB/NADH⁺ pair is rate limiting without

Scheme 14 Detailed mechanistic NADH oxidation pathway suggested by the experiments with POMs (taken from Ref. 174).



Scheme 15 The initial one-electron rate-limiting step in the oxidation of NADH by the POMs studied in this work (taken from Ref. 174).



any tendency to observe a rate-limiting electron hop. A value of $E^\circ = +0.80 \text{ V}$ was determined for the $\text{NADH}/\text{NADH}^+$ couple at $\text{pH} = 7$.

However, a pH of 8 or 9 is more favorable to shift the overall equilibrium toward the oxidized product. Taking this remark into account, Keita and Nadjio showed recently that efficient POMs exist that meet these conditions [185]. A preliminary work is being published. The series of V-substituted derivatives selected in this work contain several POMs stable in their oxidized and reduced forms in alkaline media, thus guaranteeing the stability of the species generated during the catalytic process. The preliminary study is devoted to the electrocatalytic oxidation of NADPH, a substrate closely related to NADH, with the same importance *in vivo* and *in vitro*.

Figure 35(a) shows the current enhancements accompanying the addition of increasing amounts of NADPH to a pH 8 solution of $\text{P}_2\text{V}_2\text{W}_{16}$. The current intensity increase is observed readily at the

reduction potential of the first V center. It is worth noting the high efficiency of the electrocatalysis, even though modest γ values were used (γ is the excess parameter defined here as $\gamma = C^\circ(\text{NADPH})/C^\circ(\text{POM})$). To characterize the process itself, the catalytic efficiency (CAT) is defined as follows: $\text{CAT} = 100 \times [I(\text{POM} + \text{NADPH}) - I^d(\text{POM})]/I^d(\text{POM})$, where $I(\text{POM} + \text{NADPH})$ is the current for the reduction of the POM in the presence of NADPH and I^d is the corresponding diffusion current for the POM alone. In the present experiments, CAT values of 403 and 730% were calculated for $\gamma = 10$ and $\gamma = 20$ respectively at +308 mV vs. SCE. Figure 35(b) shows the direct NADPH oxidation wave on the glassy carbon electrode surface and the rising section of the catalytic wave for $\gamma = 20$ in the same pH 8 medium. It is clear from this figure that no direct oxidation of NADPH is observed in this potential domain explored in Fig. 35(a). Furthermore, the substantial improvement in potential brought about

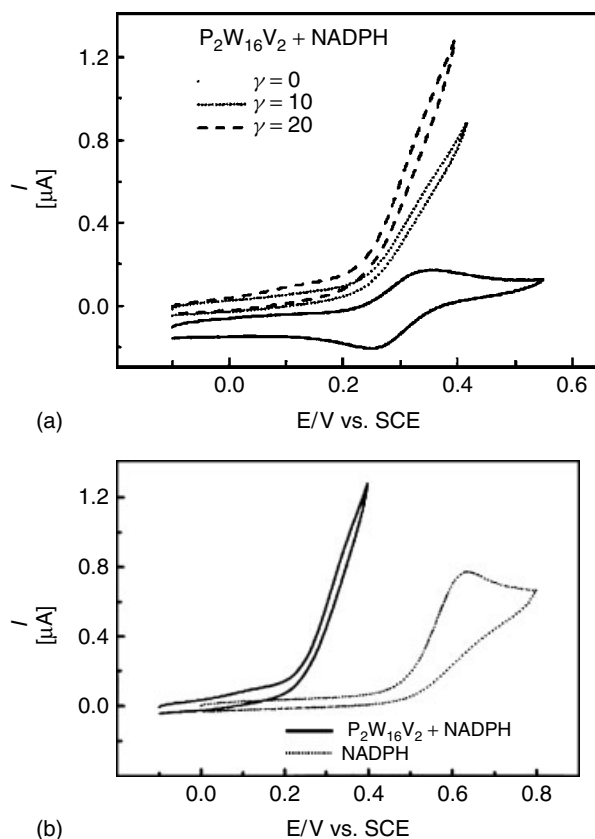


Fig. 35 Cyclic voltammograms for the electrocatalytic oxidation of NADPH by 2×10^{-4} M $\text{P}_2\text{W}_{16}\text{V}_2$, in pH 8 buffer (50 mM TRIS + 0.5 M Na_2SO_4 + H_2SO_4); the scan rate was 2 mV s^{-1} , the working electrode was glassy carbon (3 mm diameter disk), the reference electrode was SCE. (a) The excess parameter values for NADPH were $\gamma = 10$ and $\gamma = 20$ respectively; (b) Comparison of the catalytic process ($\gamma = 20$) by $\text{P}_2\text{W}_{16}\text{V}_2$ with the direct oxidation of NADPH on the glassy carbon electrode (taken from Ref. 185).

by the catalysis for the oxidation of NADPH is obvious. Double potential step chronocoulometry experiments [172] performed between 0 and +400 mV vs. SCE had allowed the value of the second-order rate constant to be evaluated: $k = 3.5 \times 10^3 \text{ M}^{-1} \text{ s}^{-1}$. The present experiments were performed in deaerated solution. However, it has been checked that an inert

atmosphere was not necessary, because the V^{V} and V^{IV} forms of $\text{P}_2\text{V}_2\text{W}_{16}$ are insensitive to the presence of dioxygen. This remark is important as that it opens the way for working in conditions close to those of biological environments, in contrast with most mediators, especially quinonic mediators proposed in the literature [186].

22.8 Conclusion

This chapter describes most of the significant electrochemical behaviors of POMs. The variety of these behaviors justifies that these molecular oxides are studied in almost every domain of chemistry from synthesis, physical chemistry, catalysis through material science, and even medicine. Yet, the widespread applicability of these molecules necessitates that the interest in their study, which is growing unabated during these recent several years, result in substantial breakthrough in several directions, including the following possibilities: the possibility to finely tune the properties by varying the POM compositions and structures on purpose; find out new structures in which substituent metal cations remain electroactive and electrocatalytic; improve the stability of the POMs; improve the kinetics of reactions that are already demonstrated to be the equivalent of several processes known with organometallic species, and so on. In electrochemistry, several domains deserve further attention. Studies in nonaqueous media are scarce and the electrocatalytic processes that can be triggered by POMs in such media should be of interest. The first attempts at use of POMs in bioelectrochemistry are very promising. Continuous efforts must aim at obtaining new POMs stable in alkaline media, which could be useful in the redox processes of coenzymes and proteins in general.

In short, much work remains to be done but the perspectives might be rather bright.

Acknowledgment

We thank all our colleagues and coworkers who have participated in the work on

Polyoxometalates. As regards the synthesis and characterization of some POMs, special thanks are addressed to Dr. R. Contant (Université Paris VI), Professor C.L. Hill, Dr. T.M. Anderson and Professor I.K. Hardcastle (Emory University, Atlanta), Professor U. Kortz (International University of Bremen), Professor M.T. Pope (University of Washington), Dr. I.M. Mbomekalle and Dr. Y.W. Lu (Université Paris XI).

References

1. B. Keita, I. M. Mbomekalle, Y. W. Lu et al., *Eur. J. Inorg. Chem.* **2004**, 3462.
2. B. Keita, L. Nadj, *Curr. Top. Electrochem.* **1993**, 2, 77.
3. C. L. Hill (Guest Ed.), *Chem. Rev.* **1998**, 98, 1–389.
4. M. T. Pope, *Heteropoly and Isopoly Oxometalates*, Springer-Verlag, Berlin, 1983.
5. M. T. Pope, A. Müller, (Eds.), *Polyoxometalates: From Platonic Solids to Antiretroviral Activity*, Kluwer Academic Publications, Dordrecht, 1994.
6. (a) M. T. Pope, Polyoxo anions: synthesis and structure in *Comprehensive Coordination Chemistry II: Transition Metal Groups 3–6* (Ed.: A. G. Wedd), Elsevier Science, New York, 2004, pp. 635–678, Vol. 4, Chapter 4.10; (b) R. Contant, G. Hervé, *Rev. Inorg. Chem.* **2002**, 22, 63; (c) J. J. Cruywagen, *Adv. Inorg. Chem.* **2000**, 49, 127; (d) J. Berzélius, *Pogg. Ann.* **1826**, 6, 369–380; (e) L. Svanberg, H. Struve, *J. Prakt. Chem.* **1848**, 44, 257–291; (f) C. Marignac, *C. R. Acad. Sci.* **1862**, 55, 888.
7. C. L. Hill, Polyoxometalates: reactivity in *Comprehensive Coordination Chemistry II: Transition Metal Groups 3–6* (Ed.: A. G. Wedd), Elsevier Science, New York, 2004, pp. 679–759, Vol. 4, Chapter 4.11.
8. M. Sadakane, E. Steckhan, *Chem. Rev.* **1998**, 98, 219.
9. B. Keita, L. Nadj, *Electrocatalysis by Chemically Modified Electrodes of the Main Inorganic Chemicals, Encyclopedia of Electrochemistry, Vol. 10* (Eds.: A. J. Bard, M. Stratmann), Wiley-VCH, Weinheim, 2003.

10. A. Belhouari, B. Keita, L. Nadjo et al., *New J. Chem.* **1998**, 83.
11. R. Contant, M. Abbessi, J. Canny et al., *Inorg. Chem.* **1997**, 36, 4961.
12. B. Keita, L. Nadjo, R. Contant, *J. Electroanal. Chem.* **1998**, 443, 168–174.
13. (a) R. Contant, M. Abbessi, J. Canny, et al., *Eur. J. Inorg. Chem.* **2000**, 567; (b) R. Belghiche, R. Contant, Y. W. Lu et al., *Eur. J. Inorg. Chem.* **2002**, 1410.
14. B. Keita, Y. W. Lu, L. Nadjo et al., *J. Electroanal. Chem.* **1999**, 477, 146–157.
15. B. Keita, F. Girard, L. Nadjo et al., *J. Electroanal. Chem.* **1999**, 478, 76–82.
16. R. C. Chambers, C. L. Hill, *Inorg. Chem.* **1991**, 30, 2776.
17. L. C. Baker, *Plenary Lecture Proceedings of XV International Conference on Coordination Chemistry 15th*, Moscow, 1973.
18. M. Fournier, Contribution à l'étude des hétéropolyanions molybdiques et des ions mixtes qui en dérivent, Thesis, Université Paris VI, 1976.
19. (a) G. Hervé, *Ann. Chim. Paris* **1971**, 6, 219; (b) G. Hervé, *Ann. Chim. Paris* **1971**, 6, 287; (c) G. Hervé, *Ann. Chim. Paris* **1971**, 6, 337.
20. G. Hervé, Contribution à l'étude des hétéropolyanions tungstiques, Thesis, Université Paris VI, 1970.
21. J. P. Launay, Contribution à l'étude de la réduction électrochimique de l'ion métatungstique et des complexes chlorés de W(VI). Propriétés des produits obtenus, Thesis, Université Paris VI, 1974.
22. J. P. Ciabrini, Contribution à l'étude des 18-tungsto-2-phosphates et de leurs dérivés lacunaires, Thesis, Université Paris VI, 1982.
23. M. Abbessi, Synthèse et propriétés d'hétéropolyanions vanado-molybdo-tungsto-phosphoriques en vue d'une application en catalyse d'oxydation, Thesis, Université Paris VI, 1989.
24. G. A. Tsirlina, V. Yu. Kotov, *Rossiiskii Khim. Z.* **1998**, 42, 96–102.
25. I. A. Weinstock, *Chem. Rev.* **1998**, 98, 113–170.
26. M. T. Pope, *Introduction to Polyoxometalate Chemistry, NATO Science Series, II: Mathematics, Physics and Chemistry, Vol. 98*. (Polyoxometalate Molecular Science), Kluwer Academic Publishers, Dordrecht, Boston, London, 2003, pp. 3–31.
27. L. E. Briand, G. T. Baronetti, H. J. Thomas, *Appl. Catal., A: Gen.* **2003**, 256, 37–50.
28. B. Keita, L. Nadjo, *Mater. Chem. Phys.* **1989**, 22, 77.
29. (a) L. P. Maslov, N. A. Tsvetkov, *Chem. Abstr.* **79** **1973**, 58,263k; (b) *Chem Abstr.* **85** **1976**, 149,794z.
30. (a) M. T. Pope, G. M. Varga, *Inorg. Chem.* **1966**, 5, 1249; (b) T. J. R. Weakley in *Structure and Bonding* (Ed.: J. O. Dunitz), Springer, Berlin, p. 131, Vol 18; (c) P. Stonehart, J. G. Koren, J. S. Brinen, *Anal. Chim. Acta* **1968**, 40, 65; (d) J. P. Launay, R. Massart, P. Souchay, *J. Less-Common Met.* **1974**, 36, 139; (e) M. T. Pope, E. Papaconstantinou, *Inorg. Chem.* **1967**, 6, 1147; (f) G. M. Varga Jr., E. Papaconstantinou, M. T. Pope, *Inorg. Chem.* **1970**, 9, 662; (g) E. Papaconstantinou, M. T. Pope, *Inorg. Chem.* **1967**, 6, 1152.
31. M. Otake, T. Onodo, *J. Catal.* **1975**, 38, 494.
32. P. Souchay, R. Massart, G. Hervé, *Rev. Polarography (Japan)* **1967**, 14, 723.
33. (a) B. Keita, T. Lucas, L. Nadjo, *J. Electroanal. Chem.* **1986**, 208, 343; (b) B. Keita, L. Nadjo, *J. Electroanal. Chem.* **1987**, 217, 287; (c) B. Keita, L. Nadjo, *J. Electroanal. Chem.* **1987**, 227, 77; (d) B. Keita, L. Nadjo, *J. Electroanal. Chem.* **1987**, 230, 267.
34. B. Keita, D. Bouaziz, L. Nadjo, *J. Electrochem. Soc.* **1988**, 135, 87.
35. P. D. Prenzler, C. Boskovic, A. M. Bond, et al., *Anal. Chem.* **1999**, 71, 3650–3656.
36. T. Fujinaga, I. Sakamoto, *J. Electroanal. Chem.* **1977**, 85, 185.
37. S. Himeno, M. Takamoto, T. Ueda, *J. Electroanal. Chem.* **2000**, 485, 49–54.
38. C. Reichardt, *Solvent Effects in Organic Chemistry*, VCH, New York, 1990.
39. J. A. Riddick, W. B. Bunger, T. K. Sakano in *Techniques in Chemistry, Organic Solvents, Vol. II* (Ed.: A. Weissberger), Wiley, New York, 1986.
40. S. Himeno, M. Takamoto, *J. Electroanal. Chem.* **2000**, 492, 63–69.
41. (a) A. M. Bond, T. Vu, A. G. Wedd, *J. Electroanal. Chem.* **2000**, 494, 96–104; (b) D. M. Way, J. B. Cooper, M. Sadek et al., *Inorg. Chem.* **1997**, 36, 4227.
42. M. Mastragostino, L. Nadjo, J. M. Saveant, *Electrochim. Acta* **1968**, 13, 721.
43. (a) E. Laviron, *J. Electroanal. Chem.* **1984**, 164, 213; (b) *J. Electroanal. Chem.* **1984**, 169, 23.

44. D. O. Wipf, K. F. Wehmeyer, R. M. Wightman, *J. Org. Chem.* **1986**, 51, 4760.
45. D. S. Polcyn, I. Shain, *Anal. Chem.* **1966**, 38, 370.
46. R. L. Myers, I. Shain, *Anal. Chem.* **1969**, 41, 980.
47. C. P. Andrieux, L. Nadjo, J. M. Saveant, *J. Electroanal. Chem.* **1973**, 41, 137.
48. C. Amatore, M. Gareil, J. M. Saveant, *J. Electroanal. Chem.* **1983**, 147, 1.
49. B. Keita, L. Nadjo, *J. Electroanal. Chem.* **1987**, 219, 355.
50. (a) R. A. Marcus, *Can. J. Chem.* **1959**, 37, 155; (b) R. A. Marcus, *J. Chem. Phys.* **1965**, 43, 679; *J. Chem. Phys.* **1956**, 24, 966; (c) R. A. Marcus in *Dahlem Workshop on the Nature of Seawater* (Ed.: E. D. Goldberg), Verlag Chemie, Weinheim, Berlin, 1975, p. 477.
51. (a) R. Samuelsson, M. Sharp, *Electrochim. Acta* **1978**, 23, 315; (b) T. W. Rosanske, D. H. Evans, *J. Electroanal. Chem.* **1976**, 72, 277; (c) A. Capon, R. Parsons, *J. Electroanal. Chem.* **1973**, 46, 215; (d) C. Rüssel, W. Jaenicke, *J. Electroanal. Chem.* **1986**, 200, 249; (e) A. Kapturkiewicz, *J. Electroanal. Chem.* **1986**, 201, 205.
52. (a) Y. Izumi, K. Urabe, M. Onaka, *Zeolite, Clay and Heteropoly Acid in Organic Reactions*, Kodansha, Tokyo, 1992, Chapter 3; (b) M. T. Pope, A. Müller, *Angew. Chem., Int. Ed. Engl.* **1991**, 30, 34; (c) T. Okuhara, M. Misono, *J. Synth. Org. Chem. Jpn* **1993**, 51, 128.
53. A. Tézé, J. Canny, L. Gurban et al., *Inorg. Chem.* **1996**, 33, 1001.
54. (a) J. J. Altenau, M. T. Pope, R. A. Prados et al., *Inorg. Chem.* **1975**, 14, 417; (b) T. Okuhara, N. Misuno, M. Misono, *Adv. Catal.* **1996**, 41, 113; (c) C. L. Hill, C. M. Prosser-McCartha, *Coord. Chem. Rev.* **1995**, 143, 407; (d) K. Maeda, H. Katano, T. Osakai, et al., *J. Electroanal. Chem.* **1995**, 389, 167.
55. M. Nakayama, T. Ii, H. Komatsu et al., *Chem. Commun.* **2004**, 1098.
56. P. J. S. Richardt, J. M. White, P. A. Tregloan et al., *Can. J. Chem.* **2001**, 79, 613.
57. (a) V. Gutmann, *The Donor-Acceptor Approach to Molecular Interactions*, Plenum Press, New York, 1978, p. 29; (b) G. Gritzner, *J. Phys. Chem.* **1986**, 90, 5478; (c) P. C. Maria, J. F. Gal, *J. Phys. Chem.* **1985**, 89, 1926.
58. (a) G. Gritzner, K. Danksagmuller, V. Gutmann, *J. Electroanal. Chem.* **1976**, 72, 177; (b) G. Gritzner, K. Danksagmuller, V. Gutmann, *J. Electroanal. Chem.* **1978**, 90, 203; (c) A. Messina, G. Gritzner, *J. Electroanal. Chem.* **1979**, 101, 201; (d) G. Gritzner, *J. Electroanal. Chem.* **1983**, 144, 259.
59. (a) J. L. Kavanau, *Water and Solute-Water Interactions*, Holden Day, San Francisco, London, Amsterdam, 1964; (b) J. Broadhead, P. J. Elving, *J. Electrochem. Soc.* **1971**, 118, 63; (c) P. G. Wolynes, *Ann. Rev. Phys. Chem.* **1980**, 31, 345; (d) H. L. Friedman, *Ann. Rev. Phys. Chem.* **1981**, 32, 179; F. Franks, (Ed.), *Water, a Comprehensive Treatise*, Plenum Press, New York, London, 1972–1975, Vols. 1–5.
60. M. Matsumoto, N. I. Neuman, T. W. Swaddle, *Inorg. Chem.* **2004**, 43, 1153.
61. (a) L. Ebersson, *J. Am. Chem. Soc.* **1983**, 105, 3192; (b) P. Carloni, L. Ebersson, *Acta Chem. Scand.* **1991**, 45, 373; (c) V. A. Grigoriev, D. Cheng, C. L. Hill, et al., *J. Am. Chem. Soc.* **2001**, 123, 5292; (d) V. A. Grigoriev, C. L. Hill, I. A. Weinstock, *J. Am. Chem. Soc.* **2000**, 122, 3544.
62. (a) P. G. Rasmussen, C. H. Brubaker Jr., *Inorg. Chem.* **1964**, 3, 977; (b) J. F. Kirby, C. L. W. Baker, *Inorg. Chem.* **1998**, 37, 5537.
63. S. K. Saha, M. Ali, P. Banerjee, *Coord. Chem. Rev.* **1993**, 122, 41; (b) L. Ebersson, M. Ekström, *Acta Chem. Scand. B* **1988**, 42, 101.
64. J. F. Keggin, *Proc. Roy. Soc.* **1934**, A144, 75.
65. C. Sanchez, J. Livage, J. P. Launay et al., *J. Am. Chem. Soc.* **1983**, 105, 6817.
66. M. Kozik, C. F. Hammer, L. C. W. Baker, *J. Am. Chem. Soc.* **1986**, 108, 2748.
67. M. Kozik, C. F. Hammer, L. C. W. Baker, *J. Am. Chem. Soc.* **1986**, 108, 7627.
68. M. Kozik, L. C. W. Baker, *J. Am. Chem. Soc.* **1990**, 112, 7604.
69. N. Casañ-Pastor, L. C. W. Baker, *J. Am. Chem. Soc.* **1992**, 114, 10384.
70. R. A. Prados, M. T. Pope, *Inorg. Chem.* **1976**, 15, 2547.
71. S. P. Harmalker, M. T. Pope, *J. Am. Chem. Soc.* **1981**, 103, 7381.
72. (a) F. Ammar, J. M. Savéant, *J. Electroanal. Chem.* **1973**, 47, 115; (b) F. Ammar, J. M. Savéant, *J. Electroanal. Chem.* **1973**, 47, 215; (c) J. B. Flanagan, S. Margel, A. J. Bard et al., *J. Am. Chem. Soc.* **1978**, 100, 4248;

- (d) A. J. Bard, *Pure Appl. Chem.* **1971**, 25, 379; (e) A. J. Bard, J. Phelps, *J. Electroanal. Chem.* **1970**, 25, A2–A5; (f) J. M. Fritsch, H. Weingarten, *J. Am. Chem. Soc.* **1968**, 90, 793; (g) C. P. Andrieux, J. M. Savéant, *J. Electroanal. Chem.* **1970**, 28, 339–348; (h) V. D. Parker, K. Nyberg, L. Ebersson, *J. Electroanal. Chem.* **1969**, 22, 150.
73. (a) B. Dawson, *Acta Crystallogr.* **1953**, 6, 113; (b) H. D'Amour, *Acta Crystallogr.* **1976**, B32, 729.
74. R. Acerete, S. Harmalker, C. F. Hammer et al., *J. Chem. Soc., Chem. Commun.* **1979**, 777.
75. L. Kazansky, M. Fedotov, *J. Chem. Soc., Chem. Commun.* **1980**, 644.
76. A. Chemseddine, C. Sanchez, J. Livage et al., *Inorg. Chem.* **1984**, 23, 2609.
77. J. N. Barrows, M. T. Pope, *Inorg. Chim. Acta* **1993**, 213, 91.
78. B. Keita, Y. Jean, B. Levy et al., *New J. Chem.* **2002**, 26, 1314–1319.
79. J. P. Ciabrini, R. Contant, J. M. Fruchart, *Polyhedron* **1983**, 2, 1229.
80. R. Contant, R. Thouvenot, *Can. J. Chem.* **1991**, 69, 1498.
81. S. P. Harmalker, M. A. Leparulo, M. T. Pope, *J. Am. Chem. Soc.* **1983**, 105, 4286.
82. B. Keita, K. Essaadi, L. Nadjo et al., *Chem. Phys. Lett.* **1995**, 237, 411.
83. M. Abbessi, R. Contant, R. Thouvenot et al., *Inorg. Chem.* **1991**, 30, 1695.
84. (a) L. Barcza, M. T. Pope, *J. Phys. Chem.* **1973**, 77, 1795; (b) L. Barcza, M. T. Pope, *J. Phys. Chem.* **1975**, 79, 92.
85. C. Rong, M. T. Pope, *J. Am. Chem. Soc.* **1992**, 114, 2932.
86. (a) B. Keita, Y. W. Lu, L. Nadjo et al., *Eur. J. Inorg. Chem.* **2000**, 2463; (b) B. Keita, Y. W. Lu, L. Nadjo et al., *Electrochem. Commun.* **2000**, 2, 720.
87. (a) F. Ortega, M. T. Pope, *Inorg. Chem.* **1984**, 23, 3292; (b) F. Ortega, M. T. Pope, H. T. Evans, *Inorg. Chem.* **1997**, 36, 2166.
88. C. M. Tourné, G. F. Tourné, A. Malik et al., *J. Inorg. Nucl. Chem.* **1970**, 32, 3875.
89. B. Keita, A. Belhouari, L. Nadjo et al., *J. Electroanal. Chem.* **1998**, 442, 49.
90. B. Keita, E. Abdeljalil, L. Nadjo et al., *Electrochem. Commun.* **2000**, 2, 145.
91. R. Contant, J. P. Ciabrini, *J. Chem. Res.* **1977**, S, 222; *M*, 2601.
92. J. Bartis, Y. Kunina, M. Blumenstein et al., *Inorg. Chem.* **1996**, 35, 1497.
93. C. Rocchiccioli-Deltcheff, R. Thouvenot, *Spectrosc. Lett.* **1979**, 12, 127.
94. (a) J. E. Toth, F. C. Anson, *J. Electroanal. Chem.* **1989**, 256, 361; (b) S. Dong, M. Liu, *J. Electroanal. Chem.* **1994**, 372, 95.
95. R. D. Peacock, T. J. R. Weakley, *J. Chem. Soc. A* **1971**, 1937.
96. J.-M. Fruchart, G. Hervé, J. P. Launay et al., *J. Inorg. Nucl. Chem.* **1976**, 18, 1627.
97. R. Contant, Thesis, Université Paris VI, 1972.
98. (a) M. Bösing, A. Nöh, I. Loose et al., *J. Am. Chem. Soc.* **1998**, 120, 7252; (b) U. Kortz, N. K. Al-Kassem, M. G. Savelieff et al., *Inorg. Chem.* **2001**, 40, 4742; (c) U. Kortz, S. Nellutla, A. C. Stowe et al., *Inorg. Chem.* **2004**, 43, 144.
99. (a) T. J. R. Weakley, H. T. Evans, J. S. Showell et al., *J. Chem. Soc., Chem. Commun.* **1973**, 139; (b) T. J. R. Weakley, R. G. Finke, *Inorg. Chem.* **1990**, 29, 1235; (c) N. Casañ-Pastor, J. Bas-Serra, E. Coronado, et al., *J. Am. Chem. Soc.* **1992**, 114, 10380; (d) X. Zhang, Q. Chen, D. C. Duncan et al., *Inorg. Chem.* **1997**, 36, 4208; (e) J. M. Clemente-Juan, E. Coronado, J. R. Galán-Mascarós, et al., *Inorg. Chem.* **1999**, 38, 55; (f) L.-H. Bi, E.-B. Wang, J. Peng et al., *Inorg. Chem.* **2000**, 39, 671; (g) U. Kortz, S. Nellutla, A. C. Stowe et al., *Inorg. Chem.* **2004**, 43, 2308.
100. (a) I. Loose, E. Droste, M. Bösing et al., *Inorg. Chem.* **1999**, 38, 2688; (b) B. Krebs, E. Droste, M. Piepenbrink et al., *C. R. Acad. Sci. Paris, Ser. IIc* **2000**, 3, 205; (c) U. Kortz, M. G. Savelieff, B. S. Bassil et al., *Inorg. Chem.* **2002**, 41, 783.
101. (a) W. H. Knoth, P. J. Domaille, R. D. Farlee, *Organometallics* **1985**, 4, 62; (b) W. H. Knoth, P. J. Domaille, R. L. Harlow, *Inorg. Chem.* **1986**, 25, 1577; (c) R. G. Finke, B. Rapko, T. J. R. Weakley, *Inorg. Chem.* **1989**, 28, 1573; (d) F. B. Xin, M. T. Pope, *J. Am. Chem. Soc.* **1996**, 118, 7731; (e) N. Laronze, J. Marrot, G. Hervé, *Inorg. Chem.* **2003**, 42, 5857.
102. (a) J. M. Clemente-Juan, H. Andres, J. J. Borrás-Almenar et al., *J. Am. Chem. Soc.* **1999**, 121, 10021; (b) D. Sloboda-Rozner, P. Witte, P. L. Alsters et al., *Adv. Synth. Catal.* **2004**, 346, 339.
103. B. Keita, I. M. Mbomekalle, L. Nadjo et al., *Electrochem. Commun.* **2001**, 3, 267.

104. L. H. Bi, E. B. Wang, J. Peng et al., *Inorg. Chem.* **2000**, 39, 671.
105. (a) L. H. Bi, J. Y. Liu, Y. Shen et al., *Gaodeng Xuexiao Huaxue Xuebao* **2002**, 23, 472; (b) L. Bi, J. Liu, Y. Shen et al., *New J. Chem.* **2003**, 27, 756.
106. U. Kortz, I. M. Mbomekalle, B. Keita et al., *Inorg. Chem.* **2002**, 41, 6412.
107. (a) U. Kortz, M. G. Savelieff, B. S. Bassil et al., *Inorg. Chem.* **2002**, 41, 783; (b) L.-H. Bi, U. Kortz, S. Nellutla et al., *Inorg. Chem.* **2005**, 44, 896; (c) L. H. Bi, M. Reicke, U. Kortz et al., *Inorg. Chem.* **2004**, 43, 3915; (d) L. H. Bi, U. Kortz, B. Keita et al., *Inorg. Chem.* **2004**, 43, 8367.
108. I. M. Mbomekalle, B. Keita, M. Nierlich et al., *Inorg. Chem.* **2003**, 42, 5143.
109. I. M. Mbomekalle, B. Keita, L. Nadio et al., *Eur. J. Inorg. Chem.* **2003**, 3924.
110. I. M. Mbomekalle, B. Keita, L. Nadio et al., *Dalton Trans.* **2003**, 13, 2646.
111. (a) I. M. Mbomekalle, B. Keita, L. Nadio et al., *Inorg. Chem.* **2003**, 42, 1163; (b) B. Keita, I. M. Mbomekalle, L. Nadio, et al., *Eur. J. Inorg. Chem.* **2002**, 473.
112. X. Zhang, G. B. Jameson, C. J. O'Connor et al., *Polyhedron* **1996**, 15, 917.
113. D. Jabbour, B. Keita, I. M. Mbomekalle et al., *Eur. J. Inorg. Chem.* **2004**, 2036.
114. I. M. Mbomekalle, B. Keita, L. Nadio et al., *Inorg. Chem. Commun.* **2003**, 6, 435.
115. B. Keita, I. M. Mbomekalle, L. Nadio, *Electrochem. Commun.* **2003**, 5, 830.
116. B. Keita, I. M. Mbomekalle, L. Nadio et al., *Inorg. Chem.* **2004**, 43, 3257.
117. W. Song, X. Wang, Y. Liu et al., *J. Electroanal. Chem.* **1999**, 476, 85.
118. L. Ruhlmann, L. Nadio, J. Canny et al., *Eur. J. Inorg. Chem.* **2002**, 975.
119. L. Ruhlmann, J. Canny, J. Vaissermann et al., *J. Chem. Soc., Dalton Trans.* **2004**, 794.
120. L. Ruhlmann, J. Canny, R. Contant et al., *Inorg. Chem.* **2002**, 41, 3811.
121. J. A. F. Gamelas, M. S. Balula, H. M. Carapuça et al., *Electrochem. Commun.* **2003**, 5, 378.
122. L. Cheng, H. Sun, B. Liu et al., *Electrochem. Commun.* **1999**, 1, 155.
123. M. Sadakane, E. Steckhan, *J. Mol. Catal. A: Chem.* **1996**, 114, 221.
124. S. M. Cohen, S. Petoud, K. N. Raymond, *Chem. – Eur. J.* **2001**, 7, 272.
125. I. M. Mbomekalle, B. Keita, Y. W. Lu et al., *Eur. J. Inorg. Chem.* **2004**, 276.
126. I. M. Mbomekalle, B. Keita, Y. W. Lu et al., *Eur. J. Inorg. Chem.* **2004**, 4132.
127. I. M. Mbomekalle, B. Keita, L. Nadio et al., *J. Chem. Soc., Dalton Trans.* **2004**, 4094.
128. N. Belai, M. H. Dickman, M. T. Pope et al., *Inorg. Chem.* **2005**, 44, 169.
129. B. Keita, A. Belhouari, L. Nadio, *J. Electroanal. Chem.* **1993**, 355, 235.
130. A. Mahmoud, B. Keita, L. Nadio et al., *J. Electroanal. Chem.* **1999**, 463, 129.
131. J. B. Moffat, *J. Mol. Catal.* **1984**, 26, 385.
132. D. Masure, P. Chaquin, C. Louis et al., *J. Catal.* **1989**, 119, 415.
133. M. K. Awad, A. B. Anderson, *J. Am. Chem. Soc.* **1990**, 112, 1603.
134. R. S. Weber, *J. Phys. Chem.* **1994**, 98, 2999.
135. H. Taketa, S. Katsuki, K. Eguchi et al., *J. Phys. Chem.* **1986**, 90, 2959.
136. K. Eguchi, T. Seiyama, N. Yamazoe et al., *J. Catal.* **1988**, 111, 336.
137. J. Y. Kempf, M.-M. Rohmer, J.-M. Poblet et al., *J. Am. Chem. Soc.* **1992**, 114, 1136.
138. M. Bénard, M.-M. Rohmer, *J. Am. Chem. Soc.* **1994**, 116, 6959.
139. M.-M. Rohmer, J. Devémy, R. Wiest et al., *J. Am. Chem. Soc.* **1996**, 118, 13007.
140. J. M. Maestre, J. M. Poblet, C. Bo et al., *Inorg. Chem.* **1998**, 37, 3444.
141. H. Duclusaud, S. A. Borshch, *Chem. Phys. Lett.* **1998**, 290, 526.
142. J. M. Maestre, J. P. Sarasa, C. Bo et al., *Inorg. Chem.* **1998**, 37, 3071.
143. B. B. Bardin, S. V. Bordawekar, M. Neurock et al., *J. Phys. Chem.* **1998**, 102, 10817.
144. M.-M. Rohmer, M. Bénard, J.-P. Blaudeau et al., *Coord. Chem. Rev.* **1998**, 178–180, 1019.
145. H. Duclusaud, S. A. Borshch, *Inorg. Chem.* **1999**, 38, 3489.
146. H. Duclusaud, S. A. Borshch, *J. Am. Chem. Soc.* **2001**, 123, 2825.
147. X. Lopez, J. M. Maestre, C. Bo et al., *J. Am. Chem. Soc.* **2001**, 123, 9571.
148. J. M. Maestre, X. Lopez, C. Bo et al., *J. Am. Chem. Soc.* **2001**, 123, 3749.
149. X. López, C. Bo, J. M. Poblet, *J. Am. Chem. Soc.* **2002**, 124, 12574.
150. X. López, J. M. Poblet, *Inorg. Chem.* **2004**, 43, 6863.
151. T. A. Albright, J. K. Burdett, M. H. Whangbo, *Orbital Interactions in Chemistry*, John Wiley & Sons, New York, 1985, pp. 82–86.

152. W. Kutner, J. Wang, M. L'Her et al., *Pure Appl. Chem.* **1998**, 70, 1301.
153. (a) S. Dong, X. Xi, M. Tian, *J. Electroanal. Chem.* **1995**, 385, 227; (b) K. Unoura, A. Iwashita, E. Itabashi et al., *Bull. Chem. Soc. Jpn.* **1984**, 57, 597; (c) X. Xi, S. Dong, *J. Mol. Catal. A: Chem.* **1996**, 114, 257; (d) J. E. Toth, F. C. Anson, *J. Am. Chem. Soc.* **1989**, 111, 2444–2451; (e) X. Xi, G. Wang, S. Dong, *Electrochim. Acta* **1995**, 40, 1025; (f) L. Cheng, X. Zhang, X. Xi et al., *J. Electroanal. Chem.* **1996**, 407, 97; (g) M. Sadakane, E. Steckhan, *J. Mol. Catal. A: Chem.* **1996**, 114, 221; (h) E. Steckhan, G. Hilt, E. Kempf et al., *Organic Synthesis via Organometallics* (Ed.: G. Helmchen), OSM5, Heidelberg, 1997.
154. B. Keita, L. Nadjo, J. P. Haeussler, *J. Electroanal. Chem.* **1988**, 243, 481.
155. B. Keita, A. Belhouari, L. Nadjo et al., *J. Electroanal. Chem.* **1995**, 381, 243.
156. J. E. Toth, J. D. Melton, D. Cabelli et al., *Inorg. Chem.* **1990**, 29, 1952.
157. B. Keita, L. Nadjo, R. Contant et al., Process for the selective catalytic reduction of nitrogen compounds and catalysts used. (CNRS) French Patent 89/1,728, 1989.
158. B. Keita, L. Nadjo, R. Contant et al., Process for the selective catalytic reduction of nitrogen compounds and catalysts used. (CNRS) Europe Patent Applied EP 382,644, 1990; *Chem. Abst.* **1991**, 114, 191882u.
159. B. Keita, F. Girard, L. Nadjo et al., *J. Electroanal. Chem.* **2001**, 508, 70.
160. (a) B. Keita, E. Abdeljalil, L. Nadjo et al., *Electrochem. Commun.* **2001**, 3, 56; (b) I. R. Epstein, K. Kustin, L. J. Warshaw, *J. Am. Chem. Soc.* **1980**, 102, 3751.
161. B. Keita, M. Benaïssa, L. Nadjo et al., *Electrochem. Commun.* **2002**, 4, 663.
162. I. M. Mbomekalle, R. Cao, K. I. Hardcastle et al., *C. R. Acad. Sci. Paris* **2005**, Special Issue, 8, 1077.
163. R. Greef, R. Peat, L. M. Peter et al., *Instrumental Methods in Electrochemistry*, Ellis Horwood, Chichester, England, 1985, Chapter 6.
164. A. Hiskia, E. Papaconstantinou, *Inorg. Chem.* **1992**, 31, 163.
165. D. C. Duncan, C. L. Hill, *J. Am. Chem. Soc.* **1997**, 119, 243.
166. J. Zhang, F. C. Anson, *J. Electroanal. Chem.* **1992**, 341, 323.
167. N. Alonso-Vante, H. Tributsch, O. Solorza-Feria, *Electrochim. Acta* **1995**, 40, 567.
168. A. I. Vogel, *Quantitative Inorganic Analysis*, Longmans, London, 1960.
169. K. Inoura, A. Iwashita, E. Itabashi et al., *Bull. Chem. Soc. Jpn.* **1984**, 57, 597.
170. R. Neuman, C. Abu-Gnim, *J. Chem. Soc., Chem. Commun.* **1989**, 1324.
171. D. E. Katsoulis, M. T. Pope, *J. Chem. Soc., Chem. Commun.* **1986**, 1186.
172. K. Essaadi, B. Keita, L. Nadjo et al., *J. Electroanal. Chem.* **1994**, 367, 275.
173. B. Keita, K. Essaadi, L. Nadjo et al., *J. Electroanal. Chem.* **1996**, 404, 271.
174. B. Keita, K. Essaadi, A. Belhouari et al., *C. R. Acad. Sci. Paris, Sér. IIc* **1998**, 343.
175. J. C. Bart, F. C. Anson, *J. Electroanal. Chem.* **1995**, 390, 11.
176. R. Neuman, C. Abu-Gnim, *J. Am. Chem. Soc.* **1990**, 112, 6025.
177. E. Steckhan, C. Kandzia, *Synlett* **1992**, 139.
178. A. M. Khenkin, C. L. Hill, *J. Am. Chem. Soc.* **1993**, 115, 8178.
179. C. Rong, F. C. Anson, *Inorg. Chem.* **1994**, 33, 1064.
180. K. Drauz, H. Waldmann, *Enzyme Catalysis on Organic Synthesis-A Comprehensive Handbook*, VCH, Weinheim, 1995, Vol. 2.
181. E. Steckhan, *Top. Curr. Chem.* **1994**, 170, 83.
182. (a) H. Jaegfeldt, *J. Electroanal. Chem.* **1980**, 110, 295; (b) W. G. Kuhr, V. L. Barrett, M. R. Gagnon et al., *Anal. Chem.* **1993**, 65, 617.
183. (a) J. H. Christie, *J. Electroanal. Chem.* **1967**, 13, 79; (b) J. H. Christie, R. A. Osteryoung, F. C. Anson, *J. Electroanal. Chem.* **1967**, 13, 236; (c) F. C. Anson, J. H. Christie, R. A. Osteryoung, *J. Electroanal. Chem.* **1967**, 13, 343; (d) P. J. Lingane, J. H. Christie, *J. Electroanal. Chem.* **1967**, 13, 227.
184. (a) R. A. Marcus, *J. Phys. Chem.* **1968**, 72, 891; (b) C. P. Andrieux, C. Blocman, J. M. Dumas-Bouchiat et al., *J. Am. Chem. Soc.* **1979**, 101, 3431.
185. B. Keita, I.-M. Mbomekalle, L. Nadjo et al., *C. R. Acad. Sci. Paris* **2005**, Special Issue, 8, 1057.
186. L. Gorton, E. Dominguez, *Rev. Mol. Biotechnol.* **2002**, 82, 371.
187. R. Contant, S. Piro-Sellem, J. Canny et al., *C. R. Acad. Sci. Ser. IIc Chim.* **2000**, 3, 157.

23

Electrochemistry of Polycyanometalates

Fritz Scholz and Heike Kahlert
University of Greifswald, Greifswald, Germany

23.1	Introduction	703
23.2	The Structure of Polycyanometalates	703
23.3	The Electrochemistry of Polycyanometalates	708
23.3.1	General Features	708
23.3.2	Correlations between the Structures of PCMs and the Thermodynamics of their Electrochemical Reactions	710
23.3.3	Special Features	712
23.3.3.1	Metal Hexacyanoferrates	712
23.3.3.2	Hexacyanocobaltates, Hexacyanomanganates, Hexacyanochromates, Hexacyanoruthenates	715
23.3.3.3	Octacyanomolybdates, Octacyanotungstates	716
23.3.3.4	Pentacyanonitrosyl Metalates	716
23.4	Preparation of Electrodes Modified by Polycyanometalates and their Applications	716
23.4.1	Preparation of Polycyanometalate Modified Electrodes	716
23.4.2	Applications of PCM Modified Electrodes	717
	References	718

23.1 Introduction

The cyanide ion is one of the strongest ligands. It is isoelectronic with carbon monoxide and in the spectrochemical series, it is comparable with carbon monoxide. Cyanide ions act as monodentate ligands for almost all d-block elements and several f-block elements. In these complexes, it is carbon that bonds to the metal ions. The metal–cyano group $M-C\equiv N$ is linear or almost so in stable cyano complexes. Cyanide is also a bidentate ligand that is capable of forming a large number of sparingly soluble polymer metal polycyanometalates (PCMs). Mostly they are hexacyanometalates, as, for example, hexacyanoferrates; however, there are also octacyanometalates, for example, octacyanotungstates, octacyanomolybdates, and there are a few tetracyanometalates, for example, tetracyanoplatinates. Copper(I) cyanide is in fact a copper(II) dicyanocuprate(I), and in the polymeric silver(I) cyanide, the cyanide ligand is also bidentate.

The electrochemistry of dissolved cyanide complexes of metal ions is very well documented [1] and there is no need to discuss these compounds here. However, the electrochemistry of

the polymeric metal PCMs has seen tremendous development in the last few decades. This chapter is aimed at giving a conscious overview on the state of the art in this field of research.

23.2 The Structure of Polycyanometalates

1. *Hexacyanometalates*: Polymeric hexacyanometalates are by far the most important and best-studied group of metal PCMs. Prussian blue is the archetype of these compounds. The general formula of the family members of Prussian blue type compounds is $Me^{(i)}\{Me^{(N)}[Me^{(C)}(CN)_6]\}$ with (i), (N) and (C) indicating the position in the crystal lattice, where (i) means interstitial sites, (N) means metal ions coordinated by the nitrogen of the cyanides, and (C) means metal ions coordinated by the carbon of the cyanides. The braces {} include all ions that form the rigid framework of the PCMs, and the square brackets [] include the complex metal cyanide anions. From Mössbauer spectroscopy, it is known that Prussian blue and Turnbull's blue are both iron(III) hexacyanoferrate(II) with high-spin Fe(III) and low-spin Fe(II). Very early, Kegg [2] proposed a simple cubic structure for Prussian blue with $-Fe^{II}-C-N-Fe^{III}-N-C-Fe^{II}$

chains along all three crystallographic directions. In many cases, for charge compensation, additional cations must be located at interstitial positions. The idealized structure is given in Fig. 1.

The most important compounds for electrochemistry possess the d-block elements Fe, Co, Cr, Ru, and V on position $M^{(C)}$ (carbon-bonded metal ions). Position $M^{(N)}$ can be occupied by almost all d-block elements and several f-block elements. Position $M^{(i)}$ can be occupied either by alkali metal ions or by other metal ions. Metal hexacyanometalates exhibit a great variety of compositions and the real structures depend very much on the method of preparation. Most of the compounds belonging to the Prussian blue family, like metal hexacyanocobaltates and hexacyanochromates, with alkali cations on the interstitial positions, crystallize with a high symmetry and belong to the space group $Fm\bar{3}m$. Some metal hexacyanometalates, for example, hexacyanoferrates with zinc ions, silver ions, and f-block elements in position $M^{(N)}$ crystallize with hexagonal symmetry. Typical examples are given in Table 1.

Metal hexacyanoruthenates possess a lower symmetry. Several compounds have highly disordered structures, especially when no alkali cations are present for charge compensation. Such a complex defect structure has been found for a completely potassium free Prussian blue precipitated very slowly from a solution in concentrated hydrochloric acid [25, 26]. Here, the structure still remains cubic face-centered; however, one-third of the $[M^{(C)}(CN)_6]$ is vacant, randomly distributed and that space is filled with water molecules. The coordination sphere of the remaining $M^{(C)}$ ions is maintained unchanged; however, the mean coordination sphere of the $M^{(N)}$ ions is decreased ($M^{(N)}(NC)_{4.5}(H_2O)_{1.5}$). No iron ions occupy interstitial positions, that is, only two types of iron environments exist. Since that special kind of Prussian blue has been the first and hitherto only Prussian blue that could be obtained as sufficiently large crystals to perform a single crystal structure analysis, practically all textbooks, and later publications present that defect structure as the “real structure” of Prussian blue, completely forgetting that this defect structure is an extreme that forms

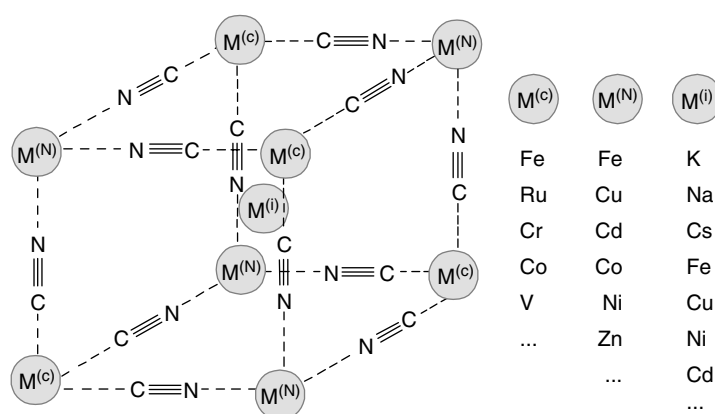


Fig. 1 Idealized structure of metal hexacyanometalates $Me^{(i)}\{Me^{(N)}[Me^{(C)}(CN)_6]\}$.

Tab. 1 Space groups of some metal hexacyanometalates. The chemical formulae indicate the coordination of the metal ions by using the notation $\text{Me}^{(i)}\{\text{Me}^{(N)}[\text{Me}^{(C)}(\text{CN})_6]\}$ (cf. Fig. 1)

Compound	Space group	Reference
$\text{Zn}\{\text{Zn}_2[\text{Co}(\text{CN})_6]_2\} \cdot 12\text{H}_2\text{O}$	$F\bar{4}3m$ (216)	3
$\text{K}\{\text{Cu}[\text{Co}(\text{CN})_6]\}$	$Fm\bar{3}m$ (225)	4, 5
$\text{K}\{\text{Ni}[\text{Co}(\text{CN})_6]\}$	$Fm\bar{3}m$ (225)	4
$\text{K}\{\text{Co}[\text{Co}(\text{CN})_6]\}$	$Fm\bar{3}m$ (225)	4
$\text{K}\{\text{Co}[\text{Fe}(\text{CN})_6]\}$	$Fm\bar{3}m$ (225)	4
$\text{K}\{\text{La}[\text{Fe}(\text{CN})_6]\} \cdot 4\text{H}_2\text{O}$	$P6_3/m$ (176)	6
$\{\text{La}[\text{Fe}(\text{CN})_6]\} \cdot 5\text{H}_2\text{O}$	$P6_3/m$ (176)	7
$\text{Na}_{0.26}\text{Ni}_{0.8}\{\text{Ni}[\text{Fe}(\text{CN})_6]\}$	$Fm\bar{3}m$ (225)	8
$\{\text{Zn}_3[\text{Fe}(\text{CN})_6]_2\} \cdot n\text{H}_2\text{O}$	$Fm\bar{3}m$ (225)	9
$\{\text{Sm}[\text{Fe}(\text{CN})_6]\} \cdot 4\text{H}_2\text{O}$	$Cmcm$ (63)	10
$\text{Fe}\{\text{Fe}_2[\text{Rh}(\text{CN})_6]_2\} \cdot 12\text{H}_2\text{O}$	$F\bar{4}3m$ (216)	11
$\{\text{Pb}_2[\text{Fe}(\text{CN})_6]\}$	$P\bar{3}$ (147)	12
$\text{K}\{\text{Ln}[\text{Fe}(\text{CN})_6]\} \cdot n\text{H}_2\text{O}$ (Ln = La–Lu)	$Cmcm$ (63)	13
$\text{Na}_2\{\text{Cu}[\text{Fe}(\text{CN})_6]\} \cdot 10\text{H}_2\text{O}$	$P2_1/m$ (10)	14
$\{\text{Cd}_2[\text{Fe}(\text{CN})_6]\} \cdot 8\text{H}_2\text{O}$	$P2_1/c$ (14)	15
$\text{Cd}\{\text{Cd}_2[\text{Fe}(\text{CN})_6]\}$	$Fm\bar{3}m$ (225)	16
$\{\text{Mn}_2[\text{Ru}(\text{CN})_6]\} \cdot 8\text{H}_2\text{O}$	$P2_1/c$ (14)	17
$\text{K}\{\text{La}[\text{Ru}(\text{CN})_6]\} \cdot 4\text{H}_2\text{O}$	$P6_3/m$ (176)	18
$\{\text{Cd}_2[\text{Ru}(\text{CN})_6]\} \cdot 8\text{H}_2\text{O}$	$P2_1/c$ (14)	15
$\{\text{Cd}_2[\text{Os}(\text{CN})_6]\} \cdot 8\text{H}_2\text{O}$	$P2_1/c$ (14)	15
$\{\text{Mn}_2[\text{Os}(\text{CN})_6]\} \cdot 8\text{H}_2\text{O}$	$P2_1/c$ (14)	19
$\{\text{Mn}_3[\text{Co}(\text{CN})_6]_2\} \cdot 12\text{H}_2\text{O}$	$Fm\bar{3}m$ (225)	20, 21
$\{\text{Cd}_3[\text{Co}(\text{CN})_6]_2\} \cdot 12\text{H}_2\text{O}$	$Fm\bar{3}m$ (225)	21
$\{\text{Co}_3[\text{Co}(\text{CN})_6]_2\} \cdot 12\text{H}_2\text{O}$	$Fm\bar{3}m$ (225)	22
$\{\text{Ag}_3[\text{Co}(\text{CN})_6]\}$	$P\bar{3}_1m$ (162)	23
$\{\text{Sm}[\text{Co}(\text{CN})_6]\} \cdot 4\text{H}_2\text{O}$	$Cmcm$ (63)	24

as a result of the complete absence of cations that could stabilize the Keggin structure. Recent attempts to prepare a potassium ion stabilized Prussian blue of a crystallinity that allows a Rietveld refinement, unambiguously show that the Keggin structure is the structure that Prussian blue assumes under the usual precipitation conditions, that is, when stabilizing potassium ions are available, just as Keggin and Miles stated long ago [27].

The most important feature of all polymeric metal hexacyanometalates is that they possess channels and holes, the size of which is mostly determined by the

large cyanide ions. The large cyanide ions also determine the unit cell dimension (ranging from 0.1 to 0.109 nm).

Since many metal hexacyanometalates have very similar structures, the formation of solid solutions is possible. The positions $\text{M}^{(C)}$, $\text{M}^{(N)}$, and $\text{M}^{(i)}$ can be occupied not only by one kind of ion, but by a variety of similar ions, allowing the existence of substitutional solid solutions with a random distribution of the different ions on their specific positions. Table 2 gives an overview of the types of solid solutions that can be formed and some examples.

Very complex mixed crystals with mixed occupation of all metal positions by

Tab. 2 Types of solid solutions of metal hexacyanometalates

Type and stability	General formula	Examples	References
Type I Very stable	$\text{Me}^{(i)}\{\text{Me}^{(N)}[\text{Me}_x^{(C)'}\text{Me}_{1-x}^{(C)''}(\text{CN})_6]\}$	$\text{K}\{\text{Cu}[\text{Fe}_x\text{Co}_{1-x}(\text{CN})_6]\}$	28
Type Ia	$\text{Me}^{(i)}\{\text{Me}^{(N)}[\text{Me}_x^{(C)'}\text{Me}_{1-x}^{(C)''}(\text{CN})_6]\}$ with $\text{Me}^{(C)'} = \text{Me}^{(C)''}$; however, in different oxidation states		
Type II Relatively stable	$\text{Me}^{(i)}\{\text{Me}_x^{(N)'}\text{Me}_{1-x}^{(N)''}[\text{Me}^{(C)}(\text{CN})_6]\}$	$\text{K}\{\text{Ni}_x\text{Co}_{1-x}[\text{Fe}(\text{CN})_6]\}$ $\text{K}\{\text{Ni}_x\text{Fe}_{1-x}[\text{Fe}(\text{CN})_6]\}$ $\text{K}\{\text{Cu}_x\text{Co}_{1-x}[\text{Fe}(\text{CN})_6]\}$ $\text{K}\{\text{Ni}_x\text{Pd}_{1-x}[\text{Fe}(\text{CN})_6]\}$	29 30 31 32
Type IIa	$\text{Me}^{(i)}\{\text{Me}_x^{(N)'}\text{Me}_{1-x}^{(N)''}[\text{Me}^{(C)}(\text{CN})_6]\}$ with $\text{Me}^{(N)'} = \text{Me}^{(N)''}$; however, in different oxidation states		
Type III Not stable	$\text{Me}_x^{(i)'}\text{Me}_{1-x}^{(i)''}\{\text{Me}^{(N)}[\text{Me}^{(C)}(\text{CN})_6]\}$		
Type IV Combination of types I (or Ia) and II (or IIa) Relatively stable	$\text{Me}^{(i)}\{\text{Me}_x^{(N)'}\text{Me}_{1-x}^{(N)''}[\text{Me}_y^{(C)'}\text{Me}_{1-y}^{(C)''}(\text{CN})_6]\}$	$\text{K}\{\text{Cu}_{0.5}\text{Ni}_{0.5}[\text{Fe}_x\text{Co}_{1-x}(\text{CN})_6]\}$	28
Type V Combination of types II and III Not stable with respect to III	$\text{Me}_x^{(i)'}\text{Me}_{1-x}^{(i)''}\{\text{Me}_y^{(N)'}\text{Me}_{1-y}^{(N)''}[\text{Me}^{(C)}(\text{CN})_6]\}$		
Type VI Combination of types I and III Not stable with respect to III	$\text{Me}_x^{(i)'}\text{Me}_{1-x}^{(i)''}\{\text{Me}^{(N)}[\text{Me}_y^{(C)'}\text{Me}_{1-y}^{(C)''}(\text{CN})_6]\}$		
Type VII Combination of all types Not stable with respect to III	$\text{Me}_x^{(i)'}\text{Me}_{1-x}^{(i)''}\{\text{Me}_y^{(N)'}\text{Me}_{1-y}^{(N)''}[\text{Me}_z^{(C)'}\text{Me}_{1-z}^{(C)''}(\text{CN})_6]\}$		

Fe(II), Fe(III), Cd(II), and K^+ have been described [33].

Generally, only the interstitial metal ions $\text{M}^{(i)}$ can diffuse through the solid polymer compounds. So far, the other metal ions have not been shown to diffuse, although very slow processes of diffusion, especially

in the structures with a high concentration of vacancies, cannot be excluded.

Mixed crystals of type I are very stable and can be used for electrochemical investigations. Recently, it has been shown that such solid solutions maintain the regular cubic structure and only a single

phase exists rather than a mixture of the phases $\text{Me}^{(i)}\{\text{Me}^{(N)}[\text{Me}^{(C)'}(\text{CN})_6]\}$ and $\text{Me}^{(i)}\{\text{Me}^{(N)}[\text{Me}^{(C)''}(\text{CN})_6]\}$ [28]. The lattice parameters obey the Vegard rule, that is, the lattice constants vary linearly with the composition of the solid solution (cf. Fig. 2).

An interesting fact is that in the case of $\text{K}\{\text{Cu}[\text{Fe}_{1-x}\text{Co}_x(\text{CN})_6]\}$, the potassium ions occupy statistically one-half of the eight cubes of one unit cell, but with a high value of the isotropic temperature factor indicating a smudgy position of the potassium ions. In the compound $\text{K}\{\text{Ni}[\text{Fe}_{1-x}\text{Co}_x(\text{CN})_6]\}$, an eccentric position of potassium ions was found. Such an eccentric position of the counteranion was also described by Bocarsly et al. for sodium-containing nickel hexacyanoferrate(II) [34].

The situation is more complex in the case of $\text{Me}^{(C)'} = \text{Fe}^{\text{II}}$ and $\text{Me}^{(C)'} = \text{Cr}^{\text{III}}$. Obviously, the incorporation of the hexacyanoferrate ions is preferred. The content of hexacyanochromate in the precipitated solid compound is less than in the solution used for precipitation [35].

Mixed crystals of type II have been used in the form of thin films on electrodes as well as in the form of chemically synthesized powders immobilized on electrodes. Depending on the radii of the ions involved in the synthesis, solid solutions can also be formed as single phases. In the case of $\text{K}\{\text{CuCo}[\text{Fe}(\text{CN})_6]\}$ films, XRD results indicated that a single phase with a cubic face-centered symmetry was formed [31]. The situation is more complex in the case of $\text{K}\{\text{NiPd}[\text{Fe}(\text{CN})_6]\}$ deposited as a thin film on electrodes [32]. Kulesza et al. have pointed out that there is a critical concentration of Pd^{2+} below which Pd^{2+} was taken as the counteranion at interstitial position, while above that value a solid solution is formed in which both Ni^{2+} and Pd^{2+} are nitrogen coordinated.

Mixed crystals of type III, V, VI, and VII are not stable, because the interstitial counteranions can be easily exchanged.

Mixed crystals of type IV are very stable. One example of such mixed crystal series is $\text{K}\{\text{Ni}_{0.5}\text{Cu}_{0.5}[\text{Fe}_{1-x}\text{Co}_x(\text{CN})_6]\}$ [28]. Also, in that case only a single phase with a cubic phase centered

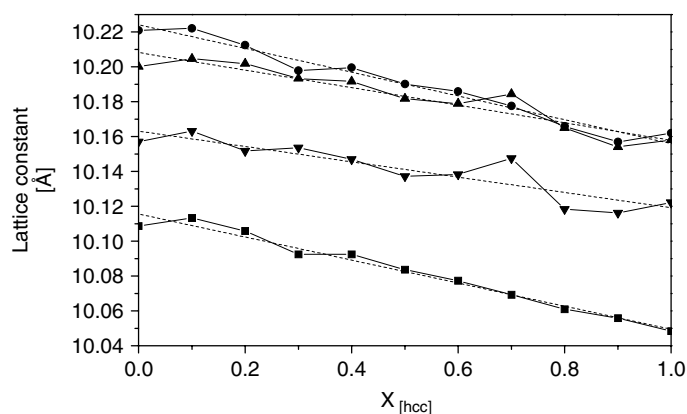


Fig. 2 Lattice constants of (●) $\text{K}\{\text{Ni}[\text{Fe}_{1-x}\text{Co}_x(\text{CN})_6]\}$, (▲) $\text{K}\{\text{Fe}[\text{Fe}_{1-x}\text{Co}_x(\text{CN})_6]\}$, (■) $\text{K}\{\text{Cu}[\text{Fe}_{1-x}\text{Co}_x(\text{CN})_6]\}$, and (▼) $\text{K}\{\text{Ni}_{0.5}\text{Cu}_{0.5}[\text{Fe}_{1-x}\text{Co}_x(\text{CN})_6]\}$ dependent on the molar ratio of cobalt. The dashed lines result from a linear fitting.

symmetry could be indexed. The lattice constants obey the Vegard rule (cf. Fig. 2). Recently [36], the structure of $K_{0.4}\{Cu_{0.65}Zn_{0.65}[Fe_{0.45}Co_{0.55}(CN)_6]\}$ has been described. Whereas the structure of $K\{Cu[Co(CN)_6]\}$ is cubic face-centered and that of $K\{Zn[Fe(CN)_6]\}$ is hexagonal, the X-ray powder analysis indicates that the structure of the solid solution is of cubic face-centered symmetry.

2. Tetracyanometalates: Solid metal tetracyanometalates with nickel(II), platinum(II), and palladium(II) ions as carbon coordinated metals are known. In such compounds, Ni, Pt, or Pd are bridged with other metal ions (e.g., Er, Tl, Nd, Eu, Co) through the cyano groups. This arrangement defines a square planar coordination environment for Ni, Pt, or Pd. The compounds contain a large amount of crystal water. Examples are: $Co(H_2O)[Ni(CN)_4]$ [37], $Cr_2[Ni(CN)_4]_3 \cdot 10H_2O$ [38], $Cd(H_2O)_2[Ni(CN)_4] \cdot 4H_2O$ [39], $Er_2[Pt(CN)_4]_3 \cdot 21H_2O$ [40], $Tl_2[Pt(CN)_4]$ [41], $Nd_2[Pd(CN)_4]_3 \cdot 12H_2O$ [42], $Eu_2[Pd(CN)_4]_3 \cdot H_2O$ [43].

3. Dicyanometalates: Dicyanometalates of silver and gold are known. Abrahams et al. [44] have described a cobalt dicyanoaurate. In these compounds, gold ions are carbon coordinated and form linear structures. Cobalt ions are coordinated by four nitrogen atoms of the cyanide group. The unit cell has a hexagonal symmetry.

23.3

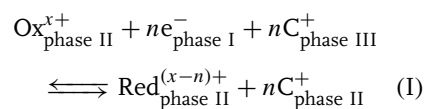
The Electrochemistry of Polycyanometalates

23.3.1

General Features

1. The insertion electrochemistry of PCMs: Most of the PCMs possess two characteristic properties, they have redox-active metal centers and they have an open

structure that allows small cations to enter the solid crystals and to diffuse inside the materials. Therefore, they are prone to undergo insertion electrochemical reactions [45]. Insertion electrochemistry means that two coupled electrochemical processes proceed across two different interfaces: (1) an electron transfer across the interface of the metal PCM with the electron conductor (metal, carbon, or, rarely, a semiconductor), and (2) an ion transfer across the interface of the PCM with an electrolyte solution. These two reactions are of truly electrochemical nature because they involve the transfer of charged particles across interfaces. Although, from time to time, reports appeared in the literature that anions could enter solid PCMs, no proof of this has ever been given. Since particles that enter the channels and holes of PCMs will see practically only the cyanide anions, it is hard to believe that anions can be forced to enter these locations. Analytical data that have indicated the presence of anions like chloride, and so on are most probably the results of contaminations since the compounds usually have a very low crystallinity and very large inner surface areas ready for absorption of various ions. In numerous studies, it has been proven that small cations are able to be housed in the PCMs, and thus another argument against the anion transfer is that in chemistry there is never a case in which anions and cations are interchangeable on the same places in a given structure. The two electrochemical reactions of PCMs can be written in one equation:



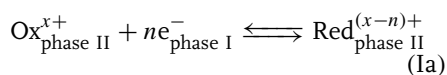
$Ox_{\text{phase II}}^{x+}$ and $Red_{\text{phase II}}^{(x-n)+}$ denote the oxidized and reduced metal ions in the

PCM and C^+ are the cations exchanged between the PCM and the electrolyte solution. In Eq. (I), three different phases are indicated, phase I being the metal that conducts the electrons to or away from the PCM, phase II being the solid PCM, and phase III being the electrolyte solution. The three phases constitute the essential feature of a so-called three-phase electrode as it is schematically depicted in Fig. 3.

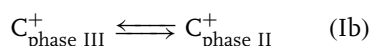
The Nernst equation corresponding to that overall chemical equation is:

$$E = E_{\text{Ox/Red/C}}^{\oplus} + \frac{RT}{nF} \ln \frac{a_{\text{Ox}^{x+}}^{\text{phase II}} a_{\text{C}^+}^n{}^{\text{phase III}}}{a_{\text{Red}^{(x-n)+}}^{\text{phase II}} a_{\text{C}^+}^n{}^{\text{phase II}}} \quad (1)$$

This equation can be divided into two equilibria, one involving the transfer of electrons



and one involving the transfer of ions



with the following Nernst equations

$$E_{\text{I/II}} = E_{\text{Ox/Red}}^{\oplus} + \frac{RT}{nF} \ln \frac{a_{\text{Ox}^{x+}}^{\text{phase II}}}{a_{\text{Red}^{(x-n)+}}^{\text{phase II}}} \quad (2)$$

$$E_{\text{II/III}} = E_{\text{C}}^{\oplus} + \frac{RT}{F} \ln \frac{a_{\text{C}^+}^{\text{phase III}}}{a_{\text{C}^+}^{\text{phase II}}} \quad (3)$$

The standard potentials for the electron- and ion-transfer reactions are interrelated by the following equation:

$$E_{\text{Ox/Red/C}}^{\oplus} = E_{\text{Ox/Red}}^{\oplus} + E_{\text{C}}^{\oplus} \quad (4)$$

An important prerequisite for reaction (I) to proceed is that both the electrons and the ions have the chance to be conducted within the PCM. For ions, it is sufficient that a system of channels exists in the solid material and that these channels need to have a sufficiently wide diameter for ions to diffuse through. For the electrons, there are two pathways that depend on the electronic structure of the PCM. Provided the PCM is a semiconductor and the conduction band is accessible at room temperature, this conduction band can support the electron conduction. When the redox centers, that is, the metal ions interact less strongly so that the band structure of a

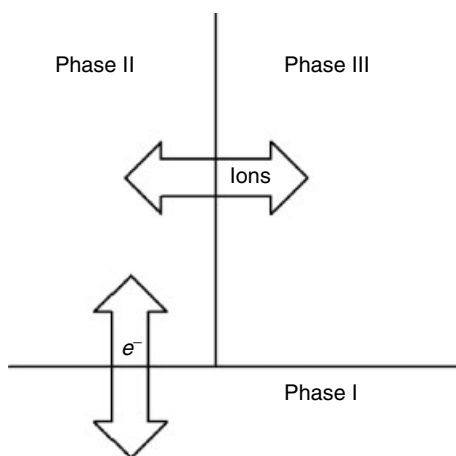


Fig. 3 Situation at a three-phase electrode where a phase II possessing redox center is in close contact with phase I that can provide or take away electrons, and with phase III that can exchange ions with phase II.

semiconductor is not built up, an electron exchange is still possible by a hopping mechanism. It seems that both pathways can be observed in PCMs, sometimes even both for one and the same PCM, but in different oxidation states. Of course, the oxidation state of the metal cations decides about the electronic structure, and hence the electronic properties of PCMs can be varied just by that parameter. Unfortunately, no conclusive and exhaustive studies of this conduction mechanism for PCMs in different oxidation states have been performed so far. An electrochemical impedance study of the reactions of copper (II) hexacyanoferrate has shown that the dependence of the charge transfer and the Warburg coefficients have a pronounced minimum at the formal potential of the redox system [46]. This indicates that the bimolecular electron hopping mechanism is operative. It was concluded in that study that the electron transport from the electrode to the reaction front inside the PCM goes via the conduction band of the semiconducting PCM, whereas the electron transport in the reaction zone proceeds via hopping.

For the case in which phase II in Fig. 3 is a solid, it is not yet clear how the activities of the species Ox, Red, and C^+ in the solid have to be defined on a strict thermodynamic basis, and how they could be determined. No experiments are known that would lead to a separation of the free energies of the equilibria Ia and Ib in the case of solids. When phase II is a solution phase, the activities of Ox, Red, and C^+ are in principle accessible; however, in that case also, it remains the problem that an extrathermodynamic assumption is necessary for quantifying the free energy of ion transfer between the liquid phases II and III.

2. Complex mechanisms of electrochemical reactions of PCMs: Frequently it can

be observed that the “simple” insertion electrochemical reactions of PCMs are associated with complex chemical reorganizations, as, for example, bond isomerization or metal ion substitution reactions. An early example of an isomerization reaction prompted by an electrochemical reaction was the transformation of iron(II) hexacyanochromate(III) to chromium(III) hexacyanoferrate(II) [47]. This reaction proceeds because a reduction of chromium(III) ions to chromium(II) leads to the well-known labilization of ligands that allows the cyanide ions to turn into the thermodynamically more favorable position with the carbon coordinated toward the iron ions and the nitrogen toward the chromium ions. A similar example was observed when iron hexacyanomanganates are subjected to electrochemical redox reactions. The electrochemical behavior is very similar to the chemical isomerizations [48].

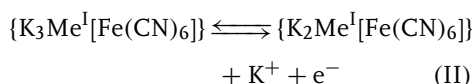
Examples of electrochemically initiated metal ion substitution reactions have been described for the case of substitution of high-spin iron by cadmium ions [49, 50], high-spin iron by nickel, and silver by nickel [51] and high-spin iron ions [52]. The reasons for the proceeding of these electrochemically initiated substitution reactions have been ascribed as well to the labilization of the cyanide ions in certain oxidation states of the metal ions of the involved PCMs.

23.3.2

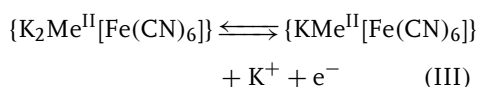
Correlations between the Structures of PCMs and the Thermodynamics of their Electrochemical Reactions

The electrochemical properties of PCMs can be tuned in certain limits by variation of the metal ions constituting the framework of these compounds. Only for the

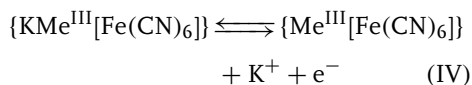
hexacyanometalates, and especially for the hexacyanoferrates, both theoretical and experimental studies have been performed so far to rationalize the dependencies between the thermodynamic electrochemical data and the structures of the compounds. Figure 4 shows a plot of the formal potentials of the following reactions versus the ion potentials of the metal ions Me^+ , Me^{2+} , and Me^{3+} [53]:



($\text{Me}^{\text{I}} = \text{Ag}$)



($\text{Me}^{\text{II}} = \text{Cd, Zn, Pb, Mn, Ni, Co}$)



($\text{Me}^{\text{III}} = \text{Ga, In, Al, Fe, Cr, Co}$).

These reactions are solid-state insertion electrochemical processes with coupled electron and ion transfers. Figure 4 includes the standard potential of hexacyanoferrate in aqueous solution. It is rather surprising that the data for the solid-state insertion electrochemistry and

that of the dissolved hexacyanoferrate in water are all situated on one and the same straight line. Obviously, this plot shows that the factor controlling the magnitude of the formal potentials is in the solid compounds and in the solution the same, that is, the ion potential of the nearest neighbor of the nitrogen end of the cyanide ions. These nearest neighbors are the metal ions Me^{I} , Me^{II} , and Me^{III} in the solid PCMs, and the proton of water in the aqueous solution! On the basis of simple thermodynamic considerations it has been shown that the following equation holds [54, 55]:

$$E_{\text{A}}^{\Phi'} = -\frac{\kappa}{zF} + \frac{\xi}{zF} \frac{a}{r_{\text{Me}}} \quad (5)$$

(κ and ξ are constants, a is the charge of the nitrogen coordinated metal ions $\text{Me}^{(\text{I}),(\text{II}),(\text{III})}$ and r_{Me} is their radius.)

The differences in formal potentials of different metal hexacyanometalates is the basis of tuning the redox properties of PCMs by synthesis of mixed solutions, as far as that is possible due to the ion radii. Examples for a continuous tuning of the hexacyanoferrate redox potential are mixed nickel/iron hexacyanoferrates [30], mixed copper/iron hexacyanoferrates [56], and mixed cadmium/iron hexacyanoferrates [33].

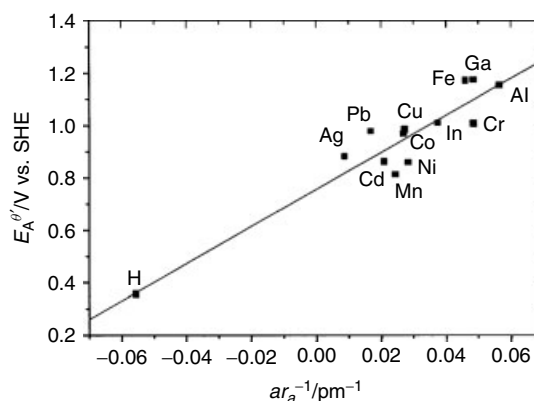


Fig. 4 Correlation between the formal potentials of the hexacyanoferrate units of the solid hexacyanoferrates and the ion potential (charge/radius) of the nitrogen coordinated metal ions [53, 55].

The formal potential of the hexacyanoferrate systems also shift by inserting different metal ions into the channels [57]. With the help of Born–Haber cycles, the following equation has been derived [55]:

$$E_A^{\Phi'} \approx -\frac{\text{const}_3}{zF} - \frac{\Phi}{zF} \frac{b_I}{r_I} \quad (6)$$

(const_3 and Φ are constants, b_I is the charge of the inserting metal ions Me^I and r_I is its radius).

Figure 5 gives the experimental proof of the validity of Eq. 6. However, some hexacyanoferrates exhibit a different affinity for the alkali metal ions. An example is samarium hexacyanoferrate [58]. The reasons for the different behavior are not yet known.

The formal potentials of solid hexacyanometalates can also be correlated with the lattice constants, that is, with a parameter that depends mainly on the radii of the two metal ions forming the framework of the compounds. This theoretically derived dependence can be verified when the nitrogen coordinated metal ion and the inserting metal ions are kept constant and the carbon coordinated metal ions are varied, for example, when hexacyanoferrate, hexacyanocobaltate, hexacyanomanganate, and so on are compared [53, 55]. The equation

that has been derived is:

$$E_A^{\Phi'} \approx -\frac{2\Psi}{zF} \left[\frac{b_C - b_B}{L} \right] - \frac{\omega_I}{zF} \quad (7)$$

(Ψ and ω_I are constants, $(b_C - b_B)$ is the difference of charges of the oxidized and reduced forms of the hexacyanometalate unit, that is, it is 1, and L is the lattice constant of the solid hexacyanometalate).

Figure 6 shows the experimental data that obviously follow Eq. (7).

The experimental data verifying the dependencies of the formal potentials on ion parameters, as shown in Figs 4, 5, and 6 have been accessible only by application of voltammetry of immobilized particles [59], since that method is the only one that allows the study of different compounds that have been chemically synthesized and completely characterized to be measured under the very same conditions. This is not, or only to some extent possible with electrochemically prepared thin films on electrodes.

23.3.3

Special Features

23.3.3.1 Metal Hexacyanoferrates

1. *Metal hexacyanoferrates possessing only one kind of redox-active metal ions:* Most of the metal hexacyanoferrates show only

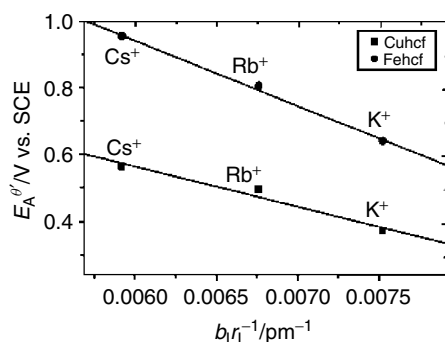


Fig. 5 Correlation between the formal potentials of the hexacyanoferrate units of the solid hexacyanoferrates and the ion potential (charge/radius) of the inserting metal ions [53, 55].

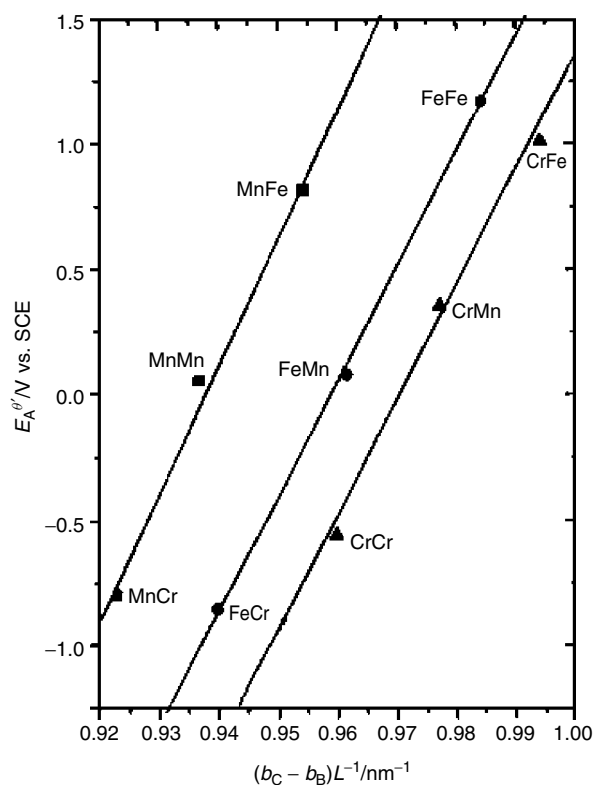


Fig. 6 Correlation between the formal potentials of the hexacyanometalate units of the solid hexacyanometalates and the inverse lattice constant L of the solid compounds [53, 55].

one electrochemically active system, that is, the hexacyanoferrate unit. This is the case for the following compounds: Cu^{2+} , Ni^{2+} , Co^{2+} , Cd^{2+} , Zn^{2+} , and other metal hexacyanoferrates. This is surprising because most of these ions are themselves electroactive in aqueous solutions. A formal reasoning is that the solubility products of these salts are so small that the reduction of the metal ions is simply shifted to inaccessible values, because even a reductive decomposition of the hexacyanometalates is not possible using aqueous electrolytes. This is not true for silver hexacyanoferrates that can be easily decomposed by reduction to metallic

silver and dissolved hexacyanoferrate ions. To this group of hexacyanoferrates belongs also vanadium hexacyanoferrate, which was described first by Shaojun [60], and studied in detail by Carpenter et al. [61], who have proved that vanadium is not active in these films, although two overlapping redox systems are present in the cyclic voltammograms. It can be supposed that different vanadium hexacyanoferrate phases may be responsible for the two systems (cf. cobalt hexacyanoferrate, although in that case cobalt is also active).

2. *Metal hexacyanoferrates possessing two kinds of redox-active metal ions:* Here we consider those hexacyanoferrates that

possess two redox systems that support insertion electrochemical reactions. The most prominent member of this group is the archetype of metal hexacyanoferrates, Prussian blue. About no other PCM so many papers have been published as on Prussian blue. Inevitably, there are contradictory and inconsistent reports among them. One reason is certainly the great variety of Prussian blues resulting from the ability to (1) house different amounts and kinds of cations in the interstitial cavities (e.g. different alkali metal ions and also high-spin Fe ions), and (2) the formation of defect structures with a considerable number of hexacyanoferrate vacancies. The latter effect is especially pronounced when no suitable cations are available during the synthesis, as in the case of the famous Ludi experiment where Prussian blue was slowly crystallized from concentrated hydrochloric acid in the absence of potassium ions [25].

Prussian blue shows two distinct redox systems, one at rather positive potentials

(around 0.8 V vs. SCE) and one at considerably more negative potentials (around 0.2 V vs. SCE) (cf. Fig. 7). Itaya et al. [62] have shown by in situ Mössbauer spectroscopy that the more negative system is caused by the nitrogen coordinated high-spin iron ions, and the other system is caused by the carbon coordinated low-spin iron ions of the hexacyanoferrate. It is a very peculiar property of Prussian blue that a cyclic electrochemical oxidation and reduction involving both redox systems, in some electrolyte solutions leads to the blocking of the low-spin iron system, that is, that voltammetric response vanishes [63]. This happens always when Ti^+ , Rb^+ , or NH_4^+ [64] ions are present in the electrolyte solution. The reason for that behavior are the small lattice constant differences between the three oxidation states of Prussian blue and the ion radii of the three earlier-mentioned cations. Both lead to a trapping of these cations in the Prussian blue that blocks ion diffusion for the interconversion of Prussian blue and

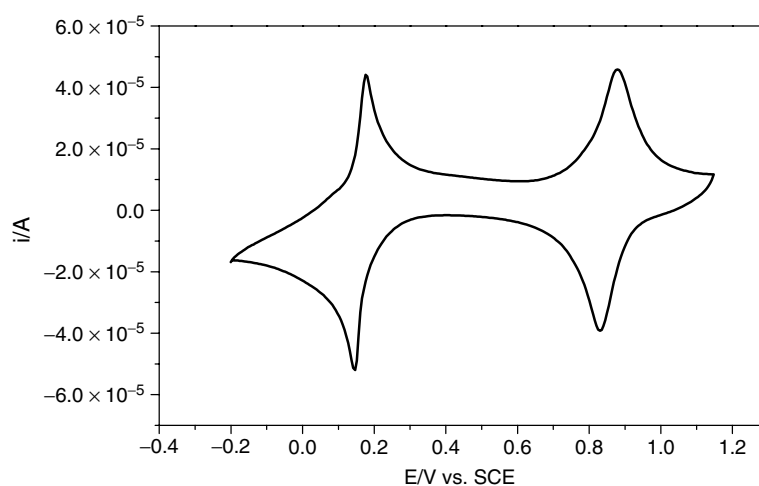


Fig. 7 Cyclic voltammogram of Prussian blue immobilized on a graphite electrode and using an electrolyte solution containing 0.1 mol L^{-1} KCl. Scan rate: 0.01 V s^{-1} .

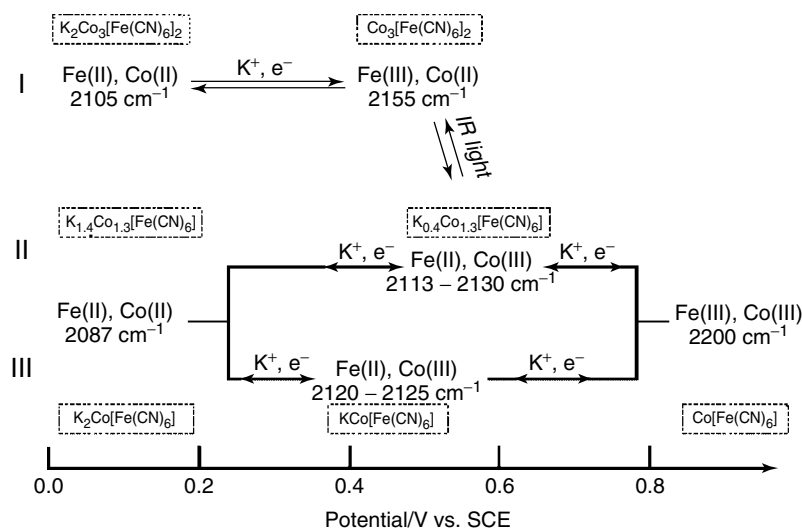


Fig. 8 Scheme of the electrochemical and photochemical conversions involved in the electrochemistry of cobalt hexacyanoferrate films according to Ref. 65.

Prussian yellow. This irreversible binding of thallium(I) ions is probably related to the well-known use of Prussian blue to bind thallium ions following poisoning.

Cobalt(II) hexacyanoferrate, formally similar to Prussian blue, exhibits a far more complex electrochemistry. Only recently, Lezna et al. [65] succeeded in elucidating this system by a combination of in situ infrared spectroscopy and electrochemistry, and ex situ X-ray photoelectron spectroscopy. Figure 8 shows the pathways of the three different phases involved in the electrochemistry, and their interconversion by electrochemical redox reactions and photochemical reactions.

23.3.3.2 Hexacyanocobaltates, Hexacyanomanganates, Hexacyanochromates, Hexacyanoruthenates

Hexacyanocobaltate(III) is not reducible and hence, most metal hexacyanocobaltates are not electrochemically active. A very interesting exception is copper(II) hexacyanocobaltate(III) that can

be reduced both chemically and electrochemically to copper(I) hexacyanocobaltate(III) coupled to a transfer of charge compensating potassium ions [28]. Hexacyanocobaltate(III) ions can be used to prepare solid solutions with hexacyanoferrate ions. In the case of mixed solid solutions of copper(II) hexacyanoferrate/hexacyanocobaltate, this causes small shifts of the formal potential of the hexacyanoferrate system, and also of the copper(II)/copper(I) system. The latter is only visible for an excess of hexacyanocobaltate [28]. Iron hexacyanochromate is not stable in electrochemical experiments, but isomerizes to chromium hexacyanoferrate [47]. Hexacyanomanganates exhibit two redox systems, corresponding to the redox states Mn(III)/Mn(II) , and Mn(II)/Mn(I) respectively. Whereas chromium(II) and iron(II) hexacyanomanganate are stable in cyclic voltammetry, the manganese(II) hexacyanomanganates(III) decomposes rapidly when the potential is cycled between 0 and -1.5 V vs. Ag/AgCl.

The latter compound, however, is completely stable when the potential is cycled only between -0.7 and -1.5 V vs. Ag/AgCl, where only the Mn(II)/Mn(I) system is active [66].

23.3.3.3 Octacyanomolybdates, Octacyanotungstates

Octacyanomolybdates and octacyanotungstates exhibit an insertion electrochemistry, which is rather similar to that of the hexacyanoferrates, [67] and the compounds show a pronounced electrochromic effect [68].

23.3.3.4 Pentacyanonitrosyl Metalates

Metal pentacyanonitrosyl metalates show an electrochemical behavior similar to that of hexacyanometalates. The compounds show electrocatalytic properties [69].

23.4

Preparation of Electrodes Modified by Polycyanometalates and their Applications

23.4.1

Preparation of Polycyanometalate Modified Electrodes

For choosing the right way of preparation of PCM modified electrodes, the decisive question is the intention of preparation. There are two principally different goals: (1) The electrodes ought to be applied for electrocatalysis, for electrochromic devices and the like, and (2) modified electrodes are prepared to study the electrochemistry of the compounds. For the first goal, there are two principally different approaches: (a) the preparation of films on electrode surfaces, and (b) the incorporation of the PCM into a matrix, for example, a mixture of graphite and a binder, leading to composite electrodes.

1. *The preparation of film electrodes:* Prussian blue films are usually prepared by cycling an electrode in a freshly prepared solution containing iron(III) and hexacyanoferrate(III) ions [70–72]. As substrate, mostly platinum is used, sometimes glassy carbon [73] is used, and very frequently ITO electrodes [74] are used because the latter are very useful for electrochromism studies. Similar procedures using solutions containing metal ions and hexacyanoferrate(III) have been used to deposit cobalt hexacyanoferrate [75] and chromium hexacyanoferrate [76, 77]. Crumbliss et al. reported a plasma deposition of iron species from a plasma containing iron pentacarbonyl and ethane, followed by electrochemical derivatization of the deposited iron sites with the help of hexacyanoferrate solutions [78].

To prepare metal hexacyanoferrate films, very frequently the following procedure was followed: first a film of the respective metal, for example, cadmium [79], copper [80], silver [81], or nickel [82, 83] was electrochemically plated on the surface of a platinum electrode, and that was followed by chemical oxidation of the metal film in a solution of $K_3[Fe(CN)_6]$, leading to the formation of the metal hexacyanoferrates. The same method has been used to produce films of nickel hexacyanoruthenate and hexacyanomanganate using the appropriate anions [83]. It is also possible to perform the oxidation of the deposited metals in solutions containing hexacyanoferrate(II) by cyclic oxidation/reduction of the latter. In a similar way, films of copper heptacyanonitrosylferrate have been deposited [84].

Sauter and Wittstock [85] have described a method for local deposition of cobalt and nickel hexacyanoferrates using the technique of electrochemical scanning

microscopy and sacrificial electrodes from cobalt and nickel.

2. The preparation of electrodes with immobilized PCM: If the purpose of modifying an electrode is the study of the electrochemistry of PCMs, of course, the best choice is to use those compounds that have been synthesized in larger amounts, and that have been characterized by all available analytical techniques, as, for example, X-ray diffraction, infrared spectroscopy, elemental analysis, and so on. (This is usually rather difficult if not impossible with the thin films precipitated on electrode surface by the techniques discussed previously.) Such well-defined samples can be very advantageously investigated by immobilizing microparticles on suitable electrodes [59], mostly on graphite electrodes. The technique of mechanical immobilization has been described in detail [59, 86–89], and it may suffice here to say that, usually, a very tiny amount (around 1 mg) of the powder sample is placed on a glass plate or tile and a graphite electrode is gently rubbed on the sample spot to press some of the microparticles into the electrode surface. This technique proved to be highly useful in systematic studies of the PCMs (see [28, 47, 50, 53, 54]). The technique of immobilizing microparticles on electrodes has also been utilized for in situ calorimetric studies of the insertion electrochemical reactions of PCMs [90, 91]. In this case, very small gold and graphite electrodes had been used and the immobilization technique was slightly different from the procedure described earlier.

23.4.2

Applications of PCM Modified Electrodes

1. Electrochromic devices: The strong differences in the spectra of the PCMs in their various oxidation states, the ease

with which the insertion electrochemical reactions can be performed, their rather good reversibility, and the low price of the PCMs has led to serious expectations for an exploitation in electrochromic windows and displays [92]. Prussian blue is still the compound exhibiting the most pronounced absorption differences, and many attempts have been made to codeposit Prussian blue with other PCMs [93] or with organic conducting polymers to get improved electrochromic properties.

2. Electrocatalysts for electroanalysis: Since PCMs contain transition metal ions that can easily undergo electron exchange reactions, they can act as effective mediators in electron transfer reactions, and thus as catalysts to bring about otherwise strongly inhibited electrode reactions. Mattos and Gorton [94] have recently reviewed the vast literature on electrocatalytic applications of metal hexacyanoferrate films. Although many examples are known, no commercial devices are known that utilize such compounds. PCMs can also be used in biosensors in combination with enzymes. A first-generation biosensor consisting of glucose oxidase immobilized onto a thin film Prussian blue electrode with a Nafion membrane was introduced by Karyakin et al. [95]. Wang et al. [96] have suggested screen printed electrodes containing cupric hexacyanoferrate and glucose oxidase. The dispersed cupric hexacyanoferrate catalyst offers the detection of glucose substrate at very low potentials (the overvoltage for the reduction of the enzymatically liberated hydrogen peroxide is decreased to around 0.1 V at physiological pH).

3. Ion Sensitive electrodes: Metal hexacyanoferrate film electrodes as well as metal hexacyanoferrate particles incorporated in solid composite electrodes have been used for the quantitative analysis of the ions

that are exchanged between the metal hexacyanoferrate and the aqueous solution. Ion selective electrodes for potentiometric sensing of intercalating ions have been described on the basis of nickel hexacyanoferrate [82, 97, 98] and copper hexacyanoferrate [99, 100]. These electrodes display a quasi Nernstian response toward cesium and potassium ions. Rotating disk electrodes modified with cobalt hexacyanoferrate or nickel hexacyanoferrate can be used as ion selective electrodes in the case of Na^+ or K^+ , respectively [101]. Nickel or cupric hexacyanoferrate film electrodes have been also used for amperometric detection of intercalating ions in a flow-injection system (K^+ and NH_4^+ in urine and K^+ in blood samples) [102]. Composite electrodes with different metal hexacyanoferrates incorporated into a graphite/paraffin matrix were used for the voltammetric determination of potassium [103]. A graphite silver hexacyanoferrate composite electrode can be used for the determination of iron(III) ions in solution [52]. Here, the silver ions are reduced to silver(0) and the liberated hexacyanoferrate anions can react with iron(III) ions to give Prussian blue. Following that preconcentration step, the iron(III) ions can be electrochemically determined by evaluating the characteristic signals of Prussian blue. Thallium ions can be determined by preconcentration in Prussian blue and using anodic stripping voltammetry, that is, the thallium ions are reduced to thallium(0), which is subsequently oxidized to give the anodic stripping signal [104]. Prussian blue immobilized in a composite electrode can also be used to determine the concentration of NH_4^+ by evaluating the decrease of the peak system of the carbon coordinated iron ion in cyclic voltammetric measurements [64].

4. *Corrosion protection*: Metal hexacyanoferrate films also attracted interest as corrosion protective layers on metals, especially as additives to conducting polymers [105, 106]. Kulesza et al. [107] reported the coating of steel with an organic anion exchanger (poly(4-vinylpyridine)) incorporating hexacyanoferrate ions that lead to the formation of a Prussian blue layer on the metal, providing surprisingly good corrosion resistance in strongly acidic solutions. This film seems to have even better properties than polyaniline/Prussian blue/hexacyanoferrate films [108].

5. *Batteries*: Metal PCMs should be useful for making rocking chair batteries because one and the same metal ions, for example, potassium ions could be shuttled between the anode and the cathode when suitable compounds are used. The published results indicate that such rocking chair batteries indeed work [109–113]; however, their properties are insufficient to be real competitors on the battery market. Despite the rather low voltages, it is also the presence of as-yet unidentified side reactions that reduces the cycleability of the batteries. Further problems are due to the bad adherence of the PCMs to the current collectors. However, it still cannot be excluded that technical developments may improve the performance of such batteries so that applications are possible.

References

1. A. G. Sharpe, *The Chemistry of Cyano Complexes of the Transition Metals*, Academic Press, London, New York, San Francisco, 1976.
2. J. F. Keggin, F. D. Miles, *Nature* **1936**, 137, 577.
3. A. Ferrari, M. E. Tani, G. Manano, *Gazz. Chim. Ital.* **1959**, 89, 2512.
4. A. Ratuszna, G. Małeck, *Mater. Sci. Forum* **2000**, 321, 947.

5. S. Ayrault, B. Jimenez, E. Garnier et al., *J. Solid State Chem.* **1998**, 141, 475.
6. G. W. Beall, D. F. Mullica, W. O. Milligan, *Acta Crystallogr., Sect. B* **1978**, 34, 1446.
7. W. E. Bailey, R. J. Williams, W. O. Milligan, *Acta Crystallogr., Sect. B* **1973**, 29, 1365.
8. M. V. Zil'berman, V. G. Kuznetsov, V. V. Vol'khin, *Zh. Neorg. Khim.* **1974**, 19, 1838.
9. P. Gravereau, E. Garnier, *Acta Crystallogr., Sect. C* **1984**, 40, 1306.
10. W. Petter, V. Gramlich, F. Hulliger, *J. Solid State Chem.* **1989**, 82, 161.
11. A. Ferrari, M. E. Tani, *Gazz. Chim. Ital.* **1960**, 90, 1565.
12. V. G. Zubkov, A. P. Tyutyunik, I. F. Berger et al., *Solid State Sci.* **2001**, 2, 361.
13. F. Goubard, A. Tabuteau, *J. Solid State Chem.* **2002**, 167, 34.
14. S. Ayrault, C. Loos-Neskovic, M. Fedoroff et al., *Talanta* **1995**, 42, 1581.
15. A. Gomez, E. Reguera, *Int. J. Inorg. Mat.* **2001**, 3, 1045.
16. H. B. Weiser, W. O. Milligan, J. B. Bates, *J. Phys. Chem.* **1942**, 46, 99.
17. M. Rueegg, A. Ludi, K. Rieder, *Inorg. Chem.* **1971**, 10, 1775.
18. D. F. Mullica, P. K. Hayward, E. L. Sappenfield, *Inorg. Chim. Acta* **1996**, 244, 273.
19. A. Gomez, V. H. Lara, P. Bosch et al., *Powder Differ.* **2002**, 17, 144.
20. A. Ludi, H. U. Guedel, N. Rueegg, *Inorg. Chem.* **1970**, 9, 2224.
21. G. W. Beall, W. O. Milligan, J. D. Korp et al., *Inorg. Chem.* **1977**, 16, 2715.
22. A. Ludi, H. U. Guedel, *Helv. Chim. Acta* **1968**, 51, 2006.
23. (a) A. Ludi, H. U. Guedel, *Helv. Chim. Acta* **1968**, 51, 1762; (b) A. Ludi, H. U. Guedel, *Helv. Chim. Acta* **1967**, 50, 2035.
24. D. F. Mullica, E. L. Sappenfield, *J. Solid State Chem.* **1989**, 82, 168.
25. A. Ludi, H. U. Guedel, *Struct. Bonding (Berlin)* **1973**, 14, 1.
26. H. J. Buser, D. Schwarzenbach, W. Petter et al., *Inorg. Chem.* **1977**, 16, 2704.
27. H. Kahlert, F. Scholz, H. Wulff, unpublished.
28. A. Widmann, H. Kahlert, I. Petrovic-Prelevic et al., *Inorg. Chem.* **2002**, 42, 5706.
29. P. J. Kulesza, M. A. Malik, J. Skorek et al., *J. Electrochem. Soc.* **1999**, 146, 3757.
30. S. J. Reddy, A. Dostal, F. Scholz, *J. Electroanal. Chem.* **1996**, 403, 209.
31. X. Ciu, L. Hong, X. Lin, *J. Electroanal. Chem.* **2002**, 526, 115.
32. P. J. Kulesza, M. A. Malik, R. Schmidt et al., *J. Electroanal. Chem.* **2000**, 487, 57.
33. N. F. Zakharchuk, N. Naumov, R. Stösser et al., *J. Solid State Electrochem.* **1999**, 3, 264.
34. M. T. Kelly, G. A. Arbuckle-Keil, L. A. Johnson et al., *J. Electroanal. Chem.* **2001**, 500, 311.
35. A. Widmann, *Insertionselektrochemie Von Festen Metallhexacyanometalaten*, Ph.D. Thesis, Universität Greifswald, 2003.
36. A. Widmann, H. Kahlert, H. Wulff et al., *J. Solid State Electrochem.* **2005**, 9, 380.
37. T. Niu, G. Crisci, J. Lu et al., *Acta Crystallogr., Sect. C* **1998**, 54, 565.
38. A. Ratuszna, S. Juszczak, G. Małeck, *Powder Differ.* **1996**, 11, 318.
39. W. K. Ham, T. J. R. Weakley, C. J. Page, *J. Solid State Chem.* **1993**, 107, 101.
40. A. Loosli, M. Wermuth, H. U. Guedel et al., *Inorg. Chem.* **2000**, 39, 2289.
41. J. K. Nagle, A. L. Balch, M. M. Olmstead, *J. Am. Chem. Soc.* **1988**, 110, 319.
42. U. Klement, *Z. Kristallogr.* **1993**, 208, 285.
43. U. Klement, *Z. Kristallogr.* **1993**, 208, 288.
44. S. C. Abrahams, L. E. Zyontz, J. L. Bernstein, *J. Chem. Phys.* **1982**, 76, 5458.
45. R. Schöllhorn, *Angew. Chem.* **1980**, 92, 1015.
46. H. Kahlert, U. Retter, H. Lohse et al., *J. Phys. Chem.* **1998**, 102, 8757.
47. A. Dostal, U. Schröder, F. Scholz, *Inorg. Chem.* **1995**, 34, 1711.
48. E. Reguera, J. F. Bertrán, L. Nuñez, *Polyhedron* **1994**, 13, 1619.
49. A. Dostal, B. Meyer, F. Scholz et al., *J. Phys. Chem.* **1995**, 99, 2096.
50. M. Hermes, M. Lovrić, M. Hartl et al., *J. Electroanal. Chem.* **2001**, 501, 193.
51. A. Dostal, M. Hermes, F. Scholz, *J. Electroanal. Chem.* **1996**, 415, 133; *J. Electroanal. Chem.* **1997**, 422, 205.
52. H. Kahlert, F. Scholz, *Electroanalysis* **1997**, 9, 922.
53. F. Scholz, A. Dostal, *Angew. Chem.* **1995**, 107, 2876; *Angew. Chem., Int. Ed. Engl.* **1995**, 34, 2685.
54. M. Bárcena Soto, *Thermodynamische Untersuchungen zur Insertionselektrochemie*

- von Metallhexacyanoferraten, Ph.D. Thesis, Humboldt-Universität, Berlin, 2000.
55. M. Bárcena Soto, F. Scholz, *J. Electroanal. Chem.* **2002**, 521, 183.
 56. D. Schwudke, R. Stößer, F. Scholz, *Electrochem. Commun.* **2000**, 2, 301.
 57. A. Crumbliss, P. S. Lugg, N. Morosoff, *Inorg. Chem.* **1984**, 23, 4701.
 58. P. Wu, C. Cai, *J. Solid State Electrochem.* **2004**, 8, 538.
 59. F. Scholz, U. Schröder, R. Gulaboski, *Electrochemistry of Immobilized Particles and Droplets*, Springer, Berlin, 2005.
 60. D. Shaojun, L. Fengbin, *J. Electroanal. Chem.* **1986**, 210, 31.
 61. M. K. Carpenter, R. S. Conell, S. J. Simko, *Inorg. Chem.* **1990**, 29, 845.
 62. K. Itaya, T. Ataka, S. Toshima et al., *J. Phys. Chem.* **1982**, 86, 2415.
 63. A. Dostal, G. Kauschka, S. J. Reddy et al., *J. Electroanal. Chem.* **1996**, 406, 155.
 64. M. Hermes, F. Scholz, *J. Solid State Electrochem.* **1997**, 3, 215.
 65. R. O. Lezna, R. Romagnoli, N. R. de Tacconi et al., *J. Phys. Chem. B* **2002**, 106, 3612.
 66. A. Dostal, *Festkörperreaktionen an Metallhexacyanometalat-Modifizierten Elektroden*, Ph.D. Thesis, Humboldt University, Berlin, 1997.
 67. U. Schröder, F. Scholz, *Inorg. Chem.* **2000**, 39, 1006.
 68. U. Schröder, B. Meyer, F. Scholz, *Fresenius' J. Anal. Chem.* **1996**, 356, 295.
 69. H. Razmi, M. Agazadeh, B. Habibi-A., *J. Electroanal. Chem.* **2003**, 547, 25.
 70. V. D. Neff, *J. Electrochem. Soc.* **1978**, 125, 886.
 71. D. Ellis, M. Eckhoff, V. D. Neff, *J. Phys. Chem.* **1981**, 85, 1225.
 72. K. Itaya, I. Uchida, V. D. Neff, *Acc. Chem. Res.* **1986**, 19, 162.
 73. C. Kuhnhardt, *J. Electroanal. Chem.* **1994**, 369, 71.
 74. A. Roig, J. Navarro, R. Tamarit et al., *J. Electroanal. Chem.* **1993**, 360, 55.
 75. P. J. Kulesza, M. A. Malik, S. Zamponi et al., *J. Electroanal. Chem.* **1995**, 397, 287.
 76. M. Jiang, X. Zhou, Z. Zhao, *J. Electroanal. Chem.* **1990**, 287, 389.
 77. Z. Gao, *J. Electroanal. Chem.* **1994**, 370, 95.
 78. A. L. Crumbliss, P. S. Lugg, D. L. Patel et al., *Inorg. Chem.* **1983**, 22, 3541.
 79. C. H. Luangdilok, D. J. Arent, A. B. Bocarsly, *Langmuir* **1992**, 8, 650.
 80. L. M. Siperko, T. Kuwana, *J. Electrochem. Soc.* **1983**, 130, 396.
 81. S. Moon, J. D. Moon, *Bull. Korean Chem. Soc.* **1994**, 15, 1042.
 82. L. F. Schneemeyer, S. E. Sprengler, D. W. Murphy, *Inorg. Chem.* **1985**, 24, 3044.
 83. S. Sinha, B. D. Humphrey, A. B. Bocarsly, *Inorg. Chem.* **1984**, 23, 203.
 84. Z. Gao, Y. Zhang, M. Tian et al., *J. Electroanal. Chem.* **1993**, 358, 161.
 85. S. Sauter, G. Wittstock, *J. Solid State Electrochem.* **2001**, 5, 205.
 86. F. Scholz, B. Lange, *Trends Anal. Chem.* **1992**, 11, 359.
 87. F. Scholz, B. Meyer, *Chem. Soc. Rev.* **1994**, 23, 341.
 88. F. Scholz, B. Meyer, Voltammetry of solid microparticles immobilized on electrode surfaces in *Electroanalytical Chemistry, A Series of Advances* (Eds.: A. J. Bard, I. Rubinstein), Marcel Dekker, New York, 1998, p. 1, Vol. 20.
 89. D. A. Fiedler, F. Scholz, Electrochemical studies of solid compounds and materials in *Electroanalytical Methods - Guide to Experiments and Applications* (Ed.: F. Scholz), Springer, Berlin, p. 331.
 90. M. Bárcena Soto, G. Kubsch, F. Scholz, *J. Electroanal. Chem.* **2002**, 528, 18.
 91. M. Bárcena Soto, F. Scholz, *J. Electroanal. Chem.* **2002**, 528, 27.
 92. P. M. S. Monk, R. J. Mortimer, D. R. Rosseinsky, *Electrochromism: Fundamentals and Applications*, VCH, Weinheim, 1995.
 93. L.-C. Chen, Y.-H. Huang, K.-C. Ho, *J. Solid State Electrochem.* **2002**, 7, 6.
 94. I. L. de Mattos, L. Gorton, *Quim. Nova* **2001**, 24, 200.
 95. A. A. Karyakin, O. V. Gitelmacher, E. E. Karyakina, *Anal. Chem.* **1995**, 67, 2419.
 96. J. Wang, X. Zhang, *Anal. Lett.* **1999**, 32, 1739.
 97. M. Giorgetti, E. Scavetta, M. Berrettoni et al., *Analyst* **2001**, 126, 2168.
 98. L. J. Amos, A. Duggal, E. J. Mirsky et al., *Anal. Chem.* **1988**, 60, 245.
 99. D. Engel, E. W. Grabner, *Ber. Bunsen-Ges. Phys. Chem.* **1985**, 89, 982.
 100. Y. Tani, H. Eun, Y. Umezawa, *Electrochim. Acta* **1998**, 43, 3431.
 101. L. Muresan, I. C. Popescu, L. Oniciu, *Stud. Univ. Babes-Bolyai, Chem.* **1995**, 40, 161.
 102. K. N. Thomsen, R. P. Baldwin, *Electroanalysis* **1990**, 2, 263.

103. H. Düssel, A. Dostal, F. Scholz, *Fresenius' J. Anal. Chem.* **1996**, 355, 21.
104. H. Kahlert, Š. Komorsky-Lovrić, M. Hermes et al., *Fresenius' J. Anal. Chem.* **1996**, 356, 204.
105. D. E. Tallman, G. Spinks, A. Dominis et al., *J. Solid State Electrochem.* **2002**, 6, 73.
106. G. Spinks, A. Dominis, G. G. Wallace et al., *J. Solid State Electrochem.* **2002**, 6, 85.
107. M. T. Galkowski, P. J. Kulesza, K. Miecznikowski et al., *J. Solid State Electrochem.* **2004**, 8, 430.
108. M. Galkowski, M. A. Malik, P. J. Kulesza et al., *J. Electrochem. Soc.* **2003**, 150, B249.
109. V. D. Neff, *J. Electrochem. Soc.* **1985**, 132, 1382.
110. E. W. Grabner, S. Kalwellis-Mohn, *J. Appl. Electrochem.* **1987**, 17, 653.
111. K. Kuwabara, J. Nunome, K. Sugiyama, *Solid State Ionics* **1991**, 48, 303.
112. M. Jayalakshmi, F. Scholz, *J. Power Sources* **2000**, 87, 212.
113. M. Jayalakshmi, F. Scholz, *J. Power Sources* **2000**, 91, 217.

24

Electrochemistry of Zinc, Cadmium, Lead, Gold, Silver, Mercury, and Copper

Part A:	Electrochemistry of Zinc, Cadmium and Lead	725
	<i>Jadwiga Stroka, Krzysztof Maksymiuk, and Zbigniew Galus</i>	
24.1	Electrochemistry of Zinc	725
24.2	Electrochemistry of Cadmium	767
24.3	Electrochemistry of Lead	804
Part B:	Electrochemistry of Gold, Silver, and Mercury	839
	<i>Marek Orlik and Zbigniew Galus</i>	
24.4	Electrochemistry of Gold	839
24.5	Electrochemistry of Silver	913
24.6	Electrochemistry of Mercury	958
Part C:	Electrochemistry of Copper	992
	<i>David B. Rorabacher and Ronald R. Schroeder</i>	
24.7	Electrochemistry of Copper	992

Part A:

Electrochemistry of Zinc, Cadmium, and Lead*

Jadwiga Stroka, Krzysztof Maksymiuk, and Zbigniew Galus
Department of Chemistry, University of Warsaw, Warsaw,
Poland

**Dedicated to the memory of Professor Robert A. Osteryoung, prominent electrochemist and analyst*

24.1

Electrochemistry of Zinc

24.1.1	Double-layer Properties of Zinc Electrodes	726
24.1.1.1	Pc-Zinc in Aqueous Solutions	726
24.1.1.2	Zn Single Crystals in Aqueous Solutions	727
24.1.2	Electrochemical Properties and Kinetics of the Zn(II)/Zn(Hg) and Zn(II)/Zn Systems	727
24.1.2.1	Electrochemistry in Aqueous Solutions	727
24.1.2.2	Electrochemistry in Water-organic Solvent Mixtures	731
24.1.2.3	Electrochemistry in Nonaqueous Solvents	733
24.1.2.4	The Influence of Organic Compounds on the Electrode Processes . .	734
24.1.2.5	The Electrochemical Properties of the Zinc Complexes	736
24.1.2.6	Properties of Zinc Oxide Electrode	737
24.1.2.7	Electrode Processes in Molten Salts	738
24.1.3	Deposition and Underpotential Deposition of Zn on Solid Electrodes	740
24.1.3.1	Underpotential Deposition of Zinc	740
24.1.3.1.1	Zn UPD on Pt	740
24.1.3.1.2	Zn UPD on Au	741
24.1.3.2	Zinc Electrodeposition on Solid Electrodes	742
24.1.3.2.1	Electrodeposition on Zn Electrodes	742
24.1.3.2.2	Electrodeposition on Other Electrodes	744
24.1.4	Passivation and Corrosion of Zinc	745
24.1.4.1	Anodic Dissolution and Passivation of Zinc	745
24.1.4.2	Corrosion	747

24.1.5	Applied Electrochemistry	748
24.1.5.1	Batteries	748
24.1.5.1.1	Ni–Zn Cells	748
24.1.5.1.2	Zn–Air Batteries	749
24.1.5.1.3	Zn–MnO ₂ Batteries	749
24.1.5.1.4	Zn–Ag Batteries	750
24.1.5.1.5	Other Cells	751
24.1.5.2	Electrowinning	751
24.1.5.3	Zinc Electroplating	753
24.1.5.4	Zinc Alloys Electroplating	753
24.1.5.5	Electrochemical Sensors and Modified Electrodes	754
24.1.5.5.1	Potentiometric Sensors	754
24.1.5.5.2	Voltammetric/Amperometric Sensors	755
24.1.5.5.3	Modified Electrodes	755
	References	756

This chapter is a supplement to the issue of *Encyclopedia of Electrochemistry of the Elements*. Owing to limited space, not all relevant work could even be briefly discussed. In this review, mainly the recent papers published in the last 10 years have been presented, with some relation to earlier works published after 1977, when the chapters on lead, cadmium, and zinc electrochemistry appeared.

24.1.1

Double-layer Properties of Zinc Electrodes

Electrical double-layer (edl) properties of solid polycrystalline zinc (pc-Zn) electrodes and single-crystal zinc electrodes in aqueous solution were studied in many works, which are reviewed in Refs 1, 2.

24.1.1.1 Pc-Zinc in Aqueous Solutions

The pc-Zn electrode was found to be nearly ideally polarizable at sufficiently wide negative polarization range [3–8]. The differential capacitance of zinc electrode was

studied in aqueous electrolytes: KCl (pH 7) [6], Na₂SO₄ [7], NaClO₄, KCl, KNO₃, and Na₂SO₄ (pH 6.6–7) [9]. Minima on the differential capacitance (*C*–*E*) curves on the pc-Zn electrodes were observed. In 0.01 M KCl aqueous solutions, the minimum was broader.

For pc-Zn/H₂O, the value of zero charge potential (E_{pzc}) was found to be equal to about –1.15 V (versus saturated calomel electrode (SCE)) [10, 11]. The same values of E_{pzc} were obtained by a scrape method in a neutral NaClO₄ aqueous solution [12].

In the presence of tetrabutylammonium iodide (TBAI) in its adsorption region on the pc-Zn electrode, the *edl* capacitance decreased with increasing TBAI concentration and the capacity minimum shifted to more negative potentials [13]. At still more negative potentials, a well-defined adsorption–desorption peak was observed. Splitting of this peak was explained by the presence of different faces on the surface of pc-Zn electrode.

24.1.1.2 Zn Single Crystals in Aqueous Solutions

Zinc crystallizes in a hexagonal close-packed system; its basal face (0001) was prepared by cleavage of single crystal at the temperature of liquid nitrogen, and the prismatic face (10 $\bar{1}$ 0) and the face (11 $\bar{2}$ 0) were prepared by polishing in nitric acid [2].

The first attempt to determine zero charge potential for single-crystal sp metal was described for zinc [3, 6] from $C-E$ capacitance curves in dilute solutions. E_{pzc} for the face of Zn(0001) was about 80 mV more positive than that for Zn(10 $\bar{1}$ 0). Later, it was pointed out [6, 10] that the determination of E_{pzc} directly from $C-E$ dependencies was not possible for zinc because the potential is close to the reversible standard potential of zinc in aqueous solution.

Therefore, E_{pzc} was determined using the indirect methods valid for single-crystals electrodes and pc-Zn electrodes [1, 2, 14, 15]: (1) salting-out of organic compounds from surface inactive electrolyte solutions, (2) from the potential corresponding to maximum on $C-E$ curves for organic compounds with high attractive interaction constant a , and (3) from the dependence of the capacitance minimum on thiourea (TU) concentration. The obtained values of zero charge potentials were in good agreement with other results [7, 8]. For various faces of Zn single-crystal electrode, the maximum difference between E_{pzc} was about 90–100 mV [2, 15, 16].

Most investigations on edl of zinc single-crystal faces were made in solutions containing organic compounds: tetraethylammonium cations [7], hexanol [17–19], tetrabutylammonium cations [13, 14, 18, 19], camphor [18–20], cyclohexanol [14, 21], and TU [22, 23]. For these substances, dependence of adsorption properties on

crystal face was observed. The potential of adsorption–desorption peak on $C-E$ curves shifts to more negative potentials in the order Zn(0001) < Zn(10 $\bar{1}$ 0) < Zn(11 $\bar{2}$ 0), and this sequence was explained by increasing the negative values of E_{pzc} .

The adsorption–desorption peaks on the single-crystal faces were narrower and higher than the peaks on the polycrystalline electrodes.

The adsorption of some neutral organic compounds on the individual faces of zinc single-crystal electrodes was described by the Frumkin-Damaskin theory with the use of two parallel capacitors model [14]. For pc-Zn electrode, a departure from the two parallel capacitors model due to the energetic inhomogeneity of the surface was observed.

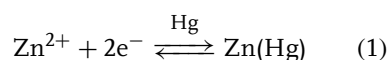
The edl parameters and adsorption parameters for various electrodes are presented by Lust et al. [24].

24.1.2

Electrochemical Properties and Kinetics of the Zn(II)/Zn(Hg) and Zn(II)/Zn Systems

24.1.2.1 Electrochemistry in Aqueous Solutions

The electroreduction of Zn(II) at a mercury electrode has been studied in aqueous media [25–38]. In noncomplexing media, this reaction can be described as



Two different mechanisms have been proposed to explain Zn(II) electroreduction in aqueous solutions, either a simple two-electron transfer in one step [28–30, 32, 33, 35, 37] or two successive one-electron transfer processes [25–27, 30] with Zn(I) as an intermediate.

From the galvanostatic and chronopotentiometric polarization measurements

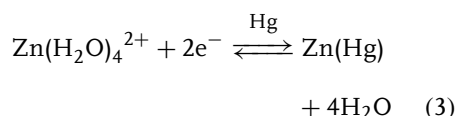
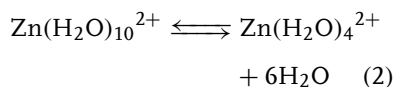
in both directions of the Zn(Hg)/Zn(II) electrode process at 25°C in 1 M chloride solutions ($1 \text{ M Cl}^- = c(\text{ZnCl}_2) + c(\text{MgCl}_2) + c(\text{HCl})$) of pH 3, Hurlen and Eriksrud [25] have found that the charge transfer occurs in two consecutive steps and that both steps are essentially symmetric. For both steps the quantitative kinetic data were presented and discussed.

Eriksrud [26] has also studied the Zn(II)/Zn(Hg) system in $x \text{ M KI} + (1-x) \text{ M KCl}$, 1 M KBr , and 1 M MeCl ($\text{Me} = \text{Li}, \text{Na}, \text{K}, \text{and Cs}$) solutions of pH 3. The substitution of chloride by bromide or iodide ions increases the rate of the Zn(I)/Zn(Hg) step more significantly than that of the Zn(II)/Zn(I) step. At iodide concentrations higher than 0.1 M , the rate of the Zn(I)/Zn(Hg) step is too high for the used experimental methods to be measured. Contrary to the Zn(I)/Zn(II) system, the rate of charge transfer for Zn(I)/Zn(Hg) step is practically independent of the kind of alkali metal cation supporting electrolyte. It can be explained by the change of Zn(II) activity in dependence on a type of cation of the supporting electrolyte.

In work [27], the Zn(II)/Zn(Hg) electrode process was investigated in 0.5 M MgSO_4 solutions at 25°C by ac and faradic rectification polarography. The Zn(II)/Zn(Hg) electrode reaction was considered as a two-step process. The kinetic parameters of both steps were evaluated.

Jindal et al. [28] have determined the kinetic parameters of Zn(II) reduction on the dropping mercury electrode (DME) in concentrated NaNO_3 , LiNO_3 , NH_4NO_3 , $\text{Mg}(\text{NO}_3)_2$, $\text{Ca}(\text{NO}_3)_2$, and NaClO_4 as supporting electrolytes, using the square-wave polarographic method. Diffusion coefficient of Zn(II) decreases with increasing concentration of supporting electrolyte caused by the change of solution viscosity.

The reversible half wave potential ($E_{1/2}$) values became higher with the increase of the concentration of supporting electrolyte, but the α values were practically constant. The rate parameters decreased with increase of radius and charge of the cation of supporting electrolyte at the same ionic strength. The number of water molecules associated with zinc ions in the solutions and with reactant, which directly takes part in the charge-transfer process, was estimated and the following reaction scheme was proposed.



The electrode reaction of Zn(II) on the DME was also studied in aqueous solutions of $(\text{NH}_4)_2\text{SO}_4$ and the kinetic parameters were determined [29].

The double-layer influence on the electrode reaction of Zn(II)/Zn(Hg) on DME in NaNO_3 solutions was studied in the concentration range from 0.01 to 1 M , using dc and ac polarography [30]. The apparent rate constants of the Zn(II)/Zn(Hg) system increase with dilution of the NaNO_3 supporting electrolyte. However, after the Frumkin correction, the rate constant was virtually independent of the supporting electrolyte concentration.

Go and Osteryoung [31] presented the alternative interpretation of the data for electroreduction of Zn(II) on the mercury electrode. They have found that in non-complexing media, zinc electroreduction may be represented by a single step with transfer of both electrons.

Osteryoung and coworkers [32, 33] optimized the square-wave voltammetry and

rapid-scan voltammetry to determine the kinetic parameters of the Zn(II)/Zn(Hg) system in 1 M NaNO₃ [32] and KNO₃ solutions with different concentrations [33].

Sluyters and coworkers [34] have studied the mechanism of Zn(II) reduction on DME in NaClO₄ solutions at different water activity (a_w) using faradaic impedance method. D_{Ox} and $E_{1/2}^r$ were determined from dc polarographic curves. Hydration numbers of Zn(II) ion were estimated from the dependence of $E_{1/2}^r$ on $\ln a_w$. The obtained standard rate constant was changing with a NaClO₄ concentration and the slope of the dependence of $\ln k_f$ on potential was changing with potential (see Fig. 1). Therefore, the following mechanisms were proposed:

1. Fast partial dehydration of electroactive species $Zn(H_2O)_{19.6}^{2+}$, which loses in average 9.3 water molecules.
2. Fast transport of reactant from solution into diffusion layer.
3. Slow transfer of first electron with $\alpha_{e1} = 0.4$.
4. Fast loss of the remaining 10.3 water molecules.
5. Slow transfer of the second electron with $\alpha_{e2} = 0.4$.

In 7 M NaClO₄ solution, the hydration number of Zn(II) decreased to about 8.6.

The authors believe that the reaction plane is situated at a greater distance from the electrode surface than the Helmholtz outer plane.

The kinetic parameters of Zn(II)/Zn(Hg) electrode reaction in aqueous solution containing perchlorate, nitrate, chloride, and bromide ions were measured at different temperatures (5–50°C) [35]. The Arrhenius activation energy and thermodynamic parameters for the Zn(II)/Zn(Hg) system

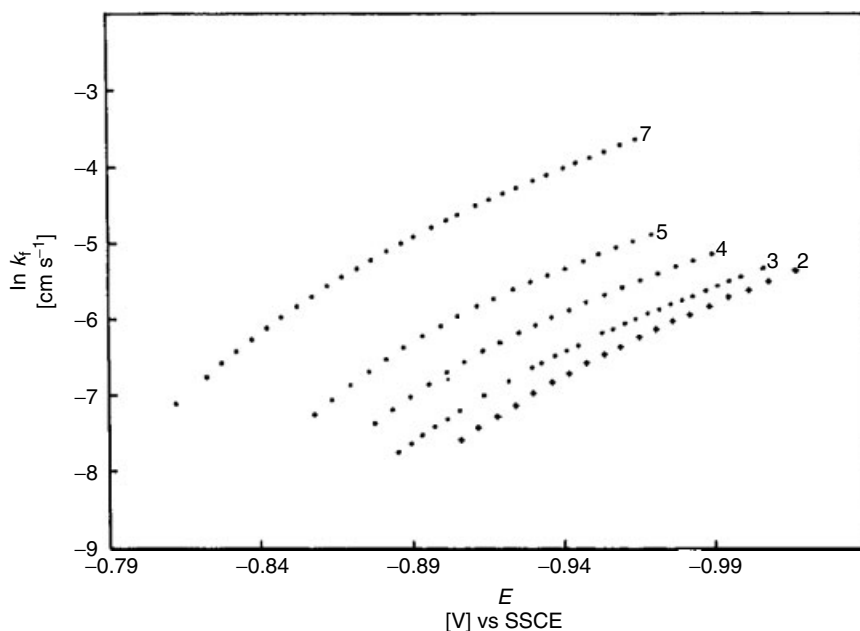
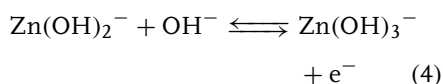


Fig. 1 Plots of $\ln k_f$ versus potential for the Zn(II) reduction in concentrated NaClO₄ supporting electrolytes. The molarity of NaClO₄ is indicated at each curve [34].

were determined from the temperature dependence of the rate constant and equilibrium potential, respectively. Empirical correlations between some pairs of kinetic and thermodynamic quantities were observed.

Hendrikx et al. [36] investigated the reaction kinetics and mechanism of zinc and amalgamated zinc electrode in KOH solutions in the concentration range 1.5–10 M using galvanostatic methods. On the basis of Tafel slopes and reaction orders for OH^- , the following rate determining step (rds) in anodic and cathodic processes was postulated:



The obtained results are in agreement with the mechanism suggested by Bockris and Nagy [37].

Sluyters and coworkers [38] have studied the catalytic influence of adsorbed iodide ions on the electroreduction of Zn(II) on the mercury electrode. It was found that the charge-transfer process proceeds through two consecutive one-electron transfer steps. Logarithms of the rate constant of both steps are linearly dependent on the amount of adsorbed iodides (Fig. 2). The experimental data were compared with the existing theoretical anion-binding model used to describe the observed results.

The $\text{Zn(II)}/\text{Zn(Hg)}$ was also studied at dropping mercury microelectrodes.

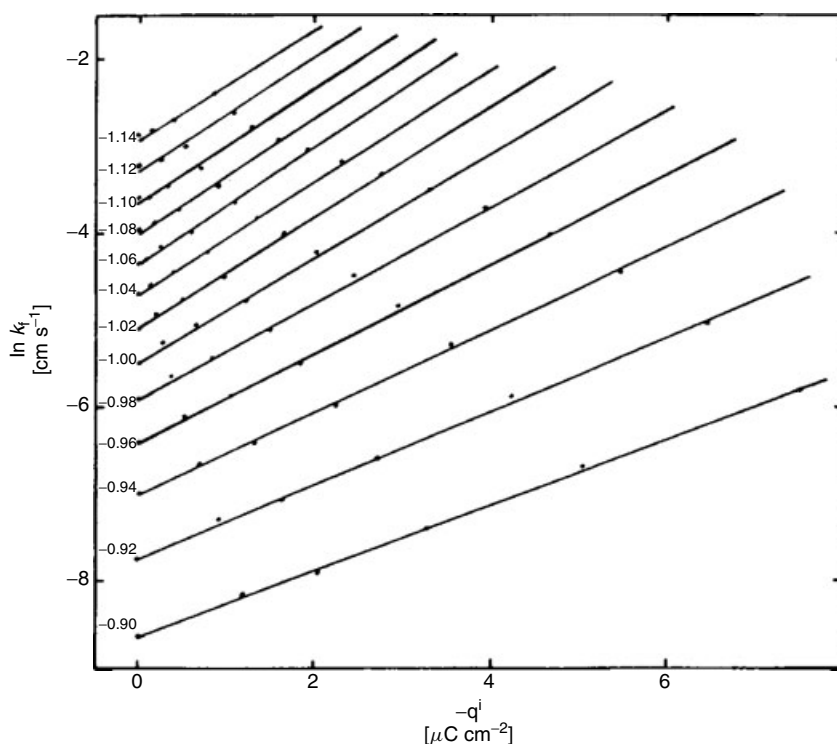


Fig. 2 The relationship between the electroreduction rate constant of Zn(II) and the amount of specifically adsorbed anion obtained at constant potentials in x M $\text{NaI} + (1-x)$ M NaClO_4 electrolyte [38]. The potentials are indicated at each curve.

Kinetic parameters were found similar to those obtained with classical mercury electrodes [39].

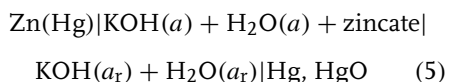
Using the dropping zinc amalgam microelectrode, detailed kinetic data were obtained [40], and the two consecutive electron transfers followed by a chemical reaction (EEC) mechanism of Zn(II) reduction could be revealed.

Dropping indium and thallium amalgam electrodes [41] were used to determine kinetic parameters of Zn(II) reduction as a function of the amalgam composition. The formal potentials were shifted to more negative values with increasing thallium and indium amalgam concentrations.

The reduction of Zn(II) from 1 M NaClO₄ in the presence of 1 mM HClO₄ was studied at the dropping gallium and mercury electrodes [42]. Zn(II)/Zn(Ga) waves were obtained after subtraction of the H₃O⁺ reduction current recorded in the absence of Zn(II)/Zn(Ga) couple.

Reduction of Zn(II) on the above mentioned electrodes [40–42] proceeds via the same two-step electron transfer mechanism that was established earlier at mercury [34].

The redox equilibria of the amalgamated zinc electrode in unsaturated and saturated zincates solutions were studied in the cell [43]



where a is the activity of species in the working compartment and a_r is the activity of species in the reference compartment solutions. It was found that the equilibrium potential of the amalgamated zinc electrode first increases and then decreases with increase of zincates concentration in the solutions. The influence of zincates concentration and its activity coefficient

on the equilibrium potential of the amalgamated zinc electrode were discussed.

Temperature effect on the electrodeposition of zinc on the static mercury drop electrode (SMDE) and glassy carbon (GC) electrode was studied in acetate solutions [44]. From the obtained kinetic parameters, the activation energies of Zn(II)/Zn(Hg) process were determined.

Quantum chemical calculations concerning reduction of the Zn(II) aqua complexes on metal electrodes were also presented [45].

24.1.2.2 Electrochemistry in Water-organic Solvent Mixtures

Kinetic parameters of zinc electrode processes in water-organic mixtures depend strongly on the composition of the surface layer, which is modified by the adsorption of organic solvent on the electrode and also on reactant solvation [46], which is changing with a solvent composition.

The electrode behavior of the Zn(II)/Zn(Hg) system was investigated in mixtures of water with several organic solvents – *N,N*-dimethylformamide (DMF) [47], dimethylsulfoxide (DMSO) [48–50], hexamethylphosphortriamide (HMPA) [51, 52], 1,3-dimethyl-3,4,5,6-tetrahydro-2(1*H*)-pyrimidinone (DMPU) [53], ethylene glycol [54], and 1,2-propanediol [55]. The obtained values of Gibbs energies of transfer (ΔG_{tr}) of Zn(II) ion from water to water-organic mixtures are negative in the case of mixtures with DMF [47], DMSO [48], DMPU [53], and HMPA [51]. This suggests that Zn(II) ions are preferentially solvated by the organic components of these mixtures.

In the mixtures of water with solvents that are characterized by donor numbers (DN) higher than that of water, such as DMF, DMPU, DMSO, and HMPA, the rate of the electrode process

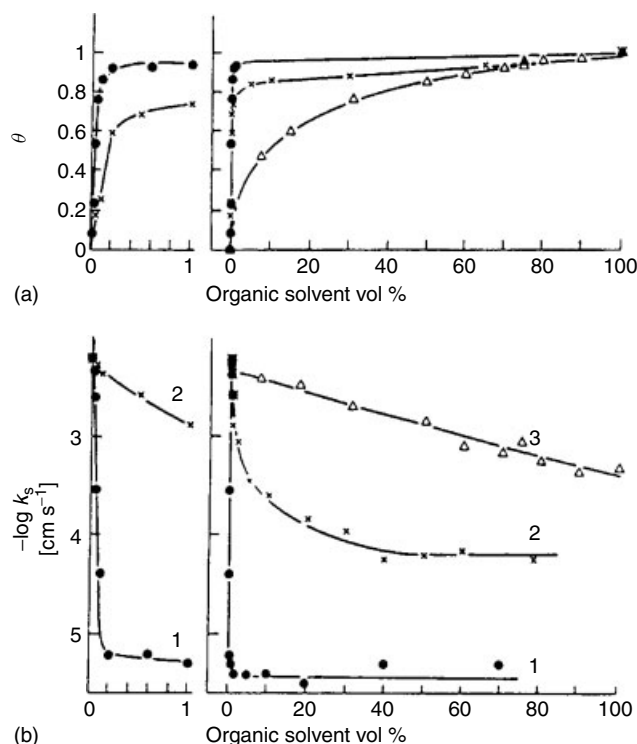


Fig. 3 (a) Adsorption isotherms of organic solvents on the mercury electrode at the formal potential of the Zn(II)/Zn(Hg) system: (1-●-) HMPA, (2-x-) DMPU, (3-Δ-) DMSO. (b) Dependence of the standard rate constant of the Zn(II)/Zn(Hg) system on the mixed solvent composition: (1) HMPA + water, (2) DMPU + water, (3) DMSO + water mixtures [53].

of the Zn(II)/Zn(Hg) system decreased at concentrations corresponding to the rising part of adsorption isotherm of the organic component of the mixture on the mercury electrode (see Fig. 3) [53]. In these mixtures the following equation was obeyed

$$k_s = k_w(1 - \theta)^a + k_{\text{sol}}\theta^b \quad (6)$$

where k_s , k_w , and k_{sol} denote the standard rate constants in mixtures, water, and organic solvent respectively, and a and b denote the number of molecules of water and organic solvents, respectively, that interact with one reactant ion when it is penetrating the surface layer.

In the mixtures of water with organic solvents of lower than water donicity such as water-methanol [56, 57] and water-ethanol [58], the rate constant of the Zn(II)/Zn(Hg) system changes nonmonotonically with solvent composition and exhibits a minimum for such concentration of organic component in the mixture, at which the Zn(II) ions are solvated by water molecules but the electrode is already solvated by the organic solvent. The influence of the composition of such mixtures on the rate of the Zn(II)/Zn(Hg) electrode processes was described by the equation [56, 57, 59]

$$c^s = c^b \exp[-\Delta G_{\text{tr}}/RT] = c^b P \quad (7)$$

where c^s and c^b are the reactant concentrations in the surface and bulk phase respectively, and P is the partition coefficient of the reactant between bulk and surface phase.

The influence of concentration and type of supporting electrolyte [49, 52] and also temperature [50] on the Zn(II) electroreduction was investigated in water–DMSO and water–HMPA mixtures. The change of kinetic parameters under the influence of these factors was similar to that observed in pure aqueous solutions.

The influence of TU on the electroreduction of Zn(II) at the mercury electrode has been investigated in several water-organic solvent mixtures. It was found that in water–DMSO 1 M NaClO₄ solutions [60–63], the presence of TU in the solutions accelerated the rate of Zn(II) electroreduction. This accelerating effect was lower at higher DMSO content in the mixture. The acceleration of the Zn(II)/Zn(Hg) electrode process is connected with the structure of the primary solvation shell of Zn(II) ions [61]. The kinetics of Zn(II) electroreduction in water–DMSO mixtures containing 1 M NaClO₄ and TU was also investigated as a function of temperature [62]. The diffusion coefficients, formal potentials, standard rate constants, and the real activation energy of the electrode reaction were determined. The presence of TU decreased the values of real energy of activation in all investigated solutions.

The influence of TU on Zn(II) electroreduction at the mercury electrode was also investigated in mixtures of water with DMF [63, 64], methanol [62, 63, 65], ethanol, and acetone [66, 67] with NaClO₄ as a supporting electrolyte. In all these mixtures, the rate of Zn(II)/Zn(Hg) process was accelerated by adsorbed TU molecules. It was postulated that the composition

of the activated complex formed on the electrode plays the dominant role in the acceleration of the electrode processes.

The kinetics of Zn(II) electroreduction in water–methanol mixtures containing 1 M NaClO₄ and TU was also investigated as a function of temperature [62]. The values of activation energy of Zn(II) electroreduction in these mixtures reached a maximum in the solution with 20 vol % of methanol. The apparent and true rate constants of the first and second electron charge transfer of Zn(II) electroreduction on Hg electrode in aqueous solution, and in the mixtures of water with methanol 91 vol %, DMSO 70 vol %, and DMF 90 vol % containing TU were estimated [63]. The data have shown acceleration of Zn(II) electroreduction in examined solutions. Very high catalytic influence of TU was observed in the mixtures in which Zn(II) ions were specifically hydrated.

The influence of *p*-toluidine [68], 1,5-diaminonaphthalene (DAN), and *N,N'*-diphenylthiourea (DFTU) [69] in water-organic mixtures on the two-step electroreduction of Zn(II) was also examined. The presence of *p*-toluidine accelerated the first electron transfer in water –90 vol % DMF and water –91 vol % methanol [68]. DAN and DFTU had no effect on Zn(II) electroreduction in aqueous solutions but they also catalyzed this process in water–methanol mixtures [69].

24.1.2.3 Electrochemistry in Nonaqueous Solvents

The behavior of the Zn(II)/Zn(Hg) system in nonaqueous solvents containing tetraalkylammonium perchlorate ions was presented in works [70–73]. The data show that the standard rate constant, k_s , in DMF and DMSO [70] solutions changes with size of the electrolyte cation in the order $k_s(\text{TPA}^+) > k_s(\text{TBA}^+) > k_s(\text{TEA}^+)$; k_s

values also become lower with increasing concentration of the electrolyte [70, 71]. The rate of the reaction for a given supporting electrolyte is always lower in DMSO than in DMF. It is connected with a stronger solvation of Zn(II) ions by DMSO than by DMF. In DMSO solutions [71] the dependence of the logarithm of the rate constant on the electrode potential indicated a two-step process. The possible mechanisms were discussed, namely, (1) two one-electron reduction processes and (2) cation transfer through the double layer.

The electrochemical rate constants of the Zn(II)/Zn(Hg) system obtained in propylene carbonate (PC), acetonitrile (AN), and HMPA with different concentrations of tetraethylammonium perchlorate (TEAP) decreased with increasing concentration of the electrolyte and were always lower in AN than in PC solution [72]. The mechanism of Zn(II) electroreduction was proposed; in PC and AN the electroreduction process proceeds in one step. In HMPA, the Zn(II) electroreduction on the mercury electrode is very slow and proceeds according to the mechanism in which a chemical reaction was followed by charge transfer in two steps (CEE). The linear dependence of logarithm of heterogeneous standard rate constant on solvent DN was observed only for values corrected for the double-layer effect.

The electrode kinetics of the Zn(II)/Zn(Hg) system was investigated in PC + DMSO mixtures [73] containing 0.1 M TEAP. It was found that the $\log k_{s, \text{corr}}$ varies linearly with the Gibbs energy of transfer of the Zn(II) ion.

Anastopoulos [74–76] has investigated the inhibition of the Zn(II) electroreduction in organic solvents. The electroreduction of Zn(II) on the mercury electrode was inhibited by the adsorbed molecules

of triphenylphosphine oxide (TPO) in PC and AN [74, 76] and formamide [75, 76] solutions. The reaction rate decreased with increasing electrode coverage, θ , by TPO molecules. The dependences of $\ln k_f$ on $\ln (1 - \theta)$ at constant potential were linear [74] with different slopes, $r \neq$. The size parameter, $r \neq$, of the activated complex was changing from 3.0 to 5.5. It was concluded that the most probable mechanism for electroreduction Zn(II) on the mercury electrode in AN, PC, and formamide solutions is the ion transfer–adsorption mechanism.

24.1.2.4 The Influence of Organic Compounds on the Electrode Processes

The organic substances adsorbed on the mercury electrodes exert either inhibiting or catalytic influence on the process of Zn(II)/Zn(Hg) system. The inhibiting influence was observed in the presence of butyl acetate [77] and was dependent on the electrolyte concentration probably owing to the “salting-out” effect.

The catalytic influence of several organic substances on the electrode process of the system Zn(II)/Zn(Hg) was investigated intensively. In the presence of anthranilic and thiosalicylic acids [78], the rate constant of the first electron transfer k_{s1} increased with increasing surface concentration of acids, while the rate constant of the second electron transfer decreased. The catalytic effect of thiosalicylic acid is higher than that of anthranilic acid.

In the presence of TU [79, 80], the rate constant of Zn(II) electroreduction changes nonmonotonically with surface concentration of TU and a maximum was observed for $\Gamma_{\text{TU}} = 3 \times 10^{-7} \text{ mol m}^{-2}$. The accelerating effect of TU was larger at more negative potentials. The adsorbed TU molecules accelerated the first and second electron transfer. The activation enthalpies

of both steps were determined from the measurements at different temperatures.

The catalytic effect of N,N' -dialkylthioureas on Zn(II) electroreduction was also observed by Dalmata [81]. In this case, the rate constant of the first electron transfer increased with increasing concentration of N,N' -dialkylthioureas, whereas the rate constant of the second electron transfer was largely dependent on the double-layer effect.

The studies on catalytic influence of diaminotoluene isomers on zinc reaction have shown the highest accelerating effect for 3,4-diaminotoluene [82–85]. The difference in catalytic activity of these isomers resulted from the difference in complex formation with Zn(II) ions because the adsorption properties of these isomers on the mercury electrode are similar [82, 84]. Two steps of Zn(II) electroreduction were postulated in the presence of diaminotoluene isomers, with the first electron transfer as a rate-determining step. The influence of diaminotoluene isomers and pH on this electrode process was studied in acetate buffers [86].

The influence of mixed adsorption layer on the Zn(II) electroreduction was also

studied [87–90]. n -Butanol (BU) is an inhibitor of the $\text{Zn(II)}/\text{Zn(Hg)}$ electrode process, whereas TU accelerates this process [87]. With the increase of TU concentration, the standard rate constant values increased to the maximum value of 0.1 cm s^{-1} , which is reached at the concentration of 0.33 M TU. When BU was added to TU solutions, the rate of the $\text{Zn(II)}/\text{Zn(Hg)}$ process decreased. For the molar concentration ratio $[\text{BU}]/[\text{TU}] \approx 12$, the inhibition was compensated by the accelerating effect.

A similar influence was observed for mixed adsorption layers of BU/toluidine isomers [88, 89].

The obtained values of true standard rate constants of transfer of the first electron, $k_{s,1}^t$, and second electron step, $k_{s,2}^t$, show that the charge transfer in the first step is stronger accelerated by toluidine than the second one [89]. Greater catalytic activity of p -toluidine compared with m -toluidine was observed (see Fig. 4).

In the presence of poly(ethyleneglycols) (PEG)–TU layers [90], the $\text{Zn(II)}/\text{Zn(Hg)}$ process could be accelerated by TU, inhibited by PEG, or the compensation of these effects could occur depending on

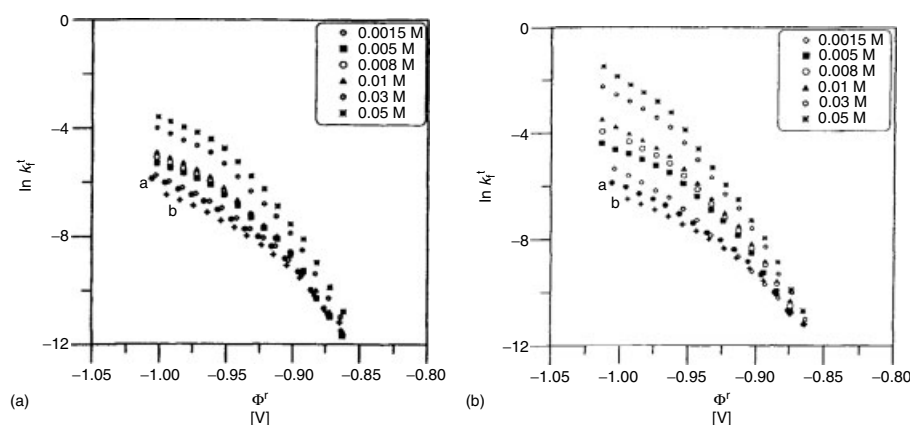


Fig. 4 Natural logarithms of corrected rate constant versus Φ^r for the $\text{Zn(II)}/\text{Zn(Hg)}$ system in $1 \text{ M NaClO}_4 + 0.11 \text{ M } n\text{-butanol}$ and various concentration of (a) m -toluidine, (b) p -toluidine [89].

the ratio of the molar concentrations of PEG to TU.

The quasi-reversible electroreduction processes of Zn(II) in the absence and in the presence of *N,N'*-dimethylthiourea (DMTU) were quantitatively compared by Sanecki [91]. It has been shown that in the presence of DMTU enhanced response of cyclic voltammetry and normal pulse polarography was complex and could be resolved into its regular reduction part and a part caused by the catalytic influence of adsorption of organic substance.

24.1.2.5 The Electrochemical Properties of the Zinc Complexes

The early electrochemical studies of Zn(II) complexes with inorganic ligands were reviewed in Volume 5 of the Encyclopedia [92]. In this part, only the later studies are covered.

Kinetics and mechanism of electroreduction of Zn(II) ammonia and hydroxy-ammonia complexes on the DME were investigated by Kravtsov and coworkers [93]. The reduction of Zn(II) on DME in solution of pH 9.2–12 and $[\text{NH}_3] = 0.05\text{--}2\text{ M}$ occurred in one irreversible diffusion-limited cathodic wave. In dilute supporting electrolyte, the maximum on the polarographic waves was observed, which is connected with accumulation of insoluble reduction product on the electrode surface. The apparent rate constant for cathodic reduction process of ammonia complexes of Zn(II) was obtained.

The equilibrium potentials of saturated zinc amalgam were determined [94] as a function of concentration of free ethylenediamine in the solutions of pH 9.5, 10.5, and 11.5. The stability constants of complexes with different compositions, which were formed, have been estimated.

The effect of ligands on the character and degree of the inner-sphere reorganization during electroreduction of aqua-, aquahydroxy-, hydroxy-, and ethylenediamine tetraacetic acid (EDTA) complexes of Zn(II) [95] and electrochemical process of Zn(II) complexed by different ligands – glycinate [96], ethanol amine [97], azinyl methyl ketoximes [98], aspartame [99], glutathione [100, 101] and several cephalosporin antibiotics [102] – were studied at mercury electrodes in aqueous solutions.

The polarographic method has been used to determine the stability constants and kinetic parameters of ternary complexes of Zn(II) with L-lysine, L-ornithine, L-serine, L-phenylglycine, L-phenylalanine, L-glutamic acid, and L-aspartic acid as primary ligands and picoline as secondary ligand at pH 8.5 [103] and also of zinc complexation by extracellular polymers extracted from activated sludge [104].

Zn(II) complexes with glycine, *N*-acetyl, and *N*-benzoyl glycine were investigated in DMSO, CH_3CN , and DMF solutions [105]. Voltammetric study of the redox chemistry of 2,3-dihydroxy-quinoxaline and its zinc complexes in nonaqueous medium was also presented [106].

Metal ions, especially Zn(II), play an important role in many enzyme-catalyzed reactions involving nucleic acids, such as DNA cleavage by zinc nuclease. Therefore, the binding of Zn(II) to a 19-mer double-stranded oligodeoxyribonucleotide was investigated to understand the role of zinc in DNA cleavage catalyzed by mung bean nuclease [107].

Also, the electrochemical behavior of copper–zinc superoxide dismutase ($\text{Cu}_2\text{Zn}_2\text{SOD}$) [108] and porcine superoxide dismutase (PESOD) [109] were studied on the mercury electrode.

Metallothioneins (MT), low molar mass proteins, have been studied electrochemically alone and in the presence of Cd(II) and Zn(II) ions [110–115]. The electrochemical behavior of zinc MTs from rabbit liver, with respect to solution pH, as well as the influence of the addition of zinc [116] and also zinc MT from rat liver, was investigated [117] using electroanalytical techniques. Studies of complexing properties of the alpha-MT with Zn(II) were carried out using differential pulse polarography [118].

The Zn(II) complexes with acetylacetone – Zn(acac)₂, Zn(OEt)₂(acac)₂, Zn(Obu)₂(acac)₂, and also Zn(OR)₂ [119] as well as binuclear bis{1-phenylglyoxal bis(3-piperidylthiosemicarbazone) Zn(II)}, [Zn(C₂₀H₂₆N₆S₂)]₂, complexes [120] were synthesized electrochemically using zinc metal as an anode.

The series of Zn(II) complexes with 1-amidino-3-aryl-substituted-thioureas [121], acetamidomalondihydroximate [122], benzilbisthiosemicarbazone [123], novel fluorene-substituted terpyridine [124], perfluoroalkoxy-substituted phthalocyanine [125], and 3-carboxylacetonehydroxamic acid [126] were synthesized. The behavior of these complexes was investigated by spectroscopic and electrochemical methods.

The preparation of a novel pentadentate ligand, 2-hydroxy-5-methylisophthalaldehyde bis(*p*-methoxy thiobenzoylhydrazone), was described together with the chloro-bridged Zn(II) complexes [127]. Synthesis and electrochemical properties of some long-chain 1,4,8,11,15,18,22,25-octa-alkylated metal-free and zinc phthalocyanines were presented by Swarts et al. [128]. The zinc derivatives show higher liquid crystalline behavior than the free-metal compounds.

In the last three decades, the complexes formed with macrocyclic ligands were intensively studied. The thermodynamic data of Zn(II)–macrocyclic complexes were collected and presented by Izatt et al. [129–131]. Examples of studies of Zn(II) complexes with macrocyclic ligands were described ([132–137] and works cited therein).

Macrocyclic ligands of biological importance as thiophenolate-containing Schiff-base macrocycles and their amine analogs (see review [138]) and new helical complexes with bis(bidentate) Schiff-base ligand [139] were also described.

The metalloporphyrins were very intensively studied and their properties are presented in monographs [140–142]. The synthesis and properties of Zn(II)–porphyrin complexes are presented in selected works [143–154].

24.1.2.6 Properties of Zinc Oxide Electrode

A number of works are devoted to the electrochemical preparation of ZnO, which may have application in photocatalysis, ceramics, piezoelectric transducers, chemical sensors, photovoltaics, and others. ZnO has the same band-gap energy as TiO₂, and the oxygenation capacities for both compounds should be similar. Yamaguchi et al. [155] prepared photoactive zinc oxide films by anodizing a zinc plate. Such films could decompose gaseous acetaldehyde with the aid of black lights.

Izaki [156] has developed the two-step electrolysis technique in order to prepare a transparent and conductive ZnO film.

Pauporte and Lincot [157, 158] have developed the preparation of zinc oxide thin films by cathodic deposition at 70°C from chloride aqueous solutions with dissolved zinc(II) chloride and hydrogen peroxide.

Potential modulation method in electrodeposition of ZnO on indium tin oxide

(ITO) electrode was used by Lee and Tak, [159]. Zinc oxide with strong photoluminescence at room temperature was prepared by electrolyzing a zinc plate in ethanol solution [160]. The particles of ZnO were initially suspended in the solution and later deposited on the Pt cathode by electrophoresis. A similar method was used by Tang et al. [161]

ZnO thin films doped with In or Al were electrodeposited at a constant potential at 80°C from aqueous solutions of $\text{Zn}(\text{NO}_3)_2$ with InCl_3 or $\text{Al}(\text{NO}_3)_3$ [162].

ZnO-based organic (eosin) inorganic hybrid semiconductor compounds have been grown heteroepitaxially in one step at low temperature by a simple electrochemical method from an oxygenated zinc chloride aqueous solution [163].

Karappuchamy et al. [164] have described cathodic electrodeposition of porous ZnO thin film modified with the dye in an aqueous solution of zinc nitrate and riboflavin 5'-phosphate.

The surface morphology of films was dependent on the dye concentration, suggesting its strong interaction with the growing surface of ZnO.

Recently, the mechanism of cathodic electrodeposition of ZnO thin films from aqueous $\text{Zn}(\text{NO}_3)_2$ baths has been studied using a rotating disc electrode [165]. Non-electrochemical methods of preparation of ZnO were also described, but they are not covered in this review.

Photocurrent generation was observed after illumination of the cell with ZnO electrode; see for instance, Refs 166–169.

24.1.2.7 Electrode Processes in Molten Salts

The combination of quaternary ammonium chloride salt, such as 1-ethyl-3-methylimidazolium chloride (EMIC), with

anhydrous metal chlorides generally produces molten salts that exhibit a melting point much lower than that of the conventional inorganic molten salt systems [170, 171]. The low melting temperatures of such molten salt systems make them easier to handle, and these molten salts can be very useful for the electrodeposition of pure metals and alloys. Studies on electrodeposition of zinc have been carried out in acidic AlCl_3 –EMIC melt [172] and in acidic AlBr_3 –dimethylethylphenylammonium bromide (DMEPB) melt [173]. While good zinc deposits could be obtained from the acidic AlCl_3 –EMIC melt [172], aluminum was codeposited with zinc from the AlBr_3 –DMEPB melt [173].

The electrodeposition of zinc on polycrystalline Au, Pt, and tungsten electrodes was preceded by underpotential deposition (UPD) [172]. The formal potential of $\text{Zn}(\text{II})/\text{Zn}(0)$ couple and diffusion coefficient of $\text{Zn}(\text{II})$ were also determined [172].

The mixtures of ZnCl_2 –EMIC also exhibit a lower melting temperature than the conventional inorganic molten salts. The Lewis acidity of ZnCl_2 –EMIC ionic liquid can be adjusted by varying the molar ratio of ZnCl_2 to EMIC [174]. The ionic liquids that have a ZnCl_2 mole fraction higher than 33 mol % are acidic because there are not enough chloride ions to fully coordinate with $\text{Zn}(\text{II})$. The melts containing less than 33 mol % ZnCl_2 are basic. In such liquids, the major zinc species is probably ZnCl_4^{2-} . Underpotential deposition of zinc was observed on Pt and Ni electrodes in acidic liquids.

The electrodeposition of zinc on GC, nickel, and tungsten electrodes was investigated in ZnCl_2 –EMIC, and AlCl_3 –EMIC [175, 176]. The nucleation on GC required a larger overpotential than on the other used electrodes. The addition of

PC [175] or benzene [176] as a cosolvent in the plating solution hinders the zinc nucleation.

The zinc electrodeposition on Au(111) from molten salts containing 58–42 mol % AlCl_3 –1-methyl-3-butylimidazolium chloride (MBIC) and 1 mM Zn(II) was investigated also using scanning tunneling microscopy (STM) [177]. In the underpotential range, three successive Zn monolayers were resolved, and the thickness of the Zn layers in the UPD range had a value of $2.4 \pm 0.2 \text{ \AA}$.

The influence of ethylene glycol and water content on the zinc electrodeposition from ZnBr_2 –1-ethyl-3-methylimidazolium bromide (EMIB) was investigated [178]. The structure of the deposits was dependent on the mole ratio of ZnBr_2 to EMIB, water concentration, and presence of ethylene glycol.

The zinc electroreduction investigated [179] in urea-chlorides melts was found to be reversible with two-electron transfer.

In ZnCl_2 –EMIC (1:1) melt containing Cu(I), the electrodeposition of Cu–Zn alloys on tungsten and nickel electrodes was carried out [180]. The composition of the Cu–Zn deposit was changed by deposition potential, temperature, and Cu(I) concentration in a plating bath.

Zinc telluride was obtained by deposition on the nickel electrode from 40 to 60 mol % ZnCl_2 –EMIC melt containing Te(IV) and PC [181]. The composition of the Zn–Te deposits was dependent on the deposition potential and Te(IV) concentration in the plating solution.

Electrodeposition of Zn–Co alloys on Ni, W, and GC electrodes from 40 to 60 mol % ZnCl_2 –EMIC melt containing Co(II) was investigated [182]. X-ray measurements indicated that Zn–Co alloy deposits with low zinc content are amorphous and the crystalline nature of Zn–Co alloys

increases as the zinc content in deposits rises.

The Zn–Cd alloys were obtained from ZnCl_2 –EMIC melt containing Cd(II), during reduction on Pt, Ni, or W electrodes at the potentials sufficient to reduce Zn(II) to metal [183]. The composition of Zn–Cd alloys was dependent on the deposition potential, temperature, and Cd(II) concentration.

The same researchers [184] studied electrodeposition of Zn–Sn alloys on tungsten and GC electrodes from ZnCl_2 –EMIC ionic liquid containing Sn(II). The Zn–Sn codeposits consist of two-phase mixtures of Zn and Sn.

Also, the Pt–Zn electrodeposition on tungsten electrode was studied in ZnCl_2 –EMIC melts containing Pt(II) [185]. The morphology of Pt–Zn alloys is dependent on the deposition potential and Pt(II) concentration in the plating solution. Pt–Zn alloys were also obtained on the electrode surface when Zn(II) was reduced on Pt electrode.

For Zn–Mg alloys in ZnBr_2 –EMIB–ethylene glycol melts [186] and ZnBr_2 –EMIB–glycerin containing Mg(II) [187], the grayish metallic colored electrodeposits were obtained. The Mg content in Zn–Mg electrodeposits varied from 12 to 25 mol % [187].

Zn–Fe alloys were deposited and studied on the nickel electrode in ZnCl_2 –EMIC melts [188]. The composition of Zn–Fe alloy was also dependent on the deposition potential and Fe(II) concentration in the plating solution.

The electrolysis of a mixture of ZnCl_2 with alkaline chlorides and the effect of different elements were investigated as a method to extract zinc from ores and industrial wastes. The studies on electrolysis of ZnCl_2 in molten ZnCl_2 –KCl–NaCl

chlorides at 450°C have shown ohmic limitations [189]. The energy consumption is to a large extent determined by the anodic process of chlorine evolution.

24.1.3

Deposition and Underpotential Deposition of Zn on Solid Electrodes

24.1.3.1 Underpotential Deposition of Zinc

There was significant interest in zinc UPD, since zinc plays a major role in plating technology. Underpotential deposition of zinc in acidic solutions on polycrystalline Pt electrode was shown by using cyclic voltammetry [190]. Later, Zn UPD was also demonstrated on Au and Pd electrodes in acidic and alkaline solutions [191, 192].

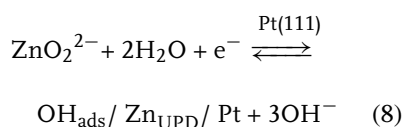
In recent years, there have been a number of works on Zn UPD on single-crystal electrodes.

UPD of various metal ions is accompanied by the adsorption of anions. Evidently, such additional adsorption makes stoichiometric calculations based on the determined charge value misleading.

24.1.3.1.1 Zn UPD on Pt Underpotential deposition of zinc was observed on Pt(111) in alkaline solution as a sharp cyclic voltammetric (CV) peak, in contrast to the behavior on polycrystalline Pt, when several broad UPD peaks were observed [193]. The changes of the peak potential with concentration of ZnO_2^{2-} were equal to 60 mV/log $[\text{ZnO}_2^{2-}]$ and led to the apparent electron transfer number $n_a = 1$.

This value is discussed in terms of two-electron transfer when Zn^{2+} is reduced to free zinc on Pt(111) surface with a true electron transfer number of $n = 2$. Also, induced adsorption of OH^- ions takes place to give OH_{ads} in an oxidative process.

Therefore, the overall UPD process may be represented by the reaction



to give the apparent electron transfer number $n_a = 1$.

The UPD of Zn on Pt(111) electrode in phosphate solutions (pH 4.6 or 3.0) was studied by Aramata and coworkers [194] in the presence of adsorbed anions. In phosphate solutions, the Zn UPD obeyed the Langmuir adsorption mechanism. On the addition of 10^{-3} M Br^- ions, the Zn^{2+} ion UPD potential shifts 120 mV to more negative values. The desorption of specifically adsorbed anions is suggested to trigger the UPD of Zn.

The effect of adsorbed anions on Zn UPD has been studied using CV [195] in 0.1 M KH_2PO_4 of pH 4.4 with and in the absence of halide ions. The charge transfer to Zn^{2+} was initiated near the desorption potential of adsorbed anions. The Zn UPD potentials moved to more negative values following the order of the anion adsorption strength $\text{H}_2\text{PO}_4^- < \text{Cl}^- < \text{Br}^- < \text{I}^-$. In the presence of Br^- and I^- ions, the CV peaks were narrower than in the presence of Cl^- or H_2PO_4^- anions. The number of transferred electrons to one Zn^{2+} ion was estimated to be about two by correlating with the number of electrons for the anion discharge with and without Br^- ions.

The specific adsorption of H_2PO_4^- ions that accompany the UPD of Zn^{2+} ions on Pt (platinized electrodes obtained by Pt electrodeposition on the gold-plated plastic foil) electrodes was studied by using a radiotracer method with ^{32}P phosphate species in the presence of a great excess of ClO_4^- ions [196]. It was found that the specific adsorption of species induced

by Zn adatoms depends on the pH value and at constant potential on Zn^{2+} concentration.

The same authors [197] have studied the specific adsorption of other anions, which accompany the Zn UPD on Pt electrodes. Again, radiotracer technique with ^{35}S -labeled sulfate and ^{36}Cl -labeled chloride ions has been used. It was found that sulfate ions adsorb on the top of Zn adatoms, and the adsorption strength of Cl^- ions on the Zn adlayer is significantly lower than that of HSO_4^- (SO_4^{2-}) ions.

Comparative studies of Zn UPD on Pt(111) and Au(111) electrodes were carried out with consideration of the anion adsorption/desorption process [198].

In the case of Zn UPD, the number of electrons transferred, n , was two, which implies that adsorbed anions are desorbed in the UPD region and readsorbed on the UPD metal in a similar amount.

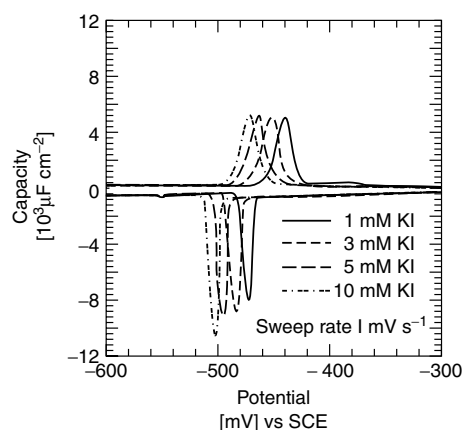
Underpotential codeposition of Cu^{2+} and Zn^{2+} at Pt(111) was examined using voltammetry [199]. In phosphate solutions of pH = 4.5, the codeposition of Cu^{2+} and Zn^{2+} was found to occur when Cu^{2+} concentration was lower than that of Zn^{2+} ions.

24.1.3.1.2 Zn UPD on Au In the case of Au(111) [198], specifically adsorbed anions are not present in the UPD region, and the value n_a equal to one was explained by the anion adsorption on the UPD Zn by the oxidative process.

The UPD of Zn^{2+} on Au(111), Au(100), and Au(110) was studied in phosphate buffer with addition of NaClO_4 and NaCl [200]. The apparent number of electrons transferred in the UPD process was nearly one, irrespective of the single-crystal face. Although UPD shift potential ΔE_p was independent of the kind of solutions, the CV characteristics were altered in different solutions. In NaCl solutions, two UPD peaks appeared in contrast to the case of phosphate and perchlorate solutions.

The influence of anion adsorption on Zn UPD on Au(111) was further studied in the presence of halide ions [201]. The order of the adsorption strength of the anions on Zn UPD was found to be different from that of specific adsorption on a substrate Au electrode $\text{ClO}_4^- < \text{SO}_4^{2-} \leq \text{PO}_4^{3-} < \text{Cl}^- < \text{Br}^- < \text{I}^-$. In phosphate solutions, chloride and bromide ions did not influence the Zn UPD, and iodide ions inhibited this process (see Fig. 5).

Fig. 5 Cyclic voltammograms of the Zn(II)/Zn system obtained at 1 mV s^{-1} on Au(111) in the solutions with 0.1 M $\text{K}_2\text{H}_2\text{PO}_4$, 1 mM Zn(II), and various KI concentrations [201].



The UPD of zinc on Au(111) in phosphate solutions at pH 4.6 was also studied using the STM method [202]. It was shown that the oxidative adsorption of phosphates occurs on the UPD Zn at Au(111) by the UPD-induced adsorption.

24.1.3.2 Zinc Electrodeposition on Solid Electrodes

Various processes are generally involved in metals electrodepositions – ion transport, ion adsorption, nucleation and growth from adions, and multistep charge transfer [203–206]. The electrodeposition process can be perturbed by the presence of inhibiting species adsorbed at the electrode. The impedance spectroscopy was used for elaboration of the reaction models accounting for the experimental data obtained during electrodeposition from various electrolytes. In alkaline solutions, the discharge of zincate ions takes place in multisteps [36, 37, 207, 208]. In acidic solutions, the electroreduction of Zn(II) ions proceeds in several steps with the participation of the intermediate adions Zn^+_{ad} [25]. Usually, small amounts of organic additives improve the homogeneity and the surface state of the zinc deposit.

24.1.3.2.1 Electrodeposition on Zn

Electrodes Rezaite and Vishomirskis [209, 210] have investigated the effect of potassium cyanide on the electrodeposition of zinc from zincate solutions on the Zn electrode. It is known that cyanide added to the zincate solution led to high-quality zinc coatings. The presence of KCN decreased the limiting current of Zn(II).

The behavior of zinc and zinc oxide electrode in 5.3 M KOH in the presence of alkaline earth oxides, SnO, $\text{Ni}(\text{OH})_2$ and $\text{Co}(\text{OH})_2$, was examined using cyclic voltammetry by Renuka et al. [211].

The aging behavior of the porous zinc electrode in 6 M KOH in the presence of different electrolyte additives such as ZnO, LiOH, and KF has been studied using cyclic voltammetry by Shivkumar et al. [212]. The mechanism of the electrode reaction in all these electrolytes was investigated.

Wang et al. [213] investigated the effect of bismuth ion and tetrabutylammonium bromide (TBAB) on the dendritic growth of zinc in alkaline zincate solution on Zn electrode. It was found that this growth is inhibited by the synergistic effect of Bi(III) and TBAB at higher overpotentials. The zinc electrodeposits

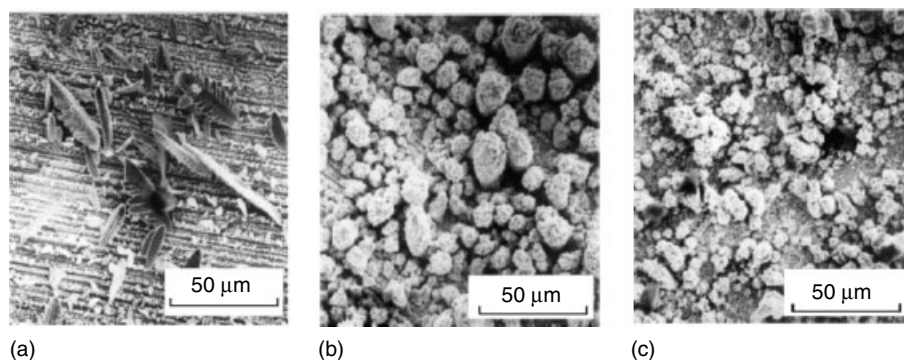


Fig. 6 Zinc electrodeposits at $\eta = -0.200$ V (a) from the alkaline solutions, (b) from the alkaline solutions containing 0.1 g l^{-1} Bi(III) [213], (c) as in b but with addition of 0.02 g l^{-1} TBAB.

obtained at the cathodic overpotential equal to -200 mV in alkaline solutions with and without additives are presented in Fig. 6.

Using the rotating disk electrode, Selivanov et al. [214] have investigated the zinc electrodeposition from zincate electrolyte containing polyethylene polyamine. The limiting current density of $[\text{Zn}(\text{OH})_4]^{2-}$ ion diffusion through a film of zinc oxides and hydroxides is shown to be responsible for the formation of dark zinc deposits in the potential range from -1.33 to -1.47 V.

The thermal phenomena – heat flux, heat quantity, and temperature gradient – occurring at the zinc electrode during the electrolysis from aqueous solutions containing zinc salt were investigated [215].

Zinc electrodeposition on zinc electrode with rough surface exhibited potential oscillations accompanied by fern-leaf-shaped deposits, contrary to the case

of zinc electrode with a smooth surface. A new autocatalytic mechanism was proposed [216] to explain these phenomena systematically.

The influence of Pb^{2+} ions on the kinetics of zinc electrodeposition on Zn electrode in acidic sulfate electrolyte was discussed [217] in terms of a reaction model involving hydrogen adsorption and evolution, a multistep mechanism for zinc deposition and the overall reaction for zinc dissolution. The strongly adsorbed Pb_{ads} inhibited all the reactions taking place on the zinc electrode.

The kinetics of zinc deposition on Zn electrode from a concentrated $\text{ZnCl}_2 + \text{KCl}$ electrolyte containing commercial long-chain polymer additives was investigated using impedance spectroscopy [218]. The additive modifies the deposit morphology by changing some specific rates of the electrode reaction surface steps (see Fig. 7).

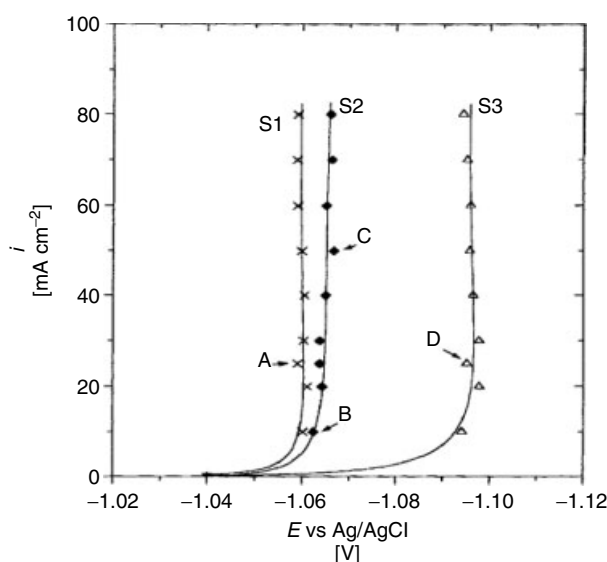


Fig. 7 Experimental steady state polarization curves of Zn(II) electroreduction for various electrolytes: (S1) additive-free bath (1.6 M $\text{ZnCl}_2 + 5.3$ M KCl); (S2) industrial bath (1.6 M $\text{ZnCl}_2 + 5.3$ M KCl + long-chain polymer + pH buffer of pH 4.7); solution (S3) (1.6 M $\text{ZnCl}_2 + 5.3$ M KCl + long-chain polymer with the same additive at the concentration of 10^{-3} M in volume) [218]; $t = 62^\circ\text{C}$.

Zhu et al. [219] have also investigated the influence of surfactants on the electrochemical behavior of zinc electrodes in alkaline solutions. In the presence of surfactants, the dendrite growth is reduced and the zinc deposit is more uniform and compact. Therefore, perfluorosurfactants can be used for decreasing the corrosion of zinc batteries.

The influence of the nonionic surfactant Forafac F1110 on the kinetics of zinc deposition in sulfate or chloride solutions was investigated using voltammetry and impedance spectroscopy [220]. The additive slightly modifies the rate of the reactions corresponding to the adsorption and evolution of hydrogen on the zinc electrode, thus affecting very little the current efficiency of zinc deposition. The additives (1) inhibit different steps of charge transfer leading to the zinc deposit and (2) modify the kinetic parameters of the slow reactions involved in the formation and destruction of the active sites for zinc deposition.

The electrochemical properties of secondary zinc electrodes after La addition (by the solid-phase diffusion method) have been investigated by Yang et al. [221]. The results showed that the La addition to the zinc electrode significantly improved the life cycle. After 80 cycles at 100 mA g^{-1} , the zinc electrode with 0.5 atom % La addition showed the best cyclic behavior. La addition significantly suppressed the corrosion behavior of secondary zinc electrodes, and the growth of zinc dendrites was effectively inhibited and the formation of zinc deposition was changed. On the Zn electrode surface, $\text{La}_2\text{O}_3/\text{La}(\text{OH})_3$ was formed and this prevented the discharge products of zinc electrodes from dissolving in the alkaline electrolyte and suppressed the dendrite growth during charging.

Similar results were obtained by Zhu et al. [222], who have investigated the influence of lanthanum and neodymium hydroxides on the properties of secondary alkaline zinc electrode.

The kinetics of cathodic deposition and anodic dissolution of zinc on Zn or Pt electrodes in DMSO, DMF, and AN solution was investigated by Białozór and Bandura [223].

24.1.3.2.2 Electrodeposition on Other

Electrodes Trejo et al. [224] have investigated the influence of the zinc chloride concentration on the zinc nucleation process on GC electrode in KCl solutions under conditions close to those employed in commercial acid deposition baths for zinc. The results show that the nucleation process and the density number of sites are dependent on ZnCl_2 concentration. The deposits are homogeneous and compact, although a change in morphology is observed as a function of ZnCl_2 concentration.

Trejo et al. [225, 226] have also investigated the influence of several ethoxylated additives (ethyleneglycol and PEG polymers of different molecular weights) on the nucleation, growth mechanism, and morphology of zinc electrodeposited on GC from an acidic chloride bath. Results have shown that the presence of additives modifies the nucleation process and determines the properties of the deposits.

Chronoamperometric experiments on zinc electroreduction on GC from acetate solutions showed that the nucleation density increases with increase of temperature [44]. Moreover, the nucleation rate constant is always very large, equal to $1.41 \times 10^9 \text{ s}^{-1}$. This indicates that the mechanism of zinc electrodeposition on the GC electrode follows a three-dimensional instantaneous nucleation and growth model within the controlled temperature range.

The same mechanism of zinc electrodeposition on the GC electrode was observed in sulfate, chloride, and acetate ion solutions [227]. The anions mainly affected the nucleation densities during zinc deposition, which resulted in a different surface morphology. The nucleation rate constant was the same in the chloride and sulfate solutions and was equal to $1.22 \times 10^9 \text{ s}^{-1}$. In the presence of acetate and chloride ions, the deposited zinc film tends to grow in a multilayered pattern, while in sulfate solution, the zinc deposition forms irregular grains. A new approach to the estimation of zinc electrocrystallization parameters on the GC electrode from acetate solutions was described by Yu et al. [228].

The influence of convection, pH, and Zn(II) of solution on electrodeposition on GC electrode of zinc–cobalt alloys was studied by Gómez and Vallés [229]. The presence of zinc in the bath always decreases the rate of the cobalt deposition.

The influence of quaternary aliphatic polyamine (QAA) on zinc electrodeposition from an alkaline non-cyanide bath was investigated [230]. In the presence of QAA, the exchange current density decreased and zinc deposit had a smaller grain size.

The electrodeposition of Zn on highly oriented pyrolytic graphite from $\text{ZnSO}_4 + \text{Na}_2\text{SO}_4$ solution was analyzed in the presence and absence of gelatin [231]. The morphology of the Zn-formed crystals was affected by the gelatin adsorption and the nucleation rate was decreased.

An experimental study of zinc electrodeposition on copper wire from 0.1 M zincate solution in 1.0 M KOH was presented by Simićić et al. [232]. A possible mechanism of the formation of spongy zinc deposits was considered. Also, it was shown that in the case of a square-wave pulsating overpotential regime, the deposit was less

agglomerated than the one obtained in the case of direct overpotential regime.

The Zn electrodeposition [233] on gold electrode was investigated in a solution of $\text{H}_3\text{BO}_3 + \text{NH}_4\text{Cl} + \text{Na}_2\text{SO}_4$ at pH 4.4 using electrochemical impedance spectroscopy and electrochemical quartz crystal microbalance (EQCM).

Also, the influence of benzylideneacetone on the mechanism of zinc electrodeposition on Pt electrode in a chloride acidic bath was studied [234].

Rodríguez-Torres et al. [235] have used ammonia-containing baths for Zn–Ni alloy electrodeposition on Pt. Zinc and nickel species exist in the form of $[\text{Zn}(\text{NH}_3)_4]^{2+}$ and $[\text{Ni}(\text{NH}_3)_6]^{2+}$ complexes in such solutions. The deposition at pH 10 was investigated and compared with deposition from ammonium chloride baths at pH 5. The Ni content in the alloys was found to be 40–60% higher from the ammonia-containing bath than from the acidic baths. The deposition mechanism was found to be affected by complexation of the metal cations by ammonia.

Raeissi et al. [236, 237] showed that temperature, pH, and current density affected the morphology and texture, as well as the nucleation mechanism of the zinc deposits on carbon steel electrode.

Zn_3N_2 reversibly reacts with lithium in electrochemical conversion reaction to give LiZn and a matrix of $\beta\text{-Li}_3\text{N}$ [238]. Upon oxidation, LiZn transformed into metallic Zn, while $\beta\text{-Li}_3\text{N}$ contributed to the transformation into LiZnN.

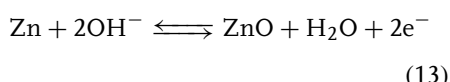
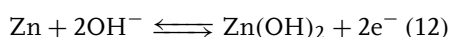
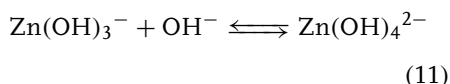
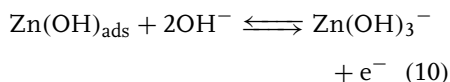
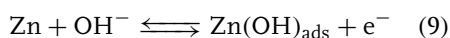
24.1.4

Passivation and Corrosion of Zinc

24.1.4.1 Anodic Dissolution and Passivation of Zinc

The electrochemical behavior of zinc anode was intensively investigated. A survey

of the literature data indicates that the nature and mechanism of the zinc passivation in alkaline solutions is the subject of debate. Various mechanisms involving several intermediate species have been proposed for passivation of Zn in alkaline solutions [36, 37, 92, 207, 208, 239–246]. In some works, Zn(OH)_2 has been proposed to be the passivating species [243, 244], while other authors assume that this role is played by ZnO [240, 245]. Moreover, in certain cases, the passive film consists of a dual layer, composed of ZnO and Zn(OH)_2 [243, 247, 248] or of two types of ZnO [240, 243, 247, 248]. The oxide growth on the zinc electrode under prevailing experimental conditions could be explained on the basis of the following reactions [249, 250]:



The thickness of the passive layer formed on Zn electrode in alkaline solutions changes with operating conditions and reaches about 50 nm [244, 251]. Recently, it was found that the rate of oxide growth in the passive region increases with decreasing concentration of borate and increases with the imposed current density [252].

Influence of pH, solvent composition, type of anions and surfactants on zinc electrochemical dissolution, and passivation was studied intensively. The nature

of the passive state on zinc was investigated in alkaline [253–256] and borate solutions [253, 257]. It was found that the metal is covered by a duplex film comprising a highly defective ZnO barrier layer covered by a precipitated outer layer of ZnO or Zn(OH)_2 . The formation of the latter can be inhibited by optimal solution composition.

Zinc dissolution was also investigated in phosphate solutions over a wide pH range of 4.5–11.7 [258], in aerated neutral perchlorate [259], and in sulfate solutions [260, 261]. In the phosphate solutions [258], zinc phosphates were present in a passive layer of zinc electrode, while for sulfate solutions a kinetic model of spontaneous zinc passivation was proposed [261].

The anodic dissolution of bulk zinc [262] and zinc-coated steel sheet [263] in aerated sulfate media was studied. During this process, a compact nonstoichiometric zinc oxide layer was formed on the surface of zinc.

The anodic dissolution of zinc [233, 264] was investigated in solution $\text{H}_3\text{BO}_3 + \text{NH}_4\text{Cl} + \text{Na}_2\text{SO}_4$ at pH 4.4 using electrochemical impedance spectroscopy and EQCM. In the same solution, zinc anodic dissolution of different galvanized steel sheets of zinc [265] was studied. The postulated [41, 266] mechanism of Zn oxidation in acidic solution corresponds to two consecutive monoelectronic transfers.

The anions such as halogenides stimulate the active dissolution of zinc and tend to break down the passive film. Therefore, the effect of halogenide anions [267–270], thiocyanate [271], and sulfur-containing anions [272–274] in different media was studied. There are also anions that inhibit active dissolution and pitting corrosion, and this effect decreases in the

order $\text{Cr}_2\text{O}_7^{2-} > \text{CrO}_4^{2-} > \text{WO}_4^{2-} > \text{MoO}_4^{2-}$ [274].

Addition of sodium dodecyl benzene sulfonate to dilute alkaline electrolyte depresses the passivation of zinc surface [275]. Owing to the dodecyl benzene sulfonate adsorption, the passive layer on zinc has a loose and porous structure. Zinc electrodisolution was inhibited by the presence of sodium metasilicate [276] and some acridines [277]. The protection effect was described by a two-parameter equation.

The anodic dissolution experiments of zinc rotating disk electrode were carried out in alkaline electrolyte [278] and in solution at pH 5.5 containing NH_4Cl and $\text{NH}_4\text{Cl} + \text{ZnCl}_2$ [279], $\text{NH}_4\text{Cl} + \text{NiCl}_2$, and $\text{NH}_4\text{Cl} + \text{NiCl}_2 + \text{ZnCl}_2$ [280, 281]. The zinc electrode was covered by a porous film composed of a mixture of metallic zinc and zinc hydroxide [279]. In Ni-containing solutions, the passivation of Zn was a result of Zn–Ni alloy formation and $\text{Zn}(\text{OH})_2$ precipitation [280].

The influence of illumination [255, 282] and magnetic field [256] on the passive layer behavior and anodic current oscillations was also studied.

24.1.4.2 Corrosion

Zinc and zinc-coated products corrode rapidly in moisture present in the atmosphere. The corrosion process and its mechanism were studied in different media, nitrate [283], perchlorate [259], chloride ions [284], and in simulated acid rain [285]. This process was also investigated in alkaline solutions with various iron oxides or iron hydroxides [286] and in sulfuric acid with oxygen and Fe(III) ions [287]. In the solution with benzothiazole (BTAH) [287], the protective layer of BTAH that formed on the electrode surface inhibited the Zn corrosion.

Youssef et al. [288] studied the corrosion of nanocrystalline zinc produced from chloride electrolyte with polyacrylamide and TU as additives.

The influence of several anions such as perchlorate [259], halogenide [267–270], sulfate ions [272, 273], and their concentration on breakdown of the passive layer and pitting corrosion was also analyzed.

A great research interest concerns zinc corrosion inhibition. Chromate solutions were used [289–293] for the inhibition of zinc corrosion. The surface film contained a mixture of zinc oxide and hydroxide of chromium(III). Different behaviors of the passivated zinc electrode was observed depending on the cation of the used chromate [293].

Because Cr(VI) is very toxic, the chromate ions were replaced by other solutions or reagents in corrosion protection. Therefore, a chromate-free, self-healing protective film was prepared on a zinc electrode using as inhibitors $\text{Ce}(\text{NO}_3)_3$ and sodium phosphate Na_3PO_4 [294–299]. The film was composed of an inner layer of Ce_2O_3 with small amounts of Ce^{4+} and an outer layer of Na_3PO_4 containing CePO_4 . The formed layer suppressed the cathodic process. The anodic process was inhibited by coverage of surface with precipitates of $\text{Zn}(\text{OH})_2$, $\text{Zn}_3(\text{PO}_4)_2 \cdot 4 \text{H}_2\text{O}$, and CePO_4 .

The corrosion of zinc was also inhibited by Al^{3+} , La^{3+} , Ce^{3+} , and Ce^{4+} cations [300].

An important group of zinc corrosion inhibitors are compounds that are adsorbed on the metal surface and/or that form precipitate with Zn(II) on the zinc surface together with zinc hydroxide and oxide [301–307].

Synergistic influence of Ce(III) ions and sodium silicate $\text{Na}_2\text{Si}_2\text{O}_5$, [308] and

octylthiopropionate [302] was also discussed.

Some ligands chelating Zn(II) ions were also found to be effective corrosion inhibitors [309, 310] owing to the growth of an organometallic layer strongly attached to the metal surface, which prevent the formation of porous corrosion products.

The corrosion behavior of zinc-coated steel electrodes electrochemically modified by polypyrrole [311] and zinc electrode in solution containing reducing polymer (Polyox WSR-301) [312] was investigated.

Photocorrosion of zinc [282, 313] and zinc alloys [314–316] was studied in NaCl solution.

The spatial distribution of Zn(II) during galvanic corrosion of a Zn/steel couple in 0.01 M NaCl was studied by Tada et al. [317].

Park and Szpunar [318] have shown that the texture, surface morphology, alloy composition, and phase composition of zinc-based coatings strongly influence corrosion resistance.

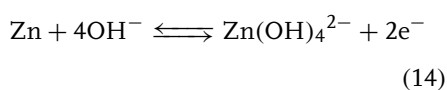
24.1.5

Applied Electrochemistry

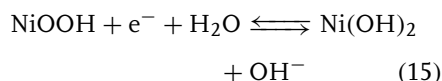
24.1.5.1 Batteries

There is significant interest in the development of batteries, which have zinc as one of the electrodes. General information about such devices is given in the book of Vincent and Scrosati [319]. In recent years, several types of batteries, which use zinc, were developed and/or improved.

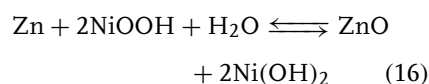
24.1.5.1.1 Ni–Zn Cells These alkaline storage batteries exhibit good performance. They are based on the following electrochemical processes:



and



and the overall reaction is



In a rechargeable battery, the initial material is the ZnO powder, which is dissolved in KOH to form $\text{Zn}(\text{OH})_4^{2-}$. Zincate is reduced to Zn during the charging process.

The progress in sealed-type Ni–Zn cells has been reviewed by Jindra [320, 321]. In the first paper, the period 1991–1995 and in the second paper the period 1996–1998 was covered. One may find here the novelties in the development of this type of batteries.

Later, a polymerized zinc electrode was developed [322] using wetting polymer and plastically shaping polymer materials, which improved the performance of batteries for many cycles.

There were also studied processes that cause passivation of the zinc electrode in many cycling operations of Ni–Zn batteries [323]. Positive effect for increasing the reaction reversibility was found when zinc-ion additives were introduced to the positive electrode [324].

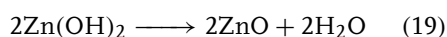
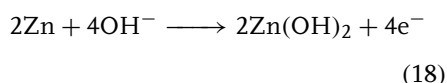
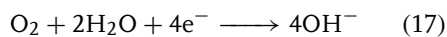
The same group have also studied [325] a mechanism of zinc(II) transfer from the negative to positive electrode of a Ni–Zn battery.

The influence of zinc intercalation on processes in nickel oxide electrode and on the long life of Ni–Zn batteries was also studied.

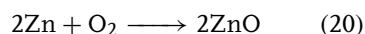
Also, an improved method for the fabrication of zinc electrodes was presented [326], which consists of electrolytic

deposition of active zinc material on very thin microfibrinous copper substrates. Such zinc electrodes with various additives were examined and tested for performance. A new structure of electrode design was employed.

24.1.5.1.2 Zn–Air Batteries The reactions occurring in these batteries may be represented by the following equations:



Overall reaction is



with the theoretical voltage 1.65 V.

For good performance of the battery, both reactions, oxygen reduction (positive electrode) and zinc oxidation (negative electrode), should be fast. It is known that the oxygen electroreduction reaction is quite complex and relatively slow. Therefore, the acceleration of the rate of this reaction in the Zn–air battery is important for the good performance of the battery. For this purpose, Wang et al. [327] prepared a perovskite-type $\text{La}_{0.6}\text{Ca}_{0.4}\text{CoO}_3$ compound as a catalyst, which improves such properties as discharge capacity.

Earlier, such catalyst was used for the preparation of a 100 W rechargeable bipolar zinc–oxygen battery [328]. Also, nanostructured MnO_2 combined with mesocarbon microbeads was prepared and used [329] in such batteries as a catalyst for oxygen reduction, which has a very good electrocatalytic activity with respect to oxygen, and in comparison with electrolytic MnO_2 . Prepared with this material, the all solid-state zinc–air cell

has good discharge characteristics at room temperature.

For the development of a long-lived, electrically rechargeable zinc–air battery, the structure and wettability of pasted zinc electrodes (with 1–10% cellulose) were optimized [330]. It was found that the addition of 10 wt % cellulose to the pasted zinc electrode, improved the life cycle and peak power drain capacity of the battery substantially.

The zinc electrode in such batteries was also modified by making porous zinc anodes from a mixture of zinc and graphite powder using gelatinized agar solution [331] as a binding agent. In the cell design, a thin agar layer was introduced between the electrode-gelled electrolyte interfaces, which resulted in substantial improvement of a cell discharge performance.

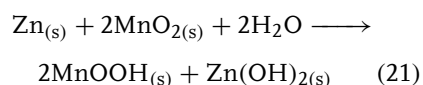
Such thin KOH-treated gelatinized agar electrolyte was also applied between the electrode-gelled electrolyte interfaces [332].

The agar layer improved the interface and simultaneously served as the electrolyte reservoir to both electrodes.

Modeling of rechargeable alkaline Zn–air batteries was also described [333], useful for optimizing zinc cell designs for specific applications.

24.1.5.1.3 Zn– MnO_2 Batteries Though this classical type with the Leclanché electrolyte has now decreasing importance, its improved modifications based on Zn (anode) and MnO_2 (cathode) as basic materials are in wide use.

The reaction of such a cell with alkaline electrolyte may be represented by the following reaction:



The nature of reactions that occur in the Leclanché cell [334] and ZnO–MnO₂ alkaline cell [335] have been studied and discussed.

Such alkaline cells have become the standard by which primary cells are judged in North America, Europe, and Japan. Approximately 12 billion cells were produced worldwide in 2001 [336].

The zinc powder has new alloying elements such as bismuth and indium to control zinc corrosion and reduce hydrogen evolution and leakage [337, 338]. Kumar and Sampath [339] have prepared a gel-polymer electrolyte based on a zinc salt for applications in a rechargeable solid-state zinc battery. The charge–discharge behavior of the cells with such zinc electrode and MnO₂ showed no significant changes during 70 cycles.

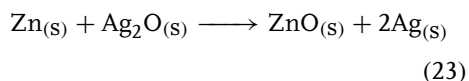
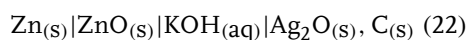
The same authors [340] have proposed another polymer gel electrolyte for Zn–MnO₂ cells.

Also, a new composite consisting of a mixture of zinc and hydrated ammonium zinc sulfate has been elaborated and studied [341] as anode material for all solid-state protonic cells. Zn–MnO₂ cells with this composite have a relatively high specific capacity.

An application of thick-film printing technology for the fabrication of a Zn–MnO₂ alkaline batteries [342] was also described. The mechanism of the capacity fade of rechargeable alkaline zinc–manganese cell was studied and discussed [343]. Zinc electrode with addition of several oxides (HgO, Sb₂O₃) for alkaline Zn–MnO₂ cells [344] was also studied.

Czerwiński and coworkers [345] reviewed the electrochemical applications of reticulated vitreous carbon (RVC). Special attention was paid to the use of RVC as an electrode support in zinc–manganese and zinc–halogen batteries.

24.1.5.1.4 Zn–Ag Batteries The cell may be represented by the scheme



The electromotive force (EMF) of this cell calculated from the potentials of the half-cells is equal to 1.593 V. Basic information about this cell are given by Vincent and Scrosati [319].

Though these alkaline silver–zinc batteries are quite expensive, they are frequently used in aerospace and military applications because they have high specific and volumetric energy density. These batteries may be kept in a dry state for several years and may be activated by introducing the electrolyte into the cells. Their status of technology and applications was presented by Karpinski et al. [346]

Various problems related to the construction and performances of these batteries, such as changes in materials of membranes and additives both to the electrode materials and to the electrolyte, were studied in recent years. Some instability of the silver electrode during such storage period and the ways of avoiding these difficulties were studied and discussed [347]. Reserve activated silver oxide–zinc cells were constructed [348] with synthetic Ag₂O and Pb-treated zinc electrodes were produced by a nonelectrolytic process. The cells were tested before and after thermally accelerated aging.

The study on the characterization of alkaline silver–zinc cells and composite electrodes for such cells was carried out [349, 350]. The improved silver–zinc battery with new developments in additives (Bi₂O₃) to the negative electrode and separator coatings for underwater

applications was also described [351]. A micromachined battery based on liquid electrolyte with gold as the positive electrode and zinc as the negative electrode was described [352].

24.1.5.1.5 Other Cells Several other cells with zinc as an active material have been studied in recent years. The zinc-containing compounds were used as anodes in lithium-ion batteries [353–355]. One such compound is nanocrystalline ZnFe_2O_4 and $\text{Ag}_x\text{ZnFe}_2\text{O}_4$ ($x = 0.16, 0.37, \text{ and } 0.50$) [355], which have been prepared as thin films, by reactive pulsed laser deposition. Especially good performance in the battery of the $\text{Ag}_{0.37}\text{ZnFe}_2\text{O}_4$ film electrode has been shown.

ZnO displays similar redox and alloying chemistry to the tin oxides on Li insertion [353]. Therefore, it may be an interesting network modifier for tin oxides. Also, ZnSnO_3 was proposed as a new anode material for lithium-ion batteries [354]. It was prepared as the amorphous product by pyrolysis of $\text{ZnSn}(\text{OH})_6$. The reversible capacity of the ZnSnO_3 electrode was found to be more than 0.8 Ah/g. Zhao and Cao [356] studied antimony–zinc alloy as a potential material for such batteries. Also, zinc-graphite composite was investigated [357] as a candidate for an electrode in lithium-ion batteries. Zinc particles were deposited mainly onto graphite surfaces. Also, zinc–polyaniline batteries were developed [358]. The authors examined the parameters that affect the life cycle of such batteries. They found that Zn passivation is the main factor of the life cycle of zinc–polyaniline batteries. In recent times [359], zinc-poly(aniline-co-*o*-aminophenol) rechargeable battery was also studied. Other types of batteries based on zinc were of some interest [360].

24.1.5.2 Electrowinning The earlier works on electrowinning of zinc from ore or waste are well described [92].

The electrowinning process is connected with higher power consumption; but, on the other hand, the electrolytically produced zinc has higher purity. Therefore, further investigations are in progress. The main factors that must be considered in electrowinning process are (1) the electrochemical properties of the cathode materials, (2) the effect of ionic impurities in the electrolyte, and (3) the cohesion strength between the deposited metal and its substrate.

Metallic impurities complicated zinc electrowinning [361–368] from acidic sulfate solutions and can adversely affect the cathodic current efficiency, cell potential, power consumption, deposit quality, and the overall polarization behavior of the cathode.

This effect was mainly studied for cadmium, iron, copper [369], nickel [370, 371], antimony [372–378], manganese [371, 379], and iron impurities [376]. Electrowinning of zinc from acidified zinc chloride solutions was investigated [380]. The deposits having lesser surface defects, which act as the active sites of hydrogen adsorption, exhibited higher current efficiency. The presence of gelatin inhibited the H_2 evolution and significantly improved the current efficiency (see Fig. 8).

The organic additives have been employed to counteract the harmful effects of different metallic impurities. Such additives act by increasing the induction period, by complexing the harmful impurities, or by suppressing the hydrogen evolution reaction. The additives also increase the current efficiency, reduce the power consumption, and improve the surface morphology.

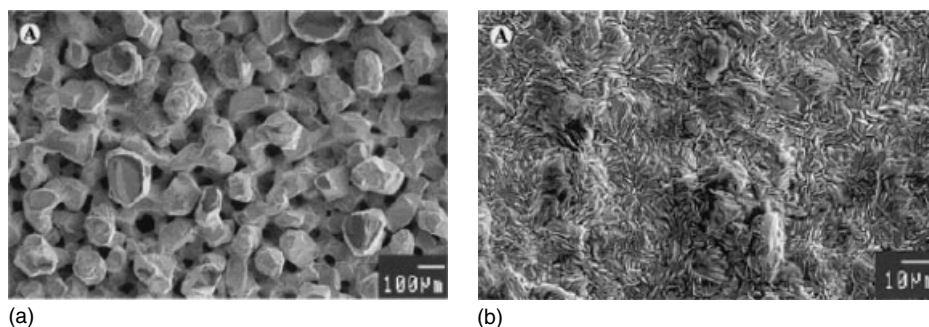


Fig. 8 Surface morphology of zinc deposits from (a) the gelatin-free solution 0.5 M ZnCl_2 + 2 M HCl and (b) gelatin-containing solution 0.75 M ZnCl_2 + 1.5 M HCl [380].

Traditionally, glues [362, 381–383] and arabic gum [384] were used as organic additives in the electrowinning of zinc. Hosny [385] and Karavasteva et al. [386, 387] used surfactants to improve the deposit morphology and current efficiency.

The influence of a number of organic additives—2-butyne-1,4-diol [388], 2-picoline [389], sodium lauryl sulfate [372], 4-ethylpyridine, 2-cyanopyridine [373], hydroxyethylated-butyne-2-diol-1,4 [376, 377, 379]—on the zinc electrowinning was studied. This influence is also presented and discussed in a review paper [390].

MacKinnon and coworkers [391–393] have studied a number of organic compounds as additives and have shown that tetrabutylammonium chloride improves surface morphology and current efficiency during zinc electrowinning from acidic chloride solutions. A similar influence was observed using other tetraalkylammonium compounds as additives [371, 374, 375, 394].

The applications of commercially available perfluorinated compounds have been reported in a number of recent publications [395–397]. In the presence of perfluorocarboxylic acids, the current efficiency increased, and surface morphology

of zinc was better during its electrowinning from acidic sulfate solutions [378]. The perfluorocarboxylic acids were found to be better additives for zinc electrodeposition when Sb(III) was absent from the zinc electrolyte.

Fluorinated organic compounds have also been used as suppressant of hydrogen evolution on zinc [395, 398].

The influence of orthophenylene diamine and sodium lignin sulfonate on zinc electrowinning from industrial zinc electrolyte was studied [399]. A very negative effect of orthophenylene diamine on current efficiency was found.

The effect of antimony, germanium, and nickel ions, and the organic additives on the zinc electrowinning from sulfuric acid electrolytes was also studied by Ivanov [400].

Also, the influence of aluminum sulfate, animal glue, and an extract of horse-chestnut nuts on zinc electrowinning from a weak acidic sulfate electrolyte prepared from an industrial waste product was investigated [401]. The use of additives mixture has a beneficial effect on zinc electrowinning and results in smooth, slightly bright zinc deposits.

Synthetic and pure zinc(II) solutions produced from laboratory leached,

oxidized zinc ores, under controlled temperature and pH were subjected to continuous electrowinning operations [402, 403]. Copper and iron additives were found to decrease the current efficiency and worsen the quality of the deposited zinc, while manganese and silica slightly influenced the properties of the deposit. Organic additives, gelatin, and TU have good leveling effects on the cathode deposits.

Lead–cobalt anodes used for electrowinning of zinc from sulfate solutions were investigated by Rashkov et al. [404].

The zinc electrowinning was also studied in alkaline solutions [405–407].

24.1.5.3 Zinc Electroplating

The deposits of zinc on different metals, especially on steel, have special relevance because of their anticorrosive properties by the formation of passive layers on contact with air, and in aqueous medium.

Mechanism of zinc electrodeposition on steel in acidic solution of zinc chloride was investigated [408] as a function of pH, grain-refining additives, and current density.

The effects of organic additives, such as benzoic acid (BA) and PEGs, on the initial stage of the zinc electrodeposition on iron have been investigated [409, 410] in an acidic zinc chloride solution. Benzoic acid molecules control the deposition rate at the dendritic sites by blocking the active surface through adsorption. PEGs are adsorbed with a well-ordered structure on the iron surface and appear to desorb in the underpotential deposition region of zinc, which helps to inhibit proton reduction by effective blocking of the electrode surface.

Effects of other additives such as *o*-vanilline [411], Triton X-10, sodium methylene bis(naphthalene sulfonate),

phenylbenzylketone, and a CH-1 brightener [412] on the electrodeposition of zinc were studied. It was found that the electrocrystallization mechanisms of zinc and microstructure of deposits are sensitive to the identity of organic additives.

Zinc electrodeposition was studied using three-dimensional electrodes [413, 414] or rotating disc electrodes (Cu, Al, and stainless steel) [415].

The effect of potential on the cathodic efficiency of a zinc electrodeposition in a cyanide-free alkaline bath was also investigated [416].

Chandran et al. have intensively studied electrodeposition of zinc on steel from noncyanide plating bath [417] and bromide electrolytes [418, 419].

The details of zinc plating from an acetate-based electrolyte were also presented [420].

24.1.5.4 Zinc Alloys Electroplating

The earlier papers on zinc alloys plating were described by Brodd and Leger [92]. In the last 10 years, the electrodeposition of the new Zn–Me alloys and ternary alloys was studied. The influence of plating conditions and different additives for deposition of alloys of Zn with iron group metals was studied in detail.

Electrochemical behaviors of Zn–Fe alloy and Zn–Fe–TiO₂ composite electrodeposition were studied in alkaline zincate solutions [421]. From the results, it can be concluded that Zn shows underpotential deposition. The content of Fe in the Zn–Fe coating changes with the composition of the electrolyte.

Electrodeposition of Zn–Ni alloys attracted considerable attention. The influence of electrolyte composition [422–428] hydrodynamic conditions [424] and the electrochemical polarization mode [424, 426, 428] on the properties of Zn–Ni

deposit were studied. The composition, morphology, and structure of the Zn–Ni alloys coatings, cathode current efficiency, and corrosion resistance were determined. Corrosion resistance of compositionally modulated multilayered Zn–Ni alloys deposited from a single bath was investigated [427]. Thermal stability of Zn–Ni alloys [425] and also their structures using X-ray diffraction [422] were studied.

Relative contributions of Ni(II) and Zn(II) reduction to anomalous electrodeposition of Zn–Ni alloys from solutions containing and not containing organic additives were reported [429].

In the presence of organic additives such as benzyl triethanol ammonium bromide [430], the smooth and uniform deposits that exhibited superior corrosion resistance were obtained.

The composition, surface morphology, and appearance of Zn–Co alloy deposits were studied as a function of experimental conditions [431–435]. These alloys were also found to be more corrosion resistant than zinc but less resistant than cobalt [432].

The influence of benzylidene acetone on the electrodeposition mechanism of Zn–Co alloy was investigated [436]. A relationship between corrosion resistance, microstructure, and cobalt content in Zn–Co alloys was investigated [437] using X-ray photoelectron spectroscopy (XPS) and Auger spectroscopy [438]. The role of vitreous carbon, copper, and nickel substrates in Zn–Co deposition from chloride bath was analyzed [439].

The electrodeposition of Zn–Sn alloys was studied using the EQCM method [440]. The influence of electrolyte composition on the Zn–Sn alloys properties was investigated and discussed [440–442].

The electrodeposition of zinc and iron group metal alloys (Zn–Co, Zn–Ni, Zn–Fe) on Cu electrode was also studied in methanol bath [443].

In addition, other zinc binary Zn–Te [444, 445] and ternary alloys such as Zn–Co–Cu [446], Zn–Ni–Co [447], Zn–Cu–Sn [448], Zn–Co–TiO₂ [435], and Ni–Zn–P [449] were also investigated.

24.1.5.5 Electrochemical Sensors and Modified Electrodes

24.1.5.5.1 Potentiometric Sensors The ion-selective electrodes have seen spectacular achievements in the last decade. Selective complexation of ligands and Zn(II) was used in the construction of chemical sensors, using different excluder and solvent mediators.

Using a typical poly(vinyl chloride) (PVC)-based membrane with different ionophores – Zn-bis(2,4,4-trimethylpentyl) dithiophosphinic acid complex [450], protoporphyrin IX dimethyl ester [451], porphyrin derivative [452] and hematoporphyrin IX [453], tetra(2-aminophenyl) porphyrin [454], cryptands [455, 456], 12-crown-4 [457], benzo-substituted macrocyclic diamide [458], 5,6,14,15-dibenzo-1,4-dioxo-8,12, diazacyclopentadecane-5,14-diene [459], and (*N*-[(ethyl-1-pyrrolidinyl-2-methyl)] methoxy-2-sulfamoyl-5-benzamide [460] – the sensors for zinc ions were prepared and investigated. The armed macrocycle, 5,7,7,12,14,14-hexamethyl-1,4,8,11-tetraazacyclo tetradeca-4,11-diene dihydrogen perchlorate was used for the preparation of polystyrene-based Zn(II)-sensitive electrode [461].

Dumkiewicz et al. [462, 463] have investigated the ion-selective electrode with a chelating pseudo-liquid membrane for zinc determination.

These electrodes exhibit a working concentration range from 1.0×10^{-5} to 1.0×10^{-1} M with a Nernstian slope of 29 ± 1 mV per decade activity and a fast response time (10–30 s). In some cases, the slope was lower [455, 456, 459].

The tetraphenylborate ion-doped polypyrrole electrode was sensitive to zinc ions [464, 465], and its sensitivity was dependent on the polymer macrostructure.

Zinc-selective electrodes based on a solid solution of $\text{Na}_{2-x}\text{Zn}_x\text{V}_{12}\text{O}_{30}$ ($x = 0.4$ or 0.6) [466] as well as sensor containing highly lipophilic $[(\text{CH}_3)_3\text{N}(\text{C}_{43}\text{H}_{79}\text{O}_3)]_2\text{Zn}(\text{SCN})_4$ ion exchanger [467] were examined. A zinc-selective electrode with low detection limit was used for the determination of Zn(II) in environmental samples [467].

The ion-selective electrodes based on different types of zinc-Schiff's bases were used for the determination of SO_4^{2-} [468] and thiocyanate ions concentration [469].

Zirconia solid electrolyte and zinc oxide sensing electrodes were used as a high-temperature NO_x sensor [470, 471]. The response of the electrode potential was linear for the logarithm of NO_x (NO) concentration from 40 to 450 ppm.

A solid-state potassium-selective electrode based on potassium zinc hexacyanoferrates, $\text{K}_2\text{Zn}_3[\text{Fe}(\text{CN})_6]_2$, ion exchanger is described [472]. The sensor can be used in the determination of K^+ ion in concentration range 10^{-4} – 1 M KCl.

24.1.5.5.2 Voltammetric/Amperometric

Sensors Thick-film carbon-containing screen-printed electrodes modified with formazan [473] were used for zinc determination.

The electrochemical properties of immobilized copper, zinc superoxide dismutase, and their interaction with super oxide radicals were investigated [474].

The modified Zn/polytetrafluoroethylene electrode can be used at high negative potentials (to -2.5 V versus Ag/AgCl) without significant hydrogen evolution [475]. Such electrode was used to detect organochloride compounds in water–AN mixtures.

Zinc hexacyanoferrate was supported on the surface of Ti(IV) oxide grafted on a silica gel [476]. Electrochemical behavior of this electrode was dependent on alkaline metal cations and acetate anion concentrations.

24.1.5.5.3 Modified Electrodes A carbon paste electrode modified with zinc diethyldithiocarbamate was used for selective accumulation and stripping analysis of mercury(II) [477].

Electrochemical and electrocatalytic behavior of zinc hexacyanoferrate directly formed on Zn electrode [478] and on carbon substrates [479] were studied.

Also, the catalytic ability of Zn electrode modified by Pt-doped nickel hexacyanoferrate for methanol electrooxidation was investigated [480].

Preparation, electrochemical, and spectroscopic properties of zinc-porphyrins and anthraquinone-based polymers [481] and also conducting polymers with Zn(II)-5-vinyl-10,15,20-triphenylporphyrin [482] coated electrodes were described.

Electropolymerized thin films of Zn(II)-4,9,16,23-tetraaminophthalocyanine immersed in a solution of relatively high pH have been studied using electrochemistry and spectroelectrochemistry [483].

The ZnO/eosinY hybrid films were prepared by cathodic electrodeposition from a hydrogen peroxide oxygen precursor in chloride medium [484], and the role of reduced eosin bound to ZnO in the electrocatalysis was discussed.

The electrochemical formation of zinc selenide from acidic solutions [485] and electrodeposition of zinc telluride thin films, its properties, and photoelectrochemical applications were presented and discussed by Mahalingam et al. [486, 487].

References

1. S. Trasatti, E. Lust, in *Modern Aspects of Electrochemistry* (Eds.: R. E. White, B. E. Conway, J. O. M. Bockris), Kluwer Academic/Plenum Publisher, New York and London, 1999, p. 1, Vol. 33.
2. A. Hamelin, T. Vitanov, E. Sevastyanov et al., *J. Electroanal. Chem.* **1983**, *145*, 225–264.
3. V. L. Heyfets, B. S. Krasikov, *Dokl. Akad. Nauk SSSR* **1956**, *109*, 586–588.
4. A. Marshall, N. A. Hampson, *J. Electroanal. Chem.* **1974**, *53*, 133–144.
5. V. V. Batrakov, A. I. Sidnin, *Elektrokhimiya* **1972**, *8*, 122–125.
6. B. S. Krasikov, V. Sisoeva, *Dokl. Akad. Nauk SSSR* **1957**, *114*, 826–828.
7. T. Chuan-Sin, Z. A. Iofa, *Dokl. Akad. Nauk SSSR* **1960**, *131*, 137–140.
8. P. Caswell, N. A. Hampson, *J. Electroanal. Chem.* **1969**, *20*, 335–338.
9. D. S. Brown, J. P. G. Farr, N. A. Hampson et al., *J. Electroanal. Chem.* **1968**, *17*, 421–424.
10. V. Ya. Bartenev, E. S. Sevastyanov, D. I. Leikis, *Elektrokhimiya* **1970**, *6*, 1868–1870.
11. A. I. Danilov, V. V. Batrakov, V. A. Safonov, *Elektrokhimiya* **1980**, *16*, 100–104.
12. T. N. Anderson, J. L. Anderson, H. Eyring, *J. Phys. Chem.* **1969**, *73*, 3562–3570.
13. A. N. Frumkin, V. V. Batrakov, A. I. Sidnin, *J. Electroanal. Chem.* **1972**, *39*, 225–228.
14. V. V. Batrakov, B. B. Damaskin, *J. Electroanal. Chem.* **1975**, *65*, 361–372.
15. Yu. P. Ipatov, V. V. Batrakov, V. V. Salaginov, *Elektrokhimiya* **1976**, *12*, 286–290.
16. E. J. Lust, K. K. Lust, A. A. J. Jänes, *Elektrokhimiya* **1990**, *26*, 1627–1632.
17. V. V. Batrakov, A. I. Sidnin, *Elektrokhimiya* **1972**, *8*, 743–747.
18. V. V. Batrakov, A. N. Frumkin, A. I. Sidnin, *Elektrokhimiya* **1974**, *10*, 216–222.
19. V. V. Batrakov, A. I. Sidnin, *Elektrokhimiya* **1974**, *10*, 1757–1761.
20. V. V. Batrakov, B. B. Damaskin, Yu. P. Ipatov, *Elektrokhimiya* **1974**, *10*, 144–148.
21. Yu. P. Ipatov, V. V. Batrakov, *Elektrokhimiya* **1975**, *11*, 1717–1720.
22. Yu. P. Ipatov, V. V. Batrakov, *Elektrokhimiya* **1980**, *16*, 624–630.
23. Yu. P. Ipatov, V. V. Batrakov, *Elektrokhimiya* **1980**, *16*, 630–638.
24. E. J. Lust, A. Jänes, K. Lust et al., *J. Electroanal. Chem.* **1997**, *431*, 183–201.
25. T. Hurlen, E. Eriksrud, *J. Electroanal. Chem.* **1973**, *45*, 405–410.
26. E. Eriksrud, *J. Electroanal. Chem.* **1977**, *76*, 27–49.
27. F. van der Pol, M. Sluyters-Rehbach, J. H. Sluyters, *J. Electroanal. Chem.* **1975**, *58*, 177–188.
28. H. L. Jindal, K. Matsuda, R. Tamamushi, *J. Electroanal. Chem.* **1978**, *90*, 185–196.
29. H. L. Jindal, K. Matsuda, R. Tamamushi, *J. Electroanal. Chem.* **1978**, *90*, 197–201.
30. S. Vavříčka, J. Kuta, L. Pospíšil, *J. Electroanal. Chem.* **1982**, *133*, 299–305.
31. W. S. Go, J. Osteryoung, *J. Electroanal. Chem.* **1987**, *233*, 275–281.
32. J. J. O'Dea, J. Osteryoung, R. A. Osteryoung, *J. Phys. Chem.* **1983**, *87*, 3911–3918.
33. W. S. Go, J. J. O'Dea, J. Osteryoung, *J. Electroanal. Chem.* **1988**, *255*, 21–44.
34. R. Andreu, M. Sluyters-Rehbach, A. G. Remijnse et al., *J. Electroanal. Chem.* **1982**, *134*, 101–115.
35. S. Kang, K. Matsuda, R. Tamamushi, *Collect. Czech. Chem. Commun.* **1982**, *47*, 1433–1443.
36. J. Hendrikx, A. van der Putten, W. Visscher et al., *Electrochim. Acta* **1984**, *29*, 81–89.
37. J. O. M. Bockris, Z. Nagy, A. Dajmjanovic, *J. Electrochem. Soc.* **1972**, *119*, 285–295.
38. R. Andreu, M. Sluyters-Rehbach, J. H. Sluyters, *J. Electroanal. Chem.* **1984**, *171*, 139–155.
39. A. Baars, M. Sluyters-Rehbach, J. H. Sluyters, *J. Electroanal. Chem.* **1994**, *364*, 189–197.
40. M. Pérez, A. Baars, S. J. M. Zevenhuizen et al., *J. Electroanal. Chem.* **1995**, *397*, 87–92.
41. L. Koene, M. Sluyters-Rehbach, J. H. Sluyters, *J. Electroanal. Chem.* **1996**, *402*, 57–72.

42. T. G. J. van Venrooij, M. Sluyters-Rehbach, J. H. Sluyters, *J. Electroanal. Chem.* **1996**, 419, 61–70.
43. C. Zhang, J. M. Wang, L. Zhang et al., *J. Electrochem. Soc.* **2001**, 148, E310–E312.
44. J. X. Yu, L. Wang, L. Su et al., *J. Electrochem. Soc.* **2003**, 150, C19–C23.
45. R. R. Nazmutdinov, W. Schmickler, A. M. Kuznetsov, *Chem. Phys.* **2005**, 310, 257–268.
46. Y. Marcus, *Ion Solvation*, Wiley, Chichester, 1985.
47. J. Taraszewska, A. Wałęga, *J. Electroanal. Chem.* **1986**, 200, 261–277.
48. J. Taraszewska, A. Wałęga, *J. Electroanal. Chem.* **1984**, 171, 243–256.
49. J. Taraszewska, A. Wałęga, *J. Electroanal. Chem.* **1985**, 185, 3–13.
50. J. Taraszewska, J. Śledzik, *J. Electroanal. Chem.* **1986**, 215, 287–291.
51. J. Stroka, K. Maksymiuk, Z. Galus, *J. Electroanal. Chem.* **1984**, 167, 211–226.
52. K. Maksymiuk, J. Stroka, Z. Galus, *Pol. J. Chem.* **1987**, 61, 529–536.
53. J. Stroka, W. Górski, H. Schneider, *J. Electroanal. Chem.* **1990**, 288, 143–152.
54. R. M. Rodriguez, E. Brillas, J. A. Garrido et al., *Can. J. Chem.* **1986**, 64, 891–896.
55. E. Brillas, J. A. Garrido, R. M. Rodriguez et al., *Electrochim. Acta* **1993**, 38, 2459–2465.
56. J. Taraszewska, A. Broda, *J. Electroanal. Chem.* **1983**, 153, 243–254.
57. B. Behr, J. Taraszewska, J. Stroka, *J. Electroanal. Chem.* **1975**, 58, 71–80.
58. B. Marczewska, *Collect. Czech. Chem. Commun.* **1994**, 59, 1545–1550.
59. Z. Galus, in *Advances in Electrochemical Science and Engineering* (Eds.: H. Gerischer, Ch. Tobias), VCH Publishers, Weinheim, 1995, p. 217.
60. B. Marczewska, *Pol. J. Chem.* **1993**, 67, 2205–2211.
61. B. Marczewska, *Collect. Czech. Chem. Commun.* **1997**, 62, 843–848.
62. B. Marczewska, J. Włoszek, U. Kozłowska, *Electroanalysis* **1999**, 11, 243–248.
63. B. Marczewska, *Electroanalysis* **1998**, 10, 50–53.
64. B. Marczewska, *Gazz. Chim. Ital.* **1996**, 126, 259–263.
65. B. Marczewska, *Monatsh. Chem.* **1996**, 127, 859–866.
66. B. Marczewska, *J. Electroanal. Chem.* **1994**, 374, 251–254.
67. B. Marczewska, *Indian J. Chem. A* **1997**, 36, 440–445.
68. B. Marczewska, *Collect. Czech. Chem. Commun.* **1999**, 64, 585–594.
69. B. Marczewska, *Electroanalysis* **1999**, 11, 1101–1107.
70. W. R. Fawcett, A. Lasia, *J. Electroanal. Chem.* **1990**, 279, 243–256.
71. A. Lasia, M. Bouderbala, *J. Electroanal. Chem.* **1990**, 288, 153–164.
72. M. Manzini, A. Lasia, *Can. J. Chem.* **1994**, 72, 1691–1698.
73. C. Cronnolly, K. Ch. Pillai, W. E. Waghorne, *J. Electroanal. Chem.* **1986**, 207, 177–187.
74. A. G. Anastopoulos, *Electrochim. Acta* **1998**, 43, 2273–2279.
75. A. G. Anastopoulos, *J. Electroanal. Chem.* **1997**, 424, 179–183.
76. A. G. Anastopoulos, G. N. Nikolaidis, *J. Electroanal. Chem.* **2004**, 571, 309–317.
77. D. Gugala, D. Sieńko, J. Saba, *Collect. Czech. Chem. Commun.* **2001**, 66, 411–422.
78. G. Dalmata, *J. Electroanal. Chem.* **1997**, 431, 67–75.
79. J. Saba, K. Sykut, G. Dalmata et al., *Monatsh. Chem.* **1999**, 130, 1453–1459.
80. B. Marczewska, A. Persona, T. Gęca, *J. Electroanal. Chem.* **2004**, 562, 267–271.
81. G. Dalmata, *Collect. Czech. Chem. Commun.* **1998**, 63, 749–760.
82. G. Dalmata, *Croat. Chem. Acta* **1996**, 69, 85–94.
83. G. Dalmata, *Gazz. Chim. Ital.* **1997**, 127, 419–424.
84. G. Dalmata, *Electrochim. Acta* **1997**, 42, 1307–1314.
85. K. Sykut, G. Dalmata, B. Marczewska et al., *Pol. J. Chem.* **2004**, 78, 1583–1596.
86. G. Dalmata, A. Nosal-Wiercińska, T. Zięcina, *Collect. Czech. Chem. Commun.* **2004**, 69, 267–278.
87. J. Saba, *Electrochim. Acta* **1994**, 39, 711–717.
88. J. Saba, *Collect. Czech. Chem. Commun.* **1995**, 60, 1457–1468.
89. J. Saba, J. Nieszporek, D. Gugala et al., *Electroanalysis* **2003**, 15, 33–39.
90. J. Saba, *Electrochim. Acta* **1996**, 41, 297–306.
91. P. Sanecki, *Electrochem. Commun.* **2004**, 6, 753–756.
92. B. J. Brood, V. E. Leger, in *Encyclopedia of Electrochemistry of the Elements* (Ed.: A. J. Bard), Marcel Dekker, New York, 1976, Vol. 5, Chapter 1.

93. V. I. Kravtsov, E. G. Tsventarnyi, O. Yu. Kurtova et al., *Russ. J. Electrochem.* **2001**, 37, 559–568.
94. O. Yu. Kurtova, V. I. Kravtsov, E. G. Tsventarnyi, *Russ. J. Electrochem.* **2004**, 40, 893–897.
95. R. R. Nazmutdinov, M. S. Shapnik, E. E. Starodubets et al., *Russ. J. Electrochem.* **2002**, 38, 1339–1345.
96. N. B. Berezin, K. A. Sagdeev, N. V. Gudina et al., *Russ. J. Electrochem.* **2005**, 41, 203–205.
97. C. S. Kumar, V. S. Muralidharan, S. S. Begum et al., *Indian J. Chem. Technol.* **2000**, 7, 202–204.
98. R. Cibulka, I. Cisařová, J. Ondráček et al., *Collect. Czech. Chem. Commun.* **2001**, 66, 170–184.
99. S. Çakir, E. Coskun, E. Biçer et al., *Carbohydr. Res.* **2003**, 338, 1217–1222.
100. M. S. Díaz-Cruz, J. Mendieta, A. Monjonell et al., *J. Inorg. Biochem.* **1998**, 70, 91–98.
101. M. S. Díaz-Cruz, J. M. Díaz-Cruz, J. Mendieta et al., *Anal. Biochem.* **2000**, 279, 189–201.
102. N. Abo El-Maali, A. H. Osman, A. A. M. Aly et al., *Bioelectrochem. Bioenerg.* **2005**, 65, 95–104.
103. S. Vajhallya, F. Khan, *J. Indian Chem. Soc.* **1999**, 76, 292–295.
104. G. Guibaud, N. Tixier, A. Bouju et al., *Process Biochem.* **2004**, 39, 833–839.
105. R. Andreoli, L. Benedetti, G. Grandi et al., *Electrochim. Acta* **1984**, 29, 227–231.
106. M. E. Bodini, M. A. del Valle, G. E. Copia et al., *Polyhedron* **1998**, 17, 2109–2114.
107. C. S. Pires de Castro, J. R. SouzaDe, C. B. Júnior, *Biophys. Chem.* **2004**, 112, 59–67.
108. A. Gartner, U. Weser, in *Molecular and Functional Aspects of Superoxide Dismutases* (Eds.: F. Vögtle, E. Weber), Springer, Berlin, 1986, p. 1.
109. Z. L. Wang, W. Qian, Q. H. Luo et al., *J. Electroanal. Chem.* **2000**, 482, 87–91.
110. A. Muñoz, A. R. Rodriguez, *Electroanalysis* **1995**, 7, 674–680.
111. J. Mendieta, A. R. Rodriguez, *Electroanalysis* **1996**, 8, 473–479.
112. O. Nieto, A. R. Rodriguez, *Bioelectrochem. Bioenerg.* **1996**, 40, 215–222.
113. C. Harlyk, G. Bordini, O. Nieto et al., *J. Electroanal. Chem.* **1998**, 446, 139–150.
114. C. Harlyk, O. Nieto, G. Bordini et al., *J. Electroanal. Chem.* **1998**, 451, 267–272.
115. C. Harlyk, O. Nieto, G. Bordini et al., *J. Electroanal. Chem.* **1998**, 458, 199–208.
116. M. Dabrio, A. R. Rodriguez, *Anal. Chim. Acta* **1999**, 385, 295–306.
117. M. Dabrio, A. R. Rodriguez, *Electroanalysis* **2000**, 12, 1026–1033.
118. M. Dabrio, A. R. Rodriguez, *Anal. Chim. Acta* **2000**, 424, 77–90.
119. X. F. Zhou, A. J. Han, D. B. Chu et al., *Acta Chim. Sin.* **2002**, 60, 2064–2068.
120. M. L. Duran, A. Sousa, J. Romero et al., *Inorg. Chim. Acta* **1999**, 294, 79–82.
121. C. P. Joshua, M. Avaudeen, A. George, *J. Indian Chem. Soc.* **2003**, 80, 171–173.
122. F. Yilmaz, V. T. Yilmaz, S. Topcu, *J. Coord. Chem.* **2004**, 57, 525–534.
123. E. Lopez-Torres, M. A. Mendiola, J. Rodriguez-Procopio et al., *Inorg. Chim. Acta* **2001**, 323, 130–138.
124. K. R. J. Thomas, J. T. Lin, C. P. Chang et al., *J. Chin. Chem. Soc.* **2002**, 49, 833–840.
125. T. Sugimori, S.-I. Horike, M. Handa et al., *Inorg. Chim. Acta* **1998**, 278, 253–255.
126. F. Yilmaz, V. T. Yilmaz, S. Topcu et al., *J. Coord. Chem.* **2003**, 56, 903–911.
127. A. Naik, S. Annigeri, U. Gangadharath et al., *Bull. Chem. Soc. Jpn.* **2002**, 75, 2161–2167.
128. J. C. Swarts, E. H. G. Langner, N. Krokeide-Hove et al., *J. Mater. Chem.* **2001**, 11, 434–443.
129. R. M. Izatt, J. S. Bradshaw, S. A. Nielsen et al., *Chem. Rev.* **1985**, 85, 271–339.
130. R. M. Izatt, K. Pawlak, J. S. Bradshaw et al., *Chem. Rev.* **1991**, 91, 1721–2085.
131. R. M. Izatt, K. Pawlak, J. S. Bradshaw et al., *Chem. Rev.* **1995**, 95, 2529–2586.
132. V. W. W. Yam, Y. L. Pui, K. K. Cheung et al., *New J. Chem.* **2002**, 26, 536–542.
133. M. Peters, L. Siegfried, T. A. Kaden, *J. Chem. Soc., Dalton Trans.* **2000**, 24, 4664–4668.
134. K. M. Kadish, J. G. Shao, Z. P. Ou et al., *J. Porphyr. Phthalocya.* **2000**, 4, 639–648.
135. V. B. Arion, E. Bill, M. T. Reetz et al., *Inorg. Chim. Acta* **1998**, 282, 61–70.
136. M. Raidt, M. Neuburger, T. A. Kaden, *Dalton Trans.* **2003**, 7, 1292–1298.
137. J. Costamagna, G. Ferraudi, B. Matsuhira et al., *Coord. Chem. Rev.* **2000**, 196, 125–164.
138. S. Brooker, *Coord. Chem. Rev.* **2001**, 222, 33–56.

139. M. Vazquez, M. R. Bermejo, M. Fondo et al., *Eur. J. Inorg. Chem.* **2002**, 2, 465–472.
140. K. M. Kadish, K. M. Smith, R. Guilard, (Eds.), *The Porphyrin Handbook*, Academic Press, 2000.
141. R. A. Sheldon, *Metaloporphyrins in Catalytic Oxidations*, Marcel Dekker, New York, 1994.
142. F. Montanari, L. Casella, *Metaloporphyrins in Catalyzed Oxidations*, Kluwer, Academic Publishers, Dordrecht, 1994.
143. Y. Terazono, B. O. Patrick, D. H. Dolphin, *Inorg. Chem.* **2002**, 41, 6703–6710.
144. Y. X. Zhou, Z. X. Wang, D. K. Wang et al., *J. Porphyr. Phthalocya.* **2001**, 5, 523–527.
145. A. Giraudeau, S. Lobstein, L. Ruhlmann et al., *J. Porphyr. Phthalocya.* **2001**, 5, 793–797.
146. C. Y. Lin, Y. C. Hung, C. M. Liu et al., *Dalton Trans.* **2005**, 2, 396–401.
147. J. Bley-Escrich, S. Prikhodovski, C. D. Brandt et al., *J. Porphyr. Phthalocya.* **2003**, 7, 220–226.
148. J. G. Goll, K. T. Morre, A. Ghosh et al., *J. Am. Chem. Soc.* **1996**, 118, 8344–8354.
149. K. Ozette, P. Leduc, M. Palacio et al., *J. Am. Chem. Soc.* **1997**, 119, 6442–6443.
150. E. K. Woller, S. G. DiMagno, *J. Org. Chem.* **1997**, 62, 1588–1593.
151. Y. Amao, T. Kamachi, I. Okura, *Inorg. Chim. Acta* **1998**, 267, 257–263.
152. J. T. Fletcher, M. J. Therien, *J. Am. Chem. Soc.* **2002**, 124, 4298–4311.
153. N. Armaroli, F. Diederich, L. Echegoyen et al., *New J. Chem.* **1999**, 23, 77–83.
154. C.-L. Lin, M.-Y. Fang, S.-H. Cheng, *J. Electroanal. Chem.* **2002**, 531, 155–162.
155. Y. Yamaguchi, M. Yamazaki, S. Yoshihara et al., *J. Electroanal. Chem.* **1998**, 442, 1–3.
156. M. Izaki, *J. Electrochem. Soc.* **1999**, 146, 4517–4521.
157. Th. Pauporte, D. Lincot, *J. Electroanal. Chem.* **2001**, 517, 54–62.
158. Th. Pauporte, D. Lincot, *J. Electrochem. Soc.* **2001**, 148, C310–C314.
159. J. Lee, Y. Tak, *Electrochem. Solid State Lett.* **2001**, 4, C63–C65.
160. H. X. Li, R. H. Wang, C. H. Guo et al., *Mater. Sci. Eng., B* **2003**, 103, 285–288.
161. F. Q. Tang, Y. Sakka, T. Uchikoshi, *Mater. Res. Bull.* **2003**, 38, 207–212.
162. M. Kemell, F. Dartigues, M. Ritala et al., *Thin Solid Films* **2003**, 434, 20–23.
163. T. Pauporte, T. Yoshida, R. Cortes et al., *J. Phys. Chem. B* **2003**, 107, 10077–10082.
164. S. Karappuchamy, T. Yoshida, T. Sugiura et al., *Thin Solid Films* **2001**, 397, 63–69.
165. T. Yoshida, D. Komatsu, N. Shimokawa et al., *Thin Solid Films* **2004**, 451–452, 166–169.
166. J. Katayama, M. Izaki, *J. Appl. Electrochem.* **2000**, 30, 855–858.
167. T. N. Rao, L. Bahadur, *J. Electrochem. Soc.* **1997**, 144, 179–185.
168. T. Hirano, H. Kozuka, *J. Mater. Sci.* **2003**, 38, 4203–4210.
169. N. G. Park, M. G. Kang, K. M. Kim et al., *Langmuir* **2004**, 20, 4246–4253.
170. S. P. Wiceliński, R. J. Gale, J. S. Wilkes, *J. Electrochem. Soc.* **1987**, 134, 262–263.
171. M. K. Carpenter, M. W. Verbrugge, *J. Mater. Res.* **1994**, 9, 2584–2591.
172. W. R. Pitner, C. L. Hussey, *J. Electrochem. Soc.* **1997**, 144, 3095–3103.
173. L. Simanavicius, A. Stakenas, A. Sarkis, *Electrochim. Acta* **1997**, 42, 1581–1586.
174. S. I. Hsiu, J. F. Huang, I. W. Sun et al., *Electrochim. Acta* **2002**, 47, 4367–4372.
175. Y. F. Lin, I. W. Sun, *Electrochim. Acta* **1999**, 44, 2771–2777.
176. Y. F. Lin, I. W. Sun, *J. Electrochem. Soc.* **1999**, 146, 1054–1059.
177. J. Dogel, W. Freyland, *Phys. Chem. Chem. Phys.* **2003**, 5, 2484–2487.
178. T. Iwagishi, H. Yamamoto, K. Koyama et al., *Electrochemistry* **2002**, 70, 671–674.
179. P. Liu, Q. Q. Yang, G. K. Liu, *Trans. Nonferrous Metal. Soc. China* **1996**, 6, 41.
180. P. Y. Chen, M. C. Lin, I. W. Sun, *J. Electrochem. Soc.* **2000**, 147, 3350–3355.
181. M. C. Lin, P. Y. Chen, I. W. Sun, *J. Electrochem. Soc.* **2001**, 148, C653–C658.
182. P. Y. Chen, I. W. Sun, *Electrochim. Acta* **2001**, 46, 1169–1177.
183. J. F. Huang, I. W. Sun, *J. Electrochem. Soc.* **2002**, 149, E348–E355.
184. J. F. Huang, I. W. Sun, *J. Electrochem. Soc.* **2003**, 150, E299–E306.
185. J. F. Huang, I. W. Sun, *Electrochim. Acta* **2004**, 49, 3251–3258.
186. T. Iwagishi, K. Sawada, H. Yamamoto et al., *Electrochemistry* **2003**, 71, 318–321.
187. T. Iwagishi, T. Nakamuka, H. Yamamoto et al., *Electrochemistry* **2004**, 72, 618–623.
188. J. F. Huang, I. W. Sun, *J. Electrochem. Soc.* **2004**, 151, C8–C14.

189. S. C. Lans, A. van Sandwijk, M. A. Reuter, *J. Appl. Electrochem.* **2004**, 34, 1021–1027.
190. A. Aramata, M. A. Quaiyyum, W. A. Balais et al., *J. Electroanal. Chem.* **1992**, 338, 367–372.
191. M. A. Quaiyyum, A. Aramata, S. Taguchi et al., *Denki Kagaku Oyobi Kogyo Butsuri Kagaku* **1993**, 61, 847–848.
192. M. A. Quaiyyum, A. Aramata, S. Moniwa et al., *J. Electroanal. Chem.* **1994**, 373, 61–66.
193. K. Igarashi, A. Aramata, S. Taguchi, *Electrochim. Acta* **2001**, 46, 1773–1781.
194. S. Taguchi, T. Fukuda, A. Aramata, *J. Electroanal. Chem.* **1997**, 435, 55–61.
195. S. Taguchi, A. Aramata, *J. Electroanal. Chem.* **1995**, 396, 131–137.
196. G. Horányi, A. Aramata, *J. Electroanal. Chem.* **1997**, 437, 259–262.
197. G. Horányi, A. Aramata, *J. Electroanal. Chem.* **1997**, 434, 201–207.
198. A. Aramata, S. Taguchi, T. Fukuda et al., *Electrochim. Acta* **1998**, 44, 999–1007.
199. S. A. Abd El-Maksoud, S. Taguchi, T. Fukuda et al., *Electrochim. Acta* **1996**, 41, 1947–1952.
200. S. Moniwa, A. Aramata, *J. Electroanal. Chem.* **1994**, 376, 203–206.
201. S. Takahashi, K. Hasebe, A. Aramata, *Electrochim. Commun.* **1999**, 1, 301–304.
202. M. Nakamura, A. Aramata, A. Yamagishi et al., *J. Electroanal. Chem.* **1998**, 446, 227–231.
203. J. O. M. Bockris, G. A. Razumney, *Fundamental Aspect of Electrocrystallization*, Plenum Press, New York, 1967.
204. A. R., Despic, in *Comprehensive Treatise of Electrochemistry*, (Eds.: B. E. Conway, J. O. M. Bockris et al.) Plenum Press, New York, 1983, p. 399, Vol. 7.
205. J. H. Lindsay, T. J. O’Keefe, in *Modern Aspects of Electrochemistry* (Ed.: B. E. Conway, J. O. M. Bockris, R. E. White), Plenum Press, New York, 1994, p. 165, Vol. 26.
206. E. Budevski, G. Stoikov, W. J. Lorenz, *Electrochemical Phase Formation and Growth*, VCH Publishers, Weinheim/New York, 1996.
207. Y. C. Chang, G. Prentice, *J. Electrochem. Soc.* **1984**, 131, 1465–1476.
208. Y. C. Change, G. Prentice, *J. Electrochem. Soc.* **1985**, 132, 375–381.
209. V. Rezaite, R. Vishomirskis, *Prot. Met.* **2001**, 37, 25–30.
210. V. Rezaite, R. Vishomirskis, *Prot. Met.* **2001**, 37, 310–313.
211. R. Renuka, L. Srinivasan, S. Ramamurthy et al., *J. Appl. Electrochem.* **2001**, 31, 655–661.
212. R. Shivkumar, P. Manikandan, G. P. Kalaigannan et al., *Bull. Electrochem.* **1998**, 14, 204–210.
213. J. M. Wang, L. Zhang, C. Zhang et al., *J. Power Sources* **2001**, 102, 139–143.
214. V. N. Selivanov, I. G. Bobrikova, S. V. Molchanov et al., *Russ. J. Electrochem.* **1997**, 33, 166–169.
215. Y. Y. Tevtul, *Russ. J. Electrochem.* **1996**, 32, 535–540.
216. S. Nakanishi, K. Fukami, S. Sakai et al., *Chem. Lett.* **2002**, 6, 636–637.
217. R. Ichino, C. Cachet, R. Wiert, *Electrochim. Acta* **1996**, 41, 1031–1039.
218. F. Ganne, C. Cachet, G. Maurin et al., *J. Appl. Electrochem.* **2000**, 30, 665–673.
219. J. L. Zhu, Y. H. Zhou, C. Q. Gao, *J. Power Sources* **1998**, 72, 231–235.
220. C. Cachet, R. Wiert, *Electrochim. Acta* **1999**, 44, 4743–4751.
221. H. B. Yang, X. L. Meng, E. D. Yang et al., *J. Electrochem. Soc.* **2004**, 151, A389–A393.
222. J. Zhu, Y. H. Zhou, H. X. Yang, *J. Power Sources* **1997**, 69, 169–173.
223. S. Białozór, E. T. Bandura, *Electrochim. Acta* **1987**, 32, 891–894.
224. G. Trejo, R. Ortega, Y. Meas et al., *J. Electrochem. Soc.* **1998**, 145, 4090–4097.
225. G. Trejo, H. Ruiz, R. Ortega Borges et al., *J. Appl. Electrochem.* **2001**, 31, 685–692.
226. G. Trejo, R. Ortega, Y. Meas, *Plat. Surf. Finish.* **2002**, 89, 84–87.
227. J. X. Yu, H. X. Yang, X. P. Ai et al., *Russ. J. Electrochem.* **2002**, 38, 321–325.
228. J. X. Yu, H. Q. Cao, Y. Y. Chen et al., *J. Electroanal. Chem.* **1999**, 474, 69–73.
229. E. Gómez, E. Vallés, *J. Electroanal. Chem.* **1995**, 397, 177–184.
230. V. Zuniga, R. Ortega, Y. Meas et al., *Plat. Surf. Finish.* **2004**, 91, 46–51.
231. A. E. Alvarez, D. R. Salinas, *J. Electroanal. Chem.* **2004**, 566, 393–400.
232. M. V. Simičič, K. I. Popov, N. V. Krstajić, *J. Electroanal. Chem.* **2000**, 484, 18–23.
233. D. Giménez-Romero, J. J. García-Jareño, F. Vicente, *J. Electroanal. Chem.* **2003**, 558, 25–33.
234. P. Díaz-Arista, Y. Meas, R. Ortega et al., *J. Appl. Electrochem.* **2005**, 35, 217–227.

235. I. Rodríguez-Torres, G. Valentin, F. Lapique, *J. Appl. Electrochem.* **1999**, 29, 1035–1044.
236. K. Raeissi, A. Saatchi, M. A. Golozar, *J. Appl. Electrochem.* **2003**, 33, 635–642.
237. K. Raeissi, A. Saatchi, M. A. Golozar, *J. Appl. Electrochem.* **2004**, 34, 1249–1258.
238. N. Pereira, L. C. Klein, G. G. Amatucci, *J. Electrochem. Soc.* **2002**, 149, A262–A271.
239. P. L. Cabot, M. Cortes, F. A. Centellas et al., *J. Electroanal. Chem.* **1986**, 201, 85–100.
240. R. W. Powers, M. W. Breiter, *J. Electrochem. Soc.* **1969**, 116, 719–729.
241. N. A. Hampson, G. A. Herdman, R. Taylor, *J. Electroanal. Chem.* **1970**, 25, 9–18.
242. D. A. Payne, A. J. Bard, *J. Electrochem. Soc.* **1972**, 119, 1665–1674.
243. M. C. H. McKubre, D. D. Macdonald, *J. Electrochem. Soc.* **1981**, 128, 524–530.
244. X. Shan, P. Scholl, G. Prentice et al., *J. Electrochem. Soc.* **1989**, 136, 3594–3599.
245. S. B. Saidman, J. R. Vilche, A. J. Arvia, *Electrochim. Acta* **1994**, 39, 1401–1407.
246. G. Prentice, Y. C. Chang, X. Shan, *J. Electrochem. Soc.* **1991**, 138, 890–895.
247. N. A. Hampson, M. J. Tarbox, *J. Electrochem. Soc.* **1963**, 110, 95–103.
248. R. D. Armstrong, M. F. Bell, *J. Electroanal. Chem.* **1974**, 55, 201–211.
249. G. Zhang, *Corrosion and Electrochemistry of Zinc*, Plenum Press, New York, 1996.
250. W. Fürbeth, M. Stratmann, *Corros. Sci.* **2001**, 43, 207–227.
251. P. Scholl, X. Shanb, D. Bonham et al., *J. Electrochem. Soc.* **1991**, 138, 895–900.
252. E. E. Abd El Aal, *Corrosion* **1999**, 55, 582–589.
253. D. D. Macdonald, K. M. Ismail, E. Sikora, *J. Electrochem. Soc.* **1998**, 145, 3141–3149.
254. M. Cai, S. M. Park, *J. Electrochem. Soc.* **1996**, 143, 2125–2131; 3895–3902.
255. A. L. Rudd, C. B. Breslin, *Electrochim. Acta* **2000**, 45, 1571–1579.
256. I. Mogi, H. Kikuya, K. Watanabe et al., *Chem. Lett.* **1996**, 8, 673–674.
257. C. V. Dalkaine, M. N. Boucherit, *J. Electrochem. Soc.* **1997**, 144, 3331–3336.
258. L. P. Podgornova, Y. I. Kuznetsov, S. V. Gavrilova, *Prot. Met.* **2003**, 39, 217–221.
259. H. H. Hassan, *Appl. Surf. Sci.* **2001**, 174, 201–209.
260. N. Ibrığ, J. C. Mirza-Rosca, A. Santana et al., *J. Solid State Electrochem.* **2002**, 6, 119–125.
261. L. Sziráki, Á. Cziráki, I. Geröcs et al., *Electrochim. Acta* **1998**, 43, 175–186.
262. C. Cachet, F. Ganne, G. Maurin et al., *Electrochim. Acta* **2001**, 47, 509–518.
263. C. Cachet, F. Ganne, S. Joiret et al., *Electrochim. Acta* **2002**, 47, 3409–3422.
264. D. Giménez-Romero, J. J. García-Jareño, F. Vicente, *Electrochem. Commun.* **2003**, 5, 722–727.
265. D. Giménez-Romero, J. J. García-Jareño, F. Vicente, *Electrochem. Commun.* **2004**, 6, 148–152.
266. R. Wiart, *Electrochim. Acta* **1990**, 35, 1587–1593.
267. S. S. Abd El Rehim, S. M. Abd El Wahab, E. E. Fouad et al., *Mater. Corros.* **1995**, 46, 633–638.
268. E. E. Abd El Aal, *Corros. Sci.* **2000**, 42, 1–16.
269. E. E. Abd El Aal, *Corros. Sci.* **2004**, 46, 37–49.
270. F. H. Assaf, S. S. Abd El-Rehiem, A. M. Zaky, *Mater. Chem. Phys.* **1999**, 58, 58–63.
271. S. S. Abd El Rehim, E. E. Foad El-Sherbini, M. A. Amin, *J. Electroanal. Chem.* **2003**, 560, 175–182.
272. S. S. Abd El Rehim, E. E. Fouad, S. M. Abd El Wahab et al., *J. Electroanal. Chem.* **1996**, 401, 113–118.
273. E. E. Abd El Aal, *Corros. Sci.* **2002**, 44, 2041–2053.
274. E. E. F. El Sherbini, S. S. Abd El Rehim, *Corros. Sci.* **2000**, 42, 785–798.
275. H. X. Yang, Y. L. Cao, X. P. Ai et al., *J. Power Sources* **2004**, 128, 97–101.
276. Y. C. Chang, G. Prentice, *J. Chinese Inst. Chem. Eng.* **1996**, 27, 17–24.
277. V. V. Ekilik, A. G. Berezhnaya, M. N. Svyataya, *Prot. Met.* **2001**, 37, 525–528.
278. S. C. Barton, A. C. West, *J. Electrochem. Soc.* **2001**, 148, A490–A495.
279. A. B. Velichenko, J. Portillo, M. Sarret et al., *J. Appl. Electrochem.* **1999**, 29, 1119–1123.
280. A. B. Velichenko, J. Portillo, M. Sarret et al., *Electrochim. Acta* **1999**, 44, 3377–3387.
281. A. B. Velichenko, J. Portillo, M. Sarret et al., *Appl. Surf. Sci.* **1999**, 148, 17–23.
282. E. Juzeliūnas, P. Kalinauskas, P. Micinskis, *J. Electrochem. Soc.* **1996**, 143, 1525–1531.
283. F. Roubani-Kalantzopoulou, G. Patermarakis, K. Karayianni, *Anti-Corros. Methods Mater.* **1998**, 45, 84.
284. S. C. Chung, J. R. Cheng, S. D. Chiou et al., *Corros. Sci.* **2000**, 42, 1249–1268.

285. S. Magaino, M. Soga, K. Sobue et al., *Electrochim. Acta* **1999**, *44*, 4307–4312.
286. V. Alonzo, A. Darchen, D. Hauchard et al., *Electrochim. Acta* **2003**, *48*, 951–955.
287. P. Jinturkar, Y. C. Guan, K. N. Han, *Corrosion* **1998**, *54*, 106–114.
288. Kh. M. S. Youssef, C. C. Koch, P. S. Fedkiw, *Corros. Sci.* **2004**, *46*, 51–64.
289. I. M. Baghni, S. B. Lyon, B. Ding, *Surf. Coat. Technol.* **2004**, *185*, 194–198.
290. R. Sarmaitis, V. Dikinis, V. Rezaite, *Prot. Met.* **2003**, *39*, 316–324.
291. A. I. Marshakov, T. I. Sokolova, Y. N. Mikhailovskii, *Prot. Met.* **1997**, *33*, 29–36.
292. S. F. L. Mertens, E. Temmerman, *Corros. Sci.* **2001**, *43*, 301–316.
293. E. Frąckowiak, J. M. Skowroński, *J. Power Sources* **1998**, *73*, 175–181.
294. K. Aramaki, *Corros. Sci.* **2002**, *44*, 2621–2634.
295. K. Aramaki, *Corros. Sci.* **2003**, *45*, 199–210.
296. K. Aramaki, *Corros. Sci.* **2003**, *45*, 451–464.
297. K. Aramaki, *Corros. Sci.* **2003**, *45*, 1085–1101.
298. K. Aramaki, *Corros. Sci.* **2004**, *46*, 1565–1579.
299. K. Aramaki, *Corros. Sci.* **2003**, *45*, 2361–2376.
300. K. Aramaki, *Corros. Sci.* **2001**, *43*, 1573–1588.
301. K. Aramaki, *Corros. Sci.* **2002**, *44*, 1375–1389.
302. K. Aramaki, *Corros. Sci.* **2002**, *44*, 1361–1374.
303. K. Aramaki, *Corros. Sci.* **2001**, *43*, 1985–2000.
304. K. Wang, H. W. Pickering, K. G. Weil, *J. Electrochem. Soc.* **2003**, *150*, B176–B180.
305. C. Huang, W. Zhang, X. Cao, *J. Appl. Electrochem.* **1997**, *27*, 695–698.
306. R. T. Vashi, V. A. Champaneri, *Indian J. Chem. Technol.* **1997**, *4*, 180–184.
307. T. I. Devyatkina, Y. L. Gun'ko, M. G. Mikhaleiko, *Russ. J. Appl. Chem.* **2001**, *74*, 1122–1125.
308. K. Aramaki, *Corros. Sci.* **2002**, *44*, 871–886.
309. S. Manov, A. M. Lamozeuere, L. Aries, *Corros. Sci.* **2000**, *42*, 1235–1248.
310. S. Manov, F. Noli, A. M. Lamazeuere et al., *J. Appl. Electrochem.* **1999**, *29*, 995–1003.
311. J. I. Martins, T. C. Reis, M. Bazzoui et al., *Corros. Sci.* **2004**, *46*, 2361–2381.
312. R. R. Zahran, G. H. Sedahmed, *Mater. Lett.* **1997**, *31*, 29–33.
313. P. Kalinauskas, I. Valsiūnas, M. Samulevičienė et al., *Corros. Sci.* **2001**, *43*, 2083–2092.
314. X. G. Zang, *J. Electrochem. Soc.* **1996**, *143*, 1472–1484.
315. I. Milosev, A. Minovic, *Ann. Chim. Rome.* **2001**, *91*, 343–354.
316. M. A. Pech-Canul, R. Ramanauskas, L. Maldonado, *Electrochim. Acta* **1997**, *42*, 255–260.
317. E. Tada, S. Satoh, H. Kaneko, *Electrochim. Acta* **2004**, *49*, 2279–2285.
318. H. Park, J. A. Szpunar, *Corros. Sci.* **1998**, *40*, 525–545.
319. C. A. Vincent, B. Scrosati, *Modern Batteries. An Introduction to Electrochemical Power Sources*, Arnold, London, 1997.
320. J. Jindra, *J. Power Sources* **1997**, *66*, 15–25.
321. J. Jindra, *J. Power Sources* **2000**, *88*, 202–205.
322. M. Geng, D. O. Northwood, *Int. J. Hydrogen Energy* **2003**, *28*, 633–636.
323. M. E. Alekseeva, Z. P. Arkhangel'skaya, R. P. Ivanova et al., *Russ. J. Appl. Chem.* **1998**, *71*, 1759–1761.
324. H. K. Liu, B. Bright, C. Y. Wang et al., *J. New Mater. Electrochem. Syst.* **2002**, *5*, 47–52.
325. Z. P. Arkhangel'skaya, R. P. Ivanova, T. B. Kas'yan et al., *Russ. J. Appl. Chem.* **2001**, *74*, 607–610.
326. W. H. Zhu, M. E. Flanzer, B. J. Tatarchuk, *J. Power Sources* **2002**, *112*, 353–366.
327. X. Y. Wang, P. J. Sebastian, M. A. Smit et al., *J. Power Sources* **2003**, *124*, 278–284.
328. S. Muller, O. Hass, C. Schlatter et al., *J. Appl. Electrochem.* **1998**, *28*, 305–310.
329. G. Q. Zhang, X. G. Zhang, *Electrochim. Acta* **2004**, *49*, 873–877.
330. S. Muller, F. Holzer, O. Hass, *J. Appl. Electrochem.* **1998**, *28*, 895–898.
331. R. Othman, A. H. Yahaya, A. K. Arof, *J. Appl. Electrochem.* **2002**, *32*, 1347–1353.
332. R. Othman, A. H. Yahaya, A. K. Arof, *J. New Mater. Electrochem. Syst.* **2002**, *5*, 177–182.
333. E. Deiss, F. Holzer, O. Hass, *Electrochim. Acta* **2002**, *47*, 3995–4010.
334. J. Larcin, W. C. Maskell, F. L. Tye, *Electrochim. Acta* **1997**, *42*, 2649–2658.
335. Q. C. Horn, Y. Shao-Horn, *J. Electrochem. Soc.* **2003**, *150*, A652–A658.
336. R. J. Brodd, K. R. Bullock, R. A. Leising et al., *J. Electrochem. Soc.* **2004**, *151*, K1–K11.

337. W. Glaeser, *ITE Lett.* **1999**, 1, 59.
338. W. Glaeser, S. Kunzel-Keune, P. Merkel, *ITE Lett.* **1999**, 1, 91.
339. G. G. Kumar, S. Sampath, *J. Electrochem. Soc.* **2003**, 150, A608–A615.
340. G. G. Kumar, S. Sampath, *Solid State Ionics* **2003**, 160, 289–300.
341. L. Telli, A. Hammouche, B. Brahimi et al., *J. Power Sources* **2002**, 103, 201–206.
342. G. A. Ghiurcan, C. C. Liu, A. Webber et al., *J. Electrochem. Soc.* **2003**, 150, A922–A927.
343. Y. W. Shen, K. Kordesch, *J. Power Sources* **2000**, 87, 162–166.
344. R. Shivkumar, G. P. Kalaignan, T. Vasudevan, *J. Power Sources* **1998**, 75, 90–100.
345. Z. Rogulski, W. Lewdorowicz, W. Tokarz et al., *Pol. J. Chem.* **2004**, 78, 1357–1370.
346. A. P. Karpinski, B. Makovetski, S. J. Russell et al., *J. Power Sources* **1999**, 80, 53–60.
347. D. F. Smith, C. Brown, *J. Power Sources* **2001**, 96, 121–127.
348. D. F. Smith, J. A. Gucinski, *J. Power Sources* **1999**, 80, 66–71.
349. B. Hariprakash, S. K. Martha, A. K. Shukla, *J. Power Sources* **2003**, 117, 242–248.
350. E. P. Koval'chuk, O. R. Artymyshyn, O. V. Reshetnyak et al., *Pol. J. Chem.* **1998**, 72, 1089–1095.
351. J. Skelton, R. Serenyi, *J. Power Sources* **1997**, 65, 39–45.
352. K. B. Lee, L. W. Lin, *J. Microelectromech. Syst.* **1997**, 12, 840–847.
353. F. Belliard, J. T. S. Irvine, *J. Power Sources* **2001**, 97–98, 219–222.
354. Z. Y. Yuan, F. Huang, J. T. Sun et al., *Chem. Lett.* **2002**, 3, 408–409.
355. Y. N. Nuli, Y. Q. Chu, Q. Z. Qin, *J. Electrochem. Soc.* **2004**, 151, A1077–A1083.
356. X. B. Zhao, G. S. Cao, *Electrochim. Acta* **2001**, 46, 891–896.
357. A. Dailly, J. Ghanbaja, P. Willmann et al., *J. Appl. Electrochem.* **2004**, 34, 885–890.
358. M. S. Rahmanifar, M. F. Mousavi, M. Shamsipur et al., *J. Power Sources* **2004**, 132, 296–301.
359. S. L. Mu, *Synth. Met.* **2004**, 143, 269–275.
360. W. Kautek, A. Conradi, M. Sahre et al., *J. Electrochem. Soc.* **1999**, 146, 3211–3216.
361. C. L. Mantell, *Electrochemical Engineering*, 4th ed., McGraw-Hill, New York, 1980, p. 210.
362. D. J. Robinson, T. J. O'Keefe, *J. Appl. Electrochem.* **1976**, 6, 1–7.
363. D. R. Fosnacht, T. J. O'Keefe, *Met. Trans. (B)* **1983**, 14, 645–655.
364. P. A. Adcock, A. R. Ault, O. M. G. Newmann, *J. Appl. Electrochem.* **1985**, 15, 865–878.
365. D. J. MacKinnon, R. M. Morrison, J. M. Brannen, *J. Appl. Electrochem.* **1986**, 16, 53–61.
366. M. Karavasteva, E. Maahn, *Hydrometallurgy* **1993**, 34, 255–261.
367. A. R. Ault, E. J. Frazer, *J. Appl. Electrochem.* **1988**, 18, 583–589.
368. E. J. Frazer, *J. Electrochem. Soc.* **1988**, 135, 2465–2471.
369. L. Muresan, G. Maurin, L. Oniciu et al., *Hydrometallurgy* **1996**, 43, 345–354.
370. C. Cachet, R. Wiart, *J. Electrochem. Soc.* **1994**, 141, 131–139.
371. Y. Stefanov, I. Ivanov, *Hydrometallurgy* **2002**, 64, 193–203.
372. B. C. Tripathy, S. C. Das, G. T. Hefter et al., *J. Appl. Electrochem.* **1997**, 27, 673–678.
373. S. C. Das, P. Singh, G. T. Hefter, *J. Appl. Electrochem.* **1997**, 27, 738–744.
374. B. C. Tripathy, S. C. Das, G. T. Hefter et al., *J. Appl. Electrochem.* **1998**, 28, 915–920.
375. B. C. Tripathy, S. C. Das, P. Singh et al., *J. Appl. Electrochem.* **1999**, 29, 1229–1235.
376. Y. Stefanov, I. Ivanov, S. Rashkov, *Hydrometallurgy* **1997**, 44, 71–81.
377. I. Ivanov, Y. Stefanov, *Hydrometallurgy* **2002**, 64, 111–117.
378. B. C. Tripathy, S. C. Das, P. Singh et al., *J. Electroanal. Chem.* **2004**, 565, 49–56.
379. I. Ivanov, Y. Stefanov, *Hydrometallurgy* **2002**, 64, 181–186.
380. D. S. Baik, D. J. Fray, *J. Appl. Electrochem.* **2001**, 31, 1141–1147.
381. D. J. MacKinnon, J. M. Brannen, *J. Appl. Electrochem.* **1977**, 7, 451–459.
382. D. J. MacKinnon, J. M. Brannen, P. L. Fenn, *J. Appl. Electrochem.* **1987**, 17, 1129–1143.
383. D. J. MacKinnon, R. M. Morrison, J. E. Moulard et al., *J. Appl. Electrochem.* **1990**, 20, 728–736.
384. R. Sato, *J. Electrochem. Soc.* **1959**, 106, 206–211.
385. A. Hosny, *Hydrometallurgy* **1993**, 32, 261–269.
386. M. Karavasteva, St. Karaivanov, *J. Appl. Electrochem.* **1993**, 23, 763–765.
387. M. Karavasteva, *Hydrometallurgy* **1994**, 35, 391–396.

388. M. Sider, D. L. Piron, *J. Appl. Electrochem.* **1988**, 18, 54–61.
389. S. C. Das, P. Singh, G. T. Hefter, *J. Appl. Electrochem.* **1996**, 26, 1245–1252.
390. B. C. Tripathy, I. N. Bhattachary, P. G. Krishna et al., *Trans. Indian Inst. Met.* **1998**, 51, 303–310.
391. D. J. MacKinnon, J. M. Brannen, R. M. Morrison, *J. Appl. Electrochem.* **1988**, 18, 252–256.
392. D. J. MacKinnon, J. M. Brannen, *J. Appl. Electrochem.* **1982**, 12, 21–31.
393. D. J. MacKinnon, J. M. Brannen, R. M. Morrison, *J. Appl. Electrochem.* **1983**, 13, 39–53.
394. B. C. Tripathy, S. C. Das, P. Singh et al., *Bull. Electrochem.* **1998**, 14, 436–438.
395. G. Juhel, B. Beden, C. Lamy et al., *Electrochim. Acta* **1990**, 35, 479–481.
396. C. Cachet, Z. Chami, R. Wiart, *Electrochim. Acta* **1987**, 32, 465–474.
397. C. Cachet, B. Saidani, R. Wiart, *J. Electrochem. Soc.* **1991**, 138, 678–687.
398. M. Naja, N. Penazzi, G. Farnia et al., *Electrochim. Acta* **1993**, 38, 1453–1459.
399. A. M. Alfantazi, D. B. Dreisinger, *Hydrometallurgy* **2003**, 69, 99–107.
400. I. Ivanov, *Hydrometallurgy* **2004**, 72, 73–78.
401. L. Muresan, G. Maurin, L. Oniciu et al., *Hydrometallurgy* **1996**, 40, 335–342.
402. A. E. Elsherief, A. S. Saba, *Trans. Indian Inst. Met.* **1996**, 49, 769–779.
403. A. S. Saba, A. E. Elsherief, *Hydrometallurgy* **2000**, 54, 91–106.
404. St. Rashkov, Ts. Dobrev, Z. Noncheva et al., *Hydrometallurgy* **1999**, 52, 223–230.
405. J. St. Pierre, D. L. Piron, *J. Appl. Electrochem.* **1986**, 16, 447–456.
406. J. St. Pierre, D. L. Piron, *J. Appl. Electrochem.* **1990**, 20, 163–165.
407. Z. Youcai, R. Stanforth, *J. Hazard. Mater. B* **2000**, 80, 223–240.
408. J. R. Park, H. T. Kim, *Plat. Surf. Finish.* **1999**, 86, 108–112.
409. J. Y. Lee, J. W. Kim, M. K. Lee et al., *J. Electrochem. Soc.* **2004**, 151, C25–C31.
410. J. W. Kim, J. Y. Lee, S. M. Park, *Langmuir* **2004**, 20, 459–466.
411. S. J. Kim, H. T. Kim, S. M. Park, *J. Electrochem. Soc.* **2004**, 151, C850–C854.
412. J. X. Yu, Y. Y. Chen, H. X. Yang et al., *J. Electrochem. Soc.* **1999**, 146, 1789–1793.
413. M. Wery, J. C. Catonné, V. Ligier et al., *J. Appl. Electrochem.* **1999**, 29, 729–739.
414. M. Wery, J. C. Catonné, J. Y. Hihn, *J. Appl. Electrochem.* **2000**, 30, 165–172.
415. V. S. Kolsnitsyn, O. A. Yapyntseva, *Russ. J. Appl. Chem.* **2004**, 77, 222–225.
416. J. A. Diez, C. Muller, H. Grande, *Rev. Metal. Madrid* **2004**, 40, 182–187.
417. M. Chandran, R. L. Sarma, R. M. Krishnan, *Trans. Inst. Met. Finish.* **2003**, 81, 207–209.
418. M. Chandran, R. L. Sarma, R. M. Krishnan, *Bull. Electrochem.* **1999**, 15, 242–247.
419. M. Chandran, R. L. Sharma, R. M. Krishnan, *Plat. Surf. Finish.* **2001**, 88, 74–77.
420. R. Sekar, S. Sriveeraraghavan, R. M. Krishnan, *Bull. Electrochem.* **1999**, 15, 219–222.
421. Y. Y. Wang, W. J. Peng, L. Y. Chai et al., *J. Cent. South. Univ. Technol.* **2003**, 10, 183–189.
422. Z. Wu, L. Fedrizzi, P. L. Bonora, *Surf. Coat. Technol.* **1996**, 85, 170–174.
423. Y. S. Jin, T. Y. Kim, K. Y. Kim, *Surf. Coat. Technol.* **1998**, 106, 220–227.
424. E. Bełtowska-Lehman, P. Ozga, Z. Swiatek et al., *Surf. Coat. Technol.* **2002**, 151–152, 444–448.
425. C. Bories, J.-P. Bonino, A. Rousset, *J. Appl. Electrochem.* **1999**, 29, 1045–1051.
426. G. Roventi, R. Fratesi, R. A. Della Guardia et al., *J. Appl. Electrochem.* **2000**, 30, 173–179.
427. I. Ivanov, I. Kirilova, *J. Appl. Electrochem.* **2003**, 33, 239–244.
428. J. B. Bajat, M. D. Maksimovic, G. R. Radovic, *J. Serb. Chem. Soc.* **2002**, 67, 625–634.
429. B. Y. Chang, S. M. Park, *J. Electrochem. Soc.* **2004**, 151, C786–C788.
430. Z. A. Hamid, *Anti-Corros. Methods Mater.* **1998**, 45, 31.
431. R. Fratesi, G. Roventi, G. Giuliani et al., *J. Appl. Electrochem.* **1997**, 27, 1088–1094.
432. I. Kirilova, I. Ivanov, S. Rashkov, *J. Appl. Electrochem.* **1997**, 27, 1380–1384.
433. C. R. Tomachuk, C. M. D. Freire, M. Ballester et al., *Surf. Coat. Technol.* **1999**, 122, 6–9.
434. K. Hayashi, Z. Tanaka, K. Kondo, *J. Iron Steel Inst. Jpn.* **1999**, 85, 314–318.
435. Z. A. Hamid, *Anti-Corros. Methods Mater.* **2001**, 48, 235–240.
436. G. Trejo, R. Ortega, Y. Meas et al., *J. Appl. Electrochem.* **2003**, 33, 373–379.

437. A. Cunha, S. D. Carpenter, J. Z. Ferreira et al., *Corros. Eng. Sci. Technol.* **2003**, 38, 313–316.
438. D. E. O. S. Carpenter, M. Ashworth, J. P. G. Farr, *Trans. Inst. Met. Finish.* **2003**, 81, 177–181.
439. E. Gómez, X. Alcobe, E. Vallés, J. *Electroanal. Chem.* **2001**, 505, 54–61.
440. K. Wang, H. W. Pickering, K. G. Weil, *Electrochim. Acta* **2001**, 46, 3835–3840.
441. E. Gaus, J. Torrent-Burgués, *J. Electroanal. Chem.* **2005**, 575, 301–309.
442. E. Gaus, J. Torrent-Burgués, *J. Electroanal. Chem.* **2003**, 549, 25–36.
443. T. Tsuru, S. Kobayashi, T. Aktiyama et al., *J. Appl. Electrochem.* **1997**, 27, 209–214.
444. A. E. Rakhshani, B. Pradeep, *Appl. Phys. Mater. Sci. Process.* **2004**, 79, 2021–2025.
445. A. E. Rakhshani, *Semicond. Sci. Technol.* **2004**, 19, 543–547.
446. S. M. Rashwan, *Mater. Chem. Phys.* **2005**, 89, 192–204.
447. M. M. Younan, *J. Appl. Electrochem.* **2000**, 30, 55–60.
448. W. S. Miu, J. Ross, F. Lau et al., *Trans. Inst. Mater. Met. Finish.* **1997**, 73, 137–139.
449. M. Bouanani, F. Cherkaoui, M. Cherkaoui et al., *J. Appl. Electrochem.* **1999**, 29, 1171–1176.
450. V. K. Gupta, A. K. Jain, L. P. Sing et al., *Electrochim. Acta* **1998**, 43, 2047–2052.
451. V. K. Gupta, A. Kumar, R. Mangla, *Sens. Actuators, B* **2001**, 76, 617–623.
452. V. K. Gupta, D. K. Chauhan, V. K. Saini et al., *Sensors* **2003**, 3, 223–235.
453. A. K. Jain, S. M. Sondhi, S. Rajvanshi, *Electroanalysis* **2002**, 14, 293–296.
454. A. R. Fakhari, M. Shamsipur, K. Ghanbari, *Anal. Chim. Acta* **2002**, 460, 177–183.
455. S. K. Srivastava, V. K. Gupta, S. Jain, *Anal. Chem.* **1996**, 68, 1272–1275.
456. H. R. Pouretedal, M. Shamsipur, *Fresenius' J. Anal. Chem.* **1998**, 362, 415–418.
457. V. K. Gupta, *Sens. Actuators, B* **1999**, 55, 195–200.
458. M. Shamsipur, S. Rouhani, M. R. Ganjali et al., *Sens. Actuators, B* **1999**, 59, 30–34.
459. A. R. Fakhari, M. Alaghemand, M. Shamsipur, *Anal. Lett.* **2000**, 33, 2169–2181.
460. M. B. Saleh, A. A. Abdel Gaber, *Electroanalysis* **2001**, 13, 104–108.
461. A. K. Singh, G. Bhattacharjee, M. Singh et al., *Electroanalysis* **1997**, 9, 1005–1008.
462. R. Dumkiewicz, C. Wardak, S. Zaręba, *Analyst* **2000**, 125, 527–530.
463. R. Dumkiewicz, C. Wardak, J. Lenik et al., *Chem. Anal. (Warsaw)* **2002**, 47, 257–265.
464. P. C. Pandey, G. Singh, *Sens. Actuators, B* **2002**, 85, 256–262.
465. P. C. Pandey, G. Singh, P. K. Srivastava, *Electroanalysis* **2002**, 14, 427–432.
466. O. I. Gyrdasova, V. L. Volkov, *J. Anal. Chem.* **1998**, 53, 535–538.
467. E. M. Rakhman'ko, V. V. Egorov, M. Ya. Tarazevich et al., *J. Anal. Chem.* **2003**, 58, 691–697.
468. M. R. Ganjali, M. Rezapour, M. R. Pourjavid et al., *Anal. Lett.* **2003**, 36, 881–894.
469. P. Buhlmann, L. Yahya, R. Enderes, *Electroanalysis* **2004**, 16, 973–978.
470. S. Zhuiykov, T. Ono, N. Yamazoe et al., *Solid State Ionics* **2002**, 152, 801–807.
471. N. Miura, K. Akisada, J. Wang et al., *Ionics* **2004**, 10, 1–9.
472. H. A. Arida, R. F. Aglan, *Anal. Lett.* **2003**, 36, 895–907.
473. N. Y. Stozhko, G. N. Lipunova, T. I. Maslakova et al., *J. Anal. Chem.* **2004**, 59, 179–184.
474. B. Ge, F. W. Scheller, F. Lisdat, *Biosens. Bioelectron.* **2003**, 18, 295–302.
475. W. Wiyaratn, M. Somasundrum, W. Surareungchai, *Electroanalysis* **2003**, 15, 1719–1722.
476. D. R. do Carmo, D. W. Franco, U. P. Rodrigues et al., *J. Coord. Chem.* **2001**, 54, 455–468.
477. S. B. Khoo, Q. T. Cai, *Electroanalysis* **1996**, 8, 549–556.
478. A. Eftekhari, *J. Electroanal. Chem.* **2002**, 537, 59–66.
479. J. Joseph, H. Gomathi, G. P. Rao, *J. Electroanal. Chem.* **1997**, 431, 231–235.
480. M. H. Pournaghi-Azar, H. Nahalparvari, *J. Solid State Electrochem.* **2004**, 8, 550–557.
481. N. Allietta, R. Pansu, C. Bied-Charreton et al., *Synth. Met.* **1996**, 81, 205–210.
482. S. N. Kuester, M. M. McGuire, S. M. Drew, *J. Electroanal. Chem.* **1998**, 452, 13–18.
483. K. L. Brown, J. Shaw, M. Ambrose et al., *Microchem. J.* **2002**, 72, 285–298.
484. T. Pauporte, T. Yoshida, A. Goux et al., *J. Electroanal. Chem.* **2002**, 534, 55–64.
485. M. Bouroushian, T. Kosanovic, Z. Loizos et al., *J. Solid State Electrochem.* **2002**, 6, 272–278.

486. T. Mahalingam, V. S. John, P. J. Sebastian, *J. Phys.: Condens. Matter* **2002**, *14*, 5367–5375.
487. T. Mahalingam, V. S. John, S. Rajendran et al., *Semicond. Sci. Technol.* **2002**, *17*, 465–470.

24.2**Electrochemistry of Cadmium**

24.2.1	Double-layer Properties of Cadmium Electrodes	768
24.2.2	Electrochemical Properties and Kinetics of the Cd(II)/Cd(Hg) Systems	770
24.2.2.1	Electrochemistry in Aqueous Solutions	770
24.2.2.1.1	Kinetics of Simple Ions	770
24.2.2.1.2	Influence of a Catalyst	771
24.2.2.1.3	Influence of Inhibitors	773
24.2.2.2	Electrochemistry in Mixed and Nonaqueous Solvents	774
24.2.2.3	Electrochemical Properties of the Cadmium Complexes	775
24.2.2.3.1	Determination of Stability Constants	777
24.2.2.3.2	Electrochemical Preparation of Cadmium Complexes	778
24.2.2.4	Preparation and Electrochemical Properties of Cadmium Chalcogenides	779
24.2.2.4.1	CdS	779
24.2.2.4.2	CdSe	780
24.2.2.4.3	CdTe	781
24.2.2.5	Properties of Cadmium Intermetallic Compounds	782
24.2.3	Cadmium Underpotential Deposition and Electrodeposition on Solid Electrodes	782
24.2.3.1	Deposition of Cd on Cadmium Electrode	782
24.2.3.2	Electrodeposition of Cd on Other Solid Substrates	783
24.2.3.2.1	Gold	783
24.2.3.2.2	Platinum	786
24.2.3.2.3	Silver	787
24.2.3.2.4	Copper	787
24.2.3.2.5	Silicon	788
24.2.3.2.6	Other Substrates	788
24.2.4	Passivation and Corrosion of Cadmium	789
24.2.4.1	Passivation of Cadmium Electrode	789
24.2.4.2	Corrosion of Cadmium	789
24.2.5	Applied Electrochemistry	790
24.2.5.1	Batteries	790
24.2.5.1.1	Cadmium–Mercuric Oxide Primary Cells	790

24.2.5.1.2	Cadmium–Nickel Oxide (Ni–Cd) Secondary Cells	790
24.2.5.1.3	Cadmium–Silver Oxide Secondary Cells	791
24.2.5.2	Application in Electrochemical Sensors	792
24.2.5.2.1	Potentiometric Sensors	792
24.2.5.2.2	Amperometric-voltammetric Sensors	793
	References	794

24.2.1

Double-layer Properties of Cadmium Electrodes

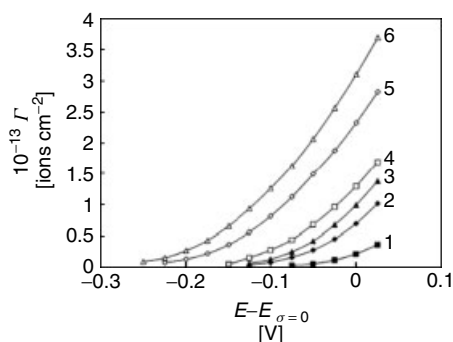
The electrical double-layer (edl) properties pose a fundamental problem for electrochemistry because the rate and mechanism of electrochemical reactions depend on the structure of the metal–electrolyte interface. The theoretical analysis of edl structures of the solid metal electrodes is more complicated in comparison with that of liquid metal and alloys. One of the reasons is the difference in the properties of the individual faces of the metal and the influence of various defects of the surface [1]. Electrical double-layer properties of solid polycrystalline cadmium (pc-Cd) electrodes have been studied for several decades. The dependence of these properties on temperature and electrode roughness, and the adsorption of ions and organic molecules on Cd, which were studied in aqueous and organic solvents and described in many works, were reviewed by Trasatti and Lust [2].

In recent years, similar studies have been carried out for Cd single crystal electrode. Korotkov et al. [3] showed that the zero charge potential (E_{pzc}) of a Cd(11 $\bar{2}$ 0) in surface inactive electrolytes, NaF and Na₂SO₄, was shifted slightly in the negative direction in comparison with E_{pzc} of pc-Cd.

Naneva and Popov et al. [4, 5] have studied Cd(0001) grown electrolytically in a Teflon capillary in NaF aqueous solution. A value of E_{pzc} equal to -0.99 V (versus saturated calomel electrode (SCE)) was evaluated from minimum potential (E_{min}) on the differential capacity C – E curves obtained in dilute electrolyte. The zero charge potential was found to be practically independent of the crystallographic orientation. The E_{pzc} and the inner layer capacity of Cd(0001) single crystals were determined in KF solution as a function of temperature [5]. The positive values of $\Delta E_{\text{pzc}}/\Delta T$ indicated that the water dipoles in the inner part of the double layer were orientated with their negative part to the electrode surface. It was found that the hydrophilicity of the electrodes was increasing in the order Cd(0001) < Ag(100) < Ag(111).

The capacitance-potential dependences of Cd(0001) in dilute solutions of ClO₄[–], NO₂[–], and NO₃[–] were also studied [6]. A weak specific adsorption of anions increasing in the order ClO₄[–] < NO₂[–] < NO₃[–] was observed. The adsorption of halides on the Cd(0001) single crystal electrode was studied [7], and was found to increase in the sequence Cl[–] < Br[–] < I[–] [8]. Analysis of the impedance data does not point to the specific adsorption of Cl[–] ions, and shows that the surface excess (Γ) of halide ions changes with potential and increases from Br[–] to I[–] (Fig. 1) [7]

Fig. 1 Surface concentration of adsorbed ions versus rational electrode potential curves for the Cd(0001) electrode in aqueous solution with constant ionic strength $0.1x$ M $\text{KA}^* + 0.1(1-x)$ M KF, where A^* is the surface-active halide ion (Br^- curves 1–3) and (I^- curves 4–6), and x is its mole fractions. $x = 0.1$ (curves 1, 4); $x = 0.5$ (curves 2, 5); and $x = 1.0$ (curves 3, 6) [7].



in accordance with the hydration energy of the anions. To describe adsorption of halide ions, the cluster model and quantum chemical calculations were used.

The double-layer structure at the electrochemically polished and chemically treated Cd(0001), Cd(10 $\bar{1}$ 0), Cd(11 $\bar{2}$ 0), Cd(10 $\bar{1}$ 1), and Cd(11 $\bar{2}$ 1) surface electrodes was studied using cyclic voltammetry, impedance spectroscopy, and chronocoulometry [9, 10]. The limits of ideal polarizability, E_{pzc} , and capacity of the inner layer were established in the aqueous surface inactive solutions. The values of E_{pzc} decrease, and the capacity of the inner layer increases, if the superficial density of atoms decreases. The capacity of metal was established using various theoretical approximations. The effective thickness of the thin metal layer increases in the sequence of planes Cd(11 $\bar{2}$ 0) < Cd(10 $\bar{1}$ 0) < Cd(0001). It was also found that the surface activity of ClO_4^- was higher than that of F^- anions [10].

The experimental data concerning capacitance of edl at the selected faces of Bi, Sb, and Cd single crystals in solutions of surface inactive electrolytes in water and organic solvent were analyzed in terms of various models [11]. From these data, it follows that the interface electrode/electrolyte properties depend both on the crystallographic and electronic characteristics of the metal and on the nature of the solvent.

Lust et al. have also investigated the adsorption of cyclohexanol [12] and various organic compounds [13, 14] on several cadmium single crystal electrodes. It was also found that the zero charge potential depended on the crystallographic structure (plane) of the electrode surface and on the nature of the solvent studied [12]. The Gibbs energy of metal–water interaction depends weakly on the chemical nature of the metal and aliphatic organic compound [13]. The edl properties of cadmium electrode were studied [15, 16] in terms of the Debye length dependent roughness theory recently developed by Daikhin et al. [17, 18]. This theory was used for the interpretation of capacitance data for cadmium electrode with various surface roughness and energetic inhomogeneity.

Structural aspects of electrochemical adsorption of inorganic ions and neutral organic molecules and water dipoles on quasi-perfect cadmium electrode were also studied [19].

The edl structure of a Cd–Ga (0.3 atom % Cd) liquid electrode in aqueous [20, 21], methanol, and propylene carbonate (PC) [21, 22] solutions with inactive electrolyte (LiClO_4 , LiBF_4) was investigated. The double layer at the liquid Cd–Ga alloy differs from that of a Ga electrode, and was virtually identical with edl at the Cd electrode.

24.2.2

Electrochemical Properties and Kinetics of the Cd(II)/Cd(Hg) Systems**24.2.2.1 Electrochemistry in Aqueous Solutions**

24.2.2.1.1 Kinetics of Simple Ions The electroreduction of Cd(II) ions to its amalgam was investigated in aqueous 1 M KF [23] and 1 M (KF + KCl) mixed electrolyte solutions at dropping mercury electrode (DME) using the faradaic impedance method [24]. From the analysis of the impedance data, it follows that the electrode process is described by mechanism with chemical step followed by two one-electron transfers (CEE). The kinetic parameters of both steps are reported and discussed. The rate constant of the chemical step increases rapidly with chloride concentration.

In mixed $(0.8 - x)$ M NaClO₄ + x M NaF supporting electrolyte the electroreduction of Cd(II) was also studied by Saakes et al. [25]. The kinetic parameters were analyzed using CEE mechanism. The obtained chemical rate constants $k_{s,0}^c$ at both steps, $k_{s,1}$ and $k_{s,2}$, decreased with increasing NaF concentration. The data were corrected for nonspecific double-layer effect (Frumkin correction). The interpretation of CEE mechanism with parallel pathways connected with coexisting cadmium complexes was presented.

The mechanism of the reduction of cadmium ions at DME in NaClO₄ solutions with varied water activity was also studied [26]. In these solutions, the electrode process of the Cd(II)/Cd(Hg) system was described by the mechanism that includes: (1) fast loss of 12.5 water molecules in a preceding equilibrium, (2) a slow “chemical” step, which is not a desolvation, (3) slow transfer of the first electron,

$k_{s,1}$, (4) fast loss of four water molecules, (5) slow transfer of the second electron $k_{s,2}$, and (6) fast loss of the remaining nine water molecules. The $k_{s,1}$ and $k_{s,2}$ values increase with decreasing water activity.

The reduction of Cd(II) ions on DME was also investigated in 1 M perchlorate, fluoride and chloride solutions using dc, ac admittance, and demodulation methods [27]. It was found that in the perchlorate supporting electrolyte, the reduction mechanism is also CEE, and that the rate constant of the chemical step is quite close to the value characteristic for fluoride solutions. The theories available at present could not be applied to the Cd(II) reduction in chloride solution because of the inapplicability of the Randles equivalent circuit.

The combination of three transient techniques – coulostatic, modified coulostatic, and galvanostatic methods was applied for the study of the electrode reaction Cd(II)/Cd(Hg) in aqueous solution of 1 M Na₂SO₄, pH 4 [28].

Recently, Darowicki [29, 30] has presented a new mode of electrochemical impedance measurements. This method employed a short time Fourier transformation to impedance evaluation. The digital harmonic analysis of cadmium-ion reduction on mercury electrode was presented [31]. A modern concept in nonstationary electrochemical impedance spectroscopy theory and experimental approach was described [32]. The new investigation method allows determination of the dependence of complex impedance versus potential [32] and time [33]. The reduction of cadmium on DME was chosen to present the possibility of these techniques. Figure 2 illustrates the change of impedance for the Cd(II) reduction on the hanging drop mercury electrode obtained for the scan rate 10 mV s⁻¹.

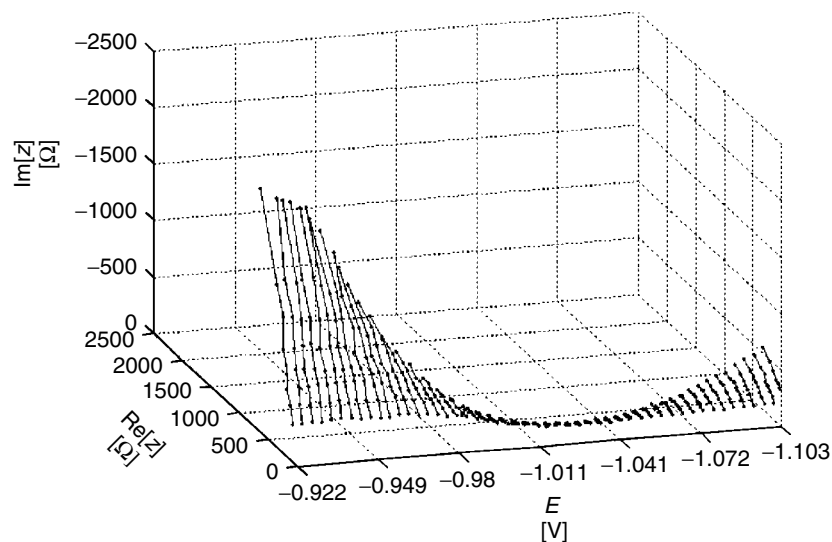


Fig. 2 Changes of impedance during reduction of 2 mM Cd(II) in 0.5 M Na₂SO₄ on HDME. Potential scan rate 10 mV s⁻¹ [32].

A uniform approach to trace the analysis and evaluation of electrode kinetics of the Cd(II)/Cd(Hg) system with fast Fourier transform electrochemical instrumentation was presented by Schiewe et al. [34].

The principles of thin-layer anodic stripping voltammetry were discussed, and a model for the stripping stage was developed for anodization by a linear potential ramp [35]. The experimental test of the theories was carried out for cadmium and lead amalgams.

The convolution–deconvolution voltammetry, combined with digital simulation techniques, was applied [36] to determine the electrochemical and chemical parameters for the Cd(II)/Cd(Hg) system in aqueous NaNO₃ solution. The agreement between experimental and theoretical data indicated that the reduction mechanism at the mercury electrode proceeds via consisting in chemical step (C) followed by charge transfer step (E)-so-called CE mechanism [37].

The dropping mercury microelectrode (DM_μE) technique was used for the mechanistic study of Cd(II) reduction in aqueous KF [38] and 0.5 M Na₂SO₄ [39] solutions.

24.2.2.1.2 Influence of a Catalyst From the data obtained with impedance and demodulation voltammetry for a solution of x M KCl + $(1 - x)$ M KF [40], it follows that chloride ions catalyze the Cd(II)/Cd(Hg) process (Fig. 3); the cadmium reduction proceeds according to several chemical (C) and charge transfer (E) steps, so-called CE-CEC mechanism. The catalyst accelerates specifically the first chemical and the first electrochemical step.

The adsorption of reactant in the system Cd(II) + 1 M KBr/Cd(Hg) was investigated by using chronocoulometry [41]. The values of the reactant surface excess were calculated. The authors proposed the adsorption isotherm, which allows the adsorption of the reactant and ligand to

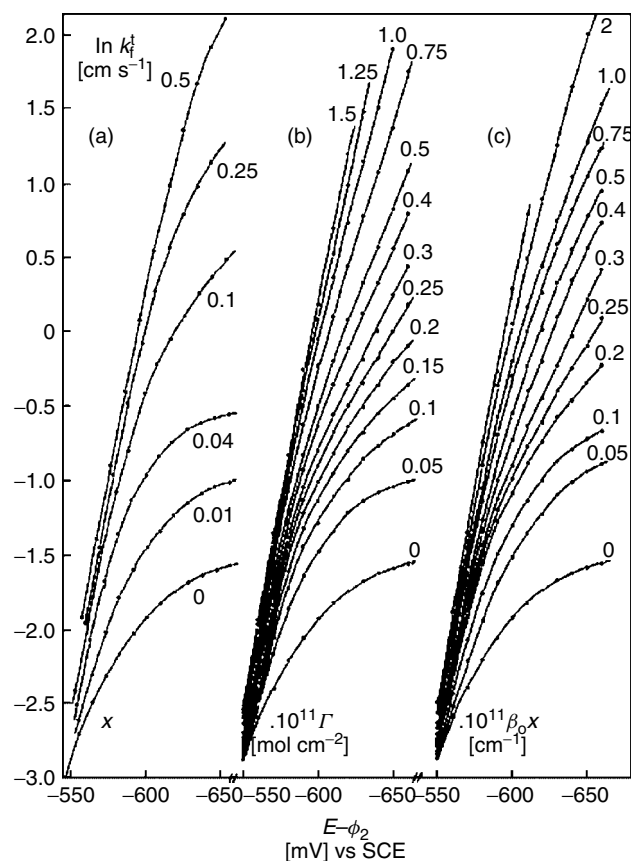


Fig. 3 The natural logarithms of “true” rate constants of Cd(II)/Cd(Hg) system versus $E - \phi_2$, depending on: (a) Cl^- concentration – (x); (b) surface excess of Cl^- ions – (Γ_{Cl^-}) and (c) $\beta_0 x$ values at each curve [40].

be correlated. A statistical thermodynamic approach to the study of anion-induced adsorption of Cd(II) from halide solutions was also presented by Guaus et al. [42]. The simultaneous adsorption of metal complex and ligand was introduced in the isotherms by considering two possible mechanisms (1) competitive adsorption of metal complex and (2) surface complexation. These isotherms were tested for the Cd(II)–KBr system at several ionic strengths. It was found that CdBr_3^- and CdBr_4^{2-} are the adsorbed species.

This approach was also applied for the investigation of anion-induced adsorption in the Cd(II)–KI system at several ionic strengths [43].

The adsorption of reactant in the Cd(II)– I^- system [44], and the influence of electrolyte concentration (1–6 M NaClO_4) on the parameters of the Frumkin isotherm system were investigated [45]. The obtained data indicated that the maximum surface concentration of CdI_2 ($\Gamma_{\text{max}} = 1 \times 10^{-10}$ to $(2.2 \pm 0.2) \times 10^{-10} \text{ mol cm}^{-2}$), adsorption constant ($\beta = 3.1 \times 10^5$ to

$(1.55 \pm 0.35) \times 10^7 \text{ l mol}^{-1}$) and Frumkin coefficient ($a = 0$ to 0.5 ± 0.1) all increase with increasing electrolyte concentration.

The catalytic effect of thiourea on the electrochemical reduction of Cd(II) ions at the DME from aqueous 1 M KF solutions was investigated [46] and described by the equation $k_f^t = k_f^{t,0} (1 + B \Gamma_{\text{Tu}})$, where B is a proportionality constant, Γ_{Tu} is the surface excess of thiourea, while k_f^t and $k_f^{t,0}$ denote the true rate constant determined at certain potential in the presence and absence of thiourea, respectively. Because of the stepwise reaction mechanism, an explanation in terms of the bridging or the surface reaction model fails. A possible alternative interpretation of the effect was given.

The formalism developed to describe current-potential characteristics for the Cd(II)/Cd(Hg) multistep electrode reaction [47] was used for the investigation of catalytic and inhibiting influence connected with variation of electrolyte composition.

A theoretical model of square-wave voltammetry (SWV) combined with adsorptive accumulation of reactant was presented [48].

24.2.2.1.3 Influence of Inhibitors The Cd(II) reduction at the mercury electrode from aqueous 1 M NaClO₄ in the presence of sucrose was described [49] by CEE mechanism. An attempt was made to correlate the individual standard rate constants that became lower with increasing concentration of sucrose, with (1) the surface coverage by sucrose, and (2) the viscosity of the solution layer adjacent to the electrode surface.

Catalysis and inhibition of the electroreduction of cadmium ions at a partially blocked DM_μE by 1-butanol was

studied [50]. The rate constant showed nonlinear dependence on the coverage; it was enhanced by the adsorption of 1-butanol at potentials $E < -0.85 \text{ V}$ versus SCE, whereas it was inhibited at $E > -0.75 \text{ V}$. A statistical model interpreting both the catalytic and the inhibiting influence was proposed.

The mechanism of Cd(II) discharge and cadmium amalgam dissolution in the absence and presence of adsorbed aliphatic alcohols and acids [51], and also the inhibiting influence of the adsorbed aliphatic alcohols and acids on the kinetics of the Cd(II)/Cd(Hg) system was studied [52, 53]. The role of the steric factors on the electrode reaction occurring in the presence of adsorbed inhibitors was investigated.

The behavior of the Cd(II)/Cd(Hg) system in the absence and presence of *n*-pentanol in noncomplexing media was analyzed using reciprocal derivative and double derivative chronoamperometry with programmed current (RDCP and RDDCP respectively) [54]. The RDCP and RDDCP are very versatile in the determination of kinetic parameters of electrode processes.

Marczewska [55] has found that the Cd(II) electroreduction in water-*N,N*-dimethylformamide (DMF) + NaClO₄ solutions was inhibited in the presence of thiourea.

The inhibiting influence of cyclodextrins on the Cd(II)/Cd(Hg) electrode processes was studied [56]. It was found that the inhibition coefficient increases in the series α -cyclodextrin < γ -cyclodextrin < β -cyclodextrin. It was observed [57] that the reduction current of Cd(II) ions was affected by the condensed film of α -cyclodextrin formed on the mercury electrode.

In the presence of methylated β -cyclodextrin [58,] the reaction rate of

the Cd(II)/Cd(Hg) system decreases in the order *per*-(2,3-di-*O*-methyl)- β -cyclodextrin > *per*-(2,3,6-tri-*O*-methyl)- β -cyclodextrin > *per*-(6-amino-2,3-di-*O*-methyl)- β -cyclodextrin.

24.2.2.2 Electrochemistry in Mixed and Nonaqueous Solvents

For the rapid electron transfer process, which follows a reversible chemical step (CE), a procedure is presented for the determination of chemical and electrochemical kinetic parameters. It is based on convolution electrochemistry and was applied for cyclic voltammetry with digital simulation [59] and chronoamperometric curves [60]. The analysis was applied to both simulated and experimental data. As an experimental example, the electroreduction of Cd(II) on HMDE electrode in dimethylsulphoxide (DMSO) [59] and DMF [60] with 0.5 M tetraethylammonium perchlorate (TEAP) was investigated.

The electrode process of the Cd(II)/Cd(Hg) system was investigated in water–DMSO [61] and hexamethylphosphortriamide (HMPA) solutions [62]. The formal potentials, charge-transfer rate constant, and diffusion coefficients were determined. In the presence of adsorbed HMPA molecules, the rate constant was found to be dependent only on the surface phase composition.

It was concluded that the change in the kinetics of the Cd(II)/Cd(Hg) system with mixed solvent composition may be described by different model equations in water–DMSO [61], and water–HMPA solvents [62].

Generally, the influence of solvent adsorption and reactant solvation on electrochemical rate constants of the Cd(II)/Cd(Hg), Zn(II)/Zn(Hg), and Pb(II)/Pb(Hg) systems in mixed solvents

was theoretically described and compared with experimental data [63].

The kinetics of the Cd(II)/Cd(Hg) reaction was also studied in organic solvents [64–66]. The double-layer effect on electroreduction of Cd(II) ions at mercury electrode was investigated in DMF solution with various concentrations of tetraalkylammonium salts [64]. The standard rate constant decreased with increasing concentration of TEAP, tetrapropylammonium perchlorate (TPAP), and tetrabutylammonium perchlorate (TBAP), while the diffusion coefficient and cathodic transfer coefficient of the cadmium electrode process changed only slightly. At constant concentration of the electrolyte, the standard rate constant decreased with increase in the size of the supporting electrolyte cation in the order $k_s(\text{TEA}^+) > k_s(\text{TPA}^+) > k_s(\text{TBA}^+)$. The change of the kinetic parameters with the nature of the base electrolyte was discussed in terms of double-layer effect and nature of the rate-determining step. The low values of the transfer coefficients were explained, assuming slow transfer of the reactant across the inner layer.

In DMSO solution, the standard rate constant and cathodic transfer coefficient of the Cd(II)/Cd(Hg) system decreased with increasing concentration of TEAP [65]. It was found that a chemical reaction, probably partial desolvation of the reactant, precedes the electron transfer, and Cd(II) is reduced according to the CEE mechanism. The kinetic parameters of this process were determined.

The standard rate constants of the Cd(II)/Cd(Hg) system measured in several solvents [66] corrected for the double-layer effect, decrease in the order $k_{s,a}, \text{AN} > k_{s,a}, \text{PC} > k_{s,a}, \text{formamide} > k_{s,a}, \text{DMF} > k_{s,a}, \text{DMSO} > k_{s,a}, \text{HMPA}$ (see Fig. 4). Solvent

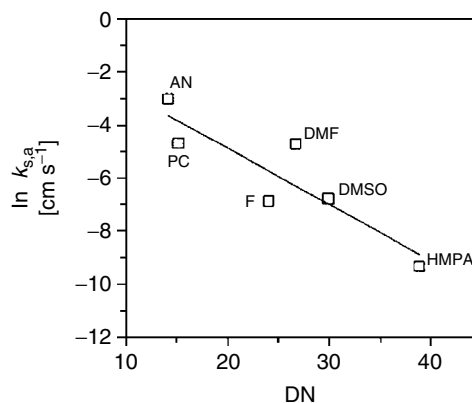


Fig. 4 Dependence of the logarithm of standard rate constant corrected for the double-layer effect of the Cd(II)/Cd(Hg) system on donor number of the solvents [66].

effects were analyzed in terms of the solvation parameters of the cation and dynamic properties of the solvent.

The double-layer effect in the electrode kinetics of the amalgam formation reactions was discussed [67]. The dependences on the potential of two reduction (EE) mechanisms of divalent cations at mercury electrode, and ion transfer–adsorption (IA) were compared. It was suggested that a study of temperature dependence of the course of these reactions would be helpful to differentiate these two mechanisms.

The half-wave potentials of Cd(II), Zn(II), and Pb(II) ions electroreduction in 22 nonaqueous solvents were used in the analysis of solvent effect on electrode potential [68].

The literature data on the kinetics of Cd(II), Zn(II), and Pb(II) electrodeposition on mercury electrode in different organic solvents were also analyzed [69].

The solvation number of reactants and reaction orders of the electrode processes of Cd(II)/Cd(Hg), Zn(II)/Zn(Hg), and Pb(II)/Pb(Hg) systems were evaluated in nonaqueous media [70].

The mechanism of Cd(II) transfer in methanol across saturated organic compounds monolayers adsorbed on the mercury electrode was also studied [71].

24.2.2.3 Electrochemical Properties of the Cadmium Complexes

The electrochemical properties of Cd(II) complexes with inorganic ligand presented in early papers were discussed by Hampson and Latham [72]. Later, electrochemical investigations of cadmium complexes were oriented on the mechanism of complex formation, determination of stoichiometry and stability constants, mechanisms of reduction on the electrodes, and evaluation of kinetic parameters of these processes. The influence of ligands and solvents on stability and kinetic parameters of electroreduction was also studied.

Electroreduction of Cd(II)–nitrilotriacetic acid and Cd(II)–aspartic acid systems was studied on DME using SWV [73]. The CE mechanism in which the chemical reaction precedes a reversible electron transfer was established. Also, the rate constants of dissociation of the complexes were determined. Esteban and coworkers also studied the cadmium complexes with nitrilotriacetic acid [74, 75] and fulvic acid [76]. The complexation reaction of cadmium by glycine was investigated by different electrochemical methods using HMDE and mercury microelectrode [77, 78].

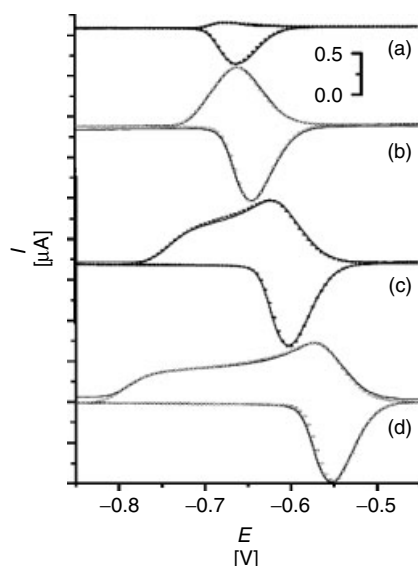


Fig. 5 Experimental (—) and calculated (symbols) square-wave voltammograms (SWV) for 3.9×10^{-7} M $\text{Cd}(\text{NO}_3)_2 + 1.35 \times 10^{-5}$ M oxine in 0.1 M buffer solution pH 6.7 $E_A = -0.1$ V. The SWV were obtained for frequency $-f = 300$ Hz, step height $-dE = 5$ mV and varied E_{sw} : (a) 8; (b) 35; (c) 80; and (d) 130 mV [84].

The electrode reaction of $\text{Cd}(\text{II})$ complexes with acetylacetone (acac) was investigated on the mercury electrode in the absence and in the presence of *n*-pentanol and *n*-octanol [79]. The kinetics parameters were evaluated, and the ionophoretic effect of acac was postulated on the basis of the interaction of the reactant with the adsorbed surface layer.

The electrochemical behavior of Cd –oxine complexes was analyzed by square-wave stripping voltammetry [80] from the mechanistic point of view, applying the theoretical model developed previously [81–83]. Influence of ligand and reactant adsorption, and the ligand concentration on the Cd –oxine electroreduction were also examined [84] using SWV. Typical curves recorded and calculated for several E_{sw} are shown in Fig. 5.

The reduction of $\text{Cd}(\text{II})$ on mercury electrode was used to study the interaction of $\text{Cd}(\text{II})$ ions with β -cyclodextrin. It was found that $[\text{Cd}(\beta\text{-cyclodextrin})(\text{OH})_2]^{2-}$ complex is formed in alkaline solutions [85].

The reduction of the $\text{Cd}(2,2,2)^{2+}$ complex on mercury electrodes was studied in aqueous solutions free and saturated with *n*-pentanol and *n*-octanol [86] and also in acetonitrile [87]. The corresponding reduction mechanism was established and the kinetic parameters were calculated.

The synthesis, structure, and complexing properties of new triazacoronands with respect to $\text{Cd}(\text{II})$, were presented [88].

The $\text{Cd}(\text{II})/\text{Cd}(\text{Hg})$ system was investigated in the presence of 2-mercaptoacetic acid as a function of pH [89]. The bidentate complexes of $\text{Cd}(\text{II})$ with 2-mercaptoacetic acid are stable and undergo a reversible two-electron reduction on the mercury electrode.

The effect of the solvent properties on the polarographic behavior of $\text{Cd}(\text{II})$ complexes with glycine, *N*-acetyl, and *N*-benzoylglycine was studied in DMSO, acetonitrile (AN), and DMF solutions [90]. The stability constants were found to depend linearly on the acceptor numbers of the solvents.

Synthesis, photophysical, and electrochemical properties of dinuclear $\text{Cd}(\text{II})$ diimine complexes with bridging chalcogenolate ligands were described [91].

The reduction mechanism of $\text{Cd}(\text{II})$ –ferrocene complexes accumulated on static mercury electrode was studied using square wave voltammetry (SWV) [92]. The electrochemical behavior of $\text{Cd}(\text{II})$ complexes with cysteine and folic acid was investigated. Folic acid forms adducts

with cysteine thiolate at the electrode surface, which influence the process of electroreduction of Cd(II)–cysteine complex [93]. The kinetics of cadmium binding by surface groups of *Chlorella marina* cells [94, 95] was studied, and stability constants were determined.

An important mechanism of metal-detoxification involves intercellular thiol-containing compounds, such as glutathione (γ -glutamyl-cysteinyl glycine, denoted as GSH) and phytochelatins. Therefore, different electrochemical techniques and multivariate curve resolutions were used by Esteban with coworkers [96–103] for the investigation of Cd(II) complexes with such ligands. Complexes of Cd(II) with GSH [96–98], were studied and used as a model for coordination of Cd(II) by thiol-containing peptides [97]. Two complexes, Cd(GSH)₂ and Cd₂(GSH)₂ were formed in this system. The complexation of Cd(II) by GSH fragments [99], phytochelatine (γ -Glu-Cys)₃Gly [100, 101], and C-terminal hexapeptide of mouse metallothionein [102, 103], were also investigated.

The polarographic characteristics of Cd(II) and Zn(II) complexes with phytochelatin extracted from marine alga *Phaeodactylum tricornutum* [104] were presented.

The peptide fragments of metallothioneins Lys-Cys-Thr-Cys-Cys-Ala [56–61] (FT) were studied by different electrochemical techniques. The cyclic voltammetric behavior of the peptide fragment in the presence of Cd(II) indicated two reversible electrochemical processes due to the oxidation of the mercury electrode in the presence of CdFT and reduction of CdFT complex, both from the dissolved and adsorbed state [105]. The influence of the experimental conditions on electroreduction of Cd–metallothioneins

complexes was also studied [106–111]. The cadmium(II) complexes with two different metallothioneins from rabbit liver were investigated by cyclic voltammetry [112].

24.2.2.3.1 Determination of Stability

Constants For the determination of the complexing ability of Cd(II) ions, the potentiometric and different polarographic methods were used [113–116]. The composition and the stability constants of Cd(II) complexes with phthalic acid [113], some benzene polycarboxylic acids [114], glycnamide [115] and crystal structure of Cd(II) phthalate hydrate were determined. The influence of basicity of ligand on the stability of Cd(II) mixed ligand complexes with glycine, alpha-alanine, L-valine, L-leucine, L-asparagine, and L-glutamine as the primary ligands and vitamin B₆ as secondary ligand was studied [116].

A polarographic study of the composition and stability constant of 2-aminoquinoxaline complex with Cd(II) in methanol–water mixtures was published by Pratihari [117].

The polarographic experimental and calculated curves of complex formation with the following ligands: *N, N'*-bis(2-pyridyl methyl)-1,2-diaminoethane [118], picolinic acid [119], *N*-(2-hydroxyethyl)ethylenediamine [120], 1-hydroxyethylenediphosphonic acid [121], and *N*-(2-hydroxyethyl)iminodiacetic acid [122] was used for modeling the Cd(II)–ligand systems. The stoichiometry and stability constants of formed complexes were evaluated. The same method was used for determinations of stability constants of Cd(II) complexes with monoaza-12-crown-4 ether in aqueous solution in the presence of an excess of sodium ions [123].

A polarographic study of Cd(II) complexes with macrocyclic ligands 18-crown-6, 1,10-diaza-18-crown-6 and cryptand (222) [124] and 18-crown-6 [125], dicyclohexano-18-crown-6 [126] in water-organic mixtures and aza-18-crown-6 and dibenzopyridino-18-crown-6 in nonaqueous solvents [127] was presented and stability constants were evaluated.

The cadmium complexes were also investigated potentiometrically. Using this method, the complexes of cadmium with asparagine [128], taurine [129], *N*-(6-amino-3-methyl-5-nitroso-4-oxo-3,4-dihydropyrimidin-2-yl)glycine [130], succinate and malate [131], acetate at different temperatures [132], pyridine oxime ligands [133], 2-hydroxypropene-1,3-diamine-*N,N,N',N'*-tetraacetic acid [134] were studied. The stoichiometry and stability constants of these complexes were determined.

The stability constants of the formed chloro-cadmium complexes in aqueous solution [135] and water-2-butanone mixtures [136] were also determined, using potentiometric measurements. The influence of hydrogen bonding of the solvent on the stability of Cd(II)-ethylenediamine complexes in water-DMSO mixtures was analyzed using pH and calorimetric measurement [137]. In five water-acetonitrile mixtures, the stability constants of Cd(II) and Zn(II) cyanide complexes were determined [138].

The complexation of Cd(II) with polymethacrylic acid, and humic acid [139] was studied potentiometrically using the Cd(II) ion-selective electrode.

In the last three decades, the complexes of many metal ions including Cd(II) with macrocyclic ligands were studied intensively. The thermodynamic data of Cd(II)-macrocyclic complexes were presented by Izatt et al. ([140–142] and literature cited therein).

24.2.2.3.2 Electrochemical Preparation of Cadmium Complexes

The application of electrochemical procedures for the preparation of cadmium complexes was studied intensively. In these syntheses, the cadmium metal or its amalgam was anodically oxidized in the presence of a ligand in an appropriate solution. Electrochemical synthesis of cadmium with 4-methyl-6-trifluoromethylpyrimidine-2-thione [143], 6-*tert*-butyldimethylsilylpyridine-2-thionate [144], 2,6-bis(1-salicyloylhydrazonoethyl)pyridine [145], and pentadentate ligand 1,6-bis{1-[2-(tosylamino)phenylimino]ethyl}pyridine [146] were carried out. Using the same method, the cadmium complexes with *N*-[(2-hydroxyphenyl)methylidene]-*N'*-tosylbenzene-1,2-diamine were obtained. When 1,10-phenanthroline or 2,2'-bipyridine was added to the cell, mixed ligand complexes were formed [147].

Pedrido et al. [148] also described the electrochemical synthesis and characterization of new neutral Zn(II), Cd(II), and Pb(II) complexes with bis(4-*N*-methylthiosemicarbazone)-2,6-diacetylpyridine. The properties and crystal structure of the obtained complexes were studied.

Electrochemical oxidation of cadmium in a solution of [(4-methylphenyl)sulfonyl]-2-pyridylamine (HL) in acetonitrile/dichloromethane mixtures resulted in CdL₂ complex formation [149]. The electrochemical oxidation of cadmium amalgam in nonaqueous solvents CH₂Cl₂, 1,2-C₂H₄Cl₂, and PC was also used for the preparation of cadmium complexes with 18-membered macromonocyclic ligands, 18-O₆, 18-S₆, 18-N₂O₄, and 18-N₆ [150]. The stoichiometry and stability of resulted complexes were determined. The same method was used to examine the complexation of Cd(II) cation with 12-crown-4 ether, azacrown ether 1,4,8,11-tetraazacyclotetradecane, and thiaazacrown

ether 1,4,6,11-tetrathiacyclotetradecane in dichloromethane [151].

The electrochemical synthesis of cadmium and zinc thiolate complexes and their properties were reviewed in addition to other metal ion complexes [152].

24.2.2.4 Preparation and Electrochemical Properties of Cadmium Chalcogenides

24.2.2.4.1 CdS CdS is a typical example of semiconductor material; its properties and applications were presented in a review by Koval and Howard [153].

Cadmium chalcogenides CdS, CdSe, and CdTe (CdX) are important in a variety of applications ranging from solar cells to chemical/biological sensors. Thin films of these materials can be prepared by using many methods (e.g. vacuum evaporation, chemical bath deposition, and electrodeposition). Three types of electrochemical methods were used for growing thin films of CdX: (1) anodic oxidation of cadmium in a chalcogenide-containing electrolyte, (2) cathodic coreduction of Cd(II) and a chalcogenide oxyanion on an inert substrate, and (3) cathodic reduction of Cd(II) ions in nonaqueous solvent containing chalcogen in elemental form [154–156]. An alternative two-step method is based on initial electrochemical modification of the

substrate, usually polycrystalline gold, with the chalcogen. Then voltammetric stripping of the chalcogen (X) in an aqueous solution containing Cd(II) ions generates the CdX compound *in situ* on the electrode surface. This approach was used for CdS and CdSe formation [157–159].

The two-step synthesis of CdS on sulfur or thiol modified polycrystalline gold electrode was described [160]. The morphologies of CdS formed in both cases and the electrochemical behavior of these compounds were compared.

An electrochemical scanning probe microscopy and Raman spectroscopy investigation of thin CdS films grown by electrochemical atomic layer epitaxy (ECALE) aimed at understanding the role played by the order of deposition on film quality were reported [161].

Using the ECALE method, thin films of CdS were deposited on Ag (111). The deposit and its morphology were characterized [162].

Synthesis and characterization of nearly monodispersed CdX semiconductor nanocrystallites were studied [163].

The hybrid electrochemical/chemical synthesis of epitaxially oriented CdS nanocrystallites-size selectively on graphite surface was described by Anderson et al. [164]. A schematic diagram of such synthesis is presented in Fig. 6.

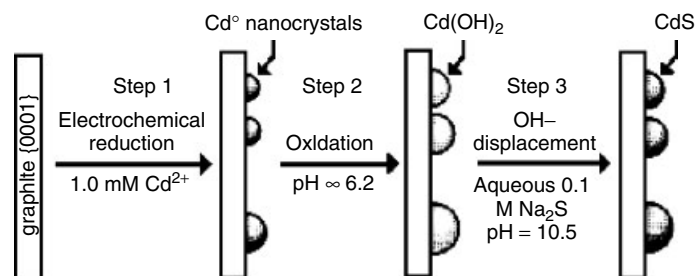


Fig. 6 Schematic diagram illustrating the three-step electrochemical/chemical epitaxial synthesis of CdS nanocrystals [164].

Synthesis and characterization of CdS nanoparticles embedded in a polymethylmethacrylate matrix was presented [165]. The assembly of CdS semiconductor nanoparticle monolayer on Au electrode was obtained, and its structural properties and photoelectrochemical applications were studied [166].

Rapid formation of CdS thin films by microwave-assisted chemical bath deposition and electrical properties of the films were studied [167].

Uniform thin films of CdS were prepared by template-assisted electrochemical deposition on Au electrodes covered with Langmuir-Blodgett (LB) films of cadmium arachidate [168]. It was found that different CdS films could be produced depending on the type of LB film used.

CdS thin films were also prepared on indium tin oxide (ITO)-covered glass by successive ionic layer adsorption and reaction (SILAR) techniques [169]. The thickness of the CdS film increased with the number of SILAR cycles. The surface roughness increased with the growth of CdS films. To increase the film thickness and to reduce roughness, the chelating agent was added to the solution. The effect of the chelating reagents, triethanolamine and cysteine, on the layer by layer CdS film formation in the electroless and electrochemical deposition process was studied [170, 171].

Thin films of CdS were also prepared by the SILAR method on the (100)GaAs [172–174], ITO [174], and glass [175, 176] substrates.

The electrodeposition of CdS films on conductive substrates from aqueous solutions is a low-cost process, which is well suited for the preparation of film solar cells. Polycrystalline CdS films of good quality were obtained by electrolysis with rectangular voltages on indium

tin oxide/glass substrate from low concentration CdSO₄ and Na₂S₂O₃ aqueous solutions [177].

CdS thin films were prepared by electrodeposition from an aqueous solution containing Cd(II) and Na₂S₂O₃ in the presence of colloidal sulfur [178].

The electrodeposition of cadmium sulfide thin films was carried out by the electroreduction of the aqueous thiocyanate complex of Cd(II). Formation of CdS is supposed to proceed by metal-catalyzed ligand reduction [179].

Studies of the kinetics and photoelectrochemistry of nanocrystalline composite films of CdS/Ni in aqueous sulfite [180] and thin film CdS/electrolyte interface were carried out [181].

Thiols were adsorbed on a CdS surface and used to control the growth of CdS particles [182].

The Cd/CdS electrode was also prepared in solutions containing cadmium sulfate and sodium thiosulfate using the potentiodynamic method [183]. The electrochemical behavior of such electrodes in electrolytes containing sulfide ions was studied.

24.2.2.4.2 CdSe CdSe was deposited on different substrates. The two-step method of the electrosynthesis of CdSe films, based on the initial chemical modification of polycrystalline gold surface with selenium overlayer was described [157]. In the second step, this overlayer was cathodically stripped as a Se²⁻ in a Se(IV)-free electrolyte medium that was dosed with the requisite amounts of Cd(II) ions.

The electrochemical preparation of CdSe nanoparticles at gold electrodes modified with molecular templates was reported [159]. The molecular templates were obtained by arranging thiolated

β -cyclodextrin self-assembled monolayers on gold electrodes.

The ECALE method was used for the growth of CdSe on Ag(111) electrode [184].

The thermodynamic analysis of Se(IV) electroreduction and CdSe electrolytic formation on Ni, Ti, and Pt cathodes in acidic aqueous solution were presented [185].

Semiconducting thin films of CdSe were electrochemically deposited on Ti substrates [186, 187]. The film electrodes were characterized with photoelectrochemical imaging, optical microscopy, and scanning electron microscopy (SEM)/energy-dispersive X-ray analysis.

The CdSe was used as a photoelectrode in photoelectrochemical cells. The CdSe film doped with Zn, has favorable states in band gap and enhances charge-transfer kinetics at the interface.

CdSe thin films and CdSe nanocrystal layers were electrodeposited on Ti or ITO substrates in solutions containing CdSO₄ and H₂SeO₃ at pH 2.5 [188, 189]. The influence of different deposition potentials on the surface morphology and crystal structure of CdSe films was studied.

Under potentiostatic conditions, CdSe films were deposited on titanium substrate from a bath containing sodium selenosulfite, cadmium sulfate, and sodium citrate [190].

CdSe films of variable composition were prepared using electrochemical codeposition under potentiostatic control [191,] and the photoelectrochemical behavior of such films was investigated.

The structure, morphology, and photoelectrochemical properties of CdSe and CdSe_xTe_{1-x} semiconductor thin films prepared by cathodic electrodeposition on Ni and Ti electrodes from acidic solution containing CdSO₄, SeO₂, and TiO₂ were investigated [192].

In sulfuric acid solution containing selenous acid and uncomplexed Cu(II) and Cd(II) ions, the formation of ternary Cu–Cd–Se thin film layers on a polycrystalline Pt electrode during the voltammetric scanning was studied [193].

24.2.2.4.3 CdTe The mechanism of CdTe electrodeposition was studied intensively [194–197]. Electrodeposition of CdTe semiconductor thin films was carried out in acidic aqueous solutions at pH 1–3 [195–197]. To prevent accumulation of tellurium in CdTe film, the concentration of Te(IV) ions in acidic electrolyte must be much lower than the concentration of Cd(II).

The electrochemical aspects of CdTe growth on Ag(111) by ECALE were studied [198].

The electrodeposition of CdTe films from various ammonia-alkaline solutions at low cathodic overpotential [199, 200] was also studied, and the mechanism of CdTe formation was discussed [201, 202]. The properties of films were electrochemically characterized.

The nucleation and growth mechanism of CdTe thin films at polycrystalline gold surface [203] and on the rough face side of a Si(100) were studied as a function of different potential steps. Schematic representation of CdTe formation is shown in [204].

CdTe was also obtained using rotating disc electrode; the kinetics of tellurium deposition process on solid tellurium electrode was analyzed, and the kinetic parameters were calculated [205].

Electrodeposition and stripping of tellurium and CdTe in sulfate electrolyte was studied by voltammetric and electrogravimetric experiments [206].

Cathodic electrodeposition of CdTe in acidic solutions with higher tellurium

concentrations was studied [207]. The effects of the deposition potential and the hydrodynamic regime were investigated.

Voltammetry at a glassy carbon (GC) electrode was used to study of the electrochemical deposition of CdTe from the Lewis basic 1-ethyl-3-methylimidazolium chloride/tetrafluoroborate room temperature ionic liquid [208].

Electrochemistry and electrogenerated chemiluminescence of CdTe nanoparticles was also studied [209].

Electrodeposition of $\text{Cd}_x\text{Hg}_{1-x}\text{Te}$ films on a titanium [210] and stainless steel substrates [211] from a bath containing CdSO_4 and TeO_2 and HgCl_2 was investigated. Film composition and band-gap energy were evaluated.

24.2.2.5 Properties of Cadmium Intermetallic Compounds

The mechanism of the formation of intermetallic compounds between cadmium and nickel during the storage of charged cadmium electrodes and the kinetics and mechanism of anodic dissolution of $\text{Cd}_{21}\text{Ni}_5$ in alkaline solutions were investigated [212]. This study helped to eliminate the negative effect of $\text{Cd}_{21}\text{Ni}_5$ on the discharge characteristics of nickel–cadmium batteries.

The structural and electrochemical characteristics of cadmium electrodes with nickel introduced in metallic state into the active material of the electrode by electrodeless plating were studied [213]. The specific role played by hetero phase interactions between nickel and cadmium in the mechanism of the Cd electrode activation was substantiated experimentally.

The identification of intermetallic compounds in electrodeposition of copper–cadmium alloys by electrochemical techniques was described [214].

The mechanism of anodic dissolution of the intermetallic compound CdSb was studied in concentrated KOH solutions [215].

The properties of Cd species formed by the dissolution of cadmium metal in molten cadmium halides and at electrode interface were investigated [216].

24.2.3

Cadmium Underpotential Deposition and Electrodeposition on Solid Electrodes

24.2.3.1 Deposition of Cd on Cadmium Electrode

The cadmium electrodeposition on the solid cadmium electrode from the sulfate medium was investigated [217]. The following kinetic parameters were obtained: cathodic transfer coefficient $\alpha = 0.65$, exchange current density $I_0 = 3.41 \text{ mA cm}^{-2}$, and standard rate constant $k_s = 8.98 \times 10^{-5} \text{ cm s}^{-1}$. The electrochemical deposition of cadmium is a complex process due to the coexistence of the adsorption and nucleation process involving Cd(II) species in the adsorbed state.

Surfaces of cadmium with various morphological properties were electro-formed on the Cd electrode from sulfate solutions by varying current densities, temperature, and pulse electrolysis conditions [218]. The surface properties were defined by the values of slopes of quasi-steady state E versus logarithm current density dependencies and exchange current densities in $0.5 \text{ M CdSO}_4 + 0.15 \text{ M H}_2\text{SO}_4$ solution. The dependence of the slope values on surface properties was explained in terms of the influence of crystallization overpotential.

Thermal phenomena at the Cd electrode during the electrolysis of aqueous solutions of Cd(II) were investigated [219]. The determination of heat flux, heat quantity, and temperature gradient at the

Cd/solution interface under galvanostatic conditions was carried out.

The blocking effect of benzyl and substituted benzyl alcohol additives on the electrodeposition of cadmium [220] and stabilization of cadmium electrode properties [221] were studied voltammetrically.

The cadmium electrodeposition on the cadmium electrode from water–ethanol [222, 223], water–DMSO [224], and water–acetonitrile mixtures [225–229] was studied intensively. It was found that promotion of Cd(II) electrodeposition [222] was caused by the formation of unstable solvates of Cd(II) ions with adsorbed alcohol molecules or by interaction with adsorbed perchlorate anions. In the presence of I^- anions, the formation of activated Cd(II)– I^- complex in adsorbed layer accelerated the electrode reaction [223].

In water–DMSO mixtures in the presence of ClO_4^- and I^- anions, the electroreduction of Cd(II) ions was influenced by competitive adsorption of DMSO molecules and anions [224] and the rate of the Cd(II)/Cd process changed nonmonotonically with solvent composition. In water-rich mixtures, the electrode process was accelerated by the formation of activated complex Cd(II)–anion (ClO_4^- , I^-). At higher DMSO concentration, the rate of the Cd(II)/Cd process was found to decrease and reach minimum at DMSO concentration equal to 9 M. At $c_{DMSO} > 9$ M, the rate of the process increased again.

The effect of perchlorate ions on cadmium electrodeposition was investigated in water–AN mixtures [227, 228]. The formation of ionic associates in the surface layer inhibited cadmium electrodeposition, and promoted the formation of higher quality coatings.

It was found that the competitive adsorption of I^- and AN molecules on the Cd electrode affected the kinetics of the Cd(II) electroreduction [226]. The physicochemical properties of coatings and effects of organic additives on cadmium deposition from iodide–water–AN mixtures were also studied by Kuznetsov et al. [225].

The same authors have found that the inhibition effect of crown ethers [230] and crown esters [229] on cadmium electrodeposition from water–AN mixtures was caused by the competitive adsorption of macrocycles and organic solvents molecules. The effect of structure and concentration of crown ethers on the cadmium electrodeposition from aqueous sulfate solutions was also studied [231].

The solution composition and the nature of particles adsorbed and reduced on the electrode, as well as ϵ -caprolactam additive, affected the electroreduction of cadmium ions [232, 233].

The experimental data for the rate of stationary two-dimensional nucleation in electrocrystallization of cadmium on the surface of the Cd(0001) crystal face in 2.5 M $CdSO_4$ aqueous solution at 45 °C were presented [234]. The overpotential dependence of the nucleus size was determined.

A method was proposed for electrolytic cadmium refining in molten $CdCl_2$ using electrolyzer with bipolar cadmium electrode [235]. The results demonstrated that high-purity Cd could be obtained in a single electrolysis cycle.

24.2.3.2 Electrodeposition of Cd on Other Solid Substrates

24.2.3.2.1 Gold Electrodeposition of Cd on gold was studied by many Scientists (early papers [72, 236–239]). A considerable effort was made to study and

understand the underpotential deposition (UPD) processes, both on single crystal and polycrystalline gold surfaces [240]. The influence of Cd–Au alloy formation on gold electrodes was underlined [241–245], and details were studied on the basis of electrochemical and electrochemical quartz crystal microbalance (EQCM) results [246]. The two-step process of fast turnover reaction – replacement of surface atoms and slow solid-state diffusion was postulated. The influence of anions on UPD process of polycrystalline electrodes was analyzed on the basis of voltammetric and EQCM data [247].

The UPD process was studied most intensively on Au(111) plane, where scanning tunneling microscopy (STM) measurements revealed a series of linear structures [248, 249]. The influence of coadsorbed anions on deposit morphology based on electrochemical and STM data, was also discussed [250, 251]. In the presence of chloride ions, nanostructures such as “nanowires” were observed by STM, the surface alloy structure following the morphology of Au(111) reconstruction [252]. The UPD process was affected not only by the applied potential and electrolyte, but also by its concentration, as shown for H₂SO₄ solutions using specular X-ray reflectivity measurements [253]. The mechanism of the process has been described in other papers. These works [254–259] also point to UPD process on reconstructed Au(111) surface and its relation with lifting the reconstruction. The early stages of Cd–Au alloy growth accompanying UPD were studied recently by del Barrio et al. [260] and Schmuki with coworkers [257–259]. Atomic size clusters start to nucleate at a relatively high underpotential, close to 0.35 V. Two-dimensional islands can grow and coalesce with the formation of new two-dimensional islands on top of

the partially formed first monolayer [260]. Alternatively, the growing clusters arrange linearly until overgrowth takes place and a complete layer is formed at underpotential close to 80 mV [257]. Atomic resolution images revealed a hexagonal structure with an interatomic distance of 0.29 nm [260]. Owing to alloying, the UPD layer contains both Cd and Au atoms. Dissolution of the Cd layer is coupled with dealloying and formation of mono- or 2–3 atomic holes resulting in surface roughening [259, 260]. Figure 7 presents STM images of Cd nanoclusters, produced at different potentials, and their anodic dissolution, confirming the presence of the interfacial dealloying process. Higher deposition potentials result in smaller and less stable clusters. The site selective mechanism of early-stage Cd clusters nucleation at the elbow sites of the Au (111) herringbone reconstruction was also postulated [258]. This process can result in self-organized patterning consisting of Cd nano-islands on the surface. Cd UPD process was also studied in organic solvents such as PC, tetrahydrofuran, and dimethoxyethane [261, 262]. The observed differences, compared to aqueous solutions, were ascribed to differences in anion adsorption and the influence of solvent on metal–substrate interactions, resulting from the partial discharge state of Cd adatoms. Electrocatalytic influence of Cd UPD on nitrate reduction [251, 263] or glucose oxidation [264] was described.

UPD Cd can also be used to obtain cadmium sulfide, an important semiconductor for electronics. Electrochemical epitaxial growth of organized CdS structures, involving underpotentially deposited Cd on Au(111) was thus reported [161, 265].

The atomic structures corresponding to Cd UPD on Au (100) plane were revealed using electrochemical atomic force microscopy (AFM) technique [241, 266].

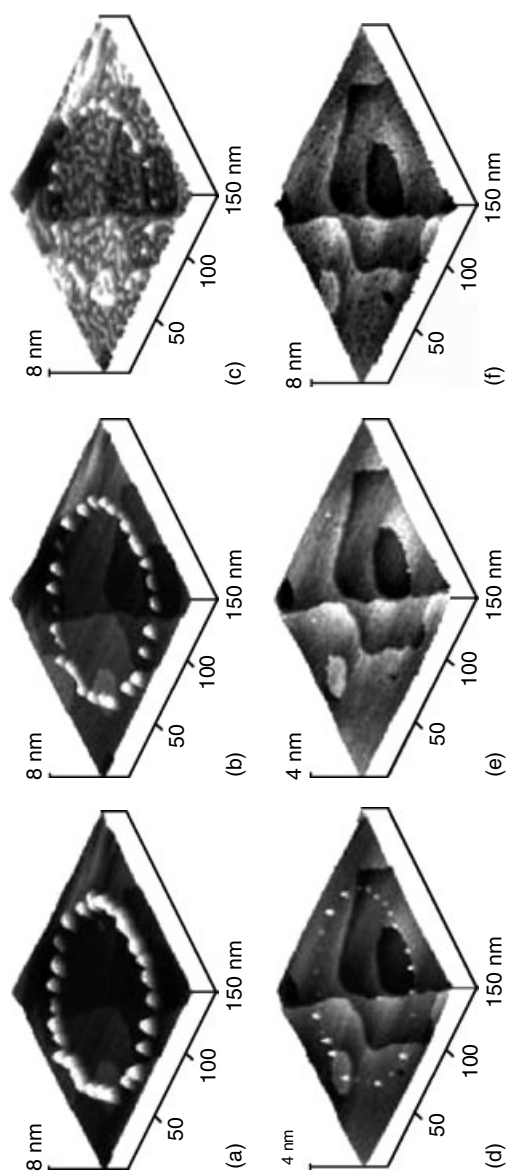


Fig. 7 Anodic dissolution of STM-tip--induced Cd nanoclusters on Au(111). The first row (a–c) shows clusters obtained at potential of 50 mV, at (a) 50; (b) 300; (c) 1000 mV. Second row (d–f) shows clusters obtained at potential of 100 mV, at (d) 100; (e) 200; (f) 200 mV [259].

Within the potential range from -0.3 to -0.45 V, a quick surface-alloying process occurs, with dynamics depending on polarization conditions [266]. A turnover mechanism was proposed for the surface-alloying process, while for long polarization times, the surface alloy formation process was determined by solid-state diffusion of Cd or Au atoms across the alloy phase [242, 267]. In sulfuric acid solutions, the diffusion coefficients corresponding to the fast process occurring within two monolayers is approximately $10^{-16} \text{ cm}^2 \text{ s}^{-1}$, while the second slow solid diffusion process is characterized by diffusion coefficient in the range 10^{-18} [243] or $10^{-19} \text{ cm}^2 \text{ s}^{-1}$ [245]. The alloying process was also studied using EQCM and X-ray diffractometry techniques [268]. On the basis of temperature dependence of the inward diffusion rate, activation energies of the surface and bulk solid-state processes were estimated [268]. In the presence of chloride ions in solution, the inward diffusion of Cd to the Au(100) phase is promoted [269]. Electrochemical atomic force microscopy (EC-AFM) observations for the Cd stripping process confirmed that the removing of Cd from the alloy phase resulted in surface roughening [266].

Cadmium bulk deposition was found to occur according to Stranski-Krastanov mechanism, with the Cd(0001) plane parallel to Au(100) [241, 266].

Cd UPD process on Au(100) and Au(110) was also studied in the presence of Te, leading to CdTe formation [270–272].

For Au (111) coated by self-assembling monolayers of alkanethiols, the Cd UPD process occurs if the alkyl chain of the thiol is shorter than eight carbon atoms [273].

The electrochemical deposition of metal (Cd, Zn, Pb) from Me(II)–ethylenediaminetetraacetic acid (EDTA) complexes

studied by quartz crystal microgravimetry [274] may be important for the development of environmental cleanup processes.

24.2.3.2.2 Platinum Electrodeposition of Cd on platinum has been described in early papers [for example [72, 239, 275]. Considerable attention has also been paid to UPD processes. This process occurring on Pt(111) was studied using electrochemical and radiotracer methods [276]. Bisulfate ions adsorption promotes the formation of a Cd adlayer, at potentials much lower than those typical for the bare Pt(111) surface. This effect was explained by lower work function for Cd, compared to Pt. Voltammetric and charge displacement (Cd displaced by anions and CO) studies of Gómez and Feliu pointed out the deposition of two UPD layers before the onset of the bulk deposition process [277]. The first layer was found open (surface coverage degree near 0.31), probably due to Cd–Cd repulsion, while the second layer was found more compact. Due to strong attractive interactions with adsorbing Br^- or Cl^- anions, voltammetric peaks are very sharp.

The process of Cd UPD on polycrystalline Pt was investigated by Machado et al. [278–280], and adsorption electrovalence of Cd adions was found to be close to 0.5 [280]. The detailed mechanism was also studied, using electrochemical and EQCM measurements [281, 282]. The formal partial charge number was found to vary between 1 and 2, for higher and lower potentials, respectively. A mechanism involving two adsorption sites and the presence of Cd^+ adsorbed ions was proposed.

The influence of surface roughness, surface diffusion of metal atoms, and exchange current density of the Cd(II)/Cd

couple on the early stages of cadmium deposition was analyzed [283]. Studies of the Cd UPD process from ionic liquid: acidic zinc chloride-1-ethyl-3-methylimidazolium chloride were also reported [284].

24.2.3.2.3 Silver Early descriptions of Cd deposition process on Ag can be found in Ref. 285. Cadmium UPD studies were carried out on Ag(111) and Ag(100) single crystals. For Ag(111) at high underpotentials (up to 0.3 V), the process is characterized by a quasi-reversible adsorption/desorption of Cd, while at lower underpotentials (below 50 mV), Ag–Cd alloy formation occurs [286]. The influence of different anions (sulfate, perchlorate, citrate) was also studied [287]. In the presence of adsorbed chloride ions, the Cd UPD occurs by replacement of Cl adatoms (not desorption), which remain adsorbed and discharged on top of Cd layer [288]. The first combined electrochemical and STM studies revealed some details of the UPD process [289]. It starts with a formation of an expanded adlayer, which at lower underpotentials transforms to a condensed close-packed Cd monolayer. This monolayer is not quite stable, because it slowly transforms with place exchange between Cd and Ag surface atoms. A formation of a second monolayer and a significant Ag–Cd surface alloying occurs at underpotentials lower than 50 mV. The anodic process is connected with dealloying resulting in the appearance of 2D islands and monoatomically deep pits, quickly disappearing at higher underpotentials, pointing to high surface mobility of Ag atoms. Cd UPD process was also studied in organic solvents such as PC, tetrahydrofuran, and dimethoxyethane [261, 262]. Similarly, as for Au(111), the observed differences, compared to aqueous solutions,

were ascribed to difference in anion adsorption and influence of solvent on metal–substrate interactions, resulting from the partial discharge state of Cd adatoms. Electrochemical epitaxial growth of organized CdS structures involving UPD Cd on Ag(111) was described [290]. Electrocatalytic influence of Cd UPD on nitrate ions reduction was revealed, as for Au (111) [263].

For Ag(100) crystals, a similar electrochemical behavior was observed with quasi-reversible adsorption/desorption of Cd and surface alloying, faster than for Ag(111) [286]. Electrochemical and AFM experiments have shown that the alloying process consisted of two steps: a very fast reaction occurring within a few atomic layers, and a much slower one, represented by a solid-state diffusion process [244].

UPD process and surface Cd–Ag alloying were also studied on polycrystalline Ag electrode [285, 286]. The surface alloy formation rate was similar to that for Ag(100) [286]. The dynamics of surface alloying promoted by Cd UPD was studied on irregular Ag substrates, dendritic, and columnar Ag deposits [291].

24.2.3.2.4 Copper Early studies of electrochemical deposition of Cd have been described in Refs 236, 239. These studies were also carried out on single crystal Cu(111), Cu(110), and Cu(100) planes. On Cu(111) different structures were proposed. The bulk deposited cadmium forms a close-packed hexagonal lattice in perchlorate solutions, growing according to modified Stranski-Krastanov mechanism [292]. UPD of Cd has been described in a few papers. Ge and Gewirth [292], using voltammetric methods and AFM, found the interatomic distance 0.343 nm for UPD Cd(4 × 4) structure, with a slightly open structure due to retained partial

charge of Cd adatoms, while Stuhlmann et al., using voltammetry and ultrahigh vacuum (UHV) based spectroscopy, reported 0.371 nm for $(\sqrt{19} \times \sqrt{19}) R23.4^\circ$ structure [293]. In both cases, this distance is higher than that for bulk Cd. In situ STM studies confirmed the $(\sqrt{19} \times \sqrt{19}) R23.4^\circ$ structure [294]. The reduction process is characterized by two pairs of UPD peaks, where the peak at lower potential, close to reversible Nernstian potential, corresponds to Cd–Au alloying [295]. The role of adsorbed chloride ions was discussed, pointing to stabilization of open Cd structure [293] and surface site exchange between Cl^- ions and Cd^{2+} cations [294, 295]. The influence of potential on Cd UPD structure studied by STM and comparison of results with predictions of hard sphere model (Cd–Cd distance 0.38 nm) was recently discussed [296]. Deposition of CuCd alloys was also studied [297, 298].

For Cu(100) in the presence of chloride ions, the structure of UPD Cd is dependent on the deposition rate [296]. For high deposition rate, nearly defect-free films were obtained with domains as large as Cu(100) terraces previously coated by chloride ions. For low deposition rate, Cd films with a high density of domain boundaries can be obtained.

The Cd UPD behavior on Cu(110) was found similar to that for Cu(111), with more pronounced alloying, resulting in irreversible changes of the original (110) surface of copper [295].

Electrodeposition of Cd on polycrystalline copper was analyzed from the point of view of oxide influence [299], and a comparison of electrochemical data with results of numerical calculations was presented.

24.2.3.2.5 Silicon The Cd deposition process was studied on H-terminated

n-Si(111) plane [300]. Because the redox potential of the Cd^{2+}/Cd couple is much lower than the flat band potential of Si substrate, the surface electron concentration is sufficiently high. Thus the process occurs similarly as on a metal surface at relatively low cathodic overpotentials. The initial stages of Cd deposition were explained by progressive nucleation and cluster growth controlled by hemispherical diffusion. CdTe deposition on Si was also studied due to interest in application in IR radiation detectors. Mechanisms of this process on different planes of *n*-Si(100) was also discussed ([203, 301, 302] and references given therein).

24.2.3.2.6 Other Substrates Deposition of cadmium was also studied on Bi, Sn and Pb [303], Ni [304], reticulated vitreous carbon [305], Ti [306], and indium tin oxide [307]. UPD of Cd on tellurium results in CdTe formation [270, 308]. Electrodes coated with conducting polymers were also used to deposit cadmium electrochemically. In the case of polyaniline, the metal reduction potential corresponds to the neutral (nonconducting) state of the polymer, therefore cadmium was found to deposit on the substrate–glassy carbon electrode surface, in the open pores of the polymer film [309, 310].

The electrowinning of cadmium from dilute sulfate solution was studied using rotating GC and spiral wound steel electrodes [311].

The electrochemistry of Cd(II) was investigated at different electrodes (GC, polycrystalline tungsten, Pt, Ni) in a basic 1-ethyl-3-methylimidazolium chloride/tetrafluoroborate, at room temperature molten salt [312], and in acidic zinc chloride-1-ethyl-3-methylimidazolium [284].

24.2.4

Passivation and Corrosion of Cadmium24.2.4.1 **Passivation of Cadmium****Electrode**

The electrochemical behavior of the cadmium electrodes in alkaline solutions was intensively studied [313–318]. It was suggested [314–318] that during anodic dissolution of the Cd electrode in alkaline solutions, a passive layer consisting of $\text{Cd}(\text{OH})_2$ and CdO is formed, and $\text{Cd}(\text{II})$ soluble species are also generated. The composition of the anodically formed layer on cadmium in alkaline solution was dependent on the electrolyte cation [319]. In 1 M NaOH and KOH solutions, both $\beta\text{-Cd}(\text{OH})_2$ and $\gamma\text{-Cd}(\text{OH})_2$ were formed, while in 1 M LiOH, $\beta\text{-Cd}(\text{OH})_2$ was the only product.

The electrochemical behavior of Cd electrode in 1 M NaOH solutions was studied in detail [320]. It was found that the passive film formed on Cd electrode was composed of two layers: a barrier layer CdO and/or $\text{Cd}(\text{OH})_2$ covered with porous layers of $\text{Cd}(\text{OH})_2$.

The influence of concentration of KOH and separator materials on the soluble cadmium compounds, for example, cadmium hydroxyl complexes formed near the Cd electrode during the anodic process was also studied [321, 322].

The passivating layer formed on Cd electrode in alkaline solution in the presence of Na_2S was studied voltammetrically [323]. At low Na_2S concentrations, CdO , $\text{Cd}(\text{OH})_2$, and CdS layer were produced during the anodic oxidation of the Cd electrode. At higher Na_2S content, a few monolayers of thick CdS film were formed.

24.2.4.2 **Corrosion of Cadmium**

From the point of view of environmental stability, cadmium represents an

intermediate case between noble and base metals. It is relatively corrosion-resistant. However, dangerous environmental pollution by cadmium required studies concerning the corrosion behavior of this metal. The influence of solution pH on cadmium corrosion was studied using classical electrochemical methods, as well as electrochemical impedance spectroscopy, X-ray photoelectron spectroscopy, and SEM observations [324–327]. In acidic solutions, continuous corrosion takes place, while in neutral and alkaline solutions, the passivation process occurs, and is enhanced by higher oxygen concentration. Polycrystalline cadmium undergoes crystallographic etching after breakdown of the passive layer in NaCl solutions alkalinized to $\text{pH} = 11$ [328]. In alkaline solutions, the inhibiting influence of aliphatic alcohols (methanol, ethanol, propanol) was studied [329]. The inhibiting influence was ascribed to alcohol molecules adsorption on the cadmium surface, increasing with growing chain length. In borate solutions, in the absence and presence of Cl^- ions, the pitting corrosion of Cd electrode was studied. The corrosion potential was a linear function of logarithm of chloride concentration; the inhibiting influence of fatty acid sulfonate was also investigated [330].

In acidic solutions, the corrosion rate is relatively high. Studies on cadmium monocrystals and polycrystals in acidic chloride solutions revealed anodic dissolution independent of the crystallographic orientation; the dissolution rate was controlled by the mass transport of CdCl^+ ions [331]. The inhibitive influence of adsorbed organic substances, for example, alcohols [332], phenotiazine [333], and some polymers (e.g. poly(vinyl alcohol), poly(acrylic acid), sodium polyacrylate,

poly(ethylene glycol), etc.) [334] on the corrosion process in acidic solutions was studied.

A protective influence of commercial coatings [335] and chromates [335, 336] as well as surface coating formation in water-acetonitrile mixed solvents [227] was analyzed.

Corrosion studies on cadmium alloys, for example, [337–339], also from the point of view of stress corrosion cracking [340, 341] have been described recently.

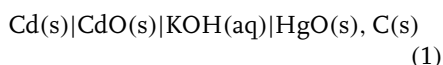
24.2.5

Applied Electrochemistry

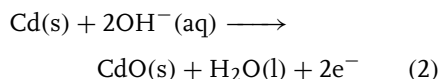
24.2.5.1 Batteries

24.2.5.1.1 Cadmium–Mercuric Oxide Primary Cells

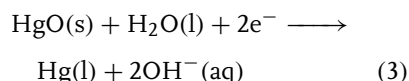
The scheme of the cell is:



The anode reaction is:



and the cathode reaction is:



The electrolyte is usually 40% KOH aqueous solution. The open-circuit voltage of this system is 0.90 V. The battery can be used and stored in a wide range of temperatures, from -55 to 80°C , due to low solubility of cadmium oxide in concentrated KOH solutions [342].

The kinetics of electrode processes on Cd electrode of an alkaline accumulator in dependence on changes in concentration of cadmium species in near-electrode layer of electrolyte was studied [343].

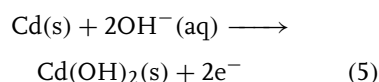
24.2.5.1.2 Cadmium–Nickel Oxide

(Ni–Cd) Secondary Cells

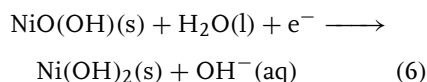
Besides lead-acid batteries, cadmium–nickel oxide cells represent the most popular type of rechargeable batteries [344]. The scheme of the cell is:



The discharge of the negative electrode is described by equation:



while the discharge of the positive electrode is:



The open-circuit voltage of the charged cell is 1.30 V.

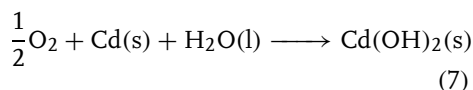
The electrolyte is usually 20–28% aqueous solution of KOH. Solid-state compositions of KOH aqueous electrolyte obtained by addition of poly(ethylene oxide) [345] or polymer based electrolyte (based on polyacrylates) were also proposed [346]. For low temperature applications, higher concentrations of KOH were used, while for higher temperatures, sodium hydroxide was sometimes applied. The influence of the temperature from 0 to 200°C , pressure and electrolyte concentration on the thermodynamic parameters of the cells, was studied in detail [347].

The active material of the negative electrode consists of metallic cadmium. Addition of iron (up to 25%), nickel, and graphite, prevents agglomeration [348]. Cadmium does not undergo corrosion, since the equilibrium potential is higher than that of hydrogen in the same solution.

However, it can undergo self-reductive dissolution (loss of active material) accompanied by oxygen evolution [349]. The active material of the positive electrode (in pocket plate cells) consists of nickel hydroxide mixed with small additions of cobalt and barium hydroxides to improve the capacity and charging/discharging performance and graphite to improve conductivity [348].

The sintered electrode constructions are gradually replaced with structures of higher capacity as, for example, felted nickel fibril or foam structures [350–352]. An open nickel foam structure can be obtained by vapor deposition of nickel from nickel carbonyl into a bed of urethane foam and then burning off the polymer. The porosity increases from 80% typical for sinter electrodes and reaches 90–95% for felted or foam structures. Application of polymer bonded cadmium electrodes significantly reduces environmentally dangerous dusting during cell production [350].

In sealed cells, which are the most important kind of Ni–Cd batteries, the gas (H_2 and O_2) evolution accompanying discharge should be minimized. This can be achieved by incorporation of “antipolar mass” – cadmium hydroxide in the positive electrode. In this case overdischarge results in reduction of $Cd(OH)_2$ to Cd, instead of hydrogen evolution [348]. On the other hand, oxygen evolved on the positive electrode during overcharging can react with cadmium [348]:



The negative electrode is thus designed to be larger than the positive one to avoid full charging of the negative electrode [351].

The state of charging, mainly of sealed cells, can be studied using galvanostatic methods [353] and electrochemical impedance spectroscopy [354–356] (see reviews [357, 358]). The battery behavior was analyzed using electronic network modeling [359, 360].

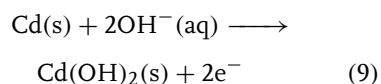
The cadmium–nickel oxide cell is the most robust secondary cell which can deliver a high charge in a short time, withstand overcharge, over discharge, and operate at temperatures as low as $-40^\circ C$ [350]. The vented Ni–Cd cells dominate in commercial jet-aircraft applications [350]. Ni–Cd batteries are gradually replaced by nickel–metal hydride and lithium-ion cells, especially in consumer electronics devices, due to higher energy storage capability and low weight. However, they are still useful for applications that require low temperatures and high-rate capability [361, 362].

24.2.5.1.3 Cadmium–Silver Oxide

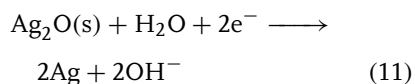
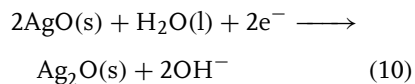
Secondary Cells The scheme of the cell is:



The discharge of the negative electrode is described by equation:



while the discharge of the positive electrode is a two-step process:



The positive electrodes are usually fabricated by sintering of silver powders and

slurry pasting [348]. The negative electrode and electrolyte are similar as in Ni–Cd batteries, but the energy density is about 30% higher. The open-circuit voltage is 1.2–1.4 V, depending on the reaction at the positive electrode. Applications are practically limited to small button cells [348].

24.2.5.2 Application in Electrochemical Sensors

24.2.5.2.1 Potentiometric Sensors The determination of cadmium is important due to its toxic nature [363]. It comes to water and soil through wastewater from metal plating industries, nickel–cadmium batteries and alloys.

Crown ethers [364] have proved to be an excellent choice as ionophores for the fabrication of ion sensors because of their ability to complex selectively a particular ion. The cadmium selective sensors have been fabricated from poly(vinyl chloride) (PVC) matrix membranes containing macrocyclic ionophores: benzo-15-crown-5 [365], monoaza-18-crown-6 [366], dibenzo-24-crown-8 [367], dicyclohexano-18-crown-6 [368], 3,4:11,12-dibenzo-1,6,9,14-tetraazacyclohexadecane [369], and polystyrene based membrane of 3,4:12,13-dibenzo-2,5,11,14-tetraoxo-1,6,10,15-tetraazacyclooctadecane [370]. Javanabakht et al. [371] have investigated Cd(II)-selective PVC membranes based on the synthesized tetrol compound. These membranes give a linear potential response in the concentration range 1.6×10^{-6} to 1.0×10^{-1} M with a Nernstian slope 28 ± 3 mV per decade of Cd(II) concentration. The cadmium ion–selective electrode based on tetrathia-12-crown-4 [372] is very sensitive, and exhibits Nernstian response for Cd(II) ions in the concentration range 4.0×10^{-7} to 1.0×10^{-1} M with a slope of 29 ± 1 mV per decade.

Gupta and D’Arc [373] have prepared the Cd(II) ion–selective electrode based on cyanocopolymer using 8-hydroxyquinoline as an electroactive ionophore. The effect of concentration of ion exchanger, plasticizer, and molecular weight of cyanocopolymers on selectivity and sensitivity of Cd(II) ion–selective electrode was also investigated [374].

Prodi et al. [375] have characterized a 5-chloro-8-methoxyquinoline appended diaza-18-crown-6 as a chemosensor for cadmium ions.

New PVC membrane sensors for Cd(II) ions based on 2-(3',4'-dihydroxyphenylazo-1')-1,3,4-thiadiazole [376] and 3-(2',4'-dihydroxyphenylazo-1')-1,2,4-triazol [377] were prepared. Their basic analytical parameters were established.

Selectivity of liquid membrane cadmium microelectrode based on the ionophore *N, N, N', N'*-tetrabutyl-3,6-dioxaoctanedithioamide was characterized by Pineros et al. [378].

The electrochemical flow sensor for in situ monitoring of total cadmium concentration in the presence of EDTA and nitrilotriacetic acid (NTA) ligands has been described [379].

The octamethyl-1,1'-di(2-pyridyl)ferrocene, redox-active ligand was used as an electrochemical sensor for Cd(II) and Zn(II) ions in acetonitrile [380].

The PVC membrane electrode based on new Schiff base complexes of 2,2-[(1,3-dimethyl-1,3-propanediylidene)dinitrilo]bis-benzenethiolato with Cd(II) [381] and cadmium-salen (*N, N'*-bis-salicylidene-1,2-ethylenediamine) complex [382] were used as the selective electrodes for thiocyanate ions.

The preparation and investigation of a stable, long lived, and highly selective fast-response novel solid-state cadmium-ion electrode, based on the ion pairing

compounds of the tetraiodocadmiate and tetrabromocadmiate anions with cetylpyridinium cations has been described by Abbas and Zahran [383]. The two sensors exhibit near Nernstian slopes independently of pH over a wide range with very fast-response time.

A number of Cd(II) sensors based mainly on the $\text{Ag}_2\text{S}/\text{CdS}$ mixtures [384, 385] and cadmium chelates [386] were described. Ito et al. [387] used an $\text{Ag}_2\text{S}/\text{CdS}$ ion-selective electrode for determination of cadmium ion in industrial wastewater by titration method.

Solid-state cadmium sensors based on chalcogenide thin film layer were prepared [388]. The electrochemical behavior of the sensor in terms of ionic sensitivity, detection limit, Nernstian response interval and effect of pH was evaluated.

Recent research in the field of polymer membrane ion-selective electrodes [389–391], has revealed that their selectivities [392–396] and limits of detections [394–397] could be improved by several orders of magnitude. The review of Bakker and Pretsch [398] summarized recent progress in the development and application of potentiometric sensors with low detection limit in the range 10^{-8} – 10^{-11} M.

Potentiometric Cd(II)-selective electrode with detection limit in ppt range has

been described [399]. The selectivity behavior was determined for two membranes based on the ionophore N, N, N', N' -tetradodecyl-3, 6-dioxaocanedithioamide, having different concentrations of ionophore and ion exchanger. The detection of 10^{-10} M Cd(II) was achieved at pH 7 with an ionic background of 10^{-4} M NaNO_3 (see Fig. 8).

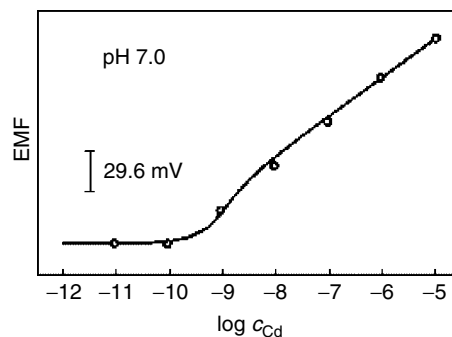
24.2.5.2.2 Amperometric-voltammetric

Sensors Thick-film screen-printed carbon containing electrodes modified with formazan were used for determination of Pb(II), Zn(II), and Cd(II) concentration [400].

A 1-(pyridylazo)-2-naphthol modified glassy carbon electrode was investigated as a voltammetric sensor for the Cd(II) ions [401], its detection limit was 5×10^{-10} M Cd(II).

The concentration of Cd(II) was determined using a carbon paste electrode modified with organofunctionalized amorphous silica with 2-benzothiazolethiol [402] or diacetyldioxime [403] and differential pulse anodic stripping voltammetry. The same method was used for determination of Cd(II) ion using GC electrode modified by anthraquinone improved Na-montmorillonite nanoparticles [404].

Fig. 8 The dependence of the electromotive force (EMF) of Cd(II) ion-selective electrode on logarithm of Cd(II) concentration in 10^{-4} M NaNO_3 at pH 7. Solid lines, calculated response curves on the basis of Eq. (7) in Ref. 399.



Voltammetric behavior in trace determination of cadmium at a calixarene modified screen-printed carbon paste electrode was investigated [405].

The GC electrode modified by dithizone was used for determination of Cd(II) and Pb(II) concentration using anodic stripping voltammetry [406].

Chow et al. have described [407] the electrochemical sensor for cadmium ions with gold electrode modified by 3-mercaptopropionic acid followed by covalently coupling the cadmium selective hexapeptide His-Ser-Gln-Lys-Val-Phe.

Roa et al. reported [408] the determination of Pb(II) and Cd(II) ions concentration using a polyclodextrin-modified carbon paste electrode with anodic stripping voltammetry.

The electrodes modified by hexacyanoferrates compounds were also used as voltammetric sensors [409–412]. The cadmium hexacyanoferrate-based composite ion-sensitive electrode for voltammetry was explored by Scholz and coworkers [409]. The potential of such electrode depends linearly on the logarithm of concentration of alkali and alkaline-earth metals ions in the solutions. Bo and Lin have studied [410] Prussian blue (PB)/Pt modified electrode in CdCl₂ electrolyte by cyclic voltammetry and in situ Fourier transform IR spectroscopy (FTIR) spectro-electrochemistry. Cadmium hexacyanoferrates were formed on a PB film.

The solid-state electrochemical formation of bilayer electrode structures of different hexacyanoferrates was studied, and a theoretical model was proposed for cyclic voltammetric behavior of the transformation of PB into cadmium hexacyanoferrates [411].

Solid-state electrochemistry of mixed iron(III)–Cd(II) hexacyanoferrates was also developed [412].

References

1. A. Hamelin, T. Vitanov, E. Sevastyanov et al., *J. Electroanal. Chem.* **1983**, 145, 225–264.
2. S. Trasatti, E. Lust, in *Modern Aspects of Electrochemistry*, (Eds.: R. E. White, B. E. Conway, J. O. M. Bockris), Kluwer Academic/Plenum Publisher, New York and London, 1999, p. 1, Vol. 33.
3. A. Korotkov, E. Bezlepina, B. B. Damaskin et al., *Elektrokhimiya* **1985**, 22, 1298–1304.
4. R. Naneva, V. Bostanov, A. Popov et al., *J. Electroanal. Chem.* **1989**, 274, 179–183.
5. A. Popov, N. Dimitrov, R. Naneva et al., *J. Electroanal. Chem.* **1994**, 376, 97–100.
6. R. Naneva, T. Vitanov, N. Dimitrov et al., *J. Electroanal. Chem.* **1992**, 328, 287–293.
7. R. R. Nazmutdinov, T. T. Zinkicheva, M. Probst et al., *J. Electroanal. Chem.* **2005**, 577, 112–126.
8. R. Naneva, N. Dimitrov, A. Popov et al., *J. Electroanal. Chem.* **1993**, 362, 281–286.
9. E. Lust, K. Lust, A. Jänes, *Russ. J. Electrochem.* **1995**, 31, 807–821.
10. E. Lust, K. Lust, A. Jänes, *J. Electroanal. Chem.* **1996**, 413, 111–121.
11. E. Lust, A. Jänes, K. Lust et al., *Russ. J. Electrochem.* **1996**, 32, 552–564.
12. E. Lust, A. Jänes, K. Lust et al., *Electrochim. Acta* **1997**, 42, 771–783.
13. E. Lust, A. Jänes, K. Lust et al., *J. Electroanal. Chem.* **1997**, 431, 183–201.
14. E. Lust, A. Jänes, K. Lust et al., *Electrochim. Acta* **1997**, 42, 2861–2879.
15. E. Lust, A. Jänes, V. Sammelselg et al., *Electrochim. Acta* **1998**, 44, 373–383.
16. E. Lust, A. Jänes, V. Sammelselg et al., *Electrochim. Acta* **2000**, 46, 185–191.
17. L. I. Daikhin, A. A. Kornyshev, M. Urbakh, *Electrochim. Acta* **1997**, 42, 2853–2860.
18. L. I. Daikhin, A. A. Kornyshev, M. Urbakh, *Phys. Rev. E* **1996**, 53, 6192–6199.
19. A. Popov, *Electrochim. Acta* **1995**, 40, 551–559.
20. V. V. Emets, B. B. Damaskin, I. A. Bogotchkaya et al., *Russ. J. Electrochem.* **2000**, 36, 661–667.
21. V. V. Emets, B. B. Damaskin, *J. Electroanal. Chem.* **2000**, 491, 30–38.
22. V. V. Emets, B. B. Damaskin, I. A. Bogotchkaya, *Russ. J. Electrochem.* **2001**, 37, 88–94.

23. C. P. M. Bongenaar, A. G. Remijnse, M. Sluyters-Rehbach et al., *J. Electroanal. Chem.* **1980**, *111*, 139–153.
24. C. P. M. Bongenaar, A. G. Remijnse, E. Temmerman et al., *J. Electroanal. Chem.* **1980**, *111*, 155–162.
25. M. Saakes, M. Sluyters-Rehbach, R. M. Souto et al., *J. Electroanal. Chem.* **1989**, *264*, 217–234.
26. M. Saakes, M. Sluyters-Rehbach, J. H. Sluyters, *J. Electroanal. Chem.* **1989**, *259*, 265–284.
27. J. Struijs, M. Sluyters-Rehbach, J. H. Sluyters, *J. Electroanal. Chem.* **1984**, *171*, 177–193.
28. E. Kirowa-Eisner, A. Kaplevatsky, Ch. Yarnitzky et al., *J. Electroanal. Chem.* **1995**, *394*, 127–139.
29. K. Darowicki, *J. Electroanal. Chem.* **2000**, *486*, 101–105.
30. K. Darowicki, J. Orlikowski, G. Lentka, *J. Electroanal. Chem.* **2000**, *486*, 106–110.
31. K. Darowicki, A. Krakowiak, *Russ. J. Electrochem.* **2003**, *39*, 134–140.
32. K. Darowicki, P. Ślepski, *J. Electroanal. Chem.* **2003**, *547*, 1–8.
33. K. Darowicki, P. Ślepski, *Electrochim. Acta* **2004**, *49*, 763–772.
34. J. Schiewe, J. Hazi, V. A. Vicente-Beckett et al., *J. Electroanal. Chem.* **1998**, *451*, 129–138.
35. J. Schiewe, K. B. Oldham, J. C. Myland et al., *Anal. Chem.* **1997**, *69*, 2673–2681.
36. I. S. El-Hallag, M. M. Ghoneim, E. Hammam, *Anal. Chim. Acta* **2000**, *414*, 173–180.
37. I. S. El-Hallag, *Anal. Chim. (Rome)* **1994**, *84*, 443.
38. A. Baars, F. J. C. Bijl, M. Sluyters-Rehbach et al., *J. Electroanal. Chem.* **1996**, *404*, 149–152.
39. F. J. C. Bijl, M. Sluyters-Rehbach, J. H. Sluyters, *J. Electroanal. Chem.* **1997**, *435*, 137–147.
40. R. M. Souto, M. Saakes, M. Sluyters-Rehbach et al., *J. Electroanal. Chem.* **1988**, *245*, 167–189.
41. E. Glaus, F. Sanz, M. Sluyters-Rehbach et al., *J. Electroanal. Chem.* **1994**, *368*, 307–314.
42. E. Glaus, F. Sanz, M. Sluyters-Rehbach et al., *J. Electroanal. Chem.* **1995**, *385*, 121–134.
43. E. Glaus, F. Sanz, *Electroanalysis* **1999**, *11*, 424–431.
44. M. Zelić, I. Pizeta, *Electroanalysis* **1997**, *9*, 155–160.
45. M. Zelić, M. Lovrić, *J. Electroanal. Chem.* **2003**, *541*, 67–76.
46. R. M. Souto, M. Sluyters-Rehbach, J. H. Sluyters, *J. Electroanal. Chem.* **1986**, *201*, 33–45.
47. M. Sluyters-Rehbach, J. H. Sluyters, *Electrochim. Acta* **1988**, *33*, 983–989.
48. M. Lovrić, *Electroanalysis* **2002**, *14*, 405–414.
49. M. Saakes, M. Sluyters-Rehbach, J. H. Sluyters, *J. Electroanal. Chem.* **1990**, *282*, 161–174.
50. A. Baars, K. Aoki, Y. Numata, *J. Electroanal. Chem.* **1997**, *436*, 133–140.
51. M. L. Kisova, M. Gołędzinowski, J. Lipkowski, *J. Electroanal. Chem.* **1979**, *95*, 29–42.
52. M. Gołędzinowski, L. Kisova, J. Lipkowski et al., *J. Electroanal. Chem.* **1979**, *95*, 43–57.
53. G. Pezzatini, M. L. Foresti, R. Guidelli, *J. Electroanal. Chem.* **1982**, *138*, 139–153.
54. A. Molina, J. Gonzalez, M. M. Moreno, *Electroanalysis* **2002**, *14*, 281–291.
55. B. Marczevska, *Gazz. Chim. Ital.* **1996**, *126*, 259–263.
56. M. Gołędzinowski, *J. Electroanal. Chem.* **1989**, *267*, 171–189.
57. M. Hromádova, R. de Levie, *J. Electroanal. Chem.* **1999**, *465*, 51–62.
58. D. Trzciński, W. Kośnik, J. Stroka et al., *Pol. J. Chem.* **2004**, *78*, 1149–1163.
59. Y. I. Moharram, *Anal. Chim. (Rome)* **1999**, *89*, 309.
60. Y. I. Moharram, *J. Electroanal. Chem.* **2004**, *563*, 283–290.
61. J. Taraszewska, A. Wałęga, *J. Electroanal. Chem.* **1984**, *171*, 243–256.
62. J. Stroka, K. Maksymiuk, A. Mital, *J. Electroanal. Chem.* **1989**, *272*, 145–160.
63. K. Maksymiuk, J. Stroka, Z. Galus, *J. Electroanal. Chem.* **1988**, *248*, 35–53.
64. W. R. Fawcett, A. Lasia, *J. Phys. Chem.* **1985**, *89*, 5695–5698.
65. G. M. Brisard, A. Lasia, *J. Electroanal. Chem.* **1987**, *221*, 129–141.
66. G. M. Brisard, A. Lasia, *J. Electroanal. Chem.* **1991**, *314*, 103–116.
67. W. R. Fawcett, *J. Electroanal. Chem.* **1991**, *302*, 13–29.
68. G. Gritzner, *J. Phys. Chem.* **1986**, *90*, 5478–5485.

69. J. Broda, Z. Galus, *J. Electroanal. Chem.* **1986**, 198, 233–244.
70. K. Maksymiuk, J. Stroka, Z. Galus, *J. Electroanal. Chem.* **1990**, 279, 1–18.
71. A. Anastopoulos, I. Moutziz, *Electrochim. Acta* **1990**, 35, 1805–1808.
72. N. A. Hampson, R. S. Latham, in *Encyclopedia of Electrochemistry of the Elements*, (Ed.: A. J. Bard), Marcel Dekker, New York, 1973, p. 156, Vol. 1.
73. M. M. Correia dos Santos, M. L. Simões Gonçalves, J. C. Romão, *J. Electroanal. Chem.* **1996**, 413, 97–103.
74. M. Torres, J. M. Diaz-Cruz, C. Ariño et al., *Anal. Chim. Acta* **1998**, 371, 23–37.
75. M. Torres, J. M. Diaz-Cruz, C. Ariño et al., *Electroanalysis* **1999**, 11, 93–100.
76. M. M. Antunes, J. E. Simao, A. C. Duarte et al., *Anal. Chim. Acta* **2002**, 459, 291–304.
77. M. M. Correia dos Santos, M. L. Simões Gonçalves, S. Capelo, *Electroanalysis* **1996**, 8, 178–182.
78. M. Fernandez, C. Ariño, J. M. Diaz-Cruz et al., *J. Electroanal. Chem.* **2001**, 505, 44–53.
79. R. Schmidt, J. Stroka, Z. Galus, *J. Electroanal. Chem.* **1998**, 456, 131–137.
80. F. Garay, V. Solis, *J. Electroanal. Chem.* **1999**, 476, 165–170.
81. M. Lovrič, I. Pižeta, Š. Komorsky-Lovrič, *Electroanalysis* **1992**, 4, 327–337.
82. M. Lovrič, *Russ. J. Electrochem.* **1996**, 32, 988–995.
83. M. Lovrič, Š. Komorsky-Lovrič, *J. Electroanal. Chem.* **1988**, 248, 239–253.
84. F. Garay, V. Solis, *J. Electroanal. Chem.* **2001**, 505, 109–117.
85. E. Norkus, G. Grinciene, T. Vuorinen et al., *Int. J. Biol. Macromol.* **2003**, 33, 251–254.
86. M. Łobacz, J. Stroka, Z. Galus, *Chem. Anal. (Warsaw)* **2002**, 47, 347–359.
87. J. Stroka, B. G. Cox, H. Schneider, *J. Electroanal. Chem.* **1989**, 266, 337–348.
88. A. Nikonowicz, P. Grzegorzewski, M. Pałys et al., *Polish. J. Chem.* **2004**, 78, 1785–1793.
89. I. Turyn, D. Mandler, *Electrochim. Acta* **1995**, 40, 1093–1100.
90. R. Andreoli, L. Benedetti, G. Grandi et al., *Electrochim. Acta* **1984**, 29, 227–231.
91. V. W. W. Yam, Y. L. Pui, K. K. Cheung, *New J. Chem.* **1999**, 23, 1163–1169.
92. F. Garay, V. Solis, *Electroanalysis* **2004**, 16, 450–457.
93. S. Cakir, E. Bicer, O. Cakir, *J. Inorg. Biochem.* **1999**, 77, 249–255.
94. M. C. E. Rollemberg, M. L. S. Simões Gonçalves, A. M. A. Mota et al., *Anal. Chim. Acta* **1999**, 384, 17–26.
95. M. C. Rollemberg, M. S. L. Simões Gonçalves, *Bioelectrochem.* **2000**, 52, 57–62.
96. J. Mendieta, M. S. Diaz-Cruz, R. Tauler et al., *Anal. Biochem.* **1996**, 240, 134–141.
97. M. S. Diaz-Cruz, J. Mendieta, R. Tauler et al., *J. Inorg. Biochem.* **1997**, 66, 29–36.
98. M. S. Diaz-Cruz, J. Mendieta, R. Tauler et al., *Anal. Chem.* **1999**, 71, 4629–4636.
99. B. H. Cruz-Vasquez, J. M. Diaz-Cruz, C. Arino et al., *Analyst* **2002**, 127, 401–406.
100. B. H. Cruz, J. M. Diaz-Cruz, I. Šestáková et al., *J. Electroanal. Chem.* **2002**, 520, 111–118.
101. B. H. Cruz, J. M. Diaz-Cruz, C. Arino et al., *Environ. Sci. Technol.* **2005**, 39, 778–786.
102. M. Esteban, C. Harlyk, A. R. Rodriguez, *J. Electroanal. Chem.* **1999**, 468, 202–212.
103. J. Mendieta, M. S. Diaz-Cruz, A. Monjonell et al., *Anal. Chim. Acta* **1999**, 390, 15–25.
104. G. Scarano, E. Morelli, *Electroanalysis* **1998**, 10, 39–43.
105. C. Harlyk, G. Bordin, O. Nieto et al., *Electroanalysis* **1997**, 9, 608–613.
106. C. Harlyk, G. Bordin, O. Nieto et al., *J. Electroanal. Chem.* **1998**, 446, 139–150.
107. M. Erk, B. Raspor, *J. Electroanal. Chem.* **1999**, 466, 75–81.
108. M. Erk, B. Raspor, *Anal. Chim. Acta* **2001**, 442, 165–170.
109. M. Erk, B. Raspor, *J. Electroanal. Chem.* **2001**, 502, 174–179.
110. O. Nieto, A. R. Rodriguez, *Electroanalysis* **1999**, 11, 175–182.
111. I. Sestakova, M. Kopanica, L. Havran et al., *Electroanalysis* **2000**, 12, 100–104.
112. C. Harlyk, O. Nieto, G. Bordin et al., *J. Electroanal. Chem.* **1998**, 458, 199–208.
113. J. L. L. Vaz, G. Duc, M. Petit-Ramel et al., *Can. J. Chem.-Rev. Can. Chim.* **1996**, 74, 359–364.
114. A. Assabbane, M. Belmouden, A. Albourine et al., *Bull. Electrochem.* **2000**, 16, 497–499.
115. J. M. Zhang, Z. W. Wang, Q. Z. Shi, *Chinese J. Inorg. Chem.* **2004**, 20, 324–330.
116. P. L. Sahu, F. Khan, *Bull. Electrochem.* **2000**, 16, 449–452.
117. P. L. Pratihari, *Asian J. Chem.* **2000**, 12, 1146–1158.
118. I. Cukrowski, *Analyst* **1997**, 122, 827–833.

119. I. Cukrowski, S. A. Loader, *Electroanalysis* **1998**, *10*, 877–885.
120. I. Cukrowski, *Electroanalysis* **1997**, *9*, 1167–1173.
121. I. Cukrowski, J. R. Zeevaert, N. V. Jarvis, *Anal. Chim. Acta* **1999**, *379*, 217–226.
122. I. Cukrowski, N. Maseko, *Electroanalysis* **2003**, *15*, 1377–1388.
123. E. Cukrowska, I. Cukrowski, *Talanta* **1998**, *47*, 1175–1189.
124. H. Parham, M. Shamsipur, *J. Electroanal. Chem.* **1991**, *314*, 71–80.
125. G. Rounaghi, M. Chamsaz, A. Nezhadali, *J. Incl. Phenom. Macrocycl. Chem.* **2000**, *38*, 153–161.
126. G. Rounaghi, A. S. Yazdi, Z. Monsef, *J. Incl. Phenom. Macrocycl. Chem.* **2002**, *43*, 231–237.
127. Z. Monsef, G. Rounaghi, A. Sarafraza, *J. Incl. Phenom. Macrocycl. Chem.* **2001**, *39*, 321–325.
128. E. Bottari, M. R. Festa, *Chem. Spec. Bioavailab.* **1996**, *8*, 75–83.
129. E. Bottari, M. R. Festa, *Talanta* **1998**, *46*, 91–99.
130. P. Arranz-Mascarós, R. López-Garzón, M. L. Godino-Salino et al., *Transition Met. Chem.* **1998**, *23*, 501–505.
131. M. Filella, R. M. Town, M. G. Bugarin, *J. Chem. Eng. Data* **1999**, *44*, 1009–1019.
132. P. Benezeth, D. A. Palmer, *Chem. Geol.* **2000**, *167*, 11–24.
133. M. Salonen, H. Saarinen, M. Orama, *J. Coord. Chem.* **2003**, *56*, 1041–1047.
134. V. P. Vasil'ev, S. N. Gridchin, L. A. Kochergina et al., *J. Anal. Chem.* **2003**, *58*, 47–49.
135. R. Tomas, M. Visic, I. Tominic et al., *Croat. Chem. Acta* **2001**, *74*, 91–101.
136. R. Tomas, I. Tominic, V. Sokol et al., *Croat. Chem. Acta* **2004**, *77*, 519–527.
137. S. F. Ledenkov, V. A. Sharnin, G. V. Chistyakova, *Russ. Chem. Bull.* **2004**, *53*, 758–765.
138. K. Kurnia, D. E. Giles, P. M. May et al., *J. Coord. Chem.* **1996**, *38*, 183–197.
139. R. Serra, F. Mas, J. M. Diaz-Cruz et al., *Electroanalysis* **2000**, *12*, 60–65.
140. R. M. Izatt, J. S. Bradshaw, S. A. Nielsen et al., *Chem. Rev.* **1985**, *85*, 271–339.
141. R. M. Izatt, K. Pawlak, J. S. Bradshaw et al., *Chem. Rev.* **1991**, *91*, 1721–2085.
142. R. M. Izatt, K. Pawlak, J. S. Bradshaw et al., *Chem. Rev.* **1995**, *95*, 2529–2586.
143. J. A. Castro, J. Romero, J. A. Garcia-Vázquez et al., *Polyhedron* **1996**, *15*, 2741–2745.
144. P. Perez-Lourido, J. A. Garcia-Vazquez, J. Romero et al., *Inorg. Chim. Acta* **1998**, *271*, 1–8.
145. M. Fondo, A. Sousa, M. R. Bermejo et al., *Eur. J. Inorg. Chem.* **2002**, *3*, 703–710.
146. R. Pedrido, M. R. Bermejo, A. M. Garcia-Deibe et al., *Eur. J. Inorg. Chem.* **2003**, *17*, 3193–3200.
147. M. Bernal, J. A. Garcia-Vázquez, J. Romero et al., *Inorg. Chim. Acta* **1999**, *295*, 39–47.
148. R. Pedrido, M. R. Bermejo, M. J. Romero et al., *Dalton Trans.* **2005**, *3*, 572–579.
149. S. Cabaleiro, E. Vázquez-Lopez, J. Castro et al., *Inorg. Chim. Acta* **1999**, *294*, 87–94.
150. C. Boudon, J. P. Gisselbrecht, M. Gross, *Electroanalysis* **1992**, *4*, 19–26.
151. A. Bobrowski, A. M. Bond, S. R. Ellis, *Inorg. Chim. Acta* **1999**, *293*, 223–228.
152. A. José, J. A. Garcia-Vázquez, J. Romero et al., *Coord. Chem. Rev.* **1999**, *193*–195, 691–745.
153. C. A. Koval, J. N. Howard, *Chem. Rev.* **1992**, *92*, 411–433.
154. K. Rajeshwar, *Adv. Mater.* **1992**, *4*, 23–29.
155. G. Hodes, in *Physical Electrochemistry* (Ed.: I. Rubinstein), Marcel Dekker, New York, 1995, p. 515.
156. R. K. Pandey, S. N. Sahu, S. Cahndra, *Handbook of Semiconductor Electrodeposition*, Marcel Dekker, New York, 1996.
157. N. Myung, N. R. de Tacconi, K. Rajeshwar, *Electrochem. Commun.* **1999**, *1*, 42–45.
158. N. Myung, S. Kim, D. Lincot et al., *Electrochim. Acta* **2000**, *45*, 3749–3756.
159. S. J. Choi, D. H. Woo, N. S. Myung et al., *J. Electrochem. Soc.* **2001**, *148*, C569–C573.
160. N. Myung, S. Ham, B. Choi et al., *J. Electroanal. Chem.* **2005**, *574*, 367–373.
161. A. Gichuhi, B. E. Boone, U. Demir et al., *J. Phys. Chem. B* **1998**, *102*, 6499–6506.
162. M. Innocenti, S. Cattarin, M. Cavallini et al., *J. Electroanal. Chem.* **2002**, *532*, 219–225.
163. C. B. Murray, D. J. Norris, M. G. Bawendi, *J. Am. Chem. Soc.* **1993**, *115*, 8706–8715.
164. M. A. Anderson, S. Gorer, R. M. Penner, *J. Phys. Chem. B* **1997**, *101*, 5895–5899.
165. L. Pedone, E. Caponetti, M. Leone et al., *J. Colloid Interface Sci.* **2005**, *284*, 495–500.
166. E. Granot, F. Patolsky, I. Willner, *J. Phys. Chem. B* **2004**, *108*, 5875–5881.

167. R. Zhai, S. B. Wang, H. Y. Xu et al., *Mater. Lett.* **2005**, 59, 1497–1501.
168. X. Xu, J. Cesarano, E. Burch et al., *Thin Solid Films* **1997**, 305, 95–102.
169. M. Sasagawa, J. Nishino, Y. Nosaka, *Electrochem.* **1999**, 67, 1237–1239.
170. M. Sasagawa, Y. Nosaka, *J. Electroanal. Chem.* **2002**, 536, 141–144.
171. M. Sasagawa, Y. Nosaka, *Electrochim. Acta* **2003**, 48, 483–488.
172. S. Tamulevicius, M. P. Valkonen, G. Laukaitis et al., *Thin Solid Films* **1999**, 356, 430–434.
173. G. Laukaitis, M. Lindroos, S. Tamulevicius et al., *Appl. Surf. Sci.* **2001**, 185, 134–139.
174. M. P. Valkonen, T. Kanninen, S. Lindroos et al., *Appl. Surf. Sci.* **1997**, 115, 386–392.
175. B. R. Sankapal, R. S. Mane, C. D. Lokhande, *Mater. Res. Bull.* **2000**, 35, 177–184.
176. C. D. Lokhande, B. R. Sankapal, H. M. Pathan et al., *Appl. Surf. Sci.* **2001**, 181, 277–282.
177. J. Nishino, S. Chatani, Y. Uotani et al., *J. Electroanal. Chem.* **1999**, 473, 217–222.
178. M. Takahashi, S. Hasegawa, M. Watanabe et al., *J. Appl. Electrochem.* **2002**, 32, 359–367.
179. T. Yoshida, K. Yamaguchi, T. Kazitani et al., *J. Electroanal. Chem.* **1999**, 473, 209–216.
180. N. R. de Tacconi, H. Wenren, K. Rajeshwar, *J. Electrochem. Soc.* **1997**, 144, 3159–3163.
181. S. K. Haram, A. J. Bard, *J. Phys. Chem. B* **2001**, 105, 8192–8195.
182. Y. Nosaka, N. Ohta, T. Fukuyama et al., *J. Colloid Interface Sci.* **1993**, 155, 23–29.
183. N. N. Gudeleva, F. S. Bekmukhametova, Z. P. Salaeva et al., *Russ. J. Gen. Chem* **1999**, 69, 1548–1552.
184. F. Loglio, M. Innocenti, F. D'Acapito et al., *J. Electroanal. Chem.* **2005**, 575, 161–167.
185. M. Bouroushian, T. Kosanovic, Z. Loizos et al., *Electrochem. Commun.* **2000**, 2, 281–285.
186. S. Eriksson, T. Gruszecki, P. Carlsson et al., *Thin Solid Films* **1995**, 269, 14–17.
187. M. Ramrakhiani, *Mater. Sci. Eng., B* **1995**, 35, 493–496.
188. C. M. Shen, X. G. Zhang, H. L. Li, *Appl. Surf. Sci.* **2005**, 240, 34–41.
189. C. M. Shen, X. G. Zhang, H. L. Li, *Mater. Sci. Eng., B* **2001**, 84, 265–270.
190. C. D. Lokhande, E. H. Lee, K. D. Jung et al., *Mater. Chem. Phys.* **2005**, 91, 399–403.
191. M. D. R. Tanveer, *Bull. Electrochem.* **2000**, 16, 370–375.
192. M. Bouroushian, J. Charoud-Got, Z. Loizos et al., *Thin Solid Films* **2001**, 381, 39–47.
193. N. Dukstiene, *Russ. J. Electrochem.* **2003**, 39, 1331–1337.
194. A. Saraby-Rentjes, L. M. Peter, M. E. Ozsan et al., *J. Electrochem. Soc.* **1993**, 140, 2880–2888.
195. R. D. Engelken, T. P. Van Doren, *J. Electrochem. Soc.* **1985**, 132, 2910–2919.
196. M. W. Verbrugge, C. W. Tobias, *J. Electrochem. Soc.* **1987**, 134, 3104–3109.
197. E. A. Meulenkaamp, L. M. Peter, *J. Chem. Soc., Faraday Trans.* **1996**, 92, 4077–4082.
198. F. Forni, M. Innocenti, G. Pezzatini et al., *Electrochim. Acta* **2000**, 45, 3225–3231.
199. K. Murase, H. Uchida, T. Hirato et al., *J. Electrochem. Soc.* **1999**, 146, 531–536.
200. M. B. Dergacheva, V. N. Statsyuk, L. A. Fogel, *J. Electroanal. Chem.* **2005**, 579, 43–49.
201. K. Murase, H. Watanabe, T. Hirato et al., *J. Electrochem. Soc.* **1999**, 146, 1798–1803.
202. K. Murase, H. Watanabe, S. Mori et al., *J. Electrochem. Soc.* **1999**, 146, 4477–4484.
203. H. Gómez, R. Henríquez, R. Schrebler et al., *Electrochim. Acta* **2001**, 46, 821–827.
204. H. Gómez, R. Henríquez, R. Schrebler et al., *Electrochim. Acta* **2005**, 50, 1299–1305.
205. T. Montiel-Santillán, O. Solorza-Feria, H. Sánchez-Soriano, *Int. J. Hydrogen Energy* **2002**, 27, 461–464.
206. J. G. N. Matias, J. F. Juliao, D. M. Soares et al., *J. Electroanal. Chem.* **1997**, 431, 163–169.
207. C. Lepiller, D. Lincot, *J. Electrochem. Soc.* **2004**, 151, C348–C357.
208. S. I. Hsiu, I. W. Sun, *J. Appl. Electrochem.* **2004**, 34, 1057–1063.
209. Y. Bae, N. Myung, A. J. Bard, *Nano Lett.* **2004**, 4, 1153–1161.
210. M. B. Dergacheva, V. N. Statsyuk, L. A. Fogel et al., *Russ. J. Appl. Chem.* **1998**, 71, 634–636.
211. A. E. Rakhshani, *Phys. Status Solidi A-Appl. Res.* **2002**, 191, 179–187.
212. I. A. Kazarinov, A. N. Stepanov, N. N. Kutnaeva et al., *Russ. J. Electrochem.* **1998**, 34, 1282–1289.
213. I. A. Kazarinov, M. M. Burashnikova, A. N. Stepanov, *Russ. J. Appl. Chem.* **2001**, 74, 430–433.

214. V. D. Jović, A. R. Despić, J. S. Stevanović et al., *Electrochim. Acta* **1989**, *34*, 1093–1102.
215. I. A. Kazarinov, N. N. Kutnaeva, E. L. Vlasova, *Russ. J. Electrochem.* **1999**, *35*, 463–466.
216. B. Borresen, G. A. Voyiatzis, G. N. Papatheodorou, *Phys. Chem. Chem. Phys.* **1999**, *1*, 3309–3314.
217. T. Montiel, O. Solorza, H. Sanchez, *J. Electrochem. Soc.* **2000**, *147*, 1031–1037.
218. E. Juzeliūnas, M. Samulevičiene, *Surf. Coat. Technol.* **1996**, *80*, 293–294.
219. Y. Y. Tevtul, *Russ. J. Electrochem.* **1996**, *32*, 535–540.
220. T. C. Franklin, T. S. N. S. Narayanan, *J. Electrochem. Soc.* **1996**, *143*, 2759–2764.
221. M. E. Alekseeva, F. K. Mansurov, V. A. Nikolskii, *Russ. J. Appl. Chem.* **1995**, *68*, 1753–1755.
222. V. V. Kuznetsov, L. M. Skibina, A. I. Sokolenko, *Prot. Met.* **2004**, *40*, 77–81.
223. V. V. Kuznetsov, L. M. Skibina, I. N. Loskutnikova et al., *Prot. Met.* **2004**, *40*, 331–336.
224. V. V. Kuznetsov, O. V. Fedorova, O. A. Gulidova, *Russ. J. Electrochem.* **1995**, *31*, 1252–1258.
225. V. V. Kuznetsov, L. M. Skibina, I. N. Loskutnikova, *Prot. Met.* **1998**, *34*, 363–367.
226. V. V. Kuznetsov, L. M. Skibina, I. N. Loskutnikova et al., *Prot. Met.* **1998**, *34*, 465–469.
227. V. V. Kuznetsov, L. M. Skibina, I. N. Loskutnikova, *Prot. Met.* **2000**, *36*, 565–570.
228. V. V. Kuznetsov, L. M. Skibina, I. N. Loskutnikova, *Prot. Met.* **2000**, *36*, 571–574.
229. V. V. Kuznetsov, L. M. Skibina, I. N. Loskutnikova et al., *Prot. Met.* **2001**, *37*, 31–34.
230. V. V. Kuznetsov, L. M. Skibina, I. N. Loskutnikova, *Prot. Met.* **2002**, *38*, 37–44.
231. V. V. Kuznetsov, L. M. Skibina, R. A. Levochkin et al., *Prot. Met.* **2003**, *39*, 154–159.
232. V. V. Kuznetsov, L. M. Skibina, I. N. Loskutnikova et al., *Prot. Met.* **2003**, *39*, 81–86.
233. V. V. Kuznetsov, L. M. Skibina, A. I. Sokolenko et al., *Prot. Met.* **2004**, *40*, 310–315.
234. V. Bostanov, E. Mladenova, D. Kashchiev, *J. Electroanal. Chem.* **2000**, *481*, 7–12.
235. V. F. Kozin, A. A. Omel'chuk, *Inorg. Mater.* **2002**, *38*, 207–211.
236. D. M. Kolb, M. Przasnyski, H. Gerischer, *J. Electroanal. Chem.* **1974**, *54*, 25–38.
237. J. W. Schultze, F. D. Koppitz, M. M. Lohrenge, *Ber. Bunsen-Ges. Phys. Chem.* **1974**, *78*, 693–701.
238. F. M. Romeo, R. I. Tucceri, D. Posadas, *Surf. Sci.* **1988**, *203*, 186–200.
239. B. W. Gregory, M. L. Norton, J. L. Stickney, *J. Electroanal. Chem.* **1990**, *293*, 85–101.
240. E. Herrero, L. J. Buller, H. D. Abruña, *Chem. Rev.* **2001**, *101*, 1897–1930. and the references given therein.
241. R. Vidu, S. Hara, *Scripta Mater.* **1999**, *41*, 617–624.
242. R. Vidu, S. Hara, *J. Electroanal. Chem.* **1999**, *475*, 171–180.
243. R. Vidu, S. Hara, *Surf. Sci.* **2000**, *452*, 229–238.
244. G. Horanyi, *J. Solid State Electrochem.* **2000**, *4*, 177–180.
245. R. Vidu, N. Hirai, S. Hara, *Phys. Chem. Chem. Phys.* **2001**, *3*, 3320–3324.
246. G. Inzelt, G. Horanyi, *J. Electroanal. Chem.* **2000**, *491*, 111–116.
247. M. C. Santos, D. W. Miwa, S. A. S. Machado et al., *Quim. Nova* **2001**, *24*, 465–472.
248. A. A. Gewirth, B. K. Niece, *Chem. Rev.* **1997**, *97*, 1129–1162. and the references given therein.
249. J. C. Bondos, A. A. Gewirth, R. G. Nuzzo, *J. Phys. Chem.* **1996**, *100*, 8617–8620.
250. B. K. Niece, A. A. Gewirth, *Langmuir* **1997**, *13*, 6302–6309.
251. S.-J. Hsieh, A. A. Gewirth, *Langmuir* **2000**, *16*, 9501–9512.
252. M. D. Lay, J. L. Stickney, *J. Am. Chem. Soc.* **2003**, *125*, 1352–1355.
253. H. Kawamura, M. Takahashi, J. Mizuki, *J. Electrochem. Soc.* **2002**, *149*, C586–C591.
254. B. Pettinger, A. Friedrich, C. Shannon, *Electrochim. Acta* **1991**, *36*, 1829–1833.
255. D. Lee, T. Rayment, *Electrochem. Commun.* **2002**, *4*, 832–837.
256. M. D. Lay, K. Varazo, N. Srisook et al., *J. Electroanal. Chem.* **2003**, *554*–555, 221–231.
257. S. Maupai, Y. Zhang, P. Schmuki, *Surf. Sci.* **2003**, *527*, L165–L170.
258. S. Maupai, Y. Zhang, P. Schmuki, *Electrochem. Solid State Lett.* **2003**, *6*, C63–C65.
259. Y. Zhang, S. Maupai, P. Schmuki, *Surf. Sci.* **2004**, *551*, L33–L39.
260. M. C. del Barrio, S. G. Garcia, D. R. Salinas, *Electrochem. Commun.* **2004**, *6*, 762–766.

261. X. Xing, P. Abel, R. McIntyre et al., *J. Electroanal. Chem.* **1987**, 216, 261–271.
262. X. Xing, I. Tae Bae, D. A. Scherson, *Electrochim. Acta* **1995**, 40, 29–36.
263. X. Xing, D. A. Scherson, C. Mak, *J. Electrochem. Soc.* **1990**, 137, 2166–2175.
264. S. B. Aoun, Z. Dursun, T. Koga et al., *J. Electroanal. Chem.* **2004**, 567, 175–183.
265. U. Demir, C. Shannon, *Langmuir* **1996**, 12, 6091–6097.
266. R. Vidu, S. Hara, *J. Vac. Sci. Technol., B* **1999**, 17, 2423–2430.
267. R. Vidu, S. Hara, *Electrochem.* **1999**, 67, 1240–1242.
268. T. Tanaka, K. Kubo, N. Hirai et al., *Mater. Trans.* **2003**, 44, 688–691.
269. K. Kubo, N. Hirai, S. Hara, *J. Jpn. Inst. Met.* **2002**, 66, 881–884.
270. D. W. Suggs, J. L. Stickney, *Surf. Sci.* **1993**, 290, 362–374.
271. B. W. Gregory, D. W. Suggs, J. L. Stickney, *J. Electrochem. Soc.* **1991**, 138, 1279–1284.
272. D. W. Suggs, J. L. Stickney, *Surf. Sci.* **1993**, 290, 375–387.
273. D. Oyamatsu, S. Kuwabata, H. Yoneyama, *J. Electroanal. Chem.* **1999**, 473, 59–67.
274. E. Juzeliunas, H. W. Pickering, K. G. Weil, *J. Electrochem. Soc.* **2000**, 147, 1088–1095.
275. R. R. Adžić, D. N. Simić, D. M. Dražić et al., *J. Electroanal. Chem.* **1975**, 61, 117–120.
276. K. Varga, P. Zelenay, G. Horanyi et al., *J. Electroanal. Chem.* **1992**, 327, 291–306.
277. R. Gómez, J. M. Feliu, *J. Electroanal. Chem.* **2003**, 554–555, 145–156.
278. S. A. S. Machado, A. A. Tanaka, E. R. Gonzalez, *Electrochim. Acta* **1992**, 37, 2559–2564.
279. M. C. dos Santos, S. A. S. Machado, *J. Brazil. Chem. Soc.* **1998**, 9, 211–218.
280. M. C. Santos, S. A. S. Machado, L. A. Avaca et al., *Quim. Nova* **2000**, 23, 392–400.
281. V. Daujotis, R. Randonis, *J. Electroanal. Chem.* **1992**, 326, 253–275.
282. V. Daujotis, *Pol. J. Chem.* **1998**, 72, 2432–2439.
283. M. E. Martins, R. C. Salvarezza, A. J. Arvia, *Electrochim. Acta* **1996**, 41, 2441–2449.
284. J. F. Huang, I. W. Sun, *J. Electrochem. Soc.* **2002**, 149, E348–E355.
285. E. Schmidt, M. Christen, P. Beyeler, *J. Electroanal. Chem.* **1973**, 42, 275–289.
286. H. Bort, K. Jüttner, W. J. Lorenz et al., *Electrochim. Acta* **1983**, 28, 993–1001.
287. V. D. Jović, B. M. Jović, A. R. Despić, *J. Electroanal. Chem.* **1990**, 288, 229–243.
288. V. D. Jović, B. M. Jović, *Electrochim. Acta* **2002**, 47, 1777–1785.
289. S. G. Garcia, D. R. Salinas, G. Staikov, *Surf. Sci.* **2005**, 576, 9–18.
290. M. L. Foresti, G. Pezzatini, M. Cavallini et al., *J. Phys. Chem. B* **1998**, 102, 7413–7420.
291. M. E. Martins, A. Hernández-Creus, R. C. Salvarezza et al., *J. Electroanal. Chem.* **1994**, 375, 141–155.
292. M. Ge, A. A. Gewirth, *Surf. Sci.* **1995**, 324, 140–148.
293. C. Stuhlmann, Z. Park, C. Bach et al., *Electrochim. Acta* **1998**, 44, 993–998.
294. J. Hommrich, S. Hümann, K. Wandelt, *Faraday Discuss.* **2002**, 121, 129–138.
295. V. D. Jović, B. M. Jović, *J. Serb. Chem. Soc.* **2001**, 66, 345–357.
296. S. Hümann, J. Hommrich, K. Wandelt, *Thin Solid Films* **2003**, 428, 76–82.
297. A. Budniok, *J. Electroanal. Chem.* **1981**, 123, 365–372.
298. A. Budniok, *Thin Solid Films* **1981**, 81, 289–299.
299. M. A. Lovell, D. Roy, *Electrochim. Acta* **1998**, 43, 2117–2130.
300. R. Krumm, B. Guel, C. Schmitz et al., *Electrochim. Acta* **2000**, 45, 3255–3262.
301. Y. Sugimoto, L. M. Peter, *J. Electroanal. Chem.* **1995**, 381, 251–255.
302. Y. Sugimoto, L. M. Peter, *J. Electroanal. Chem.* **1995**, 386, 183–188.
303. E. Schmidt, H. R. Gygas, *J. Electroanal. Chem.* **1966**, 12, 300–319.
304. G. E. Badea, T. Badea, *Rev. Roum. Chim.* **2003**, 48, 843–848.
305. J. Tramontina, D. S. Azambuja, C. M. S. Piatnicki, *J. Brazil. Chem. Soc.* **2002**, 13, 469–473.
306. H. D. Shih, F. Jona, D. W. Jepsen et al., *Phys. Rev. B* **1977**, 15, 5550–5560; 5561–5666.
307. F. Kadirgan, S. Kutun, S. Suzer, *Ann. Chim.* **1998**, 88, 705–718.
308. E. A. Streltsov, N. P. Osipovich, *Dokl. Akad. Nauk Belarus.*, **1998**, 42, 58–63.
309. V. D. Jović, T. Trišović, B. M. Jović et al., *J. Electroanal. Chem.* **1996**, 408, 149–155.
310. V. D. Jović, B. M. Jović, E. R. Stojilković et al., *J. Serb. Chem. Soc.* **1999**, 64, 265–273.
311. A. E. Elsherief, *Electrochim. Acta* **2003**, 48, 2667–2673.

312. P. Y. Chen, I. W. Sun, *Electrochim. Acta* **2000**, 45, 3163–3170.
313. R. Barnard, *J. Appl. Electrochem.* **1981**, 11, 217–237.
314. S. B. Saidman, J. R. Vilche, A. J. Arvia, *Electrochim. Acta* **1987**, 32, 395–409.
315. J. O. Zerbino, S. B. Saidman, J. R. Vilche et al., *Electrochim. Acta* **1989**, 34, 1167–1167.
316. J. O. Zerbino, S. B. Saidman, J. R. Vilche et al., *Electrochim. Acta* **1990**, 35, 605–612.
317. Y. Duhirel, B. Beden, J. M. Léger et al., *Electrochim. Acta* **1992**, 37, 665–671.
318. J. I. De Urreza, C. A. Gervasi, S. B. Saidman et al., *J. Appl. Electrochem.* **1993**, 23, 1207–1213.
319. N. Simic, A. Ahlberg, *J. Electroanal. Chem.* **1998**, 451, 237–247.
320. K. M. Ismail, *J. Appl. Electrochem.* **2001**, 31, 1333–1338.
321. T. G. Dmitrienko, E. A. Khomskaya, N. F. Burdanova et al., *Russ. J. Electrochem.* **1997**, 33, 910–914.
322. T. G. Dmitrienko, E. A. Khomskaya, N. F. Burdanova et al., *Russ. J. Electrochem.* **1998**, 34, 423–428.
323. S. B. Saidman, J. R. Vilche, A. J. Arvia, *Electrochim. Acta* **1987**, 32, 1153–1157.
324. W. A. Badawy, F. M. Al-Kharafi, E. Y. Al-Hassan, *Corros. Prevent Contr.* **1998**, 45, 95–108.
325. W. A. Badawy, F. M. Al-Kharafi, E. Y. Al-Hassan, *Mater. Sci. Forum* **1998**, 289–2, 849–859.
326. W. A. Badawy, F. M. Al-Kharafi, E. Y. Al-Hassan, *Bull. Electrochem.* **1998**, 14, 449–455.
327. W. A. Badawy, F. M. Al-Kharafi, E. Y. Al-Hassan, *Corros. Prevent Contr.* **1999**, 46, 51–62.
328. M. G. Alvarez, J. R. Galvele, *J. Electrochem. Soc.* **1980**, 127, 1235–1241.
329. W. A. Badawy, F. M. Al-Kharafi, *Bull. Electrochem.* **2000**, 16, 155–160.
330. M. Abdullah, *Bull. Electrochem.* **1997**, 13, 149–155.
331. D. Tromans, B. Foster, F. Weinberg, *Corros. Sci.* **1997**, 39, 1291–1305.
332. W. A. Badawy, F. M. Al-Kharafi, E. Y. Al-Hassan, *Corros. Prevent Contr.* **1998**, 45, 145–155.
333. A. El-Sayed, *J. Appl. Electrochem.* **1997**, 27, 193–200.
334. K. S. Khairou, A. El-Sayed, *J. Appl. Polym. Sci.* **2003**, 88, 866–871.
335. L. A. S. Silva, L. Sathler, *Plat. Surf. Finish.* **2003**, 90, 38–42.
336. T. Dobrev, M. Monev, I. Krastev et al., *Trans. Inst. Metal Finish.* **1996**, 74, 45–50.
337. A. Durairajan, B. S. Haran, R. E. White et al., *J. Electrochem. Soc.* **2000**, 147, 1781–1786.
338. P. W. Haberecht, B. R. W. Hinton, *Trans. Inst. Met. Finish.* **2000**, 78, 17–22.
339. H. S. Kim, B. N. Popov, K. S. Chen, *Corros. Sci.* **2003**, 45, 1505–1521.
340. J. R. Galvele, *Electrochim. Acta* **2000**, 45, 3537–3541.
341. M. L. Montoto, G. S. Duffó, J. R. Galvele, *Corros. Sci.* **2001**, 43, 755–764.
342. M. Lazzari, C. A. Vincent, in *Modern Batteries* (Eds.: C. A. Vincent, B. Scrosati), Arnold, London, 1997, p. 65.
343. V. V. Tenkovtsev, L. S. Nadezhina, B. A. Borisov et al., *Russ. J. Appl. Chem.* **1995**, 68, 980–984.
344. J. McBreen, in *Handbook of Battery Materials* (Ed.: J. O. Besenhard), Wiley-VCH, New York, 1999, p. 135.
345. S. Guinot, E. Salmon, J. F. Penneau et al., *Electrochim. Acta* **1998**, 43, 1163–1170.
346. X. Zhu, H. Yang, Y. Cao et al., *Electrochim. Acta* **2004**, 49, 2533–2539.
347. S. N. Lvov, D. D. Macdonald, *J. Power Sources* **1998**, 72, 136–145.
348. F. Bonino, C. A. Vincent, in *Modern Batteries*, (Eds.: C. A. Vincent, B. Scrosati), Arnold, London, 1997, p. 162.
349. G. P. Kalignan, C. Umapratheswaran, B. Muralidharan et al., *J. Power Sources* **1996**, 58, 29–34.
350. R. J. Brodd, K. R. Bullock, R. A. Leising et al., *J. Electrochem. Soc.* **2004**, 151, K1–K11.
351. Y. Morioka, S. Narukawa, T. Itou, *J. Power Sources* **2001**, 100, 107–116.
352. D. Ohms, M. Kohlhase, G. Benczúr-Ürmössy et al., *J. Power Sources* **2002**, 105, 127–133.
353. X. Y. Xiong, H. Van der Porten, M. Crappe, *Electrochim. Acta* **1996**, 41, 1267–1275.
354. J. P. Diard, B. Le Gorrec, C. Montella et al., *Electrochim. Acta* **1997**, 42, 3417–3420.
355. J. P. Diard, B. Le Gorrec, C. Montella, *J. Power Sources* **1998**, 70, 78–84.
356. A. Hammouche, E. Karden, R. W. De Doncker, *J. Power Sources* **2004**, 127, 105–111.
357. F. Huet, *J. Power Sources* **1998**, 70, 59–69.

358. S. Rodrigues, N. Munichandraiah, A. K. Shukla, *J. Power Sources* **2000**, *87*, 12–20.
359. W. S. Kruijt, H. J. Bergveld, P. H. L. Notten, *J. Electrochem. Soc.* **1998**, *145*, 3764–3773.
360. P. H. L. Notten, W. S. Kruijt, H. J. Bergveld, *J. Electrochem. Soc.* **1998**, *145*, 3774–3783.
361. M. Winter, R. J. Brodd, *Chem. Rev.* **2004**, *104*, 4245–4269.
362. U. Köhler, C. Antonius, P. Bäuerlein, *J. Power Sources* **2004**, *127*, 45–52.
363. J. K. Dunnick, B. A. Flower, in *Cadmium in Handbook on Toxicity of Inorganic Compounds*, (Eds.: H. G. Seiler, H. Sipel, M. Dekker), New York, 1988, Chapter 14.
364. H. Tsukube, *Talanta* **1993**, *40*, 1313–1324.
365. S. K. Srivastava, V. K. Gupta, S. Jain, *Electroanalysis* **1996**, *8*, 938–940.
366. V. K. Gupta, P. Kumar, R. Mangla, *Electroanalysis* **2000**, *12*, 752–756.
367. V. K. Gupta, P. Kumar, *Anal. Chim. Acta* **1999**, *389*, 205–212.
368. V. K. Gupta, S. Chandra, R. Mangla, *Electrochim. Acta* **2002**, *47*, 1579–1586.
369. A. K. Singh, P. Saxena, R. Singh, *Anal. Sci.* **2005**, *21*, 179–181.
370. A. Panwar, S. Baniwal, C. L. Sharma et al., *Fresenius' J. Anal. Chem.* **2000**, *368*, 768–772.
371. M. Javanbakht, A. Shabani-Kia, M. R. Darvich et al., *Anal. Chim. Acta* **2000**, *408*, 75–81.
372. M. Shamsipur, M. H. Mashhadizadeh, *Talanta* **2001**, *53*, 1065–1071.
373. K. C. Gupta, M. J. D'Arc, *Electroanalysis* **2000**, *12*, 1408–1413.
374. K. C. Gupta, M. J. D'Arc, *Talanta* **2000**, *52*, 1087–1103.
375. L. Prodi, M. Montalti, N. Zaccheroni et al., *Tetrahedron Lett.* **2001**, *42*, 2941–2944.
376. C. Wardak, B. Marczevska, *Chem. Anal. (Warsaw)* **2004**, *49*, 497–508.
377. C. Wardak, B. Marczevska, J. Lenik, *Desalination* **2004**, *163*, 69–75.
378. M. A. Pinos, J. E. Shaff, L. V. Kochian et al., *Electroanalysis* **1998**, *10*, 937–941.
379. J. Wang, B. M. Tian, J. Y. Wang, *Anal. Commun.* **1998**, *35*, 241–243.
380. U. Siemeling, B. Neumann, H. G. Stammeler et al., *Z. Anorg. Allg. Chem.* **2002**, *628*, 2315–2320.
381. M. M. Ardakani, M. Salvati-Niassari, A. Sadeghi, *New J. Chem.* **2004**, *28*, 595–599.
382. M. R. Ganjali, T. Poursaberi, F. Basiripour et al., *Fresenius' J. Anal. Chem.* **2001**, *370*, 1091–1095.
383. M. N. Abbas, E. Zahran, *J. Electroanal. Chem.* **2005**, *576*, 205–213.
384. Y. G. Vlasov, E. A. Bychkov, A. D. Safarov et al., *Zh. Anal. Khim.* **1985**, *40*, 1438–1446.
385. R. D. Tsingarelli, I. P. Nikolenko, A. F. Radchenko et al., *Zh. Anal. Khim.* **1986**, *41*, 449–452.
386. O. P. Ryabushko, A. T. Pilipenko, Yu. S. Savin, L. A. Batkovskaya, *Ukr. Khim. Zh.* **1990**, *56*, 263–267.
387. S. Ito, Y. Asano, H. Wada, *Talanta* **1997**, *44*, 697–704.
388. Y. G. Mourzina, M. J. Schöning, J. Schubert et al., *Anal. Chim. Acta* **2001**, *433*, 103–110.
389. Y. Umezawa, *Handbook of Ion-Selective Electrodes: Selectivity Coefficients*, CRC Press, Boca Raton, 1990.
390. P. Bühlmann, E. Pretsch, E. Bakker, *Chem. Rev.* **1998**, *98*, 1593–1687.
391. E. Bakker, P. Bühlmann, E. Pretsch, *Electroanalysis* **1999**, *11*, 915–933.
392. E. Bakker, *J. Electrochem. Soc.* **1996**, *143*, L83–L85.
393. E. Bakker, *Anal. Chem.* **1997**, *69*, 1061–1069.
394. T. Sokalski, A. Ceresa, T. Zwickl et al., *J. Am. Chem. Soc.* **1997**, *119*, 11347–11348.
395. T. Sokalski, A. Ceresa, M. Fibbioli et al., *Anal. Chem.* **1999**, *71*, 1210–1214.
396. W. Qin, T. Zwickl, E. Pretsch, *Anal. Chem.* **2000**, *72*, 3236–3240.
397. S. Mathison, E. Bakker, *Anal. Chem.* **1998**, *70*, 303–309.
398. E. Bakker, E. Pretsch, *Trends Anal. Chem.* **2005**, *24*, 199–207.
399. A. C. Ion, E. Bakker, E. Pretsch, *Anal. Chim. Acta* **2001**, *440*, 71–79.
400. Y. Stozhko, G. N. Lipunova, T. I. Maslakova et al., *J. Anal. Chem.* **2004**, *59*, 179–184.
401. S. S. Hu, K. B. Wu, H. C. Yi et al., *Fresenius' J. Anal. Chem.* **2001**, *370*, 101–103.
402. G. Marino, M. F. Bergamini, M. F. S. Teixeira et al., *Talanta* **2003**, *59*, 1021–1028.
403. C. G. Hu, K. B. Wu, X. Dai et al., *Talanta* **2003**, *60*, 17–24.
404. S. Yuan, W. H. Chen, S. H. Hu, *Talanta* **2004**, *64*, 922–928.
405. K. C. Honeychurch, J. P. Hart, D. C. Cowell et al., *Electroanalysis* **2002**, *14*, 177–185.
406. W. S. Huang, C. H. Yang, S. H. Zhang, *Chinese J. Anal. Chem.* **2002**, *30*, 1367–1370.

407. E. Chow, D. B. Hibbert, J. J. Gooding, *Electrochem. Commun.* **2005**, 7, 101–106.
408. G. Roa, M. T. Ramirez-Silva, M. A. Romero-Romo et al., *Anal. Bioanal. Chem.* **2003**, 377, 763–769.
409. H. Düssel, A. Dostal, F. Scholz, *Fresenius' J. Anal. Chem.* **1996**, 355, 21–28.
410. A. L. Bo, X. Q. Lin, *Chinese J. Anal. Chem.* **1999**, 27, 392–397.
411. M. Hermes, M. Lovrić, M. Hartl et al., *J. Electroanal. Chem.* **2001**, 501, 193–204.
412. N. F. Zakharchuk, N. Naumov, R. Stösser et al., *J. Solid State Electrochem.* **1999**, 3, 264–276.

24.3**Electrochemistry of Lead**

24.3.1	Double-layer Properties of Pb Electrodes	805
24.3.1.1	Properties of Solid Electrodes	805
24.3.1.2	Properties of Liquid Electrodes	805
24.3.1.3	Adsorption on Solid Electrodes	806
24.3.2	Electrochemical Properties and Kinetics of Lead and Lead Compounds	806
24.3.2.1	Pb(II)/Pb(Hg) System	806
24.3.2.1.1	Studies in the Presence of Inhibitors and Organic Solvents	806
24.3.2.1.2	Other Phenomena	807
24.3.2.2	Complexes of Pb(II) and Related Phenomena	808
24.3.2.3	Electrochemical Processes of Liquid Lead in Molten Salts	808
24.3.2.4	Voltammetric Behavior of Lead	808
24.3.2.4.1	Sulfuric Acid Solutions	808
24.3.2.4.2	Nitric Acid Solutions	812
24.3.2.4.3	Phosphoric Acid Solutions	812
24.3.2.4.4	Sodium Hydroxide Solutions	812
24.3.2.4.5	Different Salt Solutions	814
24.3.2.5	Voltammetric Behavior of Several Lead Compounds	815
24.3.2.5.1	PbO	815
24.3.2.5.2	PbO ₂	816
24.3.2.5.3	Pb chalcogenides	816
24.3.3	Electrodeposition and Underpotential Deposition of Lead on Solid Substrates	817
24.3.3.1	Platinum	817
24.3.3.2	Gold	818
24.3.3.3	Silver	820
24.3.3.4	Copper	821
24.3.3.5	Carbon	821
24.3.3.6	Silicon	822
24.3.3.7	Germanium	822
24.3.3.8	Other Materials	822
24.3.4	Corrosion and Passivation	823

24.3.5	Applied Electrochemistry	825
24.3.5.1	Lead-acid Batteries	825
24.3.5.2	Electrocatalytic Properties	826
24.3.5.2.1	Pb	826
24.3.5.2.2	PbO ₂	827
24.3.5.3	Electrochemical Sensors	828
24.3.5.3.1	Potentiometric Sensors	828
24.3.5.3.2	Amperometric/Voltammetric Sensors	828
	References	829

24.3.1

Double-layer Properties of Pb Electrodes

24.3.1.1 Properties of Solid Electrodes

The main properties of the double layer of solid lead electrodes have been already described in the Encyclopedia [1]. New achievements in this field have been the subject of reviews [for example [2–6]. Some of the new results relate to impedance of polycrystalline Pb electrodes in aqueous [7–9] and nonaqueous solvents (references in [3, 6]). Special attention has been paid to chemically and electrochemically polished polycrystalline electrodes, mainly in aqueous [10–12] and methanolic [13] fluoride solutions.

The influence of the single crystal face of the Pb electrode on zero charge potential has been analyzed. The difference between these potentials is within the range of 60 mV [8] and the potential value increases with lowering atomic density [11]. The increase of the inner layer capacitance at zero charge in the sequence $\text{Pb}(100) \leq \text{Pb}(110) \leq \text{Pb}(112) < \text{polycrystalline Pb} < \text{Pb}(111)$ has been explained by increasing hydrophilicity of the surface [6, 11].

A solid drop Pb electrode with additionally remelted surface has been studied in KF and NaClO₄ solutions; the

minimum capacitance versus potential curve is practically independent of the electrolyte solution concentration [6].

24.3.1.2 Properties of Liquid Electrodes

Double-layer properties as capacitance and potential of zero charge obtained for both single crystal and polycrystalline Pb electrodes differ significantly, depending also on the pretreatment procedure [6]. Therefore, some studies concern liquid electrodes containing lead. Liquid lead in molten NaX–KX (X = Cl, Br, I) eutectic mixtures has been studied using electrochemical impedance spectroscopy [14]. The double-layer capacitance at the rest potential is of the order of 0.9, 0.6, and 0.2 $\mu\text{F cm}^{-2}$, for Cl[–], Br[–], and I[–] melts, respectively. These values are much lower than those obtained previously, in the sixties of the twentieth century, because of the improvement of experimental technique and detailed studies on the influence of frequency on the measured parameters. The measured capacitance is affected by reduction of alkali metal cations to alloy with Pb (at negative potentials), substitution of metal cations by anions for more positive potentials, and also anodic dissolution of lead at highly positive potentials. An influence of possible spontaneous dissolution

of lead electrode in molten alkali metal halides has also been considered.

Double-layer properties in aqueous, propylene carbonate and formamide solutions have been studied at room temperature for liquid Ga–Pb alloy (0.06 atom % of Pb) [15], as a model of Pb electrode with renewable surface. The electrode behaves as an ideally polarizable electrode in a wide potential range, and its capacitance is intermediate between that of Ga and Hg electrodes and is independent of the solvent. This electrode is much less lipophilic than Ga. Adsorption of anions on this electrode increases in the sequence $-\text{BF}_4^- = \text{SO}_4^{2-} < \text{Cl}^- < \text{Br}^- < \text{I}^-$.

24.3.1.3 Adsorption on Solid Electrodes

Adsorption studies in $(\text{C}_4\text{H}_9)_4\text{NI}$ solution, showing splitting of adsorption–desorption peaks, point to energetic inhomogeneity of the surface [6]. This inhomogeneity has been analyzed using the concept of constant phase element affecting the impedance spectra [9]. It has been found that incomplete reduction of the Pb surface lowers the double-layer capacitance and increases the surface inhomogeneity [6]. Compact layer capacity has been found to be in quantitative agreement with that for Hg at negative charges.

The influence of organic additives on the properties of lead electrodes has been studied from the viewpoint of application in lead-acid batteries, to improve the properties of the negative electrode. These materials can be classified into two types [16]: inhibitors and expanders. Inhibitors increase the overpotential for the hydrogen evolution reaction and lower the self-discharge of the negative plate. Expanders are used to restrain the surface area shrinkage of electrode active material during cycling and to inhibit the passivation of the negative plate. The inhibitor

and expander role of different surfactants in H_2SO_4 solutions has been studied – of the cationic type (cetyltrimethyl ammonium bromide), anionic type (sodium dodecyl benzenesulfonate, sodium dodecyl sulfate, sodium lignosulfonate, amine perfluoroalkylsulfonates), and some non-ionic surfactants [16–20]. The influence of adsorbed lignin, an important additive for the negative electrode in lead-acid batteries, has been studied using the electrochemical atomic force microscopy (AFM) method [21, 22]. The presence of surfactants usually moves the hydrogen evolution potential to more negative values; however, some perfluorinated substances exert an opposite or negligible effect [16]. On the other hand, only nonionic surfactants can raise the discharge capacity of the negative electrode of lead-acid batteries [16]. Perfluorinated surfactants are more resistant to oxidation.

Specifically adsorbed inorganic ions as halide anions [23] and organic substances can inhibit corrosion (see e.g. [24]).

24.3.2

Electrochemical Properties and Kinetics of Lead and Lead Compounds

24.3.2.1 Pb(II)/Pb(Hg) System

This system with lead amalgam is especially suitable to determine thermodynamic and electrochemical kinetic data related to Pb(II) owing to renewability of the mercury electrode surface.

24.3.2.1.1 Studies in the Presence of Inhibitors and Organic Solvents

The charge-transfer rate constant for the Pb(II)/Pb(Hg) couple in aqueous solution is very high [1]; therefore, the kinetics of electrode processes of this system has been

studied in the presence of inhibitors adsorbed on the electrode surface – aliphatic alcohols [25, 26], amines [27], or complexes with organic ligands [28]. In the case of full surface coverage by an inhibitor, the logarithm of standard rate constant is linearly dependent on the logarithm of bulk inhibitor concentration with the slope determined by the so-called steric factor, which represents the ratio of surface area occupied by the activated complex and inhibitor molecules, both for noncomplexed ions [29] and Pb(II) complexes [30]. This relation also discloses stereochemical information, concerning orientation of adsorbed molecules, as confirmed on the basis of quantum chemical calculations [31].

Studies in nonaqueous and aqueous organic mixed solvents have shown the influence of two factors on charge-transfer kinetics – adsorption of the organic component of the mixture and solvation of reactant ions [32–34]. Adsorption of the organic solvent on the electrode surface decreases the electrode reaction rate in a similar manner as in the case of adsorbed inhibitors, as discussed above. On the other hand, stronger solvation of metal cations results in lower charge-transfer rate. Both the solvation and activation energy of electrodeposition reactions in pure solvents, rise with increasing basicity of the solvent, expressed, for example, by donor number. A separate influence of adsorption and solvation on the electrode kinetics of the Pb(II)/Pb(Hg) couple has been shown for water–hexamethylphosphoramide mixed solvents [34]. Moreover, on the basis of formal potential values and electrochemical rate constants in mixed solvents, solvation numbers and reaction orders with respect to the organic solvent have been determined [35]. Half-wave potentials of

the Pb(II)/Pb(Hg) in numerous organic solvents have been presented [36].

Diffusion coefficients of Pb(II) determined in organic solvents – dimethylsulfoxide and hexamethylphosphoramide – are about 1 order of magnitude lower than in aqueous solutions [33, 34, 37].

24.3.2.1.2 Other Phenomena Interaction of metallic Pb in the mercury phase [38] and amalgam decomposition in alkaline medium [39] have also been discussed. Formation of anodic monolayer PbCO_3 or $\text{Pb}_3(\text{CO}_3)_2(\text{OH})_2$ on Pb(Hg), depending on pH, in carbonate or bicarbonate solutions, has been detected using electrochemical methods (chronoamperometry and linear sweep voltammetry) and powder X-ray diffractometry [40].

The Pb(II)/Pb(Hg) electrode process has been analyzed using digital simulation and the results have been compared with experiments carried out in aqueous sodium nitrate solutions applying convolution/deconvolution voltammetry to determine charge-transfer rate constants and transfer coefficients [41]. Principles of thin-layer anodic stripping voltammetry have been discussed and a model for the stripping step has been proposed. This model has been tested experimentally for amalgams of Cd and Pb [42]. Fast Fourier transform instrumentation has been shown to be advantageous, both in the analytical and kinetic applications of voltammetry, for example, on Cd and Pb redox systems [43]. Active/passive transition for the Pb(Hg)/ PbCl_2 system has been studied using digital simulation [44].

Pb(Hg) electrode in the presence of PbSO_4 and H_2SO_4 has been used in thermodynamic studies and equilibrium potential determination [45].

The Pb(II)/Pb(Hg) system has been studied under high-pressure conditions

[[46] and the references given therein). Pb dissolution process has not been found to be favored by increased pressure.

Surface tension of Pb amalgams in relation to the electronic structure of the metal and adsorption properties has been discussed [47].

24.3.2.2 Complexes of Pb(II) and Related Phenomena

Complexation equilibria and complexation processes have been studied mainly on mercury electrodes (see book [48]), for Pb(II) with, for example, oxalates, maleates, tartrates, citrates [49], phytochelatin [50], amino acids [51–57], carboxylic acids [53], cyclodextrins and their derivatives [58, 59], ferrocene derivatives [60], picolinic acid [61], sulfonic acids derivatives [62], fulvic like organic ligands/acids [63, 64], ligands involving cephalosporins [65], phthalocyanines [66], organic ligands giving pentagonal symmetry [67], or cryptands and other macrocyclic ligands (see reviews [68–70] and [71–77]). Complexation by other systems as dissolved organic matter from an estuarine sample [78], components of oxic and sulfidic waters [79] as well as red wines [80] have also been studied. The role of ligand adsorption in stripping voltammetry has been reviewed [81]. The Pb(II)/Pb(Hg) has been used as a redox probe to study complexation processes between macrocyclic ligands and several cations competing with Pb²⁺ ions (e.g. [82]).

Electrochemical formation of Pb(II) complexes by anodic dissolution of lead [83–89] and studies on electrochemical properties of Pb(IV) complexes as well as organo-lead compounds have been reported [90, 91]. Electrogenenerated chemiluminescence of Pb(II)-bromide complexes has been described [92]. Reduction of lead to Zintl ions, such as Pb₉^{4–}, has been

observed in liquid ammonia, accompanied by intermetallic phase formation, as a result of alkali metal incorporation into lead [93, 94].

Complexation of Pb(II) by cyclic thioethers facilitates reversible interfacial transfer in ion-transfer voltammetry for the water–nitrobenzene and water–1,2-dichloroethane systems [95, 96].

24.3.2.3 Electrochemical Processes of Liquid Lead in Molten Salts

The oxidation/reduction processes of Pb(II) with formation of liquid Pb(0) have been studied in molten halides ([97, 98] and references given therein). Most authors have concluded that Pb(II) species are reduced to the metal in the course of the single two-electron process. PbO₂ has been found unstable because of the reduction by Cl[–] ions to Pb(II). On the other hand, in the presence of Zn(II), lead(II) oxide, PbO, transforms to Pb(II) with ZnO formation. In ZnCl₂–2NaCl melts, using a tungsten electrode, kinetic parameters of the charge-transfer reaction for the couple Pb(II)/Pb(0) at 450 °C have been determined, log k_s^0 and α values are equal to -4.3 ± 0.1 and 0.48 ± 0.06 , respectively [98]. The diffusion coefficient value for Pb(II) is $(7.5 \pm 0.7) \cdot 10^{-6} \text{ cm}^2 \text{ s}^{-1}$ [98]. The influence of electrolyte cation [99] and anion [100] on the kinetics of lead in molten halides has been studied.

24.3.2.4 Voltammetric Behavior of Lead

24.3.2.4.1 Sulfuric Acid Solutions Voltammetric properties of pure lead electrodes have been studied in different media, but owing to obvious applications in lead-acid batteries, most data relate to sulfuric acid solutions. Typically, voltammetric curves of lead, limited by hydrogen

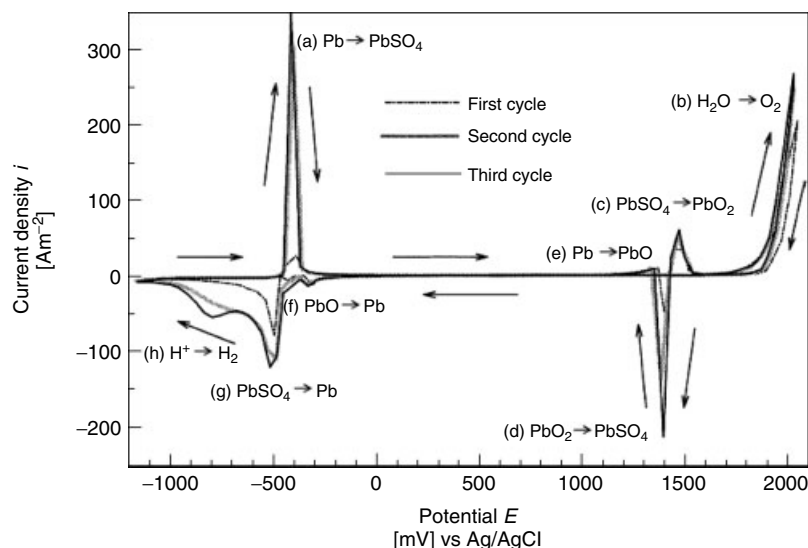


Fig. 1 Cyclic voltammetric curves of Pb electrode in 4.5 M H_2SO_4 solution [103].

and oxygen evolution processes, exhibit several peaks, for example [101, 102]. An example is presented in Fig. 1 [103] with four anodic peaks:

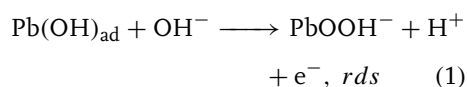
- (a) oxidation of Pb to PbSO_4 ,
 - (b) oxygen evolution,
 - (c) oxidation of PbSO_4 to PbO_2 (usually β form),
 - (e) oxidation of Pb to PbO ;
- and with four cathodic peaks:
- (d) reduction of PbO_2 to PbSO_4 ,
 - (f) reduction of PbO to Pb,
 - (g) reduction of PbSO_4 to Pb, and
 - (h) hydrogen evolution.

The inner PbO layer is formed because of the impermeability of PbSO_4 layer for SO_4^{2-} ions; only Pb^{2+} , OH^- , and H^+ ions can transfer across this film. Thus, in the course of anodic scan, H^+ ions can flow from the reaction site into solution, resulting in alkaline medium formation near the electrode surface. With increasing H_2SO_4 concentration, the lead sulfate layer is more compact and electrolyte ions

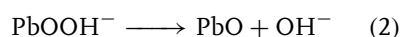
access to the inside layer is hindered [104, 105]. A characteristic, and not quite a clear feature, is the presence of a small anodic peak (*anodic excursion* peak [101, 106, 107]) recorded in the course of the cathodic scan, if the electrode potential is cycled in a potential range limited by hydrogen and oxygen evolutions. This peak is located either before [107, 108] or after [101, 106] the reduction peak (d), in low or high H_2SO_4 concentration in solution, respectively [102, 109, 110]. The presence of *anodic excursion* peak has been explained in different ways (see literature review [110]). The most probable explanation is based on the large increase of molar volume accompanying reduction peak (d) – from $25 \text{ cm}^3 \text{ mol}^{-1}$ for $\beta\text{-PbO}_2$ to $48 \text{ cm}^3 \text{ mol}^{-1}$ for PbSO_4 [101], resulting in cracks on the electrode surface. Thus, the metallic lead surface, which can be oxidized by sulfuric acid, is exposed. Water oxidation by Pb(III) , generated during surface reduction of PbO_2 has also been postulated [106, 107]. The electrochemical

properties of Pb in sulfuric acid solutions have been studied and described mainly by Pavlov (see e.g. [111, 112] and references given therein), some mathematical models concerning nucleation and growth of solid phases have been proposed, for example [113].

However, the process of Pb oxidation/reduction is more complicated because of the presence of different Pb oxides (as e.g. $3\text{PbO} \cdot \text{H}_2\text{O}$, $\alpha\text{-PbO}_2$, and also non-stoichiometric oxides) on the surface [111, 114] as electrochemical impedance spectroscopy [115], photocurrent [116], or grazing incidence X-ray diffraction studies [117] show. Soluble Pb(II) and Pb(IV) species have also been revealed on the basis of measurements obtained with the use of rotating ring-disk electrode [118]. The size and amount of PbSO_4 crystals [104, 105] and the charge-transfer rate [119] is dependent on acid concentration. Current transient experiments have pointed to two-dimensional nucleation and growth of PbSO_4 , electrodisolution of lead electrode in the zones not covered by PbSO_4 as well as passive layer growth due to lead electrodisolution, and Pb(II) transport across the PbSO_4 layer [120, 121]. Proposed mechanism of PbO formation points to intermediate $\text{Pb(OH)}_{\text{ad}}$ oxidation to PbOOH^-



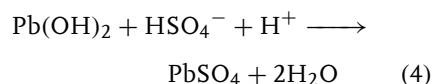
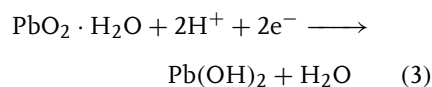
and then the final product is obtained [115]:



Diffusion of O^{2-} ions has also been taken into account as rate determining step (rds) and the value of their solid phase diffusion coefficient has been determined as $2.4 \times 10^{-15} \text{ cm}^2 \text{ s}^{-1}$ [122].

Current transient studies have also demonstrated instantaneous nucleation and two-dimensional growth mechanism of $\beta\text{-PbO}_2$ [123] and a higher rate of reduction of small PbSO_4 crystals, compared to greater ones [124].

On the basis of electrochemical results, scanning electron microscopy (SEM) images and X-ray diffraction analysis, Pavlov et al. have discussed the influence of sulfuric acid concentration on the mechanism and rate of $\text{Pb-PbSO}_4\text{-PbO}_2$ transformations [125]. Three acid concentration ranges have been distinguished. The first is active H_2SO_4 concentration range (from 0.5 to 5 M), where the concentration of HSO_4^- is the highest and $\beta\text{-PbO}_2$ phase is formed. This phase is reached in hydrated gel areas (PbO(OH)_2), which are ionically (H^+) and electronically conductive, necessary for the electrochemical process to occur, for example, for hydrated PbO_2 reduction:



Concentrations higher than 5 M correspond to a passive high concentration region, where $\alpha\text{-PbO}_2$ crystals are formed. In passive, low concentration region (H_2SO_4 concentration lower than 0.5 M), the content of $\alpha\text{-PbO}_2$ is also high. In both passive regions, the amount of gel zones is low, resulting in low electroactivity. For very low H_2SO_4 concentrations (not buffered), the changes in the potential can result in the formation of a diffusion layer at the PbO_2 surface with different pH, which can considerably affect the formation of complexes.

Formation of $3\text{PbO} \cdot \text{PbSO}_4 \cdot \text{H}_2\text{O}$ depends on the properties of PbSO_4 passivation layer. When the anodic film is passivated significantly, the diffusion of ions across the PbSO_4 becomes a rate-determining step [126]. After reactivation of the passive layer, the rate is controlled by diffusion-limited nucleation and growth. The process is promoted by decreasing acid concentration and by the presence of small amounts of Sb in alloy with Pb.

The hydrogen and oxygen evolution processes on Pb are affected by other metal additions to Pb, for example, addition of bismuth enhances both the hydrogen and oxygen evolution [127], while addition of silver inhibits hydrogen ions reduction [128].

In the presence of Pb(II) ions in sulfuric acid, potential oscillations have been observed for galvanostatic oxidation of hydrogen on platinum electrode [129]. This behavior has been attributed to adsorption/oxidation/desorption processes of lead on the platinum surface. Lead at high values of coverage is oxidized to insoluble PbSO_4 , which blocks the Pt surface.

Oxidation/reduction of Pb electrode has been studied using in situ spectroscopic techniques – Raman [114, 130–132], fourier transform infrared (FTIR) [133–135], Auger [136], and photocurrent spectroscopy [131, 137–141]. Ellipsometric studies underlined nonuniform PbSO_4 film growth; a dissolution–precipitation mechanism with nucleation and three-dimensional growth has been proposed as a result of large oversaturation of Pb(II) ionic species [142]

and formation of thin and flat PbO_2 layers [143]. In situ studies using electrochemical quartz crystal microbalance (EQCM) under galvanostatic conditions have confirmed the oxidation of Pb to PbSO_4 at low current densities and transformation of PbSO_4 to PbO_2 at higher current densities [103]. AFM studies, coupled with X-ray photoelectron spectroscopy (XPS) and X-ray diffraction (XRD) measurements give better insight into the PbSO_4 and PbO_2 structure details and have pointed to dissolution–precipitation mechanism of PbSO_4 formation [144]. Figure 2 presents AFM images of Pb electrode hold at reduction or oxidation

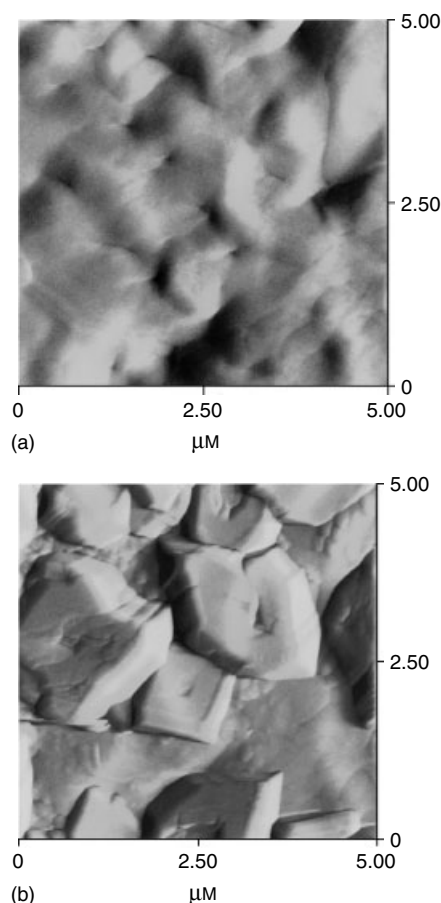


Fig. 2 AFM images of lead surface in sulfuric acid (density: 1.25 g cm^{-3}) after holding: (a) for 2 min at reducing potential -1050 mV , (b) for 6 min at oxidizing potential -1035 mV versus $\text{Hg/Hg}_2\text{SO}_4$ [145].

potential, showing the structure of metallic lead or PbSO_4 , respectively [145]. On the basis of AFM studies under potentiostatic conditions, a new mechanism of “sulfation” reaction has also been proposed [145]. It has been shown that the lead surface is covered with a lead oxide film and the lead sulfate crystals grow up on the surface. Lead sulfate crystals formed by electrochemical reaction have been found rougher than those obtained by a chemical reaction and thus, chemically more active. Therefore, during longer standing, lead sulfate recrystallizes and a new, chemically obtained PbSO_4 is formed of lower activity. This results in lower charge storage ability in lead-acid batteries. An electrochemical method to reactivate the “sulfated” lead electrode has been proposed [102].

Voltammetric experiments have revealed that lead oxidation is a fast reaction and thus, PbSO_4 deposition occurs by nucleation in supersaturated solution of Pb^{2+} , followed by the growth process. The reduction process is slower because of the slow dissolution of PbSO_4 . The crystal size becomes smaller when the potential scan rate is fast or the electrolyte concentration is high [146]. Other AFM experiments have been described elsewhere [21, 22]. Electrochemical atomic force microscopy (EC-AFM) potentiostatic studies have also been carried out at $\text{Pb}(100)$ and $\text{Pb}(111)$ single crystals in 0.05 M H_2SO_4 solutions [147]. The top faces of PbSO_4 crystals formed on $\text{Pb}(100)$ and $\text{Pb}(111)$ have been found to be $\text{PbSO}_4(001)$ and $\text{PbSO}_4(100)$, respectively. The comparison of voltammetric curves for $\text{Pb}(100)$ and $\text{Pb}(111)$ and AFM image is presented in Fig. 3 [147].

The effect of immobilizing the electrolyte using sodium silicate as thixotropic agent on electrochemical properties of lead in sulfuric acid has been described [148].

24.3.2.4.2 Nitric Acid Solutions The voltammogram of Pb in nitric acid shows two well-defined anodic peaks (first peak – PbO and lead nitrate formation, and second peak – PbO_2 deposition) in the course of the positive scan [149]. In the reverse scan, either a wide plateau followed by a cathodic peak at very negative potentials or two cathodic peaks have been observed [150]. The inhibition of Pb dissolution process in more concentrated HNO_3 results from the presence of a protective PbO_2 layer [149]. Successive cycling results in increasing current due to increasing electrode surface area by deposited PbO_2 [150].

24.3.2.4.3 Phosphoric Acid Solutions In phosphoric acid (pure liquid or concentrated aqueous solution, 12 and 6 M), a pair of peaks has been recorded corresponding to the redox couple PbHPO_4/Pb as confirmed by XRD studies and SEM photographs [151]. The presence of chloride or bromide ions also results in precipitation of $\text{Pb}_5(\text{PO}_4)_3\text{Cl}$ and $\text{Pb}_5(\text{PO}_4)_3\text{Br}$, respectively, while in the presence of iodide ions PbI_2 is formed. Addition of H_3PO_4 to H_2SO_4 , changes the voltammetric behavior (references in [151] and [152]). The lead phosphate formation blocks the lead surface oxidation to PbO_2 . For higher H_3PO_4 concentration (5 M), the *anodic excursion* peak is visible on voltammograms as in H_2SO_4 solutions, located after PbO_2 reduction peak [152].

24.3.2.4.4 Sodium Hydroxide Solutions In NaOH solutions, two main lead anodic peaks owing to the formation of PbO and PbO_2 have been recorded, followed by oxygen evolution ([153–156] and the references given therein). In the step preceding PbO production, the formation of

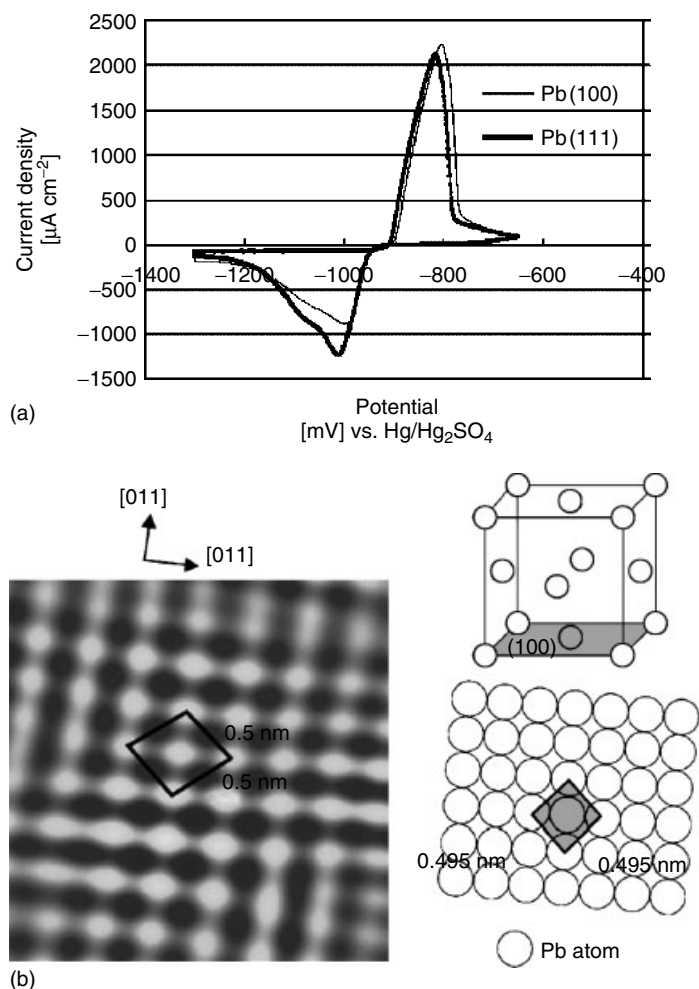


Fig. 3 (a) Cyclic voltammetric curves of Pb(100) and Pb(111) in 50 mM H₂SO₄ solution, scan rate: 1 mV s⁻¹. (b) EC-AFM high resolution image (3 nm × 3 nm) on Pb(100) in 50 mM H₂SO₄ solution at -1040 mV versus Hg/Hg₂SO₄ and schematic illustration of the image [147].

adsorbed PbOH or Pb(OH)₂ can occur, while PbO₂ formation has been assumed to be preceded by Pb₃O₄ production; however, this has not been unequivocally confirmed. The electrochemical processes are accompanied by partial dissolution of PbO and PbO₂ to HPbO₂⁻ and PbO₃²⁻, respectively. A longer conditioning of PbO film results in slow dissolution to HPbO₂⁻.

Addition of anions to NaOH solution affects the anodic film formation kinetics and morphology. These films are mainly α -PbO, with the exception of chloride ions solution, where β -PbO is formed [157]. Anodic oxidation of Pb electrode in hot alkaline solution (containing NaOH) facilitates selective growth of α -PbO, β -PbO, and PbO_{2-x} ($x = 0-1$) phases, depending

on the applied potential, as confirmed by XPS spectroscopy [158].

24.3.2.4.5 Different Salt Solutions In alkaline Na_2HPO_4 solutions, anodization of lead results in the formation of several peaks observed at a potential lower than that of oxygen evolution, Fig. 4 [159]. On the basis of cyclic voltammetry and X-rays surface analysis, the shoulder A

and peak A have been assigned to Pb oxidation to $\text{Pb}(\text{OH})_2$ (accompanied by possible dehydration to PbO). At higher anodic potentials, two-dimensional nucleation and spreading of PbO (peak B) followed by three-dimensional nucleation and growth of PbO (region C) and then PbO_2 formation (D) occurs. Figure 4 also presents a schematic illustration of the anodic process.

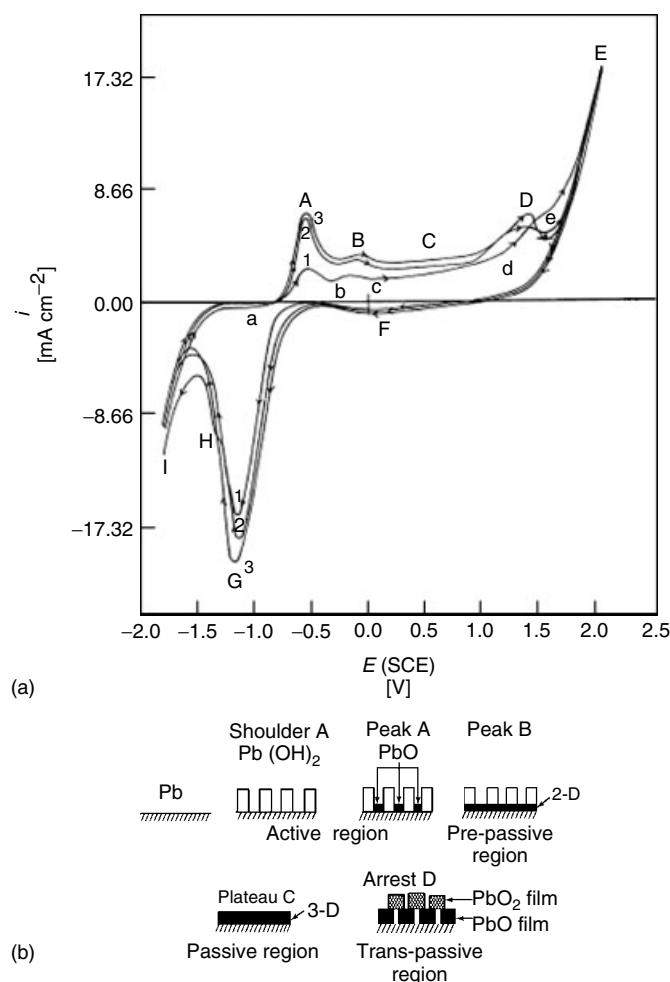


Fig. 4 Three successive sweeps of Pb electrode in 0.10 M Na_2HPO_4 solutions at scan rate of 25 mV s^{-1} (a). Schematic simplified illustration of films formation on Pb in Na_2HPO_4 solution (b) [159].

In the cathodic scan, reduction of PbO_2 (peak F), reduction of PbO (peak G), and reduction of Pb(OH)_2 (shoulder H) can be observed on the voltammetric curve.

A more complicated pattern is recorded in Na_2SO_4 solutions [160, 161], where a behavior, typical for H_2SO_4 can also be observed. Additionally, some phenomena that are typical for alkaline solutions are visible as presence of soluble species HPbO_2^- [160, 162]. The voltammetric anodic oxidation is characterized by peaks of PbSO_4 , PbO , PbO_2 , and by the transformation of PbSO_4 to PbO_2 , as well as by the formation of intermediate oxides in the second and following scans. During reverse cathodic scan, peaks are formed, corresponding to the reduction of PbO_2 to PbSO_4 , PbO_2 to PbO and PbO with PbSO_4 to Pb , and finally PbH_2 formation is observed just before hydrogen evolution. In sulfuric acid solution containing sodium sulfate, an additional oxidation process has been recorded owing to the higher conductivity of lead sulfate in the presence of sodium ions [163].

Voltammetric characteristics of lead electrodes have also been studied in sodium borate solutions [164], where formation/dissolution of lead oxides can be accompanied by lead borate precipitation on the electrode.

24.3.2.5 Voltammetric Behavior of Several Lead Compounds

24.3.2.5.1 PbO PbO exists in two polymorphic forms – tetragonal α - PbO and orthorhombic β - PbO ; they are photosensitive substances. Basic electrochemical properties of PbO have been studied in acidic [105, 111], neutral [165,] and alkaline [153] media. In acidic solutions, the β - PbO formation is followed by transformation to α - PbO [166, 167]. In sulfuric acidic

solution, the α - PbO formation/dissolution is accompanied by processes involving lead sulfate. PbO growth rate has been found to be dependent on the migration of Pb^{2+} and OH^- ions into the oxide layer, as well as of H^+ ions into the PbSO_4 layer [104, 105]. PbO reduction process to Pb has been postulated to occur according to progressive nucleation and growth path [132, 168, 169], assisted with OH^- ion diffusion through the PbSO_4 layer [104]. With decreasing concentration of sulfuric acid, the structure of PbSO_4 layer becomes looser, facilitating mass transfer of H^+ and SO_4^{2-} ions. Therefore, in the cathodic voltammetric scan, the transformation of a part of α - PbO into basic lead sulfate or lead sulfate occurs [105], followed then by lead deposition. The reduction rate can be controlled by the nucleation and growth of metallic lead and OH^- ions diffusion across the PbSO_4 layer [105]. With decreasing sulfuric acid concentration, the reduction of tetragonal PbO to Pb changes from two- to three-dimensional progressive nucleation and growth [105]. A solid-state mechanism related to migration of O^{2-} anions has also been postulated [170]. Oxidation of lead-tin alloy results in PbO of increased conductivity compared to pure PbO [171].

PbO is more stable in alkaline solutions. Anodic oxidation of Pb leads to the selective growth of β - PbO , which transforms into α - PbO in the course of prolonged polarization, as supported by X-ray diffraction studies and photoelectrochemical experiments [172]. In the presence of sulfate ions, simultaneous formation of basic lead sulfate with PbO has been observed, until the formation of $4\text{PbO} \cdot \text{PbSO}_4$. At higher potentials, the oxide film in sulfate ions solution has a strong (110) orientation with microporous structure. X-ray diffractometry and photocurrent measurements have confirmed the presence of

highly oriented (110) α -PbO phase, obtained in 0.05–0.5 M NaOH solutions, while the films obtained at higher NaOH concentrations exhibit submicrocrystalline or amorphous nature [155, 173]. In dilute solutions (0.01 M NaOH), the presence of β -PbO has also been detected. In neutral KCl solutions, X-ray diffraction [165] and AFM studies [174] show that the α -PbO reduction to Pb is an epitactic solid-state reaction occurring with conservation of the initial crystal orientation on the electrode surface. Dissolution of PbO in molten carbonates has been studied, from the point of view of materials stability in molten carbonate fuel cells [175].

24.3.2.5.2 PbO₂ PbO₂ has two crystallographic forms – orthorhombic α -PbO₂ and tetragonal β -PbO₂. PbO₂ has been electrochemically obtained on different substrates – platinum [176–178], gold [177, 179–181], nickel [182], glassy carbon [183, 184], vitreous carbon [185], titanium [180, 186–188], tin or indium-tin oxide [189, 190], stainless steel [188], titanium oxides [191], polystyrene templates enabling macroporous PbO₂ formation [189], and in acetonitrile solutions [192]. Nanostructured PbO₂ obtained by hydrolysis of Pb(CH₃COO)₄ has been found to exhibit high electrochemical activity [193]. The preparation and properties of lead dioxide electrodes have been reviewed [194–196]. α -PbO₂ has a more compact structure, is more stable mechanically, and can be obtained electrochemically in alkaline solutions, while β -PbO₂, which is thermodynamically stable, is obtained in acidic solutions and is more porous [177, 183, 197]. The morphology of PbO₂ depends on temperature, solution composition (e.g. [182, 186, 198]), and applied current density. Lower current density leads to β -PbO₂ deposition [182].

The mechanism of nucleation and growth of PbO₂ in H₂SO₄ has been described in Ref. 199 and references cited there. In sulfuric acid solutions, the phase composition (α - and β -PbO₂ content, determined on the basis of X-ray diffraction) and structure depend on many factors [196, 200, 201], as well as on the time duration of continuous cycling. The amount of β -PbO₂ phase increases in the cycling process [201, 202]. Properties of PbO₂ have also been studied in perchlorate [179, 202] and HNO₃ solutions (e.g. [150, 178]). The lead dioxide that is obtained is a non-stoichiometric compound, for example, PbO_{2- δ} · *n*H₂O [203], and more complex formulae have also been proposed. Influence on PbO₂ properties by doping with Bi [204], Fe [205], and Co [206] has been analyzed.

EC-AFM studies have shown that the two-step reduction process of lead dioxide is the dissolution process of PbO₂ and the deposition process of PbSO₄ crystals after saturation of the electrolyte with lead ions [207]. Two reduction peaks of PbO₂ can be ascribed to the partial reduction of larger and smaller crystals of electrodeposited PbO₂ [196]. Other mechanisms such as “hydrogen loss” [208] or “proton–electron mechanism” in gel zones of PbO₂ in all-solid-state systems [209] have also been discussed. Cathodic reduction of PbO₂ in alkaline media has been postulated to proceed with the formation of soluble PbO₃²⁻ and then HPbO₂⁻ [154].

24.3.2.5.3 Pb chalcogenides PbS is an important semiconductor material, which can find application in photoelectric devices owing to its low-band gap energy, depending on the size of PbS particles (0.41 eV for bulk PbS). Methods of PbS synthesis have been summarized

in, for example [210], and electrochemical deposition of PbS has been described in Refs 211–215. Using electrochemical atomic layer epitaxy, underpotential deposition (UPD) growth of each element (Pb and S) follows layer-by-layer, forming a cubic rock salt crystal structure with (200) plane parallel to the Au(111) substrate surface [210]. The obtained PbS film shows anodic photocurrents. Nanocrystals of PbS have also been obtained using electrochemical methods [214, 216]. Electrochemical properties of synthesized and natural PbS have been studied in aqueous solutions using electrochemical methods [217–220], FTIR-spectroelectrochemical methods [221–225], and synchrotron radiation excited photoelectron spectroscopy [226]. One of the main products of PbS oxidation, involving holes, has been found to be $\text{Pb}(\text{OH})_2$ [221]. Analytical applications of PbS nanoparticles as oligonucleotides labels for electrochemical stripping detection of DNA hybridization have been reported [227].

Electrochemical deposition and electrochemical properties of other Pb chalcogenides – PbSe [228–233], PbTe [234, 235], and mixed $\text{PbSe}_{1-x}\text{Te}_x$ [236–238] have also been studied.

24.3.3

Electrodeposition and Underpotential Deposition of Lead on Solid Substrates

Studies on lead electrodeposition on conducting solid substrates are related mainly to electrocatalysis, searching for alternative collectors/grids for lead-acid batteries, as well as for removing Pb(II) ions from aqueous solutions and stripping for analytical purposes.

An important group of works relates to problems of UPD. Processes of lead

electrodeposition are presented systematically depending on the substrate material.

24.3.3.1 **Platinum**

Voltammetric behavior of UPD of Pb has been studied on polycrystalline Pt electrodes and on defined Pt faces [239–241]. Earlier works have pointed to irreversible adsorption of lead and anionic species on Pt(111) [242, 243]. Ex situ XPS studies have revealed adsorption of Pb and Pb^{2+} on Pt(111) surface [244], and thermal properties of emersed adlayers have been studied [245]. UPD on Pt(111), using rotating ring-disk electrode in perchloric acid solutions [246], has pointed to two-step process of Pb deposition in the presence of adsorbed OH^- ions and desorption of adsorbed OH^- concurrent with Pb deposition. Similar studies in the presence of bromide ions have shown competitive influence of anion adsorption [247], since deposition of Pb adatoms is associated with desorption of bromide ions. Pb UPD process on Pt(111) in mixed solutions of perchloric and sulfuric acid has shown a large influence of sulfuric acid addition, and adsorption of Pb has been found on the surface already covered by HSO_4^- or SO_4^{2-} anions [248]. The influence of CO adsorption on Pb UPD process has also been studied [249]. On Pt(100) face, in perchloric acid, deposition of Pb adatoms is accompanied by displacement of adsorbed OH^- anions [250], and in the presence of bromide ions, these anions are desorbed by Pb adatoms. Thus, the potential range of a closely packed monolayer is shifted to lower values [250]. Scanning tunneling microscopy (STM) studies on Pt(001) face have shown Pb islands covering the entire Pt surface [251] but with no long range order in the surface plane, as confirmed by in situ X-ray diffraction studies [252]. The presence of strongly adsorbed Br at

step edges on the Pt(001) surface and the competitive nature of Pb–Br interactions result in a rapid exchange of Pb and Br on the Pt terraces. Thus, Pb forms a strongly bonded $c(2 \times 2)$ adlayer. The role of electrode smoothness and potential scan rate at early stages of electrodeposition have been analyzed from the point of view of the deposit structure (presence of Pb–Pb and Pb–Pt domains) and its accompanying rearrangement/equilibration by surface diffusion of metal atoms [253].

24.3.3.2 Gold

Pb UPD on Au electrodes has been studied by numerous authors, using various classical electrochemical and optical methods (e.g. Refs 254–260 and references given therein), as well as using AFM [261] and STM techniques [262, 263]. Voltammetric depositions on Au single crystals have revealed complex peaks, which have been ascribed to different structures observed by low-energy electron diffraction (LEED) experiments [257]. A range of lead layer structures, changing with surface coverage of lead, with possible formation of AuPb_2 , has also been detected by LEED and Auger spectroscopy [264]. Pb UPD has been intensively studied on polycrystalline gold and defined $\text{Au}(h, k, l)$ planes [255–258], and comparison of voltammetric curves recorded on different planes has been discussed in [256]. Pb UPD process on different $\text{Au}(h, k, l)$ planes has been reviewed by Herrero et al. [265]. Owing to a large difference in the atomic sizes of gold and lead (lead atom is ca. 20% larger than gold), formation of incommensurate adlayers is favored (see [265] and references given therein). Alloy formation is not unequivocally confirmed [265]; its formation is suggested to occur only at edges and on defect sites.

The UPD process has been studied mainly on Au(111) plane [261, 262, 266–268]. Voltammetric curves exhibit a pair of peaks (splitting in two) and a series of irreversible peaks at higher underpotentials [265]. Splitting results from kinetics of the process, growth of lead deposited islands (at higher underpotentials), and coalescence process (at lower underpotentials) [263, 265]. The initial step of Pb UPD on Au(111) is a decoration of monoatomic steps. At higher coverages, the uncompleted Pb monolayer is relatively unstable owing to surface alloy formation. Then, two-dimensional Pb islands of hcp structure are observed. Stability of two-dimensional islands on Au(111) has been recently confirmed by atom dynamics simulation studies [269]. At high surface coverages in situ STM and AFM images point to compressed and rotated hcp structures of Pb [270]. An overview of processes occurring on Au(111) surface is presented in Table 1 [268].

Stability of lead monolayers [271] and a dependence of the Pb UPD layer structure on surface coverage have also been studied on Au(100) face [272]. A phase transition from an expanded Pb overlayer to compressed hcp structure has been considered [270]. A coupled process of gold and Pb UPD oxidation process on single crystal Au(110) has been studied using XPS method [273].

The process of Pb deposition depends on the presence of adsorbed species. On polycrystalline gold, in HClO_4 acid solutions, a combined quartz crystal microbalance and probe beam deflection methods have pointed to three stages of the process – (1) water molecules release from gold surface, (2) metal UPD associated with adsorbed OH^- ions replacement, followed by (3) water formation [274]. In the presence of adsorbed anions or organic

Tab. 1 Phenomena accompanying Pb UPD on Au(111) substrate [268]

<i>Scan direction</i>	<i>Potential range [ΔE/mV]</i>	<i>Description</i>
Cathodic	220–255	Growth at existing step edges
	235–250	First nuclei form, some unstable
	210–230	Stable nuclei and other islands grow and join
	195–215	Most rapid visible change
	170–190	Continued slow filling of plane
Anodic	190–225	Small islands shrink and disappear
	210–240	Terrace edges recede
	220–245	Appearance and growth of pits
	240–250	Most rapid visible change
	245–275	Slight continued shrinking of remaining islands

molecules, competition with Pb adatoms can occur [275–277]. Using EQCM, XPS, and time of flight secondary ion mass spectrometry [275, 276] the presence of adsorbed anions has been demonstrated. The deposition process involves reduction of both adsorbed lead complex with anions and lead(II) present in the electrolyte bulk. The PbCl_4^{2-} complex has been found to be adsorbed before the potential of its reduction to Pb. On the basis of voltammetric experiments, carried out at different temperatures, standard entropies of Pb adatoms have been evaluated [278]. These data point to surface mobility of Pb adatoms, significantly dependent on the solvent, where the deposition process occurs. Frumkin isotherm of Pb adsorption has been used to explain the shape of voltammetric peaks [279].

Spontaneously adsorbed monolayers possessing sulfonate terminal groups on gold electrodes can enhance the lead UPD current, for example [280], see also Chapter Electrochemistry of Gold (24.4) in the present book.

Surface stress measurements also reveal useful data concerning surface processes.

Changes in surface stress of Au(111) electrode during Pb UPD have been measured using the bending beam method [281, 282]. A maximal surface stress appears at the onset of UPD, corresponding to the formation of a completed incommensurate monolayer. The shape of surface stress versus cathodic charge for UPD has been explained by change in rotation angle of hexagonal close packed Pb layer. Coadsorption of chloride ions promotes the structural changes of the UPD lead. Studies on Pb deposition on gold colloids have pointed to similarity of the deposition process to that on bulk electrode [283].

In the oxide region of gold electrodes, residual lead can be present, resulting from irreversible adsorption, and presence of hydroxide species has been postulated [265]. Pb UPD on Au(111) has also been studied in selected organic solvents, mainly propylene carbonate [284]. Results similar to those in aqueous solutions have been obtained. Deposition of Pb on Au electrodes coated by silver has also been studied [285]. Depending on the silver layer thickness, results typical for Pb deposited on Au or Ag have been obtained.

24.3.3.3 Silver

Pb UPD on Ag(111) and Ag(100) has been studied using X-ray diffraction method, electrochemical impedance spectroscopy, and in situ scanning probe microscopy [272, 286–288]. This process has been reviewed in [265, 270], see Table 2. Both structure and voltammetric behavior are dependent on the Ag(*h, k, l*) plane [265, 289].

On Ag(111) in perchloric acid solutions, three pairs of voltammetric peaks have been observed, prior to bulk deposition [265]. The first and third peaks have been ascribed to adsorption at defect sites, the middle (the highest) peak represents the major deposition process, and it appears owing to the first-order phase transition. In the presence of adsorbing anions, owing to blocking effects, only a single peak representing deposition/stripping is observed. The deposited zero-valent lead layer has been found incommensurate with the silver substrate. Extended polarization of the electrode

induces transformation of the lead overlayer, also represented by changes of the voltammetric curves. STM studies have revealed the presence of hcp, which can change under the influence of extended polarization [290]. The influence of adsorbed Cl[−] ions results in narrowing of potential ranges corresponding to Pb adsorption [288]. Pb nanostructures have been observed using STM method [291]. Pb UPD on Ag(111) has also been studied in selected organic solvents [284]. Results similar to those observed in aqueous solutions have been obtained.

For Ag(100), the voltammetric curve exhibits two main pairs of peaks and a pair of smaller peaks at lower potentials [265]. The first peak has been ascribed to adsorption, while the second to filling of the remaining sites to a closely packed monolayer and a phase transition. Under conditions of extended polarization, a transformation occurs, similar to that in Ag(111). However, in contrast to Ag(111), this transformation relates to

Tab. 2 Phenomena accompanying Pb UPD on silver substrates [270]

Ag plane	Potential range [Δ <i>E</i> /mV]	Description
Ag(111)	150–250	Step decoration and formation of expanded 2D Pb _{ads} phase at terraces
	120–150	Formation of a condensed 2D hcp Pb _{ads} phase from an expanded 2D Pb _{ads} phase via first-order phase transition starting at steps
	0–120	Completion and compression of 2D hcp Pb _{ads} phase at terraces
Ag(100)	140–250	Step decoration and formation of expanded Ag(100)-c(2 × 2) Pb _{ads} structure at terraces
	100–140	Formation of a condensed 2D hcp Pb _{ads} phase from an expanded 2D Pb _{ads} phase via first-order phase transition starting at steps
	100–120	Formation and limited growth of 2D Pb _{ads} clusters on top of the first Pb _{ads} monolayer
	0–100	Completion and compression of the 2D hcp Pb _{ads} phase at terraces

the adsorption layer or the competitive adsorption of anions. A dependence of the Pb UPD layer structure on surface coverage has been studied on the Ag(100) face [272].

On Ag(110), three voltammetric peaks have also been observed [265], owing to adsorption, phase transformation, and deposition on the previously formed monolayer.

Frumkin isotherm of Pb adsorption has been used to explain the shape of voltammetric peaks on polycrystalline electrodes and on the polycrystalline gold surface [279].

Comparison of electrochemical data with Monte Carlo simulation of Pb UPD on Ag(111) has enabled discussion on mechanism details [292].

UPD process has also been studied on screen-printed silver electrodes using voltammetric techniques and scanning electron microscope analysis [293]. The relative occurrence of UPD and bulk Pb process has been dependent on the scan rate, with increasing role of UPD process in higher rates. Studies on Pb deposition on silver colloids have pointed to its similarity to bulk electrode [283].

The effect of adsorbed albumin on Pb UPD has been recently studied using Ag rotating disk electrode [294].

24.3.3.4 Copper

Good adhesion of electrodeposited lead to copper substrates has been reported [295–299]. Voltammetric curves of Pb deposition on Cu in alkaline solution with glycerol [299] are characterized by two peaks, corresponding to film and mass transfer–controlled bulk deposition, respectively. SEM results have not confirmed the propagation of dendrites, even at very low deposition potentials. Lead film deposition occurs prior to lead bulk

process, explaining the adherence of the deposit. Pb UPD on Cu electrodes has been studied using voltammetric methods, rotating ring, and disk electrodes, as well as LEED, surface X-rays diffraction, and reflectivity measurements [297, 300–303]. Deposition occurs through a single process, the nucleation and growth of Pb islands. The Cu crystal face affects the deposit structure, it is hexagonally ordered on Cu(111) and disordered on Cu(100) surface [297, 301]. This difference has been ascribed to lower mobility of Pb adatoms in the latter case because of the greater atomic corrugation of the (100) surface [301]. Surface alloys can be formed, accompanied by a possible replacement of a pair of neighboring Cu atoms by two Pb atoms [302, 303]. Chloride anions significantly enhance the reduction rate of Pb^{2+} ions, probably because of the formation of Cl bridges between Cu support and reacting cations [300, 301]. The surface chloride anions also form a highly ordered structure, which can act as a template for Pb adatoms deposition [302].

24.3.3.5 Carbon

Properties of thin layers of lead electrodeposited on vitreous carbon have been found identical with that of metallic lead [304]. Therefore Pb and PbO_2 coated reticulated vitreous carbon (RVC) electrodes [185] can be applied as electrodes in lead-acid batteries, as reviewed in [305]. The deposition of lead on carbon is through the diffusion-controlled process with instantaneous or progressive nucleation, for high and low Pb^{2+} concentration, respectively, and three-dimensional growth mechanism. The number of nucleation sites increases with deposition overpotential, as shown for vitreous [306] and glassy carbon [307] electrodes. The concentration dependence of the nucleation

rate points to the incorporation of atoms to clusters directly from the bulk, and not through adsorbed intermediates [306]. This deposition process can be enhanced because of the creation of active sites by chloride ions adsorption [308, 309]. However, electrochemical pretreatment process accompanied by exposure to chloride or nitrate ions has resulted in the decrease of lead deposition efficiency. This is caused by smoother electrode surface and lower number of steps and grain edges, as shown by AFM images [310]. The greater efficiency of Pb deposition in chloride solutions has been ascribed to interactions between deposited lead and chloride ions.

On highly ordered pyrolytic graphite, HOPG(0001) electrodes, no UPD has been detected owing to weak carbon–lead interactions [311]. Deposition occurs by three-dimensional island growth according to Volmer-Weber mechanism. Initial steps are controlled by progressive nucleation on active sites and hemispherical diffusion.

Electrodeposition on boron-doped diamond has pointed to progressive growth mechanism, as confirmed by chronoamperometric transients and ex situ AFM images [312]. At lower concentrations, lead ions are deposited directly on the diamond substrate, while at higher concentrations, deposits overlap and further deposition occurs on lead. At higher temperatures, the size of the nuclei is bigger.

24.3.3.6 Silicon

Electrodeposition on semiconductor surfaces is useful from the point of view of application in metal/semiconductor – Schottky and ohmic contacts. Cyclic voltammetry, current transient methods, STM, and AFM techniques have been used to study Pb electrodeposition on *n*-Si(111) surface [311, 313–315]. Lead deposition on the H-terminated Si(111) is

reversible. Using Scharifker and Hills model [316] for three-dimensional growth under diffusion control, progressive [311] or instantaneous [314] nucleation behavior at early deposition steps has been postulated. This process occurs mainly at steps and other surface inhomogeneities. UPD has not been detected [311]. Surface X-rays diffraction studies have shown epitaxial growth of Pb clusters with Pb(111) plane predominantly aligned parallel to Si(111) plane [317]. In the case of rough silicon surfaces, this in-plane orientation is lost. Larger crystallites grow at the expense of smaller ones. The activation energy of exchange between Pb and Si atoms has been found to be 1.2 eV [318].

24.3.3.7 Germanium

In the case of *n*-Ge(111) substrates, surface states affect electrochemical deposition of Pb [319]. At high cathodic potentials, the deposition occurs by instantaneous nucleation and diffusion-controlled three-dimensional growth of lead clusters. Comparing H- and OH-terminated *n*-Ge(111) surfaces, the nucleation is more inhibited at *n*-Ge(111)-OH, which can be explained by the different densities of Ge surface free radicals, being nucleation sites. In this case, nucleation site density is about 1 order of magnitude lower than that for *n*-Ge(111)-H.

24.3.3.8 Other Materials

UPD of Pb on *n*-Se is induced by illumination [320]. The Pb adatoms modify the Se surface and form surface states in the band gap. In the dark, the Pb UPD occurs only on the Se surface where PbSe clusters have been deposited. The deposited Pb atoms interact irreversibly with surface Se atoms to form PbSe monolayer [320, 321]. The

UPD process is significantly enhanced by introducing lead into Se [322]. Pb UPD has also been studied on palladium [323], from the point of view of catalytic applications and on tellurium using electrochemical impedance spectroscopy [324]. The latter process has been found irreversible owing to the Pb–Te bonds formation. Periodic multilayer structures in Pb–Se–Te system have been studied using pulse potentiostatic methods [325].

Incorporation of Pb into nanoparticulate iridium oxide films has been realized by initial electrodeposition of Pb metal on Au substrate, followed by Ir metal coating [326].

Barium metaplumbate, being a good conductor, has been used as a substrate to deposit lead, for possible use in lead-acid batteries [327].

Electrodeposition on transparent material such as indium tin oxide (ITO) can be used for electrochromic applications [328]. Pb deposition on indium–tin oxide electrode occurs by three-dimensional nucleation with a diffusion-controlled growth step for instantaneous nucleation [329], and the electrode process has also been studied using electrochemical impedance spectroscopy [328].

24.3.4

Corrosion and Passivation

The corrosion of lead has been studied in various media, and this process has been found to be dependent on the properties of the water layer that is present on the metal surface, which is a medium for the dissolution of atmospheric gases, resulting in the formation of lead salts – chlorides, sulfates, and carbonates [24, 141, 167, 330]. Electrochemical AFM images reveal the structure of PbO and PbSO₄ on lead immersed in water or sulfuric

acid, respectively, Fig. 5 [145]. Application of different spectroscopic techniques for corrosion studies in sulfuric acid solutions has been reviewed by Bullock [131]. Influence of Pb alloy components as Ag, Sb, Bi, and Sn on passivation processes and corrosion resistance in sulfuric acid solutions has also been studied [128, 331–334].

In alkaline (NaOH) solutions [153], the role of Pb(OH)₂ and PbO is important for passivity phenomena, and the voltammetric curves represent active, passive, and transpassive regions [335]. The active region is displayed by a peak corresponding to Pb oxidation to PbO [153]. The passivity results from PbO film present on the surface. The transpassive region is represented by two peaks, ascribed to oxidation of PbO to Pb₃O₄ and PbO₂. Some anions can initiate pitting corrosion, for example, ClO₄[−], ClO₃[−], and NO₃[−] [335, 336]. The corrosion in carbonate solutions [24, 153, 337, 338] is connected with the oxidation of Pb (three voltammetric peaks) to PbCO₃ and PbO as well as PbO to PbO₂. The formation of PbO can be attributed to the oxidation of Pb within the pores of PbCO₃ and/or the transformation of PbCO₃ to the oxide. Pb dissolution is enhanced by perchlorate [339] and nitrate ions [337] causing pitting corrosion. In perchlorate ions solutions, the pitting corrosion extent, expressed by integrated anodic voltammetric charge, is linearly dependent on the logarithm of ClO₄[−] anions concentration. In the presence of nitrate ions, the pitting corrosion rate increases with rising NO₃[−] concentration and temperature. Chronoamperometric transients point to incubation time (needed for NO₃[−] ions to reach and initiate metal dissolution) before pit nucleation and instantaneous three-dimensional pit growth. The rate

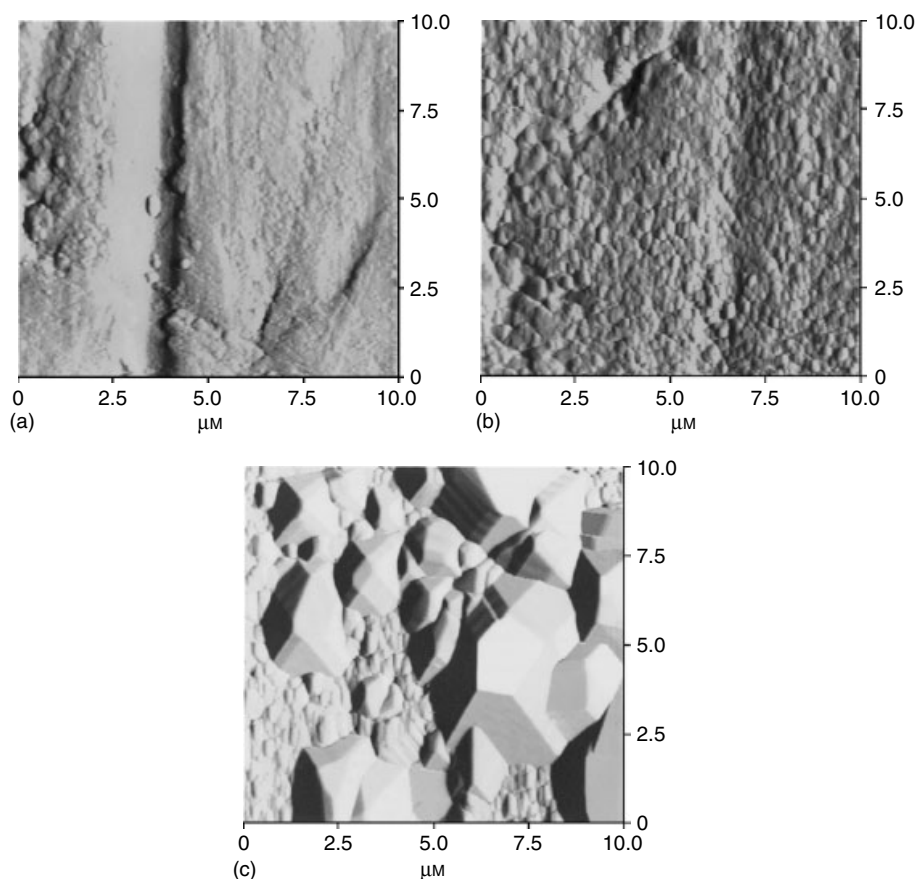


Fig. 5 AFM images of lead surface: (a) in air at room temperature, (b) in pure water after holding for 20 min at room temperature, (c) in 0.05 M sulfuric acid after holding for 60 min at room temperature [145].

of pit nucleation rises with increasing nitrate ions concentration, temperature, and applied anodic potential. In neutral nitrate solutions, the rate of metal dissolution is dependent on cation kind, and the dissolution rate is much slower in NaNO_3 than in NH_4NO_3 solutions [340]. XPS confirms formation of passive oxide layers containing a nitrogen compound (a product of nitrate reduction). The layer formed in NH_4NO_3 solution has been hydrolyzed and cracked, probably owing to locally acidified medium (from NH_4^+

acidic cation) at the oxide/solution interface, promoting hydrolysis of the oxide.

In carboxylic acid solutions, the corrosion rate increases with acid concentration (acetic, lactic); however, in oxalic and tartaric acid solutions, the dissolution of metal is associated with the formation of passive lead salt layer [341].

The oxygen and oxidants (as $\text{Cr}_2\text{O}_7^{2-}$) affect the corrosion rate [342, 343]. A decrease in the corrosion resistance after longer time (3 h) in oxygen-rich solutions has been observed.

The corrosion process can be inhibited by the addition of phosphate or polyphosphate ions [344], inorganic inhibitors as, for example, chromate ions [336], adsorbed alcohols [345], adsorbed amines, competing with anions for adsorption sites [339], as well as saturated linear aliphatic monocarboxylate anions, $\text{CH}_3(\text{CH}_2)_{n-2}\text{COO}^-$, $n = 7 - 11$, [24]. In the latter case, the formation of the passive layer requires Pb oxidation to Pb^{2+} by dissolved oxygen and then precipitation of hardly soluble lead carboxylate on the metal surface. The corrosion protection can also be related to the hydrophobic character of carboxylate anions, which reduce the wetting of the metal surface.

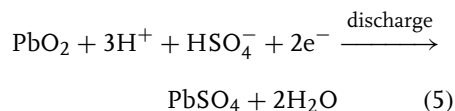
24.3.5

Applied Electrochemistry

24.3.5.1 Lead-acid Batteries

The most common applications of electrochemical processes of lead are lead-acid batteries, described in detail elsewhere ([1, 203, 346–349] and references given therein). Some detailed aspects of the electrochemistry of lead-acid batteries have already been described in the Sects 24.3.2.4 and 24.3.2.5. Therefore, only an overview of the main properties of this kind of power sources will be presented.

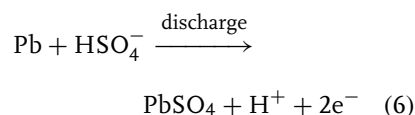
The discharge process at the positive electrode is



and the charging reaction proceeds in the opposite direction. In order to obtain high current densities, it is necessary to use the highly porous structure of PbO_2 in the β -form, which in contrast to α - PbO_2 is not isomorphic with PbSO_4 .

Therefore, passivation of the positive electrode by poorly conducting PbSO_4 can be reduced [348]. The porosity is important because it enables the expansion during the solid phase volume increase, which accompanies the transformation of PbO_2 to PbSO_4 . In the most popular construction, the electrode paste material (mixture of metallic lead with lead oxides) is held in a framework composed of lead alloys with additions of tin, antimony, selenium, and calcium [348]. Antimony improves the mechanical stability; however, it increases the resistance and facilitates the self-discharge of the battery. Better results are obtained for low antimony content and/or for lead–calcium alloys [203]. Methods of positive electrodes improvement, from the point of view of lead oxide technology have been discussed [350]. Influence of different factors on life cycle, nature, and composition of the positive active mass has been studied by Pavlov with coworkers [200, 351, 352].

The discharge process at the negative electrode is



Negative electrodes are pasted plates using grids covered with perforated lead foil and the same paste as that used in positive electrode plates [203, 348]. Under specified conditions, the paste material is reduced to sponge lead of high porosity, assuring a high electrode surface area. Additions of expanders as surface-active substances (e.g. lignosulfonic acid) is useful to lower the surface energy of lead and thus to reduce large crystals formation. The crystal formation is also damped by the addition of fine BaSO_4 , isomorphic with PbSO_4 [348]. Influence of charge mode on

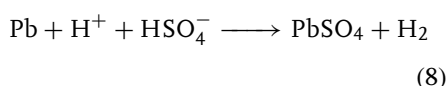
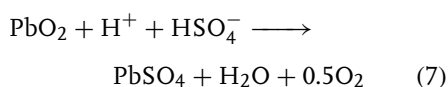
the capacity and cycle life of negative plates has been analyzed [353].

Separators used in lead-acid batteries are usually produced from synthetic polymers as sintered poly(vinylchloride) and extruded polyethylene, glass, or microglass fiber [203, 348, 354].

Properties of lead-acid cells, important from the practical point of view, related, for example, to charge/discharge process and its mechanism, conductivity, and so on are studied using different electrochemical techniques, the most powerful one being electrochemical impedance spectroscopy [355–358].

In recent years, a significant improvement of properties of the most popular automotive starting batteries has been obtained because of the technical modifications of the classical construction [349]: (1) application of thin-walled polypropylene cases, allowing more space for the plates, (2) through-the-wall intercell connections, lowering the internal resistance and also allowing more space for active elements, and (3) application of thinner polymeric separators. Also, lightweight plastic grids have been developed [359].

The stability of the charge that is stored is limited by the thermodynamically favored reactions connected with both hydrogen and oxygen evolution [348]



enhanced by impurities (e.g. Fe^{2+} ions) and presence of antimony.

These processes should be minimized, especially in maintenance free (MF) batteries because they lead to undesirable water losses. MF batteries have a grid

with reduced antimony amount, and other metals such as calcium, strontium, tin or aluminum are used [348, 360, 361]. Valve-regulated lead-acid (VRLA) batteries have been constructed to enhance the recombination of the oxygen at the negative electrode [362–364]. The oxygen transport and recombination in VRLA batteries have been discussed by Pavlov with coworkers [365, 366] and Guo with coworkers [367, 368]. Simulations and results of current-interrupt experiments for VRLA have been compared [369]. These batteries can be scaled from a few to several thousand amperes per hour and are suitable for almost all battery applications [349]. In VRLA batteries, the electrolyte amount is reduced, it is immobilized by gel formation [370] using silica or calcium sulfate, or by the incorporation of microporous glass separators [203, 348]. Leak-proof constructions with one-way vent – semisealed systems, exhibit significantly higher charge retention compared with conventional units [203, 348]. Properties of different size VRLA batteries have been studied and modeled using electrochemical impedance spectroscopy and fuzzy logic methodology of data analysis [371, 372].

A novel kind of flow lead-acid battery with no separator and single electrolyte, lead(II) in methanesulfonic acid has been proposed recently [373].

24.3.5.2 Electrocatalytic Properties

24.3.5.2.1 Pb Lead, and particularly underpotentially deposited Pb, exhibits electrocatalytic properties in numerous electrode processes. The model reaction can be oxygen reduction with slow step of peroxide reduction [374–376] or reduction of nitrobenzene and other nitrocompounds [377, 378]. In the case of

nitrocompounds, the catalytic effect observed at medium degrees of UPD adatom coverages has been interpreted in terms of strong adsorption of the nitro group with a bridged complex involving the substrate (Au) and adsorbate atom (Pb), favoring N–O bond cleavage. STM studies of Pb deposited on Au(111) suggest that the active sites are edges of the circular Pb islands [379, 380]. This activity can be reduced by the addition of adsorbing species.

Other model reactants are simple organic molecules, for example, formic acid [381, 382]. Pt(111) exerts lower catalytic influence on HCOOH oxidation than do Pt(100) and Pt(110) faces. However, in the presence of Pb adatoms on Pt(111) a strong catalytic influence has been observed [383]. The poisonous species production in HCOOH oxidation is then inhibited. Electrochemical reduction of CO₂ to glycolate/glyoxylate and oxalic acid has been studied [384]. Other products such as formic acid accompanied by CO and methane have also been detected [385]. In the latter case, the efficiency of the competing process of hydrogen evolution has been suppressed to less than 3.5%.

Other electrochemical processes of organic compounds on Pb electrodes or electrodes with UPD Pb have been studied – formaldehyde [323], oxalic acid [386], trichloro- and trifluoroethane [387], 1-phenylethylamine [388], 3-hydroxychinulidine [388], dichlorodifluoromethane [389], polychlorobenzenes [390], 1-propanol [391], pyrrole polymerization [392], and inorganic compounds – phosphine [388] and sulfate(IV) ions [393]. Simultaneous catalytic or inhibiting influence of organic solvents – acetonitrile, dimethylsulfoxide, and Pb²⁺ presence on electrooxidation of small organic molecules on Pt electrodes has been studied using on-line mass spectroscopy [394].

The influence of Pb alloy components on electrocatalytic processes has been discussed, for example, in Refs 386, 395.

24.3.5.2.2 PbO₂ Lead dioxide is an electrode material of relatively high electronic conductivity and high stability in acidic media, useful at high positive potentials. AFM studies have revealed the influence of PbO₂ structure on its electrocatalytic activity [150]. In model glucose oxidation process, the role of hydrated gel layer in the interaction between OH radicals and glucose, as well as coordination of the carbonyl atom to Pb(IV) center [150, 396, 397] has been analyzed.

The oxygen evolution overpotential on PbO₂ electrodes is high. The role of adsorbed intermediates in this process for both α - and β -forms of PbO₂ has been discussed [197]; Pavlov and Monahov proposed a mechanism of O₂ evolution with elementary reactions taking place at active centers in the hydrated zones of the electrode [398, 399]. The formation and properties of the hydrous layer can be affected by anions owing to the exchange reaction of OH[−] ions by these anions [400]. These adsorbed anions can inhibit both water electrode reactions and desorption of reaction intermediates. Low temperature inhibits the reaction by slowing down desorption of reaction intermediates [400]. The role of nonstoichiometry of PbO_{2−x} in oxygen evolution has been analyzed [401].

Another group of anodic reactions is connected with the electrogeneration of strong oxidants as ozone or persulfate, with efficiency decreasing with increasing efficiency of O₂ evolution (e.g. [191, 205, 400, 402–406]). Owing to high oxygen overpotential and high oxygen radicals formation efficiency, mainly OH radicals ([407] and references given therein), and lead dioxide electrodes are used as

anodes for the destruction of organic compounds because rates of such reactions are higher than on other traditional anodes ([408] and references given therein). Oxidation of different organics as, for example, glucose, acetic, oxalic [407] and 4-hydroxy-cinnamic acids [407, 409], phenol [204, 410, 411], 4-chlorophenols [412, 413], nitrocompounds [412–414], benzene and dimethylsulfoxide [204], 2-thiophene carboxylic acid [415], Mn(II) [415], and cyanides [188] has been reported to point to the role of the substrate molecules and intermediates adsorption. Conducting polymers – polypyrrole [416], polyaniline [417], polythiophene [418], poly(3-methylthiophene) [418], as well as copolymers of aniline and thiophene [419] have been obtained by electropolymerization onto PbO₂ electrodes.

24.3.5.3 Electrochemical Sensors

The literature concerning electrochemical sensors, where lead electrochemistry can be applied, is extremely vast. Therefore, only some representative papers will be presented. More information can be found in recent reviews [420–423].

24.3.5.3.1 Potentiometric Sensors In the field of ion-selective electrodes, considerable progress has been achieved in the last few years. By buffering the primary ions concentration on a low level in the internal solution, ionic fluxes in the membrane are affected [424–426]. Thus, primary ion leakage into sample solution is hindered, resulting in a tremendous shift of detection limits to lower values; for Pb²⁺-selective electrodes, the detection limit up to 10^{−12} M level has been achieved for internal solution electrodes [424, 427] and below 10^{−9} M for all-solid-state electrodes with conducting polymer solid

contact ([428, 429], see also recent review [423]). Efforts have been made to monitor ion fluxes in the membranes using electrochemical microscopy, potentiometric studies, and galvanostatic polarization [427, 430]. Both stability of Pb²⁺ complexes with several ionophores used in ion-selective membranes and selectivities have been discussed [431]. Recently, a new kind of Pb²⁺-selective electrode containing nonfunctionalized porous glassy carbon, loaded with ionophore/plasticizer/additive cocktail has been proposed [432]. Glassy carbon acts both as the support for the membrane and signal transducer. The reported detection limit is close to 10^{−11} M.

24.3.5.3.2 Amperometric/Voltammetric Sensors

Amperometric sensors, based on lead accumulation by interaction with electrode components, for example, adsorbed ligand, forming products that can be stripped by anodic polarization [81] have been elaborated. Although mercury and mercury film electrodes are claimed to have the highest sensitivity for Pb²⁺ determination [433, 434], other electrode materials have also been tested: amalgams [435], silver [436–440], gold [439], gold–silver alloys [441], carbon [442–446], diamond [447, 448], mesoporous silica on carbon [449], Nafion on graphite [450], conducting polymers as polyaniline [451–454], polypyrrole [455, 456] or poly(1,8-diaminonaphthalene) [457], and microelectrodes [458–460]. Quartz crystal microgravimetry has been used to study Pb deposition from ethylenediamine tetraacetic acid (EDTA) complexes [461]. The multivariate calibration transfer method has been applied to routine polarographic determination of lead [462], and multisensor systems have been developed (e.g. [463]). There are numerous papers that reveal the very

promising areas related to stripping voltammetric and chronopotentiometric determination of lead using disposable screen-printed electrodes ([464–468] as also shown by review article [469]). Sono-electroanalytical methods have been also used to determine lead for example ([470–473] and review [474]).

References

1. T. F. Sharpe, in *Encyclopedia of Electrochemistry of the Elements* (Ed.: A. J. Bard), Marcel Dekker, New York, 1973, p. 235, Vol. 1.
2. A. Frumkin, *Zero Charge Potentials* (in Russian), Nauka, Moscow, 1979.
3. M. A. Vorotyntsev, in *Modern Aspects of Electrochemistry* (Eds.: J. O. M. Bockris, B. E. Conway, R. E. White), Plenum Press, New York, 1986, p. 131, Vol. 17.
4. R. Parsons, *Chem. Rev.* **1990**, 90, 813–826.
5. A. Hamelin, T. Vitinov, E. Sevastyanov et al., *J. Electroanal. Chem.* **1983**, 145, 225–264.
6. S. Trasatti, E. Lust, in *Modern Aspects of Electrochemistry*, (Eds.: R. E. White, J. O. M. Bockris, B. E. Conway), Kluwer Academic/Plenum Publishers, New York, 1999, p. 1, Vol. 33.
7. V. Y. Mishuk, E. A. Solomatin, V. V. Elkin, *Elektrokhimiya* **1978**, 14, 1135–1135.
8. L. P. Khmelevaya, B. B. Damaskin, A. I. Sidnin, *Elektrokhimiya* **1981**, 17, 436–439.
9. E. S. Sevastyanov, V. K. Chubarova, N. A. Morozova et al., *Elektrokhimiya* **1992**, 28, 720–729.
10. V. A. Safonov, B. B. Damaskin, M. A. Choba, *Elektrokhimiya* **1989**, 25, 1432–1438.
11. L. P. Khmelevaya, A. V. Chizhov, B. B. Damaskin et al., *Elektrokhimiya* **1980**, 16, 257–260.
12. K. V. Rybalka, D. I. Leikis, *Elektrokhimiya* **1967**, 3, 383–386.
13. Z. N. Ushakova, V. F. Ivanov, *Elektrokhimiya* **1976**, 12, 485–487.
14. A. Kiszka, J. Kaźmierczak, B. Meisner, *Pol. J. Chem.* **2004**, 78, 561–573.
15. V. V. Emets, B. B. Damaskin, *J. Electroanal. Chem.* **2002**, 528, 57–68.
16. Z. Shi, Y.-H. Zhou, C.-S. Cha, *J. Power Sources* **1998**, 70, 214–221.
17. B. K. Mahato, *J. Electrochem. Soc.* **1981**, 128, 1416–1422.
18. Z. Shi, Y.-H. Zhou, C.-S. Cha, *J. Electroanal. Chem.* **1995**, 399, 213–221.
19. Z. Shi, H. Zhan, Y.-H. Zhou et al., *J. Power Sources* **1996**, 62, 135–139.
20. L. A. Beketayeva, V. I. Beklemyshev, I. I. Makhonin et al., *Russ. J. Electrochem.* **1997**, 33, 1242–1245.
21. I. Ban, Y. Yamaguchi, Y. Nakayama et al., *J. Power Sources* **2002**, 107, 167–172.
22. N. Hirai, D. Tabayashi, M. Shiota et al., *J. Power Sources* **2004**, 133, 32–38.
23. S. S. Mahmoud, G. A. El Mahdy, *Bull. Electrochem.* **1997**, 13, 75–79.
24. E. Rocca, J. Steinmetz, *Corros. Sci.* **2001**, 43, 891–902.
25. G. Pezzatini, M. L. Foresti, R. Guidelli, *J. Electroanal. Chem.* **1982**, 138, 139–153.
26. B. N. Afanasev, G. I. Merkulova, *Elektrokhimiya* **1985**, 21, 739–746.
27. J. Kůta, L. Pospíšil, J. Smoler, *J. Electroanal. Chem.* **1977**, 75, 407–420.
28. V. I. Kravtsov, V. N. Statsyuk, *Russ. J. Electrochem.* **1997**, 33, 377–384.
29. J. Lipkowski, Z. Galus, *J. Electroanal. Chem.* **1979**, 98, 91–104.
30. E. Muszalska, W. Górski, Z. Galus, *J. Electroanal. Chem.* **1990**, 294, 87–95.
31. S. Romanowski, K. Maksymiuk, Z. Galus, *J. Electroanal. Chem.* **1995**, 385, 95–103.
32. G. J. Hills, L. M. Peter, *J. Electroanal. Chem.* **1974**, 50, 175–185.
33. A. Broda, J. Stroka, Z. Galus, *Electrochim. Acta* **1983**, 28, 817–823.
34. J. Stroka, K. Maksymiuk, Z. Galus, *J. Electroanal. Chem.* **1984**, 167, 211–226.
35. K. Maksymiuk, J. Stroka, Z. Galus, *J. Electroanal. Chem.* **1990**, 279, 1–18.
36. G. Gritzner, *J. Phys. Chem.* **1986**, 90, 5478–5485.
37. S. Kariuki, H. D. Dewald, *Electroanalysis* **1996**, 8, 307–313.
38. P. Paklepa, P. K. Wrona, *J. Electroanal. Chem.* **1998**, 453, 205–210.
39. E. F. Speranskaya, V. A. Speranskii, *Russ. J. Appl. Chem.* **1996**, 69, 1319–1325.
40. R. G. Barradas, T. J. Vandernoot, *J. Electroanal. Chem.* **1987**, 233, 237–250.
41. I. S. El-Hallag, *Bull. Electrochem.* **1998**, 14, 44–47.
42. J. Schiewe, K. B. Oldham, J. C. Myland et al., *Anal. Chem.* **1997**, 69, 2673–2681.

43. J. Schiewe, J. Hazi, V. A. Vicente-Beckett et al., *J. Electroanal. Chem.* **1998**, 451, 129–138.
44. R. G. Barradas, F. C. Benson, S. Fletcher, *J. Electroanal. Chem.* **1977**, 80, 305–313.
45. P. Fusi, P. R. Mussini, *J. Solution Chem.* **1997**, 26, 337–353.
46. D. Giovanelli, N. S. Lawrence, R. G. Compton, *Electroanalysis* **2004**, 16, 789–810.
47. K. I. Ibragimov, V. S. Savvin, *Inorg. Mater.* **1996**, 32, 963–970.
48. A. T. Kuhn, (Ed.), *The Electrochemistry of Lead*, Academic Press, New York, 1979.
49. R. J. Barrio Diez-Caballero, J. F. Arranz Valentin, A. Arranz Garcia et al., *J. Electroanal. Chem.* **1985**, 196, 43–51.
50. G. Scarano, E. Morelli, *Electroanalysis* **1998**, 10, 39–43.
51. M. M. Correia Dos Santos, M. L. S. Simões Gonçalves, *J. Electroanal. Chem.* **1986**, 208, 137–152.
52. T. M. Borges Miquel, M. L. Sánchez, J. C. Macias et al., *Can. J. Chem.* **1996**, 74, 2454–2459.
53. S. K. Singh, C. P. S. Chandel, *Asian J. Chem.* **2002**, 14, 53–56.
54. S. K. Singh, C. P. S. Chandel, *Bull. Electrochem.* **2002**, 18, 1–6.
55. S. K. Singh, C. P. S. Chandel, *Bull. Electrochem.* **2003**, 19, 119–126.
56. J. C. Rodriguez Placeres, J. C. Macias, M. L. Sánchez et al., *Collect. Czech. Chem. Commun.* **2003**, 68, 663–671.
57. E. Bottari, M. R. Festa, *Chem. Spec. Bioavailab.* **1996**, 8, 75–83.
58. M. Ben Ali, R. Kalfat, H. Sfihi et al., *Mater. Sci. Eng., C* **1998**, 6, 53–58.
59. G. Roya-Morales, L. Galicia, A. Rojas-Hernández et al., *Electrochim. Acta* **2005**, 50, 1925–1930.
60. A. Ion, M. Buda, J. C. Moutet et al., *Eur. J. Inorg. Chem.* **2002**, 6, 1357–1366.
61. I. Cukrowski, S. A. Loader, *Electroanalysis* **1998**, 10, 877–885.
62. H. M. V. M. Soares, M. G. R. T. Barros, *Electroanalysis* **2001**, 13, 325–331.
63. J. Buffle, A. M. Mota, M. L. S. Simoes Goncalves, *J. Electroanal. Chem.* **1987**, 223, 235–262.
64. R. Mandal, M. S. A. Salam, C. L. Chakrabarti et al., *Electroanalysis* **2003**, 15, 903–906.
65. A. A. A. Gaber, M. A. Ghandour, H. S. El-Said, *J. Indian Chem. Soc.* **2001**, 78, 455–459.
66. Y. Z. Bian, L. Li, J. M. Dou et al., *Inorg. Chem.* **2004**, 43, 7539–7544.
67. R. Pedrido, M. R. Bermejo, M. J. Romero et al., *Dalton Trans.* **2005**, 3, 572–579.
68. R. M. Izatt, J. S. Bradshaw, S. A. Nielsen et al., *Chem. Rev.* **1985**, 85, 271–339.
69. R. M. Izatt, K. Pawlak, J. S. Bradshaw et al., *Chem. Rev.* **1991**, 91, 1721–2085.
70. R. M. Izatt, K. Pawlak, J. S. Bradshaw et al., *Chem. Rev.* **1995**, 95, 2529–2586.
71. A. Lehmani, T. Cartailier, S. Rossy-Deluc et al., *J. Electroanal. Chem.* **1996**, 416, 121–125.
72. G. Rounaghi, M. Chamsaz, A. Nezhadali, *J. Incl. Phenom. Macrocycl. Chem.* **2000**, 38, 153–161.
73. G. Rounaghi, A. S. Yazdi, Z. Monsef, *J. Incl. Phenom. Macrocycl. Chem.* **2002**, 43, 231–237.
74. Z. Monsef, G. Rounaghi, A. Sarafraza, *J. Incl. Phenom. Macrocycl. Chem.* **2001**, 39, 321–325.
75. E. Cukrowska, I. Cukrowski, *Talanta* **1998**, 47, 1175–1189.
76. R. Luckay, R. D. Hancock, I. Cukrowski et al., *Inorg. Chim. Acta* **1996**, 246, 159–169.
77. C. Caltagirone, A. Bencini, F. Demartin et al., *Dalton Trans.* **2003**, 5, 901–909.
78. M. C. Ezequiel Rollemberg, M. L. S. Simões Gonçalves, A. M. Almeida Mota et al., *Anal. Chim. Acta* **1999**, 384, 17–26.
79. T. F. Rozan, G. W. Luther, D. Ridge et al., *Environ. Sci. Technol.* **2003**, 37, 3845–3852.
80. M. T. Vasconcelos, M. Azehna, V. de Freitas, *Analyst* **2000**, 125, 743–748.
81. O. Abollino, M. Aceto, C. Sarzanini et al., *Electroanalysis* **1999**, 11, 870–878.
82. M. R. Ganjali, M. Shamsipur, *J. Inclusion Phenom.* **1995**, 23, 41–51.
83. P. Perez-Lourido, J. Romero, J. A. Garcia-Vázquez et al., *J. Chem. Soc., Dalton Trans.* **2000**, 5, 769–774.
84. E. Labisbal, A. Sousa, A. Castineiras et al., *Polyhedron* **2000**, 19, 1255–1262.
85. V. N. Kokozay, O. Y. Vassilyeva, P. Weinberger et al., *Rev. Inorg. Chem.* **2000**, 20, 255–282.
86. G. M. Barnard, M. A. Brown, H. E. Mabrouk et al., *Inorg. Chim. Acta* **2003**, 349, 142–148.
87. J. N. Liu, X. Q. Yu, Y. J. Dong et al., *Chin. J. Inorg. Chem.* **1999**, 15, 680–684.
88. S. Kumar, D. Kishore, R. K. Mehta, *J. Indian Chem. Soc.* **2000**, 77, 254–255.

89. A. Bobrowski, A. M. Bond, S. R. Ellis, *Inorg. Chim. Acta* **1999**, 293, 223–228.
90. F. Marken, W. M. Leslie, R. G. Compton et al., *J. Electroanal. Chem.* **1997**, 424, 25–34.
91. A. Morales-Pérez, M. Bernabe, G. Roa et al., *Electroanalysis* **2001**, 13, 541–548.
92. P. Singh, M. M. Richter, *Inorg. Chim. Acta* **2004**, 357, 1589–1592.
93. J. B. Chlistunoff, J. J. Lagowski, *J. Phys. Chem. B* **1997**, 101, 2867–2873.
94. J. B. Chlistunoff, J. J. Lagowski, *J. Phys. Chem. B* **1998**, 102, 5800–5809.
95. H. Katano, M. Senda, *Anal. Sci.* **1996**, 12, 683–689.
96. G. Lagger, L. Tomaszewski, M. D. Osborne et al., *J. Electroanal. Chem.* **1998**, 451, 29–37.
97. T. Store, G. M. Haarberg, R. Tunold, *J. Appl. Electrochem.* **2000**, 30, 1351–1360.
98. Y. Castrillejo, S. Palmero, M. A. Garcia et al., *Electrochim. Acta* **1996**, 41, 2461–2468.
99. V. P. Yurinskii, D. V. Makarov, *Russ. J. Appl. Chem.* **1995**, 68, 1285–1288.
100. D. V. Makarov, V. P. Yurinskii, *Russ. J. Appl. Chem.* **1996**, 69, 220–223.
101. R. L. Deutscher, S. Fletcher, J. A. Hamilton, *Electrochim. Acta* **1986**, 31, 585–589.
102. Y. Yamamoto, M. Matsuoka, M. Kimoto et al., *Electrochim. Acta* **1996**, 41, 439–444.
103. M. Taguchi, H. Sugita, *J. Power Sources* **2002**, 109, 294–300.
104. Y. Guo, *J. Electrochem. Soc.* **1995**, 142, 3378–3382.
105. Y. L. Guo, Z. Wei, S. Hua, *Electrochim. Acta* **1997**, 42, 979–984.
106. S. Fletcher, D. B. Matthews, *J. Electroanal. Chem.* **1981**, 126, 131–144.
107. J. G. Sunderland, *J. Electroanal. Chem.* **1976**, 71, 341–345.
108. M. Metikoš-Huković, R. Babić, S. Omanović, *J. Electroanal. Chem.* **1994**, 374, 199–206.
109. Y. Yamamoto, K. Fumino, T. Ueda et al., *Electrochim. Acta* **1992**, 37, 199–203.
110. A. Czerwiński, M. Żelazowska, M. Grdeń et al., *J. Power Sources* **2000**, 85, 49–55.
111. D. Pavlov, *Electrochim. Acta* **1978**, 23, 845–854.
112. D. Pavlov, T. Rogachev, *Electrochim. Acta* **1978**, 23, 1237–1242.
113. J. R. Vilche, F. E. Varela, *J. Power Sources* **1997**, 64, 39–45.
114. K. R. Bullock, M. A. Butler, *J. Electrochem. Soc.* **1986**, 133, 1085–1089.
115. M. Ma, C.-X. Yang, W.-B. Cai et al., *J. Electrochem. Soc.* **2003**, 150, B325–B328.
116. Y.-Q. Wan, Q.-Z. Wang, H.-T. Liu et al., *J. Electroanal. Chem.* **1996**, 414, 159–161.
117. G. E. Nauer, *Sci. Forum* **1996**, 228, 387–392.
118. T. Laitinen, B. Monahov, K. Salmi et al., *Electrochim. Acta* **1991**, 36, 953–963.
119. Z. Takehara, K. Kanamura, *J. Electrochem. Soc.* **1987**, 134, 1604–1610.
120. F. E. Varela, M. E. Vela, J. R. Vilche et al., *Electrochim. Acta* **1993**, 38, 1513–1520.
121. L. I. Espinoza-Ramos, C. Ramirez, J. M. Hallen-López et al., *J. Electrochem. Soc.* **2002**, 149, B543–B550.
122. W.-B. Cai, H.-T. Liu, W.-F. Zhou, *J. Power Sources* **1996**, 63, 131–135.
123. E. N. Codaro, J. R. Vilche, *Electrochim. Acta* **1997**, 42, 549–555.
124. Y. L. Guo, L. Niu, S. Zhang et al., *J. Power Sources* **2000**, 85, 38–43.
125. D. Pavlov, A. Kirchev, M. Stoycheva et al., *J. Power Sources* **2004**, 137, 288–308.
126. Q. J. Sun, Y. L. Guo, *J. Electroanal. Chem.* **2000**, 493, 123–129.
127. S. Zhong, J. Wang, H. K. Liu et al., *J. Power Sources* **1997**, 66, 159–164.
128. S. Zhong, J. Wang, H. K. Liu et al., *J. Appl. Electrochem.* **1999**, 29, 1–6.
129. E. Expósito, C. M. Sánchez-Sánchez, J. Solla-Gullón et al., *J. Power Sources* **2002**, 104, 169–174.
130. P. Varma, C. A. Melendres, N. Yao, *J. Electrochem. Soc.* **1980**, 127, 1416–1418.
131. K. R. Bullock, *J. Electroanal. Chem.* **1987**, 222, 347–366.
132. Y. Guo, *J. Electrochem. Soc.* **1991**, 138, 1222–1227.
133. G. L. J. Trettenhahn, G. E. Nauer, A. Neckel, *Ber. Bunsen-Ges. Phys. Chem.* **1993**, 97, 422–426.
134. G. L. J. Trettenhahn, G. E. Nauer, A. Neckel, *J. Power Sources* **1993**, 42, 137–144.
135. G. L. J. Trettenhahn, G. E. Nauer, A. Neckel, *Electrochim. Acta* **1996**, 41, 1435–1441.
136. S.-J. Xia, W.-F. Zhou, *J. Appl. Electrochem.* **1994**, 24, 894–899.
137. D. Pavlov, S. Zanova, G. Papazov, *J. Electrochem. Soc.* **1977**, 124, 1522–1528.
138. J. S. Buchanan, L. M. Peter, *Electrochim. Acta* **1988**, 33, 127–136.
139. Y. Yang, X. G. Chen, X. D. Zhuo et al., *J. Electroanal. Chem.* **1994**, 367, 255–258.
140. J. Han, C. Pu, W.-F. Zhou, *J. Electroanal. Chem.* **1994**, 368, 43–46.

141. R. Peat, P. T. Moseley, A. F. Hollenkamp et al., *J. Power Sources* **1993**, 42, 119–135.
142. N. Stein, E. Rocca, R. Kleim et al., *Electrochim. Acta* **1998**, 44, 445–454.
143. N. Stein, G. Bourguignon, L. Raboin et al., *Thin Solid Films* **2004**, 455–456, 735–741.
144. K. Uosaki, K. Konishi, M. Koinuma, *Langmuir* **1997**, 13, 3557–3562.
145. Y. Yamaguchi, M. Shiota, Y. Nakayama et al., *J. Power Sources* **2000**, 85, 22–28.
146. Y. Yamaguchi, M. Shiota, Y. Nakayama et al., *J. Power Sources* **2001**, 93, 104–111.
147. N. Hirai, K. Takeda, S. Hara et al., *J. Power Sources* **2003**, 113, 329–334.
148. M. P. Vinod, A. B. Mandle, S. R. Sainkar et al., *J. Appl. Electrochem.* **1997**, 27, 462–468.
149. M. M. EL-Naggar, *Monatsh. Chem.* **2001**, 132, 1189–1200.
150. M. E. Hyde, R. M. L. Jacobs, R. G. Compton, *J. Phys. Chem. B* **2004**, 108, 6381–6390.
151. M. Chatelut, S. Chah-Bouzziri, O. Vittori et al., *J. Solid State Electrochem.* **2000**, 4, 435–443.
152. I. Paleska, R. Pruszkowska-Drachal, J. Kotowski et al., *J. Power Sources* **2003**, 113, 308–317.
153. V. I. Birrs, M. T. Shevalier, *J. Electrochem. Soc.* **1990**, 137, 2643–2647.
154. B. Centeno, M. L. Tascón, M. D. Vázquez et al., *Electrochim. Acta* **1991**, 36, 277–282.
155. A. A. Montaser, P. Veluchamy, H. Minoura, *J. Electroanal. Chem.* **1996**, 419, 47–53.
156. S. S. Abd El Rehim, L. I. Ali, N. H. Amin et al., *Monatsh. Chem.* **1997**, 128, 245–254.
157. P. Veluchamy, H. Minoura, *J. Electroanal. Chem.* **1997**, 440, 41–49.
158. P. Veluchamy, H. Minoura, *Appl. Surf. Sci.* **1998**, 126, 241–245.
159. M. M. El-Naggar, *J. Power Sources* **2004**, 126, 207–213.
160. E. E. Abd El Aal, *J. Power Sources* **2001**, 102, 233–241.
161. E. F. El-Sherbini, S. S. Abd El Rehim, *Mater. Chem. Phys.* **2004**, 88, 17–22.
162. E. E. Abd El Aal, *J. Power Sources* **1998**, 75, 36–43.
163. M. Shiota, T. Kameda, K. Matsui et al., *Electrochemistry* **2003**, 71, 873–876.
164. J. S. Buchanan, N. P. Freestone, L. M. Peter, *J. Electroanal. Chem.* **1985**, 182, 383–398.
165. B. Meyer, B. Ziemer, F. Scholz, *J. Electroanal. Chem.* **1995**, 392, 79–83.
166. M. Dimitrov, K. Kochev, D. Pavlov, *J. Electroanal. Chem.* **1985**, 183, 145–153.
167. K. R. Bullock, G. M. Trishan, R. G. Burrow, *J. Electrochem. Soc.* **1983**, 130, 1283–1289.
168. R. G. Barradas, D. S. Nadezhdin, *Can. J. Chem.* **1984**, 62, 596–600.
169. F. E. Varela, E. N. Codaro, J. R. Vilche, *Electrochim. Acta* **1995**, 40, 1183–1189.
170. E. Rocca, J. Steinmetz, S. Weber, *J. Electrochem. Soc.* **1999**, 146, 54–58.
171. I. Petersson, E. Ahlberg, *J. Power Sources* **2000**, 91, 143–149.
172. P. Veluchamy, H. Minoura, *J. Electroanal. Chem.* **1995**, 396, 211–217.
173. M. Sharon, I. Mukhopadhyay, S. Ghosh, *J. Solid State Electrochem.* **1999**, 3, 141–147.
174. U. Hasse, F. Scholz, *Electrochem. Commun.* **2001**, 3, 429–434.
175. Q. F. Li, F. Borup, I. Petrushina et al., *J. Electrochem. Soc.* **1999**, 146, 2449–2454.
176. R. S. Robinson, *J. Power Sources* **1992**, 40, 149–156.
177. M. E. Herron, D. Pletcher, F. C. Walsh, *J. Electroanal. Chem.* **1992**, 332, 183–197.
178. A. B. Velichenko, R. Amadelli, A. Benedetti et al., *J. Electrochem. Soc.* **2002**, 149, C445–C449.
179. A. B. Velichenko, D. V. Girenko, F. I. Danilov, *J. Electroanal. Chem.* **1996**, 405, 127–132.
180. J. Lee, H. Varela, S. Uhm et al., *Electrochem. Commun.* **2000**, 2, 646–652.
181. A. A. Vertegel, E. W. Bohannon, M. G. Shumsky et al., *J. Electrochem. Soc.* **2001**, 148, C253–C256.
182. S. Tabat, A. Nowacki, B. Szczesniak, *J. Power Sources* **1990**, 31, 339–348.
183. D. Velayutham, M. Noel, *Electrochim. Acta* **1991**, 36, 2031–2035.
184. J. González-García, V. Sáez, J. Iniesta et al., *Electrochem. Commun.* **2002**, 4, 370–373.
185. A. Czerwiński, M. Żelazowska, *J. Power Sources* **1997**, 64, 29–34.
186. T. C. Wen, M. G. Wei, K. L. Lin, *J. Electrochem. Soc.* **1990**, 137, 2700–2702.
187. M. Ueda, A. Watanabe, T. Kameyama et al., *J. Appl. Electrochem.* **1995**, 25, 817–822.
188. G. Cifuentes, L. Cifuentes, R. Kammel et al., *Z. Metallkd.* **1998**, 89, 363–367.
189. C. N. Ho, B. J. Hwang, *Electrochim. Acta* **1993**, 38, 2749–2757.
190. P. N. Bartlett, T. Dunford, M. A. Ghanem, *J. Mater. Chem.* **2002**, 12, 3130–3135.

191. J. E. Graves, D. Pletcher, R. L. Clarke et al., *J. Appl. Electrochem.* **1992**, 22, 200–203.
192. S. Abaci, K. Pekmez, T. Hokelek et al., *J. Power Sources* **2000**, 88, 232–236.
193. J. Morales, G. Petkova, M. Cruz et al., *Electrochim. Solid State Lett.* **2004**, 7, A75–A77.
194. J. P. Carr, N. A. Hampson, *Chem. Rev.* **1972**, 72, 679–703.
195. J. P. Pohl, H. Rickert, in *Electrodes of Conductive Metallic Oxides* (Ed.: S. Trasatti), Elsevier, Amsterdam, 1980, Part A, Chapter 4.
196. D. Devilliers, M. T. Dinh Thi, E. Mahé et al., *J. Electroanal. Chem.* **2004**, 573, 227–239.
197. J. C. K. Ho, G. T. Filho, R. Simpraga et al., *J. Electroanal. Chem.* **1994**, 366, 147–162.
198. P. K. Shen, X. L. Wei, *Electrochim. Acta* **2003**, 48, 1743–1747.
199. J.-R. Wang, G.-L. Wei, *J. Electroanal. Chem.* **1995**, 390, 29–33.
200. B. Monahov, D. Pavlov, A. Kirchev et al., *J. Power Sources* **2003**, 113, 281–292.
201. C.-H. Yeh, C.-C. Wan, J.-S. Chen, *J. Power Sources* **2001**, 101, 219–225.
202. I. Petersson, E. Ahlberg, B. Berghult, *J. Power Sources* **1998**, 76, 98–105.
203. H. Bode, *Lead-Acid Batteries*, Wiley, New York, 1977.
204. K. T. Kawagoe, D. C. Johnson, *J. Electrochem. Soc.* **1994**, 141, 3404–3409.
205. A. B. Velichenko, R. Amadelli, G. L. Zucchini et al., *Electrochim. Acta* **2000**, 45, 4341–4350.
206. A. B. Velichenko, R. Amadelli, E. A. Baranova et al., *J. Electroanal. Chem.* **2002**, 527, 56–64.
207. M. Shiota, Y. Yamaguchi, Y. Nakayama et al., *J. Power Sources* **2001**, 95, 203–208.
208. R. Fitas, L. Zerroual, N. Chelali et al., *J. Power Sources* **1997**, 64, 57–60.
209. R. Fitas, N. Chelali, L. Zerroual et al., *Solid State Ionics* **2000**, 127, 49–54.
210. T. Torimoto, S. Takabayashi, H. Mori et al., *J. Electroanal. Chem.* **2002**, 522, 33–39.
211. M. Sharon, K. S. Ramaiah, M. Kumar et al., *J. Electroanal. Chem.* **1997**, 436, 49–52.
212. H. Saloniemi, M. Ritala, M. Leskela et al., *J. Electrochem. Soc.* **1999**, 146, 2522–2525.
213. A. A. Vertegel, M. G. Shumsky, J. A. Switzer, *Angew. Chem., Int. Ed. Engl.* **1999**, 38, 3169–3171.
214. K. K. Nanda, S. N. Sahu, *Adv. Mater.* **2001**, 13, 280.
215. H. Saloniemi, M. Kemell, M. Ritala et al., *Thin Solid Films* **2001**, 386, 32–40.
216. Y. J. Yang, L. Y. He, Q. F. Zhang, *Electrochim. Commun.* **2005**, 7, 361–364.
217. I. Cisneros-González, M. T. Oropeza-Guzmán, I. González, *Electrochim. Acta* **2000**, 45, 2729–2741.
218. G. L. Pashkov, E. V. Mikhлина, A. G. Kholmogorov et al., *Hydrometallurgy* **2002**, 63, 171–179.
219. J. L. Nava, M. T. Oropeza, I. Gonzalez, *Electrochim. Acta* **2002**, 47, 1513–1525.
220. Y. Mikhlin, A. Kuklinskiy, E. Mikhлина et al., *J. Appl. Electrochem.* **2004**, 34, 37–46.
221. I. V. Chernyshova, *J. Phys. Chem. B* **2001**, 105, 8178–8184.
222. I. V. Chernyshova, *J. Phys. Chem. B* **2001**, 105, 8185–8191.
223. I. V. Chernyshova, *Russ. J. Electrochem.* **2001**, 37, 579–584.
224. I. V. Chernyshova, *Langmuir* **2002**, 18, 6962–6968.
225. I. V. Chernyshova, *J. Electroanal. Chem.* **2003**, 558, 83–98.
226. I. Kartio, K. Laajalehto, T. Kaurila et al., *Appl. Surf. Sci.* **1996**, 93, 167–177.
227. N. N. Zhu, A. P. Zhang, Q. J. Wang et al., *Electroanalysis* **2004**, 16, 577–582.
228. E. A. Streltsov, N. P. Osipovich, L. S. Ivashkevich et al., *Electrochim. Acta* **1998**, 43, 869–873.
229. H. Saloniemi, T. Kanninen, M. Ritala et al., *J. Mater. Chem.* **1998**, 8, 651–654.
230. E. A. Streltsov, N. P. Osipovich, L. S. Ivashkevich et al., *Electrochim. Acta* **1999**, 44, 2645–2652.
231. H. Saloniemi, M. Kemell, M. Ritala et al., *J. Mater. Chem.* **2000**, 10, 519–525.
232. D. K. Ivanov, C. K. Poznyak, N. P. Osipovich et al., *Russ. J. Electrochem.* **2004**, 40, 1044–1051.
233. R. Vaidyanathan, J. L. Stickney, U. Happek, *Electrochim. Acta* **2004**, 49, 1321–1326.
234. H. Saloniemi, T. Kanninen, M. Ritala et al., *Thin Solid Films* **1998**, 326, 78–82.
235. H. Saloniemi, M. Kemell, P. Ritala et al., *J. Electroanal. Chem.* **2000**, 482, 139–148.
236. E. A. Strel'tsov, N. P. Osipovich, L. S. Ivashkevich et al., *Russ. J. Appl. Chem.* **1997**, 70, 1651–1653.
237. E. A. Streltsov, N. P. Osipovich, L. S. Ivashkevich et al., *Electrochim. Acta* **1998**, 44, 407–413.

238. E. A. Strel'tsov, N. P. Osipovich, L. S. Ivashkevich et al., *Russ. J. Appl. Chem.* **1998**, 71, 1756–1758.
239. D. M. Kolb, R. Kotz, K. Yamamoto, *Surf. Sci.* **1980**, 101, 490–498.
240. B. Beden, F. Kadirgan, C. Lamy et al., *J. Electroanal. Chem.* **1981**, 127, 75–85.
241. J. M. Feliu, A. Fernández-Vega, J. M. Orts et al., *J. Chim. Phys.* **1991**, 88, 1493–1518.
242. F. El Omar, R. Durand, *J. Electroanal. Chem.* **1984**, 178, 343–350.
243. J. Clavilier, J. M. Orts, J. M. Feliu et al., *J. Electroanal. Chem.* **1990**, 293, 197–208.
244. R. L. Borup, D. E. Sauer, E. M. Stuve, *Surf. Sci.* **1993**, 293, 10–26.
245. R. L. Borup, D. E. Sauer, E. M. Stuve, *Surf. Sci.* **1993**, 293, 27–34.
246. B. N. Grgur, N. M. Marković, P. N. Ross, *Langmuir* **1997**, 13, 6370–6374.
247. N. M. Marković, B. N. Grgur, C. A. Lucas et al., *J. Electroanal. Chem.* **1998**, 448, 183–188.
248. C. Nishihara, K. Iwata, T. Tai et al., *Electrochem. Commun.* **1999**, 1, 104–107.
249. N. Hoshi, I. Tae Bae, D. A. Scherson, *J. Phys. Chem. B* **2000**, 104, 6049–6052.
250. N. M. Markovic, B. N. Grgur, C. A. Lucas et al., *J. Chem. Soc., Faraday Trans.* **1998**, 94, 3373–3379.
251. R. R. Adzic, J. Wang, C. M. Vitus et al., *Surf. Sci.* **1993**, 293, L876–L883.
252. C. A. Lucas, N. M. Markovic, P. N. Ross, *Langmuir* **1997**, 13, 5517–5520.
253. M. E. Martins, R. C. Salvarezza, A. J. Arvia, *Electrochim. Acta* **1996**, 41, 2441–2449.
254. R. Adzic, R. Yeager, B. D. Cahan, *J. Electrochem. Soc.* **1974**, 121, 474–484.
255. J. Schultze, D. Dickermann, *Surf. Sci.* **1976**, 54, 489–505.
256. K. Engelsmann, W. J. Lorenz, E. Schmidt, *J. Electroanal. Chem.* **1980**, 114, 1–10.
257. K. Engelsmann, W. J. Lorenz, E. Schmidt, *J. Electroanal. Chem.* **1980**, 114, 11–24.
258. A. Hamelin, J. Lipkowski, *J. Electroanal. Chem.* **1984**, 171, 317–330.
259. D. M. Kolb, D. Leutloff, M. Przasnyski, *Surf. Sci.* **1975**, 47, 622–634.
260. F. M. Romeo, R. I. Tucceri, D. Posadas, *Surf. Sci.* **1988**, 203, 186–200.
261. C. Chen, N. Washburn, A. A. Gewirth, *J. Phys. Chem.* **1993**, 97, 9754–9760.
262. M. Green, K. J. Hanson, *Surf. Sci.* **1991**, 259, L743–L749.
263. N. J. Tao, J. Pan, Y. Li et al., *Surf. Sci.* **1992**, 271, L338–L344.
264. J. Perdureau, J. P. Biberian, G. E. Rhead, *J. Phys. F: Met. Phys.* **1974**, 4, 798–806.
265. E. Herrero, L. J. Buller, H. D. Abruña, *Chem. Rev.* **2001**, 101, 1897–1930.
266. B. K. Niece, A. A. Gewirth, *J. Phys. Chem. B* **1998**, 102, 818–823.
267. M. P. Green, K. J. Hanson, D. A. Scherson et al., *J. Phys. Chem.* **1989**, 93, 2181–2184.
268. M. P. Green, K. J. Hanson, R. Carr et al., *J. Electrochem. Soc.* **1990**, 137, 3493–3498.
269. M. Mariscal, W. Schmickler, *J. Electroanal. Chem.* **2005**, 582, 64–68.
270. E. Budevski, G. Staikov, W. J. Lorenz, *Electrochemical Phase Formation and Growth*, VCH Publishers, Weinheim, 1996.
271. M. I. Rojas, *J. Electroanal. Chem.* **1996**, 405, 33–38.
272. U. Schmidt, S. Vinzelberg, G. Staikov, *Surf. Sci.* **1996**, 348, 261–279.
273. P. Hale, S. Thurgate, P. Wilkie, *Surf. Interface Anal.* **2003**, 35, 842–851.
274. M. J. Henderson, E. Bitziou, A. R. Hillman et al., *J. Electrochem. Soc.* **2001**, 148, E105–E111.
275. X. Q. Zeng, S. Bruckenstein, *J. Electrochem. Soc.* **1999**, 146, 2549–2554.
276. X. Q. Zeng, S. Bruckenstein, *J. Electrochem. Soc.* **1999**, 146, 2555–2561.
277. X. Q. Zeng, R. Hatton, *Electrochim. Acta* **2000**, 45, 3629–3638.
278. B. E. Conway, J. C. Chacha, *J. New Mater. Electrochem. Syst.* **2004**, 7, 231–240.
279. E. Kirowa-Eisner, Y. Bonfil, D. Tzur et al., *J. Electroanal. Chem.* **2003**, 552, 171–183.
280. D. W. M. Arrigan, L. Le Bihan, M. J. Pickup, *Analyst* **1999**, 124, 1797–1802.
281. T. A. Brunt, T. Rayment, S. J. O'Shea et al., *Langmuir* **1996**, 12, 5942–5946.
282. M. Seo, M. Yamazaki, *J. Electrochem. Soc.* **2004**, 151, E276–E281.
283. Y. V. Bokshits, N. P. Osipovich, E. A. Strel'tsov et al., *Colloids Surf. Physicochem. Eng. Aspects* **2004**, 242, 79–83.
284. X. Xing, I. Tae Bae, D. A. Scherson, *Electrochim. Acta* **1995**, 40, 29–36.
285. H. J. Pauling, K. Jüttner, *Electrochim. Acta* **1992**, 37, 2237–2244.
286. K. J. Stevenson, D. W. Hatchett, H. S. White, *Langmuir* **1996**, 12, 494–499.
287. J. Sackmann, A. Bunk, R. T. Pötzschke et al., *Electrochim. Acta* **1998**, 43, 2863–2873.

288. R. Widmer, H. Siegenthaler, *J. Electrochem. Soc.* **2004**, 151, E238–E245.
289. W. J. Lorenz, G. Staikov, *Surf. Sci.* **1995**, 335, 32–43.
290. D. Carnal, P. I. Oden, U. Müller et al., *Electrochim. Acta* **1995**, 40, 1223–1235.
291. R. Widmer, H. Siegenthaler, *Electrochem. Commun.* **2005**, 7, 421–426.
292. W. Obretenov, N. Dimitrov, A. Popov, *J. Cryst. Growth* **1996**, 167, 253–259.
293. J.-M. Zen, C.-C. Yang, A. S. Kumar, *Electrochim. Acta* **2001**, 47, 899–904.
294. M. Hepel, *Electroanalysis* **2005**, 17, 1401–1412.
295. L. Bonou, M. Eyraud, J. Crousier, *J. Appl. Electrochem.* **1994**, 24, 906–910.
296. J. Horkans, I. H. Chang, H. Deligianni et al., *J. Electrochem. Soc.* **1995**, 142, 2244–2249.
297. Y. S. Chu, I. K. Robinson, A. A. Gewirth, *Phys. Rev. B* **1997**, 55, 7945–7954.
298. K. I. Popov, M. G. Pavlović, E. R. Stojilković et al., *Hydrometallurgy* **1997**, 46, 321–336.
299. I. A. Carlos, T. T. Matsuo, J. L. P. Siqueira et al., *J. Power Sources* **2004**, 132, 261–265.
300. G. M. Brisard, E. Zenati, H. A. Gasteiger et al., *Langmuir* **1995**, 11, 2221–2230.
301. G. M. Brisard, E. Zenati, H. A. Gasteiger et al., *Langmuir* **1997**, 13, 2390–2397.
302. T. P. Moffat, *J. Phys. Chem. B* **1998**, 102, 10020–10026.
303. H.-C. Wu, S.-L. Yau, *J. Phys. Chem. B* **2001**, 105, 6965–6971.
304. A. Czerwiński, M. Żelazowska, *J. Electroanal. Chem.* **1996**, 410, 55–60.
305. Z. Rogulski, W. Lewdorowicz, W. Tokarz et al., *Pol. J. Chem.* **2004**, 78, 1357–1370.
306. J. Mostany, J. Mozota, B. R. Scharifker, *J. Electroanal. Chem.* **1984**, 177, 25–37.
307. I. Petersson, E. Ahlberg, *J. Electroanal. Chem.* **2000**, 485, 166–177.
308. J. Mostany, J. Parra, B. Scharifker, *J. Appl. Electrochem.* **1986**, 16, 333–338.
309. G. Carreño, E. Sosa, I. González et al., *Electrochim. Acta* **1999**, 44, 2633–2643.
310. E. Sosa, G. Carreño, C. Ponce de León et al., *Appl. Surf. Sci.* **2000**, 153, 245–258.
311. B. Rashkova, B. Guel, R. T. Pötzschke et al., *Electrochim. Acta* **1998**, 43, 3021–3028.
312. C. Prado, S. J. Wilkins, P. Gründler et al., *Electroanalysis* **2003**, 15, 1011–1016.
313. J. C. Ziegler, G. E. Engelmann, D. M. Kolb, *Z. Phys. Chem.* **1999**, 208, 151–166.
314. J. C. Ziegler, R. I. Wielgosz, D. M. Kolb, *Electrochim. Acta* **1999**, 45, 827–833.
315. R. T. Pötzschke, G. Staikov, W. J. Lorenz et al., *J. Electrochem. Soc.* **1999**, 146, 141–149.
316. B. Scharifker, G. Hills, *Electrochim. Acta* **1983**, 28, 879–889.
317. J. C. Ziegler, G. Scherb, O. Bunk et al., *Surf. Sci.* **2000**, 452, 150–160.
318. H. Hibino, T. Ogino, *Surf. Sci.* **1995**, 328, L547–L552.
319. C. Elers, U. König, G. Staikov et al., *Electrochim. Acta* **2001**, 47, 379–385.
320. E. A. Streltsov, S. K. Poznyak, N. P. Osipovich, *J. Electroanal. Chem.* **2002**, 518, 103–114.
321. N. P. Osipovich, E. A. Streltsov, *Russ. J. Electrochem.* **2000**, 36, 1–7.
322. D. K. Ivanov, N. P. Osipovich, S. K. Poznyak et al., *Surf. Sci.* **2003**, 532–535, 1092–1097.
323. G. Ritzoulis, N. Georgolios, *J. Electroanal. Chem.* **1994**, 370, 219–222.
324. G. A. Ragoisha, A. S. Bondarenko, N. P. Osipovich et al., *J. Electroanal. Chem.* **2004**, 565, 227–234.
325. E. Streltsov, N. P. Osipovich, L. S. Ivashkevich et al., *Dokl. Akad. Nauk Belarus* **1997**, 41, 62–65.
326. A. Piekarska, H. Elżanowska, V. I. Birss, *Pol. J. Chem.* **2004**, 78, 1391–1412.
327. I. Paleska, R. Pruszkowska-Drachal, J. Kotoski et al., *J. Power Sources* **2004**, 129, 326–329.
328. C. O. Avellaneda, M. A. Napolitano, E. K. Kaibara et al., *Electrochim. Acta* **2005**, 50, 1317–1321.
329. L. O. Bulhões, L. H. Mascaro, *J. Solid State Electrochem.* **2004**, 8, 238–243.
330. T. E. Graedel, *J. Electrochem. Soc.* **1994**, 141, 922–927.
331. P. Mattesco, N. Bui, P. Simon et al., *J. Power Sources* **1997**, 64, 21–27.
332. S. Zhong, J. Wang, H. K. Liu et al., *J. Power Sources* **1997**, 66, 107–113.
333. S. Zhong, J. Wang, H. K. Liu et al., *J. Appl. Electrochem.* **1999**, 29, 177–183.
334. E. Rocca, J. Steinmetz, *J. Electroanal. Chem.* **2003**, 543, 153–160.
335. S. S. Abd El Rehim, N. F. Mohamed, *Corros. Sci.* **1998**, 40, 1883–1896.
336. E. E. Abd El Aal, *Corrosion* **1992**, 48, 482–488.
337. M. A. Amin, S. S. Abdel Rehim, *Electrochim. Acta* **2004**, 49, 2415–2424.

338. S. S. El Egamy, W. A. Badawy, *Indian J. Chem. Technol.* **1996**, 3, 37–43.
339. E. E. Abd El Aal, *Anti-Corros. Methods Mater.* **2001**, 48, 116–125.
340. M. Uchida, A. Okuwaki, *Corros. Sci.* **1999**, 41, 1977–1986.
341. S. S. Abd El Rehim, N. H. Amin, L. I. Ali et al., *J. Chem. Technol. Biotechnol.* **1998**, 72, 197–201.
342. F. M. Al-Kharafi, W. A. Badawy, *Corros. Prev. Control* **1998**, 45, 75–86.
343. W. A. Badawy, F. M. Al-Kharafi, *Bull. Electrochem.* **1998**, 14, 1–9.
344. B. P. Boffardi, A. M. Sherbondy, *Corrosion* **1991**, 47, 966–975.
345. S. Abd El Wanees, E. E. Abd El Aal, A. Abd El Aal, *Bull. Soc. Chim. Fr.* **1991**, (Nov.–Dec.) 889–893.
346. K. V. Kordesch, *Batteries, Vol. 2, Lead Acid Batteries and Electric Vehicles*, Marcel Dekker, New York, 1977.
347. D. Linden, *Handbook of Batteries*, McGraw-Hill, New York, 1995.
348. K. R. Bullock, C. A. Vincent, in *Modern Batteries* (Eds.: C. A. Vincent, B. Scrosati), Arnold, London, 1997, p. 142.
349. R. J. Brodd, K. R. Bullock, R. A. Leising et al., *J. Electrochem. Soc.* **2004**, 151, K1–K11.
350. M. G. Mayer, D. A. J. Rand, *J. Power Sources* **1996**, 59, 17–24.
351. T. Rogachev, D. Pavlov, *J. Power Sources* **1997**, 64, 51–56.
352. D. Pavlov, G. Petkova, M. Dimitrov et al., *J. Power Sources* **2000**, 87, 39–56.
353. G. Petkova, D. Pavlov, *J. Power Sources* **2003**, 113, 355–362.
354. N. Clement, R. Kurian, *J. Power Sources* **2003**, 116, 40–46.
355. J. P. Diard, B. Le Gorrec, C. Montella et al., *Electrochim. Acta* **1997**, 42, 3417–3420.
356. G. Lindbergh, *Electrochim. Acta* **1997**, 42, 1239–1246.
357. J. P. Diard, B. Le Gorrec, C. Montella, *J. Power Sources* **1998**, 70, 78–84.
358. J. M. Skowroński, T. Doczekalski, *J. Power Sources* **2004**, 126, 175–181.
359. B. Hariprakash, A. U. Mane, S. K. Martha et al., *Electrochem. Solid State Lett.* **2004**, 7, A66–A69.
360. C. S. Lakshmi, J. E. Manders, D. M. Rice, *J. Power Sources* **1998**, 73, 23–29.
361. Y. B. Zhou, H. T. Liu, W. B. Cai et al., *J. Electrochem. Soc.* **2004**, 151, A978–A982.
362. A. Cooper, P. T. Moseley, *J. Power Sources* **2003**, 113, 200–208.
363. D. Pavlov, V. Naidenov, S. Ruevski et al., *J. Power Sources* **2003**, 113, 209–227.
364. R. J. Ball, R. Stevens, *J. Power Sources* **2003**, 113, 228–232.
365. D. Pavlov, *J. Power Sources* **1997**, 64, 131–137.
366. A. Kirchev, D. Pavlov, B. Monahov, *J. Power Sources* **2003**, 113, 245–254.
367. Y. L. Guo, J. Y. Wu, L. K. Song et al., *J. Electrochem. Soc.* **2001**, 148, A1287–A1293.
368. Z. H. Li, Y. L. Guo, L. Z. Wu et al., *J. Electrochem. Soc.* **2002**, 149, A934–A938.
369. V. Srinivasan, G. Q. Wang, C. Y. Wang, *J. Electrochem. Soc.* **2003**, 150, A316–A325.
370. M. P. Vinod, K. Vijayamohanan, *J. Power Sources* **2000**, 89, 88–92.
371. A. Salkind, T. Atwater, P. Singh et al., *J. Power Sources* **2001**, 96, 151–159.
372. A. J. Salkind, P. Singh, A. Cannone et al., *J. Power Sources* **2003**, 116, 174–184.
373. A. Hazza, D. Pletcher, R. Wills, *Phys. Chem. Chem. Phys.* **2004**, 6, 1773–1778.
374. G. Kokkinidis, D. Sazou, *J. Electroanal. Chem.* **1986**, 199, 165–176.
375. K. Jüttner, *Electrochim. Acta* **1984**, 29, 1597–1604.
376. K. Jüttner, *Electrochim. Acta* **1986**, 31, 917–927.
377. G. Kokkinidis, A. Papoutsis, G. Papanastasiou, *J. Electroanal. Chem.* **1993**, 359, 253–271.
378. A. Papoutsis, G. Kokkinidis, *J. Electroanal. Chem.* **1994**, 371, 231–239.
379. S. J. Hsieh, A. A. Gewirth, *Surf. Sci.* **2002**, 498, 147–160.
380. I. Oh, A. A. Gewirth, J. Kwak, *J. Catal.* **2003**, 213, 17–22.
381. D. Pletcher, V. Solis, *J. Electroanal. Chem.* **1982**, 131, 309–323.
382. X. H. Xia, T. Iwasita, *J. Electrochem. Soc.* **1993**, 140, 2559–2565.
383. H.-W. Lei, H. Hattori, H. Kita, *Electrochim. Acta* **1996**, 41, 1619–1628.
384. B. R. Eggins, C. Ennis, R. McConnell et al., *J. Appl. Electrochem.* **1997**, 27, 706–712.
385. S. Kaneco, R. Iwao, K. Iiba et al., *Energy* **1998**, 23, 1107–1112.
386. S. Q. Xia, S. P. Chen, S. G. Sun, *Acta Phys. Chem Sin.* **2001**, 17, 140–143.
387. P. L. Cabot, M. Centelles, L. Segarra et al., *J. Electrochem. Soc.* **1997**, 144, 3749–3757.

388. I. M. Osadchenko, A. P. Tomilov, *Russ. J. Appl. Chem.* **1998**, 71, 719–721.
389. N. Georgolios, G. Kyriacou, G. Ritzoulis, *J. Appl. Electrochem.* **2001**, 31, 207–212.
390. S. T. Lin, R. Y. H. Chao, S. C. Lin et al., *J. Chin. Chem. Soc.* **2002**, 49, 539–544.
391. B. F. Gianetti, C. M. V. B. Almeida, S. H. Bonilla et al., *Z. Phys. Chem.* **2003**, 217, 35–44.
392. M. Bazzaoui, E. A. Bazzaoui, L. Martins et al., *Synth. Met.* **2002**, 130, 73–83.
393. K. Wandachowicz, R. Dylewski, *Przem. Chem.* **1999**, 78, 187–190.
394. S. Wasmus, W. Vielstich, *J. Electroanal. Chem.* **1993**, 359, 175–191.
395. J. S. Ge, D. C. Johnson, *J. Electrochem. Soc.* **1996**, 143, 2543–2548.
396. W. Gorski, R. T. Kennedy, *J. Electroanal. Chem.* **1997**, 424, 43–48.
397. F. Bonfatti, S. Ferro, F. Lavezzo et al., *J. Electrochem. Soc.* **1999**, 146, 2175–2179.
398. D. Pavlov, B. Monahov, *J. Electrochem. Soc.* **1996**, 143, 3616–3629.
399. D. Pavlov, B. Monahov, *J. Electrochem. Soc.* **1998**, 145, 70–77.
400. R. Amadelli, A. Maldotti, A. Molinari et al., *J. Electroanal. Chem.* **2002**, 534, 1–12.
401. S. Abaci, K. Pekmez, A. Yildiz, *Electrochem. Commun.* **2005**, 7, 328–332.
402. A. A. Babak, R. Amadelli, A. De Battisti et al., *Electrochim. Acta* **1994**, 39, 1597–1602.
403. A. B. Velichenko, D. V. Girenko, S. V. Kovalyov et al., *J. Electroanal. Chem.* **1998**, 454, 203–208.
404. C. N. Ho, B. J. Hwang, *J. Electroanal. Chem.* **1994**, 377, 177–190.
405. R. Amadelli, L. Armelao, A. B. Velichenko et al., *Electrochim. Acta* **1999**, 45, 713–720.
406. L. M. Da Silva, L. A. De Faria, J. F. C. Boodts, *Electrochim. Acta* **2003**, 48, 699–709.
407. U. Schümann, P. Gründler, *Water Res.* **1998**, 39, 2835–2842.
408. M. Panizza, G. Cerisola, *Electrochim. Acta* **2003**, 48, 3491–3497.
409. R. Amadelli, A. De Battisti, D. V. Girenko et al., *Electrochim. Acta* **2000**, 46, 341–347.
410. N. B. Tahar, A. Savall, *J. Appl. Electrochem.* **1999**, 29, 277–283.
411. S. Abaci, U. Tamer, K. Pekmez et al., *Appl. Surf. Sci.* **2005**, 240, 112–119.
412. C. Borrás, T. Laredo, J. Mostany et al., *Electrochim. Acta* **2004**, 49, 641–648.
413. C. Borrás, T. Laredo, B. R. Scharifker, *Electrochim. Acta* **2003**, 48, 2775–2780.
414. S. Abaci, U. Tamer, K. Pekmez et al., *J. Appl. Electrochem.* **2002**, 32, 193–196.
415. I. H. Yeo, S. Kim, R. Jacobson et al., *J. Electrochem. Soc.* **1989**, 136, 1395–1401.
416. B. J. Hwang, K. L. Lee, *Thin Solid Films* **1996**, 279, 236–241.
417. S. Abaci, K. Pekmez, N. Pekmez et al., *J. Appl. Polym. Sci.* **2003**, 87, 599–605.
418. S. Abaci, A. Yildiz, *J. Electroanal. Chem.* **2004**, 569, 161–168.
419. S. Abaci, Y. Aslan, A. Yildiz, *J. Mater. Sci.* **2005**, 40, 1163–1168.
420. P. Bühlmann, E. Pretsch, E. Bakker, *Chem. Rev.* **1998**, 98, 1593–1687.
421. E. Bakker, M. Telting-Diaz, *Anal. Chem.* **2002**, 74, 2781–2800.
422. E. Bakker, *Anal. Chem.* **2004**, 76, 3285–3289.
423. E. Bakker, E. Pretsch, *Trends Anal. Chem.* **2005**, 24, 199–207.
424. T. Sokalski, A. Ceresa, T. Zwickl et al., *J. Am. Chem. Soc.* **1997**, 119, 11347–11348.
425. E. Bakker, E. Pretsch, *Trends Anal. Chem.* **2001**, 20, 11–19.
426. E. Bakker, P. Bühlmann, E. Pretsch, *Electroanalysis* **1999**, 11, 915–933.
427. É. Pergel, R. E. Gyurcsányi, K. Tóth et al., *Anal. Chem.* **2001**, 73, 4249–4253.
428. J. Sutter, E. Lindner, R. E. Gyurcsányi et al., *Anal. Bioanal. Chem.* **2004**, 380, 7–14.
429. J. Sutter, A. Radu, S. Peper et al., *Anal. Chim. Acta* **2004**, 523, 53–59.
430. R. E. Gyurcsányi, É. Pergel, R. Nagy et al., *Anal. Chem.* **2001**, 73, 2104–2111.
431. A. Ceresa, E. Pretsch, *Anal. Chim. Acta* **1999**, 395, 41–52.
432. M. Fouskaki, N. A. Chaniotakis, *Anal. Chem.* **2005**, 77, 1780–1784.
433. N. P. R. Andersen, *Anal. Chim. Acta* **1998**, 368, 191–196.
434. E. Fischer, C. M. G. van den Berg, *Anal. Chim. Acta* **1999**, 385, 273–280.
435. O. Mikkelsen, K. H. Schroeder, *Electroanalysis* **2003**, 15, 679–687.
436. M. Brand, I. Eshkenazi, E. Kirowa-Eisner, *Anal. Chem.* **1997**, 69, 4660–4664.
437. O. Mikkelsen, K. H. Schroeder, *Electroanalysis* **2001**, 13, 687–692.
438. Y. Bonfil, E. Kirowa-Eisner, *Anal. Chim. Acta* **2002**, 457, 285–296.
439. Y. Bonfil, M. Brand, E. Kirowa-Eisner, *Anal. Chim. Acta* **2002**, 464, 99–114.

440. B. Krasnodębska-Ostregę, J. Piekarska, *Electroanalysis* **2005**, *17*, 815–818.
441. Y. Bonfil, M. Brand, E. Kirowa-Eisner, *Electroanalysis* **2003**, *15*, 1369–1376.
442. P. N. Bartlett, G. Denault, M. F. B. Sousa, *Analyst* **2000**, *125*, 1135–1138.
443. J. M. Zen, H. H. Chung, G. Hangovan et al., *Analyst* **2000**, *125*, 1139–1146.
444. S. M. Silva, A. M. Bond, *Anal. Chim. Acta* **2003**, *500*, 307–321.
445. E. A. Osipova, V. E. Sladkov, A. I. Kamenev et al., *Anal. Chim. Acta* **2000**, *404*, 231–240.
446. M. A. Rahman, M. S. Won, Y. B. Shim, *Anal. Chem.* **2003**, *75*, 1123–1129.
447. C. Prado, S. J. Wilkins, F. Marken et al., *Electroanalysis* **2002**, *14*, 262–272.
448. R. I. Stefan, S. G. Bairu, *Talanta* **2004**, *63*, 605–608.
449. A. M. Bond, W. J. Miao, T. D. Smith et al., *Anal. Chim. Acta* **1999**, *396*, 203–213.
450. Z. Hu, C. J. Seliskar, W. R. Heineman, *Anal. Chim. Acta* **1998**, *369*, 93–101.
451. K. Wagner, J. W. Strojek, K. Koziel, *Anal. Chim. Acta* **2001**, *447*, 11–21.
452. K. Wagner, J. W. Strojek, K. Koziel, *Chem. Anal. (Warsaw)* **2002**, *47*, 385–397.
453. K. Wagner, J. W. Strojek, K. Koziel, *Anal. Chim. Acta* **2002**, *455*, 69–81.
454. A. M. Zimer, R. Bertholdo, M. T. Grassi et al., *Electrochem. Commun.* **2003**, *5*, 983–988.
455. M. Hepel, L. Dentrone, *Electroanalysis* **1996**, *8*, 996–1005.
456. A. Wanekaya, O. A. Sadik, *J. Electroanal. Chem.* **2002**, *537*, 135–143.
457. S. Majid, M. El Rhazi, A. Amine et al., *Microchim. Acta* **2003**, *143*, 195–204.
458. J. Wang, *Anal. Chem.* **1982**, *54*, 221–223.
459. P. R. M. Silva, M. A. El Khakani, B. Le Drogoff et al., *Sens. Actuators, B* **1999**, *60*, 161–167.
460. B. Le Drogoff, M. A. El Khakani, P. R. M. Silva et al., *Electroanalysis* **2001**, *13*, 1491–1496.
461. E. Juzeliunas, H. W. Pickering, K. G. Weil, *J. Electrochem. Soc.* **2000**, *147*, 1088–1095.
462. A. Herrero, M. C. Ortiz, *Anal. Chim. Acta* **1997**, *348*, 51–59.
463. Y. G. Mourzina, J. Schubert, W. Zander et al., *Electrochim. Acta* **2001**, *47*, 251–258.
464. G. S. Reeder, W. R. Heineman, *Sens. Actuators, B* **1998**, *52*, 58–64.
465. I. Palchetti, A. Cagnini, M. Mascini et al., *Mikrochim. Acta* **1999**, *131*, 65–73.
466. K. C. Honeychurch, J. P. Hart, D. C. Cowell, *Electroanalysis* **2000**, *12*, 171–177.
467. J. M. Zen, H. H. Chung, A. S. Kumar, *Anal. Chim. Acta* **2000**, *421*, 189–197.
468. N. Y. Stozhko, G. N. Lipunova, T. I. Maslakova et al., *J. Anal. Chem.* **2004**, *59*, 179–184.
469. I. Palchetti, G. Marazza, M. Mascini, *Anal. Lett.* **2001**, *34*, 813–824.
470. R. P. Akkermans, J. C. Ball, F. Marken et al., *Electroanalysis* **1998**, *10*, 26–32.
471. R. P. Akkermans, J. C. Ball, T. O. Rebbitt et al., *Electrochim. Acta* **1998**, *43*, 3443–3449.
472. A. N. Blythe, R. P. Akkermans, R. G. Compton, *Electroanalysis* **2000**, *12*, 16–20.
473. C. E. West, J. L. Hardcastle, R. G. Compton, *Electroanalysis* **2002**, *14*, 1470–1478.
474. C. E. Banks, R. G. Compton, *Electroanalysis* **2003**, *15*, 329–346.

Part B:

Electrochemistry of Gold, Silver, and Mercury*

Marek Orlik and Zbigniew Galus

Department of Chemistry, University of Warsaw, Warsaw, Poland

**Dedicated to the memory of Professor Ralph N. Adams, a respected and unforgettable electrochemist and man*

24.4

Electrochemistry of Gold

24.4.1	Preparation of Au Surfaces and Double-layer Properties	841
24.4.1.1	Polycrystalline (pc-Au) and Single-crystal Au/H ₂ O Interface	841
24.4.1.2	pc-Au and Single-crystal Au/Nonaqueous Solutions Interface	844
24.4.2	Adsorption of Inorganic Compounds on Gold Electrodes	845
24.4.2.1	Sulfate	845
24.4.2.2	Hydroxide	847
24.4.2.3	Nitrate	847
24.4.2.4	Chloride	847
24.4.2.5	Bromide	848
24.4.2.6	Iodide	849
24.4.2.7	Cyanide	851
24.4.2.8	Thiocyanate	852
24.4.2.9	Other Inorganic Species	852
24.4.3	Adsorption of Organic Compounds on Gold Electrodes	853
24.4.3.1	Adsorption of Sulfur-containing Compounds	853
24.4.3.1.1	Adsorption of Thiols	853
24.4.3.1.2	Adsorption of Modified Thiols	860
24.4.3.1.3	Adsorption of Thiourea	861
24.4.3.1.4	Adsorption of Disulfides and Related Compounds	861
24.4.3.1.5	Other Sulfur Compounds and Complex Adsorption Layers	863
24.4.3.2	Adsorption of Selenium-containing Compounds	866
24.4.3.3	Adsorption of Nitrogen-containing Compounds	866
24.4.3.3.1	Pyridine and its Derivatives	866
24.4.3.3.2	Pyrazine	870
24.4.3.3.3	Amines and Other Nitrogen-containing Compounds	870

24.4.3.4	Adsorption of Other Organic Compounds	870
24.4.3.4.1	Alcohols	870
24.4.3.4.2	Aminoacids	871
24.4.3.4.3	Other Organic Acids	872
24.4.3.4.4	Nucleic Bases and Other Biochemical Compounds	872
24.4.3.4.5	Other Compounds	875
24.4.4	Reconstruction of the Surface of Gold Electrodes	876
24.4.5	Formation of Oxides on Gold Electrodes	879
24.4.6	Underpotential Deposition of Various Metals on Au	883
24.4.6.1	Cu	883
24.4.6.2	Cd	886
24.4.6.3	Pd	888
24.4.6.4	S, Se, and Te	889
24.4.6.5	Sulfur	889
24.4.6.6	Selenium	889
24.4.6.7	Tellurium	890
24.4.6.8	Bi	890
24.4.6.9	Pt	892
24.4.6.10	Ni	892
24.4.6.11	Co	892
24.4.6.12	Sb	893
24.4.6.13	Sn	894
24.4.6.14	Al	894
24.4.6.15	Tl	894
24.4.6.16	Pb	895
24.4.6.17	Zn	895
24.4.6.18	Ge	895
24.4.6.19	Rh	896
24.4.6.20	Li	896
24.4.6.21	Fe	896
24.4.6.22	Ag	896
24.4.6.23	Hg	897
24.4.7	Electrochemistry of Coordination Compounds of Gold. Electrodissolution and Electrodeposition of Au	897
24.4.7.1	Au Electrodeposition	898
24.4.7.2	Au Electrodissolution	899
24.4.8	Gold Clusters	899
	References	900

In this chapter recent studies on electrochemistry of three noble metals, gold, silver, and mercury are presented.

In recent years, electrochemical studies of these metals and their compounds have been dominated by surface studies.

Three main groups of processes related to these metals have been intensively investigated:

1. underpotential deposition of different metals (ions),

2. specific adsorption of various neutral compounds and ions, and
3. self-assembling of various mostly sulfur-containing compounds on the surfaces of these noble metals.

In the study of solid metals, gold and silver single-crystal electrodes with well-defined surfaces were preferentially used.

A chapter on the electrochemistry of gold was published in the 4th volume of *Encyclopedia of Electrochemistry of the Elements* in 1975. At that time, mostly polycrystalline gold (pc-Au) electrodes were used, although already in the early sixties, the studies involving single-crystal electrodes had also been published. It appears from a review of the recent literature that polycrystalline gold electrodes are still in use; however, the following trends are emphasized the most:

1. wide use of single-crystal electrodes;
2. modification of gold electrode surfaces.

This review should, in principle, cover the literature on the electrochemistry of gold, which has been published over the last decade, though in some cases, the earlier literature also is discussed. However, a large number of papers on this subject make a comprehensive description difficult. Therefore, this chapter is focused only on the selected papers, which present the most representative trends and the most important results.

24.4.1

Preparation of Au Surfaces and Double-layer Properties

24.4.1.1 Polycrystalline (pc-Au) and Single-crystal Au/H₂O Interface

Detailed reviews on the properties of the pc-Au/H₂O interface have been published earlier by Frumkin [1], Hamelin [2], and

Vorotyntsev [3], and more recently by Trasatti and Lust [4]. From the above papers, selected data have been taken and are presented below.

The potential corresponding to the minimum capacitance of the diffusion layer at the pc-Au|H₂O interface was found to be equal to -0.04 V (versus saturated calomel electrode, SCE), independently of the solution pH and NaF concentration studied. However, a slight negative shift of this potential with the increasing concentration of perchlorate ions was observed, thus suggesting a weak specific affinity of these anions to the gold surface. The role of surface contaminations could not be excluded as well. In spite of certain controversies, it seems that the GCSG theory is applicable to the description of the pc-Au|H₂O interface (taking into account the roughness factor), without any corrections for the crystallographic inhomogeneity of the metal surface [4–6]. This conclusion has become, however, also a subject of discussion since the crystalline Au faces of low indices, present on the pc-Au surface, have a characteristic size of 5–6 nm, which seems to be large enough to contribute to the surface inhomogeneity [4]. Noteworthy is the fact that the potential at the C_i minimum is not equivalent to the zero charge potential [4].

In more recent studies, the double layer of a pc-Au electrode has been probed by atomic force microscopy (AFM) measurements [7]. The properties of the Au/solution interface were changed by variations in pH, salt concentration, and electrode potential.

Piela and Wrona [8] have employed impedance spectroscopy to study capacitance of the pc-Au electrode in 0.5 M H₂SO₄ in the double-layer potential region (-0.25 to 1.05 V versus SSCE) and

in the range corresponding to the formation of the oxide monolayer (1.05–1.4 V). In the latter case, it has been found that capacitance depends on the surface coverage with partially pure gold surface, MOH dipoles, oxide, or reconstructed gold surface. A simple equivalent circuit (without the constant phase element (CPE)) was found to be appropriate for the interpretation of the impedance data for both the pure gold surface and the surface covered with the oxide layer. The observed capacity versus electrode potential dependence, different from that for the mercury electrode, was attributed to the strong adsorption of (bi)sulfate ions. However, the roughness factor for the Au surface, both in the double layer and in the oxide formation region, was very low and comparable to that for the Hg electrode.

Hoogvliet et al. [9] have proposed a pulsed-potential pretreatment procedure, which allows one to decrease, in a reproducible manner, surface roughness of mechanically polished polycrystalline gold electrodes by a factor of 2.

Some methods of nanoscale preparation of gold surfaces have also been described. For instance, gold nanowell electrode arrays of a well depth of about 50 nm were prepared [10] by electrodeposition of Au through the pores of a porous alumina membrane. Nanoelectrode arrays were characterized using scanning tunneling microscopy (STM), AFM, scanning

electron microscopy, and electrochemical methods.

While considering single-crystal Au electrodes, attention should be drawn to the quite comprehensive review of the most recent achievements in the studies on the properties of these electrodes brought in contact with different solutions [4].

In electrochemical practice, mainly three types of gold surfaces, that is, Au(111), Au(110), and Au(100) are of the greatest importance, whereas other surfaces, as, for example, Au(210) are less frequently described in electrochemical papers.

The potentials of zero charge of single-crystal Au electrodes of various crystallographic orientations in contact with aqueous electrolyte solutions are given in Table 1.

It follows from the above data, similarly as for Ag, that the potential of zero charge increases with the surface density of atoms.

In Ref. 13, a new approach toward the preparation of Au(111) nanoisland-arrayed electrode based on fine colloidal nanolayer-directed seeding growth has been presented.

Chemically prepared colloidal gold nanoparticles were immobilized as a submonolayer on Au(111) surface modified with self-assembled monolayers (SAMs) of 4-aminothiophenol [14]. This submonolayer of Au nanoparticles was subsequently characterized using STM.

Tab. 1 Surface density of atoms, σ_{at} , and potentials of zero charge, E_{pzc} (versus SHE) for various crystal planes of Au electrodes [4, 11, 12]. Lattice constant $d = 0.2884$ nm

Au crystal plane	$\sigma_{\text{at}}[\text{at.} \cdot \text{nm}^{-2}]$	$E_{\text{pzc}}[\text{V}](0.05\text{M NaF})$	$E_{\text{pzc}}[\text{V}](0.01\text{M HClO}_4)$
(111)	13.88	0.56 ± 0.01	0.52 ± 0.01
(100)	12.02	0.30 ± 0.01	0.29 ± 0.01
(110)	8.50	0.19 ± 0.01	0.19 ± 0.01

Dieluweit and Giesen [15] have presented STM studies on the dynamics of monolayer Au islands on Au(100) electrode surface in sulfuric acid solutions. The authors have given a quantitative description of the equilibrium shape of Au islands on Au(100) electrodes and of their thermal fluctuations around the equilibrium shape. Later, the same researchers [16] have applied STM to investigate a monolayer of Au islands on Au(100) electrode in H_2SO_4 solutions.

Bilger and Pettinger [17] have applied second-harmonic generation (SHG) method to study the anisotropy of Au(110) electrode in a wide potential range from -0.60 to 0.60 V, corresponding to the transition from the microfaceted to the unreconstructed surface.

Also, modulation resistometry of a gold electrode has been applied [18]. Mazine et al. [19] have used in situ reflectance anisotropy spectroscopy and in situ STM to characterize Au(100) surface in 0.1 M Na_2SO_4 solutions. Three ranges of the applied potential were distinguished: (1) negative potentials up to about -0.6 V (versus $\text{Ag}|\text{AgCl}$), for which clear (1×3) reconstruction is obtained, (2) positive potentials up to about $+0.6$ V, for which the surface remains unreconstructed, and (3) intermediate potential range corresponding to the mixed domains.

Au(111) and Au(210) electrodes have been investigated [20] using electrochemical impedance spectroscopy in aqueous solutions of HClO_4 and KF in the double-layer potential region, in order to identify and explain frequency dispersion of interfacial capacitance. At negative potentials, the behavior closest to the ideal dispersionless behavior has always been observed. In KF solutions, at positive potentials, dispersion on both electrodes may be attributed

to the adsorption of either OH^- or HF species.

Adsorption of some inorganic or organic compounds can facilitate formation of well-defined Au surfaces. Trevor et al. [21] have found that a roughened Au(111) surface undergoes “electrochemical annealing” associated with surface migration of Au atoms. It has also been observed that the step motion is significantly accelerated by the adsorbed chloride ions. Baumgärtel and coworkers [22, 23], using cyclic voltammetry (CV), capacitance measurements, in situ STM, and combined in situ IR and STM, have studied adsorption of tetramethylthiourea (TMTU) and adsorbate-induced etching of Au(111). It has been found that etching at sufficiently anodic potentials leads to the formation of Au–TMTU complexes soluble in the electrolyte solution. This soluble complex can be subsequently electrodeposited at more negative potentials. Etching and deposition processes are schematically depicted in Fig. 1 [23].

In a detailed discussion about the properties of single-crystal Au electrodes in contact with aqueous solutions, it is necessary to consider water molecules adjacent to the Au surface. Hydrophilic properties of single-crystal Au electrodes have been studied by determining the dependence of the Gibbs energy of adsorption of 2-ethylether on the electrode potential [24]. It has been found that water molecules particularly are strongly bound to Au(110) surfaces, accordingly to the sequence of the decreasing Gibbs energies of adsorption of 2-ethylether: $\text{Au}(111) > \text{Au}(100) > \text{Au}(110)$. The structure of various Au surfaces has also been inferred from the studies on temperature coefficient of pzc (for a concise review, see Ref. 4). Finally, Ignaczak and Gomes

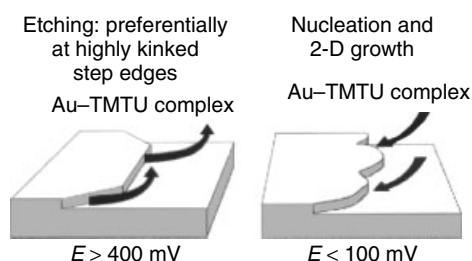


Fig. 1 The scheme of anisotropic surface etching and isotropic deposition of Au-TMTU complexes at step edges of the Au(111) surface in TMTU-containing electrolytes [23].

[25] have studied theoretically, an interaction of water molecule with Au(100), Ag(100), and Cu(100) surfaces, applying a cluster model approximation with Au-12, Ag-12, and Cu-12 clusters to mimic the (100) crystallographic plane. Two preferred conformations: bridge-perpendicular and top-tilted have been found indistinguishable in terms of adsorption energy. In both conformations, water molecule adsorbs via oxygen atom.

Under specific conditions, the potential of zero charge does not appear to be constant during electrochemical experiment, which makes the double-layer effect more complex. For example, the shift of the potential of zero charge during electroreduction of $S_2O_8^{2-}$, combined with the Frumkin-type double-layer effect, has been proposed [26] as an explanation for the oscillatory reduction of peroxodisulfate on Au(110) in diluted solutions of NaF.

24.4.1.2 pc-Au and Single-crystal Au/Nonaqueous Solutions Interface

Double layer at both pc-Au and single-crystal Au electrodes brought in contact with such nonaqueous solvents as dimethylsulfoxide (DMSO), dimethylformamide (DMF), acetonitrile, propylene carbonate (PC), and selected alcohols has also been studied. The experimental methods used involved CV and impedance measurements, except for butanol isomers, for which surface-enhanced

Raman spectroscopy (SERS) technique was also employed [27].

For example, Jarzabek and Borkowska [28] have found that the double-layer capacitance for the pc-Au|DMSO interface is significantly lower than for mercury (except for very negative charge densities). However, reproducibility of the results concerning double layer at pc-Au, as well as at single-crystal (111), (110), (100), and (210) Au electrodes, was limited, since the capacitance-potential relationships were time-dependent and, for instance, after about 1 h, a pseudostable C_d-E dependence was observed [4]. In consequence, conclusions could be drawn only for these pseudostable states. For DMSO solutions, the following sequence of the potentials of the capacitance minimum has been found: $(111) \leq (100) < \text{pc-Au} \leq (110) < (210)$, whereas for aqueous solutions, this sequence is reversed [4]. Another conclusion from these studies was that Au-DMSO interactions are stronger than Au-H₂O interactions, the former ones also being more sensitive to the atomic structure of the Au surface [29].

More data regarding Au|nonaqueous solvent interfaces, including surface preparation problems, can be found elsewhere [4] and in references cited therein. Table 2 summarizes selected values of the potential of zero charge for the pc-Au electrodes in contact with some solvent-electrolyte systems.

Tab. 2 Potentials of zero charge (E_{pzc}) for pc-Au electrode in contact with selected nonaqueous solvent–electrolyte systems. The pzc for pc-Au|H₂O is equal to 0.20 V versus aqueous standard hydrogen electrode (SHE) and 0.85 V versus bis(biphenyl)chromium(I)/(0) redox couple (BBCr) [4]

Solvent–electrolyte system	E_{pzc} [V versus aqueous SHE]	E_{pzc} [V versus BBCr]	References
Dimethylsulfoxide + LiClO ₄	0.39	0.99	28
Acetonitrile + KPF ₆	0.90	1.49	30
Propylene carbonate + NaClO ₄	0.44	1.11	28, 31
<i>N, N</i> -Dimethylformamide + LiClO ₄	0.51	1.02	32
MeOH + 0.4M LiBr + 0.1M LiClO ₄	0.25	0.81	33

24.4.2

Adsorption of Inorganic Compounds on Gold Electrodes

The effect of the supporting electrolyte on the E_{pzc} of Au electrodes indicates specific affinity of either cations or anions of the dissolved salt to the given surface. For example, the studies performed by Hamelin [34] have shown the effect of the supporting electrolyte on the double-layer capacity – potential curves (see Table 3).

From these data, it follows that in aqueous solutions, sulfate ions exhibit relatively high affinity to the gold surface, which is reflected in the least positive value of E_{min} . In view of this important role of sulfate ions, their adsorption will be described below in more detail.

24.4.2.1 Sulfate

Adsorption of sulfate species at pc-Au electrode has been studied [35] in HF–KF buffer of pH = 2.8 applying Fourier transform infrared spectroscopy (FTIR). Adsorption of sulfate starts at 0.4 V versus Pd/H₂ (which is about 0.28 V more positive than the zero charge potential). Adsorption reaches a maximum at 1.2 V. At any potential applied, a band between 1165 and 1193 cm^{−1} was observed. It was ascribed to the adsorbed SO₄^{2−}. Adsorption

Tab. 3 The effect of the supporting electrolyte (in aqueous solution) on the potential (versus SHE) of the minimum of the double-layer capacitance [11, 34] of the Au(100) electrode surface

Electrolyte	E_{min} [V]
1 mM KPF ₆	+0.325 ± 0.005
10 mM LiClO ₄	+0.308 ± 0.01
10 mM NaF	+0.333 ± 0.01
2 mM H ₂ SO ₄	+0.242 ± 0.01
1 mM HClO ₄	+0.253 ± 0.005

of sulfate anions on Au(111) electrodes has been discussed later by Lipkowski and coworkers [36]. Quantitative characteristics of this process (together with the data for halide ions) are presented in Fig. 2.

Więckowski and coworkers [37] have reported adsorption of bisulfate anions on Au(111), Pt(111), and Rh(111) electrodes in sulfuric acid solution using electrochemical and several nonelectrochemical techniques. It was concluded from the low-energy electron-diffraction data that the structure of bisulfate on gold is different from that on Pt(111) and Rh(111). Adsorption of bisulfate on Au(111) is associated with a charge transfer from the electrode to the adsorbate. However, the formation of this particular bond does

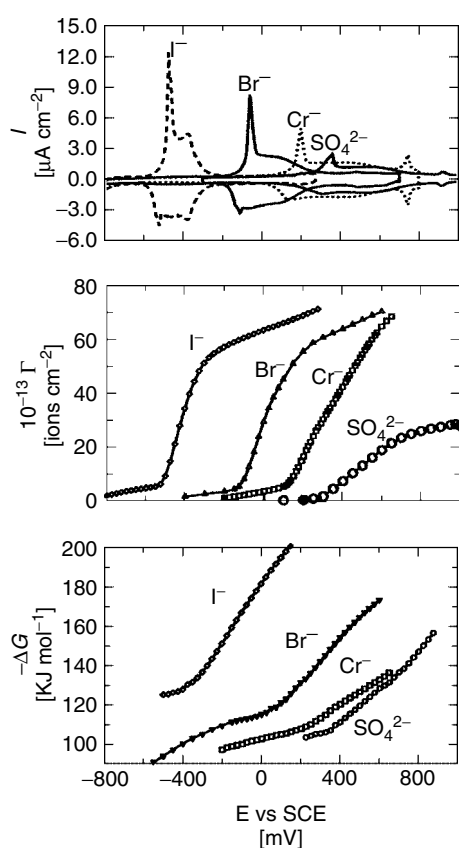


Fig. 2 Comparison of SO_4^{2-} , Cl^- , Br^- , and I^- adsorption at the Au(111) electrode surface from 0.1 M $\text{HClO}_4 + 10^{-3}$ M K_2SO_4 and 0.1 M $\text{KClO}_4 + 10^{-3}$ M KCl , KBr , and KI solutions. (a) Cyclic voltammograms at $\nu = 10 \text{ mV s}^{-1}$. (b) Gibbs surface excess versus potential. (c) Gibbs energy of adsorption versus potential. The standard state corresponds to the surface coverage $\Gamma = 1 \text{ ion per cm}^2$ and bulk concentration $c = 1 \text{ mol dm}^{-3}$ [36].

not significantly modify the band structure of the metal, which suggests that electrostatic forces mainly contribute to this bonding [38, 39]. Kolb and coworkers [40], using in situ STM, have observed an ordered adlayer of either sulfate or bisulfate ions at the unreconstructed Au(100) surface in 0.1 M H_2SO_4 . This adlayer is formed concomitantly with the lifting of the (hex)-reconstruction. In consequence, the newly generated layer consists of sulfate/bisulfate molecules ordered in rows that run parallel to the edges of the islands formed in the (hex) \rightarrow (1 \times 1) transition. Kolb and coworkers [41] have studied adsorption of sulfate anions (from 0.1 M H_2SO_4 and 0.1 M

Na_2SO_4), also in the presence of phosphates (from 0.1 M H_3PO_4 and 0.1 M $\text{KH}_2\text{PO}_4 + 0.1 \text{ M K}_2\text{HPO}_4$), on Au(111) and Au(100) using in situ STM. Hirai et al. [42] have investigated the potential dependence of the decay of multilayered islands on Au(100) electrode in 0.05 M aqueous solution of H_2SO_4 , applying in situ AFM.

In all the above cases, surface distribution of anions was nonuniform. Apparently, this is a characteristic feature common to oxoanion adlayers because of their ability to form bridging hydrogen bonds via the lone electron pairs at their oxygen atoms. Since, in neutral solution, no ordered adsorption was

observed, one may deduce that coadsorption of hydronium ions is necessary to stabilize an ordered oxoanion lattice.

Recently, the change in the interfacial free energy and surface stress has been determined for Au(111) electrodes in electrolytes containing nonspecifically adsorbed F^- anions. This behavior was compared to that of specifically adsorbed SO_4^{2-} anions [43]. It was found that the surface stress is more sensitive to the changes in electrode potential than the interfacial free energy.

Some attention has also been paid to the simultaneous adsorption of sulfate anions and organic compounds. Futamata [44] has detected coadsorption of water molecules and sulfate species with uracil on polycrystalline gold electrode, applying attenuated total reflection-infrared spectroscopy. The adsorbed sulfate species appeared either as SO_4^{2-} or HSO_4^- , depending on the pH of the electrolyte solution. Skořuda [45] has presented a voltammetric study of the Au(100) electrode in the presence of alkyl sulfate. Dutkiewicz and Skořuda [46] have investigated adsorption of benzenesulfonate anions at the Au(111) electrode, using CV and differential capacity measurements.

24.4.2.2 Hydroxide

Hamelin [47] has shown that specific adsorption of OH^- ions increases in the following order: Au(111) < Au(100) < Au(311). Chen and Lipkowski [48] have applied chronocoulometry and subtractively normalized interfacial Fourier transform infrared spectroscopy to study adsorption of hydroxide ions on Au(111) electrode. This process proceeded in three steps. Bonding of OH^- with gold atoms that is quite polar at negatively charged surface becomes less polar at positively

charged electrode surface. Oxide formation starts at higher charge densities, when surface concentration of hydroxide ions exceeds one-third of a monolayer. Interfacial properties of pc-Au electrode in tetramethylammonium hydroxide solutions of concentrations ranging from 5×10^{-3} to 4.0 M have been studied using CV and impedance spectroscopy [49]. At highly negative potentials, the double-layer capacity has been found to depend on the kind of cations and to remain independent of their concentration. Strong adsorption of hydroxide anions was observed in wide concentration and potential ranges.

24.4.2.3 Nitrate

Marinkovic et al. [50] have used in situ IR reflection spectroscopy to study adsorption of nitrate ions on Au(111) electrodes. The ions were bonded to the gold surface via one of their oxygen atoms. Within the double-layer NO_3^- formed contact ion pairs with hydronium ions. The extent of this process depended on the applied potential.

24.4.2.4 Chloride

Więckowski and coworkers [51] have carried out electrochemical and radiochemical studies of Cl^- adsorption using radioactive ^{36}Cl . By combining radiochemical measurements with CV experiments, the potential dependence of adsorption and surface-bulk exchange processes has been studied.

Also, Cuesta and Kolb [52] have employed STM to investigate adsorption of chloride ions on Au(100) surfaces.

Shi and Lipkowski [53] have presented a thermodynamic analysis of charge density data. The study aimed at the description of adsorption of chloride on Au(111)

electrode surface and calculation of basic corresponding parameters. Chloride ions were attached to gold via chemisorption. Polarity of the formed bond strongly depended on the charge of the metal. Polarity decreased significantly when the charge attained positive values.

The role of chloride ions in the anodic dissolution of Au(111) in perchloric acid solutions has been studied in Ref. 54. The mechanism of anodic dissolution was discussed in relation to the structure of the chloride adlayer on the Au(111) electrode surface.

24.4.2.5 Bromide

Thermodynamic analysis of charge density resulted in the description of bromide adsorption on Au(111) electrode [55]. Bromide ions are chemisorbed at the gold surface and polarity of the formed bonds strongly depends on the metal charge. Polarity drops significantly when the surface charge changes from negative to positive values. The second-harmonic generation studies indicate that adsorption of bromide ions strongly affects electronic structure of the metal surface.

Bromide adsorption on Au(111) has also been studied, applying in situ surface X-ray scattering (SXS) and STM [56]. The potential-dependent adlayer density agreed well with the earlier published bromide surface excess densities, obtained in electrochemical measurements. At very positive potentials, a bromide-induced step-flow etching of Au occurred.

Ocko et al. [57, 58] have studied adsorption of bromide on Au(100) using in situ surface X-ray diffraction (SXD) in combination with electrochemical measurements. Low surface excess of bromide ions at Au(100)-(hex) caused a lifting of the

surface reconstruction. This process proceeded at high overpotentials via instantaneous nucleation and two-dimensional growth. Two ordered bromide adlayer phases were found at unreconstructed Au(100)-(1 × 1) surface.

These studies led to the detailed assignment of voltammetric features of bromide adsorption to the respective structural properties, stability, and transition kinetics.

Adsorption of Br[−] on Au(111) has already been exemplified in Fig. 2, taken from Ref. 36. In Ref. 59, in turn, the dependence of phase transition on the electrode potential accompanying adsorption of Br[−] on Au(100) has been investigated (see Figs 3 and 4).

Cuesta and Kolb [52] have studied bromide adsorption on Au(100) electrodes using in situ STM. Two quasi-hexagonal structures were found, which was in agreement with the previously published SXS data.

Wang and Rikvold [60] have applied *ab initio* total-energy density-functional methods in combination with supercell models to calculate the c(2 × 2) structure of bromide adsorbed on Au(100) and Ag(100) surfaces. The preferred bonding sites have been determined. The calculations have shown that bromide favorably binds the bridge site on the Au(100) surfaces. These results explain experimental observations that adsorption of bromide on the Au(100) and Ag(100) surfaces proceeds via different bonding configurations.

Lipkowski and coworkers [61] have analyzed the relationship between the changes in the bromide surface composition on Au(100) electrode and its specific behavior observed in CV.

Finally, Adzic and Wang [62], and Wang et al. [63] have studied the formation of thallium bromide on Au(111) electrode

Fig. 3 Linear sweep voltammogram ($\nu = 10 \text{ mV s}^{-1}$) for Au(100) in 0.05 M NaBr [59].

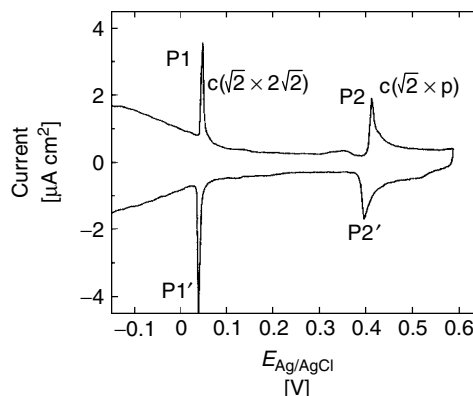
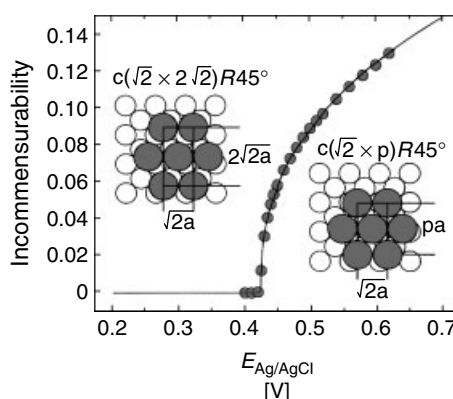


Fig. 4 The incommensurability versus electrode potential dependence for adsorption of Br^- on Au(100). Insets: atomic models of Br^- adlayers corresponding to the potentials below and above the critical point of phase transition [59].



induced by bromide adsorption. They have observed: (1) an underpotential shift for deposition of Tl on Au(111) in the presence of Br^- , (2) a formation of two mixed adlayers of two surface compounds TlBr_2^- and TlBr , and (3) a very complex structural behavior of this system. The above phenomena are related to underpotential deposition (UPD) that is reviewed in more detail in a later section.

Mitchell and Koper [64] have involved the density-functional theory to determine the parameters necessary for the construction of an off-lattice model with no freely adjustable parameters for Br^- electrodeposition on Au(100).

The simulation results were satisfactorily consistent with the experimental findings.

24.4.2.6 Iodide

Electrochemical quartz crystal microbalance (EQCM) has been used [65] to study adsorption/desorption of iodide on Au(111) electrodes. The coverages obtained at different potentials were quite close to those estimated from STM images and SXS measurements.

Iodine adlayers covering an Au(111) electrode have been characterized [66] and shown to be convenient substrates for the studies on adsorption of various organic molecules [66, 67].

Chen et al. [68] have performed chronocoulometric studies of adsorption of iodide on Au(111) electrode and calculated the parameters describing this process quantitatively. As in the case of chloride and bromide adsorption, iodide also formed quite polar chemisorption bond at the negatively charged surface. However, the polarity dropped significantly when the charge of the electrode attained positive values. At high charge densities and coverages, the chemisorption bond had a predominantly covalent character. The strength of halide adsorption and covalent character of the bond increased progressively from chloride to iodide.

It has been found [69] that alkali metal cations coadsorb with iodide ions on Au(110) electrode at potentials more positive than the potential of Au(110) reconstruction and more negative than the potential of the formation of iodine monolayers. The coverages of both the cationic and anionic species in KI, NaI, and LiI solutions decrease with the increasing electrode potential.

Seo and Ueno [70] have used a piezoelectric technique to detect the changes in the surface energy of gold electrode in 1.0 M NaClO₄ solutions in the presence and absence of iodide ions. Additions of iodide moved the potential of zero charge to the negative direction, compared to the value determined from the piezoelectric signal curve, which points at the strong contact adsorption of iodide ions.

Chang et al. [71] have studied adsorption of iodine, iodobenzene, iodoheptane, and 1,4-dihydroxy-2-iodobenzene on Au(111) electrode from 0.1 M HClO₄ solutions using CV and STM. The results obtained indicate that organic iodide molecules are significantly decomposed upon their adsorption to give an iodine layer and alkyl

and aryl organic fragments dissolved in the solution.

A physical model and a theory have been proposed [72], which might be helpful in comparative studies on electrocompressive behavior of electrodeposited chloride, bromide, and iodide monolayers on the Au(111) electrode. The theoretical results were in good agreement with the experimental data, which evidence that the adatom–adatom interactions (especially repulsive ones) and electrosorption valency of halide anions determine the compressibility within halide adlayers. Also, Lipkowski et al. have discussed various aspects of adsorption of halide anions on Au(111) in a review paper [36]. From this paper, we have taken quantitative data concerning adsorption of halide anions on Au(111) (cf. Fig. 3).

Kerner and Pajkossy [73] have measured impedance spectra for Au(111) electrode in perchlorate solutions additionally containing SO₄²⁻, Cl⁻, Br⁻, and I⁻ at concentrations of about 10⁻⁴ M. Measurements were performed at adsorption potentials of these anions. Analysis of the impedance spectra led the authors to the conclusion that the adsorption rates of SO₄²⁻ and Cl⁻ are immeasurably high. For halide anions, the apparent rate coefficient changes in the order I⁻ < Br⁻ < Cl⁻ and decreases with the increasing electrode potential and coverage.

The SHG surface spectroscopy is another method useful in the studies on halide adsorption. Applicability of the SHG spectroscopy method to Au surface properties has been discovered by Pettinger, Kolb, and coworkers [74, 75]. It has also been shown that reconstruction of Au(111) and Au(100) electrodes remarkably affects SHG anisotropy [74]. For this reason, an interference second-harmonic generation anisotropy (ISHGA)

method has been recently applied to the analysis of structural changes of Au(110) surface and to study the effect of adsorption of halide ions on Au(111) (see Ref. 74 and references cited therein). In the light of these studies, it is interesting to note that Gao et al. [76] have performed surface reconstruction of Au(110) in 0.1 M HClO_4 solution as a function of electrode potential using atomic resolution STM.

24.4.2.7 Cyanide

Studies on adsorption of CN^- ions (and other pseudohalide ions) on both pc-Au and single-crystal electrodes are particularly important in view of their role in

metal etching and dissolution processes [77]. From potential-evolved differential frequency generation (DFG) measurements, it has been found that in the aqueous solution: 0.1 M NaClO_4 + 0.025 M KCN, adsorption of CN^- starts at -1.35 V (SCE) on Au(110), at -1.05 V on Au(100), and at -0.85 V on Au(111) [78]. The results of electrochemical measurements are concordant with these findings (see Fig. 5) and have been compared with earlier electrochemical studies using the pc-Au electrode [79].

Evidently, the CN^- -Au interactions are the strongest at more open Au(110) surface, and this conclusion correlates well with the dependence of pzc on the type

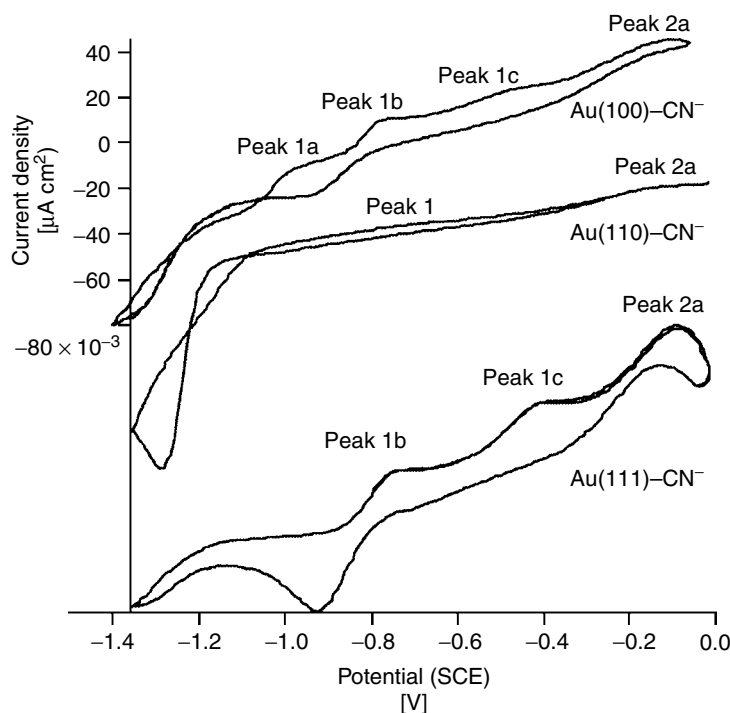
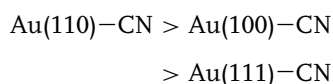


Fig. 5 Cyclic voltammograms of Au(110), Au(100), and Au(111) electrodes brought in contact with an aqueous solution of 0.1 M NaClO_4 and 0.025 M KCN; direction of polarization: from -1.35 to 0 V (versus SCE), sweep rate: 200 mV s^{-1} , CV after 10 cycles [77].

of Au surface (the pzc value in CN^- -free solutions attains the most negative value) [77, 80]. It has also been found that the rate of CN^- adsorption is roughly the same for all surface orientations, while the rate of CN^- desorption is the highest for Au(111), compared to Au(100) and Au(110) [77].

Adsorption of cyanide anions can be affected by adsorption of cations. In the solutions containing nonspecifically adsorbed anions, the nature of alkali metal cations was found to influence the measured value of the electrode capacitance at potentials more negative than -0.6 V (versus standard hydrogen electrode (SHE)). At $E < -1.0\text{ V}$ adsorption of CN^- ions was enhanced in the presence of Li^+ and Na^+ cations, and inhibited in the presence of Cs^+ ions [81]. A combined SERS and density-functional theory has been applied to study cyanide adsorption at Au electrode [82]. The authors have arrived at the conclusion that the polarity of Au–CN bonds falls between that of Au–Cl and Au–Br surface bonds. The binding strength for three different gold surfaces decreased in the order:



and agreed with the order of bond ionicity.

24.4.2.8 Thiocyanate

Adsorption of thiocyanate ions on Au electrodes from alkaline solutions has been studied using *in situ* IR spectroscopy and SERS [83]. Even at negative potentials, adsorption of thiocyanate was observed, which occurred via Au–S interaction. At higher concentration of OH^- ions, the bond strength between the adsorbed SCN^- ion and the surface was decreased. At very positive potentials, both the oxidation of thiocyanate to cyanate and the

formation of a gold–thiocyanate complex were observed.

24.4.2.9 Other Inorganic Species

Jusys and Bruckenstein [84] have used electrochemical quartz crystal microbalance to study adsorption/desorption of perchlorate and perrhenate ions on a bare polycrystalline Au electrode. The change in the equivalent mass was undoubtedly assigned to the adsorption of both anions in the double-layer region of Au electrode.

Adsorption of ammonia on the Au(111) surface at $1/4$ and $1/9$ of the monolayer coverage has been theoretically modeled [85].

Hexacyanoferrates were immobilized on Au covered with SAM of 3,3'-thiodipropionic acid [86]. It has been found from voltammetric studies that the surface coverage of hexacyanoferrate is close to one monolayer and such an electrode exhibits very good surface redox behavior. Cheng et al. [87] have described the formation of an extremely thin multilayer film of polybasic lanthanide heteropolytungstate–molybdate complex and cationic polymer of quaternary poly(4-vinylpyridine), partially complexed with osmium bis(2,2'-bipyridine) on a gold electrode precoated with a cysteamine SAM. Consequently, adsorption of inorganic species might also be related to the properties of SAMs. This problem will be discussed in detail in a separate section later.

Oznuluer and Demir [88] have employed electrochemical atomic layer epitaxy (ALE) to the investigations of kinetics of structural changes occurring within initial monolayers of thin Bi_2S_3 films on Au(111).

Finally, adsorption of CO on Au(111) surface has been investigated under reduced pressure in the range from 10^{-3} to 10^3 Tr at the room temperature [89].

24.4.3

Adsorption of Organic Compounds on Gold Electrodes**24.4.3.1 Adsorption of Sulfur-containing Compounds**

Evidently, adsorption of chemical compounds at gold surfaces via specific Au–S interactions has been very intensively studied for the last twenty years. In a recent review [90], Vericat et al. have described their own results of electrochemical, in situ STM, X-ray photoelectron spectroscopy (XPS), and SXD studies on adsorption of sulfur on Au(111). It has been stated that S–Au bonds determine the structure and adsorption/desorption kinetics for both S–Au(111) and alkanethiolate/Au(111) systems in NaOH.

Application of self-assembling has given a great impetus for the studies of Au surfaces modified with sulfur compounds. Such processes were already described a long-time ago [91], however, more intensive investigations have been initiated by seminal paper of Nuzzo and Allara [92], published in 1983. Self-assembling is very well suited to easily obtain well-ordered structures as very strong, specific adsorption of molecules with a sulfur atom in their terminal groups directs these molecules exactly to the gold surface.

Interest in these studies arises from fundamental research where monolayers serve as models of biomimetic systems, as well as from important applications of such systems in molecular and bioelectronic devices, in sensors constructions, corrosion/inhibition phenomena, and synthesis of nanostructures [93]. Although self-assembly processes of sulfur-containing compounds occur at the surfaces of many metals, especially the copper-group metals (Cu, Ag, Au), the most extensive studies have been

carried out on the modification of gold electrodes.

Even a very brief description of numerous papers published in the recent years was often beyond the scope of this work. Instead, a concise presentation of general properties of adsorption and desorption processes and electrochemical properties of such modified electrodes will be given.

24.4.3.1.1 Adsorption of Thiols

Self-assembly of alkanethiols (RSH) on gold has especially been studied intensively. In this case, adsorption proceeds via formation of chemical bond between surface gold atoms and sulfur atoms of alkanethiols. Adsorption is further supported by hydrophobic interactions between the alkyl chains. The quality of self-assembled layers depends on a number of factors, such as morphology of the substrate [94], and temperature [95]. For successful deposition, it is very important to use highly purified solvent and reagents [96]. The electrode surface should also be thoroughly cleaned; however, some researchers claim that very careful cleaning is less important in view of the very strong interaction of sulfur with gold [97]. Concentration of the solution used for deposition and duration of deposition also play a key role in the preparation of the layers of good quality. The above factors are interrelated. The lower the thiol concentration, the longer the deposition time that is required to achieve a given surface coverage. In order to investigate the influence of these and other parameters on the quality of a monolayer, as well as the completeness of the surface coverage, the process of reductive desorption has been employed.

Modification of the gold surface in the self-assembly approach proceeds after dipping the gold electrode into the solution

containing the corresponding thiol [98]:



Porter and coworkers [98] who have used pc-Au electrodes and have examined monolayers of *n*-alkanethiols $\text{C}_n\text{H}_{2n+1}\text{SH}$ with $n = 3-10, 12, 16$, and 18 , have found the surface coverage to be independent of n and equal to $9.3 (\pm 0.6) \times 10^{-10} \text{ mol cm}^{-2}$. Assuming that the real surface area of pc-Au electrode is 1.2 times larger than the geometric surface area, this is consistent with structures proposed on the basis of different experiments in which monolayers of various long-chain *n*-alkanethiols were found to form a $(\sqrt{3} \times \sqrt{3})R30^\circ$ overlayer structure on Au surfaces of predominantly (111) character. The charge associated with the reduction of monolayers of above-mentioned *n*-alkanethiols was found to be $(90 \pm 7) \mu\text{C cm}^{-2}$ and was independent of the chain length of the studied alkanethiols.

Taking into account the above-given surface coverage, the final result of Porter and coworkers [98] is written in the form of the reaction:



This 1e electrode reaction implies the loss of the thiol hydrogen and the oxidation of the S to a formal oxidation state of -1 upon adsorption of *n*-alkanethiol (RSH) at Au.

The results obtained on the double-layer properties show that the studied monolayers may be represented by a two-capacitors-in-series model. One capacitor corresponds to the thiol head-group region of the monolayer and the second to the hydrocarbon phase.

Porter and coworkers [98] have been the first to have performed electroreductive desorption of alkanethiols from the gold

surface. The charge, the shape, and the potential of the cathodic peak provided important information on the SAMs. Electroreduction was carried out in alkaline (KOH) solution. Desorption process was easily observable in cyclic voltammograms. Depending on the conditions, reductive desorption peak appeared between -0.7 and -1.4 V (versus SCE) [99–101]. The value of the peak potential depended on several parameters, including the length of the carbon chain in thiol molecule.

Formation of the thiol layer may occur also in the anodic process.

It is, however, noteworthy that despite quite intensive studies, the *detailed* mechanism of thiol adsorption is still not well known [102]. Even the most commonly accepted fact that the adsorbed species are thiolate anions (RS^-) is also questioned. In order to elucidate adsorption mechanism in more detail, Cohen-Atiya and Mandler [102] have studied potentiometrically, the effect of chain length of solvent molecules, end groups, and the nature of surface (Au, Ag, and Hg). The obtained results have confirmed again that thiol adsorption process is complex and is affected by the solvent, the nature of the surface, and also by the presence of additional functional groups in thiol molecules. When thiol was added to the electrolyte solution, a sudden shift of the potential to the negative range was noticed in the open-circuit potential experiment. This is indicative of the transfer of negative charge from the thiol group to the electrode surface during adsorption process and formation of the M–S bond. As a result, the H–S bond should be cleaved. In some cases, the authors have observed that negative potential shift is followed by a gradual shift to positive potentials, reflecting a discharge process, which probably might proceed via a reduction process.

The scheme in Fig. 6 illustrates the mechanism proposed by Cohen-Atiya and Mandler [102].

Cohen-Atiya and Mandler have also found that the extent of discharging process is significantly decreased in aprotic solutions and in the absence of oxygen. However, the influence of additional functional groups located at the other end of thiol molecules on the discharging process is still not fully understood. Possibly, such groups (e.g. carboxylic) affect accessibility of water to the electrode surface.

Brett et al. [103] have studied self-assembling of 1-decanethiol at the fixed positive potentials of pc-Au electrode in chronoamperometry and quartz crystal microgravimetry. The obtained layers appeared to have improved quality and were produced faster than in the open-circuit deposition. The factors possibly influencing the fine structure of monolayers observed in voltammetric reductive desorption and oxidative redeposition of long-chain alkane-thiolates, for example, hexadecanethiol (HT) and octadecanethiol on smooth Au electrodes have been discussed [104]. It has been shown that the local order of adlayer has a role to play in the formation of that fine structure.

There are also some papers in electrochemistry aimed at the estimation of

properties of generated monolayers. Since these papers are only loosely connected with the electrochemistry of gold, we refer to them very briefly. French and Crea-ger [105] have found that oxidation of gold at the electrode surface and oxidation of $\text{Fe}(\text{CN})_6^{4-}$ is inhibited up to +1.6 V (versus Ag|AgCl electrode) when octanol-saturated solutions of pH 5 (buffer) and dodecanethiol monolayer-coated Au electrode are used. Octanol molecules fill in the defects in the monolayer and thus make the thickness of the barrier layer increase, causing inhibition of electrode reactions.

Passivating behavior of self-assembled octadecanethiol on pc-Au electrodes has been tested by CV using $\text{Ru}(\text{NH}_3)_6\text{Cl}_3$, $\text{K}_4\text{Fe}(\text{CN})_6$, and benzoquinone [106] as the redox probes. Inhibiting properties toward these reactants were found to be different.

Inhibiting properties may be influenced by the solvent molecules trapped within the monolayer during self-assembly of octadecanethiol molecules on gold electrodes [107].

Capacitance and charge-transfer rates of SAM of ω -(4'-methyl-biphenyl-4-yl)-alkanethiols ($\text{CH}_3-\text{C}_6\text{H}_4-\text{C}_6\text{H}_4-(\text{CH}_2)_n-\text{SH}$, $n = 0-6$) adsorbed on pc-Au have also been investigated. For $n = 1-6$, the reciprocal capacity exhibited a linear dependence on the alkane spacer

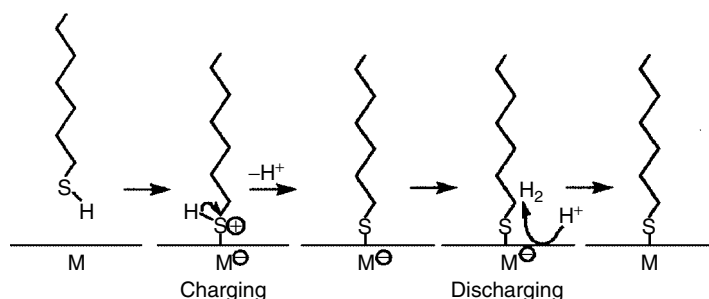


Fig. 6 Schematic representation of the mechanism of thiol adsorption on different metal surfaces [102].

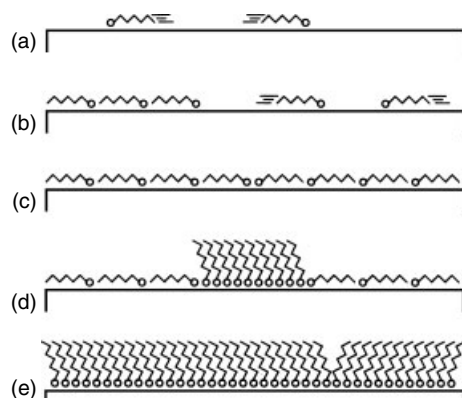


Fig. 7 Schematic of self-assembly mechanism for alkanethiols on Au(111). (a) Thiols adopt the highly mobile lattice-gas phase at very low coverage. (b) Above a critical value of surface coverage, striped-phase islands, characterized by surface-aligned molecular axes, nucleate heterogeneously, and grow in equilibrium with a constant pressure lattice gas. (c) Surface reaches saturation coverage of striped phase. (d) Surface undergoes lateral-pressure-induced solid–solid phase transition by nucleation of high-density islands at striped-phase domain boundaries. (e) High-density islands grow at the expense of the striped phase until the surface reaches saturation [110].

length. The incremental change of $0.054 \pm 0.0036 \text{ cm}^2 \mu\text{F}^{-1}$ per CH_2 group and the calculated dielectric permittivity of $\epsilon = 2.5$ agreed well with the data for *n*-alkanethiols [108].

For Hg–Au junctions containing bilayers of alkanethiols of different chain lengths, *I*–*E* curves were symmetrical with respect to the polarity of the voltage bias. Larger current was measured when a negative bias was applied to the metal modified with a monolayer of longer alkanethiol chains [109].

Au(111) electrodes. The schematic representation of the formation of the SAM of alkanethiols on Au(111) is shown in Fig. 7 [110].

Beardmore et al. [111] have presented a realistic empirical potential function to model the head-group interaction for SAMs of alkanethiols on Au(111). The main result of these calculations is that the barriers within the surface corrugation potential are too small to pin S atoms at any particular site.

It has been shown [112] that for low concentrations of thiols in the solution,

the kinetics of their self-assembly as a monolayer on Au(111) surface is limited by diffusion, and not by surface kinetics. When the coverage is low, alkanethiols are arranged on Au(111) in the striped structures and vacancy islands of the gold surface are created. At high coverages, the structure is $(\sqrt{3} \times \sqrt{3})R30^\circ$ and/or $c(4 \times 2)$ with a tilt angle of approximately 30° from the surface normal [113–115]. Alkanethiols are adsorbed on Au(111) in such a way that one sulfur atom corresponds to three gold atoms at the surface. STM studies have shown that the monolayers are seriously subjected to defects by missing rows and pits [116–118]. The missing-row defects arise from the orientational and translational domain boundaries. Density of the pits was found to be strongly dependent on the solvent [119] and the temperature [120] at which the self-assembly process was carried out. Wano and Uosaki [121] have studied electrochemical desorption process of hexanethiol from Au(111) surfaces in H_2SO_4 and KOH aqueous solutions. They have found that desorption begins at the defects

of monolayers. They have also found that desorbed thiolates form aggregates in H_2SO_4 solution. In CV experiments, after electroreduction, the electrode potential was scanned to positive values and a smaller anodic peak corresponding to the oxidative readsorption of some of the desorbed alkanethiolates was observed (see, for instance, Ref. 122). The anodic and cathodic peak potentials depended on the concentration of thiols [122]. Kolb and coworkers [123] have applied in situ STM and CV to study SAMs of ethanethiol on Au(111) electrodes. Electrochemical studies in 0.1 M H_2SO_4 have shown that at -0.31 V versus SCE, ethanethiol is reductively desorbed, while oxidative desorption of this thiol occurs at $+1.15$ V. Both processes were monitored in STM measurements. At potentials slightly negative of 0 V, the adlayer underwent structural transformation, which finally led to the formation of small pits and islands on the surface. In case of decanethiol on Au(111) and with an increasing concentration of decanethiol, both cathodic and anodic peaks were shifted to negative potentials by about 57 mV/decade, independently of the sweep rate (in the range $0.01 - 0.2 \text{ V s}^{-1}$). Assuming that the electrode reaction occurred according to Eq. (1) in both directions, and that the monolayer activity a_{Mon} was independent of the thiol concentration, one arrives at [122]:

$$E_{1/2} = E'_0 - 0.059 \log a_{\text{C}_{10}\text{S}} - \text{constant} \quad (3)$$

where $a_{\text{C}_{10}\text{S}}$ is the activity of decanethiol. This equation is consistent with the experimental results [122] and confirms that oxidation and reduction proceeded as one-electron processes.

From electrochemical and STM experiments, as well as from density

functional theory (DFT) calculations, it can be concluded [124] that the difference between experimentally observed peak potentials for reductive desorption of a given alkanethiolate from Ag(111) and Au(111) surfaces is determined by the energy required to introduce an electron into the adsorbed alkanethiolate-metal species, by desorption energy of the alkanethiolate anion, and by the solvent/metal interaction energy. Moreover, the position of the peak depends on the alkyl chains. It has been found that the longer the alkyl chain, the more negative the reduction peak potential is, probably due to stronger attractive interaction between alkyl chains [98].

The measurement of the charge involved in the reductive desorption of layers prepared under various conditions provides very important information about the surface coverage and the nature of the oxidative adsorption. The influence of time and thiol concentration on both the potential and the charge of the reductive desorption has been investigated for decanethiol adsorbed on Au(111) [125] (see Fig. 8).

In these experiments, Au(111) electrode was immersed in 0.1 M KOH solutions with 10 μM , 100 μM and 1 mM C_{10}SH and kept at the constant potential of $+0.1$ V for a certain time. After that, the potential was scanned to more negative values in order to record the cathodic peak current. These and other experiments have proved that the saturated coverage is obtained after a sufficiently long holding time. The same applies to the cathodic peak potential also. Sumi and Uosaki [125] have found that the maximum reaction charge is equal to $103 (\pm 5\%) \mu\text{C cm}^{-2}$. Two components contribute to the measured total charge: the first is produced in reaction (1), and the second is the capacitance charge

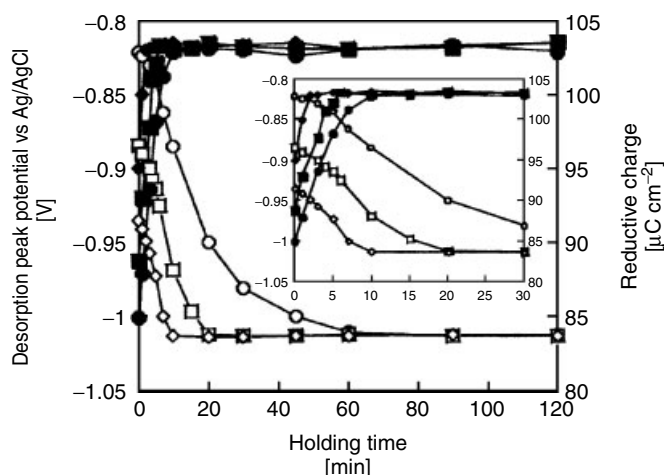


Fig. 8 Cathodic peak potential (empty symbols) and cathodic wave charge (filled symbols) as a function of holding time at +0.1 V in 0.1 M KOH ethanolic solutions containing 10 μM (○, ●), 100 μM (□, ■), and 1 mM (◇, ◆) decanethiol. Inset shows the initial stage of the above relations. All data concerning reductive charge contain $\pm 5\%$ error [125].

arising from the difference in the double-layer capacity of the thiol-covered and bare surface. The value of $103 (\pm 5\%) \mu\text{C cm}^{-2}$ agrees with the values reported for the reductive desorption of SAMs of other thiols with saturated coverage and a $(\sqrt{3} \times \sqrt{3})R30^\circ$ structure, which were formed in ethanol solutions containing only alkanethiol without the potential control [126–128]. The determined total charge equaled $103 (\pm 10\%) \mu\text{C cm}^{-2}$ and comprised $73.3 \mu\text{C cm}^{-2}$ of the Faradaic charge contribution due to reaction (1) and $30 \mu\text{C cm}^{-2}$ of double-layer recharging contribution [126, 127, 129]. Also, the rate constant of the reductive desorption of decanethiol was determined from the peak potential versus scan rate relationship and equaled to 0.24 s^{-1} . A very close value was found for nonanethiol [125, 130].

In the formation of self-assembled layer, one can distinguish three steps [131, 132]. The first step lasts for several seconds and obeys chemisorption and formation

of Au–S bond. In this step, a coverage of about 80–90% is achieved. The second step consists of straightening of the alkyl chains. The third step is the slowest and obeys reorientation of terminal group. Reorientation is accompanied by some changes in the reduction peak potential, although the surface coverage remains practically unchanged. Reorganization may take several hours and has been monitored in contact angle, ellipsometry, and FTIR studies [93, 133–135].

In situ and ex situ STM studies of self-assembled butanethiol/Au(111) have been performed [136] in order to determine the ground-state configuration and long-term behavior of this system at room temperature. The results have shown that the most stable surface structure is a $c(4 \times 2)$ reconstruction of the basic $(\sqrt{3} \times \sqrt{3})R30^\circ$ adsorption site geometry containing four distinguishable molecules. This structure is extremely sensitive to the presence of defects in the substrate. Probably, the

limiting factor leading to the formation of $c(4 \times 2)$ domains is the preexistence of large atomically flat Au(111) terraces that cover evenly at least 200–400 nm² without any defects.

Yang and Morin [137] have presented vibrational studies of reorganization of the electrical double layer, following reduction of the self-assembled nonanethiol monolayer on Au(111). The absence of changes in the vibrational spectra recorded at potentials covering the double-layer range confirmed the stability of this monolayer over the range of 800 mV. Significant changes in the vibrational spectra of water molecules were observed when the applied potential was more negative than the reduction potential of the thiol monolayer. Interactions between water molecules and gold electrode support were modified by the electrode potential.

Poirier [138] has studied phase stability of decanethiol on the Au(111) surface.

In the voltammogram of Au(111) modified with binary SAM of 1-undecanethiol and 11-mercaptoundecanoic acid, only one reductive desorption peak was formed for any value of mixing ratio of both thiols [139]. Such a response suggests that both thiols are well mixed in the SAM.

Arce et al. [140, 141] have studied the dynamics of 1-dodecanethiol and butanethiol SAMs on Au(111), applying *ex situ* and *in situ* STM. The potential of zero charge for the thiol-modified Au(111) electrode was determined for self-assembled monolayers of octadecanethiolate (−0.52 V), undecanethiolate (−0.49 V), propanethiolate (−0.3 V), and 1*H*,1*H*,2*H*,2*H*-perfluorodecanethiolate (1.04 V) [142]. The potentials (expressed versus Ag|AgCl|saturated KCl electrode) were determined from the measurements of the contact angle for a droplet of 0.1 M NaClO₄ aqueous solution.

Also, the potential dependence of ultrafast relaxation at electrochemical interfaces of 1-dodecanethiol- and 1-HT-modified Au(111) electrodes has been investigated in HClO₄ and H₂SO₄ solutions, applying transient reflectivity measurements [143]. The decay time constants found ranged from 100 to 300 fs and depended on the potential, interface modification, and the electrolyte used.

Hara et al. [144] have observed, in STM studies, an ordered nucleation of two-dimensional molecular islands at the initial growth stage.

It has been found [145] that the self-assembly of thiol molecules on Au(111) from ethanolic solution depends significantly on the electrode potential. Especially at cathodic potentials, chemisorption of thiol molecules and the development of a highly ordered structure are slowed down significantly.

Self-assembly of alkanethiols on Ag(1 × 1)-Au(111) obtained under conditions of UPD has been studied applying STM, Auger electron spectroscopy, and electrochemical techniques [146]. Even for the adsorbed short-chain alkanethiolates, the surface structure exhibited an incommensurable hexagonal lattice with the nearest-neighbor distances of approximately 0.48 nm that is usually found for long-chain alkanethiolates adsorbed on Ag(111).

Au(100) electrodes. Self-assembled thiol layers on Au(100) have also been studied. Kolb and coworkers [147] have investigated the potential-induced structure transitions in SAMs of ethanethiol in 0.1 M H₂SO₄ using STM. After modification, the STM images obtained in air exhibited a disordered thiol adlayer and Au islands of monoatomic height on about 25% of the surface. The islands originated from the lifting of the (hex) reconstruction during

thiol adsorption. In contrast to alkanethiol monolayers on Au(111), no vacancy islands were seen on the Au(100) surface.

Kolb and coworkers [148] have investigated SAMs of butanethiol applying CV and in situ STM. Adlayers comprised ordered domains of a striped structure, with the stripes running parallel to the main crystallographic axes of the substrate. Adsorption and desorption of butanethiol on Au(100)-(5 × 20) in ultrahigh vacuum have been studied using temperature-programmed desorption/reaction, low-energy electron diffraction, and Auger electron spectroscopy [149]. Physisorbed and chemisorbed states were shown to exist and desorb at quite different temperatures. Yamada and Uosaki [150] have presented structural investigations on decanethiol SAMs on the reconstructed and Au(100)-(1 × 1) surfaces using STM in air. Molecular arrangements of monolayers on both surfaces were similar to the c(2 × 8) structure with (1 × 4) gold row missing.

24.4.3.1.2 Adsorption of Modified Thiols
Amino-amido-thiol HS-(CH₂)₁₀-CO-NH-CH₂-NH₂ adsorbed on Au(111) has been studied by sum frequency generation and infrared reflection absorption spectroscopy (IRAS) in the CH₂ stretching vibration region [151].

Organized multilayers of ferrocene alkyl thiol have been self-assembled on Au(111) under conditions of controlled thiol concentration. Several methods, such as CV, ellipsometry, STM, AFM, and in situ FTIR spectroscopy have been applied in these studies in order to find out the differences between mono- and multilayers of the same compound [152]. Similar compounds, namely, short-chain alkyl thiols ($n = 3-10$) with ferrocene terminal group were allowed to form organized monolayers at Au(111) surfaces [153].

Applying subtractively normalized interfacial Fourier transform infrared spectroscopy, it has been found that electrooxidation of ferrocene groups is accompanied by rotation of these groups in such a manner that the plane of cyclopentadienyl rings turns to the position normal to the electrode surface. Also, biferrocenyl alkanethiols self-assembled on Au(111) surface and gold nanoclusters have been studied using various spectroscopic and electrochemical methods (CV) [154]. In the voltammogram, two reversible one-electron peaks were observed for both surfaces. Also, multilayered Au nanoclusters covered with mixed self-assembled alkanethiol monolayers containing methyl, ferrocene, or carboxylic terminal groups were obtained on Au(111) surface, and electrochemically characterized [155].

Gold electrodes covered with nonelectroactive alkanethiolate monolayers with amide bonds have been used to study the kinetics of long-range electron transfer, applying hexachloroiridate(IV) ion as the redox probe [156]. Ferrocene units were also attached [157] as terminal groups to alkanethiol molecules bonded via sulfur to the gold electrode support. These molecules were diluted with alkanethiol molecules without any reactive groups attached. Again, the rate of charge transfer between the ferrocene group and the electrode was calculated using voltammetry and chronoamperometry. Similarly, charge transfer occurring between the gold electrode and the ferrocene group attached to organic monolayer films with oligoglycine spacers has been studied [158].

Benzenethiol adsorbs on Au(111) from the aqueous solution to form a well-ordered monolayer of a commensurate ($\sqrt{13} \times \sqrt{13}$)R13.9° symmetry [159]. It has been found that the ordered phase

is formed in 0.1 mM aqueous solution in several minutes. Further immersion results in the formation of multilayers.

Oxidative electrodeposition of three isomers of benzenedimethanethiol on Au(111) from alkaline aqueous solutions has been studied by Rifai and Morin [160]. All isomers were found to adsorb onto gold via sulfur and to form complete monolayers.

Kuwabata et al. [161] have prepared, via electrochemical polymerization on Au(111), SAMs comprising aminobenzenethiol and 3-aminophenethylthiol units. Polymerization of aminobenzenethiol required the use of ortho and meta isomers in the molar ratio of 1:1, whereas, in contrast, 3-aminophenethylthiol was easily polymerized as a pure substance. The monolayers obtained exhibited electrochemical properties very similar to those of polyaniline and their derivatives.

24.4.3.1.3 Adsorption of Thiourea Earlier study of adsorption of thiourea on pc-Au electrode from aqueous solutions of KClO_4 and HClO_4 were carried out by Holze and Schomaker [162]. The adsorbed compound is perpendicularly oriented with sulfur atom interacting with the gold surface.

Azzaroni et al. [163] have used STM to study electrochemical reactivity of thiourea toward Au(111). Sequential STM imaging has shown that thiourea adsorbs as striped arrays that evolve to the hexagonal close-packed structure when surface charge density is decreased. The transient hcp structure undergoes electrooxidation to formamidine disulfide, which slowly yields adsorbed sulfur. Adsorption of thiourea on the pc-Au electrode from KClO_4 solutions has also been studied [164]. The film pressure and the Gibbs surface

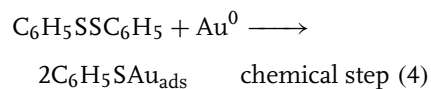
excess were determined as a function of potential applying CV differential capacity measurements and chronocoulometry.

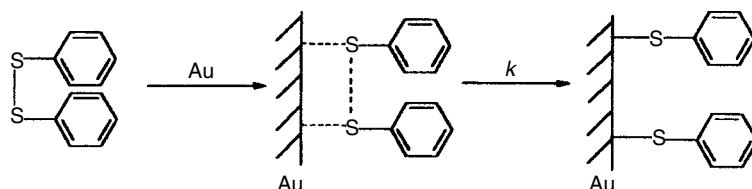
Oxidation of thiourea adsorbed on Au(111) and pc-Au electrode in 0.1 M HClO_4 has been investigated using CV, in situ Fourier transform infrared spectroscopy, and differential electrochemical mass spectrometry [165]. Two reaction mechanisms were proposed for the oxidation of the adsorbed and nonadsorbed thiourea. For both types of Au electrodes, similar results were obtained.

24.4.3.1.4 Adsorption of Disulfides and Related Compounds

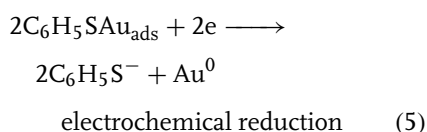
Adsorption and further electrode reactions of different disulfides at gold electrodes depend on chemical properties of the adsorbates. It has been evidenced in some papers that at least for some disulfides, adsorption process involves the cleavage of the S–S bond. Adsorption of diphenyl disulfide on a polycrystalline gold electrode has been studied in detail by Borsari et al. [166]. They have proposed the mechanism of adsorption shown in Scheme 1:

The gas–liquid chromatography with mass spectrometric detection (GLC-MS) analysis of the electrolyzed solution has shown that thiophenol is the only reduction product and the S–S bond cleavage is quantitative. Such a mechanism of bond breaking was confirmed by electrochemical studies. In cyclic voltammograms, anodic and cathodic peak potentials were the same for thiophenol and diphenyl disulfides; thus the same species were participating in these processes. Electrode reactions of diphenyl disulfide are given by the following equations [166]:

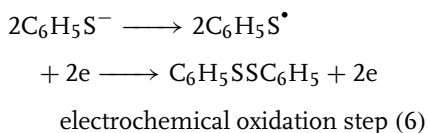




Scheme 1



and finally:



Similar behavior of other aromatic disulfides and thiols on gold electrodes has been described based on the SERS experiments [167]. Adsorption of benzenethiol, benzenemethanethiol, *p*-cyanobenzenemethanethiol, diphenyl sulfide, and dibenzyl sulfide was studied on the roughened gold electrode. All these species adsorb dissociatively as the corresponding thiolates. Monolayers formed from symmetric disulfides were exactly like those formed from the corresponding thiols. These monolayers were stable in a wide potential window: from +800 to −1000 mV (versus SCE), which was limited by the oxidation of the Au surface from the positive side and hydrogen evolution at −1000 to −1200 mV at the negative side.

Also, reductive desorption of SAMs of such asymmetrical disulfides as butyl hexadecyl disulfide and decyl-2(perfluorohexyl)ethyl disulfide has been studied on Au(111), using CV [168]. Peak potentials corresponding to electrochemical desorption waves of the adsorbed species were different from those obtained for monolayers

of the corresponding symmetrical disulfides (containing two identical chains). Possibly, these results reflect the process of mixing of the two constituent chains in the molecular scale.

Electrochemistry of disulfide unit present in cytochrome *c* (cyt *c*) molecules on gold electrodes has also been reported [169]. Disulfide unit in cytochrome *c* is strongly adsorbed on Au electrodes and this slows down the electron-transfer rate to the heme group. More recently, Krylov et al. [170] have immobilized cytochrome *c* by self-assembling on the surface-modified Au electrodes. CV was applied to study how denaturation and renaturation of cytochrome *c* depend on the solution composition.

Investigation of thiol- and disulfide-modified oligonucleotides with either 25 or 10 bases, or base pairs immobilized on polycrystalline and Au(111) electrodes has also been carried out [171]. In these studies, several techniques were employed, including X-ray photoelectron spectroscopy, cyclic and differential pulse voltammetry, interfacial capacitance data, and in situ STM.

Photoelectrochemical assemblies consisting of gold nanoparticles and a tris (2,2'-bipyridine)ruthenium(II)-viologen – disulfide derivative ([RuVS]₂) were obtained at gold electrodes by virtue of combination of the salting-out effect and self-assembly process [172].

The adsorbed state of heptyl viologen on the Au(111) electrode surface was

interrogated by in situ IRAS [173]. Both the dication HV^{2+} and the monocation HV^+ were detected. Complex spectral changes were observed when the electrode potential was varied. Recrystallization phenomena in bulk deposits of cation radical salts occurred more readily at Au(100) than Au(110) and Au(111) surfaces. Atomic arrangement of the gold electrode surface significantly affected the structure of adsorbed viologens.

Cysteine and cystine. Monolayers of L-cysteine and L-cystine assembled on Au(111) form highly ordered network-like clusters of a $(3\sqrt{3} \times 6)R30^\circ$ structure, as it has been shown in in situ STM and electrochemical studies [174]. Each cluster includes six molecules of cysteine or three molecules of cystine. One may assume that inter- and intramolecular hydrogen bonds between the adsorbed cysteine or cystine units are responsible for the observed structures, as they are not observed for 1-butanethiol adlayer under identical conditions. Adsorption of cysteine on Au(111) surface has been studied theoretically [175], involving periodic supercell density-functional theory calculations. Different adsorption modes were considered in these calculations. The strength of N–Au and S–Au adsorption bonds for amino-thiolate was estimated to be of the order of 6 and 47 kcal mol^{−1}, respectively. Hager and Brolo [176] have studied adsorption and desorption processes of the cysteine/cystine (thiol/disulfide) redox couple in neutral (0.1 M KClO₄) and basic (0.1 M NaOH) media on Au(111) electrodes. In 0.1 M KClO₄, adsorption peaks corresponding to cysteine and cystine were formed at 0.43 and 0.57 V (versus SCE), respectively. This difference in peak potentials reflects different adsorption properties of the thiol and disulfide species. Similar behavior was also

observed in 0.1 M NaOH. Disulfide was adsorbed when the applied potential was held at values more positive than +0.25 V in KClO₄ and −0.20 V in NaOH (versus SCE). The corresponding thiol (cysteine) was the only adsorbed species when the applied potentials were more negative than +0.25 V and −0.20 V in KClO₄ and NaOH, respectively. Thiol monolayers exhibited higher packing density than their disulfide counterparts.

24.4.3.1.5 Other Sulfur Compounds and Complex Adsorption Layers

Adsorption of 5-(octyldithio)-2-nitrobenzoic acid on a gold electrode has been investigated using a quartz crystal microbalance [177]. This adsorption follows the Freundlich isotherm. AFM images of the films obtained in 10 mM ethanolic solution of the studied acid exhibited dramatically different morphologies, which were ascribed to the formation of multilayered aggregates.

Dijksma et al. [178] have described the formation of SAMs of thiocetic acid on pc-Au electrodes in phosphate buffer of pH = 7.4. It has been found that potentiostatically formed monolayers of this acid have better characteristics than those generated under the open-circuit conditions. Also, a new strategy toward fast immobilization of thiocetic SAM has been described [179]. It involved placing the known quantity of thiocetic acid solution on a gold electrode surface. This way, one obtained modified electrodes that can be used in the preparation of sensors.

Yong and Beng [180] have deposited monolayers of 2-mercaptobenzothiazole and 2-mercaptobenzimidazole on Au surfaces from diluted ethanolic solutions and have studied their electrochemical behavior.

Che and Cabrera [181] have investigated molecular recognition based on

self-assembled (3-mercaptopropyl) trimethoxysilane monolayer on a gold surface.

Electrochemical dimerization of 2(2'-thienyl)pyridine adsorbed on Au(111) has been observed, applying in situ fluorescence [182]. The structure and electrochemical properties of 4,4'-dithiopyridine (PySSPy) on Au(111) have been investigated as well [183]. The S–S bond was broken during adsorption and the compound was attached to the Au surface via sulfur. Coadsorption of 2-mercaptopyrimidine and 2,2'-bipyridine on Au(111) has been studied by STM [184]. 2,2'-Bipyridine molecule was adsorbed vertically via nitrogen. Mutual adsorbate–adsorbate interactions occurred as π -stacking. The behavior of 2-mercaptopbenzimidazole SAM monolayer at the Au(111) electrode has been examined using CV and in situ FTIR spectroscopy [185]. The charge involved in reductive desorption was pH independent, while the oxidative partial redeposition charge increased with the decreasing pH. In alkaline and neutral media, 2-mercaptopbenzimidazole desorbs as the thiolate anion, and in acidic solutions, as the neutral thiol [185].

CV investigations of 6-mercaptopurine and 8-mercaptoquinoline SAMs on pc-Au electrodes have been presented by Madueno et al. [186] and He et al. [187], respectively. Several model electrode reactions involving various redox probes were studied using such modified electrodes. Baunach and Kolb et al. [188] have deposited copper on disordered benzyl mercaptan film on Au(111) surfaces. They have also studied the behavior of benzyl mercaptan SAM on Au(111) in H₂SO₄ solution using CV and STM. Structural and electrical properties of SAMs based on tetrathiafulvalene derivatives on Au(111) were investigated. These monolayers were disordered, or at least loosely

packed. Conduction through these molecular SAMs is remarkably high (due to the tetrathiafulvalene moiety).

Also, self-assembled layers of functionalized oligo(cyclohexylidene) molecules on Au(111) electrodes have been studied [189]. Their morphology has been investigated using STM and AFM. Dudek et al. [190] have studied electrochemical properties of SAMs comprising the mixture of ferrocene-terminated oligo(phenylenevinylene) methyl thiol and an alkanethiol diluent on gold electrodes. Szafranski et al. [191] have applied SERS to characterize monolayers of *p*-substituted benzenethiols and *p*-substituted benzenemethanethiols (substituents–F, Cl, Br) on gold electrodes. The studied compounds (six) existed on the surface as thiolate molecules of aromatic rings tilted with respect to the surface normal. They formed monolayers, which were stable at the surface in the potential range from +800 mV to –1000 mV (versus SCE) in neutral solutions.

It has been described [192] that the orientation of 2-mercaptopmethylthiophene molecules adsorbed on Au(111) is almost vertical at the saturation coverage. At low coverage, in turn, the molecules form striped islands, within which the thiophene rings are tilted by $45 \pm 10^\circ$ with respect to the surface normal.

Mazur and Krysiński [193] have presented a comparative study of electrodeposition of poly(3-octylthiophene) films on gold electrodes – bare and modified with a dodecanethiol monomolecular layer. The polymer deposited on the thiol-coated electrode was more compact. There is also a significant interest in adsorption of organic compounds containing two functional groups in their molecules. Sulfur-containing group directly participates in the formation of bond with the gold surface, while another group, such as

—COOH, —NH₂, or —OH, participates in the interaction with other molecules in the solutions. We briefly present the selected papers on this topic below.

Adsorption of 2,3-dimercaptopropane sulfonate on Au(111) in alkaline solutions has been studied by Yang et al. [194]. STM studies have revealed that adsorption involves reorientation in the primarily formed adlayer and a slow lifting of the reconstruction. It has been shown that ω -mercaptohexanoic acid SAMs on pc-Au electrodes are stable and exhibit catalytic property toward redox reaction of chlorophylls [195]. Using SERS, it has been demonstrated that mercaptoethylamine is adsorbed on a gold electrode in the mixed trans and gauche conformations [196], initially at 0.0 V (versus Ag|AgCl). When the potential is changed anodically or cathodically over the range: +0.4 to −0.8 V, the population of adsorbate molecules switches mostly to the gauche conformation.

Zhang et al. [197] have studied adsorption of DL-homocysteine and L-homocysteine thiolactone on Au(111) electrode in 0.1 M HClO₄ using CV and STM. Both compounds formed highly ordered adlayer on Au(111). For both adlayers, structural models have been proposed.

Dopamine β -hydroxylase adsorbed on gold electrode has been investigated electrochemically and applying quartz crystal microbalance [198]. In the neutral phosphate buffer solution, the adsorbed layer was stable and did not desorb within the potential range of 0.6 to −0.7 V (versus Ag|AgCl −1 M KCl). At potentials more positive than 0.8 V, the adsorbed compound was oxidized and, probably, residual tyrosine, tryptophan, and histidine participated in this process.

Nishizawa et al. [199] have analyzed electroreductive desorption of a mixed

self-assembled 3-mercaptopropionic acid (MPA) and HT monolayer in 0.5 M KOH on Au electrode. The monolayer prepared from 1 mM MPA and 0.2 mM HT gave two cathodic signals at different potentials, suggesting phase segregation within the mixed layer. Electrode behavior accompanying selective cathodic desorption of MPA was characteristic for an array of microelectrodes. This observation indicates that MPA domains are dispersed in the original mixed monolayer. Potential permeability of monolayers toward ionic species present in the solution has been investigated using mixed SAMs composed of MPA and poly(3-dodecylthiophene) adsorbed on gold electrodes [200]. Quartz crystal microgravimetric study of self-assembled thioglycolic acid on polycrystalline gold electrode in 0.5 M KOH has revealed formation of the monolayer. In 0.5 M HCl, in contrast, the frequency changes rather suggest the formation of a bi- or multilayer owing to the presence of hydrogen bonds.

Other studies on gold electrodes have been focused on various self-assembled reactants attached to Au via sulfur-containing groups. Some of these reactants may exhibit catalytic activity or participate in the electron transfer between the electrode and other reactants present in the solution (mediation). Thiol- or disulfide-modified gold electrodes are frequently used to attach other species to already modified surfaces, and form bilayers. Since such systems are very loosely connected with the electrochemistry of gold, only selected examples are given below. One among such compounds is metalloporphyrin deposited on a gold electrode modified with L-cysteine SAM [201]. A cupric-porphyrin-L-cysteine film exhibited good catalytic activity toward

reduction of H_2O_2 . Octabutylthiophthalocyaninato-cobalt(II) forming a SAM on gold electrodes has potential application as an electrochemical sensor in alkaline solutions [202], yet only in the potential range of -0.20 to $+0.55$ V (versus $\text{Ag}|\text{AgCl}$). Self-assembly of 4-ferrocene thiophenol immobilized on gold electrode modified with electroactive gold has been described as well [203]. Other immobilized compounds that have been studied include DNA and a C-reactive protein [204], DNA [205], fullerenes $\text{C}_{60}(\text{OH})_n$ [206], cytochrome *c* [170], bovin serum albumin [207], dipalmitoylphosphatidylcholine [208], J-aggregates of cyanine dyes [209], naphthoquinone [210], proteins [211], and α -cyclodextrin [212]. Other biologically or technically important compounds, for example, porphyrine [213] and metalloporphyrins [214], in combination with thiols or other sulfur-containing compounds have also been attached to gold electrodes. Iron(III) protoporphyrin IX and hematoporphyrin have been covalently bonded to dimercaptoalkane-modified gold electrodes [215]. Electrochemical reversibility of the attached complexes has been confirmed by CV. Heterogeneous rate constant of charge transfer between the iron protoporphyrin and the Au substrate has been found to decrease exponentially with the spacer length.

DNA has also been immobilized on Au electrode by its interaction with gemini surfactants [216]. Moreover, inclusion complexes of viologen-attached alkanethiols and α - and β -cyclodextrins that spontaneously assemble on Au electrodes have been studied [217, 218].

24.4.3.2 Adsorption of Selenium-containing Compounds

Only a few papers on the self-assembled organoselenol monolayers are available.

Samant et al. [219] have prepared a compact layer of docosaneselenol on Au(111). On the basis of X-ray scattering experiments, they have proposed a structure similar to that of thiol monolayers. Also, diphenyl diselenide forms a SAM on polycrystalline Au [220]. This compound is adsorbed even stronger than the corresponding sulfur analog [221]. Benzene-selenol chemisorbed on Au(111) forms initially only small islands, which develop later to large hexagonal-shaped facets, as it has been shown in STM studies [222]. Protsailo et al. [223] have studied adsorption of *n*-dodecaneselenol on Au(111) from ethanolic solutions. They have found that this process occurs in two steps; in the first step, lasting for several seconds, a monolayer is formed, and during the next few hours, a film is organized and self-ordering processes advance.

Employing STM, Monnell et al. [224] have characterized coexisting adsorbate phases in high-coverage decaneselenolate and dodecaneselenolate SAMs on Au(111). Two structure types have been distinguished: a densely packed distorted hexagonal lattice incommensurate to the underlying gold substrate, and a commensurate linear missing row. The differences between these structures and structurally analogous phases of alkanethiolate monolayers on Au(111) may be explained in terms of head group–head group and head group–substrate interactions guiding the self-assembly process.

24.4.3.3 Adsorption of Nitrogen-containing Compounds

24.4.3.3.1 Pyridine and its Derivatives

Adsorption of pyridine and its derivatives on different metal electrodes has been studied very intensively [11], both at polycrystalline Au surface and different

single-crystal Au surfaces. Using ellipsometry, Chao et al. [225] have detected that at positive potentials, pyridine molecules are oriented vertically on pc-Au, whereas they attain flat orientation at negative potentials. Lipkowski and coworkers, in a series of papers, have undertaken systematic studies on adsorption of pyridine from aqueous solutions at various gold electrodes. Adsorption of pyridine on polycrystalline Au electrodes has been studied first, using chronocoulometry [226]. In later studies, the results obtained from chronocoulometry and Raman spectra were compared to those from SERS [227] and radiochemical methods [228]. It has been shown that at a negatively charged surface, pyridine molecules adsorb in the flat orientation and the corresponding maximum surface concentration reaches $3 \times 10^{-10} \text{ mol cm}^{-2}$ [226]. At positively charged surface, the adsorbed pyridine molecules reorient to a vertical position, presumably with nitrogen atoms facing the gold surface. Reorientation is accompanied with the increase in the limiting surface concentration up to $7 \times 10^{-10} \text{ mol cm}^{-2}$. The change of orientation of Py molecules at the pzc is a two-dimensional phase transition. The standard Gibbs energy of adsorption equals to -38 kJ mol^{-1} . Also, a partial charge transfer has been found to be involved in the pyridine adsorption process [226]. Pyridine adsorption at single-crystal electrodes has been performed on Au(100) [229], Au(110) [230], Au(111) [231], Au(311) [232], and Au(210) [233]. The corresponding values of the standard Gibbs energy of adsorption (in kJ mol^{-1}) have been determined: -36 for Au(111) and Au(100), -42 for Au(311) and Au(110), and -47 for Au(210). According to these numbers, $\Delta G^\circ_{\text{ads}}$ decreases when densely packed surface layer is converted into the more

open one. Such an orientation is also typical of the Au lattice planes of high Miller indices. Reorientations of Py molecules on Au(100) are initially [229] analogous to those on pc-Au at negative and positive charges. Additionally, transitional orientation was suggested for the potentials close to the zero charge potential and intermediate surface concentrations. Later, however, Skořuda et al. [234] have shown that adsorption of pyridine on Au(100) is a more complex process than it appeared before, since at the unreconstructed Au(100) face, it is hampered by negative potential-induced reconstruction into the (111)-like structure. Therefore, in order to derive the adsorption isotherm for Py on unreconstructed Au(100), it is necessary to apply negative potential for the minimum time to reach the adsorption equilibrium. Consequently, Py molecules adsorbed on Au(100)-(1 \times 1) exhibit vertical orientation within the entire potential range studied. The studies of Au(110) [230] have revealed that Py molecules adsorb vertically also on this surface and are attached to the metal via the nonbonding orbital of the nitrogen atom. For Au(111), the dependence of the orientation of Py molecules on the surface charge has been found [231]. Several modern spectroscopies, for example, SHG [235, 236], DFG on Au(111) [237] and SERS on Au(210) [238], have been employed to determine the orientation of Py molecules at Au surfaces. At Au(210) and Au(311), the adsorbed Py molecules attain vertical N-bonded orientation. In general, the studies on different types of Au surfaces have shown that it is not always clear whether Py molecules desorb from the electrode or only change their orientation [11].

Arvia and coworkers [239] have investigated adsorption of pyridine on Au(111) in the potential range $0.15 \text{ V} < E < 0.55 \text{ V}$

(versus SHE) using in situ STM. At potentials higher than or equal to the pzc, both disordered and ordered domains were observed. For potentials lower than E_{pzc} , the ordered structure disappeared. In the ordered domain, pyridine molecules were adsorbed vertically and formed a (4×4) hexagonal lattice of the nearest-neighbor distance of 0.38 nm.

On a pc-Au electrode in 1 M NaF vertically oriented pyridine molecules have been observed at 0.7 V (versus Ag/AgCl), applying in situ IR. In contrast, they have not been detected at this potential in electrochemical method [240]. Considering the fact that adsorption of pyridine on gold electrodes is a replacement reaction and taking into account the results obtained from quartz crystal microbalance experiments, the conclusion has been made that adsorption of one pyridine molecule is accompanied by the removal of 10–12 water molecules [241].

Subtractively normalized interfacial FTIR has been employed [242] to study the changes in the surface coordination of pyridine molecules on Au(111). It has been deduced from the experiments that pyridine molecule is positioned upright at positive potentials and its plane rotates somewhat with respect to the electrode surface. In situ FTIR has also been used [243] to investigate adsorption of pyridine on Au(111), Au(100), and Au(110) electrodes. For the low-index electrodes, the behavior of band intensity located at 1309 cm^{-1} and corresponding to the total adsorbed pyridine, agreed with the surface excess results obtained earlier from chronocoulometry.

Hush and coworkers [244] have calculated theoretically, the binding energy and the dipole moment of isolated pyridine molecules adsorbed on Au(111) surfaces, and have determined the structure of this

system. Significant binding was found only for atop configurations, in which pyridine molecule is positioned directly above a single gold atom with its nitrogen atom bound to it.

Electrochemical and subtractively normalized interfacial FTIR studies of 4-cyanopyridine adsorption on Au(111) electrode [245] have shown that this compound is totally desorbed at potentials lower than -0.7 V versus SCE. At less negative potentials, the molecules were flatly oriented (π bonded) on the surface and reoriented to the vertical position, when potential approached 0 V. At potentials higher than 0.05 V, adsorption of 4-cyanopyridine becomes dissociative and the compound is partially hydrolyzed to isonicotinamide.

Electrochemical and SERS studies [246] have revealed strong adsorption of 4-phenylpyridine to pc-Au electrode in a wide potential range. The molecule was adsorbed via nitrogen in almost vertical orientation at electrode potentials $\leq 0 \text{ V}$ (versus Ag/AgCl), followed by the subsequent tilting of the molecular plane to adopt a more flat orientation. This reorientation resembled the behavior of 4-cyanopyridine on Au(111) [247].

Adsorption of three isomeric pyridine-carboxylic acids on pc-Au electrode in HClO_4 solutions has been investigated [248], applying in situ IRAS. When the potential was changed to more positive values, the adsorbed 3- and 4-picolinic acids were reoriented from the flat to the vertical configuration and thereafter bounded to the surface via lone electron pairs present at two oxygen atoms of the $-\text{COOH}$ group. No significant adsorption of the ortho isomer has been detected.

Using SERS, Brolo et al. [249] have studied the potential-dependent orientation of 2,2'-bipyridine molecules adsorbed on a

SERS-active Au(111) surface electrode. It has been found that at a positively charged surface, 2,2'-bipyridine adsorbs end-on via both nitrogen atoms. STM images have shown that [60]-fullerene-substituted 2,2'-bipyridine forms spontaneously, a SAM on Au(111) surface [250].

There is a class of compounds, known as promoters in redox reaction of horse cytochrome *c*, which increase the electron-transfer rate by several orders of magnitude [251]. Czerwiński et al. have studied electrochemically, using pc-Au electrodes, one of these compounds, 4,4'-bipyridyl (PyPy). It has been shown that adsorption of PyPy is governed by the Langmuir isotherm and is a one-center reaction involving the displacement of water molecules from the metal surface. In the adsorbed state, the PyPy molecules attain the perpendicular orientation toward the electrode surface. Later, Czerwiński et al. [252] have carried out CV studies of other compounds of that type, bis(4-pyridyl)disulfide (PySSPy) and 1,2-bis(4-pyridyl)ethylene (BPE). Adsorption of BPE has been found to be fast and increased with the adsorption time, whereas electrode coverage with PySSPy decreased with the adsorption time, suggesting that PySSPy molecules undergo a surface transformation.

Applying in situ infrared spectroscopy and STM, Cai et al. [253] have studied adsorption of pyridine on Au(111) electrodes from aqueous NaClO₄ solutions. It has been found that pyridine molecule is flatly adsorbed on the surface at negative potentials. Its molecular plane rises up as the applied potential and surface concentration increase. Moreover, orientation of pyridine molecule changed with the applied STM potential. Ikezawa et al. [243] have used in situ FTIR spectroscopy to investigate adsorption of pyridine on Au(111), Au(100),

and Au(110) electrodes in 0.1 M NaF solution containing 2 mM pyridine-*d*₅.

In situ subtractively normalized interfacial FTIR spectroscopy has been employed [254] to study adsorption of pyridine on the Au(110) electrode surface. The compound adsorbed via the nitrogen atom and the tilting angle decreased progressively with the increasing electrode potential, as it appeared from the IR data. At low charge density, the film of N-bonded pyridine molecules was less rigid and the molecules exhibited a waving motion.

Adsorption of pyridine on Au(110) electrodes was also studied using reflection anisotropy spectroscopy [255]. Reflection anisotropy of pyridine/Au(110) system has been attributed to $n-\pi^*$ transitions, the band of which was shifted compared to their spectral position in the gas phase, due to the interaction of the lone electron pair orbitals at N atom with the gold surface.

Ikezawa and Kosugi [256] have studied 2-chloropyridine adsorbed on Au(111) and Au(110) electrodes in 0.1 M KClO₄ using in situ infrared spectroscopy and differential capacity measurements. Relative band intensity of N-bonded adsorbate for Au(110) was much stronger than for Au(111). Apparently, at Au(111), the adsorbed 2-chloropyridine molecules either exhibited flat configuration, or the tilting angle was large.

From electrochemical measurements, the dependence of adsorption of *N*-4-pyridinyl-hexadecanamide and *N*-pentadecyl-4-pyridinecarboxamide on the Au(111) electrode potential has been determined [257]. The results were compared to the behavior of 4-pentadecylpyridine described in the previous reports.

Neutron reflectometry (NR) has been employed to study the structure and

composition of thin films of 4-pentadecylpyridine at a Au(111) electrode surface [258]. At very negative potentials, the film was desorbed from the electrode surface. With the help of NR, it has been demonstrated that at these potentials, amphiphilic molecules remain in close proximity to the gold surface as a thick and water-rich film.

Using reflectometry, Barten et al. [259] have investigated adsorption of quaternized poly-2-vinyl pyridine, of a fixed charge per monomer, on a gold electrode. The total adsorbed amount of the compound decreased linearly with the double-layer potential of gold. Adsorption proceeded up to a relatively high double-layer potential and was accompanied by a relatively high contribution of nonelectrostatic interactions.

24.4.3.3.2 Pyrazine Adsorption of pyrazine on a pc-Au electrode has been studied [260]. The obtained relationships between the SERS intensity and the surface coverage, as well as the surface morphology have been analyzed. Later, adsorption of pyrazine on a pc-Au electrode has been investigated by Cai et al. [261], who have applied in situ surface-enhanced infrared absorption spectroscopy, chronocoulometry, and impedance spectroscopy. The infrared spectra have been compared to the earlier published SERS spectra [260] in order to get a better understanding of electrochemical interface. Pyrazine was adsorbed on the surface in a vertical end-on configuration via one N atom. Pyrazine adsorption has also been studied on single-crystal electrodes: Au(111), Au(100), and Au(110) using in situ FTIR [262]. It has been concluded that pyrazine molecules attain tilted orientation at negative potentials and undergo transition to the vertical position as the potential becomes more

positive. A new band at 1035 cm^{-1} observed for all the electrodes at positive potentials can be explained in terms of adsorption-related change in vertical orientation of the molecules. Earlier, Kolb and coworkers [263] have studied adsorption of pyrazine on Au(111) and Ag(111) electrodes using ex situ X-ray photoelectron spectroscopy. Ikezawa et al. [262] have investigated adsorption of pyrazine on Au(111), Au(100), and Au(110) electrodes in 0.1 M NaF, employing in situ infrared spectroscopy.

24.4.3.3.3 Amines and Other Nitrogen-containing Compounds

Adsorption of *n*-octylamine, *n*-dodecylamine, *n*-hexadecylamine, and octadecylamine from LiClO₄ methanolic solution on Au electrodes has been studied using capacitance measurements [264]. Also, adsorption of benzylamine from aqueous solutions of KClO₄ and HClO₄ on pc-Au electrodes [265] has been investigated, applying capacitance measurements and SERS.

Lipkowski and coworkers [266] have studied adsorption of benzonitrile on the Au(111) electrode using electrochemical and subtractively normalized interfacial FTIR.

Xiao and Sun [267] have investigated adsorption of *p*-nitrobenzoic acid at a gold electrode in 0.1 M HClO₄, using various methods. At potentials more positive than 0.3 V, the molecules tended to adsorb in a vertical orientation via their carboxylic group directed toward the Au surface.

24.4.3.4 Adsorption of Other Organic Compounds

24.4.3.4.1 Alcohols Richer and Lipkowski [268, 269] have performed extensive studies on adsorption of *tert*-pentanol

on single-crystal Au surfaces of low Miller indices. They have shown that adsorption characteristics of this compound are similar to those observed for the mercury electrode [11]. The lowest Gibbs adsorption energy found for Au(110) indicated the strongest binding of water molecules to the folded surface, compared to the smoother Au(111) and Au(100) surfaces. Adsorption of *n*-tetradecanol, *n*-hexadecanol, and *n*-octadecanol from LiClO₄ methanolic solutions has also been studied by capacitance measurements [270]. Yang and Bizzotto [271] have studied the influence of electrolyte concentration on adsorption of octadecanol on Au(111), applying electrochemical methods and elastically scattered light measurements. Electrolyte concentration most significantly influenced adsorption and desorption potentials, which opens up possibilities of investigating the dynamics of adsorption/desorption processes.

Lipkowski and coworkers [272] have studied adsorption of *n*-octadecanol monolayer on Au(111) electrode. Octadecanol molecules formed a two-dimensional film at any film pressures. At film pressures exceeding 12 mN m⁻¹, the film had low compressibility and the constituting molecules were slightly tilted with respect to the surface normal. At lower pressures, the film was compressed and the tilting angle increased with the decreasing surface pressure.

Sottomayor et al. [273] have investigated adsorption of *n*-hexanol on Au(111) electrode from 0.2 M NaClO₄ aqueous solution, applying chronocoulometry to measure dynamic capacitance and capacitive charge. They have found that in this case, adsorption may be described by the Frumkin isotherm and have determined the corresponding parameters. The obtained results were discussed and

compared to the literature data reported for adsorption of *n*-hexanol on Hg and single-crystal Ag electrodes.

Some conclusions pertaining to adsorption of 1-pentanol riboflavin and thiocetic acid on Au electrode have been drawn from differential capacity-potential curves [274]. It has been found, for instance, that adsorption of these compounds obeys the Langmuir isotherm. Moreover, the free energies of adsorption have been determined.

It has also been evidenced [275] that octadecanol and pyrenenonanol form a mixed monolayer during adsorption, yet they do not mix ideally.

24.4.3.4.2 Aminoacids Adsorption of serine, tyrosine, and histidine [276], as well as asparagine [277] on a pc-Au electrode from 0.1 M LiClO₄ aqueous solutions has been investigated, applying ac-impedance measurements. For asparagine, Gibbs energy of adsorption (-47 kJ mol^{-1}) was calculated by fitting Henry's and Frumkin's isotherms to the experimental results. Electrochemical and IRAS results have revealed that asparagine interacts with Au surface via oxygen atoms of $-\text{COO}^-$ and amide carbonyl groups [277]. Adsorption strength of the studied amino acids on gold electrode was decreased in the sequence: tyrosine \geq histidine $>$ serine.

Li et al. [278] have studied adsorption of L-phenylalanine at Au(111) electrodes using electrochemical and subtractively normalized interfacial FTIR methods. It has been found that the adsorbed molecules change their orientation with the electrode potential. At a negatively charged surface, the compound was predominantly adsorbed in the neutral form of the amino acid. At potentials positive with respect to pzc, L-phenylalanine was adsorbed predominantly as zwitterion with $-\text{COO}^-$

group directed toward the surface and $-\text{NH}_3^+$ group facing the solution. At even more positive potentials, electrocatalytic oxidation of phenylalanine occurred, accompanied by the formation of CO_2 .

24.4.3.4.3 Other Organic Acids Adsorption of aliphatic acids on single-crystal Au electrodes has been studied by Dutkiewicz and coworkers [279, 280]. Specific adsorption of citrate from perchloric acid solutions at Au(111) electrodes has been investigated using *in situ* FTIR spectroscopy and CV [281]. The authors have discussed the models of surface coordination of citrate. Based on subtractively normalized interfacial FTIR spectra, Lipkowski and coworkers [282] have found that citric acid fully deprotonates during adsorption on Au(111) and the surface-bound carboxylate groups adopt a tilted orientation. They have also found that the limiting coverage is $3 \times 10^{-10} \text{ mol cm}^{-2}$. Employing *in situ* reflection-adsorption IR spectroscopy and CV, it has been shown [283] that 2-, 3-, and 4-fluorobenzoic acids adsorb at positive potentials on Au(100) from 0.1 M HClO_4 solutions. The adsorbate molecules were oriented vertically, with both oxygen atoms oriented toward the metal surface. Adsorption/desorption processes of 1-hydroxyethane-1,1-diphosphonic acid molecules on Au(111) surface have been investigated [284] in perchlorate solutions using CV and STM.

Adsorption of humic acid on Au(111) and pc-Au electrodes has been studied [285], employing several electrochemical techniques and electromicrogravimetry.

Zelenay et al. have applied CV and radiotracer technique to study adsorption of benzoic acid from 0.1 M HClO_4 solution on a pc-Au electrode prepared by electroplating [286]. Chemisorption occurred within the entire potential range

(0.05 to 1.75 V versus SHE); however, orientation of the adsorbed molecules was potential dependent, that is, at less positive potentials, flat orientation predominated, while at more positive potentials, vertical orientation was the most pronounced. It is noteworthy, that although desorption of benzoic acid to the pure supporting electrolyte solution was insignificant and extremely slow, its surface/bulk exchange was much faster. Later, Sobkowski et al. [287] have found that adsorption of benzoic acid on Au, Ag, and Cu electrodes from HClO_4 solution is reversible, whereas at Pt, it appears to be partly irreversible. For pc-Au, the following parameters of the Frumkin isotherm were found: $\Delta G_{\text{ads}}^\circ = -16.4 \text{ kJ mol}^{-1}$ (for the standard state defined as $c = 1 \text{ M}$, $\Gamma = 0.5\Gamma_\infty$, lateral interaction parameter $a = 0$), $\Gamma_\infty = 2.4 \times 10^{-14} \text{ molecules/cm}^2$, $a = 1.5$. Adsorption of benzoic acid on Au(111) and Au(110) electrodes in 0.1 M HClO_4 has been investigated, applying IRAS, voltammetry, and differential capacity measurements [288]. For both electrodes, the presence of vertically adsorbed anion at positive potentials has been confirmed by IRAS. Other orientations also occurred at negative potentials, as it followed from the IRA spectrum.

Finally, the structure of 3,4,8,10-perylene-tetracarboxylic-dianhydride grown on reconstructed and unreconstructed Au(100) has been investigated [289].

24.4.3.4.4 Nucleic Bases and Other Biochemical Compounds

It has been found that cytosine is physisorbed at negative potentials and chemisorbed at positive potentials on Au electrodes from 0.1 M NaClO_4 and HClO_4 aqueous solutions [290]. In cyclic voltammogram

of cytosine, one pair of peaks was observed, which can be ascribed to the transition between the physisorbed and chemisorbed states. In both states, the molecules were oriented with N(3), C=O and NH₂ moieties toward the surface. Adsorption of uracil on Au(100) has been studied using in situ STM [291]. Depending on the Au electrode potential, uracil formed three highly ordered monolayers, which were imaged with a molecular resolution. Pronkin and Wandlowski [292] have studied adsorption and phase formation of uracil on massive Au[*n*(111)-(110)] single-crystal and Au(111–20 nm) film electrodes in 0.1 M H₂SO₄ using electrochemical measurements and attenuated total reflection (ATR) surface-enhanced infrared reflection/absorption spectroscopy. At $E < 0.15$ V, uracil molecules were disordered and planar oriented. Close to the zero charge potential, a 2D condensed physisorbed film of planar-oriented molecules, interconnected via directional hydrogen bonds, was formed. The formation of organic adlayers on single-crystal Au electrodes has been studied for such compounds as uracil, methyluracils, and uridine. Cyclic voltammograms of such compounds on, for example, Au(111) surface, typically exhibited broad peaks and sharp spikes, associated

with significant structural modifications of the interfacial region [293–297]. For the above-mentioned compounds, four such regions can be distinguished (see Fig. 9 as an example): (I) random adsorption and gradual desorption, (II) 2D condensed film, (III) charge-transfer process of physisorbed species (II) to the chemisorbed-like state (IV). As Roelfs and Baumgärtel [298] have shown, this CT process involves deprotonation of organic molecules, which makes the reaction pH dependent.

Adsorption and phase formation of uracil on massive Au[*n*(111)-(110)] single-crystal and Au(111–20 nm) film electrodes in 0.1 M H₂SO₄ has been studied in electrochemical measurements and applying ATR surface-enhanced infrared reflection absorption spectroscopy [299]. At $E < 0.15$ V (versus trapped hydrogen electrode), uracil molecules are disordered and planar oriented. Close to the pzc, a 2D condensed physisorbed film of planar-oriented molecules interconnected by directional hydrogen bonds, is formed.

Adsorption of adenine and coadsorption of adenine–thymine and uracil–thymine on Au(111) has been reported [300]. Adenine was chemisorbed in two different states. Mutual interaction between adenine and thymine was detectable only at

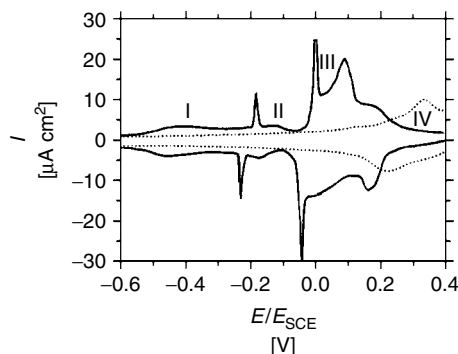


Fig. 9 Cyclic voltammograms recorded at Au(111) in the aqueous solution of 0.5 M NaF in the absence (.....) and the presence (—) of 12 mM uracil [297]. Temperature: 15 °C. See text for the description of the indicated regions.

negative potentials when both molecules had their planes oriented parallel to the surface.

Shen et al. [301] have used quartz crystal microbalance to study electrochemical behavior of guanine, guanosine, and guanosine phosphate at gold electrodes.

Hason and Vetterl [302] have studied adsorption of cytidine on Au(111) and mercury film electrodes.

Surface-enhanced near-infrared Raman spectroscopy has been utilized to study the behavior of nicotinamide adenine dinucleotide on a gold electrode [303]. It has been found that either adenine or nicotinamide moiety changes its adsorption states during potential scanning.

Adsorption of azurin – a copper-containing protein on Au electrodes under physiological conditions – has been monitored at the molecular level, applying STM [304].

It has been found that at Au electrode exposed to the solutions of human serum albumin and immunoglobulin in the phosphate buffer, the double-layer capacity is decreased, while charge-transfer resistance at the Au/solution interface increases [305, 306]. These changes were attributed to the formation of proteinaceous layer at the electrode.

Adsorption of putidaredoxin on gold electrodes has been studied using dynamic spectroscopic ellipsometry and differential capacitance measurements [307]. In Ref. 307, a method for the measurement of metal surface optical perturbation during protein adsorption at a constant potential has been described. The method is based on the concept that the charged transition layer develops between the electrode substrate and the adsorbate.

A simultaneous use of quartz crystal microgravimetry and fluorescence has

been proposed [308] to study adsorption/desorption and oxidation of vitamin B₆ at a pc-Au electrode in aqueous KOH solutions. Oxidation of vitamin was irreversible and was accompanied by strong electrogenerated fluorescence at the wavelength of 443 nm (excitation wavelength 360 nm).

Zerbino and Sustersic [309] have presented electrochemical and ellipsometric studies of dopamine adsorbed on gold electrodes in aqueous H₂SO₄ solutions of pH = 1.

Adsorption of glutathione on a gold electrode has been studied [310] using electrochemical quartz crystal impedance, electrochemical impedance spectroscopy, and CV.

Chronocoulometry and photon polarization modulation infrared reflection/absorption spectroscopy have been employed [311] to study the fusion of dimyristoylphosphatidylcholine vesicles onto an Au(111) electrode. The fusion was controlled either by the electrode potential, or charge. Film characteristics was also potential dependent. After removing the film from the electrode surface (negative potential), phospholipid molecules remained in its close proximity, in the ad-vesicle state. Several electrochemical and nonelectrochemical methods have been applied [312, 313] to investigate the spreading of small unilamellar vesicles onto Au(111) electrode. Vesicles fused onto the surface at $E > -0.5$ V (versus SSCE), to form defected bilayers in contact with the metal surface. At more negative potentials, the film was removed from the electrode surface, but it still remained in its close proximity.

A new approach to a directly controlled deposition of long DNA molecules on bare gold electrode array without any modification of gold electrodes and DNA

molecules has been described in Ref. 314. AFM studies have shown that DNA molecules are significantly less stable on bare gold surface than on the one modified with aminothiols.

24.4.3.4.5 Other Compounds Recently, low-temperature STM has been used [315] to characterize variously structured submonolayers and near monolayers of benzene on Au(111).

Adsorption of chlorobenzene on pc-Au electrode has been studied by Czerwiński and Sobkowski [316] as early as in 1980, using a ^{14}C radiotracer technique. The rate-determining step of this adsorption was diffusion of the reactant. Chlorobenzene was adsorbed in multilayers at sufficiently high bulk concentration. The adsorbed molecules were probably oriented vertically with respect to the Au surface and bounded to it via a Cl atom.

STM and CV have been applied [317] to investigate adsorption of three semi-crown ligands on Au(111) surface under conditions of potentiostatic control. Adsorption of alkanes on Au(111) surface was simulated by applying a simple computational scheme [318]. The calculated values of adsorption energies of 10 short-chain alkanes were reproducible with an average error below 1 kcal mol^{-1} . Adsorption of camphor on Au(111) and its effect on electroreduction of IO_4^- has been studied by Pettinger and coworkers [319]. Adsorption of camphor on Au(111) electrodes has also been investigated [320] by generating the second harmonic and applying CV. Also, Kolb and coworkers [321] have studied adsorption of camphor-10-sulfonic acid on reconstructed Au(111) electrode from perchlorate and sulfate solutions. In both solutions, the above compounds formed two-dimensional condensed phases. IR spectra have shown that urea molecule

is adsorbed on Au(100) with a molecular plane normal to the electrode surface. On Au(111) surface, in contrast, coordination of urea molecules was different [322]. Earlier, the adsorption of urea on pc-Au electrode from aqueous solutions of KClO_4 and HClO_4 has been studied by Holze and Schomaker [162]. The free energy of adsorption points toward strong adsorption of thiourea and less strong adsorption of urea in KClO_4 solutions. In acidic solutions, both compounds were not stable.

Structural differences between the monolayers of anthraquinone derivatives self-assembled on silver and gold electrodes have been investigated using CV and in situ SERS spectroscopy [323]. Neves et al. [324] have described Monte Carlo simulations of phenol adsorption on gold electrodes.

Potential-induced phase transition of trimesic acid on Au(111) electrode has been studied using in situ STM and CV [325]. In cyclic voltammograms, a pair of peaks was formed, which was ascribed to the structural transformation. On the basis of high-resolution STM images in 0.1 M HClO_4 , it has been proposed that trimesic acid molecules assume flat-lying and vertical orientations at 0.25 V and 0.85 V , respectively. Both orientations coexisted at 0.65 V .

In situ STM has been applied [326] to study the potential-induced self-organization of α -cyclodextrin on Au(111) surfaces in NaClO_4 solutions. The adsorbed molecules formed an ordered array of a cylindrical structure in the potential range 0.20 to -0.15 V (versus SCE), while they were desorbed at potentials lower than -0.40 V .

Self-organized adlayer of calix[4]arene on Au(111) has been obtained by potential-controlled adsorption [327]. In situ STM

images have shown that the compound molecules are adsorbed as dimers.

Lipkowski and coworkers [328] have employed STM to study the spreading of 1,2-dimyristoyl-*sn*-glycero-3-phosphatidylcholine vesicles into the film at the Au(111) electrode surface. During the initial stage, phospholipid molecules were adsorbed flatly with the acyl chains oriented parallel to the surface and assembled into an ordered monolayer similar to that formed by alkanes. Later, the molecules reoriented and the monolayer was transformed into a hemimicellar film.

Brooksby and Fawcett [329] have studied adsorption of ethylene carbonate at Au(110) electrode from aqueous solutions of HClO_4 , NaClO_4 , and Mt_4NClO_4 , using in situ infrared spectroelectrochemical method.

Growth morphology, long-range ordering, and evolution of the valence bond electronic states of ultrathin films of copper phthalocyanine deposited on the Au(110)-(1 × 2) reconstructed surface have also been investigated as a function of organic molecule coverage [330]. Also, on Au(110)-(1 × 2) surface, growth morphology and electronic structure of 2D-ordered pentacene layers have been studied [331].

Lipkowski and coworkers [332] have applied several electrochemical techniques to study adsorption of *N*-dodecyl-*N*, *N*-dimethyl-3-ammonio-1-propanesulfonate, a model zwitterionic surfactant, on Au(111) electrode. Adsorption of this compound proceeded via a few states. The first two states were observed at potentials close to the zero charge potential. At low bulk concentrations, a nearly flat film of the adsorbed molecules was formed, which was converted into a hemimicellar state at higher concentrations. The second state at negative potentials corresponded to

the film of molecules oriented with their polar head directed toward the solution. Bizzotto and Lipkowski [333] have studied adsorption of insoluble surfactants on Au(111) in order to explain the mechanism of potential-induced adsorption and desorption of 12-(9-anthroloxy) stearic acid, a surfactant dye. Applying electroreflectance spectroscopy and light scattering measurements, they have evidenced that desorbed surfactant molecules form micelles (flakes or vesicles) that are trapped under the electrode surface. The micelles spontaneously spread back on the electrode surface, when charge density at the metal approached zero.

Petri and Kolb [334] have studied the properties of sodium dodecyl sulfate adsorbed on Au(111) in H_2SO_4 solutions, using in situ STM.

24.4.4

Reconstruction of the Surface of Gold Electrodes

When using single-crystal electrodes, it is assumed that the structure of their surfaces reflects the structure of the bulk crystal. However, it appears that, frequently, the surface structure is different from that of the bulk due to their different atomic surroundings. In the bulk crystal, each metal atom is surrounded by identical atoms fixed within the well-defined structure. In contrast, the surface atoms participate in the interactions with metal atoms forming the crystal, and are involved as well in the interactions with the components of the solution at the solid/liquid interface. These asymmetrical interactions of the surface atoms may lead to the breakage of the old and formation of the new bonds, followed by the displacement of the surface atoms to the positions of the lower surface energy. The process of formation

of a new surface structure is known as *surface reconstruction*.

The process of reconstruction of gold electrode has already been mentioned in this chapter several times, for instance, in the discussion of adsorption of selected compounds, as these two processes may be coupled. We present a more systematic review of the papers devoted specifically to the problem of reconstruction of an Au surface below.

Reconstruction of all the three low-index faces of Au single crystal under elevated temperature has been described in several papers. This subject has been discussed in detail by Dakkouri and Kolb [335], as well as (also for other metals) by Kolb [336], and Gao et al. [337, 338]. A recent concise review of Au reconstruction, including experimental details of the surface preparation, has been published by Trasatti and Lust [4].

The studies under ultrahigh vacuum have shown that adsorption and surface charging influence the stability of the reconstructed surfaces. A similar influence has been observed for metal surfaces in contact with electrolyte solutions [336]. In this case, the separation of these two influences is not simple, since the surface charging and adsorption processes are interdependent. Generally, it has been concluded [4] that Au surface reconstruction occurs for negative electrode charges and disappears for positive surface charges. It is noteworthy that as early as in 1984, Kolb and coworkers [339, 340], who carried out systematic study on all three low-index faces Au electrodes, showed that the reconstructed surfaces can be stable in electrolyte solutions.

Reconstruction of Au(100) surface has been reported by Kolb and Schneider [341]. The Au(100) surface reconstructs to the hexagonal close-packed structure

(called *hex*) [342–345]. In in situ STM images, the hexagonal structure of surface atoms is easily observed. Model calculations have been performed [346, 347] to evidence that negative surface charge favors reconstruction, as arises from the comparison of the calculated surface energies for reconstructed and unreconstructed Au(100) [347].

Initial reconstruction caused by flame annealing is stopped when the surface is cooled in the atmosphere, though not in water. The rate of transition from unreconstructed to reconstructed surface is determined by the height of the activation barrier [348], especially at the room temperature. Reconstruction may be removed by adsorption of atoms and molecules [349], since unreconstructed, and thus, more open surface, interacts with the adsorbates stronger than does the densely packed surface. Therefore, the removal of reconstructed surface proceeds from the less to the more energetically favored state [348]. Reconstruction coupled with the formation of more dense surface structure may lead to quite a strong increase in the number of surface atoms. For instance, the $\text{Au}(100)-(1 \times 1) \rightarrow \text{Au}(100)\text{-(hex)}$ reconstruction is accompanied by the increase in the number of surface atoms by 24%. In consequence, the reverse change connected with the expansion of the surface lattice leads to some surface roughening, owing to the formation of small, yet high monoatomic islands. This behavior for the Au(100) surface has been shown in STM images by Kolb and coworkers [350]. Also, Bohnen and Kolb [351] have calculated the surface energies γ of Au(100)-(1 × 1) and Au(111)-(1 × 1) as a function of the surface charge, applying ab initio local density-functional method. The obtained results suggest that the lifting of the Au(100) reconstruction in HClO₄ solution at +0.55 V

(versus SCE) is caused by specific adsorption of the anion, and not by a charge effect.

Since negative surface charge favors reconstruction of the gold surfaces, it occurs under the influence of the potential negative to the potential of zero charge [341, 352] Dakkouri and Kolb [335] have stressed that the immediate quenching after flame annealing is often advised to prevent the surface contamination, yet it leads to the rough and structurally ill-defined surfaces. In view of this fact, in STM studies of Au single-crystal electrodes, they were cooled down in a gentle stream of nitrogen [335]. Dakkouri [353], applying in situ STM, has determined the conditions required to preserve thermally induced reconstruction of Au(100) electrode surface both during and after the contact with the electrolyte. Structural changes of such electrode surface may occur in the potential range used in electrochemical experiments. The kinetics and a mechanistic model of structural transition have been briefly discussed.

Since specific adsorption of anions is harmful for the reconstructed surfaces, the immersion potential of the electrode should be negative to keep the surface free from the specifically adsorbed anions. In practice, it should be 0.5 to 0.6 V more negative than the zero charge potential. The influence of the anion adsorption on the potential of the reversed transition is shown in Fig. 10.

Transition potentials have been determined from cyclic voltammograms of Au(100)-(hex) in various solutions. For 0.05 M anion concentration, the (hex) \rightarrow (1 \times 1) transition for a freshly prepared reconstructed Au(100) surface occurs at -0.62 , -0.23 , $+0.02$, $+0.2$, $+0.33$, and $+0.58$ V (versus SCE), for I^- , Br^- , Cl^- , OH^- , HSO_4^- , and ClO_4^- , respectively. Obviously, the above sequence of potentials follows the sequence of the decreasing specific adsorption. Also, the adsorption of other adsorbates influences the stability potential of the reconstructed surfaces. Lipkowski and Stolberg [355], and Hamm

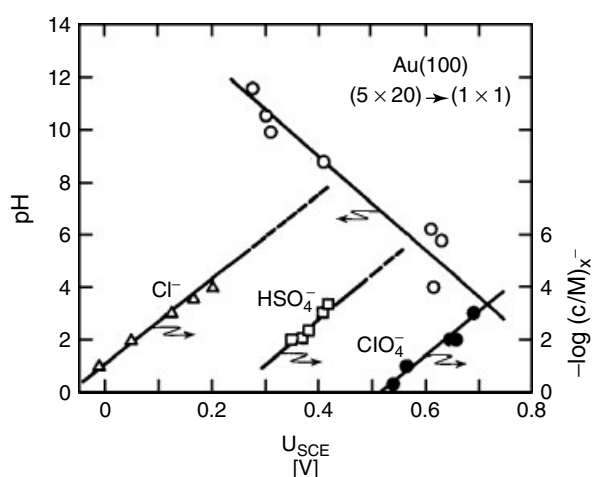
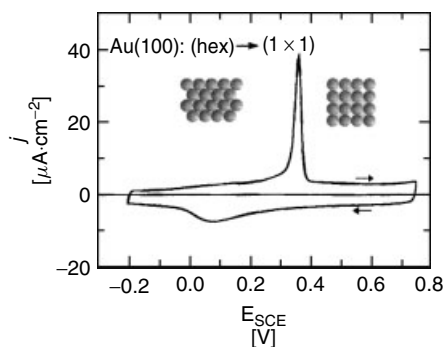


Fig. 10 Transition potential for Au(100): (5 \times 20) \rightarrow (1 \times 1) as a function of anion concentration and pH. Stability region of the (5 \times 20) structure is located to the left from the respective line (from Ref. 354).

Fig. 11 Cyclic current-potential curve for Au(100) in 0.1 M H₂SO₄ solution; beginning of polarization: -0.2 V (versus SCE) using a freshly prepared reconstructed surface. Scan rate: 50 mV s⁻¹. The peak formed in the positive scan corresponds to the lifting of the (hex) reconstruction. The subsequent scan in negative direction reflects electrochemical behavior of Au(100)-(1 × 1) [335].



and Kolb [356] have evidenced a significant influence of pyridine concentration on the potential of the (hex) \rightarrow (1 \times 1) transition.

Figure 11 exhibits the CV curve for Au(100) surface undergoing reconstruction.

Recently, the influence of γ -butyrolactone cyclohexanone [357] and propanal [358] on the stability range of the reconstructed Au(100) surface has been studied by CV.

A brief summary of reconstruction processes at other gold surfaces is given below. In order to obtain the reconstructed Au(110) surfaces after the flame annealing below the red heat, the cooling rate should be decreased [335]. Keefe et al. [359] have used the SHG method to study in situ potential-induced reconstruction of Au(110) electrode in 0.01 M HClO₄ aqueous solution. The influence of potential on the atomic structure of the ordered Au(110) in bromide solutions has been investigated, applying in situ STM [360]. A special attention has been paid to the adsorbate-induced nanoscale restructuring, which occurs at higher potentials. The observed behavior was compared to that of Au(110) surface in iodide solutions. Also, it has been found that clean Au(110) surface exhibits a (1 \times 2) structure. However, after immersion into 0.01 M HClO₄ solution and under potentiostatic control in

the range 0.9–1.0 V (versus Ag|AgCl), it changes to the centered rectangular structure [361]. After the initial oxidation, this structure prevails up to the potentials of 1.2–1.3 V, whereupon oxidation occurs on a large scale and the surface structure becomes (1 \times 1). After reduction of the oxide, these structures return to the (1 \times 2) configuration.

Reconstruction of Au(111) is observed in STM images as double rows separated from each other by 6.3 nm [335]. Some model calculations have been performed [362] to show that the energy difference of the reconstructed and unreconstructed Au(111) is small. The effect of Triton X-100 on the reconstruction process of Au(111) surface has been studied in chloride media [363] applying CV and double potential-step chronocoulometry. It has been found that adsorption of Triton X-100 stabilizes the reconstructed face of Au(111). Hobara et al. [364] have used in situ STM to study reconstruction of Au(111), following reductive desorption of 2-mercaptoethanesulfonic acid SAMs.

24.4.5

Formation of Oxides on Gold Electrodes

Oxide layers on gold electrode surfaces are interesting, mainly due to their electrocatalytic properties.

A growth of a gold oxide on Au electrodes in aqueous H_2SO_4 and KOH solutions has been observed and investigated by many researchers (see, for instance, the reviews by Jerkiewicz [365] and Burke and Nugent [366]).

A detailed behavior of gold electrodes in 0.50 M H_2SO_4 and KOH aqueous solutions has been presented by Jerkiewicz and coworkers [367]. In CV experiments,

the upper oxidation potential limit was being changed from 1.30 to 1.90 V (RHE) in the forward scan to form the oxide. After that, the direction of polarization was reversed and a single peak corresponding to the reduction of the generated oxide was formed in the voltammogram, as shown in Fig. 12 [367].

In Fig. 12, it is shown that the oxide reduction current (and charge) increases

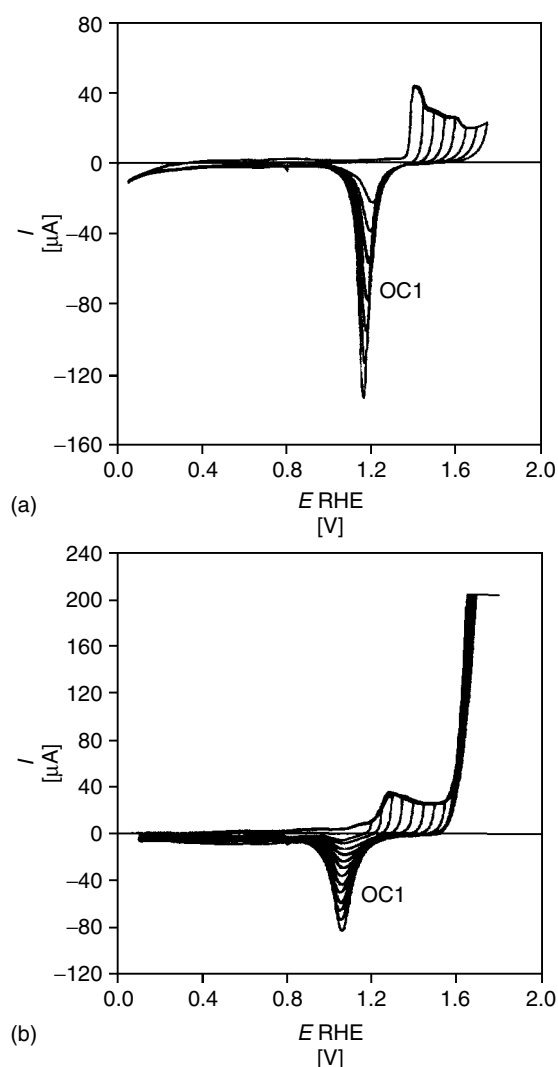


Fig. 12 (a) A series of CV profiles for Au electrode in 0.50 M aqueous H_2SO_4 solution: $T = 298 \text{ K}$, sweep rate $\nu = 50 \text{ mV s}^{-1}$, electrode surface area $A = 0.495 \text{ cm}^2$. The figure shows gradual development of the OC1 state and the changes in the oxide formation/reduction profiles upon the increase of the upper potential limit E_p . (b) A series of CV profiles for Au electrode in 0.5 M aqueous KOH solution: $T = 298 \text{ K}$, sweep rate $\nu = 50 \text{ mV s}^{-1}$, electrode surface area $A = 0.490 \text{ cm}^2$. The figure shows gradual development of the OC1 state and the changes in the oxide formation/reduction profiles upon the increase of the upper potential limit E_p (see text for the explanation of other symbols) [367].

as the upper oxidation potential limit is increased. In general, the higher the anodic polarization potential and the longer the polarization time, the thicker the oxide film that is obtained. Reduction of oxidation products occurs at potentials significantly less positive than oxidation potentials. It may point toward some transformations of the products of the electrooxidation reaction. In order to estimate the kinetics of the oxide growth, the $1/\rho_{\text{ox}}$ versus $\log t_p$ plots were constructed [367] (ρ_{ox} is the oxide reduction charge density, and t_p denotes polarization time). For electrode potentials of 2.05–2.20 V (RHE) in aqueous H_2SO_4 solution, such plots exhibit two linear regions of different slopes (indicating different mechanisms). The inflection point between these two linear ranges appears close to $1/\rho_{\text{ox}} = 0.10 \text{ mC}^{-1} \text{ cm}^2$. This agrees well with the fact that the oxide formation is preceded by chemisorption of OH, which competes with specifically adsorbed anions. However, the potential of OH/ H_2O couple is very positive (2.85 V versus SHE) and thus, adsorption of OH is rather limited. Instead, the formation of some type of polar covalently bonded $\text{Au}^{\delta+} \dots \text{OH}^{\delta-}$ species is more probable [366].

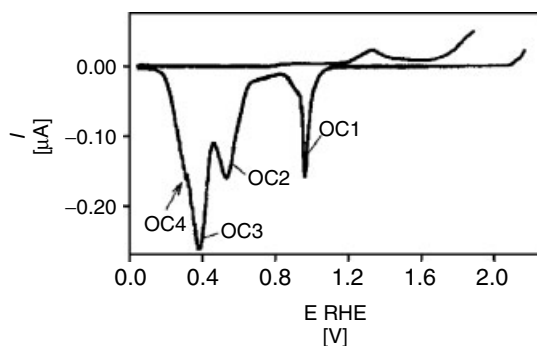
Cathodic behavior after the prolonged (up to 10^4 s) potentiostatic polarization in

the range 2.00–2.43 V is more complex. It is presented in Fig. 13 [367].

Apart from the cathodic peak observed in Fig. 12, there are three additional peaks, which correspond to new oxide states. The peak described as OC1 corresponds to either AuO or $\text{Au}(\text{OH})_2$ [367], depending on the pH of the solution. Other peaks denoted as OC2, OC3, and OC4 refer to either Au_2O_3 or $\text{Au}(\text{OH})_3$. Burke and Nugent [366] have described similar cathodic behavior. They have assumed that during oxidation at positive potentials, oxygen evolution, and production of oxides is accompanied by the formation of unstable gold peroxide species. In general, several cathodic peaks or steps observed during reduction of Au oxide may also result from the existence of several types of hydrous oxide species or several activity states of the produced gold atoms. It has been found by Jerkiewicz and coworkers [367] that the OC1 state grows to the limiting thicknesses of either three or one monolayer for AuO and $\text{Au}(\text{OH})_2$ in acidic and basic solutions, respectively. During the same time, other oxide states grow unlimitedly, even up to 100 equivalent monolayers of Au_2O_3 or $\text{Au}(\text{OH})_3$.

The combination of the electrochemical and ellipsometric data has led to the conclusion that Au oxides are composed of two layers: the inner film α and the outer

Fig. 13 Linear sweep voltammetry (LSV) oxide reduction profile for an Au electrode after polarization at $E_p = 2.23$ V (RHE) for $t_p = 900$ s in 0.50 M aqueous KOH solution; $T = 298$ K, sweep rate $\nu = 50 \text{ mV s}^{-1}$, electrode surface area $A = 0.280 \text{ cm}^2$. The LSV profile reveals the OC1, OC2, and OC3 states; the onset of OC4 is marked with an arrow [367].



film β . From ellipsometry, it is known [367] that the α film thickness reaches 0.55 nm and 0.28 nm in acidic and basic solutions, respectively. α film is adjacent to the metallic substrate with a second film β growing on the top of α without any limit. It follows from the above that α film (AuO or Au(OH)_2) is sandwiched between the Au metal substrate and β film, composed most probably of a hydrous form of either Au_2O_3 or Au(OH)_3 .

In case of thicker layers, α -oxide is reduced as first [366] giving a peak at ca 1.0 V. Reduction potential depends on several factors, including oxide coverage and scan rate. Burke and Nugent [366] have assumed that the Au^{3+} transfer across α layer is quite slow. An α film passivates the surface to some extent with regard to the hydrous β oxide growth. However, the passivating layer does not form a barrier against electroreduction of β layer, especially in basic media.

According to the presented model of oxides formation on Au, the outer surface of the thick oxide film exposed to the solution is either Au_2O_3 or Au(OH)_3 . The type of oxide determines the surface electronic structure and electrocatalytic properties. Electrocatalytic properties of gold oxide-covered electrodes have been discussed by Burke and Nugent [366, 368].

Kolb and coworkers [369, 370] have studied and observed initial stages of anodic oxidation of Au(111) in H_2SO_4 solutions, oxide formation, and topography of the oxide layer. In these studies, apart from CV, STM and AFM methods have been employed.

The redox behavior of a polycrystalline gold electrode in 0.1 M NH_3 + 0.1 M NaClO_4 solution has been investigated using electrochemical and spectrometric techniques [371]. Two gold compounds: AuO and AuNH_2 were distinguished at

the surface at +0.6 V (versus SCE) in amounts depending on the holding time at this potential. When the potential was held at +0.60 V for a longer time, other oxidized gold species might be formed at the surface.

Conway and coworkers [372] have studied anodic dissolution of gold coupled with anodic oxide formation in HClO_4 solutions with addition of bromide ions. It was observed that gold initially dissolves in a 3e oxidation process.

In recent years, Burke and coworkers have found [373] that severe cathodization of pc-Au in acid solution resulted in the appearance of faradaic responses in the double-layer region. Such anomalous behavior may be explained by the presence of active gold atoms on the electrode surface. These active atoms appear as a result of the pretreatment process, when the part of inserted energy into the gold sample is retained mostly by the surface atoms and atoms of the outer layers, in the form of various types of defects, for example, adatoms, vacancies, grain boundaries, and others.

Active low coordination, metastable state of the metal leads to anomalous electrochemical response in which hydrous (β) oxide species ($\text{Au}_2\text{O}_3 \cdot n\text{H}_2\text{O}$) are produced in a premonolayer oxidation. In contrast, conventional response yields a monolayer (α) oxide species (Au_2O_3). Since the activity of the active Au state is variable, the nature of the β oxide is also variable. Burke and Nugent [374] write about at least three forms of that oxide.

The authors [373] have studied the effect of prolonged cathodic polarization at negative potentials ($E \leq 0.00$ V) using both gold wire and rotating disc electrodes. They have shown that Au electrode prepolarized at -0.60 V for 20 min reveals in

the anodic scan, a significant anodic current peak at $E_p = 0.42$ V. This peak was followed by the flow of a relatively large anodic current in the range 0.60–1.10 V. Finally, at about +1.4 V, the large second anodic peak was observed, which corresponded to the formation of a monolayer oxide film.

In the second sweep, the first anodic peak at about +0.50 V was observed, but it was much smaller. These unusual effects observed for Au electrodes were enhanced by raising the solution temperature.

In order to explain the observed phenomena, it is assumed that during prolonged cathodic polarization, there occurs an activation of the outer gold atom layers via hydrogen embrittlement.

The authors also discuss the electrocatalytic properties of gold active state at low potentials. There are no studies of such states by surface science techniques and the authors [373] claim that such active states would be very difficult to detect using such techniques.

The effect of severe thermal pretreatment of Au wire in an inert gas atmosphere [375] on the anodic behavior of gold was also considered. In some instances, premonolayer oxidation commenced at 0.25 V (SHE).

Also, in this case, such behavior was explained by the formation of a very active metastable state with low lattice stabilization energy.

The formation of the active surface states of gold was also found in an alkaline solution [376]. Both cathodic and thermal pretreatments were used. As a result, up to five distinct premonolayer oxidation responses in the range 0–1.0 V (SHE) were observed. In a separate paper, a study of gold electrodes in the metastable states in acid and base solutions was made. The active electrodes were prepared by

rapid thermal quenching [377]. When the gold electrode was cooled rapidly from the molten state, oxidation responses were observed for gold in base at $E < 0.0$ V.

One should add that the formation of such nonequilibrium surface states may be important for electrocatalytic properties.

Redox and electrocatalytic activity in base at unusually low premonolayer potentials were observed also for copper [378, 379].

24.4.6

Underpotential Deposition of Various Metals on Au

UPD of various metals on different gold surfaces is one of the most intensively studied subjects. Abruña and coworkers have reviewed [380] the UPD deposition at single-crystal surfaces of Au, Pt, Ag, and other materials. More recently, Magnussen [381] has described ordered anion adlayers on metal electrode surface, which can affect the UPD process.

24.4.6.1 Cu

As early as in 1987, Kolb and coworkers used Auger electron spectroscopy (AES) to study UPD of Cu on Au [382].

Zeng and Bruckenstein [383] have studied UPD of Cu at polycrystalline gold in 0.1 M NH_3 + 0.1 M NaClO_4 electrolyte using the rotating disk electrode, electrochemical quartz crystal microbalance, and time-of-flight secondary ion mass spectrometry (TOF-SIMS). The experiments have revealed that Cu(0) UPD occurs in the potential range -0.4 V $< E < 0.1$ V, at three different sites. The rate-determining step was the reduction of the dissolved copper ammonia complexes to Cu(0).

For single-crystal electrodes, an extended hexagon model, in which the adsorbate interactions are averaged, has

been applied [384] for Cu UPD on Au(111). Using this model, coupled adsorption isotherms for copper and sulfate ions were obtained and numerically solved. The isotherms obtained were in good agreement with the experimental dependences. Chabala and coworkers [385] have studied Cu UPD on Au(111). They have utilized X-ray diffraction in situ and in the real time. Both potentiodynamic and potential-step polarizations were applied and the adlayer spacing of Cu on Au(111) was determined as a function of several parameters, such as potential and time. Stimming and coworkers [386] have studied experimentally, Cu UPD on Au(100), applying in situ X-ray surface diffraction. The structure of the Cu UPD layer has been studied as a function of the applied potential and Cu(II) concentration in the solution. In another paper [387], the same group of researchers studied the influence of anions on Cu deposition on Au(100) using CV.

Xia et al. [388] have investigated the kinetics and phase transitions of Cu UPD on Au(111) using in situ STM.

It has been found that Cu electroreduction from perchloric acid solution on Au(100) exhibits the UPD properties [389]. X-ray surface diffraction measurements have shown that the Cu UPD layer has a primitive (1×1) structure and that the adsorbed Cu species are located in four-fold hollow sites, with a vertical distance between the Cu adlayer and the Au surface of 0.14 nm.

Early stages of copper electrodeposition and coadsorption of chloride on the Au(111) electrode surface have been studied by Wu et al. [390] applying electrochemical methods and in situ X-ray absorption measurements. The results indicate a large degree of static disorder and exclude the presence of high-symmetry structures. Krznaric and Gorcicnik [391]

have studied, applying CV, Cu UPD on Au(111) electrode in the presence of chloride ions at various concentrations ranging from trace amounts to 0.55 M. At NaCl concentrations exceeding 5×10^{-3} M, Cu(I) was stabilized by chloride and reduction of copper proceeded as the one-electron process at the Au(111) surface covered with Cu and chloride bilayer but not on Au(111) free from Cu.

Combined X-ray and electrochemical studies on Cu UPD at Au(111) in the presence of bromide have been carried out by Abruña and coworkers [392]. At the potentials more positive than +0.55 V (versus Ag/AgCl), bromide anions adsorbed at the electrode surface and formed an ordered and rotated hexagonal structure. Initial stages of Cu deposition were observed at ca +0.36 V. In the potential range of +0.32 to +0.20 V, two voltammetric signals were observed, associated with additional copper deposition and giving rise to the stoichiometric CuBr layer. At +0.147 V, a sharp voltammetric peak was formed, corresponding to the phase transition and formation of a (1×1) copper layer with a bromide (4×4) structure adsorbed on the Cu layer. At potentials less positive than +0.147 V, bulk copper deposition occurred. In another work, Abruña and coworkers [393] have compared the results of electrochemical and in situ SXS studies on Cu UPD at Au(111) and Pt(111) surfaces in the presence of bromide. The differences in the behavior of Cu UPD at these two electrodes were ascribed not to energetic reasons, but rather to geometric constraints imposed by the lattice structure of the metal on the deposited adlayer.

Initial stages of bulk Cu deposition onto Au(100) have been investigated, applying STM [394]. Many monolayers of Cu were deposited, with the first monolayer formed via UPD, growing pseudomorphic.

Later, Kolb and coworkers [395] have studied copper deposition on Au(100) using in situ STM and in situ SXS. At the potentials positive with respect to the reversible Nernstian potential in sulfuric acid solutions, pseudomorphic (1×1) copper monolayer was formed. In STM studies at negative potentials, it was observed that bulk copper nucleates at the surface defects, step edges, or island rims. STM images have shown that the copper film up to 10 layers has a pseudomorphic structure. On the other hand, SXS measurements allowed one to precisely measure the copper layer spacing ($1.45 \pm 0.02 \text{ \AA}$). The obtained number is in good agreement with the value determined from the copper–copper step height in STM measurements.

Sanchez and Leiva [396] have considered density functional in the investigations of Cu UPD on Au(111) and Au(100). The analysis of different energetic contributions to the underpotential shift has shown that deposition of Cu on these surfaces should occur at overpotentials. The authors have arrived at the conclusion that other factors, such as anion coadsorption, should be considered in order to explain their experimental observations.

UPD of Cu on Au(111) electrodes in the presence of sulfate anions has been particularly intensively studied, both experimentally and theoretically [397] (for the review covering the literature up to 1995, see Ref. 398). Sulfate ions are specifically coadsorbed with underpotentially deposited Cu at negative potentials. For this system, a very striking phenomenon is the appearance of two voltammetric peaks, separated by 50–150 mV, upon addition of Cu^{2+} ions to the H_2SO_4 solution [382, 397, 399–401]. For the potential range separating the peaks, the existence of adsorbate layer of the $(\sqrt{3} \times \sqrt{3})$ structure,

consisting in 2/3 of a copper monolayer and in 1/3 of sulfate ions monolayer, has been suggested [402] Xu and Wang [403] have carried out the first-principles total-energy calculations to study the structure of Cu UPD on Au(111) in H_2SO_4 solutions. It has been evidenced that the proposed honeycomb structure comprising in 2/3 a copper monolayer is unstable without the coadsorbed sulfate, which bound to copper. Sulfate anions bind much more weakly to the clean Au(111) surface. Więckowski and coworkers [404] have presented the simulated dynamics of Cu UPD with sulfate ions present at the Au(111). Uchida et al. [405] have applied EQCM to study adsorption of anions (perchlorate, sulfate) on pc-Au electrodes with and without copper adatoms. It has been shown that the ratio of the number of Cu adatoms to the number of adsorbed anions is close to two when Cu coverage ranges from 0.2 to 0.5. Later, Uchida et al. [406] have studied adsorption of bisulfate and perchlorate on Au(111) electrodes, with and without Cu adatoms, applying electrochemical quartz crystal microbalance. Więckowski and coworkers [398] have applied combined computational statistical mechanics-based lattice-gas modeling, CV, coulometry, ex situ Auger electron spectroscopy, and low-energy electron diffraction to study Cu UPD on Au(111) electrodes in sulfate-containing electrolytes. Using group-theoretical ground-state calculations and Monte Carlo simulations, they have estimated effective electrovalencies and lateral adsorbate–adsorbate interactions, which cannot be calculated yet by the first-principles methods. Nakamura et al. [407] have applied in situ SXD to study the structure of coadsorbed copper bisulfate anion and hydration water molecule on Au(111) electrode in 0.5 M H_2SO_4 solution, in the potential range from 0.250 V

to 0.400 V. Two-thirds of the surface was occupied by Cu and 1/3 by the coadsorbed sulfate. On each Cu atom, one hydration water molecule was placed, forming a stable structure.

Recently, Kuzume et al. [408] have studied copper UPD at high-index single-crystal Au surfaces.

The mechanism of dissolution of the Cu UPD layer on Au(111) has been studied by Ataka et al. [409]. The monolayer comprised Cu in 2/3 and sulfate in 1/3 proportions. It has been found by applying time-resolved surface-enhanced infrared absorption spectroscopy and chronoamperometry that dissolution proceeds in two steps. In the first step, 1/3 Cu monolayer and all sulfate anions are removed via the Langmuir-type kinetics. In the second step, the rest of Cu is desorbed via nucleation and growth kinetics.

Copper was also deposited on gold electrodes modified by chemisorption with different substances. Nishizawa et al. [410] have studied Cu deposition on Au(111) electrode coated with a SAM of propanethiol in the potential region covering UPD. It has been found that the SAM remains at the electrode surface without significant changes in its amount and structure, even after repeating Cu deposition and stripping cycles. Similarly, Kolb and coworkers [411] have performed CV studies on the kinetics of Cu UPD from H_2SO_4 solutions on Au(111) modified with alkanethiol. They have found that Cu UPD proceeds on such surfaces, yet the UPD current peak is shifted to the overpotential region at typical scan rates. Also, in the underpotential region close to the Nernstian potential, the formation of the monolayer occurs, but it lasts for more than 1 h. Martinez-Ruiz et al. [412] have studied UPD of Cu on iodine-modified Au(111) using in situ STM and CV in

sulfuric acid solutions. In the UPD process, a (1×1) Cu monolayer was formed of a lattice parameter equal to that of Au(111). The results suggest that iodine adlayer is constantly present at the top layer during electrodeposition and stripping of Cu and no noticeable loss of iodine is observed. Kinetics of Cu UPD on iodine-modified Au(111) electrodes has also been studied by the same group of researchers [413] in 1 mM solution of CuSO_4 in 0.05 M H_2SO_4 , applying CV and chronoamperometry. The presence of iodine adlayer slowed down the kinetics of Cu UPD compared to the iodine-free surface. The kinetics of deposition was described applying a model with three types of contributions.

Epitaxial electrodeposition has been applied to crystallize a 0.5- μm -thick Cu_2O film on Au(100) from an alkaline copper lactate solution [414].

Zhang et al. have studied the influence of bromine adsorption on copper electrodeposition on pc-Au electrodes modified with SAMs [415].

24.4.6.2 Cd

The formation and growth of thin alloy film at underpotentials during electrodeposition of Cd on Au(100) in 50 mM H_2SO_4 + 1 mM CdSO_4 solution has been studied using EC-AFM [416].

Santos et al. [417] have studied UPD of Cd on polycrystalline Au electrodes using voltammetry and microgravimetry.

Atomic structures of several adlayers of Cd deposited underpotentially on Au(111) surface in H_2SO_4 solution have been visualized applying in situ STM [418]. Three ordered adlattices have been observed, all of which had a long-range linear morphology and were rotated by 30° with respect to the substrate lattice directions. The same system has been studied later

[419] applying in situ and real-time surface differential diffraction. It has been found that at the initial stages of UPD, Cd atoms bind to the surface at the bridging sites. This was followed by the formation of an adlayer structure of Cd atoms adsorbed at the threefold hollow sites, before the Au–Cd intermixing took place.

Formation of the Au–Cd alloy during Cd UPD on Au(111) has been investigated by del Barrio [420]. Apart from electrochemical methods, in situ STM has also been used. It appears from STM investigations that the alloy can be formed at relatively high underpotentials accompanied by the formation of 2D Cd islands. When appropriately large, these islands coalesce to form a new 2D island on the top of the partially formed first Cd monolayer. These islands exhibit hexagonal atomic structure of the interatomic distance of 0.29 ± 0.01 nm.

Kawamura et al. [421] have studied the effect of electrolytic conditions on the coverage of an Au(111) electrode with underpotentially deposited layer of Cd. The Cd atomic layer was located on the Au(111) surface similar to the reconstructed structure. Also, a layer of sulfate anions was positioned on the Cd atomic layer. Cd coverage was found to be dependent on the concentration of H_2SO_4 .

Schmuki and coworkers [422] have studied initial stages of Cd electrodeposition on the Au(111) surface from H_2SO_4 solutions. The results have shown that in such solutions (Cd(II) in H_2SO_4), the Au(111) surface starts to reconstruct at potentials around 850 mV versus bulk formal potential of cadmium electrode. Nucleation of Cd started in the potential range 350–300 mV as the formation of separated islands of monoatomic height. Further, cathodic polarization led to the formation of strings and finally to the cadmium layer

with the expected surface alloying. The same group of researchers [423] studied electrodeposition of Cd on a herringbone reconstructed Au(111) surface from the same solution as before, by also applying EC-STM. Distinct dots of monoatomic height were formed in the UPD region. At these potentials, nucleation proceeded exclusively at the elbow sites of the Au(111) herringbone reconstruction, leading to a self-organized surface patterning of nanoscale Cd islands.

Vidu et al. [424] have studied the kinetics of thin alloy film formation and growth during Cd electrodeposition on Au(100) and Ag(100) within the Cd UPD range from -0.3 to -0.45 V. Electrochemical and AFM experiments in 1 mM CdSO_4 and 0.05 M H_2SO_4 solutions have revealed that the overall alloying process comprises two processes: the first occurring relatively fast within a few atomic layers ($D \sim 10^{-16} \text{ cm}^2 \text{ s}^{-1}$), and the second much slower ($D \sim 10^{-19} \text{ cm}^2 \text{ s}^{-1}$), indicating a solid-state diffusion. In the later work [425], the process of inward diffusion of Cd UPD into an Au(100) substrate has been studied in the temperature range 295–333 K, applying voltammetry, microgravimetry, and X-ray diffractometry. Activation energy of the above-mentioned fast diffusion step is about 70 kJ mol^{-1} . It has been found that the amount of Cd UPD increases with the temperature. From X-ray diffraction studies, it was concluded that β -Au–Cd layer is formed on the sample after keeping the electrode in the UPD region at -1100 mV (versus $\text{Hg}|\text{Hg}_2\text{SO}_4$) for 1 h at 333 K. Vidu and Hara [426] have studied the kinetics of thin alloy film formation and growth on Au(100) from 1 mM CdSO_4 and 50 mM H_2SO_4 within the underpotential range of Cd electrodeposition. The distribution of Cd atoms on the Au electrode surface has

been estimated on the basis of the calculated diffusion coefficients of Cd. The mechanism of the surface alloying process in the UPD region has also been proposed.

Cd deposited underpotentially on Au(111) reaches a limiting coverage of 0.66 monolayer. Electrosorption valency corresponding to this coverage is equal to 0.5, which indicates that Cd adatoms are not fully discharged at the surface [427].

Surface alloy formation during Cd UPD on Au(110) in H_2SO_4 solutions has been investigated, applying long-time polarization experiments and in situ AFM [428]. The dynamics of this process depended on the polarization conditions. Moreover, alloying process competed with surface diffusion and further adsorption processes. Cd UPD on Au(111) from sulfate solutions has also been studied by Lay et al. [429], who have utilized electrochemical STM ultrahigh vacuum emersion techniques and quartz crystal microgravimetry. According to STM results, the Au(111)-(1 × 23) reconstruction is not lifted up by Cu UPD. Also, morphology of reconstruction indicates formation of the adlayer structure on the surface. EQCM studies suggest coadsorption of anions. Also, there are indications of a surface alloy formation.

24.4.6.3 Pd

In a series of papers, Kolb and coworkers have presented CV and in situ STM studies on palladium deposition on various gold single-crystal electrodes. They have found [430] that PdCl_4^{2-} is adsorbed on Au(111), forming a distorted hexagonal structure, which plays a crucial role in Pd deposition and dissolution. It has also been found that Pd deposition starts from the formation of a pseudomorphic layer in the underpotential region, followed by the formation of the second Pd monolayer at overpotentials. Pd nucleated

at monoatomic high steps and grows two dimensionally. Morphology of the overlayers changed with the increasing Pd coverage from the flat and well ordered for the first two monolayers to the increasingly rough and defect rich.

Electrochemical properties of Pd adlayers on Au(111) have also been compared to the behavior of massive Pd(111) [431]. Gradual transition to the bulk properties with increasing Pd coverage has been observed.

Similar to Pd UPD on Au(111), Pd deposition on unreconstructed Au(100) has also been studied applying CV and in situ STM by Kolb and coworkers [432]. They have investigated both an island-free surface and the surface covered with the islands originating from the lifting of the (hex)-reconstruction. It has been found that approximately one Pd monolayer accompanied with a distorted-hexagon chloride adlayer is formed in the UPD process. First Pd layers on Au(100) had different electrochemical behavior than large Pd(100) single crystals.

In another work from this series [433], deposition of Pd on the unreconstructed Au(110) has been studied. An ordered adlayer of PdCl_4^{2-} was imaged with atomic resolution. Pd deposition started at monoatomic high steps. From the coulometric data, it follows that approximately three monolayer equivalents are deposited in the UPD range, what may, in turn, be a result of the surface alloy formation.

Naohara et al. [434] have also studied electrodeposition of Pd from PdCl_4^{2-} complex on Au(100) electrode using in situ STM. Electrochemical deposition of Pd on Au(100) occurred at potentials more negative than 1.0 V. The first Pd layer was deposited not only on the terrace but also on gold islands, which were formed as a result of the lifting process

of the reconstructed Au(100). The bulk and surface structures of the deposited Pd layers were investigated by X-ray diffraction. The formation of a Pd(100) phase of a (1×1) surface structure has been confirmed.

Electrochemical behavior of ultrathin Pd epitaxial layers deposited electrochemically on Au(111) and Au(100) has been found to be strongly dependent on the surface structures and the thickness of the Pd thin films [435]. From the kinetic studies of Pd deposition on Au(111) electrode from K_2PdCl_4 in 0.1 M H_2SO_4 , it has been deduced [436] that this process proceeds via an instantaneous nucleation and two-dimensional (2D) growth. Initial stages of Pd deposition on Au(110) have also been studied by Robach et al. [437], who have applied STM, low-energy electron diffraction, and Auger electron spectroscopy for this purpose.

24.4.6.4 S, Se, and Te

Also, thin films of semiconducting compounds were formed on a gold electrode. To obtain them, a methodology called *electrochemical ALE* (electrochemical atomic layer epitaxy) has been developed. This procedure is based on the formation of individual atomic layers of particular elements, which may further form a compound. Accordingly, in each cycle, a controlled formation of a monolayer of the particular compound occurs. The advantage of this methodology is that three-dimensional growth of one-elemental deposit is inhibited.

The above method combined with UPD of atomic layers has been used for the preparation of such compounds as CdTe, CdSe, CdS, and others. A paper reviewing the formation process of such compounds has been published by Wade et al. [438]. Preparation of such compounds is usually

carried out on gold electrodes. In that case, the first atomic layer of the particular element is obtained via UPD at the gold surface.

We briefly present below the papers dealing with deposition of S, Se, and Te on Au electrodes and with the formation of semiconducting compounds at their surfaces.

24.4.6.5 Sulfur

Gichuhi et al. [439] have used Au(111) electrode covered with the initial underpotentially deposited Cd layer. When H_2S was electrolyzed at this surface, applying underpotential, an adlattice of the S–S interatomic spacing equal to 0.34 nm was obtained. The second monolayer of Cd and S had the same structure as the first CdS monolayer, showing that these two CdS monolayers were epitaxial. However, the third deposited monolayer of CdS exhibited interatomic spacing as observed for the bulk CdS. A direct fabrication of monodispersed, ultrasmall nanocrystals from the SAMs at Au(111) substrate has also been described [440]. Reconstruction of CdS monolayers has been studied by Demir and Shannon [441].

24.4.6.6 Selenium

Huang et al. have studied electrodeposition of selenium on Au(100) [442]. The structures of submonolayer coverages have been identified using ultrahigh vacuum electrochemical techniques, as well as STM. Selenium atomic layers were formed electrochemically by (1) direct electroreduction of $HSeO_3^-$, (2) anodic stripping of previously formed bulk Se. Alanyalioglu et al. [443] have investigated electroreduction of Se atomic layers on Au(111) from aqueous SeO_2 solutions. Two waves at the potentials more negative than that

expected for the Se(IV)/Se couple were observed. Therefore, Se deposition could not be accomplished via UPD. In addition, Ruach-Nir et al. [444] have analyzed structural effects in electrodeposition of CdSe quantum dots on mechanically strained gold.

24.4.6.7 Tellurium

Ikemiya et al. [445] have investigated both the atomic structure and growth of electrodeposited Te films on Au(100) and Au(111) with large lattice misfits. Deposition was performed in sulfuric acid solutions using in situ AFM. On both substrates, bulk-deposited Te films were formed according to the Stranski-Krastanov mechanism. Their atomic structures changed with the increasing film thickness.

It has been found [446] that in situ optical second-harmonic rotational anisotropy was significantly changed along with the first UPD of Te, and that bulk Te deposition attenuated the anisotropic character of the overall surface symmetry.

Later, Sorenson et al. [447] have studied electrochemical formation of tellurium atomic layers on Au(100) and phase transitions within these layers. They used voltammetry, in situ STM, and low-energy electron-diffraction methods. Two sub-monolayer reduction steps of HTeO_2^+ were observed. Three-dimensional nucleation progressed at potentials corresponding to the bulk Te deposition. The structures of electrodeposited atomic layers of Se and Te on Au(100) and Au(111) have been studied and compared [448]. At each surface, both elements formed a low-coverage structure, with atoms packed in high coordinate sites at distances just above their van der Waals diameters. When the coverage was increased, chalcogenide atoms formed either chains or rings. In

Ref. 448, a discussion concerning the appearance of triangular phase boundaries for both chalcogenide atoms on Au(111) is also presented.

Sorenson et al. [449] have carried out similar studies on electrodeposition of atomic Te layers on Au(111) surfaces from aqueous solutions. Similarly as in earlier works, in this study also, the following techniques were utilized: voltammetry, in situ STM, low-energy electron diffraction, and Auger electron spectroscopy. Prior to the deposition, tellurium oxide species coated the surface. Two steps were distinguished in the UPD process. Deposition process was kinetically slow.

Nicic et al. [450] have applied chronocoulometry and EQCM to perform UPD of Te monolayers on Au surfaces from HClO_4 solution.

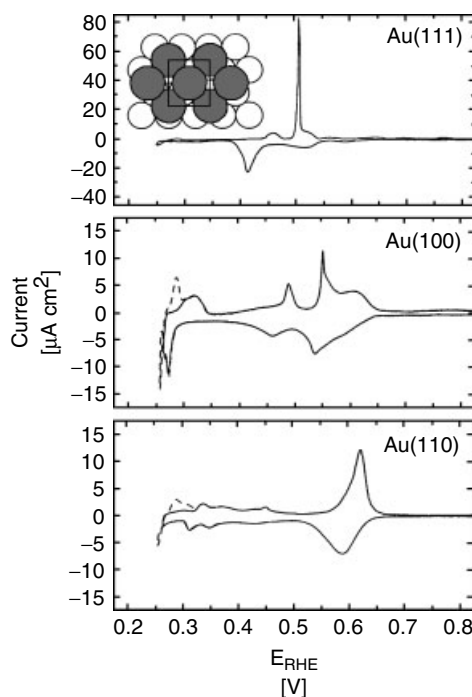
Auger electron spectroscopy, X-ray photoelectron spectroscopy, low-energy electron diffraction, and in situ STM have been employed to investigate two-step alternate electrodeposition of Cd and Te atomic layers, forming finally, CdTe monolayers (electrochemical ALE on Au(111)) [451]. STM images suggest that previously proposed hexagonal structures for CdTe may not be correct.

24.4.6.8 Bi

Wang et al. have compared UPD of Bi on different Au surfaces (see Fig. 14). It has been found that chemisorbed Bi adatoms bound preferably at more open surface.

From the CV data, the following charges associated with Bi^{3+} deposition have been estimated: 445, 472, and $357 \mu\text{C cm}^{-2}$ for Au(111), Au(100), and Au(110), respectively. The charges involved in the deposition of one Bi atom per one surface gold atom are 666, 576, and $408 \mu\text{C cm}^{-2}$, for the same sequence of the surface

Fig. 14 Linear sweep voltammograms for UPD of Bi on three low-index gold surfaces in 0.1 M HClO₄ containing 2.5 mM Bi₂O₃. Scan rate: 2 mV s⁻¹. Dashed line shows the onset of bulk deposition. Inset: atomic model of the close-packed 2Bi-($p \times \sqrt{3}$) monolayer on Au(111) (after Ref. 59).



types [59]. Hence, the following values of Bi coverage (with respect to monolayer) were calculated: 0.67 for Au(111), 0.82 for Au(100), and 0.88 for Au(110). These values are close to those determined from the SXS studies [59, 452]. It is noteworthy that Bi–Au bonding was found to be more non-metallic than those of Tl–Au and Pb–Au monolayers. Therefore, Bi monolayer differs substantially from the layers of the above-mentioned two elements [59].

Underpotential and overpotential deposition of Bi on Au(111) have been studied applying in situ STM [453]. It has been found that the adsorbed bismuth lifts the reconstruction of the Au(111) surface, leading to the formation of Au islands at potentials more cathodic than 0.170 V versus SCE. Atomic images of UPD Bi layer have shown the formation of a nearly rectangular unit cell of dimension $0.39 \pm 0.02 \times 0.43 \pm 0.02$ nm.

5–10-nm-diameter and 3–4 atomic layers deep nanometer-sized zero-dimensional (0D) cavities have been obtained at Au(111) surface applying short (80 ns) voltage pulses to the STM tip [454]. In these nanocavities, localized UPD of 0D bismuth dots has been observed applying in situ STM. The authors have discussed and compared the investigated system with the behavior of the Au(111)/Ag⁺,NO₃⁻ system.

Itaya and coworkers [455] have studied Bi UPD on Au(100) in HClO₄ solutions using in situ STM. It has been found that UPD occurs in three steps involving the formation of an A(3 × 3) structure and a square lattice has been found for the first layer.

Tamura et al. [456] have studied the kinetics of UPD of Bi monolayer on Au(111) applying simultaneously, electrochemical methods, current transients, and SXS.

Langmuir adsorption kinetics of Bi adsorption was observed for transients.

Du and Wang [457] have developed a method for bismuth determination, based on good electrochemical properties of gold electrode covered with underpotentially deposited Bi. In this method, Bi was preconcentrated at the Au surface and this step was followed by anodic stripping.

24.4.6.9 Pt

Electrochemical deposition of Pt on Au(111) electrode in acidic H_2PtCl_6 solutions has been studied [458] using STM and EQCM. The formation of the Pt(111) bulk phase and the surface structure of Pt(111)-(1 × 1) were confirmed by X-ray diffraction and UPD of copper and hydrogen, respectively.

Waibel et al. [459] have studied deposition of Pt on unreconstructed Au(111) and Au(100) applying CV and in situ STM. STM studies revealed that PtCl_4^{2-} complex is adsorbed on both surfaces and Pt is further deposited at rather high overpotential. Nucleation of Pt started mainly at the defects, like step edges, at low deposition rates. Due to the high overpotential, some nuclei also appeared on terraces at the random sites.

Also, Nagahara et al. [460] have employed in situ STM to study molecular adlayers of haloplatinate complexes and electrochemically generated Pt monoparticles on Au(111). In atomic resolution STM images, pinwheel features of planar PtX_4^{2-} adsorbates ($\text{X} = \text{Cl}^-$, Br^- , I^-) were observed. Reduction potentials of these overlayers to metallic Pt decreased in the order $\text{PtCl}_4^{2-} > \text{PtBr}_4^{2-} > \text{PtI}_6^{2-}$. The Pt deposit existed in the form of nanoparticles of an average diameter of 3.0 nm and height of 0.46 nm. They were uniformly distributed on the Au(111) substrate.

24.4.6.10 Ni

Bubendorff et al. [461] have reported, on the basis of CV and STM studies, that it is possible to deposit, applying UPD, a Ni monolayer on Au (111) from a sulfamate solution. It has been found using high-resolution STM that the formation of Ni layer occurs via complexation of Ni(II) by sulfamate adlayer on the Au surface.

Moller et al. [462] have performed in situ STM observations of Ni electrodeposition on reconstructed Au(111) electrodes. Ni nucleation proceeded in three distinct potential-dependent steps. The same group of researchers [463] has studied electrodeposition and electrodisolution of Ni on Au(100) electrodes. Pronounced differences were observed for the nucleation and submonolayer growth on the reconstructed and unreconstructed surfaces. On perfectly reconstructed Au(100), the formation of Ni islands started at overpotentials significantly higher ($\eta \geq 100$ mV) than on unreconstructed surface ($\eta \geq 40$ mV), where Ni monolayer islands were formed. Dissolution of the Ni film exhibited better monolayer stability in comparison to the multilayer deposit.

Allongue et al. [464] have studied nucleation and growth mechanisms of Co and Ni on Au(111) using in situ STM and electrochemical methods.

Submonolayer of Ni deposited in the temperature range of 130–180 K on the missing-row reconstructed Au(110)-(1 × 2) surface has been analyzed using STM [465]. An order within the thin epitaxial AuNi film deposited on an Au(100) surface, accompanying temperature changes, has been investigated by applying X-ray diffraction [466].

24.4.6.11 Co

Repain et al. [467] studied a growth of cobalt on Au(111) vicinal surfaces in

the submonolayer range. The presence of surface reconstruction led to self-organized nanostructures, such as very regular arrays of clusters or nanowires. The obtained results may be useful in the development of the fabrication procedure of cobalt nanostructures or ultrathin films of unique magnetic properties.

Also, Kolb and coworkers [468] have studied initial stages of Co deposition on Au(111) and Au(100) using CV and STM. Depending on the crystallographic orientation of the substrate and electrochemical properties, either three- or two-dimensional growth has been observed. The influence of surface reconstruction on the nucleation and growth behavior has also been discussed.

Formation and stripping of a cobalt adlayer on/from a polycrystalline Au electrode have been studied [469] applying electrochemical methods under underpotential conditions. The kinetics of deposition fitted a model of a simultaneous adsorption and diffusion-controlled two-dimensional instantaneous nucleation of cobalt on the electrode surface.

Nucleation and growth of cobalt nuclei on a polycrystalline gold electrode have been studied by the same group of researchers [470] using electrochemical methods in 10^{-2} M CoCl_2 and 1 M NH_4Cl solutions of $\text{pH} = 9.5$. The authors have studied the transition accompanying the change of electrode potential from underpotential to overpotential deposition (OPD) region. The corresponding current-time transients were explained in terms of a kinetic mechanism involving three different contributions: (1) Langmuir-type adsorption process, (2) 2D diffusion-controlled instantaneous nucleation, and (3) mass transfer-limited 3D nucleation.

Stepanyuk et al. [471] have applied local approximation of the density-functional theory and the Korringa-Kohn-Rostoker (KKR) Green's function method to determine the energy of Co adatoms located at the ideal Au(100) surface. Total-energy calculations have shown that Co atoms and small Co clusters are preferably embedded inside the substrate.

24.4.6.12 Sb

Jung and Rhee [472] have reported voltammetric studies on the deposition of Sb on Au(111) and Au(100) electrodes. In the formation of the metallic Sb layer, two processes were involved. The first one was the reduction of the irreversibly adsorbed oxygeneous Sb layer. The other was completing the full monolayer of Sb via UPD of oxygeneous Sb species in the solution.

Later, Wu et al. [473] presented an in situ STM study of Sb electrodeposition on Au(111). The authors have studied irreversible adsorption of Sb and redox behavior of Sb(III) adspecies with and without the influence of UPD, and vice versa.

The process of irreversibly adsorbed Sb on Au(111) at the open-circuit potential (close to 0.2 V) has been investigated using in situ STM [474]. The oxygenated Sb adlayer was nucleated and grown on terraces and at step edges. The oxygenated Sb domains present on terraces were round-shaped islands of a diameter ranging between 3 and 6 nm.

Wang et al. [475] have proposed a similar analytical method as that for bismuth for antimony determination based on Sb UPD on gold electrode. In the proposed procedure, Sb was accumulated at the gold surface, and this step was followed by anodic stripping. A detection limit 2.1×10^{-9} M was reported for a 120 s electrochemical deposition.

Yan et al. [476] have presented in situ STM results of a structural transition of Sb on Au(100). Remarkable structural transition took place at the potential, sufficient to initiate UPD. Both the coverage and potential-dependent Sb–Au interactions were responsible for the structural transition. The formation of the surface compound AuSb₂ has been suggested.

24.4.6.13 Sn

UPD of Sn on Au(100) has been studied applying electrochemical methods and in situ STM [477]. Three stages of Sn UPD have been distinguished: (1) reversible submonolayer UPD, (2) surface alloying, and (3) bulk-extended alloying. Reversible UPD of a submonolayer proceeds in the form of 2 nm clusters at 0.04 V itself. The surface alloying took place at –0.04 V, and the bulk alloying at –0.3 V, which quickly changed the surface morphology.

Mao et al. [478] have applied in situ STM to study Sn UPD on reconstructed and unreconstructed Au(111) electrodes. On the unreconstructed Au(111), Sn formed size-confined two-dimensional clusters of 1–2 nm. At more negative potential, surface alloying was observed. On the reconstructed Au(111) surface, in turn, Sn preferably nucleated at face-centered cubic regions. The nuclei expanded toward the hexagonal close-packed regions to build up deposit domains.

24.4.6.14 Al

Aluminum underdeposited on gold electrodes from AlCl₃ + NaCl melts at 200–300 °C. The process has been studied [479] applying CV, potentiostatic deposition, and galvanostatic oxidation. The obtained deposits were characterized by electron microprobe analysis and glancing incidence by X-ray diffraction.

Formation of several successive layers of bulk intermetallic compounds has been shown. Also, Lee et al. [480] have detected, during Al UPD, the formation of two alloys on polycrystalline Au electrodes from acidic 1-ethyl-3-methylimidazolium chloroaluminate that melt at room temperature. Moreover, in the Al UPD region, fast phase transition between these two intermetallic compounds has been evidenced. Later, the same group of researchers [481] has performed EQCM studies on Al deposition and alloy formation on Au(111) in ambient temperature molten salts/benzene mixtures.

24.4.6.15 Tl

Thallium UPD on Au(111) has been studied, applying potential-step chronocoulometry and quartz crystal microbalance [482]. The UPD surface coverage increased with the increasing cathodic potential. At low coverage, the sublayer was not completely discharged, as it appeared from electrosorption valency.

Poškus and Agafonovas [483] have applied radioactive Tl-204 to study its UPD on a polycrystalline gold electrode in alkaline solutions. The potential dependence of the equilibrium surface concentration obtained from the radiometric method has been compared to that calculated from CV. Surface concentration of Tl decreased monotonically as the potential was changed from the more positive Nernstian values. This dependence exhibited a minimum without reaching zero. At more positive potentials (with respect to the minimum), adsorption of Tl⁺ induced by specifically adsorbed hydroxyl anions occurred.

It has also been found that metal-halide coadsorption of Tl–Br and Tl–I proceeds on Au(111). This was a proof that UPD

of metals can be affected by specific adsorption of anions [59].

24.4.6.16 Pb

Pb UPD on polycrystalline Au electrode in 0.1 M perchloric acid solution has been studied by Henderson et al. [484]. In this study, CV, electrochemical quartz crystal microbalance (EQCM), and probe beam deflection methods have been used. It has been found that Pb UPD proceeds in three steps. The first step comprised water ejection from the gold surface. This step was followed by metal UPD accompanied by the removal of the adsorbed OH. Also, Zeng and Bruckenstein have studied UPD and adsorption of Pb on pc-Au electrodes, applying XPS and TOF-SIMS method in case of 0.1 M NaCl electrolyte [485], and EQCM in case of 0.1 M NaClO₄ and 0.1 M NaCl electrolytes [486]. In the presence of chloride anions, the adsorption of Pb–Cl[–] complex has been found.

A relation between the surface stress and the structural change within the Pb UPD layer on Au film electrode has been studied, applying a bending beam method [487]. A maximum in the surface stress versus potential dependence emerged at the onset of UPD, similarly as in electrocapillary curve.

Hale et al. [488] have studied Pb UPD on Au(110), applying XPS and ultrahigh vacuum apparatus with a chamber for electrochemical experiments. Lead was detected at the gold surface in the entire considered potential range: –0.5 to 1.5 V (versus Ag/AgCl). A large increase in the surface concentration of oxygen was found for lead-containing solutions.

Rojas [489] has investigated theoretically, the stability of either different submonolayers of Pb adsorbed on Au(100) or grown as the first monolayer. Calculations were performed using the atom

superposition and electron delocalization molecular orbital methodology in the cluster approximation.

Deposition of Pb has also been carried out at modified gold electrodes. The films of 3-mercaptopropene sulfonate on polycrystalline gold electrodes were prepared from an acidic solution. At such electrodes, UPD current corresponding to voltammetric reduction of lead(II) was enhanced, compared to the current observed at a clean polycrystalline gold electrode [490].

Also, epitaxial electrodeposition of Pb–Ti–O superlattices on single-crystal Au(100) has been carried out [491]. The films were formed at room temperature from aqueous solutions of 5×10^{-3} M TiNO₃ and 0.1 M Pb(NO₃)₂ in 5 M NaOH. Applying current density of 0.05 mA cm^{–2}, a bulk film of a composition of Pb_{0.46}Ti_{0.54}O_{1.7} was formed.

Finally, UPD of Pb on silver and gold colloids has been described by Bokshits et al. [492].

24.4.6.17 Zn

Takahashi et al. [493] have applied CV for UPD of Zn on an Au(111) electrode from phosphate solutions containing Cl[–], Br[–], and I[–].

24.4.6.18 Ge

Nanoscale electrodeposition of Ge on Au(111) from an ionic liquid has been studied [494] utilizing in situ STM. At underpotentials, a thin rough layer is formed. In turn, at overpotentials close to 250 mV, 50-nm-diameter nanoclusters of the initial height of several nanometers were grown. Interestingly, at overpotential of 50 mV, the deposits could be transformed within several hours into a layered structure, indicative of Ge(111) bilayers.

24.4.6.19 Rh

Kibler et al. [495] have studied electrochemical deposition of Rh on Au(111) using CV and in situ STM. Rhodium started to deposit irreversibly around 200 mV versus SCE. First, a Rh bilayer was grown, which exhibited electrochemical behavior similar to that of well-ordered Rh(111) surface.

24.4.6.20 Li

Li UPD on highly oriented Au(111) electrodes has been performed [496] from LiAsF_6 solutions in PC using quartz crystal microgravimetry, CV, and UV–visible reflectance spectroscopy simultaneously.

Saito and Uosaki [497] have studied the formation and morphological changes of the surface Li film on Au(111) electrode in 0.1 M LiClO_4 solution in PC applying STM. The surface film was observed at potentials more negative than 1.5 V (Li^+/Li). Many nuclei appeared on the flat terrace of the electrode at potentials more negative than 0.9 V, where UPD of lithium on Au was started.

24.4.6.21 Fe

Kawagoe et al. [498] have investigated the growth of Fe submonolayer films on Au(001) in the temperature range of 300 to 500 K using STM. The STM images have shown that growth and morphology of the films markedly depend on the growth temperature. Fe islands of a monolayer-height nucleated and grew on Au(001) terraces at 300 K. At 353 and 393 K, Fe islands with double-layer height and small pinholes were observed on terraces. Step edges were decorated by Fe dendrites.

24.4.6.22 Ag

Więckowski and coworkers [499] have used AES to study UPD of Ag on the Au surface.

Chabala and Rayment [500] performed a time-resolved in situ and real-time X-ray diffraction study of Ag UPD on the Au(111) surface. Later, the same researchers [501] described an in situ surface differential diffraction and anomalous scattering of surface relaxation accompanying Ag UPD on Au(111). Time-resolved surface differential diffraction has been used [502] to study the mechanism and kinetics of Ag electrodeposition on Au(111). Also, the effect of the surface stress in the surface differential diffraction measurements has been investigated. Gimenez et al. [503] have performed Monte Carlo simulation of the formation and growth of low-dimension phases in Ag UPD on Au(111). From Monte Carlo simulations, it has also been found [504] that energetic atoms can promote nucleation and island growth at early stages of film growth and thus improve the smoothness of the film surface. Whelan et al. [505] have studied structural surface transitions induced by repetitive UPD of Ag on Au(111). More recently, Kondo et al. [506] have published the results concerning in situ structural study on Ag UPD on Au(111) electrode, applying SXS technique. In situ STM has been used to investigate electrodeposition of silver on Au(111) electrodes from H_2SO_4 solution [507]. STM images of Ag UPD have revealed a series of ordered adlayer structures of increasing coverage with decreasing potential.

Ag UPD onto gold substrates covered previously with SAMs of alkanethiols in order to induce penetration of silver between the monolayer and the gold substrate has been described by Oyamatsu et al. [508]

Wang et al. [509] have reported overpotential deposition of Ag monolayer and bilayer on Au(111) mediated by the Pb adlayer UPD/stripping cycles.

Brankovic et al. [510] have described the surfactant-mediated electrochemical deposition of Ag on Au(111). Also, Reyes-Cruz et al. [511] have studied electrochemical deposition of Ag and Au from cyanide leaching solutions.

24.4.6.23 Hg

Inukai et al. [512] have used STM to study Hg UPD on Au(111) in sulfuric and perchloric acid solutions. For sulfuric acid, the influence of adsorption of bisulfate was indicated. It has been found that after the formation of the first UPD adlayer, two different structures were simultaneously formed on the same terrace. For perchloric acid, only a single structure was found. These results reflected a significant influence of the supporting electrolyte anions on the UPD structure. Recently, Abaci et al. [513] have presented the temperature-dependent studies on the influence of counteranions on Hg UPD on Au(111).

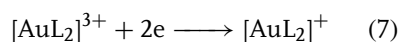
Finally, we should mention the paper by Oyamatsu et al. [514] who have studied UPD of Tl, Pb, Ag, Cd, Cu, and Bi on an Au(111)/mica electrode coated with a SAM of alkanethiols, applying CV and STM. UPD proceeded for the alkyl chain length shorter than C8. It has also been suggested that the blocking effects of the SAM depend on the Stokes radius of metal ions. For a particular case of Ag deposition, the formation of islands of atomic monolayers on which octanethiol molecules were adsorbed hexagonally has been noticed.

24.4.7

Electrochemistry of Coordination Compounds of Gold. Electrodisolution and Electrodeposition of Au

For the general characteristics of complex compounds, it is useful to remember that both Au(I)/Au(0) and Au(III)/Au(I)

aqua complex systems have very positive potentials and thus exhibit strong oxidative properties. These potentials may be changed considerably when gold ions form complexes with different ligands, which stabilize both oxidation states [515–518]. Warren and Bennett [515] have prepared Au(III) complexes with diphos [*o*-phenylenebis(dimethylphosphine)] and its arsenic analog – diars. They were irreversibly reduced in acetonitrile at Pt electrode at the potentials of –0.45 and –0.17 V for diphos and diars complexes, respectively (versus Ag|10^{–2} M AgClO₄ in CH₃CN).



Basil et al. [518] have studied theoretically and experimentally dinuclear phosphorus ylide complexes of Au(I) and Au(II). These compounds revealed irreversible redox behavior in CV experiments.

McArdle and Bossard [516] have performed a CV study on electrochemical properties of Au(I) and Au(III) complexes with four bis(diphenylphosphines) at a gold working electrode. Two-electron processes (Au³⁺/Au⁺) of these species were either reversible or quasi-reversible at moderate scan rates. Earlier papers were discussed in the 4th volume of *Encyclopedia of Electrochemistry*, published in 1975. More recently, Lagerge et al. [519], for example, have studied adsorption of potassium gold cyanide from water onto industrial activated carbon, widely used for the recovery of gold at pH = 6.0. In the applied concentration range, two distinct mechanisms of adsorption, either successive or overlapping, were experimentally proved to proceed at room temperature. At low concentrations, gold was reversibly adsorbed as Au(CN)₂[–] anions.

Koelle and Laguna [520] have carried out a systematic study on gold complexes at both oxidation states with phosphine and tetrahydrothiophene as neutral ligands, halide ions, as well as C_6F_5 (C_6Cl_5) as anionic ligands. The prepared complexes (15) were investigated using CV at a Pt working electrode. CH_2Cl_2 or acetonitrile served as a solvent with tetrabutylammonium hexafluorophosphate as a supporting electrolyte. All complexes were irreversibly reduced and only voltammetric peak potentials were reported.

The results obtained allowed one to establish the sequence of electroreduction potentials for Au complexes with π -acceptor ligands.

Both electroreductions occur at potentials considerably more negative than those observed for halide or oxosystems. Obviously, phosphine ligands stabilize Au(I) more than, for instance, CN^- and, consequently, shift the respective potential to more negative values compared to the potential of $Au(CN)_2^-$. Even stronger effect is caused by C_6F_5 (C_6Cl_5) groups.

Bond and coworkers [521] have described Au(III) electroreduction and Au(0) oxidation stripping processes in dilute aqua regia utilizing platinum, rhodium, iridium, gold, and glassy carbon electrodes. Sorption of tetrachloroaurate ions on carbon paste electrode modified with montmorillonite has been performed as a preconcentration step in the determination of gold in pharmaceutical preparation [522].

Further review of the latest literature allows one to claim that the recent electrochemical studies on gold complexes involve mainly electrodisolution of gold in the complexing media and its further electrodeposition from the complexing solution. Obviously, a large number of such investigations is related to practical

applications, since gold is frequently used as a coating metal.

24.4.7.1 Au Electrodeposition

The influence of different metal ions on the kinetics of gold electrodeposition on gold from alkaline cyanide solutions has been studied by Bek and coworkers [523–527]. Au was also deposited on glassy carbon and Pt electrodes from Au(I) ammonium solutions [528]. Nucleation mechanism was temperature dependent. Also, Marquez et al. [529] have investigated, applying electrochemical and spectroscopic methods, deposition of Au, Ag, and Au–Ag alloys on glassy carbon, and silicon electrodes from alkaline cyanide electrolytes. Also, electroreduction of $AuCl_4^-$ at boron-doped diamond electrodes has been studied [530]. Boxley et al. [531] have carried out electrochemical deposition and reoxidation of Au on highly oriented pyrolytic graphite in 5 mM $AuCl_4^-$ and 6 M LiCl solution. It has been noticed from double potential-step chronocoulometry that electrodeposition is reversible. Au nanoparticles were preferentially deposited on the upper plane of the step edges. It has also been shown that Au(I)–thiourea aqueous baths are a promising alternative to cyanide solutions for electrodeposition of Au and its alloys [532]. Free thiourea molecules were found to be adsorbed on the electrode at cathodic potentials in a vertical configuration, interacting with the metal surface via amino groups. The same authors [533] have performed in situ spectroelectrochemical Raman investigations of Au deposition and electrodisolution in $KAu(CN)_2$ solutions at pH = 6.3. Under anodic conditions, enhanced formation of $Au(CN)_2^-$ and OCN^- was observed. Also, in situ SERS has been employed to study Au deposition from sulfite electrolytes [534] and in the presence of benzyldimethylphenylammonium

chloride [535]. In recent years, electrodeposition of gold from thiosulfate-sulfite baths has been investigated [536, 537]. Gold single crystals were prepared via periodic reverse current electrodeposition in organic ion-track membranes used as templates and in the presence of either $\text{KAu}(\text{CN})_2$ or $\text{Na}_3\text{Au}(\text{SO}_3)_2$ solution. Au single crystals were successfully grown only from the cyanide solutions. There is a large interest in deposition of gold on silicon (see, for instance, [538–540]) considering the applications in microelectronics. Electrodeposition of gold has been carried out on different *n*-GaAs crystal faces [541] at the water–1,2-dichloroethane interface [542] into three-dimensional polypyrrole film [543]. Electrodeposition of thin gold films on indium-tin oxide and platinum substrates from an aminosilicate-stabilized gold sol has been described [544]. The obtained films were conductive, semitransparent, and comprised 4–6 nm Au particles, each coated with a thin aminosilicate shell. Sih et al. [545] have electrodeposited and characterized conducting thin films of gold nanoparticles bridged with oligothiophene linkers. Electrochemical oxidation of these particles resulted in the deposition of thin films consisting of intact nanoparticles linked by oligothiophene moieties. Finally, Lasia and coworkers have studied nucleation and crystal growth accompanying soft [546] and hard gold deposition [547–550].

24.4.7.2 Au Electrodisolution

Dissolution of gold and silver from Au/Ag alloys in aerated cyanide solutions has been investigated using rotating disc electrodes [551]. Dissolution was partially controlled by transport of either oxygen or cyanide. Kinetics of anodic dissolution of gold in cyanide solutions containing different metal ions has been extensively

studied by Bek and coworkers [552–566] (see also [567]). Also, the effect of temperature on dissolution has been studied [79, 568]. Electrochemical studies on dissolution of gold in thiosulfate solution [569–571] and in ammonia solutions at temperatures above 100 °C have been carried out [572]. Anodic dissolution of gold and its associated elements, for example, silver, copper, nickel, and iron in alkaline thiourea solution has also been accomplished [573, 574]. Gold was passivated by elemental sulfur produced from irreversible decomposition of thiourea. Addition of Na_2SO_3 improved the stability of thiourea in alkaline media and decelerated selective dissolution of gold (see also [575]). In HClO_4 solutions containing chloride ions, it has been noticed, using EQCM, that Au(111) dissolves in the three-electron oxidation process [576] and no evidence for one-electron oxidation has been found. Oscillatory electrodisolution of Au in 2 M HCl solutions has been investigated in Raman spectroscopy studies [577]. The obtained results indicate that the transition between active and passive states of Au account for current oscillations in a very narrow potential range.

24.4.8

Gold Clusters

The color of the colloidal solutions of gold depends on the size of colloidal particles (clusters). Several methods have been used for the preparation of such clusters (for a review see [578]). Since the size of clusters may change from one to several hundred angstroms, their electronic structure may vary between that of single atoms and the solid metal.

Gold clusters are stabilized by the adsorption of surfactants. Alkanethiols play an important role in this stabilization,

since – as we discussed earlier – they are adsorbed strongly on gold surfaces. Therefore the synthesis of clusters is carried out frequently in the presence of thiols. The adsorption of surfactants on the surface of growing clusters is useful in controlling of their size. In the core of such clusters there are Au atoms, while on the surface Au^+ ions are present which interact with thiols as shown by XPS [579].

The energy of Au-S surface bond on a cluster is 490 kJ/mol and the surface coverage by sulfur atoms is high (30 percent), compared to Au(111) surface.

One may obtain a stabilized cluster having different terminal groups.

The protective layer of surfactants may be exchanged for another, more appropriate surfactants [580]. The kinetics of such substitution has been studied [580].

Such nanoparticles may be deposited on different surfaces also, either by electrodeposition or by interaction with the surface. Various methods were used to combine clusters with the surfaces of solid substrates [578]. Some of them are based on the interaction of terminal groups of protective thiols with surface atoms or compounds attached to the surface earlier. In the formation of the cluster monolayer on the surface of solid substrates, the electrostatic interaction of clusters, with surfactants having charged terminal groups with the surfaces modified with thiols, also with charged terminal groups ($-\text{NH}_3^+$, $-\text{COO}^-$) is very important (see for instance [581]). There are also modifications of solid substrates several layers thick [581] obtained with the use of linkers such as dithiols, which combine gold clusters with the gold support by the chemical Au-S bond.

Gold clusters were also attached to the Au electrode by dithiols with the reactive bipyridyl group (Bpy) incorporated into

their structure [582, 583]. The electrode reaction of Bpy was fast on gold electrode modified by such dithiol and also with attached Au clusters.

After application of a proper potential to the tip of STM, the oxidized form of Bpy was reduced. Such a system represents the electrochemical nanoswitch. For gold clusters tunneling of single electrons was also observed. This effect was observed for nanosystems separated from two electrodes by a tunneling layer, either using STM or electrochemical methods [584, 585].

The electron tunneling on Au clusters shows that the monolayer of alkanethiols has good insulating properties. The transfer of a single electron between a STM tip and cluster occurs if the charging energy $E = e^2/2C$ (C is the capacity of cluster and e the charge of electron) is higher than the thermal energy $E_T = kT$.

The transfer of single electrons is observed on the current-potential dependence as a sequence of steps. This shows that clusters behave as redox reactants. There are many applications of gold clusters in various fields, such as preparation of new materials, electronics, heterogeneous catalysis and electrocatalysis, biosensors and others.

In medicine and biology quantum dots (composed of several gold atoms) are used as markers of chemical substances.

We present gold clusters very briefly, because recently there an extensive review [578] on their preparation, properties and applications in various fields was published.

References

1. A. N. Frumkin, *Zero Charge Potentials*, Nauka, Moscow, 1979 (in Russian).

2. A. Hamelin, in *Modern Aspects of Electrochemistry* (Eds.: B. E. Conway, R. E. White, J. O. M. Bockris), Plenum Press, New York, 1985, p. 1, Vol. 16.
3. M. A. Vorotyntsev, in *Modern Aspects of Electrochemistry* (Eds.: J. O. M. Bockris, B. E. Conway, R. E. White), Plenum Press, New York, 1986, p. 131, Vol. 17.
4. S. Trasatti, E. Lust, in *Modern Aspects of Electrochemistry* (Eds.: R. E. White, J. O. M. Bockris, B. E. Conway), Plenum Press, New York, 1999, Vol. 33.
5. R. Yu. Beck, N. V. Makurin, A. G. Zelinsky, *Elektrokhimiya* **1975**, 11, 1607.
6. A. G. Zelinsky, B. P. Tolochko, *Double Layer and Adsorption at Solid Electrodes*, VI, University of Tartu, 1981, p. 139.
7. D. Barten, J. M. Kleijn, J. Duval et al., *Langmuir* **2003**, 19, 1133.
8. B. Piela, P. K. Wrona, *J. Electroanal. Chem.* **1995**, 388, 69.
9. J. C. Hoogvliet, M. Dijkema, B. Kamp et al., *Anal. Chem.* **2000**, 72, 2016.
10. M. S. Doescher, U. Evans, P. E. Colavita et al., *Electrochem. Solid State Lett.* **2003**, 6, C112.
11. J. Sobkowski, M. Jurkiewicz-Herbich, *Wiad. Chem. (Poland)* **2004**, 58, 449.
12. A. Hamelin, J. Lecour, *Surf. Sci.* **1976**, 57, 771.
13. Y. D. Jin, S. J. Dong, *Chem. Commun.* **2002**, 16, 1780.
14. Q. Peng, E. K. Wang, *Chin. J. Chem.* **2000**, 18, 698.
15. S. Dieluweit, M. Giesen, *J. Phys.: Condens. Mat.* **2002**, 14, 4211.
16. S. Dieluweit, M. Giesen, *J. Electroanal. Chem.* **2002**, 524, 194.
17. C. Bilger, B. Pettinger, *J. Chem. Soc., Faraday Trans.* **1998**, 94, 2795.
18. D. Bigeliene, G. Valincius, *Russ. J. Electrochem.* **2000**, 36, 431.
19. V. Mazine, Y. Borensztein, L. Cagnon et al., *Phys. Status Solidi A* **1999**, 175, 311.
20. A. Sadkowski, A. J. Motheo, R. S. Neves, *J. Electroanal. Chem.* **1998**, 455, 107.
21. D. J. Trevor, C. E. D. Chidsey, D. N. Loiacono, *Phys. Rev. Lett.* **1989**, 62, 929.
22. E. Bunge, R. J. Nichols, B. Roelfs et al., *Langmuir* **1996**, 12, 3060.
23. E. Bunge, S. N. Port, B. Roelfs et al., *Langmuir* **1997**, 13, 85.
24. J. Lipkowski, C. N. Van Huong, C. Hinnen et al., *J. Electroanal. Chem.* **1983**, 143, 375.
25. A. Ignaczak, J. A. N. F. Gomes, *J. Electroanal. Chem.* **1997**, 420, 209.
26. L. Treindl, K. Doblhofer, K. Krischer et al., *Electrochim. Acta* **1999**, 44, 3963.
27. J. E. Pemberton, S. L. Joa, A. Shen et al., *J. Chem. Soc., Faraday Trans.* **1996**, 92, 3683.
28. G. Jarzabek, Z. Borkowska, *J. Electroanal. Chem.* **1987**, 226, 295.
29. Z. Borkowska, A. Hamelin, *J. Electroanal. Chem.* **1988**, 241, 373.
30. A. Hamelin, L. Doubova, D. Wagner et al., *J. Electroanal. Chem.* **1987**, 220, 155.
31. N. van Huong, *J. Electroanal. Chem.* **1985**, 194, 131.
32. Z. Borkowska, W. R. Fawcett, *Elektrokhimiya* **1980**, 16, 1092.
33. M. Brzostowska-Smolksa, S. Minc, *Pol. J. Chem.* **1983**, 106, 1005.
34. A. Hamelin, *J. Electroanal. Chem.* **1995**, 386, 1.
35. M. Weber, F. C. Nart, *Langmuir* **1996**, 12, 1895.
36. J. Lipkowski, Z. Shi, A. Chen et al., *Electrochim. Acta* **1998**, 43, 2875.
37. S. Thomas, Y. E. Sung, A. Wieckowski, *Solid-Liquid Electrochem. Interfaces ACS Symp. Ser.* **1997**, 656, 126.
38. Z. Shi, J. Lipkowski, S. Mirwald et al., *J. Electroanal. Chem.* **1995**, 396, 115.
39. P. Paredes Olivera, M. Patrino, H. Sellers, Electronic structure calculations of polyatomic oxyanions adsorbed on metal surfaces in *Interfacial Electrochemistry. Theory, Experiment and Applications* (Ed.: A. Więckowski), Marcel Dekker, New York-Basel, 1999, p. 63.
40. M. Kleinert, A. Cuesta, L. A. Kibler et al., *Surf. Sci.* **1999**, 430, L521.
41. A. Cuesta, M. Kleinert, D. M. Kolb, *Phys. Chem. Chem. Phys.* **2000**, 2, 5684.
42. N. Hirai, K. Watanabe, S. Hara, *Surf. Sci.* **2001**, 493, 568.
43. N. Vasiljevic, T. Trimble, N. Dimitrov et al., *Langmuir* **2004**, 20, 6639.
44. H. Futamata, *Chem. Phys. Lett.* **2000**, 317, 304.
45. P. Skołod, *J. Electroanal. Chem.* **1996**, 406, 235.
46. E. Dutkiewicz, P. Skołod, *J. Chem. Soc., Faraday Trans.* **1996**, 92, 3763.
47. A. Hamelin, in *Trends in Interfacial Chemistry* (Ed.: A. F. Silva), Reidel, Dordrecht, 1986, p. 3.

48. A. C. Chen, J. Lipkowski, *J. Phys. Chem. B* **1999**, 103, 682.
49. A. Tymosiak-Zielińska, Z. Borkowska, *Electrochim. Acta* **2000**, 45, 3105.
50. N. S. Marinkovic, J. J. Calvente, A. Kloss et al., *J. Electroanal. Chem.* **1999**, 467, 325.
51. A. Kolics, A. E. Thomas, A. Wieckowski, *J. Chem. Soc., Faraday Trans.* **1996**, 92, 3727.
52. A. Cuesta, D. M. Kolb, *Surf. Sci.* **2000**, 465, 310.
53. Z. C. Shi, J. Lipkowski, *J. Electroanal. Chem.* **1996**, 403, 225.
54. S. Ye, C. Ishibashi, K. Shimazu et al., *Langmuir* **1999**, 15, 807.
55. Z. C. Shi, J. Lipkowski, S. Mirwald et al., *J. Chem. Soc., Faraday Trans.* **1996**, 92, 3746.
56. O. M. Magnussen, B. M. Ocko, J. X. Wang et al., *J. Phys. Chem.* **1996**, 100, 5500.
57. B. M. Ocko, O. M. Magnussen, J. X. Wang et al., *Phys. Rev. B* **1996**, 53, R7654.
58. T. Wandlowski, J. X. Wang, O. M. Magnussen et al., *J. Phys. Chem.* **1996**, 100, 10277.
59. J. X. Wang, R. P. Adzic, B. M. Ocko, In situ surface X-ray scattering studies of electrosorption in *Interfacial Electrochemistry. Theory, Experiment and Applications* (Ed.: A. Więckowski), Marcel Dekker, New York-Basel, 1999, p. 175.
60. S. W. Wang, P. A. Rikvold, *Phys. Rev. B* **2002**, 65, art. No. 155406.
61. F. Reniers, D. H. Fairbrother, S. Wu et al., *Surf. Sci.* **1999**, 435, 12.
62. R. R. Adzic, J. X. Wang, *J. Phys. Chem. B* **1998**, 102, 6305.
63. J. X. Wang, I. K. Robinson, R. R. Adzic, *Surf. Sci.* **1998**, 413, 374.
64. S. J. Mitchell, M. T. M. Koper, *Surf. Sci.* **2004**, 563, 169.
65. H. W. Lei, H. Uchida, M. Watanabe, *J. Electroanal. Chem.* **1996**, 413, 131.
66. K. Itaya, N. Batina, M. Kunitake et al., *Solid-Liquid Electrochem. Interfaces, ACS Symp. Ser.* **1997**, 656, 171.
67. O. Endo, Y. Fukushima, H. Ozaki et al., *Surf. Sci.* **2004**, 569, 99.
68. A. C. Chen, Z. C. Shi, D. Bizzotto et al., *J. Electroanal. Chem.* **1999**, 467, 342.
69. J. X. Wang, G. M. Watson, R. M. Ocko, *J. Phys. Chem.* **1996**, 100, 6672.
70. M. Seo, K. Ueno, *J. Electrochem. Soc.* **1996**, 143, 899.
71. C. C. Chang, S. L. Yau, J. W. Tu et al., *Surf. Sci.* **2003**, 523, 59.
72. X. Q. Wang, R. Chen, Y. L. Wang et al., *J. Phys. Chem. B* **1998**, 102, 7568.
73. Z. Kerner, T. Pajkossy, *Electrochim. Acta* **2002**, 47, 2055.
74. B. Pettinger, C. Bilger, J. Lipkowski, Second harmonic generation anisotropy from single crystalline electrode surfaces in *Interfacial Electrochemistry. Theory, Experiment and Applications* (Ed.: A. Więckowski), Marcel Dekker, New York-Basel, 1999, p. 373.
75. A. Friedrich, B. Pettinger, D. M. Kolb et al., *Chem. Phys. Lett.* **1989**, 163, 123.
76. X. Gao, A. Hamelin, M. J. Weaver, *Phys. Rev. B* **1991**, 44, 10983.
77. A. Tadjeddine, A. Le Rille, Sum and difference frequency generation at electrode surfaces in *Interfacial Electrochemistry. Theory, Experiment and Applications* (Ed.: A. Więckowski), Marcel Dekker, New York-Basel, 1999, p. 317.
78. A. Le Rille, A. Tadjeddine, A. Peremans et al., *Chem. Phys. Lett.* **1997**, 271, 95.
79. C. P. Thurgood, D. W. Kirk, F. R. Foulkes et al., *J. Electrochem. Soc.* **1981**, 128, 1680.
80. S. Trasatti, *Surf. Sci.* **1995**, 335, 1.
81. N. A. Rogozhnikov, N. M. Zakharova, *Russ. J. Electrochem.* **1997**, 33, 131.
82. G. L. Beltramo, T. E. Szubina, S. J. Mitchell et al., *J. Electroanal. Chem.* **2004**, 563, 111.
83. M. Bron, R. Holze, *Electrochim. Acta* **1999**, 45, 1121.
84. Z. Jusys, S. Bruckenstein, *Electrochem. Commun.* **2000**, 2, 412.
85. A. Bilic, J. R. Reimers, N. S. Hush et al., *J. Chem. Phys.* **2002**, 116, 8981.
86. D. N. Upadhyay, V. Yegnaraman, G. P. Rao, *Langmuir* **1996**, 12, 4249.
87. Z. L. Cheng, L. Cheng, S. J. Dong et al., *J. Electrochem. Soc.* **2001**, 148, E227.
88. T. Oznuher, U. Demir, *J. Electroanal. Chem.* **2002**, 529, 34.
89. L. Piccolo, D. Loffreda, F. J. C. S. Aires et al., *Surf. Sci.* **2004**, 566, 995.
90. C. Vericat, M. E. Vela, J. Gago et al., *Electrochim. Acta* **2004**, 49, 3643.
91. W. G. Bigelow, D. L. Pickett, W. A. Zisman, *J. Colloid Sci.* **1946**, 513, 1.
92. R. G. Nuzzo, D. Allara, *J. Am. Chem. Soc.* **1983**, 105, 4481.
93. A. Ulman, *Chem. Rev.* **1996**, 96, 1553.
94. G. G. Roberts, *Langmuir-Blodgett Film*, Plenum Press, New York, 1990

95. O. Cavalleri, A. Hirstein, J. P. Bucher et al., *Thin Solid Films* **1996**, 284–285, 392.
96. C. J. Zhong, R. C. Brush, J. Anderegg et al., *Langmuir* **1999**, 15, 518.
97. C. D. Bain, E. B. Troughton, Y. T. Tao et al., *J. Am. Chem. Soc.* **1989**, 111, 321.
98. C. A. Widrig, C. Chung, M. D. Porter, *J. Electroanal. Chem.* **1991**, 310, 335.
99. C. J. Zhong, M. D. Porter, *J. Electroanal. Chem.* **1997**, 425, 147.
100. C. J. Zhong, J. Zak, M. D. Porter, *J. Electroanal. Chem.* **1997**, 421, 9.
101. M. M. Walczak, D. D. Weisshaar, M. D. Porter, *Langmuir* **1993**, 9, 323.
102. M. Cohen-Atiya, D. Mandler, *J. Electroanal. Chem.* **2003**, 550–551, 267.
103. C. M. A. Brett, S. Kresak, T. Hianik et al., *Electroanalysis* **2003**, 15, 557.
104. S. S. Wong, M. D. Porter, *J. Electroanal. Chem.* **2000**, 485, 135.
105. M. French, S. E. Creager, *Langmuir* **1998**, 14, 2129.
106. P. Krysinski, M. Brzostowska-Smolka, *J. Electroanal. Chem.* **1997**, 424, 61.
107. A. Kudelski, P. Krysinski, *J. Electroanal. Chem.* **1998**, 443, 5.
108. T. Felgenhauer, H. T. Rong, M. Buck, *J. Electroanal. Chem.* **2003**, 550–551, 309.
109. M. Galperin, A. Nitzan, S. Sek et al., *J. Electroanal. Chem.* **2003**, 550–551, 337.
110. G. E. Poirier, E. D. Pyland, *Science* **1996**, 272, 1145.
111. K. M. Beardmore, J. D. Kress, N. Gronbech-Jensen et al., *Chem. Phys. Lett.* **1998**, 286, 40.
112. N. Camillone, *Langmuir* **2004**, 20, 1199.
113. R. Yamada, K. Uosaki, *Langmuir* **1997**, 13, 5218.
114. R. Yamada, K. Uosaki, *Langmuir* **1998**, 14, 855.
115. G. E. Poirier, *Chem. Rev.* **1997**, 97, 1117.
116. C. Schönenberger, J. A. M. Sondag-Huethorst, J. Jorritsma et al., *Langmuir* **1994**, 10, 611.
117. J. A. M. Sondag-Huethorst, L. G. J. Fokink, *Langmuir* **1994**, 10, 4380.
118. C. Schönenberger, J. Jorritsma, J. A. M. Sondag-Huethorst et al., *J. Phys. Chem. B* **1995**, 99, 3250.
119. R. Yamada, H. Sakai, K. Uosaki, *Chem. Lett.* **1999**, 667.
120. R. Yamada, H. Wano, K. Uosaki, *Langmuir* **2000**, 16, 5523.
121. H. Wano, K. Uosaki, *Langmuir* **2001**, 17, 8224.
122. T. Sumi, H. Wano, K. Uosaki, *J. Electroanal. Chem.* **2003**, 550–551, 321.
123. H. Hagenstrom, M. A. Schneeweiss, D. M. Kolb, *Langmuir* **1999**, 15, 2435.
124. O. Azzaroni, M. E. Vela, G. Andreassen et al., *J. Phys. Chem. B* **2002**, 106, 12267.
125. T. Sumi, K. Uosaki, *J. Phys. Chem. B* **2004**, 108, 6422.
126. D. F. Yang, C. P. Wilde, M. Morin, *Langmuir* **1996**, 12, 6570.
127. D. F. Yang, C. P. Wilde, M. Morin, *Langmuir* **1997**, 13, 243.
128. T. Kawaguchi, Y. Yasuda, K. Shimazu et al., *Langmuir* **2000**, 16, 9830.
129. D. Qu, M. Morin, *J. Electroanal. Chem.* **2000**, 517, 45.
130. I. A. Vinokurov, M. Morin, J. Kankare, *J. Phys. Chem. B* **2000**, 104, 5790.
131. M. Himmelhaus, F. Eisert, M. Buck et al., *J. Phys. Chem. B* **2000**, 104, 576.
132. F. Schreiber, *Prog. Surf. Sci.* **2000**, 65, 151.
133. R. G. Nuzzo, L. H. Dubois, D. L. Allara, *J. Am. Chem. Soc.* **1990**, 112, 558.
134. M. W. Walczak, C. Chung, S. M. Stole et al., *J. Am. Chem. Soc.* **1991**, 113, 2370.
135. M. A. Bryant, J. E. Pemberton, *J. Am. Chem. Soc.* **1991**, 113, 8284.
136. E. Paradis, P. Rowntree, *J. Electroanal. Chem.* **2003**, 550–551, 175.
137. D. F. Yang, M. Morin, *Can. J. Chem.* **1997**, 75, 1680.
138. G. E. Poirier, *Langmuir* **1999**, 15, 3018.
139. T. Kakiuchi, M. Iida, N. Gon et al., *Langmuir* **2001**, 17, 1599.
140. F. Teran Arce, M. E. Vela, R. C. Salvarezza et al., *Electrochim. Acta* **1998**, 44, 1053.
141. F. Teran Arce, M. E. Vela, R. C. Salvarezza et al., *Langmuir* **1998**, 14, 7203.
142. Y. Iwami, D. Hobara, M. Yamamoto et al., *J. Electroanal. Chem.* **2004**, 564, 77.
143. T. Sugiyama, T. Ishioka, A. Harata, *Anal. Sci.* **2001**, 17, S237.
144. M. Hara, H. Sasabe, W. Knoll, *Thin Solid Films* **1996**, 273, 66.
145. M. Rohwerder, K. de Weldige, M. Stratmann, *J. Solid State Electrochem.* **1998**, 2, 88.
146. M. Fonticelli, O. Azzaroni, G. Benitez et al., *J. Phys. Chem. B* **2004**, 108, 1898.
147. M. Schweizer, H. Hagenstrom, D. M. Kolb, *Surf. Sci.* **2001**, 490, L627.

148. F. Loglio, M. Schweizer, D. M. Kolb, *Langmuir* **2003**, 19, 830.
149. V. Bondzie, S. J. Dion-Warren, Y. Yu et al., *Surf. Sci.* **1999**, 431, 174.
150. R. Yamada, K. Uosaki, *Langmuir* **2001**, 17, 4148.
151. A. M. Bittner, M. Epple, E. Kuhnke et al., *J. Electroanal. Chem.* **2003**, 550–551, 113.
152. A. S. Viana, L. M. Abrantes, G. Jin et al., *Phys. Chem. Chem. Phys.* **2001**, 3, 3411.
153. A. S. Viana, A. H. Jones, L. M. Abrantes et al., *J. Electroanal. Chem.* **2001**, 500, 290.
154. T. Y. Dong, L. S. Chang, I. M. Tseng et al., *Langmuir* **2004**, 20, 4471.
155. T. Kondo, M. Okamura, K. Uosaki, *Chem. Lett.* **2001**, 930.
156. S. Søk, R. Bilewicz, *J. Electroanal. Chem.* **2001**, 509, 11.
157. S. Søk, A. Misicka, R. Bilewicz, *J. Phys. Chem. B* **2000**, 104, 5399.
158. S. Søk, R. Moszyński, A. Sepiol et al., *J. Electroanal. Chem.* **2003**, 55, 359.
159. L. J. Wan, M. Terashima, H. Noda et al., *J. Phys. Chem. B* **2000**, 104, 3563.
160. S. Rifai, M. Morin, *J. Electroanal. Chem.* **2003**, 550–551, 277.
161. S. Kuwabata, R. Fukuzaki, M. Nishizawa et al., *Langmuir* **1999**, 15, 6807.
162. R. Holze, S. Schomaker, *Electrochim. Acta* **1990**, 35, 613.
163. O. Azzaroni, G. Andreasen, B. Blum et al., *J. Phys. Chem. B* **2000**, 104, 1395.
164. G. Garcia, V. A. Macagno, G. I. Lacconi, *Electrochim. Acta* **2003**, 48, 1273.
165. G. Garcia, J. L. Rodriguez, G. I. Lacconi et al., *Langmuir* **2004**, 20, 8773.
166. M. Borsari, M. Cannio, G. Gavioli, *Electroanalysis* **2003**, 15, 1192.
167. C. A. Szafranski, W. Tanner, P. E. Laibinis et al., *Langmuir* **1998**, 14, 3570.
168. H. Azebara, S. Yoshimoto, H. Hokari et al., *J. Electroanal. Chem.* **1999**, 473, 68.
169. Y. X. Zhou, T. Nagaoka, G. Y. Zhu, *Biophys. Chem.* **1999**, 79, 55.
170. A. V. Krylov, W. Pfeil, F. Lisdat, *J. Electroanal. Chem.* **2004**, 569, 225.
171. H. Wackerbarth, R. Marie, M. Grubb et al., *J. Solid State Electrochem.* **2004**, 8, 474.
172. T. Akiyama, K. Inoue, Y. Kuwahara et al., *J. Electroanal. Chem.* **2003**, 550–551, 303.
173. K. Arihara, F. Kitamura, *J. Electroanal. Chem.* **2003**, 550–551, 149.
174. J. D. Zhang, Q. J. Chi, J. U. Nielsen et al., *Langmuir* **2000**, 16, 7229.
175. R. D. Felice, A. Selloni, *J. Chem. Phys.* **2004**, 120, 4906.
176. G. Hager, A. G. Brolo, *J. Electroanal. Chem.* **2003**, 550–551, 291.
177. M. Darder, E. Casero, D. J. Diaz et al., *Langmuir* **2000**, 16, 9804.
178. M. Dijkstra, B. Kamp, J. C. Hoogvliet et al., *Langmuir* **2000**, 16, 3852.
179. M. Akram, M. C. Stuart, D. K. Y. Wong, *Anal. Chim. Acta* **2004**, 504, 243.
180. Y. J. Yong, K. S. Beng, *Electrochem. Commun.* **2004**, 6, 87.
181. G. Che, C. R. Cabrera, *J. Electroanal. Chem.* **1996**, 417, 155.
182. E. Chung, J. L. Shepherd, D. Bizzotto et al., *Langmuir* **2004**, 20, 8270.
183. W. P. Zhou, T. Baunach, V. Ivanova et al., *Langmuir* **2004**, 20, 4590.
184. L. S. Pinheiro, M. L. A. Temperini, *Surf. Sci.* **1999**, 441, 45.
185. T. Doneux, C. Buess-Herman, J. Lipkowski, *J. Electroanal. Chem.* **2004**, 564, 65.
186. R. Madueno, J. M. Sevilla, T. Pineda et al., *J. Electroanal. Chem.* **2001**, 506, 92.
187. L. Y. He, B. J. Xiang, Y. J. Yang, *Russ. J. Electrochem.* **2004**, 40, 849.
188. T. Baunach, D. M. Kolb, *Anal. Bioanal. Chem.* **2002**, 373, 743.
189. F. Reincke, S. G. Hickey, J. J. Kelly et al., *J. Electroanal. Chem.* **2002**, 522, 2.
190. S. P. Dudek, H. D. Sikes, C. E. D. Chidsey, *J. Am. Chem. Soc.* **2001**, 123, 8033.
191. C. A. Szafranski, W. Tanner, P. E. Laibinis et al., *Langmuir* **1998**, 14, 3580.
192. H. Kondoh, T. Nakamura, F. Matsui et al., *Mol. Cryst. Liq. Cryst.* **2002**, 377, 45.
193. M. Mazur, P. Krysiński, *Langmuir* **2000**, 16, 7962.
194. Y. Yang, O. Valet, C. Donner et al., *Z. Phys. Chem.* **2003**, 217, 493.
195. R. N. Gu, R. Sun, P. G. Cao et al., *Spectrosc. Spect. Anal.* **1999**, 19, 50.
196. L. S. Wong, V. L. Vilker, W. T. Yap et al., *Langmuir* **1995**, 11, 4818.
197. H. M. Zhang, G. J. Su, D. Wang et al., *Electrochim. Acta* **2004**, 49, 1629.
198. A. Ion, T. Ljones, F. G. Banica, *Collect. Czech. Chem. Commun.* **2004**, 69, 759.
199. M. Nishizawa, T. Sunagawa, H. Yoneyama, *J. Electroanal. Chem.* **1997**, 436, 213.
200. Z. Q. Gao, K. S. Siow, *Anal. Commun.* **1996**, 33, 223.
201. S. Wang, D. Du, X. Xu, *J. Appl. Electrochem.* **2004**, 34, 495.

202. K. Ozoemena, P. Westbroek, T. Nyokong, *J. Porphyrins Phthalocyanines* **2002**, 6, 98.
203. D. Li, J. H. Li, *Surf. Sci.* **2003**, 522, 105.
204. W. J. Miao, A. J. Bard, *Anal. Chem.* **2003**, 75, 5825.
205. C. W. Ge, J. H. Liao, W. Yu et al., *Biosens. Bioelectron.* **2003**, 18, 53.
206. A. H. Zhou, J. D. Zhong, Q. J. Xie et al., *Biomaterials* **2001**, 22, 2515.
207. Q. J. Xie, Y. Y. Zhang, M. C. Xu et al., *J. Electroanal. Chem.* **1999**, 478, 1.
208. M. Tarek, K. Tu, M. L. Klein et al., *Biophys. J.* **1999**, 77, 964.
209. M. Kawasaki, D. Yoshidome, T. Sato et al., *J. Electroanal. Chem.* **2001**, 543, 1.
210. T. Ohtsuka, M. Nagata, H. Komori et al., *Electrochemistry* **1999**, 67, 1184.
211. J. Zhang, Q. Chi, J. U. Nielsen et al., *Russ. J. Electrochem.* **2002**, 38, 68.
212. N. Nakashima, Y. Miyata, M. Tominaga, *Chem. Lett.* **1996**, 9, 731.
213. H. Imahori, H. Norieda, Y. Nishimura et al., *J. Phys. Chem. B* **2000**, 104, 1253.
214. X. Q. Li, B. Q. Lv, Z. H. Xue et al., *Anal. Lett.* **2002**, 35, 1811.
215. D. L. Pilloud, X. X. Chen, P. L. Dutton et al., *J. Phys. Chem. B* **2000**, 104, 2868.
216. F. Q. Zhao, L. J. Huang, B. Z. Zeng et al., *Electrochem. Commun.* **2004**, 6, 319.
217. J. C. Yan, S. J. Dong, *Electroanalysis* **1997**, 9, 1219.
218. J. C. Yan, S. J. Dong, J. H. Li et al., *J. Electrochem. Soc.* **1997**, 144, 3858.
219. M. G. Samant, C. A. Brown, J. G. Gordon II, *Langmuir* **1982**, 8, 1615.
220. K. Bandyopadhyay, K. Vijayamohanan, *Langmuir* **1998**, 14, 625.
221. F. K. Huang, R. C. Horton, D. C. Myles et al., *Langmuir* **1998**, 14, 4802.
222. M. H. Dishner, J. C. Hemminger, J. C. Feher, *Langmuir* **1997**, 13, 4788.
223. L. V. Protsailo, W. R. Fawcett, D. Russell et al., *Langmuir* **2002**, 18, 9342.
224. J. D. Monnell, J. J. Stapleton, J. J. Jackiw et al., *J. Phys. Chem. B* **2004**, 108, 9834.
225. F. Chao, M. Costa, A. Tadjeddine, *Bull. Soc. Chim. France* **1971**, 7, 5193.
226. L. Stolberg, J. Richer, J. Lipkowski, *J. Electroanal. Chem.* **1986**, 207, 213.
227. L. Stolberg, J. Lipkowski, D. E. Irish, *J. Electroanal. Chem.* **1991**, 300, 563.
228. J. Lipkowski, L. Stolberg, S. Morin et al., *J. Electroanal. Chem.* **1993**, 355, 147.
229. L. Stolberg, J. Lipkowski, D. E. Irish, *J. Electroanal. Chem.* **1987**, 238, 333.
230. L. Stolberg, J. Lipkowski, D. E. Irish, *J. Electroanal. Chem.* **1990**, 296, 171.
231. L. Stolberg, J. Lipkowski, D. E. Irish, *J. Electroanal. Chem.* **1991**, 307, 241.
232. L. Stolberg, J. Lipkowski, D. E. Irish, *J. Electroanal. Chem.* **1992**, 322, 357.
233. D. F. Yang, L. Stolberg, J. Lipkowski, *J. Electroanal. Chem.* **1992**, 329, 259.
234. P. Skořuda, M. Holze, J. Lipkowski et al., *J. Electroanal. Chem.* **1993**, 358, 343.
235. B. Pettinger, S. Mirwald, J. Lipkowski, *Ber. Bunsenges. Phys. Chem. Chem. Phys.* **1993**, 95, 395.
236. B. Pettinger, J. Lipkowski, S. Mirwald et al., *J. Electroanal. Chem.* **1992**, 329, 289.
237. P. Hebert, A. Le Rille, W. Q. Zeng et al., *J. Electroanal. Chem.* **1998**, 447, 5.
238. A. G. Brolo, D. E. Irish, J. Lipkowski, *J. Phys. Chem. B* **1997**, 101, 3906.
239. G. Andreassen, M. E. Vela, R. C. Salvarezza et al., *Langmuir* **1997**, 13, 6814.
240. Y. Ikezawa, T. Sawatari, T. Kitazume et al., *Electrochim. Acta* **1998**, 43, 3297.
241. G. Zilberman, V. Tsionsky, E. Gileadi, *Can. J. Chem.* **1997**, 75, 1646.
242. M. Hoon-Khosla, W. R. Fawcett, A. C. Chen et al., *Electrochim. Acta* **1999**, 45, 611.
243. Y. Ikezawa, T. Sawatari, H. Terashima, *Electrochim. Acta* **2001**, 46, 1333.
244. A. Bilic, J. R. Reimers, N. S. Hush, *J. Phys. Chem. B* **2002**, 106, 6740.
245. A. C. Chang, D. F. Yang, J. Lipkowski, *J. Electroanal. Chem.* **1999**, 475, 130.
246. M. Jurkiewicz-Herbich, R. Słojkowska, K. Zawada et al., *Electrochim. Acta* **2002**, 47, 2429.
247. O. Pluchery, A. Tajeddine, *J. Electroanal. Chem.* **2001**, 500, 379.
248. N. Nanbu, F. Kitamura, T. Ohsaka et al., *Electrochemistry* **1999**, 67, 1165.
249. A. G. Brolo, Z. Jiang, D. E. Irish, *J. Electroanal. Chem.* **2003**, 547, 163.
250. C. M. Xu, B. Xi, Y. L. Li et al., *New J. Chem.* **2001**, 25, 1191.
251. M. J. Eddowes, H. A. O. Hill, *J. Chem. Soc., Chem. Commun.* **1977**, 771.
252. A. Czerwiński, J. Sobkowski, S. Zamponi et al., *J. Electroanal. Chem.* **1990**, 288, 271.
253. W. B. Cai, L. J. Wan, H. Noda et al., *Langmuir* **1998**, 14, 6992.
254. N. H. Li, V. Zamylny, J. Lipkowski et al., *J. Electroanal. Chem.* **2002**, 524, 43.

255. C. I. Smith, A. J. Maunder, C. A. Lucas et al., *J. Electrochem. Soc.* **2003**, 150, E233.
256. Y. Ikezawa, T. Kosugi, *Electrochim. Acta* **2002**, 47, 2921.
257. T. Sagara, K. Uematsu, K. Nagata, *J. Electroanal. Chem.* **2003**, 550–551, 219.
258. I. Burgess, V. Zamylny, G. Szymanski et al., *J. Electroanal. Chem.* **2003**, 550–551, 187.
259. D. Barten, J. M. Kleijn, M. A. C. Stuart, *Phys. Chem. Chem. Phys.* **2003**, 5, 4258.
260. A. G. Brolo, D. E. Irish, G. Szymanski et al., *Langmuir* **1998**, 14, 517.
261. W. B. Cai, T. Amano, M. Osawa, *J. Electroanal. Chem.* **2001**, 500, 147.
262. Y. Ikezawa, Y. Koda, M. Shibuya et al., *Electrochim. Acta* **2000**, 45, 2075.
263. U. W. Hamm, V. Lazarescu, D. M. Kolb, *J. Chem. Soc., Faraday Trans.* **1996**, 92, 3785.
264. M. Brzostowska-Smolka, P. Krysiński, *Pol. J. Chem.* **1997**, 71, 1293.
265. T. Luczak, M. Beltowska-Brzezinska, M. Bron et al., *Vib. Spectrosc.* **1997**, 15, 17.
266. A. C. Chen, J. Richer, S. G. Roscoe et al., *Langmuir* **1997**, 13, 4737.
267. X. Y. Xiao, S. G. Sun, *Electrochim. Acta* **2000**, 45, 2897.
268. J. Richer, J. Lipkowski, *Langmuir* **1986**, 2, 630.
269. J. Richer, J. Lipkowski, *J. Electroanal. Chem.* **1988**, 251, 217.
270. M. Brzostowska-Smolka, P. Krysiński, *Colloids Surf., A – Physicochem. Eng. Aspects* **1998**, 131, 39.
271. Y. G. Yang, D. Bizzotto, *J. Electroanal. Chem.* **2001**, 500, 408.
272. I. Zawisza, I. Burgess, G. Szymanski et al., *Electrochim. Acta* **2004**, 49, 3651.
273. M. J. Sottomayor, V. Coelho, A. P. Ferreira et al., *Electrochim. Acta* **1999**, 45, 775.
274. H. Sawamoto, S. Kashimori, *Bunseki Kagaku* **2002**, 51, 1041.
275. D. Bizzotto, E. Wong, Y. G. Yang, *J. Electroanal. Chem.* **2000**, 480, 233.
276. R. Słojkowska, M. Jurkiewicz-Herbich, *Colloids Surf.* **2001**, 178, 325.
277. R. Słojkowska, B. Pałys, M. Jurkiewicz-Herbich, *Electrochim. Acta* **2004**, 49, 4109.
278. H. Q. Li, A. C. Chen, S. G. Roscoe et al., *J. Electroanal. Chem.* **2001**, 500, 299.
279. E. Dutkiewicz, P. Skołod, A. Hamelin, *J. Electroanal. Chem.* **1988**, 240, 291.
280. E. Dutkiewicz, P. Skołod, A. Hamelin, *J. Electroanal. Chem.* **1988**, 248, 209.
281. S. Floate, M. Hosseini, M. R. Arshadi et al., *J. Electroanal. Chem.* **2003**, 542, 67.
282. R. J. Nichols, I. Burgess, K. L. Young et al., *J. Electroanal. Chem.* **2004**, 563, 33.
283. Y. Ikezawa, A. Yoshida, R. Sekiguchi, *Electrochim. Acta* **2000**, 46, 769.
284. E. Szocs, I. Felhosi, U. Schmidt et al., *Mater. Corros. – Werkstoffe Korrosion* **2002**, 53, 631.
285. D. Krznaric, T. Goricnik, M. Vukovic et al., *Electroanalysis* **2001**, 13, 109.
286. P. Zelenay, P. Waszczuk, K. Dobrowolska et al., *Electrochim. Acta* **1994**, 39, 655.
287. J. Sobkowski, P. Waszczuk, P. Zelenay, *Russ. J. Electrochem.* **1995**, 31, 850.
288. Y. Ikezawa, R. Sekiguchi, T. Kitazume, *Electrochim. Acta* **2000**, 46, 731.
289. T. Schmitz-Hubsch, T. Fritz, R. Staub et al., *Surf. Sci.* **1999**, 437, 163.
290. K. Ataka, M. Osawa, *J. Electroanal. Chem.* **1999**, 460, 188.
291. T. Dretschkow, T. Wandlowski, *Electrochim. Acta* **1998**, 43, 2991.
292. S. Pronkin, T. Wandlowski, *J. Electroanal. Chem.* **2003**, 550, 131.
293. R. Roelfs, E. Bunge, C. Schröter et al., *J. Phys. Chem. B* **1997**, 101, 754.
294. M. Scharfe, A. Hamelin, C. Buess-Herman, *Electrochim. Acta* **1995**, 40, 61.
295. M. H. Hölzle, D. M. Kolb, D. Krznaric et al., *Ber. Bunsenges. Phys. Chem.* **1996**, 100, 1779.
296. T. Wandlowski, M. H. Hölzle, *Langmuir* **1996**, 12, 6604.
297. C. Buess-Herman, S. Baré, M. Poelman, Ordered organic adlayers at electrode surfaces in *Interfacial Electrochemistry. Theory, Experiment and Applications* (Ed.: A. Więckowski), Marcel Dekker, New York-Basel, 1999, p. 427.
298. R. Roelfs, H. Baumgärtel, *Ber. Bunsenges. Phys. Chem.* **1995**, 100, 677.
299. S. Pronkin, Th. Wandlowski, *J. Electroanal. Chem.* **2003**, 550–551, 131.
300. A. P. M. Camargo, H. Baumgärtel, C. Dinner, *PHYSICHEMCOM* **2002**, 151–152.
301. H. B. Shen, J. F. Xia, Z. S. Wang et al., *Chem. J. Chinese Univ. – Chinese* **2001**, 22, 962.
302. S. Hason, V. Vetterl, *Bioelectrochemistry* **2002**, 56, 43.
303. Y. J. Xiao, T. Wang, X. Q. Wang et al., *J. Electroanal. Chem.* **1997**, 433, 49.

304. J. J. Davis, C. M. Halliwell, H. A. O. Hill et al., *New J. Chem.* **1998**, 22, 1119.
305. S. E. Moulton, J. N. Barisci, A. Bath et al., *Electrochim. Acta* **2004**, 49, 4223.
306. E. P. Friis, J. E. T. Andersen, L. L. Madsen et al., *Electrochim. Acta* **1998**, 43, 2889.
307. V. Reipa, A. K. Gaigalas, V. L. Vilker, *Langmuir* **1997**, 13, 3508.
308. Z. J. Cao, Q. J. Xie, M. Li et al., *J. Electroanal. Chem.* **2004**, 568, 343.
309. J. O. Zerbino, M. G. Sustersic, *Langmuir* **2000**, 16, 7477.
310. A. H. Zhou, Q. J. Xie, Y. H. Wu et al., *J. Colloid Interface Sci.* **2000**, 229, 12.
311. S. L. Horswell, V. Zamylnny, H. Q. Li et al., *Faraday Discuss.* **2002**, 121, 405.
312. I. Zawisza, X. M. Bin, J. Lipkowski, *Bioelectrochemistry* **2004**, 63, 137.
313. I. Zawisza, A. Lachenwitzer, V. Zamylnny et al., *Biophys. J.* **2003**, 85, 4055.
314. Z. W. Xiao, M. X. Xu, T. Ohgi et al., *Physica E – Low Dimens. Syst. Nanostruct.* **2004**, 21, 1098.
315. P. Han, B. A. Montooth, E. C. H. Sykes et al., *J. Am. Chem. Soc.* **2004**, 126, 10787.
316. A. Czerwiński, J. Sobkowski, *Electrochim. Acta* **1980**, 25, 1313.
317. G. B. Pan, H. J. Li, Q. H. Yuan et al., *Sci. China, Ser. B – Chem.* **2004**, 47, 320.
318. R. J. Baxter, G. Teobaldi, F. Zerbetto, *Langmuir* **2003**, 19, 7335.
319. M. Danckwerts, Y. J. Li, J. Oslonovitch et al., *J. Phys. Chem. B* **2004**, 108, 14398.
320. B. Pettinger, M. Danckwerts, K. Krischer, *Faraday Discuss.* **2002**, 121, 153.
321. H. Striegler, D. Krznaric, D. M. Kolb, *J. Electroanal. Chem.* **2002**, 532, 227.
322. M. Nakamura, M. B. Song, M. Ito, *Surf. Sci.* **1999**, 428, 167.
323. K. Nishiyama, S. Tahara, Y. Uchida et al., *J. Electroanal. Chem.* **1999**, 478, 83.
324. R. S. Neves, A. J. Motheo, F. M. S. S. Fernandes et al., *J. Brazil. Chem. Soc.* **2004**, 15, 224.
325. G. J. Su, H. M. Zhang, L. J. Wan et al., *J. Phys. Chem. B* **2004**, 108, 1931.
326. A. Ohira, T. Ishizaki, M. Sakata et al., *J. Electroanal. Chem.* **1999**, 472, 163.
327. T. Sakai, A. Ohira, M. Sakata et al., *Chem. Lett.* **2001**, 8, 782.
328. S. Xu, G. Szymanski, J. Lipkowski, *J. Am. Chem. Soc.* **2004**, 126, 12276.
329. P. A. Brooksby, W. R. Fawcett, *Electrochim. Acta* **2003**, 48, 807.
330. F. Evangelista, A. Ruocco, V. Corradini et al., *Surf. Sci.* **2003**, 531, 123.
331. V. Corradini, C. Menozzi, M. Cavallini et al., *Surf. Sci.* **2003**, 532, 249.
332. E. Cholewa, I. Burgess, J. Kunze et al., *J. Solid State Electrochem.* **2004**, 8, 693.
333. D. Bizzotto, J. Lipkowski, *Prog. Surf. Sci.* **1995**, 50, 237.
334. M. Petri, D. M. Kolb, *Phys. Chem. Chem. Phys.* **2002**, 4, 1211.
335. A. S. Dakkouri, D. M. Kolb, Reconstruction of gold surfaces in *Interfacial Electrochemistry. Theory, Experiment and Applications* (Ed.: A. Więckowski), Marcel Dekker, New York-Basel, 1999, p. 151.
336. D. M. Kolb, *Prog. Surf. Sci.* **1996**, 51, 109.
337. X. Gao, A. Hamelin, M. J. Weaver, *Surf. Sci. Lett.* **1992**, 274, L588.
338. X. Gao, G. J. Edens, A. Hamelin et al., *Surf. Sci.* **1993**, 296, 333.
339. D. M. Kolb, G. Lehmpfuhl, M. S. Zei, *J. Electroanal. Chem.* **1984**, 179, 289.
340. M. S. Zei, G. Lehmpfuhl, D. M. Kolb, *Surf. Sci.* **1984**, 221, 23.
341. D. M. Kolb, J. Schneider, *Electrochim. Acta* **1986**, 31, 929.
342. D. G. Fedak, N. A. Gjostein, *Surf. Sci.* **1967**, 8, 77.
343. M. A. Van Hove, R. J. Koestner, P. C. Stair et al., *Surf. Sci.* **1981**, 103, 189.
344. M. A. Van Hove, R. J. Koestner, P. C. Stair et al., *Surf. Sci.* **1981**, 103, 218.
345. O. K. Binnig, H. Rohrer, Ch. Gerber et al., *Surf. Sci.* **1984**, 144, 321.
346. K. M. Ho, K. P. Bohnen, *Phys. Rev. Lett.* **1987**, 59, 1833.
347. C. L. Fu, K. M. Ho, *Phys. Rev. Lett.* **1989**, 63, 1617.
348. G. Ertl, *Surf. Sci.* **1985**, 152–153, 328.
349. G. A. Samorjai, M. A. Van Hove, *Prog. Surf. Sci.* **1989**, 30, 201.
350. R. J. Nichols, O. M. Magnussen, J. Hotlos et al., *J. Electroanal. Chem.* **1990**, 290, 21.
351. K. P. Bohnen, D. M. Kolb, *Surf. Sci.* **1998**, 407, L629.
352. J. Schneider, D. M. Kolb, *Surf. Sci.* **1988**, 193, 579.
353. A. S. Dakkouri, *Solid State Ionics* **1997**, 94, 99.
354. D. M. Kolb, Surface reconstruction at metal-electrolyte interfaces in *Structure of Electrified Interfaces* (Eds.: J. Lipkowski, Ph. N. Ross), VCH, N.Y.-Weinheim-Cambridge, 1993, p. 65.

355. J. Lipkowski, L. Stolberg, Molecular adsorption at gold and silver electrodes in *Adsorption of Molecules at Metal Electrodes* (Eds.: J. Lipkowski, Ph. N. Ross), VCH, N.Y.-Weinheim-Cambridge, 1992, p. 171.
356. U. W. Hamm, D. M. Kolb, *J. Electroanal. Chem.* **1992**, 332, 339.
357. P. Skořuda, *Electrochem. Commun.* **2003**, 5, 142.
358. P. Skořuda, *Pol. J. Chem.* **2004**, 78, 583.
359. C. D. Keefe, E. Revesz, M. Dionne et al., *Can. J. Chem.* **1997**, 75, 449.
360. S. Z. Zou, X. P. Gao, M. J. Weaver, *Surf. Sci.* **2000**, 452, 44.
361. P. Hale, S. Thurgate, P. Wilkie, *Surf. Interface Anal.* **2001**, 32, 240.
362. S. Narasimhan, D. Vanderbilt, *Phys. Rev. Lett.* **1992**, 69, 1564.
363. D. Krznarić, *Electroanalysis* **2002**, 14, 657.
364. D. Hobara, M. Yamamoto, T. Kakiuchi, *Chem. Lett.* **2001**, 11, 1200.
365. G. Jerkiewicz, Surface oxidation of noble metal electrodes in *Interfacial Electrochemistry. Theory, Experiment and Applications* (Ed.: A. Więckowski), Marcel Dekker, New York-Basel, 1999, p. 559.
366. L. D. Burke, P. F. Nugent, *Gold Bull.* **1997**, 30, 43.
367. G. Tremiliosi-Filho, L. H. Dall'Antonia, G. Jerkiewicz, *J. Electroanal. Chem.* **1997**, 422, 149.
368. L. D. Burke, P. F. Nugent, *Gold Bull.* **1998**, 31, 39.
369. M. A. Schneeweiss, D. M. Kolb, D. Z. Liu et al., *Can. J. Chem.* **1997**, 75, 1703.
370. M. A. Schneeweiss, D. M. Kolb, *Solid State Ionics* **1997**, 94, 171.
371. X. Q. Zeng, S. Bruckenstein, *J. Electroanal. Chem.* **1999**, 461, 131.
372. M. Tian, W. G. Pell, B. E. Conway, *J. Electroanal. Chem.* **2003**, 552, 279.
373. L. D. Burke, A. P. O'Mullane, *J. Solid State Electrochem.* **2000**, 4, 285.
374. L. D. Burke, P. F. Nugent, *J. Electroanal. Chem.* **1998**, 444, 19.
375. L. D. Burke, L. M. Hurley, V. E. Lodge et al., *J. Solid State Electrochem.* **2001**, 5, 250.
376. L. D. Burke, L. M. Hurley, *J. Solid State Electrochem.* **2002**, 6, 101.
377. L. D. Burke, J. M. Moran, P. F. Nugent, *J. Solid State Electrochem.* **2003**, 7, 529.
378. L. D. Burke, J. A. Collins, M. A. Murphy, *J. Solid State Electrochem.* **1999**, 4, 34.
379. L. D. Burke, M. A. Murphy, *J. Solid State Electrochem.* **2001**, 5, 43.
380. E. Herrero, L. J. Buller, H. D. Abruña, *Chem. Rev.* **2001**, 101, 1897.
381. O. M. Magnussen, *Chem. Rev.* **2002**, 102, 679.
382. M. S. Zei, G. Qiao, G. Lehmpfuhl et al., *Ber. Bunsenges. Phys. Chem.* **1987**, 91, 349.
383. X. Q. Zeng, S. Bruckenstein, *J. Electroanal. Chem.* **1999**, 461, 143.
384. M. Legault, L. Blum, D. A. Huckaby, *J. Electroanal. Chem.* **1996**, 409, 79.
385. E. D. Chabala, J. Cairns, T. Rayment, *J. Electroanal. Chem.* **1996**, 412, 77.
386. M. Cappadonia, K. M. Robinson, J. Schimberger et al., *J. Electroanal. Chem.* **1997**, 436, 73.
387. M. Cappadonia, U. Linke, K. M. Robinson et al., *J. Electroanal. Chem.* **1996**, 405, 227.
388. X. H. Xia, L. Nagle, R. Schuster et al., *Phys. Chem. Chem. Phys.* **2000**, 2, 4387.
389. M. Cappadonia, K. M. Robinson, J. Schimberger et al., *Surf. Rev. Lett.* **1997**, 4, 1173.
390. S. Wu, Z. Shi, J. Lipkowski et al., *J. Phys. Chem. B* **1997**, 101, 10310.
391. D. Krznarić, T. Gorcnić, *Langmuir* **2001**, 17, 4347.
392. E. Herrero, S. Glazier, H. D. Abruña, *J. Phys. Chem. B* **1998**, 102, 9825.
393. E. Herrero, S. Glazier, L. J. Buller et al., *J. Electroanal. Chem.* **1999**, 461, 121.
394. R. Randler, M. Dietterle, D. M. Kolb, *Z. Phys. Chem. – Int. J. Res. Phys. Chem. Chem. Phys.* **1999**, 208, 43.
395. R. J. Randler, D. M. Kolb, B. M. Ocko et al., *Surf. Sci.* **2000**, 447, 187.
396. C. Sanchez, E. P. M. Leiva, *Electrochim. Acta* **1999**, 45, 691.
397. G. Brown, P. A. Rikvold, S. J. Mitchell, Monte Carlo methods for equilibrium and nonequilibrium problems in interfacial electrochemistry in *Interfacial Electrochemistry. Theory, Experiment and Applications* (Ed.: A. Więckowski), Marcel Dekker, New York-Basel, 1999, p. 47.
398. J. Zhang, Y. E. Sung, P. A. Rikvold et al., *J. Chem. Phys.* **1996**, 104, 5699.
399. J. W. Schultze, D. Dickertmann, *Surf. Sci.* **1976**, 54, 489.
400. D. Dickertmann, F. D. Koppitz, J. W. Schultze, *Electrochim. Acta* **1976**, 21, 967.
401. D. M. Kolb, *Z. Phys. Chem. Neue Folge* **1987**, 154, 179.

402. D. A. Huckaby, L. Blum, *J. Electroanal. Chem.* **1991**, 315, 255.
403. J. G. Xu, X. W. Wang, *Surf. Sci.* **1998**, 408, 317.
404. G. Brown, P. A. Rikvold, M. A. Novotny et al., *J. Electrochem. Soc.* **1999**, 146, 1035.
405. H. Uchida, N. Ikeda, M. Watanabe, *J. Electroanal. Chem.* **1997**, 424, 5.
406. H. Uchida, M. Hiei, M. Watanabe, *J. Electroanal. Chem.* **1998**, 452, 97.
407. M. Nakamura, O. Endo, T. Ohta et al., *Surf. Sci.* **2002**, 514, 227.
408. A. Kuzume, E. Herrero, J. M. Feliu et al., *J. Electroanal. Chem.* **2004**, 570, 157.
409. K. Ataka, G. Nishima, W. B. Cai et al., *Electrochem. Commun.* **2000**, 2, 417.
410. M. Nishizawa, T. Sunagawa, H. Yoneyama, *Langmuir* **1997**, 13, 5215.
411. H. Hagenstrom, M. A. Schneeweiss, D. M. Kolb, *Electrochim. Acta* **1999**, 45, 1141.
412. A. Martinez-Ruiz, J. Valenzuela-Benavides, L. Morales de la Garza et al., *Surf. Sci.* **2001**, 476, 139.
413. A. Martinez-Ruiz, M. Palomar-Pardave, J. Valenzuela-Benavides et al., *J. Phys. Chem. B* **2003**, 107, 11660.
414. E. W. Bohannon, M. G. Shumsky, J. A. Switzer, *Chem. Mater.* **1999**, 11, 2289.
415. X. G. Zhang, X. H. Li, H. L. Li, *J. Colloid Interface Sci.* **2001**, 234, 68.
416. R. Vidu, S. Hara, *Electrochemistry* **1999**, 67, 1240.
417. M. C. Santos, D. W. Miwa, S. A. S. Machado et al., *Quim. Nova* **2001**, 24, 465.
418. J. C. Bondos, A. A. Gewirth, R. G. Nuzzo, *J. Phys. Chem.* **1996**, 100, 8617.
419. D. Lee, T. Rayment, *Electrochem. Commun.* **2002**, 4, 832.
420. M. C. del Barrio, S. G. Garcia, D. R. Salinas, *Electrochem. Commun.* **2004**, 6, 762.
421. H. Kawamura, M. Takahashi, J. Mizuki, *J. Electrochem. Soc.* **2002**, 149, C586.
422. S. Maupai, Y. Zhang, P. Schmuki, *Surf. Sci.* **2003**, 527, L165.
423. S. Maupai, Y. Zhang, P. Schmuki, *Electrochem. Solid State Lett.* **2003**, 6, C63.
424. R. Vidu, N. Hirai, S. Hara, *Phys. Chem. Chem. Phys.* **2001**, 3, 3320.
425. T. Tanaka, K. Kubo, N. Hirai et al., *Mater. Trans.* **2003**, 44, 688.
426. R. Vidu, S. Hara, *Surf. Sci.* **2000**, 452, 229.
427. B. K. Niece, A. A. Gewirth, *Langmuir* **1997**, 13, 6302.
428. R. Vidu, S. Hara, *J. Electroanal. Chem.* **1999**, 475, 171.
429. M. D. Lay, K. Varazo, N. Srisook et al., *J. Electroanal. Chem.* **2003**, 554–555, 221.
430. L. A. Kibler, M. Kleinert, R. Randler et al., *Surf. Sci.* **1999**, 443, 19.
431. L. A. Kibler, A. M. El-Aziz, D. M. Kolb, *J. Mol. Catal. A – Chem.* **2003**, 199, 57.
432. L. A. Kibler, M. Kleinert, D. M. Kolb, *Surf. Sci.* **2000**, 461, 155.
433. L. A. Kibler, M. Kleinert, V. Lazarescu et al., *Surf. Sci.* **2002**, 498, 175.
434. H. Naohara, S. Ye, K. Uosaki, *J. Electroanal. Chem.* **1999**, 473, 2.
435. H. Naohara, S. Ye, K. Uosaki, *J. Electroanal. Chem.* **2001**, 500, 435.
436. M. E. Quayum, S. Ye, K. Uosaki, *J. Electroanal. Chem.* **2002**, 520, 126.
437. Y. Robach, M. Abel, L. Porte, *Surf. Sci.* **2003**, 526, 248.
438. T. L. Wade, Th. A. Sorenson, J. L. Stickney, *Epitaxial compound electrodeposition in Interfacial Electrochemistry. Theory, Experiment and Applications* (Ed.: A. Więckowski), Marcel Dekker, New York-Basel, 1999, p. 757.
439. A. Gichuhi, B. E. Boone, U. Demir et al., *J. Phys. Chem. B* **1998**, 102, 6499.
440. P. Jiang, Z. F. Liu, S. M. Cai, *J. Mater. Sci. Lett.* **2003**, 22, 577.
441. U. Demir, C. Shannon, *Langmuir* **1996**, 12, 594.
442. B. M. Huang, T. E. Lister, J. L. Stickney, *Surf. Sci.* **1997**, 392, 27.
443. M. Alanyalioglu, U. Demir, C. Shannon, *J. Electroanal. Chem.* **2004**, 561, 21.
444. I. Ruach-Nir, H. D. Wagner, I. Rubinstein et al., *Adv. Funct. Mater.* **2003**, 13, 159.
445. N. Ikemiyu, D. Iwai, K. Yamada et al., *Surf. Sci.* **1996**, 369, 199.
446. I. Yagi, S. Nakabayashi, K. Uosaki, *J. Phys. Chem. B* **1998**, 102, 2677.
447. T. A. Sorenson, D. W. Suggs, I. Nandhakumar et al., *J. Electroanal. Chem.* **1999**, 467, 270.
448. T. A. Sorenson, T. E. Lister, B. M. Huang et al., *J. Electrochem. Soc.* **1999**, 146, 1019.
449. T. A. Sorenson, K. Varazo, D. W. Suggs et al., *Surf. Sci.* **2001**, 470, 197.
450. I. Nicic, J. Liang, V. Cammarata et al., *J. Phys. Chem. B* **2002**, 106, 12247.
451. K. Verazo, M. D. Lay, T. A. Sorenson et al., *J. Electroanal. Chem.* **2002**, 522, 104.

452. C. H. Chen, K. D. Keple, A. A. Gewirth et al., *J. Phys. Chem.* **1993**, 97, 7290.
453. C. A. Jeffrey, D. A. Harrington, S. Morin, *Surf. Sci.* **2002**, 512, L367.
454. T. Solomun, W. Kautek, *Electrochim. Acta* **2001**, 47, 679.
455. M. Hara, Y. Nagahara, S. Yoshimoto et al., *J. Electrochem. Soc.* **2004**, 151, E92.
456. K. Tamura, J. X. Wang, R. R. Adzic et al., *J. Phys. Chem. B* **2004**, 108, 1992.
457. Y. L. Du, C. M. Wang, *Chinese J. Chem.* **2002**, 20, 596.
458. K. Uosaki, Z. Ye, H. Naohara et al., *J. Phys. Chem. B* **1997**, 101, 7566.
459. H. F. Waibel, M. Kleinert, L. A. Kibler et al., *Electrochim. Acta* **2002**, 47, 1461.
460. Y. Nagahara, M. Hara, S. Yoshimoto et al., *J. Phys. Chem. B* **2004**, 108, 3224.
461. J. L. Bubbendorff, L. Cagnon, V. Costakie-ling et al., *Surf. Sci.* **1997**, 384, L836.
462. F. A. Moller, O. M. Magnussen, R. J. Behm, *Phys. Rev. Lett.* **1996**, 77, 5249.
463. F. A. Moller, O. M. Magnussen, R. J. Behm, *Z. Phys. Chem. – Int. J. Res. Phys. Chem. Chem. Phys.* **1999**, 208, 57.
464. T. Allongue, L. Cagnon, C. Gomes et al., *Surf. Sci.* **2004**, 557, 41.
465. A. Hitzke, M. B. Hugenschmidt, R. J. Behm, *Surf. Sci.* **1997**, 389, 8.
466. I. Schuster, G. Abadias, B. Gilles et al., *J. Phys. IV* **1998**, 8, 231.
467. V. Repain, J. M. Berroir, S. Rousset et al., *Surf. Sci.* **2000**, 447, L152.
468. M. Kleinert, H. F. Waibel, G. E. Engelmann et al., *Electrochim. Acta* **2001**, 46, 3129.
469. L. H. Mendoza-Huizar, J. Robles, M. Palomar-Pardave, *J. Electroanal. Chem.* **2002**, 521, 95.
470. L. H. Mendoza-Huizar, J. Robles, M. Palomar-Pardave, *J. Electroanal. Chem.* **2003**, 545, 39.
471. V. S. Stepanyuk, W. Heigert, P. Rennert, *Comput. Mater. Sci.* **2000**, 17, 309.
472. G. Jung, C. K. Rhee, *J. Electroanal. Chem.* **1997**, 436, 277.
473. Q. Wu, W. H. Shang, J. W. Yan et al., *J. Mol. Catal. – A Chem.* **2003**, 199, 49.
474. C. H. Jung, C. K. Rhee, *J. Electroanal. Chem.* **2004**, 566, 1.
475. C. M. Wang, Y. L. Du, Z. L. Zhou, *Electroanalysis* **2002**, 14, 849.
476. J. W. Yan, Q. Wu, W. H. Shang et al., *Electrochem. Commun.* **2004**, 6, 843.
477. J. W. Yan, J. Tang, Y. Y. Yang et al., *Surf. Interface Anal.* **2001**, 32, 49.
478. B. W. Mao, J. Tang, R. Randler, *Langmuir* **2002**, 18, 5329.
479. B. S. Radovic, R. A. H. Edwards, J. N. Jovicevic, *J. Electroanal. Chem.* **1997**, 428, 113.
480. J. J. Lee, I. T. Bae, D. A. Scherson et al., *J. Electrochem. Soc.* **2000**, 147, 562.
481. J. J. Lee, Y. B. Mo, D. A. Scherson et al., *J. Electrochem. Soc.* **2001**, 148, C799.
482. B. K. Niece, A. A. Gewirth, *J. Phys. Chem. B* **1998**, 102, 818.
483. D. Poškus, G. Agafonovas, *J. Electroanal. Chem.* **2000**, 493, 50.
484. M. J. Henderson, E. Bitziou, A. R. Hillmann et al., *J. Electrochem. Soc.* **2001**, 148, E105.
485. X. Q. Zeng, S. Bruckenstein, *J. Electrochem. Soc.* **1999**, 146, 2549.
486. X. Q. Zeng, S. Bruckenstein, *J. Electrochem. Soc.* **1999**, 146, 2555.
487. M. Seo, M. Yamazaki, *J. Electrochem. Soc.* **2004**, 151, E276.
488. P. Hale, S. Thurgate, P. Wilkie, *Surf. Interface Anal.* **2003**, 35, 842.
489. M. I. Rojas, *J. Electroanal. Chem.* **1996**, 405, 33.
490. D. W. M. Arrigan, L. Le Bihan, M. J. Pickup, *Analyst* **1999**, 124, 1797.
491. H. M. Kothari, A. A. Vertegel, E. W. Bohannan et al., *Chem. Mater.* **2002**, 14, 2750.
492. Y. V. Bokshits, N. P. Osipovich, E. A. Strel'tsov et al., *Colloids Surf. A* **2004**, 242, 79.
493. S. Takahashi, K. Hasebe, A. Aramata, *Electrochem. Commun.* **1999**, 1, 301.
494. F. Endres, S. Z. El Abedin, *Phys. Chem. Chem. Phys.* **2002**, 4, 1640.
495. L. A. Kibler, M. Kleinert, D. M. Kolb, *J. Electroanal. Chem.* **1999**, 467, 249.
496. Y. B. Mo, Y. Gofer, E. J. Hwang et al., *J. Electroanal. Chem.* **1996**, 409, 87.
497. T. Saito, K. Uosaki, *J. Electrochem. Soc.* **2003**, 150, A352.
498. T. Kawagoe, T. Kotaki, T. Shibasaki et al., *Surf. Sci.* **2000**, 468, 1.
499. P. Mrozek, Y.-E. Sung, M. Han et al., *Electrochim. Acta* **1995**, 40, 17.
500. E. D. Chabala, T. Rayment, *J. Electroanal. Chem.* **1996**, 401, 257.
501. A. R. Ramadan, E. D. Chabala, T. Rayment, *Phys. Chem. Chem. Phys.* **1999**, 1, 1591.

502. D. Lee, T. Rayment, *Phys. Chem. Chem. Phys.* **1999**, 1, 4389.
503. M. C. Gimenez, M. G. Del Popolo, E. P. M. Leiva, *Electrochim. Acta* **1999**, 45, 699.
504. Q. Y. Zhang, T. C. Ma, Z. Y. Pan et al., *Surf. Coat. Technol.* **2000**, 128, 175.
505. C. M. Whelan, M. R. Smyth, C. J. Barnes et al., *J. Electroanal. Chem.* **1999**, 474, 138.
506. T. Kondo, J. Morita, M. Okamura et al., *J. Electroanal. Chem.* **2002**, 532, 201.
507. M. J. Esplandin, M. A. Schneeweis, D. M. Kolb, *Phys. Chem. Chem. Phys.* **1999**, 1, 4847.
508. D. Oyamatsu, M. Nishizawa, S. Kuwabata et al., *Langmuir* **1998**, 14, 3298.
509. J. X. Wang, B. M. Ocko, R. R. Adzic, *Surf. Sci.* **2003**, 540, 230.
510. S. R. Brankovic, N. Dimitrov, K. Sieradzki, *Electrochem. Solid St.* **1999**, 2, 443.
511. V. Reyes-Cruz, C. Ponce-de-Leon, I. Gonzalez et al., *Hydrometallurgy* **2002**, 65, 187.
512. J. Inukai, S. Sugita, K. Itaya, *J. Electroanal. Chem.* **1996**, 403, 159.
513. S. Abaci, L. S. Zhang, C. Shannon, *J. Electroanal. Chem.* **2004**, 571, 169.
514. D. Omayatsu, S. Kuwabata, H. Yoneyama, *J. Electroanal. Chem.* **1999**, 473, 59.
515. L. F. Warren, M. A. Bennett, *Inorg. Chem.* **1976**, 15, 3126.
516. J. V. McArdle, G. E. Bossard, *J. Chem. Soc., Dalton Trans.* **1990**, 2219.
517. M. Bardaj, N. G. Connelly, M. C. Gimeno et al., *J. Chem. Soc., Dalton Trans.* **1994**, 1163.
518. J. D. Basil, H. H. Murray, J. P. Fackler Jr. et al., *J. Am. Chem. Soc.* **1985**, 107, 6908.
519. S. Lagerge, J. Zajac, S. Partyka et al., *Langmuir* **1997**, 13, 4683.
520. U. Koelle, A. Laguna, *Inorg. Chim. Acta* **1999**, 290, 44.
521. A. M. Bond, S. Kratsis, S. Mitchell et al., *Analyst* **1997**, 122, 1147.
522. P. Kula, Z. Navratilova, *Electroanalysis* **2001**, 13, 795.
523. R. Y. Bek, N. A. Rogozhnikov, L. I. Shuraeva, *Russ. J. Electrochem.* **1996**, 32, 1337.
524. R. Y. Bek, *Russ. J. Electrochem.* **2002**, 38, 1237.
525. R. Y. Bek, L. I. Shuraeva, *Russ. J. Electrochem.* **2003**, 39, 872.
526. R. Y. Bek, L. I. Shuraeva, *Russ. J. Electrochem.* **2003**, 39, 229.
527. R. Y. Bek, L. I. Shuraeva, *Russ. J. Electrochem.* **2004**, 40, 704.
528. G. Trejo, A. F. Gil, I. Gonzalez, *J. Appl. Electrochem.* **1996**, 26, 1287.
529. K. Marquez, R. Ortiz, J. W. Schulze et al., *Electrochim. Acta* **2003**, 48, 711.
530. K. B. Holt, G. Sabin, R. G. Compton et al., *Electroanalysis* **2002**, 14, 797.
531. C. J. Boxley, H. S. White, T. E. Lister et al., *J. Phys. Chem. B* **2003**, 107, 451.
532. A. Fanigliulo, C. Mele, B. Bozzini, *Trans. Inst. Met. Finish.* **2003**, 81, 75.
533. B. Bozzini, A. Fanigliulo, *J. Appl. Electrochem.* **2002**, 32, 1043.
534. A. Fanigliulo, B. Bozzini, *Trans. Inst. Met. Finish.* **2002**, 80, 132.
535. A. Fanigliulo, B. Bozzini, *J. Electroanal. Chem.* **2002**, 530, 53.
536. T. Osaka, A. Kadera, T. Misato et al., *J. Electrochem. Soc.* **1997**, 144, 3462.
537. T. A. Green, M. J. Liew, S. Roy, *J. Electrochem. Soc.* **2003**, 150, C104.
538. G. Oskam, P. C. Searson, *J. Electrochem. Soc.* **2000**, 147, 2199.
539. K. Marquez, G. Staikov, J. W. Schulze, *Trans. Inst. Met. Finish.* **2002**, 80, 73.
540. L. Magagnin, V. Bertani, P. L. Cavallotti et al., *Microelectron. Eng.* **2002**, 64, 479.
541. L. M. Depestel, K. Strubbe, *J. Electroanal. Chem.* **2004**, 572, 195.
542. Y. F. Cheng, D. J. Schiffrin, *J. Chem. Soc., Faraday Trans.* **1996**, 92, 3865.
543. B. J. Hwang, R. Santhanam, Y. L. Liu, *Electroanalysis* **2003**, 15, 1667.
544. S. Bharathi, J. Joseph, O. Lev et al., *Electrochem. Solid State Lett.* **1999**, 2, 284.
545. B. C. Sih, A. Teichert, M. O. Wolf, *Chem. Mater.* **2004**, 16, 2712.
546. Y. G. Li, W. Chrzanowski, A. Lasia, *J. Appl. Electrochem.* **1996**, 26, 843.
547. Y. G. Li, A. Lasia, *J. Appl. Electrochem.* **1996**, 26, 853.
548. W. Chrzanowski, Y. G. Li, A. Lasia, *J. Appl. Electrochem.* **1996**, 26, 385.
549. Y. G. Li, A. Lasia, *J. Appl. Electrochem.* **1997**, 27, 643.
550. Y. G. Li, A. Lasia, *J. Electrochem. Soc.* **1997**, 144, 1979.
551. X. W. Sun, Y. C. Guan, K. N. Han, *Metall. Mater. Trans. B – Process Metall. Mater. Process. Sci.* **1996**, 27, 355.
552. R. Y. Bek, N. A. Rogozhnikov, G. V. Kosolapov, *Russ. J. Chem.* **1997**, 33, 119.
553. Y. Bek, N. A. Rogozhnikov, G. V. Kosolapov et al., *Russ. J. Electrochem.* **1998**, 34, 918.

554. R. Y. Bek, N. A. Rogozhnikov, G. V. Kosolapov, *Russ. J. Electrochem.* **1998**, 34, 1162.
555. R. Y. Bek, N. A. Rogozhnikov, L. I. Shuraeva, *Russ. J. Electrochem.* **2000**, 36, 726.
556. R. Y. Bek, *Russ. J. Electrochem.* **2000**, 36, 721.
557. R. Y. Bek, *Russ. J. Electrochem.* **2001**, 37, 250.
558. R. Y. Bek, G. V. Kosolapov, L. I. Shuraeva et al., *Russ. J. Electrochem.* **2001**, 37, 244.
559. R. Y. Bek, *Russ. J. Electrochem.* **2001**, 37, 387.
560. R. Y. Bek, *Russ. J. Electrochem.* **2001**, 37, 723.
561. R. Y. Bek, *Russ. J. Electrochem.* **2002**, 38, 407.
562. R. Y. Bek, *Russ. J. Electrochem.* **2002**, 38, 398.
563. R. Y. Bek, L. I. Shuraeva, *Russ. J. Electrochem.* **2002**, 38, 526.
564. R. Y. Bek, *Russ. J. Electrochem.* **2003**, 39, 1036.
565. R. Y. Bek, *Russ. J. Electrochem.* **2004**, 40, 130.
566. R. Y. Bek, A. G. Zelinskii, S. N. Ovchinnikova et al., *Russ. J. Electrochem.* **2004**, 40, 123.
567. H. K. Lin, X. Chen, *Miner. Metall. Proc.* **2001**, 18, 147.
568. R. Y. Bek, G. V. Kosolapov, L. I. Shuraeva, *Russ. J. Electrochem.* **2001**, 37, 256.
569. S. C. Zhang, M. J. Nicol, *J. Appl. Electrochem.* **2005**, 35, 339.
570. S. C. Zhang, M. J. Nicol, *J. Appl. Electrochem.* **2003**, 33, 767.
571. I. Chandra, M. I. Jeffrey, *Hydrometallurgy* **2004**, 73, 305.
572. Y. C. Guan, K. N. Han, *J. Electrochem. Soc.* **1996**, 143, 1875.
573. L. Y. Chai, M. Okido, *Trans. Nonferr. Met. Soc. China* **1999**, 9, 145.
574. L. Y. Chai, M. Okido, *Trans. Nonferr. Met. Soc. China* **1999**, 9, 383.
575. R. Y. Beck, *Russ. J. Appl. Chem.* **1997**, 70, 400.
576. S. Ye, C. Ishibashi, K. Shimazu et al., *J. Electrochem. Soc.* **1998**, 145, 1614.
577. Z. L. Li, T. H. Wu, Z. J. Niu et al., *Electrochem. Commun.* **2004**, 6, 44.
578. M.-C. Daniel, D. Astruc, *Chem. Rev.* **2004**, 104, 293.
579. S. R. Johnson, S. D. Evans, S. W. Mahon et al., *Langmuir* **1997**, 13, 51.
580. M. J. Hostetler, A. C. Templeton, R. W. Murray, *Langmuir* **1999**, 15, 3782.
581. F. P. Zamborini, J. F. Hicks, R. W. Murray, *J. Am. Chem. Soc.* **2000**, 122, 4514.
582. D. I. Gittins, D. Bethell, R. J. Nichols et al., *J. Mater. Chem.* **2000**, 10, 79.
583. D. I. Gittins, D. Bethell, D. J. Schiffrin et al., *Nature* **2000**, 408, 67.
584. S. Chen, R. S. Ingram, M. J. Hostetler et al., *Science* **1998**, 280, 2098.
585. R. S. Ingram, M. J. Hostetler, R. W. Murray et al., *J. Am. Chem. Soc.* **1997**, 119, 9279.

24.5**Electrochemistry of Silver**

24.5.1	Properties of Ag Electrodes	915
24.5.1.1	Polycrystalline Ag Electrodes	915
24.5.1.1.1	Preparation	915
24.5.1.1.2	Surface and Double-layer Properties	915
24.5.1.2	Single-crystal Ag Electrodes	917
24.5.1.2.1	Preparation	917
24.5.1.2.2	Surface and Double-layer Properties	918
24.5.1.2.3	Surface Dynamics	919
24.5.1.2.4	Affinity of Water and Nonaqueous Solvent Molecules to Ag Surfaces	920
24.5.2	Adsorption of Inorganic Species on Ag Electrodes	921
24.5.2.1	Halide Ions	921
24.5.2.1.1	pc-Ag Electrodes	921
24.5.2.1.2	Single-crystal Ag Electrodes	922
24.5.2.2	Pseudohalide	924
24.5.2.3	Oxygen and its Compounds	925
24.5.2.4	Sulfur Compounds	925
24.5.2.5	Inorganic Carbon Compounds	926
24.5.2.6	Fullerenes	927
24.5.2.7	Other Inorganic Compounds	927
24.5.2.8	Metalocenes	928
24.5.3	Adsorption of Organic Species on Ag Electrodes	928
24.5.3.1	Hydrocarbons	928
24.5.3.2	Pyridine and Other Nitrogen Compounds	929
24.5.3.3	Carboxylic Acids	930
24.5.3.4	Alcohols	931
24.5.3.5	Sulfur Compounds	931
24.5.3.5.1	Thiourea (TU)	932
24.5.3.5.2	Alkanethiols and Self-assembled Monolayers	932
24.5.3.6	Biochemically Important Compounds	933
24.5.3.6.1	Adsorption on Modified Ag Electrodes	934
24.5.3.7	Other Organic Compounds	934

24.5.4	Electrode Processes with Participation of Silver Electrodes	935
24.5.4.1	Reactions Involving Oxidation of Ag Surface	935
24.5.4.1.1	Oxygen and its Compounds	935
24.5.4.1.2	Sulfur Compounds	937
24.5.4.1.3	Carbon Compounds	938
24.5.4.2	Electrode Reactions of Selected Organic Compounds, Adsorbed on Ag Electrodes	938
24.5.4.2.1	Biochemically Important Species	938
	Bare Ag electrodes.	938
	Modified Ag electrodes.	939
24.5.5	Underpotential Deposition Processes	940
24.5.5.1	Ag UPD on Ag	941
24.5.5.2	Ag UPD on Au and Pt	941
24.5.5.3	Pb	942
24.5.5.4	Tl	943
24.5.5.5	Ni	943
24.5.5.6	Chalcogenides	943
24.5.5.7	Other Elements and Compounds	944
24.5.6	Electrodeposition and Electrodisolution Processes of Ag	944
24.5.6.1	Electrodeposition Processes	944
24.5.6.2	Electrodisolution Processes	945
24.5.7	Silver Compounds at the Oxidation States Higher Than I	946
	References	948

The chapter on the electrochemistry of silver was published in 1978 as a part of the 8th volume of *Encyclopedia of Electrochemistry of the Elements*. At that time, most of the electrochemical properties of silver were limited to polycrystalline Ag (pc-Ag) surfaces, although the first studies with single-crystal electrodes were already described. Since the time that this chapter was published, one can indicate three main trends:

1. a continuous interest in pc-Ag electrodes;
2. a significant progress in the studies on single-crystal Ag electrodes; and
3. increasing applications of various surface spectroscopy techniques combined

with traditional electrochemical techniques in the studies of processes occurring both on polycrystalline and single-crystal Ag surfaces.

It is noteworthy that recent advances in the electrochemistry of silver are related more to the role of the surface of Ag electrodes, than to the investigations of Ag compounds in solutions.

The content of this chapter is essentially limited to physicochemical literature on the electrochemistry of silver published during the last decade. Since a large number of papers related to the chemistry of silver was published, it was not possible to include all of them in this review. Moreover, many of these publications seem to

be of interest to physicists rather than to chemists, and thus, it was not thought necessary to include them in the *Encyclopedia of Electrochemistry*. This review is, therefore, a selection of papers exemplifying representative trends in the recent studies of the properties of the silver electrode surfaces and in the electrochemical characteristics of the selected processes occurring at such electrodes. It also includes some analytical papers, but the readers particularly interested in analytical applications of various types of silver electrodes in voltammetric methods (including polycrystalline and single-crystal ones) are referred to, for example, a review by Gorokhovskii [1], covering the time period 1960–2000, and references cited therein.

24.5.1

Properties of Ag Electrodes

24.5.1.1 Polycrystalline Ag Electrodes

24.5.1.1.1 Preparation As compared to single-crystal Ag surfaces, the preparation of pc-Ag electrode may seem to be a relatively simple task. However, a pc-Ag surface, which ensures reproducibility and stability, also requires a special procedure. Ardizzone et al. [2] have described a method for the preparation of highly controlled pc-Ag electrode surface (characterized by electrochemical techniques and scanning electron microscopy (SEM)). Such electrodes, oriented toward electrocatalytic properties, were successfully tested in halide adsorption experiments, using parallelly, single-crystal and conventional pc-Ag rods as references.

24.5.1.1.2 Surface and Double-layer Properties

An extensive, recent review on electrochemical properties of the (polycrystalline) pc-Ag/solution interface, together

with earlier works, is included in the paper by Trasatti and Lust [3]. Electrical double layer at the pc-Ag/aqueous solution interface was characterized with the diffuse layer minimum located on the C_d-E curve at $E = -0.94$ to -0.96 V versus saturated calomel electrode (SCE). The roughness factor for pc-Ag was found as $f_{PZ} \geq 1.2$, applying the Parsons-Zobel method [4]. The potential of zero charge (PZC) found using the capacitance method was equal to -0.944 ± 0.015 V (SCE). Other experimental methods yielded this value ranging from -0.927 to -0.890 V for NaF, HClO₄, and Na₂SO₄ solutions [3]. The effect of anions varied in the order: $F^- \geq SO_4^{2-} \geq ClO_4^-$. Ahern et al. [5] have observed four low-level redox responses within the double-layer region of pc-Ag in basic medium and hence suggested four different types of active surface state (or site) transitions. The correlation between the transition potentials and the onset/termination potentials of different electrocatalytic processes were found.

It is noteworthy that for investigating pc-Ag electrodes, various surface spectroscopic methods have been utilized recently. A majority of the relevant papers are focused on the Raman scattering phenomena, mainly on the surface-enhanced Raman scattering (SERS) and related methods. One should emphasize that silver was one of the few noble metals for which the SERS response was observed, provided that the surface was previously activated by electrochemical or other means [6] in order to roughen it. Kruszewski [7] has investigated light absorption at the SERS-active Ag electrode. The intensity of light reflected from the SERS-active electrode was measured as a function of the potential and time. It was concluded that the observed irreversible increase in the intensity of the reflected light was

caused by an irreversible decrease in light absorption, related to the irreversible decay of the number of “active sites”. Recently, Kruszewski [8] has analyzed the dependence of the SERS signal on the Ag surface roughness, which was changed by varying the parameters of oxidation–reduction procedure. The measurements of angular distribution of elastically scattered light, as well as scanning and transmission electron microscopy, were employed for the determination of roughness. The experimentally observed relationship between the roughness extent and the SERS signal was compared with the predictions of the classical electromagnetic enhancement model.

Another important technique is the second-harmonic generation (SHG) method [6]. Interestingly, ever since SHG

techniques in combination with SERS were introduced in the early 1980s to study electrode surfaces, silver surfaces have become the most investigated objects. Surface roughening supports activation of surface plasmons that cause a substantial increase of the electromagnetic field at the surface. Plasmon is a highly delocalized excitation state formed collectively via electrostatic interaction of weakly bound electrons. Since interfacial SHG depends on the fourth power of the surface electromagnetic field generated by the incident laser beam, the field enhancement at *rough* silver surfaces should also lead to the significant enhancement of SHG at these surfaces, as compared to SHG at the smooth surfaces. Since it has been found that the electrode potential significantly affects

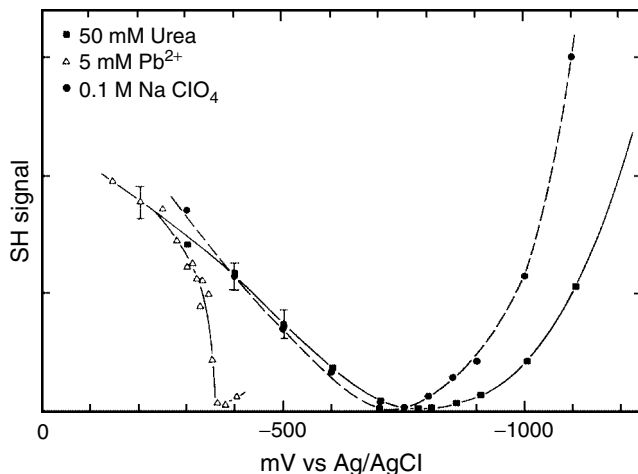


Fig. 1 Potential-dependent SHG response of a thin silver film (45 nm) in contact with a solution of 0.1 M NaClO₄ (solid circles), 0.1 M NaClO₄ + 50 mM urea (solid squares), and 0.1 M sodium acetate + 5 mM lead acetate (open triangles). Most of the crystallites of the pc-Ag film were oriented with the (111) face parallel to the surface. The minimum of the curve occurs at around -0.75 V, which is close to the PZC for Ag(111) surface. Adsorption of urea causes a little shift in PZC and a significant decrease of the SHG intensity negative of PZC point, whereas the deposition of a monolayer of Pb causes a dramatic increase in the SHG intensity [6, 9].

the SHG response, this method appeared to be interesting also for electrochemical purposes [6]. Thus, potential-dependent adsorption of neutral molecules and ions, as well as deposition processes at the Ag surface, affect the SHG signal (see Fig. 1).

One of the early examples of the application of the SHG technique in electrochemistry, proving its high sensitivity, is the investigation of the sulfate monolayers adsorbed on pc-Ag electrodes [10]. Also, one should mention the paper by Campbell and Corn [11], who have evidenced that the SHG method is also applicable to studies in nonaqueous solutions, namely, to the investigations of hydrogen evolution in acetonitrile (ACN).

Apart from the methods based on Raman spectra and SHG, the Fourier transform coupled with infrared (IR) techniques (see e.g. Ref. 12), scanning tunneling microscopy (STM), and atomic force microscopy (AFM) have also been used.

Another relatively new technique is the infrared visible sum frequency generation (SFG) spectroscopy and the difference frequency generation (DFG) spectroscopy [13], both of which represent vibrational spectroscopic techniques sensitive only to the material located at interfaces.

Apart from the above techniques, the electromodulated reflectance spectroscopy combined with cyclic voltammetry has been utilized by Gaigalas et al. [14] in the investigations of electron transfer between the {2Fe–2S} protein putidaredoxin and either bare or bekanamycin-modified Ag electrode. Of the two models considered, the free diffusion model, as compared to the adsorbed layer model, exhibited better concordance with the experimental data. After modification of the Ag electrode with bekanamycin, it exhibited only a small increase in the observed redox reaction

rates. The measured rate constants were compared to the values predicted from the Marcus theory of electron transfer.

In addition to the application of roughened Ag electrodes in SERS measurements, one should add that Geddes et al. [15] have described the use of such Ag electrodes in metal-enhanced fluorescence studies also. The constant current flowing between two silver electrodes in pure water facilitated the growth of fractal-like structures on the cathode. The electrode was coated with a monolayer of human serum albumin protein labeled with Indocyanine Green. It was observed that the fluorescence intensity on the roughened electrode increased approximately the 50-fold, compared to the unroughened electrode.

Otsuka and Iwasaki [16] have employed AFM method to observe the self-affine fractal structure of the electrochemically roughened Ag electrode surfaces [17]. Later, they have described the dynamic scaling in recrystallization of this electrode surface in water.

24.5.1.2 Single-crystal Ag Electrodes

24.5.1.2.1 Preparation A significant number of papers, which have appeared over the last decade, are focused on the studies of the Ag(*hkl*) surface in contact with various species. Our concise survey covers only those that are most relevant to electrochemists. In the electrochemical practice, the most intensively studied Ag surfaces include: Ag(111), Ag(100), Ag(110), and Ag(001), whereas the number of papers devoted to, for example, Ag(210) and Ag(410) is substantially smaller. Electrode surfaces can be prepared in various ways: electrolytic growth in a Teflon® capillary, electrolytic polishing of Ag single crystals, or chemical ($\text{CrO}_3 + \text{H}_2\text{O}$) polishing of Ag crystal

faces [3]. According to Hamelin et al. [18], during the oxidation–reduction potential cycle, surface oxide reduction and hydrogen evolution take place, and the surface roughness increases. It is also of practical importance to mention that thermal annealing, which is normally used for the preparation of an Au surface, in principle, can also be applied for single-crystal Ag electrodes; however, higher affinity of Ag to oxygen makes the experimental conditions more critical than they are for Au [3]. These difficulties in reproducible preparation of well-defined single-crystal Ag surfaces seem to limit the number of works, in which such electrodes were used.

24.5.1.2.2 Surface and Double-layer Properties Valette [19] has analyzed earlier experimental data on the inner-layer capacity at PZC for Ag(111), Ag(100), and Ag(110) surfaces in order to estimate the surface area and capacitance contributions of superficial defects for real electrodes, as compared to ideal faces. Considering the application of surface spectroscopy techniques to single-crystal Ag electrodes, one should note that anisotropy of the SHG response for metal electrode allows one to analyze and correlate its pattern with interfacial symmetries and its variations by changing nonlinear susceptibility and the surface structure. Early studies on Ag(111) single-crystal electrodes have

been performed by Shannon et al. (cf. e.g. Ref. 20). In particular, one can monitor in situ, the reconstruction of the electrode surface (cf. e.g. Ref. 21). Also, recently, the interference second-harmonic generation anisotropy (ISHGA) technique has been applied to crystalline Ag and Au electrodes [6]. This advanced technique is expected to be an even better source of information on the geometric and electronic structure of the interface and its changes upon potential scanning and adsorption.

The differences between various Ag surfaces can be distinguished by comparing their surface morphology (generally, the surface of (110) crystal is more folded than that of (111)) and other properties, such as the surface density of atoms, the PZC, and double-layer capacitance. The double-layer properties of single-crystal Ag electrodes have been studied very intensively [3, 22–27]. Selected characteristics of various Ag surfaces are compared in Table 1, which shows that the higher the surface density of atoms, the more positive PZC becomes. Furthermore, Fig. 2 exemplifies differential capacity data of those Ag surfaces.

Zheng et al. [29] have compared surface properties of the assembled silver nanoparticle electrode/indium-tin oxide (A_{Ag}NP/ITO) and roughened silver electrode, using electrochemical

Tab. 1 Surface density of atoms (σ_{at}) measured at the potentials of zero charge (PZC), and double-layer capacitances of the *inner* part of the double layer (C_i) for different crystal planes of Ag (lattice constant $d = 0.2889$ nm)

Ag plane	σ_{at} [at. nm ⁻²]	PZC [V] (versus SHE, 0.01 M KPF ₆) [3]	C_i [μF cm ⁻²] (KPF ₆ solutions) [19]	C_i [μF cm ⁻²] (LiClO ₄ solutions) [28]
(111)	13.83	-0.445 ± 0.005	77 ± 2	40
(100)	11.98	-0.615 ± 0.005	92 ± 2	42
(110)	8.47	-0.725 ± 0.005	112 ± 2	70

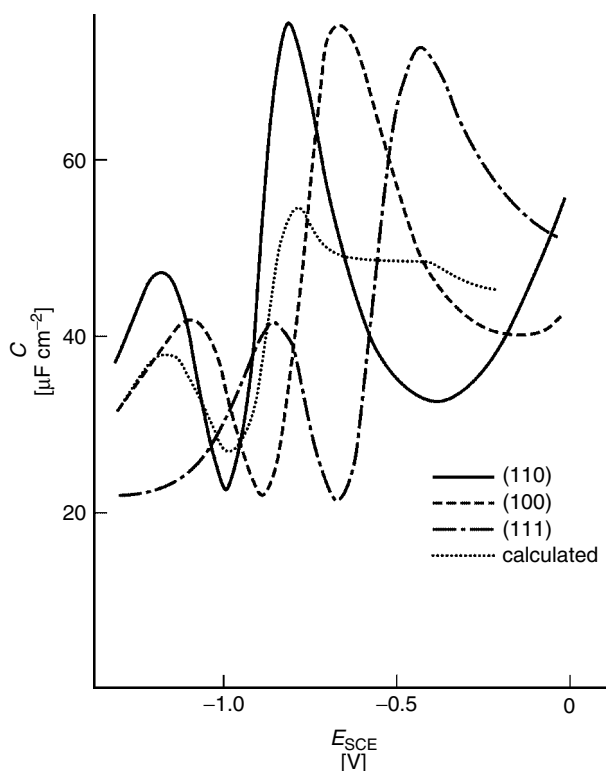


Fig. 2 Differential double-layer capacitances of Ag(111), Ag(100), and Ag(110) in 10 mM NaF determined applying an ac technique; $f = \omega/2\pi = 20$ Hz, scan rate $\nu = 5$ mV s⁻¹. The calculated curve corresponds to the model polycrystalline Ag electrode [24].

techniques and SERS, and methyl viologen (MV) and *p*-aminothiophenol (PATP) as the probing molecules. MV molecules were strongly adsorbed on the roughened Ag electrode, but not on AAgNP/ITO. Also, since no SERS spectrum was observed for AAgNP/ITO, probably no active sites were present on the surface of the isolated Ag nanoparticles to participate in the interactions between the ring plane of MV and Ag nanoparticle.

24.5.1.2.3 Surface Dynamics Quass et al. [30] have studied diffusive transport of atoms along the step edges on Ag(111).

Baier, Giesen et al. have described the dynamics of step and island on Ag(111) and Cu(100) [31], as well as on Au(100) [32] electrodes in the electrolyte. Baier and Giesen [33] have determined the activation energies of mass transport processes on Ag(111) electrodes in the aqueous electrolyte. Haftel and Einstein [34] have studied the influence of the electrochemical potential on energy landscapes close to step- and island edges: Ag(111) and Ag(100). A model of the metal/solution interface involving hydrophilicity of Ag(111) and based on the capacitance analysis, has been published by Emets et al. [35] Electron

confinement to the nanoscale Ag(111) islands on Ag(111) has been quantitatively studied by Li et al. [36]. Winkes et al. [37] have performed surface resistance measurements at the metal/electrolyte interface of Ag(110) and Ag(111) thin-film electrodes. An Ag(111)/water interface deserves special attention. The results of X-ray scattering studies [38] were consistent with the simulation results: it has been found that water is reorienting next to the charged surface and undergoes restructuring in the presence of the strong field [39]. Sun et al. [40] have described the structures of adatom clusters on Ag(111) surfaces, applying genetic algorithm. STM studies of bare Ag(100) electrode within the potential range 0.4 to -0.1 V did not reveal any potential-induced surface reconstruction (contrary to such reconstruction observed at Au(100) electrodes) [41]. Winkes et al. [37] have measured the surface resistance at the metal/electrolyte interface of Ag(100) and Ag(111) thin-film electrodes. Koga [42] has observed the diffusive motion of 2×2 adlayer formed on the Ag(100) nanoparticle facet induced by nitric acid adsorption. The adsorbates exhibited a profile image that was double-periodical to that of an Ag(100) surface along the [010] direction, and their collective diffusion was observed in the real time. A Monte Carlo simulation of submonolayer homoepitaxial growth on Ag(110) and Cu(110) has been performed by Mottet et al. [43]. Surface self-diffusion at intermediate temperatures for Ag(110) has been studied by Pedemonte et al. [44]. Substrate reconstruction and electronic surface states of Ag(001) have been studied by Savio et al. [45]. For the analysis of Ag(001) surface, Simpson and Furtak [46] have employed optical SHG spectroscopy with s-polarized excitation. The surface plasmon dispersion

on sputtered and nanostructured Ag(001) has been studied by Savio et al. [47].

24.5.1.2.4 Affinity of Water and Nonaqueous Solvent Molecules to Ag Surfaces

Hydrophilic properties of single-crystal Ag electrodes have been a subject of controversy [48]. Trasatti [49] has suggested the following series of the decreasing hydrophilicity: Ag(110) > Ag(100) > Ag(111), while Valette [50] has proposed the opposite order. Further studies, in which hydrophobicity of Ag was estimated from the adsorption energy of aliphatic alcohols [51–53], led to the following conclusion: since the adsorption energy is strongly dependent on the lattice plane of the electrode as well as on the size of the anion of the supporting electrolyte (through the salting-out effect of the adsorbate), it is not possible to indicate unambiguously the hydrophilicity series of lattice planes from electrochemical experiments [48]. Anyhow, the position of water molecules is the closest to the folded Ag(110) surface and the farthest – to the smooth Ag(111) surface [48]. As regards adsorption of anions, one should mention that the surface concentration of sulfate ions changes on particular Ag planes in the following order: Ag(111) > Ag(110) > Ag(100) (not concordant with the decreasing surface density of atoms). Such a sequence proves that for adsorption of ions, not only the electrode surface structure but also the structure of the adsorbed ions are important [54, 55]. A more detailed review of the problems of anions and water adsorption on different Ag surfaces is given in Ref. 3. Recently, Doubova et al. [56] have used ACN as either the adsorbate or the solvent to probe the crystal face specificity of Ag–water interaction at the electrode/solution interface. From the capacitance and voltammetric plots, it has been concluded that the

adsorption strength of ACN on Ag from the aqueous solution is weak and decreases in the following order: (111) > (100) > (110). It has also been suggested that ACN adsorption occurs in two alternative modes: (1) directly on the metal surface and (2) at the water layer adsorbed on the metal surface, which cause apparent inconsistencies of the adsorption parameters. Furthermore, the presence of variable amounts of water in ACN had an inhibiting effect on Ag surface oxidation. The diminution of the water content in ACN led to free anodic dissolution of the metal surface. Doubova and Trasatti [57] have investigated adsorption of isovaleronitrile versus ACN in 0.15 M NaClO₄ on Ag single-crystal face electrodes performing capacity measurements. The obtained data have shown that adsorption increases in the following sequence of crystal faces: (110) < (100) < (111) < Hg. In contrast with ACN adsorption, the mode of adsorption of isovaleronitrile is attributable to hydrophilic–hydrophobic interactions, resulting in a squeezing-out mechanism. Adsorption of neutral compounds depends on the crystallographic orientation of the metal surface, mainly because of the face specificity of metal–solvent interactions, the latter being stronger for more open surfaces (i.e. those of lower atomic density [22]). In the specific case of Ag single crystals, the following observations have been made. For linear aliphatic alcohols, the Gibbs energy of adsorption increases in the sequence: (110) < (100) < (111) [53, 58, 59], as expected from the concepts expressed above. For ACN [56, 60], in contrast, the adsorption order is: (111) < (100) < (110), although no interactions between the triple bond of the N group and the metal surface are possible.

Gu et al. [61] have studied the SERS response of Ag electrodes in ACN.

24.5.2

Adsorption of Inorganic Species on Ag Electrodes

24.5.2.1 Halide Ions

24.5.2.1.1 pc-Ag Electrodes Hecht and Strehblow [62] have utilized X-ray photoelectron spectroscopy (XPS) and ion scattering spectroscopy (ISS) in the examination of the electric double layer on Ag in NaCl solutions. It has been found that specific adsorption of Cl[−] was accompanied by coadsorption of cations and water. A layered structure of the specifically adsorbed chloride anions and the coadsorbed cations was confirmed.

Adsorption of bromide ions on pc-Ag surface has been investigated in several alcohols: C_nH_{2n+1}OH (*n* = 1–5), including butanol isomers (see e.g. Refs 63–66), with supporting electrolytes LiClO₄ and LiBr (electrochemical methods were combined with surface spectroscopy techniques). The potential-dependent orientation of the alcohol molecules was driven by the interactions of nonbonding O electrons and the alkyl chain with the electrode, as well as by hydrogen bonding of OH groups with specifically adsorbed Br[−] [3]. For a more detailed comprehensive review of the experimental procedure, the reader is referred to the original papers, cited above and summarized in Ref. 3. Later, Pemberton and Shen [67] utilized electrochemical and SERS techniques to study adsorption of bromide ions on Ag in a series of aliphatic alcohols (from methanol to pentanol, containing LiBr). An excellent correlation was observed between the SERS intensity and Br[−] surface coverage determined from differential capacitance

Tab. 2 Maximum Br[−] coverage and potentials of zero charge (PZC) values of Ag in alcohols with 0.4 M LiBr [67]

Solvent	$\Gamma \times 10^{11}$ [moles cm ^{−2}]	PZC, V versus Ag/AgCl
Methanol	110	−0.7
Ethanol	110	−0.6
Propanol	90	−1.0
Butanol	135	−0.9
Pentanol	140	−0.6

data. The double-layer data are presented in Table 2.

Shi et al. [68] have studied iodine adsorption on Ag using atomic-resolution electrochemical scanning tunneling microscopy (ECSTM) method. Distinctly different iodine adlayer structures and surface diffusion behavior were observed on mechanically polished pc-Ag in comparison with those obtained on single-crystal electrodes.

24.5.2.1.2 Single-crystal Ag Electrodes

Recently, Nazmutdinov and Zinkicheva [69] have studied adsorption of the fluoride ion from the gas phase on various single-crystal Ag surfaces, applying a density-functional method. Adsorption energy was found to increase in the series: Ag(100) < Ag(111) < Ag(311) < Ag(110). Sneddon and Gewirth [70] have published the in situ characterization of halide adsorption and Ag-halide growth on Ag(111) electrodes using AFM. The chemical bonding state of *chlorine* on Ag(100) has been studied by Chang and Lung, who applied angle-resolved secondary ion mass spectrometry [71]. It has been shown that chlorine dissociates at the surface to yield a bonding state of atomic form at room temperature and Cl adatom is chemisorbed highly above the topmost substrate layer of Ag

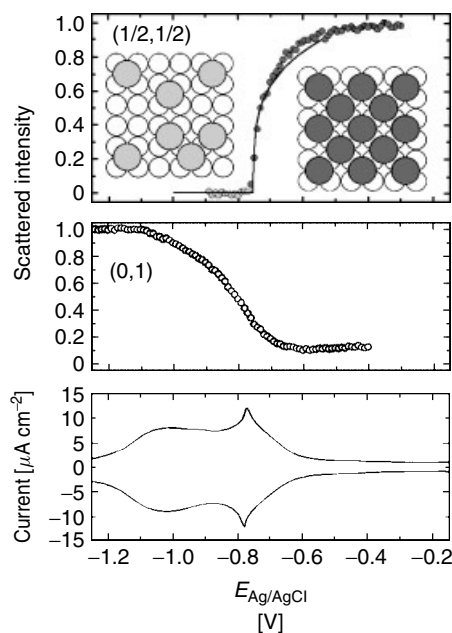
atoms. The Ag–Cl bond was oriented along the <100> azimuth with the adsorbate occupying a C-4 symmetry site. Andryushechkin et al. [72] have studied the epitaxial growth of AgCl layers on the Ag(100) surface. A potential-induced two-dimensional Ising order-disorder transition in *bromide* adsorbed on Ag(001) has been described by Ocko et al. [73]. In situ X-ray scattering studies have revealed that with the increasing potential, bromide undergoes a second-order phase transition from the lattice gas to the ordered c(2 × 2) structure. From a comparison of X-ray and electrochemical measurements, a significant lateral disorder at low coverage, decreasing with an increasing coverage, has been found. Endo et al. [74] have studied the structures of bromine adsorbed on the Ag(111) electrode at different applied potentials. They have employed for this purpose, in situ X-ray absorption fine-structure spectroscopy (XAFS). In the cyclic voltammogram, a characteristic peak was formed at 0.05 V (versus Ag/AgCl). In the region just before this peak, the Ag–Br bond length was estimated as 2.72 ± 0.05 Å, while after the peak, the spectra revealed the presence of two different Br–Ag bonds of 2.74 ± 0.05 and 2.80 ± 0.05 Å in lengths. These results were attributed to a drastic surface reconstruction taking place at the characteristic cyclic voltammetric peak potential without any changes in the surface Br density. Beltramo et al. [75] have investigated, applying SHG and impedance spectroscopy, the chloride and bromide layers adsorbed on single-crystal Ag electrodes. The SHG response at the incident wavelength of 1064 nm was measured and structural transitions in the adsorbed layer were detected. Beltramo and Santos [76] have studied further, specific adsorption of chloride and

bromide on Ag(111) surface, employing impedance spectroscopy. A physical model has been proposed to obtain different kinetic and mass transport parameters at low concentrations of halide ions. Moreover, the surface charge densities were calculated. In situ SHG studies of covered Ag(111) electrodes have also been published by Santos et al. [77]. XPS and STM studies of pseudo-AgX monolayers organized at Ag(111) and Au/Ag(111) have been published by Kawasaki et al. [78]. Recently, Jović and Jović [79] have combined differential capacitance measurements with the simulations of frequency curves for different equivalent circuits to study (111) in 0.01 M NaCl. The dependence of the capacitance on the frequency was investigated. It was suggested that in the equivalent circuit, the double-layer capacitance should be replaced with a constant phase element. The in situ X-ray adsorption studies of bromine on the Ag(100) electrode have been described by Endo et al. [80]. It was observed that the electron is transferred from the bromide anion to the silver substrate, and that the bond is partly covalent. The Br–Ag distance was determined to be $2.82 \pm 0.05 \text{ \AA}$, which is shorter than that of the bulk AgBr. The adsorption site appeared to be a fourfold hollow site. The authors have suggested that the bromide ionicity is reduced in the adsorbate phase at the electrode. Ab initio calculations for bromine adlayers on Ag(100) and Au(100) surfaces have

been performed by Wang and Rikvold [81]. Wandlowski et al. [82] have studied adsorption of bromide at the Ag(100) electrode surface. Under electrochemical conditions (similarly as in vacuum) an ordered $c(2 \times 2)$ structure was observed above a critical coverage, with halide ions located in the fourfold hollow sites of the underlying silver lattice. The difference found between Ag(100) and Au(100) is that for silver the packing arrangement is square, compared with the quasi-hexagonal structure detected for gold (Fig. 3) [83].

Hanewinkel et al. [84] have studied the change in the surface resistance of an Ag(100) electrode caused by the adsorbed bromide. It was suggested that bromide ions adsorbed in the double layer of the hollow sites do not exchange electron with the metal. Shimooka et al. [85] have studied the adlayer structures of Cl and Br, and a growth of bulk AgBr layers on Ag(100) electrodes using in situ

Fig. 3 The results of studies of electrosorption of bromide on the Ag(100) surface. The scattered intensities, after background subtraction, are shown at $(1/2, 1/2)$ and $(0, 1)$ versus the applied potential. The corresponding cyclic voltammogram (10 mV s^{-1}) is shown at the bottom [83].



STM and ex situ low-energy electron diffraction (LEED) in ultrahigh vacuum (UHV). It has been shown that the adsorbed Cl and Br monolayers possess a $c(2 \times 2)$ structure on Ag(100) in acidic solutions. At potentials corresponding to the formation of bulk AgBr, AgBr(100) layers grew epitaxially on Ag(100). On the Ag(100) surface, both Ag and Br ions in the topmost layer of the bulk AgBr were observed. LEED pattern revealed a $c(2 \times 2)$ crystallographic arrangement for the bulk AgBr(100) formed on Ag(100). Electrochemical studies and Monte Carlo simulations of electrosorption of Cl and Br on Ag(100) have been described by Rikvold, Abou Hamad et al. [86, 87], as well as by Mitchell et al. [88, 89].

Yamada et al. [90] have used in situ STM and ex situ LEED to monitor continuous variation of iodine adlattices on Ag(111) electrodes. Interestingly, contrary to the Ag(100) surface brought in contact with I^- ions, Ag(111), in the presence of I^- ions, exhibited, in cyclic voltammograms, small reversible peaks at potentials slightly negative to the bulk AgI formation. This phenomenon, in view of additional LEED and STM studies, was ascribed to the rotational phase transitions in the Ag(111)- I^- adlayer. The iodine atom adlayers on Ag(110) were studied, applying the energy band theory by Wang et al. [91]. A density-functional theory approach has been applied by Tang et al. [92] to investigate chemisorption of iodine. Ab initio pseudopotential density-functional study has been performed by Wang et al. [93] to analyze interactions of halogen atom with Ag(110). Teshima et al. [94], using in situ STM technique, have studied the effect of the adsorbed iodine on the deposition and dissolution reactions of Ag(100). It is noteworthy, in these studies, that clean Ag(100) surface was exposed

to the KI solution under potential control, since under open circuit conditions (OCP) the formation of bulk AgI and surface roughening were rather expected. Cyclic voltammetric studies have shown that Ag dissolution/deposition occurs reversibly at the same potential, regardless of the presence or absence of iodine at the Ag(100) surface. However, H_2 evolution process was shifted by ca -0.15 V when bare Ag(100) surface was replaced with the I-Ag(100) one (this is an example of the adsorbate-induced overpotential). One should add that the I-Ag(100) adlayer structure was found to be potential independent and emphasize the exceptional stability of I on Ag(100) [41]. In turn, it has appeared that the etching of Ag on I-Ag(100) is anisotropic: the etching rate along the [010] direction is faster than along the [001] direction. A model for the explanation of this phenomenon has been proposed [41].

24.5.2.2 Pseudohalide

Rogozhnikov [95] has analyzed the impedance response of an Ag electrode in cyanide solutions. The impedance spectra have shown time evolution of the surface blocking. Time evolution of the active Ag electrode area after immersion in CN^- containing solutions has been analyzed by Baltrunas et al. [96]. A time of 20–60 s was required for settling down the blocking (dependent also on CN^- concentration).

The SFG spectra of CN^- at Ag electrode at various potentials varying from -1.2 V (SCE) to the upper limit below Ag dissolution have been recorded by Tadjeddine and Le Rille [13]. Contrary to the IR spectra, in which four bands for this system were observed, SFG spectra exhibited a single band, providing direct spectroscopic information on the adsorbed species. According to the same authors, the

SFG method is also a powerful tool for a direct determination of the PZC. Tadjeddine et al. [97] have employed this method to determine the PZC of Ag(poly). The observed value was -0.95 V and -1.05 V (SCE) in the absence and in the presence of 25 mM CN^- , respectively, in the solution containing 100 mM NaClO_4 .

Vibrational properties of OCN^- adsorbed on a silver electrode from neutral solutions have been studied by Bowmaker et al. [98], applying in situ synchrotron far-infrared spectroscopy and visible-infrared SFG spectroscopy. As an example, the results of these studies are summarized below. In SFG spectra, two bands were formed; they were assigned to the antisymmetric stretching mode of OCN^- ions bound to the Ag surface: the first one in the region $2100\text{--}2130\text{ cm}^{-1}$ (for $E = -0.6$ to 0 V versus SCE, cyanate N bound to a bridging surface site), and the second in the region $2200\text{--}2240\text{ cm}^{-1}$ (for $E = 0\text{--}4$ V, cyanate in a terminal N-bonding mode). In the far-IR spectrum, the following were distinguished: (1) a broadband at about 360 cm^{-1} , at $E > 0$ V, which was assigned to the $\nu(\text{AgN})$ mode of terminally bound cyanate, in accordance with the assignment for the VIS-IR SFG band observed at these potentials, and (2) a sharper band at 90 cm^{-1} that might have arisen from a bending (or restricted rotation) of cyanate on the silver surface.

An *ab initio* study of the interaction of SCN^- with a silver electrode allowed Tielens et al. [99] to predict vibrational frequencies.

24.5.2.3 Oxygen and its Compounds

Lutzenkirchen-Hecht and Strehblow have investigated the electrochemical double layer on Ag electrodes in alkaline media [100] using *ex situ* XPS and ultraviolet photoelectron spectroscopy (UPS). An

evidence for specific adsorption of OH^- ions has been found. Noteworthy is the fact that adsorption of oxygen compounds was often coupled with the surface oxidation of Ag. The relevant papers are presented later in a separate chapter.

24.5.2.4 Sulfur Compounds

Innocenti et al. have studied the kinetics [101] of two-dimensional phase transitions of sulfide and halide ions, as well as electrosorption valency [102] of these ions adsorbed on Ag(111). The electrode potential was stepped up from the value negative enough to exclude anionic adsorption to the potential range providing stability of either the first or the second, more compressed, ordered overlayer of the anions. The kinetic behavior was interpreted in terms of a model that accounts for diffusion-controlled random adsorption of the anions, followed by the progressive polynucleation and growth. For the conditions under which a stable second overlayer is formed, the kinetic behavior was explained in terms of the transition from total desorption to the formation of the second overlayer occurring via the intermediate formation of the first monolayer [101]. Partial charge-transfer coefficients for the considered anions decreased in the order sulfide \cong iodide $>$ bromide $>$ chloride, that is, in the order of the increasing Pauling's electronegativity. Reaction of sulfur dioxide with oxygen adsorbed on Ag(110) has been studied by Alemozafar et al. [103], applying LEED, temperature programmed reaction spectroscopy (TPRS) and STM.

Theoretical calculations for the simplified systems have shown that on the Ag(110) surface, sulfate ions adsorb with the binding energy of 782 kJ mol^{-1} , whereas for carbonate ions, this energy is equal to 949 kJ mol^{-1} [104]. These

energies are higher than for Ag(111), since on the more open Ag(110) surface, the bond order between the surface metal atoms and other metal atoms is lower than in the case of closer surfaces; therefore, less coordinated surface atoms bind more strongly to the adsorbates [104]. Sobkowski et al. [105] have investigated adsorption of sulfate anions on various Ag electrodes. An effect of the surface structure on adsorption of sulfate ions on pc-Ag (and single-crystal Ag surfaces: (111), (110), and (100)) has been published by Smolinski et al. [55]. Radiometric and electrochemical methods were used in this study. On all the four studied surfaces, adsorption was reversible with respect to the potential and bulk concentration of sulfate. The pc-Ag surface exhibited intermediate adsorption properties, compared to the single-crystal surfaces, for which sulfate adsorption decreased in the sequence: $\text{Ag}(111) \geq \text{Ag}(110) > \text{Ag}(100)$ (with tetrahedral structure of the anion matching best the trigonal distribution pattern of the surface Ag atoms on (111) and (110) planes). Thermodynamic parameters of adsorption were fitted to the Frumkin isotherm. Also, Sobkowski et al. [106] have determined radiometrically, the adsorption isotherms, as well as the surface concentration/potential dependences, for various single-crystal Ag electrodes. The surface concentration sequence was found to change as follows: $\text{Ag}(111) \cong \text{Ag}(110) > \text{Ag}(100)$. Thermodynamic parameters of adsorption were calculated by fitting the experimental data to the virial, Frumkin's, and Henry's adsorption models. The sequence of the sulfate adsorption from 0.1 M NaClO_4 on three basal silver planes was quite different from that observed in acidic supporting electrolyte and agreed with the sequence of the zero-charge potentials for the investigated silver surfaces. Recently,

Schweizer and Kolb [107] have studied sulfate adsorption on Ag(111) and Ag(100) in 0.1 M H_2SO_4 , applying cyclic voltammetry and in situ STM. A new *surface preparation* method involving the inductive heating has been employed to eliminate oxygen during the annealing procedure. This method led to high quality Ag(111) and Ag(100) surfaces. An ordered adlayer of sulfate and bisulfate were found on the Ag(100) and (111) faces. An unusual $c(3 \times 3\sqrt{3})$ adlayer structure was found for Ag(111), while for Ag(100), an incommensurate (1.3×3) structure was observed. No ordered adlayer was found on Ag(110). These results constitute the first observation of ordered sulfate adlayers on single-crystal Ag electrodes. Marinkovic et al. [108] have performed the IR studies of sulfate adsorption on Ag(111) surface. Theoretical calculations have shown that at Ag(111) surface, sulfate ions have a binding energy of $159 \text{ kcal mol}^{-1}$, carbonate ions $183 \text{ kcal mol}^{-1}$, and tricoordinated bisulfate ions 58 kcal mol^{-1} (calculated at the hollow sites of Ag(111)) [104].

Recently, S and O adsorption on pure and Ge-doped Ag(111) has been studied by Blomqvist et al. [109].

24.5.2.5 Inorganic Carbon Compounds

Quantitative determination of the local adsorption structure of carbonate on Ag(110) has been done by Kittel et al. [110]. They have found that the carbonate species is essentially planar and adsorbs almost parallel to the surface at the off-atop site with respect to the outermost layer Ag atom. The C–Ag layer spacing was $0.264 \pm 0.009 \text{ nm}$, with a well-defined azimuthal orientation. This geometry is understood best in terms of the added-row model proposed by Guo and Madix. This model assumes that additional Ag atoms lie adjacent to the carbonate, such that the

bonding involves at least one of the oxygen atoms. The distance between this oxygen atom and its nearest neighbor Ag adatom is 0.19 ± 0.04 nm. The C–O distances are in the range 1.26–1.30 Å.

24.5.2.6 Fullerenes

Morphology of C_{60} thin films grown on Ag(001) has been studied by Giudice et al. [111], applying UHV-STM. C_{60} molecules were arranged in a quasi-hexagonal $c(6 \times 4)$ structure, having the long axis positioned along the (110) direction of the Ag surface. Due to the presence of two equivalent directions, the C_{60} film presented different domains, separated by dislocation lines. The same research group [112] has continued the STM studies on C_{60} thin films on Ag(001). A peculiar irreversible transition, which led to the onset of brightness differences between the molecules in the same film, was observed at around 300 K. This effect was ascribed to electronic differences caused by nonequivalent orientation of C_{60} molecules on the surface. Goldoni and Paolucci [113] have studied the interaction of fullerene C_{60} with Ag(100) and indicated the occurrence of strong, predominantly ionic, bonding. Electronic structure and growth mode of the early stages of C_{60} adsorption at the Ag(001) surface [114], electronic structure of K-doped C_{60} monolayers on Ag(001), and coexisting inequivalent orientations of C_{60} on Ag(001) have been studied by Cepek et al. [115, 116]. Grobis et al. [117] have analyzed the local electronic properties of a molecular monolayer of C_{60} on Ag(001) using STM at $T = 7$ K. It has been confirmed that the appearance of bright and dim molecules originates from Ag surface reconstruction. Peculiar STM molecular contrast (“bright” and “dim”) in C_{60} /Ag(100) has been observed by Pai et al. [118].

24.5.2.7 Other Inorganic Compounds

Valette [119] has used the dependence of the minimum of the double-layer capacitance on the concentration of the supporting electrolyte to find the adsorption sequence of anions on Ag(110) face: $F^- > ClO_4^- > PF_6^- = BF_4^-$. For the latter two ions, adsorption is practically negligible. This series shows that small ions undergo relatively strong adsorption since they can more easily penetrate the space between the silver atoms in the inner layer of the Ag(110) electrode than larger ions. It is known that the tendency of perchlorate to adsorb non-specifically is favored on metals of low work function [120], such as Ag(110) surface ($\phi = 2.3$ eV). For this reason, Stuve et al. [121, 122] have studied adsorption of perchloric acid and the reaction of adsorption products with coadsorbed H_2O . A model for tridentate adsorption of ClO_4^- on Ag(110) has been proposed [122]. It has been concluded that the chemisorbed perchlorate can be hydrated with the adsorbed H_2O under UHV conditions. Contrary to Ag(110), on Ag(100), perchlorate ions undergo stronger adsorption than F^- [123].

Niaura and Jakubenas [124] have studied the effect of alkali metal ions on the SERS spectra of phosphate anions adsorbed at Ag electrodes. The formation of ion pairs at the interface has been confirmed.

The bromide-induced adsorption of thallium complex on pc-Ag electrode has been studied using CV and chronocoulometry [125].

Electrochemical deposition of polyborate monolayers at Ag(111) electrodes has been studied by Stevenson et al. [126].

Coadsorption of ammonia and hydrogen fluoride with water on Ag(110) has been described by Krasnopoler et al. [127] as an example of hydrogen bonding and surface

interactions in protic solvents. Structural and morphological changes accompanying reaction of NH_3 with oxygen adsorbed on Ag(110) have been investigated by Guo and Madix [128].

Lee et al. [129] have studied adsorption configuration and local ordering of silicotungstate anions (STA) on Ag(100) electrode surfaces. Voltammetric studies have shown that STA passivates the Ag surface and thus slows down the electron transfer the dissolved redox species participate in. STA species is oriented with its fourfold axis perpendicular to the Ag(100) surface and the center of the STA molecule is located 4.90 Å above the top layer of the Ag substrate. From the analysis of bond lengths, it has been found that four terminal O atoms are located near the hollow sites and that an Ag–O bond length is 2.06 Å.

Jafarian et al. [130] have studied adsorption and absorption of hydrogen species on Ag electrodes in alkaline solution. Gurten et al. [131] have investigated the effect of alcohols: MeOH, EtOH, and PrOH on hydrogen evolution reaction on Ag electrode in contact with 0.01 M NaCl solution. It was observed that the presence of alcohols increased the hydrogen yield and decreased anodic overpotential (for the Pt anode).

24.5.2.8 Metalocenes

Welipitiya et al. [132] have studied adsorption and desorption of ferrocene on Ag(100), applying photoemission and thermal desorption. The initially adsorbed surface species closely resembled that of molecular ferrocene. The molecule was adsorbed with the cyclopentadienyl ring ligands parallel to the surface. Woodbridge et al. [133] have performed the high-resolution electron energy loss spectroscopy (HREELS) and XPS studies of ferrocene on Ag(100). Researchers from the

same group have also studied adsorption of other metallocenes. Langell et al. [134] have studied adsorption and decomposition of decamethylferrocene on Ag(100), while later, Pugmire et al. [135] have performed spectroscopic studies of adsorption and decomposition of nickelocene at the same surface. Also, Pugmire et al. [136] have investigated orientation of nickelocene molecules on Ag(100), following temperature-programmed desorption and applying HREELS. At relatively inert Ag(100) surface at 175 K, nickelocene was physisorbed molecularly to form a monolayer coverage. Its molecular axis was perpendicular to the surface plane. At 225 K nickelocene started to decompose to the adsorbed cyclopentadienyl and nickel. Molecular desorption was observed only for multilayer material, at 210 K, or for the first monolayer, when the adjacent surface sites were not available for decomposition.

24.5.3

Adsorption of Organic Species on Ag Electrodes

24.5.3.1 Hydrocarbons

IR reflection/absorption spectroscopic study of ethylene adsorption on Ag(110) and atomic oxygen precovered Ag(110) surfaces have been described by Akita et al. [137]. Interaction of ethylene with perfect and defective Ag(001) surfaces [138, 139], as well as coadsorption of ethylene and oxygen on Ag(001) [140], have been studied by Kokalj et al. It has been found that ethylene binds rather weakly to both clean and oxygen precovered Ag(001) surfaces, and that the molecular geometry is almost unchanged upon adsorption. The binding energy with Ag(001) increased considerably in the vicinity of steps and adatoms. Also, chemisorption energy

increased considerably in the presence of subsurface oxygen. Adsorption of ethylene on Ag(001) has also been studied by Vattuone et al. [141], who have employed vibrational excitation method to the description of the switching from the molecular to the dissociative adsorption of this compound. Later, Vattuone et al. [142] have studied ethylene adsorption on clean and oxygen-covered flat and stepped Ag(001). The final adsorption state depended on the translational and internal energies of the gas-phase molecules, as well as on the presence of defects. For instance, for low translational energy, ethylene was either physisorbed or very weakly chemisorbed at flat terrace sites. Kokalj et al. have studied adsorption of ethylene on the stepped Ag(*n*10) surfaces [143] (with *n* = 2, 3, 4) using density-functional theory. It has been found that ethylene adsorbs preferably on the top sites of the step edge. The (100) terraces were found to behave similarly to the flat Ag(100) surface, which binds ethylene only weakly.

Pawela Crew and Madix [144] have investigated desorption of propylene and propane from Ag(110) with the emphasis put on the anomalous effects of weak chemisorption on desorption kinetics of alkenes. Molecular conformation of styrene on Ag(100) related to the catalytic epoxidation of terminal alkenes has been studied by Williams et al. [145]. IR studies of the adsorption structures of 1,3-butadiene at Ag(111) and Au(111) surfaces have been published by Osaka et al. [146].

The role of water in partial oxidation of propylene on the Ag(110) surface has been shown by Gland et al. [147].

Adsorption of benzene on Ag(110) has been investigated by Pascual, Kelly et al. [148–151].

24.5.3.2 Pyridine and Other Nitrogen Compounds

Adsorption of pyridine, a rigid molecule able to attain various orientations with respect to the metal surface, evidently remains the most studied process of adsorption of organic molecules at the electrodes. Pyridine replaces water molecules at the electrode surface; the number of removed H₂O molecules depends on the orientation of pyridine molecules with respect to the electrode surface. This process is associated with the partial charge transfer across the electrode surface. Using the SERS method, Ma and Wu have studied the pyridine–iodine charge-transfer complex at the Ag electrode [152]. Yang et al. [153] have analyzed the roughened Ag electrode with the adsorbed pyridine, employing two-dimensional surface-enhanced Raman imaging and comparing the result to the AFM images. Adsorption of pyridine on Ag (and Au) has been studied by Tsionky et al. [154], who applied the electrochemical quartz crystal microbalance (EQCM) method. The frequency shift caused by adsorption of pyridine depended strongly on the nature of the metal. Furthermore, the potential-related frequency shift was observed even in the absence of specific adsorption. Interaction of water with the Ag surface was found to be much weaker than with Au. Nicholson et al. [155] have analyzed speciation of pyridine at a rough Ag electrode surface during oxidation–reduction cycles and have determined the kinetic and spectroscopic profiles of three pyridine complexes.

The studies of pyridine adsorption on Ag(110) (as well as on Ag(311) and Ag(210) surfaces) have been performed by Hamelin et al. [156–158]. An increase in the electrode potential by only 10 mV appeared sufficient for pyridine molecules to change their surface concentration from

zero to the full coverage at the positively charged electrode. The C_5H_5N molecules were then oriented vertically and attached to the Ag surface via N atom. It is noteworthy that the adsorption energy of pyridine on single-crystal Ag electrodes is lower by 15–20 kJ mol⁻¹ than that for gold electrodes.

Ma and Wu [152] have carried out SERS studies on pyridine–iodine charge-transfer complex on pc-Ag electrode.

Shi et al. [159] have performed the time-resolved surface-enhanced Raman scattering (TR-SERS) investigations of adsorption and electroreduction of 4-cyanopyridine on Ag electrode. It has been shown that the nature of the adsorbed species and the reduction products depend on the solution concentration. The rate constants of the respective reaction steps were determined. Li et al. [160] have performed SERS and surface-enhanced hyper-Raman scattering (SEHRS) studies of pyrazine and pyridine adsorbed on Ag electrodes. Lopez-Tocon et al. [161] have performed SERS studied on photoinduced charge-transfer processes of 2,4,6-trimethylpyridine on Ag electrodes. Charge transfer in SERS, based on the spectra of 3,5-dimethylpyridine at an Ag electrode, has been discussed by Arenas et al. [162]. Bukowska et al. [163], using SERS and electrochemical techniques, have investigated adsorption of 4-phenylpyridine at the Ag/solution interface in a wide range of electrode potentials. 4-Phenylpyridine was adsorbed on Ag stronger than pyridine. For saturated solutions, it has been found that 4-PhPy molecules undergo reorientation from rather “flat” at potentials more positive than –0.7 V (SCE), to rather “perpendicular” at more negative potentials. Electrochemical reduction of pyrazine on Ag electrode has been studied by Brolo and Irish [164–167], applying SERS. The

complete analysis of the SERS response of pyrazine, based on a resonant charge-transfer mechanism, has been published by Arenas et al. [168]. Also Arenas et al. [169] have applied the charge-transfer mechanism to the explanation of the SERS spectra of 2,3-dimethylpyrazine adsorbed on Ag electrode. Kudelski and Bukowska [170] have employed SERS to analyze adsorption of piperidine on a silver electrode. For this process, relative SERS enhancement factors were determined as a function of the incident wavelength and the applied potential. The effect of charge transfer on the Raman intensity was estimated from these data. Cehn et al. [171] have studied the adsorption behavior of isoquinoline on Ag surface in HCl solution utilizing SERS spectra. Isoquinoline molecule was adsorbed on Ag via Ag–N interaction at the perpendicular orientation. As the applied voltage was shifted to –0.6 V, the strength of this bond declined and the molecule orientation was tilted.

Osaka et al. [172] have also studied the adsorption structures of acrylonitrile on Ag(111) and Ag(110) surfaces using IR reflection/absorption spectroscopy. Other nitrogen compounds are discussed in the section devoted to biochemically important compounds.

24.5.3.3 Carboxylic Acids

Waszczuk et al. [173] have performed radiometric and voltammetric studies of benzoic acid adsorption on a pc-Ag electrode in contact with 0.1 M HClO₄ solution. The electrodes were obtained by electroplating Ag black onto a vacuum-deposited silver substrate. Benzoic acid appeared to be surface active in the entire range of potentials available at Ag in aqueous solutions. Adsorption of benzoic acid increased as the potential became more positive and this surface process was

fully reversible, regardless of the potential range and solution concentration. Applying the Langmuir isotherm, the apparent Gibbs energy of adsorption was estimated and equaled to -31 kJ mol^{-1} . From the kinetic analysis, it has been concluded that the surface process, rather than diffusion, is a rate-determining step in benzoic acid adsorption. Parker et al. [174] have studied deprotonation of carboxylic acid on Ag(110) and Ag(111) surfaces.

24.5.3.4 Alcohols

Adsorption of *n*-hexanol on Ag(100) and Ag(110) from aqueous 0.05 M KClO_4 solutions has been studied by Foresti et al. [59], who performed capacitive charge measurements and compared the results with those obtained for Ag(111). The calculated adsorption free energy (at the potential of maximum adsorption) was $\Delta G_{\text{ads}}^0 = -17.7 \text{ kJ mol}^{-1}$ for Ag(100), compared to $-18.4 \text{ kJ mol}^{-1}$ for Ag(111). Adsorption parameters on Ag(100) surface have been compared to the molecular model by Guidelli and Foresti [175]. It has been concluded that *n*-hexanol molecules are adsorbed in a flat orientation, similarly as on Hg and Ag(111). On the Ag(110) surface, *n*-hexanol exhibited negligible adsorptivity. Based on ΔG_{ads}^0 values, the following hydrophilicity sequence has been obtained: $\text{Hg} \ll \text{Ag}(111) < \text{Ag}(100) < \text{Ag}(110)$, with the value for Ag(110) being anomalously low. Jurkiewicz-Herbich et al. [176] have studied adsorption of 1-butanol and 2-butanol on Ag(100) and Ag(110) surfaces in two different supporting electrolytes (NaF and LiClO_4). It has been found that for weak interactions between the alcohols and the metal, all interactions occurring in the inner-layer region at the electrode contribute to the free energy of adsorption; hence, the

latter depends on the adsorbate interactions with water and supporting electrolyte ions.

Wu et al. have studied adsorption and reaction of 2-iodoethanol [177] and acetaldehyde [178] on Ag(111). Doubova et al. [179] have studied adsorption of amyl alcohol on Ag(111) electrodes in 0.05 M KClO_4 solutions and explained the observed differences and inconsistencies in the light of the applied experimental technique (e.g. the role of ac frequency) and the electrode surface preparation procedure. Generally, amyl alcohol was adsorbed less on Ag(111) than on Hg. The electron-induced surface reactions of methyl formate [180] and methanol [181] on Ag(111) have been studied by Schwaner and White. Foresti et al. [182] have investigated electrochemically, adsorption of 1,5-pentanediol on the Ag(111) and Ag(110) faces.

24.5.3.5 Sulfur Compounds

Santos et al. [183] have performed electrochemical and SHG studies of the Ag(111) electrode surface covered with various organosulfur compounds. Li et al. [184] have studied adsorption of thiophenol, 4-aminothiophenol and 1,4-dithiobenzene on the roughened Ag electrode surface employing SERS technique. The substituent in the benzene ring affected the orientation of the molecules: thiophenol ring was tilted toward the normal of the electrode surface, 4-aminothiophenol adopted an upright orientation, 2,4-dithiobenzene lay flat on the electrode surface, resulting in a strong substrate- π ring interaction. All the molecules were adsorbed via the sulfur atom by forming the Ag-S bond. Correlation of electronic and local structures of 4-hydroxy-thiophenol on $\text{NaCl}(100)$ and Ag(100) has been found by Tegenkamp and Pfnur [185].

24.5.3.5.1 Thiourea (TU) Liu and Wu [186] have presented the results of SERS studies of thiourea (TU) adsorbed on Ag electrodes. Zhong et al. [187] have studied coadsorption of TU and various electrolyte anions. Łukomska and Sobkowski [188] have compared the results from electrochemical impedance spectroscopy and radiochemical methods concerning adsorption of TU on the pc-Ag electrode in neutral solution. Adsorption parameters, in terms of the Langmuir isotherm, were calculated. TU adsorption proceeded in the entire range of the applied potentials; it was reversible with respect to the electrode potential and bulk TU concentration (with small amount of TU being irreversibly adsorbed). Smoliński and Sobkowski [189] have investigated the influence of the Ag electrode surface structure on adsorption of TU in HClO₄ solution utilizing electrochemical and radiochemical methods. Adsorption of TU was reversible with respect to the bulk concentration and the applied potential in the range of ideal polarizability of the electrodes. The maximum surface concentration of TU followed the sequence: Ag(111) > Ag(100) > Ag(110), in agreement with the atom surface density of the silver planes. For all planes, Gibbs energy of TU adsorption was similar: $25.5 \pm 1 \text{ kJ mol}^{-1}$ (in terms of the Langmuir isotherm). Yagi et al. [190] have used sulfur-K near-edge X-ray absorption fine structure (S K-edge XAFS) and XPS to study molecular adsorption of (CH₃)₂S on Ag(111). The IR reflection/absorption spectroscopic studies of the adsorption structures of dimethyl sulfide and methyl ethyl sulfide on Ag(110) and Cu(110) have been published by Kasahara et al. [191].

24.5.3.5.2 Alkanethiols and Self-assembled Monolayers The number of papers on self-assembled monolayers (SAM) on

silver surfaces is quite small compared to the papers concerning gold surfaces. This is probably because of the difficulties in preparing clean and well-ordered silver surfaces [192]. A large number of compounds contain sulfur atoms in their molecules that can interact with the Ag surface. Hatchett et al. [193, 194] have investigated electrochemical oxidative adsorption of ethanethiolate on Ag(111). Free energy of adsorption of *n*-alkanethiolates at Ag(111) was determined electrochemically [195].

Widrig et al. [196] have studied voltammetrically, the SAMs of several *n*-alkanethiols formed on pc-Ag electrodes. Analysis of data showed that during adsorption, the hydrogen of thiol group is lost and the sulfur is oxidized by one electron. Based on the charge required for the reductive desorption of the monolayer, the surface coverage was found to be $7.0 \times 10^{-10} \text{ mol cm}^{-2}$.

Further, Hatchett et al. [197] have described electrochemistry of sulfur adlayers on Ag(111) and found the evidence for the concentration- and potential-dependent surface phase transition. Electrochemical evidence for the adsorption of alkanethiols at two sites of the Ag(111) surface has been published by Mohtat et al. [198]. X-ray studies of the adsorbed monolayers of 1-octanethiol on Ag(111) and Cu(111) have been performed by Rieley et al. [199]. SAMs of 1,8-octanedithiol on Ag(111) have been investigated, applying electrochemical STM by Cavallini et al. [200]. Doomes et al. [201] have described anomalous X-ray absorption near edge structure (XANES) spectra of octadecanethiol adsorbed on Ag(111). Uibel et al. [202], utilizing electrochemical and SERS measurements, have determined the structure and free energy of adsorption of *n*-alkanethiolates at Ag(111). Lee

et al. [203] have studied nondissociative chemisorption of methanethiol on Ag(110) and compared it with adsorption on Cu(110) [204], discussing chemical aspects of the formation of SAMs. The structure and electrochemical behavior of ethanethiol SAMs on Ag(100) and Ag(111) in 0.1 M H_2SO_4 have been studied by Schweizer and Kolb [192], who have employed in situ STM and cyclic voltammetry for this purpose. Compared to the iso-electronic Au(111) and despite almost identical lattice constants, the structures of ethanethiols on Ag(111) were different and for thiols of longer chains, a distorted hexagonal structure (compared to the commensurate $(\sqrt{3} \times \sqrt{3}) R30^\circ$ structure for Au(111)) was observed. For Ag(100) and Ag(111), a double-layer capacity was equal to 4.4 and $3.4 \mu\text{F cm}^{-2}$, respectively. These values are considerably lower than those obtained for ethanethiol-modified Au(100) and Au(111) (6.5 and $8 \mu\text{F cm}^{-2}$, respectively) and probably reflect higher packing density of ethanethiol on silver surfaces. From the charges accompanying reductive desorption, assuming a one-electron process and subtracting the double-layer charge measured in 0.1 M NaOH, Schweizer and Kolb [192] have arrived at a coverage value equal to $\theta = 0.3$ (Ag(100)) and $\theta = 0.37$ (Ag(111)) for the monolayer. On Ag(100), an incommensurate structure of a next-neighbor distance of 0.44 nm was observed, while for Ag(111) a commensurate $(\sqrt{7} \times \sqrt{7}) R19.1^\circ$ structure with two different adsorption sites was found [192]. Reductive desorption of SAMs of alkanethiols on Ag(111) and Au(111) electrodes has been studied by Azaroni et al. [205]. It has been concluded that the difference in peak potentials of that desorption is determined by the energy to introduce an electron into the

adsorbed alkanethiolate-metal species, the desorption energy of the alkanethiolate anion, and the solvent/metal interaction energy. Also, Hatchett et al. [194] have studied oxidative adsorption of ethanethiolate on Ag(111) in alkaline solutions, utilizing cyclic voltammetry and SERS methods. The structure of alkanethiols of different chain lengths (from 1 to 11 C atoms), adsorbed on Ag(111), has been studied by Heinz and Rabe [206], who used ex situ STM.

24.5.3.6 Biochemically Important Compounds

Vivoni et al. [207] have employed SERS to determine orientation of 6-mercaptopurine (6MP) molecules adsorbed on the roughened Ag electrode. It has been concluded that 6MP are attached head-on via N1 atom when the molecule is adsorbed onto a silver electrode surface.

Using the SERS method, Cunha et al. [208] have studied the potential dependence of thymine coordination on pc-Ag electrodes for potentials positive to PZC up to the end of the double-layer potential range. At less positive potentials, one of the ring oxygen atoms was involved in chemical bonding and the molecule assumed a tilted position. In contrast, at more positive potentials, one of the ring nitrogen atoms (possibly, the deprotonated one) established a new bond with the surface, making the molecule's axis closer to the surface normal. Wang et al. [209] have described the SERS studies of microperoxidase-11 on roughened Ag electrodes.

Li et al. have performed a comparative study on the surface-enhanced resonance hyper-Raman scattering and surface-enhanced resonance Raman scattering (SERRS) of dyes adsorbed on Ag electrode and Ag colloid [210].

Chen et al. [211] have studied the orientation of azathioprine adsorbed on the Ag electrode using SERS and *ab initio* calculations. Brolo et al. [212] have studied adsorption of L-cysteine on a polycrystalline silver electrode utilizing SERS and surface-enhanced second-harmonic generation (SESHG) methods. L-Cys was strongly adsorbed onto Ag and remained there up to the potential of -900 mV (versus Ag/AgCl). For potentials more positive than -650 mV, L-Cys adsorbed with the protonated amino group directed toward the Ag surface; at more negative potentials, reorientation occurred. SERS investigation of NAD(+) adsorbed on Ag electrode has been performed by Chen et al. [213]. Cao et al. have published the results of SERS investigation of the interaction of imidazole with a silver electrode in ACN solution [214]. These authors, also applying SERS, have investigated interfacial water at Ag electrodes in ACN solutions [215]. Carter et al. [216] have employed SERS to determine the orientation of 1- and 2-methylimidazole molecules at Ag electrodes. Miłkowska and Jurkiewicz-Herbich [217] have investigated adsorption of tyrosine on Ag(110) and Ag(111) surfaces.

The effect of surface modifiers on electrode reactions and conformation of cytochrome *c*(3) adsorbed on Ag electrode has been investigated by Hobara et al. [218] using SERS and electroreflectance voltammetry. It has been shown that redox interactions of cytochrome *c*(3) are more reversible at Ag electrode modified with 11-mercaptoundecanoic acid compared to bare metal surface. Using nonresonant SERS technique, Niaura et al. [219] have studied adsorption of cytochrome *c* on Ag electrode. The analysis performed by Wandlowski [220] has evidenced the intermediate position of silver in the series describing the stability of the condensed

physisorbed uracil phase: $\text{Hg} < \text{Ag}(111) < \text{Au}(111)$. Guidelli et al. [221] have modeled short- and long-time behavior of two-dimensional phase transitions of chemisorbed uracil on Ag(111). Cavallini et al. [222] have performed *in situ* STM investigation of uracil on Ag(111).

24.5.3.6.1 Adsorption on Modified Ag Electrodes

Dick et al. [223] have described the SERS studies of cytochrome *c* bound to alkanethiols adsorbed on Ag electrodes. The studies were aimed at evidencing the distance and orientation dependence of heterogeneous charge transfer. Yang et al. [224] have presented *in situ* Raman spectra for the NAD⁺-modified Ag electrode at various potentials. The Ag surface was modified with a SAM. SERS studies have shown that NAD⁺ molecules undergo reorientation or desorption from the Ag electrode when potential is shifted from -0.5 to 0 V (SCE). Fang et al. [225] have studied the adsorption structure of RNA triple helix. Williams et al. [226] were the first who have observed the capping/uncapping by a ligand of Zn porphyrin adsorbed on Ag(100). Redox and conformational equilibria of cytochrome *c*(552) adsorbed on chemically modified Ag electrode probed by SERS have been further studied by Bernad et al. [227]

24.5.3.7 Other Organic Compounds

Grochala, Kudelski, and Bukowska [228] have described the anion-induced charge-transfer enhancement in SERS and SERRS spectra of rhodamine 6G on Ag electrode as a function of the electrode potential, upon addition of chloride and citrate anions. In a very recent paper, Brolo et al. [229] have discussed the ratio of the surface-enhanced anti-Stokes scattering to the surface-enhanced Stokes-Raman

scattering for molecules adsorbed on Ag electrode. For this purpose, SERS spectra for oxazine 720, rhodamine 6G, and pyridine adsorbed on a rough silver surface under controlled potential conditions were recorded. It has been concluded that the main features of the preferential enhancement of the anti-Stokes scattering for an adsorbed molecule on rough silver can be understood in the context of current SERS theories.

Electrochemical, SERS, and surface enhanced resonance Raman (SERR) studies of the reduction of methylene blue on silver electrode have been published by Nicolai et al. [230, 231]

Itaya et al. [232] have described in situ STM investigations of organic compounds adsorbed on iodine-modified Au(111), Ag(111), and Pt(111) electrodes.

Guo and Madix [233] have employed STM to study adsorption of acetylide on Ag(110). They have determined the number of metal atoms incorporated in such molecular intermediates, as, for example, imide, nitrate, and sulfite. Tautz et al. [234] have used HREELS to investigate the substrate influence on the ordering of organic submonolayers. They have also performed a comparative study of perylene-tetracarboxylic-dianhydride (PTCDA) on Ag(110) and Ag(111). The results of the studies of ultrathin films of PTCDA bear some importance in the context of organic epitaxy, which relies on the formation of highly ordered interfaces. Nowakowski et al. [235] have used STM and LEED for the analysis of the ordered structures of nonplanar derivative of perylene-tetracarboxylic-diimide (PTCDI) on Ag(110). The chosen adsorbate was perylene-3,4,9,10-tetra-carboxylic-diimide-di(2,6-isopropylphenyl), which is a derivative of organic semiconductor PTCDI. The adsorbate exhibited high

mobility on the Ag(110) surface at room temperature. In the submonolayer regime, well-ordered structures were observed. Moreover, two different structures were distinguished in the monolayer regime, depending on the preparation procedure. The first one was a random structure with the molecules lying nearly flat on the surface (relative to the perylene core). The second one was a closer-packed commensurate structure with the molecules of tilted perylene cores and forming stacks. For the second, more densely packed structure, flat-lying functional groups overlapped. The differences in submolecular image contrast between the two structures were considered to be a consequence of different tilting angles of the adsorbed molecules.

24.5.4

Electrode Processes with Participation of Silver Electrodes

24.5.4.1 Reactions Involving Oxidation of Ag Surface

24.5.4.1.1 Oxygen and its Compounds

Itagaki et al. [236] have studied electroreduction of oxygen at the oxidized Ag electrodes using channel-flow double electrode. The HO_2^- species was detected and the role of preoxidation of Ag electrode was discussed. Zabarnick et al. [237] have applied EQCM to study the silver surface corrosion and to detect sulfur. Using the TR-EQCM, Chen et al. [238, 239] have studied the mechanism of silver(I) oxide formation on a pc-Ag electrode in alkaline solution, in a series of potentiodynamic experiments. The first stage of the oxidation was unambiguously attributed to the formation of Ag_2O monolayer. In the second oxidation stage, a very small amount of Ag or its oxide was dissolved in the solution and the Ag_2O layer thickness was

gradually increased. Compact, Ag_2O layers were formed in the first two stages of the oxidation, while Ag_2O formed at more positive potential was porous. No species other than Ag_2O was detected. Anodic behavior of Ag electrode in KOH solutions has been studied by Bughiu et al. [240]. Nagle et al. [241] have investigated a growth of multilayer oxide films on pc-Ag surface in basic media, under conditions of repetitive potential cycling. Depending on the lower potential limit of the oxide growth cycles, either Ag_2O or AgOH predominated. Savinova et al. [242] have studied the structure and reactivity relations for H_2O_2 reduction at Ag electrodes in NaF/NaOH electrolytes of various pH. Cyclic voltammetry and ac-impedance spectroscopy were used. OH^- chemisorption was observed in a wide potential range (between -1.1 and 0 V (SCE), depending upon pH). The occurrence of a slow chemical step in the overall reaction mechanism has been proved. Its rate was strongly affected by the oxidation of the surface submonolayer. The proposed reaction scheme involved the structure of the adsorbate layer at the electrode/electrolyte interface at various potentials. Flätgen et al. [243] have proposed autocatalytic mechanism of H_2O_2 reduction on Ag in acidic media, which may produce negative differential resistance and current oscillations. The proposed mechanism assumed the potential-dependent coverage of the Ag electrode with the activating adsorbate $(\text{OH})_{\text{ad}}$, which is formed in the course of H_2O_2 reduction as an unstable intermediate. Experiments, as well as model calculations, have been performed. Interaction of oxygen with Ag(110) has been studied by Raukema et al. [244]. Adsorption of O_2 on Ag(110) has been investigated by Bird and Gravil [245]. Formation of d-holes at the initial stages of the oxidation of Ag(001) has been studied by Benedek

et al. [246] Cyprian et al. [247] have investigated adsorption of atomic oxygen on Ag(001) using density-functional theory. Altieri et al. [248] have studied morphological change of a MgO(001) monolayer deposited on Ag(001) induced by the application of H_2O . Jovic et al. [249] have performed cyclic voltammetric studies on Ag(111) and Ag(100) faces in NaOH solutions. In situ Raman spectroscopy was used by Savinova et al. [250] to study the interface between Ag(111) electrodes and alkaline NaF electrolytes at various pH. Submonolayer oxidation started much below the bulk silver oxide formation, namely, at the potential of ca -0.6 V versus Hg/HgO electrode at pH 11. In the Raman spectra, the bands attributed to Ag–OH stretching and AgO–H bending vibrations of electrochemisorbed hydroxide species were identified. Fluoride ions stabilized adsorption of hydroxide species. A multistep mechanism for the formation of hydroxide/oxide species at the Ag surface has been proposed. Using ex situ XPS, Savinova et al. [251, 252] have studied the interface between Ag(111) and an alkaline electrolyte. In their earlier studies, Zemlyanov and Savinova et al. have observed OH groups incorporated in the Ag(111) electrode [253]. More recently, Savinova et al. [254] have discussed the mechanism of Ag(111) submonolayer oxidation, applying combined electrochemical, in situ SERS, ex situ XPS, and UPS. The potential-dependent formation of adsorbates was observed above the zero-charge point of the Ag electrode for OH groups $(\text{OH}_{\text{ads}}^{\gamma-})$ and oxide-like species $(\text{O}_{\text{ads}}^{\delta-})$. A mechanism of the oxidation of Ag(111) submonolayer has been proposed on the basis of combined cyclic voltammetric, in situ SERS, ex situ XPS and UPS studies. Danckwerts et al. have published the results of electrochemical and SHG

studies of the Ag(111) surface [255] including coadsorption of fluoride and hydroxide ions in alkaline electrolytes, for pH ranging from 5.8 to 14 [256]. It has been found that OH^- adsorption at Ag(111)/alkaline electrolyte interface is the initial step leading to the formation of the surface oxide. A rapid transition from the F^- -dominated to the OH^- -dominated adsorption has been observed, as both species remained charged upon adsorption. At sufficiently positive potentials, yet below the reversible potential of the bulk oxide growth, OH was discharged, leading to the build up of the submonolayer oxide, whereas in acidic electrolyte, Ag was dissolved. At intermediate pH, the formation of a structured OH^-/F^- coadsorbed layer has been proposed. Shaikhutdinov [257] et al. have performed ex situ STM study of underpotential oxidation of Ag(111) electrode in alkaline ($\text{NaF} + \text{NaOH}$) electrolyte. The STM images have shown that the oxidation of the Ag(111) surface starts above the point of zero charge and proceeds according to the nucleation-growth mechanism. It started at the steps and extended to the terraces as the electrode potential was scanned in the positive direction. In the backward potential scan, the initial surface morphology was restored. Complex oxide structures formed during oxidation of Ag(111) and Ag(100) by hyperthermal atomic oxygen have been described by Li and Yang [258]. Carlisle et al. [259] have used STM for imaging the surface and the interface atoms of an oxide film on Ag(111). Recently, Kunze et al. [260] have performed an in situ STM study of the initial stages of electrochemical oxide formation at the Ag(111)/0.1 M NaOH interface. A comparative study of hydroxide adsorption from the mixed NaOH/NaF solutions, on Ag(111), Ag(110), and Ag(100) faces, using cyclic voltammetry, ex situ electron

diffraction, and in situ SHG has been recently published by Horswell et al. [261]. For all silver planes studied, two pairs of anodic and cathodic peaks were observed in cyclic voltammograms. They appeared in the potential range below the equilibrium $\text{Ag}_2\text{O}/\text{Ag}$ potential. These peaks were attributed to the specific adsorption of OH^- ions followed by submonolayer oxide formation. The differences between cyclic voltammograms for the (111), (110), and (100) planes were assigned to (1) different work functions; (2) surface atomic densities; and (3) corrugation potentials for these surfaces. Furthermore, ex situ LEED and reflection high-energy electron diffraction (RHEED) studies have shown that disordered adlayers are formed on Ag(111) and Ag(100), in contrast to Ag(110), where ordered structures are produced in the potential region corresponding to the first pair of voltammetric peaks. In the potential range of the second pair of peaks, LEED results indicated disordered oxide phases present on each crystal plane; RHEED results showed the presence of small islands of the $c(2 \times 2)$ structure at particular electrode potentials on (110) and (100). Also, isotropic (for (111), (110), and (100) planes) and anisotropic (for (110) and (111) planes) contributions to the measured SHG intensity were calculated. Recently, Kokalj et al. [262] have investigated adsorption of atomic oxygen and its inclusion into subsurface sites on Ag(210) and Ag(410) surfaces.

24.5.4.1.2 Sulfur Compounds Electrochemical growth of Ag_2S on Ag(111) electrodes has been studied using XPS by Conyers and White [263].

Flätgen et al. [264, 265] have involved surface plasmon microscopy to study the formation of spatiotemporal potential

patterns at a silver electrode during reduction of peroxodisulfate.

24.5.4.1.3 Carbon Compounds Electrochemical behavior of pc-Ag electrodes in Na_2CO_3 solution and the effect of ClO_4^- ions have been studied by Ibrahim et al. [266] under potentiodynamic and potentiostatic conditions (the results were supplemented with X-ray diffraction (XRD) analysis). It has been found that the active/passive transition (involving formation of Ag_2O and Ag_2CO_3 layers) occurs prior to oxygen evolution and that perchlorate ions stimulate active dissolution of Ag. These proceed in the passive region and lead to the pitting corrosion. Abd El Rehim et al. [267] have investigated further perchlorate pitting corrosion of a passivated silver electrode.

Constant et al. [268] have used HREELS to study the formation of carbonate on Ag(110). Also, Guo and Madix [269], using STM, have investigated the interaction of carbonate ions with Ag(110). Oxidation of CO by molecular oxygen adsorbed on Ag(110), as well as the influence of surface reconstructions on the CO oxidation reaction rate at the O/Ag(110) surface, has been investigated by Burghaus and Conrad [270, 271]. Later, Barth and Zambelli [272] have employed STM to the studies of CO oxidation by molecular oxygen at Ag(110) surface in the temperature range 60–110 K. At the lowest temperatures, CO remained weakly bound to Ag(110). Striped CO superstructures running along the [001] direction were observed at intermediate coverages, indicating weak anisotropic interactions between the molecules. Oxidation readily took place upon CO exposure, whereby single oxygen atoms were identified as an intermediate product, which could be further titrated

with CO molecules. More recently, CO oxidation on Ag(110) has also been analyzed by Burghaus et al. [273], who additionally discussed the surface reconstruction in relation to the subsurface oxygen problems. Transient CO_2 formation has been studied under “quasi-steady-state” conditions applying surface titrations. The reactivity of the surface toward CO oxidation was reduced in the course of the developing surface reconstruction and a possible influence of subsurface oxygen on CO_2 formation rates was excluded. Adsorption of oxygen and carbon dioxide on cesium-reconstructed Ag(110) surface has been studied by Guo and Madix [274].

24.5.4.2 Electrode Reactions of Selected Organic Compounds, Adsorbed on Ag Electrodes

Jones and Barteau [275] have studied the cyclization and related reactions of iodoethanol on Ag(110). The mechanism of diethyl ether formation on Ag(110) and its dependence on the coadsorbed oxygen species has been studied by Jones et al. [276].

Ab initio pseudopotential study of dehydrogenation of methanol on oxygen-modified Ag(110) surface has been described by Sun et al. [277].

24.5.4.2.1 Biochemically Important Species

Bare Ag electrodes. It is noteworthy that the recently studied electrode processes of organic compounds at pc-Ag electrodes involve mainly biochemically important species. For example, Zeng et al. [278] have investigated the voltammetric behavior of 2-mercaptopyrimidine (MPD) and have found that at appropriate potentials, MPD adsorbs on and interacts with the electrode to form an insoluble silver salt at the surface. The first of two cathodic

peaks (-0.66 V) was ascribed to the reduction of this sparingly soluble silver MPD compound, whereas the second peak (-1.28 V) was attributed to the reduction of MPD to pyrimidine. Furthermore, Zeng and Purdy [279] have investigated the influence of cetyltrimethylammonium bromide (CTAB) on the voltammetric behavior of a series of thiopurines at Ag electrode. In the presence of CTAB, cathodic accumulation of thiopurines was greatly improved and made the stripping peaks increase. Adsorptive voltammetric behavior of resveratrol (a compound present in wine) at Ag electrode has been studied by Dong et al. [280]. The Langmuir-like adsorptive behavior was assumed and the free energy of adsorption was calculated as -46.21 kJ mol $^{-1}$ at 298 K. Ye and Zhou [281] have studied the redox behavior of tyrosinase, applying cyclic voltammetry and potential-step chronoamperometry. The investigated redox process involved two electrons and was quasi-reversible. The linear dependence of the measured current versus concentration makes the studied reaction analytically applicable. Ye and Zhou [282] have investigated the electrochemical behavior of hemoglobin at bare Ag electrode, also from the point of view of potential analytical applications of this process. A pair of redox peaks was observed at $+0.26$ V (oxidation) and $+0.01$ V (reduction), at a sweep rate of 20 mV s $^{-1}$. Cai et al. [283] have applied in situ SERS technique to study irreversible adsorption of hemin and/or its reduced counterpart on the roughened Ag electrodes, as a function of the applied potential in aqueous electrolytes. The standard redox potential was found to be -0.12 V (SCE). Fast preequilibrium between the electrochemically active (monomer) and inactive (μ -oxo dimer) forms of hemin has been proposed. Later, Zheng et al. [284] studied adsorption

of hemin on a roughened Ag electrode. Li et al. [285] have described the voltammetric response of nicotinamide coenzyme I at Ag electrode. This compound was directly oxidized at a bare Ag electrode at ca 0.23 V and the resulting species yielded a cathodic peak at ca 0.12 V. Raman studies of photochemical charge-transfer excitation of trans-4-stilbazole at a silver electrode have been reported by McMahon et al. [286]. Sanchez-Cortes and Garcia-Ramos [287] have analyzed the effect of charge-transfer mechanism on the SERS response of 1,5-dimethylcytosine adsorbed on Ag electrodes, as well as on different metal colloids. Li et al. have studied electroreduction of phenazine on silver electrodes, applying SEHRS and SERS [288].

Modified Ag electrodes. A significant number of papers have been devoted recently to electrode processes of biochemically important compounds at the *modified* Ag electrodes. Li, Chen, and Zhu have studied electrochemical behavior of cytochrome *c* at the imidazole-modified silver electrode [289] and electrochemical reduction of NAD $^{+}$ at the benzoimidazole-modified silver electrode [290]. Imidazole reacted with Ag and covered the metal to give a stable and long-lasting chemically modified electrode, suitable for the electrode process of cytochrome *c* (as similar to imidazole for NAD $^{+}$ reduction). The same electrode was utilized by Li et al. in the investigation of redox process of myoglobin [291]. Zhu et al. [292] have described the voltammetric response of myoglobin at a captopril-modified silver electrode. Furthermore, Li et al. [293] have performed electrochemical studies of hemoglobin at the L-cysteine-modified Ag electrode. The covalent binding of cysteine to Ag surface via sulfur atom allowed one to obtain very stable and long-lasting chemically

modified electrode, ensuring an excellent voltammetric response in the presence of hemoglobin. Zhang et al. [294] have investigated the electrochemical properties of hemoglobin at silver electrode modified with self-assembled lipoic acid monolayer. Lipoic acid molecules were strongly adsorbed at the Ag electrode surface through the cleavage of the S–H bond and formation of the Ag–S bond. Long et al. have described electrocatalytic oxidation of NAD(P)H [295] and electrochemical regeneration of coenzyme NADH [296] on a L-histidine-modified silver electrode. They have proposed its application to the flow detection of this compound. Tian et al. [297], using EQCM, have estimated kinetic parameters of adsorption of human serum albumin onto hydroxyapatite-modified Ag electrode. The voltammetric behavior of DNA at Ag electrode has also been studied by Trnkova [298]. In particular, the influence of electrochemical pretreatment of silver electrode surfaces, as well as the choice of the starting and switching potentials, on voltammetric signals of DNA

have been discussed. The conclusion was that elimination voltammetry with silver electrodes represents a promising alternative in the construction of a biosensor for nucleic acids.

24.5.5

Underpotential Deposition Processes

Discharge of H^+ ions reveals the role played by the structure of Ag surface in the underpotential deposition (UPD) of hydrogen. Figure 4 shows that in the acidic medium, the activity of the electrode surfaces toward H^+ discharge decreases in the series: Ag(111) > Ag(poli) > Ag(100) > Ag(110), following the decrease in the surface density of atoms [48, 189].

The composition and the structure of electrodeposited metallic monolayers have always been a subject of intensive electrochemical investigations. However, the sources of information were limited by the number of available electrochemical methods. The UPD process on single-crystal surfaces (including Ag) has been summarized by Jüttner and Lorenz [299]

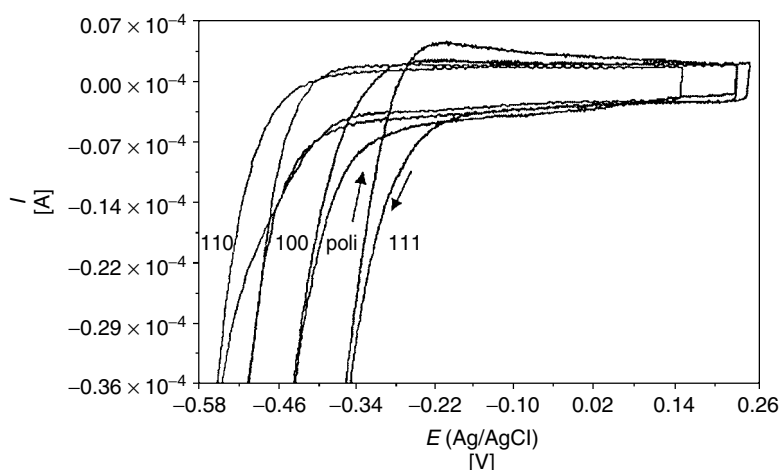


Fig. 4 Cyclic voltammograms recorded at single-crystal and polycrystalline Ag electrodes in 0.1 M $HClO_4$. Scan rate: 0.1 V s^{-1} [189].

already in 1980. At that time, UPD was a relatively new field of investigation. Recently, owing to the development of such spectroscopic surface methods as Auger electron spectroscopy (AES), LEED, STM, XPS, and XRD (grazing angle X-ray diffraction), more complete analysis of the structure of metallic monolayers on single-crystal surfaces can be performed. It is clear now that for the anodic electrodisolution of metals, the important role is played by the adlayers of various species (e.g. iodine on Ag) [41]. A more recent review of UPD at single-crystal surfaces of Au, Pt, Ag, and other materials has been published by Herrero et al. [300].

The nature of bonding of the adsorbed species to the model cluster of metal surfaces can be analyzed in terms of the so-called constrained space orbital variation (CSOV) method. For halogen anions adsorbed on various silver surfaces, it has been found that Pauli repulsion, metal polarization, and charge transfer to the metal surface mainly contribute to the binding energy of the ions [104, 301].

24.5.5.1 Ag UPD on Ag

Garcia et al. [302] have performed an in situ STM study of electrocrystallization of Ag on Ag(111) and have shown that Ag deposition occurs preferentially at the step edges following a layer-by-layer growth mechanism.

24.5.5.2 Ag UPD on Au and Pt

A series of papers have been devoted to the silver deposition on single-crystal surfaces of other metals, mainly Au(111) and Au(100). Zell et al. [303] have performed electrochemical in situ STM, cyclic voltammetric, and potential-step studies of phase formation during Ag (and Al) electrodeposition from the room-temperature molten

salts on flame-annealed Au(111). Cyclic voltammograms of Ag on Au(111) were characterized by the adsorption-controlled UPD and diffusion-controlled overpotential deposition (OPD). In the UPD range, two-dimensional Ag islands were formed, which merged into a coherent Ag monolayer. Further reduction of the potential value was followed by the formation and growth of a second monolayer. In the OPD range, a diffusion-controlled layer-by-layer growth of Ag clusters occurred. Ag UPD on Au(111) and Au(100) has been investigated by Garcia et al. [304, 305], who employed in situ STM and electrochemical techniques for this purpose. Ag UPD was found to occur stepwise and similarly on both surfaces. On Au(111), the condensed Ag phase was preferentially generated in monoatomic steps, whereas on Au(100), a simultaneous 2D nucleation of Ag on flat terraces was observed. Deposition of Ag on the Au(100) surface has been studied experimentally by Ikemiya et al. [306] (in situ AFM measurements) and theoretically by Gimenez et al. [307, 308]. Also, Chabala, Ramadan et al. [309–311] have investigated Ag UPD on Au(111) using XRD techniques. Rooryck, Buess-Herman et al. [312] have performed Auger electron spectroscopic and LEED studies of the growth of Ag on Au(111), (311), and (554) single-crystal surfaces. It has been suggested that the growth mechanism depends partly on the atomic surface roughness. Rooryck et al. [313] have revisited later silver UPD on Au(111) and stepped Au(111) in sulfuric acid using cyclic voltammetry in combination with UHV-based methodologies. They have shown that the first step of silver UPD is strongly dependent on the superficial state of the substrate and on the formation of an Ag–Au surface alloy. In the absence of surface alloy, sharp and intense UPD peak at 0.53 V

(versus Ag/Ag^+) was associated with the deposition of Ag on Au terraces. Potential cycling in the UPD region introduced some surface defects and gradually transformed the surface into the surface alloy phase, leading to the appearance of a silver UPD peak at 0.61 V. These findings constituted the basis for the discussion on voltammetric data from the previous studies on Au(111). Gimenez et al. [308] have performed theoretical (e.g. Monte Carlo) considerations of electrochemical phase formation for Ag deposited on Au(111) and Au(100). More recently, Kondo et al. [314] have employed X-ray scattering techniques for the in situ structural study of Ag UPD on Au(111) electrodes in sulfuric acid. They have found that Ag monolayer was formed in the potential range between the second and the third UPD peaks. Also, an Ag bilayer was formed in the potential range between the third UPD peak and bulk deposition potential. Recently, Cercellier et al. [315] have investigated epitaxial Ag ultrathin film grow on Au(111) using STM and angle-resolved photoemission spectroscopy (ARPES). Also, more complex deposition schemes were described. Watanabe et al. [316], using EQCM, have studied Cu and Ag adatoms at Au(111) in perchloric acid solutions. Takami et al. [317] have described the formation of a composite Ag–Cu monolayer on Au(111) applying sequential UPD. Wang et al. [318] have studied OPD of Ag monolayer and bilayer on Au(111) mediated by Pb adlayer UPD/stripping cycles.

UPD of Ag onto Au electrodes covered with SAM of alkanethiols has been described by Oyamatsu [319]. Hu et al. [320] have prepared nanoelectrode ensembles by assembling silver colloid and mercaptan on a gold electrode.

Finally, one has to mention an interesting study [321] of Ag electrodeposition onto

iodine-pretreated Pt(111). Spectroscopic studies (LEED, AES) have revealed that this deposition occurs in four steps: three subsequent underpotential processes are followed by the deposition of “bulk” Ag, while the iodine layer remains attached to the outermost layer, regardless of the number of Ag layers deposited.

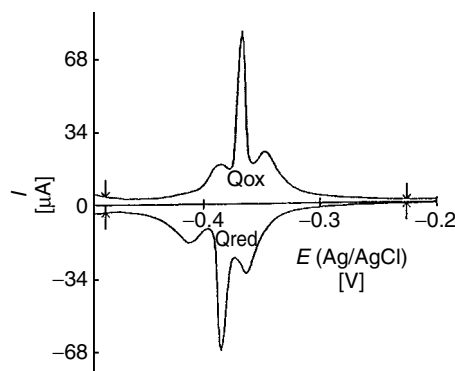
Ogura et al. [322] have studied hydrogen adsorption on Ag (and Au) monolayers grown on Pt(111).

24.5.5.3 Pb

Leiva and Schmickler [323] have employed the density-functional formalism to investigate the electronic properties of Pb monolayer deposited on Ag(111) electrode. They have predicted the enhancement of the signal observed in SHG spectroscopy. Stevenson et al. [324] have investigated the effect of the surface defect structure on the UPD deposition of Pb monolayers at Ag(111). Sackmann et al. [325] have studied Pb UPD on Ag(111) and Ag(100) using in situ scanning probe microscopy (SPM) combined with electrochemical impedance spectroscopy (EIS). Relatively simple conditions were found for Ag(111); formation of a condensed Pb monolayer, starting exclusively at monoatomic steps, was observed at low supersaturations with respect to the condensed 2D phase. The analysis of SPM and EIS data indicated that the lateral growth of the condensed Pb monolayer preferentially occurred via a direct transfer of Pb^{2+} from the electrolyte to the step edges. Smoliński and Sobkowski [189] have studied UPD of Pb on Ag(111) and have shown that the deposition/dissolution process is reversible in this sense that reduction and oxidation charges are practically equal (Fig. 5).

Widmer and Siegenthaler [326] have described STM investigation of Pb adsorption on Ag(111) surface in chloride electrolytes.

Fig. 5 Underpotential deposition of Pb on Ag(111) electrode from 0.1 M HClO₄ solution containing 1×10^{-3} M Pb²⁺ [189].



Obretenov et al. [327] have performed the Monte Carlo simulation of UPD in the Ag(111)/Pb²⁺ system. Schmidt et al. [328], using in situ STM, have studied 2D phase formation accompanying Pb UPD on Ag(100) and Au(100). Sackmann et al. [325] have performed combined in situ SPM and EIS studies of Pb UPD on Ag(100) and Ag(111).

24.5.5.4 Tl

Waszczuk et al. [329] have carried out radiometric studies of UPD of thallium on single-crystal Ag electrode from perchloric acid solutions. Deposition of Tl on Ag(100) to obtain monolayer, bilayer, and bulk crystallites has been studied by Wang et al. [330]. These studies have shown that apart from the substrate geometry, the nature of the substrate–adatom interactions also influence the structure of the UPD metal adlayers. This is because of the fact that, contrary to Au and Pt electrodes, Tl forms a well-ordered bilayer phase before bulk deposition on Ag(100) surface occurs.

24.5.5.5 Ni

Morin et al. [331] have studied electrodeposition of Ni on Ag(111) under the potential-controlled step flow conditions. Morin et al. [332], using in situ STM, have

investigated the formation of ultrathin Ni films on Ag(111) and compared the obtained results with those of analogous studies with Au(111). At multilayer coverages, atomically smooth Ni deposits were found of a lattice constant close to that observed for metallic Ni. More recently, Lachenwitzer et al. [333] from the same research group have performed the STM study of electrodeposition and anodic dissolution of Ni on Ag(111). Sztyler and Budniok [334] have studied the initial stage of nickel electrocrystallization on the Ag(111) substrate. Growth, structure, and epitaxy of ultrathin NiO films on Ag(001) have been studied by Luches et al. [335]. The early stages of NiO growth on Ag(001) have been studied by Caffio et al. [336], applying low-energy ion-scattering, XPS, and LEED.

24.5.5.6 Chalcogenides

Aloisi et al. [337] have performed in situ STM and electrochemical investigations of oxidative UPD of sulfur on Ag(111). Electrodepositions of silver selenide [338], silver telluride thin films [339], and silver selenide nanowires [340] have also been described.

Innocenti et al. [341] have studied deposition of CdS and ZnS on Ag(111), employing electrochemical atomic layer

epitaxy (ECALE). Thin films of CdS deposited on Ag(111) have been studied photometrically by Innocenti et al. [342], as well as electrochemically and microscopically (STM), by Foresti et al. [343]. Atomic structure of ultrathin CdS phase deposited on Ag(111) surface, applying ECALE, has been studied via X-ray photoelectron diffraction (XPD) by Cecconi et al. [344]. Pezzatini et al. [345] have investigated the formation of ZnSe on Ag(111) by ECALE. Cavallini et al. [346] have involved STM to the studies of Se electrodeposition on Ag(111).

24.5.5.7 Other Elements and Compounds

Electrodepositions of silver–cadmium alloys have also been described [347]. Underpotential and bulk depositions of Pb on the screen-printed Ag electrodes have been described by Zen et al. [348]. Del Popolo and Leiva [349] have studied Cu deposition on Ag(111) using embedded atom method. In situ STM study of the initial stages of Cu electrodeposition on Ag(100) has been published by Dietterle et al. [350]. A comparative kinetic study of Cd diffusion into Au(100) and Ag(100) during electrodeposition has been described by Vidu et al. [351]. The formation of a superficial alloy as a result of the initial growth, and the structure of Mn on Ag(100), have been investigated by Schieffer et al. [352]. Abt and Blugel [353] have reported the first-principles investigation of the formation of Mn/Ag(100) surface alloy. Elmouhssine et al. [354] have studied the growth and magnetic properties of Mn monolayer on Ag(100). Growth of Cr on Ag(001) has been investigated by Quinn et al. [355] using STM. Epitaxial growth of Cr on Ag(001) has been studied by Steadman et al. [356]. Two-dimensional Ising-type behavior of $c(2 \times 2)$ antiferromagnetic Mn and Cr

monolayers on Ag(001) has been studied by Hanf et al. [357]. Langelaar and Boerma [358] have studied the site exchange and mobility of Fe adatoms on Ag(100). Terreni et al. [359] have investigated the surfactant effect and dissolution of ultrathin Fe films on Ag(001). Step decoration of Co on Ag(001) has been studied by Dekoster, Degroote et al. [360, 361]. Supported magnetic Pd nanoclusters on Ag(001) have been described by Amitouche et al. [362]. Growth and temperature behavior of silicon thin films deposited on Ag(001) have been investigated by Leandri et al. [363]. Simulation of Cu growth on Ag(001) at experimental deposition rates has been published by Sprague et al. [364].

Sawaya et al. [365] have described the local density approximation studies of semiconductor metal adsorption characteristics: Ge/Ag(100).

24.5.6

Electrodeposition and Electrodisolution Processes of Ag

24.5.6.1 Electrodeposition Processes

Hasse et al. [366] have used in situ AFM for the detection of silver nucleation at the three-phase junction of the type: metal–silver halide–electrolyte solution. At this phase boundary, electrochemical reduction of submicrometer size silver halide crystals immobilized on the surface of gold and platinum electrodes took place. Following nucleation, the reaction advanced until the entire surface of the silver halide crystals was covered with 20 atomic layers of silver. Then, reduction was terminated. The obtained silver layer could be oxidized and the next layer of silver halide crystals became accessible for further reduction.

Also, single Ag₂S crystals immobilized on gold electrodes with edge lengths of

about 400 nm were electroreduced to silver [367]. In situ AFM images showed the start of the reaction at the three-phase junction Au–Ag₂S solution. The initial reduction product is a hump of silver atoms, which within minutes, recrystallize to a well-developed shape of a silver single crystal.

Initial stages of Ag electrocrystallization from silver thiosulfate complexes have been studied by Simons et al. [368] and Gonnissen et al. [369]. The formation of subcritical 2D silver clusters, preceding the formation of supercritical, stable 3D nuclei and their growth, has been suggested.

Dimitrov et al. [370] have investigated initial steps of silver deposition from nitrate solutions on silver and platinum substrates. Growth of independent large Ag grains was observed at lower overpotentials, while at higher overpotentials, dendrites were formed.

Employing in situ optical reflectivity and STM, Baltrunas et al. [371] have studied the surface roughness of an Ag electrode during electrocrystallization in cyanide electroplating bath. More recently, Baltrunas [372] has considered the role of the electrode surface inhomogeneity in the electrocrystallization mechanism in the silver/silver–cyanide system. The reaction order with respect to CN[−] was found to be close to 2, which suggests a direct participation of Ag(CN)₂[−] complex in the charge-transfer step. Daujotis et al. have studied the mechanism of electroreduction of silver–cyanide complexes in aqueous electrolyte using TR-EQCM [373] and SERS [374]. It has been shown that side by side with the electroreduction of silver–cyanide complexes, oxidation of (presumably) adsorbed cyanide ions occurs [373].

Saito et al. [375] have also studied the mechanism of silver electrodeposition from silver–cyanide complex solutions.

The kinetics of AgCl dissolution in aqueous solutions without supporting electrolyte have been studied utilizing well-defined and high mass transport properties of the scanning electrochemical microscope [376]. An ultramicroelectrode probe positioned close to the AgCl surface was used to induce and monitor dissolution of the salt via reduction of Ag⁺ from the initially saturated solution.

Scholz and Hasse [377] have shown that crystals of metallic silver can be grown at liquid/liquid interfaces (water with AgNO₃|*n*-octanol with ferrocene). Depending on the reactants concentrations in both phases, silver crystallized in the form of (1) wires (whiskers with radii from about 50 nm to 50 μm) growing into the organic phase; (2) Christmas tree-like deposits at the interface; and even (3) extremely smooth films of silver.

24.5.6.2 Electrodisolution Processes

Burke and coworkers [241] have studied the multilayer oxide films grown on silver in base during repetitive potential cycling. It was shown, on the basis of its reduction behavior, that the type of oxide obtained was dependent on the lower limit of the oxide growth cycles. Using limits of 1.03–2.60 V (SHE) the oxide film was assumed to be predominantly Ag₂O, while at limits 0.7–2.60 V, oxide deposit was assumed to be AgOH. Both types of silver oxides are assumed to be involved in premolecular oxidation and electrocatalysis at silver in base.

The mechanism of anodic dissolution of silver in cyanide solutions has been studied by Bek and coworkers [378–380]. For example, using [379] the rotating disc electrode and pulse potentiostatic method, it has been found that the limiting step involved the formation, at the electrode surface, of the adsorbed complex with two

CN⁻ ions. Anodic dissolution of silver electrode in cyanide solutions and also the behavior of Ag at potentials preceding dissolution have been studied applying electrode impedance measurements [381]. At potentials of anodic dissolution, the process was represented by the equivalent circuit with two parallel branches.

Sun et al. [382] have studied the dissolution behavior of gold and silver from Au–Ag alloys in aerated cyanide solutions using rotating disc electrodes.

Also, anodic dissolution of silver in ultrasonic field has been studied [383].

STM tip-induced local electrochemical dissolution of silver has been studied in the systems: Ag(111)/Ag⁺, ClO₄⁻ and Ag(111)/Ag⁺, SO₄²⁻ [384]

The inhibiting influence of sodium diisobutylidithiophosphinate [385] and 2-mercaptobenzothiazole [386] on silver dissolution in aqueous solutions of pH = 11 has also been investigated. Inhibition was caused by adsorption of both compounds, accompanied with the displacement of cyanides from the silver surface.

Dissolution of gold and silver from Au/Ag alloys in aerated cyanide solutions has been investigated, using rotating disc electrodes [387]. This process was partially controlled by transport of either oxygen or cyanide.

Structural changes of silver terrace domains during Ag electrodisolution in aqueous perchloric acid at constant anodic current density were followed by in situ STM sequential imaging [388].

Passivation of silver and current oscillations were observed [389] during anodic dissolution of silver in H₂SO₄ solutions. During dissolution of the electrode, silver powder was accumulated at the surface, which affected diffusion to the electrode and led to oscillations.

As regards other coordination compounds of silver, electrochemical synthesis of metallic (e.g. Ag and Cu) complexes of bidentate thiolates containing nitrogen as an additional donor atom has been described by Garcia-Vásquez et al. [390]. Also Marquez and Anaconda [391] have prepared and electrochemically studied silver(I) complex of heptaaza quinquedentate macrocyclic ligand. It has been shown that the reversible one-electron oxidation wave at +0.75 V (versus Ag|AgBF₄) corresponds to the formation of a ligand-radical cation. Other applications of coordination silver compounds in electrochemistry include, for example, a reference electrode for aprotic media based on Ag(I) complex with cryptand 222, proposed by Lewandowski et al. [392]. Potential of this electrode was less sensitive to the impurities and the solvent than the conventional Ag/Ag⁺ electrode.

24.5.7

Silver Compounds at the Oxidation States Higher Than I

Compounds containing silver at the oxidation states higher than I were not reviewed in the earlier edition of *Encyclopedia of Electrochemistry*. Therefore, it seems reasonable to fill this gap with some fundamental information on the electrochemistry of such species and an account of recent achievements made therein.

One should emphasize that in neutral aqueous solutions can only complex compounds of Ag in such high oxidation states exist, as the uncomplexed ions of that type oxidize water to oxygen. For example, $E^0(\text{Ag}^{2+}/\text{Ag}^+) = +1.980 \text{ V}$ (in 4 M HClO₄) is higher than E^0 for MnO₄⁻/Mn²⁺ [393]. Therefore, although Ag(II) ions can be, in principle, obtained by the oxidation of Ag(I) by ozone in strongly acidic solution,

the product is usually unstable. Ag(II) stability is increased in phosphoric acid media, possibly due to the complex formation between Ag(II) and phosphate anions [393]. Complex compounds of Ag(II) are, as a rule, square planar and paramagnetic ($\mu_B \sim 1.7\text{--}2.2$ BM) [393]. A variety of Ag(II) complexes with heterocyclic amines ($[\text{Ag}(\text{py})_4]^{2+}$, $[\text{Ag}(\text{bipy})_4]^{2+}$), with the accompanying nonreducing counteranions (NO_3^- , ClO_4^- , $\text{S}_2\text{O}_8^{2-}$), have been obtained by the oxidation of Ag(I) with $\text{S}_2\text{O}_8^{2-}$ [393]. Also, a violet $\text{Ba}[\text{AgF}_4]$ compound is known [393]. The importance of fluoride Ag compounds at various oxidation states is also related to their potential superconducting properties [394]. Stable Ag(II) coordination complexes can also exist in a gas phase [395].

Recently, Brückner [396] has collected the currently available data concerning compounds of silver at untypical oxidation states higher than 1. Reaction of elemental fluorine with finely powdered Ag produces $\text{Ag}^{\text{II}}\text{F}_2$, which can be further oxidized to the square-planar complex ion $[\text{Ag}^{\text{III}}\text{F}_4]^-$. By fluorinating the mixture of $\text{AgNO}_3 + \text{KCl}$ at 300°C , one obtains yellow, diamagnetic $\text{K}[\text{AgF}_4]$ compound, which is, however, unstable in contact with moist air and attacks glass [393]. Furthermore, using high-pressure fluorine in the presence of CsF, even $\text{Cs}_2[\text{Ag}^{\text{IV}}\text{F}_6]$ Ag(IV) complex can be obtained [396]. Oxidation of Ag_2O with $\text{S}_2\text{O}_8^{2-}$ at 90°C in strongly alkaline solutions generates the mixed-valence species $\text{Ag}^{\text{I}}\text{Ag}^{\text{III}}\text{O}_2$, sometimes oversimplified as “ $\text{Ag}^{\text{II}}\text{O}$ ”. Anodic oxidation of Ag in concentrated KOH solution gives a yellow $[\text{Ag}(\text{OH})_4]^-$ ion of a half-life of ~ 100 min in 1.2 M NaOH, which decomposes to AgO and O_2 [397]. Electrodeposition of Ag(II) oxide films has been described [398]. Complexes of Ag(III)

with various ligands and their reactions, including complexes with polypeptides and redox reaction of $[\text{Ag}(\text{OH})_4]^-$ with thiosulfate and arsenite, have been studied by Kirschenbaum et al. [399–402]. Eujen et al. have synthesized some di- and trifluoromethylated Ag(I) and Ag(III) complexes, and performed nuclear magnetic resonance (NMR) studies of their structures [403, 404].

Noteworthy is the fact that in spite of high oxidation potential of Ag(II) and Ag(III) ions, their complexes with various organic ligands are also known. The first known compounds of this type are: diamagnetic red ethylenedibiguanidine [393] and dibiguanidinium [396] complexes with Ag(III). Their stereochemical structures are, however, rather uncertain [396]. Later, Barefield and Mocella [405] described the synthesis of Ag(II) and Ag(III) complexes with macrocyclic tetraaza ligands. More recently, well-defined complexes of tetrapyrrolic-based ligands (porphyrin, carbaporphyrin, corrole) with Ag(II) and Ag(III) have been described (for representative examples, see e.g. Refs 406–410). The oxidation kinetics of thiosulfate ion by $[\text{Ag}(\text{cyclam})]^{2+}$, involving the inner-sphere mechanism, has been recently described by Ali et al. [411].

Redox equilibrium of Ag(II)–porphyrin /Ag(III) is characterized with $E^0 = 0.59$ V versus SCE [412]. Evidently, corroles and carbaporphyrins are able to stabilize the Ag(III) oxidation state, presumably due to the presence of π -electron donors, which reduce the formal oxidation state of the metal in such complex [396]. It is expected that such complexes have potential practical applications, for example, as the catalysts in the electron-transfer reactions.

Numerous papers devoted to Ag(II) and Ag(III) compounds represent coordination and analytical chemistry. Below, the

recently published papers of special relevance to electrochemists are discussed. Synthesis of aminomethylpyridine and its complex with Ag(III) (from AgNO₃) has been described by Kahani et al. [413] Naumann et al. [414] have described perfluoralkyl compounds of Ag(III). Li et al. have used the on-line electrogenerated Ag(II) as the oxidant in the flow-injection chemiluminescence determination of captopril [415] and sulfite [416]. Lehmani et al. have analyzed oxidation kinetics of water and organic compounds by silver(II), potentiometrically [417]. Electrochemistry and reaction kinetics of macrocyclic complexes of Ag(II) and substituted mercaptopyridines have been described by Hunting et al. [418] Sroczynski and Grzejdzia [419] have described Ag(I) and Ag(II) complexes with some tetraazamacrocyclic ligands in aqueous solutions. Electrodeposition of silver(II) oxide films has been described by Breyfogle et al. [398]. Panizza et al. [420] have reported electrochemical generation of silver(II) at boron-doped diamond electrodes. Silver(II) species served also as a mediator in electrochemical decomposition of hydrocarbons [421]. Graves et al. [422] have described electrochemical pretreatment and catalytic process for acrylonitrile-butadiene-styrene, utilizing silver(II) chemistry. Ravera et al. [423] have employed Ag(II) and peroxydisulfate reagents in the electrochemically mediated oxidation of polyaromatic sulfonates. Kumar et al. [424] have analyzed the kinetics of oxidation of 3-aminopropan-1-ol and related compounds using Ag(III) species. Zilbermann et al. [425] have described electroprecipitation of Ag(II)/Ag(III) tetraphenylsulfonate porphyrin and electrocatalytic behavior of the obtained films. Also, an Ag(II) redox mediator has been used for electroassisted elimination of ruthenium from dissolved

RuO₂ × H₂O in nitric acid solution. This process has potential application in nuclear fuel reprocessing [426].

References

1. V. M. Gorokhovskii, *J. Anal. Chem.* **2003**, 58, 198.
2. S. Ardizzone, G. Capelletti, P. R. Mussini et al., *Russ. J. Electrochem.* **2003**, 39, 107.
3. S. Trasatti, E. Lust, in *Modern Aspects of Electrochemistry* (Eds.: R. E. White, J. O. M. Bockris, B. E. Conway), Plenum Press, New York, 1999, Vol. 33. and references cited therein.
4. D. I. Leikis, K. V. Rybalka, E. S. Sevastyanov, in *Double Layer and Adsorption at Solid Electrodes* (Eds.: A. N. Frumkin, B. B. Damaskin), Nauka, Moscow, 1972, p. 5.
5. A. J. Ahern, L. C. Nagle, L. D. Burke, *J. Solid State Electrochem.* **2002**, 6, 451.
6. B. Pettinger, C. Bilger, J. Lipkowski, Second harmonic generation anisotropy from single crystalline electrode surfaces in *Interfacial Electrochemistry. Theory, Experiment and Applications* (Eds.: A. Więckowski), Marcel Dekker, New York-Basel, 1999, p. 373.
7. S. Kruszewski, *J. Raman Spectrosc.* **1996**, 27, 513.
8. S. Kruszewski, *Surf. Interface Anal.* **2004**, 21, 830.
9. R. M. Corn, M. Romagnoli, M. D. Levenson et al., *Chem. Phys. Lett.* **1984**, 106, 30.
10. G. L. Richmond, *Surf. Sci.* **1984**, 147, 115.
11. D. J. Campbell, R. M. Corn, *J. Phys. Chem.* **1987**, 91, 5668.
12. H. Seki, *IBM J. Res. Develop.* **1993**, 37, 227, and references cited therein.
13. A. Tadjeddine, A. Le Rille, Sum and difference frequency generation at electrode surfaces, in *Interfacial Electrochemistry. Theory, Experiment and Applications*. (Eds.: A. Więckowski), Marcel Dekker, New York-Basel, 1999, p. 317.
14. A. K. Gaigalas, V. Reipa, V. L. Vilker et al., *Interf. Sci.* **1997**, 186, 339.
15. C. D. Geddes, A. Parfenov, D. Roll et al., *Spectrochim. Acta, Part A* **2004**, 60, 1977.
16. I. Otsuka, T. Iwasaki, *J. Vac. Sci. Technol. B* **1996**, 14, 1153.
17. I. Otsuka, T. Iwasaki, *Surf. Rev. Lett.* **1999**, 6, 923.

18. A. Hamelin, L. Doubova, L. Stoicoviciu et al., *J. Electroanal. Chem.* **1988**, 244, 133.
19. G. Valette, *J. Electroanal. Chem.* **1987**, 224, 285.
20. V. L. Shannon, D. A. Koos, G. L. Richmond, *J. Phys. Chem.* **1987**, 91, 5548.
21. A. Friedrich, B. Pettinger, D. M. Kolb et al., *Chem. Phys. Lett.* **1989**, 163, 123.
22. S. Trasatti, L. M. Doubova, *J. Chem. Soc., Faraday Trans.* **1995**, 91, 3311.
23. S. Trasatti, *Electrochim. Acta.* **1991**, 36, 1659.
24. A. Hamelin, in *Modern Aspects of Electrochemistry* (Eds.: B. E. Conway, R. E. White, J. O. M. Bockris), Plenum Press, New York, 1985, p. 1, Vol. 16.
25. M. A. Vorotyntsev, in *Modern Aspects of Electrochemistry* (Eds.: B. E. Conway, R. E. White, J. O. M. Bockris), Plenum Press, New York, 1986, p. 131, Vol. 17.
26. S. Trasatti, *Elektrokhimiya.* **1995**, 31, 777.
27. R. Adzic, in *Modern Aspects of Electrochemistry* (Eds.: R. E. White, J. O. M. Bockris, B. E. Conway), Plenum Press, New York, 1990, p. 163, Vol. 21.
28. M. Jurkiewicz-Herbich, M. Miłkowska, *J. Solid State Electrochem.* **2001**, 5, 36.
29. J. W. Zheng, X. W. Li, R. N. Gu et al., *J. Phys. Chem. B* **2002**, 106, 1019.
30. N. Quaas, M. Wenderoth, R. G. Ulbrich, *Surf. Sci.* **2004**, 550, 57.
31. M. Giesen, R. Randler, S. Baier et al., *Electrochim. Acta.* **1999**, 45, 527.
32. S. Baier, S. Dieluweit, M. Giesen, *Surf. Sci.* **2002**, 502, 463.
33. S. Baier, M. Giesen, *Phys. Chem. Chem. Phys.* **2000**, 2, 3675.
34. M. I. Haftel, T. L. Einstein, *Appl. Surf. Sci.* **2001**, 175, 49.
35. V. V. Emets, B. B. Damaskin, V. E. Kazari-nov, *Russ. J. Electrochem.* **1996**, 32, 1313.
36. J. T. Li, W. D. Schneider, R. Berndt et al., *Phys. Rev. Lett.* **1998**, 80, 3332.
37. H. Winkes, D. Schumacher, A. Otto, *Surf. Sci.* **1998**, 400, 44.
38. M. F. Toney, J. N. Howard, J. Richer et al., *Nature* **1994**, 368, 444.
39. M. L. Berkowitz, In-Chul Yeh, E. Spohr, Structure of water at the water-metal interface: molecular dynamics computer simulations in *Interfacial Electrochemistry. Theory, Experiment and Applications* (Ed.: A. Więckowski), Marcel Dekker, New York-Basel, 1999, p. 33.
40. Z. H. Sun, Q. W. Liu, Y. F. Li et al., *Chin. Phys. Lett.* **2004**, 21, 1604.
41. K. Itaya, Atomic-scale aspects of anodic dissolution of metals: studies by In situ scanning tunneling microscopy in *Interfacial Electrochemistry. Theory, Experiment and Applications* (Ed.: A. Więckowski), Marcel Dekker, New York-Basel, 1999, p. 187.
42. K. Koga, *App. Phys. A – Mater.* **1999**, 69, 457.
43. C. Mottet, R. Ferrando, F. Hontinfinde et al., *Surf. Sci.* **1998**, 417, 220.
44. L. Pedemonte, R. Tatarek, G. Bracco, *Phys. Rev. B* **2002**, 66, art. no. 045414.
45. L. Savio, L. Vattuone, M. Rocca et al., *Surf. Sci.* **2001**, 486, 65.
46. J. J. Simpson, T. E. Furtak, *J. Electroanal. Chem.* **2001**, 500, 163.
47. L. Savio, L. Vattuone, M. Rocca, *Phys. Rev. B* **2003**, 67, art. no. 045406.
48. J. Sobkowski, M. Jurkiewicz-Herbich, *Wiad. Chem. (Poland)* **2004**, 58, 5.
49. S. Trasatti, *J. Electroanal. Chem.* **1984**, 172, 27.
50. G. Valette, *J. Electroanal. Chem.* **1987**, 230, 189.
51. B. N. Afanasjev, Yu. P. Aktslova, *Elektrokhimiya.* **1994**, 30, 1357.
52. M. Jurkiewicz-Herbich, M. Miłkowska, R. Słojkowska, *Colloids Surf. A* **2002**, 197, 235.
53. L. M. Doubova, A. De Battisti, S. Daolio et al., *J. Electroanal. Chem.* **2001**, 500, 134.
54. T. Vitanov, A. Popov, E. S. Sevastyanov, *J. Electroanal. Chem.* **1982**, 142, 289.
55. S. Smolinski, P. Zelenay, J. Sobkowski, *J. Electroanal. Chem.* **1998**, 442, 41.
56. L. M. Doubova, S. Daolio, C. Pagura et al., *Russ. J. Electrochem.* **2003**, 39, 164.
57. L. M. Doubova, S. Trasatti, *J. Electroanal. Chem.* **2003**, 550–551, 33.
58. M. L. Foresti, M. Innocenti, A. Hamelin, *Langmuir* **1995**, 11, 498.
59. M. L. Foresti, M. Innocenti, R. Guidelli, *J. Electroanal. Chem.* **1994**, 376, 85.
60. L. M. Doubova, S. Trasatti, S. Valcher, *J. Electroanal. Chem.* **1993**, 349, 187.
61. R. A. Gu, Y. H. Sun, P. G. Cao et al., *Acta Chim. Sinica.* **2001**, 59, 1522.
62. D. Hecht, H. H. Strehblow, *J. Electroanal. Chem.* **1997**, 436, 109.
63. R. L. Sobocinski, J. E. Pemberton, *Langmuir* **1990**, 6, 43.

64. R. Truu, P. Kippasto, E. Lust, *Proceedings of the Baltic Conference on Interfacial Electrochemistry*, Dept. Phys. Chem. Tartu University, Tartu, 1996, p. 232.
65. S. L. Joa, J. E. Pemberton, *Langmuir* **1992**, *8*, 2301.
66. J. E. Pemberton, S. L. Joa, A. Shen et al., *J. Chem. Soc., Faraday Trans.* **1996**, *92*, 3683.
67. J. E. Pemberton, A. J. Shen, *Phys. Chem. Chem. Phys.* **1999**, *1*, 5671.
68. C. H. Shi, X. W. Cai, Y. A. Chen et al., *Appl. Surf. Sci.* **2000**, *158*, 11.
69. R. R. Nazmutdinov, T. T. Zinkicheva, *Russ. J. Electrochem.* **2005**, *41*, 206.
70. D. D. Sneddon, A. A. Gewirth, *Surf. Sci.* **1995**, *343*, 185.
71. C. C. Chang, C. H. Lung, *J. Chin. Chem. Soc.-Taip.* **1996**, *43*, 145.
72. B. V. Andryushechkin, K. N. Eltsov, V. M. Shevlyuga et al., *Surf. Sci.* **1999**, *421*, 27.
73. B. M. Ocko, J. X. Wang, T. Wandlowski, *Phys. Rev. Lett.* **1997**, *79*, 1511.
74. O. Endo, D. Matsumura, K. Kohdate et al., *J. Electroanal. Chem.* **2000**, *494*, 121.
75. G. Beltramo, E. Santos, W. Schmickler, *Langmuir* **2003**, *19*, 4723.
76. G. Beltramo, E. Santos, *J. Electroanal. Chem.* **2003**, *556*, 127.
77. E. Santos, C. Schürrer, G. Beltramo et al., *J. Solid State Electr.* **2003**, *7*, 567.
78. M. Kawasaki, H. Ishii, H. Uchiki, *Microsc. Res. Tech.* **1998**, *42*, 100.
79. V. D. Jović, B. M. Jović, *J. Electroanal. Chem.* **2003**, *541*, 1.
80. O. Endo, M. Kiguchi, T. Yokoyama et al., *J. Electroanal. Chem.* **1999**, *473*, 19.
81. S. W. Wang, P. A. Rikvold, *Phys. Rev. B* **2002**, *65*, art. no. 155406.
82. T. Wandlowski, J. X. Wang, B. M. Ocko, *J. Electroanal. Chem.* **2001**, *500*, 418.
83. J. X. Wang, R. P. Adzic, B. M. Ocko, In situ surface X-ray scattering studies of electrosorption in *Interfacial Electrochemistry. Theory, Experiment and Applications* (Ed.: A. Więckowski), Marcel Dekker, New York-Basel, 1999, p. 175.
84. C. Hanewinkel, A. Otto, T. Wandlowski, *Surf. Sci.* **1999**, *429*, 255.
85. T. Shimooka, J. Inukai, K. Itaya, *J. Electrochem. Soc.* **2002**, *149*, E19.
86. P. A. Rikvold, I. Abou Hamad, G. Brown et al., *Abstr. Pap. Am. Chem. Soc.* **2003**, *225*, 444–COLL.
87. I. Abou Hamad, T. Wandlowski, G. Brown et al., *J. Electroanal. Chem.* **2003**, *554*, 211.
88. S. J. Mitchell, G. Brown, P. A. Rikvold, *J. Electroanal. Chem.* **2000**, *493*, 68.
89. S. J. Mitchell, G. Brown, P. A. Rikvold, *Surf. Sci.* **2001**, *471*, 125.
90. T. Yamada, K. Ogaki, S. Okubo et al., *Surf. Sci.* **1996**, *369*, 321.
91. Y. Wang, Q. Sun, K. N. Fan et al., *Acta Chim. Sinica.* **2000**, *58*, 931.
92. H. R. Tang, W. N. Wang, Z. H. Li et al., *Surf. Sci.* **2000**, *450*, 133.
93. Y. Wang, Q. Sun, K. N. Fan et al., *Chem. Phys. Lett.* **2001**, *334*, 411.
94. T. Teshima, K. Ogaki, K. Itaya, *J. Phys. Chem. B* **1997**, *101*, 2046.
95. N. A. Rogozhnikov, *Russ. J. Electrochem.* **1997**, *33*, 668.
96. G. Baltrunas, G. S. Popkairov, R. N. Schindler, *J. Electroanal. Chem.* **1997**, *435*, 95.
97. A. Tadjeddine, A. Peremans, P. Guyot-Sionnest, *Surf. Sci.* **1995**, *335*, 210.
98. G. A. Bowmaker, J. M. Leger, A. Le Rille et al., *J. Chem. Soc., Faraday Trans.* **1998**, *9*, 1309.
99. F. Tielens, M. Saeys, E. Tourwe et al., *J. Phys. Chem. A* **2002**, *106*, 1450.
100. D. Lutzenkirchen-Hecht, H. H. Strehblow, *Electrochim. Acta* **1998**, *43*, 2957.
101. M. Innocenti, M. L. Foresti, A. Fernandez et al., *J. Phys. Chem. B* **1998**, *102*, 9667.
102. M. L. Foresti, M. Innocenti, F. Forni et al., *Langmuir* **1998**, *14*, 7008.
103. A. R. Alemozafar, X. C. Guo, R. J. Madix et al., *Surf. Sci.* **2002**, *504*, 223.
104. P. Paredes Olivera, M. Patrito, H. Sellers, Electronic structure calculations of polyatomic oxyanions adsorbed on metal surfaces in *Interfacial Electrochemistry. Theory, Experiment and Applications* (Ed.: A. Więckowski), Marcel Dekker, New York-Basel, 1999, p. 63.
105. E. J. Sobkowski, S. Smoliński, P. Zelenay, *Abstr. Pap. Am. Chem. Soc.* **1996**, *212*, 49–COLL.
106. J. Sobkowski, S. Smolinski, P. Zelenay, *Colloids Surf. A* **1998**, *134*, 39.
107. M. Schweizer, D. M. Kolb, *Surf. Sci.* **2003**, *544*, 93.
108. N. S. Marinkovic, J. S. Marinkovic, R. R. Adzic, *J. Electroanal. Chem.* **1999**, *467*, 291.

109. J. Blomqvist, P. Salo, M. Alatalo, *Surf. Sci.* **2004**, 566, 1067.
110. M. Kittel, D. I. Sayago, J. T. Hoeft et al., *Surf. Sci.* **2002**, 516, 237.
111. E. Giudice, E. Magnano, S. Rusponi et al., *Surf. Sci.* **1998**, 405, L561.
112. G. Costantini, S. Rusponi, E. Giudice et al., *Carbon* **1999**, 37, 717.
113. A. Goldoni, G. Paolucci, *Surf. Sci.* **1999**, 437, 353.
114. C. Cepek, L. Giovannelli, M. Sancrotti et al., *Surf. Sci.* **2000**, 454, 766.
115. C. Cepek, M. Sancrotti, T. Greber et al., *Surf. Sci.* **2000**, 454, 467.
116. C. Cepek, R. Fasel, M. Sancrotti et al., *Phys. Rev. B* **2001**, 63, art. no. 125406.
117. M. Grobis, X. Lu, M. F. Crommie, *Phys. Rev. B* **2002**, 66, art. no. 161408.
118. W. W. Pai, C. L. Hsu, C. R. Chiang et al., *Surf. Sci.* **2002**, 519, L605.
119. G. Valette, *J. Electroanal. Chem.* **1981**, 122, 285.
120. G. Pirug, H. P. Bonzel, Electrochemical double-layer modeling under ultrahigh vacuum conditions in *Interfacial Electrochemistry. Theory, Experiment and Applications* (Eds.: A. Więckowski), Marcel Dekker, New York-Basel, 1999, p. 269.
121. N. Kizhakevariam, R. Döhl-Oelze, E. M. Stuve, *J. Phys. Chem.* **1990**, 94, 5934.
122. A. Krasnopoler, E. M. Stuve, *J. Vac. Sci. Technol. A* **1995**, 13, 1681.
123. G. Valette, *J. Electroanal. Chem.* **1982**, 138, 37.
124. G. Niaura, R. Jakubenias, *J. Electroanal. Chem.* **2001**, 510, 50.
125. T. C. Girija, M. Sangaranarayanan, *J. Colloid Interface Sci.* **2005**, 282, 92.
126. K. J. Stevenson, D. W. Hatchett, H. S. White, *Langmuir* **1997**, 13, 6824.
127. A. Krasnopoler, N. Kizhakevariam, E. M. Stuve, *J. Chem. Soc., Faraday Trans.* **1996**, 92, 2445.
128. X. C. Guo, R. J. Madix, *Surf. Sci.* **2002**, 501, 37.
129. L. Lee, J. X. Wang, R. R. Adzic et al., *J. Am. Chem. Soc.* **2001**, 123, 8838.
130. M. Jafarian, M. G. Mahjani, O. Azizi, *Indian J. Chem. A* **2003**, 42, 516.
131. A. A. Gurten, K. Kayakirilmaz, B. Yazici et al., *Int. J. Hydrogen Energy* **2003**, 28, 1083.
132. D. Welipitiya, P. A. Dowben, J. D. Zhang et al., *Surf. Sci.* **1996**, 367, 20.
133. C. M. Woodbridge, D. L. Pugmire, R. C. Johnson et al., *J. Phys. Chem. B* **2000**, 104, 3085.
134. M. A. Langell, C. M. Woodbridge, D. L. Pugmire et al., *Abstr. Pap. Am. Chem. Soc.* **2000**, 219, 124–COLL.
135. D. L. Pugmire, C. M. Woodbridge, N. M. Boag et al., *Surf. Sci.* **2001**, 471, 155.
136. D. L. Pugmire, C. M. Woodbridge, M. A. Langell, *Surf. Sci.* **1998**, 411, L844.
137. M. Akita, N. Osaka, S. Hiramoto et al., *Surf. Sci.* **1999**, 428, 374.
138. A. Kokalj, A. Dal Corso, S. de Gironcoli et al., *Surf. Sci.* **2002**, 507, 62.
139. A. Kokalj, A. Dal Corso, S. de Gironcoli et al., *J. Phys. Chem. B* **2002**, 106, 9839.
140. A. Kokalj, A. Dal Corso, S. de Gironcoli et al., *Surf. Sci.* **2003**, 532, 191.
141. L. Vattuone, L. Savio, L. Valbusa et al., *Chem. Phys. Lett.* **2000**, 331, 177.
142. L. Vattuone, L. Savio, M. Rocca, *Int. J. Mod. Phys. B* **2003**, 17, 2497.
143. A. Kokalj, A. Dal Corso, S. de Gironcoli et al., *Surf. Sci.* **2004**, 566, 1018.
144. J. Pawela-Crew, R. J. Madix, *J. Chem. Phys.* **1996**, 104, 1699.
145. F. J. Williams, D. P. C. Bird, E. C. H. Sykes et al., *J. Phys. Chem. B* **2003**, 107, 3824.
146. N. Osaka, M. Akita, K. Itoh, *J. Phys. Chem. B* **1998**, 102, 6817.
147. J. L. Gland, J. T. Ranney, S. R. Bare, *Abstr. Pap. Am. Chem. Soc.* **1999**, 217, 024–CATL.
148. J. I. Pascual, J. J. Jackiw, K. F. Kelly et al., *Phys. Rev. B* **2000**, 62, 12632.
149. J. I. Pascual, J. J. Jackiw, Z. Song et al., *Phys. Rev. Lett.* **2001**, 86, 1050.
150. K. F. Kelly, J. J. Jackiw, J. I. Pascual, *Abstr. Pap. Am. Chem. Soc.* **2000**, 220, 192–COLL Part1.
151. J. I. Pascual, J. J. Jackiw, Z. Song et al., *Surf. Sci.* **2002**, 502, 1.
152. S. G. Ma, G. Z. Wu, *J. Mol. Struct.* **1995**, 372, 127.
153. X. M. Yang, K. Ajito, D. A. Tryk et al., *J. Phys. Chem.* **1996**, 100, 7293.
154. V. Tsionsky, L. Daikhin, G. Zilberman et al., *Faraday Discuss.* **1997**, 107, 337.
155. M. A. Nicholson, J. F. Aust, H. S. Booksh et al., *Vib. Spectrosc.* **2000**, 24, 157.
156. A. Hamelin, S. Morin, J. Richer et al., *J. Electroanal. Chem.* **1989**, 272, 241.
157. A. Hamelin, S. Morin, J. Richer et al., *J. Electroanal. Chem.* **1990**, 285, 249.

158. A. Hamelin, S. Morin, J. Richer et al., *J. Electroanal. Chem.* **1991**, 304, 195.
159. C. T. Shi, W. Zhang, R. L. Birke et al., *J. Electroanal. Chem.* **1997**, 423, 67.
160. W. H. Li, X. Y. Li, N. T. Yu, *Chem. Phys. Lett.* **1999**, 305, 303.
161. I. Lopez-Tocon, S. P. Centeno, J. L. Castro, *Chem. Phys. Lett.* **2003**, 377, 111.
162. J. F. Arenas, I. L. Tocon, M. S. Woolley et al., *J. Raman Spectrosc.* **1998**, 29, 673.
163. J. Bukowska, M. Calvo, M. Jurkiewicz-Herbich et al., *Pol. J. Chem.* **2002**, 76, 1151.
164. A. G. Brolo, D. E. Irish, *J. Electroanal. Chem.* **1996**, 414, 183.
165. A. G. Brolo, D. E. Irish, *J. Chem. Soc., Faraday Trans.* **1997**, 93, 419.
166. A. G. Brolo, D. E. Irish, *Can. J. Chem.* **1997**, 75, 1643.
167. A. G. Brolo, D. E. Irish, *ACS Symp. Ser. N.* 656 ACS, Washington, DC, Ch. 22, p. 310.
168. J. F. Arenas, M. S. Woolley, I. López-Tocón et al., *J. Chem. Phys.* **2000**, 112, 7669.
169. J. F. Arenas, S. P. Centeno, I. López-Tocón et al., *Vib. Spectrosc.* **2004**, 35, 39.
170. A. Kudelski, J. Bukowska, *Surf. Sci.* **1996**, 368, 396.
171. J. Cehn, W. T. Zhao, J. M. Hu et al., *Chem. J. Chinese Univ.-Chinese.* **1995**, 16, 1697.
172. N. Osaka, M. Akita, S. Hiramoto et al., *Surf. Sci.* **1999**, 428, 381.
173. P. Waszczuk, P. Zelenay, J. Sobkowski, *Electrochim. Acta* **1998**, 43, 1963.
174. B. Parker, B. Immaraporn, A. J. Gellman, *Langmuir* **2001**, 17, 6638.
175. R. Guidelli, M. L. Foresti, *J. Electroanal. Chem.* **1986**, 197, 103.
176. M. Jurkiewicz-Herbich, M. Miłkowska, R. Słojkowska, *Colloids Surf., A* **2002**, 197, 235.
177. G. Wu, D. Stacchiola, M. Kaltchev et al., *Surf. Sci.* **2000**, 463, 81.
178. G. Wu, D. Stacchiola, M. Collins et al., *Surf. Rev. Lett.* **2000**, 7, 271.
179. L. M. Doubova, S. Valcher, S. Trasatti, *J. Electroanal. Chem.* **1994**, 376, 73.
180. A. L. Schwaner, J. M. White, *J. Phys. Chem. B* **1997**, 101, 11119.
181. A. L. Schwaner, J. M. White, *J. Phys. Chem. B* **1997**, 101, 10414.
182. M. L. Foresti, M. Innocenti, R. Guidelli et al., *J. Electroanal. Chem.* **1999**, 467, 217.
183. E. Santos, C. Schurrer, A. Brunetti et al., *Langmuir* **2002**, 18, 2771.
184. X. W. Li, J. W. Zheng, Y. G. Zhou et al., *Chinese J. Anal. Chem.* **2003**, 31, 1333.
185. C. Tegenkamp, H. Pfnur, *J. Chem. Phys.* **2003**, 118, 7578.
186. Z. J. Liu, G. Z. Wu, *Chem. Phys. Lett.* **2004**, 389, 298.
187. Q. L. Zhong, D. Q. Wang, F. M. Liu et al., *Acta Phys-Chim. Sin.* **1998**, 14, 562.
188. A. Łukomska, J. Sobkowski, *Pol. J. Chem.* **2004**, 78, 1135.
189. S. Smoliński, J. Sobkowski, *Pol. J. Chem.* **2001**, 75, 1493.
190. S. Yagi, Y. Nakano, E. Ikenaga et al., *Surf. Sci.* **2004**, 566, 746.
191. T. Kasahara, H. Shinohara, Y. Oshima et al., *Surf. Sci.* **2004**, 558, 65.
192. M. Schweizer, D. M. Kolb, *J. Electroanal. Chem.* **2004**, 564, 85.
193. D. W. Hatchett, K. J. Stevenson, W. B. Lacy et al., *J. Am. Chem. Soc.* **1997**, 119, 6596.
194. K. J. Stevenson, X. P. Gao, D. W. Hatchett et al., *J. Electroanal. Chem.* **1998**, 447, 43.
195. D. W. Hatchett, R. H. Uibel, K. J. Stevenson et al., *J. Am. Chem. Soc.* **1998**, 120, 1062.
196. C. A. Widrig, C. Chung, M. D. Porter, *J. Electroanal. Chem.* **1991**, 310, 335.
197. D. W. Hatchett, X. P. Gao, S. W. Catron et al., *J. Phys. Chem.* **1996**, 100, 331.
198. N. Mohtat, M. Byloos, M. Soucy et al., *J. Electroanal. Chem.* **2000**, 484, 120.
199. H. Rieley, G. K. Kendall, R. G. Jones et al., *Langmuir* **1999**, 15, 8856.
200. M. Cavallini, M. Bracali, G. Aloisi et al., *Langmuir* **1999**, 15, 3003.
201. E. E. Doomes, P. N. Floriano, R. W. Tittsworth et al., *J. Phys. Chem. B* **2003**, 107, 10193.
202. R. H. Uibel, D. W. Hatchett, K. J. Stevenson et al., *Abstr. Pap. Am. Chem. Soc.* **1998**, 215, 204-COLL.
203. J. G. Lee, J. Lee, J. T. Yates, *J. Am. Chem. Soc.* **2004**, 126, 440.
204. J. G. Lee, J. Lee, J. T. Yates, *J. Phys. Chem. B* **2004**, 108, 1686.
205. O. Azzaroni, M. E. Vela, G. Andreasen et al., *J. Phys. Chem. B* **2002**, 106, 12267.
206. R. Heinz, J. P. Rabe, *Langmuir* **1995**, 11, 506.
207. A. Vivoni, S. P. Chen, D. Ejeh et al., *Langmuir* **2000**, 16, 3310.
208. F. Cunha, J. R. Garcia, F. C. Nart, *J. Solid State Electr.* **2003**, 7, 576.

209. F. Wang, J. Zheng, X. Li et al., *J. Electroanal. Chem.* **2003**, 545, 123.
210. W. H. Li, X. Y. Li, N. T. Yu, *Chem. Phys. Lett.* **1999**, 312, 28.
211. S. P. Chen, Z. Qiao, A. Vivoni et al., *Spectrochim. Acta, Part A* **2003**, 59, 2905.
212. A. G. Brolo, P. Germain, G. Hager, *J. Phys. Chem. B* **2002**, 106, 5982.
213. S. P. Chen, C. M. Hosten, A. Vivoni et al., *Langmuir* **2002**, 18, 9888.
214. P. G. Cao, R. A. Gu, Z. Q. Tian, *J. Phys. Chem. B* **2003**, 107, 769.
215. P. G. Cao, R. N. Gu, L. Qiu et al., *Surf. Sci.* **2003**, 531, 217.
216. D. A. Carter, J. E. Pemberton, K. J. Woelfel, *J. Phys. Chem. B* **1998**, 102, 9870.
217. M. Miłkowska, M. Jurkiewicz-Herbich, *Pol. J. Chem.* **1998**, 72, 1096.
218. D. Hobara, K. Niki, T. M. Cotton, *Biospectroscopy* **1998**, 4, 161.
219. G. Niaura, A. K. Gaigalas, V. L. Vilker, *J. Electroanal. Chem.* **1996**, 416, 167.
220. T. Wandlowski, *J. Electroanal. Chem.* **1995**, 395, 83.
221. R. Guidelli, M. L. Foresti, M. Innocenti, *J. Phys. Chem.* **1996**, 100, 18491.
222. M. Cavallini, G. Aloisi, M. Bracali et al., *J. Electroanal. Chem.* **1998**, 444, 75.
223. L. A. Dick, A. J. Haes, R. P. Van Duyne, *J. Phys. Chem. B* **2000**, 104, 11752.
224. H. Yang, Z. Zhang, G. Shen et al., *J. Raman Spectrosc.* **2004**, 35, 190.
225. Y. Fang, C. L. Bai, Y. Wei et al., *Appl. Spectrosc.* **1996**, 50, 48.
226. F. J. Williams, O. P. H. Vaughan, K. J. Knox et al., *Chem. Commun.* **2004**, 15, 1688.
227. S. Bernad, T. Soulimane, S. Lecomte, *J. Raman Spectrosc.* **2004**, 35, 47.
228. W. Grochala, A. Kudelski, J. Bukowska, *J. Raman Spectrosc.* **1998**, 29, 681.
229. A. G. Brolo, A. C. Sanderson, A. P. Smith, *Phys. Rev. B* **2004**, 69, art. No. 045424.
230. S. H. de Araujo Nicolai, P. R. P. Rodrigues, S. M. L. Agostinho et al., *J. Electroanal. Chem.* **2002**, 527, 103.
231. S. H. A. Nicolai, J. C. Rubim, *Langmuir* **2003**, 19, 4291.
232. K. Itaya, N. Batina, M. Kunitake et al., *ACS Symp. Ser.* **1997**, 656, 171.
233. X. C. Guo, R. J. Madix, *Surf. Sci.* **2004**, 564, 21.
234. F. S. Tautz, S. Sloboshanin, V. Shklover et al., *Appl. Surf. Sci.* **2000**, 166, 363.
235. R. Nowakowski, C. Seidel, H. Fuchs, *Phys. Rev. B* **2001**, 63, art. no. 195418.
236. M. Itagaki, H. Hasegawa, K. Watanabe et al., *Electrochemistry* **2003**, 71, 536.
237. S. Zabarnick, P. Zelesnik, S. D. Whitacre, *Ind. Eng. Chem. Res.* **1996**, 35, 2576.
238. S. L. Chen, B. L. Wu, C. S. Cha, *J. Electroanal. Chem.* **1996**, 416, 53.
239. S. L. Chen, B. L. Wu, C. S. Cha, *J. Electroanal. Chem.* **1997**, 420, 111.
240. D. Bughiu, M. Buda, L. Anicai, *Rev. Roum. Chem.* **1997**, 42, 429.
241. L. C. Nagle, A. J. Ahern, L. D. Burke, *J. Solid State Electrochem.* **2002**, 6, 320.
242. E. R. Savinova, S. Wasle, K. Doblhofer, *Electrochim. Acta* **1998**, 44, 1341.
243. G. Flätgen, S. Wasle, M. Lübke et al., *Electrochim. Acta* **1999**, 44, 4499.
244. A. Raukema, D. A. Butler, A. W. Kleyn, *J. Phys. – Condens. Mat.* **1996**, 8, 2247.
245. D. M. Bird, P. A. Gravit, *Abstr. Pap. Am. Chem. Soc.* **1997**, 213, 8–PETR.
246. G. Benedek, F. B. De Mongeot, U. Valbusa et al., *Europhys. Lett.* **2001**, 53, 544.
247. G. Cipriani, D. Loffreda, A. Dal Corso et al., *Surf. Sci.* **2002**, 501, 182.
248. S. Altieri, S. F. Contri, S. Agnoli et al., *Surf. Sci.* **2004**, 566, 1071.
249. B. M. Jovic, V. D. Jovic, G. R. Stafford, *Electrochem. Commun.* **1999**, 1, 247.
250. E. R. Savinova, P. Kraft, B. Pettinger, et al. *J. Electroanal. Chem.* **1997**, 430, 47.
251. E. R. Savinova, D. Zemlyanov, A. Scheybal et al., *Langmuir* **1999**, 15, 6546.
252. E. R. Savinova, D. Zemlyanov, A. Scheybal et al., *Langmuir* **1999**, 15, 6552.
253. D. Y. Zemlyanov, E. Savinova, A. Scheybal et al., *Surf. Sci.* **1998**, 418, 441.
254. E. R. Savinova, D. Zemlyanov, B. Pettinger et al., *Electrochim. Acta* **2000**, 46, 175.
255. M. Danckwerts, E. Savinova, B. Pettinger, *Appl. Phys. B – Lasers Opt.* **2002**, 74, 635.
256. M. Danckwerts, E. R. Savinova, S. L. Horswell et al., *Z. phys. Chem.* **2003**, 217, 557.
257. S. K. Shaikhutdinov, E. R. Savinova, A. Sheybal et al., *J. Electroanal. Chem.* **2001**, 500, 208.
258. L. Li, J. C. Yang, *Mater. High Temp.* **2003**, 20, 601.
259. C. I. Carlisle, D. A. King, M. L. Bouquet et al., *Phys. Rev. Lett.* **2000**, 84, 3899.
260. J. Kunze, H. H. Strehblow, G. Staikov, *Electrochem. Commun.* **2004**, 6, 132.

261. S. L. Horswell, A. L. N. Pinheiro, E. R. Savinova et al., *G. Ertl., Langmuir* **2004**, *20*, 10970.
262. A. Kokalj, N. Bonini, A. Dal Corso et al., *Surf. Sci.* **2004**, 566, 1107.
263. J. L. Conyers, H. S. White, *J. Phys. Chem. B* **1999**, *103*, 1960.
264. G. Flätgen, K. Krischer, B. Pettinger et al., *G. Ertl., Abstr. Pap. Amer. Chem. Soc.* **1996**, 212, 69–COLL.
265. G. Flätgen, K. Krischer, B. Pettinger et al., *Science* **1995**, 269, 668.
266. M. A. M. Ibrahim, H. H. Hassan, S. S. Abd El Rehim et al., *J. Solid State Electr.* **1999**, *3*, 380.
267. S. S. Abd El Rehim, H. H. Hassan, M. A. M. Ibrahim et al., *Monatsh. Chem.* **1999**, *130*, 1207.
268. L. Constant, B. Krenzer, W. Stenzel et al., *Surf. Sci.* **1999**, 428, 262.
269. X. C. Guo, R. J. Madix, *Surf. Sci.* **2001**, 489, 37.
270. U. Burghaus, H. Conrad, *Surf. Sci.* **1996**, 352, 253.
271. U. Burghaus, H. Conrad, *Surf. Sci.* **1996**, 352, 201.
272. J. V. Barth, T. Zambelli, *Surf. Sci.* **2002**, 513, 359.
273. U. Burghaus, A. Bottcher, H. Conrad, *Surf. Rev. Lett.* **2003**, *10*, 39.
274. X. C. Guo, R. J. Madix, *Surf. Sci.* **2004**, 550, 81.
275. G. S. Jones, M. A. Barteau, *J. Vac. Sci. Technol. A* **1997**, *15*, 1667.
276. G. S. Jones, M. A. Barteau, J. M. Vohs, *J. Phys. Chem. B* **1999**, *103*, 1144.
277. Q. Sun, Y. Wang, K. N. Fan et al., *Surf. Sci.* **2000**, 459, 213.
278. B. Z. Zeng, F. Y. Ma, W. C. Purdy, *Electroanalysis* **1998**, *10*, 677.
279. B. Z. Zeng, W. C. Purdy, *Electroanalysis* **1999**, *11*, 879.
280. S. Y. Dong, J. B. Zheng, Y. L. Ning et al., *Chem. J. Chinese Univ.-Chinese* **2003**, *24*, 428.
281. B. X. Ye, X. Y. Zhou, *Talanta* **1997**, *44*, 831.
282. B. X. Ye, X. Y. Zhou, *Chem. J. Chinese Univ.-Chinese* **1996**, *17*, 33.
283. W. B. Cai, I. C. Stefan, D. A. Scherson, *J. Electroanal. Chem.* **2002**, 254, 36.
284. J. W. Zheng, X. W. Li, H. Y. Xu et al., *Spectrosc. Spect. Anal.* **2003**, *23*, 294.
285. G. X. Li, J. J. Zhu, H. Q. Fang et al., *J. Electrochem. Soc.* **1996**, 143, L141.
286. J. J. McMahon, T. J. Gergel, D. M. Otterson et al., *Surf. Sci.* **1999**, 440, 357.
287. S. Sanchez-Cortes, J. V. Garcia-Ramos, *Langmuir* **2000**, *16*, 764.
288. W. H. Li, X. Y. Li, N. T. Yu, *Chem. Phys. Lett.* **2000**, 327, 153.
289. G. X. Li, H. Y. Chen, D. X. Zhu, *Anal. Chim. Acta.* **1996**, 319, 275.
290. G. X. Lin, H. Y. Chen, D. X. Zhu, *Chem. J. Chinese Univ.-Chinese* **1996**, *17*, 553.
291. G. X. Li, H. Q. Fang, Y. Q. Qian et al., *Electroanalysis* **1996**, *8*, 465.
292. J. J. Zhu, Y. Gong, J. J. Zhang et al., *Electroanalysis* **1997**, *9*, 1030.
293. G. X. Li, H. Q. Fang, Y. T. Long et al., *Anal. Lett.* **1996**, *29*, 1273.
294. S. Zhang, W. L. Sun, W. Zhang et al., *Anal. Lett.* **1998**, *31*, 2159.
295. Y. T. Long, J. Zou, H. Y. Chen, *Anal. Lett.* **1997**, *30*, 2691.
296. Y. T. Long, H. Y. Chen, *J. Electroanal. Chem.* **1997**, 440, 239.
297. L. Tian, W. Z. Wei, Y. A. Mao, *Anal. Sci.* **2004**, *20*, 623.
298. L. Trnkova, *Talanta* **2002**, *56*, 887.
299. K. Jüttner, W. J. Lorenz, *Z. phys. Chem. NF* **1980**, *122*, 163.
300. E. Herreo, L. J. Buller, H. D. Abruña, *Chem. Rev.* **2001**, *101*, 1897.
301. G. Pacchioni, *Electrochim. Acta* **1996**, *41*, 2285.
302. S. G. Garcia, C. E. Mayer, D. R. Salinas et al., *J. Brazil. Chem. Soc.* **2004**, *15*, 917.
303. C. A. Zell, F. Endres, W. Freyland, *Phys. Chem. Chem. Phys.* **1999**, *1*, 697.
304. S. Garcia, D. E. Salinas, C. E. Mayer, *An. Asoc. Quim. Argent.* **1996**, *84*, 597.
305. S. Garcia, D. Salinas, C. Mayer et al., *Electrochim. Acta* **1998**, *43*, 3007.
306. N. Ikemiyu, K. Yamada, S. Hara, *Surf. Sci.* **1996**, 348, 253.
307. M. C. Gimenez, M. G. Del Popolo, E. P. M. Leiva, *Electrochim. Acta* **1999**, *45*, 699.
308. M. C. Gimenez, M. G. Del Popolo, E. P. M. Leiva et al., *J. Electrochem. Soc.* **2002**, *149*, E109.
309. E. D. Chabala, T. Rayment, *J. Electroanal. Chem.* **1996**, 401, 257.
310. E. D. Chabala, A. R. Ramadan, T. Brunt et al., *J. Electroanal. Chem.* **1996**, 412, 67.
311. A. R. Ramadan, E. D. Chabala, T. Rayment, *Phys. Chem. Chem. Phys.* **1999**, *1*, 1591.
312. V. Rooryck, C. Buess-Herman, G. A. Attard et al., *J. Vac. Sci. Technol. A* **1999**, *17*, 1647.

313. V. Rooryck, F. Reniers, C. Buess-Herman et al., *J. Electroanal. Chem.* **2000**, 482, 93.
314. T. Kondo, J. Morita, M. Okamura et al., *J. Electroanal. Chem.* **2002**, 532, 201.
315. H. Cercellier, Y. Fagot-Revurat, B. Kierren et al., *Surf. Sci.* **2004**, 566, 520.
316. M. Watanabe, H. Uchida, M. Hiei, *Abstr. Pap. Am. Chem. Soc.* **1996**, 212, 171–COLL.
317. S. Takami, G. K. Jennings, P. E. Laibinis, *Langmuir* **2001**, 17, 441.
318. J. X. Wang, B. M. Ocko, R. R. Adzic, *Surf. Sci.* **2003**, 540, 230.
319. D. Oyamatsu, M. Nishizawa, S. Kubawata et al., *Abstr. Pap. Am. Chem. Soc.* **1998**, 215, 071–COLL.
320. X. Y. Hu, G. Xia, R. Guo, *Bull. Electrochem.* **2002**, 18, 481.
321. D. G. Frank, O. M. R. Chyan, T. Golden et al., *J. Phys. Chem.* **1994**, 98, 1896.
322. S. Ogura, K. Fukutani, M. Wilde et al., *Surf. Sci.* **2004**, 566, 755.
323. E. Leiva, W. Schmickler, *Electrochim. Acta* **1994**, 39, 1015.
324. K. J. Stevenson, D. W. Hatchett, H. S. White, *Langmuir* **1996**, 12, 494.
325. J. Sackmann, A. Bunk, R. T. Potschke et al., *Electrochim. Acta* **1998**, 43, 2863.
326. R. Widmer, H. Siegenthaler, *J. Electrochem. Soc.* **2004**, 151, E238.
327. W. Obretenov, N. Dimitrov, A. Popov, *J. Cryst. Growth.* **1996**, 167, 253.
328. U. Schmidt, S. Vinzelberg, G. Staikov, *Surf. Sci.* **1996**, 348, 261.
329. P. Waszczuk, A. Wnuk, J. Sobkowski, *Electrochim. Acta* **1999**, 44, 1789.
330. J. X. Wang, R. R. Adzic, O. M. Magnussen, *Surf. Sci.* **1995**, 344, 111.
331. S. Morin, A. Lachenwitzer, O. M. Magnussen et al., *Phys. Rev. Lett.* **1999**, 83, 5066.
332. S. Morin, A. Lachenwitzer, F. A. Moller et al., *J. Electrochem. Soc.* **1999**, 146, 1013.
333. A. Lachenwitzer, S. Morin, O. M. Magnussen et al., *Phys. Chem. Chem. Phys.* **2001**, 3, 3351.
334. K. Sztyler, A. Budniok, *Bull. Electrochem.* **1997**, 13, 223.
335. P. Luches, S. Altieri, C. Giovanardi et al., *Thin Solid Films* **2001**, 400, 139.
336. M. Caffio, B. Cortigiani, G. Roviola et al., *J. Phys. Chem. B* **2004**, 108, 9919.
337. G. D. Aloisi, M. Cavallini, M. Innocenti et al., *J. Phys. Chem. B* **1997**, 101, 4774.
338. R. Z. Chen, D. S. Xu, G. L. Guo et al., *J. Mater. Chem.* **2002**, 12, 1437.
339. R. Z. Chen, D. S. Xu, G. L. Guo et al., *Electrochim. Acta* **2004**, 49, 2243.
340. R. Z. Chen, D. S. Xu, G. L. Guo et al., *J. Electrochem. Soc.* **2003**, 150, G183.
341. M. Innocenti, G. Pezzatini, F. Forni et al., *J. Electrochem. Soc.* **2001**, 148, C357.
342. M. Innocenti, S. Cattarin, M. Cavallini et al., *J. Electroanal. Chem.* **2002**, 532, 219.
343. M. L. Foresti, G. Pezzatini, M. Cavallini et al., *J. Phys. Chem. B* **1998**, 102, 7413.
344. T. Cecconi, A. Atrei, U. Bardi et al., *J. Electron Spectrosc. Relat. Phenom.* **2001**, 114, 563.
345. G. Pezzatini, S. Caporali, M. Innocenti et al., *J. Electroanal. Chem.* **1999**, 475, 164.
346. M. Cavallini, G. Aloisi, R. Guidelli, *Langmuir* **1999**, 15, 2993.
347. S. Jayakrishnan, *Trans. Inst. Met. Finish.* **2000**, 16, 124.
348. J. M. Zen, C. C. Yang, A. S. Kumar, *Electrochim. Acta* **2001**, 47, 899.
349. M. Del Popolo, E. Leiva, *J. Electroanal. Chem.* **1997**, 440, 271.
350. M. Dietterle, T. Will, D. M. Kolb, *Surf. Sci.* **1998**, 396, 189.
351. R. Vidu, N. Hirai, S. Hara, *Phys. Chem. Chem. Phys.* **2001**, 3, 3320.
352. P. Schieffer, C. Krembel, M. C. Hanf et al., *Solid State Commun.* **1996**, 97, 757.
353. R. Abt, S. Blugel, *Philos. Mag. B* **1998**, 78, 659.
354. O. Elmouhssine, G. Moraitis, J. C. Parlebas et al., *J. Appl. Phys.* **1998**, 83, 7013.
355. A. J. Quinn, J. F. Lawler, R. Schad et al., *Surf. Sci.* **1997**, 385, 395.
356. P. Steadman, C. Norris, C. L. Nicklin et al., *Phys. Rev. B* **2001**, 64, art. no. 245412.
357. M. C. Hanf, C. Krembel, D. Bolmont, G. Gewinner, *Phys. Rev. B* **2003**, 68, art. no. 144419.
358. M. H. Langelaar, D. O. Boerma, *Surf. Sci.* **1998**, 395, 131.
359. S. Terreni, A. Cossaro, G. Gonella et al., *Phys. Rev. B* **2004**, 70, art. no. 115420.
360. J. Dekoster, B. Degroote, H. Pattyn et al., *Appl. Phys. Lett.* **1999**, 75, 938.
361. B. Degroote, H. Pattyn, S. Degroote et al., *Thin Solid Films* **2000**, 380, 111.
362. F. Amitouche, S. Bouarab, C. Demangeat, *Catal. Today* **2004**, 89, 375.
363. C. Leandri, H. Saifi, O. Guillermet et al., *Appl. Surf. Sci.* **2001**, 177, 303.

364. J. A. Sprague, F. Montalenti, B. P. Uberuaga et al., *Phys. Rev. B* **2002**, 66, art. no. 205415.
365. S. Sawaya, J. Goniakowski, G. Treglia, *Phys. Rev. B* **1999**, 59, 15337.
366. U. Hasse, K. Wagner, F. Scholz, *J. Solid State Electrochem.* **2004**, 8, 842.
367. U. Hasse, F. Scholz, *Electrochem. Commun.* **2005**, 7, 173.
368. W. Simons, D. Gonissen, A. Hubin, *J. Electroanal. Chem.* **1997**, 433, 141.
369. D. Gonissen, W. Simons, A. Hubin, *J. Electroanal. Chem.* **1997**, 435, 149.
370. A. I. Dimitrov, S. H. Jordanov, K. I. Popov et al., *J. Appl. Electrochem.* **1998**, 28, 791.
371. G. Baltrunas, E. Pakalniene, G. S. Popkirov et al., *Z. phys. Chem.* **2002**, 216, 791.
372. G. Baltrunas, *Electrochim. Acta* **2003**, 48, 3659.
373. V. Daujotis, D. Jasaitis, R. Raudonis, *Electrochim. Acta* **1997**, 42, 1337.
374. V. Daujotis, V. Kairys, *Electrochim. Acta* **1997**, 42, 1345.
375. A. Saito, T. Shibata, H. Ohura et al., *Denki Kagaku.* **1998**, 66, 1128.
376. J. V. Macpherson, P. R. Unwin, *J. Phys. Chem.* **1996**, 100, 19475.
377. F. Scholz, U. Hasse, *Electrochem. Commun.* **2005**, 7, 541.
378. R. Y. Bek, L. I. Shuraeva, A. F. Zherebilov et al., *Russ. J. Electrochem.* **1996**, 32, 834.
379. R. Y. Bek, N. A. Rogozhnikov, *Russ. J. Electrochem.* **1995**, 31, 1125.
380. R. Y. Bek, L. Shuraeva, S. N. Ovchinnikova, *Russ. J. Electrochem.* **2004**, 40, 1079.
381. N. A. Rogozhnikov, *Russ. J. Electrochem.* **1998**, 34, 61.
382. X. W. Sun, Y. C. Guan, K. N. Han, *Metall. Mater. Trans. B* **1996**, 27, 355.
383. V. T. Yavors'kyi, O. I. Kuntiyi, S. I. Kozak et al., *Mater. Sci.* **1999**, 35, 893.
384. S. G. Garcia, D. R. Salinas, C. E. Mayer et al., *Electrochim. Acta* **2003**, 48, 1279.
385. G. A. Hope, R. Woods, K. Watling, *J. Appl. Electrochem.* **2001**, 31, 1285.
386. G. A. Hope, K. Watling, R. Woods, *J. Appl. Electrochem.* **2001**, 31, 703.
387. X. W. Sun, Y. C. Guan, K. N. Han, *Metall. Mater. Trans. B* **1996**, 27, 355.
388. M. E. Vela, G. Andreasen, R. C. Salvarezza et al., *Phys. Rev. B* **1996**, 53, 10217.
389. M. Dolata, P. Kędzierzawski, *Pol. J. Chem.* **2003**, 77, 1199.
390. J. A. Garcia-Vázquez, J. Romero, A. Souza, *Coord. Chem. Rev.* **1999**, 195, 691.
391. V. E. Marquez, J. R. Anaconda, *Polyhedron* **1997**, 16, 2375.
392. A. Lewandowski, A. Szukalska, M. Galiński, *New J. Chem.* **1995**, 19, 1259.
393. N. N. Greenwood, A. Earnshaw, *Chemistry of the Elements*, 2nd ed., Elsevier-Butterworth-Heinemann, Amsterdam, Boston, Heidelberg, 1997.
394. W. Grochala, R. Hoffmann, *Angew. Chem. Int. Ed. Engl.* **2001**, 40, 2742.
395. N. R. Walker, R. R. Wright, A. J. Stace, *J. Am. Chem. Soc.* **1999**, 121, 4837.
396. C. Brückner, *J. Chem. Educ.* **2004**, 81, 1665.
397. F. A. Cotton, G. Wilkinson, *Advanced Inorganic Chemistry*, Wiley, New York, 1988.
398. B. E. Breyfogle, C. J. Hung, M. G. Shumsky et al., *J. Electrochem. Soc.* **1996**, 143, 2741.
399. L. J. Kirschenbaum, J. D. Rush, *Inorg. Chem.* **1983**, 22, 3304.
400. L. J. Kirschenbaum, J. D. Rush, *J. Am. Chem. Soc.* **1984**, 106, 1003.
401. E. T. Borish, L. J. Kirschenbaum, *Inorg. Chem.* **1984**, 23, 2355.
402. J. D. Rush, L. J. Kirschenbaum, *Inorg. Chem.* **1985**, 24, 744.
403. R. Eujen, B. Hoge, D. J. Brauer, *Inorg. Chem.* **1997**, 36, 3160.
404. R. Eujen, B. Hoge, D. J. Brauer, *Inorg. Chem.* **1997**, 36, 1464.
405. E. K. Barefield, M. T. Mocella, *Inorg. Chem.* **1973**, 12, 2829.
406. W. R. Scheidt, J. U. Mondal, C. W. Eigenbrot et al., *Inorg. Chem.* **1986**, 25, 795.
407. H. Furuta, T. Ogawa, Y. Uwatoko et al., *Inorg. Chem.* **1999**, 38, 2676.
408. H. Furuta, H. Maeda, A. Osuka, *J. Am. Chem. Soc.* **2000**, 122, 803.
409. M. A. Muckey, L. F. Szczepura, G. M. Ferrence et al., *Inorg. Chem.* **2002**, 41, 4840.
410. C. Brückner, C. A. Barta, R. P. Briñas et al., *Inorg. Chem.* **2003**, 42, 1673.
411. M. Ali, A. I. Shames, S. Gangopadhyay et al., *Transition Met. Chem.* **2004**, 29, 463.
412. K. M. Kadish, X. Q. Lin, J. Q. Ding et al., *Inorg. Chem.* **1986**, 25, 3236.
413. A. Kahani, M. Abedini, M. Farnia, *Transition Met. Chem.* **2000**, 25, 711.
414. D. Naumann, W. Tyrre, F. Trinius et al., *J. Fluor. Chem.* **2000**, 101, 131.
415. B. X. Li, Z. J. Zhang, M. L. Wu, *Microchem. J.* **2001**, 70, 85.

416. B. X. Li, Z. J. Zhang, M. L. Wu, *Anal. Chim. Acta* **2001**, 432, 311.
417. A. Lehmani, P. Turq, J. P. Simonin, *J. Electrochem. Soc.* **1996**, 143, 1860.
418. J. L. Hunting, M. Weiss, H. N. Po, *Abstr. Pap. Amer. Chem. Soc.* **1999**, 217, 306–INOR.
419. D. Sroczynski, A. Grzejdzia, *J. Incl. Phenom. Macrocycl. Chem.* **2002**, 42, 99.
420. M. Panizza, I. Duo, P. A. Michaud et al., *Electrochem. Solid State Lett.* **2000**, 3, 550.
421. A. Paire, D. Espinoux, M. Masson et al., *Radiochim. Acta* **1997**, 78, 137.
422. J. E. Graves, M. T. Goosey, D. Hirst et al., *Trans. Inst. Met. Finish.* **2001**, 79, 90.
423. M. Ravera, C. Ciccarelli, V. Gianotti et al., *Chemosphere* **2004**, 57, 587.
424. A. Kumar, Vaishali, P. Ramamurthy, *J. Chem. Soc., Perkin Trans.* **2001**, 27, 1174.
425. I. Zilbermann, J. Hayon, E. Maimon et al., *Electrochem. Commun.* **2002**, 4, 862.
426. F. Mousset, F. Bedioui, C. Eysseric, *Electrochem. Commun.* **2004**, 6, 351.

24.6**Electrochemistry of Mercury**

24.6.1	Double-layer Properties of Hg/Water Interface	959
24.6.1.1	Potential of Zero Charge	959
24.6.1.2	Surface Charge Density and Capacitive Current	959
24.6.1.3	Experimental and Theoretical Studies of the Hg/Water Interface . . .	960
24.6.2	Double-layer Properties of Hg/Nonaqueous Media Interface	961
24.6.3	Adsorption and Electrode Reactions at Hg Surface	962
24.6.3.1	Deposition and Underpotential Deposition of Hg on Various Electrodes	962
24.6.3.1.1	Underpotential Deposition of Mercury on Gold Electrodes	962
24.6.3.1.2	Film Electrodes and Related Hg Electrodes	966
24.6.3.2	Adsorption and Electrode Reactions of Inorganic Ions and Coordination Compounds of Metal Ions	968
24.6.3.2.1	Analytical Applications	970
24.6.3.3	Adsorption and Electrode Reactions Involving Organic Compounds .	971
24.6.3.3.1	Organic Compounds Containing Sulfur, Selenium, and Tellurium .	972
	Anodization of Hg electrode	972
	Amino acids	973
	Proteins, enzymes	973
	Nucleic bases, nucleotides, and thiolipids	975
	Other sulfur-containing compounds	976
	Organic selenides and tellurides	977
24.6.3.3.2	Organic Nitrogen Compounds	977
24.6.3.3.3	Indicators and Dyes	980
24.6.3.3.4	Vitamins and Antibiotics	980
24.6.3.3.5	Enzymes and Coenzymes	981
24.6.3.3.6	Other Organic Compounds	981
	Mixed adsorption	983
24.6.3.3.7	Analytical Aspects of Adsorption of Organic Compounds	983
24.6.4	Ammonium and Quaternary-substituted Ammonium Amalgams . .	984
	References	986

The chapter on the electrochemistry of mercury was published in the IX-A volume of the *Encyclopedia of Electrochemistry of the Elements* [1] in 1982. At that time, mercury was probably the most often used electrode material. Hence the relevant chapter contained numerous data on standard and formal potentials in aqueous and nonaqueous solutions, voltammetric characteristics of mercury and double-layer properties of mercury/solution interface, electrochemical studies involving anodic dissolution and cathodic deposition of mercury, as well as examples of use of mercury and its compounds in applied electrochemistry. At present, however, it is clear that since the time that elapsed from publishing of that chapter, mercury as an electrode material partially lost its importance compared to solid (particularly single-crystal) noble metals or carbon (in electroanalysis) electrodes. The number of papers on the electrochemistry of this element is therefore also appropriately smaller than for other electrode materials, such as gold. However, a literature survey shows that a number of papers dealing with analytical studies of various compounds at mercury electrodes is still significant. Discussion of all these analytical papers is beyond the scope of this review, which is essentially focused on physicochemical aspects of electrochemistry of mercury published in the last decade. In some cases, the papers presenting analytical aspects of electrochemical processes at Hg electrodes are also briefly discussed.

24.6.1

Double-layer Properties of Hg/Water Interface

24.6.1.1 Potential of Zero Charge

Undoubtedly, the mercury/aqueous solution interface, was in the past, the most intensively studied interface, which was reflected in a large number of original and review papers devoted to its description, for example, Ref. 1, and in the more recent work by Trasatti and Lust [2] on the potentials of zero charge. It is noteworthy that in view of numerous measurements of the double-layer capacitance at mercury brought in contact with NaF and Na₂SO₄ solutions, the classical theory of Grahame [3] still holds [2]. According to Trasatti [4], the most reliable PZC value for Hg/H₂O interface in the absence of specific adsorption equals to -0.433 ± 0.001 V versus saturated calomel electrode, (SCE); residual uncertainty arises mainly from the unknown liquid junction potential at the electrolyte solution/SCE reference electrode boundary.

24.6.1.2 Surface Charge Density and Capacitive Current

R. A. Osteryoung and coworkers [5] have performed chronocoulometric measurements of surface charge density at a controlled-growth mercury electrode. After initial formation and equilibration of the mercury drop, it was expanded by further addition of mercury and the charge corresponding to the new area was directly measured. The obtained value

was used to estimate the surface charge density. Experimental studies were associated with numerical modeling, assuming stepwise spherical expansion of mercury drop. Spectral analysis of the noise was also performed. More recently, Brito et al. [6] have published a paper on accurate determination of surface charge density at mercury electrode by extrusion of mercury drops. The proposed method was free from the faradaic component contribution, originating from traces of electroactive species. This procedure involved the newly designed hanging mercury drop electrode (HMDE).

A novel method for the determination of surface charge density at a HMDE coated with a self-assembled phospholipid monolayer mimicking a biological membrane has been described by Becucci et al. [7] Charge density was calculated by integrating the capacitance current, which flows at the constant potential as a consequence of slight contraction of mercury drop.

Although the charging of the mercury surface seems to be a well-understood process, it has appeared recently that the impedance characteristics of the capacitance current at the *streaming* mercury electrode are not fully recognized yet. Jurczakowski and Orlik [8] have found in pure supporting electrolyte solutions that the capacitive current, which permanently charges fresh portions of the flowing mercury even under potentiostatic conditions, causes the impedance response qualitatively equivalent to that of the faradaic process with charge transfer as the rate-controlling step. The corresponding equivalent circuit for pure capacitive response included parallel connection of differential double-layer capacitance C_d , and virtual resistor $R_d = (2\pi r C_d \nu)^{-1}$, where r and ν denote the radius of the mercury stream, and the flow rate of mercury, respectively.

24.6.1.3 Experimental and Theoretical Studies of the Hg/Water Interface

Arihara et al. [9] have monitored in situ the Hg–Au electrode surface in HClO_4 solutions applying infrared reflection/absorption spectroscopy (IRAS). It has been found that the adsorption state of water molecules on Hg changes depending on the applied potential. The Hg–water interaction was considered stronger than the Au–water interaction. The structure of water within the dense part of electrical double layer at mercury electrode, in a wide range of surface charges, has also been analyzed theoretically by Nazmutdinov and Borisevich [10]. They used classical Monte Carlo method and ab initio quantum-chemical approach to calculate the potential for the interactions with the metal. It has been found that to theoretically explain earlier experimental data, it is sufficient to invoke dipole reorientation and the behavior of hydrogen bonds between H_2O molecules in a monolayer; any additional hypotheses on phase transitions are not necessary.

Damaskin and Grafov [11] have compared the Gonzalez-Sanz theory of the diffuse layer with the experimental data concerning mercury electrode capacitance in aqueous solutions of Na_2SO_4 and $\text{La}_2(\text{SO}_4)_3$. It has been shown that the Gonzalez-Sanz theory is rigorously consistent with the Gibbs adsorption equation, if the thickness of the inner part of the double layer (in the surface-inactive electrolyte solution) is independent of the electrode charge and the solvent concentration in the diffuse layer remains invariant. Furthermore, the experimental dependence of the capacitance of an uncharged mercury electrode on the concentration of aqueous solutions of Na_2SO_4 and $\text{La}_2(\text{SO}_4)_3$ was found to be in better agreement with the Gonzalez-Sanz theory than with the

classical Gouy-Chapman-Grahame theory. Eck and Spohr [12] have summarized earlier calculations and performed their own computer modeling of hydrated Li^+ , F^- , and Cl^- ions in the proximity of a mercury electrode. In most simulations, a simple rigid crystal model of mercury was assumed (it was also shown that the water structure is not strongly affected if a more realistic liquid model is used). The differences between the ions were explained in terms of solvation and steric interactions.

Cecchi et al. [13] have studied the influence of alkali halide compounds on photocurrent accompanying emission of electrons from dropping mercury electrode into water. Cathodic photocurrent was observed when the electrode was irradiated with UV light in nonfaradaic region of the polarographic curve in ultrapure water deaerated with pure hydrogen and in the absence of scavengers of hydrated electrons. After small additions of alkali metal halide compounds, the photocurrent was increased to an extent depending on the nature of alkali metal cations. In contrast, the current was decreased at concentrations exceeding 10^{-4} M.

24.6.2

Double-layer Properties of Hg/Nonaqueous Media Interface

An increasing interest in nonaqueous media, which began in the seventies of the XXth century, also resulted in the extended studies on the properties of the relevant Hg|solvent interface. Most of the papers discussing the dependence of E_{pzc} of Hg on the solvent used were published in the eighties [2]. The pzc values for selected solvents, including water for comparison, are collected in Table 1. They are expressed versus standard hydrogen electrode (SHE) and, in order to eliminate the unknown liquid junction potential, also versus the bis(biphenyl)chromium(I)/(0) standard potential, that was assumed to be solvent independent.

Systematic thermodynamic studies on the Hg|solvent interface led to the conclusion that entropy of its formation is always positive and lower than in the solution bulk, what suggests certain “structure making” effect of Hg for these solvents [2].

The Hg|solvent interface was intensively studied in, for example, various alcohols. For example, in EtOH and MeOH, similar data for double layer were obtained;

Tab. 1 Selected E_{pzc} values for Hg|solvent interface [2], expressed versus standard hydrogen electrode and bis(biphenyl)chromium(I)/(0) (BBCr) reference electrode

<i>Solvent</i>	<i>Electrolyte</i>	E_{pzc}/V versus aqueous SHE	$E_{\text{pzc}} (\pm 0.01 \text{ V})/\text{V}$ versus BBCr ($\pm 0.01 \text{ V}$)
H ₂ O	NaF	-0.192 ± 0.001	0.458 ± 0.001
Acetonitrile	LiClO ₄	-0.03	0.56
Dimethylsulfoxide	LiClO ₄	-0.08	0.52
<i>N,N</i> -Dimethylformamide	LiClO ₄	0.00	0.51
Propylene carbonate	NaClO ₄	-0.08	0.59
Methanol	KF	-0.05	0.51
Ethanol	LiClO ₄	-0.05	
<i>n</i> -Propanol	LiClO ₄	-0.07	

explanation for the small differences obtained (including higher capacitance at pzc in EtOH compared to MeOH) was the subject of controversy. Although some of them could be attributed to the difference in the size of EtOH and MeOH molecules, one should emphasize that the double-layer thickness was not equal to the real cross section of the solvent molecules. For EtOH, the following sequence of the surface activity of anions has been proposed: $\text{BF}_4^- < \text{ClO}_4^- < \text{Cl}^- < \text{Br}^- < \text{I}^-$ [2].

Systematic studies on double-layer properties of mercury in contact with various nonaqueous solvents were being carried out up to the beginning of the nineties of the twentieth century. A comprehensive survey of the obtained data and of the concepts used for their description is given in Ref. 2. At present, such studies are being undertaken rather occasionally. Adsorption of dimethylsulfoxide (DMSO) on mercury electrodes has been studied by Motheo and Gonzalez [14]. The Hg|0.15 M Na_2SO_4 (DMSO) interface was studied using the electrode charge density as the independent electrical variable. The observed adsorption behavior was governed by the Frumkin isotherm. Furthermore, it has been found that DMSO molecules, upon adsorption under the applied conditions, undergo partial reorientation.

Recently, Fuchs et al. [15], using the streaming mercury electrode and applying the Henderson equation, have determined the pzc value in the solutions of tetraethylammonium perchlorate in DMSO as -0.515 ± 0.001 V (versus Ag/0.01 M Ag^+ (DMSO) reference electrode). This value was corrected for the liquid junction potential and was independent of tetraethylammonium perchlorate (TEAP) concentration within the range: 0.02 to 0.75 M. Using the same methodology, Kišova et al.

[16] have determined pzc for 0.1–1.0 M sodium perchlorate solutions in DMSO as -0.527 ± 0.002 V (versus Ag/0.01 M Ag^+ (DMSO)).

24.6.3

Adsorption and Electrode Reactions at Hg Surface

24.6.3.1 Deposition and Underpotential Deposition of Hg on Various Electrodes

One of the subjects that is still quite intensively developed (using electrochemical methods frequently combined with nonelectrochemical techniques) concerns reduction of Hg compounds at various surfaces (e.g. Pt or Au), with the emphasis laid on underpotential deposition (UPD) of mercury. Deposition of mercury on other metals is generally important for better understanding of the mechanism of the formation of amalgams. Moreover, underpotential Hg deposition characteristics constitute a significant source of information on Hg–metal interactions. In turn, mercury film electrodes obtained by such deposition have a significant application in electrochemical analysis of various species.

24.6.3.1.1 Underpotential Deposition of Mercury on Gold Electrodes

Earlier studies of UPD of mercury were carried out applying only classical electrochemical methods and polycrystalline electrodes. The results have shown that UPD of Hg is accompanied by adsorption of mercury ions.

Salié and Bartels [17–20] have considered the process of Hg UPD from Hg(I) and Hg(II) perchloric acid solutions as proceeding in partial charge-transfer steps. The authors, in order to explain different experimental results, have assumed two-step process. In the first step, an intermediate is adsorbed at the gold surface and

the accompanying charge transfer is about $0.53e$ per mercury atom. At this stage, there is an interaction with Au atoms and with the species present in the solution. In the second step, full discharge of the intermediate species and formation of a full monolayer of mercury atoms occur.

Shay and Bruckenstein [21] have made an attempt to determine Hg(I) adsorption, which accompanies coulometric UPD of mercury on gold, using electrochemical quartz crystal microbalance (EQCM). It has been found from *ex situ* EQCM that the mass change accompanying coulometric deposition of mercury corresponds to the formation of one monolayer of Hg ($1.7 \times 10^{-9} \text{ mol cm}^{-2}$), with the additional adsorbed layer of Hg_2SO_4 ($2.9 \times 10^{-10} \text{ mol cm}^{-2}$). Hg_2SO_4 remained adsorbed on Hg even after rinsing the electrode with water.

In the recent years, single-crystal electrodes and new techniques, such as

scanning tunnelling microscopy (STM) and atomic force microscopy (AFM), and others, have been utilized in the studies of UPD of mercury, for example, on Au(111) [22–26]. In these papers, Abruña and coworkers have used, apart from electrochemical methods, X-ray diffraction and scattering techniques also. Cyclic voltammograms recorded using Au(111) in 0.1 M H_2SO_4 containing 1 mM Hg^{2+} are shown in Fig. 1.

Two pairs of sharp peaks around +0.93 V (see inset) correspond to adsorption of preadsorbed sulfate ions and deposition of Hg_2SO_4 . The shape of these spikes suggests that these processes are fast. An ordered coadsorbed structure of Hg_2SO_4 was observed at potentials $+0.80 \leq E \leq +0.88 \text{ V}$. Broad peak at +0.60 V corresponds to the deposition of the first Hg monolayer, which is completed at +0.52 V and reflected as sharp spikes, together with the onset of amalgam

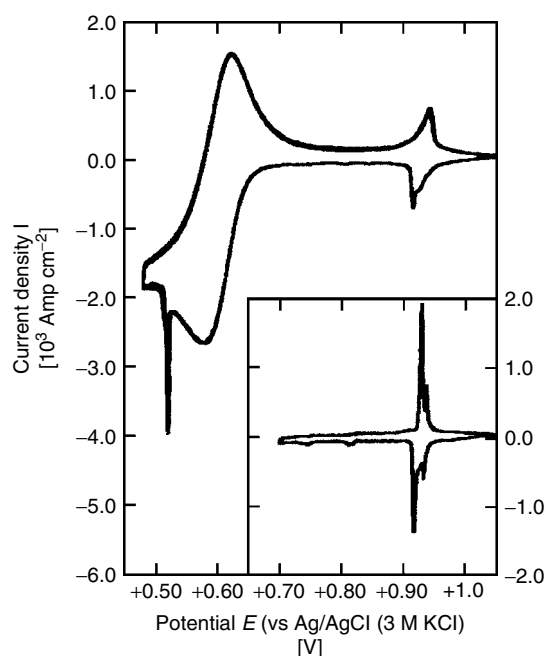
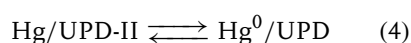
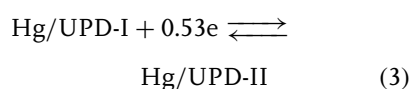
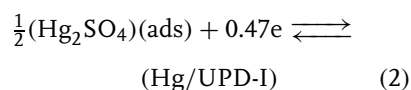
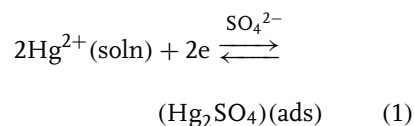


Fig. 1 Cyclic voltammogram of Au(111) electrode in 0.10 M sulfuric acid containing 1.0 mM Hg^{2+} ; scan rate: 2 mV s^{-1} . Inset: voltammetric profile over the potential range: +1.05 to +0.70 V versus Ag/AgCl (3 M KCl) (from Ref. 23).

formation. Broad shape of peaks in the potential range +0.50 to 0.70 V may suggest that these processes are slow, possibly due to the existence of intermediate states during reduction of Hg(I) to Hg(0) [17–20]. The authors have observed three UPD phases in 0.1 M H₂SO₄, at potentials preceding bulk mercury deposition. These phases consisted of two well-ordered intermediate states, which appeared to be either a fully discharged two-dimensional liquid Hg layer, or an amorphous Hg–Au monolayer [23]. Both intermediate phases had hexagonal structures with the lattice vectors rotated 30° with respect to those of the Au(111) substrate. The first phase occurred at the potential of +0.68 V (versus Ag/AgCl with 3 M KCl); it was metastable and underwent transition to the second ordered phase either at +0.68 V after longer waiting, or by moving the potential to less positive value (+0.63 V). Similar to the first phase, the second one was also metastable and might be transformed to the final, fully discharged state, being either a two-dimensional liquid Hg layer, or an amorphous Hg–Au layer. This process agreed well with the mechanism found by Salié and Bartels for polycrystalline Au electrode. The mechanism for the studied process can be represented by the following reactions:



Earlier, the first stage of Hg UPD on Au(111) in 0.10 M H₂SO₄ with 1 mM Hg²⁺ was studied by the same authors [22], who used synchrotron, X-ray scattering techniques, including grazing incidence X-ray diffraction and specular crystal-truncation rod measurements. An ordered coadsorbed structure of sulfate/bisulfate anions and mercury cations was found at the potentials between the first and the second Hg UPD peaks. The charge corresponding to the first UPD peak suggested that the coadsorbed structure is probably Hg₂SO₄. These results were consistent with those obtained for the chloride and acetate solutions [24]. Also, the voltammetric results were compared to the recent results from in situ AFM, STM, and surface X-ray scattering, in order to look for a correlation between the found voltammetric data and the surface structures and their transformations. The authors [22, 24] have proposed the following explanation for the observed processes. At potentials more positive than the first UPD peak, an ordered sulfate adlayer exists. The onset of mercury deposition triggers an order/disorder transition that, in turn, gives rise to the formation of the first set of UPD peaks. As the monolayer deposition is completed, again a disorder/order transition occurs and the second set of peaks appear. The adlayer is composed of Hg₂SO₄ with coadsorbed H₃O⁺ ions. A further voltammetric characteristic is the disappearance of the ordered coadsorbed structure. The final process is the completion of the mercury monolayer, followed by the formation of a mercury–gold amalgam.

The same group of researchers [25] has performed studies of Hg UPD on Au(111) in the presence and absence of strongly interacting anions, such as bisulfate, chloride, and acetate.

Abruña et al. [26] have carried out in situ surface X-ray diffraction studies in the following solutions: 0.1 M H_2SO_4 , 0.1 M HClO_4 , 0.1 M HClO_4 with 1 mM NaCl, and acetic buffer (0.1 M acetic acid + 0.1 M sodium acetate). They have found that anions strongly determine the structure of Hg overlayer. As before, three ordered structures were found in sulfuric acid solutions. The overlayer structure in 0.10 M HClO_4 was dominated by trace amounts of Cl^- ions and was similar to that observed in the solution containing 1.0 mM chloride ions. In acetate solutions, an incommensurate hexagonal lattice was found for a bilayer structure, which was likely formed by HgCH_3COO complexes. The lattice constant varied dramatically in a wide range of electrode potentials, which suggests that the charge of the deposited Hg atoms changed with the potential. In all four used electrolytes containing different anions, Hg UPD appeared to follow a common mechanism with desorption of preadsorbed anions at the initial step and a subsequent deposition of a coadsorbed layer comprising mercury-anion neutral species.

Hg UPD on Au(111) electrodes in the presence of bisulfate anions has been studied by Abruña et al. [27] in order to illustrate the effects of the partial charge, retained by the metal, on the interactions between the adsorbed metal and the anion. In order to obtain structural information on the adsorbed species, the authors have carried out grazing incident X-ray diffraction measurements at several potentials. Three ordered structures were observed depending on the applied potentials, which were adjusted from cyclic voltammograms. At the early stages of Hg UPD, when mercury was still partially charged, an ordered mercurous-sulfate bilayer structure was formed at the electrode

surface. At more negative potentials, two additional ordered hexagonal mercury adlayers were formed, which interacted with the anions only slightly.

Herrero and Abruña [25] have also studied the kinetics and mechanism of Hg UPD on Au(111) electrodes in the presence and absence of bisulfate, chloride, and acetate ions. In the absence of the interacting anions (in perchloric acid), the Hg UPD was significantly controlled by gold–mercury surface interactions. In sulfuric acid solutions, the kinetics of the initial and final stages of mercury deposition/dissolution was altered. The presence of two well-ordered structures at potentials below and above mercury deposition led to the formation of two pairs of sharp spikes in cyclic voltammograms. In the chloride medium, the voltammetric profile exhibited two sharp peaks and thus it was very similar to that obtained in sulfuric acid solution. Neither nucleation, nor growth kinetics mechanism was found to be linked to the process of formation/disruption of the mercury chloride adlayer. The transients obviously deviated from the ideal Langmuir behavior.

The kinetics of Hg UPD in acetate media is clearly slower than in the previous media, as voltammetric and chronoamperometric measurements have revealed [26]. A delicate interplay between the presence of the strongly interacting anions and kinetics and structure of electrochemically induced phase transitions has been shown.

One should add that Abruña and coworkers have described UPD of Hg on various $\text{Au}(h,k,l)$ electrodes in a review paper [28]. They have also studied UPD of other metals at various single-crystal metal surfaces.

Inukai et al. [29] have carried out UPD of mercury also on Au(111) and have investigated this process by in situ STM in sulfuric and perchloric acid solutions.

In sulfuric acid solution, the structure observed at potentials more positive than the first UPD peak was assigned to the adsorbed bisulfate ions. After the first UPD peak, two domains: $\begin{bmatrix} 2 & 0 \\ 3 & 3/2 \end{bmatrix}$ and $\begin{bmatrix} 1 & \bar{1} \\ 4 & 4 \end{bmatrix}$, were located always on the same terrace. In HClO_4 solution, a different structure of $\begin{bmatrix} 0 & 2 \\ 2 & 1 \end{bmatrix}$ was found after the first UPD peak. These findings have proved again that there is a large influence of anions on the UPD structure.

Abaci et al. [30] have studied the influence of temperature on Hg UPD at Au(111) electrodes. Deposition was carried out in various solutions containing anions differently interacting with the studied system: ClO_4^- ions (HClO_4) were practically inert, SO_4^{2-} (H_2SO_4) interacted with the Au(111) substrate, and $\text{C}_2\text{H}_3\text{O}_2^-$ ($\text{HC}_2\text{H}_3\text{O}_2$) interacted with the dissolved Hg^{2+} ions. At the constant Γ_{Hg} , the temperature dependence of cyclic voltammetric potentials was constructed. From the obtained plot, entropy ($\Delta S_{\text{rc}}^0(\text{upd})$) and enthalpy ($\Delta H_{\text{rc}}^0(\text{upd})$) for Hg UPD were found to be: entropies -30.9 and $-18.3 \text{ J mol}^{-1} \text{ K}^{-1}$, and enthalpies -182 and -184 kJ mol^{-1} in perchloric acid and sulfuric acids, respectively. In acetic media, these thermodynamic parameters were strongly pH dependent.

Finally, one should mention that Hg UPD on Au(111) proceeds differently on the neighboring metals in the periodic table, such as Tl, Pb, and Bi. UPD layers of Tl and Pb, just prior to the bulk deposition on Au(111), were found to be compressed by only about 3% as compared to the bulk values, and decreased with the decreasing electrode potential. At the same time, two ordered Hg UPD phases had expanded structures compared to the frozen bulk Hg [23].

24.6.3.1.2 Film Electrodes and Related Hg Electrodes

Mercury films were prepared on reticulated vitreous carbon flow-through electrodes by Hg deposition from Hg^{2+} solutions in acetic buffer [31]. Such an electrode was designed for the purposes of trace metal analysis. Mercury film deposition/oxidation on reticulated vitreous carbon and glassy carbon electrodes were compared.

Daujotis et al. [32] have described the use of electrochemical quartz microbalance for the quantitative studies on monolayer adsorption on working mercury electrodes. Mercury was deposited on Pt at negative potentials (-0.4 to -0.5 V versus $\text{Ag}|\text{AgCl}|\text{KCl}_{\text{sat}}$). In order to avoid undesirable transformation of mercury into, for example, larger droplets, the thickness of mercury film could not exceed 20 nm . Then, the linear dependence of the frequency change on the added mass was achieved. Applicability of such an electrode for EQCM measurements has been demonstrated by performing electroreduction of Pb(II) and Tl(I), as an example.

Deposition of mercury at boron-doped diamond (BDD) and platinum electrodes has also been studied [33]. Deposition and oxidation of mercury was performed by cyclic voltammetry from the solution of $1 \text{ mM Hg}_2(\text{ClO}_4)_2$ in 1 M NaClO_4 . In order to learn more about this deposition, it was carried out also under chronoamperometric conditions. The results obtained are shown in Fig. 2 in the form of dimensionless current-time transients. Experimental curves obtained at two different overpotentials were compared with the theoretical curves calculated for instantaneous and progressive nucleation. A good agreement of experimental plots with the instantaneous nucleation mechanism was

Fig. 2 Comparison of the experimental dimensionless current-time transients for electrodeposition of mercury onto boron-doped diamond electrode with the theoretical transients for instantaneous (upper curve) and progressive (lower curve) nucleation; overpotentials: (×) 0.862 V and (♦) 0.903 V (from Ref. 33).

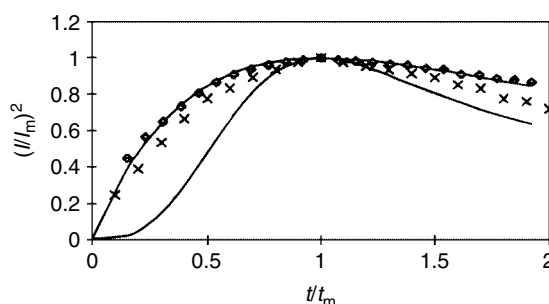
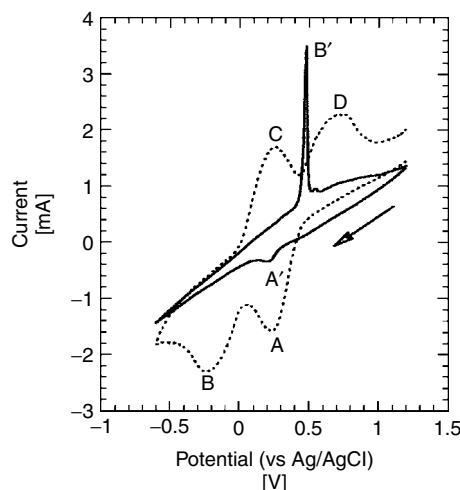


Fig. 3 A comparison of cyclic voltammograms obtained at the scan rate of 20 mV s^{-1} for reduction of Hg(II) -mesoporous silica (dotted line, $\text{Hg(II)} = 4\%$) and $1.0 \times 10^{-3} \text{ M Hg(II)}$ solution at a carbon paste electrode without mesoporous silica (solid line, current axis $\times 3$) in aqueous $0.1 \text{ M NaClO}_4 + 1.5 \text{ M HClO}_4$ (from Ref. 38).



found. One failed to describe deposition of Hg from Hg^{2+} solution either by instantaneous or progressive nucleation mechanism [33].

Wang et al. [34] have introduced a new heated mercury film electrode based on a screen printed carbon substrate. It was used in anodic stripping and exhibited a significantly improved signal-to-noise ratio. A directly heated mercury film electrode for anodic stripping voltammetry has been described by Jasinski [35]. Different factors influencing the quality of analytical determination have been investigated. Renewed mercury electrodes and examples of their various applications have been reviewed in Ref. 36. Lovric and Scholz [37] have discussed the conditions

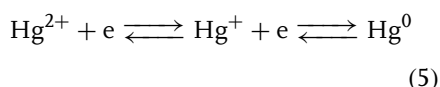
and the reasons that make anodic stripping voltammetry of mercury possible at the trace level also.

Bond et al. [38] have described a composite carbon paste electrode with mesoporous silica and Hg^{2+} metal ions adsorbed on the surface. The peak current recorded under cyclic voltammetric conditions was proportional to the amount of cation adsorbed on silica up to the surface saturation level, and also to the hydrogen ion concentration. Typical curve recorded using such electrodes is shown in Fig. 3 (dotted line).

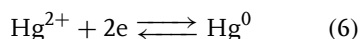
For a comparison, a cyclic voltammogram recorded at carbon paste electrode without mesoporous silica is also shown. In this case, $10^{-3} \text{ M Hg}^{2+}$ was present

in the aqueous solution containing 0.1 M NaClO₄ and 1.5 M HClO₄ as background electrolytes.

In case of Hg²⁺ adsorbed on silica, electroreduction was quasi-reversible and proceeded in two well-defined one-electron steps, according to the equation below:



For the conventional carbon paste and Hg²⁺ in the solution, reaction occurs in one step:



This can be seen in the cyclic curve in Fig. 3. In this voltammogram, relatively large anodic peak of mercury stripped from the paste electrode surface is observed. The presence of relatively stable Hg(I) at mesoporous silica carbon paste electrode may be due to adsorption.

The improvement in the preparation of renewable and reproducible mercury film-covered carbon paste electrode for use in anodic stripping voltammetry has been reported in Ref. 39. Mercury salts (mercuric oxalate) distributed in the electrode bulk served as a source of mercury.

Wang and Tsai [40] have described voltammetric behavior of chlorhexidine at film mercury electrodes in the aqueous medium.

Camarero et al. [41] have prepared graded cadmium–mercury–telluride thin films (Cd_xHg_{1-x}Te) applying cathodic electrodeposition at variable deposition voltage. Atomic proportions of mercury in the range 0.05–0.15 were considered.

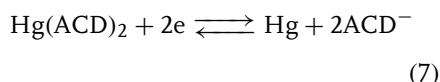
It is noteworthy that Scholz and coworkers [42] have studied electrochemical reduction of submicrometer size Hg₂Cl₂ and Hg₂Br₂ crystals immobilized on the surface of gold and platinum electrodes. The

process started at the three-phase junction, where the three phases: metal, mercury(I) halide, and electrolyte solution met. During deposition on gold electrodes, liquid mercury was transformed into a solid crystalline gold amalgam electrode. In case of Pt, liquid mercury wet the platinum surface.

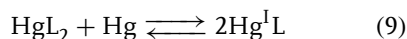
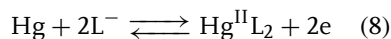
A Hg|Hg₂C₂O₄ secondary electrode has been proposed [43] for the potentiometric determination of the oxalate ion concentration.

24.6.3.2 Adsorption and Electrode Reactions of Inorganic Ions and Coordination Compounds of Metal Ions

Safavi and Gholivand [44] have studied electrochemical reduction of mercury complexes with 2-aminocyclopentene-1-dithiocarboxylic acid (ACD ≡ L) and its selected derivatives at mercury electrodes in DMSO. Reduction of Hg(ACD)₂ proceeded in a single 2-e step:



Hg(I) possibly participated as an intermediate. As a complementary study, redox behavior of the ligands themselves was investigated in DMSO solutions at Hg electrodes. 2-e oxidation of mercury proceeded according to the EC mechanism i.e. involving electrochemical step followed by chemical process:



Also, electroreduction of such complexes was studied at mercury electrodes.

The effect of the condensed adsorption layer on hydrogen evolution at mercury electrode has been studied by Ponomarev et al. [45].

Andrade and Molina [46] have performed electrochemical impedance studies of mercury electrodes with hematite particles adhered at different electrode potentials. Adhesion of such particles was strong and the decrease in the impedance was accompanied by an increase in the number of attached particles. Experimental results were analyzed in terms of an equivalent circuit including the constant phase element (CPE), the magnitude of which appeared to be directly related to the electrode coverage. A pore model for the metal/hematite particles interface has been proposed.

Anastopoulos et al. [47] have analyzed interfacial rearrangements of triphenylbismuth and triphenylantimony at mercury electrode in nonaqueous solvents of high dielectric constant. These phenomena were detected as the peaks in the capacitance-potential curves at intermediate negative potentials for triphenylbismuth and triphenylantimony in *N*-methylformamide, *N,N*-dimethylformamide, dimethyl sulfoxide, propylene carbonate, and methanol solutions.

Ramirez et al. [48] have studied adsorption of Ni(II)–dimethylglyoxime complex on mercury in ammonia and borate buffers using voltammetry and differential capacity measurements. Adsorption was found reversible and was governed by the Frumkin adsorption isotherm. The value of interaction parameter pointed toward the presence of attractive forces between the adsorbed molecules. The value of standard Gibbs energy of adsorption was close to those found for pentanol and hexanol. Later, Ramirez et al. [49] have investigated adsorption of Ni(II)–dimethylglyoxime complex on mercury in the same buffers. Electroreduction of the complex proceeded via reduction of Ni(II) to Ni with the simultaneous decomposition of the ligand.

Sander and Henze [50] have performed ac investigations of the adsorption potential of metal complexes at Hg electrode. Later, Sander et al. [51] have studied electrosorption of chromium–diethylenetriaminepentaacetic acid (DTPA) on mercury in 0.1 M acetate buffer at pH 6.2 using a drop-time method. The changes in the interfacial activity of the Cr(III)–DTPA complex with the bulk concentration obeyed the Frumkin adsorption isotherm.

Łobacz et al. [52] have described partial adsorption of Ti^+ -cryptand (2,2,2) complex on mercury electrode. From voltocoulometry, cyclic voltammetry, and chronocoulometry, it has been deduced that electroreduction of this complex proceeds via two parallel pathways: from the solution and from the adsorbed states, which are energetically close. Also, Damaskin and coworkers [53] have studied adsorption of the complexes of alkali metal cations with cryptand (2,2,2) using differential capacity measurements and a stationary drop electrode. It has been found that these complexes exhibit strong adsorption properties. Novotny et al. [54] have studied interfacial activity and adsorptive accumulation of UO_2^{2+} –cupferron and UO_2^{2+} –chloranilic acid complexes on mercury electrodes at various potentials in 0.1 M acetate buffer of pH 4.6 and 0.1 M NaClO_4 , respectively.

Kariuki and Dewald [55] have studied current oscillations accompanying reduction of indium(III) and gallium(III) in diluted chloride and nitrate solutions at a dropping mercury electrode.

Oscillations have also been reported for O_2/O_2^- redox reaction in quinoline media on HMDE, liquid Hg, and solid Hg-coated electrodes [56].

Acceleration and the associated oscillatory behavior of electroreduction of

H₂O₂ on Hg-adatom-modified polycrystalline Au electrodes have been described [57, 58].

Concerning more general application of mercury electrode in the studies on complexation equilibria, one should mention the paper by Jaworski et al. [59], who have investigated oxidation of mercury microelectrode in solutions with thiocyanates without any background electrolyte added. In the experiments, normal pulse voltammetry and staircase voltammetry were used. The authors have developed a general procedure for the determination of the stability constants, based on the data taken from the voltammograms. They have applied it to the analysis of Hg(II)–SCN[−] complexes.

Bell et al. [60] have generated two complexes by anodic oxidation of mercury in the presence of a saturated acetonitrile solution of 1-methylimidazoline-2(3*H*)-thione. Their crystalline structure has been analyzed.

Stepnicka et al. [61] have synthesized mercury(II) complexes with 1'-(diphenylphosphino)ferrocenecarboxylic acid and studied their structure and electrochemical properties.

Also, Yam and Cheung [62] have carried out the synthesis of a series of novel polynuclear mercury(II) diimine complexes with bridging chalcogenate ligands and studied their luminescence and electrochemical properties.

Complex formation of Hg²⁺, Zn²⁺, and Pb²⁺ with polyacrylic and polymethacrylic acids has been studied [63] voltammetrically, using mercury drop and glassy carbon rotating disk electrodes. The formation constants of these complexes were calculated.

Electrochemical synthesis and structural characterization of zinc, cadmium, and mercury complexes of heterocyclic

bidentate ligands (N, S) have been described by Sousa-Pedrares et al. [64].

24.6.3.2.1 Analytical Applications In addition to the above-mentioned analytical aspects of the processes at Hg electrodes, in this section, we briefly review the papers focused on the subject of the affinity of various compounds to the mercury electrode surface, which allowed one to elaborate stripping techniques for the analysis of inorganic ions. Complexes of some metal ions with surface-active ligands were adsorptively accumulated at the mercury surface. After accumulation, the ions were determined, usually applying cathodic stripping voltammetry (CSV). Representative examples of such an analytical approach are summarized as follows.

Wang et al. [65] have described adsorptive stripping determination of uranium and chromium complexes with, for example, propyl gallate, after their adsorptive accumulation. Sensitive voltammetric determination of S₂O₃^{2−} was performed, based on its electrosorption properties and utilizing the CSV analytical signal [66]. Also, Novotny and Krista [67] accumulated S₂O₃^{2−} on mercury electrodes by applying a potential of $E_{ac} = 275$ mV (versus Ag/AgCl). Reduction peak of the deposit was formed at -0.38 V. Strong adsorption of S₂O₃^{2−} was reflected in electrocapillary curves at potentials more positive than -0.4 V (SCE) in 0.1 M acetate buffer of pH 4.4 up to approximately -50 mV (SCE), where faradaic processes affected the γ versus E dependence. The potential of maximum adsorption was found to be -60 mV (SCE). After differentiation of the surface pressure π versus $\log c$ dependence, the adsorption isotherms obeying the Frumkin relation were obtained. At E_{max} , adsorption coefficient β equaled $105 \text{ m}^3 \text{ mol}^{-1}$.

Safavi et al. [68] have described an indirect method for the determination of CN^- ions and HCN. The method utilized the effect of cyanide on cathodic adsorptive stripping peak height of Cu-adenine.

The Co(II)–phenylthiourea-borax buffer system has been studied applying CSV at HMDE [69]. An irreversible peak observed at -1.5 V was attributed to the catalytic hydrogen evolution. The first reduction step, combined with the adsorptive accumulation of herbicide metribuzin at mercury electrode, has been used for its determination by adsorptive stripping voltammetry [70].

Fraga et al. [71] have proposed a new stripping voltammetric method for the determination of titanium and Co(II) [72] based on the adsorptive accumulation of its hydroxynaphthol blue complex on a static mercury drop electrode.

Traces of sulfides were determined by CSV at pH 10 in the presence of cobalt(II) ions. Cobalt sulfide was accumulated at -0.5 V (versus SCE), probably in the form of colloidal particles occluded into the mercury sulfide layer [73]. In the cathodic scan, CoS catalyzed evolution of hydrogen, which was reflected in the current peak at about -1.6 V.

Accumulation of Cu(II) complexes with xanthine and xanthosine has also been utilized in stripping analysis [74]. Copper(II) indapamide complex was adsorptively accumulated at a HMDE and used for the determination of the ligand in the cathodic stripping step [75].

Ivanov and Kaplun [76] used catechol in the determination of vanadium by adsorptive stripping voltammetry. It has been shown that the studied electrode process comprised one-electron reversible reduction of vanadium(IV) triscatecholate, previously accumulated at the electrode. It has also been found that the reduced

species, vanadium(III) complexes, were not accumulated.

Trace mercury determination by differential pulse (dp) anodic stripping voltammetry on polythiophene-quinoline/glassy carbon modified electrode has been reported [77].

Mercury electrodes were also polarized anodically in the solutions containing NaOH, HClO_4 , NaCl, NaI, NaF, Na_2SO_4 , NaHCO_3 , Na_2CO_3 , and tartaric and citric acids [78]. The solutions contained only one species, or the mixture of species, and no supporting electrolyte was added. For many of the above salts, linear calibration plots were obtained and, therefore, analytical possibilities were discovered. Anodization of mercury was also carried out in the real samples (wine, rain, tap and mineral water).

The construction and behavior of a mixed binder carbon paste electrode containing dimethylglyoxime have been described [79]. Such an electrode was used for CSV determination of mercury(II) and other metal ions. They were accumulated at the electrode surface during preconcentration step and later reduced from their complexes in the cathodic step.

Also, sodium montmorillonite-modified carbon paste electrode has been used for the determination of trace concentrations of mercury [80]. Hg^{2+} was preconcentrated at the electrode, reduced, and then stripped from the electrode surface in the positive potential scan. At a glassy carbon electrode modified with dithizone, mercury has been determined, applying anodic stripping voltammetry [81].

24.6.3.3 Adsorption and Electrode

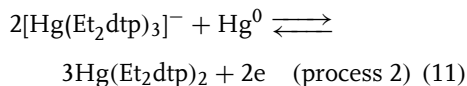
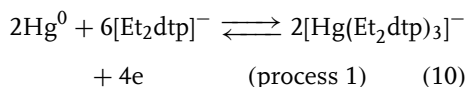
Reactions Involving Organic Compounds

Recently published studies on adsorption of organic compounds on mercury

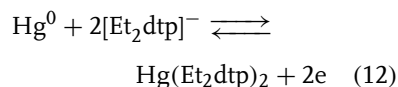
electrodes cover a relatively wide spectrum of substances, ranging from simple molecules to more complex compounds, and also of biochemical and/or pharmaceutical importance. Investigations of these compounds were performed either in the aqueous or nonaqueous media. It is noteworthy that a significant number of studies have been devoted to the sulfur-containing compounds. Typically, sulfur compounds or the products of their electrode processes adsorb or even form solid deposits at the mercury surface. For example, Mirceski et al. [82], applying polarography and cyclic and square-wave voltammetry at mercury electrodes, have described electrochemical behavior of three sulfur-containing drugs of different molecular structures. Adsorption and formation of insoluble salt at the electrode surface in this respect have been discussed.

24.6.3.3.1 Organic Compounds Containing Sulfur, Selenium, and Tellurium

Anodization of Hg electrode Polarographic studies [83, 84] have revealed that in the presence of Et_2dtp^- ($\text{Et}_2\text{dtp}^- = \text{S}_2\text{P}(\text{OEt})_2$, *o,o*-diethyldithiophosphate) in acetone mercury is oxidized in two consecutive steps:



Overall:



These processes were fast (reversible). Cathodic reduction of $\text{Hg}(\text{Et}_2\text{dtp})_2$ exhibited analogous behavior.

Bond and coworkers [85] have extended earlier [83] polarographic studies over a wider temperature range from 20 to -60°C . Assuming reversibility (processes 1 and 2), and considering the case of mercury oxidation in the presence of Et_2dtp^- , half-wave potentials depended on Et_2dtp^- concentration:

$$(E_{1/2}^r)_{\text{process 1}} = c_1 - \frac{RT}{F} \ln [(\text{Et}_2\text{dtp})^-] \quad (13)$$

$$(E_{1/2}^r)_{\text{process 2}} = c_2 + \frac{RT}{2F} \ln [(\text{Et}_2\text{dtp})^-] \quad (14)$$

where c_1 and c_2 are constants. The shapes of the waves were different. The corresponding I versus E dependencies were described by the expressions:

$$(E)_{\text{process 1}} = c_1' + \frac{RT}{2F} \ln \left[\frac{I}{(I_d - I)^3} \right] \quad (15)$$

$$(E)_{\text{process 2}} = c_2' + \frac{RT}{2F} \ln \left[\frac{I^3}{(I_d - I)^2} \right] \quad (16)$$

Additionally, the wave height ratio (process 1 : process 2) was predicted to be 2 : 1. $E_{1/2}^r$ values for the process 1 were almost independent of temperature (versus ferrocene electrode), and for the process 2, shifted to negative potentials as the temperature was lowered. Adsorption was enhanced significantly at lower temperatures, as noted previously for the room temperature [83, 84]. The third wave was observed close to the mercury electrode oxidation process. It was attributed to the formation of cationic mercury-rich dithiophosphate compounds, formed by oxidation of the mercury electrode and analogous to those characterized

for mercury dithiocarbamates [86–88]. There was no abrupt change in either the role or the nature of the electron transfer step at mercury electrode at the freezing point of mercury in both noninteracting (ferrocene) and interacting systems. $\text{Hg}(\text{Et}_2\text{dtp})_3^-$ was thermodynamically stable from 25 to -80°C . Optical studies of mercury microelectrodes have shown that their passivation, enhanced at low temperatures, is accompanied by the changes in the appearance of the surface.

Amino acids Cystine and cysteine are the amino acids, which have been the most extensively studied. Cathodic stripping of several sulfur compounds, including cysteine, cystine, and methionine has been described [89]. Voltammetric peaks were formed after accumulation at the constant potential. In case of cystine and cysteine in buffer of $\text{pH} = 8.5$, the potential of accumulation was 0.0 V versus SCE, while cathodic peaks were observed at about -0.55 V. The most important works on cystine reduction at mercury have been published by M. Heyrovsky et al. [90, 91]. They have found that cystine reacts chemically with mercury to give an adsorbed mercuric cysteine thiolate. Later, Heyrovsky and coworkers [92] have studied anodic reactions of cysteine at mercury electrodes, using several electrochemical methods. Two separate steps of mercury oxidation to cysteine mercurous and mercuric thiolates were distinguished. Both these compounds appeared to be strongly adsorbed at mercury electrodes. At low coverages of the electrode with the mercury-containing product, mercuric thiolate was formed by disproportionation of the adsorbed mercurous thiolate at the potentials of the second step. Under such conditions, only one electrode reaction

was observed. The authors have found that during the first step in acidic solutions, the molecules of mercurous cysteine thiolate in the compact film are perpendicularly oriented on the electrode, exhibiting strong lateral interactions. In alkaline solutions, S and N atoms of cysteine bind monomeric mercury(I). At the potential close to that of total mercury oxidation, the formation of cysteine mercuric thiolate occurs in the solution, followed by its adsorption at the electrode surface. Heyrovsky and Vavricka [93] have shown that adsorption and anodic reactions of homocysteine with mercury differ from those involving cysteine, due to slight differences in its hydrophilic properties and the structure of complexes with metal ions.

Proteins, enzymes Adsorption and electroreduction of proteins at mercury electrodes have been reviewed by several workers. Our short summary is partly based on the paper by Honeychurch [94]. Kuznetsov et al. [95] have suggested that the segments of the protein that interact with the surface, belong to relatively hydrophobic regions and they either denature or unfold following irreversible adsorption on mercury surface. Proteins spread on mercury electrodes [96] and form a layer of $8\text{--}10 \text{ \AA}$ in thickness, corresponding to the single polypeptide chain. This phenomenon is known as *surface denaturation*. Adsorption area and, consequently, the extent of denaturation are decreased with an increasing specific adsorption of the anion. The dependence of the molecular weight versus adsorption area shows that the proteins of large molecular weight (above 15 kD) behave differently from the smaller proteins [94], as they possibly do not denature and spread on mercury to the same extent as

smaller proteins do. It has also been suggested [94] that for adsorption of larger proteins, only the subunit attached to the surface denature. This makes the available adsorption area smaller than that predicted from the molecular weight versus adsorption area relation for smaller proteins.

Proteins can adopt several conformations at the electrode following adsorption, depending on which part of the molecules is initially bound to the electrode surface. In consequence, the number of electroactive disulfide bonds is a mean of the number of electroactive bonds corresponding to all possible conformations. Conformational variations of the adsorbed disulfide-containing proteins make the accessibility of disulfide bonds to the electrode surface to vary and may produce noninteger n values for the reduction process.

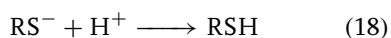
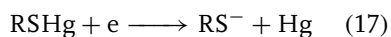
Honeychurch and Ridd [97] used chronopotentiometry to study reduction of five disulfide-containing proteins (bovine serum albumin, insulin, ribonuclease A, transferrin, and trypsin) adsorbed on HMDE. All studied proteins exhibited a reduction step at -0.6 V (versus SCE), due to reduction of disulfide groups.

The same authors [98] have presented a method for the estimation of the number of electroactive disulfide bonds in proteins adsorbed on mercury. The developed approach was based on the assumption that electroactive disulfides are located in more hydrophobic regions of the protein molecule.

Analogous to the electrode behavior of cystine and cysteine, one may expect chemical reaction occurring between mercury and protein disulfide bonds. Honeychurch and Ridd [99] have proved the correctness of such reaction pathway, applying potentiometric stripping analysis to investigate

chemical oxidation of electrolytically reduced disulfide bonds.

Electroreduction of iron-free apoferreredoxins has been studied by Ikeda et al. [100]. They have proposed the following pathway for the reaction occurring at -0.6 V versus SCE:

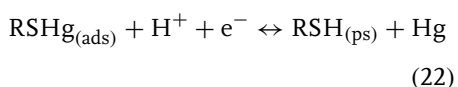
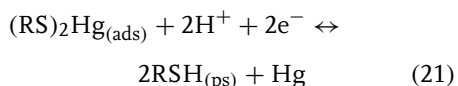
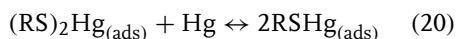
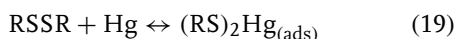


Also, different metallothioneins, a group of peptides and proteins, which play an important role in metabolism of metals in living organisms, have been studied [101, 102]. In the range of more anodic potentials, cyclic voltammograms recorded in the absence of metal ions were similar to those obtained for disulfide-containing proteins. The presence of metal ions in the solution shifted the voltammetric peaks, depending on the stability of the formed complex.

Egodage et al. [103] have described a novel application of monoclonal antibodies for the probing of conformation and orientation of the adsorbed protein using cytochrome *c*(3) films on mercury electrode. Antibodies were utilized to confirm the presence of three conformationally distinct electrochemical forms of cytochrome dependent on the applied potential.

Chen and Abruña [104] have studied, using ac and dc cyclic voltammetry, interfacial interaction between the adsorbed porcine pancreatic phospholipase A_2 and mercury. The authors have proposed reaction mechanism based on the interaction of cystine residues (disulfide) with mercury. They have found that surface reactions are complex and that several factors influence their mechanism. Their results and observations agree with the reaction pathway postulated for the

cystine/cysteine system at mercury electrodes:



Subscript (ads) denotes adsorption via a thiolate linkage, while (ps) stands for a physisorbed and/or adsorbed state via different interactions. However, large dimensions of the studied molecules and their amphiphilic nature make the surface reaction mechanism more complex than in case of cystine/cysteine. Interfacial microstructure plays an important role in the determination of the surface behavior of the adsorbed molecules. From the study on the charge-transfer kinetics, the transfer coefficient α was calculated as slightly less than 0.50, while the rate constant (based on Laviron's derivations [105]) was of the order of 10^{-3} s^{-1} . The same authors [106] have shown earlier that the adsorption rate constant of porcine pancreatic phospholipase A₂ at mercury via one of its disulfide groups is of the order of 10^4 s^{-1} .

Yang and Zhu [107] have studied, applying several electrochemical methods and mercury electrodes, electrochemical behavior of pharmaceutically important dipeptide *captopril*. In acidic solution, one-electron transfer led to the formation of a univalent mercury–sulfur compound, which was strongly adsorbed at the electrode surface and gradually transformed into the divalent mercury–sulfur compound.

Nucleic bases, nucleotides, and thiolipids

Self-assembled surface layers of 6-thioguanine (6TG) on mercury electrode have been described and electrochemically characterized by Arias et al. [108, 109]. Several condensed phases of chemically adsorbed 6TG have been described. It has been found that under conditions of complete coverage, the films of chemisorbed molecules significantly inhibit mercury oxide formation at the electrode [108]. The self-assembled monolayer had no influence on the rate of outer-sphere processes, but strongly inhibited inner-sphere processes [109]. Arias et al. [110] have also given an electrochemical characterization of the mixed self-assembled monolayer comprising chemisorbed 6TG and physisorbed guanine molecules at a HMDE. The mixed monolayer was investigated, applying chronoamperometry, cyclic voltammetry, and phase-sensitive ac voltammetry. Compact packing of the molecules within the film was found. Ex situ measurements in the presence of dissolved oxygen have proved that the mixed monolayer was stable in the solution free of 6TG and guanine. Madueno et al. [111] have also studied adsorption and phase formation of 6TG on mercury electrode. At high potentials, the molecules were chemisorbed and were able to form a self-assembled monolayer. When the potential was scanned to more negative values, reductive desorption of the monolayer was observed. Cathodic voltammetric peaks, which are typical of a 2D condensed phase transition, divided the potential window into two regions: one, in which self-assembled monolayer was stable, and the second, in which a physisorbed state existed.

Some bioelectrochemical applications of self-assembled films on mercury (including among others, chlorophyll and

channel-forming gramicidin) have been described by Guidelli et al. [112].

Recently, Moncelli et al. [113] have described tethered bilayer lipid membranes self-assembled on Hg surface. In order to incorporate integral proteins in their functionally active state, metal-supported lipid bilayers must have a hydrophilic region interposed between the bilayer and the metal. An appropriate hydrophilic molecule must be terminated at one end with either sulfhydryl or disulfide group that anchors this hydrophilic spacer to the metal surface. The other end of the hydrophilic spacer may be covalently linked to the polar head of a phospholipid molecule, giving rise to a supramolecular “thiolipid”. Compared to gold, mercury has an advantage of providing a defect-free and fluid surface for the self-assembling spacer. The use of thiolipids allowed one to obtain particularly stable mercury-supported lipid bilayers.

Heyrovsky et al. [114] have shown that voltammetric behavior of isomeric end-labeled-SH deoxyoligonucleotides on HMDE depends on the dislocation of the electroactive components along the strand, as well as on their adsorptivity compared to the adsorptivity of other parts of the molecule.

Other sulfur-containing compounds Pardo et al. [115] have studied electrochemical oxidation of 2-mercaptopyridine N-oxide on Hg electrodes in aqueous solutions. It has been found that anionic form of this compound was oxidized to yield a radical. At low concentration, oxidation was reversible and the radical was strongly adsorbed. At high concentrations, this process was accompanied by diffusive reversible oxidation. Reorientation of the adsorbed 2-mercaptopyridine N-oxide molecules on Hg electrodes in the presence of Triton X-100 has been studied

by Mellado and Galvin [116]. Safavi and Gholivand [117] have shown that reduction of di(2-iminocyclopentylidene mercapto methyl) disulfide to its monomer in DMSO is not a simple two-electron transfer process, but it occurs via mercury complex formation. Calvente et al. [118] performed voltammetric study of the oxidation of 2-mercaptoethyl ether adsorbed on mercury. They have shown that the process involves one electron and is followed by fast reversible dimerization. Later, Gil et al. [119] (the same research group) performed voltammetric studies on surface redox processes perturbed by dimerization and adsorption of the products. They have theoretically predicted voltammetric behavior of 3-mercaptopropanol on mercury as a function of the solution pH. Mandler and coworkers [120] have studied the formation and organization of *self-assembled* monolayers of alkanethiols and omega-mercaptopcarboxylic acids on mercury. The measured charging currents and the observed charge-transfer process for the $\text{Ru}(\text{NH}_3)_5^{2+/3+}$ redox system have shown that adsorption of acids on mercury was followed by the formation of a densely packed array. Finally, Muskal and Mandler [121] have described the formation of self-assembled monolayers of omega-mercaptopalkanoic acids on a mercury electrode. It has been suggested that thiols are either physisorbed or chemisorbed, depending on the applied potential. The transition between these two states occurred via a faradaic process.

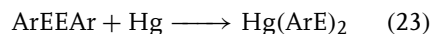
Specific conditions of the electron transfer reactions on Hg surfaces covered with sulfur compounds have been intensively investigated by Majda, Bilewicz, Słowiński, and coworkers [122–129]. The studies on electron tunneling involving Hg–Hg junction and mono- or bilayers of alkanethiolate trapped between small mercury

drops, were carried out. For example, in paper [123], it has been described that alkanethiol molecules of the chain length C-8–C-18 form densely packed, perpendicularly oriented monolayers on Hg in the course of a two-electron oxidation of Hg to mercuric thiolate. Exponential increase of the electron tunneling rate with the electrode potential, as well as exponential decay with the monolayer thickness was observed. For *n*-alkane-3-thiopropamide bilayer junctions, tunneling currents were larger than those measured for the alkanethiolate junctions involving the same number of atoms [125]. This fact suggested that the presence of amide groups increases the electronic coupling in this type of systems. More recently, asymmetric electron transmission across the Hg–Au junction containing bilayers of alkanethiols of different chain lengths has been studied both experimentally and theoretically by Majda and coworkers [130]. Also, S  k et al. [131] have investigated electrochemically controlled Ag/Hg tunneling junction, with an Ag electrode covered with a self-assembled monolayer of *n*-alkanethiol.

Finally, Gugala et al. [132] have analyzed the effect of the concentration of the base electrolyte on adsorption of 1,1,3,3-tetramethyl-2-thiourea at mercury electrode. The Flory-Huggins and the Frumkin models were utilized for the quantitative analysis of the adsorption data.

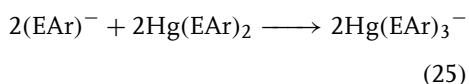
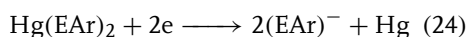
Organic selenides and tellurides Ludvik and Nyg  rd et al. [133, 134] have studied electroreduction of aromatic diselenides and ditellurides (ArEEAr) at mercury electrodes. They have found that the charge-transfer process is preceded by a spontaneous heterogeneous reaction between these compounds and mercury,

according to the equation:

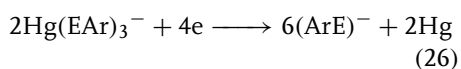


where E = Se or Te. Hg(ArE)₂ is an analog of mercury thiophenolate, which is formed in case of the corresponding sulfur-containing compounds. On the basis of electrochemical and other experiments, the following mechanism has been proposed:

First wave:



Second wave:



This mechanism is analogous to that of mercury thiophenolate [135], but different from the reduction mechanism of aromatic disulfide(I).

Recently, Alvarez et al. [136] have studied interfacial and electrochemical behavior of diphenylselenide on HMDE in DMF-water mixture (3:7, v:v). Applying ac voltammetry and chronocoulometry, it has been shown that a multilayer film of chemisorbed diselenide of the progressively increasing thickness is formed.

24.6.3.3.2 Organic Nitrogen Compounds

Theoretical quantum-chemical study of pyridine adsorption at Hg electrode (including its charged surface) has been described by Man'ko et al. [137, 138]. An ab initio Hartree-Fock-Roothaan method has been employed. The electrode was modeled as a planar seven-atomic Hg-7 cluster. The deepest minimum of the total energy of the adsorption system was found for positive charge density and Py interacting with the metal through the lone electron

pair at the nitrogen atom. For a positive surface charge, vertical orientation of the adsorbate molecule was energetically favorable, whereas for the negatively charged surface, adsorption did not occur.

Formation of 2D phase accompanying electrochemical reduction of 4,4'-pyridine on mercury in the presence of iodide ions occurred via adsorption–nucleation and reorientation–nucleation mechanisms [139]. The first reduction step of Bpy on Hg in the presence of iodide as counterion in acidic medium at 15 °C involved the $\text{BpyH}_2^{2+}/\text{BpyH}^+$ couple and led to the formation of a 2D phase. The increased contribution of the reorientation term in the formation of the condensed phase was consistent with the increased adsorption strength of the anion to the electrode surface.

Afanasev et al. [140] have analyzed the literature data concerning adsorption of N-derivatives of morpholine and cyclohexylamine at the uncharged mercury electrode. They have also determined free energy of adsorption intrinsic to the interactions of organic molecules with mercury.

Higuera et al. [141] have studied reduction of 4-chloro-2,6-diisopropylamino-s-triazine in acidic media up to pH 5, applying dc differential pulse polarography. In the recorded voltammograms, two main reduction peaks were observed, with a prepeak at less negative potentials, and a postpeak at more negative potentials, what points to adsorption of the compound at the electrode. Two main peaks corresponded to two-electron reduction process.

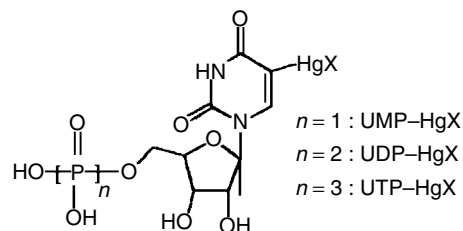
Adsorption of L-histidine (His) has been studied [142] in aqueous KF and LiClO_4 solutions on mercury electrode and at air/solution interface. The strongest adsorption of His on Hg electrode was observed in solutions of $\text{pH} \geq 8$.

There are also several papers describing adsorption of quinoline. Sawamoto [143] have studied adsorption and reorientation of quinoline molecules at Hg electrodes by recording differential capacity-potential and differential capacity-time plots using the flow-injection method. Adsorption of quinoline was found reversible at any potential, with the possibility of reorientation of the molecules at the interface. Ozeki et al. [144] have studied adsorption, condensation, orientation, and reduction of quinoline molecules at pure Hg electrode from neutral and alkaline solutions, applying electrochemistry and Raman microprobe spectroscopy. The adsorbed quinoline molecules changed their orientation from the flat at $-0.1 \text{ V} > E > -0.3 \text{ V}$, to the upright at $E < -0.5 \text{ V}$. At potentials $-0.3 \text{ V} > E > -0.5 \text{ V}$, both orientations were observed. Later, Ozeki et al. [145] have extended the studies on reorientation of quinolinium ions at the Hg|acidic aqueous solution interface. For these conditions, the specific adsorption of quinoline was not observed.

Xanthine and xanthosine were investigated on HMDE, applying out-of-phase ac and dc voltammetries [74]. It has been shown that both compounds are strongly adsorbed and interact chemically. In the cathodic stripping process, one could determine both compounds at trace level. Naidu et al. [146] have performed polarographic studies to show that the product of anodic reaction (prewave) of potassium isobutyl xanthate is strongly adsorbed at the mercury electrode.

Cyclic voltammetry and in situ IRAS have been utilized in the studies on adsorption of heptyl viologen (HV) at mercury electrode [147]. A set of very sharp cathodic and anodic peaks formed at potentials more positive than the

Scheme 1



reduction wave was ascribed to the one-electron reaction in the adsorbed state. The areas corresponding to a single molecule adsorbed on the surface were estimated and equaled to 83 and 71 square Å for Ox and Red forms, respectively. In the potential region at the negative side of the spikelike peaks, the HV cation radicals formed a bilayer with bipyridine planes positioned parallel to the surface.

McGarvey et al. [148] have studied electrochemical and adsorption properties of lumiflavin (LF) (7,8,10-trimethylbenzo[g]pteridine-2,4(3*H*,10*H*)-dione, $C_{13}H_{12}N_4O_2$) at Hg electrode in buffer solution of pH 6, 7, and 8, applying cyclic voltammetry. It has been suggested that at low-coverage, LF molecules are adsorbed in the orientation parallel to the electrode surface, independently of the potential, while at higher coverage, concerted reorientations of LF monolayer occur as the potential is changed. For the extreme potentials: positive of ca -0.35 V and negative of -1.0 V, parallel configuration has been proposed. Between these two limits, two perpendicular orientations existed, ensuring the respective increase in attainable coverage. LF exhibited striking differences from flavin adenine dinucleotides (FAD), in spite of the presence of an isoalloxazine ring system – a common electrochemically active moiety present in both compounds.

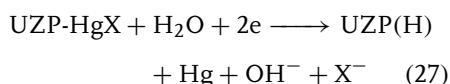
Komorsky-Lovric [149] has investigated adsorption and reduction of the plant

alkaloid berberine in electrolytes of various pH at mercury electrodes, applying ac polarography and square-wave voltammetry. Reduction of berberine appeared irreversible and occurred between -0.95 and -1.35 V, depending on the pH of the solution. The reduction product was canadine, which could not be oxidized at Hg electrodes. Both berberine and canadine formed condensed films at mercury electrodes, which limited the possibilities of analytical determination of berberine by adsorptive accumulation at the electrode. Since the condensed film of canadine was very stable, even at -0.5 V, it might prevent adsorption of berberine.

Wagner and Chambers [150] have published a study on electrochemical reduction of mono, di-, and triphosphate uridines (see Scheme 1) mercurated in 5-position of the pyrimidine ring in aqueous solutions. In 0.1 M KCl, these compounds exhibited two main electroreduction peaks in cyclic voltammograms in potential ranges -0.5 to -0.6 V and -0.8 to -0.9 V (versus SCE), respectively.

Voltammetric peaks, especially those of UDP and UTP, were sharper than those of the third compound, as they were adsorbed at the electrode surface. Coulometric studies (at -1.0 V, electroreduction) at mercury pool electrode (also glassy carbon) and analysis of the obtained products have shown that for all three compounds, the two-electron reductive cleavage of the carbon–mercury bond occurs. The electrode

process in the region of -1.0 V may be represented by the following reaction scheme:



where Z = M, D, or T signifies mono-, di-, or triphosphate nucleotide, respectively.

Philipp and Retter [151] have studied the formation of the first monolayer of adenine on mercury electrode in borate solutions. Applying potential-step method, they have proposed to explain the observed transients in terms of two-dimensional (2D) truncated progressive nucleation and constant growth of monolayer islands.

Fojta and Palecek [152] have described a supercoiled DNA-modified electrode as a highly sensitive tool for detection of DNA damage. The method is based on the measurement of an ac voltammetric peak, resulting from the scission of the single-strand in the covalently closed circular (supercoiled) DNA molecule. The method was found to be faster than gel electrophoresis. Recently, Fojta [153] has published a paper (including 188 references) reviewing applications of mercury electrodes in nucleic acid electrochemistry, emphasizing their role as sensitive analytical tools and probes of DNA structure. Generally, at mercury electrodes, nucleic acids produce (1) faradaic signals corresponding to redox processes of adenine, cytosine, and guanine residues, and (2) tensammetric signals referring to adsorption/desorption of polynucleotide chains at the electrode surface. Some of these signals appear to be highly sensitive to DNA structure. Mercury film and solid amalgam electrodes possess similar features as mercury drop electrodes in the analysis of nucleic acids.

24.6.3.3.3 Indicators and Dyes Abdel-Hamid [154] has studied adsorption of phenolphthalein at a HMDE in aqueous buffer solutions containing 10% v/v ethanol, applying cyclic voltammetry and double potential-step chronocoulometry. At pH = 3.4 and concentration at $5.1 \mu\text{mol dm}^{-3}$, phenolphthalein was adsorbed irreversibly and weakly, with triphenylmethane moiety positioned perpendicular to the electrode surface. For the solutions of pH < 3.4, adsorption of a neutral lactone form has been suggested. In alkaline solutions of pH = 10.58, no adsorption was reported. The formation and organization of a self-assembled monolayer of bromopyrogallol red in aqueous media at pH 2.16 at HMDE have been studied by El-Sagher [155]. Electroreduction process proceeded via an ECEC mechanism.

Constant current chronopotentiometry has been utilized by Honeychurch [156] to study reduction of methylene blue adsorbed at HMDE. The obtained results were interpreted in terms of a two consecutive electron transfers (EE) mechanism and the interfacial potential distribution model.

Adsorption and kinetics of electroreduction of safranin T in self-assembled phospholipid monolayer deposited on mercury have also been studied [157].

24.6.3.3.4 Vitamins and Antibiotics Gao et al. [158] have studied adsorptive voltammetric behavior of riboflavine tetrabutylate (RT) on mercury electrodes and determined the rate constant of this process. In the presence of NaOH as the supporting electrolyte, riboflavine produced one pair of cathodic and anodic peaks, separated by 0.64 V. The adsorbed species was most probably a neutral molecule of RT of the maximum surface concentration of $5.42 \times 10^{-11} \text{ mol cm}^{-2}$. Adsorption of RT

was governed by the Frumkin model: adsorption constant was 4.6×10^5 ; attractive interaction parameter equaled 1.10; and standard Gibbs free energy of adsorption was $-32.30 \text{ kJ mol}^{-1}$. Sawamoto [159] has investigated the adsorption-desorption phenomena of vitamins at a mercury electrode by recording differential capacity versus time plots, applying flow-injection method and other techniques. Adsorption of vitamins was found to be irreversible.

Gomez et al. [160] have studied specific adsorption of potassium penicillin G (salt K) on Hg electrode from electrocapillary and capacity measurements. The Frumkin isotherm has been found applicable to the quantitative description of the data; repulsive interaction parameter equaled -3.5 and standard free Gibbs energy of adsorption at the zero charge was $-38.6 \text{ kJ mol}^{-1}$. ΔG_{ads}^0 depended linearly on the surface charge. Possible orientations of antibiotic molecules on the electrode surface were also discussed. Novotny [161] has studied adsorption of polyether-antibiotic monensin applying voltammetry at new miniaturized and compressible mercury electrodes. Hason et al. [162] have used several electrochemical methods to study electrochemical behavior of echinomycin and its interaction with single-stranded (ss) and double-stranded (ds) DNA at HMDE. It has been found from the capacity measurements that echinomycin gives a pseudocapacitance peak at -0.53 V . However, this peak was observed only for ds-DNA complex with echinomycin. Accordingly, by performing capacity measurements, one could distinguish both forms of DNA.

24.6.3.3.5 Enzymes and Coenzymes Electrochemical behavior of bovine erythrocyte superoxide dismutase adsorbed on Hg electrode has been studied by Qian

et al. [163]. Adsorption of this compound was described in terms of the Langmuir model; adsorption constant equaled 8.96×10^4 and Gibbs free energy was $-28.2 \text{ kJ mol}^{-1}$. Mei et al. [164] have studied adsorption of copper-zinc superoxide dismutase on mercury electrodes. Applying double potential-step chronocoulometry, it was found that dismutase formed a monolayer at the electrode. Wittstock and Emons [165] have carried out voltammetric studies on ubiquinone adsorption at mercury electrodes. Adsorption isotherms of ubiquinones UQ(4), UQ(6), UQ(9), and UQ(10) were determined using two independent voltammetric techniques at the stationary mercury/solution interface. While the redox behavior was essentially the same for all homologs investigated, the molar Gibbs free energy of adsorption increased steadily with the number of isoprenic units in the series from UQ(4) to UQ(10).

24.6.3.3.6 Other Organic Compounds

Turowska et al. [166] have studied adsorption of *m*-hydroxybenzoic acid in aqueous solutions on the dropping mercury electrode and determined the surface tension, differential capacity, and the potential of zero charge for this system.

Gugala et al. [167] have studied adsorption of butyl acetate at mercury electrode in 1, 0.5, and 0.1 M NaClO_4 . The zero charge potential values at the streaming mercury electrode were found to shift to positive values with the increasing ester concentration, which indicated the hydrophilic part of the molecules to be directed toward the solution.

Muszalska et al. [168] have performed a comparative study on adsorption of dodecanol and cholesterol in ethylene glycol at Hg electrode and at the free surface of ethylene glycol phase. In

terms of the Frumkin model, significant differences in the quantitative adsorption characteristics of these two compounds were found and discussed.

In Ref. 169, some peculiarities associated with adsorption of alkyne peroxides from DMF–water solutions onto the mercury electrode in the presence of tetraethylammonium cations have been described. Polarography and electrocapillary measurements were employed as the experimental techniques. It has been shown that interfacial activity of these peroxides was determined by the species generated as a result of associative interactions between peroxides and DMF and tetraethylammonium cations.

Recently, Japaridze et al. [170] have investigated adsorption of some aromatic compounds, including naphthalene, naphthonitrile, naphthylamine, anthracene, and phenanthrene at the mercury electrode|ethylene glycol solution interface. The analysis of the differential capacity data obtained at the HMDE has revealed that adsorption of the above-mentioned compounds obeys the Frumkin model, with attractive interactions of the particles in the adsorption layer. The results for ethylene glycol were compared with those for other nonaqueous solvents and their role in determining the adsorption mode was discussed.

Damaskin and Baturina [171] have studied unstable states during coumarin adsorption on mercury electrode. These instabilities were attributed to the nonequilibrium phase transitions in the adsorption layer, during which the orientation of coumarin molecules changed at the electrode surface.

Adsorption of glycosidic surfactants at Hg electrode was studied by means of differential capacitance measurements

(tensammetry) [172, 173]. Monosaccharidic surfactants formed a hemimicelle monolayer, while for disaccharidic compounds, the formation of a micellar multilayer throughout the electrical double layer was suggested.

Adsorption of a condensed 1-hydroxyadamantane layer at the Hg electrode/(Na₂SO₄ or NaF) solution interface has been studied as a function of temperature by Stenina et al. [174]. Later, Stenina et al. [175] have determined adsorption parameters and their temperature dependence for a two-dimensional condensation of adamantanol-1 at a mercury electrode in Na₂SO₄ solutions. They have also studied coadsorption of halide (F[−], Cl[−], Br[−]) anions and 1-adamantanol molecules on Hg electrode [176]. More recently, Stenina et al. [177] have described a new type of an adsorption layer comprising organic molecules of a cage structure condensed at the electrode/solution interface. This phenomenon was discovered for adsorption of cubane derivatives at mercury electrode.

Moncelli et al. [178] have investigated monolayers and multilayers of chlorophyll on Hg electrode and described a novel experimental technique to investigate such thin films. Upon irradiation of the chlorophyll α -coated Hg electrode with an appropriate light, photocurrents generated by the chlorophyll aggregates were measured under short-circuit conditions. Electrochemical behavior of chlorophyll α films adsorbed at HMDE applying two different procedures has been investigated later in darkness by the same research group, who applied double potential-step chronocoulometry and cyclic voltammetry [179].

Lindholm-Sethson et al. [180] have investigated dioleoyl phosphatidylcholine

(DOPC) monolayer-coated mercury electrodes in contact with different electrolytes, using electrochemical impedance spectroscopy and a multivariate analysis of impedance data. Rueda et al. [181] have analyzed impedance spectra of DOPC-coated mercury electrodes.

Mixed adsorption Saba [182] has described the properties of the mixed adsorption layer of *m*-toluidyne/polyethyleneglycols at Hg electrode in 1 M NaClO₄. The virial and the Frumkin models were used for the quantitative analysis of the adsorption data. Mixed adsorption layer of *p*-toluidyne and polyethyleneglycol (of average molecular masses of 400 or 10⁴ u) at mercury electrode in 1 M NaClO₄ has also been studied by Saba [183]. The author determined, from the experimental data, the parameters of the Frumkin and the virial isotherms. Similar studies have been carried out [184] with thiourea instead of *p*-toluidine. Saba et al. [185] have studied further the properties of the mixed polyethylene glycols (molecular weights 400 and 10⁴ u) – iodide ions adsorption layers at mercury electrode in NaClO₄ solutions.

Formation of a mixed layer of butan-1-ol and *o*-toluidine on Hg electrode has also been studied by Sienko et al. [186].

24.6.3.3.7 Analytical Aspects of Adsorption of Organic Compounds This chapter briefly summarizes representative examples of adsorption of various organic compounds on Hg surface, which have analytical applications.

Duan et al. [187] have studied adsorptive and electrochemical behavior of estradiol valerate at a static mercury electrode using cyclic voltammetry and chronocoulometry. A sensitive and

selective adsorptive stripping square-wave voltammetric method for the determination of estradiol valerate has been developed, providing detection limit of 1.1×10^{-8} M.

Kamal et al. [188] have described adsorptive stripping voltammetric analysis of 2,3,6-tri(2'-pyridyl)-1,3,5-triazine at mercury electrode, based on preliminary adsorption and accumulation of the determined compound.

Ceftazidime was accumulated at HMDE at pH 9.5 and potential of +0.1 V in the form of the adsorbed mercury salt. The reduction peak potential at –0.7 V was used in cathodic stripping voltammetric determination of this compound [189].

Cathodic stripping voltammetric determination of nanomolar level of two anthraquinone-based chlorotriazine dyes at HMDE has also been described [190].

Kizek et al. [191] have involved catalytic reaction at mercury electrode to electrochemical determination of metallothioneins. This determination was based on catalytic processes occurring at very negative potentials and accompanied by catalytic evolution (SH group) of hydrogen.

Electrode mechanism and analytical determination of cocaine and its metabolites, such as benzoylecgonine, ecgonine, and ecgonine methyl ester have been studied [192] at HMDE. These compounds were adsorbed at the electrode. Adsorption of benzoylecgonine was stronger than that of cocaine. Consequently, adsorptive stripping voltammetric method for the determination of cocaine was based on reduction of benzoylecgonine.

Fogg et al. [193] have presented a preliminary study on the indirect cathodic stripping voltammetric determination of 2-mercaptobenzothiazole based on the accumulation of its mercury, copper(I),

and nickel(II) salts or complexes. This method, utilizing mercury, was susceptible to the interference from copper(II) and large amounts of nickel(I), and thus determination of 2-mercaptobenzothiazole was less reliable. The same group of workers [194] have developed an indirect cathodic-stripping voltammetric method for the determination of trimercapto-*s*-triazine at sub-ppb levels in standard solutions. The analyte was accumulated and determined at pH 9.0 in the form of a salt, which was reduced at -0.47 V.

Application of adsorptive stripping analysis to the determination of nucleic acids at mercury electrodes has also been reported [195]. Tomschik et al. [196] have studied reduction and oxidation of peptide nucleic acid and DNA at mercury and carbon electrodes. The authors have utilized cyclic and square-wave voltammetries to study reduction and oxidation signals of single-stranded peptide nucleic acid and DNA decamers and pentadecamers.

Farias et al. [197] have presented cathodic adsorptive stripping voltammetry of guanine in the presence of copper at static mercury electrode. Cyclic voltammetry was also employed to characterize the interfacial and redox mechanisms.

Finally, 6-benzylaminopurine has been determined [198] by applying adsorptive stripping voltammetry.

At the end of this section focused on analytical problems, it should be mentioned that Thoming et al. [199] have evidenced that electrodialysis allows one to remove heavy metals from soils. During this process, the metals, including mercury, are transferred under the applied electric field to the pore water in either dissolved form or attached to colloids. This method is especially appropriate for the purification of fine-grained soils.

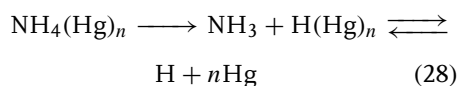
24.6.4

Ammonium and Quaternary-substituted Ammonium Amalgams

Although the properties of metal amalgams and intermetallic compounds in mercury have been investigating for many years and are already well recognized, the nature of ammonium amalgam, as well as quaternary ammonium amalgams, still remains a subject of controversy.

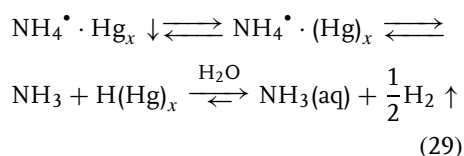
Ammonium amalgam was first reported in 1805 by Seebeck, who electrolyzed ammonium carbonate solution at mercury cathode. A concise review of the concepts on the structure of ammonium amalgam is given, for example, in Ref. 200.

Solubility of ammonium radical in Hg at 20°C reaches 1.55×10^{-2} M [201]. It has been found that redox behavior of ammonium amalgam is characterized by two equilibrium potential values, depending on the conditions of its preparation and aging [202, 203]. The more negative value of -1.7 V is typical of fresh ammonium amalgam and its concentration of 6×10^{-4} M, which is below the solubility limit and is ascribed to the $\text{NH}_4^\bullet(\text{Hg})/\text{NH}_4^+(\text{H}_2\text{O})$ couple. Saturated ammonium amalgam is characterized by less negative potential of -1.2 V, or with both values. This less negative value is associated with the $\text{H}(\text{Hg})/\text{H}_3\text{O}^+$ redox couple formed presumably in the decomposition reaction:



The studies on composition and instability of ammonium amalgam were continued later by the same group of researchers [204, 205].

Gumiński and Galus [206] critically evaluated the literature data concerning interaction of ammonium radical with mercury. It has been indicated [207] that NH_4^\bullet radical (as well as its alkyl derivatives) forms homogeneous amalgams. Significant inconsistencies of the literature data on NH_4^\bullet solubility in mercury have been emphasized. A possible role of impurities acting as decomposition catalysts has been suggested to explain these inconsistencies. The swelling phenomenon accompanying decomposition of ammonium amalgam has been described by the sequence of equilibria:



It is noteworthy that at 233 and 203 K, a NH_4^\bullet -Hg solid phase has been identified [208].

Barański and Lu [209] have carried out, applying microelectrodes, voltammetric studies on ammonium amalgam in propylene carbonate solutions at room temperatures. The sweep rates up to 80 V s^{-1} were appropriate for the analysis of the formation kinetics of this compound. Experimental and numerical simulation results have shown that ammonium amalgam was formed via fast charge-transfer process and its first-order decomposition was characterized by the rate constant of about 0.6 s^{-1} . Diffusion coefficient of NH_4^\bullet radical in mercury was estimated to be about $1.8 \times 10^{-5} \text{ cm}^2 \text{ s}^{-1}$. The formal potential of $\text{NH}_4^+ (\text{aq})/\text{NH}_4(\text{Hg})$ couple was determined as -1.723 V (SHE) .

Kovaleva and Gladyshev [210] have proposed classification of hydrogen-containing amalgams. Ammonium amalgam (NH_4^\bullet) Hg_n has been included in

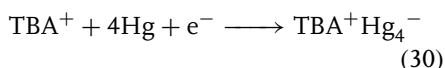
the group of binary amalgams of pseudometals (together with N_2H_5 , N_2H_6 , and $(\text{CH}_3)_n\text{NH}_{4-n}^\bullet$; $n = 1-4$ radicals). Formation of hydrogen amalgam has also been discussed.

Gumiński [211] has evaluated the equilibrium phase diagrams for the Hg-N system. For the ammonium amalgam, it has been indicated that Hg has the unique property of metallic alloying with the ammonium radical NH_4^\bullet . Lehman [212] has reported the formation of an ordered solid resulting from electroreduction of NH_4^+ on Hg, with the Hg- NH_4^\bullet layers seeming to be electrically conducting. Furthermore, Rich and Travers [213] have observed that the melting point of Hg was decreased to -45.61°C upon addition of 5.34 mol% NH_4^\bullet (a phenomenon that was analogous to the behavior of alkali metals in Hg). However, Gumiński [211] has found that this result disagrees with the solubility data of NH_4^\bullet in Hg at higher temperatures [206]. The formation of Hg-azide compound has also been discussed in this paper [211].

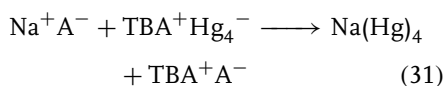
A more recent attempt to explain the structure of ammonium amalgam has been undertaken by Kariv-Miller et al. [200]. They have studied electrochemical reaction of NH_4^+ on mercury at temperatures below the freezing point of mercury, applying potential-step and linear sweep techniques. Under these conditions, "ammonium amalgam" was a solid phase stable for at least several minutes, the deposition of which at the mercury surface involved nucleation and growth steps. It has been concluded that such a phase belongs to the group of $\text{R}_4\text{N}^\bullet$ metals. Within this phase, electrons are bound by mercury in the form of negative clusters, and NH_4^+ ions act as counterions. The main role in the stability and electrochemical reversibility of ammonium amalgam has

been ascribed to the liquid–solid transition of mercury [200].

For *quaternary ammonium amalgams* it has been found that substitution of ammonium hydrogen atoms with alkyl groups increases amalgam stability [200, 214–216]. Already in 1986, Bard and coworkers [217] have suggested that “quaternary ammonium amalgams” are ammonium salts of anionic mercury species, of the type of Zintl ion salts and empirical formula $R_4N^+Hg_4^-$. These authors have studied the formation and stoichiometry of the compounds formed in the course of electroreduction of quaternary ammonium salts at mercury electrode, and also regeneration of R_4N^+ from the product upon chemical oxidation. Electrolysis of tetrabutylammonium hexafluorophosphate ($TBA^+PF_6^-$) solution in acetonitrile at $-20^\circ C$ was carried out at the potential of -4.5 V imposed on Hg (versus Ag wire quasi-reference electrode). Hg surface was covered with a black layer and finely divided particles of the product were dispersed in the solution. These phenomena have been ascribed to the reduction of tetrabutylammonium cation, which proceeded according to the equation:



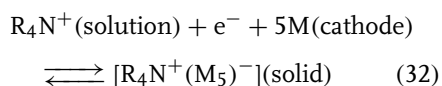
In the studies on the regeneration mechanism, addition of NaA (where $A = F^-$ or PF_6^-) caused black species to disappear, according to the reaction pathway:



The obtained product was identical (in the NMR spectrum) to the initial TBA^+ species. The latter reaction has

been suggested for easier synthesis of quaternary ammonium salts $R_4N^+A^-$.

Later, Kariv-Miller et al. have studied the properties of “tetraalkylammonium amalgams” both in situ, applying electrochemical techniques [218], and ex situ, applying solid-state techniques [219, 220]. It has been concluded that the solid products, which belong to R_4N metals, are formed in chemically and electrochemically reversible process:



Krasensky and Studnickova [221] have prepared quaternary ammonium amalgam via electroreduction of tetraethylammonium tetrafluoroborate in the aqueous medium at the room temperature. At the applied voltage of -2.8 to -2.4 V versus sodium saturated calomel electrode (SSCE) hydrogen evolution occurred simultaneously. Composition of the black precipitate formed was found to be $Et_4N \cdot Hg_x$, where $x = 2.9 \pm 0.8$.

Finally, Kovaleva and Gladyshev [222] have suggested that in the first step of electrolytic generation of either ammonium or quaternary ammonium amalgams, the amalgam of the corresponding hydride ($R^+[Hg_nH]^-$, $n = 10-12$) is formed, which is transformed to the RHg_n amalgam at more negative potentials.

To conclude, it should be said that in spite of numerous studies, the structure of ammonium amalgams has not yet been unequivocally established.

References

1. P. K. Wrona, Z. Galus, in *Encyclopedia of Electrochemistry of the Elements* (Ed.: A. J. Bard), Marcel Dekker, New York and Basel, 1982, Vol. IX-A, and references cited therein.

2. S. Trasatti, E.J. Lust, in *Modern Aspects of Electrochemistry* (Eds.: R.E. White, J.O.M. Bockris, B.E. Conway), Kluwer Academic/Plenum Publishers, New York, 1999, Vol. 33, and references cited therein.
3. D. C. Grahame, *J. Am. Chem. Soc.* **1954**, 76, 4819.
4. S. Trasatti, *Pure Appl. Chem.* **1986**, 58, 955.
5. J. J. O'Dea, M. Ciszewska, R. A. Osteryoung, *Electroanalysis* **1996**, 8, 742.
6. M. S. L. Brito, L. Angnes, C. M. A. Brett et al., *J. Electroanal. Chem.* **1999**, 468, 150.
7. L. Becucci, M. R. Moncelli, R. Guidelli, *J. Electroanal. Chem.* **1996**, 413, 187.
8. R. Jurczakowski, M. Orlik, *J. Electroanal. Chem.* **2004**, 562, 205.
9. K. Arihara, F. Kitamura, T. Ohsaka et al., *J. Electroanal. Chem.* **2002**, 518, 139.
10. R. R. Nazmutdinov, S. V. Borisevich, *Russ. J. Electrochem.* **1999**, 35, 1091.
11. B. B. Damaskin, B. M. Grafov, *Russ. J. Electrochem.* **1998**, 34, 967.
12. B. Eck, E. Spohr, *Electrochim. Acta* **1997**, 42, 2779.
13. T. Cecchi, P. Passamonti, F. Pucciarelli, *Collect. Czech. Chem. Commun.* **2002**, 67, 439.
14. A. J. Montheo, E. R. Gonzalez, *Electrochim. Acta* **1996**, 41, 2631.
15. G. Fuchs, L. Kišova, J. Komenda et al., *J. Electroanal. Chem.* **1997**, 428, 73.
16. L. L. Kišova, J. Komenda, I. Mayr et al., *J. Electroanal. Chem.* **2004**, 565, 367.
17. G. Salié, K. Bartels, *J. Electroanal. Chem.* **1988**, 245, 21.
18. G. Salié, *J. Electroanal. Chem.* **1989**, 259, 315.
19. K. Bartels, G. Salié, *Z. Phys. Chem.* **1990**, 271, 739.
20. G. Salié, K. Bartels, *Electrochim. Acta* **1994**, 39, 1057.
21. M. Shay, S. Bruckenstein, *Langmuir* **1989**, 5, 280.
22. J. Li, H. D. Abruña, *J. Phys. Chem. B* **1997**, 101, 244.
23. J. Li, H. D. Abruña, *J. Phys. Chem. B* **1997**, 101, 2907.
24. E. Herrero, H. D. Abruña, *Langmuir* **1997**, 13, 4446.
25. E. Herrero, H. D. Abruña, *J. Phys. Chem. B* **1998**, 102, 444.
26. J. Li, E. Herrero, H. D. Abruña, *Colloids Surf., A – Physicochem. Eng. Aspects* **1998**, 134, 113.
27. H. D. Abruña, J. M. Feliu, J. D. Brock et al., *Electrochim. Acta* **1998**, 43, 2899.
28. E. Herrero, L. J. Buller, H. D. Abruña, *Chem. Rev.* **2001**, 101, 1897.
29. J. Inukai, S. Sugita, K. Itaya, *J. Electroanal. Chem.* **1996**, 403, 159.
30. S. Abaci, L. Zhang, C. Shannon, *J. Electroanal. Chem.* **2004**, 571, 169.
31. S. Armalis, E. Kubiliene, *Chem. Anal.* **2001**, 46, 715.
32. V. Daujotis, C. Klingenberg, A. Teiserskien, *Anal. Chim. Acta* **2000**, 419, 243.
33. N. Vinokur, B. Miller, Y. Avyigal et al., *J. Electrochem. Soc.* **1999**, 146, 125.
34. M. Jasinski, P. Grundler, G. U. Flechsig et al., *Electroanalysis* **2001**, 13, 34.
35. M. Jasinski, A. Kirbs, M. Schmehl et al., *Electrochem. Commun.* **1999**, 1, 26.
36. L. Novotny, M. Heyrovsky, *Croat. Chem. Acta* **1997**, 70, 151.
37. M. Lovric, F. Scholz, *Electroanalysis* **1997**, 15, 1189.
38. A. M. Bond, W. Miao, T. D. Smith et al., *Anal. Chim. Acta* **1999**, 396, 203.
39. S. B. Khoo, S. X. Guo, *Electroanalysis* **2002**, 14, 813.
40. L. H. Wang, S. J. Tsai, *Anal. Chim. Acta* **2001**, 441, 107.
41. E. G. Camarero, J. Ramiro, E. Fatas, *Sol. Energy Mater. Sol. Cells* **1995**, 39, 27.
42. U. Hasse, K. Wagner, F. Scholz, *Solid State Electrochem.* **2004**, 8, 842.
43. E. Vasca, T. Caruso, M. Iuliano et al., *Ann. Chim.-Rome* **2000**, 90, 181.
44. A. Safavi, M. B. Gholivand, *Can. J. Chem.* **1996**, 74, 95.
45. E. A. Ponomarev, A. G. Krivenko, L. N. Sviridova et al., *Russ. J. Electrochem.* **2001**, 37, 435.
46. E. M. Andrade, F. V. Molina, *J. Adhes. Sci. Technol.* **2001**, 15, 1503.
47. A. G. Anastopoulos, P. Hadjiloizou, D. Nikolettou, *Langmuir* **2000**, 16, 7789.
48. S. Ramirez, G. J. Gordillo, D. Posadas, *J. Electroanal. Chem.* **1996**, 407, 219.
49. S. Ramirez, G. J. Gordillo, D. Posadas, *J. Electroanal. Chem.* **1997**, 431, 171.
50. S. Sander, G. Henze, *Electroanalysis* **1996**, 8, 253.
51. S. Sander, T. Navratil, P. Basova et al., *Electroanalysis* **2002**, 14, 1133.
52. M. Łobacz, M. Orlik, J. Stroka et al., *Electroanalysis* **2002**, 14, 583.

53. E. V. Stenina, O. A. Baturina, L. N. Sviridova et al., *Russ. J. Electrochem.* **2002**, 38, 602.
54. L. Novotny, T. Navratil, S. Sander et al., *Electroanalysis* **2003**, 15, 1687.
55. S. Kariuki, H. D. Dewald, *Electrochim. Acta* **1998**, 43, 701.
56. J. F. Wu, T. Okajima, K. Tokuda et al., *Electrochemistry* **2000**, 68, 277.
57. S. Uesugi, T. Katsumata, F. Matsumoto et al., *Electrochemistry* **2001**, 69, 681.
58. F. Matsumoto, S. Uesugi, N. Koura et al., *J. Electroanal. Chem.* **2003**, 549, 71.
59. A. Jaworski, Z. Stojek, J. G. Osteryoung, *J. Electroanal. Chem.* **2003**, 558, 141.
60. N. A. Bell, W. Clegg, J. R. Creighton et al., *Inorg. Chim. Acta* **2000**, 303, 12.
61. P. Stepnicka, I. Cisarova, J. Podlaha et al., *J. Organomet. Chem.* **1999**, 582, 319.
62. V. W. W. Yam, K. K. Cheung, *J. Chem. Soc., Dalton Trans.* **2000**, 3658.
63. K. Siegel, Ü. Mauer, H. Keis, *Electrochim. Acta* **1997**, 42, 2955.
64. A. Sousa-Pedrares, J. Romero, J. A. Garcia-Vazquez et al., *Dalton Trans.* **2003**, 7, 1379.
65. J. Wang, J. Y. Wang, B. M. Tian et al., *Anal. Chem.* **1997**, 69, 1657.
66. J. Krista, M. Kopanica, L. Novotny, *Anal. Chim. Acta* **1999**, 386, 221.
67. L. Novotny, J. Krista, *Electroanalysis* **1998**, 10, 965.
68. A. Safavi, N. Maleki, H. R. Shahbaazi, *Anal. Chim. Acta* **2004**, 503, 213.
69. N. Spataru, F. G. Banica, *Analyst* **2001**, 126, 1907.
70. J. Skopalova, K. Lemr, M. Kotoucek et al., *Fresenius' J. Anal. Chem.* **2001**, 370, 963.
71. I. C. S. Fraga, A. K. Ohara, P. A. M. Farias, *Anal. Lett.* **2001**, 34, 125.
72. I. C. S. Fraga, A. K. Ohara, P. A. M. Farias, *Anal. Lett.* **2000**, 33, 905.
73. F. G. Banica, N. Spataru, T. Spataru, *Rev. Roum. Chim.* **1998**, 43, 77.
74. Y. M. Temerk, M. M. Kamal, G. A. W. Ahmed et al., *Anal. Sci.* **2003**, 19, 1115.
75. A. Radi, *Chem. Anal. (Warsaw)* **2003**, 48, 273.
76. V. D. Ivanov, M. M. Kaplun, *J. Anal. Chem.* **1997**, 52, 321.
77. K. S. Yoo, S. B. Woo, J. Y. Jyoung, *Bull. Korean Chem. Soc.* **2003**, 24, 27.
78. M. A. Baldo, S. Daniele, G. A. Mazzocchin, *Anal. Chim. Acta* **1997**, 340, 77.
79. Z. Q. Zhang, H. Liu, H. Zhang et al., *Anal. Chim. Acta* **1996**, 333, 119.
80. W. S. Huang, C. H. Yang, S. H. Zhang, *Anal. Bioanal. Chem.* **2002**, 374, 998.
81. W. S. Huang, S. H. Zhang, *Anal. Sci.* **2002**, 18, 187.
82. V. Mirceski, B. Jordanoski, M. Avramovic, *J. Serb. Chem. Soc.* **1998**, 63, 719.
83. A. M. Bond, A. T. Casey, J. R. Thackeray, *J. Electrochem. Soc.* **1973**, 120, 1502.
84. A. M. Bond, A. T. Casey, J. R. Thackeray, *J. Electroanal. Chem.* **1973**, 48, 71.
85. A. M. Bond, R. Colton, J. Harvey et al., *J. Electroanal. Chem.* **1997**, 426, 145.
86. A. M. Bond, R. Colton, A. F. Hollenkamp et al., *J. Am. Chem. Soc.* **1987**, 109, 1969.
87. A. M. Bond, A. F. Hollenkamp, R. Colton et al., *Inorg. Chim. Acta* **1990**, 168, 233.
88. A. M. Bond, R. Colton, A. F. Hollenkamp et al., *Inorg. Chem.* **1991**, 30, 192.
89. R. von Wandruska, X. Yuan, *Talanta* **1993**, 40, 37.
90. M. Heyrovsky, P. Mader, V. Vesela et al., *J. Electroanal. Chem.* **1994**, 369, 53.
91. S. Vavricka, M. Heyrovsky, *J. Electroanal. Chem.* **1994**, 375, 371.
92. M. Heyrovsky, P. Mader, S. Vavricka et al., *J. Electroanal. Chem.* **1997**, 430, 103.
93. M. Heyrovsky, S. Vavricka, *Bioelectrochem. Bioenerg.* **1999**, 48, 43.
94. M. J. Honeychurch, *Bioelectrochem. Bioenerg.* **1997**, 44, 13.
95. B. A. Kuznetsov, G. P. Shumakovich, N. M. Mestechkina, *J. Electroanal. Chem.* **1998**, 248, 387.
96. F. Scheller, M. Jänchen, H. J. Prümke, *Biopolymers* **1975**, 14, 1553.
97. M. J. Honeychurch, M. J. Ridd, *J. Electroanal. Chem.* **1996**, 418, 185.
98. M. J. Honeychurch, M. J. Ridd, *Bioelectrochem. Bioenerg.* **1996**, 41, 115.
99. M. J. Honeychurch, M. J. Ridd, *Electroanalysis* **1996**, 8, 654.
100. T. Ikeda, K. Toriyama, M. Senda, *Bull. Chem. Soc. Jpn.* **1979**, 52, 1937.
101. R. W. Olafson, R. G. Sim, *Anal. Biochem.* **1979**, 100, 343.
102. R. W. Olafson, *Bioelectrochem. Bioenerg.* **1988**, 19, 111.
103. K. L. Egodage, B. S. da Silva, G. S. Wilson, *J. Am. Chem. Soc.* **1997**, 119, 5295.
104. S. W. Chen, H. D. Abruña, *J. Phys. Chem. B* **1997**, 101, 167.

105. E. Laviron, *J. Electroanal. Chem.* **1979**, 101, 19.
106. S. Chen, H. D. Abruña, *J. Phys. Chem.* **1995**, 99, 17235.
107. Z. Yang, S. M. Zhu, *Chinese J. Anal. Chem.* **1999**, 27, 1431.
108. Z. G. Arias, J. L. M. Alvarez, J. M. L. Fonseca, *J. Colloid Interf. Sci.* **2002**, 250, 295.
109. Z. G. Arias, J. L. M. Alvarez, J. M. L. Fonseca, *Electroanalysis* **2004**, 16, 1044.
110. Z. G. Arias, J. L. M. Alvarez, J. M. L. Fonseca, *J. Colloid Interf. Sci.* **2004**, 276, 132.
111. R. Madueno, T. Pineda, J. M. Sevilla et al., *J. Electroanal. Chem.* **2004**, 565, 301.
112. R. Guidelli, L. Becucci, A. Dolfi et al., *Solid State Ion* **2002**, 150, 13.
113. M. R. Moncelli, L. Becucci, S. M. Schiller, *Bioelectrochem* **2004**, 63, 161.
114. R. Kizek, L. Havran, T. Kubcarova et al., *Talanta* **2002**, 56, 915.
115. I. Pardo, M. Angulo, R. M. Galvin et al., *Electrochim. Acta* **1996**, 41, 133.
116. J. M. R. Mellado, R. M. Galvin, *Electrochim. Acta* **1996**, 41, 1479.
117. A. Safavi, M. B. Gholivand, *Bull. Electrochem* **1998**, 14, 218.
118. J. J. Calvente, M. L. Gil, R. Andreu et al., *Langmuir* **1999**, 15, 1480.
119. M. L. Gil, R. Andreu, J. J. Calvente et al., *J. Electrochem. Soc.* **2002**, 149, E45.
120. N. Muskal, I. Turyan, D. Mandler, *J. Electroanal. Chem.* **1996**, 409, 131.
121. N. Muskal, D. Mandler, *Electrochim. Acta* **1999**, 45, 537.
122. K. Słowiński, R. V. Chamberlain, R. Bilewicz et al., *J. Am. Chem. Soc.* **1996**, 118, 4709.
123. K. Słowiński, R. V. Chamberlain, C. J. Miller et al., *J. Am. Chem. Soc.* **1997**, 119, 11910.
124. S. Sęk, R. Bilewicz, *J. Incl. Phenom. Macrocycl. Chem.* **1999**, 35, 55.
125. K. Słowiński, H. K. Y. Fong, M. Majda, *J. Am. Chem. Soc.* **1999**, 121, 7257.
126. K. Słowiński, K. U. Słowiński, M. Majda, *J. Phys. Chem. B* **1999**, 103, 8544.
127. K. Słowiński, M. Majda, *J. Electroanal. Chem.* **2000**, 491, 139.
128. R. L. York, P. T. Nguyen, K. Słowiński, *J. Am. Chem. Soc.* **2003**, 125, 5948.
129. R. L. York, K. Słowiński, *J. Electroanal. Chem.* **2003**, 550–551, 327.
130. M. Galperin, A. Nitzan, S. Sęk et al., *J. Electroanal. Chem.* **2003**, 550, 37.
131. S. Sęk, R. Bilewicz, K. Słowiński, *Chem. Commun.* **2004**, 404.
132. D. Gugala, Z. Fekner, D. Sienko et al., *Electrochim. Acta* **2004**, 49, 2227.
133. J. Ludvik, B. Nygård, *Electrochim. Acta* **1996**, 41, 1661.
134. J. Ludvik, *Phosphorus, Sulphur Silicon* **1998**, 136–138, 413.
135. B. Person, B. Nygård, *J. Electroanal. Chem.* **1974**, 56, 373.
136. J. L. M. Alvarez, A. G. Calzon, J. M. L. Fonseca, *Electrochim. Acta* **2004**, 49, 1389.
137. L. Y. Man'ko, G. Y. Vyaseleva, V. P. Barabanov, *Russ. J. Electrochem.* **2000**, 36, 916.
138. L. Y. Man'ko, V. P. Barabanov, *Russ. J. Phys. Chem.* **2001**, 75, 943.
139. L. Gómez, J. J. Ruiz, L. Yamacho et al., *J. Electroanal. Chem.* **2004**, 564, 17.
140. B. N. Afanasev, Y. P. Akulova, G. S. Aleksandrova et al., *Russ. J. Electrochem.* **1997**, 33, 700.
141. M. J. Higuera, M. R. Montoya, J. M. R. Mellado, *Electrochem. Commun.* **1999**, 1, 184.
142. R. Słojkowska, M. Jurkiewicz-Herbich, *Polish J. Chem.* **1999**, 73, 527.
143. H. Sawamoto, *J. Electroanal. Chem.* **1997**, 432, 153.
144. T. Ozeki, M. Odziemkowski, D. E. Irish, *J. Solution Chem.* **2000**, 29, 861.
145. T. Ozeki, K. Yokoi, M. Odziemkowski et al., *J. Electroanal. Chem.* **2001**, 505, 142.
146. N. V. S. Naidu, G. Suresh, B. Prasad et al., *Anal. Sci.* **2004**, 20, 399.
147. K. Arihara, F. Kitamura, T. Ohsaka et al., *J. Electroanal. Chem.* **2000**, 488, 117.
148. C. McGarvey, S. Beck, S. Quach et al., *J. Electroanal. Chem.* **1998**, 456, 71.
149. S. Komorsky-Lovric, *Electroanalysis* **2000**, 12, 599.
150. G. J. Wagner, J. Q. Chambers, *Langmuir* **1997**, 13, 3529.
151. R. Philipp, U. Retter, Z. Phys. Chem.,-Int. J. Res. Phys. Chem. Chem. Phys **1996**, 196, 125.
152. M. Fojta, E. Palecek, *Anal. Chim. Acta* **1997**, 342, 1.
153. M. Fojta, *Collect. Czech. Chem. Commun.* **2004**, 69, 715.
154. R. Abdel-Hamid, *Monatsh. Chem.* **1998**, 129, 817.
155. H. M. El-Sagher, *Monatsh. Chem.* **1999**, 130, 295.
156. M. J. Honeychurch, *J. Electroanal. Chem.* **1998**, 445, 63.

157. R. Herrero, M. R. Moncelli, L. Becucci, R. Guidelli, *J. Electroanal. Chem.* **1997**, 425, 87.
158. H. Y. Gao, Y. L. Zhou, Y. H. Zeng, *Chinese J. Anal. Chem.* **2001**, 29, 667.
159. H. Sawamoto, *Bunseki Kagaku* **2002**, 51, 1159.
160. M. M. Gomez, A. Arevalillo, J. M. Vara, *Electrochim. Acta* **1996**, 41, 291.
161. L. Novotny, *Fresenius' J. Anal. Chem.* **1999**, 363, 55.
162. S. Hason, J. Dvorak, F. Jelen et al., *Talanta* **2002**, 56, 905.
163. W. Qian, Q. G. Meng, Q. H. Luo et al., *Chem. J. Chinese Univ-Chinese* **1996**, 17, 687.
164. G. Q. Mei, W. Qian, Q. H. Luo et al., *Chinese J. Inorg. Chem.* **2003**, 19, 774.
165. G. Wittstock, H. Emons, *Electroanalysis* **1997**, 9, 449.
166. M. Turowska, D. Kaźmierczak, T. Błaszczuk, *Polish J. Chem.* **1997**, 71, 221.
167. D. Gugala, D. Sienko, J. Saba, *Collect. Czech. Chem. Commun.* **2001**, 66, 411.
168. A. Muszalska, M. Jurkiewicz-Herbich, J. Jas-trzębska, *J. Chem. Soc., Faraday Trans.* **1996**, 92, 3859.
169. K. R. Gorbachevska, N. L. Shvarchovska, M. M. Yatsyshyn et al., *Adsorpt. Sci. Technol.* **1996**, 14, 229.
170. J. I. Japaridze, S. S. Japaridze, I. A. Gurg-enidze, *J. Electroanal. Chem.* **2003**, 552, 59.
171. B. B. Damaskin, O. A. Baturina, *Russ. J. Electrochem.* **2002**, 38, 1141.
172. C. Mousty, C. Maurice, G. Mousset et al., *J. Colloid Interf. Sci.* **1996**, 184, 671.
173. C. Mousty, C. Maurice, G. Mousset et al., *J. Colloid Interf. Sci.* **1997**, 188, 238.
174. F. V. Stenina, L. N. Sviridova, L. O. Ask-inadze, *Russ. J. Electrochem.* **1997**, 33, 1220.
175. F. V. Stenina, L. N. Sviridova, O. A. Baturina et al., *Russ. J. Electrochem.* **1999**, 35, 1313.
176. E. V. Stenina, O. A. Baturina, L. N. Sviridova et al., *Russ. J. Electrochem.* **2001**, 37, 931.
177. E. V. Stenina, L. N. Sviridova, A. G. Krivenko et al., *Russ. J. Electrochem.* **2003**, 39, 1017.
178. M. R. Moncelli, L. Becucci, A. Dolfi et al., *Bioelectrochem* **2002**, 56, 159.
179. F. T. Buoninsegni, L. Becucci, M. R. Moncelli et al., *J. Electroanal. Chem.* **2003**, 550–551, 229.
180. B. Lindholm-Sethson, P. Geladi, A. Nelson, *Anal. Chim. Acta* **2001**, 446, 121.
181. M. Rueda, I. Navarro, G. Ramirez et al., *J. Electroanal. Chem.* **1998**, 454, 155.
182. J. Saba, *Gazz. Chim. Ital.* **1997**, 127, 53.
183. J. Saba, *Monatsh. Chem.* **1997**, 128, 1.
184. J. Saba, *Electrochim. Acta* **1996**, 41, 297.
185. J. Saba, G. Dalmata, J. Nieszporek et al., *Croat. Chem. Acta* **2000**, 73, 643.
186. D. Sienko, D. Gugala, J. Nieszporek et al., *Collect. Czech. Chem. Commun.* **2002**, 67, 1579.
187. J. P. Duan, G. N. Chen, M. L. Chen et al., *Analyst* **1999**, 124, 1651.
188. M. M. Kamal, A. Z. A. Zuhri, A. A. O. Nasser, *Fresenius Z. Anal. Chem.* **1996**, 356, 500.
189. V. S. Ferreira, M. V. B. Zandoni, A. G. Fogg, *Anal. Chim. Acta* **1998**, 367, 255.
190. M. V. B. Zandoni, A. G. Fogg, J. Barek et al., *Anal. Chim. Acta* **1997**, 349, 101.
191. R. Kizek, J. Vacek, L. Trnkova et al., *Chem. Listy* **2004**, 98, 166.
192. V. Pavlova, V. Mirceski, S. Komorsky-Lovric et al., *Anal. Chim. Acta* **2004**, 512, 49.
193. A. G. Fogg, R. Ismail, R. Ahmad et al., *Analyst* **1996**, 121, 1877.
194. A. G. Fogg, R. Ismail, A. R. H. M. Yusoff et al., *Talanta* **1997**, 44, 497.
195. J. Wang, D. H. Grant, M. Ozsoz et al., *Anal. Chim. Acta* **1997**, 349, 77.
196. M. Tomschik, F. Jelen, L. Havran et al., *J. Electroanal. Chem.* **1999**, 476, 71.
197. P. A. M. Farias, A. D. R. Wagener, M. B. R. Bastos et al., *Talanta* **2003**, 61, 829.
198. D. Tarkowska, M. Kotoucek, K. Dolezal, *Collect. Czech. Chem. Commun.* **2003**, 68, 1076.
199. J. Thoming, B. K. Kliem, L. M. Ottosen, *Sci. Total Environ.* **2000**, 261, 137.
200. E. Kariv-Miller, G. K. Lehman, V. Svetličič, *J. Electroanal. Chem.* **1997**, 423, 87.
201. A. G. Stromberg, A. V. Konkova, *Zh. Fiz. Khim.* **1968**, 42, 2063. (in Russian).
202. V. P. Gladyshev, T. V. Syroeshkina, *Sov. Probl. Polar. z. Nakapl* **1975**, 136. (in Russian).
203. T. V. Syroeshkina, M. M. Raimzhanova, *Vsesoyuznoe Soveshchanie po Polarografii* **1978**, 196. (in Russian).

204. T. V. Syroeshkina, M. M. Raimzhanova, V. P. Gladyshev, *Izv. Vyssh. Uchebn. Zav* **1978**, 21, 933. (in Russian).
205. V. P. Gladyshev, A. I. Zebreva, T. V. Syroeshkina et al., *Izv. Vyssh. Uchebn. Zav, Khim. Khim. Tekhnol.* **1978**, 21, 1474. (in Russian).
206. C. Gumiński, Z. Galus, in *Solubility Data Series, Vol. 51 – Intermetallic Compounds in Mercury* (Eds.: J. G. Osteryoung, M. M. Schreiner, C. Gumiński et al.,) Pergamon Press, Oxford, New York, Seoul, Tokyo, 1992.
207. *Gmelins Handbuch der Anorganischen Chemie*, 34, Tl. A, Lfg. 2, Verlag Chemie, Weinheim, 1962, p. 1006. (see also Ref. [206]).
208. N. C. Baenziger, J. W. Nielsen, E. J. Duwell, U.S. At. Ener. Comm. Rep., COO-126, 1957.
209. A. Barański, W. Lu, *J. Electroanal. Chem.* **1993**, 355, 205.
210. S. V. Kovaleva, V. P. Gladyshev, *Zh. Obshch. Khim.* **1996**, 66, 1761. (in Russian).
211. C. Gumiński, *J. Phase Equilib.* **1997**, 18, 101.
212. (a) G. K. Lehman, *Electroorganic Reductions at High Negative Potentials and NH₄-Hg Electroformation*, Ph. D. thesis, University of Minnesota, **1989**, Minneapolis, MN; (b) *Dissert. Abstr. Intern* **1990**, 50, 2930.
213. E. M. Rich, M. W. Travers, *J. Chem. Soc.* **1906**, 89, 872.
214. J. K. S. Wan, *J. Chem. Educ.* **1968**, 45, 40.
215. H. N. McCoy, W. C. Moore, *J. Am. Chem. Soc.* **1911**, 33, 273.
216. E. Kassab, E. M. Evleth, *J. Am. Chem. Soc.* **1987**, 109, 1653.
217. E. Garcia, A. H. Cowley, A. J. Bard, *J. Am. Chem. Soc.* **1986**, 108, 6082.
218. E. Kariv-Miller, V. V. Svetličič, P. D. Christian, *J. Electrochem. Soc.* **1995**, 142, 3386.
219. E. Kariv-Miller, P. D. Christian, V. V. Svetličič, *Langmuir* **1994**, 10, 3338.
220. E. Kariv-Miller, P. D. Christian, V. V. Svetličič, *Langmuir* **1995**, 11, 1817.
221. S. Krasensky, M. Studnickova, *Collect. Czech. Chem. Commun.* **1994**, 59, 2375.
222. S. V. Kovaleva, V. P. Gladyshev, *Zh. Obshch. Khim.* **1997**, 67, 342. (in Russian).

Part C:

Electrochemistry of Copper

David B. Rorabacher and Ronald R. Schroeder
Department of Chemistry, Wayne State University, Detroit, Minnesota, USA

24.7

Electrochemistry of Copper

24.7.1	Introduction	993
24.7.1.1	Oxidation States of Copper	993
24.7.1.2	Reference Standards for Potential Values in Nonaqueous Solvent Studies	993
24.7.1.3	Methods Used for Potential Measurements	996
24.7.1.4	Potentials Involving Solvated Copper Species	996
24.7.2	Electrochemical Considerations for Copper(II/I) Complexes Involving Multidentate Ligands	997
24.7.2.1	Trends in Potentials of Copper(II/I) Complexes with Multidentate Ligands	998
24.7.2.2	Dependence of Copper(II/I) Potentials on Ligand Properties	999
24.7.2.3	Correlation of Potentials to Copper(II) Complex Stability Constants	1022
24.7.3	Mechanistic Aspects of Copper(II/I) Electron Transfer	1023
24.7.3.1	Ligand Conformational Change	1025
24.7.3.2	Complex Dissociation/Formation	1027
24.7.3.3	Interconversion of Ternary and Binary Complexes	1028
24.7.3.4	Interconversion of 1 : 2 and 1 : 1 Complexes	1029
24.7.3.5	Dimeric/Monomeric Species	1031
24.7.3.6	Other Phenomena Affecting Electrochemical Behavior	1031
24.7.3.6.1	Ligand Oxidation or Reduction	1031
24.7.3.6.2	Electroplating of Copper	1032
24.7.4	Biological Copper Systems	1032
24.7.5	Other Copper(II/I) Systems	1034
24.7.5.1	Unidentate Ligand Complexes	1035
24.7.5.1.1	Hydroxide Complexes	1035
24.7.5.1.2	Halide Complexes	1036
24.7.5.1.3	Cyanide and Thiocyanate Complexes	1036

24.7.5.1.4	Ammonia Complexes	1037
24.7.5.1.5	Complexes with Acetate and Other Common Brønsted Bases . . .	1037
24.7.5.1.6	Noncomplexing Buffer Systems	1037
24.7.5.2	Binuclear Complexes	1038
24.7.6	Copper(III/II) Systems	1039
	References	1041

24.7.1

Introduction

Elemental copper is the least easily oxidized of the first-row transition metals. This largely accounts for the extensive use of copper electrodeposition for both industrial applications and analytical purposes. Since the electrochemistry of elemental copper, including electrodeposition, electroplating, and electrowinning, was treated extensively in the previous edition of this encyclopedia [1] and detailed descriptions are to be found elsewhere [2–4], it is not covered in this treatise.

The current chapter focuses on the electrochemistry of the ionic forms of copper in solution, starting with the potentials of various copper species. This includes the effect of coordination geometry, donor atoms, and solvent upon the electrochemical potentials of copper redox couples, specifically Cu(II/I). This is followed by a discussion of the various types of coupled chemical reactions that may contribute to the observed Cu(II/I) electrochemical behavior and the characteristics that may be used to distinguish the presence of each of these mechanisms. The chapter concludes with brief discussions of the electrochemical properties of copper proteins, unidentate and binuclear complexes,

and Cu(III/II) systems. A recent review on the kinetics and mechanisms of homogeneous electron transfer involving copper can be consulted as a supplement to this chapter [5].

24.7.1.1 Oxidation States of Copper

Copper is one of the few elements for which four successive oxidation states are accessible: 0, +1, +2, and +3. As a result, copper is an important redox catalyst, having the ability to catalyze many reactions in which one reacting partner undergoes a one-electron transfer while the other reactant undergoes a two- or three-electron transfer. Among metal ions that exhibit several stable oxidation states, copper is unique in that each successive state prefers a different coordination geometry. The change in geometry that accompanies electron transfer in copper systems has a significant impact upon the electrochemistry in terms of both thermodynamics and kinetics as noted in the sections that follow.

24.7.1.2 Reference Standards for Potential Values in Nonaqueous Solvent Studies

Electrochemical studies on copper systems are frequently conducted in nonaqueous solvents, principally for the purpose of improving the solubility of complexing ligands of interest. The largest number of such studies have been reported in

acetonitrile, not only because of its ability to solubilize organic ligands, but also because of its reasonably high dielectric constant (38.8 at 20 °C) and its ability to stabilize Cu(I).

Both in acetonitrile and in other nonaqueous solvents, a major problem arises in terms of the manner in which the potential values are reported by various investigators. Koepp, Wendt, and Strehlow [6] noted that hydrogen ion is the poorest reference material on which to base nonaqueous potentials because of the extreme differences in its solvation in various solvents. On the basis of an investigation of the solvent dependence of 18 redox couples, these investigators concluded that ferrocene/ferrocenium ion (i.e. bis(cyclopentadienyl)iron(III/II), abbreviated as Fc^+/Fc^0) and/or cobaltocene/cobalticenium ion represented optimal potential reference materials for nonaqueous studies. On the basis of their minimal charge (+1, 0) and their symmetry (treated as though they were roughly spherical), the potentials of these two redox couples are presumed to be relatively independent of solvent properties.

In recognition of the work of Strehlow and coworkers, Gagne, Koval, and Lisen-sky [7] recommended that ferrocene be used as an internal standard for all potential measurements in nonaqueous solvents and that its aqueous potential of +0.400 V relative to the standard hydrogen electrode (SHE) could be considered to represent a consistent correction factor in referencing all nonaqueous potential measurements to aqueous SHE. This recommendation is somewhat in disagreement with the conclusion of Strehlow and coworkers who, on the basis of theoretical considerations, suggested that the potential of the ferrocene couple in acetonitrile should be

about +0.34 V relative to the aqueous SHE [8].

Subsequently, the International Union of Pure and Applied Chemistry (IUPAC) has recommended that all potential values in nonaqueous solvents be referenced directly to the potential of the ferrocene/ferrocenium couple or the bis(biphenyl)chromium(1/0) couple (as either an internal or external reference) without attempting to “correct” such potentials to aqueous SHE [9]. Despite this recommendation, many investigators continue to reference their nonaqueous potential measurements to the reference electrode used in their measurements such as Ag/AgCl, Ag/Ag⁺ (0.01 M), or the saturated calomel electrode (SCE). Even those workers who utilize ferrocene as a reference standard frequently report their result only in terms of values that are “corrected” to SHE without explaining the magnitude of the correction applied. This latter approach would not present a serious problem if the size of this “correction” were consistent. However, as noted above, Strehlow’s and Gagne’s recommendations are in disagreement as to whether the appropriate potential for ferrocene in acetonitrile should be +0.34 V or +0.40 V relative to SHE. And this disagreement pales in comparison with the subsequent conclusions of three other research groups that the potential of ferrocene in acetonitrile is +0.38 to +0.40 V relative to SCE, depending upon the anion present, which suggests that the appropriate correction for converting ferrocene potentials in acetonitrile to values referenced to aqueous SHE should be +0.62 to +0.64 V. (The magnitude of the correction cited here is based on the conclusion that the potential of ferrocene in acetonitrile relative to aqueous SCE is 0.38–0.40 V. Since the recognized potential of SCE is +0.241 V versus SHE,

the overall “corrected” potential of ferrocene is +0.64 V versus SHE) [10].

Pavlishchuk and Addison [11] have discussed the foregoing discrepancies and made careful measurements of the reference electrodes commonly utilized by investigators in measuring potentials in acetonitrile. The correction to be applied for converting a potential measured against a reference electrode, E_{ref} , to the ferrocene standard, E_{Fc} , can be expressed as:

$$E_{\text{Fc}} = E_{\text{ref}} - \delta \quad (1)$$

The δ values applicable in acetonitrile, as determined by Pavlishchuk and Addison, are as follows (TEAP = tetraethylammonium perchlorate):

Ag/0.1 M	AgNO ₃ ,	0.1 M	TEAP
(“ANE1”): $\delta = 0.037$ V			
Ag/0.01 M	AgNO ₃ ,	0.1 M	TEAP
(“ANE2”): $\delta = 0.087$ V			
Ag/0.001 M	AgNO ₃ ,	0.1 M	TEAP
(“ANE3”): $\delta = 0.133$ V			
Ag/0.01 M	AgClO ₄ ,	0.1 M	TEAP
(“APE”): $\delta = 0.083$ V			
Saturated calomel, aqueous (SCE): $\delta = 0.380$ V			
Saturated sodium chloride, aqueous (SSCE): $\delta = 0.384$ V			
Standard hydrogen, aqueous: $\delta = 0.624$ V			

It should be noted that Lay and coworkers [12] have made a comparative study of the electrochemical behavior of ferrocene, 1,2,3,4,5-pentamethylferrocene and decamethylferrocene in 29 solvents and have concluded that increasing substitution on ferrocene reduces the solvent dependence of the ferrocene potential. Accordingly, they recommend that decamethylferrocene be adopted as a preferred reference standard for electrochemical measurements in nonaqueous

solvents. Although this recommendation has not yet been officially adopted, their data show that the redox potential of decamethylferrocene is –506 mV relative to ferrocene in acetonitrile so that potentials referenced to either one of these standards can be readily interconverted. The relative potentials for the latter two compounds in 28 other solvents are also included in their paper.

In the current treatise, we have adopted the IUPAC recommendation in citing nonaqueous potentials relative to the value obtained for ferrocene under identical conditions wherever possible. In those instances where investigators have utilized ferrocene as a reference material but have only reported the potential values after “correction” to SHE, we have “uncorrected” the values back to the ferrocene standard whenever the magnitude of the correction applied was evident in the pertinent publication. In those cases where the magnitude of the correction is not indicated or where values are reported only with respect to the reference electrode used, we have tabulated the potential values as reported by the specific investigators and have indicated in parentheses the reference standard to which these values purportedly apply. The corrections suggested by Pavlishchuk and Addison (above) may be applied by the reader, although it is not always clear whether the conditions used warrant this. However, values for related systems reported by the same workers against a common standard can at least be compared with each other.

In the accompanying tables, all potentials are given to the same number of decimal places as were reported in the original publications. The third decimal place, when reported, is often of questionable value as is evident when potential

values for a system have been determined by more than one set of workers.

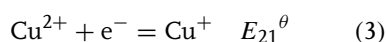
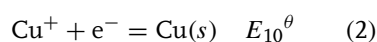
24.7.1.3 Methods Used for Potential Measurements

Redox potentials for copper systems have been based on a variety of approaches including (i) redox titrations, (ii) potentiostatic methods involving spectral monitoring, (iii) cyclic voltammetry (CV), and (iv) pulsed methods. Of these, CV measurements are by far the most prevalent. No effort has been made in this treatise to identify the method used for a specific reported potential value unless the method itself appeared to be pertinent.

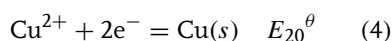
24.7.1.4 Potentials Involving Solvated Copper Species

No information is available on the solvated Cu^{3+} ion since the known solution chemistry for this oxidation state is limited

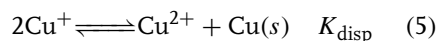
to complexes involving hard donor atoms. Thus, in the absence of complexing agents, the electrochemistry of solvated copper can be expressed by two one-electron processes:



The values of E_{10}^θ and E_{21}^θ for the solvated metal ion and the overall value of E_{20}^θ for a two-electron transfer,



have been determined in water, methanol, 80% methanol–20% water (w/w) and acetonitrile as listed in Table 1. It will be noted that, in water, methanol, and their mixtures, $E_{10}^\theta > E_{21}^\theta$, so that solvated Cu(I) is unstable with respect to disproportionation:



Tab. 1 Potential values for solvated copper ion in various solvents (all values in V versus aqueous SHE)

Solvent	E_{10}^θ	E_{21}^θ	E_{20}^θ	K_{disp}	References
Water	0.520	0.159	0.340	1.7×10^6	13
Methanol	0.64	0.40	0.513	1.1×10^4	14
80% methanol ^a	0.58	0.20	0.390 ^b	2×10^6	15
Acetonitrile	−0.344	0.133	−0.11	8.7×10^{-9}	16
Propylene carbonate ^c			0.157 ^c		17

^a Values are intended to be representative for the mixed solvent containing 80% methanol–20% water (by weight).

^b S. Minc, J. Jastrzebska, *Rocz. Chem.* **1954**, 28, 519–520. In reporting the E_{20}^θ value for copper in various methanol–water mixtures, these authors did not specify whether percent methanol referred to weight, volume, or mole per cent. Although the potential values are claimed to be referenced to aqueous SHE, the actual internal reference electrode used was not specified and no mention was made of a correction for the liquid junction potential. Since the actual liquid junction potential for aqueous reference electrodes in methanol–water mixtures was not made until a later date [$E_j \approx -0.152$ V for 80% methanol (w/w): M. Alfenaar, C. L. deLigny, *Recl. Trav. Chim. Pays-Bas* **1967**, 86, 1185–1190], it is presumed, in fact, that no correction was made for the liquid junction.

^c For propylene carbonate, the E_{20}^θ value was measured against a saturated calomel electrode for which a value of 0.2375 V versus SHE was assumed in correcting the measured value to an SHE standard.

Although the values of K_{disp} are relatively large in water and in methanol, a finite amount of Cu(I) exists in any Cu(II) solution that is in contact with metallic copper. In fact, the molecularity associated with K_{disp} dictates that the *fraction* of copper in solution in the form of Cu(I) *increases* as the total concentration of solvated copper ion *decreases*. Thus, at micromolar levels in water, for example, the two oxidation states can be maintained in essentially equal amounts. In acetonitrile, the equilibrium for reaction 5 lies far to the left so that solvated Cu(I) is readily generated by placing copper metal in contact with a Cu(II) solution (conproportionation). As a consequence, the Cu(I) salt, $[\text{Cu}(\text{CH}_3\text{CN})_4]\text{ClO}_4$, is easily prepared [18] and is temporally stable.

Due to the elongation of bonds arising from Jahn-Teller distortion, the aquated Cu(II) ion, $\text{Cu}(\text{H}_2\text{O})_6^{2+}$ is exceptionally labile with regard to inner-sphere substitution [20, 21] (A more recent neutron diffraction study has indicated that hydrated Cu(II) ion may be five coordinate. However, this latter conclusion may simply result from the asymmetric stretch of the axial waters such that, on average, the copper appears to have only five solvent bonds despite the fact that six waters may be interacting with the central copper atom.) [19] The d^{10} Cu^+ ion is also expected to be substitutionally labile in parallel to the lability of isoelectronic $\text{Zn}(\text{H}_2\text{O})_6^{2+}$ [21, 22]. Thus, other ligands can rapidly substitute into the inner-coordination sphere of both $\text{Cu}^{\text{I}}(\text{H}_2\text{O})_4^+$ and $\text{Cu}^{\text{II}}(\text{H}_2\text{O})_6^{2+}$. As a result, potential μ -bridging ligands such as Cl-, Br-, and I- (at even very low concentrations) may affect the transfer of electrons between copper ions and the electrode surface in solution. For this reason, such potentially

bridging ligands should be rigorously excluded from solution when making careful potential measurements.

24.7.2

Electrochemical Considerations for Copper(II/I) Complexes Involving Multidentate Ligands

Most of the electrochemical studies currently appearing in the literature involve copper complexes with multidentate ligands. (Unidentate ligands will be considered later.) As noted earlier, each oxidation state of copper prefers a different coordination geometry. Like Ni(II), the d^8 Cu(III) state prefers a regular octahedral geometry, which generally reverts to a square planar complex, since this oxidation state is encountered in complexes exhibiting a strong ligand field. Because of the fact that definitive data on this oxidation state are relatively sparse, Cu(III) is discussed only briefly at the end of this treatise. The d^9 Cu(II) ion tends to form six-coordinate complexes that are subject to Jahn-Teller distortion in which the coordinate bonds along one axis (usually designated as the z -axis) elongate to form a distorted octahedral (tetragonal) complex. Several cases of six-coordinate Cu(II) complexes have been reported in which one of the coordinate axes appears to be shorter than the other two, resulting in a “compressed” Jahn-Teller distortion. However, such complexes actually represent a situation where two of the axes are participating in Jahn-Teller inversion, whereas the third axis is not, so that the latter axis appears to be shorter on average. The only Cu(II) compound for which Jahn-Teller compression has been rigorously established is KAlCuF_6 . [23, 24]. This is a fluxional effect, however, and, if all donor atoms are

identical, all three axes rapidly interconvert (dynamic Jahn-Teller effect) [25, 26].

In many Cu(II) complexes, one of the axial donor atoms is missing, resulting in a square pyramidal coordination geometry in which the copper atom is slightly displaced above the xy plane in the direction of the remaining axial donor atom [27–32]. Distortions arising from ligand constraints may result in complexes that are more nearly trigonal bipyramidal. The d^{10} Cu(I) ion, having no net crystal field stabilization energy, does not exhibit an electronic preference for a specific coordination geometry. In fact, several different geometries have been observed in crystal structures, including linear, trigonal, and tetrahedral [33]; even five-coordinate Cu(I) complexes have been reported [34, 35]. However, the balance between the energy gained from coordinate bond formation and the repulsion between the coordinated donor atoms commonly results in a tetrahedral geometry for Cu(I) complexes [23].

The influence of geometric constraints imposed by coordinated ligands in combination with the differences in donor atom preferences among the various oxidation states makes it possible to exert a considerable amount of control over copper redox potentials. In fact, the influence of ligand structure upon the electrochemical properties of copper is one of the most common themes in copper studies.

24.7.2.1 Trends in Potentials of Copper(II/I) Complexes with Multidentate Ligands

The standard potential values for solvated copper, as cited in Table 1, represent thermodynamic values in terms of activities. In practice, relatively high ionic strengths (≥ 0.01 M) are used in most electrochemical measurements so that the

experimental values are generally obtained as concentration potentials:

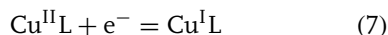
$$E = E_{21(\text{solv})}^{\theta'} - \frac{RT}{nF} \ln \frac{[\text{Cu}^+]}{[\text{Cu}^{2+}]}$$

where

$$E_{21(\text{solv})}^{\theta'} = E_{21}^{\theta} - \frac{RT}{nF} \ln \frac{\gamma_{\text{Cu}^+}}{\gamma_{\text{Cu}^{2+}}} \quad (6)$$

where γ_{Cu^+} and $\gamma_{\text{Cu}^{2+}}$ represent the relevant activity coefficients. For aquated Cu(II/I) at 25 °C and an ionic strength of 0.10 M, $E_{21(\text{solv})}^{\theta'} \approx 0.13$ V (versus SHE) [51].

In the presence of complexing agents, the potential values are usually reported in terms of the concentrations of the complexed species rather than the concentrations of the solvated copper ions:



$$E = E_{21}^{\theta'} - \frac{RT}{nF} \ln \frac{[\text{Cu}^{\text{I}}\text{L}]}{[\text{Cu}^{\text{II}}\text{L}]} \quad (8)$$

If the fraction of uncomplexed copper ion is relatively small in both oxidation states, the relationship between the concentration potential, $E_{21}^{\theta'}$, for any Cu(II/I) complex system and that for the solvated Cu(II/I) couple, can be represented as:

$$E_{21}^{\theta'} = E_{21(\text{solv})}^{\theta'} + \frac{RT}{nF} \ln \frac{K_{\text{Cu}^{\text{I}}\text{L}}}{K_{\text{Cu}^{\text{II}}\text{L}}} \quad (9)$$

Equation (9) is frequently used to estimate the value of one of the stability constants, $K_{\text{Cu}^{\text{II}}\text{L}}$ or $K_{\text{Cu}^{\text{I}}\text{L}}$, when the other stability constant has been determined experimentally.

Reported values of $E_{21}^{\theta'}$ for various Cu(II/I) complexes in aqueous solution range from approximately -0.6 to $+0.9$ V (versus SHE). Most of the potential values for Cu(II/I) currently reported in

the literature were obtained from CV determinations. The average potential of the cathodic (E_{pc}) and anodic (E_{pa}) peaks, designated as $E_{1/2}$, is assumed to approximate the value of $E_{21}^{\theta'}$ if the CV's are reasonably reversible (i.e. $\Delta E_p = E_{pa} - E_{pc} \approx 0.057$ V) [94]. The reported potential values for approximately 200 $Cu^{II/I}$ complexes are listed in Table 2. The systems included in this compilation are those for which $\Delta E_p \leq 0.090$ V [94]. The complexes are grouped according to the nature of the ligand, starting with polypyridyl ligands (2,2'-bipyridine; 1,10-phenanthroline; and substituted derivatives), followed by cyclic, acyclic, tripodal, and branched ligands.

To aid in identifying the significant features of the ligands listed in Table 2, trivial names have been assigned using the following conventions:

Cyclic ligands: Square brackets designate that the ligand is cyclic and the number within the brackets is the number of atoms in the macrocyclic ring. Saturated macrocycles are designated by "ane", while, for unsaturated ligands, "ene" is used preceded by a prefix to identify the number of double bonds (e.g. diene or tetraene). The donor atoms are then identified. Substituents attached to the macrocycle are indicated by either a prefix or suffix.

Acyclic ligands: Attached substituents are generally indicated by a prefix followed by a series of numbers representing the sequential number of carbon atoms connecting the donor atoms followed by the sequential identities of the donor atoms.

Tripodal ligands: A Greek " τ " is used to identify a tripodal ligand having a nitrogen bridgehead. This is followed by a series of three numbers that identify the number of atoms (generally carbons) connecting the

bridgehead nitrogen to the coordinating donor atoms in the three legs. Finally, abbreviations are used to indicate the nature of the appended groups.

The abbreviated prefixes and suffixes used in the foregoing trivial names are as follows:

bpy = bipyridine
 bzim = benzimidazole
 cyhx = cyclohexane
 cypt = cyclopentane
 Et = ethyl
 en = ethylenediamine
 imid = imidazole
 Me = methyl
 phen = phenanthroline
 prz = pyrazine
 py = pyridine
 quin = quinoline
 tmen = trimethylenediamine
 Φ = phenyl

The structures of all ligands listed in Table 2 are illustrated in Fig. 1.

In selecting complexes for inclusion in Table 2, preference has been given to those systems that involve a series of related compounds since these serve to show the effects of changes in structure and donor atoms upon the resulting $Cu(II/I)$ potential values. Systems in which the separation of the peak potentials (ΔE_p) exceeded 100 mV are not included.

24.7.2.2 Dependence of Copper(II/I) Potentials on Ligand Properties

For complexing agents containing several amine nitrogen donor atoms, the $Cu(II/I)$ potential tends to be so negative in aqueous solution that accurate measurements are difficult to obtain. Such measurements are generally more accessible when using acetonitrile as the solvent. For example,

Tab. 2 Potential values for mononuclear copper(II/I) redox couples involving various multidentate ligands in commonly used solvents (all values are presumed to be for 25 °C, $\mu = 0.1$ M, except as noted)

Complexed ligand ^a	Potential (V versus references indicated) ^b			References
	H ₂ O V versus SHE	CH ₃ CN V versus reference cited	Other, solvent V versus reference cited	
Polypyridyl and polyimino ligands (unsaturated nitrogen donor atoms)				
1:2 (Bis) complexes				
LAA = bpy	0.120	−0.20 (A1) ^c		36, 37 ^k
LAB = 6, 6′-Me ₂ bpy		0.38 (A1)		36 ^k
LAC = 6, 6′-Φ ₂ bpy		0.61 (A1)		36 ^k
LAD = phen	0.170		0.08 (SCE), DMF	37, 38
LAE = 2, 9-Me ₂ phen	0.603	0.28 (Fc)	0.58 (SCE), DMF	37–39
LAF = 4, 7-Me ₂ phen			0.01 (SCE), DMF	38
LAG = 5, 6-Me ₂ phen			0.05 (SCE), DMF	38
LAH = 3, 4, 7, 8-Me ₄ phen			0.02 (SCE), DMF	38
LAI = 4, 7-Φ ₂ phen	0.62		0.08 (SCE), DMF	38
LAI = Me ₂ Φ ₂ phen	0.62	0.27 (Fc)	0.59 (SCE), DMF	38, 40, 41
LAIa = Me ₂ (ΦSO ₃) ₂ phen				41
LAK = 5-Mephen			0.08 (SCE), DMF	38
LAL = 5-NO ₂ phen	0.257		0.15 (SCE), DMF	37, 38
LAM = 5-Clphen			0.14 (SCE), DMF	38
LAMa = bib		0.27 (Ag/AgCl)		42
1:1 (Mono) complexes				
LAN = Me ₄ -dioxine			−0.64 (SCE), DMF	43

<i>Macrocyclic polyamine ligands</i>		
LAO = [12]aneN ₄ (cyclen)	-0.350 (SCE)	44
LAP = Me ₄ -[12]aneN ₄	-0.280 (SCE)	44, 45
LAQ = bz ₄ -[12]aneN ₄	-0.080 (SCE)	44
LAR = [13]aneN ₄	-0.80 (SCE)	46
LAS = Me, NO ₂ -[13]aneN ₄		47
LAT = [14]aneN ₄ (cyclam)	-1.20 (SCE)	46
LAU = Me, NO ₂ -[14]aneN ₄		47
LAV = [14]aneN ₄ -b (isocyclam)	-1.10 (SCE)	46
LAW = [15]aneN ₄	-0.93 (SCE)	46
LAX = Me, NO ₂ -[15]aneN ₄		47
LAY = [16]aneN ₄	-0.70 (SCE)	46
LAZ = Me, NO ₂ -[16]aneN ₄		47
LBA = [15]aneN ₅	-0.95 (SCE)	46
LBB = [16]aneN ₅	-1.10 (SCE)	46
LBC = [17]aneN ₅	-1.10 (SCE)	46
LBD = Me-[14]dieneN ₃ py	-0.40 (SCE)	43
<i>Macrocyclic polythioether ligands</i>		
1 : 1 (Mono) complexes		
LBE = [9]aneS ₃	0.54 (Fc)	48

(continued overleaf)

Tab. 2 (continued)

Complexed ligand ^a	Potential (V versus references indicated) ^b			References
	H ₂ O V versus SHE	CH ₃ CN V versus reference cited	Other, solvent V versus reference cited	
LBF = [12]aneS ₄	0.69?		0.68 (SHE), 80% CH ₃ OH	49
LBG = oxathiane-[12]aneS ₄	0.72			50
LBH = [13]aneS ₄	0.52		0.65 (SHE), 80% CH ₃ OH	49
LBI = [14]aneS ₄ -a	0.58	0.21 (Fc)	0.69 (SHE), 80% CH ₃ OH	49, 51, 52
LBJ = [14]aneS ₄ -b	0.69			53
LBK = bz-[14]aneS ₄	0.84	0.46 (Fc)		31, 54
LBL = cis-cyhx-[14]aneS ₄	0.54	0.17 (Fc)	0.65 (SHE), 80% CH ₃ OH	54
LBM = cis-cypt-[14]aneS ₄	0.56	0.20 (Fc)		55
LBN = trans-cyhx-[14]aneS ₄	0.60	0.20 (Fc)	0.70 (SHE), 80% CH ₃ OH	54
LBO = trans-cypt-[14]aneS ₄	0.67	0.32 (Fc)		55
LBP = bz-cis-cyhx-[14]aneS ₄	0.89	0.39 (Fc)		54
LBQ = bz-trans-cyhx-[14]aneS ₄	0.78	0.38 (Fc)		54
LBR = syn-cis, cis-dicyhx-[14]aneS ₄	0.57	0.08 (Fc)	0.58 (SHE) 80% CH ₃ OH	54
LBS = syn-cis, cis-dicypt-[14]aneS ₄	0.57	0.17 (Fc)		55
LBT = anti-cis, cis-dicyhx-[14]aneS ₄	0.67	0.21 (Fc)	0.62 (SHE) 80% CH ₃ OH	54
LBU = anti-cis, cis-dicypt-[14]aneS ₄		0.28 (Fc)		55
LBV = meso-trans, trans-dicyhx-[14]aneS ₄	0.58	0.10 (Fc)	0.74 (SHE), 80% CH ₃ OH	54
LBW = meso-trans, trans-dicypt-[14]aneS ₄		0.34 (Fc)		55
LBX = dl-trans, trans-dicyhx-[14]aneS ₄	0.69	0.26 (Fc)	0.70? (SHE), 80% CH ₃ OH	54
LBZ = dl-trans, trans-dicypt-[14]aneS ₄		0.39 (Fc)		55
LBZ = cis, trans-dicyhx-[14]aneS ₄	0.60			54
LCA = cis, trans-dicypt-[14]aneS ₄	0.63	0.14 (Fc)	0.65 (SHE), 80% CH ₃ OH	55
LCD = syn-[14]aneS ₄ -diol	0.54	0.26 (Fc)		52
LCE = anti-[14]aneS ₄ -diol	≈0.49			52

LCG = [15]aneS ₄	0.64		0.74 (SHE), 80% CH ₃ OH	49
LCH = [16]aneS ₄	0.71		0.78 (SHE), 80% CH ₃ OH	49
LCL = [15]aneS ₅	0.69		0.82 (SHE), 80% CH ₃ OH	49
LCJ = [18]aneS ₆		0.38 (Fc)		56
LCK = [20]aneS ₆			0.805 (SHE), 80% CH ₃ OH	57
LCL = [21]aneS ₆			0.852 (SHE), 80% CH ₃ OH	57
1 : 2 (Bis) complex				
LBE = [9]aneS ₃	0.65	0.29 (Fc)		48
<i>Other macrocyclic complexes</i>				
LCM = [12]aneN ₂ S ₂	0.12			58, 59 ^m
LCN = Me,NEt-[12]aneN ₂ S ₂	0.15			59
LCO = [14]aneNS ₃ -a	0.38			51
LCP = [14]aneNS ₃ -b	0.41			53
LCQ = [14]aneNSNS-b	0.26			58 ^m
LCR = [14]aneN ₂ S ₂	0.04, 0.08			51, 58, 59 ^m
LCS = Me-[14]aneN ₂ S ₂	0.11			59
LCT = Me ₂ -[14]aneN ₂ S ₂	0.18			59
LCU = Me,NEt-[14]aneN ₂ S ₂	0.03			59
LCV = Me,NPr-[14]aneN ₂ S ₂	0.12			59

(continued overleaf)

Tab. 2 (continued)

Complexed ligand ^a	Potential (V versus references indicated) ^b			References
	H ₂ O V versus SHE	CH ₃ CN V versus reference cited	Other, solvent V versus reference cited	
LCW = [14]aneNSSN	−0.01			51
LCX = Me, NO ₂ -[14]aneNSSN	−0.025			60
LCY = [14]aneN ₃ S	≈ −0.24			51
LCZ = [16]aneN ₂ S ₂	0.42			58 ^m
LDA = [16]aneNSNS	0.40			58 ^m
LDB = [15]aneNS ₄	0.46			51
LDC = [15]aneN ₂ S ₃	0.10			51
LDD = [15]bpyS ₃		−0.13 (Fc)		35
LDDa = [16]S ₃ dioxime-BF ₂ (TtoxBF ₂)			−0.15 (A1)	61
LDDb = [16]SO ₂ dioxime-BF ₂ (OdtoxBF ₂)			−0.17 (A1)	61
LDE = [17]pyS ₄ bz		≈0.65 (A2)		62
LDF = dibz-[14]dieneN ₂ S ₂		−0.04 (A1)		63
LDG = dibz-[15]dieneN ₂ S ₂		0.21 (A1)		63
LDH = dibz-[16]dieneN ₂ S ₂		0.29 (A1)		63
LDHa = bz ₄ -[16]tetraeneN ₄ (TAAB)		0.13 (SCE)	0.05 (SCE), DMF	63
LDI = [18]aneN ₂ S ₄	0.30	−0.31 (Fc)		64, 65
LDJ = Me ₂ -[18]aneN ₂ S ₄		0.06 (Fc)		66
Note: The difference in the potentials of the foregoing two complexes is attributed to the fact that Cu ^{II} ([18]aneN ₂ S ₄) is racemic while Cu ^{II} (Me ₂ [18]aneN ₂ S ₄) is meso – both Cu(I) complexes having tetrahedral configurations in which Cu(I) is coordinated to one nitrogen and three sulfurs.				
LDK = bz ₂ -[18]aneN ₂ S ₄		≈ −0.27 (SCE)		67
LDL = [18]aneS ₄ O ₂		0.37 (Fc)		68
1 : 2 (Bis) complex				
LDM = [9]aneS ₂ O		≈0.36(Fc)		68

<i>Bicyclic ligands</i>			
LDN = Me ₄ -bicycloN ₆ O	-0.06		69
LDO = Me ₅ -bicycloN ₇	-0.05		69
<i>Acyclic polyamine ligands</i>			
<i>Bis complexes</i>			
LDP = en	-0.114		44
LDQ = Me ₂ en	-0.065		44
LDR = ten	-0.135		44
LDS = tmen	-0.042		44
LDT = Me ₂ -tmen	-0.044		44
LDU = <i>trans</i> -cyhx-(NH ₂) ₂	-0.250		44
<i>Mono complexes</i>			
LDV = 2, 2, 2-N ₄ (trien)		-0.28 (80% CH ₃ OH)	57
LDW = 2, 3, 2-N ₄ (2,3,2-tet)	-0.300		44
LDX = 3, 2, 3-N ₄	-0.270		44
LDY = Me-NH ₂ -2,3,2-N ₄	-0.310		44
LDZ = Me-NO ₂ -2,3,2-N ₄	-0.250		44
<i>Acyclic polythioether ligands</i>			
LEA = Me ₂ -2,3,2-S ₄	0.79		49

(continued overleaf)

Tab. 2 (continued)

Complexed ligand ^a	Potential (V versus references indicated) ^b			References
	H ₂ O V versus SHE	CH ₃ CN V versus reference cited	Other, solvent V versus reference cited	
LEB = Et ₂ -2,3,2-S ₄	0.79			49
LEC = Me ₂ -3,2,3-S ₄	0.83			70
LED = <i>cis</i> -cyhx-3,2,3-S ₄	0.75			70
LEE = <i>trans</i> -cyhx-3,2,3-S ₄	0.77			70
<i>Acyclic polyaminopyridyl ligands</i>				
LEF = 2, 2, 2-N ₂ py ₂ (pdahx)	-0.20	-0.56 (Fc)	-0.73 (Fc), DMSO	44, 71
LEG = 2, 3, 2-N ₂ py ₂ (pdahp)	-0.12	-0.55 (Fc)	-0.73 (Fc), DMSO	71, 72
LEH = 3, 2, 3-N ₂ py ₂		-0.53 (Fc)	-0.70 (Fc), DMSO	71
LEI = Me ₂ -3,2,3-N ₂ py ₂ (pdao)	0.10	-0.31 (Fc)		72
LEJ = Me ₂ -3,3,3-N ₂ py ₂ (pdan)	0.28	-0.09 (Fc)		72
LEK = 2, 2, 2-N ₂ bzim ₂		-0.40 (AT) ^d		73
LEKa = (py) ₂ DAP		-0.136 (SCE)		34
LEKb = (imidH) ₂ DAP		-0.269 (SCE)		34
LEKc = (imidR) ₂ DAP		-0.256 (SCE)		34
LEL = N ₄ -mpy		0.21 (SCE)		74
<i>Bis complex</i>				
LELa = (MeimidΦ ₂) ₂ CO		0.59 (SCE)	0.80 (SCE) CH ₂ Cl ₂	75
<i>Acyclic polyaminothioether ligands</i>				
LEM = 2, 2, 2-N ₂ SN			0.36 (SHE) 80% CH ₃ OH	57
LEN = 2, 2, 2-NSSN			0.36 (SHE) 80% CH ₃ OH	57
LEO = Me ₂ -2,2,2-SNNS	0.28			76
LEP = 2, 3, 2-NSSN			0.31 (SHE), 80% CH ₃ OH	57
LEQ = Me ₂ -2,3,2-SNNS	0.23			76

LER = Et ₂ -2,3,2-SNNS				57
LES = Me ₂ -3,2,3-SNNS				76
Other acyclic mixed-donor ligands				
1 : 2 (Bis) complexes				
LET = bzMe-S-py	0.26			
LEU = Me-imine-imid (<i>p</i> -me)		0.53 (SCE)		74
LEV = <i>i</i> Pr-imine-imid (<i>p</i> - <i>i</i> -C ₃ H ₇)			−0.61 (SCE), DMF	43
LEW = <i>i</i> Pr-imine-phenox (sal- <i>i</i> -C ₃ H ₇)			−0.53 (SCE), DMF	43
LEX = <i>t</i> Bu-imine-phenox (sal- <i>t</i> -Bu)			−0.74 (SCE), DMF	43
			−0.66 (SCE), DMF	43
Mono complexes				
LEY = 2, 3, 2-S ₄			≈0.84 (SHE), 80% CH ₃ OH	57
LEZ = bz ₂ -3,2,3-ONNO (salen)			−1.21 (SCE), DMF	43
LFA = Ac ₂ -3,2,3-ONNO (<i>l</i> -en)			−1.09 (SCE), DMF	43
LFB = bz ₂ -3,3,3-ON ₃ O (saldpt)			−1.08 (SCE), DMF	43
LFC = N ₂ S ₂ -mpy		0.77 (SCE)		74
LFD = 3, 3-bzimSpy (Biptp)		0.28 (A1)		77
LFE = 3, 2-bzimSpy (Biptb)		0.22 (A1)		77
LFF = 2, 2, 2-pyS ₂ py	0.40	0.11 (Fc)		72
LFG = 2, 3, 2-pyS ₂ py	0.47	0.15 (Fc)		72
LFH = 3, 2, 3-pyS ₂ py (pdto)	0.59	0.21 (Fc)		72, 78
LFla = 3, 2, 3-quinS ₂ quin (qdto)		0.60 (A1)		79

(continued overleaf)

Tab. 2 (continued)

Complexed ligand ^a	Potential (V versus references indicated) ^b			References
	H ₂ O V versus SHE	CH ₃ CN V versus reference cited	Other, solvent V versus reference cited	
LFI = 3, 3, 3-pyS ₂ py (pdtn)	0.59	0.26 (Fc)		72
LJ = 2, 2, 2, 2-pyS ₃ py (pttn)	0.73 ^h	0.092, ⁱ 0.069 ^j (Fc)		80, 81
LJ _a = 2, 2, 2, 2-MepyS ₃ Mepy (Mptn)		0.40 (A1)		79
LJ _b = 3, 2, 2, 3-quinS ₃ quin (qtu)		0.62 (A1)		79
LK = 2, 2, 2, 2-pySOSpy		0.054, ⁱ 0.072 ^j (Fc)		81
LF = 2, 2, 2, 2-bzimS ₃ bmim	0.73 ^h			80
LFM = Me ₄ -1,2,2,1-przS ₃ prz	0.95 ^h			80
LFN = 2, 2, 2-S ₃ dioxime (TtoxH [−])		−1.10 (A1)		61
LFO = 2, 2, 2-SOSdioxime (OdttoxH [−])		−1.15 (A1)		61
LFO _a = 2, 2-OSOdicarboxylate (ta)	0.190			37
LFO _b = 2, 1, 2-OS ₂ O-dicarboxylate (1dta)	0.266			37
LFO _c = 2, 2, 2-OS ₂ O-dicarboxylate (2dta)	0.300			37
LFO _d = 2, 3, 2-OS ₂ O-dicarboxylate (3dta)	0.310			37
LFO _e = 3, 2, 2, 3-OS ₃ O-dicarboxylate (tta)	0.439			37
<i>Tripodal ligands</i>				
LFP = τ-2,2,2-MeS ₃ (TMMEA)	0.69		0.34 (SCE) ^g , DMF	43, 82
LFQ = τ-2,2,2-EtS ₃ (TEMEA)	0.67			82
LFR = τ-2,2,2-py(MeS) ₂ (PMMEA)	0.38		0.13 (SCE) ^g , DMF	43, 82
LFS = τ-2,2,2-py(EtS) ₂ (PMAS)	0.40		0.30 (SCE), 80% CH ₃ OH −0.16 (Fc), DMF	78, 82, 83
LFT = τ-3,2,2-py(MeS) ₂ (PEMEA)	0.60			84
LFU = τ-3,2,2-py(EtS) ₂ (PEAS)	0.60		0.11 (Fc), DMF	82
LFV = τ-2,2,2-py ₂ (MeS) (BPMMEA)	0.06			82
LFW = τ-2,2,2-py ₂ (EtS) (BPMEEA)	0.08			82

LFX = τ -3,3,2-py ₂ (MeS) (BPEMEA)	0.46			82
LFY = τ -3,3,2-py ₂ (EtS) (BPEEEEA)	0.47			82
LFZ = τ -2,2,2-py ₃ (TMPA) 2	-0.11 to -0.2		-0.79 (A1) ^f , DMF	82, 85, 86
LGA = τ -3,3,3-py ₃ (TPEA,tepa)	0.17 to 0.51		0.11 (Fc), DMF	82, 86, 87
LGB = τ -2,2,2-py ₂ (quin)			-0.53 (A1), DMF	84
LGC = τ -2,2,2-py(quin) ₂			-0.41 (A1), DMF	88
LGD = τ -2,2,2-quin ₃			-0.24 (A1), DMF	88
LGH = Me- τ -2,2,2-quin ₃		-0.10 (Fc)	-0.62 (Fc), DMF	89
LGI = τ -2,2,2-py ₂ (Meimid)			-0.62 (Fc), DMF	90 ^l
LJJ = τ -2,2,2-py(Meimid) ₂		-0.19 (A2)		90 ^l
LKK = τ -2,2,2-(Meimid) ₃		-0.15 (A1)	-0.18 ^f , -0.12 ^g (SCE), DMF	91
LGL = τ -2,2,2-OH(bzim) ₂			-0.42 (A1), DMF	43
LGM = τ -2,2,2-(bzim) ₃			-0.20 ^f , -0.14 ^g (SCE), DMF	92
LGN = τ -1,1,1-(pyrz) ₃		0.49 (SCE)		43
LGO = τ -1,1,1-(Me ₂ prz) ₃	0.26	0.67 (SCE)		93
LGP = τ -1,1,1-(<i>t</i> -Bu ₂ prz) ₃		0.94 (SCE)		86, 93
LGQ = τ -2,2,2-(Me ₂ prz) ₃	0.41			93
LGR = τ -2,2,2-(<i>S</i> -Meimid) ₃			-0.09 (Fc), DMF	86
Branched ligands				84
LGS = en-2,2,2,2-OH(bzim) ₃		-0.38 (A1) ^d		73

(continued overleaf)

Tab. 2 (continued)

Complexed ligand ^a	Potential (V versus references indicated) ^b			References
	H ₂ O V versus SHE	CH ₃ CN V versus reference cited	Other, solvent V versus reference cited	
LGT = en-2,2,2,2-OH(Mebzim) ₃		−0.43 (A1) ^d		73
LGU = en-2,2,2,2-(bzim) ₄		−0.43 (A1) ^d		73
LGV = en-2,2,2,2-(Mebzim) ₄		−0.45 (A1) ^d		73
LGW = cyhxn-2,2,2,2-(bzim) ₄		−0.48 (A1) ^{d,e}		73
LGX = cyhxn-2,2,2,2-(Mebzim) ₄		−0.57 (A1) ^{d,e}		73

^a Ligand structures are illustrated in Fig. 1.

^b All aqueous potential values are referenced to the standard hydrogen electrode. Nonaqueous potential values are referenced to ferrocene (Fc) if possible. Other references are indicated in parentheses where SCE represents the standard calomel electrode, A1 represents the Ag/Ag⁺ reference electrode ([Ag⁺] = 0.01 M unless otherwise indicated) and A2 represents the Ag/AgCl reference electrode. In acetonitrile, potential values referenced to SCE may be corrected to the ferrocene reference standard by subtracting 0.380 V, depending upon the anion present: (a) Ref. 11, (b) Ref. 10c.

^c [Ag⁺] = 0.1 M.

^d In Ref. 73, text states that potentials were determined in CH₃CN, but table of values indicates that solvent was CH₃OH. It is presumed that CH₃CN was the solvent used.

^e The reference does not indicate whether the cyclohexane moiety is *cis* or *trans*.

^f Chloride ion occupies the fifth coordination site in Cu^{II}L.

^g Bromide ion occupies the fifth coordination site in Cu^{II}L.

^h Solvent used is not clearly specified.

ⁱ ClO₄[−] ion present.

^j CF₃SO₃[−] ion present.

^k The reference Ag/Ag⁺ electrode used is reported to have a potential value of +0.31 V versus SCE in acetonitrile.

^l These investigators have noted that the potential of ferrocene in DMF versus their Ag/Ag⁺ (0.01 M) reference electrode was +20 mV.

^m Values in this study were determined at 20 °C, μ = 0.2 and are slightly different from those shown in Table 4.

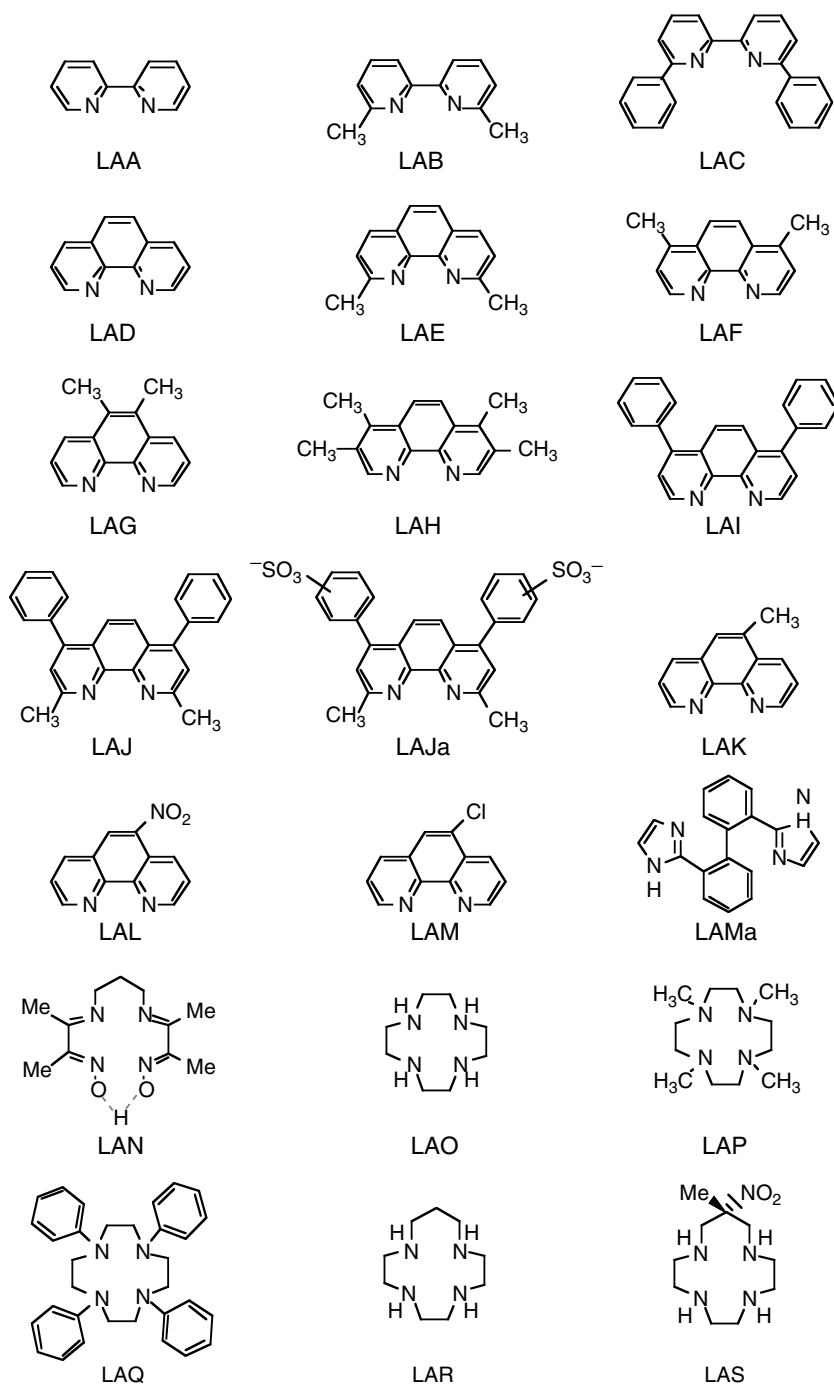


Fig. 1 Identification of ligands for which $\text{Cu}^{\text{II}}/\text{L}$ potentials are listed in Table 2.

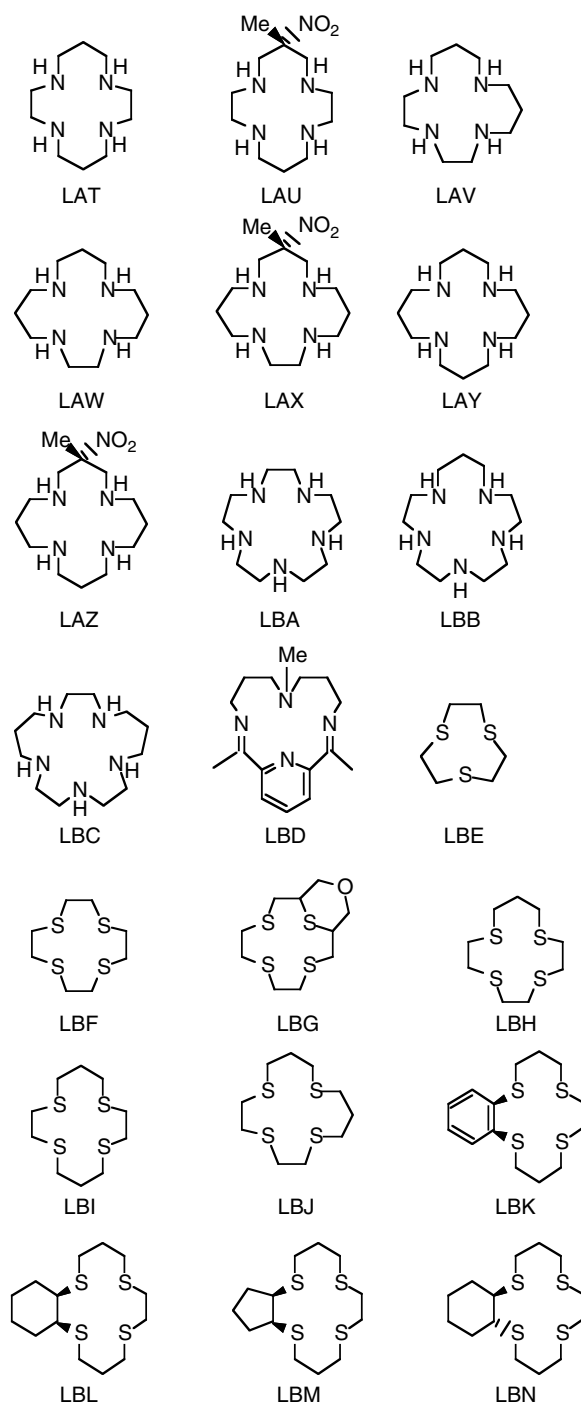


Fig. 1 (continued).

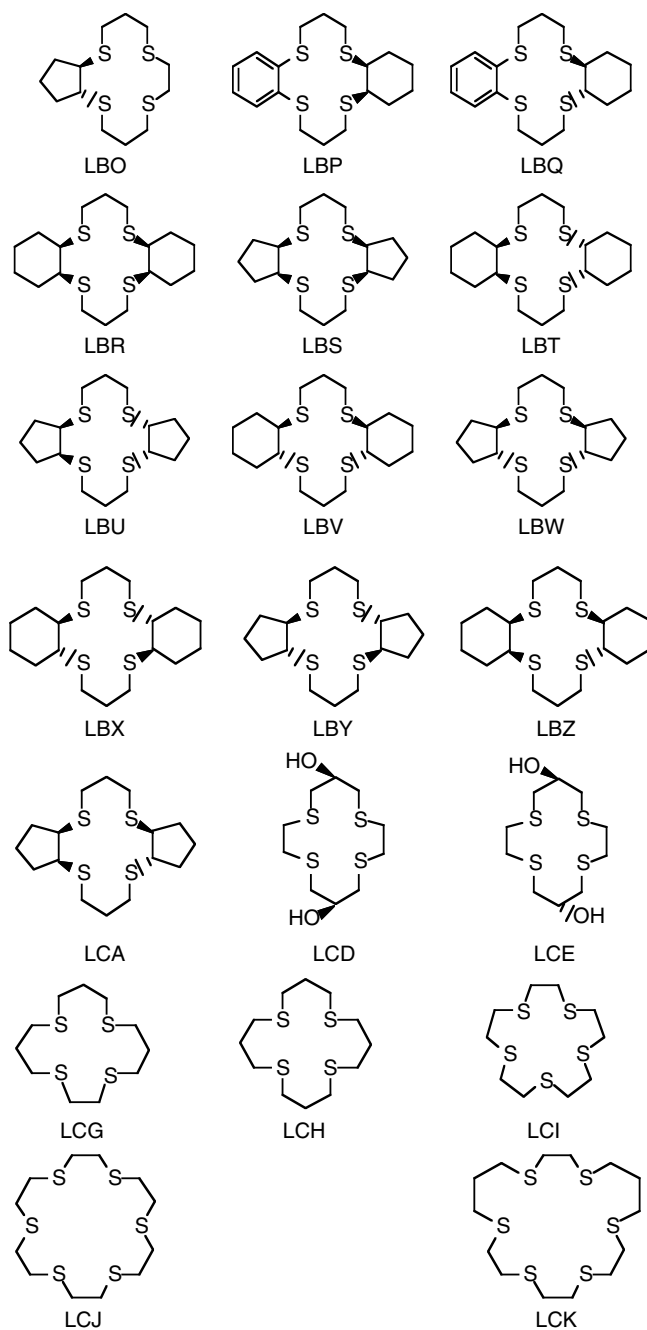


Fig. 1 (continued).

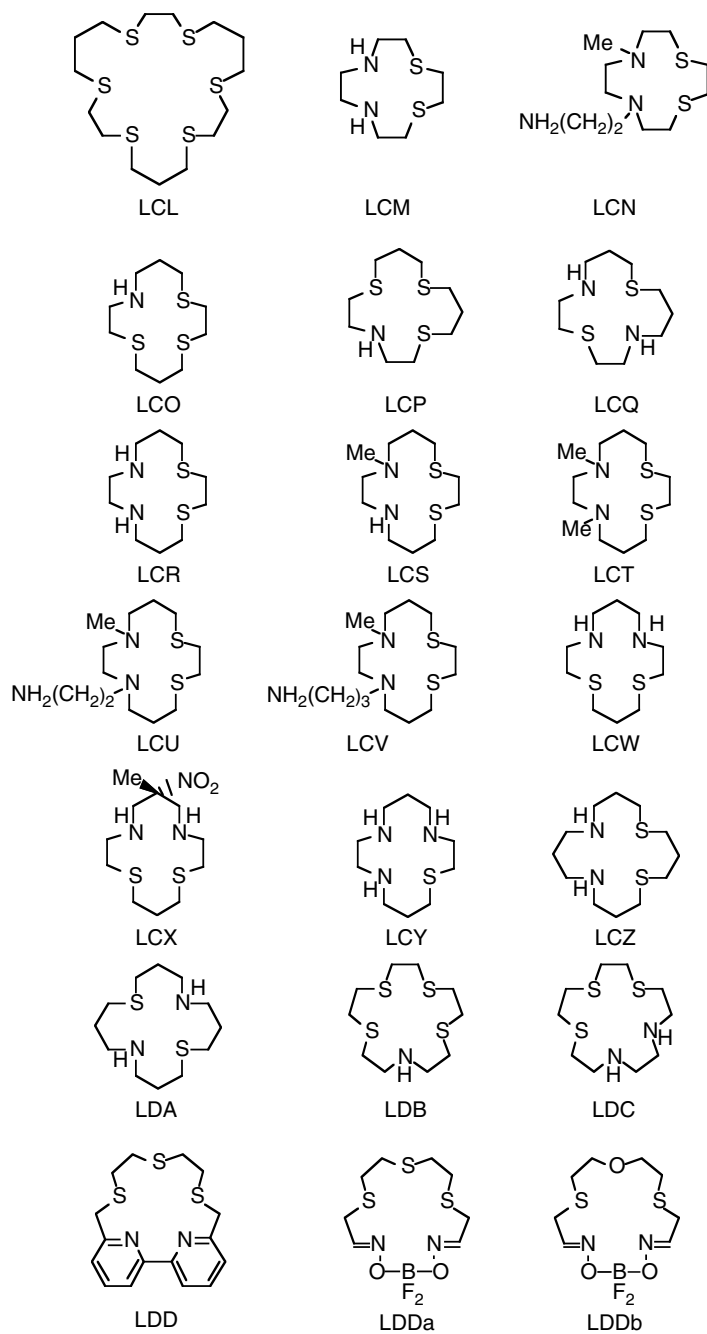


Fig. 1 (continued).

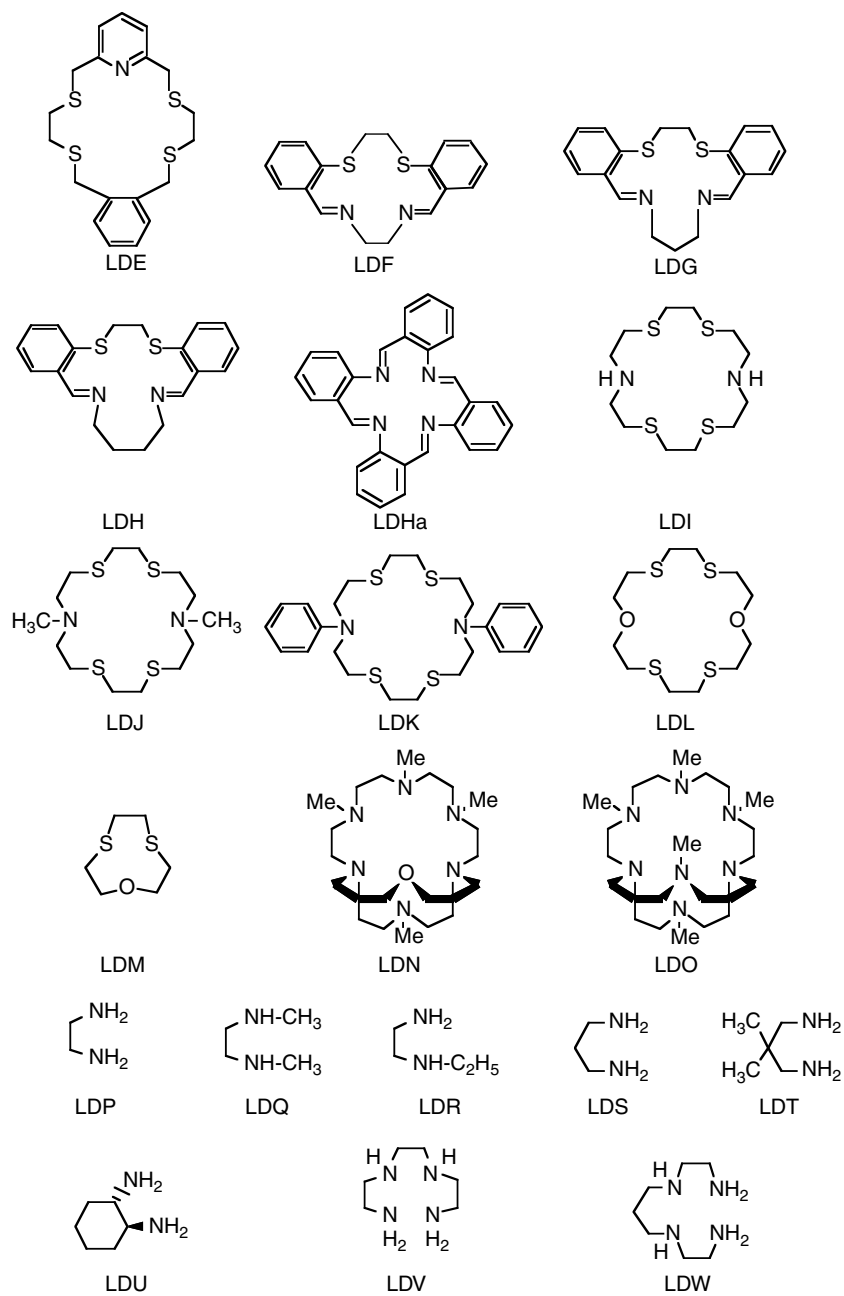


Fig. 1 (continued).

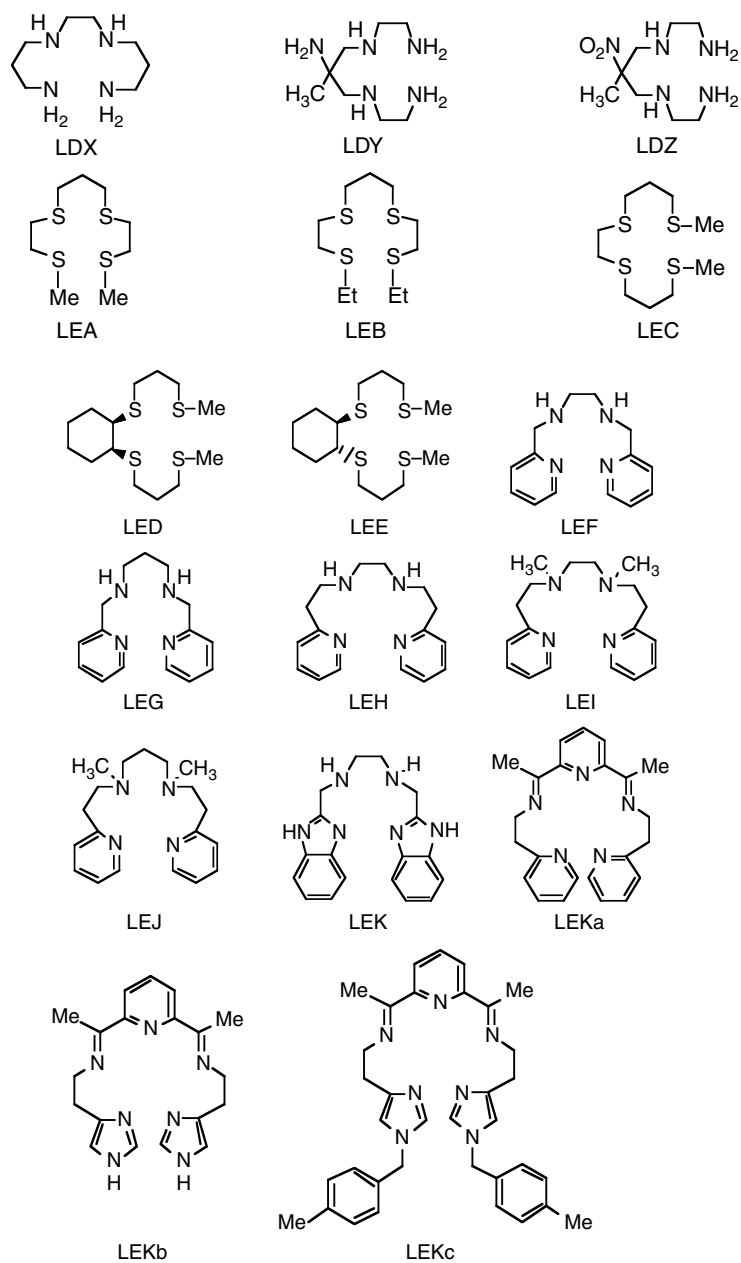


Fig. 1 (continued).

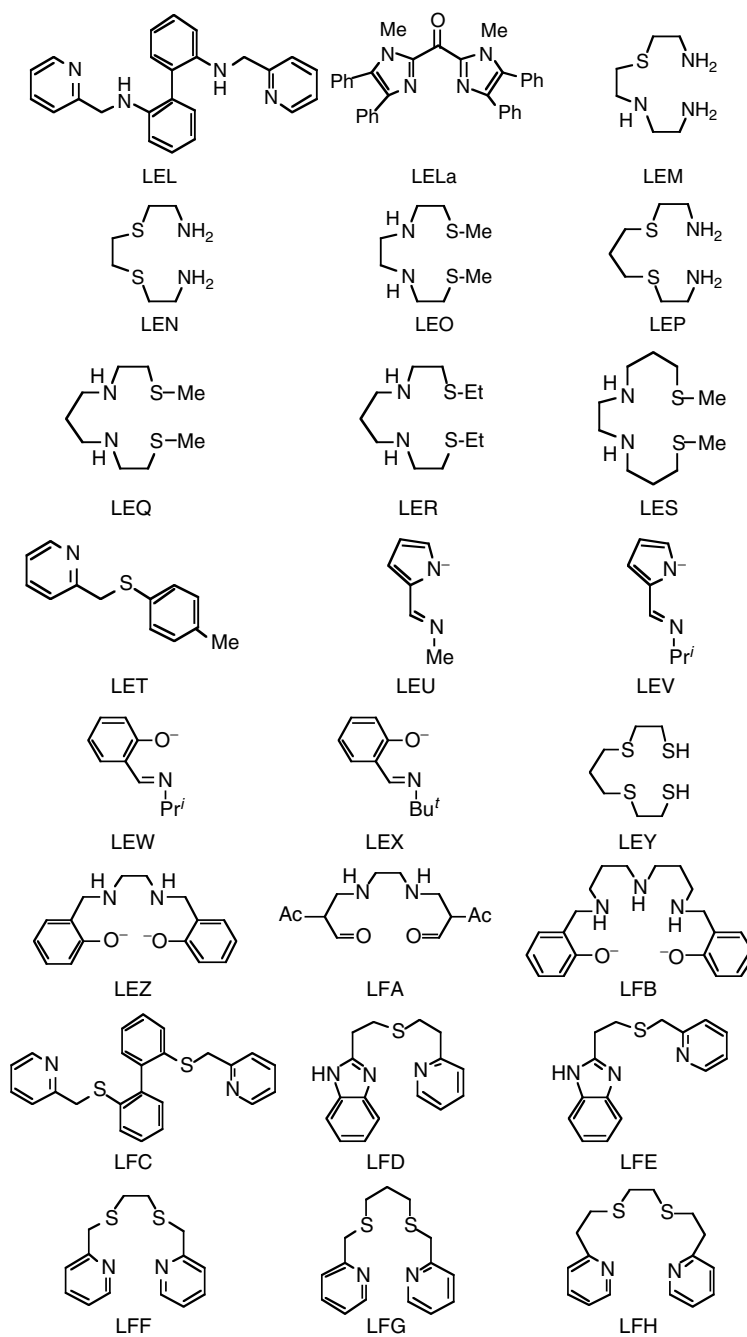


Fig. 1 (continued).

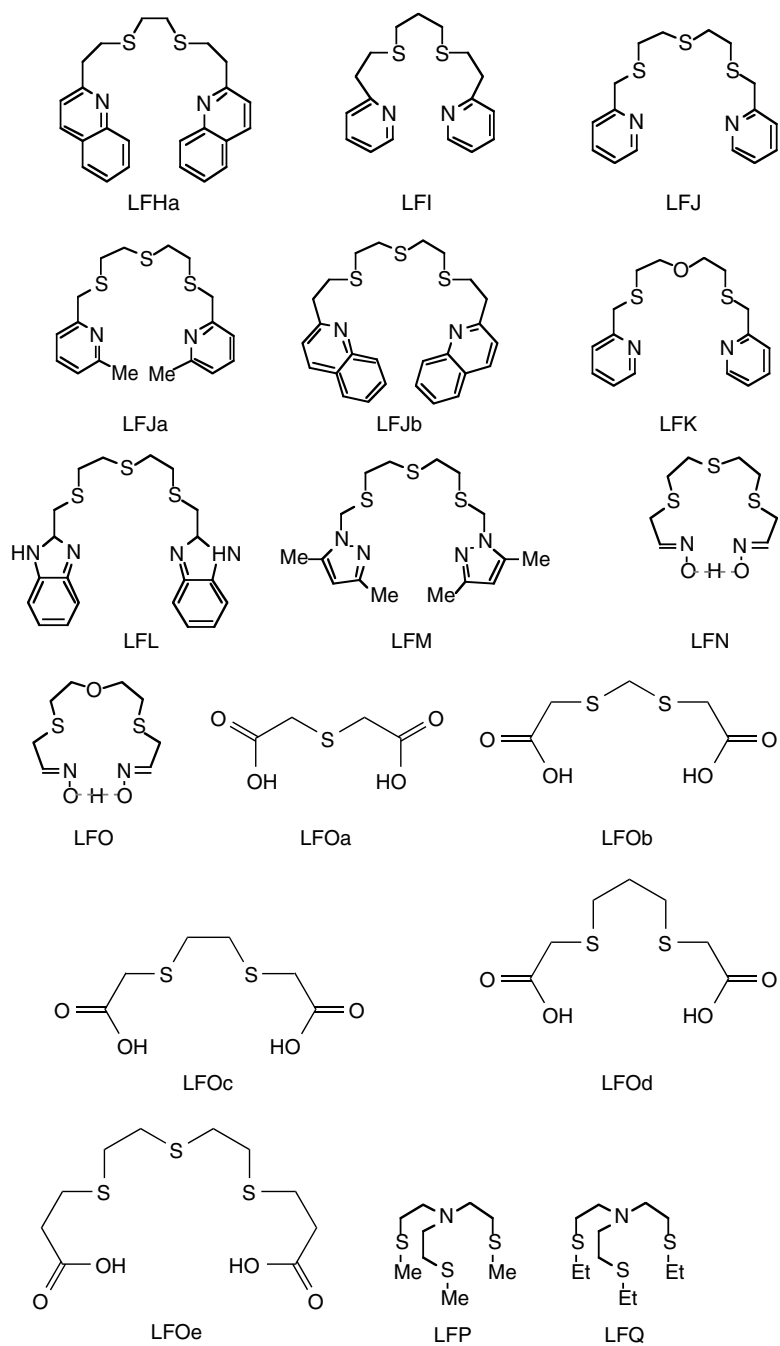


Fig. 1 (continued).

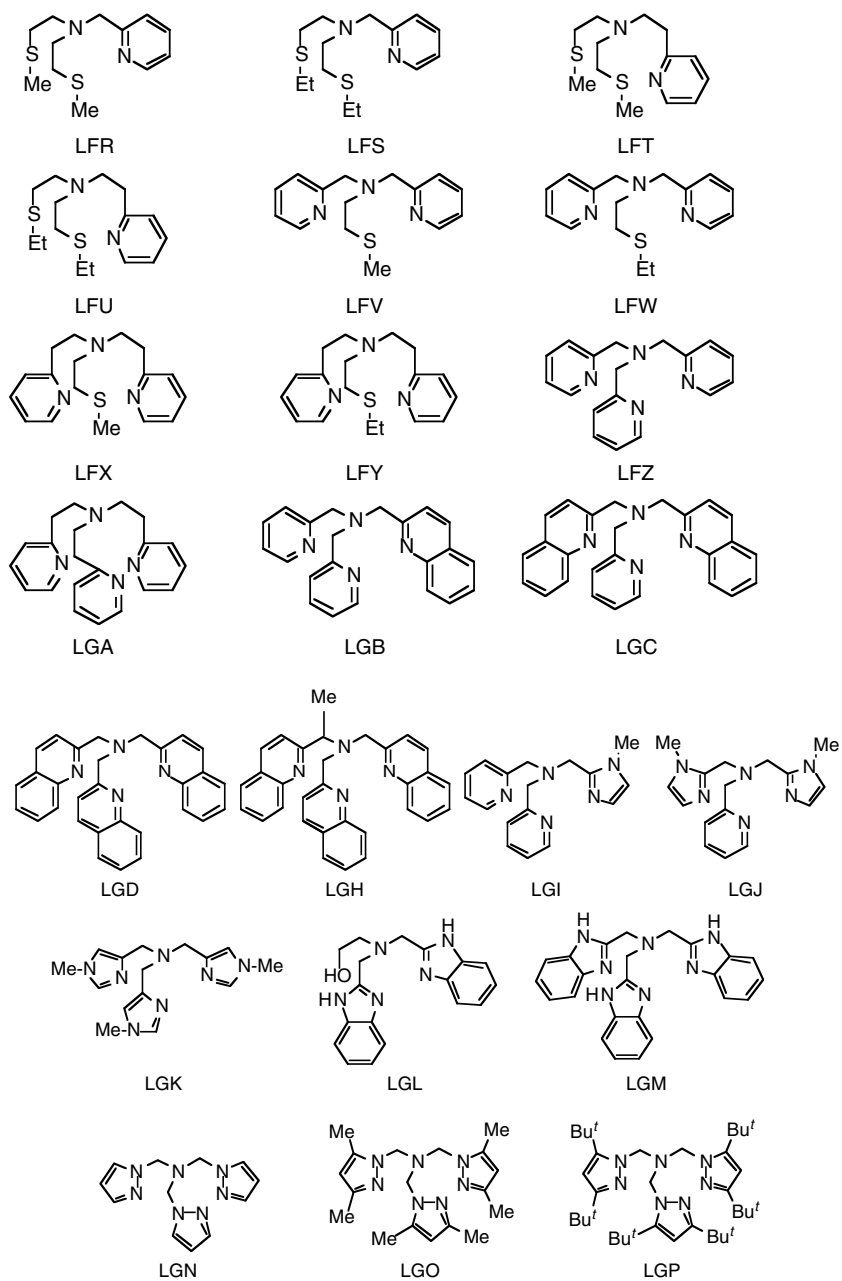


Fig. 1 (continued).

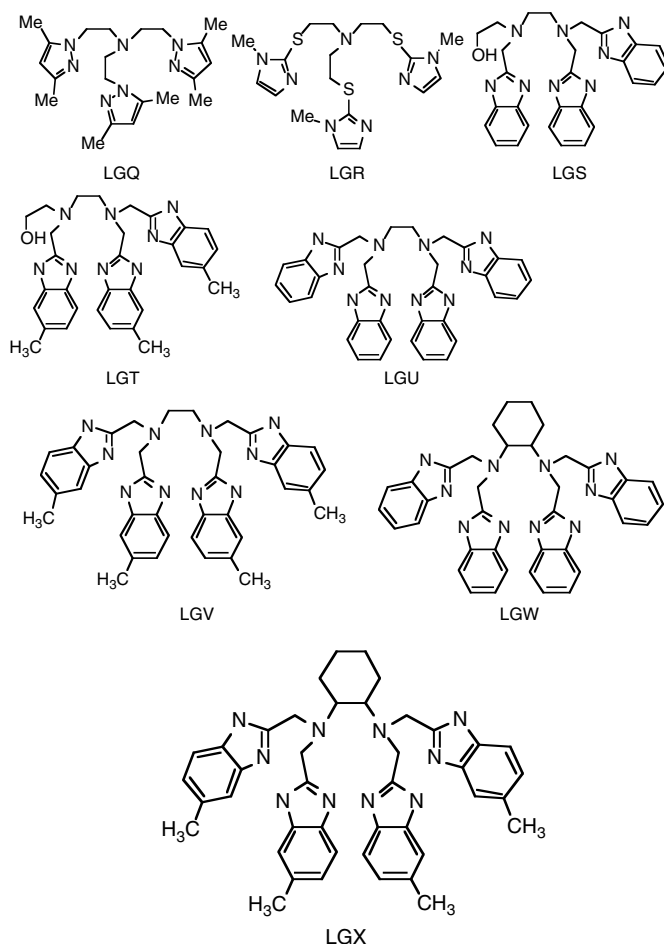


Fig. 1 (continued).

Fabrizzi, Poggi, and Zanello[46] used the latter solvent to measure the potential values of Cu(II/I) compounds involving 13- to 16-membered macrocyclic tetramines and 15- to 17-membered macrocyclic pentamines (Table 2).

As shown by Eq. (9), the relative affinity of specific ligands for the Cu(II) and Cu(I) oxidation states, as indicated by the magnitude of the stability constants, $K_{\text{Cu}^{\text{II}}\text{L}}$ and $K_{\text{Cu}^{\text{I}}\text{L}}$, respectively, is directly reflected in the Cu(II/I) redox potentials. Thus, an increase in the value of $E_{21}^{\theta'}$ is generally

interpreted to reflect either an increase in the stabilization of the Cu(I) state or the destabilization of the Cu(II) state (or both) by the complexing ligand. Because of the different geometric preferences exhibited by these two oxidation states, the influence of ligand structure upon Cu(II/I) potential values has been considered to be a matter of prime interest for more than four decades.

Patterson and Holm [95] carried out the first systematic investigation on the influence of the structure of coordinated

ligands upon Cu(II/I) potentials. Utilizing dimethylformamide (DMF) as the solvent, they made polarographic measurements on the Cu(II/I) complexes formed with 36 quadridentate and bis-bidentate ligands consisting primarily of salicylaldimine, β -ketoamine, β -iminoamine, and pyrrole-2-alimine systems. These ligands were chosen to reveal the effect of stereochemical and donor atom variations on the resultant Cu(II/I) half-wave potentials.

One of the primary observations made by Patterson and Holm was that nonplanar bis-chelate complexes were easier to reduce than their planar counterparts. In particular, the Cu^{II/I}(2,9-Me₂phen)₂ redox couple (2,9-Me₂phen = 2,9-dimethyl-1,10-phenanthroline) exhibits a potential in DMF that is more than 1 V larger than the potentials of nearly all other complex systems they studied. Molecular models readily show that, because of steric hindrance of the methyl groups in the 2,9-positions, the four nitrogen donor atoms in the Cu(II) complex are distorted out of plane. The Cu(II) presumably adopts a trigonal bipyramidal geometry by retaining an inner-sphere solvent molecule as shown in the crystal structure of a closely related bis-bipyridyl complex [96]. On the basis of the assumption that the potentials primarily reflect changes in the stabilities of the Cu(II) complexes (*vide infra*), the first observation reflects the preference of Cu(II) for four donor atoms in the *xy* plane.

Patterson and Holm also observed that rigid planar quadridentate or related planar bis-chelate complexes, and complexes differing only in donor atoms, are more readily reduced in the order N₄ < N₂O₂ < N₂S₂. This observation reflects the relative preference of Cu(II) for these donor atoms in the order N > O > S. Patterson and Holm noted that binuclear complexes were

reduced in one two-electron or two resolvable one-electron steps depending upon the ligand structure, a point that will be discussed later in this treatise.

Dockal et al. [57] used slow-scan CV to determine the $E_{21}^{\theta'}$ values for 17 Cu(II/I) complexes in 80% methanol–20% water (w/w) – including nine complexes with macrocyclic terdentate, quadridentate, quinquedentate, and sexadentate thioethers and eight complexes with acyclic quadridentate ligands containing thioether sulfur and/or amine nitrogen donor atoms. (In naming the denticity of multidentate ligands, Dwyer, Lions, and coworkers have pointed out that “dentate” is a Latin root and proper nomenclature requires that Latin prefixes be used. Thus, ter-, quadri-, quinque-, and sexa- are preferred over the Greek prefixes tri-, tetra-, penta-, and hexa-. The lone exception appears to be for ligands with two donor atoms where bidentate is universally utilized rather than the more proper didentate) [97]. The macrocyclic quadridentate tetrathioether complexes exhibit slightly lower potentials than their acyclic counterparts, but the potentials increase for larger cavity sizes. Macrocyclic ligands containing five or six thioether sulfurs exhibit the highest potential values observed. As noted by Patterson and Holm, a sharp decrease in potential was also observed by Dockal et al. when amine nitrogens were substituted for thioether sulfurs in the acyclic ligand series.

Addison [98] correlated a broad spectrum of published potential data on aqueous Cu(II/I) complexes – including those with N, S, and O donor atoms – to generate an empirical relationship between the various characteristic ligand features and the observed Cu(II/I) potentials. He concluded that closed (macrocyclic) ligand topology had little effect on the $E_{21}^{\theta'}$ values, but

certain tripodal ligands show a marked influence on the redox potentials, generally raising $E_{21}^{\theta'}$ by a few hundred millivolts. Based on 47 Cu(II/I) potential values from the literature, Addison generated the following empirical expression:

$$E_{21}^{\theta'} = E_{21(\text{soln})}^{\theta'} + \Sigma(n\Delta E_L) \quad (10)$$

In Eq. (10), ΔE_L represents the change in the Cu(II/I) potential brought about by various ligand features (such as donor atom type, number of five-membered chelate rings, etc.) and n represents the number of times that specific feature appears in a specific coordinated ligand. A tabulation of the values generated by Addison for the various ligand features is given in Table 3.

Bernardo et al. [51] subsequently determined the potentials of a series of copper(II/I) complexes formed with 14-membered macrocyclic quadridentate ligands involving amine nitrogen and thioether sulfur donor atoms and found that the substitution of each sulfur donor atom by an amine nitrogen resulted in an average decrease of 0.3 V in the Cu(II/I) potential. Since the $K_{\text{Cu}^{\text{II}}\text{L}}$ values had been determined previously for these systems [99], Bernardo et al. were able to calculate the $K_{\text{Cu}^{\text{II}}\text{L}}$ values using Eq. (9). The latter values proved to be nearly constant, indicating that Cu(I) does not discriminate

significantly between amine nitrogen and thioether sulfur donor atoms. Thus, the steady decrease in potential values as each nitrogen is substituted for a sulfur donor is almost entirely due to the *increase* in the stabilization of the Cu(II) complexes.

As noted by Addison, tripodal ligands appear to have the largest impact upon the Cu(II/I) potential values. Ambundo et al. [82] measured both the Cu(II) complex stability constants and the Cu(II/I) complex potential values for 12 different tripodal ligands containing amine nitrogen bridgeheads and thioether sulfur or aromatic nitrogen donor atoms on the three “legs”. Despite the differences in chelate ring size and donor atom type, all 12 compounds exhibit nearly constant $K_{\text{Cu}^{\text{II}}\text{L}}$ values as calculated using Eq. (9). Thus, the trend in Cu(II/I) potentials again parallels the stability of the Cu(II) complexes.

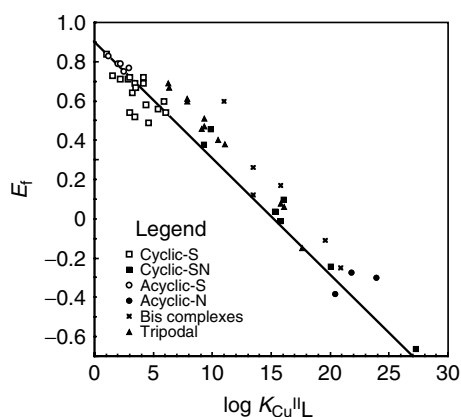
24.7.2.3 Correlation of Potentials to Copper(II) Complex Stability Constants

Based on the observations noted above, Ambundo et al. [82] plotted the aqueous $E_{21}^{\theta'}$ values for 35 Cu(II/I) systems involving neutral ligands against the corresponding $\log K_{\text{Cu}^{\text{II}}\text{L}}$ values. Their original data have been expanded in Fig. 2 to include 50 Cu(II/I) complexes, all involving uncharged ligands. The stability constant data for the systems included in

Tab. 3 Empirical parameters affecting copper(II/I) potential values (Ref. 98)

Ligand feature	ΔE_L [mV]	Error [mV]	Significance level [%]
Thioether donor	+141	± 12	>99.99
Aromatic N donor	+52	± 13	>99.9
Aliphatic N donor	−75	± 12	>99.99
Carboxylate O donor	−26	± 23	70
Macrocyclic ligand	+24	± 44	40
Five-membered chelate rings	−46	± 10	>99.99
Tripodal ligand	+291	± 52	>99.99

Fig. 2 Plot illustrating the relatively linear relationship between the $\text{Cu}^{\text{II}}/\text{I}$ redox potential and logarithmic value of the $\text{Cu}^{\text{II}}\text{L}$ stability constant, $K_{\text{Cu}^{\text{II}}\text{L}}$. The line drawn has the Nernstian slope (0.059) and represents a $\text{Cu}^{\text{I}}\text{L}$ stability constant value of 10^{13} M^{-1} . All complexes represented involve uncharged ligands (see Table 4).



this plot are given in Table 4. The resulting plot is seen to be essentially linear for $K_{\text{Cu}^{\text{II}}\text{L}}$ values differing by 26 orders of magnitude with potentials covering nearly a 1.5 V range. The line drawn in this plot is based on an average $K_{\text{Cu}^{\text{I}}\text{L}}$ value of 10^{13} (Eq. 9) and has the Nernstian slope. The close clustering of nearly all points about this line indicates that, despite the wide variety of $\text{Cu}(\text{II}/\text{I})$ systems involved, the stability of the $\text{Cu}(\text{I})$ complexes is only slightly affected by the geometry of the ligands – whether macrocyclic, acyclic or tripodal – and by the donor atoms involved. Thus, it is presumed that nearly all statements in the literature (including past comments by the current authors) are *incorrect* when they conclude that observed increases in the $\text{Cu}(\text{II}/\text{I})$ redox potentials are attributable to a *stabilization* of the $\text{Cu}(\text{I})$ complexes.

On the basis of the trend illustrated in Fig. 2, it is evident that the measured value of $E_{21}^{\theta'}$ for any aqueous $\text{Cu}(\text{II}/\text{I})$ system can be used to estimate the stability constant of the $\text{Cu}^{\text{II}}\text{L}$ complex within about 2 orders of magnitude. This is a useful tool since only a limited number of $\text{Cu}^{\text{II}}\text{L}$ stability constants have been determined in aqueous solution, whereas a large array

of $\text{Cu}(\text{II}/\text{I})$ potential values have been reported.

A similar linear relationship between $\text{Cu}(\text{II}/\text{I})$ potential values and logarithmic $\text{Cu}^{\text{II}}\text{L}$ stability constants may exist in non-aqueous solvents, but such a relationship has not been adequately established. Measurements conducted in our laboratories on a variety of polythioether complexes have shown that the $\text{Cu}^{\text{II}}\text{L}$ stability constants tend to increase by approximately 10^6 on going from water to acetonitrile, whereas the $\text{Cu}^{\text{I}}\text{L}$ stability constants tend to decrease by a similar order of magnitude [54]. These values obviously reflect the preference of $\text{Cu}(\text{II})$ to be solvated by water and the corresponding preference of $\text{Cu}(\text{I})$ to be coordinated to acetonitrile [111].

24.7.3

Mechanistic Aspects of Copper(II/I) Electron Transfer

Many electrochemical studies on $\text{Cu}(\text{II}/\text{I})$ systems exhibit irreversible or quasi-reversible behavior or involve coupled chemical reactions. There are no known examples of $\text{Cu}(\text{II}/\text{I})$ systems where irreversibility can be definitively attributed to slow electron transfer. However, many

Tab. 4 Correlation of Cu(II/I) redox potentials and stability constants of copper complexes in aqueous solution at 25 °C, $\mu = 0.1$

Complexed ligand	$\text{Log}K_{\text{Cu}^{\text{II}}\text{L}}$	$\text{Log}K_{\text{Cu}^{\text{I}}\text{L}}$	E^f , V versus SHE	References
<i>Macrocyclic ligands</i>				
[9]aneS ₃	4.14	≈14	0.72	48
[12]aneS ₄	3.39	12.0	<0.69	49, 100
Oxathiane[12]aneS ₄	3.02	12.0	0.72	101
[13]aneS ₄	3.44	10.0	≈0.52	49, 100
[13]aneS ₄ -ol	3.0	10.7	0.54	101
[14]aneS ₄	4.34	11.9	0.58	49, 100
[14]aneS ₄ -ol	4.59	10.7	0.49	101
bz[14]aneS ₄	≈1		≈0.84	31
cis-cyhx[14]aneS ₄	6.04		0.54	31
trans-cyhx[14]aneS ₄	5.90		0.60	31
cis-cypt[14]aneS ₄	5.36		0.56	31
trans-cypt[14]aneS ₄	3.48		0.67	31
[15]aneS ₄	3.17		0.64	49, 100
[15]aneS ₄ -ol	2.84	11.8	0.71	101
[16]aneS ₄	2.20		0.71	49, 100
[16]aneS ₄ -ol	1.51	11.6	0.73	101
[15]aneS ₅	4.18		0.69	49, 100
[14]aneNS ₃	9.25	13.6	0.38	51, 99
[14]aneN ₂ S ₂	15.26	13.9	0.04	51, 58, 99 ^b
[14]aneNSSN	15.72	13.5	−0.01	51, 99
[14]aneN ₃ S	≥20		≤ −0.24 (est)	51, 99
[14]aneN ₄ (cyclam)	27.20		−0.66 (est)	102
[15]aneNS ₄	9.80	15.6	0.46	51, 99
[15]aneN ₂ S ₃	16.02	15.7	0.10	51, 99
<i>Acyclic ligands</i>				
Me ₂ -2,3,2-S ₄	1.97		≈0.79	49, 100
Et ₂ -2,3,2-S ₄	2.18		0.79	49, 100
Me ₂ -3,2,3-S ₄	1.18		0.83	103
trans-cyhx-Me ₂ -3,2,3-S ₄	2.94		0.77	103
cis-cyhx-Me ₂ -3,2,3-S ₄	2.45		0.75	103
bis-en	19.60		−0.11	44, 104
bis-nncyhxn (nncyhxn = trans-1,2-diaminocyclohexane)	20.93		−0.25	44, 104
bis-phen	15.8		0.17	105, 106
bis-bpy	13.5	14.2	0.12	105, 106
bis-5-nitrophen	13.5		0.26	107, 108
bis-2,9-Me ₂ phen	11.0	19.2 ^a	0.60	108, 109
2,2,2-tet (trien)	20.4		≈ −0.38	110, 57 ^c
2,3,2-tet			−0.30	44
3,2,3-tet			−0.27	44
<i>Tripodal ligands</i>				
TMMEA	6.29	15.8	0.69	82
TEMEA	6.35	15.5	0.67	82
PMMEA	11.06	15.4	0.38	82

Tab. 4 (continued)

Complexed ligand	$\text{Log}K_{\text{Cu}^{\text{II}}\text{L}}$	$\text{Log}K_{\text{Cu}^{\text{I}}\text{L}}$	E^f , V versus SHE	References
PMAS	10.48	15.0	0.40	82
PEMEA	7.89	15.8	0.60	82
PEAS	7.87	15.9	0.61	82
BPMMEA	16.10	15.0	0.06	82
BPMEEA	15.82	15.0	0.08	82
BPEMEA	9.10	14.6	0.46	82
BPEEEA	9.29	15.0	0.47	82
TPMA	17.6	12.9	−0.15	82
TPEA	9.35	15.8	0.51	82

^aValue for $\log \beta_2$ value for $\text{Cu}^{\text{I}}(2,9\text{-Me}_2\text{phen})_2$ was determined directly.

^bValues in this study were determined at 20 °C, $\mu = 0.2$ and are slightly different from those shown in Table 4.

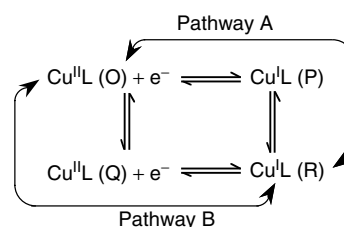
^cIn approximating the aqueous potential value, 0.10 V was subtracted from the potential value measured in 80% CH_3OH (w/w).

types of chemical processes have been proposed to account for the appearance of irreversibility in such systems. Several of the more credible reaction processes are described in the following paragraphs.

24.7.3.1 Ligand Conformational Change

The difference in the geometric preferences exhibited by $\text{Cu}(\text{II})$ and $\text{Cu}(\text{I})$ has been noted above. In the absence of complete ligand rigidity, this implies that, upon transferring an electron to or from the copper center, the ligand must undergo a change in conformation. If conformational change is rapid relative to the timescale of the experiment, the two processes will appear to

be concerted and will show no irregular behavior. In studying the homogeneous electron-transfer kinetics for a series of $\text{Cu}(\text{II}/\text{I})$ systems involving macrocyclic and acyclic polythioethers, Martin et al. [112] observed kinetic behavior that was strongly suggestive of a slow change in the ligand conformation. The CV behavior for such a mechanism was first theoretically described as a general phenomenon by Laviron and Roullier [113]. This behavior was first confirmed in the electrochemical behavior of $\text{Cu}(\text{II}/\text{I})$ systems by Bernardo et al. [114]. Their mechanism is illustrated in Scheme 1. In this mechanism, $\text{Cu}^{\text{II}}\text{L}(\text{O})$ and $\text{Cu}^{\text{I}}\text{L}(\text{R})$ represent the most stable conformational species, while $\text{Cu}^{\text{II}}\text{L}(\text{Q})$ and $\text{Cu}^{\text{I}}\text{L}(\text{P})$ represent



Scheme 1

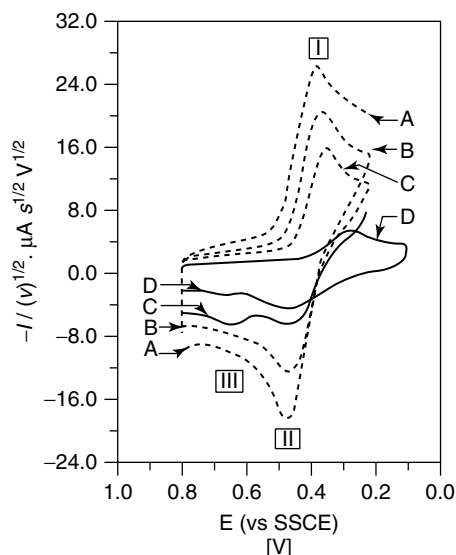


Fig. 3 Cyclic voltammetric behavior of the Cu(II) complex with [14]aneS₄ (LBI) as a function of temperature in 80% methanol (by weight) illustrating the effect of Scheme 1 upon the electron-transfer behavior. At 25 °C (curve A) and at 0 °C (curve B) a reversible voltammogram is observed in which the cathodic peak (I) represents the reduction of equilibrated O and Q and the anodic peak (II) represents the oxidation of equilibrated P and R. As the temperature is lowered to –23 °C (curve C), a second oxidation peak (III) appears at a more positive potential representing the direct oxidation of R to Q. As the temperature is decreased to –77 °C (curve D), peak III diminishes and a new peak II appears, representing the reoxidation of newly created P before it has time to convert to the more stable R. Similar behavior is observed using very fast sweep rates at ambient temperature. Reproduced with permission from Ref. 114. Copyright 1989 American Chemical Society.

metastable intermediates for which the ligand conformations are presumed to more closely approximate the stable conformations of the other oxidation state.

Since the molecularity for both reaction pathways is identical, this type of mechanism cannot be diagnosed by changes in concentration ratios. However, at sufficiently rapid-scan rates or low temperatures, the conformational changes designated by the vertical reactions in Scheme 1 can become rate limiting.

Based on CV studies carried out at low temperature (–77 °C) in 80% methanol/20% water (w/w), Bernardo et al. [114] demonstrated that Cu^{II/I}([14]aneS₄) (LBI) showed electrochemical behavior identical to that predicted by the Laviron and Roullier square scheme (Scheme 1). Subsequent CV studies by Robandt et al. [115], involving scan rates up to 80 000 V s^{–1}, made it possible to

determine the rate constants associated with all eight reaction arrows in Scheme 1 for a specific Cu(II/I) complex. Villeneuve et al. [116] later conducted a series of rapid-scan CV studies to evaluate the corresponding rate constants for seven additional related complexes that appear to conform to Scheme 1. As illustrated in Fig. 3, the primary features noted for Cu(II/I) systems corresponding to Scheme 1 is that, at sufficiently slow sweep rates, the CV's appear to be reasonably reversible with equilibrated O and Q being reduced on the cathodic sweep (peak I) and equilibrated R and P being oxidized (peak II) on the anodic sweep (Fig. 3, curves A and B). As the temperature is lowered (or as the sweep rate is increased at a constant temperature) for solutions initially containing only the oxidized complex, however, the rate of conversion of R to P becomes rate limiting and the anodic peak (III) at higher

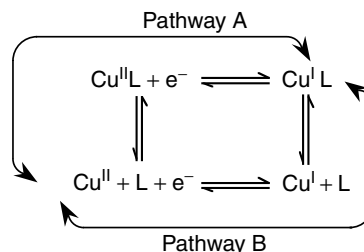
potential – representing direct oxidation of R to Q – increases in magnitude for both $\text{Cu}^{\text{II}}\text{L}$ and $\text{Cu}^{\text{I}}\text{L}$ solutions (curve C in Fig. 3). At sufficiently low temperatures (or at sufficiently high sweep rates) for $\text{Cu}(\text{II})$ solutions, the higher potential anodic peak diminishes in magnitude and eventually disappears as a new peak grows at slightly lower potential than the original equilibrated peak (curve D in Fig. 3). This new peak represents the direct oxidation of P to O, since the P intermediate produced during the cathodic sweep no longer has time to convert to the stable R conformation prior to reoxidation. For solutions containing initially only the reduced complex, $\text{Cu}^{\text{I}}\text{L}$, the initial anodic sweep shows evidence of a second peak at higher potentials, even when slow-scan rates are used, representative of the oxidation of R directly to Q. This anodic peak becomes totally dominant as the sweep rate increases (or the temperature decreases) since R, which is the dominant species present in the initial reduced solution, does not have time to convert to P before oxidation occurs.

Homogeneous cross-reaction electron-transfer kinetic studies suggest that many other $\text{Cu}(\text{II}/\text{I})$ systems obey Scheme 1. However, few $\text{Cu}(\text{II}/\text{I})$ systems have been subjected to sufficiently low temperature or rapid-scan CV measurements to demonstrate the presence of rate-limiting conformational changes.

24.7.3.2 Complex Dissociation/Formation

One of the simplest mechanisms that has been considered for $\text{Cu}(\text{II}/\text{I})$ electrochemistry involves the dissociation of either the $\text{Cu}^{\text{II}}\text{L}$ or $\text{Cu}^{\text{I}}\text{L}$ complex species to the solvated species (designated in Scheme 2 as Cu^{II} and Cu^{I}), preceding or following the electron-transfer step [117].

Since both $\text{Cu}(\text{II})$ and $\text{Cu}(\text{I})$ tend to undergo rapid inner-sphere substitution, this mechanism would appear to be viable for $\text{Cu}(\text{II}/\text{I})$ redox couples containing weakly coordinated ligands. As noted above, most $\text{Cu}(\text{I})$ complexes have reasonably high stabilities in aqueous solution while $\text{Cu}(\text{II})$ complexes cover a wide range of stabilities. This suggests that, at least in aqueous solution, some $\text{Cu}^{\text{II}}\text{L}$ complexes will be largely dissociated so that only an anodic peak may be observed. (The reverse may occur in acetonitrile solutions where $\text{Cu}^{\text{II}}\text{L}$ complexes tend to be much more stable while $\text{Cu}^{\text{I}}\text{L}$ complexes are much less stable due to the stability of $\text{Cu}^{\text{I}}(\text{CH}_3\text{CN})_4^+$.) [54] The presence of such a phenomenon can be probed by increasing the concentration of free ligand and observing whether the cathodic (or anodic) peak begins to appear and grow in magnitude in proportion to the concentration of excess ligand in solution. The possibility of observing the direct transfer of electrons via Pathway B in Scheme 2 is less likely in view of the fact that solvated copper tends to be extremely slow in undergoing



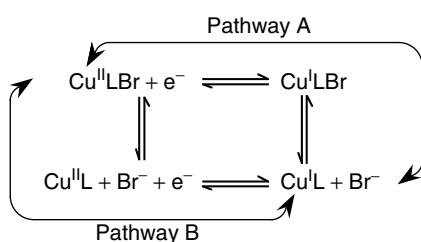
Scheme 2

electron transfer in the absence of bridging ligands [118, 119]. For ligands that protonate readily, the extent of complex formation is generally pH dependent and a study of the electrochemical behavior as a function of pH should then be diagnostic.

24.7.3.3 Interconversion of Ternary and Binary Complexes

Even when a strongly complexing multidentate ligand is coordinated to the copper ion, the differences in the preferred coordination number for Cu(II) and Cu(I) imply that one or two copper–donor atom bonds will rupture during the reduction process. Water molecules tend to

undergo rapid inner-sphere substitution with both Cu(II) and Cu(I) so that the dissociation or formation of Cu–OH₂ bonds may have no observable impact on the reversibility of the cyclic voltammograms, even at rapid sweep rates. In the case of a ternary Cu(II) complex in which Cu(II) is coordinated to a terdentate or quadridentate ligand plus a bidentate or unidentate ligand, respectively, the dissociation of the latter species upon reduction has been observed in the cyclic voltammograms for a few systems. A typical example is that postulated by Conan and coworkers as illustrated in Scheme 3 [120].



Scheme 3

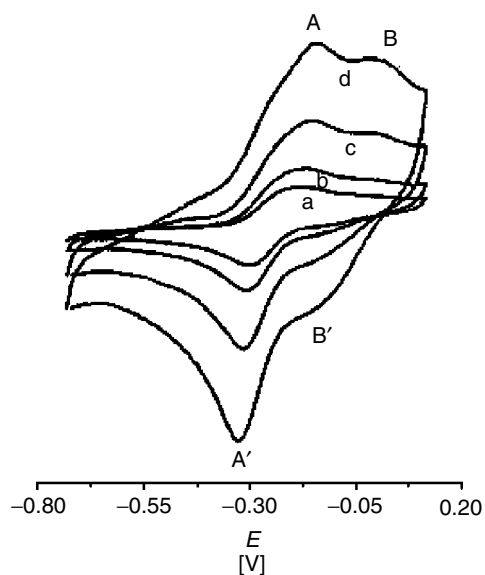


Fig. 4 Cyclic voltammetric behavior of [CuBrL]₂[Cu₂Br₄] (L = 2, 6-bis[1-(2,6-diisopropylphenylimino)ethyl]pyridine as a function of scan rate: (a) $\nu = 0.1$, (b) $\nu = 0.2$, (c) $\nu = 0.5$, and (d) $\nu = 1.0$ V s⁻¹. Peaks A and A' are attributed to the Cu^{II}/I^IBrL moiety while peaks B and B' are assigned to the Cu^{II}/I^IL redox couple in which the Cu–Br bond is dissociated. Reproduced with permission from Ref. 120. Copyright 2001 Elsevier Publishing Company.

The presence of such a mechanism was probed by varying the sweep rate as illustrated in Fig. 4. Caution must be exercised in drawing conclusions from such a study because, with halide ions (and with some other unidentate species), bridging by the halide between the copper ion and the electrode surface may accelerate the rate of electron transfer and lead to erroneous conclusions. This type of mechanism has also been proposed by Palaniandavar and coworkers [121] for the Cu(II/I) complex with deprotonated salicylidene-glycine in the presence of cytosine or cytidine in which the latter species tends to be coordinated only to the oxidized complex.

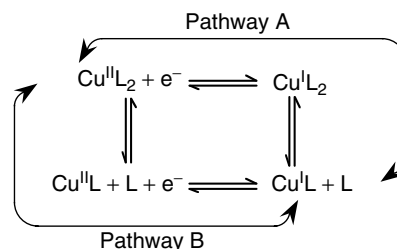
24.7.3.4 Interconversion of 1:2 and 1:1 Complexes

A similar mechanism may occur for systems involving Cu(II) coordinated to terdentate or bidentate ligands in which the oxidized complex exists primarily as a 1:2 complex while, upon reduction, the 1:1 complex predominates. Kandegedara et al. [48] reported that the system involving copper and the terdentate ligand [9]aneS₃ (LBE) appears to involve such a mechanism as illustrated in Scheme 4:

For the [9]aneS₃ system, Pathway B was not observed in homogeneous cross-reaction electron-transfer reactions [48] even when a huge excess of Cu(II) was added (up to 0.1 M) to force Cu^{II}L (the 1:1 complex) to become the dominant

oxidized form. However, the direct oxidation and reduction of the 1:1 complex can be observed electrochemically as shown by the CV trends in acetonitrile solution as a function of increasing ligand concentration (Fig. 5) [68]. In the presence of a 1:1 ratio of Cu(II) to ligand at low concentrations ($\approx 20 \mu\text{M}$), reversible peaks are observed representing the Cu^{II/I}L redox couple with a second reduction peak, representative of the 1:2 complex, Cu^{II}L₂, occurring at lower potential. As the ligand concentration is increased, the Cu^{II}L reduction peak disappears and the anodic peak representative of Cu^IL₂ begins to emerge. At sufficiently high ligand concentrations, only the reversible peaks for the Cu^{II/I}L₂ redox couple are observed. This latter ligand dependence emphasizes the necessity for utilizing a wide range of ligand concentrations to observe the changes in electrochemical behavior as a means of determining whether Scheme 4 applies (In the absence of such variations in concentrations, an earlier study mistakenly attributed the CV behavior for the Cu(II/I)-[9]aneS₄ system to Scheme 1, rather than Scheme 4.) [122].

The Scheme 4 mechanism is likely to apply to other Cu(II/I) systems involving terdentate ligands that are not sterically hindered. For example, it is suspected that the apparent irreversibility of the CV's observed by Neves and coworkers [123] for the Cu(II/I) system involving (2-hydroxybenzyl-2-pyridylmethyl) amine



Scheme 4

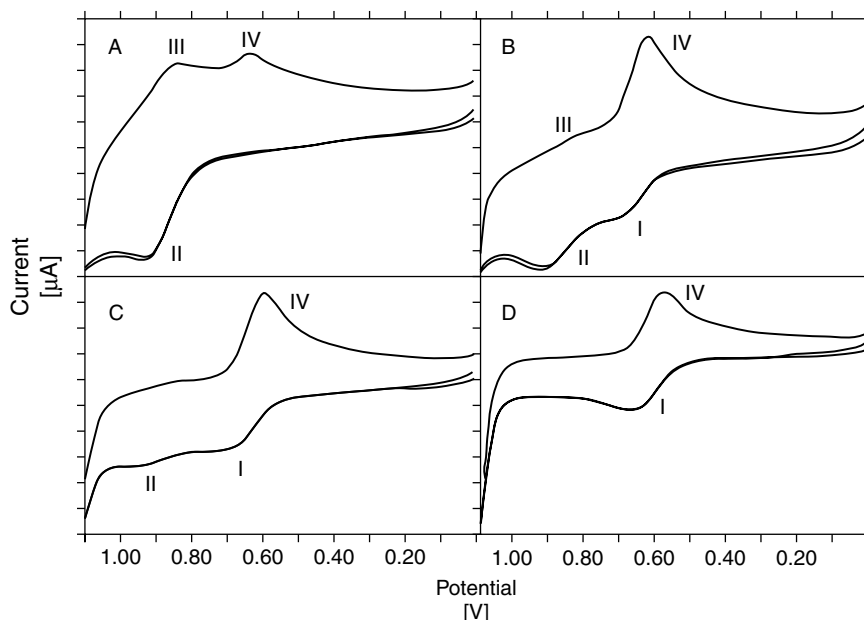
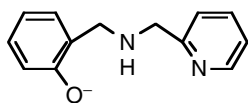


Fig. 5 Cyclic voltammograms for $\text{Cu}^{\text{I}}([\text{9}] \text{aneS}_3)_n$ in acetonitrile as a function of ligand concentration at 25°C , $\mu = 0.10 \text{ M}$ (NaClO_4). The concentration of the $\text{Cu}(\text{I})$ is $26 \mu\text{M}$ for all voltammograms. The total ligand concentration (C_L) varies as follows: (a, $C_L = 0.0228 \text{ mM}$; b, $C_L = 0.052 \text{ mM}$; c, $C_L = 0.52 \text{ mM}$; d, $C_L = 1.13 \text{ mM}$). Peaks II and III represent the 1 : 1 complex, $\text{Cu}^{\text{II/I}}([\text{9}] \text{aneS}_3)^{2+/+}$, while I and IV represent the 1 : 2 complex, $\text{Cu}^{\text{II/I}}([\text{9}] \text{aneS}_3)_2^{2+/+}$. Potentials shown are versus a Ag/AgCl reference electrode. The current scale differs slightly for each voltammogram but the peaks generally range from about -5 to $+5 \mu\text{A}$ (data from Ref. 68).

may be attributable to a mechanism of this same type.



Even more complicated behavior can be exhibited by bidentate ligand systems. For example, in acetonitrile, both $\text{Cu}(\text{I})$ and $\text{Cu}(\text{II})$ form 1 : 1 and 1 : 2 complexes with phenanthroline and bipyridine, while $\text{Cu}(\text{II})$ also forms a 1 : 3 complex. In the presence of relatively low ligand concentrations, the oxidized complex tends to be 1 : 2, while the reduced complex is 1 : 1 owing to the differing preference of the two

oxidation states for coordination to the acetonitrile solvent molecules. As the ligand concentration is increased, the oxidized species tends to convert to a 1 : 3 complex as the reduced complex becomes predominantly 1 : 2. Thus, at any specific ligand concentration, electron transfer may involve the loss of a coordinated bidentate ligand either before or following reduction. Since the dominant species for both oxidation states changes as a function of ligand concentration, the observed electrochemical behavior can be confusing and requires a comprehensive variation in ligand concentration if the contributions of the various species present are to be resolved [124, 125].

24.7.3.5 Dimeric/Monomeric Species

A number of Cu(II/I) systems have been reported where the oxidized complex tends to exist predominantly as a monomeric species while the reduced form is predominantly dimeric. This type of mechanism is illustrated in Scheme 5.

Such a dimeric/monomeric system has been proposed by Fabbri and coworkers [126] for a series of acyclic ligand systems containing four unsaturated nitrogen donor atoms. As illustrated in Fig. 6, two irreversible peaks were observed, the lone reduction peak being ascribed to monomeric $\text{Cu}^{\text{II}}\text{L}$ and the lone oxidation peak to dimeric $[\text{Cu}^{\text{I}}\text{L}]_2$, indicating that the vertical reactions are slow on the CV timescale. Takagi and coworkers [127] have proposed similar behavior for a ligand involving two covalently linked phenanthrolines where,

again, the reduced complex exists preferentially in the dimeric form. For a single scan of the $\text{Cu}^{\text{I}}_2\text{L}_2$ dimer in acetonitrile at 1.0 V s^{-1} , they observed peaks representative of only the dimeric redox couple. However, in repetitive scans, a second cathodic peak emerged at lower potential representative of the $\text{Cu}^{\text{II}}\text{L}$ monomer. Since dimers tend to be favored at higher concentrations, diagnostic studies as a function of total complex concentration are recommended for systems suspected of conforming to Scheme 5.

24.7.3.6 Other Phenomena Affecting Electrochemical Behavior

24.7.3.6.1 Ligand Oxidation or Reduction

When the CV potential range of Cu(II/I) complexes is extended to very high or

Scheme 5

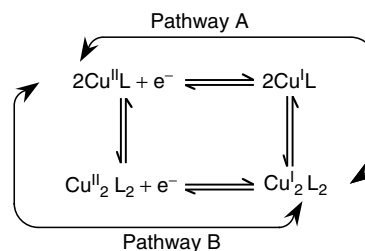
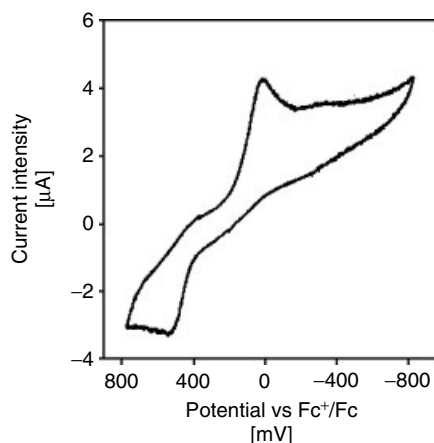


Fig. 6 Cyclic voltammogram for an acetonitrile solution initially containing a dimeric $\text{Cu}^{\text{I}}_2(\text{L})_2^{2+}$ complex involving a tetramine ligand that favors the monomeric $\text{Cu}^{\text{II}}\text{L}^{2+}$ upon oxidation. The second cycle, which features both pairs of oxidation and reductions waves, is depicted here. The peaks at lower potential represent the monomeric redox couple while those at the more positive potential are for the dimer. Reproduced with permission from Ref. 126. Copyright 2001 American Chemical Society.



low values, the complexed ligand itself may be oxidized or reduced. Owing to entropy considerations, such ligand redox reactions are not readily reversible and, thus, irreversible voltammograms are almost inevitably produced as indicated by the lack of a corresponding peak on the return scan. Studies of the electrochemical behavior of the free ligand are generally helpful in identifying such behavior.

24.7.3.6.2 Electroplating of Copper

A limiting factor in cyclic voltammograms of all copper systems is the fact that copper may be deposited on the cathode at higher potentials than for any other first-row transition element. Therefore, a large deposition peak will be observed if the cathodic sweep is extended to sufficiently low potentials. This phenomenon places severe limitations on the accessible potential range if excess uncomplexed copper is present. In the absence of excess copper, the potential at which electroplating occurs depends directly upon the concentration of excess ligand and the conditional stability constant of the copper complex. The onset of copper plating is most readily identified by the presence of a sharp anodic stripping peak during the return (anodic) scan. This

interference can be eliminated by limiting the scan range so that copper plating is avoided.

24.7.4

Biological Copper Systems

Since copper is second only to iron in its prevalence in redox-active metalloproteins, an understanding of the electron-transfer properties of copper proteins has been recognized as a matter of prime interest. However, protein systems tend to present many problems when attempting to make meaningful electrochemical measurements. The most thoroughly studied redox-active copper proteins are the cupredoxins (the simplest class of the so-called “blue” copper proteins) that contain a single copper site designated as type 1 copper. In these proteins, the copper has an elongated trigonal pyramidal coordination geometry in which the copper coordination sphere consists of a thiolate sulfur from cysteine and two histidine nitrogens forming the triangular base with an elongated bond to an apical methionine sulfur (Fig. 7) [128, 129]. In stellacyanin and related phytocyanins, the apical methionine is replaced by a glutamine [130, 131]. In some cupredoxins, such as azurin, a glycine oxygen occupies an axial site

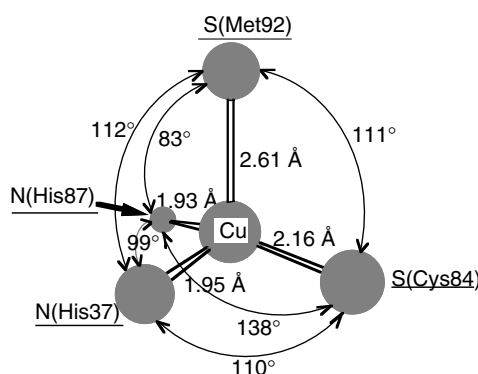


Fig. 7 Geometry of a typical type 1 copper site in plastocyanin. Bond lengths and bond angles are relatively constant upon reduction or oxidation of the copper site (J. M. Guss, P. R. Harrowell, M. Murata et al., *J. Mol. Biol.* **1986**, 192, 361–387).

opposite to the methionine sulfur to produce a trigonal bipyramidal coordination geometry [132, 133]. A primary focus of the electrochemical measurements has been the determination of the electron-transfer thermodynamics and kinetics and the correlation of these properties to the coordination geometry, particularly by generating mutant species [134, 135].

Unlike heme units, the coordination unit of the blue copper proteins does not exist outside the protein so that attempts to generate representative model compounds have been relatively unsuccessful. Electrochemical studies have been conducted directly on the native proteins, either by utilizing potentiostatic spectroelectrochemical methods [136] or by adsorbing the proteins on modified

gold, pyrolytic carbon or bare glassy carbon electrodes and conducting cyclic or square-wave voltammetric scans [137, 138]. In general, well-resolved cyclic voltammograms have been obtained with peak separations in the range of 55–100 mV. As illustrated by the values in Table 5, such measurements have yielded aqueous redox potentials that are predominantly in the region of 0.3 V (versus SHE), although the total range of potentials is 0.18–0.8 V [139–142].

The ability to obtain accurate redox potentials has played a key role in the investigation of copper proteins since it has provided investigators with data from which to generate an understanding of the factors giving rise to the unusually high potentials exhibited by some

Tab. 5 Potential values for copper(II/I) proteins (principally cupredoxins) in aqueous solution (all values are presumed to be for 25 °C, $\mu \approx 0.1$ M)

Protein type	Source	$E_{12}^{0'}$, V versus SHE	References
Amicyanin	<i>Paracoccus versutus</i>	0.255	143
Auracyanin A	<i>Chloroflexus aurantiacus</i>	0.205	138
Auracyanin B	<i>Chloroflexus aurantiacus</i>	0.215	138
Azurin	<i>Pseudomonas aeruginosa</i>	0.307	144, 145
Azurin	<i>Alcaligenes denitrificans</i>	0.276	146
Azurin	<i>Alcaligenes faecalis</i>	0.266	146
CBP	<i>Cucumis sativus</i>	0.317, 0.321	147, 148
Fungal laccase	<i>Polyporus versicolor</i>	0.780	149
Mavicyanin	Zucchini	0.215	150
Plantacyanin	Spinach	0.345	151
Plastocyanin	<i>Spinacea oleracea</i>	0.366	144
Plastocyanin	<i>Phaseolus vulgaris</i>	0.360	145
Plastocyanin	<i>Cucumis sativus</i>	0.374	144
Plastocyanin	<i>Populus nigra</i> , var. <i>italica</i>	0.375	152
Pseudoazurin	<i>Alcaligenes faecalis</i> S-6	0.275	143
Rusticyanin	<i>Thiobacillus ferrooxidans</i>	0.680	153–155
Rusticyanin	Mutant Met148Lys	0.363	135
Rusticyanin	Mutant Met148Gln	0.563	135
Rusticyanin	Mutant Met148Leu	0.798	135
SBP	<i>Spinacea oleracea</i>	0.345	151
Stellacyanin	<i>Rhus vernicifera</i>	0.1870.191	144, 145
Stellacyanin	<i>Cucumis sativus</i>	0.265	144
Urmecyanin	<i>Armoracia laphatifolia</i>	0.290	144

species. For example, a large number of mutant species of azurin have been examined to determine the effect of various alterations in the copper coordination sphere upon the resulting potential trends. The observed potentials span a range of about 0.3 V, although most were little changed from the wild-type protein [134]. Sola and coworkers [143, 156, 157] have evaluated the enthalpic and entropic contributions to the redox potentials of such mutants and concluded that entropic effects were notably influenced by the exposure of the copper site to the solvent.

As shown by the potential values in Table 5, stellacyanin exhibits one of the lowest potentials among known copper proteins. Since this protein has a glutamine amide in the axial position [130, 158] rather than the methionine thioether sulfur that commonly occupies this site in other cupredoxins, it was suspected that the Cu–S(Met) bond might be largely responsible for the high potential values of other cupredoxins. To investigate this possibility, Hasnain and coworkers prepared rusticyanin mutants in which the apical methionine was substituted by glutamine, lysine, and leucine. These mutants exhibited potentials that spanned the range from 0.37 to 0.80 V [135] (see Table 5), illustrating that the structure clearly had an effect upon the potential but that an apical sulfur was not a necessity. Olsson and Ryde [142] carried out density functional calculations and concluded that the axial ligands themselves have a small influence on the reduction potentials of the blue copper proteins. Instead, they suggested that the large variation in the reduction potentials seems to arise mainly from variations in the solvent accessibility to the copper site and in the orientation of protein dipoles around

the copper site. Subsequent theoretical calculations by Olsson and coworkers [155] led them to conclude that the reduction potential of plastocyanin is “tuned down” by the protein permanent dipole compared to the active site in regular water while in rusticyanin it is “tuned up”. They further concluded that this electrostatic environment is a property of the entire protein and solvent system and cannot be ascribed to any single interaction.

Armstrong and coworkers found that, even at scan rates up to 3000 V s^{-1} on cupredoxins adsorbed on pyrolytic graphite “edge” electrodes, the peak separation increases only slightly, indicating that electron transfer is relatively rapid [159]. These workers have also applied square-wave voltammetry to the blue copper protein azurin absorbed on both pyrolytic graphite electrodes and gold electrodes modified with self-assembled monolayers of alkanethiols [160]. The standard electron-transfer “exchange” rate constant at zero driving force was shown to depend on the nature of the electrode. However, at high driving potential, a constant rate constant of $(6 \pm 3) \times 10^3 \text{ s}^{-1}$ was reached, regardless of the electrode material, indicating that the rate of electron transfer had become “gated” by a rate-limiting conformational change in accordance with Scheme 1.

24.7.5

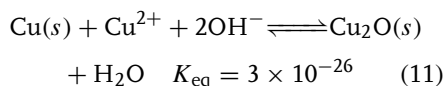
Other Copper(II/I) Systems

A large number of copper complexes involving unidentate ligands have been identified. The electrochemistry of such systems tend to be complicated by the fact that mixtures of the 1:1, 1:2, 1:3, and 1:4 complexes may be present,

each involving a different redox potential. In the case of anionic ligands with unit negative charge, the $\text{Cu}^{\text{I}}\text{L}$ complex species (i.e. the 1:1 complex) is often found to be insoluble. Unidentate ligands that can form more than one coordinate bond may act as bridging species, either to form dimers or to bridge to the electrode surface, thereby altering the observed electrochemical behavior. A number of multidentate ligands can form binuclear complexes incorporating two or more metal ions. A brief summary of the more common unidentate ligand systems and selected examples of binuclear complexes are included in the following sections.

24.7.5.1 Unidentate Ligand Complexes

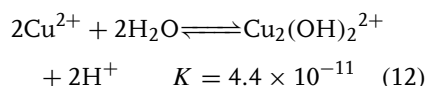
24.7.5.1.1 Hydroxide Complexes The hydrolysis of $\text{Cu}(\text{I})$ is too small to measure accurately in aqueous solution. However, the low solubility of Cu_2O limits the useful range of $\text{Cu}(\text{II})$ concentrations when in contact with elemental copper because of the following equilibrium [161]:



Since this phenomenon severely limits the concentration of Cu^{2+} that can remain in contact with the metal, the usefulness of the $\text{Cu}^{2+}/\text{Cu}(\text{s})$ electrode is severely restricted.

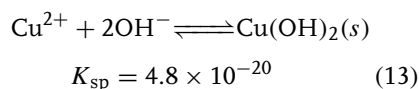
The stability of $\text{Cu}^{\text{II}}\text{OH}^+$ has been reported by several investigators, but the value is uncertain. The principal hydrolysis product is, in fact, the dimeric species, $\text{Cu}_2(\text{OH})_2^{2+}$ [161]. Higher-order species with the general formula $\text{Cu}_{n+1}(\text{OH})_{2n}^{2+}$ have been reported by many investigators, but Baes and Mesmer [161] note that these data may reflect the presence of a colloidal

or active precipitate of $\text{Cu}(\text{OH})_2$ in addition to $\text{Cu}_2(\text{OH})_2^{2+}$ at higher pH values. The formation constant for $\text{Cu}_2(\text{OH})_2^{2+}$ may be written in the following form [161]:



The introduction of hydroxide as a unique ligand into the inner-coordination sphere of solvated $\text{Cu}(\text{II})$ should diminish Jahn-Teller distortion and notably decrease the rate of inner-sphere substitution. This presumably accounts for the fact that no evidence has been found for a unique contribution of the $\text{Cu}_2(\text{OH})_2^{2+}$ ion in reactions involving solvated $\text{Cu}(\text{II})$ up to pH 5.8 [162]. (At higher pH, $\text{Cu}(\text{OH})_2$ precipitates.)

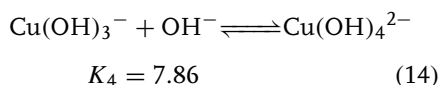
Among the divalent first-row transition metal ions, $\text{Cu}(\text{OH})_2$ (or CuO) is the least soluble hydroxide (or oxide) species [163]:



For concentrated solutions, $\text{Cu}(\text{OH})_2$ (or CuO) may begin to precipitate at pH values slightly above 4.0, thereby severely limiting the pH range in which solution electrochemical data involving $\text{Cu}(\text{II})$ can be obtained. For more dilute solutions of $\text{Cu}(\text{II})$ (e.g. $\leq 10^{-4}$ M), pH values approaching 6 may be attained before the onset of precipitate formation. A number of basic salts of $\text{Cu}(\text{II})$ are particularly insoluble, and this can further limit the range of conditions accessible for electrochemical studies involving solvated $\text{Cu}(\text{II})$. For example, nitrate ion should generally be excluded from electrochemical measurements on aqueous $\text{Cu}(\text{II})$ solutions to prevent precipitation of copper(II) trihydroxynitrate (also known as *basic copper*

nitrate), $\text{Cu}(\text{NO}_3)_2 \cdot 3\text{Cu}(\text{OH})_2$, which precipitates at pH values as low as 3 for Cu(II) solutions of intermediate concentration [164].

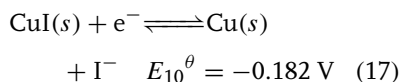
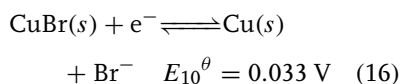
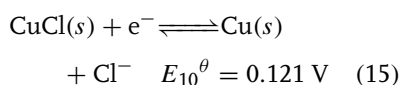
The high affinity of Cu(II) for hydroxide results in the formation of higher hydroxy species so that Cu(II) redissolves at very high pH (i.e. it is amphoteric). This permits electrochemical studies to be conducted on solvated Cu(II) in aqueous solution under high pH conditions that are not feasible for most other divalent transition metal ions [165]. McDowell and Johnston [166] measured the increasing solubility of CuO in KOH solutions and interpreted their data in terms of the formation of both $\text{Cu}(\text{OH})_3^-$ and $\text{Cu}(\text{OH})_4^{2-}$ for which they report the following equilibrium constant:



Baes and Mesmer [161] have suggested that McDowell and Johnston's data can be satisfactorily explained in terms of only the tetrahydroxy species if one allows for the probable effect of increasing ionic strength. However, this statement is presumably incorrect as McDowell and Johnston reported their equilibrium constant in terms of activities, and kinetic measurements on the complexation reactions of Cu(II) at $\text{pH} \geq 13$ indicate that two different hydroxy species exist [165].

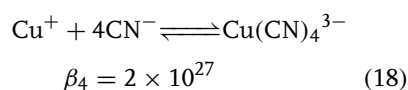
24.7.5.1.2 Halide Complexes Chloride, bromide, and iodide ions form complexes with both Cu(I) and Cu(II). Although the Cu(II) complexes are very weak (for chloride: $K_1 = 1.3$, $K_2 = 0.23$ at 25°C , $\mu = 1.0$) [167], the Cu(I) complexes are of appreciable stability (for chloride: $K_1 = 5 \times 10^2$, $K_2 = 2 \times 10^3$ at 25°C , $\mu = 5.0$) [168]. As with Ag(I), the 1:1 complexes

between Cu(I) and these halide ions are relatively insoluble (for chloride, bromide, and iodide: $K_{\text{sp}} = 4 \times 10^{-7}$, 5×10^{-9} , and $5 \times 10^{-13} \text{ M}^{-2}$, respectively) [168]. The electrochemical potentials reported for the insoluble halide salts of Cu(I) are as follows [13]:

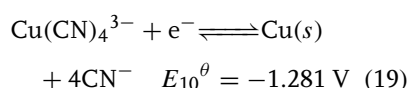


The insolubility of the Cu(I) halide salts, as well as the possibility of μ -halo-bridge formation between two copper atoms (as discussed later) or between the copper complex and the electrode surface, suggests that the presence of halides may alter the electrochemical properties observed for copper-containing solutions.

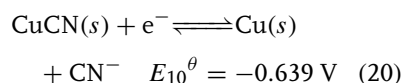
24.7.5.1.3 Cyanide and Thiocyanate Complexes Among other unidentate anionic ligands commonly encountered, cyanide forms stable complexes with both Cu(II) and Cu(I); however, the CuCN salt is so insoluble ($\text{p}K_{\text{sp}} = 19.5$) [169] that only the reduced complex has been characterized, that is, the addition of cyanide to an aqueous solution initially containing Cu(II) results in autoreduction to Cu(I). The overall equilibrium constant (β_4) for the reaction of Cu(I) with four cyanide ions was determined as early as 1904 by Kunschert [170] and subsequent measurements have yielded virtually identical values:



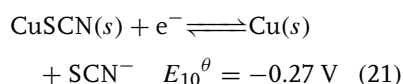
This value does not include activity corrections. The potential value reported in the literature for the electrodeposition of Cu from a solution containing high concentrations of cyanide [169, 171]



implies that $\beta_4 = 2.8 \times 10^{30}$ when expressed in terms of activities. The potential value for the reduction of solid CuCN has been determined [169]:

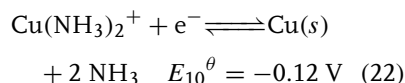


Although thiocyanate also forms an insoluble complex with Cu(I) ($\text{p}K_{\text{sp}}$ for CuSCN = 12.7) [172], the compound is more soluble than CuCN as reflected by the less negative standard potential for electrodeposition [173]:

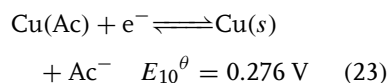


24.7.5.1.4 Ammonia Complexes Ammonia forms stronger complexes with Cu(II) than with any other divalent first-row transition metal ion. In practice, ammonia is often utilized as a masking agent to permit the study of Cu(II) at high pH by preventing the precipitation of Cu(II) hydroxide. The stepwise formation constants for Cu(II) with ammonia in aqueous solution are $K_1 = 1.3 \times 10^4$, $K_2 = 3 \times 10^3$, $K_3 = 7 \times 10^2$ and $K_4 = 1 \times 10^2$ [174]. Even stronger complexes have been reported for the addition of two NH_3 ligands to Cu(I): $K_1 = 8 \times 10^5$ and $K_2 = 8 \times 10^4$. A potential value for the reduction of the 1:2 Cu(I) complex with ammonia has been

reported as follows [175]:

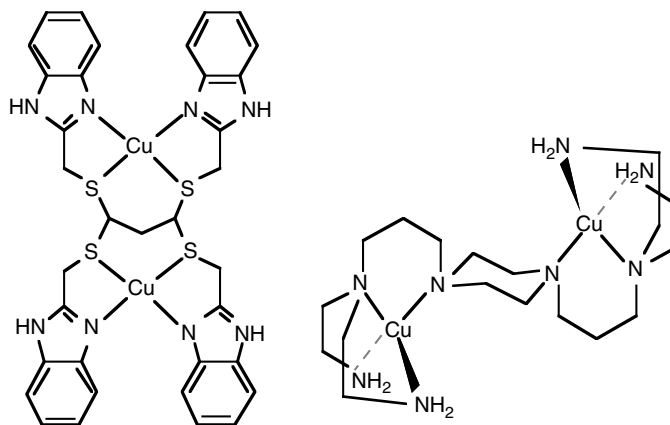


24.7.5.1.5 Complexes with Acetate and Other Common Brønsted Bases Many reactions of copper tend to be conducted in the range of pH 4.0–5.5 to avoid possible formation of hydroxycopper species. This is a range in which acetate is the most commonly used buffer. Unfortunately, acetate (Ac^-) is a very poor choice as it forms stronger complexes with Cu(II) than with any other divalent metal ion except Hg(II). The stepwise equilibrium constants for the formation of $\text{Cu}(\text{Ac})^+$, $\text{Cu}(\text{Ac})_2$, $\text{Cu}(\text{Ac})_3^-$, and $\text{Cu}(\text{Ac})_4^{2-}$ are 50, 10, 2.5, and 0.6, respectively [176]. This indicates that the apparent potential for Cu^{2+} reduction will be significantly decreased by the presence of acetate ion. Although no experimental data have been located for the reduction of Cu(II)–acetate complexes, a value has been reported for the reduction of the 1:1 Cu(I) complex with acetate [177]:



(By comparison to the aqueous E_{10}^θ value for solvated Cu^+ reduction in Table 1, this potential indicates that the K_{sp} value for Cu(Ac) is about 7.5×10^{-5} .) Thus, any electrochemical studies on copper that are conducted in the presence of acetate buffer will presumably be affected by the formation of acetate complexes.

24.7.5.1.6 Noncomplexing Buffer Systems Acetate is not the only buffer that causes difficulties when used in studies on copper systems. All Brønsted bases are also



Lewis bases and, therefore, potential complexing agents. Some investigators have attempted to avoid the problem by utilizing one of the series of buffers devised by Good and coworkers [178–180] (the so-called Good's buffers) on the basis of the assumption that these buffer compounds do not form metal complexes and are, therefore, suitable for pH control in Cu(II/I) studies. However, several studies have shown that Cu(II) is complexed by 17 of the 20 Good's buffers to a significant extent [181–186]. To prevent buffer interference when making electrochemical measurements on Cu(II)-containing solutions, noncomplexing buffers are recommended. A series of 10 sterically hindered tertiary amine compounds have recently been generated that cover the entire range of pH 3–11 and have been specifically demonstrated to provide interference-free buffering of Cu(II) solutions [181, 182].

24.7.5.2 Binuclear Complexes

A large number of binuclear complexes of copper have been reported in the literature. As first noted by Patterson and Holm [95], these systems may exhibit either two one-electron steps or a single two-electron

step. Ligands that tend to promote the formation of binuclear complexes consist of several types. The simplest systems are those in which the two copper atoms are coordinated to donor atoms that are well separated from each other, particularly within a large branched or macrocyclic ligand. Typical examples of such systems are illustrated above [187, 188].

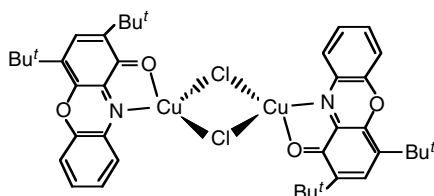
Cyclic voltammograms conducted in DMSO on the compound at left revealed two one-electron steps, both of which appear to be quasi-reversible with the differences in the potentials of the cathodic and anodic peaks for the two-electron-transfer processes being 210 and 310 mV when starting with the NO₃ salt of the oxidized complex. In the presence of chloride ion, spontaneous reduction occurred upon sitting. Subsequent analysis of the resulting product revealed that the thioether functions were partially oxidized to sulfoxide. For the compound at the right, a single two-electron-transfer step was observed in acetonitrile. Variation of the concentration ratio of copper to ligand resulted in the generation of a 3:1 complex in which the two piperazine nitrogens were coordinated to a third copper atom, the coordination sphere of all three coppers

presumably being completed by solvent molecules or anions. The latter complex showed a single three-electron transfer step.

Other binuclear complexes can be formed by ligands in which at least one of the donor atoms serves as a bridge between the two copper atoms. Two such examples are illustrated below [189, 190]:

In both cases, the two copper atoms occupy identical sites but the electronic communication between them is much more intimate. In the example at left, the two copper atoms appeared to reduce at the same potential and the cyclic voltammograms were essentially reversible.

Bridged binuclear compounds are also frequently formed by smaller ligands, particularly in the presence of chloride ions that can act as μ -bridging ligands. A typical example is illustrated below [191]:



In this compound, two separate electron-transfer peaks were observed in acetonitrile, each of which was highly irreversible. In all of the foregoing examples, each Cu(II) ion is presumably coordinated to a

fifth donor atom to complete a square pyramidal or trigonal bipyramidal coordination sphere.

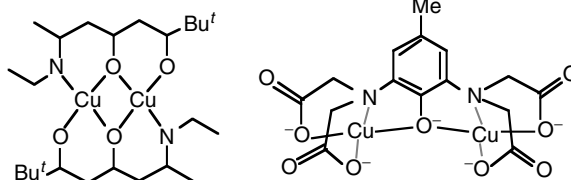
In a few instances, binuclear complexes have been reported in which the two copper atoms interact directly through a metal-metal bond. Two examples of such complexes are illustrated below [192, 193]. CV's run on the compound at left in both tetrahydrofuran and CH_2Cl_2 indicated the presence of two separate electron-transfer steps that were quasi-reversible.

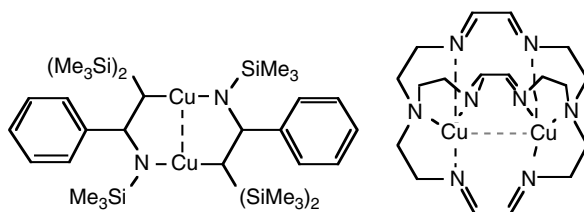
24.7.6

Copper(III/II) Systems

Copper(III)-aquo and -amine species have been generated by pulse radiolysis [194] but these are transient species that undergo rapid decay. Electrochemical generation of Cu(III) complexes of macrocyclic amines have been reported in acetonitrile [195] but they are also unstable and undergo spontaneous reduction to Cu(II). Nonetheless, it is presumed that copper(III) intermediates are generated as transients in a number of reactions, particularly those involving copper catalysis of multielectron transfer reactions.

Endicott and coworkers have measured the Cu(III/II) potentials of a few macrocyclic tetramine complexes in acetonitrile [196–198]. These values are very positive, suggesting that the Cu(III) complexes tend to undergo spontaneous reduction. Margerum and coworkers were the first to demonstrate that Cu(II) complexes with





Tab. 6 Potential values for copper(III/II) complexes in aqueous solution at 25 °C, $\mu = 0.10$ M (NaClO₄) (tetramines from Refs 196 and 197; peptides from Ref. 201)

Coordinated ligand ^a	$E_{12}^{\theta'}$	Coordinated ligand ^a	$E_{12}^{\theta'}$
<i>Tetramines in CH₃CN (V versus reference shown)</i>			
α -trans-[14]dieneN ₄	1.56 (SCE)	β -trans-[14]dieneN ₄	1.57 (SCE)
Me ₆ -[14]aneN ₄ (tet-a)	1.54, 1.62 (SCE)	Me ₂ -[14]aneN ₄	0.63 (Ag/AgCl)
<i>Tripeptides, pH 7.7 in H₂O (V versus SHE)</i>			
GGG	0.92	AGG	0.89
GAG	0.88	GGA	0.88
GGA	0.85	GAA	0.85
AAA	0.81	LGG	0.88
GGL	0.87	GLG	0.87
LGL	0.83	LLL	0.77
VGG	0.88	GGV	0.87
IGG	0.88	GGI	0.86
GGF	0.89	GG β A	0.94
<i>Dipeptide amides (hydroxide complexes) in H₂O (V versus SHE)</i>			
Gga	0.85	Gaa	0.82
Aaa	0.78		
<i>Histidine-containing peptides, pH 7.5 in H₂O (V versus SHE)</i>			
Gghis	0.98	GghisG	1.02
Asp-Ala-His-Lys	0.96		
<i>Tripeptide amides pH 9.5 in H₂O (V versus SHE)</i>			
G ₃ A	0.64	GGaA	0.60
VGGa	0.61		
<i>Higher-order peptides and peptide amides, pH 9.5 in H₂O (V versus SHE)</i>			
G ₄	0.63	AG ₃	0.61
G ₄ a	0.68	G ₅	0.66
G ₄ A	0.66	G ₆	0.67
A ₄	0.60	V ₄	0.51
<i>N-Formyl tripeptides, pH 10.0 in H₂O (V versus SHE)</i>			
NfG ₃	0.75	NfA ₃	0.66
<i>N-Formyl peptides and peptide amides, pH 11.5 in H₂O (V versus SHE)</i>			
NfG ₄	0.55	NfG ₅	0.63
NfG ₃ a	0.49	NfGGA ₃	0.45

^a G: glycyl; A: alanyl; β A: beta-alanyl; V: valyl; L: leucyl-; I: isoleucyl; F: phenylalanyl; his: histidyl; asp: aspartyl; lys: lysyl; Gga: glycylglycylamide; Nf: N-formyl.

Tab. 7 Individual contributions to the electrode potentials of Cu(III/II)–peptide couples (from Ref. 201)

Ligand property	ΔE^θ [V] ^a
1. Replacement of an equatorially bound carboxylate group by a deprotonated-peptide group	−0.28
2. Replacement of an amine group by a deprotonated <i>N</i> -formylamine group	−0.15
3. Replacement of an equatorially bound carboxylate group by a hydroxide group	−0.07
4. Leucyl, valyl, isoleucyl C substituents (per substituent)	−0.05
5. Alanyl or phenylalanyl C substituents (per substituent)	−0.04
6. A 5,5,6-membered ring system	+0.06
7. Replacement of an equatorially bound carboxylate group by an Imidazole group	+0.04
8. Axially coordinated carboxylate groups in the Cu(II) complex	+0.04

^a Relative to $[\text{Cu}^{\text{III/II}}(\text{H}_2\text{GGG})]^{0,-}$ for which $E^\theta = 0.92$ V.

deprotonated tri- and tetrapeptides can readily be oxidized to form stable Cu(III) complexes [199, 200]. These workers used CV to determine the redox potentials of 40 Cu(III/II)–peptide complexes and confirmed these values by potentiometric titrations against $\text{IrCl}_6^{4-/-3-}$ [201]. The CV's were nearly reversible with peak separations in the range of 72–89 mV. As shown in Table 6, the resultant Cu(III/II) potentials covered the range of 0.4 to 1.0 V with the di- and tripeptide complexes generally in the range of 0.77–0.99 V and the tetrapeptides at lower potentials of approximately 0.65 V (versus SHE). The potential of the Cu(III/II) complex with the quadruply deprotonated tetrapeptide C (*cyclo*-(β -alanylglycyl- β -alanylglycyl)) was subsequently shown to have an aqueous potential of only 0.48 V [202].

The coordination geometry of these Cu(III) complexes is presumed to be square planar, indicative of high field d^8 complexes. This has been demonstrated in the crystal structure of deprotonated tri- α -aminobutyric acid, $\text{Cu}^{\text{III}}(\text{H}_2\text{Aib}_3)$, in which the copper–donor atom bonds were found to be 0.12–0.17 Å shorter than for the corresponding Cu(II) complex

[203]. Since the geometries of all peptide complexes studied by Margerum and coworkers are presumed to be essentially the same, these workers were able to generate an empirical set of factors that affect the Cu(III/II) redox potentials for the peptide complexes, analogous to the empirical factors generated by Addison for Cu(II/I) redox potentials (Table 3). These empirical additivity effects for Cu(III/II)–peptide complexes are listed in Table 7 [201].

References

1. U. Bertocci, D. R. Turner, in *Encyclopedia of Electrochemistry of the Elements* (Ed.: A. J. Bard), Dekker, New York, 1973, pp. 383–497, Vol. II.
2. A. M. Alfantazi, D. Valic, *J. Appl. Electrochem.* **2003**, 33, 217–225.
3. G. K. K. Poon, D. J. Williams, *J. Electron. Manuf.* **1998**, 8, 15–37.
4. C. Leger, L. Servant, J. L. Bruneel et al., *Physica A* **1999**, 263, 305–314.
5. D. B. Rorabacher, *Chem. Rev.* **2004**, 104, 651–697.
6. H.-M. Koepp, H. Wendt, H. Strehlow, *Z. Elektrochem.* **1960**, 64, 483–491.
7. R. R. Gagne, C. A. Koval, G. C. Lisensky, *Inorg. Chem.* **1980**, 19, 2854–2855.
8. H. M. Koepp, H. Wendt, H. Strehlow, *Z. Elektrochem.* **1960**, 64, 483–491; Table 4.

9. G. Gritzner, J. Kuta, *Pure Appl. Chem.* **1984**, 56, 461–466.
10. (a) J. P. Chang, E. Y. Fung, J. C. Curtis *Inorg. Chem.* **1986**, 25, 4233–4241.
(b) D. Chang, T. Malinski, A. Ulman, K. M. Kadish *Inorg. Chem.* **1984**, 23, 817–824.
(c) N. G. Connelly, W. E. Geiger *Chem. Rev.* **1996**, 96, 877–910; Table 1.
11. V. V. Pavlishchuk, A. W. Addison, *Inorg. Chim. Acta* **2000**, 298, 97–102.
12. I. Noviadri, K. N. Brown, D. S. Fleming et al., *J. Phys. Chem. B* **1999**, 103, 6713–6722.
13. A. J. Bard, R. Parsons, J. Jordan, *Standard Potentials in Aqueous Solution*, Dekker, New York, 1985, pp. 287–293.
14. J. P. Demarquet, C. Trinh-Dinh, O. Bolck, *J. Electroanal. Chem.* **1970**, 27, 101–108.
15. L. Aronne, B. C. Dunn, J. R. Vyvyan et al., *Inorg. Chem.* **1995**, 34, 357–369 See p. 365, col. 2.
16. J. K. Senne, B. Kratochvil, *Anal. Chem.* **1971**, 43, 79–82.
17. (a) R. N. Pandey, A. K. Srivastava, M. G. Bapat *J. Electroanal. Chem.* **1988**, 245, 123–130. Cf., (b) R. A. Samant, V. S. Ijeri, A. K. Srivastava *J. Electroanal. Chem.* **2002**, 534, 115–121.
18. B. J. Hathaway, D. G. Holah, J. D. Postlethwaite, *J. Chem. Soc.* **1961**, 3215–3218.
19. (a) D. H. Powell, L. Helm, A. E. Merbach, *J. Chem. Phys.* **1991**, 95, 9258–9265.
(b) A. Pasquarello, I. Petri, P. S. Salmon et al., *Science* **2001**, 291, 856–859.
20. L. S. W. L. Sokol, T. D. Fink, D. B. Rorabacher, *Inorg. Chem.* **1980**, 19, 1263–1266.
21. A. E. Merbach, *Pure Appl. Chem.* **1987**, 59, 161–172.
22. D. B. Rorabacher, *Inorg. Chem.* **1966**, 5, 1891–1899.
23. B. J. Hathaway, *Coord. Chem. Rev.* **1981**, 35, 211–252.
24. V. M. Masters, M. J. Riley, M. A. Hitchman, *J. Synchrotron Rad.* **1999**, 6, 242–243.
25. The dynamic nature of the Jahn-Teller effect is inhibited if the inner-coordination sphere is inhomogeneous.
26. N. W. Alcock, M. Duggan, A. Murray et al., *J. Chem. Soc., Dalton Trans.* **1984**, 7–14.
27. O. P. Anderson, A. B. Packard, *Inorg. Chem.* **1979**, 18, 1940–1947.
28. M. J. Maroney, N. J. Rose, *Inorg. Chem.* **1984**, 23, 2252–2261.
29. G. Patrick, M. P. Ngwenya, S. M. Dobson et al., *J. Chem. Soc., Dalton Trans* **1991**, 1295–1299.
30. C. A. Salhi, Q. Yu, M. J. Heeg et al., *Inorg. Chem.* **1995**, 34, 6053–6064.
31. P. Wijetunge, C. P. Kulatilleke, L. T. Dressel et al., *Inorg. Chem.* **2000**, 39, 2897–2905.
32. B. J. Hathaway, *Struct. Bonding (Berlin)* **1984**, 57, 55–118.
33. F. A. Cotton, G. Wilkinson, *Advanced Inorganic Chemistry*, 2nd ed., Interscience, New York, 1962.
34. J. A. Goodwin, D. M. Stanbury, L. J. Wilson et al., *J. Am. Chem. Soc.* **1987**, 109, 2979–2991.
35. G. Chaka, M. J. Heeg, L. A. Ochrymowycz, D. B. Rorabacher, to be submitted for publication.
36. T. Maruyama, T. Yamamoto, *Inorg. Chim. Acta* **1995**, 238, 9–13.
37. J. K. Yandell, in *Copper Coordination Chemistry: Biochemical and Inorganic Perspectives*, (Eds.: K. D. Karlin, J. Zubieta), Adenine Press, Guilderland, NY, 1983, pp. 157–166.
38. (a) G. Sanna, M. I. Pilo, M. A. Zoroddu, R. Seeber *Inorg. Chim. Acta* **1993**, 208, 153–158. Cf., (b) M. I. Pilo, G. Manca, M. A. Zoroddu, R. Seeber *Inorg. Chim. Acta* **1991**, 180, 225–230.
39. N. Koshino, Y. Kuchiyama, H. Ozaki et al., *Inorg. Chem.* **1999**, 38, 3352–3360.
40. Y. Kuchiyama, N. Kobayashi, H. D. Takagi, *Inorg. Chim. Acta* **1998**, 277, 31–36.
41. A. G. Lappin, M. P. Youngblood, D. W. Margerum, *Inorg. Chem.* **1980**, 19, 407–413.
42. B. Xie, T. Elder, L. J. Wilson et al., *Inorg. Chem.* **1999**, 38, 12–19.
43. Y. Nishida, M. Takeuchi, N. Oishi et al., *Inorg. Chim. Acta* **1985**, 96, 81–85.
44. P. Comba, H. Jakob, *Helv. Chim. Acta* **1997**, 80, 1983–1991.
45. R. L. Webb, M. L. Mino, E. L. Blinn et al., *Inorg. Chem.* **1993**, 32, 1396–1402.
46. (a) L. Fabbri, A. Poggi, P. Zanello *J. Chem. Soc., Dalton Trans.* **1983**, 2191–2195. Cf., (b) P. Zanello, R. Seeber, A. Cinquantini, G. Mazzocchin, L. Fabbri, *J. Chem. Soc., Dalton Trans.* **1982**, 893–897 [for original data for CuII/[14]aneN₄] and -(u-[14]aneN₄).
47. P. Comba, N. F. Curtis, G. A. Lawrance et al., *J. Chem. Soc., Dalton Trans.* **1988**, 2145–2152.

48. A. Kandegedara, K. Krylova, T. J. Nelson et al., *J. Chem. Soc., Dalton Trans.* **2002**, 792–801.
49. M. M. Bernardo, R. R. Schroeder, D. B. Rorabacher, *Inorg. Chem.* **1991**, 30, 1241–1247.
50. K. Krylova, C. P. Kulatilleke, M. J. Heeg, C. A. Salhi, L. A. Ochrymowycz, D. B. Rorabacher, *Inorg. Chem.* **1999**, 38, 4322–4328.
51. M. M. Bernardo, M. J. Heeg, R. R. Schroeder et al., *Inorg. Chem.* **1992**, 31, 191–198.
52. N. E. Meagher, K. L. Juntunen, M. J. Heeg et al., *Inorg. Chem.* **1994**, 33, 670–679.
53. S. Galijasevic, K. Krylova, M. J. Koenigbauer et al., *Dalton Trans* **2003**, 1577–1586.
54. L. Aronne, B. C. Dunn, J. R. Vyvyan et al., *Inorg. Chem.* **1995**, 34, 357–369.
55. P. Wijetunge, Ph.D. Dissertation, “The Effect of Sterically Restricting Cyclopentane Bridges on the Electron-Transfer Behavior of Copper(II/I) Macrocyclic Tetrathiaether Complexes,” Wayne State University, 2002.
56. G. Chaka, L. A. Ochrymowycz, D. B. Rorabacher, *Inorg. Chem.* **2005**, 44, 9105–9111.
57. E. R. Dockal, T. E. Jones, W. F. Sokol et al., *J. Am. Chem. Soc.* **1976**, 98, 4322–4324.
58. K. P. Balakrishnan, T. A. Kaden, L. Siegfried et al., *Helv. Chim. Acta* **1984**, 67, 1060–1069.
59. E. Hörmann, P. C. Riesen, M. Neuberger et al., *Helv. Chim. Acta* **1996**, 79, 235–243.
60. P. Comba, G. A. Lawrance, M. Rossignoli et al., *Aust. J. Chem.* **1988**, 41, 773–781.
61. M. J. Prushan, A. W. Addison, R. J. Butcher, *Inorg. Chim. Acta* **2000**, 300–302, 992–1003.
62. M. Vetrichelvan, Y.-H. Lai, K. F. Mok, *Dalton Trans* **2003**, 295–303.
63. K. K. Nanda, A. W. Addison, R. J. Butcher et al., *Inorg. Chem.* **1997**, 36, 134–135.
64. N. E. Tokel, V. Katovic, K. Farmery et al., *J. Am. Chem. Soc.* **1970**, 92, 400–402.
65. J. Labuda, V. Plaskon, V. V. Pavlishchuk, *Inorg. Chim. Acta* **1988**, 146, 13–18.
66. N. Atkinson, A. J. Blake, M. G. B. Drew et al., *J. Chem. Soc., Dalton Trans.* **1992**, 2993–3001.
67. P. D. Beer, J. E. Nation, S. L. W. McWhinnie et al., *J. Chem. Soc., Dalton Trans.* **1991**, 2485–2492.
68. A. Kandegedara, Ph.D. Dissertation, “Electron-Transfer Kinetics of Copper Complexes with Macrocyclic Terdentate Ligands,” Wayne State University, 2001.
69. C. Bazzicalupi, A. Bencini, A. Bianchi et al., *J. Chem. Soc., Dalton Trans.* **1995**, 2377–2384.
70. B. C. Dunn, P. Wijetunge, J. R. Vyvyan et al., *Inorg. Chem.* **1997**, 36, 4484–4489.
71. E. V. Rybak-Akimova, A. Y. Nazarenko, L. Chen et al., *Inorg. Chim. Acta* **2001**, 324, 1–15.
72. D. E. Nikles, M. J. Powers, F. L. Urbach, *Inorg. Chem.* **1983**, 22, 3210–3217.
73. M. Murali, M. Palaniandavar, T. Pandiyan, *Inorg. Chim. Acta* **1994**, 224, 19–25.
74. M. R. Malachowski, M. Adams, N. Elia et al., *J. Chem. Soc., Dalton Trans.* **1999**, 2177–2182.
75. J. McMaster, R. L. Beddoes, D. Collison et al., *Chem. – Eur. J.* **1996**, 2, 685–693.
76. T. A. Kaden, S. Kaderli, W. Sager et al., *Helv. Chim. Acta* **1986**, 69, 1216–1223.
77. J. G. Gilbert, A. W. Addison, A. Y. Nazarenko et al., *Inorg. Chim. Acta* **2001**, 324, 123–130.
78. K. D. Karlin, J. K. Yandell, *Inorg. Chem.* **1984**, 23, 1184–1188.
79. R. P. F. Kanthers, R. Yu, A. W. Addison, *Inorg. Chim. Acta* **1992**, 196, 97–103.
80. B. Adhikary, C. R. Lucas, *Inorg. Chem.* **1994**, 33, 1376–1381.
81. S. Liu, C. R. Lucas, R. C. Hynes et al., *Can. J. Chem.* **1992**, 70, 1773–1783.
82. E. A. Ambundo, M.-V. Deydier, A. J. Grall et al., *Inorg. Chem.* **1999**, 38, 4233–4242.
83. K. D. Karlin, P. L. Dahlstrom, J. R. Hyde et al., *J. Chem. Soc., Chem. Commun* **1980**, 906–908.
84. K. D. Karlin, S. E. Sherman, *Inorg. Chim. Acta* **1982**, 65, L39–L40.
85. H. K. Baek, R. A. Holwerda, *Inorg. Chem.* **1983**, 22, 3452–3456.
86. M. R. Malachowski, H. B. Huynh, L. J. Tomlinson et al., *J. Chem. Soc., Dalton Trans.* **1995**, 31–36.
87. H. K. Baek, K. D. Karlin, R. A. Holwerda, *Inorg. Chem.* **1986**, 25, 2347–2379.
88. N. Wei, N. N. Murthy, K. D. Karlin, *Inorg. Chem.* **1994**, 33, 6093–6100.
89. S. Zahn, J. W. Canary, *Angew. Chem., Int. Ed. Engl.* **1998**, 37, 305–307.
90. N. Wei, N. N. Murthy, Z. Tyeklar et al., *Inorg. Chem.* **1994**, 33, 1177–1183.
91. S. Chen, J. F. Richardson, R. M. Buchanan, *Inorg. Chem.* **1994**, 33, 2376–2382.
92. A. W. Addison, H. J. Hendriks, J. Reedijk et al., *Inorg. Chem.* **1981**, 20, 103–110.

93. T. N. Sorrell, D. L. Jameson, *Inorg. Chem.* **1982**, 21, 1014–1019.
94. A. J. Bard, L. R. Faulkner, *Electrochemical Methods*, 2nd ed. Wiley: New York, 2001, p. 242, Table 6.5.1; p. 243, Table 6.5.2.
95. G. S. Patterson, R. H. Holm, *Bioinorg. Chem.* **1975**, 4, 257–275.
96. P. J. Burke, K. Henrick, D. R. McMillin, *Inorg. Chem.* **1982**, 21, 1881–1886.
97. F. P. Dwyer, N. S. Gill, E. C. Gyarmas et al., *J. Am. Chem. Soc.* **1957**, 79, 1269–1273; see footnote 2.
98. A. W. Addison, *Inorg. Chim. Acta* **1989**, 162, 217–220.
99. B. C. Westerby, K. L. Juntunen, G. H. Leggett et al., *Inorg. Chem.* **1991**, 30, 2109–2120.
100. L. S. W. L. Sokol, L. A. Ochrymowycz, D. B. Rorabacher, *Inorg. Chem.* **1981**, 20, 3189–3195.
101. K. Krylova, K. D. Jackson, J. A. Vroman et al., *Inorg. Chem.* **1997**, 36, 6216–6233.
102. M. Kodama, E. Kimura, *J. Chem. Soc., Dalton Trans.* **1977**, 1473–1478.
103. B. C. Dunn, P. Wijetunge, J. R. Vyvyan et al., *Inorg. Chem.* **1997**, 36, 4484–4489.
104. G. A. Carlson, J. P. McReynolds, F. H. Verhoek, *J. Am. Chem. Soc.* **1945**, 67, 1334–1339.
105. G. Anderegg, *Helv. Chim. Acta* **1959**, 42, 344–349.
106. M. A. Augustin, J. K. Yandell, *Inorg. Chim. Acta* **1979**, 37, 11–18.
107. C. V. Banks, R. C. Bystroff, *J. Am. Chem. Soc.* **1959**, 81, 6153–6158.
108. M. A. Augustin, J. K. Yandell, *Inorg. Chem.* **1979**, 18, 577–583.
109. B. R. James, R. J. P. Williams, *J. Chem. Soc.* **1961**, 2007–2019.
110. G. Schwarzenbach, *Helv. Chim. Acta* **1950**, 33, 974–985.
111. M. Chaudhry, I. Persson, *J. Chem. Soc., Faraday Trans.* **1994**, 90, 2243–2248.
112. M. J. Martin, J. F. Endicott, L. A. Ochrymowycz et al., *Inorg. Chem.* **1987**, 26, 3012–3022.
113. E. Laviron, L. Roullier, *J. Electroanal. Chem. Interfacial Electrochem.* **1985**, 186, 1–15.
114. M. M. Bernardo, P. V. Robandt, R. R. Schroeder et al., *J. Am. Chem. Soc.* **1989**, 111, 1224–1231.
115. P. V. Robandt, R. R. Schroeder, D. B. Rorabacher, *Inorg. Chem.* **1993**, 32, 3957–3963.
116. N. M. Villeneuve, R. R. Schroeder, L. A. Ochrymowycz et al., *Inorg. Chem.* **1997**, 36, 4475–4483.
117. D. B. Rorabacher, M. J. Martin, M. J. Koenigbauer, et al., in *Copper Coordination Chemistry: Biochemical and Inorganic Perspectives*, (Eds.: K. D. Karlin, J. Zubieta), Adenine Press: Guilderland, NY, 1983; pp. 167–202, see p 184, eq 24.
118. M. J. Sisley, R. B. Jordan, *Inorg. Chem.* **1992**, 31, 2880–2884.
119. J. Irangu, M. J. Ferguson, R. B. Jordan, *Inorg. Chem.* **2005**, 44, 1619–1625.
120. B. Le Gall, F. Conan, N. Cosquer et al., *Inorg. Chim. Acta* **2001**, 324, 300–308.
121. I. Samasundaram, M. K. Kommiya, M. Palaniandavar, *J. Chem. Soc., Dalton Trans.* **1991**, 2083–2089.
122. Sanaullah, H. Hungerbühler, C. Schöneich et al., *J. Am. Chem. Soc.* **1997**, 119, 2134–2145.
123. A. Neves, C. N. Verani, M. A. de Brito et al., *Inorg. Chim. Acta* **1999**, 290, 207–212.
124. M. P. McGillivray, Ph.D. Dissertation, “Electron-Transfer Kinetics of Copper(II/I) Complexes with 1,10-Phenanthroline and 2,2'-Bipyridine and Their Derivatives in Acetonitrile,” Wayne State University, 2005
125. M. P. McGillivray, D. B. Rorabacher, to be published.
126. V. Amendola, L. Fabbrizzi, L. Gianelli et al., *Inorg. Chem.* **2001**, 40, 3579–3587.
127. S. Itoh, S. Funahashi, H. D. Takagi, *Chem. Phys. Lett.* **2001**, 344, 441–449.
128. J. M. Guss, H. C. Freeman, *J. Mol. Biol.* **1983**, 169, 521–563.
129. E. T. Adman, *Adv. Protein Chem.* **1991**, 42, 145–197.
130. P. J. Hart, A. M. Nersissian, R. G. Herrmann et al., *Protein Sci.* **1996**, 5, 2175–2183.
131. C. Dennison, M. D. Harrison, A. T. Lawler, *Biochem. J.* **2003**, 371, 377–383.
132. G. E. Norris, B. F. Anderson, E. N. Baker, *J. Am. Chem. Soc.* **1986**, 108, 2784–2785.
133. E. N. Baker, *J. Mol. Biol.* **1988**, 203, 1071–1095.
134. T. Pascher, B. G. Karlsson, M. Nordling et al., *Eur. J. Biochem.* **1993**, 212, 289–296.
135. J. F. Hall, L. D. Kanbi, R. W. Strange et al., *Biochemistry* **1999**, 38, 12675–12680.
136. C. S. St. Clair, W. R. Ellis, H. B. Gray, *Inorg. Chim. Acta* **1992**, 191, 149–155.

137. T. Sakurai, F. Nose, T. Fujiki et al., *Bull. Chem. Soc. Jpn.* **1996**, 69, 2855–2862.
138. M. B. Rooney, M. J. Honeychurch, F. M. Selvaraj et al., *J. Biol. Inorg. Chem.* **2003**, 8, 306–317.
139. F. A. Armstrong, N. L. Barlow, P. L. Burn et al., *Chem. Commun.* **2004**, 316–317.
140. L. J. C. Jeuken, F. A. Armstrong, *J. Phys. Chem. B* **2001**, 105, 5271–5282.
141. T. Kohzuma, C. Dennison, W. McFarlane et al., *J. Biol. Chem.* **1995**, 270, 25733–25738, and references therein.
142. M. H. M. Olsson, U. Ryde, *J. Biol. Inorg. Chem.* **1999**, 4, 654–663. and references therein.
143. G. Battistuzzi, M. Bellei, M. Borsari et al., *Biochemistry* **2003**, 42, 9214–9220.
144. G. Battistuzzi, M. Borsari, L. Loschi et al., *J. Am. Chem. Soc.* **1999**, 121, 501–506.
145. V. T. Taniguchi, N. Sailasuta-Scott, F. C. Anson et al., *Pure Appl. Chem.* **1980**, 52, 2275–2281.
146. E. W. Ainscough, A. G. Bingham, A. M. Brodie et al., *Biochemistry* **1987**, 26, 71–82.
147. J. M. Guss, E. A. Merritt, R. P. Phizackerley et al., *Science* **1988**, 241, 806–811.
148. G. Battistuzzi, M. Borsari, L. Loschi et al., *J. Biol. Inorg. Chem.* **1997**, 2, 350–359.
149. V. T. Taniguchi, B. G. Malmström, F. C. Anson et al., *Proc. Natl. Acad. Sci. U.S.A.* **1982**, 79, 3387–3389.
150. G. Battistuzzi, M. Borsari, L. Loschi et al., *J. Inorg. Biochem.* **2001**, 83, 223–227.
151. G. Battistuzzi, M. Borsari, L. Loschi et al., *J. Inorg. Biochem.* **1998**, 69, 97–100.
152. J. M. Guss, P. R. Harrowell, M. Murata et al., *J. Mol. Biol.* **1986**, 192, 361–387.
153. R. L. Walter, S. E. Falick, A. M. Friedman et al., *J. Mol. Biol.* **1996**, 263, 730–751.
154. L. Harvey, Q. Hao, E. M. H. Duke et al., *Acta Crystallogr.* **1998**, D54 629–635.
155. M. H. M. Olsson, G. Y. Hong, A. Warshel, *J. Am. Chem. Soc.* **2003**, 125, 5025–5039.
156. G. Battistuzzi, M. Borsari, G. W. Canters et al., *Biochemistry* **2001**, 40, 6707–6712.
157. G. Battistuzzi, M. Borsari, L. Loschi et al., *Biochemistry* **2001**, 40, 6422–6430.
158. S. DeBeer, D. W. Randall, A. M. Nersissian et al., *J. Phys. Chem. B* **2000**, 104, 10814–10819.
159. J. Hirst, F. A. Armstrong, *Anal. Chem.* **1998**, 70, 5062–5071.
160. L. J. C. Jeuken, J. P. McEvoy, F. A. Armstrong, *J. Phys. Chem. B* **2002**, 106, 2304–2313.
161. C. F. Baes, R. E. Mesmer, Jr. *The Hydrolysis of Cations*, Wiley-Interscience, New York, 1976 Chapter 12.
162. V. B. Pett, G. H. Leggett, T. H. Cooper et al., *Inorg. Chem.* **1988**, 27, 2164–2169.
163. D. C. Harris, *Quantitative Chemical Analysis*, 4th ed., Freeman, New York, 1995 Appendix F.
164. *CRC Handbook of Chemistry and Physics*. 64th ed., (Eds.: R. C. Weast), CRC Press, Boca Raton, FL, 1983–1984, p. B90.
165. C.-T. Lin, D. B. Rorabacher, G. R. Cayley et al., *Inorg. Chem.* **1975**, 14, 919–925.
166. L. A. McDowell, H. L. Johnston, *J. Am. Chem. Soc.* **1936**, 58, 2009–2014.
167. H. McConnell, N. Davidson, *J. Am. Chem. Soc.* **1950**, 72, 3164–3167.
168. R. M. Smith, A. E. Martell, *Critical Stability Constants, Inorganic Complexes*, Plenum, New York, 1976, Vol. 4.
169. (a) M. G. Vladimirova, I. A. Kakovskii *Zh. Priklad. Khim.* **1950**, 23, 580; as cited in (b) L. G. Sillen, A. E. Martell, *Stability Constants of Metal-Ion Complexes*; Special Publication No. 17; The Chemical Society, London, 1964
170. F. Kunschert, *Z. Anorg. Chem.* **1904**, 41, 359–376.
171. R. A. Penneman, L. H. Jones, *J. Chem. Phys.* **1956**, 24, 293–296.
172. (a) A. M. Golub, *Zh. Neorg. Khim.* **1956**, 1, 2517; as cited in (b) L. G. Sillen, A. E. Martell, *Stability Constants of Metal-Ion Complexes*; Special Publication No. 17; The Chemical Society, London, 1964
173. G. Milazzo, S. Caroli, *Tables of Standard Electrode Potentials*, Wiley, New York, 1978
174. J. Bjerrum, *Metal Ammine Formation in Aqueous Solution*, P. Haase and Son, Copenhagen, 1957
175. R. Näsänen, *Suomen Kem.* **1944**, 17B, 31–33.
176. (a) S. Fronaeus, Ph.D. Dissertation, Lund University, 1948; as cited in (b) A. Ringbom, *Complexation in Analytical Chemistry*; Interscience, New York, 1963, p 320.
177. M. Lloyd, V. Wycherley, C. B. Monk, *J. Chem. Soc.* **1951**, 1786–1789.
178. N. E. Good, G. D. Winget, W. Winter et al., *Biochemistry* **1966**, 5, 467–477.

179. N. E. Good, S. Izawa, *Methods Enzymol.* **1972**, *24*, 53–68.
180. W. J. Ferguson, K. I. Braunschweiger, W. R. Braunschweiger et al., *Anal. Biochem.* **1980**, *104*, 300–310.
181. Q. Yu, A. Kandegedara, Y. Xu et al., *Anal. Biochem.* **1997**, *253*, 50–56.
182. A. Kandegedara, D. B. Rorabacher, *Anal. Chem.* **1999**, *71*, 3140–3144.
183. J. D. Gregory, S. W. Sajdera, *Science* **1970**, *169*, 97–98.
184. P. L. Lleu, G. Rebel, *Anal. Biochem.* **1991**, *192*, 215–218.
185. V. Kaushal, L. D. Barnes, *Anal. Biochem.* **1986**, *157*, 291–294.
186. L. Sigg, R. Hari, H. Xue, *Anal. Chem.* **2003**, *75*, 615–677.
187. A. Benzekri, C. Cartier, J.-M. Latour et al., *Inorg. Chim. Acta* **1996**, *252*, 413–420.
188. E. Monzani, L. Casella, G. Zoppellaro et al., *Inorg. Chim. Acta* **1998**, *282*, 180–192.
189. R. L. Lintvedt, K. A. Rupp, M. J. Heeg, *Inorg. Chem.* **1988**, *27*, 331–339.
190. L. Cai, W. Xie, H. Mahmoud et al., *Inorg. Chim. Acta* **1997**, *263*, 231–245.
191. G. Speier, J. Csihony, A. M. Whalen et al., *Inorg. Chim. Acta* **1996**, *245*, 1–5.
192. R. B. Hitchcock, M. F. Lappert, M. Layh et al., *J. Chem. Soc., Dalton Trans.* **1999**, 1455–1459.
193. J. A. Farrar, V. McKee, A. H. R. Al-Obaidi et al., *Inorg. Chem.* **1995**, *34*, 1302–1303.
194. D. Meyerstein, *Inorg. Chem.* **1971**, *10*, 2244–2249.
195. D. C. Olson, J. Vasilevskis, *Inorg. Chem.* **1971**, *10*, 463–470.
196. D. P. Rillema, J. F. Endicott, E. Papaconstantinou, *Inorg. Chem.* **1971**, *10*, 1739–1746.
197. M. Y. Udugala-Ganehenege, M. J. Heeg, L. M. Hryhorczuk et al., *Inorg. Chem.* **2001**, *40*, 1614–1625.
198. J. F. Endicott, B. Durham, in *Coordination Chemistry of Macrocyclic Compounds*, (Eds.: G. A. Melson), Plenum, New York, 1979, pp. 393–460. Chapter. 6.
199. G. L. Burce, E. B. Paniago, D. W. Margerum, *J. Chem. Soc., Chem. Commun.* **1975**, 261–262.
200. D. W. Margerum, K. L. Chellappa, F. P. Bossu et al., *J. Am. Chem. Soc.* **1975**, *97*, 6894–6896.
201. F. P. Bossu, K. L. Chellappa, D. W. Margerum, *J. Am. Chem. Soc.* **1977**, *99*, 2195–2203.
202. J. S. Rybka, D. W. Margerum, *Inorg. Chem.* **1981**, *20*, 1453–1458.
203. L. L. Diaddario, W. R. Robinson, D. W. Margerum, *Inorg. Chem.* **1983**, *22*, 1021–1025.

25 The Actinides

Michael E. Stoll
Los Alamos National Laboratory, Los Alamos, New Mexico, USA

25.1	Introduction	1049
25.2	Actinium	1049
25.2.1	Aqueous Solutions	1049
25.2.2	Electrodeposition	1050
25.3	Thorium	1050
25.3.1	Aqueous Solutions	1050
25.3.2	Nonaqueous Solutions	1051
25.3.3	Molten-salt Solutions	1051
25.3.4	Electrodeposition	1052
25.3.5	Organometallic and Coordination Compounds	1053
25.4	Protactinium	1054
25.4.1	Aqueous Solutions	1054
25.4.2	Electrodeposition	1054
25.4.3	Nonaqueous Solutions	1055
25.5	Uranium	1055
25.5.1	Aqueous Solutions	1056
25.5.2	Electrodeposition	1061
25.5.3	Molten-salt Solutions	1062
25.5.4	Nonaqueous Solutions	1063
25.6	Neptunium	1066
25.6.1	Aqueous Solutions	1066
25.6.2	Electrodeposition	1068
25.6.3	Nonaqueous Solutions	1068
25.6.4	Molten-salt Solutions	1069

25.7	Plutonium	1069
25.7.1	Aqueous Solutions	1070
25.7.2	Electrodeposition	1071
25.7.3	Molten-salt Solutions	1072
25.8	Americium	1073
25.8.1	Aqueous Solutions	1073
25.8.2	Molten-salt Solutions	1074
25.8.3	Nonaqueous Solutions	1075
25.8.4	Electrodeposition	1075
25.9	Curium	1075
25.9.1	Electrodeposition	1076
25.10	Berkelium	1076
25.11	Californium	1077
25.12	Einsteinium	1078
25.13	Fermium	1078
25.14	Mendelevium	1078
25.15	Nobelium	1079
	References	1079

25.1

Introduction

A concise review of the electrochemical behavior for the actinide elements is presented in this chapter. The material covered mainly focuses on the pertinent aspects of actinide electrochemistry covered in the latest literature reviews. For the elements for which the literature is sparse because of difficulties in handling and/or acquiring sufficient quantities of the elements owing to their radioactivity, a more general overview of their electrochemical behavior is covered. Covering the entire actinide series in a single chapter dictates a rather descriptive text, which is not possible because of space limitations. Sufficient leading references have been provided in each section to direct the interested reader to the original works. The electrochemistry of lawrencium has been omitted because of the lack of any published data.

25.2

Actinium

25.2.1

Aqueous Solutions

There is a relatively small volume of published electrochemical data on

actinium, mainly limited to aqueous electrodeposition studies. This stems in part from the intense gamma activity of the decay products from naturally occurring ^{227}Ac , making experimental work somewhat difficult. There were conclusions reached in some of the earlier literature proclaiming the existence of Ac(II) in aqueous solution on the basis of radiopolarography studies [1], a technique first described by Love [2], and a study employing 18-crown-6 to facilitate the Ac(III)/Ac(II) electron-transfer process [3]. However, the more recent literature concerning this topic contradicts the earlier reports and now suggests an irreversible Ac(III)/Ac(0) electrodeposition process at -1.96 V versus standard hydrogen electrode (SHE) in aqueous 0.1 M LiClO_4 at $\text{pH } 2.5\text{--}3.2$ [4]. Although not an electrochemical study, the chemical reduction of Ac(III) with bivalent Sm in aqueous–ethanolic solution through a cocrystallization process was observed by Mikheev et al. [5], who found no evidence for its reduction to Ac(II) . This method had been employed successfully for the production of bivalent Es and Fm in a previous study [6]. In addition, theoretical calculations predict the reduction potential for the Ac(III)/Ac(II) couple (-3.3 V) to be more negative than the Ac(III)/Ac(0) couple (-2.12 V), which is already beyond the breakdown potential of the aqueous

solvent medium [7]. It is clear from the more recent results that the existence of Ac(II) as a stable species in aqueous media is very unlikely.

25.2.2

Electrodeposition

Although the theoretical studies predict solvent medium breakdown before the onset of actinium electrodeposition, there have been reports of Ac(0) electrodeposition from aqueous solutions utilizing several different methods [8, 9]. One set of studies [8] describes the electrodeposition of actinium from nitric acid solutions, with varying pH values (1.0–4.0) being set to the appropriate level by the addition of sodium hydroxide. The anode and cathode in these studies were platinum metal, and the current density was varied from 50 to 200 mA cm⁻². The authors found that quantitative electrodeposition of actinium could be achieved under various conditions, with the shortest electrolysis time of 1 h being obtained with a current density of 200 mA cm⁻² and a pH of 2.0. A second study employed a saturated aqueous solution of urea oxalate (ca 6.6% at 30 °C) as an electrolyte for the electrodeposition of Ac onto a nickel foil cathode [9]. The authors of this study found that the yield of electrodeposited Ac increased with time and reached a near quantitative maximum yield of 97% at a current density of 53 mA cm⁻² after 2 h. The Ac electrodeposits were suitable for further study using nuclear spectroscopy.

25.3

Thorium

The previous reviews regarding the electrochemical properties of thorium and

its complexes have been covered in the literature up to approximately the mid-1980s [10, 11]. Our intent in the current volume is to just summarize, for completeness, the main findings from the earlier literature and reviews, thereby providing a focus on the more recent results of thorium electrochemistry.

25.3.1

Aqueous Solutions

In aqueous solution, thorium exists as Th(IV), and no definitive data have been presented for the presence of lower-valent thorium ions in this medium. The standard potential for the Th(IV)/Th(0) couple has not been determined from experimental electrochemical data. The values presented thus far for the standard reduction potential have been calculated from thermodynamic data or estimated from spectroscopic measurements. The standard potential for the four-electron reduction of Th(IV) ions has been estimated as -1.9 V in two separate references [12]. The reduction of Th(OH)₄ to Th metal was estimated at -2.48 V in the same two publications. Nugent et al. calculated the standard potential for the oxidation of Th(III) to Th(IV) as +3.7 V versus SHE, while Miles provides a value of +2.4 V [13]. The standard potential measurements from studies in molten-salt media have been the subject of some controversy. The interested reader is encouraged to look at the summary from Martinot [10] and the original references for additional information [14].

Polarography studies of Th(IV) in aqueous solution have been investigated by several authors under various conditions. The results from these studies generally show an irreversible and nonreproducible reduction process. In 1 M LiCl solution, the $E_{1/2}$ value for the reduction

of $\text{Th}(\text{NO}_3)_4$ was reported as -1.27 V versus saturated calomel electrode (SCE), and the authors concluded that the reduction process is catalytic in nature [15]. For the reduction of $\text{Th}(\text{NO}_3)_4$ in 1 M Li_2SO_4 , the data were inconclusive and, for that in 0.1 M KNO_3 , a Th(IV) catalytic wave at approximately -1.2 V versus SCE was observed [16]. Better results were obtained when an organic solvent was mixed with the aqueous solutions. For example, Saxena and Chaturvedi found an irreversible diffusion-controlled reduction process in 0.5 M NaClO_4 , 0.002% Triton X, 0.4 mM Th(IV), and 50% acetonitrile ($E_{1/2} = -1.440$ V versus SCE) or 50% methanol ($E_{1/2} = -1.404$ V versus SCE) [17].

25.3.2

Nonaqueous Solutions

In nonaqueous media, the polarography of Th(IV) tends to display more defined and reproducible reduction wave(s). Astheimer and Schwochau proposed a two-step reduction of ThCl_4 in dimethylsulfoxide according to the equations $\text{Th}(\text{IV}) + 2e^- \rightarrow \text{Th}(\text{II})$ and $\text{Th}(\text{II}) + 2e^- \rightarrow \text{Th}(0)$ [18]. The interpretation of these results has subsequently been called into question by Duyckaerts and Degueldre after they performed polarography and chronoamperometry studies in dimethylsulfoxide and propylene carbonate [19]. They suggested that the reduction of Th(IV) proceeds through a one-step, four-electron reduction process, with $E_{1/2} = -1.65$ V versus SCE. Additionally, to account for the observed electrochemical behavior, Duyckaerts et al. proposed the formation of an autoinhibiting layer of thorium on the surface of the mercury working electrode following initial reduction. Kolthoff and Ikeda studied the polarography of

$\text{Th}(\text{ClO}_4)_4$ in acetonitrile solvent (with 0.1 M tetraethylammonium perchlorate as the supporting electrolyte) and concluded that the reduction waves in the polarograms were due to the evolution of hydrogen and not the formation of an amalgam at the mercury surface [20]. More recently, Martinot et al. studied the reduction of ThCl_4 at 400 K in dimethylsulfoxide, $(\text{CH}_3)_2\text{SO}_2$, with LiCl as the supporting electrolyte [21]. As shown in Fig. 1, the cyclic voltammograms display an ill-defined reduction peak, with a characteristic oxidative stripping peak and a small pre-wave on the reverse scan. These results are attributed to the four-electron reduction of Th(IV) to Th(0) at the electrode with subsequent stripping of the metal from the working electrode surface on the return scan.

25.3.3

Molten-salt Solutions

Small quantities of Th metal can be electrodeposited as dendrites from molten NaCl at $\sim 800^\circ\text{C}$ by cathodic electrolysis of a ThF_4 solution at a molybdenum cathode [22]. Martinot has published several papers describing the electrodeposition of Th metal in an LiCl–KCl eutectic. Voltammetry experiments show that ThCl_4 can be reduced to Th(0) in LiCl–KCl at 400 K at a tungsten working electrode (cathode) surface in a single four-electron step with no evidence for an intermediate Th(II) species [23]. More recently, a procedure was described for converting ThO_2 to Th metal [24]. The first step was the dissolution and conversion of ThO_2 into ThCl_4 in a vitreous carbon crucible by allowing HCl gas to flow through the LiCl–KCl eutectic/ ThO_2 mixture at 400°C . The carbon crucible served as the anode and a tungsten rod as the cathode during the

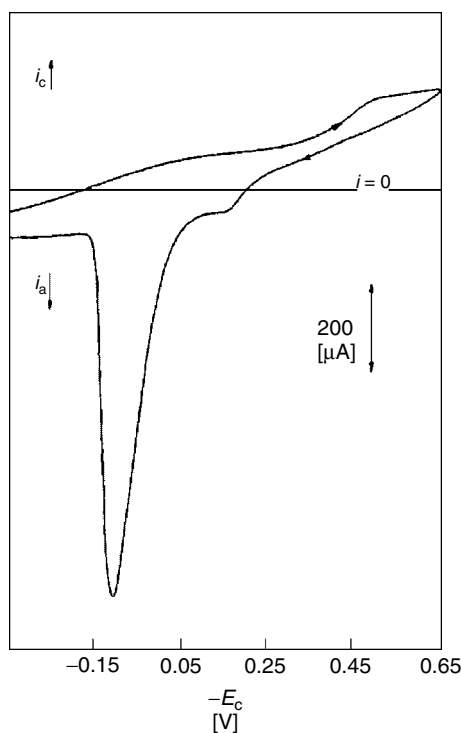


Fig. 1 Voltammetric reduction of ThCl_4 (2.6×10^{-2} M) in molten dimethylsulfone at 400 K (Pt cathode, scan rate = 0.1 V s^{-1} , 0.25 M LiCl) (reprinted from *Journal of Alloys and Compounds*, Vol. 228, L. Martinot, C. Licour, L. Lopes, Contribution to the Knowledge of the Electrochemical Properties of Actinides in Non-Aqueous Media III. The Reduction of Tetravalent Thorium and Tetravalent Neptunium in Various Organic Solvents, Pages 6–12, 1995, with permission from Elsevier).

electrolysis, with a potential difference of between 2.38 and 2.7 V.

25.3.4

Electrodeposition

The electrodeposition of thorium, typically as hydrous oxide, has been used as an efficient means of preparing samples for alpha spectrometric determination. Talvitie described a procedure at a 304 stainless steel cathode using 1 M $(\text{NH}_4)_2\text{SO}_4$ at pH 2 for 120 min, with a current density of 520 mA cm^{-2} [25]. Recently, Lee et al. compared Talvitie's method with a modified version employing the following conditions: stainless steel cathode, 300 mA cm^{-2} current density, 2 h electrolysis, pH of 1.8, and an electrolyte solution containing 0.3 M ammonium oxalate, 0.4 M ammonium sulfate, 0.1 M

hydroxyl ammonium sulfate, and 0.005 M diethyltriaminopentaacetic acid (DTPA) as chelating agents [26]. The modified procedure resulted in slightly higher deposition yields for thorium, $89.4 \pm 2.9\%$ versus $85.5 \pm 4.7\%$, and in the case of plutonium, and likely for the other actinides studied, a more uniformly electroplated analyte resulted. Glover et al. have described an optimized electrodeposition method for thorium and other actinides in which an $\text{NaHSO}_4\text{--H}_2\text{SO}_4\text{--NH}_4$ buffer was utilized [27]. The authors found close to quantitative yields ($>90\%$) for thorium recovery with a 1-h electrodeposition time at pH 1.5–2 and a constant current of 0.75 A. The thorium was plated on a 1.59-cm stainless steel planchet. For thorium determination from soil and sediment samples with sulfate electrolytes, it was recently discovered that the poor thorium recoveries

(~1%) were associated with interfering aluminum in the electrolytic solution during the electrodeposition step [28]. Higher yields were obtained when the aluminum was complexed by fluoride ions. An ammonium acetate electrolyte can be used to efficiently plate (95% recovery) thorium from solution in 2 h under the following conditions: 0.35 M $[\text{NH}_4][\text{CH}_3\text{COO}]$, pH of 1, approximately 12 V, and 400 mA stainless steel cathode [29]. Zarki et al. have employed a thorium electrodeposition step as part of their procedure for the analysis of thorium by alpha spectrometry [30]. Their method utilizes a solution of 70% ethanol, 0.45 M HCl, and 0.06 M HNO_3 for 1 h at a constant potential of 30 V and a resulting starting current of 0.95 A cm^{-2} .

25.3.5

Organometallic and Coordination Compounds

Cyclic voltammetry experiments have been performed on the complex $(\text{tren}')\text{Th}(\text{Bu}'_2\text{DAB})$, where $\text{tren}' = \text{amino-tris}[\text{ethyl(trimethylsilyl)amido}]$ and $\text{DAB} = 1,4\text{-diazabutadiene}$ [31]. The voltammetry was performed in dry tetrahydrofuran (THF) with 0.2 M tetrabutylammonium hexafluorophosphate supporting electrolyte at a Pt disc working electrode. The voltammograms were consistent with a Nernstian and chemically irreversible oxidation of the coordinated DAB ligand at $E_p = 0.20 \text{ V}$ versus Fc/Fc^+ and an electrochemically irreversible reduction process at $E_p = -1.09 \text{ V}$ versus Fc/Fc^+ . Several bent metallocene complexes of thorium were studied by polarography in a nonaqueous medium of dimethylformamide (DMF) or THF solvent with $[(n\text{-C}_4\text{H}_9)_4\text{N}][\text{PF}_6]$ as the supporting electrolyte at a dropping mercury

electrode [32]. In DMF, $(\text{C}_5\text{Me}_5)_2\text{ThCl}_2$ was reduced at -2.45 V versus SCE, while its more stable cyclohexyl isocyanide derivative $(\text{C}_5\text{Me}_5)_2\text{ThCl}_2 \cdot \text{CNC}_6\text{H}_{11}$ was reduced at -2.32 V versus SCE. In THF, $(\text{C}_5\text{Me}_5)_3\text{ThCl}$ is reduced at -2.8 V versus SCE at a Hg electrode and at -2.5 V versus SCE at a Pt working electrode surface. Through correlation with the results from pulse radiolysis experiments of $\text{Th(IV)}\text{-THF}$ solutions, the authors conclude that the reduction process can be attributed to the production of Th(III) derivatives in solution. It should be pointed out that these results contradict an earlier report by Finke et al. in which they did not observe a faradaic electrode process during voltammetry experiments on $(\text{C}_5\text{Me}_5)_2\text{ThCl}_2$ in THF up to -2.7 V versus SCE [33]. In a recent account, Morris et al. commented on the lack of metal-based reductions in “ $(\text{C}_5\text{Me}_5)_2\text{Th}$ ” derivatives [34]. Indeed, their voltammetry studies on hydrazonato ($\eta^2(N, N')\text{-RNN}=\text{CPh}_2$; $\text{R}=\text{CH}_2\text{Ph}$, Ph) and ketimido ($-\text{N}=\text{C}(\text{Ph})(\text{R})$; $\text{R}=\text{CH}_2\text{Ph}$, Ph) complexes of “ $(\text{C}_5\text{Me}_5)_2\text{Th}$ ” show an absence of a metal-based $\text{Th(IV)}/\text{Th(III)}$ reduction process in contrast to the $\text{U(IV)}/\text{U(III)}$ reduction that is observed in uranium derivatives.

The reduction of $\text{Th}(\text{acac})_4$, where $\text{acac} = \text{acetylacetonate}$, in THF at a platinum disc working electrode with $[(n\text{-C}_4\text{H}_9)_4\text{N}][\text{PF}_6]$ as supporting electrolyte shows two cathodic processes [35]. The first reduction at $E_p = -2.68 \text{ V}$ versus Ag/AgClO_4 is ascribed to the $\text{Th(IV)}/\text{Th(III)}$ couple to give $\text{Th}^{\text{III}}(\text{acac})_4$, which slowly liberates acac^- to produce the final product $\text{Th}(\text{acac})_3$. Full chemical reversibility for the $\text{Th(IV)}/\text{Th(III)}$ couple is evidenced only at sweep rates higher than 50 V s^{-1} in the cyclic voltammograms. The authors conclude from their

data that the second reduction process is associated with coordinated and uncoordinated $\text{acac}/\text{acac}^-$ ligand reductions. The electrochemical and spectroelectrochemical behavior for several porphyrin and phthalocyanine complexes containing thorium have been investigated [36]. These complexes show oxidation and reduction processes that are associated with the macrocyclic ring as opposed to the Th(IV) metal center.

25.4 Protactinium

The most stable oxidation states for protactinium are Pa(V) and Pa(IV). The chemical behavior of Pa(V) closely mimics that of Nb(V) and Ta(V), and experimental data are consistent with a $5f(1)$ rather than a $6d(1)$ electron configuration for the Pa(IV) species [37]. The electrochemical literature for Pa is mainly focused on the characteristics of the Pa(V)/Pa(IV) couple and the electrodeposition of Pa metal films from aqueous and nonaqueous electrolyte solutions. In aqueous solutions, only Pa(V) and Pa(IV) ions are known to exist, and the standard potential for the Pa(V)/Pa(IV) redox couple is in the range of -0.1 to -0.32 V [38].

25.4.1 Aqueous Solutions

As mentioned in previous reviews, the polarography of Pa(V) has been studied in aqueous fluoride, sulfate, citrate, and oxalate media [39]. The results in $[\text{NH}_4]\text{F}$ at pH 7.2 gave the most useful electrochemical data and will be discussed here briefly [40]. At a constant fluoride concentration of 3.84 M, two waves are observed in the polarogram. The first wave is the

larger of the two, is proportional to the concentration of protactinium, and has been ascribed to the Pa(V)/Pa(IV) redox couple with $E_{1/2} = -1.29$ V versus SCE. This couple approaches polarographic reversibility at low protactinium concentrations and displays a dependence on the concentration of fluoride in subsequent studies (lower fluoride concentrations give more negative $E_{1/2}$ values). The electrochemically active analyte species in the fluoride solution is thought to be $[\text{PaF}_8]^{3-}$, with the Pa(IV) electrode product likely being $[\text{PaF}_8]^{4-}$ or PaF_4 . The nature of the second reduction process ($E_{1/2} \approx -1.57$ V versus SCE) is difficult to determine and not likely because of the further reduction of Pa(IV) to Pa(III).

25.4.2 Electrodeposition

Electrodeposition of Pa metal has been performed from both aqueous and nonaqueous solutions. An isopropanol solution of $10\text{--}20\ \mu\text{g mL}^{-1}$ Pa from 8 M HCl/0.01 M HF/Pa stock was employed for quantitative electrodeposition [41]. The cell consisted of a gold-plated Al cathode and a Pt wire anode. During deposition the current was maintained at 1 mA, which produced a potential of 400–600 V during the 90-min electrolysis. The progress of the electrolysis was externally monitored by alpha-counting of the electrolysis solution before and during the electrodeposition. Deposition studies of metal from aqueous solutions are more common. Pa was electrodeposited on platinum in 95% yield at tracer concentrations from an electrolyte of $[\text{NH}_4]\text{Cl}/\text{HCl}$ [42]. Electrochemical and chemical conditions of the plating process were described for Pu solutions, which served as a model for the other actinide elements studied. Another tracer

concentration study found quantitative recovery of Pa on a stainless steel cathode from a variety of electrolyte solutions: 0.015 M $[\text{NH}_4]\text{F}/0.25 \text{ M } [\text{NH}_4]\text{Cl}$, 0.2 M $[\text{NH}_4]\text{F}$, and 0.02 M oxalic acid/0.06 M nitric acid [43]. The conditions for the electrolysis consisted of a controlled potential of 7–12 V for 4 h, with a resulting current density of approximately 160 mA cm^{-2} . Natural uranium was utilized in these experiments as a carrier, with its major influence likely associated with the evaporation and transfer steps preceding the electrodeposition. Lower deposition yields (maximum 80%) at a platinum cathode were obtained from a 0.1 N ammonium formate/0.1 N sulfuric acid electrolyte at 80 mA cm^{-2} for 8 h [44].

25.4.3

Nonaqueous Solutions

Concerning the reduction of Pa(IV), theoretical calculations have predicted a standard potential of ca -2.0 V for the Pa(IV)/Pa(III) couple [7, 45]. These results have been substantiated through a study using Tm(II) [$E^\ominus(\text{Tm}^{3+}/\text{Tm}^{2+}) = -2.22 \text{ V}$] as a reducing agent for the reduction of Pa(IV) to Pa(III) in chloride melts [2]. Due to the cathodic limit of the solvent at approximately -1.6 V the production of Pa(III) is thereby prohibited in aqueous solution. Therefore, it is likely that an error was made in the interpretation of earlier polarography data in which the authors claim to reduce Pa(IV) to Pa(III) in aqueous solution [46]. In a solution of acetonitrile with 0.1 M $[(\text{C}_2\text{H}_5)_4\text{N}][\text{ClO}_4]$ as supporting electrolyte, Schwochau and Astheimer observed a single electrochemically irreversible polarographic reduction wave for PaCl_5 ($E_{1/2} = -0.22 \text{ V}$ versus SCE), which they attribute to the two-electron reduction

of Pa(V) to Pa(III) on the basis of comparisons of limiting current values associated with NbCl_5 and TaCl_5 reductions [47]. Subsequent coulometry studies from -0.3 to -0.4 V were unable to confirm the Pa(V) to Pa(III) process in acetonitrile as reduction to the Pa(IV) species was observed [48]. The same authors studied the reduction of Pa(IV)Cl_4 in dimethylsulfoxide and identified a single electron-transfer process ($E_{1/2} = -1.49 \text{ V}$ versus SCE) consuming four electrons to give Pa(0) metal [48]. There was no evidence of the generation of a Pa(III) species in the polarograms.

25.5

Uranium

The volume of electrochemical data on uranium ions and complex compounds is substantially larger than that on the other actinides. Indeed a separate chapter just on the electrochemistry of uranium could be written without a struggle to find enough data. Our intention here is to cover the more recent literature on uranium electrochemistry and include a brief overview of the most pertinent information from earlier accounts. We have included in Table 1 the potentials for the various uranium redox couples. These potentials were obtained from the recent review by Kihara et al. in which the authors evaluated the standard redox potentials for the various uranium couples by extrapolating experimental formal potentials to the state of zero ionic strength [49]. Most of the electrochemical data in the review were obtained from the published works of Riglet et al. [50]. Additional reviews are contained within the *Gmelin Handbook of Inorganic and Organometallic Chemistry on Uranium* [51]. The earlier review covers

Tab. 1 Standard potentials for selected uranium couples

Electrode couple	E^\ominus (V versus SHE)	References
$\text{UO}_2^{2+}/\text{UO}_2^+$	0.089	50a
$\text{U}^{4+}/\text{U}^{3+}$	−0.573	49, 50b
$\text{UO}_2^{2+}/\text{U}^{4+}$	0.195	49, 54

the electrochemical properties of uranium in aqueous solutions [51a] and molten salts [51b]. The initial section contains information on the standard and formal potentials for the various uranium redox couples, a longer more detailed section follows on the polarographic and voltammetric behavior of uranium ions and complexes, and a separate chapter is included on electrochemistry of uranium in molten salts. The second, more recent review [51c] covers the electrochemistry of uranium in nonaqueous solvents and nonaqueous/aqueous mixtures. Electrochemical studies in nonaqueous solvents is oftentimes warranted because of the propensity for complex compounds of uranium that undergo hydrolysis. For a detailed and thorough analysis of the earlier literature on the electrochemistry of uranium, the interested reader is referred to the reviews mentioned above and the references contained therein.

25.5.1

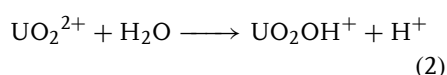
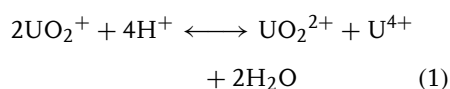
Aqueous Solutions

The general electrochemical behavior of uranium in aqueous solutions is dominated by the reduction of the hexavalent uranyl moiety, UO_2^{2+} . As shown in Table 1, the potential for the $\text{UO}_2^{2+}/\text{UO}_2^+$ couple is 0.089 ± 0.002 V versus SHE, as determined from formal potential data in ClO_4^- solutions (0.5–3.0 M) [49, 50a]. The electrochemical reduction of uranyl compounds has been a thoroughly studied

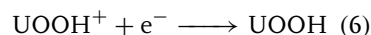
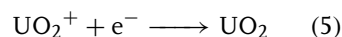
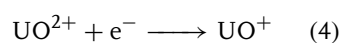
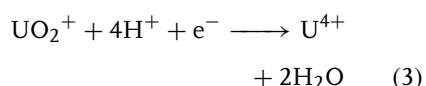
process under a range of solution conditions and typically at a mercury working electrode surface. A detailed overview of electrochemical UO_2^{2+} reduction chemistry can be found in the review by Franz and Schmitt [51a].

For most solution conditions, the initial reduction reaction is the one electron–transfer process mentioned above where the electrode product is the UO_2^+ species. The pentavalent uranyl moiety is rather unstable, although, as Morris has recently shown, it can be stabilized by the appropriate choice of ligand about the metal center [52]. The disproportionation of UO_2^+ into U(IV) and U(VI) ions is the well-known primary decomposition pathway, the specifics of which constitute a series of homogeneous chemical reactions (See Ref. 49 and references therein). A simplified overall disproportionation reaction is shown in Eq. (1). The pH of the electrolyte solutions can have a large influence on the reduction chemistry of the uranyl ion. This issue is discussed in more detail in a study by Sylva and Davidson [53]. The hydrolysis of UO_2^{2+} is more prominent in weakly acidic solutions and leads to the uranium product in Eq. (2). The UO_2OH^+ species is reduced at the electrode surface, and this further complicates the overall reductive electrochemical behavior of the uranyl ion. The electrogenerated UO_2^+ ion is most stable in a pH range of approximately 2–3 and in the absence of oxygen, whereas in strongly

acidic solutions the disproportionation reaction is facile.

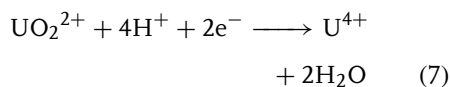


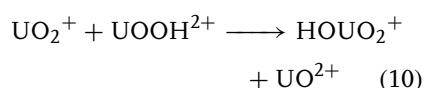
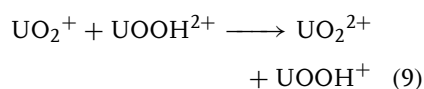
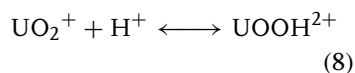
At more cathodic potentials during the reduction of UO_2^{2+} , the polarograms display a second reduction wave that is typically larger than the first wave. Depending on the solution conditions, the second wave can appear as a “composite wave” consisting of two closely spaced reduction processes usually ascribed to the $\text{U(V)}/\text{U(IV)}$ and $\text{U(IV)}/\text{U(III)}$ couples. Equations (3–6) outline the possible species involved in the reactions, in which UOOH^+ is generated during the disproportionation reactions of UO_2^+ (see Eqns (8) and (9)). Under solution conditions that produce a second reduction process displaying a wave of height equal to that of the $\text{UO}_2^{2+}/\text{UO}_2^+$ reduction, the reaction in Eq. (5) is thought to be responsible. A single two-electron wave associated with the $\text{UO}_2^{2+}/\text{U}^{4+}$ couple can be obtained in strongly acidic solutions, such as 0.5 M H_2SO_4 , 0.5 M H_3PO_4 , and 6 M HCl [54]. Experimental formal potential measurements for the $\text{UO}_2^{2+}/\text{U}^{4+}$ couple are scarce owing to the irreversibility of the electrode reaction. Sobkowski and Minc [55] performed electromotive force measurements at a Pt electrode to obtain a formal potential for the couple, from which Kihara and coauthors calculated a standard potential of 0.195 V in their recent review [49].



The recent literature in this area is focused on the electrochemistry of uranyl ions and complexes in mixtures of aqueous and organic solvents, the influence of different electrode surfaces and compositions, and the impact of the ligands surrounding the central uranyl moiety. The influence of different electrode surfaces is being investigated because of interest in using U(IV) as a reducing agent in the treatment of spent nuclear fuel. The source of U(IV) is typically from electrolytic reduction of U(VI) in nitric acid. An overview of recent literature reports is included in the following pages.

Flow coulometry experiments were performed to study the reduction of UO_2^{2+} in nitric, perchloric, and sulfuric acid solutions [56]. The results of these studies show a single two-electron reduction wave attributed to the $\text{UO}_2^{2+}/\text{U}^{4+}$ couple. The direct two-electron process is observed without evidence for the intermediate UO_2^+ species because of the relatively long residence time of the uranium ion solution at the electrode surface in comparison to the residence time typically experienced at a dropping mercury working electrode. The implication here is that as the UO_2^+ is produced at the electrode surface, it is immediately reduced to the U^{4+} ion. As the authors note a simplified equation for this process can be written, Eq. (7), but the process is more complicated. Once the UO_2^+ species is produced it experiences homogeneous reactions comprising Eqns (8) and (9) or (8) and (10) followed by chemical decomposition of UOOH^+ or UO^{2+} to U^{4+} [49].





Dueber et al. studied the voltammetric behavior of the uranyl ion at a solid graphite working electrode, Pt mesh auxiliary, and SCE reference [57]. The electrolyte was magnesium chloride in deionized water and the pH of the solutions was adjusted from 2.4 to 6.6 with appropriate quantities of HCl and NaOH. The authors observed a chemically reversible reduction process at pH of 2.4 corresponding to the $\text{UO}_2^{2+}/\text{UO}_2^+$ couple at potentials between 0 and -0.3 V versus SCE. On the return scan in the cyclic voltammograms, the wave shape is indicative of a surface confined species likely because of the adsorption of UO_2^+ . At higher pH values of approximately 4 and 6, the hydrolysis of UO_2^{2+} is greater and the resulting voltammograms show a decrease in the current for the $\text{UO}_2^{2+}/\text{UO}_2^+$ couple and the growth of a new process at more negative potentials, from -0.6 to -0.8 V versus SCE. The new process is due to the reduction of hydrolyzed uranyl complexes, likely $[(\text{UO}_2)_3(\text{OH})_5]^+$ and $[(\text{UO}_2)_4(\text{OH})_7]^+$. This second reduction process is chemically reversible and is due to the U(VI)/U(V) couple for the hydrolyzed species. Studies on uranium oxides mechanically attached to the graphite electrode show similar behavior to that obtained for the second reduction process associated with the hydrolyzed species. The authors conclude from their studies that the reductive voltammetric behavior for uranyl in magnesium chloride

electrolyte at a solid graphite electrode is simpler than the results reported for other electrodes.

Wei et al. studied the reduction of UO_2^{2+} in different concentrations of nitric acid (0.1–6 M) with added hydrazine at a glassy carbon electrode [58]. The hydrazine was added to help suppress the reduction of the concentrated nitric acid solutions. In the 0.1 M HNO_3 solutions with no hydrazine added, the reduction of UO_2^{2+} results in two ill-defined reduction features and a single anodic wave on the reverse scan at substantially more positive potentials than either cathodic reductions. The authors assign the cathodic features as the reduction of U(VI) to U(V) and the reduction of U(V) to U(IV). The anodic feature is likely the reoxidation of U(V) to U(VI). In 3 M nitric acid, only a single reduction wave was observed with no oxidation wave on the return scan. The authors suggest the single two-electron reduction of U(VI) to U(IV), $\text{UO}_2^{2+}/\text{U}^{4+}$ couple, due to the increase in the H^+ concentration in solution. Since the authors' motivation for this study is related to the processing of spent nuclear fuel and separation of uranium from plutonium, solutions with high nitric acid concentrations are advantageous for the bulk oxidation of U(VI) to the desired U(IV) product. Maximum yield of U(IV) was obtained in constant-flow bulk electrolysis experiments with 6 M HNO_3 , at an applied potential of -0.3 V versus Ag/AgCl, with 0.075–0.125 M hydrazine added as suppressor, and flow rate of $3.5\text{--}5\text{ mL min}^{-1}$.

The electrochemical reduction behavior of UO_2^{2+} was also studied in a nitric acid–hydrazine solution at a titanium electrode because of its resistance to corrosion in nitric acid [59]. It was necessary to pretreat the titanium electrode, to remove surface oxide, through cathodic

polarization at a potential of -0.9 V versus Ag/AgCl for about 25 min prior to obtaining meaningful data for UO_2^{2+} reduction. The voltammograms obtained at the oxide-free titanium electrode correspond to the irreversible $\text{UO}_2^{2+}/\text{U}^{4+}$ couple. The results from this study are intended to help understand the most desirable of conditions during operation of a U(VI)/U(IV) electrolysis process in a production facility utilizing nitric acid solutions with a titanium cathode electrode configuration.

Best and coauthors utilized IR spectroelectrochemistry to study the electrochemical reduction of UO_2^{2+} in aqueous solutions with KNO_3 as supporting electrolyte [60]. The pH of the solutions was set with appropriate quantities of HNO_3 and KOH . The optimal pH range for the study was 2.8–3.4, since within this range speciation of U(VI) is limited to UO_2^{2+} and $(\text{UO}_2)_2(\text{OH})_2^{2+}$, disproportionation of the electrogenerated U(V) species is minimized, and the U–O stretches for U(VI) are observable in the IR spectrum. The results from the study indicate that initial reduction of UO_2^{2+} at a platinum electrode surface leads to decomposition of the electrogenerated U(V) species into a film of uranium oxides on the platinum surface. After the surface is conditioned with the uranium oxides, further reduction of UO_2^{2+} produces UO_2^+ . The IR spectra show stretches associated with UO_2^{2+} and $(\text{UO}_2)_2(\text{OH})_2^{2+}$ at 954 and 938 cm^{-1} , respectively, and diminish as the electrolysis proceeds, and a new feature assigned to the asymmetric O–U–O stretch for UO_2^+ grows in at 914 cm^{-1} . The authors were unable to determine the exact nature of the electrogenerated UO_2^+ , as it could be incorporated within the uranium oxide film or dissolved in the electrolyte solution.

Ugo et al. studied the application of ion exchange voltammetry to the reduction of UO_2^{2+} at a Nafion-coated glassy carbon electrode as a possible means of detecting trace quantities of uranium in aqueous solutions [61]. The Nafion coating was employed to preconcentrate the uranyl ions within the polymeric material at the working electrode surface. Data obtained at bare glassy carbon electrodes were included in the study for comparison purposes. The reduction of UO_2^{2+} at the uncoated glassy carbon surface shows an initial reduction process associated with the $\text{UO}_2^{2+}/\text{UO}_2^+$ couple exhibiting limited chemical reversibility at pH 2.4 in 0.1 M NaCl with added HCl. As the scan is continued to more negative potentials, a second reduction process is evidenced with larger peak currents assigned to the production of U(III). This reduction process has an associated oxidation wave on the return scan with a smaller current value than its forward counterpart, again indicating limited chemical reversibility. On the return scan at potentials more anodic than the original reduction wave for the $\text{UO}_2^{2+}/\text{UO}_2^+$ couple a new anodic wave appears. The authors conclude that this wave is associated with the $\text{U}^{4+}/\text{UO}_2^{2+}$ couple, where the U^{4+} is generated from a comproportionation reaction between the two electrogenerated reduction products U(III) and U(V). Voltammetry at a Nafion-coated glassy carbon electrode in a solution identical to that described for the uncoated electrode shows different behavior. There is an increase in the current levels of approximately an order of magnitude, indicating incorporation of UO_2^{2+} into the Nafion coating. The initial reduction process is now considered to be the UO_2^{2+} to U^{4+} reduction because of the increase in H^+ activity within the Nafion coating even though the pH

of the contacting solution is identical to that employed with the uncoated electrode. This drives the disproportionation reaction of the initial electrode product UO_2^+ according to Eq. (1) and in the limiting case produces a two-electron wave. The second reduction process, which shows full chemical reversibility, is the $\text{U}^{4+}/\text{U}^{3+}$ couple.

Mizuguchi et al. performed cyclic voltammetry and UV/vis spectroelectrochemical experiments at Pt working electrodes on the reduction behavior of UO_2^{2+} in carbonate and acidic perchlorate solutions to learn about the redox behavior of uranium in groundwater environments [62]. The combined results for $\text{Na}_4[\text{UO}_2(\text{CO}_3)_3]$ reduction in 1 M Na_2CO_3 indicate a single-electron reduction (cathodic peak potential E_{pc} of -0.86 V versus Ag/AgCl) to a stable U(V) species, which the authors conclude is likely $[\text{UO}_2(\text{CO}_3)_3]^{5-}$. The potential of deep groundwater containing excess carbonate is typically about -0.3 V versus SHE and would not be adequate to reduce UO_2^{2+} complexes. In the 0.1 M HClO_4 /0.1 M LiClO_4 medium reduction of UO_2^{2+} proceeds through two reduction processes, the first being a quasi-reversible reduction at $E_{\text{pc}} = -0.2$ V versus Ag/AgCl to UO_2^+ . The second irreversible reduction at $E_{\text{pc}} = -0.4$ V versus Ag/AgCl is attributed to the reduction of UO_2^+ to U(IV). The authors' conclusion is that in a reducing acidic groundwater environment the reduction of UO_2^{2+} ultimately produces U(IV).

Gopinath et al. describe the reduction of U(VI) to U(IV) at an activated platinum electrode in 1 M H_2SO_4 for the coulometric determination of uranium [63]. The platinum working electrode is chemically and electrochemically oxidized and then electrochemically reduced to produce a surface that is more active toward uranium

reduction. Quantitative conversion of U(VI) to U(IV) with 100% current efficiency was achieved at -0.150 V versus SCE within 15–18 min. Precision and accuracy were better than 0.2% at uranium levels of 5–10 mg. The results from the study confirm the adequacy of utilizing primary coulometry at an activated platinum electrode for the determination of uranium.

In recent years, reports have appeared concerning the reduction behavior of uranyl in the presence of complexing ligand molecules that may subsequently adsorb onto the working electrode surface. These studies are aimed at developing electrochemical methods for determining the concentration of uranium in dilute solutions. As an example, Mlakar and Branica studied the voltammetric behavior of the uranyl-salicylate-tri-*n*-butyl phosphate complex at a mercury drop electrode in sodium perchlorate solution [64]. The method developed allowed for the determination of $(2.2 \pm 0.08) \times 10^{-8}$ M UO_2^{2+} in natural seawater through peak current measurements from normal pulse voltammograms. The optimized conditions consisted of an accumulation potential of -0.1 V versus Ag/AgCl, a pH of 3.6, 2×10^{-4} M tri-*n*-butyl phosphate, and 1.4×10^{-3} M salicylic acid, which yielded a peak current maximum at -0.35 V versus Ag/AgCl. Other studies of interest include the reduction behavior of UO_2^{2+} as an EDTA complex in perchlorate solutions [65] and as a cupferron complex in acetate buffer solutions [66].

Morris studied the aqueous solution voltammetric behavior of some uranyl coordination complexes to learn how changes in the ligand environment influence the redox potentials and heterogeneous electron-transfer kinetic parameters for the single-electron transfer

of the $\text{UO}_2^{2+}/\text{UO}_2^+$ couple [52]. The specific complexes studied include aquo-, hydroxo-, acetato-, carbonato-, and chloro-ligated UO_2^{2+} . The acetato complex, $[\text{UO}_2(\text{C}_2\text{H}_3\text{O}_2)_3]^-$, displays electrochemically reversible behavior at a Hg surface in 1.0 M $\text{Na}(\text{C}_2\text{H}_3\text{O}_2)/0.1 \text{ M NaNO}_3$ at pH 5.9, while the carbonato complex displays electrochemically irreversible electron transfer at a Hg surface in 0.1 M $\text{Na}_2\text{CO}_3/0.1 \text{ M NaNO}_3$ at pH 11.3. The remaining complexes display kinetic behavior that is intermediate between fully reversible and irreversible. Digital simulations of the voltammetric data were employed to quantify some of the kinetic parameters. The large spread in $E_{1/2}$ potentials, $[\text{UO}_2\text{Cl}_4]^{2-/3-} E_{1/2} = -0.065 \text{ V}$ and $[\text{UO}_2(\text{OH})_5]^{3-/4-} E_{1/2} = -0.927 \text{ V}$ versus Ag/AgCl , was ascribed to the differences in sigma-donor ability of the ligands.

Compared to studies in acidic media, studies on the electrochemical behavior of UO_2^{2+} in basic media are more limited. The report from Morris [52] describing voltammetry results for hydroxo and carbonato uranyl complexes is a recent example. Previous studies have been performed mostly in carbonate and bicarbonate solutions. Wester and Sullivan have studied the reduction of UO_2^{2+} in these solutions to find an electrochemically irreversible process but disproportionation of U(V)O_2^+ was evidenced only in the bicarbonate solutions [67].

25.5.2

Electrodeposition

The electrodeposition of uranium as an oxide is routinely employed as a means of preparing sources for quantitative analytical measurement through alpha spectroscopy. Recently dos Santos et al. studied the electrodeposition of uranium with

a focus on the characterization of the deposited film employing IR spectroscopy, Raman spectroscopy, X-ray diffraction, and thermoanalysis [68]. The optimum electrolysis conditions from a saturated NH_4Cl solution containing uranium nitrate consisted of a pH of 1, current density of 0.6 A cm^{-2} , electrolysis time of 60 min, and a distance between cathode and anode of 5 mm. The cathode was a 304 stainless steel disc coupled with a Pt wire anode. The electrodeposition is thought to proceed by precipitation of uranyl ions at the cathode surface due to the localized increased alkalinity in this area as the electrolysis progresses. The authors conclude that the deposited uranium is in the form of a polymeric hydrated uranium oxide in which some of the waters of hydration are replaced by ammonium ions. The monomeric formula of the deposit is likely $\text{UO}_2(\text{OH})_2 \cdot x\text{NH}_3 \cdot y\text{H}_2\text{O}$ and/or $\text{UO}_2(\text{OH})_{2-x} \cdot (\text{ONH}_4)_x \cdot y\text{H}_2\text{O}$. Similar electrodeposition results were obtained by Maya et al. onto stainless steel and nickel cathodes from a 0.2 M $(\text{NH}_4)_2\text{SO}_4$ electrolyte at pH of 2.5 [69]. A hydrated uranium oxide film is also advanced in this study as the composition of the electroplated uranium. The electrodeposition of uranium has been performed at aluminum cylinder cathodes from uranyl nitrate/isopropyl alcohol solutions [70].

Uranium metal can be prepared from a combination electrodeposition/thermal decomposition process by first forming a mercury amalgam and subsequently heating the amalgam to produce pure uranium metal. Hasegawa et al. utilized this methodology to prepare uranium metal with purity higher than a commercial grade of approximately 99.95% [71]. The electrochemical cell consisted of anode and cathode compartments separated by a proton-specific cation

exchange membrane. The platinum anode compartment was filled with 1 M sulfuric acid, while the cathode compartment contained 0.5–1.0 M HCl solution. The initial step in the process was reduction of U(VI) to U(IV) at -0.6 V versus SCE, followed by pH adjustment with an acetic acid/sodium acetate solution, and finally amalgamation from -2.0 to -2.3 V versus SCE. Most of the mercury was removed from the amalgam at 250°C in a vacuum ($<1 \times 10^{-6}$ torr) before heating to 1200 – 1300°C for 1 h. Martinot and coauthors have reported the electrodeposition of uranium metal from an organic solvent medium [72]. The report mostly focuses on La metal electrodeposition, but the conclusion with regard to uranium is that macroscopic quantities of metal can be deposited from γ -butyrolactone/tetrahydrofuran (60/40 vol %) solutions. The current density at the tungsten working electrode surface must be set between 20 and 40 mA cm^{-2} for plating to occur. Since reduction of the solvent is a competing process, setting the current density too high results in the inhibition of the plating of uranium. Results from Inductively Coupled Plasma (ICP) analyses of the dissolved metal were used to calculate the faradaic yield (about 39% at 20 mA cm^{-2}).

25.5.3

Molten-salt Solutions

Molten salt-based uranium electrochemistry continues to be an important area of research because of the use of pyrochemical processes within the nuclear industry. Previous reviews have covered a large portion of the literature but recent reports have added to the body of knowledge. The recent review by Willit et al. on the electrorefining of uranium and plutonium offers comprehensive literature coverage from

1943 to 1991 [73]. The majority of literature data on the electrochemical behavior of uranium in molten salts is based upon chloride melts. The typical melts are combinations of several chloride species such as NaCl–KCl, LiCl–NaCl–CaCl₂–BaCl₂, MgCl₂–NaCl–KCl, and LiCl–KCl eutectic. There have also been uranium electrochemistry results obtained in fluoride melts on the basis of the fluoride salts BaF₂, CaF₂, LiF, and UF₄ [74].

Masset and coworkers studied the electrochemistry of UCl₃ at a tungsten working electrode in LiCl–KCl eutectic through the use of cyclic voltammetry and chronopotentiometry [75]. The study was performed as part of their attempt to build an updated and accurate database on the behavior of actinides in chloride melts. The results confirm a reversible single electron-transfer process for the U(III)/U(IV) couple up to 0.3 V s^{-1} and independent of temperature from 400 to 550°C . The three electron-transfer process U(III)/U(0) is reversible up to 0.2 V s^{-1} at 550°C after which a quasi-reversible electrode process ensues. The apparent standard potentials for the U(III)/U(IV) and U(III)/U(0) couples are $-1.902\text{ V} + 0.0006104 \times T\text{ (K)}$ and $-3.099 + 0.0007689 \times T\text{ (K)}$ versus Cl₂/Cl[−], respectively. The diffusion coefficients for U(IV) and U(III) at 430°C were 2.7 and $1.9 \times 10^{-6}\text{ cm}^2\text{ s}^{-1}$, respectively. A similar study was recently performed by Kuznetsov et al., and the results were very much in line with those presented in Refs 27, 76. The potentials for the two electrode processes differ slightly in each report, with Kuznetsov et al. reporting a slightly more negative value for the U(IV)/U(III) couple (-1.517 and -1.461 V versus Cl₂/Cl[−] at 723 K) and a more positive value for the U(III)/U(0) electrodeposition step (-2.283 and -2.543 V versus

Cl_2/Cl^-). A third recent report from Reddy et al. again confirms the main findings discussed above [77].

Iizuka et al. studied the applicability of differentiated normal pulse and square-wave voltammetry to the on-line monitoring of actinide concentrations in LiCl-KCl molten salt [78]. Most of the study was focused on uranium and plutonium analysis. The results indicate that for uranium the concentration dependence of peak current from the square-wave voltammograms was not linear at higher concentration ranges. The differentiated normal pulse voltammograms yielded linear concentration/peak current responses but lacked the high sensitivity and discrimination between closely spaced peaks afforded by the square-wave method. The authors conclude that an optimized procedure could be developed for application to the on-line monitoring of actinide concentrations during molten-salt electrorefining. The electrodeposition of uranium in molten NaCl-KCl-UCl_3 from 670 to 710 °C was studied by Serrano et al. to learn more about the factors influencing the morphology of the deposited uranium [79]. As previous studies have concluded, dendrite formation is unavoidable, and the initial step in the electrodeposition is the formation of a thin layer of deposited metal on the substrate surface followed by attachment of the dendrites to the thin layer. The dendritic deposits that are formed are not influenced to any large extent by uranium ion content or current density, however, temperature does play a more dominant role on the density of the coatings.

25.5.4

Nonaqueous Solutions

In comparison to the other actinides the electrochemical behavior of uranium

in nonaqueous solutions has received considerably more attention, although in comparison to most transition metals the number of studies is limited. Coordination and organometallic complexes of uranium have been a focus of inorganic chemists because of their fundamentally interesting and unique bonding arrangements. This leads to the inevitable studies with electrochemical techniques to probe the consequence of electron transfer since the uranium metal center can exist in a number of oxidation states. Morris et al. have studied the electrochemical behavior for a series of U(IV) " $(\text{C}_5\text{Me}_5)_2\text{U}$ " complexes ligated by either σ -donor ligands (Cl , SO_3CF_3 , CH_3 , CH_2Ph) or ligands containing at least a single nitrogen-donor (imido, hydrazone, ketimido) [34]. The electrochemistry was performed in THF solvent with $[(n\text{-C}_4\text{H}_9)_4\text{N}][\text{B}(\text{C}_6\text{F}_5)_4]$ as the supporting electrolyte at platinum and graphite working electrodes. The advantageous use of the perfluoro-phenyl borate anion in low dielectric constant solvents has received considerable attention recently, [80] and in the present study the use of this anion had the added advantage of not being susceptible to fluoride abstraction by the uranium organometallics. The complexes containing the σ -donor ligands display a chemically reversible $\text{U(IV)}/\text{U(III)}$ couple between -1.8 and -2.6 V versus Fc/Fc^+ . The specific reduction potential tracks with the σ -donor ability of the coordinated ligands. The electrochemical reversibility of the couple varies because of slow electron-transfer kinetics. A metal-based oxidation process for complexes containing a σ -donor ligand is not observed. The voltammetry of the complexes containing at least one nitrogen-donor ligand show reduction behavior similar to that of the σ -donor complexes with reduction potentials from

~ -2 to -2.8 V versus Fc/Fc^+ . However, these nitrogen-donor ligand complexes also display a reversible oxidation process attributed to the metal-based $\text{U(IV)}/\text{U(V)}$ couple. The U(V) electrode product is stable on the voltammetric timescale in contrast to the typical behavior of U(V) organometallic complexes. This stability is likely because of the ability of the nitrogen ligands to engage in π -bonding with the uranium metal center increasing the electron density at the metal to stabilize the U(V) oxidation state. The nitrogen-donor complexes contain additional oxidation processes associated with ligand-based oxidations at more positive potentials than the $\text{U(IV)}/\text{U(V)}$ couple. The U(VI) bis(imido) complex, $(\text{C}_5\text{Me}_5)_2\text{U(=NPh)}_2$, shows a single electrochemically reversible $\text{U(VI)}/\text{U(V)}$ wave at -1.7 V versus Fc/Fc^+ .

Clappe et al. have studied the electrochemical behavior of $(\text{RC}_5\text{H}_4)_3\text{UCl}$ complexes ($\text{R}=\text{H}$, CH_3 , $(\text{CH}_3)_3\text{C}$, $(\text{CH}_3)_3\text{Si}$) in THF with $[(n\text{-C}_4\text{H}_9)_4\text{N}][\text{PF}_6]$ as supporting electrolyte at platinum working electrodes [81]. The results for $(\text{MeC}_5\text{H}_4)\text{UCl}$ were described in detail and for the remaining complexes the general electrochemical oxidation and reduction processes were essentially identical. The authors observe a chemically and electrochemically reversible one-electron $\text{U(IV)}/\text{U(III)}$ reduction process from 0.05 to 2.0 V s^{-1} for $(\text{MeC}_5\text{H}_4)\text{UCl}$ at -1.948 ± 0.004 V versus Fc/Fc^+ , which substantiates previous studies on the electrochemistry of Cp_3UCl in THF [82]. The oxidation wave associated with the $\text{U(IV)}/\text{U(V)}$ couple is chemically irreversible and shows an anodic peak current at slow sweep rates that is larger than anticipated for a simple one electron-transfer process. These results are explained by a disproportionation mechanism for the electrogenerated U(V) species, with an

approximate rate constant, $k_d = 6.3 \times 10^6 \text{ mol}^{-1} \text{ L s}^{-1}$. An electrochemical study of $\text{Cp}_2\text{U(BH}_4)_2$ ($E_{1/2} = -1.62$ V versus Fc/Fc^+) and $\text{Cp}_3\text{U(BH}_4)$ ($E_{1/2} = -1.92$ V versus Fc/Fc^+) in THF with $[(n\text{-C}_4\text{H}_9)_4\text{N}][\text{PF}_6]$ as supporting electrolyte shows a reversible one-electron reduction process for both complexes at slow sweep rates, 0.05 V s^{-1} [83]. Chemical reduction of both neutral complexes with Na/Hg amalgam yielded the stable anions $[\text{Cp}_2\text{U(BH}_4)_2]^-$ and $[\text{Cp}_3\text{U(BH}_4)]^-$. Voltammetry results from ultramicroelectrode studies in the absence of supporting electrolyte showed that the supporting electrolyte reacted with $\text{Cp}_2\text{U(BH}_4)_2$ giving $\text{Cp}_3\text{U(BH}_4)$ and $\text{CpU(BH}_4)_3$. The latter species further decomposed to an electrochemically inactive product(s). The electrochemical reduction of bis(dicarbollide)uranium dibromide, $[(\eta^5\text{-C}_2\text{B}_9\text{H}_{11})_2\text{UBr}_2] \cdot 2[\text{Li(THF)}_4]$, has been studied in THF with $[(n\text{-C}_4\text{H}_9)_4\text{N}][\text{PF}_6]$ supporting electrolyte at a platinum electrode [84]. The voltammograms show an electrochemically irreversible reduction with an onset potential of about -1.56 V versus Fc/Fc^+ . There is a return oxidation wave on the reverse scan well separated from the reduction process likely associated with a new species. Subsequent chemical reductions with Na/Hg amalgam in THF allowed isolation of the U(III) species $[(\eta^5\text{-C}_2\text{B}_9\text{H}_{11})_2\text{UBr(THF)}] \cdot 2[\text{Li(THF)}_2]$, resulting from loss of bromide from the parent U(IV) system.

The electrochemical behavior of UCl_4 in THF with $[(n\text{-C}_4\text{H}_9)_4\text{N}][\text{B(Ph)}_4]$ as supporting electrolyte was studied to determine the fate of the electrogenerated U(III) species [85]. The voltammograms are not straightforward and a number of additional U(IV) chloride species

were synthesized and studied to uncover the mechanism of UCl_4 reduction. The reduction of UCl_4 displaying three cathodic waves is dominated by subsequent chloride ion transfer yielding anionic U(IV) chloride complexes, which are reduced at more negative potentials than the starting UCl_4 and its equilibrium U_2Cl_8 species. The U(IV) anions formed have been described as $[\text{U}_2\text{Cl}_9]^-$ and $[\text{UCl}_5]^-$. In recent years a number of reports have appeared concerning the one-electron reduction of uranyl complexes in dimethylsulfoxide (dms) solvent with $[(n\text{-C}_4\text{H}_9)_4\text{N}][\text{ClO}_4]$ as supporting electrolyte [86–89]. The specific complexes reported contain mono-, bi-, tri-, and tetradentate ancillary ligands coordinated to the central uranyl moiety in addition to a dms solvento ligand. Most of the results have been summarized in a paper by Kim, Asakura, and coworkers, in which a clear trend toward more negative reduction potentials is presented as the denticity of the coordinated ligand(s) increases [90]. Additionally the authors have demonstrated the ability of certain ligands to stabilize the typically reactive U(V) oxidation state, allowing characterization of changes to the UO_2^{2+} moiety upon one-electron reduction. A common theme in the studies is weakened $\text{U}=\text{O}$ bonds in the U(V) derivatives in comparison to the parent U(VI) starting compounds. Some of the complexes do show evidence of limited chemical stability for the electrogenerated U(V)O_2^+ , and these results are discussed in further detail in the referenced works.

Cyclic voltammetric studies were employed to determine the stability of electrogenerated U(V) derivatives for several bis(alkoxido)-uranium-triamidoamine complexes of the general formula $\text{U}(\text{NN}_3)(\text{OR})(\text{OR}')\text{Li}(\text{THF})_n$, in which $\text{NN}_3 = \text{N}(\text{CH}_2\text{CH}_2\text{NSiMe}_3)_3$ and $\text{R}, \text{R}' =$

Bu^t or Ph [91]. The voltammetry was performed in THF with $[(n\text{-C}_4\text{H}_9)_4\text{N}][\text{PF}_6]$ as supporting electrolyte at a platinum disk working electrode. The three complexes studied, corresponding to the bis(butoxide), bis(phenoxide), and mixed butoxide/phenoxide derivatives, show a quasi-reversible, chemically reversible oxidation to the U(V) species and a second chemically irreversible oxidation that appears to be one electron in nature. The $E_{1/2}$ values for the U(IV)/U(V) couples are -1.04 V, -1.155 V, and -0.97 V versus Fc/Fc^+ for bis(butoxide), bis(phenoxide), and the mixed species. The subsequent irreversible second oxidation processes occur at E_p values of 0.86 V, 0.445 V, and 0.745 V versus Fc/Fc^+ . The stability of the U(V) derivatives evidenced in the voltammetry experiments allowed isolation and characterization from chemical oxidation experiments with the chemical oxidant $[\text{Cp}_2\text{Fe}][\text{PF}_6]$. Cathodic voltammetry scans conducted to observe the U(IV)U(III) couple in these complexes did not produce any voltammetric waves before breakdown of the solvent window. Avens et al. reported the chemically reversible oxidation of the U(III) complex $\text{U}(\text{OAr})_3$, in which $\text{OAr} = 2,6\text{-di-}t\text{-butylphenoxide}$, at -1.22 V versus Fc/Fc^+ [92]. The quasi-reversible cyclic voltammograms were recorded in THF with $[(n\text{-C}_4\text{H}_9)_4\text{N}][\text{BPh}_4]$ as the supporting electrolyte at a gold disk working electrode. Martinot et al. studied the electrochemical behavior of Cs_2UCl_6 in a series of organic solvents (dimethylsulfone -400 K, hexamethylphosphoramide -298 and 400 K, dimethylsulfoxide -298 K, propylene carbonate -298 K, 1,2-dimethoxyethane -298 K) with $\text{Li}[\text{ClO}_4]$ as the supporting electrolyte [93]. The general results in all solvents consist of two reductive electrode processes corresponding first to the one-electron reduction to a

U(III) species and a second three-electron reduction to give U(0) metal. The first reduction, U(IV)/U(III) couple, is electrochemically and chemically irreversible except in hexamethylphosphoramide at 298 K where the authors report full chemical reversibility on the voltammetric timescale. The second reduction process is electrochemically irreversible in all solvents and only in dimethylsulfone at 400 K was an anodic return wave associated with uranium metal stripping noted. Electrodeposition of uranium metal as small dendrites from Cs_2UCl_6 starting material was achieved from molten dimethylsulfone at 400 K with 0.1 M LiCl as supporting electrolyte at a platinum cathode. The deposits of uranium and the absence of UCl_3 , UCl_4 , UO_2 , and UO_3 were determined by X-ray diffraction. Faradaic yield was low at 17.8%, but the yield can be increased (55.7%) through use of a mercury pool cathode.

25.6

Neptunium

25.6.1

Aqueous Solutions

Neptunium has been characterized from the +3 to +7 oxidation states in aqueous solution. The standard potentials for various Np ions have been determined from measured formal potentials of the various redox couples. These data have been thoroughly reviewed by Martinot [94] and Fahy [95]. Recently the standard potentials for the redox couples $\text{NpO}_2^{2+}/\text{NpO}_2^+$, $\text{Np}^{4+}/\text{Np}^{3+}$, and $\text{NpO}_2^+/\text{Np}^{4+}$ in acidic aqueous solution have been reevaluated with more detailed consideration of activity coefficients [49, 50]. The standard potential accepted here for the $\text{NpO}_2^{2+}/\text{NpO}_2^+$ couple is 1.161 ± 0.011 V as determined from

formal potential measurements during voltammetry experiments at a Pt electrode in 1 M HClO_4 and 1 M HClO_4 /1 M, 2 M NaClO_4 mixtures [50a]. For the $\text{Np}^{4+}/\text{Np}^{3+}$ couple a standard potential of 0.218 ± 0.005 V is presented under similar experimental conditions.

Kihara et al. employed flow coulometry to study the electrode reactions for Np ions in various acidic media [49]. Flow coulometry has an inherent advantage over the conventional bulk coulometry methods in that the electrolysis can be achieved rapidly to aid in the characterization of unstable electrode products. The resulting coulopotentiograms for the $\text{NpO}_2^{2+}/\text{NpO}_2^+$ and $\text{Np}^{4+}/\text{Np}^{3+}$ couples indicate reversible processes in nitric, perchloric, and sulfuric acids. The differences in potentials between the various acids are attributed to the associated stability constants of the electrode products with the anion of the acid in each case. Table 2 contains the half-wave potentials for each couple in the various acids.

Kim and coworkers recently studied the reduction of NpO_2^{2+} in 3 M HNO_3 by cyclic voltammetry and UV/vis spectroelectrochemistry [96]. The authors found a quasi-reversible process for the $\text{NpO}_2^{2+}/\text{NpO}_2^+$ couple at Pt and glassy carbon (GC) working electrodes with almost identical formal potentials of 0.907 V and 0.909 V versus Ag/AgCl, respectively. Digital simulations of the cyclic voltammetry data confirmed the quasi-reversibility of the electrode couple with experimental and calculated standard heterogeneous rate constants, k° , on the order of $\text{ca } 2 \times 10^{-3} \text{ cm s}^{-1}$. The UV/vis spectroelectrochemistry results confirm the stability and identity of the electrogenerated NpO_2^+ species.

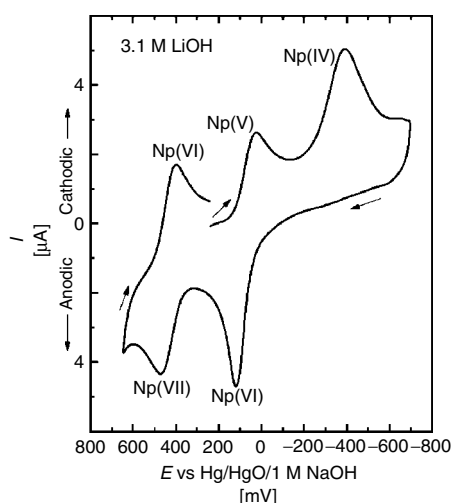
Tab. 2 Half-wave potentials (V versus Ag/AgCl) in acidic solution from flow coulometry studies [49]

Electrode couple	1 M HNO ₃	1 M HClO ₄	0.5 M H ₂ SO ₄
NpO ₂ ²⁺ /NpO ₂ ⁺	0.91	0.94	0.88
Np ⁴⁺ /Np ³⁺	−0.13	−0.06	−0.21

The electrochemical behavior of Np ions in basic aqueous solutions has been studied by several different groups. In a recent study, cyclic voltammetry experiments were performed in alkali ([OH[−]] = 0.9 – 6.5 M) and mixed hydroxo-carbonate solutions to determine the redox potentials of Np(V, VI, VII) complexes [97]. As shown in Fig. 2, in 3.1 M LiOH at a Pt electrode Np(VI) displays electrode processes associated with the Np(VI)/Np(V) and Np(VII)/Np(VI) couples, in addition to a single cathodic peak corresponding to the reduction of Np(V) to Np(IV). This latter process at $E_p \approx -400$ mV (versus Hg/HgO/1 M NaOH) is chemically irreversible in this medium. Analysis of the voltammetric data revealed an electrochemically reversible Np(VI)/Np(V)

couple at $E_c^{\oplus'} = 0.148(9)$ V versus SCE and a quasi-reversible Np(VII)/Np(VI) couple at $E_{1/2} \approx 0.450$ V versus Hg/HgO/1 M NaOH. The voltammetry of Np is independent of base concentration above 1.8 M LiOH, but below this value the Np(VI)/Np(V) couple tends toward a system with reduced electrochemical reversibility. Voltammetric behavior in NaOH solutions is very similar to the voltammograms in LiOH, with a shift in potential for the Np(VI)/Np(V) couple to $E_c^{\oplus'} = 0.106(6)$ V versus SHE in 3 M NaOH. In the mixed hydroxo-carbonate solutions (0.8 M NaOH/0.4 M Na₂CO₃ and 1.8 M NaOH/0.1 M Na₂CO₃) the Np(VII)/Np(VI) becomes chemically irreversible and the Np(VI)/Np(V) couple is quasi-reversible. This behavior is

Fig. 2 Cyclic voltammogram of Np(VI) in 3.1 M LiOH on a Pt electrode (area ~ 0.5 cm²), first scan, 20 mV s^{−1} (reprinted from *Radiochimica Acta*, Vol. 89, A. V. Gelis, P. Vanysek, M. P. Jensen, K. L. Nash, *Electrochemical and Spectrophotometric Investigations of Neptunium in Alkaline Media*, Pages 565–571, 2001, with permission from Oldenbourg Wissenschaftsverlag GmbH).



similar to that previously reported in pure carbonate and bicarbonate solutions [98]. At stronger hydroxide concentrations in the mixed media (6.2 M NaOH/0.3 M Na₂CO₃) the voltammetric behavior more closely resembles the behavior described in dilute base with no carbonate present: Np(VI)/Np(V) couple is electrochemically reversible and the Np(VII)/Np(VI) couple is quasi-reversible. The neptunium species in solution in the absence of carbonate are believed to be [NpO₂(OH)₄]^{3-/-2-} for Np(V) and Np(VI), and [NpO₄(OH)₂]³⁻ for Np(VII).

25.6.2

Electrodeposition

Neptunium has been electrodeposited from aqueous and nonaqueous solutions for the preparation of pure sources of this element for various investigations. Ramaniah et al. electroplated Np as NpO₂(OH)₂ · 2H₂O from an isopropanol solution containing Np(V) ions [99]. The deposition was performed on an aluminum disc coated with a thin layer of gold at 600 V and a current density of 1–3 mA cm⁻². From an aqueous HCl solution at pH 2.7 containing an unspecified amount of NH₄Cl, a deposition yield of 95% or better was obtained for Np in a minimum of 15 min at 2 A cm⁻² with an applied potential between 8 and 12 V on a Ti metal foil cathode [100]. Np metal can be obtained through electrodeposition at a mercury cathode and subsequent thermal decomposition of the amalgam to yield a button of pure Np metal [101]. The electrochemical step is performed in acetate buffer solutions (acetic acid/sodium acetate) of pH 3.4–3.7 with current densities varying during the experiment from ca 50 to 200 mA cm⁻². A rotating disc electrode (RDE) method was developed

for the preparation of high-quality Np α-sources [102]. The advantages of this method are high deposition yields from large volumes (>10 mL) of aqueous solutions in 1–2 h and the use of low current densities for more homogeneous deposits. A 90% deposition yield of Np is obtained in approximately 60 min at 1.4 mA cm⁻² from a pH 4.3, 0.3 M sodium sulfate solution on a stainless steel cathode rotating at 1000 rpm.

25.6.3

Nonaqueous Solutions

There are a limited number of studies for Np complexes in nonaqueous organic solvent media. Sonnenberger and Gaudiello performed voltammetry studies on several organometallic Np complexes (Cp₄Np, Cp₃NpCl, and Cp*₂NpCl₂ in which Cp = C₅H₅ and Cp* = C₅Me₅) in THF solvent to observe the influence of ligand environment on the Np(IV)/Np(III) couple [103]. At a Pt working electrode with 0.2 M [(*n*-C₄H₉)₄N][BF₄] as supporting electrolyte the measured *E*_{1/2} potentials versus the Fc/Fc⁺ couple were -1.27 V for Cp₄Np, -1.29 V for Cp₃NpCl, and -1.38 V for Cp*₂NpCl₂. While substitution of a chloride ligand for Cp did not have a large influence on the reduction potential, the more electron donating Cp* ligand shifts the reduction to a more negative potential. Detailed voltammetric data were not provided, but the electrode reaction appears to be chemically and electrochemically reversible over the sweep rates studied. The coordination compound Cs₂NpCl₆ was studied in several organic solvents with various electrochemical techniques [104]. In four of the solvents studied (hexamethylphosphoramide, dimethylsulfone, DMF, and acetonitrile) the nonideal voltammetric behavior is similar in that

two irreversible reduction waves are observed. The authors assign the first reduction to the $\text{Np}^{4+}/\text{Np}^{3+}$ couple and the second reduction to the three-electron process $\text{Np}^{3+}/\text{Np(s)}$. Controlled potential electrolyses at potentials more cathodic than the $\text{Np}^{3+}/\text{Np(s)}$ couple did not yield Np metal at a solid cathode in any solvent. In acetonitrile and dimethylsulfone small yields (7 and 0.4% current yield, respectively) of neptunium metal were obtained as amalgams at a mercury pool cathode. With formamide as a solvent only a single wave is observed during the voltammetry experiment, and no further elaboration is available from the authors.

25.6.4

Molten-salt Solutions

The electrochemistry of Np(III) has been studied in LiCl–KCl eutectic molten-salt mixtures by several research groups. The interest in the molten-salt studies stems from their use in the pyrometallurgical partitioning of actinide elements from radioactive wastes and the necessity to understand the redox behavior of the various elements in solution [78]. The general voltammetric behavior of Np(III) in the LiCl–KCl melt is that of a reversible single step three-electron transfer process in which Np metal is deposited at the working electrode surface during the cathodic sweep and stripped during the return anodic sweep. Standard potentials for the $\text{Np(III)}/\text{Np(0)}$ couple have been determined by several authors with good agreement among the different values in recent years. Sakamura et al. reported a standard potential of -1.484 V versus Ag/AgCl at 450°C with a tantalum wire working electrode [105]. Reports from Kreuger et al. [106] and Roy et al. [107] are in very good agreement with these results. At 450°C they report a standard potential

of -1.489 V versus Ag/AgCl at a tantalum surface. A slightly more negative potential of -1.519 V versus Ag/AgCl at 450°C was reported by Shirai et al. from electromotive force measurements [108]. However, in an earlier paper coauthor Shirai et al. [109] reported a potential of -1.496 V versus Ag/AgCl at 450°C , which is more consistent with the values of Roy and Kreuger.

In additional applied studies Martinot [110] and Shirai et al. [111] researched the electrodeposition of Np metal from NpO_2 and NpN, respectively. With methodology similar to that employed with ThO_2 , Martinot achieved 99.95% pure Np metal on the gram scale through dissolution of NpO_2 at 450°C in LiCl–KCl eutectic with HCl gas, followed by reduction of the resulting Np(IV) to Np(III) with H_2 , and finally electroreduction at a tungsten cathode (2.55–3.0 V potential difference) to collect Np metal. Shirai and coauthors utilized anodic electrodisolution (-0.773 V versus Ag/AgCl at 500°C) of NpN within a tungsten basket electrode in a molten solution of LiCl–KCl– NpCl_3 to produce Np(III) ions in solution. The Np(III) was then electrodeposited on a solid Mo working electrode at a potential of -1.800 V versus Ag/AgCl in approximately 90% overall yield based on the quantity of starting NpN. The redox potential for the $\text{Np(III)}/\text{Np(0)}$ couple was found to be -1.568 V versus Ag/AgCl.

25.7

Plutonium

The majority of literature concerning the electrochemical behavior of plutonium is focused on results obtained in acidic aqueous or molten salts solutions. Several reviews have appeared on the redox properties of plutonium in

solution and most include some data in relation to electrode reactions [112–114]. The redox properties of plutonium in acidic aqueous solution can be complex because of the possibility of four oxidation [Pu(III)–Pu³⁺, Pu(IV)–Pu⁴⁺, Pu(V)–PuO₂⁺, Pu(VI)–PuO₂²⁺] states to exist simultaneously. A thorough analysis of disproportionation and equilibrium reactions for plutonium ions is provided in the *Plutonium Handbook*, [115] and a brief overview of electrochemical methods for plutonium research has recently been reviewed by Peretrukhin and Maslennikov [112]. The prevalence of reported data in molten-salt solutions is due to the use of these solutions in the nuclear industry for separation and purification of plutonium metal. The recent review by Willit et al. provides a thorough coverage of the earlier literature in relation to plutonium electrorefining [73]. The more recent results (post-1991) will be covered in the present review.

25.7.1

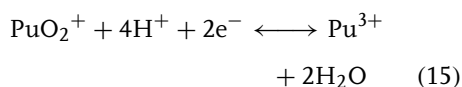
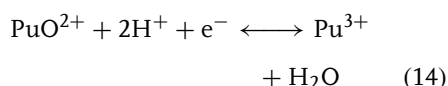
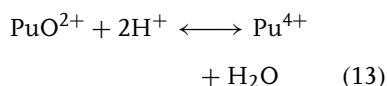
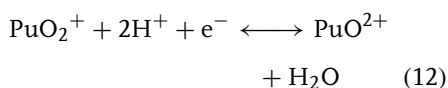
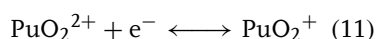
Aqueous Solutions

In acidic aqueous solution the PuO₂²⁺/PuO₂⁺ and Pu⁴⁺/Pu³⁺ couples are electrochemically reversible, while the PuO₂²⁺/Pu⁴⁺, PuO₂⁺/Pu⁴⁺, and PuO₂⁺/Pu³⁺ couples are electrochemically irreversible because of the breaking of the Pu–O bonds during the electron-transfer reactions. The earlier electrochemical data on plutonium ions were typically obtained at a single, relatively high ionic strength, thereby inhibiting the accurate extrapolation to zero ionic strength, which is needed for standard potential calculations. More recently the E^\ominus for the PuO₂²⁺/PuO₂⁺ and Pu⁴⁺/Pu³⁺ couples have been redetermined through application of the Specific Interaction

Theory (SIT) for more accurate consideration of activity coefficients [5, 49, 50b]. Kihara et al. [49] calculated values of 0.956 ± 0.010 V for PuO₂²⁺/PuO₂⁺ and 1.026 ± 0.010 V for Pu⁴⁺/Pu³⁺ from the cyclic voltammetry data of Riglet et al. [50] in perchlorate solutions. In an earlier study Capdevila and Vitorge determined E^\ominus of 0.938 ± 0.010 V for PuO₂²⁺/PuO₂⁺ and 1.044 ± 0.010 V for Pu⁴⁺/Pu³⁺ also from voltammetric data in perchlorate solutions [116]. Because of the irreversibility of the PuO₂²⁺/Pu⁴⁺ electrode reaction limited formal potential data exist in the literature for calculation of the standard potential. However, a value of 0.867 V has been calculated from the existing data and appropriate correction factors [49].

To learn more about the reduction of the electrogenerated pentavalent plutonyl species, PuO₂⁺, Kihara et al. studied the voltammetry of Pu ions in nitric and phosphoric acid mixtures at stationary and rotated glassy carbon working electrodes [49]. During the reduction of PuO₂²⁺ two waves were observed at the stationary electrode and three waves were observed when the electrode was rotated. From the rotating electrode data the three waves are thought to arise from the electrode reactions shown in Eqns (11–13), where the reaction in Eq. (11) is reversible ($E_{1/2} = 0.65$ V versus Ag/AgCl) and the reactions in Eqns (12) and (13) deviate from reversibility ($E_{1/2's} = 0.36$ V and -0.01 V versus Ag/AgCl). The $E_{1/2}$ potentials quoted here are from a mixed 1.0 M HNO₃ and 1.4 M H₃PO₄ solution. The authors believe that the Pu(IV) produced during the reduction of electrogenerated PuO₂⁺ is not Pu⁴⁺, but rather PuO²⁺ that is stabilized by the presence of the phosphate anions. The PuO²⁺ decomposes to Pu⁴⁺ according to Eq. (14), and then reduces to Pu³⁺ at a potential similar

to that for PuO_2^+ described by Eq. (12). This leads to a two-electron wave during the stationary electrode experiments as the residence time of electrogenerated PuO^{2+} is increased compared to that in the rotating electrode experiments. The overall two-electron reduction of PuO_2^+ is outlined in Eq. (15).



As with U and Np ions, flow coulometry experiments were conducted to further study the electrode reactions of Pu ions in acidic aqueous solutions [49]. The results from these studies confirm the reversibility of the one-electron couples $\text{PuO}_2^{2+}/\text{PuO}_2^+$ and $\text{Pu}^{4+}/\text{Pu}^{3+}$ in nitric, perchloric, and sulfuric acid solutions. The further reduction of PuO_2^+ resulted in an irreversible two-electron transfer yielding Pu^{3+} . The flow coulometry results in the mixed phosphoric–nitric acid solutions confirm the overall conclusions that have been reached from the stationary and rotated working electrode experiments described previously, in which PuO^{2+} is the primary Pu(IV) product from PuO_2^+ reduction.

The technique of differential pulse stripping voltammetry has been developed for the determination of plutonium in nitric acid solutions [117]. The successful determination of plutonium was demonstrated

for sample solutions containing silver ions as a possible interfering species. The procedure consisted of electrodeposition for 20 s at -0.7 V versus Ag/AgCl (Pt working electrode) followed by an anodic sweep to 0.4 V at 4 mV s^{-1} with active background subtraction of the electrochemical solvent medium. This procedure provided data applicable for construction of a Pu calibration curve from concentrations of 50–1000 ppm with an relative standard deviation (RSD) of approximately $\pm 2\%$.

The $\text{Pu}^{4+}/\text{Pu}^{3+}$ couple for a series of Pu(IV)/(EDTA $^{4-}$) based complexes, where EDTA = ethylenediaminetetraacetate, has been studied as a function of pH and EDTA concentration [118]. The voltammetry was also studied with citrate and carbonate ions present in solution. At a relatively low pH of 2.3 and equimolar $\text{Pu}^{4+}/\text{EDTA}$ concentrations a quasi-reversible one-electron reduction is observed for Pu(EDTA) at $E_{1/2} = 0.342$ V versus SHE. The quasi-reversibility of this process remains as the pH is raised to 4.6. Additional voltammetry studies are discussed in the paper for the higher coordinate Pu^{4+} species, Pu(EDTA)-L (where L = EDTA, carbonate, citrate), all of which show irreversible electron-transfer behavior.

The electrochemical behavior of plutonium ions in alkaline media has received substantially less literature coverage in comparison to results in acidic solutions. Most of the literature has been reviewed by Martinot [113], and only minimal attention has been given to the topic since this previous review [119, 120].

25.7.2

Electrodeposition

The electrodeposition of plutonium is routinely employed as a means of preparing

plutonium samples for alpha spectrometric measurements. The modification of Talvities's method by Lee and Lee [26] described in Sect. 25.3.4 for thorium electrodeposition has been applied for Pu deposition. The modified method gave a yield of $98.6 \pm 3.1\%$ compared to $92.4 \pm 2.8\%$ in the previous method in addition to slightly enhanced peak resolution in the alpha spectra. The application of this method for Pu determination in environmental samples has been reported [121]. Luskus has recently compared electrodeposition of Pu from environmental air filter samples with that of the technique of microprecipitation of Pu for preparation of alpha spectrometric sources [122]. The Pu recovered from the air filter samples was consistently higher with the microprecipitation method than that recovered by the electrodeposition procedure. In addition, microprecipitation decreases the amount of equipment and equipment maintenance time needed to perform the analyses. A rotating disc cathode cell has been developed for the electrodeposition of plutonium with resulting high-quality and thin, uniform deposits [123]. The cathode is a stainless steel disc rotated at 1200 rpm in a 0.3 M sodium sulfate solution at pH 5 with an applied current density of 1 mA cm^{-2} for 35 min. The method gave a Pu yield of $97.5 \pm 2.5\%$.

25.7.3

Molten-salt Solutions

Recent studies on the electrochemical behavior of plutonium in molten salts have mainly been performed in LiCl–KCl based melts. The electrorefining step in a pyroprocessing procedure for the recycling of nuclear fuel from the Integral Fast Reactor (IFR) Program has been

described by Laidler and coauthors [124]. The process utilizes LiCl–KCl eutectic as solvent and is based on the electrodisolution of spent metal and subsequent selective electrodeposition of uranium, plutonium, and other transuranic (TRU) elements at a solid steel (U) or liquid cadmium (Pu, U, TRU) cathode. Nishimura et al. have described a similar electrorefining/pyroprocessing procedure [125], and have also described the pyrometallurgical partitioning of actinides from rare-earth elements [126]. The foundation of these processes is related to the fundamental electrochemical behavior and thermodynamic properties of Pu and the other metals in the LiCl–KCl molten salt. Because of the importance of Pu electrorefining, researchers continue to study the details of Pu electrochemistry in molten salts. Serp et al. studied the electrochemistry of trivalent PuCl_3 reduction in LiCl–KCl eutectic from 733 to 823 K [127]. The $\text{Pu}^{3+}/\text{Pu}^0$ couple was electrochemically reversible up to 200 mV s^{-1} with quasi-reversible behavior observed at higher sweep rates. From the cyclic voltammetry and chronopotentiometry data standard potentials for the $\text{Pu}^{3+}/\text{Pu}^0$ couple were calculated at 733, 773, and 823 K. At 733 K the calculations yield an average apparent E^\ominus of -2.796 V versus Cl_2/Cl^- , which is similar to a previously reported value [107].

Uozumi, Iizuka, and coauthors have published several studies on the electrochemical behavior of Pu at liquid cadmium cathodes in LiCl–KCl eutectic melts [128–130]. In one account [130] the authors studied the reduction of Pu^{3+} to Pu^0 at the LiCl–KCl melt and liquid Cd interface and compared the results to those obtained at a solid Mo cathode surface. The electrode reaction at liquid Cd was found to be close to fully reversible with rapid,

diffusion-controlled electron transfer. At 723 K the $E_{1/2}$ value for the Pu^{3+}/Pu couple was -1.387 ± 0.002 V versus Ag/AgCl. The data reveal that the cathodic reduction peak potential for the Pu^{3+}/Pu couple is shifted to more negative potentials by about 0.340 V at a Mo electrode compared to that at the liquid Cd electrode. This difference was attributed to a lowering of the activity of Pu in the Cd phase and is similar to the Gibbs energy of formation of the intermetallic compound PuCd_6 in the liquid Cd phase. As mentioned in Sect. 25.5.3 on uranium molten-salt electrochemistry, Iizuka et al. [78] looked into the applicability of square-wave and normal pulse voltammetries for the on-line monitoring of Pu concentrations in LiCl–KCl eutectic molten salt. The results for Pu were similar to those for U in which a nonlinear relationship was found between peak current and Pu concentration from the square-wave data. Additionally, while the normal pulse method shows more promise the authors point out that there is still a problem discriminating between closely spaced redox processes.

Electrochemical studies of plutonium in NaCl-based melts are less common than that in LiCl–KCl mixtures. In a recent paper by Lambertin et al. the standard potentials for the $\text{Pu(III)}/\text{Pu(0)}$ couple were determined from cyclic voltammetry data in equimolar NaCl–KCl and CaCl_2

at 1073 K [131]. The E^\ominus in equimolar NaCl–KCl was calculated as -2.54 ± 0.01 V versus Cl_2/Cl^- and -2.51 ± 0.01 V versus Cl_2/Cl^- in CaCl_2 . This result in NaCl–KCl is similar to a previously published value of -2.585 V versus Cl_2/Cl^- [132].

25.8 Americium

25.8.1

Aqueous Solutions

The vast majority of electrochemical data on americium ions has been obtained in aqueous solutions. Americium can exist in aqueous solutions in the oxidation states III, IV, V, and VI. The divalent state is difficult to attain in aqueous solutions because of the proximity of the standard potential of the $\text{Am(III)}/\text{Am(II)}$ couple to the solvent/supporting electrolyte breakdown potential. Previous reviews have presented the formal and standard potentials for the various americium couples and these reviews should be consulted by the interested reader for more detailed discussion [133, 134]. Table 3 contains a summary of selected formal potentials E_c^\ominus from these reviews in 1 M HClO_4 for convenience. All values are calculated from various measurement techniques except for the $\text{Am(VI)}/\text{Am(V)}$ couple ($\text{AmO}_2^{2+}/\text{AmO}_2^+$), which was determined directly.

More recent experimental reports have focused on detailed electrochemical studies to characterize the different americium ions in solution in relation to their stability and molecular composition. The electrochemical behavior of americium in carbonate media has been studied by several different authors because of the tendency

Tab. 3 Formal Potentials E_c^\ominus for Am ions in 1 M HClO_4 [133, 134]

Electrode couple	Potential [V]
$\text{AmO}_2^{2+}/\text{AmO}_2^+$	+1.60
$\text{AmO}_2^{2+}/\text{Am}^{3+}$	+1.68
$\text{Am}^{4+}/\text{Am}^{3+}$	+2.6
$\text{Am}^{3+}/\text{Am}^{2+}$	–2.3
$\text{Am}^{3+}/\text{Am(s)}$	–2.07

of strong complexing agents such as carbonates to stabilize the Am(IV) oxidation state [135–138]. A common theme among these studies is the existence of four different oxidation states of americium including Am(III)/(IV)/(V)/(VI), which are dependent on the pH of the solution, the anode potential for oxidation of Am(III), and the concentration of $\text{MHCO}_3/\text{M}_2\text{CO}_3$ (where $\text{M} = \text{K}$ or Na). As an example of americium behavior in carbonate media the results from Myasoedov et al. indicate 100% production of Am(IV) at pH 8.2–9.7, 100% Am(VI) at pH 11–12.5, and 100% Am(V) at pH > 13.5 [135]. These results were obtained within 3 M $\text{KHCO}_3\text{--K}_2\text{CO}_3$ solutions at a potential of 1.25 V versus SHE. Similar results were obtained from the other referenced reports. In acetate solutions (0.05–0.4 M sodium acetate and 0.1 M acetic acid) Fedoseev and Krot found that oxidation of Am(III) led to the production of Am(VI) in solution [139]. The characterization of the different americium ions in solution was performed by absorption spectra. Kulyako et al. found that mixtures of acetonitrile with low concentrations of H_3PO_4 (0.3–2.0 M) were suitable for the oxidation of Am(III) to Am(IV) at 1.4 V versus $\text{Hg}/\text{Hg}_2\text{SO}_4$ in essentially quantitative yields [140]. This is in contrast to results obtained in H_3PO_4 solutions where a concentration ≥ 10 M is required for the production of pure Am(IV) [141].

Another strong complexing agent sodium tripolyphosphate, $\text{Na}_5\text{P}_3\text{O}_{10}$, was employed during the electrolysis of Am(III) in a dilute (2 mM) H_2SO_4 solution to attempt stabilization of Am(IV) [142]. The concentration of $\text{Na}_5\text{P}_3\text{O}_{10}$ was 0.17–0.8 M at pH 1–3 with 0.9 mM Am(III). The reported results indicate that a mixture of Am(IV) and Am(VI) was produced in solution during the electrolysis at 1.9 V versus SHE.

Additional strong complexing agents such as alkali metal tungstophosphate and tungstosilicate heteropolyanions ($[\text{P}_2\text{W}_{17}\text{O}_{61}]^{10-}$ and $[\text{SiW}_{11}\text{O}_{39}]^{8-}$) have been used to stabilize the Am(IV) oxidation state upon electrolysis of Am(III) ions in acidic aqueous media [143]. The electrogenerated Am(IV) ions form 1:1 and/or 1:2 complexes, $[\text{Am}]:[\text{anion}]$, depending on the total concentration of Am and the anion in solution.

25.8.2

Molten-salt Solutions

There is a relatively large volume of electrochemical data on americium in molten-salt media, specifically LiCl–KCl eutectic at solid (W, Mo, Ta) and liquid (Cd, Bi) electrodes. Lambertin et al. studied the electrochemical reduction of AmCl_3 in LiCl–KCl at 470 °C at a tungsten working electrode [144]. It was determined from the cyclic voltammetric data that Am(III) is first reduced to Am(II) and subsequently reduced in a second step to Am(0). The voltammetry data were used to estimate the standard potential for the Am(III)/Am(II) couple as -2.84 V versus Cl^-/Cl_2 and -2.945 V versus Cl^-/Cl_2 for Am(II)/Am(0). These results are in very good agreement with an earlier study by Fusselman and coauthors [105, 145]. They determined standard potentials for the Am(III)/Am(II) couple as -2.83 V versus Cl^-/Cl_2 and -2.852 V versus Cl^-/Cl_2 for the Am(II)/Am(0) couple at 450 °C. More recently Lambertin et al. extended their studies with a report on the stability of Am ions in molten LiCl–KCl in the presence of fluoride ions [146]. They found that Am(III) undergoes a direct three-electron reduction to Am(0) in the presence of fluoride at -2.91 V versus Cl^-/Cl_2 without voltammetric evidence

for Am(II). At more cathodic potentials the authors believe that the data are indicative of Li_xAm_y alloy formation. Serp et al. have confirmed the previously published two-step [Am(III)/Am(II) and Am(II)/Am(0)] voltammetric behavior of Am(III) in LiCl–KCl at a W working electrode and extended the work by studying the behavior at an Al working electrode [147]. At an Al surface the reduction of Am(III) proceeds in a single step, Am(III) to Am(0), and occurs at more positive potentials than the corresponding values at a W surface. The shift in reduction potential is attributed to the formation of Al–Am alloys.

25.8.3

Nonaqueous Solutions

Electrochemical studies in nonaqueous media with organic solvents are limited with the published reports being relegated to experiments in acetonitrile solvent. Myasoedov and coauthors concluded from their studies of $\text{Am}(\text{ClO}_4)_3$ reduction in acetonitrile/0.1 M $[(\text{C}_2\text{H}_5)_4\text{N}][\text{ClO}_4]$ that americium can be reduced to the divalent state with a formal potential of -1.55 V versus SCE, but small amounts of water in the acetonitrile react with Am(II) to give basic precipitates of the formula $\text{Am}(\text{OH})_x^{(3-x)+}$ [148]. The stabilization of the Am(IV) oxidation state through the use of a neutral oxygen donor ligand (Ph_3AsO) was noted by Payne and Peterson from voltammetry studies in acetonitrile in the presence of the ligand [149]. The Am(IV)/Am(III) oxidation potential was reported as 0.3 V versus Ag/AgCl, although the published cyclic voltammogram appears nonideal for the determination of this potential. From an earlier study in acetonitrile/0.1 M $[(\text{C}_2\text{H}_5)_4\text{N}][\text{ClO}_4]$ a standard potential of -1.4 V versus SHE

was determined for the Am(III)/Am(II) couple [150].

25.8.4

Electrodeposition

A common method for the electrodeposition of Am is from isopropanol solutions containing small quantities of dilute acid stock solutions of Am ions. Aqueous deposition methods have also been employed, but the organic electrolyte medium is more advantageous in that it tends to produce more uniform coatings [151]. Zhi et al. prepared relatively thick targets of Am from a mixture of isopropanol and dilute (0.1 N) nitric acid stock solutions of $^{241,243}\text{Am}(\text{NO}_3)_3$ [152]. The electrolysis was typically carried out at 5 mA cm^{-2} with a resulting potential of approximately 500 V between the platinum wire anode and aluminum foil cathode. Total plating efficiencies of 98% for ^{241}Am and 94% for ^{243}Am were ultimately obtained in about 1 h of electrolysis. The thickness of the films ranged from 622 to $910 \mu\text{g cm}^{-2}$ for ^{241}Am and from 1.0 to $1.2 \mu\text{g cm}^{-2}$ for ^{243}Am . Becerril-Vilchis and coauthors performed an in-depth study on the electrodeposition of Am and physicochemical behavior of the aqueous electrolyte solutions containing Na_2SO_4 at different pH values adjusted with H_2SO_4 and NaOH [153]. The electroplating method described for thorium in Sect. 25.3.4 utilizing DTPA as a chelating agent was also employed by Lee and Lee for the preparation of ^{243}Am targets [26]. With this method a deposition yield of $93.8 \pm 3.4\%$ was achieved in 2 h.

25.9

Curium

Electrochemical studies of curium are mostly limited to radiopolarography

measurements in aqueous solution and electrodeposition from aqueous and nonaqueous media for the preparation of curium targets and sources. However, Martinot et al. have performed a chronopotentiometric study on the reduction of Cm(III) in molten LiCl–KCl in which they observe a single wave attributed to the direct reduction of Cm(III) to Cm(0) at a Pt foil cathode [154]. The radiopolarography results are well summarized in a recent paper by Yamana and Moriyama [155]. A value of -1.77 V versus SHE is presented for the $E_{1/2}$ value of the Cm(III)/Cm(0) couple at pH 3.0 in 0.10 M LiCl from the work of Shiokawa et al. [156]. Frenkel and coauthors presented results for the oxidation of Cm(III) to Cm(IV) in 2 M K_2CO_3 solution at pH 13 [157]. They concluded from their electrochemical and spectroscopic data that 20% of the Cm(III) was oxidized to a stable Cm(IV) species after a 90 min electrolysis at 1.25 V versus Hg/HgO.

25.9.1

Electrodeposition

Lobanov et al. electroplated curium (ultimately converted to CmO_2) in a series of electrodeposition steps from solutions of curium nitrate in isobutanol [158]. The electrochemical setup consisted of a Ti foil cathode, Ti or Al foil anode, potential difference of 600 V, and a plating time of 10–15 min for each plating step. Between each deposition step the deposited curium was converted to CmO_2 . The multistep procedure allowed targets of curium with the desired thickness (300 – $400 \mu g cm^{-2}$) to be obtained with a deposition yield of no less than 90%. Ramaswami and coauthors electroplated curium from isopropanol solution [159]. A 100 μL aliquot

of curium nitrate was added to 10 mL of isopropanol and plating was conducted in an electrochemical cell containing a gold-coated aluminum foil cathode, platinum wire anode, at an applied potential of 600 V. Within 2 h quantitative electrodeposition of curium was achieved at a density of 1 – $50 \mu g cm^{-2}$. Martinot [160] has previously mentioned the electroplating of curium from a solution of 50 : 45 : 5 by volume ethanol/acetone/water at pH 2–3 obtained by the addition of 0.1 N HNO_3 [161]. The electrodeposition is carried out at a stainless steel cathode, with a platinum wire anode, and a current density of $15 mA cm^{-2}$. Curium is deposited by this method at 96% efficiency within 4 h with a density of $15 \mu g cm^{-2}$. Hallstadius described a method for curium electrodeposition at 90% yield from a Na_2SO_4/H_2SO_4 medium at a stainless steel cathode [162].

25.10

Berkelium

Electrochemical studies of berkelium in aqueous media show a reversible Bk(IV)/Bk(III) couple. Indeed the Bk(IV) species is stable in aqueous media and the chemical behavior of Bk is often compared to that of Ce. The formal potential for the Bk(IV)/Bk(III) couple has been studied in a number of weakly and strongly coordinating mineral acids and carbonate solutions. The general findings from these studies indicate a shift in the oxidation potential of Bk(III) ions, with the shift correlating with the complexing ability of the anions present in the electrochemical solution: strongly complexing anions ($SO_4^{2-} < PO_4^{3-} < CO_3^{2-}$) shift the oxidation to more negative potentials [163]. This shift implies stabilization of the electrochemically generated Bk(IV)

species with strongly complexing anions. In a noncomplexing perchlorate solution (1 M HClO_4) the formal potential for the Bk(IV)/Bk(III) couple was recently determined by Atonio et al. [164] from X-ray absorption near edge structure (XANES) spectroelectrochemistry and Nernst analysis as $E^\ominus = 1.584$ V versus SHE. This result is in good agreement with previously published data from Stokely [165] and Simakina [166]. In basic solution Bk(III) is unstable and undergoes auto-oxidation from oxygen and radiolytically produced peroxide to give Bk(IV) [167].

Detailed cyclic voltammetric and bulk electrolysis studies have been performed on the Bk(IV)/Bk(III) couple in concentrated aqueous carbonate solutions (2 M and ca 5 M K_2CO_3 ; pH range from 9.5 to 13.5) [168]. The results from these studies show that solution-composition changes impart large influences on the nature of the voltammetric response for the Bk(IV)/Bk(III) couple. A quasi-reversible process is evidenced in 2 M carbonate solutions at pH 10 and 13.5 with $E_{1/2} = -0.021$ and 0.20 V versus SCE, respectively. Characterization of the heterogeneous electron-transfer parameters was performed through digital simulation of the voltammetric data. In 2 M carbonate at an intermediate pH value of 11.7 the voltammetry becomes more complicated as two electroactive Bk(IV) species are present in similar concentration in the solvent medium. The authors have invoked a square scheme involving electrochemical and chemical reactions to account for the voltammetric behavior. For a more detailed discussion the reader is referred to the original paper [168a]. In 2.5 M carbonate at pH 9.5 and 4.8 M carbonate at pH 10.4 the voltammetry exhibits behavior characteristic of a nondiffusive species that interacts strongly with the electrode surface.

Radiopolarography measurements for the cathodic reduction of Bk(III) to Bk(0) at a dropping mercury electrode in 0.1 M LiCl at pH ~ 2 give an amalgamation half-wave potential value of 1.63 V versus SHE and an estimated E^\ominus of 2.18 V [169]. Analysis of the electrochemical data leads the authors to conclude that the Bk(III)/Bk(0) electrode process is irreversible.

25.11 Californium

There is a fairly limited set of electrochemical data on Cf with previous reviews covering the most pertinent electrochemical results [170]. The oxidation of Cf(III) to Cf(IV) in aqueous media is very difficult because of the relatively positive potential of the couple, ca 3.2 V as calculated by Nugent et al. [46]. As with Am, strongly complexing anions can shift the potential of the Cf(IV)/Cf(III) couple to facilitate the electron-transfer process. Indeed it has been demonstrated that in aqueous potassium phosphotungstate solutions Cf(III) can be chemically oxidized to Cf(IV) with persulfate dianion ($\text{S}_2\text{O}_8^{2-}$) [171]. The results in carbonate solution are more ambiguous as Hobart et al. [172] were not able to oxidize Cf(III) to Cf(IV) in carbonate, but Myasoedov and coauthors [135] claim 20% oxidation of Cf(III) presumably to Cf(IV) in 2 M K_2CO_3 at pH 13.2.

Samhoun and David [169] have studied the reduction of Cf(III) by radiopolarography in 0.1 M LiCl at pH ~ 2 and found a reversible electrode process attributed to the Cf(III)/Cf(0) couple at $E_{1/2} = -1.508$ V versus SHE with an estimated standard potential of -2.030 V. These results were called into question in a subsequent paper by Musikas et al. [173] in which they determined

through voltammetry and polarography studies on larger quantities of Cf(III) that the reduction proceeds in two steps, Cf(III)/Cf(II) and Cf(II)/Cf(0), with measured $E_{1/2}$ values of -1.47 and -1.68 V versus SHE, respectively. The measurements were performed in dilute H_2SO_4 solutions (pH 2.9–3.0) with $[(\text{CH}_3)_4\text{N}]\text{I}$ as supporting electrolyte. Definitive evidence for the existence of Cf(II) in solution, albeit nonaqueous, was also noted by Friedman et al. [174] during polarography experiments on $\text{Cf}(\text{ClO}_4)_3$ in anhydrous acetonitrile at a dropping mercury electrode with 0.1 M $[(\text{C}_2\text{H}_5)_4\text{N}][\text{ClO}_4]$ as supporting electrolyte. The $E_{1/2}$ values for the Cf(III)/Cf(II) and Cf(II)/Cf(0) were -1.00 and -1.43 V versus SCE, respectively. The results for californium were substantiated by comparison with the polarographic behavior of $\text{Sm}(\text{ClO}_4)_3$, which displays an intermediate Sm(II) species, and also with $\text{Nd}(\text{ClO}_4)_3$, which displays a direct three-electron reduction to the Nd(0).

Trautmann [100] obtained better than 90% electrodeposition of Cf-nitrate from a 5-mL isopropanol solution containing 100 μL of 0.1 M HNO_3 . Electrodeposition was performed at 1000 V for 30 min onto Ti, Ta, and C cathode foils. The electrodeposition procedure can also be performed from an aqueous HCl solution at pH 2.7 with added NH_4Cl as electrolyte. With an applied potential of 8–12 V and a resulting current density of $1.6\text{--}2\text{ A cm}^{-2}$, 98% of Cf can be deposited on Ti or Ta cathode foils in 15 min.

25.12

Einsteinium

The electrochemical behavior of einsteinium has received only minimal literature coverage. Nugent et al. [175] employed

electron-transfer band and f–d absorption band measurements to determine the standard potential for the Es(III)/Es(II) couple as -1.2 ± 0.2 V. As with some of the other actinides covered in this review radiopolarography measurements on Es(III) were obtained by Samhoun and David [170]. They found a reversible electrode process for the Es(III)/Es(0) couple in 0.1 M LiCl at pH ~ 2 with $E_{1/2} = -1.460$ V versus SHE and an estimated E^\oplus of -1.98 V. Electrodeposition of Es can be performed from aqueous and nonaqueous solutions. A relatively recent paper from Fowler et al. describes the preparation of ^{254}Es targets from isopropanol for subsequent use in accelerator bombardment studies [176]. The electrodeposition was performed on a Pd coated Be foil cathode from a 1-mL isopropanol solution with 50 μL of 0.1 M HNO_3 as electrolyte.

25.13

Fermium

The calculated standard potential for the Fm(III)/Fm(II) couple is -1.1 V as determined by Nugent and coauthors [175, 177]. Radiopolarography measurements gave an $E_{1/2}$ value of -1.47 ± 0.01 V versus SHE for the Fm(II)/Fm(0) amalgamation in 0.1 M LiCl at pH ~ 2 [169].

25.14

Mendelevium

The standard potential for the Md(III)/Md(II) couple as proposed by Nugent et al. is -0.15 ± 0.05 V [175]. This value is similar to the estimated value of -0.1 V reported by Maly and Cunningham [178]. Samhoun et al. have

studied the electrochemical behavior of Md at a mercury cathode in aqueous solution in the presence of acetate and the more strongly complexing citrate ions [179]. They determined $E_{1/2}$ potentials of -1.49 ± 0.01 and -1.60 ± 0.01 V versus SCE for the Md(II)/Md(0) couple in 0.1 M acetate and citrate solutions, respectively. The results were similar to the behavior of Fm, which is known to proceed through a two-step reduction, Fm(III)/Fm(II) and Fm(II)/Fm(0), during its amalgamation with mercury.

25.15 Nobelium

In aqueous solution nobelium ions are most stable in the +2 oxidation state. In this oxidation state nobelium has a filled f-electron shell, $5f^{14}$, which is likely a major factor for its stability. The potential for the No(III)/No(II) couple has been calculated by Nugent et al. as 1.45 ± 0.05 V [177]. A value of -1.4 to -1.5 V was determined by Silva and coauthors from experimental measurements [180]. David et al. have performed electrochemical amalgamation experiments for the reduction of No(II) to No(0) in aqueous acetate and citrate solutions [181]. They determined half-wave potentials of -1.709 ± 0.006 V versus SCE in acetate and -1.780 ± 0.004 V versus SCE in citrate. Their data was consistent with a reversible two-electron reduction process for which the data in acetate solution was taken as representative of a noncomplexing medium. The $E_{1/2}$ value in acetate was converted to a value of -1.47 ± 0.01 V versus SHE and subsequently used to derive a standard potential value of -2.49 ± 0.06 V for the No(II)/No(0) couple.

References

1. F. David, *Compt. Rend. Acad. Sci. Paris, Ser. C* **1970**, 271, 440–442.
2. D. L. Love, *Anal. Chim. Acta* **1958**, 18, 72–80.
3. H. Yamana, T. Mitsugashira, Y. Shiokawa et al., *J. Radioanal. Chem.* **1983**, 76, 19–26.
4. (a) F. David, A. G. Maslennikov, V. P. Peretrushkin, *J. Radioanal. Nucl. Chem. Radioanal. Nucl. Ch.* **1990**, 143, 415–426. (b) S. H. Eberle, *Gmelin Handbook of Inorganic Chemistry-Actinium*, 8th ed. (Eds.: H. K. Kugler, C. Keller), Springer-Verlag, Berlin, 1981, pp. 205–238, Vol. 1, Chap. 12.
5. N. B. Mikheev, I. E. Veleshko, A. N. Kamenskaya et al., *Radiochemistry* **1995**, 37, 297–299.
6. N. B. Mikheev, A. N. Kamenskaya, I. A. Rumer et al., *Radiokhimiya* **1983**, 25, 143–157.
7. S. G. Bratsch, J. J. Lagowski, *J. Phys. Chem.* **1986**, 90, 307–312. and references therein.
8. (a) M. Rajagoplan, M. Ramaniah, *Radiochim. Acta* **1966**, 3, 236. (b) R. H. Iyer, H. C. Jain, M. V. Ramaniah, C. L. Rao, *Radiochim. Acta* **1964**, 3, 225.
9. A. T. Rane, K. S. Bhatki, *Int. J. Radiat. Isot.* **1973**, 24, 385–389.
10. L. Martinot, in *Encyclopedia of Electrochemistry of the Elements* (Eds.: A. J. Bard, H. Lund), Marcel Dekker, New York, 1978, pp. 153–159, Vol. VIII.
11. G. Marx, in *Gmelin Handbook of Inorganic Chemistry – Thorium* (Eds.: R. Keim, C. Keller), Springer-Verlag, Berlin, 1988, pp. 13–21, Vol. D1.
12. (a) W. M. Latimer, *Oxidation Potentials*, 2nd ed., Prentice-Hall, Englewood Cliffs, NJ, 1961, p. 299. (b) S. Ahrland, J. O. Liljenzin, J. Rydberg, in *Comprehensive Inorganic Chemistry, The Actinides, Solution Chemistry* (Eds.: J. C. Bailar, H. J. Emeléus, Sir. R. Nyholm et al.), Pergamon Press, New York, 1973, pp. 465–635.
13. (a) L. J. Nugent, R. D. Baybarz, J. L. Burnett et al., *J. Phys. Chem.* **1973**, 77, 1528–1539. (b) J. H. Miles, *J. Inorg. Nucl. Chem.* **1965**, 27, 1595–1600.
14. (a) M. V. Smirnov, L. Ivanovskii, *Zh. Fiz. Khim.* **1957**, 31, 801–806. (b) R. Srinivasan, S. Flengas, *Can. J. Chem.* **1964**, 42, 1315–1322. (c) S. Yoshida, R. Oyamada,

- T. Kuroda, *J. Electrochem. Soc.* **1967**, 35, 183–188. (d) D. Inman, G. Hills, L. Young et al., *Ann. N.Y. Acad. Sci.* **1960**, 79, 803–829. (e) M. V. Smirnov, V. Ya. Kudjakov, Yu. V. Posokin et al., *Sov. At. Energy* **1970**, 28, 419.
15. R. Saxena, M. Mittal, *Indian J. Chem.* **1964**, 2, 333–335.
16. (a) R. Kapoor, O. Agrawal, *Proc. Nat. Acad. Sci. India, Sect. A* **1960**, 29, 273–276. (b) R. Kapoor, O. Agrawal, *Vijnana Parishad Ahusandhan Patrika* **1960**, 3, 185–187.
17. R. S. Saxena, U. S. Chaturvedi, *J. Indian Chem. Soc.* **1972**, 49, 621–624.
18. L. Astheimer, K. Schwochau, *J. Inorg. Nucl. Chem.* **1973**, 35, 223–230.
19. G. Duyckaerts, Cl. Degueldre, *J. Electroanal. Chem.* **1981**, 119, 347–354.
20. I. M. Kolthoff, S. Ikeda, *J. Phys. Chem.* **1961**, 65, 1020–1026.
21. L. Martinot, C. Licour, L. Lopes, *J. Alloys Compd.* **1995**, 228, 6.
22. J. G. Reavis, D. F. Bowersox, D. C. Christensen et al., *Radiochim. Acta* **1985**, 38, 135.
23. L. Martinot, *J. Radioanal. Nucl. Chem. Lett* **1986**, 103, 357–363.
24. L. Martinot, *J. Less-Common Met.* **1989**, 147, 73–77.
25. N. A. Talvitie, *Anal. Chem.* **1972**, 44, 280–283.
26. M. H. Lee, C. W. Lee, *Nucl. Instrum. Methods Phys. Res., Sect. A* **2000**, 447, 593–600.
27. S. E. Glover, R. H. Filby, S. B. Clark et al., *J. Radioanal. Nucl. Chem.* **1998**, 234, 213–218.
28. P. Blanco Rodríguez, F. Vera Tomé, J. C. Lozano, *Appl. Radiat. Isot.* **2001**, 54, 29–33.
29. S. C. Lee, J. G. Choi, V. F. Hodge, *J. Alloys Compd.* **1994**, 213, 465–466.
30. R. Zarki, A. Elyahyaoui, A. Chiadli, *Radiochim. Acta* **2004**, 92, 161–169. and references therein.
31. P. Scott, P. B. Hitchcock, *J. Chem. Soc. Chem. Commun.* **1995**, 579–580.
32. A. M. Koulekès-Pujo, J. F. Le Maréchal, A. Dormond et al., *Inorg. Chem.* **1987**, 26, 3171–3175.
33. R. G. Finke, G. Gaughan, R. Voegeli, *J. Organomet. Chem.* **1982**, 229, 179–184.
34. D. E. Morris, R. E. Da Re, K. C. Jantunen et al., *Organometallics* **2004**, 23, 5142–5153.
35. A. Vallet, E. Laviron, A. Dormond, *J. Chem. Soc., Dalton Trans.* **1990**, 921–924.
36. K. M. Kadish, Y. H. Liu, J. E. Anderson et al., *Inorg. Chim. Acta* **1989**, 163, 201–205. and references therein.
37. S. Fried, J. C. Hindman, *J. Am. Chem. Soc.* **1954**, 76, 4863–4864.
38. M. Haissinsky, E. Pluchet, *J. Chim. Phys.* **1962**, 10, 608–610.
39. (a) N. B. Mikheev, S. A. Kulyukhin, N. A. Konovalova, *Radiokhimiya* **1992**, 34, 23–26, and references therein. (b) R. Guillaumont, G. Ionova, J. C. Krupa, F. David, *Radiochim. Acta* **1996**, 75, 97–103.
40. (a) L. Martinot, in *Encyclopedia of Electrochemistry of the Elements* (Eds.: A. J. Bard, H. Lund), Marcel Dekker, New York, 1978, pp. 151–153, Vol. VIII. (b) F. Baumgartner, D. Brown, S. H. Eberle, et al., *Gmelin Handbook of Inorganic Chemistry – Protactinium Main Series*, 8th ed., (Ed.: K.-C. Buschbeck), Springer-Verlag, Berlin, 1977, pp. 128–131–323–332, Vol. 2.
41. C. Ferriera de Miranda, A. G. Maddock, *J. Inorg. Nucl. Chem.* **1962**, 24, 1623–1633.
42. S. Prakash, R. J. Singh, M. V. Ramaniah, *Inorg. Nucl. Chem. Lett.* **1972**, 8, 113–117.
43. R. F. Mitchell, *Anal. Chem.* **1960**, 32, 326–328.
44. G. Smith, G. A. Barnett, *J. Inorg. Nucl. Chem.* **1965**, 27, 975–978.
45. H. Shimojima, J. Takagi, *J. Inorg. Nucl. Chem.* **1964**, 26, 253–255.
46. L. J. Nugent, R. D. Baybarz, J. L. Burnett et al., *J. Inorg. Nucl. Chem.* **1971**, 33, 2503–2530.
47. A. N. Nesmeyanov, *Radiochemistry* **1978**, 20, 312.
48. K. Schwochau, L. Astheimer, *J. Inorg. Nucl. Chem.* **1970**, 32, 119–126.
49. S. Kihara, Z. Yoshida, H. Aoyagi et al., *Pure Appl. Chem.* **1999**, 71, 1771–1807.
50. (a) Ch. Riglet, P. Vitorge, I. Grenthe, *Inorg. Chim. Acta* **1987**, 133, 323–329. (b) Ch. Riglet, P. Robouch, P. Vitorge, *Radiochim. Acta* **1989**, 46, 85–94.
51. (a) Ch. Franz, R.-E. Schmitt, in *Gmelin Handbook of Inorganic Chemistry – Uranium*, 8th ed., (Eds.: V. Haase, R. Keim), Springer-Verlag, Berlin, 1984, pp. 36–78, Vol. D1. (b) L. Martinot, in *Gmelin Handbook of Inorganic Chemistry – Uranium*, 8th ed., (Eds.: V. Haase, R. Keim), Springer-Verlag, Berlin, 1984, pp. 336–378, Vol. D1. (c) Z. Kolarik, in *Gmelin Handbook of Inorganic Chemistry – Uranium*, (Ed.: R. Keim),

- Springer-Verlag, Berlin, 1996, pp. 184–235 Vol. D6.
52. D. E. Morris, *Inorg. Chem.* **2002**, *41*, 3542–3547.
 53. R. N. Sylva, M. R. Davidson, *J. Chem. Soc., Dalton Trans.* **1979**, 465–471.
 54. G. L. Booman, J. E. Rein, in *Treatise on Analytical Chemistry, Part 2, Analytical Chemistry of the Elements*, (Eds.: I. M. Kolthoff, P. J. Elving), John Wiley and Sons, New York, 1962, pp. 1–188, Vol. 9.
 55. J. B. Sobkowski, S. Minc, *J. Inorg. Nucl. Chem.* **1961**, *19*, 101–106.
 56. (a) H. Aoyagi, Z. Yoshida, S. Kihara, *Anal. Chem.* **1987**, *59*, 400–405. (b) S. Kihara, Z. Yoshida, H. Muto et al., *Anal. Chem.* **1980**, *52*, 1601–1606. (c) S. Kihara, *J. Electroanal. Chem.* **1973**, *45*, 45–58.
 57. R. E. Dueber, A. M. Bond, P. G. Dickens, *J. Electrochem. Soc.* **1994**, *141*, 311–316.
 58. Y.-Z. Wei, B. Fang, T. Arai et al., *J. Radioanal. Nucl. Chem.* **2004**, *262*, 409–415.
 59. K.-W. Kim, J.-D. Kim, H. Aoyagi et al., *J. Nucl. Sci. Technol.* **1993**, *30*, 554–559.
 60. S. P. Best, R. J. H. Clark, R. P. Cooney, *Inorg. Chim. Acta* **1988**, *145*, 141–147.
 61. P. Ugo, B. Ballarin, S. Daniele et al., *J. Electroanal. Chem.* **1992**, *324*, 145–159.
 62. K. Mizuguchi, Y.-Y. Park, H. Tomiyasu et al., *J. Nucl. Sci. Technol.* **1993**, *30*, 542–548.
 63. N. Gopinath, N. N. Mirashi, K. Chander et al., *J. Appl. Electrochem.* **2004**, *34*, 617–622.
 64. M. Mlakar, M. Branica, *J. Electroanal. Chem.* **1988**, *256*, 269–279.
 65. M. Paneli, H. Ouguenoune, F. David et al., *Anal. Chim. Acta* **1995**, *304*, 177–186.
 66. K.-S. Jung, S. C. Sohn, Y. H. Ha et al., *J. Electroanal. Chem.* **1991**, *315*, 113–124.
 67. D. W. Wester, J. C. Sullivan, *Inorg. Chem.* **1980**, *19*, 2838–2840.
 68. L. R. dos Santos, M. E. Sbampato, A. M. dos Santos, *J. Radioanal. Nucl. Chem.* **2004**, *261*, 203–209.
 69. L. Maya, B. D. Gonzalez, M. J. Lance et al., *J. Radioanal. Nucl. Chem.* **2004**, *261*, 605–607.
 70. D. Luna-Zaragoza, J. Serrano, *Appl. Radiat. Isot.* **1999**, *51*, 499–503.
 71. (a) K. Hasegawa, Y. Shiokawa, M. Akabori et al., *J. Alloys Compd.* **1998**, 271–273, 680–684. (b) Y. Shiokawa, K. Hasegawa, K. Konashi et al., *J. Alloys Compd.* **1996**, 255, 98–101.
 72. L. Martinot, L. Lopes, J. Marien et al., *J. Radioanal. Nucl. Chem.* **2002**, 253, 407–412.
 73. J. L. Willit, W. E. Miller, J. E. Battles, *J. Nucl. Mater.* **1992**, 195, 229–249.
 74. (a) T. Shimada, N. Tedzuka, Y. Shimizu et al., *J. Alloys Compd.* **1994**, 204, 1–4. (b) P. A. Haas, S. P. Cooper, *J. Chem. Eng. Data Chem. Eng. Data* **1993**, 38, 26–30.
 75. P. Masset, D. Bottomley, R. Konings et al., *J. Electrochem. Soc.* **2005**, 152, A1109–A1115.
 76. S. A. Kuznetsov, H. Hayashi, K. Minato et al., *J. Electrochem. Soc.* **2005**, 152, C203–C212.
 77. B. Prabhakara Reddy, S. Vandarkuzhali, T. Subramanian et al., *Electrochim. Acta* **2004**, 49, 2471–2478.
 78. M. Iizuka, T. Inoue, O. Shirai et al., *J. Nucl. Mater.* **2001**, 297, 43–51.
 79. K. Serrano, P. Taxil, O. Dugne et al., *J. Nucl. Mater.* **2000**, 282, 137–145.
 80. (a) R. J. LeSuer, C. Buttolph, W. E. Geiger, *Anal. Chem.* **2004**, 76, 6395–6401. (b) N. Camire, U. T. Mueller-Westerhoff, W. E. Geiger, *J. Organomet. Chem.* **2001**, 637, 823–826. (c) R. J. LeSuer, W. E. Geiger, *Angew. Chem., Int. Ed. Engl.* **2000**, 39, 248–250.
 81. C. Clappe, D. Leveugle, D. Hauchard et al., *J. Electroanal. Chem.* **1998**, 448, 95–103.
 82. (a) D. Hauchard, M. Cassir, J. Chivot et al., *J. Electroanal. Chem.* **1991**, 313, 227–241. (b) D. C. Sonnenberger, J. G. Gaudiello, *Inorg. Chem.* **1998**, 27, 2747–2748.
 83. D. Hauchard, M. Cassir, J. Chivot et al., *J. Electroanal. Chem.* **1993**, 347, 399–407.
 84. F. M. de Rege, W. H. Smith, B. L. Scott et al., *Inorg. Chem.* **1998**, 37, 3664–3666.
 85. O. Maury, M. Ephritikhine, M. Nierlich et al., *Inorg. Chim. Acta* **1998**, 279, 210–216.
 86. K. Mizouka, Y. Ikeda, *Radiochim. Acta* **2004**, 92, 631–635.
 87. K. Mizouka, S.-Y. Kim, M. Hasegawa et al., *Inorg. Chem.* **2003**, 42, 1031–1038.
 88. S.-Y. Kim, H. Tomiyasu, Y. Ikeda, *J. Nucl. Sci. Technol.* **2002**, 39, 160–165.
 89. S. H. Lee, K. Mizuguchi, H. Tomiyasu et al., *J. Nucl. Sci. Technol.* **1996**, 33, 190–192.
 90. S.-Y. Kim, T. Asakura, Y. Morita et al., *Radiochim. Acta* **2005**, 93, 75–81.
 91. P. Roussel, P. B. Hitchcock, N. D. Tinker et al., *Inorg. Chem.* **1997**, 36, 5716–5721.

92. L. R. Avens, D. M. Barnhart, C. J. Burns et al., *Inorg. Chem.* **1994**, 33, 4245–4254.
93. L. Martinot, D. Laeckmann, T. Materne et al., *J. Less-Common Met.* **1990**, 163, 185–197.
94. L. Martinot, in *Encyclopedia of Electrochemistry of the Elements*, (Eds.: A. J. Bard, H. Lund), Marcel Dekker, New York, 1978, pp. 159–171, Vol. VIII.
95. J. A. Fahey, in *The Chemistry of the Actinide Elements*, 2nd ed. (Eds.: J. J. Katz, G. T. Seaborg, L. R. Morss), Chapman and Hall, New York, 1986, pp. 469–481, 487, Vol. 1, Chap. 6.
96. S.-Y. Kim, T. Asakura, Y. Morita et al., *J. Radioanal. Nucl. Chem.* **2004**, 262, 311–315.
97. A. V. Gelis, P. Vanysek, M. P. Jensen et al., *Radiochim. Acta* **2001**, 89, 565–571.
98. (a) D. W. Wester, J. C. Sullivan, *J. Inorg. Nucl. Chem.* **1981**, 43, 2919–2923. (b) P. G. Varlashkin, D. E. Hobart, G. M. Begun et al., *Radiochim. Acta* **1984**, 35, 91–96.
99. M. V. Ramaniah, R. J. Singh, S. K. Awasthi et al., *Int. J. Appl. Radiat. Isot.* **1975**, 26, 648–650.
100. N. Trautmann, H. Folger, *Nucl. Instrum. Methods Phys. Res., Sect. A* **1989**, 282, 102–106.
101. K. Hasegawa, Y. Shiokawa, M. Akabori et al., *J. Alloys Compd.* **1998**, 271–273, 680–684.
102. V. Tsoupko-Sitnikov, F. Dayras, J. de Sanoit et al., *Appl. Radiat. Isot.* **2000**, 52, 357–364.
103. D. C. Sonnenberger, J. G. Gaudiello, *Inorg. Chem.* **1988**, 27, 2747–2748.
104. L. Martinot, C. Licour, L. Lopes, *J. Alloys Compd.* **1995**, 228, 6–12.
105. Y. Sakamura, T. Hijikata, K. Kinoshita et al., *J. Alloys Compd.* **1998**, 271–273, 592–596.
106. C. L. Kreuger, T. S. Storvick, J. J. Roy et al., *J. Electrochem. Soc.* **1991**, 138, 1186–1187.
107. J. J. Roy, L. F. Grantham, D. L. Grimmer et al., *J. Electrochem. Soc.* **1996**, 143, 2487–2492.
108. O. Shirai, M. Iizuka, T. Iwai et al., *J. Appl. Electrochem.* **2001**, 31, 1055–1060.
109. Y. Sakamura, O. Shirai, T. Iwa et al., *J. Electrochem. Soc.* **2000**, 147, 642–649.
110. L. Martinot, *J. Less-Common Met.* **1991**, 170, 121–126.
111. O. Shirai, M. Iizuka, T. Iwai et al., *J. Nucl. Sci. Technol.* **2000**, 37, 676–681.
112. V. F. Peretrushin, A. G. Maslennikov, in *Transuranium Elements A Half Century*, (Eds.: L. R. Morss, J. Fuger), American Chemical Society, Washington, 1992, pp. 515–523, Chap. 50.
113. L. Martinot, in *Encyclopedia of Electrochemistry of the Elements*, (Eds.: A. J. Bard, H. Lund), Marcel Dekker, New York, 1978, pp. 171–187, Vol. VIII.
114. F. Weigel, J. J. Katz, G. T. Seaborg, in *The Chemistry of the Actinide Elements*, 2nd ed. (Eds.: J. J. Katz, G. T. Seaborg, L. R. Morss), Chapman and Hall, New York, 1986, 499–886, Vol. 1, Chap. 7.
115. J. M. Cleveland, in *Plutonium Handbook-A Guide to the Technology*, (Ed.: O. J. Wick), American Nuclear Society, Illinois, 1980, pp. 403–520, Vol. 1 and 2, Chap. 13.
116. H. Capdevila, P. Vitorge, *Radiochim. Acta* **1995**, 68, 51–62.
117. A. C. Almon, *Anal. Lett.* **1992**, 25, 119–124.
118. H. Boulhalifa, S. D. Reilly, W. H. Smith et al., *Inorg. Chem.* **2004**, 43, 5816–5823.
119. N. A. Budantseva, I. G. Tananaev, A. M. Fedoseev et al., *J. Alloys Compd.* **1998**, 271–273, 813–816.
120. M. A. Abuzwida, A. G. Maslennikov, V. F. Peretrushin, *J. Radioanal. Nucl. Chem.* **1991**, 147, 41–50.
121. M. H. Lee, M. Pimpl, *Appl. Radiat. Isot.* **1999**, 50, 851–857.
122. C. A. Luskus, *J. Radioanal. Nucl. Chem.* **1998**, 234, 287–292.
123. V. A. Becerril, V. Y. Meas, R. A. Tejera et al., *Nucl. Instrum. Methods Phys. Res., Sect. A* **1993**, 328, 512–516.
124. J. J. Laidler, J. E. Battles, W. E. Miller et al., *Prog. Nucl. Energ.* **1997**, 31, 131–140.
125. T. Nishimura, T. Koyama, M. Iizuka et al., *Prog. Nucl. Energ.* **1998**, 32, 381–387.
126. (a) K. Kinoshita, T. Inoue, S. P. Fusselman et al., *J. Nucl. Sci. Technol.* **2003**, 40, 524–530. (b) Y. Sakamura, T. Hijikata, K. Kinoshita et al., *J. Nucl. Sci. Technol.* **1998**, 35, 49–59.
127. J. Serp, R. J. M. Konings, R. Malmbeck et al., *J. Electroanal. Chem.* **2004**, 561, 143–148.
128. K. Uozumi, M. Iizuka, T. Kato et al., *J. Nucl. Mater.* **2004**, 325, 34–43.
129. M. Iizuka, K. Uozumi, T. Inoue et al., *J. Nucl. Mater.* **2001**, 299, 32–42.
130. O. Shirai, M. Iizuka, T. Iwai et al., *J. Electroanal. Chem.* **2000**, 490, 31–36.

131. D. Lambertin, S. Ched'homme, G. Bourges et al., *J. Nucl. Mater.* **2005**, 341, 124–130.
132. V. I. Silin, O. V. Skiba, M. V. Smirnov et al., *At. Energ.* **1968**, 25, 26–29.
133. L. Martinot, in *Encyclopedia of Electrochemistry of the Elements*, (Eds.: A. J. Bard, H. Lund), Marcel Dekker, New York, 1978, pp. 188–193, Vol. VIII.
134. W. W. Schulz, R. A. Penneman, in *The Chemistry of the Actinide Elements*, 2nd ed., (Eds.: J. J. Katz, G. T. Seaborg, L. R. Morss), Springer-Verlag, New York, 1986, pp. 910–919, Vol. 1. Chap. 8.
135. B. F. Myasoedov, I. A. Lebedev, P. L. Khizhnyak et al., *J. Less-Common Met.* **1986**, 122, 189–193.
136. J. Y. Bourges, B. Guillaume, G. Koehly et al., *Inorg. Chem.* **1983**, 22, 1179–1184.
137. P. Berger, P. Blanc, J. Bourges, *Radiochim. Acta* **1988**, 43, 217–222.
138. V. Ya. Frenkel, P. L. Khizhnyak, I. A. Lebedev et al., *Radiokhimiya* **1985**, 27, 576–581.
139. A. M. Fedoseev, N. N. Krot, *Radiokhimiya* **1982**, 24, 176–178.
140. M. Yu. S. S. Kulyako, V. Perevalov et al., *Radiokhimiya* **1986**, 28, 256–261.
141. (a) I. A. Lebedev, Va. Frenkel', B. F. Myasoedov, *Radiokhimiya* **1977**, 19, 570–578. (b) B. F. Myasoedov, M. S. Milyukova, I. A. Lebedev et al., *J. Inorg. Nucl. Chem.* **1975**, 37, 1475–1478. (c) B. F. Myasoedov, V. M. Mikhailov, I. A. Lebedev et al., *Radiochem. Radioanal. Lett.* **1973**, 14, 17–24.
142. Yu. M. Kulyako, S. A. Perevalov, I. A. Lebedev et al., *Radiokhimiya* **1984**, 26, 140–142.
143. (a) D. Chartier, L. Donnet, J. M. Adnet, *Radiochim. Acta* **1999**, 85, 25–31. (b) D. Chartier, L. Donnet, J. M. Adnet, *Radiochim. Acta* **1999**, 83, 129–134.
144. D. Lambertin, J. Lacquement, S. Sanchez et al., *Plasmas & Ions* **2000**, 3, 65–72.
145. S. P. Fusselman, J. J. Roy, D. L. Grimmett et al., *J. Electrochem. Soc.* **1999**, 146, 2573–2580.
146. D. Lambertin, J. Lacquement, S. Sanchez et al., *Electrochem. Comm.* **2001**, 3, 519–523.
147. J. Serp, M. Allibert, A. Le Terrier et al., *J. Electrochem. Soc.* **2005**, 152, C167–C172.
148. B. F. Myasoedov, Y. M. Kulyako, I. S. Sklyarenko, *J. Inorg. Nucl. Chem.* **1976**, 38, 827–830.
149. G. F. Payne, J. R. Peterson, *Radiochim. Acta* **1986**, 39, 155–158.
150. C. Musikas, B. Myasoedov, *Radiochem. Radioanal. Lett.* **1969**, 2, 21.
151. C. Ingelbrecht, A. Moens, R. Eykens et al., *Nucl. Instrum. Methods Phys. Res., Sect. A* **1997**, 397, 34–38.
152. Q. Zhi, G. Junsheng, G. Zaiguo, *Appl. Radiat. Isot.* **2001**, 54, 741–744.
153. A. Becerril-Vilchis, Y. Meas, A. Rojas-Hernández, *Radiochim. Acta* **1994**, 64, 99–105.
154. L. Martinot, J. Reul, G. Duyckaerts, *Anal. Lett.* **1975**, 8, 233–239.
155. H. Yamana, H. Moriyama, *J. Nucl. Sci. Technol.* **1997**, 34, 288–297.
156. Y. Shiokawa, S. Suzuki, in *Americium and Curium Chemistry and Technology*, (Eds.: N. M. Edelstein, J. D. Navratil, W. W. Schulz), D. Reidel, Boston, 1985, pp. 105–114.
157. V. Ya. Frenkel, V. M. Chistyakov, Yu. M. Kulyako et al., *J. Radioanal. Nucl. Chem. Lett.* **1986**, 107, 159–163.
158. Yu. V. Lobanov, G. V. Buklanov, F. Sh. Abdullin et al., *Nucl. Instrum. Methods Phys. Res., Sect. A* **1997**, 397, 26–29.
159. S. P. Ramaswami, S. P. Dange, S. Prakash, *Radiochim. Acta* **1973**, 19, 46–47.
160. L. Martinot, in *Encyclopedia of Electrochemistry of the Elements*, (Eds.: A. J. Bard, H. Lund), Marcel Dekker, New York, 1978, pp. 194–196, Vol. VIII.
161. J. E. Hardcastle, N. E. Levine, *Radiochim. Acta* **1972**, 18, 59.
162. L. Hallstadius, *Nucl. Instr. Meth. Phys. Res.* **1984**, 223, 266–267.
163. (a) L. Martinot, in *Encyclopedia of Electrochemistry of the Elements*, (Eds.: A. J. Bard, H. Lund), Marcel Dekker, New York, 1978, pp. 196–198, Vol. VIII. (b) D. E. Hobart, J. R. Peterson in *Chemistry of the Actinide Elements*, 2nd ed., (Eds.: J. J. Katz, G. T. Seaborg, L. R. Morss), Chapman and Hall, New York, 1986, pp. 989–1024, Vol. 2, Chap. 10.
164. M. R. Antonio, C. W. Williams, L. Soderholm, *Radiochim. Acta* **2002**, 90, 851–856.
165. J. R. Stokely, R. D. Baybarz, J. R. Peterson, *J. Inorg. Nucl. Chem.* **1972**, 34, 392–393.
166. G. A. Simakin, V. N. Kosyakov, A. A. Baranov et al., *Soviet Radiochem.* **1977**, 19, 302.
167. G. A. Timofeev, E. A. Erin, V. M. Chistyakov et al., *Soviet Radiochem.* **1987**, 29, 296–300.
168. (a) D. E. Morris, D. E. Hobart, P. D. Palmer et al., *Radiochim. Acta* **1990**, 49, 125–134.

- (b) D. E. Hobart, D. E. Morris, P. D. Palmer et al., *Radiochim. Acta* **1990**, 49, 119–124.
169. K. Samhoun, F. David, *J. Inorg. Nucl. Chem.* **1979**, 41, 357–363.
170. (a) L. Martinot, in *Encyclopedia of Electrochemistry of the Elements*, (Eds.: A. J. Bard, H. Lund), Marcel Dekker, New York, 1978, p. 198, Vol. VIII. (b) G. Haire, in *Chemistry of the Actinide Elements*, 2nd ed., (Eds.: J. J. Katz, G. T. Seaborg, L. R. Morss), Chapman and Hall, New York, 1986, pp. 1025–1070, Vol. 2, Chap. 11.
171. (a) B. F. Myasoedov, in *Actinides in Perspective* (Ed.: N. M. Edelstein), Pergamon Press, New York, 1982, pp. 509–540. (b) V. N. Kosyakov, G. A. Timofeev, E. A. Erin et al., *Radiokhimiya* **1977**, 19, 82–84.
172. D. E. Hobart, P. G. Varlashkin, K. Samhoun et al., *Rev. Chim. Miner.* **1983**, 20, 817–827.
173. C. Musikas, R. G. Haire, J. R. Peterson, *J. Inorg. Nucl. Chem.* **1981**, 43, 2935–2940.
174. H. A. Friedman, J. R. Stokely, R. D. Baybarz, *Inorg. Nucl. Chem. Lett.* **1972**, 8, 433–441.
175. L. J. Nugent, R. D. Baybarz, J. L. Burnett et al., *J. Phys. Chem.* **1973**, 77, 1528–1539.
176. M. M. Fowler, J. C. Gursky, J. B. Wilhelmy, *Nucl. Instrum. Methods Phys. Res., Sect. A* **1991**, 303, 99–101.
177. L. J. Nugent, R. D. Baybarz, J. L. Burnett, *J. Phys. Chem.* **1969**, 73, 1177–1178.
178. J. Maly, B. B. Cunningham, *Inorg. Nucl. Chem. Lett.* **1967**, 3, 445.
179. K. Samhoun, F. David, R. L. Hahn et al., *J. Inorg. Nucl. Chem.* **1979**, 41, 1749.
180. R. J. Silva, T. Sikkeland, M. Nurmi et al., *J. Inorg. Nucl. Chem.* **1969**, 31, 3405.
181. F. David, K. Samhoun, R. W. Loughheed et al., *Radiochim. Acta* **1990**, 51, 65–70.